

Batteries

2019 Annual Progress Report

Vehicle Technologies Office

(This page intentionally left blank)

Disclaimer

This report was prepared as an account of work sponsored by an agency of the United States government. Neither the United States government nor any agency thereof, nor any of their employees, makes any warranty, express or implied, or assumes any legal liability or responsibility for the accuracy, completeness, or usefulness of any information, apparatus, product, or process disclosed or represents that its use would not infringe privately owned rights. Reference herein to any specific commercial product, process, or service by trade name, trademark, manufacturer, or otherwise does not necessarily constitute or imply its endorsement, recommendation, or favoring by the United States government or any agency thereof. The views and opinions of authors expressed herein do not necessarily state or reflect those of the United States government or any agency thereof.

Acknowledgements

The projects reported in this report were supported through various contracts funded by the U.S. Department of Energy, Vehicle Technologies Office. A list of contributing authors appears in the sections for specific projects in this report.

Acronyms

AABC	Advanced Automotive Batteries Conference
ABMR	Advanced Battery Materials Research
ABR	Applied Battery research
ABRT	Applied Battery Research for Transportation
AC	Alternating current
ACS	American Chemical Society
ADF	Annular dark-field
ADF-STEM	Annular dark-field – scanning transmission electron microscope
AEGIS	Analysis of Electrochemical Gassing by Infrared Spectroscopy
AEM	Advanced Electrolyte Model
AEO	Annual Energy Outlook
AER	All-electric range
AES	Atomic emission spectroscopy
AFM	Atomic force microscopy
AGG	Aggregates
AH	Ampere hour
AI	Artificial Intelligence
AIMD	Ab initio molecular dynamics
ALD	Atomic layer deposition
AMG	Algebraic multigrid
AMO	Advanced Manufacturing Office
AMPED	Advanced Management and Protection of Energy Storage Devices
AMR	Annual Merit Review
ANL	Argonne National Laboratory
AOI	Area of Interest
AOP	Annual Operating Plan
APL	Applied Physics Laboratory
APP	Ammonium polyphosphate
APS	Advanced Photon Source (laboratory)
ARC	Accelerated rate calorimetry
ARL	Army Research Laboratory
ARPA-E	Advanced Research Projects Agency - Energy
ARR	Anionic redox reaction
ASHRAE	American Society of Heating, Refrigeration, and Air-conditioning Engineering
ASI	Area-specific impedance
ASME	American Society of Mechanical Engineers
ASR	Area-specific resistance
ASSB	All solid-state battery
ASTM	American Society for Testing and Materials
ATOF	Acoustic time-of-flight
ATR	Attenuated total reflection
BCDI	Bragg Coherent Diffraction Imaging

BESS	Battery energy storage system
BET	Brunauer, Emmett, and Teller (surface area analysis)
BEV	Battery electric vehicle
BGE	1, 4-butanediol diglycidyl ether
BGS	Block Gauss-Seidel (numerical method)
BLI	Beyond Lithium-ion
BMF	Battery manufacturing facility
BMR	(Advanced) Battery Materials Research (program)
BMS	Battery management system
BMU	Battery Management Unit
BNL	Brookhaven National Laboratory
BOL	Beginning of life
BOP	Balance of plant
BP	Budget period
BPC	Black phosphorus/Ketjenblack-multiwalled carbon nanotubes composite
BQ	1-4-benzoquinone
BSE	Backscatter and secondary electron (imaging modes)
BTC	Battery Technology Center
BTFE	Bis(2,2,2-trifluoroethyl) ether
BTM	Battery thermal management
BTMS	Behind-the-Meter-Storage
BTO	Building Technologies Office
BV	Bond valence
BYU	Brigham Young University
CABS	Consortium for Advanced Battery Simulation
CAD	Computer-aided Design
CAEBAT	Computer-aided engineering of batteries
CAFE	Corporate Average Fuel Economy
CAMP	Cell analysis, modeling, and prototyping (facility)
CB	Carbon black
CBD	Conductive binder domain
CBT	Cantilever Beam Test
CC	Constant current
CCCV	Constant current, constant voltage
CCE	Commercial carbonate electrolyte
CDFEM	Conformal decomposition finite element method
CDI	Cobalt Development Institute
CE	Coulombic efficiency
CEI	Cathode electrolyte interfaces
CERC	Clean Energy Research Center
CG	Core-gradient
CIP	Contact ion pair
CMC	Carboxymethyl cellulose
CMD	Classical molecular dynamics
CN	Coordination number

CNT	Carbon nano-tubes
COTS	Commercial-off-the-shelf
CP	Co-precipitation
CPE	Constant phase element
CPL	Cross-linked polymer layer
CSG	Core-shell concentration gradient
CSTR	Continuous stirred tank reactor
CTE	Coefficient of thermal expansion
CV	Cyclic voltammetry
CY	Calendar year
DAMFC	(Dimethylaminomethyl)ferrocene
DBBQ	2,5-di-tert-butyl-1,4-benzoquinone
DBSCAN	Density-based spatial clustering
DBU	1,8-Diazabicyclo(5.4.0)undec-7-ene (catalyst)
DCIR	Direct current inner resistance
DCR	Direct current resistance
DDR	Damaged, defective, recalled (batteries)
DDSA	Directly derived sulfur assembled
DEC	Diethyl carbonate
DEDOHC	Diethyl 2,5-dioxahexane dicarboxylate
DEDS	Diethyl disulfide
DEM	Discrete element method
DEMS	Differential electrochemical mass spectrometry
DES	Deep eutectic solvent
DFEC	Bis(trifluoroethyl) carbonate (DFEC)
DFLM	Dark field light microscopy
DFT	Density function theory
DI	De-ionized (water)
DIW	Direct Ink Writing
DMC	Dimethyl carbonate
DMDS	Dimethyl disulfide
DME	Dimethyl ether
DMS	Dimethyl sulfide
DMSO	Dimethylsulfoxide
DOD	Depth-of-discharge
DOE	Department of Energy
DOL	Dioxolane
DOS	Density of state
DOSY	Diffusion-ordered spectroscopy
DP	Dry process
DPA	Destructive physical analysis
DPDS	Dipropyl disulfide
DPS	Dipropylulfide
DRIFTS	Diffuse reflectance FTIR spectra
DRX	Disordered (rocksalt) transition metal oxides

DSC	Differential scanning calorimetry
DST	Dynamic stress test
DTS	Dimethyl trisulfide
EA	Ethyl acetate
EADL	Electrochemical Analysis and Diagnostic Laboratory (at ANL)
EB	Electron beam
EBOS	3. Electrical balance of system
EBS	Electron back-scattering diffraction
EC	Ethylene carbonate
ECM	Equivalent circuit model
ECS	Electrochemical Society
EDAX	Energy dispersive x-ray spectroscopy mapping
EDC	Ethylene decarbonate
EDS	Energy dispersive spectroscopy
EDTA	Ethylenediaminetetraacetic acid
EDV	Electric Drive Vehicle
EDX	Energy-dispersive x-ray (spectroscopy)
EDXRD	Energy Dispersive X-ray Diffraction
EEI	Electrode/electrolyte interface
EELS	Electron energy loss spectroscopy
EERE	Energy Efficiency and Renewable Energy (DOE Office)
EES	Electrical energy storage system
EHA	Effective host alloy
EIA	Energy Information Administration
EIC	Energy Innovation Center
EIS	Electrochemical impedance spectroscopy
ELF	Electron localization function
EM	Electro-mechanical
EMC	Ethylmethyl carbonate
ENA	Effective nucleating agents
ENHA	Effective nucleating host alloys
EOL	End of life
EPA	Environmental Protection agency
EPC	4. Engineering procurement and construction
EPMA	Electron probe micro-analysis
EQCM	Electrochemical quartz crystal microbalance
ESIF	Energy Systems Integration Facility
EV	Electric vehicle
EVI	Electric Vehicle Initiative
EVSE	Electric-vehicle supply equipment
EXAFS	Extended X-ray absorption fine structure
FC	Fast-charge
FCE	First cycle efficiency
FCG	Full concentration-gradient
FDM	Fused Deposition Modeling

FEA	Finite element analysis
FEC	Fluoro ethylene carbonate
FEM	Finite element method
FEP	Fluorinated ethylene propylene
FF	Force field
FFT	Fast Fourier-transform
FIB	Focused ion beam
FIB-SEM	Focused Ion Beam Scanning Electron Microscopy
FOA	Federal opportunity announcement
FRS	Filtered Rayleigh Scattering
FSI	(Lithium) bis(trifluoromethanesulfonyl)imide
FSP	Flame spray pyrolysis
FSS	Functional porous sponge sulfur (electrode)
FTC	Freeze tapecasting
FTIR	Fourier transform infrared spectroscopy
FWHM	Full width at half maximum
FY	Fiscal year
GB	Grain boundary
GCE	Gel composite electrolytes
GC-MS	Gas chromatography - molecular spectroscopy
GDOES	Glow discharge optical emission spectrometry
GF	Glass fiber
GGA	Generalized gradient approximation
GHG	Green-house gases
GITT	Galvanostatic intermittent titration
GMRES	Block generalized minimal residual
GO	Graphene oxide
GPE	Gel polymer electrolyte
GREET	Greenhouse gas regulated energy and emissions and transpiration
GSIR	Gas-solid interface reaction
GTP	Gibbs Thomson parameter
HAADF	High-angle annular dark-field
HCE	High concentration electrolyte
HDI	Hexamethylene diisocyanate
HEMM	High energy mechanical milling
HEV	Hybrid electric vehicle
HEXRD	High-energy XRD
HF	Hydrofluoric acid
HFDEC	Bis (2,2,2 trifluoroethyl) carbonate
HFE	Hydrocarbon vs. fluoroether
HFP	Hexafluoropropylene
HIL	Hardware in the loop
HOPG	Highly oriented pyrolytic graphite
HOR	Hydrogen oxidation reaction
HPC	Highly porous carbon

HPLC	High-performance liquid chromatography
HPPC	Hybrid pulse power characterization
HRTEM	High-resolution transmission electron microscopy
HR-TEM	High resolution transmission electron microscopy
HT	High temperature
HVAC	Heating, Ventilating, and Air-Conditioning
HXN	Hard x-ray nanoprobe
ICBR	International Congress for Battery Recycling
ICE	Internal combustion engine
ICESI	International Coalition for Energy Storage and Innovation
ICEV	Internal combustion engine vehicle
ICL	Initial capacity loss
ICP	Inductively coupled plasma
IEEE	Institute of Electrical and Electronics Engineers
IFFT	Inverse-FFT
IFM	Inorganic filler molecules
INL	Idaho National Laboratory
IR	Infra-red
ISS	Inner-shell spectroscopy
ITO	Indium tin oxide
JACS	Journal of the American Chemical Society
KF	Karl Fischer (titration)
KMC	Kinetic Monte Carlo (simulations)
LAM	Loss of active materials
LAMMPS	Large-scale atomic/molecular massively parallel simulator
LATP	$\text{Li}_{1.17}\text{Al}_{0.17}\text{Ti}_{1.83}(\text{PO}_4)_3$
LBNL	Lawrence Berkeley National Laboratory
LCA	Life cycle analysis
LCO	Lithium cobalt oxide
LCV	Lower-cutoff voltage
LDH	Layered double hydroxide
LDOS	Lower density of states
LEDC	Lithium ethylene dicarbonate
LEFM	Linear elastic fracture mechanics
LEMC	Lithium ethylene monocarbonate
LFO	Li_5FeO_4
LFP	Li-iron phosphate
LHCE	Localized high concentration electrolyte
LIB	Lithium-ion battery
LIBRA	Lithium Ion Battery Recycling Analysis
LIC	Lithium-ion conducting
LISO	$\text{Li}_2\text{Ir}_{1-y}\text{Sn}_y\text{O}_3$
LL	Layered-layered
LLNL	Lawrence Livermore National Laboratory
LLS	Layered-layered spinel

LLTO	(Li,La)TiO ₃
LLZ	Li ₇ La ₃ Zr ₂ O ₁₂
LLZO	Lithium lanthanum zirconate
LLZTO	Li _{6.75} La ₃ Zr _{1.75} Ta _{0.25} O ₁₂
LMA	Lithium metal anode
LMB	Lithium metal battery
LMC	Lithium methyl carbonate
LMNO	Lithium manganese nickel oxide
LMNOF	Li-Mn-Nb-O-F
LMO	Lithium manganese oxide
LMR	Lithium manganese-rich (layered cathode material)
LMRNC	Lithium- and manganese-rich nickel manganese cobalt oxide
LMTOF	Li-Mn-Ti-O-F
LNMO	LiNi _{0.5} Mn _{0.5} O ₂
LNMT	LiNi _{0.5} Mn _{1.2} TiO _{0.3} O ₄
LNO	Lithium-nickel oxide
LNTMO	Li _{1.25} Nb _{0.15} Ti _{0.2} Mn _{0.4} O ₂
LNTMOF	Li _{1.15} Ni _{0.45} Ti _{0.3} Mo _{0.1} O _{1.85} F _{0.15}
LPS	Li ₃ PS ₄
LPSBI	Li ₇ P ₂ S ₈ Br _{0.5} I _{0.5}
LRCDRS	Li-rich cation-disordered rocksalts
LRLO	Lithium-rich layered oxide
LSB	Lithium sulfur batteries
LSV	Linear scanning voltammetry
LT	Low-temperature
LTMO	Lithium-rich transition metal oxide
LTO	Lithium titanate, Li ₄ Ti ₅ O ₁₂
LZO	La ₂ Zr ₂ O ₇
MACHT	Micro-aerosol and controlled high temperature
MAS	Magic angle spinning
MCA	Multicomponent alloys
MCSP	Minimum cathode material selling price
MD	Molecular dynamics
MECT	Mechanical/ electrochemical/thermal
MERF	Materials Engineering Research Facility
MIT	Massachusetts Institute of Technology
MLCT	Metal to ligand charge transfer
MOF	Metal Organic Framework
MOSS	Multibeam optical stress sensor
MRS	Materials Research Society
MSCP	Multifunctional sulfur-containing polymer
MSD	Mean square displacements
MSMD	Multi-scale, multi-domain
MSP	Minimum sustainable price
MSU	Michigan State University

MUMPS	Multifrontal Massively Parallel sparse direct Solver
NASICON	(Na) Super Ionic CONductor
NBO	Non-bridging oxygens
NCA	$\text{LiNi}_{0.8}\text{Co}_{0.15}\text{Al}_{0.05}\text{O}_2$
NCL	Nafion- Al_2O_3 composite layer
NCM	$\text{Li}_{1+w}[\text{Ni}_x\text{Co}_y\text{Mn}_z]_{1-w}\text{O}_2$
NDI	Naphthalene diimide
NEB	Nudged elastic band (method)
NECST	Nanomaterials for Energy Conversion and Storage Technology
NETL	National Energy Technology Laboratory
NFA	$\text{LiNi}_x\text{Fe}_y\text{Al}_z\text{O}_2$
NHTSA	National Highway Transportation Safety Administration
NIST	National Institute of Standards and Technology
NMC	Nickel manganese cobalt (oxide)
NMP	N-methylpyrrolidone
NMR	Nuclear magnetic resonance
NNT	Sodium nonatitanate
NOMAD	Nanoscaled-Ordered Materials Diffractometer
NP	Nanoparticles
NPD	Neutron power diffraction
NR	Neutron reflectometry
NREL	National Renewable Energy Laboratory
NSLS	National Synchrotron Light Source
NSLSII	National Synchrotron Light Source II
OAS	Open Architecture Software
OBD	On-board diagnostics
OCP	Open-circuit potential
OCV	Open circuit voltage
OE	Organic electrolyte
OEM	Original equipment manufacturer
OEMS	Online electrochemical Mass Spectrometry
OER	Oxygen evolution reactions
OES	Optical Emission Spectroscopy
OIM	Organic insertion material
OL	Overlithiation
ORNL	Oak Ridge National Laboratory
ORR	Oxygen reduction reaction
OTE	1H,1H,5H-Octafluoropentyl 1,1,2,2-Tetrafluoroethyl ether
PAD	Polymer Assisted Deposition
PAI	Polyamide-imide
PARC	Palo Alto Research Center
PAW	Projected augmented wave
PBE	Perdew, Burke, and Ernzerhof (parameters)
PC	Propylene carbonate
PCA	Principal Component Analysis

PCM	Phase change material
PCS	Power conversion system
PDF	Pair density function
PDMS	Polydimethylsiloxane
PDOS	Projected Density of States
PE	Polyethylene
PECVD	Plasma-enhanced chemical vapor deposition
PEDOT	Poly(3,4-ethylenedioxythiophene)
PEEK	Polyetheretherketone
PEG	Polyethylene glycol
PEGDA	Poly(ethylene glycol) diacrylate
PEGDMA	Polyethylene glycol dimethacrylate
PEIPU	Polyethylenimine-based polyurea
PEO	Polyethyleneoxide
PETA	Pentaerythritol tetraacrylate
PEV	Plug-in electric vehicle
PFIB	Plasma focused ion beam
PFO	Perfluorooctene
PHEV	Plug-in hybrid electric vehicle
PI	Principal investigator
PIP	Polyisoprene
PIPS	Polyisoprene-sulfur
PLD	Pulsed laser deposition
PLIF	Planar Laser Induced Fluorescence
PNNL	Pacific Northwest National Laboratory
POS	Point-of-sale
POSS	Poly(acryloisobutyl polyhedral oligomeric silsesquioxane)
PPS	Polyphenylene Sulfide
PQILE	$\text{Li}(\text{DME})_{0.7}\text{FSI-PEO}_{0.6}$
PSU	Pennsylvania State University
PTA	Polysulfide trapping agent
PTA-DDSA	Polysulfide trapping agent - directly derived sulfur assembled
PTF	Post-Test Facility
PTFE	Poly(tetrafluoroethylene) (cathode)
PV	Photovoltaic
PVD	Physical vapor deposition
PVDF	Poly(vinylidene fluoride)
QC	Quality control
QOCV	Quasi-open-circuit voltage
R&D	Research and Development
RE	Reference electrode
RF	Radiofrequency
RGB	Red, green, blue
RH	Relative humidity
RIXS	Resonant inelastic x-ray scattering

RMS	Root mean square
ROI	Return on investment
RPC	Red phosphorus-carbon
RPT	Reference performance test
RRDE	Rotating ring disk electrode
RS	Rocksalt
RST	Reactive Spray Technology
RT	Room temperature
RVE	Representative volume element
SAE	Society of Automotive Engineers
SAED	Selected area electrode diffraction
SAM	Self-assembled molecular (film)
SAXS	Small angle X-Ray scattering
SBIR	Small Business Innovation Research
SBOS	Structural balance of system
SCP	Sulfur containing polymer
SDS	Safety data sheet
SE	Solid electrolyte
SECM	Scanning electrochemical microscope
SEET	Structural, electrical, electrochemical and thermal
SEI	Solid electrolyte interphase
SEM	Scanning electron microscopy
SEM-AFM	Scanning electron microscopy - atomic force microscopy
SERS	Surface-enhanced Raman spectroscopy
SHE	Self-healing elastomer
SHP	Self-healing polymer
SIA	Structurally isomorphous alloy
SIE	Solvation-ion-exchange
SIG	Solvate ionogel
SIL	Solvated ionic liquid (electrolyte)
SIMS	Secondary ion mass spectrometry
SLAC	Stanford acceleration laboratory
SLD	Scattering length density
SLMP	Stabilized lithium metal powder
SLPC	Single layer pouch cell
SMPS	Scanning mobility particle sizing
SNL	Sandia National Laboratories
SNS	Spallation Neutron Source
SOA	State of the art
SOC	State of charge
SOH	State of health (for battery)
SPH	Smooth particle hydrodynamics
SPME	Solid-phase microextraction
SPN	Secondary pore network
SPRDE	Stationary probe rotating disk electrode

SR	Surface reconstruction
SRL	Surface reconstruction layer
SRO	Short-range order
SS	Solid-state
SSB	Solid-state battery
SSE	Solid-state electrolyte
SSIP	Solvent-separated ion pair
SSN	Self-healable single-ion-conductive network
SSRM	Solvent-separated ion pair
STEM	Scanning transmission electron microscopy
STTR	Small Business Technology Transfer Program
STXM	Scanning transmission X-ray microscopy
SUNY	State University of New York
SWRI	Southwest Research Institute
SXRD	Surface X-ray diffraction
TAC	Technical Advisory Committee
TAMU	Texas A&M University
TARDEC	(U.S. Army) Tank Automotive Research, Development and Engineering Center
TCD	Thermal conductivity detector
TCP	Technology Collaboration Program
TCR	Thermal contact resistance
TD	Transverse direction
TDOS	Total density of states
TEA	Triethylamine
TEGDME	Tetraethyleneglycoldimethyl
TEM	Transmission electron microscopy
TEP	Triethyl phosphate
TES	Tender-energy x-ray absorption spectroscopy
TEY	Total electron yield
TFPC	3,3,3-Trifluoropropylene carbonate
TFSI	Bistriflimide (anion)
TFY	Total fluorescence yield
TGA	Thermal gravimetric analysis
THF	Tetrahydrofuran
TM	Transition metal
TMO	Transition metal oxide
TMP	Trimethyl phosphate
TMSML	4-(Trimethylsilyl)morpholine
TMSPL	1-(Trimethylsilyl)pyrrolidine
TNO	Titanium niobium oxide
TOF	Time-of-flight
TOF-SIMS	Time-of-flight SIMS
TOU	Time-of-use
TPQD	2,3,4,6,8,9,10,12- Octathia biscyclopenta [b,c]-5,11-antraquinone-1,7-dithione
TPS	Transient plane source

TR-XAS	TR-XRD and absorption
TR-XRD	Time-resolved X-ray diffraction
TTF	Tris(2,2,2,-trifluoroethyl)
TTFP	Tris(2,2,2,-trifluoroethyl)phosphite
TVR	Taylor Vortex Reactor
TXM	Transmission X-ray microscopy
UAH	University of Alabama in Huntsville
UCD	University of Colorado at Denver
UCL	University College, London
UCP	Upper cut-off potential
UCSD	University of California, San Diego
UCV	Upper cutoff voltage
UHV	Ultra-high vacuum
UIUC	University of Illinois, Urbana Champaign
UM	University of Michigan
UMD	University of Maryland
UMEI	University of Michigan Energy Institute
USABC	United States Advanced Battery Consortium
USANS	Ultra-small angle neutron scattering
USCAR	United States Council for Automotive Research
USDRIVE	Driving Research and Innovation for Vehicle efficiency and Energy sustainability
USEPA	United States Environmental Protection Agency
UTA	University of Texas, Austin
UTK	University of Tennessee, Knoxville
UU	University of Utah
UV	Ultraviolet
UW	University of Washington
VASP	Vienna <i>ab initio</i> Simulation Package
VB	Valence bond
VBM	Valence bond maximum
VBO	Valence-band offset
VC	Vinylene carbonate
VEC	Vinyl ethylene carbonate
VIBE	Virtual integrated battery environment
VOC	Volatile organic compounds
VTO	Vehicle Technologies Office
WL	White line (energy)
WOT	Wide-open-throttle
WPI	Worcester Polytechnic Institute
WVU	West Virginia University
XANES	X-ray absorption near edge structure
XAS	X-ray absorption spectroscopy
XCEL	EXtreme Fast Charge Cell Evaluation of Lithium-ion Batteries
XCT	X-ray computed tomography
XFC	Extreme fast charging

XPD	X-ray powder diffraction
XPS	X-ray photoelectron spectroscopy
XRD	X-ray diffraction
XRF	X-ray fluorescence (microscopy)
XRR	X-ray reflectivity
XRS	X-ray Raman Spectroscopy
YSZ	Yttria stabilized zirconia

Executive Summary

Introduction

The Vehicle Technologies Office (VTO) of the Department of Energy (DOE) conducts research and development (R&D) on advanced transportation technologies that would reduce the nation's use of imported oil and would also lead to reductions in harmful emissions. Technologies supported by VTO include electric drive components such as advanced energy storage devices (primarily batteries), power electronics and electric drive motors, advanced structural materials, energy efficient mobility systems, advanced combustion engines, and fuels. VTO is focused on funding early-stage high-reward/high-risk research to improve critical components needed for more fuel efficient (and cleaner-operating) vehicles. One of the major VTO objectives is to enable U.S. innovators to rapidly develop the next generation of technologies that achieve the cost, range, and charging infrastructure necessary for the widespread adoption of plug-in electric vehicles (PEVs). An important prerequisite for the electrification of the nation's light duty transportation sector is development of more cost-effective, longer lasting, and more abuse-tolerant PEV batteries. One of the ultimate goals of this research, consistent with the current vehicle electrification trend, is an EV which can provide the full driving performance, convenience, and price of an internal combustion engine (ICE) vehicle. To achieve this, VTO has established the following overarching goal (Source: FY2021 Congressional Budget Justification¹):

...identify new battery chemistry and cell technologies with the potential to reduce the cost of electric vehicle battery packs by more than half, to less than \$100/kWh (ultimate goal is \$60/kWh battery cell cost), increase range to 300 miles, and decrease charge time to 15 minutes or less by 2028.

VTO works with key U.S. automakers through the United States Council for Automotive Research (USCAR) – an umbrella organization for collaborative research consisting of Fiat Chrysler Automobiles (FCA), the Ford Motor Company, and General Motors. Collaboration with automakers through the partnership known as U.S. Driving Research and Innovation for Vehicle Efficiency and Energy Sustainability (U.S. DRIVE) attempts to enhance the relevance and the success potential of its research portfolio. VTO competitively selects projects for funding through funding opportunity announcements (FOAs). Directly-funded work at the national laboratories are awarded competitively through a lab-call process. During the past year, VTO continued R&D in support of PEVs. Stakeholders for VTO R&D include universities, national laboratories, other government agencies and industry (including automakers, battery manufacturers, material suppliers, component developers, private research firms, and small businesses).

This document summarizes the progress of VTO battery R&D projects supported during the fiscal year 2019 (FY 2019). In FY 2019, the DOE VTO battery R&D funding was approximately \$106 million. Its R&D focus was on the development of high-energy batteries for EVs as well as very high-power devices for hybrid vehicles. The electrochemical energy storage roadmap (which can be found at the EERE Roadmap web page²) describes ongoing and planned efforts to develop electrochemical storage technologies for EVs. To advance battery technology, which can in turn improve market penetration of PEVs, the program investigates various battery chemistries to overcome specific technical barriers, e.g., battery cost, performance, life (both the calendar life and the cycle life), its tolerance to abusive conditions, and its recyclability/sustainability. VTO R&D has had considerable success, lowering the cost of EV battery packs to \$185/kWh in 2019 (representing more than 80% reduction since 2008) yet even further cost reduction is necessary for EVs to achieve head-to-head cost competitiveness with internal combustion engines (without Federal subsidies). In addition, today's batteries also need improvements in such areas as their ability to accept charging at a high rate, referred to as extreme fast charging (XFC) (15 minute charge) – to provide a “refueling” convenience similar to ICEs, and

¹ https://www.energy.gov/sites/prod/files/2020/02/f72/doe-fy2021-budget-volume-3-part-1_1.pdf, Volume 3, Part 1, Page 17.

² <http://energy.gov/eere/vehicles/downloads/us-drive-electrochemical-energy-storage-technical-team-roadmap>.

the ability to operate adequately at low temperatures. Research into “next-gen lithium-ion” batteries which would provide such functionalities is one of the R&D focus areas. VTO is funding research on both “next gen” chemistries (which employ an alloy anode and/or a high voltage cathode) and beyond lithium-ion (BLI) chemistries (which can, for example, employ a lithium metal anode). Current cycle and calendar lives of next gen and BLI chemistries are well short of goals set for EVs. To quantify the improvements needed to accelerate large-scale adoption of PEVs and HEVs, certain performance and cost targets have been established. Some sample performance and cost targets for EV batteries, both at cell level and at system (pack) level, are shown in Table ES- 1.

Table ES- 1: Subset of EV Requirements for Batteries and Cells

Energy Storage Goals (by characteristic)	Pack Level	Cell Level
Cost @ 100k units/year (kWh = useable energy)	\$100/kWh*	\$75/kWh*
Peak specific discharge power (30s)	470 W/kg	700 W/kg
Peak specific regen power (10s)	200 W/kg	300 W/kg
Useable specific energy (C/3)	235 Wh/kg*	350 Wh/kg*
Calendar life	15 years	15 years
Deep discharge cycle life	1000 cycles	1000 cycles
Low temperature performance	>70% useable energy @C/3 discharge at -20°C	>70% useable energy @C/3 discharge at -20°C
	*Current commercial cells and packs not meeting the goal	

The batteries R&D effort includes multiple activities, ranging from focused fundamental materials research to prototype battery cell development and testing. It includes, as mentioned above, R&D on “next-gen” and BLI materials and cell components, as well as on synthesis and design, recycling, and cost reduction. Those activities are organized into mainly two program elements:

- Advanced Battery and Cell R&D
- Advanced Materials R&D

A short overview of each of those program elements is given below.

Advanced Battery and Cell R&D

The *Advanced Battery and Cell R&D* activity focuses on the development of robust battery cells and modules to significantly reduce battery cost, increase life, and improve performance. This work mainly spans the following general areas:

- United States Advanced Battery Consortium (USABC)-supported battery development & materials R&D (8 projects)
- Processing science and engineering (17 projects)
- Computer-aided engineering for batteries (CAEBAT) (five projects)
- Recycling and sustainability (three projects)
- Extreme fast-charging (11 projects)

- Beyond batteries (one project)
- Testing and Analysis (seven projects)
- Small business innovative research (SBIR) (multiple Phase I and Phase II projects)

Chapter I of this report describes projects under the *Advanced Battery and Cell R&D* activity. This effort involves close partnership with the automotive industry, through a USABC cooperative agreement. In FY 2019, VTO supported eight USABC cost-shared contracts with developers to further the development of advanced automotive batteries and battery components. The estimated DOE share of those USABC contracts (over the life of the contracts) is approximately \$39M. These include high performance battery cells by 24M Technologies and Farasis Energy, high-energy anode materials by NanoGraf Technologies, lithium-ion cell manufacturing from recycled active materials by Farasis Energy, recycling process for lithium-ion batteries by Worcester Polytechnic Institute, high-energy EV batteries by Zenlabs Energy, thicker cathode coatings by PPG Industries, and benchmarking activities by the Southwest Research Institute (SWRI).

In addition to the USABC projects listed above, VTO also supports multiple *processing science and engineering* projects: including two battery and material supplier R&D projects funded/administered by the National Energy Technology Laboratory (NETL), two projects at universities also funded via NETL and 13 projects at the national labs. Most strategies for increasing the performance (and reducing cost) of lithium-ion batteries focus on novel battery chemistries, material loading modifications, and increasing electrode thickness. The latter approach is generally considered useful for increasing energy density (and in turn, the overall cell capacity). However, practical thicknesses are constrained by ionic transport limitations (which limit cell power) and processing issues. Project participants in this area include Group14, PPG, the University of Missouri, Vanderbilt University and several national labs (ANL, LBNL, NREL, and ORNL). The estimated value of those advanced processing projects (over project lifetime) is approximately \$35M.

The advanced cell and battery research activity also includes several projects categorized under the previous *Computer Aided Engineering for (Electric-Drive Vehicle) Batteries* (CAEBAT) Program – which evolved into the current Advanced Computer Aided Battery Engineering Consortium. The Consortium seeks to enable safer design of batteries by enhancing the predictive capability of computationally efficient electrochemical models for mechanical/electrochemical/thermal simulation models of battery physiochemical processes (in the event of a vehicle crash or internal short/thermal runaway). The participants include the National Renewable Energy Laboratory (NREL), Argonne National Laboratory (ANL) and Sandia National Laboratories (SNL). The consortium for advanced battery simulation (CABS) is an integrated partnership between Oak Ridge National Laboratory (ORNL), Lawrence Berkeley National Laboratory (LBNL), and SNL. Its projects highlight new experiments to develop relations for mechanical response of constituent materials, effective transport properties for electrochemical behavior of electrodes under deformation, and coupled simulations at layer-resolved scale to predict the behavior of the damaged batteries. The approximate value of the CAEBAT and associated programs is \$14M.

The *Recycling and Sustainability* activity involves studies of the full life-cycle impacts and costs of lithium-ion battery production/use; cost assessments and impacts of various recycling technologies; and the available material and cost impacts of recycling and secondary use. The participants include ANL, ORNL, and NREL and the associated budget is approximately \$10M.

To become truly competitive with the internal combustion engine vehicle (ICEV) refueling experience, EV charging times must also be significantly shorter than at present. A research project to understand/enable extreme fast charging (XFC) in enhanced lithium-ion systems – charging an EV at power rates of up to 400 kW, began in FY 2017. Projects on numerous XFC topics are taking place at ANL, INL, NREL, ORNL, SNL, the University of Tennessee, and at industry partner Microvast, Inc. In addition, a “behind the meter” storage project is taking place by a team which includes NREL, INL, ORNL, and SNL. This area focuses on novel battery technologies to facilitate the integration of high-rate EV charging, solar power generation technologies, and energy-efficient buildings while minimizing both cost and grid impacts.

The *battery testing and analysis* activity develops requirements and test procedures for batteries (to evaluate battery performance, battery life and abuse tolerance). Battery technologies are evaluated according to USABC-stipulated battery test procedures. Benchmark testing of an emerging technology is performed to remain abreast of the latest industry developments. The *battery testing* activity includes performance, life and safety testing, and thermal analysis and characterization. It currently includes four projects based at ANL, INL, SNL, and NREL. The testing activity also supports cell analysis, modeling, and prototyping (CAMP) projects at ANL, which include benchmarking and post-test analysis of lithium-ion battery materials at three labs (ANL, ORNL, and SNL). Projects include testing (for performance, life and abuse tolerance) of cells (for contract, laboratory-developed and university-developed cells), and benchmarking systems from industry; thermal analysis, thermal testing, and modeling; cost modeling; and other battery use and life studies. *Cost assessments and requirements analysis* includes an ANL project on developing the performance and cost model BatPaC. This rigorously peer-reviewed model developed at ANL is used to design automotive lithium-ion batteries to meet the specifications for a given vehicle, and estimate its cost of manufacture. An analysis using BatPaC compared the estimated costs of cells and packs for different electrode chemistries (Figure ES-1).

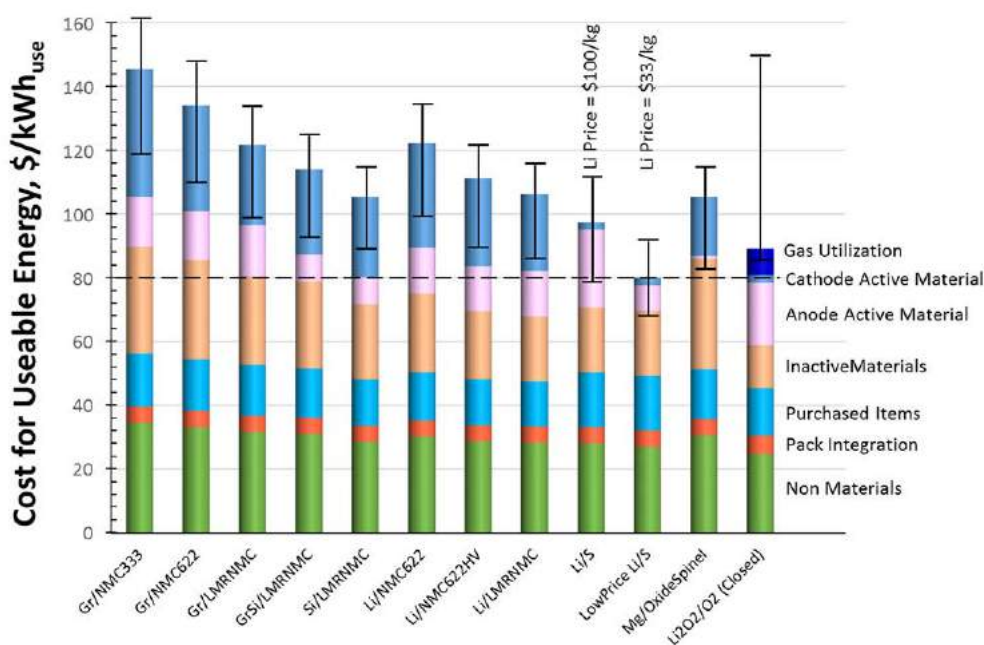


Figure ES- 1. Estimated costs of cells in automotive battery packs with different combination of electrodes. The packs are rated for 100 kWh_{Total} (85 kWh_{Useable}), 300 kW, 315 V, 168 cells, and produced at a plant volume of 100K packs/year

VTO also supports several *small business innovation research* (SBIR) contracts. These SBIR projects focus on development of new battery materials and components and provide a source of new ideas and concepts. The section on SBIR projects includes a short list of recent Phase I and Phase II projects awarded during FY 2019.

Advanced Materials R&D

The *Advanced materials research & development* activity addresses fundamental issues of materials and electrochemical interactions associated with rechargeable automotive batteries. It develops new/promising materials and makes use of advanced material models to discover them, utilizing scientific diagnostic tools and techniques to gain insight into their failure modes and processes. It is conducted by various national labs, universities, and industry partners. The work is divided into two general areas –“next gen” chemistries (which can, for example, employ an alloy anode and/or a high voltage cathode) and beyond lithium-ion (BLI) chemistries (which can, for example, employ a lithium metal anode). The projects are distributed as follows:

- Next generation (next-gen) lithium-ion battery technologies (45 projects)
 - Advanced anodes (five projects)
 - Advanced cathodes (eight projects)
 - Frontier science at interfaces (seven projects)
 - No-cobalt/Low-cobalt cathodes (seven projects)
 - Diagnostics (nine projects)
 - Modeling of electrode material (nine projects)
- Beyond lithium-ion battery technologies (24 projects)
 - Metallic lithium (nine projects)
 - Solid-state batteries (nine projects)
 - Lithium sulfur (seven projects)
 - Lithium-air Batteries (three projects)
 - Sodium-ion batteries (four projects)
 - Battery500 Consortium (five keystone projects and 16 seedling projects)

The *next generation lithium-ion battery* R&D area's goal is to advance material performances, designs, and processes to significantly improve performance and reduce the cost of lithium-ion batteries using an alloy or intermetallic anode and/or high voltage cathode. Specific areas of investigation include high-energy anodes (e.g., those containing silicon or tin), high voltage cathodes, high voltage and non-flammable electrolytes, novel processing technologies, high-energy and low-cost electrode designs, and certain other areas. This work spans a range of U.S. DRIVE activities.

- *Advanced anodes* R&D includes five multi-lab collaborative projects. In the first project, a team consisting of ANL, LBNL, ORNL, SNL, and NREL provides research facility support for the next-generation lithium-ion anodes. A second project, conducted by the five-member National Laboratory Consortium, includes the **silicon deep-dive** project. Silicon is a viable alternative to graphitic carbon as an electrode in lithium-ion cells and can theoretically store >3,500 mAh/g (i.e., about ten times more than graphite). However, lifetime problems severely limit its use in practical systems – this project is focused on those problems. The third project probes functional electrolytes structure and SEI property for Si materials. A fourth project conducted by PNNL in collaboration with the University of Pittsburgh is focused at developing high capacity silicon-based anodes. The third collaborative project (NREL, ANL, ORNL, PNNL, LBNL Stanford University, and GM) is the **silicon electrolyte interface stabilization (SEISta)** project which develops a foundational understanding of the formation/evolution of the solid electrolyte interphase on silicon.
- *Advanced cathodes* R&D includes two sets of projects:
 - *National Laboratory-based cathode projects*: These include seven projects. A collaborative project on diagnostic testing and evaluation is being conducted by a team consisting of ANL, ORNL, and NREL. Another team consisting of ANL, LBNL, and PNNL is working on the design, synthesis, and characterization of low-cobalt cathodes, including its theory and modeling by ANL, LBNL, and ORNL. ANL is working on the design and synthesis of high energy, manganese rich oxides for lithium-ion batteries and BNL on the *in situ* solvothermal synthesis of novel high-capacity cathodes. There are two projects being conducted on disordered rocksalt structured cathode materials by a team which includes LBNL, ORNL, PNNL, as well as team member University of California at Santa Barbara.
 - *Industry/university-based low-cobalt/no cobalt cathodes R&D* includes seven projects. A team headed by Cabot is developing aerosol manufacturing technology for the production of low-cobalt lithium-ion battery cathodes. A UCSD project focuses on novel architectures for cobalt-free cathode materials and another at ORNL on novel lithium iron and aluminum nickelate (NFA). The University of California at Irvine is attempting to enhance the oxygen stability in low-cobalt layered oxide cathode materials by three-dimensional targeted doping and the University of Texas at Austin on developing high-nickel cathode materials for lithium-ion batteries. In addition, Nexceris and Pennsylvania State University are also working on cobalt-free/low-cobalt projects. Although it is not a low-cobalt/no cobalt project,

the University of Texas at Austin is also working on advanced cathode materials for lithium batteries with higher capacity and voltage.

- *Frontier science at interfaces R&D* includes seven projects. In one of them, SLAC is developing a molecular-level understanding of cathode-electrolyte interfaces and ANL is working on developing an understanding of the stability of cathode/electrolyte interfaces in high voltage lithium-ion batteries and of fluorinated deep eutectic solvent (FDES)-based electrolytes. In another, LBNL is carrying out interfacial studies of emerging cathode materials. Additional interface projects are taking place at PNNL, NREL, and Daikin America.
- *Diagnostics R&D* includes nine projects ranging from interfacial processes to *in situ* diagnostic techniques and advanced microscopy, thermal diagnostics, and synthesis and characterization. The various researchers for these projects are based at LBNL, BNL, PNNL, SLAC, GM and the University of California at San Diego.
- Of the seven *modeling of advanced electrode materials* projects, one focuses on novel electrode materials from first principles and another on large-scale *ab initio* molecular dynamics simulation of liquid and solid electrolytes. Yet another modeling project is concerned with electrode materials design and failure prediction. Three more modeling projects are based at various universities (including the University of California at Berkeley, Brigham Young University, and the Michigan State University).

R&D on *beyond lithium-ion battery technologies* includes solid-state technology, lithium metal systems, lithium sulfur, lithium air, and sodium-ion. The main areas of focus include new methods to understand/stabilize lithium metal anodes; lithium polysulfides to enable the use of sulfur cathodes; and developing electrolytes for lithium air and lithium sulfur cells. These systems offer further increases in energy and potentially reduced cost compared to the next-gen lithium-ion batteries. However, they also require additional breakthroughs in materials (often at a fundamental level) before commercial use. VTO is investigating the issues and potential solutions associated with cycling metal anodes. The main research topics include: coatings, novel oxide and sulfide-based glassy electrolytes, and *in situ* diagnostics approaches to characterize and understand Li metal behavior during electrochemical cycling.

- *Metallic lithium R&D* includes nine projects. A team consisting of ORNL, Michigan Technological University, and the University of Michigan is working on the mechanical properties at the protected lithium interface. ORNL is also working on composite electrolytes to stabilize metallic lithium anodes. Of the remaining projects, two focus on dendrite suppression and one on understanding strategies for controlled interfacial phenomena. Additional projects are concerned with self-formed lithium-ion conductors for high performance Li metal anodes, multiscale modeling, 3D printing, and advanced polymer materials. The lithium metal R&D involves three national laboratories (ORNL, PNNL, LLNL, and SLAC) and five universities (University of Michigan, Texas A&M University, Purdue University, the University of Pittsburgh, and Pennsylvania State University).
- *Solid state batteries R&D* includes nine projects. Three of them are taking place at three national labs (ANL, LBNL, and ORNL) and focus on topics like advancing solid-solid interfaces, improving the stability of lithium-metal anodes and inorganic-organic solid electrolytes, and on lithium thiophosphate-based solid electrolytes and cathodes. There are also three university solid-state battery projects (based at the Stony Brook University, West Virginia University, and Rutgers University) covering a dual function solid state battery with self-forming self-healing electrolyte and separator, inorganic nanofiber network-polymer composite electrolytes, and self-forming thin interphases and electrodes. In addition, there are also three collaborative U.S.-German R&D projects in the solid-state batteries area, two of which are based at ANL and the third at ORNL.
- *Lithium sulfur R&D* includes seven projects – four of them based at national laboratories and the remaining three at universities. The lab-based projects include one on lithium-selenium and selenium-sulfur couple (ANL), the development of high energy lithium sulfur batteries (PNNL), nanostructured design of sulfur cathodes (SLAC), and a new electrode binder (LBNL). The three universities for lithium

sulfur projects include the Stanford University, the University of Wisconsin at Madison, and the University of Pittsburgh.

- Additional *beyond lithium-ion* projects include three on *Lithium-Air batteries* (one at PNNL and two at ANL) and four on *Sodium-ion batteries* (based at ANL, BNL, LBNL, and PNNL).

The *Battery500 Innovation Center* is a combined effort by a team of four national labs (PNNL, INEL, BNL and SLAC) and five universities (University of Texas-Austin, Stanford University, Binghamton University, University of Washington, and University of California, San Diego) with the goal to develop commercially viable lithium battery technologies with a cell level specific energy of 500 Wh/kg while simultaneously achieving 1,000 deep-discharge cycles. The consortium keystone projects focus on innovative electrode and cell designs that enable maximizing the capacity from advanced electrode materials. The consortium works closely with the R&D community, battery/materials manufacturers and end-users/OEMs to ensure that these technologies align well with industry needs and can be transitioned to production.

Recent Highlights

Nobel Prizes in Chemistry awarded to battery researchers. On October 9, 2019, the Royal Swedish Academy of Sciences awarded the 2019 Nobel Prize in Chemistry to three scientists who developed lithium-ion batteries. The scientists include Prof. John B. Goodenough at the University of Texas at Austin, Prof. M. Stanley Whittingham at Binghamton University and Prof. Akira Yoshino at the Meijo University in Nagoya, Japan. VTO has partially funded the R&D for the first two researchers (see Figure ES- 2) over the long term. The U.S. DOE Secretary of Energy congratulated the researchers in a statement issued by DOE³. Descriptions of their VTO-supported projects have been regularly included in all VTO Batteries R&D annual progress reports over the past 20-plus years.



John B. Goodenough, University of Texas, Austin



Stanley Whittingham, Binghamton University

Figure ES- 2. 2019 Nobel Laureate battery researchers partially funded by VTO

Battery cost reduction. DOE-funded research has helped reduce the current cost projection for an EV battery (for three DOE-funded battery developers) to an average of \$185/kWh of useable energy. This cost projection is calculated using ANL's public domain Battery Production and Cost model (BatPaC). It assumes a production volume of at least 100,000 batteries per year, the batteries meeting DOE/USABC system performance targets. DOE's goal is to continue to drive down battery cost to \$100/kWh by 2028.

Battery500 Cell Achieves 350Wh/kg and 350 cycles. The Battery500 team succeeded in preparing rechargeable Li metal batteries that achieved 275 cycles with an initial specific energy of 310 Wh/kg. A second generation Li metal/NMC811 cell that is currently cycling shows a beginning of life (BOL) specific

³ <https://www.energy.gov/articles/statement-secretary-perry-2019-nobel-prize-chemistry>.

energy of 350Wh/kg and has reached 350 cycles of operation with less than 10% capacity fade, see Figure ES-3. PNNL prepared the cells and INL performed validation and electrochemical analysis.

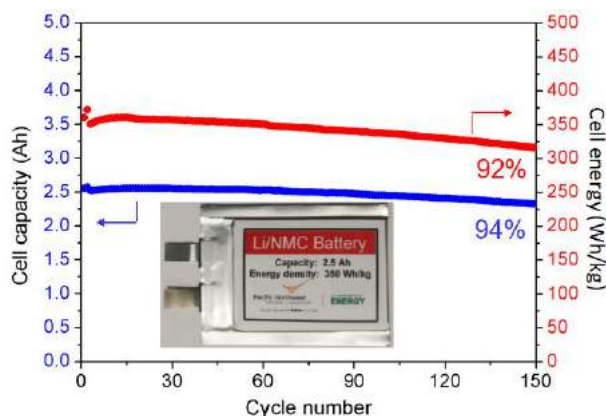


Figure ES- 3. Cell capacity (blue) and the energy (red) of a 2.5 Ah pouch cell as a function of cycling. The cell energy was measured based on the weight of the whole pouch cell including all cell components. The cell was charged within 10 hours (C/10) and discharged within 3 hours (C/3)

Collaborative Activities

In addition to the above, VTO has in place extensive and comprehensive ongoing coordination efforts in energy storage R&D across all of DOE and with other government agencies. It coordinates efforts on energy storage R&D with both the Office of Science and the Office of Electricity. Coordination and collaboration efforts also include program reviews and technical meetings sponsored by other government agencies and inviting participation of representatives from other government agencies to contract and program reviews of DOE-sponsored efforts. DOE coordinates such activities with the Army's Advanced Vehicle Power Technology Alliance, the Department of Transportation/National Highway Traffic Safety Administration (DOT/NHTSA), the Environmental Protection Agency (EPA), and the United Nations Working Group on Battery Shipment Requirements. Additional international collaboration occurs through the International Energy Agency's (IEA's) Hybrid Electric Vehicles Technology Collaboration Program (HEV TCP); and bilateral agreements between the U.S. and China. The *U.S. China Clean Energy Research Center* conducts collaborative research both on rechargeable lithium-ion and beyond lithium-ion battery technologies to help develop the next generation of advanced batteries to help expand electrification of vehicles and enable smart grids internationally and its main objective is to understand and develop advanced battery chemistries based on lithium-ion and beyond lithium ion that meet 300Wh/kg energy density.

Organization of this Report

This report covers all the FY 2019 projects as part of the advanced battery R&D (i.e., energy storage R&D) effort in VTO. We are pleased with the progress made during the year and look forward to continued cooperation with our industrial, government, and scientific partners to overcome the remaining challenges to delivering advanced energy storage systems for vehicle applications.



David Howell, VTO Deputy Director
Vehicle Technologies Office



Steven Boyd, Program Manager, Batteries and
Electrification Program
Vehicle Technologies Office



Tien Q. Duong
Manager, Advanced Battery Materials Research and
VTO Battery500 Consortium,
Vehicle Technologies Office



Peter W. Faguy
Manager, Applied Battery Research and Advanced
Processing R&D
Vehicle Technologies Office



Brian Cunningham
Manager, Battery Development; and Battery
Testing, and Analysis and Design
Vehicle Technologies Office



Samuel Gillard
Manager, Battery Testing, Analysis and Design; and
Small Business Innovation Research for Batteries
Vehicle Technologies Office

Table of Contents

Vehicle Technologies Office Overview	1
Annual Progress Report	1
Organization Chart.....	2
Batteries Program Overview	3
Introduction	3
Goals	3
State of the Art	4
Battery Technology Barriers	6
Program Organization Matrix	6
Battery Highlights from FY 2019	8
I Advanced Battery and Cell R&D	22
I.1 USABC Battery Development & Materials R&D	22
I.1.A High-Performance Semi-Solid Cell for EV Applications (24M Technologies, Inc.)	22
I.1.B Development of High Performance Li-ion Cell Technology for EV Applications (Farasis Energy)	28
I.1.C Rapid Commercialization of High Energy Anode Materials (SiNode Systems)	34
I.1.D Li-Ion Cell Manufacturing Using Directly Recycled Active Materials (Farasis Energy).....	39
I.1.E A Closed Loop Recycling Process for End-of-Life Electric Vehicle Li-ion Batteries-Phase II (Worcester Polytechnic Institute)	49
I.1.F Perform USABC/USCAR Benchmarking Activities (Southwest Research Institute).....	55
I.1.G Fast-Charge and Low-Cost Lithium Ion Batteries for Electric Vehicle Applications (Zenlabs Energy)	60
I.1.H Enabling Thicker Cathode Coatings for Lithium Ion EV Batteries (PPG Industries)	66
I.2 Processing Science and Engineering	74
I.2.A Low-cost Manufacturing of Advanced Silicon-Based Anode Materials (Group14 Technologies, Inc.)	74
I.2.B Electrodeposition for Low-Cost, Water-Based Electrode Manufacturing (PPG Industries, Navitas, ORNL).....	79
I.2.C Towards Solventless Processing of Thick Electron-Beam (EB) Cured LIB Cathodes (ORNL).....	85
I.2.D Performance Effects of Electrode Processing for High-Energy Lithium-Ion Batteries (ORNL).....	91

I.2.E	Process R&D for Next Generation Cathode Materials (ANL)	100
I.2.F	Novel R&D for Manufacturing of SS Electrolyte Materials (ANL).....	106
I.2.G	Supercritical Fluids Process R&D for LIB Materials (ANL)	110
I.2.H	Integrated Flame Spray Process for Low Cost Production of Battery Materials for Lithium Ion Batteries and Beyond (University of Missouri).....	115
I.2.I	High Performance Li-Ion Battery Anodes from Electrospun Nanoparticle/Conducting Polymer Nanofibers (Vanderbilt University).....	121
I.2.J	Continuous Flow R&D for Advanced Electrolytes (ANL).....	126
I.2.K	Optimizing Co-sintering of Ceramic Components for Manufacturing of All-Solid-State Lithium-Ion Battery (LLNL)	133
I.2.L	Structure-Activity Relationships in the Optimizing Electrode Processing Streams for LiBs (LBNL)	138
I.2.M	Fabricate and test solid-state ceramic electrolytes and electrolyte/cathode laminates (LBNL)	140
I.2.N	Higher Energy Density via Inactive Components and Processing Conditions (LBNL)	144
I.2.O	Novel data-mining and other AI approaches for synthesis and processing of cathode materials (LBNL).....	149
I.2.P	Minimizing Side-Reactions in Next Generation Lithium Ion Battery Cathodes Through Structure-Morphology Optimization (ANL).....	154
I.2.Q	High Energy, Long Life Lithium-Ion Battery (NREL).....	162
I.2.R	Co-Extrusion (CoEx) for Cost Reduction of Advanced High-Energy-and-Power Battery Electrode Manufacturing (PARC)	169
I.3	Computer-Aided Engineering for Batteries (CAEBAT)	175
I.3.A	Advanced Computer-Aided Battery Engineering Consortium (NREL, ANL, SNL, Purdue Univ.).....	175
I.3.B	Consortium for Advanced Battery Simulation (SNL)	184
I.3.C	Advanced Tool for Computer Aided Battery Engineering (ANL)	190
I.3.D	Development and Validation of a Simulation Tool to Predict the Combined Structural, Electrical, Electrochemical and Thermal Responses of Automotive Batteries (Ford Motor Company)	196
I.3.E	Consortium of Advanced Battery Simulation (ORNL)	205
I.4	Recycling and Sustainability	213
I.4.A	Battery Production and Recycling Materials Issues (ANL).....	213
I.4.B	Lithium-Ion Battery Recycling Prize Support (NREL)	217
I.4.C	ReCell Advanced Battery Recycling Center (ANL).....	225

I.5	Extreme Fast Charging (XFC).....	285
I.5.A	High Temperature Electrolytes for Extreme Fast Charging (ANL).....	285
I.5.B	XFC R&D: Battery Testing Activities (INL)	291
I.5.C	XFC R&D: MSMD Modeling & Thermal Testing (NREL).....	297
I.5.D	Research on high power, doped titanium-niobium oxide anodes (ORNL).....	310
I.5.E	Research three-dimensional hierarchical graphite architectures for anodes for fast charging (SNL)	316
I.5.F	Develop new electrolyte additives, optimized active materials, and electrode formulations (ANL)	323
I.5.G	Enabling Extreme Fast Charging through Control of Li Deposition Overpotential on Graphite Electrodes (Stony Brook University)	329
I.5.H	Detecting Lithium Plating during Fast Charging, Heterogeneity Effects during Fast Charging, and Graphite Anodes with Directional Pore Channels Made by Freeze Tape Casting (LBNL)	336
I.5.I	Novel Electrolyte Development with High Lithium-Ion Transference Number (Hi-LiT) for Extreme Fast Charging (ORNL).....	345
I.5.J	New High-Energy & Safe Battery Technology with Extreme Fast Charging Capability for Automotive Applications (Microvast, Inc.)	351
I.5.K	XFC R&D: CAMP, Testing & Post-Test Characterization and Modeling (ANL, SLAC) ..	355
I.6	Beyond Batteries	364
I.6.A	Behind-the-Meter Storage (NREL, INL, ORNL, SNL).....	364
I.7	Testing and Analysis	401
I.7.A	BatPaC Model Development (ANL)	401
I.7.B	Battery Performance and Life Testing (ANL)	408
I.7.C	Battery Safety Testing (SNL)	411
I.7.D	Battery Thermal Analysis and Characterization Activities (NREL).....	417
I.7.E	Cell Analysis, Modeling, and Prototyping (CAMP) Facility Research Activities (ANL)...	424
I.7.F	Materials Benchmarking Activities for CAMP Facility (ANL).....	441
I.7.G	Electrochemical Performance Testing (INL).....	449
I.8	Small Business Innovation Research (SBIR)	453
II	Battery Materials R&D	461
II.1	Next Generation Lithium-Ion Batteries: Advanced Anodes.....	461
II.1.A	Next Generation Anodes for Lithium-Ion Batteries: Silicon (ANL, LBNL, ORNL, SNL, NREL).....	461

II.1.B	Silicon Electrolyte Interface Stabilization (SEISa) (NREL, ANL, ORNL, LBNL, SNL) ..	512
II.1.C	Probe the Relationships between Functional Electrolytes Structure and SEI Property for Si Materials (LBNL)	610
II.1.D	Development of Si-based High-Capacity Anodes (PNNL)	616
II.1.E	Pre-Lithiation of Silicon Anode for High Energy Li Ion Batteries (Stanford University)...	623
II.2	Next Generation Lithium-Ion Batteries: Advanced Cathodes R&D	628
II.2.A	Diagnostic Testing and Evaluation (ANL, ORNL, NREL)	628
II.2.B	Design, Synthesis, & Characterization of Low-Cobalt Cathodes (ANL, LBNL, PNNL)....	654
II.2.C	Theory and Modeling (ANL, LBNL)	670
II.2.D	Design & Synthesis of High Energy, Mn-Rich Oxides for Li-Ion Batteries (ANL).....	679
II.2.E	<i>In situ</i> Spectroscopy of Solvothermal Synthesis of Next-Generation Cathode Materials (BNL).....	686
II.2.F	Lithium Batteries with Higher Capacity and Voltage (UTA).....	693
II.2.G	Disordered RockSalt Structured Cathode Materials: Electrochemistry and Synthesis (LBNL)	699
II.2.H	Disordered RockSalt Structured Cathode Materials: Characterization and Modeling (LBNL, ORNL, PNNL, UC Santa Barbara).....	707
II.3	Next Generation Lithium-Ion batteries: Frontier Science at Interfaces.....	716
II.3.A	Molecular-level Understanding of Cathode-Electrolyte Interfaces (SLAC).....	716
II.3.B	Stability of Cathode/Electrolyte Interfaces in High Voltage Li-ion Batteries (ANL).....	723
II.3.C	Interfacial Studies of Emerging Cathode Materials (LBNL)	729
II.3.D	Understanding and Modification of High-Energy Cathodes and Their Interfaces with Electrolytes for Next-Generation Li-Ion Batteries (PNNL).....	736
II.3.E	Fluorinated Deep Eutectic Solvent (FDES)-Based Electrolytes (ANL)	741
II.3.F	Developing <i>In situ</i> Microscopies for the Model Cathode/Electrolyte Interface (NREL)	748
II.3.G	Advanced Lithium Ion Battery Technology – High Voltage Electrolyte (Daikin America, Inc.).....	756
II.4	Next Generation Lithium-Ion batteries: Low-Cobalt/No Cobalt cathodes.....	765
II.4.A	Aerosol Manufacturing Technology to Produce Low-Cobalt Li-ion Battery Cathodes (Cabot)	765
II.4.B	Cobalt-free Cathode Materials and Their Novel Architectures (UCSD)	772
II.4.C	Novel Lithium Iron and Aluminum Nickelate (NFA) as Cobalt-Free Cathode Materials (ORNL).....	782

II.4.D	Enhancing Oxygen Stability in Low-Cobalt Layered Oxide Cathode Materials by Three-Dimensional Targeted Doping (UC Irvine)	789
II.4.E	High-Nickel Cathode Materials for High-Energy, Long-Life, Low-Cost Lithium-Ion Batteries (UTA)	800
II.4.F	Cobalt-Free Cathodes for Next Generation Li-Ion Batteries (Nexceris)	807
II.4.G	High-Performance Low-Cobalt Cathode Materials for Li-ion Batteries (PSU).....	813
II.5	Next Generation Lithium-Ion Batteries: Diagnostics	826
II.5.A	Interfacial Processes (LBNL)	826
II.5.B	Advanced in situ Diagnostic Techniques for Battery Materials (BNL).....	833
II.5.C	Advanced Microscopy and Spectroscopy for Probing and Optimizing Electrode-Electrolyte Interphases in High Energy Lithium Batteries (UCSD)	841
II.5.D	Microscopy Investigation on the Fading Mechanism of Electrode Materials (PNNL)	849
II.5.E	<i>In Operando</i> Thermal Diagnostics of Electrochemical Cells (LBNL)	854
II.5.F	Solid Electrolyte Interphases on Lithium Metal for Rechargeable Batteries (General Motors).....	858
II.5.G	High-Conductivity, Low-Temperature Polymer Electrolytes for Lithium-Ion Batteries (LBNL)	865
II.5.H	Development of High Energy Battery System with 300Wh/kg (ANL)	870
II.5.I	Correlative Microscopy Characterization of Oxide Electrodes (SLAC National Accelerator Laboratory)	879
II.6	Next Generation Lithium-Ion batteries: Modeling Advanced Electrode Materials.....	884
II.6.A	Electrode Materials Design and Failure Prediction (ANL).....	884
II.6.B	Design and Synthesis of Advanced High-Energy Cathode Materials (LBNL).....	891
II.6.C	Design of High-Energy, High-Voltage Lithium Batteries through First-Principles Modeling (LBNL)	899
II.6.D	First Principles Investigation of Existing and Novel Electrode Materials (LBNL)	904
II.6.E	Addressing Heterogeneity in Electrode Fabrication Processes (Brigham Young University)	911
II.6.F	Large scale <i>ab initio</i> molecular dynamics simulation of liquid and solid electrolytes (LBNL)	918
II.6.G	Dendrite Growth Morphology Modeling in Liquid and Solid Electrolytes (MSU).....	924
II.7	Beyond lithium-Ion R&D: Metallic Lithium.....	931
II.7.A	Mechanical Properties at the Protected Lithium Interface (ORNL)	931
II.7.B	Composite Electrolytes to Stabilize Metallic Lithium Anodes (ORNL)	937

II.7.C	Lithium Dendrite Prevention for Lithium Batteries (PNNL).....	943
II.7.D	Understanding and Strategies for Controlled Interfacial Phenomena in Li-Ion Batteries and Beyond (TAMU, Purdue)	949
II.7.E	Engineering Approaches to Dendrite Free Lithium Anodes (University of Pittsburgh).....	956
II.7.F	Electrochemically Responsive Self-Formed Li-ion Conductors for High Performance Li Metal Anodes (Penn State University)	966
II.7.G	Integrated Multiscale Modeling for Design of Robust 3D Solid-State Lithium Batteries (LLNL)	979
II.7.H	3D Printing of All-Solid-State Lithium Batteries (LLNL)	984
II.7.I	Advanced Polymer Materials for Batteries (Stanford University).....	991
II.8	Beyond Lithium-Ion R&D: Solid-State Batteries.....	999
II.8.A	Solid-State Inorganic Nanofiber Network-Polymer Composite Electrolytes for Lithium Batteries (WVU)	999
II.8.B	Improving the Stability of Lithium-Metal Anodes and Inorganic-Organic Solid Electrolytes (LBNL)	1003
II.8.C	U.S.-German Cooperation on Energy Storage: Lithium-Solid-Electrolyte Interfaces (ORNL).....	1014
II.8.D	Lithium Thiophosphate-Based Solid Electrolytes and Cathodes for All-Solid-State Batteries (ORNL).....	1020
II.8.E	Advancing Solid-State Interfaces in Lithium-Ion Batteries (ANL)	1028
II.8.F	Self-Forming Thin Interphases and Electrodes Enabling 3-D Structures High Energy Density Batteries (Rutgers, The State University of New Jersey)	1035
II.8.G	U.S.-German Co-operation: Lillint (ANL)	1044
II.8.H	U.S.-German Co-operation: CatSE (ANL)	1049
II.8.I	Dual Function Solid State Battery with Self-forming Self-healing Electrolyte and Separator (Stony Brook University).....	1052
II.9	Beyond Lithium-Ion R&D: Lithium Sulfur Batteries	1058
II.9.A	Novel Chemistry: Lithium-Selenium and Selenium-Sulfur Couple (ANL)	1058
II.9.B	Development of High Energy Lithium-Sulfur Batteries (PNNL)	1065
II.9.C	Nanostructured Design of Sulfur Cathodes for High Energy Lithium-Sulfur Batteries (Stanford University)	1072
II.9.D	Mechanistic Investigation for the Rechargeable Li-Sulfur Batteries (University of Wisconsin)	1082
II.9.E	Electrochemically Stable High Energy Density Lithium Sulfur Batteries (University of Pittsburgh).....	1090

II.9.F	New electrolyte binder for Lithium sulfur battery (LBNL)	1098
II.9.G	Multifunctional, Self-Healing Polyelectrolyte Gels for Sulfur Cathodes in Li-S Batteries (University of Washington)	1103
II.10	Beyond Li-ion R&D: Lithium-Air Batteries	1119
II.10.A	Rechargeable Lithium-Air Batteries (PNNL)	1119
II.10.B	Li-Air Batteries (ANL)	1125
II.10.C	Lithium Oxygen Battery Design and Predictions (ANL)	1131
II.11	Beyond Lithium-Ion R&D: Sodium-Ion Batteries	1137
II.11.A	Exploratory Studies of Novel Sodium-Ion Battery Systems (BNL)	1137
II.11.B	Development of Advanced High-energy and Long-life Sodium-ion Battery (ANL)	1144
II.11.C	High Capacity, Low Voltage Titanate Anodes for Sodium Ion Batteries (LBNL)	1151
II.11.D	Electrolytes and Interfaces for Stable High-Energy Sodium-ion Batteries (PNNL)	1157
II.12	Beyond Lithium-Ion R&D: Battery500	1162
II.12.A	Battery500 Innovation Center (PNNL, SLAC)	1162
II.12.B	Battery 500 Seedling: Composite Cathode Architecture for Solid-State Batteries (LBNL)	1197
II.12.C	Battery500 Seedling Projects	1203

List of Figures

Figure ES- 1. Estimated costs of cells in automotive battery packs with different combination of electrodes. The packs are rated for 100 kWh _{Total} (85 kWh _{Useable}), 300 kW, 315 V, 168 cells, and produced at a plant volume of 100K packs/year	xix
Figure ES- 2. 2019 Nobel Laureate battery researchers partially funded by VTO	xxii
Figure 1. Chemistry classes, status, and R&D needs	5
Figure 2. Potential for Future Battery Technology Cost Reductions	5
Figure 3. Battery R&D Program Structure	7
Figure 4. The whole cell capacity (blue) and the specific energy (red) of a 2.0 Ah pouch cell as a function of charge and discharge cycles. More than 90% of the cell capacity and specific energy can be retained after 250 cycles	10
Figure 5. (a) EverBatt's flowsheet, (b) Example breakdown of a lithium-ion battery recycling cost, including transportation, and (c) Chart comparing battery manufacturing cost and environmental impacts from virgin material and material provided by several different recycling technologies.....	11
Figure 6. Effect of using mixed-salt electrolytes on 7mAh full cells in xx3450 single layer pouch cell format assembled versus LMR-NMC with 80% Si nanoparticles, 10% hard carbon and 10% LiPAA binder, anodes without any graphite	12
Figure 7. (a) First discharge curve of S ₅ Se ₂ /C cathode in DME-based electrolyte and TTE-based electrolyte; (b) In-situ Se K-edge XANES spectra of S ₅ Se ₂ /C cathode in TTE-based electrolytes at C/10	13
Figure 8. Rate performance and d) cycling performance at high rates of S _{22.2} Se/KB cathode and S/KB cathode in TTE-based electrolyte.....	13
Figure 9. Schematic illustration of the approach for rational synthesis of high-Ni layered oxides with a "closed" loop, specifically, through studying the surface reconstruction, its impact to electrochemical properties, and its formation process (using in situ synchrotron X-ray techniques).....	14
Figure 10. (a) Rate performance and (b) impedance of the LiNi _{0.7} Mn _{0.15} Co _{0.15} O ₂ samples by slow cooling and quenching.....	14
Figure 11. Key parameters which need to be controlled during the technology development and evaluation process. From Chen et. al, Joule 3, 1-12, 2019	15
Figure 12. Universal test fixture designed to enhance data fidelity and repeatability while also providing advanced safety features	16
Figure 13. The SEM micrographs of secondary cathode particles (~10μm diameter) show the extent of interprimary particle separation (cracking) at fresh (no fast charge cycling) and the end of cycling (up to 450 cycles) at different charging rates. A 2 hour (C/2) slow discharge was used in all cases. The cycling voltage were between 3 to 4.1V	17
Figure 14. a) X-ray diffraction spectra of PVdF films produced by drying NMP-based slurries at different temperatures. b) log-log plot of room temperature conductivity data versus inverse of the absolute temperature during drying	17
Figure 15. Resistance <i>versus</i> DOD for electrodes dried at different temperatures a) active material and carbon black mixed together first; b) carbon black and polymer slurry mixed together first.....	18
Figure 16. (a) Optical image of cathode infiltrated LLZO bilayer. Cathode infiltrated porous layer surface (left) and dense layer surface (right) are shown. (b) SEM fracture surface image of cathode infiltrated bilayer. Images were taken prior to SCN electrolyte infiltration. (c) Same cell at higher magnification showing cathode infiltrate. (d) Nyquist plot of the constructed ASSB. (e) Initial charge/discharge profiles of the ASSB.....	18

Figure 17. (a) Representative HAADF-STEM image of $\text{Li}_{1.2}\text{Ni}_{0.4}\text{Ru}_{0.4}\text{O}_2$, showing the layered-rocksalt intergrown structure along the [110] zone axis; (b) charge-discharge voltage profiles during the first five cycles; (c) O <i>K</i> -edge resonant inelastic X-ray scattering map at charged state, red arrow indicating the fingerprinting feature of oxidized oxygen; and (d) X-ray diffraction patterns of $\text{Li}_x\text{Ni}_{0.4}\text{Ru}_{0.4}\text{O}_2$ ($x = 1.2, 0.5, 0.2, 0$) at different delithiated states, showing the isotropic structural evolution upon delithiation	19
Figure 18. (a) The relative surface oxygen release energies of doped LiNiO_2 with respect to the pristine phase. Yellow-orange color indicates an improved oxygen retention, while the purple color indicates a reduced oxygen retention as compared to the pristine phase. (b) Schematic illustration of surface doped LiNiO_2 model. Blue: dopant, green: Li, grey: Ni, red: oxygen. (c) 2D electron localization function contour plot for the surface slice of Sb-doped LiNiO_2	20
Figure 19. (A) NFA cathode particles synthesized through a co-precipitation reaction in a CSTR and (B) Charge/Discharge curves indicating the good capacity and performance delivered by the NFA cathode material	21
Figure I.1.A.1 18-layer densified NMC811 and un-densified graphite containing cell (52.6Ah) dimensions ...	24
Figure I.1.A.2 Program final deliverable cells weight, thickness and capacity @ C/3 discharge rate and 30° ..	25
Figure I.1.A.3 Program final deliverable cells full HPPC performance at 30°C	26
Figure I.1.B.1 a DST Cycle life for Gen1 Cells 1b) Cycle life data@ different pressure.....	30
Figure I.1.B.2 a) Calendar life capacity retention for the Gen 1 deliverable chemistry & b) DCIR.....	31
Figure I.1.B.3 a and b Capacity retention and capacity for the double layer pouch cells targeting ~ 300-310Wh/Kg in the 77-80Ah cell form factor.....	31
Figure I.1.B.4 shows the initial result for the silicon materials with cathode for a fixed capacity of 4.35mAh/cm ²	32
Figure I.1.B.5 shows the initial result for high efficiency anode with Gen1 cathode in double layer pouch cell.....	32
Figure I.1.C.1. Si anode failure mechanisms (left), NanoGraf graphene-wrapped silicon anode architecture (right).	34
Figure I.1.C.2 Normalized full cell capacity versus cycles for pure NanoGraf anodes with NMC523 cathodes	35
Figure I.1.C.3 Normalized full cell capacity versus cycles for assorted electrolyte compositions.....	36
Figure I.1.C.4 NanoGraf anode coating on pilot-scale equipment with 4mAh/cm ² and 10wt% binder content	37
Figure I.1.C.5 NanoGraf materials production quantities through FY19 (top) and improved consistency between batches and production scales (bottom).....	38
Figure I.1.D.1 Pictorial representation of the direct recycling process which largely relies on physical separation processes; compared to other recycling technologies, the positive electrode active material is recovered intact, preserving some of the value added during its synthesis.....	40
Figure I.1.D.2 Electrode scrap direct recycling process overview. First manufacturing residues such as off-spec coated electrodes and dried out slurry residue are milled to produce coarse shreds. The scrap is heated at moderate temperature to decompose the binder and the fine powders are separated from the current collector shreds using vibratory screen or air classifier. The crude recovered active material is then fired at higher temperature to remove residues and improve powder characteristics.....	42
Figure I.1.D.3 Distribution of cells between test facilities (ANL = Argonne National Laboratory; FEI = Farasis Energy USA) and conditions (DST = Dynamic Stress Test; “1C disch.” = constant current discharge; Storage = 100% SOC storage)	43

Figure I.1.D.4 Normalized C/3 static capacity test results from RPT0 and RPT1 for all cells. A0 = pristine graphite, A1 = recycled graphite, C0 = pristine NCM111, C1 = recycled NCM111. Error bars represent 1 standard deviation of the 3 cells in each test condition.....	44
Figure I.1.D.5 HPPC pulse resistance data for all cells and test conditions. Some of the data from RPT0 indicate an anomalously high resistance near mid-SOC and do not represent the normal trend of resistance as a function of SOC for Li-ion cells; the accuracy of these data are suspect and most likely are due to inaccuracies caused by the test equipment performance limitations. These anomalous trends are not subsequently observed in RPT1	45
Figure I.1.D.6 Capacity retention as a function of cycle number for cells under 1C constant current discharge test condition.....	46
Figure I.1.D.7 Process diagram for direct recovery of valuable materials from Li-ion cells.....	46
Figure I.1.E.1 Hardware Strategy of the Program	50
Figure I.1.E.2 Synthesized NMC622 with Different Magnifications	51
Figure I.1.E.3 Summary of NMC622 Coating.....	51
Figure I.1.E.4 Characterization of WPI and Control Powder	52
Figure I.1.E.5 Cycling Performance of Single Layer Pouch Cells, TXS10222: dry coating, TXS10227: wet coating, TXS10228: no coating, TXS10229: A123 control powder.....	52
Figure I.1.E.6 Cathode powder in different milling batches.....	53
Figure I.1.E.7 Coin Cell Testing Results for the 6kg NMC622.....	54
Figure I.1.F.1 High-voltage measurement schematic (left). Power electronics breakout for voltage and current measurement (right).....	56
Figure I.1.F.2 OBD e-PID messages reverse engineered.....	56
Figure I.1.F.3 HwFET engine & motor torque during charge-sustaining operation.....	57
Figure I.1.F.4 HPPC results from the cell-level testing	58
Figure I.1.F.5 Cell teardown.....	58
Figure I.1.G.1 Projected cell development progression throughout the USABC program.....	62
Figure I.1.G.2 Cycling performance from 12 Ah capacity pouch cells at 1C rate (a) and 15 minute fast charge (b) conditions	62
Figure I.1.G.3 Cycling performance in coin-cell full-cells from different electrolyte formulations	63
Figure I.1.G.4 Specific capacity (a), specific energy (b) and energy density (c) at C/3 rate from CB#1 cells...64	
Figure I.1.H.1 Long term cycling of pouch cells with baseline thickness, 93/3/4 and with NMC622 cycled under C/3	67
Figure I.1.H.2 Details of different UMEI trials	67
Figure I.1.H.3 Long term cycling of baseline pouch cells (NMC622 cathode at 22 mg/cm ² coating weight) made in June 2018 and November 2018.....	68
Figure I.1.H.4 Long term cycling of 1 st target cells (NMC 622 cathode at 30 mg/cm ² coating weight) made in November 2018 and April 2019	68
Figure I.1.H.5 a. Discharge capacity and b. Capacity retention of first target pouch cells (NMC622 cathode at 30 mg/cm ² coating weight) fabricated in April 2019	69
Figure I.1.H.6 Long term cycling of pouch cells with final target thickness, 93/3/4 and with NMC622 cathodes and matching anodes, cycled under C/3 at 30°C	70

Figure I.1.H.7 a. Discharge capacity of single layer pouch cells with final target cathode (40 mg/cm ²) and matching anodes with different binders. b. Capacity retention of SLPs with final target cathode and matching anodes	71
Figure I.1.H.8 a. Discharge capacity and b. capacity retention of 5 Ah Multi-layer pouch cells with final target cathode (40 mg/cm ²) and matching anode E coated at pilot scale	72
Figure I.1.H.9 Discharge capacity of 2 Ah Multi-layer pouch cells (N/P ~ 1.1) with final target cathode (40 mg/cm ²) and matching anode E with different electrolyte volume. Standard is refer to 4 times of cells capacity (8 ml), high is 5 times of cells capacity (10 ml) and low is 3 times of cells capacity (6 ml).....	72
Figure I.1.H.10 Comparison of discharge capacities of SLPs (0.5 Ah) and MLPs (5 Ah and 2 Ah with low electrolyte volume)	73
Figure I.2.A.1 3 rd Party data for G14's lab-pilot scale Si-C: Confirmation of high FCE	75
Figure I.2.A.2 3 rd Party data for G14's lab-pilot manufactured Si-C: > 800 Cycle stability	76
Figure I.2.A.3 Cost model (BatPaC 2018 v. 3) using increasing amount of Si-C in the anode.....	77
Figure I.2.B.1 Side-to-side coating weight comparison between Coating Conditions 1 (black) and Coating Conditions 2 (red) (left) and coating weight of NMC 622 electrodes coated on the mini-coater using a single bath with Conditions 2. Approximate coating ranges used for defining "Foot 150" and "Foot 300" that are used throughout this chapter are depicted in blue (right).....	80
Figure I.2.B.2 analysis of digested cathode electrode from the 150th and 300th foot of coating (left) Coin cell half-cell performance of NMC 622 Build 2 electrodes produced on the mini-coater using Conditions 2 (right).....	81
Figure I.2.B.3 Lab-scale film build of NMC 622 electrodes coated using Coating Conditions 2 (red) and 3 (black) (left) and coin cell half-cell performance of lab scale NMC 622 electrodes produced using Coating Conditions 2 (red) and 3 (black) (right).....	82
Figure I.2.B.4 Discharge capacity retention vs. cycle number of electrocoat-based cells (blue) and PVDF/NMP control (black) (left). DCR measurements of electrocoat-based cells (blue) and PVDF/NMP control (black) (right).....	82
Figure I.2.B.5 Cycling performance for pouch cells with PPG cathodes secondary dried at 100, 120, 140, and 160°C for 4h at ORNL R2R Manufacturing Group comparing rate capability (left) and C/10 cycle life (right).....	83
Figure I.2.C.1 cycling performance of 200 mAh pouch cell using NMC811 electrodes processed using two different curing conditions: 500 fpm/290kV/60kGy with 820 ppm O ₂ and 400 fpm/290 kV/75kGy with 180 ppm O ₂	88
Figure I.2.C.2 Voltage-capacity curves of EB cured NMC cathodes at different rates	88
Figure I.2.C.3 Cycling performance of full coin cells with NMC cathodes using different binders	89
Figure I.2.C.4 (a) DSC curve of an EB cured resin with T _g appearing at -36.38°C. (b) full coin cell cycling performance using resin with low T _g , which shows similar cycling performance compared to the baseline NMP/PVDF case.....	89
Figure I.2.D.1 a) Capacity retention comparison between NMC 811 cathodes made via NMP-processing, aqueous-processing, and NMP-processing with the NMC811 powder pre-exposed to water (1000 USABC 0.33C/-0.33C cycles); b) discharge voltage profiles at different C rates	92
Figure I.2.D.2 Top left) Comparison of USABC 0.33C/-0.33C cycle life, and top right) rate performance between three different aqueous-processed NMC811 cathodes, and an NMP-processed NMC811 baseline cathode. Bottom) SEM image of the four various electrodes showing the differences in coverage of NMC811 particles with carbon black and binder network	93

Figure I.2.D.3 HPPC of full cells made with NMP-and aqueous-processed NMC811 cathodes	94
Figure I.2.D.4 Left) Comparison of 0.33C/-0.33C cycle life between three aqueous-processed NMC 811 and NMP-processed NMC811 baseline cathode cycled at 30°C and 45°C. Right) HPPC of the corresponding cells after 200 and 400 cycles	94
Figure I.2.D.5 Comparison of rate performance of a thick (~7 mAh/cm ²) aqueous-processed NMC 811 cathode with two thick NMP-processed NMC811 baseline cathodes in coin cell configuration.....	95
Figure I.2.D.6 Optical micrographs of aqueous NMC811 coatings of various thicknesses made on aluminum (left) and copper foil (right) substrates.	95
Figure I.2.D.7 Optical micrographs of aqueous NMC811 coatings of various thicknesses made on copper foil substrate using carbon black (bottom) and carbon fibers (VGGT)(top) as the conductive additive.....	95
Figure I.2.D.8 SEM and optical microscope images of aqueous-processed cathode coatings (500 μ m coating wet gap) on copper foil comprising VGGT conductive additive, and NMC811 with particle size of (a, b) D50/ μ m = 13.8, and (c, d) D50/ μ m = 7.4.	96
Figure I.2.D.9 Electrolyte imbibition coefficient dependence on salt concentration (a) and porosity of NMC532 cathode (b) and A12 anode (c).....	97
Figure I.2.E.1 Morphologies and XRD profile of nickel-rich compositions at different temperatures; table shows the Rietveld refinement analysis.....	102
Figure I.2.E.2 Voltage profile of nickel-rich compositions with different lithium ratios at different temperatures. Bottom row shows rate capabilities (3.0–4.3 V cycling at 30°C; 1C = 200 mA/g)	103
Figure I.2.E.3 DSC profiles of some of the nickel-rich compositions compared to commercially available NMC532 and NMC811 chemistries	103
Figure I.2.E.4 Scaled-up NCM811 ~7 μ m particles at 1-kg scale in support of “Thick, Low-Cost, High-Power Lithium-Ion Electrodes via Aqueous Processing (BAT164)”	104
Figure I.2.E.5 Chemistries for advanced particle coatings: ~4–5 μ m NCM622, NCM811, and LNO particles, Volexion Inc. (Image Credit: Jung Woo Seo, Volexion).....	104
Figure I.2.E.6 Morphology of single-crystal NMC cathodes; former precursors were made by using a 1-L TVR.....	105
Figure I.2.F.1 In situ electrochemical testing of LLZO+NCM622 composite cathode showing compatibility of the LLZO and NMC622 phases	107
Figure I.2.F.2 The cycle life of NCM622 (left) and NCM811 (right) fabricated by FSP powders	108
Figure I.2.F.3 (a) In situ Raman spectrometer and (b) Flame emission spectroscopy sample data from the multi-fiber probe array of FSP flame in the OH region	109
Figure I.2.G.1 Installed supercritical fluids system for processing battery cathode materials.....	111
Figure I.2.G.2 Optimization of synthesis variables to achieve final target properties of battery materials	111
Figure I.2.G.3 Preliminary synthesized NMC811 precursor using sulfate starting materials.....	112
Figure I.2.G.4 Preliminary synthesized NMC811 precursor using acetate starting materials	112
Figure I.2.G.5 Synthesized NMC811 precursors with various particle sizes and morphologies using acetate starting materials.....	112
Figure I.2.G.6 Three-dimensional reconstructed image and element percentage plot of the synthesized single-crystal-like NMC811 precursor	113
Figure I.2.G.7 Two-dimensional concentration distribution image of the synthesized single-crystal-like NMC811 precursor	113

Figure I.2.G.8 Preliminary coin cell result of 1- μm NMC811 using supercritical fluids synthesis process.....	114
Figure I.2.H.1 SEM image of NCA powders after annealing at 800°C.....	116
Figure I.2.H.2 Charge-discharge of the NCA powders and cycling performances at 1C.....	116
Figure I.2.H.3 Charge-discharge of NCA powder made from the flame spray process with further improved capacity.....	117
Figure I.2.H.4 Cycling performances of the NCA powders at 1C and 5C, showing extraordinary retention rates.....	117
Figure I.2.H.5 Charge-discharge of NMC811 powder made from the flame spray process at 0.1C.....	118
Figure I.2.H.6 NMC811 cycling performances at 1C.....	118
Figure I.2.H.7 Effect of NMC cathode material components on (a) MCSP and (b) cost of cells.....	119
Figure I.2.I.1 (a) As-spun Si/PAA-C/PAI mat (20% C, 45% Si, 35% binder (3% PAI, 32% PAA); scale bar = 2 μm , (b) Cross section of Si/PAA-C/PAI compacted and welded mat; scale bar = 2 μm . C) Cycling performance of two Si/PAA-C/PAI anodes.....	123
Figure I.2.I.2 (a) SEM image of an as-spun Si/PAA-C/PVDF raw mat, composition: 20% C, 45% Si, 35% binder (3% PVDF, 32% PAA) scale bar = 2 μm , (b) Cycling performance of the Si/PAA-C/PVDF anode.....	123
Figure I.2.I.3 SEM images of (a) Raw electrospun Si/PAA (40 wt.% PAA) fiber mat, (b) Final electrode obtained after mat densification; magnification 3,000x, and (c) Cycling performance of Si/PAA anode (40 wt.% PAA) compared to that of Si/PAA/C anode (40wt.% PAA, 3 wt.% C).....	124
Figure I.2.J.1 Reaction to produce F-DEC.....	127
Figure I.2.J.2 Reaction to produce F-EMC.....	127
Figure I.2.J.3 Catalyst screen results and reaction calorimetry for flow condition of F-EMC.....	128
Figure I.2.J.4 Corning flow reactor and close up of the dual plate system for the synthesis of F-EMC.....	128
Figure I.2.J.5 Catalyst screen results and NMR study showing selective catalyst activity.....	129
Figure I.2.J.6 Proposed flow chemistry process for TFPC.....	129
Figure I.2.J.7 Catalyst activity and solvent screen for TFPC.....	129
Figure I.2.J.8 Full scale reaction conversion results.....	130
Figure I.2.J.9 Synthesis of salt-free Ionic Liquids.....	130
Figure I.2.K.1 Optimized amorphous(top) and crystalline(bottom) structures of $\text{Al}_x\text{Li}_{7-3x}\text{La}_3\text{Zr}_2\text{O}_{12}$	135
Figure I.2.K.2 Optimized surface structures of Al doped cubic LLZO. Only Li (green) and Al (grey) are shown as spheres, the La-O and Zr-O bonds are shown as sticks. ΔE represents the energy difference for a single Al atom to occupy the Li-site in the sub-surface vs. in the bulk. A positive value indicates occupying the sub-surface site is energetically favored and a negative value suggests the bulk site is preferred.....	136
Figure I.2.M.1 Impact of sintering atmosphere on phase purity and sintering behavior. (Left) XRD patterns and (right) derivative of dilatometry shrinkage curves.....	141
Figure I.2.M.2 Optimization of Li loading and sintering parameters. (Left) Density and conductivity of LLZO pellets sintered for various hold times at 1075°C with 3wt% Li_2CO_3 . (Right) Overview of pellet density and conductivity optimization efforts. Points in each group represent different sintering times.....	142
Figure I.2.M.3 (Left) Tape casting dispersant optimization and (right) photograph of optimized LLZO tape.....	142
Figure I.2.N.2 The adhesion and cohesion of laminates of cathode material dried at different temperatures from 80 to 190°C.....	145

Figure I.2.N.1 The resistance of laminates dried at different temperatures as measured by applying a current pulse for 30 seconds and measuring the change in voltage divided by the change in current. This was performed at 10% discharge increments	145
Figure I.2.N.3 The spectroscopic results of x-rays taken of films prepared with different levels of carbon black dried at different temperatures. The ratio of PVdF to carbon black is indicated in the insets as zero carbon, 5:1, 5:2, and 5:4. The films were dried at 80, 130, or 180°C	146
Figure I.2.N.4 The film on the top was formed from the Solids process and dried at 170°C; the film on the bottom was formed from the Glue process and dried at 180°C. The film on the left dries in 4.5 minutes but shows cracking; the film on the right dries in 12 minutes but shows no cracking.....	147
Figure I.2.N.5 Resistance of the electrodes dried at different temperatures versus depth of discharge for 30 second discharge pulses	147
Figure I.2.N.6 SEM of electrode surface.	147
Figure I.2.O.1 Sintering temperature versus fraction of Ni in M content for various NMC cathode materials found in our solid-state synthesis dataset. As shown by the plateaus, high Ni content NMC materials have to be sintered at lower temperatures and often use O ₂ instead of air as the sintering atmosphere.....	152
Figure I.2.O.2 K-means clustering of synthesis products in our database with the developed features. Materials with different chemistry are clustered into different groups in the feature space	152
Figure I.2.P.1 (a) During coprecipitation of NMC352 carbonates, the residual amounts of metal cations within the reacting solution at different values of pH are shown. (b) Comparison between the amount of carbonate and hydroxide precipitates at different values of pH. In order to minimize the amount of hydroxide precipitates, coprecipitation of carbonates must be conducted at a pH range between 5 and 8.5	155
Figure I.2.P.2 (a) SEM image of precipitated MnCO ₃ particles obtained with 1.5mM concentration of Mn ²⁺ . (b) SEM image of precipitated MnCO ₃ particles obtained with 4.5mM concentration of Mn ²⁺ . (c) Bar chart demonstrating the fraction of rhombohedral, cubic and spherical particles observed at 1.5mM and 4.5mM concentrations of manganese. The relative fractions of various particles have been obtained from simple visual inspection. It is evident that more rhombohedral particles evolve at 1.5mM concentration, whereas, more cubic particles form at 4.5mM concentration of Mn ²⁺ cations	156
Figure I.2.P.3 As the free energy for the (102) surface decreases, the equilibrium shape converts from a hexagonal unit cell to a rhombohedral particle. The surface energy of the rhombohedral particles is 1.05 J/m ²	157
Figure I.2.P.4 (a) Cubic shape of the MnCO ₃ particles can be obtained with (103) facets. (b) At higher concentrations of Mn ²⁺ , the (103) facets demonstrate lower surface energy as compared to the (102) facets, which indicates that the cubic shape is favorable during coprecipitation at 4.5mM concentration.....	157
Figure I.2.P.5 (a-b) Phase field variables indicating the shape of the MnCO ₃ particles obtained at 1.5mM and 3.0mM concentrations. It is evident that the aspect ratio decreases from 1.26 to 1.05 with increasing metal concentration within the reacting solution. (c-d) Variation in salt concentration within the reacting solution around the growing particle at metal concentrations of 1.5mM and 3.0mM	158
Figure I.2.P.6 Growth of particle size with time as observed for the initial metal concentration of 4.5mM. The growth rate is also denoted by the red circles, which clearly indicates that at longer times, the growth rate decreases substantially. The experimentally observed size of the final particle is denoted by blue cross.....	158
Figure I.2.P.7 (a) Evolution in size of the LZO precursors with increasing temperature. These LZO particles convert to cubic- LLZO. (b) Formation of LLZO and increase in their particle size is demonstrated. Major growth happens within 870°C to 950°C. Beyond 960°C, the size of LLZO particles almost stabilizes	159
Figure I.2.P.8 Comparison between the experimental (blue diamond) and computational (black solid line) results for particle growth observed in LLZO during the formation step of synthesis. The red line indicates	

increase in temperature over 10 minutes from 860 ⁰ C to 960 ⁰ C. Location of the particles and corresponding grain-boundary domains, as predicted by the phase field based computational model, are also shown.....	160
Figure I.2.P.9 Comparison of densification observed in small, large and bimodal shaped LLZO particle. It is evident that bimodal particles experience the maximum amount of increase in relative density, and large particles densify very slowly. The corresponding particle microstructures for the small and bimodal particles are shown in right side images.....	160
Figure I.2.Q.1 Cycling of 400 mAh Si pouch cells at C/3 and room temperature with and without continuous relithiation using L3B passive control. (Left) Number of cycles to 80% remaining capacity is more than doubled. (Right) Cell resistance is not affected by relithiation.....	164
Figure I.2.Q.2 Demonstration of estimation algorithm with 10% initial error in positive electrode capacity (left) and lithiation extent (right)	166
Figure I.2.Q.3 Real time estimation framework for individual electrode algorithm developed by UCD.....	166
Figure I.2.Q.4 Demonstration of prelithiation for 15 wt% Si pouch cells. Yellow and Blue lines represent capacity during C/3 cycling for cells with 15% prelithiation done over 1 week using inserted device. The black and grey lines are for cells without any prelithiation.....	167
Figure I.2.Q.5 Moles of lithium versus distance from lithium reservoir predicted from 2D transport model for prelithiation over different lengths of time. The moles of lithium is relative to number of moles of lithium in cell prior to any SEI formation/growth.....	167
Figure I.2.R.1 3-D Microscope images of as-printed and dried (a) and post-calendered (b) cathode electrodes produced via CoEx. Images illustrate the corrugated topography that persists after the calendaring process.	170
Figure I.2.R.2. Electrochemical Performance of 1 Ah pouch cells, comparing thin and thick baselines vs. CoEx cathodes. Error bars represent +/- 1 standard deviation. Quadratic curve fits are intended to guide the eye. All cells were made with 1.2 M LiPF ₆ in 3:7 wt% EC/EMC electrolyte	172
Figure I.2.R.3 Normalized capacity of large format pouch cells at discharge rates from D/10 to 7.5D, comparing thin and thick baselines vs. CoEx cathodes. Data points are median values, and error bars represent minimum and maximum of data set (4 cells for each baseline, 5 CoEx cells). Quadratic curve fits are intended to guide the eye. All cells were made with 1.2 M LiPF ₆ in 3:7 wt% EC/EMC electrolyte.....	173
Figure I.3.A.1 Effect of aging on mechanical properties of anode versus the cathode: the moduli were dominated by that of the current collector material and there was noticeable difference between the bulk modulus and that from calendaring. Calendaring lowered the mechanical strength of the electrodes considerably: these results are comparable to what is reported in the literature. The samples were aged over a period of 5 years and drop in elastic modulus for the cathode was noticed; the differences on the anode samples were relatively minimal	177
Figure I.3.A.2 (Top) Microstructure model 3D computational domain. (Bottom) Schematic of static scaling numerical test applied in the paper [18] using high-performance computing.....	178
Figure I.3.A.3 (a) Silicon/NMC cell voltage variation during 1C charging and (b) porosity distribution within the electrode at the end of C/50 charge with and without large deformation and stress effects.	179
Figure I.3.A.4 (a) EBSD mapping of NMC polycrystalline architecture. (b) Discontinuous and continuous damage models, respectively resolving and homogenizing polycrystalline architecture.....	180
Figure I.3.A.5 Schematic of 1D Li-sulfur model and polysulfide reaction sequence.	180
Figure I.3.B.1 Workflow for converting 3D imaging to simulation including the conductive binder domain.	185
Figure I.3.B.2 Planar snapshots from a full 3D mesostructure under 5C constant current discharge. In all cases, the current collector is at the top of the image, with the separator at the bottom. When not colored, the electrolyte and particle regions are light grey (particles are approximately spherical) and the binder region is	

dark grey. Figure sublabels (a-f) refer to rows containing information about a parameter of interest at four different states of charge.....	186
Figure I.3.B.3 Electrolyte phase tortuosity for both in-plane (top) and out-of-plane (bottom) directions. Markers represent mean values across simulated subdomains while error bars represent two standard deviations. The traditionally used Bruggeman equation is plotted for comparison, and a Bruggeman model form best fit to the simulation results is also provided.	187
Figure I.3.B.4 Simulation methodology: (I) The manufacturing of three-phase electrodes, from slurry drying to calendering, is simulated using granular and colloidal dynamics. The AM particles (red) are poly-disperse granular particles, and the CBD phase is represented by coarse-grained colloidal particles (blue) of a uniform size. Cross sections in the middle of the electrode are displayed after slurry drying and calendering. The white region around AM and CBD particles represents the pore space. (II) The simulated electrode in (I) is first swelled to introduce 50% nanoporosity, and then mapped onto a regular lattice to provide a spatial distribution of AM (red), CBD (blue), and pore (white) phases. (III) The effective transport properties are calculated using finite element analyses, with the spatial distribution of current density shown. All images are from the same mesostructure realization.	187
Figure I.3.C.1 (a) Relaxation dynamics for cell voltage U at different C-rates. The constant-current charging was terminated when U reached 4.39 V. The solid lines are least squares fits to eq. 1. (b) The plots of τ_s and τ_f vs. the reciprocal C-rate during charge; smaller the τ_s value, faster the cell relaxation.....	192
Figure I.3.C.2 Extrapolated voltages U for relaxation kinetics of cell-I shown in Figure I.3.C.1 and plotted vs. C-rate during charge. Traces i, ii, and iii correspond to the voltage before and after the Ohmic drop at $t=0$ (U_0), and voltage at $t=\infty$ (U_∞), respectively, that was estimated using eq. 1. The solid lines are linear fits ..	192
Figure I.3.C.3 Relaxation dynamics of the (a) anode and (b) cathode potentials for voltage-limited charging of cell I shown in Figure I.3.C.1 and Figure I.3.C.2. The C-rates are color coded as shown in panel a. The vertical arrow in panel a indicates maxima in the $\phi_a(t)$ kinetics that are most clearly seen at a rate of 6C	193
Figure I.3.C.4 (a) Voltage changes induced by $\tau=10$ s pulses applied at 4.2 V. The C-rates during the pulse are given in the inset. (b) The initial (<i>open circles</i>) and end-of-pulse (<i>filled circles</i>) voltages. The straight lines are linear fits. In panel a, the lines represent least squares fits to eq. 1 after the pulse and exponential fits during the pulse	194
Figure I.3.C.5 Relaxation kinetics for U after a 10 s long charge pulse applied at 4.2 V (<i>solid lines</i>). The dashed lines are least squares fits to eq. 1. (b) A plot of time constants for the fast (τ_f) and slow (τ_s) components of kinetics plotted vs. the reciprocal C-rate. The fast component is C-rate independent, while the slow component scales with the C-rate.....	194
Figure I.3.D.1. Project schematic showing major constituents and progression of Alpha and Beta versions ..	196
Figure I.3.D.2 Model setup for a pouch cell impacted by (a, b, c) a semi-sphere and (d, e, f) a semi-cylinder indenter, where the cell bulk is represented by (a, d) standard solid elements, (b, e) composite tshell elements and (c, f) macro model	198
Figure I.3.D.3 Comparison of (a) loading force, (b) cell voltage and (c) state of charge in models with different indenters and element types.....	198
Figure I.3.D.4 Temperature distribution in (a, d) solid element model, (b, e) composite tshell model and (c, f) macro model when a pouch cell is impacted by a (a, b, c) semi-sphere and (d, e, f) semi-cylinder indenter ...	199
Figure I.3.D.5 Comparison of the relative computational time in different models	199
Figure I.3.D.6 Layered element model for (a) spherical and (b) cylindrical indentation.....	202
Figure I.3.D.7 Indentation loads obtained by different active material model formulations and comparison with experiments for (a) spherical and (b) cylindrical indentation	202
Figure I.3.D.8 Shear test. (a) experimental setup, and (b) simulation model	203

Figure I.3.D.9 Load displacement curve for the shear test. Label “Shear phase” denotes the reacting force on the supports to the shear loading step	203
Figure I.3.E.1 Fragmentation of copper current collectors observed by 3D XCT in a small prismatic cell (a), (b) and (c), and the top cell of large format LG-Chem 10-cell stack (d), (e) and (f) after indentations	206
Figure I.3.E.2 (a) EPMA element maps of a used anode and (b) line profiles of four elements across one interface, (c) STEM image and element mapping, and (d) Line profiles of four elements across the interface	207
Figure I.3.E.3 Comparison of charge and discharge voltages with the experiments	208
Figure I.3.E.4 Lithium ion concentration through thickness of the cell during charge cycle at 5C rate.....	209
Figure I.3.E.5 Discharge voltage (left) and temperature (right) profiles for a battery cell at 1C, 2C, and 3C discharge rates. Experiment data shown as dotted lines and model results as solids lines	210
Figure I.3.E.6 Voltage (left) and temperature (right) profiles for cells in a battery pack under constant discharge conditions. Each line represents a single battery cell in the pack.....	210
Figure I.3.E.7 EOL cycle and SOH decay rate as a function of C-rate and temperature	211
Figure I.3.E.8 Normalized battery capacity compared to number of cycles at different temperatures	211
Figure I.4.A.1 Supply from recycling depends on demand growth	214
Figure I.4.A.2 Need for upcycling of recovered material	215
Figure I.4.B.1 Materials Research Plan with three major areas of research to address critical materials issues for lithium-ion batteries and recovery of materials for reintroduction into the supply chain	218
Figure I.4.B.2 Left: Logo of the Lithium-Ion Battery Recycling Prize. Right: The Lithium-Ion Battery Recycling Prize consists of three progressive phases from concept through pilot validation, over about three years.....	219
Figure I.4.B.3 There are five main areas of interest within Phase I of the prize to help address the various issues that arise in the battery recycling supply chain	220
Figure I.4.B.4 The 15 Phase I winning teams submitted innovative proposals from across the United States	223
Figure I.4.B.5 Assistant Secretary Daniel Simmons announced the 15 winners of Phase I at NREL on September 25, 2019	223
Figure I.4.C.1 ReCell organization chart as of the end of FY19Q2.....	226
Figure I.4.C.2 ReCell Pilot Scale High-bay located at Argonne National Laboratory Building 369	227
Figure I.4.C.3 ReCell Laboratory off the High-bay.....	227
Figure I.4.C.4 XRD patterns of Relithiated NMC versus starting lithia source.....	230
Figure I.4.C.5 Rate performance of LiOH•H ₂ O relithiated NMC (650°C) half-cell	232
Figure I.4.C.6 (a) and (b) XRD patterns for pristine NMC111, chemically delithiated NMC111, and relithiated NMC111 (reaction condition: LiCl, [C2OHmim][NTf2], 150°C, 24 h). (c) and (d) TGA results for samples recovered under different reaction conditions	234
Figure I.4.C.7 Comparison of TGA plots of black powder from (a) LiBr-in three different ionic liquids and (b) three large scale experiments with pristine and delithiated NMC111	235
Figure I.4.C.8 1 st and 2 nd charge-discharge curves for the pristine, delithiated, and relithiated samples before (a) (b) and after calcination at 500°C (c) (d).....	236
Figure I.4.C.9 (a) 2 nd charge-discharge curves and (b) cycle performance for the pristine, delithiated, and relithiated samples	237

Figure I.4.C.10 High resolution XPS spectra of T-NCM111 (a), D-NCNM111 (b), HT-220C-1h-NCM111(c) and HT-220C-2h-NCM111 (d)	239
Figure I.4.C.11 High resolution XPS spectra of HT-160C-1h-NCM111(a), HT-160C-2h-NCM111 (b) and HT-160C-4h-NCM111 (c)	239
Figure I.4.C.12 Cycling stability of D-NCM111 after hydrothermal lithiation at 220C (a) and 160C (b) for different time	240
Figure I.4.C.13 Cycling stability (a) and lithium content (b) of D-NCM111 after pre-removal of PVDF binder with and without lithium source, as well as the corresponding regenerated products	241
Figure I.4.C.14 Electrochemical cycling of 10% chemically delithiated NCM 111 with 3 wt.% PVDF binder and 5 wt.% carbon black after various annealing procedures. Pristine material is pure NCM 111 without any processing, pristine binder removal is with PVDF and carbon black heated to 500°C with 4 wt.% LiOH·H ₂ O. The one step process uses 15 wt.% LiOH·H ₂ O heated to 500°C, and the two step process uses 7.5 wt.% LiOH·H ₂ O in each step both with heats to 500°C. The 850C processes use 15 wt.% LiOH·H ₂ O heated 500°C at 0.5°C/min and then to 850°C at 2°C/min	241
Figure I.4.C.15 Electrochemical rate performance of 10% delithiated NMC 111 with 3 wt.% PVDF binder and 5 wt.% carbon black after heat treating with a) 15 wt.% LiOH·H ₂ O, and b) at 850°C for 8 hr with different amounts of LiOH·H ₂ O per 5 g of bound cathode material	242
Figure I.4.C.16 Triboelectric separation operating	243
Figure I.4.C.17 Adjustable baffle system	243
Figure I.4.C.18 Yield vs. applied voltages for NMC/LMO separation.....	244
Figure I.4.C.19 Results of triboelectric separation of NMC111 and LMO	244
Figure I.4.C.20 Yield vs purity curves for separations of selected cathode mixtures.....	245
Figure I.4.C.21 Recovered mass and purity of magnetic and non-magnetic fractions	245
Figure I.4.C.22 Purity and yield of each LMO rich and NMC111 rich fractions	246
Figure I.4.C.23 SEM image of 45-125 µm shredded copper foil.....	247
Figure I.4.C.24 Mass percent of copper added to cathode powder.....	247
Figure I.4.C.25 Separations conducted at 7 different rotational speeds.....	247
Figure I.4.C.26 Mass percentage of copper remaining after classification at different rotational speeds	248
Figure I.4.C.27 Recovery of pristine cathode materials at different Ph using collector A, B, and C	249
Figure I.4.C.28 XRD analysis of black mass. Assessment is summarized in the preceding table.....	251
Figure I.4.C.29 SEM/EDX analysis of the black mass cathodes	252
Figure I.4.C.30 Annealing at 800 °C for 20h, the only observed change in the mixture was that the structure of layered LiNiO ₂ converted to a disordered rock salt structure	254
Figure I.4.C.31 Effect of nickel salt on the formation of the desired 622 phase (black – nickel sulfate; red – nickel acetate)	254
Figure I.4.C.32 Images showing (a) the SolveX process for the delamination of cathode materials from aluminum current collector and (b) the delaminated electrode of different sizes. (c) The delamination time dependence on the reaction temperature.....	255
Figure I.4.C.33 SEM-EDX results for the recovered cathode materials.....	256
Figure I.4.C.34 Characterizations on the recovered aluminum foils. (a) XRD pattern, (b) SEM image, (c) EDX image, and (d) EDX spectra.....	256

Figure I.4.C.35 Voltage profiles for the recovered NMC622	257
Figure I.4.C.36 Effect of shredding	257
Figure I.4.C.37 (a) Recovered black mass and aluminum foil via the SolveY process. Characterizations on the recovered black mass: (b) FTIR, (c) SEM, and (d) EDX mapping.....	258
Figure I.4.C.38 Diagram of benchtop fluidized magnetic separation apparatus.....	259
Figure I.4.C.39 Purity of graphite powder as a function fluidization time for 50/50 and 80/20 mixtures	259
Figure I.4.C.40 Triboelectric separation operating principles	260
Figure I.4.C.41 Adjustable baffle system	260
Figure I.4.C.42 Data tables for triboelectric separation of graphite.....	260
Figure I.4.C.43 Composition of electrolytes as determined by NMR recovered from commercial cells with different heat treatments under an argon atmosphere	261
Figure I.4.C.44 Full cell cycling results from electrolyte recovered from commercial cells dried at 90°C under air, and 100°C under vacuum compared to gen 2 electrolyte (1.2 M LiPF ₆ in 3:7 EC:EMC)	262
Figure I.4.C.45 Full cell cycling results of recovered electrolyte from commercial cells dried at 90°C under argon with different additives. The additives are VC (2 wt.% vinylene carbonate), VEC (0.5 wt.% vinyl ethylene carbonate), and PS (5 wt.% 1,3-propane sulfone)	262
Figure I.4.C.46 Cycle life of the 800 mAh pouch cell.....	264
Figure I.4.C.47 Li/transition metal ratio in the rinsed NMC622 cathodes.....	264
Figure I.4.C.48 First cycle voltage profile a) and dQ/dV curve of the rinsed electrodes b)	265
Figure I.4.C.49 Cycle life of the coin cells with fresh electrolyte a) and voltage profile at the end of 00 cycles b)	265
Figure I.4.C.50 Morphology of electrodes washed by various solvents	266
Figure I.4.C.51 Specific capacity (left) and HPPC ASI at 50% DoD (right) for the baseline electrodes (NMC622 and SLC1520P) under test in coin cells (single-sided) and 500-mAh pouch cells (double-sided)..	267
Figure I.4.C.52 Quantifying lattice strains as a function of statistical spreads in grain orientation provides detailed information about wear down of cathodes with resolutions down to the primary particle level. Figure Credit: Helio Moutinho.....	268
Figure I.4.C.53 Superior Graphite/Toda 1520P/NMC-111, 532,622, and 811 heat generation curves for a 2C full discharge (2a - top) and 2C full charge (2b - bottom)	270
Figure I.4.C.54 Efficiency of 1520P/NMC cells under Various Charge/Discharge Currents over an SOC range of 80% to 20%	271
Figure I.4.C.55 Simulated global Co reserves over the time period 1998–2040. Results of 3,427 sensitivity runs are shown	273
Figure I.4.C.56 LIBRA Model Interface.....	274
Figure I.4.C.57 LIBRA Model Sensitivity Analyses	275
Figure I.4.C.58 NREL's updated supply chain model resultd (Sources: NREL Analysis; Campagnol, N. et al. 2017; BNEF 2019; LME 2019; Daly, T. 2019; Stringer, 2019)	276
Figure I.4.C.59 Test matrix developed for evaluating ReCell baseline electrodes in coin-cell format	277
Figure I.4.C.60 Summary of the discharge capacity from the full-cell coin-cell test matrix results for pristine NMC111 versus SLC1520P graphite under the Life Cycle test protocol (see legend for details).....	277

Figure I.4.C.61 Summary of the discharge capacity from the full-cell coin-cell test matrix results for pristine NMC111 versus SLC1520P graphite under the Aging test protocol (see legend for details).....	278
Figure I.4.C.62 Summary of HPPC ASI from the full-cell coin-cell test matrix results for pristine NMC111 versus SLC1520P graphite under the Life Cycle test protocol (see legend in Figure 2 for details)	278
Figure I.4.C.63 Single-layer pouch cells made with 1 wt.% metallic impurity in anode and cathode electrodes for micro-calorimetry studies at NREL	279
Figure I.5.A.1 (a) Picture of assembled NMR experimental setup (b) diagram of experimental setup.....	285
Figure I.5.A.2 (a) ^{19}F NMR of Gen 2 electrolyte heated at 80°C for increasing lengths of time (b) Integrated peak area of PF5-Lewis base species relative to PF6-	286
Figure I.5.A.3 (a) ^{19}F spectra after aging of, from bottom to top: Gen 2 + NMC @ 55°C , Gen 2 @ 55°C , Gen 2 + H_2O @ 55°C , and Gen 2 @ 80°C (b) Peak width at half maxima of different chemical species over time	287
Figure I.5.A.4 Chemical structure of cyclotriphosphazenes, and the derivatives synthesized for this experiment	287
Figure I.5.A.5 (a) Integrated peak area of PF5-Lewis base species relative to PF6- for three different electrolyte systems (b) dQ/dV of the first cycle of a Gr/Li half cell with increasing concentrations of PzTFE	288
Figure I.5.A.6 (a) Capacity retention and (b) coulombic efficiencies of NMC622/Gr cells when cycled at 55°C with phosphazene additives	288
Figure I.5.A.7 Capacity retention and coulombic efficiencies of PzTFE in combination with (a) vinylene carbonate, (b) 1,3-propanesultone, and (c) triallylphosphate.....	289
Figure I.5.A.8 Area-specific of PzTFE in combination with (a) vinylene carbonate, (b) 1,3-propanesultone, and (c) triallylphosphate	289
Figure I.5.B.1 Analysis of reversible and irreversible Li plating along with capacity from graphite delithiation as a function of OL extent. (a) 1.5% OL (c) 5.5% OL. (b) Capacity associated with different stages of graphite at the beginning of life (BOL) and after OL. (d) Coulombic and stripping efficiency as multiple OL cycles are used. Figure from Tanim et al, 2019.....	293
Figure I.5.B.2 Focused-ion beam SEM (FIB-SEM) images of positive electrodes before (left) and after 450 cycles at 4C (middle) and 6C (right). Increasing the rate of charge led to distinct intergranular separation and increased capacity fade due to loss of active positive electrode material	294
Figure I.5.B.3 Coin cell data for various electrolyte blends identified using AEM. Cells were cycled using Round 2 positive and negative electrode laminates from Argonne. Cell capacity is shown on the left horizontal axis.....	295
Figure I.5.C.1 Model predictions for achievable energy density during 4C and 6C constant current charging to 4.2V for cells with a loading of $3\text{ mAh}\cdot\text{cm}^{-2}$ (left) and $4\text{ mAh}\cdot\text{cm}^{-2}$ (right). The white section of bars represents where model predicts lithium plating will occur.	299
Figure I.5.C.2 Comparison of gas-titration results from LBNL and macro-homogeneous model predictions for lithium plated during 3 cycles vs. charge rate. Half-cells were fully lithiated to graphite's theoretical capacity of 372 mAh/g -graphite and then discharged to an upper voltage of 1.5V vs Li.	300
Figure I.5.C.3 (Left) Lithiation heterogeneity induced by particle size distribution: large particle lithiation is lagging due to solid-state diffusion limitation. (Right) Anode state of charge associated with lithium plating onset calculated for different particle alignment and compared with spherical reference case.	301
Figure I.5.C.4 (a) Anode state of charge associated with lithium plating onset calculated for different dual coating architectures and compared with non-graded reference case, (b) schematic of a secondary pore network, (c) higher overall diffusion gain is achieved for higher tortuosity coefficient α	302

Figure I.5.C.5 (a) Illustration showing the design of cell for operando high-speed X-ray diffraction (XRD). (b) Illustration showing a magnified view of the cell, and a further magnified view of the graphite electrode with yellow points throughout the depth indicating the locations of each XRD measurement. (c) An example of a quantified profile of state of charge as a function of depth and time.....	303
Figure I.5.C.6 (a) Illustration showing the depth of the electrode with yellow points highlighting XRD measurements. The highlighted yellow region indicates where Li plating was present and depth-dependent colors (pink to blue) are for reference in the neighboring plots. (b) State of lithiation over time for each color-coded depth (blue near the separator and pink near the current collector) during 6C charge and (c) 6C discharge, where residual lithiated states are observed near the separator upon full discharge.....	303
Figure I.5.C.7 Effect of charging protocol on charge capacity and minimum (phis-phie) in 10 mins. (left) 2 steps and 3 steps constant current charging. (right) positive pulse current charging.....	304
Figure I.5.C.8 Full cell discharge capacity measured at C/3 using NMC-622 and graphite electrodes from Targray following a 5C charge to 4.2 V	305
Figure I.5.C.9 Cyclic voltammetry verifies electrochemical stability of Round-2 solvents against Li/Li+.	305
Figure I.5.C.10 Fast charge algorithms used to assess heat generation and efficiency.....	306
Figure I.5.C.11 Efficiency, heat rate, and capacity under various constant-current discharge and charge rates.....	307
Figure I.5.C.12 (a) Grey-level image after contrast correction, vertical direction is along electrode thickness, with lithium plating on top, and graphite layer at the bottom. (b) After segmentation. (c) Probability density function of lithium plating and graphite layer thickness. (d) Tentative correlation between volume ratio of lithium plating and graphite porosity near the separator.....	308
Figure I.5.D.1 Rate performance and coulombic efficiencies of TNO and TNO@C half cells (electrode loading 2.3 mg cm^{-2}).....	311
Figure I.5.D.2 Rate performance and coulombic efficiencies of NMC622 (18 mg/cm^2) and TNO@C (13.5 mg/cm^2) half-cells.....	311
Figure I.5.D.3 Discharge capacities and coulombic efficiencies of full cells (a) based on TNO and TNO@C with the same loading of 9.41 mg cm^{-2} and (b) based on TNO@C with different mass loadings.....	312
Figure I.5.D.4 (a) Voltage profiles and (b) cycling performance of NMC622/TNO@C full cells under different charging protocols with a total charge time of 10 min and discharge at C/3	312
Figure I.5.D.5 Effect of additives on capacity, coulombic efficiency and cycling stability of NMC622/TNO@C full cells at 5C fast charge condition.....	313
Figure I.5.D.6 Rate performance of (a) p-TNO and b-TNO half-cells with the same TNO loading of 10 mg/cm^2 ; (b) b-TNO half-cells with various TNO loadings	313
Figure I.5.D.7 (a) Rate performance and (b) Electrochemical Impedance Spectroscopy (EIS) of b-TNO half-cells with different TNO mass loadings.....	314
Figure I.5.D.8 Charge-discharge capacities, coulombic efficiencies, and energy densities of (a) p-TNO and b-TNO full cells with the same TNO loading of 10 mg/cm^2 ; and (b) b-TNO full-cells with various TNO mass loadings.....	314
Figure I.5.E.1 Voltage and Current during rate capability testing of NMC/Graphite UMich cell.....	318
Figure I.5.E.2 dQdV of charge steps during rate capability testing of NMC/Graphite cell.....	318
Figure I.5.E.3 Rate capability and long 6C/1C cycling for NCA/Hard Carbon cell.....	319
Figure I.5.E.4 Charge dQdV for NCA/Hard Carbon cells	320
Figure I.5.E.5 Efficiency for NMC/Graphite and NCA/Hard Carbon cells.....	320

Figure I.5.E.6 Temperature profile for 6C/1C cycling, with and without temperature control plates	321
Figure I.5.E.7 Cycle to cycle efficiency for 6C/1C cycling, with and without temperature control plates	322
Figure I.5.F.1 The bulk composition and surface composition are analyzed by XRF and TEM-EDS mapping	324
Figure I.5.F.2 The EELS spectra offset for clarity to show the intensity of the Mn and Ni are changing with position along the primary particle	325
Figure I.5.F.3 (a) The initial capacity of FCG85-5-10; (b) cycle data of plain FCG Ni85 material, and after a treatment with Al and Ti. (c) and (d) The qQ/dV of the untreated FCG and FCG altered with Al is shown to demonstrate how the material degradation is impeded thru treatment.....	325
Figure I.5.F.4 FCG 85-5-10 and FCG 85-10-5 (Ni-Mn-Co) comparing the first cycle load curve, capacity retention during coin cell cycling, and half-cell rate performance	326
Figure I.5.F.5 Graph comparing the two in situ cell HE-XRD (003) peak positions during charge and discharge. The shape during charge and discharge are obviously different.....	326
Figure I.5.F.6 (a) The cycle data for different LiDFOB added in Gen2 electrolyte tested in a half cell. (b) The rate performance comparison of Gen2 and Gen2 electrolyte with 1wt% LiDFOB	327
Figure I.5.F.7 15AH pouch cells energy density and energy retention over 500 cycles tested under XFC cycling conditions	327
Figure I.5.G.1 (a-i) SEM backscatter images of graphite electrodes(a,d,g,) pristine, (b,e,h) sputter coated with 10 nm Cu, and (c, f, i) sputter coated with 10 nm of Ni. Images a-i show the samples measured top-down while j-m show cross sectional images of the electrodes. (j, l) SEM secondary electron images and (k, m) corresponding composite EDS maps for graphite electrodes sputtered with (j, k) 10 nm Cu and (l, m) 10 nm Ni. (n,o) High resolution SEM-SE images for electrodes sputtered with (n) 10 nm Cu and (o) 10 nm Ni	330
Figure I.5.G.2 (a, b) Representative atomic force microscopy images of ultra-flat SiO_2 wafers sputtered with (a) 10 nm of Cu, and (b) 10 nm of Ni. (c-f) XPS spectra of (c, d) Cu $2p_{3/2}$ region of (c) pristine 10 nm Cu-graphite electrode and (d) 10 nm Cu-graphite electrode after formation cycling (charged state); (e,f) Ni $2p_{3/2}$ region of (e) pristine 10 nm Ni-graphite electrode and (f) 10 nm Ni-graphite electrode after formation cycling (charged state).....	331
Figure I.5.G.3 Operando XANES results for (a-c) Cu-graphite electrodes and (d-f) Ni-graphite electrodes during a formation cycle at C/5 rate between 0.01 – 1.4 V vs. Li/Li^+ . (a, d) Voltage profiles of operando cells. (b, c, e, f) Linear combination fit results for operando spectra during (b, e) discharge and (c, f) charge.....	332
Figure I.5.G.4 LABE SEM images displaying the morphologies of Li plated at -20 mV on the (g) uncoated graphite, (h) Cu-coated graphite, and (i) Ni-coated graphite electrodes	333
Figure I.5.G.5 Cycling of single layer full cells with NMC 622 cathodes and uncoated graphite (control), Cu-graphite, or Ni-graphite anodes between 3.0 – 4.3 V at C/2 rate	333
Figure I.5.G.6 Cycling of single layer full cells with NMC 622 cathodes and uncoated graphite (control), Cu-graphite, or Ni-graphite anodes between 3.0 – 4.3 V with 10 minute charge (CC/CV) and 1C discharge.....	334
Figure I.5.G.7 EDS mapping images for the top down view of Cu and Ni deposited on graphite. (a-f) Ni deposited on graphite with thickness of 5, 10 and 20 nm. (g-l) Cu deposited on graphite with thickness of 5, 10 and 20 nm. Magnification is 3000x	334
Figure I.5.H.1 a) DEMS titration setup schematic. b) Measured dead Li amount after 2 C/10 formation cycles and 3 cycles of varying intercalation rates to 372 mAh/g and deintercalation to 1.5 V. c) DEMS data for Li-graphite cell with following cycling procedure: (i) 5 hour OCV, (ii) one C/5 cycle (cutoff at 10 mV and 1.5 V), (iii) C/2 intercalation for 5 hours (overlithiation), (iv) 5 hour OCV	337

Figure I.5.H.2 a) 1 st cycle charge/discharge voltage profiles of the in situ optical cell when cycled at C/10 rate between 0.01 and 3 V, b) and c) in situ optical images of the graphite electrode before and after the 1 st lithiation process. d) Schematic configuration of an optical cell	338
Figure I.5.H.3 (a) Schematic of X-ray tomography cell. (b) Slice of an X-ray tomogram of micro-cell after 3 formation cycles (C/10 intercalation, C/5 deintercalation) and (c) slice of an X-ray tomogram of the same cell after 20 cycles (6C intercalation, C/2 deintercalation).....	339
Figure I.5.H.4 a) The evolution of thermal resistance in 100+ cycles, b) 3w sensor on separator for ex situ measurements, c) the impact of external pressure on thermal contact resistance	339
Figure I.5.H.5 (a) Graphite/Li cell cycling to generate OCV data after fast charge for various SOC and c-rates. (b) Coulombic efficiencies (CE) for these half cell cycles. We believe the drop in CE's at 6C and 40% SOC corresponds to the onset of Li plating.....	340
Figure I.5.H.6 OCV's (top row) and differential OCV's (bottom row) during relaxation after graphite intercalation at 1C, 2C, and 6C. Each window shows the OCV's after intercalation to the designated SOC .	341
Figure I.5.H.7 (a) Lithiation voltage profiles for graphite electrode between 0.20 and 0.00 V, inset showing full profile from 1.00 to 0.00 V, (b) charge voltage profiles for NMC electrode, (c) average negative graphite and (d) positive NMC half-cell resistance of four cells from 10 to 90% lithiation with range bars. Range bar represents the minimum and maximum values for each set of cells.....	342
Figure I.5.H.8 (a) CV formation of the basal HOPG/Li half-cell. (b) Current ramp behavior of basal HOPG/Li half-cell, after CV formation. (c) Image of cell	343
Figure I.5.H.9 SEM (a)(b) fracture surface and (c) surface images of freeze tape cast graphite anode. Graphite layer is 150 μm thick, showing vertical pore channels. Graphite columns are composed of 1506T graphite, Timcal C45 conductive additive, NaCMC and SBR binders. Porosity is 58 vol.%	343
Figure I.5.I.1 the ionic conductivities of 5 electrolytes under different temperatures: (a) the ion conductivities at 20°C; (b) the ion conductivities at 30°C; (c) the ion conductivities at 40°C	346
Figure I.5.I.2 (a) the rate performance for the 5 electrolyte systems with LiPF ₆ concentration of 1.2 M. (b) the long-term cycling performance with different electrolytes.....	346
Figure I.5.I.3 (a) Conductivity of LiFSI and LiPF ₆ in (EC:EMC) (30:70 wt%) as function of concentration and temperature. (b) Voltage (V) and Current (I) versus charging time for cells charged at (a) 1C, (b) 2C, (c) 3C and (d) 5C, with time cut-off of 1 hour, 30 minutes, 20 minutes and 12 minutes, respectively. The voltage (V) curves correspond to the y-axis on the far left while the current (I) curves correspond to the y-axis on the right of each corresponding panel	347
Figure I.5.I.4 (a) Charge (different C rate) and discharge voltage curves (all at C/2) of NMC/graphite cells with LiPF ₆ and LiFSI electrolyte. (b) Long term cycling performance of the cells with LiFSI and LiPF ₆ electrolytes with 12 minutes fast charging. Inserted photos show the extent of Li plating on each graphite electrode.....	348
Figure I.5.I.5 (a) Voltage (V) and Current (I) versus charging time for cells charged at 6C with time cut-off of 10 minutes. (b) Cycling performance of the 500 mAh at fast charging rate.....	349
Figure I.5.J.1 15AH pouch cells energy density and energy retention over 500 cycles tested under XFC cycling conditions.....	352
Figure I.5.J.2 Projects final 21AH Generation 1 pouch cells capacity and energy density cycling results, (including retention) over 500 cycles of 6C/1C conditions with periodic reference cycles	353
Figure I.5.J.3 Concentration gradient cathode with NMC ratio of 6:3:1 tested in half cell at 4.3V and 4.4V with and without a lower resistance titania coating	353
Figure I.5.K.1 Electrode composition and design parameters for Round 2-Batch 1 pouch cell design. The Round 1 electrodes had the same composition but had less mass loading (and thickness)	357

Figure I.5.K.2 Comparison of optical and XRD spatial map of the anode, showing Li intensities across the electrode.....	358
Figure I.5.K.3 Photo of the fully transparent (left, PET/PE [Kapak SealPAK 400]) and the windowed (right, PP window heat-sealed on layered pouch material) pouch cells designed for brief XRD experiments.....	359
Figure I.5.K.4 Correlation between mass of plated Li (as a % of initial mass of Li before cycling) and capacity fade in Round 2 cells. While cells charged at 4C (red) show negligible plating independent of the capacity fade, the other cells (#3–#7) show a direct correlation between the amount of plating and capacity fade.....	360
Figure I.5.K.5 microCT of a Round 2 anode cycled at the 9C charging rate for 450 cycles. (a) Projection of the tomographic reconstruction showing anode (gold) and Li in the form of LiOH (purple). (b) Segmentation, with the Li layer on top and the graphite layer below, showing the pore structure in each layer.....	361
Figure I.5.K.6 Left: schematic depicting a graphite anode strip with different regions of lithium plating indicated by bright regions. The strip was vacuum sealed in a glass capillary in a kapton tube. Right: top-view diagram of the perpendicular neutron and X-ray beams in NeXT with the rotation angle (yaw).....	361
Figure I.5.K.7 (a) The configuration of operando pressure measurement: a multilayer pouch cell is stacked with a metal plate and load cell and contained in a bench vise to define a fixed thickness. (b) A typical voltage profile versus pressure and $dP/d Q $ profiles are shown for a 70-mAh multilayer pouch cell under slow charging/discharging (0.5 C). (c) SEM images of the top surface of graphite electrodes under different charging condition. From left to right: after 50 cycles under 0.5 C, the graphite surfaces are smooth and clean; after 1 min, the dP/dQ curve passes the threshold (SH) and lithium droplets nucleate on the graphite surface; after 3 min, passing the SH, lithium dendrites can be clearly observed. (d) The dP/dQ curve during cycling in which slow 0.5 C cycles are followed by a fast-charging (3C) cycle. The blue and orange dots indicate the time points where the cells were open for SEM imaging	362
Figure I.6.A.1 Overview of BTMS relevance.....	366
Figure I.6.A.2 BTMS System Modeled in FY19.....	367
Figure I.6.A.3 Aggregate demand by time of day for EV charging.....	369
Figure I.6.A.4 Utility rate structure for PG&E customers, demonstrating the time-variability in electricity price and demand charges.....	369
Figure I.6.A.5 Block schematic based on signal flow graph representing the overall electrical and thermal model for the entire system.....	370
Figure I.6.A.6. Illustrative discharge curves for sensible and latent thermal storage materials (left) and for electrochemical and capacitor energy storage (right). This shows a drop in potential during discharge, with sensible storage and capacitors losing their potential more quickly than phase-change and electrochemical storage.....	372
Figure I.6.A.7. Discharge curves at different C rates, and corresponding Ragone plots for electrochemical batteries (top) and phase-change thermal energy storage (bottom). V_{OC} = open-circuit voltage; T_t = transition temperature. The y-axis on the bottom-left plot is inverted because these data are for cooling applications....	372
Figure I.6.A.8 Capital cost for EV charging station with BTMS	373
Figure I.6.A.9 EV charging demand shifting with a behind-the-meter battery.....	373
Figure I.6.A.10 Block schematic of an electric vehicle supply equipment.....	376
Figure I.6.A.11 Block-tree-type categorization of the various aspects of installation-oriented design of EVSE [1],[2],[3],[4],[5].....	378
Figure I.6.A.12 Capacity data throughout life testing is shown for LFP/graphite EV cells DST cycled to full depth of discharge.....	380

Figure I.6.A.13 INL cycling data at 1C/1C is shown overlaid on 5C/10C cycling data published by the developer.....	380
Figure I.6.A.14 Calendar- and cycle-life data for LMO-NMC/LTO cells.....	381
Figure I.6.A.15 Cycle-life data for LMO/graphite cells	381
Figure I.6.A.16 Cycle-life data for NMC-LMO/graphite cells	382
Figure I.6.A.17 Preliminary test matrix for cells with 6-XFC and 1 MWh ESS and accelerated aging conditions.....	383
Figure I.6.A.18 Cycle-life testing results for the NMC/graphite cells	384
Figure I.6.A.19 Calendar testing results for the NMC/Graphite cells, shown with the baseline cycling condition results.....	384
Figure I.6.A.20 Cycle-testing reference-performance-test (RPT) capacity results for the NMC/LTO cells	385
Figure I.6.A.21 Cycle-by-cycle testing capacity results for each cycling condition for the NMC/LTO cells..	385
Figure I.6.A.22 LFP/graphite cycling results.....	386
Figure I.6.A.23 Differential capacity test for LFP/graphite cells	386
Figure I.6.A.24 Capacity decay rate for each LFP/graphite cell type and condition	387
Figure I.6.A.25 Example of physics-based life predictive model (NREL) applied to 2012 Nissan Leaf fast charge data (INL).....	389
Figure I.6.A.26 Example local model fit of Kokam 75-Ah cell data using machine-learning elastic-net regularization algorithm.....	390
Figure I.6.A.27 Voltage measurement as a function of cycle using the original data (blue) and clean data after removal of data outliers (orange).....	391
Figure I.6.A.28 Comparison of predicted and observed reference performance test capacity after 900 cycles for the test and training datasets. Analysis performed using Nissan Leaf test data	391
Figure I.6.A.29 Comparison of observed and predicted reference performance test capacity for each cell in the analysis. Of note is that the data were collected at three different temperatures and three different cycling conditions [1]	392
Figure I.6.A.30. (a) Expanded graphite (EG), thermally expanded after acid intercalation. EG flakes are compressed in (b) die fixture using (c) pneumatic press. (d) Graphite matrix is soaked in PCM, resulting in (e) composite PCM	393
Figure I.6.A.31. DSC curves (melting) of several PCM composites with varying mass fraction of PCM.....	394
Figure I.6.A.32 Experimental setup (left), and CAD rendering showing each component	395
Figure I.6.A.33 4ergy storage capacity during cycling	395
Figure I.6.A.34. Experimental hardware in the loop (HIL), focusing on multi-system level integration of the building and behind-the-meter storage assets. In this case, storage assets are in hardware, with the building, grid, and photovoltaics (PV) simulated. The conditions applied to the hardware is from these simulations or from a specified weather file.....	396
Figure I.7.A.1 Simplified process diagram for LMO production using sol-gel method (P2)	403
Figure I.7.A.2 Simplified process diagram for LMO production using solid state synthesis (P1)	403
Figure I.7.A.3 Effect of cathode active material and temperature on the area specific impedance measured in coin cells.	404
Figure I.7.A.4 Comparison of estimated costs of lithium ion battery packs.....	406

Figure I.7.B.1 Average, relative capacity vs. cycle count for cells undergoing XCEL and standard charging	410
Figure I.7.C.1 Force against mechanical test apparatus of a cell fixed in place within the test fixture as temperature is increased. Used to evaluate cell swelling, this shows little to no swelling up to 90-100°C. Above this the force begins to rapidly increase until venting occurs at ~150°C	413
Figure I.7.C.2 Voltage vs temperature of cell tested in Figure I.7.C.1 above. A slight drop in voltage is observed with increasing temperature, indicating potential feasibility of rendering the cell inert through self-discharge over time. Voltage rapidly drops to 0 when cell failure occurs	414
Figure I.7.C.3 DPA and abuse test behaviors of cells with reduced n:p ratios to force significant lithium plating. Visible deposits are observed in the low n:p cell, with a significant thermal runaway event observed	415
Figure I.7.D.1 Efficiency summary of cells tested at 30°C in NREL's calorimeters. Caption Credits/Source: NREL- Aron Saxon	419
Figure I.7.D.2 Efficiency of silicon blended cells tested at 30°C in NREL's calorimeters under various charge/discharge currents and SOC ranges. Caption Credits/Source: NREL- Aron Saxon	420
Figure I.7.D.3 Calorimeter normalized heat rate for a graphite/high nickel content NMC cells under C/10 charge. Caption Credits/Source: NREL- Aron Saxon	421
Figure I.7.D.4 Large format graphite/NMC cell under a 3.2C fast charge. The calorimeter test temperature was 30°C. Caption Credits/Source: NREL- Aron Saxon	422
Figure I.7.D.5 Infrared image of lithium battery cell (graphite-silicon/high nickel content NMC) at the end of a 2C discharge. Caption Credits/Source: NREL- Aron Saxon	423
Figure I.7.E.1 Pictorial of cathode particle cross-sections produced in MERF	426
Figure I.7.E.2 Electrochemical performance high-nickel content NMC cathode powders produced by MERF compared to a baseline NMC811 (Targray). All electrodes and pouch cells were fabricated and tested by the CAMP Facility	427
Figure I.7.E.3 Images of a researcher scraping the laminate off of the substrate foil in an inert glovebox and the parts used for the DSC experiment	427
Figure I.7.E.4 Test conditions and sample preparation procedure used for DSC experiment	428
Figure I.7.E.5 Voltage profiles and energy-capacity relationship for NMC111, NMC622, NMC811, NMC811-core-gradient, NMC811-core-shell, and NMC811-core-multishell with respect to the energy cutoff of 750 mWh/g of NMC	428
Figure I.7.E.6 Exothermic heat released (integrated DSC peak area), half-cell charged specific capacity, and half-cell voltage before cell disassembly DSC results (left) and total heat released of the materials (right)	429
Figure I.7.E.7 Cell design options the CAMP Facility explored for coating materials onto an existing electrode. The green lines indicate the interface of film coating on to the anode	430
Figure I.7.E.8 Voltage profiles of graphite electrodes with selected ceramics (Al_2O_3 and MgO) coated graphite electrodes coatings vs. lithium metal made in coin cells. The left plot show the performance when the polymer separator is present in the system and the right plot shows when the polymer is absent from the system. This test was a scoping experiment to observe the performance and test if there would be any capacity loss due to the ceramic coating	430
Figure I.7.E.9 SEM images of the surface of the graphite electrodes with and without various coatings. The various ceramic coatings appear to provide a uniform coverage over the surface of the calendered graphite baseline anode	431
Figure I.7.E.10 Cross section SEM images of the various ceramic coatings generally indicate a more uniform thickness is achieved using the comma coater compared to a hand coating	432

Figure I.7.E.11 SEM cross section image (left) and a surface SEM image (right) for the Al_2O_3 coating on the graphite anode. The image was provided by Nancy Dietz Rago (PTF).....	432
Figure I.7.E.12 Electrochemical performance of the baseline full-cell pouch-cell build using a typical polymer separator with no ceramic coating on the anode against 8 other data sets where the cells contain ceramic coatings on the anode.....	432
Figure I.7.E.13 Coating methods used in the CAMP Facility for coating ceramics onto graphite electrodes..	433
Figure I.7.E.14 Influence of oxide nanoparticles on the electrochemical cycling of NCM811//Gr cells	435
Figure I.7.E.15 Influence of oxide nanoparticles on the Area specific impedance (ASI) of NCM811//Gr cells. ASI for Gen2 electrolyte (panel <i>a</i>) is reproduced in gray in panels <i>b-h</i> for comparison. Impedance was measured at the cycles indicated in Figure I.7.E.14.....	436
Figure I.7.E.16 Correlation of (a) initial ASI at 3.7 V (y-axis) and ASI rise (<i>x-axis</i>) and (b) ASI rise (y-axis) and capacity retention (<i>x-axis</i>) for NCM811/Gr cells containing various electrolytes	436
Figure I.7.E.17 Representation of the effect of oxide particles on cell performance.....	437
Figure I.7.E.18 The effect of added water on electrochemical performance of NCM811//Gr cells. Cycle life (panels a , b , and c) and impedance rise (panels d , e , and f) for multiple cells containing baseline electrolyte with (panels b , c , e , and f) or without (panels a and d) 1,000 ppm water. Different color hues represent different cells. The dashed horizontal lines are visual guides to compare different systems.....	439
Figure I.7.F.1 a) Cycle performance of SiO/NCM523-LFO full cells, b) discharge capacity with C/10 rate as a function of time.....	443
Figure I.7.F.2 a) 3 rd cycle voltage profile of NMC and NCA half cells, b) cycle performance of NMC and NCA full cells	444
Figure I.7.F.3 DSC of NMC (left) and NCA (right) for delithiated material.....	445
Figure I.7.F.4 a) pouch cell assembly, b) prelithiation setup, c) electrode before and after prelithiation.....	445
Figure I.7.F.5 a) 1 st cycle differential capacity and b) Coulombic efficiency plots of pristine and prelithiated graphite electrodes	446
Figure I.7.F.6 (a) Differential capacity plot and (b) cycle performance of full cells with prelithiated graphite electrode.....	446
Figure I.7.F.7 (a) Differential capacity plot and (b) cycle performance of full cells with prelithiated SiO electrode.....	447
Figure II.1.A.1 Battery Performance and Cost (BatPaC) model utilized to establish relevance by connecting pack to anode targets.....	462
Figure II.1.A.2 Program participants including Laboratories, research facilities, and individual contributors	463
Figure II.1.A.3 Lithiation capacity versus lithium metal for various graphite-free silicon electrodes fabricated by the CAMP Facility. These cells were cycled between 0.05 to 1.5 V or 0.1 to 1.5 V vs. Li^+/Li as noted in the legend.....	465
Figure II.1.A.4 Full cell results using the silicon DeepDive protocol for the high-silicon graphite-free anodes and 15 wt.% Si in graphite composite. All anodes were tested against a capacity-matched NMC532 cathode. The anode to cathode capacity pairing for the electrode couples was based on the anode capacities achieved upon a 50-mV lithiation cutoff	466
Figure II.1.A.5 (Left) Raman mapping of pristine electrode. (Right) – cycling data for the electrodes.....	467
Figure II.1.A.6 Variations in coating quality as a function of wet gap setting for 23 wt.% SFG-6-L flakey graphite with 60 wt.% silicon	468

Figure II.1.A.7 Final specification for the two trial electrodes produced in this quarter based on 23 wt.% electrochemically active carbon (SFG-6-L flakey graphite and hard carbon) with 60 wt.% silicon	468
Figure II.1.A.8 Lithiation & delithiation capacity versus lithium metal for 60 wt.% Si electrodes with 23 wt.% of either SFG-6-L flakey graphite or hard carbon. Comparison made to 80 wt.% graphite-free silicon electrodes (A-A017 “4 Kd Si” and A-A018 “Dec 2018 Si”; 10 wt.% C45 and 10 wt.% LiPAA), all fabricated by the CAMP Facility. These cells were cycled between 0.1 to 1.5 V vs. Li ⁺ /Li	469
Figure II.1.A.9 Viscosity vs. shear rate for 80 wt.% Si using LiPAA binder with PAA dispersant (LN3174-115) and without PAA dispersant (LN3174-116). Rheology measurement performed using a cone-plate geometry with a cone diameter of 20 mm and an angle of 2°. The temperature was held at 25°C	470
Figure II.1.A.10 Viscosity vs. shear rate for a SFG-6L graphite electrode (no silicon) using LiPAA binder dispersant (black curve, LN3174-111), and for a SFG-6L graphite electrode (no silicon) with PAA binder (magenta curve, LN3174-112). Slurries consisted of 88 wt.% graphite, 2 wt.% C45 carbon, and 10 wt.% binder. Rheology measurement performed using a cone-plate geometry with a cone diameter of 20 mm and an angle of 2°. The temperature was held at 25°C	470
Figure II.1.A.11 Viscosity versus shear rate curve for silicon electrode slurry. Inset schematic from left to right depict 1) extremely collapsed polymer chains on a silicon particle, 2) a mixture of extremely collapsed polymer chains and extended polymer chains as well as polymer that has been sheared and is now in the water phase, and 3) silicon particle aggregation at high shear rates. The line is added to guide the eye	472
Figure II.1.A.12 Intensity versus Q ultra small angle neutron scattering plots of (a) 14 wt% solution of 450,000 g/mol poly(acrylic acid) in deuterated water at 0 Hz and 30 Hz and (b) a 10 wt% solution of 450,000 g/mol poly(acrylic acid) and silicon nanoparticles (17 wt%) in deuterated water at 0 Hz (experimental data=blue circles, fitted data=blue lines) and 30 Hz (experimental data=red circles, fitted data=red lines)	473
Figure II.1.A.13 Specific delithiation capacity profiles of Li half cells using electrodes containing 73 wt% graphite, 15 wt% Si, 10 wt% modified PAA binders, and 2 wt% C45 over 100 cycles at C/3 rate	475
Figure II.1.A.14 (a) Small angle X-Ray scattering (SAXS) profiles for binder solutions; (b) Sample information and R _g of the modified PAA solutions	476
Figure II.1.A.15 (a) Sample information and R _g of PAA solutions; (b) Specific delithiation capacity profiles of half cells using electrodes containing 73 wt% graphite, 15 wt% Si, 10 wt% PAA binders in organic processing solvent, and 2 wt% C45 over 100 cycles at C/3 rate; (c) Specific delithiation capacity profiles of half cells using electrodes containing 73 wt% graphite, 15 wt% Si, 10 wt% PAA binders in mixed processing solvent, and 2 wt% C45 over 100 cycles at C/3 rate	477
Figure II.1.A.16 Synthetic scheme of PAA analogues with modified properties	477
Figure II.1.A.17 Electrochemically Induced Fracture Method. LEFT: Electrochemical cycling conditions used to induce fracturing, where arrows represent times where samples were analyzed via SEM. RIGHT: SEM data of sample in pristine state (a) and following (b,d) 2 h and (c,e) 6 h lithiation	478
Figure II.1.A.18 Limitations of the linear elastic fracture mechanics (LEFM) model based on the thickness of the silicon wafer. For thick wafers (1 mm), crack propagation occurs along crystallographic directions. For thinner wafers (675 μ m), LEFM mechanics cannot be applied. Rather, plastic deformation occurs resulting in a number of different failure modes including compression, slabbing, shear, microcracking, and pseudoplastic behavior—similar to the cracking behavior expected from silicon nanoparticles. SEM data and schematic on left from NREL	478
Figure II.1.A.19 TOP: Chemical structures of polymer capping layers used in this study; MIDDLE: Plan view SEM images. BOTTOM: Cross-sectional SEM images after FIB milling. The trench from the FIB milling is seen in the plan view images for CMC- and PAA-capped wafers	479
Figure II.1.A.20 LEFT: Cantilever Beam Test (CBT) instrument showing the cantilever bound to a polymer-capped silicon wafer; MIDDLE: Schematic of the single cantilever beam method. RIGHT: Representative load versus displacement plot obtained during a v-G measurement. Load reversals are conducted to extract dC/da	

(change in beam compliance C as a function of extended debond length a) and obtain G_c values as the debond extends	480
Figure II.1.A.21 Synthesis of surface-functionalized silicon nanoparticles SF-SiNPs	481
Figure II.1.A.22 (a) TEM images of H-SiNPs and (b) Si-C3-(EO) ₁ -epoxy SiNPs (the specimens were prepared from a 1 mg g ⁻¹ SiNP aqueous suspension by casting the nanoparticles on a carbon-coated copper grid); (c) aqueous dispersions of H-SiNPs and Si-C3-(EO) ₁ -epoxy SiNPs (left: after 10 min sonication, right: the same dispersions rested for 24 h)	481
Figure II.1.A.23 Electrochemical performance of Si composite electrodes. (a) Cycling performance and Coulombic efficiency, and (b) Nyquist plots of H-SiNP and SF-SiNP electrodes after 150 cycles	482
Figure II.1.A.24 SEM images and EDX elemental mappings (colored images) of composite electrodes. (a) H-SiNP anode and (b) surface functionalized Si-C3-(EO) ₂ -epoxy SiNP anode before cycling, (c) H-SiNP anode, and (d) Si-C3-(EO) ₂ -epoxy SiNP anode after 150 cycles (C, Si, O, F, and P)	484
Figure II.1.A.25 (a) Capacity retention and Coulombic efficiency of the pure silicon anodes using H-SiNPs and Si-C3-(EO) ₄ -epoxy SiNPs as active material, and (b) F1s XPS spectra of H-SiNPs and Si-C3-(EO) ₄ -epoxy-SiNPs anodes after 200 cycles at delithiated stage	485
Figure II.1.A.26 (a) Cycling performance of Si-Sn and Si films of similar thickness. (b) XRD patterns of co-sputtered Si _x Sn _{1-x} thin films along with Sn reference	486
Figure II.1.A.27 SEM images of co-sputtered Si _x Sn _{1-x} thin films	486
Figure II.1.A.28 Charge-discharge voltage profiles of the co-sputtered Si _x Sn _{1-x} thin films during the first two cycles	487
Figure II.1.A.29 (a) Lithiation capacity, (b) delithiation capacity, (c) coulombic efficiency and (d) capacity retention of co-sputtered Si _x Sn _{1-x} thin films upon cycling	487
Figure II.1.A.30 dQ/dV plots of co-sputtered Si _x Sn _{1-x} thin films during the first two cycles	488
Figure II.1.A.31 C 1s spectra from the 15 wt% Si/C, 70 wt% Si/C, 90 wt% Si/C, 70 wt% Si/C/PEG, 70 wt% Si/C/PVdF, and 70 wt% Si/C/PFO-based electrodes	490
Figure II.1.A.32 Si 2p spectra from the 15 wt% Si/C, 70 wt% Si/C, 90 wt% Si/C, 70 wt% Si/C/PEG, 70 wt% Si/C/PVdF, and 70 wt% Si/C/PFO-based electrodes	490
Figure II.1.A.33 O 1s spectra from the 15 wt% Si/C, 70 wt% Si/C, 90 wt% Si/C, 70 wt% Si/C/PEG, 70 wt% Si/C/PVdF, and 70 wt% Si/C/PFO-based electrodes	491
Figure II.1.A.34 F 1s spectra from the 15 wt% Si/C, 70 wt% Si/C, 90 wt% Si/C, 70 wt% Si/C/PEG, 70 wt% Si/C/PVdF, and 70 wt% Si/C/PFO-based electrodes	492
Figure II.1.A.35 Electrode potential changes during the first lithiation/delithiation of half-cells with the 15 wt% Si / C, 70 wt% Si / C, 90 wt% Si / C, 70 wt% Si / C/PEG, 70 wt% Si / C/PVdF, and 70 wt% Si / C/PFO electrodes	493
Figure II.1.A.36 Differential capacity (dQ/dV) as a function of voltage during the first lithiation of half-cells with the 15 wt% Si / C, 70 wt% Si / C, 90 wt% Si / C, 70 wt% Si / C/PEG, 70 wt% Si / C/PVdF, and 70 wt% Si / C/PFO electrodes. The peak observed at ~1.0 – 1.1 V is not observed during subsequent lithiation cycles	493
Figure II.1.A.37 Comparing the discharge capacity vs. cycle number for full cells containing (a) 15 wt% Si / C, 70 wt% Si / C, 90 wt% Si / C and (b) 70 wt% Si / C, 70 wt% Si / C/PEG, 70 wt% Si / C/PVdF and 70 wt% Si / C/PFO electrodes. Cycles 1-3 and 97-100 are at a ~C/20 rate, where C refers to the initial C/1 capacity of the cells; cycles 4-94 are at a ~C/3 rate	494
Figure II.1.A.38 Full-cell electrochemical test results. Cells in panels (a)-(d) consist of NMC532 cathodes and Si or Graphite anodes (formation cycles are not shown). Cells in panels (e)-(h) consist of HE5050 cathodes and	

Si or graphite anodes (formation cycles are not shown). At the end of each charge step the cells were held at 4.1 V until the current dropped below C/50. The discharge capacities in panels (a) and (c) are normalized by the weights of cathode materials (NMC523 or HE5050). The discharge capacities and discharge energy densities in panels (b), (c), (f), and (g) are normalized by the total weights of cathode materials (NMC523 or HE5050) and anode materials (Si or graphite). Error bars represent the standard deviations of at least three measurements for each sample. Trend lines for the coulombic efficiencies in (d) and (h) were calculated by a moving average of 15 adjacent points..... 497

Figure II.1.A.39 Discharge capacities of full cells using GenF, GenFM, GenFA, and GenFC electrolytes with extended cycles. (a) The full cells consist of NMC532+Si electrodes were cycled between 3.0 and 4.1 V at C/3 after three formations cycles between 3.0 and 4.1 V at C/20 (formation cycles are not shown). (b) The full cells consist of HE5050+Si electrodes were cycled between 3.0 and 4.1 V at C/3 after three formations cycles between 3.0 and 4.5 V at C/20 (formation cycles are not shown). At the end of each charging process during aging cycles the cells were held at 4.1 V until the current dropped below C/50. Two cells were tested for extended cycles on each cathode to show that the lifetime of the full cells are repeatable..... 498

Figure II.1.A.40 Frequency shift for the early SEI formation for the 0.2 M Zn(TFSI) and 0.2 M Mg(TFSI)₂ as electrolyte additives to the baseline electrolyte (Gen2+10%FEC) on a Si thin film anode. Lithiation depth is 0.115 V 498

Figure II.1.A.41 Voltage, current and frequency versus time plots of the early SEI formation of Zn(TFSI)₂ additive into the Gen2 electrolyte from OCV to lithiation depth of 0.4 V 499

Figure II.1.A.42 Schematics of the gradient polarity solvent wash technique..... 500

Figure II.1.A.43 Gradient polarity solvent wash was applied to a Cu electrode polarized to 10 mV Li/Li+ ... 501

Figure II.1.A.44 Three different scanning rates of CV at 1, 10 and 60 mV min⁻¹ were applied to the Cu electrodes respectively with baseline electrolyte and two additives-based electrolytes. The Cu surface species vary due to both the additives and scan rates..... 501

Figure II.1.A.45 Si N-type disk electrode voltammetric results shown for the reductive side of the voltage window where SEI first cycle is shown. (a.) Slow CV at 6 μV/s between 0.01 to 1.5 V vs. LiLi⁺ RE/CE electrode. (b.) Fast frequency electrode disk sweeping at 100 mV/s for 10 cycles between 0.01 to 1.5 V vs. LiLi⁺ RE/CE electrode..... 502

Figure II.1.A.46 (a.) Si N-type disk electrode voltammetric results shown for the oxidative side of the voltage window with 10 mM ferrocene in GEN2 + 10% FEC. (b.) RRDE result showing the limiting current on the Si N-type disk and the Pt ring response to oxidation (disk) and reduction (ring) of ferrocene as a function of rotation rate..... 503

Figure II.1.A.47 (a.) Si N-type disk electrode and Pt ring RRDE results shown for the oxidative side of the voltage window with 10 mM ferrocene in GEN2 + 10% FEC. This SEI was grown using 60 μV/s rate, and (b.) 10 cycles at 100 mV/s SEI cycling formation..... 503

Figure II.1.A.48 Synthetic scheme of PAA analogues with modified properties 504

Figure II.1.A.49 Voltage and current versus time, showing the testing regimen used for these short tests..... 505

Figure II.1.A.50 Schematic of electrolyte extraction steps 505

Figure II.1.A.51 Molecular structure and properties of several diluents and the recipes of new LHCEs..... 506

Figure II.1.A.52 Charge-discharge curve, cycling stability, and Coulombic efficiency of DeepDive anodes in new LHCEs in half-cell (a-c) and full-cells (d-f) with NMC532 cathodes..... 507

Figure II.1.B.1 Energy per atom of two relaxed crystalline interfaces between i) SiO₂ (001) and Si (111), and ii) SiO₂ (110) and Si (100) as a function of SiO₂ film thickness 516

Figure II.1.B.2 Energy per atom of interfaces between i) amorphous SiO₂ and ii) crystalline SiO₂ (001) with Si (111) 516

Figure II.1.B.3 Energy per atom of slabs of a) Li_xSi and b) Li_xSiO_y as a function of thickness, with the bulk energies shown to the right. Error bars shown represent 1 standard deviation among five sample slabs. The dotted lines show the regression for energy vs thickness	517
Figure II.1.B.4 a) Schematic of film expansion during lithiation; b) Lithiation profile for amorphous Si films; c) Lithiation profile for amorphous SiO_2 films	518
Figure II.1.B.5 Left: Galvanostatic cycling results obtained with an O-ring cell and Si wafer anode as a function of current density at NREL (4-h half-cycles for 5 and 2 μAcm^{-2} , 12 h for 0.7 μAcm^{-2}). Right: Comparable results reported by LBL for a single lithiation cycle	519
Figure II.1.B.6 Cycling of Si wafer anodes with variation of SiO_2 coating thickness at 20 μAcm^{-2} with no lower voltage cut-off. Top: 1 st and 9 th cycles as a function of SiO_2 thickness (left, middle), and Coulombic efficiency as a function of cycle number (right). Bottom: Photographs of Si wafers after 10 cycles.....	520
Figure II.1.B.7 Chronoamperometry at 0.01 V/Li for different SiO_2 thicknesses. Photographs of selected samples at the end of testing are shown.....	520
Figure II.1.B.8 Changes in Si, Li, O, and F bonding studied by the XPS. Colors of the XPS curves correspond to the lithiation-delithiation stages in the voltage-time plot on the left (2 half-cycles, 2 h each)	521
Figure II.1.B.9 Two-dimensional TOF-SIMS map of Li, Si, O, and carbon-containing sputtering fragments, along with the optical micrograph. The mapping area was 500x500 microns and is shown in the micrograph by the orange contour	522
Figure II.1.B.11 CVs of a) 2 nd cycle, b) 7 th cycle, and c) 14 th cycle of $\text{Si}_x\text{Li}_y\text{O}$ samples under slow-scan CV (same conditions as above)	524
Figure II.1.B.12 Nyquist plots of SiO_2 film exposed to Gen-2 electrolyte at 30C for various times. Film evolution is very slow, with little change after several days.....	524
Figure II.1.B.13 Nyquist plots of SiO_2 film exposed to Gen 2 electrolyte at 60°C (left) and 80°C (right) over time. Both the electrical model and the film evolution are dramatically changed from the room-temperature case	525
Figure II.1.B.14 a) 1 st -cycle and b) 2 nd -cycle CV curves of Si, Si with native oxide layer, and four SiO_x anodes with different oxygen level tested under the scan rate of 0.1 mV/s in the potential range of 0.05–1.5 V	525
Figure II.1.B.15 Galvanostatic charge-discharge profiles of Si, Si with native oxide layer, and SiO_x anode under the current of 1 C (6 μA) in the potential range of 0.05–1.5 V	526
Figure II.1.B.16 CV curves and galvanostatic charge-discharge profiles of Si prepared under different sputtering conditions under the scan rate of 0.1 mV/s in the potential range of 0.05–1.5 V	527
Figure II.1.B.17 A) Moiré in situ cell design with PEEK pieces in white and the metal heating elements in beige. B) Current custom microscope with optical illumination arm complete. C) Schematic of the targeted design of the final Moiré microscope	528
Figure II.1.B.18 A) Moiré fringe pattern using 470-nm incident light for the Si wafer thermal expansion experiments. B) Cross-sectional average of the Moiré fringe pattern given in A with the data in blue and the fit in orange. C) Dimensionless frequency obtained from the sine-wave fit for each temperature with the slope giving the CTE of the silicon wafer substrate. D) Cyclic voltammogram of the 50-nm Si on 2- μm Cu in blue and 2- μm Cu in orange. The working electrode was the silicon on copper foil and the counter/reference electrode were lithium metal. The electrolyte was the Gen 2 electrolyte. The scan rate was 0.1 mV/s at room temperature. Contamination peaks seem to be present during the first cycle	529
Figure II.1.B.19 Summary of optimized nonthermal plasma growth conditions for preparing 30-nm-diameter Si NPs at gram scale	530
Figure II.1.B.20 Left: C_{65}/Si ratio must increase as the Si NP size decreases to ensure an electrical percolation network for active anode material as the surface area/volume ratio increases. Center: Normalized dQdV versus	

potential plot of the 1st cycle of the same samples showing that only the air-free-processed Si NP electrode undergoes reversible lithiation and delithiation, whereas SiO₂ electrodes do not exhibit reversible lithiation. Right: Capacity and Coulombic efficiency of half-cell anodes made from plasma-grown Si NPs (blue) fabricated air-free using NMP solvent or (red) in air using H₂O solvent 530

Figure II.1.B.21 (a) Normalized cycling data for a range of SiH_x-terminated Si NP anodes. The data here have been normalized to their capacity at cycle number 50. (b) Scatter plot of the average capacity fade rate as determined by fitting the last 50 cycles of each of the different-diameter Si NP-based anodes. The data in the blue open circles represent silicon with SiH_x-termination, and the data in red are those from oxidized (SiO₂) Si NPs. The black dashed line is a power function fit to the SiH_x-data with the form $\text{cap. fade} = ax^n + b$, where x represents the Si NP diameter. The inset is the same data plotted as a function of Si NP surface-area-to-volume (SA/V) ratio 531

Figure II.1.B.22 (a) Representative Nyquist plots for Si NP-based anode half-cells with (red) and without (blue) an intentionally grown surface oxide (SiO₂) layer. The equivalent circuit used to model these data are shown in the top of panel (a), and fits to the data using this circuit are shown in the dashed lines. (b) Normalized scan-rate-dependent data for SiH_x- (blue) and SiO₂- (red) terminated Si NPs for 3.9 nm (open circles), 11.6 nm (light-colored circles), and 30.3 nm (dark-colored circles). The inset shows the non-normalized data. (c) Values of the resistance of the SEI layer (R_{SEI}) extracted from fitting the impedance data. (d) Values of the capacitance of the SEI layer (R_{SEI}) extracted from fitting the impedance data. (e) RC time constants for impedance process associated with the SEI layer..... 532

Figure II.1.B.23 Neutron PDF data collected for Li₂SiO₃ (top), Li₂Si₂O₅ (middle), and Li₄SiO₄ (bottom) for the raw material (black line) and material exposed to electrolyte (red dashed line)..... 534

Figure II.1.B.24 a) Heat flow and voltage curves for NMC vs Paraclete-G18 coin cell subjected to electrochemical microcalorimetry. b) The cell capacities and generated heat per cycle derived from these curves..... 536

Figure II.1.B.25 (a) Photograph of the 1-cycle, 200-mV, and 10-mV GenF or GenFM samples in the air-free holder used for micro-Raman analysis. (b) Optical micrographs of the samples imaged through a 20x objective on the Raman microscope. Samples from GenF and GenFM looked the same. (c) Raman spectra of the samples 537

Figure II.1.B.26 (a) ATR-FTIR and (b) DRIFTS-FTIR spectra of 1 cycle, 200 mV, and 10 mV GenF or GenFM samples 538

Figure II.1.B.27 XPS spectra of the Si electrodes cycled in GenF. Peak assignments are preliminary..... 539

Figure II.1.B.28 XPS spectra of the Si electrodes cycled in GenFM. Peak assignments are preliminary (N.A. denotes “not assigned”) 539

Figure II.1.B.29 STEM EDS atomic % maps of particles of first-cycle GenFM sample 540

Figure II.1.B.30 STEM EDS spectra obtained from particles of 1-cycle GenFM sample..... 540

Figure II.1.B.31 Optical microscope images of composite electrodes after cycling and disassembly. Scale is visible in the width of the visible AFM cantilever, which measures 40 μm in width..... 541

Figure II.1.B.32 5 \times 5- μm AFM images and RMS roughness calculated from AFM images..... 541

Figure II.1.B.33 Summary of XPS measurements for the O 1s, Si 2p, and valence-band (VB) regions during in situ lithiation of 5-nm SiO₂ / Si(001) sample. For these measurements, the Li⁺ ion gun was pulsed (square wave, 50% duty cycle) at 200 μHz with a current density $\sim 55 \text{ nA/cm}^2$. The top row represents core-level spectra from the as-received sample. The middle and lower rows show spectra acquired when the Li⁺ ion gun was on and off, respectively. The dashed vertical lines are a guide to the eye to illustrate core-level shifts associated with the lithiation overpotential..... 543

Figure II.1.B.34 (a) Summary of time evolution of SiO₂ O 1s binding energy and overpotential during VE-GITT (i.e., the pulsed in situ lithiation experiment). (b)–(f) O 1s core-level spectra at various times illustrating

that the core-level shifts associated with the overpotential become progressively smaller in magnitude as the lithiation proceeds. (Note that the black trace in (b) corresponds to the initial, pre-lithiated state)	544
Figure II.1.B.35 (a) XPS spectra from the (a) O 1s and (b) Si 2p core levels, as well as the (c) valence-band regions. The top row of spectra (black traces) show spectra from the pre-lithiated sample. The Si 2p and VB spectra both show clear features associated with both SiO ₂ and Si ⁰ , whereas the O 1s spectra each show a single feature associated with SiO ₂ . O 1s. The bottom row of spectra (red traces) shows the sample at an early stage of lithiation (cf. Figure II.1.B.34(b) and (c)) with the Li ⁺ ion gun in the off state.....	545
Figure II.1.B.36 Schematic illustration of the observed change in interfacial band alignment that occurs during early-stage lithiation of the 5-nm SiO ₂ / Si(001) model-system interface	545
Figure II.1.B.37 Schematic representation of the electrochemical cell set up, cell components, and protocols employed in the Corrosion Task.....	547
Figure II.1.B.38 (a) First lithiation–delithiation process of 500-nm Si thin film on Cu foil observed by cyclic voltammetry by using four different electrolyte solutions. A scan rate of 0.1 mV s ⁻¹ has been applied within the 0.05–1.5 V potential range. Inset shows the enlarged potential region of the electrolyte decomposition. (b) Galvanostatic cycling test of the same systems performed at 50 μA cm ⁻²	548
Figure II.1.B.39 Application of Protocol 1 (GCPL + CA) to the 500-nm Si thin-film model electrode by using (a, b) 1.2 M LiPF ₆ EC:EMC (3:7 wt%), (c, d) 1.2 M LiPF ₆ EC:EMC (3:7 wt%) + 10% FEC, and (e, f) 1.2 M LiTFSI EC:EMC (3:7 wt%). (a, b, c) show the galvanostatic cycling with associated potentiostatic step at 0.05 V. (b, d, f) reports the related current-density measurement during the potentiostatic step	549
Figure II.1.B.40 Summary of XPS measurements on 50-nm a-Si / 3-nm SiO ₂ films at varying states of lithiation and delithiation. Peak assignments are preliminary, N.A. denotes “not assigned”	551
Figure II.1.B.41 Summary of XPS measurements on 50-nm a-Si / 10-nm SiO ₂ films at varying states of lithiation and delithiation. Peak assignments are preliminary, N.A. denotes “not assigned”	552
Figure II.1.B.42 The voltage profiles of LiFePO ₄ /Si cells containing the 500-nm Si thin-film model electrodes (1 st , 2 nd , 5 th , and 10 th cycle) with (a) 1.2 M LiPF ₆ EC:EMC (3:7 wt%), (b) 1.2 M LiPF ₆ EC:EMC (3:7 wt%) + 10% FEC, and (c) 1.2 M LiTFSI EC:EMC (3:7 wt%).....	554
Figure II.1.B.43 Cycling performance and efficiency of LiFePO ₄ /Si cells containing the 500-nm Si thin-film model electrodes with different electrolyte solutions	555
Figure II.1.B.44 Schematic of the procedure to estimate the actual state of charge (SOC) of silicon electrodes. From (a) the GITT profile, (b) the relation between quasi-open-circuit voltage (QOCV) and SOC is obtained. At the end of each lithiation step, the SOC is extrapolated from (c), the observed QOCV in relation to the QOCV value on the GITT profile.....	556
Figure II.1.B.45 The calculated capacity loss from electrolyte decomposition and lithium trapping in LiFePO ₄ /Si cells containing the 500-nm Si thin-film model electrodes with different electrolyte solutions ...	556
Figure II.1.B.46 Schematics of the gradient polarity solvent wash technique.....	557
Figure II.1.B.47 Gradient polarity solvent wash was applied to a Cu electrode polarized to 10 mV Li/Li ⁺	558
Figure II.1.B.48 Three different scanning rates of CV at 1, 10, and 60 mV min ⁻¹ were applied to the Cu electrodes, respectively, with baseline electrolyte and two additives-based electrolytes. The Cu surface species vary due to both the additives and scan rates.....	558
Figure II.1.B.49 Cyclic voltammograms of a-Si thin-film anodes cycled in various electrolytes between 1.5 V and 50 mV vs. Li/Li ⁺ at a scan rate of 0.1 mV/s showing the (a) first and (b) sixth cycles.....	559
Figure II.1.B.50 Summary of the parasitic current density during the galvanostatic cycling (GC) – chronoamperometry (CA) test for a-Si cycled in various electrolytes. During the formation cycle, the a-Si was first discharged to 50 mV vs. Li/Li ⁺ and then galvanostatically cycled between 1.5 V and 50 mV at 1C (41.7	

$\mu\text{A}/\text{cm}^2$). In between each charge-discharge cycle, a 24-hour potential hold at 50 mV vs. Li/Li^+ was performed, and the steady-state current at the end of this step was recorded.....	560
Figure II.1.B.51 Variation of normalized discharge/lithiation capacity with cycle number (up to 110 cycles) of the a-Si anodes using multiple electrolytes at a 1C equivalent current density. All capacity values were normalized with respect to that of the Gen2 at Cycle 0	561
Figure II.1.B.52 SEM micrographs of the a-Si anodes after 110 cycles.....	561
Figure II.1.B.53 Elemental analysis of the a-Si anodes after five cycles and after 110 cycles using EDX. Error bar indicates the standard deviation of three measurements on three different locations of each sample	562
Figure II.1.B.54 Electrochemical results of 319 cycles on native SiO_x -terminated Si wafer. Panel (a) shows potential vs. time for periodic cycles, with 0.2 V incremental offset, whereas (b) depicts the final lithiation potential and initial delithiation potential vs. number of cycles	563
Figure II.1.B.55 STEM HAADF image and EELS areal density maps for a FIB-prepared cross section of SEI formed on Si wafer after 50 cycles. C K, Si L, O K, Li K, and F K EELS areal density maps, with map area shown in the green box on the HAADF image, depict elemental composition of SEI.....	564
Figure II.1.B.56 SIMS depth profiles on formed SEI after 1 cycle (left) and 319 cycles (right). All series are normalized to their maximum intensity	565
Figure II.1.B.57 Changes in the current density over time during the potentiostatic hold at 1.0, 0.5, 0.2, and 0.01 V (vs. Li/Li^+) in Gen2 (left) and Gen2 + $\text{H}_2\text{O}_{50\text{ppm}}$ (right). Corresponding images of the Si wafers after the potentiostatic hold are shown below each Current Density vs. Time plot	566
Figure II.1.B.58 Roughness, thickness, and resistivity of the SiEI measured with AFM and SSRM. Mean results are plotted and the standard deviations are shown as error bars. Schematic diagram of the SiEI layer formed at different voltages is shown on the right.....	567
Figure II.1.B.59 XPS spectra of the SiEI layers formed in Gen2 (top) and Gen2+ $\text{H}_2\text{O}_{50\text{ppm}}$ (bottom) at 1.0, 0.5, 0.2, and 0.01 V as indicated in the figure. Si 2p, O 1s, C 1s, F 1s, P 2p, and Li 1s core levels are presented..	568
Figure II.1.B.60 ATR-FTIR spectra of the SiEI layers formed in Gen2 and Gen2+ $\text{H}_2\text{O}_{50\text{ppm}}$ at 1.0, 0.5, 0.2, and 0.01 V	569
Figure II.1.B.61 Gas chromatograms of electrolytes recovered from the cells after the potentiostatic holds (left) and the chemical equations of the LiPF_6 hydrolysis reaction (right)	569
Figure II.1.B.62 High-resolution elemental maps of SiEI layers formed at 0.2 V (left) and 0.5 V (right) in Gen2 (top) and Gen2+ $\text{H}_2\text{O}_{50\text{ppm}}$ (bottom). The intensity is on a blue-to-red color scale, with red being the highest intensity.....	570
Figure II.1.B.63 (a) Cycling performances and Columbic efficiencies of Si/C-P and Si/C-S electrodes at C/10, from 1.00 V to 0.01 V; (b) Galvanostatic discharge/charge profiles of Si/C-P electrode from 2 nd to 50 th cycles at C/10, from 1.00 V to 0.01 V; (c) Differential capacity vs. potential curves of Si/C-P electrode from 2 nd to 50 th cycles at C/10, from 1.00 V to 0.01 V (1C = 2,000 mAh g ⁻¹).....	572
Figure II.1.B.64 Three representative solvation structures in Gen2 electrolyte: (a) solvent-separated ion pairs (SSIP), (b) contact ion pairs (CIP), and (c) aggregates (AGG). The light blue, dark blue, and light yellow line representations denote the EMC, EC, and PF_6^- clusters, respectively. The purple and red ball representations denote Li ions and coordinating carbonyl O atoms, respectively	573
Figure II.1.B.65 The proportions of SSIP, CIP, and AGG in (a) the EC electrolyte and (b) the Gen2 electrolyte	574
Figure II.1.B.66 The coordination number of solvent molecules for SSIP, CIP, and AGG species in (a) EC electrolyte and (b) Gen2 electrolyte.....	574
Figure II.1.B.67 AGG species in the Gen2 electrolyte	575

Figure II.1.B.68 The proportions for SSIP, CIP, and AGG in (a) the ECF electrolyte and (b) the GenF electrolyte	576
Figure II.1.B.69 The coordination number of solvent molecules for SSIP, CIP and AGG species in a) ECF electrolyte and b) GenF electrolyte.....	576
Figure II.1.B.70 Variation of normalized discharge capacity with cycle number (up to 110 cycles) of the a-Si anodes using multiple electrolytes at a 1 C equivalent current density	578
Figure II.1.B.71 SEM micrograph of the a-Si anodes after 110 cycles	578
Figure II.1.B.72 Elemental analysis of the a-Si anodes after 5 cycles and after 110 cycles. Error bars indicate the standard deviations of the three measures on three different locations of each sample	579
Figure II.1.B.73 Synthesis of LMC	580
Figure II.1.B.74 FTIR data collected for LMC.....	580
Figure II.1.B.75 Synthesis of LMC	580
Figure II.1.B.76 Synthesis of LEDC.....	581
Figure II.1.B.77 FTIR spectra of the synthesized LEDC, stirred under CO ₂ for 1 day (blue curve) and 7 days (red curve).....	581
Figure II.1.B.78 NMR spectra of LEDC compounds under various conditions	581
Figure II.1.B.79 Left: Current density study for 5–10 $\Omega\cdot\text{cm}$ resistivity Si wafers in the ATR-FTIR spectroelectrochemical cell. A voltage drop of ~300 mV is caused by poor contact to the Si wafer. Right: Cycling behavior of the same cell indicating points where ATR-FTIR spectra were collected (see Figure II.1.B.74 for ATR-FTIR data).....	582
Figure II.1.B.80 Left: Current density study for 5–10 $\Omega\cdot\text{cm}$ resistivity Si wafers in the ATR-FTIR spectroelectrochemical cell. A voltage drop of ~300 mV is caused by the resistivity of the low doping density Si wafer. Right: Cycling behavior of the same cell indicating points where ATR-FTIR spectra were collected (see Figure II.1.B.74 for ATR-FTIR data).....	583
Figure II.1.B.81 Cyclic voltammograms for heavily surfaced p ⁺ -doped Si wafers (bulk resistivity 5–10 $\Omega\cdot\text{cm}$) in the ATR-FTIR spectroelectrochemical cell. These surface-doped wafers feature an ~100 nm-deep surface p ⁺ layer (doping density 10^{19} – 10^{20} cm ⁻³), resulting in a highly conductive working electrode (<1 m $\Omega\cdot\text{cm}$).....	583
Figure II.1.B.82 Chronoamperograms of silicon wafers with native oxide (left, SiO _x) and hydrogen terminated (right, SiH) at 400 and 150 mV vs. Li/Li ⁺ (gray and blue, respectively). The wafers used in this experiment feature a highly p ⁺ -doped surface layer (doping density = 10^{19} – 10^{20} cm ⁻³) to allow for high conductivity and IR transparency. The chronoamperograms show the greater reactivity of the SiH samples compared to SiO _x	584
Figure II.1.B.83 Carbonyl region of FTIR spectra corresponding to the chronoamperograms shown in Figure II.1.B.82, showing loss of uncoordinated (uc) EMC relative to other electrolyte components during the 18-hour potentiostatic holds	585
Figure II.1.B.84 Galvanostatic cycling voltage profiles and corresponding in situ Raman spectra collected at specific voltages: (a) the 1 st cycle and (b) the 2 nd cycle. The spectra were obtained with a 632.8-nm He-Ne laser, and all spectra were baseline corrected	587
Figure II.1.B.85 Schematic (a), scattering orientation (b), and photo (c) of the in situ electrochemical cell ...	589
Figure II.1.B.86 Neutron reflectivity curves (open circles) and fits (grey line) for PAA on a-Si thin film anode at different states of charge (curves offset for clarity)	590
Figure II.1.B.87 The resulting SLD plots from reflectivity fitting routine representing a one-dimensional view of the film heterostructures separated by interfacial roughness.....	590
Figure II.1.B.88 A summary of the SLD (left) and thickness (right) values obtained from NR refinements...	591

Figure II.1.B.89 Neutron reflectivity data with open holes representing collected data and the fit, shown as a solid line (top). The SLD profile from resulting fit (bottom)	593
Figure II.1.B.90 Schematic of the SEI chemistry with various binders (top) and a schematic representation of the relative fraction of inorganic versus organic SEI components (bottom).....	596
Figure II.1.B.91 Headspace Solid-Phase Microextraction Gas Chromatography Mass Spectrometry (HS-SPME GC-MS) prevents injection of LiPF_6 salt into the gas chromatographer while still providing detection of electrolyte solvents, decomposition products, and soluble SiEI components.....	597
Figure II.1.B.92 (a) Electrochemical performance of coin-type cells (with Si wafer vs. Li metal): Half of the samples were rested at OCV, while the other half were galvanostatically cycled between 0.1 and 1.5 V at an applied current of $30 \mu\text{A}/\text{cm}^2$. (b) Gas chromatograms using HS-SPME to sample the headspace above the separators (red and green lines) and pristine Gen2 electrolyte for comparison (black line); inset in part (b) is a zoom-in at retention times between 10 and 14 minutes	598
Figure II.1.B.93 (top) Comparison of GC-MS gas chromatographs of the recovered electrolyte from potentiostatic holds at 1, 0.5, and 0.2 V for 10 hrs. (bottom) Reaction mechanism for some of the soluble SiEI species detected in the GC-MS	599
Figure II.1.B.94 Comparison of GC-MS gas chromatographs of pristine Gen2 electrolyte and the electrolyte from a half-cell containing silicon, lithium, and Gen2 held at 60°C	599
Figure II.1.B.95 (a) Cycle data for $d = 30 \text{ nm}$ SiH_x -terminated (black) and dodecyl-terminated (blue) in a half-cell configuration. The first three cycles are at a C-rate of C/20, and the latter 13 are C/5. The error bars represent $\pm 1 \sigma$ from the mean of three electrodes. (b) Plots the dQdV of the first cycle for the same $d = 30 \text{ nm}$ SiH_x -terminated (black) and dodecyl-terminated (blue) samples	601
Figure II.1.B.96 SEM images of milled silicon powders.....	602
Figure II.1.B.97 Zeta potential of Deep Dive silicon (left) and milled silicon powders (right).....	602
Figure II.1.B.98 Representative cycling data measured for milled silicon electrodes	603
Figure II.1.C.1 (a) Cycling performances and Coulombic efficiencies of Si/C-P and Si/C-S electrodes at C/10, from 1.00V to 0.01V; (b) Galvanostatic discharge/charge profiles of Si/C-P electrode from 2nd to 50th cycles at C/10, from 1.00V to 0.01V; (c) Differential capacity vs. potential curves of Si/C-P electrode from 2nd to 50th cycles at C/10, from 1.00V to 0.01V ($1\text{C}=2,000 \text{ mAh g}^{-1}$)	612
Figure II.1.C.2 Schematics of the gradient polarity solvent wash technique	613
Figure II.1.C.3 Gradient polarity solvent wash was applied to a Cu electrode polarized to 10 mV Li/Li+	613
Figure II.1.C.4 Three different scanning rates of CV at 1, 10 and 60 mV min^{-1} were applied to the Cu electrodes respectively with baseline electrolyte and two additives-based electrolytes. The Cu surface species vary due to both the additives and scan rates	614
Figure II.1.D.1 (a) Cycling performance of NMC532 Si/Gr (CAMP electrodes) in BTFE-based electrolytes with different salt concentrations; (b) cycling performance of NMC532 Si/Gr (CAMP electrodes) in BTFE, TTE, and BTFE-based electrolytes.....	617
Figure II.1.D.2 (a) Cycling performance of NMC532 Si/Gr (CAMP electrodes) in BTFE-based electrolytes with different salt concentrations at 0.05C and 0.33C; (b) high voltage stability of NMC532 Li in E-104 and baseline electrolytes	618
Figure II.1.D.3 Photographs of ignition tests of glass fibers saturated with E-control-3 (a) and NFE-2 LHCE. (c) Long-term cycling performance and Coulombic efficiency of Li Si/Gr half cells in different electrolytes.....	620
Figure II.1.D.4 Electrochemical behavior of Si/Gr NMC333 full cells in different electrolytes. (a) Long-term cycling performance of Si/Gr NMC333 full cells with different electrolytes at 25°C . (b) Rate capability of the Si/Gr NMC333 cells in different electrolytes at 25°C . (c-e) Voltage profiles upon cycling in electrolyte-	

control-3 (c), NFE-1 (d) and NFE-2 (e). f) Long-term cycling performance of Si/Gr NMC333 cells cycled at 45°C in different electrolytes. g) Cycling performance of full cell with high loading in NFE-2 at 25°C	621
Figure II.1.E.1 Schematic illustration of the prelithiation of Si electrode film.....	624
Figure II.1.E.2 The effects of pressure and pressing duration on ICE of Si anode-based half cell	625
Figure II.1.E.3 Morphology evolution of Si anode before (a,c,e) and after (b,d,f) prelithiation treatment. (a,b) TEM images, (c,d) in-plane and (e,f) cross-section SEM characterization of Si anode	626
Figure II.1.E.4 (a) First cycle voltage curves and (b) cycling stability of Si-LiFePO ₄ and Li _x Si-LiFePO ₄ full cells operated between 2.5 and 3.8 V	627
Figure II.2.A.1 Standard diagnostics protocol	630
Figure II.2.A.2 (Left) Galvanostatic first-cycles capacities (without a potentiostatic hold on the discharge) and (right) sources of first-cycle capacity loss of the four cathodes examined	630
Figure II.2.A.3 “(Left) Capacity vs. cycle number for the LCV (4.2-2.5 V) cycles and (right) the UCV (4.5-2.5 V) cycles used in the standard protocol. Cycles 4 and 10 were not included. The capacity for cycle 1 includes the potentiostatic hold at the LCV of 2.5 V. Closed symbols are charge capacities and open symbols are discharge capacities	631
Figure II.2.A.4 (Left) Capacities during the potentiostatic-hold cycle and (right) effect of the potentiostatic hold on discharge capacities, where discharge capacities from cycles 6 and 9 are used for “Pre-hold” and “Post-hold” capacities, respectively.....	631
Figure II.2.A.5 Polarizations at various SOC as determined by current interrupts for cycles 4 (orange) and 10 (green).....	632
Figure II.2.A.6 Average rate performance of the four cathodes surveyed. Discharge current (mA/g) is indicated in each 3-cycle subdivision, 20 mA/g used for all charge cycles	633
Figure II.2.A.7 Schematic of in situ MS set up for gas analysis using direct sampling method from pouch cell (left image) and for thermal stability test (right image).....	633
Figure II.2.A.8 Gas generation during cycling with UCVs of 4.2 V (top left panel), 4.4 V (top right panel), and 4.6 V (bottom panel).....	634
Figure II.2.A.9 O ₂ (upper left) and CO ₂ (upper right) generation rate during thermal stability test of composite electrode without the presence of electrolyte. Neutron diffraction of composite materials after undergoing thermal stability test (lower panel)	636
Figure II.2.A.10 O ₂ and CO ₂ generation rate during thermal stability test of composites with the presence of electrolyte	637
Figure II.2.A.11 DSC results of five samples with various amounts of electrode material and electrolyte	638
Figure II.2.A.12 ICP-MS quantification results. (a) Concentration of Mn (blue, circle), Ni (red, square) and Co (orange, diamond) from anodes cycled with various NMC cathodes. (b) Concentration of Mn and Ni from various NMC cathodes versus ideal stoichiometry in Li(Ni _x Mn _y Co _{1-x-y})O ₂	639
Figure II.2.A.13 SICs of m/z detected via HPLC/ESI-MS that are present in the aged Gen2 electrolyte samples from the cycled pouch cells composed of graphite anodes against NMC-532(orange), NMC-622(blue) and NMC-811(red)	639
Figure II.2.A.14 Concentrations of Mn, Co and Ni in solution from the cathode materials used in this study. The concentrations of the metals without the additive are given as blue bars; and with it, as orange ones. It should be noted that, due to the large differences in the relative concentrations, the blue bar may not be visible in all plots	641
Figure II.2.A.15 Concentrations of the transition metals vs. various combinations of the ideal stoichiometries with bifluoride present. Markers represent the data, and dotted lines, the least squares fit. The regression	

yielded the following equations (value of r^2): (a) $[\text{Ni}] = 203.07X_{\text{Co}}(X_{\text{Ni}})^3 + 1.23$ (0.97); (b) $[\text{Ni}] = -77.04(X_{\text{Mn}})^2 + 12.76$ (0.96); (c) $[\text{Mn}] = 275.67X_{\text{Co}}(X_{\text{Ni}}) - 10.71$ (0.97); and (d) $[\text{Co}] = 28.09X_{\text{Co}} - 1.61$ (0.99)	642
Figure II.2.A.16 In situ ATR-FTIR cell design	642
Figure II.2.A.17 ATR-FTIR spectra showing the changes in peak intensities during electrochemical delithiation of NMC-622 cathode for electrolyte components—EMC, EC, and PF_6^- —associated with a Li^+ ion or “free” in the solution near the cathode surface	644
Figure II.2.A.18 ATR-FTIR and Raman spectra comparing the pristine and aged NMC-811 composite electrodes	644
Figure II.2.A.19 (Left) C/10 galvanostatic cycle of an NMC-622 cathode (left), with $\text{d}q/\text{d}V$ (inset). (Right) FTIR-ATR spectra	645
Figure II.2.A.20 ATR-FTIR spectra at OCV and after the 3 rd galvanostatic charge/discharge cycles of NMC-622. After cycling, new peaks emerge that indicate formation of CEI species, containing carboxylate and carbonate functional groups.....	645
Figure II.2.A.21 Potential change during the 0.95 V potentiostatic hold in an oxide(+)/oxide(-) symmetric cell for a total of 300 h. (a) Full-cell and (b) electrode potentials. (c) Current flow through the cell during the 100 h hold cycles	647
Figure II.2.A.22 Current flow through an oxide(+)/oxide(-) symmetric cell during the first (<i>left</i>) and second (<i>right</i>) 100 h potentiostatic holds at 0.6 V (<i>black</i>), 0.8 V (<i>blue</i>), and 0.95 V (<i>red</i>)	647
Figure II.2.A.23 Nyquist plots (100 kHz – 0.01 Hz, 30°C, 0 V) for oxide(+)/oxide(-) symmetric cells after (a) 0 h, (b) 100 h and (c) 200 h at 0.6 V (<i>black</i>), 0.8V (<i>blue</i>) and 0.95 V (<i>red</i>). Mind the different scales in the three panels	648
Figure II.2.A.24 Nyquist plots (100 KHz-0.01 Hz, 0 V) for oxide(+)/oxide(-) symmetric cells comparing the effect of 0-0.8 V cycling at a C/15 rate vs. 0.8 V potentiostatic hold. Panel a is for 10 cycles (100 h hold) and panel b is for 20 cycles (200 h hold).....	649
Figure II.2.A.25 In situ formed additives 2a and 2b and their precursors 1a and 1b	649
Figure II.2.A.26 (A) Specific capacity per weight of lithiated oxide of NMC-622//Gr cells containing additives and the baseline electrolyte (<i>black line</i>) obtained for cycling at a rate of C/3 with a 3 hour hold at the top of each charge. The discontinuities correspond to HPPC tests performed every 20th cycle. The coulombic efficiency for these cells is shown to the right; (B) Full cell area specific impedance (ASI) for the NMC-622//Gr cells with electrolyte containing 1 wt% MS and baseline Gen2 electrolyte (HPPC test). ASI of baseline Gen2 cell is shown in black while the cell containing 1 wt% MS is shown in red. The traces in the graph correspond to 7, 30, 53, 76, and 99 cycles (<i>from bottom to the top</i>), respectively.....	650
Figure II.2.A.27 (A) Pictures of the Gen2 electrolytes with intentionally added 2 vol % water without and with 0.2 vol% TMSML stored at room temperature (25°C) original and after 1 day, 1 week and 1 month; (b) ^{19}F NMR spectra of Gen2 electrolytes with intentionally added 2 vol % water without and with 0.2 vol% TMSML stored at room temperature after 1 day	651
Figure II.2.B.1 (a) Ternary phase diagram of high-Nickel NMCs including the $\text{Ni}_{94}\text{Co}_6$ composition (gray sphere), (b) SEM-images of $\text{Ni}_{94}\text{Co}_6$ particles showing a narrow particle size distribution, and (c) Rietveld refinement results obtained from data taken at beamline 13-BM-C of the Advanced Photon Source (ANL)..	655
Figure II.2.B.2 (a) Initial voltage profiles and (b) magnified view of high-voltage region for the $\text{Ni}_{94}\text{Co}_6$. Cells used Li-metal anodes and were cycled at C/5 ($1\text{C}=180\text{mA/g}$) after 3 formation cycles at C/10.....	657
Figure II.2.B.3 (a) Illustration of concentration gradient materials using an in-house built, co-precipitation reactor for full-concentration gradient particles, (b) core-shell gradient particle, (c) a scheme of as-synthesized materials for different metal gradients with an NMC-811 composition and the corresponding capacity retention results.....	658

Figure II.2.B.4 SEM images of baseline, Ni-rich compositions annealed at different temperatures	659
Figure II.2.B.5 (a) and (b) SEM images, (c) and (d) STEM images of pristine NMC-333 and NMC-622 crystal samples, (e) indexed facets on platelet NMC particles and (f) XRD patterns of pristine NMC-333 and NMC-622 crystal samples	660
Figure II.2.B.6 First 100-cycle charge-discharge profiles of (a, c) NMC333 and (b, d) NMC622 in the voltage window of (a, b) 3-4.3 V and (c, d) 3-4.6 V. e) and f) Comparison of discharge capacity and capacity retention at a cycling rate of C/10	660
Figure II.2.B.7 HAADF STEM imaging shows facet-dependent surface reconstruction on (a, b) pristine NMC-333 and c, d) pristine NMC-622 particles. SRL was found on non-(001) surface (a, c) while no SRL was observed on (001) surfaces.	661
Figure II.2.B.8 Atomic-resolution HAADF STEM images of SRL formation on: non-(001) surfaces (a and c) and (001) surfaces (b and d) of cycled NMC-333 (a and b) and NMC-622 (c and d) platelet crystals	662
Figure II.2.B.9 Phase transitions at open surfaces, closed surfaces, and grain boundaries. (a) Cross-sectional SEM image of a secondary particle. (b) HAADF-STEM image of the NMC76, (c-d) HAADF-STEM image of the primary particles. The blue, red, and green arrows point to the inter-granular GBs, inter-granular channels, and intra-granular boundaries, respectively. (e) Surface configurations of pristine NMC76 at the basal plane. The blue arrow points to the Li layer occupied by TM ions. (f) Surface configurations of pristine NMC76 at the edge plane. (g) Surface configurations of NMC76 at the basal plane after 200 cycles. (h) Surface configurations of NMC76 at the edge plane after 200 cycles. The white dashed lines in (f) and (h) outline the boundary between the layered structure and the converted phase. h1 represents the thickness of converted phase/cation mixed phase. (i) The construction of a typical sealed surfaces. The black rectangle, 2, outlines the sealed surface area. The black rectangles 1 and rectangle 3 indicate the entrances to the area 2. The inserts are a magnified view of the two entrances. (j) Atomic resolution imaging of the sealed surface from rectangle 2 in (i). (k-l) The configurations of incoherent boundaries after prolonged cycling. The white and blue lines indicate the (003) planes of upper and low grains	663
Figure II.2.B.10 ^6Li solid-state NMR analysis of pristine NiMn5050 and NMC-442 compositions.....	664
Figure II.2.B.11 Comparison of ^6Li solid-state NMR analysis of cycled and pristine NiMn5050 and NMC-442 compositions	664
Figure II.2.B.12 Comparison of ^6Li solid-state NMR analysis of pristine and cycled samples having different dopants	665
Figure II.2.B.13 Comparison of ^6Li solid-state NMR of model systems: The effect of synthesis conditions and the presence of Co on Li/Mn ordering ('clustering')	666
Figure II.2.B.14 (a) Ni K-edge XANES for the LC-NMC compared to data from standard NMC compositions and NCA. (b) Corresponding magnitudes of the Fourier transformed EXAFS of the samples in (a)	667
Figure II.2.B.15 (a) Rate data of the LC-NMC cathode conducted between 4.45-2.5V at 30°C. Charge and discharge currents were the same and are as listed in the plot (mA g^{-1}). (b) Ragone plot derived from the data in (a), based on active weight of the cathode only	668
Figure II.2.C.1 Schematic representation of the slab model for NMC-111 (104) facet (top view): (a) stoichiometric amount of Co, (b) excess of one Co ion per surface, (c) excess of two Co ions per surface. Small red spheres represent oxygen, green, grey, purple and blue spheres represent Li, Ni, Mn and Co respectively	671
Figure II.2.C.2 Lowest energy configuration of electrolyte components at or near the (012) facet of (a-d) fully lithiated or (e-f) fully delithiated NMC-532. (a) EMC, (b) EC, (c) HFDEC, (d) DFEC, (e) TTFP on delithiated NMC, and (f) TTFPa detached from NMC surface	673
Figure II.2.C.3 Projected Density of States (PDOS) on the TMs in fully lithiated (pristine) NMC. The dashed line indicates the Fermi level	674

- Figure II.2.C.4 Li/Ni anti-site formation energy change with number of defects. The defects are located in the same Li layer forming a row of continuous defects..... 674
- Figure II.2.C.5 Total energy of $\text{LiNi}_{0.5}\text{Ni}_{0.5}\text{O}_2$ for different ionic configurations within the transition metal layer. Grey represent Ni, purple represents Mn and green represents Li in the layer underneath the transition metal layer 675
- Figure II.2.C.6 Total energy of $\text{LiNi}_{0.5}\text{Ni}_{0.5}\text{O}_2$ for different ionic configurations within the transition metal layer. (a) Configurations sorted by energies and the number of TM-TM bonds (where TM = Co, Ni, Mn). (b) Total energy as a function of the number of Ni-Mn bonds in the system. Grey represents Ni, purple represents Mn and green represents Li in the layer underneath the TM layer 676
- Figure II.2.C.7 Total energy change of $\text{LiNi}_{0.5}\text{Ni}_{0.5}\text{O}_2$ for five different ionic configurations within the transition metal layer, as a function of Li-Ni defect exchange concentration..... 677
- Figure II.2.D.1 (a) High resolution X-ray data on four LLS samples fired at different temperatures as noted in the figure. The inset shows a magnified view of the (003) peaks and the table shows how the full width at half maximum changes as a function of the firing temperature. SEM images showing the morphology of the primary (inset) and secondary particles of the samples fired at: (b) 925°C (c) 950°C (d) 975°C and (e) 1000°C..... 680
- Figure II.2.D.2 Refinements neutron powder diffraction data (ANSTO) showing (a) the weight fraction of C2/m and (b) % Li/Ni exchange as a function of secondary firing temperatures 681
- Figure II.2.D.3 Electrochemical performance of samples fired at different temperatures: 925°C, 950°C, 975°C, and 1000°C. The current for all cycles was 20 mA/g. The first cycle activation was between 4.6 – 2.5 V. All other cycles were between 4.5 – 2.5 V. (a) Capacity (filled symbols) and coulombic efficiency (open symbols) for the 1st, 4th, 7th, and 10th cycles. The charge/discharge curves for the (b) 1st cycle and (c) 10th cycle. (d) 1st cycle charge/discharge curve between 4.6 – 2.5 V at 20 mA/g with a 20 hour voltage hold at 2.5 V. dQ/dV of the (e) 1st cycle and (f) 10th cycle 682
- Figure II.2.D.4 Representative DSC data (baseline-subtracted, mass-normalized) from each charged cathode sample, all charged to the same calculated lithium content after formation cycles. 682
- Figure II.2.D.5 Operando synchrotron XRD analysis of a Li/LT- $\text{LiCo}_{0.85}\text{Al}_{0.15}\text{O}_2$ cell cycled between 4.2 – 3.5 V vs. Li at 15 mA/g: (a) changes to strong peaks (selected regions) and corresponding initial charge/discharge profile; variation of the (b) (840) peak, (c) unit cell volumes, and (d) Li occupancies as function of Li content. 683
- Figure II.2.D.6 (a) Capacity vs. cycle number for lithium cells with LT- $\text{LiCo}_{1-x}\text{Al}_x\text{O}_2$ electrodes ($0 \leq x \leq 0.5$), (b) rate performance data ($0 \leq x \leq 0.3$). 684
- Figure II.2.E.1 In situ tracking of cationic ordering/disordering in $\text{LiNi}_{0.7}\text{Mn}_x\text{Co}_{0.3-x}\text{O}_2$ ($0 \leq x \leq 0.3$) during calcination at 850°C. (A) Schematic illustration of the experimental setup for in situ synchrotron XRD measurements. (B) Time-resolved XRD patterns recorded at 850°C during the synthesis of $\text{LiNi}_{0.7}\text{Mn}_{0.1}\text{Co}_{0.2}\text{O}_2$ (NMC712), with wavelength $\lambda = 0.2953 \text{ \AA}$. (C) Intensity maps of characteristic peaks (003), (104) in Figure 1B. (D–G) Evolution of the I(003)/I(104) ratio, lattice parameter a, c, and occupancy of Ni at 3b sites, respectively, as a function of holding time for NMC712 (black square), NMC721 (red circle), and NM73 (blue triangle). The solid lines in (E, G) represent the fitting of lattice parameter a and the anti-site occupancy of Ni at 3b sites, Ni(3b), as a function of time, by using an exponential-linear function $y = A \exp(-kt) + bt + y_0$; the error bars represent standard deviations derived from the Rietveld refinements. (H) Dependence of the kinetics of cationic ordering on Mn stoichiometry. 687
- Figure II.2.E.2 Li/Ni mixing as a function of composition in the series of $\text{LiNi}_{0.7}\text{Mn}_x\text{Co}_{0.3-x}\text{O}_2$ ($0 \leq x \leq 0.3$). 688
- Figure II.2.E.3 Dependence of cationic ordering and electrochemical performance in NMC71515 on sintering temperature and holding time. (A) Synchrotron XRD patterns from NMC71515 sintered at 775 °C (data were also taken from samples sintered at other different temperatures and not shown here). (B) Schematic

illustration of cationic ordering and disordering processes with holding time. (C, D) Galvanostatic charge/discharge profiles and rate performances of NMC 71515, respectively, sintered for optimized time at different temperatures. 689

Figure II.2.E.4 Schematic illustration of the approach with a “closed” loop for rational design of synthesis in making high-Ni layered oxides, specifically, through studying the surface reconstruction and its impact to electrochemical properties, and its formation process (via in situ X-ray study). a,b) Formation of a surface layer, and the potential impact on the electrochemical performance due to impedance to the Li extraction/insertion during charging/discharging. c) In situ X-ray studies of the synthesis process using temperature-resolved synchrotron X-ray diffraction technique that has high enough detection efficiency to track the formation of Li_2CO_3 (despite its weak scattering of X-ray; inset)..... 690

Figure II.2.E.5 In situ tracking of the structural evolution and formation of Li_2CO_3 in NMC71515 upon cooling during synthesis. a) Temperature-resolved in situ XRD patterns recorded during the slow cooling process. Inset: temperature profiles of in situ experiments during slow cooling and quenching (as labeled), using cooling rates of 2 and $200^\circ\text{C min}^{-1}$, respectively. b) Zoom-in view of the diffraction patterns associated with Li_2CO_3 , as marked by the black dashed square in (a). c) The evolution of the percentage of Ni at 3b sites, Ni(3b), as a function of temperature; Inset: schematic illustration of Li/Ni ordering process, showing inter-diffusion of Li/Ni ions between 3a sites (in the TM layers) and 3b sites (in the Li layers). d) The evolution of the integrated area of 002 peak associated with Li_2CO_3 (denoted as I(002), and normalized by I(104) of the layered oxides) as a function of temperature. The dashed lines are extended from the fitting lines and crossed at the gray square, indicating the initial formation of Li_2CO_3 at around 750°C . No obvious increase of the peak intensity at temperatures below 350°C (as marked with a dotted line)..... 691

Figure II.2.F.1 Discharge capacity and coulombic efficiency of full-cells with SiO_2 electrode coating as a separator (a) and a sheet of polypropylene as a separator (b) 694

Figure II.2.F.2 SEM images of SiO_2 electrode coating and a sheet of polypropylene representative of the separator schemes used for cells in Figure II.2.F.1 694

Figure II.2.F.3 (a) TEM image and (b) XRD pattern of the $\text{Na}_3\text{MnZr}(\text{PO}_4)_3$ cathode material prepared by the sol-gel method..... 695

Figure II.2.F.4 (a) Charge/discharge profiles of the $\text{Na}_3\text{MnZr}(\text{PO}_4)_3$ cathode at different current densities. (b) Charge/discharge cycling performance of the $\text{Na}_3\text{MnZr}(\text{PO}_4)_3$ cathode at the rate of 0.5 C..... 695

Figure II.2.F.5 The structure and characteristic of $\text{Li}_6\text{PS}_5\text{Cl}$ sulfide solid electrolyte. (a) XRD. (b) The Nyquist plots at different temperatures. (c) Temperature dependence of the ionic conductivity. (d) Cyclic voltammogram of stainless steel/SE/Li cell at a scanning rate of 0.5 mV/s between -0.5 V and 5 V . (e) SEM images and corresponding element mapping 696

Figure II.2.F.6 (a) The structure of $\text{Li}_2\text{S}/\text{Li}_6\text{PS}_5\text{Cl}/\text{Li}$ battery. (b-c) Electrochemical performance of $\text{Li}_2\text{S}/\text{Li}_6\text{PS}_5\text{Cl}/\text{Li}$ battery at 25°C and 55°C , respectively 696

Figure II.2.F.7 Structure and electrochemical performance of $\text{Na}_{0.6}(\text{Li}_{0.2}\text{Mn}_{0.8})\text{O}_2$ (a) XRD pattern. The inset is ordered Li/Mn atoms. (b) the $P3$ structure. (c) Charge and discharge profiles and cycle stability at 10 mA g^{-1} between $3.5\text{--}4.5 \text{ V}$. (d) Charge and discharge profiles and cycle stability at 15 mA g^{-1} between 2 and 4.5 V . 697

Figure II.2.F.8 (a) XPS patterns of Mn during the initial charge and discharge process. (b) Ex situ XRD patterns of $P3\text{-Na}_{0.6}(\text{Li}_{0.2}\text{Mn}_{0.8})\text{O}_2$ at different states..... 698

Figure II.2.G.1 Synthesis and electrochemistry of LMNOF baseline. (a) XRD pattern and Rietveld refinement of optimized cathode, (b) voltage profiles in cycle 1-20, dQ/dV curves for voltage window tests at various (c) charge and (d) discharge cutoff voltages, and GITT plots with a voltage range of (e) $4.8 - 1.5 \text{ V}$ and (f) $4.0 - 1.5 \text{ V}$ 700

Figure II.2.G.2 Synthesis and electrochemistry of LNTMOF baseline. (a) XRD pattern and Rietveld refinement of optimized cathode, (b) voltage profiles of the baseline in cycle 1-20, dQ/dV curves for voltage

window tests at various (c) charge and (d) discharge cutoff voltages, and GITT plots with a voltage range of (e) 4.8 – 1.5 V and (f) 4.15 – 1.5 V.....	701
Figure II.2.G.3 Left: Cell resistance plotted against OCV for LNTMOF with and without carbon ball milling. Right: voltage profile during the 30-second pulse at an OCV close to 3.3 V.....	702
Figure II.2.G.4 SEM images and XRD patterns of a) $L_{1.3}M_{0.4}NO$, b) $L_{1.3}M_{0.5}NOF$, c) $L_{1.2}M_{0.4}TO$, and d) $L_{1.2}M_{0.6}TOF$ samples. EDX mapping results on b) and d) are shown at the bottom	703
Figure II.2.G.5 a)-d) First 20-cycle voltage profile of $L_{1.3}M_{0.4}NO$, $L_{1.3}M_{0.5}NOF$, $L_{1.2}M_{0.4}TO$, and $L_{1.2}M_{0.6}TOF$ half cells. e) and g) capacity retention of the half cells. f) and g) discharge voltage retention of the half cells. The current density is 10 mA/g.....	703
Figure II.2.G.6 First-cycle incremental capacity (dQ/dV) profiles of: a) $L_{1.3}M_{0.4}NO$ and $L_{1.3}M_{0.5}NOF$ half cells and b) $L_{1.2}M_{0.4}TO$ and $L_{1.2}M_{0.6}TOF$ half cells. The current density is 10 mA/g.	704
Figure II.2.G.7 Setup of the fluidized bed reactor (left) and XRD patterns of pristine LNTMO and the F-LNTMO at different conditions (right). The F content was determined by EDX analysis.....	704
Figure II.2.G.8 Summary of XPS depth-profiling experiments for pristine and F-LNTMO.....	705
Figure II.2.G.9 Electrochemical cycling for first few cycles for pristine LNTMO and 30min, 3hrs and 12hrs F-LNTMO	705
Figure II.2.H.1 7Li (a, c) and ^{19}F (b, d) spin echo NMR spectra of LMNOF (a, b, in black), LNTMOF (c, d, in black) and LiF (a-d, in blue) obtained at $B_0 = 7$ T and 60kHz (a, b) or 55kHz (c, d) magic angle spinning (MAS). Asterisks indicate spinning sidebands. Isotropic 7Li (a, c) and ^{19}F (b) pj-MATPASS spectra collected on LMNOF (a) and LNTMOF (c, d) are represented with a gray shading. (e) $^7Li\{^{19}F\}$ 2D TEDOR spectrum of LiF obtained at $B_0 = 7$ T and 45kHz MAS using a 45 us recoupling time. The TEDOR projections in black are compared to LiF 7Li and ^{19}F MAS NMR spectra in blue.	708
Figure II.2.H.2 Raman spectra collected on a) LMNOF and b) LNTMOF. Schematics of the Mn-O symmetric stretch are also shown.....	709
Figure II.2.H.3 mRIXS results of Mn-L (a) and O-K (b) collected on LMNOF cycled to different electrochemical potentials. The red rectangular in (a) indicates the area that non-distorted Mn-L spectra could be extracted for absolute quantification of the Mn redox reactions. Red arrows in (b) indicates the oxidized oxygen feature that could be quasi-quantified to reveal the reversibility and cyclability of the oxygen redox in DRX-based electrodes. The quantification results of Mn redox and the evolution of the oxidized oxygen feature are displayed in (c) in blue and red dashed lines, respectively	710
Figure II.2.H.4 a) Comparison of F K-edge XAS of pristine $L_{1.3}M_{0.5}NOF$ and LiF, b) a schematic showing covalent and ionic bonding environment of F. Comparison of F K-edge XAS of $L_{1.3}M_{0.5}NOF$ cathode after: c) charged to 4.8 V and d) discharged to 1.5 V after various cycles. All spectra were collected under TEY mode. Each spectrum was fitted via linear combination fitting of covalent and ionic components (green lines) and the fitted spectra are shown in dotted lines. e) Changes in ionic fraction as a function of cycle number.....	711
Figure II.2.H.5 a) DEMS measurements of O_2 and CO_2 evolution during cycling of LMNOF and b) fluoride-scavenging coupled with DEMS to examine fluoride dissolution from LMNOF. The cell is cycled in $LiClO_4$ instead of $LiPF_6$ to remove other sources of fluoride	712
Figure II.2.H.6 Atomic structures of $Li_{1.2}Ti_{0.2}Mn_{0.6}O_{1.8}F_{0.2}$. (a) As-captured atomic-scale HAADF STEM image and (b) corresponding Fast Fourier transform (FFT). (c) Filtered HAADF STEM image from the masked FFT pattern in (d) showing atomic structures that correspond to the long-range ordered cubic lattice. (e) Filtered HAADF STEM image from the masked FFT pattern in (f) showing the quasi-periodic pattern, as typified by the dashed line marked regions as indicated by 1-4. (g) Atomic models for 4 different nanosized regions highlighted in (e), indicating quasi-periodic patterns over long ranges	713
Figure II.2.H.7 (a) Evolution of the amount of percolating Li as a function of F content obtained from Monte Carlo simulations at 1873 K, a temperature representative of typical synthesis conditions for this class of	

materials, in four $\text{Li}_{1.2}(\text{M}, \text{M}')_{0.8}\text{O}_{2-y}\text{F}_{2y}$ DRX systems: $(\text{M}, \text{M}') = (\text{Mn}^{3+}, \text{Ti}^{4+}), (\text{Ni}^{2+}, \text{Ti}^{4+}), (\text{Ni}^{2+}, \text{Nb}^{5+})$ and $(\text{Mn}^{2+}, \text{Ti}^{4+})$. (b) Li percolation map as a function of both Li and F contents in $\text{Li}_x(\text{Ni}^{2+}, \text{Ti}^{4+})_{2-x}\text{O}_{2-y}\text{F}_{2y}$, obtained from Monte Carlo simulations at 1873 K. The color scale represents the amount of accessible Li through the 0-TM percolation network, while solid lines indicate the theoretical $\text{Ni}^{2+}/\text{Ni}^{4+}$ redox capacity. (c) First-cycle voltage profiles of $\text{Li}_{1.3}\text{Mn}_{0.267}\text{Nb}_{0.433}\text{O}_2$ (LMNO), $\text{Li}_{1.3}\text{Mn}_{0.3}\text{Nb}_{0.4}\text{O}_{1.9}\text{F}_{0.1}$ (LMNF10), and $\text{Li}_{1.3}\text{Mn}_{0.367}\text{Nb}_{0.333}\text{O}_{1.7}\text{F}_{0.3}$ (LMNF30) within a voltage window of 1.5–4.5 V 714

Figure II.3.A.1 The electrochemical stability window of different electrolytes and the degradation of electrolytes on cathode surface as-revealed by theoretical modeling and experiments. (a) The linear sweep voltammetry (LSV) studies of baseline carbonates (1.2 M LiPF₆ in EC/ethylene carbonate : EMC/ethyl methyl carbonate), sulfones (3.25M LiFSI in sulfolane), as well as fluorinated carbonates (1 M LiPF₆ in FEC/fluoroethylene carbonate : EMC, and LiPF₆ in FEC : FEMC/methyl (2,2,2-trifluoroethyl) carbonate): HFE/2,2,2-Trifluoroethyl 1,1,2,2-tetrafluoroethyl ether); (b) The most probable decomposition reactions and the reaction energy (Er_{rxn}) of EMC (top) and FEC (bottom) on Li_{0.5}NiO₂, respectively; (c) The reaction energy of LiPF₆ salt decomposition on LiNiO₂. Colors: Li (green), O (red), Ni (dark grey), F (light grey), P (light grey) 718

Figure II.3.A.2 Structure characterization of PLD-grown NMC thin-films with different oxygen pressure. The SXRD (a) and XRR (b) of NMC thin-films grown at an oxygen pressure of 75mT, inserted are the scheme of the structure and thickness of NMC thin-film, and SrRuO₃ buffer layers. The crystalline thickness and d spacing of (108) Bragg peak as a function of oxygen pressure conditions in PLD growth 718

Figure II.3.A.3 The electrochemical characterization of PLD-derived NMC thin-films of different thickness. The cyclic voltammograms and potential-capacity curves of NMC thin-films grown under an oxygen pressure of 75mT in a thickness of 10 nm (a, b) and 25 nm (c, d), respectively (with a scan rate of 0.2 mV.S⁻¹ and in the electrolyte of 1M LiPF₆ in commercial EC : DMC/dimethyl carbonate)..... 719

Figure II.3.A.4 The evolution of interphase from the chemical reactions between NMC and carbonate electrolytes (1M LiPF₆ in EC : DMC). The surface-sensitive total reflection X-ray absorption near edge structure (XANES) and Fourier transformed extended X-ray absorption fine structure (FT-EXAFS) of NMC thin-films with and without electrolyte at Co K-edge (a, b) and Ni K-edge (c, d), respectively 720

Figure II.3.B.1 a) Electrochemical response of Cu, Ni and Pt electrodes in 1 M LiPF₆ in EC/EMC 3:7w. b) % of metal dissolution in each response as measured by ICP-MS. c) Schematic of the Stationary Probe Rotating Disk Electrode (SPRDE) System Coupled to Inductively Coupled Plasma Mass Spectrometry (ICP-MS).... 724

Figure II.3.B.2 Online Electrochemical Mass Spectrometry. a) Gas detection following linear potential sweep to 6 V of C-65 carbon electrode. Signals for HF, CO₂ and POF₃ are clearly visible. b) Picture of the OEMS apparatus 725

Figure II.3.B.3 Rotating ring disk proton detection method. a) Cyclic voltammogram of hydrogen oxidation/evolution reaction in a H₂ saturated electrolyte. b) Polarization curves for HOR at different rotation rates on the Pt disk and the measured responses on Pt ring. c) Electrochemical decomposition of 1M LiClO₄ EC/EMC electrolyte on Glassy carbon electrode. d) Proton reduction current on the Pt ring. e) Proton/electron ratio obtained from disk vs. ring current, corrected for the ring collection efficiency 726

Figure II.3.B.4 Effects of anion, solvent, substrate and rotation rate on the electrolyte oxidation. a) Comparison of the electrochemical responses on Pt(111) electrode in LiClO₄ and LiPF₆ based electrolytes with and without rotation. b) Comparison of electrochemical responses in EC, EMC and EC/EMC based LiClO₄ electrolytes on Pt electrode. c) Comparison of electrochemical responses in EC, EMC and EC/EMC based LiClO₄ electrolytes on graphene electrode 727

Figure II.3.C.1 XRD pattern of as-synthesized Li₄Mn₂O₅ with an SEM image shown in the inset 730

Figure II.3.C.2 Upper left: charge and discharge profiles of Li₄Mn₂O₅ in a lithium half cell when cycled between 4.8-1.2V and (lower left) capacity as a function of cycle number. Upper right: charge and discharge profiles of Li₄Mn₂O₅ in a lithium half cell when cycled between 4.4-1.2V and (lower right) capacity as a function of cycle number 731

Figure II.3.C.3 Left: X-ray Raman Mn L-edge spectra on pristine and charged $\text{Li}_4\text{Mn}_2\text{O}_5$ electrodes as a function of charging potential. Right: X-ray Raman O K-edge spectra.....	732
Figure II.3.C.4 Left: XRD pattern of $\text{Li}_2\text{Ru}_{0.75}\text{Sn}_{0.25}\text{O}_3$ with its structure and the particle morphology indicated in the insets. Right: XRD pattern of $\text{Li}_2\text{Ru}_{0.75}\text{Ti}_{0.25}\text{O}_3$	732
Figure II.3.C.5 Upper left: Voltage profiles of a $\text{Li}/\text{Li}_2\text{Ru}_{0.75}\text{Sn}_{0.25}\text{O}_3$ cell cycled between 4.6 and 2.0V. Upper middle capacity as a function of cycle number. Bottom left : cyclic voltammogram of a $\text{Li}/\text{Li}_2\text{Ru}_{0.75}\text{Sn}_{0.25}\text{O}_3$ cell cycled between 4.8 and 2.0V and (bottom center) voltage profiles over the same potential range. Right: Voltage profiles of a $\text{Li}/\text{Li}_2\text{Ru}_{0.75}\text{Ti}_{0.25}\text{O}_3$ cell between 4.8-2.0V	733
Figure II.3.D.1 Morphology and phase characterization of polycrystalline and single crystalline NMC76. (a, b) SEM images of polycrystalline and single crystalline NMC76. (c, d) Cross section images of polycrystalline and single crystalline NMC76. (e, f) STEM images of polycrystalline and single crystalline NMC76. (g, h) Selected area electron diffraction (SAED) of polycrystalline and single crystalline NMC76.....	737
Figure II.3.D.2 (a) Cross section images of polycrystalline NMC76 cathodes with different mass loadings. (b) Cross section images of single crystalline NMC76 cathode with different mass loadings. (c) Comparison of the first charge-discharge curves for polycrystalline and single crystalline NMC76 based thick cathodes. The corresponding coulombic efficiencies of single crystalline and polycrystalline cathodes are 85% and 91%, respectively	738
Figure II.3.D.3 (a) First charge and discharge curve of single crystal NMC76 in a graphite/NMC76 full cell between 2.7 and 4.4 V at 0.1C (1C = 200 mA/g). (b) Cycling stability of single crystal NMC76 in the graphite/NMC full cell using thick electrode. The full cell is charged at C/10 and discharged at C/3	738
Figure II.3.D.4 (a) Cyclic voltammetry curve of polycrystalline NMC76 under in situ AFM testing, inserted figure is the demonstration of in situ AFM experimental setup. (b, c, d, e, f, g, h and i) AFM images of polycrystalline NMC76 at different potentials obtained from in situ measurements.....	739
Figure II.3.E.1 (a) PMpipFSI/LiFSI electrolyte conductivity dependence on temperature measured by electrochemical impedance spectroscopy, and (b) Raman spectra (600-1500 cm^{-1}) for PMpipFSI/LiFSI electrolyte with different LiFSI salt concentrations.....	742
Figure II.3.E.2 (a-d) Pairwise radial distribution functions $g(r)$ computed from MD simulations.3-4 (Strong spatial coordination between Li^+ and FSI $^-$ within 5Å can be observed. In contrast, the coordination shells of other type ion-ion pairs extend to 10Å and exhibit significantly weaker spatial coordination than Li^+ - FSI $^-$.	743
Figure II.3.E.3 Cyclic voltammograms of (a) 1 M LiFSI-PMpipFSI, (b) 5 M LiFSI-PMpipFSI and (c) Gen 2 electrolyte using Al working electrode in an Al-coated 2032-coin cell setup (Figure II.3.E.1b). (Working electrode: Al, counter and reference electrode: Li, scan rate: 10 mV/s).....	744
Figure II.3.E.4 (a) Cyclic voltammograms of ILEs scanned to 6.0 V vs Li^+/Li and (b) scanned to 5.0 V vs Li^+/Li using Pt as working electrode and Li as counter and reference electrode; (c) Al-coated 2032-coin cell configuration with two stainless steel spacers placed on anode side; (d) capacity retention and Coulombic efficiency of NMC532/Li cells with 1 M and 5 M ILE with a cutoff voltage 4.5 V-3.0 V, and (e) 4.7-3.0 V. 745	745
Figure II.3.E.5 C-rate capability of NMC532/Li cells with 1 M and 5 M LiFSI-PMpipFSI electrolyte cycled between (a) 4.3-3.0 V, and (b) 4.7-3.0 V; snapshots randomly selected from equilibrated MD trajectory for (c) 1 M and (d) 5 M-LiFSI concentration, respectively. (The two concentrations exhibit sharply different coordination structure, where one Li^+ and four FSI $^-$ constitute an isolated Li^+ solvation structure at 1 M concentration while at 5 M concentration a deadlocked Li^+ -FSI $^-$ - Li^+ -FSI $^-$... coordination network is established. For a center Li^+ (labeled with 0), each of its four coordinated FSI $^-$ also is paired with another Li^+ (labeled by 1, 2, 3, 4)).....	746
Figure II.3.F.1 Schematic representation of a scanning electrochemical microscope (SECM).....	749
Figure II.3.F.2 Schematic Representation of the Polymer Assisted Deposition (PAD) Process	750

Figure II.3.F.3 (A) Photograph of PAD films coated on ~ 1cm ² silicon samples, (B) XRD for LMO deposited on Si substrates (C) AFM of PAD LMO films on Si.....	751
Figure II.3.F.4 (A) XRD for LMO PAD film on stainless steel (B) Cyclic Voltammetry for PAD Film on stainless steel (C) XRD of LMO(111) deposited via PAD on STO (111).....	751
Figure II.3.F.5 Cyclic Voltammetry for a 2 mm Pt disk electrode in 1M LiClO ₄ :PC, with 1mM Mn(II) and Mn(III) acac.....	753
Figure II.3.F.6 SECM Tip Voltammetry collected at a 25 μm tip electrode placed near an LMO substrate. Data was collected following 30-minute intervals of holding the LMO substrate at 4.5V vs Li/Li+	754
Figure II.3.G.1 Calibration curve of Keyence contact sensors in the 0 – 1 mm range (left). Custom device configuration to measure thickness changes in 200 mAh cells (right)	758
Figure II.3.G.2 Thickness changes of NMC532 cells as a function of electrolyte, with the baseline hydrocarbon (left) and HFE/FEC electrolyte (middle). Electrochemical performance of NMC532 cells normalized to 1st CC/CC cycle (right).....	758
Figure II.3.G.3 Prototype setup of the non-contact thickness measurement system (left) and laser position calibration (middle). The pixels from the laser is tracker using the ImageJ software package (NIH).....	759
Figure II.3.G.4 Dissolved Co concentrations in tested LCO cells as a function of time (200 cycles), voltage (4.5 and 4.6V), and electrolyte (EC/EMC, HFE, HFE/FEC).....	760
Figure II.3.G.5 Dissolved metals concentration (Ni, Mn, Co) in tested NMC532 and NMC622 cells as a function of time (200 cycles), voltage (4.2 and 4.5V), and electrolyte (EC/EMC, HFE, HFE/FEC).....	760
Figure II.3.G.6 Dissolved metals (Ni, Mn, Co) in tested NMC532 cells at 4.6V (left). NMC532 and NMC622 cells with the HFE electrolyte at 4.6V (middle). Stoichiometric ratios of HFE cells at 4.6V post mortem versus theoretical (right)	761
Figure II.3.G.7 Powder X-ray diffraction patterns for LCO and all NMC cathodes studied to date. LCO (black), NMC111 (red), NMC532 (blue), NMC622 (teal), and NMC811 (violet) are depicted	762
Figure II.3.G.8 Custom gas manifold control plate (left) is comprised of a series of needle and ball valves, and monitored using the digital pressure gauge (± .1 torr). A typical sample cylinder containing the desired mixture allows for the direct sampling of the gas without contaminating the bulk mixture (right)	762
Figure II.3.G.9 Cross sections of 50 nm (far and middle-left) and 100 nm (middle and far-right) following Pt deposition and FIB milling	763
Figure II.4.A.1 Reactive spray technology system set up and optimized at ANL to produce cathode material	767
Figure II.4.A.2 (a) XRD patterns and (b) SEM pictures of the layered NCM811 by RST. (e) Formation and cycle life testing plots for NCM811 electrodes made with active material synthesized with the RST system.	767
Figure II.4.A.3 NCM 811 produced by FSP with different precursor and flame conditions. XRD pattern and SEM (a) and (b) nitrate precursors, (c) and (d) nitrate precursors with excess Li, (e) and (f) nitrate precursors, acetate with acetic acid, (g) and (h) nitrate precursors, acetate with propionic acid and excess Li.	769
Figure II.4.A.4 (a) Different milling and sieving conditions used to post process NCM811 powder.(b) XRD pattern of NCM811 (a) as prepared, milled for (b) 1 and (c) 3 hours. Crystallite size decreases as milling energy process increases	769
Figure II.4.A.5 Half-cell data for electrode made with NCM811 by FSP using nitrate precursors. (a) Formation data for large scale sample (>350g per batch), (b) Cycling data for sample at different scales, the larger batches were milled and classified using an improved method (better particle distribution)	770

Figure II.4.A.6 Scanning electron micrographs of NCM 811 coated with 1wt% nano NCM111, (a) before and (b) after thermal treatment. Dark and light patches on particle surface may indicate uneven coating. Half coin cell for NCM811 cathodes with nano NCM111. (c) rate capability plots and (d) cycling data.....	770
Figure II.4.B.1 Initial charge-discharge profile of different LNMO samples with 3 mAh/cm ² loading thick electrode.....	773
Figure II.4.B.2 Galvanostatic cycling (left) and associated Coulombic efficiencies (right) for industry-partner LNMO with different novel electrolytes in half cells	774
Figure II.4.B.3 Charge-discharge profiles (Left) and cycle performances at C/3 (Right) of the LNMO samples synthesized with different excess lithium in the reaction mixture	774
Figure II.4.B.4 SEM images of the LNMO-3 and LNMO-5 samples and the corresponding electrochemical performances in half cells.	775
Figure II.4.B.5 Cycling results for LNMO-graphite full cells cycled within a confined (green) and expanded (blue) voltage window.	775
Figure II.4.B.6 Cycling results for LNMO-graphite full cells with 3 mAh/cm ² loading and Gen2 electrolyte.	776
Figure II.4.B.7 STEM/HAADF images of the (a) pristine LNMO and (b) LNMO after 225 cycles in Gen2 electrolyte. (c, d) Spatially resolved EELS spectra from the surface to the bulk of the cycled LNMO in Gen2 electrolyte and (e) Mn L3/L2 ratio fit results from the EELS spectra compared to literature values for various oxidation states of Mn species.	776
Figure II.4.B.8 Performance metrics per cycle at C/3 in terms of coulombic efficiency, energy efficiency, and energy and capacity on charge and discharge of LNMO/graphite cells with different electrolytes (electrolyte composition identified at the bottom of each figure)	778
Figure II.4.B.9 (a) cross-section SEM image of dry coated LNMO thick electrode with Haldor Topsoe material. (b) EDX mapping of the cross-section of the electrode. (c) voltage profile of formulation #3 LNMO/Li half cell assembled in CR2032 with Gen2 electrolyte. (d) capacity retention and (e) energy density retention of formulation #3 LNMO/Li half cells cycled at C/10	779
Figure II.4.B.10 (a) 1st cycle voltage profile of the LNMO/graphite full cell using formulation #3 cathode and dry coated graphite with capacity matching. Cycling performance of this full cell in terms of (b) capacity and (c) energy density are shown in the figure. The full cell was cycled between 3.3 V to 4.85 V with C/10	780
Figure II.4.B.11 (a) OCV of half cells with Gen2 stored at room temperature (black) and at 55°C (red). (b) OCV of half cells with Gen2 (red) and Daikin electrolyte (blue) as a function of the rest time. (inset) Expanded view of the OCV with Gen2 electrolyte between 0 and 4 days.	780
Figure II.4.C.1 (A) Sol Gel method for preparation of NFA cathode powders, (B - C) Scanning electron micrographs of the sol-gel synthesized NFA cathode powders, (D) EDS spectra of the sol-gel synthesized NFA powders.....	783
Figure II.4.C.2 Crystallographic assessment of the NFA compositional variants (A) X-Ray diffractograms, (B) Mossbauer spectra, (C) Schematic representation of the crystal structure of NFA class and with the corresponding lattice parameters	784
Figure II.4.C.3 Electrochemical assessment of the NFA compositional variants (A) Cyclic voltammograms, (B) Charge/Discharge curves, (C) Cycling performance	785
Figure II.4.C.4 (A) Schematic representation of the co-precipitation process for the scale-up of the NFA class, (B) Scanning electron micrographs of the NFA cathode powders synthesized using co-precipitation process and calcined in oxygen atmospheres, (C) X-Ray Diffractogram of the NFA powders synthesized using co-precipitation process and (D) Electrochemical assessment of the NFA powders synthesized using co-precipitation process	786

Figure II.4.D.1 Characterizations of the pristine Mg/Ti-LNO material. (a) Ni/Ti L-edge and O K-edge soft XAS spectra, the * represents carbonate species; (b) neutron diffraction and Rietveld refinement; (c-d) annular dark-field STEM images of the primary particle; (e) EELS spectra scanning pathway from the surface to subsurface with the increment of 0.8 nm for each spectrum; (f) Ti L-edge EELS spectra recorded with the scanning pathway (from the bottom purple to the top dark red spectra); (g) normalized peak area of Ti L-edge EELS as a function of the scanning depth; (h) STEM-EDS mapping of the Ni (red), and Ti (green) in the composition scale and (i-j) concentration scale on the selected particle.....	791
Figure II.4.D.2 Electrochemical performance of the half cells containing the Mg/Ti-LNO cathode at 22°C within 2.5-4.4 V. (a) The voltage profiles of the LNO and Mg/Ti-LNO at C/10 (20 mA/g), the insert shows the discharge capacity as a function of cycle number; (b) the voltage profiles in the first 50 cycles at C/10; (c) the dQ/dV curves of the two cathodes derived from the voltage profiles at C/10; (d) discharge voltage profiles at the symmetrical constant currents of C/10, C/5, C/2, 1C and 2C; (e) long-term cycling performance; (f) specific energy retention at different C-rates.	792
Figure II.4.D.3 STEM-EDS tomographic reconstruction of the primary cathode particles with Gen-2 chemistry. Surface dopant is shown in red, bulk dopant is shown in blue, and Ni is shown in green.....	793
Figure II.4.D.4 (a) Atomic-resolution HAADF-STEM image of pristine VT Gen-3 Sb-doped LNO and (b) Sb distribution in VT Gen-3 Sb-doped LNO	793
Figure II.4.D.5 In situ probing structural degradation of delithiated LNO during oxygen loss. (a) Atomic-resolution TEM image of delithiated LNO. The insets shows FFT and enlarged image showing local O1-O3-O1 stacking. (b) Layered structure to disordered spinel transformation in delithiated LNO upon heating at 230°C. (c) Disordered spinel to rock-salt transformation with prolonged heating at 230°C	794
Figure II.4.D.6 (a) 3D electron tomography of a delithiated LNO particle at room temperature. (b) 3D electron tomography of the delithiated LNO with severe oxygen loss after in situ heating at 500°C. Pores/cracks formed along (003) planes of layered structure as indicated by the arrow.....	794
Figure II.4.D.7 (a) HAADF-STEM image and (b) Bright-field image of a delithiated TiMg-doped LNO after in situ heating at 250 for 1 h. (c) Atomic-resolution TEM image of the delithiated TiMg-doped LNO in (b).	795
Figure II.4.D.8 (a) The relative surface oxygen release energies of doped LiNiO ₂ with respect to the pristine phase. An orange color indicates an improved oxygen retention, while a purple color indicates a reduced oxygen retention as compared to the pristine phase. (b) Schematic illustration of surface doped LiNiO ₂ model. Blue: dopant, green: Li, grey: Ni, red: oxygen. (c) 2D electron localization function contour plot for the surface slice of Sb-doped LiNiO ₂	795
Figure II.4.D.9 Battery performances of Gr NMC811 coin cells using different electrolytes between 2.5 and 4.4 V. (a) Voltage profiles of the first formation cycle at C/20 and 25°C. (b-c) Long-term cycling stability at C/3 at (b) 25°C and (c) 60°C after three formation cycles at 25°C. (d,e) Rate capabilities under (d) varying discharge rates (xC) with the same charge rate at C/5 and (e) varying charge rates (xC) with the same discharge rate at C/5. f, Low-temperature discharge performance at C/5 discharge rate, with all charging process at 25°C while the discharging at 25°C, 0°C, -10°C, -20°C, -30°C and -40°C, and then back to 25°C. 1C = 2.8 mAh cm ⁻²	796
Figure II.4.D.10 Cycling performance of Gr NMC811 coin cells with five different electrolytes. The Gr NMC811 cells were subjected to two formation cycles at C/20 and then cycling at C/2 charge and 1C discharge in the cutoff voltage range of 2.8-4.3 V and 1C = 200 mAh g ⁻¹ or 1.5 mAh cm ⁻² based on the weight of the NMC811 active material.....	797
Figure II.4.D.11 Discharge voltage profiles of the Project Progress Cells (PPC) at different currents and at room temperature.....	797
Figure II.4.D.12 Charge and discharge capacity of the Project Progress Cells (PPC) during cycling at room temperature.	798

Figure II.4.E.1 SEM images of various low-cobalt or cobalt-free, high-nickel compositions prepared through metal hydroxide co-precipitation, <i>i.e.</i> , NCM-900505 ($\text{LiNi}_{0.9}\text{Co}_{0.05}\text{Mn}_{0.05}\text{O}_2$), NCA-900505 ($\text{LiNi}_{0.9}\text{Co}_{0.05}\text{Al}_{0.05}\text{O}_2$), NMA-900505 ($\text{LiNi}_{0.9}\text{Mn}_{0.05}\text{Al}_{0.05}\text{O}_2$), and NCMAM-9004040101 ($\text{LiNi}_{0.9}\text{Co}_{0.04}\text{Mn}_{0.04}\text{Al}_{0.01}\text{Mg}_{0.01}\text{O}_2$)	802
Figure II.4.E.2 Pouch cell cycling performances of NCMAM-9004040101, NCA-900505, and NMA-900505 (voltage window 2.5 – 4.2 V; active material loading: 2.0 mAh cm ⁻² ; single stack).....	802
Figure II.4.E.3 SEM images of $\text{LiNi}_{0.85}\text{Co}_{0.05}\text{Mn}_{0.075}\text{Al}_{0.02}\text{Mg}_{0.005}\text{O}_2$ prepared through metal co-precipitation, which has been delivered to Tesla, Inc. for making thirty 2 Ah pouch cells for performance evaluation by DOE	802
Figure II.4.E.4 Coin cell performances of $\text{LiNi}_{0.85}\text{Co}_{0.05}\text{Mn}_{0.075}\text{Al}_{0.02}\text{Mg}_{0.005}\text{O}_2$ (Ni-85): (left) coin-cell performance evaluation of samples from varying 200 g batches; (right) pouch-cell performance evaluation of samples from batches 4 & 5.....	803
Figure II.4.E.5 Preliminary cycling performances of Ta ⁵⁺ -doped LiNiO_2 in both coin and pouch cells.....	803
Figure II.4.E.6 Cyclability of graphite/ $\text{LiNi}_{0.94}\text{Co}_{0.06}\text{O}_2$ pouch cells in LiFSI/EMC-based electrolyte with lithium difluoro(oxalato)borate (LiDFOB) as the SEI-forming additive.....	804
Figure II.4.E.7 Cycling performances in coin cells of $\text{LiNi}_{0.94}\text{Co}_{0.06}\text{O}_2$ treated with various ALD coating cycles	804
Figure II.4.E.8 Electrode thickness as a function of Ink flow rate. Web rate was held at 0.7 m/min.	804
Figure II.4.E.9 Roll of NC-9604 on an 8-inch-wide Al foil. 10 x 10 cm wide defect free electrodes were punched out of the roll	805
Figure II.4.F.1 Schematic of the technical approach for creating high-performance LNMTO Li-ion cathodes	808
Figure II.4.F.2 Key unit operations and process variables for the solid-state synthesis of high voltage spinel cathode powders	808
Figure II.4.F.3 Charge/Discharge-voltage profiles and cycle performance for coin-type half-cells at 25°C made with LNMTO cathodes from different production size batches, 20 g, 200 g, and 2 kg. Electrolyte 1 M LiPF ₆ in 1:1 wt. EC/EMC (no additive). Cycling conditions: Cycle 1: C/10 then C/5 (Ch) and C/2 (dis).....	809
Figure II.4.F.4 Charge/Discharge-voltage profiles and cycle performance for coin-type half-cells at 25°C with LNMTO cathodes made with baseline and modified solid-state processes. Electrolyte 1 M LiPF ₆ in 1:1 wt. EC/EMC (no additive). Cycling conditions: Cycle 1: C/10 then C/5 (Ch) and C/2 (dis).....	809
Figure II.4.F.5 Charge/Discharge-voltage profiles and cycle performance coin-type half-cells made with LNMO and LNMTO cathodes synthesized using solid-state (SS) and co-precipitation (CP) processes. Electrolyte 1 M LiPF ₆ in 1:1 wt. EC/EMC (no additive). Cycling conditions: Cycle 1: C/10 then C/5 (Ch) and C/2 (dis)	810
Figure II.4.F.6 Comparison of the cycle performance of half-cell and full-cells made with baseline solid-state (SS) LNMTO cathode and preliminary core/shell LNMTO cathode. Anode: Li (half) and graphite (full) Electrolyte 1 M LiPF ₆ in 1:1 wt. EC/EMC (no additive). Cycling conditions: Cycle 1: C/10 then C/5 (Ch) and C/2 (dis)	810
Figure II.4.F.7 Cycle performance of coin-type full-cells and single-layer pouch cells at 25°C made with the baseline LNMTO cathode with LiPAA binder, Electrolyte 1 M LiPF ₆ in 1:1 wt. EC/EMC (no additive) and graphite anode. Cycling conditions Cycle 1: C/20, Cycle 2/3: C/10 rate, then coin-cell: C/5 (Ch) and C/2 (dis), and pouch cell: C/3 (Ch) and C/3 (dis)	811
Figure II.4.F.8 Charge/Discharge-voltage profiles and cycle performance of SLPC with baseline LNMTO cathode with LiPAA binder, Electrolyte 1 M LiPF ₆ in 1:1 wt. EC/EMC (with additive) and graphite anode.	

Cycling conditions Cycle 1: C/20, Cycle 2/3: C/10 rate, then coin-cell: C/5 (Ch) and C/2 (dis), and pouch cell: C/3 (Ch) and C/3 (dis)	811
Figure II.4.G.1 XRD patterns of $\text{LiNi}_{0.83}\text{Co}_{0.11}\text{Mn}_{0.06}\text{O}_2$ materials calcined at 480°C first, and then at various high temperatures from 725°C to 800°C	814
Figure II.4.G.2 SEM images of as-synthesized $\text{LiNi}_{0.83}\text{Co}_{0.11}\text{Mn}_{0.06}\text{O}_2$ material at 700°C (a and b) and 800°C (c and d)	815
Figure II.4.G.3 a) Capacity retention of $\text{LiNi}_{0.83}\text{Co}_{0.11}\text{Mn}_{0.06}\text{O}_2$ synthesized at various temperatures. b) Capacity retention of LFP-coated $\text{LiNi}_{0.83}\text{Co}_{0.11}\text{Mn}_{0.06}\text{O}_2$ with different LFP amount	816
Figure II.4.G.4 Capacity retention of the LFP-coated NCM/Graphite full-cells during 1 C cycling at room temperature and 40°C	816
Figure II.4.G.5 (a) HAADF-STEM image of LFP-NCM and (b-f) corresponding EDX elemental maps	816
Figure II.4.G.6 Image of twenty cells to be delivered to Idaho National Laboratory	817
Figure II.4.G.7 C-rate performance of Cells #1 and #2	818
Figure II.4.G.8 a) Charge/discharge curves b) capacity retention and coulombic efficiency of the low-cobalt material $\text{LiNi}_{0.92}\text{Co}_{0.055}\text{Mn}_{0.025}\text{O}_2$ synthesized at 715°C	818
Figure II.4.G.9 XRD patterns of various Mo content in $\text{LiNi}_{0.5-x/2}\text{Mn}_{0.5-x/2}\text{Mo}_x\text{O}_2$ (where $x = 0, 0.01, 0.03, 0.05$)	819
Figure II.4.G.10 Charge and discharge curves at different cycles in the voltage range between 2.0-4.5 V at current density of 20mA/g for (a) Undoped LNMO and (b) Mo-doped LNMO	820
Figure II.4.G.11 TEM images, STEM images and corresponding EDS maps of (a, b) $\text{LiNi}_{0.5}\text{Mn}_{0.5}\text{O}_2$ and (c, d) $\text{LiNi}_{0.4995}\text{Mn}_{0.4995}\text{O}_2$	820
Figure II.4.G.12 HAADF-STEM and EELS analysis of Mo doped and undoped $\text{LiNi}_{0.5}\text{Mn}_{0.5}\text{O}_2$	821
Figure II.4.G.13 STEM-HAADF images of $\text{LiNi}_{0.5}\text{Mn}_{0.5}\text{O}_2$ (a) before and (b) after cycling. STEM-HAADF images of Mo-doped $\text{LiNi}_{0.5}\text{Mn}_{0.5}\text{O}_2$ (e) before and (f) after cycling	821
Figure II.4.G.14 Electrochemical performance of LNMO with 0 – 1 at% Mo substitution showing: (a) Galvanostatic charge/discharge curves collected during the first cycle and (b) capacity stability over 65 cycles. Cells were cycled between 2.0 – 4.5 V vs. Li/Li^+ at a specific current of 20 mA/g	822
Figure II.4.G.15 Rate capabilities of LNMO with 0 – 1 at% Mo substitution when cycled between 2.0 – 4.5 V vs. Li/Li^+ at specific currents of 10 – 200 mA/g	822
Figure II.4.G.16 Atomic structures of pristine undoped and Mo-doped LNMO. (a) HAADF STEM image of a near-surface region in undoped LNMO. (b) Magnified HAADF STEM image of undoped LNMO aligned with STEM-image intensity profiles. (c) Corresponding atomic model the layered LNMO structure marked with strong cation mixing. (d) HAADF STEM image of a near-surface region in Mo-doped LNMO. (e) Magnified HAADF STEM image of Mo-doped LNMO aligned with STEM-image intensity profiles. (f) Corresponding atomic model the layered LNMO structure marked with weak cation mixing	823
Figure II.4.G.17 Morphology, composition, and atomic structures of cycled undoped and Mo-doped LNMO particles. (a) STEM image and corresponding EDS elemental maps of an undoped LNMO particle after 100 cycles. (b) STEM image and corresponding EDS elemental maps of a Mo-doped LNMO particle after 100 cycles. (c) Atomic-resolution STEM image of local regions in 3 different undoped LNMO particles after 100 cycles, in which strong cation mixing and phase transitions (layered-to-spinel-like or layered-to-rocksalt) are observed. (d) Atomic-resolution STEM image of local regions in 3 different Mo-doped LNMO particles after 100 cycles. The layered structures were well-preserved without any significant cation mixing or phase transitions	824

Figure II.5.A.1 (a) S K-edge XANES spectra of LPS mixed with NCM333, 523, 811 and 811 coated with LiNbO ₃ , (b) 1st cycle charge and discharge profile of NCM333 and NCM811 cathode. S K-edge XANES spectra of cycled solid state batteries which assembled with (c) LPS-NCM33 and (d) LPS-NCM811	828
Figure II.5.A.2 Optical images (a) and UV-vis absorbance spectra (b) of and PVdF co-block polymer (65% PEO, 82% PEO) binder in 0.05 mmol/L polysulfide solution in DOL/DME.....	829
Figure II.5.A.3 Discharge capacity and coulombic efficiency at 0.2 C (a), and discharge/charge voltage profiles at 0.05 C of sulfur composite cathodes with PVdF and co-block polymer binder. In operando sulfur K-edge XAS spectrum of PVdF (c) and co-block polymer-based (d,e) composite cathodes after 1st discharge. 2472 eV polysulfides peak normalized intensity (f).....	829
Figure II.5.A.4 Raman spectrum of pristine LiPF ₆ salt collected with a 400 nm laser wavelength in (i) CW, (ii) Kerr gated mode, (iii) baseline correction of Kerr gated spectrum. The intensity of the (i) CW spectrum has been scaled by x0.001 in order to observe all three spectra on the same axis	830
Figure II.5.B.1 Optimized structure and bond length of TPQD obtained by DFT calculation (grey denotes to the carbon, yellow for sulfur and red for oxygen)	835
Figure II.5.B.2 O K-edge XANES spectra of TPQD electrodes at the different states of charge.....	835
Figure II.5.B.3 (b) S-K edge XAS spectra of TPQD electrodes at different state of charge. (c) The structural evolution of TPQD electrodes during the lithiation process	836
Figure II.5.B.4 Digital photograph for sulfur cathode obtained from the cycled pouch cell (schematic illustration) with indicating boxes for three selected spots of interest; outer region nearby electrode-tab (R1), central region (R2) and outer corner region (R3). Corresponding mappings of XRF at two different energy levels (2469 and 2480 eV) to investigate the status and distribution of sulfur species at the regions of R1 (b and c), R2 (e and f), and R3 (h and i). XAS spectra (d , g , and j) within an energy scanning range of 2468–2488 eV at two strong contrasted areas in XRF image respectively.....	837
Figure II.5.B.5 Spatially-resolved XAS and XRF imaging for cycled Li metal anode (inner side)	838
Figure II.5.C.1 (a). SEM images taken at different magnifications. (b). Rietveld refinement of the XRD pattern of LR-NCM. (c). The discharge capacity and energy density of the modified LR-NCM (d). Voltage profiles of the modified LR-NCM at different cycle numbers.	842
Figure II.5.C.2 (a). Voltage profiles and (b). cycling performance of the LR-NCM cycled in standard electrolyte. (c). Voltage profiles and (d). cycling performance of the LR-NCM cycled in 2% LiBOB electrolyte. (e). XPS C 1s and (f). XPS O 1s comparison of pristine LR-NCM electrode and LR-NCM cycled in different electrolyte after 50 cycles.....	843
Figure II.5.C.3 Cryo-TEM images of the (a). cycled LR-NCM in the Baseline electrolyte and (b). in 2% LiBOB electrolyte. (c). XPS spectra of the pristine and cycled LR-NCM.	844
Figure II.5.C.4 STEM/HAADF images of the (a). cycled LR-NCM in the Baseline electrolyte and (b). cycled LR-NCM in 2% LiBOB electrolyte. Spatially resolved EELS spectra from the surface to the bulk of the (c). cycled LR-NCM in the Baseline electrolyte and (d). cycled LR-NCM in 2% LiBOB electrolyte.	845
Figure II.5.C.5 Electrochemical performance of the (a). initially cycled LR-NCM and (c). initially cycled NMC811 with or without heat treatment. The changes in the occupancy of Li in TM layer during heat treatment in the (b). initially cycled LR-NCM and (d). initially cycled NMC811 obtained from operando neutron diffraction. HRTEM images and corresponding FFT pattern of the (e).10-cycled NMC811 and (f). 10-cycled NMC811 after annealing at 300°C for 1 hour.	846
Figure II.5.C.6 (a-c), results for HCE. (e-g), results for CCE. (a, e), Inactive Li morphology at low magnifications for both electrolytes. (b, f), HRTEM shows that a different amount of metallic Li ₀ is wrapped by SEI in the two types of electrolyte. (c, g), FFT patterns of corresponding HRTEM indicate the SEI component, which contains crystalline Li ₂ CO ₃ , Li ₂ O, and LiF. (d, h), XPS analysis of inactive Li SEI components formed in HCE (d) and CCE (h) for various stripping rates.....	847

Figure II.5.D.1 Spatial and temporal evolution of structural degradation from the surface into the bulk STEM-HAADF images of the $\text{Li}_{1.2}\text{Mn}_{0.6}\text{Ni}_{0.2}\text{O}_2$ cathode show the gradual propagation of the nanovoid-populated zone from the particle surface towards the interior of the particle with increasing cycles of the battery. a,b, After five cycles, formation of the nanovoid-populated region at the particle surface region is indicated by the yellow arrows in a, where the nanovoid shows as a dark contrast. c,d, After 45 cycles, the nanovoid-populated zone thickens. The red dashed line in d indicates a nanovoid. e,f, After 200 cycles, further thickening of the nanovoid-populated zone occurs. Note that the small particle as indicated by the blue arrow in e has been fully populated by nanovoids. The dashed yellow lines in b, c and e mark the boundary between the nanovoid-populated zone near the surface and the region free of nanovoids within the bulk lattice..... 850

Figure II.5.D.2 Atomic-resolution TEM of electrochemically deposited Li metal (EDLi) and SEI interface. (a) Bright-field TEM image of the EDLi at a low magnification. (b) Atomic-resolution image of the EDLi and SEI interface. (c) Schematic of the observed SEI formed on EDLi..... 852

Figure II.5.E.1 Design of 3-omega thermal sensors and how they are incorporated into an electrochemical battery pouch cell for *in-operando* measurements. (A) Sensor and sample design and operation. (B) Sensors fabricated on a cathode. (C) Sensors embedded within pouch cell; assembled in a glove box. (D) *Operando* measurement of a battery while it powers an LED (for illustrative purposes only; actual data collected using batter cyclers, not LED)..... 855

Figure II.5.E.2 Results of *operando* measurements. (A) Thermal contact resistance (TCR) between separator and electrodes as a function of pouch age during formation cycling. (B) Representative raw 3-Omega data for pouch cell 1 before and after 2 formation cycles, showing it is not possible to fit data without including a TCR. (C) Breakdown of relative contribution of each battery layer to total thermal resistance. (D) Representative voltage traces of battery cycling during 3-omega measurement..... 856

Figure II.5.F.1 Change in stress-thickness vs. time for respective cycles from the MOSS studies. Left plot is the response with soft (PEO) artificial layer. Right plot is the response with stiff (LiF) artificial layer. 859

Figure II.5.F.2 Delamination of PAA oligomers by (a) breaking all Li-O bonds, (b) breaking all Li-Li bonds, and (c) breaking mixed Li-O and Li-Li bonds. (d) The work of separation in terms of energy, 860

Figure II.5.F.3 The microstructure of mossy Li on the stripping side under different pressures: (a) 0.05 MPa, (b) 0.11 MPa, and (c) 0.17 MPa. The current density is 1 mA/cm² and the areal capacity of plating and stripping is 4 mAh/cm² 860

Figure II.5.F.4 (a) EIS curves for the three pressures of 0.23, 0.35, and 0.61 MPa. (b) EIS results..... 861

Figure II.5.F.5 The microstructure of mossy Li electroplated at different current densities in the DOL-DME electrolyte 861

Figure II.5.F.6 The reaction mechanism of lithium surface treatment with chlorosilanes and simulation results of intermolecular interaction in resulted siloxane coating film on lithium surface..... 862

Figure II.5.F.7 Galvanostatic cycling voltage profiles for symmetric cells using coated (TMCS or PhDMCS modified) or uncoated lithium electrodes under (a) low (0.25 mA/cm², 1 mAh/cm²) and (2) high (1 mA/cm², 4 mAh/cm²) current density and areal capacity 862

Figure II.5.F.8 in situ characterization of symmetric cells using PhDMCS treated or untreated lithium electrodes. (a) and (b): Impedance before and during cell cycling. (c) and (d): Height change by dilatometer. 863

Figure II.5.G.1. Conductivity of Li⁺-neutralized sulfonated PSf-co-PEO polymer solutions with added LiTFSI salt. Polymer concentration is reported as sulfonate concentration. 866

Figure II.5.G.2. Conductivity and viscosity of a range of potential additives to improve conductivity of the control 0.1 M polymer in 2:1 (vol.) EC:DMC. Each additive is introduced at 0.1 M to match the lithium content of the solution. The structure of the polymer, EC, and DMC in the control solution are also included. 867

Figure II.5.G.3. Second charge and discharge curves at C/20 for batteries fabricated with the 0.1 M polymer in 2:1 (vol.) EC:DMC solution containing no additives (control), containing stabilizing additives FEC and VC, and containing 15-crown-5 and the stabilizing additives. The calculated theoretical maximum capacity of the cell is also shown.	867
Figure II.5.G.4. RAFT polymerization synthesis scheme for triflimide-based styrene polymer (PS-LiTFSI).	868
Figure II.5.G.5. Conductivity (mS/cm) & viscosity (mPa s) as a function of concentration for PS-LiTFSI in carbonate solutions.	868
Figure II.5.G.6. Ideal transference number versus Li concentration (molal) for LiTFSI in EC:EMC (3:7). Each color represents a separate cell, with each cell polarized subsequently to ± 5 , ± 10 , ± 15 , & ± 20 mV.	868
Figure II.5.H.1 Theoretical design of the roadmap for an advanced Ti & LaMO dual modification	872
Figure II.5.H.2 ^7Li MAS NMR spectra obtained before cycling and after cycling of NCM and NCM with modification. Morphology characterization of NCM and NCM with modification using TXM	873
Figure II.5.H.3 The ultrafine coating on both primary and secondary particle surface for the cathode	874
Figure II.5.H.4 The effects of PEDOT coating on electrochemical performance.....	875
Figure II.5.H.5 In situ synchrotron HE-XRD characterization on the structural evolution of LMO and LR-LMO during the first charge/discharge	876
Figure II.5.H.6 Qualitative structural analysis of LMO with different potentials and cycles.....	877
Figure II.5.I.1 Computational predictions of M-O decoordination and Ir=O/O-O mediated anion redox. (a) Local coordination environments predicted by DFT in a $\text{Li}_{0.5}\text{Ir}_{0.75}\text{Sn}_{0.25}\text{O}_3$ structure showing the consequence of SnLi/VM defect formation when the vacancy neighbors only Ir: contraction of the Ir—O bonds (left) and the resulting changes in local oxygen environment (right). Note that the presence of Li neighboring O negligibly affects the O 2p states due to minimal hybridization between Li and O. (b) Projected DOS of the individual oxygen atoms involved in the Ir—O bond contraction before (top) and after (bottom) forming the SnLi/VM defect, demonstrating the shift of the O 2p states above the Fermi level, indicating oxygen redox. (c) Local coordination environments when the migrating Sn initially neighbors another Sn, resulting in the formation of a 1.44 Å O—O dimer. (d) Projected DOS of the individual oxygen atoms involved in the O—O bond formation before (top) and after (bottom) forming the SnLi/VM defect and O—O dimer, also showing a shift of the O 2p states above the Fermi level.....	881
Figure II.5.I.2 Spatial distribution of the Ni and O oxidation state in the charged state after 125 cycles determined through STXM. The far left shows the distribution over an “electrode scale” ($\sim 30 \times 30 \mu\text{m}$) determined with only three energies, while the zoomed in images show the distribution within the boxed region determined by fitting of spectra containing > 40 energies. The reduced fraction as a function of thickness is taken using the zoomed in images, although there is no qualitative difference when using the “electrode scale” Ni map instead. The scale bar in each image is 1 micron.....	882
Figure II.6.A.1 (a) GI/GB microstructure with average grain size 167 nm. (b) GI/GB microstructure with average grain size 60 nm. (c) Current focusing observed at the GB region plotted with respect to grain size. Decrease in grain size helps to distribute the current and reduce the current focusing observed at the GB regions.....	886
Figure II.6.A.2 (a) GI/GB microstructure with larger grains (LG). (b) Strain energy (SE) and cracking at GB for LG. (c) GI/GB microstructure with small grains (SG). (d) SE and cracks at GB for SG.....	886
Figure II.6.A.3 (a) Computational domain of the cathode/SSE interface with presence of grain boundaries (GB). (b) Distribution of current density at the interface during the charge process (magnitude of current is positive, because anodic current is active). (c) Distribution of current density at the interface during the discharge process (magnitude of current is negative, because cathodic current is active).....	887
Figure II.6.A.4 (a) Schematic diagram of the cathode/SSE interface where delamination can occur during the first charge or delithiation process. (b) Charge and discharge curves obtained during the first delithiation and	

lithiation of the cathode particles. Delamination during the charge process manifests as a capacity fade during discharge	887
Figure II.6.A.5 (a) Computational domain with large grain size of approximate diameter around 150nm. (b) Computational domain with smaller grain sizes of diameter approximately 75nm. In both (a) and (b), the orange portion indicates cathode (NMC 111), the red domain denotes grain interior, and the yellow region stands for the grain-boundary. (c) Capacity fade due to interfacial delamination as observed in different LLZO microstructures with various grain sizes. Decreasing the grain size helps to minimize capacity fade	888
Figure II.6.A.6 (a) The voltage vs. capacity performance curves as observed during the first, third and ninth CC-CV charge and CC discharge cycle as observed in the LLZO microstructures with large grain sizes. (b) Interfacial delamination induced capacity fade observed in three different LLZO microstructures with large, medium and small grain sizes. The rate of capacity fade is much less in the smaller grain, due to the limited mechanical degradation observed there	888
Figure II.6.A.7 (a) Demonstration of change in potential with stoichiometry of Li in NMC cathodes during the charge process. Impedance analysis has been conducted at three different SOC values. (b) The impedance curves at three different points denoted by A, B and C	889
Figure II.6.A.8 (a) Potential vs. Li stoichiometry curves as obtained during the charge and discharge processes. (b) Variation in charge transfer resistance with Li stoichiometry during charge (red) and discharge (black) process. The experimental results are denoted by symbols	889
Figure II.6.B.1 a-c) Cyclic voltammograms of LNMO, LNTMO and LTMO half cells in the first 10 cycles. The scan rate is 5 mV/min. d-f) Voltage profiles of LNMO, LNTMO and LTMO half cells in the first 50 cycles. Data plotted in every 5 cycles. g-i) First-cycle incremental capacity (dQ/dV) profiles of the half cells. Half-cell cycling current density is 10 mA/g	892
Figure II.6.B.2 Comparison of operando DEMS measurements on a) LNMO and b) LTMO half-cells. The dQ/dV profiles (top panel) during the 1st charge are added to correlate with the gas analysis. Middle panels show gas evolution as a function of cell voltage while bottom panels show the cumulative O ₂ evolved during the 1st charge. The charge rate is 25 mA/g	893
Figure II.6.B.3 O K-edge mRIXS maps collected at pristine (P), charged (Ch) and discharged (D) states after various cycles: a) LNMO and b) LTMO. The voltage profiles of the selected cycles are also shown	894
Figure II.6.B.4 a) mRIXS map and the corresponding RIXS cut emission spectrum collected at the excitation energy of 531 eV, b) and c) RIXS cut spectra of LNMO and LTMO collected at the pristine state and after various cycles, and d) changes in area intensity of RIXS O ⁿ⁻ feature as a function of cycle number.....	894
Figure II.6.B.5 a, b) Schematics showing the probing depth of hard XAS (for Mn K-edge XANES) and soft XAS (for Mn L-edge), c, e) average Mn oxidation states derived from K-edge XANES edge energy of spectra collected on charged and discharged electrodes after various cycles, respectively, d, f) average Mn oxidation states derived from PCA analysis of Mn L-edge sXAS spectra collected on charged and discharged electrodes after various cycles, respectively	896
Figure II.6.B.6 Schematics showing the effect of d^0 TM on O redox behavior and subsequent degradation of the Mn redox-active cation-disordered rocksalt cathodes.....	897
Figure II.6.C.1 Schematic illustrations of different Li transport models in amorphous coating.....	900
Figure II.6.C.2 (a) Trajectory of one Li ⁺ atom in Li _{0.3} Al ₂ O _{3.15} (electrolyte model) for 40 ps at 2000K. Yellow and green dots represent vibrational and translational motions, respectively. (b) Number of O ²⁻ neighbors during Li translational and vibrational motions. The white dots represent the median values.	901
Figure II.6.C.3 Coordination number of Li ⁺ with PC computed in the present work and compared to experimental values (left) and fraction of Li ⁺ with n PF ₆ ⁻ anions (middle). Representative solvation structures are shown on the right.....	901

Figure II.6.C.4 Bulk electrolyte conductivity of LiPF_6 electrolyte as a function of salt concentration. Experimental data taken from Takeuchi et al. [3].....	902
Figure II.6.C.5 Diffusion constants of Li^+ and BF_4^- in propylene carbonate as a function of concentration....	902
Figure II.6.D.1 Calculated Li_2S - P_4S_7 - S phase diagram using SCAN functional	905
Figure II.6.D.2 (a) Comparison of binary sulfide formation energy calculated from PBE and SCAN with experimental measurement. (b) ΔG vs. T for $\text{Li}_7\text{P}_3\text{S}_{11}$ & $\text{Li}_4\text{P}_2\text{S}_7$	905
Figure II.6.D.3 (a) Comparison between calculated and experimental PDFs for amorphous LPS. (b) Raman spectra calculated for different LPS crystalline phases.....	906
Figure II.6.D.4 (a) Electrochemical stability windows of 1,600 phase-stable materials categorized by anion chemistry. (b) Chemical reaction energy ΔE_{ext} with LPS and fully lithiated NCM for the 302 screened materials enclosed in the green box in (a) [18].	907
Figure II.6.D.5 Computational structures of the amorphous Li-P-S systems including different types of anion building blocks at same composition. Green, purple and yellow balls denote Li, P and S ion, respectively ...	908
Figure II.6.D.6 Arrhenius plots of AIMD simulation on the Li-P-S systems with different concentrations of anion building blocks, PS_4^{3-} , $\text{P}_2\text{S}_6^{4-}$ and $\text{P}_2\text{S}_7^{4-}$	908
Figure II.6.E.1 A Newman-type model was adapted to rapidly predict the effects of heterogeneity by placing dissimilar regions in parallel. The model is able to show why lithium plating occurs preferentially in some regions.....	912
Figure II.6.E.2 Temperature, current, and positive and negative electrodes states of charge (SOCs) distributions, along with charge curves for the charging aligned resistances case (hot-hot, middle-middle, and cold-cold)	913
Figure II.6.E.3 (a) Conceptual geometry (not to scale) of revised local conductivity probe and (b) XYZ stage for automated measurement of local conductivity	914
Figure II.6.E.4 An example localized conductivity measurement with ionic conductivity given in terms of dimensionless MacMullin Number, for a commercial LCO electrode	915
Figure II.6.E.5 Schematic of XYZ stage and head unit for local electronic conductivity probe. This unit was adapted for use in measuring ionic conductivity as well, as shown in the adjacent figure (b).	915
Figure II.6.E.6 Snapshots of beginning and ending particle configurations for drying and calendering SPH simulations. The colored spheres indicate active material (blue), carbon/binder (yellow), and solvent (gray)	916
Figure II.6.F.1 The Li diffusion pathways for different solid electrolytes (the yellow isosurfaces), compared with the ab initio calculated transition pathways (the arrows).....	920
Figure II.6.F.2 (a) Side view of schematic representation of liquid electrolytes. (b) One representative local structures of the coordination environments around a Li-ion. (c) Li-O and (d) Li-F pair correlation functions (solid lines) and their integrals (dash lines) for LE from NVT AIMD simulation at 600 K.....	920
Figure II.6.F.3 mean square displacement (MSD) plots of Li-ion and PF_6^- -ion taken from 30 ps NVT at 600 K simulations in bulk LE and LiF/LE interface.....	921
Figure II.6.F.4 the stacking structure of $\text{Li}_x\text{S}_y/2\text{D-HAB-CP}$ at different level of lithiations.	921
Figure II.6.F.5 Li-migration barriers distribution (a) and diffusion coefficients as a function of temperature (b) of Mn-HAB- Li_5S_8 , Mn-HAB- Li_{10}S_8 , and Mn-HAB- Li_{15}S_8 , in the X and Z-directions. The diffusion coefficients curves of Li on graphene and $\text{Li}_{10}\text{GeP}_2\text{S}_{12}$ are also presented as a reference.	921
Figure II.6.F.6 (a) vulcanization of 5-Decene in two methods (cycloaddition and crosslinking); (b) two different positions of C=C in Decene are considered as vulcanization sites. The numbers in the table are the vulcanization energies in eV for different S chains and different binding configurations.....	922

Figure II.6.F.7 the lithiation process of S vulcanized 5-Decene	923
Figure II.6.G.1 The calculated total density of states (TDOS) for the four SE surface structures aligned with the vacuum level. The position of CBM of the corresponding bulk structure is labeled as the cyan dot lines. The position of the vacuum level, and the Fermi level of Li metal (Li EF), and the potential corresponding to the Li+/Li0 deposition are labeled. Eg,surface stands for the surface bandgap, and Tg is the energy difference from Li-metal in vacuum to the CBM of the SE.	925
Figure II.6.G.2 The distribution of additional electrons (yellow region), which is calculated from the difference in charge density before and after inserting additional electrons.....	926
Figure II.6.G.3 Phase-field simulation results on the impacts of surface trapped electrons and grain size on the morphologies and electric potential distributions after 800s Li electrodeposition. A comparison of the final phase morphologies in (a1-d1) the ideal SEs with excess electron-free surfaces and (e1-h1) the real SEs with the calculated surface electron concentrations from DFT, in a series of grain sizes. And a comparison of their corresponding final electric overpotential distributions for the SEs in (a1-h1). The dynamic evolution of (i) the Li dendrite penetration depths and (j) the total amount of metallic Li in SEs of different grain sizes. The initiation of isolated dendrite nucleation is demonstrated by (k1) the phase morphology and (k2) the corresponding electric potential distribution in the SE of the 75 μm grain size at 200s.....	927
Figure II.7.A.1 Discharge of the Li-solid electrolyte interface is sensitive to pressure. Comparison (left) of the pressure-induced creep-strain rate and the current-induced strain rate for stripping Li at 0.1 mA/cm ² . The point where the current-induced strain rate becomes dominant is when unstable void growth occurs at the Li interface, reducing the contact area, A. Stepwise reduction in stack pressure (right) while stripping Li at different currents identifies the maximum discharge rate that can be accessed for a stack pressure.....	934
Figure II.7.A.2 Typical load displacement curves (a) show the punch-in displacement that occurs at a range of displacement. An undulation in the surface (b) is proposed to model an interface defect and the corresponding state of stress as a function of the electrochemical cycling conditions. The model yields the deformation mechanism map for Li (c). Here the average current density at the interface and the Young's modulus of Li are taken to be 1 mA/cm ² and 9 GPa, respectively.	935
Figure II.7.B.1 a , In-plane scanning electron microscopy (SEM) image of sintered LICGC TM thin film. b , cross-section view of the LICGC TM /xPEO composite thin film. c and d , equibiaxial flexural strength measurement of the composite electrolyte. e and f , schematics of the composite pellet (e) and thin film (f), showing that the effects of surface xPEO layer and interfacial resistance. Schematics are not drawn to scale. g , the ionic conductivity of composite pellet and thin film as a function of inverse temperature, compared to neat polymer, pristine ceramic, and a composite without the interconnected ceramic structure.....	939
Figure II.7.B.2 a . composition of the gel composite electrolyte. b . storage moduli of gel composite electrolytes as a function of temperature, measured by dynamic mechanical analysis. c . Li ⁺ transference number of the gel composite electrolytes. d and e , ionic conductivity in the dry (d) and plasticized states (e). f , Li symmetrical cell cycling at room temperature.....	940
Figure II.7.B.3 Composites consisting of LICGC TM ceramic and 3 different polymers: PEGDMA crosslinked with LiTFSI free salt, with covalently bound styrene sulfonate anion and with covalently bound styrene TFSI anion. Right, ionic conductivity of the polymers and their respective composite with 50 wt% Ohara ceramic.....	941
Figure II.7.B.4 Cycling of Li/LiFePO ₄ solid state cells with dry composite and polymer electrolytes. a , cells at cycle 10 with different thicknesses of excess Li, 0-120 μm ; b , reduced polarization when thin PEO+salt fills interface between the cathode and electrolyte composites; c , one of the longest cycling cells with Lipon at the cathode interface.	941
Figure II.7.C.1 Temperature dependence of ionic conductivity of (a) carbonate SCEs, (e) ether SCEs, (i) alkylphosphate SCEs. Electrochemical stability of (b) carbonate SCEs, (f) ether SCEs, (j) alkylphosphate SCEs in Li Li Pt cells at a scan rate of 0.5 mV s ⁻¹ and room temperature. CE of Li Cu cells at 0.5 mA cm ⁻² with (c)	

carbonate SCEs, (g) ether SCEs, (k) alkylphosphate SCEs. SEM images of deposited Li particles at 0.1 mA cm⁻² with capacity of 1.5 mAh cm⁻² with (d) LiFSI-1.1DMC, (h) LiFSI-1.2DME, (l) LiFSI-1.3TMPa..... 944

Figure II.7.C.2 (a) Linear sweep voltammetry curves of PQILEs of Li(DME)_xFSI-PEO_{0.6} on Pt electrode in a three-electrode cell with a scan rate of 0.5 mV s⁻¹. (b) Temperature dependence of ionic conductivity of Li(DME)_xFSI-PEO_{0.6} (c) Average Li CE values of Li(DME)_xFSI-PEO_{0.6} at 60°C with Celgard 3501. (d) Cycling performance of Li||NMC cells using Li(DME)_{0.7}FSI-PEO_{0.6} under different charge cut-off voltages. (e) Cycling performance of Li||NMC cells with different cathode materials and the optimal PQILE cycled in the voltage range of 3.0-4.3 V 945

Figure II.7.C.3 (a) XPS profiles of the pristine NMC333 cathode and NMC333 cathodes after 300 cycles with different charge cut-off voltages of 4.2, 4.3, 4.4 and 4.5 V. TEM images of NMC cathodes after 300 cycles at 60°C with the charge cutoff voltage of (b) 4.4 V and (c) 4.5 V. Insets are the fast Fourier transform (FFT) patterns of selected regions 946

Figure II.7.C.4 (a) Nucleation overpotentials of Li plating on Li, Li-Ag, and Li-Ag-LiF surfaces in a carbonate electrolyte of 1 M LiPF₆ in EC-DMC (1:2 by vol.) (b) Cycling performance of Li||NMC333 full cells. SEM images of the cycled (c, f) Li, (d, g) Li-Ag/Li, and (e, h) Li-Ag-LiF/Li anodes disassembled from the Li||NMC333 full cells after 100 cycles at 1C/1C rates 947

Figure II.7.D.1 (a) Energy profile of Li deposition on Cu(001) from DME-solvated LiFSI in absence of an external field. ΔE values are energies relative to the initial configuration shown at the left. (b) Projected density of states (DOS) of the partially reduced Li 1s orbital, after adsorption on Cu(001). The Li 1s orbital is usually located in the unoccupied region, right of the Fermi level. At the surface, the Li 1s peak shifts toward the Fermi level, indicating partial reduction. The inset shows the charge density distribution. (c) Polarization orbitals (yellow) created on the Li/Cu(001) system by an external electric field of 0.2 V/Å. (d) Electric field dependence of the kinetic energy profile of Li deposition on Cu(001). Substrate and molecules are placed between two electrodes (not shown), within the Effective Screening Medium framework. Adapted from J. Mater. Chem. A, 7, 8527-8539, (2019)..... 950

Figure II.7.D.2 Effects of reaction rate and surface diffusion barrier on the development of metal nucleation morphology as calculated from KMC simulations. From *Energy Storage Materials*, 20, 1 (2019)..... 951

Figure II.7.D.3 LiTFSI decomposition on LiOH/Li. (a) Snapshots illustrating decomposition dynamics. (b) Net Bader charges of system components for DME and 1 M LiTFSI with Li/LiOH. (c) Bader charges of elements in Li and OH layer by layer, numbered as in (d). (d) Snapshot of the system at the end of dynamics. Color code: Li: purple; O: red; S: yellow; N: blue; F: light blue; C: gray 952

Figure II.7.D.4 Simulation cell contains Li metal surface (red atoms) interfacing with a solid-state electrolyte Li₉N₂Cl₃ (Li: purple, N: brown, Cl: green). (a) Input potential (red line) and potential energy profile with (black line) and without (yellow line) the application of an external electric field at 0 ps. (b) Potential energy profile (black line) at 20 ps under an external electric field along the z-axis pointing to the right. The asymptotic slope of the input potential along the slab tends to the external field of 0.5 V/Å..... 953

Figure II.7.E.1 (a) Equilibrium plating potential of Li arising due to compositional variation at the Li-metal/electrolyte interface illustrating the condition for dendrite formation. (b) Variation of Li metal plating and stripping potential for 5th-10th cycles of positive interfacial energy current collector. The plot shows large nucleation underpotential (-100mV) with growth potential of -21mV cycled at a current density of 1mA cm⁻² with plating areal capacity 2mAh cm⁻² (c) Plating and stripping potential variation with time for 92 cycles, and areal capacity 2mAh/cm² with cycle number for positive interfacial energy current collector showing poor cycle life after 60 cycles 958

Figure II.7.E.2 (a) Variation of Li metal plating and stripping potential for 25th cycles of SIA cycled at a current density of 1mA cm⁻² with plating areal capacity 0.5mAh cm⁻² (b) Variation areal capacity with cycle number of SIA showing excellent cycle life, however, low CE for first 10th cycles due to low Li ion diffusivity 958

Figure II.7.E.3 (a) Variation areal capacity with cycle number of MCA showing excellent cycle life with CE ~99.9% cycled at 1mA/cm ² . (b) Variation of Li metal plating and stripping potential for 50 th cycles of MCA showing zero nucleation underpotential and 15mV growth potential.....	959
Figure II.7.E.4 (a) Variation areal capacity with cycle number of IES showing excellent cycle life with CE ~99.4%. (b) Variation of Li metal plating and stripping potential for 96 th -100 th cycles showing 58mV growth potential	959
Figure II.7.E.5 SEM micrograph of Li metal growth front obtained after 100 cycles.....	960
Figure II.7.E.6 a) Electrochemical cycling, b) Voltage profile after 40 cycles, c) SEM after 200 cycles showing absence of dendrites, scale bar 10 microns	960
Figure II.7.E.7 Nucleation and growth behavior of carbon nano -architectures at different current rates.....	961
Figure II.7.E.8 Variation of potentials of Li plating on carbon nanoarchitectures at different current densities	961
Figure II.7.E.9 Columbic Efficiency of Li plating and deplating @1mA/cm ² , 4mAh/cm ² in Li/Li ⁺ cell.....	962
Figure II.7.E.10 Voltage vs. time (hours) profile of carbon-based electrodes at the transition region in traditional coin cell testing.....	962
Figure II.7.E.11 Schematic of the traditional and insulated coin cell testing along with the recorded performance for copper foils.....	963
Figure II.7.E.12 Columbic Efficiency of Li plating and de-plating @4mAh/cm ² , 4mAh/cm ² in Li/Li ⁺ cell (Insulated coin cell).	964
Figure II.7.F.1 (a) Electrokinetic phenomena (e.g. electrokinetic surface conduction and electroosmosis) in 3D PPS under electric field. (b) Electro-diffusion of Li ions in traditional cells under electric field. (c) Photograph of bare Cu foil and 3D PPS@Cu. (d) SEM morphology of 3D PPS@Cu (top view). (e) SEM morphology of 3D PPS@Cu (cross-section view).	967
Figure II.7.F.2 The Li-ion electrokinetic self-concentrating and pumping features of the 3D PPS. (a) Linear sweep voltammeteries of 3D PPS@Cu and bare Cu electrode, (b,c) Equilibrium Li-ion concentration profiles with constant-reaction-current electrode surfaces at the enlarged 10×10 μm ² sponge-pore scale for (b) 3D PPS@Cu and (c) bare Cu electrode. (d,e) Initial phase morphologies of 250×250 μm ² (d) 3D PPS@Cu and (e) bare Cu half-cell systems. (f,g) Equilibrium Li-ion concentration profiles with constant-reaction-current electrode surfaces at the 250×250 μm ² scale for (f) 3D PPS@Cu and (g) bare Cu electrode. (h), 1D cross-sectional equilibrium Li-ion concentration profiles along Y direction in 3D PPS@Cu and bare Cu electrode.....	967
Figure II.7.F.3 The morphology of Li metal deposited on the different electrodes. SEM images of Li metal deposited on the bare Cu electrode (a-b) and 3D PPS@Cu (c-f) at a deposition capacity of 2 mA h cm ⁻² and current density of 2 mA cm ⁻² . SEM images of Li metal deposited on the bare Cu electrode (g-h) and 3D PPS@Cu (i-l) at a deposition capacity of 6 mA h cm ⁻² and current density of 6 mA cm ⁻² . The electrolyte used here is 1.0 M LiTFSI in DOL and DME (V/V = 1) with 1 wt% LiNO ₃	968
Figure II.7.F.4 The morphology of Li metal deposited on the 3D PPS@Cu at different deposition capacities and current densities. LiTFSI/DOL+DME+1 wt% LiNO ₃	968
Figure II.7.F.5 The morphology of Li metal deposited on the 3D PPS@Cu at extremely high current densities and a deposition capacity of 4 mA h cm ⁻² . (a-d) At a current density of 12 mA cm ⁻² . (e-h) At a current density of 20 mA cm ⁻² . The electrolyte used here is 1.0 M LiTFSI/DOL+DME+1 wt% LiNO ₃	968
Figure II.7.F.6 The morphology of Li metal deposited on the bare Cu electrode and 3D PPS@Cu at -10°C with a high current density of 20 mA cm ⁻² and a deposition capacity of 4 mA h cm ⁻²	968
Figure II.7.F.7 The morphology of Li metal deposited on the bare Cu electrode and 3D PPS@Cu at -10°C with a high current density of 20 mA cm ⁻² and a deposition capacity of 4 mA h cm ⁻²	968

- Figure II.7.F.8 (a), CE of Li deposition on 3D PPS@Cu and bare Cu electrode at a current density of 2 mA cm^{-2} and a deposition capacity of 2 mA h cm^{-2} . (b), CE of Li deposition on 3D PPS@Cu and bare Cu electrode at a current density of 4 mA cm^{-2} and a deposition capacity of 4 mA h cm^{-2} . (c), CE of Li deposition on 3D PPS@Cu and bare Cu electrode at a current density of 6 mA cm^{-2} and a deposition capacity of 6 mA h cm^{-2} . (d), Cycling performance of full cells (N/P ratio: 0.6) using 1.5 mA h cm^{-2} Li on 3D PPS@Cu and bare Cu electrode as anodes, respectively. (e-h), SEM images of Li@3D PPS@Cu in full cell after 50 cycles. (i), Cycling performance of full cells (N/P ratio: 2) using 7.7 mA h cm^{-2} Li on 3D PPS@Cu as anodes and high-areal-capacity LiFePO_4 as cathodes (3.8 mA h cm^{-2})..... 969
- Figure II.7.F.9 Optical images of (a) just mixed solution of starting materials, (b) after 10 h. Optical images of (c) just mixed solution of starting materials on SS foil and (d) after drying overnight under vacuum..... 969
- Figure II.7.F.10 High-resolution XPS spectra of Cl 2p, C 1s and S 2p for (a and b) pure chlorine-rich polymer, (c) Sn--containing trifunctional crosslinker lithium polysulfidophosphate and (d-f) polymer-PxSy film..... 970
- Figure II.7.F.11 (a,b) Top-view and (c) side-view SEM images of the as-prepared MSCP film on SS foil 971
- Figure II.7.F.12 (a,b) Top-view and (c) side-view SEM images of deposited Li on bare SS foil after 10 cycles. (d,e) Top-view and (f) side-view SEM images of deposited Li on MSCP protected SS foil after 10 cycles. The cells were cycled at 2 mA cm^{-2} and 2 mAh cm^{-2} 971
- Figure II.7.F.13 S 2p, P 2p, Cl 2p, and Li 1s XPS spectra of (a)–(d) MSCP-SEI and (e)–(h) control SEI. (i) Elemental composition comparison of control SEI and MSCP-SEI calculated on the basis of the XPS spectra 971
- Figure II.7.F.14 C 1s, F 1s, and N 1s XPS spectra of (a-c) MSCP-SEI and (d-f) control SEI..... 972
- Figure II.7.F.15 CEs of cells using bare (black) and MSCP protected (red) SS foil versus cycle number at (a) 1 mA cm^{-2} and 1 mAh cm^{-2} , (b) 2 mA cm^{-2} and 2 mAh cm^{-2} , (c) 2 mA cm^{-2} and 3 mAh cm^{-2} , and (d) 2 mA cm^{-2} and 4 mAh cm^{-2} 972
- Figure II.7.F.16 (a) Cycling performance of symmetric cells using bare (black) or MSCP protected (red) Li metal foils cycled at 2 mA cm^{-2} and 2 mAh cm^{-2} . (b) Cycling performance of $\text{Li}||\text{LFP}$ full cells using bare (black) and MSCP protected (red) Li metal as anode at 0.5 C ($1 \text{ C} = 170 \text{ mAh/g}$). (c) Cycling performance of anode-free $\text{SS}||\text{LFP}$ cells using bare SS foil (black) and MSCP protected (red) SS foil as anode at 0.5 C 973
- Figure II.7.F.17 (a) Electrokinetic phenomena (i.e. electrokinetic surface conduction) enhance Li-ion transport in the leaky film under applied electric field in the electrolyte. (b-d) SEM morphology of the PPS leaky film. e) The linear sweep voltammetries of PPS@stainless steel (PPS@SS) and bare SS electrodes..... 974
- Figure II.7.F.18 The morphologies of Li metal deposited on the PPS@Cu at (a–c) a deposition capacity of 2 mAh cm^{-2} and a current density of 1 mA cm^{-2} , (d–f) a deposition capacity of 4 mAh cm^{-2} and a current density of 2 mA cm^{-2} , (g–i) a deposition capacity of 6 mAh cm^{-2} and a current density of 2 mA cm^{-2} 974
- Figure II.7.F.19 The morphology of Li metal deposited on the PPS@Cu at different deposition capacities and current densities. (a-c) 6 mA h cm^{-2} and 6 mA cm^{-2} . (d-f) 4 mA h cm^{-2} and 10 mA cm^{-2} . (g-i) 4 mA h cm^{-2} and 20 mA cm^{-2} . (j-l) 4 mA h cm^{-2} and 40 mA cm^{-2} 974
- Figure II.7.F.20 Electrochemical performance of PPS@Cu and bare Cu foil electrodes. CE of Li plating/stripping on PPS@Cu and bare Cu foil at a current density of 1 mA cm^{-2} and a deposition capacity of 2 mA h cm^{-2} (a), at a current density of 2 mA cm^{-2} and a deposition capacity of 4 mA h cm^{-2} (b), and at a current density of 2 mA cm^{-2} and a deposition capacity of 6 mA h cm^{-2} (c). (d) Cycling stability of symmetric cells using PPS leaky film protected Li metal as electrodes 975
- Figure II.7.F.21 Cycling performance of full cells using PPS leaky film protected Li metal as anodes and NCM-811 as cathodes. (a) Flooded electrolyte. (b) Lean electrolyte of $5 \text{ }\mu\text{l}/\text{mA h}$. (c) Lean electrolyte of $3 \text{ }\mu\text{l}/\text{mA h}$. The photo image of Li foil protected by PPS leaky film ($20 \text{ cm} \times 15 \text{ cm}$) is shown as an inset in (a), the thickness of Li foil is $120 \text{ }\mu\text{m}$. The areal capacity of NCM-811 cathode is around 4.2 mA h cm^{-2} 975
- Figure II.7.F.22 (a) The photos of prepared FSS electrodes. (b) FT-IR spectra of FSS electrode..... 976

Figure II.7.F.23 Li_2S_6 adsorption of FSS electrodes.....	976
Figure II.7.F.24 (a) The cycling performance of the FSS electrode with various S mass loading of 6, 8.78 and 10 mg cm^{-2} at an E/S ratio of 10 $\mu\text{l mg}^{-1}$. The cycling performance of the FSS electrodes with the S mass loading of 11 mg cm^{-2} at the E/S ratios of 5 $\mu\text{l mg}^{-1}$ (b) and 3 $\mu\text{l mg}^{-1}$ (c). The electrolyte used here is 1 M LiTFSI/DOL+DME+4 wt% LiNO_3	977
Figure II.7.F.25 (a) Cycling performance of the FSS electrodes with the S mass loading of $\sim 11.67 \text{ mg cm}^{-2}$ at the E/S ratios of 5 $\mu\text{l mg}^{-1}$. (b) Cycling performance of the FSS electrodes with the S mass loading of $\sim 8.3 \text{ mg cm}^{-2}$ at the E/S ratios of 3.5 $\mu\text{l mg}^{-1}$	977
Figure II.7.G.1. Examples of generated digital microstructures of polycrystalline LLZO with (a) different grain sizes; and (b) different grain boundary thicknesses.....	981
Figure II.7.G.2. Workflow for computing the effective ionic diffusivity/conductivity of reconstructed digital representation of a solid electrolyte microstructure.....	981
Figure II.7.G.3. Characterized kink temperatures of computed temperature-dependent ionic conductivities of polycrystals with (a) increasing grain size; and (b) increasing grain boundary thickness.....	982
Figure II.7.H.1 Morphology of LLZTO powders under various high-energy ball milling conditions. (a) Raw powders purchased from MTI Corporation. (b) Dry milled powders. (c-i) powders milled in medium including (c) H_2O , (d) hexane, (e) acetonitrile, (f) mineral oil, (g) hexane with oleic acid, (h) acetonitrile with Triton X-100, (i) ethanol. Milling beads are 0.1-0.2 mm YSZ, time is 60 min.....	986
Figure II.7.H.2 (a) XRD of powders before ball milling (black), and after ball milling in acetonitrile/Triton X-100 (red) and ethanol (blue). x values in (Li_x) represent Li contents in $\text{Li}_x\text{La}_3\text{Zr}_{1.4}\text{Ta}_{0.6}\text{O}_y$ measured from ICP-OES. (b) XRD of corresponding 1100 °C sintered pellets. (c-e) SEM images of corresponding 1100 °C sintered pellets.....	986
Figure II.7.H.3 (a-d) and (e-h) are SEM images of pristine and MT-milled LLZTO powder pellets sintered at 950°C, 1000°C, 1050°C, and 1100°C, respectively. (i) Relative density of LLZTO pellets (black: raw powder; Red: MT-milled powder; Green: ball milled LLZTO with 5 wt% Li_3BO_3 powder) sintered at different temperatures. The green circle is the density of sintered LLZO with Li_3BO_3 additive reported in the literature. [7].....	987
Figure II.7.H.4 PEGDA recipe: 3D printing and post sintering. PEGDA/LLZTO ink was first printed as a thin film using the paste PuSL system, and then zig-zag structures with varying spacings (a-c) were printed on top using DIW. (d) A honeycomb structure on a film substrate. Inset is an 3D optical image of a piece after 1100°C sintering. (e) Cross-section SEM image of the printed film after sintering, showing high densification with thickness of $\sim 50 \mu\text{m}$. (f) Surface.....	988
Figure II.7.H.5 Sintering of DIW-extruded LLZTO filaments. (a) 1100°C furnace-sintered filament from raw powder LLZTO/NMP (83 wt%) ink. (b) 1100°C furnace-sintered filament from ball milled LLZTO/NMP (73 wt%) ink. (c-e) In situ tomography results from halogen lamp sintering of ball milled LLZTO filament. Sintering temperature is proportional to the applied current of the lamp heating source.....	989
Figure II.7.I.1 (a) Chemical structures of the liquid compounds studied in this work. (b) Lithium/Lithium cycling at 0.5 mA/cm^2 to 0.5 mAh/cm^2 as a function of electrolyte content. (c) Li/Li cycling at 1 mA/cm^2 to 1 mAh/cm^2 as a function of hexane content in the electrolyte. The ratios (e.g., 1:1) represent volume ratios. Salt concentration: 0.1 M LiTFSI.....	993
Figure II.7.I.2 (a) SEM image of the lithium deposition morphology at a current rate of 1 mA/cm^2 to 0.1 mAh/cm^2 as a function of electrolyte content. (b) ^7Li NMR chemical shifts of 0.1 M LiTFSI in the respective electrolytes. The dashed line in (b) demarcates the ^7Li chemical shift of LiTFSI in DOL, and the ‘deshielding’ and ‘shielding’ is made with respect to the peak.....	994
Figure II.7.I.3 a, Chemical structure of PDMS Self-Healing Polymer (SHP). b, FTIR Spectra of the PDMS-IDPI with varying size of PDMS soft block in the co-polymer. c, Oscillatory shear measurements at stain 1% for the different PDMS based self-healing polymers.....	995

- Figure II.7.I.4 **a**, Chemical structure of PDMS-IDPI Self-Healing Polymer. **b**, FTIR Spectra of the PDMS SHP with varying size of PDMS soft block in the co-polymer..... 996
- Figure II.7.I.5 **a**, Typical voltage profile of Li||PDMS-SHP@Cu cells. **b**, Coulombic efficiency comparisons of the PDMS SHP with varying size of PDMS soft block as well as H-bonding strengths in the co-polymer..... 996
- Figure II.7.I.6 **a**, Oscillatory shear measurements at strain 1% for the different self-healing polymers. **b**, Coulombic efficiency comparisons of the polymer SHP with varying H-bonding strengths in the co-polymer 997
- Figure II.8.A.1 (a) Voltage profiles of Li plating/stripping cycling with a current density of 0.5 mAcm^{-2} at room temperature (inserted: voltage profiles of PEO and PEO/LLTO tested at 201–203 cycles - left; voltage profile of PEO/LLTO at 990–1000 cycles - right). (b) Cycling performance of full-cell battery tested at 0.05 C (0.084 mAcm^{-2}) with a sulfur loading of 1.27 mg cm^{-2} . (c) Charge/discharge curves and (d) rate capability of the full cell tested at 0.05 C (0.084 mAcm^{-2}), 0.1 C (0.168 mAcm^{-2}) and 0.2 C (0.335 mAcm^{-2}) 1000
- Figure II.8.B.1 (a) POSS-PEO-POSS (5-35-5) chemical structure (b) Example of a routine used to test the limiting current of POSS-PEO-POSS (5-35-5)..... 1004
- Figure II.8.B.2 Voltage as a function of time during preconditioning cycles for a lithium symmetric cell and a POSS-PEO-POSS/LiTFSI $r = 0.04$ electrolyte. This cell was cycled at a current density of 0.02 mA cm^{-2} without significant increase in resistance over 10 cycles..... 1005
- Figure II.8.B.3 Nyquist plot of a lithium symmetric cell before and after the conditioning cycles shown in Fig. 1. Bulk resistance was unchanged and interfacial resistance increased by approximately 10%. Frequencies sampled were 1 Hz to 1 MHz with 30 mV perturbations 1005
- Figure II.8.B.4 Interfacial resistance of PEO-POSS 5k-1k with ethyl, isobutyl, and isoctyl end groups as a function of salt concentration..... 1006
- Figure II.8.B.5 ^7Li NMR spectra (open circles) of (a) 5 kg mol^{-1} (b) 35 kg mol^{-1} and (c) 275 kg mol^{-1} PEO annealed against lithium metal for 12 days at 130°C in a coaxial NMR tube with a reference solution in the outer compartment. Red lines are fits to the experimental data. (d) Lithium molality as a function of PEO molecular weight..... 1007
- Figure II.8.B.6 Conductivity of 35 kg mol^{-1} PEO, containing no lithium salts, annealed at 120°C in a lithium symmetric cell (closed symbols) and a stainless-steel symmetric cell (open symbols) as a function of time 1008
- Figure II.8.B.7 (a) Impurities are present in lithium as-received. Cross-sectional slice through cell with additional cross section of pure lithium showing impurity particles. (b) Volume reconstruction of volume of lithium as-received with highlighted impurity particles and a volume density 1009
- Figure II.8.B.8 Correlation between current density and defect density in failed cells. The areal density of protruding defects, P , increases with current density 1009
- Figure II.8.B.9 Slice through a reconstructed volume imaged using X-ray tomography. This Li/POSS-PEO-POSS/Li cell was cycled at 0.175 mA cm^{-2} and failed after 17 cycles 1010
- Figure II.8.B.10 Strategy of the electrochemical filtering treatment to push impurity particles away from the interface. (a) Schematic of the electrochemical filtering treatment. After symmetric cell fabrication, some impurity particles, shown as white triangles, lie at the electrode-electrolyte interface. Step 1: with a sufficiently low current density, new planar lithium, highlighted in orange, can be deposited onto the bottom electrode to create a layer free of impurity particles. Step 2: by reversing the direction of current, planar lithium may be plated on to the upper electrode, such that the both electrodes now have a layer of impurity-free lithium at the electrode-electrolyte interface. (b) Current density and voltage of one electrochemical treatment over time. Lithium was charged at 0.04 mA cm^{-2} for 43.75 h ($8.5 \text{ }\mu\text{m}$ of Li calculated) and discharged at the same current density for 8.75 h ($1.7 \text{ }\mu\text{m}$ of Li calculated). (c) Slice through a reconstructed volume of a symmetric cell as-fabricated after 14 conditioning cycles. No inhomogeneities were observed at the interfaces. (d) Slices through a reconstructed volume of the symmetric cell in Fig. 2c after an electrochemical filtering treatment. Yellow dashed lines indicate the calculated height of lithium after the treatment. This cell charged a calculated $38 \text{ }\mu\text{m}$

of lithium, and discharged a calculated 19 μm of lithium. Impurity particles are visibly pushed away from the electrode-electrolyte interface. (e) Slices through a reconstructed volume of the symmetric cell in Fig. 2d after an electrochemical filtering treatment. Yellow dashed lines indicate the calculated height of lithium after the treatment. Some impurity particles still remain adhered to the polymer electrolyte after the treatment 1010

Figure II.8.B.11 Galvanostatic cell cycling example and results. (a) Current density and voltage of the first cycles at 0.12 mA cm^{-2} for one cell. During each cycle, current was applied for 4 h at -0.12 mA cm^{-2} (2.3 μm of Li calculated), no current was applied for 45 minutes, current was applied for 4 h at 0.12 mA cm^{-2} , and no current was applied for 45 minutes. (b) Charge passed before failure, Cd, plot for each group's control and treated cells. Details of the electrochemical filtering treatment are found in Figure II.8.B.4. The transparent circles indicate control cells, while the filled-in squares indicate treated cells. Hollow diamonds indicate the average of cells in the column. Dashed lines connect the averages of control and treated cells in each group. The asterisk indicates a cell which has not yet failed. Treatment 1 cells were cycled at 0.12 mA cm^{-2} , while Treatment 2 and 3 cells were cycled at 0.175 mA cm^{-2} 1011

Figure II.8.B.12 Representative cross section of cell polarized at $i = 0.04 \text{ mA cm}^{-2}$ for $t = 900 \text{ h}$ acquired using X-ray tomography. Lithium was deposited downward through the polymer electrolyte, which appears as a light band extending across the cell near the top of the cross-section. No lithium protrusions were observed. This cell did not short circuit. The yellow arrow shows the thickness of the electrochemically deposited lithium, 190 μm , at a representative location based on the analysis of the tomograms, using the electrolyte's original position at the edge of the cell as a reference point. The light blue arrow shows for comparison the estimated thickness of electrochemically deposited lithium, 175 μm , based on the current passed through the cell 1011

Figure II.8.B.13 Comparison of the calculated and experimental limiting currents of a POSS-PEO-POSS hybrid inorganic-organic block copolymer electrolyte and a PS-PEO all-organic block copolymer electrolyte. In each case, the calculated limiting current is higher than the experimental limiting current due to considerations for transport in the concentrated solution regime. The limiting current of the POSS-PEO-POSS electrolyte is both higher and proportionally closer to its calculated limiting current than the PS-PEO 1012

Figure II.8.C.1 (a) Schematic of the experimental design in the initial state, after plating Li on the Ni current collector and after interface formation and stripping of the Li. (b) Photographs of one cell taken through the Sapphire wafer in the initial state, after the first plating, and after the first stripping cycle. (c) Plating and stripping curves for a representative cell. (d) Nyquist plots for electrochemical impedance spectroscopy (EIS) of the cell in (c) in its initial state and after plating Li metal 1017

Figure II.8.C.2 Plating and stripping profile of a Cu foil/PEO-LiTFSI/Li metal cell 1018

Figure II.8.D.1 Structural characterization of $\beta\text{-Li}_3\text{PS}_4$ prepared through a solution-based route showing (a) X-ray diffraction (XRD) patterns and (b) Raman spectra of the precursors and annealed powders. (c) Crystallographic structure of $\beta\text{-Li}_3\text{PS}_4$. In (b), the broad background at $2\theta < 30^\circ$ are due to the Kapton film which was used to prevent air exposure during the XRD measurements 1021

Figure II.8.D.2 Ionic conductivity measurements of $\beta\text{-Li}_3\text{PS}_4$ solid electrolyte pellets. (a) Conductivity cell configuration, (b) representative Nyquist plots of a C/ $\beta\text{-Li}_3\text{PS}_4$ /C cell at 23-78°C, and (c) Arrhenius plots showing ionic conductivity as a function of temperature for C/ $\beta\text{-Li}_3\text{PS}_4$ /C and Li/ $\beta\text{-Li}_3\text{PS}_4$ /C cells 1022

Figure II.8.D.3 AC impedance measurements on a Li/ $\beta\text{-Li}_3\text{PS}_4$ /C cell used to determine the oxidative stability limit of the $\beta\text{-Li}_3\text{PS}_4$ solid electrolyte. (a) Nyquist plots collected by polarizing the C electrode between 2.2 – 3.7 V vs. Li/Li⁺ and (b) effective total cell capacitance as a function of cathode potential. The sharp decrease in capacitance at potentials > 2.6 V vs. Li/Li⁺ is attributed to formation of a passive film at the C electrode ... 1022

Figure II.8.D.4 Structural characterization of a- Li_3PS_4 + PEO composite solid electrolytes. (a) XRD patterns of composites containing 0.2 – 56 wt% PEO. (b) XRD patterns of a- Li_3PS_4 + 1 wt% PEO after heating for 12 h at 25 – 250°C. The broad background at $2\theta < 30^\circ$ are due to the Kapton film which was used to prevent air exposure during the XRD measurements..... 1023

Figure II.8.D.5 Raman spectra of a- Li_3PS_4 + 1 wt% PEO after heating for 12 h at 25 – 250°C showing (a) 100-1,000 cm^{-1} and (b) 1,000 – 3,500 cm^{-1} regions 1024

Figure II.8.D.6 Li^+ conductivity for several $\alpha\text{-Li}_3\text{PS}_4 + \text{PEO}$ composite solid electrolytes. The sample denoted $\alpha\text{-Li}_3\text{PS}_4 + 5\%$ PEO/LiTFS contained PEO/lithium trifluoromethanesulfonate (LiTFS) in a 12/1 molar ratio, and the total PEO+LiTFS content was 5 wt%. Li^+ conductivity of crystalline $\beta\text{-Li}_3\text{PS}_4$ is shown for comparison.....	1024
Figure II.8.D.7 (a) Li-P-S ternary phase diagram. Due to limited available thermodynamic quantities (e.g., free energies of formation), not all tie lines are known for this system. (b) X-ray diffraction (XRD) patterns of LiPS_3 and catenated $\text{LiPS}_3\cdot\text{S}$ cathode powders. The sloping profiles at $2\theta < 30^\circ$ are due to the Kapton film which was used to prevent air exposure during the XRD measurements	1025
Figure II.8.E.1 Bulk Stability of doped-LLZO in Contact with Metallic Li: (a) Nb 3d and (b) Zr 3d core level XPS spectra and (c) Al L-edge XAS spectra reveals (a) the reduction of Nb, (b) no reactivity of Zr for all doped LLZO, and (c) no reactivity of Al	1029
Figure II.8.E.2 Galvanostatic cycling of Al- doped LLZO: a) Symmetric Li/Al-LLZO /Li coin cell cycled with the current density of 4 mA cm^{-2} b) Charge and discharge voltage profiles after 3h of cycling c) Charge and discharge voltage profiles after 14h of cycling	1031
Figure II.8.E.3 Effect of LLTO Crystallinity on Reactivity with Metallic Li (a) XPS and (b) XAS spectra of amorphous LLTO film after contacting with Li metal. (c) XAS of crystalline LLTO films after reaction with Li	1032
Figure II.8.E.4 Li-LLTO Ab Initio Molecular Dynamics: AIMD trajectories for (a) Li/LLTO (001) interface; (b) Li/LLTO (100) interface and (c) Li/amorphous LLTO interface. Initial atomic positions are shown with balls, and Li ion trajectories are shown with black lines	1033
Figure II.8.F.1 Illustration of transport challenges, both ionic and electronic identified and addressed in this work	1036
Figure II.8.F.2 Illustration of the transport challenges, both ionic and electronic identified and addressed in this work	1037
Figure II.8.F.3 Voltage profile of a 12 V cell architecture with a modified electrode aspect ratio. The cell cycled between 7.5 V and 13.5 V following a charge protocol with incremental capacity cutoffs of 13%, 26%, and 52% of the theoretical capacity in the first 3 cycles and maintaining its maximum cutoff after the 3 rd cycle.....	1037
Figure II.8.F.4 Impact of electrolyte additive on the utilization of the positive electrode for 12 V self-formed cells cycled between 7.5 and 13.5 V. The cells were charged at constant voltage with incremental capacity cutoffs of 13%, 26%, and 52% of the theoretical capacity in the first 3 cycles showing that when the capacity limitation is lifted, the solid state electrolyte additive improves the performance appreciatively	1038
Figure II.8.F.5 Comparison of the positive electrode utilization and electrode pairs' energy density for the 12 V cell configuration with variations on the cell design. The variations that were tested include electrode aspect ratio, electrolyte thickness, and electrode spacing	1039
Figure II.8.F.6 Comparison of the positive electrode utilization and electrode pairs' energy densities for the single cell configuration with variations in cell design. Variations include orientation, electrode aspect ratio and electrode spacing	1039
Figure II.8.F.7 Positive electrode utilization (%) for single cell configurations with different lithium ion dopant quantities, in the first cycle. The cells were cycled between 1.5 V and 3.5 V	1040
Figure II.8.F.8 Positive electrode utilization (%) of optimized single cell designs, without and with nanolayered multicomponent electrodes in the first two cycles. Cells were cycled between 1.5 V and 3.5 V	1041
Figure II.8.F.9 Positive electrode utilization (%) for the first cycle of single cell configurations with 90 micron spacing and different hybrid electrolyte compositions. The cells were cycled between 1.5 V and 3.5 V	1041

Figure II.8.F.10 Cycling efficiency (%) comparison for the first four cycles of single cell configurations with lithium enrichment, nanolayered electrode composition, and the optimized cell design. The charge capacity cutoffs were varied. The cells were cycled between 1.5 V and 3.5 V	1042
Figure II.8.G.1 ^1H DOSY-NMR spectra of (a) 1:1 VC:EMC, (b) 1:4:4 LiPF_6 :VC:EMC, (c) 1:1 VEC:EMC and (d) 1:4:4 LiPF_6 :VEC:EMC with toluene added as an internal reference	1046
Figure II.8.G.2 Voltage profiles for Li/Li symmetric cells cycled at 2 mA cm^{-2} with Gen2 with 2% VC and Gen2 with 2% VEC electrolytes	1047
Figure II.8.H.1 Structure of LLZO (001) and NMC (10 –14) interface that is calculated using density functional theory	1050
Figure II.8.I.1 Cell Design A: (A) pre-charge AC Impedance, (B) Comparison of first cycle charge curve.	1054
Figure II.8.I.2 Coulombic efficiency under extended cycling in cell constructions B I-B IV with comparison to A I.	1054
Figure II.8.I.3 Cell Design A: (A) EIS (B) Resistance v. cycle, (C) Cycling, (D) Coulombic efficiency v. cycle number.	1054
Figure II.8.I.4 Coulombic efficiency in cell constructions B I, B III, B IV and A I at (A) higher and (B) lower DoD at 40°C and Impedance measurements at elevated temperature prior to charging, charged, and fully discharged for cell designs B I, B III, and A I.	1055
Figure II.8.I.5 X-ray diffraction of composite solid electrolyte A) Prior to cell assembly, B) Removed from cell after charge	1055
Figure II.8.I.6 SEM/EDS analysis of cells post charge, L) Cathode side, R) Anode side	1055
Figure II.8.I.7 EDXRD stack plot for uncharged LiI solid electrolyte with LiI(HPN)_2 additive.....	1056
Figure II.8.I.8 EIS of Control, Process I, II, III A) Before charge, B) After charge to 0.5%, and C) Discharge profile.....	1056
Figure II.8.I.9 Demonstration of self-healing A) Under high current density, B) Same cell cycled under lower current density.....	1057
Figure II.9.A.1 Raman spectra of siloxane, DOL and siloxane-based electrolytes with increased concentration in the Raman shift range of (a) 580-650 cm^{-1} and (b) 730-760 cm^{-1} . Typical snapshot of the optimized structures of (c) 1M and (d) 5M siloxane-based electrolytes using ab initio molecular dynamics (AIMD) simulation. (e) Small angle X-ray scattering (SAXS) result of siloxane-based electrolytes with increased concentration. (f) calculated solvation-ion-exchange energy in different solvents. (g) Snapshot of simulated structure of Li_2S_6 in 5M siloxane-based electrolyte determined by AIMD simulation	1059
Figure II.9.A.2 BET measurement results of two highly porous carbon (HPC) hosts in this study: (a) HPC1 and (b) HPC2	1060
Figure II.9.A.3 Cycle performance of S-HPC1 (70 wt.% S) composite in (a) dilute ether, (b) concentrated ether and (c) concentrated siloxane electrolytes. (d) Coulombic efficiency comparison in different electrolytes. (e) Charge/discharge profiles and (f) cycling performance of S-HPC2 (70 wt.%) composite in concentrated ether electrolytes	1060
Figure II.9.A.4 (a) Representative current relaxation curve collected to extract the static leakage current. (b) Leakage current measurement of S-HPC1 composite in different electrolytes. (c) in situ HEXRD characterization on S-HPC1 composite in concentrated ether electrolytes.....	1060
Figure II.9.A.5 Li metal plating/stripping in Li/Li symmetric cells in (a) dilute ether and (b) concentrated electrolytes at 1.25 mA cm^{-2} with an areal capacity of 1.25 mAh cm^{-2} . SEM image of Li metal and corresponding EDX mapping in different electrolytes: (c, f) dilute ether, (d, g) concentrated ether and (e, h) concentrated siloxane electrolytes	1061

- Figure II.9.A.6 (a) S 2p spectra of Li metal in the Li/S-HPC1 cells after 20 cycles in different electrolytes at C/10. F 1s spectra of Li metal in Li/S-HPC1 cells after 20 cycles in different electrolytes: (b) dilute ether; (c) concentrated ether and (d) concentrated siloxane 1062
- Figure II.9.A.7 Flammability test: (a) dilute ether; (b) concentrated ether and (c) concentrated siloxane 1063
- Figure II.9.B.1 Schematic of the hybrid electrode design, in which solid electrolyte and liquid electrolyte are filled in the big voids and small pores of electrode, respectively, to enable the robust Li-ion conduction networks in sulfur cathode. 1066
- Figure II.9.B.2 (a) XRD patterns of the glass phase (bottom), LT-LPSBI (middle) and HT-LPSBI (top). (b) Nyquist plot of an In-SE-In (SE = LT-LPSBI) cell tested at various temperatures. (c) STEM of LT-LPSBI powder. (d) Low magnification TEM image of the primary particle edge. (e) Electron diffraction of the circled region in panel d 1067
- Figure II.9.B.3 (a) Cyclic voltammogram for a C-SSE/SSE/Li cell at a scan rate of 5 mV/s (SSE=LT-LPSBI). (b) Nyquist plots of a Li/SSE/Li cell at room temperature as a function of time (voltage modulation was 5 mV). (c) The effect of exposure to dry room atmosphere on the ionic conductivity of LT-LPSBI. σ_x is the ionic conductivity at x h. (d) Li/SSE/Li cell cycling at different areal current densities with 1h duration for each step..... 1067
- Figure II.9.B.4 (a) Nyquist plot of a S-SE/SE/Li cell at room temperature for the frequency range of 100 kHz to 0.01 Hz (voltage modulation was 5 mV, SE=LT-LPSBI). (b) First two cycle charge/discharge curves of the S/SE/Li cell. (c) Photo image of the high-loading and free-standing sulfur cathode. (d) Cross-section SEM of the S electrode (S 4.4mg/cm²) 1068
- Figure II.9.B.5 Interfacial stability of liquid electrolytes with Li anode and SSE contained sulfur cathode. Nyquist plots of Li/Li symmetric cells with (a) 1M LiTFSI/DOL/DME+0.3M LiNO₃ (E-121), (b) solvated ionic liquid electrolyte (E-SIL), (c) room temperature ionic liquid electrolyte (E-IL), and (d) corresponding overall resistance evolution with a test duration of 10 hours. Nyquist plots of Li-S cells with a) E-121, b) E-SIL, c) E-IL, and d) corresponding overall resistance evolution with a test duration of 10 hours 1069
- Figure II.9.C.1 (a) Schematic of the electrochemical cell design that allows in-operando dark field light microscopy (DFLM) observation. (b and c) DFLM images of the metal grid (50 nm thick, 1 μ m wide) fabricated on glass slide as a substrate for the electrochemical cell. (d) Voltage profile of the cell. Time-lapse DFLM images (e-i) showing the formation and dissolution of super-cooled sulfur droplets. (j, k) Two sets of time-lapse images showing rapid merging of neighboring droplets and relaxation to spherical shape within one second, indicating the liquid nature of sulfur. (l) In situ Raman spectra of super-cooled sulfur droplets. Corresponding bright field light microscopy images captured by the Raman microscope are shown on the right. The spectra match that of solid S₈ powder, and the signals are not from electrolyte or substrate 1074
- Figure II.9.C.2 (a) *In-operando* DFLM images of sulfur droplets electrochemically formed on Pd, Pt, indium tin oxide (ITO) and cobalt sulfide (CoS₂) substrates. (b) Time-lapse *in-operando* DFLM images of crystalline sulfur formation and dissolution on glassy carbon substrate 1075
- Figure II.9.C.3 (a) DFLM image of exfoliated graphite nano-platelets dispersed on Ni metal grid for growing solid and liquid sulfur in the same cell. (b) High-magnification bright field light microscopy image of a single nano-platelet sitting on Ni grid, as shown in the red box in (a). (c) *In-operando* DFLM image of the cell after charging, showing co-existing needle-shape sulfur microcrystals and metastable sulfur droplets. (d-h) Time-lapse DFLM images showing the approaching of a needle-shaped sulfur microcrystal towards a sulfur microdroplet and its rapid solidification upon touching 1076
- Figure II.9.C.4 (a and b) Time-lapse light microscopy images of the initial formation of sulfur droplets, one on the Ni grid (a) and another off the Ni grid on glass (b). (c) Two general mechanisms for the nucleation and growth of sulfur on electrodes. The solution mechanism is consistent with the results in both (a) and (b) ... 1077
- Figure II.9.C.5 (a) Charge/discharge voltage profiles of the Ni, C, and Al electrodes at a current density of 0.05 mA cm⁻². (b) Cycling stability of the Ni, C, and Al electrodes at a current density of 0.05 mA cm⁻² for 50 cycles. (c) Comparison of the rate capacity of the Ni, C, and Al electrodes. (d) Nyquist plots of the Ni and C

electrodes at open circuit before cycling at room temperature. Inset is the Nyquist plot of the Al electrode at open circuit before cycling at room temperature	1078
Figure II.9.C.6 Optical images of the Al electrode in lithium polysulfide electrolyte (a) at initial state, (b) after charging to 3.0 V, and (c) after discharging to 1.0 V. Optical images of the C electrode in lithium polysulfide electrolyte (d) at initial state, (e) after charging to 3.0 V, and (f) after discharging to 1.0 V. Optical images of the Ni electrode in lithium polysulfide electrolyte (g) at initial state, (h) after charging to 3.0 V, and (i) after discharging to 1.0 V	1079
Figure II.9.C.7 SEM images of the discharging products formed on the (a) Al, (b) C, and (c) Ni substrates. Inset in (c) is the magnified area indicated by the red circle. SEM images of the charging products formed on the (d) Al, (e) C, and (f) Ni substrates. Inset in (e) is the magnified area indicated by the red circle. (g) Li 1s XPS spectra of the Ni and C substrates. (h) S 2p XPS spectra of the Ni and C substrates.....	1080
Figure II.9.C.8 Schematic illustration of the sulfur species evolution on (a) Ni, (b) C, and (c) Al substrates during charging and discharging processes	1081
Figure II.9.D.1 Prevent dissolution of the polysulfide ions and their reaction with the anode	1083
Figure II.9.D.2 Example of synthesis route of a sulfur co-polymer compound. Chalker et al, Green Chem. 2017,19,2748	1084
Figure II.9.D.3 The selection of possible cross-linking groups for the co-polymers.....	1084
Figure II.9.D.4 Comparison of relative capacity retention of three selected copolymer cathodes	1085
Figure II.9.D.5 Copolymerize sulfur with p-Phenylene vinylene to form crosslinked sulfur-rich S/Xant-copolymer	1086
Figure II.9.D.6 Rate performance of a coin cell made of fully prelithiated Phosphorus anode and 75% Sulfur/carbon cathode (up); the cyclability of the cell (low). copolymer	1086
Figure II.9.D.7 Schematic illustration of the S/P batteries (low/left); rate and cycling performance of a fully prelithiated P/C anode prepared through patented chemical methods (up); typical voltage profiles at different current densities (d). Insert is the theoretical and practical energy densities of the S/P LIB (low/right).....	1088
Figure II.9.D.8 (A) The sulfur cathode is a polymeric sulfur (co-polymerization with monomer) electrode, the averaged capacity is 0.805 mAh discharge/charge; (B) The sulfur cathode is an elemental sulfur electrode, the averaged capacity is 2.075 mAh discharge/charge at 50uA between 1.8 to 2.8V	1088
Figure II.9.D.9 Cycle life of sulfur and polymer sulfur cathodes with metal sulfide additives	1088
Figure II.9.E.1 Schematic representation of the FC surface with attached polysulfide molecule (removal of Li or S atom represents reaction 1 or 2, respectively) and free energies of reaction 1 and 2 for different FCs and polysulfides.....	1092
Figure II.9.E.2 Electrochemical cycling of PTA-DDSA electrode using the Batt 500 lean electrolyte protocol	1093
Figure II.9.E.3 Li ion conductivity of the doped LICs predicted by theoretical analysis using DFT	1093
Figure II.9.E.4 a) EIS analysis of the Li-S batteries fabricated using the doped LIC coated sulfur electrodes as cathodes; Figure b) Cycle life performance of the doped and undoped LIC coated sulfur cathodes cycled at a rate of 0.2C	1094
Figure II.9.E.5 Synthesis of Cu-bpy-CFM and sulfur infiltrated S-Cu-bpy-CFM electrodes (EnergyTechnol.2019, 1900141, https://doi.org/10.1002/ente.201900141)	1094
Figure II.9.E.6 (a): Cycling performance of doped and undoped LIC coated S-Cu-bpy-CFM cathodes cycled at a rate of 100 mA/g. Figure II.9.E.2(b): Rate capability performance of the doped and undoped LIC coated S-Cu-bpy-CFM cathodes.....	1095
Figure II.9.E.7 a: Cycling performance of EC-CFM-S and 7b: Cycling performance of LIC-CFM-S	1095

Figure II.9.E.8 Free energies of reaction 1 and 2 for different metal oxides as functional catalytic materials and polysulfides..... 1096

Figure II.9.F.1 Left section. Long chain polysulfides confinement mechanism is illustrated at the upper part: the C-S bonds generated after vulcanization provide a reservoir for long chain polysulfides so that the polysulfides would not directly diffuse into electrolyte. The chemical transformation and material processing for PIPS preparation are shown at the lower part: polysulfides are immobilized in the polymer network. Right section. FT-IR spectra of starting materials sulfur (blue) and PIP (orange), and product PIPS (yellow). 1099

Figure II.9.F.2 SEM images of (a, b, c) commercially available micron sulfur and (d, e, f) vulcanized PIPS and sulfur nanocomposite materials particles. The particle sizes of the samples vary from several microns to tens of microns. The PIPS and sulfur nanocomposite materials particles show evident network structure on the surface..... 1100

Figure II.9.F.3 Electrochemical characterization of PIPS and sulfur nanocomposite materials based sulfur electrode and comparison to micron sulfur based electrode. The composition of cathode is PIPS and sulfur nanocomposite materials: C45:Graphene:binder=6:2:1:1 (weight ratio). The sulfur content in PIPS and sulfur nanocomposite materials is 90 wt%. a, b, c, Cycling stability comparison of PIPS and sulfur nanocomposite materials based sulfur electrode versus micron sulfur based electrode at around 0.47 mA/cm^2 at 30°C . d, e, f galvanostatic lithiation and delithiation. 1101

Figure II.9.G.1 a) Specific capacity ($\text{mAh/G}_{\text{sulfur}}$) for Li-S cells of indicated cell structure [anode | electrolyte-separator | binder/gel-cathode] during Galvanostatic cycling at 0.1C (calculated based on $1672 \text{ mAh/G}_{\text{sulfur}}$ theoretical capacity). b) 3rd cycle voltage profiles for indicated cells at 0.1C . c) 3rd cycle voltage profiles for indicated cells at 0.05C . d) Cycling of symmetric cells [electrolyte-separator-electrodes] at $\pm 0.1 \text{ mA/Cm}^2$ using a 6h cycle period. e) Cycling of symmetric cells [electrolyte-separator-electrodes] with varying current density and cycle period. f) Ionic/electrical conductivity vs temperature for gel cathodes and gel separators, extracted from frequency-dependent impedance between stainless steel blocking electrodes 1106

Figure II.9.G.2 GITT results for six different Li-S coin cell designs, with the cell structure indicated as Li | (electrolyte) | (cathode). All data was collected at 30°C and C/10 rate (assuming $1672 \text{ mAh/g}_\text{s}$), with GITT being performed on the 3rd cycle. All cathodes have $\sim 1 \text{ mg}_\text{s}/\text{cm}^2$ areal loading. The blue and red curves connect the current-applied voltages and open-circuit voltages, respectively, measured directly before current interruption and after a 1hr rest, respectively. Their difference represents the cell overpotential at that point of charge/discharge. The point of minimum overpotential during the lower discharge plateau of each cell is labeled on the corresponding graphs..... 1107

Figure II.9.G.3 a) Cycling performance of QSS and OE cells, with a 100h rest during 7th cycle discharge. Some irreversible capacity loss is observed for both designs, but the OE cell exhibits accelerated redox shuttling after the self-discharge test, while the QSS cell continues to cycle stably; b) OE voltage profiles for the 6th, 7th, and 8th cycles; c) QSS voltage profiles for the 6th, 7th, and 8th cycles; d) Cycling performance of two representative high-loading QSS cells. Available capacity is quite low at C/10 due to large internal resistance in the thick cathodes; e) 2nd and 10th voltage profiles for the representative high-loading cells. Increasing resistance during discharge prevents the cells from accessing their lower plateau capacity, especially at C/10..... 1109

Figure II.9.G.4 a) Visual test of the reaction/interaction between Li_2S_8 (1 mM) in DOL/DME (1;1, v:v) with 1 M LiTFSI. b) UV-vis spectra of solutions with various ratio between dbNDI and Li_2S_8 in DOL/DME (1;1, v:v) with 1 M LiTFSI. The concentration of dbNDI was kept constant as 0.1 mM in the mixture. c) CV spectra of dbNDI (10 mM) and Li_2S_8 in DOL/DME (1;1, v:v) with 1 M LiTFSI (scan rate = 10 mV/s). d) Two-step reductions of NDI moiety and illustration of ion-dipole interaction between NDI moiety and polysulfides. e) Schematic illustration of redox-mediator effect of NDI moiety 1111

Figure II.9.G.5 a) Cycling performances of S cathodes with PP and PVDF as binder, respectively; b) S cathodes fabricated using PP as binder with different ratio between PENDI-350 and tri-Py; c) Cycling performances of S cathodes with PP (PENDI-350: tri-Py = 1 : 1) as binder with different loading amount of S..... 1112

Figure II.9.G.6 a) Cycling performances of S cathodes with PENDI-350 (2.0 mgS/cm²) and PVDF (3.1 mgS/cm²) as binder, respectively; b) SEM images of cathodes with PENDI-350 and PVDF as binder after 20 cycles; c) Cycling performance of sulfur cathode with PENDI-350/PVDF as binder and the SEM image of the cathode after 20 cycles; d) Cycling performance of sulfur cathode with PENDI-350/PVDF 1114

Figure II.9.G.7 Cycling performances of cells with S cathodes with a) PENDI-350/PEO as binder (3.71 mgS/cm²) and b) PENDI-350/triPy/PEO (PPP) as binder (2.91 mgS/cm²). All cells were cycled with C rate of C/10 in the first 5 cycles and then 1C in the remaining cycles; c) Image of S cathode using PPP as binder (5.04 mgS/cm²); XPS spectrum of d) Li₂S₄ reacted with mesoporous carbon and e) Li₂S₄ and dbNDI mixture reacted with mesoporous carbon; f) Possible reaction route of lithium polysulfides in the presence of NDI..... 1115

Figure II.10.A.1 (a) Schematic images of Li-O₂ cells composed of Li metal anodes and CNT air cathodes with different electrolytes: PEO with 1 M LiTf-TEGDME (left), PEO with 3 M LiTf-TEGDME (center), and 3 M LiTf-TEGDME (right). (b) Cycling stability performance of the above Li-O₂ cells at 25°C at a current density of 0.1 mA cm⁻² under a capacity protocol of 1,000 mAh g⁻¹ 1120

Figure II.10.A.2 (a) Schematic of traditional artificial membrane on as-received Li foil surface and current CPL applied by direct casting on Li foil. (b) Cyclic stability tests based on Li||Li cells with or without CPL on Li metal containing 1 M LiFSI-DME electrolyte at 25°C. Current density: 0.2 mA cm⁻²..... 1121

Figure II.10.A.3 (a) Schematic images of different anodes and improvement by 3D carbon host for Li/C composite anodes and protective layer (NCL) coating for surface stabilization. (b) Cyclic stability tests based on Li-O₂ cells composed of RuO₂-CNTs air cathodes and 1 M LiTf-TEGDME electrolyte at 25°C at a current density of 0.1 mA cm⁻² under a capacity protocol of 1,000 mAh g⁻¹ with Li metal anode (left), Li/C composite anode (center), and NCL-protected Li/C composite anode (right) 1122

Figure II.10.A.4 (a, b) TEM image and corresponding FFT pattern of (a) pristine RuO₂/CNT electrode and (b) pretreated electrode. (c, d) Cyclic stability tests of Li-O₂ cells composed of RuO₂/CNTs air cathodes, 1 M LiTf-TEGDME electrolyte, and protected Li/C composite anode at 25°C at a current density of 0.1 mA cm⁻² under a capacity limited protocol of 1,000 mAh g⁻¹ (c) without or (d) with electrochemical pretreatment . 1123

Figure II.10.B.1 SEM of (a) 1st discharge and (b) charge products in Li-O₂ batteries with the Co₂Ni@LiOH cathode. (c) XRD of the 1st, 20th, 30th, and 40th discharge and the 1st charge products, (d) Raman spectrum of the 1st discharge and charge products in Li-O₂ battery (Amine et al, ACS Applied Materials & Interfaces, 11, 811–818 (2019)) 1127

Figure II.10.B.2 (a) Discharge profile of Ir-rGO under O₂ followed by discharge profile under Ar flow (b) PEIS measurements performed on pristine cathode, after O₂ discharge, after Ar discharge and after re-charge of the discharged cathode 1129

Figure II.10.C.1 Voltage profiles for Li-O₂ battery with LiNO₃ salt (left), and LiI redox mediator (right) .. 1132

Figure II.10.C.2 (left) Voltage profiles for Li-O₂ battery with 1M LiNO₃ and 1M LiI in 75% TEGDME/ 25% IL; (right) Raman spectra showing the presence of Li₂O₂ in the discharge product 1133

Figure II.10.C.3 AIMD simulation of eight LiNO₃ molecules added to electrolyte showing them forming a layer on the lithium anode 1133

Figure II.10.C.4 Redox potentials (vs Li⁺/Li) of redox mediators measured from CV experiments in DMSO 1134

Figure II.11.A.1 Structure evolution during Na extraction and insertion. In situ XRD patterns of Na_{0.7}[Cu_{0.15}Fe_{0.3}Mn_{0.55}]O₂ electrode collected during a) the first and b) the fifth charge/discharge process. c) In situ XRD patterns of Na_{0.7}[Cu_{0.2}Fe_{0.2}Mn_{0.6}]O₂ electrode collected during the first charge/discharge. All cycled between 2.5 and 4.2 V under a current rate of C/15 1139

Figure II.11.A.2 XAS analysis of a-c) Na_{0.7}[Cu_{0.15}Fe_{0.3}Mn_{0.55}]O₂ and d-f) Na_{0.7}[Cu_{0.2}Fe_{0.2}Mn_{0.6}]O₂ electrodes at different SOC during the 1st and 11th cycle: XANES spectra at a), d) Fe K-edge, b), e) Cu K-edge and c), f) Mn K-edge 1140

Figure II.11.A.3 sXAS of $\text{Na}_{0.7}[\text{Cu}_{0.15}\text{Fe}_{0.30}\text{Mn}_{0.55}]\text{O}_2$ (a–c) and $\text{Na}_{0.7}[\text{Cu}_{0.20}\text{Fe}_{0.20}\text{Mn}_{0.60}]\text{O}_2$ (d–f) samples. The Cu L-edge, (a and d), Fe L-edge (b and e), and O K-edge (c and f) sXAS data for the $\text{Na}_{0.7}[\text{Cu}_x\text{Fe}_y\text{Mn}_{1-x-y}]\text{O}_2$ cathode were collected at different cycle states, including pristine, charge 3.9 V, charge 4.3 V, and discharge 2.5 V during the first cycle and charge 4.3 V and discharge 2.5 V during the 15th cycle. The spectra in solid lines were collected in TFY mode, while those in dotted lines demonstrate sXAS collected in TEY mode. Schematic of metal to ligand charge transfer (MLCT) is shown in the inset of (a). The spectral evolution is highlighted with shaded areas	1141
Figure II.11.A.4 Crystal Structural Evolution of $\text{Na}_{0.72}[\text{Li}_{0.24}\text{Mn}_{0.76}]\text{O}_2$ Electrodes. (A) In situ XRD patterns collected during the first charge/discharge and the second charge of the $\text{Na}_{0.72}[\text{Li}_{0.24}\text{Mn}_{0.76}]\text{O}_2$. (B–D) Evolution of the lattice parameters during the charge/discharge process: a axis (B); c axis (C); and unit cell volume (D)	1142
Figure II.11.B.1 (a) X-ray Diffraction and (b) Raman spectra of Black Phosphorus-Carbon Composite. SEM images of (c) Bulk phosphorus and (d) black phosphorus-carbon composite, (e) High magnification and (f) high resolution TEM images of BPC composite	1146
Figure II.11.B.2 (a) Initial voltage profile of black phosphorus-carbon composite at 0.416 A g^{-1} ; (b) Cyclic voltammogram of black phosphorus-carbon composite at 0.1 mV s^{-1} ; Cycle performance of black phosphorus-carbon composite anode at (c) 0.416 A g^{-1} and (d) 1.3 A g^{-1} . The specific capacities were calculated based on the mass of BP. (e) The effect of Na salts on the cycle performance of BPC anode using different electrolytes at 0.416 A g^{-1} . (f) Comparison for the cycle performance of red phosphorus-carbon and black phosphorus-carbon composite at 0.416 A g^{-1}	1147
.Figure II.11.B.3 (a) XRD patterns and (b) SEM images of the Pb-PbO-C composite samples prepared by SPEX mill with various milling times	1147
Figure II.11.B.4 (a) XRD and (b) initial voltage profiles of the Pb-O-C electrodes prepared in air and in Ar-filled glove box	1148
Figure II.11.B.5 (a) Cycle performance of optimized Pb-PbO-O anode in sodium half cells. Carbonate electrolytes are used and 100 mA g^{-1} current density was applied. Initial voltage profiles of the Pb-PbO-C nanocomposite anode cycled in different electrolytes: (a) 1M NaPF_6 in EC/DEC, and (b) 1M NaTFSI in TEGDME.....	1148
Figure II.11.C.1 Structures of $\text{Na}_2\text{Ti}_3\text{O}_7$ (left), $\text{NaTi}_3\text{O}_6(\text{OH})\cdot 2\text{H}_2\text{O}$ or NNT (middle) and lepidocrocite –type titanate $\text{AxTi}_2\text{-yMyO}_4$ (right)	1152
Figure II.11.C.2 Top left: images of a pristine carbon-free electrode containing NNT, and a carbon-free electrode discharged to 0.1V. The color change is a qualitative indicator of reduction to trivalent titanium. The first and second discharge profiles of a Na/NNT cell is shown at bottom left (taken from reference [3]) showing the sloping voltage profile. Ti K-edge hard XAS spectra of pristine, cycled, and discharged NNT electrodes are shown on the right. These results are also consistent with $\text{Ti}^{3+}/\text{Ti}^{4+}$ redox.....	1153
Figure II.11.C.3 First and second cycles of a carbon coated nanowire NNT electrode made with CMC binder (left) discharged in a sodium half cell at low rates. Cycling behavior of nanowire electrodes with PVdF binder (red), CMC binder (blue) and carbon coated with CMC binder (black) in sodium half cells at moderate rates.....	1153
Figure II.11.C.4 High-resolution TEM image of NNT dehydrated at 600°C (left), its electron diffraction pattern (middle) and a simulated pattern for $\text{Na}_2\text{Ti}_6\text{O}_{13}$ (right).....	1154
Figure II.11.C.5 Second cycle discharge profiles of NNT heated to different temperatures (upper left) in sodium half cells. Comparison of second cycle discharge profiles of NNT heated to 500°C and 600°C (upper right). Cycling data for NNT heated to 800°C (lower left) and that of the hydrous (unheated) sample, lower right.....	1154
Figure II.11.C.6 First and second cycle discharge profiles of $\text{Na}_{0.7}\text{Ti}_{1.825}\square_{0.175}\text{O}_4$ in sodium half cells (left). Cycling data at different rates on right	1155

Figure II.11.D.1 (a) Raman spectra of EC-DMC mixed solvent and 1 M NaPF ₆ /EC-DMC electrolyte. (b) ¹³ C Chemical shift deduced from ¹³ C NMR spectra of different carbonates based electrolyte	1158
Figure II.11.D.2 (a) Rate performance and (b) Coulombic efficiency of Na HC cells (HC electrode: HC:PVDF:CB = 90:5:5; mass loading: 2–3 mg. cm ⁻²) in 1 M NaPF ₆ electrolyte with different solvents (c) Three-electrode EIS measurement for HC electrodes in different electrolytes. (d) Rate performance of HC in electrolytes with different salts (1 M) in EC+DMC mixture (1:1 by mass)	1159
Figure II.11.D.3 (a) Cycling stability of Na HC cells (HC electrode, HC:binder:CB = 90:5:5; mass loading: 2–3 mg. cm ⁻²) in 1 M NaPF ₆ /EC+DMC electrolyte. (b) Charge profile of Na HC cells (HC coated with alginate acid binder)	1159
Figure II.11.D.4 (a) Molecular structure of TEP and TMP (b) Ionic conductivity of TEP:NaFSI and TMP:NaFSI (2:1) at different temperatures (c) The effect of BTFE or TTE diluent on the conductivity of TEP-based electrolyte	1160
Figure II.11.D.5 (a) ¹³ C NMR spectra (b) Raman spectra of TEP-based electrolyte and with TTE or BTFE diluent	1160
Figure II.11.D.6 (a) Cycling performance at different discharge rates and (b) Charge-discharge profiles of Na HC in phosphate-based LHCE (NaFSI:TEP:TTE= 1:2:2). The HC electrode consists of HC:PVDF:CB = 90:5:5; mass loading: 2–3 mg. cm ⁻²	1161
Figure II.12.A.1 (a-c) Cryo-EM images of SEI formed in 1M LiPF ₆ in EC/DEC without FEC on CuO nanowires at electrode potentials of (a) 0.5 V, (b) 0.0 V, and (c) below 0.0 V vs. Li/Li ⁺ . (d-f) Cryo-EM images of SEI formed in 1M LiPF ₆ in EC/DEC with 10% FEC on CuO nanowires at electrode potentials of (a) 0.5 V, (b) 0.0 V, and (c) below 0.0 V vs. Li/Li ⁺ . (g,h) Series resistance (R ₁), SEI ionic conductivity, and interfacial resistances (R ₂) extracted from EIS measurements for SEI formed in electrolyte (g) without and (h) with 10% FEC additive. Na _{0.7} [Cu _{0.2} Fe _{0.2} Mn _{0.6}]O ₂ electrode collected during the first charge/discharge. All cycled between 2.5 and 4.2 V under a current rate of C/15	1164
Figure II.12.A.2 In situ optical microscopy used to visualize the electrodeposition of Li and long-term cycling on symmetric cells. (a) The optical images of the bare Li (left column) and GF-LiF-Li (right column) interfaced with electrolyte after 0, 10, 15, and 20 minute Li plating at a current rate of 3 mA cm ⁻² . The scale bars are 200 μm. (b) to (d) Cycling curves in symmetric cells for bare Li foil (black) and GF-LiF-Li (red) at various current densities: (b) 1 mA cm ⁻² , (c) 5 mA cm ⁻² , and (d) 10 mA cm ⁻² . The specific capacity of the cell is 1 mAh cm ⁻² . (e) Cycling performance of symmetric GF-LiF-Li cells cycled at 2 mA cm ⁻² rates for 2, 4, and 6 mAh cm ⁻² capacity cells	1165
Figure II.12.A.3 (a) Comparison between model prediction and experimental voltage response for lithium symmetric cells. (b) Simulated electrode overpotentials as a function of time.....	1166
Figure II.12.A.4 Compare of 1st cycle of ECOPRO NMC811 vs. Li with cycled with different upper limit voltages (2.8 ~ 4.4, 4.6 and 4.8 V) at (a) room temperature (RT) and (b) 45 °C. (c) Cycling performance of the Li NMC811 pouch cells using bare PP and LATP-coated PP separators	1166
Figure II.12.A.5 Large scale synthesis of NMC811, showing (left) the material formed; (center) the uniformity of the “meatballs” formed, top is 20 g batch and bottom is 220 g batch; and (right) the consistency of discharge capacity and capacity retention between the different size batches	1167
Figure II.12.A.6 Schematic of the tools Battery500 are employing to study thick electrodes.....	1167
Figure II.12.A.7 Abnormal d-spacing observed in NMC622 cathode material at highly charged state (> 4.5 V). (a) Large d-spacing peak at 7 Å. (b) Neutron pair distribution function (nPDF) analysis with (c) supercell model. (d) TEM observation of the abnormal structure formed at highly charged state	1168
Figure II.12.A.8 Cycling performances of Li NMC811 batteries in different electrolytes (conventional electrolyte (1 M LiPF ₆ in EC-EMC (3:7 by wt.) with 2 wt.% of VC); dilute electrolyte (LiFSI-9DME); HCE (LiFSI-1.2DME), and LHCE (LiFSI-1.2DME-3TTE) under the charge cutoff voltage of 4.4 V (a) and 4.5 V (b), respectively. The electrolyte amount in each coin cell is 75 μl.....	1169

- Figure II.12.A.9 SEI on Li metal anode. (a)–(c) Cryo-EM images of Li deposited on a TEM grid at different scales. Insert in (a) shows corresponding selected area electron diffraction (SAED) pattern. Insert in (c) shows corresponding reduced fast Fourier transform (FFT) (up) and the energy-dispersive X-ray spectroscopy (EDS) spectra (bottom) of the SEI layer, where the yellow lines shows the lattice space of the crystalline Li. (d) Schematic of the observed single-layer SEI structure on deposited Li in the 1 M LiFSI/DME-TFEO electrolyte. (e) Li||NMC811 cell cycling performances of the investigated electrolytes, where the lines with full and hollow circles represents specific capacity and CE of the cells, respectively 1170
- Figure II.12.A.10 (Left) 1st cycle behavior of NMC811 in voltage range 2.8–4.6 V; (middle) rate capability of NMC811 with a LiBO₂/LiF coating in voltage range 2.8–4.6 V, and (right) rate capability of LiNi_{0.94}Co_{0.06}O₂ after storage in voltage range 2.8–4.4 V 1171
- Figure II.12.A.11 (a) Cycle performance of Li₂S electrodes with high sulfur mass loading. (b) Voltage profiles of Li₂S charging with and without quinone redox mediator. (c) Comparison of redox potentials of different redox mediator candidates 1172
- Figure II.12.A.12 First cycle voltage profiles of (a) NMC622 and (b) NMC811 thick electrodes with various active mass loading and porosity, at C/10, 2.8 – 4.4 V. Electrodes are provided by Maxwell Technologies 1173
- Figure II.12.A.13 (a) SEM cross-section image of pristine NMC811 thick electrode, (b) PFIB large volume serial section of the thick electrode, (c) 3D reconstructed volume and phase segmentation calculated using the PFIB-SEM data, and (d) EDX mapping of NMC811 thick electrode on one serial section obtained from PFIB 1173
- Figure II.12.A.14 (a) Photo of an eggplant and its cross-section morphology. (b) Schematic illustration for a carbonized EP with interconnected channel-like structure. (c) Carbonized EP after Li metal melt infusion. (d) Carbonized EP-Li metal composite anode further coated with a layer of LiF thin film NMC811 thick electrode on one serial section obtained from PFIB 1174
- Figure II.12.A.15 Top view SEM image of EP–LiF anode after (a) 1 cycle and (b) 10 cycles under 1 mA cm^{−2} and 1 mAh cm^{−2} in a symmetric cell. Top view SEM image of Li foil anode after (c) 1 cycle and (d) 10 cycles under 1 mA cm^{−2} and 1 mAh cm^{−2} in a symmetric cell. Cross section of (e) a pristine EP–LiF electrode, (f) an EP–LiF electrode after stripping ≈10 mAh cm^{−2} of capacity and (g) an EP–LiF electrode after stripping ≈10 mAh cm^{−2} of capacity and plate it back anode further coated with a layer of LiF thin film NMC811 thick electrode on one serial section obtained from PFIB 1175
- Figure II.12.A.16 Quantitative differentiation of inactive Li by the hydrogen evolution method. (a) Average CE of Li||Cu cells under different testing conditions. (b) Representative voltage profiles of Li||Cu cells under different testing conditions in the first cycle. (c) Summarized quantitative contribution of capacity loss from the SEI Li⁺ and metallic Li⁰. (d) Total capacity loss as a function of CE. (e) Inactive metallic Li amount measured by the TGC method as a function of CE. (f) Calculated SEI Li⁺ amount as a function of CE 1176
- Figure II.12.A.17 (a) Schematic of the structure of a 3D mesoporous carbon host that encourages Li wetting and pore filling. (b) Capacity retention of Li||NMC cells with cycling. NMC622 is LiNi_{0.6}Co_{0.2}Mn_{0.2}O₂, NMC811 is LiNi_{0.8}Co_{0.1}Mn_{0.1}O₂, E/C is electrolyte/capacity ratio 1176
- Figure II.12.A.18 A schematic comparison of the structure of Li-rGO (reduced graphene oxide) and Li-SirGO where the presence of silicon between the GO layers helps to maintain the gaps (a–d); SEM images of electrode cross-section demonstrating that the Li-SirGO structure maintains its overall thickness after removal of 1 mAh/cm² of lithium 1177
- Figure II.12.A.19 Microstructures of inactive Li generated in HCE (a–f) and CCE (g–l) imaged by Cryo-FIB-SEM. (a–c) and (g–i) are top view of the inactive Li at 52° tilted stage. (d–f) and (j–l) are cross-sections obtained by cryo-FIB. Each column represents a stripping rate. (a, d, g and j) are at 0.5 mA cm^{−2}. (b, e, h and k) are at 2.5 mA cm^{−2}. (c, f, i and l) are at 5.0 mA cm^{−2} 1177
- Figure II.12.A.20 Nanostructures of inactive Li generated in HCE (a–d) and CCE (e–h) by Cryo-TEM. a, e, inactive Li morphology at low magnifications for both electrolytes. b, f, HRTEM shows a different amount of metallic Li⁰ is wrapped by SEI in the two types of electrolytes. The highlighted metallic Li⁰ region in green is

identified through FFT-mask filtering-inverse FFT-image overlay process. c, g, FFT patterns of corresponding HRTEM indicate the SEI component which contains crystalline Li_2CO_3 , Li_2O , and LiF . d, h, Schematic of inactive Li nanostructure in both electrolytes. Small area of metallic Li^0 is embedded in a sheet-like SEI layer for HCE, while a large bulk of metallic Li^0 is isolated in whisker-like SEI layer in CCE 1178

Figure II.12.A.21 Molecular design and chemical structures of SSN and derivatives. (a-c) Conceptual sketch of SSN (a), B-SSN (b), and Si-SSN (c). Blue spheres: Li^+ ; orange spheres: Al; purple spheres: B; olive spheres: Si; tetrahedra: anion centers; grey chains: soft ligands. (d) The reaction to synthesize SSN. (e) Detailed chemical structure of SSN. (f, g) Photos of an as-synthesized viscous SSN/DME solution (f) and a free-standing SSN film (g) 1179

Figure II.12.A.22 A) Cycling data for a Li/NMC622 cell developed in FY17. The cell achieved 200 cycles. B) Variation in NMC loading content from ex-situ XRD analysis following the completion of testing C) SOC in the NMC cathode from ex-situ XRD analysis 1180

Figure II.12.A.23 Post-test Li metal electrode at the completion of 200+ cycles. Circles indicate areas of disconnected Li after cycling 1181

Figure II.12.A.24 Uneven reaction was identified by XRF (b ~ g) and XAS spectra (h ~ i) at different locations of sulfur cathodes harvested from the cycled Li-S pouch cell. (a) Photo image of the cycled cathode with labeled locations for XRF and XAS analysis: R1(b, e, and h), R2 (c, f, and i) and R3 (d, g, and j). b, c, and d are XRF collected at 2469 eV. e, f and g are XRF collected at 2480 eV. h, i, and j are XAS collected in the b, c, and d, respectively within a energy range of 2468-2488 eV. Yellow and blue lines in the XAS spectra were collected at the yellow and blue dots of corresponding XRF image at 2469 eV..... 1181

Figure II.12.A.25 Pressure evolution over the first 28 cycles for a cell with 21 psi of external pressure applied. Similar, but more pronounced variation was observed at lower pressures which also exhibited decreased cycle life 1182

Figure II.12.A.26 Cycle life data for a 2.5 Ah Li||NMC cell. Cycling was at a C/10 charge and a C/3 discharge 1182

Figure II.12.A.27 Left) Differential capacity analysis on the impact of three different pressure regimes for cycling of a single layer Li||NMC pouch cell. Right) Model framework and predicted, local current density for real electrode during early cycling..... 1183

Figure II.12.A.28 (a) Cycling performance of the pristine and LiF/LiBO₂-coated NMC811 cathodes. Selected charge-discharge curves of (b) the pristine and (c) LiF/LiBO₂-coated NMC811 cathodes. The dQ/dV plot of the pristine and LiF/LiBO₂-coated NMC811 thick electrodes at the (d) 5th and (e) 50th cycles. The tests were conducted using the Battery500 testing protocol at 20°C within the voltage range of 2.8-4.4 V at C/3. There was a 4-h rest between charge and discharge regimes during cycle aging. The formation was performed at C/10 for two cycles with 1-h rest between charging and discharging 1184

Figure II.12.A.29 The electrochemical analytical diagnosis (eCAD) technique revealed (a) the attributes to the capacity fade of an early failed Li | standard electrolyte | NMC622 coin cell and the significant impact from the loss of Li inventory. (b) The SEM micrographs showed the impact of the dead Li on the Li inventory that failed the cell..... 1185

Figure II.12.B.1 (a) Nyquist plot of Au interface engineered Li/LLZO/Li cell. (b) DC cycling of Au interface engineered Li/LLZO/Li cell with a step current of 20 $\mu\text{A cm}^{-2}$ starting from 20 $\mu\text{A cm}^{-2}$. (c) SEM fracture surface image showing superior interfacial bonding of Li and LLZO. (d) DC cycling of Au interface engineered Li/LLZO/Li cell at selected current densities. (e) SEM surface image of typical sintered LLZO thin films 1199

Figure II.12.B.2 Fracture surface SEM micrographs of green tapes freeze tape cast from slurries containing (a) 7.5 vol.% LLZO / 400 μm , (b) 10 vol.% LLZO / 220 μm , and (c) 10 vol.% LLZO / 150 μm . Fracture surface micrographs of (d) sintered porous/dense (140/36 μm) bilayer, (e) porous/dense/porous (130/37/130 μm) trilayer, and (f) porous/dense/porous trilayer with a 14 μm dense layer. (g) Surface SEM micrograph of the

porous layer. (h) 3D reconstruction of micro-CT scan of the trilayer. Subvolume size is 400 (width) \times 280 (height) \times 530 (depth) μm^3 . Inset shows an optical image of a typical trilayer 1200

Figure II.12.B.3 (a) Optical image of cathode infiltrated LLZO bilayer. Cathode infiltrated porous layer surface (left) and dense layer surface (right) are shown. (b) SEM fracture surface image of cathode infiltrated bilayer (c) Same cell at higher magnification showing cathode infiltrate. (d) Nyquist plot of the constructed all solid state battery. (e) Initial charge/discharge profiles of the ASSB at room temperature..... 1200

List of Tables

Table ES- 1: Subset of EV Requirements for Batteries and Cells	xvii
Table 1: Subset of Requirements for Advanced High-Performance EV Batteries and Cells. (Cost and Low Temperature Performance are Critical Requirements).	3
Table 2: Subset of Targets for 12V Start/Stop Micro-hybrid Batteries (Cost and Cold Cranking are Critical Requirements).....	4
Table 3: Lithium-ion battery recycling prize Phase I contest winners.....	9
Table I.1.A.1 Characteristics of the Annual Cell Deliverables in the Program	23
Table I.1.A.2 Phase 3 Deliverable Cell Initial Performance	25
Table I.1.A.3 Phase 3 Deliverable Abuse Tolerance Results	27
Table I.1.B.1 Gen1 Cell Builds with the Down Selected Chemistry	30
Table I.1.D.1 Overview of Program Hardware Deliverables and Build Strategy	41
Table I.1.D.2 Material Properties Comparison of NMC111 Recovered from Electrode Scrap with Pristine NMC111 from the Same Lot	42
Table I.1.D.3 Material Properties Comparison of Graphite Recovered from Electrode Scrap with the Same Type of Pristine Graphite	42
Table I.1.D.4 Cell Build 1 Test Article Characteristics	43
Table I.1.D.5 Material Properties Comparison of Direct-recycled NMC111 Recovered from Whole Cells with Pristine NMC111	47
Table I.1.D.6 Material Properties Comparison of Graphite Recovered from Whole Cells with the Same Type of Pristine Graphite	47
Table I.1.F.1 PHEV-20-mile Target Comparison.....	59
Table I.1.H.1 Formulation Details of Final Target Anodes	70
Table I.1.H.2 Physical Parameters of 1 st and Final Target Anode Coating	70
Table I.1.H.3 Details of Anode Coatings for Single Layer Pouch Cells.....	71
Table I.1.H.4 Formulation and Coating Details of Anode E Coated at UMEI	71
Table I.2.A.1 3 rd Party Confirmation of High FCE	75
Table I.2.A.2 3 rd Party Confirmation of High FCE (Graphite Blend)	76
Table I.2.C.1 Summary of the High Speed Curing Experimental Runs at Ebeam Technologies	86
Table I.2.C.2 Summary of the High Speed Curing (A-dosimeter under NMC622 Coating, B-dosimeter under NMC811 Coating)	87

Table I.2.K.1: Elastic Moduli of Al-doped LLZO	134
Table I.2.K.2: Calculated Amorphization Energy of $\text{Al}_x\text{Li}_{7-3x}\text{La}_3\text{Zr}_2\text{O}_{12}$	135
Table I.2.K.3: Calculated Surface Energy of La-terminated (011) Surface of Al-doped LLZO	136
Table I.2.M.1 Impact of Sintering Atmosphere on Density and Conductivity	141
Table I.2.O.1 Amounts of Reaction of Various Well-researched Li-ion Battery Materials	151
Table I.2.O.3 Most Common Precursors and Occurrence Frequencies for NMC Cathodes.....	151
Table I.2.Q.1 Calculations for Device Volume Inside EV Type 30 Ah Pouch Cell.....	165
Table I.2.R.1. Electrode Dimensions and Loadings for 1 Ah Cells.....	171
Table I.2.R.2. Energy Density Comparison Between CoEx Cathodes and Baseline Cathodes	172
Table I.2.R.3. Capacity of Large Pouch Cells at Varying Discharge Rates.....	173
Table I.2.R.4. Energy Density Improvement of CoEx Over Baseline in Large Format Cells.....	174
Table I.3.D.1 Impact test conditions for pouch and prismatic cells.....	200
Table I.3.D.2 Quasi-static test conditions for pouch and prismatic cells.....	200
Table I.3.D.3 Material parameters for active materials for material models MAT_025 and MAT_145.	201
Table I.3.E.1 EPMA Quantitative Analysis: Average Normalized Mass% of 10 Spots Measured on Used and Pristine Cu Current Collectors	207
Table I.3.E.2 Charging Times and Efficiency with C-Rate	209
Table I.4.A.1 Challenges for Li-Ion Battery Recycling.....	215
Table I.4.C.1 Modeling and Analysis Focus Area Major Efforts in Q3 FY2019	229
Table I.4.C.2 GDOES-determined Lithium Content as a Function of Lithia Source at 500°C	231
Table I.4.C.3 GDOES-determined Lithium Content as a Function of Lithia Source at 650°C	231
Table I.4.C.4 Comparison of Relithiation, Delithiation and Reversible Capacities for Half Cells Relithiated at Room Temperature or 50°C.....	233
Table I.4.C.5 Summary of Large Scale Ionothermal Experiments, TGA, ICP, and XRD Results.....	234
Table I.4.C.6 ICP-OES Results.....	236
Table I.4.C.7 Cycle Performance.....	237
Table I.4.C.8 Result of NMC111/LMO Separation via Froth Flotation Using Collector A.....	249
Table I.4.C.9 Result of NMC111/LCO separation via froth flotation using collector A.....	249
Table I.4.C.10 Result of NMC111/LMO Separation via Froth Flotation Using Collector B	250
Table I.4.C.11 Result of NMC111/LMO Separation via Froth Flotation with Collector A in Flotation Column	250
Table I.4.C.12 ICP Analysis of Black Mass used for Impurity Discovery	251
Table I.4.C.13 Element Ratios Measured Using GDOES	255
Table I.4.C.14 Electrode Information	263
Table I.4.C.15 Preliminary Estimate of Rejuvenation Hardware on Pack Energy Density from BatPaC.....	267
Table I.4.C.16 CAMP Cells to be Used for Thermal Characterization (Cathode Material supplied by Toda and Anode Material by Superior Graphite)	269

Table I.4.C.17 Progress of EverBatt Customization in Q4 FY2019	272
Table I.4.C.18 Sample Information: XPS/SEM Study	280
Table I.5.B.1 Conductivity of Different New Electrolyte Blends to Enable Fast Charge	295
Table I.5.C.1 Heat Efficiency and Heat Rate for Fast Charge Algorithms	306
Table I.5.E.1: Cycling Profile for Baseline COTS and UM Cells	317
Table I.5.E.2: Cells used to establish baseline lithium plating performance.	317
Table I.5.G.1 Normalized Lithium Plating Capacities for Fully Lithiated Electrodes Subjected to Voltage Holds of -10 mV, -15 mV and -20 mV for 6 hours	332
Table I.5.G.2 Normalized Li(110)/Cu(220) Peak Area Ratios from XRD Measurements of Electrodes Recovered from Half Cells Subjected to Voltage Holds of -10 mV, -15 mV and -20 mV for 6 hours	332
Table I.6.A.1 Cost Data for Extreme Demand Scenario.....	374
Table I.6.A.2 Cost Data for Seasonal Demand Scenario	375
Table I.6.A.3 Design Considerations for Cost and Thermal Model of an EVSE	377
Table I.6.A.4 EVSE Component-wise Cost Estimate for a 1-MW, 13.8-kV Setup [1]–[5]	379
Table I.6.A.5 EVSE PE Total Cost Estimate for a 1-MW, 13.8-kV Setup [1]–[5].....	379
Table I.6.A.6 Pack Estimation Calculation Table (Shaded Row Represents the C/2 Discharge Rate)	383
Table I.6.A.7 Degradation Mechanism Models	388
Table I.6.A.8 Acceleration Factors Used for Building Degradation Rate Laws.....	388
Table I.6.A.9. Heat of Fusion and Transition Temperature for Several PCM Composites with Varying Mass Fraction of PCM	394
Table I.7.A.1. Input Values and Results from BatPaC 3.1 for a 94 kWh Battery Pack for a Battery Electric Vehicle (BEV)	405
Table I.7.B.1 Status of Deliverables for Testing.....	409
Table I.7.E.1 Capacity Values for Cathodes Made in MERF	426
Table I.7.E.2 Delithiation Capacity and Voltage for Cathodes Made in MERF.....	429
Table I.7.E.3 Ceramic Materials Under Test as Coatings on Anode	431
Table I.7.E.4 Oxofluorophosphate and HF Yields after 1 Week of Aging in Electrolyte with 8,300 ppm Water.....	438
Table I.7.E.5 Summary of Electrode Library Distributions.....	440
Table I.7.F.1 Electrode Composition and Physical Properties.....	443
Table I.7.G.1 Articles Tested for USABC	451
Table I.7.G.2 Articles Tested for Benchmark.....	451
Table II.1.A.1 Summary of Grafting Density, Loading Density, Initial Capacity, Coulombic Efficiency, Capacity Retention, and Charge-transfer Resistance (R_{ct}) of Graphite/silicon Composite Electrodes Fabricated using H-SiNPs or SF-SiNPs.	483
Table II.1.A.2 Si Powder Description.....	488
Table II.1.A.3 Electrodes with Silicon, Graphite (Gr), Carbon Black (CB) and LiPAA.....	489
Table II.1.A.4 Surface Compositions of the Electrode Samples Measured by XPS.....	489

Table II.1.A.5 First Cycle Capacities and Coulombic Efficiencies of Half Cells with Si Electrodes.....	491
Table II.1.A.6 Discharge Capacities (1 st and 99 th cycle) and Capacity Retention of the Full Cells	494
Table II.1.A.7 Formulations and Notations of the Electrolytes Used in this Study.....	495
Table II.1.A.8 Proposed Compounds from HPLC Data	506
Table II.1.B.1. Quantified Energy Generation Based on the Fit Curve of the Paraclete-4KD + CB Sample as well as predicted material and performance loss based on the formation of silica	535
Table II.1.B.2 Copper-based Substrates Investigated With Protocol 1	547
(The values of the residual current observed after 24 hours of potentiostatic step at 0.05 V are reported. The thin copper foil presents the lower values on the order of 1 $\mu\text{A cm}^{-2}$.).....	547
Table II.1.B.3 Summary of the Investigated Effects on the Passivating Properties of Silicon and Preliminary Conclusions.....	549
Table II.1.B.4 Summary of Results: SSRM 3D Resistivity vs. Depth Profiling of SEI and AFM Roughness	564
Table II.1.B.5 Raman Peak Assignments	586
Table II.1.D.1 Electrochemical Performance of NMC532 Si/Gr (CAMP Electrodes) Full Cells in BTFE-based Electrolytes with Different Salt Concentrations	617
Table II.1.D.2 Swelling of Si/Gr Anode in Different Electrolytes	618
Table II.1.D.3 Molarity, Viscosities and Self-extinguish Time (SET) of Three Baseline Electrolytes and Two Localized High Concentration Electrolytes	619
Table II.1.E.1 Electrochemical Performance of Si Anode after being Preliathiated under Different Conditions.....	625
Table II.2.A.1 DSC Samples with Various Amounts of Active Material and Electrolyte.....	638
Table II.2.A.2 Twelve Most Intense Ions Detected via HPLC and Corresponding Chemical Structures	640
Table II.2.A.3 FTIR Peak Assignments for Gen2 Electrolyte	643
Table II.2.B.1 Rietveld Refinement and Particle Size Analysis Results of $\text{LiNi}_{0.94}\text{Co}_{0.06}\text{O}_2$	656
Table II.2.B.2 Summary of Electrochemical Properties of $\text{Ni}_{94}\text{Co}_6$	656
Table II.2.B.3 Rietveld Refinement Analysis of Samples	659
Table II.2.B.4 Model Systems Prepared with Various Synthesis Conditions for NMR Studies	665
Table II.2.D.1 Theoretical and Experimental Properties of $\text{LT-LiCo}_{1-x}\text{Al}_x\text{O}_2$ Electrodes for $0 \leq x \leq 0.5$	684
Table II.3.E.1. Summary of Physical Properties, Ionic Conductivity and Li^+ Transference Number of PMpipFSI with Different LiFSI Concentrations.....	742
Table II.3.G.1 200 mAh Cell Thickness Changes Following 200 Charge/discharge Cycles at .7C	759
Table II.4.A.1 Project performance targets for cathode active material and cell made with this material	765
Table II.4.A.2 Summary of Samples and Precursors Used to Synthesize NCM811	768
Table II.4.C.1 Equilibrium Reactions, Solubility Product Constant and pH of Precipitation.....	786
Table II.4.E.1 Performance Targets.....	801
Table II.4.F.1 Rietveld Analysis of LNMTO Cathode Powders.....	809
Table II.4.G.1 $I_{(003)}/I_{(104)}$ Values of the $\text{LiNi}_{0.83}\text{Co}_{0.11}\text{Mn}_{0.06}\text{O}_2$ Materials Synthesized at Various Temperatures	815

Table II.4.G.2 C/3 Capacity of the Cells Measured at Room Temperature	817
Table II.6.G.1 Comparison of the Intrinsic Material Properties of Different Solid Electrolytes	928
Table II.7.G.1 Calculated elastic constants for Li metal, cubic LLZO and hexagonal LiCoO ₂	980
Table II.7.G.2: Calculated strain-depedent activation energy of Li-hopping in LiCoO ₂	980
Table II.7.G.3: Effects of vacancy on the activation energy of Li-ion diffusion in cubic LLZO	981
Table II.7.H.1 Development of Ink Recipes for 3D Printing.....	988
Table II.8.D.1 Chemically Titrated Capacities of LiPS ₃ and LiPS ₃ •S cathode powders	1026
Table II.8.G.1 Coordination Ratio α and the Ratio of Diffusion Coefficients of Toluene, VC and EMC Before and After the Addition of LiPF ₆	1046
Table II.8.G.2 Coordination Ratio α and the Ratio of Diffusion Coefficients of Toluene, VEC and EMC Before and After the Addition of LiPF ₆	1046
Table II.8.I.1 Quarterly Milestones and Verification for FY19.....	1053
Table II.9.D.1 Test results of ten synthesized co-polymer electrodes in 2018, but with improved electrode processes.	1085
Table II.9.E.1 Battery Specifications for the Battery 500 Program	1091
Table II.9.G.1 Breakdown of SIG/S/C slurry (and subsequent cathode) composition by weight. The demonstration cell formula was used for QSS cells with ~1 mg _s /cm ² cathode loading, while the updated formula is intended for high-loading (4-5 mg _s /cm ²) cells.	1110

Vehicle Technologies Office Overview

Vehicles move our national economy. Annually, vehicles transport 11 billion tons of freight—about \$35 billion worth of goods each day⁴—and move people more than 3 trillion vehicle-miles.⁵ Growing our economy requires transportation and transportation requires energy. The transportation sector accounts for approximately 30% of total U.S. energy needs⁶ and 70% of U.S. petroleum consumption.⁷ The average U.S. household spends over 15% of its total family expenditures on transportation, making it the most expensive spending category after housing.⁸

The Vehicle Technologies Office (VTO) has a comprehensive portfolio of early-stage research to enable industry to accelerate the development and widespread use of a variety of promising sustainable transportation technologies. The research pathways focus on fuel diversification, vehicle efficiency, energy storage, and mobility energy productivity that can improve the overall energy efficiency and efficacy of the transportation or mobility system. VTO leverages the unique capabilities and world-class expertise of the National Laboratory system to develop innovations in electrification, including advanced battery technologies; advanced combustion engines and fuels, including co-optimized systems; advanced materials for lighter-weight vehicle structures; and energy efficient mobility systems.

VTO is uniquely positioned to address early-stage challenges due to strategic public-private research partnerships with industry (e.g. U.S. DRIVE, 21st Century Truck Partnership) that leverage relevant expertise. These partnerships prevent duplication of effort, focus DOE research on critical R&D barriers, and accelerate progress. VTO focuses on research that industry does not have the technical capability to undertake on its own, usually due to a high degree of scientific or technical uncertainty, or that is too far from market realization to merit industry resources.

Annual Progress Report

As shown in the organization chart (below), VTO is organized by technology area: Batteries & Electrification R&D, Materials Technologies, Advanced Engine & Fuel R&D, Energy Efficient Mobility Systems, Technology Integration, and Analysis. Each year, VTO's technology areas prepare an Annual Progress Report (APR) that details progress and accomplishments during the fiscal year. VTO is pleased to submit this APR for Fiscal Year (FY) 2019. In this APR, each project active during FY 2019 describes work conducted in support of VTO's mission. Individual project descriptions in this APR detail funding, objectives, approach, results, and conclusions during FY 2019.

⁴ Bureau of Transportation Statistics, Department of Transportation, Transportation Statistics Annual Report 2018, Table 4-1. <https://www.bts.gov/tsar>.

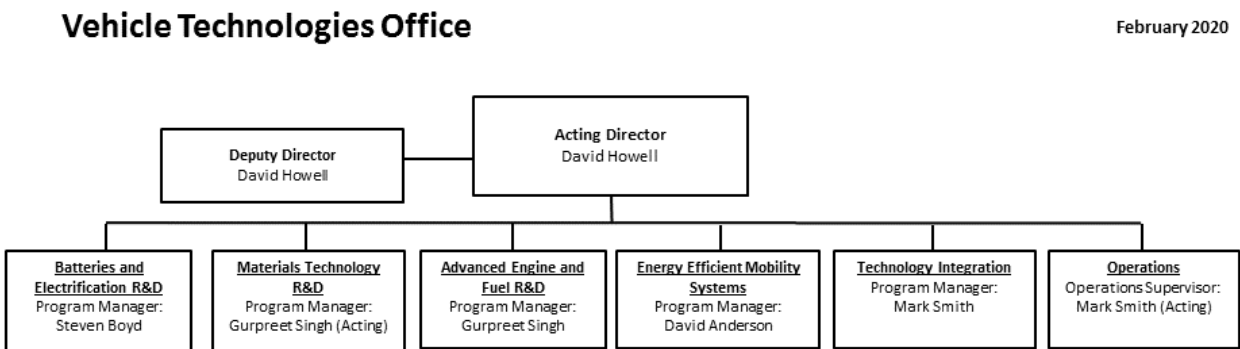
⁵ Transportation Energy Data Book 37th Edition, Oak Ridge National Laboratory (ORNL), 2019. Table 3.8 Shares of Highway Vehicle-Miles Traveled by Vehicle Type, 1970-2017.

⁶ Ibid. Table 2.1. U.S. Consumption of Total Energy by End-use Sector, 1950-2018.

⁷ Ibid. Table 1.12. U.S. Transportation Petroleum Use as a Percent of U.S. Petroleum Production, 2018.

⁸ Ibid. Table 10.1, Average Annual Expenditures of Households by Income, 2016.

Organization Chart



Batteries Program Overview

Introduction

During the fiscal year 2019 (FY 2019), the Vehicle Technologies Office (VTO) battery program continued research and development (R&D) support of technologies for plug-in electric vehicles (PEVs), e.g., plug-in hybrids, extended range electric vehicles, all-electric vehicles, and some hybrid electric vehicles (including 12 volt start/stop hybrid). One objective of this support is to enable U.S. innovators to rapidly develop next generation of technologies that achieve the cost, range, and charging infrastructure necessary for the widespread adoption of PEVs. Stakeholders involved in VTO R&D activities include universities, national laboratories, other government agencies and industry partners – including automakers, battery manufacturers, material suppliers, component developers, private research firms, and small businesses. VTO works with key U.S. automakers through the United States Council for Automotive Research (USCAR) – an umbrella organization for collaborative research consisting of Fiat Chrysler LLC, the Ford Motor Company, and the General Motors Company. Collaboration with automakers through the U.S. DRIVE (Driving Research and Innovation for Vehicle Efficiency and Energy Sustainability) partnership enhances the relevance and the success potential of the research platform. An important prerequisite for the electrification of the nation's light duty transportation sector is the development of more cost-effective, longer lasting, and more abuse-tolerant PEV batteries and accordingly, VTO battery R&D is focused on the development of high-energy batteries for PEVs and very high-power devices for hybrid vehicles.

Goals

The goals of this research are to address barriers to EVs reaching the full driving performance, convenience, and price of an internal combustion engine (ICE) vehicle. EVs have the advantage of a very high efficiency compared to other vehicle types, a simplified drive train, and a flexible primary energy source (i.e., the electricity needed to charge an EV can come from coal, natural gas, wind turbines, hydroelectric, solar energy, nuclear, or any other resource). Another current focus is the 12V start/stop (S/S) micro-hybrid architecture, in which the engine is shut down whenever a vehicle stops. Vehicles with the S/S functionality are being deployed worldwide. The 12V battery provides power for auxiliary equipment (e.g., the radio and air conditioning) and then restarts the engine when the vehicle moves. Current 12V S/S batteries, typically lead-acid batteries, have a poor life. Table 1 and Table 2 show a subset of the targets for high-performance EVs and 12V start/stop micro hybrid batteries that have been set by U.S. DRIVE⁹, respectively.

Table 1: Subset of Requirements for Advanced High-Performance EV Batteries and Cells.
(Cost and Low Temperature Performance are Critical Requirements).

Energy Storage Goals (by characteristic)	System Level	Cell Level
Cost @ 100k units/year (kWh = useable energy)	\$125/kWh*	\$100/kWh
Peak specific discharge power (30s)	470 W/kg	700 W/kg
Peak specific regen power (10s)	200 W/kg	300 W/kg
Useable specific energy (C/3)	235 Wh/kg*	350 Wh/kg
Calendar life	15 years	15 years
Deep discharge cycle life	1000 cycles	1000 cycles
Low temperature performance	>70% useable energy @C/3 discharge at -20 °C	>70% useable energy @C/3 discharge at -20 °C

⁹ https://www.uscar.org/guest/article_view.php?articles_id=85

Table 2: Subset of Targets for 12V Start/Stop Micro-hybrid Batteries
(Cost and Cold Cranking are Critical Requirements)

Energy Storage Goals (by characteristic)	Under the hood	Not under the hood
Maximum selling price (@220k units/year)	\$220*	\$180*
Discharge pulse (1s)	6 kW	
Cold cranking power, (-30 °C)	6 kW for 0.5s followed by three 4 kW/4s pulses*	
Available energy (750W acc.)	360 Wh	
Peak recharge rate (10s)	2.2 kW	
Sustained recharge rate	750 W	
Cycle life	450 k	
Calendar life	15 years at 45 °C*	15 years at 30 °C**
Maximum weight	10 kg	
Maximum volume	7 liters	
	*Current commercial cells do not meet this goal **Current cells almost meet this goal	

State of the Art

Battery R&D attempts to advance battery technology to help improve the market penetration of PEVs and hybrid vehicles by overcoming the current barriers. To accomplish this, it focuses on: (1) a significantly reduced battery cost, (2) increased battery performance, e.g., extreme fast charge (XFC) and low temperature performance for enhanced lithium-ion, (3) improved life advanced chemistry cells, (4) increased tolerance to abusive conditions; and (5) more cost-effective recycling and sustainability.

The current status of the broad battery chemistry types (current lithium-ion, next gen, and BLI) is summarized in Figure 1. Battery R&D spans mainly three areas:

- **Current technology (enhanced lithium-ion):** including cells with current materials (graphite anode/transition metal oxide cathode) and features like XFC compatibility, low temperature performance and improved abuse tolerance.
- **Next-gen lithium-ion:** Cells containing an alloy anode, usually silicon-based, and/or a high voltage (>4.5 V) cathode.
- **Beyond lithium-ion (BLI):** Cells containing Li metal anodes.

Over the past nine years, PEVs have become more commercially viable, with battery costs dropping almost 80% since 2010. Further cost reductions in high-energy batteries for PEVs are always desirable. In addition, although today's batteries approach very attractive cost numbers, they still need the ability to accept extreme fast charging (XFC) and to perform better in low-temperature operations to compete with ICEs in all-weather performance and "refueling" convenience. Research into "enhanced lithium-ion" batteries (which would provide these functionalities) is one of the R&D focus areas. For further gains in energy density and cost reduction, research is needed in both "next gen" chemistries (which employ an alloy anode and/or a high voltage cathode) and BLI chemistries (see Figure 1). Cycle and calendar lives of next-gen and BLI chemistries fall well short of EV goals. Most cells employing a significant amount of silicon provide around 1,000 deep-discharge cycles but with less than two years of calendar life; BLI cells typically provide much less of a cycle life (250 cycles or less). In addition, the requisite low temperature performance and extreme fast charge capability are lacking in all chemistries.

Current Technology Lithium-ion Graphite/NMC	Next Generation Lithium-ion Silicon Composite/High-voltage NMC	Longer-term Battery Technology Lithium Metal
Battery Pack Cost	Battery Pack Cost	Battery Pack Cost
<ul style="list-style-type: none"> Current: \$235/kWh Potential: \$100-160/kWh 	<ul style="list-style-type: none"> Current: \$256/kWh Potential: \$90-125/kWh 	<ul style="list-style-type: none"> Current: ~\$320/kWh Potential: \$70-120/kWh
Large-format EV cells: 20-60 Ah	Large-format EV cells: 20-60 Ah	Large-format EV cells: TBD (Today)
Current cycle life: 1000-5000	Current cycle life: 500-700	Current cycle life: 50-100
Calendar life: 10-15 years	Calendar life: Low	Calendar life: TBD
Mature manufacturing:	Mature manufacturing:	Mature manufacturing:
Fast-charge:	Fast-charge:	Fast-charge:
R&D Needs	R&D Needs	R&D Needs
<ul style="list-style-type: none"> High-voltage cathode/electrolyte Lower-cost electrode processing Extreme-fast charging 	<ul style="list-style-type: none"> High-voltage cathode/electrolyte Lower-cost electrode processing Durable silicon anode with increased silicon content 	<ul style="list-style-type: none"> High-voltage cathode Lithium protection High-conductive solid electrolyte

Figure 1. Chemistry classes, status, and R&D needs

An overview of the candidate battery technologies and their likely ability to meet the DOE cost goals are shown in Figure 2. Because of the large variation in different battery technologies, battery research also includes multiple activities focused to address remaining high cost areas within the entire battery supply chain.

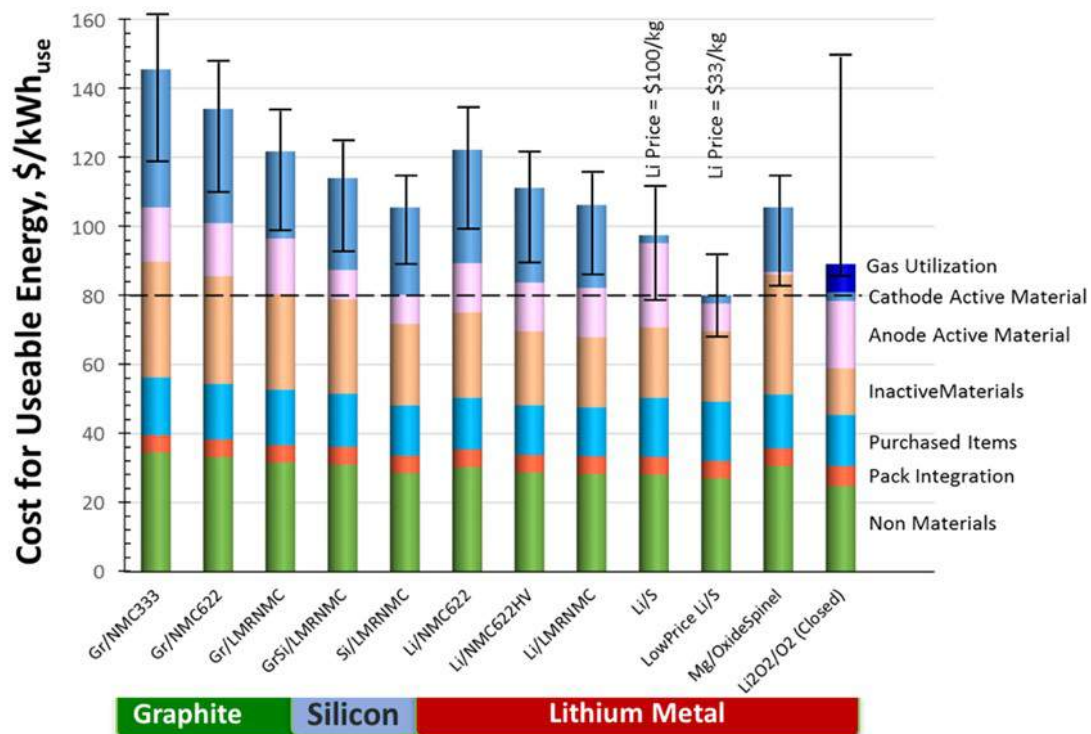


Figure 2. Potential for Future Battery Technology Cost Reductions

Battery Technology Barriers

The major remaining challenges to commercializing batteries for EVs (as well as 12V start-stop micro-hybrid batteries) are as follows:

A. Cost. The current cost of high-energy lithium-ion batteries is approximately \$150 – \$200/kWh (on usable energy basis), a factor of two-three times too high from where it needs to be. The cost of lithium-ion-based 12V micro-hybrid batteries (which offer significantly better life and higher capacity than conventional lead acid batteries) is approximately 50% too high compared to lead acid. The main cost drivers are the high cost of raw materials, costs associated with materials processing, the cell and module packaging, and manufacturing.

B. Performance. Historically, a higher energy density was needed to reduce the weight and volume of PEV batteries, but those weight and volume issues have been to a large degree been addressed. The use of higher energy materials is still an effective way to reduce costs further and extend driving range, but cell chemistries that provide higher energy have life and performance issues. Also, existing chemistries (e.g., graphite anodes paired with transition metal oxide cathodes) need improvement in XFC and low temperature performance to compete favorably with gas-powered vehicles in the areas of performance and customer convenience. The main performance issue with lithium-ion 12V start/stop batteries is a challenging “cold start” requirement at -30°C coupled with high or room temperature life.

C. Life. The life issue for mature lithium-ion technologies has mainly been mostly addressed. However, both next-gen and BLI cell technologies still suffer major cycle and calendar life issues. The life of lithium-ion-based 12V start/stop micro-hybrid batteries is relatively good at room temperatures. However, enhancing cold crank performance often shortens battery life at the high temperatures found in the under the hood application.

D. Abuse Tolerance. Many lithium-ion batteries are not intrinsically tolerant to abusive conditions; however, full packs have been engineered by automotive OEMs to mitigate much of the risk. The reactivity of high nickel cathodes and flammability of current lithium-ion electrolytes are areas for possible improvement. The characteristics of next-gen and BLI chemistries to abusive conditions are not well-understood. However, silicon anode cells show very high temperatures during thermal runaway and lithium metal-based batteries have a long history of problematic dendrite growth which can lead to internal shorts and thermal runaway. Thus, research into enhanced abuse tolerance strategies will continue.

E. Recycling and Sustainability. Currently, automotive OEMs pay a relatively large cost (5-15% of the battery cost) to recycle end of life PEV batteries. The various chemistries used in lithium-ion cells results in variable backend value. Alternatively, unless they get recycled, lithium-ion batteries could lead to a shortage of key materials (lithium, cobalt, and nickel) vital to the technology. Finding ways to decrease the cost of recycling could thus significantly reduce the life cycle cost of PEV batteries, avoid material shortages, lessen the environmental impact of new material production, and potentially provide low-cost active materials for new PEV battery manufacturing.

Program Organization Matrix

VTO's energy storage effort includes multiple activities, ranging from focused fundamental materials research to prototype battery cell development and testing. The R&D activities can involve either shorter-term pre-competitive research by commercial developers or exploratory materials research generally spearheaded by national laboratories and universities. The program elements are organized as shown in Figure 3. Battery R&D activities are organized into the following program elements: Advanced Batteries and Cells R&D, Battery Materials R&D, and the current focus.

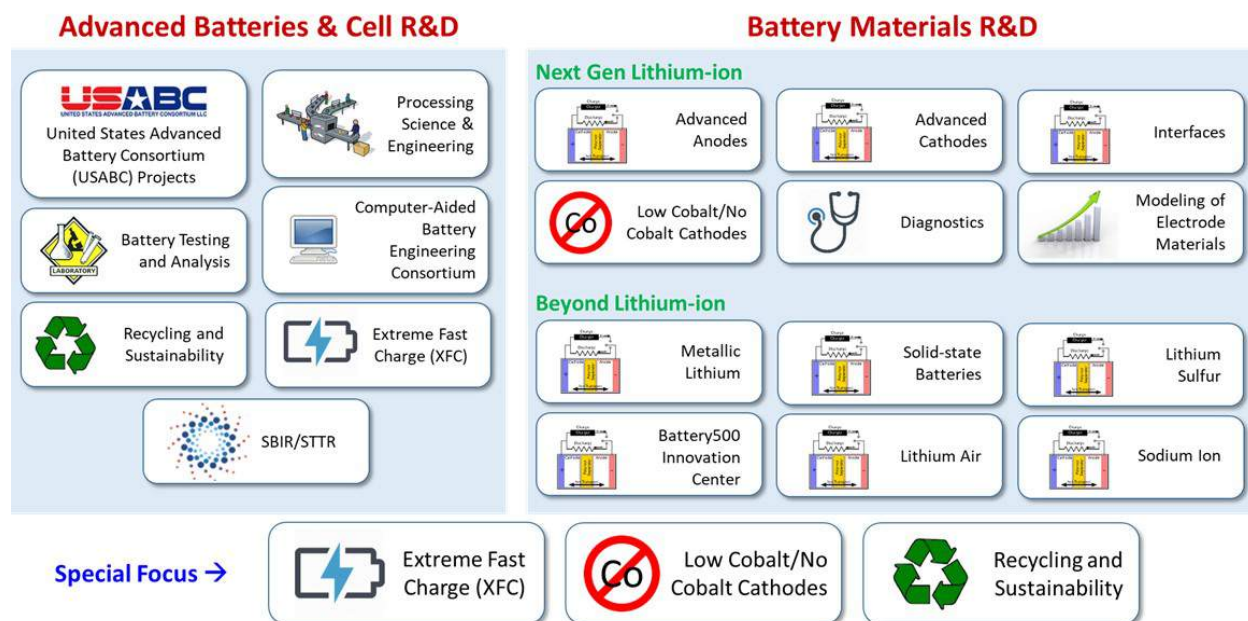


Figure 3. Battery R&D Program Structure

Advanced Cell and Battery Research and Development activity. This activity focuses on the development of robust battery cells and modules to significantly reduce battery cost, increase life, and improve performance. In this report, Part of this effort takes place in close partnership with the automotive industry, through a cooperative agreement with the *United States Advanced Battery Consortium* (USABC). In FY 2019, the USABC supported eight cost-shared contracts with developers to further the development of batteries and battery components for PEVs and HEVs. In addition to the USABC projects, DOE supports battery and material suppliers via contracts administered by the National Energy Technology Laboratory (NETL). Other projects in this area include performance, life and abuse testing of contract deliverables, laboratory- and university-developed cells, and benchmarking new technologies from industry; thermal analysis, thermal testing and modeling; cost modeling; secondary usage and life studies; and recycling studies for core materials. The *processing science & engineering* activity supports the development and scale-up of manufacturing technologies needed to enable market entry of next-generation battery materials and cell components – emphasizing disruptive materials and electrode production technologies that could significantly reduce cost and environmental impact while increasing yield and process control relative to existing production technologies. Several *small business innovation research* (SBIR) projects, also supported by VTO, are focused on the development of new battery materials/components and are the source of new ideas and concepts and are covered in that chapter.

Advanced Materials Research activity. This activity addresses fundamental issues of materials and electrochemical interactions associated with rechargeable automotive batteries. It develops new/promising materials and uses advanced material models to discover them and their failure modes, as well as scientific diagnostic tools and techniques to gain insight into why they fail. This work is carried out by researchers at national labs, at universities, and at commercial facilities. It includes the *next generation lithium-ion* research activity focused on the optimization of next generation, high-energy lithium-ion electro-chemistries that incorporate new battery materials. It emphasizes identifying, diagnosing, and mitigating issues that impact the performance and lifetime of cells constituted of advanced materials. Research continues in the six areas of advanced anodes, advanced cathodes, advanced electrolytes, electrode issues, interfaces, diagnostics, and modeling. The *beyond lithium-ion* (BLI) Technology activity addresses fundamental issues associated with lithium batteries, develops new/promising materials and uses advanced material models to discover such

materials using scientific diagnostic tools/techniques. It includes solid-state battery technologies, lithium metal, lithium sulfur, lithium air, and sodium-ion systems. The newly-started VTO *Battery500* projects are also managed in conjunction with this program element.

Special Focus. The current focus targets three areas of battery research. The first area is concerned with enabling *extreme fast charging* (XFC) in enhanced lithium-ion systems. It started with a 2017 research project to understand XFC, followed by a set of XFC awards (listed in the last year's report). In the second area, recognizing the issues of price volatility and supply reliability with cobalt DOE recently started new projects to develop and optimize low cobalt cathode materials. The third area consists of a set of *recycling and sustainability* projects, which involve studies of full life-cycle impacts and costs of battery production and use; cost assessments and impacts of various battery recycling technologies; and the material availability for recycling and secondary usage and their cost impacts.

As a further resource, the Electrochemical Energy Storage Roadmap describes ongoing and planned efforts to develop battery technologies for PEVs and can be found at the EERE Roadmap page <http://energy.gov/eere/vehicles/downloads/us-drive-electrochemical-energy-storage-technical-team-roadmap>. VTO also has extensive ongoing *collaboration* efforts in batteries R&D across the DOE and with other government agencies. It coordinates efforts on energy storage with the DOE Office of Science, and the DOE Office of Electricity. Coordination and collaboration efforts include membership and participation in program reviews and technical meetings by other government agencies, and the participation of representatives from other government agencies in the contract and program reviews of DOE-sponsored efforts. DOE also coordinates with the Department of Army's Advanced Vehicle Power Technology Alliance, the Department of Transportation/National Highway Traffic Safety Administration (DOT/NHTSA), the Environmental Protection Agency (EPA), and the United Nations Working Group on Battery Shipment Requirements. Additional international collaboration occurs through a variety of programs and initiatives. These include: the International Energy Agency's (IEA's) Hybrid Electric Vehicles Technology Collaboration Program (HEV TCP); the G8 Energy Ministerial's Electric Vehicle Initiative (EVI); and bilateral agreements between the U.S. and China. The collaborative activities with China under U.S. China CERC.

Battery Highlights from FY 2019

The following are some of the highlights associated with battery R&D funded by VTO (including highlights related to market developments, R&D breakthroughs, and commercial applications).

Advanced Battery Recycling Center (ReCell) Launched: The ReCell Center is a national collaboration of industry, academia (University of California San Diego, Worcester Polytechnic Institute, and Michigan Technological University) and national laboratories (Argonne National Laboratory, National Renewable Laboratory, and Oak Ridge National Laboratory) working together to advance recycling technologies along the entire battery life-cycle for current and future battery chemistries. The recycled materials can be reused in new batteries, helping to drive down the overall production cost of electric vehicle batteries to the national goal of \$80/kWh. The Center will test new recycling techniques in order to develop new battery designs that will enable greater material recovery at end of life. The most promising new recycling processes and battery designs will be demonstrated at pilot scale Center. Validated processes and designs will be licensed to industry for further commercialization. The center collaborators will use existing modeling and analysis tools to help industry determine how to optimize value. Argonne's EverBatt model evaluates the techno-economic and environmental impacts of each stage of a battery's life, including recycling. NREL's supply chain analysis tool provides a birds-eye view of the interconnections between raw material availability, primary manufacture, recycling, and demand. The ReCell Center had its kickoff meeting November 1-2, 2018, at Argonne National Laboratory. The ribbon-cutting celebration for the Center was held on February 15th, 2019 at ANL. The four focus areas include direct cathode recycling, recovery of other materials, design for recycle, and modeling and analysis. A total of 17 projects across the four focus areas identified as the initial work to be performed within the center.

Battery Recycling Prize Phase I Winners Declared: The purpose of the Lithium-Ion Battery Recycling Prize is to incentivize American entrepreneurs to develop and demonstrate processes that, when scaled, can potentially capture 90% of all lithium-based battery technologies in the U.S., covering consumer electronics, stationery, and transportation applications. A 90% recycling rate of lithium-based batteries would be a significant achievement compared to today's 5% recycling rate. NREL was selected as the Battery Recycling Prize administrator to support DOE with implementation and execution of the prize elements. Over 50 submissions were received for Phase I of the Prize. After review from industry experts and the Federal Consensus Panel, DOE determined that 15 of the submissions (see Table 3) adequately met the criteria for innovativeness, impact, feasibility, and technical approach outlined in the Prize Rules¹⁰. Assistant Secretary Daniel Simmons presented the winner announcement at NREL on September 25, 2019.

Table 3: Lithium-ion battery recycling prize Phase I contest winners

Winner	Project Title
Admiral Instruments	Battery Sorting with Voltammetry and Impedance Data
EEDD	Battery Self-Cooling for Safe Recycling
Holman Parts Distribution	Holman Parts Reverse Logistics Recycling Solution
Li Industries	Smart Battery Sorting System
LIBIoT	Innovative Battery Collection System by Lithium-Ion Battery Internet-of-Things (LIBIoT)
OnTo Technology	Li-Ion Identification
Powering the Future	Banking Today's Materials to Power Tomorrow
Renewance	Reverse Logistics Marketplace
Smartville	Distributed Battery Conditioning HUB
SNT Laser Focused	Utilizing Laser Cutting for Efficient Battery Pack Dismantling
Store Packs Umicore	Development of Four U.S. Collection and Storage Sites for Lithium-Ion Automotive Battery Packs
Team EVBs	A Circular Economy for Electric Vehicle Batteries
Team Portables	Reward to Recycle – Closing the Loop on Portables
Team RRCO	Composite Discharge Media
Titan AES	IonView-Ultrasonic LIB Automated State of Health (SoH) 1 Second Test

Battery500 Consortium. Lithium (Li)-ion batteries have found wide applications in electric vehicles and grid-scale energy storage systems, but it difficult to further increase the energy density to beyond 300 Wh kg⁻¹. The Battery500 Consortium is a multi-institute Department of Energy (DOE) program to develop next generation high energy and low cost lithium (Li) batteries with a specific energy up to 500 Wh kg⁻¹.

- The Battery500 Consortium deploys a multi-disciplinary strategy to use high capacity Li metal anode, and nickel manganese cobalt oxide (NMC) or sulfur (S) cathode for high energy cells.
- The Consortium aims to overcome fundamental scientific barriers in the fabrication and performance of pouch cells.
- The Battery500 team is made of leading scientists and engineers in the United States, including the 2019 Nobel Laureates in Chemistry, Professor Stanley Whittingham and Professor John Goodenough.
- The Consortium leverages the latest advances in battery research and state-of-the-art facilities supported by DOE, implements and optimizes the most advanced electrode materials on industry relevant pouch cells.

¹⁰ <https://americanmadechallenges.org/batteryrecycling>

The Battery500 Consortium has made significant progress in developing electrolyte and electrode materials, and in integrating and optimizing these materials on industry relevant pouch cells.

- The team has implemented and optimized strategies for the design, fabrication and testing of high energy pouch cells.
- The team has developed and implemented standard testing protocols, and safety procedures for cell fabricating and testing.
- The team developed new stable electrolytes for Li anode, and optimized electrode materials and architectures for high energy cells with lean electrolyte and thin Li foil. The team also developed large-scale synthesis techniques for optimized high-nickel (>80%) cathodes.
- The team developed and used advanced tools to characterize thick cathode, Li dendrite formation and pressure effect to extend cell cycling life.
- The consortium fabricated and tested 350Wh/kg Li-NMC pouch cells cycled >250 cycles (>95% capacity retention), and reduced cell swelling by 40%. (Figure 4)

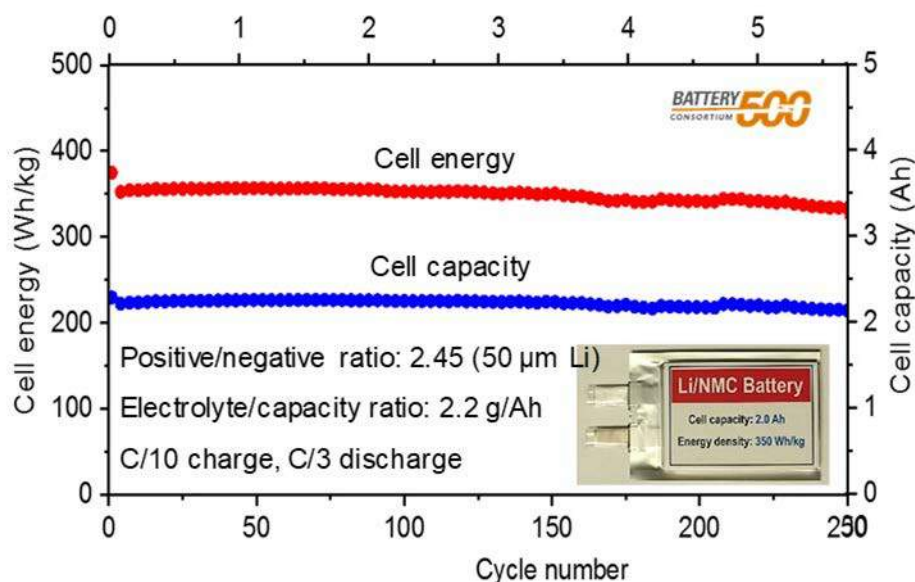


Figure 4. The whole cell capacity (blue) and the specific energy (red) of a 2.0 Ah pouch cell as a function of charge and discharge cycles. More than 90% of the cell capacity and specific energy can be retained after 250 cycles

EverBatt: Battery Lifecycle Cost and Environmental Impacts Modeling Findings. EverBatt is a closed loop model used to estimate cost and environmental impacts throughout a products lifespan for lithium-ion batteries. Figure 5(a) shows all the lifecycle stages of a battery included in the model (except the “Battery Use” stage). The model has been used by industry, academia and government to help identify and evaluate many battery lifecycle questions. Though it can be used for any stage of battery life, the initial focus of the model is on battery recycling. Some examples of how this new type of model can be useful include:

- Identification of the highest impact lifecycle stages of a product’s life
- Comparison of processes within a particular lifecycle stage
- Comparison of a virgin battery to a battery manufactured with recycled content

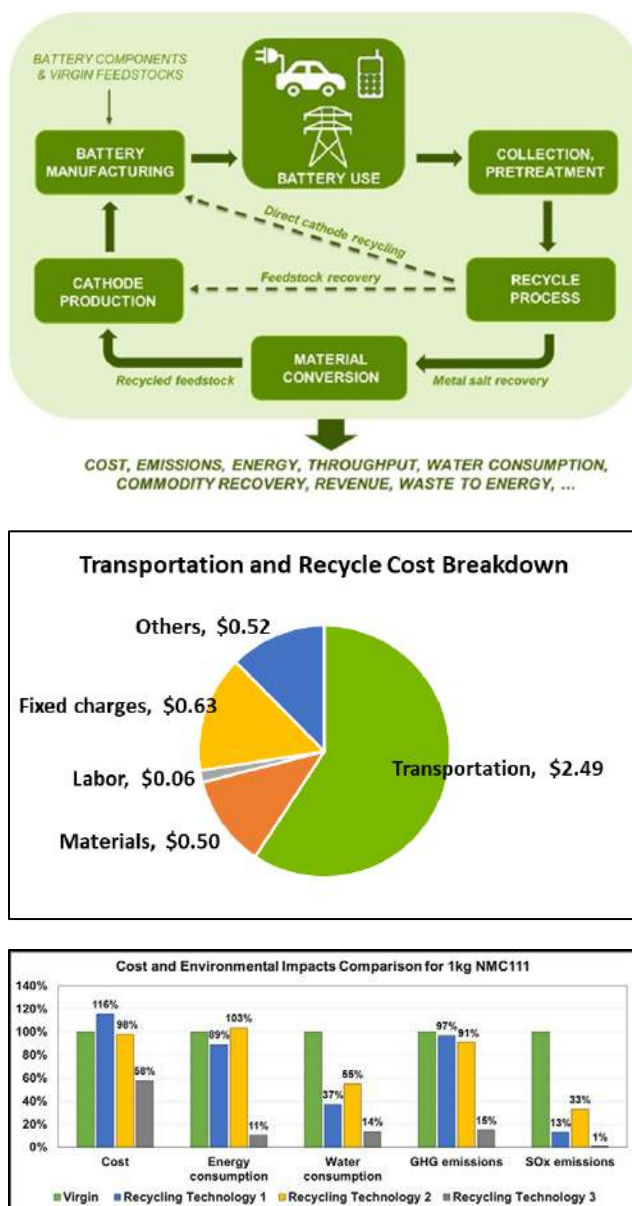


Figure 5. (a) EverBatt's flowsheet, (b) Example breakdown of a lithium-ion battery recycling cost, including transportation, and (c) Chart comparing battery manufacturing cost and environmental impacts from virgin material and material provided by several different recycling technologies

When comparing different lifecycle stages of a lithium-ion battery the model identified that transportation costs could, in some instances, be higher than the cost of recycling itself (Figure 5 (b)), helping push the search for improved methods of transporting batteries at end of life to help reduce the overall consumer cost. Another important finding (Figure 5 (c)) is that closed loop recycling via any technology provides a much lower environmental impact during the battery manufacturing stage than battery manufacture from scratch, but at a higher cost. It was also found that direct cathode recycling may dramatically improve the economics and environmental impacts of recycling and lower the cost of new batteries.

Stabilizing Silicon Anodes via Mg- and Ca-salt Electrolyte Additives to Enable Graphite Replacement.

While the commercial graphite anode has excellent properties, its relatively low capacity has become a limiting factor for improved cells. Replacing the traditional graphite anode with a silicon anode would create

an electrode with 10 times the volumetric and gravimetric capacity of graphite. In practice, this enhanced capacity is tied to a lithium storage mechanism that requires bond-breaking within the silicon lattice (with a large volume expansion), in addition to creating reactive lithiated silicon electrodes at top of charge built from various negatively charged Si_2^{-2} and/or Si^{-4} cluster anions that can chemically reduce common binders and electrolyte components. ANL successfully controlled the reactivity of the surface while maintaining performance by adding 0.1M $\text{M}(\text{TFSI})_x$ ($\text{M} = \text{Mg, Zn, Al and Ca}$) salt in addition to standard LiPF_6 into the electrolyte, stabilizing the anode through *in situ* formation of surface Li-M-Si phases during charging. These new electrolytes were tested in commercially relevant but non-optimized electrodes in xx3450 format single layer pouch cells made by Argonne's *Cell Analysis Modeling and Prototyping (CAMP)* Facility. Cells tested showed superior cyclability and higher Coulombic efficiencies in both half-cell and full-cell configurations (except for Zn) when compared with state-of-the-art electrolytes, as shown in Figure 6. In fact, the best cell (for Ca) demonstrated 65% capacity retention after 300 cycles at C/3 rate. This study opens a new industry-friendly scalable way with a simple and universal additive to stabilize silicon anodes to enable widespread application of Si anodes for lithium-ion batteries.

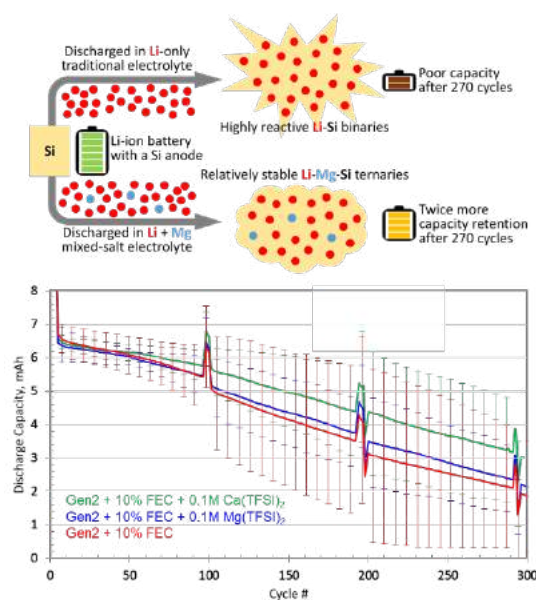


Figure 6. Effect of using mixed-salt electrolytes on 7mAh full cells in xx3450 single layer pouch cell format assembled versus LMR-NMC with 80% Si nanoparticles, 10% hard carbon and 10% LiPAA binder, anodes without any graphite

New electrolytes eliminate shuttle effect in sulfur systems. Lithium/sulfur (Li/S) batteries are attractive for automotive and grid application because of their high theoretical energy density (2600 Wh kg^{-1}) and the abundance of sulfur. However, two major obstacles resulting from poor electronic conductivity of sulfur and lithium polysulfides shuttle significantly impede their practical implement. Integrating sulfur with various carbon hosts has been the most common approach to improve the electrochemical performance of Li/S batteries due to the high electronic conductivity and polysulfides confinement effect from carbon hosts. Researchers at ANL developed a new strategy by using fluorinated ether electrolyte ($1.0 \text{ M LiTFSI/DOL+TTE+0.2M LiNO}_3$) and Se doping to significantly improve the electrochemical performance of Li/S batteries. This TTE-based electrolyte can directly eliminate the formation of polysulfides and enable a solid-solid lithiation process, which is significantly different from the two-step solid-liquid-solid lithiation process in the conventional DME-based electrolytes (Figure 7a). In the meantime, researchers use Se doping to increase the utilization of S due to the comparable volumetric capacity and high electronic conductivity of Se compared to S. The electrochemical test results showed that by using only 10wt.% Se doping, it significantly improved the rate and cycling performance of S cathode (Figure 8). Researchers believe that this strategy could serve as a promising solution for fast-charging Li/S batteries with high coulombic efficiency and long life.

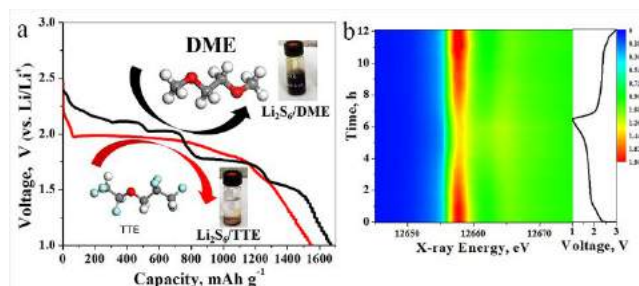


Figure 7. (a) First discharge curve of S_5Se_2/C cathode in DME-based electrolyte and TTE-based electrolyte; (b) In-situ Se K-edge XANES spectra of S_5Se_2/C cathode in TTE-based electrolytes at C/10

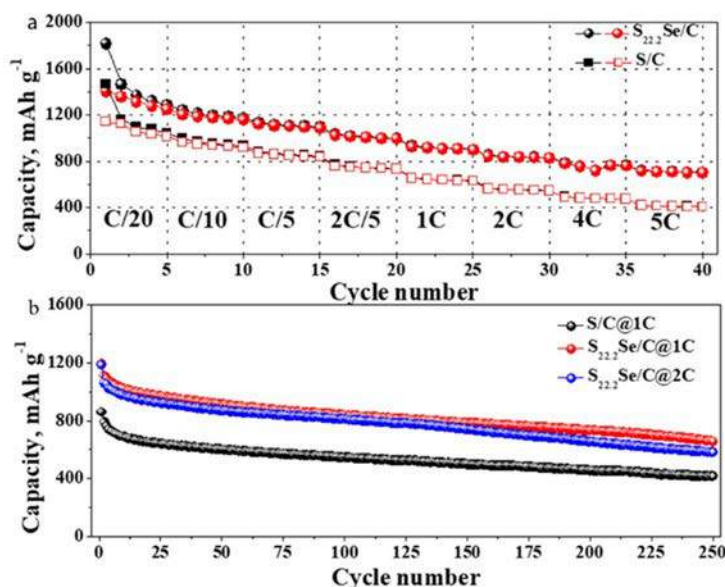


Figure 8. Rate performance and d) cycling performance at high rates of $S_{22.2}Se/KB$ cathode and S/KB cathode in TTE-based electrolyte

Surface Conditioning of High-Nickel Cathodes. High-nickel (Ni) layered oxides (with $\geq 70\%$ Ni) are promising candidates for cathodes in lithium (Li)-ion batteries (LIBs) for electric vehicles, due to their high capacity and low cost. The high Ni loading, on the other hand, gives rise to poor cycling and rate performance. Significant efforts on developing practically viable high-Ni cathodes have been given to materials synthesis/processing, mostly on tuning the structural ordering in the bulk. It is not until recently that researchers started to pay close attention to surface reconstruction as evidences have been growingly reported, showing it is an inherent issue in high-Ni cathodes and the resulted inactive surface layer causes high impedance to Li^+ (de)intercalation (Figure 9(a, b)). However, it's unclear how the reconstruction occurs and how the issue should be alleviated during synthesis.

At Brookhaven National Laboratory (BNL), scientists have developed *in situ* techniques for real-time monitoring of synthesis reactions at various length scales. Using that capability, the BNL team studies the process of synthesizing high-Ni layered oxides by tracking intermediates and their structural (re)orderings, not only in the bulk but also at the surface (Figure 9 (c)). Through the efforts, they reveal the accumulation of carbonate (Li_2CO_3), formation of a Li-deficient layer and Ni reduction at the particle surface, as a result of the near-surface Li/oxygen loss in the final cooling stage of synthesis. The kinetic reconstruction process occurs predominantly at high temperatures (above 350 °C) and is highly cooling-rate dependent.

With these findings, the BNL team has developed protocols for synthesizing high-Ni layered oxides with greatly reduced interfacial impedance and improved rate capability (Figure 10). Results are published in the *Advanced Energy Materials* at: <https://doi.org/10.1002/aenm.201901915>. They will test the protocols in future studies, in developing other high-Ni, low-cobalt (Co) or Co-free cathodes, of the immediate interest to commercial use in next-generation LIBs.

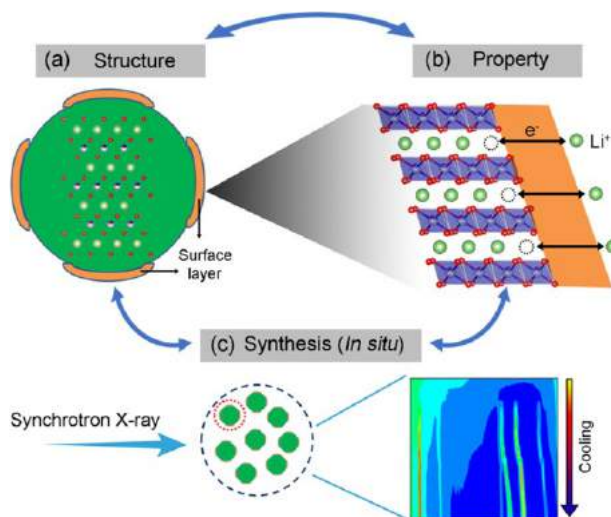


Figure 9. Schematic illustration of the approach for rational synthesis of high-Ni layered oxides with a “closed” loop, specifically, through studying the surface reconstruction, its impact to electrochemical properties, and its formation process (using in situ synchrotron X-ray techniques)

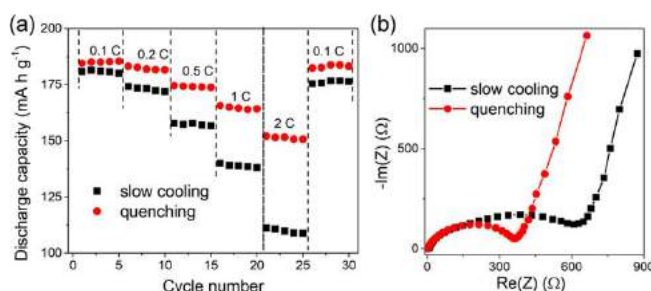


Figure 10. (a) Rate performance and (b) impedance of the $\text{LiNi}_{0.7}\text{Mn}_{0.15}\text{Co}_{0.15}\text{O}_2$ samples by slow cooling and quenching

Appropriate cell design for evaluating high energy cells. As part of the Battery500 Consortium research activities, investigators at Pacific Northwest National Laboratory, Idaho National Laboratory, UC San Diego and Binghamton University identified conditions necessary for evaluation of new materials and electrode designs for high energy batteries. Traditional efforts in this area have used reproducible methods for evaluation, but a significant gap exists in key experimental parameters directly linking early research advances to improved life and performance in realistic cell designs of 1 Ah and above. As part of the effort to transition early research successes to full rechargeable lithium metal pouch cells the team developed sets of guidelines and best practices that ease the transition and enable better comparison across the research community.

To facilitate high energy, rechargeable lithium metal batteries key parameters need to be considered during all stages of the technology development. As shown in Figure 11, three of the most distinct considerations are the use of lean electrolyte, thin lithium metal and cathode loadings that are sufficiently high to meet the desired cell-level specific energy.

Based on results that the use of excess electrolyte or lithium metal or the use of low cathode loadings can artificially extend the cycle life of cells by 10's if not 100's of cycles, the team developed a set of recommendations for use in coin cell and pouch cell evaluation. These include using a thin Li metal negative electrode (50 μm thickness or less), a certain volume of electrolyte (less than 3 g/Ah of cathode capacity) and a minimum cathode loading (at least 3.5 mAh/cm²). Using these three primary recommendations the team completed evaluations in both coin cells and in a 1+ Ah cell to demonstrate the effectiveness of the use of more direct and prescribed limiting conditions that align with a realistic full cell design. The team has also developed recommendations for lithium-sulfur batteries.

Using these recommendations as a backdrop the Battery500 team has cascaded new technology advancements into the full cell design which have enabled increasing specific energy to 350 Wh/kg and over 250 cycles.

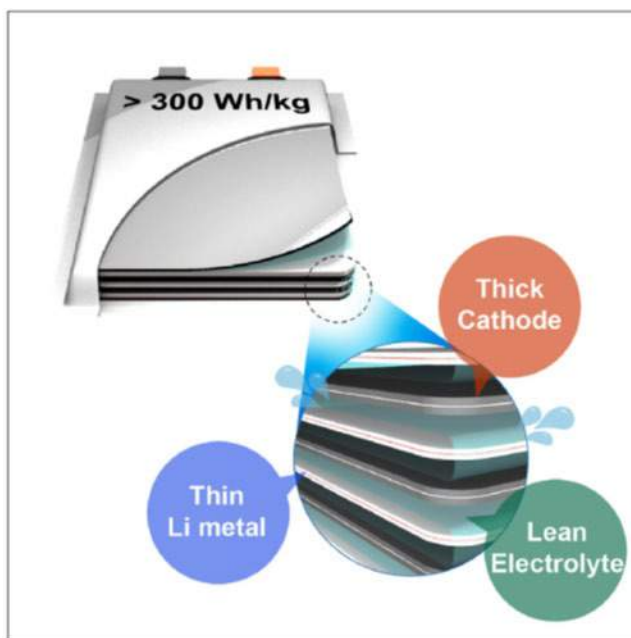


Figure 11. Key parameters which need to be controlled during the technology development and evaluation process. From Chen et. al, Joule 3, 1-12, 2019

Safety guidelines for energy storage testing. As research and development of new batteries expands and additional researchers look to evaluate technology developments in realistic formats and conditions there has been an identified gap in how to effectively and reproducibly perform analysis in laboratories across the R&D spectrum. Building on significant prior experience working with the U.S. Department of Energy, a recommendations set was published to help advance research in larger battery systems.

Since starting characterization in 1983 researchers at INL have developed sets of best practices which facilitate high fidelity data collection and safe operation. In an article published in a perspective article to the Journal of the Electrochemical Society (R. Bewley et. al, J. Electrochem. Soc, 166(8), E263, 2019), many of these best practices were disseminated to the research community as an effort to facilitate enhanced technology development and integration for high energy and high power batteries.

Key aspects covered in the perspective

- Proper planning including test plan development covering possible failure routes
- Appropriate loading levels for environmental chambers to limit propagation risk
- Best practices for fixturing and cabling
- Use of secondary safety measures and independent confirmation of profiles and protocols
- End of test disposition and treatment of cells

The design of universal test fixtures (Figure 12) that can be readily adapted to different cell sizes and formats was one of the distinct contributions that has arisen from the work. The fixtures provide the ability to reduce the possibility of researcher exposure to cell terminals, provide enhanced isolation between cells and can be modified to accommodate several different secondary sensors including thermocouples and pressure sensors. While the design of the fixtures provides distinct safety advantages it also helps in the reproducible fixturing of cells which is increasingly being shown to directly impact performance for many different battery chemistries.

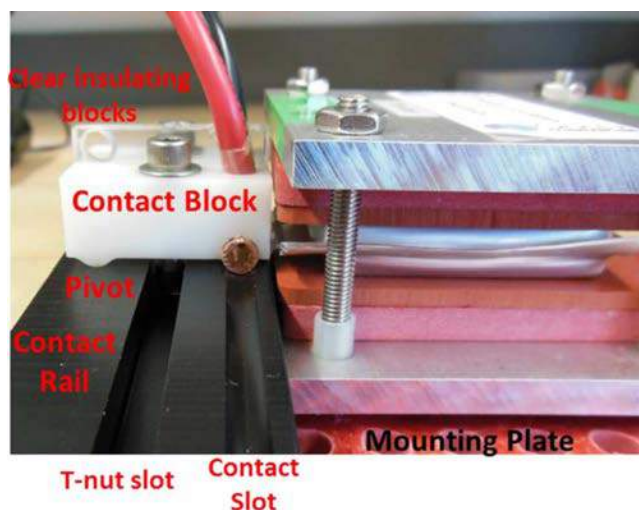


Figure 12. Universal test fixture designed to enhance data fidelity and repeatability while also providing advanced safety features

Cathode cracking during fast charge. Enabling extreme fast charging (XFC: $\geq 6C$ in ≤ 10 min) of lithium-ion battery could spur the wider adoption of battery electric vehicles, by making recharging times comparable to refueling times in traditional gasoline vehicles. Undesirable lithium plating at the anode is considered to be the key barrier to fast charging. The scientific community devotes significant efforts to better understand the lithium-plating issue and identify solution pathways during XFC. The effects of XFC on the cathode side have been largely unexplored. Understanding the full suite of limitations which occur in full cells during XFC conditions is required to enable XFC.

During evaluation of cells for XFC conditions, researchers at Idaho National Laboratory has characterized the failure mechanisms that were related to both positive and negative electrodes. Using well-defined single-layer pouch cells (gr/NMC₅₃₂), the Laboratory performed extended fast-charge cycling (up to 450 cycles) at multiple charging rates (C-rates). Comprehensive electrochemical analyses accompanied by targeted post-testing were carried out to identify the central constraints of XFC.

Comparison of cycle-life capacity fade at different charging rates (or C-rates) showed distinct and more-global cathode cracking (primary particle separation within the secondary particle) when cells are charged at higher C rates (Figure 13). Such cracking resulted in significant loss of cathode-active material, which subsequently manifested as cell capacity loss and impedance rise. For the extreme charging conditions—i.e., 6C and above—the cathode-capacity loss (due to cracking) dominated the overall cell capacity loss in cells which did not have favorable conditions for Li plating (relatively low loading cell typical for high-power applications).

INL's finding highlights that, besides focusing on loss of Li through plating, attention needs to be paid to the positive electrode during XFC, in particular when the charging rate exceeds 6C. Follow on efforts include detailed characterization of cracking, its evolution with cycling and when it becomes the limiting factor and advanced modeling of the cathode by incorporating cathode-cracking phenomena for better predictability, and identification and verification of ways to mitigate cracking during XFC conditions.

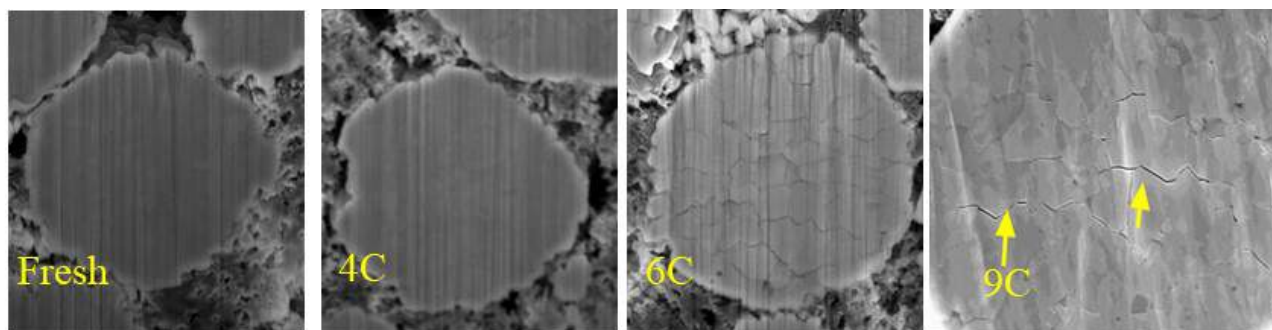


Figure 13. The SEM micrographs of secondary cathode particles ($\sim 10\mu\text{m}$ diameter) show the extent of interprimary particle separation (cracking) at fresh (no fast charge cycling) and the end of cycling (up to 450 cycles) at different charging rates. A 2 hour (C/2) slow discharge was used in all cases. The cycling voltage were between 3 to 4.1V

Impact of Binder Morphology and Crystal Structure on Electrode Performance. Electrode construction can have as much of an impact on a battery's life and performance as does the active material that assumes an overwhelming fraction of the electrode's overall composition. Recent research is starting to shed some light on how the binder may play a critical role in this regard.

To better understand the polymer's impact, one needs to understand the morphology of the polymer. PVDF takes on several forms of crystallinity depending upon the temperature at which it is formed as it transitions from a solubilized state to a dried structure. The data provided in Figure 14.a) confirms the transition of the polymer crystallinity from β -phase crystallinity to α -phase when formed from NMP slurries dried at several different temperatures.

Investigation of the conductivity of the films at different temperatures when saturated with electrolyte revealed that the crystalline phase formed at lower temperatures is more ionically conductive than films formed at higher temperatures. This is illustrated in Figure 14.b).

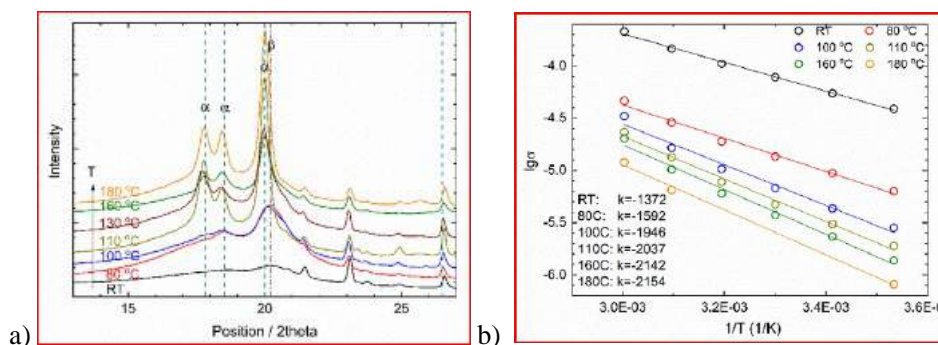


Figure 14. a) X-ray diffraction spectra of PVdF films produced by drying NMP-based slurries at different temperatures. b) log-log plot of room temperature conductivity data versus inverse of the absolute temperature during drying

We have previously shown that mixing order of electrode components can have an impact on battery cycle life. We revisited this aspect with regard to drying rate and pulse power performance. What we discovered is that electrodes prepared by mixing the active material and carbon black in NMP prior to adding dissolved binder could be dried at temperatures up to 140°C without cracking but electrodes prepared by mixing the carbon black with dissolved binder prior to adding the active material could be dried to as high as 180°C without cracking. However, the former process led to electrodes that dried 3 times faster than the latter process when dried at comparable temperatures. This suggests that the former mixing sequence leads to a polymer morphology that is thinly spread over all of the solid materials and easily accessible for heat and mass transfer

during drying whereas the latter process leads to agglomeration of conductive carbon and polymer that takes longer to remove the absorbed NMP.

We also discovered that the electrodes produced that lead to a thin layer of polymer over the active material relied on the conductivity of the film to enhance performance (Figure 15a) whereas binder agglomerated with carbon may rely on strong mechanical properties between particles for better performance (Figure 15b).

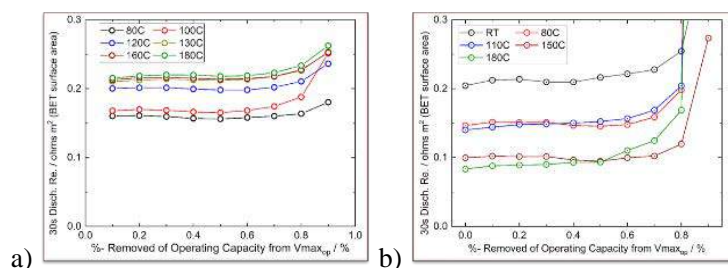


Figure 15. Resistance versus DOD for electrodes dried at different temperatures a) active material and carbon black mixed together first; b) carbon black and polymer slurry mixed together first

Composite Cathode Architectures Made by Freeze Casting for All Solid-State Lithium Batteries.

Functioning bulk-type all-solid-state batteries in a practical form factor with composite positive electrodes, using Al-substituted $\text{Li}_7\text{La}_3\text{Zr}_2\text{O}_{12}$ (LLZO) as the solid electrolyte, have been demonstrated for the first time. The devices incorporate bilayers composed of dense LLZO membranes and porous LLZO scaffolds infiltrated with $\text{LiNi}_{0.6}\text{Mn}_{0.2}\text{Co}_{0.2}\text{O}_2$ (NMC-622) and other components as positive electrodes, combined with lithium anodes. The porous scaffolds are prepared using an easily scaled freeze-tape-casting method. The unidirectional pores of the scaffold facilitate infiltration of cathode components and shorten lithium ion diffusion path-lengths, while the addition of a soft ionically conductive solid to the scaffold ensures good contact among the components. (Figure 16)

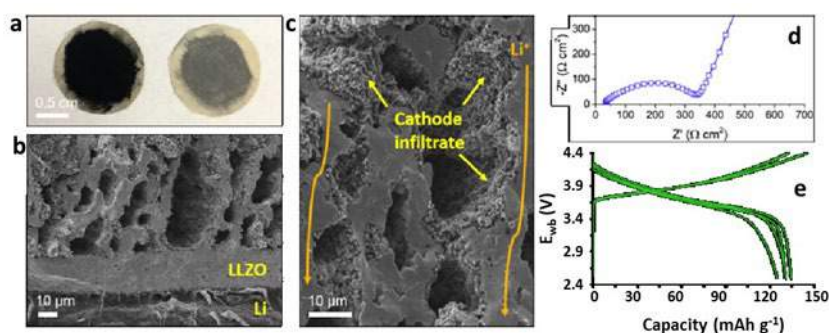


Figure 16. (a) Optical image of cathode infiltrated LLZO bilayer. Cathode infiltrated porous layer surface (left) and dense layer surface (right) are shown. (b) SEM fracture surface image of cathode infiltrated bilayer. Images were taken prior to SCN electrolyte infiltration. (c) Same cell at higher magnification showing cathode infiltrate. (d) Nyquist plot of the constructed ASSB. (e) Initial charge/discharge profiles of the ASSB

To the best of our knowledge, this is the first report of successful room temperature cycling of a bulk type all solid-state battery using a LLZO separator and composite electrode in a practical form factor. Almost all studies reporting solid-state-batteries use thick LLZO pellets (3-5 mm) and apply/attach active materials to complete a cell. While those studies are useful for answering fundamental questions, they are not in a practical form factor. The use of thick pellets and thin cathode layers greatly compromises energy density. The LLZO should be in a thin film form, to minimize weight and volume as well as impedance. Examples of LLZO thin films or bilayer/trilayer architectures involving a thin LLZO layer have been reported previously. However, the constructed cells all use liquid electrolytes to address the cathode/LLZO interfacial contact issue and are therefore not truly solid state.

The superior electrochemical performance can be ascribed to several factors including the use of a thin, dense LLZO separator layer, seamless Li/LLZO contact, a low tortuosity pore structure and intimate contact among the components in the composite cathode structure. The concept of combining a rigid scaffold with a soft, yet solid, conductor is quite general and can be expanded to other types of systems, including those that conduct, e.g., sodium.

Layered-Rocksalt Intergrown Cathode for High-Capacity Zero-Strain Operation. Li-rich metal oxides of layered and rocksalt structure that can exhibit a high capacity of 250-300 mAh g⁻¹ are considered as promising cathode candidates for high-energy lithium-ion batteries. Although both materials share a similar close-packed oxygen framework, layered oxide cathode suffers from an irreversible phase transformation as well as oxygen loss, while rocksalt oxide exhibits a minimal isotropic structural change upon electrochemical cycling. It would be principally ideal to harness the combined figures of merit from each individual phase. So far, very limited success has been demonstrated to utilize the structural compatibility of layered and rocksalt phases for the development of high-performance lithium-ion cathodes.

At LBNL, we propose a concept of layered-rocksalt intergrown structure for the development of advanced lithium-ion cathode. For the proof of concept, we have successfully designed and synthesized lithium nickel ruthenium oxide based on Ni²⁺/Ru⁵⁺ combination, Li_{1.2}Ni_{0.4}Ru_{0.4}O₂, which exhibits a main layered R $\bar{3}$ m structure with well-grown rocksalt Fm $\bar{3}$ m nanodomains. High-angle annular dark-field scanning transmission electron microscopy (HAADF-STEM) image (Figure 17) clearly reveals an intergrown structure with the rocksalt domain embedded in the main layered phase. This layered-rocksalt intergrown oxide displays an initial Li⁺ extraction and insertion of ~ 1.1 and 0.95 (244 mAh g⁻¹) out of total 1.2 Li⁺ inventory during charge and discharge, respectively. Such a high reversible capacity is enabled by combined cationic and anionic redox reactions.

We further probe the phase evolution of layered-rocksalt intergrown oxide upon electrochemical cycling. There is no new phase formation upon the extraction of Li⁺. Strikingly, the lattice parameters *a* and *c* of the layered R $\bar{3}$ m component exhibit an isotropic change. It is worthwhile noting that both lattice parameter *a* and *c* of the layered R $\bar{3}$ m component show a minimal change of ~1%, hence referred to as “zero-strain” electrode. The layered-rocksalt intergrown phase displays an excellent structural robustness with the minimal change in lattice parameters upon delithiation/lithiation. The success of such layered-rocksalt intergrown structure exemplifies a new concept of battery electrode design and opens up a vast space of compositions to develop high-performance intergrown cathode for advanced energy storage devices.

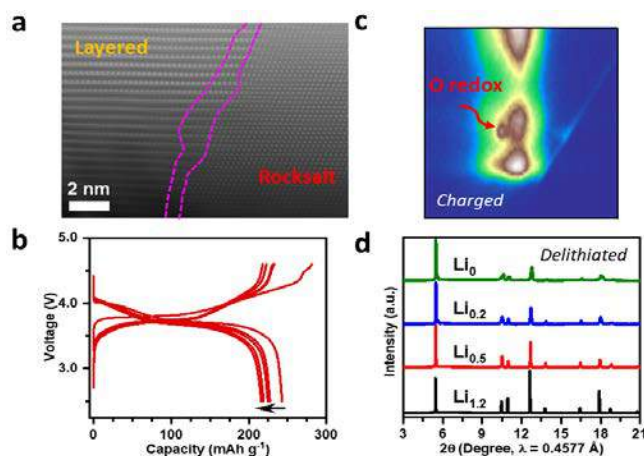


Figure 17. (a) Representative HAADF-STEM image of Li_{1.2}Ni_{0.4}Ru_{0.4}O₂, showing the layered-rocksalt intergrown structure along the [110] zone axis; (b) charge-discharge voltage profiles during the first five cycles; (c) O K-edge resonant inelastic X-ray scattering map at charged state, red arrow indicating the fingerprinting feature of oxidized oxygen; and (d) X-ray diffraction patterns of Li_xNi_{0.4}Ru_{0.4}O₂ (*x* = 1.2, 0.5, 0.2, 0) at different delithiated states, showing the isotropic structural evolution upon delithiation

Surface Dopants to Stabilize High Ni Cathodes. Layered transition-metal oxides remain the majority of the cathode materials in commercialized lithium-ion batteries (LIBs). To further increase the energy density and decreasing the reliance on Co, the Ni content in the current Ni-rich cathodes has been progressively increased. However, deteriorating cycling performance currently limits widespread deployment. One major culprit is oxygen loss, which increases the surface impedance and undermine the thermal stability of LIBs.

Lawrence Berkeley National Laboratory (LBNL) has used a theory-guided screening to discover a number of surface dopants that alleviate oxygen evolution from LiNiO_2 . To evaluate each dopant's ability to suppress the surface oxygen loss, we calculated the relative oxygen release energy during delithiation of doped- LiNiO_2 with respect to the pristine phase (Figure 18a). Figure 18b shows a surface model of doped- LiNiO_2 majority (104) surface facet. It was found that the calculated oxygen release energies of Sb-, Ta-, and Ti-doped LiNiO_2 are higher than that of the pristine phase, which implies that Sb, Ta, and Ti can enhance the surface oxygen retention of LiNiO_2 and Sb is predicted to be the most promising dopant.

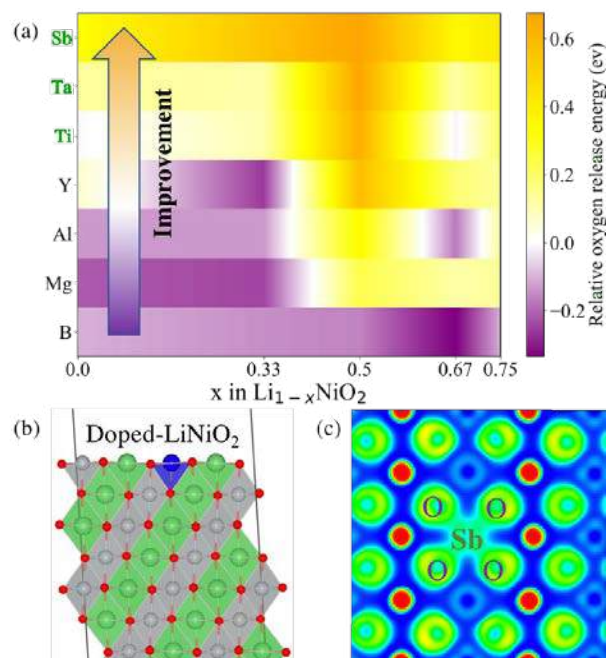


Figure 18. (a) The relative surface oxygen release energies of doped LiNiO_2 with respect to the pristine phase. Yellow-orange color indicates an improved oxygen retention, while the purple color indicates a reduced oxygen retention as compared to the pristine phase. (b) Schematic illustration of surface doped LiNiO_2 model. Blue: dopant, green: Li, grey: Ni, red: oxygen. (c) 2D electron localization function contour plot for the surface slice of Sb-doped LiNiO_2

Further insight into the nature of the dopant-oxygen bonding is provided by an electron localization function (ELF) analysis, as shown in Figure 18c. The green regions between the Sb and O atoms correspond to shared electrons, which is a signature of covalent bonding. Therefore, a higher degree of electrons sharing between Sb and O leads to a stronger Sb-O bond and better oxygen retention.

In summary, Sb, Ti as well as Ta were identified as promising dopants to mitigate surface oxygen loss from LiNiO_2 . The effectiveness of Sb doping was rationalized based on the bond strength between the dopant and oxygen.

As part of the EERE-funded Co-free program, the theory team at LBNL is working closely with experimental collaborators from Virginia Tech to verify the predictions. The initial results show a superior capacity retention in Sb-doped LiNiO_2 over the pristine phase.

NFA Synthesis, Scale-up, and Performance. Commercial present-day cathode materials used in lithium ion batteries such as $\text{LiNi}_x\text{Mn}_y\text{Co}_z\text{O}_2$ (NMC) and $\text{LiNi}_x\text{Co}_y\text{Al}_z\text{O}_2$ (NCA) contain cobalt in their compositions. Recently, cobalt prices however, have undergone rapid fluctuations and have nearly tripled in the last decade. This trend has become quite unsustainable for the battery manufacturing industry especially at a time when lithium-ion batteries are poised to usher in the era of electric automobiles. The availability of cheap cobalt is a potential problem which can derail the hopeful future projections of renewable energy storage and electric vehicles.

To address this challenge, researchers have embarked on developing novel classes of cobalt free cathode materials which contain low-cost constituents aimed specifically at replacing the cobalt in conventional NMC and NCA type cathode systems. The developed cobalt free chemistries would facilitate seamless integration into existing global battery manufacturing infrastructures without compromising material and electrochemical performance metrics. In this context, our team of researchers have developed a new class of nickelate cathodes, the lithium, iron and aluminum nickelate ($\text{LiNi}_x\text{Fe}_y\text{Al}_z\text{O}_2$) termed the NFA class of cathodes. Our team initially synthesized these materials using the sol-gel process to quickly explore their compositional landscape. Specific compositions starting with 80% nickel content (NFA Gen-1) and the rest a combination of iron and aluminum were selected after thorough evaluations of their compositional and crystallographic purities determined using advanced characterization techniques such as ICP-MS, XRD and Neutron diffraction following which electrochemical evaluations were carried out. The best performing composition was down selected for scale-up through the coprecipitation process using a continuous stirred tank reactor (CSTR). The NFA cathode particles synthesized using the CSTR is shown in the Figure 19(A). The electrochemical half-cell performance of the cathode material is shown in Figure 19(B). The NFA cathode delivers a capacity of ~ 180 mAh/g at a c-rate of C/3 in the voltage range of 3V-4.5V.

The insights and advancements developed through our work highlights the potential of cobalt free cathode materials such as the NFA class to provide a commercially viable pathway towards successful development of next-generation electric automobiles.

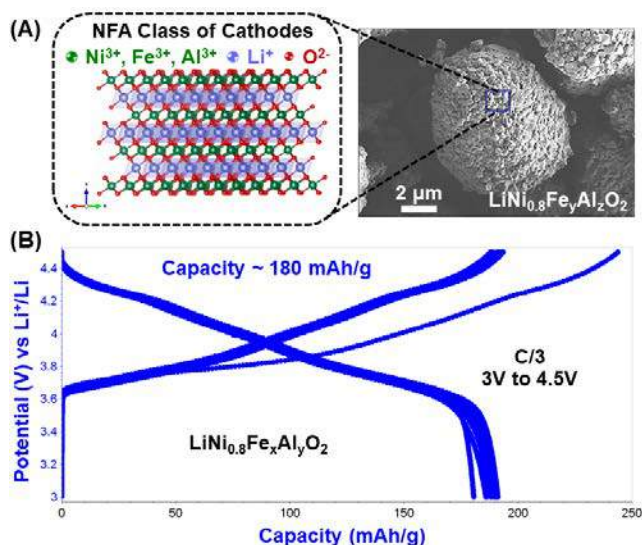


Figure 19. (A) NFA cathode particles synthesized through a co-precipitation reaction in a CSTR and (B) Charge/Discharge curves indicating the good capacity and performance delivered by the NFA cathode material

I Advanced Battery and Cell R&D

I.1 USABC Battery Development & Materials R&D

I.1.A High-Performance Semi-Solid Cell for EV Applications (24M Technologies, Inc.)

Mohamed Taggougui, Principal Investigator

24M Technologies, Inc.

130 Brookline Street

Cambridge, MA 02139

E-mail: Mtaggougui@24-m.com

Brian Cunningham, DOE Technology Development Manager

U.S. Department of Energy

E-mail: Brian.Cunningham@ee.doe.gov

Start Date: June 15, 2016

End Date: June 14, 2019

Total Project Cost: \$6,998,594

DOE share: \$3,499,297

Non-DOE share: \$3,499,297

Project Introduction

24M Technologies has developed a breakthrough manufacturing process that leverages proven and emerging chemistries to deliver lithium-ion batteries with lower cost and less inactive materials content than any existing lithium-ion cell. In this program, 24M will develop large-format, automotive-capable cells leveraging high-energy advanced lithium-ion chemistries. 24M's unique electrode and cell architectures are inherently capable of accommodating large volume-change active materials, and 24M's cells exhibit unprecedented levels of abuse tolerance. The manufacturing process requires less than one half the number of unit operations of conventional lithium-ion technology and has been demonstrated in automated pilot production.

24M's proprietary flowable (SemiSolid) electrode technology enables unique cell architectures with several advantages compared to conventional Li-ion batteries. For automotive applications, a key advantage is the novel manufacturing method, which dramatically reduces manufacturing complexity and cost. Additionally, it is readily scalable according to market demand. The small footprint for equipment and comparatively low capital equipment investment needed further reduce the manufacturing risk.

24M's unique electrode and cell architectures significantly lower the materials cost in each cell. 24M believes that its cell design has lower materials cost per energy (\$/kWh) than any Li-ion cell of comparable energy and power in the market or under development. Cells based on SemiSolid electrodes have a higher ratio of active materials to inactive materials than conventional Li-ion cells, providing an inherent, sustainable advantage in the cell bill of materials.

Finally, unlike most development approaches in advanced batteries, 24M's core technologies is a platform for electrode and cell design and manufacturing that are not limited to any particular set of active materials. Therefore, 24M's cells can leverage all of the active materials available today and those developed in the future. As a platform player, 24M maintains the flexibility to drop-in next generation active material as lithium-ion chemistries evolve and as alternative chemistries (such as Na-ion or Mg-ion) emerge.

Objectives

24M will demonstrate that its novel electrode, cell and manufacturing approach can be applied to high-energy density lithium-ion chemistries to enable mass production of automotive-capable prismatic Li-ion cells with dramatically lower cost. The approach outlined below has been planned to develop high energy density SemiSolid electrode formulations, and to demonstrate the manufacturing of prototype cells based on those formulations that meet or exceed the USABC targets outlined in Table I.1.A.1 for each phase of the program.

Table I.1.A.1 Characteristics of the Annual Cell Deliverables in the Program

	Phase 1	Phase 2	Phase 3
Cell Footprint (cm ²)	80	250	250
Capacity (Ah)	6	11	11
Energy Density* (Wh/L)	400	640	800
Specific Energy** (Wh/kg)	200	290	350
Number of Cells	30	18	18

*Assuming 87% volumetric packing efficiency, End of Life requirement

**Assuming 95% gravimetric packing efficiency, End of Life requirement

Approach

24M has planned activities designed to achieve the objectives identified in the preceding section. For each activity, the task-specific objectives and approaches are described below.

1. High Energy Materials Evaluation and Selection

Developing new SemiSolid electrode formulations utilizing high energy active materials requires evaluation and selection of materials comprising a SemiSolid suspension—active materials, additives, and electrolyte—as well as developing an appropriate mixing procedure that yields a SemiSolid suspension with excellent electrochemical performance. Different combinations of active materials and additives will be formulated into SemiSolid suspensions where the physical properties will be evaluated and ranked. The rheology of the material suspension will also be tested in order to determine the consistency and repeatability of the electrode forming process. Candidate electrode formulations will then be used in cell fabrication to evaluate the electrochemical performance of the electrode. Ultimately, active materials and electrode formulations will be selected that optimally balance the tradeoffs of power performance, safety, processability, and life (cycle and calendar) in a 24M automotive cell.

2. Processing Methods for Increased Active Solids Loading

Although increases in active solids loading may seem incremental, each time solids loading is increased, an entirely new formulation must be developed, and processing method evaluated to ensure that ion and electron transport and rheological properties are optimized for manufacturing and cell performance. In this activity, 24M's current and alternative mixing methods will be evaluated and developed to obtain SemiSolid electrodes with active materials loadings necessary for target high energy densities while achieving cycle life and safety performance targets. This activity is complementary to, but distinct from, the active material evaluation and selection activity outlined above. New mixing methods and equipment are continuously improved at 24M and these will be evaluated, and as necessary, developed to achieve the active materials loading levels required for a cell meeting the USABC targets. 24M will create quality control metrics and measure electrochemical performance to evaluate the performance of the SemiSolid suspensions from the various processing methods.

3. Electrode Architecture Development

24M's current electrode manufacturing process is based on automated dispensing and coating of both anode and cathode SemiSolid slurries, using conventional foil current collectors. This activity will evaluate alternative electrode forming methods and cell architectures, including current collectors and investigations into cell formats with increased volumetric efficiency. As 24M continues to transition from pilot manufacturing to high volume manufacturing methods, we anticipate continual improvements in the electrode and cell making operations. Additionally, the ideal processing methods for highly-loaded SemiSolid slurries based on high-energy active materials may differ from those developed for earlier electrode formations. Initially, this activity will evaluate current electrode structure and forming methods for compatibility with high energy active materials. Throughout the program, there will be continual evaluations to ensure that the developed cells are capable of meeting or exceeding the automotive power performance requirements. Finally,

this area of activity will include a specific focus on safety and abuse testing of the developed 24M automotive cell.

4. Cost Modeling

24M's novel manufacturing approach is so different from traditional Li-ion manufacturing methods that conventional cost models cannot be directly applied for cost forecasting. Therefore, this additional activity is planned to develop and commission a cost model for 24M automotive cells to understand the cost at scale and the necessary level of capital investment. In Phase 1, the developed cost model for automotive cells will be developed and commissioned in consultation with USABC. Throughout the duration of the program, it will be applied to scrutinize the viability of the developing 24M automotive cell.

Results

We have successfully completed this 3 year program and achieved tremendous progress along numerous development pathways, some of the most notable being in the following categories:

Delivered Phase 3 deliverable cells:

During this program, the team successfully demonstrated that 24M SemiSolid technology can meet EV requirements. Phase 3 deliverable cells are expected to meet DST cycle life requirement using the cell full DOD range. The team developed a unique unit cell architecture that enables excellent safety behavior under extreme abuse conditions, both mechanical and electrical. Using NMC811 high energy cathode chemistry, 24M demonstrated EUCAR4 in a Pin test, EUCAR1 in crush, EUCAR2 in overcharge and external short. The team successfully increased the cell beginning of life energy density by 35% since the start of the program. Table I.1.A.2 below summarizes the initial performance of phase 3 deliverable cells. The reported values are for an 18-layer densified NMC811 and un-densified graphite containing cells (52.6Ah nominal capacity cell). The final deliverable cell dimensions are shown below (Figure I.1.A.1).

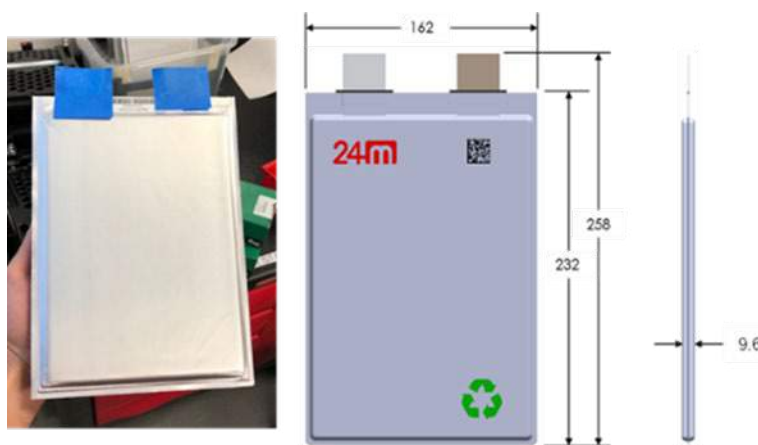


Figure I.1.A.1 18-layer densified NMC811 and un-densified graphite containing cell (52.6Ah) dimensions

Table I.1.A.2 Phase 3 Deliverable Cell Initial Performance

	Phase 3 Deliverable
Nominal Capacity, C/3, 25 °C	52.6 Ah
Discharge Power Density, 30 s Pulse, 20%SOC	1730 W/L
Specific Discharge Power, 30 s Pulse, 20%SOC	850 W/kg
Specific Regen Power, 10 s Pulse, 10%SOC	360 W/kg
Total Specific Energy @ C/3 Discharge Rate	272 Wh/kg
Areal Capacity	9.7 mAh/cm ²
Nominal Roundtrip Energy Efficiency, C/3 rate	94%
Maximum Operating Voltage, Continuous/Pulse (V)	4.2/4.3
Minimum Operating Voltage, Continuous/Pulse (V)	2.8/2.7
Maximum Self-discharge	<1.5%/month

Program Final Deliverable Cell Energy:

The 24M USABC team built 39 phase 3 cells toward the final deliverable. To evaluate the cells energy density, the team measured all cells weights, thicknesses and capacities at C/3 discharge rate. Figure I.1.A.2 below summarizes those data.

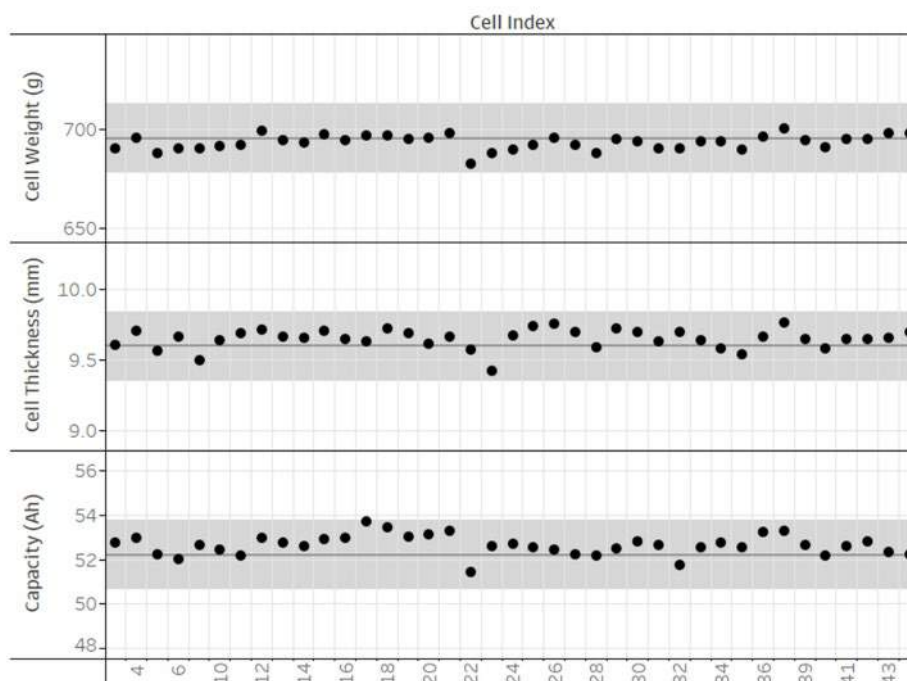


Figure I.1.A.2 Program final deliverable cells weight, thickness and capacity @ C/3 discharge rate and 30 °

The cells mean weight is 694grs with a standard deviation of 4grs. The cells mean final thickness measured 9.5mm with a standard deviation of 0.07mm. the cells delivered mean discharge capacity is 52.6Ah at C/3

discharge rate from 4.2V to 2.8V. The standard deviation on cells capacity is 0.5Ah. The cells tolerance on those metrics is below $\pm 3\%$.

Program Final Deliverable Cell Power:

The final deliverable cells power capability was evaluated by completing a full HPPC test at 30°C. the full HPPC results of 5 cells are represented in Figure I.1.A.3 below.

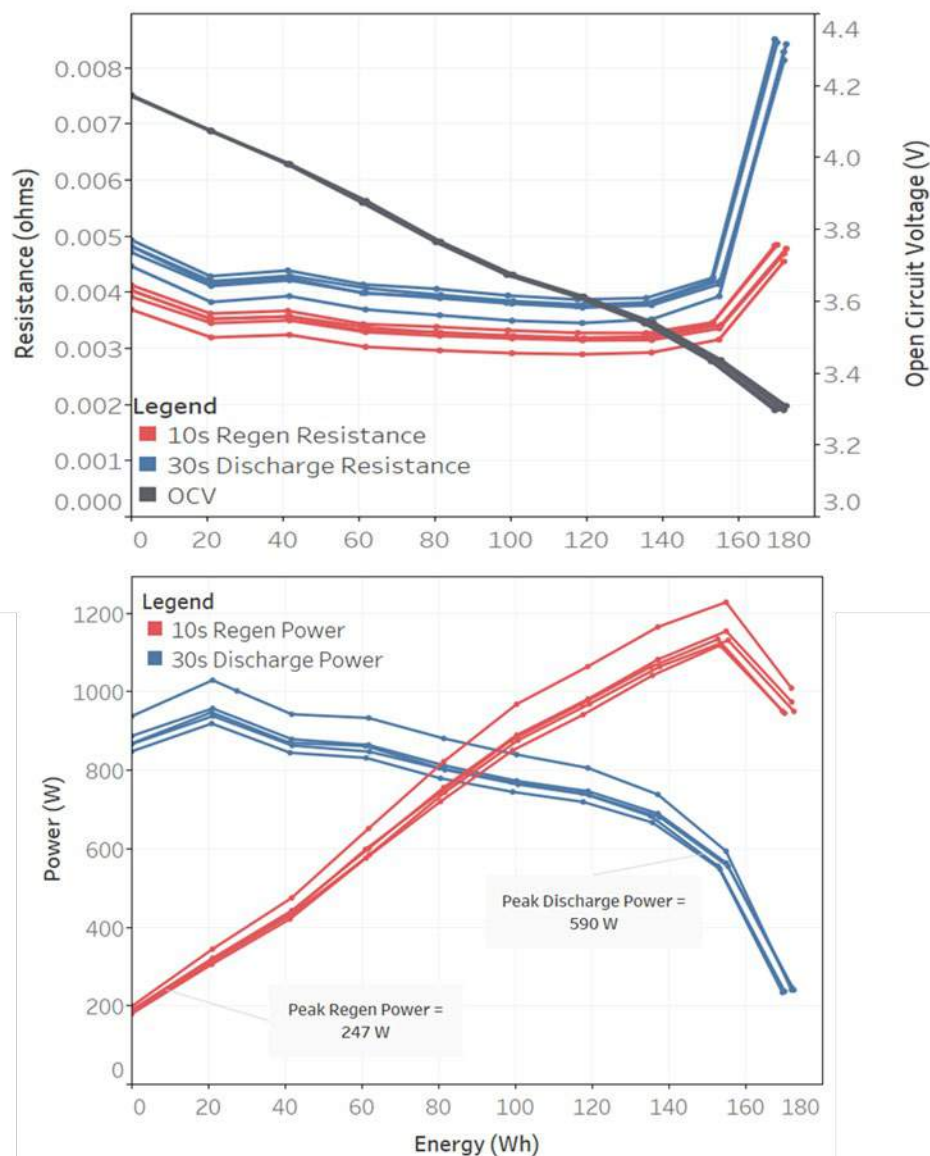


Figure I.1.A.3 Program final deliverable cells full HPPC performance at 30 °C

The analysis of the HPPC data confirmed that the final deliverable cells have a 30sec peak discharge power density of 1730 W/L, a peak specific discharge power of 850 W/kg and a 10sec peak specific regen power of 360 W/kg. the phase 3 final deliverables exceeded the program initial performance power requirement.

Program Final Deliverable Cell Abuse Tolerance:

24M USABC team completed extreme mechanical and electrical abuse testing of phase 3 deliverable cells. in all testing, the cell reacted with a EUCAR level 4 or lower. In overcharge to 200%SOC, the program final

deliverable large format design achieved an impressive EUCAR level 2. Phase 3 deliverable cells abuse tolerance results are summarized in Table I.1.A.3 below.

Table I.1.A.3 Phase 3 Deliverable Abuse Tolerance Results

Reference	Test Conditions	# of Cells Tested	Results
Overcharge	1C to 200%SOC or 8.4V @ 60 °C	6	EUCAR2
External Short circuit	100%SOC (4.2V), 60 °C, 3.5mOhm	6	EUCAR2
Internal Short circuit (Pin penetration)	100%SOC, 1.5mm, Voltage drop of $\leq 5\text{mV}$	4	EUCAR4
Over-discharge	1C to voltage reverse voltage	3	EUCAR2
Crush	100%SOC, 50%deformation or 200kN	2	EUCAR1
Thermal Stability	100%SOC, 5 °C/min ramp to 130 °C	4	EUCAR2

Conclusions

24M has successfully completed this 3 year program. 24M has successfully demonstrated that its semisolid electrode and unique unit cell architecture enables high energy density with excellent abuse tolerance. 24M has successfully demonstrated that its manufacturing method of semisolid electrode format for lithium-ion battery is scalable and agnostic to active materials chemistry. Project phase 3 deliverable cells, the last deliverable of this program, were produced and delivered to USABC national labs for independent testing.

Key Publications

1. “SemiSolid Lithium-ion: A Breakthrough Battery and Manufacturing Platform,” Naoki Ota (invited speaker), International Conference on Advanced Lithium Batteries for Automotive Applications, 2017.

Acknowledgements

Li Yang at General Motors in Warren, MI served as the USABC program manager for this project.

I.1.B Development of High Performance Li-ion Cell Technology for EV Applications (Farasis Energy)

Madhuri Thakur, Principal Investigator

Farasis Energy
21363 Cabot Boulevard
Hayward, CA 94545
E-mail: mthakur@farasis.com

Brian Cunningham, DOE Technology Development Manager

U.S. Department of Energy
E-mail: Brian.Cunningham@ee.doe.gov

Start Date: February 2017	End Date: September 2020	
Total Project Cost: \$5,900,000	DOE share: \$2,950,000	Non-DOE share: \$2,950,000

Project Introduction

The goal of this project is to develop a high energy density, low cost Li-ion cell technology that meets the USABC goals for Advanced Batteries for EV's. Farasis headed the development effort which will bring together technical contributions from a large number of leaders in the Li-ion technology industry including subcontractors Argonne National Laboratory (ANL) and Lawrence Berkeley National Laboratory (LBNL), and material suppliers for anode, cathode, electrolyte and separator etc. The project will build on technology development efforts at Farasis and our collaborators that have been supported, in some cases, through previous Department of Energy sponsored projects. The development effort will be iterative, with an intermediate Go/No Go Milestone based on cell performance goals and progress tracked against the USABC Battery goals. The major objective of this program is to develop cell technology capable of providing 350 Wh/kg after 1000 cycles at a cost target of \$100/kWh. The beginning of life (BOL) target for the cell level specific energy is ~ 400 Wh/kg, which is approximately 12% higher than the energy needed to meet the USABC end of life (EOL) cell level targets. To achieve the desire target of 350Wh/Kg the anode needs to be pre-lithiated with a capacity $\geq 1500\text{mAh/g}$ and cathode with a capacity higher then 220mAh/g. The pre-lithiation of anode is done by adding sacrificial lithium source into the cathode. The past two years we try to optimize the amount of sacrificial lithium source added to the cathode. The addition of sacrificial lithium source leads to decrease in the capacity of cathode and increase the impedance of the cells. To overcome all the problems associated with the Li source, requires more work on the stabilization of this material, and would be difficult to implement in the time frame required for the program builds. During the Go/No Go Milestone based on cell performance, a change in the chemistry of is done to meet the deliverable energy target of 330Wh/Kg. The final deliverable must achieve specific energy of 330Wh/Kg at the beginning of life without pre-lithiation at a cost target of \$100/ KWh. The major objective of this project is to develop a cell technology capable of providing 280 Wh/kg after 1000 cycles at end of life. The specific energy of the cell at the beginning of life will be approximately 15% higher than the energy needed to achieve the cell level target for this program.

Objectives

- Develop an EV cell technology capable of providing 280 Wh/kg after 1000 cycles at a cost target of \$0.10/Wh.
- Develop high capacity cathode materials to meet USABC EV goals through collaborative development efforts with partner organizations.
- Develop high capacity Silicon based anode
- Develop and optimize electrolyte and conductive additives to stabilize high voltage cathode/ Ni rich cathode and improve the safety

- Optimization of negative electrode formulation for maximum energy density and cycle life, calendar life, power, safety, and low/high temperature cell requirements.
- Investigate effect of Si incorporation on conductivity and mechanical stability of negative electrode relative to graphite electrodes.

Approach

- Phase I of the project, which lasted for approximately 15 months, was focused on the development and characterization of materials and optimization of electrolyte technology. Initial sets of small cells (ca. 1-2 Ah) was used to evaluate different positive/negative electrode composites, material combinations and for electrolyte development in an iterative manner. The specific plan was to optimize the electrode compositions during the first build of cells focused on chemistry optimization in which various active material compositions for the cathode and anode were evaluated in half cells and then in small full cells against a baseline anode or cathode electrode respectively. A second iteration leads to narrow down the range of electrode designs, introduce materials improvements, and pre-lithiation techniques into the design. The electrolyte development effort was conducted in parallel with the cell optimization work, initially using baseline cells made from the baseline composite cathode and silicon anode of the first cell builds. The results from this initial screening was used to narrow the electrolyte compositions best suited for this chemistry and to be used for further optimization in the second round of small cell builds. The electrolyte work will focus on exploiting the high-voltage stability of advanced solvents along with new salts and additives from leading electrolyte technology developers across the U.S.. A combination of device level testing and fundamental electrochemical measurements will be used to guide the development of large form factor cells for Phase II of the project. End of the phase I the cells was built with down-selected chemistry for a capacity of 41.5Ah and delivered to the National Labs.
- Phase II of the project is scheduled for approximately 17 months and shifts to manufacturing and testing of larger format pouch cells using a refined subset of cell chemistries. Some ongoing chemistry development will continue at this stage to address specific issues identified in Phase I builds and to pursue further optimization of cell level performance. To achieve the targeted energy density of 330Wh/Kg we need to evaluate silicon material with higher first cycle coulombic efficiency which does not required pre-lithiation as well as the Ni rich cathode with a capacity in between 200-210mAh/g. Other cell components such as foil, separators, electrolyte, conductive additives and pouch materials is also get evaluated for higher amount of the Si. This will occur in two iterations starting with ca. 41 Ah Gen1 form factor cells for the internal evaluation and progressing to the final deliverable cells based on a larger pouch cell form factor, which will be ca. 87Ah using the optimized high-energy cell chemistry. Phase II of the program will also include testing to guide system development in future applications; these tests will characterize cells in small groups to efficiently evaluate their behavior on a large scale where thermal management, cycling-induced gradients, and failure isolation become important.

Results

Gen1: Technology Development: The Gen 1 cells build with the down-select chemistry of Ni rich and high voltage NCM as cathode and SiO/C composite as an anode. The Table I.1.B.1 shows the number of cells build at the factory after down selecting the cathode and anode before delivering the cells to the National Labs. The first cell build was done to do the internal testing before finalizing the cell design for the Gen1 cell build. The cell was built for a capacity of 35Ah and 2.3Ah to do the internal testing. The cells tested internally to understand the failure mechanism so that we can modify or optimize Gen1 deliverable chemistry

Table I.1.B.1 Gen1 Cell Builds with the Down Selected Chemistry

Test Item	Cell Type & Site	Gen1 -35Ah	Gen1-2.3Ah	Gen1- 3Ah	Gen 1 Delivered Cells, 41.5Ah	
		Farasis	Farasis	Farasis	Farasis	USABC
Capacity and Energy		2X	2X	2X	2X	17 Cells
HPPC		2X			2X	
Peak Power Test					2X	
Discharge Rate Capability					2X	
Cold Crank						
Cycling (1C/1C & DST)		4X	4X	4X	2X	
Calendar Life (30°C)		2X	2X	2X	3X	
Calendar Life (45°C)		2X	2X	2X	2X	
Calendar Life (55°C)			2X	2X	2X	10 Cells
Overcharge test						
Nail Penetration						
Thermal Ramp test						
External and Internal Short						3 Cells
Thermal Test/Calorimetry Evaluation						
Qty Needed					10	7
Qty Delivered					-	30

After evaluating the results in 35Ah cells for cycle life, safety and calendar life the chemistry if further optimized for Gen1 deliverables. Gen1 cells were built to a capacity of 41.5Ah and an energy density of 270Wh/Kg. Figure I.1.B.1a shows the dynamic stress testing (DST) cycling data and Figure I.1.B.1b shows the cycle life for the Gen1 cells (41.5 Ah) under different pressure with Ni-rich NCM and SiO/C composite delivered to National Labs. Figure I.1.B.2a & b shows the calendar life capacity retention and DCIR for Ni-rich cathode and SiO/C anode for the Gen1 cells.

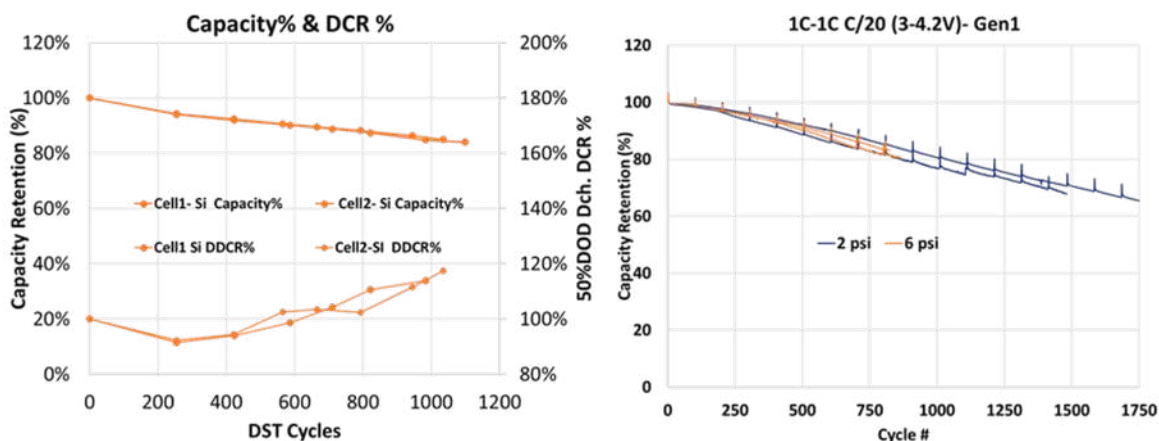


Figure I.1.B.1 a DST Cycle life for Gen1 Cells 1b) Cycle life data@ different pressure

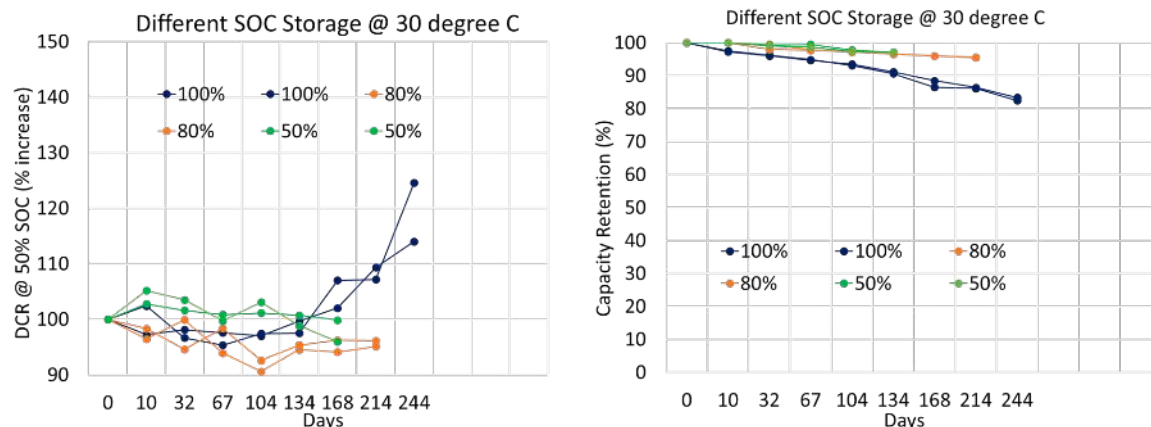


Figure I.1.B.2 a) Calendar life capacity retention for the Gen 1 deliverable chemistry & b) DCIR

In parallel we are doing the optimization of the Gen1 cells to improve the overall performance and optimization of Si amount. Figure I.1.B.3a and b shows the capacity retention of anode for different capacity with same capacity of the cathode.

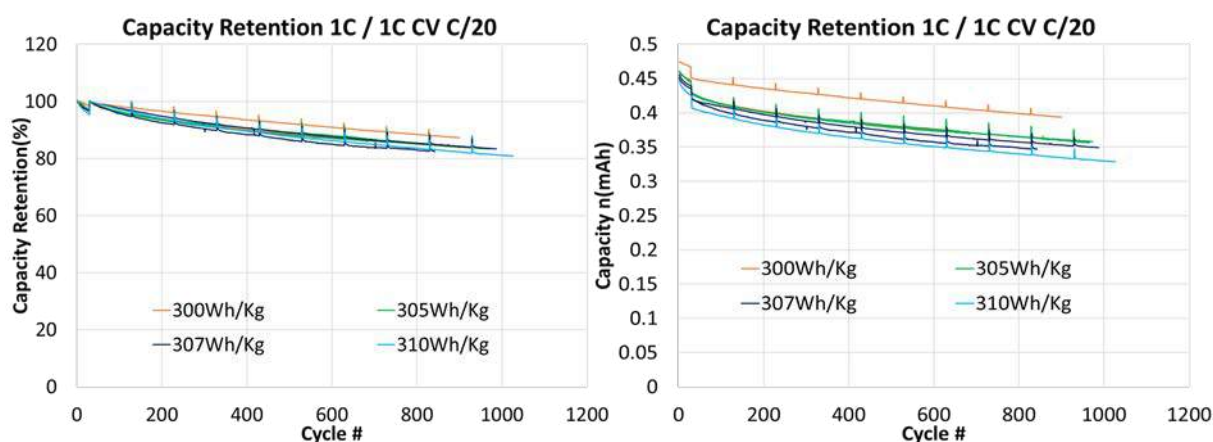


Figure I.1.B.3 a and b Capacity retention and capacity for the double layer pouch cells targeting ~ 300- 310Wh/Kg in the 77-80Ah cell form factor

Gen2 Deliverable

To achieve the specific energy of 330Wh/Kg we need an electrode (cathode capacity $\geq 200\text{mAh/g}$ and anode capacity $\geq 450\text{mAh/g}$). To hit the target energy density, we need silicon material with higher coulombic efficiency to avoid the pre-lithiation of anode. The 1st cycle efficiency of 100% silicon material need to be more than 85%. Depending up on the cathode material we are using we can optimize the amount of the silicon material in the cell design. Figure I.1.B.4 shows the initial result for the silicon materials with the discharge capacity of 540mAh/g, but different coulombic efficiency.

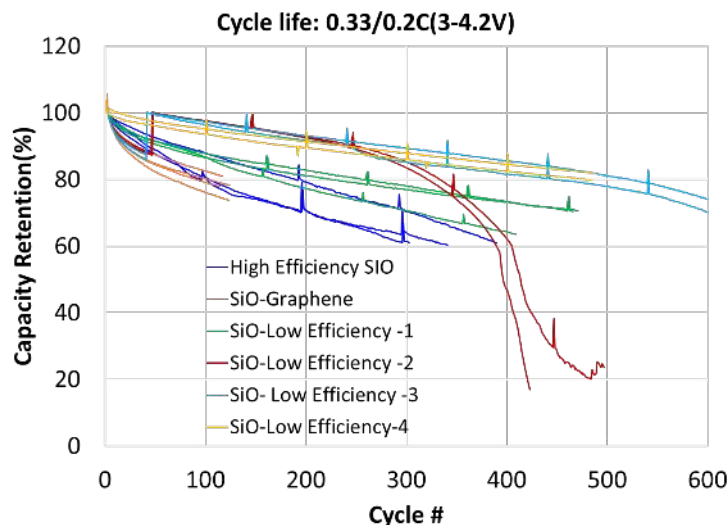


Figure I.1.B.4 shows the initial result for the silicon materials with cathode for a fixed capacity of 4.35mAh/cm²

Figure I.1.B.4 show the initial results for SiO/graphite composite for a capacity ranging in between 4.3-4.75 mAh/cm² with fixed capacity cathode. The 1st cycle efficiency of SiO-Low efficiency is lower than 80%, so it can't be a good candidate for the final deliverable. The first cycle efficiency for the high efficiency SiO is higher than 87%. The high efficiency material can achieve the targeted energy density of 330Wh/Kg in 87Ah cell form factor with an anode loading of 4.74 mAh/cm².

The high efficiency Si anode with capacity ranging from 4.7-4.75mAh/cm² are tested with Gen1 cathode in a double layer pouch cell for the targeted capacity of 330Wh/Kg in 80-87Ah form factor cells. Figure I.1.B.5 shows the cycle life and capacity of the double layers pouch cells.

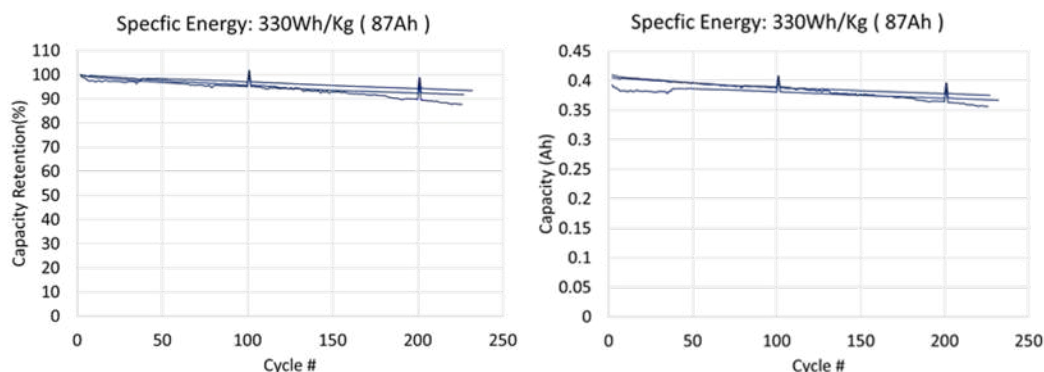


Figure I.1.B.5 shows the initial result for high efficiency anode with Gen1 cathode in double layer pouch cell

Conclusions

Farasis has shown more than 1000 cycle before reaching 80% capacity retention in 41.5Ah Gen1 cells with a specific energy of 270Wh/Kg. Farasis delivered 41.5Ah Gen1 pouch cells to National Labs for testing, abuse testing and thermal testing (INL, SNL and NREL). To improve the calendar life of Gen1 cells further optimization in chemistry is going on by testing different electrolyte additives. The down-selection of the material is done for the Gen2 deliverable in the proto-type double layer pouch cells. Farasis will continues to use a system level approach to meet the USABC goals by optimization of material, cell components and cell design.

Key Publication

1. “Development of High-Performance Lithium-Ion Cell Technology for Electric Vehicle Applications“, bat355_thakur_2018_p, U.S. DOE Vehicle Technologies Program Annual Merit Review, AMR, 2018.
2. “Development of High-Performance Lithium-Ion Cell Technology for Electric Vehicle Applications“, bat355_thakur_2018_p, U.S. DOE Vehicle Technologies Program Annual Merit Review, AMR, 2019.

Acknowledgements

Meng Jiang, GM R&D Center, Battery Systems Group, CMS, in Warren, MI served as the USABC Program Manager for this project.

I.1.C Rapid Commercialization of High Energy Anode Materials (SiNode Systems)

Cary Hayner, Principal Investigator

NanoGraf Corporation
3440 S. Dearborn Street, #113N
Chicago, IL 60616
E-mail: cary@nanograf.com

Brian Cunningham, DOE Technology Development Manager

U.S. Department of Energy
E-mail: Brian.Cunningham@ee.doe.gov

Start Date: May 23, 2019

End Date: June 30, 2022

Project Funding (FY19): \$994,560

DOE share: \$497,280

Non-DOE share: \$497,280

Project Introduction

As global usage of electric vehicles steadily increases, so does the power/energy requirement to meet mainstream needs. Performance trajectories of traditional lithium-ion technology, despite an annual 3-5% improvement in energy density since inception, suggest that long-term electric vehicle needs will not be met without an evolution beyond traditional energy storage materials (i.e., graphitic anodes). NanoGraf Corporation has developed a novel Si-based, negative-electrode material which can enable a quantum leap in battery energy and power density, and significantly impact battery weight and run-times that burden today's electric vehicles.

Objectives

The project entitled “Rapid Commercialization of High Energy Anode Materials” has been established with the aim of extending, benchmarking, and demonstrating the performance of NanoGraf’s advanced silicon-based anode materials in battery form factors and designs relevant for electric vehicle applications.

Approach

NanoGraf Corporation has demonstrated a novel high energy density ($>1,000$ mAh/g) Si-based negative-electrode materials technology with a long-term potential to replace graphitic-based anodes in lithium-ion batteries. NanoGraf’s technology uses a proprietary silicon alloy-graphene material architecture to achieve: i) category-leading performance and ii) solutions to long-standing Si anode technical hurdles. The proprietary combination of silicon-based alloys and a flexible 3D graphene network helps to stabilize the active material during charge and discharge by providing an interfacial barrier between the active material and the electrolyte which can accommodate large volumetric changes through a laminar graphene sliding mechanism. The 3D graphene-silicon architecture results in a minimization of capacity losses due to electrical disconnection, significantly improved active utilization (mAh/g), and partial stabilization of the SEI interface with a flexible physical barrier between electrolyte and active material (Figure I.1.C.1).

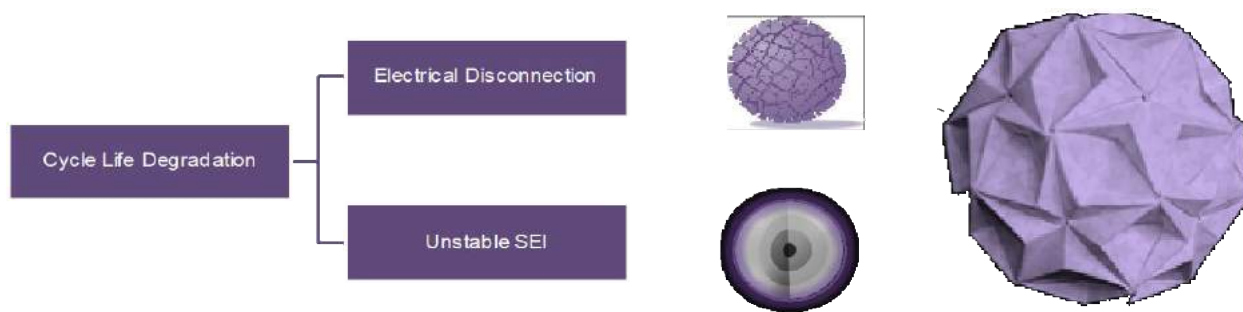


Figure I.1.C.1. Si anode failure mechanisms (left), NanoGraf graphene-wrapped silicon anode architecture (right).

NanoGraf has made continuous improvements against key USABC advanced electrode metrics over time, and has demonstrated an attractive trajectory towards USABC advanced electrode goals. The goal of the program is the advancement and commercialization of advanced silicon-based active materials for high energy and high power EV batteries. Specifically, the program aims to demonstrate that NanoGraf technologies can exceed USABC electric vehicle performance targets in USABC-recognized form factors, be produced at-scale by commercially viable methods and reach USABC cost targets at scale. To this end, a series of tasks have been developed to address the core technology gaps and their associated barriers: Task 1: Electroactive Synthetic Design & Optimization, 2. Electroactive Barrier Design & Optimization, 3. Anode/Cathode/Electrolyte/Binder Design Optimization, 4. Material Production & Process Development, 5. System Integration & Cell Production and 6. Electrochemical & Safety Testing.

NanoGraf has two strategic partners for this program. A123 Systems works with NanoGraf on Tasks 5 and 6 for the cell deliverables and PPG works with NanoGraf on Task 3 to assist with electrode design and optimization.

Results

During FY19 for Task 1, NanoGraf has explored treatments to the SiOx to impact the microstructure configuration in an effort to both improve the overall cycling stability and to advance the energy density of the electroactive components. As shown in Figure I.1.C.2, NanoGraf has been able to achieve more than 270 cycles to 80% for a pure NanoGraf material (>1300 mAh/g) without any graphite addition. Additionally, through microstructural development, NanoGraf was able to achieve a 24% increase in cycle life compared to previous product variants (Sample MT1 and ST3a). The improved material will be constructed into 1 Ah cell deliverables in collaboration with A123 Systems. Key learnings on this topic have included progress on identifying preferred SiOx structures and sub-structures, internal morphologies, and distributions.

For Task 2, NanoGraf focused on continued development and improvement of their novel SiOx precursor material with high stability has been integrated into NanoGraf's 3D graphenic architecture. Experiments were undertaken with the goal of improving the graphene morphology and architecture to maximize the barrier quality. Throughout this work, NanoGraf was better able to understand and optimize the graphene coating procedure.

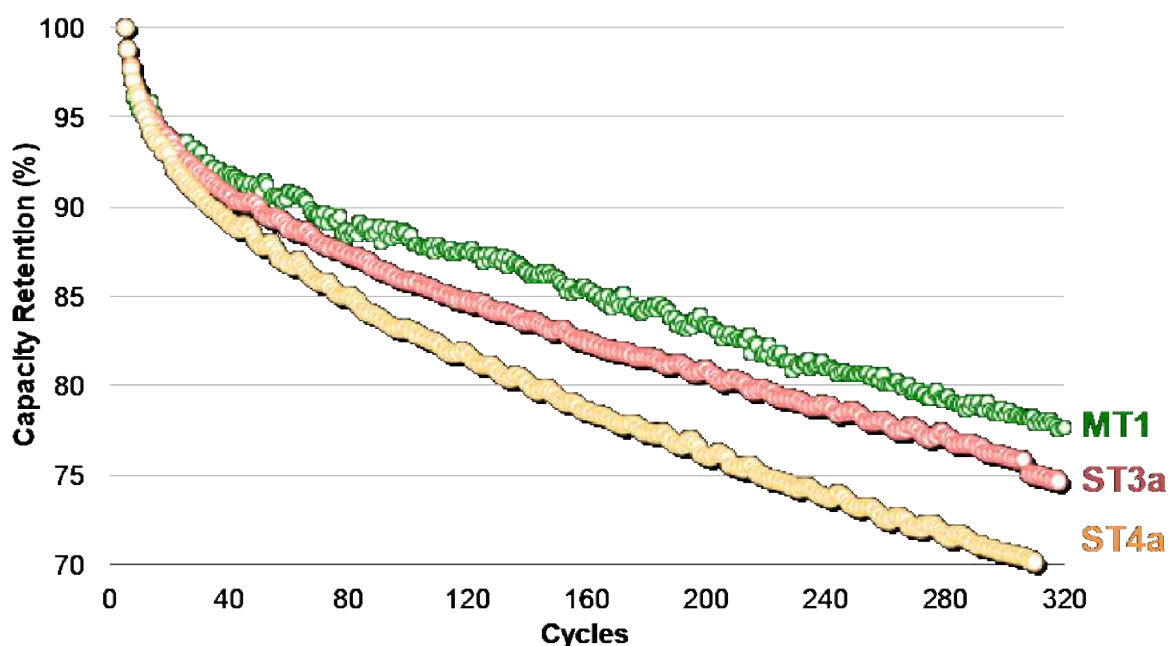


Figure I.1.C.2 Normalized full cell capacity versus cycles for pure NanoGraf anodes with NMC523 cathodes

As part of Task 3, NanoGraf has investigated various electrolyte formulations and additive packages to further improve the cycling stability of the graphene-SiOx composite materials in full cell configuration. As shown in Figure I.A.5.3, NanoGraf has been able to demonstrate improved cycling stability by an additional 30% over conventional electrolyte formulations via studies using scalable chemicals.

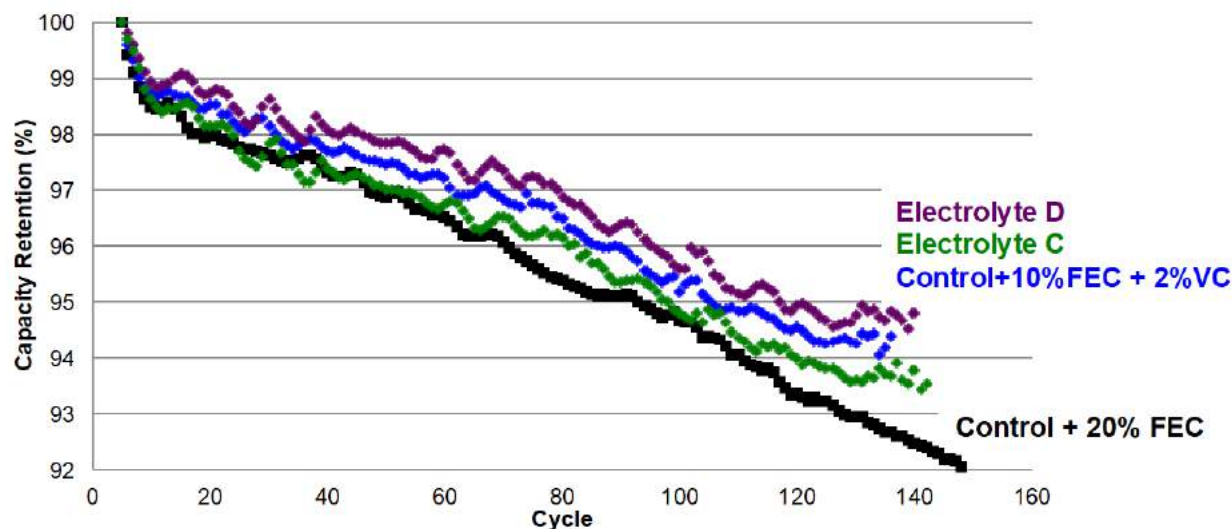


Figure I.1.C.3 Normalized full cell capacity versus cycles for assorted electrolyte compositions

In Task 3, NanoGraf has also focused on developing improved anode and cathode electrodes with good adhesion and minimal binder to decrease inactive components and maximize energy density. On the anode side, NanoGraf has investigated binder systems and additives to improve electrode coatings at high areal loading ($>4 \text{ mAh/cm}^2$) and low content. So far, NanoGraf has successfully reduced binder content to $<10\text{wt}\%$ for many high-capacity formulations at 4 mAh/cm^2 with good uniformity, adhesion, and flexibility. Figure I.1.C.4 demonstrates these anode electrode formulations (4 mAh/cm^2 , 10% binder) have been successfully coated on pilot-line equipment with good properties.

On the cathode side, PPG developed a new binder system capable of providing improved peel strength at a high areal loadings ($>4 \text{ mAh/cm}^2$) including a 50% increase in peel strength over control PVDF/NMP systems at 5 mAh/cm^2 and 2wt% binder content. These improved binder materials also enable high capacity and stable cycling performance of NMC-based materials that are on-par or better than control PVDF systems and should enable higher energy density when integrated into prototype cells.



Figure I.1.C.4 NanoGraf anode coating on pilot-scale equipment with 4mAh/cm² and 10wt% binder content

Through Task 4, NanoGraf has also made advancements on production scale-up and cost reduction segments. During FY19, NanoGraf produced kg-quantity materials monthly (Figure I.1.C.5 top) and is capable of producing >25 kg/month using existing validated pilot-scale equipment. In particular, NanoGraf has focused on improving QA/QC processes, including narrowing particle size variability between batches, to improve product quality and consistency – a key customer metric (Figure I.1.C.5 bottom). NanoGraf will scale its most advanced materials developed in Task 1 and 2 to be integrated into prototype cells by A123 Systems for Task 5 and 6 development.

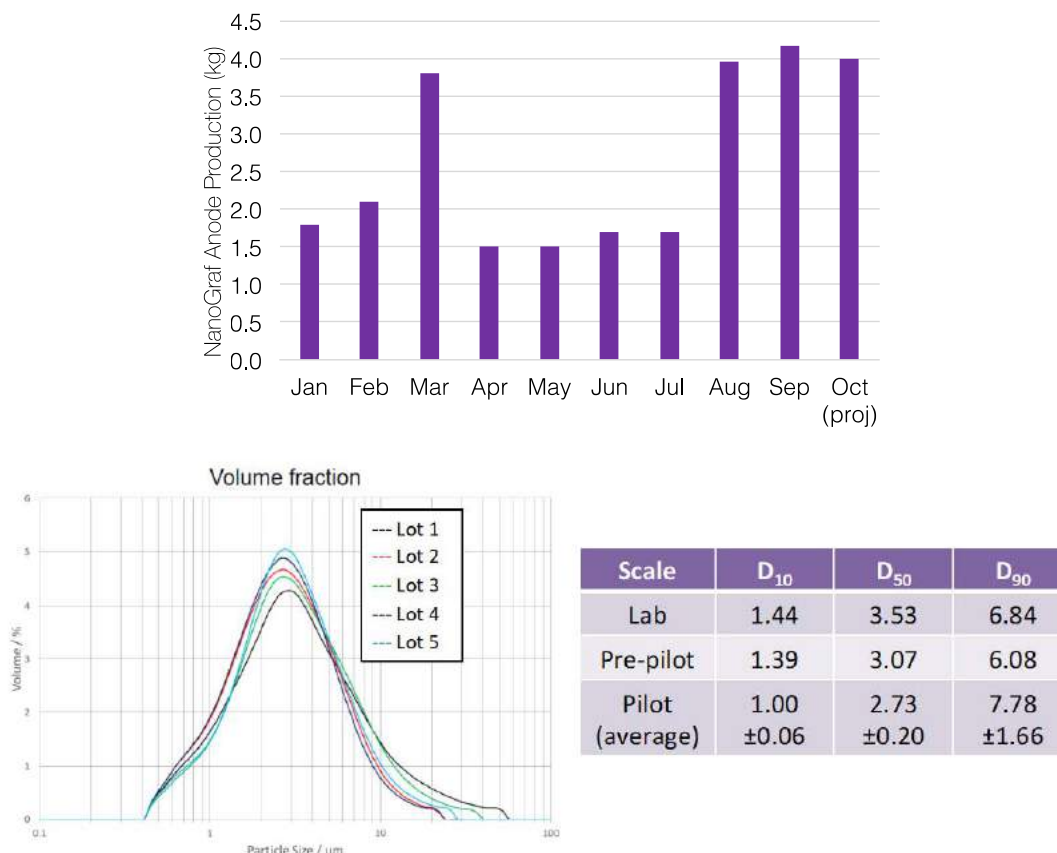


Figure I.1.C.5 NanoGraf materials production quantities through FY19 (top) and improved consistency between batches and production scales (bottom)

Conclusions

NanoGraf has concluded the 4th month of the 36-month long project. The 1 Ah cell deliverables will be delivered in Q1 2020 and cylindrical cells will also be constructed. A major milestone was achieved in the improved cycle life of the SiOx materials via structural changes and improved barrier properties.

Several challenges need to be surmounted over the coming year, including consistent improvements to the energy, cycle life, calendar life, scale and cost of the NanoGraf material in order to successfully surpass USABC key metrics.

NanoGraf has demonstrated a cadence of innovation and product development throughout the project, and looks optimistically towards demonstration of viable performance in commercially relevant EV cells.

I.1.D Li-Ion Cell Manufacturing Using Directly Recycled Active Materials (Farasis Energy)

Michael Slater, PhD, Principal Investigator

Farasis Energy, Inc.
21363 Cabot Boulevard
Hayward, CA 94545
E-mail: mslater@farasis.com

Brian Cunningham, DOE Technology Development Manager

U.S. Department of Energy
E-mail: Brian.Cunningham@ee.doe.gov

Start Date: February 1, 2017
Project Funding: \$1,639,044

End Date: February 1, 2019
DOE share: \$819,522

Non-DOE share: \$819,522

Project Introduction

The rapid performance gains of Li-ion batteries in the past few decades have led to accelerating implementation of this electrochemical energy storage technology on an unprecedented scale. For this growth to be sustainable, the entire life cycle of the batteries must be accounted for, from raw material sourcing to end-of-life disposal and reuse. So far, the cost associated with end-of-life disposition of these batteries has not been included in the product price; coupled with a drive to use less costly materials in the batteries themselves we are arriving at a situation in which there is less intrinsic value in the elemental composition of the battery than it costs to recycle/dispose of them in a responsible manner. Thus, there is a need for a recycling method that goes beyond treating the battery as an ore and can harvest some of the additional value that is invested in the product during complex raw material and cell manufacturing processes.

Objectives

There are four main objectives for this project:

1. Optimize direct recovery processes at larger scale (>8 kg cell/module input)
2. Optimize electrode formulations to make best use of refurbished active materials
3. Manufacture full-size LiBs on commercial production line using direct-recycled active materials
4. Quantify impacts of using recycling active materials on technology cost

Approach

Farasis Energy has been working on recycling technology for Li-ion batteries for a number of years. We have addressed the challenges of closing the loop of the Li-ion product life cycle by developing methods for recovery and reuse of valuable components in the batteries largely based on the direct recycling approach. “Direct Recycling” refers to battery recycling technology in which material recovery is performed using physical separation processes and active materials are reused with minimal processing, ideally without the need for extensive chemical transformation. In this way, some of the value invested in the materials (e.g., synthesis process energy, particle size distribution and shape) can be recovered without the need to resynthesize these materials from their lowest value elemental form. Figure I.1.D.1 shows a flow chart for a straightforward direct recycling process used to recover the high value components of the Li-ion battery. In this approach the entire cell or module is shredded after being fully discharged and deactivated. Safety is a key requirement for this step, and therefore measures to prevent release of hazardous materials and fires are a primary consideration. The shredded material is subjected to a solvent extraction step, which removes the electrolyte while also stabilizing the cell chemistry by removing a source of hydrofluoric acid, which can damage the valuable active materials upon exposure to air and water during subsequent processing. The shredded mass is then screened/sieved to remove other battery components from the micron-sized active

materials. This leaves the “Black Mass,” a mixture of active anode and cathode powders with some binder, carbon, and small amounts of other components as contaminants. Separation of the cathode and anode active materials from each other is achieved using a liquid with density between that of graphite and the metal oxide. In this state, the recovered active materials are not immediately ready for use in new lithium ion cells; the recovered cathode material is missing some lithium due to the inherent losses during the formation process and extended cycling while the graphite active material contains some lithium and surface species generated during the formation and cycling processes. Regeneration of the active materials by removing contaminants, restoring the lithium inventory, and final annealing in which the structural integrity of the materials is returned to its pristine state. Farasis has developed proprietary approaches to achieve these final steps that are chemistry independent and have demonstrated the capability to achieve good separation yields, high purity, and high performance materials.

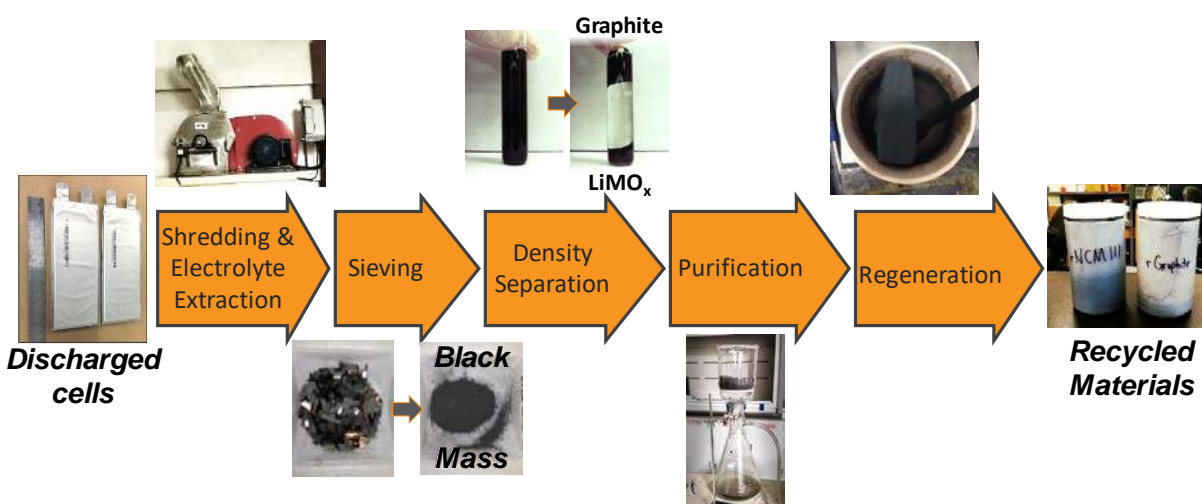


Figure I.1.D.1 Pictorial representation of the direct recycling process which largely relies on physical separation processes; compared to other recycling technologies, the positive electrode active material is recovered intact, preserving some of the value added during its synthesis

Available evidence to-date suggests that modified surface chemistry of the isolated active materials is the primary technological challenge to address from a process perspective, while any intervention in this domain also provides an opportunity for improvements over the properties of the pristine materials. Detailed structural investigations as to the nature of material changes during recycling processes are being explored in collaboration with Robert Kostecki at Lawrence Berkeley National Laboratory. The suite of analytical tools that will be used to inform the optimization of the recycling steps include:

- High resolution X-ray instrumentation at DOE’s Synchrotron User Facilities, enabling detailed investigation of structural parameters such as microstrain and lattice defects
- SEM will be used for imaging particle morphology and surface chemical analysis by EDAX
- Electrochemical Impedance Spectroscopy will be used to determine intrinsic conductivity of materials and for electrode-level characterization during formulation research with recycled materials
- Particle size distribution measurements and gas adsorption analysis will be used to determine material physical characteristics such as particle size, surface area, and internal microporosity
- Raman spectroscopy will be used to study surface and near surface changes in material structure and chemistry which are difficult to characterize by other methods

- Neutron diffraction will be employed in conjunction with XRD to more accurately characterize the structure of Li-containing materials. Due to the extremely weak scattering cross section of Li for X-rays, neutron diffraction is required to positively locate Li in the crystal structures.

The direct recycled active materials will be used in iterative cell builds through which insight will be gained on how to best incorporate recycling technologies in battery manufacturing, resulting in more environmentally friendly, lower cost production of Li-ion batteries. A high-level summary of project deliverables (internal and external) may be found in Table I.1.D.1.

Table I.1.D.1 Overview of Program Hardware Deliverables and Build Strategy

Hardware Deliverable	Description	Source Material	Quantity ANL/FEI*	Delivery Date
Cell Build 1 (84 x ~1 Ah cells)	Control: pristine Graphite//pristine NMC	commercial powders	9/24	Month 27
	recycled Graphite//recycled NMC	manufacturing scraps	9/24	Month 27
	pristine Graphite//recycled NMC	manufacturing scraps	0/18	Month 27
Cell Build 2 (60 x ~2 Ah cells)	Control: pristine Graphite//pristine NMC	commercial powders	9/12	Month 35
	pristine Graphite//40 % recycled NMC	BOL cells/QC rejects	9/12	Month 35
	pristine Graphite//100 % recycled NMC	BOL cells/QC rejects	0/12	Month 35
Final Build (54 x ~2 Ah cells)	Control: pristine Graphite//pristine NMC	commercial powders	15/12	Month 38
	optimized maximum recycled content in each electrode (<i>tbid</i>)	EOL cells and module parts	15/12	Month 38

* Each build will include cells for external (USABC/ANL) and internal (Farasis Energy) testing and evaluation

The measure of success of the program is being quantified by measuring the gap between recovered material and equivalent control test articles made using commercial grade active materials, which will be included with each build to allow comparative evaluation. While not included in the final deliverables, there will be development work addressing how best to handle mixed chemistry feed streams, which is an inherent challenge for direct recycling processes. Specifically, recovery of feed streams with NMC532 and mixed NMC/spinel compositions will be studied. Another important outcome of the program will be to refine current assumptions of a scaled production process (including milling, separation, purification and regeneration operations) and evaluate revenue potential against capital and energy requirements and operating costs, thus ensuring that the technology is economically relevant.

Results

Kilogram quantities of recycled anode and cathode active materials were recovered from electrodes scrap in FY18. This feedstock is less complex than entire cells or batteries; a simplified process pictorial for isolation of active materials in this case is presented in Figure I.1.D.2. The overall scheme is the same for both anode and cathode feedstocks, with some difference in parameters for each stage. The material properties of recycled active materials recovered at kg-scale using this process are presented in Table I.1.D.2 and Table I.1.D.3. The recycled NMC111 is very similar to its pristine counterpart, with only a small decrease in specific capacity and first cycle efficiency. A few of the trace impurity elements increased during the recycling process; the iron is an artefact of the process equipment that can be addressed using more appropriate equipment at larger scale, while the fluoride is a byproduct of the electrode binder. The recycled graphite exhibits slightly lower specific capacity, first cycle efficiency, and tap density and increased ash residue and specific surface area compared with the same graphite in pristine form. These differences are due to residual nanocarbon and copper oxide impurities; additional effort can always further increase material purity, but time constraints forced us to utilize the recycled graphite in this state. In this way the project is probing the impacts of the particular contaminants that direct recycling processes have to deal with and their impacts on Li-ion cell performance.

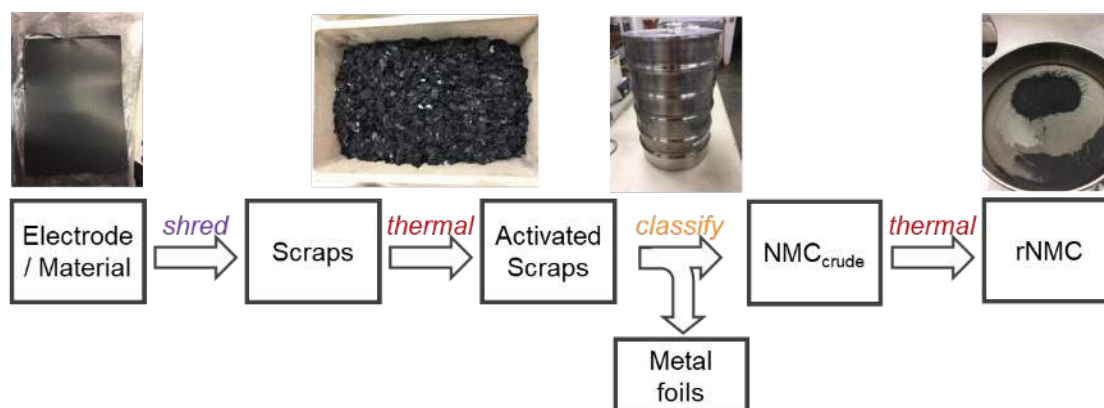


Figure I.1.D.2 Electrode scrap direct recycling process overview. First manufacturing residues such as off-spec coated electrodes and dried out slurry residue are milled to produce coarse shreds. The scrap is heated at moderate temperature to decompose the binder and the fine powders are separated from the current collector shreds using vibratory screen or air classifier. The crude recovered active material is then fired at higher temperature to remove residues and improve powder characteristics

Table I.1.D.2 Material Properties Comparison of NMC111 Recovered from Electrode Scrap with Pristine NMC111 from the Same Lot

Characteristic	Units	Pristine	Recycled NMC
Particle size (D_{50})	μm	11	12
Tap Density	(g/cm^3)	2.5	2.3
Reversible capacity (4.2 - 3.0 V vs. Li/Li ⁺ , 0.1 C)	(mAh/g)	150	145
Specific Surface Area (BET method)	(m^2/g)	0.23	0.28
First cycle efficiency	%	91	88
Impurities	%w/w	0.11 < Na < 1 Mg < 0.026 Ca < 0.07 Fe = 0.022 Cu < 0.0014 Al < 0.072	0.11 Na < 1 Mg < 0.026 Ca < 0.07 Fe = 0.1 Cu < 0.0014 Al < 0.072
pH assay	$-\log [\text{H}^+]$	11.0	11.1

Table I.1.D.3 Material Properties Comparison of Graphite Recovered from Electrode Scrap with the Same Type of Pristine Graphite

Characteristic	Units	Pristine	Recycled Graphite
Particle size (D_{50})	μm	15	14
Tap Density	(g/cm^3)	1.1	0.97
Reversible capacity	(mAh/g)	322	315
First Cycle Efficiency	%	89	88
Specific Surface Area	(m^2/g)	1.3	1.6
Ash content	%w/w	<0.1	0.6

The materials recovered from electrode scrap were used in Cell Build 1 to fabricate small pouch cells different combinations of recycled and pristine active materials. The experimental design for this cell build examines sensitivity of cell performance to characteristic impurities present in the recycled active materials. The distribution of cells amongst test conditions and test laboratory are displayed in Figure I.1.D.3. Further details on these test protocols can be found in the Vehicle Technologies Program Battery Test Manual for Electric Vehicles revision 3. The cells were all subject to a reference performance test (RPT) set at 30 °C approximately once per month, consisting of the C/3 static capacity test and hybrid pulse power characterization (HPPC).

Graphite//NCM			Graphite//recycledNCM			recycledGraphite//recycledNCM		
	ANL	FEI		ANL	FEI		ANL	FEI
DST, 30 °C		3	DST, 30 °C			DST, 30 °C		3
DST, 45 °C	3	3	DST, 45 °C		3	DST, 45 °C	3	3
DST, 55 °C		3	DST, 55 °C		3	DST, 55 °C		3
1C disch., 45 °C		3	1C disch., 45 °C		3	1C disch., 45 °C		3
Storage, 30 °C			Storage, 30 °C			Storage, 30 °C		
Storage, 45 °C	3	3	Storage, 45 °C		3	Storage, 45 °C	3	3
Storage, 55 °C		3	Storage, 55 °C		3	Storage, 55 °C		3
TOTAL	6	18	TOTAL	0	15	TOTAL	6	18

Figure I.1.D.3 Distribution of cells between test facilities (ANL = Argonne National Laboratory; FEI = Farasis Energy USA) and conditions (DST = Dynamic Stress Test; “1C disch.” = constant current discharge; Storage = 100% SOC storage)

The cells were built to a common design scheme (*i.e.*, identical electrode loadings, porosities, *etc.*) regardless of pristine or recycled material combination. In terms of processability (slurry mixing, electrode coating), the recycled active materials behaved similarly to pristine materials. The initial cell characteristics for the different material configurations are assembled in Table I.1.D.4. The available Li inventory of the cells reflects the properties of the type of NCM used. Thus, cells that utilized recycled NCM have slightly lower cell capacities and first cycle efficiencies; the recycled status of the graphite does not have any apparent impact because it was not independently tested against pristine cathode. In the recycled graphite//recycled NCM cells, the low first cycle efficiency of the NCM masks the lower first cycle efficiency of recycled graphite.

Table I.1.D.4 Cell Build 1 Test Article Characteristics

Active Material Configuration		Cell Capacity		First Cycle Efficiency		NCM Specific Capacity
Anode	Cathode	mAh	+/- 1 σ	%	+/- 1 σ	mAh/g
pristine	pristine	630	12	90.1	1.1	152
pristine	recycled	591	9	88.6	1.0	145
recycled	recycled	587	14	87.4	1.8	144

At the end of FY18, the cells had completed 2 RPT sets (including the beginning-of-life RPT0). The C/3 static capacity test results are displayed in Figure I.1.D.4. Comparing A0//C1 and A1//C1 configurations, which represent pristine graphite//recycled NCM and recycled graphite//recycled NCM respectively, reveals that the recycled graphite is responsible for an increase in the rate of capacity loss across all test conditions. This is most likely due to the impurities present in the recycled graphite causing incomplete passivation of the negative electrode, although data from additional RPTs will be required to further characterize this behavior.

Although the recycled NCM causes a decrease in the initial cell capacity, the relative rate of capacity loss in A0//C1 cells is identical to A0//C0 cells (pristine graphite//pristine NCM).

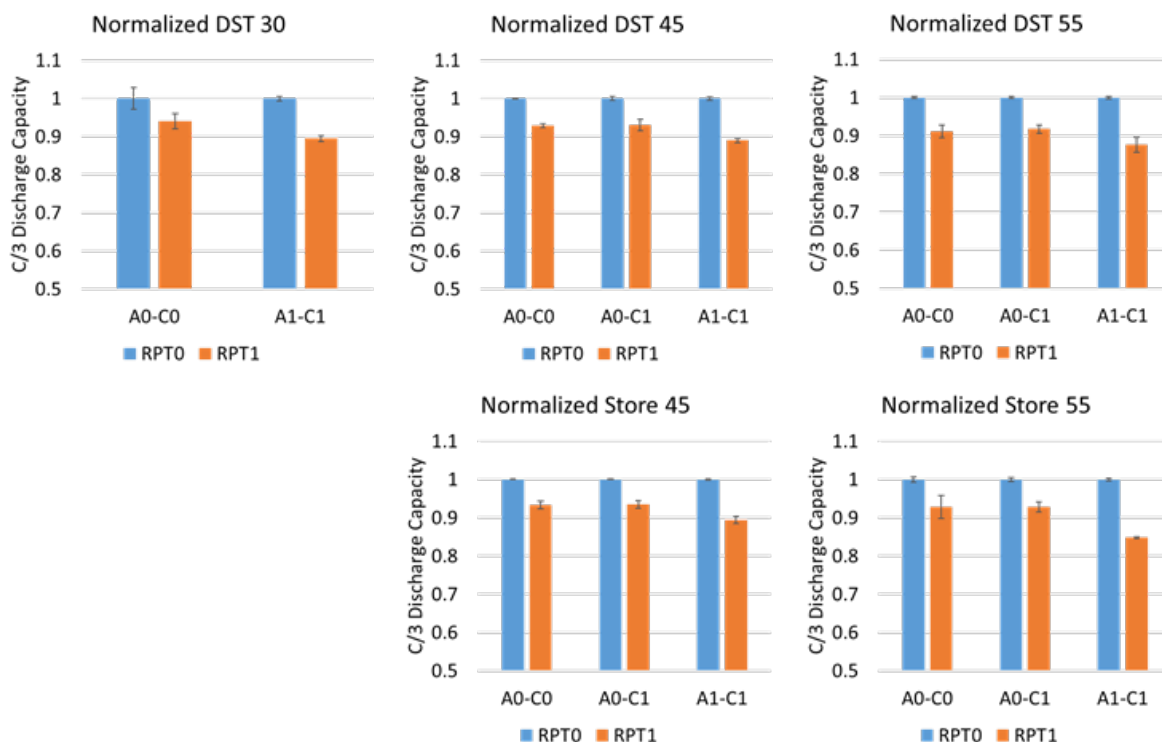


Figure I.1.D.4 Normalized C/3 static capacity test results from RPT0 and RPT1 for all cells. A0 = pristine graphite, A1 = recycled graphite, C0 = pristine NCM111, C1 = recycled NCM111. Error bars represent 1 standard deviation of the 3 cells in each test condition

The pulse resistance data from the HPPC tests are plotted in Figure I.1.D.5. All cells show increased pulse resistance between RPT0 and RPT1. Cells with pristine graphite and recycled NMC exhibit slightly higher resistance in RPT0, although some anomalous data makes direct comparisons at a single state-of-charge (SOC) difficult (see figure caption); in RPT1 pristine graphite//pristine NCM cells and pristine graphite//recycled NCM cells both show similar resistances. Cells with both recycled NCM and recycled graphite have higher resistance at BOL and this persists through RPT1. The lowest resistance cell group at RPT 1 is pristine graphite//pristine NCM in 30°C DST, while the highest resistance group is recycled graphite//recycled NCM in 55°C storage.

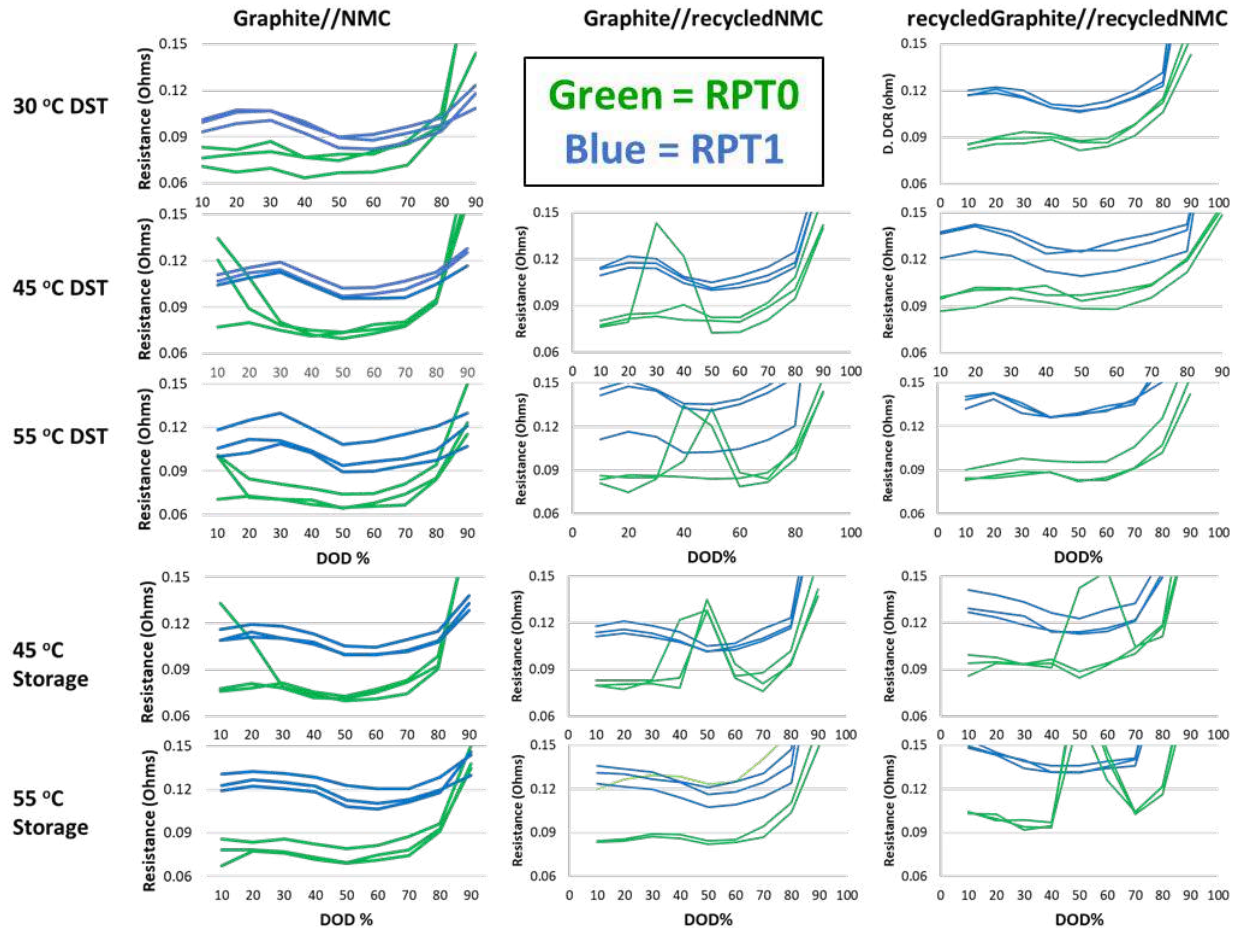


Figure I.1.D.5 HPPC pulse resistance data for all cells and test conditions. Some of the data from RPT0 indicate an anomalously high resistance near mid-SOC and do not represent the normal trend of resistance as a function of SOC for Li-ion cells; the accuracy of these data are suspect and most likely are due to inaccuracies caused by the test equipment performance limitations. These anomalous trends are not subsequently observed in RPT1

Three cells for each material configuration were also subject to a simpler test protocol consisting of 1C constant current discharge at 45°C. This test protocol, while not representative of EV battery use conditions, are typical for developmental work with Li-ion cells. The capacity retention as a function of cycle number are plotted in Figure I.1.D.6. In this case, the rate of capacity fade is similar for both sets of cells containing recycled active materials. These cells were also subject to RPT test sets although the data has not yet been analyzed and will be included in future reporting.

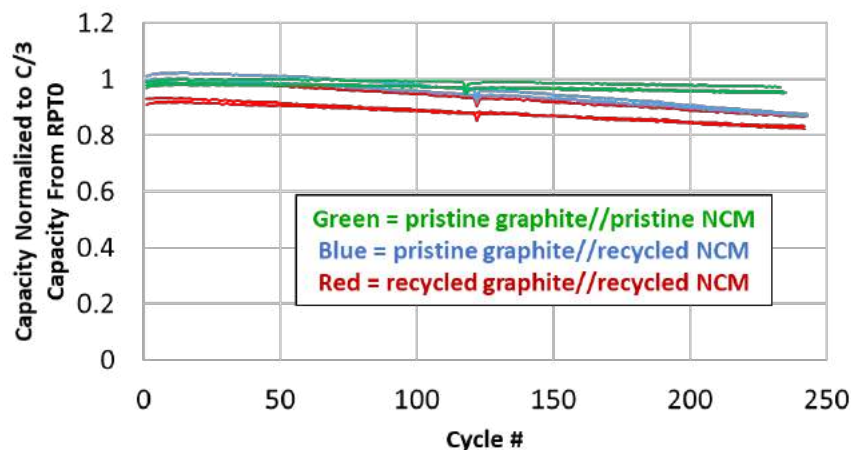


Figure I.1.D.6 Capacity retention as a function of cycle number for cells under 1C constant current discharge test condition

As a feedstock for recycling operations, electrode scrap is the least complex in terms of number of components and how much each of those components deviates from their pristine state. Direct recycling of whole, functional Li-ion cells requires several additional separation and chemical transformation steps. Figure I.1.D.7 illustrates the overall process flow and outputs. Cells are first discharged which is important for safety in the subsequent shredding step, but also returns some lithium to the cathode. The cells are shredded under inert atmosphere to prevent possible combustion and protect the materials from reaction with atmospheric gasses. The shredded scrap is then extracted to recover soluble electrolyte components and stabilize the scrap for further processing. A thermal treatment is used to degrade the binders and black mass (mixed fine powder active materials) are recovered using a size-based separation. The active materials are separated into crude graphite and crude NCM and then each crude material is independently processed via selective extraction and thermal treatment to produce the recycled active materials.

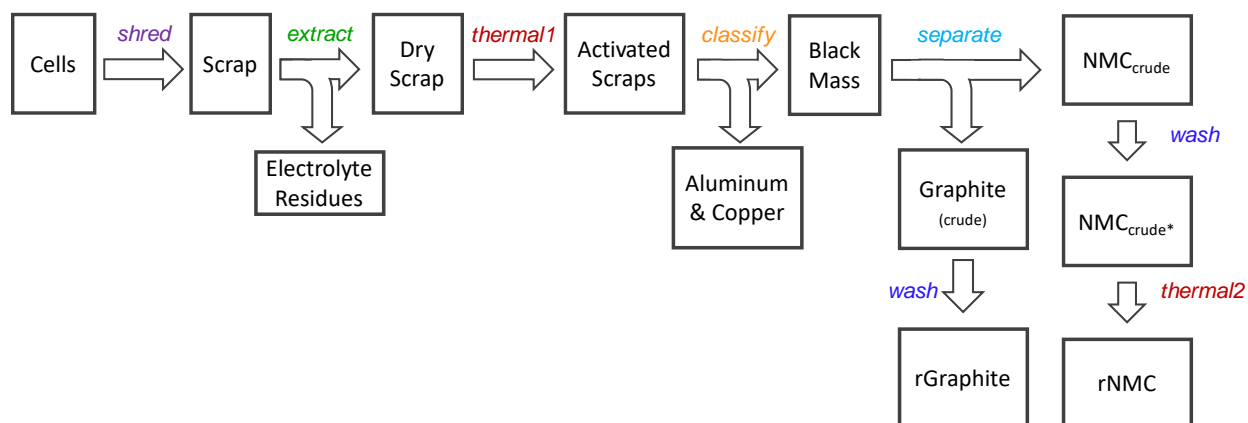


Figure I.1.D.7 Process diagram for direct recovery of valuable materials from Li-ion cells

The properties of active materials produced via this process are presented in Table I.1.D.5 and Table I.1.D.6. These recycled active materials will be incorporated in Cell Build 2 which explores blending of recycled active materials with pristine materials. The recycled NMC recovered from whole cells has significantly degraded performance characteristics compared to pristine materials or recycled NMC recovered from electrode scrap. This reflects the significant material alterations that occur during cell formation and the complexity of the separations and restoration process steps. Additional process optimization is in progress and will be reflected

in the materials used in the final cell build. Graphite recovered from whole cell feedstock is similar to graphite recovered from electrode scrap.

Table I.1.D.5 Material Properties Comparison of Direct-recycled NMC111 Recovered from Whole Cells with Pristine NMC111

Characteristic	Units	Pristine	Recycled NMC
Particle size (D_{50})	μm	11	12
Tap Density	(g/cm^3)	2.5	2.1
Reversible capacity (4.2 - 3.0 V vs. Li/Li ⁺ , 0.1 C)	(mAh/g)	150	130
Specific Surface Area (BET method)	(m^2/g)	0.23	0.74
First cycle efficiency	%	91	86
Impurities	%w/w	0.11 < Na < 1 Mg < 0.026 Ca < 0.07 Fe = 0.022 Cu < 0.0014 Al < 0.072	Metals quantification pending
pH assay	$-\log [\text{H}^+]$	11.0	11.9

Table I.1.D.6 Material Properties Comparison of Graphite Recovered from Whole Cells with the Same Type of Pristine Graphite

Characteristic	Units	Pristine	Recycled Graphite
Particle size (D_{50})	μm	15	13
Tap Density	(g/cm^3)	1.1	0.78
Reversible capacity	(mAh/g)	322	304
First Cycle Efficiency	%	89	89
Specific Surface Area	(m^2/g)	1.3	3.2
Ash content	%w/w	<0.1	0.3

Conclusions

Valuable active materials, both graphite and NMC, have been recovered from two different potential direct recycling feedstocks: electrode scrap and whole cells. The materials recovered from electrode scrap were used to build a series of small pouch cells with different combinations of pristine or recycled active materials. Between the different materials configurations, the cells in which NMC is the only recycled component perform more like the pristine material cells. Cells with both recycled NMC and recycled graphite are performing significantly worse in terms of capacity fade and rate of impedance increase. The different performance characteristics can be traced back to residual impurities that are not fully removed during the recycling process and we are confident that additional process refinement will further improve the performance characteristics of direct recycled active materials.

Key Publications

1. "Li-Ion Cell Manufacturing Using Directly Recycled Active Materials," bat356_Slater_2098_p, U.S. DOE Vehicle Technologies Office Annual Merit Review, 2019.

Acknowledgements

Farasis Energy would like to extend special thanks to Renata Arsenault, who manages this project for USABC, for her collaboration and dedicated effort to advance Li-ion battery recycling technology. The PI would also like to extend special recognition to Farasis Energy researchers Benjamin Little and Martin Grodzicki who contribute to the success of this project on a daily basis.

I.1.E A Closed Loop Recycling Process for End-of-Life Electric Vehicle Li-ion Batteries-Phase II (Worcester Polytechnic Institute)

Yan Wang, Principal Investigator

Worcester Polytechnic Institute
100 Institute Road
Worcester, MA 01609
E-mail: yanwang@wpi.edu

Brian Cunningham, DOE Technology Development Manager

U.S. Department of Energy
E-mail: Brian.Cunningham@ee.goe.gov

Start Date: March 26, 2018	End Date: September 30, 2020	
Project Funding (FY19): \$1,083,610	DOE share: \$541,808	Non-DOE share: \$541,808

Project Introduction

During the course of the Phase I USABC program, the team has observed that the xEV battery industry is moving to higher nickel NMCs. Although the team has successfully synthesized NMC111 which has similar performance with the commercial powder, it is considered necessary to be able to synthesize high nickel NMC (for example NMC622) from the recycling stream in order to compete in the market and successfully commercialize the technology. Therefore, in the Phase II (follow-on) of the USABC project, the team has been developing the capability to synthesize NMC622, once again striving to demonstrate both flexibility to accommodate recycling streams diverse in EV battery chemistry, and the ability to generate NMC622 with similar performance to commercial grade powder. The impacts of emerging new anode materials and adhesives is also being examined. Finally, the recycling process is being further refined and scaled, with the cost model being updated accordingly.

Objectives

The overall objective of the Phase II program is to demonstrate the recovery of NMC622 cathode materials from cycled lithium ion batteries with mixed and emergent cathode and anode chemistries, and adhesives. In comparison to NMC111, NMC622 offers higher energy density, which is increasingly demanded by the EV industry. In addition, the recycling process and cost model will be further developed based on the process update and scale-up.

Approach

Similar to the phase I program, WPI collaborated with A123 Systems and Battery Resources for this phase II program. WPI's primary focus was developing the recycling process and recovering NMC622 powder, A123's focus was on powder characterization, cell fabrication and testing, and Battery Resources' focus was on scale up and cost analysis. In addition, the cells will be delivered to Argonne National Laboratory for independent testing and evaluation. Figure I.1.E.1 shows the hardware strategy of the program. The project included 3 phases: initial scale-up, optimization and final deliverables. During the initial scale-up, the synthesis parameters of NMC622 precursor and cathode materials were determined and electrochemical testing was conducted using coin cells and single layer pouch cells. During the optimization phase, 1~2 different spent battery streams (30kg each) were utilized for recycling experiments to generate NMC622 for 1Ah cells. At the same time, virgin NMC622 was used to fabricate 1Ah control cells for side by side evaluation. For the final deliverables phase, 1 spent battery stream, with intentionally different input chemistry combinations, was utilized for recycling experiments to generate NMC622 for 10Ah cells. At the same time, virgin (commercial) NMC622 was again used to fabricate 10Ah control cells.

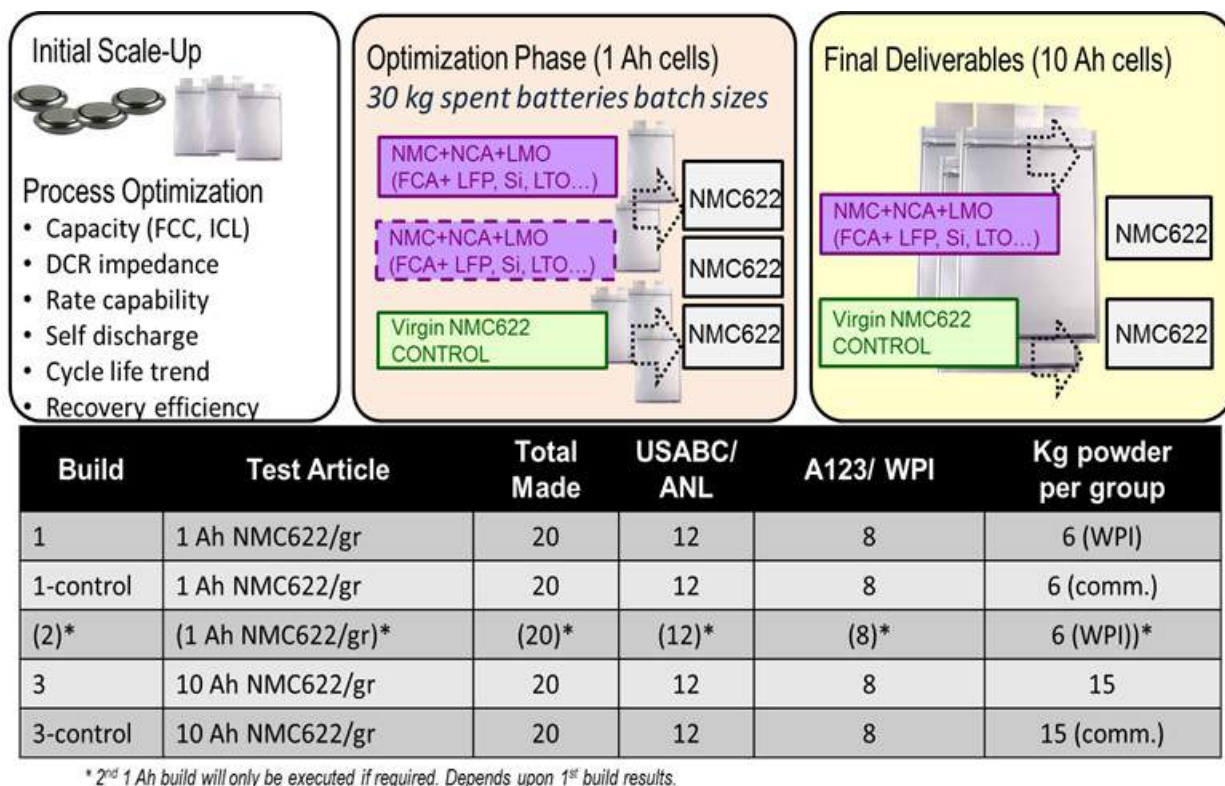


Figure I.1.E.1 Hardware Strategy of the Program

Results

Synthesized NMC622 and coating technology: The team found that most commercial NMC622 has a stabilizing coating (mainly Al_2O_3). Therefore, the team had to likewise develop an effective coating strategy to enable a fair evaluation of the coated (recycled) powder and the A123 sourced coated control powder. To this end, WPI ran a co-precipitation reaction to generate enough NMC622 precursor for the coating development. The precursor was sintered with a lithium source to generate NMC622 cathode powder. Figure I.1.E.2 shows the SEM results of NMC622 powder with different magnifications. The particles are spherical shape and the tap density is $\sim 2.7\text{g/cc}$. A123 tested electrochemical performance for the powder, and determined it to be on par with the control powder. The team used this powder to develop Al_2O_3 coating technology, comparing the two established methods:

Dry Al_2O_3 coating technology: The team first used a dry Al_2O_3 coating technology. The experimental procedure consisted of mixing nano-sized Al_2O_3 with synthesized NMC622 cathode powder and sintering for 3 hours at different temperatures.

Wet Al_2O_3 coating technology: The team also used a wet Al_2O_3 coating technology. The experimental procedure involved filtering synthesized NMC622 cathode powder in $\text{Al}(\text{NO}_3)_3$ solution, drying at 80°C and sintering at 600°C for 3 hours.

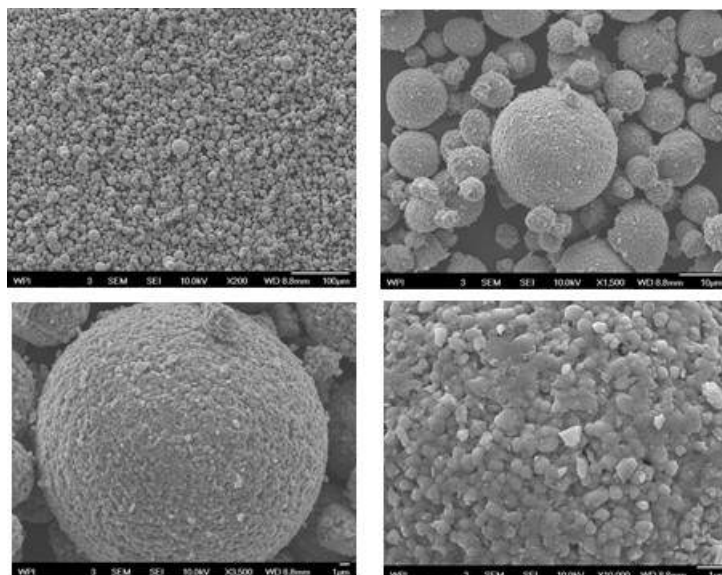


Figure I.1.E.2 Synthesized NMC622 with Different Magnifications

Figure I.1.E.3 summarizes 8 NMC622 cathode powders (1 uncoated, 7 coated) made with the same precursor. Two different coating methods (dry and wet) were used to coat Al_2O_3 onto NMC622. From the analysis, the Al_2O_3 coating of both methods seemed uniform and the FCC and FDC did not change after coating. The team selected two coating powder (one dry coating: #10302018, one wet coating: #11132018) for further analysis, mainly pouch cell cycle performance.

Lot#	Precursor lot #	Sintering setting conditions	Furnace door and Grinding time	Actual sintering conditions	Lithium source	Coating	FCC(0.1C) (mAh/g)	FDC(0.1C) (mAh/g)
10152018	09272018	450c-5hrs Mix it 850c-18hrs	Closed 30mins	450c-5hrs 850c-18hrs	Li_2CO_3 -5% excess	No coating	193.9	170.1
10222018-C1	09272018	450c-5hrs Mix it 850c-18hrs	Closed 30mins	450c-5hrs 850c-18hrs	Li_2CO_3 -5% excess	0.5 wt% Al_2O_3 600c-3hrs	196.3	171.2
10222018-C2	09272018	450c-5hrs Mix it 850c-18hrs	Closed 30mins	450c-5hrs 850c-18hrs	Li_2CO_3 -5% excess	5wt% $\text{Al}(\text{NO}_3)_3$ 600c-3hrs	192.1	173.5
10302018	09272018	450c-5hrs Mix it 850c-18hrs	Closed 30mins	450c-5hrs 850c-18hrs	Li_2CO_3 -5% excess	0.35 wt% Al_2O_3 600c-3hrs	194.9	170.1
10312018	09272018	450c-5hrs Mix it 850c-18hrs	Closed 30mins	450c-5hrs 850c-18hrs	Li_2CO_3 -5% excess	0.5 wt% Al_2O_3 500c-3hrs	195.6	171.4
11012018	09272018	450c-5hrs Mix it 850c-18hrs	Closed 30mins	450c-5hrs 850c-18hrs	Li_2CO_3 -5% excess	0.5 wt% Al_2O_3 400c-3hrs	196.2	171.4
11132018-C1	09272018	450c-5hrs Mix it 850c-18hrs	Closed 30mins	450c-5hrs 850c-18hrs	Li_2CO_3 -5% excess	0.2 wt% Al_2O_3 600c-3hrs	196.6	172
11132018-C2	09272018	450c-5hrs Mix it 850c-18hrs	Closed 30mins	450c-5hrs 850c-18hrs	Li_2CO_3 -5% excess	10wt% $\text{Al}(\text{NO}_3)_3$ 600c-3hrs	195.2	175.1

Figure I.1.E.3 Summary of NMC622 Coating

A123 testing results of coating technology: A123 Systems has evaluated WPI synthesized NMC622 with and without coating. Figure I.1.E.4 shows the physical, electrode and electrochemical properties measured. All WPI synthesized powder (uncoated and coated) shows similar performance with A123 control powder. Most of WPI powder has slightly better rate performance (2C and 5C). We also noticed that wet coated powder normally has very large BET.

Phase 2 - WPI NMC622 Powder Results with Coating		Physical Properties					Electrode		Echem								
Lot #	Wet Coating (WC) or Dry Coating (DC)	BET (m ² /g)	Tap Density (g/cm ³)	D10 (μm)	D50 (μm)	D90 (μm)	Load mg/cm2	Press Density (g/cc)	FCC (0.1C) (mAh/g)	FDC (0.1C) (mAh/g)	First Cycle Eff (%)	0.2C (mAh/g)	0.5C (mAh/g)	1C (mAh/g)	2C (mAh/g)	5C (mAh/g)	10C (mAh/g)
10152018	Uncoated	0.362	2.66	7.1	12.8	22.1	21.02	2.85	193.9	170.1	87.7	166.8	160.7	154.8	144.2	61.1	14.3
10222018-C1	DC	0.562	2.70	6.5	11.6	20.1	22.16	2.87	195.0	171.9	88.2	167.6	160.9	154.3	143.5	57.6	14.6
10222018-C2	WC	1.695	2.78	6.7	11.5	19.4	21.11	3.15	191.6	175.5	91.6	169.3	161.8	155.5	146.8	69.9	16.4
10302018	DC	0.389	2.73	7.9	14.4	25.0	22.42	3.09	194.9	170.1	87.3	167.5	162.1	154.4	136.6	37.4	10.8
10312018	DC	0.641	2.62	7.9	14.7	26.4	21.58	2.96	195.6	171.4	87.6	168.1	162.2	156.2	145.8	68.6	16.5
11012018	DC	0.322	2.59	7.9	15.0	26.8	21.37	2.93	196.2	171.4	87.4	167.4	161.2	155.2	144.9	70.8	17.2
11132018-C1	DC	0.593	2.67	6.5	11.6	20.3	21.88	2.92	196.6	172.0	87.5	167.2	160.8	153.7	141.3	57.9	13.7
11132018-C2	WC	1.388	2.78	6.5	12.6	23.7	22.42	2.99	195.2	175.1	89.7	170.8	165.2	159.4	149.1	58.0	14.7
Control		0.23	2.99	6.2	11.4	20.4	21.27	2.98	196.0	175.5	89.6	171.2	166.3	159.9	137.2	32.4	9.3

Figure I.1.E.4 Characterization of WPI and Control Powder

In addition to coin cells, single layer pouch cells were used to further evaluate cycle performance of the different powder samples. Figure I.1.E.5 shows the updated cycling performance of single layer pouch cells representing the different powder lots (A123 powder, synthesized NMC622 without coating, synthesized NMC622 with dry coating and synthesized NMC622 with wet coating). The cells were cycled at 1C charge and discharge for over 350 cycles. Although there was some variation even within a given group of material, the dry coated NMC622 had the highest capacity retention overall, and thus the dry coating technique was selected for the 1Ah and 10Ah cell builds.

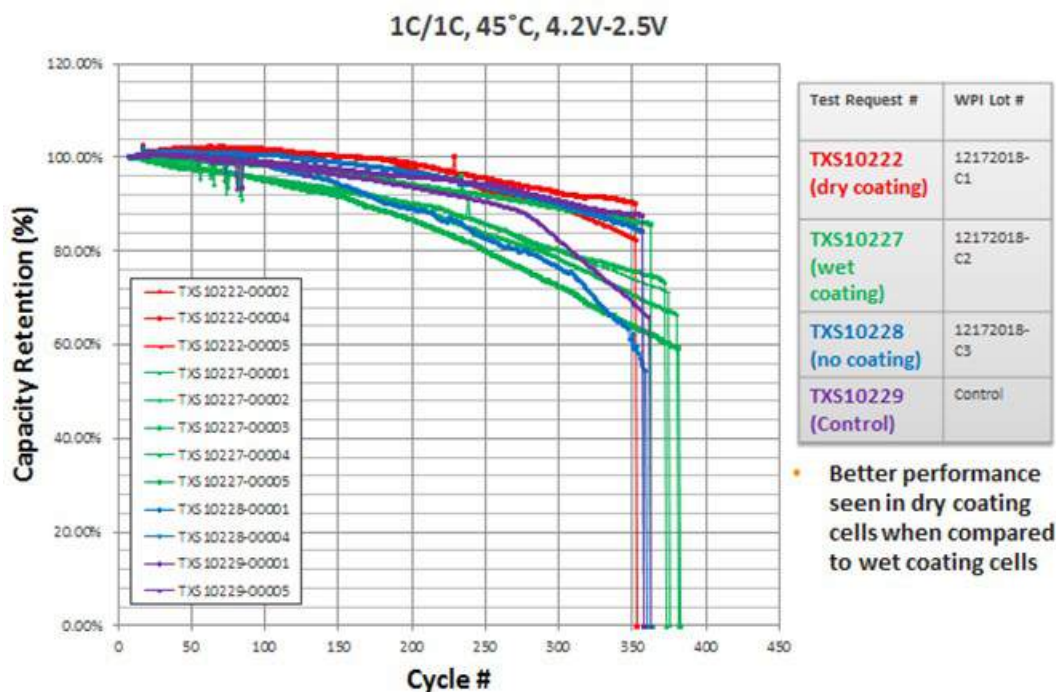


Figure I.1.E.5 Cycling Performance of Single Layer Pouch Cells, TXS10222: dry coating, TXS10227: wet coating, TXS10228: no coating, TXS10229: A123 control powder

6kg cathode powder for 1Ah cells: A 14 day co-precipitation reaction was conducted in order to generate enough NMC622 powder (6kg) for the 1Ah cells. Precursor from days 8-14 and the material gathered from the main and aging reactors was used for final cathode sintering. The precursor sintering was conducted using a large furnace at BRs. After sintering, the uncoated cathode powder was milled. Since the jet mill at BRs was not functional, the WPI team had to mill the powder by mortar and pestle. Each day, roughly 700-800g powder was milled. Figure I.1.E.6 shows the SEM images of the different batches of milled powder. To minimize any adverse effects from potential variability in the hand-milled ‘batches’, the all of the uncoated NMC622 powder was mixed together after milling. Then Al_2O_3 was coated onto the cathode powder using the previously described dry method.

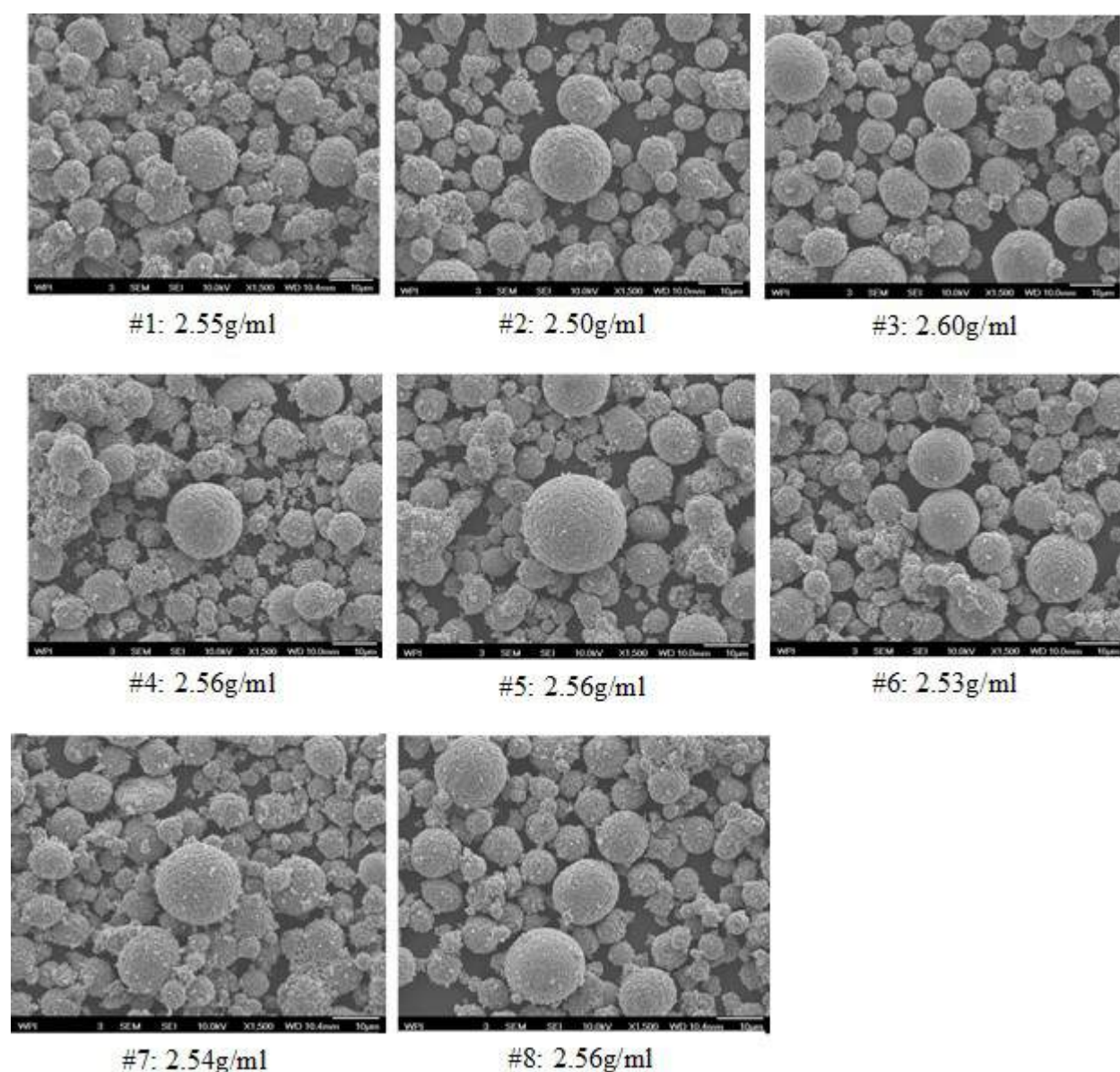


Figure I.1.E.6 Cathode powder in different milling batches

A123 testing results of 6kg powder: A123 Systems first evaluated 6kg NMC622 powder using coin cells and the results are shown in Figure I.1.E.7. The synthesized powder (from recycled battery feed) shows similar

performance with the A123 control powder with slightly higher rate performance. Currently, A123 has coated electrodes for the 1Ah cells, and is fabricating the Build 1 cell deliverables.

Phase 2 - WPI NMC622 Powder Results with Coating		Physical Properties	Electrode		Echem								
Lot #	Comment	BET (m ² /g)	Load mg/cm2	Press Density (g/cc)	FCC (0.1C) (mAh/g)	FDC (0.1C) (mAh/g)	First Cycle Eff (%)	0.2C (mAh/g)	0.5C (mAh/g)	1C (mAh/g)	2C (mAh/g)	5C (mAh/g)	10C (mAh/g)
08192019	6kg batch for 1Ah Cells		19.66	3.12	194.2	175.2	90.2	170.5	164.1	157.9	143.2	47.3	12.3
Control	Control	0.23	21.27	2.98	196.0	175.5	89.6	171.2	166.3	159.9	137.2	32.4	9.3

Figure I.1.E.7 Coin Cell Testing Results for the 6kg NMC622

Conclusions

In this USABC project, the team has successfully recycled multiple 30 kg size batches of end of life EV batteries consisting of different incoming cathode chemistries and producing NMC622 powder. In addition, the team developed two scalable surface coating techniques to stabilize the NMC622 active material and mitigate cycling and calendar aging-induced degradation. The dry coating method was selected due to the observed higher stability of the dry coated powder. Throughout the extensive material analysis and electrochemical testing performed on coin cells and single layer pouch cells, the recovered NMC622 powder continues to demonstrate similar performance to commercial control powder. The team has successfully synthesized and delivered 6kg powder to A123 Systems for 1Ah cell fabrication, and is presently generating powder for the final program deliverables.

Key Publications

1. Zhangfeng Zheng, Mengyuan Chen, Qiang Wang, Yubin Zhang, Xiaotu Ma, Chao Shen, Dapeng Xu, Jin Liu, Yangtao Liu, Paul Gionet, Ian O'Connor, Leslie Pinnell, Jun Wang, Eric Gratz, Renata Arsenault, Yan Wang, High Performance Cathode Recovery from Different Electric Vehicle Recycling Streams, ACS Sustainable Chemistry & Engineering, 6 (2018) 13977-13982.
2. Mengyuan Chen, Zhangfeng Zheng, Qiang Wang, Yubin Zhang, Xiaotu Ma, Chao Shen, Dapeng Xu, Jin Liu, Yangtao Liu, Paul Gionet, Ian O'Connor, Leslie Pinnell, Jun Wang, Eric Gratz, Renata Arsenault, Yan Wang, Closed Loop Recycling of Electric Vehicle Batteries to Enable Ultra-high Quality Cathode Powder, Scientific Reports, 9 (2019) 1654.
3. Mengyuan Chen, Xiaotu Ma, Bin Chen, Renata Arsenault, Peter Karlson, Nakia Simon, Yan Wang, Recycling End-of-Life Electric Vehicle Lithium Ion Batteries, Joule, DOI: 10.1016/j.joule.2019.09.014.
4. Bin Chen, Xiaotu Ma, Mengyuan Chen, Dennis Bullen, Jun Wang, Renata Arsenault, Yan Wang, Systematic Comparison of Al³⁺ Modified NMC 622 from Recycling Process, ACS Applied Energy Materials, DOI: 10.1021/acsaem.9b01814.

Acknowledgements

The development team (WPI/A123/BRs) would like to thank the following for all of the help, advice, support and suggestions: USABC program manager Renata Arsenault (Ford) and USABC work group members Nakia Simon (FCA), Peter Karlson (GM), Brian Cunningham (DOE), and David Robertson (ANL).

I.1.F Perform USABC/USCAR Benchmarking Activities (Southwest Research Institute)

Bapiraju Surampudi, Principal Investigator

Southwest Research Institute
6220 Culebra Road
San Antonio, TX 78258
E-mail: bapiraju.surampudi@swri.org

Ian Smith, Principal Investigator

Southwest Research Institute
6220 Culebra Road
San Antonio, TX 78258
E-mail: ian.smith@swri.org

Brian Cunningham, DOE Technology Development Manager

U.S. Department of Energy
E-mail: Brian.Cunningham@ee.doe.gov

Start Date: February 23, 2018

End Date: October 31, 2019

Project Funding: \$529,253

DOE share: \$150,000

Non-DOE share: \$379,253

Project Introduction

Development of new powertrains for hybrid electric vehicles requires knowledge of similar and past powertrains' proficiencies and shortcomings. This knowledge is gained through benchmarking and additional data analysis and can help drive the direction of product development and influence goals and targets such as range and production price for the U.S. Department of Energy Vehicle Technologies Program. A vehicle- and component-level technical benchmark study and detailed cost analysis was performed on the 2018 Audi A3 eTron plug-in hybrid electric vehicle (PHEV).

Objectives

Vehicle-level benchmarking included on-road testing at various battery pack state of charge (SOC) to examine vehicle performance (acceleration and regenerative braking) along with chassis dynamometer testing to determine vehicle fuel economy over various emissions certification drive cycles.

Component-level benchmarking included battery pack and cell performance testing (static capacity and HPPC), pack teardown and cost analysis and motor performance testing.

Approach

For vehicle-level benchmarking the PHEV was instrumented to acquire voltage and current at various locations in the high-voltage system (battery pack, electric motor, inverter, etc.) and 12 V system. CAN data on the engine, transmission, electric motor, inverter and power electronics was also recorded. The coolant loop for the power electronics and high-voltage battery pack was instrumented to provide insight into the thermal management strategies for the vehicle under different dynamic and charging tests.

For component-level testing, the various subsystems of the vehicle were removed and installed in test cells for evaluation. The battery pack was tested using a high-voltage power supply to determine its pulse power and static capacity under ambient conditions. The battery pack was disassembled, and individual cells were evaluated under various temperatures ranging from -30°C to 45°C. A third-party worked with SwRI and USABC to conduct a cost analysis on the battery pack.

The electric motor was tested with an industrial inverter due to the difficulty in operating the OEM inverter and motor outside of the vehicle. Steady-state efficiency mapping was conducted from 0 to 3000 rpm and 0 to

110 N-m with the motor and transaxle at normal operating temperature. Spinloss testing was conducted to provide information on the parasitic losses from the electric motor and transmission with the motor de-energized.

Results

In 2018 the vehicle was acquired and instrumented for vehicle/on-track testing. Instrumentation included current sensors and voltage taps on each phase of the electric motor, high-voltage battery pack, high-voltage accessories (air conditioning compressor & PTC heater), on-board charger and DC/DC converter. The electric motor and high-voltage battery pack were connected to a power analyzer in order to determine the power factor and electrical efficiency of the electric motor. Thermocouples were placed in various locations along the cooling circuit for the high-voltage system along with flow meters to accurately account for the cooling requirements for the powertrain. (See Figure I.1.F.1.)

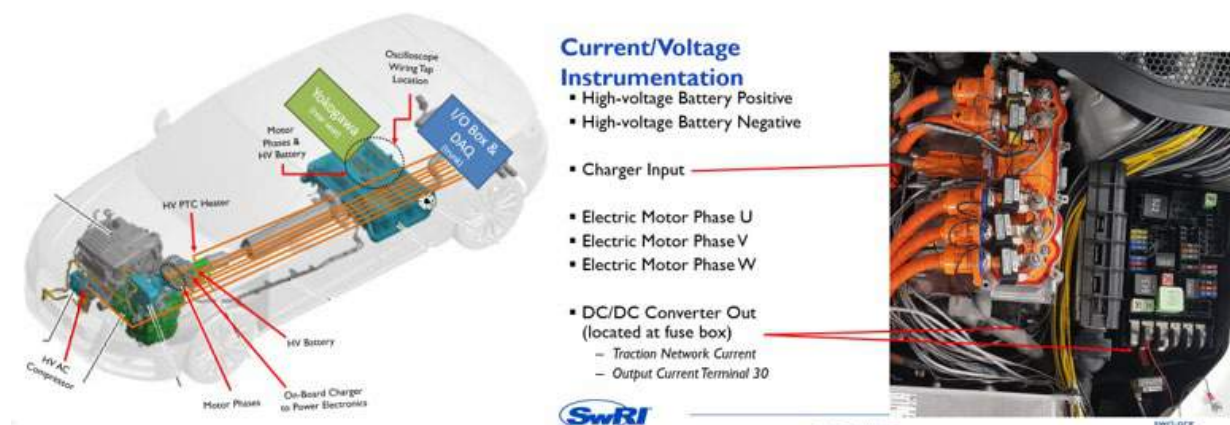


Figure I.1.F.1 High-voltage measurement schematic (left). Power electronics breakout for voltage and current measurement (right)

Over 55 OBD-II extended PID messages were reverse engineered on the engine, transmission, electric drive, battery and steering assist modules. A sample of these messages is shown in the figure below. These messages include electric motor commanded torque and speed, driver requested torque, transmission input/output speeds, battery temperatures and various currents and voltages. (See Figure I.1.F.2.)

OBD CAN Data			
▪ The following messages have been reverse engineered over the OBD CAN bus			
Battery	Engine	Electric Drive	Auto Trans
Current of HV/High battery*	Throttle Valve Position	Phase current U*	Engine Speed*
Battery Temperature	Absolute load value	Phase current V*	Transmission Output Speed*
Battery Charge Condition	Normalized load value	Phase current W*	Accelerator position*
HV battery voltage	Selected Gear-kits 0-7	RPM of electric machine*	Brake pressure*
Temperature Sensors 1	Coolant Temperature at Radiator	Cr-machine speed: actual value*	Transmission fluid temperature
Temperature Sensors 2	Engine oil temperature	Temperature of electric machine*	Driver Request Torque*
Temperature Sensors 3	High fuel pressure	Torque: current value*	Transmission Input Speed*
Temperature Sensors 4	Low fuel pressure	Specified torque*	Vehicle Speed Sensor
Temperature Sensors 5	Throttle valve position: normed	Calculated actual torque of electric machine*	Trans Input Speed Shaft 1*
Temperature Sensors 6	Shift lever position	Output current of DC/DC converter*	Trans Input Speed Shaft 2*
Temperature Sensors 7	Vehicle Speed	Electric Motor: electric power*	Trans Output Speed Shaft 1*
Temperature Sensors 8	Engine Torque*	Electric motor: RMS current*	Trans Output Speed Shaft 2*
Cell 1 SOC	Brake Torque*	DC/DC Converter circuit voltage	Current of Gear Solenoid A*
...	Brake Pressure		Current of Gear Solenoid B*
Cell 96 SOC			Current of Gear Solenoid C*
Min Cell SOC			Current of Gear Solenoid D*
Max Cell SOC			
Cell 1 Voltage			
...			
Cell 96 V			
Min Cell V			
Max Cell V			

*Indicates investigating HS CAN buses for this signal.

The more messages you request the more traffic on the OBD CAN bus and the slower the response.

Some messages found on multiple modules.

POWERTRAIN ENGINEERING
swri.org

Figure I.1.F.2 OBD e-PID messages reverse engineered

In addition to the OBD-II CAN traffic that was being requested, SwRI tapped into two high-speed, proprietary CAN bus lines (the Powertrain CAN bus and Hybrid CAN bus) located underhood. Unlike OBD, these two buses openly broadcast hundreds of frames of messages with update rates ranging from 2 ms to 0.5 seconds. SwRI reverse engineered a number of these high-speed CAN messages pertaining to the transmission and electric motor using a SwRI proprietary algorithm.

Results from the track testing of the instrumented vehicle showed that wide-open-throttle (WOT) acceleration was independent of battery state of charge. The electric motor provided a peak torque of 320 N-m for the first 1.5 seconds of acceleration at which point the engine would turn on and provide the majority (67%) of the torque requested. The vehicle used all-regenerative braking below 0.1 g of deceleration and limited the peak power into the battery pack at 42 kW (~4.4 C rate). At deceleration rates greater than 0.1 g the vehicle blended braking torque demand between the electric motor and friction brakes.

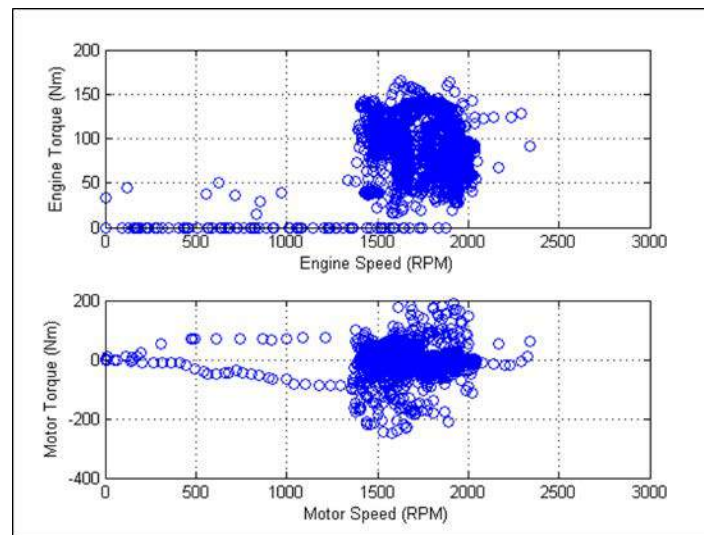


Figure I.1.F.3 HwFET engine & motor torque during charge-sustaining operation

Chassis dyno testing allowed SwRI to compare measured fuel economy to the manufacturer and EPA published fuel economy data. In general, the fuel economy was very similar, with the exception of the Cold CO and SC03 drive cycles. SwRI measured fuel economy significantly lower than the manufacturer published values (up to 20% lower) for both the Cold CO and SC03 drive cycles. SwRI was able to determine the thermal management strategy for the battery pack, as well as, the conditions under which the engine would turn on and when the vehicle would change from charge-depleting to charge-sustaining operation. Sample data from the chassis dyno test of the HwFET drive cycle is shown above and illustrates the area of operation for the engine and electric motor. (See Figure I.1.F.3.)

After the vehicle was tested the battery pack and electric motor and transmission were removed. The battery pack was tested independent of the BMS to determine its capacity, charge/discharge resistance & power at ambient conditions.

After the battery pack was tested it was disassembled to conduct cell-level HPPC and static capacity testing along with material and construction analysis of the battery cell. HPPC testing was conducted at -30, 0, 30 and 45°C from 90 to 10% SOC. The results from the analysis are shown below. (See Figure I.1.F.4.) As temperature increased, charge and discharge resistance decreased. This decrease in resistance allowed for an increase in charge and discharge power. Charge and discharge resistance were, in general, insensitive to state of charge. However, charge and discharge power did show a slight sensitivity to state of charge (see curved contour lines).

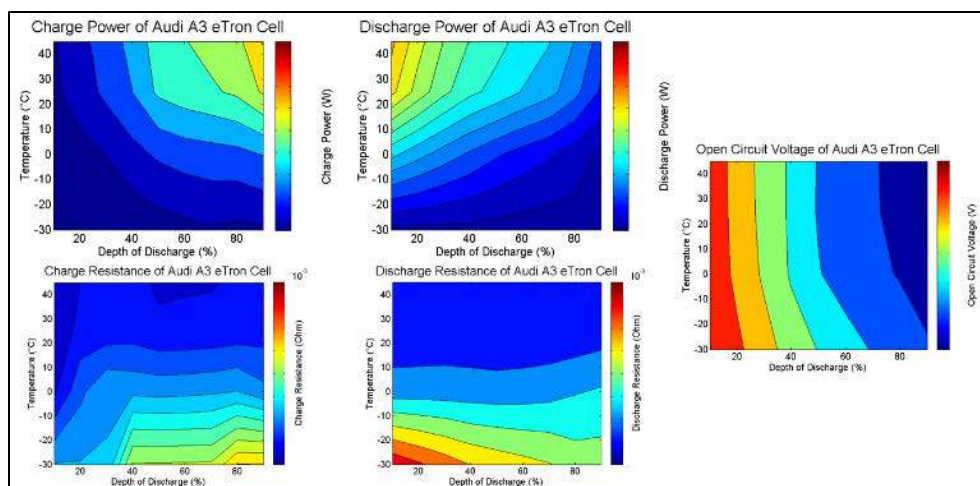


Figure I.1.F.4 HPCC results from the cell-level testing

A single battery cell was destructively tested to provide insight into the materials used in the anode, cathode, separator and electrolyte. Scanning electron microscopy (SEM) was used to determine the particle size for the anode and cathode along with the thickness for the anode, cathode and separator. Raman spectroscopic micro-analysis was conducted on both the anode and cathode to discern the composition/structure of the materials used (e.g., amorphous or crystalline carbon). Energy dispersive x-ray spectroscopy (EDS) analysis was used to provide a semi-quantitative elemental makeup for the anode and cathode (i.e., how much Nickel, Cobalt, Manganese and Silicon). (See Figure I.1.F.5.)

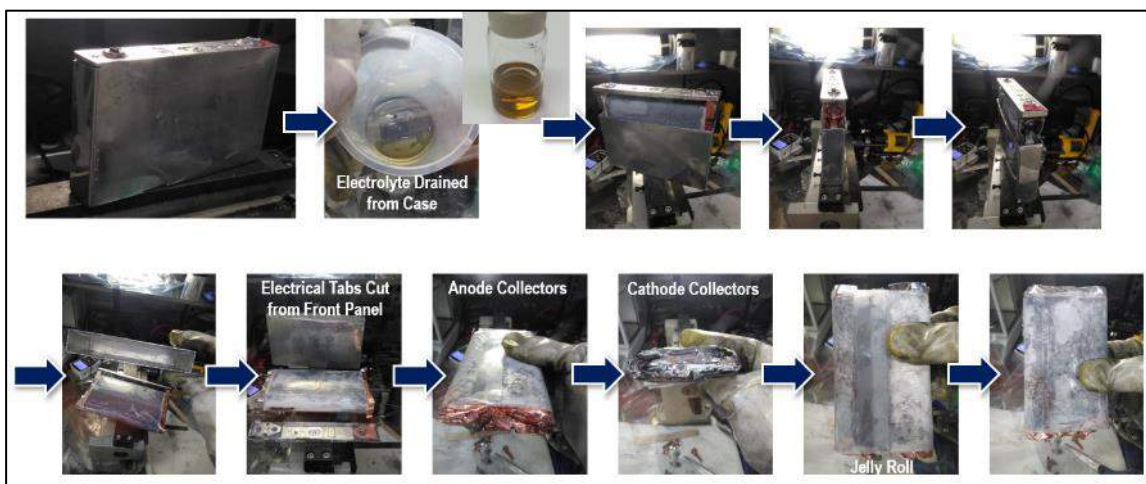


Figure I.1.F.5 Cell teardown

A third-party provided a cost analysis on the battery pack and estimated the volume-cost of the 8.7 kWh battery pack to be \$2,547.16 with the largest portion (70%) of the cost being associated with the battery modules. The normalized cost of the battery pack was 292.78 \$/kWh.

The electric motor and transaxle were installed in a test cell and connected to a dynamometer and industrial inverter to power the motor. An industrial inverter was used due to the difficulty in getting the electric motor and OEM inverter operational with them being removed from the vehicle. Because the electric motor was so tightly integrated with the transaxle, the two components were tested together. Spinloss testing revealed that the parasitic losses from driving the transaxle were very low. The majority of the parasitic losses came from driving the de-energized permanent magnet electric motor. Efficiency testing of the electric motor indicated that the base speed of the motor was between 2000 and 2400 rpm as the efficiency of the system increased

sharply from 1750 to 2000 rpm. SwRI was able to test the electric motor at higher torque levels with lower motor temperatures.

Conclusions

The fully instrumented vehicle was tested over various drive cycles and on-road conditions to provide SwRI and USABC insight into control and thermal management strategies. Additionally, the high-voltage battery pack was tested and disassembled for cell-level testing to provide information on the capacity (Ah), power and cold-cranking performance. The electric motor was also removed from the vehicle and tested to determine its efficiency. The Table I.1.F.1 below compares the results from this benchmarking program to that of the system performance targets for PHEV-20-mile vehicle.

Table I.1.F.1 PHEV-20-mile Target Comparison

Characteristic	PHEV-20 Mile Target	Meet/Exceed?
All Electric Range (AER)	20 mi	Yes
Peak Discharge Pulse Power (10 sec)	37 kW	Yes
Peak Discharge Pulse Power (2 sec)	45 kW	Yes
Peak Regen Pulse Power (10 sec)	25 kW	Yes
System Recharge Rate at 30 °C	3.3 kW (220 V/16A)	Yes
Maximum Discharge Pulse Current (≤ 10 s)	300 A	Yes
Max System Production Price at 100,000 units/year	\$2,200	Yes ¹¹

¹¹ Cost analysis was done assuming actual volume of 8,500/year. Should one extrapolate to 100,000 units/year the price would decrease.

I.1.G Fast-Charge and Low-Cost Lithium Ion Batteries for Electric Vehicle Applications (Zenlabs Energy)

Herman Lopez, Principal Investigator

Zenlabs Energy Inc.
3390 Gateway Boulevard
Fremont, CA 94538
E-mail: herman@zenlabsinc.com

Brian Cunningham, DOE Technology Development Manager

U.S. Department of Energy
E-mail: Brian.Cunningham@ee.doe.gov

Start Date: February 1, 2019	End Date: August 31, 2021	
Project Funding (FY19): \$1,724,320	DOE share: \$862,160	Non-DOE share: \$862,160

Project Introduction

In order to reduce our dependence on fossil fuels and decrease greenhouse gas emissions, electric vehicles (EVs) have received intense attention as a possible solution. Electrification of automobiles is slowly gaining momentum with the main barrier preventing widespread adoption being the lack of available low cost, high energy, fast-charging and safe energy storage solutions. Lithium ion batteries (LIBs) are presently the best energy storage solution used in current and upcoming EVs. Further improvements to the performance of LIBs by integrating high capacity active materials, novel passive components and unique cell designs will be critical for the success and mass adoption of EVs.

This project is developing novel electrolyte formulations, optimized cell designs and a scalable pre-lithiation solution that enables the use of high capacity silicon oxide anodes that will result in lithium-ion batteries capable of meeting the Low-Cost and Fast-Charge (LC/FC) USABC goals for advanced EV batteries in CY 2023. High specific capacity anodes containing high amounts of active silicon (>50%), Nickel-rich Ni-Co-Mn (NCM) cathodes and uniquely tailored electrolytes will be integrated in large capacity (10-60 Ah) pouch cells targeting Fast-Charge and Low-Cost energy solutions. At the conclusion of the program, Zenlabs aims to demonstrate Fast-Charge and Low-Cost LIBs also maintaining other performance requirements of EV cells, including specific energy greater than 300 Wh/Kg, power, cycle life, calendar life, and safety.

Objectives

- Develop unique electrolyte formulations integrating commercially available organic solvents, salts and additives that will perform well with Silicon anodes and Ni-rich NCM cathodes.
- Evaluate and support the develop of a pre-lithiation solution for high capacity and high percent active silicon anodes addressing manufacturability, reproducibility, accuracy, cost and safety.
- Develop optimized cell designs to build and deliver cells that will meet the USABC EV battery goals for commercialization in calendar year 2023.
- Evaluate and integrate cost effective and high performing active and passive materials, processing steps and cell designs to meet the low-cost and fast-charge targets.
- Design and develop large format (10 - 60 Ah capacity) pouch cells to meet the USABC EV cell goals.
- Build, deliver and test large format (10 - 60 Ah capacity) pouch cells integrating optimized high capacity Si-based anode, NMC cathode, electrolyte, separator and pre-lithiation to meet the USABC fast-charge, low cost, energy, power, cycle life, calendar life, safety and temperature EV goals.

Approach

Zenlabs is utilizing a system-level approach to screen, develop and optimize the critical cell components (cathode, anode, electrolyte, separator), pre-lithiation process (process, dose), cell design (N/P ratio, electrode design) and cell formation and testing protocols that will enable meeting the USABC EV cell level goals for the year 2023. The development consists in integrating pre-lithiated silicon-based high capacity anodes, high capacity Ni-rich NCM cathodes, high voltage electrolytes and composite separators into large capacity (10-60 Ah) pouch cells. The developed cells will target low-cost and fast-charge along with high energy density and power, good cycle life and calendar life, safety and low and high temperature performance. During the program, Zenlabs will utilize three cell build iterations to meet the program targets that will deliver cells to the National Laboratories for testing. Cells will be tested both at Zenlabs and independently by three National Laboratories: Idaho National Laboratory (INL), Sandia National Laboratories (SNL) and National Renewable Energy Laboratory (NREL).

During the program, Zenlabs will leverage its material, processing and cell design and development expertise to screen, engineer and optimize various electrolytes, pre-lithiation approaches and cell design solutions addressing the challenges associated with meeting the USABC Low-Cost and Fast-Charge cell targets. Zenlabs has identified development areas that will be addressed and improved during the program. Significant material and cell development (electrolyte engineering, pre-lithiation development and cell design engineering) will take place to meet USABC cell targets.

Zenlabs believes that it will be able to meet the program cell cost targets. First, the high energy density of the cells increases the kWh of a given system, which reduces the \$/kWh ratio and reduces the cost target gap. In addition, by utilizing a high capacity silicon-based anode, the quantity of material needed is reduced and cost decreases. While the current costs for silicon and pre-lithiation can be relatively high, Zenlabs will continue to evaluate and qualify cost effective options and believes that the cost of these important components and processes will decrease significantly in the near future as existing suppliers scale production and additional suppliers come online. Zenlabs is also partnering with a cell manufacturing partner and equipment vendors to build pre-lithiation equipment capable of meeting the low-cost and manufacturing program targets.

The program is 2 ½ years where Zenlabs will meet the USABC low-cost and fast-charge cell specifications by integrating unique electrolyte formulations and cell designs that will improve fast charging, cycle life and calendar life, as well as, focusing on the best pre-lithiation solutions and material options to reduce cost and improve performance from high capacity silicon oxide anodes. At the conclusion of the program, the cells will meet the USABC EV cell goals for the year 2023.

The program has been structured in a way that as it progresses, the cell targets increase with respect to specific energy, energy density, cycle life and lower cell cost. The program consists of 3 cell builds during the 2 ½ year program that include a baseline build at the beginning of the program (CB#1), a second cell build (CB#2) midpoint in the program and a final cell build (CB#3) at the conclusion of the program. Cells from each of the builds will be delivered and independently tested by the National Laboratories. Figure I.1.G.1 shows the projected usable BOL (beginning of life) and EOL (end of life) cycle life (a), cell cost (b), specific energy (c) and energy density (d) for three program cell builds. Different cell builds will focus on different size and capacity cells. Where CB#1 focused on 12 Ah cells, CB#2 will focus on both 12Ah and 50 Ah capacity cells and CB#3 will primarily focus on the larger 50 Ah capacity cells.

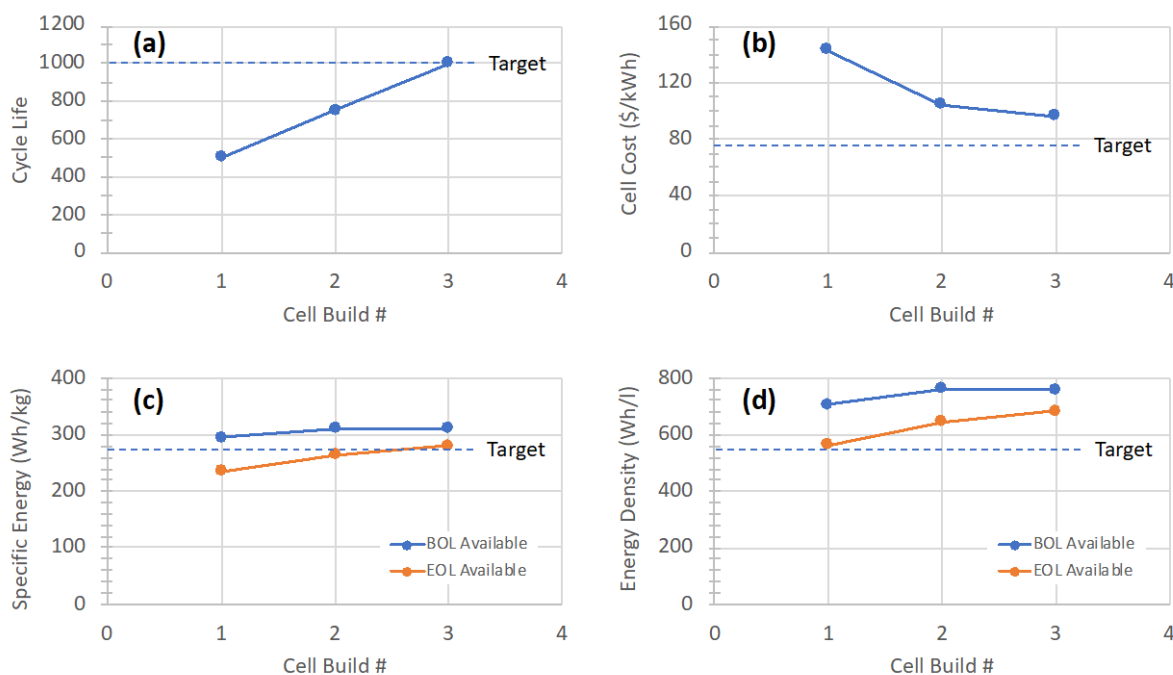


Figure I.1.G.1 Projected cell development progression throughout the USABC program

Results

Zenlabs has demonstrated 1,000 cycles at 1C rate from 12 Ah capacity high silicon containing (>50%) pouch cells with an energy density >300 Wh/Kg before reaching 80% capacity retention. The same cells have also shown fast-charging capability recovering >90% of the capacity for a 15-minute charge and showing >600 fast-charge (15 minute) cycles before reaching 80% capacity retention. Figure I.1.G.2 shows the 1C rate charge and discharge cycling (a) and the fast charge cycling (b) composed of a 4C rate charge followed by a CV for a total charge time of 15 minutes followed by a 1C rate discharge. The fast charge cycling also contains a 1C charge and discharge capacity check every 50 fast charge cycles.

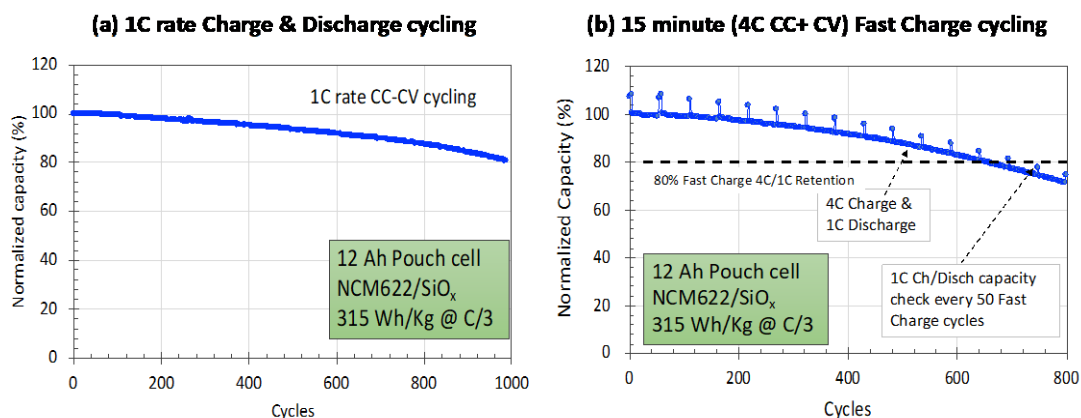


Figure I.1.G.2 Cycling performance from 12 Ah capacity pouch cells at 1C rate (a) and 15 minute fast charge (b) conditions

The program will further improve the fast charging performance and reduce cost by developing unique electrolyte formulations, pre-lithiation solutions to enable high capacity silicon oxide anodes and optimized

cell designs to build and deliver pouch cells that meet the USABC EV battery goals for commercialization in CY 2023.

Electrolyte Development

The stability and properties of the electrolyte will be critical to ensure good cell performance with respect to fast rate charging, cycle life, calendar life, gassing, low and high temperature operation and safety. Decomposition of the electrolyte at the negative electrode can take place under the highly reducing and oxidative high voltage environments. The only reason graphite electrodes remain dormant to the reduction process is due to the formation of a stable protective film at the interface of the anode electrode and the electrolyte which is termed as the solid electrolyte interface (SEI). Si-based materials also require an SEI, that is chemically and potentially structurally different than graphite. A similar passivating SEI film can also form at the cathode surface. The chemical nature and stability of the SEI films are highly dependent on the type of electrolyte with respect to the organic solvents, additives and salts used. The SEI is electronically insulating but allows lithium ions to conduct through them. Having a stable and highly conductive electrolyte capable of rapidly and reversibly shuttling lithium ions in and out of the cathode and anode will be necessary for meeting the fast charge cell targets.

Zenlabs is evaluating various electrolyte formulations containing different commercially available linear and cycling organic carbonate solvents, solvent ratios, lithium salts, salt concentrations and various additives known to perform well with silicon anodes and Ni-rich NCM cathodes. Various anti-gassing additives, anode and cathode SEI forming additives, hydrofluoric (HF) acid scavenging additives, and fire-retardant additives are also being evaluated. Initially the electrolyte formulations are screened and evaluated in coin-cell full-cells under identical cell design conditions used in the high energy pouch cells. After promising electrolyte formulations based on capacity, rate, and cycle life are identified from the coin-cells, evaluation in large capacity pouch cells will follow. Figure I.1.G.3 shows the coin-cell full-cell cycle life data at 1C rate for various electrolyte formulations where different solvents and additives (a) and salt types and concentrations (b) were evaluated. The results show a number of promising electrolyte formulations with respect to cycle life that will be integrated in pouch cells where additional tests like power, energy, gas evolution, calendar life and safety tests will be performed.

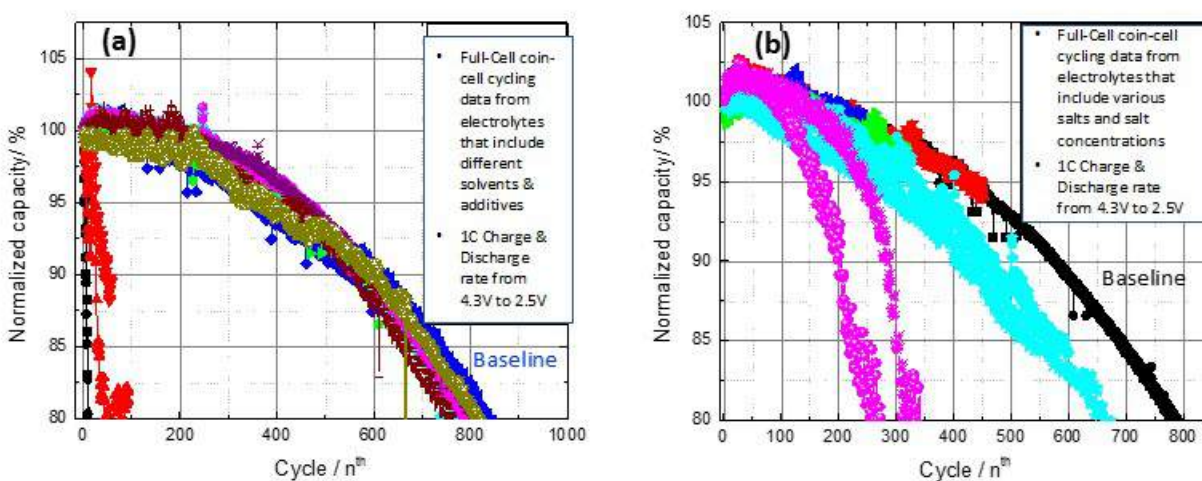


Figure I.1.G.3 Cycling performance in coin-cell full-cells from different electrolyte formulations

Cell Development

Zenlabs is leveraging its cell development and design know-how to meet the challenging fast-charge and low-cost USABC cell targets, by optimizing various cell design parameters from the anode, cathode, electrolyte, and separator. The ongoing cell development has focused on understanding and optimizing the anode and cathode electrode loading and porosity, electrode formulation with respect to carbon additives and ratios, N/P balancing, pre-lithiation dose and testing protocols. Zenlabs has built and delivered baseline cells from cell build #1 (CB#1) to the National Labs for independent testing. Testing of the CB#1 cells is ongoing both at the National Labs and at Zenlabs focusing on cycle life, calendar life, safety, and temperature performance. Figure I.1.G.4 shows the beginning of life (BOL) specific capacity (a), specific energy (b) and energy density (c) from 19 cells from CB#1. The 19 cells exhibit reproducible BOL values at C/3 rate from 2.5V to 4.3V with an average specific capacity of 12.2 Ah \pm 0.1, average specific energy of 319.6 Wh/Kg \pm 1.5 and average energy density without terraces of 734.2 \pm 8.0.

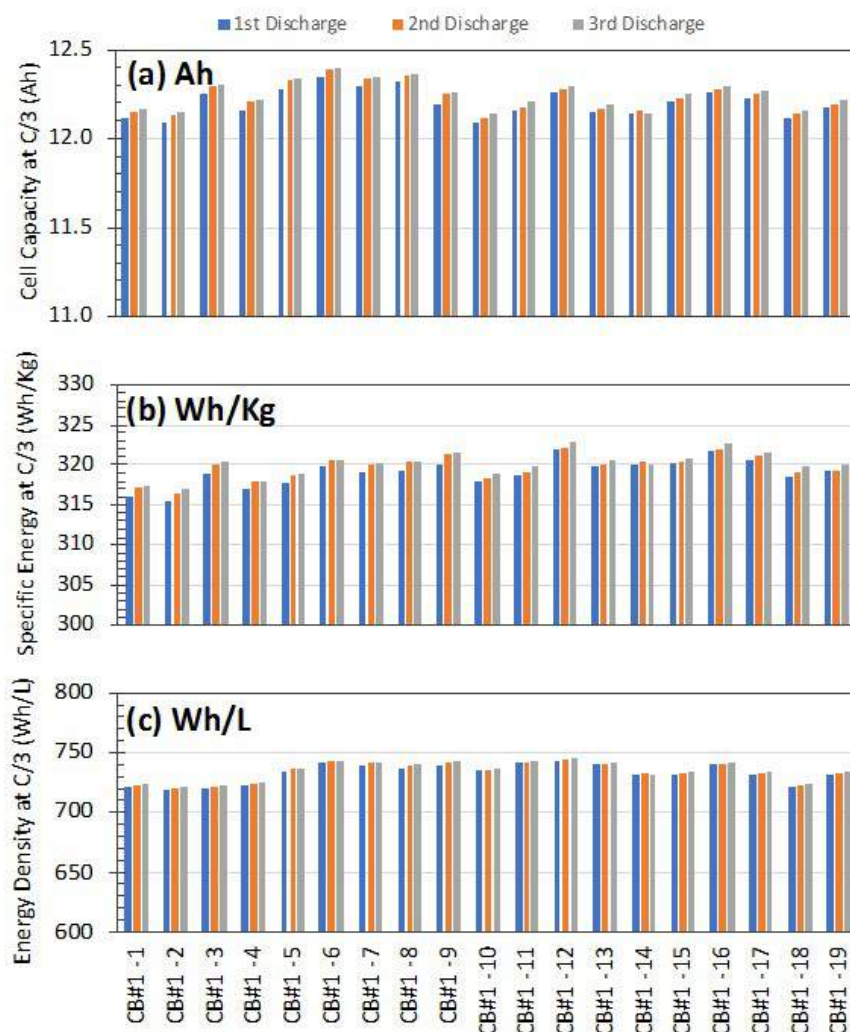


Figure I.1.G.4 Specific capacity (a), specific energy (b) and energy density (c) at C/3 rate from CB#1 cells

Zenlabs continues cell development focused on understanding and improving the calendar life. Zenlabs has developed a protocol to evaluate calendar life from coin-cells as a screening tool, where promising conditions and designs will be evaluated in large capacity pouch cells. Additional development is ongoing to further improve the fast-charge capability and fast-charge cycle life of the cells while continuing to meet the rest of

the USABC cell specifications (energy, power, safety, cost, calendar life, temperature, etc.). Results will be reported in future reports.

Conclusions

Zenlabs has shown 1,000 cycles at 1C rate from 12 Ah capacity high silicon containing (>50%) pouch cells with an energy density >300 Wh/Kg before reaching 80% capacity retention. The cells have also shown fast-charging capability recovering >90% of the capacity for a 15-minute charge and showing >600 fast-charge (15 minute) cycles before reaching 80% capacity retention. Zenlabs has completed and delivered the baseline cells from cell build #1 (CB#1) to the National Labs and cell testing both at Zenlabs and the National Labs is ongoing. Electrolyte and cell development continues focusing on the down-selection of cell build #2 (CB#2) to further meet the USABC EV cell targets.

Key Publications

1. “High Energy Lithium Batteries for Electric Vehicles”, ES247_Lopez_2019_p, U.S. DOE Vehicle Technologies Program Annual Merit Review, AMR, 2019.

Acknowledgements

This work is being performed under the guidance and support from the USABC technical work group: Oliver Gross (program manager), Meng Jiang, Minghong Liu, Jack Deppe, Brian Cunningham, Lee Walker, Aron Saxon and Joshua Lamb

I.1.H Enabling Thicker Cathode Coatings for Lithium Ion EV Batteries (PPG Industries)

Stuart Hellring, Principal Investigator

PPG Industries Inc
4325 Rosanna Drive
Allison Park, PA 15101
E-mail: hellring@ppg.com

Brian Cunningham, DOE Technical Development Manager

U.S. Department of Energy
E-mail: Brian.Cunningham@nrel.gov

Start Date: February 1, 2017	End Date: June 30, 2020	
Project Funding (FY19): \$1.24 Million	DOE share: \$618,654.50	Non-DOE share: \$618,654.50

Project Introduction

To lower the overall cost of the electric vehicle (EV) lithium ion battery, PPG Industries, Inc. will develop and demonstrate NMP-free cathode and matching anode coatings with higher achievable thickness compared to conventional state of the art coatings. These thicker coatings will permit fabrication of higher energy density batteries with improved electrochemical performance. Additional cost savings and reduced environmental impact will be realized through the elimination of NMP-based manufacturing.

Objectives

The objective of this program is to develop solvent based binder systems for lithium ion cathode coatings that do not require the use of NMP and can be coated at a thickness of 150 μm and beyond. NMC622 cathodes at 22, 30 and 40 mg/cm^2 coating weight using PPG's NMP-free binder is fabricated and these cathodes show high flexibility and passed 1/8" Mandrel bend test. The 90° peel strength of pressed coating is higher than 66 N/m. Thick graphite anode coatings (up to 22 mg/cm^2) using PPG waterborne binder is prepared to match the NMC622 cathodes. Full cells were fabricated at pilot facility for performance evaluation.

Approach

Reconfigure the electrode design using a novel NMP-free cathode binder. The unique design of PPG's NMP-free binders along with optimized processing parameters will mitigate film stress and enable the preparation of thicker, more flexible, homogeneous cathode coatings with higher energy density.

Cathodes with PPG binder system show excellent electrochemical properties such as low impedance, and improved cycle performance. PPG also developed waterborne anode coatings to match the cathodes at different coating weights for performance evaluation in full cells. Cell performance is demonstrated in single and multi-layer pouch cells format.

Results

PPG has successfully done several slurry scale-ups and enabled pilot line application to prepare double-sided cathode coatings. PPG baseline cathode coatings (22 mg/cm^2) with 93/3/4 NMC622/Carbon/Binder formulation has shown good adhesion, flexibility and excellent capacity retention (93-96% after 1000 C/3 cycles) and meets the project baseline goal. Cells with binder A shows 93.2% retention at 1000 cycles while cells with binder B are 95.7% retention at 1000 cycles (Figure I.1.H.1). Deliverable cells were fabricated using cathode made with binder B and shipped to INL. Unfortunately, these deliverable baseline cells showed lower than expected performance and didn't match the USABC qualification criteria.

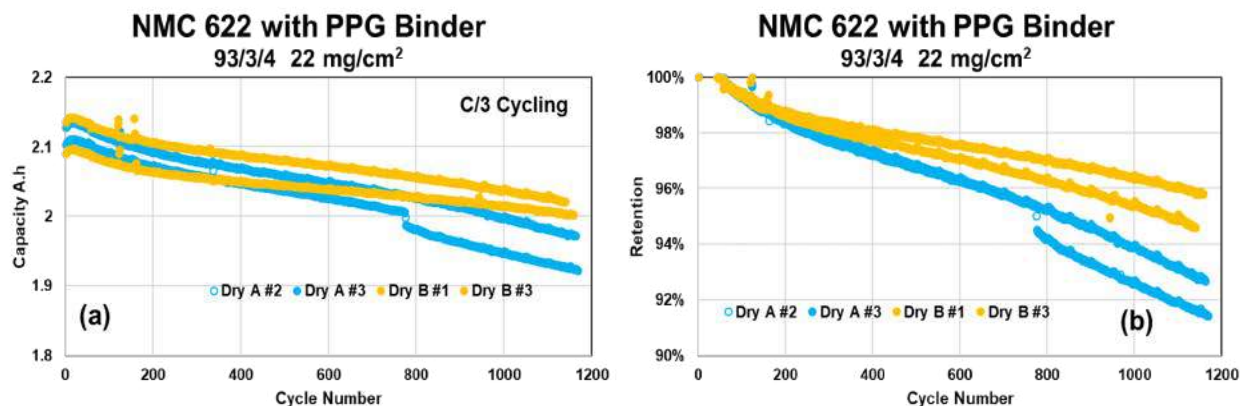


Figure I.1.H.1 Long term cycling of pouch cells with baseline thickness, 93/3/4 and with NMC622 cycled under C/3

PPG performed root cause analysis to find out the poor performance of baseline deliverable cells made in November UMEI trial. In November 2018 UMEI trial, PPG fabricated the deliverable baseline cells (20 mg/cm² cathode) with PPG binder and a graphite based anode to match, the combination of which has previously shown good performance. Fourteen pouch cells with 2.3 Ah capacity were fabricated at UMEI and were delivered to INL for testing. PPG also fabricated first target (30 mg/cm²) pouch cells with 3.1 Ah capacity with cathode coatings of 30 mg/cm² and matching anode coating of 15.6 mg/cm² with CMC/SBR. Unfortunately, none of the cells (baseline and first target cells) from this batch showed a satisfactory performance.

PPG reviewed multiple batches of NMC622 cells coated and fabricated at UMEI in the past year using the same PPG binder and graphite anode. As shown in the Figure I.1.H.2, only cells made during November 2018 trial had unsatisfactory performance. All other cells using the same PPG binder and graphite anode have good performance. For easy comparison, cell performance of 20 mg/cm² and 30 mg/cm² cells made between November 2018 and other trials was plotted together in Figure I.1.H.3 and Figure I.1.H.4. Out of these four batches of NMC622 cells, cells made in June 2018 used a dry mix procedure, all three other trials used the carbon dispersion mixing procedure. PPG does not believe the unsatisfactory cell performance of November 2018 cells was caused by the use of carbon dispersion mixing procedure.

UMEI Trial Date	Jun-18	Nov-18	Jan-19	Apr-19
cathode formulation (NMC622/Carbon/Binder)	93/3/4	93/3/4	2% binder customer project	93/3/4
Cathode loading	20 mg/cm ²	20 mg/cm ² 30 mg/cm ²	20 mg/cm ²	30 mg/cm ²
Anode formulation (graphite/CMC/SBR)	97/1.5/1.5	97/1.5/1.5	97/1.5/1.5	97/1.5/1.5
Cell Performance	good	bad	good	good
Charge/Discharge rate	C/3	C/3	1C	C/3
Cycle Life (20mg/cm ²)	92% at 1300 cycles	78% at 400 cycles	90% at 700 cycles	
Cycle Life (30mg/cm ²)		78% at 225 cycles		95% at 175 cycles

Figure I.1.H.2 Details of different UMEI trials

In order to find possible cause of poor cell performance in November 2018 trial, PPG reviewed lab notebooks, trial reports and logs for all four trials. No significant difference in raw material use was noticed between these trials. However, PPG noticed two factors that could contribute to the poor performance for cells made in November 2018.

1. Cathode slurry was initially mixed in 10L planetary mixer and coated on the pilot line. The coated electrodes had different coating weights on two sides of the coating and those electrodes were discarded. With limited materials left during that trial, cathode slurry was remade using 5L planetary mixer and shorter mixing time. Baseline deliverable cells were fabricated using the electrodes made of the 5L cathode slurry mix. In all other trials, cathode slurry was mixed using 10L planetary mixer and longer mixing time before coating and drying. PPG suspects that insufficient mixing of cathode slurry for cells made in November 2018 could contribute to poor cell performance.
2. The associate who participated in November 2018 trial is no longer with PPG. But PPG was able to get some information from that associate. According to the associate, lower porosity of anode coating made in November 2018 could also contribute to the poor cell performance.

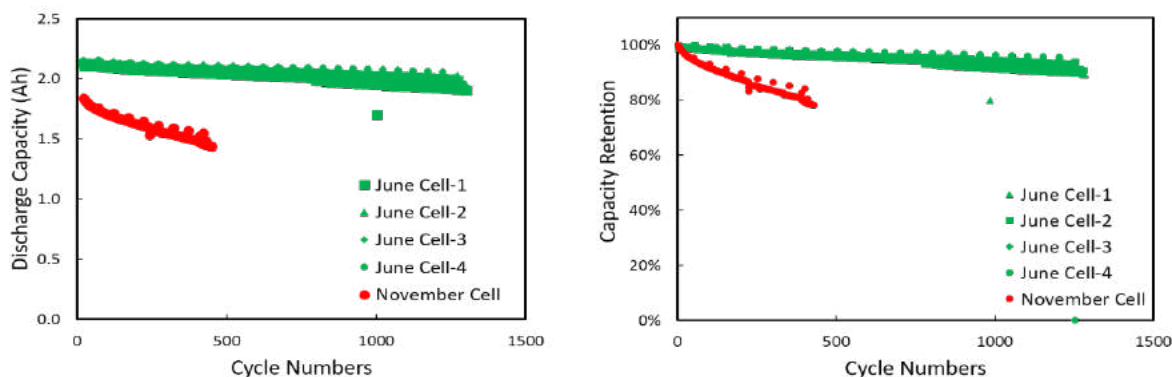


Figure I.1.H.3 Long term cycling of baseline pouch cells (NMC622 cathode at 22 mg/cm² coating weight) made in June 2018 and November 2018

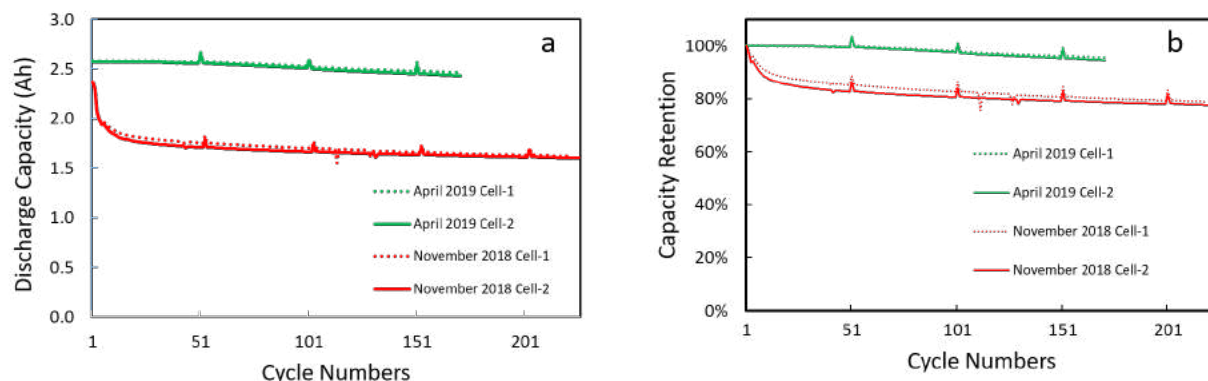


Figure I.1.H.4 Long term cycling of 1st target cells (NMC 622 cathode at 30 mg/cm² coating weight) made in November 2018 and April 2019

PPG successfully coated 1st target NMC622 cathode, PPG binder cathode (30 mg/cm²) showed excellent flexibility (pass 1/8" mandrel) and peel strength (64 N/m). PPG also optimized graphite/CMC/SBR based matching anodes (16 mg/cm²) and assembled pouch cells. These 3 Ah Pouch cells with ~ 1.1 N/P ratio were assembled at UMEI in April 2019. Cells with 1st target 93/3/4 NMC622/Carbon/Binder formulation cathode (C44) and matching graphite anode (Anode AR) with 97/1.5/1.5 Graphite/CMC/SBR formulation show the best cycling performance. These cells completed 500 C/3 cycles with 89% capacity retention (Figure I.1.H.5) and match the USABC qualification criteria.

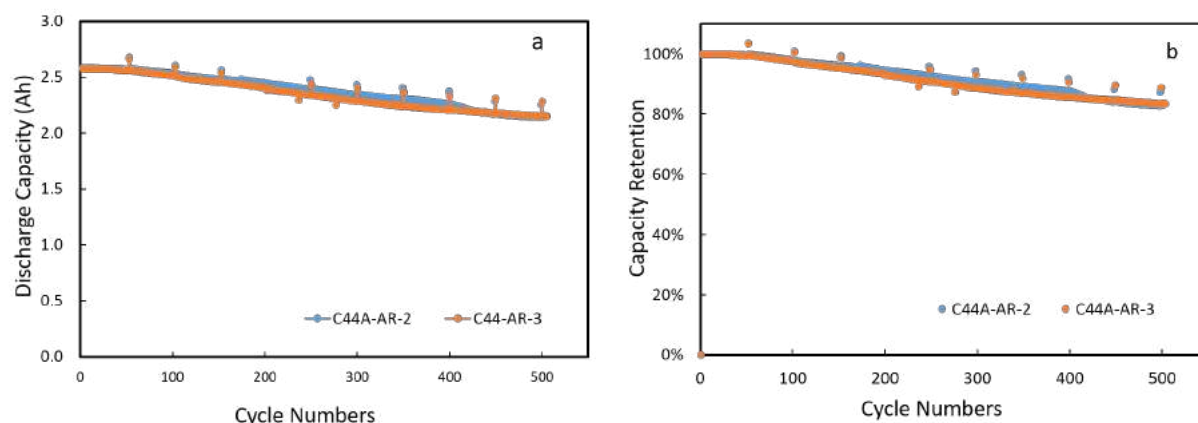


Figure I.1.H.5 a. Discharge capacity and b. Capacity retention of first target pouch cells (NMC622 cathode at 30 mg/cm² coating weight) fabricated in April 2019

After successful demonstration of cells with baseline and first target cathodes, PPG fabricated final target (40 mg/cm²) NMC 622 cathode with PPG binders. These final target cathode coating show excellent flexibility (pass 1/8" mandrel) and peel strength (~ 60 N/m). PPG developed three anode formulations (Anode O, Anode Q and Anode S, see Table I.1.H.1 and Table I.1.H.2 for details). Total nine cells were fabricated at UMEI in Q2 2019. These cells were shipped to BIC for cycling test, and were cycled at C/3, 30°C to evaluate cycling performance. The capacity data of these pouch cells are very different from each other and highly depend on the anode choice. Cell with anode O (AO, refer to Table I.1.H.1) show highest capacity retention (~70% at 100 cycles), whereas the cell with anode Q (AQ, refer to Table I.1.H.1) show the lowest capacity retention (40%) (Figure I.1.H.6) after 100 cycles at C/3, which is lower than the USABC qualification criteria. These results clearly indicate that a better anode is required to improve the performance of the final target cells.

Table I.1.H.1 Formulation Details of Final Target Anodes

Targets	Electrodes	Coating Facility	Formula	Binder	Active Material	Mass Loading mg/cm ²
Final Target	Anode S	UMEI	97/1.5/1.5	CMC/SBR	Superior Graphite	21.3
	Anode O	UMEI	95.37/1.2/3.43	CMC/SBR	Oxidized Graphite	21.2
	Anode Q	UMEI	93.08/1.68/5.32	CMC/SBR	Oxidized Graphite	21.9

Table I.1.H.2 Physical Parameters of 1st and Final Target Anode Coating

Targets	Electrodes	Areal Density (mg/cm ²)	Flexibility before press	Flexibility after press	Peel strength	Thickness after press
Final Target	Anode S	21.3	3/8"	1/4"	28.8 N/m	138 um
	Anode O	21.2	3/8"	1/4"	11.9 N/m	141 um
	Anode Q	21.9	3/8"	1/4"	28.3 N/m	150 um

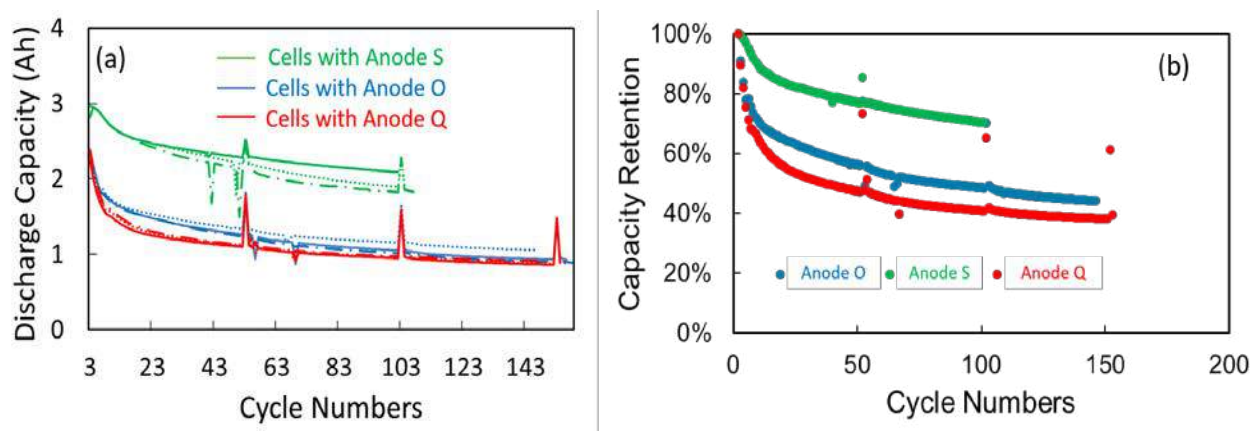


Figure I.1.H.6 Long term cycling of pouch cells with final target thickness, 93/3/4 and with NMC622 cathodes and matching anodes, cycled under C/3 at 30 °C

PPG optimized the graphite sources, PPG waterborne binders and carbon addition to develop the final target anodes (see Table I.1.H.3 for details). These anodes were coated by draw-down method at PPG facility. These anode coatings were pressed to 32% porosity. Anodes with CMC/SBR were also prepared for comparison. PPG fabricated single layer pouch cells (SLP) of 0.52 Ah and 1.1 N/P ratio from these new anode formulations and final target cathode (40 mg/cm²) from April 2019 trial at UMEI. This final target cathode was coated on both sides, so one side of the coating was removed by careful rubbing with NMP. These final target SLP cells were assembled and formed at UMEI and brought back to CIC for C/3 cycle analysis. These cells are cycling at PPG and completed 300 C/3-cycles with 90-93% capacity retention (Figure I.1.H.7). Cells with binder E anode show the highest capacity and capacity retention (93%). PPG decided to coat binder E anode at pilot scale and fabricate multi-layer pouch cells.

Table I.1.H.3 Details of Anode Coatings for Single Layer Pouch Cells

Anodes	Graphite Sources and formulation	Binders	Loading (mg/cm ²)	Peel Strength (N/m)	Flexibility
Control	SLC1520T 95/2/2/1:Graphite/ CMC/Binder/Carbon	SBR	21.7	32	1/4"
A35		PPG Binder D	21.3	37	1/8"
A37		PPG Binder E	21.4	39	1/8"

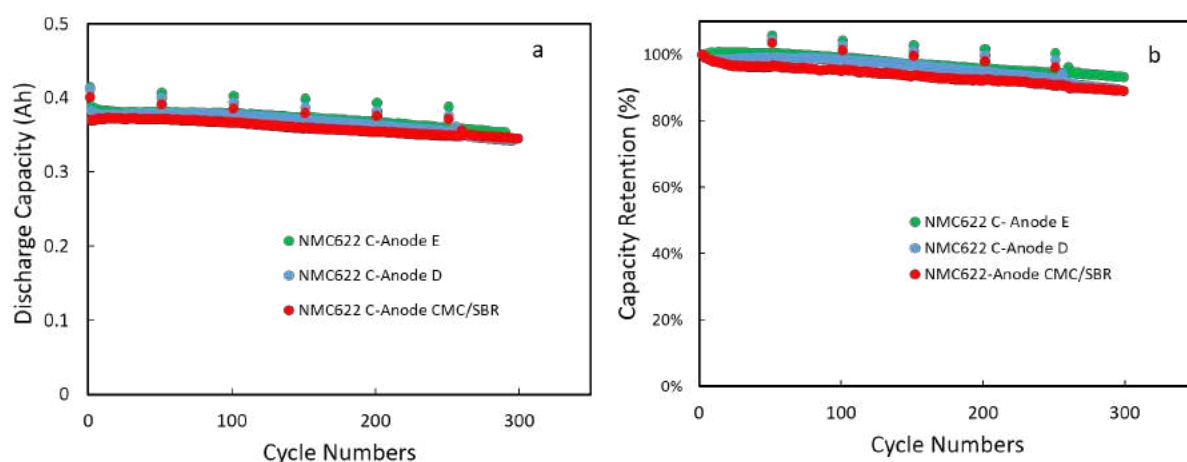


Figure I.1.H.7 a. Discharge capacity of single layer pouch cells with final target cathode (40 mg/cm²) and matching anodes with different binders. b. Capacity retention of SLPs with final target cathode and matching anodes

Anode E was coated at pilot scale (UMEI facility) to match the final target cathode (40 mg/cm²) in multi-layer pouch cells (Table I.1.H.4). Anode E developed cracks during drying at UMEI, whereas we didn't see any cracks in Anode E coating at lab scale in PPG. This discrepancy is due to different mixing, coating and drying procedures used at lab and pilot scale. These cracks were not visible after calendaring. PPG fabricated 5 Ah multi-layer pouch cells (N/P ~ 1.12) from final target NMC622, PPG binder cathode (40 mg/cm²) and matching Anode E (22 mg/cm²). These cells completed ~250 C/3 cycles and show 84% capacity retention (Figure I.1.H.8), which is lower than the USABC qualification criteria (85% after 300 C/3 cycles). We believe that the poor performance of 5 Ah MLPs is due to the cracks in Anode E coated in pilot scale.

Table I.1.H.4 Formulation and Coating Details of Anode E Coated at UMEI

Anodes	Graphite Source and formulation	Binders	Loading (mg/cm ²)	Peel Strength (N/m)	Flexibility
Anode E	SLC1520T Graphite 95/2/2/1:Graphite/ CMC/Binder E/Carbon	PPG Binder E	22	26	1/4"

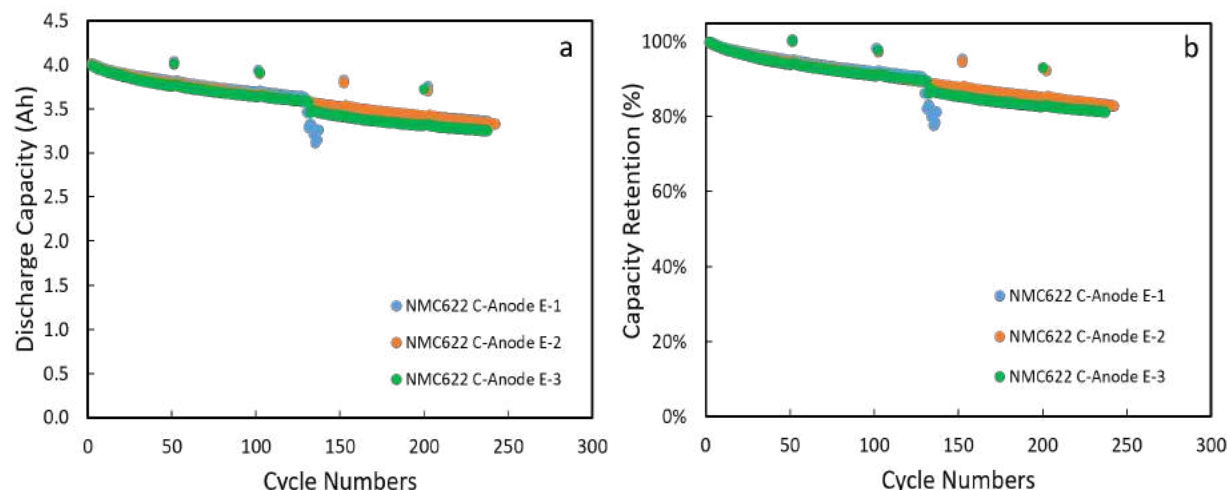


Figure I.1.H.8 a. Discharge capacity and b. capacity retention of 5 Ah Multi-layer pouch cells with final target cathode (40 mg/cm²) and matching anode E coated at pilot scale

PPG also assembled three sets of 2 Ah multi-layer pouch cells (N/P ~1.1) with final target NMC622, PPG Binder cathode (40 mg/cm²), Anode E (22 mg/cm²) and three different electrolyte volumes (3, 4 and 5 times of cells capacity). Cells with low electrolyte volume (3 times of cells capacity) show the highest capacity and capacity retention (Figure I.1.H.9). These cells have completed 100 C/3 cycles and exhibit 96% capacity retention (Figure I.1.H.9). PPG will continue to monitor these cells performance and will report in next quarterly meeting.

We also compared the electrochemical performance of SLPs (0.5 Ah) and MLPs (5 Ah and 2 Ah with low electrolyte volume) (Figure I.1.H.10). These results suggest that 2 Ah cells with NMC622 cathode and Anode E with low electrolyte volume may be able to meet the USABC qualification criteria (85% capacity retention after 300 C/3 cycles). PPG is also working to address the crack issue in Anode E in pilot scale application.

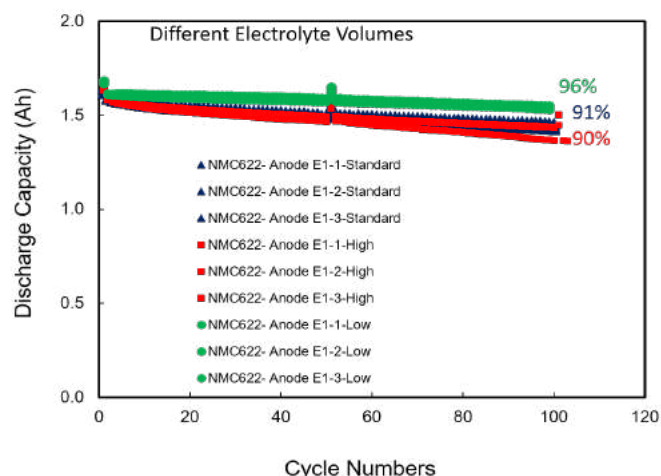


Figure I.1.H.9 Discharge capacity of 2 Ah Multi-layer pouch cells (N/P ~ 1.1) with final target cathode (40 mg/cm²) and matching anode E with different electrolyte volume. Standard is refer to 4 times of cells capacity (8 ml), high is 5 times of cells capacity (10 ml) and low is 3 times of cells capacity (6 ml)

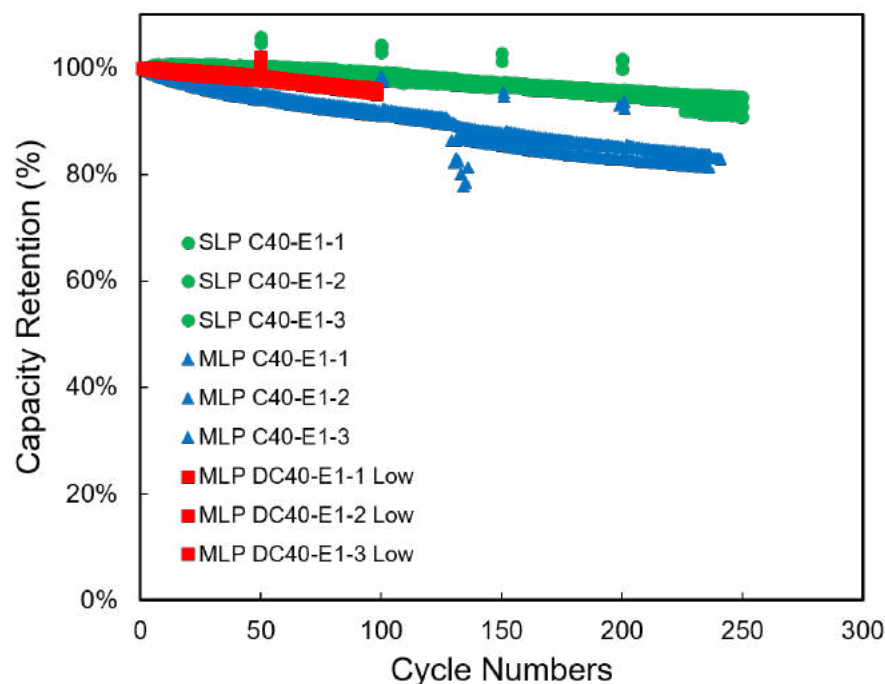


Figure I.1.H.10 Comparison of discharge capacities of SLPs (0.5 Ah) and MLPs (5 Ah and 2 Ah with low electrolyte volume)

Conclusions

PPG demonstrated excellent cycle performance of multilayer pouch cells of baseline and first target (22 and 30 mg/cm²) with NMC 622 and PPG NMP-free binder. Baseline and first target (30mg/cm² cathode) multi-layer pouch cells with 93/3/4 NMC622/carbon/PPG binder completed 1000 and 500 C/3 cycles with ~96% and 89% capacity retention respectively. Baseline deliverable cells underperform at ANL is due to the issue with cathode slurry preparation at UMEI for the delivery cells. PPG optimized anode formulation to match the final target cathode in pouch cells. Single layer pouch cells with final target cathode (40 mg/cm²) and Anode E coated in lab scale completed 300 C/3 cycles with 93% capacity retention. When coated in pilot scale at UMEI, cracks was observed in anode E before calendaring pressing. 5 Ah multi-layer pouch cells with final target NMC622 cathode (40 mg/cm²) and matching Anode E coated in pilot scale at UMEI completed ~ 250 C/3 cycles with 84% capacity retention. Cracks in Anode E coated in pilot scale is the main reason of 5 Ah cells poor performance. PPG also assembled 2 Ah pouch cells with final target NMC622 cathode and Anode E at three different electrolyte volumes. Cells with low electrolyte volume (3 times of cells capacity) exhibit highest capacity retention (96% after 100 C/3 cycles). Additional anode optimization is needed to achieve good performance for final target cells.

Conclusions

Matthew Denlinger, Ford Motor Company, from Dearborn, MI served as the USABC Program Manager for this project. Ahmad Peseran, from NREL, served as the Technical Liason with DOE.

I.2 Processing Science and Engineering

I.2.A Low-cost Manufacturing of Advanced Silicon-Based Anode Materials (Group14 Technologies, Inc.)

Henry R. Costantino, Principal Investigator

Group14 Technologies, Inc.
5809 238th St SE, Suite 1
Woodinville, WA 98072
E-mail: rcostantino@group14technologies.com

Peter Faguy, DOE Technology Development Manager

U.S. Department of Energy
E-mail: Peter.Faguy@ee.doe.gov

Start Date: January 1, 2016
Project Funding: \$3,940,113

End Date: June 30, 2019
DOE share: \$2,728,079

Non-DOE share: \$1,212,034

Project Introduction

Despite substantial investment in Lithium-Ion Battery (LIB) technology, most commercial cells still rely on graphite anodes—originally deployed in the ‘90’s, because of their low cost and acceptable lithium capacity. A shift is underway to replace the graphite anode with a silicon containing material, but due to elaborate manufacturing techniques current costs exceed \$100/kg. It is our vision to develop new anode materials that are high performance, and also easily scalable, employing low-cost materials and manufacturing processes. To this end, we have launched Group14 Technologies, spun out of EnerG2 Inc., a leader in carbon materials development, manufacturing, and commercialization. Group14’s strategy is to develop low cost processes for manufacturing silicon-carbon (Si-C) composite materials that will enable a dramatic reduction in the cost structure of silicon-carbon anodes, i.e., by an order of magnitude, while maintaining the high performance that the LIB industry demands of these advanced anodes.

Objectives

The objective of this project is to develop a new low cost production process that is capable of mass-producing silicon-based lithium ion battery (LIB) anode material that can reach 1000 mAh/g after 1000 cycles and with a cell level cost target of < \$125/kWh, validate performance in LIB full cells, and prove the cost basis at pilot scale.

Approach

At Group14, we are leveraging EnerG2’s carbon technology as our foundation to develop new approaches for low-cost manufacturing of high-performing Si-C composites. These Si-C composites comprise nano-sized and/or nano-featured silicon. Our approach focuses on raw materials that are low cost and readily sourced. Likewise, our approach focuses on manufacturing processes that are low-cost and readily scalable. Specifically, both carbon and silicon components within the Si-C composite are based on low-cost precursors.

Our approach is to down-select Si-C composite materials and manufacturing processes at lab-scale, supported by robust characterization, including electrochemical characterization with a focus on electrochemical testing of the Si-C composite anode materials in full cell Li-ion batteries such as coin cells or pouch cells. Our philosophy for the electrochemical characterization is to employ relatively standard procedures and materials, i.e., industry-standard electrolyte, cathode, and battery cycling conditions. While we are interested in potential synergies with our Si-C composite materials and the next generation of other battery materials (cathodes, electrolyte, etc.) our current intent is that our Si-C composite materials are a “drop-in” replacement for graphite powder as an anode materials, compatible with current commercial anode and Li-ion battery manufacturing lines.

Consistent with our project plan, we have down-selected materials and processes, and have established a facility for manufacturing Si-C at pilot scale (~kg). We are currently producing materials for external and internal performance evaluations. The latter includes electrode and device development towards achieving our final DOE project goal.

Results

During the current FY19, the primary project focus was production of silicon-carbon (Si-C) composite at lab-pilot scale (~kg). To that end, we produced multi-kg quantities of Si-C, thus facilitating shipments to numerous 3rd parties (for instance potential customers). Those shipments, in turn, have provided us with important feedback from the receiving 3rd parties, including confirmation of high first cycle efficiency and excellent cycle stability in a graphite blend. Importantly, several 3rd parties have provided us permission to share their data with the DOE. As discussed during a telecon with the DOE on May 24, 2019, that data, along with our own modeling employing the BatPaC model, satisfies the final project milestone, namely synthesis of 1 kg completes a demonstration 1000 mAh/g and predicted 1000 cycles at < \$125/kWh at full scale volume.

Table I.2.A.1 and Figure I.2.A.1 provide an illustration of 3rd party feedback for pilot-plant produced Si-C, specifically with regards to first cycle efficiency. These data were generated in Swagelok half cells, collected in triplicate (three individual cells). The anode comprised 90% Group14's Si-C, 5% conductivity enhancer, and 5% SBR-CMC binder. Lithium metal provided the counter electrode and reference. The electrolyte was 1 M LiPF₆ in 3:7 ethylene carbonate: diethylene carbonate to which 10% fluoroethylene carbonate (FEC) was added. Cycling was accomplished at a rate of C/25 between 5 mV and 1.5V.

Table I.2.A.1 3rd Party Confirmation of High FCE

Cell #	Capacity ^a	First Cycle Efficiency (%)
1	1658	89
2	1710	89
3	1601	90

^a Swagelok half-cell, working electrode 90/5/5 AM/C/SBR-CMC, Counter electrode and reference: Li metal, electrolyte: 1M LiPF₆ in EC/DEC 3:7 with 10% FEC, formation: CC charge-discharge at C/25 between 5 mV and 1.5V.

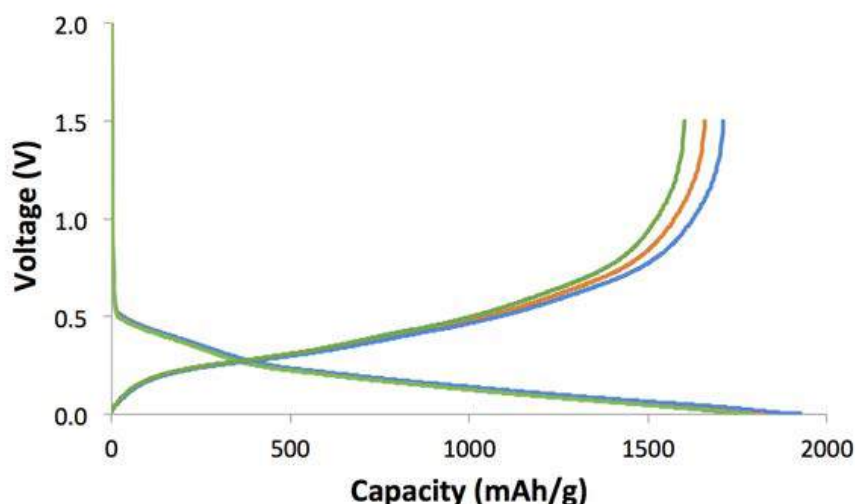


Figure I.2.A.1 3rd Party data for G14's lab-pilot scale Si-C: Confirmation of high FCE

The measured capacity for the Group14 Si-C was 1601-1710 mAh/g. The measured first cycle efficiency was 89-90%. The charge and discharge curves are presented graphically in Figure I.2.A.1. The three curves in green, red, and blue, depict the individual charge/discharge curves for the three replicate cells.

Yet another example of positive 3rd party feedback regarding G14 Si-C's high FCE is presented in Table I.2.A.2. In this example, the anode comprised a blend of Group14's Si-C with graphite to yield a gravimetric capacity of ~550 mAh/g reversible capacity. The data presented in Table I.2.A.2 are for half cell, coin cell format, wherein the anode comprised ~12% Si-C diluted in graphite. The data were generated for two different samples. The measured FCE was 90.5% to 92.0%. These data were also employed to back calculate the capacity and first cycle efficiency of non-diluted Si-C. The calculated value for capacity was 1918 to 2092 mAh/g, and the calculated value for first cycle efficiency was 88.7 to 92.1. It is important to note that Sample 2 had a lower surface area than Sample 1 with a consequently further improved (lowered) first cycle efficiency. It is remarkable to note that for Sample 2 the calculated first cycle efficiency for the non-diluted Si-C was higher than the case for the blend of Si-C diluted in graphite.

Table I.2.A.2 3rd Party Confirmation of High FCE (Graphite Blend)

Sample ^a	Initial Charge Capacity (mAh/g)	Initial Discharge Capacity (mAh/g)	Initial Coulombic Efficiency (%)	Calculated Discharge Capacity [no dilution] (mAh/g)	Calculated Initial Coulombic Efficiency [no dilution] (mAh/g)
1	604	547	90.5	1918	88.7
2	604	556	92.0	2092	92.1

^a Data for half-cell coin cells, anode ~12% Si-C diluted in graphite, counter electrode Li metal, discharge: 0.1 C CC-CV 5 mV 0.005 C cutoff, charge: 0.1 C CC 1.5V cutoff.

The same 3rd party also generated data for cycling performance in full cells (see Figure I.2.A.2). The anode gravimetric capacity was ~ 550 mAh/g and the anode density was ~1.6 g/cm³ (therefore the anode volumetric density was ~880 mAh/cm³).

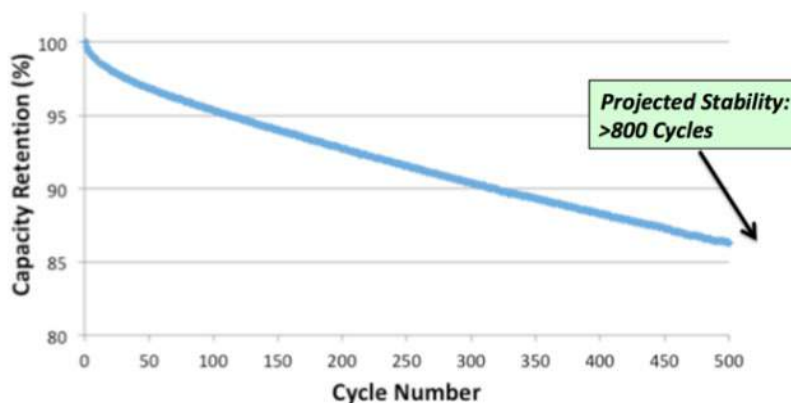


Figure I.2.A.2 3rd Party data for G14's lab-pilot manufactured Si-C: > 800 Cycle stability

Presented are the average data for two full cell pouch cells, anode ~12% Si-C diluted in graphite, NMC 622 cathode, cycled at 1C rate between 4.3V (CV charge 0.05C cut-off) and 3.0 V, electrolyte 1M LiPF₆ in EC:EMC:DEC = 3:5:2 v/v% + Additive. As can be seen, Group14's Si-C is achieving a projected stability (i.e., capacity retention of 80%) of greater than 800 cycles.

Beyond high first cycle efficiency and cycling stability, another attractive attribute of Group14's Si-C is projected low cost at full scale volume. To that end, we used BatPaC model (2018 version 3), developed by Argonne National Laboratory, to validate the cost benefit of including G14 Si-C material in a battery pack.¹³ We chose this model since it has a comprehensive list of considerations to evaluate the battery pack cost and has been used by EPA for cost estimations of battery technologies.

For the BatPaC cost calculation, we used default values provided in the model with few exceptions. In the “chemistry” part of the model, our input parameters in the model are NMC622 cathode, capacity of the graphite/G14 Si-C blend, and cost of anode active material. Other input parameters are not changed as we expect G14 Si-C graphite blend to have similar resistance and electrode density as pure graphite based on preliminary data from our customers.

For the cost calculation, we assumed that the specific capacity of Si-C material is 1500 mAh/g. G14 has the ability to tune the capacity based on Si content of our composite and as such we are able to produce material with capacity as high as 1900 mAh/g. Our baseline case assumed a \$40/kg selling price, which is based on a detailed cost of goods sold model at full scale volume, taking into account projected raw material costs, labor costs (standard U.S. rates), electricity costs, process yields, equipment depreciation, etc. As a sensitivity analysis, we also considered the case for a higher (e.g., \$50/kg) and a lower (e.g., \$30/kg) Si-C selling price than the \$40/kg baseline selling price.

We have examined scenarios wherein G14 Si-C was blended into the anode from 0-50% wherein we considered the cost of a unit battery pack assuming 200,000 units manufactured per year. For the pack design, we picked 88 kWh battery with 300-mile range (typical objective for a sedan type vehicle). As can be seen in Figure I.2.A.3, from the assumptions above and employing the BatPaC model, we project that blending G14 Si-C into the anode of lithium ion batteries can achieve the project goal of attaining <\$125/kWh. Note that the analysis was conducted for 88 kWh battery pack for 300 mi range vehicle, Si-C cost of \$30/kg, \$40/kg, and \$50/kg, 200,000 battery system manufactured per year, graphite cost of \$12.50/kg, NMC622 cathode.

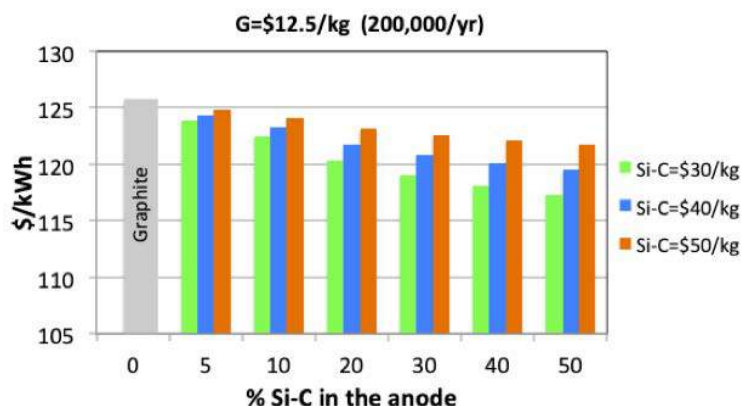


Figure I.2.A.3 Cost model (BatPaC 2018 v. 3) using increasing amount of Si-C in the anode

Conclusions

Over the course of the project we advanced from lab to lab-pilot scale manufacturing of G14 Si-C. Specifically, we demonstrated ability to produce Si-C at pilot scale in excess of the 1 kg goal. Importantly, the product performance of the pilot-scale synthesized Si-C has been validated in the lab. This performance includes demonstration of gravimetric capacity well in excess of 1000 mAh/g, successfully demonstrating the achievement of the second aspect of the final project goal. Regarding the objective to achieve a predicted 1000 cycle stability, we have achieved this goal in combination with device-level enhancements, as discussed above. Based on our in-house electrochemical testing, G14 Si-C has the ability to boost anode energy density by at least ~30% with at least 600 cycle stability. Furthermore, we have obtained 3rd party feedback of achieving even greater stability, for example >800 cycle stability. Importantly, this result was obtained for lab-pilot scale manufactured G14 Si-C. Finally, we have employed the BatPaC model to determine that incorporation of G14 Si-C into the anode of lithium ion batteries can achieve < \$125/kWh. Given this information, in discussion with the DOE we have agreement that G14 Si-C has met the project milestones and deliverables.

In conclusion, G14 has developed a novel Si-C composite that has been proven by industry-leading battery manufacturers to dramatically increase anode capacity with at least 90% first cycle efficiency and 800 cycle stability. This technology is anticipated to lower the cost of Li-ion batteries on a \$/kWh basis by 30%, enabling electric vehicle cost parity with internal combustion engines.

Key Publications

1. Poster entitled “Low Cost Manufacturing of Advanced Silicon-Based Anode Materials,” presented on June 11, 2019 at the Annual Merit Review (AMR) meeting in Washington, DC.

References

1. DOE Telecon for Project ES268, “Low Cost Manufacturing of Advanced Silicon-Based Anode Materials,” presented on May 24, 2019.

Acknowledgements

Walter G. Parker, NETL, served as the Technical Project Officer for this project. The PI also thanks Avery Sakshaug, Chris Timmons, and Dr. Abirami Dhanabalan (Group14 Technologies, Inc) for critical contributions to the project. The PI also thanks Dr. Matt Lim and Professor Peter Pauzauskie (University of Washington) for investigations on material properties as described herein.

I.2.B Electrodeposition for Low-Cost, Water-Based Electrode Manufacturing (PPG Industries, Navitas, ORNL)

Stuart Hellring, Principal Investigator

PPG Industries
4325 Rosanna Drive
Allison Park, PA 15101
E-mail: hellring@ppg.com

Peter Faguy, DOE Technology Development Manager

U.S. Department of Energy
E-mail: Peter.Faguy@ee.doe.gov

Start Date: January 1, 2016	End Date: December 31, 2019	
Project Funding (FY19): \$2,399,034	DOE share: \$1,399,275	Non-DOE share: \$999,759

Project Introduction

The state of the art for the manufacture of lithium ion battery (LIB) cathodes is slot-die coating of a high-viscosity slurry of active battery materials, conductive additives, and a polymeric binder that is dissolved in N-methyl-2-pyrrolidone (NMP). NMP is an expensive consumable in electrode manufacturing with serious health concerns. With the high cost of raw materials and operating costs associated with 2-coat/2-cure electrode processing, this approach results in LIB costs that exceed the DOE target. In order to realize cost-effective, environmentally friendly processes for battery electrode manufacture, binder systems must be developed that enable compatibility of lithium-ion active materials with water and are amenable to coating processes that reduce the cost of electrode manufacturing compared to the current state of the art. One promising approach to achieve this is the use of waterborne binder systems applied to metal foils using electrocoat. Electrocoat is a process widely recognized to be a high-throughput, low cost coating application method that allows both sides to be coated simultaneously, enabling single cure processing.

Solvent-based electrodeposition of pre-formed cathode active powders for producing electrodes for secondary lithium ion batteries has been evaluated by several groups. Cathodes produced by solvent-based electrodeposition showed promising battery performance for metrics which include discharge capacity/rate capability, Coulombic efficiency and cycle life retention. However, the use of volatile organic solvents for manufacturing electrode coatings by electrodeposition has a number of serious drawbacks including volatile organic compound (VOC) emissions, explosion risk, health risks from worker exposure, and cost. Using waterborne coatings significantly mitigates most of the concerns associated with organic solvent-based coating formulations. Benefits include lower voltage/current, better process temperature control and faster deposition rates due to a higher dielectric constant. Binder design, proprietary additives, and electrochemical processing methods are used to ensure quality during manufacturing, to disperse pigment particles and stabilize the aqueous formulation bath against agglomeration and settling.

Objectives

The objective of the project is to develop and demonstrate novel binders and cathode active materials to enable a low-cost, water-based, electrodeposited lithium-ion battery electrode coating system and manufacturing process capable of reducing cell costs by at least 20% while improving battery performance. The project will also demonstrate a battery supply chain model that mirrors traditional automotive Original Equipment Manufacturer (OEM) supply chain models to reduce the risk of electric vehicles (EVs) and increase adoption.

Approach

The approach employed to reach project objectives:

- Develop a viable electrodeposition process through the design and synthesis of electrodepositable binders with flexibility and ionic mobility.
- Tailor and fabricate high-energy density active materials for compatibility while formulating stable water-based cathode coating systems.
- Establish electrodeposition process parameters and validate the performance and economics of the technology at a 1Ah scale, ensuring a path to commercialization.

Specifically, Budget Period 1 included the development of the materials necessary for a successful electrocoated electrode. Work was split between concurrent active materials modification and electrocoat system development. At the end of BP 1, targeted materials were selected based on their performance characteristics.

Budget Period 2 refined the coatings system to improve baseline performance. Cell validation scale increased, enabling refined quantification of the achievable cost reductions. The design and build of a bench scale coater for representative evaluation supported the scale up in Budget Period 3.

The Budget Period discussed throughout this chapter, Budget Period 3, optimized the coating system components to the point that large format cells were built and evaluated. This budget period included obtaining optimized, representative electrodes that were tested for performance properties both independently and within cells. Included within, the possible areas for improvement were identified and next-generation formulations are proposed.

Results

Continued mechanical modification and formulation development of the mini-coater resulted in cathode electrodes with sufficient electrochemical stability, adhesion, and electrocoat performance under high turbulence conditions. In terms of formulation development, the electrode constituent ratio was modified (90% NMC622 material and 10% carbon/binder) and the coating was performed with the application of 100 volts with a line speed of 1.0 m/min. The combination of multiple mechanical modifications and a revised set of coating conditions (Coating Conditions 2) resulted in the production of cathode electrodes with sufficient areal density and uniformity (Figure I.2.B.1, left).

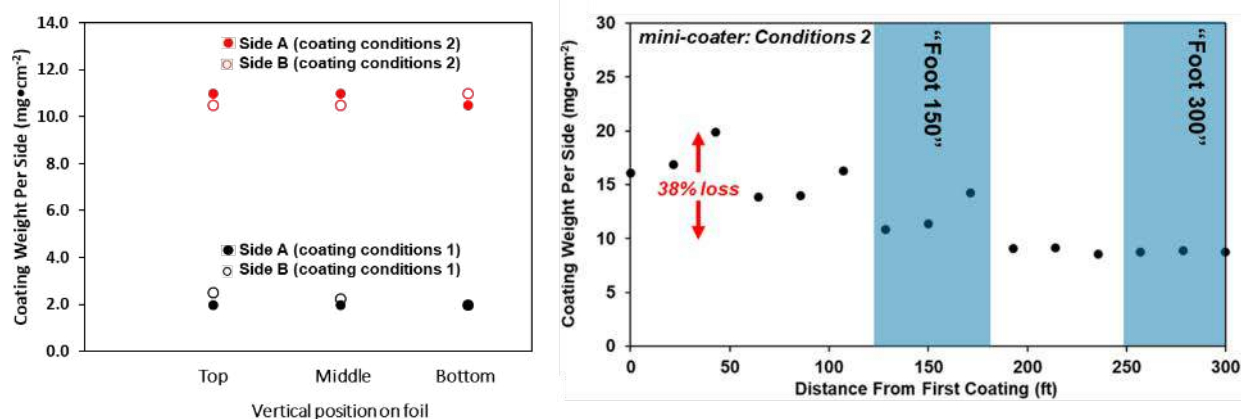


Figure I.2.B.1 Side-to-side coating weight comparison between Coating Conditions 1 (black) and Coating Conditions 2 (red) (left) and coating weight of NMC 622 electrodes coated on the mini-coater using a single bath with Conditions 2. Approximate coating ranges used for defining “Foot 150” and “Foot 300” that are used throughout this chapter are depicted in blue (right)

With these optimized coating conditions and substrate parameters, over 300 feet of NMC 622-based electrodes were produced on the mini-coater system from a single bath. The length of foil coated each run was limited by

the length of the oven due to excessive foil fluctuation during continuous operation. As a result, operation was conducted in a semi-continuous operation in 8-foot lengths of coating to allow for sufficient cure time. As mention in the previous update, we believe that while Coatings Conditions 2 increased active material loading, the settling of the total solids in the bath still remains due to the initial mini-coater design. As shown within Figure I.2.B.2 (right), settling led to an approximately 38% decrease in coating weight per side as the distance from first coating to those produced at Foot 300.

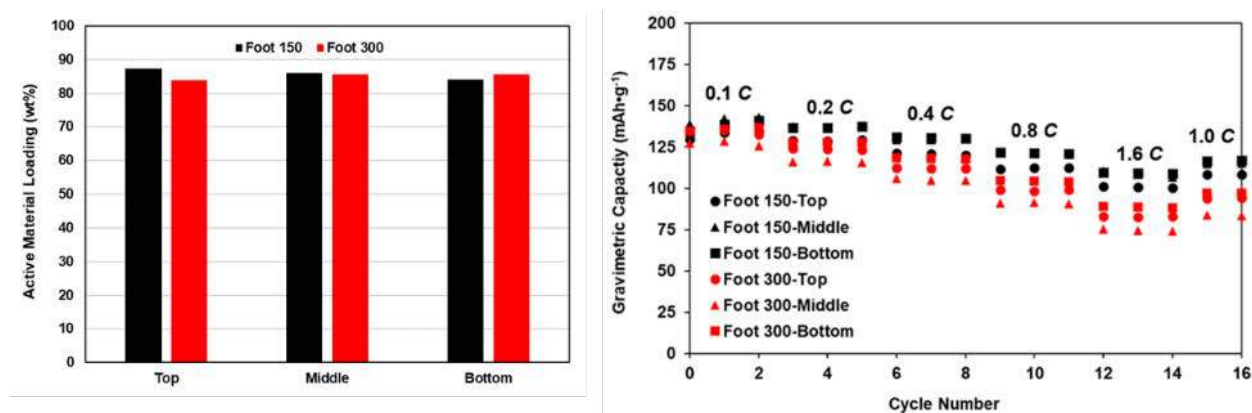


Figure I.2.B.2 analysis of digested cathode electrode from the 150th and 300th foot of coating (left) Coin cell half-cell performance of NMC 622 Build 2 electrodes produced on the mini-coater using Conditions 2 (right)

While the film build rate of the mini-coater decreased over time, ICP-OES analysis of the digested coating reveals similar active material loading between the 150th foot and 300th foot of coating (Figure I.1.2, left). While all coatings show a slightly decreased active material loading relative to the 90% bath composition the loading remains relatively constant. In addition, the top-middle-bottom film uniformity remains as the length of coating increases from a single bath. To evaluate cell performance of electrode films as the coating length increases, coin cell half-cells were fabricated with lithium metal as the negative electrode, 1.2 M LiPF₆ in EC:EMC (3:7 by wt) + 2 wt% VC, and ceramic-coated Celgard separators. Cells were cycled between 3.0 and 4.3 V at room temperature with 3x 0.1C formation cycles followed by a rate test using charge-discharge rates of 0.2C, 0.4C, 0.8C, and 1.6C and finally 3 cycles at 1.0C rate. On average, 140 and 100 mAh·cm⁻² of discharge capacity is delivered at 0.1C and 1.0C, respectively. We note that while the active material loading is expected to remain constant between these two data sets (*vide supra*), the decreased performance of the 300th foot of coating at C-rates >0.1C suggests a different carbon/binder ratio. Further support comes from the through-plane resistance measurements, where coatings near the 150th foot show a lower resistance (29.0 Ω·cm⁻³) than those produced after coating approximately 300 feet of foil (65.0 Ω·cm⁻³). This approximate 2-fold increase in resistance suggests preferential settling of carbon during the operation of the mini-coater.

In effort to improve coating consistency during extended coating sessions we propose that by implementing an unstirred rest time prior to electrodeposition on the bench that we will be able to probe the rate of settling during mini-coater operation. That is, a “10-minute unstirred rest period” will be performed such that an electrodeposition solution is stirred until a homogenous slurry results, stirring is removed and a delay of 10 minutes is implemented prior to electrodeposition. To test this hypothesis, Coating Conditions 2 were conducted after a series of unstirred rest times: 30 seconds, 10 minutes, 30 minutes and 60 minutes, where the resulting coating weights are shown in Figure I.2.B.3 (left). As illustrated below, the next generation Coating Conditions 3 retain similar coating weight even after an unstirred rest time of 60 minutes, significantly improving upon the decay that is observed for Coating Conditions 2. With a drastic improvement in coating weight retention, electrodes fabricated with Coating Conditions 3 were cycled between 3.0 and 4.3 V at room temperature with 3x 0.1C formation cycles followed by a rate test using charge-discharge rates of 0.2C, 0.4C, 0.8C, and 1.6C followed by 50 cycles at 1.0C rate (Figure I.2.B.3). Here, little-to-no difference is observed when comparing lab scale prepared cathode electrodes from Coating Conditions 2 or 3. Overall, demonstrating the importance of formulation development on waterborne bath stability.

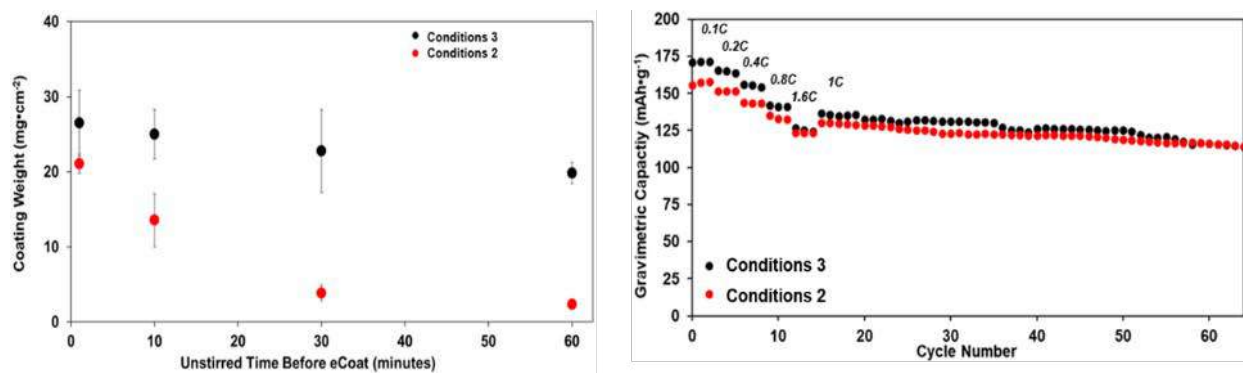


Figure I.2.B.3 Lab-scale film build of NMC 622 electrodes coated using Coating Conditions 2 (red) and 3 (black) (left) and coin cell half-cell performance of lab scale NMC 622 electrodes produced using Coating Conditions 2 (red) and 3 (black) (right)

Fabrication and Evaluation of NMC Single Layered Pouch Cells

Navitas Systems fabricated and evaluated mini-coater produced cathode electrodes produced using Coating Conditions 2 vs. a PVDF/NMP control of identical electrode constituent ratio. Both sets of electrodes were paired across a graphite-based anode and formed at C/10 rate from 2.7 V to 4.3V. The cells were then cycled at +0.5C/-1C rates between 3.0V and 4.2V at room temperature. The electrocoated NMC cells showed comparable capacity retention to the baseline electrodes up to 200 cycles and then showed a reduced capacity fade over time (Figure I.2.B.4 (left)). The baseline NMP formulation fell below 80% retention after 550 cycles while the electrocoated-based cells remained >80% capacity retention after 1500 cycles. Electrocoated NMC formulations show a lower DCR than the baseline cells, possibly due to a higher carbon/binder ratio than expected for these initial coatings (Figure I.2.B.4, right). This is further supported with low initial discharge capacity (120 mAh·cm⁻²) relative to the NMP baseline at 175 mAh·cm⁻².

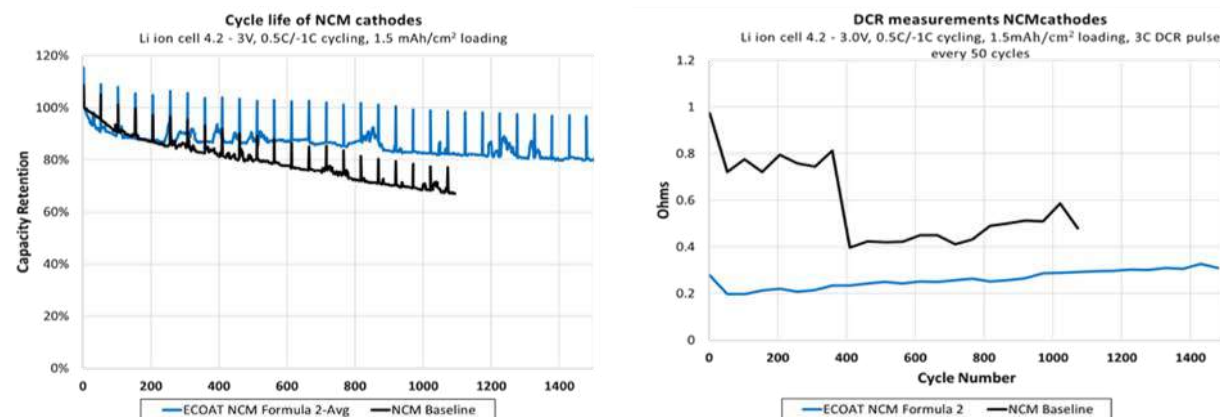


Figure I.2.B.4 Discharge capacity retention vs. cycle number of electrocoat-based cells (blue) and PVDF/NMP control (black) (left). DCR measurements of electrocoat-based cells (blue) and PVDF/NMP control (black) (right)

Secondary Drying for Electrocoat Electrodes

Oak Ridge National Laboratories (ORNL) performed a comprehensive secondary drying study on the un-calendared, double-sided electrocoated that were provided by PPG via Coating Conditions 2. Testing electrodes were calendared to target thickness, and the residual water in the samples was measured by Karl Fischer (KF) titration after drying at four different temperatures (100°C, 120°C, 140°C, 160°C) for 4 hours. Pouch cell fabrication was performed by sandwiching the double-layered cathode from PPG in between two symmetric single-layer graphite-based anode (4 mg·cm⁻²) that was coated by ORNL. To down-select cells for extended cycling, rate performance for each secondary drying group was evaluated with the protocol of constant current + constant voltage (until $I \leq C/20$) between 3.0 and 4.3 V at room temperature with 3x 0.1C

formation cycles ($1C=157 \text{ mAh}\cdot\text{g}^{-1}$) followed by 3 cycles each at 0.5C charge and 0.1C, 0.2C, 0.5C, 1C, 2C, 5C and 10C discharge rates. As shown within Figure I.2.B.5 (left), as the secondary drying temperature increases the discharge capacity retention increases with applied currents $>5C$. In terms of cycle life, the 160°C-based cell continues to maintain discharge capacities at C/10 greater than the other cells investigated, likely the result of a small sample size employed within this study (Figure I.2.B.5, right).

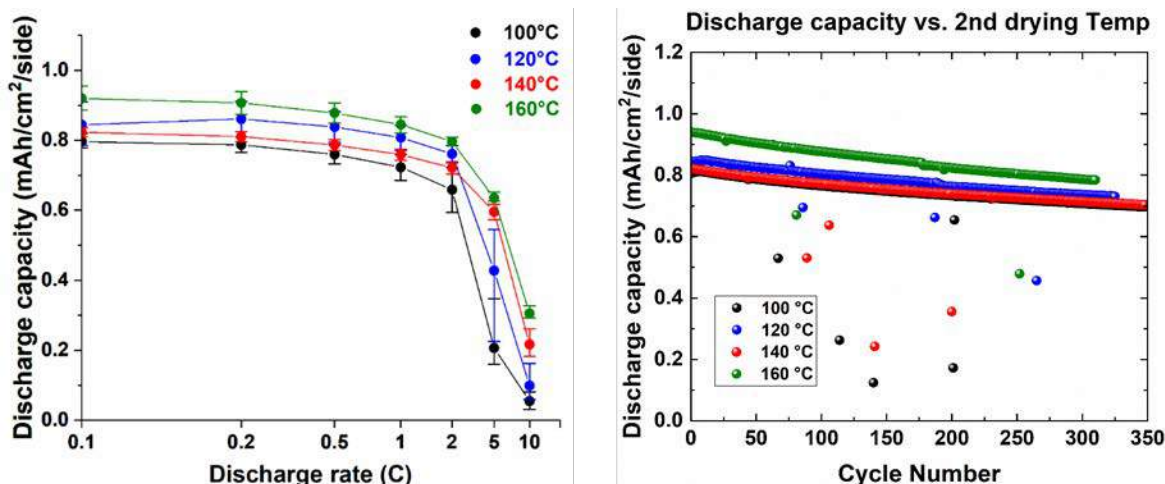


Figure I.2.B.5 Cycling performance for pouch cells with PPG cathodes secondary dried at 100, 120, 140, and 160 °C for 4h at ORNL R2R Manufacturing Group comparing rate capability (left) and C/10 cycle life (right)

Test Plan for 1Ah Prismatic cells

Navitas has successfully delivered 18 large format pouch cells, consisting of 15 x electrocoated cells and 3 x Baseline cells, to Idaho National Laboratories (INL) for testing. PPG provided the double-sided NMC cathode (90% active / 5% conductive carbon / 5% binder), prepared by employed Coating Conditions 2, with the following loadings; 1.13, 1.31, 1.48, 1.71, 1.98, 2.14, 2.54 and $3.2 \text{ mAh}\cdot\text{cm}^{-2}$. The baseline cathode was prepared by Navitas, coating the PPG provided NMC active with a commercial PVDF (in NMP) binder (90% active / 5% conductive carbon / 5% binder) at a loading of $2.21 \text{ mAh}\cdot\text{cm}^{-2}$ and the anode loadings were maintained at 10% higher than the cathode. Electrodes were separated with a $20 \mu\text{m}$ polyethylene film employing a 1M LiPF_6 in EC:EMC (3:7 by wt) + 2 wt% VC. The semi-continuous electrocoated cathodes were punched to 5.1 mm x 9.2 mm pieces, producing a single sided active area of 46.92 cm^2 . Electrodes were weighed and organized according to their chemical loading and placed into individual cell groups based off of their expected aerial capacity. An analogous set of cells was constructed using baseline NMC cathodes.

All NMC-based cells were first charged at C/20 rate up to 4.2V with a taper charge. The cells were then placed in a 50°C oven for 24hrs to allow the electrolyte to fully wet the electrodes. Cells were then discharged at C/10 rate to 2.7V and drained of excess electrolyte. After being placed back onto the Maccor unit, each cell went through 5 additional cycles, charging up to 4.2V at a rate of C/5 with a taper charge. The rate of discharge increased with each cycle through the following procedure: C/10, C/5, C/2, 1C and 2C. The last discharge was followed by C/5 charge to 30% SOC. Here, the best performing cells within each group were selected (15x electrocoated cells and 3x Baseline cells) and shipped to INL. The remaining cells of the build were continued to cycle (C/3) at Navitas.

PPG worked with Idaho National Laboratories (INL) to develop a test plan for the final deliverable cells. The intent of the tests described in the test plan is to characterize the performance of 16 cells with different cathode loading resulting in capacity range from 0.75 Ah to 1.13 Ah supplied to INL by PPG. This testing will benchmark the performance capability of these cells relative to the EV targets and is under the oversight of the Department of Energy, Vehicle Technologies Office. These test articles will be subjected to the performance test procedures defined for the EV Program and as outlined within this project's 2019 3rd quarter research performance progress report.

Conclusions

The viability of electrocoat to produce cathode electrodes at commercially relevant formulations has been demonstrated at both the bench-scale and the pilot-scale roll-to-roll coating system (mini-coater). Over the course of this initial demonstration, bath stability has been continuously improved through mini-coater mechanical modifications and formulation development. With the optimized coating conditions (Coating Conditions 2), over 300 feet of NMC 622-based electrodes were produced on the mini-coater system using the optimized conditions and substrate parameters from a single bath. Evaluating these coating conditions through full cell pouch cells vs. a PVDF/NMP control of identical electrode constituent ratio, the electrocoat-based cells demonstrate improved discharge capacity retention over the control cell group. In addition, a drying study completed by ORNL suggests that employing a secondary drying temperature $\geq 160^{\circ}\text{C}$ may improve the rate capability of electrocoat produced cathode electrodes. While the possible areas for improvement are determined and discussed throughout this chapter, current efforts involve monitoring the cell performance in collaboration with INL.

Key Publications

1. Oral presentation at the 2019 Department of Energy Vehicle Technologies Office Annual Merit Review

Acknowledgements

Adam Crowe, Landon Oakes, Haley Orlor, Peter Votruba-Drzal and Zhilian Zhou at PPG. Mike Wixom and Robert Sosik at Navitas Systems. David Wood III, Marissa Wood, Jianlin Li and Mengya Li at ORNL.

I.2.C Towards Solventless Processing of Thick Electron-Beam (EB) Cured LIB Cathodes (ORNL)

David L Wood, III, Principal Investigator

Oak Ridge National Laboratory
Energy & Transportation Science Division
2370 Cherahala Boulevard, GRID Center, MS-6479
Knoxville, TN 37932
E-mail: wooddl@ornl.gov

Zhijia Du, Principal Investigator

Oak Ridge National Laboratory
Energy & Transportation Science Division
2370 Cherahala Boulevard, GRID Center, MS-6479
Knoxville, TN 37932
E-mail: duz1@ornl.gov

Peter Faguy, DOE Technology Development Manager

U.S. Department of Energy
E-mail: Peter.Faguy@ee.doe.gov

Start Date: October 1, 2015

End Date: September 30, 2022

Project Funding (FY19): \$400,000

DOE share: \$400,000

Non-DOE share: \$0

Project Introduction

There are a variety of technical attributes to electron beam (EB) curing of LIB binders. EB curing uses solvent-free compositions that have low emissions (VOCs, etc.) and are recognized by federal, state and local governments as being a more desirable technology. Solvent or water-based processing requires high drying energy and results in significant CO₂ emissions. EB curing offers significant process energy savings, is ultra-high speed, and utilizes much more compact equipment than conventional drying ovens (much less plant floor space required). Furthermore, it is a relatively cool process and is compatible with heat-sensitive substrates. Conventional thermal drying of LIB electrodes is typically conducted using multiple temperature stages; however, EB can be conducted in a single step. Solvent-free electrode compositions are rated as non-flammable, which translates into lower insurance costs, less stringent storage requirements and, a reduction in handling hazards.

EB treatment is a fast, robust materials processing technology that commonly delivers low cost and excellent performance for high-volume materials production. Based on decades of development and commercial deployment, self-shielded machines routinely operate with high reliability and low maintenance in industrial roll-to-roll production environments. ORNL is developing, demonstrating, and transitioning technology for high-speed roll-to-roll EB processing of LIB electrodes (i.e., coating formation and binder curing). Further specific advantages of this processing route for LIBs are:

- Unmatched throughput – We estimate $\geq 600 \text{ m}^2/\text{min}$ throughput can be achieved based on $\geq 300 \text{ m/min}$ line speed for roll widths up to 2 m (\$1.5-2.0M installed with machine footprint $\sim 10 \text{ m}^2$).
- Thicker electrodes (synergy with Task 1) – Up to 150 microns can be achieved at the throughput rate mentioned above. Coatings of several hundred microns could be processed at higher capital cost per unit throughput, modest reduction in energy efficiency, and larger equipment footprint.
- Excellent energy efficiency – Electrical efficiencies $\geq 60\%$ are possible, including voltage transformer losses (i.e., $\geq 60\%$ of electrical line energy is converted to productive EB energy).

- Environmentally friendly – EB processing requires no solvent and no initiator and has low emissions.

Objectives

- Significant process energy savings
- Ultra-high electrode processing speed
- Utilize much more compact and less expensive capital equipment than conventional drying ovens.

Approach

ORNL is working on a multiphase approach to develop, demonstrate, and transition EB processing of roll-to-roll battery materials:

- Phase 1 – Demonstrate the technology’s key differentiating attributes of high throughput and thick layer processing (FY15-16).
- Phase 2 – Address the key challenges of EB curing parameters and resulting material performance; develop coating methods requiring little or no solvent. (FY17-18).
- Phase 3 – Demonstrate an optimized curing system placed at ORNL in conjunction with a high-speed coating line together with a key equipment supplier (FY19-20).
- Phase 4 – Transfer technology to a key U.S. battery manufacturer based on collaborative scale-up trials at ORNL and PCT Engineered Systems, LLC (FY21-22).

Results

High speed electron beam curing line speed experiments were conducted on several of ORNL’s cathode electrodes at PCT Engineered Systems, LLC in Davenport, Iowa on September 25-September 28. The purpose of the visit was to demonstrate the feasibility of processing NMC622 and NMC811 electrodes with EB curable binder (Ucecoat 7689) at high speed. The electrodes were prepared at ORNL using the slot-die coater with formulation of NMC/Binder/carbon black at 90/5/5. Three different loadings were prepared at 12 mg/cm², 24 mg/cm² and 30 mg/cm². The cathode samples were taped around the periphery onto a paper leader material using clear packaging tape. To ensure that the coating was free of oxygen during irradiation a 15 µm thick clear film (Stretch-Tite film) was placed over the entire cathode sample and was then taped down around the periphery using clear packaging tape. For each run three dosimeters were placed directly on top of the coating and three dosimeters were placed directly underneath the end of the coated aluminum foil. Prior to taping down the last side of the clear films that was placed over the samples it was purged several times with nitrogen, then the film was pressed down along the length of the sample to remove most of the nitrogen and quickly taped closed to minimize any air intrusion.

Table I.2.C.1 Summary of the High Speed Curing Experimental Runs at Ebeam Technologies

Run No.	Sample Name	Experimental details	EB conditions
1	NMC622 - 12 mg/cm ² NMC811 - 12mg/cm ²	covered and N ₂ inerted using Stretch-tite film.	275kV/60kGy 500 fpm
2	NMC622 - 24 mg/cm ² NMC811 - 24 mg/cm ²	covered and N ₂ inerted using Stretch-tite film.	275kV/60kGy 500 fpm
3	NMC622 - 30 mg/cm ² NMC811 - 30 mg/cm ²	covered and N ₂ inerted using Stretch-tite film.	290kV/60kGy 500 fpm
4	NMC622 - 30 mg/cm ² NMC811 - 30 mg/cm ²	covered and N ₂ inerted using Stretch-tite film.	290kV/75kGy 400 fpm

Table I.2.C.2 Summary of the High Speed Curing (A-dosimeter under NMC622 Coating, B-dosimeter under NMC811 Coating)

Test #1: 60 kGy / 275 kV / 500 fpm / 125gsm									
Dose (kGy)		Dose (kGy)		*Estimated* Dose (kGy)		Dose (kGy)		*Estimated* Dose (kGy)	
Top L	49.9	A1 Bottom	55.2	A1 Bottom No Al	55	B1 Bottom	55.2	B1 Bottom No Al	55
Top C	52.8	A2 Bottom	54.1	A2 Bottom No Al	54	B2 Bottom	52.8	B2 Bottom No Al	53
Top R	52.2	A3 Bottom	55.2	A3 Bottom No Al	55	B3 Bottom	53.2	B3 Bottom No Al	53
Test #2: 60 kGy / 275 kV / 500 fpm / 250gsm									
Dose (kGy)		Dose (kGy)		*Estimated* Dose (kGy)		Dose (kGy)		*Estimated* Dose (kGy)	
Top L	63.9	A1 Bottom	49.6	A1 Bottom No Al	67	B1 Bottom	51.1	B1 Bottom No Al	67
Top C	64.1	A2 Bottom	49.4	A2 Bottom No Al	67	B2 Bottom	51.1	B2 Bottom No Al	67
Top R	64.2	A3 Bottom	55.6	A3 Bottom No Al	67	B3 Bottom	50.1	B3 Bottom No Al	67
Test #3: 60 kGy / 290 kV / 500 fpm / 300gsm									
Dose (kGy)		Dose (kGy)		*Estimated* Dose (kGy)		Dose (kGy)		*Estimated* Dose (kGy)	
Top L	68.3	A1 Bottom	55.3	A1 Bottom No Al	68	B1 Bottom	51.2	B1 Bottom No Al	68
Top C	69.2	A2 Bottom	53.2	A2 Bottom No Al	69	B2 Bottom	50.3	B2 Bottom No Al	69
Top R	66.8	A3 Bottom	56.6	A3 Bottom No Al	67	B3 Bottom	47.8	B3 Bottom No Al	67
Test #4: 75 kGy / 290 kV / 400 fpm / 300gsm									
Dose (kGy)		Dose (kGy)		*Estimated* Dose (kGy)		Dose (kGy)		*Estimated* Dose (kGy)	
Top L	Over Range	A1 Bottom	55.9	A1 Bottom No Al	80	B1 Bottom	57.5	B1 Bottom No Al	80
Top C		A2 Bottom	53.4	A2 Bottom No Al	80	B2 Bottom	57.5	B2 Bottom No Al	80
Top R	78.3	A3 Bottom	53.9	A3 Bottom No Al	78	B3 Bottom	56.1	B3 Bottom No Al	78

Evaluation of thick NMC622 and NMC811 cathode electrodes EB cured at high speed. Six pouch cells were assembled using EB cured NMC811 cathode electrodes with two different EB curing conditions: one using 290 kV/60kGy/500fpm with 820 ppm O₂ and the other one using 290 kV/75 kGy/400fpm with 180 ppm O₂. As shown in Figure I.2.C.1, the electrode cured at higher speed 500 fpm shows lower capacity, which is due to the high oxygen level in the chamber during the EB curing. The oxygen will react with the free radical and terminate the propagation process. The electrode cured at a slightly lower speed 400 fpm shows normal capacity behavior and the oxygen level in the chamber was 180 ppm which is sufficiently low to avoid oxygen scavenge for free radicals. Figure I.2.C.1 shows the cycling performance. The cells with electrodes cured at 400 fpm shows very stable cycling up to 75 cycles (still cycling). The three cells show good repeatability.

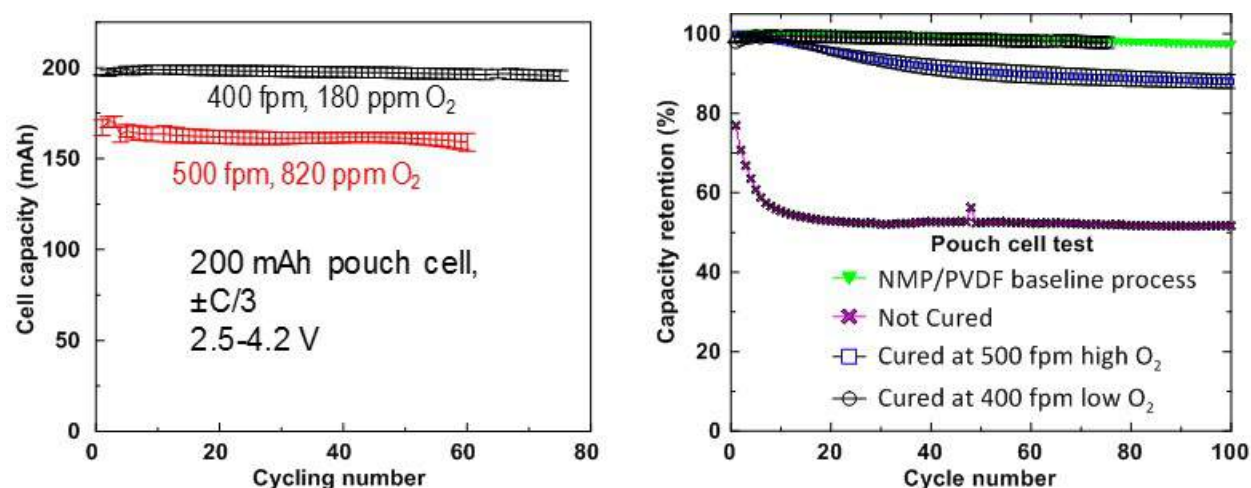


Figure I.2.C.1 cycling performance of 200 mAh pouch cell using NMC811 electrodes processed using two different curing conditions: 500 fpm/290kV/60kGy with 820 ppm O₂ and 400 fpm/290 kV/75kGy with 180 ppm O₂

ORNL is collaborating with Keyland Polymer for the development of this technology. ORNL received more proprietary waterborne resins from Keyland Polymer. The resins were used directly for lithium ion battery slurry formulations. The slurry formulations were prepared using a planetary mixer and consisted of the waterborne resin, carbon black and lithium nickel manganese cobalt oxide (NMC622). Additional water was added into the formulation. The slurry was spread onto aluminum foil. The water was evaporated prior to curing, and the EB curing was conducted using the EB lab unit at PCT Ebeam and Integration, LLC in Davenport, IA. Half coin cells and full coin cells were assembled using EB cured cathodes paired with Li foil and graphite electrodes, respectively. Figure I.2.C.2 shows the voltage curves of the EB cured NMC electrode in half coin cell. This voltage behavior is typical for NMC materials, which demonstrate the feasibility of using Keyland resins in Li-ion cells. Long term cycling performance in full coin cells is shown in Figure I.2.C.3. The cell with the Keyland resin showed good performance, and, although it is not as good as the PVDF baseline or Ucecoat, the performance can be further improved to be on par with the other formulations.

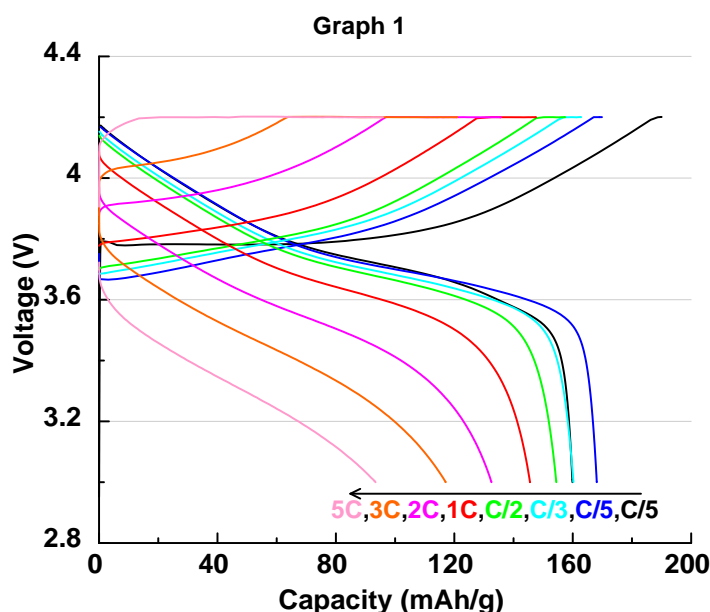


Figure I.2.C.2 Voltage-capacity curves of EB cured NMC cathodes at different rates

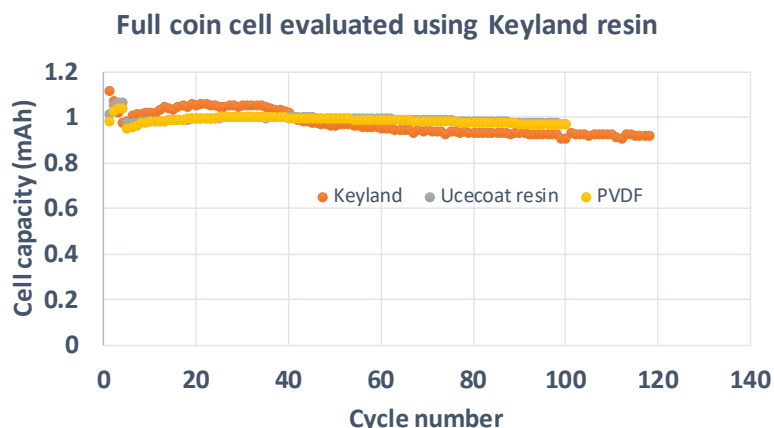


Figure I.2.C.3 Cycling performance of full coin cells with NMC cathodes using different binders

High solids loading slurry formulation is under development at ORNL using acetone as the solvent to replace the electrostatic spraying for compatibility with high-speed coating techniques. The electrostatic spraying encountered a loading limitation when thick electrodes were investigated. This is possibly due to the limited charge attraction when the coating builds up during spraying. The high solids loading slurry formulation using acetone as the solvent enabled a solid loading of 85-90 wt% since the resin is low molecular weight oligomers. Acetone has a much higher evaporation rate compared to water and NMP; therefore, it has promising compatibility with high speed coating processes without using large footprint drying ovens. Acetone is also listed as a VOC exempt solvent which will boost the environmental friendliness of this methodology.

Radiation curable resins with low T_g after curing were evaluated for giving more flexibility of the final electrode coatings. Figure I.2.C.4a shows the DSC curve of the cured resin where the heating/cooling rate was $2^\circ\text{C}/\text{minute}$. The data was processed using Universal Analysis 2000, and the glass transition of the cured resin was found to begin at -44.42°C and end at -30.21°C with a T_g of -36.38°C . A composite electrode using NMC622, carbon black and the resin at 88/5/7 wt% ratio was prepared and EB cured. Full coin cells were prepared using the cathode and graphite anode. The cycling performance shown in Figure I.2.C.4b demonstrates promise of this low T_g resin as Li-ion cell binder materials.

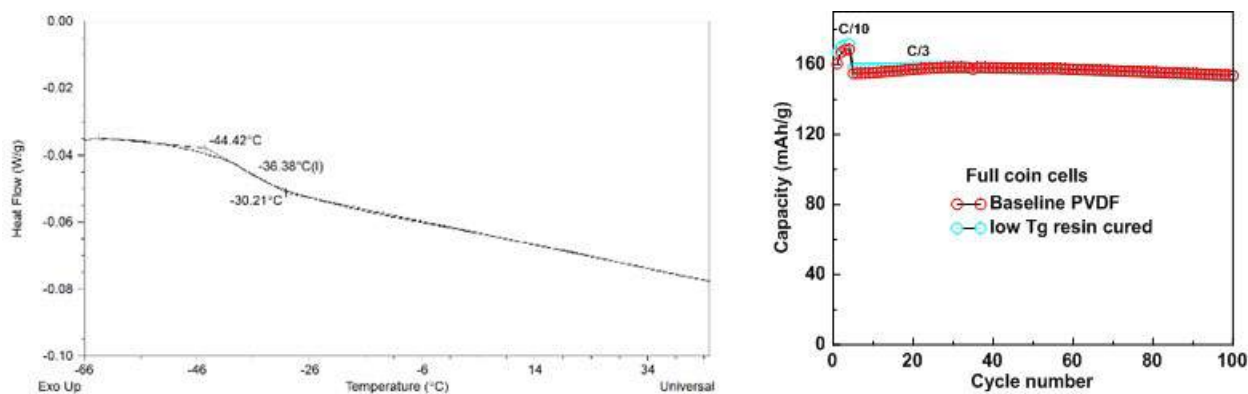


Figure I.2.C.4 (a) DSC curve of an EB cured resin with T_g appearing at -36.38°C . (b) full coin cell cycling performance using resin with low T_g , which shows similar cycling performance compared to the baseline NMP/PVDF case

Conclusions

This research demonstrated the feasibility of using high speed electron beam curing to manufacture thick Li-ion battery cathodes, which can significantly reduce the manufacturing cost compared to conventional fabrication processes. Pilot-scale manufacturing equipment was used to validate the suitability of the scaling process. Oxygen inhibition of the cross-linking led to the poor adhesion in the coating. With improvement in

nitrogen protection, a high speed EB curing at 400 fpm with 75 kGy dose under 275 kV was successfully implemented. The electrochemical performance was tested in the format of pouch cells produced at the DOE Battery Manufacturing R&D Facility at ORNL (BMF). High speed EB cured electrodes showed similar cycling performance compared to PVDF/NMP baseline processing. High solid loading slurry formulation was also developed so that it is compatible with the EB curing speed. Low Tg resins were also evaluated for coatings with more flexibility at low temperature. High speed EB curing technology can be utilized in manufacturing low-cost and high energy density Li-ion battery electrodes.

Key Publications

1. Z. Du, C.J. Janke, J. Li, C. Daniel, and D. L. Wood III, High speed EB curing of thick electrode for high energy density Li-ion batteries, *Green Energy & Environment*, 4 (2019) 375-381.
2. Z. Du, C. J. Janke, J. Li, and D. L. Wood. "Radiation Curing and Its Application in Li Cells." In *Meeting Abstracts*, no. 2, pp. 392-392. The Electrochemical Society, 2019.

I.2.D Performance Effects of Electrode Processing for High-Energy Lithium-Ion Batteries (ORNL)

David L. Wood, III, Principal Investigator

Oak Ridge National Laboratory
Energy & Transportation Science Division
2370 Cherahala Boulevard, GRID Center, MS-6479
Knoxville, TN 37932
E-mail: wooddl@ornl.gov

Jianlin Li, Principal Investigator

Oak Ridge National Laboratory
Energy & Transportation Science Division
2370 Cherahala Boulevard, GRID Center, MS-6479
Knoxville, TN 37932
E-mail: lij4@ornl.gov

Peter Faguy, DOE Technology Development Manager

U.S. Department of Energy
E-mail: Peter.Faguy@EE.Doe.Gov

Start Date: October 1, 2014

End Date: September 30, 2022

Project Funding (FY19): \$400,000

DOE share: \$400,000

Non-DOE share: \$0

Project Introduction

This project at the DOE Battery Manufacturing R&D Facility (BMF) at ORNL builds on past research successes in the areas of battery electrode process development and optimization, cost reduction, cell energy density improvements, and manufacturability advancements, which support the Vehicle Technologies Office (VTO) and Electrochemical Energy Storage Tech Team ultimate targets of \$80/kWh-usable system cost, 500 Wh/kg cell energy density, 800 W/kg cell power density, and 10-15 min extreme fast charging times. Our goal is to perform the science needed to reduce high-risk, high-payoff technologies to lower risk levels, such that U.S. industry will consider their integration in future products. Once a new material, process, or concept has demonstrated feasibility for integration and scaling, the BMF will work to make it a viable processing methodology (preferably with industry partners) with validated performance in a full pouch cell design. While doing so, the BMF will leverage a large array of complimentary projects and sponsors that will provide additional experience and a fast, efficient methodology for solving problems faced by the domestic lithium-ion battery (LIB) industry.

Objectives

To generate a deep understanding of process-property-performance relationships that lead to lower cost and higher performing lithium-ion cells:

- To improve cell energy and power density and reduce battery pack cost by implementing tailored electrode architectures via aqueous processing while simultaneously utilizing high-energy, high-voltage cathode materials.
- Fabricate thick (6-8 mAh/cm²) composite NMC811 cathodes via aqueous processing.
- Create laser structured electrodes.
- Characterize electrolyte imbibition rate and understand the electrolyte imbibition-processing relationship.

- Evaluate processability of thick NMC811 cathode via aqueous processing.
- Initially characterize the electrochemical performance of the aqueous processed thick NMC811 cathode.
- Demonstrate energy density ≥ 225 Wh/kg (BMF pouch cell level).

Approach

- Evaluate stability of Ni-rich cathodes (NMC811) during aqueous processing.
- Incorporate aqueous processing to fabricate NMC811 cathodes.
- Synthesize small NMC811 particles to improve electrode integrity and power density.
- Fabricate crack-free NMC811 cathodes with high areal loading ($6\text{--}8$ mAh/cm²) via aqueous processing.
- Increase energy and power density through laser structuring of electrodes.
- Characterize electrolyte imbibition in porous electrodes.
- Characterize electrode microstructure.
- Evaluate rate performance and long term cyclability at room temperature and high temperature in pouch cells.

Rate and cycle life assessment of aqueous processed NMC811 in pouch cells

Pouch cells were assembled with NMC811 cathodes processed by three approaches: 1) conventional NMP-processing; 2) aqueous-processing; and 3) conventional NMP-processing with pre-exposure of the NMC811 powder to water. This study aimed to isolate the combined effects of exposing the NMC811 powder to water (i.e., Li dissolution) and binder. As shown in Figure I.2.D.1, pouch cells in all three cases demonstrated outstanding cycle life and rate performance. The cells made via aqueous processing and water pre-exposure showed slightly greater capacity fade, which can be ascribed to the dissolution of Li. The aqueous processed cells also showed lower rate performance at high discharge rates, while the other two were identical at all evaluated rates. The former was found to be caused by excessive binder coverage, which was confirmed by cathode morphology evaluation where binder coverage was much larger for the water soluble binder. The data in Figure I.2.D.1 indicates that through optimized formulation chemistry for the aqueous processed case, long-term cycling data on par with the NMP/PVDF baseline can be achieved and that Ni-rich NMC processing is ready for LIB industry adoption.

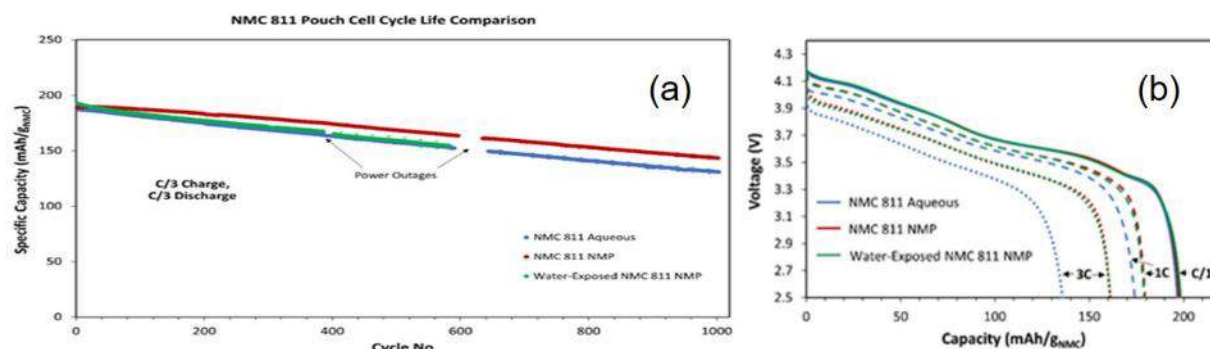


Figure I.2.D.1 a) Capacity retention comparison between NMC 811 cathodes made via NMP-processing, aqueous-processing, and NMP-processing with the NMC811 powder pre-exposed to water (1000 USABC 0.33C/-0.33C cycles); b) discharge voltage profiles at different C rates

Further, we also investigated binder effect on cycle life. NMC811 cathodes were fabricated with three different aqueous slurry formulations where the binder type was varied while keeping everything else constant. Rate and cycling performance were evaluated in single-layer pouch cell format by pairing with graphite anodes. An NMP-processed NMC811 cathode was also tested as a baseline. Active material loading in all cathodes was between 11.4-11.6 mg/cm². Figure I.2.D.2 (top left) shows the cycling performance over 1000 USABC 0.33C/-0.33C cycles with HPPC tests after every 200 cycles, and Figure I.2.D.2 (top right) shows the rate performance. It is seen that two of the three aqueous-processed cathodes match the NMP-processed cathode baseline after 1000 cycles, showing excellent cyclability. The rate performance of all three aqueous cathodes was slightly lower than the NMP-baseline, which is thought to be due to higher binder coverage on the carbon black network and NMC811 particles impeding electronic and lithium-ion transport, as seen in the SEM images in Figure I.2.D.2 (bottom).

NMP: 90 wt.% NMC811/ 5 wt.% Carbon Black/ 5 wt.% PVDF Binder; 11.5 mg/cm²

Aqueous 1: 90 wt.% NMC811/ 5 wt.% Carbon Black/ 1 wt.% CMC Binder/ 4 wt.% Solvay Latex Emulsion Binder; 11.4 mg/cm²

Aqueous 2: 90 wt.% NMC811/ 5 wt.% Carbon Black/ 1 wt.% CMC binder/ 4 wt.% JSR TRD202A Emulsion Binder; 11.4 mg/cm²

Aqueous 3: 90 wt.% NMC811/ 5 wt.% Carbon Black/ 5 wt.% LiPAA Binder; 11.6 mg/cm²

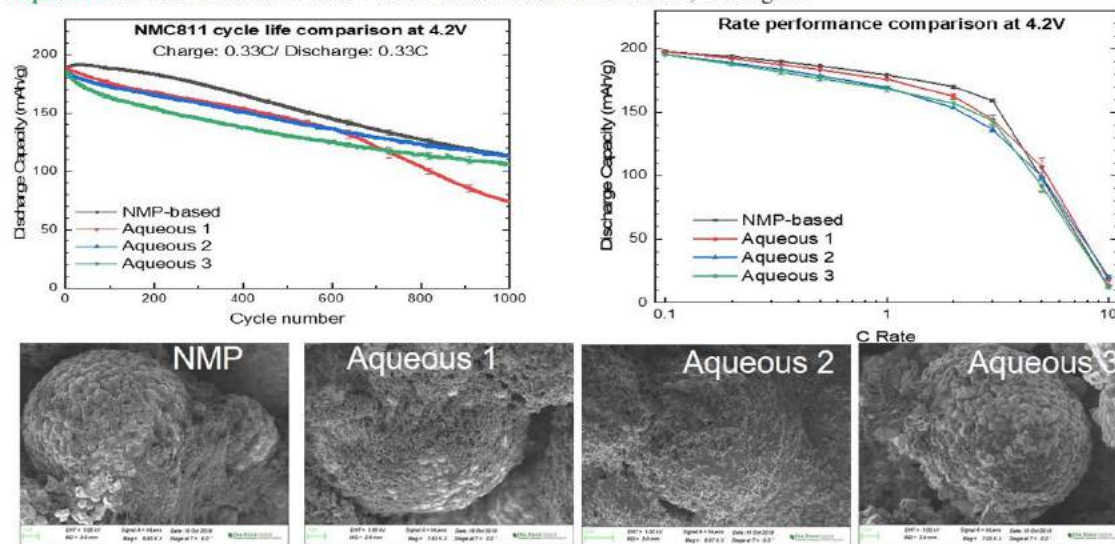


Figure I.2.D.2 Top left) Comparison of USABC 0.33C/-0.33C cycle life, and top right) rate performance between three different aqueous-processed NMC811 cathodes, and an NMP-processed NMC811 baseline cathode. Bottom) SEM image of the four various electrodes showing the differences in coverage of NMC811 particles with carbon black and binder network

In Figure I.2.D.3, the evolution of area-specific impedance (ASI) during cycling for all four types of cells is shown. While the ASI of all cells was similar before cycling, differences in ASI emerged over cycling. Cells with NMP-based cathodes had the least ASI throughout the cycling. In addition, no clear dependence of ASI evolution on cycling performance was observed for the aqueous-processed cathodes containing cells.

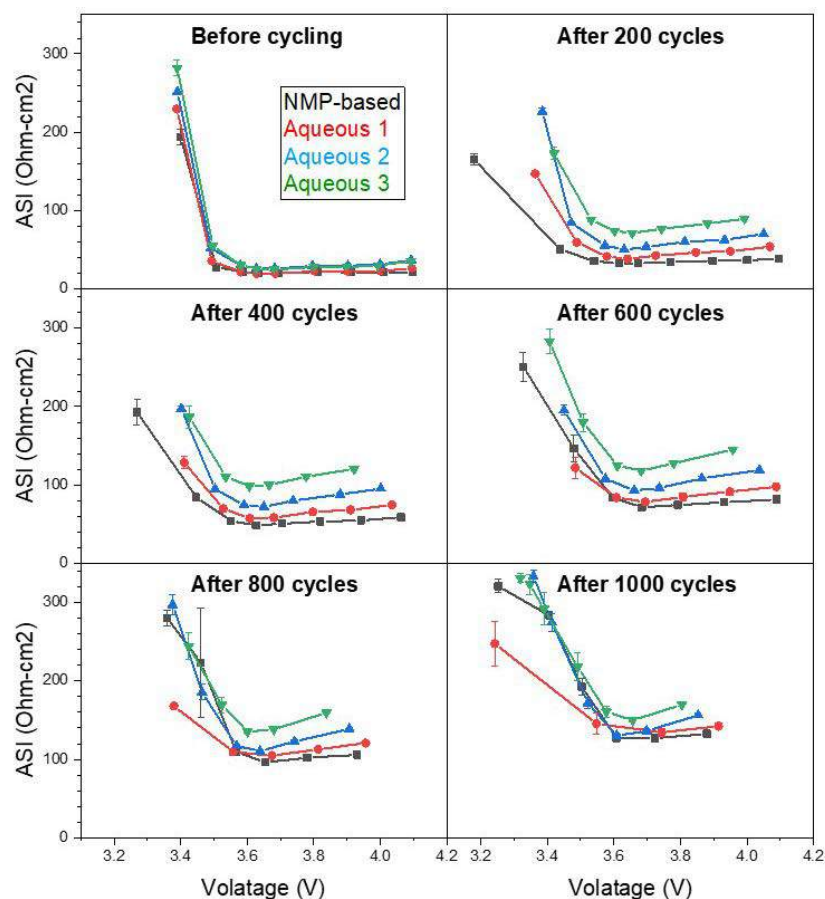


Figure I.2.D.3 HPPC of full cells made with NMP- and aqueous-processed NMC811 cathodes

Cycle life and HPPC testing at high-temperature (45°C) of aqueous-processed NMC811 cathodes was also performed in single-layer pouch cell format and compared with an NMP-based NMC811 cathode (Figure I.2.D.4). It was observed that ASI of cells with aqueous-processed cathodes remained higher than NMP-based cathodes throughout the cycling. It was also observed that capacity retention of cells with aqueous-processed cathode was only ~6% lower than NMP-based at both 30°C and 45°C.

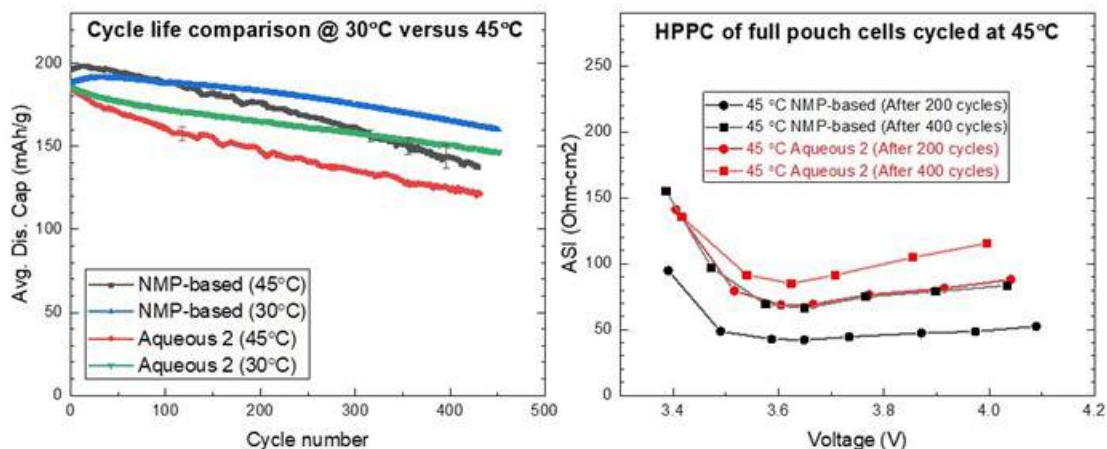


Figure I.2.D.4 Left) Comparison of 0.33C/-0.33C cycle life between three aqueous-processed NMC 811 and NMP-processed NMC811 baseline cathode cycled at 30°C and 45°C. Right) HPPC of the corresponding cells after 200 and 400 cycles

Rate performance of $\sim 7 \text{ mAh/cm}^2$ aqueous-processed NMC811 cathode

Crack-free thick ($\sim 7 \text{ mAh/cm}^2$) aqueous-processed NMC811 were successfully made using our IPA co-solvent (IPA/H₂O 2/8) approach. To compare the rate performance to our baseline, NMP based thick (6 mAh/cm^2 and 8 mAh/cm^2) NMC811 cathodes were also successfully fabricated. Figure I.2.D.5 shows rate-performance of the three thick cathodes. Severe mass transport limitations are seen with all three cathodes above a C/3 discharge rate, and the discharge capacity at 1C dropped below 30 % of the capacity obtained at 0.1C. The rate performance of the aqueous-processed 7 mAh/cm^2 cathode lies in between that of NMP-based 6 mAh/cm^2 and 8 mAh/cm^2 cathodes, which also suggests the comparable performance of aqueous and NMP-based cathodes. In addition, it was noted that flexibility of the thick aqueous-processed electrode needs to be improved in order to allow roll-to-roll fabrication while the NMP-processed one showed superior flexibility.

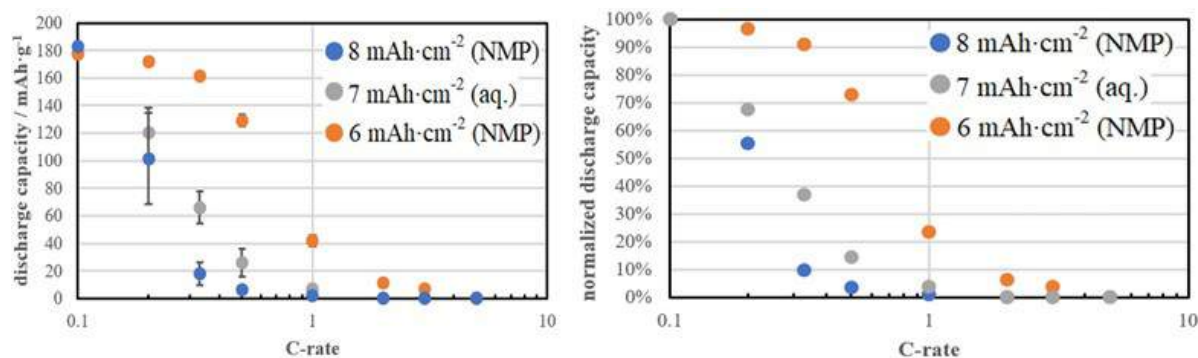


Figure I.2.D.5 Comparison of rate performance of a thick ($\sim 7 \text{ mAh/cm}^2$) aqueous-processed NMC 811 cathode with two thick NMP-processed NMC811 baseline cathodes in coin cell configuration

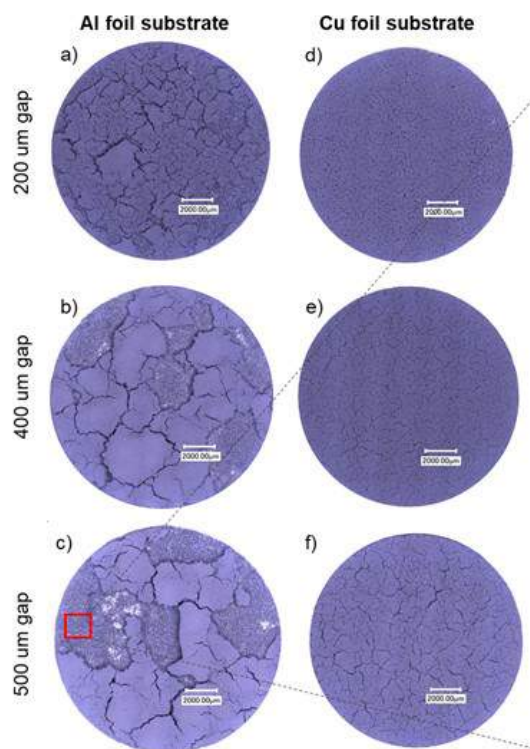


Figure I.2.D.6 Optical micrographs of aqueous NMC811 coatings of various thicknesses made on aluminum (left) and copper foil (right) substrates.

Understanding cracking evolution during drying of thick aqueous-processed NMC811 cathodes

The contributions of various factors towards cracking during drying of thick aqueous-processed NMC811 cathodes were identified. Hydrogen gas generation due to corrosion of the

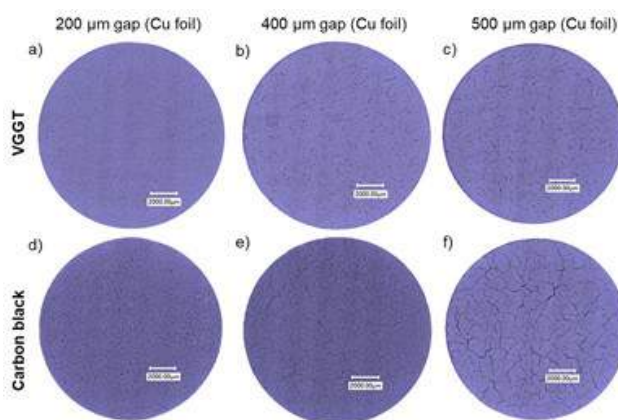


Figure I.2.D.7 Optical micrographs of aqueous NMC811 coatings of various thicknesses made on copper foil substrate using carbon black (bottom) and carbon fibers (VGGT)(top) as the conductive additive.

aluminum current collector caused by the highly basic ($\text{pH} > 12$) aqueous NMC811 slurry was identified to be the primary cause of cracking. Figure I.2.D.6 shows optical micrographs

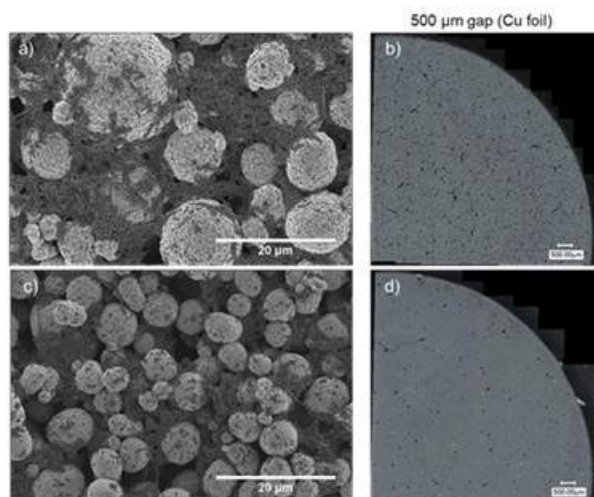


Figure I.2.D.8 SEM and optical microscope images of aqueous-processed cathode coatings (500 μm coating wet gap) on copper foil comprising VGGT conductive additive, and NMC811 with particle size of (a, b) $D_{50}/\mu\text{m} = 13.8$, and (c, d) $D_{50}/\mu\text{m} = 7.4$.

of 15 mm diameter electrode discs punched out of aqueous-processed NMC811 coatings made with different thicknesses (200, 400, and 500 μm) on aluminum foil (left) and copper foil (right) substrates. Copper foil substrates were chosen to distinguish the contribution of hydrogen gas generation towards cracking, as no corrosion of copper occurs from the basic slurry. However, there were still some secondary cracks/defects remaining even after elimination of hydrogen gas generation. These defects were further reduced by switching the carbon black conductive additive to carbon fibers (Figure I.2.D.7). The reason for improvement was found to be due to modification of distribution of the conductive additive and binder network within the coating. It is thought that the carbon fiber anchored the electrodes improving the electrode integrity. In addition, as carbon fibers have smaller surface area compared to carbon black, the emulsion binder has a smaller area to cover and could cover more of the NMC811 particles, improving the coating's ability to absorb drying stresses without cracking.

Further understanding was also developed regarding the working mechanism of IPA as a co-solvent to reduce the cracks in aqueous-processed NMC cathodes. It is shown that IPA not only reduces the cracking by lowering the capillary pressures between particles during drying, but it eases the escape of hydrogen generated due to aluminum corrosion reducing the bubble formation in the coatings that evolve into cracks during drying. The areal defect density of aqueous-processed cathode coatings (wet gap of 500 μm) was further reduced when NMC811 particles of smaller size were used (Figure I.2.D.8 b and d) compared to the larger ones (Figure I.2.D.8 a and c).

Determining the electrolyte imbibition in electrodes and its correlation with processing conditions

Electrolyte imbibition was investigated using NMC532 and graphite electrodes, which were fabricated via conventional NMP-based processing. Various parameters were evaluated for their effect on electrolyte imbibition, including salt contents in electrolyte and electrode porosity. As shown in Figure I.2.D.9, when increasing the LiPF_6 concentration, the electrolyte imbibition coefficient decreased in both NMC532 and A12 electrodes, which was due to the increase in electrolyte viscosity (μ). This resulted in reduce in $\frac{\gamma}{\mu}$, which is proportional to the imbibition coefficient. In addition, the electrolyte imbibition rate was $\sim 2\times$ in the A12 anode compared to the NMC532 cathode. The lower imbibition rate with higher salt concentration was consistent regardless of the electrode porosity. Furthermore, it decreased with decreasing porosity. When reducing the porosity from as coated ($\sim 55\%$) to 35%, the imbibition reduced by $\sim 50\%$. This indicates that a longer aging period is required when reducing electrode porosity for higher volumetric energy density.

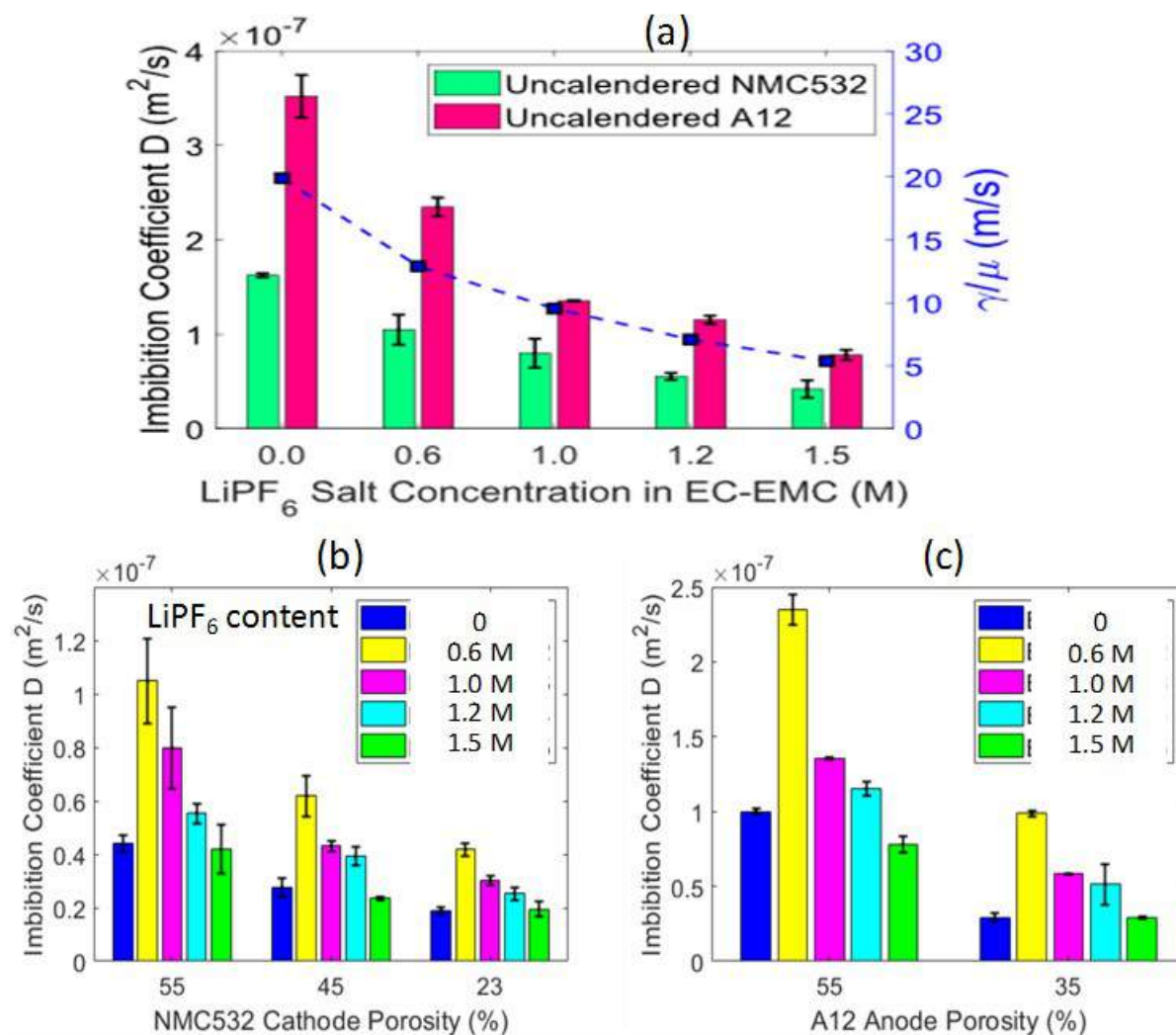


Figure I.2.D.9 Electrolyte imbibition coefficient dependence on salt concentration (a) and porosity of NMC532 cathode (b) and A12 anode (c)

Conclusions

Excellent cycle life was demonstrated with the aqueous processed NMC811 cathodes. The hydrophilic nature of the binders from aqueous processing resulted in more coverage on the active material particles, which increased resistance and resulted in slightly lower performance at high current density. There were more challenges in fabricating thick and crack-free electrodes via aqueous processing. Utilizing a co-solvent (i.e., adding IPA) and replacing carbon black with carbon fiber significantly mitigated the cracking issues, although electrode flexibility needs further improvement. Thick NMC811 cathodes showed poor high rate performance regardless of processing methods, whether they were made with water or NMP as the solvent. Electrode architecture needs to be optimized in order to take advantage of high energy and power density from thick electrode design. Electrolyte imbibition rate was investigated in both the anode and cathode, and it was found that the rate was ~2× in the anode compared to that of the cathode. Increasing the salt concentration and reducing electrode porosity slowed the imbibition coefficient, requiring a longer aging process during cell assembly.

Key Publications, Patents, and Invited Presentations

1. A. Davoodabadi, J. Li, H. Zhou, D. Wood III, T. Singler, C. Jin, “Effect of calendaring and temperature on electrolyte wetting in lithium-ion battery electrodes”, *Journal of Energy Storage*, 26 (2019) 101034-101043.
2. D.L. Wood, III, J. Li, and S.J. An, “Formation Challenges of Lithium-Ion Battery Manufacturing,” *Joule*, in press, 2019. **(Invited)**
3. D. Parikh, T. Christensen, C. Hsieh, J. Li, “Elucidation of separator effect on energy density of Li-ion batteries”, *Journal of the Electrochemical Society*, 166(14) (2019) A3377-A3383.
4. W. B. Hawley, J. Li, “Beneficial rheological properties of lithium-ion battery cathode slurries from elevated mixing and coating temperatures”, *Journal of Energy Storage*, 26 (2019) 100994-101001.
5. M. Wood, J. Li, R. Ruther, E. Self, H. Meyer III, C. Daniel, I. Belharouak, D. Wood III, “Chemical stability and long-term cell performance of low-cobalt, Ni-rich layer oxide cathodes prepared by aqueous processing for high-energy lithium-ion batteries”, *Energy Storage Materials*, In Press, [10.1016/j.ensm.2019.08.020](https://doi.org/10.1016/j.ensm.2019.08.020)
6. W. B. Hawley, J. Li, “Electrode manufacturing for lithium-ion batteries-analysis of current and next generation processing”, *Journal of Energy Storage*, 25 (2019) 100862-100877.
7. S. J. An, J. Li, C. Daniel, David. Wood III, “Effect of ultraviolet light treatment in ambient air on lithium-ion battery graphite and PVDF binder”, *Journal of the Electrochemical Society*, 166(6) (2019) A1121-A1126.
8. A. Davoodabadi, J. Li, Y. Liang, D. Wood III, T. Singler, C. Jin, “Analysis of electrolyte imbibition through lithium-ion battery electrodes”, *Journal of Power Sources*, 424 (2019) 193-203.
9. R. Sahore, J. Li, D. Wood III, “A study of factors responsible for cracking during drying of thick aqueous-processed NMC811 cathodes”, 236th Meeting of the Electrochemical Society, Atlanta, GA, October 13-17, 2019.
10. A. Davoodabadi, J. Li, D. Wood III, C. Jin, “A novel technique to analyze the electrolyte wetting rate through Li-ion battery electrode”, 236th Meeting of the Electrochemical Society, Atlanta, GA, October 13-17, 2019.
11. W. B. Hawley, J. Li, “Elevated mixing and coating temperatures yield beneficial processing properties of organic solvent-based lithium-ion battery cathode slurries”, 236th Meeting of the Electrochemical Society, Atlanta, GA, October 13-17, 2019.
12. J. Wu, J. Li, “Asymmetric membrane for high capacity lithium ion batteries: a low cost, efficient, and scalable method”, 236th Meeting of the Electrochemical Society, Atlanta, GA, October 13-17, 2019.
13. J. Li, A. Davoodabadi, C. Jin, D. Wood III, “Characterizing surface free energy of composite electrodes for lithium-ion battery electrodes”, 235th Meeting of the Electrochemical Society, Dallas, TX, May 26-30, 2019.
14. J. Li, “Overview of electrode processing and engineering at BMF”, GT-ORNL Energy Storage Manufacturing Workshop, Georgia Institute of Technology, Atlanta, GA, April 30, 2019. **(Invited)**
15. D. Wood III, M. Wood, S. J. An, J. Li, Z. Du, R. E. Ruther, C. Mao, “Electrode and cell processing considerations of Ni-rich/low-Co cathodes for lithium-ion batteries”, 2019 International Battery Seminar, Fort Lauderdale, FL, March 25-28, 2019. **(Invited)**
16. J. Li, A. Davoodabadi, C. Jin, D. Wood III, “Understanding materials processing effect on surface energy and electrolyte wettability of lithium-ion battery electrodes”, 2019 International Battery Seminar, Fort Lauderdale, FL, March 25-28, 2019. **(Invited)**

17. J. Li, M. Wood, Z. Du, D. Wood III, “Advanced materials processing for low-cost and high energy density electrodes”, KNMF User Meeting 2019, Karlsruhe, Germany. **(Invited)**
18. J. Li, “Advanced Materials Processing and Tailored Electrode Architectures for Low-Cost and High Energy Density Batteries”, A123 Systems, Waltham, MA, November 29, 2018. **(Invited)**
19. W. Pfleging, P. Smyrek, Y. Zheng, J.-H. Rakebrandt, Y. Sheng, M. Wood, David Wood III, J. Li and H. J. S., “Laser-engineering and analytics in electrode manufacturing for lithium-ion batteries”, Materials Research Society Conference 2018 Fall, Boston, MA, November 25-30, 2018.
20. A. Davoodabadi, J. Li, D. Wood III, and C. Jin, “A systematic approach for characterizing the surface free energy of composite electrodes for Li-ion batteries”, Materials Research Society Conference 2018 Fall, Boston, MA, November 25-30, 2018.

Acknowledgements

The PIs are grateful to ORNL team members Ritu Sahore, Blake Hawley, Alexander Kukay, Dhrupad Parikh and Marissa Wood, for valuable data collection and analysis, and Binghamton University for completing the electrolyte wetting experiments. We also thank Dr. Ozge Kahvecioglu at the Materials Engineering Research Facility (MERF), Argonne National Laboratory, for providing the NMC811 powder with smaller particle size, which is through [project I.2.F](#) “Process R&D for Next Generation Cathode Materials (BAT167)”.

I.2.E Process R&D for Next Generation Cathode Materials (ANL)

Ozge Kahvecioglu, Principal Investigator

Argonne National Laboratory
9700 South Cass Avenue
Lemont, IL 60439-4837
E-mail: okahvecioglu@anl.gov

Peter Faguy, DOE Technology Development Manager

U.S. Department of Energy
E-mail: Peter.Faguy@ee.doe.gov

Start Date: October 1, 2018

End Date: September 30, 2019

Project Funding: \$900,000

DOE Share: \$900,000

Non-DOE share: \$0

Project Introduction

Nickel-rich cathode materials with low or no cobalt content are the key to the development of less expensive batteries with higher energy densities that meet DOE goals. Although the theoretical capacity of lithium-nickel oxide (LiNiO₂, LNO) is high the capacity fade rapidly rendering the material unusable for practical application. Thermal stability and capacity fade are common issues when the nickel content in the cathode active material is 80% or above. The first step to solve the problem is to gain an ultimate understanding on an atomic level what is the role of nickel substitutes (e.g., cobalt, manganese, aluminum, and the like) in pure LiNiO₂ (LNO) that stabilized the material. Material of various structures at various percentages and combinations of elements are needed for the study. There is no reliable source of such materials available to the research community. The availability of hard-to-make, on-demand materials is critical to battery research community to explore and progress toward developing advanced LIBs chemistry. In a close collaboration with other partners in the program, the Materials Engineering Research Facility (MERF) at Argonne National Laboratory is utilizing non-traditional, advanced co-precipitation synthesis methods, such as the Taylor Vortex Reactor (TVR), to produce large quantity of high, uniform quality materials. Sample of the materials are distributed to collaborating research groups for investigation and performance evaluation. By evaluating new precipitation technologies, the Process R&D for Next Generation Cathode Materials project is establishing new platform for scalable and economically feasible manufacturing of advanced cathode materials. The results presented in the report demonstrate that the MERF's developed TVR technology is capable of producing high quality materials with desirable composition and morphology at scale for ultimate deployment if a full-scale manufacturing.

Objectives

The multifaceted objective of the program is to provide the research community with materials they want to investigate, ascertain the key missing link between discovery of advanced active battery materials, market evaluation of these materials, and high-volume manufacturing to reduce the risk associated with their commercialization. We perform systematic process and material engineering research to develop cost-effective customized processes and to produce sufficient quantities of high-quality target materials by optimizing synthesis processes and material compositions, evaluating material purity profiles, and applying emerging manufacturing technologies to address challenges associated with manufacturing of advanced materials. The technical targets of this program are the development of customized synthesis processes for each material selected, scaling up of multi-kilogram material with reproducibility under rigorous quality control, and evaluation of emerging manufacturing technologies to assist fundamental research and to reduce the commercialization risk of newly invented active battery materials.

Approach

In previous fiscal years, the advantages of utilizing an emerging synthesis technology, the TVR, for the production of cathode precursors for lithium-ion batteries, were demonstrated. This reactor has a cylindrical

rotor and tremendous Taylor vortices in the annulus. It produces homogenous micro-mixing and high mass and heat transfer, enabling a high degree of uniform supersaturation. This results in faster kinetics and denser particles with minimal optimization. The TVR continuously produces spherical precursors with a narrow particle size distribution, which is critical to achieving high-quality battery material, and now it is the preferred platform for rapidly making new chemistries that are not commercially available. In support of the Realizing Next Generation Cathode Materials program, six different cathode chemistries were synthesized at a 1-L TVR, more than a 500 g scale. Some of the promising candidates were then scaled up to a 10-L TVR to generate multiple kilograms of material. While TVR utilization speeds up the synthesis of new chemistries, it is the only reactor type that can produce the cathode secondary particles in very small sizes, down to 3 μm , without compromising its performance. The advantages of TVR over the Continuously Stirred Tank Reactor (CSTR) operation are its easy scalability, unique flow pattern, and dead-zone-free design, which bypasses the scale-up issues encountered with CSTRs.

Within this context, different scales of TVR and 4-L CSTR operations were used in fiscal year 2019 to support basic R&D groups at national laboratories, universities, and startup companies with the cathode chemistries, such as LNO, $\text{LiNi}_{0.90}\text{Co}_{0.05}\text{Mn}_{0.05}\text{O}_2$, $\text{LiNi}_{0.90}\text{Co}_{0.10}\text{O}_2$, $\text{LiNi}_{0.90}\text{Mn}_{0.10}\text{O}_2$, $\text{LiNi}_{0.80}\text{Co}_{0.10}\text{Mn}_{0.10}\text{O}_2$, $\text{LiNi}_{0.75}\text{Mn}_{0.25}\text{O}_2$, and $\text{LiNi}_{0.60}\text{Co}_{0.20}\text{Mn}_{0.20}\text{O}_2$. Among those, LNO, NMC811, and NMC622 were the commercially available cathode chemistries. However, good performing, small, and spherical NMC secondary particles, below and/or around 5 μm , are not commercially available. Current research is trending toward advanced particle coatings because of the undesirable surface interaction of nickel-rich compositions with ambient atmosphere (carbon dioxide, humid) along with rapid capacity fading and thermal runaway issues upon cycling, so coating technologies are seeking small but excellent performing NMC particles for conformal and efficient coatings. Based on requests from companies, various small NMC particles with a D50 value of $\leq 5 \mu\text{m}$ were generated using TVR to enable an advanced coating technology compatible with particle sizes ranging from 100 nm up to 8 μm . All preliminary syntheses were conducted at a 1-L TVR and scaled up to a 10-L TVR to validate the scalability of this advanced reactor.

While the use of small secondary particles is of huge interest (for advanced coatings, solid state batteries, fast charging), their higher surface area, in the case of nickel-rich compositions, creates postprocessing problems. Another approach was to make single crystals using small and dense TVR-made hydroxide precursors and apply long-term and high-temperature calcinations at the lithiation step.

Results

Materials in Support of “Deep-Dive into Next Generation Cathode Materials”

The majority of our effort was spent on generating off-the-shelf nickel-rich NMC chemistries for BAT375. Five different compositions were synthesized at either a TVR (1 L and 10 L) or a CSTR (4 L). Some of these chemistries were also scaled up to kilogram quantities upon request.

In general, coprecipitation reactions at TVRs were successfully conducted with *minimal to no optimization* for most of these compositions, generating spherical and dense particle morphology. The second step of synthesizing the actual cathode powders (calcination step) was challenging because excess lithium was being used; this typically creates surface impurities (lithium species, electrochemically inactive and chemically reactive towards air, humidity) along with strong agglomeration at the secondary particle level. These impurities caused high pH levels of the cathode slurry, resulting in postprocessing problems with these powders, such as gelling and inhomogeneous electrode lamination. Figure I.2.E.1 shows the morphology of the nickel-rich secondary particles generated by a 1-L TVR and then calcined at either 725°C or 775°C, including X-ray Diffraction (XRD) profiles of each composition at different temperatures.

To eliminate these problems, surface treatment is needed. However, prior to any surface treatment, the excess lithium that is binding the secondary particles together should be removed by conventional washing, drying, and recalcining; these steps are expected to help in de-agglomerating the particles to some extent.

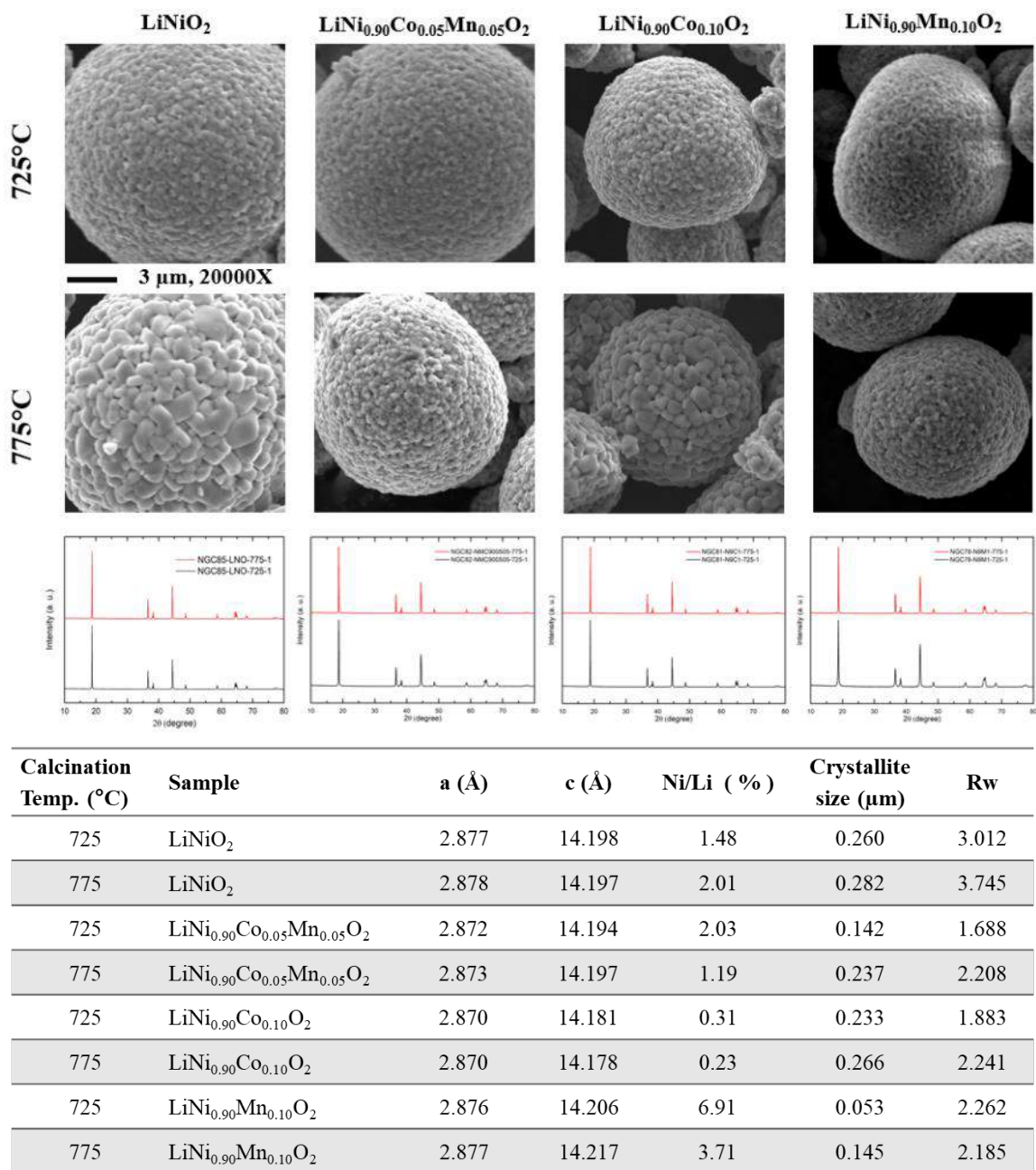


Figure I.2.E.1 Morphologies and XRD profile of nickel-rich compositions at different temperatures; table shows the Rietveld refinement analysis

In Figure I.2.E.2, the top two rows show the voltage profiles of the cathode materials synthesized at different calcination temperatures, and the bottom row shows the rate capabilities of the cathodes with various lithium ratios synthesized at either 725°C or 775°C. All cathode chemistries displayed different electrochemical behavior, as expected.

Differential scanning calorimetry (DSC) was also performed on the nickel-rich compositions (except LNO), as well as on the commercially available compositions, in order to investigate the effects of cobalt and manganese on thermal stability. All cathodes were first charged to 4.3V prior to DSC analysis. Figure I.2.E.3 shows the DSC profiles of commercial NCM523 and NCM811 materials that Argonne's Cell Analysis, Modelling and

Prototyping (CAMP) facility made and nickel-rich compositions that MERF made. Onset of main peaks for 90% nickel-containing cathodes occurs at a lower temperature than that for NCM811, as expected.

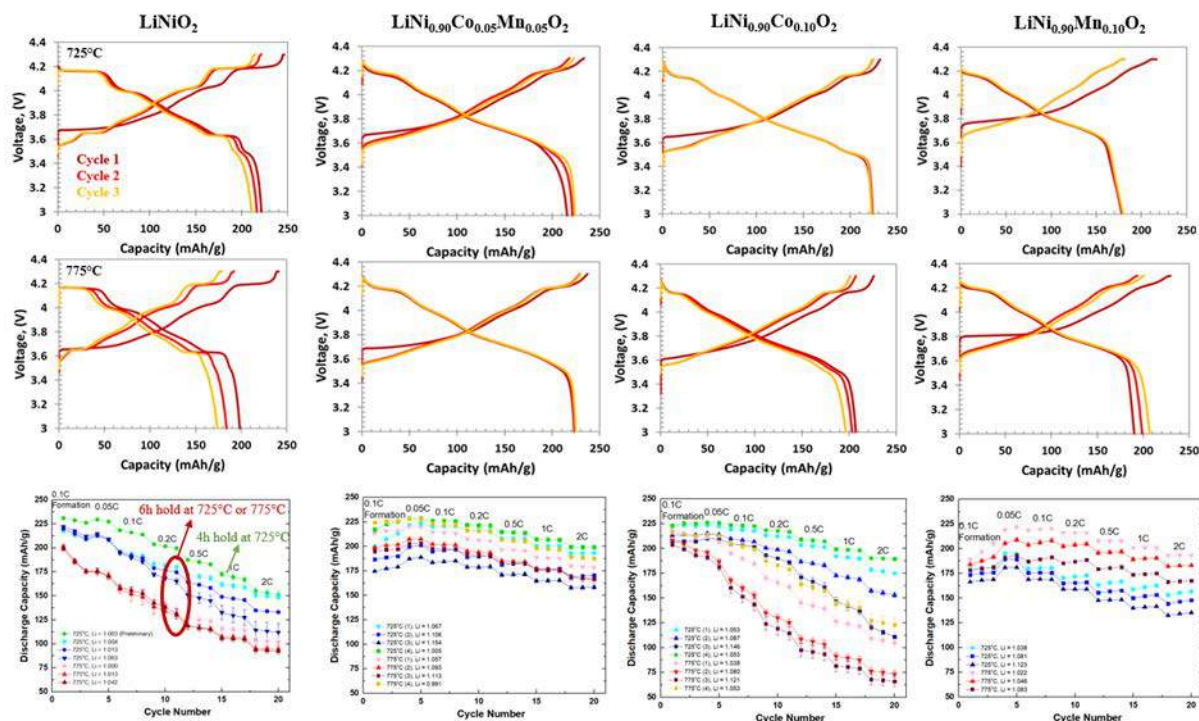


Figure I.2.E.2 Voltage profile of nickel-rich compositions with different lithium ratios at different temperatures. Bottom row shows rate capabilities (3.0–4.3 V cycling at 30 °C; 1C = 200 mA/g)

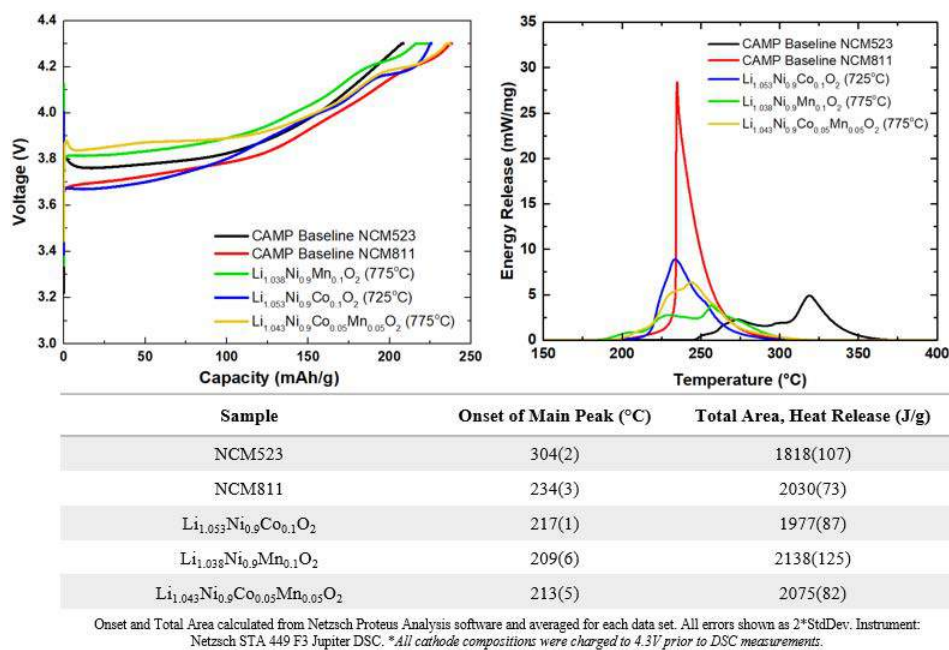


Figure I.2.E.3 DSC profiles of some of the nickel-rich compositions compared to commercially available NMC532 and NMC811 chemistries

Materials in Support of “Thick, Low-Cost, High-Power Lithium-Ion Electrodes via Aqueous Processing”

NCM811 small size particles, with a target D50 value of 5–8 μm , were synthesized at two different scales to support BAT164. Figure I.2.E.4 shows the scanning electron microscope (SEM) images of the hydroxide precursor (top left) and the calcined cathode powders (bottom left) that were synthesized using a 10-L TVR (at the 2-kg scale). Voltage profiles of the two different scales were plotted for comparison, revealing similar profiles with expected capacity values. Slight differences in the rate capabilities might be due to the fact that a 1-L TVR-made product had a particle size (D50) of $\leq 5 \mu\text{m}$, while the scaled-up product had a slightly larger ($\sim 6\text{--}7 \mu\text{m}$) particle size.

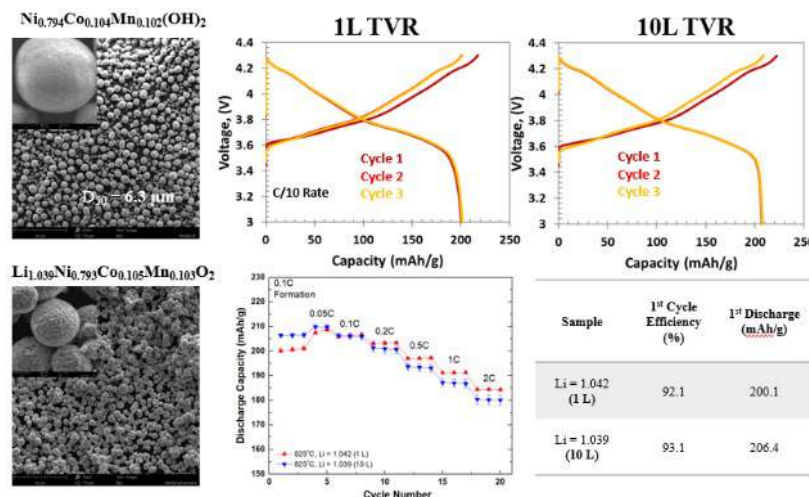


Figure I.2.E.4 Scaled-up NCM811 $\sim 7 \mu\text{m}$ particles at 1-kg scale in support of “Thick, Low-Cost, High-Power Lithium-Ion Electrodes via Aqueous Processing (BAT164)”

Materials in Support of Startup Companies and Universities

Three different cathode chemistries including LNO, NCM622, and NCM811 were synthesized at a 1-L TVR, targeting small secondary particles down to 5 μm and below. These spherical and dense small particles were delivered to (1) Volexion, in order to enable their proprietary graphene coating; (2) BlueCurrent, for the development of all-solid-state batteries; and (3) Northwestern University (LNO only), for “locking the high-voltage phase transition for better cycle life of LNO material” by applying a graphene coating. Figure I.2.E.5 shows the SEM images of TVR-made small secondary NCM cathode particles, the snapshot of Volexion’s graphene coating, and the electrochemical behavior of the pristine and graphene-coated NMC particles (data provided by Jung Woo Seo, Volexion).

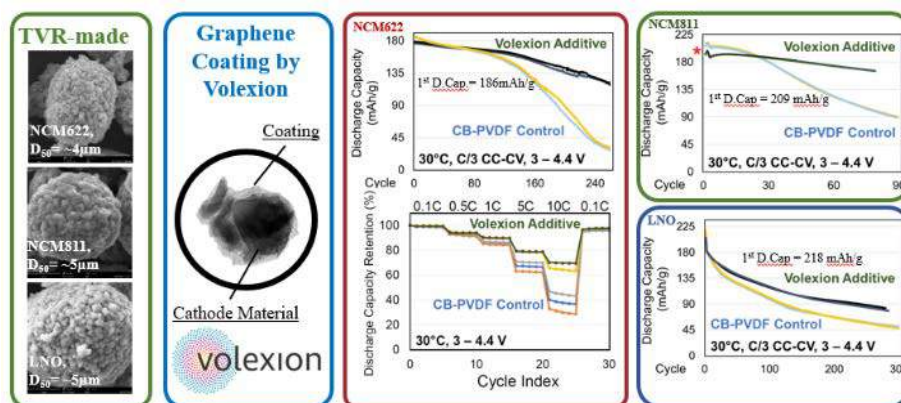


Figure I.2.E.5 Chemistries for advanced particle coatings: $\sim 4\text{--}5 \mu\text{m}$ NCM622, NCM811, and LNO particles, Volexion Inc. (Image Credit: Jung Woo Seo, Volexion)

Single-Crystal NMC Chemistries

Preliminary single crystals were synthesized from TVR-made small and dense secondary particles for commercially available chemistries. Figure I.2.E.6 shows the morphologies of TVR-made precursors and the single crystal after calcination. Single crystals up to 6 μm were synthesized; however, adjusting the lithium ratio was challenging because of high-temperature, long-duration calcination; in addition, isolating the single crystals required postprocessing, like milling, because of the strong agglomeration. This work requires optimization of the calcination step.

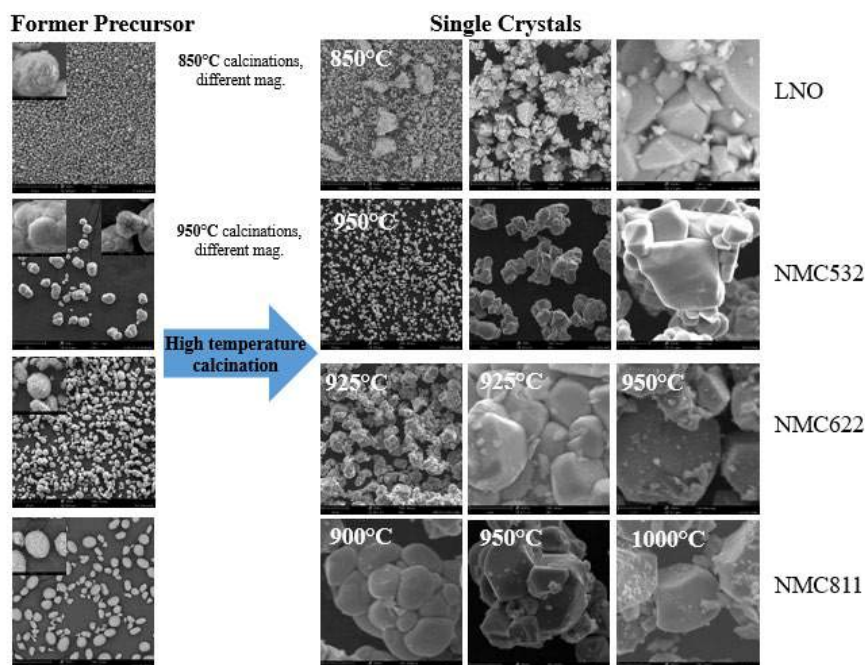


Figure I.2.E.6 Morphology of single-crystal NMC cathodes; former precursors were made by using a 1-L TVR

Conclusions

MERF's experimental materials scale-up program assists the battery research community, allows for a comprehensive evaluation of new materials by industrial laboratories, and supports basic research. In fiscal year 2019 the program provided several new, not commercially available, materials. Samples of high, uniform-quality materials were distributed for further evaluation and research. A total of eight different compositions have been synthesized at a 1-L TVR, and some of those were scaled up to a 10-L TVR. All these compositions were shared with the collaborators either in the form of precursor or cathode, ranging from 50 to 1,000 g.

Key Publications

1. O. Kahvecioglu Feridun, and G. K. Krumdick, 2019, "Carbon dioxide treatment of cathodes," U.S. Pat. Appl. Publ. US 20190326591 A1.
2. Y. Shin, O. Kahvecioglu Feridun, and G. K. Krumdick, 2019, "Pressurized Taylor Vortex Reactor," U.S. Patent No. 10,335,755.
3. J. L. Durham, O. Kahvecioglu Feridun, A. L. Lipson, S. Aryal, K. Z. Pupek, "Controlling NMC Particles by Selecting co-Precipitation Technique ", TechConnect World Innovation Conference & Expo, June 17-19, 2019, Boston, MA

I.2.F Novel R&D for Manufacturing of SS Electrolyte Materials (ANL)

Joseph Libera, Principal Investigator

Argonne National Laboratory
9700 S Cass Avenue
Lemont, IL 60439
E-mail: jlibera@anl.gov

Peter Faguy, DOE Technology Development Manager

U.S. Department of Energy
E-mail: Peter.Faguy@ee.doe.gov

Start Date: October 1, 2018
Project Funding (FY19): \$600,000

End Date: September 30, 2019
DOE share: \$600,000

Non-DOE share: \$0

Project Introduction

Combustion synthesis by flame spray pyrolysis is a materials synthesis technique that uses solution of organic and/or inorganic metal salts in flammable liquids. The liquid solution is atomized using oxygen and combusted to atomic species from which particles condense and are collected in exhaust filters. The composition of the particles is precisely determined by the solution composition. Any ceramic oxide can be produced by this method as well as reduced phases. This technique is amenable to continuous powder manufacture and is used to industrial scale production of carbon black, silica and titania for example. LLZO, LMO, NCM, NCA, and LNMO have been successfully manufactured in the ANL FSP facility. The as-synthesized particle size range is 30-140 nm. The particle size increases with solution concentration up to the limit of solubility of the precursor chemicals. Modifications to combustion chamber and burner design were implemented and found to be a strong factor in controlling material properties. These improvements made it possible to optimize the synthesis of LLZO to produce a “green” powder (a precursor) that anneals to the cubic desirable phase at lower temperature than any precursor chemistry including the lowest-cost raw chemicals that are suitable for combustion synthesis.

Objectives

Develop Flame Spray Pyrolysis as a mass manufacturing option for Li-ion battery active cathode phase and for solid electrolyte powder for use in conventional and solid state Li-ion batteries for the automotive sector. Obtain economically competitive protocols and recipes using the lowest cost precursor and solvent options. Produce optimized LLZO for separator and catholyte applications. Leverage the advantages of the atomically mixed nano-powder produced by FSP to access otherwise difficult to produce cathode materials.

Approach

Flame Spray Pyrolysis is a commodity scale powder production method and is successfully deployed for simple materials. Adoption of this technology for complex materials such as multi-element battery electrolyte or cathode active materials is challenging due to the greater number of possible materials phases and limited thermodynamic data to refer to. However, there are two viable strategies both of which can produce a useful product that can be used in the production of energy storage devices. Ideally, the target phase with optimized crystal structure and particle size is obtained and used directly in applications. However, even when the desired final phase is not produced, the resulting powder which may consist of several phases, will be a nano-mixed material that is amenable to sintering to the final desired product. FSP can take advantage of rapid quenching inherent in the flame synthesis process which allows in some cases metastable phases to be synthesized.

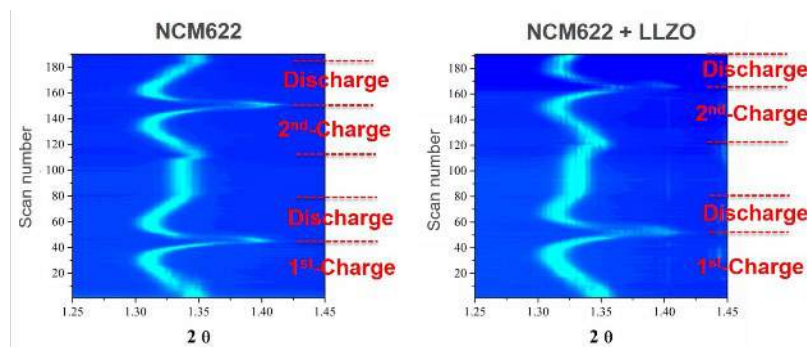


Figure I.2.F.1 In situ electrochemical testing of LLZO+NMC622 composite cathode showing compatibility of the LLZO and NMC622 phases

The ANL FSP facility has features that allow for convenient and high throughput sample production. A glovebox design filter box allows for collection of nanomaterials and restoration of the filter media within 15 minutes of a run completion allowing for up to 6 generated and collected samples per workday. Material that deposits on the walls of the reactor does not significantly cross-contaminate from sample to sample. On a day to day basis, a clean-in-place brushing fixture allows for the combustion tube to be cleaned of wall deposits for changeover to new material systems further assuring no cross contamination between runs.

The ANL FSP facility has been designed to produce powder materials in an industrially relevant way using liquid spray (droplet) combustion which can produce materials at the highest possible rate compared to ultrasonic atomization or gas-fed precursor introduction. In order to best navigate the complexities of spray combustion, the ANL FSP facility has been provided with a suite of in situ advanced diagnostics: (a) laser diagnostic system for Filtered Rayleigh Scattering (FRS) and Planar Laser Induced Fluorescence (PLIF) imaging of temperature and species distribution respectively, (b) Optical Emission Spectroscopy (OES) of the flame zone, (c) In situ Raman spectroscopy and (d) particle size analysis using Scanning Mobility Particle Sizing (SMPS). Ex situ diagnostics are also applied including (a) XRD and temperature programmed XRD, (b) BET-SA, (c) DSC-IR/MS, (d) electrochemical testing and electron microscopy (SEM and TEM).

Results

In FY2019, the ANL FSP facility was first used to research synthesis of (a) solid-state electrolyte materials, (b) Li-ion battery cathode active phases, (c) Platinum titania catalyst and (d) silica as a model system for the development of machine learning tools and strategies for FSP. The FSP facility was further built out by acquiring and installing a medium resolution ANDOR Kymera spectrograph which will be used flame emission spectroscopy and Raman spectroscopy. A custom built UV-Raman spectrometer was added to the FSP with the capability to use 266, 355, 532 and 780 nm excitation to analysis an in situ collection of FSP green powder.

Solid Electrolyte

In 2018 Al-doped LLZO powder was made using the University of Michigan (UM) protocol (Yi et al.) to obtain tetragonal LLZO upon calcination at 700-800°C and cubic LLZO at 1050°C while a new solution chemistry (recipe LLZO-ANL) that gives the cubic phase LLZO at temperatures as low as 670°C (48 hours) was discovered. The ability to process LLZO green powders into the cubic phase at lower temperatures is desirable due to the compatibility for co-sintering with active phase materials and the avoidance of Li loss during higher temperature annealing. However, both the UM and LLZO-ANL protocols are based on metal-organic precursors that may be cost prohibitive for adoption into the mass SSB market. Subsequently several advances were made toward understanding the FSP synthesis to always produce green powder that give the low-T to cubic characteristic. It was found that certain modifications to the combustion zone are critical to achieving this goal and we demonstrated that the U/M recipe could be processed into a low-T to cubic green

powder. For economically viable LLZO, nitrate and acetate salts were used to produce LLZO green powder. It was found that these systems could also be optimized in the ANL FSP process to produce

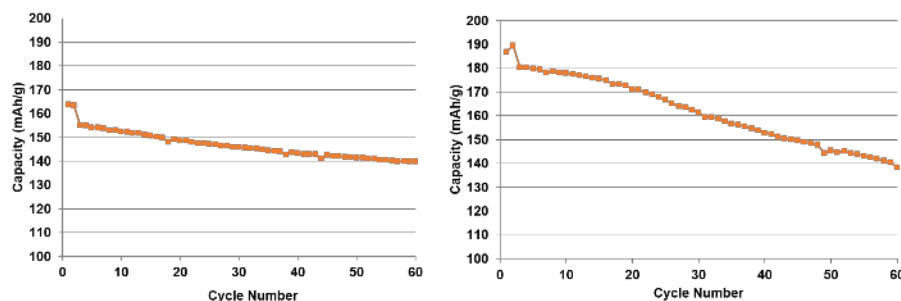


Figure I.2.F.2 The cycle life of NCM622 (left) and NCM811 (right) fabricated by FSP powders

low-T to cubic LLZO green powder. It now remains to optimize the lower cost precursor routes to cubic LLZO relative to a particular downstream processing strategy in SSB manufacture. The current strategies for using LLZO in SSB's involves either >1000 °C sintering or lower temperature composite electrolyte assembly using a finished LLZO cubic input. There are no developed manufacturing strategies to take advantage of the low-T to cubic property of the FSP material. Final optimization of LLZO material requires different strategies for the separator and catholyte components. For separators, high temperature and pressure can be used to produce these parts as this could happen prior to cell assembly but a mass production option is still very difficult. For the cathode layer, a low temperature catholyte is desirable in order to synthesize a cathode layer with good sintering of the catholyte and active phases. Towards this end preliminary co-sintering experiments were performed. In Figure I.2.F.1, the compatibility of NMC622 and LLZO in co-sintering is demonstrated. In this experiment performed in situ at the APS, lattice changes were monitored during cycling for pristine 622 and 622+LLZO each calcined at 900°C prior to cycling.

It should be noted that while the low-T to cubic is a promising development, the production of commodity c-LLZO using FSP where a high temperature anneal (>1000°C) is required remains as an option for FSP production of cubic LLZO powder. Continuing efforts are now focused on optimizing the green powder synthesis together with various downstream application strategies including cold press/anneal, slurry processing, and tape casting in order to produce SSB separators and cathode composite phases. Co-processing of cathode phases and solid electrolyte are most advantageously performed at the same temperature so that the availability of LLZO green powder that anneals to cubic at a temperature that does not compromise the cathode phase is critical. Typically, 750-850°C is a well-established limit for many cathode active phases. Optimization of the LLZO synthesis follows different criteria for separator and cathode composite production. In particular, the maximum processing temperature together with the dwell time determine the necessary excess Li required to account for Li loss during sintering, similar to what is experienced during the calcination of cathode phases. Thus, the optimization of FSP LLZO synthesis must follow a co-optimization with SSB manufacturing steps which may vary depending on the cathode phase and component in the SSB. Samples of FSP LLZO have been distributed to collaborators at ANL for the study of application into all aspects of SSB manufacture including (a) APS in situ examination of the grain growth of LLZO during calcination (b) in situ cosintering and phase formation using FSP-LLZO (c) tape casting method development (d) Raman analysis of carbonate and hydroxide formation of LLZO exposed to air.

Cathode Phase Synthesis

Many of the common cathode phases were synthesized by FSP using acetylacetonate, nitrate and acetate based transition metals salts for the FSP solutions. NMC 111, 622, 811, 9055 and NCA were explored with NMC811 being the material chosen for the year 1 PPC cell demonstration for the low-Co project. In general, similar capacity and cycling performance is observed for FSP powders compared to other synthesis methods reported

in the literature without extensive optimization of the FSP process. Several general features have been observed during this initial exploration of NMC phases: (a) the best results are obtained when Li is included in the FSP solutions (b) across all of the NMC family, the FSP green powder consists of a mixture of the TM rock salt phase and Li carbonate, much like the LLZO green powder. (a) the green powders produced by FSP are nanopowders that upon calcination tend to assemble in a very wide particle size dispersion ranging from 100nm up to tens of microns primary particle size with the bulk of the annealed layered phase occurring as micron sized primary particles which are possibly single crystal in nature. As such, most conventional wisdom on the proper calcination protocols are not optimal for the FSP powders and thus some optimization for calcination and slurry preparation is required to achieve the optimal result using FSP powders.

FSP Facility

Improvement of the FSP processing and diagnostic capabilities were implemented. An ANDOR Kymera 328 medium resolution spectrograph was deployed for use in flame emission spectroscopy and an in situ Raman spectrometer which was custom built for the FSP facility. The Raman spectrometer uses 266, 355, 532, and 730 nm excitation to optimally probe Raman features. The flame emission data is gathered by an 8-to-1 fiber optic coupler that allows for simultaneous light gathering along the axis of the flame. The 8 fiber sources simultaneously project onto the spectrograph sensor as shown in Figure I.2.F.3b. Together these capabilities along with the PLIF diagnostic provide extensive diagnostic capability for monitoring the FSP combustion process and chemical properties through use of the in situ Raman spectrometer. In addition, two-solution blending was added to facilitate rapid screening of solution chemistries using the in situ Raman and particle size analysis instruments. In this mode, individual solution composition points can be processed in ~15 minutes. A generation 2 burner was designed and will be deployed in the 1st quarter of FY2020. The new burner uses the same nozzle as previously but adds temperature control of the burner body and a motorized air-gap of the atomizing nozzle. These parameters were found to be very influential on FSP processing especially for short duration 20-50g sample runs so that some inherent variability in sample production causes suboptimal perspective on the potential of FSP processing. It was also found that the air gap is a particularly sensitive parameter affecting flame character which is very difficult to optimize as this requires stopping and starting the burner in the present case. The ability to dynamically adjust the air-gap during operation of the laser diagnostics will provide significantly faster optimization and approach to the optimal performance of FSP.

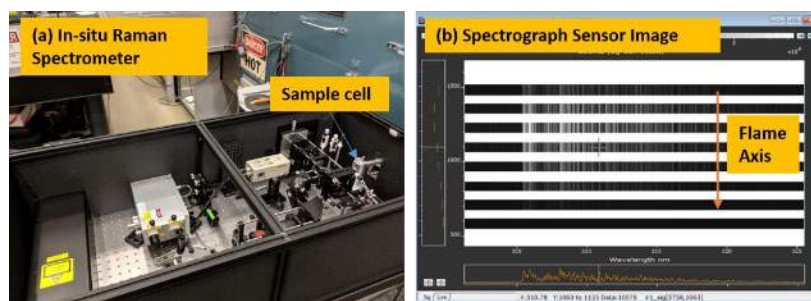


Figure I.2.F.3 (a) In situ Raman spectrometer and (b) Flame emission spectroscopy sample data from the multi-fiber probe array of FSP flame in the OH region

Conclusions

The ANL FSP facility has continued to expand its capability and experience during the pursuit of economically manufactured LLZO solid electrolyte and NMC cathode phases. Synthesis diagnostics were improved with the addition of a medium resolution spectrograph and an in situ Raman spectrometer. Low cost precursor recipes and processing conditions for LLZO with a low-T to cubic property were discovered and materials were distributed into the SSB research community. A broad survey of NMC materials using FSP was conducted and it was found that FSP has the potential to be competitive in performance and economics to other methods of cathode manufacture.

I.2.G Supercritical Fluids Process R&D for LIB Materials (ANL)

Youngho Shin, Principal Investigator

Argonne National Laboratory
9700 S Cass Avenue
Lemont, IL 60439
E-mail: yshin@anl.gov

Peter Faguy, DOE Technology Development Manager

U.S. Department of Energy
E-mail: Peter.Faguy@ee.doe.gov

Start Date: October 1, 2018
Project Funding: \$300,000

End Date: September 30, 2019
DOE Share: \$300,000

Non-DOE Share: \$0

Project Introduction

The development of novel technologies for manufacturing battery materials is important for improving performance, increasing lifespan, ensuring security, and reducing prices of lithium-ion batteries. Supercritical fluids technology, an emerging manufacturing process, provides a high electrode density due to a robust single crystal without internal void fraction, an improved rate capability due to submicron particle size, cycling stability due to suppressed particle crack and resistance layer, and a facet-controlled particle, thus enabling the production of high-performance battery cathode materials. These material properties are a result of the higher degree of supersaturation and the formation of single-crystal cathodes due to the reduced solubility of metal ions under supercritical fluids conditions. The supercritical fluids process is an important route for single-crystal preparation, and crystallization can be customized by changing the reactant, solvent, temperature, and mineralizer. The technology although commercially available for a simple chemistry yet to be developed for more advanced materials that meets current DOE specification for active cathode materials. A customized system is under development. The preliminary experiments to verify the ability to produce an advanced cathode material by the supercritical fluids process has been validated. High-quality materials at the kilogram scale with quality control and reproducibility will be produced for both fundamental research and industrial validation.

Objectives

The aim of the program is to develop a robust and rapid process for manufacturing battery cathode materials using supercritical fluids. This process is one of the emerging manufacturing technologies and aims to reduce the risks associated with the discovery of advanced active battery materials, market evaluation of these materials, and their commercialization with mass production. We perform systematic process and material engineering research to develop a cost-effective supercritical fluids process, to produce sufficient quantities of target materials with high quality by optimizing the synthesis process and material composition, to assist fundamental research, and to reduce the commercialization risk of advanced battery cathode materials.

Approach

A multipurpose supercritical fluids reaction system is developed that allows the synthesis and surface treatment of battery cathode materials. The first step is to develop a batch-type supercritical fluids process to optimize the material synthesis condition, produce the battery cathode material, and analyze the material performance. This step focuses on improving the particle size, distribution, morphology, mechanical strength, and electrochemical performance of the material, as well as studying the process design fundamentals of the continuous-flow supercritical fluids process to be performed in the second step. The second step is to develop a robust and rapid continuous-flow supercritical fluids manufacturing process with a production capacity of more than a kilogram per day.

In the batch-type supercritical fluids system installed, the main material selected for optimizing synthesis conditions is nickel-rich NMC 811 cathode material. In order to optimize the synthesis process, various feed

precursors, additives, reaction pressures, reaction temperatures, pHs, residence times, and stirring speed conditions are applied to carry out material synthesis. We perform material characterization of these synthesized cathode particles with particle cross-sectional mapping and evaluate electrochemical performance, such as discharge capacity, capacity retention, thermal stability, impedance rise, and oxygen release.

Results

A multipurpose supercritical fluids reaction system was set up. Figure I.2.G.1 shows the installed system, which comprises high-pressure pumps, feed lines, valves, a reactor, an electrical heater, a heat exchanger, and a pressure control unit. The main specifications of the system are as follows:

- Maximum allowable working pressure, 340 atm;
- Maximum allowable working temperature, 510°C;
- Maximum stirring speed, 1,700 rpm; and
- Production capacity, ~40 grams per batch.



Figure I.2.G.1 Installed supercritical fluids system for processing battery cathode materials

Input parameters for installed supercritical fluids reaction systems include reaction pressure, reaction temperature, reaction pH, residence time, stirring speed, feed precursors, and additives. Depending on synthesis conditions, the dependent variables are particle size, size distribution, morphology, surface area, capacity, rate performance, and cyclability of battery cathode materials. We correlate these process input variables with the physical electrochemical properties of the product; see Figure I.2.G.2. Efforts are being made to predict the synthesis conditions for materials with the required physical properties and to make these conditions possible at the synthesis stage.

Correlation between process input variables and battery performance

Customized synthesis to predict the performance of the products demanded by the market

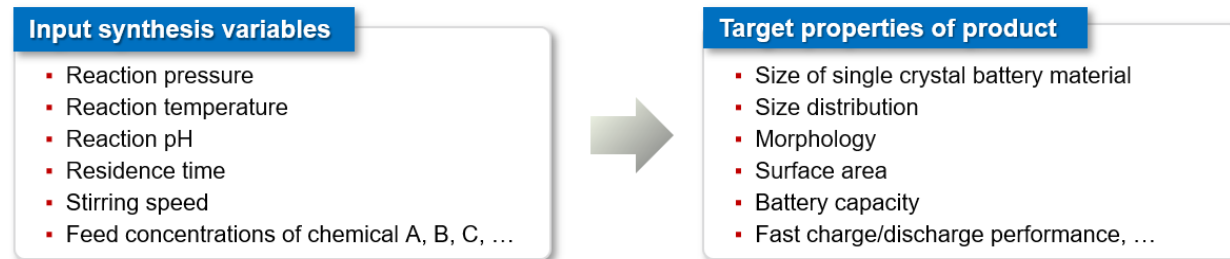


Figure I.2.G.2 Optimization of synthesis variables to achieve final target properties of battery materials

After the permit for operation of the system was obtained, preliminary synthesis of NMC811 was carried out. Sulfate starting chemicals such as nickel, manganese, and cobalt sulfate were used. As shown in Figure I.2.G.3, the synthesized particles were flattened hexagonal single crystal, about 20 μm in size. This preliminary result confirmed the formation of a single-crystal-like NMC811 precursor. However, these 20- μm particles are too big for cathode applications. So efforts to synthesize smaller NMC811 particles have begun.

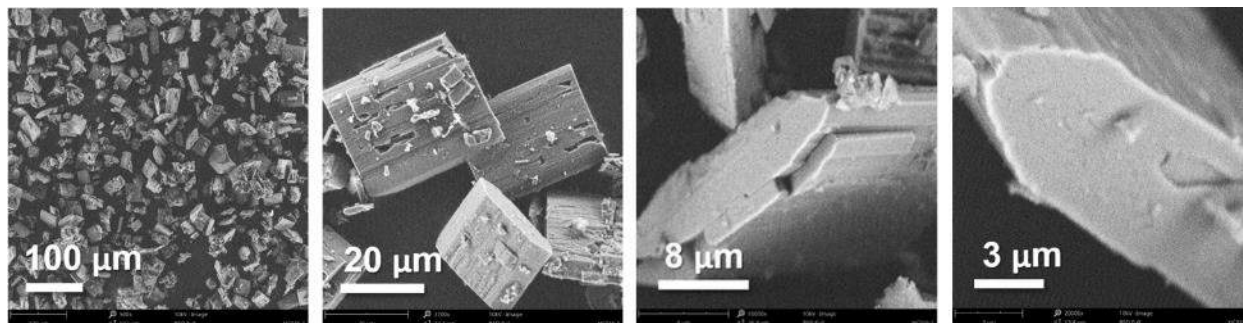


Figure I.2.G.3 Preliminary synthesized NMC811 precursor using sulfate starting materials

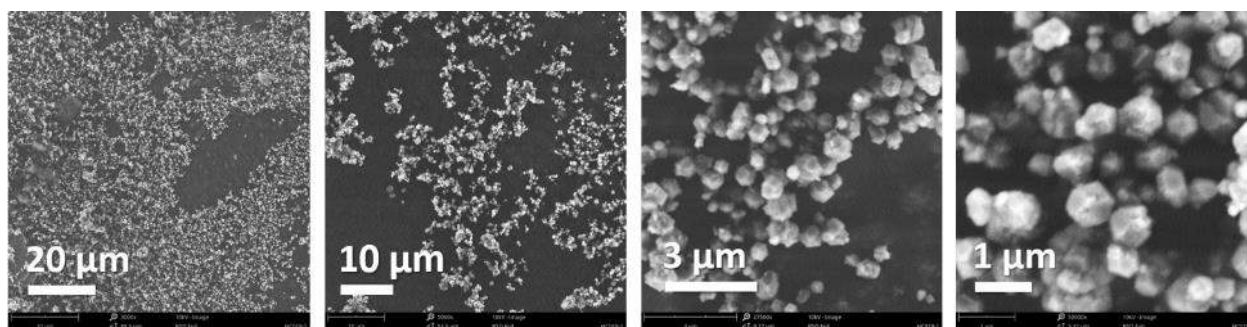


Figure I.2.G.4 Preliminary synthesized NMC811 precursor using acetate starting materials

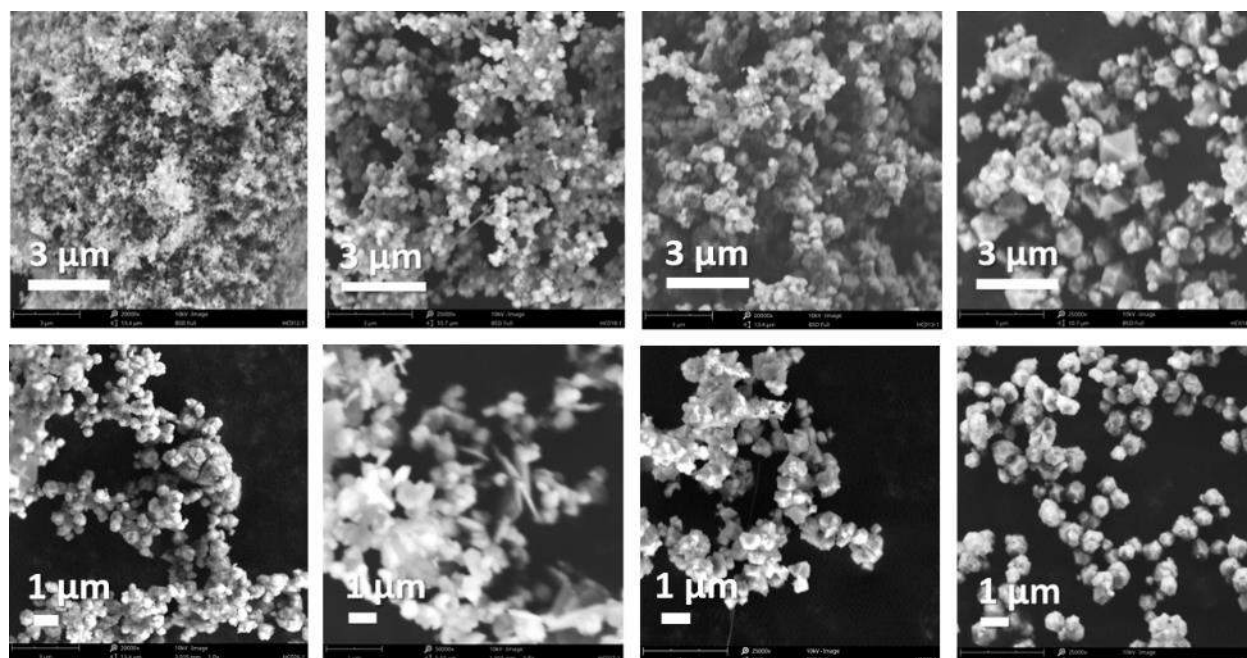


Figure I.2.G.5 Synthesized NMC811 precursors with various particle sizes and morphologies using acetate starting materials

In another approach, we applied acetate starting materials. As shown in the SEM images in Figure I.2.G.4, dodecahedron-type single-crystal particles without agglomeration were synthesized. The particle size is preferably 1 μm . Figure I.2.G.5 shows synthesized NMC811 precursors with various particle sizes and morphologies using acetate starting materials obtained by varying the synthesis process conditions. These results demonstrate that, despite the same starting materials, product morphology, particle size, size distribution, and crystallization can be adjusted by changing reaction conditions, such as solvent, pressure, temperature, reaction pH, stirring speed, and mineralizer.

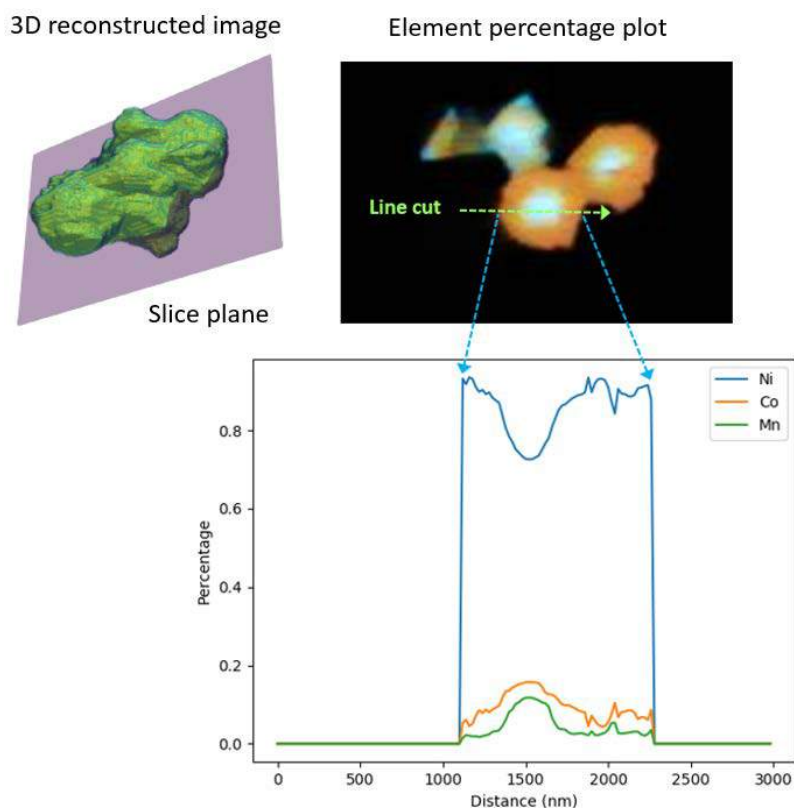


Figure I.2.G.6 Three-dimensional reconstructed image and element percentage plot of the synthesized single-crystal-like NMC811 precursor

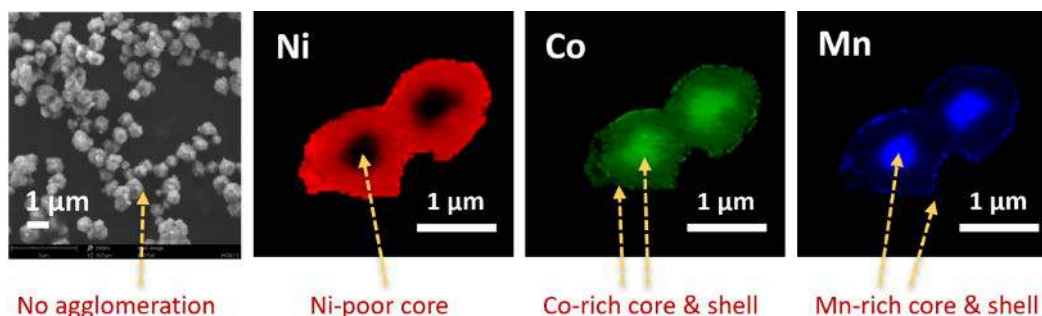


Figure I.2.G.7 Two-dimensional concentration distribution image of the synthesized single-crystal-like NMC811 precursor

In collaboration with BNL (Dr. Seongmin Bak), we analyzed the synthesized single-crystal-like NMC811 precursor shown in Figure I.2.G.6 and Figure I.2.G.7. The three-dimensional XRF image shows an elemental distribution of nickel, cobalt, and manganese in the particles. The synthesized NMC811 precursor shows clear concentration gradients for nickel, cobalt, and manganese, despite being a 1- μm single-crystal-type particle. In the element percentage plot, the overall composition is NMC811, but inside the 1- μm single particle, there is

less nickel and more cobalt and manganese. On the contrary, the outside of the particles is more nickel and less cobalt and manganese. These results demonstrate that we can freely adjust the element concentration at the particle center or surface at the 1- μm single-particle level. This is a new, noteworthy, and interesting result that has not been reported, so various applications can be considered. It is also worth noting that the synthesized 1- μm single-crystal-like material has very desirable properties with no agglomeration between particles.

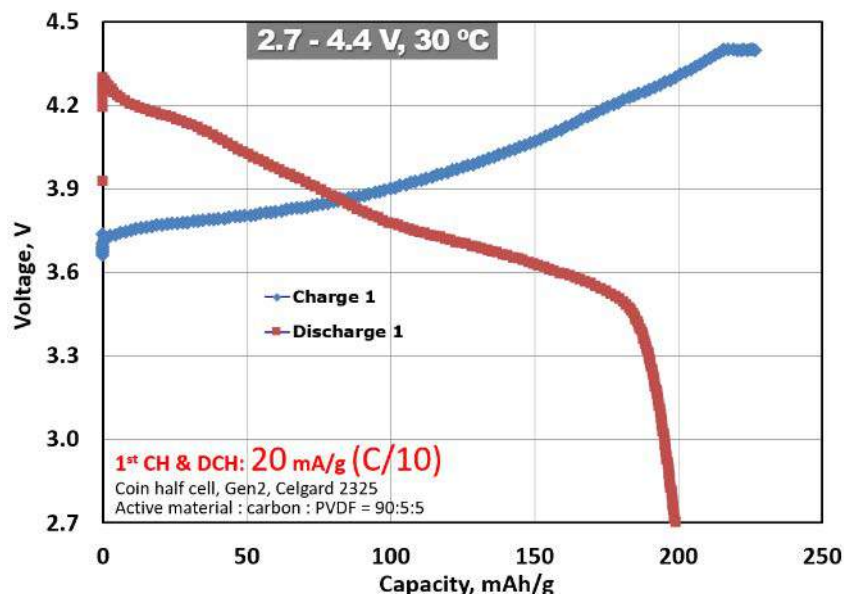


Figure I.2.G.8 Preliminary coin cell result of 1- μm NMC811 using supercritical fluids synthesis process

Figure I.2.G.8 shows the preliminary electrochemical performance results. The voltage window is from 2.7 to 4.4 V, and the charge-discharge rate is C/10. The initial discharge capacity is similar to that of NMC811 cathode material synthesized in a typical coprecipitation process. In an effort to achieve even better electrochemical performance, we are improving the cathode laminate preparation procedure optimized for a single-particle size of 1 μm .

Conclusions

An emerging capability for manufacturing battery cathode material using supercritical fluids technology has been established at the Argonne Materials Engineering Research Facility (MERF). This supercritical fluids system is a material synthesis platform that produces single-crystal cathode materials with a solid structure and unique mechanical, optical, and electrochemical properties. The platform provides convenient and efficient battery materials that can be distributed to collaborators and that meets the requirements of the battery community. Nickel-rich NMC811 materials were selected for the evaluation of the installed synthesis process. The synthesis process and conditions are being optimized to achieve better particle morphology, size distribution, and electrochemical performance.

Key Publications

1. Chung, Y., Y.H. Shin, Y. Liu, J.S. Park, C.L. Margez, and T.A. Greszler, 2019, "Synergetic effect of carbon and AlF_3 coatings on the lithium titanium oxide anode material for high power lithium-ion batteries," *Journal of Electroanalytical Chemistry* 837: 240–245.
2. Maeng, S., Y. Chung, S. Min, and Y.H. Shin, 2019, "Enhanced mechanical strength and electrochemical performance of core-shell structured high-nickel cathode material," *Journal of Power Sources*, <https://doi.org/10.1016/j.jpowsour.2019.227395>.
3. Shin, Y.H., O.K. Feridun, and G.K. Krumdick, 2019, "Pressurized Taylor vortex reactor," U.S. Patent No: 10,335,755.

I.2.H Integrated Flame Spray Process for Low Cost Production of Battery Materials for Lithium Ion Batteries and Beyond (University of Missouri)

Yangchuan (Chad) Xing, Principal Investigator

University of Missouri
416 S. 6th Street
W2033 Lafferre Hall
Columbia, MO 65211
E-mail: xingy@missouri.edu

Peter Faguy, DOE Technology Development Manager

U.S. Department of Energy
E-mail: Peter.Faguy@ee.goe.gov

Start Date: January 1, 2016
Project Funding: \$2,526,250

End Date: September 30, 2020
DOE share: \$2,215,556

Non-DOE share: \$310,694

Project Introduction

Flame (combustion) processes have been demonstrated to be the most economical way to produce fine powders. Pigment titanium oxide and fused silica are produced in millions of tons per year worldwide using flame processes. One of the challenges in these flame processes is that multiple metal oxides, like those used in lithium ion batteries, are difficult to produce due to the lack of appropriate gasified chemical precursors. As a result, oxides of multiple metals are often produced in flame spray pyrolysis processes in which liquid precursors of metal salts dissolved in water are used. The precursor salt solutions are then atomized and sprayed into a flame and are burned to make metal oxide powders. These processes consume a large amount of water and energy, and are prone to producing pollutants. They also do not show much advantage in cost reduction.

This project is aimed at developing an integrated flame spray process (iFSP) to produce battery materials. The technology is based on our innovations in spray processes, chemical precursors, and process integrations. The process is a green chemical process and does not use water. It has the potential to reduce the cost of battery materials significantly. A full-scale production process beyond the performance period is expected to reduce cathode powder cost by 50%.

For the reported period of FY19, we have demonstrated the production of NCA and NMC811 powders with good capacity and excellent capacity retention. We have also demonstrated that our technology would enable reaching the \$125/kWh battery target of DOE using various NMC powders from our process.

Objectives

The overall objective of this project is to develop advanced process technology for battery material production at low cost and in a green chemical process using glycerol as solvent to replace water. The specific objectives in 2019 were to understand the process science in powder synthesis of nickel rich powders and evaluate the economics of the NMC powders from the iFSP technology to reduce battery cost and reach DOE target.

Approach

The approach is to develop the iFSP process into a cost effective process to produce battery materials. The innovations of the proposed technology can be summarized in the following three technical aspects:

- (1) DES as novel chemical precursors.
- (2) Innovative spray process.
- (3) Integrated downstream processing.

Results

(a) NCA powders from iFSP processes

To achieve higher capacities, $\text{Li}(\text{Ni}_{0.8}\text{Co}_{0.15}\text{Al}_{0.05})\text{O}_2$ (NCA) powders were made in the flame spray reactor. The glycerol-based DES precursors were made from metal acetates of Li, Ni, and Co, with a small, but preset, amount of aluminum salt added. The powders can be generally controlled to have spherical shape, whereas their size can be controlled in the micron size ranges. Depending on the operation conditions of the flame reactor, the powders can be highly wrinkled. Process conditions were studied to control morphology of NCA powders. It was observed that processing conditions have a significant effect on powder morphologies. Powders made at a low temperature (e.g., 400°C) show a wrinkled morphology, but powders made at a higher temperature can mainly have a denser spherical morphology. It was assumed that the surface wrinkles were formed due to a slow drying process where surface tension can create non-uniform surface structures as a result of high viscosity of the glycerol-based DES precursors. At high temperatures, the wrinkles were smoothed out leading to smoother spherical particles. Depending on need, the powder morphologies can be controlled to a certain degree through temperature controls in the flame reactor. Figure I.2.H.1 shows a typical morphology of the produced NCA powders after annealing at 800°C .

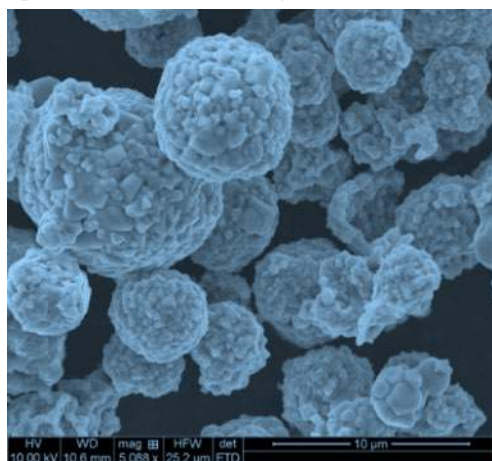


Figure I.2.H.1 SEM image of NCA powders after annealing at 800°C

The NCA powders were tested in coin cells. It was found that an initial discharge capacity of 190 mAh/g can be achieved at 0.1 C in 4.3–2.8 V, as shown in Figure I.2.H.2. This was what we have been targeted in terms of the capacity. The NCA powders showed very a good retention rate of 91.6% or more after 180 cycles in 4.3–3.0 V at 1C.

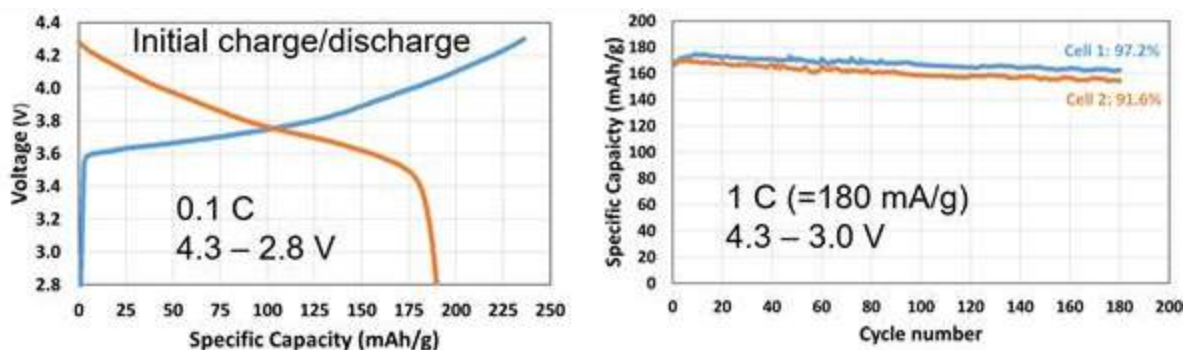


Figure I.2.H.2 Charge-discharge of the NCA powders and cycling performances at 1C

Further improvement of the NCA powders has been made towards increasing their capacity by improving the flame reactor heating conditions. NCA powders made after the improvement showed a better capacity in coin cell tests as shown in Figure I.2.H.3. A capacity of 203 mAh/g (5 cell average) at 0.1C in 4.3 – 3.0 V was achieved, which is better than that in the previous effort [1].

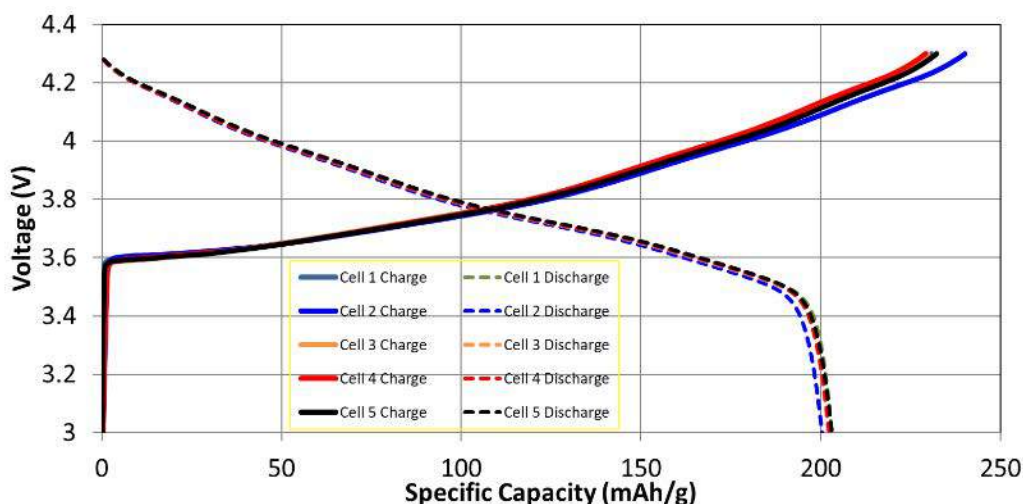


Figure I.2.H.3 Charge-discharge of NCA powder made from the flame spray process with further improved capacity

It was also found that the capacity retention is extraordinary at high rates in these NCA powders. Without any surface coating, the retention rate of about 90% for both 1C and 5C has been achieved (see Figure I.2.H.4). This result may imply that these NCA powders would not need any surface coatings that would introduce inert mass and reduce the overall capacity of the powders. Surface coating is also an extra process that would increase material cost.

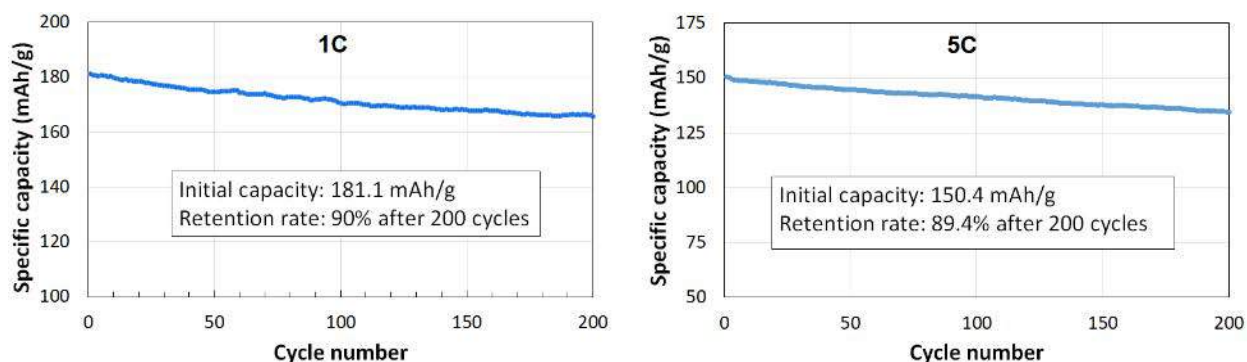


Figure I.2.H.4 Cycling performances of the NCA powders at 1C and 5C, showing extraordinary retention rates

(b) NMC 811 powders from iFSP processes

$\text{Li}(\text{Ni}_{0.8}\text{Co}_{0.1}\text{Mn}_{0.1})\text{O}_2$ (NMC811) powders were also made in the flame spray process. The performance result of the NMC811 material was shown in Figure I.2.H.5, demonstrating an initial discharge capacity of ~185 mAh/g at 0.1 C in 4.3-3.0 V. While the capacity is good in agreement with those powders from other spray processes reported, further improvement is expected in future work. The cycling results of the NMC811 powders at 1C rate were shown in Figure I.2.H.6, which demonstrates an initial discharge capacity of 166.2

mAh/g. This capacity at 1C is comparable to many literature reports. However, the retention rate of the NMC811 powder (94.4% at 165 cycles) was found to be better than most reported values in the literature.

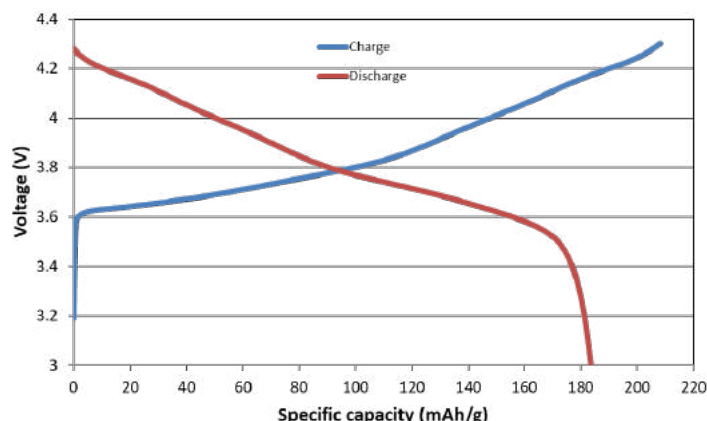


Figure I.2.H.5 Charge-discharge of NMC811 powder made from the flame spray process at 0.1C.

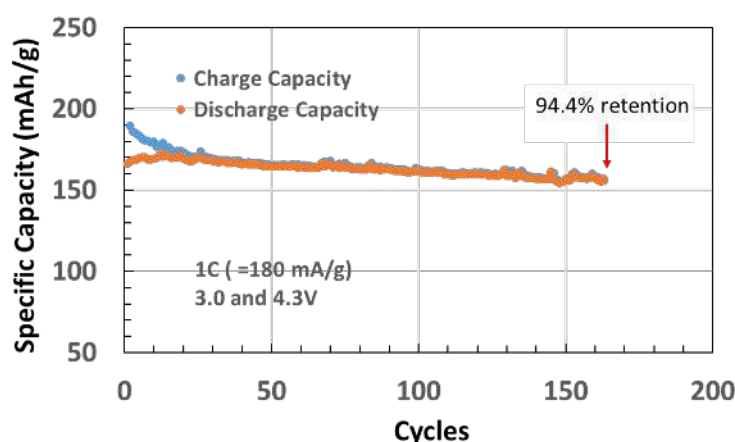


Figure I.2.H.6 NMC811 cycling performances at 1C

(c) Economic analysis of the iFSP process for NMC materials

The techno-economic analysis of the iFSP process was based on a two-steps economic analysis model, and the minimum cathode material selling price (MCSP) is used as the major economic indicator [2]. Results show that when compared with the benchmark co-precipitation carbonate process for NMC333 production [3], the new flame spray process has lower water and energy consumption, and minimum environmental impact. The MCSP of the iFSP process is \$19.1/kg, which is 83% of that of the carbonate process. When the calcination process is integrated within the iFSP, the MCSP of NMC333 is as low as \$15.6/kg, or 68% of that of the co-precipitation carbonate process, demonstrating that the flame spray process is a promising manufacturing process for NMC cathode materials.

Further analysis of different NMC powders shows that NMC532 and NMC811 have lower MCSP than NMC333 and NMC622, as shown in Figure I.2.H.7 (a). The lower material prices further translate into lower battery cell cost. The cost of cells is calculated using BatPac Version 3.1 (Argonne National Laboratory) by the assumptions of 180 kW power and 52.94 kW energy. The NMC333 cell cost based on the flame spray process is \$125.2/kWh, which is at about the DOE target, but still ~10% more expensive than other NMC cells, as shown in Figure I.2.H.7 (b). According to the BatPac simulation results, the NMC811 has the most potential to

realize the DOE battery price target of \$125/kWh. It is noted that these results are obtained without an integrated calcination process. If it is incorporated, the price would be further reduced.

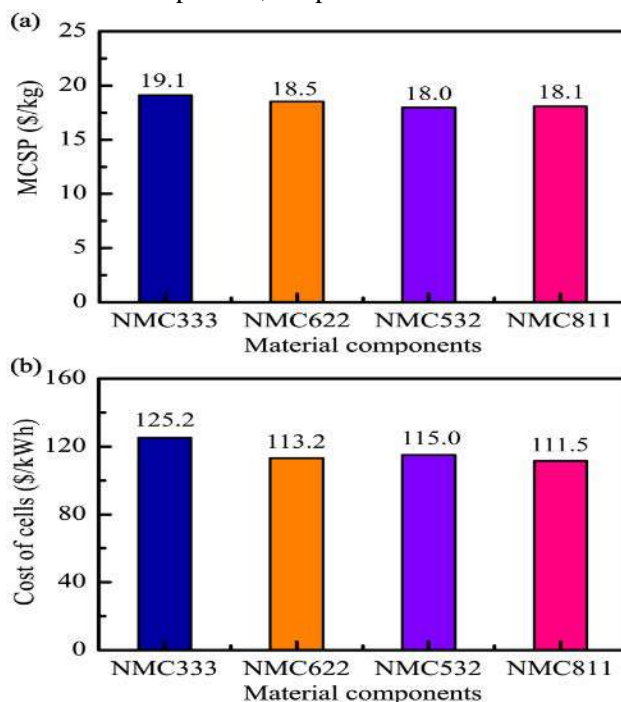


Figure I.2.H.7 Effect of NMC cathode material components on (a) MCSP and (b) cost of cells

Conclusions

1. The iFSP process is demonstrated to produce NCA powders with a capacity of ~200 mAh/g, comparable to or better than reported values from other processes. The retention rates (~ 90% at 200 cycles) are much better than reported values, even without any surface coating for protection.
2. NMC811 powders produced in the iFSP process show good capacity and retention. They are expected to be much improved in the future work.
3. Techno-economic analysis shows that the iFSP process has a lower production cost of NMC333 than the co-precipitation carbonate process with a 17% cost reduction using a separate calcination process and a 32% cost reduction using an integrated calcination process.
4. Battery cell cost analysis shows that while all NMC cathode materials components can reach the DOE \$125/kWh target, the NMC811 material produced in the iFSP process has the most potential to enable battery cells to reach the target or go beyond it.

Key Publications

1. Zhang, J., Xu, S., Hamad, K.I. and Xing, Y. "High Retention Rate NCA Cathode Powders from Spray Drying and Flame Assisted Spray Pyrolysis Using Glycerol as the Solvent". *Powder Technology*, under review, 2019.
2. Zang, G., Zhang, J., Xu, S., and Xing, Y. "Economic analysis of battery NMC cathode material production in a flame spray process with sustainable solvents". *To be submitted*, 2019.
3. Hamad, K.I. and Xing, Y., "Improving Retention-Rate of NCA Cathode Material Synthesized Using Glycerol Solvent", *Journal of Electrochemical Energy Conversion and Storage*, in press, 2019.
4. Jasim, A.M., He, X., White, T.A. and Xing, Y. "Nano-Layer Deposition in Liquid Hydrocarbons using Condensed Water Film". *(Nature) Communications Materials*, under review, 2019.

5. Hamad, K.I. and Xing, Y., “Stabilizing Li-rich NMC Materials by Using Precursor Salts with Acetate and Nitrate Anions for Li-ion Batteries”, *Batteries*, 5(4), 69, 2019.
6. Jasim, A.M., Xing, Y., He, X., and White, T.A., “Nanocoating of Metals Oxides on Nanoscale Substrates in Organic Solvents”, 2019 AIChE Annual Meeting. Orlando, FL, November 10-15, 2019.
7. Hamad, K.I. and Xing, Y., “Effect of Cobalt and Nickel Contents on the Performance of Lithium Rich Materials Synthesized in Glycerol Solvent”, *Journal of The Electrochemical Society*, 165, A2470-A2475, 2018.
8. Hamad, K.I. and Xing, Y. “Lithium Ion Cathode Materials Prepared Using Glycerol as Solvent and Reactant”, presented at the 2018 AIChE Annual Meeting, Pittsburg, PA, October 28 - November 2, 2018.

References

1. Zhang, Jianan, Siqi Xu, Khaleel I. Hamad, and Yangchuan Xing. 2019. High Retention Rate NCA Cathode Powders from Spray Drying and Flame Assisted Spray Pyrolysis Using Glycerol as the Solvent. *Powder Technology*, under review.
2. Zang, Guiyan, Jianan Zhang, Siqi Xu, and Yangchuan Xing. 2019. Economic analysis of battery NMC cathode material production in a flame spray process with sustainable solvents. *To be submitted*.
3. Ahmed, S., P.A. Nelson, K.G. Gallagher, N. Susarla, and D.W. Dees. 2017. Cost and energy demand of producing nickel manganese cobalt cathode material for lithium ion batteries, *Journal of Power Sources* 342, 733.

Acknowledgements

EaglePicher Technologies is a partner in this project with Dr. Hyun Joo Bang as project lead. We thank Walter G. Parker at NETL and Dr. Ahmad Pesaran and Dr. Jack Deppe for their project management and support in this work.

I.2.I High Performance Li-Ion Battery Anodes from Electrospun Nanoparticle/Conducting Polymer Nanofibers (Vanderbilt University)

Peter N. Pintauro, Principal Investigator

Vanderbilt University
Department of Chemical and Biomolecular Engineering
Nashville, TN 37235
E-mail: pn.pintauro@vanderbilt.edu

Peter Faguy, DOE Technology Development Manager

U.S. Department of Energy
E-mail: Peter.Faguy@ee.doe.gov

Start Date: October 1, 2015

End Date: September 20, 2019

Project Funding: \$706,062

DOE share: \$590,000

Non-DOE share: \$117,062

Project Introduction

Si is an attractive replacement for graphite in Li-ion battery anodes due to its high theoretical capacity (3,579 mAh/g for $\text{Li}_{15}\text{Si}_4$ vs. 372 mAh/g for LiC_6) and low operating potential (< 0.5 V vs. Li/Li^+). However, Si-based anodes often exhibit poor stability during charging and discharging due to large volume changes and particle pulverization during cycling as well as instabilities associated with the solid electrolyte interphase (SEI) layer. The use of Si nanoparticles and nanowires has shown promise, but the active material loading in such nano-Si anodes is low, resulting in low areal and volumetric capacities. Thus, there is a need for new anode designs that can tolerate Si volumetric changes while maintaining high gravimetric, areal, and volumetric capacities over many charge/discharge cycles at low and high C-rates.

Objectives

The objectives of this project are to fabricate an electrospun Li-ion battery nanofiber anode and demonstrate its superior performance in half-cell and full-cells. The fiber mat anode is expected to outperform current state-of-the-art thin film slurry anodes, in terms of volumetric capacity and rate capability, and could enable a substantial reduction in the weight and size of an electric vehicle battery. The project will also demonstrate that the fiber mat anode can be manufactured in large scale at a commercial electrospinning facility. Experiments will focus on optimizing the composition and morphology of Si-based nanofiber anodes with a non-conducting polymer binder for lithium ion batteries. Such anodes will be designed for high gravimetric and volumetric energy densities, e.g., an initial capacity of 1,200 mAh/g and 1-2 mAh/cm² with 90% capacity retention after 200 cycles at 0.1C and a capacity of 500 mAh/g after 200 cycles at 2C which is recoverable to at least 1,000 mAh/g at the lower charge rate of 0.1C. The project will also generate useful correlations and insightful understandings regarding the composition, structure, and performance of electrospun Si anodes.

Approach

This project is an extension of the PI's prior successes in using neat polymer and particle/polymer nanofiber electrospinning for membranes and electrodes in electrochemical devices. In prior published studies, fiber-based Li-ion battery electrodes were prepared by carbonizing polymeric electrospun fiber precursors at high temperature. In particle/polymer electrospinning, there is no fiber pyrolysis; the electrospinning and post-processing are performed at room temperature to preserve the beneficial properties of the polymer binder and to insure an electrode with a high fiber volume fraction. High gravimetric, areal, and volumetric capacities are achieved at fast charge/discharge rates through the use of thick, densely packed particle/polymer nanofiber mats. The project has four key tasks: (1) Synthesis, optimization and testing of conducting polymer binders; (2) Electrospinning and post-processing of composite nanofiber mat anodes of Si nanoparticles with a conducting binder or with electrically conducting carbon powder and a non-conducting binder; (3) Evaluation of short-term and long-term performance of electrospun anodes in half-cells and full-cells (with a NMC

cathode) followed by post-mortem characterization; and (4) Preliminary scale-up of anode fiber mat manufacturing at a commercial electrospinning facility, where the resultant materials meet the project performance targets. Experiments during this reporting period focused on: (a) single fiber mats composed of Si and carbon particles in a suitable polymer binder; (b) dual fiber mat anodes, where one fiber type contains Si nanoparticles and binder and the second fiber is composed of carbon powder and binder; and (c) an electrospayed anode composed of Si nanoparticles and carbon powder with a new thermally crosslinked polymer binder. The partner on this project is Dr. Jagjit Nanda at the Oak Ridge National Laboratory (ORNL) who is overseeing electrode characterization experiments.

Results

Fiber-Particle Anodes Made by Simultaneous Electrospinning/Electrospraying

Silicon/poly(acrylic acid) (Si/PAA) electrospun fiber mats with electrospayed carbon black/binder droplets were fabricated to decrease the relative amount of binder in the anode while maintaining high electrical conductivity from the current collector to the anode/separator interface. Areal capacities as high as 1.3 mAh/cm² were achieved with this method. The carbon/binder/solvent ink compositions were optimized to ensure a small average particle sizes during spraying. Two carbon binders, poly(vinylidene fluoride) (PVDF) and polyamide-imide (PAI) were evaluated.

Anodes Fabricated by Concurrent Electrospinning of Si/PAA and Electrospraying of C/PVDF

Anode mats were made with Si/PAA electrospun fibers (with a 60/40 w/w Si/PAA) and C/PAI electrospayed droplets (83/17 w/w C/PAI), where the overall composition of the final fiber mat was 20% carbon, 45% Si nanoparticles, 32% PAA, and 3% PAI. Anode mats were further processed by interfiber welding (one-hour exposure to dimethylformamide vapor), fiber mat densification (compaction at room temperature for 1 minute and a pressure of 28 MPa) and annealing for 2h at 120°C. The surface of a raw electrospayed/electrospun mat is shown in Figure I.2.I.1a; fibers of uniform diameter with small carbon particle clusters dispersed throughout the mat are evident. A cross sectional SEM image of the welded and compacted mat is shown in Figure I.2.I.1b, highlighting the fiber structure of the processed electrode. Anodes were evaluated in CR2032 half-cells, with a Li metal counter/reference electrode, a Celgard porous separator, and an electrolyte of 1.2 M LiPF₆ in 3/7 EC/EMC with 10 wt.% FEC additive. The half-cells were galvanostatically charged/discharged between 0.015 V and 1.5 V, for 5 cycles at a rate of 0.1C and then for 100 cycles at 1C. The cycling performance of one of the best fiber-particle anodes is shown in Figure I.2.I.1c at two different Si loadings. The terminal discharge capacity after 100 cycles at 1C is 900 mAh/g (gravimetric) and 0.92 mAh/cm² (areal) for a 0.46 mg Si/cm² anode loading. A higher loading anode (0.89 mg Si/cm²) had a terminal gravimetric capacity of 700 mAh/g and an areal capacity of 1.29 mAh/cm². The lower Si loading anode exhibited a capacity retention of 98.6% over 100 cycles at 1C. The higher Si loaded anode was less effective in maintaining a high gravimetric and areal capacity during charge/discharge cycling, with a capacity retention of 90% over 100 cycles at 1C. Thus, an increase in Si loading resulted in a significantly increased areal capacity at the expense of slightly greater capacity fade over 100 cycles.

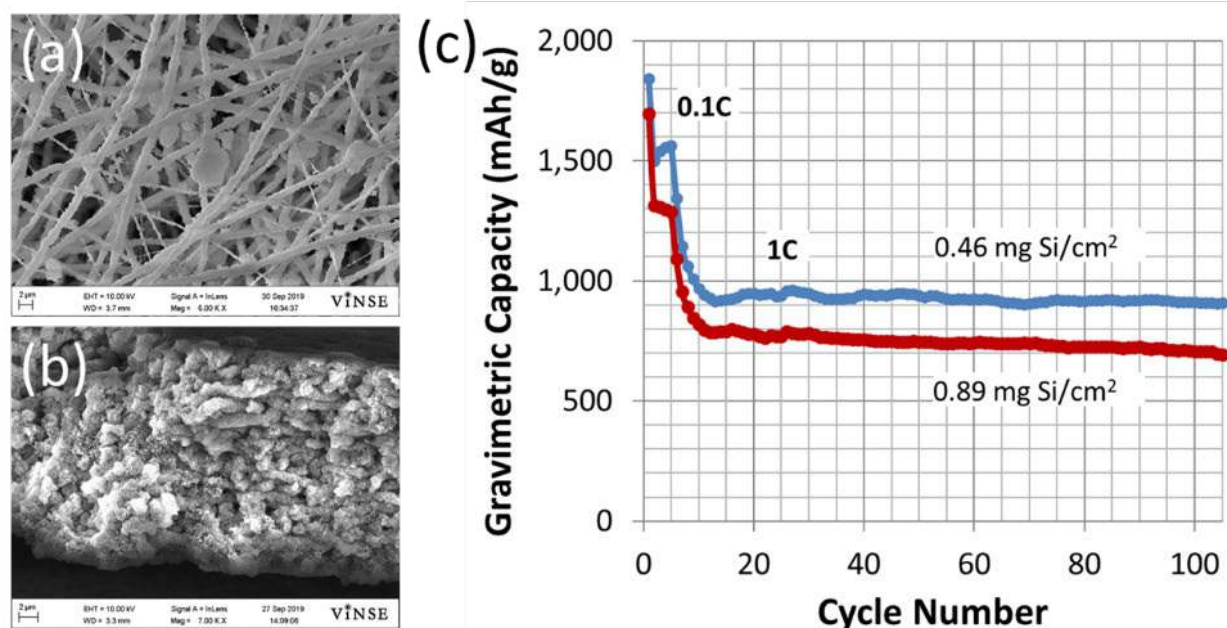


Figure I.2.I.1 (a) As-spun Si/PAA-C/PAI mat (20% C, 45% Si, 35% binder (3% PAI, 32% PAA); scale bar = 2 μm), (b) Cross section of Si/PAA-C/PAI compacted and welded mat; scale bar = 2 μm . C) Cycling performance of two Si/PAA-C/PAI anodes

Anodes Fabricated by Concurrent Electrospinning of Si/PAA and Electrospinning of C/PVDF

A second series of experiments were performed with anodes composed of Si/PAA electrospun fibers (60/40 w/w Si/PAA) and C/PVDF electrospun droplets (83/17 w/w C/PVDF), with an overall anode composition of 20% carbon, 45% silicon, 32% PAA, and 3% PVDF, and with varying silicon areal loading. A representative SEM image of an as-spun mat is shown in Figure I.2.I.2a (Si areal loading of 0.92 mg/cm^2). The morphology is similar to that shown in Figure I.2.I.1a for a Si/PAA-C/PAI mat.

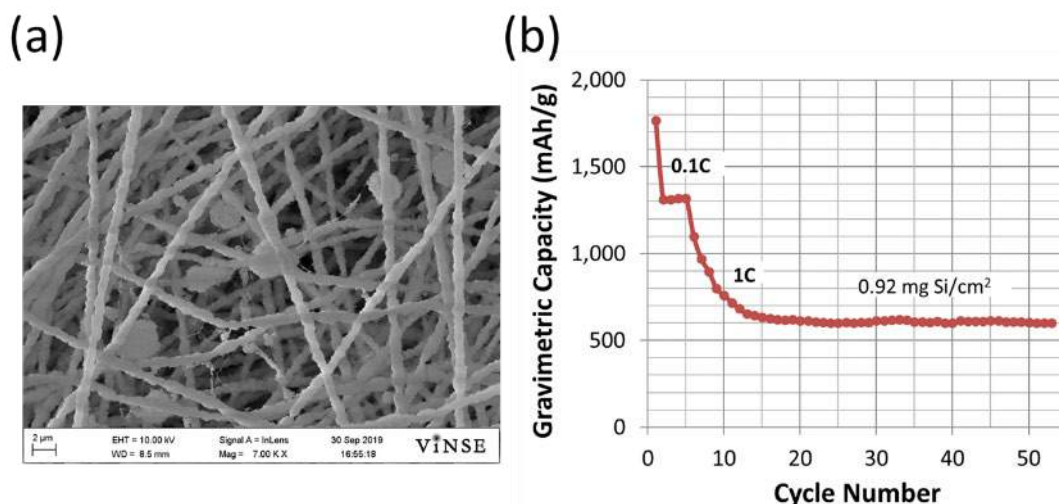


Figure I.2.I.2 (a) SEM image of an as-spun Si/PAA-C/PVDF raw mat, composition: 20% C, 45% Si, 35% binder (3% PVDF, 32% PAA) scale bar = 2 μm , (b) Cycling performance of the Si/PAA-C/PVDF anode

Anode mats were further processed by interfiber welding (one-hour exposure to dimethylformamide vapor), fiber mat densification (compaction for 1 minute at a pressure of 28 MPa) and annealing for 2h at 120°C. Anodes were evaluated in a CR2032 coin cells with a Li metal counter/reference electrode and an electrolyte

of 1.2 M LiPF_6 in 3/7 EC/EMC with 10 wt.% FEC additive. Galvanostatic charge/discharge experiments were conducted by polarizing the cells between 0.015 and 1.5 V vs. Li/Li^+ . Cycling performance of the Si/PAA-C/PVDF anode with an areal loading of 0.92 mg Si/cm^2 is shown in Figure I.2.I.2b. At 1C, the anodes exhibited an initial (10 cycles) drop in capacity followed by 93% capacity retention over the remaining 40 cycles. The terminal gravimetric capacity was 600 mAh/g and a terminal areal capacity was 1.15 mAh/cm^2 .

Electrospun Si/PAA and Si/C/PAA Single Fiber Anodes

Two different types of single fiber Si anodes were prepared, one with Si, C, and PAA (at a composition of 3 wt.% C, 57 wt.% Si, 60 wt.% PAA) and the second anode with just Si (60 wt.%) and PAA binder (40 wt.%). These two anodes were tested in CR2302 half-cells with a Li metal counter/reference electrode using an electrolyte of 1.2 M LiPF_6 in 3/7 EC/EMC with 10 wt.% FEC additive. Galvanostatic charge/discharge experiments were conducted by polarizing the cells between 0.015 and 1.5 V vs. Li/Li^+ . The coin cells were first charged/discharged at 0.1C for 5 cycles and then at 1C for 50 cycles. In Figure I.2.I.3, SEM images are shown of a raw Si/PAA (40 wt.% PAA) electrospun mat (Figure I.2.I.3a) and the final electrode after welding and compaction (Figure I.2.I.3b). Good fiber quality with uniform fiber diameters is evident. Similar fiber structures were obtained for an electrospun, welded, and compacted Si/C/PAA mat. A comparison of the charge/discharge behavior of the two anodes is presented in Figure I.2.I.3c. The Si/PAA (40 wt.% PAA, 0.98 mg Si/cm^2) anode showed stable cycling with a terminal gravimetric capacity of 640 mAh/g and an areal capacity of 1.1 mAh/cm^2 , after 50 cycles at 1C. Addition of 3 wt.% of carbon black to the Si/PAA fibers (0.97 mg Si/cm^2 loading) led to an increase of gravimetric capacity (832 mAh/g) and areal capacity (1.38 mAh/cm^2) after 50 cycles at 1C.

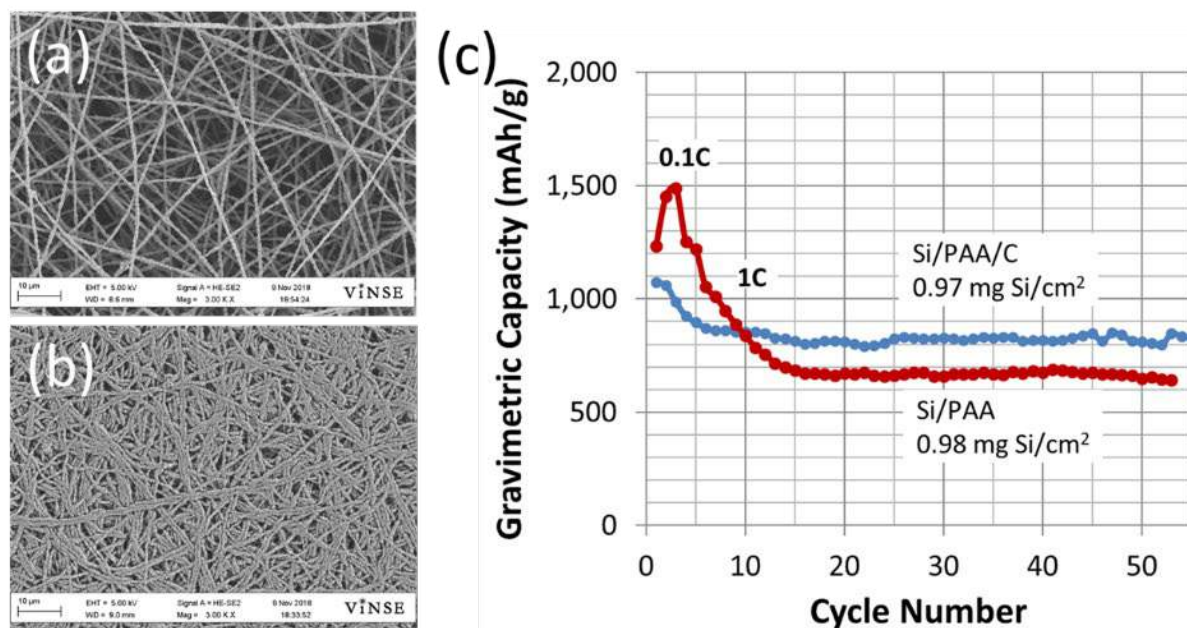


Figure I.2.I.3 SEM images of (a) Raw electrospun Si/PAA (40 wt.% PAA) fiber mat, (b) Final electrode obtained after mat densification; magnification 3,000x, and (c) Cycling performance of Si/PAA anode (40 wt.% PAA) compared to that of Si/PAA/C anode (40wt.% PAA, 3 wt.% C)

We found that, surprisingly, there was a significant capacity decay when the carbon content was further increased to 6 wt.% and 12 wt.% in single fiber Si/PAA/C anodes. In addition, in the absence of carbon, the areal loading was limited to about 1.0 mg Si/cm^2 ; at higher loadings, there was a gradual loss in gravimetric capacity.

Conclusions

1. A maximum gravimetric capacity of 900 mAh/g at 1C after 100 cycles was achieved using Si-PAA/C-PAI electrospun/electrosprayed anodes, with an areal capacity of 1.3 mAh/cm².
2. Si-PAA/C-PVDF electrospun/electrosprayed anodes exhibited a gravimetric capacity of 700 mAh/g with an areal capacity of 1.4 mAh/cm² after 50 cycles at 1C.
3. Single fiber Si anodes with PAA binder and a small amount of carbon black (Si/PAA/C, 3 wt.% C) showed stable charge/discharge cycling behavior with gravimetric capacity significantly greater than fibers with no carbon (Si/PAA). For example, a terminal capacity of 832 mAh/g (1.38 mAh/cm²) was obtained after 50 cycles at 1C with the Si/PAA/C anode, vs 641 mAh/g (1.1 mAh/cm²) for a Si/PAA anode.

Key Publications

1. Peter N. Pintauro, Nanofiber Electrospinning for Battery Electrodes and Membranes, invited paper, International Coalition for Energy Storage and Innovation (ICESI) and Pacific Power Source Symposium, Waikoloa, Hawaii, January 7, 2019
2. Abhishek N. Mondal, Ryszard Wycisk, Peter N. Pintauro, Ethan C. Self, and Jagjit Nanda, New Si Nanofiber Mat Designs for Li-Ion Battery Anodes, paper presented at the Electrochemical Society Meeting, Dallas, TX, May 2019.
3. A. Mondal, R. Wycisk, J. Nanda, E. Self, and P. N. Pintauro Dual Fiber Electrospun Anodes for Li-Ion Batteries – in preparation
4. A. Mondal, R. Wycisk, and P. N. Pintauro Single Fiber Electrospun Si-PAA and Si/C/PAA Fiber Anodes for Li-Ion Batteries – in preparation
5. J. Waugh, A. Mondal, R. Wycisk, J. Nanda, E. Self, and P. N. Pintauro, Electrospun/Electrosprayed Hybrid Mat Si Anodes for Li-Ion Batteries – in preparation.

Acknowledgements

The PI would like to acknowledge Mr. John Waugh, Dr. Abhishek N. Mondal and Dr. Ryszard Wycisk from Vanderbilt University and Dr. Ethan Self and Dr. Jagjit Nanda from ORNL for their contributions to the project.

I.2.J Continuous Flow R&D for Advanced Electrolytes (ANL)

Trevor Dzwiniel, Principal Investigator

Argonne National Laboratory
9700 S Cass Avenue
Lemont, IL 60439
E-Mail: tdzwiniel@anl.gov

Peter Faguy, DOE Technology Development Manager

U.S. Department of Energy
E-mail: Peter.Faguy@ee.doe.gov

Start Date: October 1, 2018
Project Funding: \$1,000,000

End Date: September 30, 2019
DOE share: \$1,000,000

Non-DOE share: \$0

Project Introduction

Innovative, experimental materials are being constantly developed to improve the safety, energy density, cycle, and calendar life of lithium ion batteries for EV, HEV and PHEV applications. These materials are typically synthesized in discovery laboratories in small batches providing amounts sufficient for limited basic evaluation only but not in quantities required for full scale validation and prototyping. In addition, bench-scale processes are often un-optimized, not validated, and generate materials with inconsistent purity and yield that varies from lab to lab and from batch to batch. This project aims to assist advanced battery research community by enabling access to larger quantities of high, uniform quality innovative materials. The objective of the program is also to evaluate an emerging technology to lower cost of advanced materials manufacturing without compromising quality and performance. The current focus of the program is on continuous flow chemistry, a technology with disruptive potential to rapidly bring to the market an advanced material at lower manufacturing cost.

Objectives

The objective of this project is to conduct research toward scaling up production of advanced materials for Li-ion batteries originally created in small quantities by discovery scientists and proven to be promising. Scaling up the original route used by discovery scientists often requires an extensive modification of the bench-scale chemistry and systematic, science-based process research and development to allow for 1) safe and cost effective production, 2) development of an engineering flow diagram, 3) design of a mini-scale system layout, 4) construction of the experimental system, and 5) validation of the optimized process, all of which are needed for full industrial implementation. The experimental system will be assembled, and the materials will be manufactured in quantities sufficient for prototyping and full-scale industrial evaluation. The materials produced by the program will be fully characterized to confirm chemical identity and purity. Analytical methods will be developed for quality control. The electrochemical performance of the materials will be validated to confirm that these properties match the original data generated by the discovery scientist. Sample of the materials produced by the project will be available to the advanced lithium ion battery research community to support basic development, prototyping and large-scale performance validation.

Approach

New materials for experimental electrolyte formulations often have complex molecular structure and difficult synthesis procedure that translates frequently into increased manufacturing cost. The Materials Engineering Research Facility (MERF) at Argonne is evaluating emerging production technologies to address the challenges. A comprehensive, systematic approach to scale-up of advanced battery materials has been defined. This approach starts with the original route the new material was first made in the discovery lab and initial electrochemical evaluation. This determines if the material is to be added to the inventory database, ranked, prioritized and selected for scale up. MERF prioritizes new materials based on level of interest, validated

performance and scale up feasibility. The new candidate materials for scale up are discussed with DOE for final approval. MERF evaluates several approaches, including non-standard manufacturing technologies, to determine the best approach to scale up of each particular material. One such technology is a Continuous Flow Chemical Reactor that enables the continuous synthesis of materials from discovery through process development and production scale. Continuous flow reactor technology can be used for rapid screening of reaction conditions to better understand the fundamentals of process kinetics and thermodynamics. The technology offers a cost-effective and safer alternative to traditional batch processes by improving material and energy usage and minimizing the environmental impact of the manufacturing operation. At this point, the scale-up process begins with a feasibility study, followed by proof of concept testing, 1st stage scale-up and, as needed, further scale-up cycles. Several Go/No Go decisions are located after feasibility determination and electrochemical validation testing. For each material, we will develop a scalable manufacturing process, analytical methods and quality control procedures. We also prepare a “technology transfer package” which includes detailed procedures of the revised process for material synthesis, materials balance, analytical methods and results (Specification Sheet) and the SDS for the material. The detailed process description allows for preliminary estimates of production cost, an important factor for decision making in industry. We apply the newly developed process to manufacture kilogram quantities of the material. We fully chemically characterize each material and make samples available for industrial evaluation and to the research community. We will also provide feedback to discovery chemists helping to guide future research.

Results

Flow Chemistry Synthesis of Fluorinated Electrolyte Solvents F-EMC and F-DEC.

As reported earlier, we have developed workable batch syntheses for these two materials, which are promising solvents^{1,2} for high voltage LIBs electrolyte formulations. We also have reported that the reactions are highly exothermic in nature, making them good candidates for synthesis via a continuous flow platform.

We first examined the synthesis of bis (2,2,2-trifluoroethyl)carbonate (F-DEC) in flow synthesis (Figure I.2.J.1). The original procedure was adapted to flow chemistry by changing the reaction solvent to acetonitrile, which solubilized the reagents at a concentration of roughly 0.5M. The separate reactants are then combined using a simple T-mixer and allowed to react in a reaction coil to furnish the product with only imidazole as a byproduct. Although the reaction was initially successful at a high temperature, it was found that a soluble amine catalyst allowed the process to run at slightly above ambient. This finding was applied to other reactions in flow. This process was ultimately determined to be less economical than the batch process due to the lower concentrations required to solubilize the reagents and the higher cost of acetonitrile relative to the batch solvents.

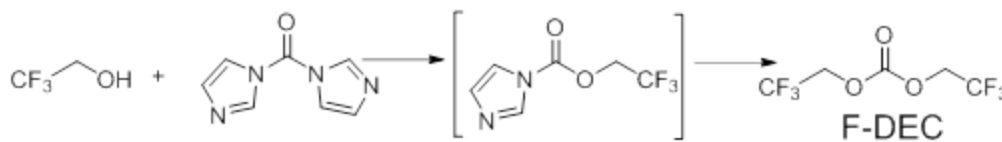


Figure I.2.J.1 Reaction to produce F-DEC

We also investigated the synthesis of methyl 2,2,2-trifluoroethyl carbonate (F-EMC) using flow conditions (Figure I.2.J.2). The original batch process using acetone and potassium carbonate were less amenable to direct translation to flow processes.



Figure I.2.J.2 Reaction to produce F-EMC

A solvent screen was carried out to uncover a solvent/base combination that both remained soluble and effectively carried out the reaction. After several screening experiments (Figure I.2.J.3), the combination of diisopropylethylamine and acetonitrile was chosen. This reaction was found to be significantly exothermic, with a

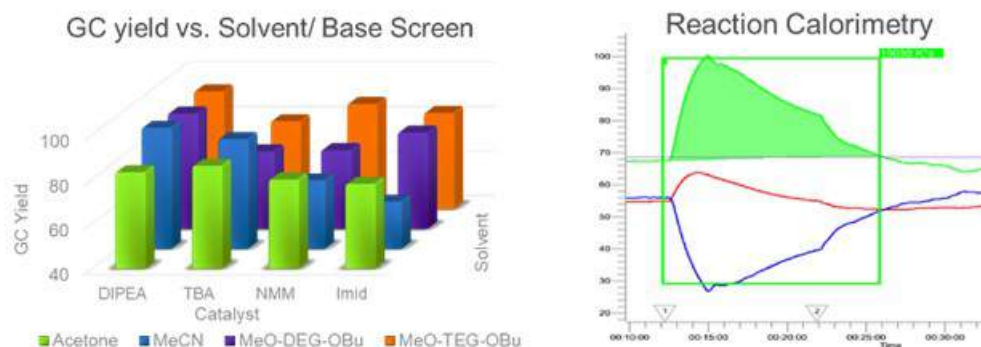


Figure I.2.J.3 Catalyst screen results and reaction calorimetry for flow condition of F-EMC

heat of reaction of approximately 120 kJ/mol and a maximum heat flux of 560 W/L (Figure I.2.J.3). This ironically makes this new procedure ill-suited for batch reactions, yet readily carried out with flow chemistry. This reaction was run in two separate reaction plates in the Corning flow reactor (Figure I.2.J.4). The first plate was used for the reaction, while the second plate was adapted for an aqueous quench. This prevented any possibility of

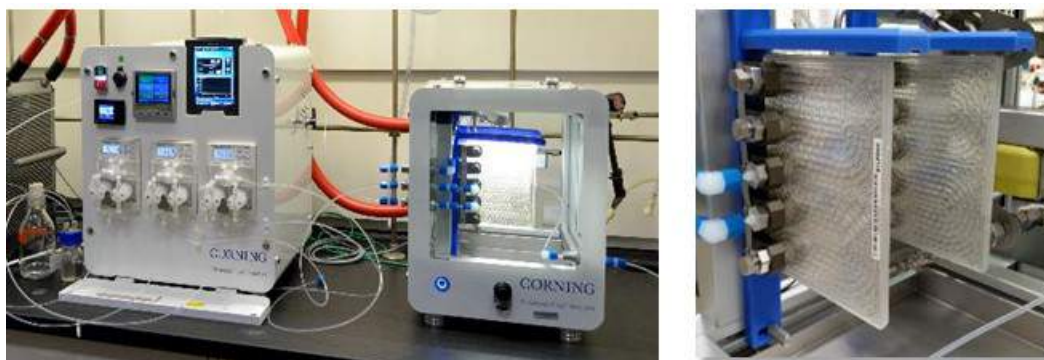


Figure I.2.J.4 Corning flow reactor and close up of the dual plate system for the synthesis of F-EMC

crystallization or precipitation to occur in the eluent mixture. The eluent layers were separated and a simple distillation gave pure F-EMC. This reaction was carried out on several hundreds of grams over an 8 hour period. Although this has an estimated 16% increase in materials costs, there is a 45% saving in time due to automation.

Flow Chemistry Synthesis of BTSMC.

We recently reported that the novel silicon-containing carbonate bis (trimethylsilylmethyl) carbonate (BTSMC) outperformed the standard Gen 2 electrolyte when cycled at high voltage. However, the synthesis of the material was slow and tedious, requiring several days to react and constant monitoring and addition of extra catalyst. We now report that flow chemistry gave valuable insight how to optimize this reaction. We initially sought to increase the reaction rate by running at above-boiling temperatures, and found that although the first reaction occurs rapidly, the second addition is extremely slow. Following the synthesis of F-DEC, we then sought to use a soluble amine catalyst, but unlike F-DEC, found that most standard amines were unreactive (Figure I.2.J.5). Fortunately, we also looked at stronger bases and found that select cyclic amines

were effective in catalyzing these reactions. Tests with TBD and DBU were so effective that in a simple NMR study (Figure I.2.J.5) showed that even at room temperature, the reaction is complete within 30 minutes.

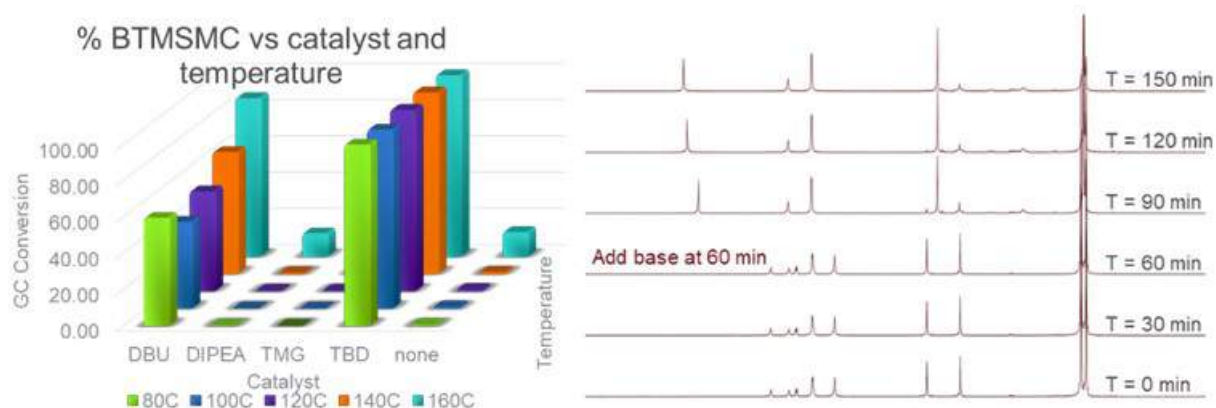


Figure I.2.J.5 Catalyst screen results and NMR study showing selective catalyst activity

Flow Chemistry Synthesis of TFPC.

3,3,3-Trifluoropropylene carbonate (TFPC) has shown excellent properties for several areas of lithium ion battery design.³ This solvent has been investigated extensively in recent years but is not widely available due to the difficulty in its synthesis. We reported earlier on a batch process to make this material from commercially available ethyl trifluoropyruvate, which is now optimized for material with purity >99.5% in a chlorine-free, safe, and environmentally friendly process. We further adapted this route to a semi-batch process using continuous flow chemistry; however, this overall process still did not seem to be the best overall method to manufacture the product. We therefore have begun investigations on a fully continuous method of production using a different chemistry. This new process uses carbon dioxide and a catalyst to ring-expand trifluoropropylene oxide (Figure I.2.J.6), known for small-scale batches using high pressure autoclaves, but is not suitable for commercial manufacturing.⁴ Many of these catalysts are heterogeneous and incompatible with flow processes.

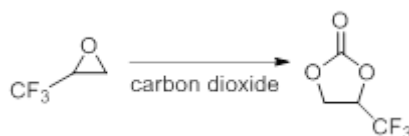


Figure I.2.J.6 Proposed flow chemistry process for TFPC

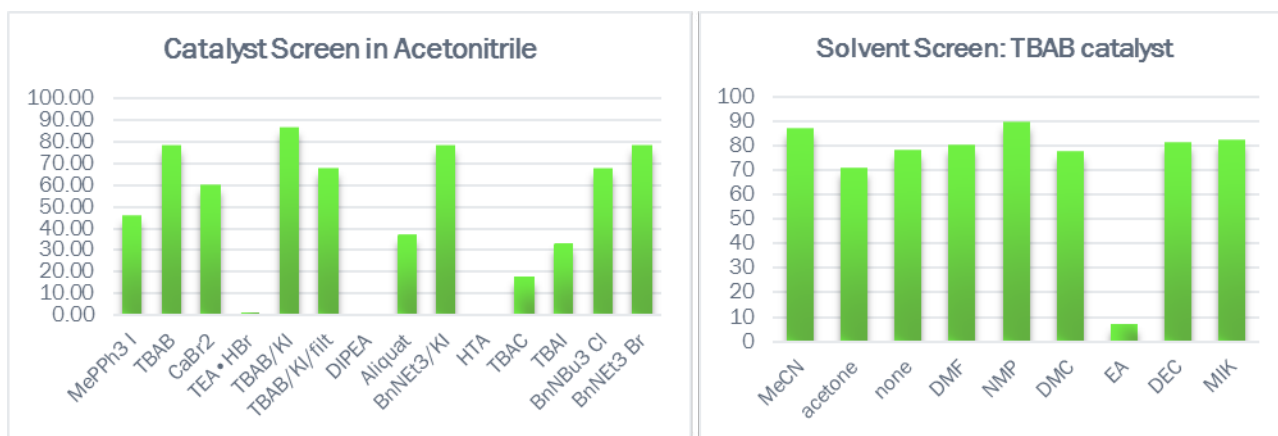


Figure I.2.J.7 Catalyst activity and solvent screen for TFPC

We initially investigated catalysts for activity and solubility in acetonitrile, observing that tetrabutylammonium salts were generally effective (Figure I.2.J.7). Having identified a reasonable catalyst, we examined different solvents, finding little effect on conversion. Many of these either showed poor solubility or were likely to interfere with the isolation of TFPC. Acetonitrile was again selected as the best compromise of workability, solubility, and cost.

Finally, we ran several full scale reactions in order to confirm the screening experiments in the actual manufacturing equipment (Figure I.2.J.8). Conditions were set using 10mol% TBAB catalyst, CH₃CN, and 75°C. The solutions were pumped at a rate of 0.5 ml/min solution, with a gas flow rate of 10 ml/min CO₂. The back pressure was set at 2.5 bar pressure. Several hundreds of grams have been synthesized.

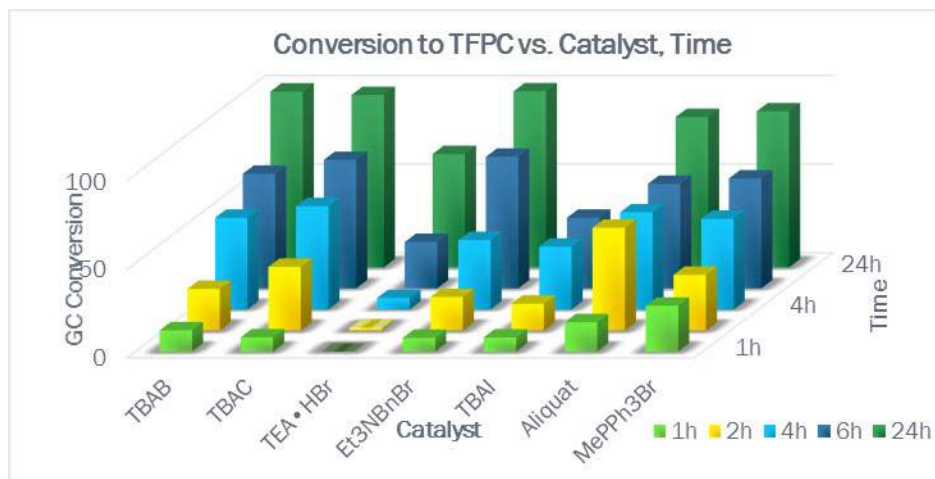


Figure I.2.J.8 Full scale reaction conversion results

Synthesis of Ionic liquids for non-flammable electrolytes.

Ionic liquids have been proposed and used as non-flammable solvents for lithium ion batteries, but generally exhibit less than ideal behavior, mainly attributed to high viscosity and low lithium-ion conductivity. In cooperation with the Zhang group, we have scaled up methyl bis(fluorosulfonyl)imide, a reagent that can be used in a one-step synthesis of high purity ionic liquids (Figure I.2.J.9). This process was modified to address the exothermic reactions in both the reaction and workup procedures. High purity Me-FSI was provided to the Zhang group and further IL studies are in progress.

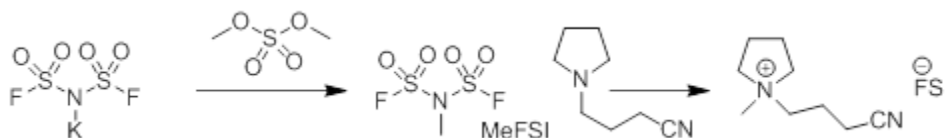


Figure I.2.J.9 Synthesis of salt-free Ionic Liquids.

Samples of selected electrolyte formulations containing the new materials will be provided to Argonne's CAMP facility for throughout evaluation. Materials (electrolyte formulations) with acceptable electrochemical performance will be used to manufacture larger cell formats for safety and abuse tolerance tests.

Conclusions

MERF's experimental materials scale-up program assists the battery research community and allows for a comprehensive evaluation of new materials by industrial laboratories as well as supports basic research. In FY19 the program provided several new, not commercially available materials in sufficient quantities for throughout investigation. Samples of high, uniform quality materials were distributed for further evaluation

and research. Over 200 samples, ranging from grams to hundreds of grams of experimental battery materials have been provided to researchers in industry, national labs and academia since the program inception.

MERF continues to design and synthesize new compounds in a series of silicon-containing carbonate solvents. The materials have significantly higher flash point than solvents commonly used to formulate LIBs electrolytes. Preliminary electrochemical evaluation revealed that the materials can improve safety of LIBs without performance degradation.

Evaluate emerging manufacturing technologies such as continuous flow reactors, microwave assisted reactions, acoustic mixing or reactive distillations to improve product quality while lowering manufacturing costs are all under consideration. MERF utilized recently acquired a customized Syrris ASIA320 and Corning Advanced-Flow™ continuous flow chemical reactors to develop expedient manufacturing processes for new electrolyte solvents, salts and additives by improving safety, minimize waste stream and lower material and energy cost

Key Publications

Issued Patents

1. Dzwiniel, Trevor; Pupek, Krzysztof; Krumdick, Gregory “Process for The Production Of High Voltage Electrolyte Solvents For Li-Ion Batteries” U.S. Patent 10,099,994 October 16, 2018.
2. Dzwiniel; Trevor, Pupek; Krzysztof, Krumdick; Gregory K. “Process for producing fluorinated electrolyte solvent” U.S. Patent 10,294,189 May 21, 2019.

Patent Applications

1. Dzwiniel, Trevor L.; Pupek, Krzysztof; Krumdick, Gregory K. “Process For Producing Fluorinated Electrolyte Solvent” U.S. Pat. Appl. Publ. (2018), U.S. 20180079708 A1 20180322.
2. Dzwiniel, Trevor L.; Pupek, Krzysztof “Method For Preparing Bis-(Silylalkyl) Carbonate Esters “ filed July 11, 2019 as Application #16/508,550.
3. Liao; Chen; Dzwiniel; Trevor L ; Pan; Baofei; Han; Sang-Don; Burrell; Anthony. “Salts For Multivalent Ion Batteries” U.S. Pat. Appl. Publ. (2018), 20180316060 A1 November 1, 2018

Presentations

1. Dzwiniel, Trevor; Pupek, Krzysztof. “Continuous Flow Processes as an Advanced Manufacturing Platform for Electrolyte Materials” 7th Flow Chemistry Congress, Miami, FL, Nov. 12-13, 2018.
2. Pupek, Krzysztof; Dzwiniel, Trevor “Continuous Flow Processes – A Platform for Manufacturing of Advanced Electrolyte Materials” International Battery Seminar & Exhibit, Fort Lauderdale, FL, March 25-28, 2019.
3. Dzwiniel, Trevor; Pupek, Krzysztof. “Continuous Flow Chemistry: Advanced Manufacturing for Electrolyte Materials” Flow Chemistry & Continuous Processing, Boston, MA, April 08-09, 2019.

References

1. a) Hamada, T. et al. “Improved Synthesis of Unsymmetrical Carbonate Derivatives Using Calcium Salts” Organic Process Research & Development (2019), 23(4), 667-673. b) Amine, K. et al. “Solvating power series of electrolyte solvents for lithium batteries” Energy & Environmental Science (2019), 12(4), 1249-1254. c) Fan, X. et al. “Non-flammable electrolyte enables Li-metal batteries with aggressive cathode chemistries” Nature Nanotechnology (2018), 13(8), 715-722.
2. a) Zhang, Z et al. “Polyfluorinated carbonate electrolyte for high-voltage lithium batteries” U.S. Pat. Appl. Publ. (2019), U.S. 20190288340 A1 20190919. b) Tornheim, A et al. “Preformed anodes for

high-voltage lithium-ion battery performance: fluorinated electrolytes, crosstalk, and the origins of impedance rise” *Journal of the Electrochemical Society* (2018), 165(14), A3360-A3368.

3. a) Mueller, G et al. “Fluorinated liquid electrolyte for electrochemical cells having a lithium metal anode” *PCT Int. Appl.* (2019), WO 2019042741 A1 20190307. b) Yun, J et al. “A Binary Cyclic Carbonates-Based Electrolyte Containing Propylene Carbonate and Trifluoropropylene Carbonate for 5 V Lithium-Ion Batteries” *Electrochimica Acta* (2015), 167, 151-159.
4. Tan J et al. “Novel and effective strategy of dual bis(trifluoromethylsulfonyl)imide imidazolium ionic liquid immobilized on periodic mesoporous organosilica for greener cycloaddition of carbon dioxide to epoxides” *New Journal of Chemistry*, 43(6), 2583-2590, 2019. b) Yu, L. H. et al. “Quaternary phosphonium cationic ionic liquid/porous metal–organic framework as an efficient catalytic system for cycloaddition of carbon dioxide into cyclic carbonates” *Environmental Chemistry Letters*, 17(1), 501-508, 2019.

I.2.K Optimizing Co-sintering of Ceramic Components for Manufacturing of All-Solid-State Lithium-Ion Battery (LLNL)

Brandon C. Wood

Lawrence Livermore National Laboratory
7000 East Avenue
Livermore, CA 94550
E-mail: wood37@llnl.gov

Peter Faguy, DOE Technology Development Manager

U.S. Department of Energy
E-mail: Peter.Faguy@ee.doe.gov

Start Date: April 1, 2019

End Date: September 9, 2020

Project Funding (FY19): \$150,000

DOE share: \$150,000

Non-DOE share: \$0

Project Introduction

The performance of solid-state batteries is greatly limited by the high interfacial impedance experienced between the solid components of the batteries. Unlike conventional liquid electrolytes, which can provide sufficient wetting of the solid electrodes, ceramic solid-state electrolytes often form poor physical contact with the solid electrodes, which impedes Li-ion transport across the interfaces. One approach to improve the physical contact between the solid-state electrolyte and the anode is to use post-annealing processing to premelt Li metal; however, this approach is far less effective at the interface with the cathode because very high ceramic processing temperatures are required to produce full densification at the interfaces. Unfortunately, at these elevated temperatures, the electrode materials are often prone to decomposition that lead to formation of ionically resistive secondary phases at the interfaces.

One relevant example can be found in solid-state batteries based on garnet oxides, including lithium lanthanum zirconate oxide (LLZO). This material is (electro)chemically stable against Li metal, and upon heating, forms a robust LLZO|Li metal interfacial structure. The main challenge of employing LLZO in a full electrochemical cell lies in the difficulty of fabricating a densified ceramic interface against typical cathode materials. Depending on particle size and shape, LLZO is typically sintered at a temperature above 1100°C.¹ However, most cathode materials, such as LiCoO₂, cannot survive a temperature above 900°C, either decomposing or reacting with the LLZO electrolyte. Lowering the LLZO sintering temperature to below 900°C has therefore become a critical step toward the commercialization of LLZO-based all-solid-state batteries.

It has been reported that the sintering temperature of LLZO can be lowered by doping LLZO with different elements.^{2,3} This is a promising strategy that is based on altering fundamental materials chemistry rather than introducing an external sintering agent, which may produce unwanted side reactions or residual byproducts. However, while doping may help lower the LLZO sintering temperature, it is likely to reduce grain size, which may affect the lithium ion conductivity due to diffusion limitations across grain boundaries. Finding the proper trade-off between sintering temperature and conductivity through a laboratory approach is time consuming and costly. Instead, this project leverages computational approaches, combined with controlled experiments, to explore the implications of chemical modification of the solid-state electrolyte LLZO on sintering temperature and microstructure as a first step towards enabling co-sintering of the electrolyte and cathode materials in ceramic solid-state batteries.

Objectives

This project aims to identify LLZO based solid electrolyte compositions and/or processing conditions that could lead to sintering temperatures below 900°C while preserving ionic conductivities above 0.3 mS/cm. Key descriptors of sintering temperature will be computed and calibrated to experimental data. Microstructures that

evolve from the sintering process will also be used to predict implications for Li-ion conductivity within the polycrystalline solid electrolytes.

Approach

This project utilizes *ab initio* and multiscale simulations to provide an efficient and unbiased way of exploring the effects of composition (doping) and microstructure on the performance of LLZO based solid electrolytes. *Ab initio* molecular dynamics (AIMD) simulations, along with custom codes developed at LLNL for studying polycrystalline systems, form the cornerstone methodology of our computational studies. Because directly predicting quantitative sintering temperatures is challenging, we instead invoke an approach that relies on candidate descriptors that we expect to track with the sintering temperature. These candidate descriptors for sintering temperature will be computed for selected LLZO compositions and calibrated against experimental sintering temperatures to downselect those descriptors that are found to be most effective. Next, these descriptors will be applied to other compositions to predict trends in sintering temperature. Promising LLZO compositions will then be used to calculate Li-ion conductivities for bulk and selected grain boundaries. These conductivity data will be integrated within our code to predict effective Li-ion conductivities of polycrystalline solid electrolytes with different grain sizes and morphologies, and the minimum grain sizes that maintain suitable ionic conductivity will be determined.

Results

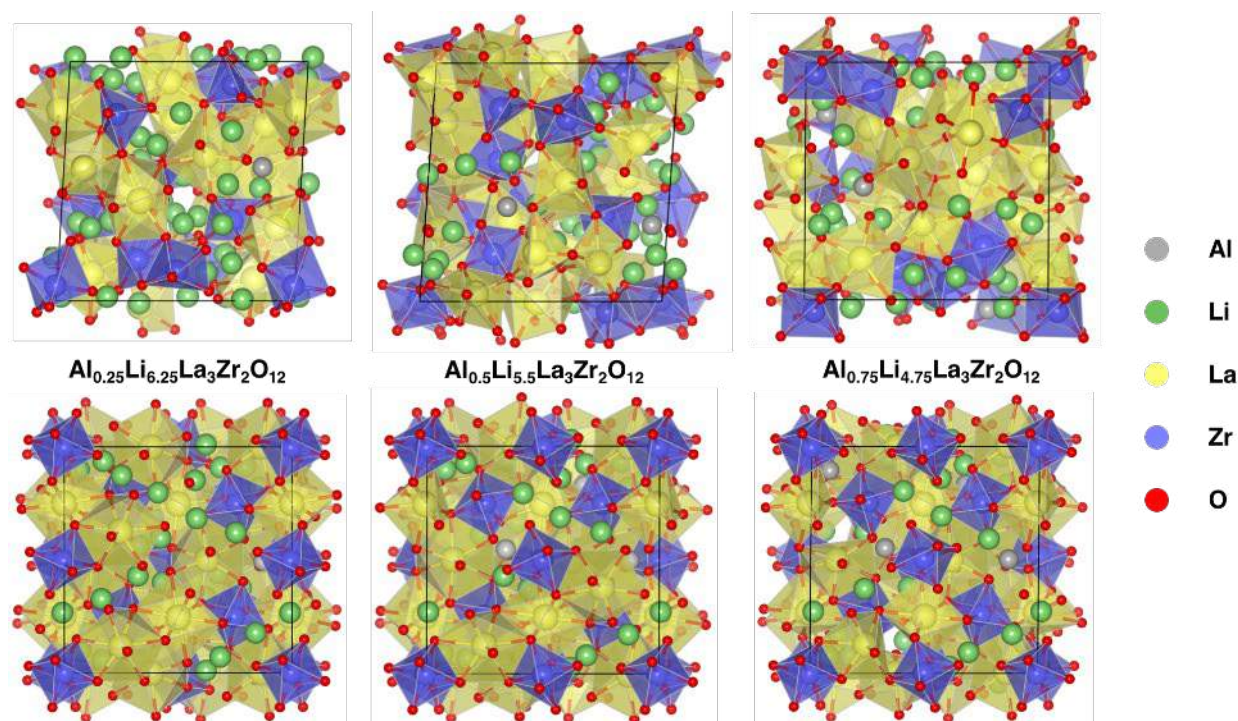
To predict sintering temperatures, our project is pursuing both static descriptors, which are relatively simple to compute, and dynamic descriptors, which require much longer and more cumbersome simulation techniques. This year, we focused primarily on testing the efficacy of static descriptors based on elastic moduli, amorphization energy, and surface energy of the materials. For these tests, the compositions and structures considered were Al-doped cubic LLZO, i.e., $\text{Al}_{0.25}\text{Li}_{6.25}\text{La}_3\text{Zr}_2\text{O}_{12}$, $\text{Al}_{0.5}\text{Li}_{5.5}\text{La}_3\text{Zr}_2\text{O}_{12}$ and $\text{Al}_{0.75}\text{Li}_{4.75}\text{La}_3\text{Zr}_2\text{O}_{12}$.

The elastic properties of Al-doped LLZO were determined by calculating the total energy of the system as a function of applied strain. For the calculation of bulk modulus and C_{11} and C_{12} constants, strain fields of ($\pm 2\%$, $\pm 1.5\%$, $\pm 1\%$, $\pm 0.5\%$) were used, and for the calculation of C_{44} constant, strain fields of ($\pm 4\%$, $\pm 3\%$, $\pm 2\%$, $\pm 1\%$) were used. Table I.2.K.1 shows a summary of calculated elastic moduli for different compositions of Al-doped LLZO compared with previous experiments.

Table I.2.K.1: Elastic Moduli of Al-doped LLZO

Composition	Bulk modulus (GPa)	Shear modulus (GPa)	Young's modulus (GPa)
$\text{Al}_{0.25}\text{Li}_{6.25}\text{La}_3\text{Zr}_2\text{O}_{12}$	99.6	60.3	150.5
$\text{Al}_{0.5}\text{Li}_{5.5}\text{La}_3\text{Zr}_2\text{O}_{12}$	91.5	56.2	139.9
$\text{Al}_{0.75}\text{Li}_{4.75}\text{La}_3\text{Zr}_2\text{O}_{12}$	87.7	47.2	120.2
$\text{Al}_{0.25}\text{Li}_{6.25}\text{La}_3\text{Zr}_2\text{O}_{12}$ (Exp. from Ref. 4)	102.8 ± 0.3	59.6 ± 0.1	149.8 ± 0.4

We also pursued descriptors based on the amorphization energy, defined as the energy difference between the ground state structure and the amorphous structure. An amorphous model for Al-doped LLZO was created using *ab initio* molecular dynamics by heating the ground state structure to 3000K and equilibrating for ~ 10 ps. Fifty structures were selected from the dynamics trajectory, within internal degrees of freedom relaxed. The amorphization energy was then computed as the average of these structures with respect to the crystalline variant. Examples of the amorphous structure of each LLZO composition, along with their crystalline structure is shown in Figure I.2.K.1, and the average amorphization energy of each LLZO composition is tabulated in Table I.2.K.2. The differences in amorphization energy with composition lies outside the standard deviation, affording confidence in the general approach.

Figure I.2.K.1 Optimized amorphous(top) and crystalline(bottom) structures of $\text{Al}_x\text{Li}_{7-3x}\text{La}_3\text{Zr}_2\text{O}_{12}$.**Table I.2.K.2: Calculated Amorphization Energy of $\text{Al}_x\text{Li}_{7-3x}\text{La}_3\text{Zr}_2\text{O}_{12}$**

	$\text{Al}_{0.25}\text{Li}_{6.25}\text{La}_3\text{Zr}_2\text{O}_{12}$	$\text{Al}_{0.5}\text{Li}_{5.5}\text{La}_3\text{Zr}_2\text{O}_{12}$	$\text{Al}_{0.75}\text{Li}_{4.75}\text{La}_3\text{Zr}_2\text{O}_{12}$
Average amorphization energy (eV)	23.3	21.1	18.5
Standard deviation (eV)	1.40	1.34	1.73

A third possible descriptor being pursued is the surface energy, defined as $\gamma = 1/2A [E_{\text{surface}} - E_{\text{bulk}}]$, where A is the surface area and E_{surface} and E_{bulk} are the total energies of the surface slab and bulk structure, respectively. According to Ref. 5, the La-terminated (011) surface shows the lowest surface energy among all stoichiometric surfaces studied. Hence, we chose this surface as a stable representative to study how the surface energy change as a function of Al doping level. It is found that at low Al doping levels ($\text{Al}_{0.25}\text{Li}_{6.25}\text{La}_3\text{Zr}_2\text{O}_{12}$), Al prefers to occupy sub-surface Li positions (see Figure I.2.K.2). As the Al doping level increases, the energy difference for Al to reside near the surface versus in the bulk decreases. Eventually, at high Al doping level, Al atoms saturate near the surface, causing Al atoms to favor Li-sites in the bulk region. Based on the lowest energy obtained for different Al doping sites, we compute the surface energy and present the results in Table I.2.K.3.

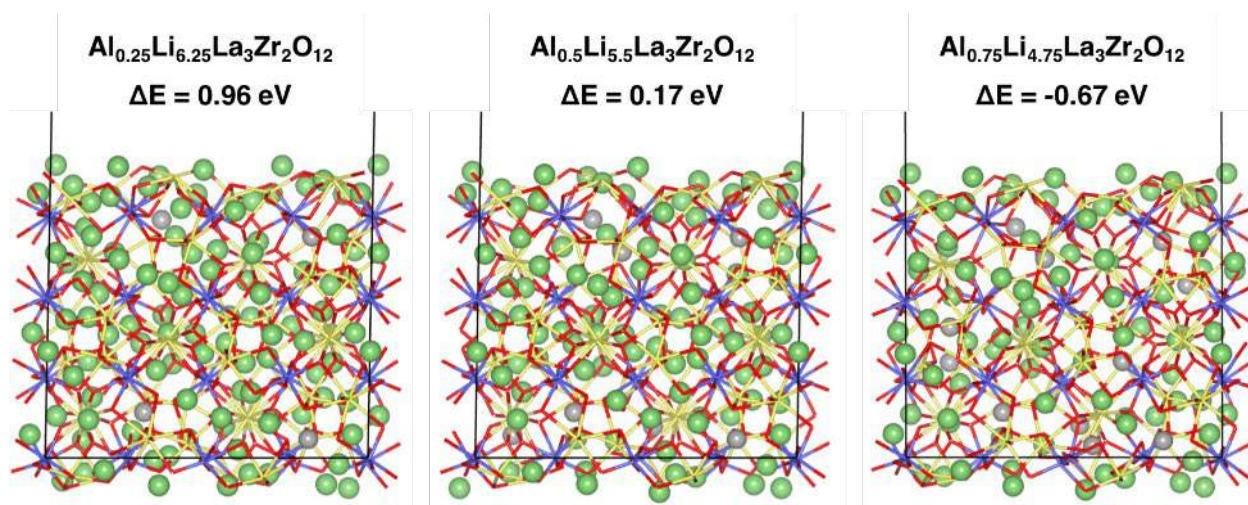


Figure I.2.K.2 Optimized surface structures of Al doped cubic LLZO. Only Li (green) and Al (grey) are shown as spheres, the La-O and Zr-O bonds are shown as sticks. ΔE represents the energy difference for a single Al atom to occupy the Li-site in the sub-surface vs. in the bulk. A positive value indicates occupying the sub-surface site is energetically favored and a negative value suggests the bulk site is preferred

Table I.2.K.3: Calculated Surface Energy of La-terminated (011) Surface of Al-doped LLZO

	$\text{Al}_{0.25}\text{Li}_{6.25}\text{La}_3\text{Zr}_2\text{O}_{12}$	$\text{Al}_{0.5}\text{Li}_{5.5}\text{La}_3\text{Zr}_2\text{O}_{12}$	$\text{Al}_{0.75}\text{Li}_{4.75}\text{La}_3\text{Zr}_2\text{O}_{12}$
Surface energy (J/m^2)	0.40	0.38	0.83

We note that both elastic moduli and amorphization energy seem to predict a linear relation with respect to the Al doping level—at higher Al doping, the material becomes mechanically softer and it requires less energy to become amorphized or disordered, which should track favorably with the sintering temperature. The surface energy, on the other hand, does not show a linear trend, suggesting it is likely unsuitable as a predictor of sintering behavior. Our next step will be to incorporate dynamical descriptors and begin our calibration procedure against experimentally measured sintering temperatures.

Conclusions

The goal of this project is to find appropriate dopants (and doping levels) to lower the sintering temperature of LLZO, while preserving the desired ionic conductivity. To efficiently screen the space of possible dopants and compositions, we need to identify computationally efficient and accurate descriptor based on examinations of selected dopants (in this case, Al) and doping level. Once the descriptor is successfully identified, we will use this descriptor to screen a larger pool of dopants and compositions. Our early efforts are focused on establishing this descriptor. In this fiscal year, we have focused on “static” descriptors, *i.e.*, elastic moduli, amorphization energy and surface energy, which can be easily computed using density functional theory. The elastic moduli and amorphization energy vary monotonically with Al doping level, suggesting these may be viable candidates. On the other hand, due to the structure and chemical complexity of the LLZO surfaces, the surface energy may not be a good choice as descriptor for further screening of dopants and doping levels. In the coming quarters, we will extend our descriptor search to include dynamical quantities derived from molecular dynamics, which we expect may be better predictors of sintering temperature. In addition, in order to identify the most relevant descriptor, we will proceed to calibrate our results with the experimentally determined sintering temperatures of exact compositions.

Key Publications

1. B.C. Wood, “Optimizing co-sintering of ceramic components for manufacturing of all-solid-state batteries,” VTO Annual Merit Review (June 2019).

References

1. R. Murugan, V. Thangadurai and W. Weppner, “Fast lithium ion conduction in garnet-type $\text{Li}_7\text{La}_3\text{Zr}_2\text{O}_{12}$ ”, *Angew. Chem. Int. Ed.* **46**, 2007, 7778-7781.
2. R.-J. Chen, M. Huang, W.-Z. Huang, Y. Shen, Y.-H. Lin and C.-W. Nan, “Effect of calcining and Al doping on structure and conductivity of $\text{Li}_7\text{La}_3\text{Zr}_2\text{O}_{12}$ ”, *Solid State Ionics* **265**, 2014, 7-12.
3. S. Ohta, T. Kobayashi and T. Asaoka, “High lithium ionic conductivity in the garnet-type oxide $\text{Li}_{7-x}\text{La}_3(\text{Zr}_{2-x}\text{Nb}_x)\text{O}_{12}$ ($x=0-2$)”, *J. Power Sources* **196**, 2011, 3342-3345.
4. J. Ni, E. Case, J. Sakamoto, E. Rangasamy and J. Wolfenstine, “Room temperature elastic moduli and Vickers hardness of hot pressed LLZO cubic garnet”, *J. Mater. Sci.* **47**, 2012, 7978–7985.
5. P. Canepa, J. A. Dawson, G. S. Gautam, J. M. Statham, S. C. Parker and M. S. Islam, “Particle morphology and lithium segregation to surfaces of the $\text{Li}_7\text{La}_3\text{Zr}_2\text{O}_{12}$ solid electrolyte”, *Chem. Mater.* **30**, 2018, 3019-3027.

Acknowledgements

This work was performed under the auspices of the U.S. Department of Energy by Lawrence Livermore National Laboratory under contract DE-AC52-07NA27344.

Collaborations. The LLNL computational modeling team includes Liwen Wan, Tae Wook Heo, and Aniruddha Jana. The project also collaborates with Jianchao Ye and Marissa Wood from LLNL on determining experimental sintering conditions for LLZO-cathode interfaces in solid-state batteries.

I.2.L Structure-Activity Relationships in the Optimizing Electrode Processing Streams for LiBs (LBNL)

Vincent Battaglia, Principal Investigator

Lawrence Berkeley National Laboratory
1 Cyclotron Road, MS 70R0108B
Berkeley, CA 94720
E-mail: vsbattaglia@lbl.gov

Peter Faguy, DOE Technology Development Manager

U.S. Department of Energy
E-mail: Peter.Faguy@ee.doe.gov

Start Date: February 1, 2019

End Date: September 30, 2019

Project Funding: \$200,000

DOE share: \$200,000

Non-DOE share: \$0

Project Introduction

The processing of dispersion components into porous electrodes for lithium ion batteries involves a large number of variables in component selection, and mixing, coating, and drying procedures. These choices can have an enormous effect on electrode performance, but are typically made through trial-and-error because little is understood about the behavior of the dense electrode dispersions (Kraytsberg, Alexander, and Ein-Eli 2016), (Kwade, Arno, *et al.* 2018), (Hawley, W. Blake, and Li 2019). The aim of this project is to connect interactions among battery porous electrode dispersion components and processing conditions to electrode properties, in the interest of providing understanding that can be used to guide optimization of electrode fabrication processes. This will involve the development of novel experiments and corresponding mathematical models that connect experimental results.

Objectives

The ultimate objective of this project is to develop a method for creating models that connect battery electrode dispersion component-level information and processing variables to porous battery electrode properties. These models will require the design and execution of a collection of novel experiments, which will involve:

- Characterization of dispersion component association
- Characterization of dispersion component interaction strengths
- Creating modifications and/or additions to drying coating observation apparatus (developed primarily under the AMO roll-to-roll consortium) as needed specifically for battery electrode dispersions
- Measurement of coating drying rates

Approach

This project will heavily leverage our efforts under the AMO roll-to-roll consortium, but with emphasis on examining battery porous electrode dispersions and the dispersion components.

We will begin by using customized, computer-controlled disperser equipment and battery electrode dispersion materials to produce dilute single-component dispersions (one solute or solid in solvent or suspension fluid). These will be examined using dynamic light scattering and/or a particle size analyzer in order to determine how mixing conditions affect evolution of size distributions, providing an indication of the cohesiveness of each component of interest. This will be repeated with mixtures of single-component dispersions, providing an indication of the strength of interactions among different components.

Dilute, and later, concentrated dispersions will then be examined through FTIR, in order to obtain an indication of the freedom of polymer chain movement, which should reflect polymer entanglement and adsorption on dispersed particles.

Subsequent experiments will be planned based on the results of these early experiments, and are expected to include techniques such as thermogravimetric analysis, differential scanning calorimetry, and optical microscopy, Raman microscopy at the Molecular Foundry, and IR spectroscopic mapping, X-ray fluorescence microprobe / X-ray absorption spectroscopy, X-ray radiography and tomography, and X-ray diffraction at the Advanced Light Source.

A new experimental apparatus for observation of dispersion coating and drying processes is being developed primarily under our AMO roll-to-roll consortium efforts, and will be applied both to dispersions of interest to AMO and to battery dispersions under the present project. VTO funding will be used for modifications or additions that are specifically needed for examining battery electrode dispersions. This apparatus will allow observation of drying coatings under conditions that simulate roll-to-roll processing.

Results

This project started mid-year and has primarily involved planning and procurement. Funding was largely reserved for postdoctoral scholar effort. We have hired one postdoctoral scholar, who started in late June 2019, and a second postdoctoral scholar, who is anticipated to start in January 2020. Both will devote approximately 50% time to this project.

Much of the project effort up to this point has been in developing the approach outlined in the previous section, through literature surveys and through consulting with collaborators within LBNL and in the AMO roll-to-roll consortium.

Conclusions

None, this project started mid-year and has primarily involved planning and procurement.

Key Publications

None, this project started mid-year and has primarily involved planning and procurement.

References

1. Kraytsberg, Alexander, and Yair Ein-Eli. 2016. "Conveying Advanced Li-ion Battery Materials into Practice: The Impact of Electrode Slurry Preparation Skills." *Adv. Energy Mater.*, 6, 1600655. DOI: 10.1002/aenm.201600655.
2. Kwade, Arno, Wolfgang Haselrieder, Ruben Leithoff, Armin Modlinger, Franz Dietrich, and Klaus Droeder. 2018. "Current status and challenges for automotive battery production technologies." *Nature Energy*, vol. 3, 290-300. <https://doi.org/10.1038/s41560-018-0130-3>.
3. Hawley, W. Blake, and Jianlin Li. 2019. "Electrode manufacturing for lithium-ion batteries—Analysis of current and next generation processing." *Journal of Energy Storage*. 25, 100862. <https://doi.org/10.1016/j.est.2019.100862>.

Acknowledgements

Other LBNL personnel participating in this project include Ravi Prasher (associate laboratory director / division director), Kenneth Higa (project scientist), and Zhi Huang (postdoctoral scholar).

I.2.M Fabricate and test solid-state ceramic electrolytes and electrolyte/cathode laminates (LBNL)

Michael Tucker, Principal Investigator

Lawrence Berkeley National Laboratory
1 Cyclotron Road
Berkeley, CA 94720
E-mail: MCTucker@LBL.gov

Peter Faguy, DOE Technology Development Manager

U.S. Department of Energy
E-mail: Peter.Faguy@ee.doe.gov

Start Date: March 1, 2019

End Date: September 30, 2019

Project Funding (FY19): \$350,000

DOE share: \$350,000

Non-DOE share: \$0

Project Introduction

Ceramic solid state battery technology is limited by processing constraints such as Li loss during sintering, reaction between active materials and electrolyte during processing, and non-ideal microstructure and electrochemical/mechanical properties of layers fabricated via conventional processing routes. This project will address these limitations by elucidating behavior of the key materials during processing, including sintering behavior, reactivity, and phase stability. Of particular importance is the fabrication of thin, completely dense electrolyte and thick, highly porous cathode scaffold layers using high-volume, low-cost fabrication processes. Initial work focuses on $\text{Li}_{6.25}\text{Al}_{0.25}\text{La}_3\text{Zr}_2\text{O}_{12}$ (LLZO).

Objectives

The project objectives are: to determine processing methods and conditions that enable high-volume, low-cost production of solid state battery ceramic electrolyte and electrolyte-cathode bilayer structures; and, demonstrate improved electrochemical and mechanical performance for these structures.

Approach

The impact of processing conditions and precursor properties on layer structure, electrochemical performance, and mechanical properties will be determined. Diagnostic tools such as dilatometry, mechanical testing, and synchrotron techniques will be used to interrogate the relationship between processing and layer quality. Viability of alternative processing routes will be assessed, such as solid state reactive sintering and infiltration/impregnation of active materials. Commercially-available LLZO powder is used for all experiments to eliminate batch variations and ensure experimentally observed processing improvements and not due to variation of powder properties.

Results

Sintering atmosphere

Sintering atmosphere is expected to impact sintering behavior, lithium evaporation, LLZO oxidation state, and choice of kiln furniture materials. Pellets of LLZO with additional 5wt% lithium carbonate were sintered in various atmospheres presenting a range of oxygen partial pressure between pure oxygen and reducing conditions. In all cases, cubic LLZO phase was obtained, and for oxygen a minor amount of $\text{La}_2\text{Zr}_2\text{O}_7$ was also detected. The derivative of shrinkage curves obtained in a vertical dilatometer indicate that sintering is delayed by approximately 50°C for reducing (hydrogen-containing) atmosphere relative to air, oxygen, and inert atmospheres. Pellets sintered in a tube furnace with various atmospheres exhibited a range of density and conductivity, but very similar microstructure. Sintering in argon provided the highest conductivity, and also enables the use of graphite setter plates that avoid reaction with LLZO, and was therefore chosen as the preferred processing atmosphere.

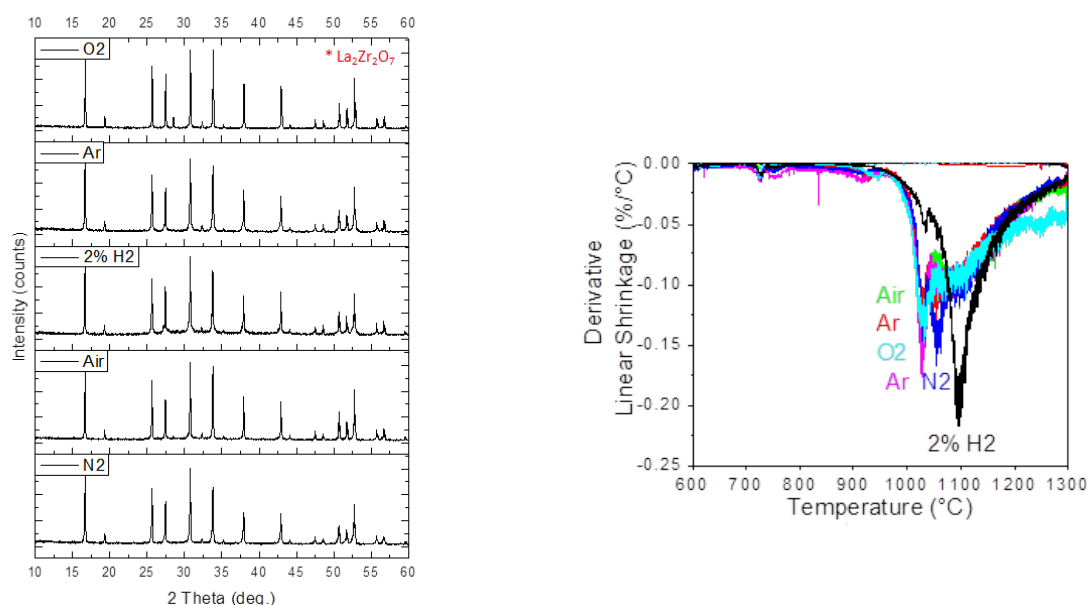


Figure I.2.M.1 Impact of sintering atmosphere on phase purity and sintering behavior. (Left) XRD patterns and (right) derivative of dilatometry shrinkage curves

Table I.2.M.1 Impact of Sintering Atmosphere on Density and Conductivity

Atmosphere	Density (% Theoretical)	Conductivity (S/cm $\times 10^{-4}$)
Ar	90.6	3.60
N2	92.2	3.34
2% H2	92.0	2.55
Air	88.8	2.13

Sintering protocol

Sintering temperature and time must be optimized for each sample geometry, as the rate of Li evaporation depends on temperature, time, and surface-area-to-volume of the sample. Furthermore, the sintering protocol impacts microstructure, including residual porosity, grain size, and grain size distribution. Excess Li is typically added to offset Li evaporation during sintering. If too much Li remains after sintering, the low-conductivity tetragonal LLZO phase dominates. If too little Li is retained, the inactive $\text{La}_2\text{Zr}_2\text{O}_7$ phase is produced. Careful co-optimization of the excess Li content and sintering protocol is therefore required to optimize properties of the sintered LLZO structure.

Based on the sintering curve in Ar presented above, sintering temperature in the range 1075 to 1150°C was chosen for further optimization. Pellets of LLZO with 3wt% Li_2CO_3 were sintered in Ar at 1075°C for various times. The density plateaus after 5h, but the conductivity continuously increases from 1h to 7h, as the ratio of cubic to tetragonal LLZO phase increases due to Li evaporation. A wide variety of excess Li loading and sintering time were explored, with a wide resulting range of conductivity and density. Addition of MgO was found to significantly increase the densification without sacrificing conductivity.

Similar optimization of the excess Li content, MgO loading, and sintering protocol for thin tapes is ongoing.

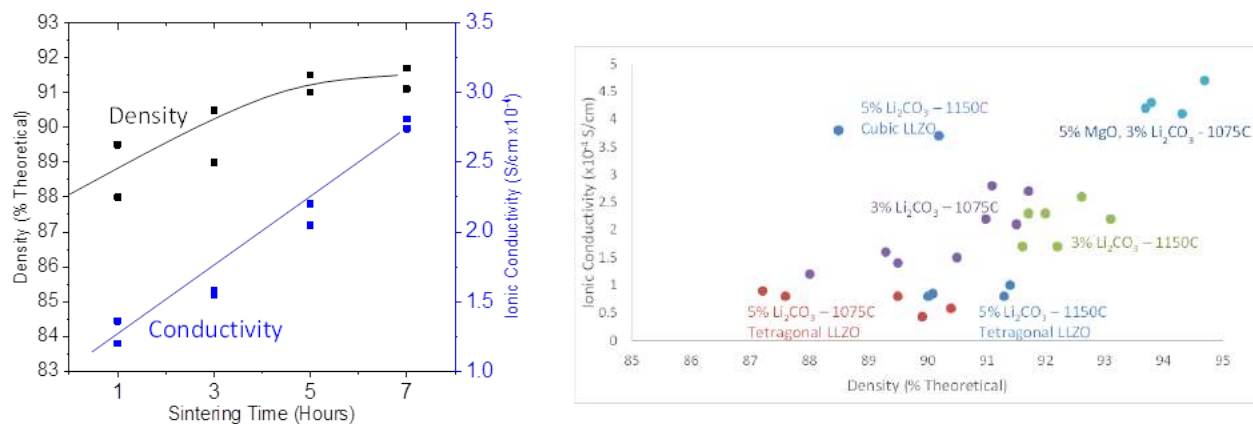


Figure I.2.M.2 Optimization of Li loading and sintering parameters. (Left) Density and conductivity of LLZO pellets sintered for various hold times at 1075 °C with 3wt% Li₂CO₃. (Right) Overview of pellet density and conductivity optimization efforts. Points in each group represent different sintering times

Tape casting

Several solvent and binder systems were evaluated on the basis of compatibility with LLZO, quality of casting slurry, release from carrier substrate, mechanical properties, and green density. The most promising system is toluene/xylene solvent with a proprietary binder. Loadings of ceramic particles and binder were optimized for slurry viscosity, casting quality, and tape strength. Dispersant loading was optimized by conducting settling experiments, where the lowest bed height after settling indicates the best dispersion of ceramic powder in the solvent. Adding 0.025 weight ratio of Dispersant B to LLZO resulted in a strong, flexible LLZO cast tape, with green oxide-only density of 2 g/cm³. Optimization of the addition of lithium carbonate to the tape to offset Li loss during sintering is ongoing.

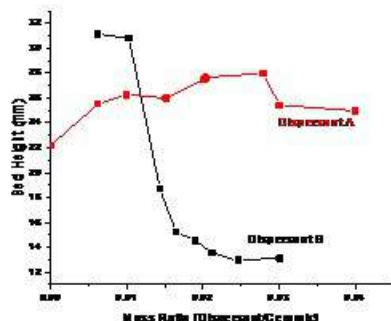


Figure I.2.M.3 (Left) Tape casting dispersant optimization and (right) photograph of optimized LLZO tape

Conclusions

This project aims to prepare LLZO-based electrolyte and electrolyte/cathode scaffold structures using scalable processing techniques such as tape casting and furnace sintering. The initial work during this project period focused on optimizing the sintering protocol and atmosphere for a commercially-available LLZO powder composition and particle size. It was found that sintering atmosphere has a moderate impact on pellet properties, and Ar was chosen as the preferred atmosphere. Li content, sintering temperature, and sintering time were optimized to obtain pellets with high density and near-theoretical conductivity.

Various tapecasting solvent and binder systems were screened for compatibility with LLZO. Promising systems were optimized in terms of slurry loading and dispersant concentration. Strong, thin, flexible tapes were prepared. The next project period will focus on optimizing sintering of thin electrolyte and electrolyte/cathode scaffold tapes to achieve high density and conductivity.

Acknowledgements

All data presented in this report was generated by Robert Jonson.

I.2.N Higher Energy Density via Inactive Components and Processing Conditions (LBNL)

Vincent Battaglia, Principal Investigator

Lawrence Berkeley National Laboratory
1 Cyclotron road
Berkeley, CA 94720
E-mail: vsbattaglia@lbl.gov

Peter Faguy, DOE Technical Development Manager

U.S. Department of Energy
E-mail: Peter.Faguy@ee.doe.gov

Start Date: October 1, 2016

End Date: September 30, 2020

Project Funding (FY19): \$750,000

DOE share: \$750,000

Non-DOE share: \$0

Project Introduction

To increase market penetration of EVs will require further reductions in the cost of the battery. One means of doing this with today's SOA chemistry is to find a way to produce thick electrodes with small levels of inactive components that can still deliver most of their energy at C-rates of C/3. Higher energy density should translate to more miles per charge or smaller, less expensive batteries. Unfortunately, the limit to making thicker electrodes is presently not based on the limited rate capability of today's Li-ion cells. Today's electrodes are fabricated at thicknesses of around 100 μ m. These electrodes can be discharged at a rate of C/1, which is considered three times faster than what is necessary for a battery designed for an EV. The reasons for this is that most major cell manufacturers have found these thicknesses adequate for the portable electronic devices that they sell in mass quantities. Changes in the formulations would require changes in slurry formulations and changes in their roll-to-roll processing speeds. At this point in time, such changes have not appeared warranted.

Objectives

The objective of this research is to bring as much understanding as possible to current electrode processing conditions at the particle to particle and particle to binder interactions level to help us better understand slurry rheology, slurry mixing, laminate coating, and laminate drying. Such an understanding would allow innovative companies to consider physical and surface chemical changes to the particles that should allow for significant penetration into the market.

Approach

Our approach is to investigate all aspects of the electrode processing conditions from initial mixing of materials to the final coated laminate drying step using the capabilities found collectively at a national lab. This initial work will focus on today's SOA Li-ion chemistry, which involves active materials, high surface area, conductive carbon additives, and PVdF binder mixed and dried in an NMP based solution. We will investigate changes in electrode performance as it relates to the distribution of the materials in the dried electrodes and the properties that lead to this distribution as a result of the rheological properties of the slurry. Techniques employed will include electrode cross sectioning, SEM, EDX, XRD, different mixing orders, different drying conditions, peel testers, rheometers, potentiostats, and battery cyclers.

Results

As work concluded in FY'18, we discovered that when the cathode material and carbon black are first mixed together in NMP and then a mixture of binder dissolved in NMP added to it and then thick coatings are cast and dried at temperatures between 80 and 190°C that the electrodes formed displayed significant levels of cracking when dried above 140°C but below this temperature, the laminates showed reduced electrochemical

performance with increase in drying temperature and improved mechanical properties. This is presented in Figure I.2.N.2 and Figure I.2.N.1.

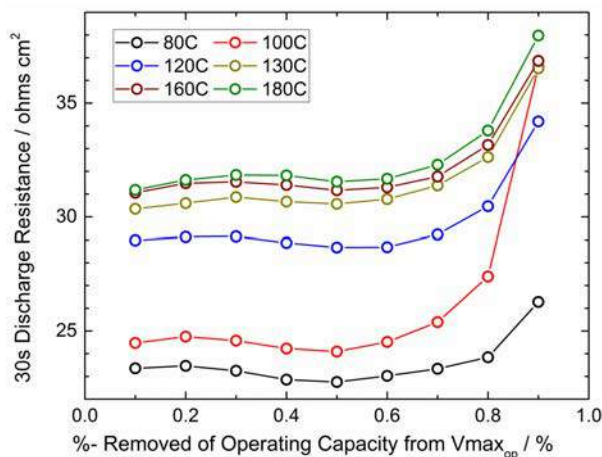


Figure I.2.N.2 The resistance of laminates dried at different temperatures as measured by applying a current pulse for 30 seconds and measuring the change in voltage divided by the change in current. This was performed at 10% discharge increments.

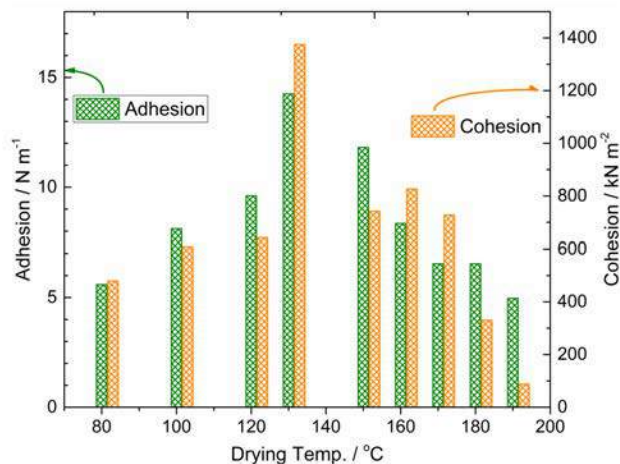


Figure I.2.N.1 The adhesion and cohesion of laminates of cathode material dried at different temperatures from 80 to 190°C.

We also demonstrated that if a film of PVDF is cast and dried from NMP (solvent), the temperature at which the slurry is dried, impacts the crystalline structure of the dried polymer. We believe that this micro structure affects the transport of lithium ions. Thus, in general, polymer crystallinity impacts the mechanical properties and the ionic conductivity of the polymer film formed. High levels of crystallinity improve the mechanical properties and reduce the ionic conductivity. Drying at high temperatures provides enough energy for the polymer to reconfigure itself into its preferred thermodynamic state of crystallinity. Above 110°C the preferred crystalline state is referred to as the α -phase.

Based on this, we started the new year investigating the conditions that impact the crystallinity of the polymer.

Films of polymer were cast onto sheets of glass consisting of different levels of carbon black and dried at different temperatures. X-rays were then taken of the dried films to assess the crystallinity. The results are displayed in the three figures of Figure I.2.N.3.

Looking down through the three figures, one sees that the level of crystallinity increases as the drying temperature is increased (the peaks are sharper and taller at higher drying temperatures.) Looking from top to bottom in each figure one sees the same trend of crystallinity with addition of carbon but exhibited at different levels of carbon black addition. For drying at 80°C (top figure), there is a distinctive change in the spectra between 5:1 and 5:2 PVdF:carbon. With the crystallinity becoming noticeably less at the higher carbon fraction. At 130°C, there is a noticeable change in the spectra between 5:2 and 5:4 PVdF:carbon ratio. Finally, at 180°C drying temperature, the spectra looks the same for all three compositions. Thus, crystallinity can be improved for high carbon content binders if the drying is performed at high temperatures.

It thus appears that the addition of carbon to the slurry may impede the formation of polymer crystallization and promote the formation of β -phase over α -phase. We've measured β -phase to be more conductive of lithium ions than α -phase but that the α -phase is more mechanically favored. Because we have previously seen an impact on performance based on mixing order of components, we decided to investigate the order in which the high-surface area carbon is added to the slurry.

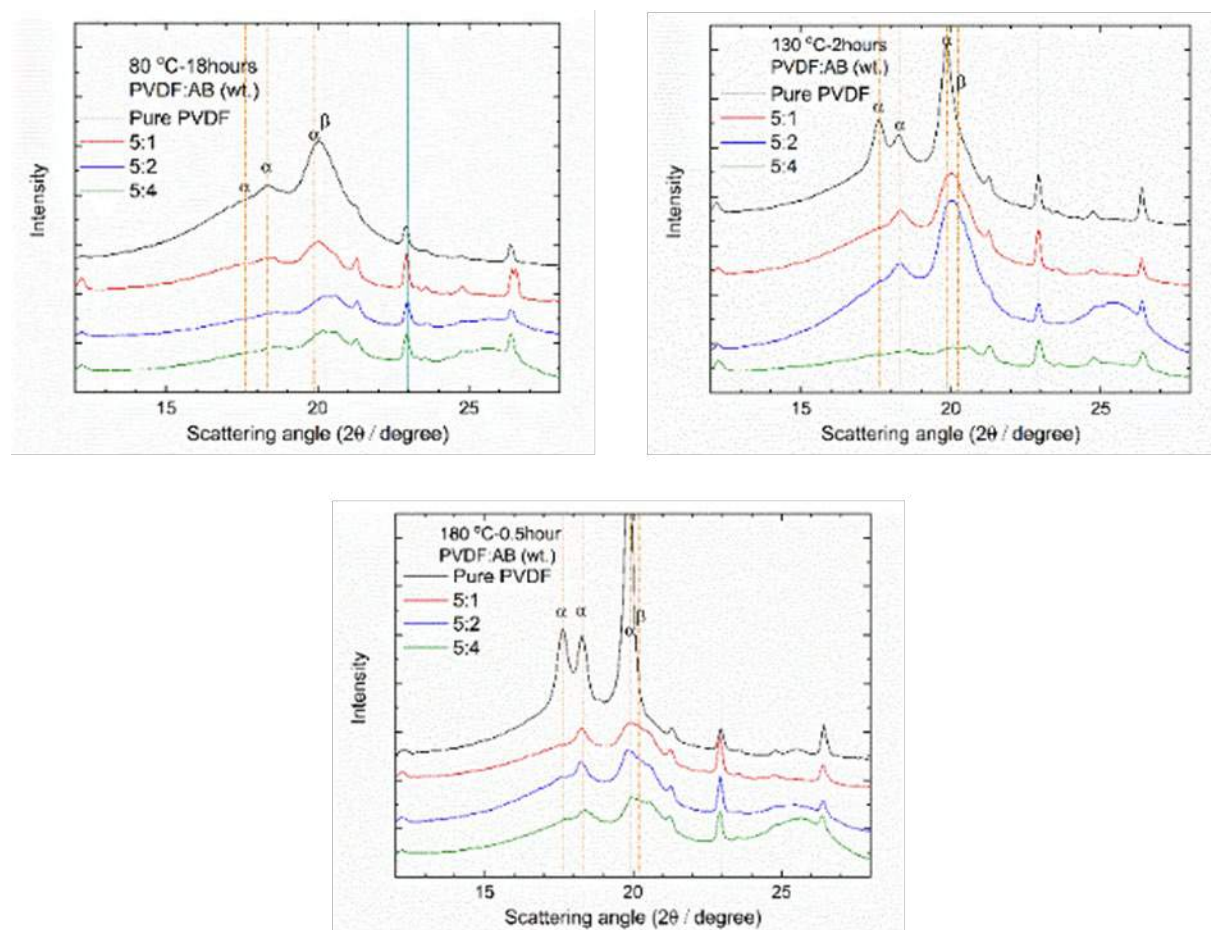


Figure I.2.N.3 The spectroscopic results of x-rays taken of films prepared with different levels of carbon black dried at different temperatures. The ratio of PVdF to carbon black is indicated in the insets as zero carbon, 5:1, 5:2, and 5:4. The films were dried at 80, 130, or 180 °C

In one slurry, we mixed the carbon and active material together in NMP, then added solubilized binder to the mix (referred to as the Solids process); in another, we mixed carbon and solubilized binder together and then added the active material (referred to as the Glue process). Laminates were then cast of the slurries, dried at different temperatures, and their properties measured. The result of drying the electrodes at high temperatures are shown in the SEMs of Figure I.2.N.4. The film on the top of Figure I.2.N.4 was dried at 170 °C. It took less than 4 minutes to dry but showed significant cracking. The film on the bottom of Figure I.2.N.4 was dried at 180 °C. It took 12 minutes to dry but showed no visible cracking. The rheology of the slurries indicated that the Solid process has a higher viscosity than the Glue process, which suggests that the solid process leads to a more uniform slurry or one where the carbon agglomerations were more broken down to some extent but maintained a structure of strands connecting nanoparticle to nanoparticle. Alternatively, the slurry from the Glue process resulted in larger agglomerates of carbon black that was less broken down. The larger agglomerates of binder and carbon contain more of the solvent, which reduces the rate of drying. On a positive note, the slower rate of drying appears to stop the cracking. In the past we've shown that the solids process leads to better long-term cycleability than the Glue Process, which suggests better mechanical properties coming from the Solids process.



Figure I.2.N.4 The film on the top was formed from the Solids process and dried at 170°C; the film on the bottom was formed from the Glue process and dried at 180°C. The film on the left dries in 4.5 minutes but shows cracking; the film on the right dries in 12 minutes but shows no cracking

The sum of this research appears to point to a possible optimization of the mixing that would incorporate both processes – mixing the carbon with the soluble binder and with the active material and then a mix of the two. Drying at different temperatures for different lengths of time should also have an impact. The goal will be to produce a highly functional, thick electrode that is dried in under three minutes.

In the third quarter we focused most of our effort on what we referred to as process IV, which is a combination of the solid and glue mixing processes where 25% of the carbon was premixed with the active material and the other 75% premixed with the polymer. Those two solutions were then mixed together. The slurry was then cast and dried at different temperatures, ranging from room temperature up to 180°C. SEM of an electrode dried at 150 °C is provided in Figure I.2.N.6. If one looks closely, one can see islands of agglomerated carbon nanoparticles sparsely covering the large secondary cathode particles. Electrodes of this material were tested in half cells and an HPPC test run to establish the resistance of the electrodes produced under different drying temperatures *versus* depth of discharge, Figure I.2.N.5.

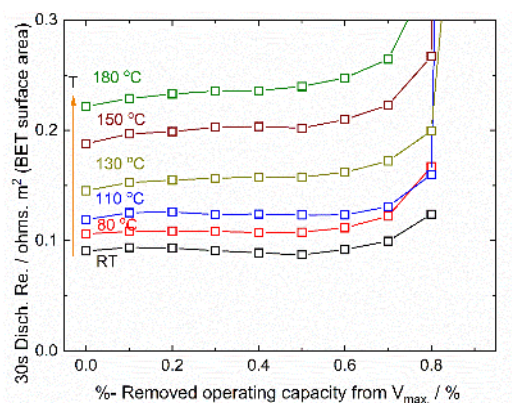


Figure I.2.N.5 Resistance of the electrodes dried at different temperatures versus depth of discharge for 30 second discharge pulses

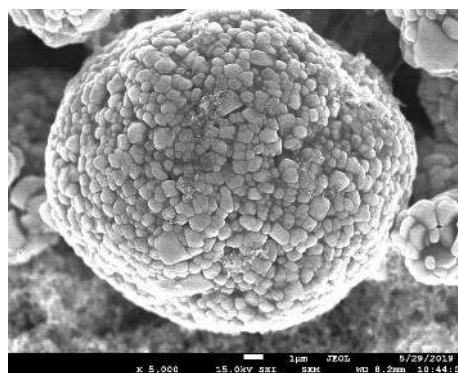


Figure I.2.N.6 SEM of electrode surface.

The data are similar to the data seen for electrodes where the impedance rises with drying temperature; however, for these electrodes the rise in impedance was more gradual with temperature.

In the final fraction of the year, we repeated our work on the hybrid processing but with even thicker electrodes. Results are pending. We have also gone back to investigate the impact of polymer crystallinity

versus carbon content in order to directly measure the impact of crystallinity in the electrode on electrolyte transport *and* mechanical strength. Also, a second set of polymer film experiments are being conducted to assess polymer morphology and function as it depends upon the rate of cooling.

Conclusions

The experiments conducted this year clearly indicate that the quality of a thick electrode will highly depend upon the breakdown of the carbon aggregates and the final crystal structure of the polymer binder. The former can be highly impacted by the order of mixing and the probably by the shear rate of mixing. To date, all of our experiments have been conducted *via* a spindle run at 3000 rpm, which translates to a shear rate of $2\pi f = 314 \text{ s}^{-1}$. Moving forward we plan to investigate the impact of mixing shear rate on slurry rheology and ultimately electrode performance. Our experiments with drying temperature indicate that there is a significant impact on polymer crystallinity, which in turn impacts the electrode mechanical properties and electrochemical performance properties. This can also be impacted by the carbon configuration and level of deaggregation. Further experiments are needed to better understand how different modes of mixing and drying can lead to robust, thick electrodes with low impedance that can be dried in three minutes or less.

Acknowledgements

The PI would like to acknowledge the efforts of Yanbao Fu and Xiangyun Song, wholly responsible for the work presented here.

I.2.0 Novel data-mining and other AI approaches for synthesis and processing of cathode materials (LBNL)

Gerbrand Ceder, Principal Investigator

Lawrence Berkeley National Laboratory
One Cyclotron Road, Bld. 33, Rm. 142B
Berkeley, CA 94720
E-mail: gceder@lbl.gov

Peter Faguy, DOE Technology Manager

U.S. Department of Energy
E-mail: Peter.Faguy@ee.doe.gov

Start Date: January 1, 2019
Project Funding (FY19): \$200,00

End Date: September 30, 2022
DOE share: \$200,000

Non-DOE share: \$0

Project Introduction

A major obstacle to large-scale manufacturing and utilization of advanced materials arises from the inability to devise synthesis methods for materials in a rational manner. This is an issue for novel predicted materials, which have never been synthesized, as well as for existing materials, which often have to be synthesized in a particular particle form, with particular surface chemistry, or with very targeted structure and composition, in order to have optimized behavior in the dispersions used to cast electrodes.

To bridge the gap between materials prediction and production, we envision the following for this project:

- 1) An automatic materials synthesis design solution, which employs machine-learning approaches to learn synthesis concepts from scientific publications, and design efficient synthesis routes for novel materials.
- 2) Predictive tools which can modify a synthesis method to achieve optimal particle size, shape and surface chemistry for a given application and performance requirement.

Objectives

Use Machine Learning and First Principles Calculations to develop the ability to predict the appropriate synthesis routes for battery cathode materials, their surface chemistry and their interaction with solutions.

Approach

The project will be approached in two aspects.

1. **Automated materials synthesis design solution.** Our objective is to extract all known synthesis methods for battery cathode materials from publications and patents, organize them, make them available, and use them for machine learning of novel synthesis recipes. In order to obtain details of synthesis procedures from publications and convert them into a machine-readable format, we developed a data mining pipeline which uses machine learning techniques to retrieve “codified synthesis recipes” of inorganic compounds from available scientific publications. The most important steps of pipeline include: i) collecting research articles available online using our own web scraper; ii) extraction of experimental sections and identification of paragraphs describing ceramics synthesis, made in unsupervised way by using topics modeling approaches; iii) extraction of so-called “codified recipes” of the synthesis procedures which include final product, starting materials, operations and conditions of synthesis; iv) accumulating all recipes in the database and their subsequent mining.
2. **Optimization of particle shape, size and surface chemistry.** The geometry and surface chemistry of oxide particles is important for their behavior in solution when they are cast into electrodes, and for the ultimate electrochemical performance of the cast electrode. Our objective is to design the modeling tools to predict the shape and size of particles, and their surface chemistry as function of

applied synthesis conditions (synthesis from solution or solid-state synthesis). This will be critical inputs for higher length scale models used to predict casting behavior of electrodes.

Results

A complete data pipeline for extracting synthesis information from literature

We have developed a fully functional data-mining pipeline that downloads online journal articles and extracts synthesis information from natural language text. The input data of this pipeline include 4.1 million articles downloaded from 8 major publishers: Elsevier, Royal Society of Chemistry, Nature Publishing Group, Wiley, Springer, American Chemical Society, American Physical Society, and the Electrochemical Society. To parse articles in HTML/XML format, we developed a markup parser that is capable of parsing these 4.1 million articles into 100 million plain text paragraphs. Using a semi-supervised machine learning approach consisting latent Dirichlet allocation and random forests, we have classified and identified around 190k synthesis paragraphs in four categories: conventional solid-state synthesis, sol-gel precursor synthesis, co-precipitation synthesis, and hydrothermal synthesis, all of which are typical preparation methods for battery materials.

To extract and codify synthesis information written in the natural language text, we have built an extraction pipeline. The extraction pipeline contains 5 components:

- We implemented a Bi-Directional Long-Short Term Memory Neural Network with a Conditional Random Field layer (BiLSTM-CRF) to read the paragraphs and extract starting materials and final products of each reaction.
- We implemented an algorithm consisting of a Neural Network and natural language Sentence Dependency tree analysis to identify key experimental steps of each synthesis, such as “mixing”, “heating”, “drying”, “shaping”, and “quenching”.
- We used Regular Expression and a keyword-based screening method to find the synthesis conditions for each experimental step, such as time, heating temperature, and heating atmosphere.
- We developed a Materials Parser that converts ambiguous forms of materials descriptions, such as chemical formulas, material names, doped materials, abbreviations, into a unified data structure.
- We created codes for balancing valid solid-state synthesis Reaction Equations using the starting materials and final products based on symbolic linear algebra manipulation libraries.

To evaluate the performance of our developed data extraction pipeline, we performed similar data extraction tasks by human. Human extraction results are retreated as the “ground truth” to estimate extraction precision (number of correct items in all extracted data). We found that the extraction precision for starting materials, final products, and balanced synthesis equations are 97%, 99%, and 95%. The extraction precision for experimental steps and experimental conditions are 86% and 82%. These results indicate our extraction pipeline successfully extracts relevant synthesis information in a high accuracy.

A database of solid-state synthesis reactions and battery materials

We maintain a database of solid-state synthesis reactions automatically compiled by the above data pipeline. As of November 2019, the current database consists of $\approx 30,000$ reactions. Although the database extracts synthesis reactions on all inorganic materials, a considerable amount of the reactions is related to battery materials research. Table I.2.O.1 shows the amounts of reactions of various Li-ion battery materials in our database. The total number of Li-ion battery related materials is more than 3000, making our database an important data source for building machine-learning synthesis prediction models of battery materials.

Table I.2.O.1 Amounts of Reaction of Various Well-researched Li-ion Battery Materials

Material	Type	Compositions	Reactions in DB
LMO	Cathode	Li Mn O	357
LCO	Cathode	Li Co O	104
NMC	Cathode	Li Ni Mn Co O	778
LFP	Cathode	Li Fe P O	204
NCA	Cathode	Li Ni Co Al O	7
LTO	Anode	Li Ti O	204
Li-materials	/	Containing Li O	3341

Case study: data-mined synthesis insights for NMC cathodes

NMC cathodes (cathodes that have Li, O elements as well as various compositions of Ni, Mn, and Co) are a well-studied type of battery materials in our database. As shown in Table I.2.O.1, more than 700 NMC synthesis reactions have been extracted from more than 700 unique journal articles. Our data-mined database contains synthesis information, such as sequences of experimental steps, experimental conditions, sintering temperature and time, enabling us to perform big-data and machine learning analysis for NMC cathodes.

Table I.2.O.2 shows the most common precursors and their frequencies of occurrence in NMC cathode syntheses in our database. LiCO_3 is by far the most commonly used Li precursor. Oxides of Ni, Mn, Co are more frequently used than their hydroxides, carbonates, nitrates, and acetates. Note that we reckon the first most common precursor is often used for its abundance, not necessarily for its better results. Nevertheless, precursor distributions in Table I.2.O.3 can serve as a starting point for a machine predicted NMC cathode synthesis route.

Table I.2.O.3 Most Common Precursors and Occurrence Frequencies for NMC Cathodes

Li precursors	Ni precursors	Mn precursors	Co precursors
LiCO_3 (2323)	NiO (175)	MnO_2 (232)	Co_3O_4 (155)
$\text{LiOH}\cdot\text{H}_2\text{O}$ (298)	Ni(OH)_2 (80)	MnCO_3 (188)	CoO (32)
LiOH (184)	$\text{Ni(CH}_3\text{COO)}_2\cdot x\text{H}_2\text{O}$ (39)	Mn_2O_3 (117)	$\text{Co(CH}_3\text{COO)}_2\cdot x\text{H}_2\text{O}$ (28)
LiNO_3 (107)	$\text{Ni(NO}_3)_2$ (35)	$\text{Mn(CH}_3\text{COO)}_2\cdot x\text{H}_2\text{O}$ (58)	CoCO_3 (26)
LiF (61)	NiCO_3 (22)	MnOOH (31)	$\text{Co(NO}_3)_2$ (22)

Figure I.2.O.1 shows the distribution of temperatures and atmosphere used in the synthesis of NMC cathode materials as a function of the Ni content in the NMC. The color of each point represents the sintering atmosphere. While there is a lot of scatter in the data the trend that higher Ni content materials require lower synthesis temperature and more oxidizing conditions clearly emerges, consistent with the fact that Ni needs to be oxidized to Ni^{3+} .

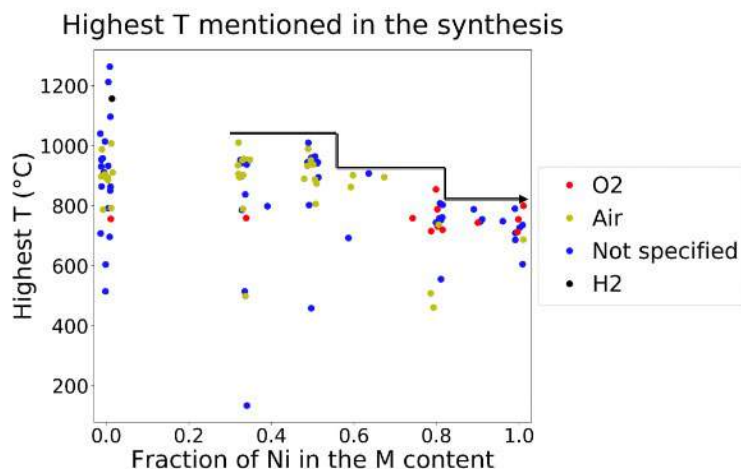


Figure I.2.O.1 Sintering temperature versus fraction of Ni in M content for various NMC cathode materials found in our solid-state synthesis dataset. As shown by the plateaus, high Ni content NMC materials have to be sintered at lower temperatures and often use O₂ instead of air as the sintering atmosphere.

Developing a framework for cathode synthesis prediction

A machine learning framework of materials synthesis requires a proper set of numerical representations, or features of materials and synthesis routes. While a few representations have been studied and benchmarked in the machine learning synthesis prediction field, no successful features exist for cathode materials. To fill this gap, we started by incorporating our synthesis database with several materials features that convert synthesis product materials into numerical vectors:

- Linear combinations of elemental material features.
- Linear combinations of materials word embeddings.
- Neural Network representation of materials learned by multi-task learning developed in our group.

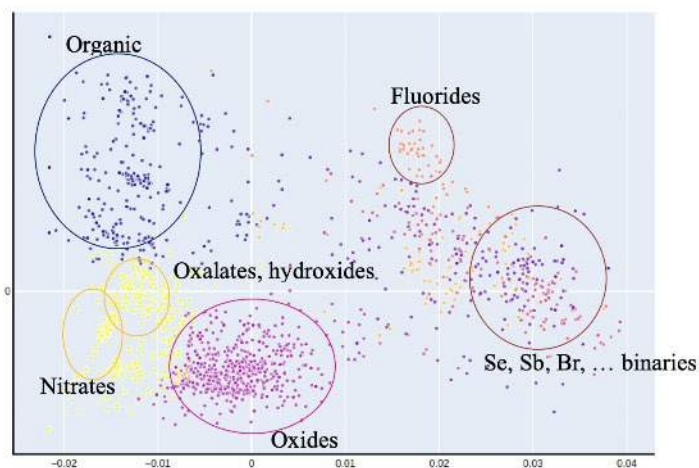


Figure I.2.O.2 K-means clustering of synthesis products in our database with the developed features. Materials with different chemistry are clustered into different groups in the feature space

As shown in Figure I.2.O.2, our preliminary K-means clustering results show the features allow computers to capture and group synthesis products by their chemistry. Materials that belong to similar categories, such as oxides, nitrates, etc., are clearly found to be in the same clusters. While the features are currently still being

developed and benchmarked, they are necessary input parameters of prediction models for cathode materials synthesis.

Conclusions

During the first year of this project, we have successfully implemented a synthesis information extraction pipeline, and extracted a 30k solid-state synthesis database. More than 3000 reactions in our database synthesize Li-ion cathode materials and will be used as training data to machine-learn Li-ion cathode synthesis prediction models.

We made preliminary attempts on the cathode synthesis prediction problem. The NMC cathode synthesis data demonstrate that patterns existing in our synthesis database can be mined and reveal synthesis knowledge. To machine-learn this knowledge, we have developed feature representations of materials, upon which cathode materials synthesis predictors will be built in the future.

Key Publications

No publications yet.

I.2.P Minimizing Side-Reactions in Next Generation Lithium Ion Battery Cathodes Through Structure-Morphology Optimization (ANL)

Venkat Srinivasan, Principal Investigator

Argonne National Laboratory
9700 S Cass Avenue
Lemont, IL 60439
E-mail: vsrinivasan@anl.gov

Hakim H. Iddir, Principal Investigator

Argonne National Laboratory
9700 S Cass Avenue
Lemont, IL 60439
E-mail: iddir@anl.gov

Peter Faguy, DOE Technology Development Manager

U.S. Department of Energy
E-mail: Peter.Faguy@ee.doe.gov

Start Date: October 1, 2018

End Date: September 30, 2019

Project Funding (FY19): \$460,000

DOE share: \$460,000

Non-DOE share: \$0

Project Introduction

The goal of this project is to improve the performance of next-generation Li-ion battery cathodes by synergistically tuning the structure of the cathode along with its morphology. Understanding the densification behavior of LLZO type oxide based ceramic SSEs, and how that improves its overall conductivity, is another major aim of this project. Improvement in performance will be achieved by developing multi-scale theoretical methods, coupled with in situ operando experimentation to create a one-of-a-kind “particles by design” framework. This framework will go beyond the traditional “materials by design” approach used today, wherein the focus is on calculating material crystal structure, by incorporating morphological features to create particles in which the exposed surfaces are tuned to maximize performance. In the first year, we focused on the carbonate based coprecipitation process for making cathode precursors, and high temperature calcination process for making cubic-LLZO solid-state electrolytes (SSEs). NMC352-carbonate and Mn-carbonate was coprecipitated to understand the growth process of these carbonate cathode precursors. For SSEs, LZO ($\text{La}_2\text{Zr}_2\text{O}_7$) precursors were heated with Li_2CO_3 to form LLZO at high temperature conditions to understand the growth process of LLZO particles during the formation step. Understanding the evolution of particle morphology during the synthesis of cathode precursors and SSEs will help to improve the performance of next generation lithium ion batteries.

Objectives

The overall objectives of this project can be divided into two parts. The first component deals with the investigation of the impact of solution pH, ammonia content, and transition metal concentration on the size, shape, porosity, tap density and facet dependent reactivity of cathode precursors during the coprecipitation process. As a part of this task we aim to determine the equilibrium Wulff shape and corresponding surface energies of cathode precursors and final lithiated oxide materials. We also aim to elucidate the impact of thermodynamic and kinetic factors in determining the size and shape of primary and secondary particles. In the second task of the project, the main objective is to understand the densification and grain growth mechanism observed during the sintering of LLZO pellets. To accomplish this, we will develop a phase-field based mesoscale models capable of capturing the sintering process between multiple LLZO particles. We will also experimentally measure the densification and growth of LLZO particles during the sintering process.

Approach

To understand how the structure and morphology of cathode and electrolyte particles evolve during the synthesis steps, experimental techniques as well as computational methodologies have been developed. Attempts have been made to establish good correlation between the two for proper elucidation of the physical and chemical phenomena that controls the structure and morphology of these battery particles. For the coprecipitation of NMC352 carbonate precursors, the conventional CSTR reactors have been used. The pH has been maintained at 8.3, and Na_2CO_3 was used as the source of carbonate ions. Transition metal sulfate acted as the source of metal cations within the solution. The coprecipitation of MnCO_3 was conducted in a beaker with stirring speed 500 rpm, and NH_4HCO_3 was used as the source of carbonate ions. During the coprecipitation of MnCO_3 , mili-molar concentrations of the transition metal were used. In the CSTR, the reactants were added in a drop-by-drop fashion, whereas, in the beaker all the reactants were added all together. This led to much higher initial concentration of the reactants within the reacting solution. Calcination of the LZO with Li-carbonate was conducted in an in situ setup at APS to understand the reaction mechanism that leads to the formation of cubic-LLZO. The powders were held in an alumina capillary, which was heated by flowing hot helium gas through it. During the calcination step, the evolution of LLZO particle size was extracted from the width of the x-ray diffraction peaks. Elucidation of the densification of LLZO particles has also been attempted using similar in situ setup.

From the computational modeling perspective, both atomistic as well as continuum level schemes have been developed for capturing the formation and growth of carbonate based cathode precursors (MnCO_3) as well as LLZO SSEs. All the atomistic calculations were conducted by spin polarized density-functional-theory (DFT) as implemented in Vienna Ab Initio Simulation Package (VASP). Exchange correlation potentials were treated by generalized gradient approximation (GGA). Interaction between valance electron and ion core have been implemented as described by the projected augmented wave (PAW) method. In the mesoscale level, continuum based mass balance equations have been solved to capture the growth of precipitated particles, as well as to predict the densification and sintering of LLZO particles. Phase field based techniques have been used for capturing the sharp interface observed in both the systems. The facet dependent growth of primary particles has been captured in the coprecipitation model. However, the impact of different surface energies along the various crystal facets has not been taken into account in the LLZO sintering model. Competition between reaction rate, surface diffusion and grain boundary mobility dictates the final shape and size of the cathode and SSE particles.

Results

We tried to understand the physico-chemical phenomena that occurs during the synthesis of carbonate based cathode precursors, as well as the sintering of LLZO SSEs. The results obtained for both the studies are summarized below.

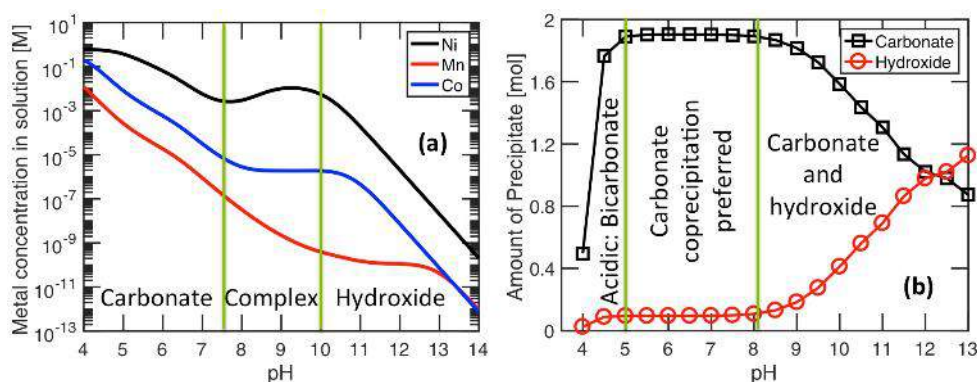


Figure I.2.P.1 (a) During coprecipitation of NMC352 carbonates, the residual amounts of metal cations within the reacting solution at different values of pH are shown. (b) Comparison between the amount of carbonate and hydroxide precipitates at different values of pH. In order to minimize the amount of hydroxide precipitates, coprecipitation of carbonates must be conducted at a pH range between 5 and 8.5

Carbonate cathode precursor synthesis: Equilibrium equations have been solved to determine the suitable range of pH where coprecipitation of carbonates should be conducted. Figure I.2.P.1(a) demonstrates the residual amount of metal cations within reacting solution. Figure I.2.P.1(b) compares the magnitude of carbonate and hydroxide precipitates with increasing solution pH. It is evident that coprecipitation of carbonates must be conducted at $\text{pH} < 8.5$ in order to minimize the extent of hydroxide precipitates. Also, at higher pH (> 8.5), more metal ammonia complex is formed with Ni, and the stoichiometry of the NMC cathodes may change. Also, coprecipitation of carbonates is not desired at $\text{pH} < 5$, because at such acidic environments, not enough metal carbonates precipitate and majority of the CO_3^{2-} ions react with H^+ to form bicarbonates.

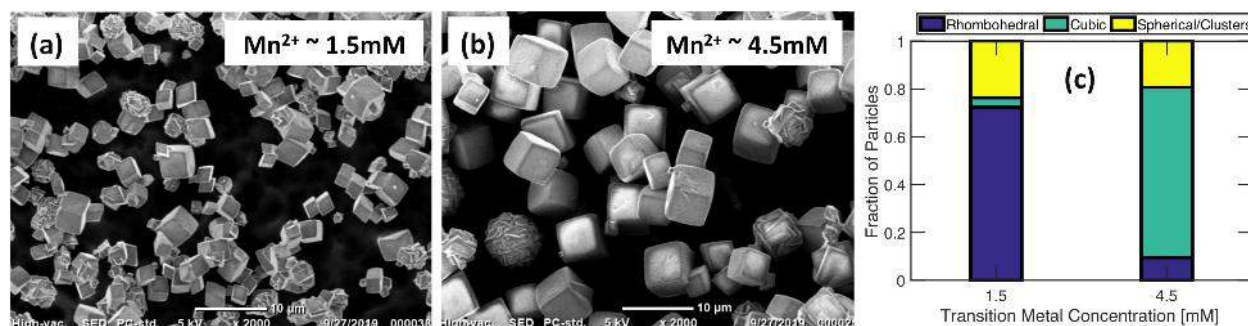


Figure I.2.P.2 (a) SEM image of precipitated MnCO_3 particles obtained with 1.5mM concentration of Mn^{2+} . (b) SEM image of precipitated MnCO_3 particles obtained with 4.5mM concentration of Mn^{2+} . (c) Bar chart demonstrating the fraction of rhombohedral, cubic and spherical particles observed at 1.5mM and 4.5mM concentrations of manganese. The relative fractions of various particles have been obtained from simple visual inspection. It is evident that more rhombohedral particles evolve at 1.5mM concentration, whereas, more cubic particles form at 4.5mM concentration of Mn^{2+} cations

In order to understand the growth of carbonate based cathode precursors, we conducted simple coprecipitation experiments of MnCO_3 in simple beakers, which was stirred at 500 rpm using magnetic stirrers. Consistent with the results reported in Figure I.2.P.1, pH of the solution was maintained at 7.5 during the coprecipitation of metal carbonates. SEM image of the resulting particles are shown in Figure I.2.P.2, which clearly reveals that at lower concentration of Mn^{2+} , rhombohedral particles evolve, whereas, at higher concentrations, cubic shaped particles are formed. Some spherical clusters are observed at both the concentrations, which can be attributed to local inhomogeneity in concentration due to improper mixing of the reactants. Next, we try to understand this transition in particle shape with increasing metal concentration within the solution. Based on DFT based atomistic calculations, it is evident that MnCO_3 type particles should demonstrate minimum surface energy along the (102) plane. The Wulff shape of particles surrounded by (102) planes takes a rhombohedral shape, which is clearly demonstrated in Figure I.2.P.3. Also, according to DFT calculations, the surface energy of these (102) facets is estimated to be 1.05 J/m^2 . At lower concentrations of Mn^{2+} ($\sim 1.5\text{mM}$), growth of the particles occur according to a thermodynamically equilibrium condition. Hence, the minimum energy rhombohedral shape of the metal carbonate precursors is obtained at lower concentrations of transition metal cations.

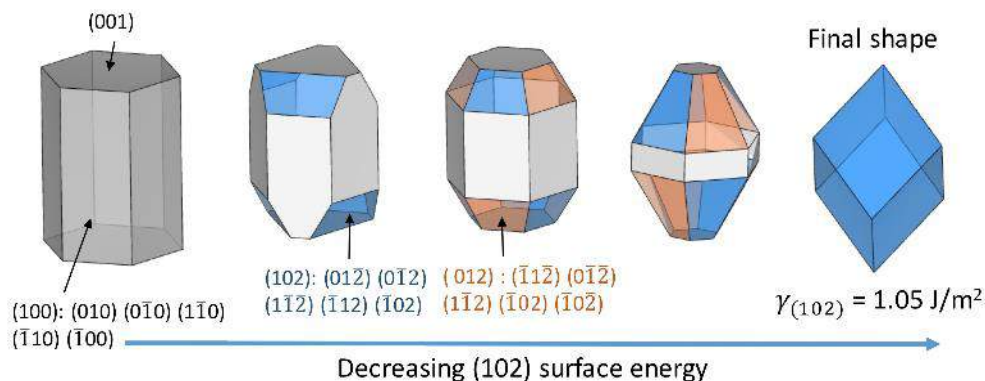


Figure I.2.P.3 As the free energy for the (102) surface decreases, the equilibrium shape converts from a hexagonal unit cell to a rhombohedral particle. The surface energy of the rhombohedral particles is 1.05 J/m²

Experimentally, it has also been observed that as the concentration of metal cations increase from 1.5mM to 4.5mM, the shape of the particles change from rhombohedral to cubic. DFT based atomistic calculations revealed that the Wulff shape of a particle surrounded by (103) surfaces can demonstrate a cubic shape. Such a cubic particle is shown in Figure I.2.P.4(a). For MnCO₃, there does not exist any particular (103) facet. However, by combining a series of (102) facets and defects in the form of jumps in between them, it is possible to form a (103) facet. It is also clearly demonstrated in Figure I.2.P.4(b) that with increasing Mn²⁺ concentration within the reactor, the surface energy of the (103) facet decreases to a level even smaller than the energy of (102). Hence, certain high concentrations of Mn²⁺ do stabilize the (103) facets, and eventually the cubic shape of MnCO₃ particles, and the precipitation at 4.5mM concentration of metals reside within this range. However, please note that this cubic shape with (103) facets do contain defects on top of the surface, and it is not a stable equilibrium, rather a metastable one.

Solving the non-conserved phase field models using the Allen-Cahn equations, growth of these MnCO₃ primary particles have been captured. Evolution of concentration within the reacting solution has also been predicted.

Figure I.2.P.5 clearly demonstrates that at smaller concentrations of Mn²⁺, the rhombohedral shapes are preferred. The cubic shapes become favorable at higher concentrations, such as, 3.0mM. This transition in shape of the particles is attributed to the competition between rate of reaction on top of the surface, and surface diffusion of the atoms/ions on the particle surface that leads to the thermodynamically equilibrium rhombohedral shape. At lower supersaturation ratios, the rate of reaction is slow enough, such that the atoms/ions can diffuse on top of the primary particles to obtain the equilibrium rhombohedral shape. However, at higher supersaturation ratios, the reaction rate is extremely high. Arrival of new atoms is much faster than the distribution of those atoms through surface diffusion process. Hence, the atoms/ions do not have sufficient time to reorganize themselves to form the thermodynamically equilibrium rhombohedral shape. Rather, it gets stuck in an intermediate cubic shape, which consists of

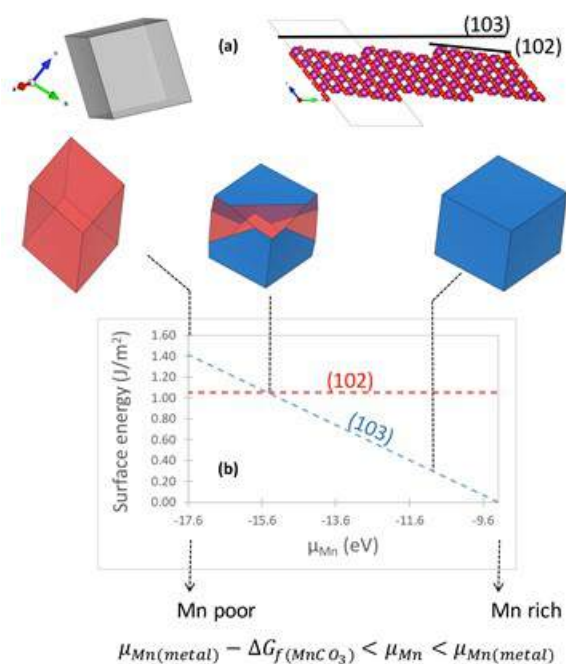


Figure I.2.P.4 (a) Cubic shape of the MnCO₃ particles can be obtained with (103) facets. (b) At higher concentrations of Mn²⁺, the (103) facets demonstrate lower surface energy as compared to the (102) facets, which indicates that the cubic shape is favorable during coprecipitation at 4.5mM concentration.

equilibrium (102) facets along with some jumps/kinks/defects. This metastable (103) covered cubic shape also demonstrates lower surface energy than the (102) facets at higher concentrations of Mn^{2+} . The corresponding variation in salt concentration within the reacting solution is also provided in Figure I.2.P.5(c) and Figure I.2.P.5(d). Since the concentration of salt remains well above the solubility limit, it is evident that the growth of these particles occurs in a rate-limited fashion. Transport limitation within the reacting solution is not observed. This can be attributed to the higher diffusivity of cations within water and relatively smaller domain size.

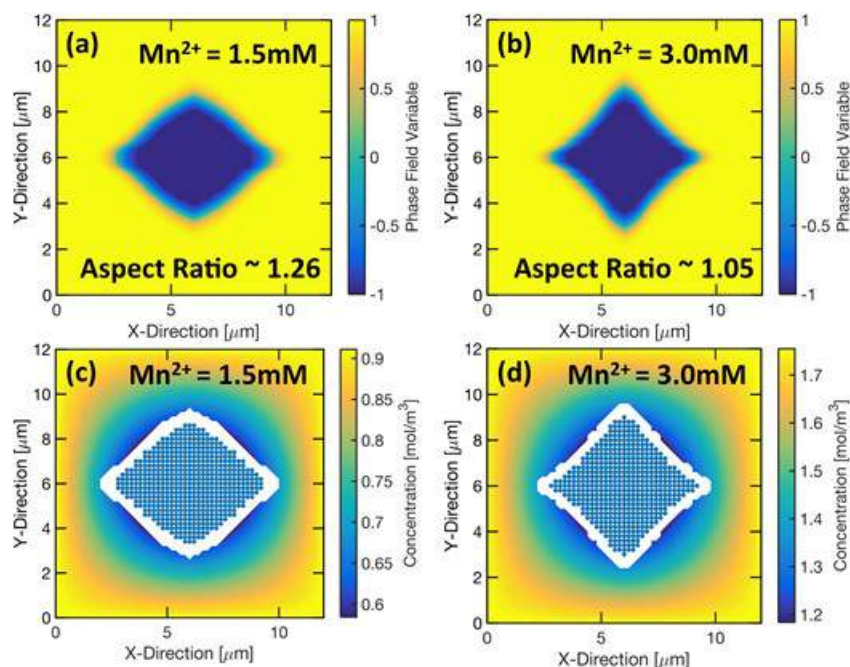


Figure I.2.P.5 (a-b) Phase field variables indicating the shape of the MnCO_3 particles obtained at 1.5mM and 3.0mM concentrations. It is evident that the aspect ratio decreases from 1.26 to 1.05 with increasing metal concentration within the reacting solution. (c-d) Variation in salt concentration within the reacting solution around the growing particle at metal concentrations of 1.5mM and 3.0mM

The next question that arrives is what limits the size of these MnCO_3 particles. To provide a reasonable answer, in Figure I.2.P.6 we plot the time dependent increase in particle size and change in particle growth rate, as observed during precipitation with metal concentration of 4.5mM. It is evident that initially these particles grow very fast, then their growth rate stabilizes, and towards the end it slows down substantially. Decrease in growth rate is attributed to the drop in salt concentration within the reacting solution. As the particles grow, they consume reactants from the solution, and the available amount of reactants within the solution decreases. This slows down the growth of the particles. Eventually, when the ion concentration within the solution becomes very small, the growth rate decreases, and the particle cease to grow in size. The experimentally observed final size of the particle is also shown in Figure I.2.P.6 by the blue cross symbol. There exist very good correlation between the computational prediction and the experimental observation. This clearly indicates that the particle growth is

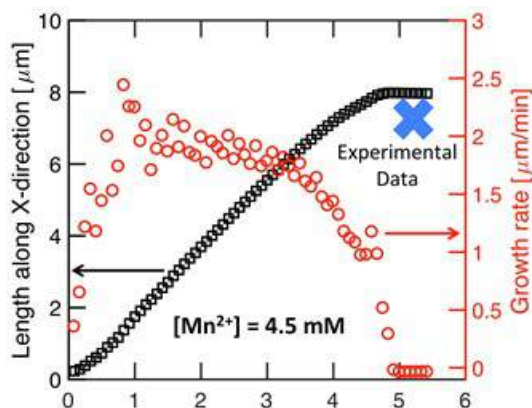


Figure I.2.P.6 Growth of particle size with time as observed for the initial metal concentration of 4.5mM. The growth rate is also denoted by the red circles, which clearly indicates that at longer times, the growth rate decreases substantially. The experimentally observed size of the final particle is denoted by blue cross.

indeed limited by the lack of reactants, and stirring induced shear force does not have a huge impact in limiting the size of these MnCO_3 particles.

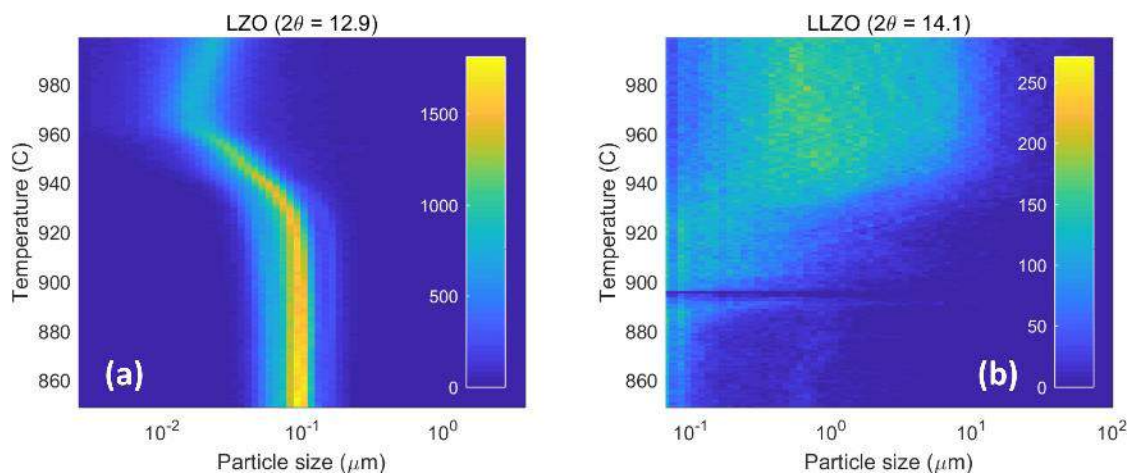


Figure I.2.P.7 (a) Evolution in size of the LZO precursors with increasing temperature. These LZO particles convert to cubic-LLZO. (b) Formation of LLZO and increase in their particle size is demonstrated. Major growth happens within 870°C to 950°C. Beyond 960°C, the size of LLZO particles almost stabilizes

Densification of LLZO cathode particles: As the second task of this project, we looked into the formation and densification of LLZO particles. Usually, LLZO is synthesized by mixing LZO with some lithium source (usually Li_2CO_3), and then heated to high temperatures ($\sim 800^\circ\text{C}$ to 1000°C). This causes the lithium carbonate to decompose and release Li, which then reacts with the LZO to form LLZO particles. It is important to understand that LLZO may exist in tetragonal or cubic form, and some dopants are usually used to stabilize the cubic phase that demonstrates much higher ionic conductivities. Figure I.2.P.7 shows the formation of cubic-LLZO particle from a mixture of LZO and lithium carbonate. The growth of LLZO particles during the formation process is successfully captured here. Please note that, the initial LZO particles are in the nanometer range. However, the final LLZO particles grow substantially larger during the formation process, and the size of the final cubic-LLZO particles are around 500nm to 1micron. A continuum based phase field model has been developed to capture the sintering of LLZO particles. We use the same scheme to understand the growth of LLZO particles during the formation process. The comparison between computational and experimental results regarding the growth of LLZO particles is shown in Figure I.2.P.8. A decent correlation between the two indicates that the developed computational model can capture the particle growth process to certain accuracy. The evolution of particle microstructure is also demonstrated in the surrounding images in Figure I.2.P.8. Towards the end, even though the particles look very dense, there still exists voids at the surface, and it is far away from the relative density observed in this type of freshly formed LLZO particles. To capture the realistic density, even more number of particles should be used. Please note that activation energy of 260kJ/mol has been used to capture the particle size growth during the LLZO formation process.

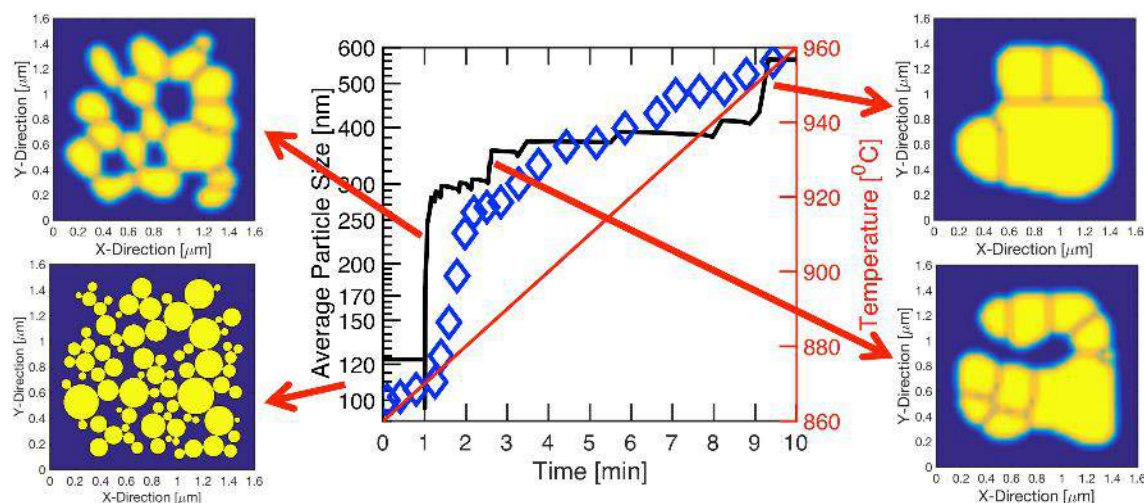


Figure I.2.P.8 Comparison between the experimental (blue diamond) and computational (black solid line) results for particle growth observed in LLZO during the formation step of synthesis. The red line indicates increase in temperature over 10 minutes from 860°C to 960°C. Location of the particles and corresponding grain-boundary domains, as predicted by the phase field based computational model, are also shown

In general, the as formed LLZO particles are 2 microns to 5 microns in size, and pellets are formed out of them, which are later densified (through high temperature sintering) to minimize the volume fraction occupied by pores. We developed computational methodologies at the mesoscale level to capture the densification process observed at higher temperatures, and used it to analyze the impact of particle size and size-distribution on the overall densification process. Comparing with experimental results obtained from literature, the activation energy of LLZO densification has been estimated to be ~ 330 kJ/mol. Using this number, we studied the densification experienced by small, large, and bimodal shaped LLZO particles. The results are shown in Figure I.2.P.9, where densification has been conducted for 8 hours, including the time taken to heat-up the sample. Maximum tendency to densify has been observed in bimodal shaped particles. The large particles experienced the least amount of densification. Whereas, the small particles did show quick initial densification, but once they grew large, their tendency to densify decreased. From this analysis, we can conclude that maximum densification is observed within the bimodal shaped particles. Hence, bimodal particles within the LLZO pellet can lead to higher relative density, and subsequently higher ionic conductivity.

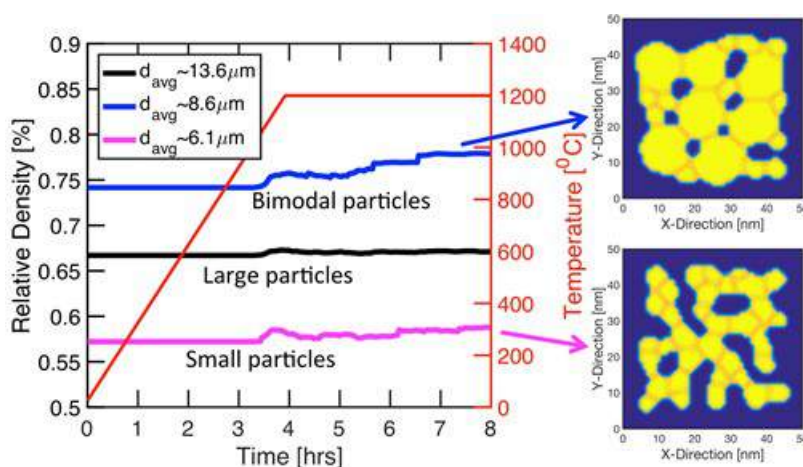


Figure I.2.P.9 Comparison of densification observed in small, large and bimodal shaped LLZO particle. It is evident that bimodal particles experience the maximum amount of increase in relative density, and large particles densify very slowly. The corresponding particle microstructures for the small and bimodal particles are shown in right side images

Conclusions

In the present project, we tried to understand the growth process of MnCO_3 precursor particles and studied the densification observed in LLZO during the sintering step. Based on our study, we arrived at the two following conclusions:

1. Growth of MnCO_3 precursors is governed by the concentration of metal cation within the solution. At lower concentrations, the particles can adopt the thermodynamically equilibrium rhombohedral shape. However, as the concentration of reactants increase within the solution, growth rate of the particles overrun the surface diffusion of atoms on top of the particles. This leads to the formation of other cubic type shapes that are locked in an intermediate metastable state. Also, growth of these primary particle ceases due to depletion of reactants from the reacting solution after long time operation.
2. During the formation of LLZO from LZO precursors, growth of the particles occur at a much faster rate as compared to the densification of LLZO pellets. Hence, the size of the as formed cubic-LLZO particles is in the micron range, even though the size of the LZO-precursors is around 100 nanometers. Further study on the densification behavior of the LLZO particles reveal that highest relative density of the LLZO pellets can be obtained by using bimodal particle size distributions.

Aggregations of particles, as observed in CSTR reactors, are being modeled right now. Also, new techniques are being developed to understand the particle densification under externally applied stress fields.

Key Publications

1. P. Barai, Z. Feng, H. Kondo, and V. Srinivasan. Multiscale Computational Model for Particle Size Evolution During Coprecipitation of Li-Ion Battery Cathode Precursors. *The Journal of Physical Chemistry B* 123 (15) 3291 – 3303.

Acknowledgements

We acknowledge Arturo Gutierrez and Jiajun Chen for their kind help in generating the MnCO_3 precursor particles following techniques adopted from published articles.

I.2.Q High Energy, Long Life Lithium-Ion Battery (NREL)

Kandler Smith, Principal Investigator

National Renewable Energy Laboratory
15013 Denver West Parkway
Golden, CO 80401
E-mail: Kandler.Smith@nrel.gov

Brian Cunningham, DOE Technology Development Manager

U.S. Department of Energy
E-mail: Brian.Cunningham@ee.doe.gov

Start Date: October 1, 2016
Total Project Cost: \$1,200,000

End Date: September 30, 2019
DOE share: \$1,200,000

Non-DOE share: \$0

Project Introduction

Energy-dense, long-life energy storage is needed to improve market readiness and enable higher penetration of electric vehicles. Today's state-of-the-art lithium-ion EV battery lasts around 10 years and provides just 100-250 miles range, both inferior to conventional vehicles. Across virtually all of today's Li-ion chemistries, Li loss capacity fade is the dominant mechanism that limits lifespan. High-energy Li-ion electrode materials presently under research and development (e.g., silicon) suffer even shorter life than today's materials because of large volume change during cycling that fractures electrode surface films and accelerates Li loss. In addition to lifetime challenges, large irreversible Li loss on the first cycle limits the beginning-of-life performance of these high-energy electrodes. To boost initial capacity, these materials presently require prelithiation as an extra manufacturing step, adding unwanted cost to the cell. This project seeks to overcome the barrier presented by limited useable Li inventory in order to enable higher energy, longer life batteries.

Objectives

The objective of the High-Energy, Long-Life Li-ion Battery (L3B) Project is to increase cycle and calendar lifetime of both graphite and silicon (Si) based Li-ion cells. For cells employing Si, the proposed technology will also increase initial capacity. The L3B device will be low cost, passively controlled, and occupy minimal weight and volume. Specific objectives include:

- Extend calendar and cycle life by 50% for Li-ion graphite/NMC (nickel-manganese-cobalt) and Si-X/NMC systems
- Re-lithiate the Si anode following formation cycle to increase Si-anode Li-ion cell energy density by 20%
- Design the Li reservoir and release-control device such that it adds less than 5% to the cost, weight, and volume of Li-ion cells, and is compatible with cell manufacturing and safety
- Use modeling and experiments to quantify the uniformity of lithium distribution throughout the cell at multiple rates of relithiation

Approach

The proposed objectives will be met by introducing an excess Li reservoir into Li-ion cells that can be released to boost capacity upon demand, increasing initial performance and extending lifetime. Different from previous concepts, the proposed technology is controlled by a passive internal circuit and can deliver a slow, continuous release of Li ions throughout the cell lifetime and/or a faster, triggered release of Li ions on demand. No third electrode or external circuitry is needed to control Li release. The device is projected to add less than 5% to the cost, weight, and volume of today's cells. In addition to extending lifetime, the device is a practical way to pre-

lithiate Li-starved systems to boost their initial capacity, addressing a present roadblock hindering commercialization of high-energy anode materials such as silicon. The project is demonstrating the proposed device on cells using both today's graphite-based and tomorrow's high-energy Si-based negative electrode material presently under investigation by the DOE Applied Battery Research for Transportation (ABRT) program.

The team leverages unique expertise at NREL and ANL. NREL is a recognized expert in the electrochemical characterization and model-based design of electrochemical couples and large-format cells under DOE's CAEBAT program, including diagnosis and modeling of degradation mechanisms in automotive systems and environments. ANL's Cell Analysis, Modeling, and Prototyping (CAMP) laboratory is the leading DOE facility for producing high-quality electrochemical couples in partnership with DOE's Si Deep-Dive project. (See Section II.H.1 of this report for additional description of the CAMP facility.) ANL's high energy density Si anodes when demonstrated together with NREL's supplemental Li technology may represent the best progress to date amongst labs, universities, and industry to reach DOE's VTO Battery500 Strategic Goal for EV batteries of 500Wh/kg and 1000 cycles.

Results

The L3B device is a combination of excess lithium reservoir and passive control. Experiments have been conducted with and without the passive control. During FY 2017-2019, NREL demonstrated significant life extension for Si/graphite-NMC based cells using L3B, as well as conventional graphite/LMO and graphite/LFP cells. Capacity recovery was initially performed in a triggered fashion using a second cyclers channel with the cell resting in a deep discharged state. Next, NREL starting using passive control to continuously release lithium during cycling. Major accomplishments included:

- >2X life extension for 400 mAh Si-based pouch cells with passive control. The cells were fabricated by ANL-CAMP and, with 73% graphite and 15% Si, have an anode specific capacity of 600 mAh/g
- 50% capacity recovery demonstrated for Si-based pouch cells using multiple triggered relithiations
- Prototype cells built with Li reservoir and passive control inserted inside of cell packaging
- Measurement of lithium distribution via extensive coin cell harvesting after relithiation within 18650 commercial graphite cells and Si pouch cells after high rate relithiation.
- Development of 2D transport model through comparison with experimentally measured results. Used model to predict distributions at lower rates that have not been measured within the program due to time constraints (experiments would take several years)
- Published manuscript in *Electrochimica Acta* quantifying fade mechanisms for state-of-the-art (SOA) high-energy density 18650 cell.

To prove the capability of the proposed Li reservoir/passive control, NREL inserted metallic lithium electrodes into ANL-CAMP fabricated Si/graphite-NMC pouch cells. NREL received an initial batch of 33 cells. The anodes consisted of 15 wt% Si, 73 wt% graphite, 2 wt% carbon black and 10% binder with a specific capacity of ~600 mAh/g-electrode. The anode had a high porosity of 44% to allow for expansion of Silicon during lithiation. The high porosity is also beneficial for enabling uniform relithiation. Baseline data was collected for the cells without the device inserted and with the device inserted but idle. In either case, the cell capacity rapidly faded to 80% of the initial value in only 40-50 cycles.

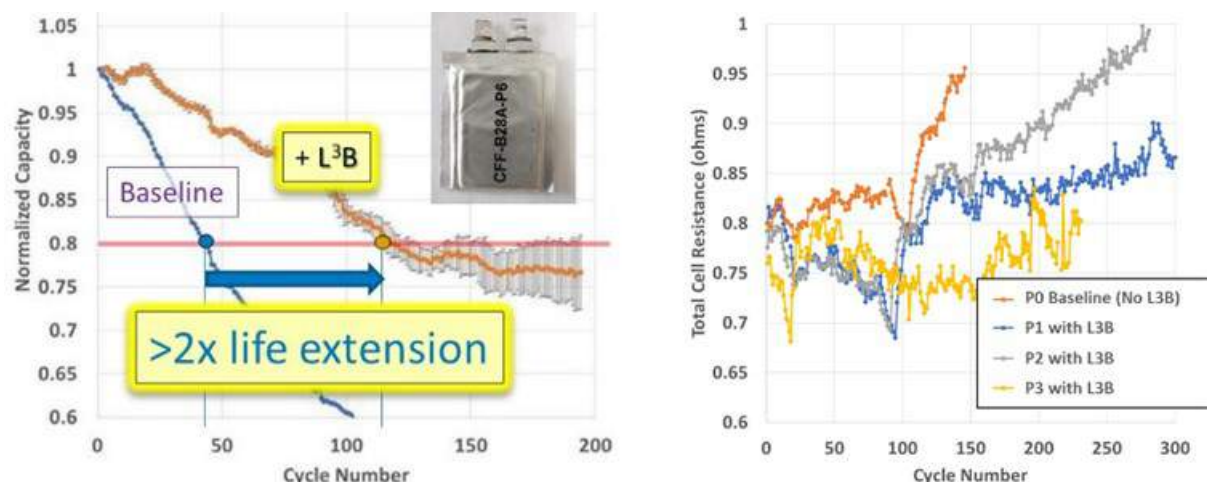


Figure I.2.Q.1 Cycling of 400 mAh Si pouch cells at C/3 and room temperature with and without continuous relithiation using L3B passive control. (Left) Number of cycles to 80% remaining capacity is more than doubled. (Right) Cell resistance is not affected by relithiation

The capacity of Si cells was initially recovered by pausing cycling at various levels of capacity fade and using a second cyler channel to control relithiation from the Li reservoir. During relithiation, the cell was resting in a deeply discharged state. Initial recovery was done at a relatively high rate of 100 μ A discharge for Li. For these cells, this would represent 20% lithium capacity inserted in one month. Cells were then re-lithiated multiple times using triggered, externally controlled release. A possible concern for cells with Si-based anodes is that other physical phenomena besides loss of lithium could result in significant capacity loss, such as loss of active material or electrolyte dry out. The large volume expansion of Si can result in tremendous stress and cracking of SEI layers. This process results in continuous SEI growth and loss of lithium, for which the reservoir can be used to recover capacity. The large stresses can also crack particles and isolate them from electronic percolation paths leading to a loss of active material. Further, SEI growth may result in too much electrolyte consumption and lead to dry out. To investigate, two cells that had faded to around 150 mAh capacity from 350 mAh were relithiated at 100 μ A multiple times. The capacity of both cells was restored to 300+ mAh. These tests showed a very large amount of capacity can be restored with relithiation and that at least 75% of the capacity fade for these Si cells was due to loss of available lithium. Other degradation mechanisms play a minor role compared to Li inventory loss. With multiple relithiations, cycle life was extended from 60 cycles to 180+ cycles – a 3x improvement. The ability to replenish lithium throughout cell lifetime is one of the major benefits of the proposed technology compared to prelithiation.

In a separate experiment demonstrating the passive control circuit, the Li reservoir was used to extend life during continuous cycling within 400 mAh Si cells. In Figure I.2.Q.1a, the blue dots/line represent cycling for the baseline cell which rapidly falls to 80% capacity in ~40 cycles. The orange circles/line represent the average of two cells cycling with continuous relithiation using passive control. The bars on individual circles represents the standard deviation for replicate cells. The end of life capacity of 80% is reached after 110+ cycles.

Resistance growth was also tracked during these experiments to test the baseline cell's resistance growth and monitor whether relithiation affected the cell's power fade characteristics. Figure I.2.Q.1b shows that relithiation causes no discernable change to the cell's resistance growth. Both pulse resistance and total cell resistance, calculated from the voltage difference between the charge and discharge directions, showed similar trends, with no discernable difference between the baseline and re-lithiated cells. So while the L3B technology is not helping reduce power fade, it is not exacerbating the problem either.

With the lithium reservoir placed on the edge of the jellyroll, a concern of the proposed technology is the ability to uniformly insert lithium throughout the entire cell. Due to relatively slow in-plane electrolyte transport properties, lithium will preferentially insert near the lithium reservoir when the recovery/lithium discharge rate is too high. The discharge/charge capacity of harvested coin cells was used to measure lithium concentration as a function of distance from the reservoir. For the ANL pouch cells, the lithium must only move across a total distance of 3.2 cm for the 3450 cell. Further, the porosity of the cells is relatively high and there is a large variation in anode and cathode OCP with intercalation fraction that promotes uniformity. These 3 factors resulted in a very uniform lithium distribution even at a high recovery rate of 100 μA . In 2018, a 2D electrochemical transport verified safe rates of relithiation to achieve uniformity and avoid excessive Li in the region of electrodes nearest the Li reservoir.

In 2019, NREL performed analysis to demonstrate the device occupies less than 4% of cell volume while adding >100% life improvement. The proposed device has been demonstrated to increase lifetime of 15 wt% Si pouch cells from 40-50 cycles to 110+ as shown in Figure I.2.Q.1a. Calculations were performed to determine the volume needed for device in high energy density EV type cell and summarized in Table I.2.Q.1. The calculations are based on a 30 Ah pouch cell with a high energy density of 650 Wh/L and average discharge voltage of 3.7V. End of life was defined as 80% remaining capacity and the reservoir was sized to supply lithium needed to regain 20% of capacity. Assuming constant SEI growth/loss of lithium, this amount of lithium is expected to roughly double the lifetime of cell. The specific capacity of lithium is 1.9 Ah/cm³. Thus, a volume only of 3.1 cm³ or 1.8% of nominal cell volume is needed to double lifetime. Considering a design factor of 2 for extra lithium and packaging/circuitry, the device would occupy less than 4% of the cell volume.

Table I.2.Q.1 Calculations for Device Volume Inside EV Type 30 Ah Pouch Cell

30-Ah cell volume	170 cm ³
Li capacity to double life	6 Ah
Li specific capacity	1.9 Ah cm ⁻³
Volume of Li needed	3.1 cm ³
% volume of Li	1.8%

A potential concern for the proposed device is over-lithiation/lithium plating from over discharging the inserted lithium reservoir to the anode. To mitigate this concern, NREL initiated a subcontract with professor Satadru Dey from the University of Colorado at Denver (UCD) to estimate individual electrode state of charge. The real-time algorithm estimates individual electrode capacity, electrode SOC, and lithium inventory based on measured cell voltage and current [3]. By providing the battery management system individual electrode information, safe bounds are determined for charging/discharging. The algorithm can also alert the BMS system if lithium inventory is excessive and if the device control circuit needs to be opened. Further, the developed algorithm is very beneficial for cells without the inserted device to improve battery safety and lifetime.

The first step in demonstrating the model-based estimation is to perform parameter identification for specific 15 wt% Si CAMP pouch cells. For parameter identification, the measurement of individual electrode potentials via the inserted device with an exposed third terminal is very insightful. However, the identification can be performed on a standard 2-electrode cells given the open circuit potential for each electrode has been well characterized or cell chemistry is known. A schematic of how individual electrode capacity and SOC can be estimated in real-time and converge despite incorrect initialization is illustrated in Figure I.2.Q.3. An illustration of the real time estimation framework is shown in Figure I.2.Q.2. The initial cathode capacity and state of charge were incorrectly initialized with a 10% error. Even with the relatively large initialization error, the estimator converges rapidly to the experimental measurement. The steady state error for both capacity and

lithiation extent are less than 0.5%. Moving forward the algorithm will be used with continuous cycling to track changes in electrode parameters from loss of active material and lithium inventory.

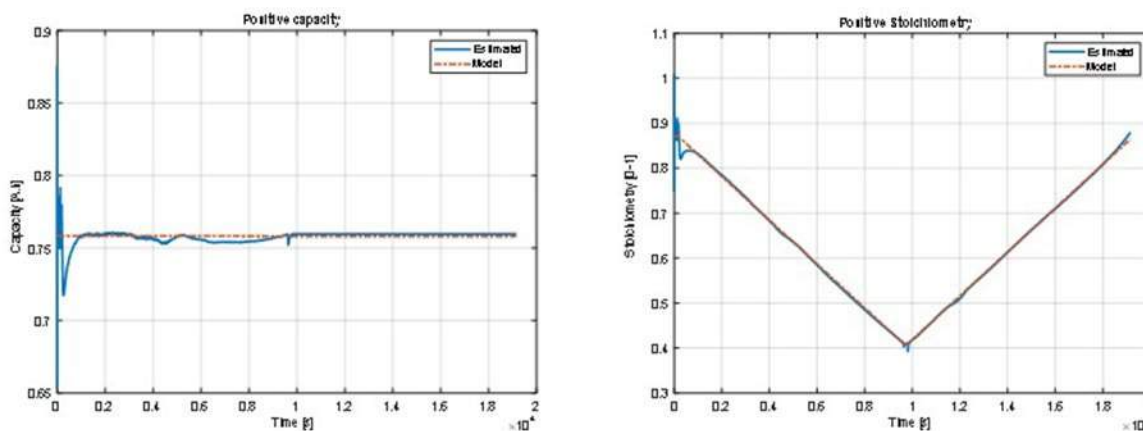


Figure I.2.Q.2 Demonstration of estimation algorithm with 10% initial error in positive electrode capacity (left) and lithiation extent (right)

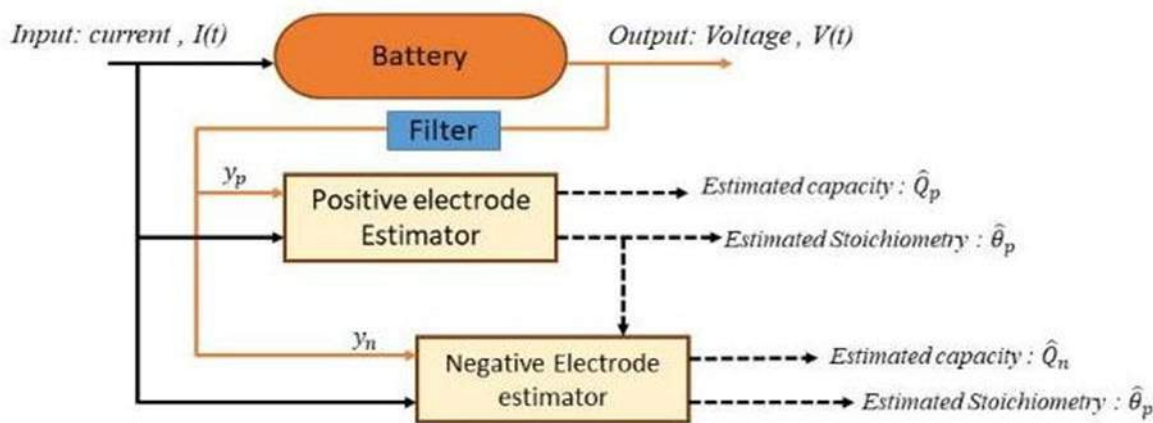


Figure I.2.Q.3 Real time estimation framework for individual electrode algorithm developed by UCD

Also in FY19, NREL investigated the suitability of the proposed technique for prelithiation. To date, companies manufacturing Si cells have been most interested if the proposed device can be used as an alternative to expensive prelithiation techniques used for cells with a high Si/SiO_x loading (>50%). An uncertainty for the proposed device, is that rate at which lithium can be discharged from the device and uniformly inserted throughout the entire cell. Also, the number of days acceptable for this prelithiation step is a question, but probably the timeframe acceptable to cell manufacturers is likely less than a month. Prelithiation up to 15% capacity was performed for the 15 wt% Si pouch cells. Cells were formed and a few baseline C/3 cycles were collected. The cell was then pre-lithiated at a very high rate of 300-400 μ A over the course of 7 days and results are illustrated in Figure I.2.Q.4. The grey line represents fade for a standard cell without prelithiation. The black line represents the average of ~ 10 cells tested without any prelithiation or lithium recovery. The typical fade rate for these cells was 1.6 mAh/cycle. The blue and yellow lines are cells with the 15% prelithiation. There is not a rapid jump in capacity after prelithiation due to relatively low loading of only 15% Si. The extra lithium results in a shift in the voltage window such that NMC is operating at lower potentials (equivalently higher amount of lithiation). However, the prelithiated cells have significant capacity

gains over baseline cells as cycles are accumulated and lithium inventory is lost. Figure I.2.Q.4 shows a 9% capacity gain is achieved at cycle 15. The capacity gains will be higher for cells with higher Si content and NREL is working to demonstrate in state-of-the-art higher Si-content cells.

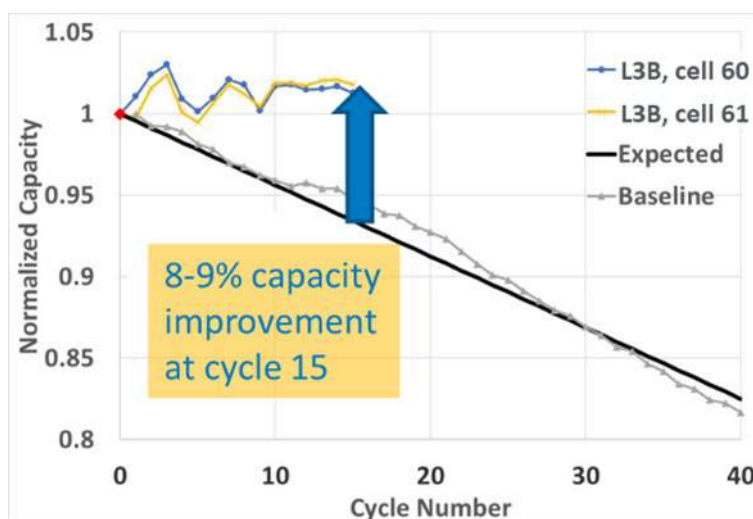


Figure I.2.Q.4 Demonstration of prelithiation for 15 wt% Si pouch cells. Yellow and Blue lines represent capacity during C/3 cycling for cells with 15% prelithiation done over 1 week using inserted device. The black and grey lines are for cells without any prelithiation

To further investigate the suitability of the proposed device for prelithiation, NREL modeled prelithiation for a high energy density Si cell with 700 Wh/L. The 2D transport model was used to predict lithium concentration as a function of position from the reservoir. For the hypothetical high energy density cell, lithium must be transported 6.5 cm from the reservoir. Figure I.2.Q.5 illustrates model prediction for number of moles vs. distance from lithium reservoir. Due to relatively slow in-plane transport, if the relithiation rate is too high then the lithium is preferentially inserted close to the reservoir. The number of moles of lithium is relative to the number of moles in the cell initially before any SEI formation. When this number goes above 1, lithium plating is a concern. At times of around 1 month or more lithium plating is not predicted. In general, the model has been shown to be conservative. Thus, the device can likely be used to prelithiate a high energy density Si cell over the timeframe of weeks. Also, electrolytes with enhanced transport properties would enable shorter prelithiation times.

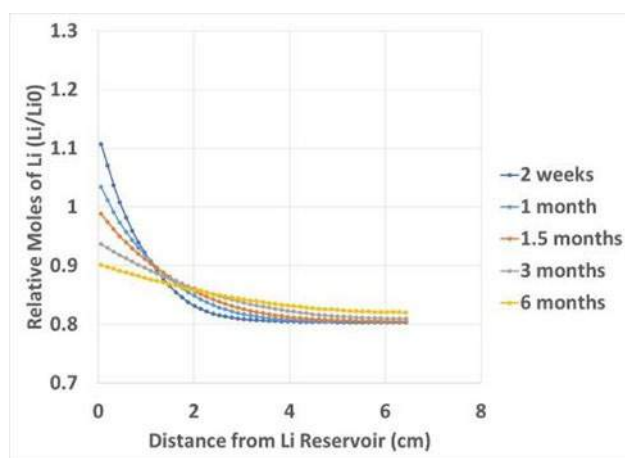


Figure I.2.Q.5 Moles of lithium versus distance from lithium reservoir predicted from 2D transport model for prelithiation over different lengths of time. The moles of lithium is relative to number of moles of lithium in cell prior to any SEI formation/growth

Conclusions

NREL has demonstrated significant life extension and capacity recovery for Si based cells using the proposed L3B Li reservoir and passive control. More specifically, a life extension of >2X and capacity recovery of 50% have been demonstrated for 400 mAh pouch cells with anodes containing 15 wt% Si. The technology has also been demonstrated with more conventional graphite type cells. The variation of lithium concentration from relithiation has been measured for a worst-case scenario at high rate and with electrodes having flat OCP. A 2D lithium-transport model compared well with the result for the tested graphite/LFP cells. For high energy density graphite/NMC cells, the 2D model prediction shows relithiation over the course of 1 year or more should result in relatively uniform lithium distribution and well avoid any concerns of lithium plating. The team investigated chemistry and loss mechanisms for SOA commercial Si-Gr/NMC LG MJ1 18650 cells and a journal article has been accepted.

In FY19, the team demonstrated inserting the proposed device entirely within cells. Detailed analysis was performed to confirm the device occupies less than 5% of volume for high energy density EV type cell while doubling expected lifetime. NREL partnered with UCD to employ its individual electrode estimation algorithm to alleviate concerns with over-lithiation/plating. Parameters were identified for electrode capacity, SOC, and resistance. The framework combined with feedback correction/filtering rapidly converged to correct estimates of electrode capacity and lithium content despite with large initial errors in parameters. Thus, the algorithm can be employed and beneficial for standard two-terminal cells and act as a virtual reference electrode. Lastly, NREL demonstrated how the device can be used as a substitute for expensive external prelithiation. Cells with 15% internal prelithiation had a boosted capacity of 9% at cycle 15 compared to cells without any prelithiation. An even higher initial capacity boost from the device is expected for cells with higher Si loading. A 2D transport model predicts prelithiation should be feasible in reasonable time frame for Si cells with very high energy densities.

Key Publications

1. X. Li, A. Colclasure, D. Finnegan, D. Ren, Y. Shi, X. Feng, L. Cao, Y. Yang, and K. Smith. "Degradation Mechanisms of High Capacity 18650 Cells Containing Si-Graphite Anode and Nickel-Rich NMC Cathode." *Electrochimica Acta*. (2019).
2. M. Keyser, A. Colclasure, X. Li, D. Finegan, K. Smith, "High-Energy Long-Life Li-ion Battery: L3B," DOE Innovation XLab Energy Storage Summit, SLAC National Accelerator Laboratory, Sept. 18-19 (2018).
3. S. Dey, Y. Shi, K. Smith, A. Colclasure, X. Li, "From Battery Cell to Electrodes: Real-time Estimation of Charge and Health of Individual Battery Electrodes," *IEEE Trans. On Industrial Electronics*, 67 (2) 2167-2175 (2019).

Acknowledgements

This section was co-authored by Andrew Colclasure, Donal Finegan, and Satadru Dey. Thanks are also due to Drs. Andy Jansen, Bryant Polzin and Steven Trask of the ANL-CAMP facility for supplying high-quality Si cells and for helpful discussions regarding Si chemistry.

I.2.R Co-Extrusion (CoEx) for Cost Reduction of Advanced High-Energy-and-Power Battery Electrode Manufacturing (PARC)

Ranjeet Rao, Principal Investigator

Palo Alto Research Center (PARC)
3333 Coyote Hill Road
Palo Alto, CA 94304
E-mail: ranjeet.rao@parc.com

Peter Faguy, DOE Technology Development Manager

U.S. Department of Energy
E-mail: Peter.Faguy@ee.doe.gov

Start Date: December 1, 2015

End Date: August 30, 2019

Project Funding (FY19): \$3,790,000

DOE share: \$3,000,000

Non-DOE share: \$790,000

Project Introduction

Most strategies for increasing the performance and reducing the cost of lithium-ion batteries have focused on novel battery chemistries, material loading modifications, and increasing electrode thickness. Increasing electrode thickness is a known approach to increase energy density and in turn overall cell capacity. However, practical thicknesses are constrained by ionic transport limitations that occur with increasing thickness, limiting cell power. We believe PARC's Co-Extrusion (CoEx) technology can overcome this limitation, enabling a substantial improvement in the performance of thick electrodes for most lithium-ion chemistries. CoEx has the potential to disrupt current manufacturing processes and enable the DOE 2022 goal of \$125/kWh by enabling the simultaneous deposition of alternating regions of high ionic transport and high lithium density.

Objectives

Our overall project objectives are to demonstrate Co-Extrusion (CoEx) printing technology at electric vehicle (EV) relevant scales by assembling large, 14 Ah pouch cells. These pouch cells will demonstrate an estimated $\geq 30\%$ reduction in \$/kWh costs through thick, structured high energy and high power electrodes, and a gravimetric energy density improvement of $\geq 20\%$ relative to conventional electrodes of the same chemistry.

Approach

Co-Extrusion (CoEx) Cathode

Co-Extrusion (CoEx) is a deposition technology developed at PARC that uses engineered fluidic channels to cause multiple streams of dissimilar fluids to impart shape to one another[1]. The result is a high-speed, continuous deposition process that can create fine structures much smaller than the smallest physical feature within the printhead. By eliminating the small channels necessary for conventional extrusion and injection processes, CoEx is able to deposit highly loaded and viscous pastes at high process speeds under reasonable operating pressures. Depending on particle size, the CoEx process is capable of direct deposition of features as small as 25 μm with aspect ratios of 5 or greater, and print speeds $> 400 \text{ mm/s}$ ($\sim 80 \text{ ft./min}$). A CoEx printhead can serve the same function as the slot die printhead in modern battery manufacturing lines, depositing the electrode slurry onto the current collector web in a continuous roll-to-roll process. The thicknesses, widths, and lengths of the deposited CoEx features are dependent on the internal printhead geometry, slurry rheology, and process conditions. The precise flow paths are constructed out of a stack of replaceable printhead layers that can be easily exchanged, allowing for precise tailoring of the final deposited features within a single printhead design. PARC's scale-up of CoEx batteries for EVs builds on a solid base of experience in applying CoEx to solar cell manufacturing[2]. We have chosen a commercially relevant chemistry, $\text{LiNi}_{0.5}\text{Mn}_{0.3}\text{Co}_{0.2}\text{O}_2$ (NMC 532) and our strategy is to scale the technology from coin cells (BP1) to large pouch cells (BP3) by project completion. Our partner, Ford Motor Company, will provide PARC with

baseline cell specifications in addition to EV-relevant cell characterization on the pouch cells developed during the course of the project.

High Capacity Graphite Anode

While PARC will use CoEx to develop thick, high performance cathode electrodes, ORNL will develop the thick, high capacity anode that will match the CoEx cathode. In addition, they will utilize ORNL's Battery Manufacturing Facility (BMF) to fabricate small scale pouch cells in BP2 and assist PARC with technology scale-up on ORNL's roll coater, in addition to running electrochemical rate and cycling tests. As part of the anode development, ORNL will refine graphite-based anode slurries for improved coating adhesion, agglomerate cohesion, and high ionic and electronic conductivity by modifying binder and conductive additive. Anodes will be prepared with an NMP/PVDF solvent/binder system and slot-die coated to a sufficient thickness to balance the CoEx cathodes. Beginning with baseline anode coatings with targets of 50-80 μm in thickness after calendaring, 2.5-3.0 mAh/cm² in loading, and capacity > 350 mAh/g, ORNL will then work to demonstrate anodes that are thick (125 – 200 μm) to match the high capacity CoEx cathodes. These anodes will be shown to maintain their integrity after drying and calendaring to 30-40% porosity

Results

As was described in the FY2018 annual report, work in BP1 focused on developing the CoEx cathodes and thick conventional anodes separately at PARC and ORNL, respectively. In this way, CoEx cathodes were tested in half-cell configuration and structure-performance relationships were tested without concern that anode limitations would obscure results. The CoEx printhead takes two inks or slurries as inputs, and interdigitates the fluid streams to create a patterned thick film on a substrate. By depositing inks with different solvent loadings, we are able to create films that, after drying, result in a cathode electrode with periodic grooves. These grooves get filled with electrolyte during battery assembly, and these periodic regions of reduced tortuosity result in overall improved utilization of a highly loaded electrode. Figure I.2.R.1 is a 3-D microscope (Keyence VHX-500) image of a representative CoEx electrode region both before (a) and after (b) calendaring. In these images, one can see the general topology of the CoEx electrode, with a narrow groove or “valley” and a wider, thicker “ridge” region. This image also illustrates that CoEx features survive the calendaring process. Modeling work done in the first budget period [3] provided guidance on the types of CoEx structures to make, indicating that the best performance, in terms of gravimetric and volumetric energy density, would be achieved by having a ridge:valley width ratio ≥ 4 and with an electrode thickness $\sim 120 \mu\text{m}$. We control the relative width ratio of these ridge and valley regions by controlling the relative input pressures and thus volumetric flow rates of the two inks.

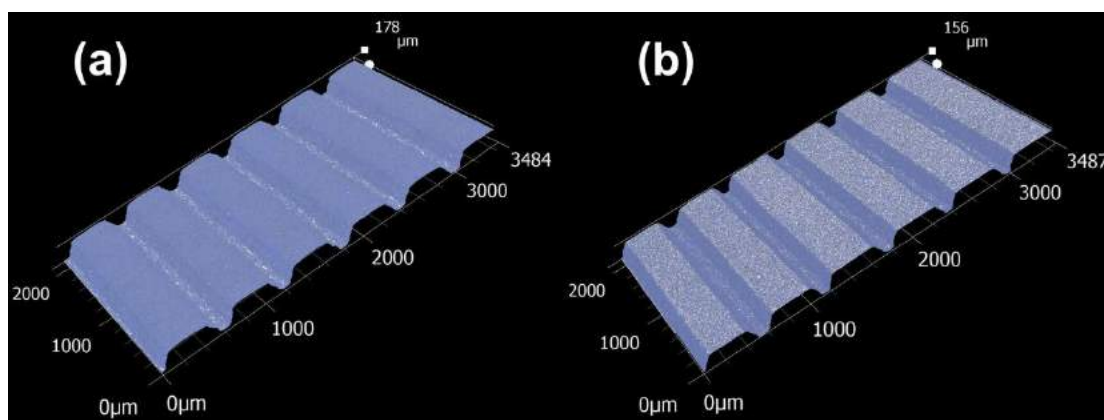


Figure I.2.R.1 3-D Microscope images of as-printed and dried (a) and post-calendared (b) cathode electrodes produced via CoEx. Images illustrate the corrugated topography that persists after the calendaring process

In Budget Period 1, we used results from coin sized half cells to demonstrate how CoEx structuring improved the performance of cathode electrodes compared to homogeneous electrodes. These electrodes were made

with a CoEx printhead with a maximum print width of about 20 mm, which limited the size and capacity of the assembled batteries. As part of achieving the overall goals of creating high capacity pouch cells in the remaining budget periods, major project tasks included scaling up the printhead hardware to enable larger format battery cells. During this project, we have designed, fabricated, and tested a CoEx printhead with a 90 mm print width (CoEx90), sufficient to make 1 Ah pouch cells (nominal cathode dimensions of 56.0 x 84.4 mm), and as well as a larger, 180 mm wide printhead (CoEx180) that was installed on the Frontier web coater at ORNL's Battery Manufacturing Facility to manufacture electrodes for 10+ Ah pouch cells (nominal cathode dimensions of 110 x 150 mm). As part of this process development, we have demonstrated print speeds as high as 400 mm/s (24 m/min) as well as the capability for double-sided printing. For these larger pouch cells, CoEx cathodes were matched with graphite anodes produced via dual-layer slot-die coating. These CoEx cells were compared against two baseline cases representing conventional coating technologies. In one baseline ("thin baseline"), cathode active material loading is $\sim 15 \text{ mg/cm}^2$, while in the other baseline ("thick baseline"), cathode active material loading is $\sim 25 \text{ mg/cm}^2$, similar to the CoEx active material loading. In this way, we compare CoEx against a typical cathode to illustrate energy density improvements as well as a conventional thick cathode to illustrate power improvements.

Table I.2.R.1 shows electrode dimensions and loadings for 1 Ah pouch cells, comparing CoEx cells against both conventional baselines. All cells were chosen to have similar overall capacity, and since the CoEx and thick baseline cells have higher loading in their cathodes, this results in fewer overall electrode layers. Figure I.2.R.2 shows the rate performance of the CoEx pouch cells along with baseline and thick homogeneous cathodes for comparison. Referring to, both the CoEx and thick baseline cells have similar thicknesses and electrode loadings, approximately twice that of the thinner baseline. As a result, 40% fewer electrode layers are required to reach 1 Ah capacity, with a concurrent decrease in the number of current collector and separator layers. With regards to electrochemical performance, all pouch cells show high utilization at low discharge rates, with similar performance out to approximately D/2 discharge rate. At higher discharge rates, the thick baseline shows much reduced capacity compared to both the CoEx (which contains cathodes of the same thickness and loading) and the baseline pouch cells, again showing that structuring the cathode electrode results in improved utilization of the active material. These electrochemical results, combined with the physical parameters of the pouch cells (mass, thickness) can be used to calculate the performance in terms of gravimetric and volumetric energy density. Table I.2.R.2 summarizes this data, showing how the CoEx pouch cells compares to the thin and thick baseline cells. Since the CoEx pouch cell needs fewer electrode layers in order to achieve a 1 Ah capacity, it contains fewer current collector and separator layers, resulting in improved energy density at discharge rates $\leq 1D$. The improved ionic transport within the CoEx cathodes improves performance relative to the thick baseline pouch cells, with gains of 11% and 9% at 1D discharge in gravimetric and volumetric energy density, respectively. At higher discharge rates (2D), the energy density of CoEx pouch cells is even greater, 2.5x that of the thick baseline cells.

Table I.2.R.1. Electrode Dimensions and Loadings for 1 Ah Cells

	CoEx		Baseline		Thick Baseline	
	NMC532	Graphite	NMC532	Graphite	NMC532	Graphite
Active Material Loading (mg/cm^2)	23.0	12.3	13.2	6.9	24.8	12.3
Electrode Thickness (μm)	111	109	55	63	106	109
# of cathode layers	6		3		3	

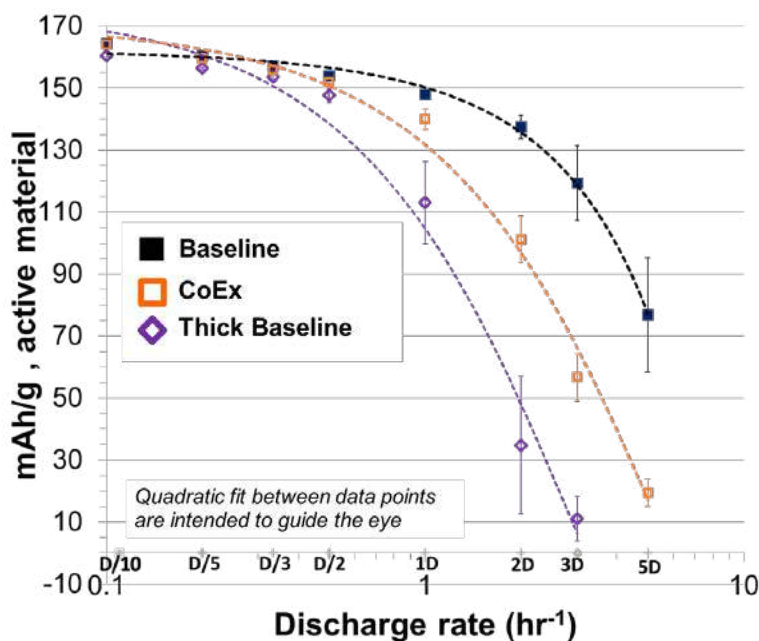


Figure I.2.R.2. Electrochemical Performance of 1 Ah pouch cells, comparing thin and thick baselines vs. CoEx cathodes. Error bars represent +/- 1 standard deviation. Quadratic curve fits are intended to guide the eye. All cells were made with 1.2 M LiPF₆ in 3:7 wt% EC/EMC electrolyte

Table I.2.R.2. Energy Density Comparison Between CoEx Cathodes and Baseline Cathodes

Discharge Rate	CoEx Vs. Thin Baseline			CoEx Vs. Thick Baseline		
	mAh/g	Wh/kg	Wh/L	mAh/g	Wh/kg	Wh/L
D/10	5%	6%	9%	-5%	-6%	-7%
D/5	5%	5%	8%	-6%	-6%	-8%
D/3	5%	4%	7%	-6%	-7%	-9%
D/2	4%	2%	5%	-5%	-7%	-8%
1D	0%	-4%	-2%	15%	11%	9%
2D	-22%	-29%	-24%	169%	149%	145%

With validation of CoEx structuring demonstrated at the small pouch cell level, we continued to scale up the CoEx process to enable the capability to make pouch cells with an order of magnitude more capacity. Accomplishing this goal required two main changes to the print process. The CoEx printhead was scaled up to 180 mm wide, enabling printing of larger format cells (nominal cathode dimensions of 110 x 150 mm), and the print hardware was adapted to run off on a web rather than in batch mode. These changes allowed us to print multiple meters of electrode length at the desired width and active material loading (~ 25 mg/cm²). A CoEx printhead and associated fluid delivery equipment was installed on the Frontier web coater at the Battery Manufacturing Facility at ORNL. In a similar manner to the 1 Ah cell testing, large format pouch cells were made using CoEx cathodes as well as two different conventional baseline cathodes (thick and thin). The CoEx and thick baseline cells contained 28 cathode electrodes, while the thin baseline required 44 cathodes to achieve a similar capacity. These pouch cells were tested at discharge rates ranging from D/10 up through 7.5D, and the resultant capacity data is shown in Table I.2.R.3, which shows capacity for each pouch cell for each discharge rate. Due to variations in coating thickness, these cells have capacities ranging from 15 – 18 Ah.

Table I.2.R.3. Capacity of Large Pouch Cells at Varying Discharge Rates

Discharge Rate	CoEx Cell Capacity (Ah)					Thin Baseline Capacity (Ah)				Thick Baseline Capacity (Ah)			
	Cell 1	Cell 2	Cell 3	Cell 4	Cell 5	Cell 1	Cell 2	Cell 3	Cell 4	Cell 1	Cell 2	Cell 3	Cell 4
D/10	16.6	10.2	17.9	17.4	16.2	15.6	16.0	15.4	16.1	17.1	17.2	17.6	15.4
D/5	16.2	10.0	17.5	17.0	15.8	15.4	15.8	15.2	15.8	16.9	17.0	17.3	15.0
D/3	15.7	9.7	17.1	16.6	15.5	15.2	15.4	15.0	15.4	16.7	16.7	16.8	14.5
D/2	15.3	9.5	16.7	16.2	15.2	15.0	15.0	14.8	15.0	16.3	16.2	16.3	13.9
1D	14.7	9.2	16.3	15.7	14.6	14.5	14.6	14.3	14.7	15.4	15.0	15.2	12.3
2D	12.6	7.8	14.5	10.0	12.0	14.1	14.5	13.9	14.5	11.3	10.4	10.1	5.7
3D	8.5	5.0	10.5	6.4	6.9	13.9	14.3	13.6	14.3	4.9	4.1	4.1	0.0
5D	3.2	1.9	3.8	2.7	2.3	13.3	13.7	13.2	13.5	0.7	0.4	0.3	0.0
7.5D	1.5	0.9	1.6	0.9	1.3	11.5	11.7	10.9	10.1	0.0	0.0	0.0	0.0

As we do not have individual cathode mass data, we were unable to plot this data in terms of specific capacity, but Figure I.2.R.3 shows normalized performance data, where each data point is the median performance and error bars represent the highest and lowest capacities for each discharge rate. Like the results seen at the 1 Ah level, CoEx cells performed better than the thick baseline cells despite being of similar thickness, especially at the higher discharge rates. Based on the weight and volume of these pouch cells, we can use this electrochemical data to calculate the volumetric and gravimetric energy densities for these pouch cells. Table I.2.R.4 shows how CoEx cells compare to the thick and thin baseline cells for these metrics. Similar trends exist for the larger pouch cells compared to the thinner ones, and although all cells performed better compared at high discharge rates compared to the 1 Ah case, the CoEx cells showed greater improvements, resulting in modest gains in energy density relative to the 1 Ah pouch cells.

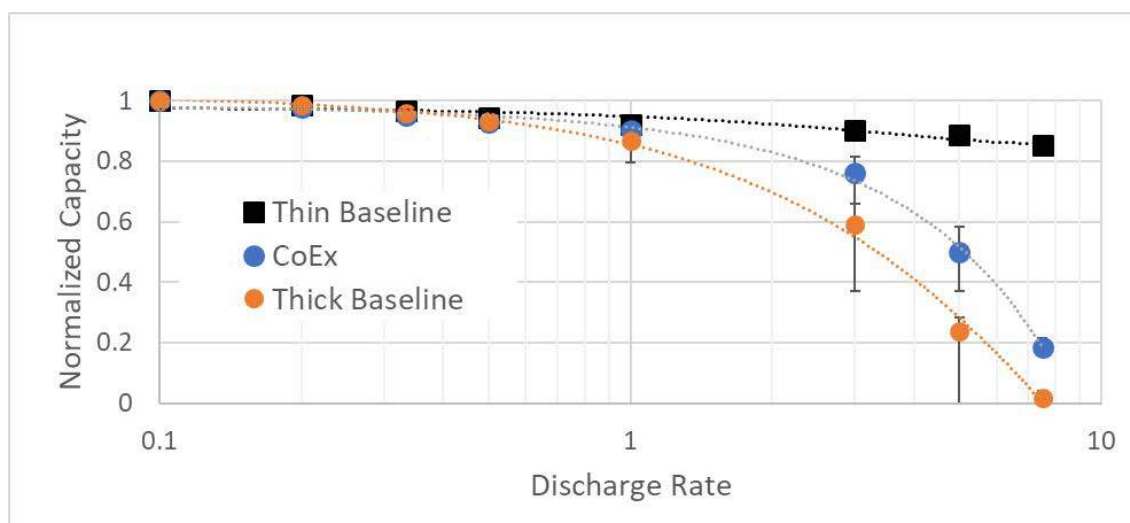


Figure I.2.R.3 Normalized capacity of large format pouch cells at discharge rates from D/10 to 7.5D, comparing thin and thick baselines vs. CoEx cathodes. Data points are median values, and error bars represent minimum and maximum of data set (4 cells for each baseline, 5 CoEx cells). Quadratic curve fits are intended to guide the eye. All cells were made with 1.2 M LiPF₆ in 3:7 wt% EC/EMC electrolyte

Table I.2.R.4. Energy Density Improvement of CoEx Over Baseline in Large Format Cells

Discharge Rate	CoEx Vs. Thin Baseline		CoEx Vs. Thick Baseline	
	Wh/kg	Wh/L	Wh/kg	Wh/L
D/10	11%	7%	0%	2%
D/2	3%	7%	-1%	2%
1D	1%	6%	5%	7%
2D	-15%	-13%	31%	31%
5D	-77%	-77%	1000%	983%

Conclusions

PARC, ORNL, and Ford have collaborated to create a pilot scale demonstration of PARC's CoEx battery manufacturing technology for structured high energy and high power cathodes for cost-effective EVs. Over the course of this project, we have successfully scaled up our electrode printhead from 20 mm wide to 180 mm wide, enabling large (> 15 Ah) pouch cells. We have demonstrated that CoEx structuring leads to improved utilization over homogeneous (*i.e.* non-structured) electrodes of similar loading. These improvements lead to energy density improvements of 3 – 7% over conventional (thin) battery cathodes at D/2 discharge rates while avoiding the

Key Publications

1. Cobb, C.L. and Scott E. Solberg, "Analysis of Thick Co-Extruded Cathodes for Higher-Energy-and-Power Lithium-Ion Batteries," *J. Electrochem. Soc.*, **164** (7), A1339-A1341, 2017
2. Rao, R.B., "Co-Extrusion of Electrodes for Both Energy and Power." Presentation, *U.S. Drive Electrochemical Energy Storage Technology Discussion*, Southfield, MI, May 16, 2017
3. Cobb, C.L., "Co-Extrusion: Advanced Manufacturing for Energy Devices." Presentation, *2016 AIChE Annual Meeting, Battery and Energy Storage Technologies*, San Francisco, CA, November 14, 2016. (Session Keynote)
4. Cobb, C.L., "Modeling Co-extruded Cathodes for High Energy Lithium-ion Batteries." Presentation, *229th ECS Meeting*, San Diego, CA, June 1, 2016.
5. Rao, R.B. *et al.*, "Thick Co-Extruded Cathode Electrodes for High Energy Lithium-Ion Batteries." Presentation, *2018 Fall MRS Meeting and Exhibition*, Boston, MA, November 27, 2018

References

1. Fork, David, and Thomas Hantschel. Extrusion/dispensing Systems and Methods. U.S. Patent US7765949B2, filed May 17, 2007, and issued September 21, 2010
2. L.P. Richter *et al.*, "Progress in Fine Line Metallization by Co-extrusion Printing on Cast Mono Silicon PERC Solar Cells," *Solar Energy Materials and Solar Cells*, 142 (2015): 18-23
3. Cobb, C.L., and Scott E. Solberg, "Analysis of Thick Co-Extruded Cathodes for Higher-Energy-and-Power Lithium-Ion Batteries." *Journal of The Electrochemical Society* 164, no. 7 (2017): A1339-A1341

Acknowledgements

We would like to acknowledge the help of Bryant Polzin & Daniel Abraham at Argonne National Laboratories for early assistance in developing formation protocols, as well as Michael Wixom and Christopher Silkowski at Navitas Systems for large format pouch cell assembly and testing.

I.3 Computer-Aided Engineering for Batteries (CAEBAT)

I.3.A Advanced Computer-Aided Battery Engineering Consortium (NREL, ANL, SNL, Purdue Univ.)

Dr. Kandler Smith, Principal Investigator

National Renewable Energy Laboratory
15013 Denver West Pkwy
Golden, CO 80401
E-mail: kandler.smith@nrel.gov

Dr. Shriram Santhanagopalan, Principal Investigator

National Renewable Energy Laboratory
15013 Denver West Pkwy
Golden, CO 80401
E-mail: shriram.santhanagopalan@nrel.gov

Brian Cunningham, DOE Technology Development Manager

U.S. Department of Energy
E-mail: Brian.Cunningham@ee.doe.gov

Start Date: October 1, 2015	End Date: September 30, 2019	
Total Project Cost: \$5,150,000	DOE share: \$5,150,000	Non-DOE share: \$0

Project Introduction

DOE's Computer Aided Engineering for Electric-Drive Vehicle Batteries (CAEBAT) Program seeks to accelerate the battery research, development and design processes by developing and coupling computational simulation models of battery physics. First generation CAEBAT tools focused on coupling particle- and electrode-scale electrochemistry with 3D cell- and pack-scale electron and heat transport. NREL's multiscale multidimensional (MSMD) model efficiently captured these physics at the cell scale. Commercial software companies adopted and validated similar approaches serving industry's needs for 3D cell, pack and thermal management design tools.

The Advanced Computer Aided Battery Engineering Consortium was formed in response to DOE's 2015 CAEBAT lab call, and consists of a partnership between NREL, Argonne National Laboratory (ANL), Sandia National Laboratories (SNL) and Purdue University conducting complementary modeling/experimental studies in battery simulation R&D. Achievements in FY2017 and FY2018 included development of parameter identification algorithms for electrochemical models, an open-source electrode microstructure library, a microstructure-scale 3D electrochemical model, characterization tools for predicting electrode tortuosity, and 3D mechanical/ electrochemical/thermal (MECT) simulation models that describe the physiochemical processes encountered by batteries in the event of vehicle crash.

In FY2019, the team worked in two major thrust areas: (1) to further develop and validate MECT based on evaluation and feedback from the USCAR industry working group, and (2) to extend the electrochemical models to represent emerging battery chemistries and align future modeling projects with material-scale R&D. SNL experimental studies are further described in separate sections of this report. The project has resulted in 22 archival publications, an open-source electrode microstructure library [17] and an open-source plug-in for the FEniCS finite-element software [18] used for 3D microstructure simulation. An open-source microstructure characterization toolbox will be released in FY2020.

Objectives

The Advanced Computer Aided Battery Engineering Consortium is working to develop modeling capabilities that help industry accelerate development of electric-drive vehicle (EDV) batteries, promote deeper and

quantitative physical understanding and thereby improve battery performance, energy density, cost, safety and life. Specific objectives for the past year included to

- Develop 3D models of battery crush/crash events, predicting sequence of internal/external short phenomena, thermal runaway and design of safe battery systems that avoid thermal runaway
- Model, understand physical limitations and aid the design of energy-dense thick battery electrodes
- Predict the impact of electrode/particle morphology, size distribution, alignment and other microstructural features on device-level performance
- Scale 3D microstructure models using high-performance computing so that they can simulate statistically representative volumes of electrodes (solving some 2M degrees of freedom) in a few days
- Capture the physics important for emerging battery chemistries including
 - Large volume deformation and solid mechanics (e.g., for silicon electrodes)
 - Mechanical stress/damage-coupled degradation processes
 - Multi-reaction (electro)chemistry (e.g., for Li-sulfur systems and side reaction processes)

Approach

Results below describe major achievements in the following five areas:

- 1) Mechanical abuse (MECT)
- 2) Efficient scale-up of 3D microstructure electrochemical model
- 3) Electrochemical modeling of large volume-change materials
- 4) Mechanical stress/damage-coupled degradation processes
- 5) Multi-reaction (electro)chemistry

Results

1) Mechanical abuse (MECT)

In FY19, NREL built six different case files for distribution to the USCAR Crash Safety Workgroup as well as other industry partners to get feedback on the implementation of the electrochemical models in LS-DYNA. These case files serve as the benchmark for each of our implementation approaches encompassing different mechanical models (lumped model, representative sandwich and detailed layer-by-layer model). These were each coupled with an electrochemical-thermal model implemented using a user-defined material model for the first set of case studies and as in custom-built user-defined elements for the next set of case studies. These are currently being evaluated by the Crash Safety Workgroup under a research license.

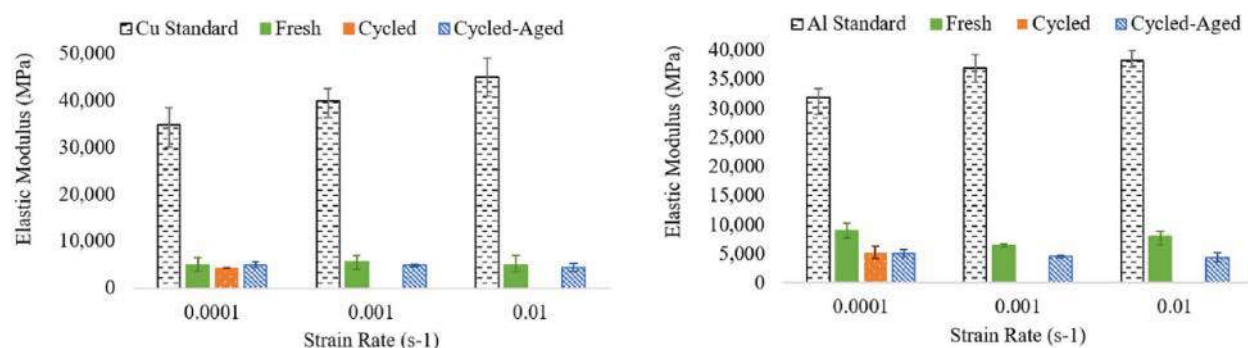


Figure I.3.A.1 Effect of aging on mechanical properties of anode versus the cathode: the moduli were dominated by that of the current collector material and there was noticeable difference between the bulk modulus and that from calendaring. Calendaring lowered the mechanical strength of the electrodes considerably; these results are comparable to what is reported in the literature. The samples were aged over a period of 5 years and drop in elastic modulus for the cathode was noticed; the differences on the anode samples were relatively minimal

In general, the user-defined elements show higher computational efficiencies compared to calling the electrochemical-thermal subroutines from every element as a material model. We also verified that the approach presented is scalable across large geometries. For defining the user-defined-elements, some input from the software developer (Livermore Software Technology Corporation LLC) will enable quicker implementation of the models for large format test articles (modules to packs). We are collecting input from industry partners towards the different implementation schemes. On the technical aspects of the project, we implemented shear-induced failure as part of our improvements to the mechanical models. This enables us to simulate complex loading conditions that go beyond the quasi-steady-state one-dimensional loading. These results were documented in two different manuscripts [24]. To populate the parameters in these models, the team built a custom shear-test fixture that was used to collect shear deformation data on cell-components. This fixture provides a reliable alternate to the picture frame test recommended by the ASTM standards – especially for thin-film samples that suffer from through plane buckling during the picture frame tests. We also completed measurement of mechanical properties on electrode samples aged to 5 years (Figure I.3.A.1). These results show faster degradation of the cathode compared to the anode – and the results are dominated by the properties of the current collector.

2) Efficient scale-up of 3D microstructure electrochemical model

Battery performance is strongly correlated with electrode microstructure. Electrode materials for lithium-ion batteries have complex microstructure geometries that require millions of degrees of freedom to solve the electrochemical system at the microstructure scale. A fast-iterative solver with an appropriate preconditioner is thus required to simulate large representative volume in a reasonable time. In a recently submitted article [18], a finite element electrochemical model was developed to resolve the concentration and potential within the electrode active materials and the electrolyte domains at the microstructure scale, with an emphasis on numerical stability and scaling performance. The block Gauss-Seidel (BGS) numerical method was implemented because the system of equations within the electrodes is coupled only through the nonlinear Butler-Volmer equation, which governs the electrochemical reaction at the interface between the domains. The best solution strategy consisted of splitting the system into two blocks—one for the concentration and one for the potential field—and then performing block generalized minimal residual (GMRES) preconditioned with algebraic multigrid (AMG), using the FEniCS and the Portable, Extensible Toolkit for Scientific Computation

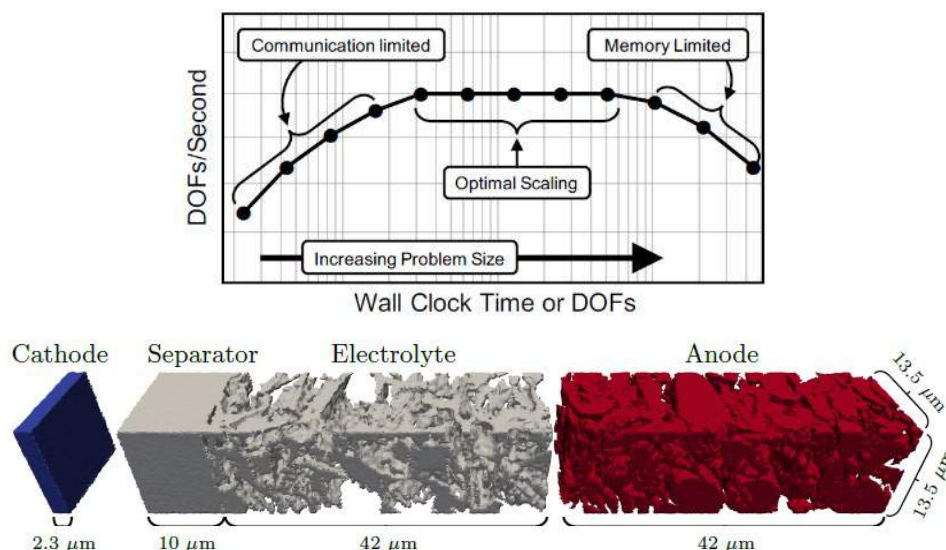


Figure I.3.A.2 (Top) Microstructure model 3D computational domain. (Bottom) Schematic of static scaling numerical test applied in the paper [\[18\]](#) using high-performance computing.

(PETSc) libraries. Significant improvements in terms of time to solution (six times faster) and memory usage (halving) are achieved compared with the Multifrontal Massively Parallel sparse direct Solver (MUMPS). Additionally, BGS experiences decent strong parallel scaling within the electrode domains. Last, the system of equations is modified to specifically address numerical instability induced by electrolyte depletion, which is particularly valuable for simulating fast-charge scenarios relevant for automotive application. The model is presently being used for design of fast-charge electrodes under DOE's XCEL program and identify methods to suppress the lithium plating side reaction. Described elsewhere in this annual report, the XCEL simulations capture representative electrode volumes $100 \times 100 \times 100\text{-}\mu\text{m}^3$ in size, solving on the order of 2M degrees of freedom in several days.

3) *Electrochemical modeling of large volume-change materials*

Emerging battery chemistries such as silicon and intermetallics suffer from several-hundred-percent volume change of their active materials during each charge/discharge cycle. Without sufficient porosity, the active material expansion can close pores, shutting off electrolyte-phase ion transport. The mechanical stress of volume change also causes damage to the electrode if not properly designed. The traditional Pseudo2D electrochemical reaction/transport model—widely popular for electrode design of conventional Li-ion systems—does not capture these effects and must be reformulated to adapt to emerging chemistries.

In a published article [\[21\]](#), the Pseudo2D electrochemical reaction/transport battery model is reformulated based on the finite strain theory to incorporate the coupled effects of large electrochemical-mechanical deformations at both particle and electrode levels. The active material volume change due to lithium insertion/extraction causes the electrode deformation and porosity variation. The porosity variation affects the mechanical properties of each component of the cell as well as the transport processes. In turn, the electrode deformation also affects porosity variation and the electrochemical processes (transport and equilibrium potential). Variables such as particle size and specific surface area are also simultaneously updated based on the approximated electrode deformation and porosity distributions. The model is applied to simulate the performance of a cell composed of a Si anode and NMC532 cathode to study the effect of active material

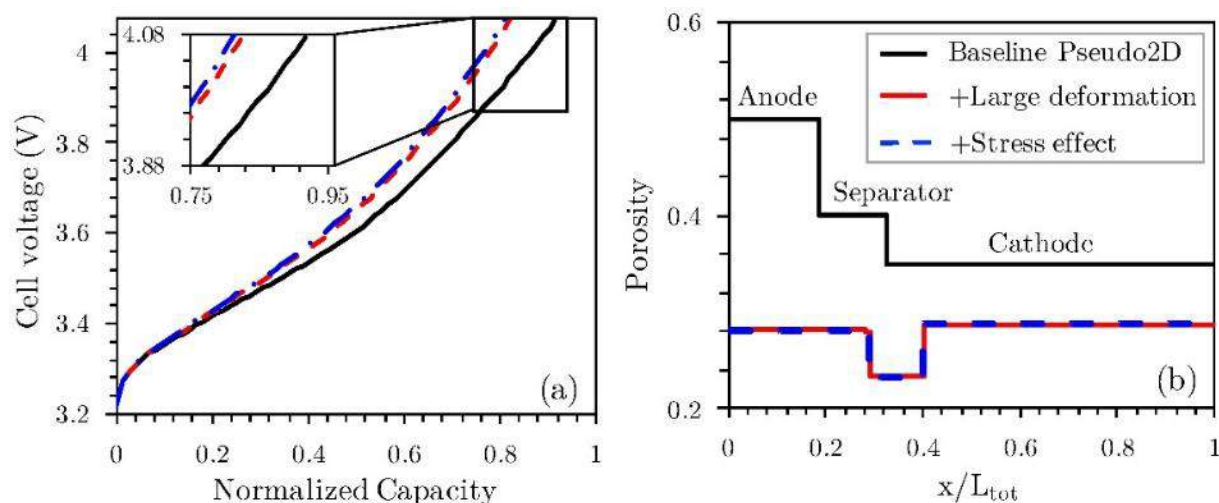


Figure I.3.A.3 (a) Silicon/NMC cell voltage variation during 1C charging and (b) porosity distribution within the electrode at the end of C/50 charge with and without large deformation and stress effects.

volume change on cell performance. The simulation results show that during the charging process the porosity of each cell component experiences significant reduction due to the large expansion of Si particles. Also, a notable hydrostatic stress develops within the cell, which introduces an overpotential in addition to that caused by porosity reduction. The model is also employed to study the effects of charging rate, initial anode porosity, cell loading and fixture condition. This model is a significant step forward from the traditional Pseudo2D model, adding large deformation mechanics applicable to many emerging battery chemistries. In FY20, the model will be enhanced with Si surface chemistry evolution under the SEIsta program.

4) Mechanical stress/damage-coupled degradation processes

Cathode particle cracking or pulverization is a mechanism limiting the lifetime of Li-ion batteries during high-voltage and fast charge operation. High-voltage stability is particularly important to realize the full capacity of high-nickel cathodes. Figure I.3.A.3a shows a cross section revealing the polycrystalline architecture of a NMC532 secondary particle using electron back-scattering diffraction (EBSD). NREL developed a 2D cohesive zone model to simulate the transport/mechanical damage processes within the particles, as well as a separate continuum damage model to map the damage process to larger length-scales, e.g., entire electrodes. The model predicts particle damage increases proportional to the square-root of C-rate, to be validated in future experiments. In FY20 under the XCEL program, the models will be expanded to 3D and applied to improve charging strategies and explore future material architectures (single crystal particles, directionally oriented crystals, etc.) less susceptible to damage.

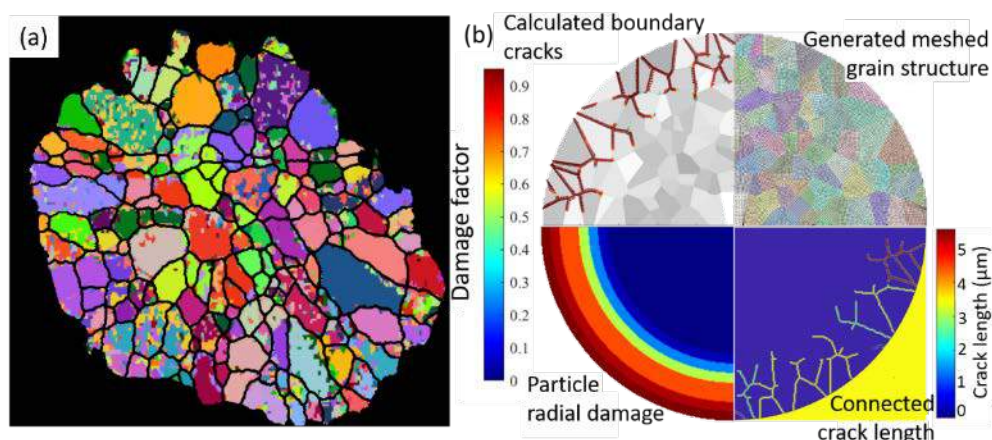


Figure I.3.A.4 (a) EBSD mapping of NMC polycrystalline architecture. (b) Discontinuous and continuous damage models, respectively resolving and homogenizing polycrystalline architecture.

5) Multi-reaction (electro)chemistry

Lithium-sulfur (Li-S) is an emerging rechargeable battery chemistry notable for its high energy density. With complex reaction chemistry, its lifetime is presently limited to around a hundred cycles. Research is needed to precisely identify reaction sequences on discharge and charge and minimize the polysulfide shuttle effect that limits cathode lifetime. Colorado School of Mines worked with NREL to develop a preliminary multi-reaction Li-S electrochemical model that, once verified and validated, will help complement experimental studies, clarify reaction sequences and offer solutions to optimize the chemistry. The model uses Cantera open-source software to provide flexibility for evaluating multiple reaction, dissolution and precipitation hypotheses.

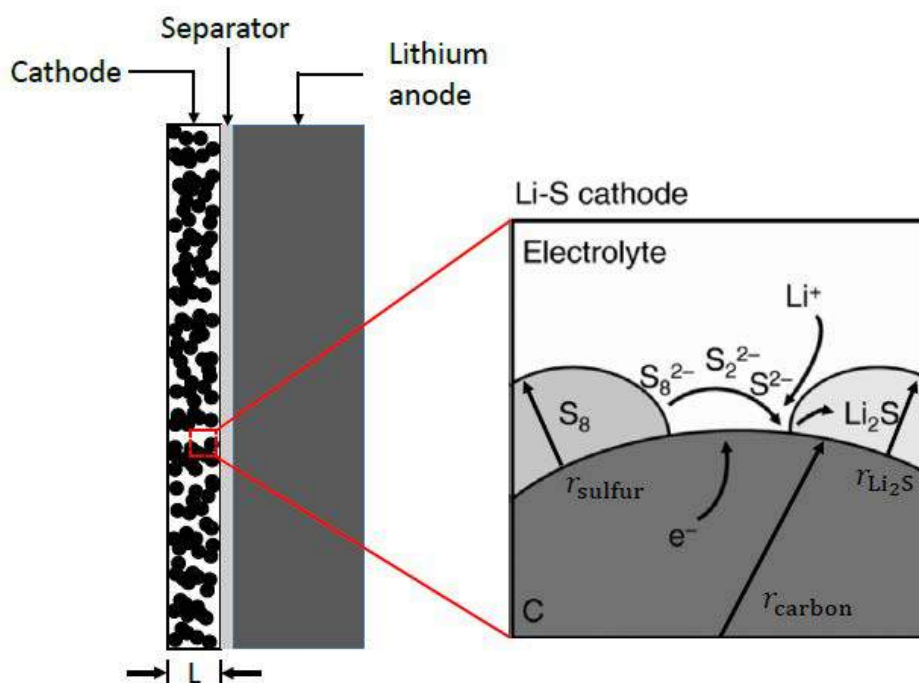


Figure I.3.A.5 Schematic of 1D Li-sulfur model and polysulfide reaction sequence.

Conclusions

The Advanced Computer Aided Battery Engineering Consortium – a partnership between NREL, ANL, SNL and Purdue University – develops and validates simulation models that promote deeper understanding of battery physics and enables acceleration of next generation designs. In this final year of the four-year project, NREL carried out additional high-strain rate tests to mechanically characterize battery components, including in fresh and aged condition. Those results were incorporated into mechanical/ electrochemical/thermal abuse models and shared with USCAR working group for further feedback and validation. Also in the past year, NREL numerically enhanced its 3D microstructure model such that it can carry out large-scale simulations of representative volumes of battery electrodes in just a few days and submitted a journal article for publication. The 3D microstructure model is being used under the XCEL program to investigate fast charge electrode and material design strategies that enhance transport and suppress Li plating. Several models were adapted to consider emerging Li-ion chemistries. The widely popular pseudo2D electrochemical model was enhanced with large deformation mechanics and an exemplar study was published on the silicon anode system. In FY20-22, that model will be merged with detailed models of silicon solid/electrolyte interfacial side reaction chemistry under the SEIsta program. Finally, a detailed model of the Li-sulfur polysulfide reaction sequence during charge/discharge was built in the Cantera framework. Pending resources, that model will be used to explore reaction sequence hypotheses and identify pathways for continued improvement of the high energy density Li-sulfur chemistry.

Key Publications

1. G-H. Kim, K. Smith, J. Lawrence-Simon, and C. Yang, “Efficient and Extensible Quasi-Explicit Modular Nonlinear Multiscale Battery Model: GH-MSMD,” J. Electrochem. Soc., A1076-1088, 2017.
2. Verma, K. Smith, S. Santhanagopalan, D. Abraham, K.P. Yao, P.P. Mukherjee, “Galvanostatic Intermittent Titration and Performance Based Analysis of LiNi_{0.5}Co_{0.2}Mn_{0.3}O₂ Cathode,” J. Echem. Soc., 164 (13), A3380 – A3392, 2017.
3. Z. Wu, L. Cao, J. Hartig, S. Santhanagopalan, “Effect of Aging on Mechanical Properties of Lithium-Ion Battery Components,” ECS Trans., 77 (11) 199-208 (2017).
4. C. Zhang, J. Xu, L. Cao, Z. Wu and S. Santhanagopalan, “Constitutive Behavior and Progressive Mechanical Failure of Electrodes in Lithium-ion Batteries,” J. Power Sources, 2017.
5. C. Zhang, S. Santhanagopalan, and A. Pesaran, “Simultaneously Coupled Mechanical-Electrochemical-Thermal Simulation of Lithium-Ion Cells,” ECS Trans., 72 (24) 9-19 (2016).
6. S. Santhanagopalan, C. Zhang, M.A. Sprague, and A. Pesaran, “A Representative-Sandwich Model for Simultaneously Coupled Mechanical-Electrical-Thermal Simulation of Lithium-ion Battery Cell under Quasi-Static Indentation Tests,” J. Power Sources, 298, p. 102-113 (2016).
7. F. Usseglio-Viretta, K. Smith, “Quantitative Microstructure Characterization of a NMC Electrode,” ECS Transactions, 77 (11) 1095-1118 (2017).
8. Mistry, D. Juarez-Robles, M. Stein IV, K. Smith, and P.P. Mukherjee, “Analysis of Long-Range Interaction in Lithium-Ion Battery Electrodes,” J. Echem. Energy Conversion & Storage, 13 (3) 031006, 2016.
9. C.-F. Chen, A. Verma and P. P. Mukherjee, “Probing the Role of Electrode Microstructure in the Lithium-ion Battery Thermal Behavior”, J. Electrochem. Soc., 164 (11), E3146 – E3158 2017.
10. Mistry, K. Smith and P. P. Mukherjee, “Secondary-Phase Stochastics in Lithium-ion Battery Electrodes”, ACS Appl. Mater. Interfaces, 10 (7), 6317 – 6326, 2018.
11. Mistry, K. Smith and P. P. Mukherjee, “Electrochemistry Coupled Mesoscale Complexations in Electrodes Lead to Thermo-Electrochemical Extremes”, ACS Appl. Mater. Interfaces, 10 (34), 28644 – 28655, 2018.

12. Mistry and P. P. Mukherjee, “Probing Spatial Coupling of Resistive Modes in Porous Intercalation Electrodes through Impedance Spectroscopy”, *Phys. Chem. Chem. Phys.* In press (doi: 10.1039/C8CP05109G), 2018.
13. F. L. E. Usseglio-Viretta, A. Colclasure, A. N. Mistry, K. P. Y. Claver, F. Pouraghajan, D. P. Finegan, T. M. M. Heenan, D. Abraham, P. P. Mukherjee, D. Wheeler, P. Shearing, S. J. Cooper, and K. Smith, “Resolving the Discrepancy in Tortuosity Factor Estimation for Li-Ion Battery Electrodes through Micro-Macro Modeling and Experiment”, *J. Electrochem. Soc.*, 165 (14) A3404 – A3426, 2018.
14. L. Trembacki, A. N. Mistry, D. R. Noble, M. E. Ferraro, P. P. Mukherjee, and S. A. Roberts, “Mesoscale Analysis of Conductive Binder Domain Morphology in Lithium-ion Battery Electrodes”, *J. Electrochem. Soc.*, 165 (13), E725 – E736, 2018.
15. Qibo Li, Chuanbo Yang, Shriram Santhanagopalan, Kandler Smith, Joshua Lamb, Leigh Anna Steele, and Loraine Torres-Castro, “Numerical Investigation of Thermal Runaway Mitigation through a Passive Thermal Management System” *J. Power Sources*, (429) 80-88 (2019).
16. Koffi P.C. Yao, John S. Okasinski, Kaushik Kalaga, Ilya A. Shkrob, and Daniel P. Abraham, “Quantifying lithium concentration gradients in the graphite electrode of Li-ion cells using operando energy dispersive X-ray diffraction”, *Energy and Environmental Science*, accepted for publication (2018).
17. “Battery Microstructures Library,” <https://www.nrel.gov/transportation/microstructure.html>
18. “pFIBS: A Parallel FEniCS implementation of Block Solvers,” <https://github.com/nrel/pfibs>
19. J.M. Allen, J. Chang, F. Usseglio-Viretta, P. Graf, K. Smith, “A Segregated Approach for Modeling the Electrochemistry in the 3-D Microstructure of Li-Ion Batteries and its Acceleration Using Block Preconditioners,” *Computer Methods in Applied Mechanics and Engineering*, submitted.
20. A.M. Colclasure, A.R. Dunlop, S.E. Trask, B.J. Polzin, A.N. Jansen, K. Smith, “Requirements for Enabling Extreme Fast Charging of High Energy Density Li-Ion Cells while Avoiding Lithium Plating,” *J. Electrochem. Soc.* 166 (8) A1412-A1424 (2019).
21. A.C. Colclasure, T.R. Tanim, A.N. Jansen, S.E. Trask, A.R. Dunlop, B.J. Polzin, I. Bloom, D. Robertson, L. Flores, M. Evans, E.J. Dufek, K. Smith, “Electrode scale and electrolyte effects on extreme fast charging of lithium-ion cells,” *Electrochimica Acta*, submitted.
22. W. Mai, A. Colclasure, K. Smith, “A novel reformulation of the Pseudo2D battery model coupling large electrochemical-mechanical deformations at particle and electrode levels”, *J. Electrochem. Soc.*, 166 (8) A1330-A1339 (2019).
23. K. Fink, S. Santhanagopalan, J. Hartig, L. Cao, Characterization of Aged Li-Ion Battery Components for Direct Recycling Process Design, *J. Electrochem. Soc.*, 166(15) A3775-A3783 (2019).
24. Y. Chen, S. Santhanagopalan, V. Babu and Y. Ding, “Dynamic mechanical behavior of lithium-ion pouch cells subjected to high-velocity impact”, *Composite Structures* 218 50-59 (2019).
25. A. Subramaniam, S. Kolluri, C.D. Parke, M. Pathak, S. Santhanagopalan, V.R. Subramanian, “Properly Lumping Lithium-Ion Battery Models: A Tanks-in-Series Approach”, *J. Electrochem. Soc.* In Press (2019).

Acknowledgements

This report was coauthored by Andrew Colclasure, Francois Usseglio-Viretta, Chuanbo Yang, Jeff Allen, Justin Chang, Peter Graf, Partha Mukherjee, Ankit Verma, Daniel Abraham, Josh Lamb, Daniel Korff, and Steven Decaluwe. We wish to thank DOE and CAEBAT program manager Brian Cunningham for funding and guidance as well as collaborators from Univ. College of London (Paul Shearing group) for microstructure imaging and Brigham Young University (Dean Wheeler group) for tortuosity measurement. We also wish to

thank Drs. Andrew Jansen, Bryant Polzin, Steven Trask and Alison Dunlop from the ANL-CAMP facility for providing electrodes and cells in previous years' validation efforts.

I.3.B Consortium for Advanced Battery Simulation (SNL)

Scott A. Roberts, Principal Investigator

Sandia National Laboratories
1515 Eubank SE
Albuquerque, NM 87123-0836
Email: sarober@sandia.gov

Brian Cunningham, DOE Technology Development Manager

U.S. Department of Energy
E-mail: Brian.Cunningham@ee.doe.gov

Start Date: October 1, 2015
Project Funding: \$1,600,000

End Date: September 30, 2019
DOE share: \$1,600,000

Non-DOE share: \$0

Project Introduction

Multi-physics simulations of battery performance are typically performed at the macroscale, including entire cells, cells stacks, batteries, packs, and modules. Classically, these types of simulations model the electrodes using homogenized equations and properties, often utilizing porous electrode theory. These electrodes, however, are comprised of packs of active material particles, polymeric binders, and conductive additives. These materials are combined to form a complex mesostructure that is influenced by material choices and processing conditions. This mesostructure strongly influences the macroscopic performance of the electrode and is of particular importance in abuse scenarios, where it is difficult to experimentally determine mesostructure evolution and properties and during extreme fast charge, where transport through this complex mesostructure can be rate limiting.

Study of the influence of these mesoscale effects on the macroscale behavior of electrodes is the focus of this project. We are utilizing microtomography of nickel-manganese-cobalt oxide (NMC) cathodes to create detailed simulation domains within Sandia's Sierra/Aria code suite using the Conformal Decomposition Finite Element Method (CDFEM). These imaging-derived particle networks are augmented with a conductive binder morphology that we designed. We created discrete element method (DEM) capabilities informed by image data to computationally predict electrode mesostructures. Physics simulations are then performed on these mesostructures, including the calculation of effective properties (e.g., electrical conductivity, ionic tortuosity, Young's modulus) and fully coupled electrochemical-mechanical (dis)charge simulations.

Objectives

The objective of this project is to improve the fidelity of battery-scale simulations of abuse scenarios through the creation and application of microscale (particle-scale) electrode simulations. Our specific FY2019 objectives are twofold:

- Complete an accurate, robust coupled electrochemical-mechanical simulation of NMC discharge at the mesoscale, including the active binder phase.
- Computationally generate realistic mesostructures using discrete element techniques and predict effective properties using these mesostructures, enabling design optimization of particle sizes and binder chemistry/morphology.
- Successfully accomplishing these objectives will impact the VTO by improving the ability to assess battery response to abuse scenarios (e.g., crush) computationally, enabling many parametric computer tests rather than expensive and dangerous experiments.

Approach

Our approach centers around simulations performed using Sandia's Sierra Mechanics suite of codes. In particular, physics simulations are performed using the Sierra/Aria multi-physics code and the mesoscale geometric representation is performed using CDFEM implemented within Sierra/Krino. Additionally, we have begun the use of the LAMMPS code for DEM-based predictions of electrode mesostructures.

Experimentally gathered electrode tomography data forms the foundation of our mesostructure representation. We have utilized microtomography from Vanessa Wood's group from ETH-Zurich. Specifically, Ebner *et al.* [1], published and made publicly available a high-quality data set of NMC electrodes. Material properties were gathered from a variety of sources detailed in our FY2016 report.

Computational representations of the NMC particle mesostructures are created using the CDFEM algorithm. This workflow has been discussed in detail in two journal publications [2] [3] [4], but will be summarized here for completeness. Image processing software is used to binarize, label, and surface mesh individual particles from the images. CDFEM is then used to decompose the background mesh to be conformal to the particles. Conductive binder domain (CBD) phases are added to the mesostructure mesh using the "binder bridge" morphology approach [5], including nanoporosity [6]. This workflow is illustrated in Figure I.3.B.1.

Additionally, DEM simulation were performed to generate mesostructures including both particle and CBD phases. The LAMMPS simulation code is used to uniaxially compress a collection of NMC particles (modeled using 10-micron diameter spheres) and coarse-grained CBD particles (modeled as 500 nm cohesive colloidal particles) from the as-coated condition (roughly 90% porous) all of the way through calendaring (as low as 20% porosity).

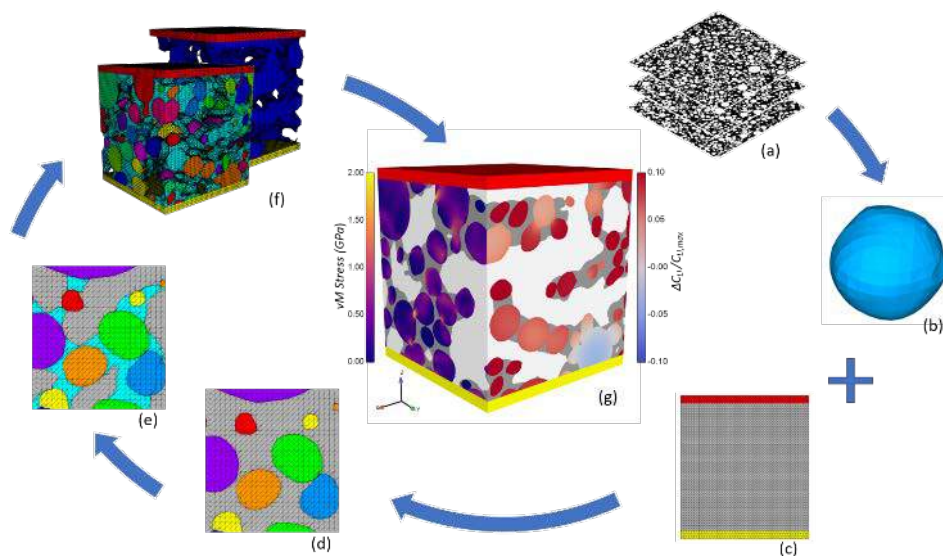


Figure I.3.B.1 Workflow for converting 3D imaging to simulation including the conductive binder domain.

Results

The key technical results arising from our FY2019 research are presented in the following subsections.

Coupled Electrochemical and Mechanical Analysis of NMC Cathodes

Battery electrodes are composed of polydisperse particles and a porous, composite binder domain. These materials are arranged into a complex mesostructure whose morphology impacts both electrochemical performance and mechanical response. We present image-based, particle-resolved, mesoscale finite element model simulations of coupled electrochemical-mechanical performance on a representative NMC electrode domain. Beyond predicting macroscale quantities such as half-cell voltage and evolving electrical

conductivity, studying behaviors on a per-particle and per-surface basis enables performance and material design insights previously unachievable. Voltage losses are primarily attributable to a complex interplay between interfacial charge transfer kinetics, lithium diffusion, and, locally, electrical conductivity. Mesoscale heterogeneities arise from particle polydispersity and lead to material underutilization at high current densities. Particle-particle contacts, however, reduce heterogeneities by enabling lithium diffusion between connected particle groups. While the porous CBD may have slower ionic transport and less available area for electrochemical reactions, its high electrical conductivity makes it the preferred reaction site late in electrode discharge. This work enables improvements in materials design by providing a tool for optimization of particle sizes, CBD morphology, and manufacturing conditions. Highlights of the insights available from this study are found in Figure I.3.B.2 and is published as [7].

Mesoscale Effects of Composition and Calendering in Lithium-Ion Battery Composite Electrodes

Macrohomogeneous battery models are widely used to predict battery performance, necessarily relying on effective electrode properties, such as specific surface area, tortuosity, and electrical conductivity. While these

properties are typically estimated using ideal effective medium theories, in practice they exhibit highly non-ideal behaviors arising from their complex mesostructures. In this paper, we computationally reconstruct electrodes from x-ray computed tomography of 16 nickel-manganese-cobalt-oxide electrodes, manufactured using various material recipes and calendering pressures. Due to imaging limitations, a synthetic conductive binder domain (CBD) consisting of binder and conductive carbon is added to the reconstructions using a binder bridge algorithm. Reconstructed particle surface areas are significantly smaller than standard approximations predict, as the majority of particle surface area is covered by CBD, affecting electrochemical reaction availability. Finite element effective property simulations are performed on 320 large electrode subdomains to analyze trends and heterogeneity across the electrodes. Significant anisotropy of up to 27% in tortuosity and 47% in effective conductivity is observed. Electrical conductivity increases up to 7.5x with particle lithiation. We compare results to traditional Bruggeman approximations and offer improved alternatives for use in cell-scale modeling, with Bruggeman exponents ranging from 1.62-1.72 rather than the

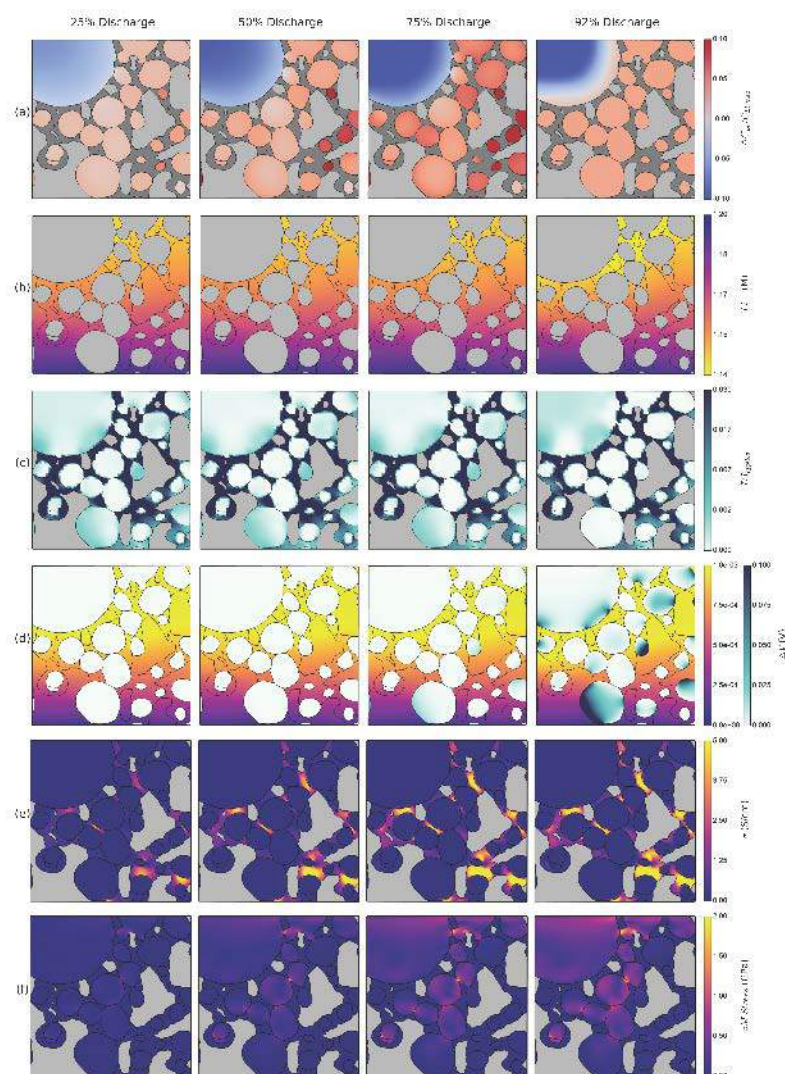


Figure I.3.B.2 Planar snapshots from a full 3D mesostructure under 5C constant current discharge. In all cases, the current collector is at the top of the image, with the separator at the bottom. When not colored, the electrolyte and particle regions are light grey (particles are approximately spherical) and the binder region is dark grey. Figure sublabels (a-f) refer to rows containing information about a parameter of interest at four different states of charge.

theoretical value of 1.5. Results for tortuosity are found in Figure I.3.B.4. We also conclude that the CBD phase alone, rather than the entire solid phase, should be used to estimate effective electronic conductivity. This study provides insight into mesoscale transport

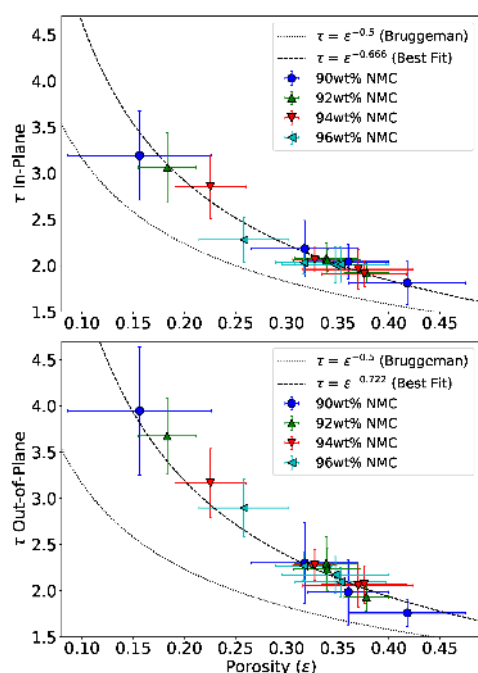


Figure I.3.B.3 Electrolyte phase tortuosity for both in-plane (top) and out-of-plane (bottom) directions. Markers represent mean values across simulated subdomains while error bars represent two standard deviations. The traditionally used Bruggeman equation is plotted for comparison, and a Bruggeman model form best fit to the simulation results is also provided.

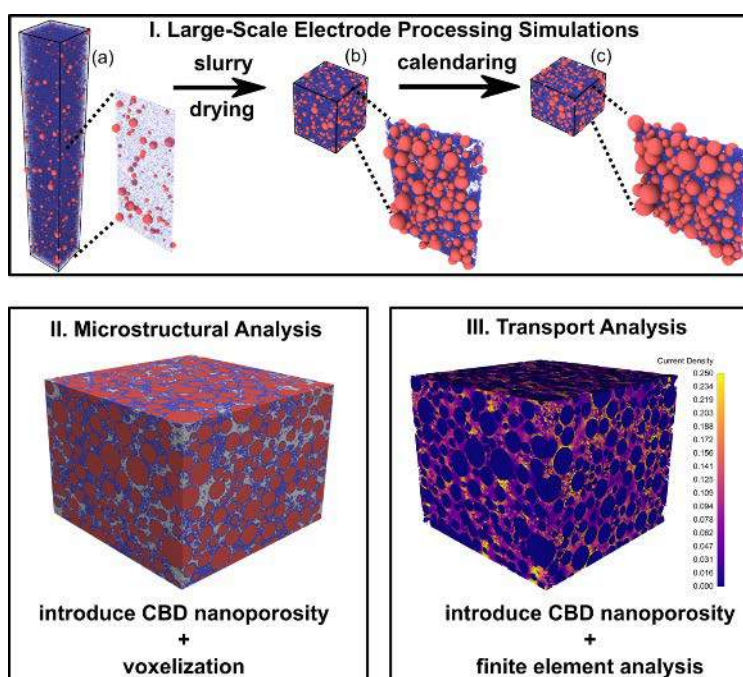


Figure I.3.B.4 Simulation methodology: (I) The manufacturing of three-phase electrodes, from slurry drying to calendaring, is simulated using granular and colloidal dynamics. The AM particles (red) are poly-disperse granular particles, and the CBD phase is represented by coarse-grained colloidal particles (blue) of a uniform size. Cross sections in the middle of the electrode are displayed after slurry drying and calendaring. The white region around AM and CBD particles represents the pore space. (II) The simulated electrode in (I) is first swelled to introduce 50% nanoporosity, and then mapped onto a regular lattice to provide a spatial distribution of AM (red), CBD (blue), and pore (white) phases. (III) The effective transport properties are calculated using finite element analyses, with the spatial distribution of current density shown. All images are from the same mesostructure realization.

phenomena and results in improved effective property approximations founded on realistic, image-based morphologies. This work is published as [8].

Controlling Binder Adhesion Towards Mesostructural and Transport Enhancement in Lithium-ion Battery Electrodes

The complex three-phase composition of lithium-ion battery electrodes—containing an ion-conducting pore phase, a nanoporous electron-conducting carbon binder domain (CBD) phase, and an active material (AM) phase—provides several avenues of microstructural engineering to enhance battery performance. In this paper, a promising strategy is demonstrated for engineering electrode mesostructures for enhanced electrochemical transport by controlling the strength of adhesion between the AM and CBD phases. Using high-fidelity, physics-based, colloidal, and granular dynamics simulations, it is predicted that this strategy can provide significant control over electrode mesostructure and transport-relevant properties such as ionic conductivity, electronic conductivity, and AM-electrolyte surface area. Importantly, the proposed strategy could be experimentally realized through surface functionalization of the AM and CBD phases and would be

compatible with traditional electrode manufacturing methods. This work and procedure is summarized in Figure I.3.B.3 and is submitted for publication as [8].

Conclusions

We have used mesoscale computational models of NMC cathodes, combining image-based particles with synthetic CBD phases, to provide insight into the performance of these cathode materials. Coupled electrochemical-mechanical simulations of half-cell discharge highlight the complex interplay between ionic conductivity, surface electrochemical kinetics, and electrical transport in controlling electrochemical performance. A careful study of effective thermal conductivity and tortuosity as a function of conductive binder loading and calendaring pressure provides macroscale properties and improved effective media theory calibrations for use in battery-scale simulations. To supplement the image-based simulations, discrete element simulations demonstrate the interplay between conductive binder cohesion and adhesion in determining electrode mesostructure and therefore performance.

Key Publications

1. S. Roberts, V. Brunini, K. Long and A. Grillet, "A Framework for Three-Dimensional Mesoscale Modeling of Anisotropic Swelling and Mechanical Deformation in Lithium-Ion Electrodes," *Journal of The Electrochemical Society*, vol. 161, pp. F3052-F3059, 2014.
2. S. Roberts, H. Mendoza, V. Brunini, B. Trembacki, D. Noble and A. Grillet, "Insights Into Lithium-Ion Battery Degradation and Safety Mechanisms From Mesoscale Simulations Using Experimentally Reconstructed Mesostructures," *Journal of Electrochemical Energy Conversion and Storage*, vol. 13, pp. 031005--031005, 2016.
3. S. A. Roberts, H. Mendoza, V. E. Brunini and D. R. Noble, "A verified conformal decomposition finite element method for implicit, many-material geometries," *Journal of Computational Physics*, pp. 352 - 367, 2018.
4. B. Trembacki, D. Noble, V. Brunini, M. Ferraro and S. Roberts, "Mesoscale Effective Property Simulations Incorporating Conductive Binder," *Journal of The Electrochemical Society*, vol. 164, pp. E3613-E3626, 2017.
5. B. L. Trembacki, A. N. Mistry, D. R. Noble, M. E. Ferraro, P. P. Mukherjee and S. A. Roberts, "Editors' Choice—Mesoscale Analysis of Conductive Binder Domain Morphology in Lithium-Ion Battery Electrodes," *Journal of The Electrochemistry Society*, pp. E725-E736, 2018.
6. M. E. Ferraro, B. L. Trembacki, V. E. Brunini, D. R. Noble and S. A. Roberts, "Electrode Mesoscale as a Collection of Particles: Coupled Electrochemical and Mechanical Analysis of NMC Cathodes," *Journal of the Electrochemical Society*, 2020.
7. B. L. Trembacki, D. R. Noble, D. R. Ferraro and S. A. Roberts, "Mesoscale Effects of Composition and Calendaring in Lithium-Ion Battery Composite Electrodes," *Journal of Electrochemical Energy Conversion and Storage*, 2020.
8. I. Srivastava, D. S. Bolintineanu, J. B. Lechman and S. A. Roberts, "Controlling Binder Adhesion Towards Mesostructural and Transport Enhancement in Lithium-ion Battery Electrodes," 2020.

References

1. M. Ebner, F. Geldmacher, F. Marone, M. Stampanoni and V. Wood, "X-Ray Tomography of Porous, Transition Metal Oxide Based Lithium Ion Battery Electrodes," *Advanced Energy Materials*, vol. 3, pp. 845--850, 2013.
2. K. Higa, S.-L. Wu, D. Parkinson, Y. Fu, S. Ferreira, V. Battaglia and V. Srinivasan, "Comparing Macroscale and Microscale Simulations of Porous Battery Electrodes," *Journal of The Electrochemical Society*, vol. 164, pp. E3473-E3488, 2017.

Acknowledgements

We would like to acknowledge members of the Sandia CAEBAT team, namely Bradley Trembacki, Mark Ferraro, Ishan Srivastava, and David Noble. We also appreciate our collaboration through the CAEBAT project, including ORNL partners John Turner and Srikanth Allu and our co-authors at Purdue Partha Mukherjee and Aashutosh Mistry.

Sandia National Laboratories is a multi-mission laboratory managed and operated by National Technology and Engineering Solutions of Sandia, LLC., a wholly owned subsidiary of Honeywell International, Inc., for the U.S. Department of Energy's National Nuclear Security Administration under contract DE-NA0003525.

I.3.C Advanced Tool for Computer Aided Battery Engineering (ANL)

Dr. Daniel Abraham, Principal Investigator

Argonne National Laboratory
9700 Cass Avenue
Lemont, IL 60439
E-mail: abraham@anl.gov

Brian Cunningham, DOE Technology Development Manager

U.S. Department of Energy
E-mail: Brian.Cunningham@ee.doe.gov

Start Date: October 1, 2016
Total Project Cost: \$300,000

End Date: September 30, 2019
DOE share: \$300,000

Non-DOE share: \$0

Project Introduction

The main goals of DOE's Computer Aided Engineering for Electric-Drive Vehicle Batteries (CAEBAT) Program were introduced in section I.C.1. In this section we describe the experimental studies conducted at Argonne National Laboratory (ANL) to support the development of 3D models of electrochemical processes on the electrode microstructure length scale and to provide an understanding of factors that limit electrode performance and cause premature degradation. These studies are intended to complement and enhance the experimental and computational work being conducted at the partner national laboratories and universities.

Objectives

The key objectives of our work can be summarized as follows:

- 1) To provide the positive and negative electrodes needed to accomplish the various tasks.
- 2) To characterize the electrodes using conventional electrochemical techniques, both in half-cell and full-cell configurations, and to provide the data for the development of 3D electrochemistry models.
- 3) To develop advanced tools, including spectroscopy and diffraction, to obtain deeper insights on the correlations between electrode microstructure and electrochemical performance.

Approach

Commercial lithium-ion batteries (LIBs) predominantly use porous graphite (Gr) anodes (negative electrodes) and layered metal oxide cathodes (positive electrodes). At cycling rates below 1C (full discharge in 1 hour), these LIBs can go through hundreds of cycles of operation with minimal performance degradation. However, at higher cycling rates, the capacity, cycle life, and thermal stability of these LIBs is known to degrade. Theoretical studies of lithium intercalation using Newman-type models attribute these effects to lithium plating, kinetic losses, and Li^+ concentration gradients occurring both in the electrolyte filling the matrix pores and in the graphite electrode itself. These concentration gradients are problematic for a number of reasons: they polarize the cell, lowering capacity by causing the cell to reach its cut-off voltage before all the lithium is fully extracted from the cathode; they create heterogeneous conditions at the anode that can result in localized lithium plating; and they generate stresses, within the active material particles causing their fracture, and in the electrode coating causing it to peel off the current collector.

We have been using a microprobe reference electrodes (RE) to characterize lithium ion cells charged at high rates. [1] The RE can independently determine potentials in the cathode and anode during the electrochemical test. Specifically, the RE is used to diagnose two detrimental conditions: metallic lithium deposition on the graphite anode and impedance rise in the oxide cathode. The effects of anode polarization caused by the high currents is particularly important because the close proximity of lithiated graphite to Li plating potentials can

result in lithium plating. In this report we focus on the voltage relaxation dynamics at the electrodes *after* abrupt stopping of the current flows. The transient phenomena during this relaxation can limit the rates of charging and discharging during braking and acceleration of electric cars. Equally important is to consider how such phenomena affect the time-dependency of the open circuit voltage (OCV), as the effective control of battery packs rely on state-of-charge (SOC) estimations entirely based on known OCV values.

All cells in this study included a NCM523 cathode ($\text{Li}_{1.03}(\text{Ni}_{0.5}\text{Co}_{0.2}\text{Mn}_{0.3})_{0.97}\text{O}_2$), a graphite anode and the standard “Gen2” electrolyte (1.2 M LiPF_6 in a 3:7 wt/wt mixture of ethylene and ethyl methyl carbonates). The anode contained 91.8 wt% graphite (CGP-A12, Philips 66), 2 wt% of carbon black (C45, Timcal), 0.2 wt% oxalic acid and 6 wt% poly(vinylidene difluoride) (PVdF) binder (KF-9300, Kureha). The cathode contained 90 wt% NCM523 (Toda) and 5 wt% of both C45 and PVdF (Solvay 5130). Slurries were coated on battery grade copper and aluminum foils, respectively. The electrodes were calendared after drying, resulting in a thickness of 44 μm (38.4% porosity) for the anode and 34 μm (33.5% porosity) for the cathode. The cells (20.3 cm^2 electrode area) also contained a microprobe reference electrode (RE), which is a 25 μm thick insulated Cu wire with an electrochemically lithiated tip (2 mm). [1] This microprobe was placed at the center of the electrode stack and sandwiched between two microporous Celgard 2325 separators.

All measurements were conducted on cells conditioned after two formation cycles at C/10 followed by a capacity measurement at a C/25 rate. During voltage-limited charging, the graphite cell was cycled at a constant rate between 3.0 V (lower cutoff voltage, LCV) and 4.39 V (UCV). After reaching the UCV, the cells were allowed to rest for >1 h at open circuit. During capacity-limited tests, the graphite cell was charged to a set capacity at a constant rate, followed by the rest step. In each case, the cell was exposed to cycles with progressively increasing current from low C-rates (C/5) to high C-rates (6C). Discharge was always carried out at C/5, followed by a potentiostatic hold at the LCV until the measured current was below C/25. For studies of cell response to current pulses, cells were first charged at a C/10 rate to the specified voltage, followed by a potentiostatic hold for 1 h. Single or hybrid current pulses with duration $\tau=0.2\text{--}30$ s and the C-rate up to 16C were used. The anode and cathode potentials (ϕ_a and ϕ_c) and full-cell voltage (U) were independently logged during and after these pulses.

Results

Switching off constant charging currents. Figure I.3.C.1a shows a set of relaxation kinetics $U(t)$ for voltages observed after galvanostatic charging of a cell to a UCV of 4.39 V at varying rates. Comparing curves of different rates, two behaviors stand out. First, the starting voltage (at $t=0$) is progressively lower at increasing rates, due to the ohmic drop. At higher charging rates, the UCV is achieved at a lower SOC due to increasing polarization of the cell, causing the cell to relax to a lower voltage. Second, the initial relaxation (< 2 min) comprises an increasingly greater fraction of voltage change when the cell is charged at higher rates. After the initial decay, the cell voltage continues to decrease over several decades in time. A closer examination suggests that kinetics in Figure 1a are bimodal. Empirically, these kinetics can be fit to a master equation

$$U(t) \approx U_{\infty} + (U_0 - U_{\infty}) \{1 - \eta [1 - e^{-t/\tau_f}]\} e^{-(t/\tau_s)^{\nu}} \quad (1)$$

where η is the fraction of the fast (exponential) component with the time constant τ_f and the slow, dispersive decay is represented by a stretched exponential component with $\nu \approx 1/2$ and the time constant τ_s . The extrapolated initial (U_0) and terminal (U_{∞}) voltages scale linearly with the C-rate (Figure I.3.C.2). The solid lines in Figure I.3.C.1a are least squares fits with eq. (1), and the associated time constants are shown in Figure I.3.C.1b. While the time constant τ_f of the fast component is rate-independent, the time constant τ_s of the slow component is inversely proportional to the C-rate. We have examined numerous cells containing graphite electrodes, varying the electrode material and porosity and thickness of the matrix, as well as the lithium salt in the electrolyte, and in each case obtained dispersive kinetics similar to the ones shown in Figure I.3.C.1b. While the absolute values for these two time constants somewhat varied, the general behavior remained the same: there was a fast rate-independent component and a slow rate-dependent component comprising 20% to 50% of the total response.

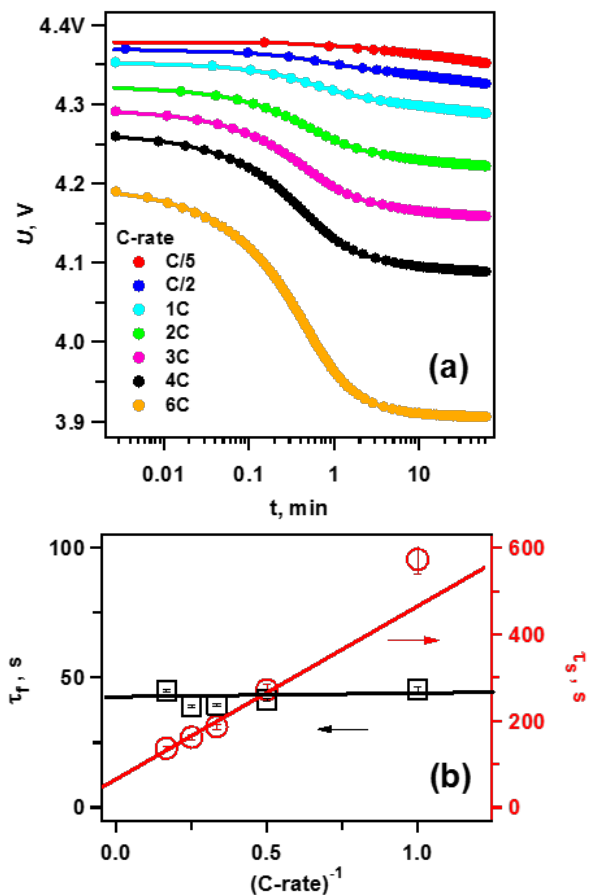


Figure I.3.C.1 (a) Relaxation dynamics for cell voltage U at different C-rates. The constant-current charging was terminated when U reached 4.39 V. The solid lines are least squares fits to eq. 1. (b) The plots of τ_s and τ_r vs. the reciprocal C-rate during charge; smaller the τ_s value, faster the cell relaxation

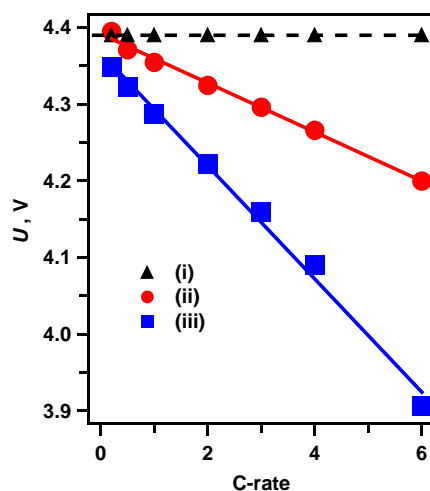


Figure I.3.C.2 Extrapolated voltages U for relaxation kinetics of cell-I shown in Figure I.3.C.1 and plotted vs. C-rate during charge. Traces i, ii, and iii correspond to the voltage before and after the Ohmic drop at $t=0$ (U_0), and voltage at $t=\infty$ (U_∞), respectively, that was estimated using eq. 1. The solid lines are linear fits

The relaxation dynamics of the full-cell potential is determined by the electrode potentials ϕ_a and ϕ_c . These are shown separately in Figure I.3.C.3a and b: greater potential variations are also seen after higher charging rates. The graphite OCV of ~ 88 mV is eventually reached during resting, regardless of the charging current (Figure I.3.C.3a). At higher rates, however, ϕ_a exhibits a maximum before equilibrating to the OCV value. For this cell chemistry, the anode potential vs. Li/Li^+ becomes negative at rates above $\sim 3\text{C}$, indicating that Li plating occurs on the electrode. The maximum seen in Figure I.3.C.3a only appears when the cell enters Li plating condition. The feature is intensified with repeated cycling and/or when ϕ_a decreases below -50 mV vs. Li/Li^+ . It is likely that the maximum is associated with rapid insertion of plated Li into the under-lithiated graphite during equilibration of the anode.

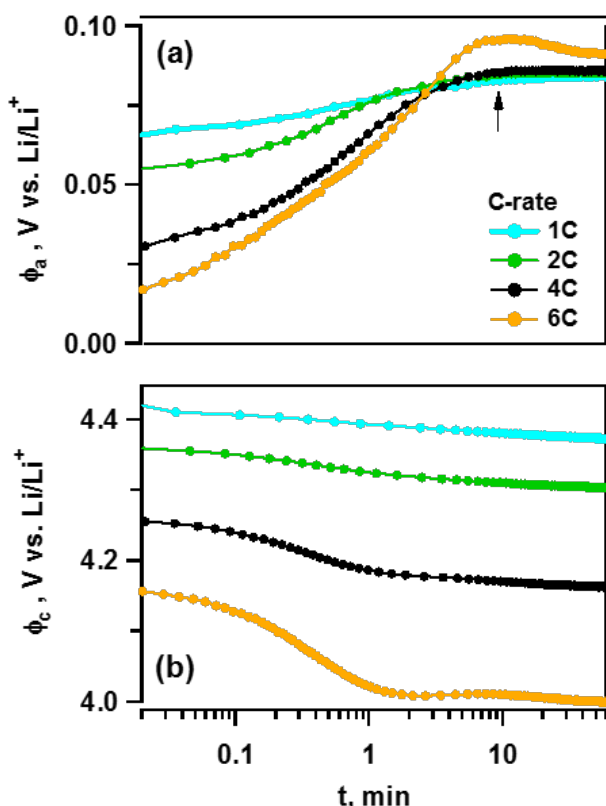


Figure I.3.C.3 Relaxation dynamics of the (a) anode and (b) cathode potentials for voltage-limited charging of cell I shown in Figure I.3.C.1 and Figure I.3.C.2. The C-rates are color coded as shown in panel a. The vertical arrow in panel a indicates maxima in the $\phi_a(t)$ kinetics that are most clearly seen at a rate of 6C

Polarity and duration of current pulses. Having covered the time response to fast switching off of a steady current, we now examine short current pulses. In these tests, successive pulses with increasing rate or pulse duration were applied to the cell, with each pulse being applied after the cell was equilibrated at a same voltage.

Figure I.3.C.4a shows the response to 10 s long *charge* pulses applied at 4.2 V as the rate increased from C/2 to 10C. It is seen from Figure I.3.C.4b that the voltages at both edges of the pulse increase proportionally to the rate, so for a fixed pulse duration the impedance is constant at all rates, i.e., a linear response is observed. The voltage relaxation of the cell *after* the current pulses is presented in Figure I.3.C.5a (*solid lines*). We used eq. 1 to fit these kinetics (*dashed lines*), and in Figure I.3.C.5b time constants are plotted vs. the reciprocal C-rate. Comparison with Figure I.3.C.1b indicates that time responses after a 10 s pulse and after abrupt termination of steady current follow the same trends.

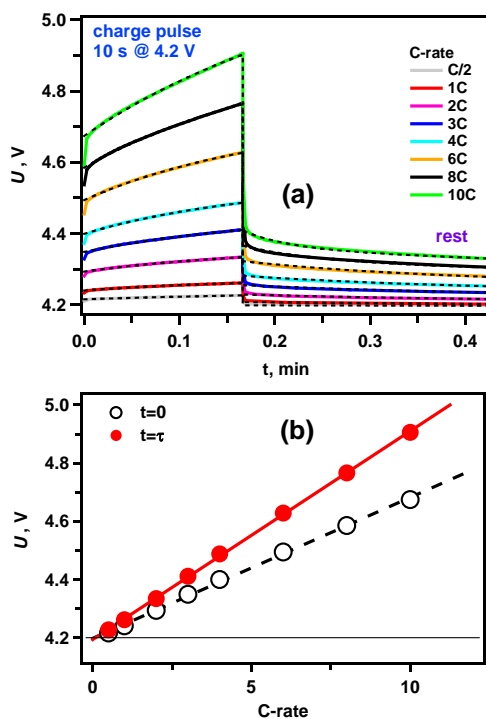


Figure I.3.C.4 (a) Voltage changes induced by $\tau=10$ s pulses applied at 4.2 V. The C-rates during the pulse are given in the inset. (b) The initial (open circles) and end-of-pulse (filled circles) voltages. The straight lines are linear fits. In panel a, the lines represent least squares fits to eq. 1 after the pulse and exponential fits during the pulse

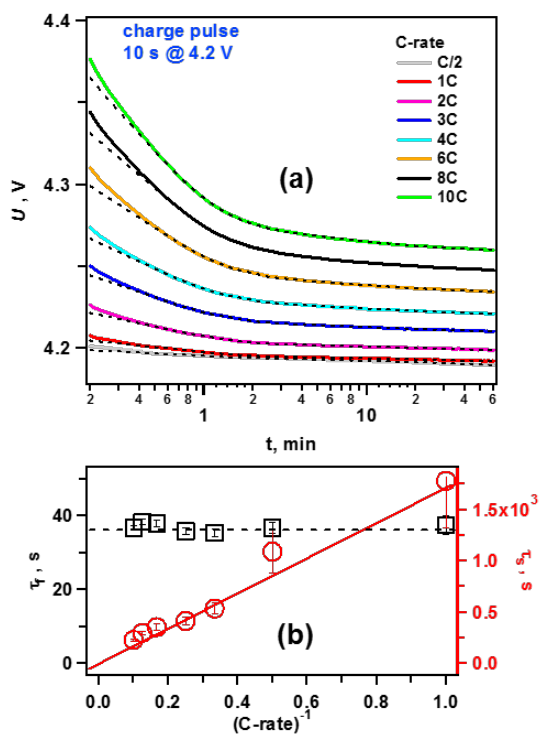


Figure I.3.C.5 Relaxation kinetics for U after a 10 s long charge pulse applied at 4.2 V (solid lines). The dashed lines are least squares fits to eq. 1. (b) A plot of time constants for the fast (τ_f) and slow (τ_s) components of kinetics plotted vs. the reciprocal C-rate. The fast component is C-rate independent, while the slow component scales with the C-rate

Conclusions

Our results reveal that potential responses to trailing edges of pulsed or steady currents are qualitatively similar. The time response weakly depends on the cell voltage, state-of-charge and current polarity, but strongly depends on the current amplitude. There is a fast component that is rate- and pulse length independent. This component reflects rapid equilibration of the cell described by Newman type models. In addition to this fast component, there is also a slow component with stretched-exponential profile; this component, as far as we can tell, is not predicted by contemporary models. For a sufficiently long current pulse, the rate constant for this component is proportional to the C-rate, but for very short pulses it becomes independent of the C-rate. There is a small minimum charge that needs to be passed through the cell for the slow component to become rate-dependent, and this charge is equivalent to a minute fraction of the total charge stored in the cell. The time constant for this slow component is weakly dependent of the voltage, polarity, and even the pulse duration, provided that this duration is sufficiently long.

We note that the relaxation behavior can be described by stretched-exponential kinetics (equation 1, also known as the Kohlrausch function), which is the universal feature of relaxation in disordered and/or microheterogeneous media. The stretch factors ν in eq. 1 are close to $3/5$ and $3/7$ that are typical for regimes in which short-range (e.g., dispersive) or long-range (e.g., Coulomb) interactions prevail, respectively. We propose that the stretched-exponential kinetics can be explained by trap-limited transport; i.e., diffusion of charge carriers between randomly dispersed static traps in the medium that capture and release these carriers as they travel through the medium. Given that most of phases in Li-ion cells are well ordered, such dispersive kinetics almost certainly involve migration of Li^+ ions through a disordered interphase, which is consistent with our observation that speeding of time response requires passing a small fraction of the total charge. Our data suggests that the dispersive kinetics is likely dominated by the cathode response. Experiments are underway to determine the origin and mechanisms of the slow response, as these same mechanisms likely contribute to cell polarization during rapid charging of lithium-ion battery cells.

Key Publications

1. Ilya A. Shkrob, Marco-Tulio F. Rodrigues, and Daniel P. Abraham, “Fast Charging of Li-ion Cells: Part 3. Relaxation Dynamics and Trap-Controlled Lithium Ion Transport”, *under review* by Journal of the Electrochemical Society (2019).

References

1. M.-T. F. Rodrigues, K. Kalaga, S. E. Trask, D. W. Dees, I. A. Shkrob and D. P. Abraham, J. Electrochem. Soc., 166, A996 (2019).
2. M.-T. F. Rodrigues, V. A. Maroni, D. J. Gosztola, K. P. C. Yao, K. Kalaga, I. A. Shkrob and D. P. Abraham, ACS Appl. Energy Mater., 2, 873 (2019).

Acknowledgements

The electrodes used in this article are from Argonne’s Cell Analysis, Modeling and Prototyping (CAMP) Facility, which is supported within the core funding of the Applied Battery Research (ABR) for Transportation Program. We are grateful to colleagues, both at Argonne and elsewhere for their support during this effort.

I.3.D Development and Validation of a Simulation Tool to Predict the Combined Structural, Electrical, Electrochemical and Thermal Responses of Automotive Batteries (Ford Motor Company)

Dr. Chulheung Bae, Principal Investigator

Ford Motor Company
Energy Storage Research
2101 Village Road
Dearborn, MI 48121
E-mail: cbae@ford.com

Brian Cunningham, DOE Technology Development Manager

U.S. Department of Energy
E-mail: Brian.Cunningham@ee.doe.gov

Start Date: January 1, 2016
Total Project Cost: \$4,375,000

End Date: December 31, 2019
DOE share: \$3,500,000

Non-DOE share: \$875,000

Project Introduction

This is the fourth and last year of a (originally three-year) project to develop a practical simulation tool for predicting battery abuse response. However, due to unexpected problems in cell testing, model validation fell behind schedule, and a one-year no-cost extension was approved. The project will now conclude by the end of 2019.

The project plan including major constituents and progression based on case studies is shown in Figure I.3.D.1. The first half of the project was focused on developing an Alpha version of the model. This included developing new, battery-specific keywords within LS-DYNA, identifying electrical, thermal, and mechanical input parameters, validating the model for performance situations where the cells are cycling in their intended operating mode, demonstrating preliminary abuse simulations for external short and crush, and enhancing the composite element formulations within LS-DYNA to provide accurate representations of battery material mechanics. Importantly, one-way coupling mechanisms linking the structural response to the electrical and thermal response were implemented and initial simulation predictions compared to test results from previous studies to confirm that the solvers are directionally accurate. Physical testing of full cells, begun for model validation in the second year, was insufficient and will be completed during the final year of the project.

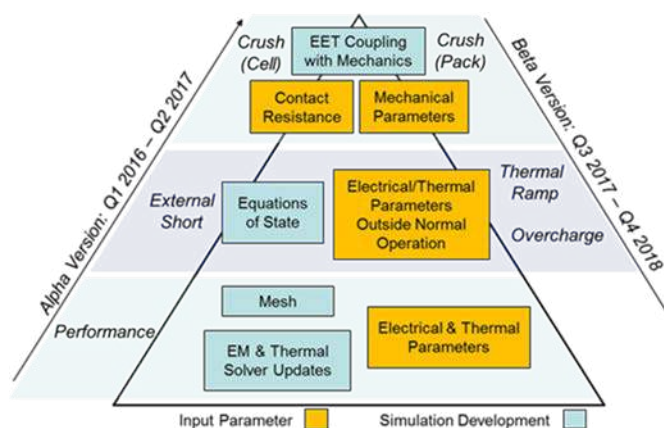


Figure I.3.D.1. Project schematic showing major constituents and progression of Alpha and Beta versions

Objectives

Develop and validate a simulation tool to predict the combined structural, electrical, electrochemical and thermal (SEET) response of automotive batteries to crash-induced crush and short circuit, overcharge, and thermal ramp, and validate it for conditions relevant to automotive crash.

Approach

Develop material constitutive models and finite element method (FEM) element formulations that capture the mechanical response of cell components, including the case material, electrodes, separator, and their interactions with electrolyte.

Clearly identify the required input parameters for the constitutive models, FEM element formulations, and exothermic, electrochemical reaction state equations governing multi-physics phenomena during crush-induced electrical short, thermal ramp, and overcharge conditions.

Design and execute a test matrix encompassing automotive crash strain rates, at a number of kinetic energy levels and physical orientations likely to occur in vehicle impacts.

Develop integrated modeling tools that demonstrate high-fidelity predictions of the onset of thermal runaway from the experimental test matrix using commercially available cells, modules, and packs, spanning multiple chemistries relevant to automotive applications.

Maintain high-fidelity predictions while exploring methods to reduce the computational complexity of the model, and deliver a practical tool that is integrated with the laboratory's Open Architecture Software (OAS), for a broad customer base within automotive product development.

Results

Development of LS-DYNA Solvers

Work continued in refining the mechanical, EM and thermal solvers for three types of models: solid model, composite t-shell model and macro model. In solid models, each individual layers of batteries are resolved. In composite t-shell models, composite t-shell elements are used to represent the cell, which can save simulation time in the mechanical solver while still distinguishing different properties of each component. In macro models, a battery cell is treated as a homogenous part, where a coarse mesh with standard solid elements are utilized.

To examine the performance of these three models, we built three models for two scenarios: a pouch cell placed on a rigid wall is impacted by either a semi-sphere or a semi-cylinder indenter, see Figure I.3.D.2. In each simulation, the indenter moves toward to the cell at a constant speed for 0.5ms (semi-sphere) or 0.6ms (semi-cylinder), after which all parts become rigid and the EM and thermal solvers continue to run until the end of simulations. It is assumed that a short circuit occurs when the distance between positive and negative current collectors decreases 10% of its original value in solid and composite t-shell models. The short-circuit condition in the macro model is based on effective strain and its critical value is calibrated to match the solid element model.

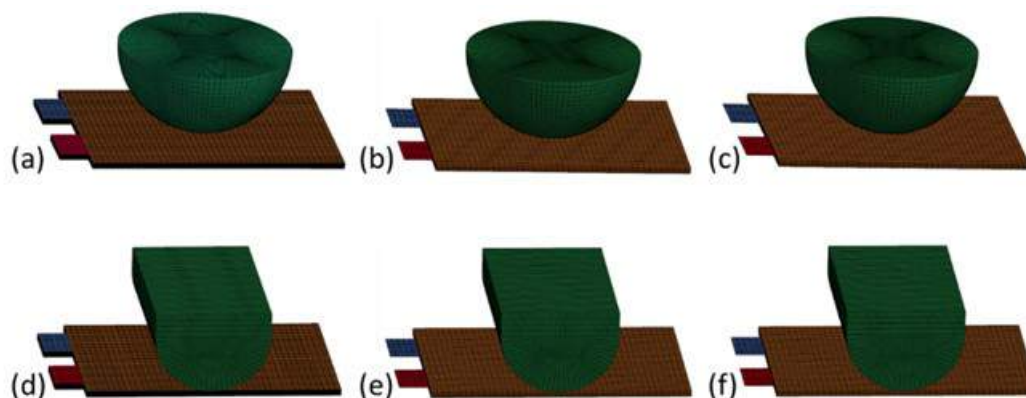


Figure I.3.D.2 Model setup for a pouch cell impacted by (a, b, c) a semi-sphere and (d, e, f) a semi-cylinder indenter, where the cell bulk is represented by (a, d) standard solid elements, (b, e) composite tshell elements and (c, f) macro model

Comparison of loading force, voltage, state of charge and temperature distribution in different models is shown in Figure I.3.D.3 and Figure I.3.D.4. It can be seen that in all simulations, the cell is shorted during the impact period, during which voltage and state of charge (SOC) drop rapidly. After that, voltage and SOC decrease gradually and then temperature starts to increase due to Joule heating. Moreover, it is found that the three types of models give almost the same results. The relative simulation time between them is given by Figure I.3.D.5. It shows that the composite t-shell model is more than one order of magnitude faster than the solid model due to time savings in the mechanical solver. In addition, the macro model is more than two orders of magnitude faster than the solid model since it uses coarse mesh and homogeneous material properties. It demonstrates that with calibration, the macro model can achieve the similar results using much less time compared with the solid model. This time saving is critical to large-scale simulations and allows us to extend the simulations from cell to module/pack level. On the other hand, in order to capture the detailed behaviors of each individual layers, composite t-shell model is preferred.

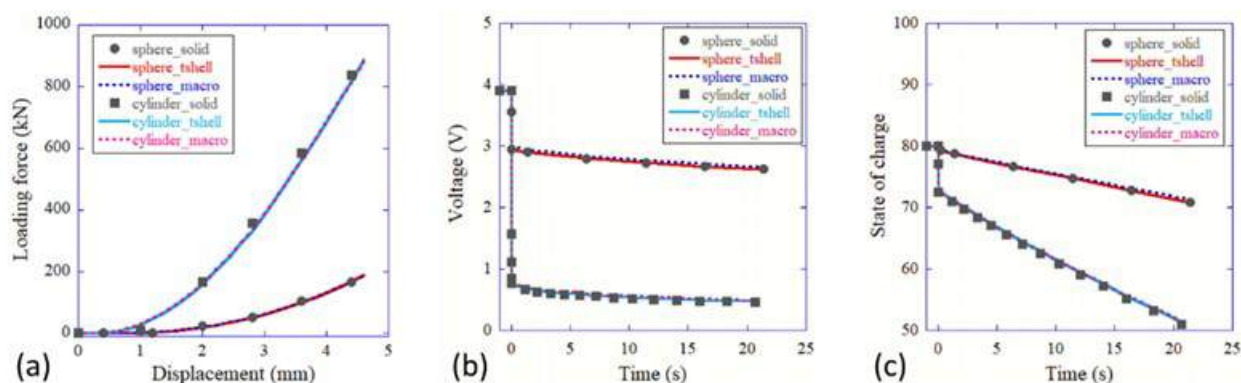


Figure I.3.D.3 Comparison of (a) loading force, (b) cell voltage and (c) state of charge in models with different indenters and element types

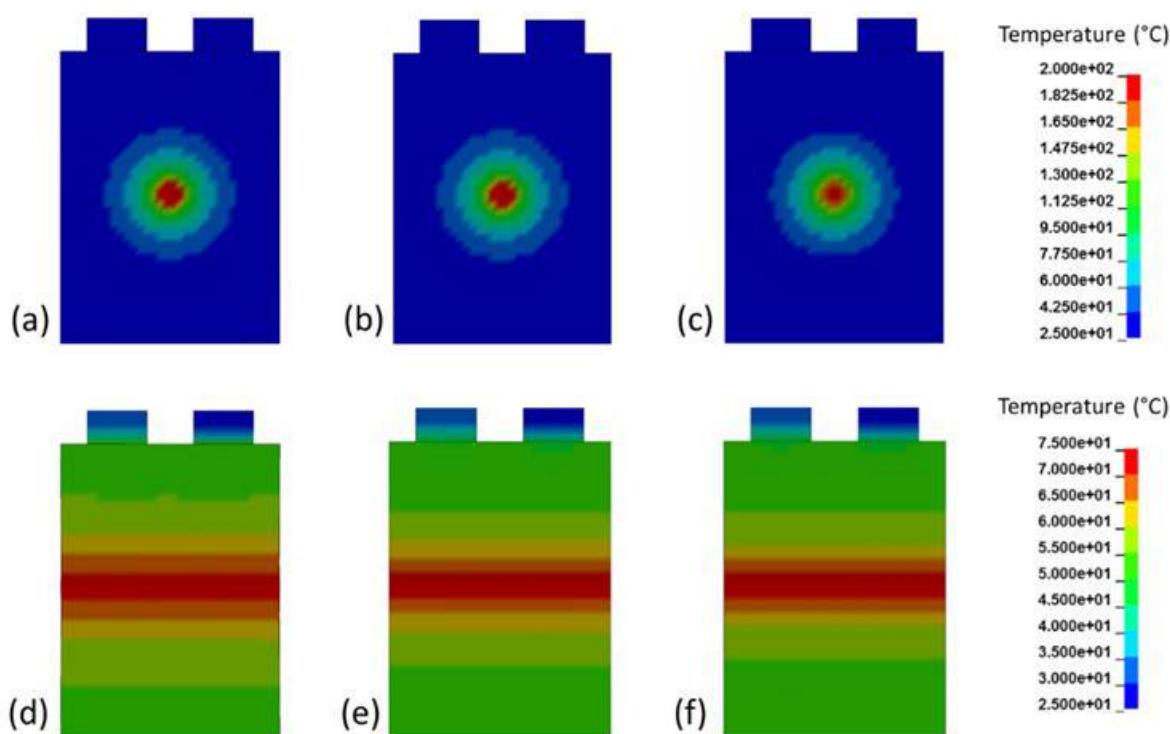


Figure I.3.D.4 Temperature distribution in (a, d) solid element model, (b, e) composite tshell model and (c, f) macro model when a pouch cell is impacted by a (a, b, c) semi-sphere and (d, e, f) semi-cylinder indenter

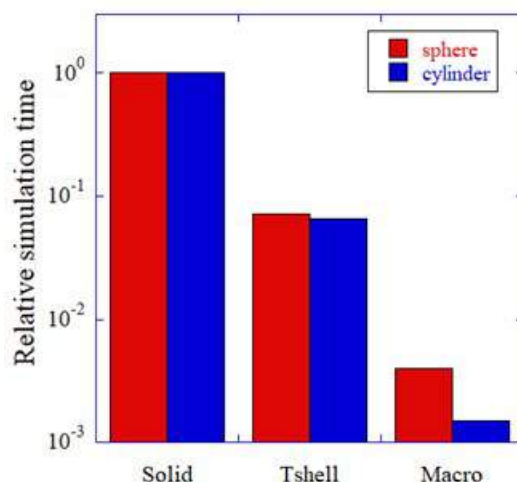


Figure I.3.D.5 Comparison of the relative computational time in different models

Along with the solver development, the impact and quasi-static tests for both pouch (type D) and prismatic (type E) cells are completed. Different loading conditions are selected, see Table I.3.D.1 and Table I.3.D.2. Test results show that the cell behaviors depend on the indenter type such that the peak force with semi-cylinder indenter is higher than semi-sphere indenter due to its larger contact area with cell. Moreover, the cell behavior does not show strong dependence of the state of charge. In addition, it is found that, when the platen has trough in the center, the loading force is higher while the cell is less likely to fail (be shorted) compared with the flat platen case. Furthermore, it is shown that the cell behavior depends on the strain rate such that the response under impact is different from the quasi-static case. These results not only improve our understanding of cell behaviors in abuse conditions, but also provide data to calibrate and validate the model predictions.

Table I.3.D.1 Impact test conditions for pouch and prismatic cells.

Cell Type	Impact energy	Indenter shape	SOC	Platen type				
				flat	41%t	100%t	170%t	200%t
D	High	Cylinder	100	X	X	X	X	X
			20	X	X	X	X	X
		Sphere	100	X				
			20	X				
	Low	Cylinder	100	X	X	X	X	X
		Sphere	100	X				
E	High	Cylinder	100	X				
			20	X				
		Sphere	100	X				
			20	X				
	Low	Cylinder	100	X				
		Sphere	100	X				

Table I.3.D.2 Quasi-static test conditions for pouch and prismatic cells.

Cell Type	Indenter shape	SOC	Platen type				
			flat	41%t	100%t	170%t	200%t
D	Cylinder	100	X	X	X	X	X
	Sphere	100	X				
E	Cylinder	100	X				
	Sphere	100	X				

Constitutive Material Model Development for Active Materials

Battery jellyrolls are made from a stack of alternating layers of electrodes and separators. The electrodes consist of layers of active materials laminated on the conductive metal foils. The active materials are porous, loosely bonded particulate assemblies that are permeated with electrolyte. The mechanical strength of the active material layers is relatively low as active material particles have cohesive and adhesive bonding with a small quantity of binders. However, they make up the largest volume fraction in the jellyroll and thereby control the mechanical response of the assembly. The models and mechanical properties of separators and current collectors are well established. However, material models and parameters for active materials are still under development.

Our experiments have indicated that active materials in the cell have similar response to geologic materials. That is not surprising because of their constitution, which resembles soils with cohesion and loosely bonded aggregates. In this task, we calibrated the parameters for soil material models to resemble the observed response of the active materials in mechanical experiments. The difference in length scales between the standard equipment for soil characterization and active materials in cells does not allow for application of standard test equipment for soil characterization. We have developed and conducted mechanical tests on active materials in the previous project year. During this fiscal year, we have calibrated the material model properties for different soil constitutive models available in LS-DYNA. The candidate material models were

MAT_025 (MAT_GEOLOGIC_CAP_MODEL),

MAT_63 (MAT_CRUSHABLE_FOAM),

MAT_145 (MAT_SCHWER_MURRAY_CAP_MODEL),

MAT_173 (MAT_MOHR_COULOMB), and MAT_193 (MAT_DRUCKER_PRAGER).

The foam material model, MAT_063, was used in the earlier phase of this project and is the main material model used for the modeling of battery cell deformation in the open literature. However, MAT_063 cannot model the shear dominance in the deformation, shear dilatation, and various strength deterioration mechanisms. While material parameters were fit from experiments to the above constitutive models and used in simulations, the two principal models for this project phase were MAT_025, and MAT_145. These two materials are capable of modeling characteristic responses of bonded particulate materials and can represent the deformation modes observed in the cell indentation experiments.

The MAT_025 model was used first. This material model does not have limit values for strength, and cannot model damage or strain rate effects. The fitting procedure and parameter identification has been developed and reported to the project participants. The process will be described and submitted to a journal publication. MAT_145 is an extension of MAT_025. It adds sub-models for variation of strength with respect to loading configuration, damage sub-models and strain rate sensitivity. It can be used to simulate processes of brittle and ductile failure in active materials. The reduction in strength in active materials under load then creates additional loading in other cell components and can lead to the overall mechanical failure. The layered thick shell formulation developed in this project and implemented in LS-DYNA can be used for simulating the mechanical response of the cell jellyroll with low computational cost. Current material parameters for MAT_025 and MAT_145 are shown in Table I.3.D.3.

Simulations of SWRI Indentation Tests of Pouch Cells using Geological Cap Model for Active Materials

In this task, we have developed models for simulation of the quasi-static indentation tests performed at the South West Research Institute (SWRI). The models use geological cap model (MAT_025) and crushable foam (MAT_063) from LS-DYNA to model active materials. Other jellyroll components are modeled with isotropic elasto-plastic material (MAT_024) as described in previous reports. The parameters for MAT_025 have been developed during this period based on the experiments at ORNL and data reported in the literature on the testing of cell active materials.

Table I.3.D.3 Material parameters for active materials for material models MAT_025 and MAT_145.

Anode Active Material		Cathode Active Material	
MAT_025	MAT_145	MAT_025	MAT_145
G = 0.082 GPa	G = 0.082 GPa	G = 0.082 GPa	G = 0.082 GPa
K = 0.06 GPa	K = 0.06 GPa	K = 0.06 GPa	K = 0.06 GPa
$\alpha = 0.578$ MPa	$\alpha = 0.578$ MPa	$\alpha = 2.31$ MPa	$\alpha = 2.31$ MPa
$\theta = 0.333$	$\theta = 0.333$	$\theta = 0.4131$	$\theta = 0.4131$
R = 3.64	R = 3.64	R = 4.16	R = 4.16
W = 0.50	W = 0.50	W = 0.70	W = 0.70
D = 0.00952 MPa ⁻¹	D = 0.00952 MPa ⁻¹	D = 2.8 MPa ⁻¹	D = 2.8 MPa ⁻¹
X ₀ = 2.10 MPa	X ₀ = 2.10 MPa	X ₀ = 9.61 MPa	X ₀ = 9.61 MPa
	$\alpha_1 = \alpha_2 = 1.0$		$\alpha_1 = \alpha_2 = 1.0$
	$\theta_1 = \theta_2 = 0$		$\theta_1 = \theta_2 = 0$
	AFIT = CFIT = EFIT = 1.0		AFIT = CFIT = EFIT = 1.0
	BFIT = DFIT = FFIT = 0.0		BFIT = DFIT = FFIT = 0.0

Table I.3.D.3 only describes mapping of material model parameters. It does not include models for damage (shear, ductile, damage) in MAT_145 that we are currently calibrating to the impact experiments.

The indentation tests were performed with spherical and cylindrical indenters as described in the previous reports. The schematics of the spherical and cylindrical indentation models are shown in Figure I.3.D.6. Type-D (pouch) cell is deformed with rigid indenters of spherical and cylindrical shapes. The radius of the spherical indenter is 75mm, and the radius of the cylindrical indenter is 25mm. We used layered thick shell elements to model the cell. The layered thick shell element allows for modeling of the layered configuration of the jellyroll without having to discretize individual layers with separate solid elements. We have exploited symmetries in the model to speed up computations.

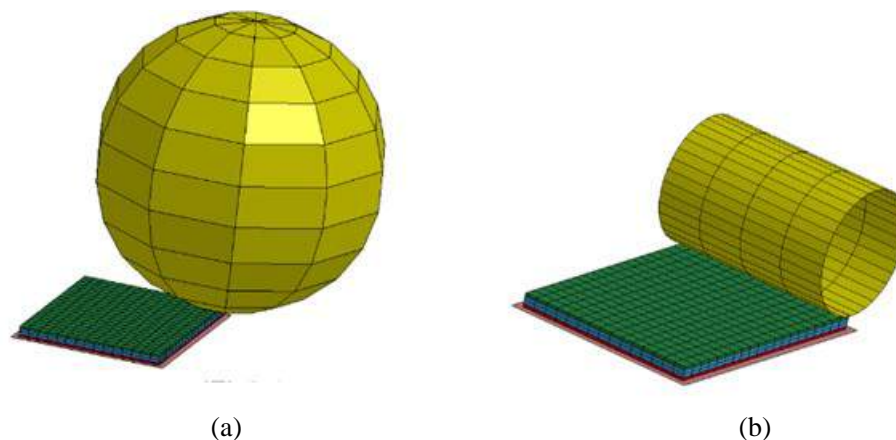


Figure I.3.D.6 Layered element model for (a) spherical and (b) cylindrical indentation

The comparison of the simulation results and experiments in Figure I.3.D.7. The agreement between the simulations based on MAT_025 material model is much closer to the experiments compared to the MAT_063 that was used earlier in the project.

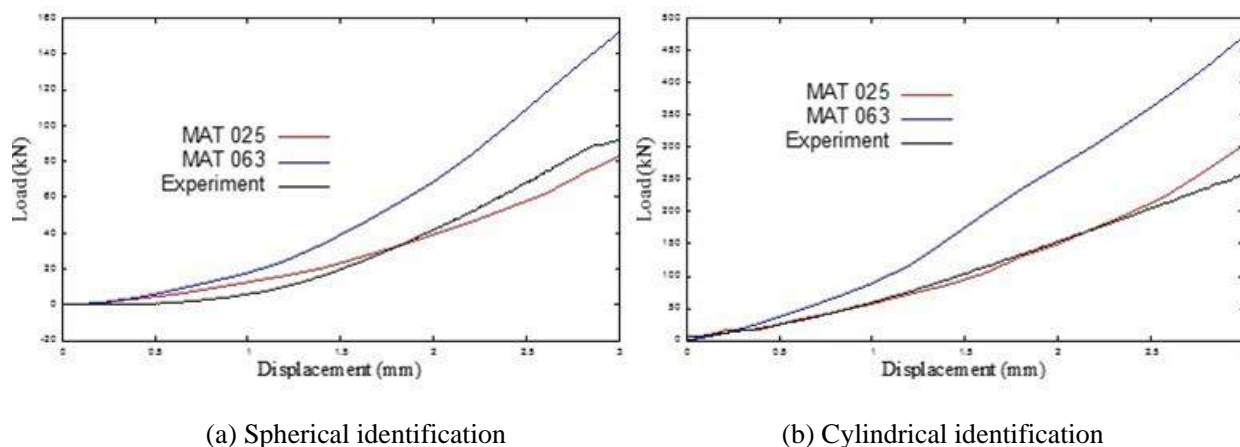


Figure I.3.D.7 Indentation loads obtained by different active material model formulations and comparison with experiments for (a) spherical and (b) cylindrical indentation

Simulations of Pouch Cell Shear Tests using Geological Cap Model for Active Materials

In the earlier work, the simulations of the shear tests of Type D cells were yielding much higher reaction forces compared to experiments. In those shear models, the crushable foam material model (MAT_063) was used to model active materials. Crushable foam formulations are not as compliant to the shear loading as the geologic cap formulations. As we have mentioned above, it has been shown in the experiments and reported in the

literature that active materials' mechanical response resembles the response of granular cohesive materials. These materials are very sensitive to shear loading and are better represented by the material model formulations for soils and concrete. Therefore, we used MAT_025 as in the previous task to represent the active materials in the cell.

The experiment setup and its simulation model are shown in Figure I.3.D.8. The model uses a cross section of the cell (20 mm x 1.5 mm x 5.4mm). The shear loading in the experiment is imposed after an initial compression. This compression step is performed in order to hold the cell in place during the shear by restricting its slipping into the shear cavity. The simulation consists of two steps. In the first step of the simulation, the cell is uniaxially compressed by 0.4 mm in the z direction. In the second step, it is deformed under shear loading. In the simulation, we measure a total force on the support plates on one side of shear support. This force contains both compression and shear responses. In order to obtain only the shear testing force component, we subtracted the compression value from the total simulation, as shown in Figure I.3.D.9.



Figure I.3.D.8 Shear test. (a) experimental setup, and (b) simulation model

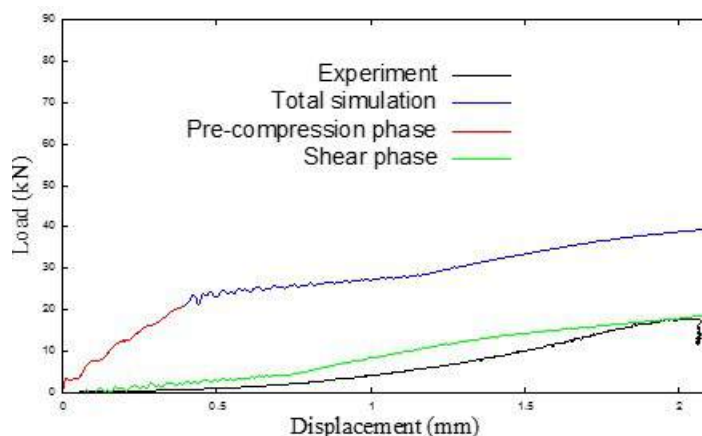


Figure I.3.D.9 Load displacement curve for the shear test. Label "Shear phase" denotes the reacting force on the supports to the shear loading step

The results of the simulation using geologic cap model (MAT_025) are now close to the experimental response. The material model does not contain any failure models so it cannot account for internal damage that was shown to be very extensive in the shear test. We are currently calibrating model MAT_145 to account for strain rate sensitivity and damage mechanisms in the jellyroll active materials.

Conclusions

The third year has been successful and we expect to complete the project by the end of 2019. Particular accomplishments include:

- Enhanced the capabilities of the mechanical, electromagnetic (EM) and thermal solvers in three types of models: solid (detailed) model, composite t-shell model and macro model.
- Developed solid, composite t-shell and macro models under different loading conditions and demonstrated the advantages and limitations of each type of model.
- Completed the quasi-static and impact tests for pouch and prismatic cells.

Key Publications

1. Jie Deng, Chulheung Bae, Theodore Miller, Pierre L'Eplattenier, Inaki Caldichoury, "Communication – Multi-Physics Battery Safety Simulations across Length Scales", Journal of The Electrochemical Society, 166, A3119-A3121, 2019.

Acknowledgements

Adrienne Riggi served as the DOE-NETL Program Manager for this project.

I.3.E Consortium of Advanced Battery Simulation (ORNL)

Srikanth Allu, Principal Investigator

Oak Ridge National Laboratory
1 Bethel Valley Road
Oak Ridge, TN, 37831-6164
E-mail: allus@ornl.gov

Brian Cunningham, DOE Technology Development Manager

U.S. Department of Energy
E-mail: Brian.Cunningham@ee.doe.gov

Start Date: October 1, 2015
Project Funding: \$3,180,000

End Date: September 30, 2019
DOE share: \$3,180,000

Non-DOE share: \$0

Project Introduction

CABS is an integrated partnership between Oak Ridge National Laboratory (ORNL), Argonne National Laboratory (ANL), and Sandia National Laboratories (SNL). The project report is divided into three sections (I.C.3, I.C.4, I.C.5) that includes contributions from individual Laboratories. Sections I.C.4 and I.C.5 also report updates from industry-led projects. In this final report, we discuss experiments conducted to understand failure of the cells, development of physics-based models for understand the fast charge cycling and composite ageing models for battery modules under realistic driving conditions are introduced into the software release.

Objectives

The objective of this project is to characterize the failure of the cells, develop upscaled coupled simulation tools to predict electrochemical behavior under extreme conditions, and software improvements that allows users to configure and launch simulations within a browser. The progress towards these objectives is achieved by delivering the following milestones for FY19:

1. Experimental data and diagnosis on deformation leading to mud-cracks.
2. Development of framework to model primary effects under fast charge condition.
3. Deployment of virtual integrated battery environment (VIBE) on cloud platform

Approach

During the previous year, we reported progress on development of new experimental protocols to study failure leading to internal short circuit. In the current year, we conducted indentation tests till failure and followed with microscopy experiments for diagnostic analysis. The diagnosis from this experimental evidence is used to develop formulation of new models for mechanical behavior of battery components. These various efforts allowed us to investigate some of the challenging internal short simulations under extreme mechanical deformations and predict the behavior of the batteries. Also, as part of improving the capability of models deployed through VIBE, we have demonstrated the coupling of lower order models with physics-based models in simulating the dynamic discharge of the battery modules.

Results

Microscopic analysis of fragmentation mechanisms of current collectors under compressive loads:

Fragmentation of copper current collectors was observed by 3D X-ray computed tomography (XCT) after spherical indentation on both prismatic and large-format pouch Li-ion cells. Microscopic analysis including scanning electron microscopy (SEM), scanning transmission electron microscopy (STEM) and x-ray photoelectron microscopy (XPS) was carried out on copper current collectors from used commercial cells and pristine anodes. The copper-graphite cross-section images showed rough interface areas affected by reactions

and diffusion in the used cell. Electron probe micro-analysis (EPMA) element mapping showed the interface area was rich in oxygen and phosphorus. A detectable amount of phosphorus was also distributed uniformly inside the current collector. The same oxygen and phosphorus distributions were confirmed in STEM analysis. XPS depth profiles on multiple elements revealed the interface area of the aged anode was rich in Li, F, P, O and C and diffused at least 50 nm into the copper. In comparison, the pristine anode showed a very smooth C/Cu interface. No other elements were detectable. For commercial cells, the reactions in the interface area and diffusion of multiple elements into the lattice were responsible for the embrittlement of the copper current collectors.

The indented prismatic and large format cells were examined by 3D XCT after an initial short circuit was detected by a 0.1 V open circuit voltage drop. Figure I.3.E.1(a), (b) and (c) are images from three different directions of a prismatic cell. The cathodes are thicker layers with light grey color because of the presence of cobalt. Since x-ray can penetrate carbon in anodes, only the copper current collectors contributed to the signals. As observed previously, the copper layers were fragmented, and they showed as discontinuous lines in the cross-sectional views (Figure I.3.E.1(a) and Figure I.3.E.1(b)), but as mud-cracks when viewed in the plane parallel to the layers (Figure I.3.E.1(c)). For the large format cell, the top cell in the 10-cell stack was selected for XCT. An external DC power source was connected to the top cell and voltage drop was monitored from the positive and negative tabs. Because of the restriction of sample holder to scan a 5.5 mm x 50 mm x 145 mm strip, spatial resolution was not very high in cross-sectional images Figure I.3.E.1(d) and Figure I.3.E.1(e). However, the discontinuous copper layers were also observed. In the plane parallel to the layers, Figure I.3.E.1(f), the layers are shown as rings due to the curvature from indentation. The copper current collectors had the same mud cracks as the prismatic cells. The indentation of 10-cell stack has conditions of realistic battery backing in an electric vehicle battery module. The displacement was a few times the cell thickness because of the “crushable” cells underneath. Large cracks through the cell were developed. However, the evidence of fragmentation of copper layers was very clear. Because the aluminum layers in the cathode did not show any sign of fragmentation under spherical indentation, the focus of this study is on the copper current collector.

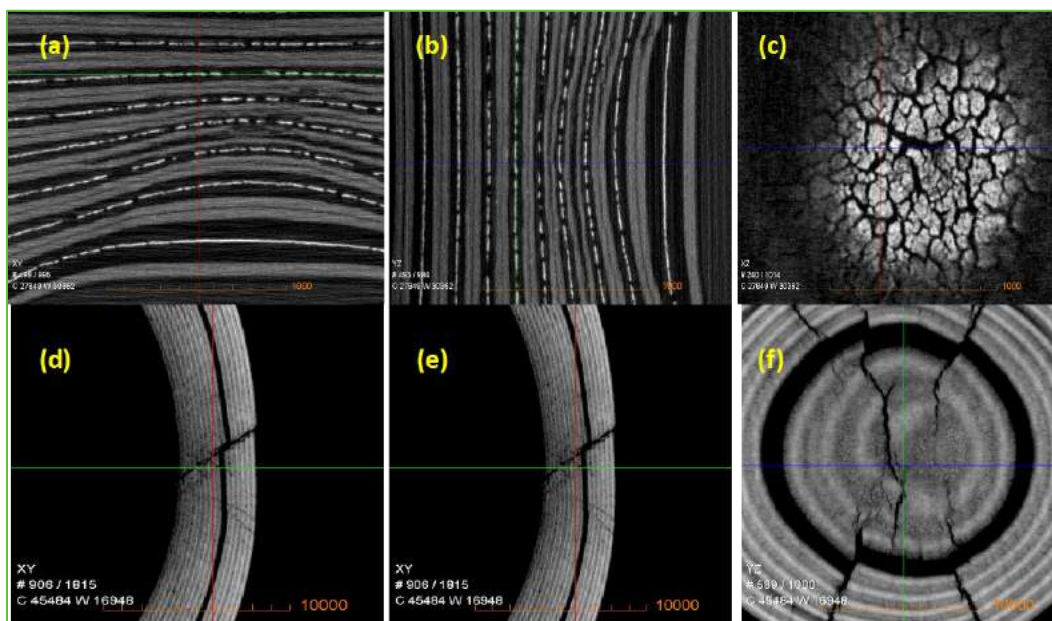


Figure I.3.E.1 Fragmentation of copper current collectors observed by 3D XCT in a small prismatic cell (a), (b) and (c), and the top cell of large format LG-Chem 10-cell stack (d), (e) and (f) after indentations

EPMA was carried out on the interface areas using element mapping. Ten points from the cross-sectional areas of the used and pristine Cu were measured with quantitative element analysis. Table I.3.E.1 shows the average mass % of the main elements. The used and pristine copper were from different suppliers. The copper in used

cell has higher carbon contents than the pristine copper. Both copper foils had 0.19-0.20 mass % of phosphorus. As shown in Figure I.3.E.2 (a), the anode cross-section maps of Cu, C, O and P indicated interface regions on both sides of the current collector. The Cu and C maps showed a transition region about 1-2 microns. The oxygen and phosphorus maps showed these two elements co-exist at the boundaries possibly as deposits from electrolyte and surface oxidation of Cu. It is also noticeable that phosphorus also evenly distributed inside the copper. This is consistent with EPMA mapping of both used and pristine anodes showing P as an alloying element. Figure I.3.E.2(b) are line profiles of elements C, Cu, O and P across the interface area. The intensities of the four elements were scaled to maximize the contrast in each map while the counts for C and Cu are much higher than O and P. The step-transition of Cu and C indicated the spatial resolution at the interface. There are two oxygen peaks at the interface along with smaller peaks of phosphorus. The wider peaks of oxygen and phosphorus extended into the copper foil. Both O and P intensities did not go to zero as the carbon indicating the presence of a diffusion region. High-resolution STEM studies, in Figure I.3.E.2(c), also showed maps C, Cu, O and P with similar distributions. The higher spatial resolution images showed oxygen and phosphorus concentrated at the interface 100-500 nm in depth. The lower portion of the interface was affected by reactions and showed a thicker diffusion layer with additional O and P into the current collector. The upper portion of the images was smoother and the O and P distributions at the interface were similar to the bulk area. Line profiles of the elements are shown in Figure I.3.E.2(d). The high spatial resolution clearly showed a transition region of oxygen and phosphorus with a diffusion depth of 0.5 microns.

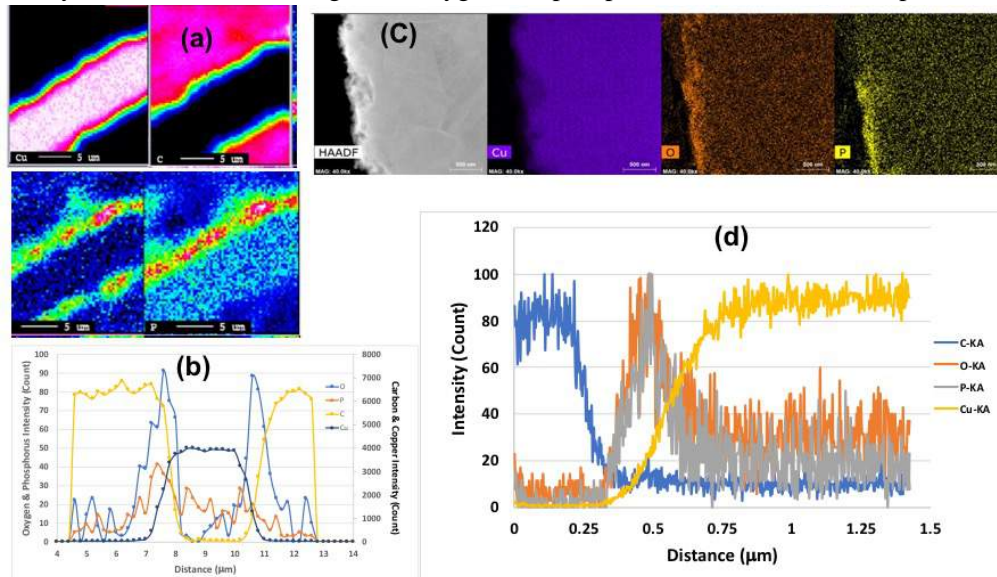


Figure I.3.E.2 (a) EPMA element maps of a used anode and (b) line profiles of four elements across one interface, (c) STEM image and element mapping, and (d) Line profiles of four elements across the interface

Table I.3.E.1 EPMA Quantitative Analysis: Average Normalized Mass% of 10 Spots Measured on Used and Pristine Cu Current Collectors

Sample	Cu	C	P	Cl	Total
Used	95.5594	4.2497	0.1853	0.0056	100
Pristine	98.4259	1.3566	0.1991	0.0184	100

In summary, fragmentation of copper current collector was observed and confirmed in both small prismatic and large pouch cells. Detailed microscopy analysis showed significant corrosion at the copper surface and formation of interface area between graphite and copper. The corrosion and diffusion of elements into the

copper are the sources for its brittle behavior. The mechanism of alloying embrittlement was proposed and the results were compiled into journal article [1].

Understanding limiting conditions during various charging protocols:

An important step toward understanding the limitations such as lithium plating and other degradation mechanism on fast charging of batteries, we need to quantitatively analyze the lithium distributions under various stages in battery charge cycles. Experiments were conducted at Battery Manufacturing facility at ORNL using a large-format 0.5Ah NMC532/graphite pouch cell with thickness values of 60 μm for anode, 25 μm for separator, and 60 μm for cathode. In the Figure I.3.E.3(a/b) we show comparison of the ampere-hours electrochemical model under various charge and discharge rates in good agreement with the experimental curves.

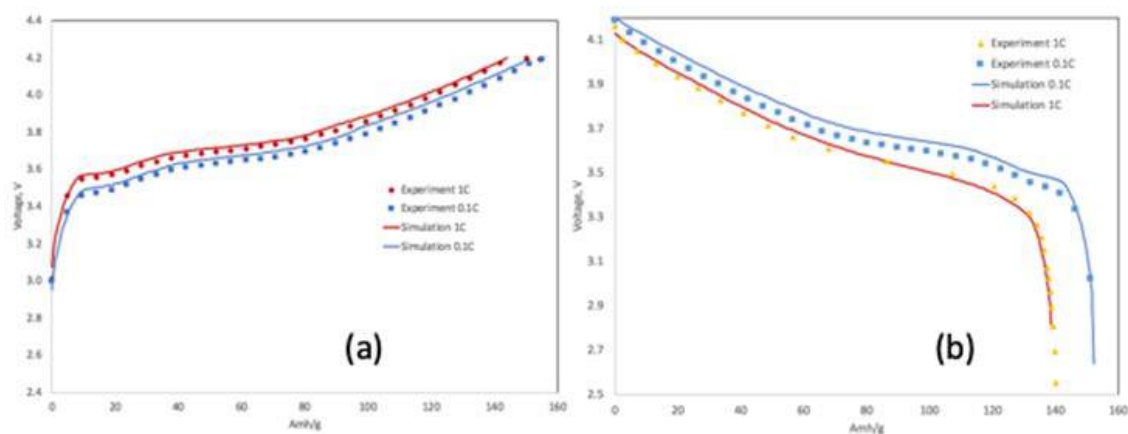


Figure I.3.E.3 Comparison of charge and discharge voltages with the experiments

We will begin our study of the lithium-ion distributions by analyzing the distributions in the entire charge cycle: discharge, constant current charge, constant voltage (CV) charge/relaxation. The discharging phase starts for a lithium-ion battery with full capacity, which means that the lithium-ion concentration in electrode is set to a pre-defined high value on the anode side and a low value on the cathode side. Uniform values are set for both anode and cathode, as will be discussed later that the uniform distributions are usually achieved on both anode and cathode after an adequate rest period. On the electrolyte, the lithium-ion concentration is set to a uniform value provided from the experiment data. As illustrated in Figure I.3.E.4(a), the lithium concentration on electrode starts high on anode and low on cathode. As the discharge progresses, lithium ions concentration reduces in anode and increases in cathode. In the charging process, the reverse occurs as the lithium moves back from cathode to anode. Figure I.3.E.4(b) shows the lithium concentration in the electrolyte which serves as the carrier for the lithium ion intercalation. Note that the x-axis denotes the dimension in thickness, where left side is for anode, right side is for the cathode, and middle region is for separator. During discharge, the positive lithium ion de-intercalation from the electrode on the anode side, and intercalate on the cathode side, while the lithium-ion transport in the electrolyte by both migration and diffusion. During constant current (CC) charge, the intercalation process reverses the direction, i.e., the positive lithium ion moves from cathode and enters anode through the electrolyte solution. A constant voltage (CV) charge can follow CC charge after the cell voltage has reached a pre-set maximum value, typically 4.2 V. Increasing the charge current, or fast charging, does not hasten the full-charge state significantly. Although the battery reaches the designated voltage (e.g., 4.2 V) quicker, the saturation charge will take longer to recover full capacity/SOC. With higher current, Stage 1 is shorter but the saturation during Stage 2 will take longer. A high current charge will, however, quickly fill the battery to about 74%. This is demonstrated by the simulation results in Table I.3.E.2. A CV charge starts with the same current load as the CC stage, e.g., CV with 4.2 V after 5C CC will start with 5C current, but the current quickly reduces to zero as the slope of the lithium-ion distribution starts to even out.

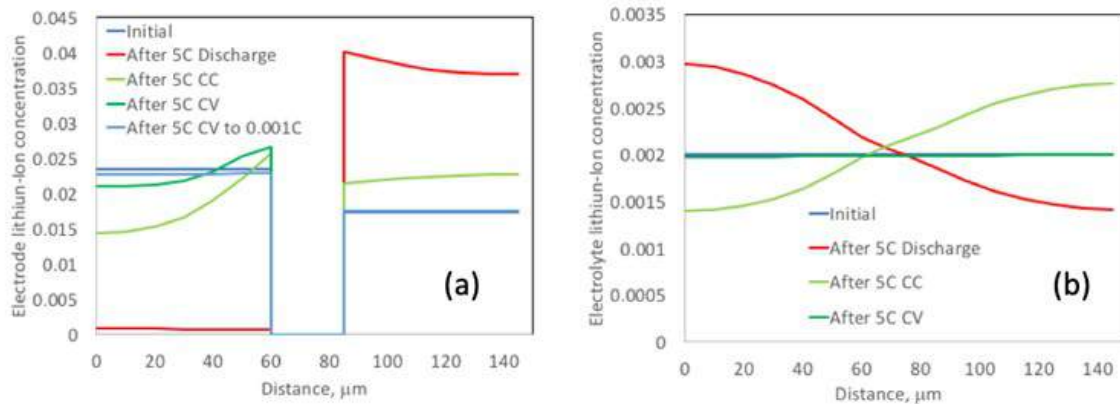


Figure I.3.E.4 Lithium ion concentration through thickness of the cell during charge cycle at 5C rate

Table I.3.E.2 Charging Times and Efficiency with C-Rate

Charge Rate	CC (to 4.2V)		CV (to 0.1C)	
	SOC(%)	Time(sec)	SOC(%)	Time(sec)
0.1 C	99.36	35575	-	-
1C	94.09	3594	98.6	432.7
3C	84.43	1008	97.53	628.8
5C	74.71	536.7	97.03	797

This is consistent with the fact that the lithium gradient after CC is larger than that from the discharge with the same C-rate. Leaving a higher gradients in the lithium distribution, and consequently restoring less capacity back to the battery cell, i.e., 75% capacity for 5C CC alone. CV (e.g., with 0.1C termination current) charging which makes up the most lost capacity requires a longer time if it follows a high C rate CC charge.

Development of coupled ageing models with thermal transport of battery pack:

The equivalent circuit battery cell model (ECM) for large format cell (33Ah) was coupled with a thermal component and could be easily extended to model a battery pack. Initial validation of equivalent circuit model under constant current discharge are executed and associated voltage and battery temperature plots are shown in the Figure I.3.E.5 below.

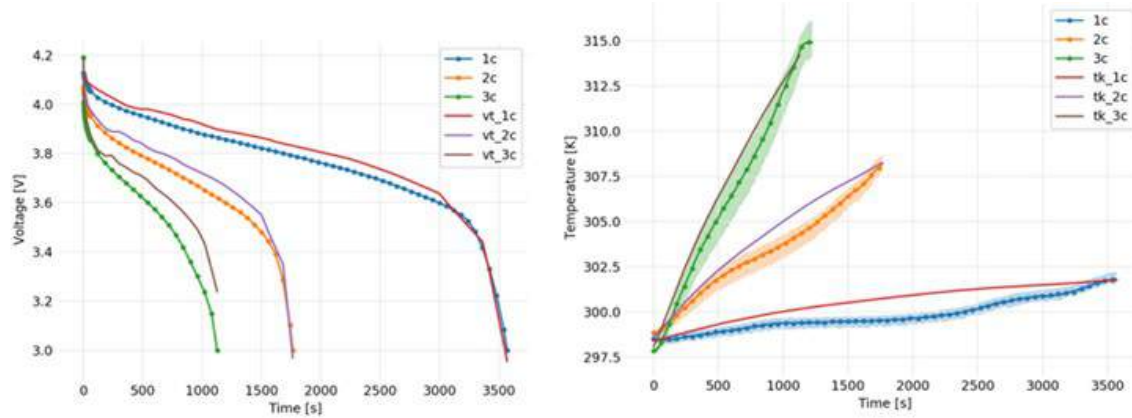


Figure I.3.E.5 Discharge voltage (left) and temperature (right) profiles for a battery cell at 1C, 2C, and 3C discharge rates. Experiment data shown as dotted lines and model results as solids lines

An example battery modules connected in series where each module contains several battery cells connected in parallel is constructed. As proof of concept, each cell is initialized with a random state of charge and capacity as well as an initial constant temperature. Voltage and temperature profiles of the cells in this battery module during a constant discharge event are shown in Figure I.3.E.6. Two of the cells become fully discharged due to their low initial capacity and high branch current.

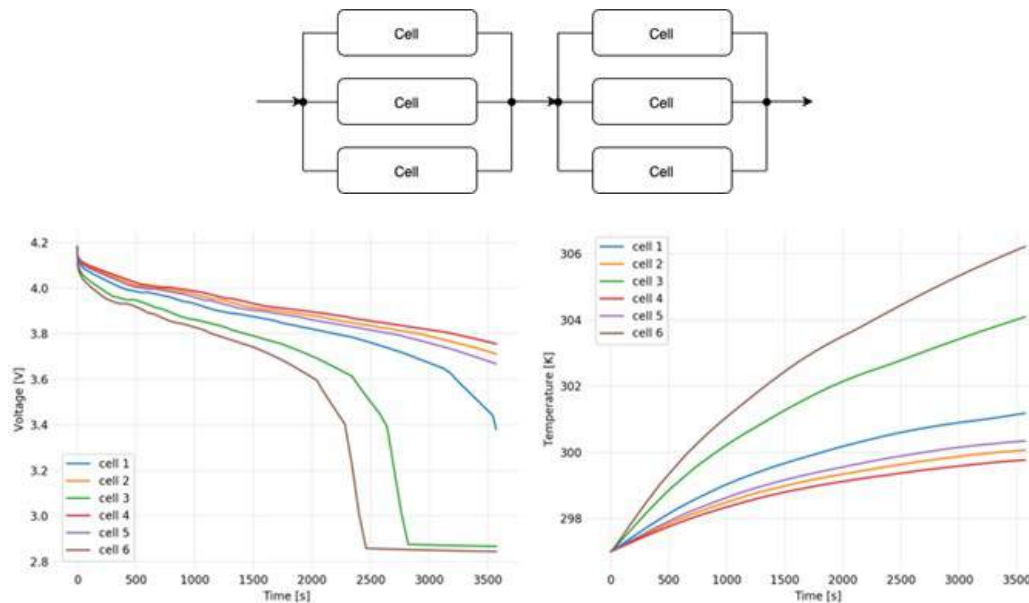


Figure I.3.E.6 Voltage (left) and temperature (right) profiles for cells in a battery pack under constant discharge conditions. Each line represents a single battery cell in the pack

Simultaneously, a battery ageing model based on the work [1] was developed to estimate end-of-life (EOL) and state-of-health (SOH) of a battery cell as a function of current (C-rate) and core temperature. The paper combines an electro-thermal model with an aging model to determine a charging protocol that shortens charge time while minimizing the effect on battery health. The expression around which the aging model is given by $\Delta Q_b = M(c) \cdot \exp\left(\frac{-E_a(c)}{RT_c}\right) \cdot A(c)^z$, where ΔQ_b is capacity fade as a percent, $M(c)$ is the pre-exponential factor shown earlier, $E_a(c)$ is activation energy as a function of C-rate, T_c is core temperature (computed by the thermal model), $A(c)$ is discharge current throughput in amperes, and z is the empirical power law factor, given as $z = 0.55$. The Figure I.3.E.7 shows plots of end-of-life (EOL) cycles $N(c, T_c)$ and SOH decay versus

current for various temperatures. The model predict the increase in the C-rate or temperature increases the SOH decay rate and more EOL cycles can be obtained at C-rates of 2-5C and low temperatures. The next Figure I.3.E.8 shows a plot of normalized capacity fade for various temperatures with respect to cycle number. Temperature has a significant effect on the decay; for example, the 45°C curve reaches 80% capacity compared to the 15°C curve which is near 95% capacity at 2500 cycles.

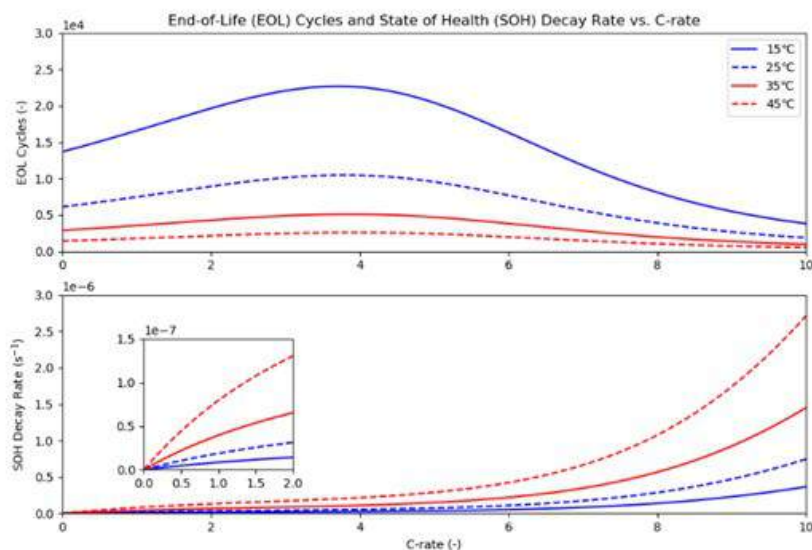


Figure I.3.E.7 EOL cycle and SOH decay rate as a function of C-rate and temperature

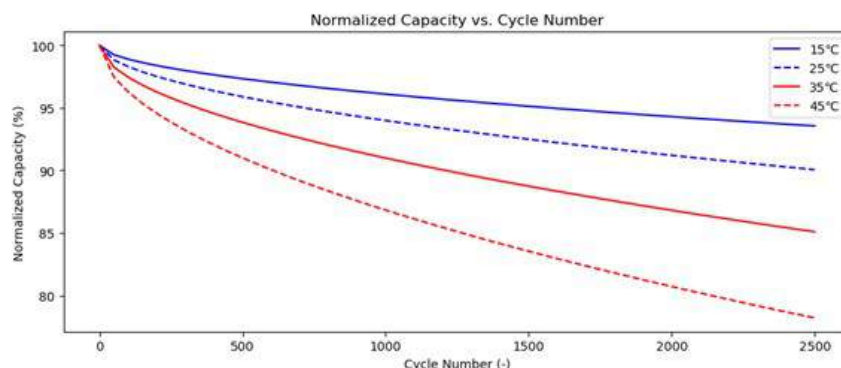


Figure I.3.E.8 Normalized battery capacity compared to number of cycles at different temperatures

Deployment of cloud infrastructure for battery simulations:

A public battery simulation environment called “VIBE cloud” has been set up at vibe.ornl.gov/jupyter. This online resource provides tools for modeling batteries and energy storage systems without the need for user to download and install the software stacks on HPC hardware. Jupyter notebooks are used to interface with the VIBE framework to aid in the development of realistic and predictive battery performance and safety models. This allows for inline configuration and setup of simulations, launching simulations and processing results with advanced plotting tools within the internet browser. Users can upload their experimental data and develop custom models within the Jupyter notebook and integrate seamlessly to the cloud instance of the software stack. The figure below represents a screen capture of VIBE running in a web browser.

Conclusions

During this final year, using no cost extension, we have wrapped the diagnostic studies on the origin of failure of battery components. We have also developed physics-based models for understand the fast charge cycling behavior and associated limitations. Also, composite models for simulations of battery module and packs under realistic driving conditions are introduced into the software release.

Key Publications

1. Hsin Wang, Donovan N Leonard, Harry M Meyer III, Thomas R Watkins, Sergiy Kalnaus, Srdjan Simunovic, Srikanth Allu, John A Turner, “Microscopic Analysis of Copper Current Collectors and Mechanisms of Fragmentation Under Compressive Forces”. Submitted to Journal of Power Sources.
2. Gavin Wiggins, David West, Srikanth Allu, “Understanding the temperature distribution impacts on the ageing of battery packs”, article under preparation.
3. VIBE manual version 2.0a, <https://vibe.ornl.gov/jupyter> (under construction)

References

1. Hector E. Perez, Xiaosong Hu, Satadru Dey and Scott J. Moura. “Optimal Charging of Li-Ion Batteries with Coupled Electro-Thermal-Aging Dynamics.” IEEE Transactions on Vehicular Technology, vol. 66, no. 9, pp. 7761-7770, 2017.

Acknowledgements

The current CABS team members, Hsin Wang (ORNL), Kevin Lai (ORNL) and Gavin Wiggins (ORNL) contributed to this project. We would like to acknowledge SNL, ANL and NREL CAEBAT team members for sharing experimental data and technical discussions.

I.4 Recycling and Sustainability

I.4.A Battery Production and Recycling Materials Issues (ANL)

Linda Gaines, Principal Investigator

Argonne National Laboratory
9700 S Cass Avenue
Lemont, IL 60439
E-mail: lgaines@anl.gov

Samuel Gillard, DOE Technology Development Manager

U.S. Department of Energy
E-mail: Samuel.Gillard@ee.doe.gov

Start Date: October 1, 2018
Total Project Cost: \$250,000

End Date: September 30, 2019
DOE share: \$250,000

Non-DOE share: \$0

Project Introduction

Examination of the production of batteries from raw material acquisition to assembly illuminates the stages of this supply chain that incur the greatest energy and environmental burdens. Recycling of material from spent batteries will be a key factor in alleviating potential environmental and material supply problems. We examine battery material production, battery assembly, and battery recycling processes that are available commercially now or have been proposed. Battery materials, assembly, and recycling processes are compared on the basis of energy consumed and emissions, suitability for different types of feedstock, and potential advantages relating to economics and scale. We compare the potential of recycling processes to displace virgin materials at different process stages, thereby reducing energy and scarce resource use, as well as potentially harmful emissions from battery production. Although relatively few automotive batteries have been produced to date, viable processes will be required to recycle them when they are no longer usable. Secondary use of the batteries could delay return of material for recycling. Economic and institutional factors impact recycling as well.

This project identified the recycling technologies that would maximize energy, environmental, and economic benefits, and laid the foundation for the process R&D at the ReCell Center, aimed at developing a commercially-viable process.

Objectives

- Follow developing and potential material scarcity issues that may influence viability of automotive lithium-ion batteries
- Characterize lithium-ion battery recycling in the United States and abroad to identify the most promising recycling technologies as they evolve, barriers to recycling, and influence of recycling on material scarcity
- Engage with the international battery recycling community to exchange information and identify paths to advancing battery recycling technology and enabling adoption
- Postulate improved recycling processes to maximize material recovery
- Determine impact of battery reuse on recycling processes and economics
- Formulate actions to address developing technical and institutional issues concerning used batteries

- Coordinate ongoing analysis and modeling projects related to battery recycling

Approach

Life cycle analysis (LCA) was used to further identify potential environmental and economic roadblocks to battery production, and to compare energy savings and emissions reductions enabled by different types of recycling processes. Economic analysis of recycling processes revealed cathode recovery as a way to achieve economic viability for recycling of low-Co cathodes. This research forms the basis for the work of the new ReCell advanced battery recycling research center. Projections of material demand identified cobalt as the first target for recovery to displace scarce, imported material. Further study determined that nickel, while not as scarce globally as cobalt, could experience bottlenecks in supply because of the higher costs involved in production of the very pure Class I nickel required for battery manufacture. This highlights the importance of recycling as an additional source of supply.

Close interactions with stakeholders are sustained to remain on top of technological and legislative developments associated with LIB production and recycling, and to maintain Argonne's position as the world's leader in battery recycling research and analysis. During FY19, Argonne staff 1) gave invited talks and presentations to government, industry, and academia, and to numerous visitors; 2) interacted with international groups like the IEA and the Faraday institution to coordinate research, 3) obtained process data from visits to Chinese plants, 4) served on SAE and NAATBatt recycling committees and the Science Advisory Board of the Responsible Battery Coalition; 5) negotiated potential battery recycling and modeling work with several organizations; and 6) responded to countless requests for information. Argonne has also examined recycling processes and businesses for other battery types to determine what lessons can be learned from successfully established systems.

Results

We also examined the extent to which recycling could alleviate U.S. dependence on imported battery materials. This depends directly on the growth of demand; as long as demand continues rapid growth, recovered material can only contribute minimally to supply. But as soon as demand turns over, recycling can play an important role. Figure I.4.A.1 illustrates that maximum material from recycling (assumed recovered after 10 years) varies with different assumed demand growth curves. In addition, we addressed a criticism of direct recycling presented by conventional recyclers, who pointed out that the material recovered would be a 10-year-old formulation no longer in demand. Figure I.4.A.2 shows that until about 2040, recovered material will still see significant demand; after that there will be a need for material to be upcycled from current formulations to new ones.

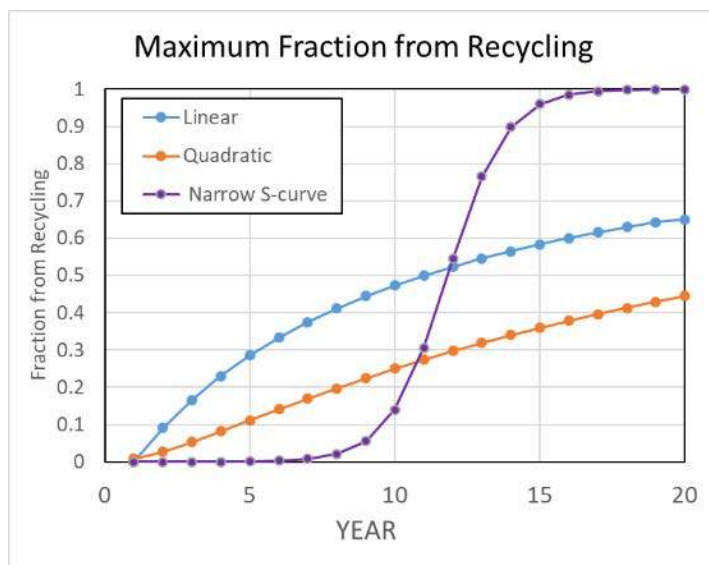


Figure I.4.A.1 Supply from recycling depends on demand growth

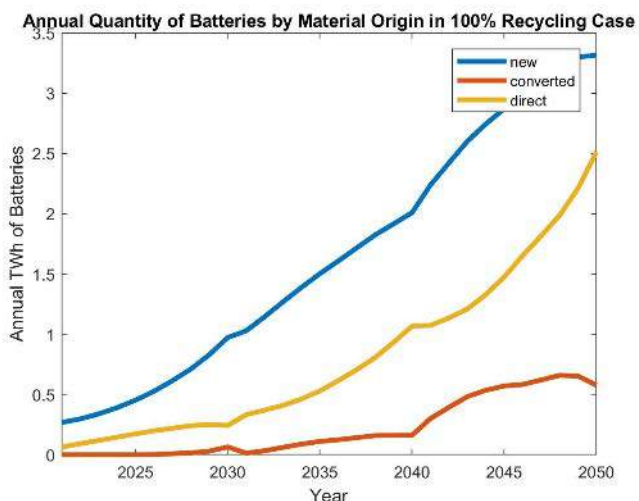


Figure I.4.A.2 Need for upcycling of recovered material

Based on our analysis, recycling provides energy conservation benefits and reduces the local impacts of metal recovery and purification. Benefits differ by recycling process and increase as more materials are recovered. Recycling is especially beneficial when cathode materials contain nickel or cobalt. In the case of LiCoO_2 , the recovery and purification of the metal dominates the overall energy consumption of producing this cathode material, so recycling results in significant energy savings (and sulfur emission reductions).

Although recycling technologies have been demonstrated, basic process R&D is needed to develop the optimal recycling method for each Li-ion chemistry, especially lower cobalt cathode materials. For such materials, it

appears that direct recycling, still only demonstrated at bench scale, offers the only real prospect of being economically feasible, but a segregated feed stream would be required. For any process, the goal is to maximize the yield of valuable materials at lower recycling cost. Optimized processes would then require demonstration on a larger scale, but this might not be sufficient because manufacturers are skeptical about putting recycled material back into batteries. Therefore, we will need to develop product specifications that recycled materials must meet. Furthermore, there is not yet enough material available to support full-scale infrastructure for collection and processing. There should be enough material from consumer electronics, but those batteries are generally not getting collected, let alone recycled. This realization contributed to the development of DOE's Recycling Prize, recently making 15 Phase I awards. The potential for restrictive government regulations also hinders recycling business development, so the industry could consider pre-emptive self-regulation. Some of the challenges to Li-ion battery recycling are shown in Table I.4.A.1, with proposed R&D to address them.

Table I.4.A.1 Challenges for Li-Ion Battery Recycling

Challenge	R&D to address
Many of the constituents have low market value	Process development to recover multiple high-value materials
Low value of mixed streams	Separation of mixed cathode material
Loss of lithium in spent cathode material	Relithiation of cathode
Obsolete cathode recovered	Upcycle to new configuration

Detailed understanding of recycling processes will be necessary to maximize material recovery. Low-temperature processes that can recover usable cathode material are of particular interest.

In contrast to China and Korea, LIB recycling has yet to be fully commercialized in the U.S. Retriev operates a plant that recovers black mass, but it is not running at capacity. Europe relies primarily on pyrometallurgy. Great Britain and Australia are exploring their options. In the U.S., the ReCell Center has been established to develop direct recycling technology to pilot-scale because it has the biggest potential to be economic and to reduce energy use and environmental impacts of LIB. Barriers to growth of LIB recycling in the U.S. include low collection rate of spent LIB, unstandardized LIB designs, confusion over liability for LIB recycling, and uncertainty in the market for recovered materials. Several companies are moving forward with plans for

hydrometallurgical recycling in the U.S., and each employs a different set of process steps. We continue to gather detailed recycling process information to include in our EverBatt closed-loop lifecycle model, which will serve as an important tool in vetting processes developed by the center. Transportation cost is another issue, which leads to our new interest in pretreatment to enable cheaper transport.

Conclusions

Recycling has the potential to significantly reduce both demand for raw materials and energy and environmental impacts of battery production. However, technical and economic barriers must be overcome before recycling will be available on a large scale. Through engagement with stakeholders, publications and presentations, Argonne has disseminated its research results in this area and fostered open discussion of technical, institutional, and economic issues involved in recycling of lithium-ion batteries. With the establishment of the ReCell Center, this function has developed even greater importance.

Key Presentations/Publications

1. Paper: Dai, Qiang, Jarod Kelly, Linda Gaines and Michael Wang. "Life Cycle Analysis of Lithium-ion Batteries for Automotive Applications." Batteries 5, no. 2 June, 2019 doi: 10.3390/batteries5020048.
2. Paper: Gaines, Linda, Kirti Richa and Jeffrey Spangenberg. "Key issues for lithium-ion battery recycling." MRS Energy and Sustainability, Volume 5, E14 22 November 2018 doi: 10.1557/mre.201.
3. Report: Dai, Qiang, Jeffrey Spangenberg, Shabbir Ahmed, Linda Gaines, Jarod Kelly and Michael Wang. "EverBatt: A Closed-loop Battery Recycling Cost and Environmental Impacts Model." Argonne National Laboratory, ANL-19/16, April, 2019.
4. Presentation: Gaines, Linda. "Research Directions for Lithium-Ion Battery Recycling." Pacific Power Sources Symposium and International Coalition for Energy Storage and Innovation, January 5, 2019 - January 10, 2019.
5. Presentation: Gaines, Linda. "Why Direct Recycling is Promising." 2019 NAATBatt Annual Meeting and Conference, March 11, 2019 - March 14, 2019.
6. Invited presentation: Gaines, Linda. "EV Battery Lifecycle issues." 2019 Which Way to Electrification of the U.S. Transportation System?, Washington, DC, April 3, 2019 - April 4, 2019.
7. Invited presentation: Gaines, Linda. "LCA and Direct Recycling for Lithium-Ion Batteries." 2019 International Energy Agency Task 30 Meeting, Washington, DC U.S., June 13, 2019 - June 14, 2019.
8. Presentation: Dai, Qiang, Jennifer Dunn, Linda Gaines, Jarod Kelly, Amgad Elgowainy and Michael Wang. "Life Cycle Analysis of Automotive Lithium-ion Batteries (LIBs): the Real Story." 18th LCA, September 25, 2018 - September 27, 2018.
9. Presentation: Dai, Qiang, Jeff Spangenberg and Linda Gaines. "ReCell: A Closed-loop Battery Recycling Economics and Environmental Impacts Model." 233rd Electrochemical Society Meeting, May 13, 2018 - May 17, 2018.
10. Presentation: Gaines, Linda. "Lithium-ion battery recycling research at the Recell center." 19th Advanced Automotive Battery Conference, San Diego, CA, June 24, 2019 - June 27, 2019.
11. Presentation: Gaines, Linda. "LCA and Economics of Recycling Lithium-Ion Batteries." 19th Advanced Automotive Battery Conference, June 24, 2019 - June 27, 2019.
12. Invited presentation: Gaines, Linda. "Lithium-Ion Battery Recycling." Molecular Foundry Meeting, Lawrence Berkeley Laboratory, August 22, 2019.
13. Panel: Storage and the Grid- Current Options, Applications, and Possible Futures. Energy Security Meeting, NREL, October 2, 2018.

I.4.B Lithium-Ion Battery Recycling Prize Support (NREL)

Ahmad Pesaran

National Renewable Energy Laboratory
15013 Denver West Parkway
Golden, CO 80401
Email: ahmad.pesaran@nrel.gov

Samuel Gillard, DOE Technology Development Manager

U.S. Department of Energy
Email: Samuel.Gillard@ee.doe.gov

Start Date: October 1, 2018	End Date: December 31, 2021	
Project Funding (FY19): \$4,570,000	DOE share: \$4,570,000	Non-DOE share: \$0

Project Introduction

Lithium-ion batteries have become the main choice for portable electronics (such as smart phones, tablets, and laptops), power tools, and electric vehicles (EVs) for personal, commercial, industrial, and military applications. The demand for lithium-ion batteries for EVs is expected to grow as the cost of manufacturing and materials is reduced, while performance improves. The U.S. Energy Information Administration (EIA) projects that U.S. light-duty battery EV sales will reach 1.3 million by 2025, and others project even higher sales growth. Global EV sales are expected to reach 30 million by 2030, up from 1.1 million in 2017. This growth in EV sales, as well as increased demand for consumer and stationary uses, are expected to double the demand for lithium-ion batteries by 2025 and quadruple the demand by 2030.

Demand for global production of battery materials such as lithium, cobalt, manganese, nickel, and graphite will grow at similar rates, depending on changes on the composition of future chemistries. In fact, the growth in demand for lithium-ion batteries for EVs is expected to establish EVs as the largest end-user of cobalt and lithium, and could create a particularly high supply risk for cobalt, both because of its potential rise in cost and because its availability depends on foreign sources for production. To address this potential risk, the DOE Vehicle Technologies Office (VTO), within the Office of Energy Efficiency and Renewable Energy (EERE), developed a “Research Plan to Reduce, Recycle, and Recover Critical Materials in Lithium-Ion Batteries.” A goal identified in the plan is to reduce the cost of electric vehicle battery packs to less than \$150/kWh with technologies that significantly reduce or eliminate the dependency on critical materials (such as cobalt) and utilize recycled material feedstocks. However, lithium-ion batteries are currently only recycled at a rate of about 5%. Analysis has shown that recycled materials could potentially provide one-third of cathode material needs for lithium-ion batteries in the United States by 2030. The current recycling supply chain for collecting, sorting, and safe storing and transporting of lithium-ion batteries and recovery of valuable materials is limited, particularly for larger batteries used in EVs and industrial applications. Preventing lithium-ion batteries—particularly those in consumer electronics—from going to waste disposal facilities (as some of them have caused fires) and landfills is important not only for the recovery of key materials, but also for the benefit of the economy and the environment.

To achieve the above goals and address potential critical materials issues, VTO has initiated three key areas of research and development (R&D): 1) supporting laboratory, university, and industry research to develop low-cobalt (or no-cobalt) active cathode materials for next-generation lithium-ion batteries; 2) establishing the ReCell Lithium Battery Recycling R&D Center, focused on cost-effective recycling processes to recover lithium battery critical materials; and 3) launching the Lithium-Ion Battery Recycling Prize to incentivize American entrepreneurs to find innovative solutions to solve current challenges associated with **collecting, sorting, storing, and transporting** discarded lithium-ion batteries safely and economically, for eventual recovery of valuable materials for reintroduction to the battery production supply chain.

Critical Materials Research Plan for Batteries

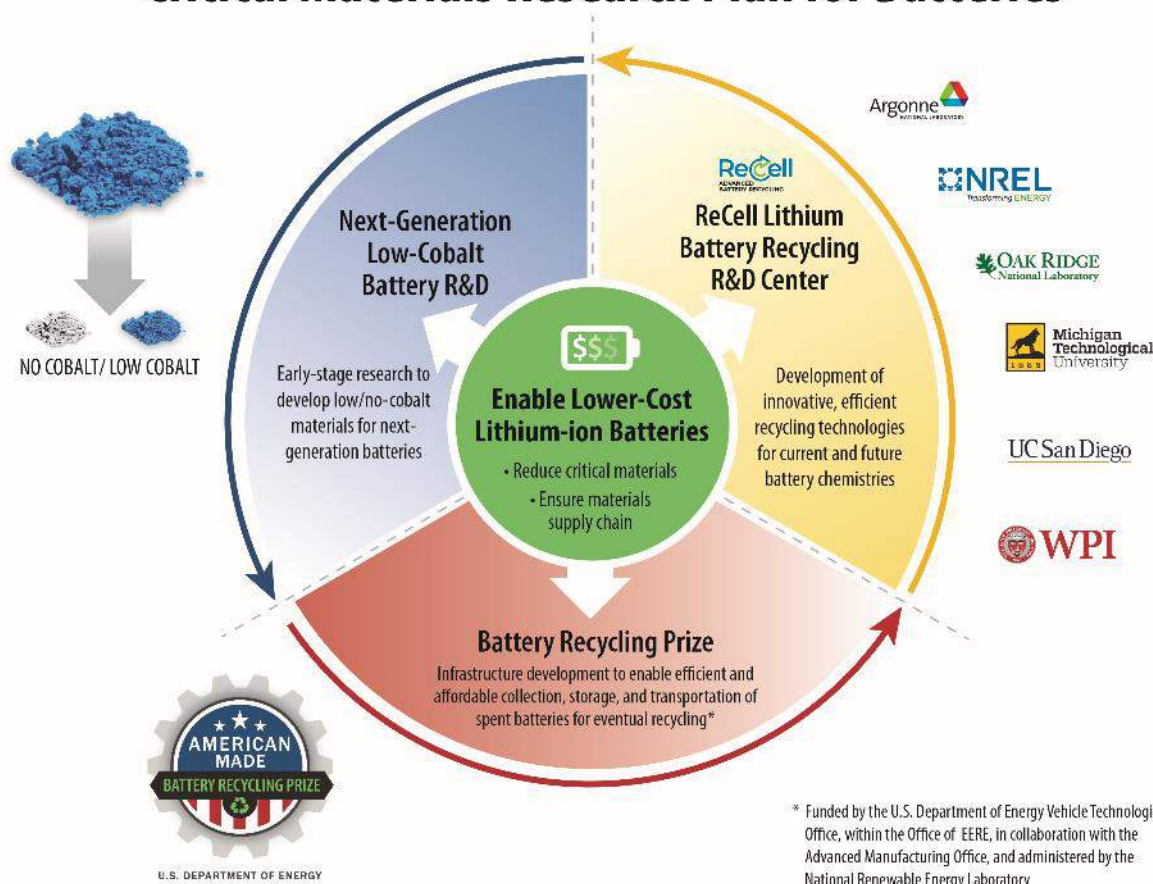


Figure I.4.B.1 Materials Research Plan with three major areas of research to address critical materials issues for lithium-ion batteries and recovery of materials for reintroduction into the supply chain

While the first two initiatives focus on creating next-generation cobalt-free lithium-ion batteries, conducting research into the recovery of critical materials, and reintroducing these materials into recycled batteries, the \$5.5 million Lithium-Ion Battery Recycling Prize leverages innovative ideas from American entrepreneurs to develop and demonstrate a supply chain that safely transitions spent batteries to specialized battery recycling facilities. The Recycling Prize is a joint collaboration between VTO and DOE's Advanced Manufacturing Office (AMO), with \$4.5 million in funding support from VTO and \$1.0 million from AMO.

The \$5.5 million prize is designed to be implemented in three progressive phases over three years to bring ideas from concept to prototype and partnering through pilot validation. In each phase, submissions will be evaluated by expert reviewers and a federal consensus panel for recommendation to the DOE selection officials. DOE assigned the administration and execution of the Battery Recycling Prize to the National Renewable Energy Laboratory (NREL) to use an already-established framework for American-Made Challenges that has been used to administer prizes for other EERE offices such as the Solar Energy Technologies Office. Figure I.4.B.2 provides an overview of the three phases of the contest and the number and dollar amounts of awards available in each phase.

This progress report provides a summary of activities of the prize for the first year and Phase I: Concept Development and Incubation, with the aim of awarding \$1 million to Phase I winners.



Figure I.4.B.2 Left: Logo of the Lithium-Ion Battery Recycling Prize. Right: The Lithium-Ion Battery Recycling Prize consists of three progressive phases from concept through pilot validation, over about three years

Objectives

The purpose of Lithium-Ion Battery Recycling Prize is to incentivize American entrepreneurs to develop and demonstrate processes that, when scaled, have the potential to capture 90% of ALL lithium-based battery technologies in the U.S., covering consumer electronics and both stationary and transportation applications. A 90% recycling rate of lithium-based batteries would be a significant achievement compared to today's 5% recycling rate. It is the goal of this prize to find innovative solutions to current challenges in safe and economical collecting, sorting, storing, and transporting discarded (or end-of-life) lithium-ion batteries for eventual recycling so that the 90% target can be achieved.

Approach

NREL was selected as the Battery Recycling Prize administrator to support DOE with implementation and execution of the prize elements such as planning, communication, technical insight, outreach, promotion, training, writing content for documents and websites, and the submission review process. NREL used the same framework for the Battery Recycling Prize that another team at NREL developed for the Solar Prize under the American-Made Challenges. For interactions with the public for providing information on the prize and its rules, and for exchange of information between the potential applicants and reviewers, the American-Made Challenges and NREL have been using a hosting platform developed by HeroX (www.HeroX.com). HeroX provides a flexible two-sided marketplace where innovators interact with one another to form teams, and where clients such as NREL have the flexibility to design their challenges in a way that will work for them.

The NREL Prize Team supported the DOE Prize Team with development of the battery recycling framework, messaging strategy, communication strategy, technical information gathering, developing rules, finding stakeholders, and writing content for outreach documents and videos. In order to document and clearly define the parameters of the prize, NREL supported DOE in developing an extensive rules document for Phase I (<https://americanmadechallenges.org/batteryrecycling/battery-recycling-prize-rules-and-scoring-criteria.pdf>). The rules identified five areas of interest (collection, separating and sorting, safe storage and transportation, reverse logistics, and other innovative ideas) for the prize for the three applications: consumer electronics, electric vehicles, and stationary/industrial, as indicated in Figure I.4.B.3.

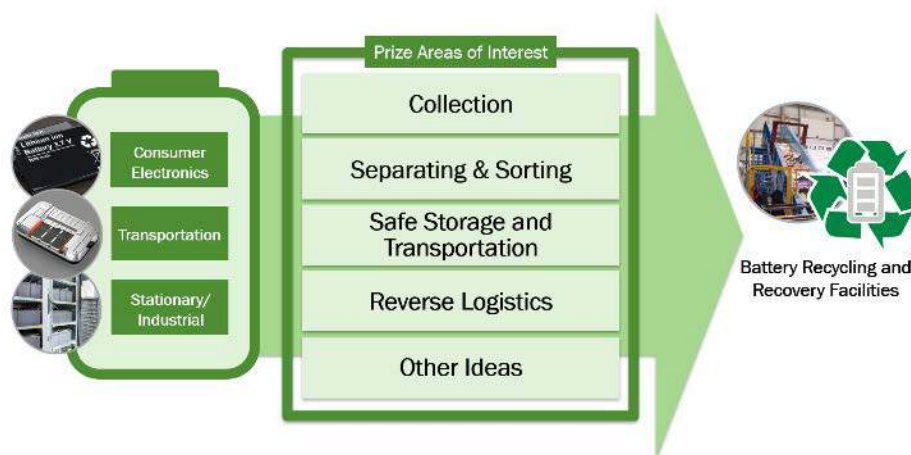


Figure I.4.B.3 There are five main areas of interest within Phase I of the prize to help address the various issues that arise in the battery recycling supply chain

Here are key dates for execution of Phase I of the prize:

- January 17, 2019: Energy Secretary Rick Perry announced the establishment of the Lithium-Ion Battery Recycling Prize and the ReCell Lithium Battery Recycling R&D Center at the Bipartisan Policy Center's American Energy Innovation Council meeting
- February 15, 2019: EERE Assistant Secretary Daniel Simmons launched the Lithium-Ion Battery Recycling Prize with the release of the website (<https://americanmadechallenges.org/batteryrecycling/>)
- February 15–September 26, 2019: Outreach and communication activities in FY19 to inform the public and interested parties about the prize for their potential participation
- April 10, 2019: An informational webinar was conducted on the objectives, rules, eligibility, and submission process. Recording and transcript were posted on the Battery Recycling Prize HeroX website (<https://www.herox.com/BatteryRecyclingPrize/resource/335>)
- August 1, 2019: Submission deadline (58 submissions were received by the deadline)
- August 2–September 13, 2019: Review and Selection Process that included:
 - *Compliance Review* – The Prize Administrator, in concurrence with DOE VTO Prize Manager, identified the eligible submitters and submissions
 - *Advisory Review* – The designated independent advisory reviewers evaluated and scored the submissions assigned to them.
 - *Federal Consensus Panel* – The Federal Consensus Panel reviewed all submissions and associated advisory reviewer scores, and then made recommendations on submission rankings and selections
 - *Selection Official* – The Selection Official(s) made the final determination of winners.
- September 25, 2019: EERE Assistant Secretary Daniel Simmons announced Phase I Contest winners at NREL.

Throughout the course of Phase I, NREL maintained the website and email account for the prize, answering questions and providing updates, and provided support for ongoing outreach efforts including the coordination of an informational webinar. NREL further promoted Phase I through social media outreach via NREL and

American-Made Challenges social media properties, as well as articles posted to www.NREL.gov that were extended through NREL e-newsletters. To reach attendees at relevant conferences, NREL created [a postcard](#) to drive traffic to the Lithium-Ion Battery Recycling Prize website, as well as a pop-up banner to attract conference participants.

NREL coordinated the review of all Phase I submissions by industry experts by assembling a panel of advisory reviewers. NREL then compiled all feedback and presented the DOE Federal Consensus Panel with a document highlighting the comments and scores awarded to each submission.

Once the winning submissions were selected, NREL facilitated and hosted the September 2019 announcement of the 15 winning teams of Phase I.

Results

Over 50 submissions were received for Phase I of the Lithium-Ion Battery Recycling Prize. After review from industry experts and the Federal Consensus Panel, the DOE Selection Official determined that 15 of the submissions adequately met Phase I criteria for innovativeness, impact, feasibility, and technical approach outlined in the Prize Rules. Assistant Secretary Daniel Simmons presented the winner announcement at NREL on September 25, 2019.

The Phase I contest winners, titles, and *description* of their submissions are:

- Admiral Instruments – Battery Sorting with Voltammetry and Impedance Data
 - *Novel algorithms and hardware to use cyclic voltammetry (CV) and electrochemical impedance spectroscopy (EIS) for battery chemistry, state of charge (SOC), and state of health (SOH) determination.*
- EEDD – Battery Self-Cooling for Safe Recycling
 - *Developing a thermoelectric cooler using energy from the batteries to keep batteries safe during transportation.*
- Holman Parts Distribution – Holman Parts Reverse Logistics Recycling Solution
 - *Develop partnership with automotive manufacturers, recyclers, and distributors to collect lithium-ion batteries at dealership locations across the U.S.*
- Li Industries – Smart Battery Sorting System
 - *Automated battery sorting using machine learning and chemical/physical property measurements for more effective direct battery recycling.*
- LIBIoT – Innovative Battery Collection System by Lithium-Ion Battery Internet-of-Things (LIBIoT)
 - *Methodologies found in IoT and Data Analytics are used for an innovative approach to lithium-ion battery collection for recycling purposes.*
- OnTo Technology – Li-Ion Identification
 - *A technology to engineer and automate a reliable end-of-life lithium-ion battery (EOL-LIB) sorting approach using analytical inputs and artificial intelligence.*
- Powering the Future – Banking Today's Materials to Power Tomorrow

- *Build on the company's existing auto battery collection network for lead acid; without reinventing the wheel, this solution will offer a complete closed-loop system.*
- Renewance – Reverse Logistics Marketplace
 - *Closed-loop model combined with on-demand service mechanism utilizing existing infrastructure delivers cost-effective reverse logistics.*
- Smartville – Distributed Battery Conditioning HUB
 - *Smartville will deploy distributed battery conditioning “HUBs,” or Heterogeneous Unifying Battery Facilities, to reduce costs and create value in the reverse logistics supply chain.*
- SNT Laser Focused – Utilizing Laser Cutting for Efficient Battery Pack Dismantling
 - *Developing a solution utilizing laser cutting to access battery pack casing efficiently.*
- Store Packs Umicore – Development of Four U.S. Collection and Storage Sites for Lithium-Ion Automotive Battery Packs
 - *Creating four collection and storage sites around the country to collect EV LIBs from automotive scrapyards, test for second life, then recycle.*
- Team EVBs – A Circular Economy for Electric Vehicle Batteries
 - *A demonstration whereby electric vehicle batteries are given a digital identity to connect all stakeholders in the lifecycle.*
- Team Portables – Reward to Recycle – Closing the Loop on Portables
 - *A demonstration whereby portable LIBs and the products they power will be given a digital identity to support final recycling.*
- Team RRCO – Composite Discharge Media
 - *Flowable media with tailored electrical properties allows the safe bulk discharge of LIBs.*
- Titan AES – IonView-Ultrasonic LIB Automated State of Health (SoH) 1 Second Test
 - *IonView – A commercial ultrasound-enabled second-life lithium-ion state-of-health battery test performed at 99% accuracy in under one minute.*



Figure I.4.B.4 The 15 Phase I winning teams submitted innovative proposals from across the United States



Figure I.4.B.5 Assistant Secretary Daniel Simmons announced the 15 winners of Phase I at NREL on September 25, 2019

The Phase I winners are posted in the prize website (<https://americanmadechallenges.org/batteryrecycling/>). The announcement of Phase I winners was covered in *E&E News* and later picked up by *Scientific American* in a positive story.

Conclusions

After one year of planning, content development, announcements, outreach, receiving submissions, review, and selection for Phase I, DOE selected 15 winning teams to receive the \$1 million prize, resulting in \$67,000 awarded to each team. These innovative concepts include ideas on how blockchain, car sharing, existing reverse logistics industries, and sorting technologies can be utilized to potentially collect 90% of discarded lithium batteries when scaled across the nation. Moving forward into Phase II: Partnering and Prototyping, these teams will build prototypes of their concepts while partnering with stakeholder to address the goal of capturing 90% of all lithium-ion batteries for recycling.

Key Publications

1. Phase I Lithium-Ion Battery Recycling Prize Rules
2. Informational Webinar
3. Promotional Video
4. Postcard
5. Pop-Up Banner
6. VTO's Research Plan to Reduce, Recycle, and Recover Critical Materials in Lithium-Ion Batteries (<https://www.energy.gov/sites/prod/files/2019/07/f64/112306-battery-recycling-brochure-June-2019%202-web150.pdf>)

References

1. EERE. 2019. "Energy Department Announces Battery Recycling Prize and Battery Recycling R&D Center." January 17, 2019. <https://www.energy.gov/articles/energy-department-announces-battery-recycling-prize-and-battery-recycling-rd-center>.
2. EERE. 2019. "Energy Department Announces Phase 1 Winners of Battery Recycling Prize." September 25, 2019. <https://www.energy.gov/eere/articles/energy-department-announces-phase-1-winners-battery-recycling-prize>.
3. Fialka, John. 2019. "Don't Junk That EV Battery—It Might Power a Town." Scientific American, September 26, 2019. <https://www.scientificamerican.com/article/dont-junk-that-ev-battery-it-might-power-a-town/>.

Acknowledgments

DOE Battery Recycling Prize Team:

- Connie Bezanson
- Samuel Gillard
- Helena Khazdozian
- Kate McMahon

NREL Battery Recycling Prize Team:

- Barbara Khan
- Nick Langle
- Lauren Lynch
- Rebecca Martineau
- Julie Sodano

I.4.C ReCell Advanced Battery Recycling Center (ANL)

Jeff Spangenberg, Principal Investigator

Advanced Materials Division
Argonne National Laboratory
9700 South Cass Avenue
Lemont, IL 60439
E-mail: jspangenberg@anl.gov

Samuel Gillard, DOE Technology Development Manager

U.S. Department of Energy
E-mail: Samuel.Gillard@ee.doe.gov

Start Date: October 1, 2018	End Date: December 31, 2021	
Project Funding (FY19): \$1,875,000	DOE share: \$1,875,000	Non-DOE share: \$0

Project Introduction

The use of lithium-ion batteries has surged in recent years, starting with electronics and expanding into many applications, including the growing electric and hybrid vehicle industry. But the technologies to optimize recycling of these batteries has not kept pace.

The launch of the U.S. Department of Energy's (DOE) first lithium-ion battery recycling center, called the ReCell Center, will help the United States grow a globally competitive recycling industry and reduce our reliance on foreign sources of battery materials.

Objectives

DOE sees an opportunity to de-risk the recycling of lithium-ion batteries and future battery chemistries to help accelerate the growth of a profitable recycling market for spent EV, electronics, and stationary storage batteries. This can be done by developing novel recycling techniques that will make lithium-ion recycling cost-effective by using less energy-intensive processing methods and capturing more metals and other high-value materials in forms that make reuse easier.

Accelerating and advancing industry adoption of EV battery recycling will help meet the Vehicle Technology Office goals of pushing down the cost of EV battery packs for consumers and increasing the use of domestic recycled sources of battery materials.

These recycled materials can be recycled for use in new batteries, helping to drive down the overall production cost of electric vehicle batteries to the national goal of \$80/kWh.

Approach

A collaboration of researchers from industry, academia, and national laboratories will test new recycling techniques at their home institutions and at Argonne National Laboratory in order to develop new battery designs that will enable greater material recovery at end of life. The most promising new recycling processes and battery designs will be demonstrated at pilot scale at the ReCell Center based at Argonne. Validated processes and designs will be licensed to industry for further commercialization.

The center collaborators also will use existing modeling and analysis tools to help industry determine how to optimize value. Argonne's EverBatt model evaluates the techno-economic and environmental impacts of each stage of a battery's life, including recycling. NREL's supply chain analysis tool provides a birds-eye view of the interconnections between raw material availability, primary manufacture, recycling, and demand.

The ReCell Center had its kickoff meeting November 1-2, 2018, at Argonne National Laboratory. The three laboratory partners (Argonne National Laboratory, National Renewable Laboratory, and Oak Ridge National

Laboratory) were all present, as well as the three collaborating universities (University of California San Diego, Worcester Polytechnic Institute, and Michigan Technological University). The center organization is shown in Figure I.4.C.1.

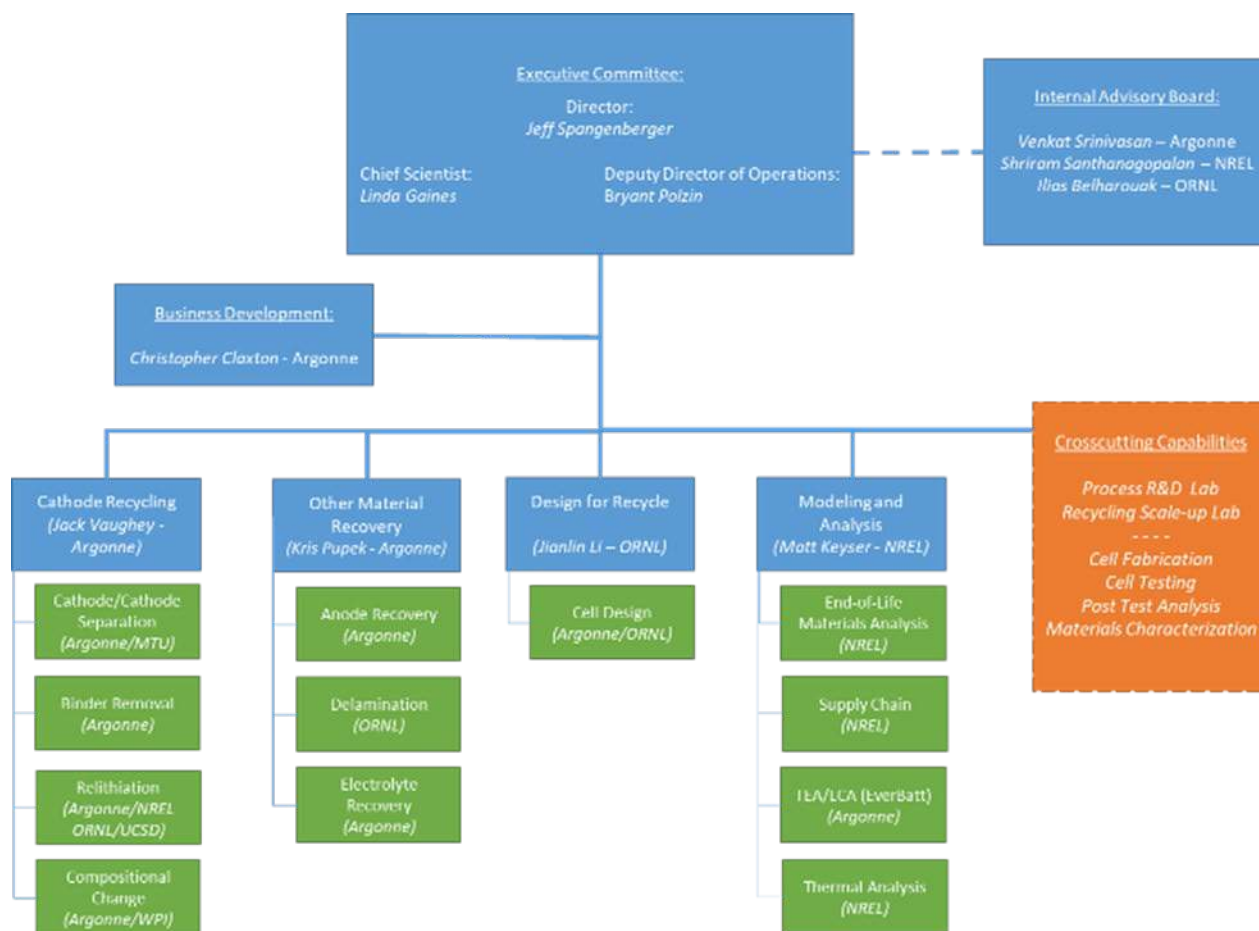


Figure I.4.C.1 ReCell organization chart as of the end of FY19Q2

The four focus areas include Direct Cathode Recycling, Recovery of Other Materials, Design for Recycle, and Modeling and Analysis. A total of 17 projects across the four focus areas identified as the initial work to be performed within the center.

In addition to the focus areas, each organization has crosscutting capabilities that will be utilized throughout this program.

Energy Secretary Rick Perry announced the ReCell Center on January 17, 2019 (at the Bipartisan Policy Center's American Energy Innovation Council) as a national security initiative that will bolster economic growth, strengthen our energy security and improve the environment. Daniel Simmons, Assistant Secretary for Energy Efficiency and Renewable Energy, and Alex Fitzsimmons, Chief of Staff for the Office of Energy Efficiency and Renewable Energy, and many others joined the ribbon-cutting celebration on February 15th, 2019 at Argonne, where equipment for scale-up demonstrations will be housed. Bench- and pilot-scale laboratories are under construction at Argonne and scheduled to be completed at the end of FY19.

Milestone FY19Q4

The center's FY19Q4 milestone was to establish the ReCell Center's Battery Recycling Laboratory and Scale-up Facilities

The ReCell center will ultimately have three laboratories located at Argonne National Laboratory; a bench scale laboratory used for small scale research, a Process Scale-up facility for larger equipment R&D, and a third, Pilot Scale High-bay facility that will house large equipment and equipment. The ReCell Bench Scale and Process Scale-up Laboratories are located within Argonne's Materials Engineering Research Facility (MERF) in building 370 and these facilities are scheduled to be move-in ready in February 2020. The ReCell Pilot Scale High-bay is currently functional and is populated with equipment that will both stay in the laboratory or will be moved to the bench scale and process scale-up laboratories when they are ready. The ReCell Pilot Scale High-bay has been able to accommodate all of the equipment received so far within the program, but is near capacity. The new space in the MERF will alleviate the space restriction.

The ReCell Pilot Scale High-bay is located at Argonne National Laboratory in Building 369. Flooring, lighting, exhaust ventilation and building cooling has been updated in this facility as well as the installation of a. A walk in powder handling hood has been installed so that battery processing equipment can be wheeled in and out as needed. The two pictures below are of the facility. (See Figure I.4.C.2.)



Figure I.4.C.2 ReCell Pilot Scale High-bay located at Argonne National Laboratory Building 369

Additionally, there is a small laboratory, pictured below (see Figure I.4.C.3), off the high bay space that has been improved as well. In this lab space casework, air conditioning and plumbing have been installed. This area is used for analytical and some small processing equipment. An FTIR, CSTR system and vacuum oven have been installed as well. More equipment will populate this area as projects in the ReCell research program begin to mature.



Figure I.4.C.3 ReCell Laboratory off the High-bay

Direct Cathode Recycling

In 2018, production of lithium-ion batteries (LIB) in the world consumed > 50,000 tons of various transition metals and lithium salts to meet the world's energy storage needs. For the manufacture of LIBs, the consumption of these critical materials represents a significant market for suppliers, mineral companies, and materials processors. Most notably, at present rates of production, over 50% of the world's output of cobalt is used to make LIBs, with projections that demand will increase significantly as various countries attempt to reduce fossil fuel consumption. An alternative to increased mine output and exploration is to utilize recycling of out-of-service LIBs as a source of various critical metals or as a feedstock for new low-cobalt compositions. Within this program we are seeking to understand how to address the various types of cathode materials that are used in the marketplace, the state of their performance at end-of-life, and to develop processes to, with minimal input, recover, rejuvenate, and reuse these cathode electrode materials. In this section we are seeking to address the issue that at end of life, due to side reactions, salt precipitation, and corrosion, the amount of useable lithium within the cathode structure is typically about 15-20% below the initial formulation, e.g., $\text{Li}_{0.8}(\text{Ni}_{0.33}\text{Mn}_{0.33}\text{Co}_{0.33})\text{O}_2$. Within Direct Recycling, there are four efforts focused on cathode separation and isolation processes (froth flotation, magnetic separation, electrode binder removal, impurity incorporation into the cathode), and four pathways that seek to address relithiation of the recovered cathode (chemical relithiation, electrochemical relithiation, ionothermal relithiation, and hydrothermal relithiation). All will be evaluated in terms of relithiation extent, relithiation rate, and eventually by cost of the relithiation process (with Q. Dai, EverBatt Model). In addition, an effort that addresses the role of altering the metal ratio will be undertaken, focused on using the relithiated Co-rich cathodes as feedstock for low-cobalt, Ni-rich cathodes.

Recovery of Other Materials

Lithium-ion cells contain a number of valuable materials. In the first area of this program, cathode recovery was the focus of the work. Valuable metals and high processing cost contribute to making cathode materials important to recover as close to a reusable form as possible. There are other materials that are present in lithium-ion batteries that are just as critical and are costly to produce.

In this area of the program, Other Materials Recovery, the projects are focusing on recovering those materials. Graphite and lithium-containing compounds (electrolyte salt) are two other critical materials that are present in cells. These materials are defined as critical due to their limited quantity around the world or the geographical location that they are produced. By recovering these materials, we will be securing a source of these materials, therefore reducing the foreign dependence on these materials and increasing our national security.

Again, just like the cathode, lithium hexafluorophosphate (LiPF_6 , one of the electrolyte salts), has a high production cost and detrimental effect on the environment if discarded. By recovering LiPF_6 , this material can be reused in batteries, thus reducing the cost and environmental impact.

By recovering additional materials, the recycling process maximizes the reuse of lithium-ion cell components and therefore increasing the revenue in the recycling process and driving the overall process to profitability.

This section covers projects on: Hydrothermal Recovery Process for the Black Mass, Anode/ Cathode Separation and Purification, and Electrolyte Components Removal and Recovery. Each of these projects addresses an additional material stream that can be recovered and sold to drive the recycling process towards profitability.

Design for Recycle

Millions of batteries are approaching their end of life and need to be recycled. While many efforts have been focused on recycling the elements and/or compounds from spent cells through various techniques, this project aims to create cell designs that will enable rejuvenation of a spent cell, and/or improve the ease of recycling at the end of life. The ability to regenerate a cell with an electrolyte flush/rejuvenation has the potential to extend the life of a lithium-ion battery far beyond its 10-year life. This will reduce the quantity of packs requiring recycling and/or enable easier target material extraction.

Modeling and Analysis

The modeling and analysis focus area includes four subareas: diagnostics on aged materials, microcalorimetry on recycled materials, cost and environmental impacts modeling, and battery supply chain modeling. The first two subareas characterize battery materials via electron backscattering diffraction (EBSD) and with a microcalorimeter, respectively, to evaluate the performance of battery materials under various conditions, while the last two subareas evaluate the economic and environmental impacts, as well as the material flows, pertaining to the battery supply chain. The four subareas will work together to identify the optimal recycling processes for batteries and will serve to inform and direct R&D efforts under the ReCell Center.

Major efforts made under the modeling and analysis focus area during the fourth quarter of fiscal year (FY) 2019 are summarized in Table I.4.C.1. Detailed information about individual project progress and the latest results are provided in the subarea reports below.

Table I.4.C.1 Modeling and Analysis Focus Area Major Efforts in Q3 FY2019

Subarea	Major Efforts
Diagnostics on Aged Materials	Established improved sampling and analytical tools have been established to quantify strain mapping at the primary particle level via EBSD.
Microcalorimetry on Recycled Materials	Thermally tested the new/pristine 1520P/NMC cells in the microcalorimeter.
Cost and Environmental Impacts Modeling	Developed customized versions of EverBatt have been developed to evaluate the electrolyte recovery process, the hydrothermal relithiation process, and the ionothermal relithiation process
Battery Supply Chain Modeling	Development of a user interface, LIBRA Model Interface, and a sensitivity app, LIBRA Sensitivity Analyzer.

Cross-Cutting Activities

Crosscutting research takes advantage of established facilities and capabilities of individuals and combines them together to accelerate R&D for deployment into industry. This project uses crosscutting capabilities to address specific Tasks in the projects, to enable a successful outcome in the allotted timeframe. This program will leverage prior efforts at the labs, funded by lab LDRD's, CEMAC, AMO, and VTO programs.

Results

Chemical Relithiation of NMC Cathodes

A significant underlying cause of performance degradation for cathode lithium-ion battery materials is the gradual cycle to cycle loss of active lithium from the system. Due to SEI formation, corrosion, and electronic isolation of particles, the active lithium initially supplied by the NMC cathode can be irreversibly trapped in a variety of forms that affects long-term battery performance. On cycling, the amount of lithium trapped and rendered inactive increases at a slow rate (after losses involved in the initial break-in cycling), gradually decreasing the cell's capacity until performance is noticeably affected or the commonly used 80% of initial capacity value is reached. The 80% value (stoichiometry: $\text{Li}_{0.8}(\text{NiMnCo})\text{O}_2$) is associated with rises in impedance, stability, and a decrease in capacity in the standard window (lifetime). The structure of this end of life (EoL) product is a lithium deficient version of the starting materials, although some further structural changes can be related to the temperature of operation, initial stoichiometry, or processing conditions. Typical structural changes include site mixing of lithium and nickel (similar size), oxygen loss, or degradation of the surface layers to similar (but electrochemically less desirable) materials, including various defect spinel or rocksalt structures. In this section we are establishing the conditions required to convert a lithium-deficient NMC cathode material back to a stoichiometric material using low- to mid ($< 400^\circ\text{C}$) temperature annealing in the presence of a lithium source, O_2 -containing atmosphere, and lithium source material. Re-lithiated materials will be characterized and studied for electrochemical activity, extent of anti-site mixing, and sample purity. Data and insights will be provided to the EverBatt team led by Qiang Dai (ANL) and modeled for cost and performance metrics.

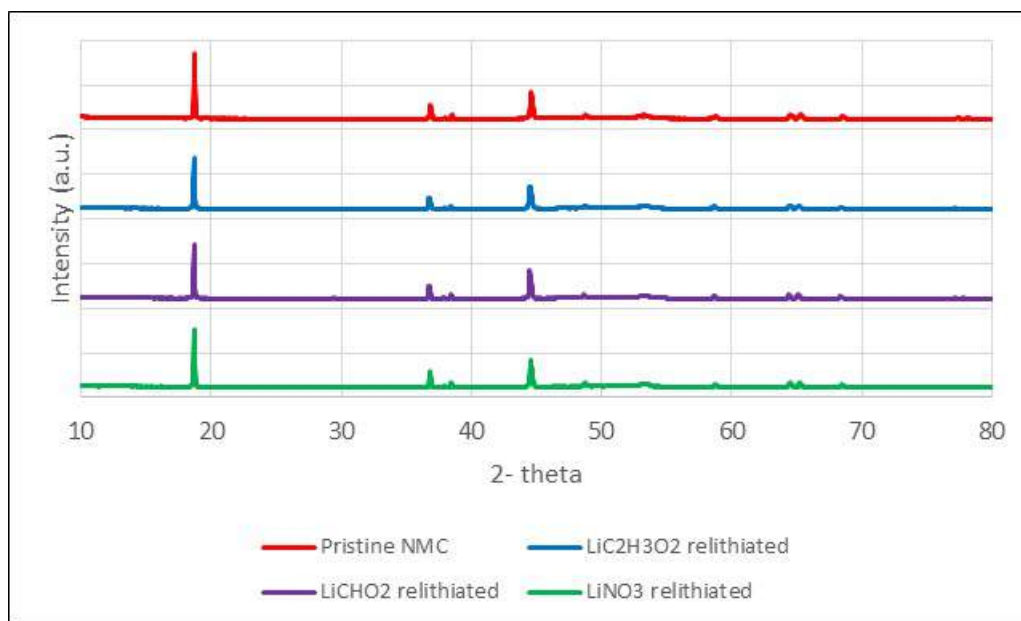


Figure I.4.C.4 XRD patterns of Relithiated NMC versus starting lithia source

In this quarter we evaluated the relithiation versus temperature and lithia (lithium oxide) source for baseline delithiated NMCs (MERF/ANL). At a recent industrial conference (NaatBatt 2019), several industrial recyclers noted that while dissolution of the NMC recycled material into salts was the state-of-the-art method, direct relithiation was under discussion and evaluation. Specific suppliers noted that the impedance rise we have discussed previously, and they had been evaluating methods to reverse this (perceived) surface-degradation phenomenon. Specific directions included identifying lithia sources that produced active lithia at the appropriate temperature range and looking at the role of temperature. Additionally, the role of time at temperature was evaluated as longer times at a lower temperature was compared to shorter times at higher temperatures. Alternative relithiation sources to lithium hydroxide or carbonate were also tested (LiCHO_2 ,

$\text{LiC}_2\text{H}_3\text{O}_2$, LiNO_3) in reactions at 500°C . By XRD, these products were comparable to the pristine NMC and the previous sets of relithiated products. Observationally the LiCHO_2 (lithium formate) relithiated product showed decreased high temperature thermal stability relative to the others compared to lithium acetate or lithium nitrate. Further analysis for lithium content was done using GDOES and is presented in Table I.4.C.2. These values are comparable to those of the other lithium sources.

Table I.4.C.2 GDOES-determined Lithium Content as a Function of Lithia Source at 500°C

Relithiation Source	Li content (st.dev.)
$\text{Li}(\text{C}_2\text{H}_3\text{O}_2) \cdot 4\text{H}_2\text{O}$	1.17 (0.04)
LiCHO_2	1.07 (0.04)
LiNO_3	1.07 (0.03)

In association with CAMP (ANL) and EverBatt, we have started scale-up relithiation reactions (2-3x lab scale) using Li_2O , $\text{LiOH} \cdot \text{H}_2\text{O}$, and Li_2CO_3 heated to $650\text{--}700^\circ\text{C}$ to have more material for electrochemical, structural, and surface characterization, and cell testing. Table I.4.C.3 highlights select lithiation data for the products versus lithiation salt for the scale-up processing.

Table I.4.C.3 GDOES-determined Lithium Content as a Function of Lithia Source at 650°C

Relithiation Source (Temperature)	Li content (st.dev.)
$\text{LiOH} \cdot \text{H}_2\text{O}$ (650°C)	1.14 (0.02)
Li_2O (650°C)	1.08 (0.05)
$\text{LiOH} \cdot \text{H}_2\text{O}$ (700°C)	1.06 (0.09)

Electrochemical evaluation of the hydroxide-sourced lithia is shown in Figure I.4.C.5. Preliminary rate studies on the re-lithiated 20% delithiated starting materials indicate similar low rate capacity as the pristine but some drop-off in capacity is noted. Preliminary studies point to impedance rise within the window used for evaluation. Previous TGA studies indicated that delithiated materials were stable to $\sim 300^\circ\text{C}$ before oxygen loss. The 650°C annealing temperature thus is in competition with surface decomposition (reduction of the oxidized surface species, i.e., Ni^{+3}) and the relative speeds should be taken into account for higher temperature studies.

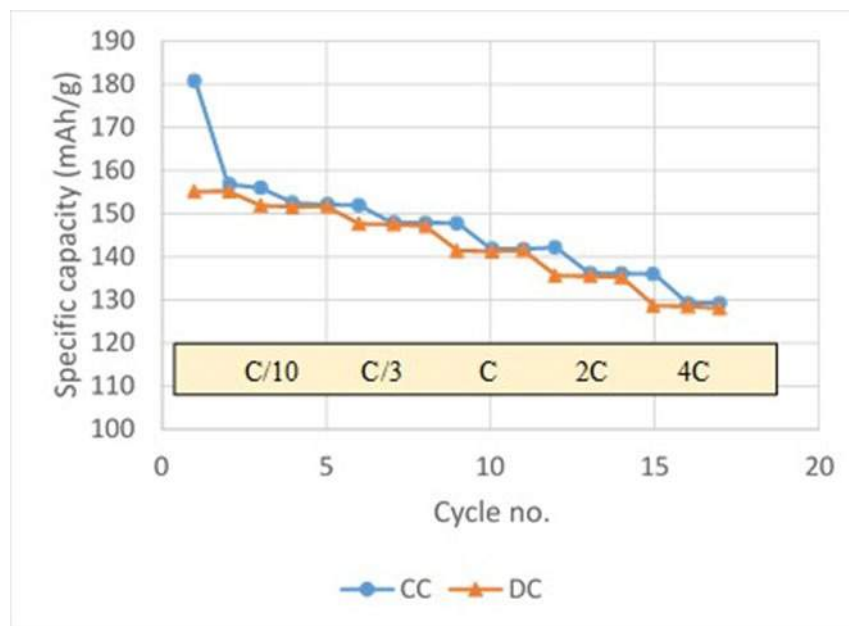


Figure I.4.C.5 Rate performance of LiOH • H₂O relithiated NMC (650 °C) half-cell

Electrochemical Relithiation (NREL)

The objective of this project is to develop an electrochemical recycling method for EoL (End of Life) LIB cathode materials. Restoring the EoL cathode performance and recreating initial (pristine-like) structure are to be achieved using electrochemical relithiation with a lithium metal sacrificial anode as the electrochemical Li ion (Li⁺) source to counteract the cathode lithium deficiency. The electrochemical relithiation process developed is being optimized for application to large-scale direct recycling such as roll to roll processes. One critical aspect is that the electrochemical relithiation must be optimized for high speed in order to minimize the amount of time the EoL cathodes must be in an electrochemical bath during lithiation. Previous studies have shown that NMC cathodes can be relithiated to the original pristine oxide crystal structure utilizing at long (72 hour) voltage hold at 3.0V. This method will be optimized using voltage range, temperature and electrolyte as variables to fine-tune the fastest and most effective electrochemical relithiation method to restore EoL cathodes to pristine condition.

The impedance rise in the delithiated samples was evaluated and compared to the baseline cells created last quarter (Q3). Several cathode electrodes using pristine and delithiated NMC powders (MERF/ANL) were prepared with the composition of 90% NMC, 5% of PVDF, and 5% of conductive carbon. The chemically delithiated NMC cathodes were paired with Li metal in the coin cells for cycling between different voltage windows using either 1.2M LiPF₆ in EC:EMC 3:7 wt% (Gen2) electrolyte or a higher temperature stable alternative (1M LiPF₆ in PC). Half cells with gen 2 electrolyte and chemically delithiated NMC 111 cathodes were discharged (lithiated) at a C/10 rate based on the full NMC 111. Average capacities of 145 mAh/g on first discharge were seen, with a theoretical capacity of 161 mAh/g. Reported work by the Direct Recycling team in ReCell has noted that this difference could be due to impedance rise from the processing of the samples and its temperature history. MAS-NMR work noted at the last face-to-face (at Argonne) highlighted that little secondary lithium phases existed at the surface and the stoichiometries (bulk) appeared to be in good agreement with ICP and GDOES data. The observation that the samples appeared not be homogeneous lent credence to the proposal that the delithiation process preferably delithiated the surface layers (over bulk) and this might create a surface instability if heating or chemical reactions with the electrolyte resulted in an impedance rise.

As our methods are typically room temperature and can be evaluated using standard tools, impedance was measured for optimizing electrochemical relithiation to understand the kinetically limited relithiation of the chemically delithiated NMC 111 cathodes. The two most apparent methods to do this are to either increase the

temperature at which this reaction occurs or to decrease the lithiation rate by decreasing the applied current. In the spirit of our programmatic goals, the latter option is not available since we are aiming to make the relithiation process as swift as possible for it to be applied to a roll-to-roll direct relithiation approach.

The method explored to address the kinetically limited relithiation process was the use of elevated testing temperatures to increase lithium cation diffusion. Table I.4.C.4 depicts the results from the first discharge (relithiation) of chemically delithiated NMC111 half cells with one set relithiated at a CC 10C_r rate to 3.0V with a subsequent 1 hour CV hold at 3.0V, one set relithiated at 50°C at a CC 10C_r rate to 3.0V with a subsequent 1 hour CV hold and one set relithiated at 50°C at a CC 10C_r rate to 2.2V with a subsequent 1 hour CV hold. Each of these procedures was followed by a 30-minute rest at the set relithiation temperature followed by three cycles at C/10 in order to evaluate the stability of the restored capacity. The elevated temperature cells were removed and allowed to come back to room temperature because the following three C/10 cycles. From these experiments the lithiation kinetics for cells at an elevated temperature are found to be improved compared to room temperature based on the higher initial charge (lithiation) capacity that can be achieved at elevated temperatures. There is also evidence that using lower cut off voltages could even over-lithiate the cathode in comparison to the NMC111 capacity from the baseline studies. These results are consistent with the higher degree of homogeneity the higher temperature induces in the samples. This may have the effect of gradually lowering the formal oxidation state of the surface cations and inducing higher levels of stability against the electrolyte. This is supported additionally by the observation that the electrochemically delithiated NMC111 samples showed lower impedance on re-lithiation than the samples exposed to higher temperatures associated with chemical relithiation.

Table I.4.C.4 Comparison of Relithiation, Delithiation and Reversible Capacities for Half Cells Relithiated at Room Temperature or 50 °C

	RT 1 hour CV hold 3.0V (mAh/g)	50 °C 1 hour CV hold 3.0V (mAh/g)	50 °C 1 hour CV hold 2.2V (mAh/g)
1st Discharge	5.43	15.84	18.42
1st Charge	140	147	163
Reversible Charge	125	130	134
Reversible Discharge	117	123	131

Direct Regeneration of NMC Cathodes through Ionothermal Lithiation (ORNL)

The objective of this project is to develop a low-cost ionothermal lithiation process to relithiate and/or upgrade used cathode at ambient pressure. Ionic liquids (ILs) are a family of non-conventional molten salts that offer many advantages, such as negligible vapor pressures, negligible flammability, wide liquidus ranges, good thermal stability, and much synthesis flexibility. The unique solvation environment of these ionic liquids provides new reaction or flux media for controlling formation of solid-state materials with a minimum perturbation of morphologies¹. In addition, the ionic liquid can be readily recycled and reused after ionothermal lithiation.

In this quarter, we focused on scale-up of our ionothermal lithiation and three large-scale relithiation experiments were performed. New lithium precursor, LiBr, was investigated in three ionic liquids and two temperatures (150°C and 120°C) were used. The relithiated samples were characterized by various techniques including XRD, TGA, ICP-OES. Half-cells were prepared with relithiated black powder and electrochemical tests were performed. Typical large scale reaction conditions were: 5.93 g of delithiated NMC111, ~55 mL (74.93 g) of ionic liquid, [C₂mim][NTf₂], LiBr as lithium precursor, 150°C for 6 hours. The black powder was

washed with acetone, ethanol, and acetone, and finally dried at 100°C for 1 hour. The black powder was calcined at 500°C for 4 hours.

Results from three large-scale experiments are summarized in Table I.4.C.5 and Figure I.4.C.6. As shown in Table I.4.C.5, large-scale experiments work as well as small-scale. LiBr seems to be a better lithium precursor than LiCl. These results indicated that black powder prepared from LiBr as lithium precursor reaches 99.88% thermal stability close to that of pristine NMC111 and Li ratio of 1.07, which is the same as that of pristine NMC111.

Table I.4.C.5 Summary of Large Scale Isothermal Experiments, TGA, ICP, and XRD Results

Ionic liquid	Lithium precursors	Temperature	Black powder recovered (%)	IL recovered (%) and color	TGA (%)	Li ratio from ICP	XRD 108/110 gap
[C ₂ mim][NTf ₂]	LiBr	150°C, 6 h + 500 °C calcine 4 h	98.2	84.6, green	99.88	1.07	0.75
[C ₂ OHmim][NTf ₂]	Li Cl	150°C, 24 h	95.4	97.4, green	98.75	1.03	0.72
		150°C, 24 h + 500 °C calcine 4 h	95.5	95.4, green	99.68	1.01	0.72
Pristine NMC111	As received				99.80	1.07	0.76
Delithiated NMC111	As received				97.84	0.93	1.05

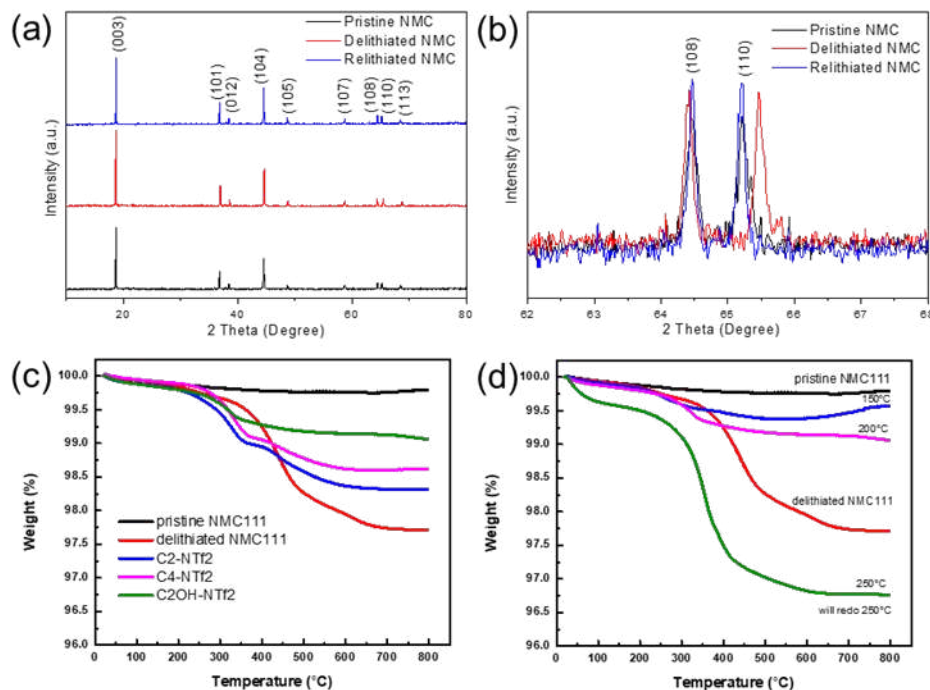


Figure I.4.C.6 (a) and (b) XRD patterns for pristine NMC111, chemically delithiated NMC111, and relithiated NMC111 (reaction condition: LiCl, [C₂OHmim][NTf₂], 150 °C, 24 h). (c) and (d) TGA results for samples recovered under different reaction conditions

Typical XRD patterns are shown in Figure I.4.C.6 (a) and (b). The peak splitting between (108) and (110) narrowed from 1.05 to 0.75 degree after ionothermal lithiation process, indicating Li restoring to some degree according to literature³. TGA data in Figure I.4.C.6 (c) and (d) demonstrates that the thermal stability of the NMC sample was enhanced after ionothermal relithiation and varied from reaction conditions, such as type of ionic liquid and reaction temperature. It can also be concluded that relithiation under reaction temperature of 150°C and in the ionic liquid of [C₂mim][NTf₂] using LiBr as a lithiated precursor resulted in samples with higher thermal stability and high Li ratio.

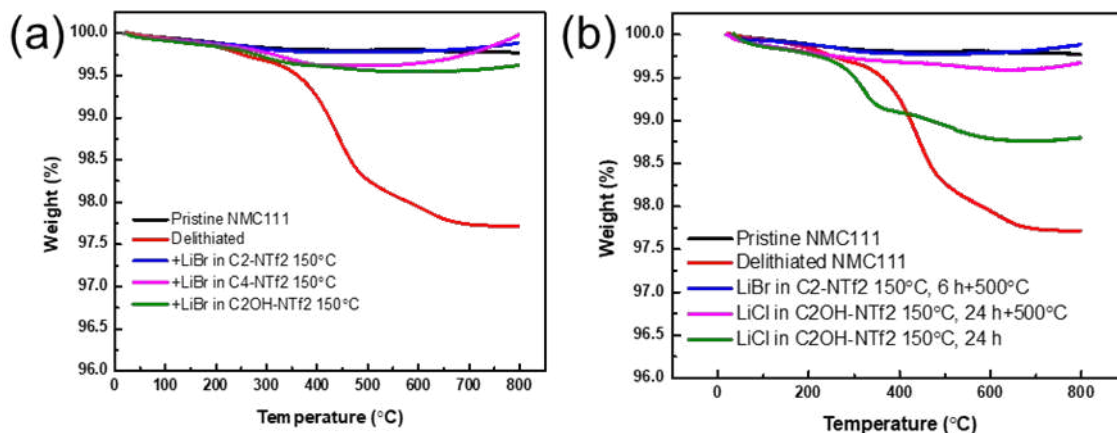
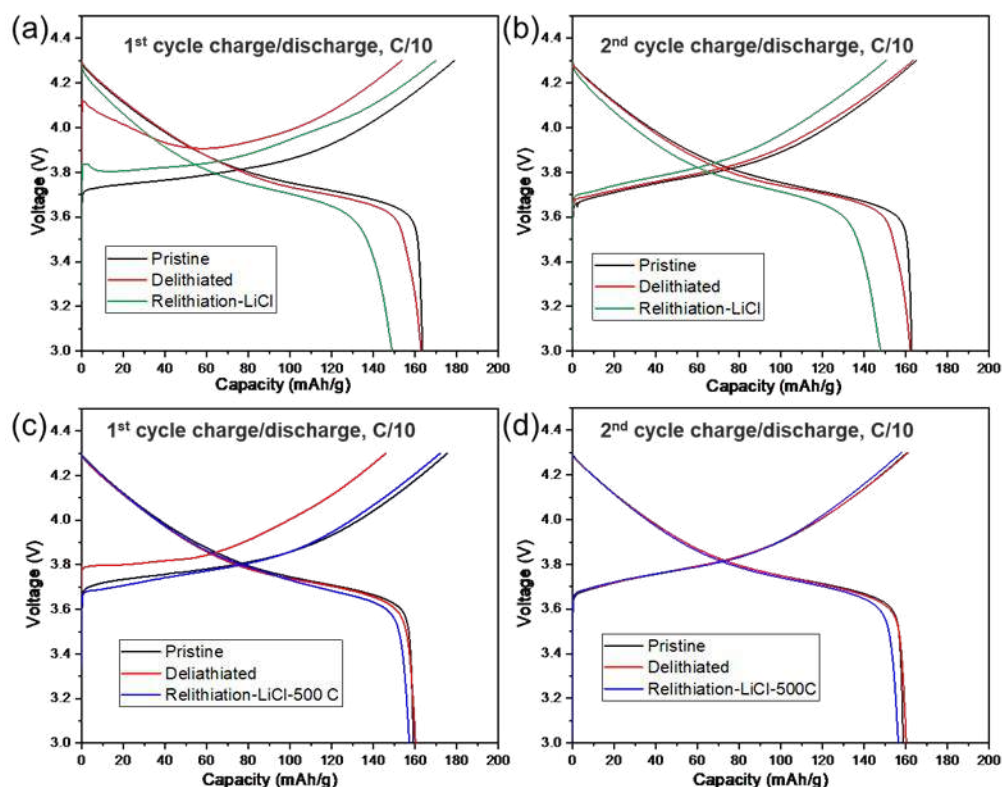


Figure I.4.C.7 Comparison of TGA plots of black powder from (a) LiBr-in three different ionic liquids and (b) three large scale experiments with pristine and delithiated NMC111

ICP-OES measurements were conducted to analyze the lithium content in the relithiated NMC111 and the results are listed in Table I.4.C.6. Our ICP measurements of both pristine and delithiated NMC111 are consistent with ANL's measurements. ICP results are also consistent with our TGA results (see Figure I.4.C.6 (c) and (d)). The lithium can be restored to ~1.07 after ionothermal reaction. As illustrated in Table I.4.C.6 and Figure I.4.C.7, when LiBr was used as lithiating agent lithium ratio is higher than 1.04 no matter which ionic liquid is used. TGA demonstrated that all three ionic liquids gave higher stability close to that of pristine NMC111. Therefore, we conclude that the better lithium precursor is determined to be LiBr among many agents studied so far.

Table I.4.C.6 ICP-OES Results

Sample ID	Mole ratio			
	Li	Ni	Co	Mn
Pristine NMC111 (ORNL)	1.071723	0.336569	0.331692	0.33174
Pristine NMC111 (ANL)	1.073	0.327	0.336	0.336
Delithiated NMC 111 (ORNL)	0.927183	0.336627	0.331569	0.331804
Delithiated NMC 111 (ANL)	0.935	0.336	0.336	0.328
LiCl, [C ₂ OHmim][NTf ₂], 150 °C	1.050938	0.337895	0.334309	0.327796
LiCl, [C ₂ mim][NTf ₂], 200 °C	0.985426	0.337594	0.333826	0.32858
LiCl, [C ₄ mim][NTf ₂], 200 °C	0.997455	0.341654	0.337617	0.320729
LiCl, [C ₂ OHmim][NTf ₂], 200 °C	1.035736	0.338916	0.334575	0.326508
LiBr, [C ₂ OHmim][NTf ₂], 150 °C-16h	1.063703	0.334784	0.325532	0.339681
LiBr, [C ₂ OHmim][NTf ₂], 120 °C-5h	1.048	0.339	0.329	0.332
LiBr, [C ₄ mim][NTf ₂], 150 °C-16h	1.069626	0.339126	0.329244	0.331630
LiBr, [C ₂ mim][NTf ₂], 150 °C-16h	1.07959	0.338330	0.330595	0.331075
LiBr, [C ₂ mim][NTf ₂], 120 °C-5h	1.053	0.338	0.329	0.332
LiBr, [C ₂ mim][NTf ₂], 120 °C-2h	1.042	0.337	0.330	0.333

Figure I.4.C.8 1st and 2nd charge-discharge curves for the pristine, delithiated, and relithiated samples before (a) (b) and after calcination at 500 °C (c) (d)

The electrochemical performance for the relithiated samples was evaluated in half-cell configuration. Figure I.4.C.8(a) and (b) show the voltage profiles for the relithiated NMC111 using LiCl as lithium precursor. Lithium was restored as proved by higher 1st charge capacity. However, relithiated sample displayed reduced discharge capacities and large polarization. The possible reason is that ionic liquids were not completely washed off. To solve that problem, we washed the sample with solvent that is miscible with ILs and calcined the sample at low temperature (e.g., 500°C). As plotted in Figure I.4.C.8(c) and (d), the relithiated sample displayed higher discharge capacities and less polarization after heat treatment at 500°C.

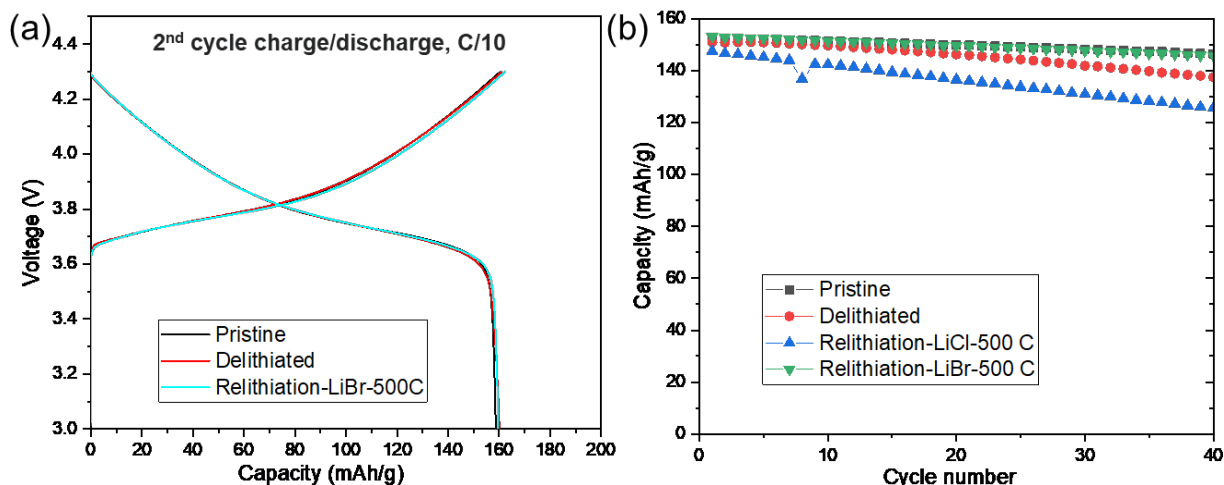


Figure I.4.C.9 (a) 2nd charge-discharge curves and (b) cycle performance for the pristine, delithiated, and relithiated samples

As above mentioned, LiBr is demonstrated as a better lithium precursor for the relithiation process. The relithiated NMC111 sample obtained by combining LiBr as lithium precursor and heat treatment at 500°C was also evaluated in a half-cell. As illustrated in Figure I.4.C.9 (a), the relithiated sample displayed good electrochemical performance, which is similar as the pristine sample. The cycle performance for the relithiated samples is plotted in Figure I.4.C.9 (b) and summarized in Table I.4.C.7. After 40 cycles, 94.5% of the initial capacity was retained for the relithiated NMC111 using LiBr, while only 83.4% remained for the relithiated NMC111 using LiCl, suggesting the importance of bromide, which serves as the reducing agent.

Table I.4.C.7 Cycle Performance

Sample	1 st discharge capacity at C/3 mAh/g	40 th discharge capacity at C/3 mAh/g	Capacity retention
Pristine	152.6	146.5	96.00%
Delithiated	151.0	135.2	89.53%
Relithiation-LiCl-500 C	147.6	123.1	83.40%
Relithiation-LiBr-500 C	153.2	144.8	94.52%

Hydrothermal Relithiation of Chemically Delithiated NMC111 Cathodes

A facile regeneration strategy with combination of hydrothermal lithiation and appropriate thermal annealing is proposed here to regenerate the delithiated NCM111 (D-NCM111). An optimal condition of the relithiation of D-NCM111 is fixed at 220°C hydrothermal treatment for 2h and 850°C sintering for 4h through systematic

investigations. The layered crystal structure and electrochemical performance including capacity (154 mAh g⁻¹) and cycling stability (96% capacity retention after 50 cycles) could be recovered to the level of pristine Toda NCM111 (T-NCM111). This direct cathode-to-cathode regeneration method displays several advantages over the traditional recycling techniques involved smelting or leaching processes and even solid sintering routes: (i) the energy consumption and greenhouse emission are effectively decreased without high temperature smelting and the acid solution waste treatment is eliminated without leaching; (ii) tedious chemical analysis to determine the amount of additional lithium source is unnecessary and it is compatible with cathodes with different capacity fading conditions. (iii) the embedded energy in the spent material is retained during the non-destructive regeneration process and resynthesis of cathode from precursor is not needed. Therefore, this method provides a promising strategy to regenerate used Li-ion battery cathodes.

The chemically delithiated NCM111 cathode (provided by the Materials Engineering Research Facility at Argonne) was successfully regenerated by the hydrothermal lithiation at 220°C for 2h followed by short sintering at 850°C for 4h in the air/pure oxygen atmosphere. The capacity could be recovered to the level of pristine materials. The mechanism was firstly investigated by X-ray photoelectron spectroscopy (XPS). Figure I.4.C.10 shows the high resolution XPS spectra in Ni 2p region of Toda NCM111 (T-NCM111), chemically delithiated NCM111 (D-NCM111), hydrothermally lithiated NCM111 at 220°C for 1h (HT-220C-1h-NCM111) and hydrothermally lithiated NCM111 at 220°C for 2h (HT-220C-2h-NCM111). All the spectra display two main peaks and two side peaks, which correspond to Ni 2p_{1/2} and Ni 2p_{3/2}, accompanying two satellite peaks, respectively. For the T-NCM111 spectra in Figure I.4.C.10a, the fitting peaks located at 854.4 eV and 871.8 eV indicate the valance state of Ni is 2+, which is in accordance with other reports. Interestingly, after chemical delithiation, the two main peaks could be fitted into two peaks, respectively. The peaks from 854.4 eV and 871.9 eV are the signs of Ni²⁺ and the peaks at 855.7 eV and 873.4 eV demonstrate the existence of Ni³⁺.⁴ The Ni is oxidized because the compensation of charge balance due to the lithium ions loss. After the hydrothermal lithiation at 220°C for 1h, the peaks from Ni³⁺ still exist. According to the integration of peaks, the Ni³⁺ content is up to 84%, which is even higher than that of D-NCM111 (42%). However, when the hydrothermal treatment time is prolonged to 2h, the Ni element valence state only displays a valence state of 2+. Therefore, a plausible reaction process of the hydrothermal lithiation may be Ni²⁺ oxidation to Ni³⁺ firstly and then lithium ions in the solution will move into the vacancies. It should be noted that the pre-oxidization of Ni²⁺ could efficiently restrict the cation mixing and supply a path for lithium diffusion.

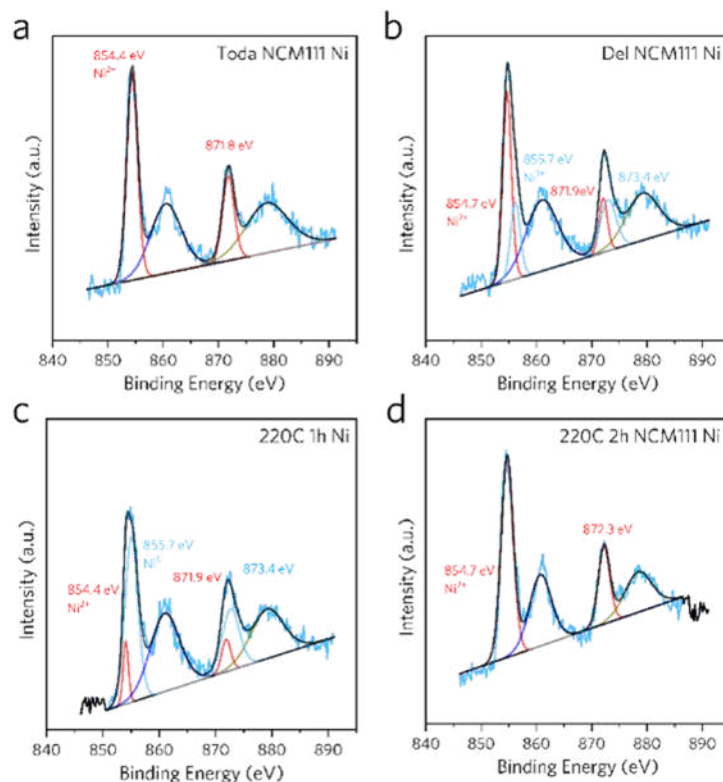


Figure I.4.C.10 High resolution XPS spectra of T-NCM111 (a), D-NCM111 (b), HT-220C-1h-NCM111(c) and HT-220C-2h-NCM111 (d)

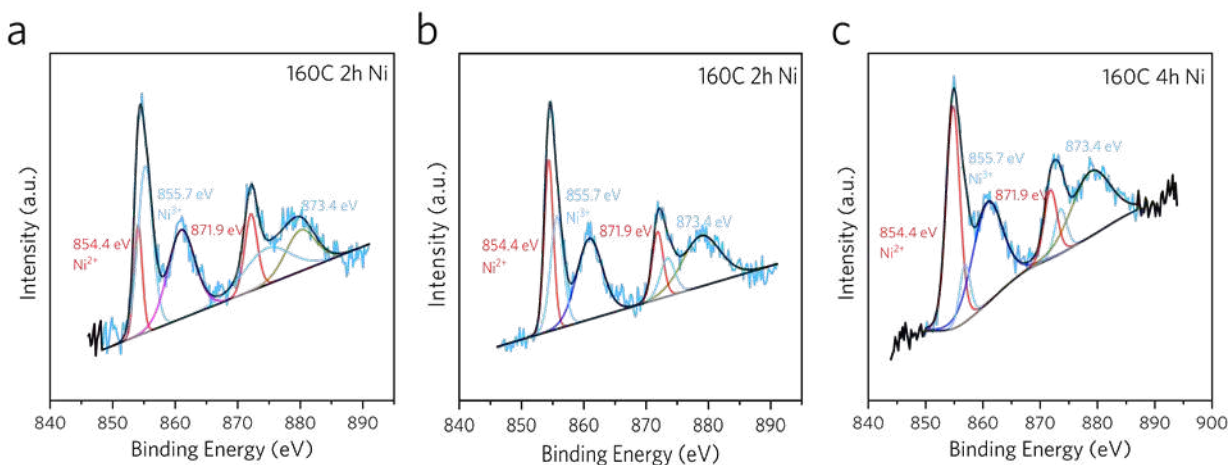


Figure I.4.C.11 High resolution XPS spectra of HT-160C-1h-NCM111(a), HT-160C-2h-NCM111 (b) and HT-160C-4h-NCM111 (c)

Besides, the samples treated at lower temperature (160 °C) for different time were also characterized by XPS. The results are shown in Figure I.4.C.11. When the D-NCM111 is lithiated for 1h, the Ni^{3+} content also increases, similar to that occurs in the 220 °C 1h case. And with the treatment time increased to 4h, the Ni^{3+} gradually decreased. The reduction may result from the insertion of lithium ions.

The electrochemical performance of the samples was evaluated by coin cells (half-cell) with cathode mass loading of $\sim 10 \text{ mg cm}^{-2}$. The electrolyte was LP40 (1M LiPF_6 in EC/DEC) and cells were cycled in the voltage

range of 3–4.3 V with first activation 4 cycles at 0.1C and following 50 cycles at 0.33C. The cycling stability of D-NCM111 after hydrothermal lithiation at 220 °C and 160 °C for different times is shown in Figure I.4.C.12. When the D-NCM111 is treated at 220 °C for 1h, the discharge capacity of the first cycle is only 137 mAh g⁻¹ and the capacity retention is only 71% after 50 cycles, both of which are even lower than that of D-NCM111 (145 mAh g⁻¹ and 90.3%). This may be because the oxidation of Ni²⁺ makes the crystal structure unstable. When the samples are treated at 220 °C for 2h, Ni³⁺ disappears completely and the capacity and retention are recovered to the level of the pristine (150 mAh g⁻¹ and 93.3%), demonstrating that the lithium ions are fully inserted into the vacancies of the layered structure. When the samples are treated at 160 °C, with the increase of treatment time, both the capacity and retention are improved, however, it is still lower than the value of pristine sample. This probably suggests that the lithiation is not complete. For a longer lithiation time, such as 6h, the XPS will be performed in future work.

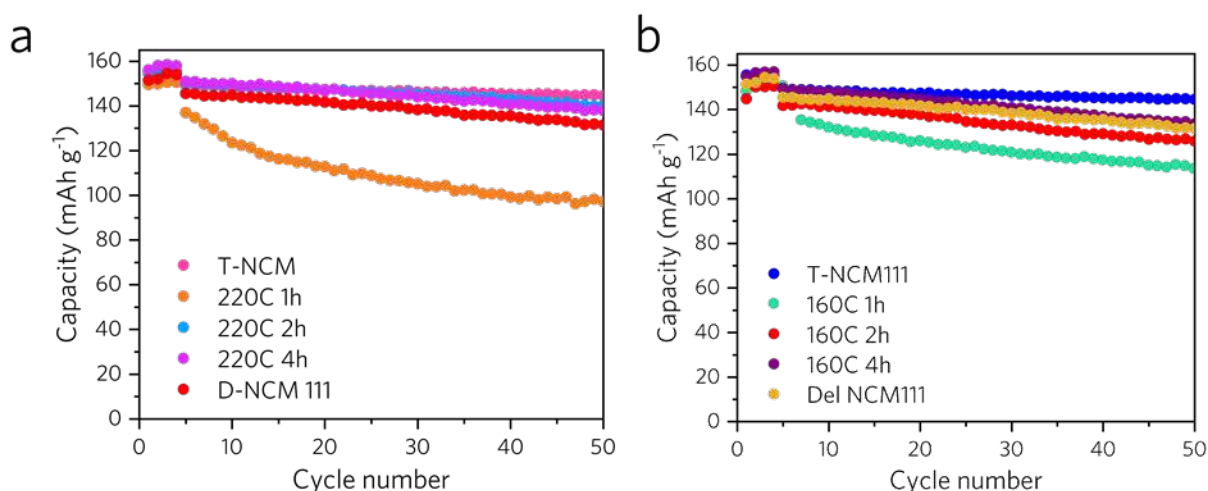


Figure I.4.C.12 Cycling stability of D-NCM111 after hydrothermal lithiation at 220°C (a) and 160°C (b) for different time

Before the regeneration of the black mass powder, removal of the residual PVDF binder might be a key step. Generally, sintering at low temperature (500 °C) is a widely considered method, of which the effect on the electrochemical performance and subsequent lithiation is investigated. Figure I.4.C.13 shows the cycling stability (a) and lithium content (b) of D-NCM111 after pre-removal of PVDF binder with and without a lithium source, as well as the corresponding regenerated products. In Figure I.4.C.13a, the capacity and stability are dropping dramatically when the D-NCM111 after 500°C sintering to remove PVDF binder without additional lithium source. The discharge capacity of the first cycle is only 92 mAh g⁻¹, which is left at 65 mAh g⁻¹ after 50 charge/discharge cycles. Because the lithium content remains the same as the D-NCM111(0.93) (Figure I.4.C.13b), the crystal structure might be destroyed. Even though an additional lithium source is added during the sintering, the capacity is increased to only 124 mAh g⁻¹, which is still lower than the D-NCM111. After the standard regeneration step (hydrothermal lithiation at 220°C for 2h followed by short sintering at 850°C for 4h), the capacity is clearly improved (148 mAh g⁻¹ and 148 mAh g⁻¹ for NCM111-500 and NCM11-500-Li), the stability is slightly poorer than the pristine material. These results show that the removal of PVDF via the suggested temperature (500°C) induces irretrievable crystal structure damage. The specific reason will be explored in the future work.

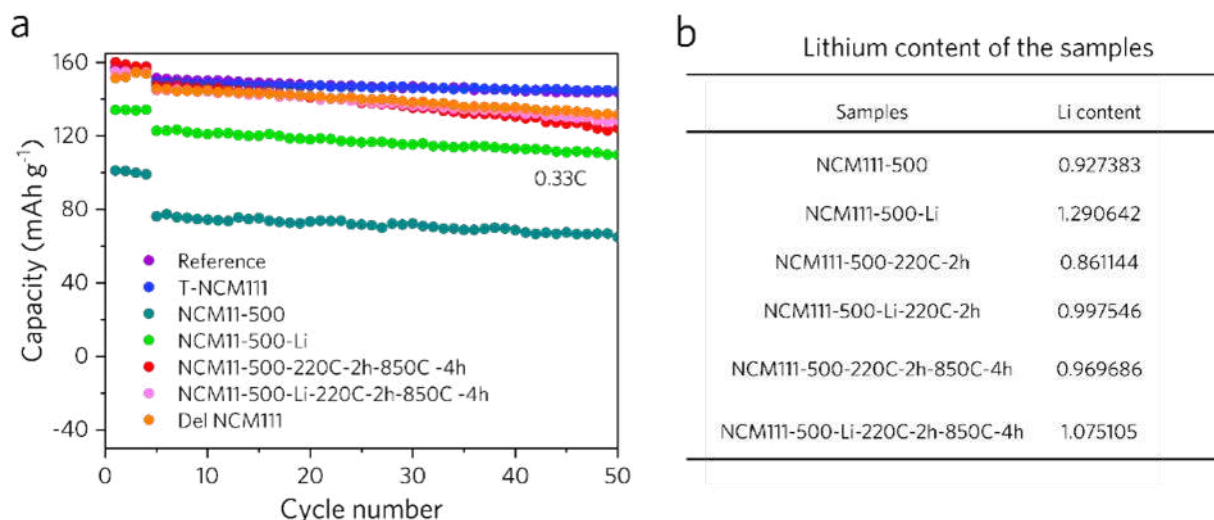


Figure I.4.C.13 Cycling stability (a) and lithium content (b) of D-NCM111 after pre-removal of PVDF binder with and without lithium source, as well as the corresponding regenerated products

Binder Removal

Once cathode materials are separated to be recycled, the poly(vinylidene difluoride) (PVDF) binder needs to be removed to allow for further processing. This can be done using a large quantity of *n*-methyl-2-pyrrolidone (NMP), but this is not cost-effective for battery recycling. Other methods need to be explored in order to enable profitable direct cathode recycling, such as thermal decomposition and mechanical methods. Both these methods require substantial development to allow for them to remove PVDF without damaging the cathode material. Thermal decomposition can result in substantial fluorine doping of the cathode material, thereby increasing impedance and reducing capacity. Various methods to prevent fluorine doping into the cathode material need to be developed, such as adding materials to absorb fluorine or create a fluorinated coating. Mechanical methods require a careful balancing to prevent cracking of the cathode while removing the binder, which could be made simpler by going to lower temperatures to embrittle the PVDF.

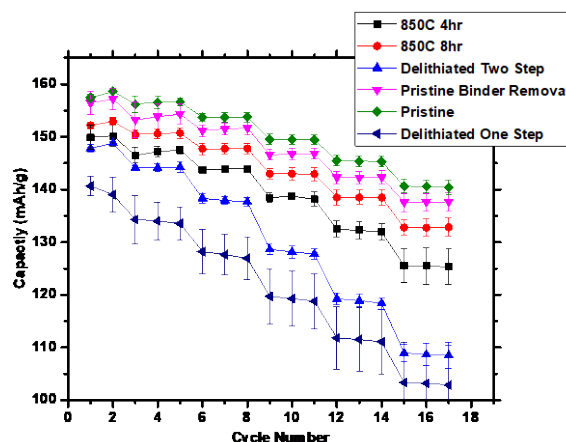


Figure I.4.C.14 Electrochemical cycling of 10% chemically delithiated NCM 111 with 3 wt.% PVDF binder and 5 wt.% carbon black after various annealing procedures. Pristine material is pure NCM 111 without any processing, pristine binder removal is with PVDF and carbon black heated to 500°C with 4 wt.% LiOH·H₂O. The one step process uses 15 wt.% LiOH·H₂O heated to 500°C, and the two step process uses 7.5 wt.% LiOH·H₂O in each step both with heats to 500°C. The 850C processes use 15 wt.% LiOH·H₂O heated 500°C at 0.5°C/min and then to 850°C at 2°C/min

Binder can be successfully be removed from pristine cathode materials at 500°C with only slight capacity loss with the addition of 4 wt.% $\text{LiOH} \cdot \text{H}_2\text{O}$. However, the situation is very different for the delithiated material where a process with sufficient LiOH to relithiated and compensate for the binder removal leads to very poorly performing material. We attempted to fix these issues by splitting the amount of LiOH into 2 separate steps, which improved the initial capacity, but has much higher impedance. Based on a variety of results we suspected that the Li wasn't able to fix the structural damage done by heating a delithiated material. To fix this structural damage much higher temperatures might be needed, and the higher temperature can remove more F from the structure. With an 850°C anneal the electrochemistry improves, and additional annealing time improves it more. After an 8 hr process the rate performance is similar to the pristine material, but the capacity is reduced. Additional optimization of the process may yield further improvements. (See Figure I.4.C.14.)

Additional binder removal attempts were made at 800°C and 900°C to see if further improvements could be achieved. With 4 hr of annealing time the initial capacity is similar to 4 hr at 850°C, but with improved rate performance. Longer annealing at 850°C starts to hinder the rate performance as too much Li is removed. Additional trials are needed with longer annealing times at 800°C and 900°C to see if further improvements can be made. Optimizing the amount of LiOH may also enable improved performance. The electrochemical performance is almost identical between 0.65 g (13 wt.%) and 0.85 g (17 wt.%) $\text{LiOH} \cdot \text{H}_2\text{O}$. (See Figure I.4.C.15.)

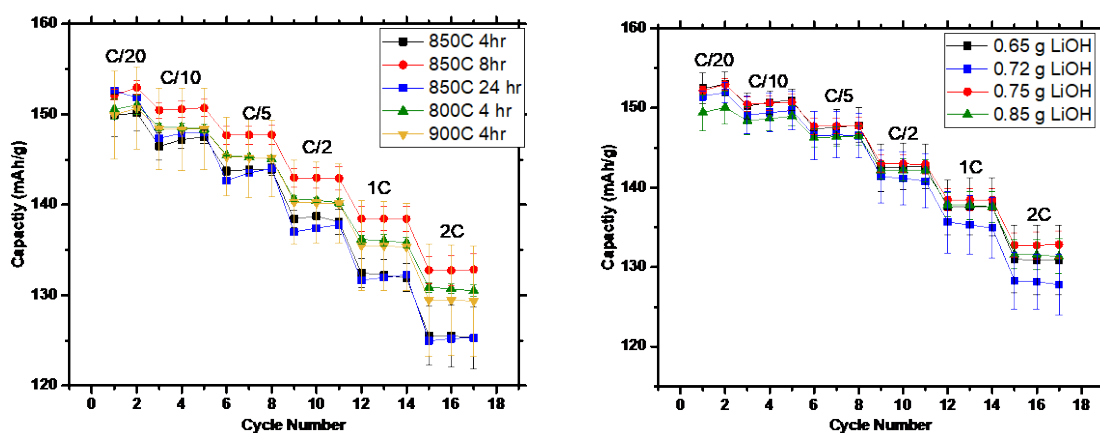


Figure I.4.C.15 Electrochemical rate performance of 10% delithiated NMC 111 with 3 wt.% PVDF binder and 5 wt.% carbon black after heat treating with a) 15 wt.% $\text{LiOH} \cdot \text{H}_2\text{O}$, and b) at 850°C for 8 hr with different amounts of $\text{LiOH} \cdot \text{H}_2\text{O}$ per 5 g of bound cathode material

Cathode/Cathode Separation Process Development (Argonne National Laboratory)

There are several methods of separation being investigated to separate different cathode chemistries by exploiting differences in physical characteristics such as magnetic susceptibility, particle size, charge etc.

1. Triboelectric separation

Triboelectric separation fractionates powders based on differences in charge and is one of the few dry powder separation techniques being used commercially for very fine particles. To determine the applicability of this technique for lithium-ion battery recycling several tests were conducted using equipment in Tribo Flow Separation's test facility.

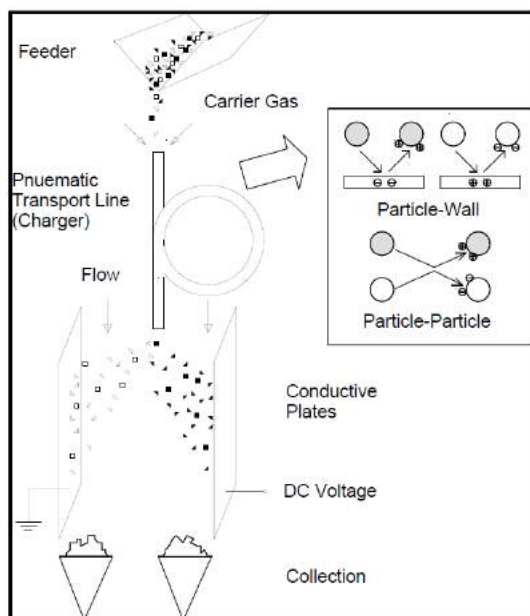


Figure I.4.C.16 Triboelectric separation operating

Figure I.4.C.16 shows the fundamental operating principles at work for tribo-electric separation. Model black mass powders are fed using a vibratory feeder into the pneumatic transport tube. Triboelectric charging of the particles occurs due to collisions of the particles with each other and the walls. The charged particles passed through an electric field created by the conductive plates. The separation occurs as the particles are drawn towards the positive or negative poles. An adjustable baffle shown in Figure I.4.C.17 is installed between the conductive plates and can be used to control the cut point between positive and negatively charged fractions.

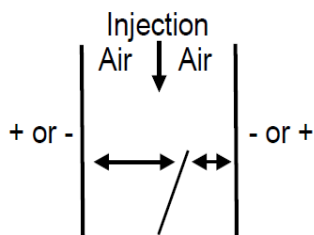


Figure I.4.C.17 Adjustable baffle system

The experiments were conducted using 500 g of a 50% lithium manganese oxide and 50% lithium nickel manganese cobalt oxide mixture. The sample was thoroughly mixed using a resonant acoustic mixer. The sample was separated into three parts and fed into the unit at a rate of approximately 650 g/hr. For each sample

the potential between the electrodes was set at voltages between 5 and 15 kV. Separated material was recovered and evaluated by ICP.

The 3 preliminary studies that were conducted resulted in 6 samples of separated material. These were labeled according to the voltage that was applied and the pole where the material was collected. The results of these tests are shown in Figure I.4.C.18 and Figure I.4.C.19. The yield at each respective pole did not vary as a function of voltage. LMO showed a preference for the positive electrode with consistent results even as the voltage was increased. The invariance of the separation was not expected. The testing conducted was limited and so it may be that the operating window was too small to identify maxima and minima. Additional testing may be able to provide better separation as several variables such as the position of the baffle, flow rates and voltages were not exhaustively investigated. Longer electrode plates may also provide additional efficiency since the charged particles will spend more time in the electrical field.

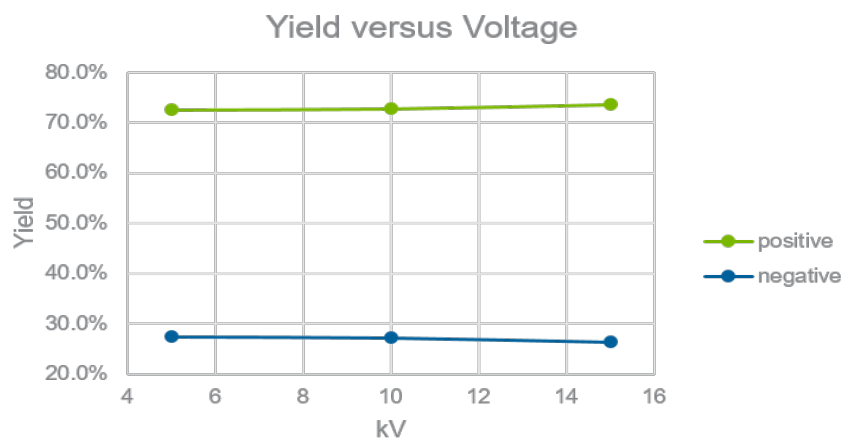


Figure I.4.C.18 Yield vs. applied voltages for NMC/LMO separation

NMC 111 and LMO mixture											
Voltage [kV]	Mass fed [g]	Mass + [g]	Mass - [g]	LMO + [%]	LMO Mass + [g]	Yield + [%]	LMO - [%]	LMO Mass - [g]	Yield - [%]	Recovery [%]	
5	170	118.8	44.9	58.1%	69.1	72.6%	42%	18.8	27.4%	96.3%	
10	165	110.7	41.4	59.2%	65.5	72.8%	41%	16.9	27.2%	92.2%	
15	165	117.3	42.1	58.6%	68.8	73.6%	41%	17.4	26.4%	96.6%	

Figure I.4.C.19 Results of triboelectric separation of NMC111 and LMO

2. Multistage magnetic separation

Many experiments have been conducted using various magnetic separation techniques. These have demonstrated the feasibility of separating cathode powders magnetically. A common trend in all of these tests was that as the amount of material in the magnetic fraction (material retained by the magnet) increased the purity of that fraction decreased. Several examples of this trend are shown in Figure I.4.C.20. To better understand this process an experiment was conducted to determine how many steps it would take to purify the product and what the final yield would be. A permanent magnet with a residual flux density of 12300 Gauss was used since previous testing showed that this field strength represented the midpoint between maximum yield and maximum purity. 150 grams of a 50/50 mixture of lithium manganese oxide and lithium nickel manganese cobalt oxide was separated. After each test the magnetic fraction of the material was saved and used in a subsequent test. This process was repeated 4 times. Unlike previously reported work this process was

repeated until both the NMC111 and LMO were highly purified. To achieve high purity for both components of the mixture required 5 stages of separation where each stage was an iteration of the 4 step process referenced above.

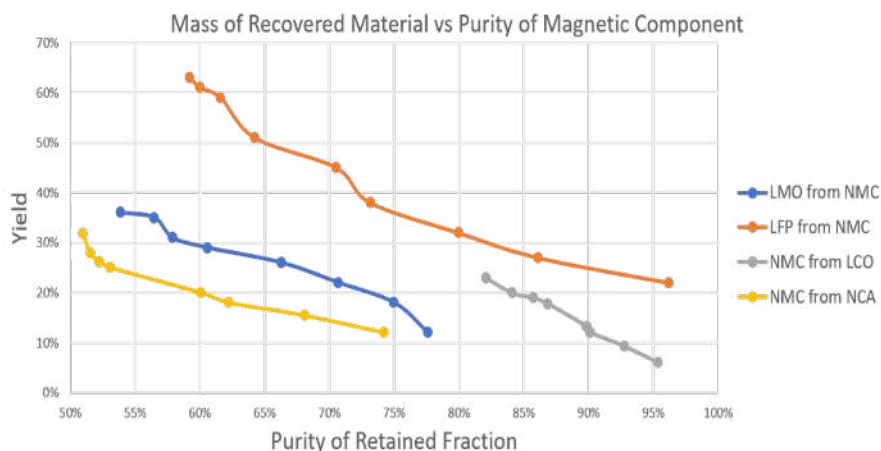


Figure I.4.C.20 Yield vs purity curves for separations of selected cathode mixtures

A total of 135 grams (90% yield) of high purity cathode powders were recovered. At each stage the purity of the magnetic fraction (LMO) was largely constant which is to be expected. The purity of the non-magnetic fraction (NMC111) increases as the total mass of the non-magnetic fraction decreases. The total mass of the non-magnetic fraction is decreasing as the LMO is removed from it. As can be seen in Figure I.4.C.21 and Figure I.4.C.22, most of the separation occurred by the end of stage 4. Very little improvement occurred after the second run of the 5th stage. The limiting factor of this process was likely the surface area of the magnetic collector. If it had been larger the separation would have occurred in fewer stages. Some disparity was seen in the amounts of the recovered LMO and NMC111. About 10 grams of NMC111 was lost while less than 4 grams of LMO was lost. This is likely because once the LMO was separated from the bulk, it was no longer handled. The NMC111 was constantly recycled through the separator which leads to more losses of material.

Stage	Magnetic		Non-magnetic	
	Mass of recovered LMO [g]	Purity	Mass of recovered NMC111 [g]	Purity
1	17.83	99.3%	120.95	57.7%
2	37.25	99.1%	107.45	67.7%
3	61.92	99.3%	79.14	88.2%
4	70.51	99.3%	68.36	98.8%
5	71.33	99.2%	65.11	99.9%

Figure I.4.C.21 Recovered mass and purity of magnetic and non-magnetic fractions

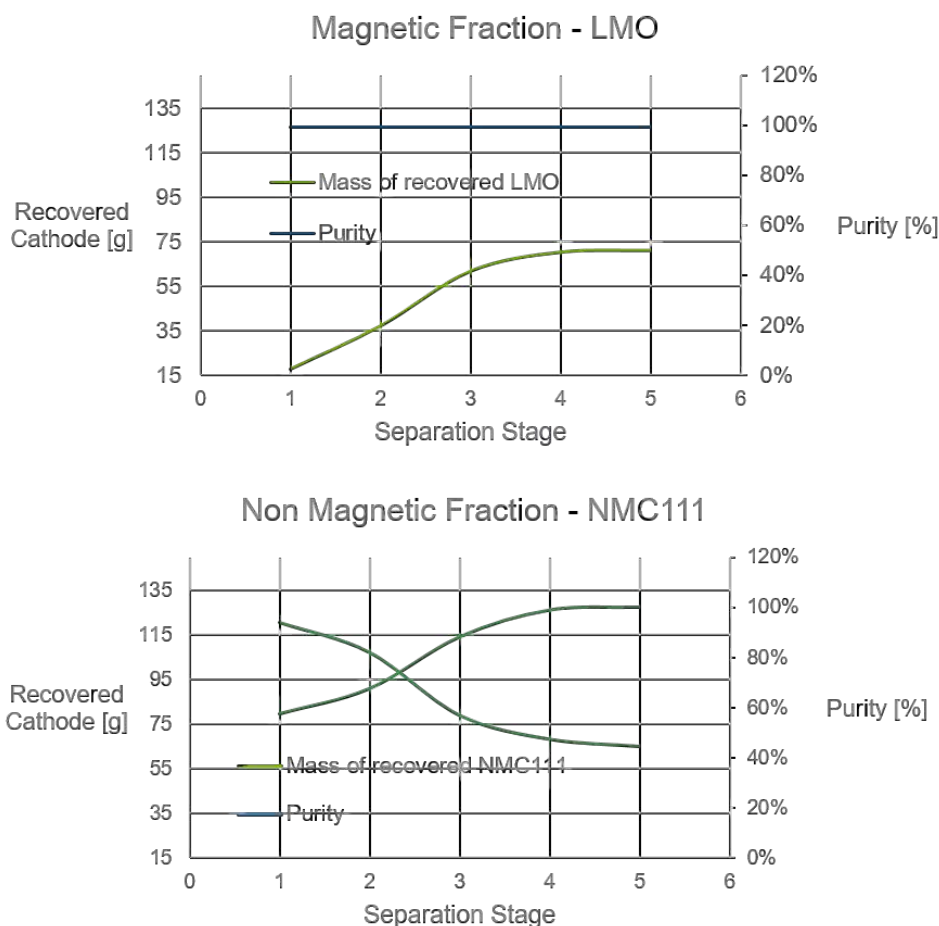
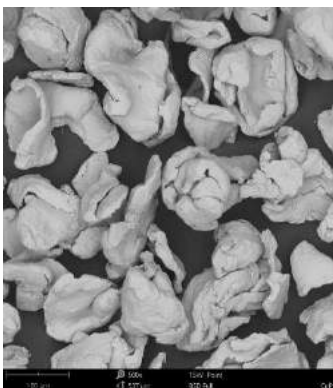


Figure I.4.C.22 Purity and yield of each LMO rich and NMC111 rich fractions

3. Current collector separation

Shredding or grinding lithium ion cells to separate their components is a common approach. This can result in the formation of small micron sized particles from the electrodes, separators, casing, etc. Large pieces can be removed in a fairly straightforward manner through sieving and flotation. Particles that are similar in size to the cathode powders may not be separated as easily. An experiment was conducted to determine the effectiveness of separating foil fines from active materials using a turbo classifier. Several yards of 9 μm copper foil were repeatedly ground and sieved. This copper fines were separated as: $>125\ \mu\text{m}$, $45\text{--}125\ \mu\text{m}$, and $<45\ \mu\text{m}$. Mixtures of NMC111 and copper were prepared at 1, 5 and 10 weight percent as shown in Figure I.4.C.23. The samples were run through the classifier at an RPM values of 1600-3700. Recovered samples were weighed and subjected to ICP analysis. (See Figure I.4.C.24.)

Figure I.4.C.23 SEM image of 45-125 μm shredded copper foil

The use of classification to remove copper foil particles was highly successful. Separations were conducted at 7 different rotational speeds with copper content reaching negligible levels between 3200-3600 RPM. (See Figure I.4.C.25 and Figure I.4.C.26.) A portion of the cathode material is lost with the copper during the separation. Optimization of process parameters is likely to improve results. Additional testing will be required with finer foil particles as well as more complex mixtures containing cathode/anode and copper.

Weighed Mass %	ICP Mass %
1	0.9301
5	4.7848
10	9.8914

Figure I.4.C.24 Mass percent of copper added to cathode powder

RPM	Fraction A Mass % Cu	Fraction B Mass % Cu	Recovery of Cathode
1600	4.9811	2.5429	89%
2000	5.4112	1.9847	86%
2400	5.8439	1.6975	85%
2800	6.2551	0.8518	81%
3200	7.2185	0.4439	78%
3600	8.0768	0.0078	76%
3700	8.1216	0.0038	76%

Figure I.4.C.25 Separations conducted at 7 different rotational speeds

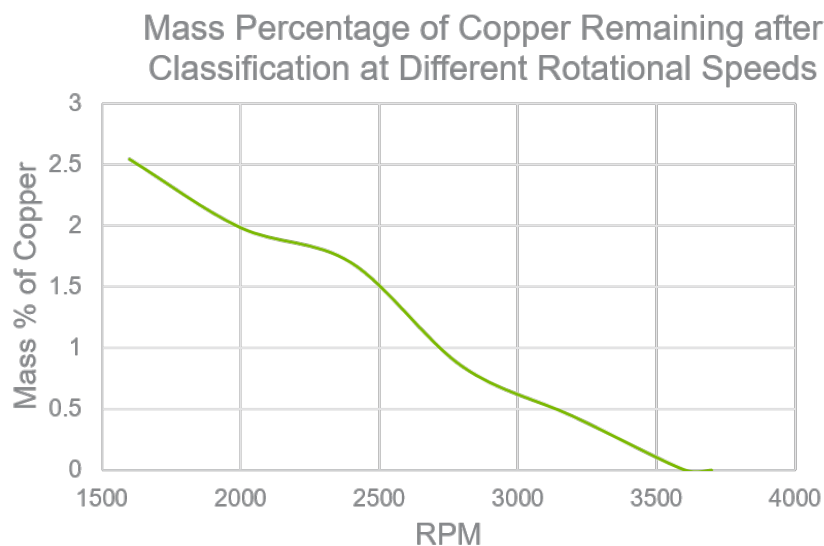


Figure I.4.C.26 Mass percentage of copper remaining after classification at different rotational speeds

Cathode-Cathode Separation via Froth Flotation (Michigan Technological University)

Unlike other recycling processes, direct recycling requires single battery chemistries or compatible chemistries to be successful. There is a need to be able to separate cathode chemistries from one another. Direct cathode recycling provides the opportunity to obtain higher-value recycling products. The success of this project is a critical piece to make direct recycling a reality. The purpose of this work is to investigate the effectiveness of the froth flotation process to separate different battery cathode chemistries in powder form. During this reporting period, we have tested separation performance of two pristine cathode mixtures. We have been focusing on the separation of NMC111, LMO, and LCO materials.

The cathode/cathode separation experiments *via* froth flotation method were continued using new chemicals (A, B and C). The new chemicals were tested as a result of the limitation previously observed with using sodium hydroxamate and oleic acid, and the limitations include low mass recovery, slow recovery kinetics and low grade (purity). During this reporting period, the experiments were carried out in a 2-L Denver cell for a batch process and a 1.5"-ID flotation column. In each experiment, a binary mixture of pristine cathode materials was fed into a flotation cell with 1.8 L of DI water. The slurry pH was adjusted to a desired value using dilute HCl or KOH solutions. The slurry pH varies with different cathode materials and might change with the amount of time being agitated in the flotation cell. A given amount of the collector was added, and the slurry was conditioned for 5 minutes. It was followed by adding frothier chemical and conditioning the slurry for 1 minute. Flotation commenced after the air was introduced. The froth products were collected in collection pans for a given period (typically 3-10 minutes). Both froth and tailing products after one-stage experiment might be used as feed for the follow-up experiments. A modified release analysis protocol was used to separate individual components from a mixture by the degree of hydrophobicity. The first froth product, namely froth 1 (F1) product, exhibit a largest degree of surface hydrophobicity that can be readily floated by air bubbles, while the tailing product is hydrophilic. This protocol is intended to provide a baseline of the separation performance in full-scale froth flotation cells/columns. For experiments using flotation columns, only froth and tailing products are collected. The obtained products were dried in a forced air oven at a temperature of 105 °C overnight and weighed. The composition of the recovered products were determined using energy-dispersive X-ray spectroscopy (EDS) and inductively coupled plasma – optical emission spectroscopy (ICP-OES). Three pristine materials were focused on for these experiments; NMC111, LMO, LCO, and they were characterized based on the recovery with the use of the three collectors.

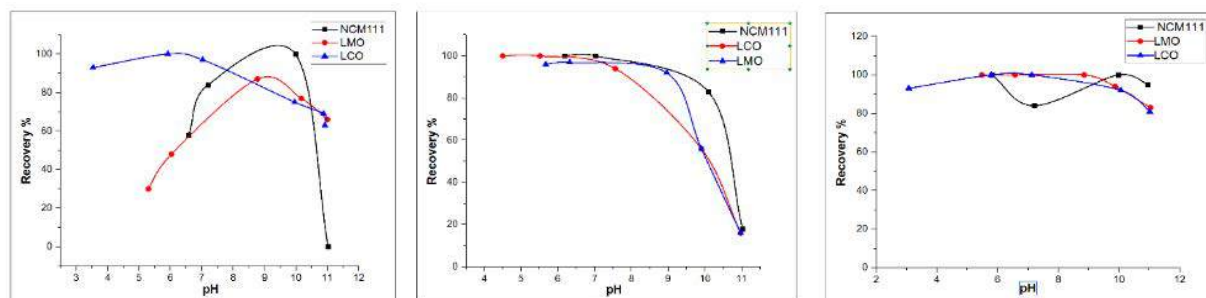


Figure I.4.C.27 Recovery of pristine cathode materials at different Ph using collector A, B, and C

Figure I.4.C.27 shows the recovery of individual pristine cathode materials using collector A, B, and C, respectively. It was observed that three collectors surveyed during this period of study exhibits strong adsorption capabilities on surfaces of pristine cathode materials, while collector A exhibits a degree of selectivity. Figure I.4.C.27a shows that at a pH of 8.5-9.0 there is a possibility of separating NMC111 and LMO, while at a pH lower than 6 it should be easy to recover LCO selectively from a binary mixture of LCO and NMC111 using collector A.

Separation experiments were performed with a binary mixture. Table I.4.C.8 shows the separation result of LMO and NMC111 in a mass ratio of 1:1 (10g each). The result shows that the first froth product has 84% of NMC111. The result suggests that most of the NMC111 is collected in the first froth and the tailing has a 94% of LMO. This result shows that separation of NMC111 and LMO was achievable. Table I.4.C.9 show the result with a binary mixture of NMC111 and LCO using collector A. The result shows that a 73% of total mass was recovered in the first froth, implying a considerable amount of LCO was also recovered. This results in a reduction of the purity of the froth collected. We hypothesize that this result may be due to a difference in kinetics. Experiments were performed on a mixture of NMC111 and LMO using collector B (Table I.4.C.10). Clearly, there is no separation between NMC111 and LMO, and the recovery was low with most of materials left in the tailing.

Table I.4.C.8 Result of NMC111/LMO Separation via Froth Flotation Using Collector A

Product	Weight (%)	%NMC111	%LMO
Froth 1	51%	84%	16%
Froth 2	6%	6%	94%
Froth 3	29%	20%	80%
Tailing	14%	6%	94%

Table I.4.C.9 Result of NMC111/LCO separation via froth flotation using collector A

Product	Weight (%)	%NMC111	%LCO
Froth 1	73%	71%	29%
Froth 2	24%	33%	67%
Tailing	2%	39%	61%

Table I.4.C.10 Result of NMC111/LMO Separation via Froth Flotation Using Collector B

Product	Weight (%)	%NMC111	%LMO
Froth 1	25%	47%	53%
Froth 2	28%	50%	50%
Tailing	47%	44%	56%

Column flotation was performed to evaluate the performance of the separation processes. Since separation was achievable using collector A, collector A was also used in the separation process. Samples were collected for a total period of two minutes. The result shown in Table I.4.C.11 reveals that is consistent with the results obtained from the Denver flotation experiment using Collector A as shown above.

Table I.4.C.11 Result of NMC111/LMO Separation via Froth Flotation with Collector A in Flotation Column

Samples	Product	%NMC111	%LMO
1	Froth	82%	18%
	Tailing	6%	94%
2	Froth	76%	24%
	Tailing	4%	96%

Due to trend observed from the use of Collector B which already showed a high adsorption in the single-phase experiment as shown in Figure I.4.C.27, less attention was paid to collector C, which showed an even higher absorption across all pH in the single-phase experiments.

Role of Impurities in Recycled Cathodes

When identifying and developing lithium-ion battery recycling technologies, understanding the role of impurities is always a concern as they may have an impact on electrochemical performance, material stability, or lifetime. While elemental doping is considered one of the most efficient ways to improve the electrochemical properties of cathode materials, the role impurities play concerning the final properties of precursor and cathode recycled materials is not fully understood. Knowing the wide variety of impurities that may be introduced in the recycling process, the objectives of this project are to determine the possible impurities, their role in structural stability, and their impacts (during synthesis and after synthesis) on the recovered NMC622 precursor and cathode materials. In the last quarterly report, the WPI team determined how Cu impurities included in the initial NMC622 synthesis affected the morphology, properties, and electrochemical properties of NMC622 precursor and cathode powder. The choice of copper came from initial analytical studies of black mass samples and the observation of copper impurities (believed to be mainly from the anode current collector). In this quarter we expanded these studies to the alumina or aluminum metal (Al) as they represent the other major impurities in the black mass studies.

For a recycled cathode material, the isolated material may also be isolated in the presence of other electrode or cell components carried through at low levels in the black mass processing. ICP analysis of sample black mass has shown that common impurities such as copper or aluminum, are present and both are known to act as dopants in NMC-type cathode materials. Previous reports highlighted the role of copper and its effect on the NMC622 cathodes under investigation. In this quarter we have initiated a similar study to identify the role of Al impurities on the properties of the cathode. Table I.4.C.12 highlights the ICP analysis that sets for us the amount of aluminum that may be typical in a black mass sample. It was evident that the aluminum is present as

both metal (from anode current collector) and as alumina. The alumina may be from the passivation coating on the anode current collector, a cathode dopant, or as a post-synthesis alumina coating applied to protect the surface of the cathode on cycling. As all are common uses for aluminum (or alumina) they probably all contribute. XRD and SEM/EDX images are shown in Figure I.4.C.28 and Figure I.4.C.29. The particles are composed of plate-shaped primary particles. As with the earlier copper-substituted NMC622 model study, when adding Al ions, the size of the secondary particles gradually increases, and the primary particles become thinner compared to the particles without Al ions. Again, as with the Cu study, it was then observed that the tap density decreases significantly when Al ions were added. In general, the tap density increases with the increased reaction time.

Table I.4.C.12 ICP Analysis of Black Mass used for Impurity Discovery

Elemental/Phase Analysis	
Cathode (NMC622)	60 wt%
Anode (graphite)	30 wt%
Conductive Additive (carbon)	5 wt%
Alumina	4 wt %
Cu metal	< 1 wt %
Al metal	< 1 wt %

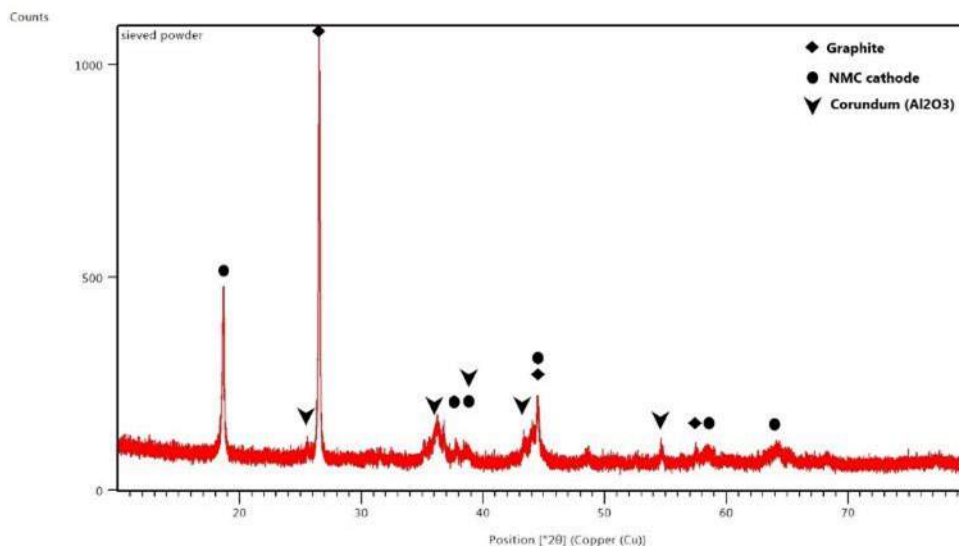


Figure I.4.C.28 XRD analysis of black mass. Assessment is summarized in the preceding table

The XRD patterns of the black mass is shown in Figure I.4.C.28. Figure I.4.C.29 highlights SEM analysis of the materials to identify issues associated with homogeneity (i.e doping) or heterogeneity (second phase).

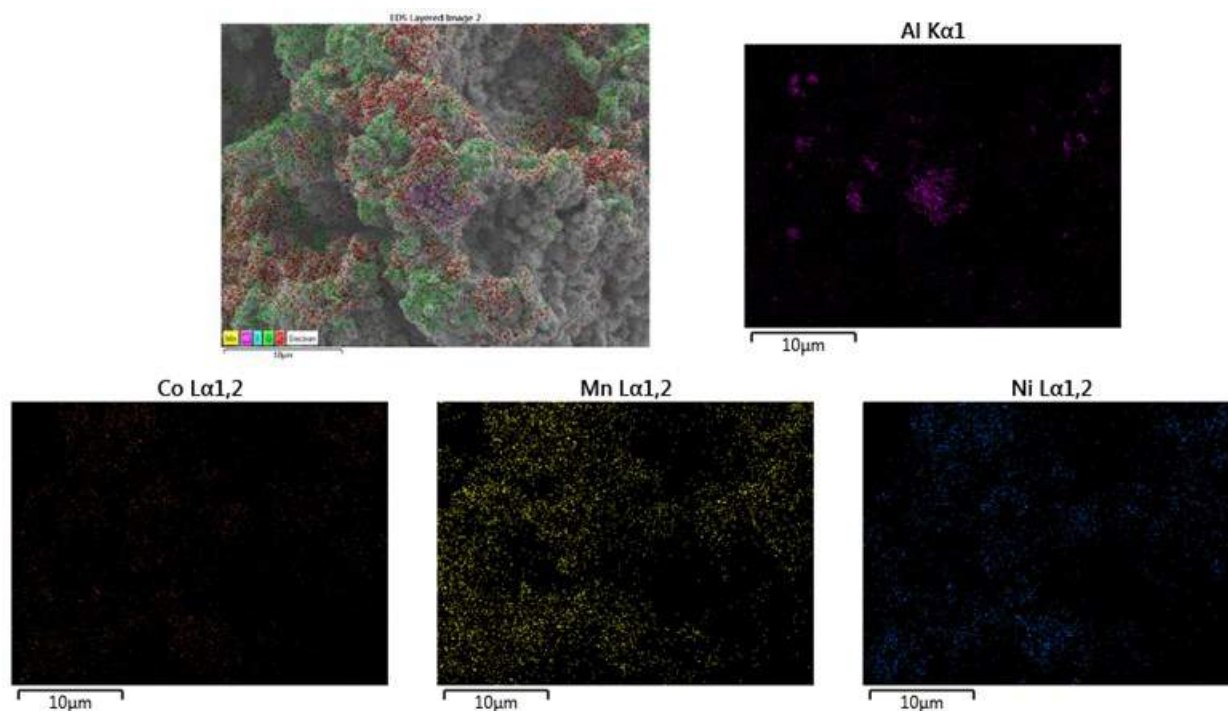


Figure I.4.C.29 SEM/EDX analysis of the black mass cathodes

Preliminary analysis shows the alumina is present as a second phase and not likely to be at the temperatures used as a cathode dopant. Published work on the role of surface alumina and alumina diffusion in NMC622 has been examined and the conclusions appear to indicate that temperatures above 600°C are needed to diffuse alumina into the lattice, although some data also show that the more likely pathway that must be examined is that the alumina will extract lithia from the cathode lattice to form LiAlO_2 before it reacts. This may be a source of cell impedance rise to be evaluated.

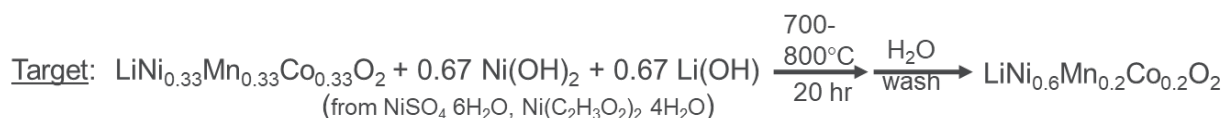
NMC622 samples created from homogenous precursors have been made in our labs using aluminum nitrate salts. As with the copper studies previously reported, the addition of Al(III) lowers the tap density in a manner that tracks aluminum content, i.e., 5% had a lower tap density than the 1% substituted samples. Early electrochemical evaluation has shown that while Al(III) is not electrochemically active and thus cannot contribute to the capacity, aluminum does improve the electrochemical performance of regenerated cathode material below a certain limit, namely an Al content less than 0.4 wt %, possibly due to oxide sublattice stability enhancements. Further evaluation on these processes is underway.

Recycled Cathodes as Materials Feedstock (Argonne National Laboratory)

The available batteries being supplied to recyclers reflect the popular battery chemistries from 5-10 years ago. This time lag between recycled materials and materials wanted by the marketplace may not be in sync over time as new chemistries and cell designs drive changes in supply and materials choices. Besides changes in the stream from material performance improvements and new chemistries, materials from non-transportation sectors may also play a role in adding anomalous materials to the waste stream, for instance LiCoO_2 from consumer electronics. In this effort we are designing and evaluating methods to change the metal ratios of recycled cathode materials to convert them to more current cathode formulations. This effort will focus on two raw materials, $\text{Li}(\text{NiMnCo})\text{O}_2$ (NMC111) and LiCoO_2 and establish methods to use them as a feedstock material to produce other stoichiometries. An initial target will be NMC622.

Based on present waste streams and historical cathode usage, the NMC cathodes used in the past ten years have gradually shifted from NMC111 to variants that are more nickel rich, such as NMC622. This trend has

been the result of the need for increased energy density, higher capacities, and advances in materials synthesis and characterization. Although other systems have been utilized, for example LiMn_2O_4 was a major component of the early Nissan Leafs, many of the recycling streams are been dominated by composition change reactions to target higher nickel content cathode from lower nickel content systems. This effort has initially followed two approaches; (1) react a physical mixture of NMC111 with a trivalent nickel source (e.g., LiNiO_2) or (2) precipitation of a stoichiometric amount of a nickel hydroxide salt onto the NMC surface followed by annealing. The reactions are shown below:



Analysis of the XRD initial product of the physical mixture reaction still showed the separate phases of NMC and LiNiO_2 , as expected. After annealing at 800°C for 20h, the only observed change in the mixture was that the structure of layered LiNiO_2 converted to a disordered rock salt structure (see Figure I.4.C.30). This loss of layering (with the same stoichiometry) is consistent with slow Ni^{+3} diffusion into the lattice and high temperature stability issues associated with oxygen loss and formation of a Ni^{+2} material.

Based on this pathway, utilizing a divalent source of nickel is a better route for investigation. Our first attempt involved precipitating a nickel oxide coating from a NiSO_4 solution using LiOH onto the surface of the NMC111 baseline cathode. This composite was then heated to 800°C in air. As with the other system, XRD analysis (see Figure I.4.C.31) identified a physical mixture of a LiNiO_2 phase in addition to NMC111. As above the role of temperature was then further investigated by using more reducible spectator anions and lower temperatures based on reported synthesis procedures for NMC622. The nickel coating was derived from nickel acetate ($\text{Ni}(\text{C}_2\text{H}_3\text{O}_2)_2$). After precipitating $\text{Ni}(\text{OH})_2$ with LiOH onto NMC111 surface and heating to 700°C , a single-phase product was obtained. Table I.4.C.13 highlights the analytically derived stoichiometric data. Preliminary GDOES and structural analysis confirms the change in lattice consistent with 622 formation with some small possible Mn deficiency. Causes are under evaluation.

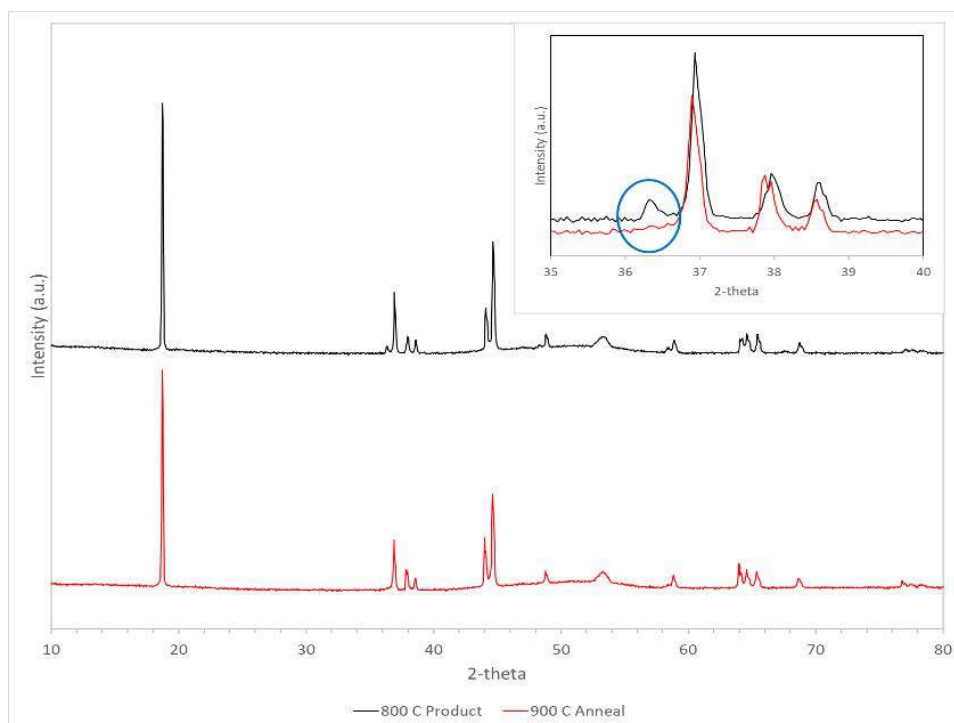


Figure I.4.C.30 Annealing at 800 °C for 20h, the only observed change in the mixture was that the structure of layered LiNiO_2 converted to a disordered rock salt structure

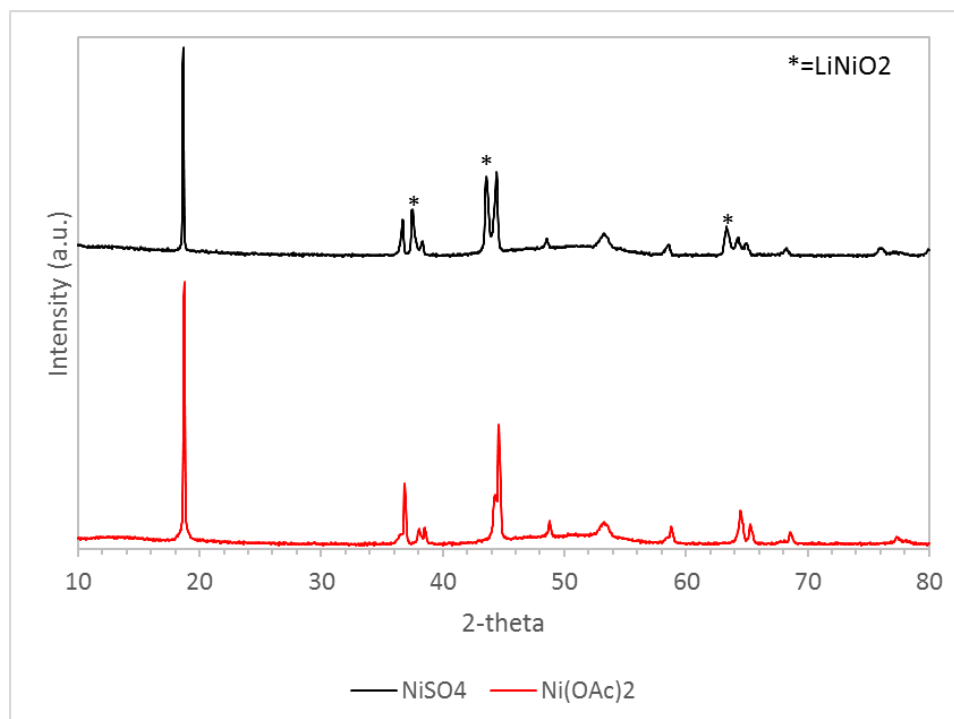


Figure I.4.C.31 Effect of nickel salt on the formation of the desired 622 phase (black – nickel sulfate; red – nickel acetate)

Table I.4.C.13 Element Ratios Measured Using GDOES

	Ni/Co	Ni/Mn	Co/Mn
Pristine NMC111	1.05	0.99	1
Targeted NMC622	3.09	2.60	1
Ideal NMC622	3	3	1

Hydrothermal recovery processes for the black mass (ORNL)

The objective of this project is to develop efficient recovery processes for separating black mass from current collectors. The separation processes are designed to be completed efficiently with minimal or no damage to either the active materials or the current collectors. This is challenging because of the strong adhesion and cohesion forces, as well as high chemical stability of the PVDF binder. In addition, the desired separation processes should possess high peeling-off efficiency and be cost effective, energy efficient, and environmentally friendly. The current state-of-art methods have many deficiencies, including high energy consumption, low peeling-off efficiency, high toxicity, causing water and air pollution, etc. As wet-chemical processes, solvent-based separation processes are promising for the recovery of black mass from spent cells because they can reduce the required energy input and can be economically favorable and environmentally friendly if green solvents are employed. In this task, we propose and demonstrate efficient wet-chemical recovery approaches for separating the black mass from metal foils with minimal deterioration and nearly 100% peeling-off efficiency.

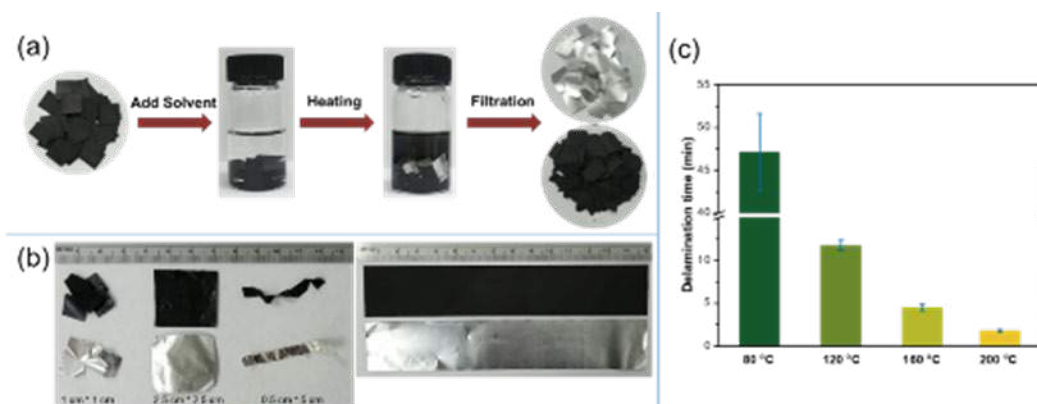


Figure I.4.C.32 Images showing (a) the SolveX process for the delamination of cathode materials from aluminum current collector and (b) the delaminated electrode of different sizes. (c) The delamination time dependence on the reaction temperature

Our SolveX process aimed to separate cathode materials from aluminum foil by weakening and breaking the interactions between the binder and the current collector. As shown in Figure I.4.C.32, the shredded cathodes (as-coated NMC622 electrode) were mixed with the solvent X, followed by heating up the mixture to certain temperature for certain time. The black mass was completely delaminated as whole pieces with no visible black mass left on the aluminum current collector, suggesting a high delamination efficiency. The SolveX process is robust and can be used to delaminate electrodes of different sizes (Figure I.4.C.32), indicating there is no electrode size limit for the SolveX process. In addition, this robust process works well for separation of aluminum foil from electrodes with various cathode chemistries, including but not limited to NCA, NMC series, and LFP.

The delamination time is highly dependent on the reaction temperature. The SolveX process can work in a wide temperature range from room temperature to 200°C. It takes more than 12 hours to complete the peel-off process at room temperature (~20°C). The delamination time is greatly decreased as increasing the reaction temperature. At high temperature (e.g., 200°C), the delamination process completes in less than 2 min, which is so far the most efficient and fastest process. The fast delamination process requires low energy input, making it an economically favorable process.

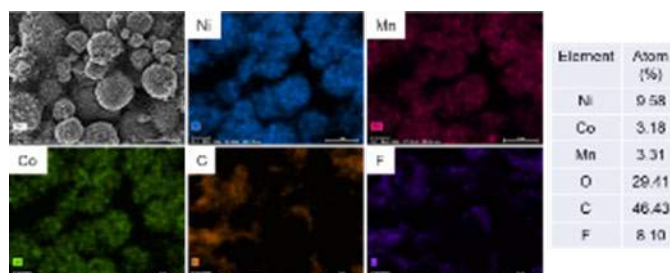


Figure I.4.C.33 SEM-EDX results for the recovered cathode materials

Direct recycling seeks to recover cathode materials with still useful morphology, which requires the separation process neither damaging the active materials nor introducing impurities. The morphology of the recovered black mass was previously reported unaffected by the delamination process. The EDX results (Figure I.4.C.33) show that the fluorine existed on the delaminated cathode, confirming the existence of PVDF, which is consistent with the fact that PVDF is insoluble in the solvent X. Thus, the SolveX process recovered the black mass without dissolving the PVDF binder, suggesting the solvent deactivates the binding capability of PVDF. The EDX results also revealed that no impurities were detected during the separation process.

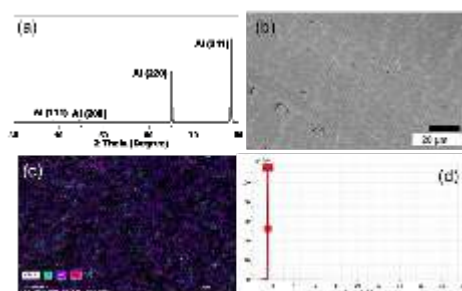


Figure I.4.C.34 Characterizations on the recovered aluminum foils. (a) XRD pattern, (b) SEM image, (c) EDX image, and (d) EDX spectra

Characterizations for the recovered aluminum foils, including XRD, SEM, and EDX mapping, were also performed, as shown in Figure I.4.C.34. All the characterizations demonstrate that no corrosion on the aluminum occurred. In addition, there are neither cathode materials nor PVDF binder left on the recovered

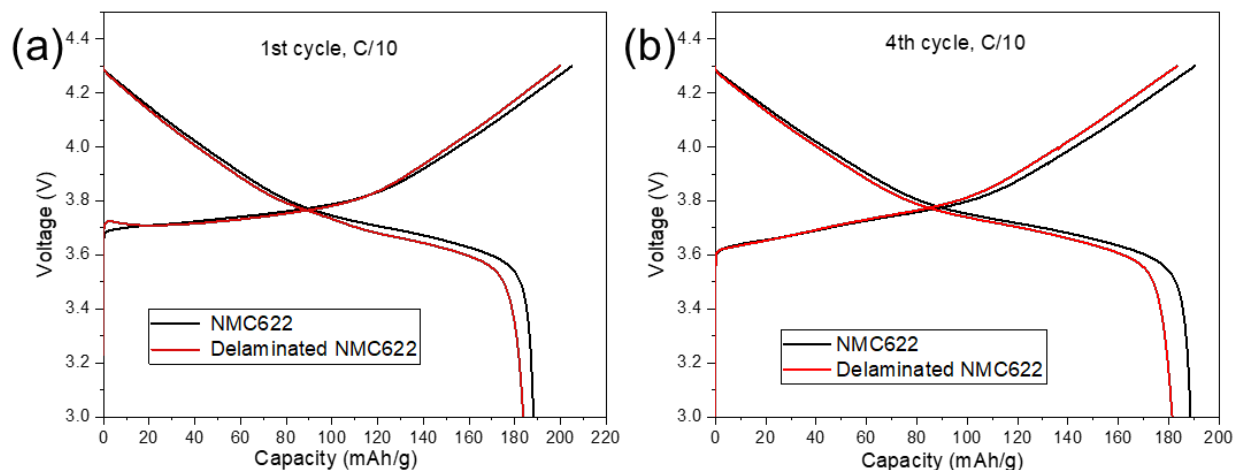


Figure I.4.C.35 Voltage profiles for the recovered NMC622

The electrochemical performance of the recovered black mass was evaluated in half-cell configuration. Figure I.4.C.35 shows the voltage profile for the 1st and 4th formation cycle. The recovered NMC622 showed similar charge and discharge capacities as the original NMC622, indicating the SolveX process has minimal effect on the electrochemical performance.

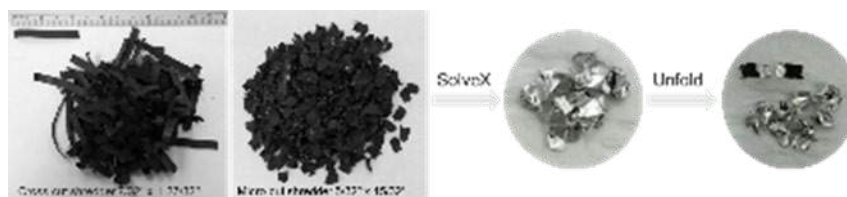


Figure I.4.C.36 Effect of shredding

The effect of shredding was investigated. Two types of shredders including cross-cut shredder and micro-cut shredder were used to shred the positive electrode, as shown in Figure I.4.C.36. The electrodes were cut into strips measuring 3/16" x 1-27/32" and tiny pieces measuring 5/32" x 15/32", respectively. However, there are two problems when using those shredded electrodes in the solvent-based separation processes. The first one is that the shredded electrodes tend to fold, resulting in the black mass being covered inside. Another problem is that aluminum burrs formed during shredding would easily fall off in the SolveX process, making it hard to separate the small pieces of Al from black mass. Thus, it is important to use better shredders to avoid and solve the above two issues. As illustrated in Figure I.4.C.32(b), there is no electrode size limit for our SolveX process, making it possible for not shredding the cells to small pieces to avoid those problems.

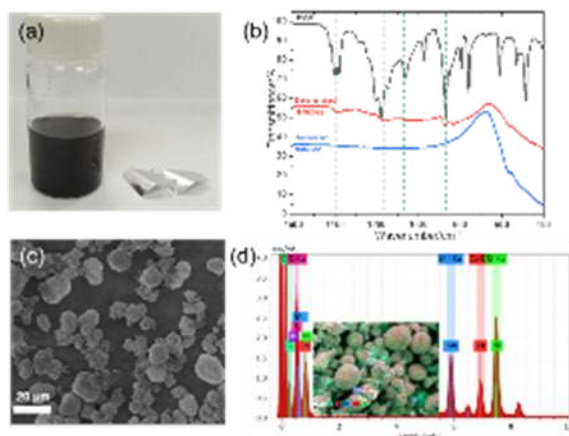


Figure I.4.C.37 (a) Recovered black mass and aluminum foil via the SolveY process. Characterizations on the recovered black mass: (b) FTIR, (c) SEM, and (d) EDX mapping

The SolveX process can be used to quickly delaminate the electrode materials from aluminum foils. However, as mentioned above, the PVDF binder still exists in the recovered black mass because PVDF is insoluble in solvent X. In this regard, another solvent Y is required to dissolve PVDF. Here, we propose the use of a green solvent Y for the removal of PVDF. In this process, the shredded cathodes were mixed with the solvent Y, followed by heating up the mixture to certain temperature for certain time. The cathode materials were peeled off, as illustrated in Figure I.4.C.37(a). Preliminary characterizations including FTIR, SEM, and EDX mapping were performed, as shown in Figure I.4.C.37. No PVDF signals were detected from FTIR, which was further confirmed by EDX mapping. Future work will be conducted to systematically investigate the removal of PVDF using solvent Y.

Anode/Cathode Separation and Purification (Argonne National Laboratory)

There are several methods for separating graphite that are being investigated, including screening, air classification, magnetic separation, and electrostatic separation. There are many process currently used commercially that separate graphite. The separation of graphite from shredded lithium-ion cells presents unique challenges because there will be many components, such as cathode powders, copper and aluminum foils, separators, and cell casing components. Graphite is not magnetic, which provides opportunities for magnetic separation. Its particle size distribution is usually larger than most cathode powders and it has far lower density.

1. Fluidized magnetic separation

There are currently several commercial techniques of magnetic separation of fluidized powders. To determine if this would be an effective method for purifying graphite a series of preliminary tests were conducted. A sample of 50% graphite and 50% NMC111 by weight was prepared and thoroughly mixed using a resonant acoustic mixer. A second mixture of 80% graphite and 20% NMC111 was prepared using the same method. A permanent magnet with a residual flux density of 14800 gauss was used as the collector. The powder was fluidized with compressed nitrogen at 10 PSI for between 1 and 30 seconds. At 30 seconds the 50/50 mixture was concentrated to 93% graphite. The 80/20 mixture reached 98.95% graphite after 20 seconds and plateaued at 99.13% at 30 seconds. (See Figure I.4.C.38 and Figure I.4.C.39.)

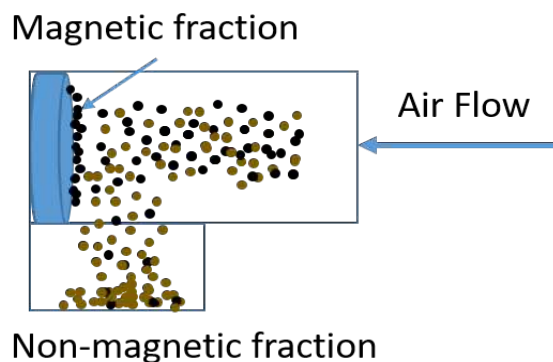


Figure I.4.C.38 Diagram of benchtop fluidized magnetic separation apparatus

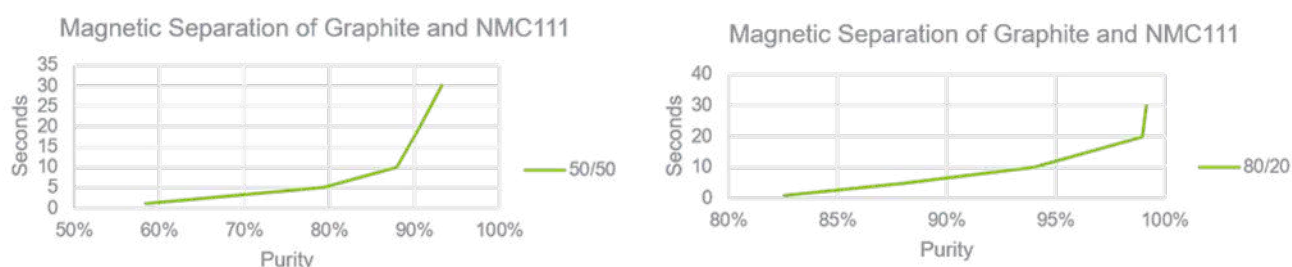


Figure I.4.C.39 Purity of graphite powder as a function fluidization time for 50/50 and 80/20 mixtures

2. Triboelectric separation

Triboelectric separation fractionates powders based on differences in charge and is one of the few dry powder separation techniques being used commercially for very fine particles. To determine the applicability of this technique for lithium-ion battery recycling several tests were conducted using equipment in Tribo Flow Separation's test facility. Figure I.4.C.40 shows the fundamental operating principles at work for tribo-electric separation. Model black mass powders are fed using a vibratory feeder into the pneumatic transport tube. Triboelectric charging of the particles occurs due to collisions of the particles with each other and the walls. The charged particles passed through an electric field created by the conductive plates. The separation occurs as the particles are drawn towards the positive or negative poles. An adjustable baffle shown in Figure I.4.C.41 is installed between the conductive plates and can be used to control the cut point between positive and negatively charged fractions.

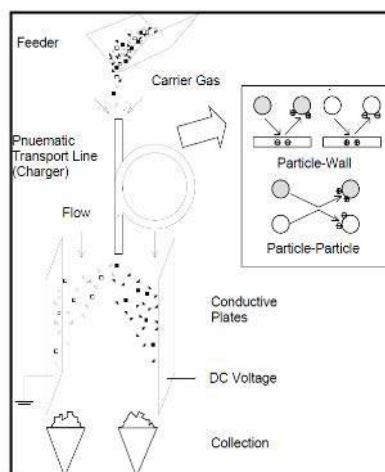


Figure I.4.C.40 Triboelectric separation operating principles

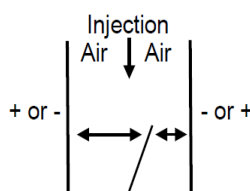


Figure I.4.C.41 Adjustable baffle system

The experiments were conducted using 500 g of 50% lithium nickel manganese cobalt oxide and 50% graphite. The sample was thoroughly mixed using a resonant acoustic mixer. The sample was separated into three parts and fed into the unit at a rates between 720-900 g/hr. For the first sample the potential between the electrodes was set to 10kV. The second and third samples were at 10 and 15kv with the polarity of the electrodes reversed. Separated material was recovered and evaluated by SEM-EDS. (See Figure I.4.C.42

Graphite is known to perform well in triboelectric separators which is why the results of this test were so surprising. In normal polarity mode the majority of the powder (73%) was collected at the positive electrode. In reverse polarity mode this trend was reversed for both voltages.

NMC 111 and graphite mixture								
Voltage [kV]	Mass fed [g]	Mass + [g]	Carbon + %	Mass - [g]	Carbon - %	Yield + [%]	Yield - [%]	Recovery [%]
10	165	119.5	54.83	43.6	44.82	73.3%	26.7%	98.8%
NMC 111 and graphite mixture - Reverse Polarity								
Voltage [kV]	Mass fed [g]	Mass + [g]	Carbon + %	Mass - [g]	Carbon - %	Yield + [%]	Yield - [%]	Recovery [%]
10	165	57.9	55.23	103.2	47.12	35.9%	64.1%	97.6%
15	165	65.4	52.96	96.7	49.33	40.3%	59.7%	98.2%

Figure I.4.C.42 Data tables for triboelectric separation of graphite

The best separation was seen in normal polarity mode with 55% of the graphite being collected at the positive electrode. Similar trends were observed in reverse polarity mode. The separation efficiency was surprisingly low. A few factors may have caused this problem. As a starting point the elemental analysis is being redone to ensure the results were accurate. Most triboelectric separation is not of 50/50 mixtures. Usually there is a much smaller fraction that is being removed. Additionally, there is not yet any expertise in separating lithium-ion battery materials. The testing conducted was limited and so it may be that the operating window was too small to identify maxima and minima. Additional testing may be able to provide better separation as several variables such as the position of the baffle, flow rates and voltages were not exhaustively investigated. Longer electrode plates may be required to provide additional efficiency since the charged particles will spend more time in the electrical field.

Electrolyte Component Removal and Recovery

Electrolyte needs to be removed from the materials during the recycling process to allow for further processing to recover other materials. This can be done in several ways including extraction with supercritical CO₂, thermal drying, water washing and solvent extraction. Of these only supercritical CO₂ with added co-solvent or solvent extraction can recover the LiPF₆, which is the most valuable component of the electrolyte. In either of these processes it is critical to know the impurities, the different electrolyte compositions and how these may impact electrochemistry and the recycling process. Alternatively, water washing can generate LiF, that could potentially be recovered, and sold to be manufactured back into LiPF₆. In addition, water washing may be able to remove SEI components from the anode, thereby recovering additional Li.

After initial studies with vacuum drying it was decided to try more realistic drying conditions under ambient inert atmosphere. Specifically, the electrolyte was extracted in DEC and then dried under vacuum to remove most of the excess solvent. The resulting material was then further dried at 90°C, 100°C, and 110°C under an argon atmosphere inside a glovebox with less than 1 ppm H₂O and O₂. Composition was then analyzed using NMR with added trifluoroethanol as an internal standard. The composition doesn't vary substantially with temperature, however the yield drops, indicating decomposition of the LiPF₆ above 90°C along with additional evaporation of the solvents. (See Figure I.4.C.43.)

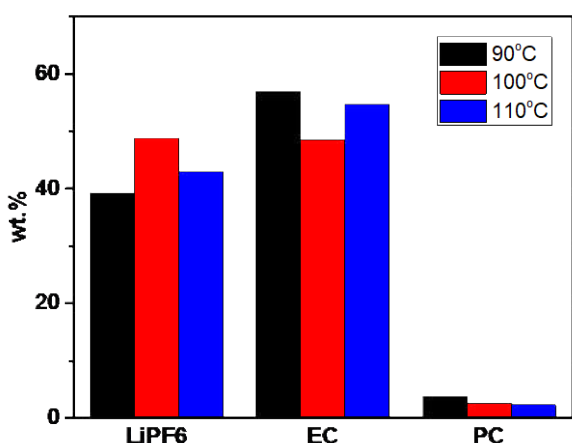


Figure I.4.C.43 Composition of electrolytes as determined by NMR recovered from commercial cells with different heat treatments under an argon atmosphere

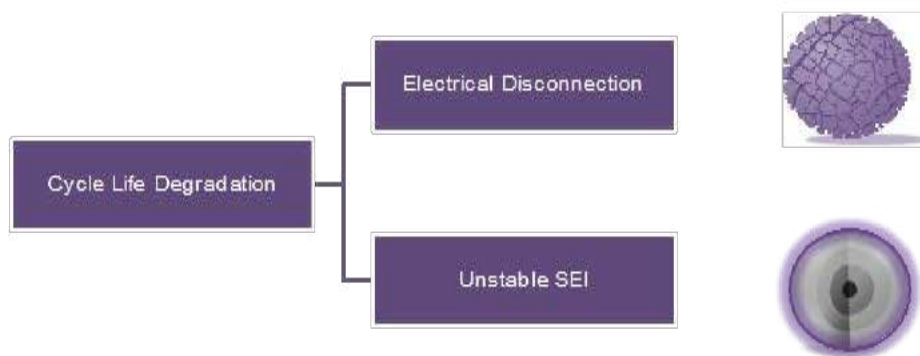


Figure I.4.C.44 Full cell cycling results from electrolyte recovered from commercial cells dried at 90°C under air, and 100°C under vacuum compared to gen 2 electrolyte (1.2 M LiPF₆ in 3:7 EC:EMC)

Once dried, the solid residue (presumably mostly LiPF₆) was used to reconstitute electrolyte, adjusting the compositions as determined by NMR to make 1 M LiPF₆ in 1:1 EC:DEC w/w solution. This electrolyte was then used to make coin cells with a graphite anode, and compared to our standard baseline electrolyte (Gen 2). This recovered and recycled electrolyte initially shows more rapid capacity fade than Gen 2 electrolyte. However, in long term cycling the recovered electrolyte substantially outperforms the Gen 2 electrolyte. In particular, Gen 2 loses 11.7 mAh/g per 100 cycles as compared to 8.5 mAh/g per 100 cycles for the recovered electrolyte. (See Figure I.4.C.44.)

During this quarter, a variety of additional additives were tried to see if they could improve the performance of the recovered electrolyte. Three different additives were used at various concentrations. All of the additives reduce the cycling performance substantially, with vinylene carbonate (VC) affecting the performance the least. Since no additives improve the electrolyte and no additive-containing electrolyte cycles better than Gen 2 there is no reason to further pursue developing an additive. (See Figure I.4.C.45.)

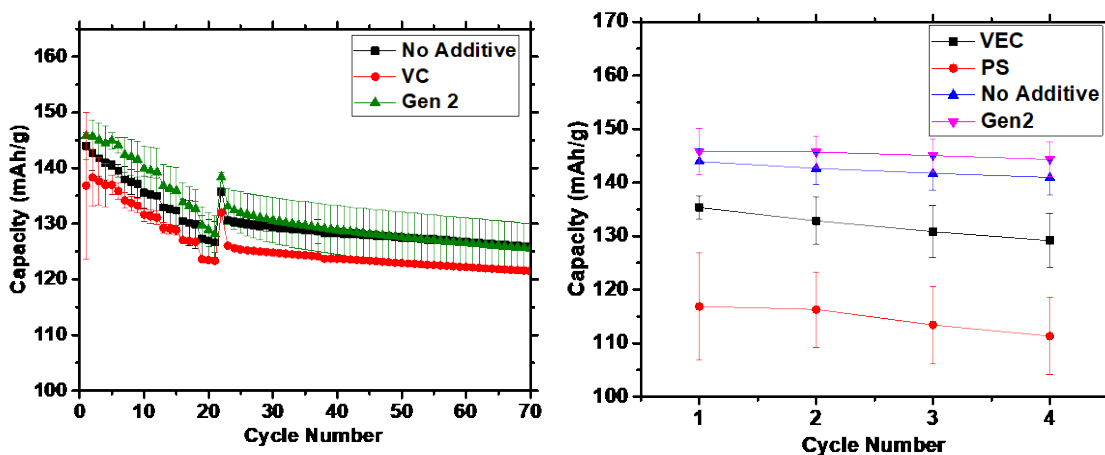


Figure I.4.C.45 Full cell cycling results of recovered electrolyte from commercial cells dried at 90°C under argon with different additives. The additives are VC (2 wt.% vinylene carbonate), VEC (0.5 wt.% vinyl ethylene carbonate), and PS (5 wt.% 1,3-propane sulfone)

Design for Recycle – Cell Design (ORNL & ANL)

The two most common cell formats used in large lithium-ion battery packs are the cylindrical and the prismatic (pouch) designs. This project will focus on the common 18650 cylindrical cell format and the xx6395 pouch

cell format. The cell-making capabilities in Argonne's Cell Analysis, Modeling, and Prototyping (CAMP) Facility (CAMP) and ORNL's Battery Manufacturing Facility (BMF) are collaborating to design, model, prototype, and test novel cell designs that can be rejuvenated based on these two cell formats. The battery techno-economic model BatPaC will later be utilized to model gravimetric and volumetric energy density of the new designs to determine their viability. Selected cell designs that meet established criteria will be tested in prototype cells.

1. Pouch cell assembly, cycling and electrode rising

A pouch cell consists of $\text{LiNi}_{0.6}\text{Mn}_{0.2}\text{Co}_{0.2}$ (NMC622) and SLC1520T has been cycled between 3.0 and 4.3V at C/3 at 30°C. It is noted that the mass loadings are slightly lower than the targets as the cells were assembled before we settled on the target loading of 3 mAh/cm² so that we have time to cycle the cells at C/3.

Table I.4.C.14 Electrode Information

Electrode	Solvent	Electrode Composition	Porosity	Loading
NMC622	NMP	NMC622/Denka CB/5130 PVDF in 90/5/5 wt%	37%	14.6 mg/cm ²
SLC1520T	NMP	SLC1520T/C65 CB/9300 PVDF in 92/2/6 wt%	33%	6.5 mg/cm ²

The pouch cell went through 4 formation cycles at C/10 before it underwent cycle life test. As shown in Figure I.4.C.46, capacity retention reduced to 79% after 716 cycles and the cell was discharged to 3 V before being disassembled in a glovebox. As the electrodes were double-sided, we washed one side off with N-methyl-2-pyrrolidone (NMP) for subsequent coin cell assembly. The electrodes were punched out for rinsing. The electrodes were washed for 5 minutes in either dimethyl carbonate (DMC), isopropanol (IPA), or ethanol (EtOH). The washed electrodes were assembled into full coin cells with both the anodes and cathodes from the pouch cell. The lithium concentration in the cathodes was characterized by inductively coupled plasma optical emission spectrometry (ICP-OES). Some of the electrodes were also sent to Argonne National Laboratory for postmortem characterization. The full coin cells were cycled at the same protocol as the pouch cells to evaluate the effect of washing.

2. Electrochemical performance of rinsed electrodes

Figure I.4.C.47 shows the ratio of lithium and transition metal in the rinsed NMC622 cathodes. Although the cell was discharged to 3V before disassembly, there is significant lithium deficit in the cathodes. Assuming negligible lithium loss during rinsing in DMC, more than 30% of lithium was lost during cycle life test, contributing to the capacity fade. There was a little more lithium loss when rinsing in ethanol and IPA. The lithium amount in the rinsed NMC622 cathode was in agreement with the capacity as shown in Figure I.4.C.48 a). Compared to the voltage profile at the end of life (EOL) of the pouch cell, all cells with fresh electrolyte showed lower polarization during charging. The discharge voltage profiles were similar for all cells while the one with unwashed electrodes showed slightly higher polarization. The unwashed electrodes demonstrated slightly lower capacity compared to the EOL of pouch cell, which was possibly due to some defect at the electrode edge during punching, resulting in poor contact of some particles. For all the cells with rinsed electrodes, the capacity was higher than the EOL one, indicating capacity recovery from the rinsing. The reduced polarization, especially during charging, where lithium intercalated into graphite, was attributed to lower polarization in the rinsed graphite anode. As indicated in Figure I.4.C.48 b), the interval between the graphite lithiation (~3.5V) and delithiation (~3.4V) peaks reduced in the rinsed electrodes while the redox peaks for the cathode, i.e., $\text{N}^{2+} \leftrightarrow \text{Ni}^{4+}$ was barely changed. This indicated that the benefit from electrode rinsing is mostly from the graphite anode.

Although the electrodes rinsed with DMC showed the highest initial capacity, it is the one washed by IPA that showed the best cyclability with ~90% capacity retention after 100 cycles compared to the 65% capacity retention for the DMC and ethanol ones. It is clearly shown in the voltage profile in Figure I.4.C.49 that the

polarization at the end of 100 cycles follows the trends: IPA<DMC<ethanol<unwashed. This verifies the benefit from electrode rinsing.

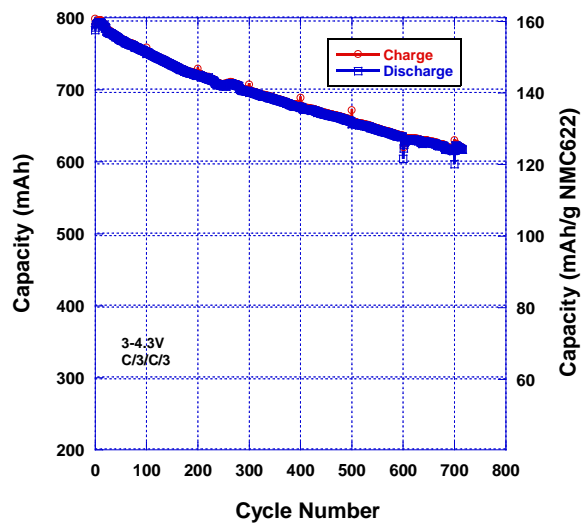


Figure I.4.C.46 Cycle life of the 800 mAh pouch cell

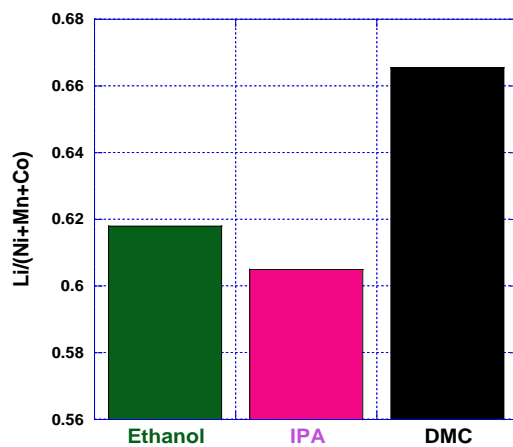


Figure I.4.C.47 Li/transition metal ratio in the rinsed NMC622 cathodes

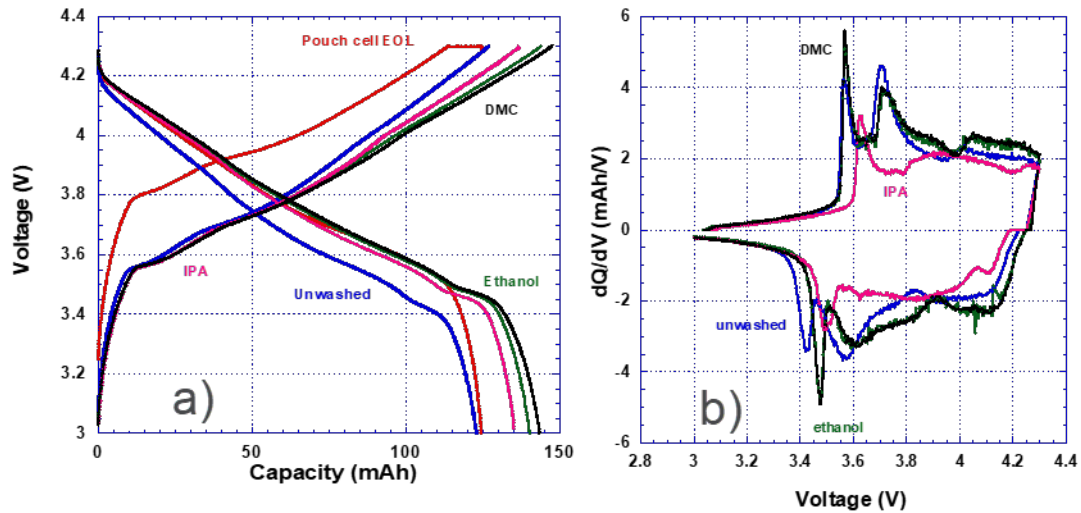
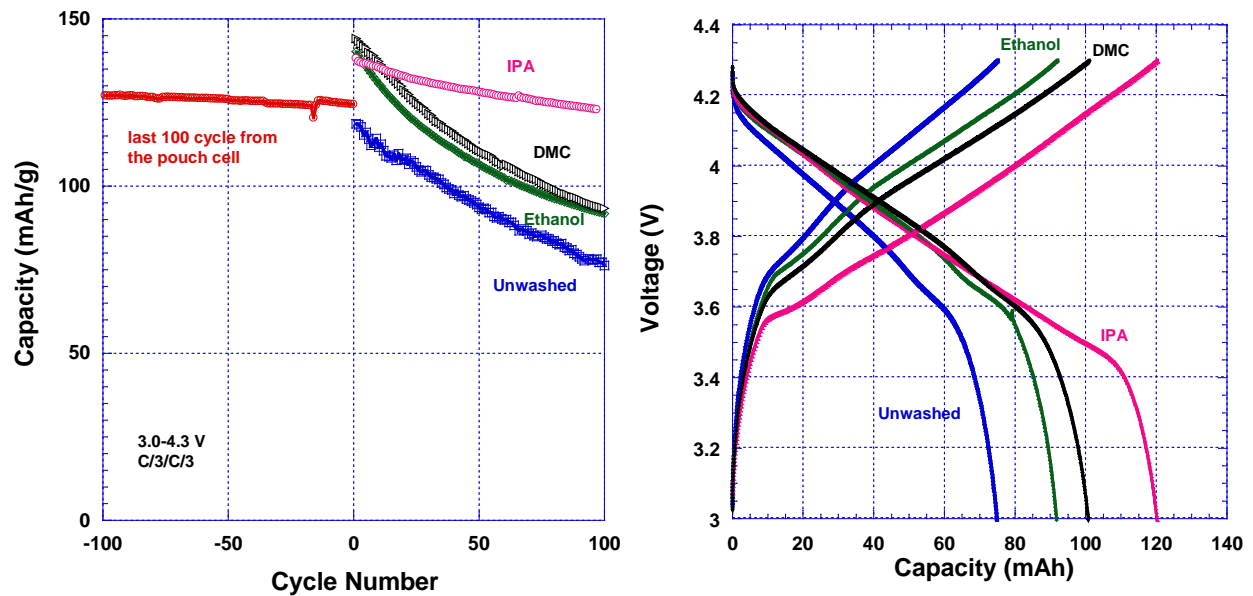
Figure I.4.C.48 First cycle voltage profile a) and dQ/dV curve of the rinsed electrodes b)

Figure I.4.C.49 Cycle life of the coin cells with fresh electrolyte a) and voltage profile at the end of 100 cycles b)

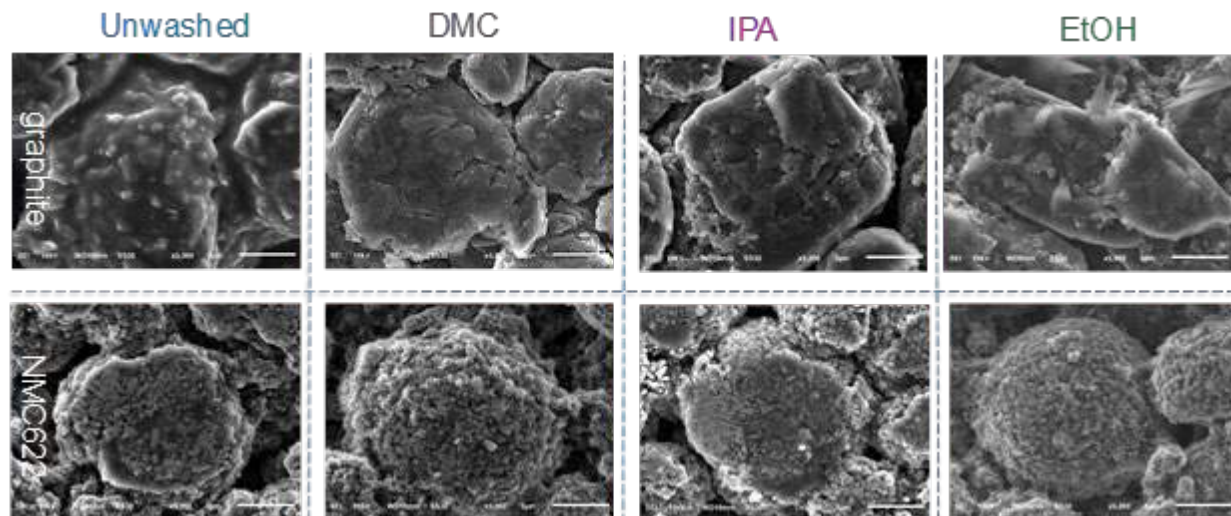


Figure I.4.C.50 Morphology of electrodes washed by various solvents

The morphology of the spent electrodes were characterized by Zhenzhen Yang and Ira Bloom at Argonne using SEM. As shown in Figure I.4.C.50, there was a shiny layer coated on the unwashed graphite particles, which was the SEI. After washing, regardless of solvent, the SEI layer was gone and the features of the graphite particles were more pronounced. This is in agreement with the reduced polarization in the rinsed anodes. In contrast, the wash effect on cathode morphology was much less significant which is consistent with the unchanged polarization in the cathode.

3. Double-sided Baseline Electrodes

The benefit of cell rejuvenation must be determined in electrodes and separators that are likely to be produced in the near future. It is anticipated that these electrodes will use NMC-based cathode powders and graphite anode powders with capacity loadings near 3 mAh/cm² on each side of the electrode. The double-sided baseline electrodes made in the 2nd Quarter are still under test now in 500-mAh pouch cells and can be compared to the single-sided baseline coin cells that began testing earlier in the program. The capacity and HPPC ASI are provided in Figure I.4.C.51 for both cell systems. It appears from this preliminary data that these baseline electrodes are suitable for use in developing cells systems designed for rejuvenation. When the cells have exceeded 20 % capacity loss, they will be cut open, flushed with a solvent(s), refilled with fresh electrolyte, and then resume cycle life testing. This method will minimize the physical damage to the cell assembly due to handling.

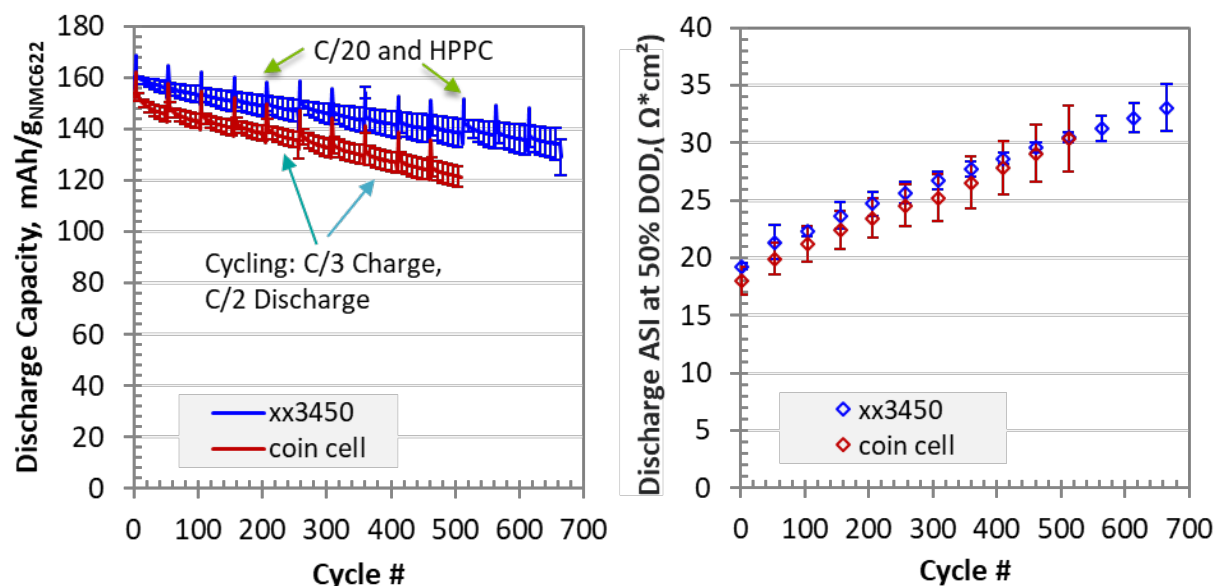


Figure I.4.C.51 Specific capacity (left) and HPPC ASI at 50% DoD (right) for the baseline electrodes (NMC622 and SLC1520P) under test in coin cells (single-sided) and 500-mAh pouch cells (double-sided)

4. Impact of Rejuvenation on Energy Density

Designing the cells, modules, and battery pack to incorporate cell rejuvenation will most likely have an impact on the energy density and specific energy of the overall battery pack. The need to estimate the magnitude of the impact of the rejuvenation hardware on energy density and cost is critical to determine if rejuvenation is practical. In this quarter, efforts were initiated to estimate this effect using the Battery Performance and Cost (BatPaC) spreadsheet model developed at Argonne. Seven pack designs were considered using BatPaC – the key results of each design are summarized in Table I.4.C.15.

Table I.4.C.15 Preliminary Estimate of Rejuvenation Hardware on Pack Energy Density from BatPaC

NMC622- Gr couple for EV battery							
Cell Level Calculated Results	Battery 1	Battery 2	Battery 3	Battery 4	Battery 5	Battery 6	Battery 7
Number of Cells in Pack	240	240	240	240	140	240	432
Pack Mass, kg	289	340	391	441	172	406	478
Specific Energy (Pack), Wh/kg	183	190	196	200	171	196	185
Pack Volume, L	178	204	230	256	107	236	286
Energy Density (Pack), Wh/L	298	317	333	345	274	336	308
Estimated Free Space in Pack (L)	2.8	2.8	2.8	2.8	2.8	2.8	2.8
Estimated Volume of Tubes & Hardware in Pack (L)	3.2	3.2	3.2	3.2	1.9	3.2	5.8

Several assumptions were made to estimate the volume of the rejuvenation hardware, which include:

- 2 tubes per cell, each 30 cm long & 0.4 cm OD (~4 mL each)
- 2 valves per module (30 cells per module), ~60 mL each
- 2 ganged tubing ports per module, ~15 mL each.

The net effect on volume is approximately 400 mL per module in an ideal case, which assumes that there is no wasted volume due to geometric limitations. Under such an ideal condition, the total volume required in each pack ranges from 1.9 to 5.8 L (see Table I.4.C.15), which is on par with the amount of free space that is estimated in each pack. This is on the order of 2 % of the pack volumes. However, if the rejuvenation hardware forces the battery pack to be increased by a couple centimeters in any direction, the volume impact would easily be in the tens of liters, or >10% of the pack volumes. These numbers will be fleshed out more in FY20.

Diagnostics of Aged Materials

There are trade-offs between recycling a vehicle battery at a set end-of-life and extending the usable range of the battery. Similar trade-offs exist between keeping recycling streams separate and co-mingling materials from cells with different histories.

This task evaluates the extent of material degradation in cell components under different life conditions and aims to provide technical rationale and diagnostic criteria to determine the suitability of specific recycling methods. In particular, characterizing aged electrode material as a function of operating voltages and C-rates will:

- 1) Identify chemical signatures corresponding to efficiency losses via calorimetry measurements;
- 2) Inform electrochemical relithiation conditions and
- 3) Match the extent and type of degradation to target recycling methods, based on load profiles, cycling windows, and cost metrics.

Standard practices in the community to characterize recovered cathodes from recycled cells include detailed measurement of particle size distribution, tap density, reversible capacity, first cycle efficiency, specific surface area, ash content, etc. However, there is still some reluctance to employing recycled material in Tier-1 applications. Towards reducing this, we track statistical distributions of structural change, composition and morphology at the level of the primary particles under this task. During the last quarter, we mapped changes to grain orientation, as well as the spread in the lattice strains across different samples from ANL (fresh, 7% chemically de-lithiated and 20% chemically de-lithiated NMC-111).

Cells undergoing electrochemical delithiation (aging under cycling conditions prescribed by ANL) at NREL have started to reach cut-off capacity fade for intermittent analysis. During the last quarter, we have cycled cells with NMC-111 and NMC-532 cathodes. The former reached ~ 80% of the design capacity while the latter cells (which we started cycling earlier than the NMC-111) have reached 60% of the design capacity. The electron back scatter measurement on these cells is currently underway.

In addition to this, we developed a methodology to map lattice strains to spread in the grain orientations of the primary particles. We used this approach to compare spreads on the fresh versus chemically delithiated samples from ANL. Two different versions of the chemically delithiated samples were analyzed. The results showed an increase in the lattice strains, even before any re-lithiation, which perhaps explains the difficulty in electrochemical re-lithiation of some of this material. We are cross-comparing these results against bulk XRD measurements. (See Figure I.4.C.52.)

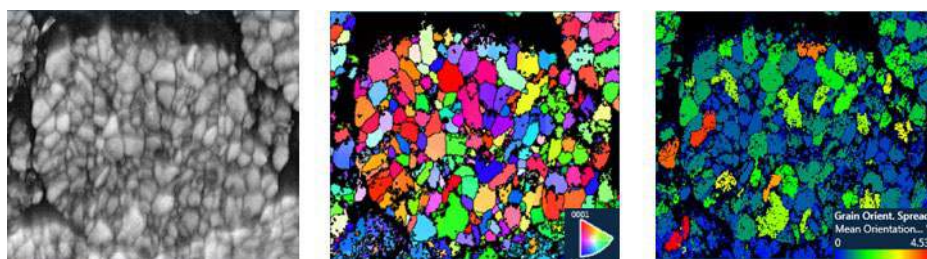


Figure I.4.C.52 Quantifying lattice strains as a function of statistical spreads in grain orientation provides detailed information about wear down of cathodes with resolutions down to the primary particle level. Figure Credit: Helio Moutinho

Microcalorimetry on Recycled Materials (NREL)

The chemistries of advanced energy storage devices are very sensitive to operating temperature. High temperatures degrade batteries faster while low temperatures decrease their power and capacity. NREL's equipment is sensitive enough to determine how changing the design of cell components affects the overall performance of the cell. We will use our isothermal calorimeters to develop an understanding of the life cycle effects on heat generation and determine if the recycling processes being developed under the ReCell program have a deleterious effect on the performance of the cells. In particular, NREL will be investigating the following:

- 1) Thermally characterize existing NMC cathode compositions to understand how the thermal signature of a battery changes from the beginning of life to the end of life. The data will be used to assess the quality of the recycled material being produced under the ReCell program.
- 2) Thermally characterize NMC/graphite cells with a known contaminant. For instance, we want to understand how much silicon material can be tolerated in the cathode without having a negative effect on heat generation and efficiency.
- 3) Match the extent and type of thermal degradation to target recycling methods, based on load profiles, cycling windows, and cost metrics.

In Q3 FY19, NREL received the ANL CAMP cells for thermal characterization. A comprehensive list is given in Table I.4.C.16. The batteries supplied by CAMP are a combination of NMC and graphite—standard material used in electric vehicles today.

Table I.4.C.16 CAMP Cells to be Used for Thermal Characterization (Cathode Material supplied by Toda and Anode Material by Superior Graphite)

Cathode Material	Anode Material	Number of Cells
NMC - 111	1506T	4
NMC - 532	1506T	4
NMC - 622	1506T	4
NMC - 811	1506T	4
NMC - 111	1520P	4
NMC - 532	1520P	4
NMC - 622	1520P	4
NMC - 811	1520P	4

During Q4 FY19, NREL measured the heat generation of two of each of the 1520P/NMC cell versions (NMC - 111, 532, 622, and 811). Figure I.4.C.53a shows the measured heat generation of the four types of cells under a 2C constant current discharge. As expected, the heat generation is at a maximum at the end of the discharge – typical for graphite cells. Unexpectedly, the 2C heat generation was the highest for the 1520P/NMC-111 and the lowest for the 1520P/NMC-811 for a given SOC. The heat generation difference between the two cells varied by as much as 200% over the discharge curve. Since both cells are using the same anode, the heat generation difference between the test runs originates from the cathode. Figure I.4.C.53b shows the heat generation of the four variants of cells under a 2C constant current charge. The difference in heat generation between the four different types of cells under charge was less than that for the discharge over the entire SOC

range. Finally, the heat generation trend reversed under charge as expected – in general, the 1520P/NMC-111 produced the least amount of heat for a given SOC and the 1520P/NMC-811 produced the most.

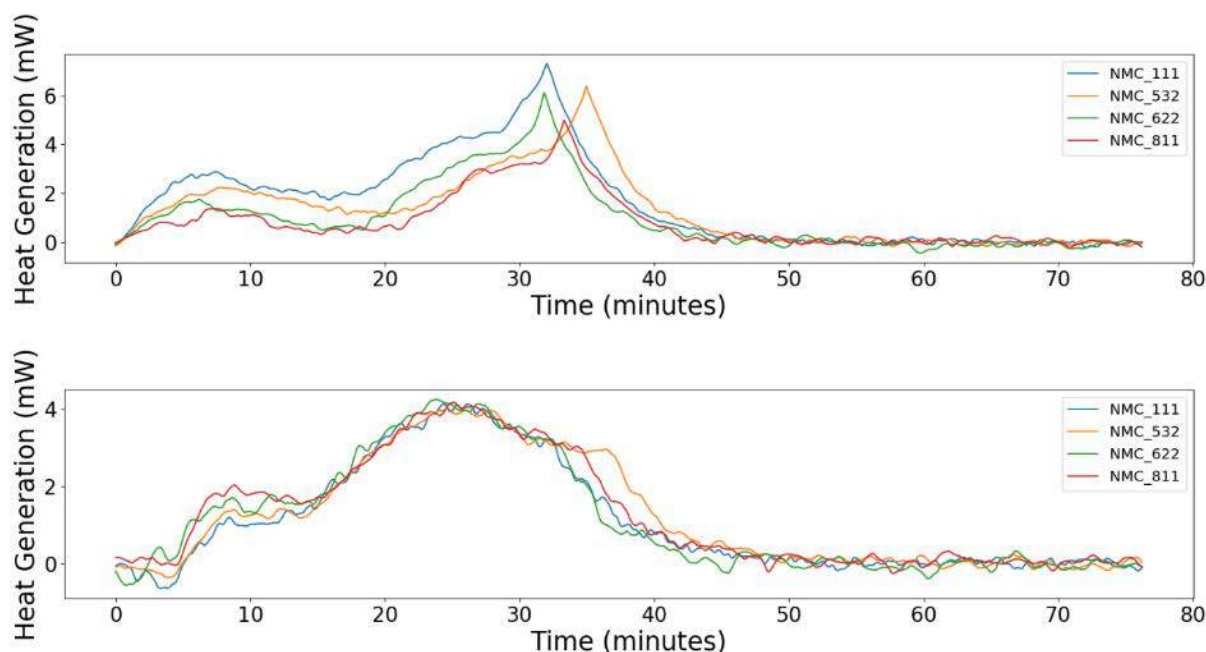


Figure I.4.C.53 Superior Graphite/Toda 1520P/NMC-111, 532,622, and 811 heat generation curves for a 2C full discharge (2a - top) and 2C full charge (2b - bottom)

NREL also measured the heat generation and efficiency of the four types of cells at various charge and discharge currents over an SOC range of 80% to 20% —the data are shown in Figure I.4.C.54. The charge efficiencies range from 99% to 96.5% for all variations of the cells. The discharge efficiencies over the same constant current range are slightly higher than the charge efficiencies for a given cell chemistry. For graphitic systems, the discharge efficiency is typically higher than the charge efficiency. For a given C-rate charge, the efficiency is consistent across the different versions of the cells – not unexpected due to the flow of ions from the cathode to the anode. However, for a given C-rate discharge, we see the expected differences in efficiency across the four variations of the cells.

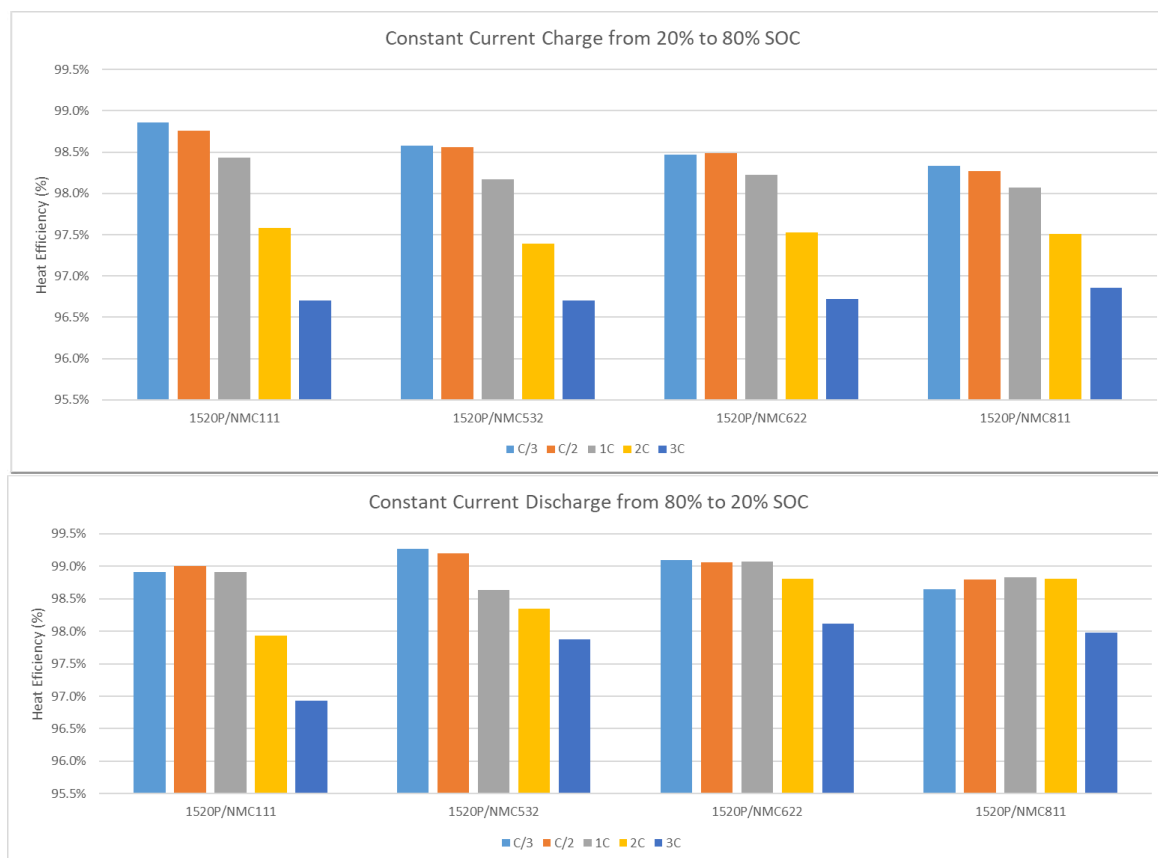


Figure I.4.C.54 Efficiency of 1520P/NMC cells under Various Charge/Discharge Currents over an SOC range of 80% to 20%

EverBatt: Cost and Environmental Impacts Modeling (ANL)

Cost and eco-friendliness are two crucial performance metrics for battery recycling technologies. Argonne has developed the EverBatt model to estimate the cost and environmental impacts associated with closed-loop recycling of lithium-ion batteries. We will use the model to evaluate the recycling processes and design-for-recycling (DfR) strategies developed under the ReCell Center, and thereby help inform and direct the R&D efforts. Specifically, we will

- 1) Expand EverBatt to include unit processes proposed for direct cathode recycling and recovery of anodes and electrolyte components; and
- 2) Increase the granularity of the battery manufacturing module and the recycling module in EverBatt to enable evaluation of DfR strategies.

During Q4 FY2019, we developed customized versions of EverBatt to evaluate

- Cost of the electrolyte recovery process developed by Dr. Lipson's team at Argonne
- Cost and environmental impacts of the hydrothermal relithiation process developed by Prof. Chen's team at University of San Diego
- Cost of the ionothermal relithiation process developed by Dr. Dai's team at ORNL.

Progress of EverBatt customization for the three projects is summarized in Table I.4.C.17.

Table I.4.C.17 Progress of EverBatt Customization in Q4 FY2019

Customization Stages	Description	Project		
		Electrolyte Recovery	Hydrothermal Relithiation	Ionothermal Relithiation
Collect Process Information	Collect information on equipment used, reagents consumed, emissions, and materials recovered	Complete	Complete	Complete
EverBatt Training (Optional)	Provide deep dive into EverBatt (e.g., how to modify model input, how to interpret model output, etc.)	N/A	Complete	N/A
Aspen Plus Modeling (Optional)	Simulate conceptual/lab-scale sub-process(es) in Aspen Plus to derive required input for EverBatt	Ongoing	N/A	N/A
Build Process in EverBatt	Add process-specific equipment and materials to EverBatt	Ongoing	Complete	Complete
Fine-tune Customized Model	Tweak model input as new/better information becomes available	On track	Complete	Ongoing

In Q4 FY2019, we also started collecting information on battery packaging, storage, and transportation. In the current version of EverBatt, the logistics for battery recycling are approximated by a simplified linear model of class 9 hazardous/non-hazardous material transportation. In light of recent developments in battery transportation regulations, we are working with personnel from the Department of Transportation (DOT) to refine EverBatt so that it can account for

- Different regulations for transportation by different modes
- Different regulations for transportation of batteries of different sizes
- Special requirements for transportation of damaged, defective, recalled (DDR) batteries
- Regulation exemption(s) for batteries transported for recycling
- Regulation exemption(s) made possible via special permit(s)

We have also learned that battery packaging, especially UN packaging if required, as well as battery storage can incur substantial cost. Therefore, in Q1 FY2020, we will expand EverBatt to include battery packaging and storage.

Analysis of Supply Chain Challenges for Battery Recycling (NREL)

Increasing demand for battery component materials combined with limited supply may put upward pressure on prices and limit the commercial potential for electrifying transportation. While industrial recycling of lithium-ion batteries is economically viable and undertaken in many countries, the long-term implications of recycling on primary battery manufacturing and material supply are largely unknown. As R&D efforts to better recycle lithium-ion batteries are undertaken, a birds-eye view of the interconnections between raw material availability, primary manufacture, recycling, and demand is needed.

In this project, NREL is incorporating previous analysis and data in a system dynamics framework, named Lithium Ion Battery Recycling Analysis (LIBRA), to explore issues related to the global and regional impacts of the interlinking supply chains associated with battery manufacturing and recycling. Electrification of the

transportation and energy storage markets is projected to result in explosive growth in the demand for batteries. In response to concern over raw material demands, increased emphasis is being placed on battery recycling capacity expansion. While some resulting impacts are anticipated, such as the shift in manufacturing costs and raw material prices, the interconnectiveness of multiple markets, operations, and policies could have unanticipated impacts on the success of electrification efforts. LIBRA analytically explores the technological and market feedback and feed-forward signals that could affect global supply chains for raw materials, primary and recycled batteries, and electric vehicles. (See Figure I.4.C.55.)

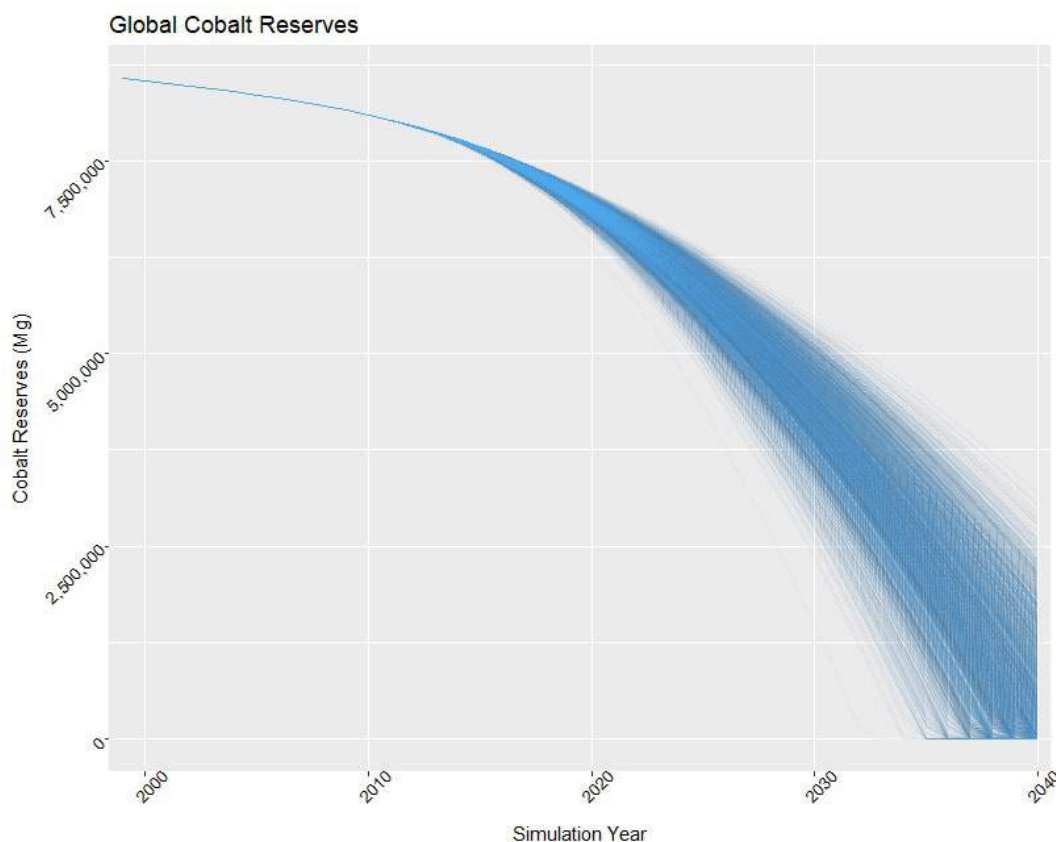


Figure I.4.C.55 Simulated global Co reserves over the time period 1998–2040. Results of 3,427 sensitivity runs are shown

Work performed this quarter has focused on the development of a user interface: [LIBRA Model Interface](#) (see Figure I.4.C.56) and a sensitivity app: [LIBRA Sensitivity Analyzer](#) (see Figure I.4.C.57).

The interface has 3 sections: input variable ranges, diffusion rates, and results. The input variables are slider bars that allow the user to provide values within a specific range for the following parameters:

- Sales of electric or plug-in hybrid vehicles
- Average battery size in kWh per vehicle
- Battery Lifetime
- Average battery size in kWh per stationary battery.

In addition, the rate of diffusion or adoption of specific technologies or behaviors can be modified: U.S. storage battery sales, recovery of Co from recycling, rate of battery recycling, and adoption of the NMC811 battery in the marketplace. Base technology diffusion curves are used to represent the rate of adoption of Co

recycling efficiency, EV battery recycling rates, and the adoption of alternative battery chemistries. Four result charts are reported for each run: Co Recycled in U.S., U.S. Cobalt Demand, Estimated Global Co Reserves and Cobalt Price Index Actual. The user can conduct a series of runs and chart each result on the same chart. The example below shows a series of 4 runs varying xEV sales.

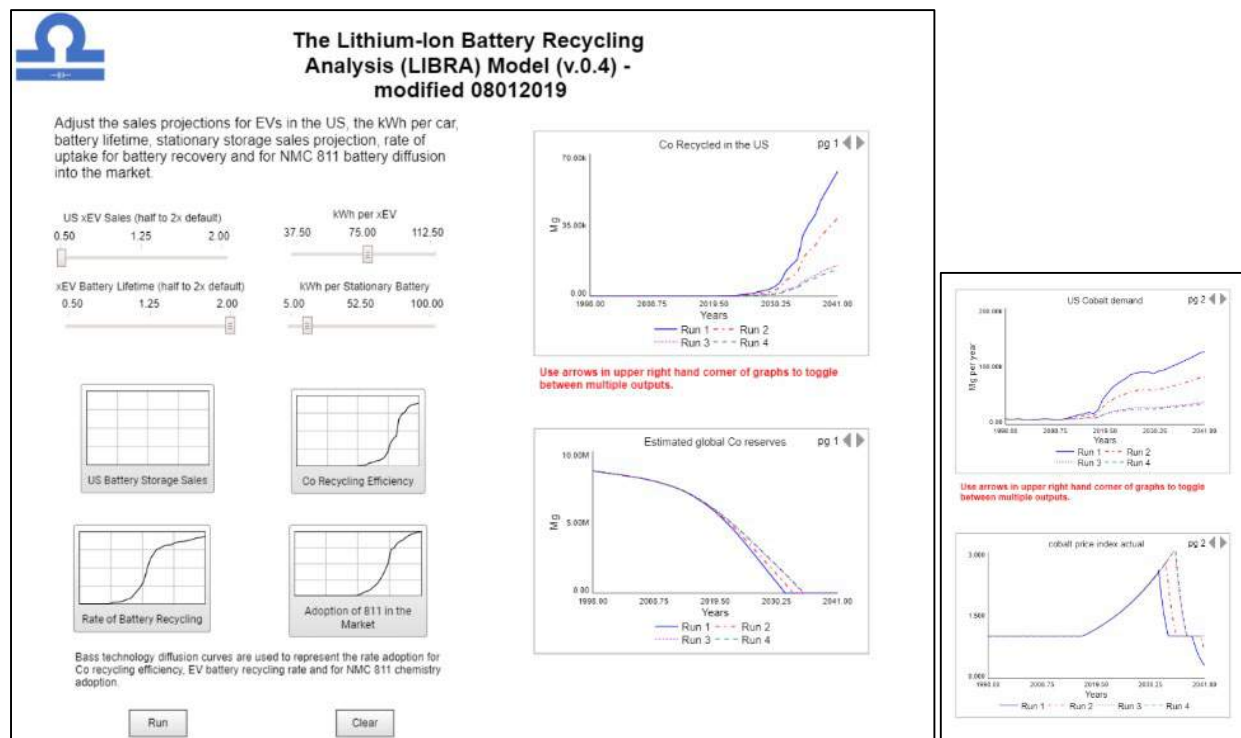


Figure I.4.C.56 LIBRA Model Interface

The sensitivity app ([LIBRA Sensitivity Analyzer](#)) runs a Monte Carlo simulation to provide a sensitivity analysis within the specified variable ranges. These runs (~7000) are shown in the chart below. The user can then select a range of values (i.e., by drawing a pink box) to obtain a local sensitivity analysis.

The local sensitivity analysis for the pink box drawn on the chart below shows the inputs that cause results to significantly different from all other runs performed. In this case, EV battery recovery fraction, U.S. EV multiplier, and Battery Share LCO. These are shown in the table below where B.mean is the mean of the current run and B.bar.mean is that from the new run.

As shown below, the results in the drawn pink box had higher EV recovery fraction (0.57. vs. 45), more EVs in the market (51% vs 5% greater than the base AEO forecast), higher penetration of high LCO batteries in EVs (59% vs 43%), with lower penetration of all other battery types (47% NCA and NMC811 and 48% for NMC622 versus 52%, 53% and 52%, respectively). Finally, the average time to recycle is about the same for both cases (i.e., ~ 9 months).

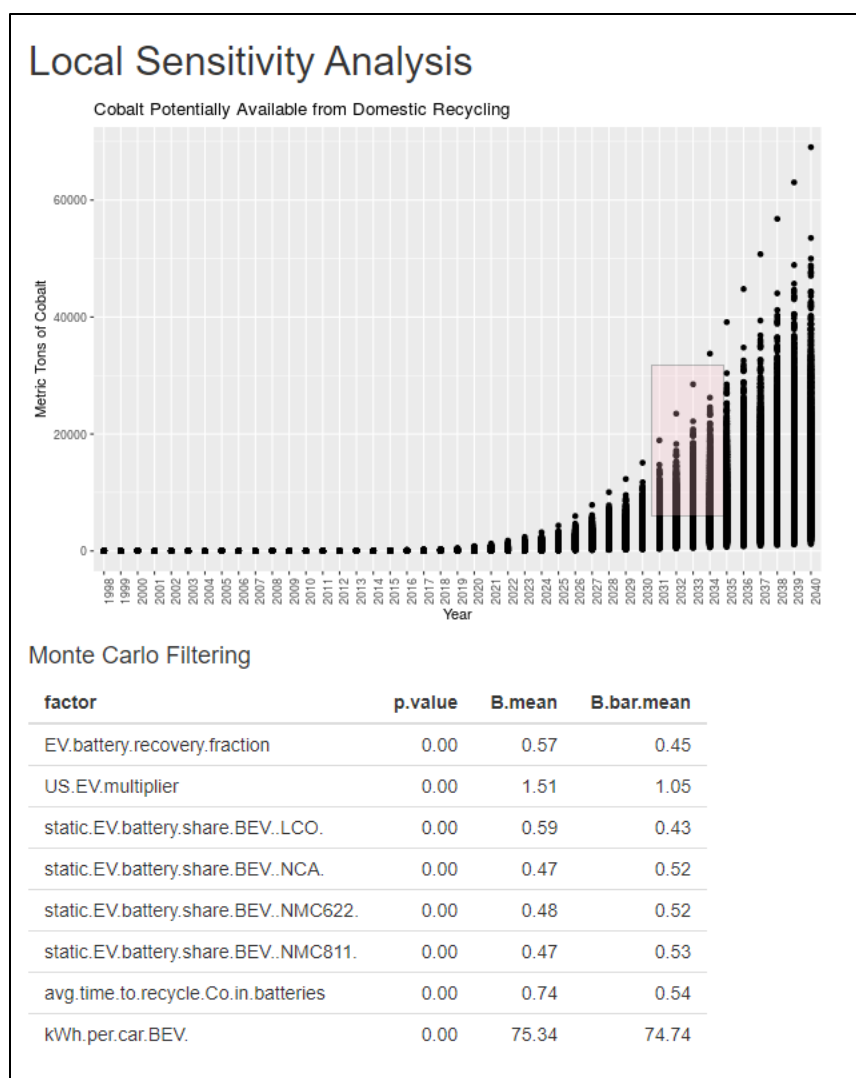


Figure I.4.C.57 LIBRA Model Sensitivity Analyses

The current sensitivity was developed by varying “all possibilities” and as such there are some combinations that are unlikely (i.e., the LCO static battery share) as LCOs are not used in xEVs. As the model is developed to add improved pricing formulation, TEA information, battery aging, recycling and adoption curves, unlikely outcomes will be minimized.

In addition to the model development, NREL has updated its supply chain analyses (see Figure I.4.C.58). NREL presented these analyses at the DOE Roundtable and the 24th International Congress for Battery Recycling (ICBR) 2019. In particular, new information on a potential nickel shortage was discussed. Low nickel prices over the last several years and greater demand from China for Grade 2 nickel, which is used in stainless steel, has resulted in an oversupply of Grade 2 but no investment in the production of the Grade 1 nickel that’s used in batteries. The capital investment for Grade 1 facilities is on the order of hundreds of millions of dollars, estimated to be approximately \$20,000 per metric tonne of nickel capacity. A shortage in supply is estimated to evolve in 5-6 years according to sources; these dates are highly dependent on growth of lithium-ion batteries and the chemistry that is adopted in the marketplace. Work in the next quarter will assess the sensitivity of the nickel supply chain on battery chemistry.



Figure I.4.C.58 NREL's updated supply chain model resultd (Sources: NREL Analysis; Campagnol, N. et al. 2017; BNEF 2019; LME 2019; Daly, T. 2019; Stringer, 2019)

Cross-Cutting Activities – CAMP Facility Support (Argonne National Laboratory)

Numerous recycled battery materials will be created in the ReCell Program that will need to be validated in prototype electrodes and pouch cells. The Cell Analysis, Modeling, and Prototyping (CAMP) Facility at Argonne will validate these materials (active cathode powders, graphite, electrolytes, etc.) and compare their electrochemical performance to baseline electrodes (and electrolyte). Validating the electrochemical performance of recycled battery materials will be critical to establishing their market viability.

In FY 2019, the CAMP Facility will use pristine NMC111 cathode material and SLC1520P graphite to fabricate baseline capacity-matched electrodes and baseline single-layer pouch cells. In addition, they will use chemically delithiated NMC111 pristine materials that are supplied by Argonne's Materials Engineering Research Facility (MERF) as tasked in the ReCell Program. The final delithiated NMC111 powder will also be fabricated into a baseline delithiated cathode electrode that is capacity-matched to the baseline SLC1520P anode electrode. All of the electrodes will first be tested in coin cells for initial validation and then tested in single-layer pouch cells for rate performance, HPPC impedance, and cycle life. All future recycled NMC111 cathode materials will be compared against these baseline electrochemical performance data, as well as other recycled battery materials that are of interest to the ReCell Program.

Preliminary experiments will be conducted to test the effects of rinsing harvested electrodes from end-of-life pouch cells and reassembled into cells. These results will be of particular use to the Cell Design efforts focused on rejuvenating electrodes/cells via an “electrolyte flush”.

A large supply (60 kg) of NMC111 was purchased from Toda and distributed as requested to other efforts in the ReCell Center. The CAMP Facility fabricated sample electrodes of the baseline NMC111 powder to establish initial specific capacity values, which were needed in designing the final electrode couple. Meanwhile, MERF conducted scale-up experiments to chemically delithiate this baseline NMC111 powder to 10% and later 25%. Samples of the both delithiated powder were provided to CAMP Facility to make sample electrodes and coin cells for electrochemical performance analysis. These cathode powders and the baseline SLC1520P graphite from Superior Graphite were tested in coin cells under several test protocols that were created to test the long-term electrochemical performance of these baseline active materials.

Figure I.4.C.59 is an update of the coin-cell test matrix that represents a summary of the baseline active materials and testing protocols. The baseline pristine NMC111 cathode, baseline graphite, and 10% delithiated NMC111 cathode electrodes finished testing in half-cells. The pristine NMC111 and SLC1520P graphite were tested in full cells, and the 10% delithiated NMC111 versus SLC1520P graphite are on their last test protocol (highlighted in yellow in Figure I.4.C.59). Also of note is that two electrolyte conditions were used: flooded and 29 μL .

Anode	Cathode	Electrolyte : Amount	Testing Protocol Order			
			Profile 1	Profile 2	Profile 3	Profile 4
Li	NMC 111	Gen 2 : Flooded	ReCell-Cathode-Half-Form.000	ReCell-Cathode-Half-Rate.000	-	-
Li	NMC 111	Gen 2 : Flooded	ReCell-Cathode-Half-Form.000	ReCell-Cathode-Half-Cyc.000	-	-
Li	Delithiated NMC 111	Gen 2 : Flooded	ReCell-Cathode-Half-Form.000	ReCell-Cathode-Half-Rate.000	<div>Test Needs to be Done</div> <div>Test is On-Going</div> <div>Test Completed</div>	
Li	Delithiated NMC 111	Gen 2 : Flooded	ReCell-Cathode-Half-Form.000	ReCell-Cathode-Half-Cyc.000		
1520P	Li	Gen 2 : Flooded	ReCell-Gr-Half-Form.000	ReCell-Gr-Half-Rate.000		
1520P	Li	Gen 2 : Flooded	ReCell-Gr-Half-Form.000	ReCell-Gr-Half-Cyc.000	-	-
1520P	NMC 111	Gen 2 : 29 μL	ReCell-FullCell-Form.000	ReCell-FullCell-Rate.000	ReCell-FullCell-HPPC.000	ReCell-FullCell-Cyc.000
1520P	NMC 111	Gen 2 : 29 μL	ReCell-FullCell-Age.000	-	-	-
1520P	Delithiated NMC 111	Gen 2 : 29 μL	ReCell-FullCell-Form.000	ReCell-FullCell-Rate.000	ReCell-FullCell-HPPC.000	ReCell-FullCell-Cyc.000
1520P	Delithiated NMC 111	Gen 2 : 29 μL	ReCell-FullCell-Age.000	-	-	-

Figure I.4.C.59 Test matrix developed for evaluating ReCell baseline electrodes in coin-cell format

The results of the full-cell coin-cell tests are shown in Figure I.4.C.60-Figure I.4.C.62 for the Pristine NMC111 versus SLC1520P graphite. Figure I.4.C.60 is a plot of the cell capacity versus cycles under the Life Cycle protocol (described in the figure legend). This protocol combines the effect of cycling and calendar aging. Note that there is little effect of the amount of electrolyte for the first 70 cycles, after which the capacity retention is greater for cells with excess (flooded) electrolyte. Figure I.4.C.61 is a plot of the cell capacity versus cycles under the Aging protocol (described in the figure legend). Under this test protocol, which is a much faster protocol than the Life Cycle protocol, the amount of electrolyte has little effect until ~400 cycles. This point in time corresponds to the same point in time of the Life Cycle protocol at 70 cycles. Figure I.4.C.62 is a summary of the HPPC area specific impedance (ASI) measured every 51 cycles in the Life Cycle test protocol for both electrolyte conditions. Here too, a flooded cell performs better than the coin cells with only 29 μL of electrolyte. A more ideal electrolyte amount would be in additions of $5+14+14 = 33 \mu\text{L}$ for this electrode loading ($\sim 1.6 \text{ mAh/cm}^2$) – more electrolyte would be needed for higher electrode loadings.

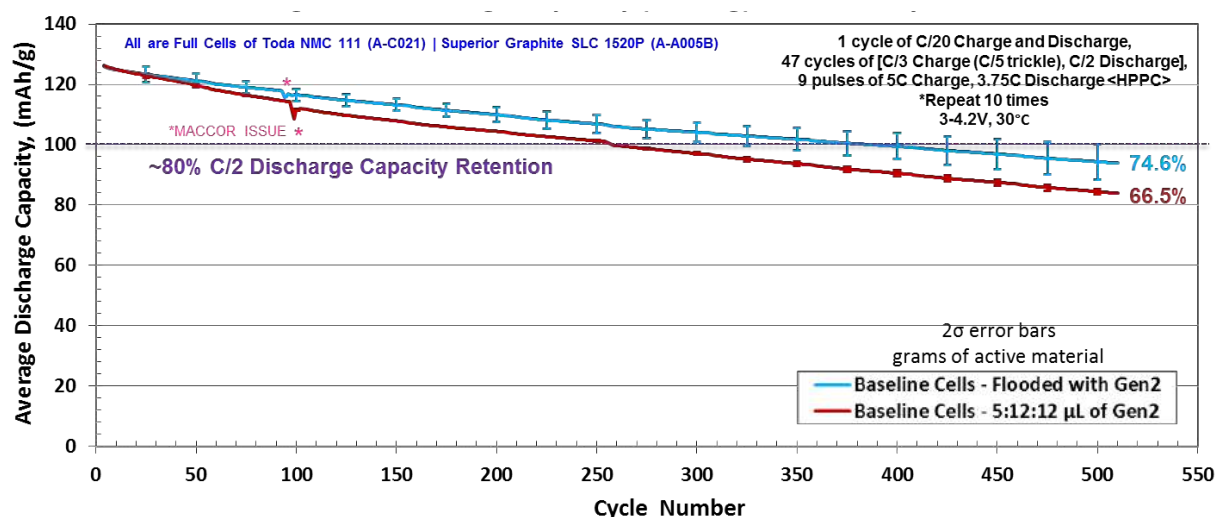


Figure I.4.C.60 Summary of the discharge capacity from the full-cell coin-cell test matrix results for pristine NMC111 versus SLC1520P graphite under the Life Cycle test protocol (see legend for details)

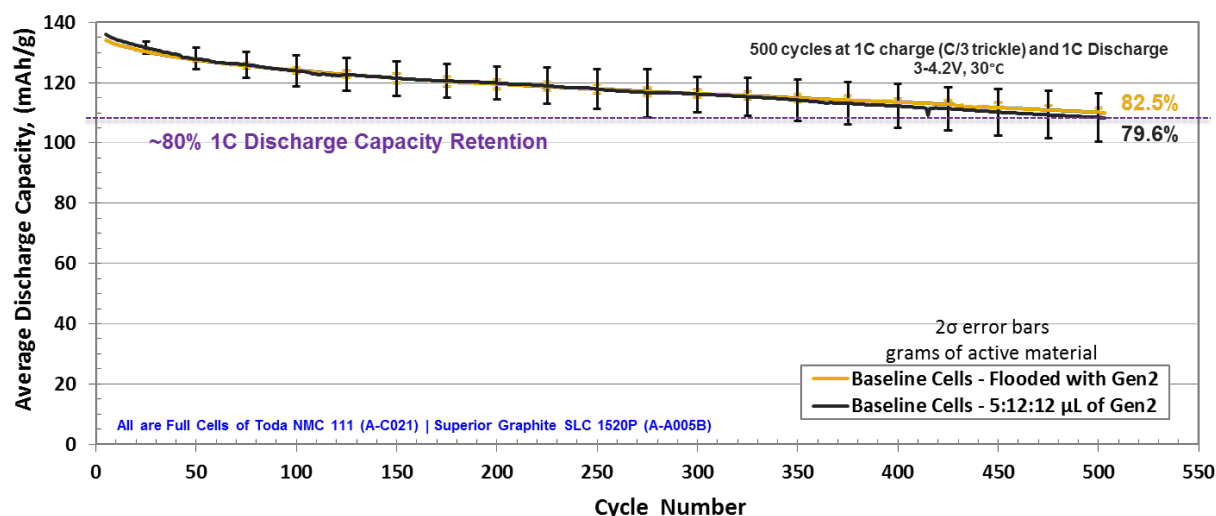


Figure I.4.C.61 Summary of the discharge capacity from the full-cell coin-cell test matrix results for pristine NMC111 versus SLC1520P graphite under the Aging test protocol (see legend for details)

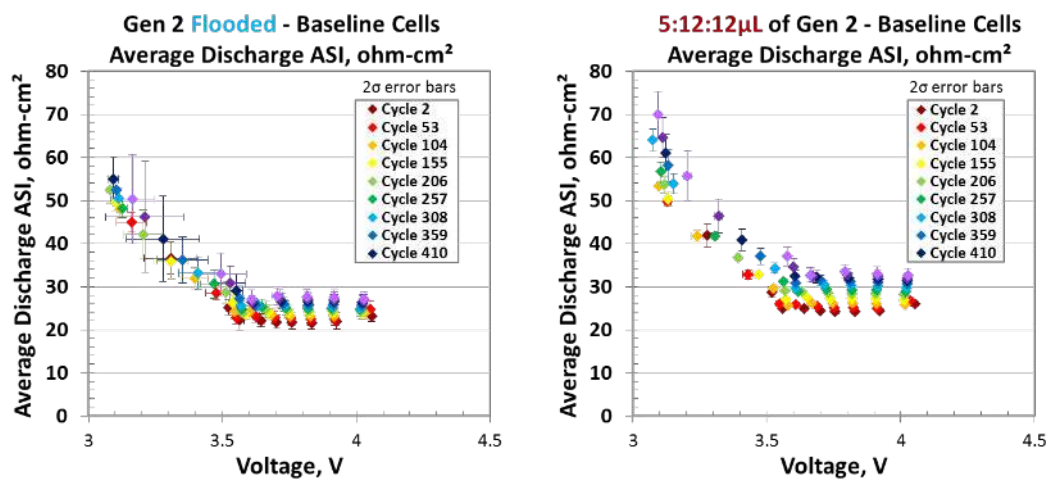


Figure I.4.C.62 Summary of HPPC ASI from the full-cell coin-cell test matrix results for pristine NMC111 versus SLC1520P graphite under the Life Cycle test protocol (see legend in Figure 2 for details)

Single-Layer Pouch Cell Build for Micro-calorimetry Study at NREL

Single-layer pouch cells were made from electrodes that contained 1 wt.% of anticipated metallic impurities in the anode and cathode recycled materials. Five cathode impurity electrodes (Cu, Al, Fe, Mg, Si in pristine NMC111) and four anode impurity electrodes (Cu, Al, Fe, Mg in pristine SLC1520P) were each paired with the corresponding baseline electrode. Three cells were made for each condition (depicted in Figure I.4.C.63). These cells were fabricated by the CAMP Facility and shipped dry to NREL for micro-calorimetry studies. This is in addition to the dozens of pouch cells made with various pristine cathode materials and two pristine graphites, which were delivered to NREL for micro-calorimetry studies.

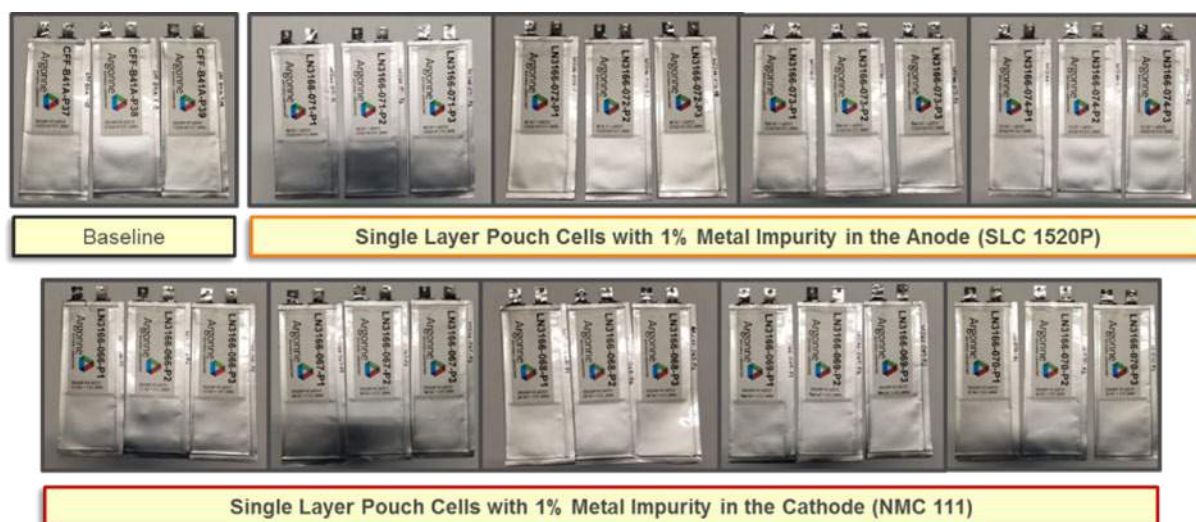


Figure I.4.C.63 Single-layer pouch cells made with 1 wt.% metallic impurity in anode and cathode electrodes for micro-calorimetry studies at NREL

Cross-Cutting Activities – Post Test Facility Support (Argonne National Laboratory)

The Post Test Facility at Argonne performs a supporting role in the ReCell Program. Post-test diagnostics of aged batteries can provide additional information regarding the cause of performance degradation, which previously, could be only inferred. The facility combines microscopy, spectroscopy and chromatography in a controlled-atmosphere glove box to the greatest extent possible to characterize materials without air exposure. These results will help us identify issues in the recycled materials, such as how well does a given recycling process separate an initial mixture of cathode, anode, supporting foils and casing materials.

Because we perform a supporting role, we depend on others for materials. This quarter we characterized the products from USCD, WPI, and NREL for different studies, which were summarized in the Table I.4.C.18 X-ray photoelectron spectroscopy (XPS) was used to determine their respective surface compositions and chemistries. Surface morphology of SEI/CEI after washing with different solvents for different periods was also characterized by SEM without any exposure to air. We already shared the results with the owners and are working together on the data, including XPS data fitting for potential publications.

Table I.4.C.18 Sample Information: XPS/SEM Study

Institutes	Sample description
UCSD (regeneration of NCM111 via hydrothermal relithiation)	1. Pristine Toda NCM111 2. Chemically delithiated NCM111 from Argonne 3. Lithiated at 220C for 1 hour 4. Lithiated at 220C for 2 hours 5. Lithiated at 160C for 1 hour 6. Lithiated at 160C for 6 hours
WPI (impurity study)	1. Pristine NMC 622 powder 2. 0.34% Cu doped NMC 622 powder 3. 5% Cu doped NMC 622 powder
ORNL (evaluation of the efficiency in cleaning the SEI/CEI with various solvents after cycling)	Group 1: Graphite anode and NMC 622 cathode without any cleaning Group 2: Anode cleaned with DMC for 5 min and 15 min Group 3: Cathode cleaned with DMC for 5 min and 15 min Group 4: Anode cleaned with IPA for 5 min and 15 min Group 5: Cathode cleaned with IPA for 5 min and 15 min Group 6: Anode cleaned with Ethanol for 5 min and 15 min Group 7: Cathode cleaned with Ethanol for 5 min and 15 min

Currently, we are continually working on 5% Cu doped NMC 622 sample from WPI from cross section to find out whether Cu preferably stays in the bulk rather than at the surface. Meanwhile, we discussed with Jaclyn Coyle from the NREL team about comparing the effect of chemically delithiated and electrochemically delithiated NMC 111 (Potentiostatic Hold at 5V) by XPS. Experiments will be carried out in the near future.

Conclusions

Chemical Relithiation of NMC Cathodes

Initial work on thermal relithiation has determined that the delithiated lattice (20%) is stable to approximately 300°C. Studies to identify lower decomposing sources of active lithia have shown that lithium acetate and nitrate produced the best samples (stability). The use of hydroxide at higher temperatures was evaluated and data show that the low rate cycling is comparable but higher rates support some minor surface degradation that may be from the competition of oxygen loss (with metal reduction) and lithia diffusion to fill vacancies.

Electrochemical Relithiation (NREL)

In this quarter for the electrochemical relithiation section of the ReCell project we identified some of the variables that have led to the noted impedance rise in some of the chemically delithiated samples. Previous ReCell work had shown that the problem was more associated with higher delithiated samples and that methods of relithiation that used moderate temperature (RTIL/ORNL, Thermal/ANL) yielded higher impedance than pristine cathodes. We have found that this may be related to sample homogeneity and have used the room temperature electrochemical measurements to identify pathways to overcome the impedance rise. Cycling at slightly higher temperatures was found to improve performance, but at temperatures that are not known to change the chemistry of the de-lithiated NMC111 samples.

Direct Regeneration of NMC Cathodes through Ionothermal Lithiation (ORNL)

In summary, ionothermal relithiation of chemically delithiated NMC111 was investigated under different reaction conditions. The recovered materials were analyzed by various characterization techniques including TGA, XRD, SEM, and ICP-OES, which demonstrate that the ionothermal approaches towards restoring Li into delithiated NMC111 for direct regeneration of cathode materials are promising and feasible. LiBr was demonstrated to be a better lithium precursor than LiCl due to the reducing capability of bromide. In addition, the scaling up of the relithiation process has been achieved. Electrochemical performance was evaluated. 94.5% of initial capacity was maintained for the ionothermally relithiated samples using LiBr as lithium precursor after 40 cycles. Further optimization the ionothermal relithiation process will continue with lower reaction temperature and ratios of ionic liquids and delithiated NMC 111 in next quarter. Hopefully even large scale-up to 25 g material will be accomplished too.

Hydrothermal Relithiation of Chemically Delithiated NMC111 Cathodes

In summary, a viable hydrothermal lithiation mechanism was explored by XPS, in which the Ni^{2+} is first oxidized to Ni^{3+} , and then the lithium ions are inserted into the vacancies of the layered structure. And the different electrochemical behavior of the samples relithiated at different temperature is due to the different Ni^{3+} content. When the Ni^{3+} is completely transferred to Ni^{2+} , the material shows the best electrochemical performance. Besides, the effect of pre-removal of PVDF binder via low temperature sintering induces irreversible microstructure damage, leading to reduced capacity and its retention.

Binder Removal

Substantial improvements in the electrochemical performance of delithiated materials after binder removal can be made by increasing annealing temperature to temperatures similar to those used for the initial calcination. Times of about 8 hr seem to result in the best performance. Despite these improvements there is still about a 3.6% capacity loss as compared to pristine material. Additional improvements might be had by increasing annealing time to 8 hr at 800°C and 900°C. Depending on these results additional optimization can be focused on those regions. In addition, experiments are needed to determine how bed depth affects performance as these results are needed to cost model the heating process.

Cathode/Cathode Separation Process Development (Argonne National Laboratory)

The most effective methods of separation studied in FY2019 have been the wet and dry magnetic separation methods. It has been shown that high purity separation can be achieved with magnetic separation. The dry method will require custom equipment to scale while the wet system is commercially available. Triboelectric separation while theoretically promising has proven less effective than hoped. Further testing would be required for this method. Acquisition of a wet high intensity magnetic separator (WHIMS) is recommended for scaling the magnetic separation process.

Cathode-Cathode Separation via Froth Flotation (Michigan Technological University)

Separation of LCO and NMC111 was achieved using collector A. The performance of collector A outperforms oleic acid and sodium hydroxamate. Future studies will focus on the separation of other combination of binary mixtures.

Role of Impurities in Recycled Cathodes

Aluminum, in the amounts present in the black mass analysis studies, has a significant impact on synthesized NMC622 in terms of morphology, properties, and electrochemical properties. As with copper addition, the tap density decreases significantly when Al ions were added. Unlike with copper no significant impurities in preliminary synthetic baseline studies were detected but additional analysis and experiments are warranted. As the state of the alumina and its reactivity are an issue, the main impurity expected ($\alpha\text{-LiAlO}_2$) under our conditions is similar in structure to the underlying cathode and small amounts at the predicted solubility limit may be hard to estimate.

Recycled Cathodes as Materials Feedstock (Argonne National Laboratory)

We have evaluated the use of various temperatures and starting materials to add stoichiometric nickel to the baseline NMC111 materials. In general, the process requires metal cation diffusion which is favored at high temperature and lower oxidation states. Studies using a Ni(III) salt resulted in reduction and phase separation. Divalent nickel salts were evaluated and temperatures of annealing above 700°C showed phase separation while inclusion of the extra nickel was observed based on XRD and GDOES data for samples around 700°C. Electrochemical evaluation continues as does assessment of homogeneity of cations.

Hydrothermal recovery processes for the black mass (ORNL)

In summary, a SolveX process has been developed for the efficient separation of the black mass from current collectors without corroding the Al or damaging the active materials. Besides, a green solvent Y was proposed and demonstrated to efficiently remove PVDF and to recover the black mass.

Anode/Cathode Separation and Purification (Argonne National Laboratory)

Magnetic separation of graphite from cathode materials can be effective and does not require especially powerful magnets. Air classifiers can be used to achieve separation of anode and cathode powders but will not be able to produce very high purity products without additional processing. Most of these technologies are relatively inexpensive. Air classification has a capital cost of \$15-20k per hourly metric ton of capacity. Triboelectric separation has an amortized cost of about \$50 per metric ton, and magnetic separation typically costs only \$0.30-1 per ton. These are all methods in wide use in industries that are producing far less valuable products than anode powders. Given the low cost of these processes, economically viable recovery of graphite from shredded lithium-ion cells is quite possible and should be given further study.

Electrolyte Component Removal and Recovery

Electrolyte can be effectively removed from black mass via solvent extraction. Lithium hexafluorophosphate can be recovered and re-used without further purification. It was found that heating at 90°C in an inert atmosphere yields an electrolyte concentrate that is about 60:40 EC:LiPF₆. The cycling performance shows slightly more capacity fade initially, but more stable cycling thereafter as compared to Gen 2 electrolyte. Combining this electrolyte with additives did not improve the cycling performance. Going forward, we need to prove that this process works equally well on other manufacturers' batteries. Cost modeling is also ongoing to determine the economic feasibility of the process.

Design for Recycle – Cell Design (ORNL & Argonne)

In this project period, we have generated spent electrodes and investigated the effect of electrode rinsing on capacity recovery. Electrode rinsing dramatically increased the capacity compared to the spent electrodes, which was mainly attributed to reduced polarization in the graphite anodes after washing. A preliminary estimate was made on the impact of the rejuvenation hardware on the battery pack volume/energy density. Under the ideal conditions of no wasted space in the battery design, the energy density would be decreased by only a few percent, but that could increase to tens of percent if the battery pack dimensions need to be increased by several centimeters.

Diagnostics of Aged Materials

Improved sampling and analytical tools have been established to quantify strain mapping at the primary particle level via EBSD, in addition to the particle size and grain orientation data we previously reported. This allows for comparison of degradation metrics on recycled cathodes, against well-established methods (e.g., monitoring lattice spacing from XRD measurements with aging). Whereas the conventional tools provide estimates of average strains across the particle (or electrode), the use of EBSD provides detailed spatial resolution of these parameters, allowing us to assess statistical significance of these measurements versus ability to relithiate. For next steps, we are also subjecting off-the-shelf NMC-532 samples to EBSD measurements in pristine (uncycled) state and after cycling to 20% and 40% capacity loss. Analysis of orientation preference and changes to grain size will continue as cells cycled to 60% and 80% capacity loss become available. We will summarize our initial results into a publication.

Microcalorimetry on Recycled Materials (NREL)

In the next fiscal quarter, NREL will continue to thermally test the various CAMP NMC/1506T graphite cells with pristine cathode/anode material. We are also beginning to cycle the CAMP NMC/1520P cells according to ReCell guidelines until 80% of the initial capacity remains. NREL will then measure the heat generation and efficiency at the end of life. The data from these tests will be used as a baseline to assess the performance of future recycled material and processes. During Q4 FY19, NREL received dry cells from ANL with a known amount of contaminant on the cathode and anode. NREL will begin using calorimetry to determine how these contaminants affect the performance of the cells. The cells will be filled at NREL and then formed and cycled in the calorimeter as the heat generation variance due to the contamination is expected to be highest during the formation cycles.

EverBatt: Cost and Environmental Impacts Modeling (Argonne)

Customized versions of EverBatt have been developed to evaluate the electrolyte recovery process, the hydrothermal relithiation process, and the ionothermal relithiation process. As previously thought, process scaling-up turns out to be a substantial challenge to modeling and analysis. We note that the reagents cost and the process yield, both of which change considerably with the production scale, can have significant impacts on the evaluation results. Therefore, we contend that for all EverBatt customization projects, sensitivity analyses of key process parameters should be conducted to examine the effect of production scale. In addition to EverBatt customization, we are also working to expand EverBatt to include battery packaging and storage, and refine the transportation modeling based on DOT's new regulations.

Analysis of Supply Chain Challenges for Battery Recycling (NREL)

Work performed this quarter has focused on the development of a user interface: LIBRA Model Interface, and a sensitivity app: LIBRA Sensitivity Analyzer. NREL has also updated its supply chain analyses, and in particular, evaluated potential problems in the nickel supply chain. Low nickel prices and a lack of investment in facilities to produce nickel in the purity required for batteries may result in a shortage in 5-6 years.

Cross-Cutting Activities – CAMP Facility Support (Argonne National Laboratory)

The CAMP Facility actively supports the efforts of the ReCell Center by providing baseline materials, fabricating trial electrodes and baseline electrodes, fabricating and testing numerous coin cells, and fabricating single-layer pouch cells. It has established a thorough test matrix and protocols that were used to conduct electrochemical evaluation of baseline active materials of interest to the ReCell Center in FY 2019. It has fabricated several dozens of unique pouch cells as needed, many of which are used in the micro-calorimetry studies at NREL.

Cross-Cutting Activities – Post Test Facility Support (Argonne National Laboratory)

The Post-Test Facility will continue to provide support for the ReCell project, providing characterization expertise where needed. The planned, future work includes characterizing recycled materials that are produced as part of this project. As the recycling processes mature, cells will be constructed from the materials. Cells containing these materials will be sent to Post-Test for additional characterization data regarding causes of loss of performance.

Acknowledgements

The following individuals worked as individual task leaders/members for the tasks described in this project: Tony Montoya, Jack Vaughney (ANL) on chemical relithiation of NMC cathodes; Jaclyn Coyle, Xuemin Li, Anthony Burrell (NREL) on electrochemical relithiation; Sheng Dai, Huimin Luo, Nitin Muralidharan, Jianlin Li, Zhijia Du, and Ilias Belharouak (ORNL) on the direct regeneration of NMC cathodes through ionothermal lithiation; Zheng Chen, UC San Diego on the Hydrothermal Relithiation of Chemically Delithiated NMC111 Cathodes; Albert L. Lipson, Bradley Ross (Applied Materials Division, Argonne National Laboratory) on binder removal; Erik Dahl (ANL) on the cathode/cathode separation process development; Lei Pan, Tinu Folayan, and Ruiting Zhan (Michigan Technological University) on the cathode-cathode separation via froth flotation; Yan Wang (WPI) on the role of impurities in recycled cathodes; Yan Wang (WPI) on recycled

cathodes as materials feedstock; Ilias Belharouak, Yaocai Bai, Nitin Muralidharan, Jianlin Li, Huimin Luo, and Sheng Dai (ORNL) on the hydrothermal recovery processes for the black mass; Erik Dahl (ANL) on the anode/cathode separation and purification; Albert L. Lipson, Seth Reed (Applied Materials Division, Argonne National Laboratory) on the electrolyte component removal and recovery; Jianlin Li, Anand Parejiya, Sergiy Kalnaus, Steve Trask, Alison Dunlop, Dave Kim, Bryant Polzin, Tony Fracaro, and Andrew Jansen on the design for recycle – cell design; Shriram Santhanagopalan, Kae Fink, Helio Moutinho, and Andrew Norman (NREL) on the diagnostics of aged materials; Matthew Keyser, Josh Major, Jeff Tomerlin, Shriram Santhanagopalan (NREL) on the microcalorimetry on recycled materials; Qiang Dai (ANL) on the EverBatt: cost and environmental impacts modeling; Margaret Mann, Daniel Inman, Darlene Steward (NREL) on the analysis of supply chain challenges for battery recycling; Alison R. Dunlop, Andrew N. Jansen, Dave Kim, Bryant J. Polzin, and Stephen E. Trask (Argonne National Laboratory) on the cross-cutting activities – CAMP Facility Support; and Nancy Dietz Rago, Zhenzhen Yang, and Ira Bloom (Argonne National Laboratory) on the cross-cutting activities – post test facility support.

I.5 Extreme Fast Charging (XFC)

I.5.A High Temperature Electrolytes for Extreme Fast Charging (ANL)

Zhengcheng (John) Zhang, Principal Investigator

Argonne National Laboratory
9700 S Cass Avenue
Lemont, IL 60439
E-mail: zzhang@anl.gov

Brian Cunningham, DOE Technology Development Manager

U.S. Department of Energy
E-mail: Brian.Cunningham@ee.doe.gov

Start Date: July 1, 2018

End Date: June 30, 2020

Project Funding (FY19): \$150,000

DOE share: \$150,000

Non-DOE share: \$0

Project Introduction

Widespread adoption of electric vehicles is limited by the current necessary charging times of greater than one hour. However, high charging rates are kinetically limited by lithium ion intercalation into graphite, which causes undesirable lithium plating and dendrite formation. High temperature charging could eliminate this issue.

Objectives

The objective of this subproject is to design and develop new electrolytes that are stable at elevated temperatures ($>50^{\circ}\text{C}$) which could support the fast charging at high temperatures while maintaining excellent cycle life and calendar life.

Approach

In this project, a targeted additive approach was employed to directly address the causes of high temperature cell degradation. Electrolyte additives that stabilize the electrolyte bulk and protect the cathode surface at high temperatures will be designed and their impact on the cell performance will be evaluated. The best-performing additives will be verified in the commercial EV cells.

Results and Discussion

1. Suppressing the thermal decomposition of LiPF_6

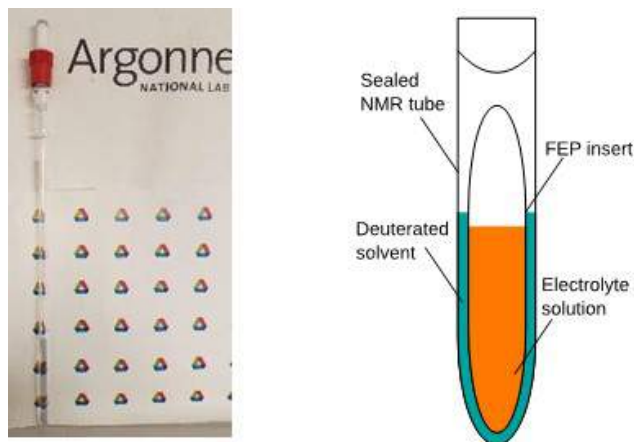


Figure I.5.A.1 (a) Picture of assembled NMR experimental setup (b) diagram of experimental setup

The degradation of electrolytes containing lithium hexafluorophosphate (LiPF_6) is well-studied subject. However, practical application of the knowledge is difficult, since the effects of the degradation process on battery performance aren't well-known. Here we propose a novel experimental setup allowing direct observation of the effects of different perturbations on the electrolyte degradation process, which allows for the design of new electrolyte additives that can improve lithium-ion battery performance at elevated temperatures.

At elevated temperatures, the commonly accepted mechanism for decomposition of LiPF_6 -based electrolyte leads to the initial generation of PF_5 and LiF through a dissociation reaction^{1, 2}. PF_5 species reacts rapidly with trace amount of protic impurities or solvent, making it difficult to detect directly^{3, 4}. As shown in Figure I.5.A.1, we have created an NMR experimental setup where the generated PF_5 could become trapped by a weak Lewis base, allowing the study of different perturbations on the electrolyte system at high temperature, and specifically determining the efficacy of additives designed to slow electrolyte decomposition.

Figure I.5.A.2a is the ^{19}F -NMR spectra of 1.2 M LiPF_6 in 3:7 ethylene carbonate/ethyl methyl carbonate (Gen 2) electrolyte at 80°C . Over time, a new peak system is generated which matches the coupling pattern of a PF_5 -Lewis base complex. Additives which act to limit the reactivity of PF_5 should be able to limit the growth of this complex, since the PF_5 would be less free to form an irreversible complex with the Lewis base, and would therefore shift the equilibrium of the dissociation reaction. One such additive is *N,N*-dimethylacetamide (DMAc), which has been demonstrated to increase the storage time of LiPF_6 -based electrolytes at elevated temperatures⁵. When our method was used on a mixture of Gen 2 with 2% (w/w) of DMAc, the concentration of generated PF_5 was significantly reduced, indicating that it is a reliable method for studying the effects of different perturbations on LiPF_6 dissociation at high temperatures.

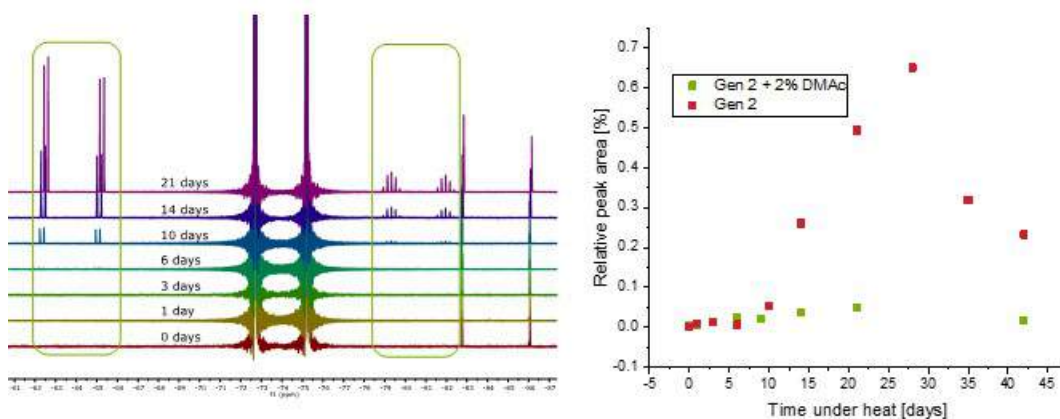


Figure I.5.A.2 (a) ^{19}F NMR of Gen 2 electrolyte heated at 80°C for increasing lengths of time (b) Integrated peak area of PF_5 -Lewis base species relative to PF_6^-

Figure I.5.A.3a shows one of the key results from this study. Different experimental conditions such as temperature, water content, and the inclusion of various cell components showed that NMC cathode material accelerated the disproportionation reaction. One potential cause of this is the dissolution of Mn^{2+} ions, which are active catalytic species that can increase the reaction rate. As Mn^{2+} is a paramagnetic species, you would expect to see peak broadening for species in its local space, which might provide some indication for the viability of this hypothesis. Figure I.5.A.3b shows the result of this analysis, where PF_6^- maintains a uniform peak width, while ROPOF_2^- species show a significant broadening as the experiment progresses.

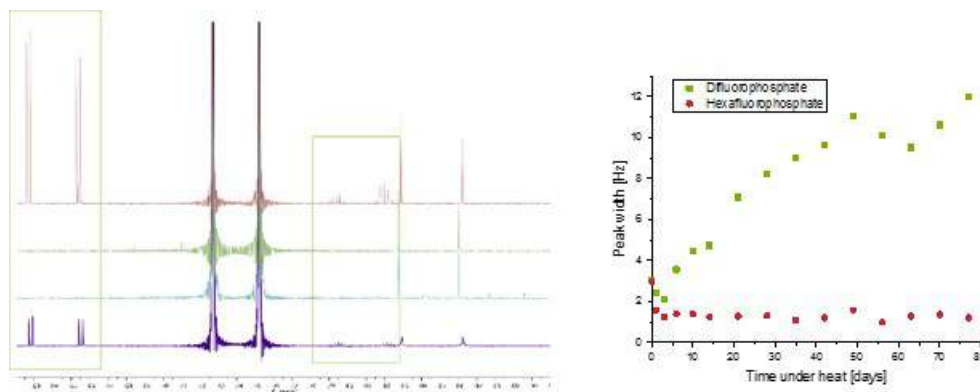


Figure I.5.A.3 (a) ^{19}F spectra after aging of, from bottom to top: Gen 2 + NMC @ 55 °C, Gen 2 @ 55 °C, Gen 2 + H₂O @ 55 °C, and Gen 2 @ 80 °C (b) Peak width at half maxima of different chemical species over time

2. Phosphazene-based electrolyte additives

Using this new analytical technique, we proceeded to evaluate a number of potential additives that might be used to slow the degradation of electrolytes based on LiPF_6 . One such candidate is the phosphazenes, which have been proposed to work via this mechanism⁶⁻⁹. As can be seen in Figure I.5.A.4, cyclotriphosphazenes have available lone pairs at the nitrogen position which can be used as a weak Lewis base, similar to DMAc. Three fluorinated ether derivatives were synthesized for the purpose of this experiment. All were synthesized via a Williamson ether synthesis, using sodium hydride as a base to create 2,2,2-trifluoroethoxy (**PzTFE**), 2,2,3,3-tetrafluoropropoxy (**PzTFP**) and 1,1,1,3,3,3-hexafluoropropoxy (**PzHFiP**) derivatives. The fluorinated ether functionality was used to stabilize the system from reductive decomposition, to not interfere with normal SEI formation. This is in line with our targeted additive strategy.

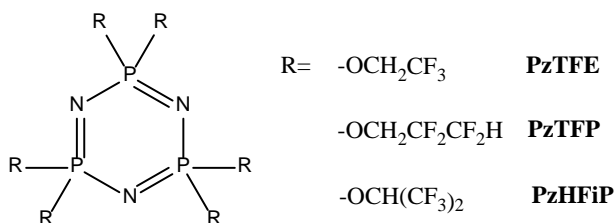


Figure I.5.A.4 Chemical structure of cyclotriphosphazenes, and the derivatives synthesized for this experiment

In Figure I.5.A.5a is the same NMR analysis used to verify the efficacy of DMAc as a stabilizing agent. It can be seen that **PzTFE** is comparable in performance, indicating that it too can be used to reduce LiPF_6 dissociation in Gen 2 electrolytes. Figure I.5.A.5b shows the first cycle of a graphite half-cell with increasing concentrations of PzTFE additive, showing the absence of a new reduction peak associated with the additive. This indicates that the fluorinated ethers are indeed stable against reductive decomposition, and any improved performance can be attributed to their ability to reduce the reactivity of PF_5 .

Figure I.5.A.6a shows $\text{LiNi}_{0.6}\text{Mn}_{0.2}\text{Co}_{0.2}\text{O}_2$ /graphite full cells cycled at 55 °C at a C/1 rate. While the starting capacity was highly variable, the capacity retention of **PzTFE** in particular was quite good relative to unprotected Gen 2. After 100 C/1 cycles, Gen 2 had faded to 65% of its starting capacity, while

PzTFE, PzTFP, and PzHFiP retained 80%, 65%, and 69%, respectively. PzTFE also maintained a very steady coulombic efficiency, as seen in Figure I.5.A.6b. The average value was maintained at 99.7%, while Gen 2 averaged 99.3%.

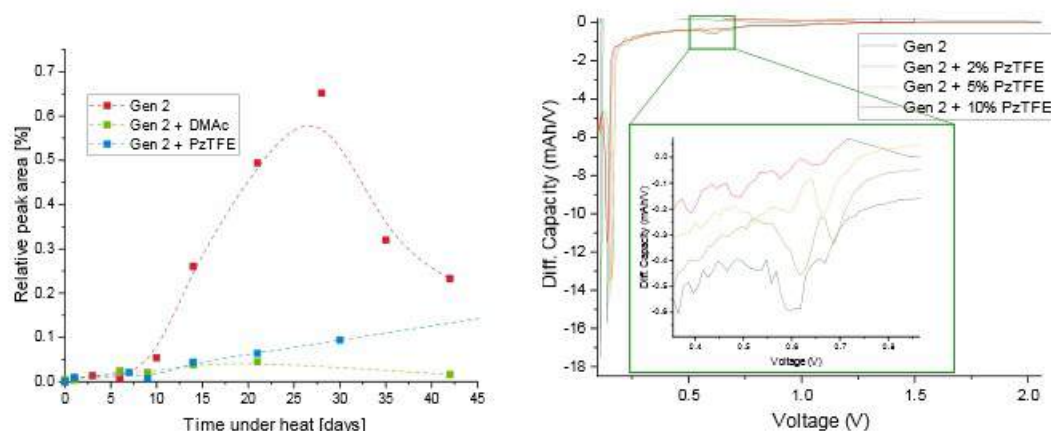


Figure I.5.A.5 (a) Integrated peak area of PF₅-Lewis base species relative to PF₆ for three different electrolyte systems (b) dQ/dV of the first cycle of a Gr/Li half cell with increasing concentrations of PzTFE

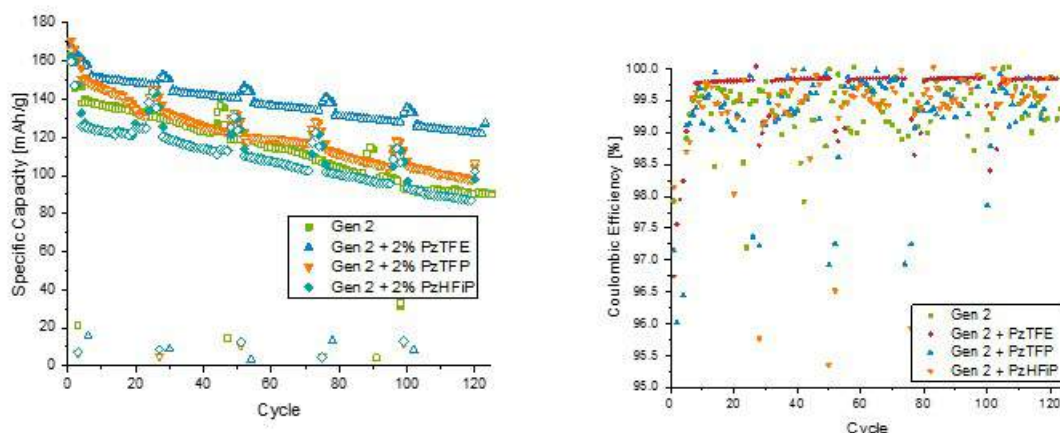


Figure I.5.A.6 (a) Capacity retention and (b) coulombic efficiencies of NMC622/Gr cells when cycled at 55 °C with phosphazene additives

3. Combinatorial Additives

Now that an additive with the potential to selectively limit the generation and reactivity of PF₅ was determined, we undertook tests to use it in combination with additives known to form a protective SEI. In theory, these should work together to create a system more stable to decomposition than either alone. In Figure I.5.A.7, those results can be seen when testing PzTFE in combination with vinylene carbonate (VC), 1,3-propanesultone (PS) and triallyl phosphate (TAP), which are three of the best additives for protecting the system against the negative effects of elevated temperature cycling. There is an improvement in capacity retention and coulombic efficiency for combinations with VC, but PS and TAP didn't show any synergistic benefit.

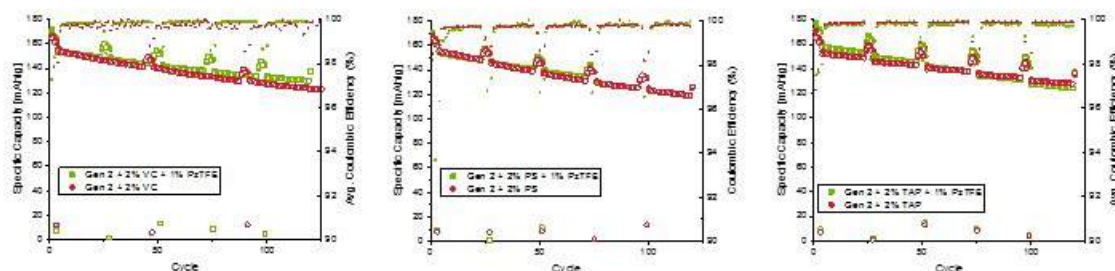


Figure I.5.A.7 Capacity retention and coulombic efficiencies of PzTfE in combination with (a) vinylene carbonate, (b) 1,3-propanesultone, and (c) triallylphosphate

The Hybrid Pulse Power Characterization Test (HPPC) shows the in-cell area-specific impedance at different voltages for different points in the cycling. As a general trend, this impedance will increase over the course of the experiment, as the different SEI layers thicken and resistances increase. As can be seen in Figure I.5.A.8, this trend does hold true for all of the cells, with different additives modifying the starting impedance and growth rate. PzTfE tends to slightly increase the starting impedance but maintains a similar or slightly slower growth rate when compared to the additives alone. This demonstrates that while modifying the reactivity of PF_5 directly is a useful strategy, the current state-of-the-art additives are excellent at protecting the system from this source of electrolyte degradation.

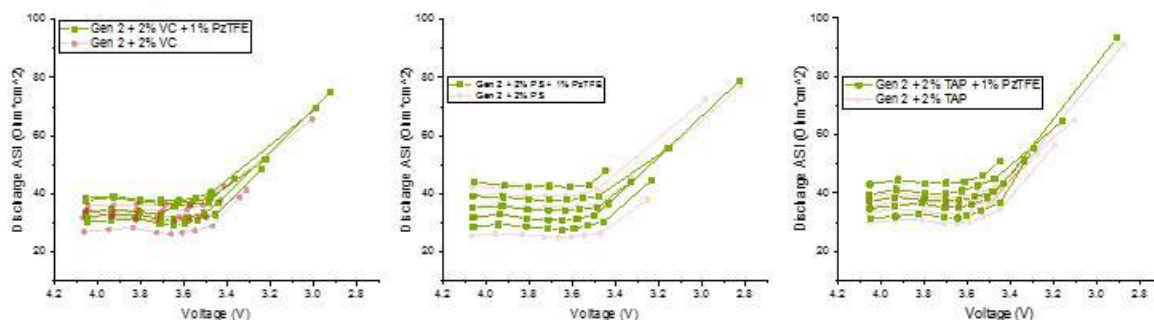


Figure I.5.A.8 Area-specific of PzTfE in combination with (a) vinylene carbonate, (b) 1,3-propanesultone, and (c) triallylphosphate

As the results from our NMR analysis showed, the next portion of cell degradation to target is the cathode. At elevated temperatures, the cathode is known to leach transition metals into solution, thickening the SEI and trapping cyclable lithium. Its interface with the electrolyte is also unstable, and can cause undesirable phase transitions and electrolyte oxidation. While additives that effectively protect the cathode have been challenging thus far, it is a necessary step to create a high-temperature fast-charging battery.

Conclusions

In FY2019, we have developed a new analytical technique for the determination of PF_5 generation in LiPF_6 -based electrolytes. This technique was used to identify a promising new additive, hexa(trifluoroethoxy)-cyclotriphosphazene (PzTfE), that can be used to improve battery performance by directly reducing the reactivity of PF_5 . It maintains high capacity retention at elevated temperatures when used with standard electrolytes and additives, and can be used in continuation of our targeted additive strategy to create a comprehensive electrolyte package capable of enabling elevated temperature fast charging lithium-ion batteries.

Key Publications

1. Noah M Johnson and Zhengcheng Zhang. A Practical NMR Study of High Temperature Electrolyte Degradation Using a Novel PF₅ Marker. **2020**, in preparation
2. Noah M Johnson and Zhengcheng Zhang. Application of Fluorinated Phosphazenes in Elevated Temperature Lithium-Ion Batteries. **2020**, in preparation

References

1. Campion, C. L.; Li, W.; Lucht, B. L., Thermal decomposition of LiPF₆-based electrolytes for lithium-ion batteries. *Journal of The Electrochemical Society* **2005**, *152* (12), A2327-A2334.
2. Ravdel, B.; Abraham, K. M.; Gitzendanner, R.; DiCarlo, J.; Lucht, B.; Campion, C., Thermal stability of lithium-ion battery electrolytes. *Journal of Power Sources* **2003**, *119*, 805-810.
3. Wiemers-Meyer, S.; Winter, M.; Nowak, S., Mechanistic insights into lithium ion battery electrolyte degradation—a quantitative NMR study. *Physical Chemistry Chemical Physics* **2016**, *18* (38), 26595-26601.
4. Grutzke, M.; Weber, W.; Winter, M.; Nowak, S., Structure determination of organic aging products in lithium-ion battery electrolytes with gas chromatography chemical ionization mass spectrometry (GC-CI-MS). *Rsc Advances* **2016**, *6* (62), S7253-S7260.
5. Smart, M. C.; Lucht, B. L.; Ratnakumar, B. V., The Use of Electrolyte Additives to Improve the High Temperature Resilience of Li-Ion Cells. *ECS Transactions* **2008**, *11* (29), 79-89.
6. Ahn, S.; Kim, H.-S.; Yang, S.; Do, J. Y.; Kim, B. H.; Kim, K., Thermal stability and performance studies of LiCo_{1/3}Ni_{1/3}Mn_{1/3}O₂ with phosphazene additives for Li-ion batteries. *Journal of Electroceramics* **2008**, *23* (2-4), 289-294.
7. Harrup, M. K.; Gering, K. L.; Rollins, H. W.; Sazhin, S. V.; Benson, M. T.; Jamison, D. K.; Michelbacher, C. J.; Luther, T. A., Phosphazene based additives for improvement of safety and battery lifetimes in lithium-ion batteries. *ECS Transactions* **2012**, *41* (39), 13-25.
8. Liu, J.; Song, X.; Zhou, L.; Wang, S.; Song, W.; Liu, W.; Long, H.; Zhou, L.; Wu, H.; Feng, C.; Guo, Z., Fluorinated phosphazene derivative – A promising electrolyte additive for high voltage lithium ion batteries: From electrochemical performance to corrosion mechanism. *Nano Energy* **2018**, *46*, 404-414.
9. Rollins, H. W.; Harrup, M. K.; Dufek, E. J.; Jamison, D. K.; Sazhin, S. V.; Gering, K. L.; Daubaras, D. L., Fluorinated phosphazene co-solvents for improved thermal and safety performance in lithium-ion battery electrolytes. *Journal of Power Sources* **2014**, *263*, 66-74.

Acknowledgements

Support from Brian Cunningham and David Howell at Vehicle Technologies Office (VTO), Office of Energy Efficiency and Renewable Energy, U.S. Department of Energy is gratefully acknowledged. Argonne, a U.S. Department of Energy laboratory, is operated by UChicago Argonne, LLC under contract DE-AC02-06CH11357.

I.5.B XFC R&D: Battery Testing Activities (INL)

Eric Dufek, Principal Investigator

Idaho National Laboratory
2525 Fremont Avenue
Idaho Falls, ID 83415
E-mail: eric.dufek@inl.gov

Samuel Gillard, DOE Technology Development Manager

U.S. Department of Energy
E-mail: Samuel.Gillard@ee.doe.gov

Start Date: October 1, 2017	End Date: September 30, 2019	
Project Funding (FY19): \$440,000	DOE share: \$440,000	Non-DOE share: \$0

Project Introduction

Extreme fast charging (XFC) of Li-ion batteries can create life and safety issues (Ahmed et al. 2017). With respect to performance loss one of the key complications is plating of Li metal on the negative electrode during fast charging. When this occurs there is a pronounced loss of Li inventory and subsequent enhanced electrolyte degradation due to the reaction of electrolyte molecules with Li metal. The detection and monitoring of Li plating onset and evolution over aging is a significant challenge. In operando detection schemes to understand the dynamics of Li plating and the role that aging has on Li plating are vital to enable fast charging of high specific energy cells.

Discreetly identifying Li plating is difficult without performing a destructive post-test analysis. The objective of the Battery Testing Activity at Idaho National Laboratory (INL) and Princeton is to overcome these limitations using electrochemical analysis and non-destructive ultrasonic acoustic methods that can be directly applied *in operando* to understand onset and growth of Li plating during XFC. The team is closely coordinating with other efforts at the National Renewable Energy Laboratory (NREL) and Argonne National Lab (Argonne) to understand the key limitations that enhance the probability of Li plating. The effort is directed at understanding the interplay between materials, electrode structure and use conditions. The ability to understand the complex interactions will be distinctly aided in this project using the joint electrochemical and ultrasonic tools which ultimately advance the scientific understanding required to facilitate the XFC of batteries for electric vehicles.

Electrochemical methods which can be used to identify Li plating include the use of differential capacity (dQ/dV), both direct (DC) and alternating current (AC) impedance measurement, and quantitative analysis of the cells charge and discharge profiles. These tools give pertinent information associated with both kinetic and thermodynamic processes which occur in batteries, and as such provide direct ability to better understand how variation in materials and electrodes have an impact across the life of a battery. There are limitations on the type of techniques which can be used to compliment electrochemistry *in operando* using standard cell formats. One method which is showing promise is the use of ultrasonic measurements. Ultrasonic measurements rely on acoustic waves propagating through a structure, such as an electrode, which are modulated by its properties and encode structure/property relationship data. These relationships are directly tied to the material and mechanical changes which occur in a cell during cycling and can be used to characterize change in a non-destructive, real time manner. Coupling ultrasonic and electrochemical measurements will enable a more complete evaluation of the impacts of XFC to be understood. In particular both electrochemical and acoustic methods are expected to produce distinct and complimentary signals which signal the deposition of Li on the negative electrode of a battery during aggressive charging conditions. Tracking changes with the coupled ultrasonic and electrochemical methods over life and as batteries age will provide information related to the distinct conditions which drive Li plating during XFC.

Objectives

This work is focused on non-destructive, principle-based evaluation methods that can be used to better identify, quantify and advance understanding of performance fade for cells which undergo XFC. Key objectives are detection of the early stages of Li metal plating on graphite negative electrodes, quantifying the cycle-to-cycle evolution of plating and understanding reproducibility of plating. With respect to detection, both electrochemical and acoustic techniques are being evaluated to provide complimentary information on cycling performance and mechanical changes within the cell. Secondary objectives lie in advancing the understanding of how to minimize ion transport limitations in cells using different charging protocols and temperature regimes. Lastly the work is focused at identifying other ways to facilitate fast charge using advanced electrolytes which have transport properties superior to existing electrolytes. At the end of the project a combined set of quantitative, non-destructive methods will be advanced to understand fade from extreme fast charging as will recommended electrolytes that both reduce the likelihood of Li metal plating and other aging factors.

Approach

This effort is a joint collaboration that includes researchers from INL, Argonne, NREL, Princeton/Columbia, the Stanford Linear Accelerator Laboratory (SLAC), and Lawrence Berkeley National Laboratory (LBNL). For analysis at INL, cells and electrode laminate prepared at Argonne were used for all studies with a base chemistry of graphite/NMC 532. Work during fiscal year 2019 cell analysis in both coin and single layer pouch cells used the second round of cell design which included negative electrode loading of 3 mAh/cm². Single layer pouch cells used a base electrolyte of 3:7 ethylene carbonate:ethylmethyl carbonate (EC:EMC) with 1.2 M lithium hexafluorophosphate (LiPF₆) (Gen 2). After receipt from Argonne single layer pouch cells were cycled using commercial battery cyclers or coin cells were prepared with laminate. Cycling focused on fast charging scenarios and different means to modify the transport of ions in the cell in a systematic manner. Different charging regimes which either used fixed or variable rates for the bulk of characterization efforts. All cycling at INL was performed at a constant temperature (25°C). For variable rate studies two different approaches were used. In the two step protocol (MS2) an initially higher current was reduced after the cell reached a maximum voltage of 4.1 V. The other multi-step protocol used five steps and was based on the overvoltage of the cell. In this, MS5, approach when the cell reached a certain overvoltage level the current was automatically reduced. This was repeated for a total of five steps over the course of the charge procedure. All the procedures used a constant voltage component at the end of charge that extended to either a total charge time of 10 or 15 min.

During cycling, periodic reference performance tests (RPTs) were used to gauge the combined thermodynamic and kinetic degradation of the cell performance. The RPTs included slow cycling steps for both charge and discharge to look for distinctive losses from Li plating and to better quantify the full set of losses in the cell over cycling. At the completion of cycling, cells were either disassembled at INL, shipped to Argonne for disassembly or shared with other team members. Key portions of the work in FY-2019 focused on aligning different methods for detection and understanding of Li metal plating. As part of this endeavor several cells cycled at INL were provided to the SLAC team for analysis at different beam line user facilities.

Studies focused on detection and fate of electrochemically deposited Li were also performed in coin cells using a graphite electrode and a Li metal counter electrode. Studies were performed as described elsewhere (Tanim et al 2019) where the graphite was purposefully overlithiated with and without rest. The electrochemical signature from Li metal stripping was then quantified to isolate capacity from graphite, reversible Li plating and irreversible loss of Li.

Electrolyte studies involved both computational and experimental activities to identify possible electrolyte blends which have transport properties above what is typically seen for the Gen 2 electrolyte. Computational screening of electrolytes occurred using the Advanced Electrolyte Model (AEM, Gering 2017) A selection of blends which had properties such as conductivity and Li-ion diffusivity which exceed those of Gen 2 were formulated in an inert atmosphere, Ar-filled glovebox. Conductivity measurements were then compared to the

computed values. Coin cell characterization of blends was also performed to compare the early life cycling efficiency and cell polarization as a function of the new electrolytes.

Activities at Princeton focused on obtaining acoustic signals using commercial ultrasound transducers during cycling of commercial and Argonne prepared cells. Cells were cycled at different temperatures and rates to better understand the acoustic time-of-flight (TOF) response from different conditions and the plating of Li metal. For both the INL and Princeton work, targeted post-test characterization of electrodes using cell disassembly was performed to identify regions of Li plating and to analyze for other degradation modes present due to fast charge.

Results

The ability to detect and understand the role of Li metal that is plated during fast charge was a primary focus during FY-2019. In coin cell studies that utilized a graphite electrode and a Li metal counter electrode it was possible to directly track the extent of overlithiation (OL) of the graphite and the subsequent capacity during delithiation (Tanim et al 2019). As shown in Figure I.5.B.1 as the level of OL increases the irreversible capacity from Li plating increases while the capacity of graphite approaches theoretical levels. The study also clearly indicated that over multiple OL cycles that there is a slight increase in the stripping efficiency and only marginally decreased coulombic efficiency. While quantifying the differences in stripping and coulombic efficiency the study also found that as the length of rest between lithiation and delithiation increases the extent of lithiation due to chemical processes increases and the overall reversible capacity from Li stripping increases.

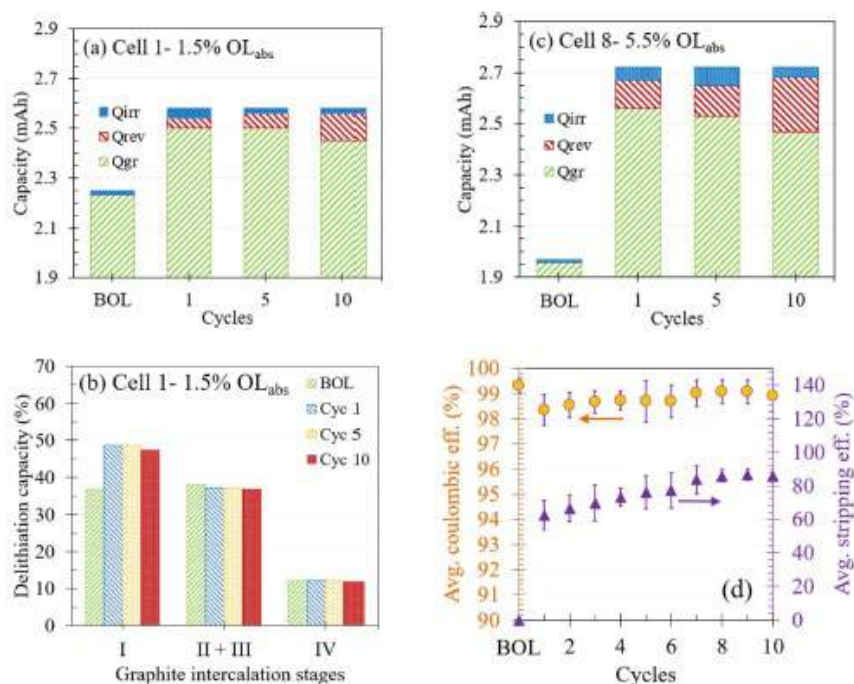


Figure I.5.B.1 Analysis of reversible and irreversible Li plating along with capacity from graphite delithiation as a function of OL extent. (a) 1.5% OL (c) 5.5% OL. (b) Capacity associated with different stages of graphite at the beginning of life (BOL) and after OL. (d) Coulombic and stripping efficiency as multiple OL cycles are used. Figure from Tanim et al, 2019

In additional studies during FY-2019 there was a focus on identifying the full set of fade modes that occurred over the course of cycling. In addition to irreversible plating of Li during fast charge analysis of the single layer pouch cells from Argonne indicate that there was a distinct increase in intergranular separation for the secondary cathode particles as the rate of charge increased. This can be seen in Figure I.5.B.2 where a cross-sectional scanning electron micrograph (SEM) comparison of pristine NMC 532 next to particles that have undergone 450 cycles at either 4C or 6C is shown. The main impact of the intergranular separation is that the

observed fade in cathode capacity increased significantly. For the 4C case loss of active material was only about 4% after 450 cycles, however increasing to 6C doubled the loss to 8%. Increasing above 6C as was done during FY-2018 resulted in even higher loss of positive electrode active material. Presently several studies are underway to better understand and determine initiating events which lead to the intergranular cracking.

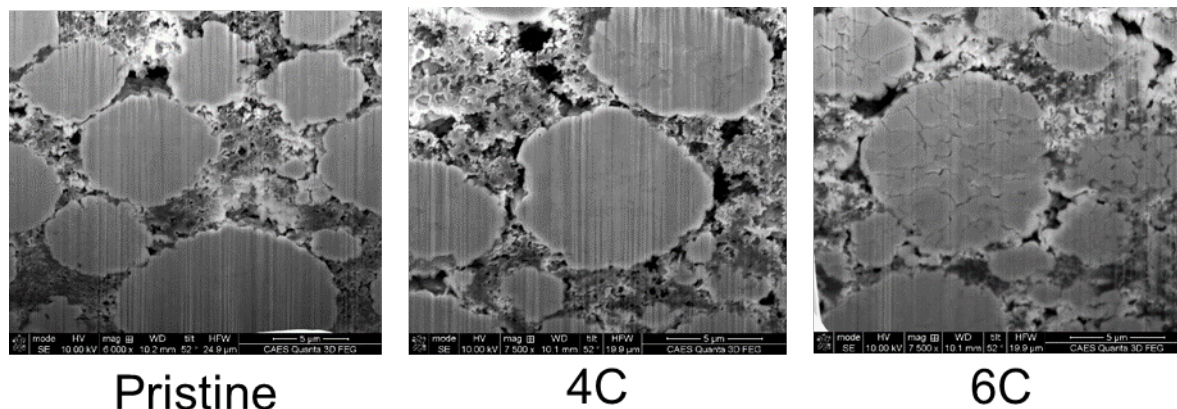


Figure I.5.B.2 Focused-ion beam SEM (FIB-SEM) images of positive electrodes before (left) and after 450 cycles at 4C (middle) and 6C (right). Increasing the rate of charge led to distinct intergranular separation and increased capacity fade due to loss of active positive electrode material

During both FY-2018 and FY-2019 cycling of cells using the Gen 2 electrolyte it readily became apparent that there is a distinct need for electrolytes which have higher conductivity and ion-transport. In an effort to increase the performance above Gen 2 AEM was used to rapidly screen and compare an assortment of different electrolytes. The AEM screening provided a wealth of information on the electrolytes including predicted conductivity, solvation and desolvation energies, transference number and diffusivity. Table I.5.B.1 includes a selection of different electrolyte blends that AEM identified as having better transport properties. To validate model performance experimental conductivity readings were measured for each electrolyte prior to building coin cells. In all, but one of the cases there was very close agreement between the model and experimental data. Subsequent analysis of the solvents used in the blend with divergent data indicated a higher level of impurities which likely caused most of the variation. With electrolyte blends identified that had conductivity values between 1.5 and 3x that of Gen2, initial coin cells studies to look at initial stability and ability to form an effective SEI were performed. The early results from this study are shown in Figure I.5.B.3. Both blend 1 (B1) and blend 6 (B6) had initial performance on par with the Gen2 electrolyte at both C/10 and C/2 rates. They also displayed high coulombic efficiency while having conductivities over 1.5x that of Gen2. Additionally, the polarization of the cells using B1 and B6 were significantly less than cells using Gen2 (data not shown). These results and subsequent studies using additional SEI forming additives are showing promise that high conductivity, stable electrolytes can be developed for fast charge purposes.

Electrolyte interactions within the porous structure of an anode material is an abiding topic that impacts initial electrode wetting, impedance and eventual achievable capacity. To support this topic area INL has developed a modeling approach that predicts surface tension of electrolytes over salt concentration and temperature, as well as the liquid electrolyte ingress rates over wide ranges of pore diameters and lengths. This will serve as a screening and characterization tool for candidate XCEL electrolytes.

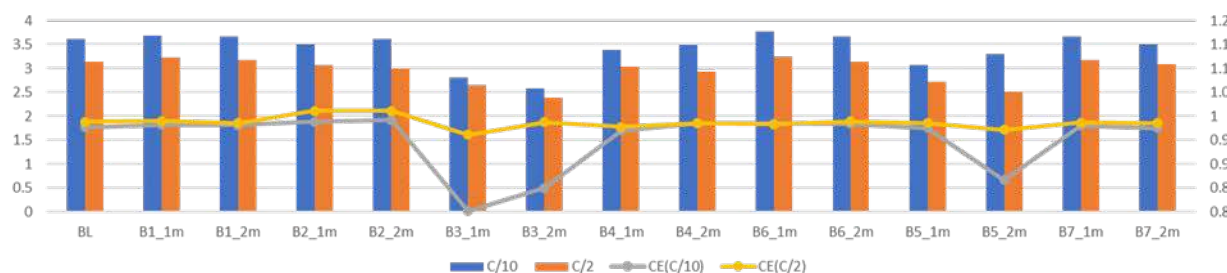


Figure I.5.B.3 Coin cell data for various electrolyte blends identified using AEM. Cells were cycled using Round 2 positive and negative electrode laminates from Argonne. Cell capacity is shown on the left horizontal axis

Table I.5.B.1 Conductivity of Different New Electrolyte Blends to Enable Fast Charge

	Baseline (BL) 1m	Blend 1 (B1) 1m	B1 2m	Blend 3 (B3) 1m	B3 2m	Blend 6 (B6) 1m	B6 2m
AEM Conductivity	8.75	13.50	12.17	25.18	29.52	16.55	16.06
Experimental Conductivity	8.66	13.92	11.49	22.1	21.2	15.84	13.65

Acoustic methods such as ultrasound where an impulse is introduced to a cell and the response is measured to directly identify changes in the condition of a cell provides opportunity to align and correlate signatures from lithium plating *in operando*. During FY-2019 the team led by Daniel Steingart observed a strong correlation and shifts in acoustic time-of-flight (ATOF) as well as acoustic transmittance (AT) with deposition of lithium metal on graphite negative electrodes. These correlations held for single layer high rate test cells designed and fabricated at the Argonne National Laboratory Cell Analysis, Modeling, and Prototyping Facility (CAMP). In separate, activities the utility of using acoustics to detect plating in multilayer, commercial-off-the-shelf cells was also confirmed. Currently both efforts are in the publication process.

During the early stages of the work it was identified that to achieve detection in single layer pouch cells that detection sensitivity was going to be a critical activity. Increased sensitivity was achieved using tight temperature control which minimized drift in signal over the course of an experiment. Different frequency ranges were also utilized to enhance sensitivity. Combined these modifications led to the observance of a shift in the ATOF during the later stages of a fast charging event at rates above 6C, in cells with a loading of 3.0 mAh/cm². Plating of lithium in these cells and at the rates used had previously been confirmed by other XCEL team members including those at INL and Argonne during cell disassembly. No observable shift in ATOF or AT was seen when cycling at lower rates which were below the threshold for lithium plating. Current activities are looking at identifying the detection limits in single and multilayer cells using this acoustic methodology.

Conclusions

Research activities have identified distinct differences in fast charging performance as different charging protocols are used. One of the main areas investigated during FY-2019 the impact of positive electrode capacity fade and associated intergranular separation. Further activities to determine the underlying causes of the intergranular separation are still on-going. Other work found that during rest periods Li metal which has been plated on graphite negative electrodes led to chemical lithiation of graphite. Analysis of the capacity for different processes led to quantification of Li metal stripping efficiency. Electrolyte blends with conductivities of 1.5-3x that of the Gen2 electrolyte have been identified using AEM with experimental confirmation of the predicted transport properties. Coin cell evaluation has found that there are many promising candidate electrolytes that can attain capacity in line with the baseline cells with reduced overpotential. The last area of

investigation centered on the use of ultrasound to detect Li plating during fast charge. Using single layer pouch cells with tight experimental control it was possible to isolate signatures from Li plating.

Key Publications

1. Tanim, Tanvir R, Eric J. Dufek, Charles C. Dickerson, Sean M. Wood. 2019 “Electrochemical Quantification of Lithium Plating: Challenges and Considerations” *Journal of the Electrochemical Society* 166(12):A2689-A2696. <https://doi.org/10.1149/2.1581912jes>.
2. Tanim, Tanvir R, Eric J. Dufek, Michael Evans, Charles Dickerson, Andrew N. Jansen, Bryant J. Polzin, Alison R. Dunlop, et al. 2019. “Extreme Fast Charge Challenges for Lithium-ion Battery: Variability and Positive Electrode Issues” *Journal of the Electrochemical Society* 166(10):A1926-A1938. <https://doi.org/10.1149/2.0731910jes>.

References

1. Ahmed, Shabbir, Ira Bloom, Andrew N. Jansen, Tanvir Tanim, Eric J. Dufek, Ahmad Pesaran, Andrew Burnham, et al. 2017. “Enabling Fast Charging – A Battery Technology Gap Assessment.” *Journal of Power Sources* 367 (Supplement C): 250–62. <https://doi.org/10.1016/j.jpowsour.2017.06.055>.
2. Gering, Kevin 2017. “Prediction of Electrolyte Conductivity; Results from a Generalized Molecular Model Based on Ion Solvation and a Chemical Physics Framework” *Electrochimica Acta* 225: 175-189. <https://doi.org/10.1016/j.electacta.2016.12.083>.
3. Tanim, Tanvir R, Eric J. Dufek, Charles C. Dickerson, Sean M. Wood. 2019 “Electrochemical Quantification of Lithium Plating: Challenges and Considerations” *Journal of the Electrochemical Society* 166(12):A2689-A2696. <https://doi.org/10.1149/2.1581912jes>.
4. Tanim, Tanvir R, Eric J. Dufek, Michael Evans, Charles Dickerson, Andrew N. Jansen, Bryant J. Polzin, Alison R. Dunlop, et al. 2019. “Extreme Fast Charge Challenges for Lithium-ion Battery: Variability and Positive Electrode Issues” *Journal of the Electrochemical Society* 166(10):A1926-A1938. <https://doi.org/10.1149/2.0731910jes>.

Acknowledgements

The work has been supported by Tanvir Tanim, Kevin Gering, Sangwook Kim, Charles Dickerson, Michael Evans, and Ryan Jackman at INL. At Princeton/Columbia efforts were led by Daniel Steingart and Clement Bommier. The INL team would also like to thank Argonne for pouch cells and electrode material and the other team members from Argonne and NREL for discussions.

I.5.C XFC R&D: MSMD Modeling & Thermal Testing (NREL)

Matthew Keyser

National Renewable Energy Laboratory
15013 Denver West Pkwy
Golden, CO 80401
E-mail: matthew.keyser@nrel.gov

Samuel Gillard, DOE Technology Development Manager

U.S. Department of Energy
E-mail: Samuel.Gillard@ee.doe.gov

Start Date: October 1, 2017

End Date: September 30, 2019

Project Funding (FY19): \$800,000

DOE share: \$800,000

Non-DOE share: \$0

Project Introduction

A 2017 DOE technology gap assessment report [1] established goals for next-generation electric vehicle (EV) batteries, namely battery cost of \$80/kWh, energy density of 275 Wh/kg and 550 Wh/L, vehicle range of 300 miles, and charge time of 80% ΔSOC in 15 minutes. Compared to thin electrodes, thick electrodes are preferred due to less inert material, higher energy density and lower cost. Unfortunately, today's thick electrodes cannot tolerate fast charge rates. The thick electrodes have increased distance for ionic transport through the liquid electrolyte. Thin electrode batteries are capable of fast charge, however they come at an almost 2x increase in cell cost (from \$103/kWh to \$196/kWh) and have around 20% less energy density (180Wh/kg vs. 220 Wh/kg) [1]. In addition to polarization and low capacity, electrolyte transport limitations can lead to lithium plating, a side reaction with degradation and safety consequences. It is uncertain what graphite materials can best tolerate fast charge and why. At the system level, fast charging presents thermal management challenges to remove the heat generated during charging.

Objectives

- Achieve 6C (10 minute) charging of low cost, thick electrodes with loadings approaching 4 mAh/cm²
- Identify material-, electrolyte- and electrode-level barriers to reach these goals
- Validate NREL's multi-scale multi-dimensional microstructure and macro-homogeneous electrochemical models versus
 - Electrochemical data from Argonne National Laboratory (ANL) and Idaho National Laboratory (INL) for cells with various materials, loadings and charged under different rates
 - Beamline X-ray diffraction and other advanced diagnostics data from NREL, ANL, SLAC and Lawrence-Berkeley National Laboratory (LBNL) providing *ex situ* and in situ spatial-temporal measurements of intercalated and plated metallic lithium
- Use modeling tools to identify what changes are needed to material, electrode architecture and electrolytes to enable 6C fast charging
- Formulate, screen and test advanced electrolytes capable of meeting 6C charge goals
- Use isothermal calorimetry to measure heat generated at various charge rates
- Provide design feedback to experimentalists.

Approach

Using continuum electrochemical transport/reaction modeling at several different length scales, NREL is exploring how to best design electrodes for fast electrolyte transport and to minimize degradation and lithium plating. Macro-scale models rank the relative benefits of how much charge batteries employing different design/thermal control strategies can accept at the 6C constant current rate. One of the compelling strategies is to introduce secondary pores into the electrode to provide fast channels for through-plane electrolyte transport. A 2D meso-scale model explores this design space. Microstructure models explore the role of different microstructures in suppressing the Li plating side reactions by reducing tortuosity and heterogeneities. Data analysis is being performed on previous diagnostic experiments that measured graphite electrode state-of-charge heterogeneity *in operando* at the 6C rate, as well as microscopy that resolved the polycrystalline architecture of nickel-manganese-cobalt (NMC) particles responsible for fracture under high C-rates. Using molecular-dynamics models, we identified several candidate solvent molecules to provide requisite solubility while retaining good transport properties (viscosity, dielectric constant). We further tested several of these solvent recipes in graphite/NMC cells and showed improved 5C fast charge acceptance compared to the standard Gen II electrolyte.

This report summarizes NREL FY19 work in seven areas:

1. Benefits analysis using macro-homogeneous electrochemical model
2. Electrode architecture optimization including secondary pore network (SPN)
3. In situ XRD measurement of graphite electrode heterogeneities and Li plating
4. Fast charge algorithms
5. Electrolyte development and characterization
6. Calorimetry
7. Li plating quantitative image analysis.

Results

1. Benefits analysis using macro-homogeneous model

NREL continues to refine its macro-homogeneous electrochemical model as validation data is collected by the XCEL team, use the model to elucidate technical approaches to achieve XFC goals and publish results [1],[2]. Cells with a low loading of 1.5 mAh.cm⁻² withstand XFC performance remarkably well even up to 9C constant current (CC) charging with high charge acceptance and very little lithium plating. For a moderate loading of 2.5 mAh.cm⁻², the 6C CC charge capacity is poor with significant amounts of lithium plating. Insufficient electrolyte transport properties are a major limitation for XFC performance of moderate and high loading cells. Charging at elevated temperature is an effective strategy for moderate loading cells enabling good 10-minute charge acceptance and mitigating lithium plating. Shown in Figure I.5.C.1, the electrochemical model is used to investigate strategies for enabling 4-6C CC charging for cells with loadings of 3 to 4 mAh.cm⁻². For a loading of 3 mAh.cm⁻², operating at 45°C with electrodes having reduced tortuosity enables an energy density of 186 and 104 Wh/kg during 4 and 6C CC charging without plating. Similar results can be realized for 4 mAh.cm⁻² and non-conventional electrodes, but the operating temperature must be raised to 60°C. Next generation electrolytes with 1.8-2.3X ionic conductivity, 3-4X diffusivity, and increased transference number of 0.05-0.15 are predicted to enable good XFC performance for high loading cells. A combination of elevated temperature, reduced tortuosity, and electrolytes with improved transport are needed to enable XFC for high energy density cells.

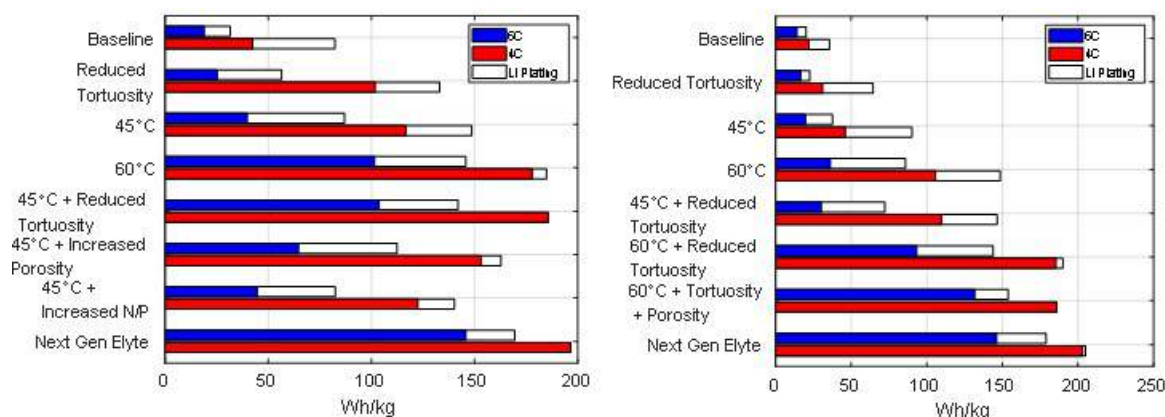


Figure I.5.C.1 Model predictions for achievable energy density during 4C and 6C constant current charging to 4.2V for cells with a loading of 3 mAh.cm⁻² (left) and 4 mAh.cm⁻² (right). The white section of bars represents where model predicts lithium plating will occur.

To better understand the onset of plating, the addition of multi-phase graphite transport and kinetics to the macro model is underway. Initial comparisons have been made to beamline X-ray diffraction (XRD) data that resolve total lithium and phase specific (LiC₆, LiC₁₂, etc.) concentrations across a 100- μ m thick electrode during operando 6C charging. Initial comparisons are reasonable, however secondary effects are present and the team is working to further understand them and decouple resultant signals in the data. For instance, lithium plated during the first 6C charge event appears to block (de)intercalation on subsequent discharge and charge events of the electrode.

Separately, NREL has added a Li plating reaction to its model and is working with Lawrence Berkeley National Laboratory (LBNL) to compare predictions of plated Li to their Round 1 half-cell experiments. In those experiments, LBNL followed electrochemical cycling with destructive tests in which de-lithiated graphite electrodes are injected with water in an air-free environment and the amount of hydrogen gas evolved is measured via mass spec and correlated with dead metallic lithium. The lithium plating is first modeled as an irreversible reaction. Thus, no lithium stripping is (initially) considered. Figure I.5.C.2 shows a comparison between titration results after 3 cycles (blue dots) and model predictions with different exchange current densities for lithium plating. The relatively thin 47-micron graphite electrodes plate lithium because cycling consists of lithiation to graphite's full theoretical capacity of 372 mAh/g, graphite is lithiated ~20% more than in standard full cell cycling. As expected, the amount of plated lithium exponentially increases with charge rate. An exchange current density for irreversible lithium plating around 0.2 A/m² best fits the measured data. At 4C, the 2500 nmoles of lithium measured corresponds to 3% of the total graphite capacity. As part of the newly formed heterogeneity workgroup, NREL is working with ORNL to develop a more detailed lithium plating/stripping model considering:

- Lithium stripping
- Electrical isolation
- SEI effects/lithium reacting with electrolyte
- Ion transport effects
- Local condition effects on reversibility.

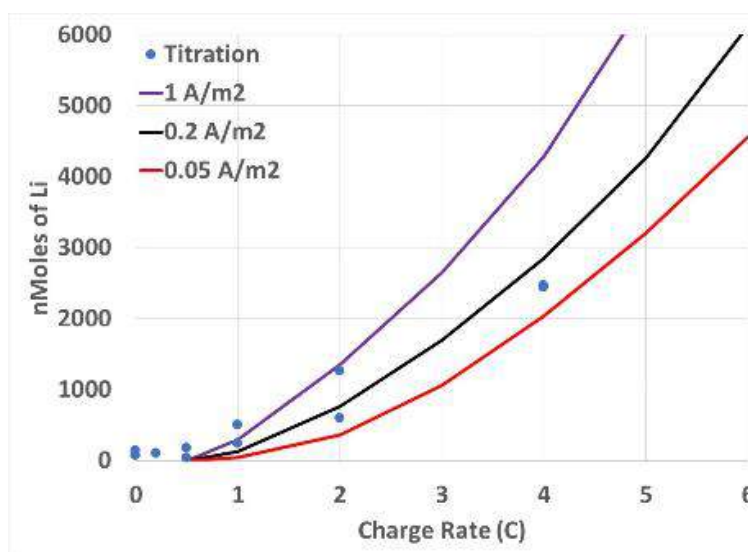


Figure I.5.C.2 Comparison of gas-titration results from LBNL and macro-homogeneous model predictions for lithium plated during 3 cycles vs. charge rate. Half-cells were fully lithiated to graphite's theoretical capacity of 372 mAh/g-graphite and then discharged to an upper voltage of 1.5V vs Li.

2. Electrode architecture optimization

NREL applied 3D microstructure and 2D meso-scale models as well as a new 3D-microstructure virtual generation algorithm to propose design guidelines for active material particle size, morphology and composite electrode tortuosity, as well as advanced strategies/architectures that can help batteries achieve 10-minute charge. Results have been submitted for publication [3],[4].

- Shown in Figure I.5.C.3b, the model predicts a linear correlation between specific surface area and lithium plating, with higher surface area delaying lithium plating due to lower local C-rate. Since higher surface area also reduces calendar life due to faster solid/electrolyte interface layer growth, it makes sense to utilize higher surface area material mainly at the front of the electrode.
- The model indicates bimodal size distribution is slightly detrimental, causing lithium plating to occur 2.5% anode-SOC earlier, not due to tortuosity difference but to higher lithiation heterogeneities (Figure I.5.C.3a). Interestingly, depending on the electrode particles, bimodal size distribution can have either a positive (NMC case) or a negative (SLC1506T round 1 case) impact on tortuosity factor.
- For ellipsoid or platelet-like particles, alignment can delay lithium plating compared with spherical particles (4% anode SOC later), if correctly aligned, i.e., with their long diameter parallel with electrode thickness (Figure I.5.C.3b). Contrarily, particle misalignment triggers earlier lithium plating and should be avoided. Tortuosity factor – correlated with particle alignment and aspect ratio – explains this difference of lithium plating. Macroscopic isotropy coupled with local anisotropy (randomly oriented particles) also triggers earlier plating.

Regarding electrode architectures, design guidelines for advanced architectures tailored for fast charging have been provided for two distinct designs: (1) a dual-coated architecture and (2) a secondary/dual pore network (SPN) architecture, relying on a newly developed analytical MATLAB model [9] complemented with a 2D electrochemical model.

- The model predicts dual coated architecture with higher porosity (i.e., lower tortuosity factor) and smaller particles (i.e., higher specific surface area and thus lower local C-rate) for the layer near the

separator delays lithium plating by 7% anode-SOC compared with the non-graded reference electrode (Figure I.5.C.4a). Adequately tuned, graded electrodes also reduce electrolyte gradient and homogenize intercalation reaction along the electrode thickness.

- An analytical transport model indicates electrodes with higher initial tortuosity benefit more from SPN (Figure I.5.C.4b,c), and that a combination of high through-plane tortuosity and low in-plane tortuosity is a good fit for SPN. The latter case corresponds to some battery electrodes, such as A12 graphite. Being extremely fast (20 million case in 10s with a laptop), the analytical model is useful for large design space.

The analytical SPN model [9] will be released open source in FY20 together with publication of a two-part journal article [3],[4] from NREL on optimal SPN architecture for fast charge. A first article documenting the microstructure scale electrochemical NREL model has been submitted [7] as well.

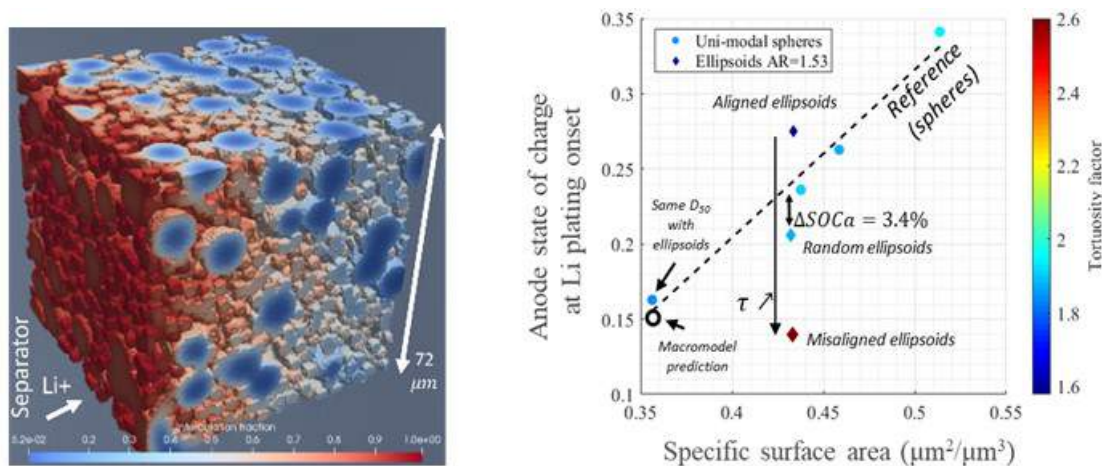


Figure I.5.C.3 (Left) Lithiation heterogeneity induced by particle size distribution: large particle lithiation is lagging due to solid-state diffusion limitation. (Right) Anode state of charge associated with lithium plating onset calculated for different particle alignment and compared with spherical reference case.

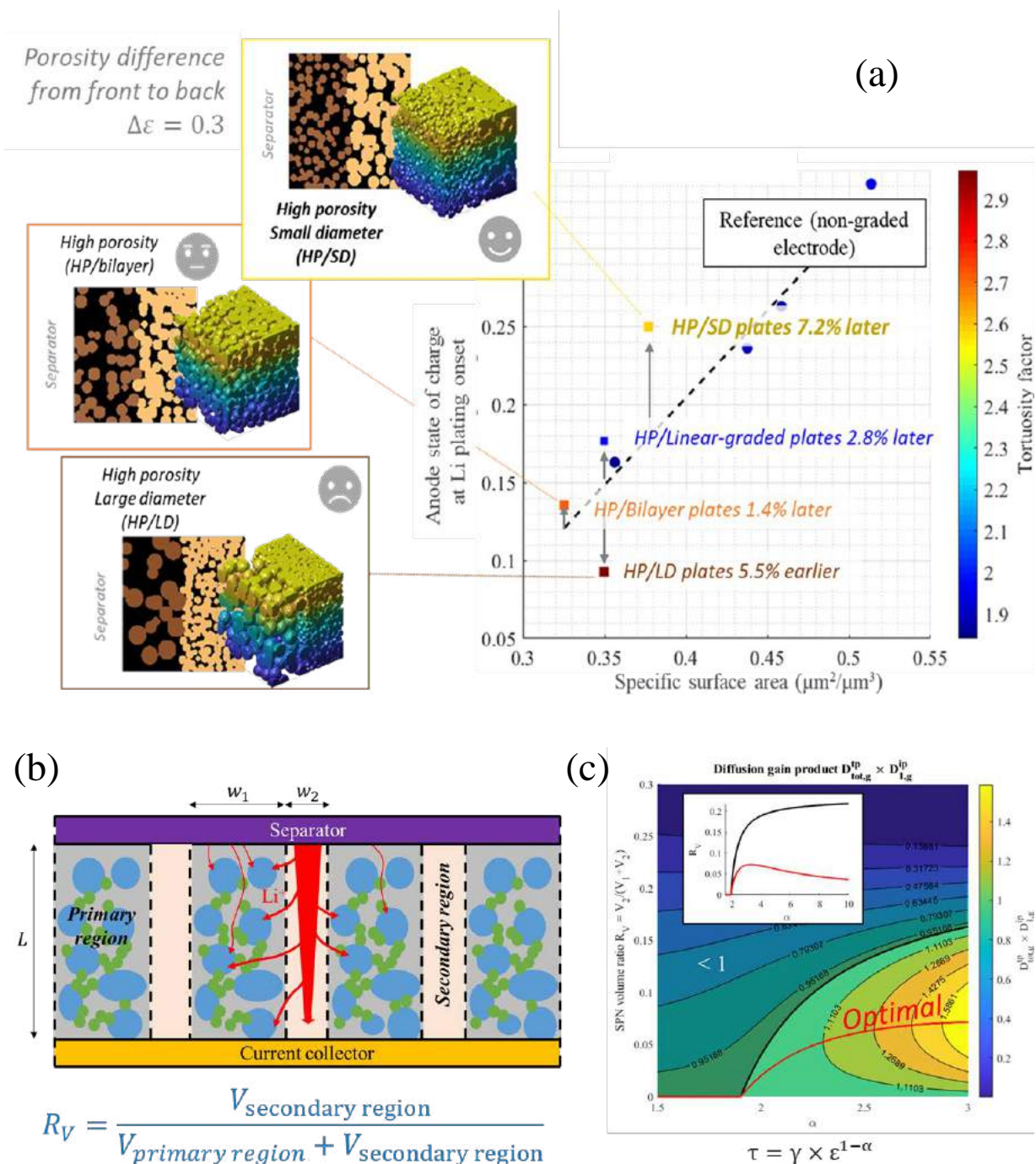


Figure I.5.C.4 (a) Anode state of charge associated with lithium plating onset calculated for different dual coating architectures and compared with non-graded reference case, (b) schematic of a secondary pore network, (c) higher overall diffusion gain is achieved for higher tortuosity coefficient α

3. *In situ* measurement of graphite electrode heterogeneities

Understanding the limitations of coated graphite electrodes during fast charging requires a spatial and temporal measurement of lithiation and Li plating. Utilizing the state-of-the-art capabilities of The European Synchrotron (ESRF), a high-resolution picture of lithiation gradients and Li plating within a graphite electrode was constructed via high-speed X-ray diffraction (XRD) measurements (Figure I.5.C.5). The measurements provided a live view of how a graphite electrode lithiates throughout its depth, from separator to current collector, and revealed conditions that lead to the onset of Li plating. New insights into the function of graphite electrodes under fast charge conditions were revealed. For example, the onset of Li plating was quantified in real time and shown to only occur over the first 20 μm of depth into the electrode. Li plating was also shown to increase and then decrease when lower charge currents during the constant voltage step were reached, indicating that some Li plating is reversible. Furthermore, regions where Li plating was detected did not fully delithiate upon discharge (Figure I.5.C.6) and the residual lithiated graphite existed as LiC_6 , which presents the first time that co-existence of delithiated graphite and fully lithiated LiC_6 was observed. This raises questions about how the behavior of graphite changes when Li plates on its surface and how this might affect the propensity of that graphite to further plate and affect the safety and performance of the cell, questions that are guiding NREL's modelling pursuits.

4. Charge algorithm development

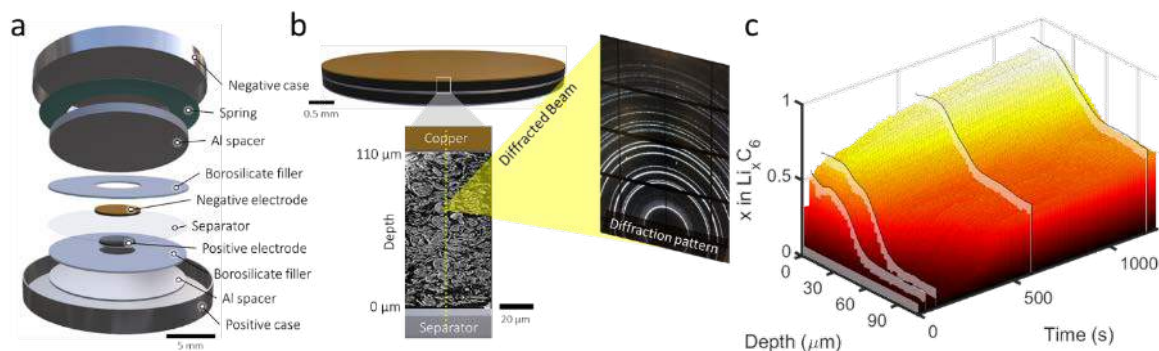


Figure I.5.C.5 (a) Illustration showing the design of cell for operando high-speed X-ray diffraction (XRD). (b) Illustration showing a magnified view of the cell, and a further magnified view of the graphite electrode with yellow points throughout the depth indicating the locations of each XRD measurement. (c) An example of a quantified profile of state of charge as a function of depth and time.

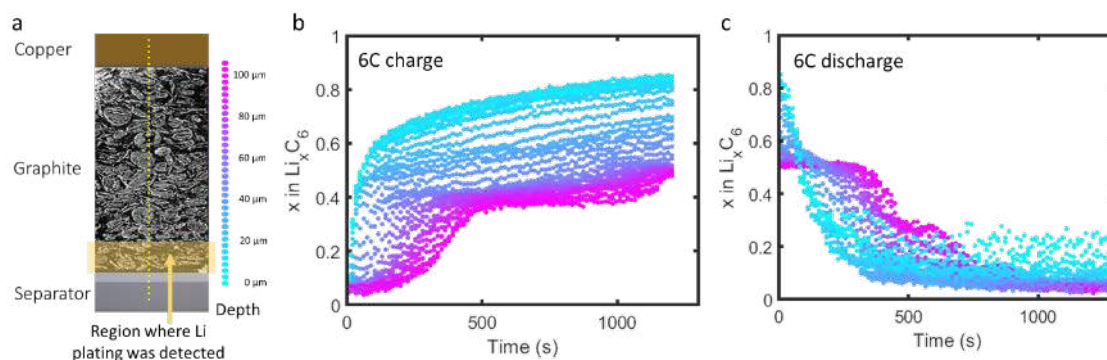


Figure I.5.C.6 (a) Illustration showing the depth of the electrode with yellow points highlighting XRD measurements. The highlighted yellow region indicates where Li plating was present and depth-dependent colors (pink to blue) are for reference in the neighboring plots. (b) State of lithiation over time for each color-coded depth (blue near the separator and pink near the current collector) during 6C charge and (c) 6C discharge, where residual lithiated states are observed near the separator upon full discharge.

The fast charging of lithium ion batteries (LIBs) is limited by degradation and safety concerns due to possible lithium plating. While the development of new active materials and electrolyte with improved properties is the key to tackle this problem, charging protocols may also increase fast charging capability of LIBs. Using the existing Pseudo2D battery model, NREL has screened hundreds of different charging protocols by simulating variations of protocols that are being experimentally investigated at INL. Metrics taken from simulations include charge capacity, minimum phis-phie potential (indicator for onset of lithium plating), average cell temperature and maximum cell temperature in 10 minutes, which corresponds to 6C charging. Figure I.5.C.7 shows the minimum phis-phie as a function of charge capacity for different charging protocols, with the colormap representing the average cell temperature. The simulation results show that there is a strong correlation between charge capacity, minimum phis-phie and average cell temperature. Higher charge capacity inevitably leads to smaller phis-phie, indicating a higher driving force for lithium plating. In Figure I.5.C.7, none of the investigated conventional charging protocols is significantly superior to the others. Other novel charging protocols are being investigated, aiming at achieving high charge capacity in 10 minutes without triggering lithium plating.

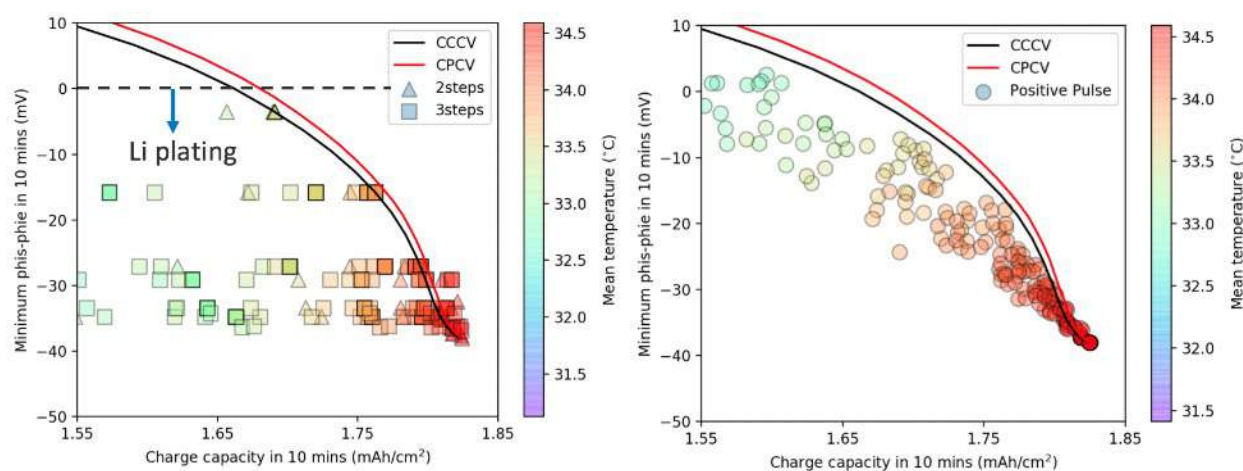


Figure I.5.C.7 Effect of charging protocol on charge capacity and minimum (phis-phie) in 10 mins. (left) 2 steps and 3 steps constant current charging. (right) positive pulse current charging.

5. Electrolyte screening for extreme fast charge

As illustrated by the macro-homogeneous model, today's liquid electrolyte transport properties are insufficient to support 6C fast charge of energy-dense high-loading electrodes, $>>3 \text{ mAh/cm}^2$. Next generation electrolytes with 1.8-2.3X ionic conductivity, 3-4X diffusivity, and increased transference number of 0.05-0.15 are needed. Using molecular-dynamics models and machine learning, we identified several candidate solvent molecules to provide requisite solubility while retaining good transport properties (viscosity, dielectric constant). The work this quarter comprised of experimental evaluation of these solvent recipes. For the first round of screening, we used ethylene carbonate, ethyl formate, methyl difluoro acetate and propionitrile in the ratio 10:25:25:40 with 3% vinylene carbonate and another with ethylene carbonate, dimethyl carbonate, methyl difluoroacetate and trimethyl phosphate in the ratio 15:45:20:20. The salt concentration was maintained at 1.2M LiPF_6 . These candidates were selected as baseline to compare against previous reports. The formate- and acetate-based recipes showed some adhesion issues, in particular of the anode active material on to the copper current collector. This is likely due to the binders used in the electrode formulation (CMC). Following these results, we screened a second batch, including some non-flat cyclic compounds as co-solvents (30% by weight) to Gen2. The electrochemical stability is comparable to Gen 2 electrolyte (Figure I.5.C.8) and the discharge capacities after a 5C charge are reasonable (Figure I.5.C.9).

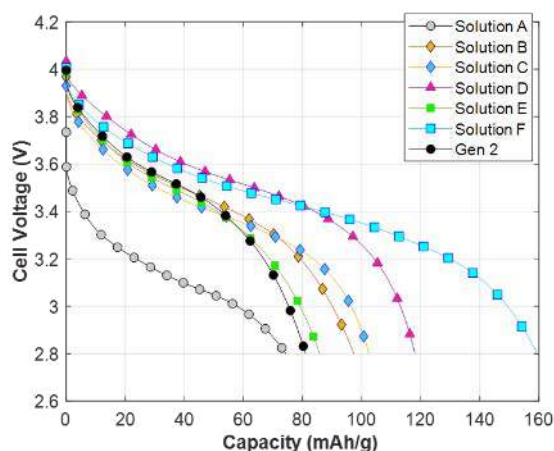


Figure I.5.C.8 Full cell discharge capacity measured at C/3 using NMC-622 and graphite electrodes from Targray following a 5C charge to 4.2 V

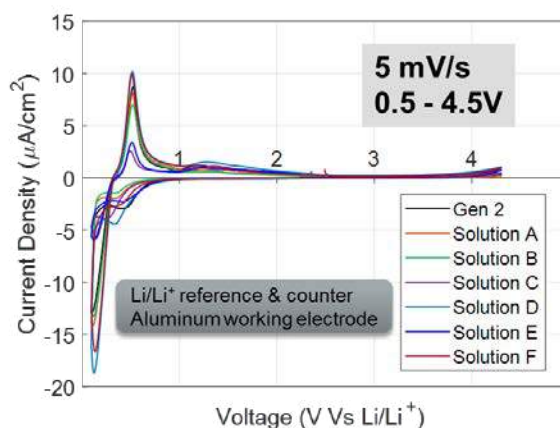


Figure I.5.C.9 Cyclic voltammetry verifies electrochemical stability of Round-2 solvents against Li/Li+.

6. Calorimetry

ANL's CAMP facility supplied NREL with multi-layer 400 mAh cells with the cathode consisting of Toda NMC 532 (90%), Timcal C-45 carbon black (5%), and Solvay 5130 PVDF binder (5%). The anode consisted of Hitachi MagE3 (91.83%), Timcal C-45 carbon black (5%), Kureha 9300 PVDF binder (6%), and with the remaining mass being oxalic acid. The cathode and anode single sided thicknesses were 58 μm and 60 μm , respectively. The estimated capacity for the cathode was between 2.11 and 2.27 mAh/cm² whereas the anode capacity was estimated to be between 2.68 and 2.73 mAh/cm².

The cells were cycled under INL-engineered fast charge profiles. INL developed algorithms that incorporated step changes and rests in order to maximize the lifetime of the cells. The constant-current constant-voltage (CCCV) charge protocols involved initial charging at 6.8C or 9C until V_{max} was reached then switched to CV charging at V_{max} until the total time reached 10 min. The two-step (multi-step 1, or MS1) constant current involved charging at either 6.8C or 9C until V_{max} was reached. Once V_{max} was reached, the cell as charged at a lower constant-current rate until total charging time reached 10 min. The lower rate is the theoretical rate required to fully charge the battery within the time left after hitting V_{max} . For the 6.8C initial rate the lower rate equated to 3.25C, and 3.5C equated to the second rate for the 9C condition. If V_{max} was reached during the lower rate of charging (prior to 10 min), a CV mode was used until the full 10 min charging time was reached. The pulse charging protocol (MS2) recharged 20% of the beginning of life C/1 capacity followed by a 17.65 s rest while charging at either 6.8C or 9C. The CV charging step was triggered when V_{max} was reached. Total charging time was maintained at 10 min. Finally, the MS5 charging protocol aims to increase the fraction of CC charging by gradually reducing the step-charging rate as the charging progressed. Such a gradual reduction in charging rate reduces the cell transport overpotential (due to concentration buildup) with the progression of charging.

As per NREL's testing, we are focused on the heat generation and efficiency of the cell under each of these fast charge regimes. Figure I.5.C.10 shows the current profiles for the six charge algorithms used in our calorimetry tests whereas Table I.5.C.1 shows the efficiency and heat generation rates for each of the profiles. The efficiencies were tightly clustered and ranged from a low of 89.01% to a high of 91.97%. The efficiencies correlated to the amount of charge capacity returned to the cell during the 10-minute-limited, charge. As expected, the higher charge capacities resulted in lower efficiencies.

NREL also tested constant-current charging at rates from 4C to 9C. The efficiency and heat generation data are shown in Figure I.5.C.11 for both constant-current charge and discharge. The efficiency at a 9C charge rate was approximately 89.3% but only returned about 10% of the cell capacity before voltage limiting at 4.1 Volts.

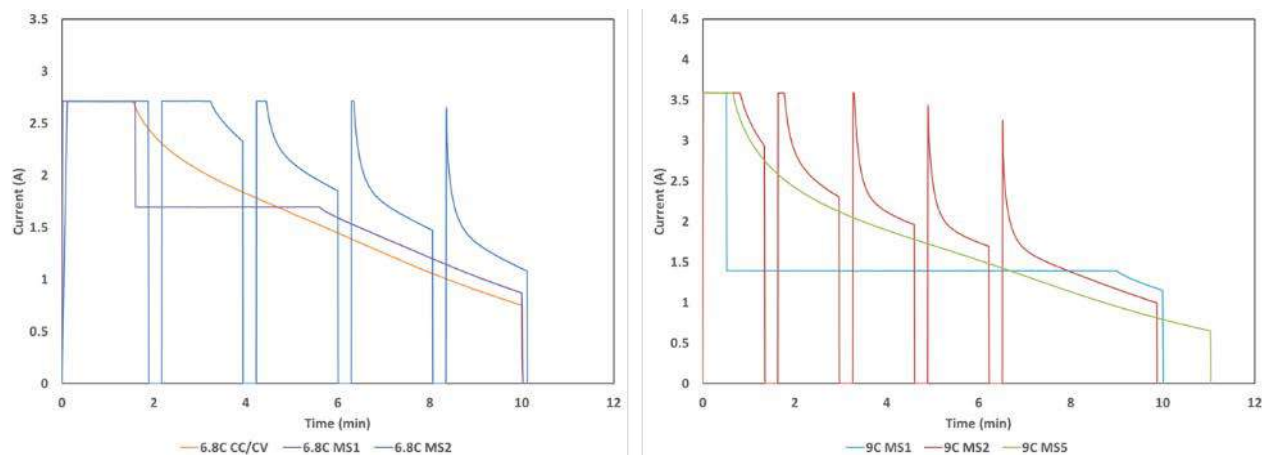


Figure I.5.C.10 Fast charge algorithms used to assess heat generation and efficiency.

For a 4C charge rate, the efficiency was approximately 92.7% with a little more than half of the capacity returned before hitting the maximum voltage limit.

Table I.5.C.1 Heat Efficiency and Heat Rate for Fast Charge Algorithms

Charge Algorithm	RMS Current (Amps)	Heat Efficiency (%)	Heat Rate (Watts)	Charge Capacity (mAh)
6.8C CC/CV	1.81	89.30	0.74	284
6.8C MS1	1.74	89.56	0.70	277
6.8C MS2	2.07	89.40	0.80	316
9C MS1	1.57	91.97	0.47	249
9C MS2	2.16	89.01	0.85	314
9C MS5	1.91	89.06	0.77	380

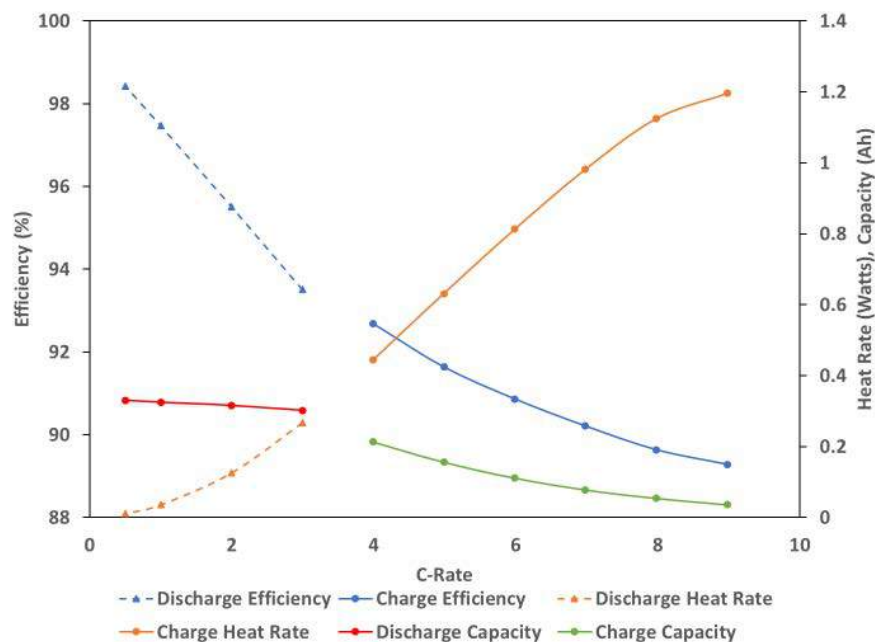


Figure I.5.C.11 Efficiency, heat rate, and capacity under various constant-current discharge and charge rates.

7. Lithium plating quantitative image analysis

Understanding the correlation between the onset and severity of lithium plating with local microstructure defects or heterogeneities requires experimental imaging at the microstructure scale. SLAC researchers imaged an 80-micrometer thick graphite electrode at the 2-BM (microCT) beamline at the Advanced Photon Source (APS) at Argonne National Laboratory, after 450 cycles performed at 9C (3-4.1V) on a round 2 full cell. Unfortunately, image quality prevented simple segmentation of the three phases (pore, graphite, lithium plating). NREL used its expertise in microstructure analysis to perform the segmentation using a combination of thresholding-based and machine learning-based methods and thereafter characterized image (Figure I.5.C.12a,b). Far from the edges, the expected graphite porosity (35%) is calculated, supporting the segmentation result. Analysis reveals plating to be heterogeneous with a wide plating layer thickness distribution (Figure I.5.C.12c). No correlations between plating heterogeneity and microstructure heterogeneity were found, as local porosity (either considering the full electrode thickness or only the region near the separator) didn't appear to control the amount of local plating (Figure I.5.C.12d). Modeling results predict that microstructure heterogeneities accelerate lithium plating onset by 2-5% state of charge [8]. This experimental result suggests that *after* a significant amount of plating, 450 cycles at 9C, any correlation between microstructure parameters and plating is lost, and that the localized plating pattern changes as more lithium is deposited at the electrode surface. Imaging performed after only few cycles should be able to correlate plating onset with microstructure heterogeneity to validate models and thereafter enabling tailoring microstructure through modeling to delay such onset.

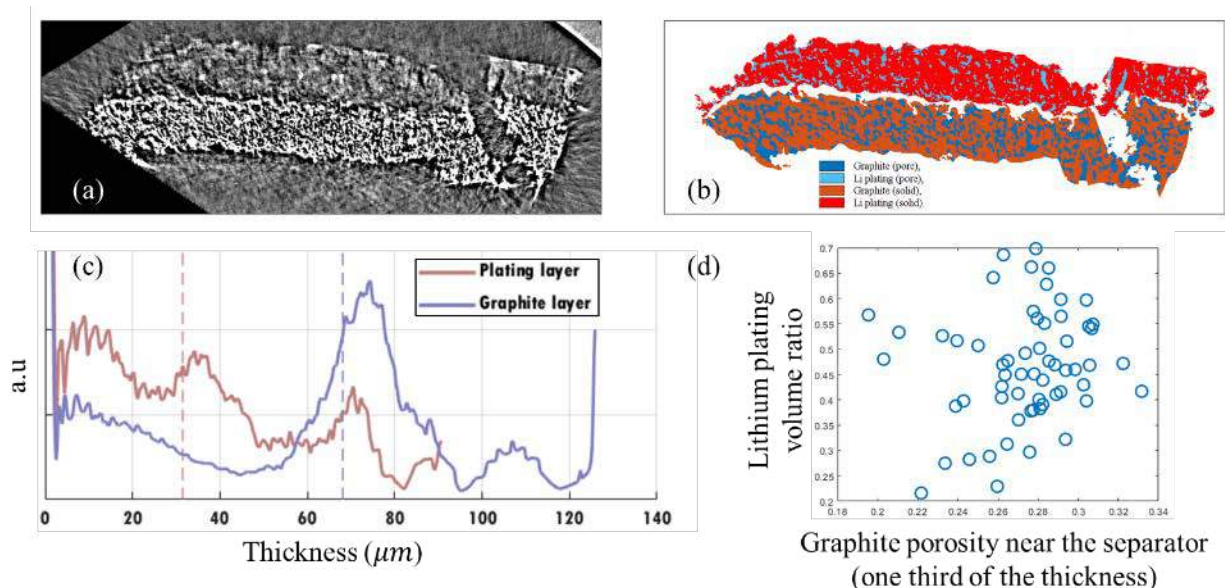


Figure I.5.C.12 (a) Grey-level image after contrast correction, vertical direction is along electrode thickness, with lithium plating on top, and graphite layer at the bottom. (b) After segmentation. (c) Probability density function of lithium plating and graphite layer thickness. (d) Tentative correlation between volume ratio of lithium plating and graphite porosity near the separator.

Conclusions

Electrochemical models at a range of length scales support deeper understanding and interpretation of experiments and guide prototype electrode designs for the XCEL team. At the electrode length scale, macro-homogeneous models quantify benefits of reducing tortuosity, adding secondary pore networks, improving charge protocols, charging at elevated temperature, and set targets for next generation electrolytes needed to enable 6C charging of energy-dense cells. The macro-homogeneous model was recently updated with multi-phase graphite transport/kinetic behavior and a Li-plating side reaction and initial comparisons made to diagnostic data from the XCEL team.

A 3D microstructure model explored how graphite electrode particle size, morphology, graded and dual-coated electrodes either suppress or accelerate the onset of the undesired Li plating side reaction. Compelling designs for suppressing Li plating include (i) single-coated electrodes with uniform particle size and particles aligned in the in-plane direction and (ii) dual-coated electrodes with higher-porosity and smaller particles near the separator. NREL is working with ANL to determine how to fabricate such electrodes. Working with SLAC, NREL applied its microstructure characterization toolbox to segment and generate quantitative statistics of lithium plating on a cycled graphite electrode. After 450 cycles and significant Li plating, no correlation was found with microstructure heterogeneity. Result suggests correlation is lost after significant plating. Follow-on diagnostic experiments are being run following fewer cycles with Li plating.

For XFC electrolyte development, NREL screened a second batch of novel co-solvents to standard Gen2 electrolyte. These novel formulations showed reasonable stability and, in some cases, significantly enhanced high-rate charge capability of graphite/NMC 622 cells.

Novel operando, in situ XRD results were presented for 100-micron thick graphite electrodes during XFC. Measurements were performed as a function of depth within the electrode with ~ 2 -micron resolution. As expected, the electrode is used preferentially near the separator interface and lithium plates near this region. XRD results are being compared with model predictions and will be written into an upcoming journal article.

NREL isothermal calorimeters measured the heat rate and efficiency of a 400 mAh cell provided by CAMP under various INL charge algorithms. The average efficiency of the cell under these conditions was approximately 90%; however, the cell tested did not meet the DOE specific energy goal. As we increase the energy density of the cells, the efficiency will decrease unless the current and ionic pathways are optimized.

Key Publications

1. A.M. Colclasure, A.R. Dunlop, S.E. Trask, B.J. Polzin, A.N. Jansen, K. Smith, “Requirements for Enabling Extreme Fast Charging of High Energy Density Li-Ion Cells while Avoiding Lithium Plating,” *J. Electrochem. Soc.* 166 (8) A1412-A1424 (2019).
2. A.C. Colclasure, T.R. Tanim, A.N. Jansen, S.E. Trask, A.R. Dunlop, B.J. Polzin, I. Bloom, D. Robertson, L. Flores, M. Evans, E.J. Dufek, K. Smith, “Electrode scale and electrolyte effects on extreme fast charging of lithium-ion cells,” *submitted*.
3. Francois Usseglio-Viretta, Weijie Mai, Andrew Colclasure, Kandler Smith, “Enabling fast charging of lithium ion battery through Secondary/dual pore network: Part I - analytical model,” *in preparation*
4. Weijie Mai, Francois Usseglio-Viretta, Andrew Colclasure, Kandler Smith, “Enabling fast charging of lithium ion battery through Secondary/dual pore network: Part II - numerical model,” *in preparation*
5. Donal Finegan, Alex Quinn, David Wragg, Andrew Colclasure, Xuekun Lu, Chun Tan, Thomas M.M. Heenan, Marco Di Michiel, Rhodri Jervis, Paul R. Shearing, Kandler Smith, “Quantifying heterogeneities in state of charge and Li plating during fast charging,” *in preparation*
6. Alex Quinn, Helio Moutinho, Ankit Verma, Francois Usseglio-Viretta, Kandler Smith, Donal P. Finegan, “The application of electron back scatter diffraction for quantifying grain orientations and transport pathways in Li-ion electrodes,” *in preparation*
7. Jeffery Allen, Justin Chang, Francois L. E. Usseglio-Viretta, Peter Graf, Kandler Smith, “Accelerating a Segregated Approach for Li-Ion Battery Modeling using Block Preconditioners,” *submitted*
8. Aashutosh Mistry, Francois L. E. Usseglio-Viretta, Andrew Colclasure, Kandler Smith and Partha P. Mukherjee, “Fingerprinting Distributed Activity of Inhomogeneous Electrodes during Extreme Fast Charging,” *submitted*
9. Software Record SWR-20-08 “Secondary pore network design optimization analytical diffusion model for lithium ion battery,” *to be released open source with upcoming journal article*.

Acknowledgements

This section was co-authored BY Andrew Colclasure, Kandler Smith, Francois Usseglio-Viretta, Weijie Mai, Shriram Santhanagopalan, Donal Finegan, Ryan Brow, AND Jeffrey Allen. We wish to acknowledge Samuel Gillard and DOE for sponsoring these efforts as well as the XCEL team from ANL, INL, LBNL and SLAC who contributed substantial test prototypes and data to this project. For beamline studies, we would like to thank The European Synchrotron (ESRF) (Marco DiMichiel), Univ. College London (Shearing group) and Oslo University (David Wragg). For tortuosity studies, we further wish to acknowledge CAEBAT collaborators (see separate section of this report) from Purdue University (Mukherjee group), ANL (Abraham group), Univ. College London (Shearing group), Brigham Young University (Wheeler group) and Imperial College of London (Cooper).

I.5.D Research on high power, doped titanium-niobium oxide anodes (ORNL)

Sheng Dai, Principal Investigator

University of Tennessee
354/502 Buehler Hall
1416 Circle Drive
Knoxville, TN 37996-1600
E-mail: sdai@utk.edu

Brian Cunningham, DOE Technology Development Manager

U.S. Department of Energy
E-mail: Brian.Cunningham@ee.doe.gov

Start Date: July 1, 2018

End Date: June 30, 2020

Project Funding: \$800,000

DOE share: \$720,000

Non-DOE share: \$80,000

Project Introduction

Commercial lithium ion batteries (LIBs) using graphite as an anode material can easily result in lithium plating during extreme fast charging or abuse conditions, leading to fast capacity fading and safety issues. To eliminate the lithium plating issue in LIBs during extremely fast charging, we proposed to use doped titanium niobium oxide (TNO) as the anode, which has not only an operation voltage of 1.66 V vs. Li/Li⁺ that is far from the lithium plating but also a high theoretical capacity of 387 mAh g⁻¹.

Objectives

The main objective of this project is to synthesize titanium niobium oxide (TNO) that has a nanoporous structure with porous channels for rapid lithium diffusion, enabling extreme fast charging (XFC). The focus of this project is to improve the electronic conductivity and ion diffusion coefficient in TNO to achieve high capacities under extreme fast charge conditions. In addition, electrolytes with additives will be formulated to promote stable interphase formation on the NMC cathode surface to improve long cycling stability.

Approach

- Enhance rate capability by formation of nanostructures.
- Improve electronic conductivity by doping and surface coating with carbon.
- Synthesize large scale TNO with low cost precursors.
- Evaluate rate performance and long term cyclability of coin cells with high loading TNO.
- Improve long term cyclability of coin full cells using functional additives.
- Evaluate rate performance and long term cyclability of pouch full cells.

Results

The focus of this project is to improve the electronic conductivity and ion diffusion coefficient of TNO to enable its high rate performance, thus we have used low-cost glucose as the carbon source to synthesize carbon coated porous TNO material (TNO@C) with 1 wt.%, 2 wt.%, and 3 wt.% carbon, respectively. As shown in Figure I.5.D.1, half cells based on TNO@C with 1 wt.% carbon coating delivers the best rate performance among the four tested samples (including the uncoated sample) under the same electrode loading of 2.3 mg cm⁻². It exhibits reversible capacities of 240 and 211 mAh g⁻¹ at 5C and 10C, respectively, which is about 50 mAh g⁻¹ higher than that of the pristine TNO. In addition, TNO@C with 1 wt.% surface carbon coating achieves a high initial coulombic efficiency of 98%, much higher than that of the pristine TNO sample (92%).

To deliver the targeted cell energy of 180 Wh kg^{-1} , active materials loading for NMC622 cathodes and TNO anodes were calculated to be 18 and 13.5 mg/cm^2 , respectively. Figure I.5.D.2 shows the high rate performance and coulombic efficiencies of the NMC622 and TNO@C half-cells. For the NMC622 half-cell, the charge rates (Li extraction) changed while the discharge (Li insertion) rate was fixed at C/3, whereas for the TNO@C half-cell, the discharge (Li insertion) rates changed while the charge (Li extraction) rates was fixed at C/3 (1C=150 mA/g for NMC622 and 200 mA/g for TNO@C). The NMC622 half-cell and the TNO@C half-cell deliver matched capacities at lower current rates of C/5 and 4C (Figure I.5.D.2), however, the TNO@C half-cell delivers much higher capacity than the NMC half-cell at higher current rates of 5C and 6C. This result indicates that the NMC cathode is limiting at this high loading of active materials.

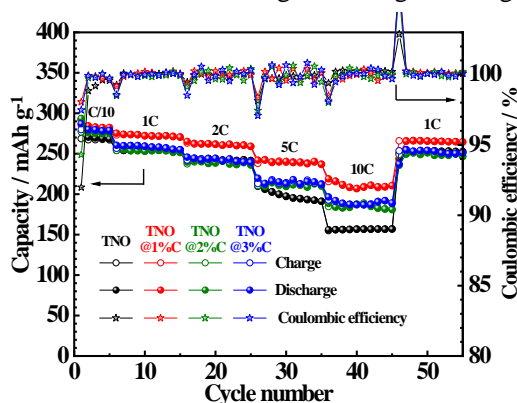


Figure I.5.D.1 Rate performance and coulombic efficiencies of TNO and TNO@C half cells (electrode loading 2.3 mg cm^{-2})

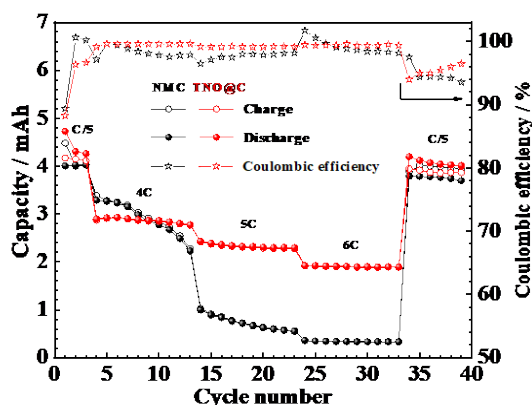


Figure I.5.D.2 Rate performance and coulombic efficiencies of NMC622 (18 mg/cm^2) and TNO@C (13.5 mg/cm^2) half-cells

Based on the half-cells results, we compared the performance of the full cells of NMC622/TNO and NMC622/TNO@C with the same TNO loading of 9.41 mg cm^{-2} while maintaining a capacity ratio of 1:1 between the cathode and anode. As shown in Figure I.5.D.3a, under a high current rate of 5C, the full cell with TNO@C delivers higher capacity, demonstrating the effectiveness of our strategy of surface coating of TNO with conductive carbons. We then investigated the effect of loading of active materials on the performance of the full cells with the capacity ratio of anode and cathode being 1:1. All the cells were charged at 5C to 2.8 V and maintained at 2.8 V until the total charge time of 10 min was reached, followed by discharging at a fixed rate of C/3. As shown in Figure I.5.D.3b, the specific capacities and cycling performance of the full cells are dramatically influenced by the loading of active materials. Subsequently, we investigated the effect of different charging protocols on the cycling stability of the full cells. Figure I.5.D.4 shows that the 4C charging protocol (600 mA/g for NMC622 and 800 mA/g for TNO@C) delivers the best cycling stability with the smallest voltage polarization. We also investigated the additive effect on the cycling stability of the full cells under fast charge conditions. We formulated electrolytes using commercially available additives such as vinylene

carbonate (VC) and fluoroethylene carbonate (FEC). To the baseline electrolyte of 1.2 M LiPF₆/EC-EMC (3:7 vol), 2 wt.% of VC or FEC was added as the additives. Under a high current rate of 5C, the baseline cell delivers the best cycling performance with high initial capacity and high capacity retention after 500 cycles. Although the capacity retention for the cell with 2 wt.% FEC is a little higher than that of the baseline cell (85.6 % vs. 84.1%), its initial capacity is much lower than that of the baseline cell, about 15 mAh/g. On the other hand, the initial capacity of the cell with 2 wt.% VC is higher than that with 2 wt.% FEC, but the coulombic efficiencies and cycling stability of the former cell are much worse than that of the latter cell. Therefore, both VC and FEC have not been evaluated further in this project.

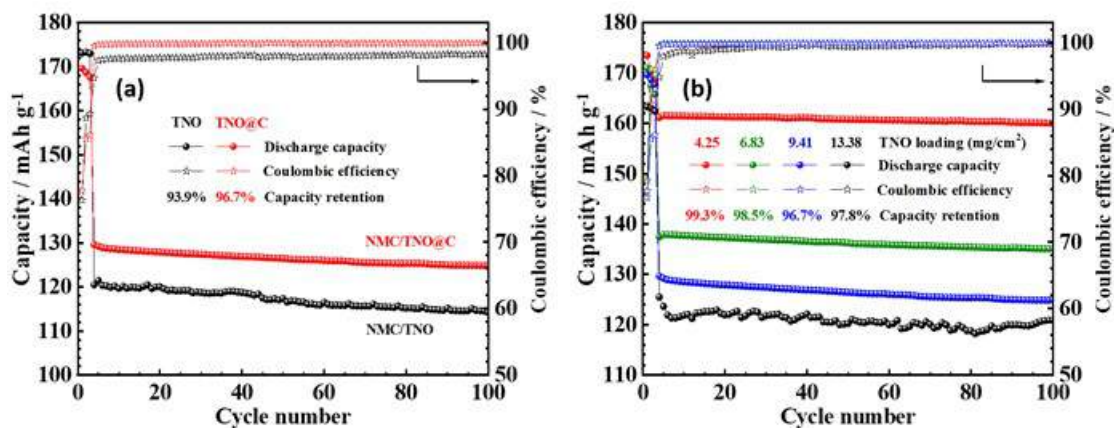


Figure I.5.D.3 Discharge capacities and coulombic efficiencies of full cells (a) based on TNO and TNO@C with the same loading of 9.41 mg cm⁻² and (b) based on TNO@C with different mass loadings

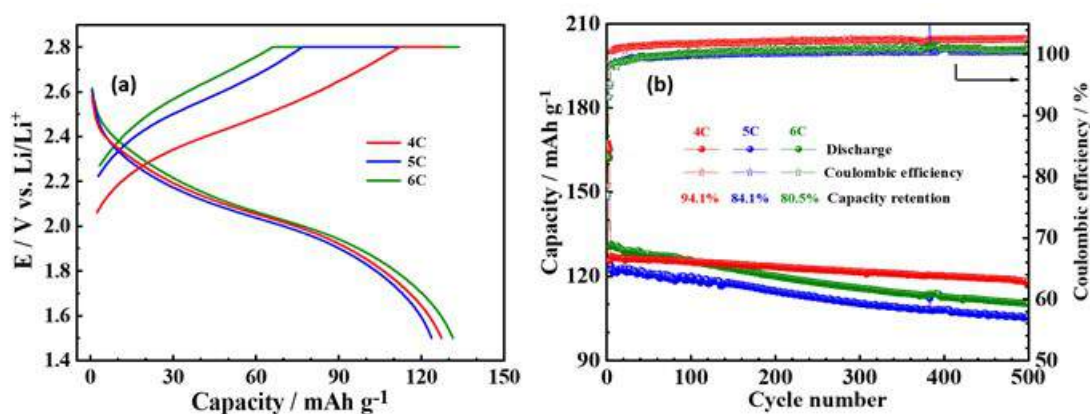


Figure I.5.D.4 (a) Voltage profiles and (b) cycling performance of NMC622/TNO@C full cells under different charging protocols with a total charge time of 10 min and discharge at C/3

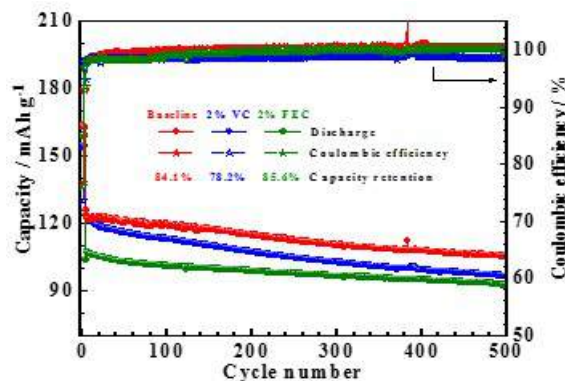


Figure I.5.D.5 Effect of additives on capacity, coulombic efficiency and cycling stability of NMC622/TNO@C full cells at 5C fast charge condition

During the evaluation of high loading TNO half-cells and NMC/TNO full-cells, it was found that all the cells had relatively low initial coulombic efficiencies, about 88% for the half-cells and 76% for the full-cells, respectively. One possible reason for low coulombic efficiency is the interfacial reactions between electrolyte and TNO electrodes in the initial formation cycles, due to the high surface area of the as-prepared TNO powders. To verify this hypothesis, we have synthesized non-porous TNO (b-TNO) powders following the same synthetic procedure without adding the templating agent F127. Consequently, the BET surface area of b-TNO ($14.4 \text{ m}^2/\text{g}$) is much lower than that of p-TNO ($46.8 \text{ m}^2/\text{g}$). To compare the rate performance, p-TNO and b-TNO electrodes with the same TNO loading of $10 \text{ mg}/\text{cm}^2$ were used to fabricate half-cells. Figure I.5.D.6a shows that the initial coulombic efficiency of the b-TNO half-cell is 93.5%, which is much higher than that of the p-TNO half-cell (87.1%), mainly due to less interfacial reactions between the electrolyte and the b-TNO particles. Moreover, the coulombic efficiencies of the b-TNO half-cells are always higher than those of p-TNO half-cells at various current rates, suggesting better reversibility of the former cells. At current rates of C/5 and 4C, the specific capacities of the p-TNO half-cells are almost the same as those of the b-TNO half-cells. However, at higher rates of 5C and 6C, the specific capacities of the b-TNO half-cell are much higher than those of the p-TNO half-cells. The better high rate performance of the b-TNO material makes it a better choice for XFC applications. To investigate the loading effect on rate performance of the b-TNO materials, b-TNO half-cells with various TNO loadings were assembled and cycled at different current rates. As shown in Figure I.5.D.6b, the specific capacities of the b-TNO half-cells decrease with increasing TNO loading, especially at 5C and 6C, confirming the active material loading is still a major issue for the high rate performance of the b-TNO half-cells. Therefore, the b-TNO electrodes with an active material loading of $10 \text{ mg}/\text{cm}^2$ were chosen for further battery evaluation. It is also noted that the high initial coulombic efficiencies of the b-TNO half-cells were always above 93%, not affected by the TNO loadings.

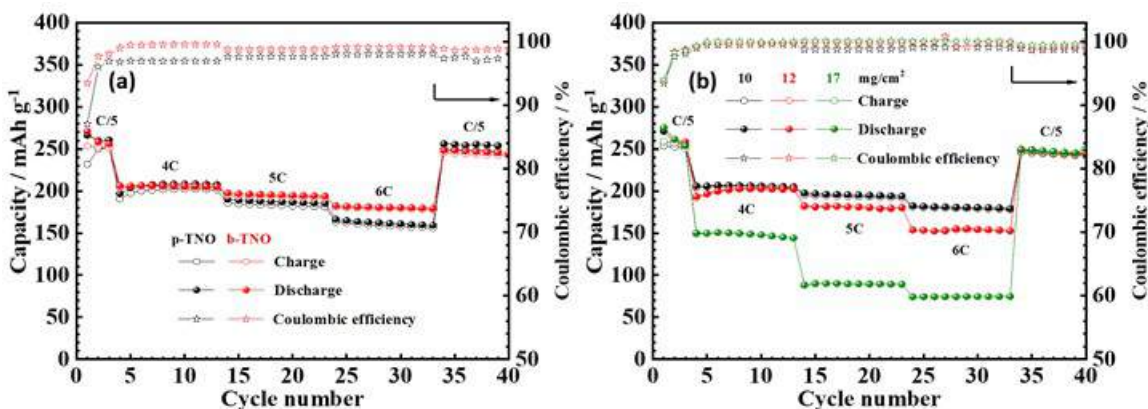


Figure I.5.D.6 Rate performance of (a) p-TNO and b-TNO half-cells with the same TNO loading of $10 \text{ mg}/\text{cm}^2$; (b) b-TNO half-cells with various TNO loadings

Besides trying to improve specific capacities, we also tried to increase the energy density by increasing the weight percentage of the active materials in the electrode fabrication. Thus, two types of b-TNO electrodes with higher weight percentage of TNO (> 80 wt.%), that is, TNO:C45: PVDF = 85:11:4 and 88:8:4, were fabricated and evaluated in half-cells. The active material loadings were kept at 10 mg/cm^2 . As shown in Figure I.5.D.7a, the specific capacities of the b-TNO half-cells at high current rates of 4C, 5C and 6C systematically decrease with increasing the weight percentage of TNO, which can be ascribed to its lower electronic conductivity due to the decreasing amount of the conductive carbon. This conclusion is supported by the Electrochemical Impedance Spectroscopy (EIS) of the b-TNO half-cells with different amount of TNO. As shown in Figure I.5.D.7b, the total cell impedance of the fresh b-TNO half-cells increases with increasing the amount of TNO material, that is, 67.6, 120.7, and $175.0 \text{ } \Omega \text{ cm}^2$ for 80%, 85%, and 88% TNO, respectively. Therefore, the b-TNO electrode with 80% TNO was used for further optimization, since it is unfavorable to lose about 20% capacity with only 5 wt.% increase in TNO loading.

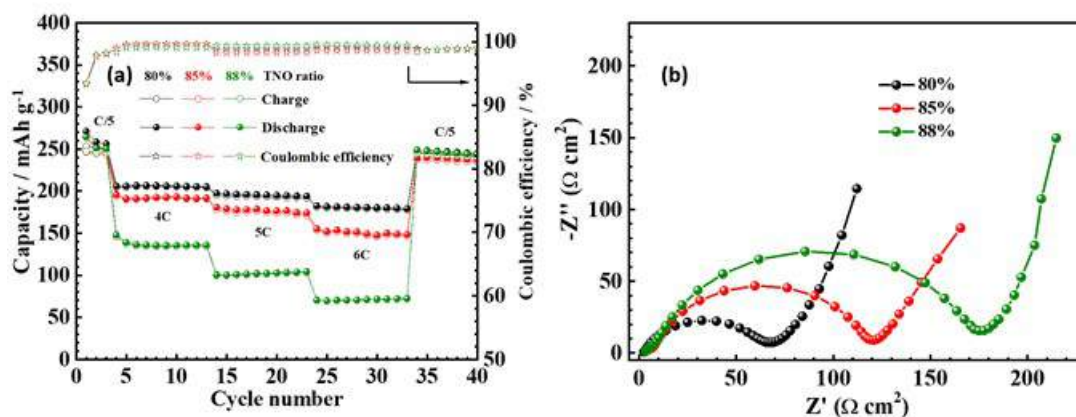


Figure I.5.D.7 (a) Rate performance and (b) Electrochemical Impedance Spectroscopy (EIS) of b-TNO half-cells with different TNO mass loadings.

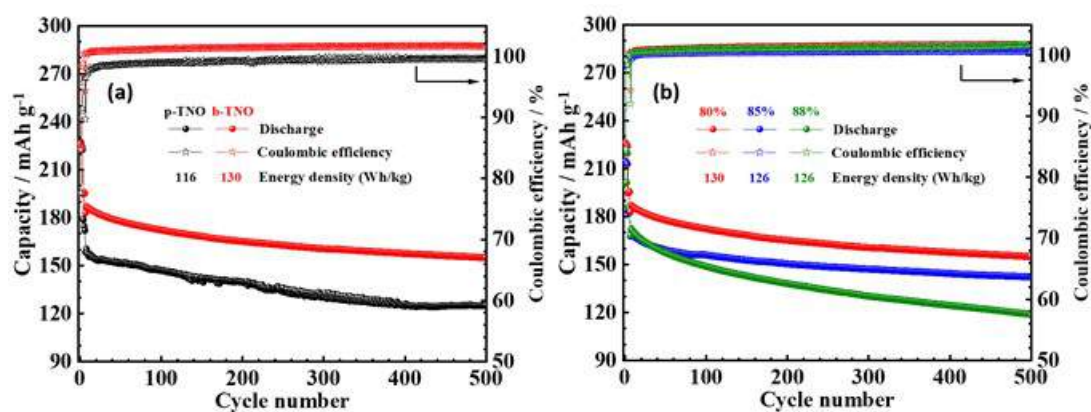


Figure I.5.D.8 Charge-discharge capacities, coulombic efficiencies, and energy densities of (a) p-TNO and b-TNO full cells with the same TNO loading of 10 mg/cm^2 ; and (b) b-TNO full-cells with various TNO mass loadings

To maximize the energy density of the full cells under high current rates, it would be much better to fully utilize both cathode and anode within their respective electrochemical stability windows. Thus, we have assembled a three-electrode cell to learn the individual profile of the NMC cathode and the TNO anode during full cell cycling. It shows that when the upper cut-off voltage of the full cell is 3.2 V, the potential of the NMC cathode reaches 4.15 V vs. Li/Li^+ , while that of the TNO anode reaches 0.95 V vs. Li/Li^+ . Therefore, 3.2 V was used as the upper cut-off voltage for evaluating the NMC and b-TNO based full cells. The full cells were pre-cycled at C/5 for three cycles, and then three cycles at 6C-10 min charge and C/3 discharge, followed by 6C-10 min charge and 1C discharge for 500 times. Figure I.5.D.8a shows the comparison between the p-TNO and b-

TNO full-cells with the same TNO loading of 10 mg/cm². The specific capacity of the b-TNO full-cell is about 30 mAh/g higher than that of the p-TNO full-cell, although the specific capacities of the two cells at C/5 are almost same. Figure I.5.D.8a also shows the energy density increases from 116 Wh/kg for the p-TNO full cell to 130 Wh/kg for the b-TNO full cell. It is also noted that the initial coulombic efficiency of the b-TNO full cell is 85%, which is much higher than that of the p-TNO full cell (77%). This result shows that the excellent high-rate performance of non-porous b-TNO, resulting in higher specific capacities and energy densities of the full cells under XFC conditions. The b-TNO full cells with different TNO mass loadings were also assembled and evaluated with the same XFC procedure. As shown in Figure I.5.D.8b, the b-TNO full cell with 80% TNO loading exhibits the highest specific capacities at various current rates and the highest energy density at the initial XFC cycle, suggesting that sufficient amount of conductive carbon is crucial for the better XFC performance of the full cells.

Conclusions

In summary, the nanoporous TiNb₂O₇ (TNO) was successfully synthesized with a low-cost niobium chloride precursor, achieving a similar performance as previously reported. Also, the carbon-coated porous TNO material (TNO@C) was synthesized with low-cost glucose and a facile hydrothermal approach. In addition, it has been demonstrated that TNO with 1 wt.% carbon coating delivered the best rate performance and the highest initial coulombic efficiency. It is further demonstrated that the lower surface area of the non-porous b-TNO synthesized without using the F127 template achieved better XFC performance than nanoporous p-TNO. Finally, with an upper cut-off voltage of 3.2 V, the energy density of the NMC/TNO full cell has been successfully increased from 93 to 130 Wh/kg by using the non-porous b-TNO material and through electrode optimization.

References

1. Guo, B. K.; Yu, X. Q.; Sun, X. G.; Chi, M. F.; Qiao, Z. A.; Liu, J.; Hu, Y. S.; Yang, X. Q.; Goodenough, J. B.; Dai, S., A long-life lithium-ion battery with a highly porous TiNb₂O₇ anode for large-scale electrical energy storage. *Energy Environ. Sci.* 2014, 7 (7), 2220-2226.
2. Li, J. L.; Daniel, C.; An, S. J.; Wood, D., Evaluation Residual Moisture in Lithium-Ion Battery Electrodes and Its Effect on Electrode Performance. *Mrs Advances* 2016, 1 (15), 1029-1035.

Acknowledgements

U.S. DOE Office of Energy Efficiency and Renewable Energy (EERE), Adrienne L. Riggi (NETL), Brian Cunningham & David Howell (VTO). ORNL contributors include Xiao-Guang Sun and Jianlin Li. The UTK contributors include Hailong Lyu and Tao Wang.

I.5.E Research three-dimensional hierarchical graphite architectures for anodes for fast charging (SNL)

Mohan Karulkar, Principal Investigator

Sandia National Laboratories
1515 Eubank Dr. SE, M/S 0613
Albuquerque, NM 87185
E-mail: mpkarul@sandia.gov

Brian Cunningham, DOE Technology Development Manager

U.S. Department of Energy
E-mail: Brian.Cunningham@ee.doe.gov

Start Date: October 1, 2018	End Date: September 30, 2019	
Project Funding (FY19): \$80,000	DOE share: \$80,000	Non-DOE share: \$0

Project Introduction

With current lithium ion batteries optimized for performance under relatively low charge rate conditions, implementation of XFC has been hindered by drawbacks including Li plating, kinetic polarization, and heat dissipation. This project will utilize model-informed design of 3-D hierarchical electrodes to tune key XFC-related variables like 1) bulk porosity/tortuosity 2) vertical pore diameter, spacing, and lattice 3) crystallographic orientation of graphite particles relative to exposed surfaces 4) interfacial chemistry of the graphite surfaces through “artificial SEI” formation using ALD 5) current collector surface roughness (aspect ratio, roughness factor, etc.).

A key aspect of implementing novel electrodes is characterizing them in relevant settings. For this project, ultimately led out of University of Michigan by Neil Dasgupta, that includes both coin cell and 2+ Ah pouch cell testing, as well as comparison testing against baselines. Sandia National Labs will be conducting detailed cell characterization on iterative versions/improvements of the model-based hierarchical electrodes, as well as COTS cells for baseline comparisons. Key metrics include performance under fast charge conditions, as well as the absence or degree of lithium plating. Sandia will use their unique high precision cycling and rapid EIS capabilities to accurately characterize performance and any lithium plating during 6C charging and beyond, coupling electrochemical observations with cell teardown. Sandia will also design custom fixturing to cool cells during rapid charge, to decouple any kinetic effects brought about by cell heating and allow comparisons between different cells and charge rates. Using these techniques, Sandia will assess HOH electrodes from the University of Michigan, as well as aiding in iterative model and electrode design.

Objectives

- Work with University of Michigan to establish cadence for receiving improved-electrode cells for characterization via in-person kickoff and weekly update meetings.
- Develop and validate a custom rapid cooling plate fixture to allow the best possible temperature control of cells during fast charging, regardless of cell design, charge current, and environmental conditions.
- Begin baseline COTS cell fast charge characterization.
- Demonstrate high fidelity dQdV measurements during 6C charging using high precision coulometry.

Accomplishments

- Completed Baseline testing of NMC/Graphite and NCA/Hard Carbon cells made at University of Michigan.

- Took possession of HOH Anode cells from UM, and completed design of experiments to test at 4C and 6C charge rates.
- Obtained dQdV measurements demonstrating lithium plating for NMC/Graphite baseline cell.
- Presented findings at Electrochemical Society meeting, Annual Merit Review, and Advanced Automotive Battery Conference (AABC).

Approach

To establish baseline performance for UM-Made cells, a combined rate capability and cycle life approach was used. Cells were cycled with increasing charge rates, followed by a charge taper to C/20, followed by a 1C discharge. After the rate capability portion, the cell was cycled at 1C charge / 1C discharge to a total of 100 cycles to monitor capacity retention after the high rate charge cycles (See Table I.5.E.1).

Table I.5.E.1: Cycling Profile for Baseline COTS and UM Cells

Cycles	CC Charge	Ch Taper	CC Discharge	Rest	Temp	Purpose
1 - 24	0.5 – 6 C	yes	1C	yes	22C, 30C	Rate capability
25-70	1C	yes	1C	yes	22C, 30C	Cycling

Baseline Cells included COTS NMC/Graphite, UM-made NMC/Graphite, and UM-made NCA/Hard Carbon, with characteristics described in Table I.5.E.2. Cycling was performed with the Arbin high precision cyclers developed through an ARPA-E AMPED program with SNL, Ford, Arbin, and Montana Tech. A rapid response cooling system was used to maintain isothermal operation and avoid complications arising from temperature rise during testing.

Table I.5.E.2: Cells used to establish baseline lithium plating performance.

	COTS NMC/Graphite	UM NMC/Graphite	UM NCA/Hard Carbon
Capacity	5Ah	2.85Ah	2.75 Ah
Anode			
<i>Loading</i>	2.6 mg/cm ²	8.4 mg/cm ²	8.3 mg/cm ²
<i>Capacity Loading</i>	0.9 mAh/cm ²	3.04 mAh/cm ²	3.0 mAh/cm ²
Cathode			
<i>Loading</i>	4.0 mg/cm ²	18.2 mg/cm ²	14.9 mg/cm ²
<i>Capacity Loading</i>	0.65 mAh/cm ²	3.0 mAh/cm ²	3.0 mAh/cm ²
N:P Ratio	1.4	1.01	1.0
Energy Density	112 Wh/kg	200 Wh/kg	165 Wh/kg

Results

Figure I.5.E.1 shows the results of rate capability testing on the NMC/Graphite cell. Voltage indicates normal cycling behavior with some capacity loss to polarization, up to 3C. During the 4C cycles, a longer Constant Voltage portion is noted, and the current trace (blue) indicates an increasing current, which is indicative of short circuit behavior. The plot also shows that the cell fails during the 5C charge section. Figure I.5.E.2 shows the dQdV calculations for the charge steps. Normal lithiation peaks are seen for the 0.5C and 1C charge steps, but at 2C a small hump is seen forming at around 4.1V. The hump groups at higher charge rates, and is clearly

distinct from the earlier lithiation humps. This is an indication of lithium plating, and represents the first time lithium plating has been demonstrated in this project. It is interesting to note that the dQdV reveals the start of plating as early as 2C, whereas the simple voltage/current profile (Figure I.5.E.1) does not indicate problems until the 4C steps. dQdV shows a clear utility in detecting plating which may otherwise go unnoticed.

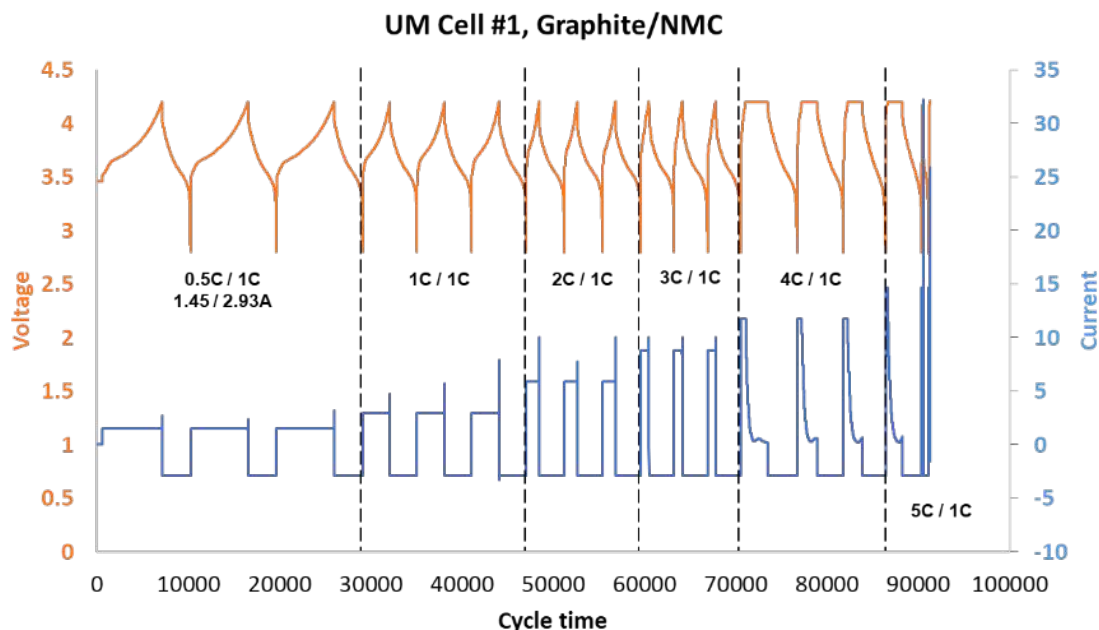


Figure I.5.E.1 Voltage and Current during rate capability testing of NMC/Graphite UMich cell

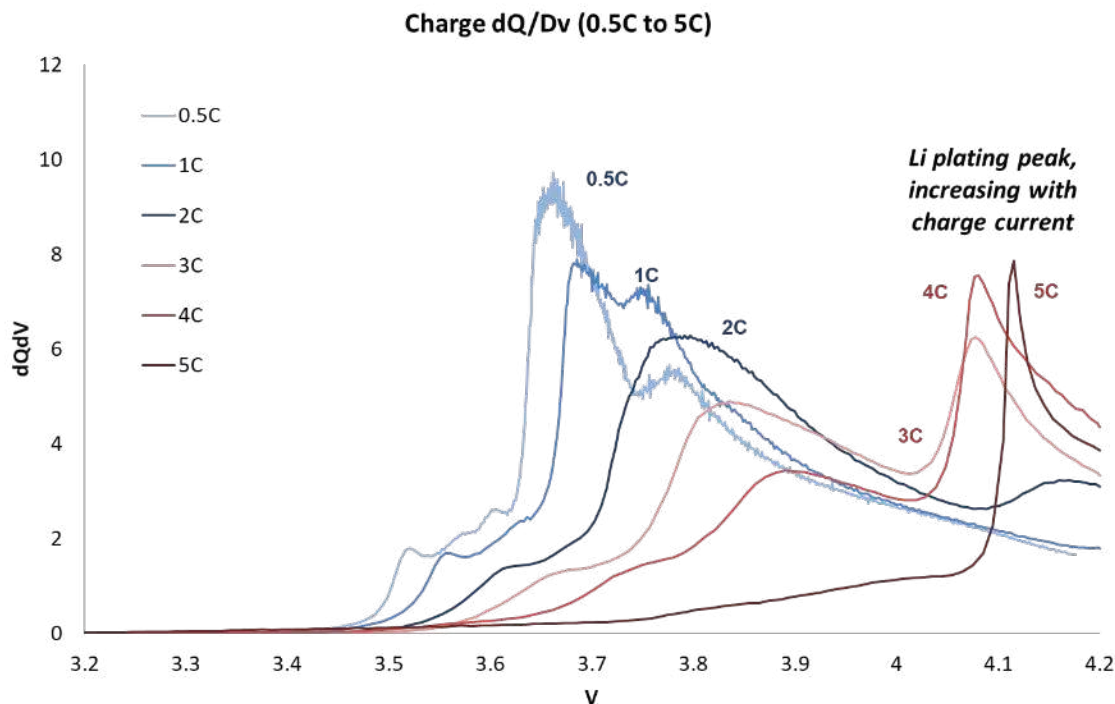


Figure I.5.E.2 dQdV of charge steps during rate capability testing of NMC/Graphite cell

Testing on the NCA/Hard Carbon Cell

Similarly to the NMC/Graphite cell, the same profile was applied to an NCA/Hard Carbon Cell. Figure I.5.E.3 shows the results, and here a 6C/1C (Charge/Discharge) profile with no CV taper steps was applied after rate capability to stress-test the cell. While large polarization is seen during the high rate charge steps, the total capacity (after charge taper) indicates a smaller loss of capacity indicative of SEI growth common to hard carbon. The sustained 6C cycling shows a steady polarized 1.75Ah, and a recoverable 2.6Ah during 1C/1C capacity check steps. There is no indication of cell failure as seen in the NMC/Graphite cell. Figure I.5.E.4 shows the dQdV results for the NCA/Hard Carbon cell. While the shape looks quite different than the NMC/Graphite cell due to the unique lithiation behavior of hard carbon, the overall trend does not show the growth of a lithiation peak. This is consistent with Figure I.5.E.3 and the lack of evidence of cell failure. It can be surmised that the hard carbon cell is much more resilient to lithium plating than the graphite anode. Figure I.5.E.5 shows the efficiency during cycling of both the NMC/Graphite cell and the NCA/Hard Carbon cell. The graphite cell hits maximum efficiency right away, which is consistent with the expected behavior for graphite. Efficiency begins to slip at 3C, and has fallen precipitously at 4C, which is consistent with the observation of lithium plating in the dQdV. The hard carbon cell takes several cycles to reach maximum efficiency, consistent with hard carbon's longer SEI Formation period, but the efficiency does not drop afterwards, which agrees with the observed lack of lithium plating in the dQdV and voltage/current plots.

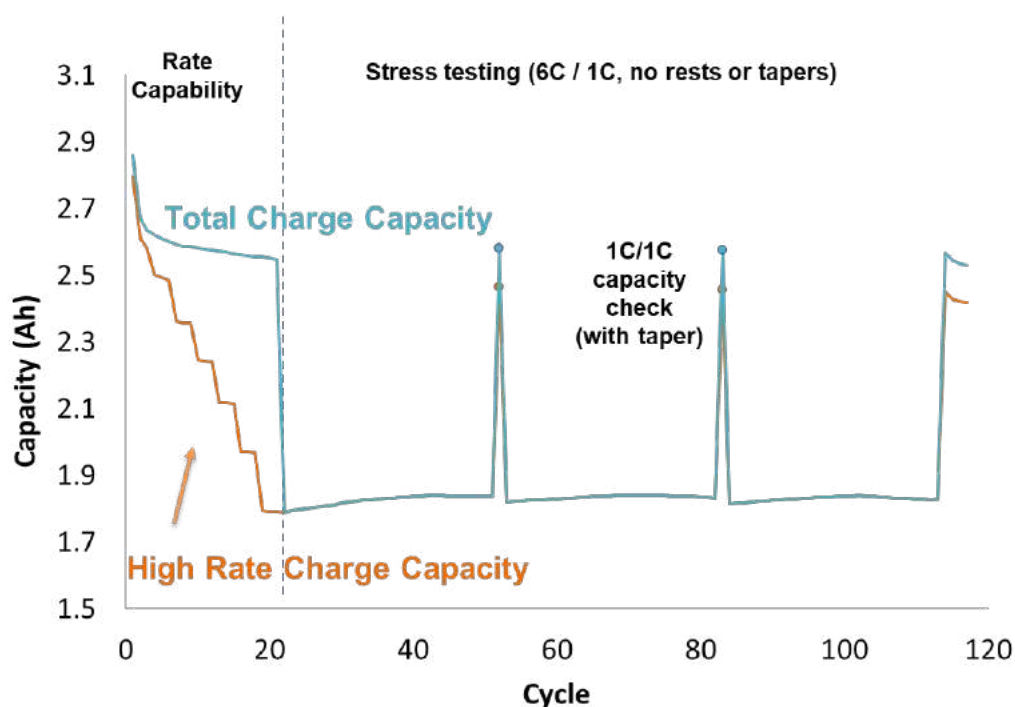


Figure I.5.E.3 Rate capability and long 6C/1C cycling for NCA/Hard Carbon cell

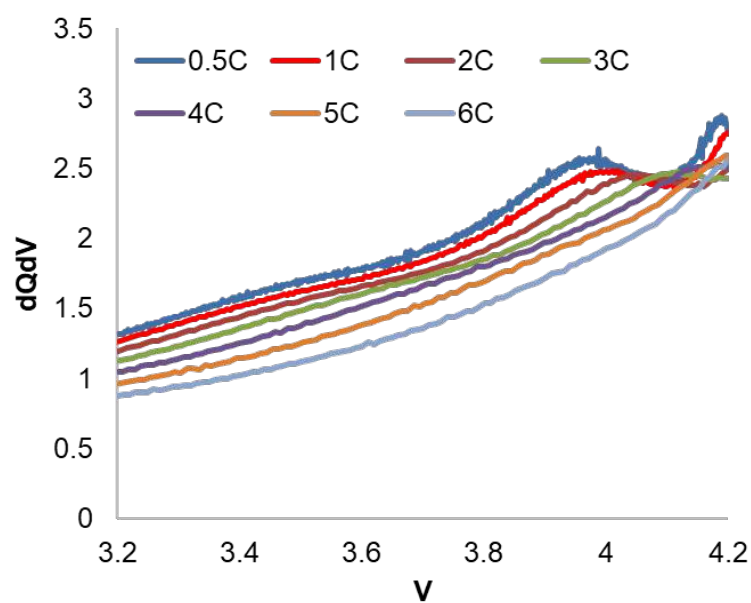
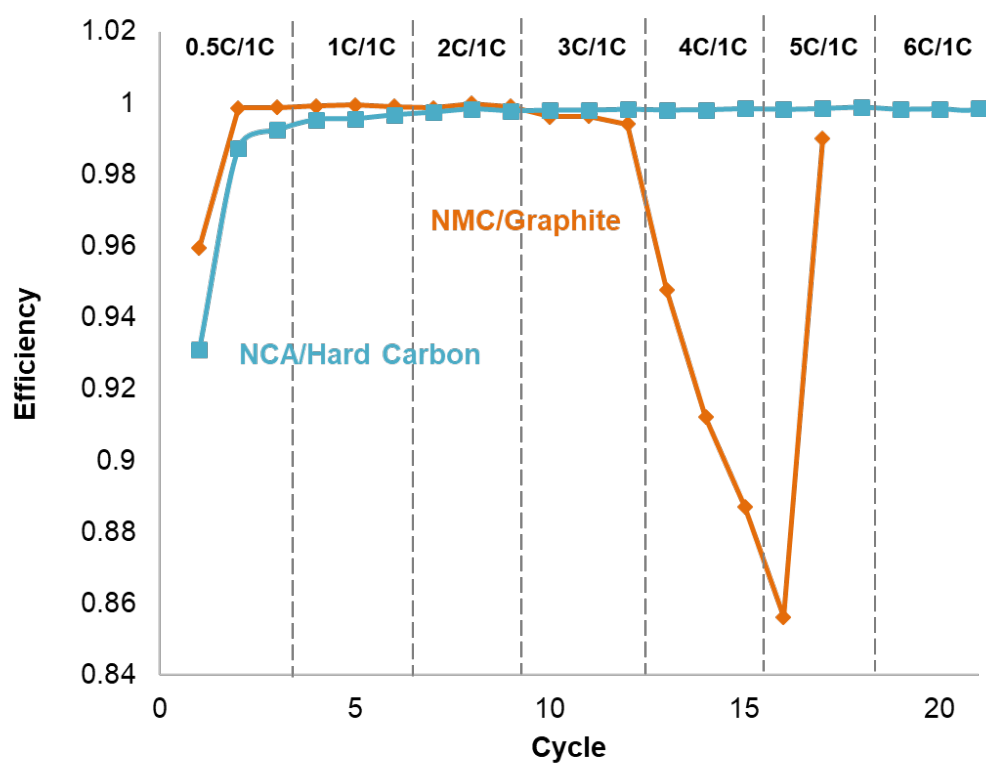
Figure I.5.E.4 Charge $dQdV$ for NCA/Hard Carbon cells

Figure I.5.E.5 Efficiency for NMC/Graphite and NCA/Hard Carbon cells

Importance of Temperature Controls

SNL's use of cooling plates is designed to minimize temperature fluctuations due to XFC heating and environmental temperature changes. A key tool in detecting lithium plating is analysis of voltage response, both in terms of intra-cycle $dQdV$, and inter-cycle efficiency. Since cell capacity is highly dependent on temperature, it follows that temperature fluctuations should be kept at a minimum if one is using those metrics to assess Li plating. Figure I.5.E.6 shows the temperature profile during 6C charge / 1C discharge cycling of the COTS 5Ah cells, with (orange) and without (blue) temperature control. The temperature swings during high rate charging are limited to 2°C with cooling plates; the swing is 6°C – three times as large – without cooling plates. Moreover, the average temperature drift due to environmental changes is significant without cooling plates, with a cyclic pattern corresponding to day-night cycles. Similar cycling is only somewhat visible with cooling plates, and the temperature swings are cut by half. Figure I.5.E.7 shows cycle-to-cycle efficiency for cycling with and without cooling plates. Temperature-induced efficiency swings are clearly visible in the case without temperature control, making efficiency tracking impossible. For the case with temperature control, no pattern is noticeable, leading one to believe that efficiency fluctuations better correlate to genuine cell events like lithium plating rather than heating.

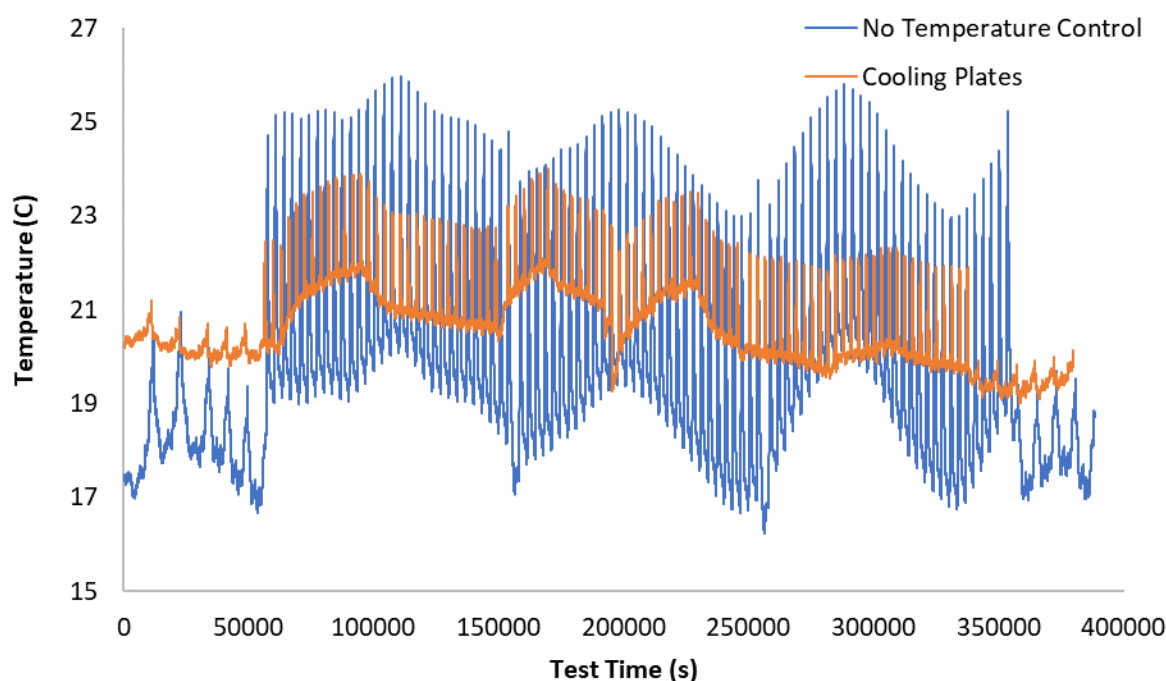


Figure I.5.E.6 Temperature profile for 6C/1C cycling, with and without temperature control plates

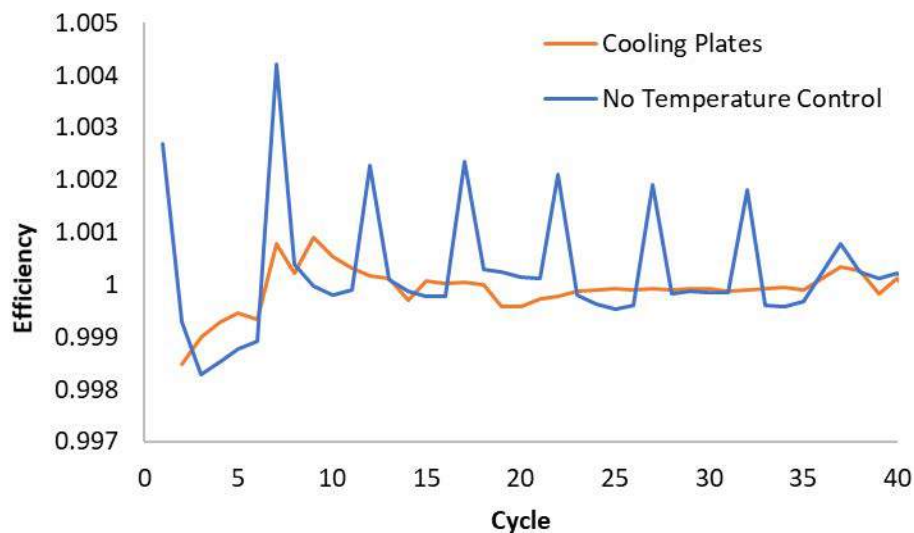


Figure I.5.E.7 Cycle to cycle efficiency for 6C/1C cycling, with and without temperature control plates

Conclusions

The work performed in FY19 demonstrated the use of High Precision dQdV analysis to detect lithium plating, at both the earliest stages when lithium appears to re-strip during discharge, and later stages when dead lithium accumulates to reduce battery capacity and ultimately cause failure. NMC/Graphite cells showed a strong relationship between increasing energy density and propensity for lithium plating. COTS cells with 112 Wh/kg showed no evidence of plating, while UM cells with 200 Wh/kg showed clear plating at as low as 3C charging. Conversely, NCA/Graphite cells with 165 Wh/kg showed no evidence of plating, though a high amount of polarization rendered most of the anode capacity inaccessible with 6C charging. FY19 work also demonstrated the importance of isothermal operation in R&D applications. Without temperature control, efficiency tracking becomes nearly impossible because of the cell heating effects brought on by fast charging.

In FY20, cells with anodes using HOH improvements will be compared to baseline cells. The methods established during FY19 will be used to quantify the improvements as they related to lithium plating.

Key Publications

1. M. Karulkar, L. Castro-Torres, J. Lamb, "High Precision Characterization of Li-Ion Batteries during Extreme Fast Charging," 235th Meeting of the Electrochemical Society, Abstract MA2019-01 47, Dallas TX (2019).
2. M. Karulkar, "Anode Improvements for Better Fast Charge Tolerance in Cells of High Energy and Powder Density," Advanced Automotive Battery Conference, San Diego CA (2019).

Acknowledgements

The Sandia co-authors for this section include Josh Lamb, Loraine Torres-Castro, June Stanley, Chris Grosso, Lucas Gray, and Christopher Orendorff.

Sandia National Laboratories is a multimission laboratory managed and operated by National Technology & Engineering Solutions of Sandia, LLC., a wholly owned subsidiary of Honeywell International, Inc., for the U.S. Department of Energy's National Nuclear Security Administration under contract DE-NA0003525.

I.5.F Develop new electrolyte additives, optimized active materials, and electrode formulations (ANL)

Khalil Amine, Principal Investigator

Argonne National Laboratory
9700 S Cass Avenue
Lemont, IL 60439
Email: amine@anl.gov

Brian Cunningham, DOE Technology Development Manager

U.S. Department of Energy
E-mail: Brian.Cunningham@ee.doe.gov

Start Date: January 1, 2018	End Date: September 30, 2019	
Project Funding (FY19): \$500,000	DOE share: \$500,000	Non-DOE share: \$0

Project Introduction

Lithium-ion batteries (LIBs) now surpass other, previously competitive battery types (for example, lead–acid and nickel metal hydride) but still require extensive further improvement to, in particular, extend the operation hours of mobile IT devices and the driving mileages of all-electric vehicles. [1],[2],[3] High energy density and fast charging of lithium-ion batteries are the main challenges that are highly desirable to drive the entire technology forward in future. [4] Because the energy density of a rechargeable battery is determined mainly by the specific capacities and operating voltages of the anode and the cathode, active materials have been the main focus of research in recent years, especially cathode materials. [5],[6] On the basis of numerous experimental results, it is currently well accepted that increasing Ni content enables to greatly improve capacity of cathode materials while in turn causes a fast capacity degradation. [7] The fast capacity degradation originate from a severe side reaction on the interface between electrodes and electrolyte. Therefore, electrolyte additives are designed to improve the properties of the electrolytes and suppress capacity degradation of electrodes. [8]

In this project, we are going to design cathode materials with full concentration gradient to simultaneously achieve targeted capacity and good cycling stability. Surface modification such as surface coating / doping will be conduct on our cathode materials to further protect particle surface and improve electronic conductive. In addition, electrolyte additives will be developed to improve the chemical stability of electrolyte and protect electrodes at a high operating voltage.

The team led by Dr. Khalil Amine at Argonne National Laboratory (ANL) is working on advanced cathode materials and electrolyte additives design. Employing advanced diagnostic tools including synchrotron X-ray probes and transmission electron microscopy, cathode structure and composition design as well as understanding of electrolyte additive chemistry can be quickly feedbacked and applied to further improve electrochemical performance.

Objectives

The objective of the project is to research, develop, and design cathode materials and electrolyte additives to achieve high capacity, good cycling performance and fast charging properties.

Approach

Our approach to meet the objectives is detailed as follows:

- For cathode materials, we design a full concentration gradient cathode, wherein 65% Ni content composition is arranged on particle surface and 90% Ni content is arranged in the particle center. The average composition includes 85% Ni, 10% Co, and 5% Mn, composing $\text{LiNi}_{0.85}\text{Mn}_{0.05}\text{Co}_{0.1}\text{O}_2$.

- LiDFOB was selected as an electrolyte additive used in Conventional electrolyte (1.2M LiPF₆ in EC/EMC) due to its bifunctional protection at the cathode and anode.
- Advanced diagnostic tools including synchrotron X-ray probes and transmission electron microscopy are employed to establish in-depth understandings of cathode composition and structure as well as electrolyte chemistry.

Results

The controllable synthesis of full-concentration gradient Ni-rich cathode materials

The FCG-NMC material is intended to be a high capacity cathode that shows improved stability and performance over NMC cathodes. The reason a varied slope material is necessary to make a higher nickel composition and simultaneously arrange a lower nickel composition on the surface that has better stability and safety. Using a CSTR reactor, a FCG cathode with average 85% Ni was successfully synthesized. As shown in Figure I.5.F.1, the FCG composition is characterized by two-slope wherein nickel composition slowly decreases in the bulk but sharply decrease on the surface. Combining advanced synchrotron XRF and TEM-EDS mapping, the two-slope gradient concentration has been confirmed. In addition, TEM-EELS results demonstrate, believed for the first time, that the gradient exists within a single primary particle rod. Synchrotron-based High-energy XRD (HEXRD) was conducted to investigate the initial structural properties of the FCG samples. The XRD results with Rietveld refinements confirmed a well-crystallized layered structure with around 4% Li/Ni disorder that is acceptable for Ni-rich cathodes.

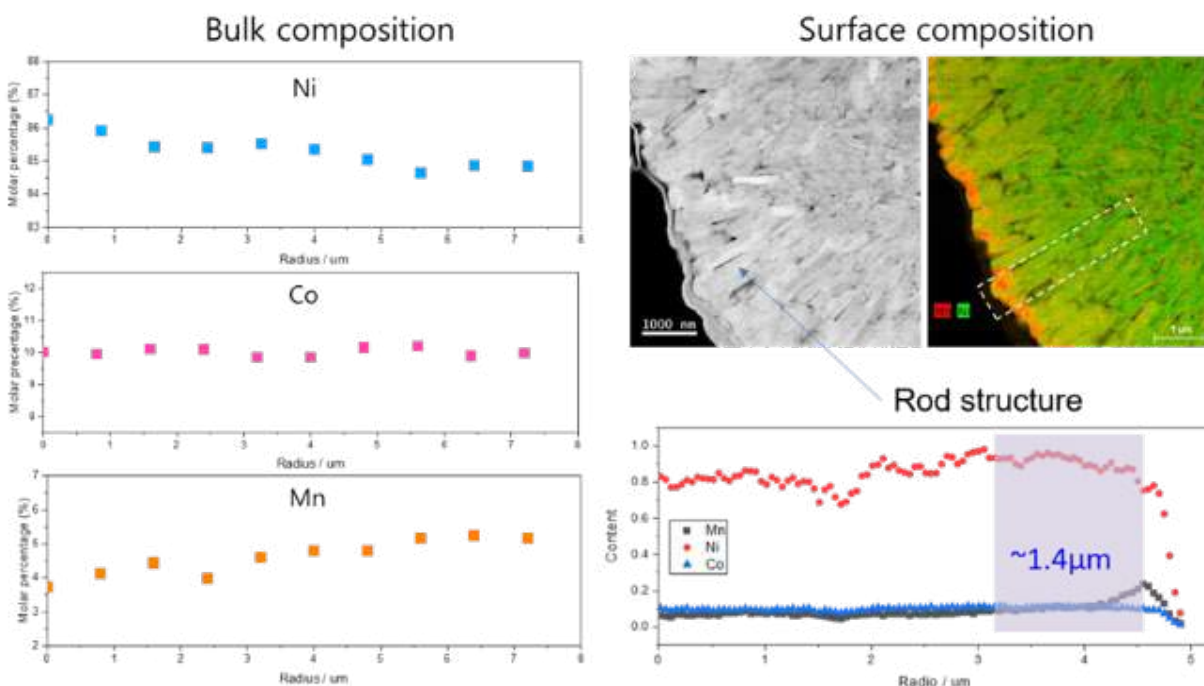


Figure I.5.F.1 The bulk composition and surface composition are analyzed by XRF and TEM-EDS mapping

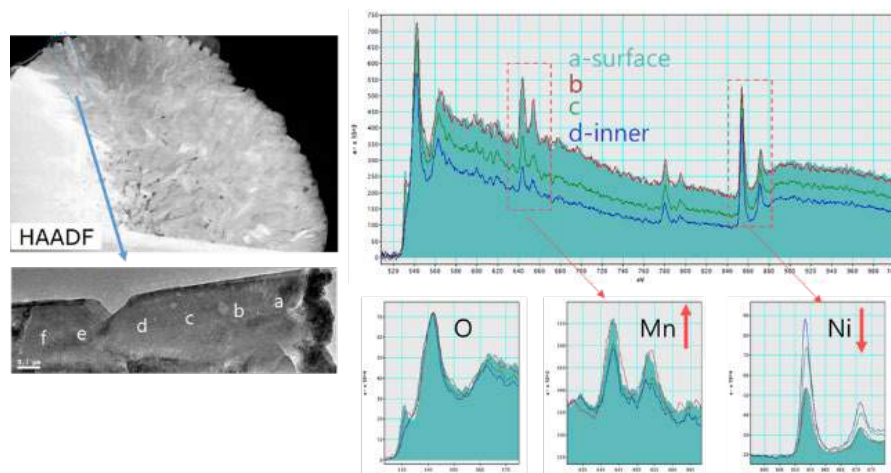


Figure I.5.F.2 The EELS spectra offset for clarity to show the intensity of the Mn and Ni are changing with position along the primary particle

The electrochemical performance of the FCG cathode sample was initially tested by half-cell. Figure I.5.F.2 shows that the FCG cathode delivers 225 mAh/g of capacity from 3-4.4V at C/10 and extremely high coulomb efficiency of 94% at 1st cycle. At the same time work has begun to incorporate Al and Ti coating/doping in the FCG precursor particle; the idea being to make a uniform Al/Ti coating layer and narrow surface doping within the material. Efforts so far show an obviously improved cycle stabilities when Al/Ti coating and surface doping are successfully prepared in the FCG particles. The dQ/dV analysis shows improved reversibility of electrochemical with the Al or Ti treatment. Efforts will be continually taken to manipulate the processing conditions to directly add Al into the precursor crystals.

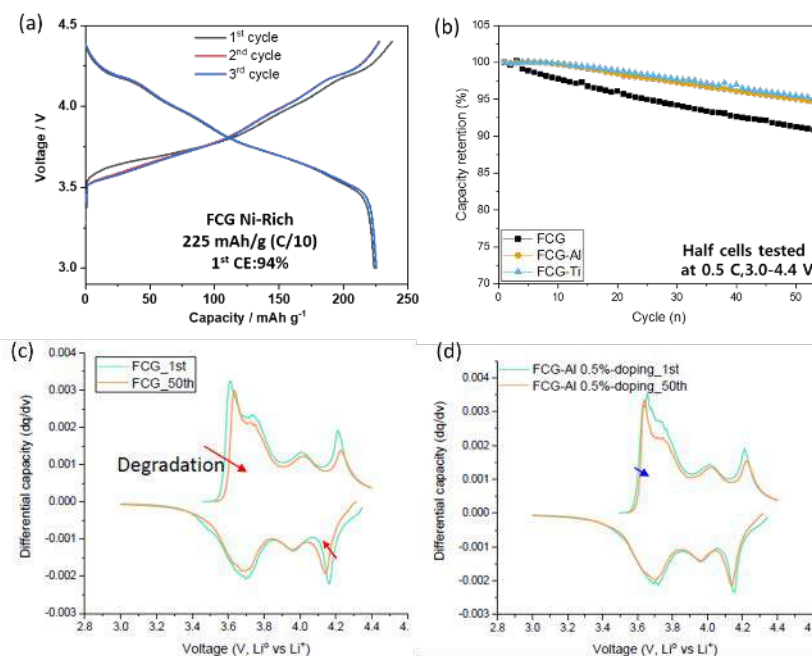


Figure I.5.F.3 (a) The initial capacity of FCG85-5-10; (b) cycle data of plain FCG Ni85 material, and after a treatment with Al and Ti. (c) and (d) The dQ/dV of the untreated FCG and FCG altered with Al is shown to demonstrate how the material degradation is impeded thru treatment

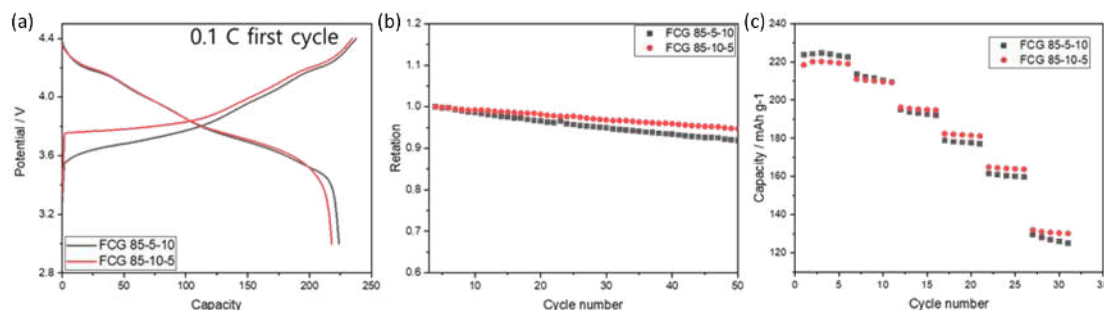


Figure I.5.F.4 FCG 85-5-10 and FCG 85-10-5 (Ni-Mn-Co) comparing the first cycle load curve, capacity retention during coin cell cycling, and half-cell rate performance

In order to further improve the stability of Ni-rich FCG materials, the FCG composition was tuned by increasing Mn content and reducing Co content because it is well accepted that Mn enables to stable the layered structure and improve cycling performance. Thus, two FCG cathode materials with 85% Ni were prepared, one with 5% Co & 10% Mn [FCG 85-5-10], while the other was 10% Co & 5% Mn [FCG 85-10-5]. The coin cell electrochemistry results for these two samples is provided in Figure I.5.F.4, and clearly show that the small change in composition has an influence on the material performance. Overall the material with more Mn performs better in cycle stability and rate capability, although the higher cobalt sample shows superior first cycle capacity and efficiency. To better understand why the materials show a difference in performance, high energy XRD measurements were performed at the beamline 11-ID-C of the Advanced Photon Source (APS) at Argonne National Laboratory to precisely identify the structural variation of these two FCG samples. The Rietveld refinement results clearly show a slightly lower Li/Ni disorder for FCG 85-10-5 over FCG 85-5-10. To probe the results even deeper, in situ XRD on a cycling coin cell was collected at Advanced Photon Source beamline 11-ID-C. The preliminary data workup shows larger parameter variations occur during charge and discharge for the FCG 85-5-10 material compared to FCG 85-10-5, so volume change is another potential reason in addition to Li/Ni disorder for comparatively worse cycling performance. The *c* axis distance solved during the refinement supports the finding that Li/Ni disorder is less, since as the site exchange occurs the *c*-axis distance usually collapses. Past scientific papers have also found there is a clear relation between the rate performance of layered cathode materials and the *c*-axis distance. In addition, the lattice parameter changes show an interesting structural difference during high states of charge, specifically an (003) asymmetry in the FCG 85-10-5 sample phase change during de-lithiation and re-insertion versus a symmetrical change for FCG 85-5-10, which directly proof the better structure reversibility of FCG85-10-5.

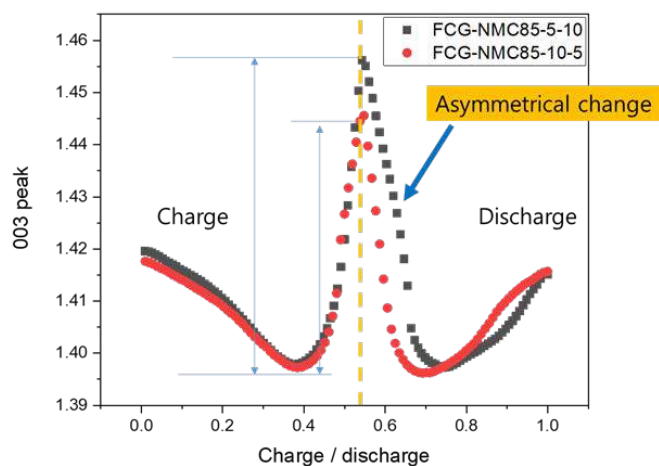


Figure I.5.F.5 Graph comparing the two in situ cell HE-XRD (003) peak positions during charge and discharge. The shape during charge and discharge are obviously different

Employing advanced electrolyte additives to improve the electrochemical performance.

Lithium difluoro(oxalato)borate (LiDFOB) with one oxalate moiety bonded to a central boron core was employed as a salt-type additive to enhance the interfacial stabilities of Ni-rich cathodes and graphite anodes. Previous literatures revealed that the LiDFOB additive modified the surface film on the electrodes and effectively restrained degradation of the cycling performance of the electrodes. [9] Different amounts of LiDFOB additives was tested in a Ni-rich cathodes (NMC85-5-10 with uniform composition) half cells. Figure I.5.F.6 shows that LiDFOB as electrolyte additive significantly improve the cycling stability and rate performance. Using the Microvast Gen1 electrode (FCG-NMC631) in a full cell with ANL's Gen2 electrolyte was compared with Gen2 + 1wt% LiDFOB, and the cycle retention and areal capacity both are improved when the additive is present in the cell.

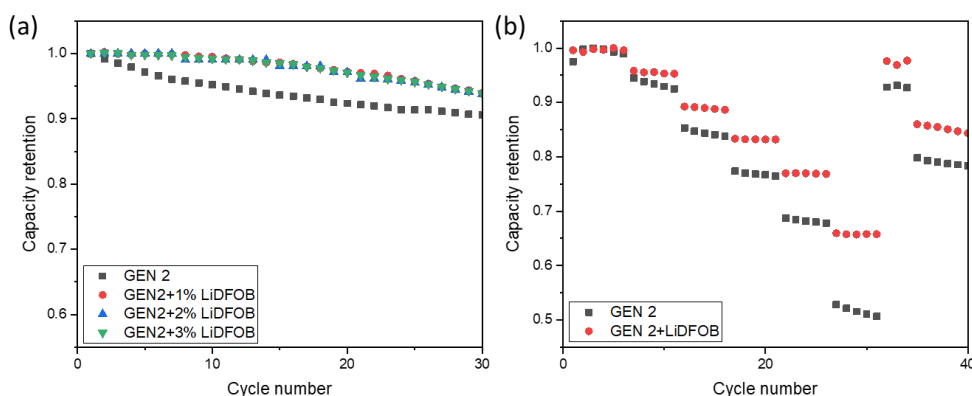


Figure I.5.F.6 (a) The cycle data for different LiDFOB added in Gen2 electrolyte tested in a half cell. (b) The rate performance comparison of Gen2 and Gen2 electrolyte with 1wt% LiDFOB

Initial achievements of extreme fast charging system.

At the initiation of the project a 200 Wh/kg pouch cell was constructed to baseline the project by Microvast and give some first impressions to the project team regarding cell performance under 6-minute charge/1C discharge cycling conditions. The cell built used a moderate nickel NCM cathode and a graphite anode. The pouch cell built was 15AH, and capable of cycling 500 cycles under XFC conditions (Figure I.5.F.7).

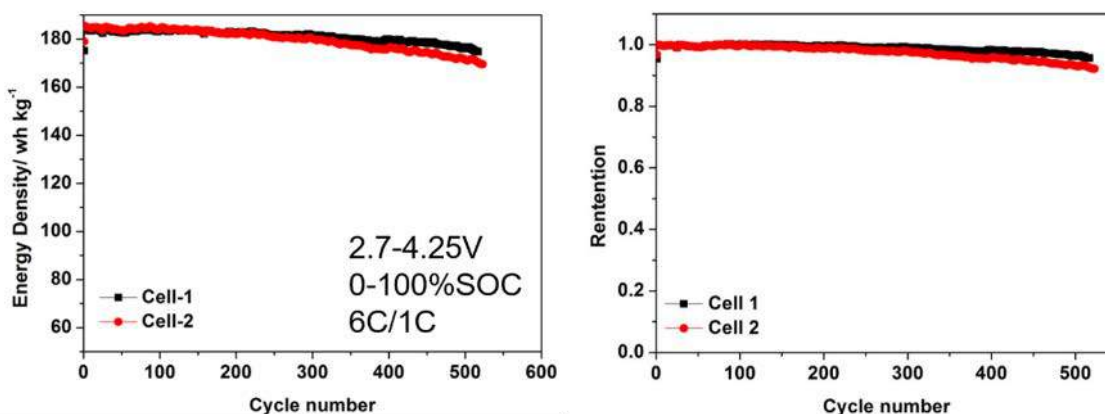


Figure I.5.F.7 15AH pouch cells energy density and energy retention over 500 cycles tested under XFC cycling conditions

After the success of the baseline cells cycling, the project commenced at the originally proposed 220 Wh/kg pouch cell target. This cell introduced a 60% Ni/NMC full concentration gradient (FCG) cathode into the cell design. The FCG originally introduced into the cell had Co/NMC ratio of 10%. Cobalt is considerably more

expensive than nickel or manganese, so limiting its input into a cell can be beneficial for the cell's cost. The cell's energy density was slightly below 180 Wh/kg when cycled at 6CCCV/1CD, though the energy density retention was above 80% after 500 cycles.

The project team has now begun to investigate the generation 2 cell performance under fast charge. The higher areal loadings and cell Wh/kg is making the fast charge performance more challenging. We believe a combination of engineering decisions regarding charge procedures and cell designs, along with materials selected is the best approach to overcome these challenges in a working large capacity cell.

Conclusions

In summary, we have successfully designed Ni-rich cathode materials with two-slope full concentration gradient. Advanced synchrotron X-ray and TEM techniques have confirmed the gradient exists even within a single primary particle rod. The FCG material delivers 225 mAh/g of capacity from 3–4.4V at C/10 and extremely high coulomb efficiency of 94% at 1st cycle. Further modification with Al and Ti coating/doping as well as improve Mn content in composition both significantly improve the capacity retention. LiDFOB was employed as an electrolyte additive to effectively enhance the interfacial stabilities of Ni-rich cathodes and graphite anodes. The first-generation extreme fast charge pouch cell has successfully been built by Microvast. The 20Ah cell, using an FCG cathode, was internally tested to deliver > 180 Wh/kg energy density at the start of XFC testing and retained > 80% of the cell's XFC energy density after 500 cycles.

References

1. Tarascon, J. M. & Armand, M. Issues and challenges facing rechargeable lithium batteries. *Nature* **2001**, 414, 359–367.
2. Etacheri, V., Marom, R., Elazari, R., Salitra, G. & Aurbach, D. Challenges in the development of advanced Li-ion batteries: a review. *Energy Environ. Sci.* **2011**, 4, 3243–3262
3. Armand, M. & Tarascon, J. M. Building better batteries. *Nature* **2008**, 451, 652–657.
4. Dunn, B., Kamath, H. & Tarascon, J.-M. Electrical energy storage for the grid: a battery of choices. *Science* **2011**, 334, 928–935.
5. Goodenough, J. B. & Kim, Y. Challenges for rechargeable Li batteries. *Chem. Mater.* **2010**, 22, 587–603.
6. Li, M., Lu, J., Chen, Z., Lu, J. & Amine, K. 30 years of lithium-ion batteries. *Adv. Mater.* **2018**, 30(33), 1800561.
7. Chapman, N.; Borodin, O.; Yoon, T.; Nguyen, C. C.; Lucht, B. L. Spectroscopic and Density Functional Theory Characterization of Common Lithium Salt Solvates in Carbonate Electrolytes for Lithium Batteries. *J. Phys. Chem. C* **2017**, 121 (4), 2135–2148.
8. Su, C.-C.; He, M.; Amine, R.; Chen, Z.; Sahore, R.; Dietz Rago, N.; Amine, K., Cyclic carbonate for highly stable cycling of high voltage lithium metal batteries. *Energy Storage Materials.* **2019**, 17, 284–292.
9. Chen, Z., Ren, Y., Jansen, A. N., Lin, C. K., Weng, W., & Amine, K. New class of nonaqueous electrolytes for long-life and safe lithium-ion batteries. *Nat. Commun.* **2013**, 4, 1513.

Acknowledgements

Support from Brian Cunningham of the U.S. DOE's Vehicle Technologies Office is gratefully acknowledged. We also want to thank all our collaborators for their significant contribution to this project: Jianguo Wen (ANL), Yang Ren (ANL), Wenjuan Liu-Mattis (Microvast), Bryan Yonemoto (Microvast), Peter Lamp (BMW), Odysseas Paschos (BMW) and Forrest Gittleman (BMW).

I.5.G Enabling Extreme Fast Charging through Control of Li Deposition Overpotential on Graphite Electrodes (Stony Brook University)

Esther Takeuchi, Principal Investigator

Stony Brook University
100 Nicolls Road, 675 Chemistry
Stony Brook, NY 11790-3400
E-mail: esther.takeuchi@stonybrook.edu

Brian Cunningham, DOE Technology Development Manager

U.S. Department of Energy
E-mail: Brian.Cunningham@ee.doe.gov

Start Date: July 1, 2018	End Date: August 31, 2020	
Project Funding (FY19): \$892,496	DOE share: \$800,000	Non-DOE share: \$92,496

Project Introduction

A major barrier facing the adoption of electric vehicles (EVs) is that currently utilized Li-ion batteries take significantly longer to recharge compared to the time necessary to refuel vehicles powered by internal combustion engines. Thus, the need to develop Li-ion batteries which can be charged in approximately 10 minutes (6 C rate) without sacrificing range, cost, or cycle life is critical for the widespread implementation of EVs. Fast charging capability of state of the art Li-ion batteries is limited by the occurrence of Li plating at the graphite anode. At fast charge rates the graphite anode is polarized below 0V, causing Li plating that results in capacity loss, increased resistance, and internal short circuits. To suppress Li plating, multiple strategies have been demonstrated with only limited effectiveness, and new approaches are needed to enable cycling at extreme fast charging rates.

Objectives

The objective of the project is to research, develop, design, fabricate, and demonstrate 2 Ah XFC cells, with an energy density ≥ 200 Wh/kg, capable of a 10-minute fast charge protocol at ≥ 6 C charging rate, cost of $\leq \$150$ /KWh, and 500 cycles with $< 20\%$ fade in specific energy.

Approach

The technological approach is to deliberately increase the overpotential for Li metal deposition at the graphite anode surface, thereby inhibiting Li metal deposition. This is accomplished by coating graphite electrodes with nanometer scale coatings of Cu or Ni metal, which have high overpotentials unfavorable for lithium deposition. During battery charging, the overpotentials for Li deposition on the metal coated electrode surface are greater in magnitude than the overpotential for intercalation into graphite, resulting in preferred lithiation of graphite and inhibited Li plating. The nanometer scale thickness of the metal coatings enable the function of the graphite electrode to be maintained and preserve state of the art energy density. The program represents an entirely novel and potentially transformative strategy for Li plating suppression.

Results

1. Preparation and Characterization of Metal Coated Graphite Electrodes

Graphite electrodes with 10 nm Ni or 10 nm Cu surface films were prepared using DC magnetron sputtering. At this thickness, the contributions of the metal coatings to the inactive mass of the electrode are insignificant: for a theoretical 1 Ah NMC622/graphite pouch cell with 20 cm² electrode area and 2.5 mAh/cm² areal capacity, the extra mass contributed by the metal coatings on the anode would result in only a 0.015% decrease in energy density. The sputter deposited electrodes were characterized using scanning electron microscopy (backscatter and secondary electron imaging modes) as well as energy dispersive x-ray spectroscopy (Figure I.5.G.1). The BSE yield dependence on Z enabled clear contrast between pristine graphite and graphite coated with the metal films. As observed in the images collected from the top-down, the upper surfaces of the electrodes appear to be uniformly coated with Cu or Ni. SEM-BSE images of the electrode cross sections were also collected to further understand the uniformity of the sputter deposited metal layers. The sputtered films are limited to the electrode surface, and crevices between adjacent graphite particles are not completely covered with the deposited Ni or Cu. EDS maps of the electrodes indicate good uniformity of the deposited Cu and Ni layers on the electrode surfaces. High resolution SEM-SE images probe the surface texture of the metal coated electrodes. This texture can be visualized as small cracks among the deposited metal grains.

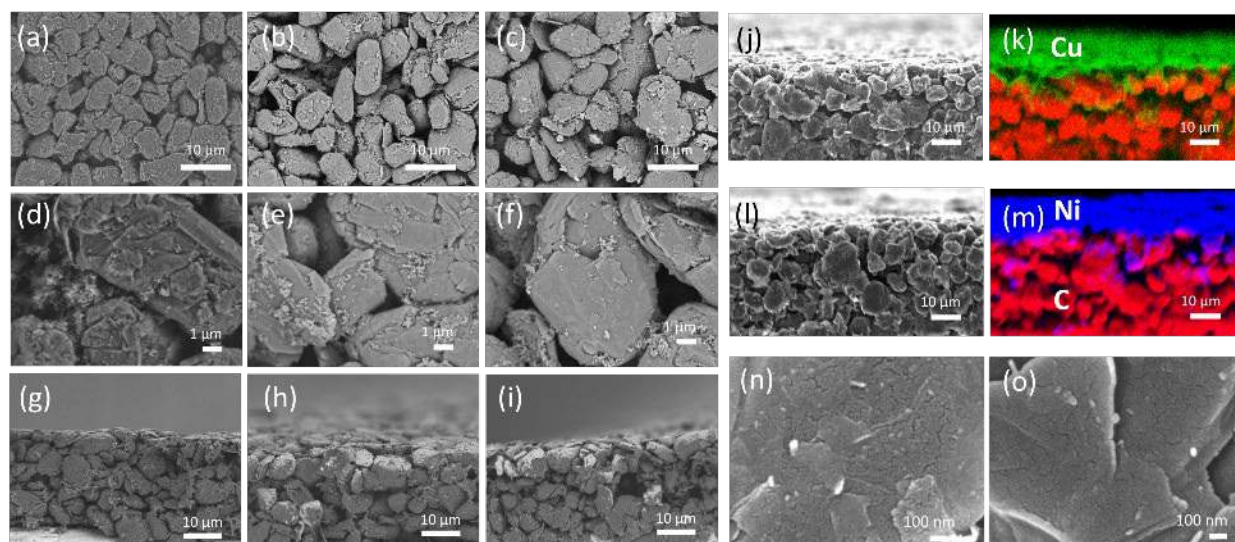


Figure I.5.G.1 (a-i) SEM backscatter images of graphite electrodes (a, d, g), pristine, (b, e, h) sputter coated with 10 nm Cu, and (c, f, i) sputter coated with 10 nm of Ni. Images a-i show the samples measured top-down while j-m show cross sectional images of the electrodes. (j, l) SEM secondary electron images and (k, m) corresponding composite EDS maps for graphite electrodes sputtered with (j, k) 10 nm Cu and (l, m) 10 nm Ni. (n, o) High resolution SEM-SE images for electrodes sputtered with (n) 10 nm Cu and (o) 10 nm Ni

The thicknesses of the deposited Ni and Cu films were verified via atomic force microscopy (AFM) analyses of ultra-flat SiO₂ wafers which were sputtered alongside the graphite anodes. Post-sputtering, a portion of the sputter deposited coating was removed, creating a step between the metal coated and uncoated areas. Non-contact AFM scanning was then performed on the stepped region to determine the thickness of the deposited film (Figure I.5.G.2a,b). The average Cu and Ni thicknesses were determined to be 10.2 ± 0.6 nm ($n=10$) and 9.7 ± 0.7 nm ($n=10$), respectively. These findings verify that 10 nm thicknesses of Cu and Ni could be consistently prepared under controlled conditions of sputtering power and argon pressure using DC magnetron sputtering.

X-ray photoelectron spectroscopy (XPS) was used to probe the surface oxidation state of the as-prepared Ni and Cu films on graphite, as well as the films after undergoing formation cycling (Figure I.5.G.2c-f). Based on the fit of the spectral data for the as-prepared Cu-coated graphite electrode, the Cu²⁺ percent composition is ~70%, indicating significant oxidation of the deposited metal. However, analysis of the electrode after

undergoing the formation cycling protocol (ending in the delithiated state) indicates that the Cu coating consists entirely of Cu^0 . This result clearly indicates that while the sputter deposited Cu film is oxidized, during formation it is electrochemically reduced to Cu metal, and does not re-oxidize during delithiation of the graphite in the potential window used. XPS analysis of the pristine Ni-coated graphite electrode indicates that the surface of the as-deposited film is comprised of NiO. After undergoing formation cycling, the spectrum was well fit to a single Ni^0 phase. Thus, both Ni and Cu as-deposited films are oxidized but electrochemically reduce to Ni^0 and Cu^0 during formation, resulting in pure metal films on the graphite electrodes. To reduce 10 nm layers of CuO to Cu^0 and NiO to Ni requires only $4.2 \mu\text{Ah}/\text{cm}^2$ and $4.8 \mu\text{Ah}/\text{cm}^2$, respectively, and thus the contribution of the reduction of the oxide films to the irreversible capacity of the electrode is negligible.

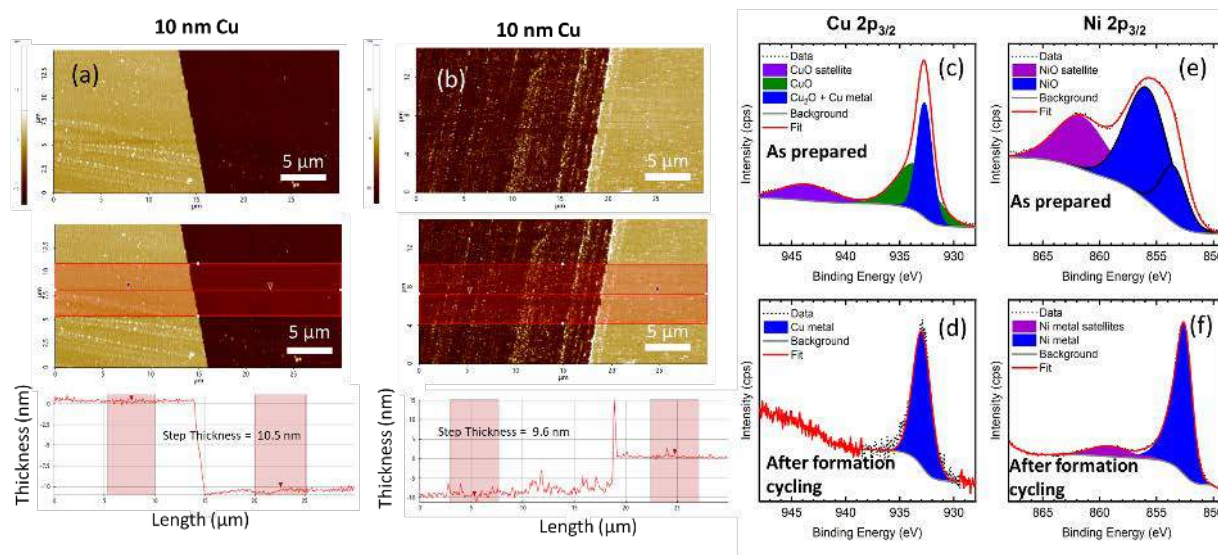


Figure I.5.G.2 (a, b) Representative atomic force microscopy images of ultra-flat SiO_2 wafers sputtered with (a) 10 nm of Cu, and (b) 10 nm of Ni. (c-f) XPS spectra of (c, d) Cu $2p_{3/2}$ region of (c) pristine 10 nm Cu-graphite electrode and (d) 10 nm Cu-graphite electrode after formation cycling (charged state); (e, f) Ni $2p_{3/2}$ region of (e) pristine 10 nm Ni-graphite electrode and (f) 10 nm Ni-graphite electrode after formation cycling (charged state)

Operando X-ray Absorption Near Edge Structure (XANES) spectroscopy measurements were collected on the electrodes during the initial formation cycle to probe the changes in the oxidation state of the films with discharge and charge (Figure I.5.G.3). Linear combination fit results relative to XANES standards show that the as prepared 10 nm Cu coated graphite electrode is a mixture of $\sim 22\%$ Cu^0 , $\sim 61\%$ Cu_2O , and $\sim 17\%$ CuO . Notably, the results demonstrate that during formation cycling the copper oxides that comprise the film are fully reduced to Cu metal during the initial lithiation, and do not re-oxidize during delithiation, in good agreement with the XPS results. Similarly, the 10 nm Ni-graphite coating in the as-prepared state shows a composition from LCF fitting of $\sim 50\%$ NiO and $\sim 50\%$ Ni^0 and irreversibly is reduced to 100% Ni metal during the formation cycle.

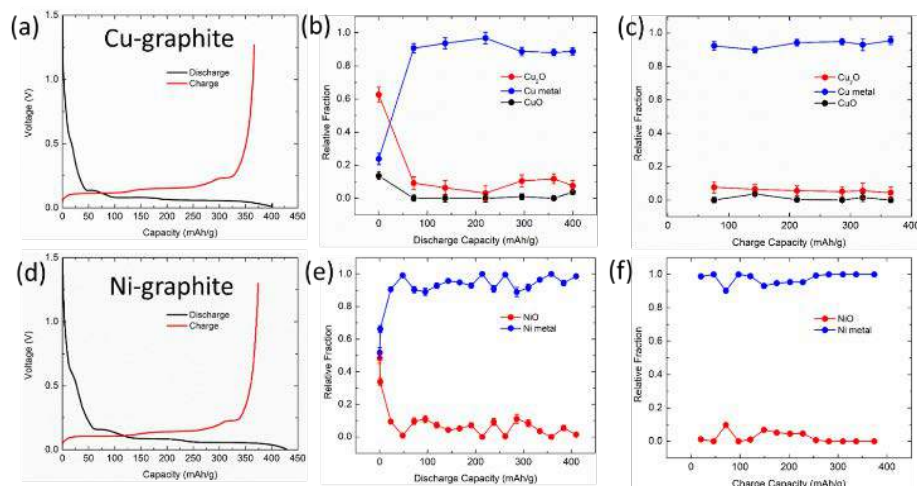


Figure I.5.G.3 Operando XANES results for (a-c) Cu-graphite electrodes and (d-f) Ni-graphite electrodes during a formation cycle at C/5 rate between 0.01 – 1.4 V vs. Li/Li⁺. (a, d) Voltage profiles of operando cells. (b, c, e, f) Linear combination fit results for operando spectra during (b, e) discharge and (c, f) charge

2. Impact of Metal Coatings on Li metal Deposition

Lithium plating experiments in half cells demonstrated the effectiveness of the Cu and Ni films at preventing Li metal deposition compared to uncoated graphite. Half cells of each electrode type with fully lithiated electrodes were subjected to voltage holds of -10 mV, -15 mV and -20 mV for 6 hours. Under each potentiostatic condition, the Cu-graphite and Ni-graphite electrodes show less plating capacity compared to the uncoated graphite electrode, providing electrochemical evidence that the metal coatings reduce lithium plating (Table I.5.G.1). Post-testing, we recovered the electrodes under inert atmosphere and measured X-ray diffraction of the Li⁰ (110) peak to determine the amount of crystalline Li plated on each electrode type. Quantified Li peak areas for metal coated electrodes are approximately 50% of the control graphite electrode at each condition, validating the electrochemical results (Table I.5.G.2). The XRD findings confirm that metal films of Cu and Ni significantly inhibit the deposition of Li metal under plating conditions.

Table I.5.G.1 Normalized Lithium Plating Capacities for Fully Lithiated Electrodes Subjected to Voltage Holds of -10 mV, -15 mV and -20 mV for 6 hours

Electrode Type	Normalized Li Plating Capacities		
	-10 mV hold	-15 mV hold	-20 mV hold
graphite	0.30 ± 0.03	0.65 ± 0.05	1.00 ± 0.05
Cu-graphite	0.20 ± 0.05	0.48 ± 0.05	0.65 ± 0.03
Ni-graphite	0.20 ± 0.08	0.48 ± 0.03	0.60 ± 0.03

Table I.5.G.2 Normalized Li(110)/Cu(220) Peak Area Ratios from XRD Measurements of Electrodes Recovered from Half Cells Subjected to Voltage Holds of -10 mV, -15 mV and -20 mV for 6 hours

Electrode Type	Normalized Li(110)/ Cu(220) Peak Area Ratio		
	-10 mV hold	-15 mV hold	-20 mV hold
graphite	0.26 ± 0.03	0.49 ± 0.09	1.00 ± 0.08
Cu-graphite	0.13 ± 0.05	0.28 ± 0.08	0.6 ± 0.1
Ni-graphite	0.08 ± 0.08	0.28 ± 0.08	0.54 ± 0.05

SEM backscatter images of the electrodes after plating at the 6 hr, - 20 mV condition are shown in Figure I.5.G.4. Graphite particles as well as Ni and Cu coatings appear brighter in the images compared to the plated Li. On the uncoated graphite electrodes, interconnected dense Li films were observed, covering much of the electrode surface. In contrast, the structure of the graphite electrodes is still apparent in the Cu- and Ni-coated electrodes, which further confirms that nm thickness films of Cu and Ni significantly inhibit the deposition of Li metal under voltage conditions where plating occurs.

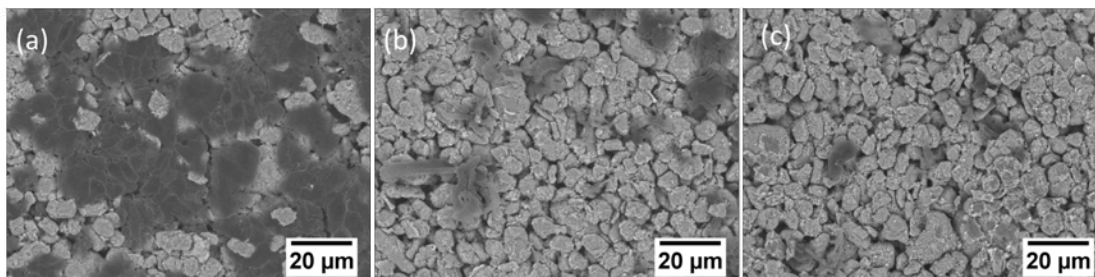


Figure I.5.G.4 LBE SEM images displaying the morphologies of Li plated at -20 mV on the (g) uncoated graphite, (h) Cu-coated graphite, and (i) Ni-coated graphite electrodes

3. Electrochemical Testing of Metal Coated Graphite Electrodes in Full Cells

The FY2019 year 1 Go/No-Go decision point was the demonstration of NMC622/graphite single layer full cells using a Cu-graphite or Ni-graphite electrode which exhibited capacity retention $\geq 80\%$ of control (uncoated) graphite electrodes when cycled at C/2 rate for 50 cycles. Graphite electrodes were prepared with composition of 90% SLC 1506T natural graphite, 3% carbon black, and 7% KF-9300 Kureha PVDF binder. Electrode loading was 8.6 mg cm^{-2} with porosity of 41 %. 10 nm was selected as the thickness of the metal coatings for the milestone. The graphite electrodes were paired with NMC 622 cathodes (90% NMC622, 5% carbon black, 5% PVDF, 15.9 mg/cm^2 loading, 35% porosity) with N:P ratio of 1.17 : 1. The paired electrodes were used to prepare single layer pouch cells with 1M LiPF₆ 30:70 EC:DMC electrolyte. Cells containing pristine, untreated graphite anodes were also prepared for comparison to cells with the metal coated electrodes. A cell formation protocol of 4 cycles at C/10 rate between 3 V – 4.3 V was used form a stable solid electrolyte interphase on the electrodes. Cells were then cycled at symmetric C/2 discharge and charge rate between 3.0 – 4.3 V for 100 cycles (Figure I.5.G.5). The Go/No-Go Decision point was met, with the capacity retention of the three electrode groups within experimental error of each other. Areal capacity was approximately 2.7 mAh/cm^2 after 100 cycles.

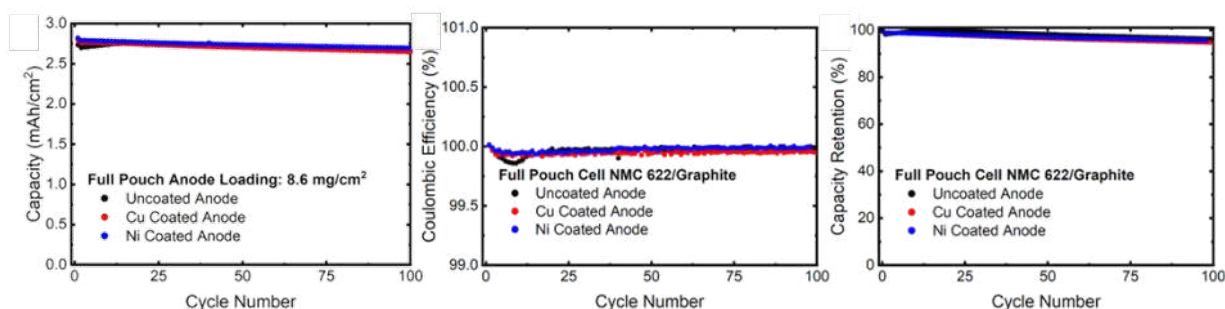


Figure I.5.G.5 Cycling of single layer full cells with NMC 622 cathodes and uncoated graphite (control), Cu-graphite, or Ni-graphite anodes between 3.0 – 4.3 V at C/2 rate

Additional testing of the full cells under a 10 minute charge protocol has been performed (Figure I.5.G.6). A constant current / constant voltage charge protocol was used for the test, where a charge rate equivalent to 6C was used for the constant current step, followed by a voltage hold at 4.3 V until the total charge time of 10 minutes was met. The cells with Ni-graphite anodes exhibited an approximate 10% improvement in capacity retention through 300 cycles relative to the control group.

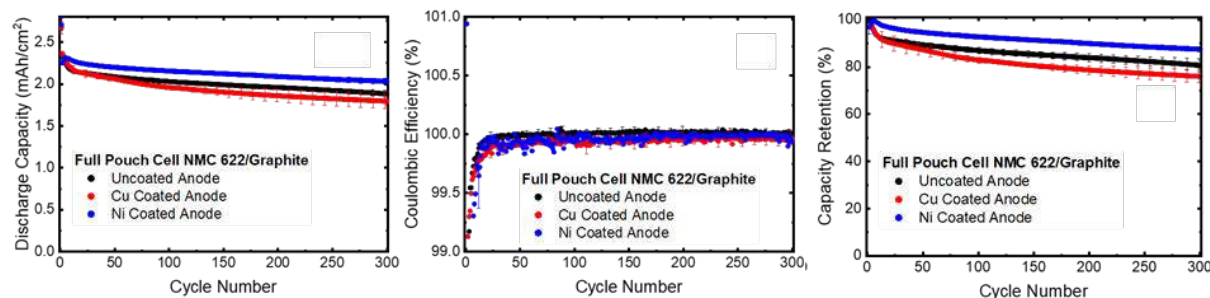


Figure I.5.G.6 Cycling of single layer full cells with NMC 622 cathodes and uncoated graphite (control), Cu-graphite, or Ni-graphite anodes between 3.0 – 4.3 V with 10 minute charge (CC/CV) and 1C discharge

A year end deliverable for the project was the delivery of nine 2 Ah cells to DOE for testing. This deliverable was completed where 9 full cells were prepared (2 cells with control (uncoated) graphite anodes, 3 cells with graphite anodes deposited with 10 nm Cu, 4 cells with graphite anodes deposited with 10 nm Ni) and shipped to DOE, with electrochemical testing currently in progress.

4. Optimization of Metal Coating Type and Thickness

Work is now underway to optimize rate capability and cycle life of Cu or Ni coated electrodes through systematic study of metal coating type and thickness. Graphite electrodes have been prepared with 5 nm, 10 nm, and 20 nm thicknesses of Cu and Ni, and electrodes have been characterized by SEM and EDS mapping (Figure I.5.G.7). Evaluation of the fast charging capability of these electrodes in single layer NMC622 pouch cells is in progress.

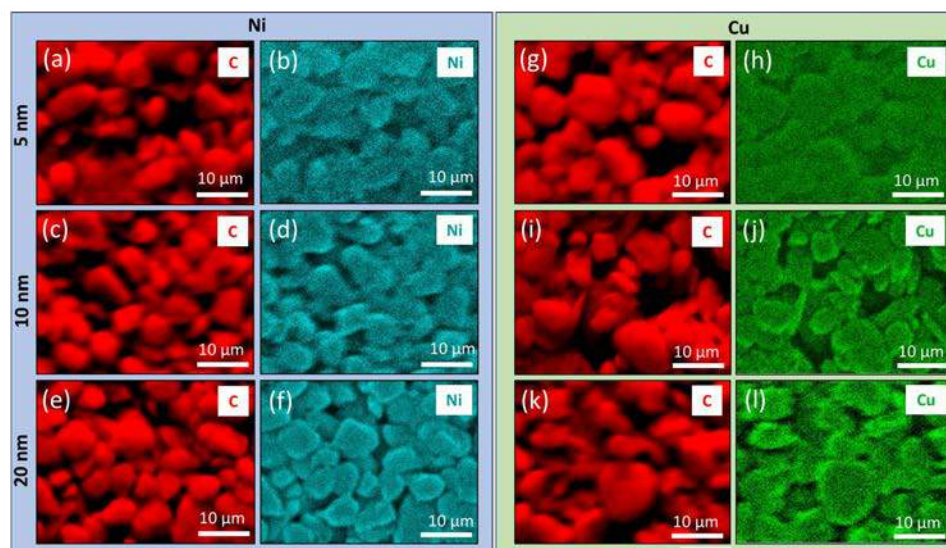


Figure I.5.G.7 EDS mapping images for the top down view of Cu and Ni deposited on graphite. (a-f) Ni deposited on graphite with thickness of 5, 10 and 20 nm. (g-l) Cu deposited on graphite with thickness of 5, 10 and 20 nm. Magnification is 3000x

Conclusions

Graphite electrodes with controlled nanometer scale thickness of Cu or Ni surface films have been prepared using a DC magnetron sputtering technique. While the pristine Ni or Cu films are oxidized on air exposure, during lithiation they are electrochemically reduced to Cu^0 and Ni^0 , and do not re-oxidize during delithiation with the potential limits used. At 10 nm thickness, the reduction of the films requires only $4.2 \mu\text{Ah}/\text{cm}^2$ (Cu) and $4.8 \mu\text{Ah}/\text{cm}^2$ (Ni), and thus first cycle irreversible capacity is not significantly increased. Li plating experiments demonstrate that the metal films reduce the quantity of plated Li metal by 40% - 50% compared to

uncoated graphite. The efficacy of the metal films, specifically for Ni-coated graphite anodes, as a modification technique to reduce Li-plating are demonstrated at high charge rates. Pouch cells containing Ni-coated anodes tested under extreme fast charging conditions (10 minute charge time) exhibit enhanced electrochemistry with ~90% capacity retention after 300 cycles, corresponding to a ~10% increase compared to cells containing pristine graphite electrodes. The findings establish an entirely new and potentially transformative concept for prevention of lithium plating on graphite via deliberate control of the overpotential for Li deposition.

Key Publications

Publications

1. Tallman, Killian; Zhang, Bingjie; Wang, Lei; Tong, Xiao; Thieme, Juergen; Kiss, Andrew; Marschilok, Amy C.; Takeuchi, Kenneth J.; Bock, David C.; Takeuchi, Esther S. “Anode Overpotential Control via Surface Treatment: Inhibition of Lithium Plating.” Under Revision.

Patents

1. Takeuchi, Esther S.; Takeuchi, Kenneth J.; Marschilok, Amy C.; Bock, David C. Device and Method for Fast Charge of Batteries. Provisional Patent Application No.: 62/618,116 (2018). (filed prior to program start).

Presentations

1. Takeuchi, Esther S.; Takeuchi, Kenneth J.; Marschilok, Amy C.; Bock, David C., “Enabling Extreme Fast Charging Through Control of Li Deposition Overpotential,” Poster Presentation at 2019 Vehicle Technologies Office Annual Merit Review, June 12, 2019, Arlington, VA 22202.
2. Takeuchi, Esther S.; Takeuchi, Kenneth J.; Marschilok, Amy C.; Bock, David C., “Enabling Extreme Fast Charging Through Control of Li Deposition Overpotential,” Oral Presentation at U.S. Drive XFC Meeting, August 20, 2019, Lemont, IL 60439.

Acknowledgements

The co-PIs for this project include Kenneth J. Takeuchi, Amy C. Marschilok, David C. Bock; all from the Brookhaven National Laboratory.

I.5.H Detecting Lithium Plating during Fast Charging, Heterogeneity Effects during Fast Charging, and Graphite Anodes with Directional Pore Channels Made by Freeze Tape Casting (LBNL)

Dr. Nitash P. Balsara, Principal Investigator

Department of Materials Sciences
Lawrence Berkeley National Laboratory
University of California, Berkeley
Berkeley, CA 94720
E-mail: nbalsara@berkeley.edu

Samuel Gillard, DOE Technology Development Manager

U.S. Department of Energy
E-mail: Samuel.Gillard@ee.doe.gov

Start Date: October 1, 2018

End Date: September 30, 2019

Project Funding (FY19): \$950,000

DOE share: \$950,000

Non-DOE share: \$0

Project Introduction

The U.S. Department of Energy's Office of Energy Efficiency and Renewable Energy (DOE-EERE) has identified fast charging — with a goal of 15-min recharge time — as a critical challenge to pursue in ensuring mass adoption of electric vehicles. Present-day high-energy cells with graphite anodes and transition metal cathodes in a liquid electrolyte are unable to achieve this metric without negatively affecting battery performance. There are numerous challenges that limit such extreme fast charging at the cell level, including Li plating, rapid temperature rise, and possible particle cracking. Of these, Li plating is thought to be the primary culprit.

Objectives

The primary goal of this project is to detect the initial nucleation event using data available in typical battery management systems. Identifying the initial onset of Li plating during fast charging is a multi-faceted, challenging “needle-in-a-haystack” problem. First, there may be a barely perceptible chemical signature of this event. For example, the presence of lithium may lead to the sudden formation of a small amount of gases due to irreversible reactions between the plated lithium and the electrolyte-soaked solid electrolyte interphase (SEI). Second, identifying the particular particle where the overlithiation and Li plating occurs can be challenging at the immediate onset of Li plating. Clearly, the particular particle that is overlithiated first will depend on the state-of-charge of the electrode, as it will be governed by the amount of lithium intercalated at that time and the lithium concentration in the surrounding liquid electrolyte. The third and final challenge is identifying electrical signatures of the overlithiation event so that our work can be used in practical battery management systems. We note here that the signatures may be different at different states-of-charge and that the electrical signature may be inherently non-linear, and thus not clearly evident in standard electrochemical measurements. Our objective is to address all three challenges.

Characterization of the onset of lithium plating and its mechanism is, in practical graphitic lithium ion battery anodes, complicated by the three-dimensional porous composite nature of the anode and its interaction with an electrolyte whose lithium concentration at the interface with the graphite varies as a function of depth within the electrode during fast charging. We aim to determine some of the fundamental factors at play by performing experiments using planar, highly oriented pyrolytic graphite (HOPG) samples. HOPG is as close to monocrystalline graphite as is commercially available, and consists of a stack of graphite planes, with in-plane grain sizes on the order of 0.1-1mm. It is therefore possible to study the difference in lithium plating behavior on edge and basal planes as a function of current density on these samples, initially and as a function of ageing.

An additional goal is to use a freeze tape casting method to develop graphite anode architectures with low tortuosity open pores parallel to the ion transport direction during cycling. Various types of commercial graphite, carbon, and binder will be tested for slurry stability. The down selected combinations will be used to produce graphite anodes with controlled porosity, pore size, and layer thickness. The final product may serve as a drop-in replacement for the conventional graphite anode, but with a goal of improved charge acceptance capability. Modeling efforts of the Kandler group (NREL) will provide guidance to the desired overall porosity and pore structure. Tomography data will be shared with NREL to improve model accuracy. The Jansen group (ANL) will aid with cycling the produced freeze tape cast graphite anodes to compare with conventional counterparts.

Approach

A wide variety of methods have been utilized to address the problems mentioned earlier. Titrations with *ex situ* differential electrochemical mass spectrometry was performed on lithium plated graphite electrodes. Optical and X-ray tomography cells are being developed to study lithiation and plating in situ and with time stop experiments. Thermal sensors were developed for *operando* measurements of thermal resistances during fast charging. Electrochemical techniques were applied to detect the onset of plating, to investigate rate limitations of NMC and graphite electrodes, and to compare the edge and basal plans of HOPG. Directional pore graphite electrodes were freeze tape casted.

Results

Quantify dead lithium on fast-charged graphite electrodes. Bryan McCloskey's group used differential electrochemical mass spectrometry (DEMS) to detect gases evolved during cycling of graphite electrodes. Figure I.5.H.1a shows the DEMS titration setup, in which water is injected air-free into a vessel containing a cycled graphite electrode, evolving an amount of H_2 equal to 1 mole H_2 per 2 moles dead Li. This titration was done for Round 1 graphite electrodes cycled at various rates, and a clear trend of increasing dead Li amount with increasing C-rate is observed in Figure I.5.H.3b. A representative gas evolution signature collected for a Li-graphite half cell is shown in Figure I.5.H.1c. A clear ethylene (C_2H_4) signature is observed during the first intercalation due to the SEI-forming reduction of ethylene carbonate, but only modest traces of gas evolution are seen thereafter, even after intentional overlithiation of the graphite. Future work will involve using this technique to quantify the sensitivity of proposed Li detection methods.

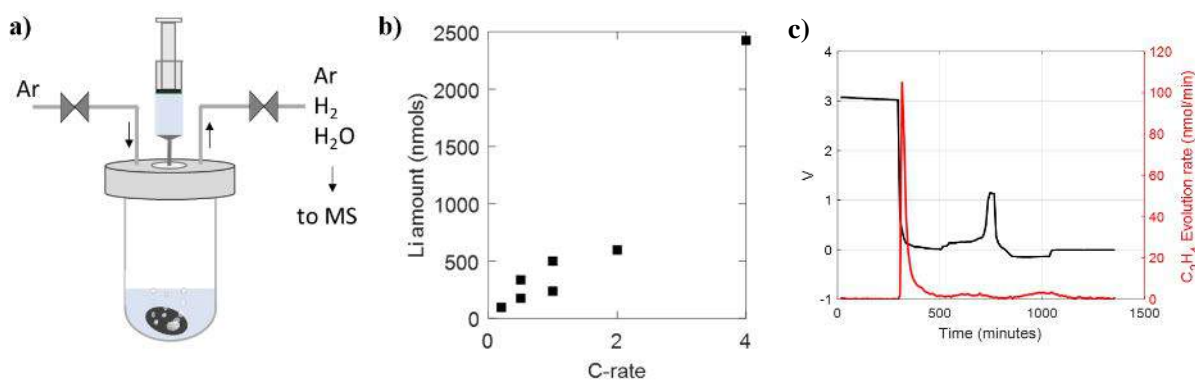


Figure I.5.H.1 a) DEMS titration setup schematic. b) Measured dead Li amount after 2 C/10 formation cycles and 3 cycles of varying intercalation rates to 372 mAh/g and deintercalation to 1.5 V. c) DEMS data for Li-graphite cell with following cycling procedure: (i) 5 hour OCV, (ii) one C/5 cycle (cutoff at 10 mV and 1.5 V), (iii) C/2 intercalation for 5 hours (overlithiation), (iv) 5 hour OCV

In situ microscopic characterization of graphite lithiation and delithiation. Guoying Chen's group constructed an optical cell with a graphite working electrode (SLC1605T, ANL), Li metal counter and reference electrodes, and a PVDF membrane separator soaked with the Gen 2 electrolyte (1.2 M LiPF₆ in EC: EMC 3:7 wt. %) for the study. Details on the cell design are shown in Figure I.5.H.2d. Figure I.5.H.2a-c show the

preliminary results obtained during the 1st charge and discharge at a C/10 rate. The voltage profile of the lithiation process (Figure I.5.H.5a) is consistent with what was reported on typical graphite half-cells in the literature, confirming that the optical cell is suitable for the in situ studies. As the lithiation process proceeded, the graphite electrode experienced a progression in colors that ranged from grey, blue, red and gold, corresponding to the different lithiated stages of C, LiC₁₈, LiC₁₂ and LiC₆, respectively. Figure I.5.H.2b and Figure I.5.H.2c compare the in situ optical images taken from the graphite electrode before and after the 1st lithiation, as indicated on the voltage profile shown in Figure I.5.H.2a. At the pristine state, large graphite particles with an average particle size of ~10–15 μm were seen uniformly in grey color. At the end of the 1st lithiation process at 0.01 V (vs. Li/Li⁺), gold-colored LiC₆ particles along with red-colored LiC₁₂ were broadly visible. Li dendrites were not observed under current conditions. The optical cell suffered large resistance during the delithiation process which prevented the graphite electrode from full extraction of the intercalated Li⁺ (Figure I.5.H.2a). This was mostly a result of electrolyte loss from the current cell. In future work, we will optimize the various fabrication steps, especially electrolyte soaking and epoxy sealing to prevent electrolyte leaking, to improve total charge and discharge capacities as well as columbic efficiency of the optical cell. Studies using various current densities will be performed to investigate the correlation between charging rate and Li dendrite formation and propagation under *operando* conditions.

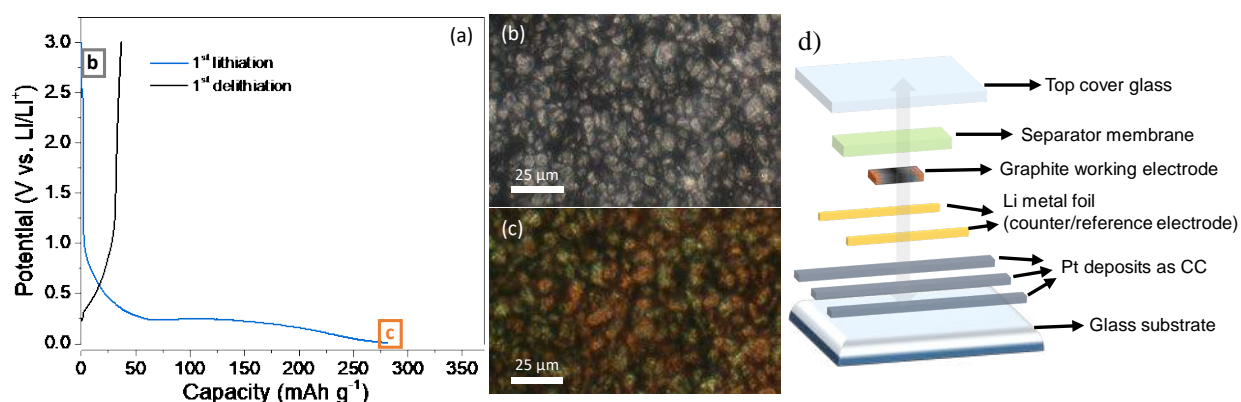


Figure I.5.H.2 a) 1st cycle charge/discharge voltage profiles of the in situ optical cell when cycled at C/10 rate between 0.01 and 3 V, b) and c) in situ optical images of the graphite electrode before and after the 1st lithiation process. d) Schematic configuration of an optical cell

Time-stop X-ray tomography study of lithiated graphite in a lithium half-cell. Nitash Balsara's group is collaborating with Finegan (NREL), and Figure I.5.H.3a shows a microtomography sample holder designed by Finegan. The Balsara group constructed Li metal/Superior graphite SLC1520P (D50 = 16.94 μm) microtomography cells with a Whatman QMA separator soaked in 1.0 M LiPF₆ 1:1 wt% EC:EMC. In an initial study, a micro-cell was imaged on the X-ray microtomography beamline at LBNL before and after 3 formation cycles of C/10 intercalation and C/5 deintercalation. The results in Figure I.5.H.3b show the presence of lithium microstructures at the interface between the separator and Li metal after formation cycles. Figure I.5.H.3c shows the formation of moss-like lithium in the same cell after 20 cycles of 6C intercalation and C/2 deintercalation. In future work, we will increase pressure via a spring within the cell and replace Whatman QMA with Celgard 2500 to help suppress these moss-like formations. Furthermore, cells made with free-standing graphite electrodes will be imaged with tomography and electrochemically tested within the micro-cell.

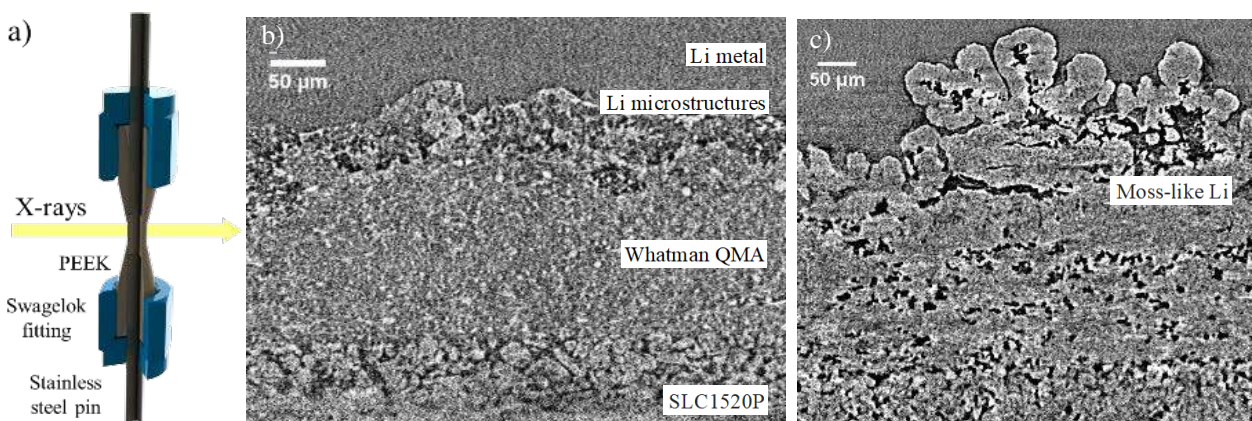


Figure I.5.H.3 (a) Schematic of X-ray tomography cell. (b) Slice of an X-ray tomogram of micro-cell after 3 formation cycles (C/10 intercalation, C/5 deintercalation) and (c) slice of an X-ray tomogram of the same cell after 20 cycles (6C intercalation, C/2 deintercalation)

Thermal analysis of fast-charging full cells. The Prasher group developed thermal sensors, which have been successfully used for *operando* measurement of thermal resistance in pouch cells. The voltage signal across a wide range of frequency enables analyzing thermal properties at different distances from sensors. Figure I.5.H.4a shows that the interface thermal resistance and total thermal resistance increases by 183% and 50% after 120 cycles charged and discharged at C/3, respectively. The total thermal resistance increases rapidly in the first 60 cycles and tends to be stable after that. To understand the evolution of thermal resistances, we performed *ex situ* measurements of interface resistance between the separator and electrode (see Figure I.5.H.4b). Preliminary results show that the thermal interface resistance between the separator and dry electrodes are $4.1 \times 10^{-5} \text{ m}^2\text{K/W}$ and $3.63 \pm 1.06 \times 10^{-5} \text{ m}^2\text{K/W}$ for cathode and anode, respectively. These measurements were done with an external pressure of 3 psi. In addition, we studied the impact of external pressure on the thermal interface resistance (see Figure I.5.H.4c). The thermal contact resistance decreases 53% from $1.35 \pm 0.25 \times 10^{-4} \text{ m}^2\text{K/W}$ to $6.38 \pm 0.38 \times 10^{-5} \text{ m}^2\text{K/W}$ as the pressure varies from 0 to 3 psi. In future work, thermal measurements at different temperatures and fast charge rates will be performed using pouch cells with new thermal sensors (see Figure I.5.H.4c).

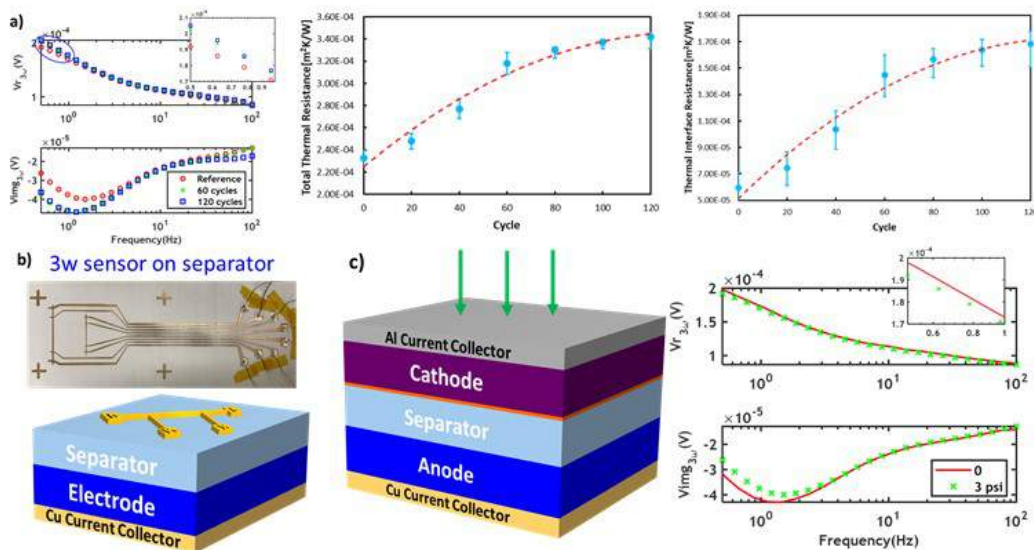


Figure I.5.H.4 a) The evolution of thermal resistance in 100+ cycles, b) 3w sensor on separator for *ex situ* measurements, c) the impact of external pressure on thermal contact resistance

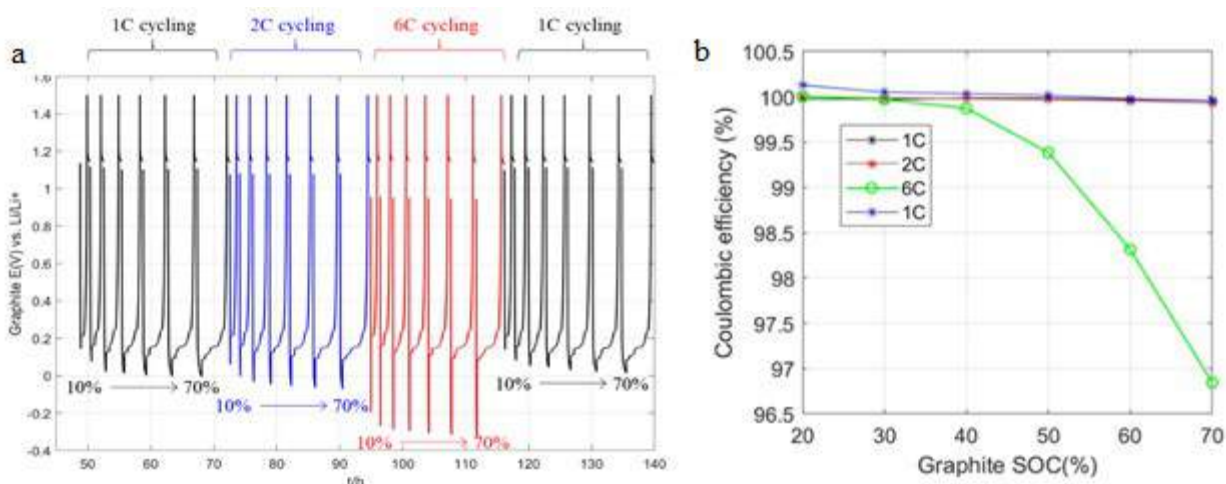


Figure I.5.H.5 (a) Graphite/Li cell cycling to generate OCV data after fast charge for various SOC and c-rates. (b) Coulombic efficiencies (CE) for these half cell cycles. We believe the drop in CE's at 6C and 40% SOC corresponds to the onset of Li plating

Electrochemically detecting the onset of lithium plating. The McCloskey group is also using differential voltage technique for detecting the onset of Li plating after fast charging. When Li plating occurs on the surface of lithiated graphite (Li_xC_6), the measured potential will be a mixed potential of the Li and Li_xC_6 . During cell relaxation after fast charge, small amounts of plated Li will chemically intercalate into graphite, resulting in a decay of the mixed Li/ Li_xC_6 potential into a pure Li_xC_6 potential. The presence of this decay feature in the open-circuit voltage (OCV) has been shown to indicate Li plating. A differential analysis of the OCV with respect to time shows a more pronounced plating signature. Our differential OCV technique analyzes the OCV after charge instead of the voltage profile during discharge. Progressive coin cell cycling enables us to use this differential OCV technique to estimate the graphite SOC at which plating begins in graphite/Li cells. Figure I.5.H.5a shows the cycling protocol used to generate abundant OCV data corresponding to different C-rates and final SOC of the graphite. Each cycle has four steps: constant-current (CC) intercalation to a varied SOC, 30 min OCV rest, CC deintercalation at $C/5$ to 1.5 V, and a final 30 min OCV before starting the next cycle. For the first 7 cycles (Figure I.5.H.3a, black), the graphite intercalation was at 1C with SOC cutoffs of 10% for cycle 1, 20% for cycle 2 etc. up to 70% for cycle 7. The next 7 cycles are identical except with an intercalation rate of 2C (Figure I.5.H.5a, blue). Plating is not expected at the 1C and 2C intercalation rates, but those cycles provide a baseline of OCV profiles for comparison with the 6C cycles. Comparing the OCV data extracted from the cycling in Figure I.5.H.5 can show the SOC onset of Li plating. All OCV profiles and derivatives are grouped by SOC and plotted in Figure I.5.H.6. At 20-30% SOC, the differential OCV profiles are similar for all c-rates, which indicates minimal plating at 6C after intercalation to 30% SOC. At 40% SOC, we attribute a shift in the 6C differential OCV to the onset of Li plating. This feature becomes more prominent at higher SOC when we expect increased Li plating. Coulombic efficiencies for all cycles, defined as a ratio of the deintercalation capacity to the intercalation capacity, support our hypothesis that this feature corresponds to Li plating (Figure I.5.H.5b). At 40% SOC, where the differential OCV suggests plating has occurred, we also see a slight drop in the coulombic efficiency that becomes larger drop at higher SOC. *Investigate the rate limitations of positive NMC and negative graphite electrodes.* Wei Tong's group used electrochemical analysis to study NMR and graphite prior to lithium metal plating. Nominal negative electrode loadings were 11.0 mg cm^{-2} , with positive loadings of 17.3 mg cm^{-2} . Graphite lithiation and NMC delithiation rate characterization was performed in half-cells. Resistance was determined from polarization vs. change in rate ($\Delta V/\Delta i$) for graphite/NMC at different percentages of lithiation/delithiation, respectively. The difference in behavior between the charge of negative graphite half cells and discharge of positive NMC half cells is clearly revealed by comparing the voltage profiles (Figure I.5.H.7a, b) at each designated rate. Increasing discharge rate clearly leads to less visible staging phenomena in the graphite electrode. In contrast, positive NMC half cells exhibit sloping charge voltage profiles from open

circuit voltage to 4.3 V cutoff with minimal change when increasing charge rate, even at 3C. The striking difference between NMC and graphite half cells implies the graphite negative electrode indeed is a key barrier to the fast charging of current Li-ion batteries. Analysis of voltage profiles (Figure I.5.H.7a, b) allows for the determination of cell resistance at each state of charge (SOC). To determine resistance, polarization from the C/25 voltage profile and change in current from C/25 rate are used. Resistance was calculated at every 10% SOC, from 10% to 90% for both graphite and NMC half-cells. Figure I.5.H.2c highlights a trend of increased resistance that occurs for a negative half-cell as percentage of lithiation increases. More specifically, the cell resistance remains relatively constant at the beginning of graphite lithiation ($\leq 30\%$), corresponding to $\sim 100 \text{ mAh g}^{-1}$ right before reaching the plateau of 0.015 V. A propensity for impedance becomes more visible towards the high percentage lithiation ($\geq 70\%$), especially near full lithiation. In contrast, the positive electrode half-cells show that cell resistance is both a function of current and SOC (Figure I.5.H.7d), where cell resistance is higher at lower rates as well as at high and low depths of charge.

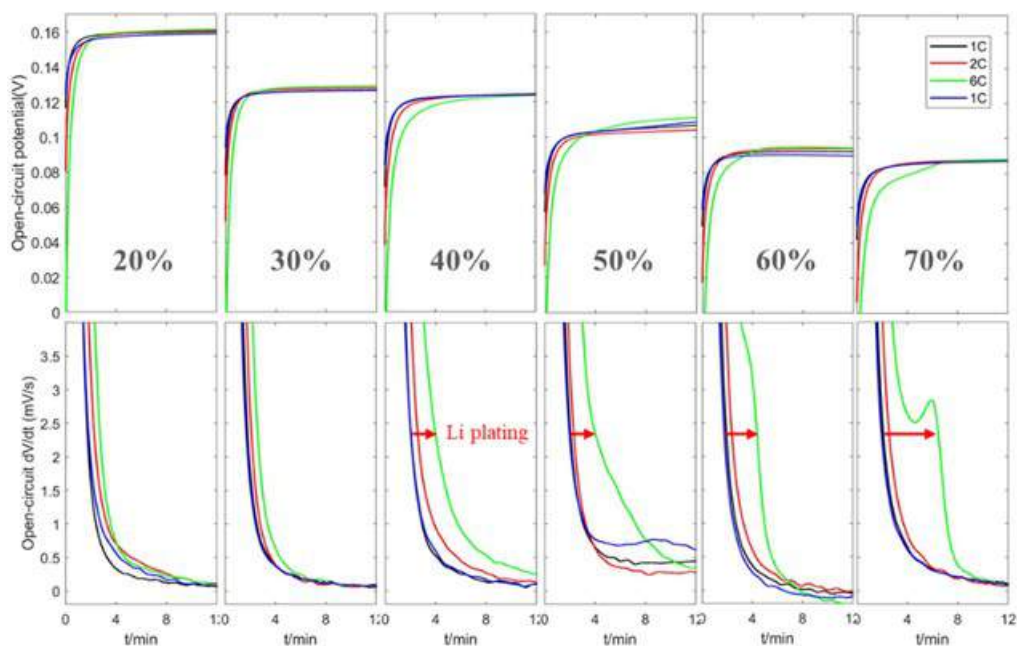


Figure I.5.H.6 OCV's (top row) and differential OCV's (bottom row) during relaxation after graphite intercalation at 1C, 2C, and 6C. Each window shows the OCV's after intercalation to the designated SOC

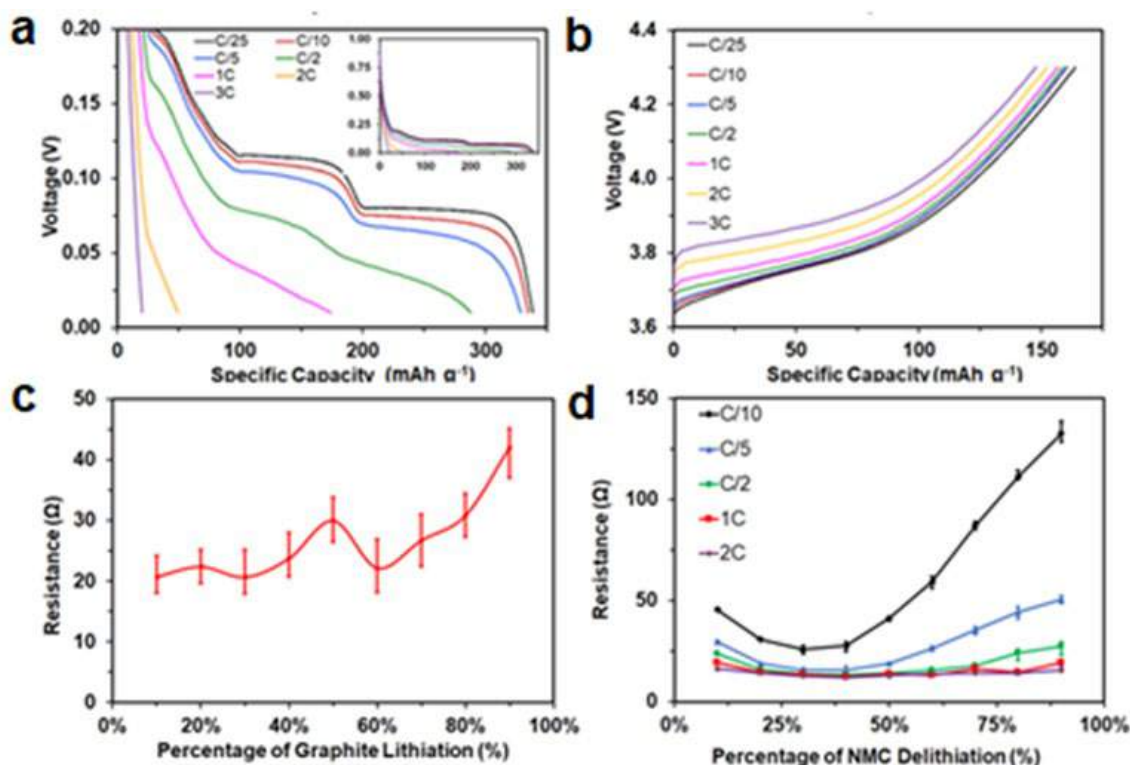


Figure I.5.H.7 (a) Lithiation voltage profiles for graphite electrode between 0.20 and 0.00 V, inset showing full profile from 1.00 to 0.00 V, (b) charge voltage profiles for NMC electrode, (c) average negative graphite and (d) positive NMC half-cell resistance of four cells from 10 to 90% lithiation with range bars. Range bar represents the minimum and maximum values for each set of cells

Compare effects of lithium plating on edge and basal planes of graphite. Robert Kostecki's group began by isolating the basal plane of graphite using a beaker cell with an O-ring. A fresh surface was created on a piece of HOPG by exfoliation with tape, and the HOPG was sealed against the O-ring, and measured against Li counter and reference electrodes. Two cyclic voltammetry (CV) cycles were performed in the range 0.01–1.5 V vs Li in order to achieve SEI-coated graphite. Then, a current ramp was applied to determine the current density that can be sustained above 0 V. The results are shown in Figure I.5.H.8. The CV formation cycles exhibit a pronounced peak at about 0.5 V vs Li, indicative of carbonate electrolyte reduction. The lack of a peak at lower voltages, and the absence of an anodic current during the sweep back to 1.5 V, indicates that no reversible process such as Li intercalation is occurring at significant current densities. It can also be seen that electrolyte reduction and the concomitant SEI formation is incomplete after the two CV cycles and continues during the current ramp. This process cannot sustain more than 46 $\mu\text{A}/\text{cm}^2$, and above this current density the potential drops below 0 V vs Li, at which point plating cannot be ruled out. Similarly, the edge plane was examined by immersing a piece of HOPG in a beaker cell with Li counter and reference electrodes. The basal areas were not isolated in this case, but it will be seen that the currents are so much higher that the basal contribution is negligible. We have found that basal and edge graphite can sustain about 46 $\mu\text{A}/\text{cm}^2$ and 4000 $\mu\text{A}/\text{cm}^2$ respectively while remaining in the plating-free regime above 0 V vs Li, although only the latter is clearly an intercalation current.

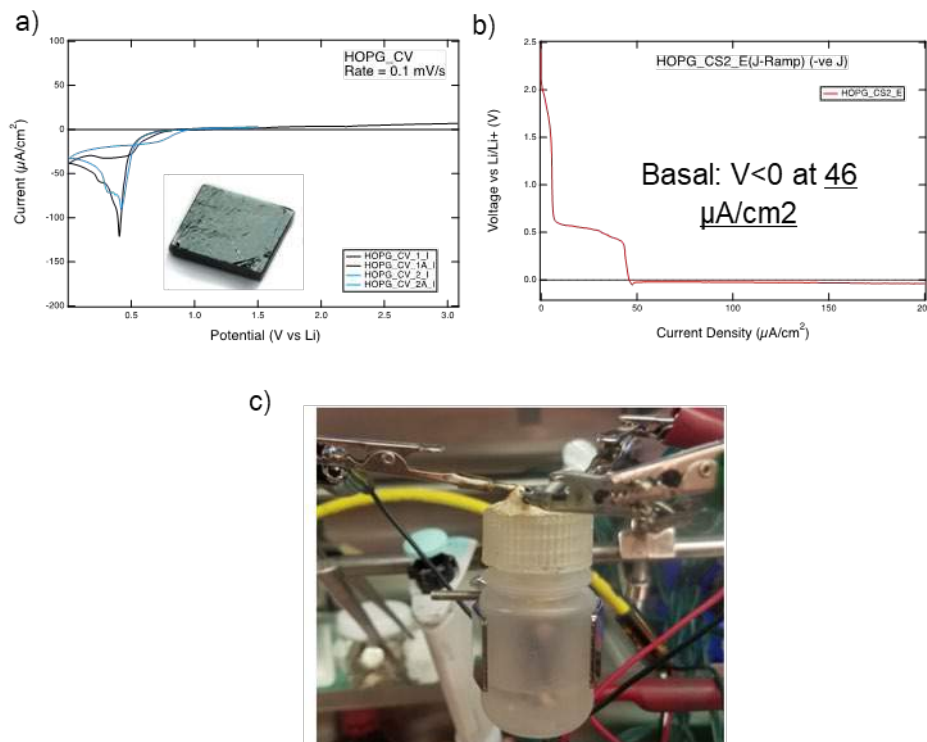


Figure I.5.H.8 (a) CV formation of the basal HOPG/Li half-cell. (b) Current ramp behavior of basal HOPG/Li half-cell, after CV formation. (c) Image of cell

Fabricate graphite electrodes with directional pores. The Doeff group tested four types of commercial graphite (1506T, BFC-10, SFG-6, KS-6) for dispersion and slurry formulation. 1506T was down-selected as optimal. We found that lower freezing temperatures result in more nucleation sites making it difficult to differentiate the pore channels from the graphite using SEM imaging. We succeeded in freeze tape casting graphite electrodes with 58 vol.% porosity. Mixed binder system of CMC/SBR was used which resulted in good adhesion and flexibility. Typical dry compositions of the electrodes were graphite (1506T): CMC binder (MW 90k): SBR binder: Timcal C45 at 90.8: 2.4: 4.8: 2 wt.%. The slurry was mixed using a centrifugal mixer (Thinky mixer) for 15 min. Casting speed was fixed at 2.5 mm/min. Figure I.5.H.9 shows SEM images of a freeze tape cast 1506T graphite anode cast at 36 vol.% graphite at -8°C with porosity of 58 vol.%. Vertical pore channels are observed with average channel widths of $8 \pm 3 \mu\text{m}$. Mixed solvent system of $\text{H}_2\text{O}/\text{PrOH}$ at selected weight ratios were also tested but did not show pore alignment on freeze tape casting likely due to poor dispersion of graphite.

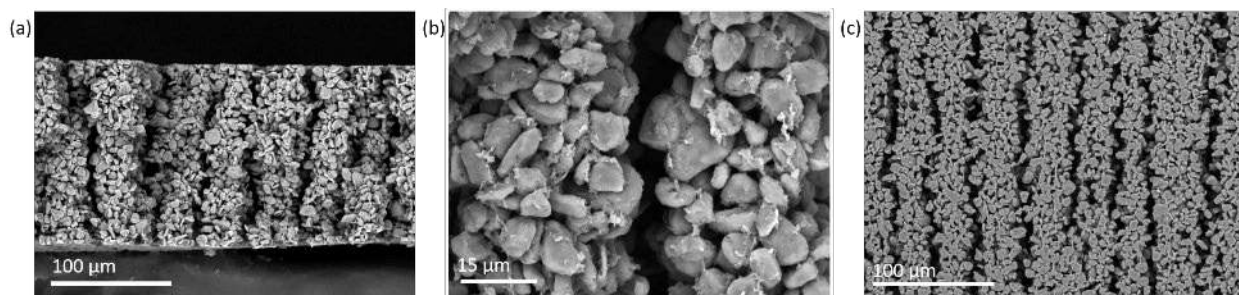


Figure I.5.H.9 SEM (a)(b) fracture surface and (c) surface images of freeze tape cast graphite anode. Graphite layer is 150 μm thick, showing vertical pore channels. Graphite columns are composed of 1506T graphite, Timcal C45 conductive additive, NaCMC and SBR binders. Porosity is 58 vol.%

Conclusions

In the present research, detecting lithium plating during fast charging, heterogeneity effects, and graphite anodes with directional pores have been investigated. The major conclusions are summarized below:

1. A trend of increasing dead Li amount with increasing C-rate was observed using *ex situ* titrations with DEMS.
2. Optical and X-ray microtomography cells have begun to show clear images of graphite. This will allow for future in situ experiments for detecting the onset of lithium plating. A signature indicating lithium plating is observed using a differential voltage technique after fast charging.
3. *Operando* measurements with thermal sensors reveal an increase in thermal resistances during fast charging.
4. The edge plane of graphite was found to sustain a much higher current density than the basal plane.
5. Graphite electrodes with directional pores were successfully freeze tape cast with 58% porosity.

Acknowledgements

Other contributors to this project include Dr. Vince Battaglia, Dr. Guoying Chen, Dr. Bryan McCloskey, Dr. Marca Doeff, Dr. Robert Kostecki, Dr. Ravi Prasher, and Dr. Wei Tong; all at the Lawrence Berkeley National Laboratory.

I.5.I Novel Electrolyte Development with High Lithium-Ion Transference Number (Hi-LiT) for Extreme Fast Charging (ORNL)

Zhijia Du, Principal Investigator

Oak Ridge National Laboratory
One Bethel Valley Road
Oak Ridge, TN 37830
E-mail: duz1@ornl.gov

Brian Cunningham, DOE Technology Development Manager

U.S. Department of Energy
E-mail: Brian.Cunningham@ee.doe.gov

Start Date: August 15, 2018
Project Funding: \$1,000,000

End Date: August 14, 2020
DOE share: \$900,000

Non-DOE share: \$100,000

Project Introduction

This project focuses on development of novel electrolyte to address AOI 2 (Batteries for Extreme Fast Charging (XFC)) in DE-FOA-0001808. The DOE has ultimate goals for EV batteries, which include reducing the production cost of a BEV cell to \$80/kWh, increasing the range of BEVs to 300 miles, and decreasing the charging time to 15 minutes or less. Increasing electrode thickness is an effective way to achieve these goals; however, thicker electrodes present several barriers to fast charging. This project is to implement a novel high-Li-ion-transport (Hi-LiT) electrolyte and enable a 10-minute charge of 180 Wh/kg energy density with less than 20% fade after 500 cycles (144 Wh/kg). The targeted improvements in the Hi-LiT electrolyte will be increasing Li ion transference number from 0.363 to 0.7-0.75 while maintaining a relatively high conductivity of 4-10 mS/cm. The improvement in electrolyte formulation will suppress the Li plating issue during cycling. This electrolyte will be implemented into high energy density Li-ion cells.

Objectives

The objective of this project is the increase of Li ion transference number while maintaining high conductivity of non-aqueous electrolyte through novel Li salt synthesis, anion receptors additives screening and solvent systems optimization, which will significantly increase the Li ion mass transport from cathode to anode during XFC to avoid abrupt end of charging and Li plating/dendrite growth. The implementation of this novel non-aqueous electrolyte system in high energy density Li-ion cells meet the battery performance goal of delivering 180 Wh/kg of stored energy to the cell in 10-minute charging at the beginning of life and achieving less than 20% fade in specific energy after 500 cycles (144 Wh/kg).

Approach

- (1) Innovative Li salts to improve Li ion mobility and increase Li ion transference number.
- (2) Formulations with multiple solvent systems to provide better Li ion mobility and suppress Li plating.
- (3) Anion receptor additives to further immobilize anions and dissociate cations in electrolyte.

Results

The utilization of various organic solvents as co-solvents, including esters and ethers, has been proved to be an effective way to lower the viscosity and thus enhance the Li ion conductivity of the electrolyte to further improve the overall performance of LIBs [1]. Various co-solvents, including MA, EA, EF, DMC are mixed with EC and EMC with LiPF₆ salt to study their effects on enhancing the fast charging performance in LiNi_{0.6}Mn_{0.2}Co_{0.2}O₂ (NMC622)/graphite cells. The physical properties of blended electrolytes, including ion conductivity and viscosity are measured first, then their cycling performance under XFC are tested and further compared with the Gen2 baseline electrolyte.

Figure I.5.I.1 shows ionic conductivities for all electrolyte with molarity from 0.5 to 1.75 mol/L at 20, 30, and 40°C. At a given temperature and solvent system, the ionic conductivity increases with the increase of salt concentration and reaches the maximum value at 1.0 M. Then the ionic conductivity decreases with further increasing salt concentration which can be attributed to the increasing viscosity and higher ion aggregation [2],[3],[4]. The conductivity of a specific electrolyte composition is improved with increasing temperature, which is ascribed to the added thermal agitation into the system to increase the ion mobility [3]. This increased conductivity at elevated temperature can be beneficial to fast charging as the cell temperature is reported to increase during fast charging [5]. The utilization of these co-solvents improves the ionic conductivity over the baseline electrolyte formulation with the trend of MA>EF>EA>DMC>baseline.

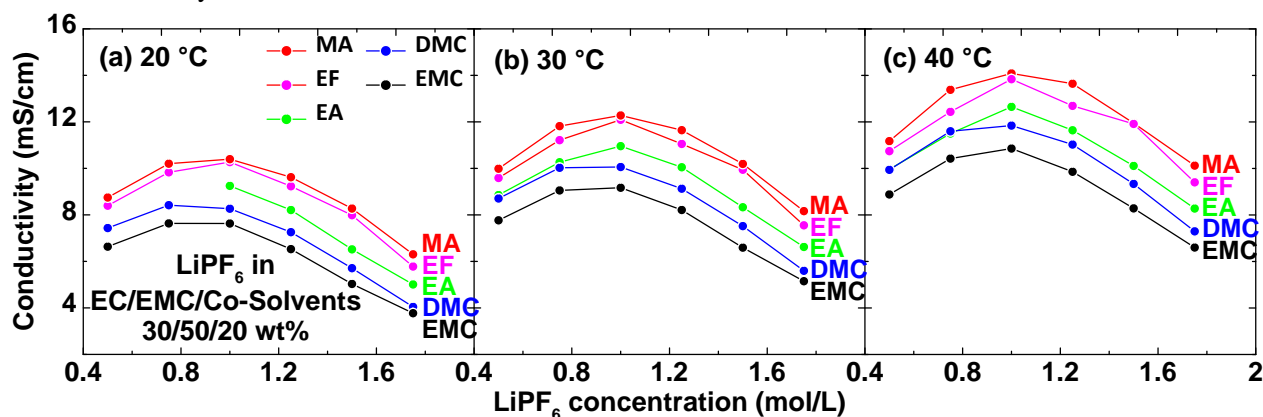


Figure I.5.I.1 the ionic conductivities of 5 electrolytes under different temperatures: (a) the ion conductivities at 20 °C; (b) the ion conductivities at 30 °C; (c) the ion conductivities at 40 °C

Pouch cells of NMC622/graphite filled with electrolyte of 1.2 M LiPF_6 in 5 different solvent systems show similar capacity at low charge/discharge rate ($\pm C/3$). The cells are then charged at different C rate at 2C (30-minute), 3C (20-minute) and 4C (15-minute), and their capacity retentions are summarized in Figure I.5.I.2a. With shorter charging time, the cell capacity retention drops gradually in all 5 cases, which largely due to the Li ions mass transport limitation in the electrolyte at higher C rate in high energy Li-ion cells [6]. However, the use of co-solvents improves the capacity retention compared to the baseline electrolyte. The improvement can be ascribed to the increased ionic conductivity with co-solvents. Under higher charging C rate, the improved ion conductivity mitigates the polarization and prompts heterogeneous distribution of Li ions in mass transport [6],[7]. Figure I.5.I.2b shows the cycling performance of the pouch cells using different electrolyte formulations discussed above. The most promising electrolyte composition is adding DMC in the formulation.

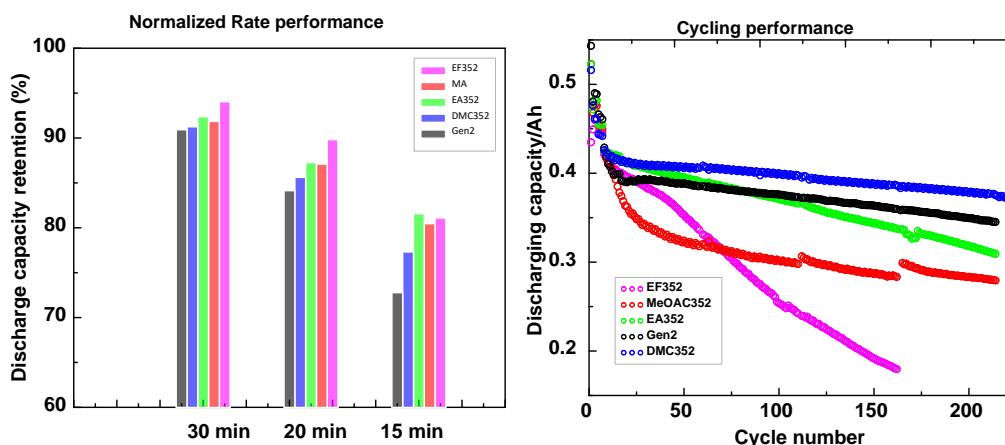


Figure I.5.I.2 (a) the rate performance for the 5 electrolyte systems with LiPF_6 concentration of 1.2 M. (b) the long-term cycling performance with different electrolytes

The project also evaluated the salt, lithium bis(fluorosulfonyl)amide (LiFSI), as a potential alternative candidate for the salt, lithium hexafluorophosphate (LiPF₆), in cells designed for fast charging. The study sheds the light on the higher Li ion conductivity and transference number in electrolytes comprising the salt LiFSI.

Figure I.5.I.3 shows the conductivity of electrolytes, measured at 20, 30 and 40°C, as a function of LiPF₆ or LiFSI concentrations in the solvent system (EC:EMC) (30:70 wt. %). With the increase of concentrations of the lithium salts from 0.5 to 1 M, the conductivity increased due to the increased number of dissociated ions in the electrolyte solutions. With further increase of the salt concentrations, the cationic and anionic species form pairs and hence do not contribute to conductivity. In our case, the conductivity reached topmost values in the range of 1–1.5 M, and then decreased thereafter. With the increase of temperature, the maximal conductivity values shifted from 1 M at 20°C to 1.5 M at 40°C, owing to higher thermal agitation that increases the dissociation of ion pairs. When comparing the two lithium salts, LiFSI consistently shows a higher conductivity compared to LiPF₆ under the same concentration and temperature. For example, the conductivity of LiFSI is 10.36 mS/cm compared to 9.35 mS/cm of LiPF₆ at the same 1.5 M concentration and same temperature 30°C. This finding agrees with a previous report ascribing the higher conductivity to a higher degree of dissociation of LiFSI. Another interesting finding is that the conductivity drop for LiFSI from 1.5 to 2.0 M concentrations was less severe than for LiPF₆, which is expected to ease the electrolyte depletion issue when fast charging and discharging is applied to Li-ion cells.

The electrolyte with the LiPF₆ salt has a t_+ of 0.382 and the t_+ of the LiFSI based electrolyte measured in this study is 0.495. Our hypothesis is that both the higher dissociation of the LiFSI salt in the electrolyte and the larger size of the FSI⁻ anion contribute to the transference number enhancement. The higher dissociation indicates that Li ions can move more freely due to less attractive forces by the anions. The larger size of FSI⁻ (95 Å³) compared to PF₆⁻ (69 Å³) suggests slower movement of FSI⁻, and as a result, Li-ions can move faster in the presence of the FSI ions.

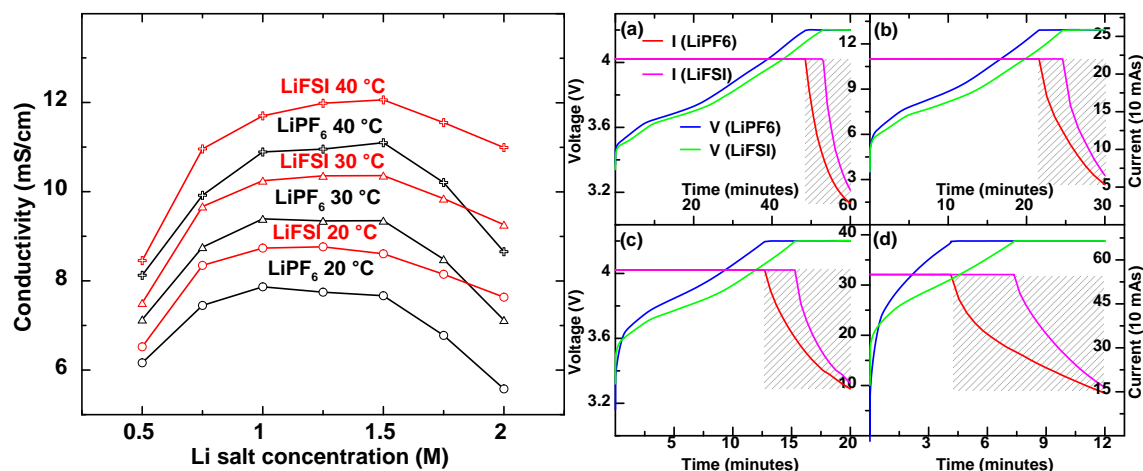


Figure I.5.I.3 (a) Conductivity of LiFSI and LiPF₆ in (EC:EMC) (30:70 wt%) as function of concentration and temperature. (b) Voltage (V) and Current (I) versus charging time for cells charged at (a) 1C, (b) 2C, (c) 3C and (d) 5C, with time cut-off of 1 hour, 30 minutes, 20 minutes and 12 minutes, respectively. The voltage (V) curves correspond to the y-axis on the far left while the current (I) curves correspond to the y-axis on the right of each corresponding panel

Figure I.5.I.3b shows the fast charging capability of the cell comprising NMC cathode and graphite as the anode and in the presence of the LiFSI and LiPF₆ based electrolytes. Under the 1C rate, the cell voltages gradually increased during the constant current (CC) charging and reached the cut-off voltage (4.2 V) around 49.5 minutes (LiPF₆) and 53.1 minutes (LiFSI). The cells were further charged under the constant voltage (CV) mode with a decreasing trickle current till the overall charging reached 60 minutes. With increasing the charge current to 2C and 3C, the cells with the LiPF₆ electrolyte attained the cut-off voltage earlier than the

ones with the LiFSI electrolyte. This gap widened even further under a the 5C charge. In this case, the cell with the LiPF₆ electrolyte had only 4.2 minutes under the CC charge while the one with the LiFSI electrolyte had 7.4 minutes under the CC charge. This large gap (shaded areas in figure), between the plots of the current (I) vs. time, indicates that more capacity can be stored when the cell has a longer CC charging time under the intended C-rate.

Figure I.5.I.4a shows the corresponding discharge voltage curves at the C/2 rate for the cells charged under 1C, 2C, 3C and 5C rate as shown in Figure I.5.I.3b. When the cells were charged in one hour, they delivered 173.8 and 170.8 mAh/g capacity in the presence of the LiFSI and LiPF₆ electrolyte, respectively. The capacity difference grew further when the charge rate was increased to 5C and charging time shortened to 12 minutes. The cell with the LiFSI electrolyte had a capacity of 153.2 mAh/g, which is a 13% improvement over the LiPF₆ electrolyte (i.e., 135.4 mAh/g).

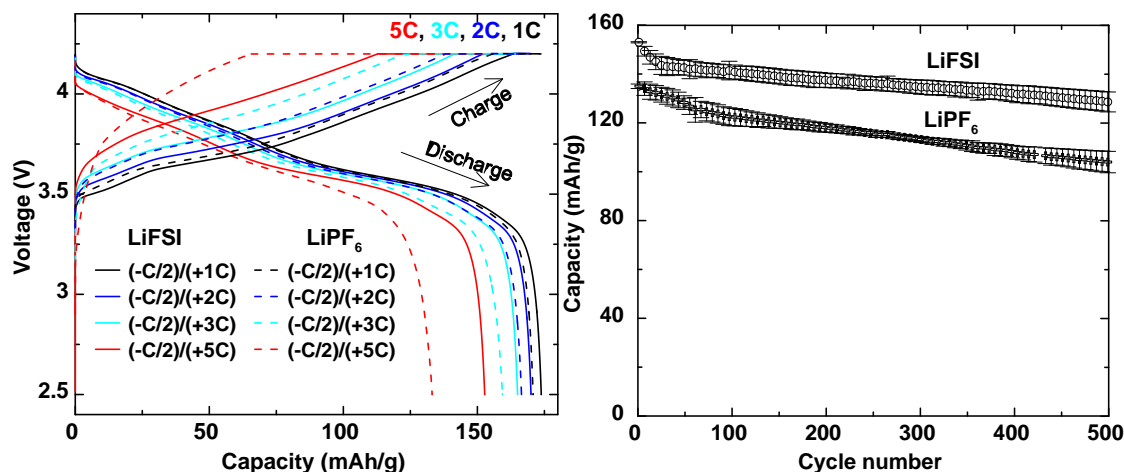


Figure I.5.I.4 (a) Charge (different C rate) and discharge voltage curves (all at C/2) of NMC/graphite cells with LiPF₆ and LiFSI electrolyte. (b) Long term cycling performance of the cells with LiFSI and LiPF₆ electrolytes with 12 minutes fast charging. Inserted photos show the extent of Li plating on each graphite electrode

Figure I.5.I.4b shows the cycling performance of under 12-minute fast charging through 500 cycles. The cell with the LiFSI electrolyte exhibited minimal capacity fading over the 500 cycles with 134.3 mAh/g capacity retained (84% retention compared to 1st cycle of 12-minute charge). The cell with LiPF₆ electrolyte showed rapid capacity fading during the first 100 cycles and then decreased steadily with further cycling. This cell only had 110.6 mAh/g capacity retained (77% retention) after 500 cycles. The cells after 500 cycles were opened inside an Ar-filled glove box after discharging to 2.0 V for observation. Both cells showed lithium plating after repeated fast charging cycles. However, the lithium plating area on the graphite electrode was much smaller for the LiFSI electrolyte compared to the LiPF₆ electrolyte, which is ascribed to the better Li-ion transport properties of the LiFSI based electrolyte compared to the LiPF₆ one.

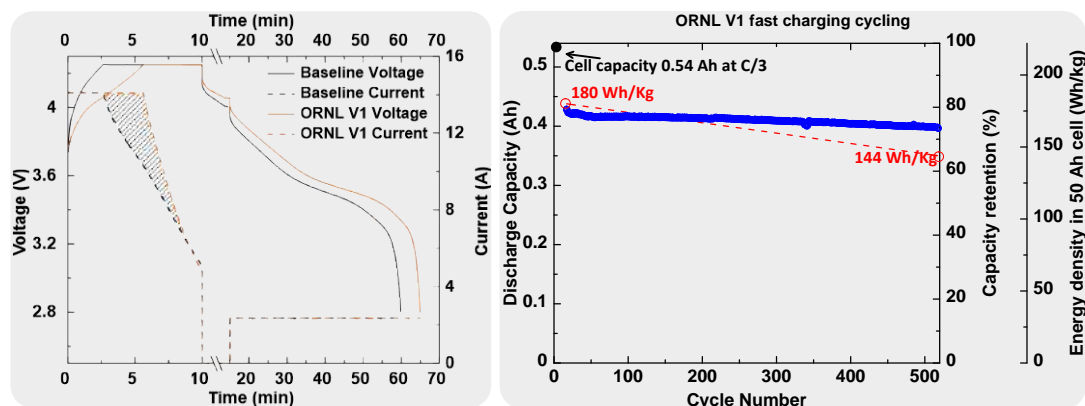


Figure I.5.I.5 (a) Voltage (V) and Current (I) versus charging time for cells charged at 6C with time cut-off of 10 minutes. (b) Cycling performance of the 500 mAh at fast charging rate

The cells were scaled up to 540 mAh and 2.3 Ah pouch cells. Figure I.5.I.5a shows the voltage and current curves vs. time. The cells were filled with electrolyte developed at ORNL at the end of year 1 project (ORNL V1). This new formulation of electrolyte is a combination of the solvent, salt and additive studied which shows the most promising performance for fast charging. The cell with the newly developed electrolyte shows a constant current charge of the cell up to 5.59 minutes compared to 2.59 minutes constant current charge of baseline cell. The cell with ORNL V1 electrolyte has 84% capacity retained in 10 minutes XFC, compared to 75% capacity retained with Gen2 (1.2 M LiPF₆ in EC/EMC 3/7 by wt.). The cycling performance of the 540 mAh pouch cell with ORNL V1 electrolyte formulation is shown in Figure I.5.I.5b. The cells show excellent cycling performance with 86% capacity retention under fast charging.

Conclusions

- Cell development of high energy cell (222 Wh/Kg at 50 Ah scale up) for fast charging.
- Studied four different co-solvents and effects on viscosity, conductivity and cycling performance.
- Successfully synthesized oligomer type Li salts.
- Electrolyte formulation with LiFSI that has higher σ and $t(\text{Li}^+)$ than LiPF₆.
- Successfully developed ORNL V1 electrolyte formulation with a combination of selected Li salt, solvent and additive.
- Achieved 166 Wh/Kg energy density (at 50Ah cell level) after 500 fast charging cycles.
- Delivered 9 cells with 2.33 Ah capacity (each cell) to ANL for evaluation.

Key Publications

1. Z. Du, D. L. Wood, and I. Belharouak. Enabling fast charging of high energy density Li-ion cells with high lithium transport electrolytes. *Electrochem Comm* 103 (2019) 109.
2. S. Huang, X. Wu, G. M. Cavalheiro, X. Du, B. Liu, Z. Du, and G. Zhang. In Situ Measurement of Lithium-Ion Cell Internal Temperatures during Extreme Fast Charging. *J Electrochem Soc* 166 (2019) A3254.
3. Z. Du, T. Liu, X. Wu, F. Lin, K. Zhao, D. L. Wood, I. Belharouak, Towards Fast Charging of High Energy Density Li-Ion Batteries (*Invited*), 236th ECS meeting.

4. T. Liu, Z. Du, X. Wu, et al, Bulk and Surface Reconstructions in High Nickel Cathodes Subjected to Fast Charging Conditions, *submitted*.
5. Xianyang Wu, Zhijia Du, Tianyi Liu, et al. Effects of various co-solvents for LiNi_{0.6}Mn_{0.2}Co_{0.2}O₂ (NMC622)/graphite battery under extreme fast charging, *submitted*.

References

1. K. Xu, Electrolytes and interphases in Li-ion batteries and beyond, *Chem. Rev.* 114 (2014) 11503–11618. doi:10.1021/cr500003w.
2. M.S. Ding, K. Xu, S.S. Zhang, K. Amine, G.L. Henriksen, T.R. Jow, Change of Conductivity with Salt Content, Solvent Composition, and Temperature for Electrolytes of LiPF₆ in Ethylene Carbonate-Ethyl Methyl Carbonate, *J. Electrochem. Soc.* 148 (2001) A1196. doi:10.1149/1.1403730.
3. M.S. Ding, T.R. Jow, Conductivity and viscosity of PC-DEC and PC-EC solutions of LiPF₆, *J. Electrochem. Soc.* (2003). doi:10.1149/1.1566019.
4. K. Xu, Nonaqueous Liquid Electrolytes for Lithium-Based Rechargeable Batteries, *Chem. Rev.* 104 (2004) 4303–4418. doi:10.1021/cr030203g.
5. S. Huang, X. Wu, G.M. Cavaleiro, X. Du, B. Liu, Z. Du, G. Zhang, In Situ Measurement of Lithium-Ion Cell Internal Temperatures during Extreme Fast Charging, *J. Electrochem. Soc.* 166 (2019) 3254–3259. doi:10.1149/2.0441914jes.
6. Z. Du, D.L. Wood, I. Belharouak, Enabling fast charging of high energy density Li-ion cells with high lithium ion transport electrolytes, *Electrochem. Commun.* 103 (2019) 109–113. doi:10.1016/j.elecom.2019.04.013.
7. Z. Du, D.L. Wood, C. Daniel, S. Kalnaus, J. Li, Understanding limiting factors in thick electrode performance as applied to high energy density Li-ion batteries, *J. Appl. Electrochem.* 47 (2017) 405–415. doi:10.1007/s10800-017-1047-4.

Acknowledgements

We would like to acknowledge the following collaborators: Prof Guangsheng Zhang (UAH), Feng Lin (Virginia Tech), Kejie Zhao (Purdue), Jue Liu (SNS).

I.5.J New High-Energy & Safe Battery Technology with Extreme Fast Charging Capability for Automotive Applications (Microvast, Inc.)

Wenjuan Liu-Mattis, Principal Investigator

Microvast, Inc.
3259 Progress Dr. OFC132
Orlando, FL 32826
E-mail: wenjuanmattis@microvast.com

Brian Cunningham, DOE Technology Development Manager

U.S. Department of Energy
E-mail: Brian.Cunningham@ee.doe.gov

Start Date: July 3, 2018	End Date: July 2, 2020	
Project Funding (FY19): \$1,615,252	DOE share: \$807,626	Non-DOE share: \$807,626

Project Introduction

Automakers worldwide have announced plans to begin transitioning from gasoline powered vehicles to ones driven via electricity. To make these bold adoption plans a reality the lithium-ion battery must continue to improve so electric drive trains can become competitive in cost and convenience to a traditional gasoline powered vehicle.

In this project technology is being explored to try and make lithium-ion batteries re-energize in a matter of minutes without making significant sacrifices to safety, cost or energy density of the cell. To that end, we are exploring extreme fast charge (i.e., under 6 minutes charge) in larger capacity (> 20AH) cells using a concentration gradient cathode chemistry, advanced impedance reduction additives, and Microvast's high performance separator.

Objectives

The objective of the project is to develop a redox couple that can be implemented into a large format automotive cell capable of 500 cycles of 10-minute fast charge and 1C discharge. The targeted cell will maximize the energy density while still being able to meet the > 180Wh/kg energy density target after fast charge. The final cell built will use advanced materials, particularly an advanced separator capable of improved thermal durability, to offer excellent abuse tolerance for cells applied towards an electric vehicle.

Approach

To achieve the end goal two thrusts are undertaken simultaneously during the project. The first thrust is related to material development, so a higher energy redox couple can be utilized in the cell and lower impedance gain during cycling via an effective interface can be realized. The second thrust is via cell design, by going thru at least 3 generations where at least one principle material – anode, cathode or separator – will be replaced to try and stepwise improve the energy density and/or performance.

For the material work, project members Microvast and Argonne National Labs will focus on developing a high nickel content concentration gradient cathode. Higher nickel cathodes are desirable for their higher gravimetric capacity, but the safety of the materials particularly when de-lithiated is a concern. As the nickel concentration of the cathode increases the performance of the gradient cathode maybe improved by manipulating the atomic concentrations of cobalt/manganese, or via the addition of other dopants and/or coatings to the cathode. At the same time, advanced electrolyte additives will be explored by Microvast and Argonne National Labs to minimize the resistance increase that negatively effects fast charge energy density.

For cell design, there will be 3 generations during the project, with each generation adding at least one significant material change to the cell. The electrodes prepared for the project by Microvast will be split, with one batch remaining at Microvast for pouch cell assembly and the second batch going to BMW to be tested in their prismatic cells. The first-generation cell design will start with a 220 Wh/kg pouch cell design goal. After each cell generation the performance will be analyzed to determine if the cycling goals are met. If met, the next round of cell design will incorporate a higher electrode loading to boost the cells 0.33C Wh/kg energy density. In the event the cell is unable to successfully meet the XFC cycling requirements a material will be upgraded and the same energy density will be repeated. Cell testing procedures will follow USABC/DOE guidelines for the project, and a yearly cell delivery will be made to the Department of Energy for independent testing of the cell generations.

Results

At the initiation of the project a 200 Wh/kg pouch cell was constructed to baseline the project and give some first impressions to the project team regarding cell performance under 6-minute charge/1C discharge cycling conditions. The cell built used a moderate nickel NCM cathode and a graphite anode. The pouch cell built was 15AH, and capable of cycling 500 cycles under XFC conditions (Figure I.5.J.1).

After the success of the baseline cells cycling, the project commenced at the originally proposed 220 Wh/kg pouch cell target. This cell introduced a 60% Ni/NMC full concentration gradient (FCG) cathode into the cell design. The FCG originally introduced into the cell had Co/NMC ratio of 10%. Cobalt is considerably more expensive than nickel or manganese, so limiting its input into a cell can be beneficial for the cells cost. The cells energy density was slightly below 180 Wh/kg when cycled at 6CCCV/1CD, though the energy density retention was above 80% after 500 cycles.

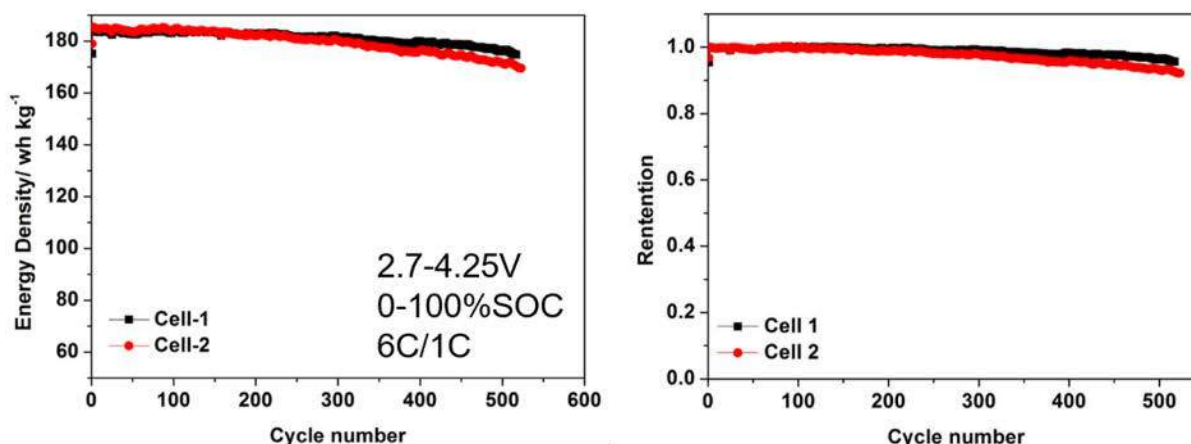


Figure I.5.J.1 15AH pouch cells energy density and energy retention over 500 cycles tested under XFC cycling conditions

It was decided that a second round of the generation 1 cell design would be prepared, except this time the FCG cathode would be changed to have 20% Co/NMC. While the pouch cell 0.33C Wh/kg energy density was not strongly affected by the cathode change, the 6CCCV/1CD cell energy density was altered to now be above 180 Wh/kg at the start of life.

The generation 1 cells performance under XFC conditions is shown in Figure I.5.J.2. The cells were cycled at 30°C under 6CCCV/1CD conditions that are periodically interrupted for 6CCCV/0.33CD + HPPC referencing cycles. The cells tested were above the target 180 Wh/kg at the start of XFC cycling, and maintained > 80% energy density retention after 500 cycles. These cells were delivered to a DOE National Laboratory for validation of the testing results.

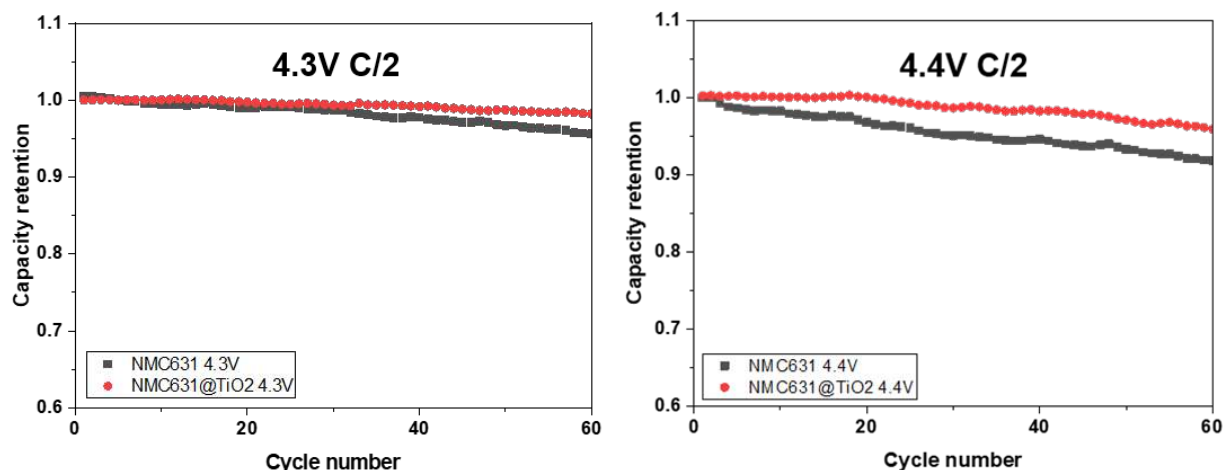


Figure I.5.J.2 Projects final 21AH Generation 1 pouch cells capacity and energy density cycling results, (including retention) over 500 cycles of 6C/1C conditions with periodic reference cycles

For the material development a titania treatment was investigated by Argonne on the Ni:Mn:Co 6:3:1 generation 1 concentration gradient cathode. At both 4.3 and 4.4V in the half-cell the treated cathode shows improved capacity retention after 60 cycles (see Figure I.5.J.3), with the improvement more obvious for the higher voltage. This titania treatment is intended to isolate the cathode materials surface from the electrolyte during cycling in an effort to reduce dense phase oxides forming at the cathode electrolyte interface. Having a stable cathode interface is especially important in fast charge cells where surface degradation leads to increased resistances.

High nickel concentration gradient cathodes were also prepared by Microvast and Argonne for consideration in generation 2 and generation 3 of the XFC cell, respectively. The generation 2 FCG material is intended as an NCM811 substitute. The targeted concentration gradient profile of the particle matches well the experimental result obtained via EDS line scan of a FIB cross sectioned particle. The generation 3 material has Ni content above 85% and the gradient presence has been confirmed within the materials via X-ray fluorescence elemental mapping at Advanced Photon Source beamline 2 ID-E. Half cell testing of this new concentration gradient material shows a stable load curve after 3 cycles and a capacity retention of 96.2% after 50 cycles between 3-4.4V at C/2.

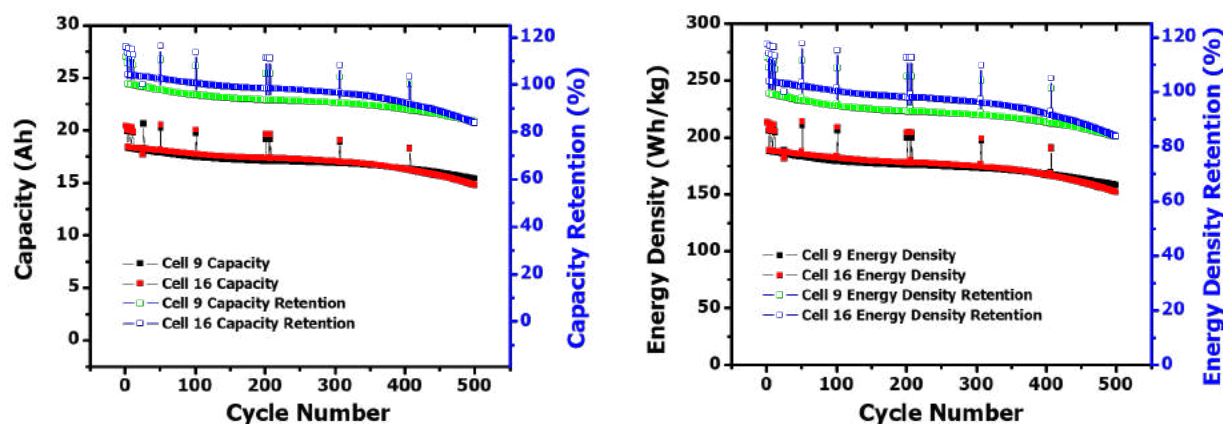


Figure I.5.J.3 Concentration gradient cathode with NMC ratio of 6:3:1 tested in half cell at 4.3V and 4.4V with and without a lower resistance titania coating

The project team has now begun to investigate the generation 2 cell performance under fast charge. The higher areal loadings and cell Wh/kg is making the fast charge performance more challenging. We believe a combination of engineering decisions regarding charge procedures and cell designs, along with materials selected is the best approach to overcome these challenges in a working large capacity cell.

Conclusions

Microvast has successfully built the first-generation extreme fast charge pouch cell. The 20AH cell, using an FCG cathode, was internally tested to deliver > 180 Wh/kg energy density at the start of XFC testing and retained > 80% of the cells XFC energy density after 500 cycles. The cell set was delivered to a Department of Energy National Laboratory for validation.

Acknowledgements

Microvast would like to thank Brian Cunningham, DOE Technology Manager, and Kimberly Nuhfer, NETL manager, for their support. The project would not be possible without the helpful discussion and collaboration of Khalil Amine (ANL), Tongchao Liu (ANL), Chicheung Su (ANL), Jihyeon Gim (ANL), Peter Lamp (BMW), Odysseas Paschos (BMW) and Forrest Gittleston (BMW).

I.5.K XFC R&D: CAMP, Testing & Post-Test Characterization and Modeling (ANL, SLAC)

Venkat Srinivasan, Principal Investigator

Argonne National Laboratory
9700 S Cass Avenue
Lemont, IL 60439
E-mail: vsrinivasan@anl.gov

Samuel Gillard, DOE Technology Development Manager

U.S. Department of Energy
E-mail: Samuel.Gillard@ee.doe.gov

Start Date: July 3, 2018	End Date: July 2, 2020	
Project Funding (FY19): \$1,615,252	DOE share: \$807,626	Non-DOE share: \$807,626

Project Introduction

The U.S. Department of Energy's Office of Energy Efficiency and Renewable Energy (DOE-EERE) has identified fast charge—with a goal of 15-min recharge time—as a critical challenge to pursue in ensuring mass adoption of electric vehicles (EVs). Present-day, high-energy cells with graphite anodes and transition metal cathodes in a liquid electrolyte are unable to achieve this metric without negatively affecting battery performance. There are numerous challenges that limit such extreme fast charging (XFC) at the cell level, including lithium (Li) plating, rapid temperature rise, and possible particle cracking. Of these, Li plating is thought to be the primary culprit. This project aims to gain an understanding of the main limitations during fast charge using a combined approach involving cell builds, tests under various conditions, characterization, and continuum-scale mathematical modeling. Researchers from five national laboratories are contributing their expertise to make progress on the eXtreme Fast Charge Cell Evaluation of Lithium-ion Batteries (XCEL) project.

Cells are built at the Cell Analysis, Modeling, and Prototyping (CAMP) Facility at Argonne National Laboratory (Argonne) using various carbons and different cell designs, in both half-cell and full-cell configurations and with reference electrodes. Cells are tested at both Idaho National Laboratory (INL) and Argonne under various operating conditions (e.g., C-rate, temperature) and under different charging protocols with the aim of identifying the onset of plating, quantifying the extent of the problem, and determining parameters and test data for mathematical models. After testing, cells are opened, and various advanced characterizations are performed at Argonne to determine the extent of plating and to determine whether other failure models, such as particle cracking, also play a role.

A critical part of the project is the use of continuum-scale mathematical models so XCEL participants can understand the limitations at high charge rates and, therefore, suggest possible solutions to pursue. Both macro-scale approaches and microstructure-based simulations are pursued and serve to complement each other. Macromodeling at the National Renewable Energy Laboratory (NREL) is used to test cell designs, accompanied by development of microstructure models to provide deeper insights into the electrochemical phenomena in the battery. This effort is complemented with development of models incorporating new physics, such as phase change and solid-electrolyte interphase growth, at Argonne.

Two exploratory projects aim to study ways to detect Li *in situ* during operation. NREL is pursuing the use of microcalorimetry to detect heat signatures during plating. INL is working with Princeton University to examine the use of acoustic methods to determine whether plating leads to a signature in the acoustic signal.

Finally, the Stanford Linear Accelerating Center (SLAC) National Acceleratory Laboratory is using synchrotron X-ray methods to guide the cell design and charging protocols of XFC of Li-ion battery cells, and

Lawrence Berkeley National Laboratory (LBNL) is investigating the initial onset of Li plating during fast charging as well as developing a strategy to detect it.

The overall project can be roughly divided into the following three project areas:

- The Cell, Analysis, Modeling and Prototyping (CAMP) Facility, at ANL
- XCEL R&D, at SLAC National Accelerator Laboratory: Project 1
- XCEL R&D, at SLAC National Accelerator Laboratory: Project 2

The Cell, Analysis, Modeling and Prototyping (CAMP) Facility continues to support the XCEL Program's objective of identifying and mitigating causes of lithium plating at fast charge ($>4C$) in single-layer pouch cells. Efforts in fiscal year 2018 (FY18) demonstrated that the choice in graphite did not significantly affect the ability to cycle under fast charge conditions (6C charge, C/2 discharge)—all six of the selected graphites were able to achieve 750 cycles with 80% capacity retention, using a 2-mAh/cm² graphite loading. The team made the decision to use the SLC1506T graphite from Superior Graphite as the baseline graphite material and NMC532 as the baseline cathode material. More than 70 single-sided, single-layer pouch cells were fabricated in the Round 1 cell build using a 2-mAh/cm² graphite loading and were delivered to lab partners (INL, Argonne, and NREL) for fast charge testing with a nominal capacity of 19 mAh capacity. Prescreening of anode-cathode pairs with varying electrode capacity loading indicated that loadings over ~ 2.5 mAh/cm² were not able to charge at a true 6C rate. Thus, the next pouch cell build was designed with a graphite loading of 3.0 mAh/cm². A total of 48 of these Round 2 pouch cells were delivered to Argonne, INL, and NREL for testing. These two cell builds are now considered the baselines for the XCEL Program.

Objectives

The goal of the FY19 work is to explore methods of preventing lithium plating via modifications of the electrode architecture. Ideally, the negative and positive electrodes should have low tortuosity to enable fast lithium ion transport to and from the active material closest to the current collector, while maintaining low porosity to maintain high energy density. In addition, the CAMP Facility will support the DOE-EERE Vehicle Technologies Office Funding Opportunity Announcement and Lab Call projects and teams that are focused on developing methods of detecting lithium plating.

Approach

The Cell, Analysis, Modeling and Prototyping (CAMP) Facility

In FY18, the CAMP Facility developed two single-layer pouch cells to benchmark the fast charge capabilities of a typical lithium-ion battery, with the main difference between the cells being electrode loading. These two electrode/cell designs will be used as the baseline designs for this program in FY19. The details of the two cell designs are as follows:

Round 1 Pouch Cells were assembled with 14.1 cm² single-sided cathodes (0.145 grams of NMC532 per pouch cell) and 14.9 cm² single-sided graphite anodes (SLC1506T from Superior Graphite) using the Celgard 2320 separator (20 μ m, PP/PE/PP) and 0.5 mL of Tomiyama 1.2 M lithium hexafluorophosphate (LiPF₆) in an EC:EMC (3:7 wt%) “Gen2” electrolyte. The n:p ratio is between 1.12 to 1.22 for this voltage window (3.0 to 4.1 V). After assembly, the pouch cells underwent formation cycles at ~ 4 psi in the 3.0 to 4.1 V window as follows: 1.5 V tap charge and hold for 15 minutes, followed by a 12-hour rest, and then three cycles at C/10, followed by three cycles at C/2. The cells were then brought to a safe state of charge by constant voltage charging to 3.5 V for 6 hours, and then degassed and prepared for shipping/delivery to the battery test labs. A nominal C/3 capacity of 19 mAh was recommended for future tests.

Round 2 Pouch Cells were assembled with 14.1 cm² single-sided cathodes (0.236 grams of NMC532 per pouch cell) and 14.9 cm² single-sided graphite anodes (SLC1506T from Superior Graphite) using the Celgard 2320 separator (20 μ m, PP/PE/PP) and 0.615 mL of Tomiyama 1.2 M LiPF₆ in an EC:EMC (3:7 wt%) “Gen2” electrolyte for an electrolyte-to-pore volume factor of 4.20. The n:p ratio is between 1.07 to 1.16 for this

voltage window (3.0 to 4.1 V). Figure I.5.K.1 details the electrode composition and design parameters for the Round 2 electrodes. The formation process was the same as that used in making the Round 1 cells. A nominal C/2 capacity of 32 mAh was recommended for future tests.

Anode: LN3107-190-4A

91.83 wt% Superior Graphite SLC1506T
2 wt% Timcal C45 carbon
6 wt% Kureha 9300 PVDF Binder
0.17 wt% Oxalic Acid

*Lot#: 573-824, received 03/11/2016
Single-sided coating, CFF-B36 anode*

Cu Foil Thickness: 10 μm

Total Electrode Thickness: 80 μm

Total Coating Thickness: 70 μm

Porosity: 34.5 %

Total SS Coating Loading: 9.94 mg/cm²

Total SS Coating Density: 1.42 g/cm³

Made by CAMP Facility

Cathode: LN3107-189-3

90 wt% Toda NMC532

5 wt% Timcal C45

5 wt% Solvay 5130 PVDF

*Matched for 4.1V full cell cycling
Prod: NCM-04ST, Lot#: 7720301
Single-sided coating, CFF-B36 cathode*

Al Foil Thickness: 20 μm

Al Foil Loading: 5.39 mg/cm²

Total Electrode Thickness: 91 μm

Coating Thickness: 71 μm

Porosity: 35.4 %

Total Coating Loading: 18.63 mg/cm²

Total Coating Density: 2.62 g/cm³

Made by CAMP Facility

Figure I.5.K.1 Electrode composition and design parameters for Round 2-Batch 1 pouch cell design. The Round 1 electrodes had the same composition but had less mass loading (and thickness)

XCEL R&D- Project 1: SLAC National Accelerator Laboratory

Our approach has been to exploit the nondestructive nature and fast acquisition times of characterization techniques at synchrotron sources to understand parasitic Li plating in LIBs under fast charging conditions and across multiple length scales. These findings will be used as inputs in simulations to guide cell design and charging protocols of extreme fast-charging LIBs. The specific aim in this quarter was to build on the mm-scale XRD studies conducted in the previous quarters by examining other length scales as well as complementary imaging techniques. This approach also allowed exploitation of the nondestructive nature of characterization of full cells using mm-scale XRD in the fully assembled conditions.

The characterization techniques were expanded in two main directions focused on complementing the structural information obtained by diffraction with some morphological information from imaging-based techniques. First, X-ray-based micro-computer tomography (microCT) was used to obtain information on the porosity of the anode after XFC charging, specifically to enable comparison between spots that did and did not show significant Li plating in the mm-scale XRD. Second, neutron-based imaging was conducted on the same areas observed using the X-ray microtomography, with the main aim of characterizing metallic Li plated on the anode. Using X-ray tomography alone cannot distinguish between graphitic carbon and metallic Li; however, neutrons can make this distinction, which is a huge advantage while studying Li plating on the graphite anode.

The plan of action was to select specific “interesting areas” on the cells based on the prior mm-scale XRD results. Toward this end, areas on the anode that showed low and high intensities for metallic Li were identified and characterized further. One caveat was that the geometry of these other techniques forced the tearing open of the cells to enable creating sample geometries better suited for that particular technique. However, this step enabled taking optical images of the anodes to provide a base comparison for the spatial maps of Li graphite intensities obtained through mm-scale XRD, as shown in Figure I.5.K.2 for one representative cell cycled 450 times with the 6C CCCV (constant current, constant voltage) protocol, where the Li intensity map corresponds very well to “bright” regions seen in the optical image.

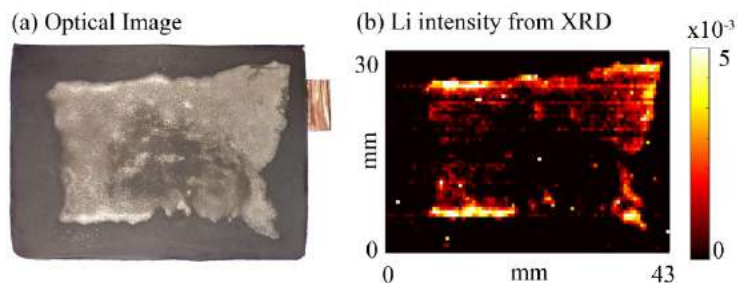


Figure I.5.K.2 Comparison of optical and XRD spatial map of the anode, showing Li intensities across the electrode

Finally, all cells presented herewith are in the fully discharged state at a nominal SOC of 0% (3.0V) after 450 XFC cycles. The cycling rate and protocols vary from cell to cell. The cells are single-layer pouch cells assembled at CAMP, with an NMC 532 cathode and graphite anode and separated by a Celgard 2320 separator. The cells have a capacity of $\sim 3.0 \text{ mAh/cm}^2$ and a nominal area of $\sim 14 \text{ cm}^2$. The Results section contains one key finding outcome from the mm-scale XRD that connects the amount of plated Li calculated from XRD to the capacity loss of the cell. Then, X-ray microCT imaging of portions of the disassembled anode are shown, followed by a novel technique of using simultaneous neutron and X-ray-based imaging on the same region of the cut-up anode.

XCEL R&D- Project 2: SLAC National Accelerator Laboratory

In recent years, lithium-ion batteries have become the battery technology of choice for portable devices, electric vehicles, and grid storage. While increasing numbers of car manufacturers are introducing electrified models into the market, range anxiety and the length of time required to recharge the batteries are still common concerns. The high currents needed to accelerate the charging process have been known to reduce energy efficiency and cause accelerated capacity and power fade. Among many of the fading mechanisms during fast charging, lithium plating is known to deleteriously affect the cycle life and safety of the lithium ion battery. Nondestructive operando diagnosis of lithium plating is of great significance for onboard application, as well as a technique to assist scientific study of fast charging.

Results

The Cell, Analysis, Modeling and Prototyping (CAMP) Facility

1. Fabrication of Transparent Pouch Cells for XRD Studies

At the last F2F meeting at INL in July, the CAMP Facility participants mentioned to the PIs that they have the capability to make a pouch cell with a polypropylene (PP) window. Colleagues from UC-Berkeley were very interested in having a transparent pouch cell for their X-ray diffraction (XRD) experiments. They are developing a technique to measure temperature in the anodes (thermal expansion of copper [Cu]) and the cathodes (thermal expansion of aluminum [Al]) separately during fast charge. Thus, they cannot have a pouch material with any blocking metal, such as aluminum. A further suggestion was made by UC-Berkeley to use the Kapak SealPAK pouch material, which is a polyester/polyethylene (PET/PE) laminate that can be heat-sealed. The CAMP Facility developed sealing processes for both materials (PP and PET/PE) that still maintained an adequate tab seal. Two pouch cell designs were developed (Figure I.5.K.3):

- Fully transparent – PET/PE (Kapak SealPAK 400), and
- Windowed – PP window heat-sealed on layered pouch material.

The cells were sent to UC-Berkeley without any electrolyte. In the interest of time, the CAMP Facility did not run any trial cycling with these cell designs. It is safe to say that these pouch cells should last several hours to several days before drying out (or springing a leak). UC-Berkeley will vacuum-impregnate the cells with electrolyte, complete a heat seal, and apply an abbreviated formation cycle right before the cell is placed in the

XRD setup. It is planned that the cells will be placed in a protective Kapak pouch envelope after heat-sealing to minimize the rate of permeation and catch any leakage. If successful, these pouch cell designs may find use in other experiments that require metal-free cell containment.

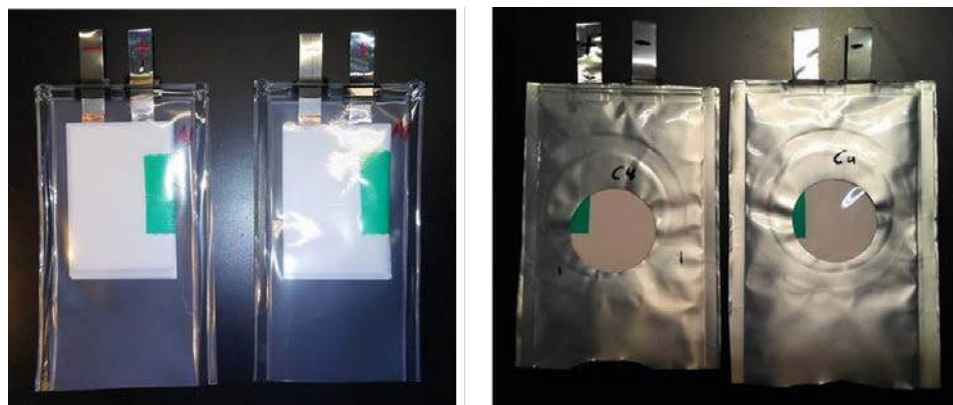


Figure I.5.K.3 Photo of the fully transparent (left, PET/PE [Kapak SealPAK 400]) and the windowed (right, PP window heat-sealed on layered pouch material) pouch cells designed for brief XRD experiments

2. Support of Electrolyte Development at INL

Lithium plating can be minimized with the use of electrolytes with high ionic conductivity. INL is exploring several electrolyte formulations that are predicted to have ionic conductivity that is better than that of the baseline Gen2 electrolyte. INL is currently scoping out these electrolytes in coin cells, with the plan that the electrolytes that pass the initial tests will be explored further in pouch cells. The CAMP Facility has supported this effort in the first quarter by fabricating 11 Round 2 pouch cells and shipping them to INL without electrolyte added. INL will add its candidate electrolyte as needed. INL requested 18 more dry-pouch cells in the fourth quarter to continue its studies in electrolytes. The CAMP Facility made 18 Single-Layer Pouch Cells with the Round 2, Batch 2 Fast Charge electrodes (LN3174-73-4 [NMC 532] | LN3174-75-3 [SLC 1506T]) and shipped them to INL in August.

3. Support of Lithium Plating Detection Teams – SLAC/Stanford University

The CAMP Facility continued its support of the lithium-plating detection activities at SLAC and Stanford University by supplying several electrode sheets, and fabricating/cycling several pouch cells in time for their beamtime experiments at Argonne's Advanced Photon Source (APS) in July. A few pouch cells required opening to harvest the electrodes. A list of items supplied in this quarter include:

- Four sheets of Round 1 positive and 2 sheets of Round 1 negative electrodes
- Two sheets each of Round 2 positive and negative electrodes
- One single-layer pouch cell xx3450 with the Round 2 material (NMC 532 | SLC 1506T) filled with Gen2 electrolyte and tap-charged

4. Support of Lithium Plating Detection Teams – Argonne

The CAMP Facility supported the lithium-plating detection activities at Argonne by fabricating and forming two Round 1 pouch cells before APS beamtime scheduled for the start of October 2019.

XCEL R&D- Project 1: SLAC National Accelerator Laboratory

1. Relating the Capacity Fade in Cells to the Amount of Dead Li

Figure I.5.K.4 shows the amount of plated Li in all the cells, normalized by the total amount of Li in the pristine cell, as a function of the capacity fade of the cell after 450 cycles. The total amount of plated Li is calculated after 450 cycles at 0% SOC, thus any Li on the anode is considered 'dead' Li. The data points of the cells are

colored by the charging rate. In general, the higher the capacity fade of the cell, the higher is the intensity of plated Li. Note that we have previously shown that the graphite near the Li metal deposits is lithiated in LiC_6 or LiC_{12} and this some of the Li loss is accounted for within the graphite. The exception is the cells colored in red, that are both charged at a 4C rate, that show negligible plating, irrespective of the capacity fade. This result showing direct correlation between capacity fade and plating differs from earlier works that report that the amount of Li plating (dead Li) is primarily a function of the C-rate. Our result also shows that cells cycled under the same charging protocols and rates, for the same number of cycles, show a significant heterogeneity in performance (in terms of capacity fade) as well as amount of Li plating over the cell. Therefore, in order to ensure the wider deployment of XFC enabled batteries commercially, addressing the root cause for this heterogeneity of behavior between similar cells is of paramount importance.

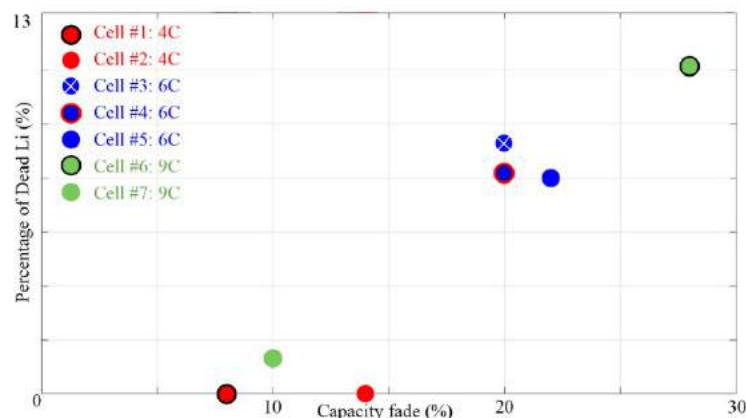


Figure I.5.K.4 Correlation between mass of plated Li (as a % of initial mass of Li before cycling) and capacity fade in Round 2 cells. While cells charged at 4C (red) show negligible plating independent of the capacity fade, the other cells (#3–#7) show a direct correlation between the amount of plating and capacity fade

2. Insights Into Porosity of Anode and Amount of Plated Li

X-ray microCT was conducted at Beamline 2BM at Argonne's APS. This technique offers a superior spatial resolution of $\sim 0.5\mu\text{m}$, which is several orders of magnitude finer than the mm-scale XRD, albeit with a proportionally smaller field of view. Therefore, this technique is ideal for studying small volumes of the electrode. In addition, microCT provides an avenue to study the heterogeneity of various species across the depth of the anode, from the separator to the current collector. The ideal geometry for such imaging characterizations involves cutting the anode into thin strips about 1–2 mm wide. These anode strips were selected based on the mm-scale XRD maps to cover regions with a large amount of Li, those with no Li, and the regions in between. Reconstruction and segmentation of the data (Figure I.5.K.5) were performed by the team at INL led by Francois Viretta, and revealed a porosity of $\sim 35\%$ in the anode, which agrees with the nominal porosity of the pristine anode. This finding points toward the regions of the anode where there is plated Li that does not have a large change in porosity as compared to regions without plating. In addition, the deposited Li is observed to be purely on the separator side, with a thickness of the order of 10s of μm . During the creation of anode strips from the anode sheet, the plated Li was converted to lithium hydroxide (LiOH), which enhanced the X-ray contrast between the graphite and Li, thus allowing for such characterization. Furthermore, calculations were performed on the thickness of each species, with the graphite showing a fairly uniform thickness of $\sim 80\mu\text{m}$ and the Li layer showing very uneven thickness. Additional calculations are ongoing, with the aim of calculating the tortuosity factor, Bruggemann exponent, and diffusion co-efficient ratio, as well as the anisotropy of each of these factors based on the direction of the calculations from tomography (in-plane versus through-plane directions).

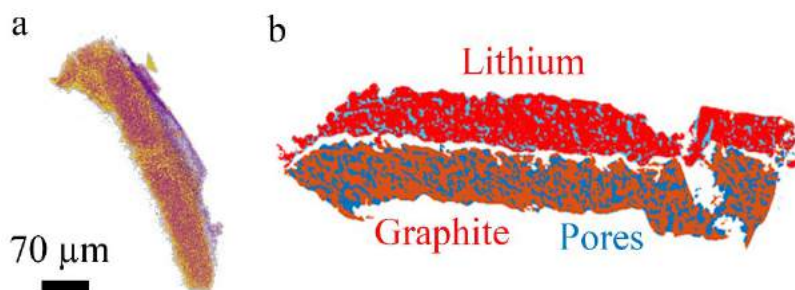


Figure I.5.K.5 microCT of a Round 2 anode cycled at the 9C charging rate for 450 cycles. (a) Projection of the tomographic reconstruction showing anode (gold) and Li in the form of LiOH (purple). (b) Segmentation, with the Li layer on top and the graphite layer below, showing the pore structure in each layer

3. Simultaneous Neutron and X-ray Tomography (NeXT)

Neutrons and X-ray-based, dual-mode tomography are advantageous for improving the estimation of the sample composition due to the complementary interaction of the two imaging modalities with the sample. A combination of X-ray and neutron imaging is useful because X-rays are sensitive to graphite in the anode, whereas neutrons are sensitive to Li (see the schematic in Figure I.5.K.6). The difference in the absorption cross-section of neutrons for carbon (0.0035) and the natural abundance of lithium (70.5) is fairly high, making neutron-based imaging a good candidate for directly detecting Li metal. The spatial resolution achieved by this technique is $\sim 15\ \mu\text{m}$, thus providing an intermediate step between the mm-scale XRD and microCT. We performed NeXT experiments at BT-2 imaging beamline at the National Institute of Standards and Technology Center for Neutron Research. The main cells characterized were the anode strips used for X-ray microCT, as described earlier. In addition, as a trial, a full pouch cell (Round 2 electrodes, assembled at CAMP) was also scanned in discharged condition and after formation cycles. The data processing is currently underway, with the aim of obtaining the total volume of plated Li on the anode. In the future, this result will be considered a substitute for X-ray microCT, especially at coarser length scales (on the order of $15\ \mu\text{m}$) due to the fewer constraints it places on sample preparation.

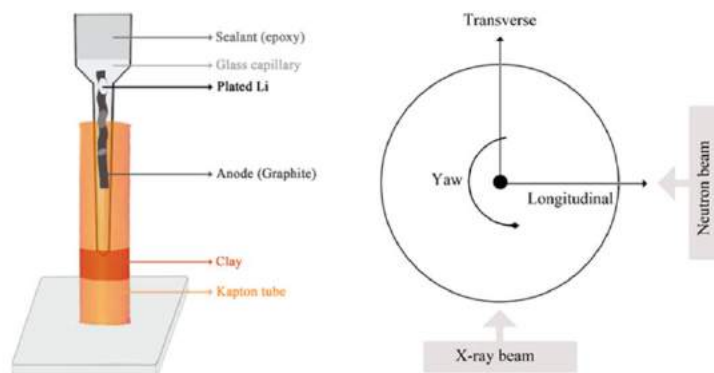


Figure I.5.K.6 Left: schematic depicting a graphite anode strip with different regions of lithium plating indicated by bright regions. The strip was vacuum sealed in a glass capillary in a kapton tube. Right: top-view diagram of the perpendicular neutron and X-ray beams in NeXT with the rotation angle (yaw)

XCEL R&D- Project 2: SLAC National Accelerator Laboratory

In the XCEL program, we have developed a platform based on uniaxial mechanical pressure measurement combining with electrochemical analysis, which enables us to detect lithium plating at a very early stage (the seeding stage) in real time. Graphite electrodes have a drastically different change of thickness during lithiation vs. during lithium plating. Graphite has a 10% volume change (3% uniaxial length change) after lithiation. The Round 2A electrodes have a coating thickness of $70\ \mu\text{m}$ with an area capacity of $2.84\ \text{mAh}/\text{cm}^2$,

which has only about a 2- μm change in thickness after full lithiation. In contrast, if the same capacity is delivered by lithium plating, the thickness change will be 14.2 μm without considering the mossy structure. The cathode side also experiences a small volume change during cycling; however, the change is negligible ($\sim 3\%$ for NMC) compared to the anode side. Therefore, the volume change in the cell is dominated by the anode. The lithium-ion battery is a fixed-volume system; any volume change in the battery material will eventually translate to pressure change. Here we describe the new method we have developed: by analyzing the pressure change per charge (dP/dQ), lithium plating can be identified easily.

The operando uniaxial pressure profile of a constrained pouch cell is measured by a load cell, as shown in Figure I.5.K.7a. Figure I.5.K.7b shows the typical operando pressure and the dP/dQ profiles versus the voltage curve of a 70-mAh NMC/Graphite 5-layer pouch cell during 0.5 C charging and discharging. The plateau on the pressure curve and the valley on the dP/dQ curve indicate the $2\text{L} \rightarrow 2$ phase transition of graphite, during which there is minimum volume change. The data from the slow (0.5 C) charging reveal the upper boundary of dP/dQ (pink dashed line) when graphite undergoes intercalation chemistry. In contrast, when lithium plating happens during fast charging, dP/dQ quickly passes the threshold as shown in Figure 29d. Scanning electron microscopy (SEM) images of the graphite anode after different lengths of time after passing the threshold show that lithium metal first appears as droplets on the surface and then evolves to a dendritic structure (Figure I.5.K.7c). This image reveals that this nondestructive technique is capable of detecting lithium plating in real time at a very early stage.

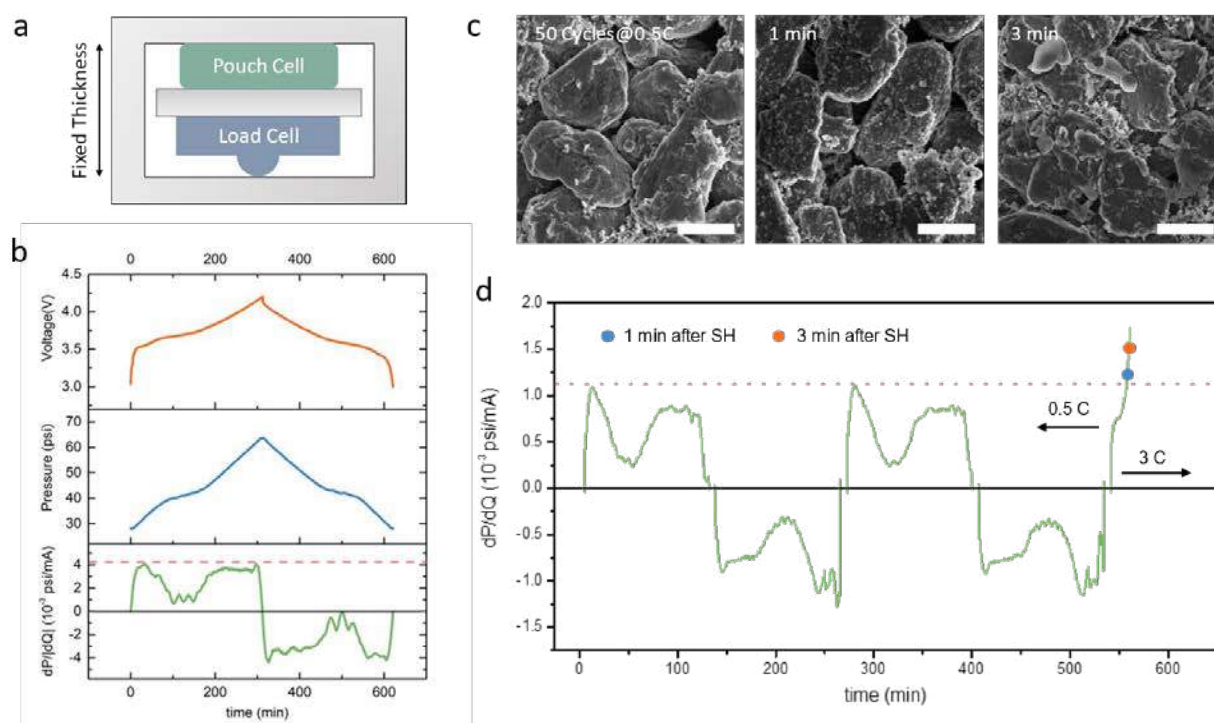


Figure I.5.K.7 (a) The configuration of operando pressure measurement: a multilayer pouch cell is stacked with a metal plate and load cell and contained in a bench vise to define a fixed thickness. (b) A typical voltage profile versus pressure and dP/dQ profiles are shown for a 70-mAh multilayer pouch cell under slow charging/discharging (0.5 C). (c) SEM images of the top surface of graphite electrodes under different charging condition. From left to right: after 50 cycles under 0.5 C, the graphite surfaces are smooth and clean; after 1 min, the dP/dQ curve passes the threshold (SH) and lithium droplets nucleate on the graphite surface; after 3 min, passing the SH, lithium dendrites can be clearly observed. (d) The dP/dQ curve during cycling in which slow 0.5 C cycles are followed by a fast-charging (3C) cycle. The blue and orange dots indicate the time points where the cells were open for SEM imaging

Conclusions

The CAMP Facility successfully designed and fabricated pouch cells with no metal in the pouch material for brief XRD experiments at UC-Berkeley. An additional 18 dry, single-layer Round 2 pouch cells were fabricated to support INL's electrolyte development effort. As in the previous quarter, the CAMP Facility continued to support several fast charge teams this quarter by supplying requested powders, electrode sheets, and pouch cells. Many of the cell builds were fabricated "just-in-time" for beamtime experiments at Argonne's APS. Technical data and electrochemical results were provided to all team members as needed to aid in their experiments and modeling efforts.

Key Publications

1. T. Tanim, E. Dufek, M. Evans, C. Dickerson, A. Jansen, B. Polzin, A. Dunlop, S. Trask, R. Jackman, I. Bloom, Z. Yang, and E. Lee, "Extreme Fast Charge Challenges for Lithium-ion Battery: Variability and Positive Electrode Issues," accepted in *J. Electrochem. Soc.*
2. M. Colclasure, A. R. Dunlop, S. E. Trask, B. J. Polzin, A. N. Jansen, and K. Smith, "Requirements for Enabling Extreme Fast Charging of High Energy Density Li-Ion Cells while Avoiding Lithium Plating," *J. Electrochem. Soc.* **166** (8) A1412–A1424 (2019).

Acknowledgments

Key contributors to the Cell, Analysis, Modeling and Prototyping (CAMP) Facility work include Alison Dunlop, Andrew Jansen, Dave Kim, Bryant Polzin, and Steve Trask (all from Argonne National Laboratory). Key contributors to the XCEL R&D- Project 1 at SLAC National Accelerator Laboratory include Hans-Georg Steinrück, Chuntian Cao, and Michael Toney. Key contributors to the XCEL R&D- Project 2 at SLAC National Accelerator Laboratory include Yi Cui, William Chueh, and Mike Toney.

I.6 Beyond Batteries

I.6.A Behind-the-Meter Storage (NREL, INL, ORNL, SNL)

Anthony Burrell

National Renewable Energy Laboratory
15013 Denver West Parkway
Golden, CO 80401
E-mail: anthony.burrell@nrel.gov

Samuel Gillard, DOE Technology Development Manager

U.S. Department of Energy
E-mail: Samuel.Gillard@ee.doe.gov

Start Date: October 1, 2018

End Date: September 30, 2022

Project Funding (FY18): \$2,200,000

DOE share: \$2,200,000

Non-DOE share: \$0

Project Introduction

This initiative, referred to as Behind-the-Meter Storage (BTMS), will focus on novel critical-materials-free battery technologies to facilitate the integration of electric vehicle (EV) charging, solar power generation technologies, and energy-efficient buildings while minimizing both costs and grid impacts. For extreme fast-charging at levels of 350 kW or higher, novel approaches are required to avoid significant negative cost and resiliency impacts. However, it is reasonable to assume that BTMS solutions would be applicable to other intermittent renewable energy generation sources or short-duration, high power-demand electric loads.

BTMS research is targeted at developing innovative energy-storage technology specifically optimized for stationary applications below 10 MWh that will minimize the need for significant grid upgrades. Additionally, avoiding excessive high-power draws will eliminate excess demand charges that would be incurred during 350-kW fast-charging using current technologies. The key to achieving this is to leverage battery storage solutions that can discharge at high power but be recharged at standard lower power rates, acting as a power reservoir to bridge to the grid and other on-site energy generation technologies such as solar photovoltaics (PV), thereby minimizing costs and grid impacts. To be successful, new and innovative integration treatments must be developed for seamless interaction between stationary storage, PV generation, building systems, and the electric grid.

Key components of BTMS will address early-stage research into new energy-generation and building-integration concepts, critical-materials-free battery energy-storage chemistries, and energy-storage designs with a focus on new stationary energy-storage strategies that will balance performance and costs for expanded fast-charging networks while minimizing the need for grid improvements.

Objectives

A cohesive multidisciplinary research effort to create a cost-effective, critical-materials-free solution to BTMS by employing a whole-systems approach will be taken. The focus of this initiative is to develop innovative battery energy-storage technologies with abundant materials applicable to EVs and high-power charging systems. Solutions in the 1–10 MWh range will eliminate potential grid impacts of high-power EV charging systems as well as lower installation costs and costs to the consumer.

Although many lessons learned from EV battery development may be applied to the BTMS program, the requirements for BTMS systems are unique—carrying their own calendar-life, cycle-life, and cost challenges. For example, EV energy-storage systems need to meet very rigorous energy-density and volume requirements to meet consumer transportation needs. Despite that, current stationary storage systems use batteries designed

for EVs due to high volumes driving down costs. This creates another market demand for EV batteries, further straining the EV battery supply chain and critical-material demand.

By considering BTMS electrochemical solutions optimized for these applications with less focus on energy density in mass and volume, the potential for novel battery solutions is very appealing. Furthermore, the balance-of-plant (BOP) for a BTMS battery system, or the cost of everything minus the battery cells, is thought to be upwards of 60% of the total energy-storage system cost. In contrast, the EV's BOP costs make up roughly 30% of the total battery cost. Therefore, BTMS will also need to focus on reducing BOP cost through system optimization to realize desired cost targets.

The design parameters are needed to optimize the BTMS system for performance, reliability, resilience, safety, and cost.

The objectives for the project are to:

- Produce BTM battery solutions that can be deployed at scale and meet the functional requirement of high-power EV charging.
- Use a total-systems approach for battery storage to develop and identify the specific functional requirements for BTMS battery solutions that will provide novel battery systems in the 1–10 MWh range at \$100/kWh installed cost—and able to cycle twice per day, discharging for at least 4 hours, with a lifetime of roughly 20 years or at least 8,000 cycles.

Approach

A cohesive multidisciplinary research effort—involving NREL, INL, SNL, and ORNL—will create a cost-effective, critical-materials-free solution to BTMS by employing a whole-systems approach. The focus of this initiative is to develop innovative battery energy-storage technologies with abundant materials applicable to PV energy generation, building energy-storage systems, EVs, and high-power charging systems. Solutions in the 1–10 MWh range will enable optimal integration of PV generation from a DC-DC connection, increase energy efficiency of buildings, eliminate potential grid impacts of high-power EV charging systems, and lower installation costs and costs to the consumer.

Many lessons learned from EV battery development may be applied to the BTMS program, but the requirements for BTMS systems are unique—carrying their own calendar-life, cycle-life, and cost challenges. For example, EV energy-storage systems need to meet very rigorous energy-density and volume requirements to meet consumer transportation needs. Despite that, current stationary storage systems use batteries designed for EVs due to high volumes that drive down the costs. This creates another market demand for EV batteries, further straining the EV battery supply chain and critical-material demand.

By considering BTMS electrochemical solutions optimized for these applications with less focus on energy density in mass and volume, the potential for novel battery solutions is very appealing. Furthermore, the BOP for a BTMS battery system, or the cost of everything minus the battery cells, is thought to be upwards of 60% of the total energy-storage system cost. In contrast, the EV's BOP costs make up roughly 30% of the total battery cost. Therefore, BTMS will also need to focus on reducing BOP cost through system optimization to realize desired cost targets.

Integration of battery storage with PV generation, energy-efficient buildings, charging stations, and the electric grid will enable new and innovative control strategies. The design parameters are needed to optimize the BTMS system for performance, reliability, resilience, safety, and cost. (See Figure I.6.A.1.)

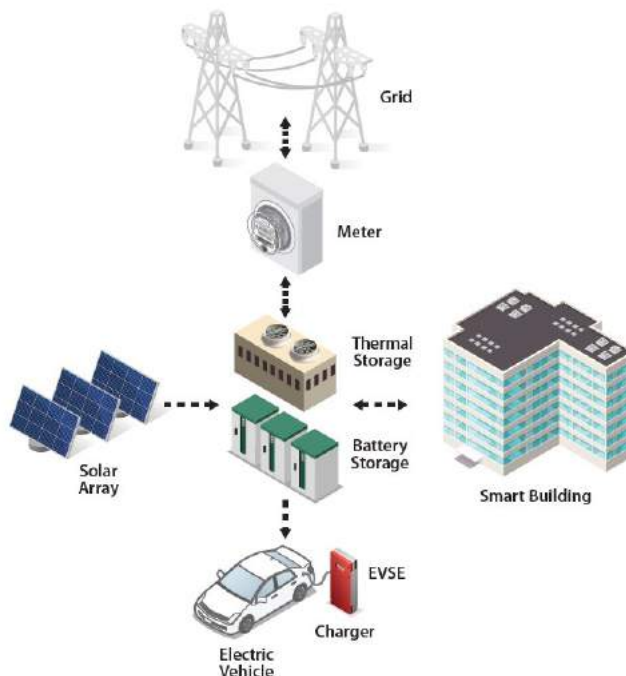


Figure I.6.A.1 Overview of BTMS relevance

This project is being conducted through a set of sub-projects, as listed below:

- BTMS Analysis (NREL) - Contributors: Margaret Mann, Samantha Reese, Tim Remo, Erin Burrell, Madeline Gilleran (NREL)
- Electrical and Thermal Design Behind the Meter System (Oak Ridge National Laboratory) – Contributors: Madhu Chinthavali, Pankaj Bhowmik (Oak Ridge National Laboratory)
- BTMS Testing (INL, SNL, NREL)
- Physics-Based Machine Learning for Behind-the-Meter Storage (INL, NREL) – Contributors: Eric Dufek, Kandler Smith, Ross Kunz
- Behind-the-Meter Energy Storage for Buildings.

BTMS Analysis (NREL)

The goal of the Behind-the-Meter Storage (BTMS) techno-economic analysis conducted in FY19 was to highlight the potential cost barriers and cost advantages that are present when coupling high-demand vehicle-charging loads with different storage configurations. The FY19 cost analysis of BTMS with DC Fast-Charging electric-vehicle supply equipment (EVSE) examined how performance, system utilization, and general changes to the demand profile could affect the minimum sustainable price that an EVSE provider would pass on to their customer.

In FY19, this analysis project focused on a high-level assessment of the potential for BTMS to reduce system costs through avoidance of demand charges. As shown in Figure I.6.A.2, the system design was limited to charging electric vehicles at a facility similar to that of today's gasoline fueling stations. This report focuses on the results from that work, with a description of the expanded effort beginning in FY20.

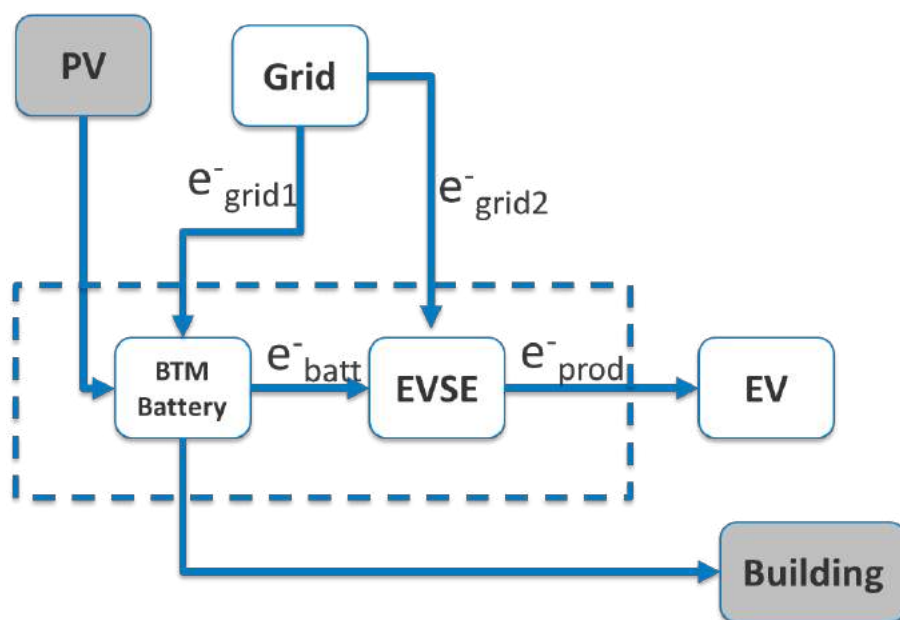


Figure I.6.A.2 BTMS System Modeled in FY19

The EVSE/BTMS model was built to incorporate the construction costs, energy load usage scenarios, geographical rate structures, and system financial requirements. The costs over the lifetime of the EVSE facility and equipment are calculated using a standard discounted cash-flow methodology to determine the minimum sustainable price (MSP) for the energy provided to the consumer, denoted as e^-_{prod} in Figure I.6.A.1. MSP is the price for which something can sell and pay back all investment and cost within analysis period. The model was designed to be technology- and location-agnostic to allow maximum sensitivity analysis. In calculating the MSP for the electricity (kWh) flowing to the electric vehicle, e^-_{prod} , the different scenarios investigated included:

- Multiple charging demand scenarios
- Multiple rate structures
- Multiple EVSEs
- Multiple battery sizes.

For this analysis, the general benchmark configuration of a DC fast-charging station was used. The targeted technology milestones and general model assumptions are listed below:

- System
 - 20-year operating lifetime
 - 90% round-trip efficiency
 - Benchmark demand profile

- EVSE Charger Configuration
 - 6 individual charging stalls
 - Rated at 350 kW power
- Behind-the-Meter Storage
 - Li-ion battery pack
 - 5 MWh capacity
 - 90% depth of discharge
 - 1 charge and discharge cycle per day
 - \$209 /kWh battery pack costs.

The structure of this model is designed to be technology-agnostic. This allows the comparison of new storage or charging components to be evaluated with respect to the current state-of-the-art designs being installed. It also allows for incorporating other subcomponent cost and construct models into this analysis. An example is the inclusion of the BacPac model developed by Argonne National Laboratory. Changes to the cell designs of the cathode material can have a significant impact on the lifetime performance and cost of a battery cell and pack. These data are computed and imported into the EVSE/BTMS model, which then shows the overall cost effect on the system's total economics.

The model was constructed to incorporate data from the consumer demand behavior, construction costs, and the electrical rate structures to understand the total economic case for the combination of storage with EVSEs.

The Electric Vehicle Infrastructure Projection (EVI-Pro) model was used to obtain a simulated demand profile for charging electric vehicles, assuming DC fast charging at 350 kW. The scenario decided upon was a “gas” station and considered that six chargers would be available. Figure I.6.A.3 graphically represents the anticipated demand modeled by EVI-Pro for the base scenario.

The model was set up to evaluate multiple utility rate structures, made available through the [Utility Rate Database](#). Two examples of the rates available for Pacific Gas and Electric (PG&E) customers in California are shown in Figure I.6.A.4.

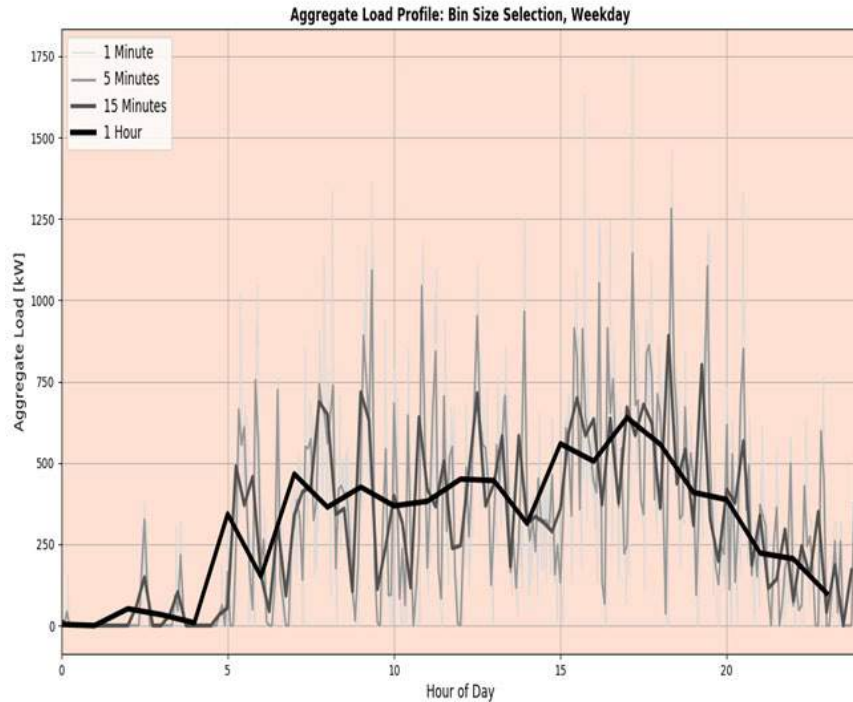


Figure I.6.A.3 Aggregate demand by time of day for EV charging

Tiered Energy Usage Charge Structure

Period	Tier	Max Usage	Max Usage Units	Rate \$/kWh	Adjustment
1	1		kWh	0.08684	
2	1		kWh	0.10163	
3	1		kWh	0.08012	
4	1		kWh	0.10749	
5	1		kWh	0.15199	

Fuel Adjustments Monthly (\$/kWh)

Jan	Feb	Mar	Apr	May	Jun	Jul	Aug	Sep	Oct	Nov	Dec

Weekday Schedule

	12 am	1 am	2 am	3 am	4 am	5 am	6 am	7 am	8 am	9 am	10 am	11 am	12 pm	1 pm	2 pm	3 pm	4 pm	5 pm	6 pm	7 pm	8 pm	9 pm	10 pm	11 pm
Jan	1	1	1	1	1	1	1	1	1	2	2	2	2	2	2	2	2	2	2	2	2	2	1	1
Feb	1	1	1	1	1	1	1	1	1	2	2	2	2	2	2	2	2	2	2	2	2	1	1	1
Mar	1	1	1	1	1	1	1	1	1	2	2	2	2	2	2	2	2	2	2	2	2	1	1	1
Apr	1	1	1	1	1	1	1	1	1	2	2	2	2	2	2	2	2	2	2	2	2	1	1	1
May	3	3	3	3	3	3	3	3	3	4	4	4	4	4	4	4	4	4	4	4	4	3	3	3
Jun	3	3	3	3	3	3	3	3	3	4	4	4	4	4	4	4	4	4	4	4	4	3	3	3
Jul	3	3	3	3	3	3	3	3	3	4	4	4	4	4	4	4	4	4	4	4	4	3	3	3
Aug	3	3	3	3	3	3	3	3	3	4	4	4	4	4	4	4	4	4	4	4	4	3	3	3
Sep	3	3	3	3	3	3	3	3	3	4	4	4	4	4	4	4	4	4	4	4	4	3	3	3
Oct	3	3	3	3	3	3	3	3	3	4	4	4	4	4	4	4	4	4	4	4	4	3	3	3
Nov	1	1	1	1	1	1	1	1	1	2	2	2	2	2	2	2	2	2	2	2	2	1	1	1
Dec	1	1	1	1	1	1	1	1	1	2	2	2	2	2	2	2	2	2	2	2	2	1	1	1

Seasonal/Monthly Demand Charge Structure

Period	Tier	Max kW Usage	Rate \$/kW	Adjustments \$/kW	Jan
1	1		15.97		+

Time of Use Demand Charge Structure

Period	Tier	Max kW Usage	Rate \$/kW	Adjustments \$/kW
1	1		0	
2	1		0.13	
3	1		5.45	
4	1		20.62	

Weekday Schedule

	12 am	1 am	2 am	3 am	4 am	5 am	6 am	7 am	8 am	9 am	10 am	11 am	12 pm	1 pm	2 pm	3 pm	4 pm	5 pm	6 pm	7 pm	8 pm	9 pm	10 pm	11 pm
Jan	1	1	1	1	1	1	1	1	1	2	2	2	2	2	2	2	2	2	2	2	2	1	1	1
Feb	1	1	1	1	1	1	1	1	1	2	2	2	2	2	2	2	2	2	2	2	2	1	1	1
Mar	1	1	1	1	1	1	1	1	1	2	2	2	2	2	2	2	2	2	2	2	2	1	1	1
Apr	1	1	1	1	1	1	1	1	1	2	2	2	2	2	2	2	2	2	2	2	2	1	1	1
May	1	1	1	1	1	1	1	1	1	3	3	3	3	3	3	3	3	3	3	3	3	1	1	1
Jun	1	1	1	1	1	1	1	1	1	3	3	3	3	3	3	3	3	3	3	3	3	1	1	1
Jul	1	1	1	1	1	1	1	1	1	3	3	3	3	3	3	3	3	3	3	3	3	1	1	1
Aug	1	1	1	1	1	1	1	1	1	3	3	3	3	3	3	3	3	3	3	3	3	1	1	1
Sep	1	1	1	1	1	1	1	1	1	3	3	3	3	3	3	3	3	3	3	3	3	1	1	1
Oct	1	1	1	1	1	1	1	1	1	3	3	3	3	3	3	3	3	3	3	3	3	1	1	1
Nov	1	1	1	1	1	1	1	1	1	2	2	2	2	2	2	2	2	2	2	2	2	1	1	1
Dec	1	1	1	1	1	1	1	1	1	2	2	2	2	2	2	2	2	2	2	2	2	1	1	1

Figure I.6.A.4 Utility rate structure for PG&E customers, demonstrating the time-variability in electricity price and demand charges

Electrical and Thermal Design Behind the Meter System (Oak Ridge National Laboratory)

The objective of this project is installation-oriented electrical and thermal design of a behind-the-meter system involving battery-based electrical energy storage system (EESS), thermal energy storage, building load, and extreme fast-charger-based electric vehicle supply equipment (EVSE). (See Figure I.6.A.5.)

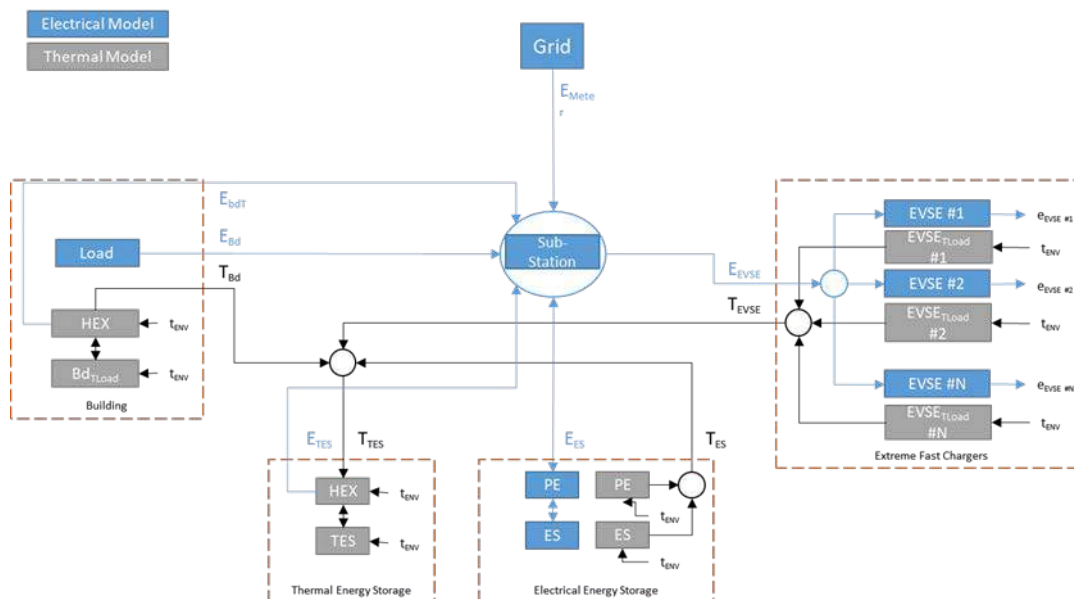


Figure I.6.A.5 Block schematic based on signal flow graph representing the overall electrical and thermal model for the entire system

Q2 Challenges

- ✓ Installation-oriented design of battery energy storage system (BESS)
- ✓ Pricing estimate of BESS
- ✓ Thermal-loss estimate of BESS

Q3 Challenges

- ✓ Installation-oriented design of electric vehicle supply equipment (EVSE)
- ✓ Pricing estimate of EVSE.

BTMS Testing (INL, SNL, NREL)

Testing activities in the first year of the program focused on several aspects of forming testing protocols to assess the gaps in performance of different battery chemistries relative to the high-level BTMS targets that were established at the program's onset. First, we performed an initial review of legacy life data from vehicle-systems energy storage testing. Next, put together preliminary testing protocols to begin cycling a few types of cells under both a single simplified use-case and under a small matrix of varied thermal and depth-of-discharge conditions that generally affect aging. We evaluated these early data along with the legacy data to aid in further testing protocol development that focused on better accelerated test methods, enhanced with machine-learning techniques, and we refined application-specific cycling protocols and performance tests.

Physics-Based Machine Learning for Behind-the-Meter Storage (INL, NREL)

Developing and deploying batteries in new, diverse applications requires that the batteries function in the necessary environment as well as a deep understanding of their performance, life, and expected failure mechanisms. In the past, the primary means to advance knowledge on performance and life was to test batteries for extended periods of time under a range of different scenarios. Testing of batteries in this manner can take upwards of a year to make reasonable estimations of life and to clearly identify failure modes and rates. The need to shorten the design and testing cycle is critical to bringing new battery chemistries and cell designs into emerging applications such as stationary energy storage to support EV charging stations capable of extreme fast charging. Connection of physics-based life models and machine learning (ML) provides the

opportunity to enable more robust assessment of battery aging, identification of failure mechanisms, and understanding as new use-case scenarios are proposed. The current project focuses on ways to apply ML to enhance the estimation of life while also identifying key failure pathways. During the first portion of the project, existing datasets will be used for both training and validating ML approaches to better characterize expected battery life. The work also looks to link ML with existing physics-based life models at INL and NREL.

Behind-the-Meter Energy Storage for Buildings: Thermal storage material characterization

Behind-the-meter storage (BTMS) is needed at buildings to mitigate high electric demand charges and to facilitate building-sited renewables and electric vehicle (EV) charging. BTMS systems can include electrochemical and/or thermal, but determining which to use—and how to size and control them together—is largely unknown.

To determine system designs for thermal and battery energy storage systems, we will use a framework that includes *multi-scale modeling* and *multi-scale experiments* for designing, sizing, characterizing, and evaluating BTMS systems, including thermal storage at multiple scales. The multi-scale experiments to validate the models are critical and ensure that the thermal + battery storage system results are meaningful and accurate. This project's goal is to evaluate today's available thermal + battery storage solutions, future possible system-level solutions, and the thermal storage R&D needs to enable these future solutions.

Behind-the-Meter Energy Storage for Buildings: Thermal storage device characterization

As with electrochemical batteries, one needs to understand not only the *material* properties of thermal storage, but also the performance when integrated into a *device*. The charging and discharging of thermal energy storage devices is analogous to the charging and discharging of electrochemical devices. The analogy is best illustrated with example discharge curves for electrical storage using electrochemical batteries and a capacitor, and for thermal storage using a sensible material and phase-change material (Figure I.6.A.6). The discharge curves for sensible storage (left) and an electric capacitor (right) have similar behavior, with their characteristic exponential decay in potential. Phase-change materials behave more like electrochemical batteries, with their slower decay in potential, because of the energy released or absorbed by the enthalpy of fusion during phase change.

For thermal storage, the temperature drop in potential is from “ qR ” losses, similar to iR losses for electrochemical batteries. The decay in temperature potential is caused by two effects: 1) at high and low state-of-charge, the PCM behaves more like a capacitor, with sensible storage above or below the phase-transition temperature, and 2) the finite temperature gradients that occur within the storage material mean that the melt (or freeze) front is further from the heat-transfer fluid, increasing the resistance between the fluid and the phase-change process. Like batteries, the potential can recover if the discharge is interrupted by equalizing temperature gradients within the material.

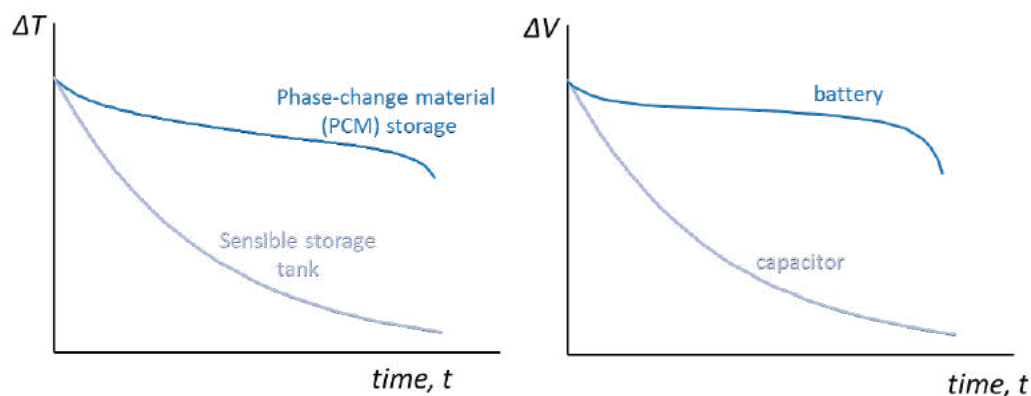


Figure I.6.A.6. Illustrative discharge curves for sensible and latent thermal storage materials (left) and for electrochemical and capacitor energy storage (right). This shows a drop in potential during discharge, with sensible storage and capacitors losing their potential more quickly than phase-change and electrochemical storage

Furthering this analogy, we can create Ragone plots for thermal energy storage using discharge curves at different C rates. Figure I.6.A.7 shows illustrative discharge curves for electrochemical energy storage (top, left), and the corresponding Ragone plot (top, right). Constant-power discharge curves for phase-change thermal energy storage (bottom, left) are also used to create corresponding Ragone plots for thermal energy storage (bottom, right). The Ragone plots require an assumed *cutoff temperature*, similar to the *cutoff voltage* used for electrical storage.

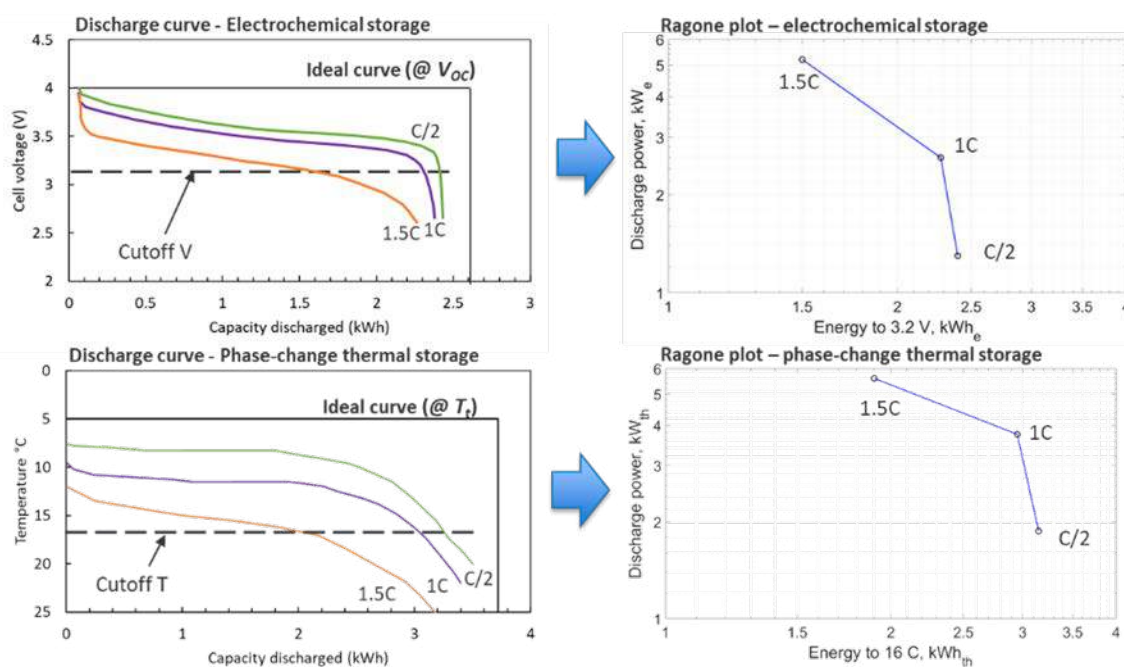


Figure I.6.A.7. Discharge curves at different C rates, and corresponding Ragone plots for electrochemical batteries (top) and phase-change thermal energy storage (bottom). V_{oc} = open-circuit voltage; T_t = transition temperature. The y-axis on the bottom-left plot is inverted because these data are for cooling applications

Results

BTMS Analysis (NREL)

The distribution of capital costs across the equipment for the EV station with BTMS is shown in Figure I.6.A.8.

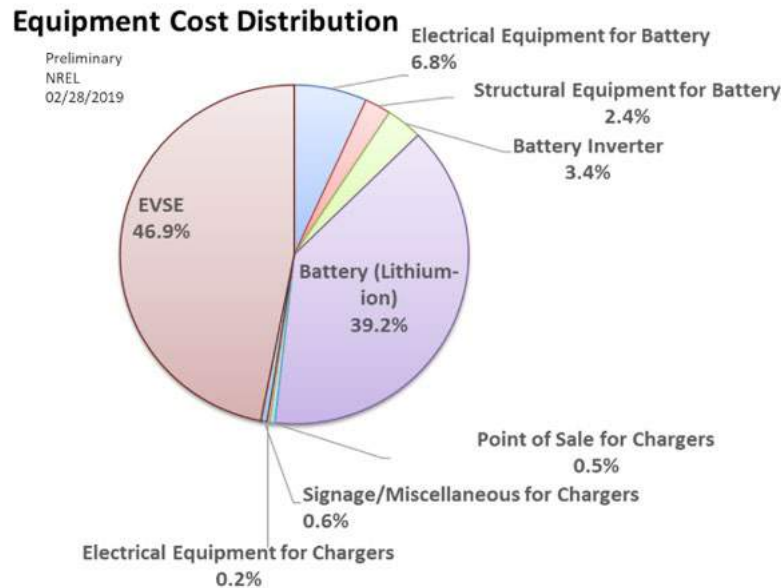


Figure I.6.A.8 Capital cost for EV charging station with BTMS

The model assessed the periods of highest demand to determine when to dispatch and charge the battery to minimize electricity cost, including demand charges. The demand for electricity from the grid during these periods was effectively shifted to other periods by using the battery to assist in charging the vehicles. Figure I.6.A.9 shows the three periods of demand and price change overlaid with the EV demand. The light blue is the original demand; the dark blue shows how that is lowered when the battery is used. Note that in the furthest left quadrant, you can see the increased demand where the battery is charging during the lowest-cost time.



Figure I.6.A.9 EV charging demand shifting with a behind-the-meter battery

With current component costs, there is only a small lifetime savings if a battery is used to offset peak demand and electricity cost. But when the battery system achieves the installed target cost, a ~40% lifetime savings would be achieved.

The initial costs for BTMS systems can be offset over time through reductions in the station's total electricity costs. The reductions are primarily through lowering demand charges, with the secondary effect of shifting electricity usages from peak to off peak times.

Reductions in peak times can offset demand charges and keep the cost for the end consumer relatively flat over the life of the system. A closer look at the rate structures show that the most impactful BTMS systems involve fewer high demand intervals followed by a low baseline energy consumption. An extreme case is highlighted in Table I.6.A.1, where the energy consumption is the same as our current baseline scenario, but the demand spike is depicted for a worst-case scenario.

Table I.6.A.1 Cost Data for Extreme Demand Scenario

Standard Scenario (Monthly Values)	Summer			
	EVSE Only		EVSE+BTMS	
Fixed Charge (Total)	\$ 1,499	1%	\$ 1,499	5%
Energy Charge (Total)	\$ 25,112	9%	\$ 23,131	7.8%
Demand Charge (Period 1)	\$ 246,986	90%	\$ 3,815	13%
Demand Charge (Period 2)	\$ 1,008	0%	\$ 1,008	3%
Demand Charge (Period 3)	\$ 24	0%	\$ 59	0%
Demand Charge (Total)	\$ 248,019	90%	\$ 4,882	17%
Total Monthly Charge	\$ 274,629	100%	\$ 29,511	100%
Cost of Electricity from Grid (\$/kWh)	\$ 1.2221		\$ 0.1245	
MSP	\$ 1.5911		\$ 0.2779	

Systems that operate under highly variable demand loads scattered throughout a daily operation, with a high average energy baseline load, require larger battery systems to impactfully reduce the total MSP. These systems can still be economically viable over the life of the system, but the high cost of the battery pack will cause a longer payback period. This leads to concerns of longer system reliability requirements. Another important aspect to properly size a BTMS storage system involves optimizing the ration of demand charge to energy charge. Future analysis will also incorporate on-site distributed generation, which will have the potential to reduce the energy charges as well as further assist to reduce demand.

Seasonal charges will also contribute to how the battery will operate. In some cases, standby or use as a backup system may extend the life of the system. This is due, in part, to demand charges that only exist during the four- to six-month summer periods. Table I.6.A.2 shows one example of the large potential price difference in seasonal operations. As these systems become more standardized, there is even the possibility that containerized systems could be considered mobile assets and moved from one location of value to another location of higher value once or multiple times during its lifetime based on system economics. This would allow for more, shorter positive payback periods over the asset's usable life.

Table I.6.A.2 Cost Data for Seasonal Demand Scenario

	Off Summer				Summer			
Standard Scenario (Monthly Values)	EVSE Only		EVSE+BTMS		EVSE Only		EVSE+BTMS	
Fixed Charge (Total)	\$ 1,499	4%	\$ 1,499	5%	\$ 1,499	3%	\$ 1,499	6%
Energy Charge (Total)	\$ 20,451	61%	\$ 20,588	74%	\$ 24,273	53%	\$ 20,136	86%
Demand Charge (Period 1)	\$ 11,407	34%	\$ 5,799	21%	\$ 14,729	32%	\$ -	0%
Demand Charge (Period 2)	\$ -	0%	\$ -	0%	\$ 4,854	11%	\$ 1,680	7%
Demand Charge (Period 3)	\$ -	0%	\$ -	0%	\$ 89	0%	\$ 135	1%
Demand Charge (Total)	\$ 11,407	34%	\$ 5,799	21%	\$ 19,672	43%	\$ 1,816	8%
						100		
Total Monthly Charge	\$ 33,357	100%	\$ 27,886	100%	\$ 45,444	%	\$ 23,451	100%
Cost of Electricity from Grid (\$/kwh)	\$ 0.1484		\$ 0.0932		\$ 0.2022		\$ 0.0989	
MSP	\$ 0.3061		\$ 0.2409		\$ 0.3696		\$ 0.2477	

One potential driver for a mobile system would be changes in the demand profile during the system's lifetime. A system that is oversized for current demand results in a large price penalty to the consumer and operator. This will be a challenge for EVSE+BTMS systems designs. The price penalty for not installing a BTMS system is severe due to potential high demand charges and grid upgrade costs that can be incurred with site construction. Oversizing a system, however, can create an upfront potential barrier to market adoption.

BTMS coupled with high demand rates and irregular demand profiles can have a positive rate of return when systems have a long operational life. The current specified system lifetimes under 10 years do fall short of a positive return. But given the ability to upgrade and extend the life of a system, a simple business model as described for this analysis is likely to change over the full operating life span. These changes could include repowering or expanding the system capacity. Given the falling cost of batteries packs and typical rising inflation values, designing a system capable of expansion in a plug-and-play fashion could provide a greater economic benefit because there could be advantages specific to permitting and soft costs. The current bottom-up analysis for systems designs shows that the battery pack itself is around 50% of the total system capital cost.

It is also important to understand how the energy rate structures may change over time given the emergence of low-cost energy from distributed generation and changing energy load profiles. Energy storage has the ability to operate under multiple use-cases, but the largest attraction to energy storage is the energy arbitrage operation of operating low-cost energy from one timeframe and dispatching the energy at expensive rate timeframes. In doing so, energy storage does not generate energy but rather shifts it from one time to another so that all energy storage systems require some generation source—whether that is the grid or distributed generation sources such as renewables. BTMS systems can smooth the operational demand for a load profile, potentially reducing demand spikes on a transmission line. This may reduce the costs of upgrading transmission and distribution systems and—of particular benefit to EV station owners—reduce the cost of interconnecting their systems to the grid. Future work should examine a wide range of current and predicted

utility rate structures, as well as grid interconnection costs, to better understand how BTMS systems should be defined to optimize cost.

Electrical and Thermal Design Behind the Meter System (Oak Ridge National Laboratory)

An installation-oriented design of an EVSE may be subdivided into two major design items, as follows:

1. Electric vehicle (EV) load
2. Power electronics (PE).

This report discusses the design of the PE that has to be installed to supply power to an EV load from the grid. The design of PE has certain aspects that must be performed alongside determining the nature of EV load. Here, we consider EV extra-fast-charging stations. These installation design aspects are also reviewed here. We also present an estimate of the costs and losses associated with the design of an EVSE (Figure I.6.A.10).

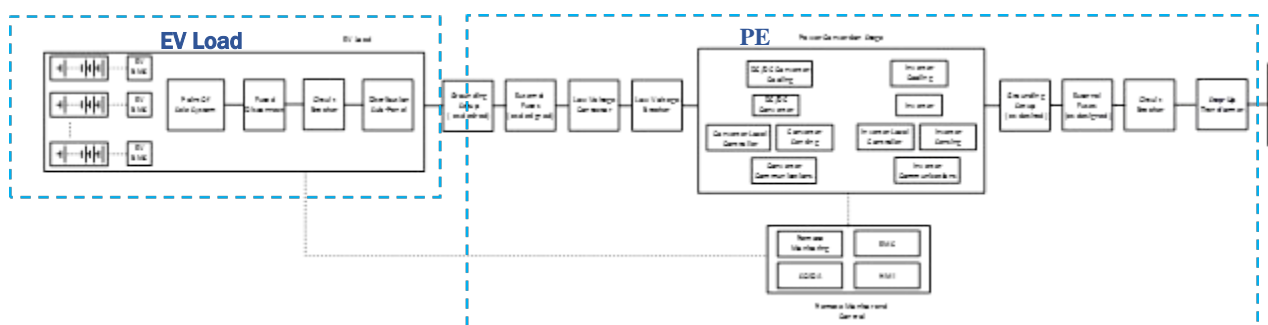


Figure I.6.A.10 Block schematic of an electric vehicle supply equipment

A simplified block schematic of a typical EVSE installation with EV load and PE is shown in Figure I.6.A.10. PE consists of three main aspects from the perspective of electrical power flow and signals:

- a. Control and Protection
- b. Power conversion
- c. Communications.

Protection may be further subdivided into DC-side and AC-side protection. Typically, both DC- and AC-side protection involve fuses, contactors, circuit breakers, and proper grounding setup. Also, a step-up transformer is added while integrating the PE to the grid, and to step up the voltage, an additional level of isolation is added to EVSE from the utility grid. Depending on the number of EVs that can be simultaneously charged, the protection design costs and losses will vary.

Power conversion incorporates the power converter, power converter cooling system, power converter sensing, and connecting cables. The designed PE system may be rated at 1 MVA power-handling capacity. But the estimated range for costs presented in this chapter may be used to evaluate PE designs up to 100 MVA.

Control and communications includes the converter controller, converter communications, remote monitoring, supervisory control, and data acquisition, EV load battery communication system, and human/machine user interface for the point-of-sale (POS) system. This element of a PE design is also responsible for the control and coordination between EV load, DC and AC protection devices, and power conversion system.

These aspects of a PE design only demonstrate the electrical power flow, signal monitoring, control, and protection perspective. To view the site installation-oriented design flow of a PE system, the various aspects such as site allocation, site building, engineering construction, labor, and costs, to name a few, have to be incorporated into the design. This particular commercial installation-oriented design will provide more insight into cost estimate and loss estimate for any proposed EVSE. The next section discusses this design flow for an EVSE system. The design considerations that will be used to estimate the costs and losses for an EVSE are presented in Table I.6.A.3

Table I.6.A.3 Design Considerations for Cost and Thermal Model of an EVSE

Parameters	Values	Units
DC Bus Voltage	1,500	V
DC Bus Current	1,000	A
DC Bus Power	1.5	MW
AC Bus Line Voltage	480	V
AC Bus Current	1,200	A
AC Bus Active Power	1	MW
Grid Line Voltage	13.8	kV

Installation-Oriented Design of Electric Vehicle Supply Equipment

The installation-oriented design for an EVSE is subcategorized into five main elements (Figure I.6.A.11):

1. Power conversion system (PCS)
2. Structural balance of system (SBOS)
3. Electrical balance of system (EBOS)
4. Engineering procurement and construction (EPC)
5. Soft cost.

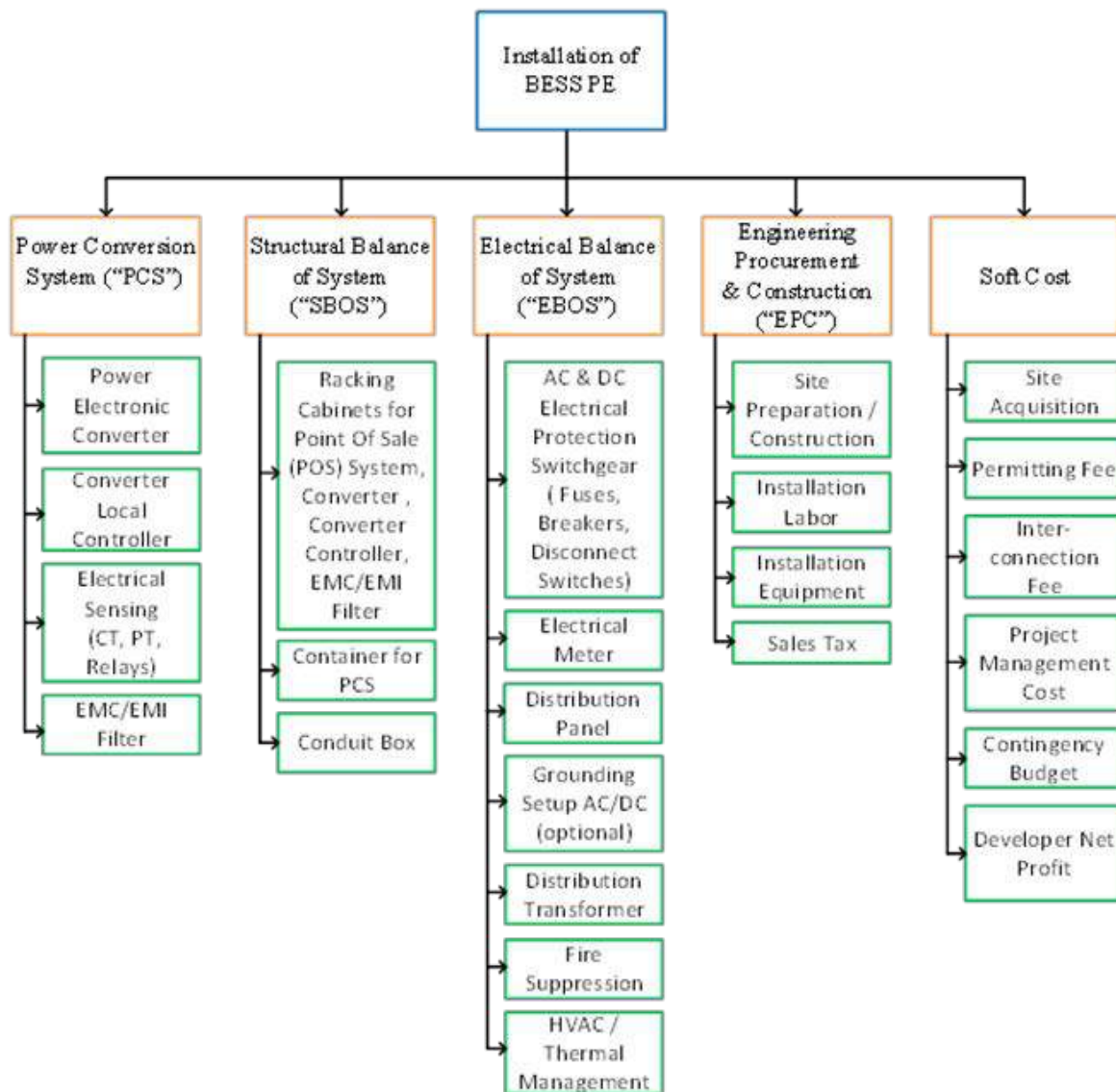


Figure I.6.A.11 Block-tree-type categorization of the various aspects of installation-oriented design of EVSE [1],[2],[3],[4],[5]

The PCS involves procuring the converter, converter local controller, electrical sensing equipment such as the current transformer (CT), potential transformer (PT) and relays, and also the EMI/EMC filter. This category has been so named because it involves conversion of the AC power obtained from the grid to DC power that is being supplied to the EV load.

The SBOS involves procuring all the components that provide structural integrity and housing to install the PCS as well as EBOS. It involves racking cabinets for the POS system, converter, converter controller, and EMC/EMI filter. It also incorporates the container for housing the PCS and conduit boxes to house the cable terminal connections.

The EBOS involves procuring all the components that monitor electrical power flow and signals and that under fault conditions protects the PCS, EV load, and grid. It also provides added functionality of fire suppression and management of the thermal energy dissipated from the PCS through HVAC or other cooling technologies. It involves AC and DC components such as fuses, breakers, meters, and disconnect switches. It also includes a

distribution transformer for isolation as well as voltage step-up purposes. In the case where no grounding is available in the PCS, a grounding setup on the DC or AC side may be considered to provide a return path to fault current or neutral current under fault or unbalanced system conditions.

EPC is a multi-faceted and human-resource intensive activity that is crucial to installing an EVSE PE. It involves preparing and constructing a site for the installation of PCS, SBOS, and EBOS. It also involves acquiring or renting equipment for installing PCS, SBOS, and EBOS. To perform all these activities in EPC, installation labor has to be hired with wages whose minimal value may vary from state to state. Most importantly, all the taxes levied on this overall EVSE installation process are included under sales tax, which may again vary by state.

Lastly, soft cost entails acquiring the site for EVSE installation, permitting fee for permission to install EVSE, interconnection fee for EVSE interconnection with the utility grid, project management cost for planning and executing the project for installation of EVSE, and the overall developer net profit generated by undertaking the EVSE installation.

Pricing Estimate of Electric Vehicle Supply Equipment

Table I.6.A.4 lists the EVSE PE installation components and presents the estimated rates for each process as a range in the units of U.S. dollars per watt (\$/W). The total estimated cost is also estimated from the rates based on the power rating of 1 MW.

Table I.6.A.4 EVSE Component-wise Cost Estimate for a 1-MW, 13.8-kV Setup [1]–[5]

EVSE Installation Components	Estimated Rate (\$/W)	Estimated Total Cost (\$)
PCS	0.11–0.16	110,000–160,000
SBOS	0.07–0.12	70,000–120,000
EBOS	0.10–0.20	100,000–200,000
EPC	0.12–0.34	120,000–340,000
Soft Cost	0.08–0.19	80,000–190,000

Table I.6.A.5 lists the complete EVSE installation total estimated rate in \$/W units, which is the summation of each component rate from Table I.6.A.5. The total estimated cost is then calculated from the total estimated cost based on the power rating of 1 MW.

Table I.6.A.5 EVSE PE Total Cost Estimate for a 1-MW, 13.8-kV Setup [1]–[5]

Cost Estimate for a 1-MW, 13.8-kVac Setup:		
Total EVSE Installation	Total Estimated Rate (\$/W)	Total Estimated Cost (\$)
	0.48–1.01	480,000–1,010,000

BTMS Testing (INL, SNL, NREL)

Legacy data review looked at both cobalt-free cell chemistries and some with cobalt-bearing cathode materials, in addition to published life and performance data. From 2010–2012, two builds of lithium iron phosphate (LFP)-graphite cells were cycled and aged under test protocols developed for EVs at 30°C. The later build reached 20% capacity fade before 1,500 full-DOD cycles were reached (Figure I.6.A.12).

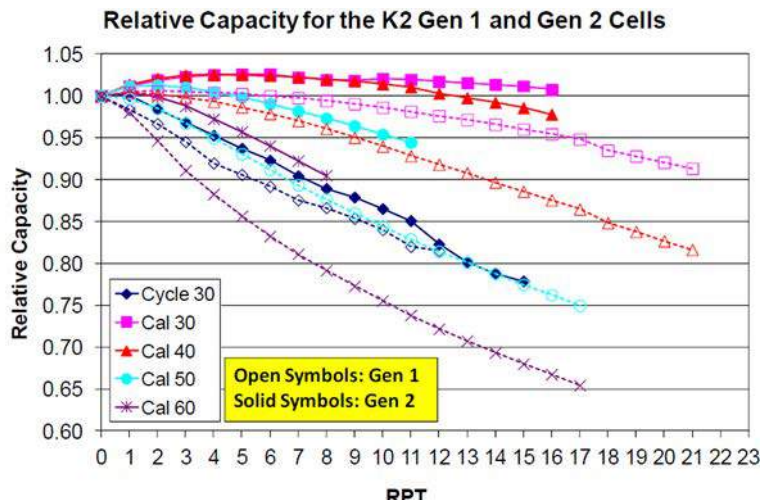


Figure I.6.A.12 Capacity data throughout life testing is shown for LFP/graphite EV cells DST cycled to full depth of discharge

LFP cells with lithium titanate oxide (LTO) anodes were reported to have extremely long cycle life, due in part to the lack of solid-electrolyte-interphase formation on the anode. Testing from 2012–2013 with continuous cycling at 30°C yielded less than 6,000 1C/1C full cycles to 20% capacity fade (Figure I.6.A.13). This did not align with the developer's testing data at the same ambient temperature, but much higher rates, using a 5C/10C cycling protocol, which yielded 20,000 cycles without appreciable fade. This specific couple is not known as being pursued because of its very low energy density, although LTO anodes are generally capable of long cycle life.

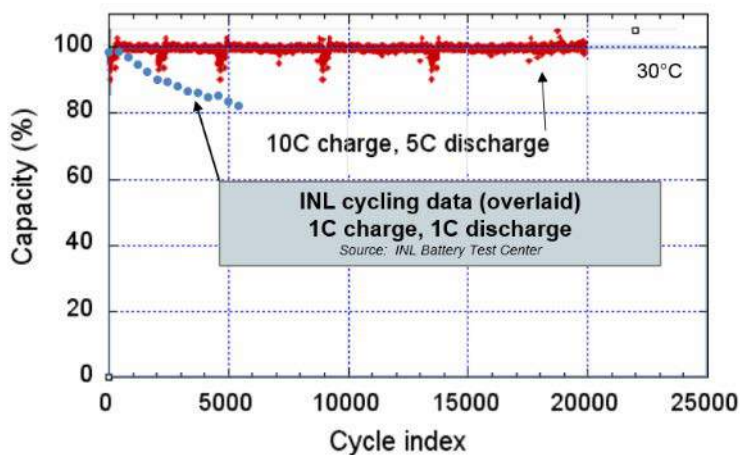


Figure I.6.A.13 INL cycling data at 1C/1C is shown overlaid on 5C/10C cycling data published by the developer

Another LTO-anode cell type, with an unspecified cathode thought to be LMO with NMC, was cycled under test protocols developed for EVs at 30°C and 52°C from 2016–2018. These prismatic cells showed no fade under DST cycling with both C/3 slow-charging and 5C fast-charging after more than 2,000 cycles. High temperature rapidly accelerates these cells' capacity loss, and that is compounded by rest at 100% SOC, as evidenced by the high fade rates of the calendar-life cells at 52°C. (See Figure I.6.A.14.)

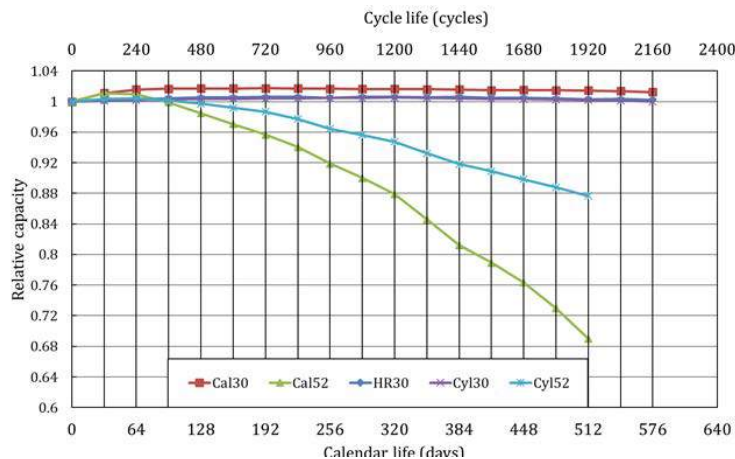


Figure I.6.A.14 Calendar- and cycle-life data for LMO-NMC/LTO cells

Early Nissan Leaf LMO/graphite EV cells, manufactured by AESC, were cycled at three different temperatures. The cells were cycled using an EV DST discharge profile, from 90% SOC, removing 60% of the total BOL energy. Recharge was done using a constant-power, constant-voltage protocol approximating a slow C/7 charge. Temperature had a primary impact on the rate of capacity loss of these cells. Because the primary purpose of this testing was to investigate the effects of charging rate on degradation, the testing was stopped after 864 cycles. Linear extrapolation of the last six 30°C data points yields an approximation of 2,100 of these 60% DOD cycles to 80% capacity remaining. Incremental capacity analysis indicated capacity loss due mainly to loss of lithium inventory and loss of active material on the anode for all three temperature conditions. (See Figure I.6.A.15.)

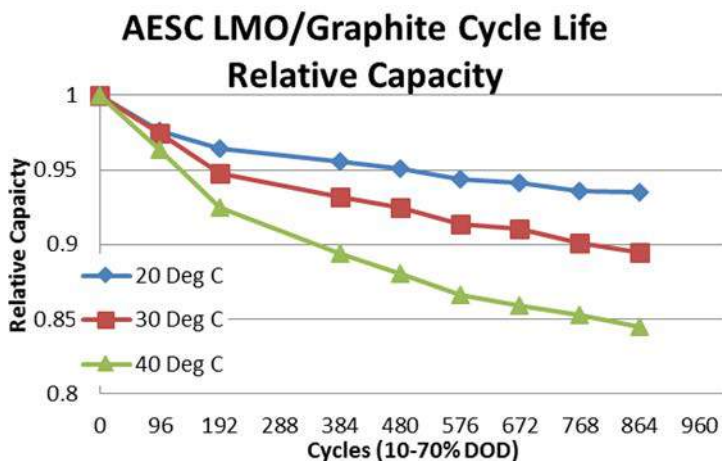


Figure I.6.A.15 Cycle-life data for LMO/graphite cells

NMC-LMO/graphite pouch cells were cycled from 2016–2019 under a plug-in hybrid EV (PHEV) charge-depleting cycling protocol from 90% SOC, removing 65% of their total energy per cycle, at 30°C. These cells retained 78.5% of their original capacity after more than 5,000 PHEV-40 CD cycles. (See Figure I.6.A.16.)

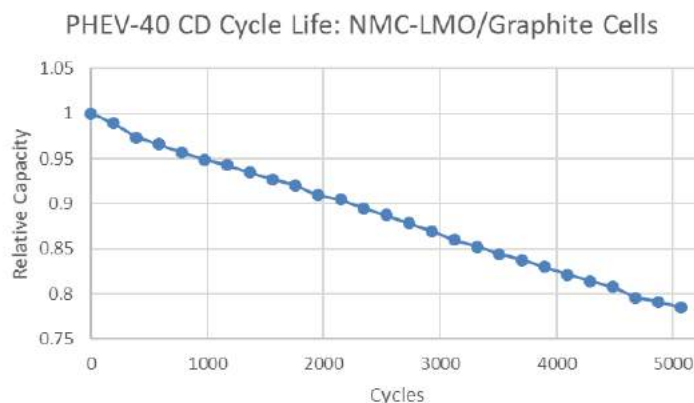


Figure I.6.A.16 Cycle-life data for NMC-LMO/graphite cells

The BTMS program specified investigation of 1–10 MWh storage systems used to support extreme fast-charging (XFC), among other co-beneficial systems including buildings electrical and thermal needs and on-site renewable electricity generation. Although complex use-cases were being discussed and developed, we selected a gas-station-like model featuring six 350-kW DC fast-chargers with 1 MWh of storage as a scenario to base initial battery rate requirements for a preliminary cycle-life protocol. Pairing the minimum energy storage system size with six XFC units that concurrently use 100% of their power from the energy storage system yields about a 2:1 power-to-energy ratio system requirement, which can be approximated by a 2C discharge of a cell. This situation could be realized when all of the energy supplied to XFC units is supplied from the BTMS system, accomplishing a full load shift of off-peak energy. It is likely that in many scenarios, simultaneous use of all XFC stations would be occasional, and XFC power would be supplied by both the grid and the BTMS system. In this case, a lower rate would be realized. A C/2 rate was chosen as a more moderate discharge rate for preliminary cycling based on discussion of these factors. This rate results in less than 6 full cycles per day, when accounting for CV charging time. High discharge rates, within cell manufacturer specifications and laboratory channel resource availability, were chosen to accompany the slow cycling, to accumulate cycles more rapidly and to accelerate capacity loss. Aside from a 30°C reference condition, 10°C and 45°C were also chosen to affect rates of capacity loss. Finally, some cells were cycled shallowly, within the middle 50% of their capacity, to investigate path dependence of capacity loss. We selected NMC/graphite, NMC/LTO, and LFP/graphite commercial cells with quick availability. (See Figure I.6.A.17.)

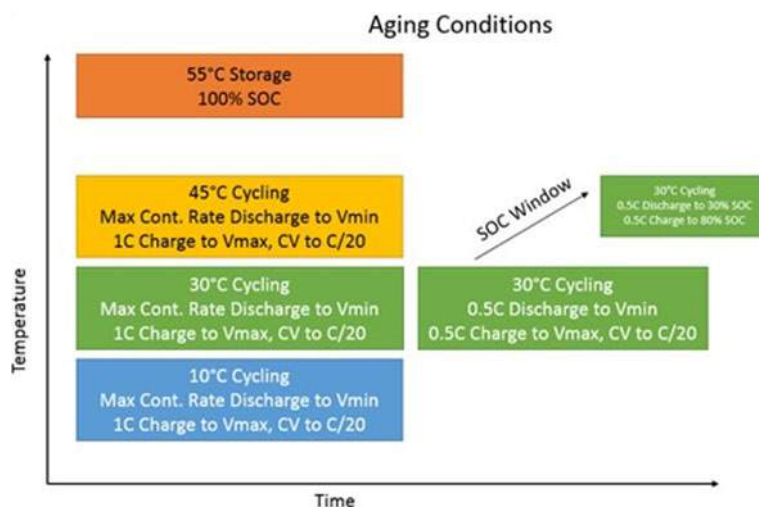


Figure I.6.A.17 Preliminary test matrix for cells with 6-XFC and 1 MWh ESS and accelerated aging conditions

Sandia National Laboratories assembled a pack-estimating table (Table I.6.A.6), and this calculation demonstrated that lowering the applied current of the string can be cost prohibitive due to the number of cells needed and the implied balance of plant. What resulted from this discussion was a test plan that spanned a variety of use cases—from pushing the limits of the cells to standard cycling—to fully understand the capabilities of the cells and their aging characteristics.

Table I.6.A.6 Pack Estimation Calculation Table (Shaded Row Represents the C/2 Discharge Rate)

Current Applied per String	Current in C rate (assuming 3.5 Ahr)	Capacity consumed	Minimum number of strings	D-Rated Voltage	Minimum Cells in String	Recommended Cells in String	Pack Power (Without Power Electronics)	Total Number of Cells	COST? (k)
50	14.29	12.5	19.4	2.8	125	138	0.374	2671	10.7
40	11.43	10	24.3	2.9	121	133	0.374	3224	12.9
30	8.57	7.5	32.4	2.95	119	131	0.374	4226	16.9
20	5.71	5	48.6	3	117	128	0.374	6233	24.9
10	2.86	2.5	97.1	3.2	109	120	0.374	11688	46.8
5	1.43	1.25	194.3	3.3	106	117	0.374	22667	90.7
1.75	0.50	0.4375	555.1	3.32	105	116	0.374	64372	257.5
1	0.29	0.25	971.4	3.35	104	115	0.374	111642	446.6

The 2-hour discharge capacity and pulse-power capability of each cell was measured monthly in a reference performance test. Every third performance test included a set of 20-hour charge and discharge cycles that can be analyzed to understand differences in aging mechanisms among test conditions, in addition to the characterization of performance loss through time and cycling. Cells were fixtured and placed in thermal chambers and connected to cycling equipment, and baseline testing and life cycling and aging commenced in Q2. Initial results showed cell-level energy densities of 485 Wh/L for the NMC/graphite cells, 133 Wh/L for the NMC/LTO cells, and 98–107 Wh/L for the LFP/graphite cells, for power and energy application types, respectively.

The NMC/graphite cells suffered rapid degradation in the first set of cycle aging, and the rate of capacity loss generally increased with increasing charge and discharge rates. Only the cells in the slowest 2-hour charge and 2-hour discharge cycling condition retained enough capacity to complete the first and second reference tests. The NMC/graphite cells in the other cycling conditions, including up to 1C charge and 1C discharge, lost more than 25% capacity before RPT1. The results from the cells tested through the third reference performance test are shown in the figures below. The shallow-cycled cells show little benefit relative to the cells cycled over the entire SOC window. (See Figure I.6.A.18 and Figure I.6.A.19)

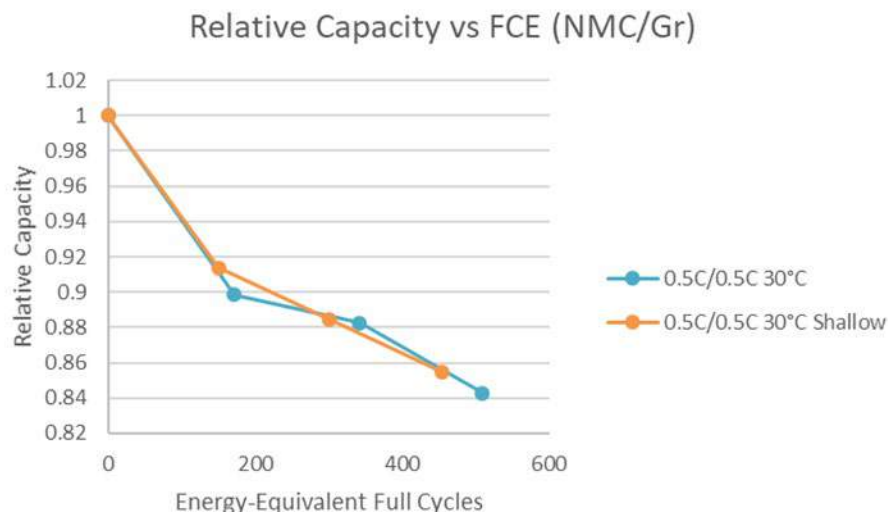


Figure I.6.A.18 Cycle-life testing results for the NMC/graphite cells

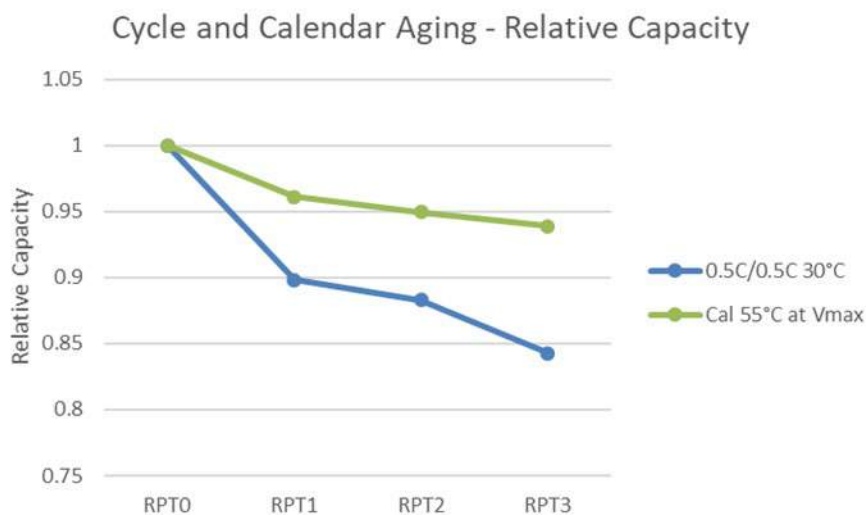


Figure I.6.A.19 Calendar testing results for the NMC/Graphite cells, shown with the baseline cycling condition results

The NMC/LTO cells had a maximum continuous discharge rate of 6C, and that condition was applied, along with 1C and C/2 cycling conditions. Only the colder cycling condition showed significant fade at the second RPT. Due to the different rates and different temperatures, varying amounts of capacity were discharged from each test condition, resulting in disparate numbers of cycles per time period. These data are shown in Figure I.6.A.20, plotted relative to the full-cycle equivalent (FCE) of cumulative energy discharged at the 30°C, 2-

hour discharge reference condition. These cells have shown less than 1% fade over more than 1,700 cycles at slow- and high-rate discharge and at both 30°C and 45°C conditions. The cycle-by-cycle discharge capacity for each condition is shown as well in Figure I.6.A.21. However, note that the cycle count is raw, and each cycle at the various conditions are not equivalent due to rate and temperature.

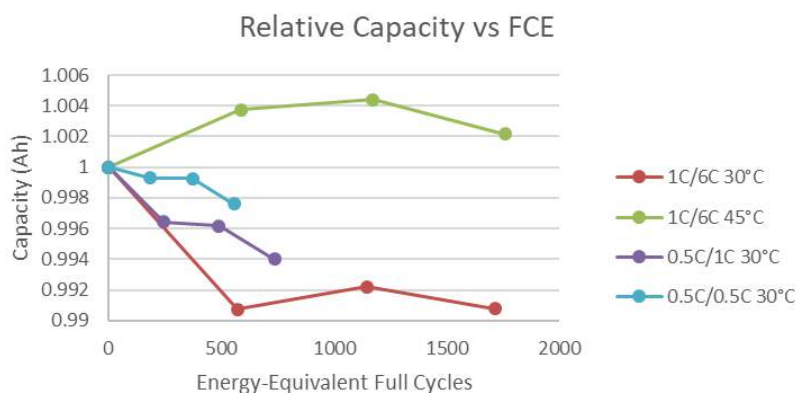


Figure I.6.A.20 Cycle-testing reference-performance-test (RPT) capacity results for the NMC/LTO cells

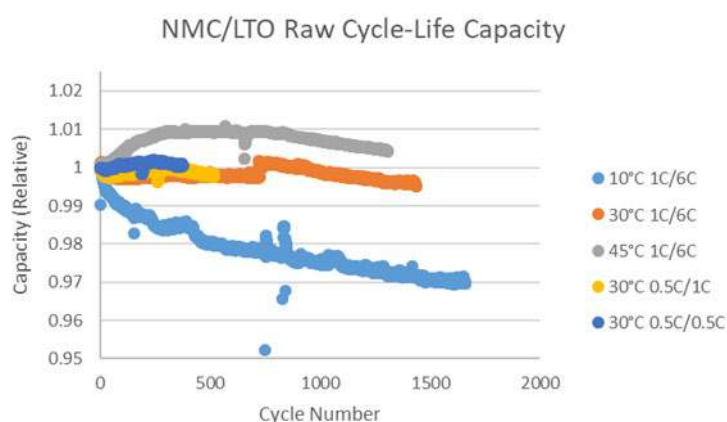


Figure I.6.A.21 Cycle-by-cycle testing capacity results for each cycling condition for the NMC/LTO cells

Two different cell constructions are currently being investigated for the LFP/graphite system. These cells have undergone close to 130 consecutive days of continuous cycling. The effects of this cycling on the capacity fade of the cells can be observed in Figure I.6.A.22. Results show that on average the power cells have lost ~10% whereas the energy cells have lost close to ~30% in the worst case. It is difficult to say that the ~30% loss in the energy cell is representative without additional cells to provide statistics. Differences in the state-of-health testing of these cells can also be observed as demonstrated in Figure I.6.A.23.

Capacity Retention of LFP/Graphite Cells Cycled at 30°C

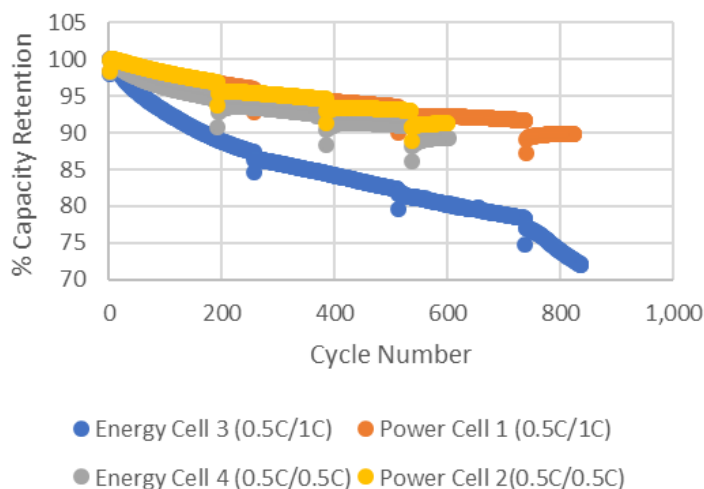


Figure I.6.A.22 LFP/graphite cycling results

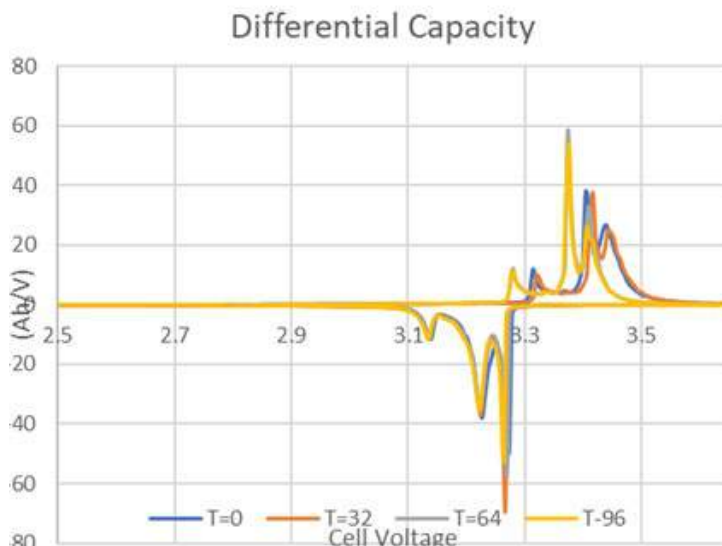


Figure I.6.A.23 Differential capacity test for LFP/graphite cells

HPPC results show that as the cell continues to cycle, it loses its ability to deliver power at low SOC's. Understanding this phenomenon will be critical for predicting end-of-life behavior of these cells. The differential-capacity results suggest that the loss of performance is most likely attributed to changes in the graphite anode. This is a known problem. Graphite is known to degrade from extensive cycling. In an effort to predict the lifetime of these cells, a simple trend line (which is an overestimate) was fitted to each curve in Figure I.6.A.22 and the calculated slopes of the line can be found in Figure I.6.A.24. These fade rates fall short of providing 10,000 cycles, even when allowing for 50% capacity loss at end of life.

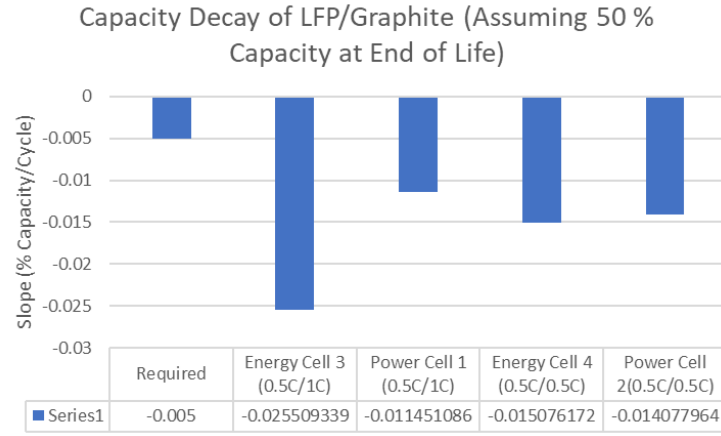


Figure I.6.A.24 Capacity decay rate for each LFP/graphite cell type and condition

Physics-Based Machine Learning for Behind-the-Meter Storage (INL, NREL)

During Q4, three primary activities were advanced toward adapting physics-based lifetime models to use ML tools to automate the process of more rapidly and accurately mapping accelerated test results to real-world lifetime predictions: 1) data transfer and analysis, 2) life model generalization, and 3) machine learning using existing datasets. Across each of these three areas, INL and NREL teams have had significant interaction to drive uniformity in analysis and to advance the overall knowledge base in the project.

Data exchange. For test datasets, the team exchanged data from 2012 Nissan Leaf cell and pack fast-charge experiments (INL) [1], as well from Kokam 75-Ah graphite/NMC grid energy storage cell life testing (NREL) [2]. These cycling sets each provide distinct information from prior testing efforts at different cycling conditions and temperature. Combined, they were chosen for these reasons as well as for their combination of summary (associated with reference performance tests) and raw data from the different cycling regimes. Initial sharing of datasets has occurred using Box, with plans in place to move forward with different sharing mechanisms during FY20.

Generalize physical lifetime model. NREL generalized and documented their battery lifetime predictive model based on experience from previous Li-ion technologies [2],[3]. With some exceptions, changes in battery performance metric, y , are represented as a linear combination of the reduced-order degradation models x_i shown in Table I.6.A.7,

$$y = \sum_i x_i.$$

Performance metrics y include battery relative resistance growth r ; relative capacity q ; or, in the case of changing mechanisms controlling capacity fade, y may represent negative electrode site inventory q_- , positive electrode sites inventory q_+ , and lithium inventory q_{Li} with overall relative capacity taken as

$$q = \min(q_{Li}, q_-, q_+,).$$

In Table I.6.A.7, x is the state variable for degradation mechanism i , p is the order of the fade mechanism (a constant), k is the rate of fade, and M is the magnitude of fade. Accelerated aging tests are generally conducted at different constant values of temperature T , depth of discharge DOD , average state of charge SOC , and discharge/charge current C_{rate} . For individual aging tests under simple aging, fade rate k is constant, and the analytical solution is used for model fitting. With fade rate k determined for multiple aging conditions, a rate-law model is fit to describe $k(T, SOC, DOD, C_{rate})$. Rate laws are generally built as multiplicative combinations of acceleration factors listed in Table I.6.A.8,

$$k_i = k_{i,ref} \prod_j \theta_j.$$

Table I.6.A.7 Degradation Mechanism Models

Mechanism	State equation	Analytical solution valid for constant k
1) Mixed diffusion/kinetic-limited side reaction ¹	$\dot{x}(t) = kp \left(\frac{k}{x(t)} \right)^{\left(\frac{1-p}{p} \right)}$	$x(t) = kt^p$
2) Site loss ²	$\dot{x}(N) = k \left(\frac{x_0}{x(N)} \right)^p$	$x(N) = [x_0^{1+p} + k' x_0^p (1+p)N]^{\frac{1}{1+p}}$
3) Break-in process ³	$\dot{x}(t) = k(M - x(t))$	$x(t) = M(1 - \exp(-kt))$

1. Order $p = 0.5$ for diffusion-limited solid/electrolyte interface (SEI) growth.
2. Order $p = 0$ for linear fade. $p \geq 1$ for accelerating fade.

Table I.6.A.8 Acceleration Factors Used for Building Degradation Rate Laws

Rate/magnitude dependence	Type of Stress	Acceleration factor, θ_j
Temperature	Chemical & Mechanical	(1.1) $\exp \left[-\frac{E_a}{R_{ug}} \left(\frac{1}{T(t)} - \frac{1}{T_{ref}} \right) \right]$
SOC	Chemical	(2.1) $\exp \left[\frac{\alpha F}{R_{ug} T(t)} \eta(t) \right]$ where $\eta(t) = U_{\pm}(t) - U_{ref}$
C-rate	Chemical	(2.2) ... where $\eta(t) = U_{\pm}(t) - U_{ref} - C_{rate}(t)R_{film}$
	Mechanical	(3.1) $C_{rate,i} \sqrt{t_{pulse,i}} = DOD_i \sqrt{C_{rate,i}}$ (3.2) $(C_{rate,i})^{\gamma}$
DOD	Chemical	(4.1) $(DOD_i)^{\beta}$
	Mechanical	(5.1) $(1 + \gamma(DOD_i)^{\beta})$ (5.2) $\exp(\gamma(DOD_i)^{\beta})$

- i is cycle index from Rainflow algorithm
- Fitting parameters are k_{ref} , E_a , α , R_{film} , γ , β
- Constants are $R_{ug} = 8.314 \text{ J K}^{-1} \text{ mol}^{-1}$, $F = 96485 \text{ C mol}^{-1}$, T_{ref} arbitrary with units [K], U_{ref} arbitrary with units [V]
- U_- and U_+ , respectively, are negative and positive electrode equilibrium potentials, and are functions of SOC.

The generalizations described above were used to refine life model parameters for graphite/NMC cells. The first step of this activity took place under the DOE's eXtreme Fast Charge and Cell Evaluation of Lithium-Ion Batteries (XCEL) program using the Kokam 75-Ah cell data. This was then transferred to the Nissan Leaf cell data from INL (Figure I.6.A.25) across three temperatures and three charge protocols. INL and NREL are both

using the initial life model analysis as the base set for work related to ML using physics-based analysis and development.

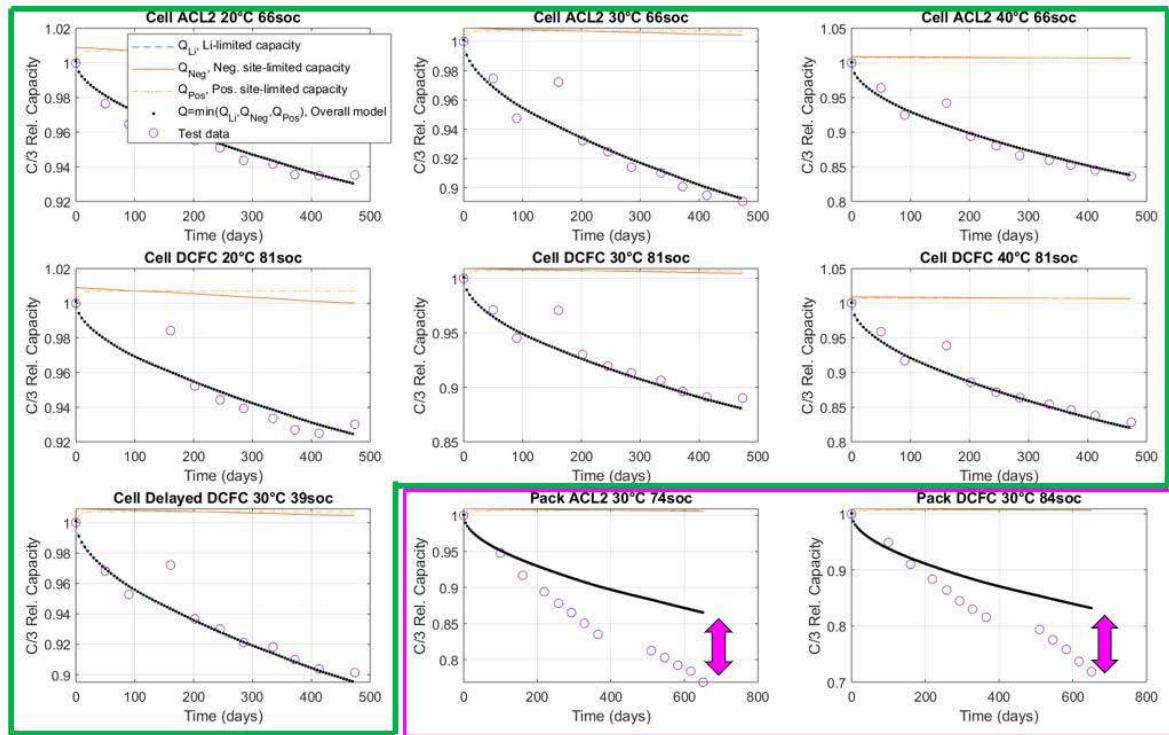


Figure I.6.A.25 Example of physics-based life predictive model (NREL) applied to 2012 Nissan Leaf fast charge data (INL)

Machine learning of physics-based life model from summary capacity/resistance data. With numerous possible degradation mechanisms (Table I.6.A.7) and dependence on operating conditions (Table I.6.A.8), identifying a life model from accelerated aging data is a time-consuming process. As a first step to automate the life model identification, the team applied the elastic net regularization algorithm to one step of the model-fitting process for the Kokam data. Popular in the ML field for its robustness in model selection, the elastic net algorithm efficiently eliminates or “turns off” extraneous terms in a model with little statistical significance. Figure I.6.A.26 shows possible fitted-model coefficients versus the regularization parameter, lambda. Many possible coefficients can reasonably represent the data, but some are unrealistic (e.g., producing negative fade rates such as the “best fit” minimum mean-square error model coefficients in green in Figure I.6.A.26). Instead, the elastic net selects more reasonable parameters within 1 standard error of the data and eliminates unneeded terms in the model. In the next quarter, the team will apply the algorithm to additional steps of the model-fitting process to automate robust life model identification.

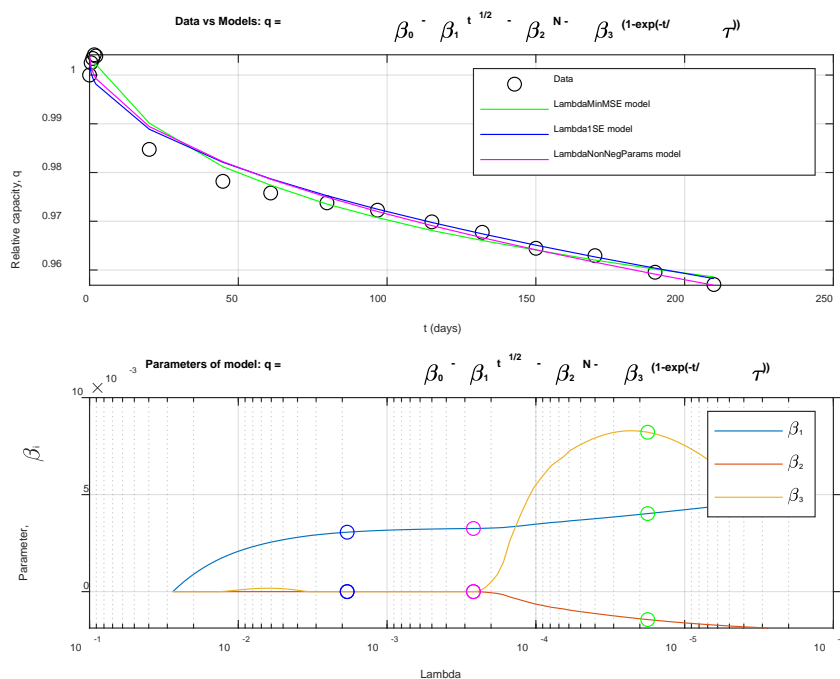


Figure I.6.A.26 Example local model fit of Kokam 75-Ah cell data using machine-learning elastic-net regularization algorithm

Machine learning of physics-based life model from raw electrochemical current/voltage data. The second ML-based activity focused on analysis using the raw electrochemical data from the Nissan Leaf dataset. Of the data used for analysis, key portions were used of the cycling profiles and rest steps. Broadly, the key points of interest were chosen due to alignment with key kinetic and thermodynamic indicators including cell impedance, state of charge, and temperature.

During early stages of the ML work, a key need identified when considering and linking physics with the life model was the need for a robust analysis that clearly assessed the adequacy of the sample set and also differentiated outliers. Figure I.6.A.27 presents an example of a voltage measurement used for ML before (orange) and after removal of outliers (blue).

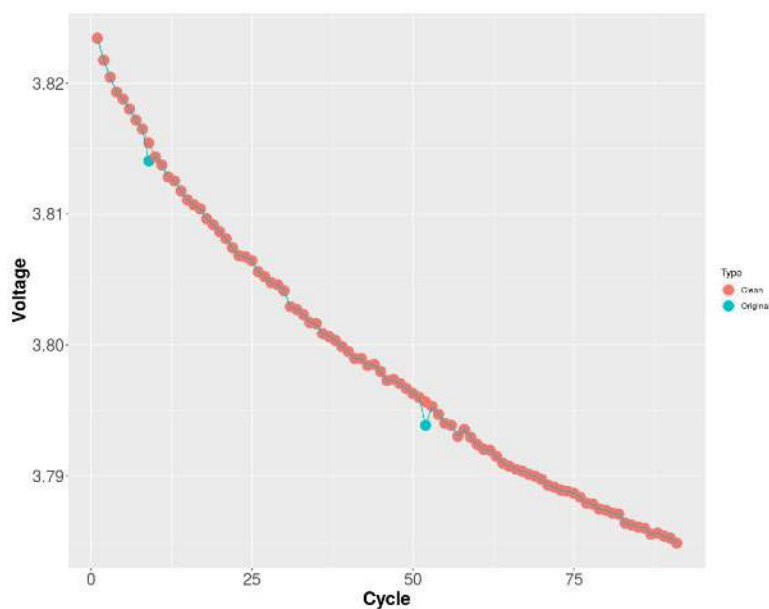


Figure I.6.A.27 Voltage measurement as a function of cycle using the original data (blue) and clean data after removal of data outliers (orange)

For the initial set of analyses, the use of different ML algorithms proceeded using the cleaned dataset. Figure I.6.A.28 shows the C/20 capacity from the reference performance test at the end of 900 cycles for the training and predicted data. Figure I.6.A.28 shows good agreement between the training and predicted sets. Further confirmation of the utility of the ML algorithms was achieved by comparing the predicted value for each of the different cycle conditions with the actual experimentally measured capacity during the reference performance test at 900 cycles (Figure I.6.A.29).

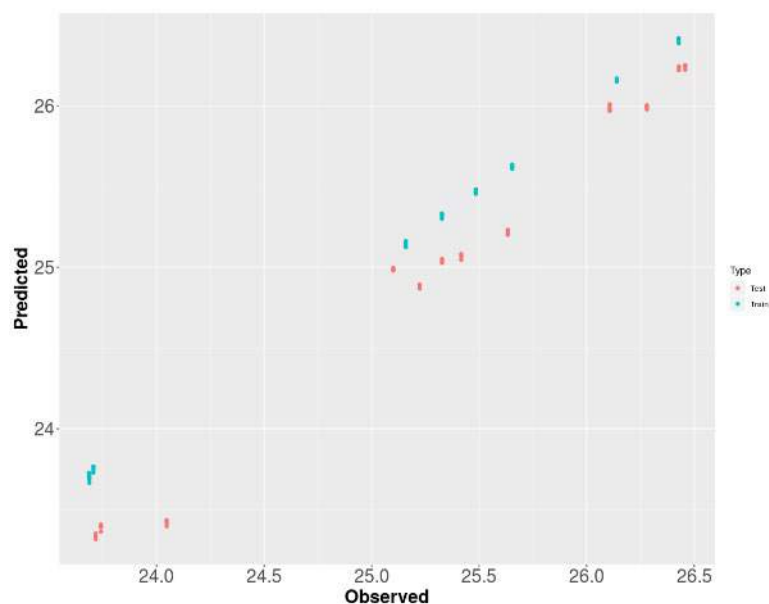


Figure I.6.A.28 Comparison of predicted and observed reference performance test capacity after 900 cycles for the test and training datasets. Analysis performed using Nissan Leaf test data

Figure I.6.A.29 shows good alignment between the different cycling conditions due to the physically linked parameters used for the ML. Distinct about the analysis is that the cycle sets included data from three different

cycling temperatures and three different charge procedures (AC Level 2, DC Fast Charge, and a combination of the two) [1]. Continued work in this area focuses on refining the analyses and further linking the life model as described above.

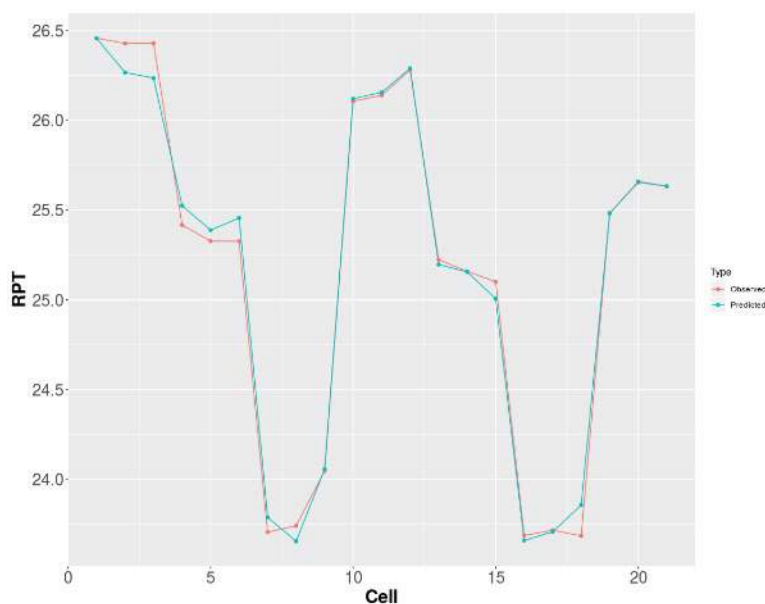


Figure I.6.A.29 Comparison of observed and predicted reference performance test capacity for each cell in the analysis. Of note is that the data were collected at three different temperatures and three different cycling conditions [1]

Behind-the-Meter Energy Storage for Buildings: Thermal storage material characterization

Traditional thermal energy storage shifts electricity use from day to night using large, custom systems, which have high initial costs for planning, engineering, and installation. Thermal energy storage that is instead integrated into a packaged system eliminates the initial cost for custom design and installation.

Solid/liquid phase-change materials (PCMs) can be designed for these packaged applications, but have several limitations, including low thermal conductivity and the need for a tank or other type of leak-free containment. PCMs with a solid-to-solid transition (e.g., amorphous to crystalline phase transformation) can overcome these limitations, but their energy densities are low, typically less than 100 J/g. An alternative is a solid/liquid PCM that is made into a solid-state composite PCM (Figure I.6.A.30). This composite PCM maintains its solid shape upon melting (the PCM remains in the nanoscale pores), provides nearly a 100x increase in thermal conductivity, and has an effective latent heat of 150-200 J/g. These composite PCMs are created by expanding natural graphite through rapid heating, after intercalation with an acid. The expanded graphite is then compressed, creating these porous graphite structures that are then soaked in PCM to create the composite PCM.

The thermal-conductivity enhancement of these composite PCMs exceeds the commonly used approach of adding thermally conductive fillers (~2–3x), which lack an interconnected (or percolated) thermal network. These composite PCMs can be well-suited for the packaged systems mentioned above, but more data are needed to evaluate their performance. The key material properties we measured were:

- Thermal conductivity
- Heat of fusion and transition temperature
- Thermal cycling performance.

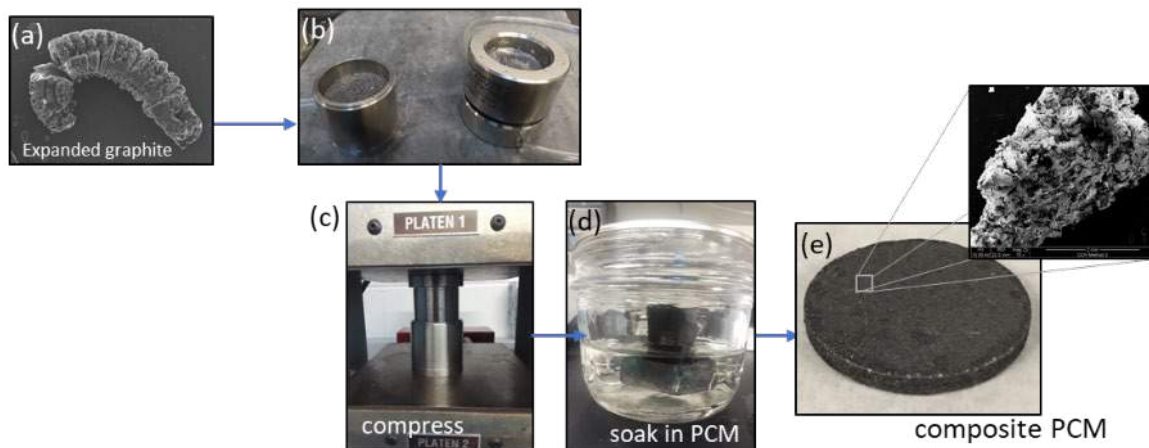


Figure I.6.A.30. (a) Expanded graphite (EG), thermally expanded after acid intercalation. EG flakes are compressed in (b) die fixture using (c) pneumatic press. (d) Graphite matrix is soaked in PCM, resulting in (e) composite PCM

Thermal conductivity. In addition to energy density, thermal conductivity (k) is an important figure of merit for thermal storage applications. Higher thermal conductivity enables faster charge/discharge rates, resulting in higher power densities. Tetradecane is an organic paraffin PCM that suffers from low k ($\sim 0.1\text{--}0.4\text{ W/m-K}$). Incorporating it into the nanoporous graphite structure greatly improves k .

The k of graphite matrices with and without infiltrated PCM were measured using a combination of measurement approaches. The ASTM D-5470 steady-state method was used to measure the k of 80% porous graphite. It was found that there is anisotropy in the k of the samples, with k being higher in the direction perpendicular to compression than the direction parallel to compression. For a sample with no PCM, k was measured to be 8.9 W/m-K in the parallel direction and 17.4 in the perpendicular direction. A sample with PCM infiltrated was measured to be 9.7 W/m-K in the parallel direction. This indicates that because the pure PCM k is so low, the composite k is dominated by the graphite and the k of the samples with and without PCM are similar. A different sample of graphite matrix with no PCM, of about 92% porosity, was measured using the transient plane source (TPS) technique. This sample was measured to have $k\ 11.7\text{ W/m-K}$ in the parallel direction. Inserting the PCM into the graphite matrix increases thermal conductivity by 50x.

Heat of fusion and transition temperature. The specific PCM studied here is n-tetradecane ($\text{C}_{14}\text{H}_{30}$), an organic paraffin PCM with transition temperature of 4°C which is suitable for air-conditioning applications. Figure I.6.A.31 shows several differential scanning calorimeter (DSC) curves of PCM composites with varying mass fraction of PCM and graphite, and Table I.6.A.9 presents their corresponding heats of fusion and transition temperatures. As can be seen, incorporation of graphite does reduce latent heat of fusion (energy density) of the PCM composite, relative to the pure PCM. However, as discussed in the previous section, incorporation of just 20% graphite results in up to 50x increase in thermal conductivity, but only $\sim 20\%$ reduction in heat of fusion.

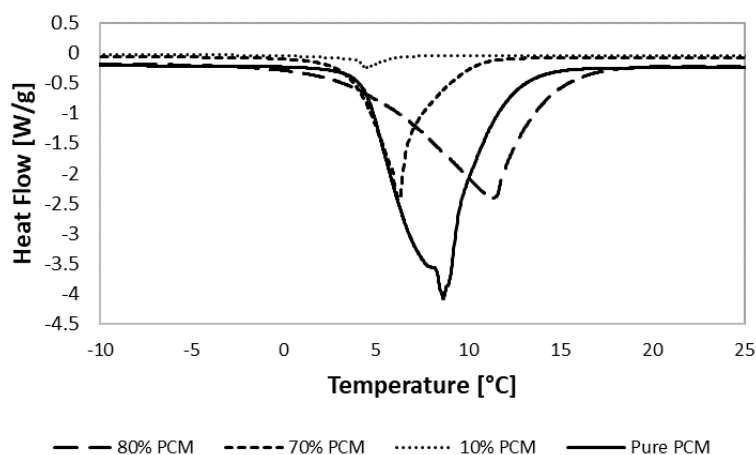


Figure I.6.A.31. DSC curves (melting) of several PCM composites with varying mass fraction of PCM

The incorporation of graphite does not change the transition temperature of the PCM, as shown in Table I.6.A.9, indicating no chemical interaction between the graphite and the PCM.

Table I.6.A.9. Heat of Fusion and Transition Temperature for Several PCM Composites with Varying Mass Fraction of PCM

Sample	T_t [°C]	ΔH_f [J/g]
Pure PCM	4.16	213.4
80% PCM/20% graphite	4.02	183.0
70% PCM/30% graphite	4.61	97.8
10% PCM/90% graphite	3.94	6.2

Dynamic performance and cycling behavior. In addition to the material properties above, we also designed, fabricated, and commissioned an experiment enabling measurements of heat transfer through the graphite-tetradecane composite PCM. This allows us to estimate thermal conductivity, heat of phase change, and the transition temperature of bulk TES materials, unlike the techniques above, which are constrained to small sample sizes. The experiment can also characterize the thermal cycling behavior of the composite PCM. A numerical heat-transfer model developed for comparison showed good agreement with experimental data.

The experiment consists of a heat source and sink as two fluid-filled plates connected to temperature-controlled baths (Figure I.6.A.32, left). The sample to be characterized is placed between the plates with silicone elastomer pads as a thermal interface material (Figure I.6.A.33, right). Insulation along the sides ensures one dimensional heat transfer through the sample.

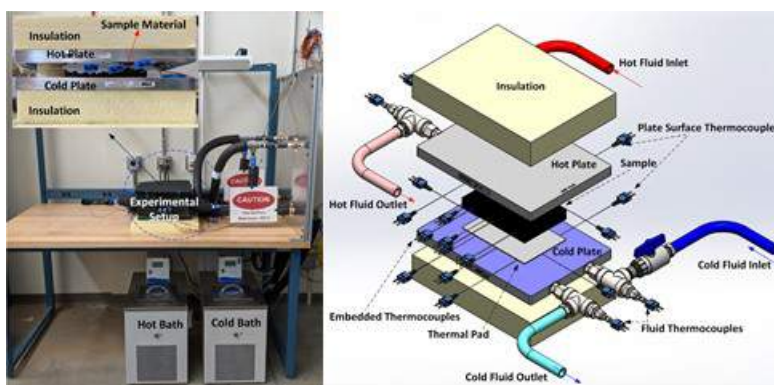


Figure I.6.A.32 Experimental setup (left), and CAD rendering showing each component

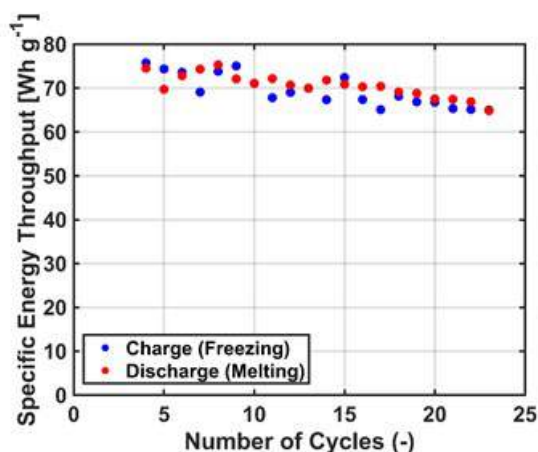


Figure I.6.A.33 Energy storage capacity during cycling

The flow rate of the heat-transfer fluid was controlled using a manual gate valve. Temperature and flow rate measurements were used to calculate heat-transfer rates. Surface thermocouples were placed on both top and bottom surfaces between the composite PCM sample and the heat-transfer plates and were used to estimate thermal conductivity. Embedded thermocouples along the centerline of the composite PCM sample allowed measurement of the temperature of the material and helped identify the transition temperature and the completion of the charging/discharging process.

Initial results from thermal cycling experiments (Figure I.6.A.33) showed a degradation in specific energy storage capacity by ~15% after 23 cycles. We observed leakage of the PCM from the composite material during multiple cycles, causing the degradation in the storage capacity. During these experiments, we observed consistent phase-transition temperature for this material at ~4.5°–5°C, which agreed well with other measurements using DSC.

We are currently modifying the experiment to ensure isothermal conditions of the heat source and sink surfaces, automating the flow control valves for improved cycling control, and developing methods to minimize thermal contact resistance by applying a consistent clamping force and identifying the most suitable thermal interface material.

Behind-the-Meter Energy Storage for Buildings: Thermal storage device characterization

In FY19, we designed and started construction on a new capability in NREL's Energy Systems Integration Facility (ESIF) to characterize thermal storage technologies. Specifically, this capability enables characterization at the device and system scales:

Thermal characterization experiments enable us to characterize the performance of components and systems, over a range of operating conditions (e.g., flow rates, temperatures, humidity (if applicable)). For example, we can generate curves of charge rates, discharge rates, and efficiency vs. temperature.

Hardware-in-the-loop (HIL) experiments enable us to measure the performance of components and systems while representing surrounding components in simulation. An example is given below, where we can emulate a building's thermal and electric loads for a specific climate, but include the chiller plant and thermal storage tank in hardware. This gives us insight into the actual performance of the system when installed in a representative environment, but without the need for a field demonstration, and with certain equipment in simulation. For example, in Figure I.6.A.34, the solar photovoltaic system is shown in simulation, while the battery is in hardware. But these could be switched, depending on which question is being answered.

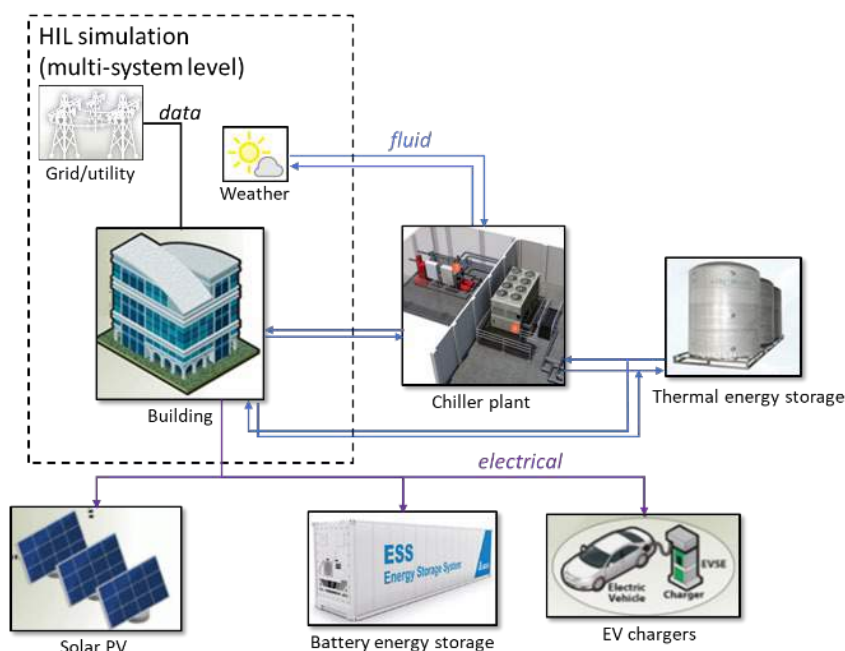


Figure I.6.A.34. Experimental hardware in the loop (HIL), focusing on multi-system level integration of the building and behind-the-meter storage assets. In this case, storage assets are in hardware, with the building, grid, and photovoltaics (PV) simulated. The conditions applied to the hardware is from these simulations or from a specified weather file

Conclusions

BTMS Analysis (NREL)

The rate structure, load profile, and system operating capacity are three of the most significant drivers to optimizing the BTMS system configuration and therefore to planning for the lowest MSP value. DC fast charging without storage has the potential to significantly increase the customer's average MSP for electricity by an order of magnitude. But simply adding storage will not reduce the cost back into 0.10–0.20 \$/kWh range. This is because the capital cost for these storage systems is significant between 300–500 \$/kWh. Research advances to reduce battery cell and balance-of-system costs can reduce the upfront costs for BTMS with EVSE.

BTMS by itself can significantly impact demand charges, but in general it will have only a small impact on shifting the energy charges. Adding distributed generation with renewables could future reduce long-term energy costs for the consumer by not only shifting electricity rates from peak to off-peak timeframes, but also, by reducing the total amount of energy pulled from the grid.

The results of this analysis show that BTMS coupled with DC fast-charging EVSE can be cost-effective today with long lifetime and high system reliability. The challenge for these assets will be how these systems will operate over their usable lifetimes and if they can achieve long life in the field. Asset operations will be influenced by changes to EVSE demand and market growth. Utility rate structure is also likely to change over time, which will impact this marketplace. Designing systems that are easily scalable, portable, and upgradeable have the potential to provide long-term profitability for these assets.

Electric-vehicle adoption is expected to grow significantly over the coming years, and it could have a significant and potentially negative effect on grid infrastructure. Additionally, the rapid penetration of solar photovoltaic generation installed on buildings is leading to new challenges for the electric grid. In response to the potentially large and irregular demand from EVs, along with changing load profiles from buildings with on-site generation, utilities are evaluating multiple options for managing dynamic loads, including time-of-use pricing, demand charges, battery storage, and curtailment of variable generation. Buildings, as well as commercial, public, and workplace EV charging operations, can use energy storage (e.g., batteries, thermal energy storage) coupled with on-site generation to manage energy costs as well as provide resiliency and reliability for EV charging and building energy loads.

The key question this project will be examining starting in FY20 is: What are the optimal system designs and energy flows for thermal and electrochemical BTMS with on-site PV generation enabling fast EV charging for three variables: climate, building type, and utility rate structure?

The previous effort created a framework for evaluating a multi-component BTMS system; however, additional work is needed to fully include and analyze on-site generation, thermal storage, building interactions, and possible energy export. This project seeks to integrate into a single interface the existing models and knowledge about PV generation, building energy use, battery storage, thermal energy storage, and EV charging. This combined framework, referred to as EnStore for Energy Storage, will be scalable and flexible, and it will answer questions about the tradeoffs between battery and thermal energy storage size, energy storage dispatch, PV size, EV charging demand, building energy demand, and use of grid energy. EnStore will be designed as a system optimization model, focused on the following metrics:

- Levelized cost of ownership (LCO) (also known as MSP, levelized cost of energy (LCOE), and profited cost; related to payback period and return on investment (ROI)) to the system owner, including Beyond LCOE project implications.
- Total system energy use (efficiency) to meet varied energy demands from the building and EV charging.
- Resiliency in terms of grid backup time (duration for supporting 100% of the loads and critical loads).
- Quantified daily load flexibility, both in terms of power and energy.

The building type and design will be the foundation for the overall system configuration, because building use is the determining factor for how people access energy, now and in the future. PV installation on the building and the addition of EV charging at the building site will be included in the configurations examined. For building energy use, the model will include representative cities for the ASHRAE climate zones. Several building types to be assessed will include the following:

- Retail big-box grocery store
- Commercial office building
- Fleet vehicle depot and operations facility
- Multi-family residential

- EV charging station (with multiple EVSEs, as determined by load projections).

For each building type, the scenarios to be evaluated include: Solar energy (PV generation, No PV generation, Selling electricity to the grid (net metering)); Energy storage (Battery, Thermal, Battery and thermal, No energy storage); EV charging (1, 6, 12 EVSEs, extreme fast charging and/or Level II charging, depending on building type and load projections, No EV charging); Rate structure (Flat rate structure, Variable demand charges (in both threshold and cost multiplier), and Time-of-use (TOU) structures: both high and low ratios between on- and off-peak rates). Net metering at both retail and bulk rates should be considered for all the preceding rate-case scenarios.

The integrated EnStore modeling framework will provide critical information to several stakeholders, such as DOE decision makers, utilities, industry players investing in EV charging, PV, and others, while avoiding duplication and divergent approaches for evaluating BTM energy storage. This model will be able to answer the following types of questions, and others related to BTMS:

Priority Questions are:

1. What is the sensitivity of analysis results to the variability of location, building loads, EV charging demands, and component costs, and combinations of each case within those categories?
2. What research achievements (e.g., material characteristics for thermal energy storage, battery material costs and lifetime, PV deployment) would increase the economic viability of the various configurations of BTMS at multiple locations?
3. What level of improved iterative feedback modeling, informed by BTO research on battery and thermal energy storage systems, would be necessary to optimize sizing and designs for subsystem components (PV, battery size and operation, thermal storage)?
4. What is the potential energy savings, PV energy generation, and EV demand coverage in different locations across the United States, as a function of technical and cost improvements?

Electrical and Thermal Design Behind the Meter System (Oak Ridge National Laboratory)

The key lessons learned from completing this quarter's project milestones are summarized as follows:

- Design of an EVSE depends much on the EV load being served.
- Installation-oriented design requires a proper understanding of the three main aspects of the entire system: protection, power conversion, control and communications.
- Pricing estimation of an EVSE has been discussed in detail in the report, and it may be seen that the estimated total cost rate, \$/W, varies greatly as the EPC and soft cost have a much greater difference between the minimum and maximum rates. It is so because these design elements contain aspects that are governed by financial constraints that vary by state, by area (location of site), or by required human resources.

BTMS Testing (INL, SNL, NREL)

Cycling under the initial protocol has shown that the commercial NMC/graphite and LFP/graphite cells, designed for purposes other than the proposed BTMS system, are not capable of meeting a 10,000 cycle life goal. Design tradeoffs taken to enhance properties (e.g., energy density) that are not critical to the BTMS application may impact their performance relative to BTMS goals. As material and design factors are investigated to address cost and cycle life, which are primary BTMS technology gaps, we will continue to develop updated testing methods to provide accelerated results that are relevant to target operating scenarios developed through modeling. The testing effort will be closely coupled with complementary machine-learning development tasks aimed at minimizing the time-on-test needed to accurately predict lifetime.

Physics-Based Machine Learning for Behind-the-Meter Storage (INL, NREL)

The team achieved significant progress in physics-based ML of life-predictive models during Q4 of FY19. During the second quarter of the project, two datasets were effectively shared between INL and NREL. One dataset was used to refine life model parameter estimation to reduce the time needed to execute and adapt the model for different cell designs and chemistries. The other dataset was used to predict capacity fade as a function of aging using small quantities of cycling data that are linked to specific kinetic and thermodynamic aging processes in the batteries. Current work is linking together the two methods.

Behind-the-Meter Energy Storage for Buildings: Thermal storage material characterization

The investigated composite PCMs show promise for thermal energy storage applications. From the above results, we conclude that:

- Composite PCMs show a large increase in thermal conductivity even for high-porosity graphite structures (>80% open volume).
- The method of creating these graphite composite PCMs leads to anisotropic thermal conductivity, with ~2x difference between the compression and non-compression directions.
- Although these materials maintain their shape, slow leakage needs to be prevented through sealing or packaging techniques.
- Contact resistance between the PCM composite and the heat-transfer surfaces are critical for the overall performance of these thermal storage devices.

Based on this research, we recommend the following next steps:

Improved graphite host matrices. More research is needed to better understand and improve the graphite host matrices, including infiltrating PCM and obtaining higher thermal conductivity with maximal porosity. This requires experiments and modeling. The experiments will characterize the structure of existing and new graphite host matrices, including pore size, pore size distribution, tortuosity, total open volume, accessible volume, and pore interconnectedness. These properties are difficult to measure with existing techniques, including intrusion porosimetry or BET. Micro-scale modeling will help identify the impact of changes to the graphite structure, and ideally determine the preferred structure through multiple model simulations.

Reducing contact resistance. The importance of contact resistance is evident through multiple projects working with this composite PCM. An inexpensive solution is needed to address this issue if this technology is to be commercialized. We are investigating thermal interface materials, composite PCM geometries, and applying pressure to reduce this contact resistance—both for implementing this PCM in practice and for minimizing error in our thermal measurements.

Cycling behavior. The cycling performance of these composite PCMs is still unknown. Initial experiments showed some degradation, but some (if not all) of this was due to leakage of the PCM. Further experiments need to eliminate this leakage to enable measurement of long-term cycling degradation. In addition, we need to develop experiment protocols to ensure we capture all the relevant degradation mechanisms.

Selectable transition temperature. The PCM investigated here has a phase-transition temperature of 4°C, which is suitable (although not optimal) for air-conditioning applications. There are many organic and inorganic PCM options, spanning the -30°C to 80°C range applicable to buildings. But their performance, particularly when impregnated within the graphite matrices, needs more research.

In FY20, we will further explore these thermal discharge curves and Ragone plots to better understand the mechanisms that cause the drop in temperature potential at high depth of discharge and at high C rates. We will also develop design rules for thermal storage devices for different C rates.

References

1. <https://smartchargeamerica.com/electric-car-chargers/commercial/chargepoint-express-250/>
2. https://afdc.energy.gov/files/u/publication/evse_cost_report_2015.pdf
3. <https://www.epri.com/#/pages/product/000000003002000577/?lang=en-US>
4. <https://www.ohmhomenow.com/electric-vehicles/electric-vehicle-charging-stations-business/>
5. <https://avt.inl.gov/sites/default/files/pdf/arra/PluggedInSummaryReport.pdf>
6. T.R. Tanim, M. Shirk, R.L. Bewley, E.J. Dufek, B. Liaw, “Fast Charge Implications: Pack and Cell Comparison and Analysis,” *J. Power Sources*, 381 (2018), 56–65.
7. K. Smith, A. Saxon, M. Keyser, B. Lundstrom, Z. Cao, A. Roc, “Life Prediction Model for Grid-Connected Li-Ion Battery Energy Storage System,” *American Control Conference*, Seattle, WA, May 30–June 1, 2017.
8. S. Santhanagopalan, K. Smith, J. Neubauer, G.-H. Kim, A. Pesaran, M. Keyser, *Design and Analysis of Large Lithium-Ion Battery Systems*, Artech House, Boston, 2015, ISBN-13: 978-1608077137.

Acknowledgements

The various contributors to this project included the following: Margaret Mann, Samantha Reese, Tim Remo, Erin Burrell, Madeline Gilleran (NREL) (BTMS Analysis); Madhu Chinthavali, Pankaj Bhowmik (Oak Ridge National Laboratory) (Electrical and Thermal Design Behind the Meter System); and Eric Dufek (INL), Kandler Smith (NREL), Ross Kunz (INL) (Physics-Based Machine Learning for Behind-the-Meter Storage).

I.7 Testing and Analysis

I.7.A BatPaC Model Development (ANL)

Shabbir Ahmed, Principal Investigator

Argonne National Laboratory
9700 S Cass Avenue
Lemont, IL 60439
E-mail: ahmeds@anl.gov

Samuel Gillard, DOE Technology Development Manager

U.S. Department of Energy
E-mail: Samuel.Gillard@ee.doe.gov

Start Date: October 2015	End Date: September 30, 2020	
Project Funding (FY19): \$900,000	DOE share: \$900,000	Non-DOE share: \$0

Project Introduction

A performance and cost model (BatPaC [1]) was developed at Argonne to design automotive Li-ion batteries that can meet the specification of a given vehicle, and then to estimate the cost of manufacturing such batteries. It is the product of long-term research and development at Argonne through sponsorship by the U.S. Department of Energy.

Over a decade, Argonne has developed methods to design Li-ion batteries for electric-drive vehicles based on modeling with Microsoft® Office Excel spreadsheets. These design models provided all the data needed to estimate the annual materials requirements for manufacturing the batteries being designed. This facilitated the next step, which was to extend the effort to include modeling of the manufacturing costs of the batteries.

The BatPaC model has been peer reviewed and is available on the web. It captures the interplay between design and cost of Li-ion batteries for transportation applications. It is used to estimate the impact of R&D advances on the mass, volume, and cost of lithium ion batteries. Moreover, BatPaC is the basis for the quantification of battery costs in U.S. EPA and NHTSA 2017-2025 Light-Duty Vehicle Technical Assessment. This assessment is then used to determine what mileage (i.e., CAFE) and CO₂ emission standards are optimal from a cost-benefit analysis.

Objectives

To develop and utilize efficient simulation and design tools for lithium ion batteries to predict

- Overall and component mass and dimensions
- Cost and performance characteristics when manufactured in large volume.

Approach

The battery pack design and cost calculated in BatPaC represent projections for a specified level of annual battery production (10,000-500,000). As the goal is to predict the future (~5 years) cost of manufacturing batteries, a mature manufacturing process is assumed. The model designs a manufacturing plant with the sole purpose of producing the battery being modeled. The assumed battery design and manufacturing facility are based on common practice today but also assume some problems have been solved to result in a more efficient production process and a more energy dense battery. Our proposed solutions do not have to be the same methods used in the future by industry. We assume the leading battery manufacturers, those having successful operations in the near future, will reach these ends by some means.

For a selected battery chemistry, BatPaC solves the governing equations to determine the size of each layer, cell, and module that make up the battery pack that can meet the desired requirements for power and energy. This allows the calculation of the mass of each material, the volume of the components, and the heat removal needed during discharge. The cost of the pack is then estimated based on a predefined manufacturing process.

Current effort is directed at

- Improving the design capability by including correlations derived from continuum modeling and updating the default material properties to reflect recent experimental and industrial performance data
- Reducing the uncertainty of model predictions by setting up independent models of the manufacturing processes
- Validating the results through discussions with manufacturers and component developers.
- Updating the cost of materials used in BatPaC calculations.

Results

Key Accomplishments

- A process model for the production of lithium manganese oxide (LMO) has been developed.
- The effect of temperature on the area specific impedance has been studied for five types of positive active materials.
- A model of the battery management unit has been developed for inclusion into BatPaC.
- A cost estimate for a BEV battery pack from BatPaC was obtained and compared to published data.

Production of Lithium Manganese Oxide (LMO)

Lithium manganese oxide, LiMn_2O_4 , is a cathode active material that is used in automotive batteries and has been attractive on account of its lower cost and that it does not require the use of cobalt (prices are high and volatile), and is safer than some of the other transition metal oxide (TMO) materials, and because its spinel structure supports high rate capability. LMO is one of the cathode material options available in BatPaC.

In an effort to better understand the key cost factors in the production of LMO, two production processes were modeled. These are the (i) Solid State Synthesis (P1), (ii) Sol-Gel Method, and are compared on the basis of plants with a capacity of 60 MT/day. Figure I.7.A.1 and Figure I.7.A.2 show simplified schematics of the processes.

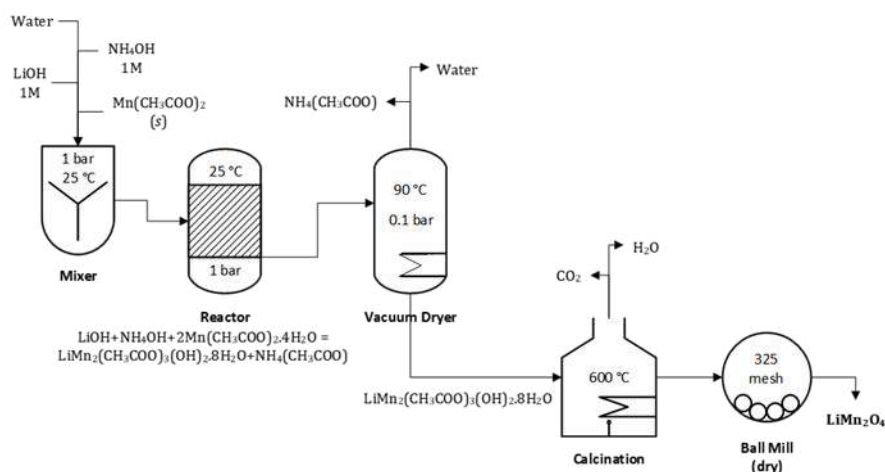


Figure I.7.A.1 Simplified process diagram for LMO production using sol-gel method (P2)

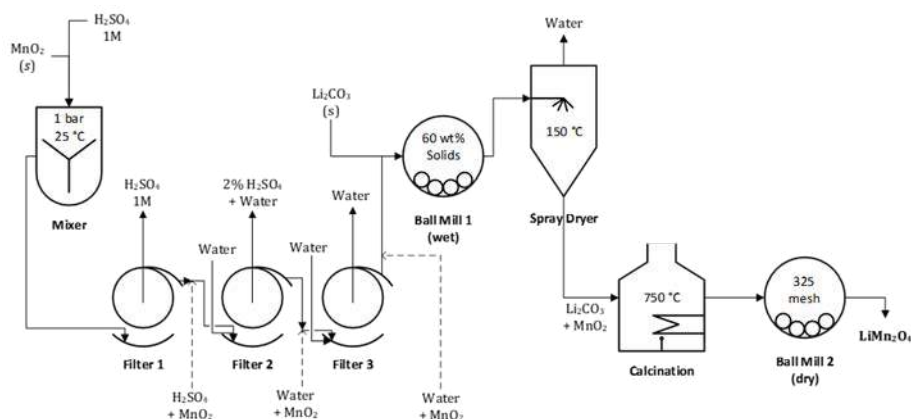


Figure I.7.A.2 Simplified process diagram for LMO production using solid state synthesis (P1)

The solid state method, P1, reacts the manganese oxide with lithium carbonate in a calcination step at $\sim 750^\circ\text{C}$ to produce the lithium manganese oxide powder. The sol-gel method, P2, first produces a gelatinous lithium-manganese complex by precipitation, which is then calcined at $\sim 600^\circ\text{C}$ to produce the desired powder. A quick comparison of the processes reveal that the raw material cost for P2 (manganese acetate and lithium hydroxide) is nearly twice that of P1 (manganese oxide and lithium carbonate), and is key to the difference in the cost of LMO estimated for the two processes. For the base case scenario, LMO cost was \$7 per kg via P1, and \$14 per kg via P2. The calcination furnace is perhaps the most expensive item in the plant and the production process has an estimated energy demand of approximately 6 kWh/kg of LMO. This study is presented in greater detail in a submitted manuscript (to be published).

Effect of Temperature on the Area Specific Impedance (ASI)

The area specific impedance represents the resistance to the flow of ions between the electrodes and results in energy loss during the charge and discharge of the cells. The ASI is an important parameter in determining the electrode area that is needed to meet the power requirements for the cell. The ASI is affected by the combination of the cell materials (properties, porosities, separator thickness), the operating conditions (state of charge, current, temperature), and the cycle history or state of health. A series of tests were run to determine the effect of temperature and cathode active material on the ASI that can be used as the default values provided for BatPaC calculations. The cathode active materials tested in the study included nickel manganese cobalt oxides (NMCs) such as NMC111, NMC532, NMC622, NMC811 and nickel cobalt aluminum oxide (NCA).

The ASI was measured at -20°C, 0°C, 20°C and 40°C. Figure I.7.A.3 shows a plot of the measured ASI (at 50% nominal state of charge) as a function of temperature for the five cathode active materials. The values show the exponential increase in the ASI at the lower temperatures. This trend supports the need for maintaining a warm battery in cold climates to ensure high power capability and efficiency. The data in Figure I.7.A.3 can be fitted across the temperature range with an Arrhenius type expression that can be incorporated into BatPaC. A more detailed analysis using the approach of equivalent circuits is in progress and will try to elucidate the rate-limiting steps.

Detailing the Battery Management Unit (BMU)

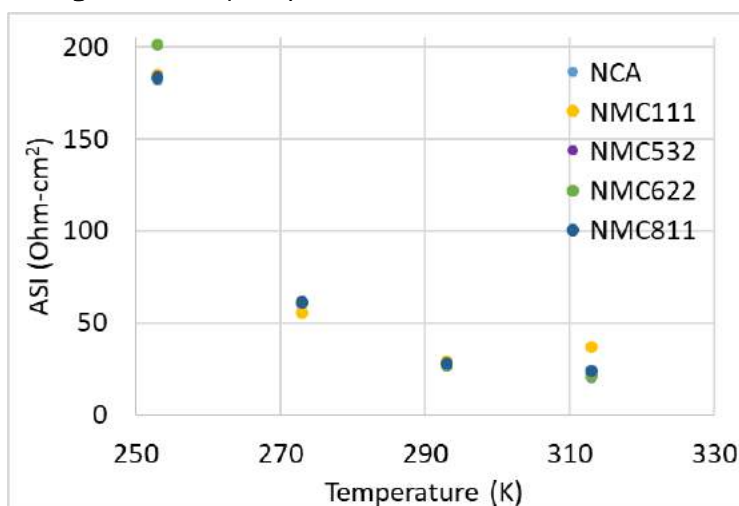


Figure I.7.A.3 Effect of cathode active material and temperature on the area specific impedance measured in coin cells.

The Battery Management Unit performs numerous operational and safety functions during the various stages of charge and discharge, and during standby. These include the monitoring of current to/from each cell, group of cells, or modules and monitoring the voltages and temperature. The BMU responds to redirect or limit the current flow and coolant flow, and in the extreme shuts down the battery pack.

A model of the BMU has been included in BatPaC that uses the number of cells and their configuration in the pack to calculate the number of components needed and then to estimate the mass, volume, and cost of the unit. For example, BMU for a 90 kWh pack may include more than 50 items that add up to over 3,000 components.

The net effect is a greater fidelity and direct dependence on the specifics of the pack needs, such as the number of cells, modules, series-parallel connections, etc. Compared to earlier versions of BatPaC, the new BMU unit indicates a cost reduction of 30-60%, lowering the pack/cell cost ratio, and a cost savings of about 3.5% in a \$14,000 Battery Electric Vehicle (BEV) pack.

The model was developed to associate different functions, such as contactor control, cell voltage monitoring or thermal management to specific mass, volume and cost such that a pack can be customized within BatPaC to remove or add specific functions to the BMU. Hardware associated with monitoring and connecting the battery, such as contactors, fuses and external sensors were also included to add more detail and flexibility to the model for electrical components associated with the BMU. This also provides opportunity to understand where further savings may be achieved within the BMU.

Pack Level Cost of Lithium Ion Batteries

The cost of a battery pack was estimated for a BEV battery pack using BatPaC 3.1. Table I.7.A.1 shows some of the input values used in the case study of a 94 kWh battery pack. The calculations assume a positive electrode thickness of 70 microns and allows 22 minutes to recharge 60% of the pack capacity (34 minutes to recharge 80% of the capacity) using a 150 kW charger. The cost of the battery pack, manufactured in a plant with a production capacity of 20,000 packs per year, is estimated at \$167/kWh. The cost of the cells is estimated at \$136/kWh.

Table I.7.A.1. Input Values and Results from BatPaC 3.1 for a 94 kWh Battery Pack for a Battery Electric Vehicle (BEV)

Electrode Combination	NMC622-Graphite
Pack Energy, kWh _r	94
Useable Energy (80% of Total), kWh _{Use}	75
Total Number of Cells	400
Cell Configuration	100S-4P
Pack Voltage, Volts	375
Cell Capacity, Ah	126
Material Prices	
NMC622, \$/kg	\$20
Carbon, \$/kg	\$7
Binder, \$/kg	\$10
Binder Solvent, \$/kg	\$3.1
Graphite, \$/kg	\$13
Separator, \$/m ²	\$1.3
Positive Electrode Current Collector, \$/m ²	\$0.4
Negative Electrode Current Collector, \$/m ²	\$1.3
Electrolyte, \$/L	\$15
Positive Electrode Thickness, μm	70
Negative Electrode Thickness, μm	79
Time to Recharge 60% of Capacity (15-75% State of Charge), min	22
Plant Production Volume, packs per year	20,000
Cost of Cells, \$/kWh _r	\$136
Cost of Pack, \$/kWh _r	\$167

Figure I.7.A.4(a) compares the above results with some estimates of average pack costs reported in the public media [2],[3]. Per the Statista [2] data, the cost has dropped 42% since 2016. BatPaC estimate for the battery in Table I.7.A.1 seems to correlate well with the public data. Figure I.7.A.4(b) compares the cost breakdown of the components with that reported by Avicennes [3] [Note: The cost components included in each category could not be ascertained for the Avicennes data]

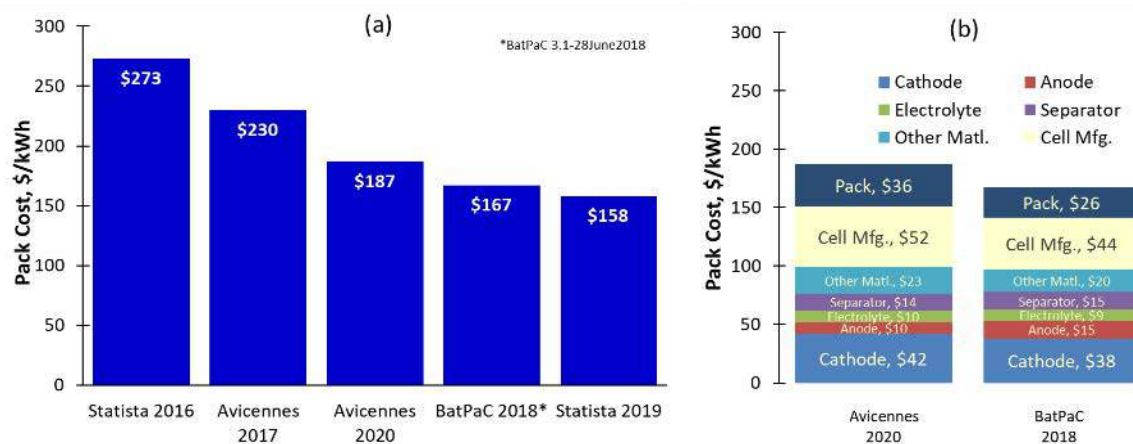


Figure I.7.A.4 Comparison of estimated costs of lithium ion battery packs

Conclusions

Lithium manganese oxide is an important cathode active material that offers high rate capability and can be cost-effective. The study explored two feasible pathways for its production and found that the solid state synthesis method is more cost-effective, with a production cost estimate of ~\$10/kg, considerable lower than some of the other cathode active materials such as the NMCs and NCA.

An experimental study of the area specific impedance has been conducted to provide data for use in BatPaC and to enable the understanding of the contributing factors and to develop representative models to anticipate the effects of temperature, voltage and charge-discharge cycles. The preliminary analysis shows a strong correlation with temperature, with the ASI increasing exponentially and follows the trend of an Arrhenius equation.

The battery management unit has been developed that accounts for the thousands of individual components in it, and its components and their costs are correlated to the cell and module design. The bottom-up accounting improves BatPaC calculations and suggests that the cost of this unit should be lower than previously estimated.

An analysis of a typical BEV battery pack was conducted with BatPaC. For the assumed design and manufacturing estimates, the cost of the pack was estimated at \$167/kWh, and compares well with the cost of lithium ion batteries reported in the public media.

Key Publications

1. Naresh Susarla and Shabbir Ahmed. "Estimating cost and energy demand in producing lithium manganese oxide for Li-ion battery cathodes," manuscript in preparation.
2. Shabbir Ahmed, Daniel Abraham and Andrew Jansen. "Lithium-Ion Starting-Lighting-Ignition Batteries." Argonne National Laboratory, ANL/CSE-19/1, 2019.
3. Paul Nelson, Shabbir Ahmed, Kevin Gallagher and Dennis Dees. "Modeling the Performance and Cost of Lithium-Ion Batteries for Electric-Drive Vehicles, Third Edition." Argonne National Laboratory, ANL/CSE-19/2, March 2019.
4. Qiang Dai, Jeffrey Spangenberg, Shabbir Ahmed, Linda Gaines, Jarod Kelly and Michael Wang. "EverBatt: A Closed-loop Battery Recycling Cost and Environmental Impacts Model." Argonne National Laboratory, ANL-19/16, April 2019.

References

1. P. Nelson, S. Ahmed, K. Gallagher and D. Dees, "Modeling the Performance and Cost of Lithium-Ion Batteries for Electric-Drive Vehicles, ANL/CSE-19/2," 2019.

2. “Statista,” [Online]. Available: <https://www.statista.com/statistics/883118/global-lithium-ion-battery-pack-costs/>. [Accessed October 2019].
3. M. Sanders, “Comparing Li-ion to Lead-Acid Batteries & Other Storage Options: Future Predictions,” March 2018. [Online].

Acknowledgements

P. Nelson, N. Susarla, A. Dunlop, A. Jansen, Cell Analysis Modeling and Prototyping Facility (CAMP),
D. Robertson, A. Meintz, D. Dees, A. Tornheim, J. Kubal, J. Song, G. Henriksen

I.7.B Battery Performance and Life Testing (ANL)

Ira Bloom, Principal Investigator

Argonne National Laboratory
9700 South Cass Avenue
Lemont, IL 60439
E-mail: ira.bloom@anl.gov

Samuel Gillard, DOE Technology Development Manager

U.S. Department of Energy
E-mail: Samuel.Gillard@ee.doe.gov

Start Date: October 1, 2018	End Date: September 30, 2019	
Project Funding (FY19): \$1,500,000	DOE share: \$1,500,000	Non-DOE share: \$0

Project Introduction

Batteries are evaluated using standard tests and protocols that are transparent to technology. These protocols are based on those developed by the USABC [1]-[4].

Objectives

- Provide DOE, USABC, and battery developers with reliable, independent and unbiased performance and life evaluations of cells, modules and battery packs.
- Benchmark battery technologies that were not developed with DOE/USABC funding to ascertain their level of maturity.

Approach

The batteries are evaluated using standardized and unbiased protocols, allowing a direct comparison of performance within a technology and across technologies. For those tested using the USABC methods, the performance of small cells can be compared to that of larger cells and full-sized pack by means of a battery scaling factor [1],[2].

Results

Batteries, which were fabricated during programs with developers, are sent to Argonne for evaluation. Here, the purpose of evaluation is two-fold: to provide confirmation of other test information and to provide an independent assessment of the state of the given battery technology, that is, how does it compare to the USABC [1]-[4] and/or project goals. A list of program deliverables associated with Argonne is given in Table I.7.B.1, along with their status.

Refilling an automobile with gasoline typically takes ten minutes or less. Decreasing the charging time of a battery to something that today's drivers are accustomed represents a technical challenge. To do this, the battery must be charged at very high rates. Here, not only does the technology have to avoid lithium deposition at the high charge rate, the technology must avoid life-shortening degradation caused by i^2R heating from the high current/power. There are, in principle, many ways to do this, including increasing the pack voltage so that the current at high power is relatively low. This is an engineering solution. Perhaps, a better way to overcome these issues is to develop or adapt lithium-ion technology to tolerate or avoid the problems.

Table I.7.B.1 Status of Deliverables for Testing

Developer	Sponsor	Quantity x System Level	Application	Status
Maxwell	USABC	15 x Cell	12-V S/S	complete
Maxwell	USABC	15 x Module	12-V S/S	complete
24-M	USABC	18 x 6 Ah 18 x 11 Ah 18 x 52 Ah	EV	complete
Navitas	DOE FOA	24 x Cell	EV	complete
XALT	DOE FOA	24 x Cell	EV	complete
WPI	USABC	40 x Cell	Recycling/PHEV-20	on-going
WPI	USABC	30 x cell	Recycling/PHV-20	On-going
SiNode	USABC	9 x 2.36 AhHalf cell	EV	complete
SiNode	USABC	8 x 1.56 Ah Cell	EV	Complete
SiNode	USABC	18 x 800 mAh	EV	Complete
SiNode/	USABC	9 x 550 mAhI	EV	Complete
SiNode/Nanograf	USABC	18 x 8.9 Ah	EV	On-going
SiNode/Nanograf	USABC	18 x 8.9 Ah	EV	Expected
Farasis	USABC	18 x 600 mAh	Recycling/EV	On-going
Farasis	USABC	24 x 2 Ah	Recycling/EV	Expected
Farasis	USABC	30 x 25 Ah	Recycling/EV	Expected
Penn State	DOE	9 x 5 Ah	XCEL	Complete
Microvast	DOE	9 x 20.6 Ah	XCEL	On-going
UCSD	DOE	9 x 2.3 Ah	XCEL	On-going
ORNL	DOE	9 x 2.33 Ah	XCEL	On-going
Stanford	DOE	TBD	XCEL	Expected
Stonybrook	DOE	9 x 2.1 Ah	XCEL	On-going
University of Michigan	DOE	9 x 2.1 Ah	XCEL	On-going
Coulometrics	DOE	TBD	XCEL	Expcted
University of Tennessee	DOE	TBD	XCEL	Expected
ORNL	DOE	15 x 2 Ah	EV (low cobalt)	Expected
Penn State	DOE	20 x 20 Ah	EV (low cobalt)	Expected
Nextech-Nexceris	DOE	30 x 2 Ah	EV (low cobalt)	Expected
University of Texas-Austin	DOE	15 x 2 Ah	EV (low cobalt)	Expected
University of California-Irvine	DOE	21 x 2 Ah	EV (low cobalt)	Expected
UCSD	DOE	20 x 2 Ah	EV (low cobalt)	expected

There were many different solutions proposed to the fast-charge problem under the XCEL Project. Some results from one of these projects is shown in Figure I.7.B.1. Figure I.7.B.1 shows a plot of average, relative capacity of two groups of cells, one being cycled at the 1-C and the other at the XFC rate. The data shows that the performance of the groups of cells is similar; the capacity decreased by about 3% after 400 cycles. The capacity fade for the fast-charged XCEL cells was slightly more than 4% after 500 cycles; these cells met the project goal.

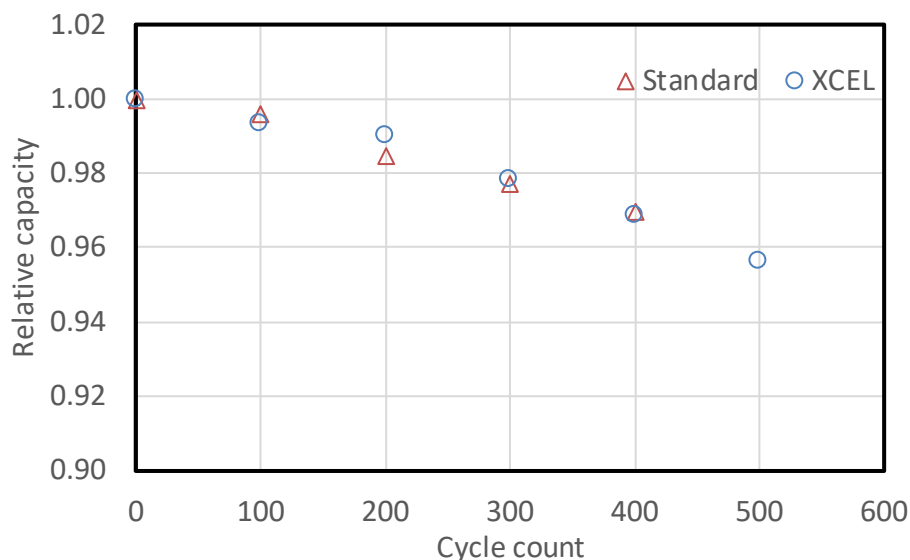


Figure I.7.B.1 Average, relative capacity vs. cycle count for cells undergoing XCEL and standard charging

Conclusions

We will continue to support DOE's and the USABC's cell development efforts by providing unbiased evaluation of cell performance. In the case cited above, there appears to be at least one solution to the general fast-charging problem.

Key Publications

1. A comparison of methodologies for the non-invasive characterisation of commercial Li-ion cells, Anup Barai, Kotub Uddin, Matthieu Dubarry, Limhi Somerville, Andrew McGordon, Paul Jennings, Ira Bloom, *Progress in Energy and Combustion Science*, 72 (2019) 1-31.
doi.org/10.1016/j.pecs.2019.01.001
2. Modeling Memoryless Degradation Under Variable Stress, Edward V. Thomas, Ira Bloom, Jon P. Christophersen, David C. Robertson, Lee K. Walker, Chinh D. Ho, and Vincent S. Battaglia, *Journal of Quality Technology*, March 2019, DOI: 10.1080/00224065.2019.1569963.

References

1. FreedomCAR Battery Test Manual for Power-Assist Hybrid Electric Vehicles, DOE/ID-11069, October 2003.
2. FreedomCAR Battery Test Manual for Plug-In Hybrid Electric Vehicles, June 2010.
3. Electric Vehicle Battery Test Procedures Manual, Revision 2, January 1996.
4. Battery Test Manual for 12 Volt Start/Stop Vehicles, Rev. 1, May 2015, INL/EXT-12026503.

Acknowledgements

David Robertson, Panos Prezas and LeRoy Flores served as co-investigators for this project.

I.7.C Battery Safety Testing (SNL)

Joshua Lamb, Principal Investigator

Sandia National Laboratories
1515 Eubank Dr. SE, M/S 0613
Albuquerque, NM 87185
E-mail: jlamb@sandia.gov

Samuel Gillard, DOE Technology Development Manager

U.S. Department of Energy
E-mail: Samuel.Gillard@ee.doe.gov

Start Date: October 1, 2018

End Date: September 30, 2019

Project Funding (FY19): \$800,000

DOE share: \$800,000

Non-DOE share: \$0

Project Introduction

Abuse tests are designed to determine the safe operating limits of HEV/PHEV energy storage devices. Testing is intended to achieve certain worst-case scenarios to yield quantitative data on cell/module/pack response, allowing for failure mode determination and guiding developers toward improved materials and designs. Standard abuse tests with defined start and end conditions are performed on all devices to provide comparison between technologies. New tests and protocols are developed and evaluated to more closely simulate real-world failure conditions. While robust mechanical models for vehicles and vehicle components exist, there is a gap for mechanical modeling of EV batteries. The challenge with developing a mechanical model for a battery is the heterogeneous nature of the materials and components (polymers, metals, metal oxides, liquids). This year saw the stand up of a new drop tower tester capable of providing dynamic mechanical test results. This work is discussed in further detail in the CAEBAT annual report section. Additional modeling efforts lie in being able to better predict failure propagation within larger battery systems. Sandia's battery safety testing provides testing support to better aid in thermoelectrical model development at NREL and SNL.

Materials characterization to better understand batteries that have undergone abusive conditions is of interest. Our partnerships with Argonne National Laboratory (ANL) and Oakridge National Laboratory (ORNL) through the Post Test Analysis Program for ABR, spans the building of cells with known materials (ORNL), overcharge testing to various states (SNL), and the posttest analysis of the cells (ANL). In addition, testing to support the Si-Deep Dive Program has been leveraged to gain a better understanding of the safety implications for these materials.

Calorimetry testing has historically been performed on 18650 cells of ~1.5 AH or lower. Testing has been performed to understand how best to apply data from this testing to larger scale formats and cells of increasing energy density. This will inform future work performing ARC testing of new high energy chemistries and how those results might apply to larger format cells.

The ability to fast charge electric vehicles addresses two major points of consumer EV adoption: range anxiety and convenience. However, fast charging also introduces new degradation mechanisms in the battery, and may contribute to new failure mechanisms. In fact, adverse effects seen during fast charge resemble battery abuse in several ways. In the cathode, fast charging is known to cause localized heating, which can lead to breakdown of active materials, electrolyte, and binder. It can also cause localized over-delithiation, damaging the cathode structure. In the anode, the primary danger is lithium plating, which occurs if lithium diffusion into the cathode can't keep pace with high rate Li⁺ delivery to the anode. The anode can also be host to Li⁺ depletion in the adjacent electrolyte, causing unexpected electrolyte changes and double layer effects. To study this cells were built in Sandia's prototyping facility at varying n:p ratios, with the low n:p ratios used as conditions highly likely to plate lithium. After charging to induce lithium plating, cells were analyzed with DPA and ultimately subjected to abuse testing to observe changes in thermal runaway severity after significant lithium plating.

Objectives

- Provide independent abuse testing support for DOE and USABC
- Abuse testing of all deliverables in accordance with the USABC testing procedures
- Evaluate the impact of high quantities of lithium plating on abuse response of cells. Evaluate control and test cells with forced lithium plating to observe the impacts to failure.
- Improve the ability of calorimetry and other test methods to withstand and provide relevant data for high energy materials, particularly their ability to withstand high temperature failure. Begin evaluations of impacts of high energy materials.
- Evaluate feasibility of using elevated temperature to render cells inert without swelling, venting or thermal runaway.
- Provide testing data to support failure propagation model (NREL).
- Provide testing support for ABR Post Test program (ORNL/ANL).

Accomplishments

- Completed testing of all USABC deliverables to date and reported results to the USABC TAC.
- Inconel alloy ARC cell holders designed, built and tested.
- Test cells at varying n:p ratios built in Sandia prototyping facility and cycled to induce plating in low n:p ratio cells. Cells were analyzed using DPA and abuse testing.
- Extended failure propagation modeling efforts with NREL using testing data. This resulted in newly published work using direct test data to establish validated models.
- Provided testing support for several cell chemistry types (NMC, LFP, and Si) to varied levels of overcharge in support of the ABR post test program (ORNL, SNL, and ANL).
- Boundary conditions determined for rendering cells inert. Heated cells were observed while fixed in mechanical test equipment to observe the onset and severity of potential temperature induced swelling.

Approach

Abuse tolerance tests evaluate the response to expected abuse conditions. The goals of abuse and safety testing include a) testing to failure of energy storage devices and documentation of conditions that caused failure, b) systematic evaluation of failure modes and abuse conditions using destructive physical analysis (DPA), c) provide quantitative measurements of cell/module response, d) document improvements in abuse response, and e) develop new abuse test procedures that more accurately determine cell performance under most probable abuse conditions. Electrical (overcharge/overvoltage, short circuit, over discharge/voltage reversal, and partial short circuit), mechanical (controlled crush, penetration, blunt rod, drop, water immersion, laser induced short circuit, mechanical shock and vibration) and thermal abuse (thermal stability, simulated fuel fire, elevated temperature storage, rapid charge/discharge, and thermal shock cycling) cover the main categories of possible conditions evaluated. These techniques are applied to USABC deliverables and the results reported to DOE and USABC.

Research and development batteries used for new test development, including stand up of the drop tower, studies to render batteries inert, and testing of temperature hardened calorimetry test cells use commercial off the shelf (COTS) 18650 and pouch format cells. Generally, NMC-graphite cells were used for testing due to the general relevance to EV applications. The testing of the hardened calorimetry test cells used high energy density materials, particularly NCA-graphite cell as the cells in question had been previously observed to

exhibit a severe runaway event. Testing of lithium plating effects on abusive battery failure used cells built within Sandia's battery prototyping facility to build NMC-graphite cells.

Results

Testing of deliverables was performed for USABC development programs, including testing deliverables from 24M, Amprius, Farasis and Zenlabs. Test results have been reported to the USABC Technical Assessment Committee.

Evaluations of determining if exposure to extended elevated temperature have begun with determine thresholds where cells in question will begin to excessively expand or vent from temperature exposure. This provides a threshold for the maximum temperatures that could reasonably be used to prevent excessive cell exposure. 5 AH commercial off the shelf NMC-graphite “energy” cells were used slowly ramped while clamped in a mechanical test fixture applying a constant position to the cell constraints. During this time the load cell of the mechanical test fixture was monitored for the onset of significant swelling. Figure I.7.C.1 shows the results of this initial testing. In this cell, we observed constant cell pressures until the cell temperature exceeded 100°C. Above this temperature, a rapid increase in cell pressure was observed until the cell ultimately went into thermal runaway. The voltage with respect to temperature is shown in Figure I.7.C.2 and this shows that some voltage drop was observed at moderately elevated temperatures as well. This presents the possibility for a high temperature induced accelerated self-discharge that could be used to render batteries inert for transport to final disposition.

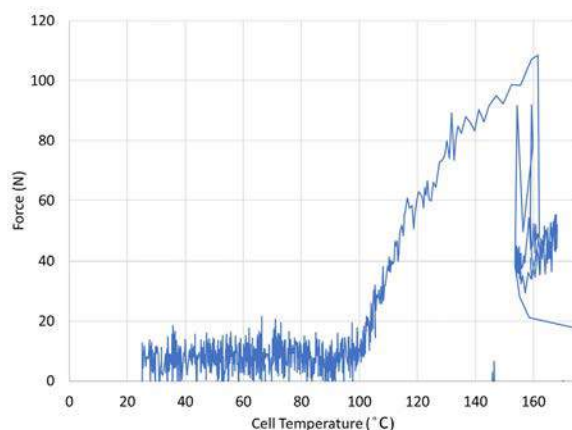


Figure I.7.C.1 Force against mechanical test apparatus of a cell fixed in place within the test fixture as temperature is increased. Used to evaluate cell swelling, this shows little to no swelling up to 90-100 °C. Above this the force begins to rapidly increase until venting occurs at ~150 °C

New trends in battery development have largely focused on the development of high energy density materials, including silicon anode materials, high nickel content cathode materials and solid state batteries to enable lithium metal rechargeable batteries. The high energy density of these cells has exposed limitations in the traditional materials used to measure and contain battery failure during abuse testing. Modifications of capabilities have been performed to better support testing of high energy anode and cathode materials. In particular, increased temperatures have been observed during thermal runaway that have damaged test equipment and exceeded monitoring capabilities. Accelerating Rate Calorimetry hardware has been modified to include high temperature alloy cell holders to replace the stainless steel holders previously used. These were tested and able to withstand a high rate runaway from a 3.1 AH NCA-graphite cell that had previously damaged a stainless steel holder. This provides the capability for planned ARC testing of silicon anode cells to better understand its role in thermal runaway. Modular data acquisition devices capable of high temperature thermocouple inputs have also been acquired to stand up high temperature thermocouple measurements for

future testing and better understand the maximum potential temperatures that are occurring in general abuse tests.

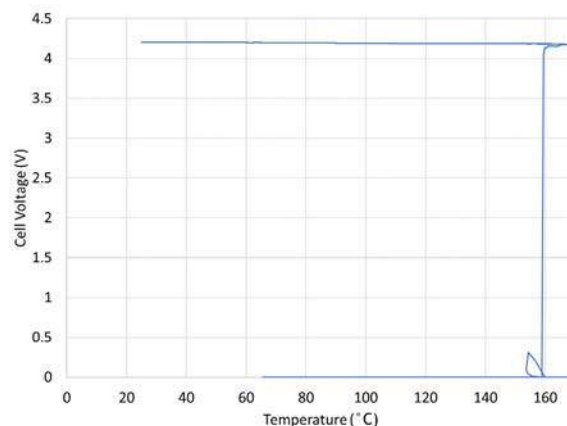


Figure I.7.C.2 Voltage vs temperature of cell tested in Figure I.7.C.1 above. A slight drop in voltage is observed with increasing temperature, indicating potential feasibility of rendering the cell inert through self-discharge over time. Voltage rapidly drops to 0 when cell failure occurs

The primary objective of the lithium (Li) plating project is to observe the effect of varying amounts of lithium plating on the safety characteristics of lithium-ion (Li-ion) cells subjected to abusive conditions. To satisfy this underlying goal, the following three objectives have been proposed: (1) Develop a method for preferentially plating Li metal on a graphitic anode, (2) Investigate the effect of Li plating on cell safety characteristics during abusive conditions, and (3) Investigate the effect of C-rate on extent of Li plating/stripping and its effect on abuse response. To eliminate variability in our results, we are utilizing a cradle-to-grave approach which includes fabrication of 1Ah pouch cells using in-house electrode and electrolyte formulations. Cell cycling schedules are consistent between cells, as are parameters during abuse testing. The use of high-rate cycling has been utilized to preferentially plate Li on anodes with variable n:p ratios. Two sets of cells have been fabricated, of which one was deconstructed to visually inspect for Li plating and the other subjected to abuse cycling. Cell teardowns (see Figure I.7.C.3) suggest that extent of Li plating scales with decreased n:p ratio. Initial results from overtemperature testing indicates that greater extent of Li plating leads to exacerbated abuse response, where cells with 1.2 and 0.75 n:p ratios failed to exhibit runaway behavior even at high temperatures (>250°C). On the other hand, the 0.5 n:p ratio cell exhibited a violent runaway reaction at ~130°C. All cells exhibited pouch bulging and subsequent venting, however it is speculated that the additional Li plating present in the 0.5 n:p ratio cell was the primary factor leading to exacerbated abuse response (see below image).

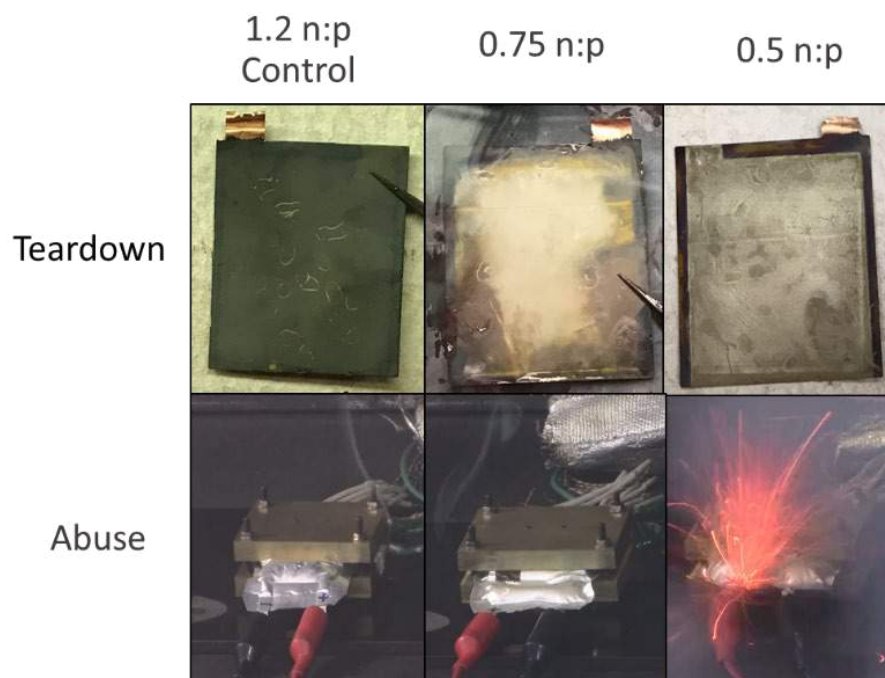


Figure I.7.C.3 DPA and abuse test behaviors of cells with reduced n:p ratios to force significant lithium plating. Visible deposits are observed in the low n:p cell, with a significant thermal runaway event observed

Continued research will involve subjecting cells to a greater array of abuse tests relevant to vehicle battery packs, including mechanical crush, overcharge and accelerated rate calorimetry (ARC). Work is also being conducted to determine whether a Li plating plateau exists beyond which exacerbated abuse response will not persist. Finally, a modified cycling schedule which involves higher rate cycling will be implemented to determine the dependence of C-rate on the safety performance of test subjects.

Conclusions

Development and testing of higher energy, larger format cells and modules continues for USABC developers in hopes to meet the EV Everywhere 2022 goals. We provide a means to field the most inherently safe chemistries and designs to help address the challenges in scaling up lithium-ion technologies of interest. This has required careful control and monitoring of tests with the potential of high energy release as well as standing up a larger facility at SNL to support module level testing this FY. This has provided critical information to cell developers to aid in the development of increasingly abuse tolerant cell chemistries and module designs. This independent testing is also necessary to perform objective evaluations of these various designs and chemistries by the DOE and U.S. automobile manufacturers. SNL has completed abuse testing support for all USABC deliverables to date.

Work has been performed this FY to expand the capabilities at SNL. A drop tower impact tester has been developed to better understand how batteries fail under dynamic loading conditions in collaboration with the CAEBAT program. Cell holder equipment for accelerating rate calorimetry has also been temperature hardened to better accommodate the high temperature failures that have been observed with high energy active materials. On going testing will evaluate the impact of increasing levels of silicon in the failure response of 18650 cells. Work is also on going to provide better detection of high temperature failures during standard abuse tests.

Low n:p ratio cells were built to force lithium plating on test cells and evaluate the impact of lithium plating on abuse response. The low n:p cells were shown through DPA to have significant lithium plating after cycling. This also resulted in a more severe abuse response in the low n:p cells that included a significant thermal

runaway in the 0.5 n:p cell. This included ejection of incandescent particles and self-ignition of the vent gasses. Higher n:p ratios did not show a significant thermal runaway event in the cells tested.

SNL continues to provide testing support and data to help build and validate models with other national lab partners through the CAEBAT VTO program. Additional abuse testing support for the VTO post mortem program and Si-Deep Dive expanded this year, which included overcharging cells of various chemistries manufactured by ORNL to different states followed by posttest analysis done by ANL. Preparations have been made as well to provide support to safety critical tests that may develop as the result of cell recycling efforts.

Key Publications

1. Q. Li, C. Yang, S. Santhanagopalan, K. Smith, J. Lamb, L. A. Steele, L. Torres-Castro, “Numerical investigation of thermal runaway mitigation through a passive thermal management system,” *Journal of Power Sources*, vol. 429, p.p. 80, 2019
2. Lamb, J. et. Al. “Evaluating the Impact of Initiation Methods on Propagating Thermal Runaway in Lithium-Ion Batteries” *Battery Safety 2018*, October 2018
3. Lamb, J. et. Al. “Mechanisms and Material Impacts of Overcharge in Lithium-ion batteries” *MRS Fall Meeting*, November 2018
4. Lamb, J. et Al. “Evaluating the Impact of Initiation Methods on Propagating Thermal Runaway in Lithium-Ion Batteries” *SAE Government Industry Meeting 2019*, March 2019
5. Lamb, J. et Al. “Scaling Accelerating Rate Calorimetry Results” *Spring Meeting of the Electrochemical Society*, May 2019
6. Torres-Castro, L. et al., Mechanisms and material impacts of overcharge in lithium ion, 235th ECS Meeting, Dallas, Texas; May 26-30, 2019
7. Karulkar, M. et al. “High Precision Characterization of Li-Ion Batteries during Extreme Fast Charging” 235th ECS Meeting, Dallas, Texas; May 26-30, 2019
8. Lamb, J. et Al. “Failure Propagation Work and Abuse Testing” *Advanced Automotive Battery Conference*, June 2019
9. Karulkar, M. et Al. “Characterization of Abuse Response during Fast Charge of Lithium Ion Batteries” *Advanced Automotive Battery Conference*, June 2019
10. Lamb, J. et Al. “Evaluating the Impact of Energy Density on Thermal Runaway” *Battery Safety Summit 2019*, October 2019
11. Lamb, J. et Al. “Battery Safety and Abuse Testing Overview” *Stanford Battery Seminar Series*, October 2019
12. Stanley, J. et al. “Li-ion Battery Impact Testing” *AMSE InterPACK Conference*, October 2019
13. Deichman, E. e al. “Analyzing the effect of lithium plating on the safety performance of lithium-ion batteries” *Fall ECS Meeting*, October 2019

Acknowledgements

The following individuals contributed to this project: from Sandia- Loraine Torres-Castro, June Stanley, Christopher Grosso, Mohan Karulkar, Lucas Gray, Eric Deichmann, and Kyle Fenton; from national labs and industry- the USABC TAC Team, Ira Bloom (ANL), Matt Keyser (NREL), Shriram Santhanagopalan (NREL), Eric Dufek (INL), and Lee Walker (INL). Sandia National Laboratories is a multi-mission laboratory managed and operated by National Technology and Engineering Solutions of Sandia, LLC., a wholly owned subsidiary of Honeywell International, Inc., for the U.S. Department of Energy’s National Nuclear Security Administration under contract DE-NA0003525.

I.7.D Battery Thermal Analysis and Characterization Activities (NREL)

Matthew Keyser, Principal Investigator

National Renewable Energy Laboratory
15013 Denver West Parkway
Golden, CO 80401
E-mail: Matthew.Keyser@nrel.gov

Samuel Gillard, DOE Technology Development Manager

U.S. Department of Energy
E-mail: Samuel.Gillard@ee.doe.gov

Start Date: October 1, 2018
Total Project Cost: \$500,000

End Date: September 30, 2019
DOE share: \$500,000

Non-DOE share: \$0

Project Introduction

While EDVs promise to curb America's need for imported oil, designing high-performance, cost-effective, safe, and affordable energy-storage systems for these cars can present challenges, especially in the critical area of battery thermal control. As manufacturers strive to make batteries more compact and powerful, knowing how and where heat is generated becomes even more essential to the design of effective thermal-management systems. NREL's thermal characterization activities provide developers, manufacturers and OEMs with the knowledge necessary to assure that batteries are designed to perform strongly, last a long time, and operate at maximum efficiency.

The Vehicle Technologies Office has a goal to reduce the cost of electric vehicle battery packs by 2022 to less than \$150/kWh with technologies that significantly reduce or eliminate the dependency on critical materials (such as cobalt) and utilize recycled material feedstocks [1]. In order to meet these metrics, the battery packs will need to have higher energy densities resulting in a very compact system. Even if the energy efficiency of the next generation of batteries increases, because of the compactness of these batteries more heat is being generated per unit volume with less heat transfer area. Thus, more advanced heat rejection systems are needed to keep the battery temperatures in the “goldilocks” zone that prevents acceleration of the aging mechanisms within the battery.

The chemistries of advanced energy-storage devices—such as lithium-based batteries—are very sensitive to operating temperature. High temperatures degrade batteries faster while low temperatures decrease their power and capacity, affecting vehicle range, performance, and cost. Understanding heat generation in battery systems—from the individual cells within a module, to the inter-connects between the cells, and across the entire battery system—is imperative for designing effective thermal-management systems and battery packs.

Inadequate or inaccurate knowledge of the thermal characteristics of batteries makes it difficult to design effective thermal-control systems. This can negatively affect lifespan, safety, and cost, ultimately resulting in negative consumer perception and reduced marketability. In 2012, Nissan had to address problems with the battery for its Leaf fully-electric vehicle (EV) losing capacity in the hot Arizona climate. Many attributed this issue to inadequate battery-thermal management.

Accurately measuring battery thermal performance under various electrical loads and boundary conditions makes it possible for battery-system engineers to design effective thermal-management systems. NREL, with the funding from DOE VTO, has developed unique capabilities to measure the thermal properties of cells and evaluate thermal performance of active, air, and liquid cooled battery packs. Researchers also use electro-thermal finite element models to analyze the thermal performance of battery systems in order to aid battery developers with improved thermal designs. In addition, our lumped capacitance multi-node battery-vehicle-ambient model can predict the temporal temperature of batteries as a function drive cycle, ambient

temperature, and solar radiation. These one-of-a-kind tools allow NREL to work with the battery manufacturers and OEMs to meet stringent EDV life, performance, cost, and safety goals

Objectives

- Thermally characterize battery cells and evaluate thermal performance of battery packs provided by USABC developers.
- Provide technical assistance and modeling support to USDRIVE/USABC and developers to improve thermal design and performance of energy storage systems.
- Evaluate extreme fast charging effects on battery thermal performance.
- Quantify the impact of temperature and duty-cycle on energy storage system life and cost.
- Address high energy storage cost due to battery packaging and integration costs
- Reduce the cost, size, complexity, and energy consumption of thermal management systems
- Optimize the design of passive/active thermal management systems—explore new cooling strategies to extend the life of the battery pack.

Approach

NREL has measured the thermal properties of the cells and batteries with many different chemistries (lead acid, NiMH, and many versions of lithium cells) through heat generation, heat capacity, and infrared thermal imaging; conducted performance thermal testing of battery and ultracapacitor modules and packs; analyzed the thermal performance of cells and modules; and developed thermal models. Researchers perform thermal testing, analysis, and modeling (1) to assist DOE/USABC battery developers in designing cells/modules/packs for improved thermal performance, and (2) to evaluate and validate the thermal performance of cell/module/pack deliverables from DOE/USABC battery developers and suppliers.

NREL's equipment can benchmark how changing the design of the cell using a different cathode, anode, current collector, electrolyte, additive, or separator affects the overall performance of the cell. The information garnered from these tests helps battery and advanced vehicle manufacturers improve their designs, while providing critical data for the development of thermal management systems that will reduce the life-cycle cost of battery systems. Using NREL's unique R&D 100 Award-winning calorimeters and infrared thermal imaging equipment, we obtain thermal characteristics of batteries and ultracapacitors developed by USABC battery developers and other industry partners. NREL supports the Energy Storage Technical Team by participating in various work groups such as the Amprius, Zenlabs, Farasis, 24M and USABC Working Groups.

Results

The following narrative outlines some of the more interesting insights garnered from NREL's testing over the past year. The outline below is not meant to be an exhaustive study of NREL's work but rather to help the reader understand how NREL's unique thermal characterization technologies are used to improve the energy storage technologies in conjunction with industry and USABC.

Calorimeter Testing

Figure I.7.D.1 shows the efficiency of cells tested in FY17/FY18/FY19 at NREL at a calorimeter temperature of 30°C. The lithium ion cells were fully discharged from 100% SOC to 0% SOC under a C/2, C/1, and 2C currents. It should be noted that the cells in the figure are for both power and energy cells and have been developed for the HEV, PHEV, EDV, and/or the 12 Volt Start/Stop programs within USABC. The figure shows a general trend with regards to the choice of anode on discharge efficiency. The graph indicates that the lithium titanate oxide (LTO) systems are the most efficient, followed by the graphite cells, and then the silicon

blended cells. One confounding factor in the data is that the LTO cells are typically formulated to be power cells. Therefore, the thickness of the electrode and current collectors will have a positive effect on the efficiency of the system. In contrast, the silicon blend cells were designed with energy density as a primary consideration resulting in these systems having slightly lower efficiencies. However, the efficiency of the silicon cells tested at NREL have improved considerably over the past two years. In FY18, the maximum 2C discharge efficiency for a silicon/graphite (> 50% silicon) blended cell was optimistically measured at about 90%. In FY19, the efficiency for a similar silicon/graphite blended cell increased to approximately 94% at a 2C discharge rate. Adjusting for the electrode thickness confounding factor, the general trend still shows that the stable structure of LTO systems allows for higher energy efficiencies and confirms that the silicon systems still need improvements with regards to their electrical conductivity when used under conditions such as fast charge. DOE and USABC are investigating each of these chemistries to improve energy density, power density, cycle life and/or cost benefits. NREL's calorimeters provide the fundamental understanding of whether the inefficiencies shown below are due to chemistry or cell design.

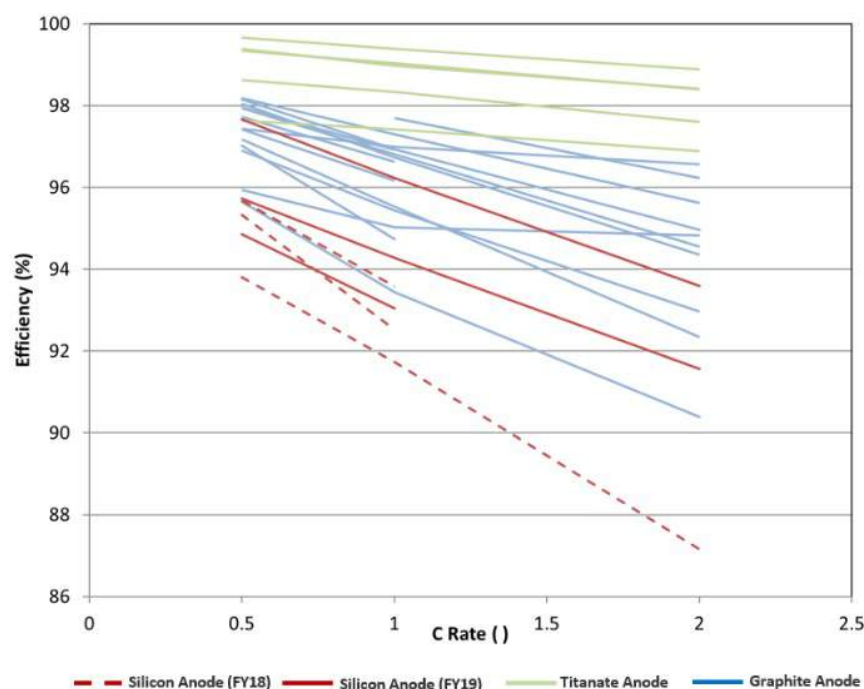


Figure I.7.D.1 Efficiency summary of cells tested at 30°C in NREL's calorimeters.
Caption Credits/Source: NREL- Aron Saxon

Over the past several years, our testing has shown that the difference in efficiency over the full SOC range as compared to the usage SOC range has decreased for PHEV and EV cells. NREL typically discharges cells under a constant current from 100% to 0% SOC for comparison purposes against other cells. However, cells are not typically used over their full capacity range due to life cycle limitations of the cell. Thus, NREL additionally tests the cells over their usage range for the cell—for a PHEV and EV cell; the usage range is approximately 95% to 20% SOC. As would be expected, the cells are less efficient over the full SOC range as compared to the partial SOC range. Figure I.7.D.2 shows a full/partial discharge efficiency comparison of a silicon-graphite/high nickel content NMC cell. The cell was tested at temperatures of 30°C and 0°C. As can be seen from the figure, the efficiency for a given temperature and C-rate decreases by approximately 2% when cycling the cell over the full SOC range as compared to the partial SOC range of 95% to 20%. Battery manufacturers use the data from the calorimeter to ensure that the cell has the desired efficiency over the usage

range while making trade-offs on other aspects of the cell design, such as low temperature operation, safety, cost, and ease of manufacturing.

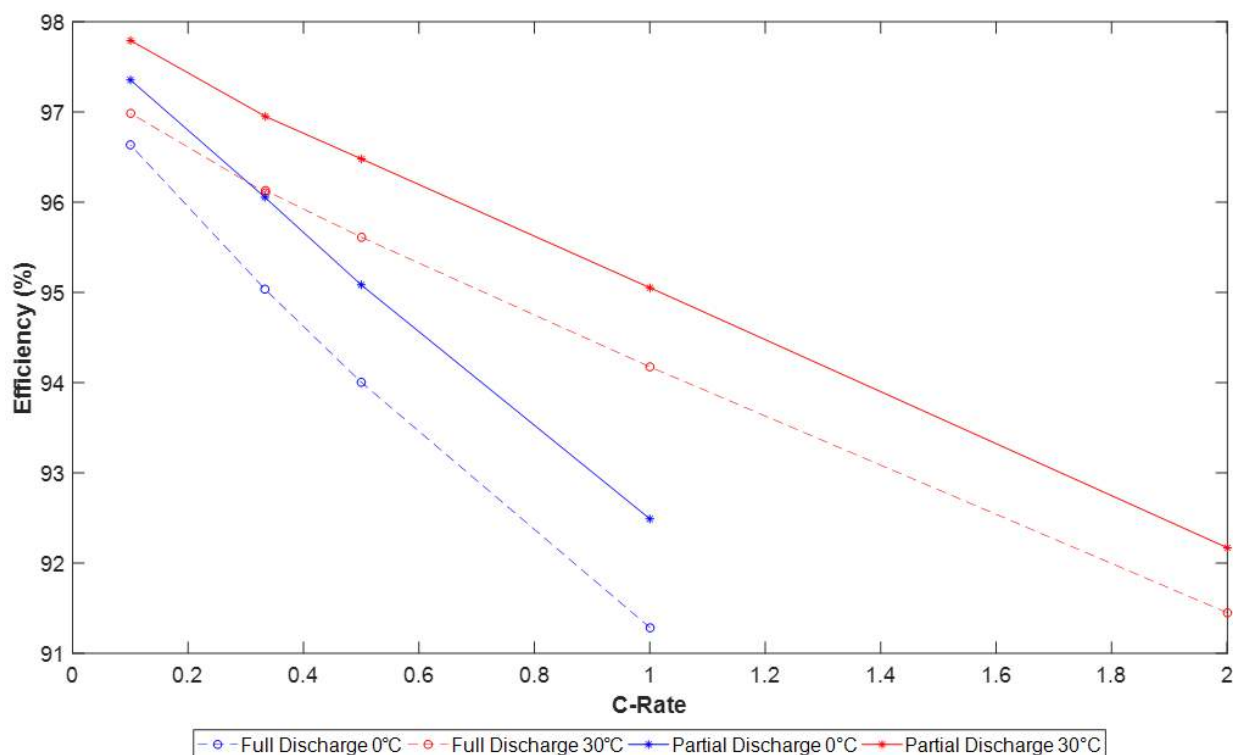


Figure I.7.D.2 Efficiency of silicon blended cells tested at 30°C in NREL's calorimeters under various charge/discharge currents and SOC ranges. Caption Credits/Source: NREL- Aron Saxon

NREL's calorimeters were designed to be accurate enough to measure the electrochemical response from batteries under test – this capability allows NREL to understand benefits associated with design and chemistry changes to the cell. Figure I.7.D.3 shows the entropic heat generation rates normalized to the Ah capacity of the cell for two temperature, 30°C and 0°C, for a graphite/high nickel content NMC under a C/10 constant current charge. The cells in this figure were cycled over their entire state-of-charge range – minimizing the current decreases the joule heating of the cell and allows for the entropic heat signature to be assessed. As shown in the figure, the cells can undergo endothermic and exothermic heat generation over the cycling range. By testing at multiple temperatures, we are able to differentiate the entropic heat contribution from the joule heating within the cell. Testing at higher temperatures allows for the entropic response to dominate, but joule heating will dominate as the temperature is lowered. Testing at low currents and multiple temperatures allows for us to understand how architecture and additive/chemistry changes affect the cells performance.

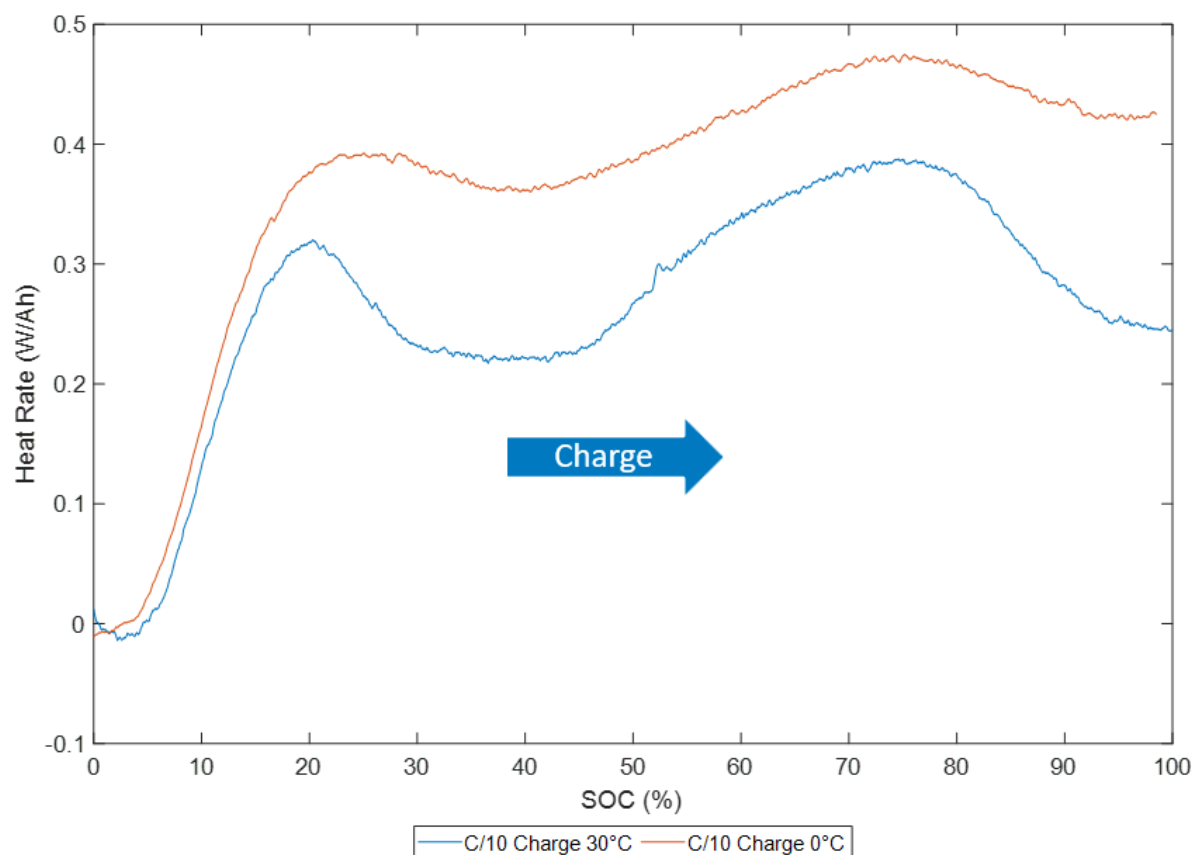


Figure I.7.D.3 Calorimeter normalized heat rate for a graphite/high nickel content NMC cells under C/10 charge.
Caption Credits/Source: NREL- Aron Saxon

During the past two years, NREL has also been testing commercially available cells under fast charge conditions. The USABC test procedure consists of a 3.2C fast charge from the minimum operational voltage to the maximum operational voltage. If the maximum operational voltage is reached during the charge, then the current is tapered to complete the 15-minute charge. NREL was able to acquire several electric vehicle cells and we tested the cells under the USABC fast charge procedure even though these cells have not been optimized for fast charge conditions. The voltage and temperature curves for a large format graphite/NMC cell are shown in Figure I.7.D.4 for the fast charge test. As the graph indicates, the test was halted after approximately 9 minutes as the cell reached the maximum operational temperature of the battery of 55°C. During our testing, the cell is not actively cooled within the calorimeter but it is sandwiched between aluminum plates to diffuse the heat generated in the cell. For the fast charge test, the cell generated 90 watts of heat with a heat efficiency of 88%. For cells used under extreme and fast charge conditions, we will need to increase the overall efficiency of the cells to meet life and warranty expectations as well as limiting safety concerns for future charging applications.

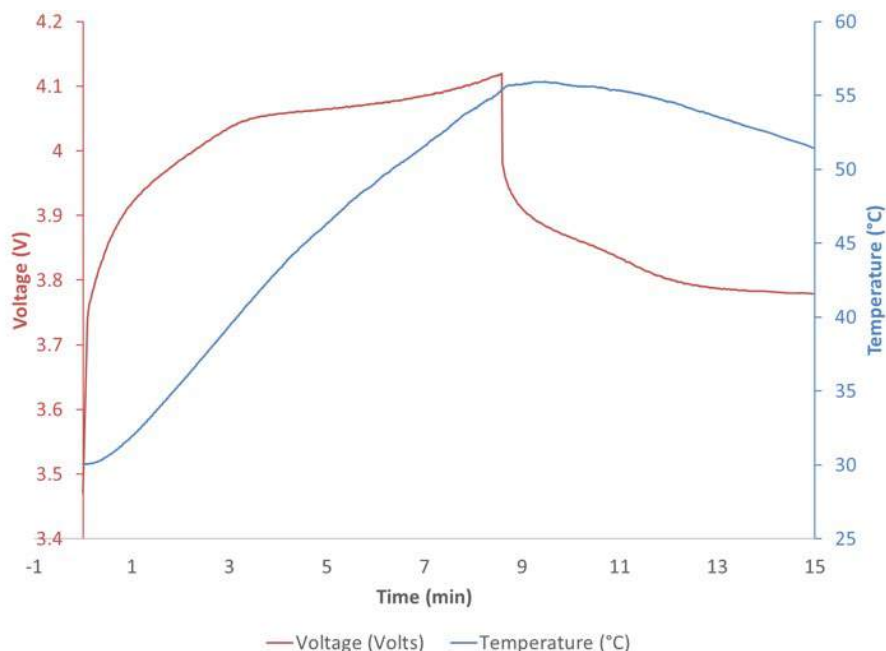


Figure I.7.D.4 Large format graphite/NMC cell under a 3.2C fast charge. The calorimeter test temperature was 30 °C.
Caption Credits/Source: NREL- Aron Saxon

Infrared Imaging of Cells

NREL performs infrared (IR) thermal imaging of battery manufacturer's cells to determine areas of thermal concern. We conduct IR thermal imaging under a set of prescribed procedures and environments to minimize the error from different sources such as reflective cell surfaces, radiation from surrounding surfaces, and cooling from the power cables attached to the cell. NREL combines the IR imaging equipment with a battery cyclers to place the cells under various drive cycles, such as a US06 charge depleting cycle for a PHEV, to understand the temperature differences within the cell. We then make recommendations to the battery manufacturers and USABC on how to improve the thermal design of the cell to increase its cycle life and safety.

Figure I.7.D.5 shows a lithium battery (Graphite-Silicon/High Nickel Content NMC) at the end of a 2C discharge. Each IR image has a temperature spread associated with it – by decreasing the temperature spread a visual reference can be used to determine where the heat is preferentially being generated within the cell. For this cell, the heat generation is biased towards the positive terminal of the battery. The point of thermal concern on this cell is due to the sizing of the aluminum tabs. During the IR imaging, we also assess the temperature uniformity across the cell surface. When the cell temperature is not uniform and consistent, individual cells within modules and packs age differently affecting the cycle life of the module. NREL is working with battery developers to understand how temperature non-uniformities affect the efficiency and cost of the cell over its life.

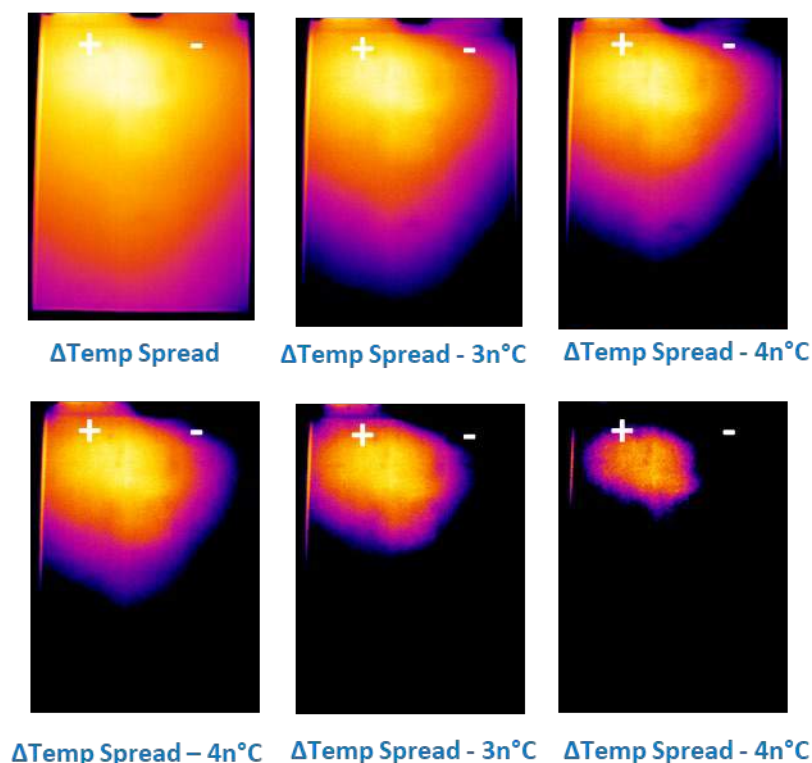


Figure I.7.D.5 Infrared image of lithium battery cell (graphite-silicon/high nickel content NMC) at the end of a 2C discharge.
Caption Credits/Source: NREL- Aron Saxon

Conclusions

NREL has thermally tested cells and modules from Amprius, Zenlabs, Farasis, and 24M during FY18. We've provided critical data to the battery manufacturers and OEMs that can be used to improve the thermal design of the cell, module, pack and their respective thermal management systems. The data included heat generation of cells under typical profiles for HEV, PHEV, and EV applications, which is essential for designing the appropriately sized battery thermal management system. In FY20, NREL will continue to thermally characterize cells and modules for USABC, DOE, and USDRIVE but the focus will shift to fast charging applications and the heat generation differences between chemistries.

Key Publications

1. Conference Presentation: Matthew Keyser, "Heat generation associated with extreme fast charging", The Battery Show, Germany, 2019.
2. Conference Presentation: Aron Saxon, "Battery thermal analysis and characterization activities", InterPack, California, 2019.
3. Quarterly meeting presentations to the battery working group and manufacturers.

References

1. Brian Cunningham, Electrochemical Energy Storage R&D Overview, Annual Merit Review, Washington DC, 2018

Acknowledgements

We wish to acknowledge Samuel Gillard and DOE for sponsoring these efforts. We would also like to acknowledge team members and co-authors of this report – Aron Saxon and Thomas Bethel.

I.7.E Cell Analysis, Modeling, and Prototyping (CAMP) Facility Research Activities (ANL)

Andrew N. Jansen, Principal Investigator

Argonne National Laboratory
9700 S Cass Avenue
Lemont, IL 60439
E-mail: Jansen@anl.gov

Peter Faguy, DOE Technology Development Manager

U.S. Department of Energy
E-mail: Peter.Faguy@EE.Doe.Gov

Start Date: September 30, 2018

End Date: September 29, 2021

Total Project Cost: \$900,000

DOE share: \$900,000

Non-DOE share: \$0

Project Introduction

The “valley of death” is a phrase often used to describe the path a new discovery must traverse to become a commercial product. This is especially true for novel battery materials invented in research laboratories around the world. Often researchers are resource limited and are only able to make gram quantities of their new material. The CAMP Facility is appropriately sized to enable the design, fabrication, and characterization of high-quality prototype cells using just a few hundred grams of the latest discoveries involving high energy battery materials. Prototype cells made in the CAMP Facility generally have 400-mAh capacity, which straddles the gap between coin cells and industrially-sized cells nicely – two orders of magnitude from each end point. Thus, a realistic and consistent evaluation of candidate chemistries is enabled in a time-effective manner with practical quantities of novel materials in cell formats commonly used in industry.

The CAMP Facility is an integrated team effort designed to support the production of prototype electrodes and cells, and includes activities in materials validation (benchmarking), modeling, and diagnostics. It is not the aim of this facility to become a small battery manufacturer, but instead to be a laboratory research facility with cell production capabilities that adequately evaluate the merits and limitations of new lithium-ion chemistries in a close-to-realistic industrial format. The source of these materials (anodes, cathodes, electrolytes, additives, separators, and binders) may originate from the ABR and BMR Programs, as well as from other domestic and foreign organizations such as universities, national labs, and industrial vendors. Electrochemical couples with high power and energy density are given extra priority.

The CAMP Facility has the capability to make three prototype cell formats in their 45 m² dry room: pouch cells (xx3450 format, with capacity around 0.5 Ah; and xx6395, with capacity around 2 Ah) and 18650 cells (with capacity around 2 Ah). Pouch cells are generally easier to assemble, and are a great indicator of gassing problems in a cell during cell aging and cycling. Central to this effort is a pilot-scale coating machine that operates with slurry sizes that range from 20 grams to a couple kilograms. This is a key feature of the CAMP Facility that enables a professional evaluation of small quantities of novel materials. If needed, the Materials Engineering Research Facility (MERF) is available for scaling up materials for these prototype cell builds.

Objectives

The objective of this core-funded effort is to design, fabricate, and characterize high-quality prototype electrodes and cells that are based on the latest discoveries involving high energy anode and cathode battery materials. Using this multi-disciplined facility, analytical diagnostic results can be correlated with the electrochemical performance of advanced lithium-ion battery technologies for electric vehicle (EV) applications.

- Link experimental efforts through electrochemical modeling studies.

- Identify performance limitations and aging mechanisms.
- Support lithium-ion battery projects within the DOE-EERE-VTO.

Approach

The general approach used in this effort is to start small and grow large in terms of cell size and amount of resources devoted to each novel battery material. At various points in the development process, decisions are made to either advance, modify, or terminate studies to maximize utilization of available resources.

Coin cells (2032 size) are used for materials validation purposes with initial studies performed at 30°C. After formation cycles, the coin cells go through rate capability testing, HPPC testing, and limited cycle life testing. Additional temperatures and test conditions are employed if warranted.

Using the results obtained by the materials validation of promising materials, single-sided electrodes are fabricated on the larger dry-room coater for diagnostic study. The new cell chemistries are studied in detail using advanced electrochemical and analytical techniques, including the employment of micro-reference electrode cells. Factors are identified that determine cell performance and performance degradation (capacity fade, impedance rise) on storage and on extensive deep-discharge cycling. The results of these tests are used to formulate data-driven recommendations to improve the electrochemical performance/life of materials and electrodes that will be incorporated in the prototype cells that are later fabricated in the dry room. This information also lays the foundation for electrochemical modeling focused on correlating the electrochemical and analytical studies, in order to identify performance limitations and aging mechanisms.

If the results from diagnostics and modeling still look promising, full cell builds are conducted using double-sided electrodes. The electrodes are then either punched in the case of pouch cells, or slit in the case of 18650 cells and assembled into full cells in the dry room using semi-automated cell assembly equipment. Formation procedures are conducted on the cells to encourage electrolyte wetting and uniform solid-electrolyte-interface (SEI) formation. These cells undergo rigorous electrochemical evaluation and aging studies under the combined effort of the CAMP Facility team, and Argonne's Electrochemical Analysis and Diagnostic Laboratory (EADL) and Post-Test Facility. After testing, select cells are destructively examined by the Post-Test Facility to elucidate failure mechanisms. This information is then used to further improve the new chemistry, as well as future electrode and cell builds.

Results

The CAMP Facility is designed to work closely with materials researchers across the many electrochemical energy storage programs throughout the DOE-EERE-VTO. In addition to its own yearly R&D tasks, it actively coordinates its efforts to provide support to other national lab teams such as: the Realizing Next Generation Cathodes, the Next Generation Anodes, Fast Charge (XCEL), and the ReCell Center programs. The Materials Benchmarking Activities (the next section) is a segment of the CAMP Facility. The CAMP Facility also complements the capabilities of other DOE support facilities such as: the Materials Engineering Research Facility (MERF - Argonne), the Post-Test Facility (PTF - Argonne), the Battery Abuse Testing Laboratory (BATLab - SNL), and the Battery Manufacturing Facility (BMF - ORNL). More information about these projects can be found in the relevant chapters and sections of this annual report. The remainder of this CAMP Facility section will discuss the results of the CAMP Facility deliverables for FY19, and include results of related topics.

Finalize Evaluation of Core-Shell and Core-Gradient Cathode Powders

The CAMP Facility evaluated full cell performance of cathode core-shell and core-gradient powders made by the MERF. These materials are of interest to the battery community because of a possible increase of energy density, while maintaining good safety. Our study investigated these potential advancements. MERF provided the CAMP Facility with NMC core-shell (CS), core-gradient (CG), and core-multi-shell (CMS) powders that they fabricated into single layer ~20 mAh pouch cells versus a baseline graphite anode. The baseline cathode

used was NMC811 from a commercial source. All cathodes had a coating composition of 90% active, 5% carbons, and 5% PVDF with an aerial capacity of ~ 1.6 mAh/cm².

Figure I.7.E.1 depicts the design and estimated result of making core-shell, core-gradient, and core multi-shell powders based on lithium-nickel-cobalt-manganese oxide (NMC) chemistries.

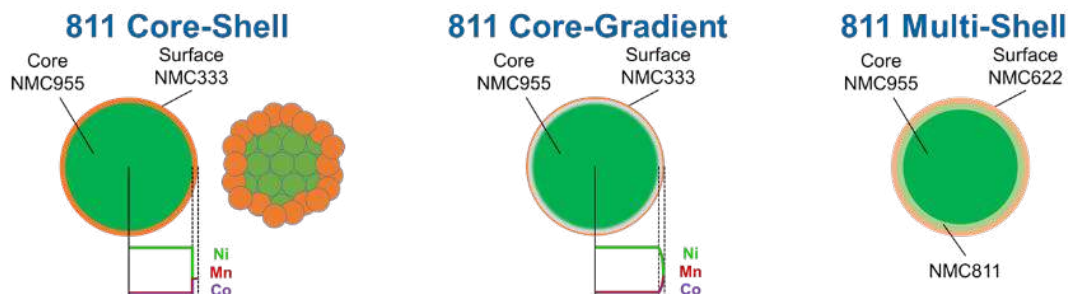


Figure I.7.E.1 Pictorial of cathode particle cross-sections produced in MERF

Table I.7.E.1 summarizes the initial results from the formation test. The 1st charge and reversible discharge capacities provide information about ICL (irreversible capacity loss). The CS, CG, and CMS powders yielded slightly lower discharge capacities compared to the baseline NMC811. The electrolyte used in this study was 1.2 M LiPF₆ in EC:EMC (3:7 by wt.), referred to as “Gen2”, and the test conditions were 3.0 to 4.3 V, C/10 current rate, and 30°C.

Table I.7.E.1 Capacity Values for Cathodes Made in MERF

Cathode	Average 1 st Charge Capacity (mAh/g)	Average Reversible Discharge Capacity (mAh/g)
NMC811	221	203
NMC811-CG	211	188
NMC811-CS	208	186
NMC811-CMS	221	193

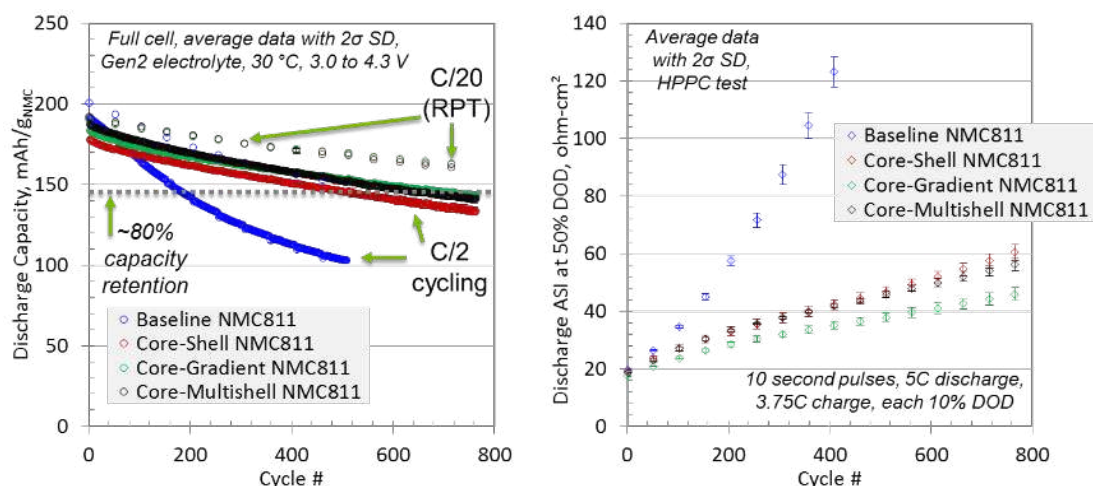


Figure I.7.E.2 Electrochemical performance high-nickel content NMC cathode powders produced by MERF compared to a baseline NMC811 (Targray). All electrodes and pouch cells were fabricated and tested by the CAMP Facility

Figure I.7.E.2 summarizes the electrochemical cycling performance of the baseline high nickel content NMC (NMC811) against 3 electrodes made by the CAMP Facility using cathode powders provided by MERF. The left plot shows discharge capacity as it relates to cycle number. The baseline has a faster capacity decay rate during cycling compared to the MERF cathode powders. The right plot shows the cell resistance changes as the cells cycle. In this study, the MERF cathode powders had slightly lower initial cycling capacities. However, as the cycle life test continued, the MERF cathode powders all had significantly better capacity retention, and considerably lower impedance rise compared to the baseline NMC811. The top performer for capacity retention and impedance was NMC811-CG.

Next, the CAMP Facility performed characterization of core-shell and core-gradient materials made in MERF with a focus on thermal stability. The CAMP Facility electrodes consisting of the NMC811 baseline and MERF cathode powders were tested by Differential Scanning Calorimetry (DSC) to study the thermal stability based on decomposition temperature and heat released. DSC measures the difference in heat required to raise the temperature of a sample relative to a reference (empty pan).

Details of the preparation and testing for the DSC evaluation are shown in Figure I.7.E.3 and Figure I.7.E.4, respectfully. The CAMP Facility chose to compare cathode materials at the same charged specific energy (\approx specific capacity) rather than same upper-cutoff voltage to help normalize the data for an effective evaluation based on the energy content of the material.



Laminate powder scraped from electrode in glovebox



Reusable steel high pressure capsules with gold-plated caps, Perkin Elmer

Figure I.7.E.3 Images of a researcher scraping the laminate off of the substrate foil in an inert glovebox and the parts used for the DSC experiment

- Cycling - CR2032 half-cells with Gen2, 30 °C
- 3 x C/10 formation cycles, 3.0–4.5V
 - Potentiostatic hold at 3.0V until C/100
 - C/50 charge to *specific energy* cutoff of 750 mWh/g
 - $\approx \text{Li}_{0.24}\text{MO}_2$, 76% State-of-Charge (SOC)

Sample Preparation

- Cell disassembled in glove box
- Cathode rinsed 2 x 60s in 1mL EMC, dried 10 min under dynamic vacuum
- Cathode laminate powder scraped from current collector
- 2–3 mg cathode powder added to DSC capsule with Gen2 electrolyte (1 μL :1mg powder)
- 2 cells, 2 samples per cell tested for each chemistry

DSC Testing

- 30–400 °C, 10 °C/min.
- Baseline of empty pan subtracted from data

Figure I.7.E.4 Test conditions and sample preparation procedure used for DSC experiment

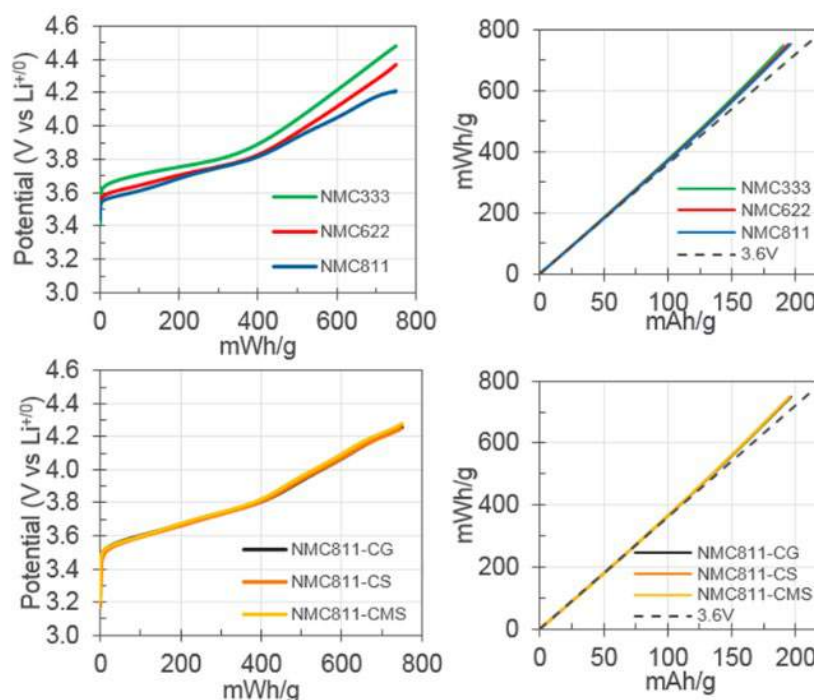


Figure I.7.E.5 Voltage profiles and energy-capacity relationship for NMC111, NMC622, NMC811, NMC811-core-gradient, NMC811-core-shell, and NMC811-core-multishell with respect to the energy cutoff of 750 mWh/g of NMC

The plots in Figure I.7.E.5 show 6 materials (NMC111, NMC622, NMC811, NMC811-core-gradient, NMC811-core-shell, and NMC811-core-multishell) voltage profiles with respect to the energy cutoff of 750 mWh/g of NMC.

Table I.7.E.2 Delithiation Capacity and Voltage for Cathodes Made in MERF

Cathode	750 mWh/g Delith. Capacity (mAh/g)	750 mWh/g Delith. Voltage (V)
NMC333	190	4.44
NMC622	194	4.36
NMC811	196	4.21
NMC811-CG	196	4.25
NMC811-CS	196	4.25
NMC811-CMS	196	4.27

Table I.7.E.2 summarizes the capacity and voltage values from charging (delithiating) each material to 750 mWh/g of NMC. NMC333 and NMC622 were also included in this study to provide a broader lens for NMC thermal stability.

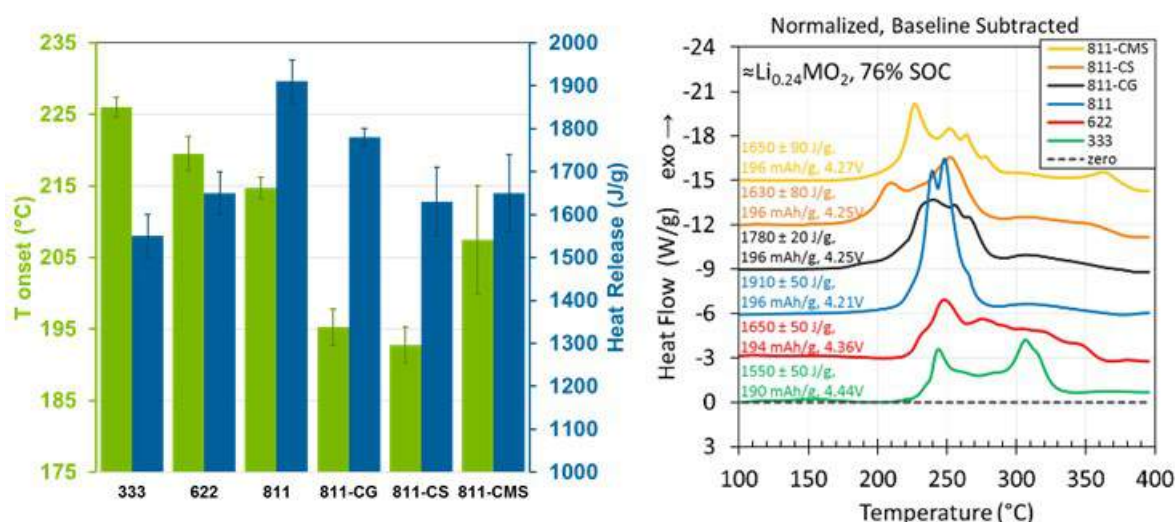


Figure I.7.E.6 Exothermic heat released (integrated DSC peak area), half-cell charged specific capacity, and half-cell voltage before cell disassembly DSC results (left) and total heat released of the materials (right)

Figure I.7.E.6 (left) lists exothermic heat released (integrated DSC peak area), half-cell charged specific capacity, and half-cell voltage before cell disassembly DSC results. DSC exothermic peaks can be associated with cathode oxygen loss and reaction with electrolyte. Figure I.7.E.6 (right) indicates the total heat released of the materials. The MERF composition gradient materials have favorably less heat released over broader range than commercial NMC811 without composition gradient. However, this benefit is offset by the lower onset temperature.

Thermal stability is known to decrease with increasing Ni content. Worse performance is not unexpected, as the core of the NMC811 gradient materials is ~90% Ni. In summary, the DSC results suggest the examined gradient/shell materials have mixed thermal stability results when compared at similar charge energy.

Develop Methods to Direct Coat Ceramics onto Lithium-Ion Electrodes

The CAMP Facility continues to develop the capability to coat specialty films onto electrodes (preferably the anode). The techniques being learned will be valuable to the adaptation of processing solid electrolyte electrode systems. The effort remains on ceramic-based films, but may later include active materials or polymer films, that could serve a variety of applications: replace polymer separator with ceramic separator (added safety); getter undesirable decomposition products with ceramic/functional film; suppress formation of lithium dendrites with novel electrode architecture; replace liquid/polymer electrolytes with solid state electrolyte. A schematic of the cell design approaches being considered are shown in Figure I.7.E.7.

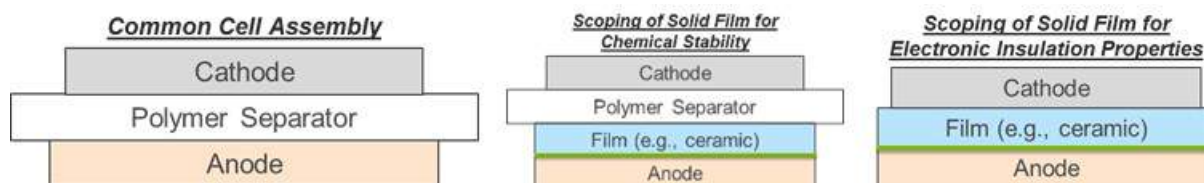


Figure I.7.E.7 Cell design options the CAMP Facility explored for coating materials onto an existing electrode. The green lines indicate the interface of film coating on to the anode

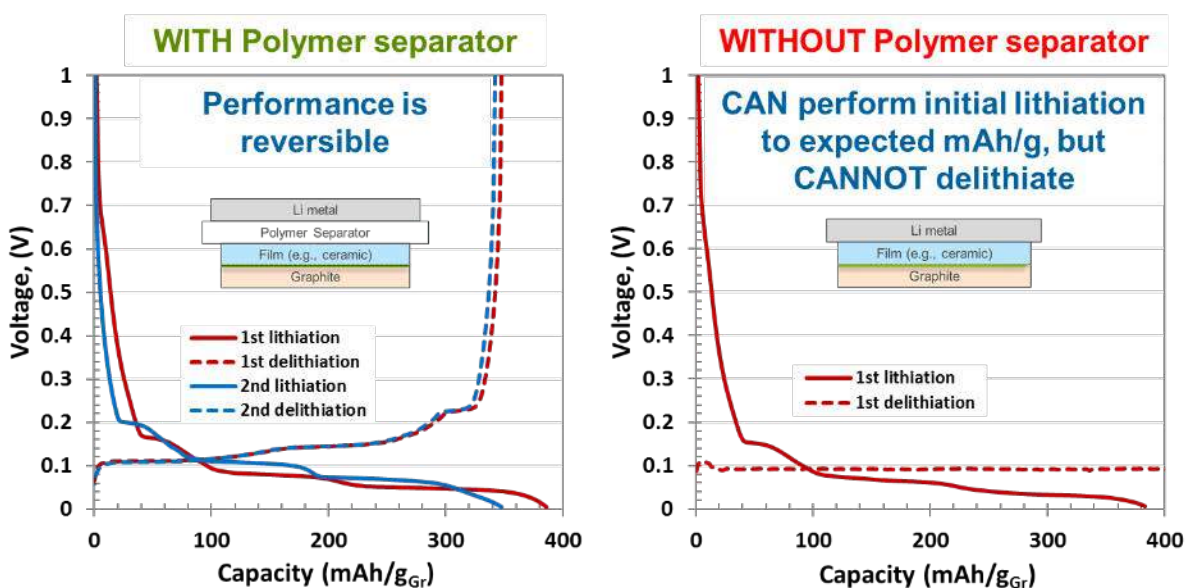


Figure I.7.E.8 Voltage profiles of graphite electrodes with selected ceramics (Al_2O_3 and MgO) coated graphite electrodes coatings vs. lithium metal made in coin cells. The left plot show the performance when the polymer separator is present in the system and the right plot shows when the polymer is absent from the system. This test was a scoping experiment to observe the performance and test if there would be any capacity loss due to the ceramic coating

The results of the study (Figure I.7.E.8) suggest that Al_2O_3 and MgO ceramic coatings both appear chemically stable with a polymer separator between it and lithium metal. However, the films and lithium metal show chemical instability when in direct contact, while maintaining electronic insulation properties (OCV after 1st delithiation remained constant near 0.1 V). This work is related to full cells made in coin cells using the same ceramic coatings paired against NMC532, reported in the previous fiscal year annual report, which resulted in not only the appearance of chemical stability but also compatible electronic insulation with NMC532 in place of the lithium metal electrode.

Table I.7.E.3 Ceramic Materials Under Test as Coatings on Anode

Name	Linear Formula	Molecular Weight	Description	Particle Size
Boron nitride	BN	24.82	powder, ~1 μm , 98%	~1 μm
Aluminum oxide	Al_2O_3	101.96	nanopowder, gamma phase, <50 nm particle size (TEM), alumina	<50 nm (TEM)
Aluminum silicate	$3\text{Al}_2\text{O}_3 \cdot 2\text{SiO}_2$	426.05	Aluminosilicate, Mullite	TBD
Zirconium(IV) oxide	ZrO_2	123.22	powder, 5 μm , 99% trace metals basis, Zirconia	5 μm
Magnesium oxide	MgO	40.3	$\geq 99\%$ trace metals basis, -325 mesh	<44 μm
Zirconium(IV) silicate	ZrSiO_4	183.31	-325 mesh, Zirconium(IV) silicon oxide	<44 μm
Aluminum oxide	Al_2O_3	101.96	powder, primarily α phase, $\leq 10 \mu\text{m}$ avg. part. size, 99.5% trace metals basis, Alumina	$\leq 10 \mu\text{m}$
Aluminum oxide	Al_2O_3	101.96	fused, powder, primarily α -phase, -325 mesh, Alumina	<44 μm
Aluminum nitride	AlN	40.99	powder, 10 μm , $\geq 98\%$	10 μm

Table I.7.E.3 lists the various materials that have been coated (95 wt.% ceramic, 5 wt.% PVDF) on graphite electrodes for single-layer full-cell pouch-cell builds. The graphite electrode was calendered before ceramic coating, then lightly re-calendered after the ceramic coating had been applied. Depending on the material chosen, these non-optimized initial ceramic coatings resulted in thicknesses of 24 to 40 μm and 2.51 to 9.27 mg/cm^2 loadings. As a reference, the Celgard 2325 Separator is 25 μm thick with a loading of 1.53 mg/cm^2 . The material selection was based on scoping a variety of ceramics with various properties in an effort to better understand potential processing challenges that may occur with solid-electrolyte systems (i.e. LLZO). A SEM analysis was performed on these coatings, and is summarized in Figure I.7.E.9 to Figure I.7.E.11.

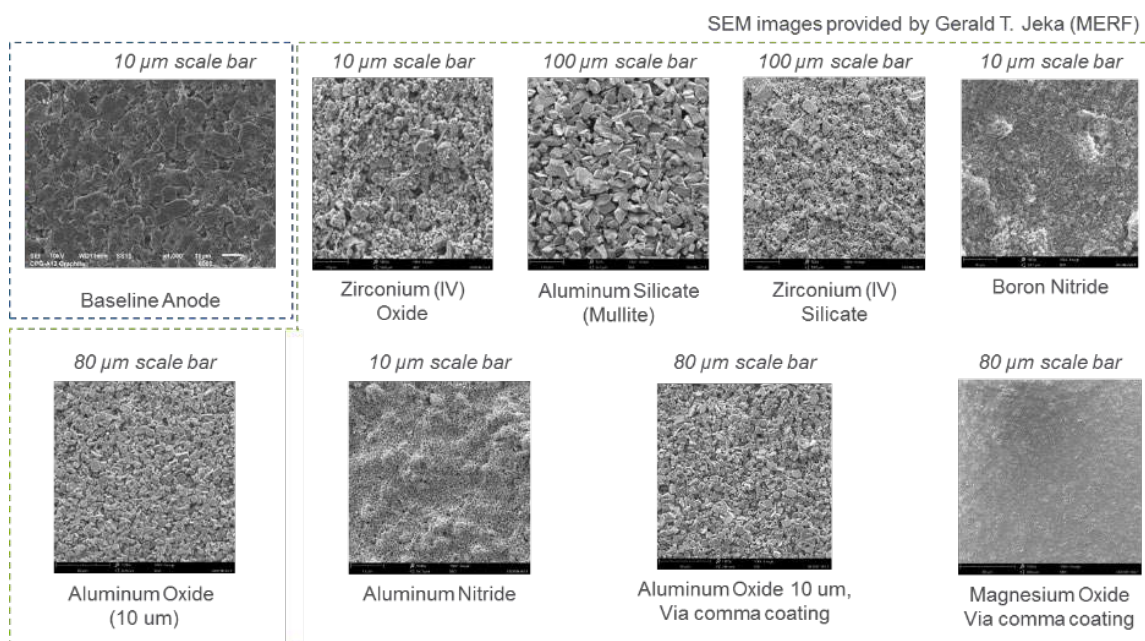


Figure I.7.E.9 SEM images of the surface of the graphite electrodes with and without various coatings. The various ceramic coatings appear to provide a uniform coverage over the surface of the calendered graphite baseline anode

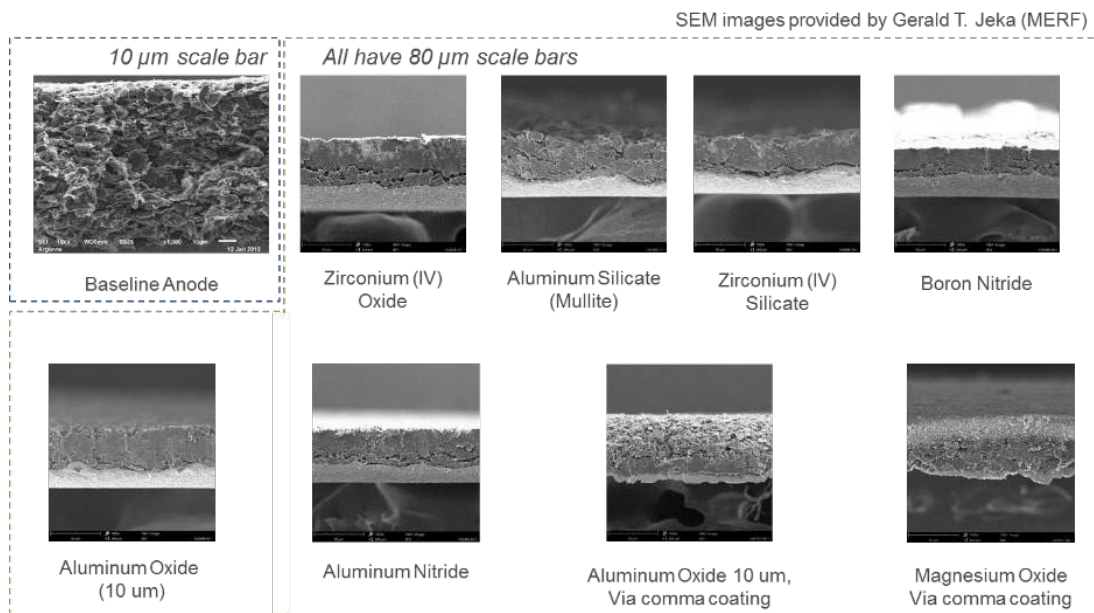


Figure I.7.E.10 Cross section SEM images of the various ceramic coatings generally indicate a more uniform thickness is achieved using the comma coater compared to a hand coating

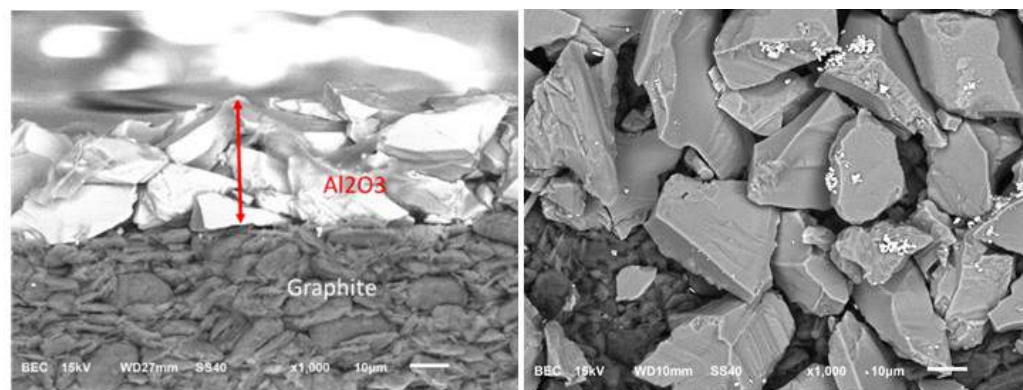


Figure I.7.E.11 SEM cross section image (left) and a surface SEM image (right) for the Al_2O_3 coating on the graphite anode. The image was provided by Nancy Dietz Rago (PTF)

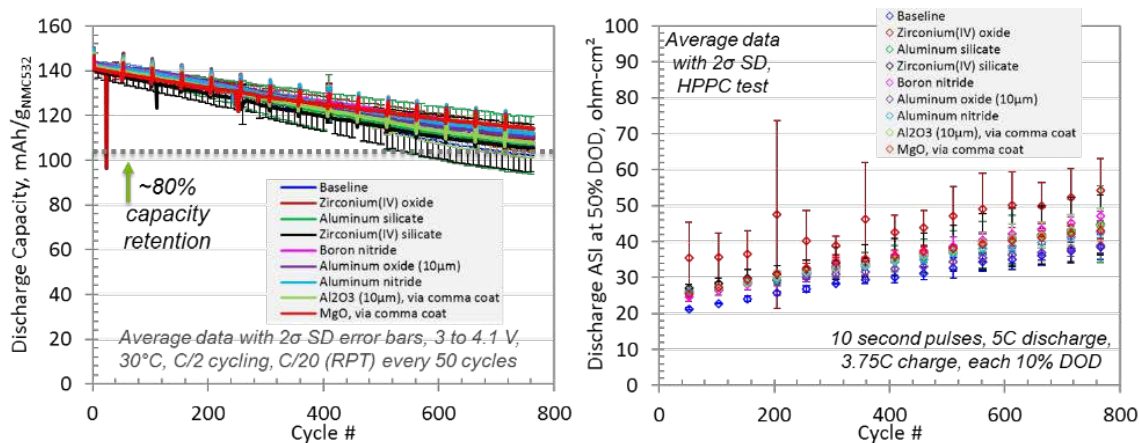


Figure I.7.E.12 Electrochemical performance of the baseline full-cell pouch-cell build using a typical polymer separator with no ceramic coating on the anode against 8 other data sets where the cells contain ceramic coatings on the anode

Figure I.7.E.12 shows the electrochemical performance of the baseline full-cell pouch-cell build using a typical polymer separator with no ceramic coating on the anode against 8 other data sets where the cells contain ceramic coatings on the anode. In this study, a polymer separator was included in all the pouch cells to study the chemical stability of the wide variety of ceramics examined. The left plot shows discharge capacity as it relates to cycle number. The baseline has a similar decay rate of capacity retention as it is cycled compared to the ceramic coated anodes. The right plot shows the cell resistance changes as the cells cycle. In this study, the baseline cell configuration showed a lower impedance and impedance rise than the ceramic coated anode data sets. The full cell cycle life testing indicates satisfactory ceramic chemical compatibility with the cell system. Further investigation is needed with testing the ceramic separators without a polymer separator present in the pouch cells to better understand the pros and cons of the system.

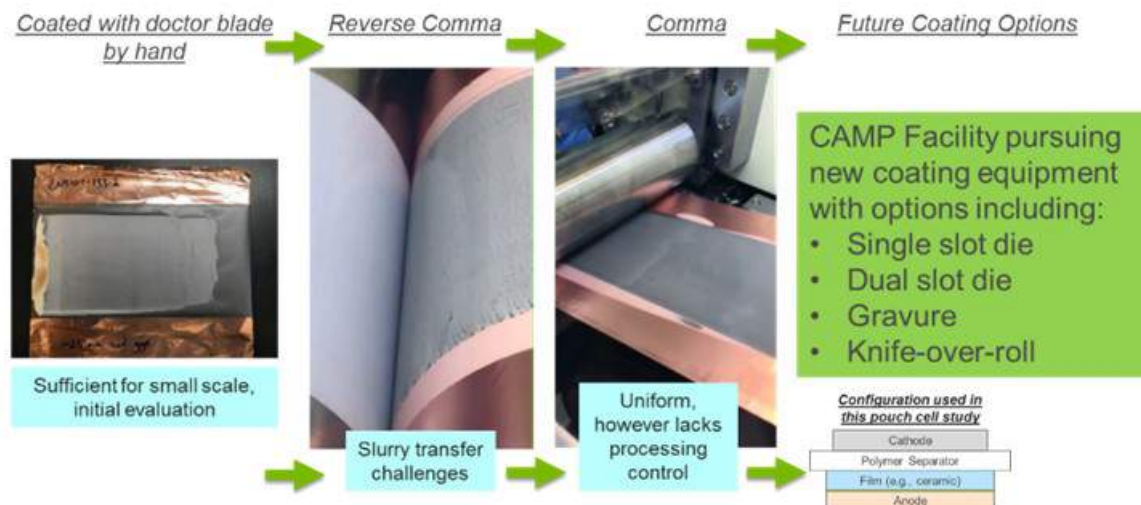


Figure I.7.E.13 Coating methods used in the CAMP Facility for coating ceramics onto graphite electrodes

Figure I.7.E.13 depicts the various coating methods the CAMP Facility has explored for coating ceramics onto graphite electrodes. While the comma coating method enables a uniform coating, other coating technologies provide application methods more conducive to enhancing the process. The CAMP Facility will be purchasing additional coating equipment in FY20 that will enable high quality coatings of solid films on porous anodes.

This work closely relates to continued efforts of incorporating LLZO ceramics into the battery system. The LLZO material exhibits slurry and electrode processing challenges. Initial slurries indicated gelation during mixing. This result could be due to the high pH that the doped LLZO materials exhibit, which would correlate with previous observations of high pH materials when mixed with PVDF in NMP. We are investigating the possibility of pH stabilization of the LLZO powders, as well as exploring other binder and solvent systems in order to achieve improved slurry and corresponding coating properties. In order to perform these studies, reasonably sized quantities are needed, thus the CAMP Facility purchased (250 grams for each powder) commercial doped LLZO materials: $\text{Li}_{6.25}\text{La}_3\text{Zr}_2\text{Al}_{0.25}\text{O}_{12}$; $\text{Li}_{6.25}\text{La}_3\text{Zr}_2\text{Ga}_{0.25}\text{O}_{12}$; $\text{Li}_{6.6}\text{La}_3\text{Zr}_{1.6}\text{Ta}_{0.4}\text{O}_{12}$. The new coating system will help advance this work.

Dehydration Explains Performance Improvements of Lithium-ion Cells by Oxide Nanoparticles

Increasing the energy density of Li-ion batteries is highly desired, as it would extend the driving range of electric vehicles. Although nickel-rich layered oxide cathodes such as $\text{LiNi}_{0.8}\text{Co}_{0.1}\text{Mn}_{0.1}\text{O}_2$ (known commercially as NCM811) can potentially supply more energy at high voltages, in their delithiated state they become thermodynamically unstable, undergoing oxygen loss from the surface that contributes to impedance rise. High voltage exposure also causes acidic dissolution of transition metal ions (in particular, Mn^{2+}) to the electrolyte; these ions migrate to the graphite (Gr) anode, where they deposit in the solid electrolyte interphase (SEI) and catalyze detrimental reactions leading to capacity fade. This process is further exacerbated by the

formation of hydrofluoric acid in the electrolyte bulk. This acid is formed by the hydrolysis of LiPF_6 , the commonly used electrolyte salt, as trace water present in the electrodes and electrolyte stepwise converts the hexafluorophosphate (PF_6^-) anion to HF molecules and oxofluorophosphate (e.g., PO_2F_2^-) anions. While it may be impossible to completely eliminate moisture (and thus HF) from the cell, mitigation strategies can be pursued to reduce acidic dissolution of metal ions. These approaches include creating physical barriers, such as protective coatings, that limit access to the oxide surface, and HF capture with electrolyte additives and dopants. Ceramic materials are well known in this regard.

Reports abound in the literature demonstrating benefits conferred by thin ceramic coating on the cathodes, anodes and separators. Incorporating these materials into electrode slurries or using them as electrolyte additives have also been shown to improve performance. Generally, it appears that having ceramic materials in the cell (regardless of their physical form) is beneficial, and the prevalent view is that such materials react with HF thereby preventing acidolysis of the cathode. However, not all observations fit into this scenario. For example, it was reported that mere exposure of the carbonate electrolyte to ceramic nanoparticles can improve the cycle life of LiCoO_2/Li half-cells *even after these particles are removed from the electrolyte*. These observations raise questions as to what aspect of chemical behavior plays the most important role in the anti-aging action of these ceramics. Here, we demonstrate that removing water (thereby suppressing HF generation) is more important than the postulated HF scavenging.

Aluminum oxide (Al_2O_3 , 80 nm) was obtained from Sigma-Aldrich; CeO_2 (50-105 nm), MgO (40-60 nm), SiO_2 (80 nm), TiO_2 (100 nm), ZnO (90-210 nm) and ZrO_2 (20 nm) were obtained from Nanostructured & Amorphous Materials, Inc. The particle sizes were provided by the manufacturer. The oxide powders were dried at 120 °C under vacuum for 48 h, and then stored under argon. Dried oxide nanoparticles (300 mg) were mixed with 10 mL of Gen2 electrolyte (1.2 M LiPF_6 in 3:7 wt/wt ethylene carbonate:ethylmethylcarbonate) in polypropylene vials for 7 days. The vials were vortexed for 1 min immediately after mixing, and also on day 2 and 4 afterwards. The solution settled by gravity for 72 hours, and the top layer of supernatant was removed and used as electrolyte.

In certain tests, Gen2 contained ~1,000 ppm of water. This electrolyte was prepared by combining 5 μL of water with 5 g of Gen2 in a stainless steel container. The mixture was vortexed for 2 min and used in the coin cells. Fluorine-19 and phosphorus-31 Nuclear Magnetic Resonance (NMR) was used to quantify LiPF_6 hydrolysis and HF yield after treating the electrolyte with ceramic nanoparticles. For these tests, 60 mg of oxide material was combined with 1.98 mL Gen2 containing 20 μL water to obtain ~8,300 ppm solutions. A control sample without ceramic particles was also prepared. The samples rested for 7 days before NMR analysis.

Electrochemical tests were carried out in 2032-type stainless steel cells, using a $\text{LiNi}_{0.8}\text{Co}_{0.1}\text{Mn}_{0.1}\text{O}_2$ (NCM811) cathode paired with a graphite anode (Gr). The positive electrode contained 90 wt% of the active oxide, 5 wt% of C45 carbon and 5 wt% PVdF binder. The anode comprised a mixture of 91.8 wt% graphite, 2 wt% C45 carbon, 6 wt% PVdF binder and 0.17 wt% oxalic acid. Celgard 2325 was used as the microporous separator. The electrolyte was either Gen2, Gen 2 aged in the presence of oxide particles (as described above) or Gen2 deliberately contaminated with water. The electrochemical cells were cycled between 3.0 V and 4.4 V. The formation cycling consisted of four constant-current, constant-voltage cycles at a C/10 rate, with the voltage held at 4.4 V for 3 h or until the current decreased to < C/20 rate. Cells were then exposed to five series of aging cycles. Each series began with diagnostic tests. These tests consisted of (i) a slow cycle at a C/10 rate (to estimate capacity loss), (ii) a fast cycle that included charge at a C/3 rate followed by discharge at an 1C rate (to characterize cell polarization), and (iii) a hybrid pulse power characterization step (HPPC) with incremental discharge, also at a C/3 rate. These diagnostic tests were followed by 20 cycles at a C/3 rate (with

a potentiostatic hold for 3 h at 4.4 V after charging in order to increase high voltage exposure). At the end of this test, each cell was subjected to 100 cycles at a C/3 rate and 300 h of combined exposure to 4.4 V.

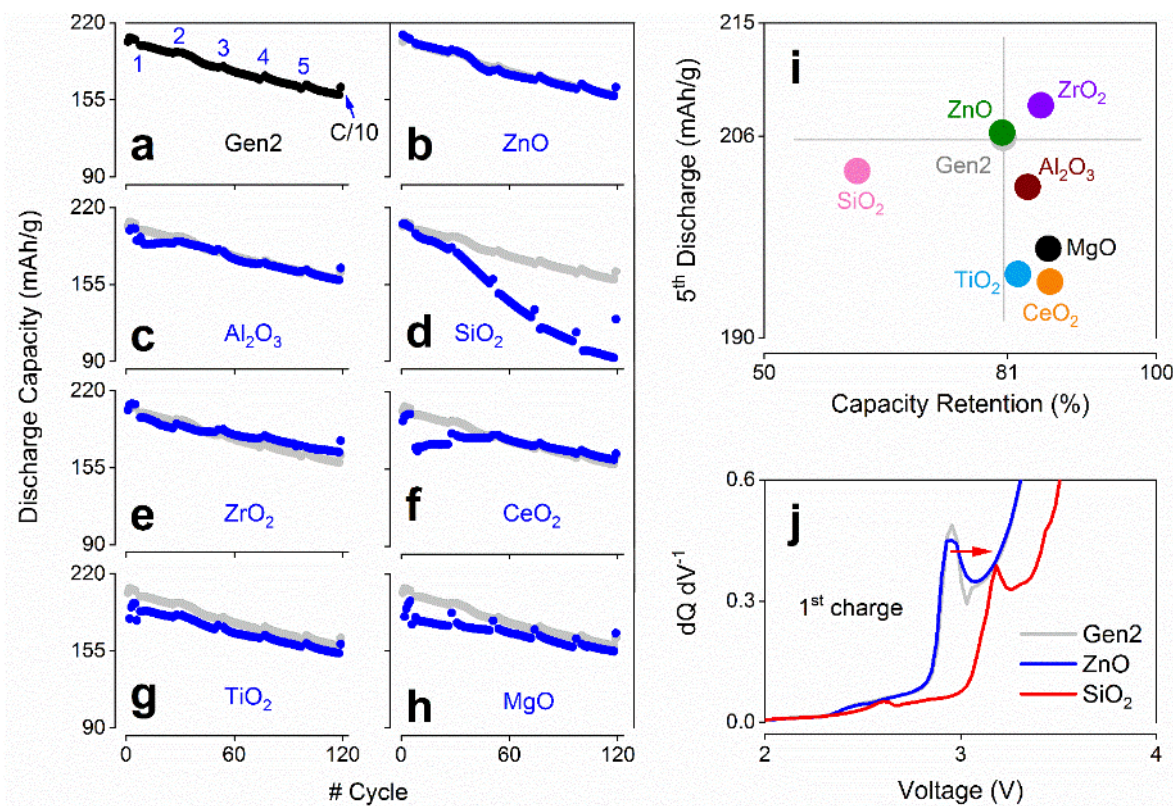


Figure I.7.E.14 Influence of oxide nanoparticles on the electrochemical cycling of NCM811//Gr cells

Electrochemical performance of the cells is briefly summarized in Figure I.7.E.14. For the baseline electrolyte (Figure I.7.E.14a), the initial specific discharge capacity was 204 mAh/g (the mass pertains to the active material in the cathode). The capacity gradually decreased over time, resulting in a final capacity of 166 mAh/g. This capacity fade (~19%) includes both the Li⁺ inventory loss (as the ions become trapped in the SEI) and slowdown of Li⁺ intercalation due to impedance rise. Turning to cells containing electrolytes pre-exposed to the nanoparticles, for some materials (e.g., ZnO and Al₂O₃ in Figure I.7.E.14b and Figure I.7.E.14c, respectively), the capacity fade is not significantly affected by the pre-exposure, while for others (e.g., SiO₂, Figure I.7.E.14d) there is significant capacity loss. When ZrO₂ and CeO₂ are used (Figure I.7.E.14e-f), the final capacity is slightly *higher* than for the baseline electrolyte, while for MgO and TiO₂ (Figure I.7.E.14g-h) it is slightly lower (though with a higher capacity *retention*). These trends are graphically summarized in Figure I.7.E.14i, in which the initial discharge capacities and capacity retention are plotted together. Systems to the right of the vertical line in this chart (ZrO₂, Al₂O₃, MgO, TiO₂ and CeO₂) have better capacity retention than the baseline electrolyte. Only SiO₂ lies to the left of the vertical line, presumably because the SEI formation chemistry is affected. Figure I.7.E.14j shows differential capacity (dQ/dV) plots during the first charge for cells containing electrolyte exposed to SiO₂ or ZnO (the latter is representative of most other systems). For SiO₂, the peak associated with electrolyte reduction deviates from ~3 V indicating interference during SEI formation, whereas for ZnO the peak is similar to that for the baseline electrolyte.

Impedance data acquired at various stages of aging (indicated by the blue numbers in Figure I.7.E.14a) are summarized in Figure I.7.E.15. The pulsed current technique gives the cell area specific impedance (ASI) at different depths of discharge. The ASI of the baseline cells increases continuously as the cell ages (Figure I.7.E.15a). After 100 cycles, the ASI at ~ 3.7 V increases by a factor of six. Previous studies using reference microelectrodes showed that this increase is predominantly from the cathode; negligible changes are observed in the graphite ASI. For the ceramic-modified electrolytes, the initial impedance was comparable to that observed in the baseline cells. For ZnO and TiO₂ (Figure I.7.E.15b-c), no change was observed in the rate of impedance rise, while for Al₂O₃ (Figure I.7.E.15d), the impedance rise accelerated. More interestingly, for ZrO₂, CeO₂, SiO₂ and MgO (Figure I.7.E.15e-h), the impedance rise slowed down. This beneficial effect is particularly notable for MgO and SiO₂ (see Figure I.7.E.16a which plots the initial ASI vs. ASI increase). The capacity retention and impedance rise for different oxides are graphically summarized in Figure I.7.E.16b. It is seen that most of the nanomaterials have relatively little effect on electrochemical performance with two outliers: SiO₂ and MgO. Both of these materials halve the rate of impedance rise, and MgO also improves capacity retention.

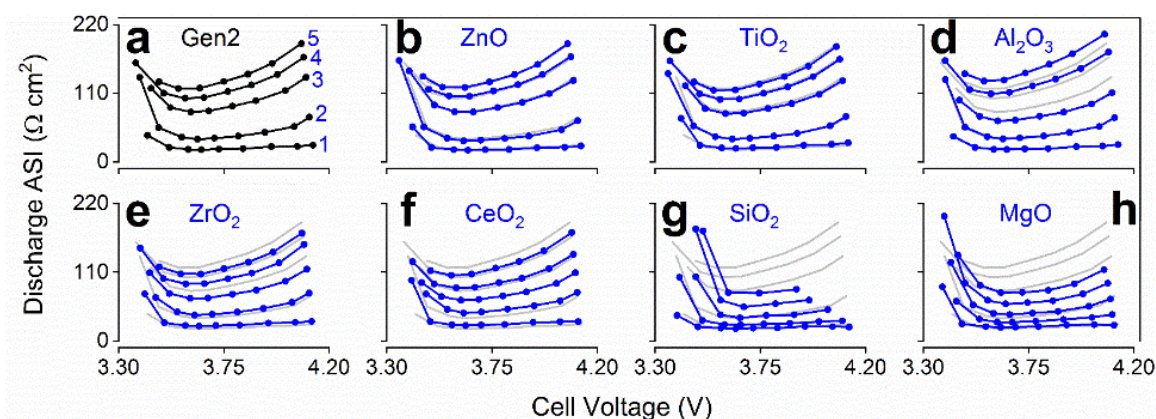


Figure I.7.E.15 Influence of oxide nanoparticles on the Area specific impedance (ASI) of NCM811//Gr cells. ASI for Gen2 electrolyte (panel a) is reproduced in gray in panels b-h for comparison. Impedance was measured at the cycles indicated in Figure I.7.E.14

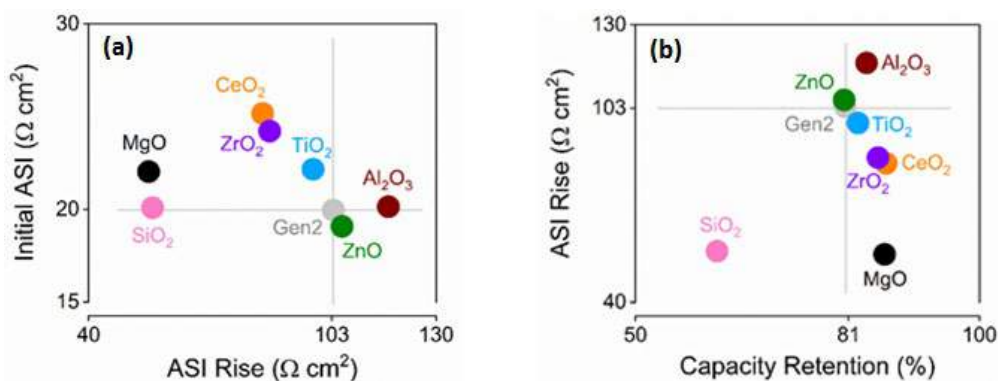


Figure I.7.E.16 Correlation of (a) initial ASI at 3.7 V (y-axis) and ASI rise (x-axis) and (b) ASI rise (y-axis) and capacity retention (x-axis) for NCM811//Gr cells containing various electrolytes

The trends for the various oxides, and the unique behavior of MgO and SiO₂, can be explained by their ability to interfere with the hydrolytic cycle of LiPF₆ in the cell as shown in Figure I.7.E.17. We observe that all oxide ceramics chemisorb and dissociate water by hydroxylation of their surfaces, forming thin hydrogel coatings. Additional water molecules then physisorb onto these hydroxylated surfaces, increasing the net moisture uptake. For a generic oxide particle (panel a), the hydrolytic cycle converting between HF and water in the electrolyte is not disrupted, and can even be facilitated by the ceramic nanoparticles. At low-to-moderate fluoride concentration, these modified surfaces undergo anion exchange, capturing and immobilizing the fluoride anion. SiO₂ is the exception to this general rule, as the fluorinated compounds solubilize, exposing fresh surface that can react with more fluoride. For MgO particles, the water is locked in a stable hydrogel on the particle surface, so LiPF₆ hydrolysis is largely suppressed and the hydrolytic cycle is disrupted (panel b).

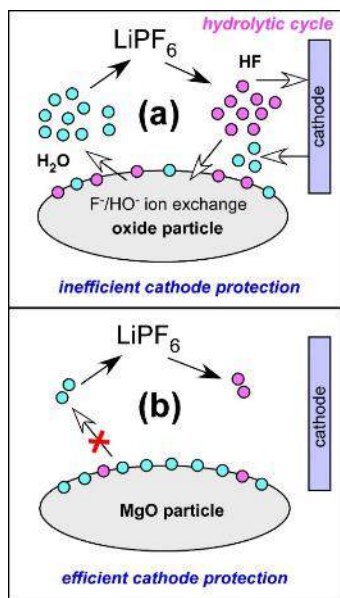


Figure I.7.E.17 Representation of the effect of oxide particles on cell performance

To estimate how the oxides interfere with the hydrolytic cycle responsible for the release of HF acid, we intentionally added ~8,300 ppm of water to freshly prepared nanoparticle-containing electrolytes. After 7 days of resting, the electrolyte samples were examined using fluorine-19 and phosphorus-31 nuclear magnetic resonance (NMR). In the presence of water, PF₆⁻ converts to HF, PO₂F₂⁻ and PO₃F₂⁻, which display resonance lines in the NMR spectra. The results of our analyses are summarized in Table I.7.E.4. Note that the baseline electrolyte contained no HF or hydrolysis products before water addition.

Advanced stages of hydrolysis are observed in most samples, the oxide particles generally catalyzing PF₆⁻ hydrolysis rather than impeding it. The behavior of silica is particularly illuminating in this respect: though less HF was detected (as can be expected given the high reactivity of SiO₂ towards HF), the high yield of oxofluorophosphate anions indicated advanced stage of hydrolysis. These analytical results suggest that the oxides benefit the cell primarily by removing water from the hydrolytic cycle. This propensity readily explains what distinguishes MgO from other oxides, as it is a well-known drying agent, readily dissociating water on its surface. For magnesia, only traces of HF and other hydrolytic products are observed, suggesting that it completely disrupts the hydrolytic cycle. When MgO was added to aged Gen2 doped with water (compare the first and last rows in Table I.7.E.1), the HF concentration before and after the addition of MgO was nearly the same, suggesting low fluoride uptake by MgO. This simple experiment demonstrates that MgO acts by removing water rather than HF from the hydrolytic cycle. We conclude that active removal of water during aging of the cell significantly improves long-term performance of cells cycled at high-voltage.

Table I.7.E.4 Oxofluorophosphate and HF Yields after 1 Week of Aging in Electrolyte with 8,300 ppm Water

Electrolyte/ceramic	% LiPF ₆ hydrolyzed ^a	% HF yield
baseline	4.0	9.7
SiO ₂	10.4	4.1
ZnO	9.9	9.0
ZrO ₂	7.4	13.5
TiO ₂	7.1	11.9
Al ₂ O ₃	6.5	9.4
CeO ₂	4.8	9.0
MgO	0.1	0.0
MgO – added after 1 week	4.6	7.3

To assess how water affects the cell operated at 4.4 V, we deliberately introduced ~1,000 ppm H₂O to our baseline electrolyte. In one series of experiments, the cells were assembled and tested immediately after water addition. In another series, the electrolyte was aged for 7 days before cell assembly to facilitate LiPF₆ hydrolysis. The results of these two series of tests are shown in Figure I.7.E.18. While the baseline cells cycle reproducibly (Figure I.7.E.18a,d), the “wet” cells display non-reproducible and erratic behavior, demonstrating sudden capacity loss and impedance rise (Figure I.7.E.18b,e and Figure I.7.E.18c,f). Such erratic behaviors have been linked to transition metal ions loss from the cathode surface, which then migrate to the anode and catalyze parasitic reactions in the SEI. In fact, even the best-performing “wet” cells (Figure I.7.E.18b,c) exhibit more capacity fade than the baseline cells, and the initial capacities are consistently lower for the *aged* hydrated electrolyte (see dashed lines along Figure I.7.E.18a-c). While the typical Li-ion cells contain much less water than these “wet” cells, our experiment proves that water can have highly detrimental effect on the long-term electrochemical performance at higher cycling voltages.

In regular Li-ion cells, the residual moisture is introduced mainly from the *electrode* matrices. The typical water content of a dry *electrolyte* is <20 ppm, while fully dried *electrodes* can still contain >100 ppm of water. The typical moisture levels listed above amounts to ~3 µg of water in our coin cells. Considering the sorption capacity of MgO suggested by Table I.7.E.4, only ~10 µg of MgO nanoparticles would be sufficient to completely dehydrate the coin cell. Given this miniscule amount, the behaviors shown in Figure I.7.E.14 and Figure I.7.E.15 could be caused by dispersed nanoparticles carried with electrolyte into the cell: even at a low concentration, MgO nanoparticles can dehydrate the cell and stall the hydrolysis of LiPF₆.

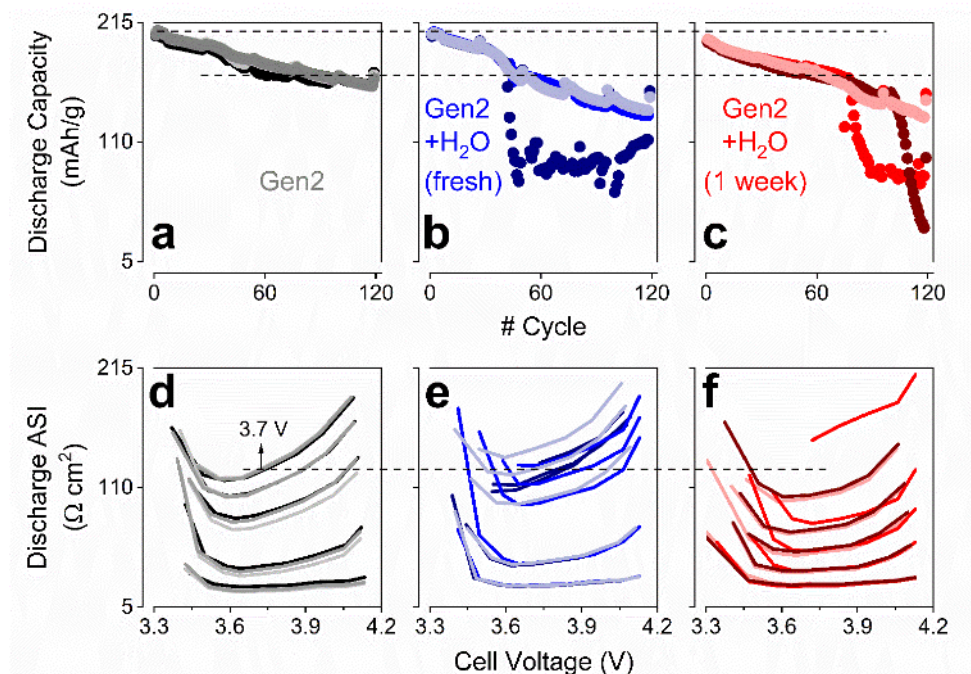


Figure I.7.E.18 The effect of added water on electrochemical performance of NCM811//Gr cells. Cycle life (panels a, b, and c) and impedance rise (panels d, e, and f) for multiple cells containing baseline electrolyte with (panels b, c, e, and f) or without (panels a and d) 1,000 ppm water. Different color hues represent different cells. The dashed horizontal lines are visual guides to compare different systems

Our experiments suggest that the beneficial effects of ceramic nanoparticles on electrochemical performance originate mainly from their ability to chemisorb water, disrupting the hydrolytic cycle that converts LiPF_6 to HF acid. Among the oxides examined, MgO is the most effective anti-aging agent precisely because it is the most efficient drying agent. The research literature indicates that the presence of water in the electrolyte has relatively little effect on electrochemical performance at low cell voltages (< 4.2 V). Here we demonstrate that this is not the case for 4.4 V operation; this is why removal of water is so important in this regime. While the oxide nanoparticles are believed to act primarily as HF scavengers, our results suggest that by the moment HF is generated, the battle is largely over, as this HF will be converted to water on their surfaces that re-enters the hydrolytic cycle generating still more HF. The most efficient way to protect the cathode is rather via the removal of water hydrolyzing LiPF_6 . Using the dehydrating MgO particles can be a simple and cost-effective approach to building longer-lasting Li-ion batteries.

Summary of Electrode Library Activities

Table I.7.E.5 shows the distribution of electrodes from the Electrode Library, which is maintained by the CAMP Facility. From October 1, 2018 to April 15, 2019, 498 sheets of electrode were fabricated and distributed by the CAMP Facility, which is ~12 square meters of electrodes. Many of these electrodes were supplied by the CAMP Facility in support of DOE-EERE's many activities in advanced battery R&D.

Table I.7.E.5 Summary of Electrode Library Distributions

Electrodes Delivered	FY16		FY17		FY18		FY19 (as of April 2019)	
Argonne	174	8 %	142	9 %	140	14 %	62	12 %
Other National Labs	726	36 %	172	11 %	172	18 %	47	9 %
Universities	117	6 %	151	10 %	175	18 %	152	31 %
Industry	1004	50 %	1083	70 %	495	50 %	237	48 %
Total:	2021		1548		982		498	

Conclusions

The CAMP Facility has had a productive year in the R&D of advanced lithium-ion electrochemical energy storage systems. We were also critical to the support of other numerous DOE-EERE programs, much of which was performed through the CAMP Facility's Electrode Library. A summary of some of the key successes in FY19 are as follows:

- Demonstrated the electrochemical performance of NMC811 cathodes made in MERF with varying gradient profiles in the particle.
- Assessed the thermal abuse response of the MERF-made NMC811 cathodes using DSC.
- Proved ceramic-coated anodes worked well under variety of testing conditions.
- Demonstrated that full cells can operate without polymer-based separators.
- Proved that the most efficient way to protect the cathode is via the removal of water from the cell system with MgO particles being a viable method.
- Provided numerous experimental electrodes and cells to DOE-EERE programs.

Key Publications

1. M.-T.F. Rodrigues, C. Liao, K. Kalaga, I.A Shkrob, D.P Abraham, "Dehydration Rather Than HF Capture Explains Performance Improvements of Li-Ion Cells by Ceramic Nanoparticles", *ACS Appl. Energy Mater.* **2**, 5380-5385 (2019).
2. CAMP Facility contributions to other papers are acknowledged in numerous other sections of this report and peer-reviewed scientific manuscripts.

Acknowledgements

Key contributors to this work include: Daniel Abraham, Shabbir Ahmed, Ira Bloom, Dennis Dees, Nancy Dietz-Rago, Fulya Dogan, Alison Dunlop, Trevor Dzwiniel, Andrew Jansen, Gerald Jeka, Chris Johnson, Ozge Kahvecioglu Feridun, Dohyeun (Dave) Kim, Joel Kirner, Gregory Krumdick, Wenquan Lu, Paul Nelson, Bryant Polzin, Kris Pupek, Yan Qin, Marco Tulio Fonseca Rodrigues, YoungHo Shin, Ilya Shkrob, Seoung-Bum Son, and Steve Trask.

I.7.F Materials Benchmarking Activities for CAMP Facility (ANL)

Wenquan Lu, Principal Investigator

Argonne National Laboratory
9700 S Cass Avenue
Lemont, IL 60439
E-mail: luw@anl.gov

Peter Faguy, DOE Technology Development Manager

U.S. Department of Energy
E-mail: Peter.Faguy@ee.doe.gov

Start Date: October 1, 2018
Project Funding (FY19): \$550,000

End Date: September 30, 2019
DOE share: \$550,000

Non-DOE share: \$0

Project Introduction

High energy density electrode materials are required in order to achieve the requirements for electric vehicle (EV) application within the weight and volume constraints established by DOE and the USABC. One would need a combination of anode and cathode materials that provide 420 mAh/g and 220 mAh/g, respectively, as predicted by Argonne's battery design model (BatPaC), if one uses a 20% margin for energy fade over the life of the battery assuming an average cell voltage of 3.6 volts. Therefore, the search for new high energy density materials for lithium ion batteries (LIB) is the focus of this material benchmarking project. In addition to electrode materials, other cell components, such as separators, binders, current collectors, etc., are evaluated to establish their impact on electrochemical performance, thermal abuse, and cost.

This benchmarking effort is conducted as part of the Cell Analysis, Modeling, and Prototyping (CAMP) Facility (please refer to the previous section) to identify and support promising new materials and components across the "valley of death", which happens when pushing a new discovery towards a commercial product. The CAMP Facility is appropriately sized to enable the design, fabrication, and characterization of high-quality prototype cells, which can enable a realistic and consistent evaluation of candidate chemistries in a time-effective manner. However, the CAMP Facility is more than an arrangement of equipment, it is an integrated team effort designed to support the production of prototypes electrodes and cells. In order to utilize the facility more efficiently and economically, cell chemistries are validated internally using coin type cells to determine if they warrant further consideration. In addition, fundamental understanding of cell materials will be improved during the bench marking, which will advance the technology development.

Objectives

- The primary objective is to identify and evaluate low-cost materials and cell chemistries that can simultaneously meet the life, performance, and abuse tolerance goals for batteries used in EV applications.
- The secondary objective is to enhance the understanding of the impact of advanced cell components and their processing on the electrochemical performance and safety of lithium-ion batteries.
- This project also provides the support to the CAMP Facility for prototyping cell and electrode library development, and the MERF facility for material scale up.

Approach

Under materials benchmarking activities, we constantly reach out to, or are approached by, material developers to seek opportunities to test their advanced or newly released products. By leveraging Argonne's expertise in electrode design and cell testing, we can provide not only a subjective third opinion to material suppliers, but also deeper understanding on their materials, which can aid their material development. This deep

understanding becomes even more important when the material developers are small companies or new players, who often overlook overall requirements of battery materials.

In addition to industrial partners, we also work closely with scientists from various research institutes, such as universities and research laboratories. They often come up with novel materials with advanced electrochemical performance, but small quantities, which is only enough for validation purpose. These test results help us to determine how much effort should be expanded to explore the material potential.

In general, we will validate any potential cell material, which has impact on the cell performance, mainly in terms of electrochemical performance, electrode optimization, and thermal stability. The electrochemical performance is the centerpiece of the materials benchmarking activities, which will be tested using 2032-sized coin-type cells under test protocols derived from USABC PHEV 40 requirements [Battery Test Manual For Plug-In Hybrid Electric Vehicles, Idaho National Laboratory]. The freshly made coin cells will undergo three formation cycles at a C/10 rate. The cells are then tested for the rate performance. For the rate test, the charging rate is set at C/5, while the discharge rate varies from C/5, C/3, C/2, 1C to 2C. Three cycles are performed for each discharge rate. After the rate test, the cells then undergo cycling test at C/3 rate. During the cycling test, we change the current rate to C/10 every 10th cycle to check the rate effect. Also, Hybrid Pulse Power Characterization (HPPC) is conducted every 10th cycle, which will be used to calculate the Area Specific Impedance (ASI).

This fiscal year, we have investigated various battery materials, such as cathode, anode, and conductive additives. In this report, selective work, including SiO anode, nickel-rich cathode material, prelithiation of graphite and SiO electrodes, will be presented.

Results

Calendar and Cycle Life of SiO Anode

Silicon monoxide (SiO) has been investigated as the next-generation anode material for lithium-ion batteries due to its high energy density. Compared to commercially used graphite, SiO has a theoretical gravimetric capacity of 1,710 mAh/g and volumetric capacity of 1,547 Ah/L and can offer an 18% increase in volumetric energy density on the cell stack level, making it a promising anode material for the next generation high energy density lithium-ion batteries.

In order to replace graphite with SiO as anode, its life time, as one of most important characteristics of LIBs, should be investigated. Life time of LIBs includes both cycle life and calendar life. The cycle life of LIBs is to measure the capacity (energy) retention during continuously charge and discharge cycles. The calendar life of LIBs is to measure the capacity (energy) retention when the LIBs are at rest at certain state of charges (SOC).

The electrode couples used in this work are SiO anode and NCM523-LFO cathode with composition of NCM523-LFO:C45:PVDF=90:5:5. The ratio of NCM523 to LFO is 10:1. [1]. Silicon monoxide (SiO) electrode composition is SiO: LiPAA:C45=7:2:1 in weight ratio. The Li_5FeO_4 (LFO) is used in the cathode as the prelithiation reagent to compensate the large irreversible capacity loss of SiO in the first cycle as reported previously [1]-[2]. The fabricated full cells were electrochemically tested between 2.5 V and 4.3 V using Maccor 4300 Series Test Unit at 30°C. First of all, the full cells underwent 3 formation cycles at C/10 rate. Then, multiple cycling-tests were applied to the full cells (Figure I.7.F.1a). The cycling-tests were numbered 1, 2, 3 and 4. There were totally 50 cycles for each cycling-test, except cycling 4, which was cut short. The rest time between cycling-test 1 and 2, cycling-test 2 and 3, and cycling-test 3 and 4 are 22, 0, and 11 days, respectively.

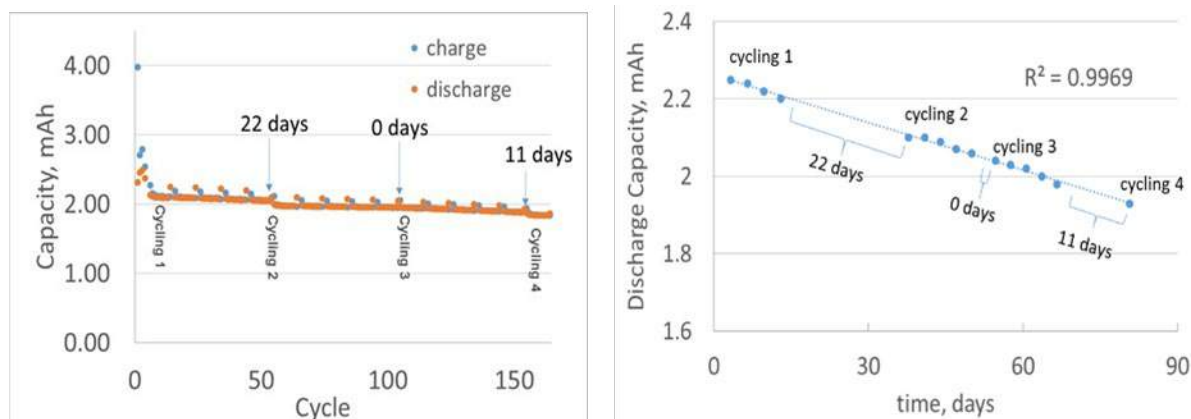


Figure I.7.F.1 a) Cycle performance of SiO/NCM523-LFO full cells, b) discharge capacity with C/10 rate as a function of time

In order to elucidate the relationship between the calendar life and cycle life of SiO/NCM523-LFO full cells, we plotted the discharge capacity of the cycles performed at C/10 rate (every 10th cycle during the cycling-tests) as a function of time, which combined both the cycling time and the rest time. A very linear relationship between the discharge capacity and the test time was obtained as shown in Table I.7.F.1b. The capacity fading rate is determined to be 0.2% per day, whether the cell was under cycling-test or not. The interesting results suggested that the capacity fading of our SiO/NCM523-LFO full cell is not cycle-number-dependent, but time-dependent. This result also suggests that the volume change of SiO electrode during cycling has minimal impact on the capacity fade of the full cell. It is rational to speculate that the SOC (if it has any impact on capacity fading) is secondary factor during the rest since the calendar life behavior of LIBs with SiO anode was obtained at fully discharged state, which is presumed to be the least reactive state.

Low-cobalt transition metal oxide cathode

Low cobalt and nickel-rich $\text{LiNi}_x\text{Mn}_y\text{Co}_z\text{O}_2$ (NMC) is gaining momentum as high energy cathode materials for EV applications. NMC532, with 50 at.% in transition metal Ni, has become a dominate NMC cathode material for EV application due to its balance of good electrochemical performance, low cost, and reasonable thermal safety. However, 20 at.% cobalt in NMC can be further reduced to increase the energy density and lower the cost of LIB to meet the target set by DOE. While NMC622 is penetrating the market, even higher nickel content cathode materials are under development. We received two cathode materials, NMC and NCA from BTR with nickel content as high as 90 at.%. Their electrochemical performance and thermal property were characterized.

The electrodes were fabricated in our lab using a hand coater and the electrode composition and physical properties are shown in Table I.7.F.1. The half cells vs. lithium metal were fabricated and tested at 30°C with voltage window between 3.0 V and 4.3 V. Both cathode materials can deliver about the same amount of reversible specific capacity, above 210 mAh/g (Figure I.7.F.2a, left), at 3rd formation cycles. The 1st cycle coulombic efficiency of NCA is about 89%, which is a little less than that of NMC (93%).

Table I.7.F.1 Electrode Composition and Physical Properties

	NMC	NCA
Active, wt.%	90%	90%
C45, wt.%	5%	5%
PVDF, wt.%	5%	5%
Electrolyte	1.2M LiPF ₆ in EC/EMC (3/7)	
Coating, mg/cm ²	7	7

In order to evaluate the cycle performance of high-nickel content cathode materials, full cells were fabricated vs. graphite (A12 from Conoco Phillips). The graphite electrode made by the CAMP Facility (Argonne) consists of 92% graphite, 2% C45, and 6% PVDF. The cells were cycled between 3.0 V and 4.2 V and their cycle performance is shown in Figure I.7.F.2b (right). It can be seen from the figure that full cells with NCA cathode show slight better capacity retention, up to 95% in 50 cycles, compared to 94% capacity retention of the full cells with NMC. We also calculated the area specific impedance (ASI) using hybrid pulse power characterization profile (HPPC with 10 second pulse at 2C rate every 10% state of charge – SOC). The ASI indicates that the full cells with NCA have less impedance value and show slower impedance rise with cycling test.

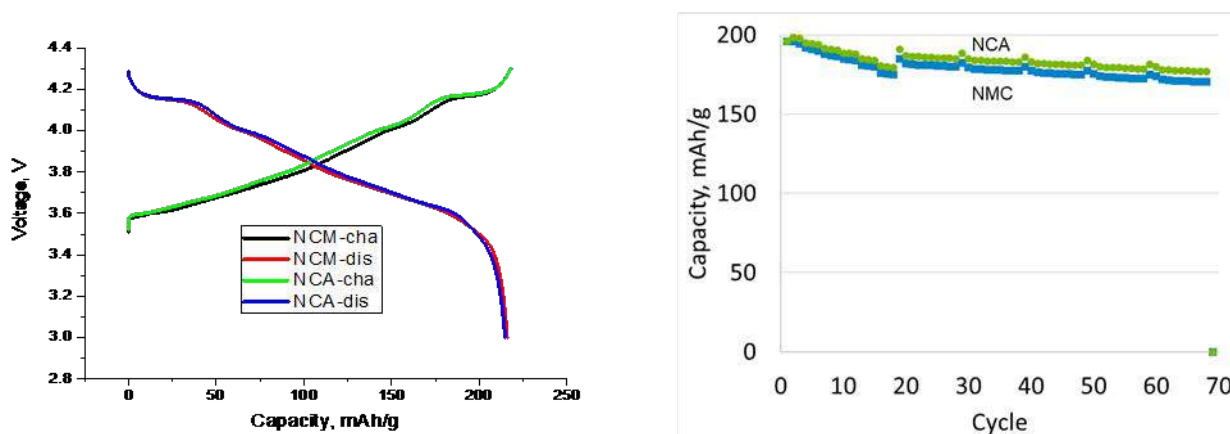


Figure I.7.F.2 a) 3rd cycle voltage profile of NMC and NCA half cells, b) cycle performance of NMC and NCA full cells

Thermal property of these two high-nickel cathode materials were investigated using differential scanning calorimetry (DSC). The half cells were cycled at C/10 rate between 3.0 V and 4.2 V at 30°C. After two formation cycles, the cathode materials were delithiated to remove 0.75 Li in Li_xMO_2 (M: Ni, Co, Mn). The charged electrode were recovered in a glove box and had laminate powder scraped from the aluminum current collector for DSC measurement. Typically, about 2 mg laminate powder was mixed with 2 μL electrolyte (1.2 M LiPF_6 in EC/EMC). The samples were heated from room temperature to 400°C with 10°C/min scan rate. The DSC results are shown in Figure I.7.F.3. Three repeats were conducted for each sample with good reproducibility. First of all, all materials show a similar decomposition onset temperature of ~200°C.

Furthermore, the first thermal peak of NCA and NMC appears at the same temperature, but was more profound for NCA. The second thermal peak of NCA appears later and smaller than that of NMC. However, the total heat generation of NMC seems less than that of NCA. Therefore, these two cathode materials definitely show different thermal behavior. However, it is hard to tell which material has better thermal stability. Further abuse testing will be required to make a complete conclusion.

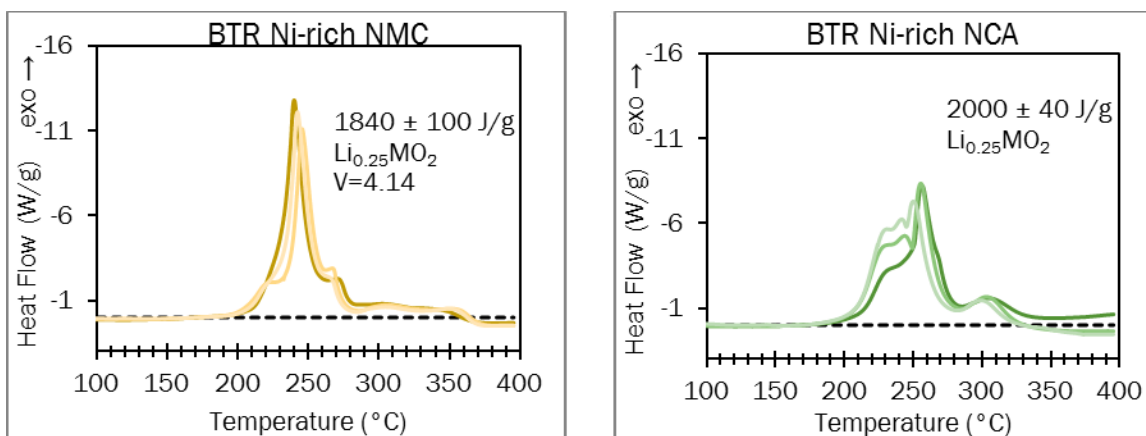


Figure I.7.F.3 DSC of NMC (left) and NCA (right) for delithiated material

Pre-lithiation of graphite and SiO

The poor 1st cycle coulombic efficiency of silicon and its derived electrodes is one of the challenges to commercialize the advanced anode materials in LIB. To address this problem, prelithiation reagents, such as lithium powder, lithium iron oxide, etc have been tried as additions to either the anode or the cathode, which were reported in our previous work [4],[5]. A prelithiation reagent provides extra lithium during the first formation cycle, therefore compensating the lithium loss caused by irreversible reactions. However, these strategies will either create safety issues or have impact on the electrode integrity in practical applications. In this work, we attempted to prelithiate the electrode or powder using an electrochemical approach.

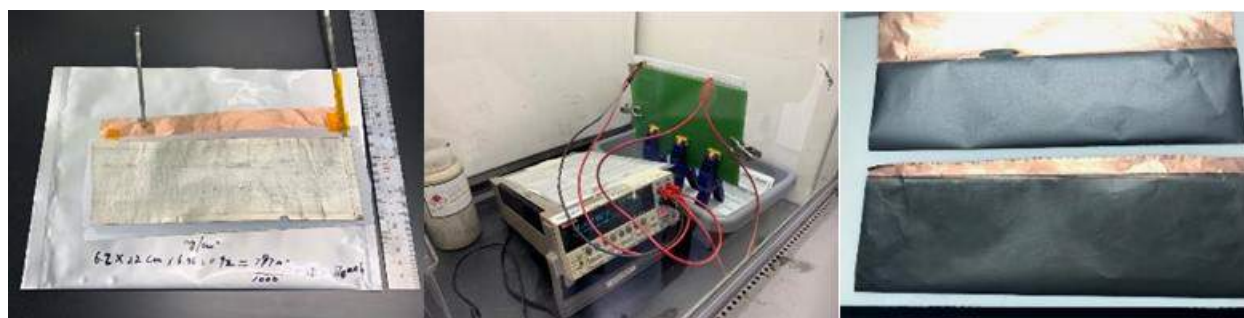


Figure I.7.F.4 a) pouch cell assembly, b) prelithiation setup, c) electrode before and after prelithiation

We started this prelithiation effort with the graphite electrode, which consists of 92% Hitachi MagE3 graphite, 2% C45, and 6% PVDF, made by the CAMP Facility. The large size graphite electrode sheet (6 x 21 cm) was put against lithium metal foil and separated by a separator. This assembly was put into a pouch and wetted with 1.2 M LiPF₆ in EC/EMC electrolyte, as shown in Figure I.7.F.4a (left). The cell assembly was then electrochemically lithiated using a Keithly source meter to 5% and 10% prelithiation, respectively (Figure I.7.F.4b, middle). The prelithiated electrode was then removed from the pouch and rinsed using EMC solvent. No difference was observed when comparing the pristine to the prelithiated electrodes (Figure I.7.F.4c, right, top: pristine, bottom: prelithiated electrode).

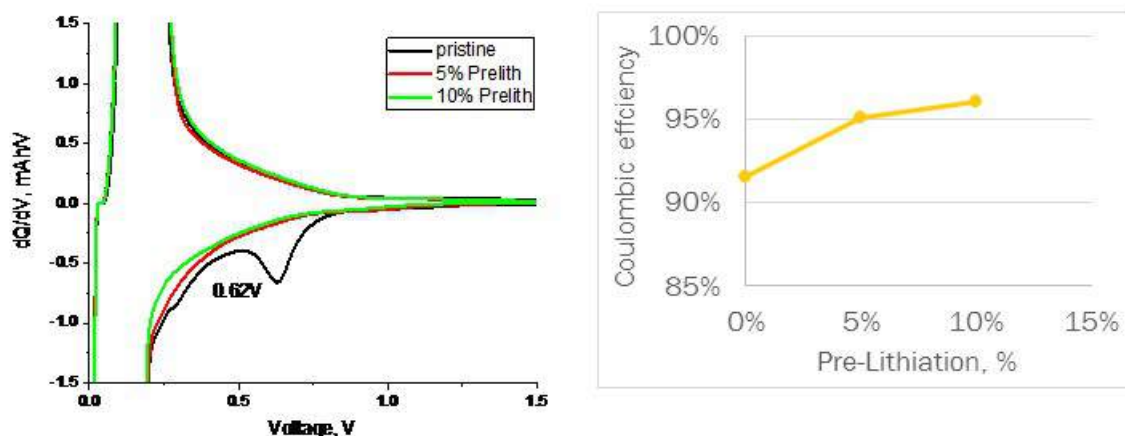


Figure I.7.F.5 a) 1st cycle differential capacity and b) Coulombic efficiency plots of pristine and prelithiated graphite electrodes

The prelithiated electrode was then fabricated into half cells and the differential capacity of the very first formation cycle is plotted in Figure I.7.F.5a (left). The pristine electrode has a downward peak around 0.62V during lithiation, which is due to the solid electrode interface (SEI) formation. This SEI formation peak is not present for the 5% and 10% prelithiated electrode. The 1st cycle Coulombic efficiency increases with increasing amount of prelithiation, as shown in Figure I.7.F.5b (right). In order to investigate the cycle performance of prelithiated electrodes, full cells were made using NMC532 electrode. Again, the SEI formation related peak was not present during the 1st formation cycle in full cells with prelithiation as shown in Figure I.7.F.6a (left). Full cell cycle performance is shown in Figure I.7.F.6b. Similar capacity retention is observed for 5% prelithiated electrode compared to pristine electrode. The full cell using 10% prelithiated electrode shows even better capacity retention.

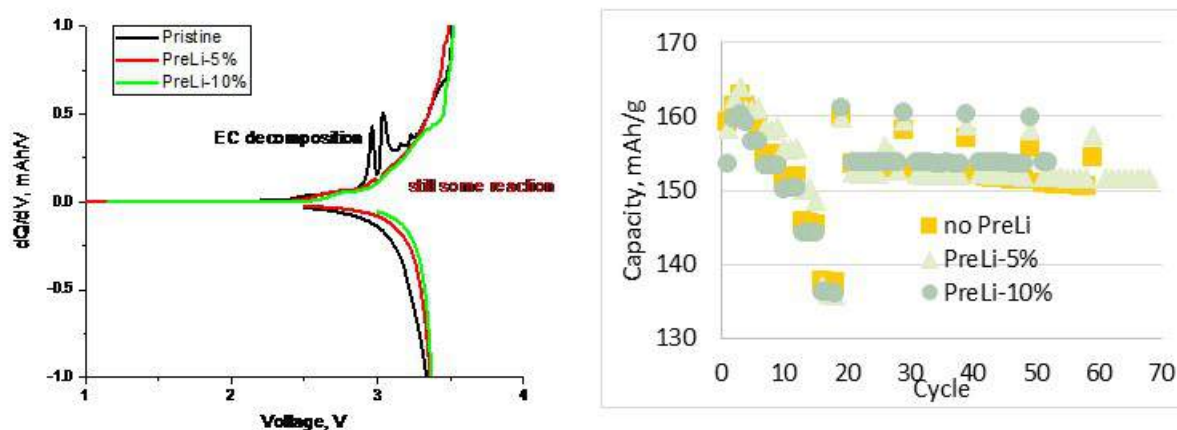


Figure I.7.F.6 (a) Differential capacity plot and (b) cycle performance of full cells with prelithiated graphite electrode

Similar prelithiation was conducted with a SiO electrode. Due to the large 1st cycle irreversible capacity loss, the SiO electrode was prelithiated with 30% of its capacity. The differential capacity plot of the SiO electrodes in half cells is shown in Figure I.7.F.7 (left). Much less integrated area can be seen for the prelithiated SiO compared to the pristine one, which suggests a better Coulombic efficiency for the prelithiated SiO electrode. As a matter of fact, close to 100% Coulombic efficiency was achieved at the 1st cycle for the prelithiated SiO electrode. Full cells vs. NMC532 were fabricated and cycled between 2.5 V and 4.2 V. As shown in Figure

I.7.F.7 (right), the utilized specific capacity of NMC532 increased from 100 mAh/g to 160 mAh/g for the full cells with prelithiated SiO electrode. Furthermore, both full cells show almost identical capacity retention during the cycling test.

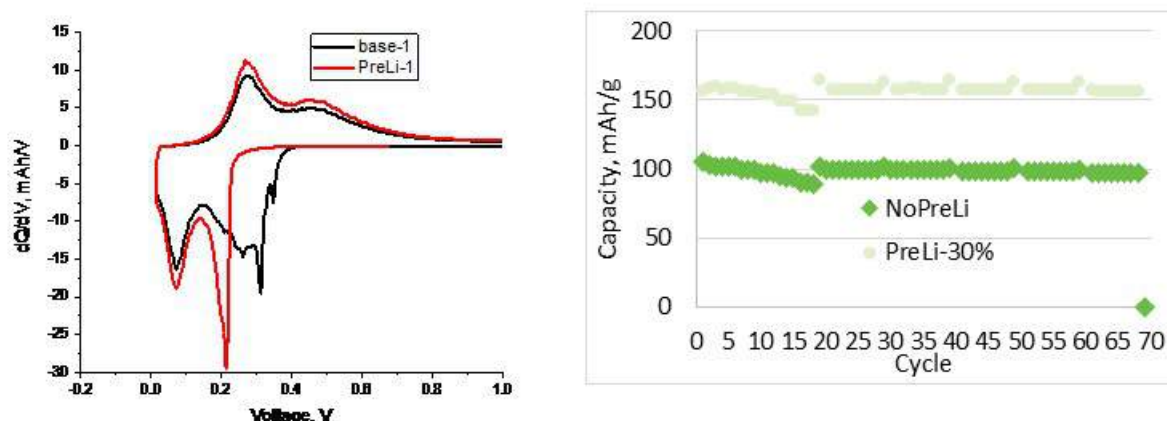


Figure I.7.F.7 (a) Differential capacity plot and (b) cycle performance of full cells with prelithiated SiO electrode

At last, we also attempted to electrochemically prelithiate graphite powder. A copper beaker was used to contain the graphite powder and connected to the source meter. The graphite powder in the copper container was stirred to create the connection between powder and copper beaker. However, the electrical connections between particles, and particles to the beaker, were so poor that the lithiation overpotential was too high to lithiate the powder.

Conclusions

The cycle life and calendar life of a SiO electrode were systematically investigated using full cells. It is found that the capacity fading of full cells consisting of SiO is mainly time dependent. The capacity fade rate is the same at rest as that during cycling. The thorough data analysis and post-mortem analysis suggest that the side reaction between electrolyte and SiO is believed to be the main contributor.

Industrial low-cobalt nickel-rich transition metal oxides, NMC and NCA with 90% Ni, were characterized electrochemically and thermally. These high-nickel metal oxides show similar electrochemical behavior. However, different thermal properties were observed according to DSC tests.

In this report, the electrochemical prelithiation of graphite and SiO electrodes were successfully demonstrated. After prelithiation, the electrode underwent rinsing and drying processes. All the half cells and full cells fabricated with prelithiated electrodes validated the improvement of 1st cycle Coulombic efficiency. No detrimental effect was observed in the electrochemical test results, i.e., the full cells with prelithiated electrodes show similar or better cycling performance. We also attempted to prelithiate the powder. However, the high impedance between the powder and current collector lead to large overpotential to such an extent that the powder was not successfully prelithiated.

Key Publications

1. Calendar and Cycle Life of Lithium Ion Batteries Containing Silicon Monoxide Anode, Wenquan Lu, Linghong Zhang, Yan Qin, and Andrew Jansen, *J. Electrochem. Soc.*, vol. 165(10), 2018, pA2179-A2183
2. Mitigating the Initial Capacity Loss and Improving the Cycling Stability of Silicon Monoxide Using Li₅FeO₄, Linghong Zhang, Wesley M. Dose, Anh D. Vu, Christopher S. Johnson and Wenquan Lu, *J. Power Sources*, vol. 400, 2018, p549-555

3. A new strategy to mitigate the initial capacity loss of lithium ion batteries, Xin Su, Chi-kai Lin, Xiaoping Wang, Victor A. Maroni, Yang Ren, Christopher S. Johnson, Wenquan Lu, J. Power Sources, vol. 324, 2016, p150-157
4. Materials benchmarking activities for CAMP Facility, Wenquan Lu, Qingliu Wu, Steve Trask, Bryant Polzin, Jai Prakash, Dennis Dees, and Andrew Jansen, 2019 DOE Vehicle Technology Office Annual Merit Review and Peer Evaluation Meeting, Washington D.C., 06/08/2015
5. Materials benchmarking activities for CAMP Facility, Wenquan Lu, Xin Su, Yan Qin, Manar Ishwait, Linghong Zhang, Steve Trask, Bryant Polzin, Dennis Dees, and Andrew Jansen, 2019 DOE Vehicle Technology Office Annual Merit Review and Peer Evaluation Meeting, Washington D.C., 06/06/2016

Acknowledgements

Contributors to this project in FY19 include: Alison Dunlop, Andrew Jansen, Joel Kirner, Yuzi Liu, Bryant Polzin, Yan Qin, Yang Ren, Steve Trask, Zhenzhen Yang, and Linghong Zhang.

I.7.G Electrochemical Performance Testing (INL)

Lee Walker, Principal Investigator

Idaho National Laboratory
2525 Fremont Ave
Idaho Falls, ID 83402
E-mail: lee.walker@inl.gov

Samuel Gillard, DOE Technology Development Manager

U.S. Department of Energy
E-mail: Samuel.Gillard@ee.doe.gov

Start Date: October 1, 2018	End Date: September 30, 2019	
Project Funding (FY19): \$4,000,000	DOE share: \$4,000,000	Non-DOE share: \$0

Project Introduction

The advancement of battery technologies that can meet the emerging demands for vehicle electrification requires in-depth understanding of the performance of early stage pre-commercial batteries, state-of-the-art commercial cells and the ability to adapt evaluation methods as mobility needs change. The Battery Test Center (BTC) at Idaho National Laboratory (INL) has been supporting the evolution of electrified transportation through high-quality, independent testing of electrical energy storage systems for more than 30 years. Independent testing provides data for quantitative assessment of the fundamental technology gaps that exist in early stage battery development. Test methods and techniques are continuously improved to offer data on relevant metrics as vehicle applications evolve and as new core gaps are identified. Advancing electrified powertrain transportation including understanding both high-energy battery chemistries and high power, extreme fast charging needs, is a top priority in advancing how people and goods are transported in the United States. As a designated core capability and lead test facility for the Vehicle Technologies Office (VTO), the BTC at INL directly supports the U.S. Advanced Battery Consortium (USABC) and other VTO programs by providing discrete information on failure modes, mechanisms and shortfalls in emerging technologies. Gaps in performance relative to targets are used as a metric to guide future R&D priorities.

Objectives

The activities at the INL BTC are focused on providing high fidelity, science-based performance and life testing, analysis, modeling, and reporting. To ensure the alignment with future industry and government needs, it is a key objective to update test and analysis procedures as new concepts and design space become achievable. Refined procedures help identify promising future research paths and identify key fundamental gaps that need to be addressed.

Approach

With 20,000 square feet of laboratory space, the INL BTC is equipped with over 800 test channels for advanced energy storage testing at the cell-level (e.g., up to 7V, 300A), module-level (e.g., up to 65V, 1200A), and pack-level (e.g., 500-1000V, 500A). Test equipment is programmed to perform distinct test profiles while simultaneously monitoring for compliance with operating limits such as voltage, current and temperature. The output from such tests enables principles-based analysis to be performed that can aid in identification of key technology gaps.

To ensure high quality, repeatable and dependable data is used for analysis, batteries and other energy storage devices are typically subjected to specific test sequences while housed inside precision thermal chambers. To enhance performance testing across a wide range of thermal conditions, driven by automotive usage scenarios, the thermal chambers can be operated across a broad temperature range (e.g., -70 to 200°C). This temperature

range enables key information to be extracted by modifying the chemical kinetic degradation rates within the evaluated items and enables accelerated aging analysis.

Successful performance testing and accurate life modeling are highly dependent on the fidelity of the acquired test data. The INL BTC has developed advanced calibration verification and uncertainty analysis methodologies to ensure that voltage, current, and temperature measurements are within the tolerance specified by the test equipment manufacturer (e.g., 0.02% of the full scale). These measured test parameters are subsequently used in various mathematical combinations to determine performance capability (e.g., resistance, energy, power, etc.). INL has also quantified the error associated with these derived parameters using the accuracy and precision of the relevant measured parameter (e.g., voltage) to ensure high-quality and repeatable results and meaningful presentation.

The INL BTC is also equipped with facilities that enable the characterization of batteries in aggressive use cases. One such use case is vibration that mimics what would be seen over the life of a battery in a typical automotive setting. Analysis of vibration on batteries at INL utilizes a high capacity vibration table to perform non-destructive tests to understand reliability and safety of new cell topologies to mechanical vibration and shock. Emerging cell designs that vary from current state of the art cell designs are the main focus of mechanical vibration and shock testing at INL.

Adjacent to the vibration table are two fire-rated isolation rooms that can be used for tests that push the known limits of battery operation. These aggressive use cases include extreme fast charging, subtle over- or under-charging, high-temperature thermal characterization for under-hood systems, among many others. The isolation rooms allow for safe testing of emerging cell technologies at or near the design limits and help characterize future use cases. The rooms also enable identification of key changes in performance fade that may emerge in aggressive use cases that can directly inform future rounds of early stage material and cell development activities. These complimentary non-destructive evaluation capabilities comprise INL's Non-Destructive Battery Evaluation Laboratory.

Results

The INL BTC continues to test articles of various sizes and configurations using standardized test protocols developed by INL with industry partnerships for different electric drive vehicle application. Table I.7.G.1 and Table I.7.G.2 summarize the testing activities under the USABC and Benchmarking programs, respectively, for FY-19. Technologies developed through USABC contracts are aged and tested against the appropriate application target (EV, HEV, PHEV, 12V S/S, 48V HEV) and, where applicable, they are compared to previous generations of test articles from the same developer. 215 articles were tested for USABC in FY-19, including 6 modules and 209 cells. The purpose of the Benchmark program is to evaluate device technologies that are of interest to VTO within DOE, but are not deliverables developed under a contract. In some cases, Benchmark devices are used to validate newly developed test procedures and analysis methodologies. Benchmark activities also are used to understand which gaps need to be fundamentally addressed to improve cell performance. 90 cells were tested for the Benchmark program in FY-19.

Analysis was performed for all articles tested, and results were presented regularly at quarterly review meetings and USABC Technical Advisory Committee (TAC) meetings to USABC representatives from different automotive manufacturers, DOE VTO representatives, developers, and National Laboratory staff. INL worked with the USABC test methods committee to develop the methodology and update the manual for testing EV batteries.

Table I.7.G.1 Articles Tested for USABC

Developer	Application	System	Number of Articles Tested	Status at Year End
LG/CPI	12V Stop/Start	Cell	15	Complete
SAFT	12V Stop/Start	Cell	4	Complete
SAFT	12V Stop/Start	Module	3	Complete
LG/CPI	12V Stop/Start	Cell	15	Complete
LG/CPI	12V Stop/Start	Module	3	Complete
Xalt	12V Stop/Start	Cell	18	Complete
PPG	EV	Cell	17	Complete
Amprius	EV	Cell	4	Complete
FARASIS	EV	Cell	8	Complete
SAFT	HEV	Cell	13	Ongoing
SAFT	12V Stop/Start	Cell	15	Ongoing
Amprius	HP-EV	Cell	24	Ongoing
Amprius	HP-EV	Cell	13	Ongoing
FARASIS	HP-EV	Cell	18	Ongoing
Zenlabs	HP-EV	Cell	17	Ongoing
Zenlabs	HP-EV	Cell	5	Ongoing
Zenlabs	LC/FC-EV	Cell	23	Ongoing

Table I.7.G.2 Articles Tested for Benchmark

Developer	Application	System	Number of Articles Tested	Status at Year End
Toshiba	12V Stop/Start	Cell	12	Complete
Toshiba	EV	Cell	3	Ongoing
Toshiba	EV	Cell	18	Ongoing
LG/CPI	EV	Cell	15	Ongoing
Microvast	EV	Cell	6	Ongoing
Microvast	EV	Cell	6	Ongoing
Diakin	EV	Cell	30	Ongoing

A key focal area for FY-19 at INL was expanded fade analysis as part of the Benchmark and USABC activities. The analysis was focused on more directly quantifying different levels of performance fade associated with more aggressive use cases, developing the ability to accurately capture non-electrochemical data including pressure evolution during cycling and alternative ways to ensure thermal equilibrium during cycling. Many of these methods were part of a refinement to enhance the utility of the Non-destructive battery

evaluation laboratory (NOBEL). In several instances, especially in the benchmark program, enhanced electrochemical analysis was performed to further isolate performance degradation pathways. In line with this work new activities using advanced data analytics were also initiated in FY-19. This work in conjunction with the National Renewable Energy Laboratory (NREL) seeks to shorten the time to characterize batteries while still providing useful, physics-backed information on performance fade and cell failure. The data analytics activity started during the last quarter of FY-19 is looks to have expanded impact in FY-20 and beyond. After refinement, it is expected that the outcomes from this project will be broadly applicable to testing and research activities alike.

Conclusions

The ability to perform discrete performance and life evaluation of emerging technologies in an independent, reliable manner is a direct aid to the identification of key technology gaps. Over the course of FY-19, the INL BTC was able to directly support many different endeavors within VTO with a keen focus on advancing battery technologies for emerging trends in electrified transportation. As a core capability in performance and life analysis for VTO, INL has identified key performance fade modes that exist in cells used for fast charging and has advanced the understanding of performance and evaluation protocols for multiple programs funded by VTO and USABC. 305 devices were tested in FY-19. The work also continues to develop the update of the USABC EV test manual and the submission/acceptance of 2 peer reviewed manuscripts. In FY-20, INL plans to continue this level of support for multiple programs with broad support for the USABC and Benchmark programs in particular. FY-19 activities will also look to more discretely probe key failure modes and how they relate to cell design and evaluation. Additional testing and data analytics activities will be started to support XCEL and BTMS activities. INL will also continue developing and refining standard test protocols and analysis procedures in collaboration with USABC and on providing information on core fundamental performance gaps that need to be addressed across VTO programs.

Key Publications

1. “Modeling memoryless degradation under variable stress” E.V. Thomas, I. Bloom, J.P. Christophersen, D.C. Robertson, L.K. Walker, C.D. Ho, V.S. Battaglia, *Journal of Quality Technology*, 51(3), (2019), 284-299
2. “Safety Aspects of Energy Storage Testing, R. Bewley, E.J. Dufek, S.E. Egan, D.K. Jamison, C. Ashton, C.D. Ho, M.C. Evans, T.L. Bennett, *Journal of the Electrochemical Society*, 166(8), (2019), E263-E265

Acknowledgements

The following staff at INL supported this work Matthew Shirk, Tanvir Tanim, Sergiy Sazhin, Eric Dufek, Boryann Liaw, Randy Bewley, Charles Dickerson, Chinh Ho, Ryan Jackman, Michael Evans, and David Jamison.

I.8 Small Business Innovation Research (SBIR)

Samuel Gillard, DOE Technology Development Manager

U.S. Department of Energy

E-mail: Samuel.Gillard@ee.doe.gov

Project Introduction

The advanced batteries effort of the Vehicle Technologies Office supports small businesses through two focused programs: Small Business Innovation Research (SBIR) and Small Business Technology Transfer (STTR). Both programs are established by law and administered by the Small Business Administration. Grants under these programs are funded by set aside resources from all Extramural R&D budgets; 3.0% of these budgets are allocated for SBIR programs while 0.45% for STTR grants. These programs are administered for all of DOE by the SBIR Office within the Office of Science. Grants under these programs are awarded in two phases: a 6-9 month Phase I with a maximum award of \$200K and a 2 year Phase II with a maximum award of \$1.1M. Both Phase I and Phase II awards are made through a competitive solicitation and review process.

Objectives

Use the resources available through the Small Business Innovation Research (SBIR) and Small Business Technology Transfer (STTR) programs to conduct research and development of benefit to the advanced batteries effort within the Vehicle Technologies Office.

Approach

The advanced batteries team participates in this process by writing a topic which is released as part of the general DOE solicitation. Starting in FY12, the advanced batteries team decided to broaden its applicant pool by removing specific subtopics and allowing businesses to apply if their technology could help advance the state of the art by improving specific electric drive vehicle platform goals developed by the DOE with close collaboration with the United States Advanced Battery Consortium.

Results

The advanced batteries team participates in this process by writing a topic which is released as part of the general DOE solicitation. Starting in FY12, the advanced batteries team decided to broaden its applicant pool by removing specific subtopics and allowing businesses to apply if their technology could help advance the state of the art by improving specific electric drive vehicle platform goals developed by the DOE with close collaboration with the United States Advanced Battery Consortium.

Phase II Awards Made in FY 2019

Under the SBIR/STTR process, companies with Phase I awards made in FY 2018 are eligible to apply for a Phase II award in FY 2019. The following four Phase II grants were awarded in FY 2019 (from among the Phase I grants that were conducted in FY 2017):

New Coulometry Technique for Li-ion Battery Durability Analysis (Xilectric, Fall River, MA)

Large Li-ion factories are being built around the world in an attempt to dramatically lower cost through economies of scale. At the same time, new market opportunities are becoming accessible to Li-ion as the technology improves. For many of these technologies, the levelized cost of energy storage is the primary metric, not \$/kWh. Cycle life varies tremendously depending on cycling conditions, chemistry, cell design, and manufacturing quality. Cell manufacturers and storage integrators are very interested in new technologies that can improve the abuse tolerance of Li-ion batteries resulting in improved cycle life. But proving new technologies or even iterating on existing formulations is challenging given that under some load profiles Li-ion chemistries can cycle for many years. Such long evaluation timeframes are not conducive to technical advancement. New characterization techniques are required that provide rapid insight on capacity loss and

degradation mechanisms with sufficient clarity to make informed design decisions. This project will develop a new battery characterization tool that allows the measuring of capacity loss rates of Li-ion batteries under a variety of specific use scenarios. Xiletric's proposed characterization technique provides insights not available from existing techniques providing a more complete picture of the capabilities of the variant of Li-ion chemistry under test. In particular, our technique is able to provide several measures of fidelity under realistic cycling conditions while avoiding artificial accelerated aging conditions such as extreme temperatures and potentials as well as full depth of discharge cycling. The information provided by the new test can be used to develop better battery management algorithms, to improve on cell design, and to select Li-ion formulations best suited to the end-user application. In Phase I, the basic performance requirements of the new coulometer system were established. Several batteries were characterized with the new technique. In phase II, the full system will be prototyped. Once validated, Xiletric would expect strong commercial interest in the new device from various Li-ion cell manufacturers, end-users, researchers, and academic institutions.

Low Cost 5V Spinel Cathode for Electric Vehicle Batteries with Enhanced Cycle Life (CAMX Power, Lexington, MA)

Broad commercialization and adoption of electric drive vehicles (EVs) that meet the market requirements for driving range necessitates development of electrochemical storage technologies that can deliver high energy density while providing requisite power, cycle life and calendar life at a low cost. Lithium-ion (Li-ion) batteries are the current technology of choice for both consumer electronics and emerging EVs. However, the highest energy density Li-ion cells currently used for commercial portable power applications are still well over 100 \$/kWh in cost. On a \$/kWh basis, Li-ion costs are more greatly driven by cathode materials than by any other component, and therefore lower cost, high-performance next generation cathode materials are needed to provide higher energy density, lower cost Li-ion cells. CAMX Power is developing a novel low-cost, high voltage Li-ion cathode chemistry with long cycle life. This novel chemistry produced via a low-cost manufacturing process, enables Li-ion electric drive vehicle batteries that are lower cost and higher energy density. CAMX Power will resolve historical challenges of high voltage cathodes by developing an inexpensive manufacturing process, developing protective coatings based on ionically and electronically conducting materials to boost high temperature cycle life, and by developing electrolyte formulations that are stable for high voltage operation. In Phase I, we demonstrated a pathway for low-cost production of LNMO cathodes. We also explored different techniques for coating the material with protective layers and demonstrated electrochemical performance of coated materials relative to uncoated controls. Materials were evaluated with a range of different electrolytes and tested in small pouch cells opposite a graphite and LTO anodes for both room temperature and high temperature cycle life. CAMX Power low-cost, high voltage spinel cathode material technology will enable achievement of DOE's energy and power goals for future EV batteries. Our high voltage cathode technology will enable use of fewer cells in EVs as well as circumvent the challenges associated with limitations in cobalt availability while achieving the lower costs that are required for widespread EV adoption.

Lithium Metal Batteries with Improved Cycle Life For Electric Vehicles (Cuberg, Emeryville, CA)

Improved battery technology is indispensable in electric vehicles (EVs) and grid-scale storage if the United States is to realize the benefits to national security and reduction of carbonaceous emissions that come of energy independence. The economic opportunity is immense; the market for the current state of the art rechargeable battery, lithium-ion (Li-ion), is already approaching \$50 billion per year, and it continues to grow with the continued adoption of EVs. Cuberg is developing a next-generation battery technology based on a non-flammable electrolyte formulation and a lithium metal anode. These cells deliver a step-change improvement in energy density and safety compared to the best lithium-ion batteries in the world today. The technology is a drop-in solution that can be manufactured and scaled using existing lithium-ion production equipment. In this project, we will assemble a battery with a new electrolyte formulation and cathode design to greatly improve the cell cycle life while retaining the excellent energy density, power, and safety profile achieved to date. Our tasks include R&D and cell design for cycle life improvement, analysis techniques, chemical approaches, electrochemical approaches, cell integration, and quality control. Our batteries will power the portable electronics of the future and help bring about mass-market electrification of UAVs, cars, air

taxis, and passenger airliners. Significant safety and energy improvements in EVs will accelerate their mass market penetration around the world which will reduce fossil fuel usage, air pollution, and cost of transportation. The focus of this proposal, cycle life improvements, will enable our products to achieve broad commercialization in EVs.

High Energy Safe Anodes for Lithium Ion Batteries (SafeLi, Madison, WI)

Electric vehicle manufacturers and the Department of Energy want safe and fast charging batteries for electric and hybrid vehicles with significant improvement in specific power. Of particular interest are new low-cost materials that can accept high-power recharging during regenerative braking and are compatible with existing manufacturing infrastructure. The applicant holds an exclusive license to patented materials with favorable properties for use in lithium-ion batteries. Moreover, these materials can improve batteries for portable tools and electronics, medical implants, military, and aerospace applications. The company's founders discovered and patented Graphene Monoxide, a novel carbon-based nanomaterial that is a 2-dimensional solid crystalline form of carbon monoxide. This is the first and only known solid form of carbon monoxide that occurs at ambient conditions; it has exciting properties suitable for marketable lithium-ion anodes. Superior battery performance arises from improved lithium+ and electron transfer. The materials actively store lithium+ during fast charging at stations and during regenerative braking. The new materials are compatible with graphite and silicon-graphite, enabling development of novel, lighter, and safer anode materials that will charge faster and increase battery specific energy and power. We will use two approaches to constrain costs: (1) maintain compatibility with existing manufacturing infrastructure and (2) enter the market as an additive to improve silicon-graphite anode performance. As economies of scale reduce costs, the applicant's materials will become a larger fraction of the anode. Phase I objectives (1) Prepare and test novel active anode compositions in half-cells; (2) Prepare and test coin and pouch batteries using anode materials from Objective 1; and (3) Plan for materials scale up. All Phase I Milestones were achieved as proposed, or with modifications guided by R&D, producing 200mAh pouch-cell batteries as a chief milestone. Half- and full-coin and pouch cell electrochemical cycling prove superior performance at fast charging (10C) and at low temperatures (-20°C), with improved specific energy and power. Phase II objectives (1) Improve and optimize novel active anode materials and composites to reduce cost and enhance desirability; (2) Achieve progressive, iterative scale-up of material manufacture to develop an industry-ready process for production of novel active anode materials; (3) Prepare & test 2Ah prototype batteries for demonstration to investors, technology transfer partners, or customers using optimized novel active anode materials. Improved anode materials will result in better batteries, consequently making electric vehicles more affordable and convenient. In addition to economic benefits (such as job creation) from the innovative electric vehicle industry, political and environmental benefits include decreased dependence on foreign oil and reduced air pollution.

Phase I Awards Made in FY 2019

Seven Phase I grants were awarded in the Summer of FY 2019.

Artificial Interphases Enable the Use of Silicon Anodes for High-Energy Vehicle Batteries (Storageenergy Technologies, Salt Lake City, UT)

Si has been considered as a potential candidate to replace the current anode material, graphite (372 mAh/g, LiC₆), because of its high capacity (3579 mAh/g, Li₁₅Si₄), low environmental impacts, and potentially low cost. However, the utilization of Si in LIBs has been hindered by two major issues: 1) Si particles experience huge volume expansion up to 300%, which causes mechanical disintegration of the electrodes; 2) sophisticated interaction between the organic carbonate electrolytes and Si particles results in the formation of unstable SEIs on the Si surface. The unstable SEI and the newly formed interface induced by repeated volumetric expansion/contraction lead to the continuous formation of SEIs, which makes the electrode more insulated and leads to low Coulombic efficiency (CE). One approach to address the unstable (non-passivating) SEI layer on silicon is the development of an artificial SEI, which can enhance the ionic and electric conductivity, accommodate volumetric changes, prevent particle agglomeration, and modify surface conditions favoring a robust interface. This functional artificial SEI can overcome the science and technology barriers to the use of silicon-based anodes in high-energy density LIBs for transportation applications. In addition, achieving stable

cycle life of Si anodes in the high-energy full cell is another tough challenge in that the capacity fading of Si anodes is pronounced in the full cells rather than in the half cells. In full cell configuration, the irreversible capacity is associated with the active material loss, whereas the reversible capacity loss is associated with side reactions. Storageenergy Technologies Inc. (Storageenergy) and Virginia Tech. (VT) propose to develop stable artificial SEI on Si anode by MLD process and an in-situ pre-lithiation method for high energy density and long cycling life LIB development. The artificial hybrid SEI on high-capacity Si anode will improve the mechanical/chemical properties and protect the Si surface from the attack of reductive electrolytes. The in-situ pre-lithiation method will significantly simplify the conventional pre-lithiation process to compensate the lithium loss during the initial electrochemical cycle. Our high-performance LIBs system with highly mechanical stability and chemical stability Si anode and in-situ pre-lithiation technology promise to transform the energy storage and distribution fields. This technology, in the distributed energy storage form, reduces greenhouse emissions by serving as a gateway technology to the widespread use of alternative and more importantly intermittent energy sources, namely wind and solar. The distributed Si anode-based LIB technology will also serve a critical need in the future Smart Grid by moderating the daily fluctuations in the power grid. And, finally, this technology will serve to re-establish the U.S. technological lead in batteries that has migrated overseas. The successful development of this technology will enable a new family of American batteries of all scales for both commercial and government sectors.

The Development of a Stabilized SEI Layer for Si-Containing Lithium Ion Battery Anodes (Edward Buie Consulting, Chattanooga, TN)

This project focuses on the development of new lithium ion battery (LIB) electrolyte/cathode combinations that enable stabilized solid electrolyte interphases (SEI) on Si- based materials. This effort focuses on negative electrodes combining synthetic graphite and Si- based materials, where Si contributes at least 30% of the reversible capacity of the electrode. This effort will result in significantly longer cycle life and calendar life for LIBs that feature Si- containing negative electrodes. Recent work has shown that the capacity fade seen in well-designed Si and Si-based negative electrodes is a consequence of an increase in surface area with cycling as the Si-based material expands and contracts. The increased surface area results in an increase in parasitic side reactions and accelerated electrolyte consumption. High precision calorimetry combined with high precision coulometry allows an early identification of the increasing parasitic thermal power that accompanies the increasing surface area. The volume changes of Si-based materials can be diluted but they cannot be suppressed. The path forward for truly enabling Si-based materials therefore lies in targeted electrolyte chemistry. Electrolyte constituents that lead to the formation of carbon dioxide (CO₂) or CO₂ precursors have recently been shown to be effective in extending the cycle life of Si. It is believed the presence of CO₂, or readily reducible intermediates, leads to the formation of an inorganic carbonate Si SEI and has a remarkable effect on extending cycle life. Early results show this approach as being superior to fluoroethylene carbonate, the gold standard electrolyte solvent for Si. The strategy of this effort will be two-fold: 1) development of electrolyte components that can provide a sustainable level of CO₂ or reducible intermediates in order to provide Si-containing electrodes capable of at least 1000 cycles and 2) engineering the cell positive electrode such that the positive electrode surface reactions lead to by-products that help stabilize the Si SEI. Early work in this area has been promising. Coulometrics, LLC will partner with Cyclikal, LLC to provide an excellent balance of cell assembly and cell testing capabilities with state-of-the-art microcalorimetry, which has proven successful in recent years in increasing the life of Si in LIBs. The combined team has excellent equipment, facilities, and 20 trained staff that have over 100 years of experience developing LIBs. Dr. Edward Buie has over 25 years of experience as CTO of two advanced energy storage companies and now CEO of Coulometrics, LLC. Joe Turner has 15 years of LIB development experience and recently was R&D director of K2 Energy before joining Coulometrics. Dr. Larry Krause has over 30 years of industrial energy storage experience, especially relating to Si. The team also benefits from Coulometrics' consulting business that has been profitable since 2008 and provides significant revenue to support this effort and any commercialization effort that may arise from this program.

Recovery of High Value Anode Materials for a Fully Closed Loop Li-ion Battery Recycling Process (Battery Resourcecs, Worcester, MA) Battery Resourcecs' goal with this Small Business Innovative Research Phase 1 project is to produce high quality and high purity graphite generated from its Li-ion battery recycling technology. This will lead to low cost anode materials for Electric Vehicle batteries and push the battery cost towards DOE's goal of \$100/kWh. Battery Resourcecs' technology recovers cathode material from a broad spectrum of Li-ion battery regardless of size, shape or chemistry. In Battery Resourcecs existing model, the graphite is recovered to be used as a reductant. However, in this application the value is low and therefore the battery materials cost or recycling cost is not lowered by the recovery of the graphite Battery Resourcecs and its subcontractor WPI intend to demonstrate the same success with the recovered graphite for anode materials. By selling high quality graphite and NMC powder to battery manufacturers, it will drastically lower the overall battery cost. This advancement is critical because traditional recycling processes only recover individual metals from the batteries, and graphite is simply burned. The success of this award will enable Battery Resourcecs offer lowest cost anode materials while reducing the carbon footprint of the battery industry. This will potentially lower the cost of EV by lowering the upfront cost of the battery and the end of life disposal costs. The technical objectives of this Phase 1 research project are to purify the recovered graphite from Battery Resourcecs leaching process and demonstrate it is viable to be used in new electric vehicle lithium ion batteries. The graphite in Battery Resourcecs recovery process contains Co, Ni, Mn, and Al₂O₃. To separate the graphite from other materials we will employ new filtering techniques and chemical processing methods. Secondly, Battery Resourcecs will develop a technology such that the anode material can be used in new batteries. If the process can be improved such that the anode material can be used in new batteries than the value recovered is such more. When successful this technology can be directly piloted on Battery Resourcecs existing pilot plant for a phase II project.

Additives for Improved Cell Reliability (Xilectric, Fall River, MA)

This Small Business Innovation Research project will develop new additive strategies to improve the cost and cell reliability of Li-ion batteries for electric vehicle applications. Xilectric's technology seeks to dramatically improve Li-ion abuse tolerance to high temperatures and voltages by better maintaining the Li-ion electrolyte. Our additives improve the capacity retention and rate capabilities of Li-ion batteries. Through this SBIR project, Xilectric will accelerate the development of our additives and begin chemical process development studies needed to bring our materials to the market. Xilectric will also develop tailored derivatives for application to emerging use-case scenarios. For example, high-nickel cathode materials are an important next-generation EV cathode due to their high capacity, rate capability, and low cost. A subset of the development work on this SBIR program will focus on the requirements of emerging high-nickel cathodes. The key to driving down the cost of Li-ion to further promote adoption of the high-value end products such as electric vehicles is to reduce the material input cost of the anodes, cathode, and other materials that comprise the cell. Despite being low-cost, the materials must also present adequate calendar and cycle life for the given product application. Li-ion manufacturers would prefer to use the lowest cost materials, but need to balance cost with customer expectations for high-quality long-lasting batteries. Through this SBIR program, Xilectric will developed a new additive strategy that enables lower-cost active materials to be used in Li-ion batteries while still presenting superior calendar and cycle life.

Development of nickel rich and concentration gradient cathode materials for high energy density and long cycle-life lithium ion batteries using controlled micro-aerosol pyrolysis Beltech (Hit Nano, Princeton, NJ)

Lithium ion batteries (LIBs) are promising candidates for next-generation energy storage and electrified transportation systems. However, continuous growth of cobalt price, low energy density, short lifetime, and high propensity in fire accidents of LIBs creates a big challenge to renewable electricity production and electrification of transportation. Therefore, there is an urgent need to develop low cost, high energy density, long cycling, and fire resistant LIBs cathode materials for the integration of renewable energy, energy storage, electrification of transportation, and smart mobility. In this project, a new type of controlled micro-aerosol pyrolysis process will be explored for the synthesis of high nickel and concentration-gradient cathode materials that will systematically improve the electrochemical performance of lithium ion batteries, reduce chemical

footprint and fire propensity, and strongly promote the utilization of renewable energy for transportation and high efficient energy storage. This Small Business Innovation Research Phase I project will develop a novel micro-aerosol and controlled high temperature (MACHT) evaporation and pyrolysis process for the synthesis of high nickel content nickel-cobalt-manganese (NCM) high-energy cathode materials using particle morphology control, concentration gradient, and precision ion-doping. By controlling the ratio of solvent evaporation time to precursor diffusion time during heating, a uniform high nickel content nanoparticle morphology is achieved which increases the energy density of LiB. The concentration gradients of nickel and doped ions, which significantly increases the LiBs cycling performance and fire resistance, are realized from the differences in precursor solubility and precipitation rate. Thus, MACHT provides a new way to precisely control nanoparticle morphology, precision ion doping and functional ion gradients to design new and advanced NCMs and nickel-cobalt-alumina NCA cathode materials for LiBs. Compared to commercial co-precipitation methods, MACHT process has the potential to significantly lower the manufacturing costs, increase the energy density and battery cycling performance, and reduce fire propensity and chemical waste production, offering the great opportunity to advance the discovery of new high performance battery materials. The success of this technology will greatly enhance the overall performance of lithium-ion batteries to meet energy density, power, lifetime, and fire safety objectives. The development of the advanced cathode materials by using the proposed technology will increase the commercial viability of LIBs and reduce battery cost, and thus accelerates the electrification of transportation and large scale energy storage for renewable energy in the near future. Moreover, MACHT technology is transformative. If successful, it will create a new LiBs cathode materials manufacture process and establish the leadership of U.S. manufactures of LiBs. In addition, MACHT increases recycling ability of key materials in battery (lithium, cobalt and nickel), eliminates the production of large amount of waste in existing commercial co-precipitation method, and reduces the propensity of fire accidents. Furthermore, MACHT method can also be used for synthesis of other nanomaterials for energy storage, catalysis, and biomedical applications to control nanoparticle morphology and functionality. As such, the proposed project will have large impact on the U.S. economics and job employment. Finally, the project will provide hands on experiences for high school and minority students to design EV batteries.

Multilayered Superionic Conductive Conformal Solid Electrolyte for Lithium Metal/High Nickel Lithium Nickel Manganese Cobalt (NMC) Cells (Akron PolyEnergy, Akron, OH)

The Department of Energy is leading efforts to develop advanced battery technologies for Electric Vehicles (EVs). Improving the performance and lowering the cost of batteries will help to further increase market penetration of EVs, consequently reducing our nation's dependence on foreign oil. The current state-of-the-art in EV battery technology is Lithium Ion batteries (LIBs); however, LIBs would significantly benefit from higher specific energy densities (currently about 170~265 Wh/kg) and improved durability. Lighter and more durable batteries will increase the range of EVs and/or lower the total battery cost per vehicle. The electrode materials determine the specific energy of LIBs. An attractive and straightforward approach to increase the specific energy is to utilize new electrode materials that have larger capacities. Among all the future electrode material candidates, lithium metal is the most promising anode due to its large capacity and largest negative voltage. However, traditional liquid electrolytes can neither prevent Li dendrite formation nor are stable with respect to lithium metal for prolonged cycles. Replacement of the liquid electrolytes with solid electrolytes could be a viable solution for lithium metal anode systems. The proposed technology in this project is to develop a superionically conductive (conductivity $> 10^{-3}$ S/cm at room temperature) solid polymer electrolyte that is suitable for Lithium Metal/High Nickel Lithium Nickel Manganese Cobalt (NMC) cells. The team will further develop a multilayered electrolyte system to allow the use of high nickel NMC cathodes which is crucial for high energy density LIBs. The lamination of two polymer electrolytes will provide both superionic conductivity and high cathode stability, allowing the utilization of the full capacity of the cathode. If successful, the resulting solid-state Li Metal/High Ni NMC cells will achieve gravimetric energy densities over 400 Wh/kg, which is 50% higher than the start-of-art lithium ion batteries. Such a high energy density certainly will be beneficial for EV applications. In addition, the solid-state cells have intrinsic safety advantages over liquid electrolyte based batteries, making them a safer choice for energy storage. Beyond the EV application, safe batteries with ultrahigh energy densities will attract attention of manufactures from consumer electronics industry.

Roll-to-Roll Production of Flexible Composite Solid-State Electrolytes for Lithium Metal Batteries in Electric and Hybrid Electric Vehicles using Gravure Printing (Amperica, Tuscon, AZ)

To make the electrical vehicles more competitive with internal combustion engine ones, the United States Advanced Battery Consortium has listed a set of goals for future lithium-ion batteries to meet, which includes a higher specific energy (275 Wh/kg) and energy output (50 kWh). Since current lithium-ion batteries aren't capable of reaching these goals, rechargeable lithium-metal batteries have been of particular interest in recent years. However, due to the dendrite growth issue of lithium metal anodes, the key factor to commercialize lithium-metal batteries is to develop suitable solid-state electrolytes to replace the organic liquid electrolytes. Among the solid-state materials, sulfide ceramics are the most promising owing to their high ionic conductivity and stability. Unfortunately, their brittleness still hinders their application in large scale production. To overcome this drawback, fabrication of composite electrolyte by the integration of sulfide ceramics with specific polymers has been proven to be a promising route. The composite electrolyte shows good flexibility, chemical compatibility with high-performance cathodes and efficient ability to block lithium dendrite growth. However, a suitable processing method should be developed to meet the high output, good reproducibility requirements for composite electrolyte production. In Phase I, a low-cost roll-to-roll method will be developed for the formation of a ceramic/polymer composite. The ceramic/polymer composite slurry will be developed so that it can be tape casted into high ionic conductive and mechanically flexible and strong membranes. The membrane will be assembled into all solid-state lithium batteries in coin cell and pouch cell format and evaluated for its performance. The slurry will be used to develop a scalable Gravure Printing process to make the process more appropriate for mass production and easily integrated with mass production assembly lines. The product will be put into pouch cells and tested under United States Battery Consortium guideline. Future Phases will focus on optimization of the roll-to-roll process in order to achieve optimal composite electrolyte. Furthermore, cells in larger format (2Ah) and different configurations such as cylindrical cells will be fabricated for practical applications. Electrochemical performance and safety testing will also be conducted at various temperatures to show the applicational capabilities of the electrolytes. It is anticipated that this solid electrolyte fabrication approach will greatly accelerate the commercialization of lithium-metal batteries in electric vehicle industries.

Manufacturing and Storage Optimization of Ultralow-cobalt Cathodes for Electric Vehicle Batteries (TexPower, Austin, TX)

Electric vehicles are approaching price and range performance targets that make them competitive against petroleum-driven internal combustion engines. Cathodes represent the largest cost component of lithium-based automotive batteries (lithium-ion batteries) and are still the limiting electrode for overall energy content. In addition, state-of-the-art cathode materials in vehicle batteries, such as $\text{Li}[\text{Ni}_{0.6}\text{Co}_{0.2}\text{Mn}_{0.2}]\text{O}_2$ and $\text{Li}[\text{Ni}_{0.85}\text{Co}_{0.10}\text{Al}_{0.05}]\text{O}_2$, utilize significant amounts of cobalt (12% and 6% by weight, respectively), a metal of high supply risks and geopolitical/ethical concerns that can lead to surging costs of vehicle batteries. Furthermore, the U.S. manufacturing base for cathode materials is limited, with most production occurring in East Asia including China, Japan, and South Korea. TexPower, Inc., in collaboration with the University of Texas at Austin, aims at developing ultralow- and cobalt-free cathode materials produced in the U.S. for lithium-ion batteries. These materials possess significant benefits including higher energy content, low cobalt reliance and affordable price compared to state-of-the-art cathode materials. TexPower's technology was developed at the University of Texas at Austin through funding from the Department of Energy over the last five years at an academic setting. The requested SBIR/STTR funding will allow TexPower scale laboratory processes for industrial production and fabrication. In phase I, TexPower and the University of Texas at Austin will optimize oxygen usage during lithiation calcination of their cathode materials to balance performance and cost at large- scale production. Additionally, formation of surface residual lithium compounds will be minimized to facilitate electrode fabrication and enhance safety during battery operation. Also, packaging options will be explored for reliable and low-cost materials shipment. The effects of these processes will be validated in large-format commercially relevant pouch full cells paired with graphite anodes (from 200 mAh to above 1 Ah). Since most battery cathode materials are currently produced overseas, a strong supply chain in the U.S. will be an enormous driver for the growth of our economy, considering the increasing vehicle electrification in upcoming decades. Funding of this proposal will facilitate TexPower in becoming a robust

domestic cathode manufacturing firm. Further, maturing of TexPower's cathode technology with significantly less dependence on cobalt will accelerate the electric vehicle propulsion that reduces air pollution imprint caused by conventional combustion engines.

II Battery Materials R&D

II.1 Next Generation Lithium-Ion Batteries: Advanced Anodes

II.1.A Next Generation Anodes for Lithium-Ion Batteries: Silicon (ANL, LBNL, ORNL, SNL, NREL)

Jack Vaughey, Principal Investigator

Argonne National Laboratory
9700 South Cass Avenue
Lemont, IL 60439
E-mail: vaughey@anl.gov

Brian Cunningham, DOE Technology Development Manager

U.S. Department of Energy
E-mail: Brian.Cunningham@ee.doe.gov

Start Date: October 1, 2016	End Date: September 30, 2020	
Project Funding (FY19): \$2,710,000	DOE share: \$2,710,000	Non-DOE share: \$0

Project Introduction

Silicon has received significant attention as an alternative to the graphitic carbon negative electrode presently used in lithium-ion batteries due to its much higher capacity and general availability. Compared to graphitic carbons, silicon has nearly an order of magnitude higher capacity (~3600 mAh/g silicon vs 372 mAh/g graphite), however, several problems that limit its utility in commercial cells have been identified including large crystallographic expansion upon lithiation (~320%), slow lithium diffusion, and high reactivity at various states of charge. Combined, these materials properties can result in active particle cracking (stress-strain), particle isolation, electrolyte reactivity, and electrode delamination issues. These chemical reactivity and volume changes are manifested in SEI stability and cycling efficiency issues for the cell. Keeping this in mind, the large number of studies focused on silicon-based electrodes is a testament to the opportunity it presents but also the size of the challenge and innovation it inspires on multiple fronts. BatPaC, a techno-economic program designed to model lithium-ion battery performance and cost, was utilized to establish program relevance by connecting DOE/USABC pack performance targets to anode targets. BatPac analysis of the needs for LIB anode science (see Figure II.1.A.1, left frame) indicated that anode volumetric capacities greater than 1000 mAh/cm³ generally minimizes battery cost when coupled to an advanced NMC cathode. Note that higher capacities result in diminishing savings in cost. The analysis (right frame) also predicts that silicon-graphite electrodes with less than 75 wt% graphite can achieve the 1000 mAh/cm³ target.

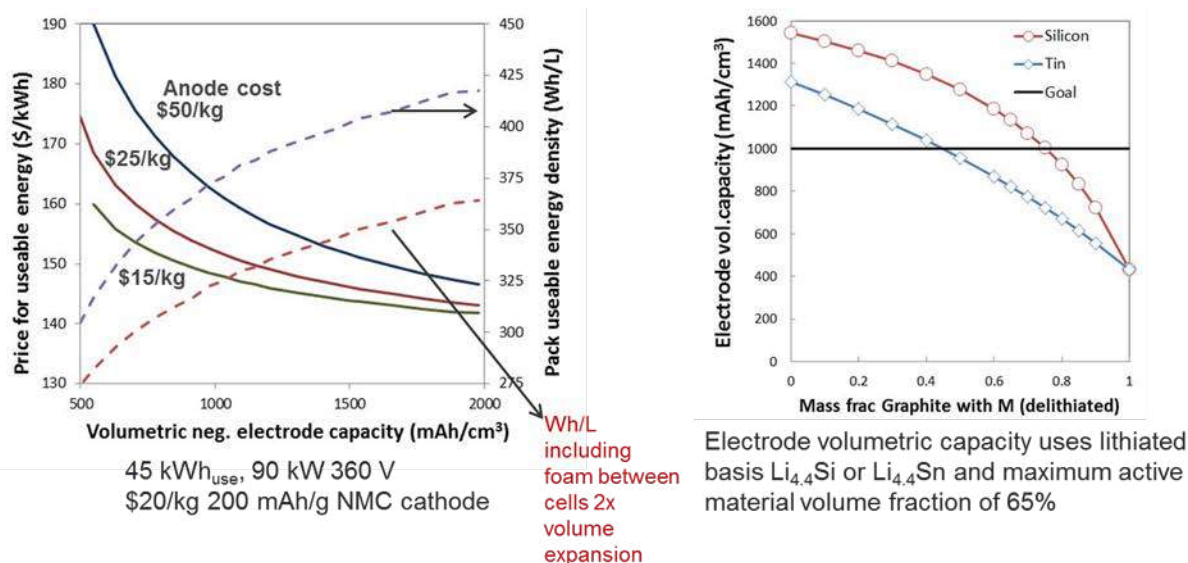


Figure II.1.A.1 Battery Performance and Cost (BatPaC) model utilized to establish relevance by connecting pack to anode targets

Next Generation Anodes for Lithium-Ion Batteries, also referred to as the Silicon DeepDive Program, is a consortium of five National Laboratories assembled to tackle the barriers associated with development of an advanced lithium-ion negative electrode based upon silicon as the active material. This research program has several goals including establishing baseline silicon materials for research consistency obtained in quantities sufficient for electrode preparation by the consortiums combined facilities and executing full cell development strategies that leverage DOE-EERE-VTO investments in electroactive materials and characterization. The primary objective of this program is to understand and eliminate the barriers to implementation of a silicon-based anode in a lithium-ion cell. The five National Laboratories involved are focused on a single program with continuous interaction, established protocols for analysis, and targets for developing both an understanding and a cell chemistry associated with advance negative electrodes for lithium-ion cells. This undertaking is a full electrode/full cell chemistry project leveraging common baseline electrodes prepared at the consortium facilities. All efforts are directed to understanding and developing the chemistry needed for advancing silicon-based anodes operating in full cells. Materials development efforts include active material development, binder synthesis, coatings, safety, and electrolyte additives. Efforts include diagnostic research from all partners, which span a wide range of electrochemical, chemical and structural characterization of the system across length- and time-scales. Specialized characterization techniques developed with DOE-EERE-VTO funding, include neutron diffraction studies, MAS-NMR and optical spectroscopy methods, and X-ray based techniques being employed to understand operation and failure mechanisms in silicon-based anodes. The project is managed as a single team effort spanning the Labs, with consensus decisions driving research directions and toward development of high-energy density lithium-ion batteries. A detailed list of participants is given in Figure II.1.A.2.

CONTRIBUTORS AND ACKNOWLEDGMENT

Research Facilities

- Post-Test Facility (PTF)
- Materials Engineering Research Facility (MERF)
- Cell Analysis, Modeling, and Prototyping (CAMP)
- Battery Manufacturing Facility (BMF)
- Battery Abuse Testing Laboratory (BATLab)

Contributors

- | | | | |
|---------------------|-----------------------|----------------------------|------------------|
| ▪ Daniel Abraham | ▪ Yeyoung Ha | ▪ Gao Liu | ▪ Stephen Trask |
| ▪ Ira Bloom | ▪ Binghong Han | ▪ Wenquan Lu | ▪ Jack Vaughey |
| ▪ Su Ahmed | ▪ Sang-Don Han | ▪ Maria Jose Piernas Muñoz | ▪ Gabriel Veith |
| ▪ Nasim Azimi | ▪ Andrew Jansen | ▪ Jagjit Nanda | ▪ Qingliu Wu |
| ▪ Beth Armstrong | ▪ Sisi Jiang | ▪ Nate Neale | ▪ Yimin Wu |
| ▪ Chunmei Ban | ▪ Haiping Jia | ▪ K. Nie | ▪ Kang Yao |
| ▪ M. Katie Burdette | ▪ Christopher Johnson | ▪ Bryant Polzin | ▪ Ji-Guang Zhang |
| ▪ Anthony Burrell | ▪ Baris Key | ▪ Krzysztof Pupek | ▪ Linghong Zhang |
| ▪ Saida Cora | ▪ Joel Kirner | ▪ Marco-Tulio F. Rodrigues | ▪ Lu Zhang |
| ▪ Jaclyn Coyle | ▪ Robert Kostecki | ▪ Rose Ruther | ▪ John Zhang |
| ▪ Dennis Dees | ▪ Bob Jin Kwon | ▪ Niya Sa | ▪ Tianyue Zheng |
| ▪ Fulya Dogan | ▪ Xiaolin Li | ▪ Yangping Sheng | ▪ Ting Zhang |
| ▪ Wesley Dose | ▪ Chen Liao | ▪ Seoung-Bum Son | |
| ▪ Alison Dunlop | ▪ Min Ling | ▪ Caleb Stetson | |
| | ▪ Michael Liu | ▪ Wei Tong | |

Support for this work from Battery R&D, Office of Vehicle Technologies, DOE-EERE, is gratefully acknowledged – Brian Cunningham, Steven Boyd, and David Howell



Figure II.1.A.2 Program participants including Laboratories, research facilities, and individual contributors

Objectives

- Understand and overcome the science and technology barriers to the use of silicon-based anodes in high-energy density lithium-ion batteries for transportation applications.
 - Stabilize the SEI
 - Stabilize the electrode structure
- Demonstrate functional prototype lithium-ion cell chemistries that include a silicon-containing anode which meet the DOE/USABC performance targets.

Approach

Oak Ridge National Laboratory (ORNL), National Renewable Energy Laboratory (NREL), Sandia National Laboratories (SNL), Lawrence Berkeley National Laboratory (LBNL), and Argonne National Laboratory (ANL) have teamed together to form an integrated program dedicated to identifying, developing an understanding, and proposing solutions to the problems associated with the commercialization of silicon as an active component of a lithium-ion electrochemical cell. Technical targets have been developed and regular communications have been established across the team. Throughout the program, there is a planned focus on understanding, insights into, and advancement of silicon-based materials, electrodes, and cells. Advancements will be verified based on life and performance of full cells. Toward that end, baseline silicon-based materials, electrodes, and cells have been adopted, along with uniform full cell testing protocols.

In examining improvements, changes to the baseline cell technology will be assessed regularly and will be updated to reflect advances, new suppliers, and treatments based on the data and assessments from team members. Studies of the present baseline systems have adopted a testing protocol from the literature that has worked well for lithium-ion cells with silicon containing anodes. The test starts with three slow (C/20) formation cycles, an HPPC cycle, and then the C/3 aging cycles. The test ends with another HPPC cycle and three slower (C/20) cycles. All constant current cycling is symmetric between charge and discharge rates. The tests are run at 30°C. If there is little or no aging in the first 100 cycles, the protocol can be repeated. This protocol effectively examines capacity, impedance, and aging effects in about a month's worth of testing. The present baseline silicon was developed and produced by Paraclete Energy (Chelsea, MI) and has been made available to all participants on demand. The silicon was purchased in bulk from Paraclete to minimize batch to batch issues and electrode fabrication was done using consistent materials, compositions, and conditions. The cathode is a commercial 532 NMC Cathode available from CAMP, and the baseline electrolyte is 1.2M LiPF₆ in a 3:7 ratio of EC/EMC by weight (Gen2) plus 10 wt% FEC. Scale-up of materials, incorporation of materials advancements into electrodes, prototype cells, characterization, safety evaluation, abuse tolerance and testing of cells, are part of a wide range of integrated studies supported by battery research facilities at the National Labs working closely with the program. These research facilities include the Battery Abuse Testing Laboratory (BATLab), the Battery Manufacturing Facility (BMF), the Cell Analysis, Modeling, and Prototyping (CAMP), and the Post-Test Facility (PTF).

The fundamental understanding developed as part of the silicon DeepDive is based on extensive electrochemical and analytical studies of the components, electrodes, and cells conducted by researchers in the program. This effort contains in situ and ex situ studies on full and specialty cells, including reference electrode cells. Overall, the diagnostic studies are intended to help establish structure-composition-property relationships, including lithium-rich surface compounds, bulk transport, and kinetic phenomena. Together they form the basis for accurately assessing component and electrode failure modes and sets a path for advancements. Supported by the diagnostic studies, materials development on silicon-based materials, electrodes, and cells has been focused on enhancement of interfacial stability, accommodation of volume changes on lithiation, improvements in overall performance and life. A key avenue of research for this goal is the development and testing of surface coatings and electrolyte additives designed to modify and stabilize the dynamic silicon-electrolyte interface. In this past year we have added more diagnostic techniques designed to probe the role of additives on the rigidity, porosity, and transport properties of the surface electrolyte interphase (SEI). Keeping with the goals of using full cell for the DeepDive effort, efforts aimed at understanding the slurry properties, role of binder protonation, and viscosity continues as a multi-Laboratory pathway to improve the baseline electrodes.

Communication of programmatic progress to battery community is critical. This will generally be accomplished through publications, presentations, reports, and reviews. Further, the program is open to industrial participation and/or collaboration that does not limit program innovation or the free flow of information. Finally, the DeepDive is highly integrated with the SEISta program, a sister program focused on stabilization of the silicon SEI layer. Generally, SEISta is focused on the development and characterization of model systems, surface analysis, well-defined thin film electrodes, and interfacial silicate phases and phenomena.

Results

1. Silicon-based Electrodes

Silicon Utilization: The silicon electrode development effort continued a focus on high-silicon (graphite-free) electrode formulations that it began in FY18. Since volume expansion issues associated with charged silicon anodes are dependent on the cell voltage, a goal was to understand with a silicon composite electrode (rather than the just the element) the role silicon particle volume expansion and contraction play in electrode performance versus extent of lithiation by evaluating multiple voltage window cutoffs for the anode. Previous efforts by CAMP utilized lithiation to as low as 10 mV versus Li⁺/Li, with limited enhancement of cycle life. The initial focus was a performance comparison of electrodes designed with 50 mV and 100 mV lithiation

cutoff potential using three batches of baseline silicon material sourced from Paraclete Energy. Sample one was a Si batch annealed in air at 400°C to remove surface silica defects using conditions optimized previously. Samples two and three were high-silicon content electrode compositions noted below:

71:10:19 wt.% (silicon: conductive additive: LiPAA binder)

80:10:10 wt.% (silicon: conductive additive: LiPAA binder)

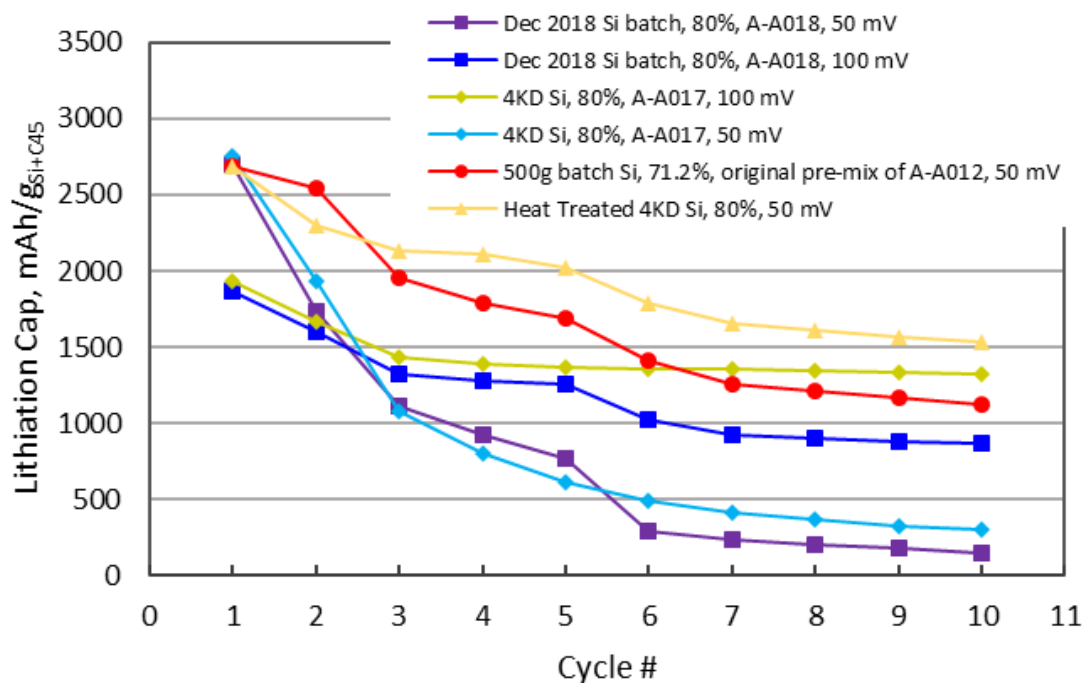


Figure II.1.A.3 Lithiation capacity versus lithium metal for various graphite-free silicon electrodes fabricated by the CAMP Facility. These cells were cycled between 0.05 to 1.5 V or 0.1 to 1.5 V vs. Li⁺/Li as noted in the legend

The half-cell performance of these cells is shown in Figure II.1.A.3. From this plot it is noted that the capacity utilization and fade rate vary significantly between electrodes, however it is clear is that the first lithiation capacity is very consistent for the electrode sets using a 50 mV and 100 mV cutoff potential. For samples that underwent the heat treatment in air at 400°C, enhanced capacity utilization of the silicon compared to baseline was observed. This is consistent with previous reports although tradeoffs in lost active material, control of passivation thickness, and lithium silicate formation and dissolution have been noted in the DeepDive and SEISta programs.

Figure II.1.A.4 is a comparison of full cell performance of the 15 wt. % silicon-graphite and a high-silicon graphite-free anodes versus a baseline NMC532 cathode baseline with the 50mV cutoff. The Si electrodes were matched to the NMC532 capacity loading that were included in this full cell study. This included the original baseline Si (electrodes: 15 wt.%) from NanoAmor (50-70 nm) from electrodes in the CAMP library at the correct loading. It is evident that both data sets have a similar but excessive capacity fade rate, regardless of the amount or source of silicon. The performance of the various sources of Si at 15 wt.% is exceptionally similar. For the 80 wt. % Si electrodes, the best capacity retention was seen for the 400°C air annealed Paraclete Si (black line) materials. While the same Si that was not heat treated resulted in a lower capacity, the capacity fade rate was similar for all Si electrodes.

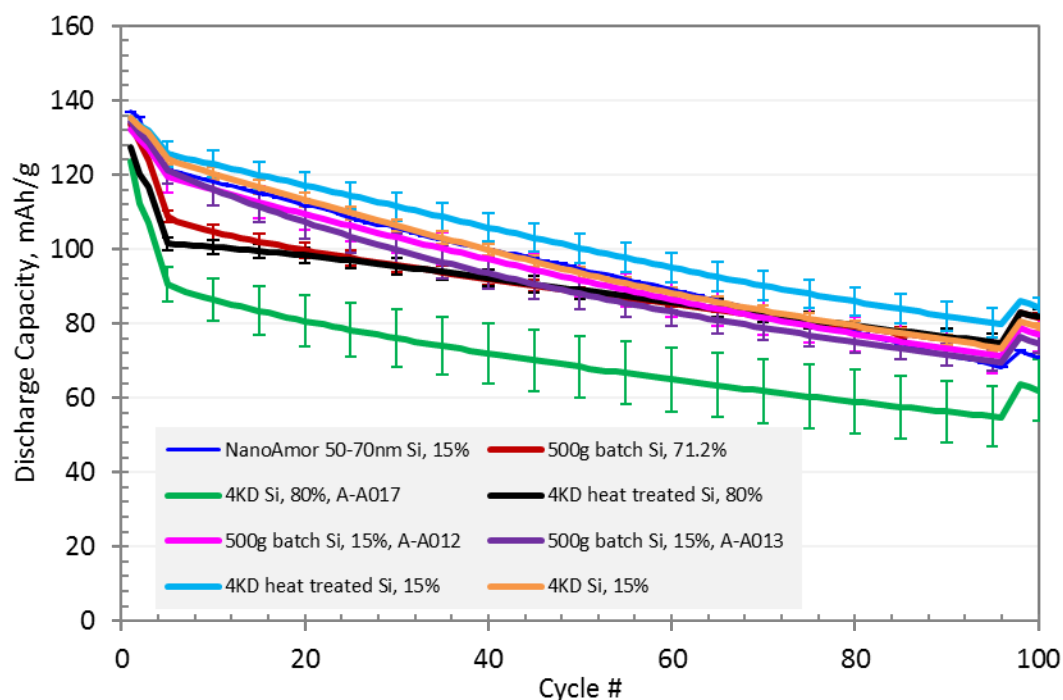


Figure II.1.A.4 Full cell results using the silicon DeepDive protocol for the high-silicon graphite-free anodes and 15 wt.% Si in graphite composite. All anodes were tested against a capacity-matched NMC532 cathode. The anode to cathode capacity pairing for the electrode couples was based on the anode capacities achieved upon a 50-mV lithiation cutoff

Comparing the half-cell and full-cell results, a portion of which was presented in Figure II.1.A.4, we believe that the difference in capacity utilization and fade rate for the high-silicon electrodes is most likely due to subtle uncontrolled variations in mixing and coating of the slurries used to create the electrodes. These subtle variations are magnified greatly due to the high capacity of silicon, which is ten times the capacity of graphite. Such an effect would be expected with the relatively lower amounts of conductive additive used in these high-silicon electrodes. Supported by microscopy studies by ANL Post Test and ORNL teams, it is possible that the silicon particles are more easily isolated and electronically disconnect (partially or completely) from the electronic matrix of the electrode during cycling. These observations have led to joint efforts between ANL and ORNL to develop slurries that lead to more homogeneous electrodes with higher amounts of conductive additive and silicon content in the 50 – 70 wt.% range. Additional and related work in conjunction with the binder development group (Lu Zhang/ANL) has been addressing the role of slurry viscosity, pH, and adhesion to the active silicon particles as a path to strengthening the physical properties of electrodes. For these tests, the silicon sources were from Paraclete Energy, the programmatic baseline material, to ensure surface chemistries are consistent.

Conductive Additives: Using Raman Spectroscopy mapping techniques, electrode homogeneity was explored and is presented in Figure II.1.A.5. The *K-means clustering* algorithm was used to analyze the Raman mapping of each sample. The purpose of using K-means analysis is to partition the large set of the Raman spectra into a small groups or clusters of spectra that have similarities. Each spectrum in a frame of Raman mapping was categorized into three clusters, with each cluster color coded in Figure II.1.A.5. The electrode is not uniform on a microscopic level. The blue region in the Raman map corresponds to a silicon rich, carbon black deficient region. The red region corresponds to a carbon black rich, silicon deficient region. The green region is the silicon/carbon black interface. As constructed the electrodes are best described as islands of carbon black dispersed in a sea of silicon. Because silicon has low intrinsic conductivity, contact between the carbon black and the majority of the silicon needs to be high to achieve the highest capacity on cycling. Inhomogeneities in the electrode structure due to particle size

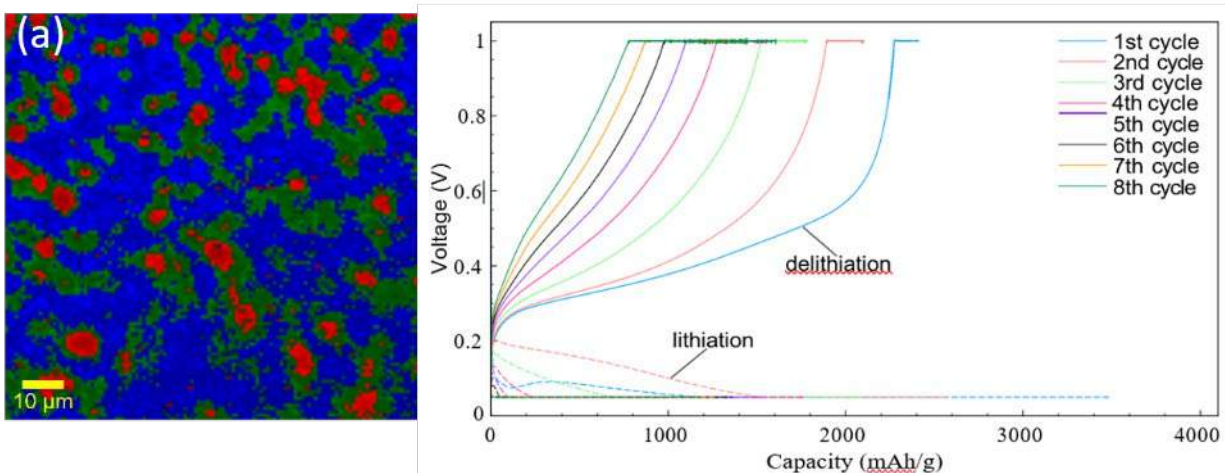


Figure II.1.A.5 (Left) Raman mapping of pristine electrode. (Right) – cycling data for the electrodes

differences, surface chemistry, incomplete polymer interactions, and processing issues may exist. This inhomogeneity may translate to poor cycling performances depending on their defect concentrations and local changes in electrode structure (Figure II.1.A.5 right) that build-up on cycling.

Based on these electrode formulation observations, a study of various types of carbon that can be used to improve electrode stability and the electronic conductivity of the electrode matrix was performed with a high-silicon content (60 wt%). Increasing the concentration of conductive additive in these high-silicon electrodes should ensure that the silicon particles are more firmly connected to the electrode's electronic matrix during cycling. Based on small scale tests and discussions, two series of electrodes were created for the CAMP electrode library, one with 23 wt% electrochemically active Timcal SFG-6-L flake graphitic carbon, 60 wt.% Paraclete Si, 2 wt.% C45 carbon additive, and 15 wt.% LiPAA binder; the second uses a Kureha hard carbon instead of the graphitic carbon. These electrodes were designed to operate with a 100 mV lithiation cutoff (vs. Li^+/Li) as discussed previously.

With these different electrode slurries, electrodes required optimization of the coating wet gap, temperature zone profile, ventilation flow, and coating line speed. This was especially so for the SFG-6-L flakey graphite, as can be seen in Figure II.1.A.6. for various wet gap settings. The final specifications for both of these trial electrodes are summarized in Figure II.1.A.7.

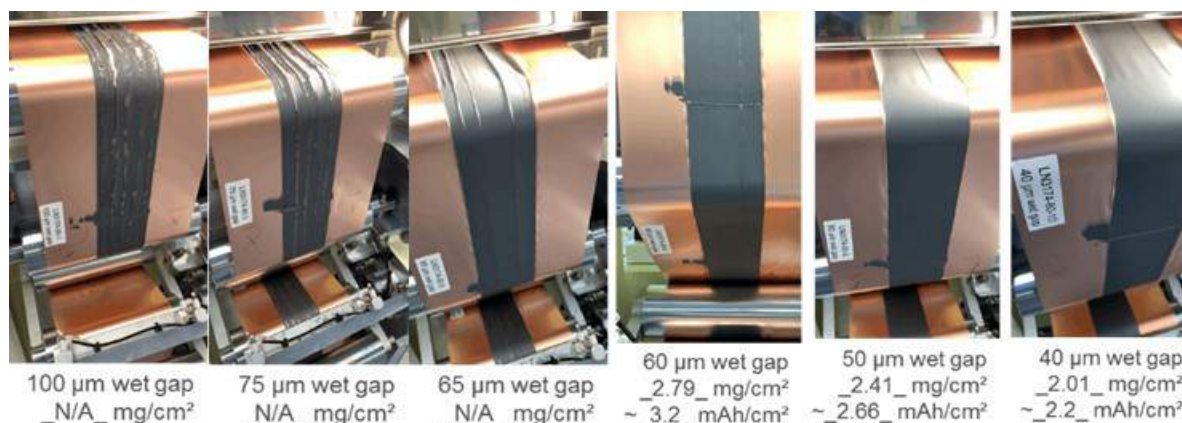


Figure II.1.A.6 Variations in coating quality as a function of wet gap setting for 23 wt.% SFG-6-L flakey graphite with 60 wt.% silicon

The half-cell performance of these two electrodes with 60 wt.% Si are shown in Figure II.1.A.8 with a comparison to two 80 wt.% Paraclete Si electrodes that are graphite-free (A-A017 “4 Kd Si” and A-A018 “Dec 2018 Si”; 10wt.% C45 and 10 wt.% LiPAA). Analysis of the data indicates that the Coulombic efficiency is significantly improved for the electrode with SFG-6-L flakey graphite compared to the 80 wt.% Si electrodes.

Anode: LN3174-80-10

60 wt% Paraclete Energy nSiO “G18-031-MM”
 23 wt% Timcal SFG-6-L flake graphite
 2 wt% Timcal C45 carbon
 15 wt% LiPAA (H₂O), LiOH titrated
Paraclete nSiO (G18-031-MM); “SS” = single sided -> Calculated by hand
 Cu Foil: 10 microns
 Total Electrode Thickness: 28 μ m (SS)
 Coating Thickness: 18 μ m (SS)
 Porosity: 44.4 %
 Total SS Coating Loading: 2.01 mg/cm²
 Total SS Coating Density: 1.12 g/cm³

Made by CAMP Facility

Anode: LN3174-81-8

60 wt% Paraclete Energy nSiO “G18-031-MM”
 23 wt% Kureha Hard Carbon
 2 wt% Timcal C45 carbon
 15 wt% LiPAA (H₂O), LiOH titrated
Paraclete nSiO (G18-031-MM); Kureha Carbon P (S/F) grade hard carbon Lot#: 220801;
 “SS” = single sided -> Calculated by hand
 Cu Foil: 10 microns
 Total Electrode Thickness: 28 μ m (SS)
 Coating Thickness: 18 μ m (SS)
 Porosity: 49.0 %
 Total SS Coating Loading: 1.84 mg/cm²
 Total SS Coating Density: 1.02 g/cm³

Made by CAMP Facility

Figure II.1.A.7 Final specification for the two trial electrodes produced in this quarter based on 23 wt.% electrochemically active carbon (SFG-6-L flakey graphite and hard carbon) with 60 wt.% silicon

After the second cycle this Si-flake graphite electrode has a delithiation specific capacity similar to the electrodes with 80 wt.% Si. Notably, the electrode made with a Kureha hard carbons had noticeably poorer Coulombic efficiency and lower specific capacity than the electrode made with a graphitic carbon.

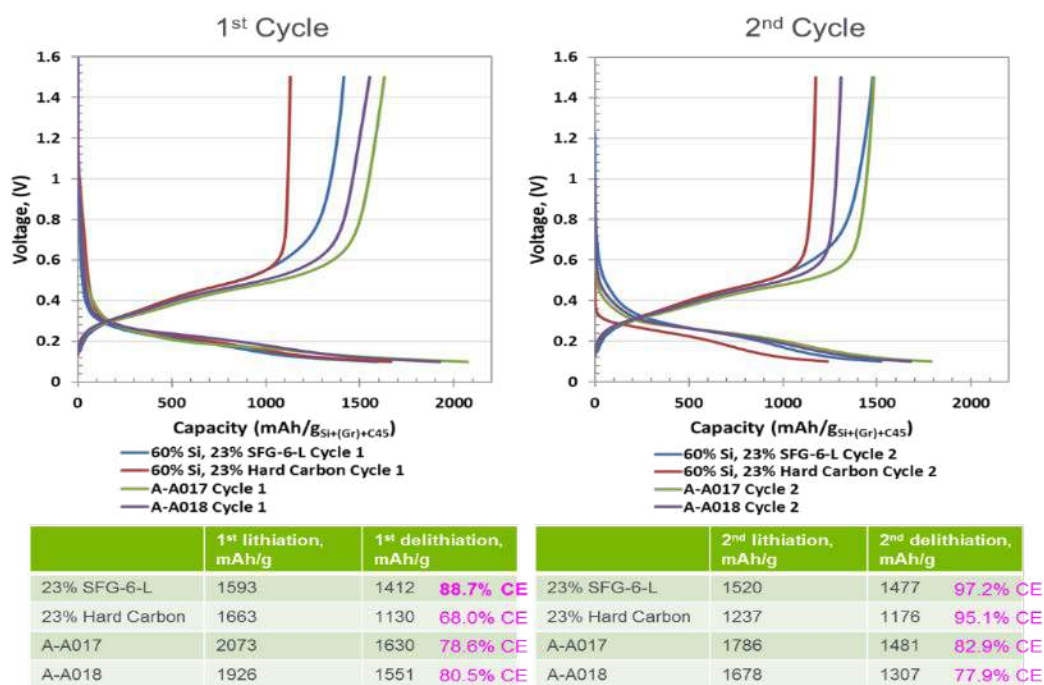


Figure II.1.A.8 Lithiation & delithiation capacity versus lithium metal for 60 wt.% Si electrodes with 23 wt.% of either SFG-6-L flakey graphite or hard carbon. Comparison made to 80 wt.% graphite-free silicon electrodes (A-A017 “4 Kd Si” and A-A018 “Dec 2018 Si”; 10 wt.% C45 and 10 wt.% LiPAA), all fabricated by the CAMP Facility. These cells were cycled between 0.1 to 1.5 V vs. Li⁺/Li

Binder Properties: To improve slurry properties, the use of PAA as a dispersant in the silicon electrode slurry was evaluated using several slurry modifications suggested by the Zeta-potential data from ORNL. Two slurries were tried with 1.8k PAA as the dispersant with either PAA as the binder, or LiPAA as the binder. Two more slurries were prepared without the dispersant to establish a baseline for this study. The PAA and LiPAA were 450k molecular weight. The compositions (dry wt. %) were as follows:

- i. 80 / 10 / 9.5 / 0.5 [Si/C-45/450k PAA binder/1.8k PAA dispersant, water based]
- ii. 80 / 10 / 10 [Si/C-45/450k PAA binder, water based]
- iii. 80 / 10 / 9.5 / 0.5 [Si/C-45/450k LiPAA binder/1.8k PAA dispersant, water based]
- iv. 80 / 10 / 10 [Si/C-45/450k LiPAA binder, water based]

Early data and discussions have highlighted that the order of addition is a variable that needs to be explored and will be a focus in FY20. The slurries above were mixed all at once in a planetary ball mill as a first trial. The rheology of the slurries was investigated and is shown in Figure II.1.A.9 for the slurries based on LiPAA as the binder, with and without the PAA dispersant. Overall, the viscosity-shear rate behavior was very similar, with the dispersant lowering the viscosity slightly, as can be expected.

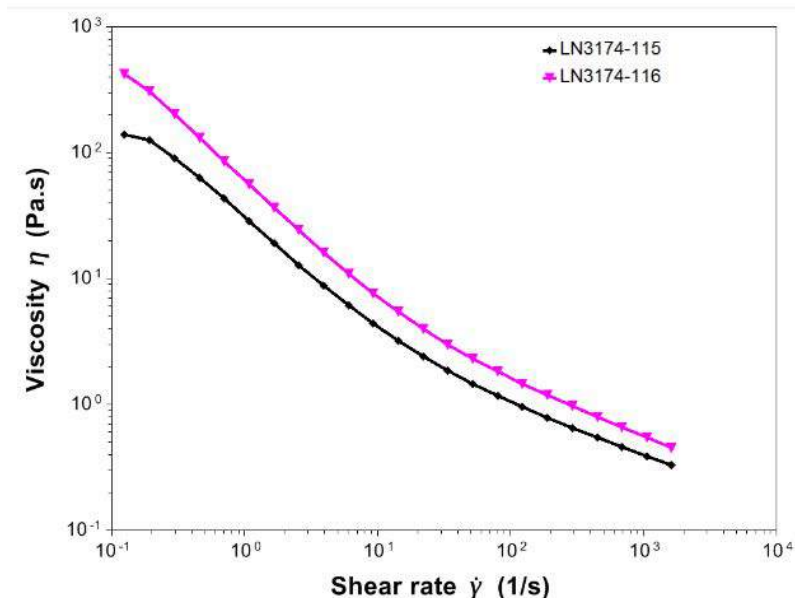


Figure II.1.A.9 Viscosity vs. shear rate for 80 wt.% Si using LiPAA binder with PAA dispersant (LN3174-115) and without PAA dispersant (LN3174-116). Rheology measurement performed using a cone-plate geometry with a cone diameter of 20 mm and an angle of 2°. The temperature was held at 25°C

Initial baseline electrode studies based on LiPAA indicated they were much more uniform than the electrodes based on PAA binder. This was consistent with previously reported CAMP studies establishing the LiPAA-based electrodes as the baseline. While previous PAA-based slurries and electrodes showed inferior lamination properties, the addition of the dispersant to date has shown only small changes in electrode quality. However early state testing of multiple electrodes in a half cell configuration indicates that the cells with PAA as the binder have far better capacity utilization. For comparison the viscosity versus shear rate plot for an SFG6 graphitic carbon electrode with a LiPAA binder is shown in Figure II.1.A.10.

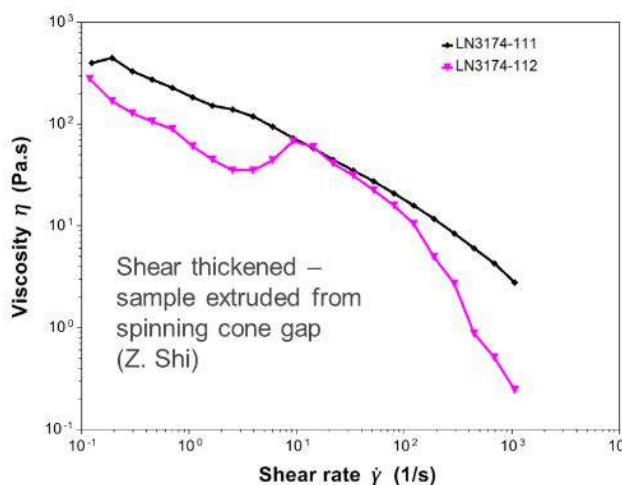


Figure II.1.A.10 Viscosity vs. shear rate for a SFG-6L graphite electrode (no silicon) using LiPAA binder dispersant (black curve, LN3174-111), and for a SFG-6L graphite electrode (no silicon) with PAA binder (magenta curve, LN3174-112). Slurries consisted of 88 wt.% graphite, 2 wt.% C45 carbon, and 10 wt.% binder. Rheology measurement performed using a cone-plate geometry with a cone diameter of 20 mm and an angle of 2°. The temperature was held at 25°C

To better understand these observations, the solution properties of the slurries were investigated. The role of the binder, in addition to adhesion to particles and the current collector foil, additionally involves mediating electrode formation and homogeneity which will influence SEI formation and electrode stability as the Si particles expand and contract. To address this interest, ultra-small angle neutron scattering (USANS) experiments on PAA solutions and PAA solutions with high concentrations of silicon with and without shear has been performed. These shear conditions reflect what occurs during electrode casting and slurry fabrication. USANS is an elastic neutron scattering method where incident neutrons are scattered at very small angles to measure large macrostructural organizations in solids, liquids and mixtures (100-3000 nm). USANS is particularly sensitive to hydrogen containing molecules (PAA) but insensitive to Si. As a result, the data fit provides insights to the polymer structure and dynamics.

For these experiments 450K MW PAA and silicon were obtained from the CAMP facility and used as received. The materials were dispersed in D₂O which allows significant contrast to observe the complex structure of the PAA. Figure II.1.A.11 shows the rheology data measured for the PAA solution and a PAA/Si/CB slurry used to fabricate electrodes at CAMP. The data for the PAA shows an initial flat (Newtonian) viscosity to about 20 Hz followed by a decrease in viscosity attributed to shear thinning due to changes in the PAA conformation within the suspension. In contrast, the slurry shows a more significant shear thinning processes followed by Newtonian behavior then a larger shear thinning behavior at shear rates greater than 20 Hz. This rheological response is indicative of complex interactions within the slurry and point to different polymer structures depending on shear rates which will influence electrode formation and could help explain the differences in performance reported in the literature for PAA-based electrodes.

The USANS data collected for the samples at 0 and 30 Hz are shown in Figure II.1.A.12. The data is presented as intensity versus \AA^{-1} . USANS data was fit with the correlation length model described by Equation 1. The correlation length model characterizes polymer and colloidal solutions on multiple length scales from polymer chain packing to agglomeration. This allows for the exploration of the slurry system on a length scale from 200 nm to 10 microns. Q is a length scale measurement in reciprocal space. The first term represents the Porod scattering at low Q ranges, the second term characterizes the Lorentzian scattering at high Q ranges, and the third term, B is a background correction term. Porod-type scattering represents large features, such as polymer aggregation, while Lorentzian scattering represents small features, such as density of polymer chains in a polymer cluster.

$$(I) \quad I(Q) = A/Q^n + C/(1 + (QL)^m) + B$$

The exponent n characterizes the shape of the particles or aggregates as surface fractals, while the exponent m represents the density of polymer chain packing. The scaling factor A has an inverse relationship with the amount of polymer agglomeration on a micron length scale, while the scaling factor C represents polymer aggregation on a 300 nm to 1-micron length scale. The final parameter L is correlation length which represents the size of a polymer cluster.

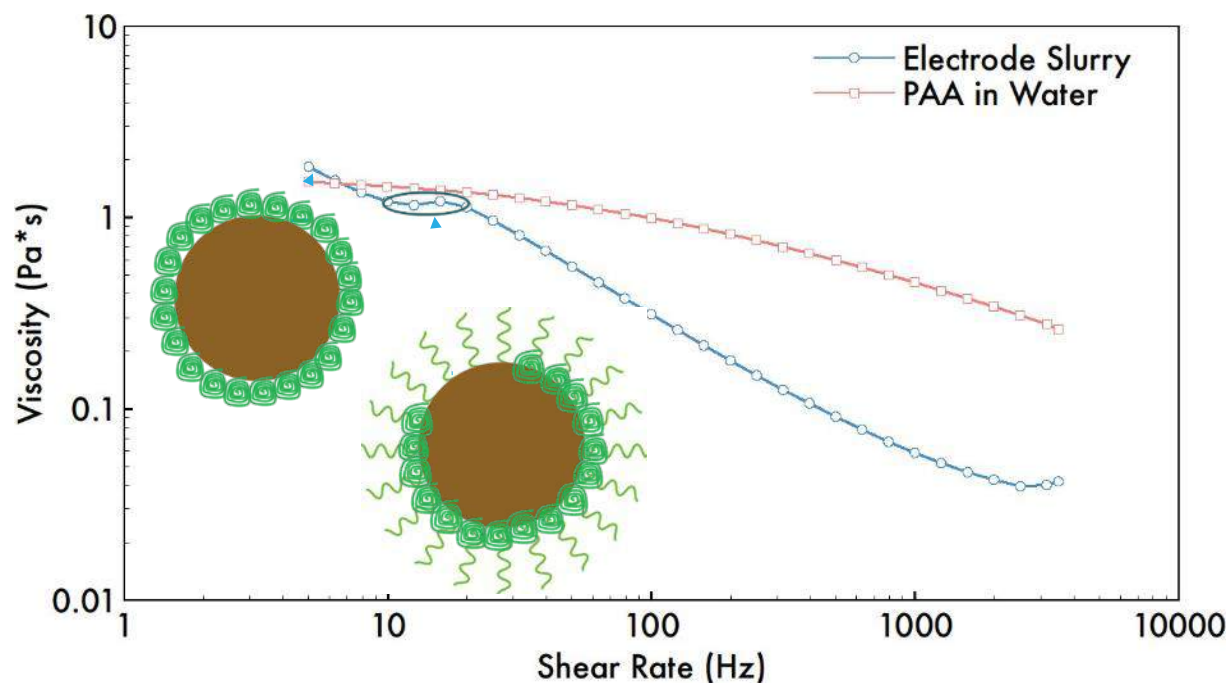


Figure II.1.A.11 Viscosity versus shear rate curve for silicon electrode slurry. Inset schematic from left to right depict 1) extremely collapsed polymer chains on a silicon particle, 2) a mixture of extremely collapsed polymer chains and extended polymer chains as well as polymer that has been sheared and is now in the water phase, and 3) silicon particle aggregation at high shear rates. The line is added to guide the eye

Based on our previous experience, a binder needs to exist as a polymer ellipsoid ($n=2-3$) where the ellipsoid can interact with other polymer chains forming a polymer network homogeneously distributed throughout the electrode slurry with and without shear. Additionally, agglomeration (1-10 μm length scale) and aggregation (0.3-1 μm length scale) of the polymers tend to mediate electrode homogeneity and dispersion. Fitting the PAA data revealed that PAA agglomerates and aggregates at shear rates less than approximately 50 Hz. (The agglomeration parameter, A , decreases from 8.9 to 4×10^{-4} , and the aggregation parameter, C , increases from 2.1×10^9 and 9.1×10^9 .) This is typical behavior in polymer solutions as the polymer becomes entangled with itself causing an increase in agglomeration. At a certain shear rate, the shear stress overcomes the critical entanglement parameter of the polymer and the polymer shear thins. Shear thinning occurs when polymer-polymer interactions are broken by the shear force. The polymer chains then align in the direction of shear and the polymer-polymer interactions are not reformed until shear is removed. The observed changes in the PAA data are consistent with the rheology data in Figure II.1.A.11 showing shear thinning behavior and is due to these changes in the PAA in solution.

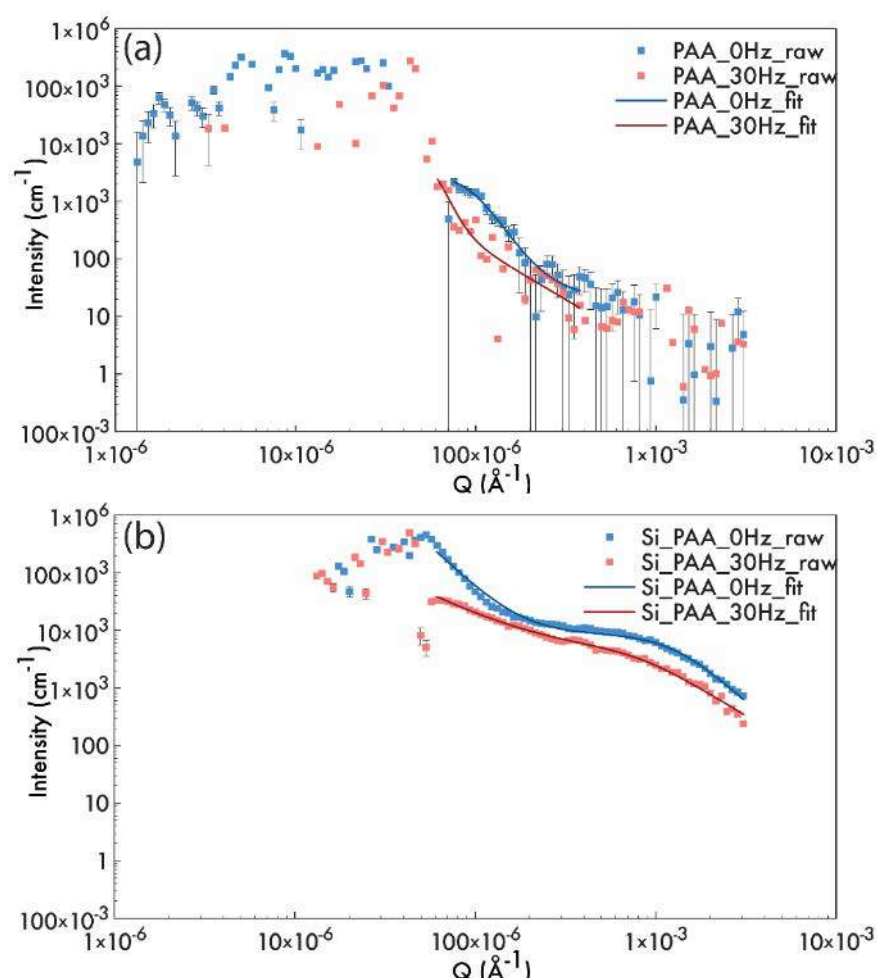


Figure II.1.A.12 Intensity versus Q ultra small angle neutron scattering plots of (a) 14 wt% solution of 450,000 g/mol poly(acrylic acid) in deuterated water at 0 Hz and 30 Hz and (b) a 10 wt% solution of 450,000 g/mol poly(acrylic acid) and silicon nanoparticles (17 wt%) in deuterated water at 0 Hz (experimental data=blue circles, fitted data=blue lines) and 30 Hz (experimental data=red circles, fitted data=red lines)

The addition of silicon results in major changes in the solution polymer structure. Agglomeration and aggregation decrease upon an increase in shear rate with the introduction of silicon. This is the opposite of what was observed with the PAA alone. This may be a result of several possibilities including: 1) PAA chains interactions strongly adsorb to the silicon surface results but the polymer chains elongate and disentangle, 2) PAA desorbs from silicon anode upon shear and disentangle from one other, and 3) extra PAA that cannot adsorb to silicon creates lubrication layers which do not allow PAA chains adhered to other silicon particles to interact with one another. Analysis of USANS data shows that the PAA chains in the Si/PAA slurry are elongating as the L parameter increases from 76 nm to 120 nm upon shear. Elongation implies that polymer chains are disentangling from one another and polymer-polymer interactions are broken. Elongation and disentanglement of the polymer chains are supported by analysis of n parameter where the aggregate goes from a hard sphere ($n=4$) to a polymer ellipsoid ($n=2.6$) as shear rate is increased. For a polymer to exhibit crystal-like scattering ($n=4$), the polymer chain must be highly collapsed and have almost no free volume. For this same polymer to morph into a polymer ellipsoid upon shear, the polymer chains must elongate and begin to fold back on themselves and one another. This data is consistent with the rheology data and demonstrates that

the origin of the shear thinning is a slight elongation of the bound polymers. A schematic of this Si/PAA architecture is shown in Figure II.1.A.12.

The data analysis reveals some surprising differences between the pure PAA and Si/PAA mixture. The PAA solution is comprised of large PAA clusters well dispersed in solution (~1000 nm). The addition of the Si particles causes PAA condensation forming ~76 nm particles, a nearly 10-fold decrease in size due to association with the silicon materials. These bound PAA molecules are strongly associated and not well dispersed in solution. This would indicate the PAA is acting to stabilize the Si in suspension but not interacting to form an extended network which we hypothesize is needed to form a stable electrode.

The properties of the polymeric binder are derived not only from the shear properties and molecular weight, but also the relative pH, functional groups, and viscosity. For baseline electrodes, LiPAA-based binders were chosen based on experimental evidence of final electrode structure. This was believed to be derived from superior viscosity properties associated with slurries with high lithiation. This advantage of better initial electrodes was in part offset by slightly better performance for cells derived from electrodes that were created using an approximately pH neutral PAA binder system. The higher pH used for the heavily lithiated PAA binder systems adversely affects chemical stability of Si particles in the slurry (dissolution of SiO₂), binding strength of PAA, and cycling performance of the silicon anodes due to the involvement of strong base of LiOH. Currently, only *N*-methyl-2-pyrrolidone (NMP) and water have been widely used as processing solvent for silicon electrodes, and the fabricated cells behave drastically differently. Despite the drastic impacts, the role of the processing solvents is not clear.

With these observations, we have investigated alternative methods to generate a more basic solution pH but at lower lithium cation contents to improve the viscosities and processing of the baseline PAA-based slurries. Initially, ammonia (NH₃) and triethylamine (Et₃N) were used as alternative neutralizing reagent to improve the rheological properties of PAA solutions. These additives were in part chosen because after the advantages associated with processing at a more neutral pH were built into the electrode, gentle heating would remove the additives from the electrode in a clean one-step process. A series of SAXS (Small Angle X-ray Scattering) experiments were used to understand the solvation behavior of PAA in various solvents as it related to the basic additives, processed into Si content electrodes and evaluated in Li half cells. These experiments are complimentary to the neutron diffraction studies noted earlier.

Slurry Properties: According to our previous study, aqueous PAA-Li solutions have higher viscosity at low shear rate and better shear thinning at high shear rate than pristine PAA solution. Therefore, more water should be needed for PAA-Li slurry to achieve the desired fluidity. For example, PAA-85% Li slurry requires three times of water to reach the ideal state for lamination compared to that of pristine PAA slurry. The resulting PAA-85% Li slurry is thus more dilute with better dispersion of electrode materials, and less effected by the water evaporation, which is observed all the time in dry rooms. However, PAA-Li binders can lead to more degradation of the fabricated electrodes, which we believe is caused by the increased pH value of the binder solution and weaker binding strength provided by lithiated binder. To address this issue, ammonia (NH₃) and triethylamine (Et₃N, TEA) were utilized as neutralizing reagent instead of LiOH. These weak bases can modify the viscosity of the PAA solution in a similar way as LiOH does but with less of an increase of pH value. As shown in Figure II.1.A.13 the viscosity and shear thinning of PAA solutions neutralized by NH₃ (i.e.,

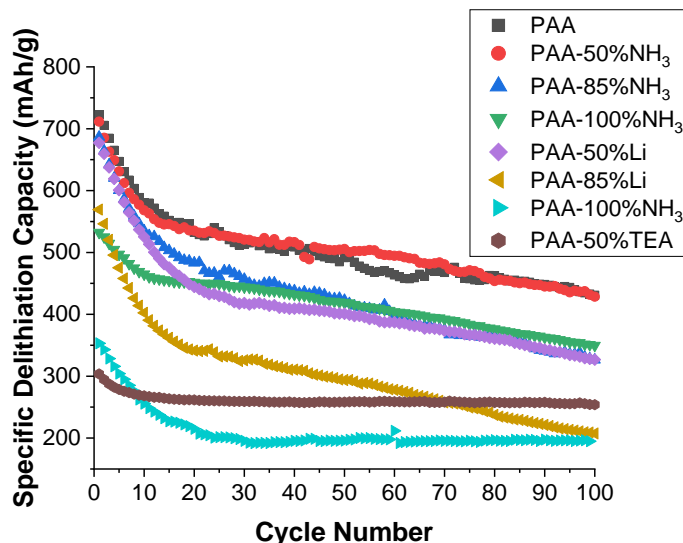


Figure II.1.A.13 Specific delithiation capacity profiles of Li half cells using electrodes containing 73 wt% graphite, 15 wt% Si, 10 wt% modified PAA binders, and 2 wt% C45 over 100 cycles at C/3 rate

PAA-NH₃) is comparable with the current standard PAA-Li binder used by CAMP (i.e., PAA-85%Li with pH of 6). The pH value of PAA-NH₃ solutions (e.g., pH of PAA-85%NH₃ = 5) is lower than that of PAA-85%Li solution. PAA solutions modified by Et₃N (i.e., PAA-TEA) showed even more viscosity improvements due to the bulky [Et₃NH]⁺ cations. For example, PAA-TEA solution with only 50% of Et₃N achieved similar viscosity and shear thinning as PAA-85%Li solution. The pH of PAA-TEA solutions is even lower (e.g., pH of PAA-50% TEA = 4.5). In addition, these weak bases could be removed from the electrode by thermal decomposition during the drying process at high temperature in vacuo. IR analysis for PAA-NH₃ binders after thermal treatment showed a distinct peak around 1700 cm⁻¹, indicating the existence of pristine PAA. Therefore, the binding strength of PAA binder could be restored since the ammonium carboxylate groups will convert to carboxylic acid groups after thermal decomposition. The capacity profiles of graphite-Si composite electrodes fabricated using these modified PAA binders were summarized in Figure II.1.A.14. The cells were subjected to three formation cycles between 0.01 V and 1.50 V at C/20 rate, followed by 100 aging cycles at C/3 rate. PAA-50%TEA cells have much lower initial capacity (303 mAh/g) than pristine PAA cells (722 mAh/g). By looking into the differential capacity profile of a PAA-50% TEA cell, most of the capacity resulting from Si was lost during formation cycles, possibly due to the increased impedance by the large [Et₃NH]⁺ cations. On the other hand, PAA-NH₃ cells have higher initial capacity, higher average capacity, and better capacity retention than those of PAA-Li cells. For example, PAA-85%NH₃ cells have initial capacity of 686 mAh/g, average capacity of 492 mAh/g while PAA-85%Li cells have initial capacity of 569 mAh/g and average capacity of 303 mAh/g. Interestingly, PAA-100%NH₃ cells have slightly lower capacity than PAA-85% NH₃ cells during the first 50 cycles, then the performance catches up and becomes pretty much identical. PAA-100%Li cell has the worst performance among the tested cells as expected due to the aforementioned reasons. Overall, PAA-50% NH₃ solution seems to achieve a good balance with significantly improved rheological properties and comparable performance as pristine PAA cells. We feel confident this new binder neutralization approach is superior to the lithiation approach.

Small-angle X-ray scattering (SAXS) analysis was utilized to investigate the solvation behavior of PAA binders at the APS facility at Argonne by beamline scientist Tao Li (Figure II.1.A.14). SAXS can detect the density difference in a sample at nanoscales and therefore determine size, and shape information of the polymers. The radius of gyration (R_g) is a key parameter that is related to the particle sizes and can be obtained from SAXS signals by applying unified fit to the broad peak composed of a Guinier part and a power law tail in each profile. As shown in Figure II.1.A.14, the results showed that R_g values dropped significantly by adding bases to PAA solution. For a given volume, smaller R_g indicates that the shape of the particle is closer to sphere (i.e., smaller surface area for a given volume) and larger R_g is related to more stretched polymer conformations. Based on the results, we suspect that the better cycling performance of PAA binders, whose solution has a large R_g value (31.63), is maybe resulting from the stretched-out conformation that could prompt the interaction or adhesion with silicon particles. This may explain why the performance of PAA-NH₃ cells compared to PAA cell as the R_g values of PAA-NH₃ solution (5.36) is much smaller.

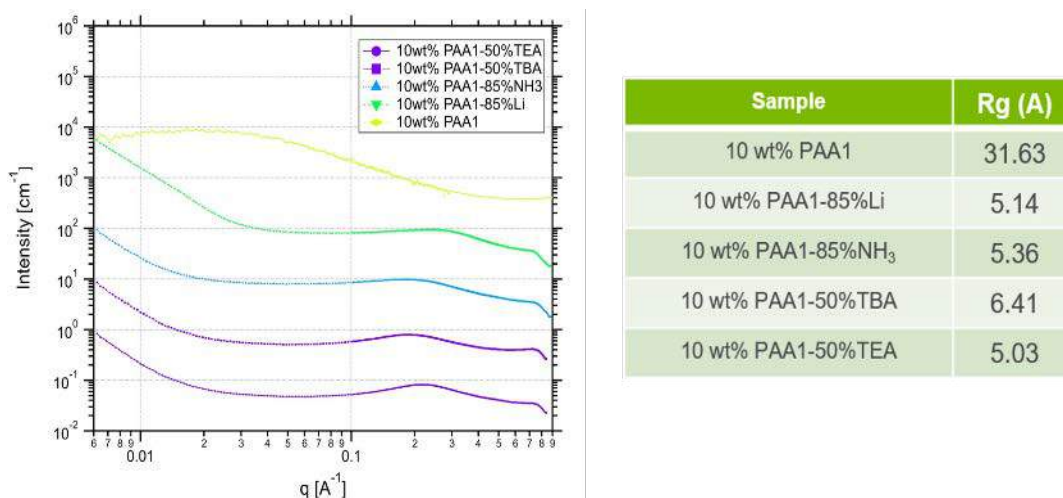


Figure II.1.A.14 (a) Small angle X-Ray scattering (SAXS) profiles for binder solutions; (b) Sample information and R_g of the modified PAA solutions

Moreover, as we observe drastic difference when NMP solvent was used to fabricate silicon electrodes, it is of crucial importance to understand why the changing of processing solvents impact the cycling performance. We adapted SAXS to probe this relationship. Several organic solvents or organic solvent/water mixtures were selected based on certain properties (e.g., boiling point, solubility of PAA, dielectric constant). By using similar testing protocols as shown above, the R_g values of PAA in these solvents as well as cycling performance of the corresponding cells were summarized in Figure II.1.A.15. Right away, we notice the bigger R_g is still from PAA/ water solution and that is also the case in cycling performance. Electrodes fabricated using 1,4-dioxane (PAA-dioxane) and N,N-dimethylformamide (PAA-DMF) have similar initial capacity compared to electrodes fabricated using water (PAA-H₂O), but suffer more severe capacity loss during the first 20 cycles. Electrodes processed via N-methyl-2-pyrrolidone (PAA-NMP) and ethanol (PAA-EtOH) showed significantly lower initial capacity than PAA-H₂O electrodes. Since PAA-H₂O electrodes outperformed all the tested electrodes fabricated using organic processing solvents, organic solvent/water mixtures were prepared to study the role of water. For example, electrodes fabricated using equal weight mixture of 1,4-dioxane and water (PAA-dioxane/H₂O) showed improved performance than PAA-dioxane, but not as good as PAA-H₂O electrodes. The R_g of PAA in 1,4-dioxane/water mixture also falls in between that of pure water and 1,4-dioxane, which is consistent with our hypothesis relating R_g and cycling performance. The outstanding performance of water might be a combined result of solubility, pH, dielectric constant, evaporation rate, and is under investigation.

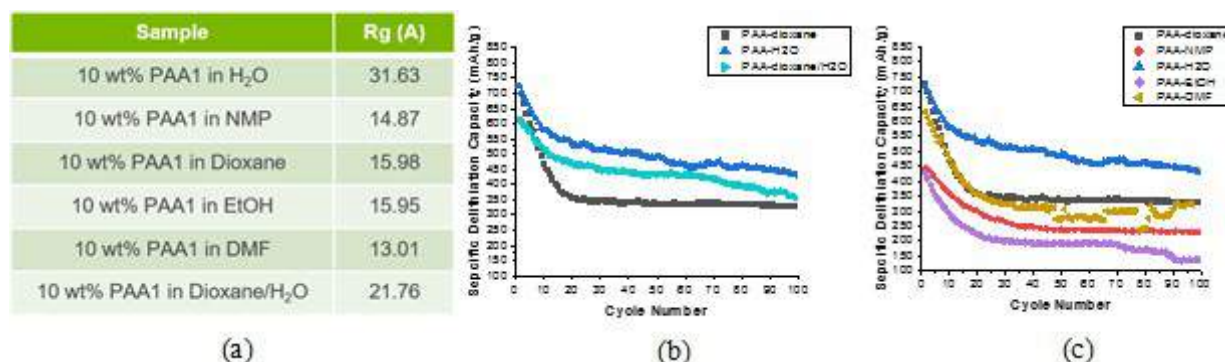


Figure II.1.A.15 (a) Sample information and R_g of PAA solutions; (b) Specific delithiation capacity profiles of half cells using electrodes containing 73 wt% graphite, 15 wt% Si, 10 wt% PAA binders in organic processing solvent, and 2 wt% C45 over 100 cycles at C/3 rate; (c) Specific delithiation capacity profiles of half cells using electrodes containing 73 wt% graphite, 15 wt% Si, 10 wt% PAA binders in mixed processing solvent, and 2 wt% C45 over 100 cycles at C/3 rate

designed to model lithium-ion battery performance and cost, was utilized to establish program relevance by connecting DOE/USABC pack performance targets to anode targets. BatPac analysis of the needs for LIB anode science (see Figure II.1.A.1, left frame) indicated that anode volumetric capacities greater than 1000 mAh/cm³ generally minimizes battery cost when coupled to an advanced NMC cathode. Note that higher capacities result in diminishing savings in cost. The analysis (right frame) also predicts that silicon-graphite electrodes with less than 75 wt% graphite can achieve the 1000 mAh/cm³ target.

Silicon-Binder Interactions: Using silicon nanomaterials is a widely accepted strategy for mitigating the volume expansion associated with the lithiation of silicon and the accompanying capacity fade. However, the high surface area of silicon nanomaterials provides more opportunity for electrolyte decomposition which leads to high irreversible capacity loss and low Coulombic efficiency. By using model crystalline electrodes, a more thorough understanding of the initial lithiation mechanics of the silicon crystalline particles is possible. This work is targeted at the initial crack formation of silicon and how the polymeric capping layers associated with binder interactions are affected by lithiation depth (state of charge) and cracking of the crystalline silicon.

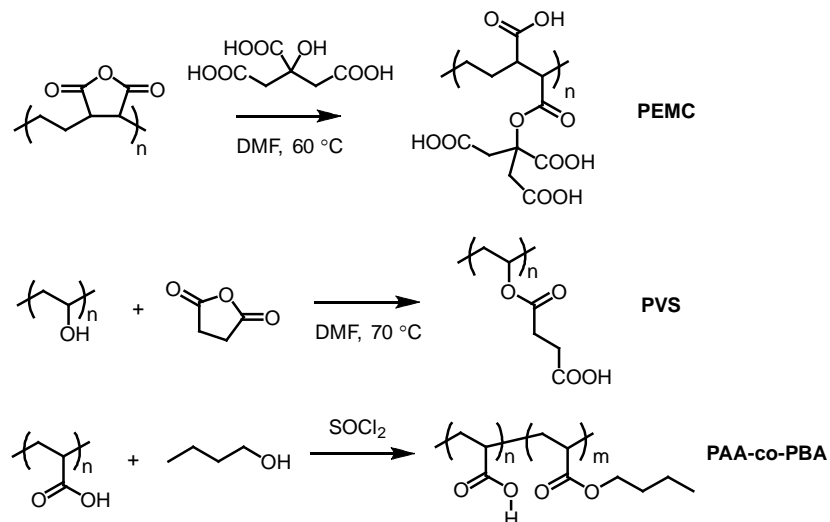


Figure II.1.A.16 Synthetic scheme of PAA analogues with modified properties

Using thin film samples, the formation of buckled silicon within a thin film induced by the anisotropic lithiation of crystalline Si during the 1st lithiation along the $\langle 110 \rangle$ direction was identified. We also noted that as the delithiation proceeded, new cracks oriented along the $\langle 100 \rangle$ direction appear in the intact area where no *geological* deformation occurred during the previous lithiation (Figure II.1.A.17). The $\langle 100 \rangle$ -oriented cracking followed the linear elastic mechanism developed for multilayer structures. Using a linear elastic fracture mechanic (LEFM) model, the results implied that the $\langle 100 \rangle$ -oriented cracking behavior depends on the mechanical properties of the Si substrate and the amorphous Li_xSi layer.

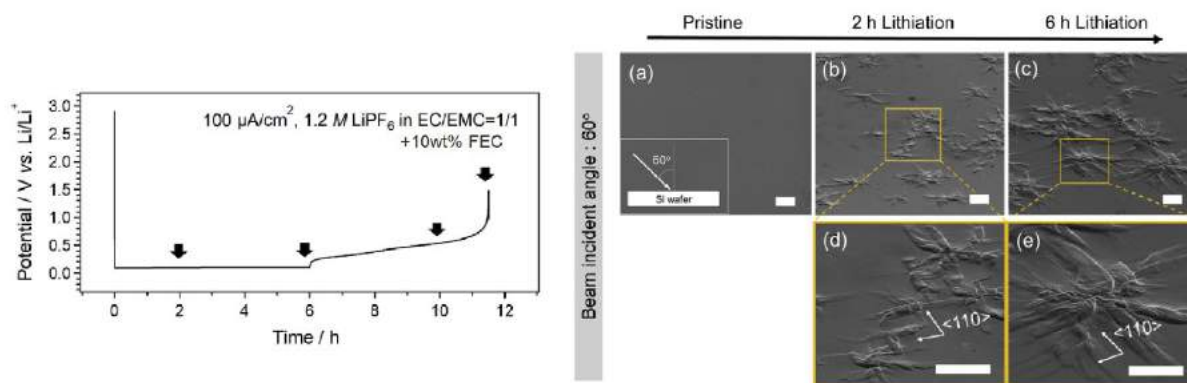


Figure II.1.A.17 Electrochemically Induced Fracture Method. LEFT: Electrochemical cycling conditions used to induce fracturing, where arrows represent times where samples were analyzed via SEM. RIGHT: SEM data of sample in pristine state (a) and following (b,d) 2 h and (c,e) 6 h lithiation

For these studies, the LEFM model assumes an elastic deformation and is known to fail at the *plastic* zone at the crack tip. For the LEFM model to be absolutely applicable, the plastic zone at crack tip must be small with respect to the crack length and dimensions of the sample. Thus, as the ratio of the crack length to the full sample thickness increases, more plastic deformation/types of fracture occur. Figure II.1.A.18 shows that the cracking behavior only follows LEFM-type mechanisms for thicknesses larger than 1 mm thickness. It has been noted that when 675 μm -thick samples are used, the failure mode also includes compression, slabbing, shearing, and microcracking behavior. In the context of the DeepDive effort, the silicon substrates used will be thin enough to exhibit the complex behavior that will be more analogous to the cracking dynamics observed in baseline silicon electrodes.

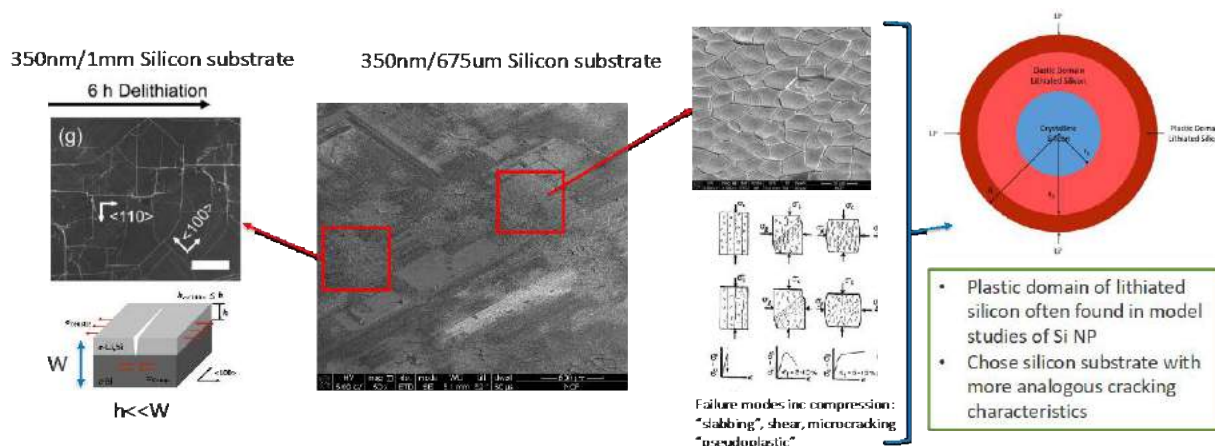


Figure II.1.A.18 Limitations of the linear elastic fracture mechanics (LEFM) model based on the thickness of the silicon wafer. For thick wafers (1 mm), crack propagation occurs along crystallographic directions. For thinner wafers (675 μm), LEFM mechanics cannot be applied. Rather, plastic deformation occurs resulting in a number of different failure modes including compression, slabbing, shear, microcracking, and pseudoplastic behavior—similar to the cracking behavior expected from silicon nanoparticles. SEM data and schematic on left from NREL

With appropriate model silicon wafer thickness established, the mechanical properties of the top surface layer of the crystalline silicon substrates were modified by adding a polymeric capping layer, designed to mimic the properties of the binders used, and observed how these polymeric layers affect the electrochemically induced fractures. Initial experiments were done using a polyvinylidene difluoride (PVDF), polyacrylic acid (PAA), or carboxymethylcellulose (CMC) polymeric binder system and were spin-coated from an NMP solution onto native oxide (SiO_x)-terminated crystalline silicon substrates. The samples were then lithiated to the same extent as control sample of an uncoated SiO_x -terminated silicon anode. For lithiation, $10 \mu\text{A cm}^{-2}$ of current was applied to the working electrode for 60 h using 1.2 M LiPF_6 in EC/EMC = 3/7 (wt%) with 10 wt% FEC electrolytes. The same current density was applied for delithiation with a cutoff voltage of 1.5 V (vs. Li/Li^+).

Plan view SEM images from these PVDF-, PAA-, CMC-coated silicon wafer samples are shown in Figure II.1.A.19 (middle row). Following the 10th charge-discharge cycle, the SEM plan view images show that the polymeric capping layers based on PVDF-capped silicon wafers exhibit extensive cracking all over the sample, whereas wafers using CMC show far less cracking, and PAA capping layers do not appear to have any cracking. Additional studies confirmed that the same level of lithiation was achieved electrochemically. Using cross-sectional SEM images after fast ion bombardment (FIB) milling, it was also observed that the extent of the amorphous silicon (a-Si) layer (thickness) was different between the samples. The PVDF sample underwent more extensive lithiation-delithiation during the electrochemical cycling as inferred from the thicker a-Si layer (several 100 nm thick) in this sample, whereas in CMC- and PAA-coated silicon wafers, show virtually no a-Si present.

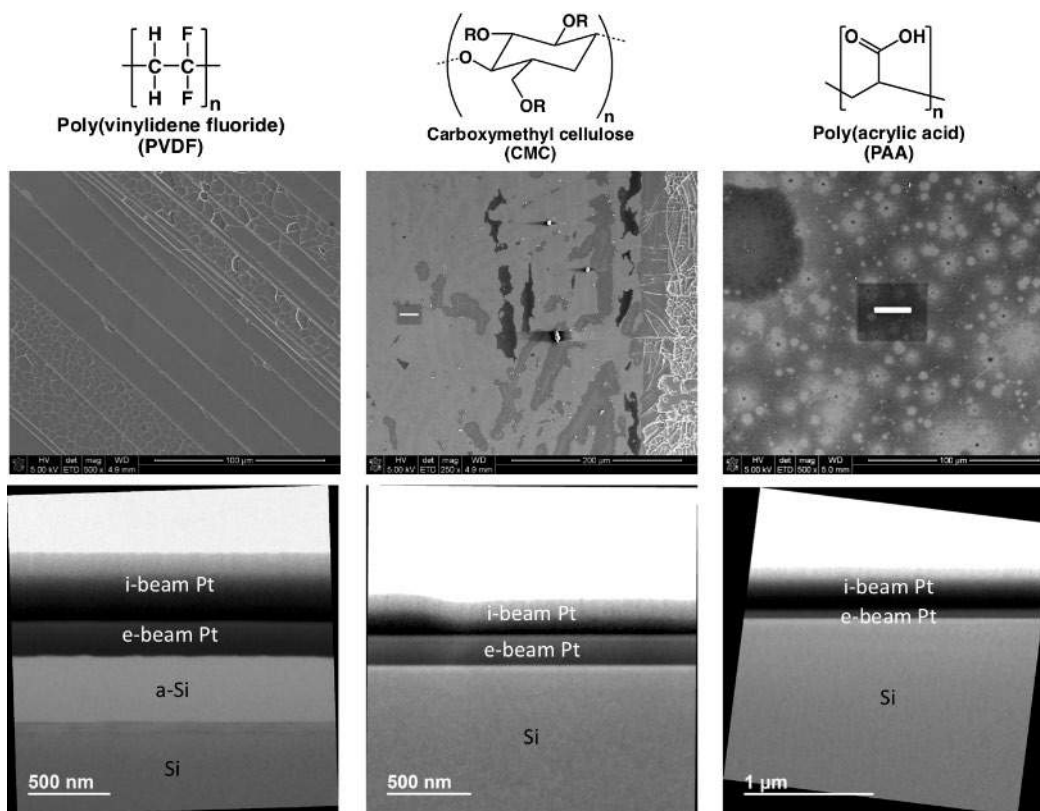


Figure II.1.A.19 TOP: Chemical structures of polymer capping layers used in this study; MIDDLE: Plan view SEM images. BOTTOM: Cross-sectional SEM images after FIB milling. The trench from the FIB milling is seen in the plan view images for CMC- and PAA-capped wafers

In addition to the FIB SEM studies, we have utilized a Cantilevered Beam Test (CBT) technique to measure polymer adhesion to silicon that was developed for photovoltaic module durability and reliability. This is an advanced version of a conventional peel test, which has been applied previously for assessing the binding strength of a polymer to silicon and correlating with the electrochemical performance. A conventional peel test used to measure adhesion force of a material to a substrate, however, does not account for *subcritical debonding*: when delamination occurs at a finite rate at driving forces below its critical strain energy release rate, G_c . This phenomenon may occur in polymer-silicon systems due to the viscoelastic behavior of the polymer and/or stress-enabled chemical reactions with environmental species, such as electrolyte and humidity. We have used this methodology and applied it to polymer-on-silicon wafer electrodes as shown in Figure II.1.A.20, and preliminary data suggests, in conjunction with electrochemical performance data and microscopy data, it can be used to quantify the relationship between the mechanical properties of the surface capping layer and the cracking propagation of underlying silicon electrodes.

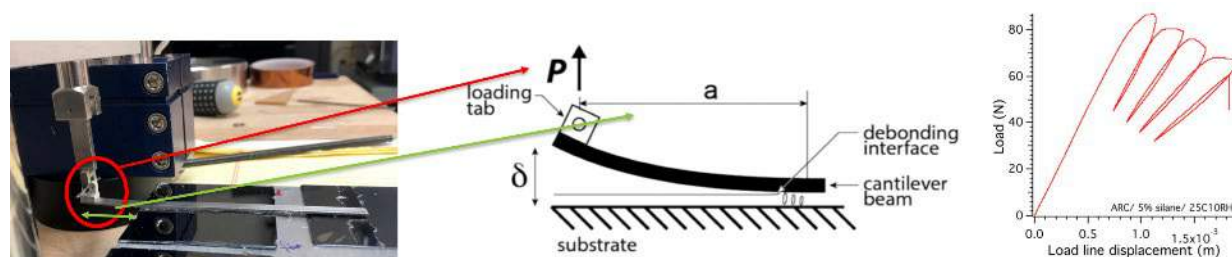


Figure II.1.A.20 LEFT: Cantilever Beam Test (CBT) instrument showing the cantilever bound to a polymer-capped silicon wafer; MIDDLE: Schematic of the single cantilever beam method. RIGHT: Representative load versus displacement plot obtained during a v-G measurement. Load reversals are conducted to extract dC/da (change in beam compliance C as a function of extended debond length a) and obtain G_c values as the debond extends

2. Silicon Surface Modifications

Understanding the electrochemical performance of silicon is dependent on several materials characteristics of the underlying active material. Understanding that the electrochemical process is mediated by the electrolyte-surface interactions, tailoring the surface can provide a pathway towards developing a more stable and robust interface. Within the DeepDive effort, several approaches are under investigation to modify this critical interface via modifications of the underlying silicon rather than by modifications of the electrolyte composition. An example of electrolyte modification may be addition of materials that polymerize to form detached but protective films on the surface, such as fluoroethylene carbonate (FEC), which is a different research pathway than a DeepDive approach of chemically attaching 1) a polymer to the surface (Zhang, Neale), 2) defect elimination in the passivation layer (Lu), or 3) adding electrochemically active interfaces with low oxophilicity to the interface (Tong). This effort supports the electrode effort as it seeks to create an understanding of the interface, active surface species, and viable surface modifications that would feed into to more stable electrode structures and electrochemical performance. In this section, advances and approaches to modifying the surface of the silicon bound within an electrode structure in an electrochemical cell will be discussed.

Functionalization: One of the most direct methods to modify the interface is to utilize the passivation coating as an anchor for a modified chemical species at the interface. While the natural passivation coating of silica has minimal reactivity and thus has limited utility for this effort, the Neale group at NREL has developed methods to scale up hydride-coated silicon particles (designated *H-SiNP*) that possess the requisite reactivity to support designer chemical modifications. In collaboration with the Zhang Group (ANL), hydride terminated silicon created by a plasma method derived from silane, was used as a base for multiple approaches to surface modification. The general approach, shown in Figure II.1.A.21, provides the synthetic route of surface-functionalization. The *H-SiNPs* were modified with an oligoether-epoxy group $((CH_2CH_2O)_n\text{-Epoxy})$ or $(EO)_n\text{-Epoxy}$ via a Pt-catalyzed hydrosilylation reaction.

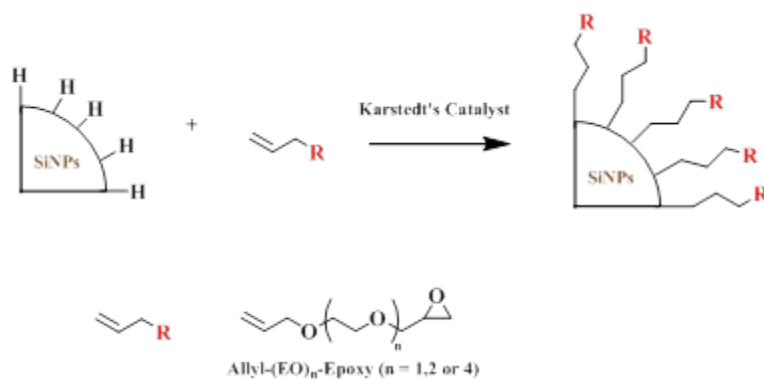


Figure II.1.A.21 Synthesis of surface-functionalized silicon nanoparticles SF-SiNPs

In Figure II.1.A.22 TEM images of the SiNPs before and after surface functionalization are shown. In the figure it is apparent that the H-SiNPs (as provided) are agglomerated into clusters, while after surface functionalization the particles show a more even distribution with no agglomeration noted. The stability of SiNPs created by surface functionalization was further verified by a dispersion experiment, illustrated in Figure II.1.A.22, where surface functionalized SiNP (designated *SF-SiNP*) were dispersed in water. After 24 hours, the sample color and appearance remained unchanged indicating significant stability in the aqueous environment, in contrast, the unfunctionalized H-SiNP when dispersed in water formed translucent solution that precipitated on standing for 24 hours.

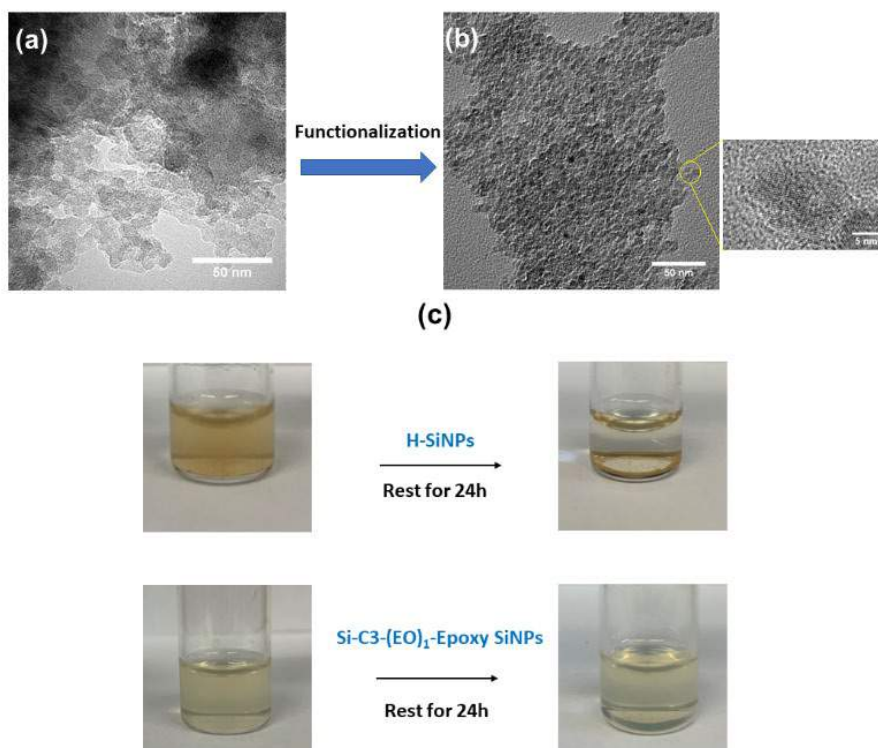


Figure II.1.A.22 (a) TEM images of H-SiNPs and (b) Si-C3-(EO)₁-epoxy SiNPs (the specimens were prepared from a 1 mg g⁻¹ SiNP aqueous suspension by casting the nanoparticles on a carbon-coated copper grid); (c) aqueous dispersions of H-SiNPs and Si-C3-(EO)₁-epoxy SiNPs (left: after 10 min sonication, right: the same dispersions rested for 24 h)

In Figure II.1.A.23 the cycling performance of a SiNP/graphite composite anode is shown. The H-SiNP based electrode showed an initial capacity of 552 mAh/g. This represents approximately 60% of the composite

electrode theoretical capacity (~ 900 mAh/g). This is indicative of high lithium-ion trapping (or loss) due to the chemical/electrochemical instability of the active H-SiNPs. In contrast the SF-SiNP anode materials demonstrated much higher initial capacities (see Table II.1.A.1) under similar conditions of testing to the H-SiNPs. When testing was modified to evaluate these materials at faster rate (C/3), the Coulombic efficiency of the SF-SiNP, specifically for this study the functionalized NP has the composition Si-C3-(EO)_n-epoxy, the electrodes electrochemical performance stabilized at a CE of 99.8% within a few cycles, whereas the anode based on H-SiNPs did not exceed a CE of 99.5% within 80 cycles. These results suggest that the introduction at the interface of these surface functional groups mitigates the surface reactivity of the SiNP anode (seen for the H-SiNP based electrode) and enables improved cycling performance. Figure II.1.A.23 shows the impedance profile of the SiNP electrodes obtained using Electrochemical Impedance Spectroscopy (EIS) measurement. The impedance data were fit to a phenomenological equivalent circuit model consisting of two Randle circuits in series followed by a Warburg diffusion polarization (inset in Figure II.1.A.23). As shown by the R_{ct} (charge transfer resistance) data in Table II.1.A.1, the major difference between the two materials was that the SF-SiNPs showed a much smaller R_{ct} than the anode made with H-SiNPs or with pristine SiNPs anode. The Si-C3-(EO)₂-epoxy electrode under evaluation exhibited the lowest $R_{ct,2}$, indicating limited SEI accumulation/growth and good stability during the cycling. Si-C3-(EO)₂-epoxy functionalized SiNPs showed the least interfacial resistance due to the combination of grafting density and the ideal -EO- geometry for facile Li^+ coordination and transport at the interphase.

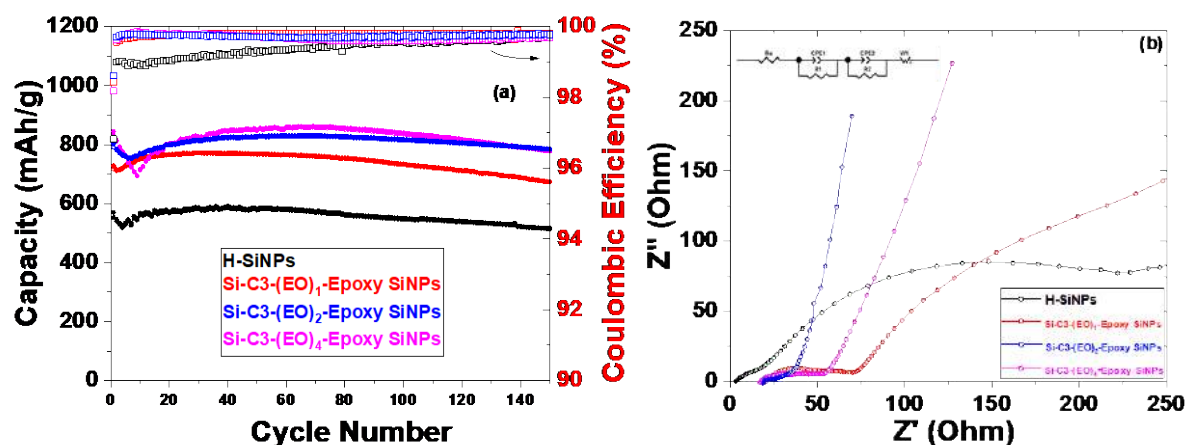


Figure II.1.A.23 Electrochemical performance of Si composite electrodes. (a) Cycling performance and Coulombic efficiency, and (b) Nyquist plots of H-SiNP and SF-SiNP electrodes after 150 cycles

Table II.1.A.1 Summary of Grafting Density, Loading Density, Initial Capacity, Coulombic Efficiency, Capacity Retention, and Charge-transfer Resistance (R_{ct}) of Graphite/silicon Composite Electrodes Fabricated using H-SiNPs or SF-SiNPs.

Anode Material	Grafting density (chains/nm ²)	Loading density (mg/cm ²)	Initial capacity ^a (mAh/g)	Initial Coulombic efficiency ^a (%)	Capacity retention (%)	Charge transfer resistance R_{ct} ^b (Ω)
Si-H SiNPs	N/A	1.6	552	96.8	93.5	$R_{ct,1}$: 7.3 $R_{ct,2}$: 178.1
Si-(EO) ₁ -epoxy	5.1	1.6	717	98.4	94.1	$R_{ct,1}$: 19.0 $R_{ct,2}$: 20.3
Si-(EO) ₂ -epoxy	4.2	1.6	803	98.2	97.9	$R_{ct,1}$: 3.2 $R_{ct,2}$: 5.6
Si-(EO) ₄ -epoxy	3.6	1.6	828	98.6	94.3	$R_{ct,1}$: 24.4 $R_{ct,2}$: 10.6

^a 1st C/3 delithiation capacity and Coulombic efficiency

^b EIS measured at the 150th cycle; $R_{ct,1}$ and $R_{ct,2}$ are obtained from the high and intermediate frequency semi-circles.

Figure II.1.A.24 shows the results of SEM/EDX analysis of the created SiNP/graphite composite anodes before and after cycling. H-SiNPs show large particle agglomeration before cycling (Figure II.1.A.24) and after cycling (Figure II.1.A.23c), whereas the surface functionalized SF-SiNPs are well distributed within the graphitic / silicon active material matrix before cycling (Figure II.1.A.24b) and the same electrode morphology was retained even after 150 cycles, as observed in Figure II.1.A.24d. This morphological difference supports the observed high utilization of the SF-SiNPs material in the composite anode where the better silicon dispersion and a more robust mechanism to prevent agglomeration is enabled. In addition, EDX analysis of the surface films shows that the as-prepared H-SiNPs have more F-rich decomposition products on the surface of the electrode when compared with the SF-SiNP anode. This is indicative that the role being played by the surface functionalization most likely includes mitigation of the parasitic reactions that occur with the electrolyte during repeated cycling.

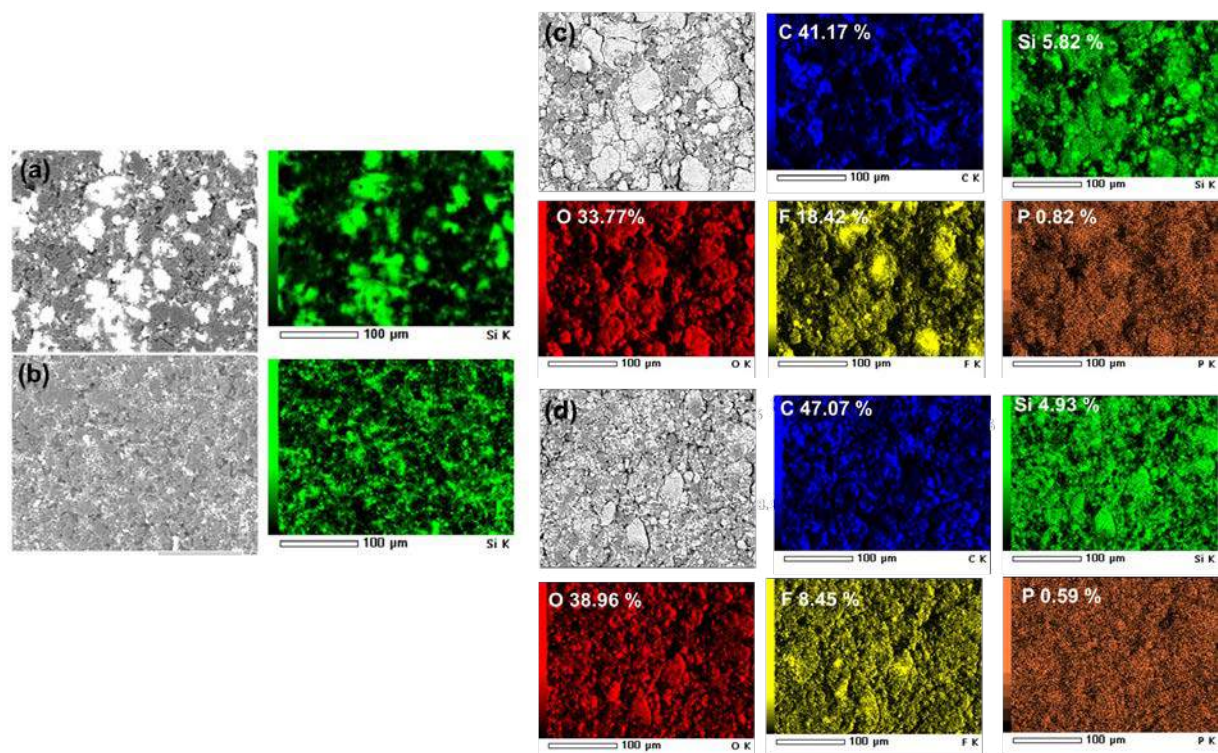


Figure II.1.A.24 SEM images and EDX elemental mappings (colored images) of composite electrodes. (a) H-SiNP anode and (b) surface functionalized Si-C3-(EO)₂-epoxy SiNP anode before cycling, (c) H-SiNP anode, and (d) Si-C3-(EO)₂-epoxy SiNP anode after 150 cycles (C, Si, O, F, and P)

Figure II.1.A.25 shows the electrochemical performance of the H-SiNP electrodes in a half cell. Due to the high reactivity of Si-H group, pristine Si-H terminated SiNPs show both low capacity and Coulombic efficiency. In contrast, after surface functionalization, initial capacities, the Coulombic efficiency and the cycling stability are significantly improved. Figure II.1.A.25b shows the F1s XPS data of the H-SiNP anodes after extended cycling. From this we can conclude that the high reactivity of the H-SiNPs is suppressed with surface functionalization as noted by the large drop off in the amount of LiF detected in the F1s XPS spectra for the SF-SiNPs.

Silicon Tin Amorphous Films: An alternative to direct surface modification of nanoparticles is the addition of a compatible lithium-ion conducting phase to the active silicon electrochemical interface. This concept can be evaluated by using a lithium ion conductor that is stable in the same electrochemical window and reversibly lithiates at a higher potential than the silicon. Literature studies on Si-Sn system, notably by the Dahn group, have demonstrated improved cycling stability of the Si-Sn thin film composite compared to Si alone and it meets the criteria proposed as a test system. Electrochemically, elimination of grain boundaries and distinct crystallites is advantageous for materials mixing and electrode homogeneity. Several methods of synthesis have been evaluated to splat quenching and Si-Sn thin films deposited directly on Cu current collectors by magnetron sputtering. Such thin

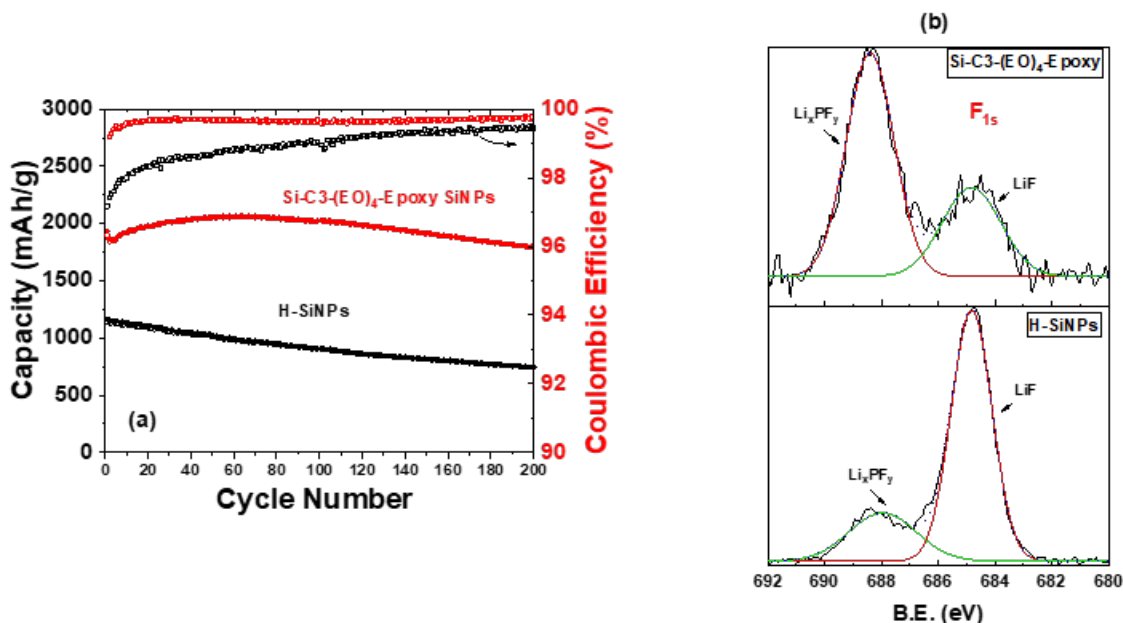


Figure II.1.A.25 (a) Capacity retention and Coulombic efficiency of the pure silicon anodes using H-SiNPs and Si-C3-(EO)₄-epoxy SiNPs as active material, and (b) F_{1s} XPS spectra of H-SiNPs and Si-C3-(EO)₄-epoxy-SiNPs anodes after 200 cycles at delithiated stage

films free of binder/conductive carbon additive offer the opportunity to enable the effective characterization of solid-electrolyte interphase (SEI) formation, mechanistic understanding of the interfaces, and phase evolution upon electrochemical cycling. The co-sputtered films were characterized by X-ray diffraction (XRD), scanning electron microscopy (SEM), energy-dispersive X-ray spectroscopy (EDS) and electrochemical method to determine the optimal composition with superior cycling performance. Postmortem analysis was carried out to gain constructive understanding on the cycling behavior of Si-Sn and compared to pure Si electrodes.

Previous work has determined that the Si-Sn films sputtered from a single target of fixed composition exhibited better electrochemical cycling stability than Si films of similar thickness (Figure II.1.A.26). To allow variation of stoichiometry, the Si-Sn materials were co-sputtering to tune the desired thin film compositions. For these samples Si_xSn_{1-x} composite films were successfully deposited onto a Cu foil current collector by pulsed direct current (DC) magnetron co-sputtering using a 3-inch p-type Si target (99.999% purity) and a 3-inch Sn target (> 99.998% purity). The film composition was tuned by adjusting the deposition power. All the as-deposited films were subsequently stored under vacuum to prevent air exposure and oxidation of the silicon to silica. For evaluation, coin cells were assembled using the films, a Li metal anode, and Gen2 electrolyte. Cells were cycled in galvanostatic mode in the voltage window 1.5 - 0.01 V at C/20. The XRD patterns of the co-sputtered Si_xSn_{1-x} thin films with Si content (x) increasing from 0.45 to 0.87 are shown in Figure II.1.A.26. EDX was used to estimate silicon content, along with a Sn reference. XRD data analysis indicates that at the crystalline Sn peaks are eliminated for x = 0.45 (black line in Figure II.1.A.26b) and films outside that range are X-ray amorphous. Note the two strong peaks around 50 and 60° 2θ are from the Cu substrate.

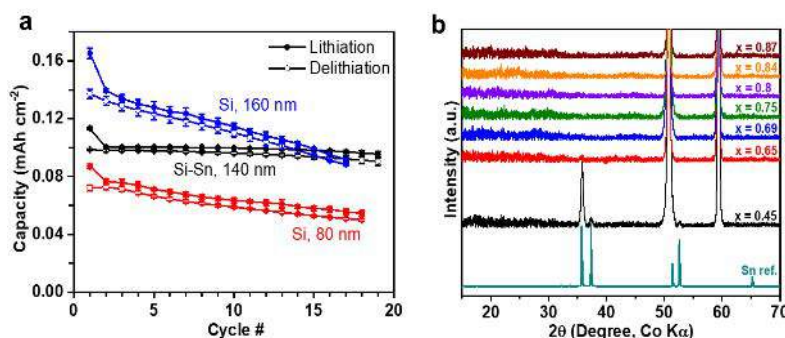


Figure II.1.A.26 (a) Cycling performance of Si-Sn and Si films of similar thickness. (b) XRD patterns of co-sputtered Si_xSn_{1-x} thin films along with Sn reference

Figure II.1.A.27 shows the SEM images of all co-sputtered Si-Sn films. The upper and lower image in each panel is obtained at a low and high magnification, with a scale bar of 1 μm and 100 nm, respectively. At low magnification (except for $x = 0.45$ which showed crystalline Sn), the films show a striated morphology consistent with the underlying Cu substrate. Higher magnification pictures reveal more variation of morphology. For the films of $0.45 \leq x \leq 0.75$, aggregated particles are observed with increasing Sn content, although the films with $0.65 \leq x \leq 0.75$ appear X-ray amorphous. With Sn content decreasing to ≤ 0.2 ($x = 0.8$), no visible particles are observed; instead, uniform films are obtained with the morphology resembling the Cu substrate.

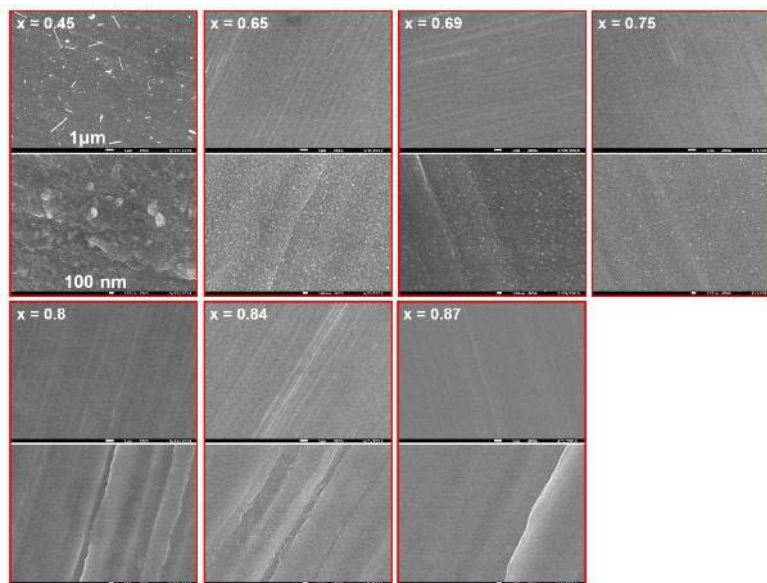


Figure II.1.A.27 SEM images of co-sputtered Si_xSn_{1-x} thin films

The Si-Sn films were evaluated electrochemically and the voltage profiles of the Si-Sn thin films and pure Sn reference for the first two cycles are shown in Figure II.1.A.28. For low Si content ($x = 0.45$) films, characteristic plateaus of Sn are clearly observed. These characteristic features diminish for films of $x = 0.65$ and 0.69 and become almost completely invisible for the films with Si contents greater than 75%. The voltage profiles of films with $x \geq 0.75$ are dominated by the typical lithiation-delithiation features of amorphous Si (a-Si) when a-Si is the major component.

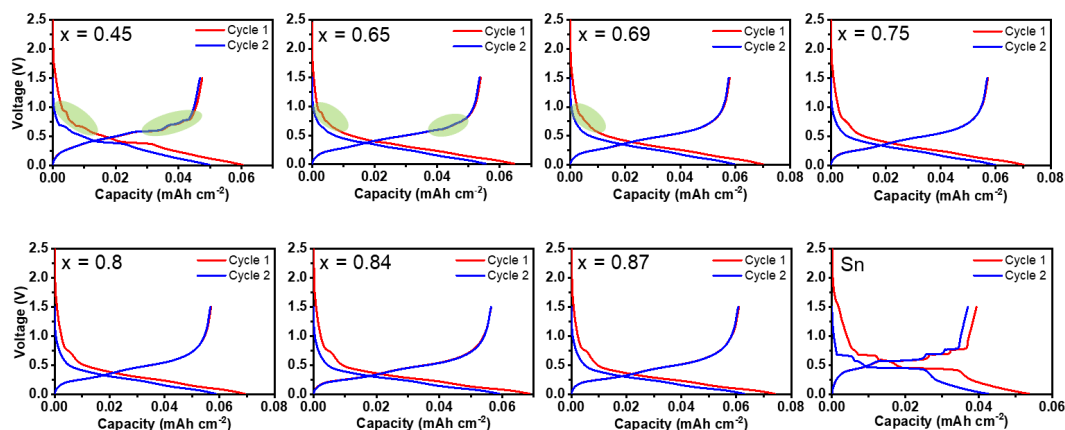


Figure II.1.A.28 Charge-discharge voltage profiles of the co-sputtered $\text{Si}_x\text{Sn}_{1-x}$ thin films during the first two cycles

The corresponding dQ/dV plots of the Si-Sn thin films (Figure II.1.A.29) highlight the role making a homogenous sample in this system aids in preventing phase separation. This was a similar conclusion in the previous electrode slurry studies that more homogenous samples with better dispersion had better electrochemical properties. The distinct sharp lithiation/delithiation peaks are attributed to Sn for $x = 0.45$, but with increasing Si content, the broad lithiation peaks below 0.3 V and delithiation peaks at ~ 0.3 and 0.5 V, characteristic of α -Si, emerge. For films $> 80\%$ Si, the silicon in a Li_xSn matrix cycles with the features of an amorphous phase and agglomeration and particle growth appear inhibited. A more detailed electrochemical cycling performance of the co-sputtered Si-Sn thin films is given in Figure II.1.A.30. The thin film data informed the splat cooling studies underway in conjunction with the Kostecki Group and compositions with approximately 20% Sn are under preparation for scale up to bulk powders.

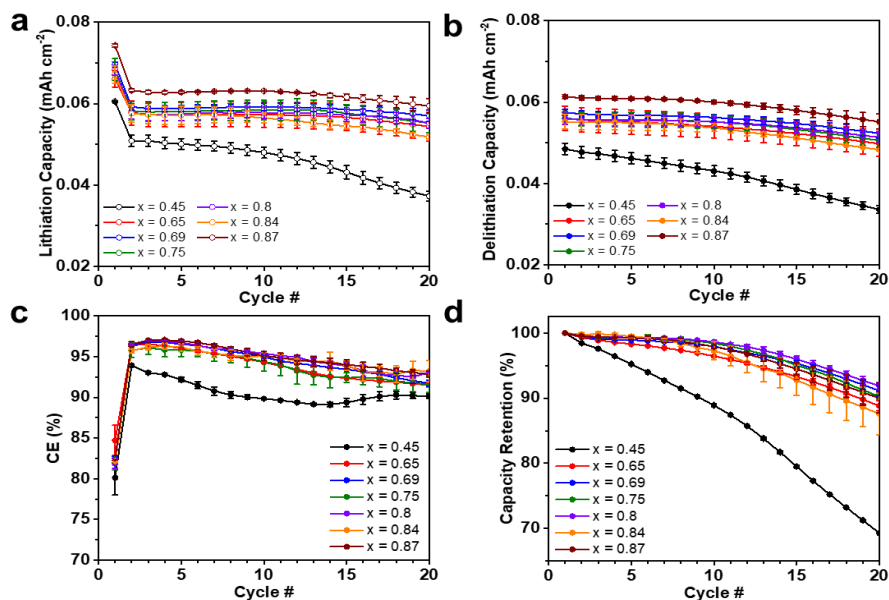


Figure II.1.A.29 (a) Lithiation capacity, (b) delithiation capacity, (c) coulombic efficiency and (d) capacity retention of co-sputtered $\text{Si}_x\text{Sn}_{1-x}$ thin films upon cycling

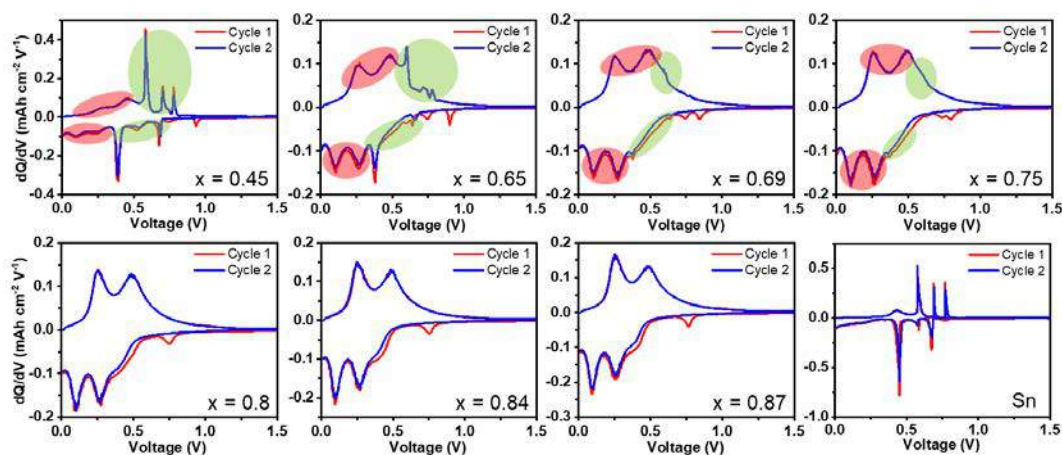


Figure II.1.A.30 dQ/dV plots of co-sputtered $\text{Si}_x\text{Sn}_{1-x}$ thin films during the first two cycles

Carbon-Coated Silicon / Binder Interactions The commercialization of silicon-based electrodes has been hindered by the large volume changes (up to 320%) that result from the insertion/extraction of lithium-ions into/from silicon particles while graphite displays a $\sim 10\%$ volume change. This volume expansion on cycling fractures the silicon particles and increases their surface area, which in turn increases parasitic side-reactions that trap lithium-ions and degrades battery performance. Efforts to modify the silicon particle surfaces to minimize reactivity with the electrolyte and maximize interactions with the polymer binder ranks high among these approaches. Utilizing polymeric coatings to enhance the electronic contact within the electrode matrix is especially important for silicon, given that these particles have an insulating oxide surface layer that forms during material synthesis or storage. Additionally, with charged state reactivity in the cell, surface modification has been proposed as a method to prevent H_2 or other degradation product gases evolution during fabrication processes and during cycling.

To gain a better understanding, X-ray photoelectron spectroscopy (XPS) data was collected from a series Si-based composite electrode containing various surface-modified silicon powders (Table II.1.A.2) obtained from baseline commercial materials vendor Paraclete Energy. The powders were produced by milling and contain Si particles with a mean diameter of ~ 150 nm. The XPS data are for Si particles coated with a thin carbonaceous layer (Si/C), and from Si/C particles with additional coatings based on polyethylene glycol (PEG), polyvinylene difluoride (PVdF), and perfluorooctene (PFO).

Table II.1.A.2 Si Powder Description

Powder	Description
Si/C	Si coated with 2.5 wt% carbon
Si/C/PEG	Si coated with 2.5 wt% carbon, further modified with 4 wt% PEG
Si/C/PVdF	Si coated with 2.5 wt% carbon, further modified with 4 wt% PVdF
Si/C/PFO	Si coated with 2.5 wt% carbon, further modified with 4 wt% PFO

In addition to the silicon, the composite electrodes (Table II.1.A.3) used also contain: carbon (for electronic conduction), graphite (for limiting overall electrode expansion) and partially-lithiated polyacrylic acid (Li-PAA, for active binding to the current collector). The Li-PAA was prepared by titrating polyacrylic acid (PAA) with 1 M LiOH in an aqueous solution; exchanging the protons with Li^+ ions reduce coiling of the PAA polymer chains and improves their adhesion to the particles. XPS measurements of the samples were

conducted at Illinois (UIUC) using a Kratos Axis Ultra X-ray photoelectron spectrometer (Kratos Analytical, Manchester, UK) with monochromatic Al K_{α} radiation (1486.6 eV).

Table II.1.A.3 Electrodes with Silicon, Graphite (Gr), Carbon Black (CB) and LiPAA

Electrode	Si type, wt%	Gr, wt%	CB, wt%	LiPAA, wt%
15 wt% Si / C	Si/C, 15%	73	2	10
70 wt% Si / C	Si/C, 70%	...	15	15
90 wt% Si / C	Si/C, 90%	10
70 wt% Si / C/PEG	Si/C/PEG, 70%	...	15	15
70 wt% Si / C/PVdF	Si/C/PVdF, 70%	...	15	15
70 wt% Si / C/PFO	Si/C/PFO, 70%	...	15	15

Figure II.1.A.31-Figure II.1.A.34 shows XPS data collected from the various electrodes. A comparison of the C 1s spectra are shown in Figure II.1.A.31 of the various components on the electrode surface. The Si 2p regions collected from electrodes are shown in Figure II.1.A.32. The O 1s spectra collected from the electrodes fabricated with the surface-modified silicon particles are shown in Figure II.1.A.33. The F 1s spectra from the electrodes are shown in Figure II.1.A.34. Surface quantification from spectral data on the electrodes is summarized in Table II.1.A.4. In general, the elemental composition trends are as expected.

Electrochemical button cells were used for the electrochemical tests. Testing was done in either half cells with a Si-composite electrode along (and a Li-metal anode) or in full cells with a capacity-matched NMC532 ($\text{LiNi}_{0.5}\text{Mn}_{0.3}\text{Co}_{0.2}\text{O}_2$) cathode. The electrolyte used was DeepDive standard baseline Gen2+10% FEC.

Table II.1.A.4 Surface Compositions of the Electrode Samples Measured by XPS

Sample	F, at%	O, at%	C, at%	Si, at%
15% Si/C	...	21.3	68.9	9.9
70% Si/C	...	25.7	52.3	22.0
90% Si/C	...	29.7	34.6	35.7
70% Si/C/PEG	...	27.0	45.5	27.5
70% Si/C/PVdF	4.0	28.4	43.2	24.5
70% Si/C/PFO	12.1	23.1	43.0	21.8

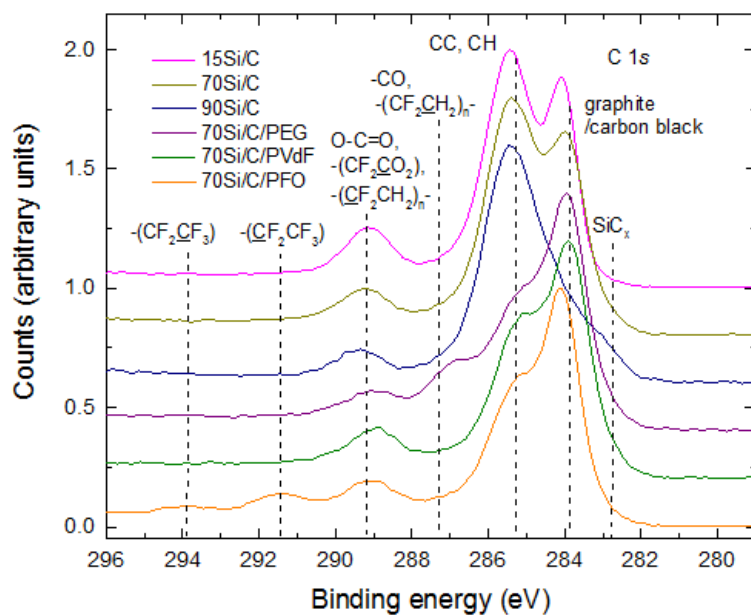


Figure II.1.A.31 C 1s spectra from the 15 wt% Si/C, 70 wt% Si/C, 90 wt% Si/C, 70 wt% Si/C/PEG, 70 wt% Si/C/PVdF, and 70 wt% Si/C/PFO-based electrodes

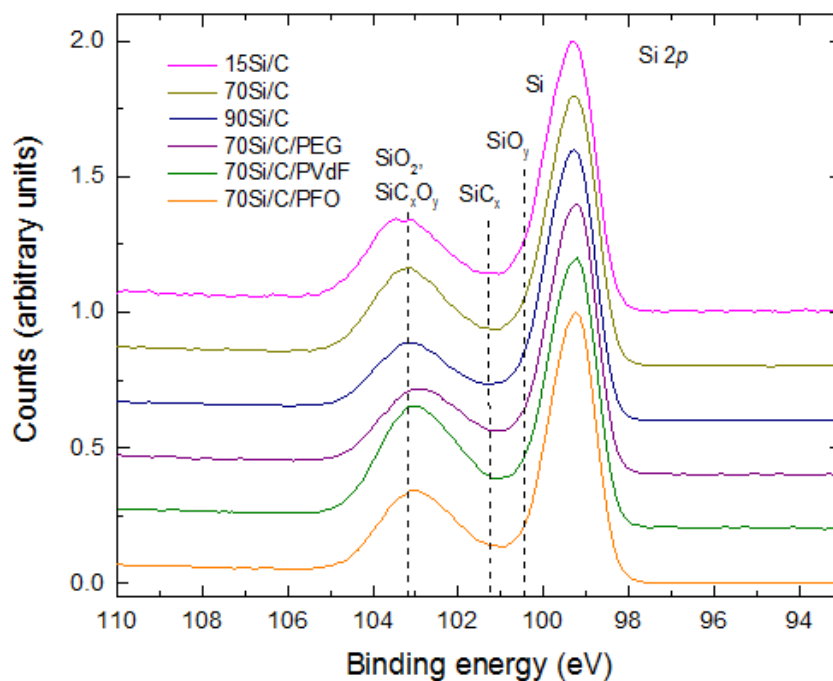


Figure II.1.A.32 Si 2p spectra from the 15 wt% Si/C, 70 wt% Si/C, 90 wt% Si/C, 70 wt% Si/C/PEG, 70 wt% Si/C/PVdF, and 70 wt% Si/C/PFO-based electrodes

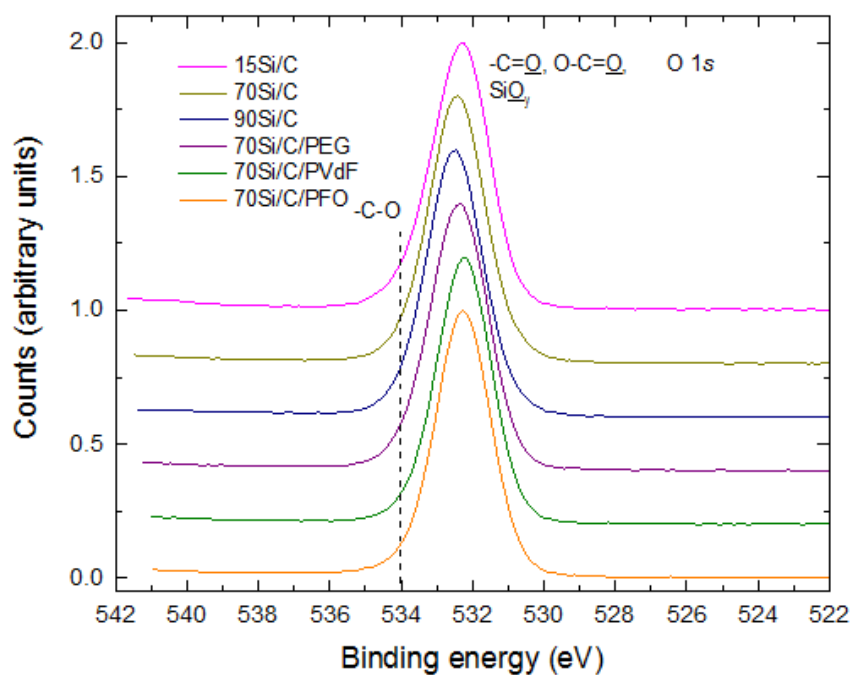


Figure II.1.A.33 O 1s spectra from the 15 wt% Si/C, 70 wt% Si/C, 90 wt% Si/C, 70 wt% Si/C/PEG, 70 wt% Si/C/PVdF, and 70 wt% Si/C/PFO-based electrodes

Table II.1.A.5 First Cycle Capacities and Coulombic Efficiencies of Half Cells with Si Electrodes

Electrode	Si type, wt%	Lithiation, mAh/g	Delithiation, mAh/g	Coulombic Efficiency, %
15 wt% Si / C	Si/C, 15%	527	460	87.3
70 wt% Si / C	Si/C, 70%	1606	1375	85.7
90 wt% Si / C	Si/C, 90%	1823	962	52.8
70 wt% Si / C/PVdF	Si/C/PVdF, 70%	1554	1264	81.3
70 wt% Si / C/PFO	Si/C/PFO, 70%	2218	1904	85.8
70 wt% Si / C/PEG	Si/C/PEG, 70%	2098	1721	82.1

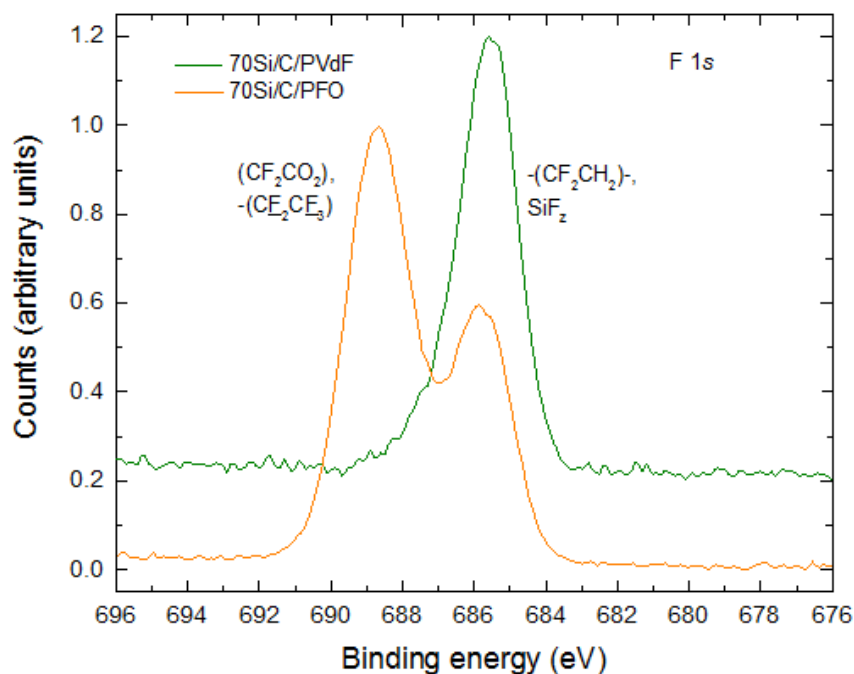


Figure II.1.A.34 F 1s spectra from the 15 wt% Si/C, 70 wt% Si/C, 90 wt% Si/C, 70 wt% Si/C/PEG, 70 wt% Si/C/PVdF, and 70 wt% Si/C/PFO-based electrodes

Figure II.1.A.36 shows the differential capacity (dQ/dV) peak associated with electrolyte reduction during the first cycle and SEI formation; peaks are present for all samples, except 90 wt% Si/C. In all cases, the peak is centered in the 1.0 – 1.1 V range, which is characteristic of FEC reduction. The small variations in peak location and intensity suggest subtle differences in electrolyte reduction (and possibly SEI composition) for the various samples. The apparent lack of a ~1.0 V peak for the 90 wt% Si/C sample maybe from the increased polarization (and hence delayed solvent reduction) resulting from the absence of carbon black in the electrode.

The full cells were cycled in the 3.0–4.1 V range; the data from the tests are given in Table II.1.A.6 and Figure II.1.A.37. The 15 wt% Si / C cell has higher initial discharge capacity than the 70 wt% Si / C and 90 wt% Si/C cells. The capacity differences arise from differences in the 1st cycle coulombic efficiencies, which are 76.1, 67.8 and 50.3% for the 15, 70 and 90 wt% Si cells, respectively. This trend is in line with expectations in line with the adage that “higher the Si content, greater the lithium losses in the solid electrolyte interphase (SEI)”. The absence of C45 carbons explains the low capacity retention (11.2%) of the 90 wt% Si/C cell because active particle isolation becomes more likely. As for the coatings on underlying Paraclete Si particles, PVdF and PFO have small effects on the capacity retention that are within the range of uncertainty. The cell with the PEG-coated particles shows a rapid loss of capacity suggesting that the reactions of PEG with the SEI yield compounds that isolate the active particles. The higher reactivity of the PEG samples on cycling is in line with the observations by Key and Vaughey (ANL) noted last year, that the charged silicon anodes showed heightened reactivity to this class of binders when compared to other available options.

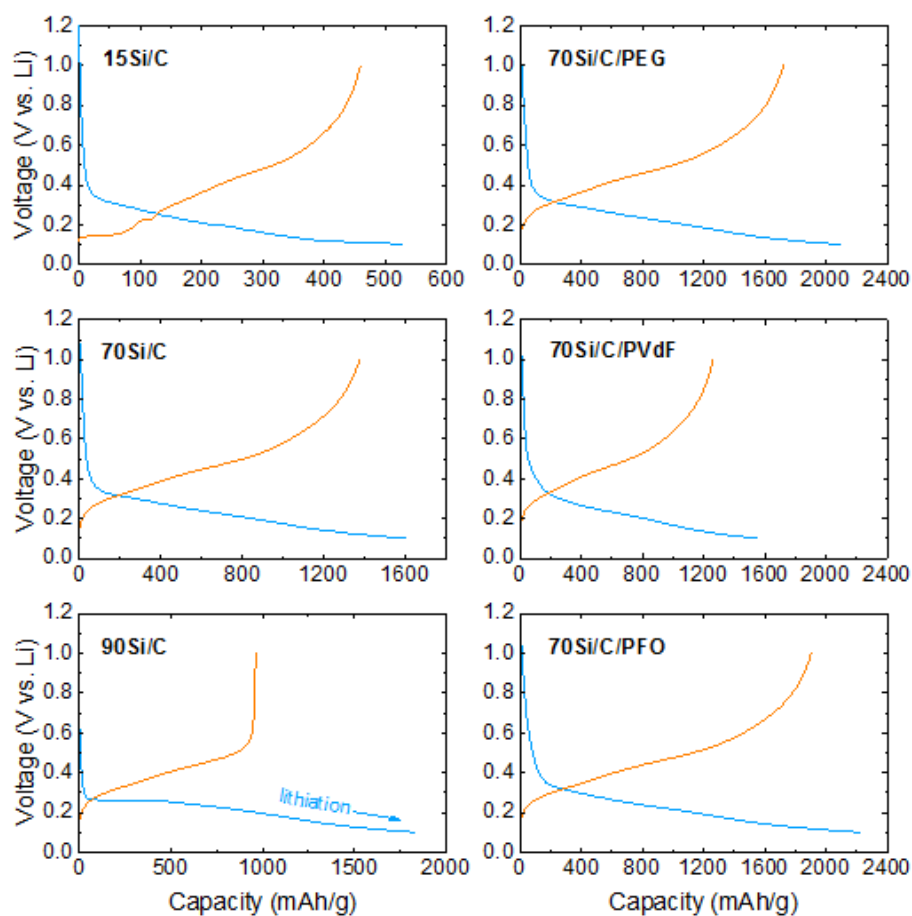


Figure II.1.A.35 Electrode potential changes during the first lithiation/delithiation of half-cells with the 15 wt% Si / C, 70 wt% Si / C, 90 wt% Si / C, 70 wt% Si / C/PEG, 70 wt% Si / C/PVdF, and 70 wt% Si / C/PFO electrodes

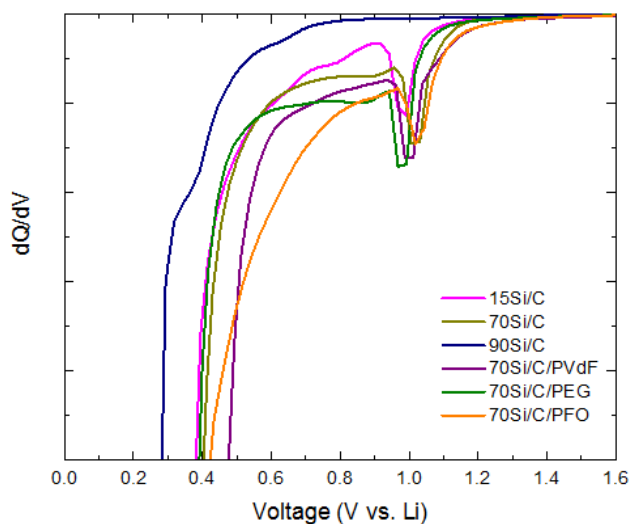


Figure II.1.A.36 Differential capacity (dQ/dV) as a function of voltage during the first lithiation of half-cells with the 15 wt% Si / C, 70 wt% Si / C, 90 wt% Si / C, 70 wt% Si / C/PEG, 70 wt% Si / C/PVdF, and 70 wt% Si / C/PFO electrodes. The peak observed at $\sim 1.0 - 1.1$ V is not observed during subsequent lithiation cycles

Table II.1.A.6 Discharge Capacities (1st and 99th cycle) and Capacity Retention of the Full Cells

Electrode	Si type, wt%	1 st cycle, mAh/g	99 th cycle, mAh/g	Retention, %
15 wt% Si / C	Si/C, 15%	136.4	85.4	62.6
70 wt% Si / C	Si/C, 70%	118.6	79.4	66.9
90 wt% Si / C	Si/C, 90%	93.2	10.5	11.2
70 wt% Si / C/PVdF	Si/C/PVdF, 70%	120.2	74.9	62.3
70 wt% Si / C/PFO	Si/C/PFO, 70%	130.0	86.7	66.6
70 wt% Si / C/PEG	Si/C/PEG, 70%	122.8	21.2	17.3

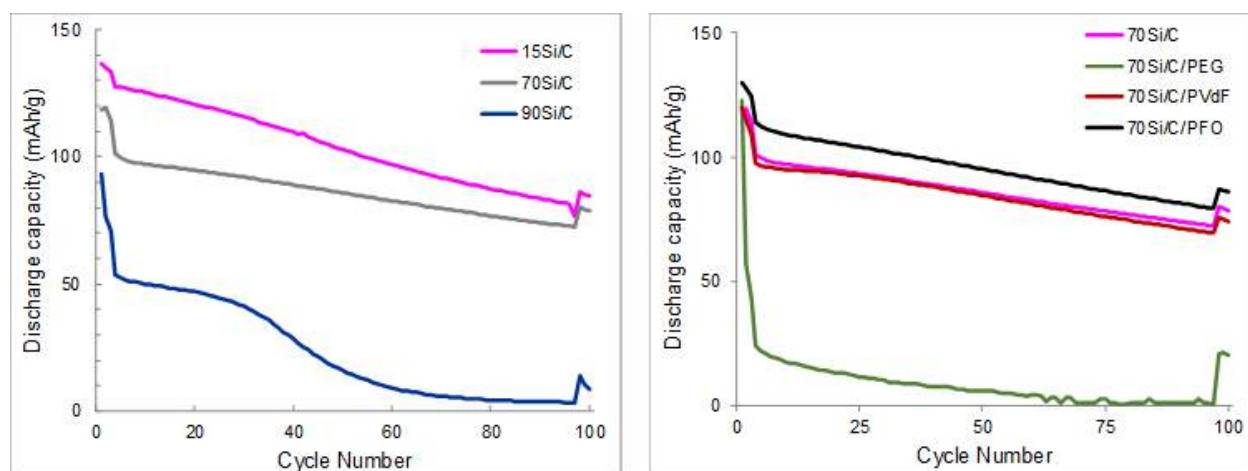


Figure II.1.A.37 Comparing the discharge capacity vs. cycle number for full cells containing (a) 15 wt% Si / C, 70 wt% Si / C, 90 wt% Si / C and (b) 70 wt% Si / C, 70 wt% Si / C/PEG, 70 wt% Si / C/PVdF and 70 wt% Si / C/PFO electrodes. Cycles 1-3 and 97-100 are at a $\sim C/20$ rate, where C refers to the initial C/1 capacity of the cells; cycles 4-94 are at a $\sim C/3$ rate

Observationally, the XPS data were consistent with expectations with peaks from silicon, the particle coatings, carbons, and binder observed in the spectra. The effect of the polymeric coatings on the silicon were minimal in either cell design scenario used. The best data were obtained for the perfluorooctene (PFO)-coated silicon particles that displayed a higher initial capacity, however, the capacity fade rate for these electrodes were similar to that of the uncoated particles indicating the method of coating and types of polymeric coating materials do not improve the performance of the underlying electrode materials beyond an initial positive effect.

Interfacial Zintl Phase Formation: Whereas the efforts noted above evaluated coatings that were associated with the surfaces of the silicon anode, the incorporation of a material into the surface, to become part of the surface aids in stability and longevity as the extra interface becomes either non-existent or can be described as a gradient. An alternative approach to the surface functionalization via surface attachment with poly-ether groups is the formation of a gradient at the interface that at the surface acts to reduce the redox activity of the electrode. In these silicide systems, the reducing power of the surface species is significant and previous work has shown that the reactivity of these phases with free solvent molecules and binders was a significant side reaction that exacerbated active lithium losses. With the introduction of various multivalent cations, we have identified a pathway that maintains the electrochemical properties of the bulk silicon electrode while reducing

the redox activity of the surface, the interface in contact with the electrolyte. Tuning the methods of introduction and identifying in situ synthesis methods can lead to control of the reactivity by tuning the reactivity and defect chemistry.

Whereas we previously reported that binary Li-Si phases are reactive against most common solvents and binder materials, Li-M-Si ternary compounds (M= Mg, Zn, Al, Ca) are chemically stable against common electrolyte solvents and they can be formed in situ through electrochemical co-insertion after adding $\text{Mg}(\text{TFSI})_2$ (or salts Zn, Al or Ca) as a second salt into the electrolyte at low concentrations. Mechanistically, it's been noted that the phenomenon changes the traditional Li-Si binary surface chemistry while minimally effecting the electrochemical profiles, capacities, and rate capabilities by stabilizing the interface and reducing side reactions with the electrolytes. Initial half-cell electrochemical testing showed higher capacity, better cycling, and improved coulombic efficiencies with the new electrolyte containing $\text{Mg}(\text{TFSI})_2$ as the secondary salts.

Table II.1.A.7 Formulations and Notations of the Electrolytes Used in this Study

Notations	Components
Gen2	1.2 M LiPF_6 in 30 wt% EC + 70 wt% EMC
GenF	Gen2 electrolyte + 10 wt% FEC
GenFM	GenF electrolyte + 0.1 M $\text{Mg}(\text{TFSI})_2$
GenFZ	GenF electrolyte + 0.1 M $\text{Zn}(\text{TFSI})_2$
GenFA	GenF electrolyte + 0.1 M $\text{Al}(\text{TFSI})_3$
GenFC	GenF electrolyte + 0.1 M $\text{Ca}(\text{TFSI})_2$
GenFL	GenF electrolyte + 0.1 M LiTFSI

NMC532: In a full cell test, two standard CAMP anode baselines (Si+GenF and Graphite+Gen2) were used with appropriate active material loadings to match CAMP NMC532 ($\text{LiNi}_{0.5}\text{Mn}_{0.3}\text{Co}_{0.2}\text{O}_2$) or Li-rich HE5050 ($\text{Li}_{1.2}\text{Ni}_{0.2}\text{Co}_{0.2}\text{Mn}_{0.6}\text{O}_2$) cathodes. The electrolyte formulations are shown in Table II.1.A.7. The full-cell configurations were chosen since neither M cation intercalates into graphite nor has an appreciable insertion chemistry related to the selected cathodes. The full-cell electrochemical performance is shown in Figure II.1.A.38. Initial analysis of the NMC532 cathode // Si anode cells, cycled between 3.0 V and 4.1 V at C/3 (with 4.1 V holds at the end of each charge cycle) was performed using the GenFM electrolyte (see Table II.1.A.7). When compared to the system without addition of the divalent cation salt, the addition of the divalent cation leads to a higher capacity retention rate of 68% (over 90 cycles) when compared with the baseline GenF electrolytes system, 49% retention (over 90 cycles). While still below the performance of the CAMP graphite anodes (96% retention over 90 cycles), additional improvements are being evaluated in conjunction with multiple SEISTA research teams as, even in these preliminary evaluations, cells using Si anodes have significant increases in energy density, as shown in Figure II.1.A.38 b,c. Adding a secondary Mg salt into the electrolyte brought an improvement of ~ 0.15% to the Coulombic efficiency (see Figure II.1.A.38d). For its uses in an electrochemical cell, impedance is always considered especially when new materials are being added to the active electrochemical interface in the electrode. We have discovered that when using a Mg-Li mixed electrolyte salts, lower initial impedance after the formation cycles as well as after 90 aging cycles was seen. This may be a result of the lower reactivity of the active interface and the resulting diminished reactions with electrolyte blocking the active surface with degradation products. Formulations that use significantly more Mg-salt additives show no obvious cycling advantages in performance, suggesting that the co-insertion process may be slowed as Mg is isolated as an insoluble salt (i.e., MgO) or, with enough SEI buildup, diffusion to the surface may be inhibited or blocked. The fact that no negative response is detected with a factor of two

increase (to 0.2 M Mg(TFSI)₂), additional salt may be useful if the mechanism for the concentration drop-off on extended cycling is determined.

LMR-NMC HE5050: To bring more active lithium into the cell design, Li-rich layered oxides (TODA HE5050 with 20% additional Li) were used with an increased voltage cutoff to 4.5V during the initial three C/20 formation cycles for the activation and the removal of extra electrochemically active Li. The additional Li extracted from the cathode can be used to compensate the greater amount of Li consumption during the initial SEI formation on Si anodes, which is commonly referred as the 1st cycle irreversible capacity loss. With this built-in prelithiation, much higher capacities can be obtained with a Li-rich HE5050 cathode // Si anode cell. In Figure 1e, cycling between 3 and 4.1 V using GenFM electrolyte is shown. The high-voltage cutoff of the formation cycles should be high enough that the additional Li available can be extracted to compensate the initial Li consumption losses often seen in non-graphitic anodes. Figure II.1.A.38 e-g show that after adding Mg into the GenF electrolyte, the discharge capacities and energy densities of the HE5050 cathode // Si anode full cells increased by a dramatic ~30%, indicating that adding Mg secondary salt is an effective way to reduce the Li losses during the SEI formation. As with the example above using NMC532, the addition of a Mg salt leads to lower initial impedance, slower impedance growth over 90 aging cycles, and a high initial Coulombic efficiency of ~99.4% for silicon, approaching levels usually obtained with graphite-only anodes. Figure II.1.A.38g shows the combined effect of using a high Si-content electrode with GenFM electrolyte against a Li-rich HE5050 cathode on the full cell electrochemical performance. The total active material weight specific energy density surpasses both graphite anode and silicon anode baselines by a remarkable 30% over 90 cycles. The cells tested above show stable extended cycling performance in Figure II.1.A.39, with ~80 mAh/g_{cathode} capacity after 270 cycles for cells with Li-rich cathodes (33% higher over baseline), and ~55 mAh/g_{cathode} after 270 cycles for cells with NMC532 cathodes (120% higher over baseline). After 270 cycles, TEM/EDX analysis of the cycled Si electrodes taken from Li-rich HE5050 cathode // Si anode cells cycled in a GenFM electrolyte, show a bulk Si:Mg ratio of ~24:1, indicating there is still some Mg left inside of the Si particles after long-term. Similar analysis of the Li-rich HE5050 cathode // Si anode cathode particles after 270 cycles shows minimal Mg presence at the cathode-electrolyte interface confirming that Mg has little influence or opportunity to insert into the cathode. The dramatic increase in performance for lithium limited systems such as NMC532 cathodes and the compounded improvement in performance gained via use of mixed salts and intrinsic prelithiation clearly rationalize further improvements in capacities, cyclabilities, and efficiencies that can be obtained by optimizing other cell components such as binders and Si materials.⁴

Moving to other multivalent salts that support formation of similar Li-M-Si ternary compounds, GenFA, GenFC, and GenFZ electrolytes (shown in Table II.1.A.7) were prepared with Al, Ca, and Zn salts and tested in full-cell configurations. In the case of the zinc-based GenFZ electrolyte, the full cell loses all capacity promptly during the first formation cycle of the cycling protocol, which is most likely due to the intercalation activity of Zn-ion in the cathode.⁵ Conversely, the Al- and Ca-salts like Mg work well in the full-cell configuration. As shown in Figure II.1.A.38, using Al-containing GenFA electrolyte leads to a lower coulombic efficiency compared with other electrolytes. When paired with NMC532 cathodes, GenFA-based electrolytes lead to lower initial capacity but better capacity retention than the GenF baseline, which let it outperform the GenF electrolyte after ~80 cycles. When paired with HE5050 cathodes, GenFA shows an initial capacity even higher than GenFM but with diminished capacity retention, which might be due to its high capacity utilization or fast rising impedance. Extended cycles for GenFA shows higher cycling decay and performance degradation when compared to GenFM (Figure II.1.A.39). Meanwhile, the GenFC electrolyte (Ca addition) brings similar improved capacities, retention rates, coulombic efficiencies and impedance as in the GenFM electrolyte in NMC532-based full-cell tests, as shown in Figure II.1.A.38 a-d. In HE5050-based full-cell tests, GenFC shows much higher capacities, better cyclability, higher efficiencies and lower impedance than GenFM (see Figure II.1.A.38 e-h).¹ To date the Ca-containing electrolyte performs better than the Mg-containing electrolyte with initial high-voltage activation process. These GenFC cells show a remarkable ~70% capacity retention after 270 cycles in extended full-cell tests as shown in Figure II.1.A.38b.

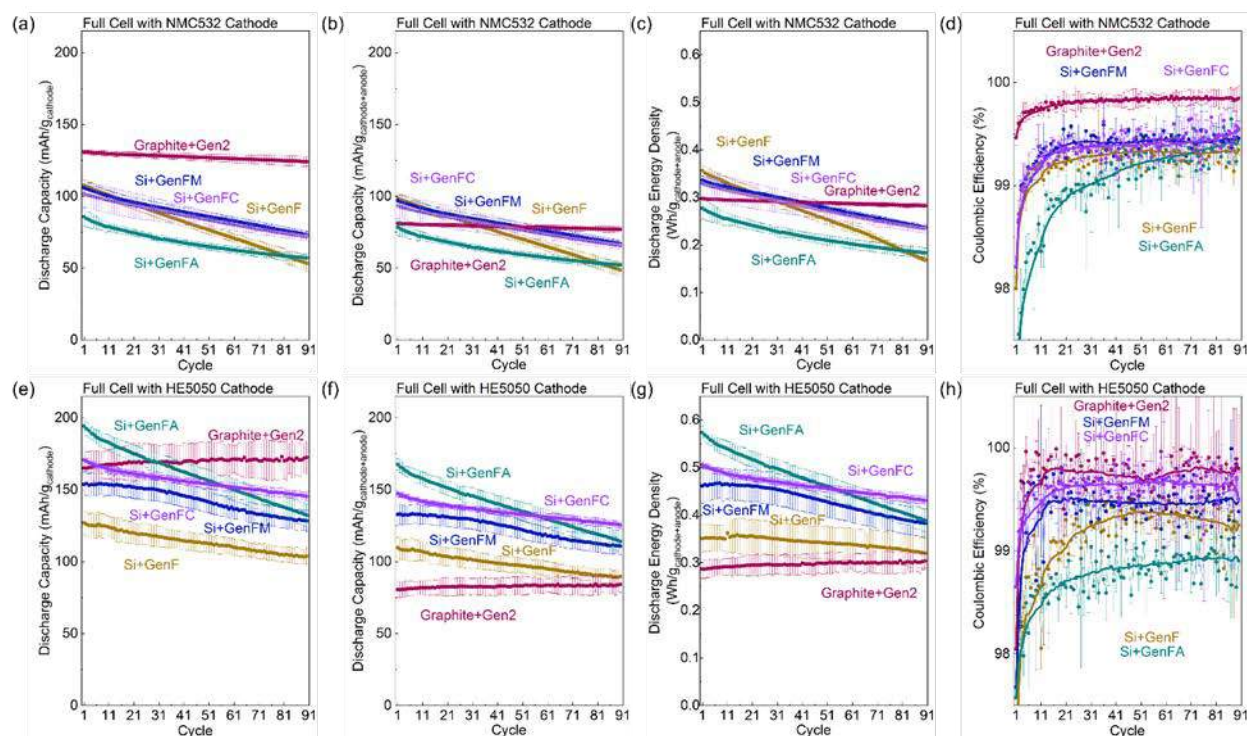


Figure II.1.A.38 Full-cell electrochemical test results. Cells in panels (a)-(d) consist of NMC532 cathodes and Si or Graphite anodes (formation cycles are not shown). Cells in panels (e)-(h) consist of HE5050 cathodes and Si or graphite anodes (formation cycles are not shown). At the end of each charge step the cells were held at 4.1 V until the current dropped below C/50. The discharge capacities in panels (a) and (c) are normalized by the weights of cathode materials (NMC523 or HE5050). The discharge capacities and discharge energy densities in panels (b), (c), (f), and (g) are normalized by the total weights of cathode materials (NMC523 or HE5050) and anode materials (Si or graphite). Error bars represent the standard deviations of at least three measurements for each sample. Trend lines for the coulombic efficiencies in (d) and (h) were calculated by a moving average of 15 adjacent points

The differences in electrochemical performance trends observed between GenFM, GenFA and GenFA can be due to several factors originating from the complexity of the battery systems, including side reactions, diffusion depth, and role the TFSI⁻ anion plays in SEI stability. Joint studies between Argonne, ORNL, and NREL are addressing these issues are underway and taking advantage of the unique resources each possesses.

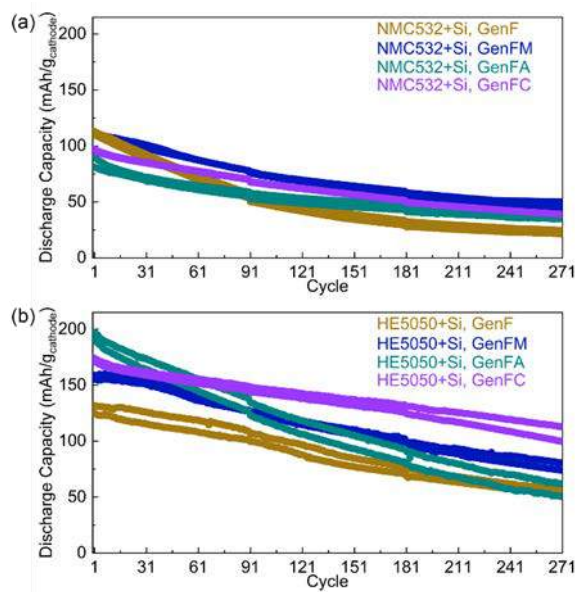


Figure II.1.A.39 Discharge capacities of full cells using GenF, GenFM, GenFA, and GenFC electrolytes with extended cycles. (a) The full cells consist of NMC532+Si electrodes were cycled between 3.0 and 4.1 V at C/3 after three formations cycles between 3.0 and 4.1 V at C/20 (formation cycles are not shown). (b) The full cells consist of HE5050+Si electrodes were cycled between 3.0 and 4.1 V at C/3 after three formations cycles between 3.0 and 4.5 V at C/20 (formation cycles are not shown). At the end of each charging process during aging cycles the cells were held at 4.1 V until the current dropped below C/50. Two cells were tested for extended cycles on each cathode to show that the lifetime of the full cells are repeatable

Zintl Electrolyte Properties: As seen, significant changes to the active electrochemical interface are observed electrochemically and physically upon addition to the electrolyte of small multivalent cations. EQCM investigations seek to assess role the cations added play in changing the electrolyte equilibriums and carrier species. Samples containing Mg^{2+} and Zn^{2+} cations in the electrolyte were evaluated against a Si thin film anode, to distinguish the early stage SEI formation from Si lithiation. Data were compared to the control electrolyte, Gen2+10% FEC.

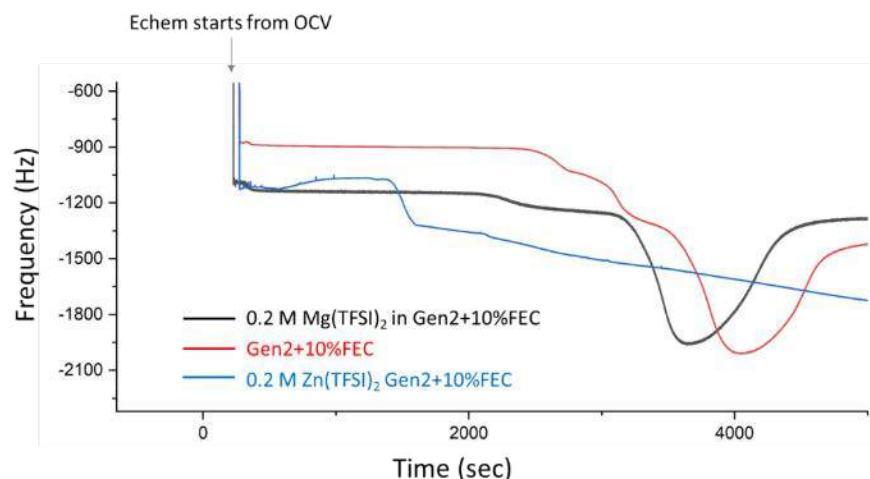


Figure II.1.A.40 Frequency shift for the early SEI formation for the 0.2 M $\text{Zn}(\text{TFSI})_2$ and 0.2 M $\text{Mg}(\text{TFSI})_2$ as electrolyte additives to the baseline electrolyte (Gen2+10%FEC) on a Si thin film anode. Lithiation depth is 0.115 V

The electrochemical performance of Si thin film anode with DeepDive GenF baseline and either 0.2 M $\text{Zn}(\text{TFSI})_2$, or a 0.2 M $\text{Mg}(\text{TFSI})_2$ as electrolyte additives were compared. Data in Figure II.1.A.40 presents the frequency shift from OCV to the first lithiation. An EQCM measurement weighs the electrode as it cycles and combining that information with the electrochemical signal, a value for the SEI weight and porosity can be deduced separate from the weight gained by addition of lithium to the silicon. For these representative cations, it can be seen that early stage SEI formation weight is highest for the Zn (GenFZ) system, and is the least for the Mg (GenFM) system. This result suggests that the SEI formed in the presence of a Mg additive is thinner than the SEI seen in similar studies for baseline GenF electrolytes. Specifically, for the Zn system, no obvious current signal is detected for the first 2 electrochemical cycles suggesting no lithiation of Si is occurring down to 0.4V, as shown in Figure II.1.A.41. This is consistent with the previous GenFZ cycling studies where rapid loss of capacity was observed. Compared to other possible cations, the Zn system is easiest to reduce to the metal and has a stable binary Laves Phase (Li_2Zn) that may play a role in removing active lithium if this poor electronic conducting phase plates out at an active interface. From OCV to the lithiation of 0.4 V, only capacitive current is detected and there is no lithium intercalation to Si, however, there is mass accumulation at the Si electrode. Pushing the electrode to lower potential (from 0.115V from 0.4V), lithiation of Si started with clear intercalation and de-intercalation observed and the corresponding reversible mass change is detected at the same time.

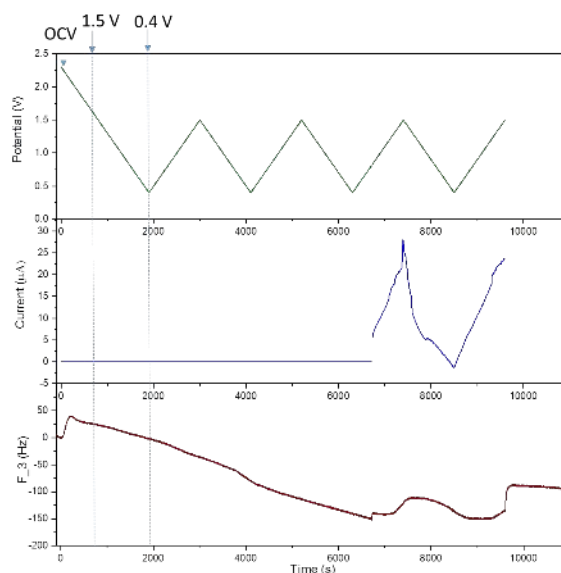


Figure II.1.A.41 Voltage, current and frequency versus time plots of the early SEI formation of $\text{Zn}(\text{TFSI})_2$ additive into the Gen2 electrolyte from OCV to lithiation depth of 0.4 V

3. SEI Stability

Soluble SEI Components: The solid electrolyte interphase (SEI) formed during the cycling of lithium-ion batteries (LIBs) by the decomposition of lithium salt and solvent molecules plays a crucial role for the device performance. On extended cycling these insoluble species precipitate on the active surface, forming the protective SEI layer. In graphitic carbon systems this layer is relatively stable as the lack of significant volume expansion and bond breaking is missing as a driving force when compared to other possible anode systems. With this different mechanism in mind, the SEI formed by silicon (or other main group elements) is different than seen with carbons and tend to have a larger percentage of inorganic phases. In addition to composition, several reports that monitor the SEI as a function of state of charge (i.e., EQCM) have noted that the SEI thickness is not consistent. As lithium is removed on discharge, the SEI thins out. This has typically been assigned to loss of soluble SEI species. However, the identification of these low concentration species is problematic as they are chemically similar to one another, may draw upon minority species in the electrolyte

(i.e., fluoride anion), or may react with the cathode. Since these species are critical to understanding the cell cycling profiles in full cells, a study of the wide variety of electrochemical pathways and development of facile analytical methods for chemical characterization of SEIs is needed. With this in mind, a gradient polarity solvent wash (gradient wash) technique

involving the use of solvents with gradually increased polarities is employed to sequentially remove different SEI components from electrode surfaces and near surface has been developed and used to identify these low concentration soluble species. A primary identification tool is Fourier Transform Infrared (FTIR) spectroscopy to quickly characterize the SEIs composition and products isolated. This study presents a new concept of rationally controlled solvent wash technique for electrode surface analysis that can selectively remove targeted components with gradient wash off the targeted electrode surface by adjusting solvent polarity to reflect the different solubility requirements of the species that may range from neutral aliphatic species to ionic salts (see Figure II.1.A.42). The gradient wash of electrodes was performed in glass vials, where the electrodes were immersed under 5 ml solvents with gentle manual agitation. The solvents used were 0% to 100% volume ratio a polar ethyl acetate (EA) solvent in a non-polar hexane (Hex) solutions with 10-percent intervals (*i.e.*, 0%, 10%, 20%, 30% EA/Hex, *etc.*). After rinsing, the electrodes were immediately dried and stored under vacuum until FTIR characterization.

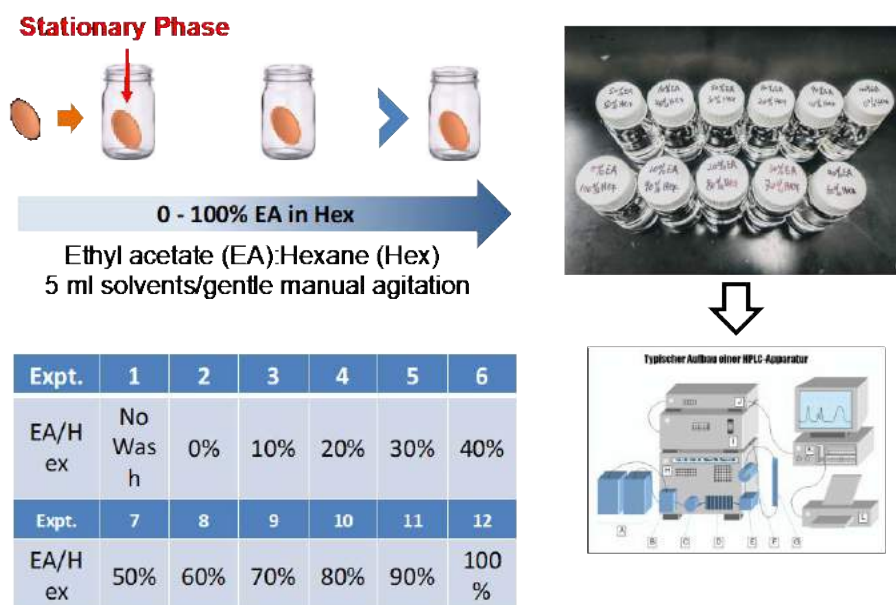


Figure II.1.A.42 Schematics of the gradient polarity solvent wash technique

Analysis of the SEI materials and near SEI materials produced using a polar methacrylate additive under different electrochemical conditions were separated by a gradient wash as described. Cu electrodes were cycled with a Gen2 electrolyte (1.2M LiPF₆ with a 3:7 ethylene carbonate/ethyl methyl carbonate (EC/EMC) containing the additive. The methacrylate additive was chosen as it is a partially reduced species similar in structure and composition to the electrolyte solvent breakdown products seen in literature studies. With a binary solvent system of a non-polar solvent and a polar solvent at various ratios, it is possible to selectively remove different SEI components formed on cycling. The electrode surfaces before and after each wash protocol are characterized with FTIR for identification of the decomposition products.

The TEGMA additive, structure shown in Figure II.1.A.43, produced a poly-TEGMA film on the Cu electrode surface, which, due to its high polarity, did not resist adsorption of residue electrolyte (EC/EMC:LiPF₆ solvates, 1809, 1780, 1269, 1196, 1082, 833 cm⁻¹) and Li₂CO₃ (1510, 1419 cm⁻¹) as shown in Figure II.1.A.43, Spectrum 1. The poly-TEGMA layer was fully exposed after gradient wash with 0-30% EA/Hex solvents. This

polar polymer film also survived all remaining washing steps. Its chemical composition was confirmed with the synthetic sample. The removal of electrolyte species with 0-30% EA/Hex solutions is consistent with the case of the base electrolyte. It is worth noting that the carbonyl peak for poly-TEGMA at 1726 cm^{-1} presented a slight red shift before removal of lithium salt species due to solvation effect.

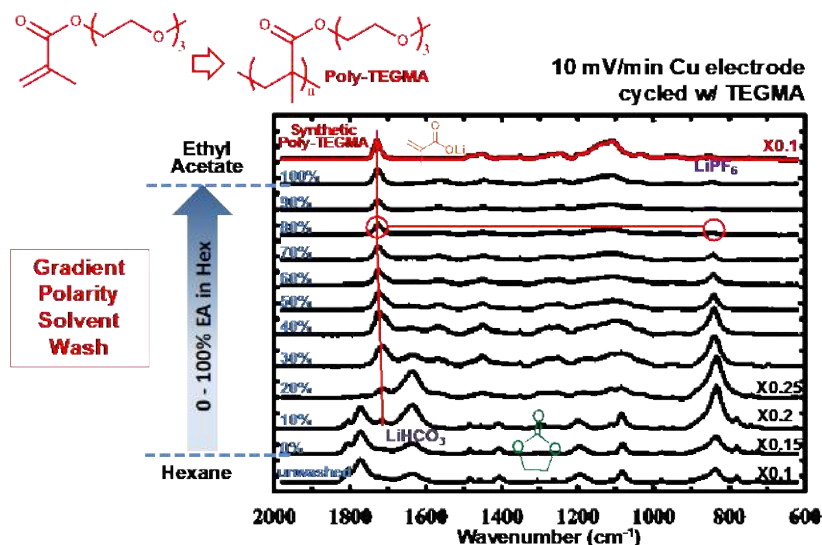


Figure II.1.A.43 Gradient polarity solvent wash was applied to a Cu electrode polarized to 10 mV Li/Li+

The scanning rate or the potential step-down rate from 3V to 50 mV has a significant impact to the surface film (SEI) and near surface species formation. At slow to mediate rate of 1 to 10 mV min^{-1} , the baseline electrolyte (EC/EMC: LiPF₆) facilitates the formation of LiEDC/LiEMC salts on the Cu surface. In the two additives-based electrolyte containing systems, they are predominantly additives derived polymer films on the Cu surface instead of lithium salt species. The species on the Cu surfaces can be clearly observed with gradient wash technique. However, when the voltage step rate is 60 mV min^{-1} , the Cu surface are free of deposition of decomposition products with the baseline electrolyte. A highly polar TEGMA additive tends to stick to the surface of the Cu at this fast scan rate. Products identified to date by FTIR as shown in Figure II.1.A.44. Therefore, the chemistry of SEI formation is dependent on the reaction rate, where lower lithiation rate favors the formation of lithium salts on the electrode surface, and faster rate promote the formation of polar organic decomposition products.

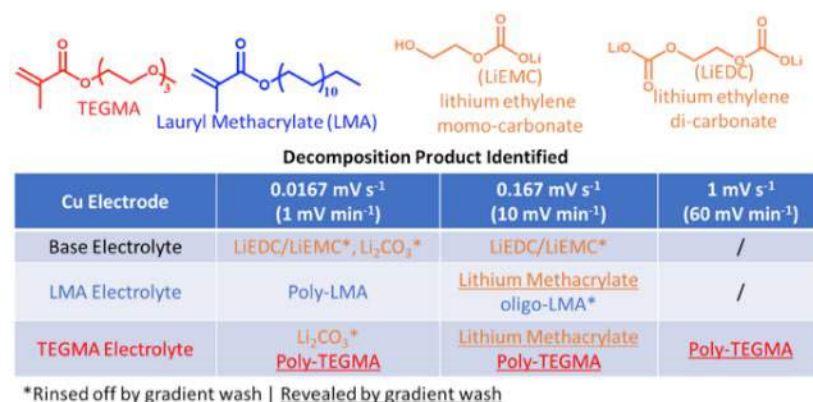


Figure II.1.A.44 Three different scanning rates of CV at 1, 10 and 60 mV min^{-1} were applied to the Cu electrodes respectively with baseline electrolyte and two additives-based electrolytes. The Cu surface species vary due to both the additives and scan rates

Besides the solvent polarity gradient techniques developed to date, SEI formation and species identification using a rotating ring disk electrode (RRDE) design rotating unit (with bi-potentiostat) has also been adapted as an analysis method. In conjunction with the ANL and ORNL materials group, several model samples of 50 nm sputtered Si thin films on the Cu disk RRDE tip were created. Notably the simplest baseline sample of Si on Cu did not maintain adherence to the substrate during measurements, however addition of a titanium or chromium adhesion layer onto the Cu gave more stable sputtered Si thin films. As our method development baseline, we have focused on the Si N-type doped disk electrode sample rather than a model silicon electrode on Cu. This combination avoids binder and carbon artifacts in the electrochemistry and instead focus on the pure SEI on Si surface, in a similar manner to the Si-Sn thin film studies allowed for good cycling and diagnostic studies to be developed with a simpler electrode design.

The SEI on the Si N-type electrode surface was grown using a variety of different protocols. First, no protracted growth of SEI was done, a ‘native’ SEI, the second SEI was a 1-cycle study sample grown at $6 \mu\text{V/s}$ down to 10 mV, and back to 1.5 V, and thirdly, an SEI formed using fast-frequency methods. This last sample was created by sweeping the voltage of the Si N-type electrode disk at 100 mV/s for 10 cycles between 0.01 V to 1.5 V. Following SEI growth, a ferrocene probe molecule was added to the electrolyte (10 mM) as a source of an electrochemical signal and tested at the silicon SEI formed using RRDE method to assess the properties related to molecule partitioning. The electrolyte was Gen 2 with 10% FEC (distilled; dry no water).

In the analysis part of the experiment, the RRDE was rotated at a variety of speeds in 150 mL of electrolyte in order to sweep away any products from the Si N-type disk to be subsequently electrochemically oxidized or reduced at the Pt ring electrode. The disk and the ring voltage were simultaneously swept at 2 mV/s from OCV ($\sim 1 \text{ V}$) to 4.2 V cutoff vs. Li/Li^+ .

Figure II.1.A.45 shows the first sweep i-V curves for the Si N-type disk electrodes in Gen2 + 10% FEC electrolyte. In the ‘native’ SEI, no low voltage sweep was conducted. In (a.), reduction current is seen indicative of SEI formation and some lithiation of Si occurs. For (b.), the fast frequency (*ff*) sweep, the current is roughly the same magnitude, but the CV is featureless. This indicates that little to no lithiation of Si occurs, because of its slow reaction. With this *ff* method, it is expected that the SEI is porous and thick, as it has had no time to age, condense, and collapse. In contrast, for the slow sweep voltage ($6 \mu\text{V/s}$), the SEI should be compact and smoother with tighter coverage.

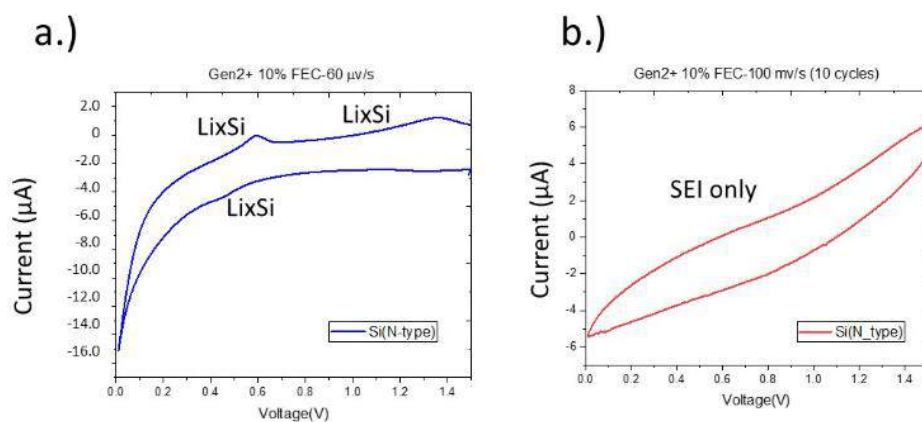


Figure II.1.A.45 Si N-type disk electrode voltammetric results shown for the reductive side of the voltage window where SEI first cycle is shown. (a.) Slow CV at $6 \mu\text{V/s}$ between 0.01 to 1.5 V vs. LiLi^+ RE/CE electrode. (b.) Fast frequency electrode disk sweeping at 100 mV/s for 10 cycles between 0.01 to 1.5 V vs. LiLi^+ RE/CE electrode

The CV response (i-V curve) at the Si N-type electrode in the presence of ferrocene (10 mM) is shown in Figure II.1.A.46. Essentially the voltammetric process is near ideal. Current increases linearly as a function of $v^{1/2}$. In addition, the RRDE output is also ideal. This result suggests that the SEI is 'native', very thin, and ferrocene can exchange electrons in a fairly facile way with the underlying Si N-type (conductive) electrode interface.

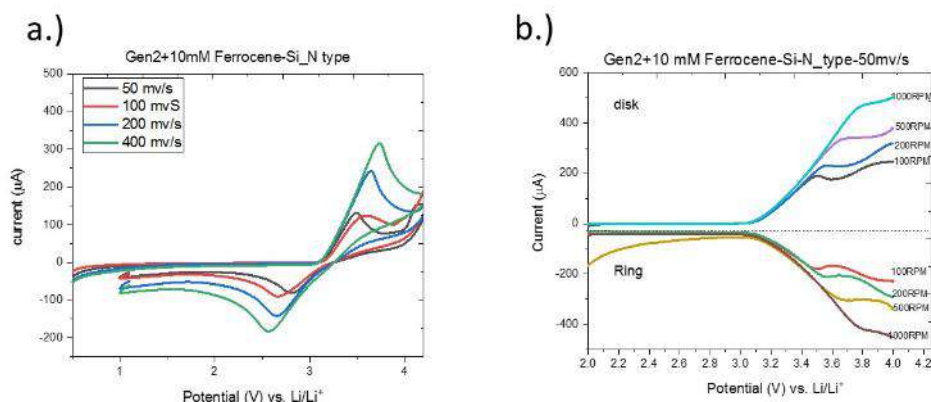


Figure II.1.A.46 (a.) Si N-type disk electrode voltammetric results shown for the oxidative side of the voltage window with 10 mM ferrocene in GEN2 + 10% FEC. (b.) RRDE result showing the limiting current on the Si N-type disk and the Pt ring response to oxidation (disk) and reduction (ring) of ferrocene as a function of rotation rate

When the thicker SEI is present on the Si N-type electrode (results in Figure II.1.A.45) either in compact form, or porous form, the ferrocene redox response is much less ideal than 'native' SEI, thus indicating poor charge transfer through the SEI to react with the ferrocene. Figure II.1.A.47 indicates that the porosity of the SEI is greater for the SEI formed with *ff* methods. An example of the data is the ring current at the Pt is more defined for Figure II.1.A.47 which indicates that an oxidized form of ferrocene has partitioned into and out of the SEI and reacted with electron exchange within the SEI. Moreover, for the Si N-type disk current (limiting for 100 mV/s, Figure II.1.A.47) at 1000 rpm (green), the limiting value is about 550 μA, while in Figure II.1.A.47a, the current (green trace) is about 330 μA. Clearly the charge transfer reaction at the SEI is hindered for the compact version versus the porous one.

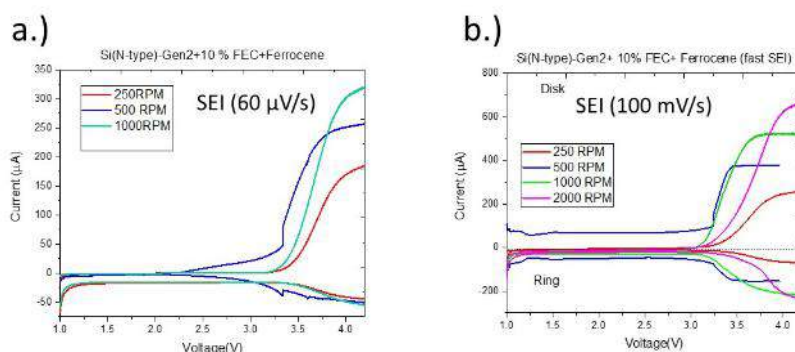


Figure II.1.A.47 (a.) Si N-type disk electrode and Pt ring RRDE results shown for the oxidative side of the voltage window with 10 mM ferrocene in GEN2 + 10% FEC. This SEI was grown using 60 μV/s rate, and (b.) 10 cycles at 100 mV/s SEI cycling formation

SEI Component Synthesis: In support of the soluble SEI species effort, the Lu Zhang group at Argonne synthesized several model compounds from the literature that have been reported to be significant components and / or stable phases in the silicon SEI. Identifying the components of the solid-electrolyte interphase (SEI) on silicon anodes is of crucial importance to enabling this promising chemistry. While many species have been synthesized and evaluated in graphite-based anodes, understanding silicon based SEI is still ongoing. This effort is to synthesize the known SEI components, such as lithium methyl carbonate (LMC), and lithium ethylene dicarbonate (LEDC), and to characterize their possible roles in the SEI formation process. As shown in Figure II.1.A.48, LMC was synthesized in high yield and purified using a modified procedure according to literature. The attempt to synthesize LMC using lithium iodide was not working well due to the low yield and iodine contamination (Figure II.1.A.48b). LEDC was synthesized using a reported procedure in moderate yield (Figure II.1.A.48c). The characterization data matched those reported for this compound. Materials have been provided to interested DeepDive and SEISTA parties for analysis.

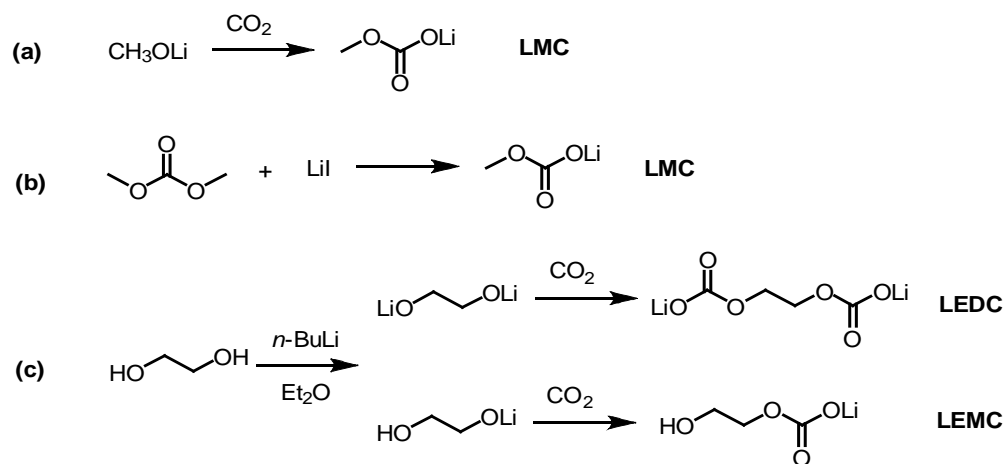


Figure II.1.A.48 Synthetic scheme of PAA analogues with modified properties

Cathode Interactions: The role of SEI speciation in a cell scan be affected by testing conditions. Previously we examined SEI components from thin film Si electrodes and via model electrode studies with no active phase. In comparison, the full Si-containing cell, with DeepDive cathodes, is the most complex test system as the number of species and the number of possible reactive sites in increased and this will affect the type and range of organics found on the silicon electrode and the SEI. For these SEI component studies, two different cathodes were used, namely LiCoO_2 (LCO) and $\text{Li}(\text{Ni}_{0.5}\text{Mn}_{0.3}\text{Co}_{0.2})\text{O}_2$ (NMC532) in combination with a 80-wt% silicon cells containing Gen2+10wt% FEC. The LCO studies, although not a DeepDive baseline electrode, were used to evaluate the role of cathode dissolution and migration and Mn-containing cathode are known to have stability problems (cathode crosstalk). The catalytic properties of deposited manganese may alter the SEI speciation.

As alluded to above, the cycling regime used was very short, consisting of three C/20 cycles, a hybrid pulse-power characterization test (HPPC), two C/3 cycles and another HPPC test. This is shown in Figure II.1.A.49.

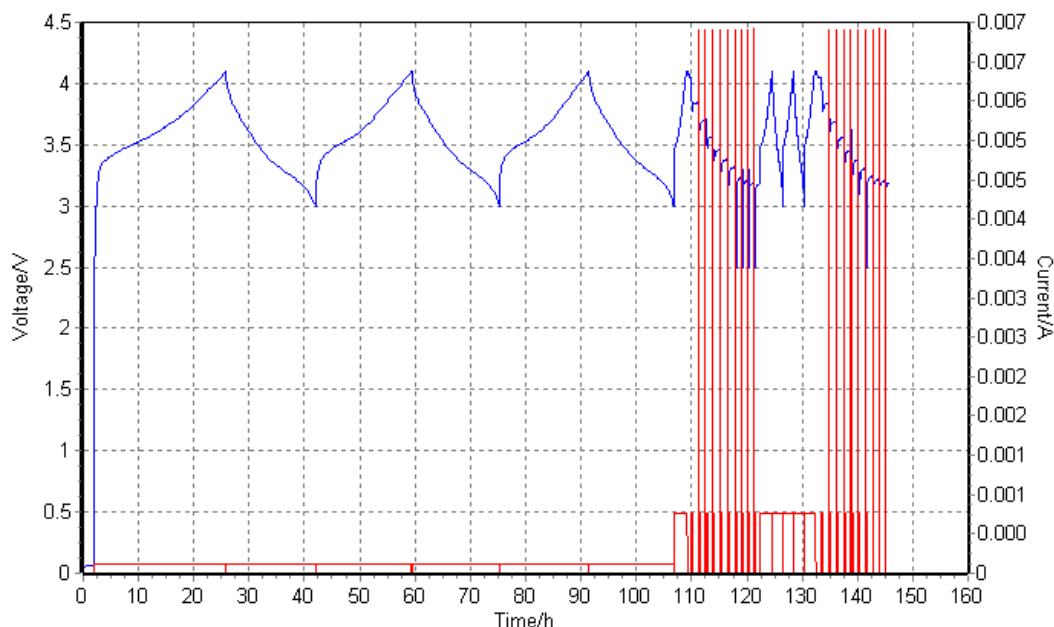


Figure II.1.A.49 Voltage and current versus time, showing the testing regimen used for these short tests

After cycling, the cells were taken apart and the electrolyte was recovered and characterized by HPLC/ESI-MS. These steps are shown schematically in Figure II.1.A.50. The CH_2Cl_2 layer was extracted and allowed to dry. The residue dissolved in acetonitrile and analyzed by HPLC.



Figure II.1.A.50 Schematic of electrolyte extraction steps

The HPLC data indicated that there were five new compounds in the LCO case and four from NMC532. Table II.1.A.8 shows the retention times, molecular ion (m/e), number of carbons atoms and proposed empirical formulae of the species. When only one sample was present, an uncertainty of 10% was assumed in the number of carbons. Identification of the compounds is still in progress.

With these analysis and combined with previous reports on the role of temperature, the nature of the cathode material has a direct impact on changes in the organics found solubilized in the electrolyte.

LHCE Electrolytes: While variables such as SOC, cathode, and temperature stability can lead to SEI dissolution and premature cycling failure, alternative electrolytes that may offer different breakdown pathways and electrochemical window stability are not readily available. One that has been evaluated in the DeepDive is based on the concept of localized high concentration electrolytes (LHCEs) as the lack of free solvent partially eliminates a side-reaction degradation pathway noted in the Zintl section above. Previous reports have noted

Table II.1.A.8 Proposed Compounds from HPLC Data

	Retention time, min	m/e, Da	No. of carbon atoms	Empirical formula
Si-LCO	3.4	408	18.4	$[\text{C}_{16}\text{H}_{32}\text{O}_{10}]^+\text{Na}^+$ (assuming $\pm 10\%$)
	5.5	215	6	$[\text{C}_5\text{H}_{11}\text{O}_7\text{P}]^+\text{H}^+$ (assuming $\pm 10\%$)
	6.6	243	6.5	?
	9.5	229	8.1	?
	13.9	90		$[\text{EC}]\text{H}^+$
	20	467	3?	?
Si-NMC	3.4	408	8.5 ± 0.6	?
	15.9	391	19.1 ± 0.5	?
	18.1	795	37.6 ± 1.6	$[\text{C}_{35}\text{H}_{70}\text{O}_{19}]^+\text{H}^+$
	20	467	21.5 ± 3.1	?

that with an alternative binder system (poly-imide), LHCEs can support cycling of silicon-based electrodes at room temperature, Figure II.1.A.51 shows the table of the LHCE diluent properties and the electrolyte compositions. The diluent 1,1,2,2-tetrafluoroethyl-2,2,3,3-tetrafluoropropyl ether (TTE) has a boiling point of 93.2°C and the 1H,1H,5H-Octafluoropentyl 1,1,2,2-Tetrafluoroethyl ether (OTE) has a boiling point of 133°C. The fundamental properties of the electrolytes were compared side-by-side.

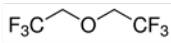
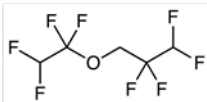
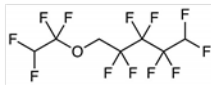
		Longer chain length →		
		BTFE (bis(2,2,2-trifluoroethyl)ether)	TTE (1,1,2,2-tetrafluoroethyl-2,2,3,3-tetrafluoropropyl ether)	OTE (1H,1H,5H-Octafluoropentyl 1,1,2,2-Tetrafluoroethyl ether)
				
DMC solvent with different diluents				
EL1	LiFSI-DMC- BTFE (molar ratio = 0.51:1:2) +1.0 wt% VC + 5 wt% FEC			
EL2	LiFSI-DMC- OTE (molar ratio = 0.51:1:2) +1.0 wt% VC + 5 wt% FEC			
Ether solvent				
EL3	1 LiFSI-1.2DME-3TTE + 1.0 wt% VC + 5 wt% FEC			
Carbonate solvent				
EL4	1.8M LiFSI in EC-EMC (3:7 by wt.) -2TTE (molar ratio to EC/EMC)+1.0 wt% VC + 5 wt% FEC			

Figure II.1.A.51 Molecular structure and properties of several diluents and the recipes of new LHCEs

The electrochemical performance was tested using standard DeepDive Si anodes in half-cell design (Figure II.1.A.52a-c) and full-cell (Figure II.1.A.52d-f) with standard NMC532 cathodes from Argonne National Laboratory. Among all the LHCE electrolytes and baseline electrolyte, EL1 and EL3 with higher conductivity delivered higher specific capacity in half-cell and better cycling stability. EL1 with DMC as bulk solvent and BTFE diluent showed the best overall performance with 91.6% first cycle Coulombic efficiency and excellent capacity retention over 50 cycles (Figure II.1.A.52a-c). In full-cell tests, cells using EL1 and EL3 showed similar specific capacity as those using baseline electrolyte and higher than those using EL2 and EL4. It confirms the trend in half cell tests. EL3 showed similar cycling performance to baseline electrolyte while EL1 showed the best cycling stability with almost no capacity fade over 50 cycles (Figure II.1.A.52d-f)

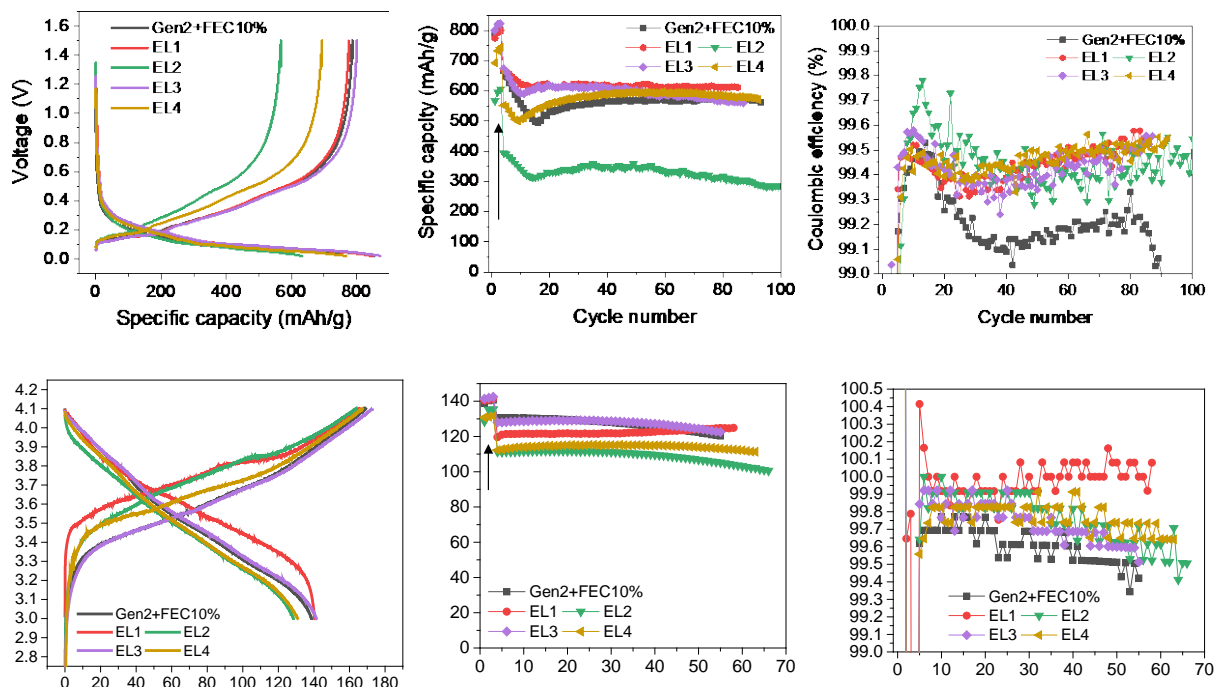


Figure II.1.A.52 Charge-discharge curve, cycling stability, and Coulombic efficiency of DeepDive anodes in new LHCEs in half-cell (a-c) and full-cells (d-f) with NMC532 cathodes

Conclusions

1. Silicon-based Electrodes

In this past year we have undertaken a significant effort studying the various components and properties of slurries and solutions to gain a better understanding of the interactions of silicon and the binder that drive electrode quality. Specific studies have included the solution structures of PAA-binders to understand the role of pH, additives, and polymer morphology. Combined with neutron diffraction, clustering and agglomeration were identified as well as an interesting change in properties when silicon was added to the mixture. In that case the properties of the slurry (i.e., viscosity) were dramatically effected as the polymers interaction with the silicon surface induced structural variations that changed fundamental properties related to shear thinning. Once properly coated it can be noted that the binding strength and coating thickness of the binder have some effect on the underlying silicon fracture properties tied in part to coating homogeneity and probably the binding mechanism used by the pair of materials. Brought together the electrode slurries, electrodes processing science, and the electrochemical evaluation protocols, form a complex problem that need insights across multiple fronts to make advances. This past year significant across-lab advances in our understanding of the

electrode slurries and binder interactions has produced more homogenous composite electrodes and a better understanding of the factors that have limited the electrochemical performance of the baseline electrodes.

2. Silicon Surface Modifications

The active interface between silicon and the electrolyte is the critical interface for SEI formation, particle isolation, agglomeration, and cell-based reactivity in general. In this section multiple efforts have been undertaken to examine the diversity of ways to modify this critical interface. In SEISTA, the initial goals included development of a better understanding of the role the natural passivation layer of silica plays in cell chemistry and electrochemical performance. Based on numerous spectroscopic studies and evaluations, the pathway from silica thru lithium silicate formation to eventual dissolution (dispersion) was identified and efforts at control were evaluated. In the DeepDive effort, the main multi-lab focus has been on system level variables and a more active stance with regard to material modifications. Work by Zhang and Neale has focused on creating a more active surface by using a silane as the source of silicon. This yields a hydride terminated surface that is amenable to controllable substitution reactions. Addition of poly-ether groups has resulted in a more homogenous and dispersed nanophase sample as the surface functionality now plays the role of buffer in addition to assisting in local lithium cation transport. In a similar manner, another joint study with SEISTA has focused on using cation additives that diffuse into the surface of the charged anode to drastically reduce the reactivity towards other cell components, notably the binder and electrolyte solvent. With the in situ formation of ternary Zintl phases, such as $\text{Li}_{14}\text{MgSi}_4$ and $\text{Li}_{14}\text{CaSi}_4$, redox activity of the surface silicon is eliminated while the close structural relationship to various lithium silicides helps mediate the formation of internal interfaces. The addition of a small amount of Mg or Ca can be readily observed to increase the Coulombic efficiency and extend cycle life significantly, especially in conjunction with a high capacity cathode such as the lithium-rich NMC materials. The performance boost is supported by EQCM data that shows the SEI formed from the Mg-containing electrolyte on silicon was much thinner than the SEI from a standard baseline Gen2 cell; indicative again of the role eliminating the redox activity of the surface silicon has on reducing electrolyte reduction reactions. Additional studies highlighting surface protection schemes, such as encasing the active silicon in an amorphous tin matrix or carbon coating, have also been evaluated. While the tin matrix studies are more analogous to the Zintl phase work, their lack of interdiffusion creates internal interfaces. As noted in this section, several ways have been identified to overcome these issues, notably RF sputtering and splat cooling, that are capable of making amorphous mixtures that do not crystallize and phase separate on cycling. Overall, controlled surface functionalization is a viable method to limit surface reactivity that drives low Coulombic efficiency and side reactions that lose active lithium. Two strategies have been examined in detail and shown promise. Addition and attachment of poly-ethers to the surface is promising as it can alleviate electrode level issues associated with particle agglomeration. While supplies are limited, mainly in the context of the sample sizes required to make a large-scale laminate run at CAMP, scale up studies of the process on commercial silicon have been initiated by Jiang and Zhang. Zintl phase studies continue and collaborative efforts at NREL, ORNL and ANL have identified research pathways and insights that are helping to better understand the limitations and process issues.

3. SEI Stability

We have continued our investigation on SEI stability in full cell and extended our SEISTA collaborations to include method development on identification of soluble species. Efforts using solvent polarity gradients have isolated various species as a function of electrochemical preparation and molecular properties. The method highlights the utility of this co-solvent approach. Studies in half cells and full cells using RRDE, HPLC, and other techniques have identified several phases that result from electrochemically mediated reactions between the silicon and the electrolyte. Collaborations with the synthetic organic synthesis group have been initiated to scale up and evaluate the properties of these identified phases as identified.

Key Publications

1. Rago, Nancy Dietz, Basco, John K, Anh Vu, Li, Jianlin, Hays, Kevin, Sheng, Yangping, Wood, DL Bloom, I “Effect of formation protocol: Cells containing Si-Graphite composite electrodes” *J. Power Sources* Vol **435** 126548 (2019) DOI: 10.1016/j.jpowsour.2019.04.076
2. Han, Binghong, Liao, Chen, Dogan, Fulya, Trask, Stephen E, Lapidus, SH, Vaughey, JT, Key, Baris “Using Mixed Salt Electrolytes to Stabilize Silicon Anodes for Lithium-Ion Batteries via in Situ Formation of Li-M-Si Ternaries (M = Mg, Zn, Al, Ca)” *ACS Appl Materials and Interfaces* **11**, 29780-29790 (2019) DOI: 10.1021/acsami.9b07270
3. Nanda, Jagjit; Yang, Guang, Hou; TZ; Voylov, DN; Li, X; Ruther, RE; Naguib, M; Persson, K; Veith,.; Sokolov, AP “Unraveling the Nanoscale Heterogeneity of Solid Electrolyte Interphase Using Tip-Enhanced Raman Spectroscopy” *Joule*, **3**, 2001-2019 (2019) DOI: 10.1016/j.joule.2019.05.026
4. Yoon, Taeho; Xiao, Chuanxiao; Liu, Jun; Wang, Yikai; Son, Seoungbum; Burrell, A; Ban, CM “Electrochemically induced fractures in-crystalline silicon anodes” *J. Power Sources*, **425** 44-49 (2019) DOI: 10.1016/j.jpowsour.2019.03.105
5. Xu, Yun; Wood, Kevin; Coyle, J; Engtrakul, C; Teeter, G; Stoldt, C; Burrell, A; Zakutayev, A “Chemistry of Electrolyte Reduction on Lithium Silicide” *J. Phys Chem C.*, **123** 13219-13224 (2019) DOI: 10.1021/acs.jpcc.9b02611
6. K.P.C. Yao, J.S. Okasinski, K. Kalaga, J.D. Almer, D.P. Abraham, “Operando Quantification of (De)Lithiation Behavior of Silicon–Graphite Blended Electrodes for Lithium-Ion Batteries”, *Adv. Energy Mater.* **9** 1803380 (2019).
7. K. Kalaga, M.-T. Rodrigues, S.E. Trask, I.A. Shkrob, D.P. Abraham, “Calendar-life versus Cycle-life aging of Lithium-ion Cells with Silicon-Graphite Composite Electrodes”, *Electrochimica Acta* **280** 221 (2018).
8. Yao, K.; Ling, M.; Liu, G.; Tong, W., Chemical Reduction Synthesis and Electrochemistry of Si-Sn Nanocomposites as High-Capacity Anodes for Li-Ion Batteries. *J. Phys. Chem. Lett.* (2018), **9** (17), 5130-5134.
9. Hannah R. Morin, María José Piernas Muñoz, Stephen E. Trask, Alison R. Dunlop, Ira Bloom “Effect of Cathode on Changes in the Electrolyte: A First Step to Understand ‘Cross-talk’ in Si-based Lithium-ion Cells” *J. Power Sources*, submitted, (2019).
10. H. Jia, L. Zou, P. Gao, Cao Xia, W. Zhao, Yang He, Mark H. Engelhard, S. D. Burton, Hui Wang, X. Ren, Q. Li, Ran Yi, Xin Zhang, C. Wang, Z. Xu, X. Li, J. Zhang, Wu Xu, “High performance silicon anodes enabled by nonflammable localized high concentration electrolytes,” *Advanced Energy Materials*, (2019) <https://doi.org/10.1002/aenm.201900784>
11. Hu, Bin; Jiang, Sisi; Shkrob, Ilya A.; Zhang, Jingling; Trask, Stephen E; Polzin, Bryant; Jansen, Andrew; Chen, W; Liao, C; Zhang, ZC ; Zhang, L. “Understanding of pre-lithiation of poly(acrylic acid) binder: Striking the balances between the cycling performance and slurry stability for silicon-graphite composite electrodes in Li-ion batteries” *J. Power Sources* **416** p 125-131 (2019) DOI: 10.1016/j.jpowsour.2019.01.068
12. Jiang, SS; Hu, Bin; Sahore, Ritu; Zhang, Linghong; Liu, HH; Zhang, L; Lu, WQ; Zhao, B; Zhang, ZC “Surface-Functionalized Silicon Nanoparticles as Anode Material for Lithium-Ion Battery” *ACS Appl Materials and Interfaces* **10** 44924-44931 (2018) DOI: 10.1021/acsami.8b17729
13. Chen, H; Ling, M; Hencz, L; Ling, HY; Li, GR; Lin, Z; Liu, G; Zhang, SQ “Exploring Chemical, Mechanical, and Electrical Functionalities of Binders for Advanced Energy-Storage Devices” *Chem Rev* **118**, 8936-8982 (2018) DOI: 10.1021/acs.chemrev.8b00241

14. Han, B.H.; Piernas-Munoz, Z.J.; Dogan, F.; Kubal, J.; Trask, S.E.; Bloom, I.D.; Vaughey, J.; Key, B. “Probing the Reaction between PVDF and LiPAA vs Li₇Si₃: Investigation of Binder Stability for Si Anodes” *J. Electrochem. Soc.*, **166**, A2396-A2402 (2019) DOI: 10.1149/2.0241912jes

References

1. M.N. Obrovac and V.L. Chevrier “Alloy Negative Electrodes for Li-Ion Batteries”, *Chem. Rev.* 2014, 114, 11444-11503.
2. P. Nelson, D. Dees, K. Gallagher, S. Ahmed “*Modeling the Performance and Cost of Lithium-Ion Batteries for Electric-Drive Vehicles*” Second Edition, Argonne National Laboratory Report, ANL-12/55.
3. Wu H.; Cui, Y. *Nano Today* **2012**, 7 (5), 414-429.
4. Hu B.; Shkrob I. A.; Zhang S.; Zhang L.; Zhang J.; Li Y.; Liao C.; Zhang Z.; Lu W.; Zhang L. *J. Power Sources* **2019**, 416, 125-131.
5. Erogbogbo F.; Lin T.; Tucciarone P. M.; LaJoie K. M.; Lai L.; Patki G. D.; Prasad P. N.; Swihart M. T. *Nano Lett.* **2013**, 13(2), 451-456.
6. G. V. Zhuang, H. Yang, P. N. Ross, Jr., K. Xu, and T. R. Jow, *Electrochem. Solid-State Lett.* **2006**, 9, A64-A68.
7. H. Liu, X. Wang, H. Zhou, H. Lim, X. Xing, Q. Yan, Y. S. Meng, and P. Liu, *ACS Appl. Energy Mater.* **2018**, 1, 1864-1869.
8. G. V. Zhuang, K. Xu, H. Yang, T. R. Jow, and P. N. Ross, Jr., *J. Phys. Chem. B* **2005**, 109, 17567-17573.
9. L. Wang, A. Menakath, F. Han, Y. Wang, P. Y. Zavalij, K. J. Gaskell, O. Borodin, D. Luga, S. P. Brown, C. Wang, K. Xu, and B. W. Eichhorn, *Nat. Chem.* **2019**, 11, 789-796.
10. Choi, S., et al., *Highly elastic binders integrating polyrotaxanes for silicon microparticle anodes in lithium ion batteries*. *Science*, 2017. **357**(6348): p. 279-283.
11. Munaoka, T., et al., *Ionically Conductive Self-Healing Binder for Low Cost Si Microparticles Anodes in Li-Ion Batteries*. *Advanced Energy Materials*, 2018. **8**(14): p. 1703138.
12. Yoon, T., “Electrochemically induced fractures in crystalline silicon anodes” *Journal of Power Sources*, 2019. **425**: p. 44-49.
13. Meyers, M.A. and K.K. Chawla, “*Mechanical Behavior of Materials*”, Upper Saddle River, New Jersey: Prentice-Hall, Inc. (1999)
14. Sarkar, A., P. Shrotriya, and A. Chandra “Fracture Modeling of Lithium-Silicon Battery Based on Variable Elastic Moduli” *Journal of The Electrochemical Society*, 2017. **164**(11): p. E3606-E3612.
15. Wei, L. “Poly (acrylic acid sodium) grafted carboxymethyl cellulose as a high performance polymer binder for silicon anode in lithium ion batteries”. *Scientific Reports*, 2016. **6**: p. 19583.
16. Bosco, N., J. Tracy, and R. Dauskardt, “Environmental Influence on Module Delamination Rate” *IEEE Journal of Photovoltaics*, 2019. **9**, p. 469-475.
17. Ahn, H.-J.; Kim, Y.-S.; Park, K.-W.; Seong, T.-Y. “Use of Sn-Si nanocomposite electrodes for Li rechargeable batteries” *Chemical Communications* 2005, (1), 43-45.
18. Hatchard, T.; Dahn, J. Study of the electrochemical performance of sputtered Si_{1-x}Sn_x films. *J. Electrochem. Soc.* **2004**, 151 (10), A1628–A1635.

19. Xiao, X.; Wang, J. S.; Liu, P.; Sachdev, A. K.; Verbrugge, M. W.; Haddad, D.; Balogh, M. P. Phase-separated silicon–tin nanocomposites for high capacity negative electrodes in lithium ion batteries. *J. Power Sources* **2012**, *214*, 258–265.
20. Xu, J.; Ling, M.; Terborg, L.; Zhao, H.; Qiu, F.; Urban, J. J.; Kostecki, R.; Liu, G.; Tong, W. Facile synthesis and electrochemistry of Si-Sn-C nanocomposites for high-energy Li-ion batteries. *J. Electrochem. Soc.* **2017**, *164* (7), A1378–A1383.
21. Yao, K.; Ling, M.; Liu, G.; Tong, W. Chemical reduction synthesis and electrochemistry of Si–Sn nanocomposites as high-capacity anodes for Li-Ion batteries. *J. Phys. Chem. Lett.* **2018**, *9* (17), 5130–5134.
22. M. -T. F. Rodrigues, S. E. Trask, I. A. Shkrob, D. P. Abraham, “Quantifying gas generation from slurries used in fabrication of Si-containing electrodes for lithium-ion cells”, *J. Power Sources* **395**, 289 (2018).
23. Han, Binghong, Liao, Chen, Dogan, Fulya, Trask, Stephen E, Lapidus, SH, Vaughey, JT, Key, Baris “Using Mixed Salt Electrolytes to Stabilize Silicon Anodes for Lithium-Ion Batteries via in Situ Formation of Li-M-Si Ternaries (M = Mg, Zn, Al, Ca)” *ACS Appl Materials and Interfaces* **11**, 29780-29790 (2019) DOI: 10.1021/acsami.9b07270
24. Dogan, F.; Croy, J. R.; Balasubramanian, M.; Slater, M. D.; Iddir, H.; Johnson, C. S.; Vaughey, J. T.; Key, B., Solid State NMR Studies of Li_2MnO_3 and Li-Rich Cathode Materials: Proton Insertion, Local Structure, and Voltage Fade. *Journal of the Electrochemical Society* **2015**, *162* (1), A235-A243.
25. Dose, W. M.; Maroni, V. A.; Piernas-Muñoz, M. J.; Trask, S. E.; Bloom, I.; Johnson, C. S., Assessment of Li-Inventory in Cycled Si-Graphite Anodes Using LiFePO_4 as a Diagnostic Cathode. **2018**, *165* (10), A2389-A2396.
26. Pan, C.; Nuzzo, R. G.; Gewirth, A. A., $\text{ZnAl}_x\text{Co}_{2-x}\text{O}_4$ Spinels as Cathode Materials for Non-Aqueous Zn Batteries with an Open Circuit Voltage of ≤ 2 V. *Chemistry of Materials* **2017**, *29* (21), 9351-9359.
27. “High performance silicon anodes enabled by nonflammable localized high concentration electrolytes,” Haiping Jia, Lianfeng Zou, Peiyuan Gao, Cao Xia, Wengao Zhao, Yang He, Mark H. Engelhard, Sarah D. Burton, Hui Wang, Xiaodi Ren, Qiuyan Li, Ran Yi, Xin Zhang, Chongmin Wang, Zhijie Xu, Xiaolin Li, Jiguang Zhang, Wu Xu, published online in *Advanced Energy Materials*, <https://doi.org/10.1002/aenm.201900784>

II.1.B Silicon Electrolyte Interface Stabilization (SEISta) (NREL, ANL, ORNL, LBNL, SNL)

Anthony Burrell

National Renewable Energy Laboratory
15013 Denver West Parkway
Golden, CO 80401
E-mail: anthony.burrell@nrel.gov

Brian Cunningham, DOE Technology Development Manager

U.S. Department of Energy
E-mail: Brian.Cunningham@ee.doe.gov

Start Date: October 1, 2016	End Date: September 30, 2020	
Project Funding (FY19): \$2,000,000	DOE share: \$2,000,000	Non-DOE share: \$0

Project Introduction

This report documents the Silicon Electrolyte Interface Stabilization team's approach in 1) characterizing the early-stage silicon solid-electrolyte interphase (SEI) including progress on identifying the specific reaction pathways present in the formation of the SEI layer, and 2) establishing a procedure for measuring SEI growth rate at fixed potentials and different cycling regimes.

Silicon is a viable alternative to graphitic carbon as an electrode in lithium-ion cells and can theoretically store >3,500 mAh/g. However, lifetime problems have been observed that severely limit its use in practical systems. The major issues appear to involve the stability of the electrolyte and the uncertainty associated with the formation of a stable SEI at the electrode. Recently, calendar-life studies have indicated that the SEI may not be stable even under conditions where the cell is supposedly static. Clearly, a more foundational understanding of the nature of the silicon/electrolyte interface is required if we are to solve these complex stability issues. A new multi-lab consortium has been formed to address a critical barrier in implementing a new class of materials used in lithium-ion batteries that will allow for smaller, cheaper, and better-performing batteries for electric-drive vehicles. This consortium, named the Silicon Electrolyte Interface Stabilization (SEISta) project, was formed to focus on overcoming the barrier to using such anode materials. Five national laboratories are involved: the National Renewable Energy Laboratory (NREL), Argonne National Laboratory (ANL), Lawrence Berkeley National Laboratory (LBNL), Oak Ridge National Laboratory (ORNL), and Sandia National Laboratories (SNL).

The SEISta project was specifically developed to tackle the foundational understanding of the formation and evolution of the solid-electrolyte interphase on silicon. This project will have as its primary goal an understanding of the reactivity of the silicon and lithiated silicon interface with the electrolyte in lithium-ion systems. It consists of researchers from NREL, ANL, LBNL, ORNL, and SNL working toward clear unified goals. The Silicon Deep-Dive team, which focuses on the science and technology barriers in functional electrodes, is a critical partner in this work. Many of the researchers are shared between both teams, and we hold joint meetings to ensure effective communication between the teams.

The current goals of SEISta are:

Quarter 1 Milestone: Have determined if the pristine surface of the silicon influences the composition and the function of the SEI after 1, 10, and 50 cycles (XPS, SIMS, IR, Raman, STEM, SSRM). (100% complete)

Quarter 2 Milestone: Have determined that the nature of the silicon surface can affect the composition, function, and thickness of the SEI. (100% complete)

Quarter 3 Milestone: Have determined how water concentration (as a function of water content up to 100 ppm) in the electrolyte affects SEI thickness and composition (electrochemistry, spectroscopy, impedance) of the SEI formed at 1.5, 1.0, 0.7, 0.4, 0.15, and 0.05 V vs Li/Li+. (100% complete)

Quarter 4 Milestone: Have determined the nature of the soluble SEI components that are formed over 10 cycles and that are soluble in the Gen 2 electrolyte. (100% complete)

Objectives

The critical issues that SEISta is attempting to address are:

- What are the properties of the lithiated silicon/electrolyte interface?
- What is the silicon SEI actually made of and what reactions are contributing to it?
- How fast does the silicon SEI grow?
- Does it stop growing?
- Is it soluble?
- Can it be stabilized?

The SEISta team works to ensure that protocols for sample preparation, experimental design, and implementation as well as data reporting are consistent across the whole team. Each laboratory is working toward the same set of quarterly milestones using its own specific talents and capabilities in a concerted effort with the other team members. This joint focus results in multiple researchers interacting to produce and analyze data to ensure that individual experimental variations will not lead to erroneous results. Critical to the success of this effort is the use of standard samples that can be shared by all parties. In addition to weekly whole-team video presentations, we have held on-site face-to-face meetings each quarter for all team members and other interested parties to brainstorm and sort out issues with existing experiments and jointly develop new experimental plans.

Approach

For FY19, the team continues to focus on three broad tasks:

Materials Standardization—This task is critical to developing and deploying standardized samples and experimental procedures across the team. We will continue to provide full characterization to any new sample that is to be used for SEI studies to ensure reproducibility and full understanding of the material. This quarter's work focused on developing new oxide coatings and methods to control the thickness and density of oxide samples. In addition, work on the silicon nanoparticles has made progress with the enhancement of the materials collection and handling system in the plasma reactor. *Although this work dominated the early part of the project and is still critical to its success, it is now only a minor part of the work, and this is reflected in the relative balance of this quarterly report.*

Model Materials Development and Characterization—The nature of the electrode-electrolyte interaction in silicon electrodes is at the heart of the formation and stability of the SEI. The synthesis of well-defined silicon nanoparticles and the different chemical markups of lithiated silicon surfaces is being probed by preparing model compounds and thin films that may/can exist in silicon anodes. Lithium silicides, silicates, and other inorganic material (LiF, Li₂O) are being prepared, and their reactivity with electrolytes is being determined. These materials also act as standard spectroscopy samples for the researchers who are looking at the formation of the SEI on different silicon materials.

SEI Characterization—The overall objective for SEISta is to understand the nature and evolution of the SEI on silicon anodes. The materials standardization and model compounds will enable the researchers to

systematically investigate the formation of the solid-electrode interphase using a wide variety of spectroscopy techniques—from different optical, microscopy, and electrochemistry—to determine how the SEI forms based on the nature of the silicon surface, and how it evolves over time. This section of work will continue to grow in scope as we move beyond the sample-characterization phase of the project and toward understanding the nature and evolution of the SEI. *This part of the project now represents the bulk of the work and, as such, this quarterly report is largely reporting on work leading to this outcome.*

The FY19 results for this project are presented by the following three topic areas/parts.

- Part 1: Studies of SiO₂ Interfaces
- Part 2: Origins of Si/Electrolyte Interface Stability
- Part 3: (Re)engineering of the Si/Electrolyte Interface via Molecular Interactions.

Results

Part 1: Studies of SiO₂ Interfaces

A central objective of the SEISta project is to understand the what role the surface SiO₂ layers on silicon have on the electrochemical cycling properties of composite electrodes. This includes how the early- and late-stage SEI is affected by the presence of SiO₂. Oxygen is almost inevitable in the Si anode where the surface of Si forms a native oxide layer when it is exposed to air. In addition, different preparation processes of Si anodes may lead to different levels of oxygen content, not only on the surface but also through the bulk. Previously, the SEISta consortium has identified the native SiO₂ as playing a major role in the surface behavior and passivation of the silicon anode. Experiments have shown non-passivating behavior and corrosion current at high voltages, well above the predicted lithiation of SiO₂ and Si.

We consider three different types of surfaces in our studies of SiO₂ on Si. First, polished silicon wafers, either directly or as a substrate for physically deposited thin films of Si, provide the most controlled silicon material with which to study the fundamental processes occurring during the lithiation of silicon from an electrolyte. In addition, they can be oxidized, resulting in dense SiO₂ layers of varying thickness whose effect on lithiation and battery electrochemistry can be studied as a model system. This includes simulations targeted at the stability of the SEI and the amorphous SiO₂ native oxide layer, and they elucidate the impact of the confining effects of a film, versus the bulk, on the lithiation behavior of the native oxide.

Second, entirely air-free routes for producing Si nanoparticles (NP) allows for the jump from the flat-surface model system to something more akin to a three-dimensional coated electrode that would ultimately be the basis for a new anode. These include synthesized particles of Si and SiO_x, because different levels of oxygen in the Si anode could affect the surface SEI formation, reversible capacity, and overall electrochemical performance. So far, most of the studies regarding the impacts of oxygen on the Si anode have focused on either the native oxide layer or the thermally grown thin SiO₂. Particles are synthesized from the gas phase, allowing the tuning of the composition of the surface from SiH_x-terminated to SiO₂-terminated, as well as particle size. Alternatively, a route to oxygen-free particle synthesis was studied by using an inert grinding method to produce particles from ingots of oxygen-free starting material. Finally, because of the recognition of the role of oxygen during either the synthesis or subsequent exposure, a series of SiO_x anodes with different oxygen levels were investigated to understand the impacts of oxygen on the SEI formation and overall electrochemical performance of the obtained SiO_x anodes.

Because of the existence of surface oxides and their role in changing the electronic density of states within the Si structure, there is concern that SEI formation will ultimately always be affected by the presence of oxygen and that oxygen can never truly be removed. One possible way to mitigate this effect of oxygen is by the addition of another species during the lithiation that can lead to formation of stabilizing phases within the SEI formation cycle. Recently, Key et al. demonstrated that adding 0.1 M M(TFSI)_x (M = Mg, Zn, Al, and Ca) as an additive salt into the Gen2 electrolyte (1.2 M LiPF₆ in ethylene carbonate (EC):ethyl methyl carbonate

(EMC) (3:7, wt%) + 10 wt% fluorinated ethylene carbonate (FEC)) stabilizes the Si anode chemistry through the in situ formation of Li–M–Si ternary phases during the charging process (lithiation into the Si anode) [1]. Such ternary Zintl phases, which are presumably formed on the Si surface, are more stable than the lithiated Si species, and hence, they demonstrate improved electrochemical performance with the possibly stabilized SEI. This program has characterized the formed SEI ternary Zintl phases, using a variety of analytical techniques (e.g., XPS, FTIR/Raman, STEM-EDS, and AFM/SSRM) to better understand the voltage- and time-dependent formation and the chemical and physical nature of the Li–Mg–Si ternary phase incorporated into the silicon anode.

As in any electrochemical system, the impact of the electrolyte and its interplay with the surface introduces complexity into the understanding of the formation of interface. This is particularly true in Si/SiO₂ interfaces, where SEIsta has previously shown that decomposition products from the electrolyte may generate species that attack the SEI at various points in the lithiation/delithiation process. Removing the impact of the liquid phase from the study requires a vacuum-phase lithium source to study the impact of just the introduction of Li to the SiO₂/Si interface without any intervening solvent or salt species. We continued the development of this virtual-electrode (VE) approach [2] for studying fundamental interfacial processes during silicon lithiation. Experiments were performed on 5-nm SiO₂/Si(001) wafer model-system anode samples to address key questions relating to how (electro)chemical evolution of inorganic phases in the solid-electrolyte interphase (SEI) affects the lithiation overpotential. Specifically, experiments were performed to determine how overpotential evolves as surface silicon oxides are converted to silicate phases according to $\text{SiO}_x + y\text{Li}^+ + y\text{e}^- \rightarrow \text{Li}_y\text{SiO}_x$.

To probe these phenomena, we developed a VE technique analogous to the galvanostatic intermittent titration technique (GITT). In the VE approach to GITT, a square-wave pulse is applied to the low-energy Li⁺ ion gun during in situ lithiation, while composition and chemical states are monitored with X-ray photoelectron spectroscopy (XPS). The in situ lithiation XPS measurements were performed using a Phi 5600 instrument equipped with a low-energy Li⁺ ion gun. For these experiments, the Li⁺ incident energy was set to 10 eV, and typical beam current densities were set in the range ~50–200 nA/cm².

Taken together, these studies of virtual electrode, model electrode, and particle electrode studies, combined with electrochemical, spectroscopic, and computational analysis, increases our understanding of the phenomena that are occurring during the initial SEI formation phases of Si anode. And they suggest pathways, such as the Zintl phase formation, that may help to stem the worst of these effects.

Simulations of Stability Studies on Li Insertion into SiO₂

Previous work in SEIsta investigated the thermodynamics of the Li–Si–O chemical system, finding that lithiation of bulk SiO₂ is thermodynamically preferred. This lithiation was found to occur at a potential of ~1.5V vs Li/Li⁺. Based on this result, the program started investigating the lithiation of SiO₂ films because the introduction of surface, interfacial, and confinement effects can impact the relative stability of various silicates and silicides.

First, we studied the relative stability of the amorphous (herein denoted “a-”) SiO₂ on crystalline (denoted as “c-”) Si (a-SiO₂/c-Si) and c-SiO₂/c-Si film interfaces. Within the c-SiO₂/c-Si system, we identified two possible low-strain epitaxial matches between SiO₂ and Si: i) SiO₂ (001) and Si (111), and ii) SiO₂ (110) and Si(100). Epitaxial matches were found using the algorithm described by Zur et al. [3]. Using our recently developed interface builder tool in pymatgen, we constructed SiO₂/Si interfaces of varying oxide thickness for density functional theory (DFT) calculations. When building the epitaxial interfaces, both the film and substrate lattices were equally distorted to accommodate the lattice mismatch. We note, however, that for a real system, where the substrate is much thicker than the film, the strain is likely to be localized to the film. Figure II.1.B.1 shows the energy per atom as a function of the thickness for both low-strain epitaxial matches. We find that the lowest-energy interface is the SiO₂(001) and Si(111), a reassuring result, given that the Si(111) surface is the most stable facet.

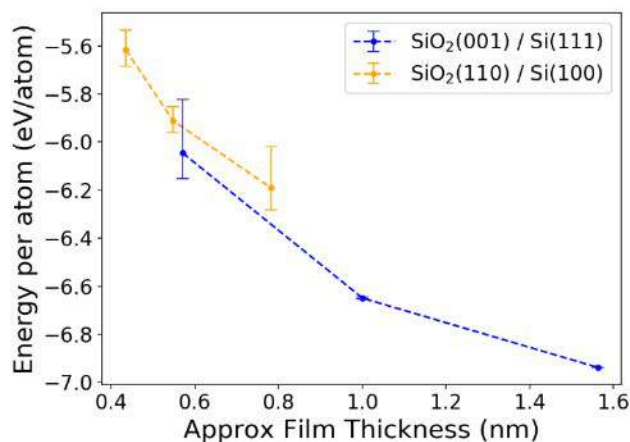


Figure II.1.B.1 Energy per atom of two relaxed crystalline interfaces between i) SiO₂ (001) and Si (111), and ii) SiO₂ (110) and Si (100) as a function of SiO₂ film thickness

Given that the native SiO₂ is well known to be amorphous, we also generate amorphous SiO₂ films and amorphous SiO₂/Si interfaces with varying SiO₂ film thicknesses and compare the energies with the crystalline films. Similar to the results found by Aykol et al. [4], we find an amorphous film to be preferred for thin films, with a crystalline film preferred when > 0.3 nm, as seen in Figure II.1.B.2. Most native SiO₂ is amorphous for thicknesses much greater than 0.3 nm; thus, we conclude that the formation of a crystalline native oxide is a kinetically hindered process. However, we assert that the choice to divide the strain between the film and substrate will decrease the stability of the crystalline film, likely increasing the 0.3-nm value, although this is currently being reinvestigated.

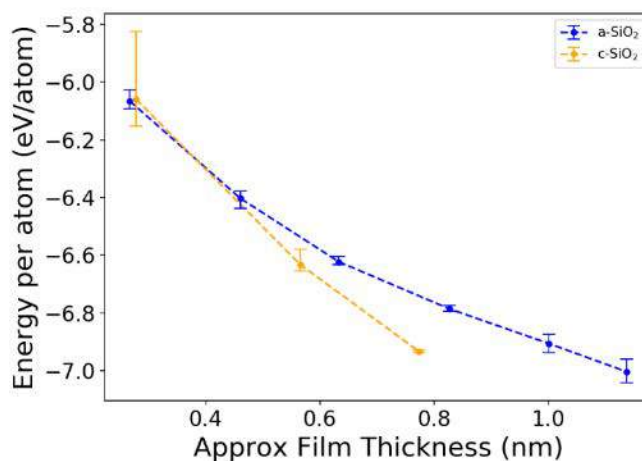


Figure II.1.B.2 Energy per atom of interfaces between i) amorphous SiO₂ and ii) crystalline SiO₂ (001) with Si (111)

We have also investigated the thermodynamics for lithiation of a SiO₂ film toward understanding the role of the SiO₂ layer. We looked at the generation of lithium silicate/silicon interfaces through epitaxial matches. The crystalline lithium silicates, however, due to the complexity and large unit cells, form limited epitaxial matches with Si, with existing matches having surface areas of > 500 Å. Such an interface would require in excess of 500 atoms and is not reasonably simulated by DFT. An amorphous interface is, however, accessible through current computational methods and is our current research direction.

As a precursor to the much more expensive amorphous interface calculations, we first studied a- Li_xSi and a- Li_xSiO_y slabs independently to eliminate interfacial effects, focusing on only the energy change due to confinement and presence of a surface. We generate amorphous slabs by adding 20 Å of vacuum sputter material to the bulk amorphous structures previously obtained through a melt-quench method. The slabs are then annealed at 500 K with ab initio molecular dynamics (AIMD) for 2 ps to allow for surface relaxation and reconstruction. Energies are calculated following a DFT-based conjugate-gradient structure optimization. Thinner films are obtained by removal of an integer multiple of the film stoichiometry. Five samples of each film are obtained using five different starting amorphous structures.

As shown in Figure II.1.B.3, the films are found to be greater in energy than their bulk counterparts, with energy decreasing as thickness increases, approaching the bulk value. The largest effects on the film energies are observed for small thicknesses, where the number of surface atoms dominates over the internal atoms. The film energies are found to follow the equation below:

$$E_{slab}(x) = E_{bulk} + \frac{2\sigma}{\rho x}$$

where E_{slab} and E_{bulk} are the energy per atom in the slab and bulk, respectively. x is the thickness of the film in Å, σ is the surface energy in units of $\frac{\text{eV}}{\text{\AA}^2}$, and ρ is the atomic density in units of $\frac{\text{atoms}}{\text{\AA}^3}$.

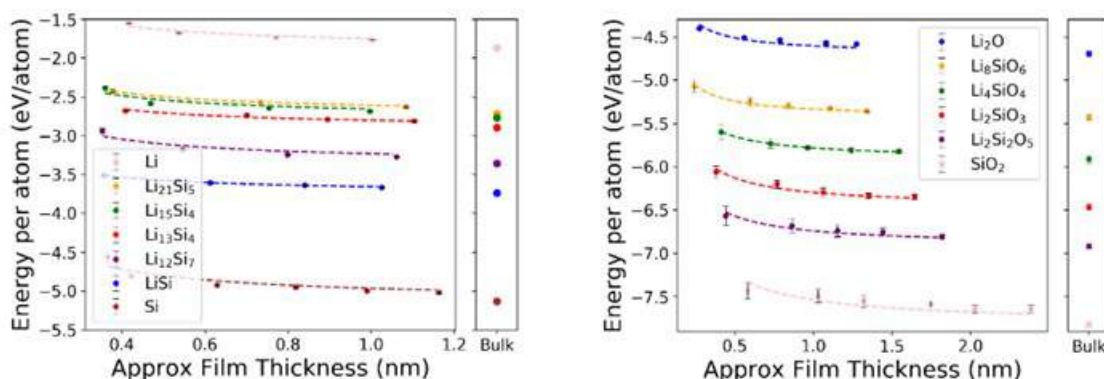


Figure II.1.B.3 Energy per atom of slabs of a) Li_xSi and b) Li_xSiO_y as a function of thickness, with the bulk energies shown to the right. Error bars shown represent 1 standard deviation among five sample slabs. The dotted lines show the regression for energy vs thickness

Starting with a fixed amount of Si or SiO_2 , we calculate the film thickness at each lithiation step, assuming the film expansion is limited to only the film-normal direction, with little stress in plane, as shown in the schematic in Figure II.1.B.4a. The film energies are then calculated for the expanding film, following the regressions shown in Figure II.1.B.3, and a convex hull is constructed. Using the chemical potential of Li in each of the hull simplices, we obtain the lithiation profiles shown in Figure II.1.B.4b and Figure II.1.B.4c. In general, we find the trend that films have a higher initial lithiation potential than bulk materials. This is primarily due to the decreased stability of the initial film. As the film grows, through lithiation, the relative number of surface atoms to internal atoms decreases, and the difference in lithiation potentials decreases.

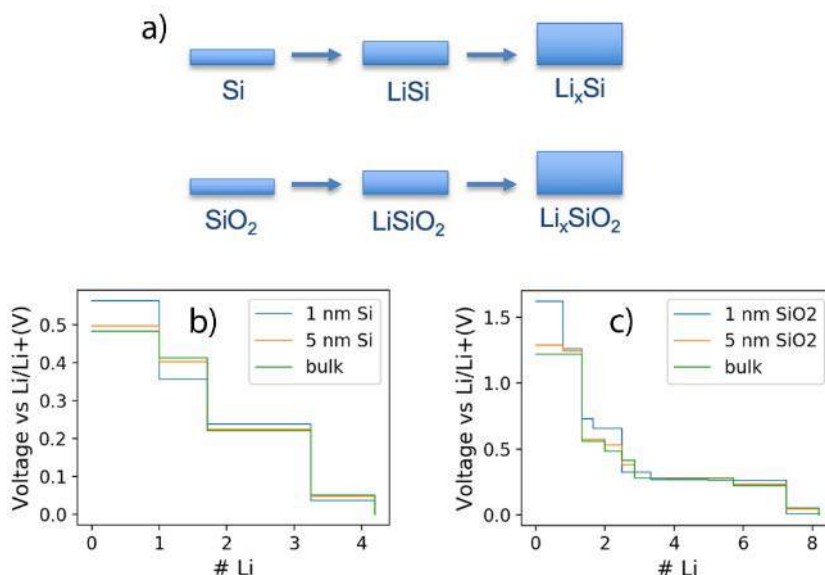


Figure II.1.B.4 a) Schematic of film expansion during lithiation; b) Lithiation profile for amorphous Si films; c) Lithiation profile for amorphous SiO₂ films

This suggests that an amorphous oxide layer is preferred initially, but the energy conditions favor recrystallization after a very thin layer has formed. Also, thin-film materials in general tend toward higher potential for lithiation than their bulk counterparts.

SiO₂ Model System Studies

In general, flat Si wafers, such as those used in the semiconductor and photovoltaics industry, provide a good model system to study electrochemistry of the SEI formation, although the perturbing factors of diffusion and permeation through a coated layer are absent in these systems. Two general types of samples are used in these studies: i) silicon wafers that are diced to test samples and used as-is after a cleaning protocol and oxidation, and ii) samples that are backed by bulk copper current collectors and that have thin (~50–100 nm) Si physically deposited onto the Cu. These thin samples are then coated with SiO₂ through physical deposition, as well.

Si wafers with SiO₂ coatings must be tested in cells that define the electrochemically active area of the wafer using an O-ring to avoid participation of the wafer edges or rear in the electrochemical processes. This is crucial because the edges are not coated with SiO₂ and are thus initially much more electronically conductive.

However, a cell with an O-ring necessarily uses a larger electrolyte volume, and we found that this can lead to more pronounced side reactions. When only cleaning cell parts in dimethyl carbonate between experiments, galvanostatic cycling at $20\ \mu\text{Acm}^{-2}$ yields continuous electrolyte reduction at voltages far above the lithiation potential. Through a series of experiments, we found that using fresh Li metal for reference and counter electrodes, using fresh electrolyte, and cleaning cell parts in organic solvents as well as water between experiments was crucial to suppress electrolyte reduction. With this procedure, we are able to achieve lithiation at current densities down to $5\ \mu\text{Acm}^{-2}$ (see Figure II.1.B.5).

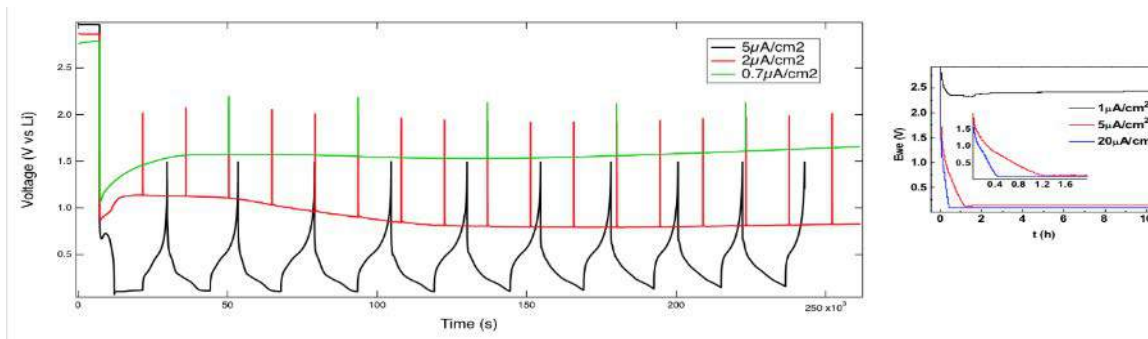


Figure II.1.B.5 Left: Galvanostatic cycling results obtained with an O-ring cell and Si wafer anode as a function of current density at NREL (4-h half-cycles for 5 and $2\ \mu\text{Acm}^{-2}$, 12 h for $0.7\ \mu\text{Acm}^{-2}$). Right: Comparable results reported by LBL for a single lithiation cycle

As seen from the figure, current densities of 2.0 and $0.7\ \mu\text{Acm}^{-2}$ do not allow lithiation even with this optimized procedure. This result agrees with earlier results, suggesting that this effect is not related to our particular cell components, but perhaps to the fact that $\sim 1.4\ \text{mL}$ electrolyte is used per cm^2 of anode area, as opposed to $\sim 20\ \mu\text{Lcm}^{-2}$ in a typical coin cell. For the following studies, the cell cycling was performed at $20\ \mu\text{Acm}^{-2}$.

Using these O-ring cells, we proceeded to study the effect of 1.4–5.2-nm thermal SiO_2 coatings on the lithiation of Si wafers. Galvanostatic cycling was performed at $20\ \mu\text{Acm}^{-2}$ in Gen2 electrolyte against Li metal counter and reference electrodes with no lower voltage cut-off; the results are summarized in Figure II.1.B.6. From the electrochemical data, there is a stark difference between samples with less than 3.0-nm SiO_2 and more than 3.0-nm SiO_2 .

Samples with less than 3.0-nm SiO_2 all cycle in the same manner: their cycling curves overlap (except for the very start, where 2.1-nm and 2.6-nm SiO_2 samples exhibit a spike to negative voltage vs Li (V_{Li}), whereas the 1.4-nm sample does not), their Coulombic efficiencies overlap at over 99% from the 2nd cycle onwards, and photographs of cycled samples indicate uniform lithiation.

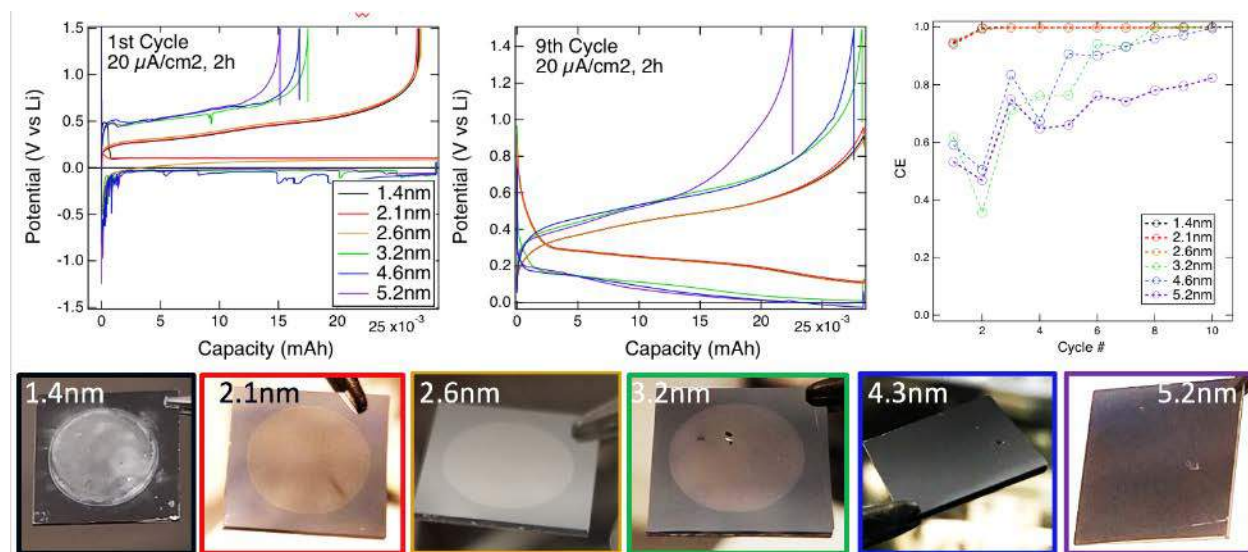


Figure II.1.B.6 Cycling of Si wafer anodes with variation of SiO_2 coating thickness at $20 \mu\text{Acm}^{-2}$ with no lower voltage cut-off. Top: 1st and 9th cycles as a function of SiO_2 thickness (left, middle), and Coulombic efficiency as a function of cycle number (right). Bottom: Photographs of Si wafers after 10 cycles

In contrast, samples with more than 3.0-nm SiO_2 initially only lithiate at negative voltages vs Li, exhibit low Coulombic efficiencies, and photographs of cycled samples at the bottom Figure II.1.B.6 show only localized lithiation or Li plating. However, by the 9th cycle, they exhibit markedly higher Coulombic efficiency, and cycling occurs at positive VLi, although the difference between lithiation and delithiation voltages is higher than for thinner oxides, indicating that a higher resistance remains. This may be correlated to the question of amorphous vs. crystalline transformations discussed in the modeling sections or may be due to strict overpotential needs due to the resistance of the films.

Nevertheless, it appears that samples with more than 3.0-nm SiO_2 undergo a change within the first 10 cycles that facilitates lithiation, allowing it to occur at positive VLi and higher Coulombic efficiency—again, possibly due to conversion of the films to lower resistance, or to a more crystalline network structure. To determine whether this is due to prolonged exposure to low VLi, we acquired a second dataset on sister samples by holding them at 0.01 VLi and recording the current. These data, along with images of tested anodes, are shown in Figure II.1.B.7.

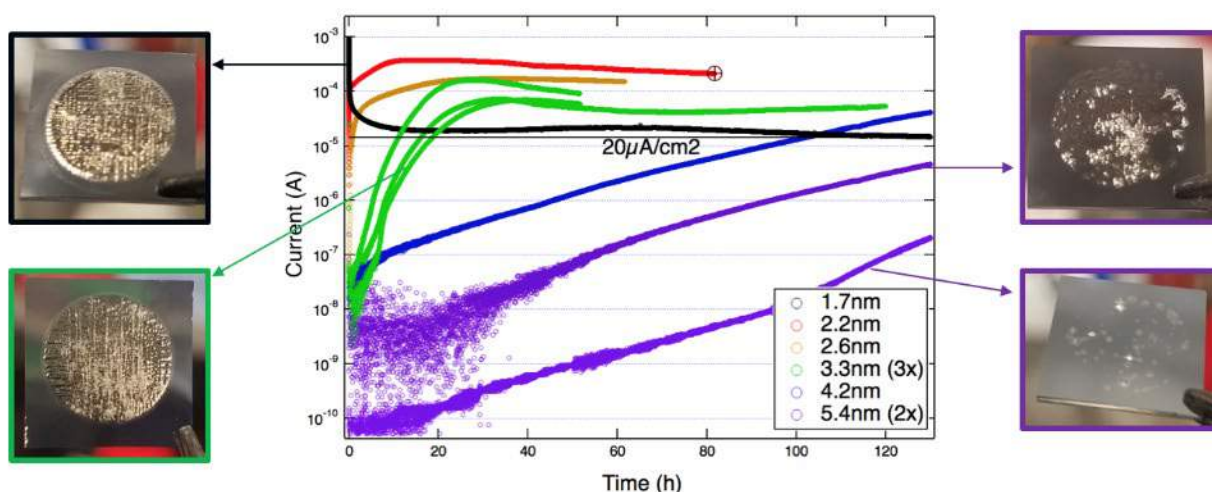


Figure II.1.B.7 Chronoamperometry at 0.01 VLi for different SiO_2 thicknesses. Photographs of selected samples at the end of testing are shown

Two regimes are apparent: samples with <3.0 -nm SiO_2 , which all cycled identically, rapidly reach currents above the $20 \mu\text{Acm}^{-2}$ previously used for cycling and reach a steady-state lithiation current after 15–20 hours. Examination of the anodes after testing reveals uniform lithiation overlaid with cracks resulting from the long duration of lithiation. On the other hand, samples with more than 4.0 -nm SiO_2 initially exhibit very low currents, which rise slowly and exponentially by 2–3 orders of magnitude. This process appears to proceed at a fixed rate (the slopes of the corresponding curves are very similar), but the starting current varies widely, even among two nominally identical samples with 5.4 -nm SiO_2 . Examination of these two anodes shows that lithiation or Li plating in this regime is highly nonuniform: the process appears to initiate at pinholes, and then spreads radially. The somewhat random pinhole density on a given sample appears to be responsible for the initial current, from which the increase in current with time proceeds. The transition between the two regimes appears to occur around 3 -nm SiO_2 ; hence, three samples with 3.3 -nm SiO_2 exhibit intermediate behavior.

We investigated the changes in Si, Li, O, and F bonding by the XPS for thin (up to 2.6 -nm) oxide overlayers, and morphology of two-dimensional (2D) chemical composition changes in Si samples with thick (~ 5 -nm) SiO_2 using time-of-flight secondary-ion mass spectrometry (TOF-SIMS) mapping. The XPS results for the two thin SiO_2 layers are compared in Figure II.1.B.8.

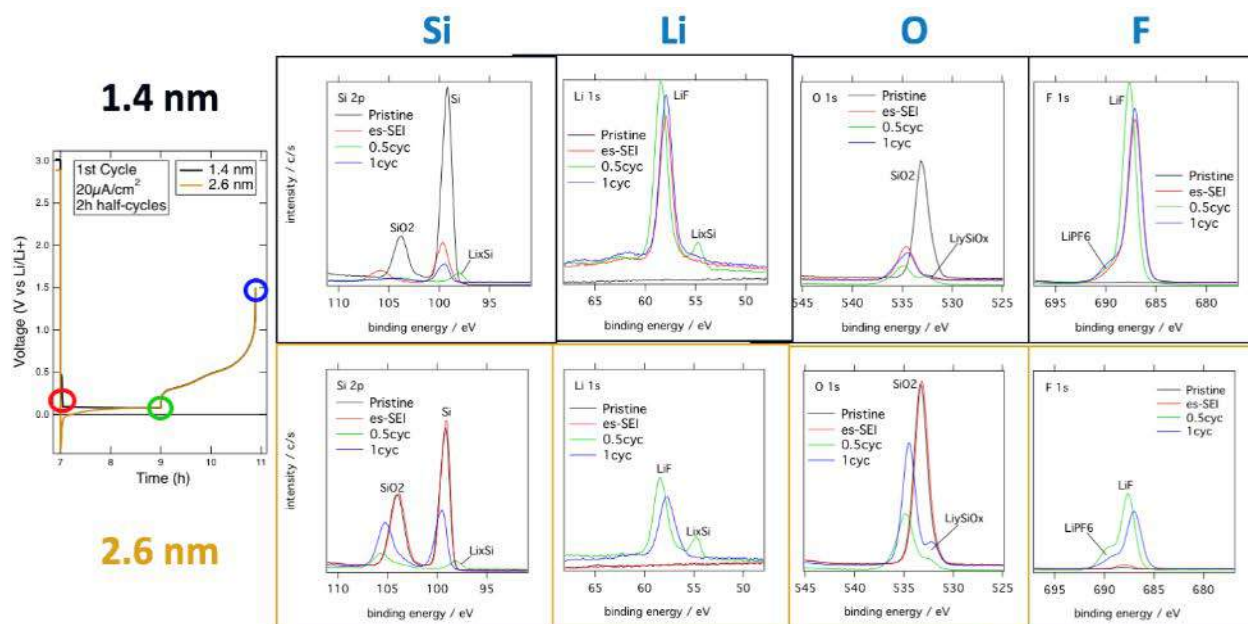


Figure II.1.B.8 Changes in Si, Li, O, and F bonding studied by the XPS. Colors of the XPS curves correspond to the lithiation-delithiation stages in the voltage-time plot on the left (2 half-cycles, 2 h each)

From these data, we conclude that 2.6 -nm SiO_2 blocks pre-lithiation SEI, because the SiO_2 remains visible after one full cycle, and that silicon wafer lithiates reversibly (LiSi_x peak appears and disappears), whereas the conversion of silicon oxide to a lithium silicate $\text{SiO}_2 \rightarrow \text{Li}_x\text{SiO}_y$ is not reversible.

In contrast, samples with >3.0 -nm SiO_2 overlayer initially only lithiated at negative voltages vs Li, exhibited low Coulombic efficiencies, and photographs of cycled samples show only localized lithiation or Li plating. To study this in more detail, as the second microscopic/compositional technique, we performed TOF-SIMS 2D compositional mapping around the lithiated spots. The results are shown in Figure II.1.B.9.

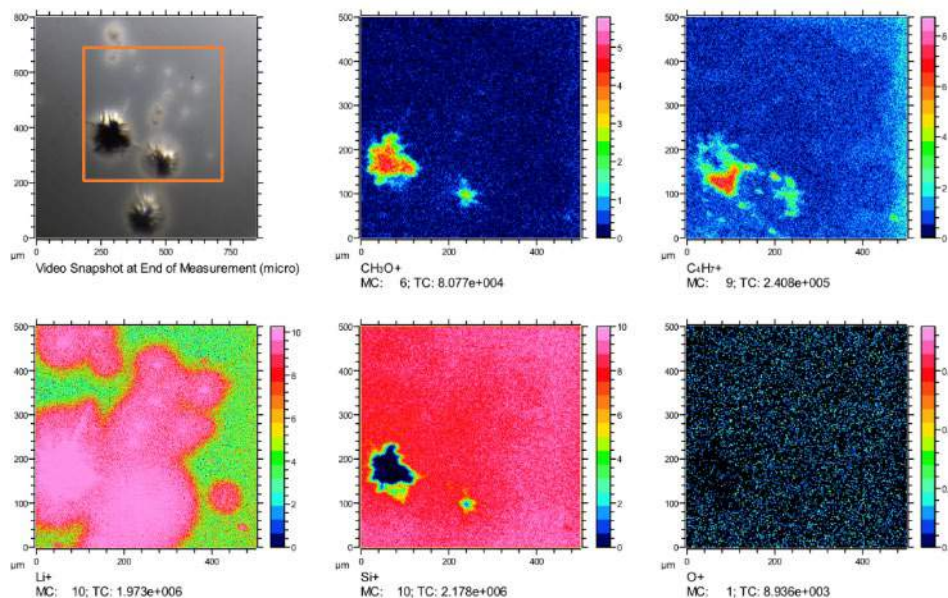


Figure II.1.B.9 Two-dimensional TOF-SIMS map of Li, Si, O, and carbon-containing sputtering fragments, along with the optical micrograph. The mapping area was 500x500 microns and is shown in the micrograph by the orange contour

These data show that the location of Li and of SEI-related organic species such as CH_3O^+ and C_4H_7^+ , correlates with the optically visible features (pinholes). However, although the SEI species are localized there, the Li has spread massively over a much larger sample area than indicated by the optical contrast. From these 2D maps alone, it is not possible to attribute Li spreading to within the wafer (underneath the SiO_2) or first lithiating the SiO_2 overlayer. However, 2D depth profile maps (not shown) indicate that Li had first entered the Si wafer through the pinholes, and then had spread underneath the thick SiO_2 . This suggests interfacial enhancement of Li diffusion. It further indicates that even if the area at which SEI is formed is limited to pinholes (which we might expect reduces the irreversible capacity loss associated with SEI formation), then lateral diffusion beyond the pinholes means that a larger area can be lithiated than had to be passivated by SEI, potentially lowering the irreversible capacity loss as a proportion of total capacity. This class of interfacial phenomena is currently used to design next-generation solid-state electrolytes [5],[6].

CV Studies of Previously Lithiated Oxides

The previous data show that, above a certain thickness, oxides are too resistive to lithiate directly, and instead, they lithiate through pinholes in the oxide. Over time, it appears that these processes give rise to less electrochemically resistive structures and result in more nominal electrochemical behavior. It is possible that this process is the actual lithiation of the oxide itself, as is predicted from the simulations. To study this possibility, physically deposited samples of previously lithiated oxides were prepared as thin-film 50-nm Si on 500-nm Cu on Si substrates. These samples were then used as substrates for the sputter deposition of 40-nm-thick lithium silicates of varying compositions (SiO_2 , $\text{Li}_2\text{Si}_2\text{O}_5$, Li_2SiO_3 , and Li_3SiO_x) expected from the tie line on the Li-Si-O ternary for lithiation of SiO_2 . Note that these substrates are substantially thicker than those studied in the previous analysis and should therefore be electrochemically inert. These correspond to a 0, 1:1, 2:1, and 3:1 composition of Li:Si. Samples were then assembled into half cells using Li metal as a counterelectrode in a standard coin-cell configuration using Gen2 electrolyte without FEC. Cyclic voltammetry (CV) was conducted at 10 uV/s sweeps from open circuit to 0.08 V. As was observed previously, in the absence of pre-existing lithium within the oxide, the onset potential for lithiation was observed at 0.23 V, in good agreement with other observations for SiO_2 -coated Si samples. However, if lithium was present at all in the oxide, the onset potential was significantly higher, near 0.35 V, and there were plateaus or peaks that manifested in the lithiation sweep. A first plateau that is present for all lithium-containing silicates exists at 0.31 V vs. Li/Li^+ , which does not exist for the pure SiO_2 film. There are additional plateaus/peaks at lower

potential, with increasing lithium content in the oxide resulting in an increasing onset potential for the second plateau. It may be that the first plateau is based on the formation of $\text{Li}_{12}\text{Si}_7$ with Li inserting into the Si substrate directly from the glass, and the lower-potential plateaus onset at the formation of $\text{Li}_{14}\text{Si}_6$ and $\text{Li}_{13}\text{Si}_4$, respectively, as the amount of available lithium for insertion from the oxide increases. These first-cycle CV curves are shown in Figure II.1.B.10.

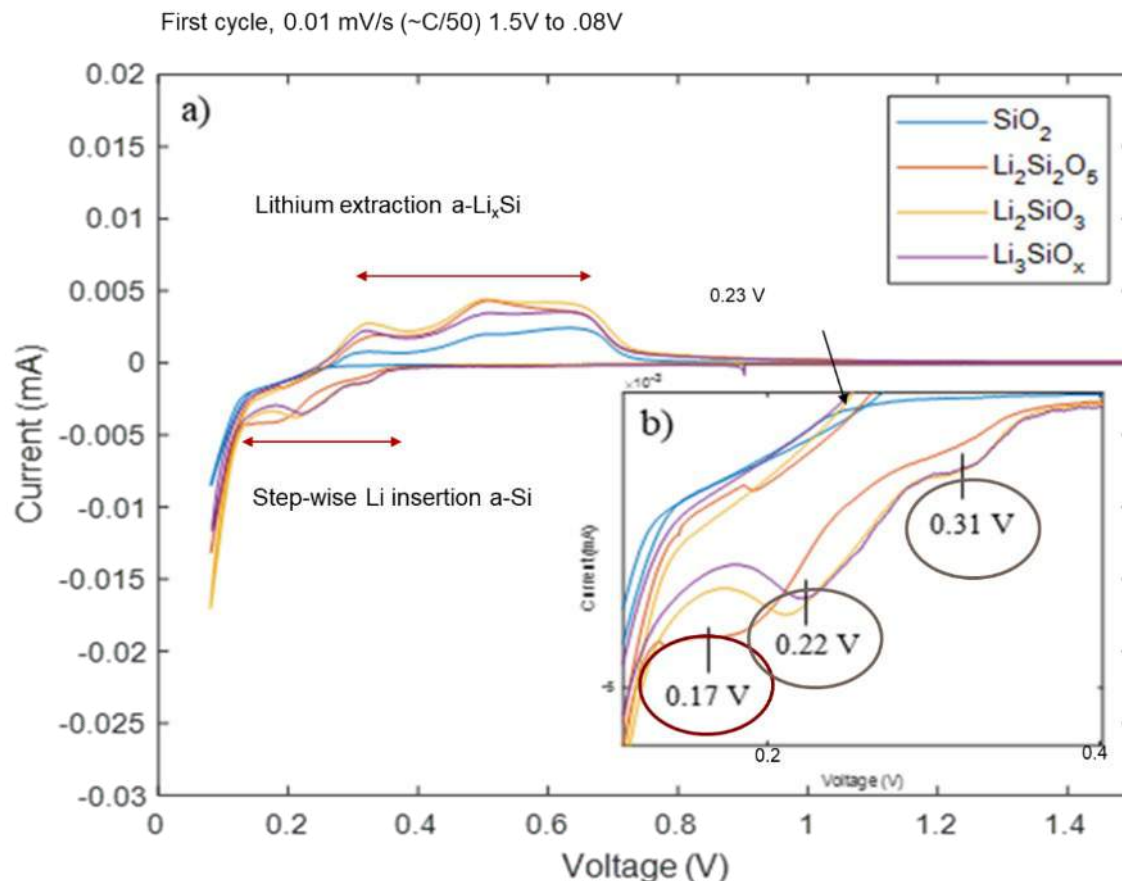


Figure II.1.B.10 CV of 50-nm-thick $\text{Si}_x\text{Li}_y\text{O}$ films under slow CV. Conditions: 25 °C, 10 $\mu\text{V/s}$, 50-nm Si/500-nm Cu/300- μm Si/20-nm Ti/200-nm Au WE, Li CE, Li RE

Further cycling of the samples in CV result in a steady evolution of both the early-onset potential plateau and the lower potential insertions. At the second cycle (see Figure II.1.B.11), SiO_2 now shows some of the peaks observed from the silicates at both the $\text{Li}_{12}\text{Si}_7$ and $\text{Li}_{14}\text{Si}_6$ state; and by the 14th cycle, the SiO_2 is closely matched to those films with the starting silicates, which potentially match to the onset of the $\text{Li}_{14}\text{Si}_6$ phase. This suggests that, upon cycling, any native starting oxide is lithiated to behave electrochemically similarly to those oxides that start with lithium in them, suggesting that evolution of the silicon oxide film toward a silicate-like structure may be happening. However, evidence of the silicates through direct beam observation are unable to identify these silicates directly, suggesting that it may just be the existence of lithium within the film that gives rise to these effects, rather than for formation of the stoichiometric silicates in the SiO_2 network. It may be that the presence of Li as a network modifier results in a substantively less ionically resistive film, as was observed in the thin-film studies above.

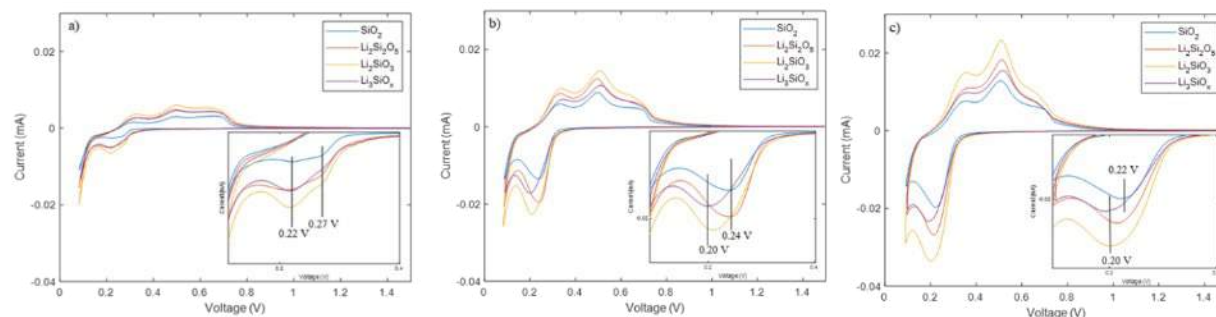


Figure II.1.B.11 CVs of a) 2nd cycle, b) 7th cycle, and c) 14th cycle of Si_xLi_yO samples under slow-scan CV (same conditions as above)

If the films are indeed becoming less resistive, such an effect should be visible as changes in their electrochemical impedance plots. To test this, films of varying composition were prepared as above and assembled into half cells with a lithium counterelectrode, with Gen2 electrolyte. Electrochemical impedance spectroscopy (EIS) was performed between 10 kHz and 0.1 Hz with 10-mV perturbation and were studied as a function of both time and temperature. The resulting impedance curves are very different between film chemistries, with elevated temperatures showing a much-changed response over time. SiO₂ films exposed to the electrolyte show little change over time at room temperature, with several days of exposure showing minimal change (Figure II.1.B.12). However, at 60°C and 80°C (Figure II.1.B.13), there is significant evolution of the film conditions over time, and at 80°C, the equivalent circuit of the resulting response is quite different than in the simple capacitive case, indicating that lithium transport may be affected at the elevated temperatures, which would be expected if the Li is penetrating faster into the film over time at elevated temperature. In the case of highly lithiated films (such as the Li₄SiO₄ films), much different impedance response is observed. At room temperature, after a few hours, the impedance response starts to show signs of a low-frequency “loop” in the data, indicative of instability within the electronic response on the timescale of the experiment. At 80°C, the kinetics of the response are fast enough to remove this low-frequency loop, but the evolution of the film is largely complete by the time the first round of EIS is complete, and the film shows little further evolution over time at the elevated temperature. Because the electrical response model is changing depending on chemistry of the film and temperature, it is difficult to coordinate a single set of parameters to extract kinetic properties from the films using EIS solely; but the obvious change in conduction and EIS behavior suggests permanent conductivity changes occurring within the film, in agreement with the other studies done here.

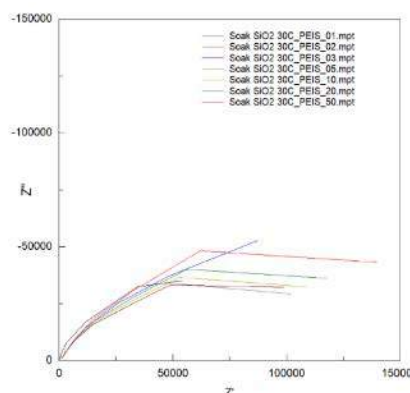


Figure II.1.B.12 Nyquist plots of SiO₂ film exposed to Gen-2 electrolyte at 30°C for various times. Film evolution is very slow, with little change after several days

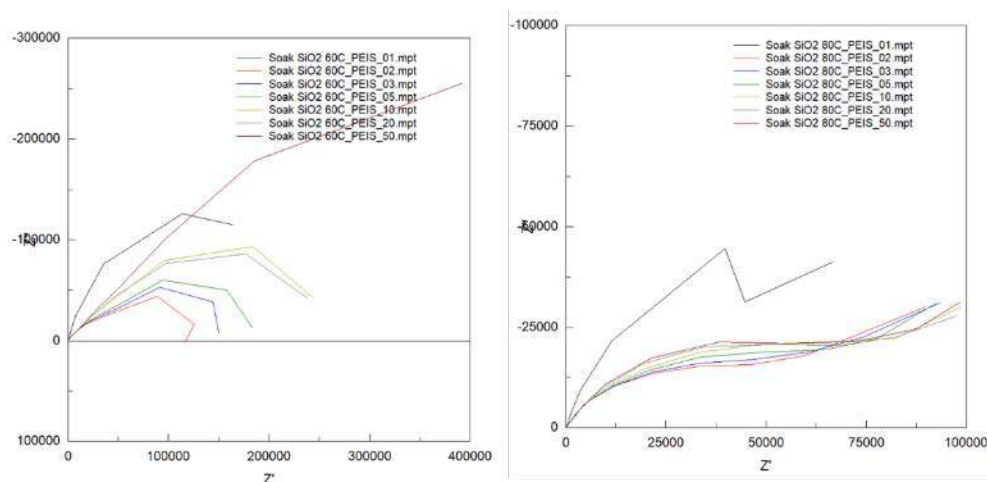


Figure II.1.B.13 Nyquist plots of SiO₂ film exposed to Gen 2 electrolyte at 60 °C (left) and 80 °C (right) over time. Both the electrical model and the film evolution are dramatically changed from the room-temperature case

Effect of Oxygen Content on Electrochemical Performance

In the final study done on flat model substrates, the question of oxygen and its role in allowing for lithiation was probed by changing the oxygen content of the starting film. SiO_x anode with minimum oxygen content (referred to as Si) was prepared by magnetron sputtering with Si target under low base pressure ($\sim 2 \times 10^{-7}$ torr), low deposition pressure (5 mtorr), and short work distance (8 cm). This Si anode was assembled into coin cells after the deposition and was not exposed to air in the process. In other samples, the prepared low-oxygen-content Si was exposed to air to obtain Si with native oxide layer. To prepare SiO_x anodes with higher oxygen level, we performed Si and SiO₂ co-sputtering with different power combinations (90–30 W, 90–60 W, 90–90 W, 60–90 W) for the Si and SiO₂ target and obtained SiO_x anodes with four different oxygen levels. We also performed Si sputtering under different base pressures, deposition pressure, and working distance to study whether these different sputtering conditions would affect the performance of the obtained Si anodes. The thickness for all the Si and SiO_x anodes reported here is around 50 nm, and all the cells were tested in Gen2 with 10% FEC.

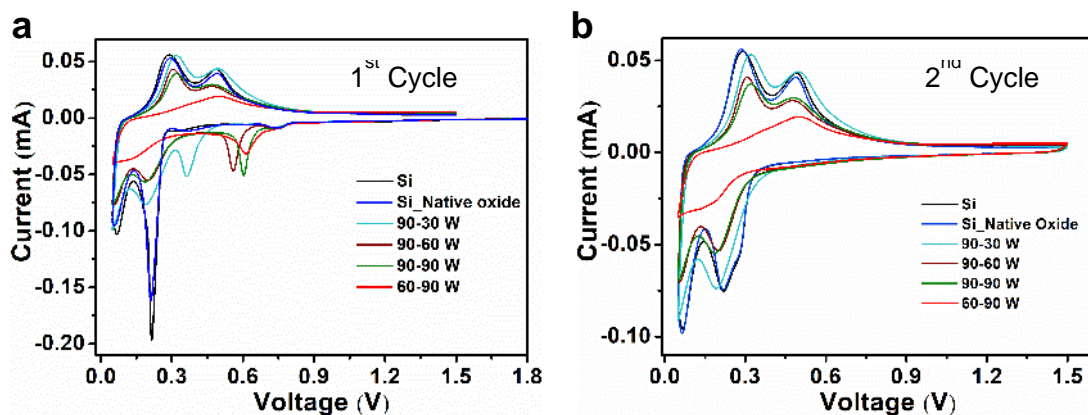


Figure II.1.B.14 a) 1st-cycle and b) 2nd-cycle CV curves of Si, Si with native oxide layer, and four SiO_x anodes with different oxygen level tested under the scan rate of 0.1 mV/s in the potential range of 0.05–1.5 V

The obtained Si, Si with native oxide layer, and SiO_x anodes with different levels of oxygen content were first evaluated with CV test at scan rate of 0.1 mV/s. As shown in Figure II.1.B.14a, all the Si, Si with native oxide layer, and SiO_x anodes exhibit a small reduction peak at around 0.7 V, which should be due to electrolyte reduction. By comparing Si, Si with native oxide layer, and SiO_x anodes, a distinct difference is observed in

the first CV cycle. All the SiO_x anodes prepared by co-sputtering show an extra reduction peak in the potential range of 0.3–0.6 V, where the peak position shifts to lower potential with possibly lower oxygen content. This peak should be due to the formation of lithium silicates during the lithiation of the surface silicon oxides. Because the Si anode has very low oxygen content, it did not show this reduction peak—once again suggesting that lithiation into an oxide has an electrochemical signature.

Even for Si anode with surface native oxide layer, the oxygen level is still not high enough to exhibit this lithium silicate formation peak. In addition, both Si and Si with native oxide layer show a much stronger peak than the other SiO_x anodes at around 0.2 V during the first cathodic process. This much stronger peak at low potential may suggest more electrolyte decomposition for Si anode and Si anode with native oxide layer. As Xu et al. have reported, lithium silicate is more stable toward the electrolyte than lithium silicide [71,8]. The formation of silicates at higher potential for SiO_x may stabilize the electrodes toward electrolyte reduction at lower potential. Note that the SiO_x anode synthesized with power combination of 60 W for the Si target and 90 W for the SiO_2 target have much broader redox peaks than other anodes, indicating a high resistivity of this anode due to its high oxygen content. All the SiO_x anodes did not show the reduction peak in the potential range of 0.3–0.6 V in the second CV cycle (Figure II.1.B.14b), which suggests that the formation of lithium silicates is irreversible. The reduction peak at around 0.2 V for Si and Si with native oxide layer was smaller during the second cycle, suggesting that there was more electrolyte decomposition during the first cathodic cycle, in agreement with other observations made for first-cycle electrochemical performance in the absence of formation cycles.

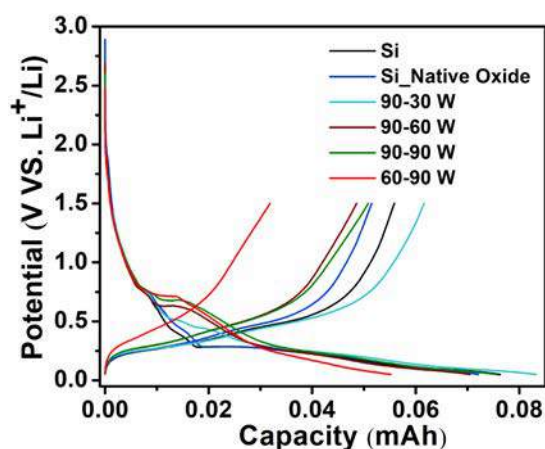


Figure II.1.B.15 Galvanostatic charge-discharge profiles of Si, Si with native oxide layer, and SiO_x anode under the current of 1 C (6 μA) in the potential range of 0.05–1.5 V

The galvanostatic charge-discharge profiles of all Si and SiO_x anodes (Figure II.1.B.15) agrees well with the CV data, where the Si and Si with native oxide layer show similar shapes during the first discharge and the SiO_x anodes with higher oxygen content have a much longer plateau in the potential range of 0.3–0.7 V. The potential of the plateau is higher for SiO_x with possibly higher oxygen levels; again, this agrees with the potential of the reduction of SiO_x during the first cathodic CV cycle. The first-cycle Coulombic efficiency for Si, Si with native oxide layer, and SiO_x with different power combination is 75%, 75%, 73% (90–30 W), 69% (90–60 W), 67% (90–90 W), and 58% (60–90 W), respectively. Increasing the oxygen content appears to lower the first-cycle Coulombic efficiency, possibly due to the irreversible formation of lithium silicates. The cycling performance of all these anodes was also evaluated, and the capacity retention at 100th cycle is 69%, 69%, 70%, 72%, 75%, and 84% for Si, Si with native oxide layer, and the SiO_x obtained at 90–30 W, 90–60 W, 90–90 W, and 60–90 W, respectively. It is worth noting that although SiO_x obtained at 60–90 W has a much better capacity retention, its reversible capacity is much lower than others due to its high oxygen content. The cycling test was performed by running three cycles at 1/10 C (6 μA) and then raising the current to 1 C. The capacity retention was calculated by comparing the capacity at 100th cycle with the 1st-cycle capacity at 1 C.

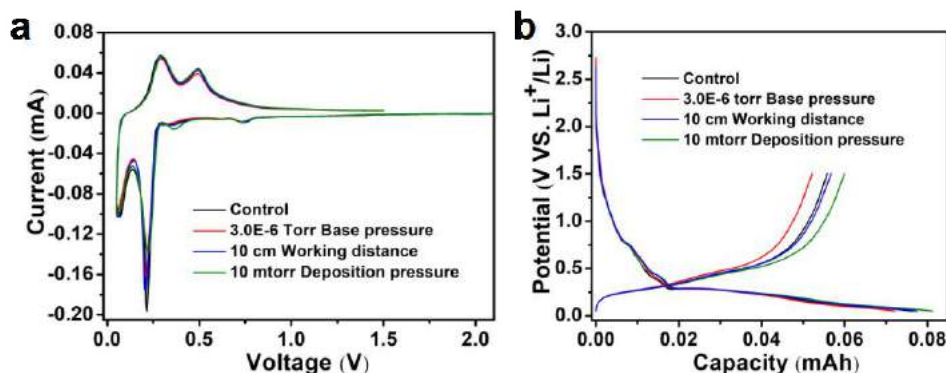


Figure II.1.B.16 CV curves and galvanostatic charge-discharge profiles of Si prepared under different sputtering conditions under the scan rate of 0.1 mV/s in the potential range of 0.05–1.5 V

The CV curves and galvanostatic charge-discharge profiles of all the pure Si anodes prepared under different conditions (changing base pressure, changing working distance, and changing deposition pressure) were also collected, and these results are shown in Figure II.1.B.16. All these Si anodes prepared under different conditions did not show a clear difference from both the CV curves and the charge-discharge profiles. In addition, their capacity retention at 100th cycle is also all around 69%. These results indicate that these different Si anode preparation conditions did not lead to a large difference in the oxygen level and electrochemical performance, therefore giving us some flexibility in preparing the Si anode with magnetron sputtering. We recognized, however, that these changes, although they may not give rise to electrochemical behavioral changes in the flat electrodes, do give rise to stress variation. Because stress applied to the SEI has previously been suggested as a reason for the loss of capacity, efforts to measure the stress in thin, flat Si films was undertaken.

Interfacial Stress Measurement

Measuring the stress in thin-film samples requires that the substrates be compliant and that the changes in shape on these thin samples can be measured accurately while in contact with the electrolyte and undergoing electrochemical cycling. To make measurements that allow simultaneous measurement of mechanical displacement and electrochemical behavior, new samples were constructed that are similar those used above, but remove the rigid Si substrate, leaving only a thin Cu layer covered by a nanometer-scale Si layer. The resulting thin samples are sufficiently compliant that stress changes due to electrochemical phenomena occurring on the silicon will register as changes in mechanical shape of the sample, which can be observed using a printed grating on the back of the substrate and Moiré interferometry.

As part of this effort, a new test cell needed to be designed that allowed for electrolyte contact with the Si continuously, even as the substrate moved during the lithiation and delithiation process. The current cell design is shown in Figure II.1.B.17A, featuring a PEEK body and metal heating block. Two chambers are used to allow for pressure equalization to prevent the thin electrodes from rupturing. The electrodes are 2- μ m copper foils with a 50-nm Si thin film held in place by an O-ring and washer. The thin foil electrodes are intended to enable magnified changes in stress in the electrode, leading to easier measurement of strain.

The first half of the custom microscope is displayed in Figure II.1.B.17B including the optical illumination arm, objective, and camera. A schematic of what the finished interferometer will consist of is shown in Figure II.1.B.17C. The Moiré illumination arm, containing the reference grating, is currently in progress.

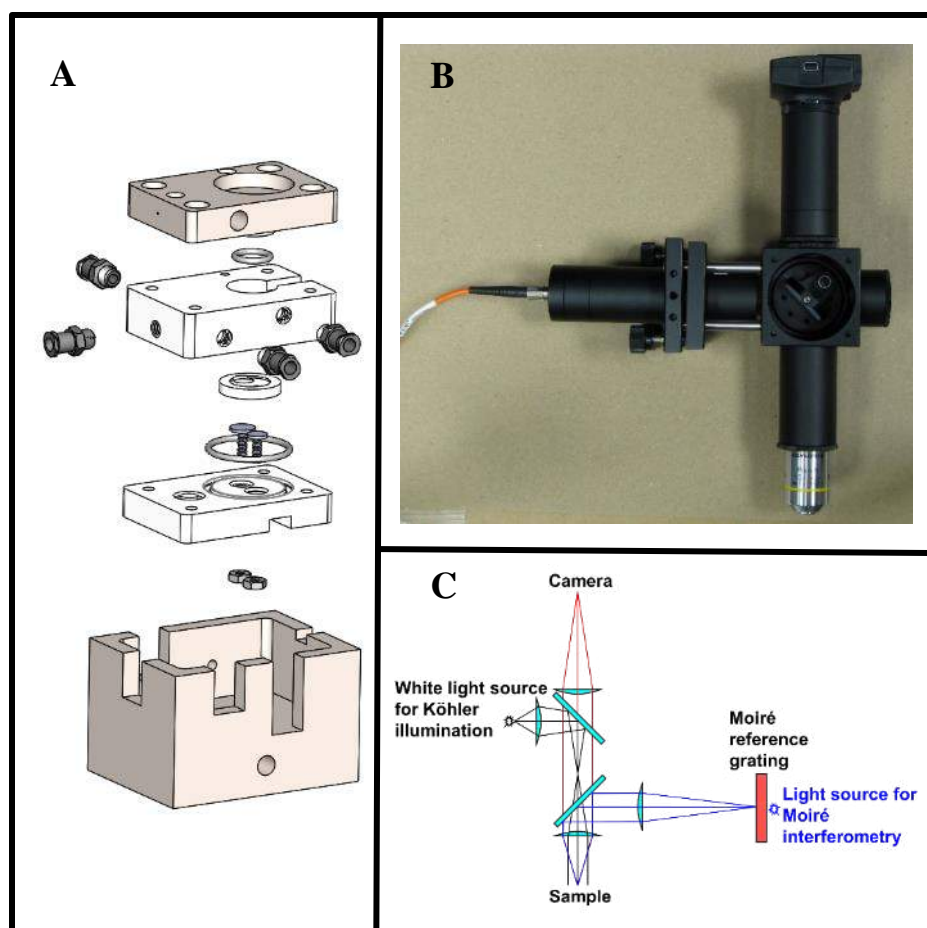


Figure II.1.B.17 A) Moiré in situ cell design with PEEK pieces in white and the metal heating elements in beige. B) Current custom microscope with optical illumination arm complete. C) Schematic of the targeted design of the final Moiré microscope

To calibrate these measurements, thermal expansion experiments were performed to verify the microscope's functionality and applicability for measuring strain in silicon and the SEI in the future. A film of 500 nm of Cu was evaporated on a silicon wafer. A grating, with a period of 4 μm was then patterned on top of the Cu. The amplitude grating consisted of 2- μm bars of 610-Å-thick Si. With an incident light wavelength of 470 nm, the silicon has near-zero reflectance while the copper has near-total reflectance. Moiré fringes that are formed due to the offset of the sample and reference gratings (Figure II.1.B.18A) create a sine wave with varying amplitude (shown in Figure II.1.B.18B). The frequency of this sine wave is consistent over the area of interest, indicating uniform heating of the sample. By fitting the sine wave and tracking the change in frequency with temperature, the strain and coefficient of thermal expansion (CTE) of the material can be determined. The silicon wafer substrate has a theoretical CTE of about 3–5 ppm/K in the temperature range studied. As seen in Figure II.1.B.18C, the experimental CTE can be found from the slope and is estimated as 4 ± 0.9 ppm/K. Each 30°C change in temperature corresponds to ~ 0.0001 change in strain whereas the lower limit of strain measured in silicon anodes in the literature is on the order of 0.003 [9],[10],[11]. This demonstrates the nondestructive ability of Moiré microscopy to measure the strain in silicon and the presumably smaller changes in strain caused by the formation of the SEI. Next will be to apply this confirmed technique to the in situ measurement of strain during the operation of a battery.

Lastly, the electrochemical behavior of the thin samples were verified in the same in situ cell assembly. The cyclic voltammograms of 2- μm Cu and 50-nm Si on 2- μm Cu are shown in Figure II.1.B.18D. In the first cycle, there are two contaminant peaks at ~ 0.74 V (Cu and Si samples) and 0.5 V (only Si samples) vs. Li/Li^+

in the first cycle that are not typically observed in the literature but are present in other samples previously reported and seem to be related to the oxide content of the films. From these data, both the electrochemical behavior of the Si and the mechanical measurements are compatible and will be used in the coming year to assess the stress in the films as the SEI is formed and evolves over time.

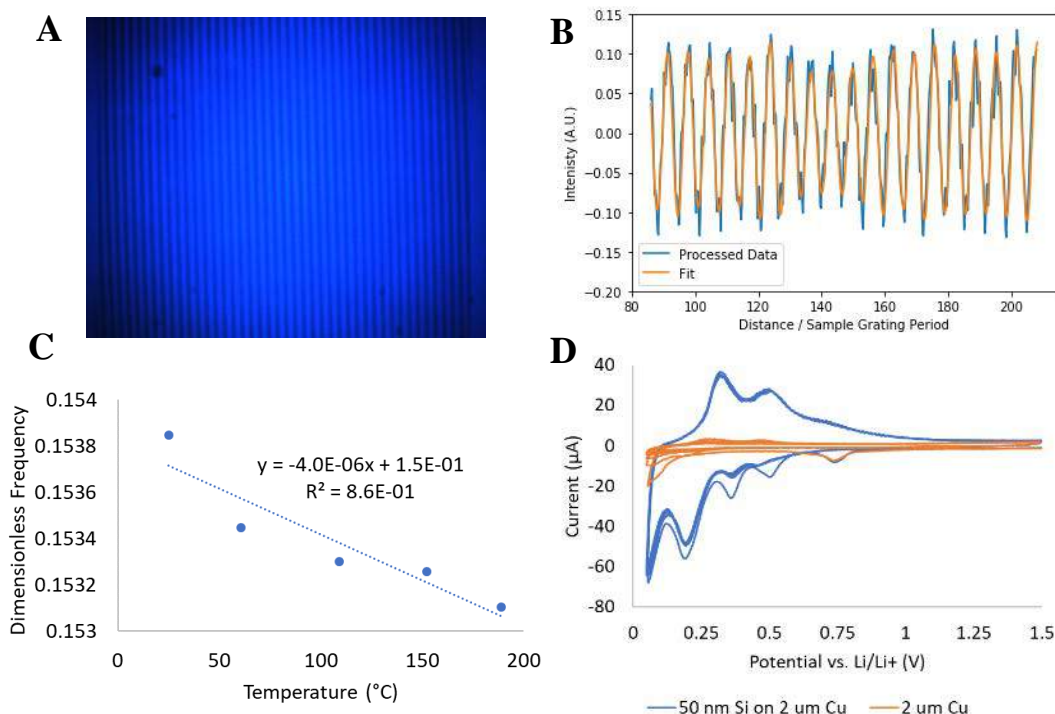


Figure II.1.B.18 A) Moiré fringe pattern using 470-nm incident light for the Si wafer thermal expansion experiments. B) Cross-sectional average of the Moiré fringe pattern given in A with the data in blue and the fit in orange. C) Dimensionless frequency obtained from the sine-wave fit for each temperature with the slope giving the CTE of the silicon wafer substrate. D) Cyclic voltammogram of the 50-nm Si on 2-μm Cu in blue and 2-μm Cu in orange. The working electrode was the silicon on copper foil and the counter/reference electrode were lithium metal. The electrolyte was the Gen 2 electrolyte. The scan rate was 0.1 mV/s at room temperature. Contamination peaks seem to be present during the first cycle

Oxygen-Free Particle Formation and Studies

The presence of oxygen, either included in the particle or as a surface oxide, is now understood to have a dramatic effect on the transport of lithium and subsequent electrochemical behavior in the model systems. Any commercially available powders that can be procured for producing Si electrodes have some (often uncontrolled) oxygen in them as part of their preparation. Removing that oxygen in the preparation allows us to study just the effects of the Si, to introduce controlled amounts of oxygen, and to study the effects of different surface modifications. Air-free Si nanoparticles (NPs) production by nonthermal plasma synthesis allows this and was developed previously under the SEISta program. This activity has been significantly expanded to enhance both the size and yield of the NPs. This effort now allows us to regularly produce 30-nm-diameter Si NPs in gram-scale quantities (Figure II.1.B.19). These are incorporated into various studies on both the inorganic chemical interface, detailed below, as well as the chemistry at the Si NP interface (included in the (Re)engineering of the Si/Electrolyte Interface via Molecular Interactions section).

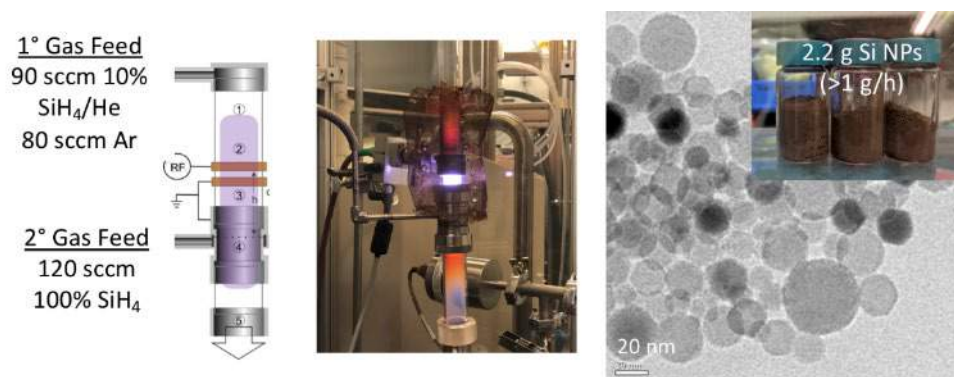


Figure II.1.B.19 Summary of optimized nonthermal plasma growth conditions for preparing 30-nm-diameter Si NPs at gram scale

All electrode slurries using these NP powders are prepared using in-house purified polyacrylic acid (PAA) binder and dried Timcal C65 conductive carbon in purified N-methyl-2-pyrrolidone (NMP) solvent. Slurries of plasma-grown 3.9–35-nm Si NPs contain 1:4:2 Si:TimcalC65:PAA. The low Si/C65 ratio ensures an effective electrical percolation network with smaller NP diameters (because percolation scales inversely with NP size, Figure II.1.B.20). We have previously determined that processing Si NPs in water results in significant surface oxidation (penetrating at least 3 nm into the particle) and that *the SiO₂ formed is electrochemically inactive toward lithiation/delithiation*, as evidenced by the lack of a delithiation peak in the dQ/dV plots in water-processed electrodes (Figure II.1.B.20). This matches previous work in the thin-film form where oxides larger than 3 nm are electrochemically inert under normal polarizations. For air-free Si NPs with no oxide, the capacity fade rate was minimal, with ≥99.0% Coulombic efficiency (CE) from cycles 20–100 (Figure II.1.B.20). However, given that the CE was constantly increasing, this suggested poor wetting of active material (slurry formulation needed to be optimized). The air-free slurry formulation process has since been optimized so that we could more definitively understand the role of the oxide SiO_x on the capacity fade rate.

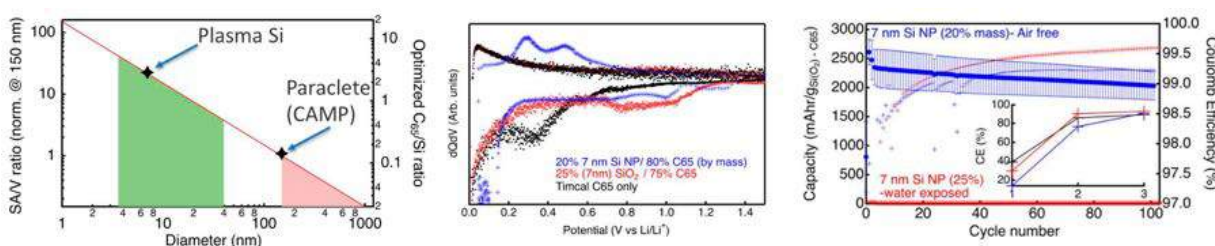


Figure II.1.B.20 Left: C₆₅/Si ratio must increase as the Si NP size decreases to ensure an electrical percolation network for active anode material as the surface area/volume ratio increases. Center: Normalized dQ/dV versus potential plot of the 1st cycle of the same samples showing that only the air-free-processed Si NP electrode undergoes reversible lithiation and delithiation, whereas SiO₂ electrodes do not exhibit reversible lithiation. Right: Capacity and Coulombic efficiency of half-cell anodes made from plasma-grown Si NPs (blue) fabricated air-free using NMP solvent or (red) in air using H₂O solvent

With an optimized slurry process, coatings of NP were made that allowed us to deduce the effects of chemical (SiO₂) and mechanical stress (Si NP size) on capacity fade. In addition, we carried out a detailed impedance spectroscopy analysis of the SEI layer for Si NPs with and without surface oxide.

Figure II.1.B.21a shows the normalized capacity at a cycle 50 using a C/5 rate for Si NP ranging from 4–35 nm in diameter. The gravimetric capacities of these anodes range between ~1700–2500 mAhg⁻¹_{Si}, and there is no obvious dependence of gravimetric capacity on NP size. We believe the range of capacities is likely related to C₆₅ percolation. Therefore, we normalize capacity data to highlight the important dependence of the capacity fade rate on the Si NP size. From Figure II.1.B.21a, the *smallest 3.9-nm-diameter Si NPs display the flattest curves and exhibit virtually no change in capacity over 100 cycles*. At Si NP diameters >10 nm (13–35 nm),

the largest 35-nm-diameter Si NPs display the steepest curves; but all Si NPs in this size regime show very similar fade rates because the traces of each are nearly superimposable on each other. To further analyze these data, we fit the traces in Figure II.1.B.21a (starting from cycle 20) to a linear function to extract an average capacity fade rate per cycle for each of the SiNP sizes measured. Those data are shown in Figure II.1.B.21b.

From Figure II.1.B.21b (blue data points), the smallest-diameter Si NPs have the lowest fade rate and the largest Si NPs have the fastest fade. From this plot, however, the trend is clearly not linear—as the SiNP size increases, the capacity fade rate appears to approach a horizontal asymptote. Thus, this scatter plot is fit with a sub-linear power function (black dashed line in Figure II.1.B.21), where the exponent = 0.75. We do not currently have an explanation for the significance of this number, other than that the fade rate is likely related to the ratio of surface area to volume (SA/V). When the same data are plotted against their SA/V (Figure II.1.B.21b inset), the data fall on a linear fit, which suggests that the origin of capacity fade is a combination of chemical (surface area, SEI) and mechanical (volume expansion/contraction) properties of the electrode.

We next performed additional experiments on water-processed Si NPs that will have a SiO₂ shell (red data points, Figure II.1.B.21b). Interestingly, these SiO₂-terminated Si NP samples overlay perfectly on the same exponential fit as the SiH_x-terminated Si NPs, suggesting that with these plasma-derived Si NPs, surface oxidation has no effect on the capacity fade rate. Another surprising result is found with Paraclete Si NPs (provided by CAMP, processed into slurries and electrodes at NREL), where these heavily oxidized SiO₂/Si NPs also fall on this curve. This result suggests that regardless of initial inorganic interface, all roads point toward the same capacity fade rate under these conditions.

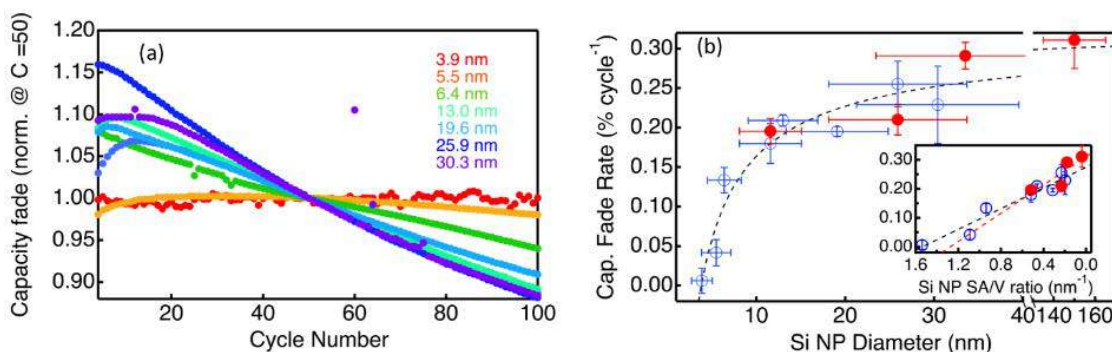


Figure II.1.B.21 (a) Normalized cycling data for a range of SiH_x-terminated Si NP anodes. The data here have been normalized to their capacity at cycle number 50. (b) Scatter plot of the average capacity fade rate as determined by fitting the last 50 cycles of each of the different-diameter Si NP-based anodes. The data in the blue open circles represent silicon with SiH_x-termination, and the data in red are those from oxidized (SiO₂) Si NPs. The black dashed line is a power function fit to the SiH_x-data with the form $\text{cap. fade} = ax^n + b$, where x represents the Si NP diameter. The inset is the same data plotted as a function of Si NP surface-area-to-volume (SA/V) ratio

We next probe the electronic properties of the SEI with and without surface oxidation on the Si NPs. EIS analysis of these composite anodes are conducted at three different states of charge after the first formation cycle (2nd-cycle delithiation). The impedance data are summarized in Figure II.1.B.22. Figure II.1.B.22a shows the Nyquist plots for 11.6-nm Si NP anodes with and without surface oxidation, as well as the equivalent circuit used to model these data. The equivalent circuit is established in the literature for silicon anodes [12]. In these measurements, there are three distinct processes occurring at different timescales. The fastest process (first semicircle) is double-layer charging (CPE_{DL}) and electrical resistance associated with electron propagation at the surface (R_{Surface}). As expected, the SiO₂ surface has a much higher R_{Surface} than the SiH_x-terminated Si NPs. The second process is associated with ion conduction through the SEI (R_{SEI}) and SEI capacitance (CPE_{SEI}). This process occurs on the 1–100-ms timescale. The third process is lithium diffusion in silicon and is accounted for with a Warburg circuit element. Because this process is slow, we are not able to make meaningful conclusions from the fits, and therefore, we analyze the characteristics of the SEI component only.

Figure II.1.B.22c displays plots R_{SEI} after the first formation cycle. For all samples measured, R_{SEI} decreases as the potential increases, indicating that the electronic character of the SEI at these Si NPs varies with potential. The SiO_2 -terminated Si NP anodes display increased R_{SEI} compared to the SiH_x -terminated Si NPs, implying that SiO_2 contributes to the SEI and that it impedes Li^+ diffusion. The capacitance for this process is shown in Figure II.1.B.22d. Interestingly, the capacitance for the SiH_x -terminated Si NP anodes is higher than that of the corresponding oxidized SiO_2 -terminated Si NP sample. This could mean that the SEI formed from SiH_x -terminated Si NP anodes accommodates more Li^+ or that the SEI is thicker. Finally, we plot the RC time constants for all of the measured anodes. As shown in Figure II.1.B.22e, the time constants are slower for the SiO_2 - versus the SiH_x -terminated Si NPs electrodes. Taken together, all these observations indicate that the electronic character of the SEI depends greatly on the inorganic surface of the Si NP. However, given that the capacity fade rate appears to be unaffected by the presence of SiO_2 and simply depends on the Si NP size, the differences in the SEI between SiH_x - and SiO_2 -terminated silicon are unimportant with respect to the overall capacity-fade mechanism.

Finally, to test whether the limited Li^+ conduction (increased R_{SEI} and decrease C_{SEI}) limits the rate capability of the electrode, we carried out a rate-dependence experiment in which the lithiation/delithiation rate capabilities are affected by the SiO_2 interface. The results are summarized in Figure II.1.B.22b. All the samples measured show a decrease in the delithiation capacity as the rate increases from C/20 to 10C. However, the magnitude of scan-rate dependence is strongly influenced by the Si NP size, where smaller-diameter Si NPs retain more capacity with increasing scan rates compared to larger-diameter Si NPs. Comparing the rate dependence for the samples of the same Si NP size, but with or without surface oxide layers, there appears to be no difference between the capacity drop between SiH_x - and SiO_2 -terminated Si NP electrodes. This surprising finding suggests that the measured SEI character is not limiting the uptake of Li^+ during lithiation/delithiation. Rather, the limiting factor is related to Si NP size, indicating the Li^+ -diffusion in silicon determines the rate dependence.

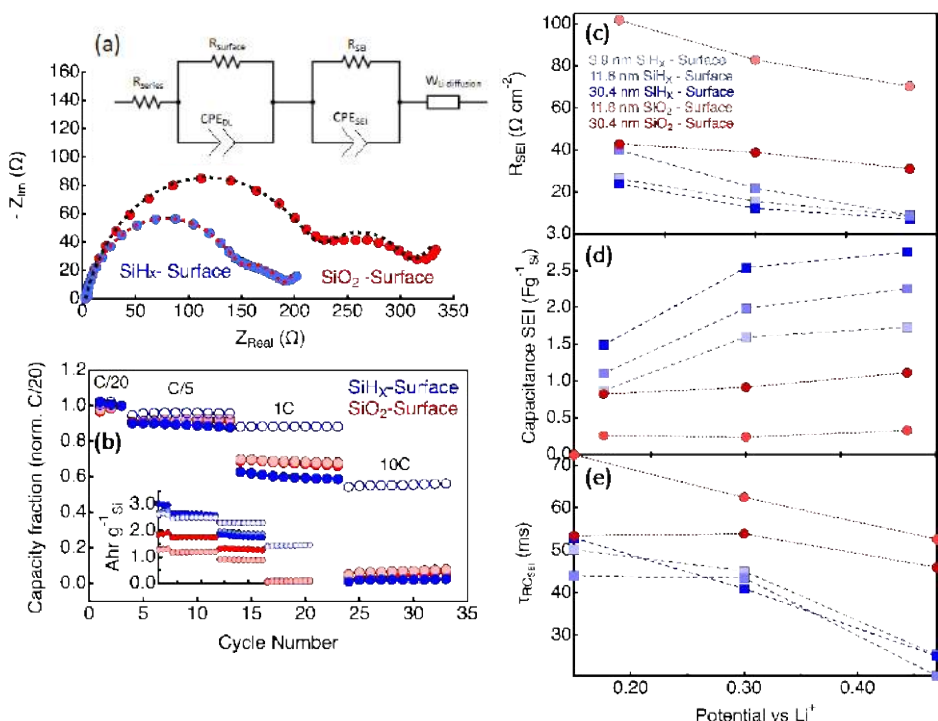


Figure II.1.B.22 (a) Representative Nyquist plots for Si NP-based anode half-cells with (red) and without (blue) an intentionally grown surface oxide (SiO_2) layer. The equivalent circuit used to model these data are shown in the top of panel (a), and fits to the data using this circuit are shown in the dashed lines. (b) Normalized scan-rate-dependent data for SiH_x - (blue) and SiO_2 - (red) terminated Si NPs for 3.9 nm (open circles), 11.6 nm (light-colored circles), and 30.3 nm (dark-colored circles). The inset shows the non-normalized data. (c) Values of the resistance of the SEI layer (R_{SEI}) extracted from fitting the impedance data. (d) Values of the capacitance of the SEI layer (R_{SEI}) extracted from fitting the impedance data. (e) RC time constants for impedance process associated with the SEI layer

LiSiO_x Powder Chemical Reactivity Study

The question of formation of the silicates during lithiation and delithiation is still debated, but there is ample evidence that a combination of Li, Si, and O are present in the SEI during formation and subsequent cycling, whether they form the crystalline silicate phases as the modeling has previously suggested. It may be that they are kinetically hampered in this formation, or that the transport of the lithium ion across the silicon oxide retards the recrystallization into the thermodynamically preferred phases, and so, only a quasi-stable amorphous structure is present in the film during electrochemical cycling. SEISta has previously reported that the presence of the electrolyte against such amorphous silicates (deposited via physical vapor deposition) results in the chemical attack of the silicate phases with increasing lithium content. This was at open-circuit potentials, and so, no current was flowing, although an exchange current would have been present in this system as it represents an electrochemical couple at dynamic equilibrium.

If the electrochemical processes are removed, there is the question of stability simply sitting against an electrolyte. Is the surface of any formed silicates intrinsically reactive enough to decompose the electrolyte salt and initiate chemical attack of the surface? To answer this question, a short study was done on powder forms of the silicates exposed to the Gen2 electrolyte, but in the absence of any electrochemical cell or exchange current. We synthesized high-purity raw silicates through the direct reaction with Li_2CO_3 and SiO_2 to form Li_2SiO_3 , $\text{Li}_2\text{Si}_2\text{O}_5$, and Li_4SiO_4 . The as-prepared materials were loaded in a glove box and subjected to a 500°C anneal for 2 hours to remove water and any surface carbonates. The dried materials were ground to a velvet-like consistency in the glove box prior to use. One gram of the resulting materials was exposed to 5 mL of the standard 1.2M LiPF_6 3:7 wt% ethylene carbonate/ethyl methyl carbonate at 60°C for 72 hours to explore the reactivity of crystalline Li-Si-O materials with the electrolyte. Previous work on amorphous films indicated that the amorphous films reacted readily with the electrolyte forming a complex Li-Si-O-P-F layer.

After aging, the powders were collected and washed four times with 15-mL aliquots of dry dimethyl carbonate to remove residual solvents. The samples were dried in vacuum for 24 hours and packed in 3-mm glass capillaries. In addition, reference samples of LiF , Li_2CO_3 , ethylene carbonate, LiPF_6 , and pristine starting materials were loaded in capillary tubes. The samples were analyzed on the Nanoscaled-Ordered Materials Diffractometer (NOMAD) located at the Spallation Neutron Source. This instrument is ideally configured to collect data suitable for pair distribution analysis, which is useful for identifying structural correlations within amorphous material. Furthermore, neutrons are especially sensitive to low-Z elements such as Li and O, allowing for structural determination of materials containing these elements.

The results of the neutron study are shown in Figure II.1.B.23. The black lines are the data collected for the pristine samples whereas the red dashed line shows the data after electrolyte exposure. From these data, there is no evidence of changes to the bulk structure of the Li-Si-O materials. Furthermore, there is no evidence of the formation of an amorphous surface phase on the crystalline materials. If there was such an amorphous phase, we would see new peaks and valleys in the data. Finally, there was no evidence for significant concentrations of organic species in or on the sample, which would attenuate the neutron signal due to the absorption of neutrons by H.

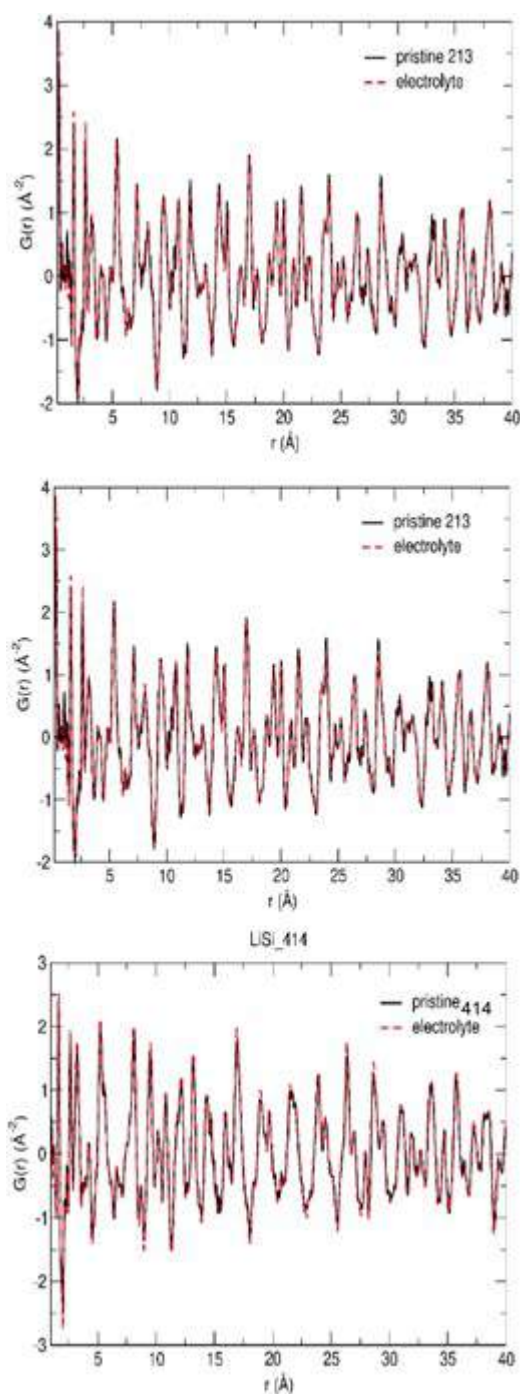


Figure II.1.B.23 Neutron PDF data collected for Li_2SiO_3 (top), $\text{Li}_2\text{Si}_2\text{O}_5$ (middle), and Li_4SiO_4 (bottom) for the raw material (black line) and material exposed to electrolyte (red dashed line)

Together, this indicates that the crystalline Li-Si-O materials are very stable against the electrolyte. This is true at high temperatures where one would expect greater reactivity. Furthermore, we see no evidence of other significant lithium or organic phases trapped on the surface. These data do not exclude catalytic activity of the materials, but do point to stability in the crystalline phase. This is in contrast to the data measured for amorphous materials reported previously, which demonstrated significant electrolyte reactivity.

Microcalorimetry

When processed and incorporated into electrodes, silicon active material surfaces such as those that are being grown under the SEISta program above are altered from their pristine conditions in a way that likely influences SEI formation and function. To understand the difference between model silicon systems and powders incorporated into electrodes, microcalorimetry has been employed to measure the heat generated from the aqueous processing of silicon powders with LiPAA binders and carbon additives, because this technique can show how different processing conditions can give rise to substantively different heat generation depending on how the surface reacts during early cycling behavior. To initiate this study, commercially available powders were used to understand how the measurement would vary under known variances of surface treatment.

Previous isothermal microcalorimetry curves of nanosilicon from various suppliers showed the Paraclete-4KD commercially available Si powder material to have one of the highest peaks and average heat generation over the test duration, correlated to its high Brunauer, Emmett and Teller (BET) surface area. Although generated heat was known to correlate to BET surface area, this material sample was noted to also have poor surface properties that impacted cycling performance. We hypothesized that these surface properties may also correlate with our high heat generation. However, similar analysis of new Paraclete-G18 material, with improved surface properties and cycling, demonstrated nearly identical heat generation. This suggests that surface area is the primary correlative property because both samples showed similar BET surface areas. These data are summarized in Table II.1.B.1.

Table II.1.B.1. Quantified Energy Generation Based on the Fit Curve of the Paraclete-4KD + CB Sample as well as predicted material and performance loss based on the formation of silica

NanoSilicon	Peak Signal, μW	Average Signal, μW	Normalized Peak Signal, $\mu\text{W/g-Si}$	Normalized Peak Signal, $\mu\text{W/m}^2\text{-Si}$
Paraclete – 4KD	90.7	64.2	468.6	13.9
Paraclete – G18	97	57.3	489	15.2

Electrochemical microcalorimetry has also been carried out on two silicon-containing coin cells. The microcalorimetry fixture was first calibrated for dynamic time correction using a “dummy” coin cell of known resistance to both confirm measurement accuracy and enable reduction of signal latency by roughly one order of magnitude [13]. Figure II.1.B.24a shows the overlay of the voltage and heat-generation curves for a full coin cell of NMC cathode vs Paraclete G18 anode. The current level of analysis does not enable us to isolate parasitic heat flow from other sources (entropic and ohmic), but it does provide quantification of the overall reduction in heat generation with subsequent cycling [14]. Figure II.1.B.24b shows the measured coin-cell capacity along with heat generated per cycle, with both showing similar decreasing trends. The values measured here also agree closely with those reported in a newly accepted paper on microcalorimetry of silicon anodes [15].

Continued electrochemical microcalorimetry testing of coin cells will enable comparison of heat generation between cathodes and anodes within cells and, through controlled discharge parameters, enable isolation of the parasitic heat flow from the entropic and ohmic heat flow coming out of the tested coin cell. This will enable us to determine the point of cycling with peak parasitic losses as well as, through charge-counting potentiostatic measurements, determine the heats of formation for SEI layers at different states of charge.

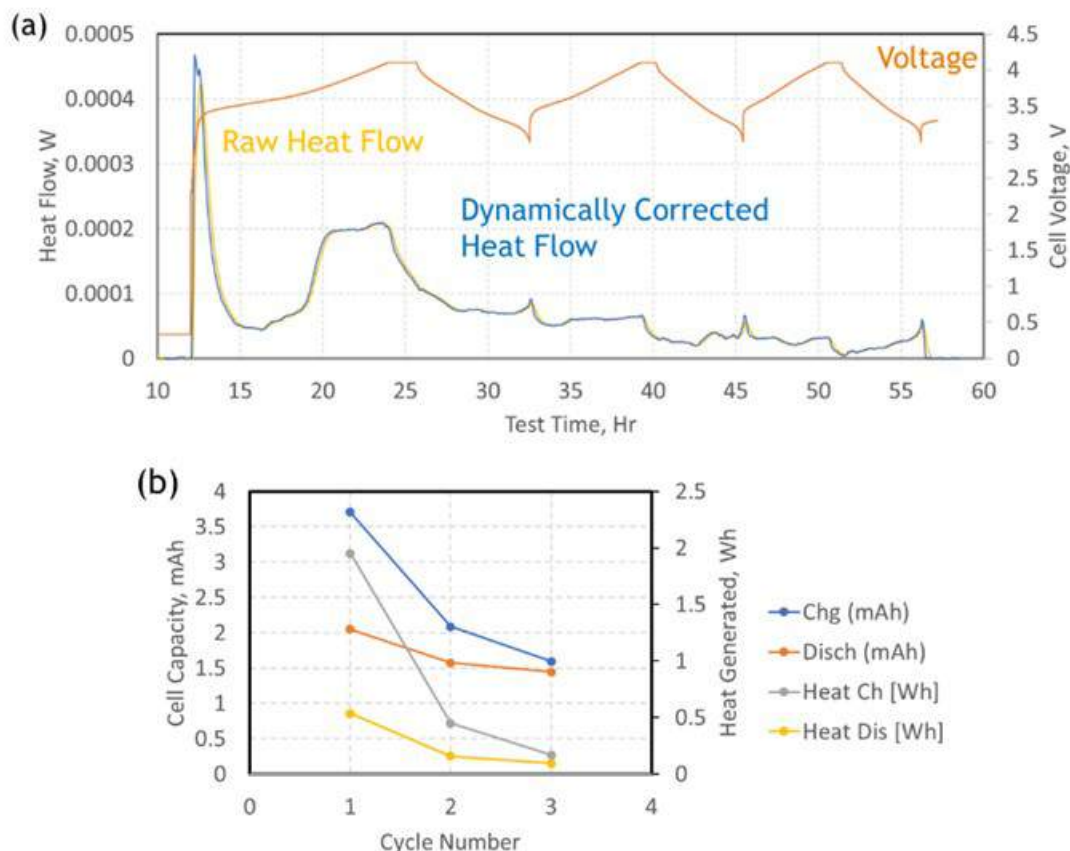


Figure II.1.B.24 a) Heat flow and voltage curves for NMC vs Paraclete-G18 coin cell subjected to electrochemical microcalorimetry. b) The cell capacities and generated heat per cycle derived from these curves

Zintl Oxide Electrochemistry

The nature and function of the reactivity of the Si surface (and of the SiO₂ surface) has been observed repeatedly to influence the formation and evolution of the SEI and to have an impact on the cycling of the Si electrode. Recently, workers in SEISta from ANL have used a small amount of metal salt additive in the electrolyte during cell construction to modify this surface. This is an attempt to stabilize its formation and evolution by supplying additional charge density at the surface of the Si to tie up uncoordinated Si near the surface and to hopefully improve the stability of this surface. To that end, experiments were done on powder-coated anodes that used a new electrolyte additive that forms a Zintl phase at the surface of the Si during assembly.

The half cells of Si electrode (CAMP A-A017, Paraclete Si nano-particle(80):C₄₅ conductive carbon(10):LiPAA binder(10)) | GenF or GenFM (GenF + 0.1 M Mg(TFSI)₂) | Li metal were electrochemically cycled using 2032-type coin-type cells. Cells were subjected to one of three electrochemical treatments: 1) 200-mV GenF or GenFM (discharge and potentiostatic hold at 200 mV until $i \leq 5.0 \times 10^{-6}$); 2) 10-mV GenF or GenFM (discharge and potentiostatic hold at 10 mV until $i \leq 5.0 \times 10^{-6}$); or 3) 1-cycle GenF or GenFM (one galvanostatic cycle from 1.5 to 0.01 V (vs. Li/Li⁺, hereafter) at a C/20 rate with potentiostatic hold at 10 mV until $i \leq 5.0 \times 10^{-6}$ between discharge and charge). The collected Si electrodes from cycled cells did not go through a rinsing process to protect formed Silicon SEI. All collected electrodes were stored in an Ar-filled glove box after vacuum drying at room temperature and transferred to each analytical equipment without air exposure.

Chemical Composition of Zintl Phase. Raman microscopy was used to investigate the chemical composition of the first cycle at 200 mV and 10 mV using both the GenF or GenFM electrolyte. Figure II.1.B.25a shows a photograph of the six types of samples, and Figure II.1.B.25b shows micrographs recorded through a 20x Raman microscope objective for the samples. Optically, GenFM samples look the same as GenF. The first-cycle GenF or GenFM composite anodes had a “powdery” appearance against the copper substrate and many individual microdomains. This surface morphology is likely due to cracking of the film after silicon expansion (during lithiation) and contraction (during delithiation). In contrast, the 200-mV GenF or GenFM samples have a very smooth crack-free appearance. Samples that were held at 10 mV in GenF or GenFM are also smooth, but many cracks exist, and the film has plate-like domains, many of which have detached from the copper foil, suggesting that lithiating the anode may have detrimental effects of anode adhesion properties. In Figure II.1.B.25c, Raman spectra of the samples are presented and show expected chemical composition signatures. A large crystalline silicon (c-Si) peak at 520 cm^{-1} and band between $920\text{--}980\text{ cm}^{-1}$ appear in the 200-mV sample, indicating that it has not been highly lithiated. These peaks are present in the 1-cycle sample as well, but to a lesser extent. In contrast, the 10-mV sample shows almost no evidence of c-Si, except a weak 520 cm^{-1} peak for GenFM (suggesting incomplete lithiation). Instead, a new peak appears at 385 cm^{-1} that is attributed to lithium silicide (Li_xSi_y) [16]. Due to a peak from the sapphire window of the sample holder at around 420 cm^{-1} , we are unable to distinguish whether the phase of the lithium silicide is Li_7Si_4 or $\text{Li}_{13}\text{Si}_4$. Also observed in the Raman spectra are peaks representing the other components of the anode: conductive carbon (1355 and 1560 cm^{-1}) and LiPAA binder (1445 cm^{-1}). In this measurement, we did not observe any specific differences between GenF and GenFM samples in terms of chemical composition.

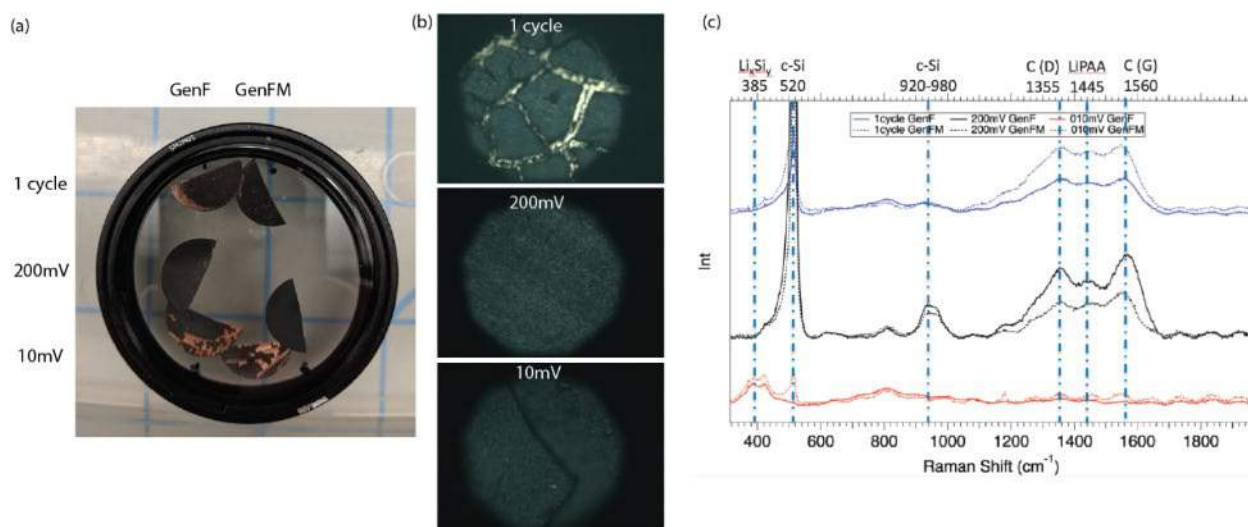


Figure II.1.B.25 (a) Photograph of the 1-cycle, 200-mV, and 10-mV GenF or GenFM samples in the air-free holder used for micro-Raman analysis. (b) Optical micrographs of the samples imaged through a 20x objective on the Raman microscope. Samples from GenF and GenFM looked the same. (c) Raman spectra of the samples

To further characterize the samples, we used two different methods of Fourier transform infrared (FTIR) spectroscopy. Figure II.1.B.26a and Figure II.1.B.26b show the attenuated total reflection (ATR)- and diffuse reflectance (DRIFTS)-FTIR spectra, respectively. For reference, a pristine electrode spectrum is presented in Figure II.1.B.26a (green line). The pristine sample matches well with previous studies [17]. Silicon oxide shows a broad peak between 1200 and 1000 cm^{-1} . A Si-O-Si absorption at 870 cm^{-1} indicates some SiO_2 surface layer to the silicon nanoparticles. In addition, we observe asymmetric and symmetric COO⁻ from the LiPAA binder at 1545 cm^{-1} and 1400 cm^{-1} , respectively. There is also a C=O peak at 1700 cm^{-1} from COOH of unreacted PAA binder. Upon lithiation of silicon and SiO_2 to form Li_xSi_y and Li_xSiO_y SiEI components, respectively, the FTIR spectra show a reduction of both the silicon oxide and LiPAA binder signals due to lithium lost in the formation of these SiEI species. ATR works well with smooth films but cannot measure rough films well. Because the 10-mV GenF or GenFM samples are so flaky and they show many spots of bare

copper, we were unable to use ATR to measure these films. Instead, at least for 10-mV GenF, we were able to use DRIFTS to acquire a well-resolved FTIR absorption spectrum. The 10-mV GenFM sample was too degraded to measure. Additionally, the DRIFTS spectra contain two peaks, 1670 cm^{-1} and 1200 cm^{-1} , that are slightly more prominent in the GenFM, compared to GenF samples, at all potentials.

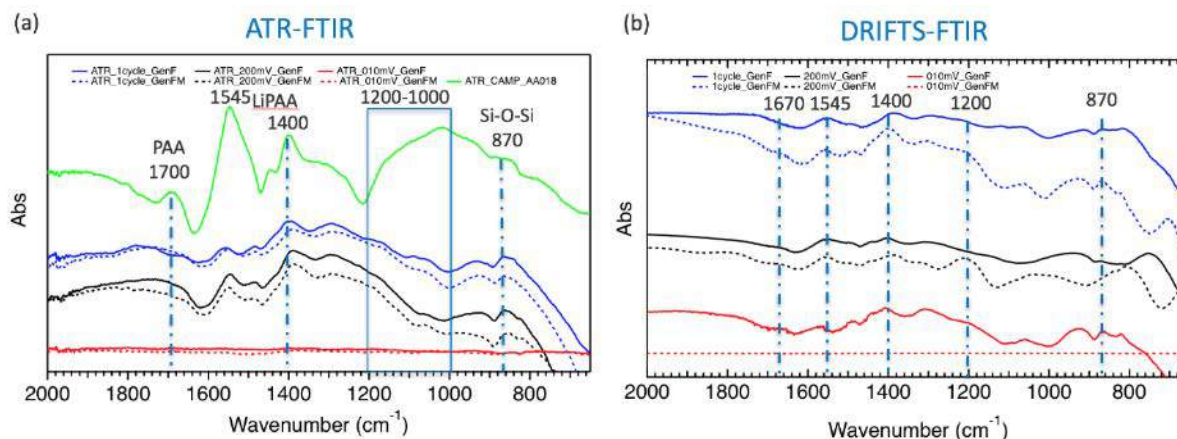


Figure II.1.B.26 (a) ATR-FTIR and (b) DRIFTS-FTIR spectra of 1 cycle, 200 mV, and 10 mV GenF or GenFM samples

The XPS spectra of 1-cycle, 200-mV, and 10-mV GenF or GenFM samples are shown in Figure II.1.B.27 and Figure II.1.B.28, respectively. In all samples, the signals from PF_6^- species are detected (P 2p and F 1s peaks at $\sim 139\text{ eV}$ and $\sim 689\text{ eV}$, respectively), which is highly attributed to the residual electrolyte on the surface of unwashed electrodes. One major difference observed between the GenF and GenFM samples, specifically for the 200- and 10-mV ones, is found in the Si 2p spectra: there are apparent peaks from lithiated Si species (Li_xSi , $\sim 98.5\text{ eV}$, bright yellow) in GenF samples (200- and 10-mV lithiated ones), but it is not the case for GenFM samples. One possible explanation for this is that a surface-sensitive XPS technique cannot detect the Li_xSi formation in the presence of a relatively thick and well-covered SiEI layer (with possible Zintl phase) formed in GenFM electrolyte. It is noted that Raman can detect 385 cm^{-1} peaks attributed to lithium silicide (Li_xSi_y) in both 10-mV GenF and GenFM samples (Figure II.1.B.25c). Another major difference in Mg 2p core level is detected in GenFM samples. The peak shape is distinctively different between 200-mV and 10-mV lithiated samples. The 1-cycle and 200-mV lithiated samples have two peaks at $\sim 53\text{ eV}$ and $\sim 52\text{ eV}$, which are tentatively assigned to MgO and MgF_2 , respectively. In the 10-mV lithiated sample, the $\sim 53\text{-eV}$ peak disappears, and a new peak is observed at a lower binding energy ($\sim 50.5\text{ eV}$), which is likely Mg^0 . $\text{Mg}(\text{TFSI})_2$ was eliminated from the assignment because there was not enough N 1s signal (not shown).

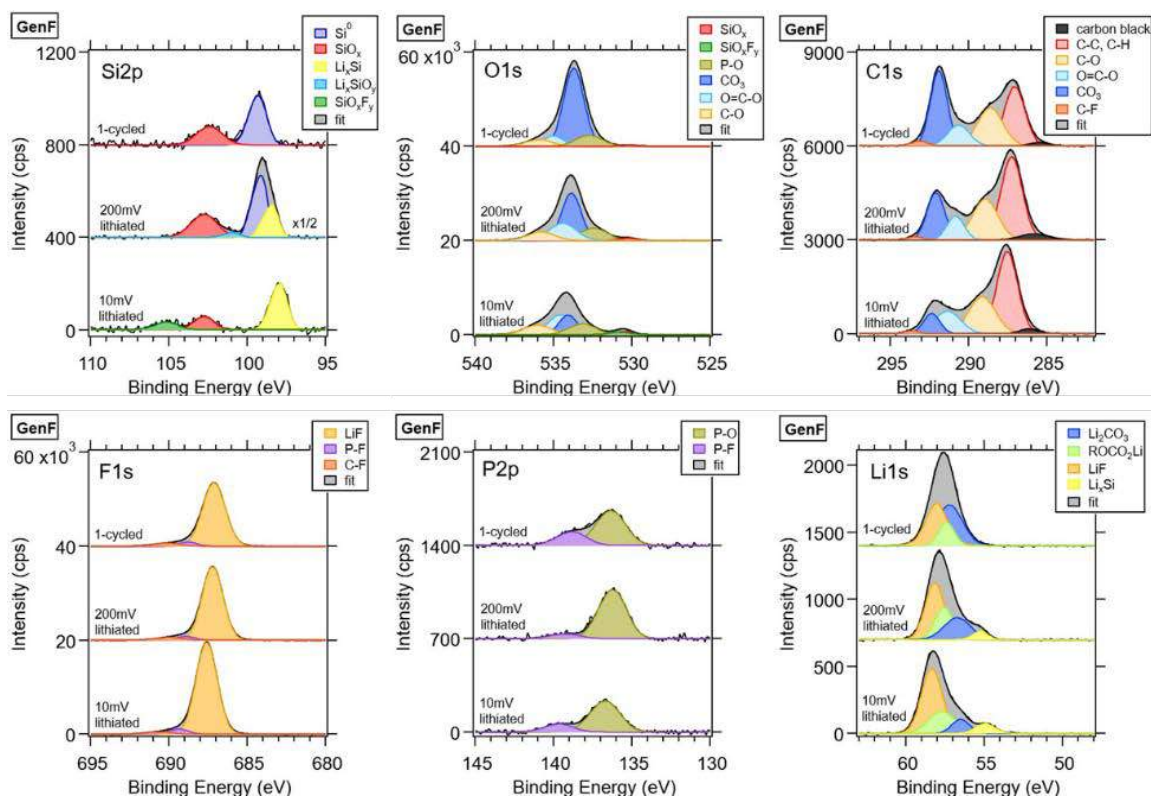


Figure II.1.B.27 XPS spectra of the Si electrodes cycled in GenF. Peak assignments are preliminary

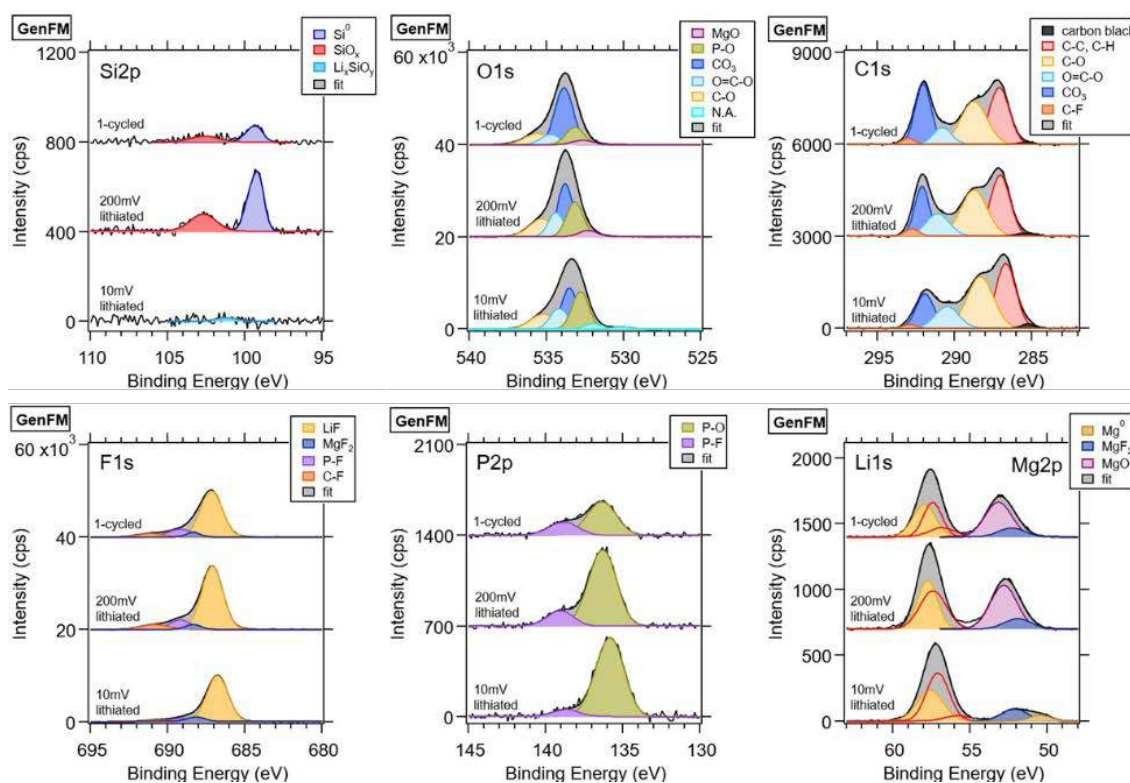


Figure II.1.B.28 XPS spectra of the Si electrodes cycled in GenFM. Peak assignments are preliminary (N.A. denotes "not assigned")

Scanning transmission electron microscopy (STEM) energy-dispersive X-ray spectroscopy (EDS) and electron energy-loss spectroscopy (EELS) analysis were performed on the first-cycle GenFM sample. A TEM sample was prepared in an Ar glove box by scraping particles of the Si-based composite electrode off the Cu foil substrate onto an ultrathin carbon support-film TEM grid. Examples of STEM EDS atomic % maps are shown in Figure II.1.B.29, and the sum EDS spectra from this map area is in Figure II.1.B.30. The results are consistent with Si nanoparticles being present either containing or being surrounded by a shell containing C, O, Mg, F, and P. STEM EELS analysis (not shown) revealed the presence of lithium in or around the Si particles. Areas of LiF were found to be present. STEM EELS mapping of Mg may be difficult due to the high energy of the Mg K edge.

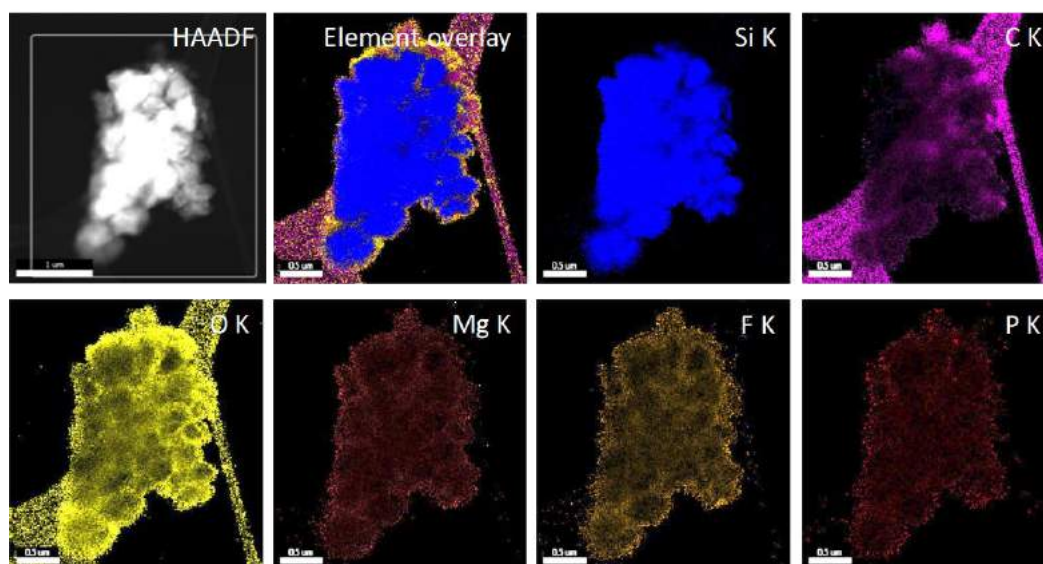


Figure II.1.B.29 STEM EDS atomic % maps of particles of first-cycle GenFM sample

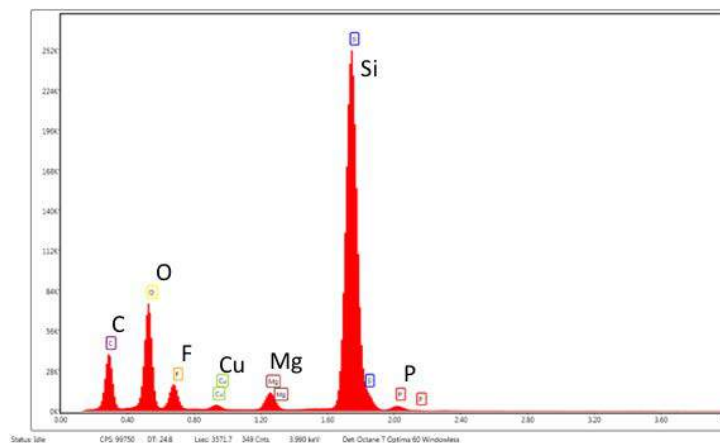


Figure II.1.B.30 STEM EDS spectra obtained from particles of 1-cycle GenFM sample

Surface Morphology and Roughness of Zintl Phase. Optical microscope images obtained in the AFM instrument are illustrative of the effect of cycling (Figure II.1.B.31). The 200-mV GenF or GenFM sample shows an undisturbed composite electrode because lithiation potentials were not reached under this condition. The effect of volume expansion during lithiation is seen in the sample held at 10-mV potential; large cracks appear where active material has delaminated from the underlying Cu current collector. The sample that underwent one full cycle of lithiation and delithiation shows the most damage, with diffuse cracking induced by volume contraction during delithiation.

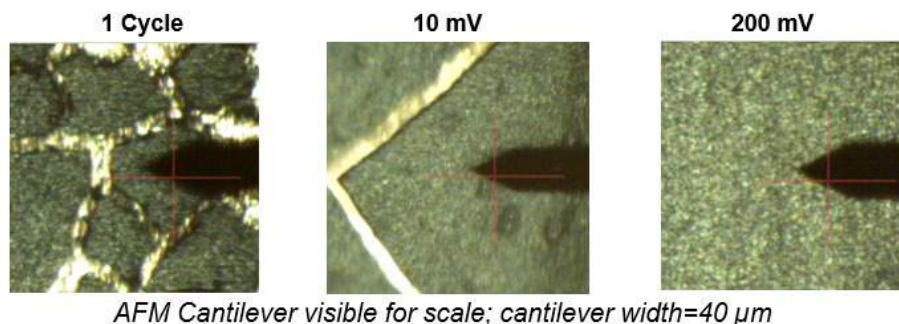


Figure II.1.B.31 Optical microscope images of composite electrodes after cycling and disassembly. Scale is visible in the width of the visible AFM cantilever, which measures 40 μm in width.

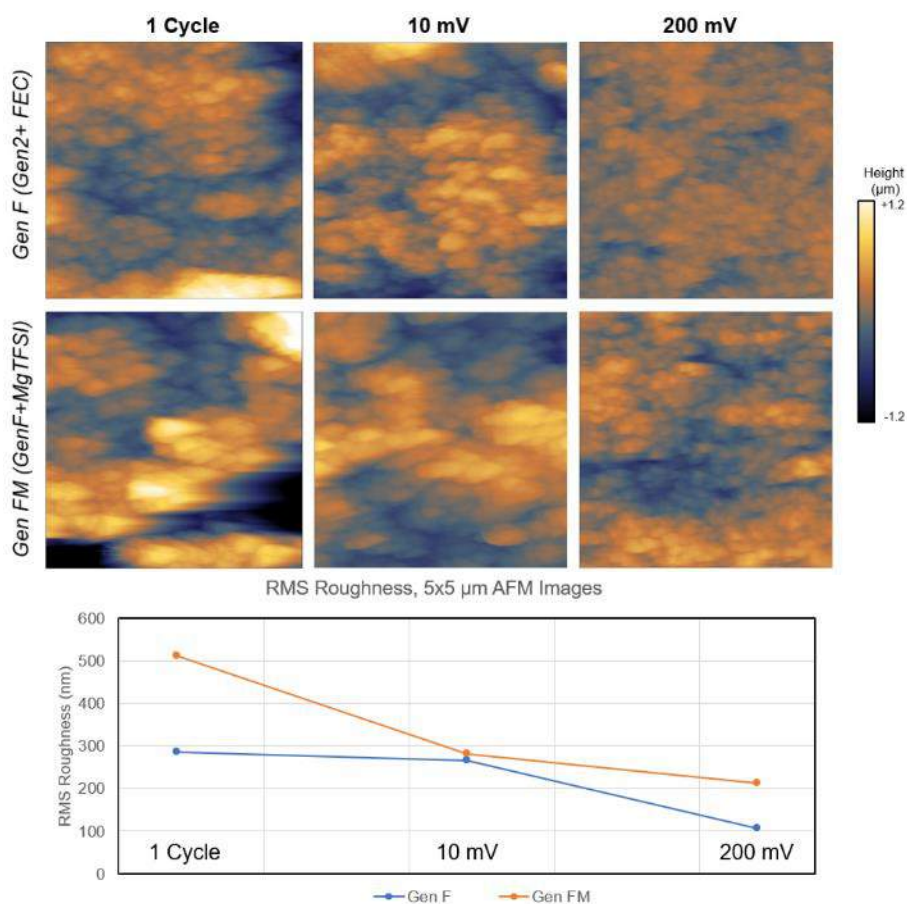


Figure II.1.B.32 5 \times 5- μm AFM images and RMS roughness calculated from AFM images

In Figure II.1.B.32, AFM images show a rough surface, with the same trend visible in the optical microscope images (1-cycle roughness > 10-mV roughness > 200-mV roughness). Minor differences were also visible in roughness between the two sample sets, with greater roughness measured for samples cycled in GenFM electrolyte. However, with such heterogeneous structures, measurements may be representative of a local area rather than the entire surface. In the future, measurements will be carried out over more locations to establish a measurement of roughness with a quantified standard deviation.

Li Beam Lithiation, Model System

All previous experiments, whether on thin film or powders, describe the interaction of Li with the Si and the oxide coating, but in the presence of electrolyte. It is clear that electrolyte decomposition plays a role in the formation and evolution of the SEI, but it was not previously possible to deconvolute the electrochemistry of electrolyte decomposition and SEI formation from the lithiation of the silica films, because they tend to occur at similar potentials in the first few cycles. Being able to independently study the process of lithium insertion into the oxide without an electrolyte or solvent present would allow us to understand the mechanisms of evolution purely of the oxide, without the salt decomposition and possible subsequent HF attack, which will give insight into the oxide layer's evolution as it accepts Li into its structure. The SEISta program has previously developed a capability to deliver Li⁺ ions of a given kinetic energy to the surface of an oxide or Si sample in vacuum conditions and study the resulting structure. We have named this process the virtual electrode (VE) because it does not require an electrode or metal surface to provide ion species for lithiation, instead relying on an ion beam to deliver these species to the surface.

A variant of the VE technique that uses a galvanostatic titration (GITT) technique, VE-GITT XPS measurements on a 5-nm SiO₂ / Si(001) wafer sample are summarized in Figure II.1.B.33. On the as-received, pre-lithiation sample, the Si 2p core-level spectrum shows features associated with SiO₂ (~104.0 eV) and Si₀ (~99.0 eV). Corresponding features are observed in the valence-band spectrum: the Si₀ and SiO₂ valence-band maxima (VBMs) appear at ~0.5 eV and 5.5 eV, respectively. The relative peak heights of these Si 2p features are consistent with an SiO₂ thickness on the order of 5 nm, and the single core level in the O 1s spectrum (O 1s to Si 2p ΔBE ~429.1 eV) supports the SiO₂ phase assignment. As observed previously, application of Li⁺ current bias (middle row of spectra in Figure II.1.B.33) causes an immediate shift to higher binding energies (BEs) for all core levels. Initially, the Si₀ peak shifts to higher BE by ~0.9 eV, and this effect is attributed to the introduction of substantial downward band bending in the Si(001) wafer, initially caused by the transient accumulation of positive charge (Li⁺ ions) on the free surface, and at later times by a shift in near-surface doping of the Si(001) from p- to n-type. A similar shift can be discerned in the VBM associated with the Si₀ region of the VB spectra.

The applied Li⁺ current bias produces substantially larger BE shifts (~2.5 eV) in the SiO₂ features for the O 1s, Si 2p, and VB spectra in Figure II.1.B.33. In part, these shifts are due to the fact that the potential at the surface of the SiO₂ layer rides atop that of the underlying Si(001) layer. As a result, the potential shift across the SiO₂ layer is additive to that of the Si(001) substrate, and consequently, one can infer that the potential difference across the SiO₂ layer is ~1.6 V. This value is significant in that it represents the overpotential (i.e., quasi-equilibrium magnitude of the potential difference) required to drive Li⁺ migration through the SiO₂ layer.

Also clearly seen in Figure II.1.B.33 is the appearance and growth of spectral features associated with an Li_ySiO_x phase. This phase forms via the reaction $\text{SiO}_x + y\text{Li}^+ + ye^- \rightarrow \text{Li}_y\text{SiO}_x$, and therefore, it represents a mechanism for transformation of the relatively resistive SiO₂ phase into less-resistive Li_ySiO_x. Lastly, comparison of core-level BEs acquired with vs. without Li⁺ current bias (middle- vs. bottom-row spectra in Figure II.1.B.33) shows how overpotential evolves over the course of lithiation.

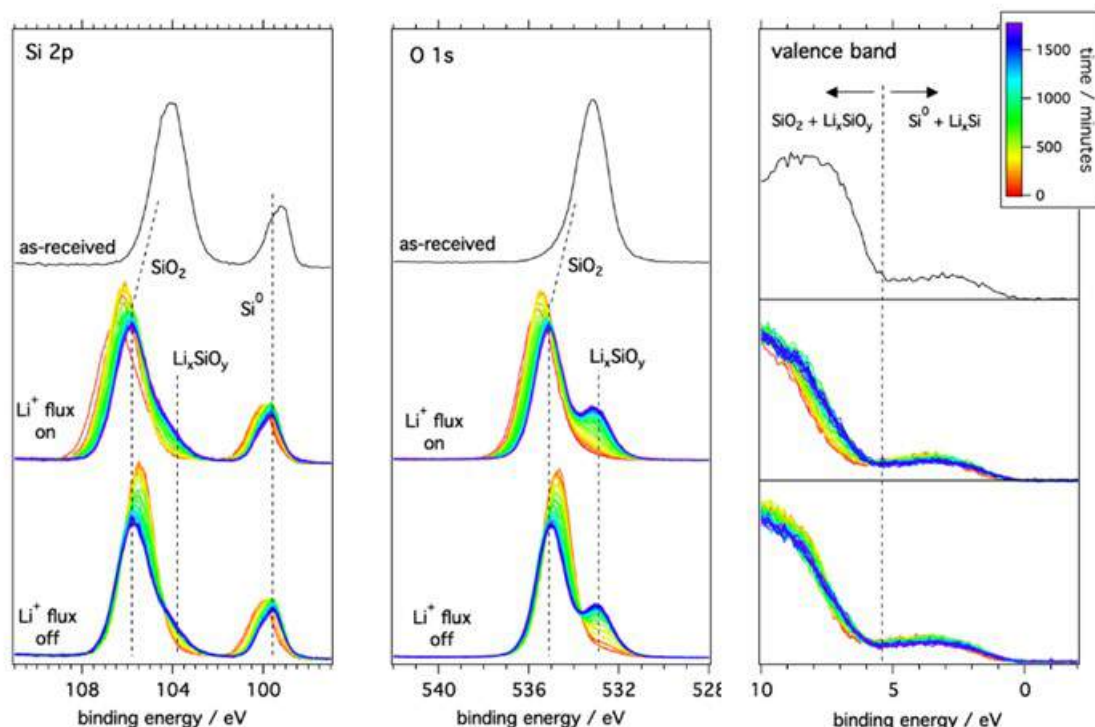


Figure II.1.B.33 Summary of XPS measurements for the O 1s, Si 2p, and valence-band (VB) regions during in situ lithiation of 5-nm SiO₂ / Si(001) sample. For these measurements, the Li⁺ ion gun was pulsed (square wave, 50% duty cycle) at 200 μ Hz with a current density \sim 55 nA/cm². The top row represents core-level spectra from the as-received sample. The middle and lower rows show spectra acquired when the Li⁺ ion gun was on and off, respectively. The dashed vertical lines are a guide to the eye to illustrate core-level shifts associated with the lithiation overpotential

The time evolution of the overpotential associated with conversion of SiO₂ to Li_ySiO_x is summarized in Figure II.1.B.34. In the top panel of Figure II.1.B.34 (a), the O 1s BE from the SiO₂ phase is plotted vs. time. The SiO₂ O 1s BE toggles between high and low values as the flux of Li⁺ ions pulses on and off. The lower panel of Figure II.1.B.34 (a) shows how the difference in upper and lower BEs changes with time: initially (\sim 0–200 s), the overpotential is nearly constant at \sim 0.7 V, but thereafter, the magnitude decreases monotonically. Figure II.1.B.34 (b)–(f) show sets of spectra at various time over the course of the in situ lithiation experiment. In each case, several spectra each are shown for the Li⁺ flux off and on conditions, and the relative shifts in these spectra directly reveal the evolution in the lithiation overpotential as SiO₂ is progressively converted to Li_ySiO_x. The effect of this phase conversion on overpotential is dramatic—whereas initially the overpotential is \sim 0.7 eV, it eventually drops to \sim 0.05 eV.

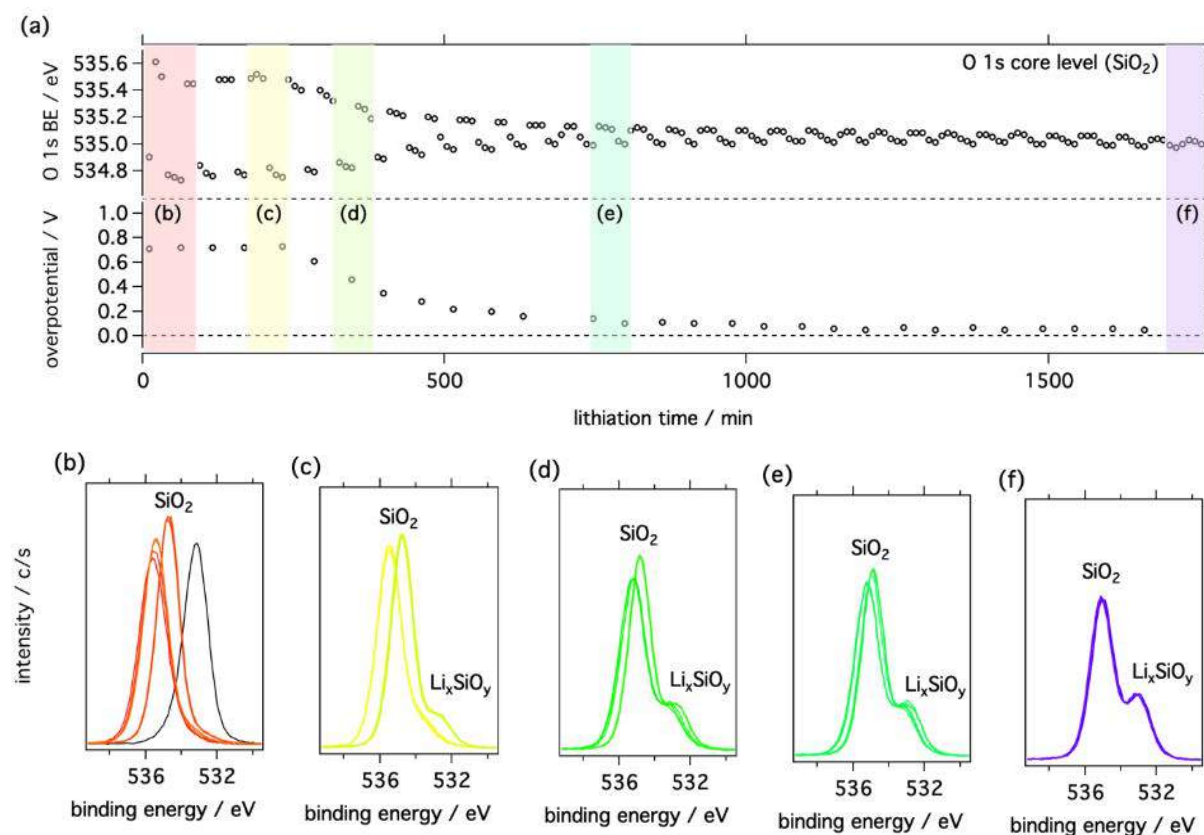


Figure II.1.B.34 (a) Summary of time evolution of SiO₂ O 1s binding energy and overpotential during VE-GITT (i.e., the pulsed in situ lithiation experiment). (b)–(f) O 1s core-level spectra at various times illustrating that the core-level shifts associated with the overpotential become progressively smaller in magnitude as the lithiation proceeds. (Note that the black trace in (b) corresponds to the initial, pre-lithiated state)

Another interesting feature revealed in the evolution of XPS spectra during the early stage of lithiation is that all spectral features associated with both Si0 and SiO₂ shift to substantially higher BE as soon as the Li⁺ current bias is applied, and thereafter, they never return to initial values, even after the current bias has been turned off. Figure II.1.B.35 compares spectra from the as-received, pre-lithiated sample to those after the first half-cycle of the VE-GITT XPS experiment. Focusing first on the Si0 features (Si 2p peaks ~99.0–100.0 eV, and VBMs ~0.0–1.0 eV), from these shifts as noted previously we can infer that the initial effect of lithiation is to induce substantial downward band bending, ~0.9 eV, in the Si(001) near the free surface. This observation is consistent with conversion of the near-surface silicon from p-type to n-type, presumably due to near-degenerate doping by Li, which acts as a shallow donor. On the other hand, the SiO₂ features (O 1s peaks ~533.0–535.0 eV, Si 2p peaks ~105.0–107.0 eV, and VBMs ~5.0–7.0 eV) shift to higher BE by ~1.6 eV. The fact that lithiation results in larger shifts in the SiO₂ relative to the Si0 features can only be explained by a change in the interfacial valence-band offset (VBO) between SiO₂ and Si(001)—from 5.1 eV to 5.8 eV—as illustrated in Figure II.1.B.36. We speculate that the change in VBO is a result in a change in the SiO₂ / Si(001) interfacial dipole, possibly as a result of changes in chemical bonding at this interface associated with the introduction of Li⁺ ions. For example, Li⁺ might effectively passivate Si dangling-bond states at this interface.

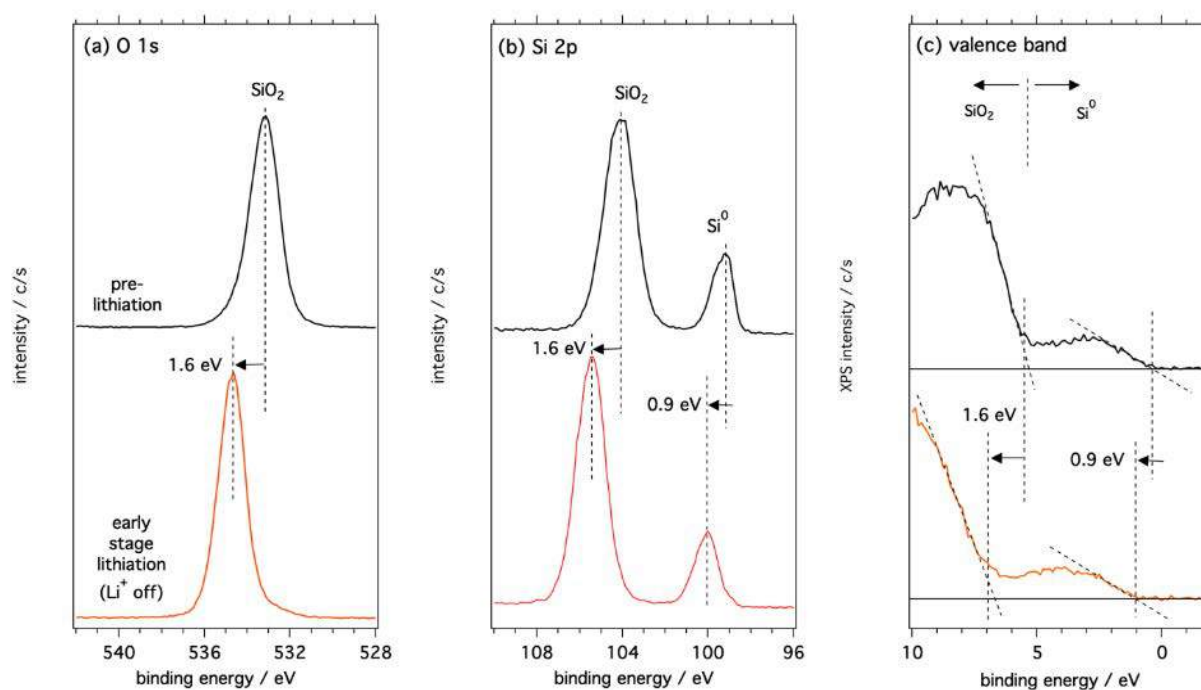


Figure II.1.B.35 (a) XPS spectra from the (a) O 1s and (b) Si 2p core levels, as well as the (c) valence-band regions. The top row of spectra (black traces) show spectra from the pre-lithiated sample. The Si 2p and VB spectra both show clear features associated with both SiO₂ and Si⁰, whereas the O 1s spectra each show a single feature associated with SiO₂. O 1s. The bottom row of spectra (red traces) shows the sample at an early stage of lithiation (cf. Figure II.1.B.34(b) and (c)) with the Li⁺ ion gun in the off state

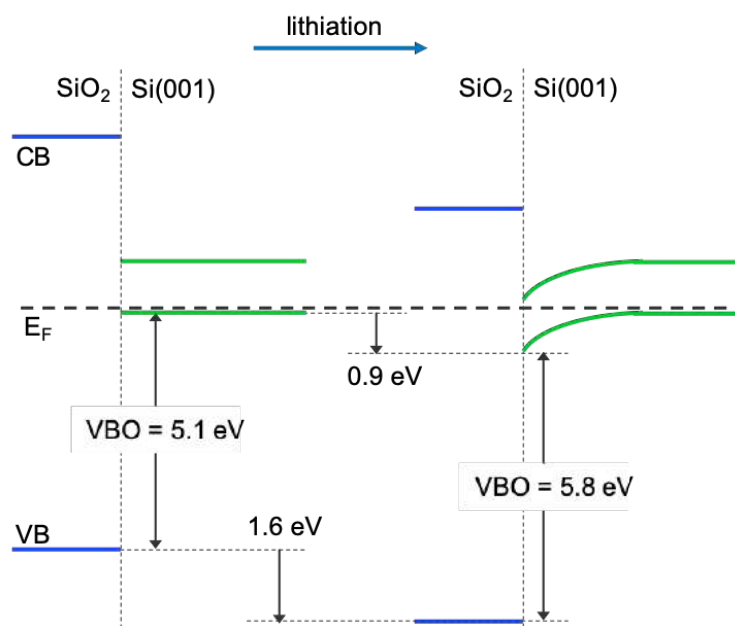


Figure II.1.B.36 Schematic illustration of the observed change in interfacial band alignment that occurs during early-stage lithiation of the 5-nm SiO₂ / Si(001) model-system interface

Part 2: Origins of Si/Electrolyte Interface Stability

The primary objective of our effort is to understand the processes occurring at the silicon/electrolyte interface (SEI). The reductive decomposition of the electrolyte in lithium-ion systems employing silicon anodes is inevitable because the working potential of the electrode is far below the electrochemical stability window of the electrolyte components. In principle, the insoluble decomposition products should precipitate on the electrode surface and result in the formation of a passivating film that suppresses further electrolyte decomposition [1],[2]. However, cycling performance is adversely impacted by the inherent instability of the silicon/electrolyte interface and the mechanical instability of the electrodes, which, upon alloying with lithium, experience a huge volume expansion and consequent cracking [3]. A better understanding of the kinetic processes occurring upon cycling will enable an efficient implementation of silicon-based electrodes in high-performance lithium-ion batteries.

To accomplish this, two model systems were used: the first consisting of thin-film electrodes, the second consisting of Si wafers. For the thin-films studies, we address the inherent non-passivating behavior of silicon model electrodes in organic electrolytes by studying the corrosion behavior and thus the evolution of the SEI as a function of cycling. In addition to understanding the fundamental shortcomings of carbonate-based electrolyte for the Si anode, we explored Glyme-based electrolyte, a potential alternative to Gen2 electrolyte and compare the performance and reactivity of the two electrolyte systems.

Likewise, for the Si-wafers model, cracking is a well-understood limitation, but the evolution of a solid-electrolyte interphase (SEI) through cycling is not fully understood, yet it plays a fundamental role in understanding of SEI stability of Si anodes. By applying microscopic and spectroscopic methods to this two-dimensional (2D) model system, we were capable of producing valuable insight into the characteristics of the SEI and its development over the lifetime of the anode material. We further investigate the role of water, a contaminant that potentially can be introduced during the battery manufacturing process. Specifically, we assessed how 50 ppm of water affects the SEI stability and evolution.

Finally, we investigate the role of carbon coatings on the stability of the SEI using nanoparticles as a model system and the use of gradient polarity solvent wash to remove sequentially different SEI components from electrode surfaces to help their precise identification.

Corrosion Task: Role of Lithium Salts on the Passivation Behavior of Si/Electrolyte Interface

The “Corrosion Task” is a coordinated research effort to provide a basic understanding and effective ways to mitigate the corrosion of Si anodes in organic carbonate-based electrolytes. For this task, Oak Ridge National Laboratory fabricated all model electrodes, the team at Lawrence Berkeley National Laboratory (LBNL) electrochemically investigated the corrosion currents involved upon cycling, and samples were further characterized in a joint-effort at LBNL and the National Renewable Energy Laboratory (NREL).

Firstly, we defined the electrochemical protocols to be employed to determine the corrosion currents. Two different electrochemical protocols have been established involving galvanostatic tests followed by chronoamperometry measurements, both in potentiostatic mode at fixed voltage values (Protocol 1), and at open-circuit voltage conditions (Protocol 2). A schematic of the electrochemical cell and a description of the two protocols is given in Figure II.1.B.37.

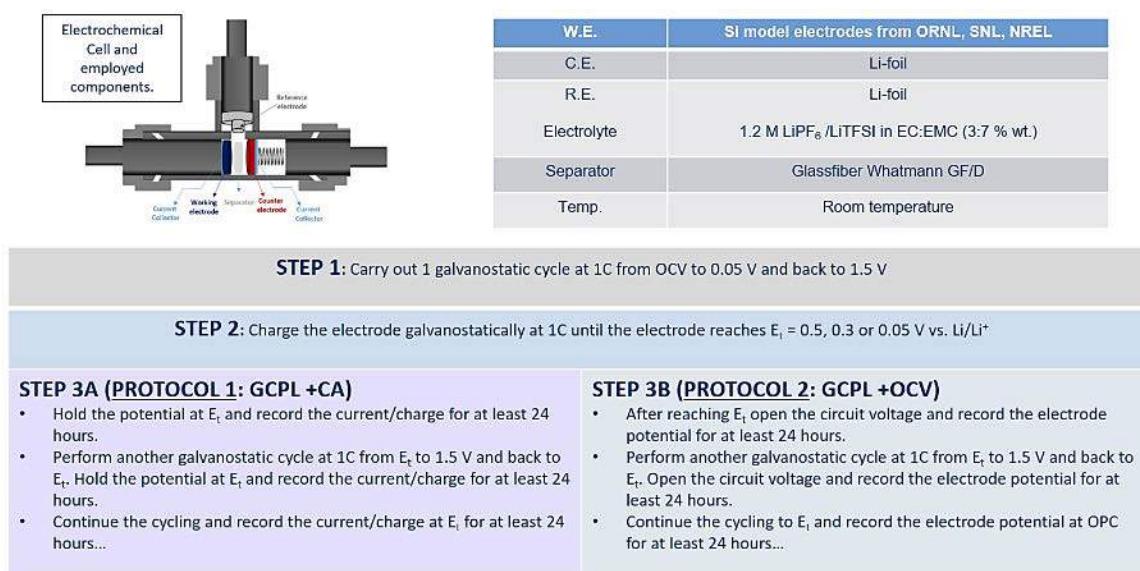

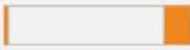




Figure II.1.B.37 Schematic representation of the electrochemical cell set up, cell components, and protocols employed in the Corrosion Task

Several configurations were tested using the developed Protocol 1 (GCPL + CA) to determine the residual currents after every lithiation, as described in details in the FY19 Q1 quarterly report. The results indicate that almost one third of the current values observed are associated with the copper piston, most likely due to the large surface area of copper exposed to the electrolyte in T-cell configuration. To find a more suitable substrate involving less exposed surface area, different copper substrates have been tested. A schematic representation of the investigated substrates and the residual current values observed after the 1st cycle by applying Protocol 1 are reported in Table II.1.B.2.

Table II.1.B.2 Copper-based Substrates Investigated With Protocol 1

Substrate				
Residual Current after 1 st cycle	2.7 $\mu\text{A cm}^{-2}$	1.8 $\mu\text{A cm}^{-2}$	2.6 $\mu\text{A cm}^{-2}$	1.0 $\mu\text{A cm}^{-2}$

(The values of the residual current observed after 24 hours of potentiostatic step at 0.05 V are reported. The thin copper foil presents the lower values on the order of $1 \mu\text{A cm}^{-2}$.)

Copper foil (12-mm diameter) presented the smaller residual current values. Accordingly, the first model electrode of choice for the evaluation of the corrosion currents has been identified as: 500-nm amorphous silicon (with 3-nm native oxide) deposited on copper foil (500-nm Si + 3-nm SiO₂ on Cu). The 500-nm Si thin film has been investigated in four electrolyte solutions, i.e., 1.2 M LiPF₆ EC:EMC (3:7 wt%), 1.2 M LiPF₆ EC:EMC (3:7 wt%) + 10% wt. FEC, 1.2 M LiTFSI EC:EMC (3:7 wt%), and 1.2 M LiTFSI EC:EMC (3:7 wt%) + 10% wt. FEC. The electrochemical characterization has been performed both in terms of cyclic voltammetry and galvanostatic cycling test as reported in Figure II.1.B.38.

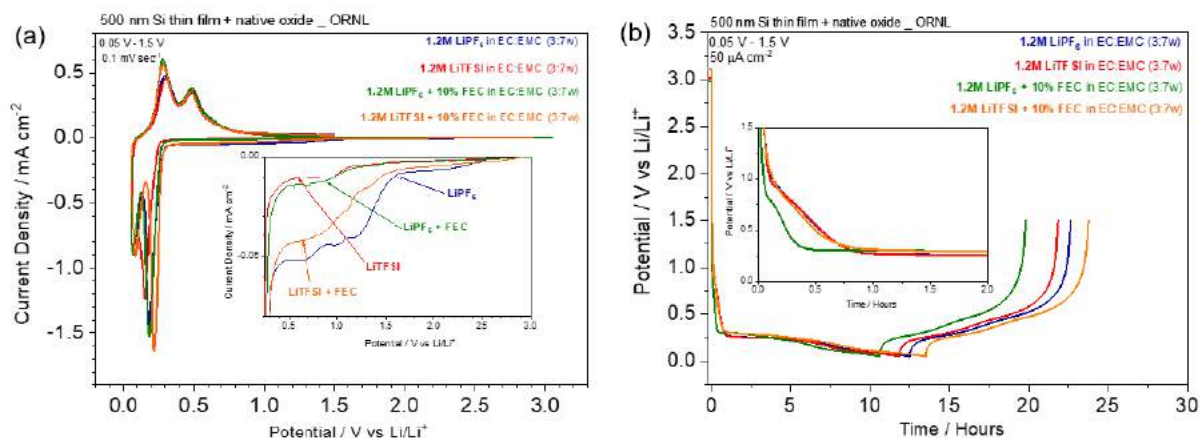


Figure II.1.B.38 (a) First lithiation–delithiation process of 500-nm Si thin film on Cu foil observed by cyclic voltammetry by using four different electrolyte solutions. A scan rate of 0.1 mV s⁻¹ has been applied within the 0.05–1.5 V potential range. Inset shows the enlarged potential region of the electrolyte decomposition. (b) Galvanostatic cycling test of the same systems performed at 50 μA cm⁻²

Interestingly, the inset of Figure II.1.B.38 reports the current values involved during the electrolyte decomposition process occurring before lithiation. The LiPF₆-based electrolyte presents the largest reductive current density, whereas the presence of FEC and the substitution of LiPF₆ with LiTFSI strongly reduce the current involved in the process.

The observation has been confirmed by galvanostatic cycling test reported in Figure II.1.B.38(b). Indeed, the first Coulombic efficiency has been calculated to be: 81.4%, 84.3%, 86.5%, and 75.8%, respectively, for the 1.2 M LiPF₆ EC:EMC (3:7 wt%), 1.2 M LiPF₆ EC:EMC (3:7 wt%) + 10% FEC, 1.2 M LiTFSI EC:EMC (3:7 wt%), and 1.2 M LiTFSI EC:EMC (3:7 wt%) + 10% FEC electrolyte solutions. Protocol 1 (GCPL + CA) has been applied to the above-mentioned system to understand and evaluate the effect of different salts (LiPF₆ vs LiTFSI) and the effect of the additive (10% wt. FEC) on the passivating properties of silicon.

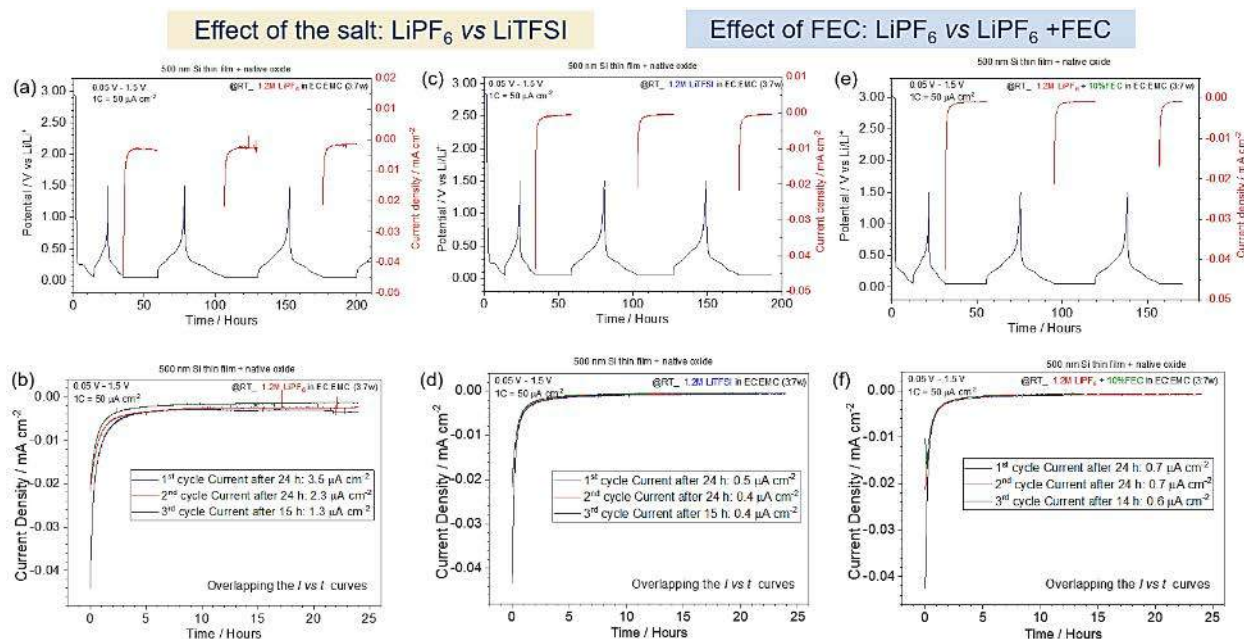


Figure II.1.B.39 Application of Protocol 1 (GCPL + CA) to the 500-nm Si thin-film model electrode by using (a, b) 1.2 M LiPF₆ EC:EMC (3:7 wt%), (c, d) 1.2 M LiPF₆ EC:EMC (3:7 wt%) + 10% FEC, and (e, f) 1.2 M LiTFSI EC:EMC (3:7 wt%). (a, b, c) show the galvanostatic cycling with associated potentiostatic step at 0.05 V. (b, d, f) reports the related current-density measurement during the potentiostatic step

Figure II.1.B.39 reports the galvanostatic cycling tests and the *I* vs *t* curves obtained during the constant voltage step at 0.05 V in three different electrolytes. Interestingly, the residual current detected after 24 hours at 0.05 V are very large for the 1.2 M LiPF₆ EC:EMC (3:7 wt%) electrolyte, whereas by substituting LiPF₆ with LiTFSI, the current value is about 7 times smaller. The same effect is observed with the addition of 10% FEC to the bare 1.2 M LiPF₆ EC:EMC (3:7 wt%) solution. The data are in agreement with the CV and GCPL tests reported in Figure II.1.B.38. It is also observed that the passivation of silicon improves upon cycling, as demonstrated by the lower current values observed after the third potentiostatic step when compared to the first one.

The same kind of analysis has also been conducted to investigate other effects on the corrosion currents and passivating properties of silicon. The investigated effects include: 1) the state of charge at which the potentiostatic step is applied (0.5 V vs 0.05 V); 2) the effect of the silicon thickness (500-nm Si vs 50-nm Si, cracking effect of silicon upon cycling); and 3) the effect of the surface silicon oxide layer on silicon, which has also been investigated by applying protocol 2 (GCPL + OCV) (3-nm native SiO₂ vs 10-nm sputtered SiO₂). All the investigated effects and related conclusions are summarized in Table II.1.B.3.

Table II.1.B.3 Summary of the Investigated Effects on the Passivating Properties of Silicon and Preliminary Conclusions

Investigated Effects	Conclusion
Effect of the salt: LiPF ₆ vs LiTFSI	LiTFSI-based electrolytes exhibit lower residual currents
Effect of additives: 10% wt. FEC addition	FEC improves the passivation properties of Si
Effect of the state of charge on corrosion current: 0.5 V vs 0.05 V	Larger currents are observed at 0.05 V than 0.5 V
Effect of silicon thickness: 500 nm vs 50 nm Si decoupling cracking effect from catalytic activity of Si	The cracking effect is responsible of about 60% of the parasitic currents observed in fully lithiated state
Effect of SiO ₂ on passivating behavior	SiO ₂ inhibits passivation of silicon surface

The 50-nm films with 3-nm and 10-nm SiO₂, respectively, were further analyzed. Galvanostatic cycling was performed by applying a constant current of 5 $\mu\text{A cm}^{-2}$ within the 0.05–1.5 V potential range in a three-electrode Swagelok T-type cell, using Gen 2 electrolyte (1.2M LiPF₆, EC:EMC 3:7 wt.%). Following galvanostatic testing, samples were rinsed with DEC, packaged and shipped to the National Renewable Energy Laboratory (NREL) for X-ray photoelectron spectroscopy (XPS) measurements. At NREL, samples were transferred from an argon-filled glove box into the XPS analysis chamber via an ultrahigh-vacuum transport pod to avoid exposure to ambient atmosphere. XPS measurements were performed in a Kratos Axis Nova instrument.

XPS measurements on the 50-nm a-Si / 3-nm SiO_x sample are summarized in Figure II.1.B.40. XPS datasets were analyzed using a method previously developed in the SEISta project, where phases are identified by constraining elemental ratios and binding-energy separation (ΔBE) values for all core-level peaks in a particular phase [4]. Initially, during the first lithiation (1.5 V), XPS spectra primarily showed the presence of SiO_x (Si 2p and O 1s peaks at ~105 eV and 534.2 eV, respectively), as well as the underlying Si⁰ (Si 2p peak at ~99.5 eV). Additionally, there appears to be a small amount of Li_ySiO_x present even at 1.5 V. As the first lithiation proceeds down to 0.05 V, the most striking changes include the appearance and growth of peaks associated with Li₂CO₃, Li₃PO₄, LiF, and a P-F-containing species. The P-F species is revealed by F 1s and P 2p peaks (~690.5 eV and ~138 eV, respectively) that are strongly correlated with respect to both ΔBE values and peak-intensity ratios. The existence of (PF₆)⁻ (or LiPF₆) as a candidate to explain the observed P-F features is tentatively ruled out, because the observed F 1s –to– P 2p ΔBE values (~553 eV) do not match the expected value for LiPF₆ (~552 eV). Also, the observed peak intensity ratios F/P are too low to be consistent with (PF₆)⁻; therefore, we tentatively assign these peaks to Li_xPF_yO_z [5],[6]. This assignment is supported by the existence of intensity-ratio- and ΔBE -correlated peaks in the O 1s core-level spectra. An additional pair of features is observed in the F 1s and O 1s spectra following the first delithiation to 1.5 V that is tentatively attributed to (SiF₆)²⁻ [7]. Lastly, SiO_xF_y is tentatively identified as a relatively strong set of peaks following the second lithiation to 0.05 V [8],[9].

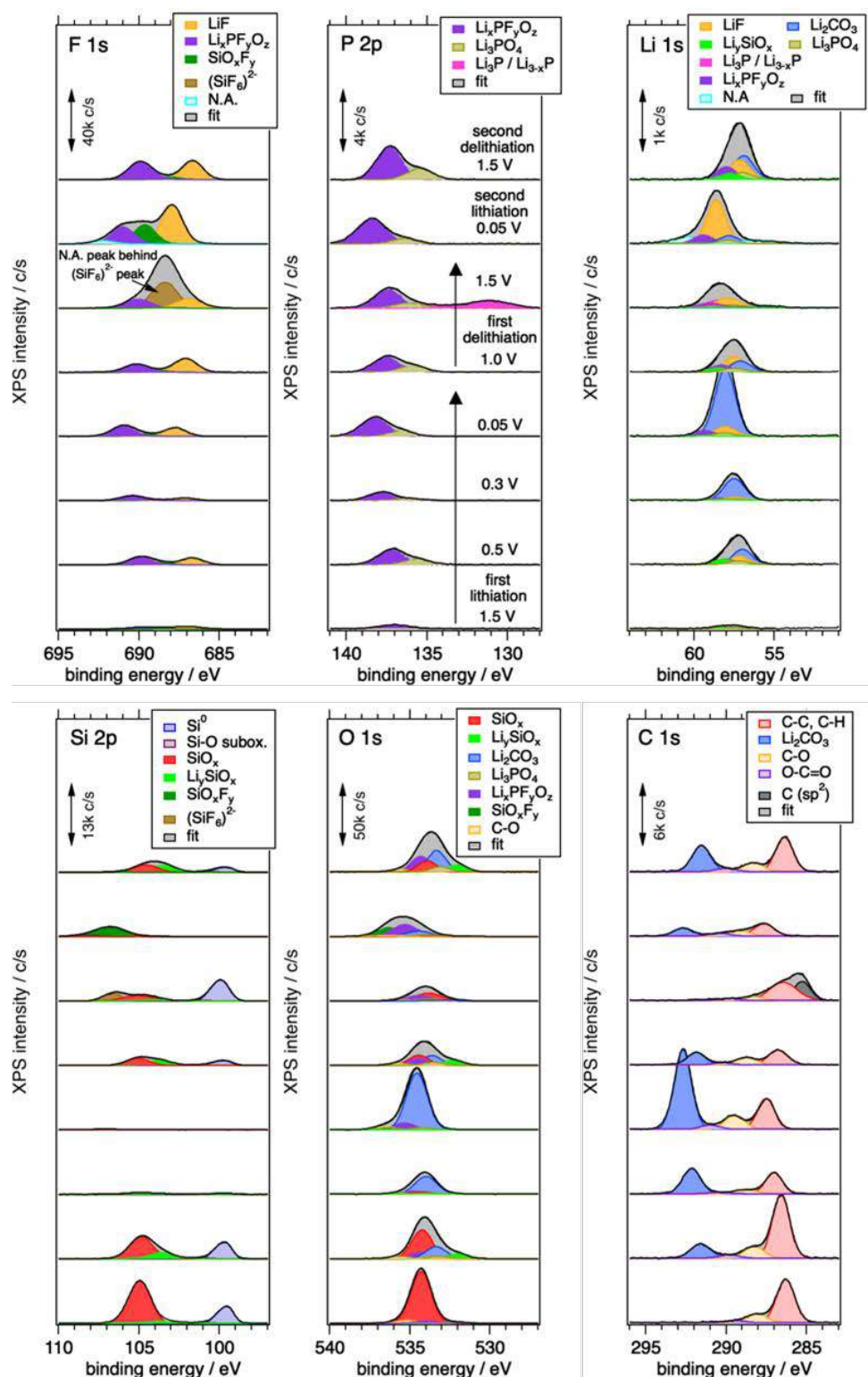


Figure II.1.B.40 Summary of XPS measurements on 50-nm a-Si / 3-nm SiO₂ films at varying states of lithiation and delithiation. Peak assignments are preliminary, N.A. denotes “not assigned”

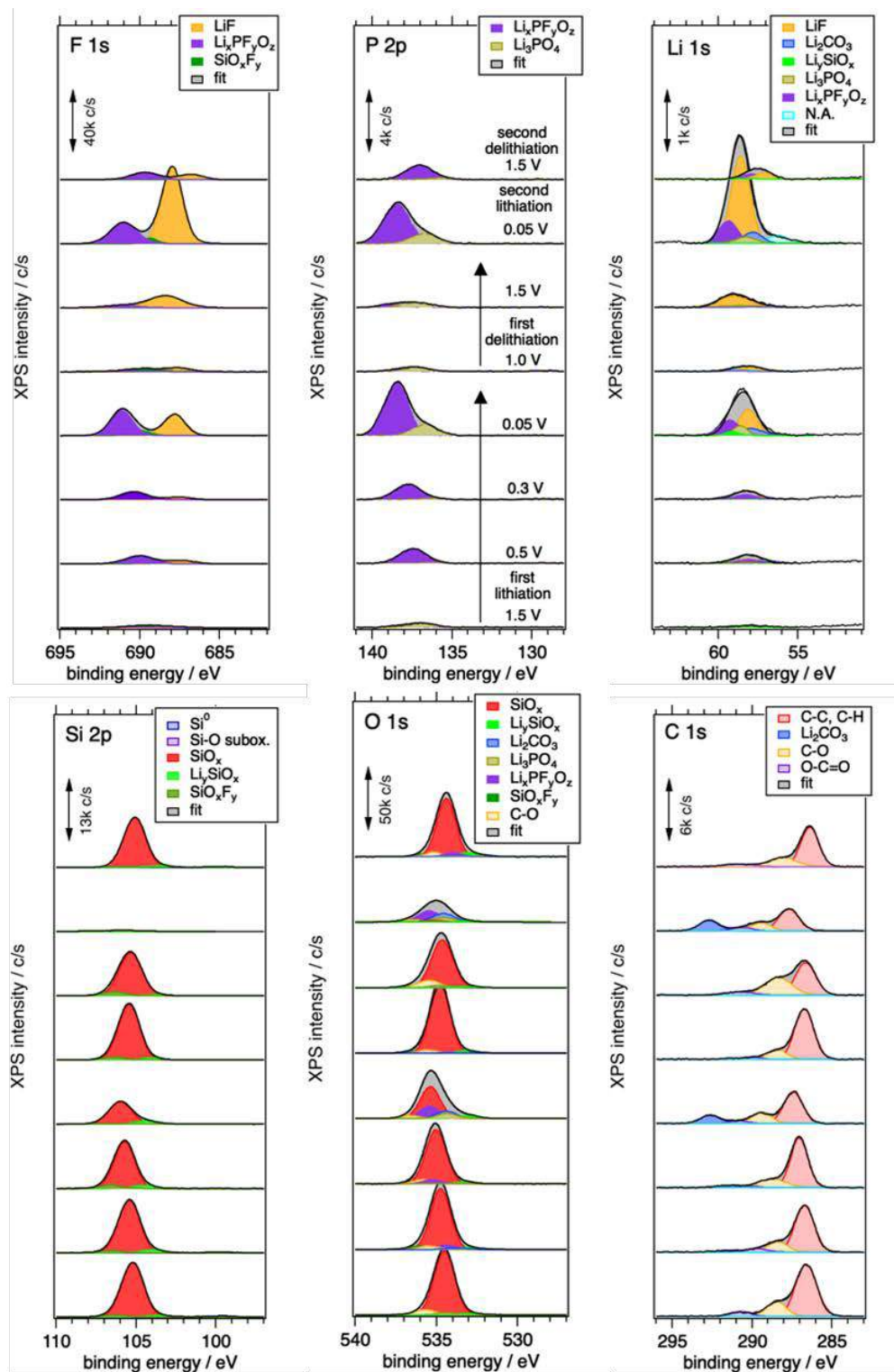


Figure II.1.B.41 Summary of XPS measurements on 50-nm a-Si / 10-nm SiO₂ films at varying states of lithiation and delithiation. Peak assignments are preliminary, N.A. denotes “not assigned”

XPS measurements for the 10-nm SiO_x samples are shown in Figure II.1.B.41. For the most part, the same phases are observed for the SEI in these samples as were seen in the native-oxide samples. On the other hand, significantly less Li_2CO_3 is seen for the 10-nm samples than for the native-oxide sample, and it forms at substantially lower potentials. Also, less Li_ySiO_x phases are observed for the 10-nm sample. In contrast to the native-oxide samples, relatively more LiF and $\text{Li}_x\text{PF}_y\text{O}_z$ -containing phases form on the 10-nm samples, especially at the lowest lithiation potential, 0.05 V.

An interesting feature for both the native-oxide and 10-nm SiO_x samples is that the peaks associated with Li_2CO_3 are most intense at the lowest lithiation potentials (0.05 V) and subsequently decrease during delithiation. Similar effects are seen with both LiF and the $\text{Li}_x\text{PF}_y\text{O}_z$ phase. Furthermore, the attenuation of Si^0 and SiO_x XPS signals also indicates that SEI layer thickness tends to increase during lithiation and decreases during delithiation. These observations suggest that formation of these phases is partially reversible, or, that after formation these phases can detach from the SEI.

C 1s spectral features tentatively assigned to C-C, C-H, C-O, and O-C=O moieties are observed on all samples, and, in general, the magnitudes of these peaks are not strongly correlated with lithiation/delithiation potential. With the exception of Si^0 peaks, there is considerable variability in measured binding-energy (BE) values for all phases, indicating varying degrees of charging during the XPS measurements. For both the native-oxide and 10-nm SiO_x samples, the observed trend is that peaks shift to higher BEs at lower lithiation potentials, consistent with lower net ionic and electronic conductivities in these SEI layers.

In summary, the key results of the XPS analysis include:

- For the native-oxide samples, a fraction of the initial SiO_x layer is converted to Li_ySiO_x phases during the first two cycles, but very little Li_ySiO_x is seen in the 10-nm SiO_x samples.
- Phases including LiF , Li_2CO_3 , Li_3PO_4 , and $\text{Li}_x\text{PF}_y\text{O}_z$ are clearly observed.
- The relative phase composition of the SEI layers evolve significantly over the course of cycling.
- SEI phase evolution in the 10-nm samples primarily takes place at markedly lower potentials than observed in the native-oxide case.

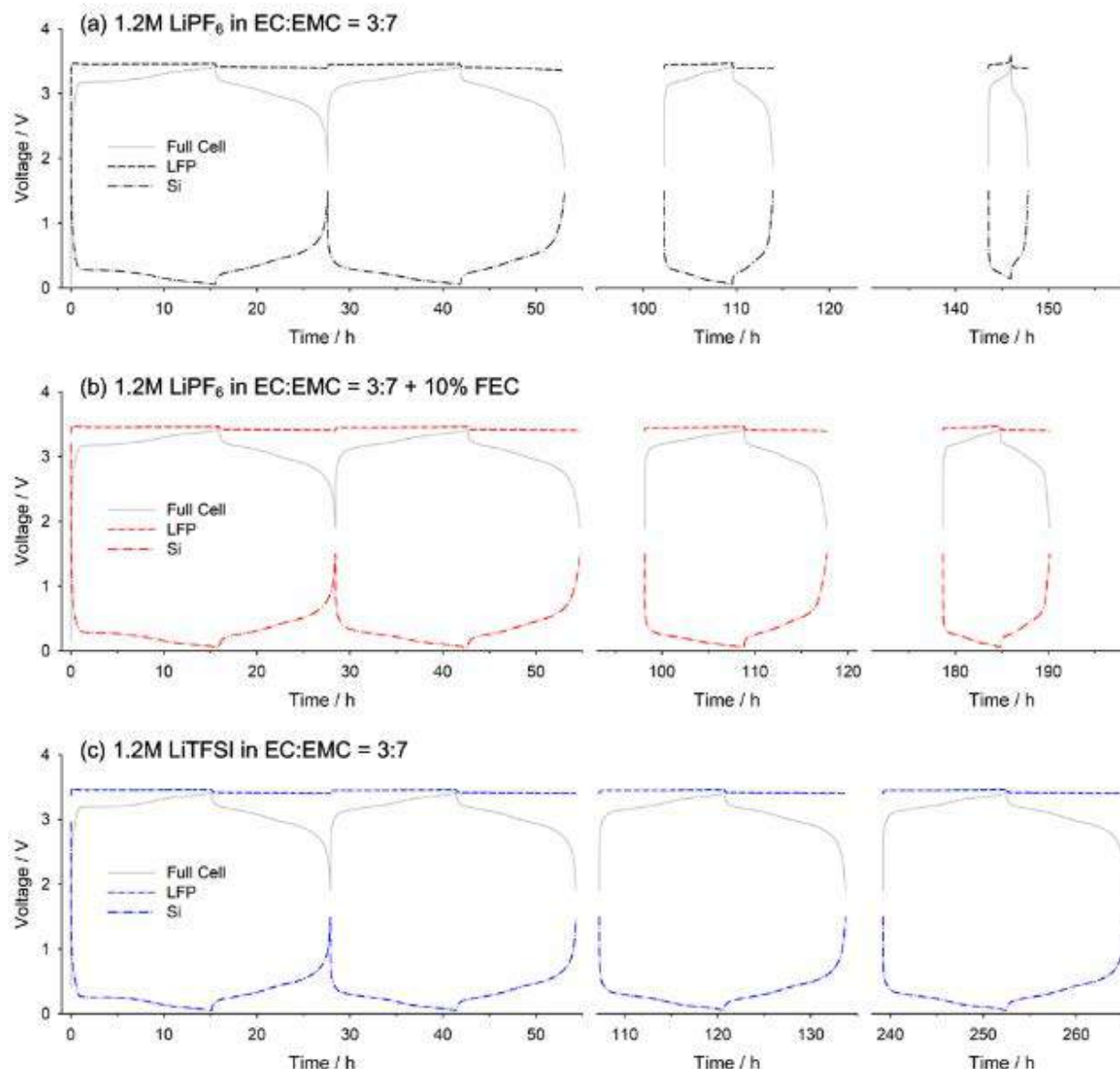


Figure II.1.B.42 The voltage profiles of $\text{LiFePO}_4/\text{Si}$ cells containing the 500-nm Si thin-film model electrodes (1st, 2nd, 5th, and 10th cycle) with (a) 1.2 M LiPF_6 EC:EMC (3:7 wt%), (b) 1.2 M LiPF_6 EC:EMC (3:7 wt%) + 10% FEC, and (c) 1.2 M LiTFSI EC:EMC (3:7 wt%)

Finally, we investigated the corrosion behavior of silicon electrodes in the full-cell configuration, in addition to the half-cell configuration, by employing LiFePO_4 (LFP) as cathode electrode. The use of LFP, which acts as source of limited amount of lithium, enables a direct visualization of the effect of the silicon corrosion and lithium consumption upon cycling. Figure II.1.B.42 and Figure II.1.B.43 show the voltage profiles (Figure II.1.B.42) and cycling performance (Figure II.1.B.43) of LFP/Si cells using three different electrolyte solutions, *i.e.*, 1.2 M LiPF_6 EC:EMC (3:7 wt%), 1.2 M LiPF_6 EC:EMC (3:7 wt%) + 10% wt. FEC, and 1.2 M LiTFSI EC:EMC (3:7 wt%). As mentioned above, this full-cell system has a very limited amount of lithium, such that lithium loss upon cycling is directly visible from the remaining capacity of LFP/Si cells. In the initial 10 cycles, the cell with 1.2 M LiPF_6 EC:EMC (3:7 wt%) solution lost almost 80% of its initial capacity, which indicates that the lithium consumption from the corrosion behavior on the silicon surface had been very severe. The presence of FEC and the substitution of LiPF_6 with LiTFSI improved the cycling performance significantly, comparable to the previous results with the half cells. It should be noted that the cell with 1.2 M

LiTFSI EC:EMC (3:7 wt%) presents remarkably good cycling performance and only loses a marginal amount of lithium upon cycling. These results suggest that the corrosion behavior on silicon affects the performance of full cells such that it needs to be reduced for the commercialization of silicon.

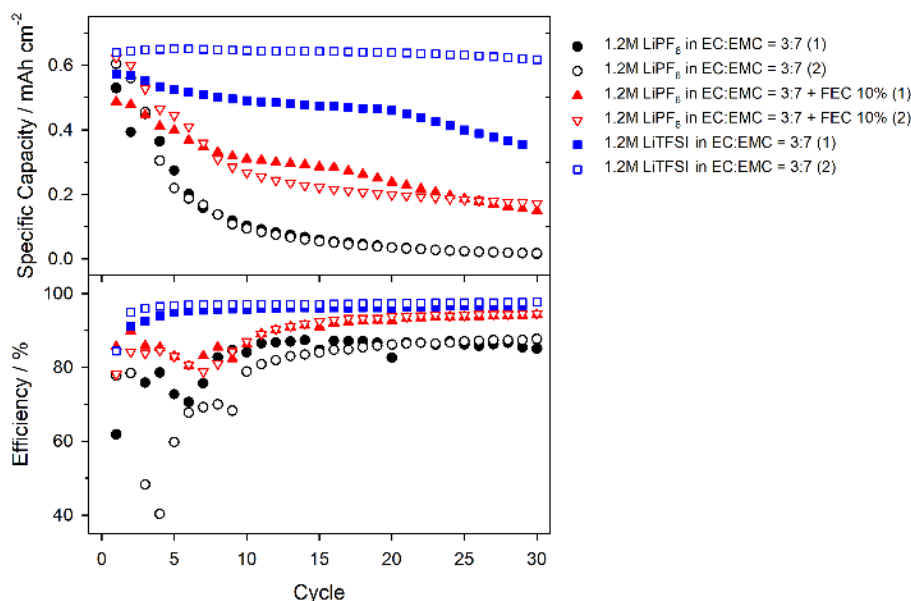


Figure II.1.B.43 Cycling performance and efficiency of LiFePO₄/Si cells containing the 500-nm Si thin-film model electrodes with different electrolyte solutions

To calculate the amount of consumed lithium from two possible sources—electrolyte decomposition and lithium trapping—we adopted a calculation model [10]. In this calculation model, the irreversible capacity originating from electrolyte decomposition is the difference between the consumed lithium during each lithiation step and the actual amount of inserted lithium to silicon in this step. The irreversible capacity originating from lithium trapping can be obtained by subtracting the delithiation capacity from the lithiation capacity in that cycle. The amount of inserted lithium (lithiation capacity) can be accessed by the quasi-open-circuit voltage (QOCV) at the end of each lithiation step. Figure II.1.B.44 presents the schematic of the approach to the state-of-charge (SOC) value of each cycle through the QOCV and the galvanostatic intermittent titration technique (GITT) profile.

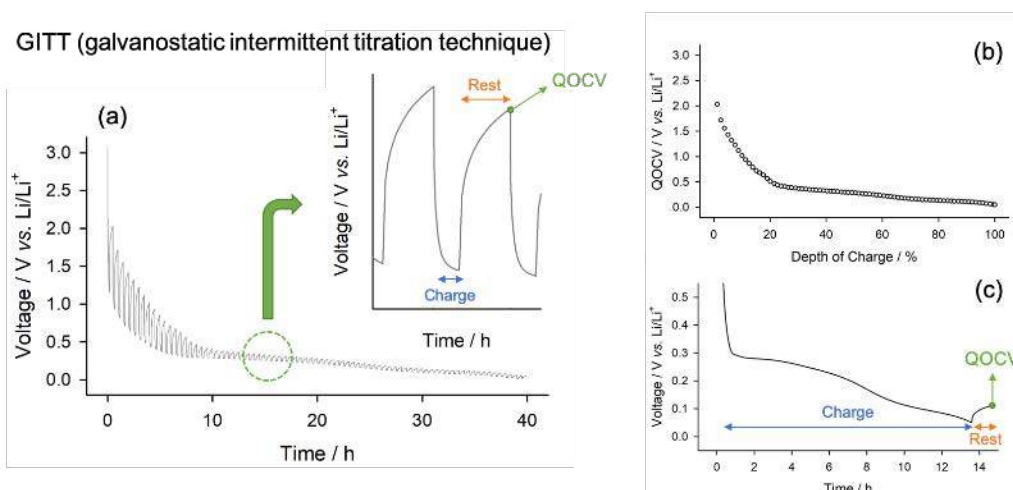


Figure II.1.B.44 Schematic of the procedure to estimate the actual state of charge (SOC) of silicon electrodes. From (a) the GITT profile, (b) the relation between quasi-open-circuit voltage (QOCV) and SOC is obtained. At the end of each lithiation step, the SOC is extrapolated from (c), the observed QOCV in relation to the QOCV value on the GITT profile

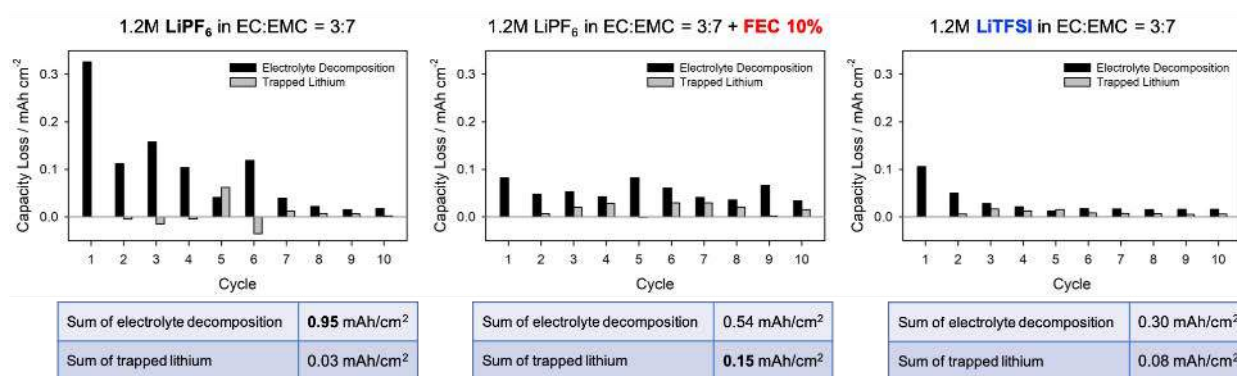


Figure II.1.B.45 The calculated capacity loss from electrolyte decomposition and lithium trapping in $\text{LiFePO}_4/\text{Si}$ cells containing the 500-nm Si thin-film model electrodes with different electrolyte solutions

Figure II.1.B.45 shows the calculated irreversible capacity (capacity loss) originating from electrolyte decomposition and lithium trapping in $\text{LiFePO}_4/\text{Si}$ full cells. Overall, electrolyte decomposition is dominant over lithium trapping regardless of electrolytes. It is noteworthy that the cell with 1.2 M LiPF_6 EC:EMC (3:7 wt%) solution loses the most lithium over the early 10 cycles, but also, that it shows surface instability (trapped lithium < 0).

Again, this suggests the non-passivating behavior of silicon anodes in the standard condition. The calculated irreversible capacity from electrolyte decomposition correlates well with the cycling performance of full cells, indicating that electrolyte decomposition is the main reason of cycling decay of $\text{LiFePO}_4/\text{Si}$ cells.

In summary, the Corrosion Task has led to the definition of standard protocols enabling a relative quantification of the non-passivating behavior of silicon model electrodes. A set of electrodes has been investigated to define the model electrodes of choice. Silicon thin films have been identified as the best model electrodes so far investigated. By applying Protocols 1 and 2 to various systems characterized by different properties (thickness of silicon, thickness of the oxide surface layer) and also different interfaces (employment of four types of electrolyte solutions), we have obtained preliminary conclusions. Specifically, the non-passivating behavior of silicon thin films has been directly observed for the first time as an independent effect

from the cracking of silicon particles due to the lithiation. A visualization of the improvement of the passivation properties upon cycling has been quantified, suggesting a thickening of the passivating film on the silicon surface. The beneficial effect of FEC for the SEI stability has been confirmed, and the use of LiTFSI as alternative salt to improve the SEI stability is proposed. Furthermore, we investigated the effect of corrosion of silicon in the full-cell configuration using LFP/Si cells. Due to the non-passivating nature of silicon thin films, the lithium consumption upon cycling was substantial for the standard electrolyte solution. The full-cell results are comparable to our previous observation with the half-cells such that the use of FEC and LiTFSI mitigates such silicon corrosion. Further, the calculation model concludes again that the electrolyte decomposition and surface instability on the silicon anode is the main reason for the irreversible capacity and capacity loss of LFP/Si cells.

Electrolyte Additives and Detection

The solid-electrolyte interphase formed during the cycling of lithium-ion batteries by the decomposition of lithium salt and solvent molecules plays a crucial role in device performance. However, the detailed decomposition process and distribution of products remains elusive due to the wide variety of electrochemical pathways and the lack of facile analytical methods for chemical characterization of SEIs. In this report, a gradient polarity solvent wash (gradient wash) technique involving the use of solvents with gradually increased polarities is employed to sequentially remove different SEI components from electrode surfaces and the near-surface. Fourier transform infrared (FTIR) spectroscopy is used to characterize the SEIs composition. The impacts of electrolyte additives and discharge rates over SEI formation are illustrated. This study presents a new concept of a rationally controlled solvent wash technique for electrode surface analysis that can selectively remove targeted components with gradient wash of the targeted electrode (Figure II.1.B.46). The gradient wash of electrodes was performed in glass vials, where the electrodes were immersed under 5-mL solvents with gentle manual agitation. The solvents used were 0% to 100% volume ratio ethyl acetate (EA) in hexane (Hex) solutions with 10% intervals (i.e., 0%, 10%, 20%, 30%, 40% EA/Hex, etc.). After rinsing, the electrodes were immediately dried and stored under vacuum until FTIR characterization.

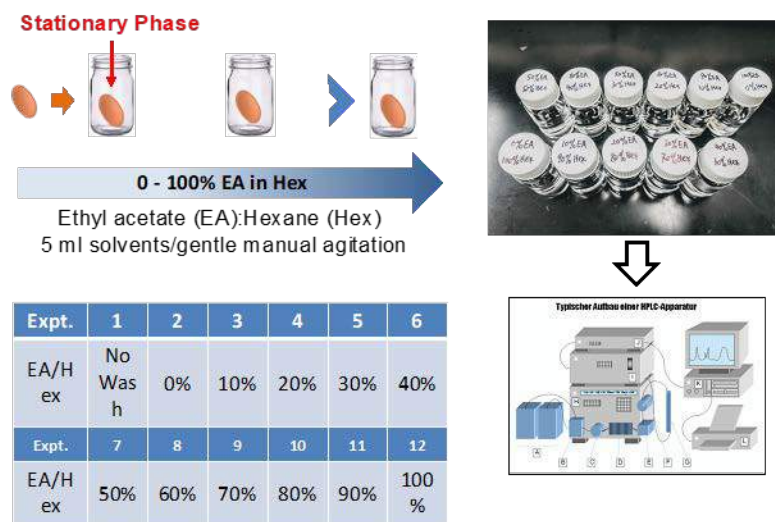


Figure II.1.B.46 Schematics of the gradient polarity solvent wash technique

We examine the SEIs and near-SEIs produced with both polar methacrylate additive under different electrochemical conditions by gradient wash. Cu electrodes are electrochemically cycled with LiPF_6 ethylene carbonate/ethyl methyl carbonate (EC/EMC) electrolyte containing the additive. With a binary solvent system of a non-polar solvent and a polar solvent at various ratios, it is possible to selectively remove different SEI components. The electrode surfaces before and after each wash protocol are characterized with FTIR to identify the decomposition products.

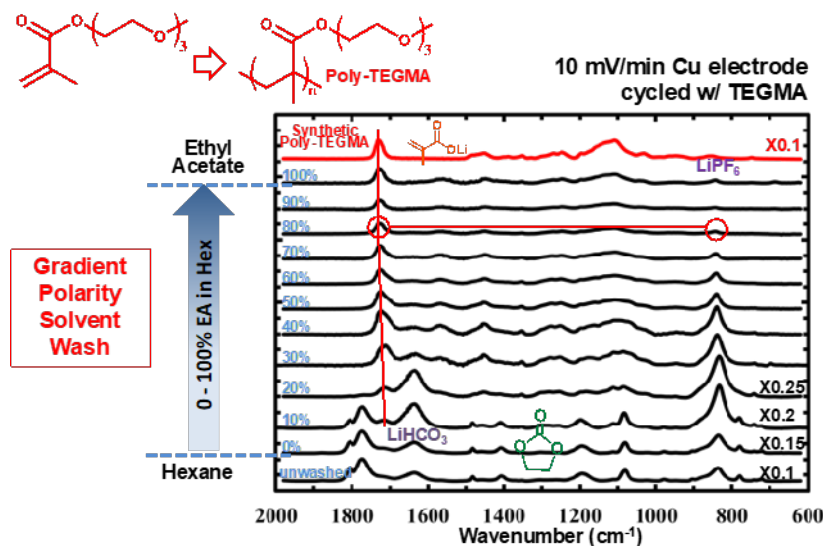


Figure II.1.B.47 Gradient polarity solvent wash was applied to a Cu electrode polarized to 10 mV Li/Li^+

TEGMA additive also produced a poly-TEGMA film on the Cu electrode surface, which, due to its high polarity, did not resist adsorption of residue electrolyte (EC/EMC: LiPF_6 solvates, 1809, 1780, 1269, 1196, 1082, 833 cm^{-1}) and Li_2CO_3 (1510, 1419 cm^{-1}) as shown in Figure II.1.B.47, Spectrum I. The poly-TEGMA layer was fully exposed after gradient wash with 0%–30% EA/Hex solvents. This polar polymer film also survived all remaining washing steps. Its chemical composition was confirmed with the synthetic sample. The removal of electrolyte species with 0%–30% EA/Hex solutions is consistent with the case of the base electrolyte. It is worth noting that the carbonyl peak for poly-TEGMA at 1726 cm^{-1} presented a slight red shift before removal of lithium salt species due to solvation effect.

CC(=C)C(=O)OCCOCCOC(=O)C
TEGMA

CC(=C)C(=O)OCCOCCOC(=O)C
Lauryl Methacrylate (LMA)

CC(=C)C(=O)OCCOCCOC(=O)C
lithium ethylene momo-carbonate (LiEMC)

CC(=C)C(=O)OCCOCCOC(=O)C
lithium ethylene di-carbonate (LiEDC)

Cu Electrode	0.0167 mV s^{-1} (1 mV min^{-1})	0.167 mV s^{-1} (10 mV min^{-1})	1 mV s^{-1} (60 mV min^{-1})
Base Electrolyte	LiEDC/LiEMC*, Li_2CO_3 *	LiEDC/LiEMC*	/
LMA Electrolyte	Poly-LMA	Lithium Methacrylate oligo-LMA*	/
TEGMA Electrolyte	Li_2CO_3 * Poly-TEGMA	Lithium Methacrylate Poly-TEGMA	Poly-TEGMA

*Rinsed off by gradient wash | Revealed by gradient wash

Figure II.1.B.48 Three different scanning rates of CV at 1, 10, and 60 mV min^{-1} were applied to the Cu electrodes, respectively, with baseline electrolyte and two additives-based electrolytes. The Cu surface species vary due to both the additives and scan rates

The scanning rate or the potential step-down rate from 3 V to 10 mV has a significant impact to the surface film (SEI) and near-surface species formation (Figure II.1.B.48). At slow to medium rate of 1 to 10 mV min⁻¹, the baseline electrolyte (EC/EMC:LiPF₆) facilitates the formation of LiEDC/LiEMC salts on the Cu surface. In the two additives-based electrolyte-containing systems, they are predominantly additives-derived polymer films on the Cu surface instead of lithium salt species. The species on the Cu surfaces can be clearly observed with the gradient wash technique. However, when the voltage step rate is 60 mV min⁻¹, the Cu surface is free of deposition of decomposition products with the baseline electrolyte. A highly polar TEGMA additive tends to stick to the surface of the Cu at this fast scan rate. Therefore, the chemistry of SEI formation depends on the reaction rate, where lower lithiation rate favors the formation of lithium salts on the electrode surface, and faster rate promote the formation of polar organic decomposition products.

Glyme-Based Electrolytes for Amorphous Silicon Anodes: An Alternative to GEN2 to Improve Passivation

The standard Gen-II electrolyte, LiPF₆ in an EC/EMC mixture, has been extensively explored for model amorphous Si (a-Si) films and composite electrodes prepared by slurry casting. The choice of this electrolyte system originates from the successful commercialization of graphite anodes. However, carbonate-based electrolytes do not form stable interfacial layers on silicon. Recent studies by LBNL using model a-Si thin films show that carbonate-based electrolytes do not passivate the silicon surface during cycling, which results in an unstable SEI layer. Based on a suite of local SEI characterization conducted on model silicon anode (with a native nanometer suboxide layer) under the SEISta program, the dominant organic SEI components on a-Si include diethyl alkyl carbonates, carboxylates, and ethers. We hypothesize that solvents containing these functionalities may lead to more stable silicon interfaces. Therefore, the goal of this current work is to investigate ether-based solvents and compatible salts for Si anodes. Specifically, a-Si electrode were cycled in the following electrolyte systems: i) Gen-II electrolyte as a benchmark, ii) lithium bis(fluorosulfonyl)imide (LiFSI) dissolved in dimethoxyethane (DME), and iii) LiFSI-DME with a fluoroether additive (1,1,2,2-tetrafluoroethyl-2,2,3,3-tetrafluoropropyl ether, TTE, and iv) 1.2 M LiPF₆ in 1,2-dimethoxyethane (DME). TTE has been shown to stabilize the lithium-sulfur (Li-S) batteries [11] and Li-metal batteries [12].

For this work, 50-nm a-Si thin films were used as a model system. First, we explored the cyclic voltammetry (CV) of the a-Si anode cycled against a lithium counter electrode using different electrolytes at a scan rate of 0.1 mV s⁻¹. The initial onset reduction potential occurred at 0.4 V vs. Li/Li⁺ for the Gen2 electrolyte, which was lower than that of the other electrolytes. Upon addition of 10 wt% FEC to Gen2, the reduction potential increased slightly to 0.42 V vs. Li/Li⁺. The comparable increment occurred to LiPF₆-DME and LiTFSI-DME electrolytes. In comparison, the initial reduction peak was at 0.5 V vs. Li/Li⁺ for LiFSI-DME and did not change with the addition of TTE. The higher reduction potential for the LiFSI-DME system suggests that this electrolyte more readily reduced on the Si surface [13]. This peak became less prominent in subsequent CV scans (see Figure II.1.B.49(b)), which indicates the presence of a passivated Si surface that inhibited further electrolyte reduction.

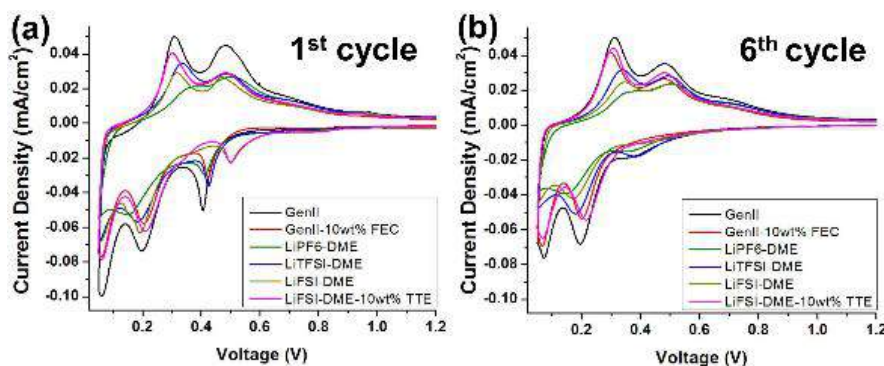


Figure II.1.B.49 Cyclic voltammograms of a-Si thin-film anodes cycled in various electrolytes between 1.5 V and 50 mV vs. Li/Li⁺ at a scan rate of 0.1 mV/s showing the (a) first and (b) sixth cycles

We further used galvanostatic cycling (GC) and chronoamperometry (CA) testing to evaluate the SEI passivation on the a-Si anode using different electrolytes. This protocol was described in the Q2 report. The steady-state current measured after a 24 h potential hold at 50 mV vs. Li/Li⁺ is attributed to continuous parasitic reactions occurring between the electrolyte and lithiated a-Si. As shown in Figure II.1.B.50, the steady-state current density decreased after cycling for many electrolytes. In general, a lower parasitic current indicates a more effective SEI film on the a-Si surface. Surprisingly, a-Si cycled in Gen2-10 wt% FEC showed a 2-fold increase in the parasitic current during the first cycle compared to other electrolytes, as shown in Figure II.1.B.50. The parasitic current of Gen2-10 wt% FEC exhibited a sharp drop during the first three cycles and became the smallest among all other electrolytes after five cycles. This result indicates that the SEI formed on a-Si anode during the first three cycles with Gen2-10 wt% FEC electrolyte was not stable. We note here that the SEI layer formed during the initial few cycles may deform and/or dissolve into the electrolyte upon extended cycling.

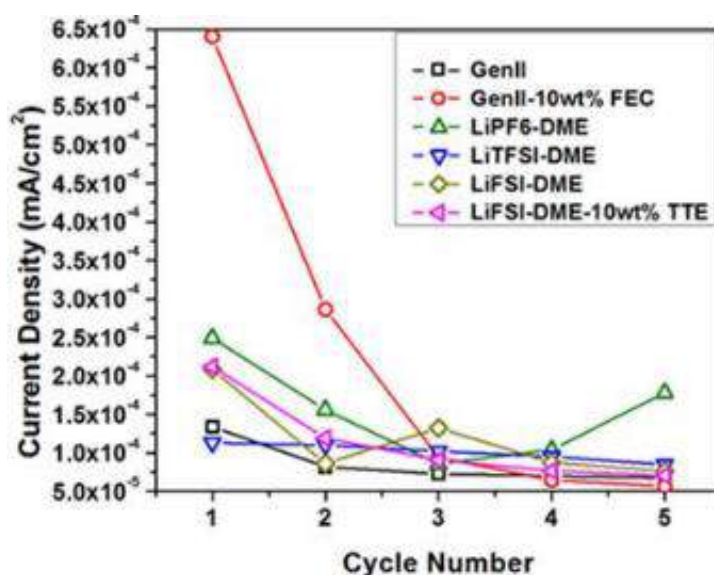


Figure II.1.B.50 Summary of the parasitic current density during the galvanostatic cycling (GC) – chronoamperometry (CA) test for a-Si cycled in various electrolytes. During the formation cycle, the a-Si was first discharged to 50 mV vs. Li/Li⁺ and then galvanostatically cycled between 1.5 V and 50 mV at 1C (41.7 $\mu\text{A}/\text{cm}^2$). In between each charge-discharge cycle, a 24-hour potential hold at 50 mV vs. Li/Li⁺ was performed, and the steady-state current at the end of this step was recorded.

The fact that the parasitic current of glyme and carbonate electrolytes became comparable after five cycles motivates us to continue researching the passivation behavior of the glyme systems after extended cycling. Among all electrolytes, a-Si cycled in Gen2 exhibited the highest initial discharge/lithiation capacity, as shown in Figure II.1.B.51. Addition of 10 wt% FEC to Gen2 stabilized the SEI formed on a-Si, as demonstrated by the improved capacity retention over 110 cycles (85% as compared to 31% for Gen2). a-Si cycled in LiPF₆-DME exhibited the lowest capacity among all electrolytes, agreeing with its unstable parasitic current as observed in the GC-CA test in Q3. The LiTFSI-DME and LiFSI-DME glyme electrolytes exhibited lower discharge capacity compared with Gen2+FEC. Although the addition of 10 wt% TTE to LiTFSI-DME and LiFSI-DME did not stabilize the a-Si well (Figure II.1.B.51), a formulation containing LiFSI-DME-TTE in a 1:3:3 molar ratio significantly improved the cyclability of the a-Si anodes with 92% capacity retention after 110 cycles. This improved performance is attributed to the formation of a stable, robust SEI layer.

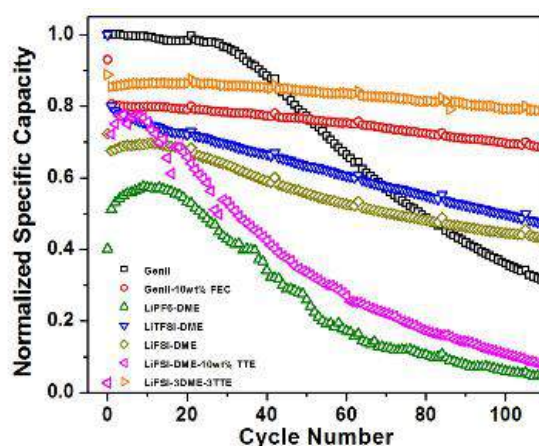


Figure II.1.B.51 Variation of normalized discharge/lithiation capacity with cycle number (up to 110 cycles) of the a-Si anodes using multiple electrolytes at a 1C equivalent current density. All capacity values were normalized with respect to that of the Gen2 at Cycle 0

We further explored the surface morphology of the a-Si anodes after prolonged cycles using scanning electron microscopy (SEM). The a-Si anodes cycled in Gen2 and Gen2+FEC electrolytes exhibited significant cracking, as shown in Figure II.1.B.52. In comparison, the a-Si cycled in LiFSI-DME was covered by a patch-like SEI layer. This may suggest the mechanical failure of the formed SEI layer during Si expansion/contraction. The a-Si anode cycled in LiFSI-3DME-3TTE glyme electrolyte had a much smoother and crack-free surface after 110 cycles, indicating the presence of a more conformal passivation layer. This observation agrees well with the cycling results shown in Figure II.1.B.51, which show excellent performance of a-Si cycled in LiFSI-3DME-3TTE.

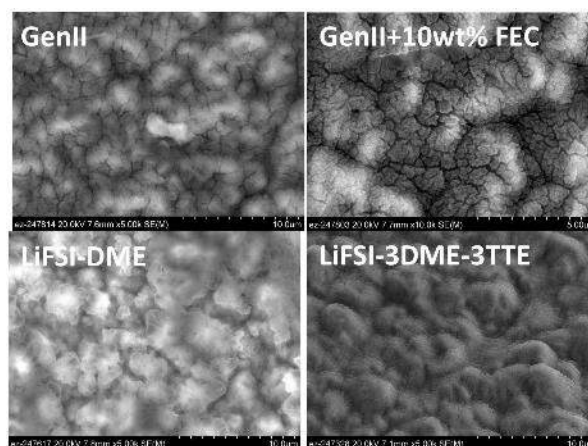


Figure II.1.B.52 SEM micrographs of the a-Si anodes after 110 cycles

The surface chemistry of the a-Si anodes during early cycles and after prolonged cycles was explored further by using energy-dispersive X-ray (EDX) spectroscopy. The surface elements in the SEI layer seen from EDX spectroscopy include carbon, oxygen, fluorine, silicon, and sulfur, as shown in Figure II.1.B.53. Intriguingly, the C-O atomic ratio was close to 2:1 for Gen2 electrolyte after five cycles, suggesting that the initial SEI largely consisted of PEO-like oligomer species as previously reported [14]. After 110 cycles, the C-O ratio for Gen2 and Gen2+FEC was about 1:1, which suggests an increased abundance of C=O groups [14]. These carbonates may include Li_2CO_3 and/or lithium ethylene dicarbonate (LEDC) species. In contrast, the C-O ratio for LiFSI-3DME-3TTE glyme electrolyte was 2:1 after prolonged cycling, indicating enrichment of the organic PEO-like SEI species. This observation agrees fairly well with the infrared (IR) spectra of various a-Si samples cycled in glyme-based electrolytes as reported in a previous quarterly report. Notably, the addition of TTE did not increase the abundance of fluorinated species, which indicates that F content in the SEI layer is largely due to LiFSI decomposition.

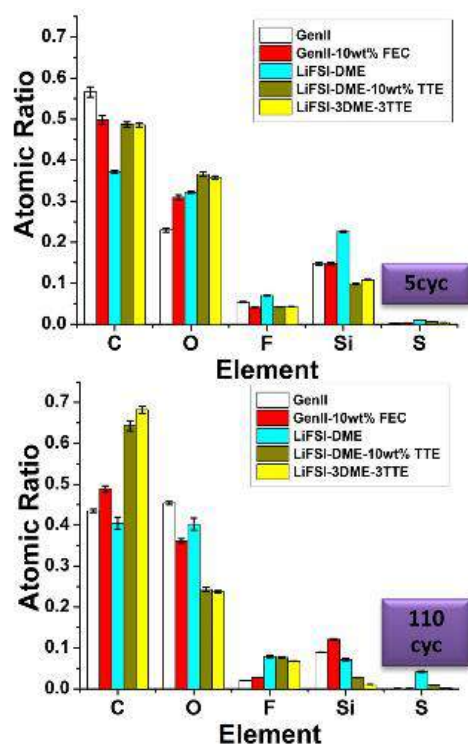


Figure II.1.B.53 Elemental analysis of the a-Si anodes after five cycles and after 110 cycles using EDX. Error bar indicates the standard deviation of three measurements on three different locations of each sample

Future research efforts will investigate the surface chemistry of the a-Si before/after cycling using X-ray photoelectron spectroscopy (XPS). We will also explore SEI formation mechanisms in different electrolyte systems. The effect of the electrolyte coordination chemistry will be evaluated for the LiFSI-3DME-3TTE using a similar method reported by Persson et al. [15]. ^1H NMR has been measured on various electrolytes after cycling to study soluble electrolyte decomposition products. These data are being analyzed and will be reported in due course.

In summary, we evaluated the passivation behavior of glyme electrolytes on a-Si thin-film anodes. CV profiles indicate that LiFSI-DME-based electrolytes passivate the a-Si better during early-stage electrochemical cycles. The GC-CA test indicates that the SEI formed on a-Si in Gen2-FEC electrolyte is metastable for the first three cycles. In comparison, our new electrolyte formulation (LiFSI-3DME-3TTE) passivates the a-Si better for prolonged galvanostatic cycling. EDX elemental analysis on post-mortem a-Si anodes indicates that the Gen2 electrolyte passivation results in formation of an SEI enriched in carbonate species (e.g., lithium carboxylate,

Li_2CO_3 , and LEDC) after extended cycling. In contrast, using glyme-based electrolytes leads to the formation of PEO-like organic species on the a-Si surface.

Evolution of SEI on Si Wafer

Si wafers are the second model system that we used for studying the stability of the SEI and its evolution with cycling. Specifically we examined SEI formed on a Si wafer at 1, 10, 50, and 319 cycles, characterizing its thickness, resistivity, surface roughness, and chemical composition.

A native SiO_x -terminated Si wafer was cycled at a fixed current density of $6.82 \mu\text{A cm}^{-2}$ for a maximum time of 2 h per half cycle. Lithiation cutoff voltage was set at 0.01 V vs. Li/Li^+ while delithiation cutoff voltage was set at 1.5 V vs. Li/Li^+ .

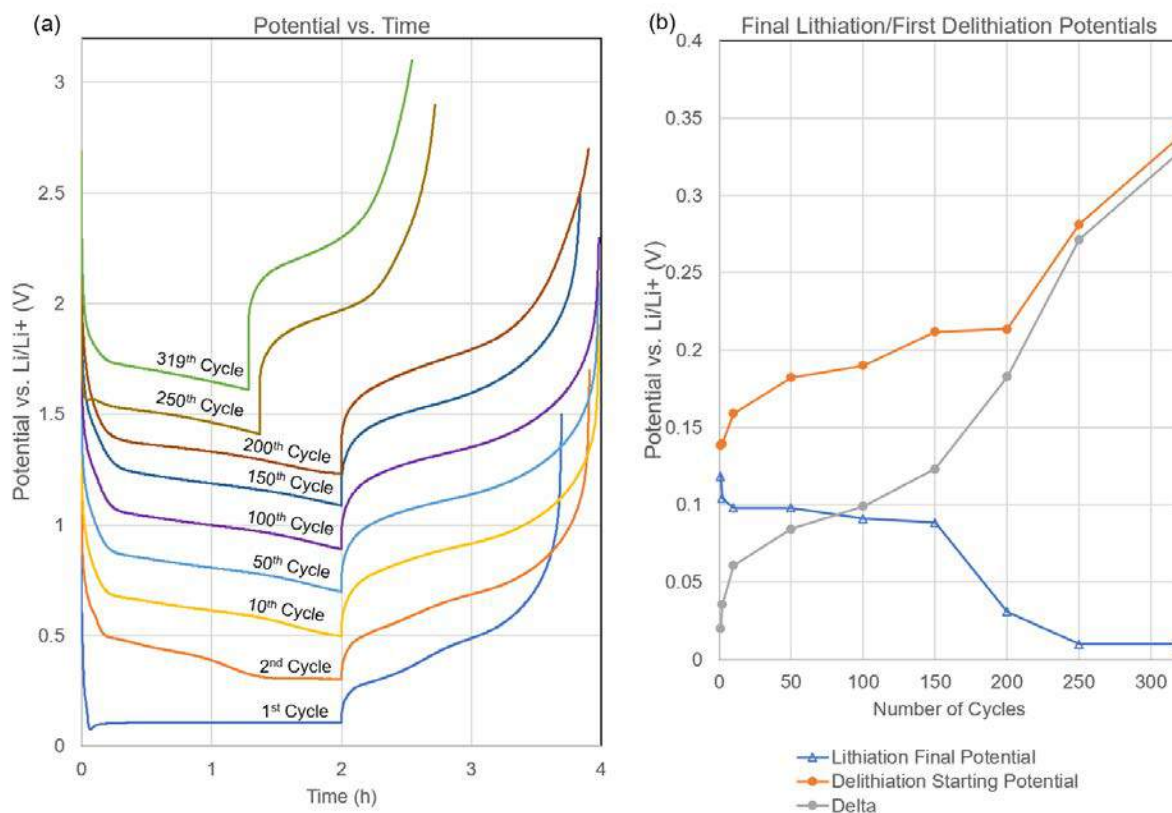


Figure II.1.B.54 Electrochemical results of 319 cycles on native SiO_x -terminated Si wafer. Panel (a) shows potential vs. time for periodic cycles, with 0.2 V incremental offset, whereas (b) depicts the final lithiation potential and initial delithiation potential vs. number of cycles

The first cycle depicts the characteristic features of lithiation of crystalline Si. In subsequent cycles, the potential reached at the end of the lithiation period drops lower, while the first potential during delithiation rises (Figure II.1.B.54(b)). By the 200th cycle, during delithiation, the potential reaches the 1.5 V cutoff before the 2 h time limitation. By the 250th cycle, potential reaches the 0.01 V potential lithiation cutoff prior to the 2 h time limitation. These results indicate that the SEI becomes a barrier to Li diffusion, and/or the condition of the Si degrades such that it becomes increasingly difficult to electrochemically drive Li^+ into the Si and recover Li^+ during delithiation.

SEIs after 1, 10, 50, and 319 cycles were disassembled, soaked in DMC to remove residual salts, and transferred without atmospheric exposure to Ar glove boxes for further characterization. The results of scanning spreading resistance microscopy (SSRM) three-dimensional (3D) resistivity vs. depth profiling and atomic force microscopy (AFM) morphology measurements are summarized in Table II.1.B.4.

Table II.1.B.4 Summary of Results: SSRM 3D Resistivity vs. Depth Profiling of SEI and AFM Roughness

SEI Development Stage	Effect on SEI Thickness, t	Per Cycle SEI Growth Rate	Effect on SEI Resistivity, ρ_{SEI}	Effect on Si Resistivity, ρ_{Si}	Effect on Surface Roughness
Pristine Si → 1 cycle	Initial SEI formation, <10 nm	Large initial SEI growth rate	Well-segregated Initial SEI, resistive outer SEI, less resistive inner SEI	Decrease	Increase
1 cycle → 10 cycles	Increase	Decreased growth rate	Increase	Increase	Increase
10 cycles → 50 cycles	Increase	Decreased growth rate	Decrease	Increase	Increase
50 cycles → 319 cycles	Increase	Decreased growth rate	Decrease	Increase	Large Increase

Scanning transmission electron microscopy (STEM) was used to examine a focused ion beam (FIB)-prepared cross-sectional sample of the SEI formed at 50 cycles. Electron energy-loss spectroscopy (EELS) was also used to examine elemental SEI composition (Figure II.1.B.55).

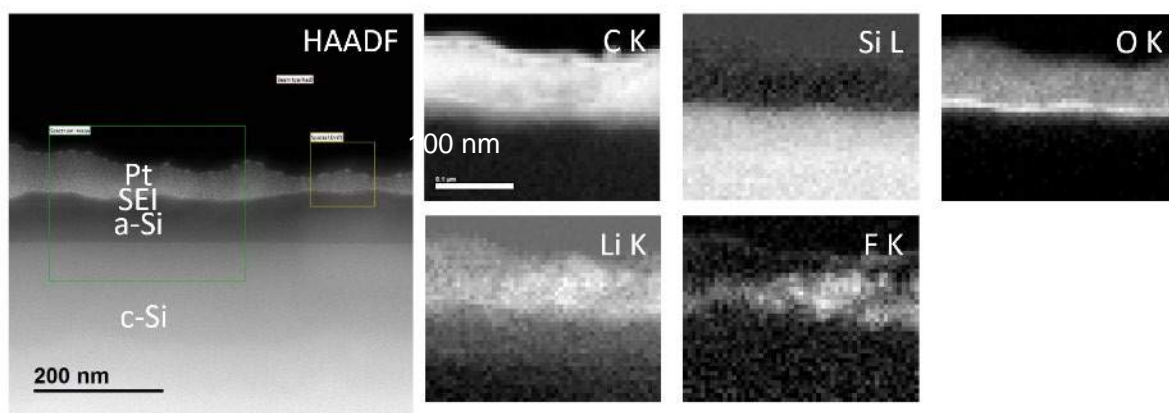


Figure II.1.B.55 STEM HAADF image and EELS areal density maps for a FIB-prepared cross section of SEI formed on Si wafer after 50 cycles. C K, Si L, O K, Li K, and F K EELS areal density maps, with map area shown in the green box on the HAADF image, depict elemental composition of SEI

STEM HAADF image shows that heterogeneity has already begun to form in the active Si material and SEI, while a linear amorphization front is achieved by lithiation. Expansion of lithiated Si forms an uneven amorphized Si layer of 80–120 nm in thickness. SEI shows a Li-, F-, O-, and C-rich composition (Figure II.1.B.56).

Secondary-ion mass spectrometry (SIMS) was carried out on formed SEI after 1 and 319 cycles. The comparative SIMS depth profiles are shown in Figure II.1.B.56.

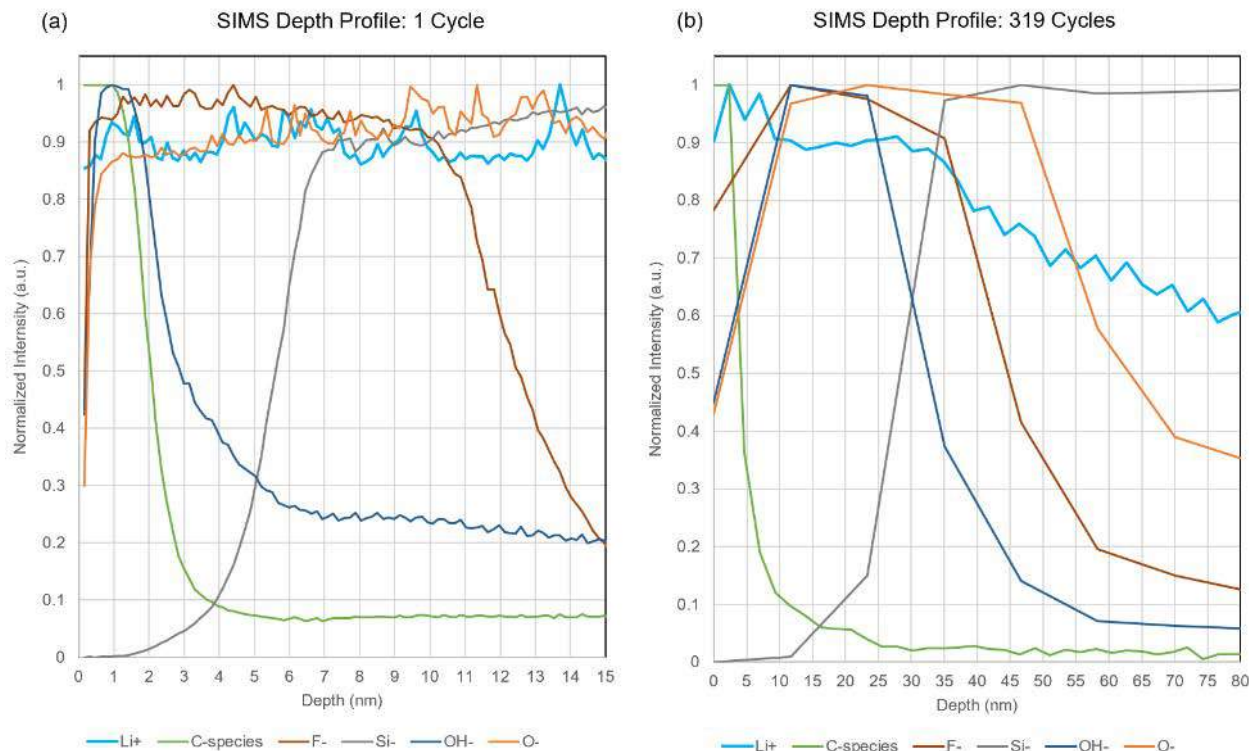


Figure II.1.B.56 SIMS depth profiles on formed SEI after 1 cycle (left) and 319 cycles (right). All series are normalized to their maximum intensity

SIMS depth profiles show that SEI composition remains somewhat consistent throughout its evolution; however, from 1 cycle to 319 cycles, there is an increase in the relative composition of hydroxides with a concurrent decrease in the relative composition of organic species. The SEI and the underlying Si show high levels of O, F, and Li. Thickness increases substantially from 1 to 319 cycles, consistent with SSRM thickness measurements.

In summary, electrochemical results show that the cyclability of Si wafer diminishes by about 250 cycles. At later stages of cycling, increasingly large potentials are required to drive lithiation and recover Li^+ from Si. SSRM results show that the thickness of SEI increases from 1→10→50→319 cycles, while surface roughness measured with AFM also increases, with a dramatic increase in roughness between 50 and 319 cycles. SIMS and STEM EELS show a layered composition of SEI, with C-rich species at the surface SEI and O, Li, and F located in the inner SEI.

Effect of Water Concentration in the Electrolyte on the Thickness and Composition of the Silicon/Electrolyte Interface

The concentration of water in an electrolyte significantly affects the stability of the silicon/electrolyte interface (SEI) and the subsequent electrochemical performance of a cell because water is known to react with LiPF_6 salt in carbonate-based electrolytes to generate corrosive HF [16], which further reacts with Si and SiO_2 . To understand how the presence of water in the system affects the interfacial chemistry and evolution of the Si anodes, we evaluated the electrochemical performance of a model Si wafer electrode in Gen2 electrolyte (1.2 M LiPF_6 in ethylene carbonate (EC): ethyl methyl carbonate (EMC), 3:7 wt%) with 50 ppm of water. The custom three-electrode O-ring cells were potentiostatically held at four different voltages, determined from the dQ/dV plot that shows redox behaviors of the electrolytes, to investigate the surface chemistry changes and

evolution within SiEI at selected specific voltages. The mechanistic analysis of formed and evolved SiEI was performed using a variety of analytical techniques including AFM, SSRM, XPS, time-of-flight SIMS (ToF-SIMS), FTIR spectroscopy, and gas chromatography-mass spectrometry (GC-MS). From these measurements, we report the thickness and composition of the SiEI layers formed at different voltages and how it changes when water is added to the electrolyte.

Electrochemical Performance

Potentiostatic hold experiments were performed using a previously described (FY19 Q3) custom three-electrode O-ring cell. The working electrode was a Si wafer (675 μm thick, 0.001–0.005 $\Omega\text{ cm}$, p-type (B), 1.2-nm native oxide on the surface) and both reference and counter electrodes were Li metal foils. The working electrode was held at 1.0, 0.5, 0.2, or 0.01 V (vs. Li/Li⁺, hereafter) for 10 hours after 2 hours rest at the OCV. The cells were immediately disassembled after the 10 hours of voltage hold to minimize the dissolution of the SiEI layer. The Si wafers were soaked in 1 mL of DMC for 60 seconds to remove residual electrolyte from the surface and further dried under dynamic vacuum for 30 min prior to being analyzed. All measurements were carried out under Ar atmosphere.

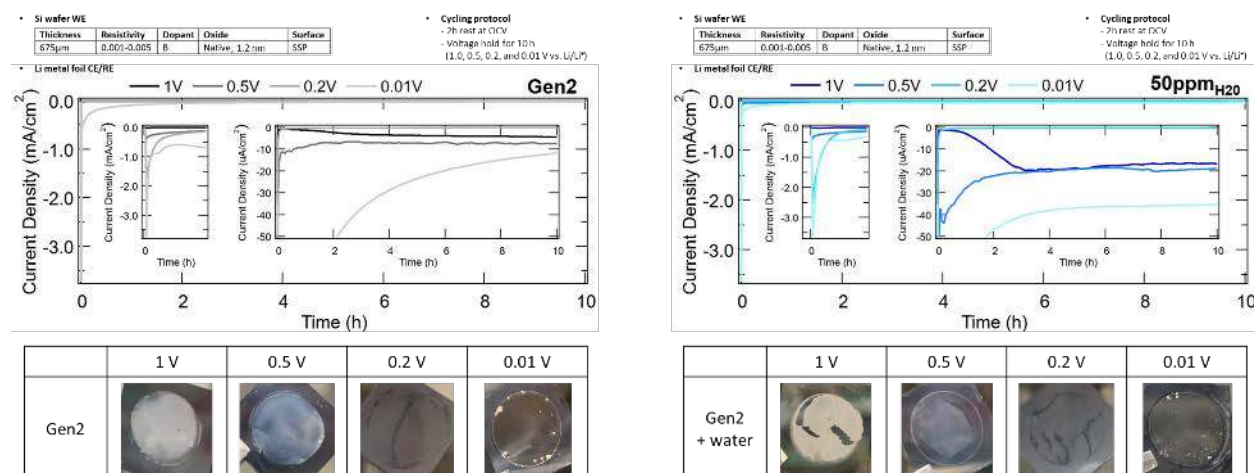


Figure II.1.B.57 Changes in the current density over time during the potentiostatic hold at 1.0, 0.5, 0.2, and 0.01 V (vs. Li/Li⁺) in Gen2 (left) and Gen2 + H₂O 50 ppm (right). Corresponding images of the Si wafers after the potentiostatic hold are shown below each Current Density vs. Time plot

In Figure II.1.B.57, changes in the current density during the potentiostatic hold are presented along with the images of electrochemically treated Si wafers. First, looking at the initial current spike immediately after applying the voltage, a larger reductive current is observed when a lower voltage is applied in both Gen2 and Gen2 with 50 ppm of added H₂O (“Gen2+H₂O_{50ppm}”). The steady-state current also follows the same trend (i.e., a larger current at a lower voltage)—except for 0.2 V, where the current decays to near zero. Such behavior indicates that a surface layer is formed between 0.5 and 0.2 V that successfully inhibits further electrolyte reduction, and additional reactions may not occur because the crystalline wafers cannot be lithiated at 0.2 V. On the other hand, at 0.01 V, we observed a large current flowing mostly due to the lithiation of the silicon. Another interesting observation is that the steady-state current is greater in Gen2+H₂O_{50ppm} than that observed in Gen2 at the same voltage. This additional charge can be attributed to the side reactions taking place in the presence of water starting at about 1.0 V. The images of the Si wafers clearly show different surface layers formed at different voltages (Figure II.1.B.57). To understand the nature and properties of these SiEI layers, we performed a series of surface chemistry and property analysis.

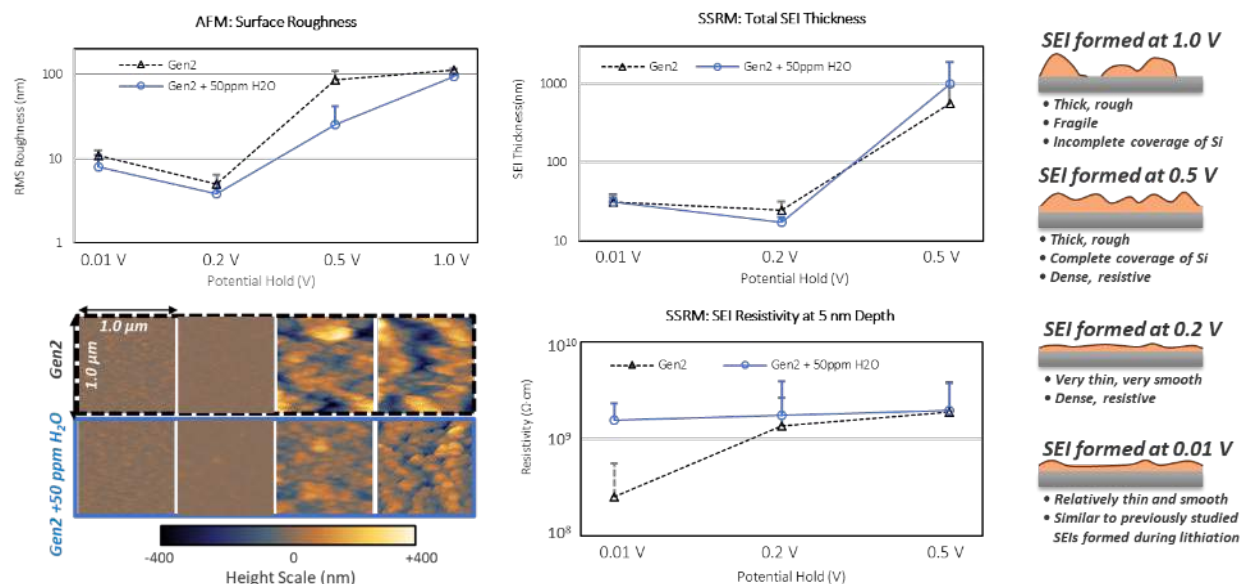


Figure II.1.B.58 Roughness, thickness, and resistivity of the SiEI measured with AFM and SSRM. Mean results are plotted and the standard deviations are shown as error bars. Schematic diagram of the SiEI layer formed at different voltages is shown on the right

Roughness, Thickness, and Resistivity of the SiEI

AFM and SSRM measurements were conducted to analyze the roughness, thickness, and resistivity of the SiEI layer. The measurements were carried out three times on freshly prepared 24 samples (6 samples—3 without water and 3 with water—for 4 voltage conditions) to validate the results and provide error bars (Figure II.1.B.58). The root-mean-square (RMS) surface roughness values measured with AFM, and the corresponding images, show that the SiEI formed in the presence of water is smoother at all voltages tested. As a function of voltage, the SiEI layers that formed at 1.0 and 0.5 V are significantly rougher than those formed at 0.2 and 0.01 V (for both Gen2 and Gen2+ H₂O_{50ppm}). Further, the SSRM results show that the thickness of the SiEI also dramatically changes between 0.2 and 0.5 V, showing that the 0.5 V layer is significantly thicker, ~700–1,000 nm (vs. ~20–40 nm at 0.2 V). Such behavior can be correlated to the electrochemical performance (Figure II.1.B.57) where the electrolyte reduction, and resulting SiEI buildup, was successfully hindered at 0.2 V. It is quite challenging to perform SSRM measurements in contact mode for the 1.0 V samples because the SiEI layer is too fragile. The SiEI formed at a higher voltage is more resistive in Gen2, whereas the resistivity does not change much among the SiEI formed at different voltages in the presence of water. At 0.01 V, we measured the SiEI resistivity to be significantly greater (almost an order of magnitude) in the presence of water. This can be explained by the fact that more charges are consumed by the side reactions in the presence of water and less lithiation of silicon occurs. The AFM and SSRM results are summarized in a schematic diagram shown in Figure II.1.B.58.

Chemical Composition of the SiEI

To understand the chemical composition of the SiEI, we used spectroscopic techniques. First, XPS spectra were collected to look at Si 2p, O 1s, C 1s, F 1s, P 2p, and Li 1s core levels (Figure II.1.B.59). Si 2p spectra in both Gen2 and Gen2+H₂O_{50ppm} show the same trend upon changing: the voltage where strong signals from Si⁰ (~99 eV) and SiO_x (~104 eV) are observed at 1.0 V and the signals vanish at 0.5 V. The high intensity of Si 2p peaks at 1.0 V can be correlated to the AFM results, where the SiEI formed at 1.0 V exhibited high roughness and incomplete coverage of Si. At 0.5 V, the SiEI is thicker and there is complete coverage of Si, which induces no Si signal detection from the XPS spectra.

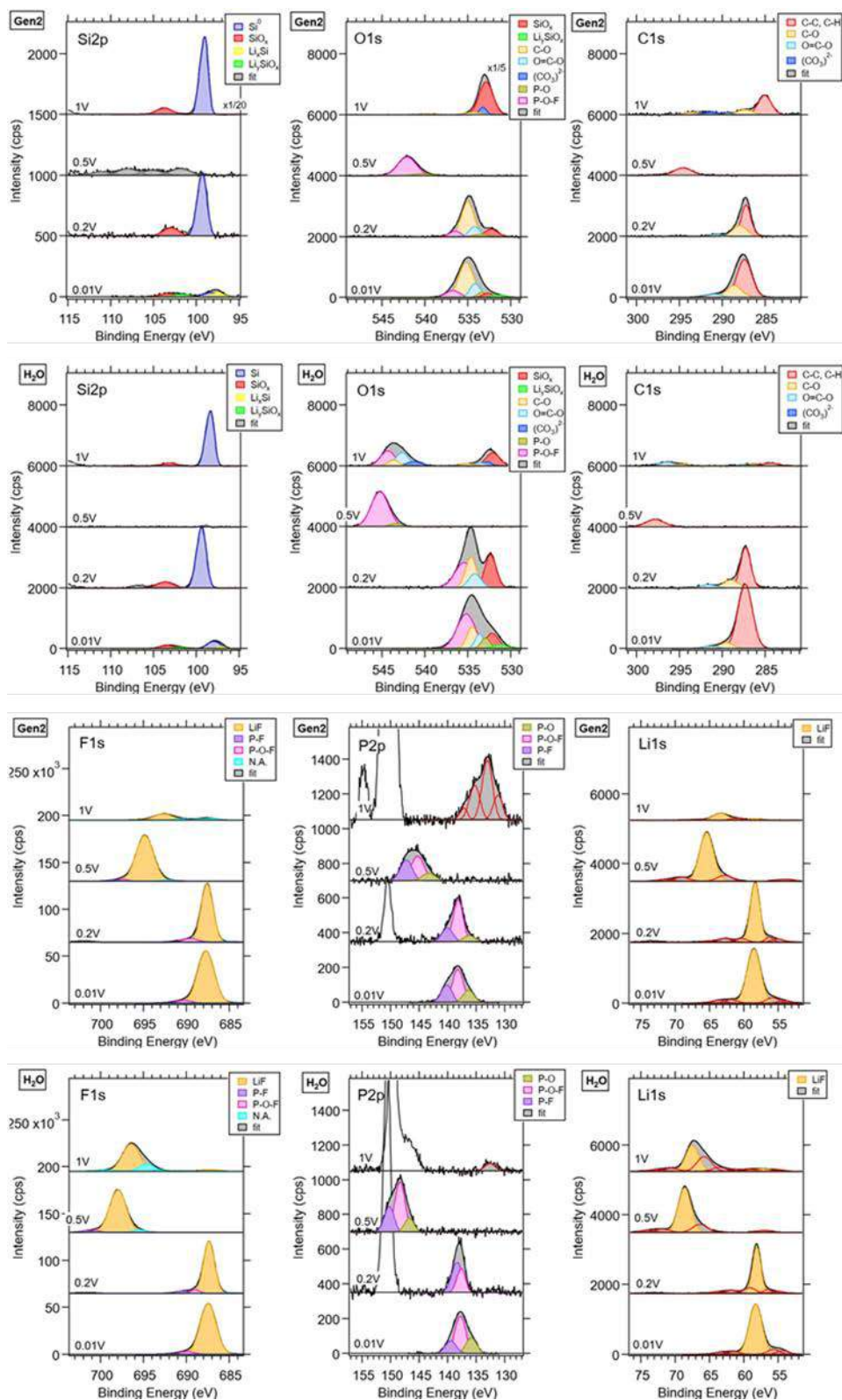


Figure II.1.B.59 XPS spectra of the SiEI layers formed in Gen2 (top) and Gen2+H₂O_{50ppm} (bottom) at 1.0, 0.5, 0.2, and 0.01 V as indicated in the figure. Si 2p, O 1s, C 1s, F 1s, P 2p, and Li 1s core levels are presented

At 0.2 V, the SiEI is thinner and more compact; thus, the Si core levels are observable, and at 0.01 V, lithiated Si species (Li_xSi at ~ 97 eV and Li_ySiO_x at ~ 102 eV) are detected. Another voltage-dependent trend is observed in the C 1s and O 1s spectra. In both Gen2 and Gen2+H₂O_{50ppm}, the SiEI formed at 0.5 V has a large amount of C-H species and fewer C-O species. These findings are corroborated using ATR-FTIR measurements (Figure II.1.B.60): strong -CH₃ and -CH₂ stretching modes are observed in the 0.5 V sample spectra between 2850 and 2950 cm⁻¹. In addition, the peaks at 1655 cm⁻¹ and 910 cm⁻¹ suggest the presence of alkene species. The ATR-FTIR spectra also reveal vibrational modes from carboxylate, ester, and ether species in 1.0 V and 0.2 V samples and not in the 0.5 V samples, in agreement with the XPS results.

Looking at other elements in Figure II.1.B.59 a significant amount of LiF (~ 58 eV and ~ 688 eV in Li 1s and F 1s core levels, respectively) is detected in all samples. Further, higher concentration of fluorophosphates are detected in the SiEI formed in Gen2+H₂O_{50ppm}. Specifically, significant amount of charging is observed (~ 9 eV) in the white layer of SiEI (Figure II.1.B.57) formed at 1.0 V as a byproduct of the reactions involving the water in the system. The layer consists of fluorophosphates, LiF, and C-O-containing species. In addition, GC-MS measurements of the electrolytes salvaged from the disassembled cells confirm the presence of fluorophosphates in the 1.0 V sample. Fluorophosphates are known reaction products in the hydrolysis of PF_6^- (Figure II.1.B.60). This agrees well with XPS results, where the effect of water in the electrolyte is maximized at 1.0 V, because not many reactions occur in Gen2 at this voltage except extensive side reactions from water.

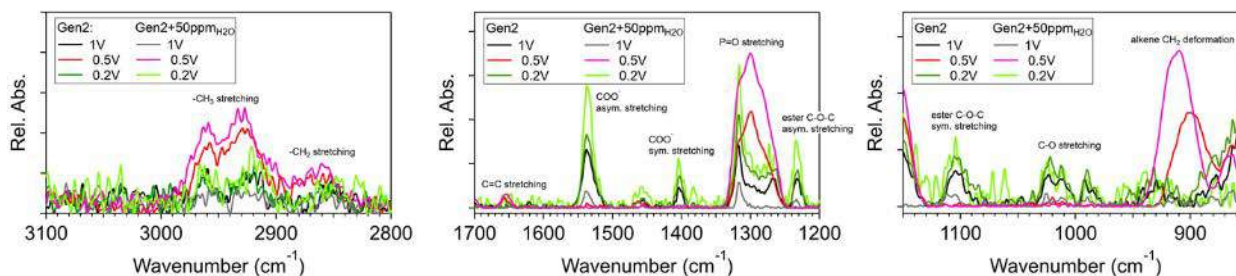
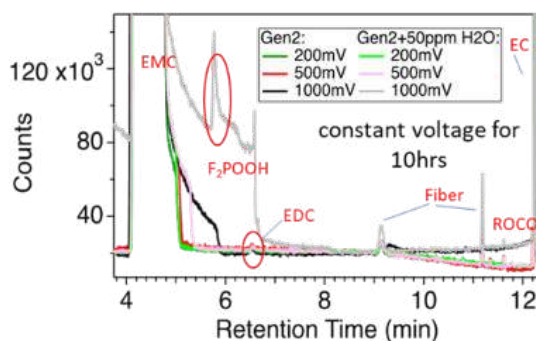


Figure II.1.B.60 ATR-FTIR spectra of the SiEI layers formed in Gen2 and Gen2+H₂O_{50ppm} at 1.0, 0.5, 0.2, and 0.01 V



LiPF₆ hydrolysis

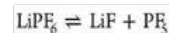


Figure II.1.B.61 Gas chromatograms of electrolytes recovered from the cells after the potentiostatic holds (left) and the chemical equations of the LiPF₆ hydrolysis reaction (right)

Three-Dimensional Elemental Maps of the SiEI

To further analyze the elemental distribution of the SiEI, we obtained ToF-SIMS 3D tomography images on selected voltages, 0.2 V and 0.5 V, as shown in Figure II.1.B.62. The SiEI layers formed at 0.2 V are relatively thin, in both Gen2 and Gen2+H₂O_{50ppm}, which agrees with the thickness measured with SSRM (Figure II.1.B.58). In addition, a similar distribution of F⁻ and Li⁺ indicates the existence of LiF, which was also observed from the XPS results (Figure II.1.B.59). One major difference is that the SiEI formed in Gen2+H₂O_{50ppm} shows a pitted structure in Si, possibly due to the reactions of Si and SiO₂ with HF formed from the LiPF₆ hydrolysis. In the case of 0.5 V, relatively thicker SiEI layers are formed—again, in agreement with the SSRM results—and the intensity of LiF is highest right on top of the Si substrate. It is obvious that more inhomogeneous layers are formed in the presence of water.

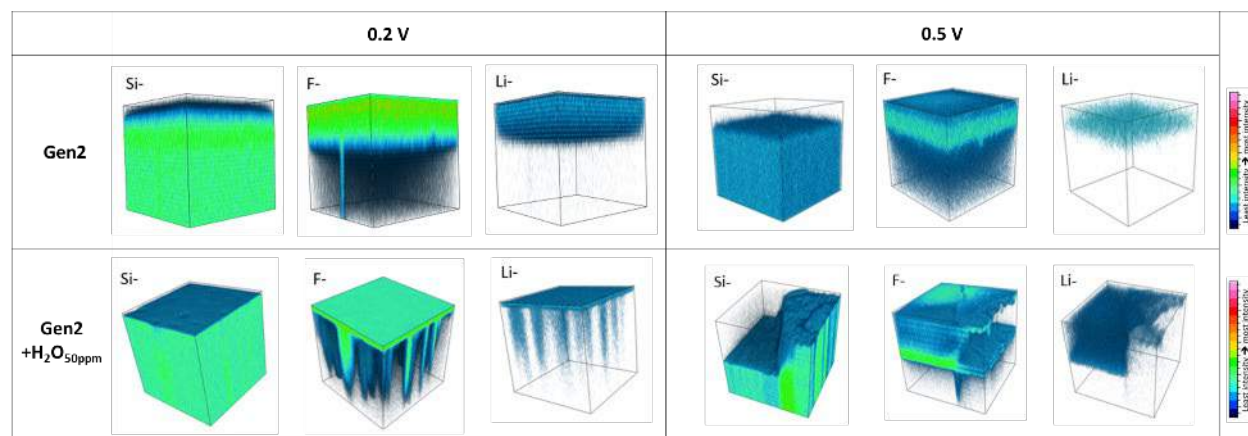


Figure II.1.B.62 High-resolution elemental maps of SiEI layers formed at 0.2 V (left) and 0.5 V (right) in Gen2 (top) and Gen2+H₂O_{50ppm} (bottom). The intensity is on a blue-to-red color scale, with red being the highest intensity

In summary, detailed analysis of the SiEI layers formed at different voltages (1.0, 0.5, 0.2, and 0.01 V vs. Li/Li⁺) was performed using a variety of techniques including AFM, SSRM, XPS, ATR-FTIR, GC-MS, and ToF-SIMS. The effect of water concentration in the electrolyte (50 ppm) on the thickness and composition of the SiEI was also studied. The SiEI layers formed at both 1.0 V and 0.5 V show a thick and rough texture, but the SiEI formed at 1.0 V has a porous structure whereas the SiEI formed at 0.5 V exhibits a complete coverage of Si. Between 0.5 V and 0.2 V, the thickness and the roughness of the SiEI dramatically decreased, possibly due to the formation of a layer that successfully hindered further electrolyte decomposition and subsequent SiEI formation. The SiEI formed at 0.5 V had more C-H and less C-O species than the SiEI formed at all the other voltages. When 50 ppm of water is added to the electrolyte, the formed SiEI has more fluorophosphates generated during the LiPF₆ hydrolysis and the Si has pitted structures with an inhomogeneous SiEI. Such behavior can be attributed to the reaction of Si and SiO₂ with HF, a product of the LiPF₆ hydrolysis reaction.

Si Electrode Investigation: Superior Carbon Coating Alters Si Materials Transformation During Electrochemical Process

To address the large volume change and excessive surface reaction of silicon materials during lithiation and delithiation reaction, carbon coating has been widely used as an electric conductive medium and electrolyte insulating buffering layer to encapsulate the silicon particles. Despite the reported improved capacity retention of Si-based material by carbon coating, there is relatively less investigation of the Si material transformation with the carbon coating. Moreover, many different precursors can be used to produce the carbon coatings, which, however, result in the coating having very different chemical and morphological characteristics. Here, we report the drastically different Si solid-state transformation during electrochemical process due to the different types of carbon precursors and carbon coatings on the same Si nanoparticles.

A high-temperature thermal-based carbonization process is used to produce carbon coating on Si nanoparticles. Organic-based precursors are used to form carbon coatings. Different precursors tend to form carbon coatings

with different morphologies. Two types of carbon coatings can be formed on Si: one is a highly graphitized and dense coating from a polymer precursor (Si/C-P), and the other is more disordered structures from a sucrose precursor. The Si materials with highly graphitized and dense coating are able to deliver higher gravimetric capacity and stable cycling compared to that of the Si with disordered carbon coating. The dramatic differences come from the Si materials transformation. The Si/C-P materials maintain a two-phase reaction during delithiation in the first 30 cycles, whereas the Si/C-S forms an amorphous structure after the 1st cycle, and it does not form a clear two-phase transformation during delithiation.

A Si/C electrode with compact and ordered carbon coating was prepared with polyvinylidene chloride (Si/C-P electrode), and a Si/C electrode with loose and porous carbon coating was made with sucrose (Si/C-S electrode) for comparison. The cells of the Si/C electrodes were cycled at C/10 between 1.00 V and 0.01 V after a formation step at C/20 ($1C = 2,000 \text{ mAh g}^{-1}$). All the reported capacities are based on the total mass of Si/C composites. Figure II.1.B.63(a) presents the cycling performance and Coulombic efficiency (CE) of Si/C-P and Si/C-S. The initial Coulombic Efficiency (ICE) of Si/C-P (72.7%) is much higher than that of Si/C-S (56.1%). The compact carbon structure in the Si/C-P sample can protect the silicon nanoparticles from direct exposure to the electrolyte, and thus, leads to improved ICE. After the formation step, the CE of the Si/C-P electrode increases to above 99.0% after 10 cycles and to 99.5% after 20 cycles. On the other hand, the CE of the Si/C-S electrode stays below 99.0%. The Si/C-P electrode exhibits a specific charge capacity of $1219.6 \text{ mAh g}^{-1}$ with the capacity retention of 98.1% after 20 cycles at C/10, which is higher than those of the Si/C-S electrode, 692.7 mAh g^{-1} and 77.0 %, respectively. At the 25th cycle, the CE of the Si/C-P electrode experiences a sharp decrease, dropping from 99.8% to 98.6%, which is rationalized as a consequence of the fracture of the carbon coating. After the fracture of the carbon coating, the CE of the Si/C-P electrode drops to about 98%, which is very similar to that of the Si/C-S electrode. During the 30th–50th cycle, the Si/C-P electrode presents a gradually decreasing capacity from 1149.5 to $1078.0 \text{ mAh g}^{-1}$, and the capacity retention ratio of the Si/C-P electrode during these 20 cycles is 93.8%. These results indicate that the more compact carbon coating of the Si/C-P material helps to decrease interface reaction and increase cell life. In addition, after the breakdown of the carbon coating on the Si/C-P sample, the interface stability of the Si/C-P sample begins to decay.

To better understand the electrochemical behavior of the Si/C-P electrode during the lithiation and delithiation process, the voltage profiles of the Si/C-P electrode from the 2nd–50th cycles are examined in Figure II.1.B.63(b). There is a major plateau at 0.43 V for the 2nd–20th delithiation curves, which disappears beyond the 30th cycle where the carbon coating is fractured. The disappearance of the voltage plateau at 0.43 V indicates a significant bulk structure change during lithiation and delithiation processes due to the carbon-coating fracturing. This is the first observation of the influence of compact and ordered carbon coating on bulk Si particle structure transformation during electrometrical process. Figure II.1.B.63(c) shows dQ/dV plots for the Si/C-P electrode for 2nd–50th cycles. During the 2nd lithiation cycle, three different processes are observed. The first discharge process at ~250 mV is associated with the gradual lithiation of the a-Si to form $\text{Li}_{-2.0}\text{Si}$, a structure that still presents extended Si networks and large Si-Si clusters. The second process at ~80 mV is related to the further lithiation of $\text{Li}_{-2.0}\text{Si}$ to $\text{Li}_{-3.5}\text{Si}$. At this stage, large Si-Si clusters broke into smaller Si clusters and isolated Si anions. The third process at ~35 mV corresponds to the formation of the crystalline phase, c- $\text{Li}_{3.75}\text{Si}$, from a- Li_xSi . The third process is not observed beyond the 30th cycle. As for the de-lithiation process, there is a strong and sharp peak at ~430 mV for the 2nd–20th cycles, which is associated with the two-phase transition from c- $\text{Li}_{3.75}\text{Si}$ to Li_xSi ($x = 0-2.0$). In this case, the x value is approaching 0 to reflect the dominating two-phase transition from $\text{Li}_{3.75}\text{Si}$ to almost delithiated amorphous Si, with minor transition from Li_xSi to a-Si phase. However, beyond the 30th cycle, where the carbon coating is fractured, two broad peaks at ~280 mV and ~500 mV are observed instead (no sharp peak at ~430 mV), which is an indicator of solid-solution reaction. This observation demonstrates that the formation of c- $\text{Li}_{3.75}\text{Si}$ is no longer the dominating process and that there is no direct transformation from c- $\text{Li}_{3.75}\text{Si}$ to amorphous Si particles. To be more specific, the two broad peaks are associated with the delithiation process of Li_xSi ($x = 3.5-3.75$) to $\text{Li}_{-3.5}\text{Si}$ (~280 mV) and $\text{Li}_{-3.5}\text{Si}$ to $\text{Li}_{-2.0}\text{Si}$ (~500 mV). The compact and unbroken carbon coating can enhance the kinetic property of the Si alloying reaction by improving the conductivity of Si and by promoting the

formation of the small Si clusters and isolated Si anions with uniformly dispersed silicon particles. Due to the enhanced alloying kinetics, the Si/C-P electrode can continuously generate c-Li_{3.75}Si during the lithiation process.

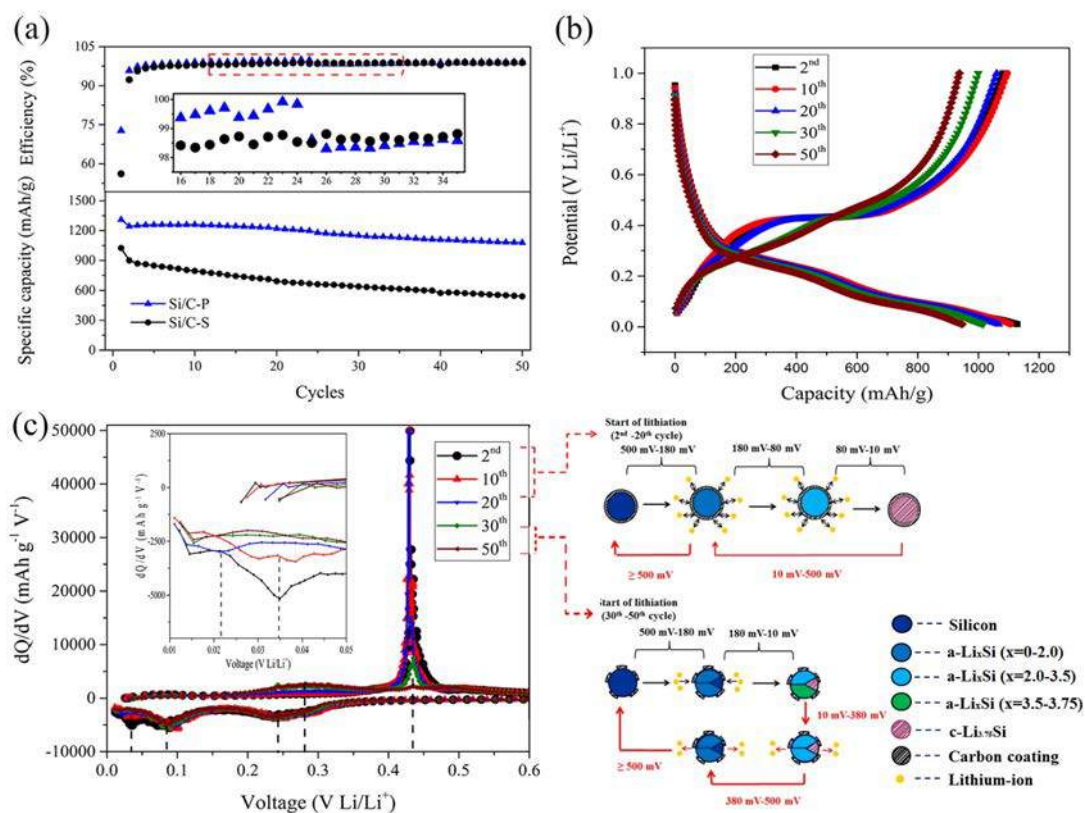


Figure II.1.B.63 (a) Cycling performances and Coulombic efficiencies of Si/C-P and Si/C-S electrodes at C/10, from 1.00 V to 0.01 V; (b) Galvanostatic discharge/charge profiles of Si/C-P electrode from 2nd to 50th cycles at C/10, from 1.00 V to 0.01 V; (c) Differential capacity vs. potential curves of Si/C-P electrode from 2nd to 50th cycles at C/10, from 1.00 V to 0.01 V (1C = 2,000 mAh g⁻¹)

Part 3: (Re)engineering of the Si/Electrolyte Interface via Molecular Interactions

Over the course of this research project it has become increasingly clear that the standard electrolyte used in batteries comprised of a graphite anode, i.e., LiPF₆ in mixtures of ethylene carbonate and ethyl methyl carbonate (referred to as Gen2), is not stable with respect to silicon anodes. Furthermore, the variability of silicon with manufacturing processes leads to intrinsic surface instabilities that often mask other problems in cell stability (i.e., gassing, poor polymer adhesion, etc.). As detailed in the previous sections, the standard Gen2 electrolyte forms a non-passivating interface that changes with time and cycling conditions. These changes effectively eliminate the use of this standard electrolyte in future applications with silicon anodes.

As a result of these observations we have executed a series of collaborative studies to (1) understand the bonding and dynamics in standard electrolytes, (2) search for new electrolytes based on what appears to be stable surface moieties (based on chemical analysis), (3) continue developing tools to characterize and understand the interfacial chemistry of *all the components* (i.e., gas, soluble and insoluble species, polymers), and (4) develop new silicon materials with specific surface functionality designed to stabilize to Si particles and improve electrode fabrication (in close collaboration with the Si Deep Dive Consortium led by ANL). In addition, we have performed studies to explore the role of common impurities (i.e., water), which are known to contaminate cells where water-loving binders are used.

Throughout the course of this work, the team has made extensive use of model thin-film electrodes. These electrodes consist of single crystal silicon wafers with well-defined geometries and amorphous silicon films grown on battery-grade copper foil. To reduce the number of variables in the collaborative studies, these single crystal or amorphous silicon films were distributed from central locations (NREL and ORNL, respectively) and used exclusively for these studies. The chemistry of these films is documented in the Fiscal Year 2017 (FY17) and FY18 annual reports for those interested. This section of the SEISTa report is divided into three topical areas, all focused on the development of a predictive understanding of the silicon/electrolyte interface and application of this knowledge to developing new, robust, electrode materials. These sections are:

- Understanding and Designing New Electrolytes
- In situ Understanding of the Growth and Evolution of the SEI on Model Electrodes
- Design of New Si Surfaces Based on Experimentally Validated Stable Chemical Moieties.

The work in these sections was done in collaboration with the results detailed in Parts 1 and 2 and should be viewed as part of the larger collaborative efforts between the teams.

Understanding and Designing New Electrolytes

Solvation Structures of Electrolyte

Based on our previous simulation work on the influence of fluorinated ethylene carbonate (FEC) on the solvation structure of ethylene carbonate (EC) electrolyte, we continue our work to include ethyl methyl carbonate (EMC), as used in the Gen2 electrolyte, to study how linear carbonate additions affect the properties of the electrolyte. Herein, we compare the difference in solvation structures between the EC electrolyte and the Gen2 electrolyte. The influence of FEC additive is also considered and compared between the EC and Gen2 electrolyte.

The solvation structures of EC and Gen2 electrolyte are compared by conducting molecular dynamics simulations for EC (1.2 M LiPF_6 in EC) and Gen2 (1.2 M Li in EC:EMC (v/v 3:7)) electrolytes. Figure II.1.B.64 shows the three representative solvation structures for Gen2 electrolyte, which are solvent-separated ion pairs (SSIP), contact ion pairs (CIP), and aggregates (AGG). For all three structure categories, both EC and EMC participate in the formation of the first solvation shell. Meanwhile, both EC and EMC coordinate with Li^+ ions via the carbonyl oxygen but not the alkoxy oxygen.

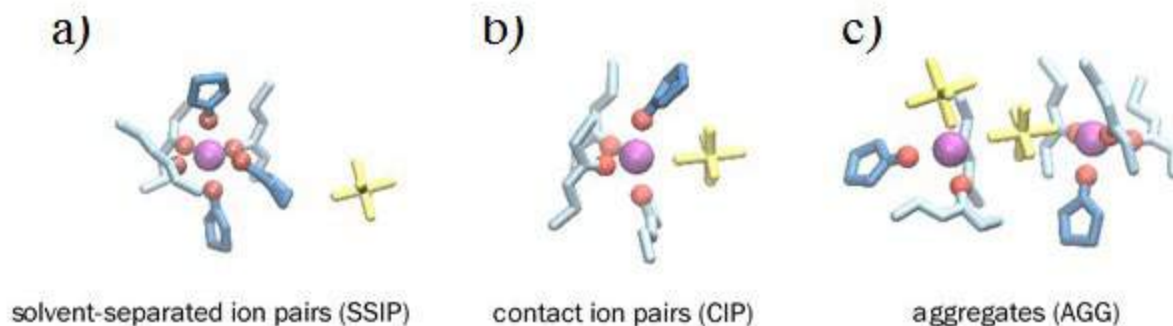


Figure II.1.B.64 Three representative solvation structures in Gen2 electrolyte: (a) solvent-separated ion pairs (SSIP), (b) contact ion pairs (CIP), and (c) aggregates (AGG). The light blue, dark blue, and light yellow line representations denote the EMC, EC, and PF_6^- clusters, respectively. The purple and red ball representations denote Li ions and coordinating carbonyl O atoms, respectively

While these three solvation structures also appear in the EC electrolyte, the proportion of each category changes between the 100% EC and Gen2 electrolyte, as analyzed by the molecular dynamic statistics. For the EC electrolyte, 86.95% of the Li ions form SSIP, while in the Gen2 electrolyte, SSIP only comprises 36.81% of the total Li⁺ ions. CIP and AGG constitute 31.79% and 31.4% in the Gen2 electrolyte, respectively, meaning that in the Gen2 electrolyte the Li⁺ cations and PF₆⁻ anions are more associated, while CIP and AGG represent 11.03% and 2.02% in pure EC, respectively. The higher SSIP population in the EC electrolyte indicates that the EC electrolyte has more ionic conduction carriers than the Gen2 electrolyte.

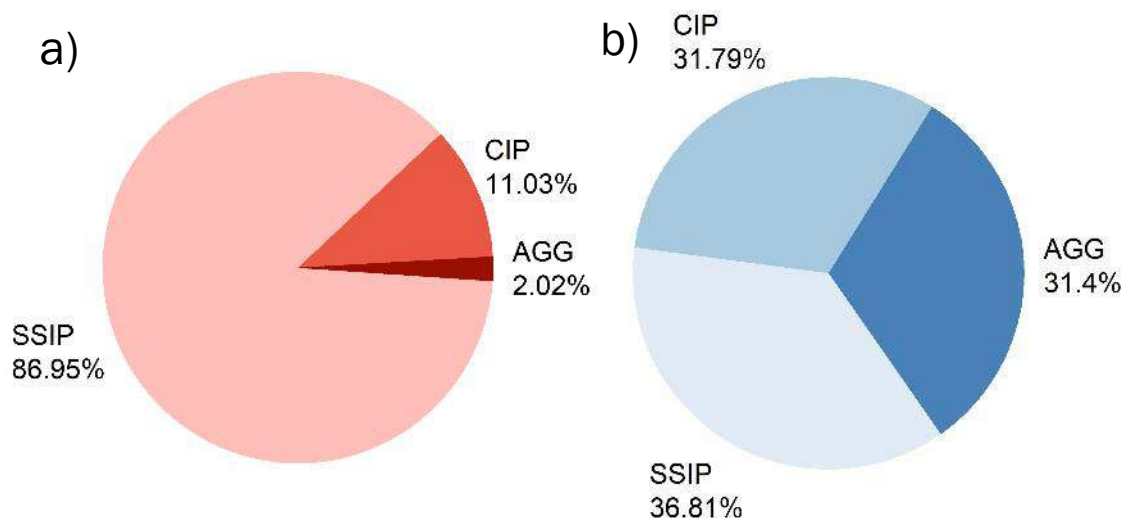


Figure II.1.B.65 The proportions of SSIP, CIP, and AGG in (a) the EC electrolyte and (b) the Gen2 electrolyte

The averaged solvent coordination numbers for these three species are statistically analyzed. For both the EC and Gen2 electrolyte, the total solvent coordination number decreases as a PF₆⁻ anion coordinates with Li to form CIP and additional PF₆⁻ anions coordinate with Li to form AGG. Interestingly, in the Gen2 electrolyte only the coordination number for EC decreases while that for EMC is preserved between species, indicating that only the EC molecules are substituted by PF₆⁻. This may be attributed to the bulky shape of EMC, which results in larger Lennard-Jones forces that confine or stabilize the coordinating structure, and renders EMC-Li⁺ a stiffer configuration. More detailed study of this phenomenon will be conducted in the future.

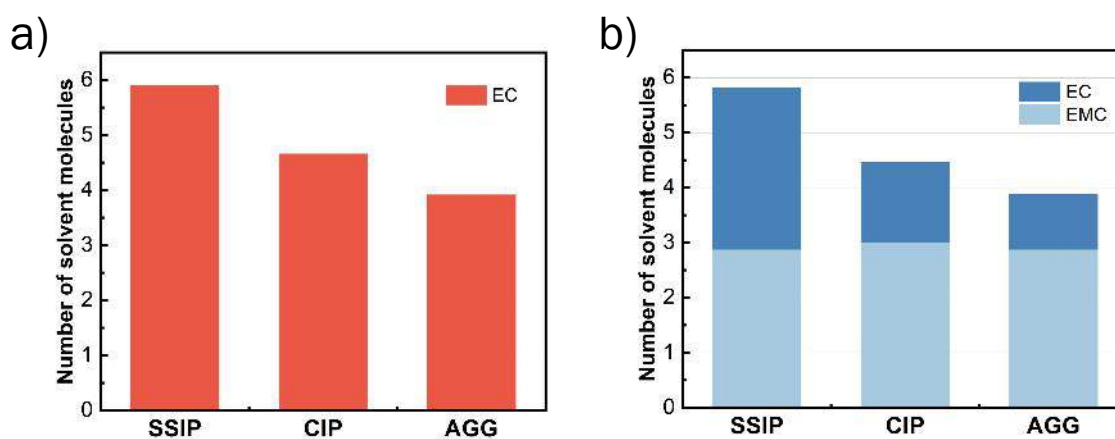


Figure II.1.B.66 The coordination number of solvent molecules for SSIP, CIP, and AGG species in (a) EC electrolyte and (b) Gen2 electrolyte

The detailed speciation of AGG in the Gen2 electrolyte is further analyzed, as shown in Figure II.1.B.67. Among the 31.4% of the AGG species, 9% are AGG1 form with 2 Li^+ and 1 PF_6^- , which is +1 charged. Meanwhile, the AGG2 form with neutral charge and the AGG3 form with -1 charge take up 8% and 7%, respectively. The remaining forms, including the AGG4 and AGG5, have a percentage of 7%. Overall, at least 19% of the 31% AGG species are charged species, which will contribute to the ionic conductivity. Subsequently, while the EC electrolyte has a much higher SSIP ratio than the Gen2 electrolyte, more than half of the AGG species in the Gen2 electrolyte narrow the gap of the proportion of ionically conductive solvation species.

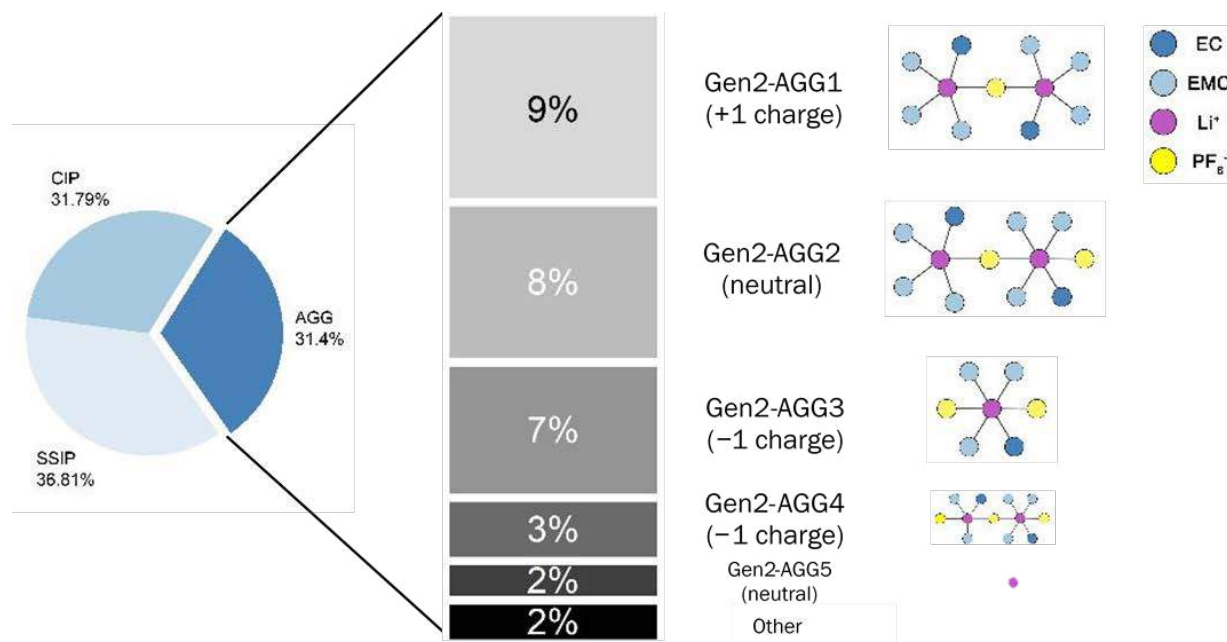


Figure II.1.B.67 AGG species in the Gen2 electrolyte

To compare the influence of FEC additive on the solvation structure of the EC and Gen2 electrolyte, 10% of FEC are added into the systems which make the ECF (EC + 10 mol% FEC) and the GenF (Gen2 + 10 mol% FEC) model electrolyte. The proportions of CIP, SSIP, and AGG of the ECF and GenF follow the same trend as the EC and Gen2 electrolyte, as shown in Figure II.1.B.68. For the ECF electrolyte, 84.73% of the Li^+ ions form SSIP, while in the GenF electrolyte, SSIP takes up 38.37% of the total Li^+ ions. The reason why the SSIP ratio decreased in the ECF and increased in the GenF might be attributed to the fact that FEC has a solvating ability that is between EC and EMC. Accordingly, the CIP and AGG ratios of the ECF change to 14.39% and 0.88%, respectively, while those of the GenF change to 34.04% and 27.59%. Consequently, the ionic conduction ability of ECF and GenF is supposed to be similar to the EC and Gen2 electrolyte. Detailed analysis of the conduction and transport properties will be addressed in the future.

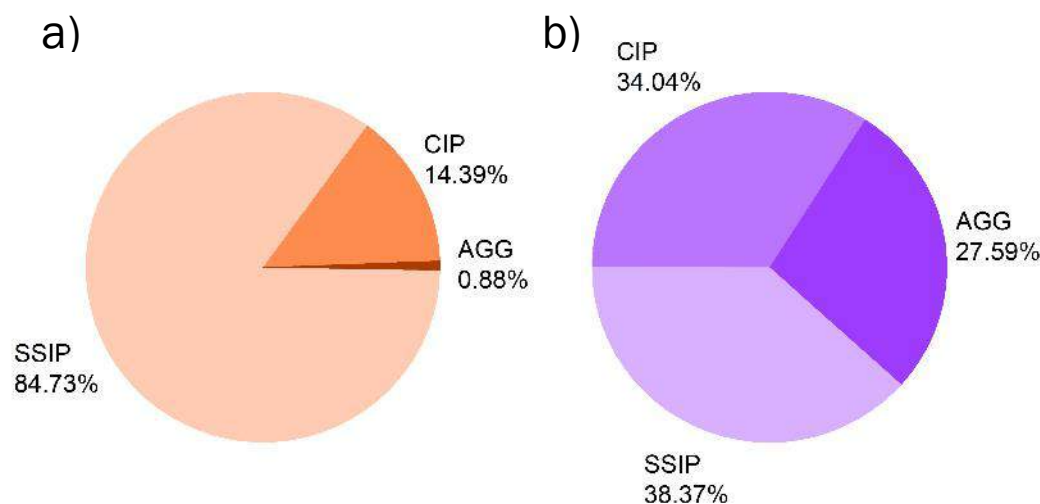


Figure II.1.B.68 The proportions for SSIP, CIP, and AGG in (a) the ECF electrolyte and (b) the GenF electrolyte

The averaged solvent coordination number for the three species in the ECF and GenF electrolyte are also analyzed. For both the ECF and GenF electrolyte, the total solvent coordination number follows a similar trend as in the EC and Gen2 electrolyte, namely that it decreases when PF_6^- coordinates with Li to form CIP and AGG. Analogously, the EC and FEC molecules are substituted by PF_6^- for both the ECF and GenF electrolyte when forming CIP and AGG, in the sense that EC and FEC have similar structures. Meanwhile, the coordination number of EMC-Li remains ~ 3 for all the species in the GenF electrolyte.

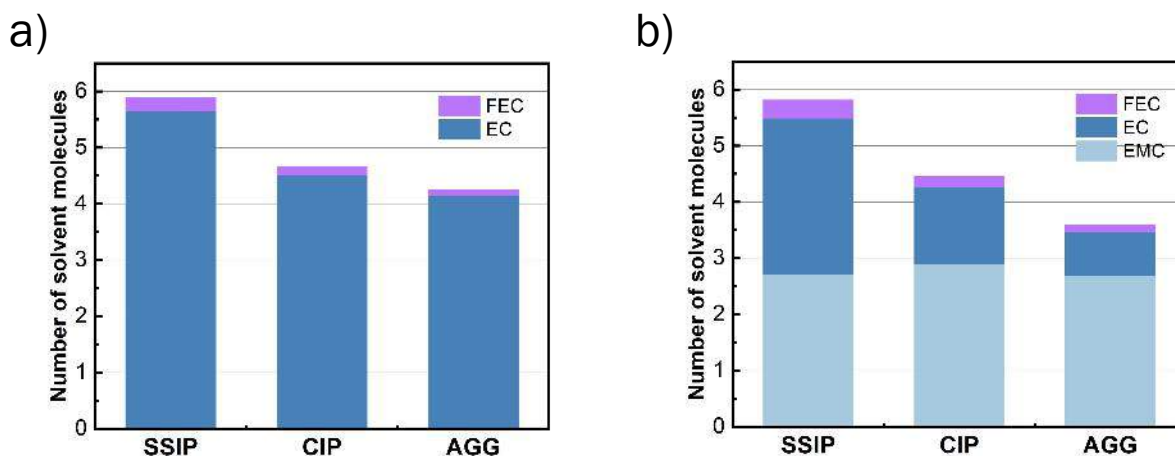


Figure II.1.B.69 The coordination number of solvent molecules for SSIP, CIP and AGG species in a) ECF electrolyte and b) GenF electrolyte

In conclusion, using a classical molecular dynamics simulation, we have found that the Gen2 electrolyte favors a much higher CIP ratio ($>30\%$) and AGG ratio ($>30\%$), while the EC electrolyte exhibits nearly 90% SSIP and 10% CIP. Hence, the EC electrolyte presents more ionic conduction carriers as compared to the Gen2 electrolyte. The EC molecule is substituted by PF_6^- for both EC and Gen2 electrolyte when forming CIP and AGG, indicating the EMC solvent forms a more stable binding with Li^+ . Further investigations will be conducted to reveal the reason why EMC is favored to coordinate, as compared to, e.g., the PF_6^- anion. One proposed method is to calculate the EMC- Li^+ and EC- Li^+ pair desolvation energy as a function of atomic

distance using density functional theory (DFT). The energy difference will be compared to the dissociation constant observed in the molecular dynamics (MD) results. Moreover, the electron density analysis will also be performed to help rationalize the energy calculation.

In Gen2 electrolyte, at least 19% out of 31% AGG species are charged species, which will contribute to the ionic conductivity. Further calculations of the conduction and transport properties of the Gen2 electrolyte will be addressed in the future. The influence of FEC additive on the solvation structure of the ECF and GenF electrolyte is also compared. It is found that FEC will participate in first solvation shell of the GenF electrolyte, as has been found in the ECF. The proportion of FEC in the solvation shell exhibits a similar changing trend as EC when Li coordinates with PF_6^- , which could be explained by their structural similarity.

New Electrolytes for Si Anodes

As noted previously, the Gen2 electrolytes are not stable. One approach to address this issue is to explore solvents and salts other than Gen2 electrolytes that could potentially demonstrate better passivating properties, specifically during early electrochemical cycles. Earlier study by the team investigating solid-electrolyte interphase (SEI) formation on amorphous silicon (a-Si) thin film indicates that polymeric ether components such as poly(ethylene oxide) (PEO) are formed during early galvanostatic cycles (GC) [1], enabling a certain degree of elasticity to buffer the volumetric change of the Si anodes. We thus hypothesize that the glyme-based system can potentially be reduced to polymeric ether-type species during the initial SEI formation, providing better passivation. Initial studies in Q3 showed that glymes have higher parasitic currents, especially during early SEI formation, as compared to their carbonate electrolyte counterpart, Gen2. However, the parasitic currents of glyme and carbonates became comparable at the fifth GC cycle. This motivates us to continue the research on the passivation behavior of the glyme electrolytes on Si at prolonged GC cycles in Q4. For this study, Gen2 and Gen2+FEC electrolytes were used as the benchmark. The 50 nm amorphous (a-Si) thin film was used as the model anode and lithium metal was used as a counter electrode.

Among all electrolytes, Gen2 exhibited the highest discharge capacity during the early GC cycling stage, as shown in Figure II.1.B.70. This agrees with data indicating that Gen2 had the lowest parasitic current for the first five GC cycles, as reported in Q3. The addition of 10 wt% FEC in Gen2 stabilized the SEI formed on a-Si, as demonstrated by the improved capacity retention (85% as compared to 31% for Gen2) during prolonged GC cycles. LiPF_6 -DME electrolyte exhibited the overall lowest capacity among all electrolytes, agreeing with its unstable parasitic current as observed in the GC-CA test in Q3. Both the LiTFSI -DME and LiFSI -DME glyme electrolytes exhibited a lower discharge capacity compared with Gen2+FEC. A fluoroether, 1,1,2,2-tetrafluoroethyl-2,2,3,3-tetrafluoropropyl ether (TTE), was further used as an additive in glyme electrolytes. While the addition of a small amount (10 wt%) of TTE didn't seem to stabilize the a-Si well (Figure II.1.B.43), a special formula of LiFSI -3DME-3TTE (the molar ratio is 1:3:3) performed best among all electrolytes, as it showed the highest specific capacity at prolonged GC cycles, with the largest capacity retention at 92%, indicative of a more robust SEI formation using this special glyme electrolyte formula.

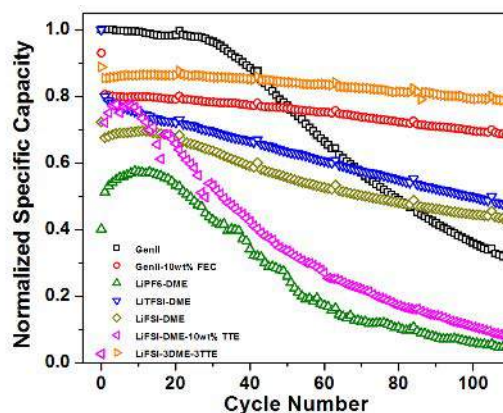


Figure II.1.B.70 Variation of normalized discharge capacity with cycle number (up to 110 cycles) of the a-Si anodes using multiple electrolytes at a 1 C equivalent current density

We further explored the surface morphology of the a-Si anodes after prolonged cycles using a scanning electron microscope (SEM). The a-Si anodes cycled in Gen2 and Gen2+FEC electrolytes exhibited crack patterns, as shown in Figure II.1.B.71. For the LiFSI-DME electrolyte, the a-Si surface was covered by a patch-like SEI layer. This may indicate the existence of an underdeveloped passivation layer on the a-Si surface. The a-Si anode cycled in LiFSI-3DME-3TTE glyme electrolyte had a much smoother and crack-free surface after 110 GC cycles, demonstrating a more conformal passivation layer formed on the a-Si surface. This agrees well with the GC cycling performance in Figure II.1.B.70, indicative of a more stable SEI formation for LiFSI-3DME-3TTE during prolonged GC cycling.

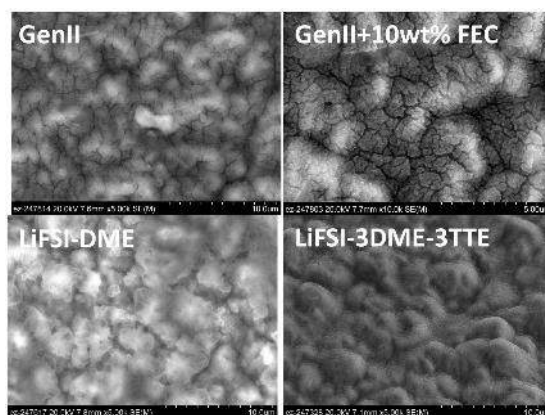


Figure II.1.B.71 SEM micrograph of the a-Si anodes after 110 cycles

The surface chemistry of the a-Si anodes during early cycles and after prolonged cycles was explored further by using energy-dispersive X-ray spectroscopy. The surface elements in the SEI layer include carbon, oxygen, fluorine, silicon, and sulphur, as shown in Figure II.1.B.72. Intriguingly, the C-O ratio is close to 2:1 for Gen2 electrolyte after 5 cycles, agreeing with that of the PEO oligomer SEI species on a-Si in an early study [1], as PEO is composed of $-\text{CH}_2-\text{CH}_2-\text{O}$ repeating units. After prolonged cycles, the C-O ratio for Gen2 and Gen2+FEC is close to 1:1. This may indicate the increased abundance of $\text{C}=\text{O}$, agreeing with evidence that carbonate electrolytes have enriched carboxylate SEI species [1]. The existence of Li_2CO_3 and lithium ethylene dicarbonate (LEDC) cannot be ruled out. In contrast, the C-O ratio for LiFSI-3DME-3TTE glyme electrolyte was increased to 1:2 after prolonged cycling, indicating enrichment of the organic PEO-like SEI species. This observation agrees fairly well with the infrared spectra of various a-Si samples GC cycled in glyme-based electrolytes, as reported in Q3. For glyme-based electrolytes, the abundance of the fluorinated species was not increased upon

adding more TTE. This indicates that the resource of the fluorinated species in the SEI layer on a-Si may stem from the decomposition of the LiFSI salt instead of the TTE additive.

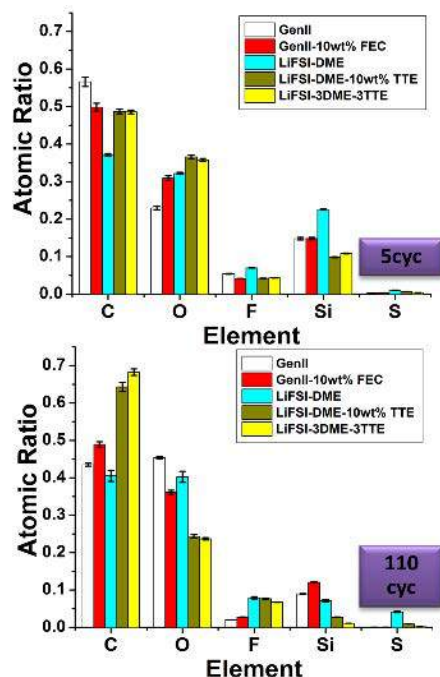


Figure II.1.B.72 Elemental analysis of the a-Si anodes after 5 cycles and after 110 cycles. Error bars indicate the standard deviations of the three measures on three different locations of each sample

Future plans for the research include elucidating and consolidating the surface chemistry of the a-Si after the short and prolonged galvanostatic cycling test using X-ray photoelectron spectroscopy (XPS). Exploring the SEI formation mechanisms following different electrolyte reaction paths in different electrolytes is another future focus. The effect of the electrolyte coordination chemistry will be evaluated for the LiFSI-3DME-3TTE using a similar method reported by Persson et al. [2]. Proton nuclear magnetic resonance (NMR) has been measured on various electrolytes after GC cycling at different stages to explore the dissolved SEI species in the electrolytes. Those data are being analyzed and will be reported in due course. In summary, we evaluate the passivation behaviour of glyme electrolytes on a-Si thin-film anodes for prolonged cycles. The galvanostatic cycling profile indicates that LiFSI-3DME-3TTE passivates the a-Si better. The energy-dispersive X-ray (EDX) elemental analysis on a-Si anodes indicate that the GenII electrolyte passivation results in formation of enriched carbonated species such as lithium carboxylate, Li_2CO_3 , and LEDC-rich SEI. In contrast, using glyme-based electrolytes leads to the formation of the PEO-like SEI on the a-Si surface.

In situ Understanding of the Growth and Evolution of the SEI on Model Electrodes

Synthesis of Reference Compounds

Through the course of this work the team has identified the formation of lithium ethylene dicarbonate as an SEI formation product that forms upon lithiation on the Si anode but dissolves into the electrolyte upon cycling. This work is to synthesize the known SEI components such as lithium methyl carbonate (LMC) and lithium ethylene dicarbonate (LEDC), and to characterize their possible roles in the SEI formation process. Specifically, they will be used as additives in the next section (“Design of New Si Surfaces Based on Experimentally Validated Stable Chemical Moieties”) and as additives to the electrolyte to drive saturation.

Synthesis of Lithium Methyl Carbonate (LMC)

Approach 1: Lithium methoxide (0.75 g, 20 mmol) and dry methanol (20 mL) were added to an oven-dried Schlenk flask under argon. Excess amount of analytical grade carbon dioxide (CO₂) was then introduced to the solution. The mixture was stirred at room temperature for 24 h, concentrated, and dried in vacuum to give LMC as a white solid (yield: 1.6 g, 97%). The Fourier-transform infrared spectroscopy (FTIR) data matched those reported results, as seen in Figure II.1.B.74 [3]. The synthesis is summarized in Figure II.1.B.73.

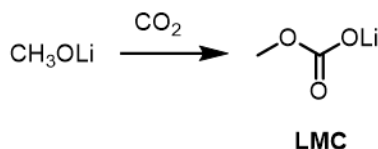


Figure II.1.B.73 Synthesis of LMC

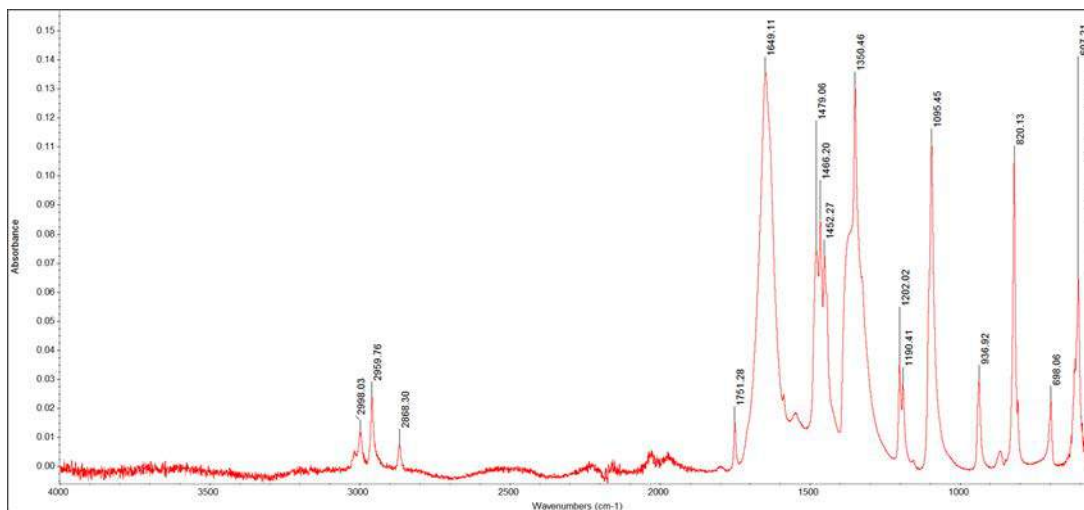


Figure II.1.B.74 FTIR data collected for LMC

Approach 2: Lithium iodide (0.27 g, 2.0 mmol) and dry dimethyl carbonate (10 mL) were added to a scintillation vial under argon. The mixture was stirred at room temperature for 24 h, filtered, washed with diethyl ether, and dried in vacuum to give LMC as a light yellow solid (yield: 0.048 g, 29%). The characterization data matched those reported for this compound [4]. The synthesis is summarized in Figure II.1.B.75. However, the yield of this method is very low, and the product might have some iodine contamination.

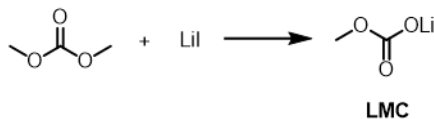


Figure II.1.B.75 Synthesis of LMC

Synthesis of Lithium Ethylene Dicarboxylate (LEDC)

LEDC was synthesized following the procedure in Figure II.1.B.76. Dry diethyl ether (40 mL) and *n*-butyllithium (1.6 M in hexane, 10 mL) were added to an oven-dried three-neck flask under argon. Ethylene glycol (0.49 g, 7.9 mmol) was then added slowly. The mixture was stirred for 2 h before excess amount of analytical grade CO₂ was introduced. The resulting suspension was then stirred for 1 week under CO₂. The precipitates were filtered, washed with acetonitrile, and dried to give a white solid (yield: 0.63 g, 49%). The characterization data matched those reported for this compound [5]. Resulting FTIR data are shown in Figure

II.1.B.77. However, a recent paper claims that lithium ethylene monocarbonate (LEMC) was formed instead of LEDC when using this method [6].

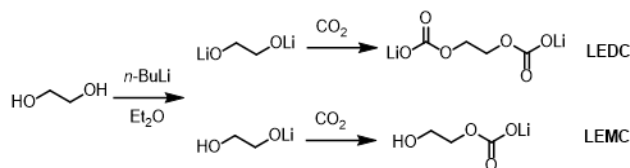


Figure II.1.B.76 Synthesis of LEDC

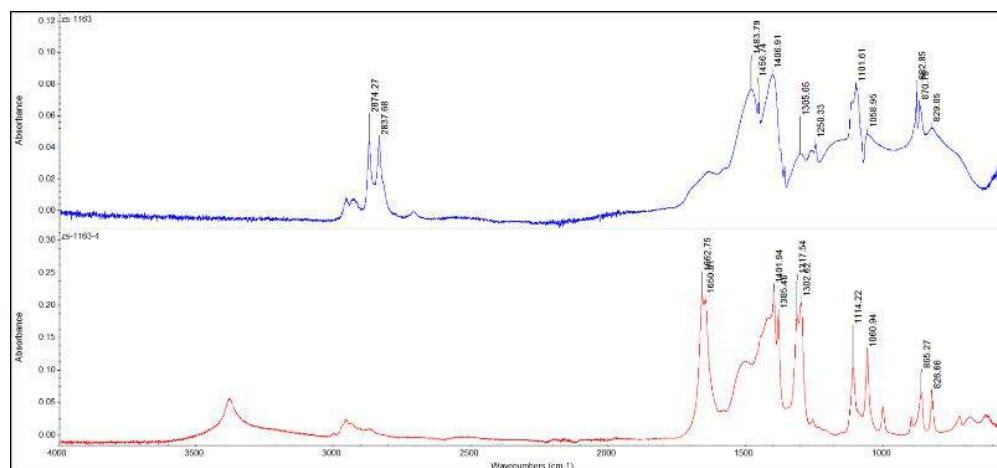


Figure II.1.B.77 FTIR spectra of the synthesized LEDC, stirred under CO_2 for 1 day (blue curve) and 7 days (red curve)

It should be noted that NMR spectra are not very useful determining the structures, as most of the compounds are not very soluble and are sensitive to water. Trace amounts of water can lead to hydrolysis of the limited amount of compounds dissolved in NMR solutions, which may lead to confusing chemical shift results. These data are presented in Figure II.1.B.78.

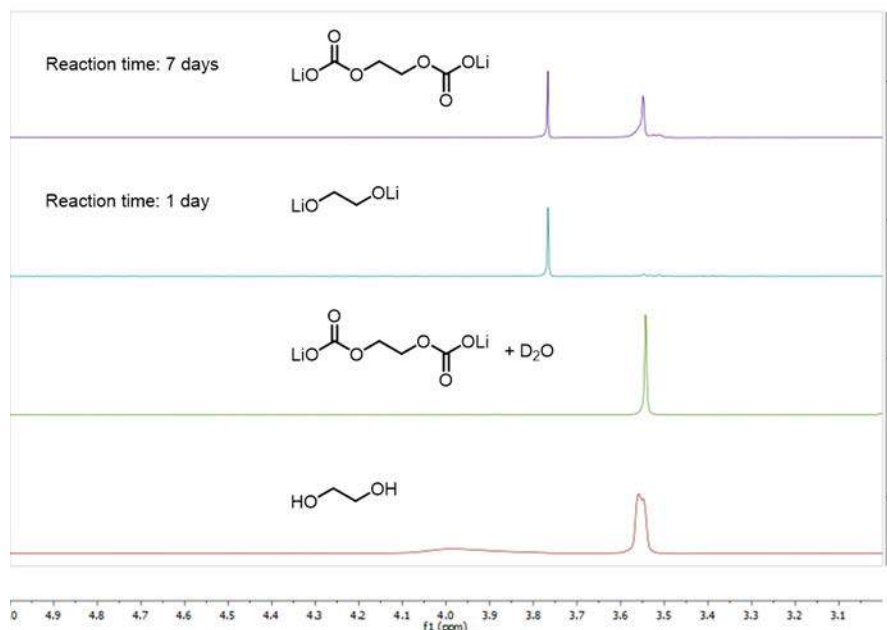


Figure II.1.B.78 NMR spectra of LEDC compounds under various conditions

Operando ATR-FTIR Spectroscopy

We have continued our development of the operando attenuated total reflectance-Fourier transform infrared (ATR-FTIR) spectroelectrochemical characterization instrument begun in FY18. Prior work in this area by Phil Ross and coworkers [7], [8] showed that the components of the SEI vary significantly as a function of applied voltage. In that work, electrolyte composed of 1.0 M LiPF_6 in EC:DEC (1:2, v/v) was used in conjunction with native oxide (SiO_x)-covered Si wafer. At 1.3 V, electrolyte reduction (DEC) to diethyl 2,5-dioxahexane dicarboxylate (DEDOHC) was found, whereas at 5 mV, selective electrolyte reduction (EC) to lithium ethylene dicarbonate (LiEDC) occurred [9]. Cycling data showed an SEI composed primarily of DEDOHC. Our goal is to extend this study of SEI dissolution and growth using other model samples (H-terminated Si, native SiO_x -terminated, and molecularly functionalized Si wafers) and eventually extend this to three-dimensional Si NP-based electrodes assembled on the Si wafer substrate.

Our new setup provides significant distinguishing features relative to that of Ross and coworkers, who used several milliliters of electrolyte in their operando experiments. Since it is well known that SEI dissolution and growth is strongly dependent on the electrolyte volume, we designed our ATR-FTIR cell to be effectively that of a coin cell, where a Celgard separator is placed directly on top of the double-polished Si wafer. The Si wafer in this configuration doubles as the ATR crystal *and* the working electrode. A Li metal foil counter electrode is placed on top of the Celgard separator, followed by a stainless-steel plate and rod. The stainless-steel plate and rod apply pressure to the electrode assembly to more closely mimic that of a coin cell battery, as well as to minimize the air gap between the ZnSe ATR prism and the double-polished Si wafer.

Using this new “coin cell ATR-FTIR” configuration, in Q1FY19 we discovered that our cycling data had a significant voltage offset due to poor contact to the Si wafer substrate. We estimate that a 1–2 k Ω resistor owing to this bad contact can account for the ~300 mV offset observed in the voltage profiles for our current density and galvanostatic cycling data (Figure II.1.B.79).

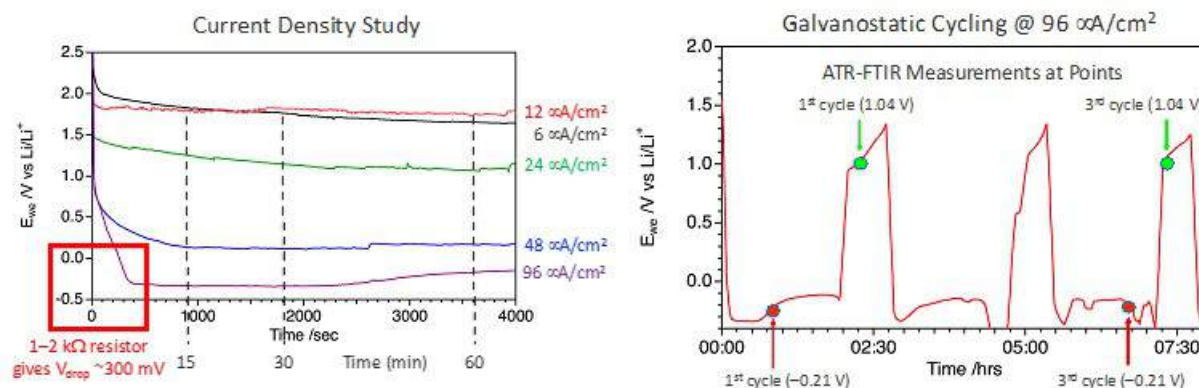


Figure II.1.B.79 Left: Current density study for 5–10 $\Omega \cdot \text{cm}$ resistivity Si wafers in the ATR-FTIR spectroelectrochemical cell. A voltage drop of ~300 mV is caused by poor contact to the Si wafer. Right: Cycling behavior of the same cell indicating points where ATR-FTIR spectra were collected (see Figure II.1.B.74 for ATR-FTIR data)

In Q2FY19 we conducted a further analysis of the 2017 paper by Ross and coworkers describing related experiments [2]. We found that a 5 $\Omega \cdot \text{cm}$ Si wafer (same doping density as in the 2017 work) results in a large potential drop due to the resistivity of the wafer. When applying sufficiently negative potentials to drive lithiation in the hundreds of $\mu\text{A}/\text{cm}^2$ range (as seen in the cyclic voltammograms in that paper [9] and Figure II.1.B.80) and a measured resistivity of ~1 k Ω from the contact to the wafer center (where the IR beam is incident), Ohm's Law tells us to expect a voltage drop of several hundred mV. This is exactly what is observed experimentally in our system, as shown in Figure II.1.B.80.

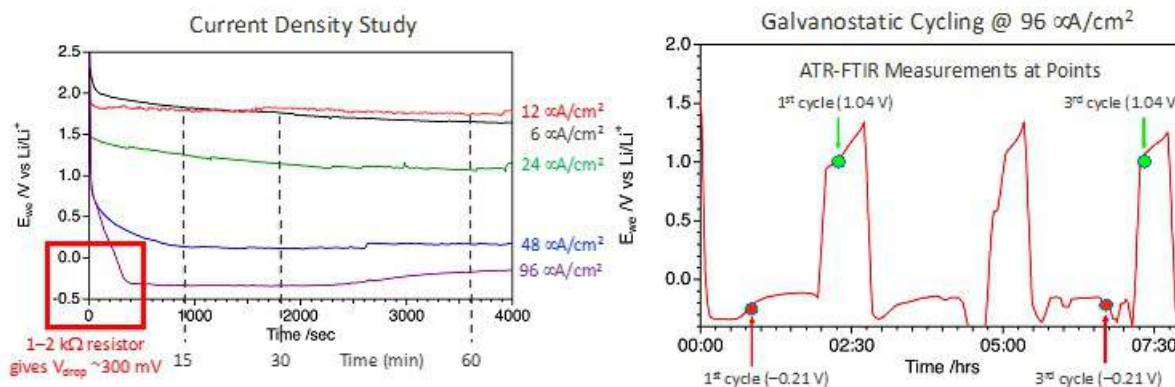


Figure II.1.B.80 Left: Current density study for 5–10 $\Omega \cdot \text{cm}$ resistivity Si wafers in the ATR-FTIR spectroelectrochemical cell. A voltage drop of ~ 300 mV is caused by the resistivity of the low doping density Si wafer. Right: Cycling behavior of the same cell indicating points where ATR-FTIR spectra were collected (see Figure II.1.B.74 for ATR-FTIR data)

Thus, we worked with our silicon photovoltaic (PV) experts to develop a protocol to selectively surface-dope the crystalline Si wafer. This provided the necessary IR transparency required to collect ATR-FTIR spectra while also allowing excellent electrochemical behavior. Figure II.1.B.81 displays representative cycling data from 1.5 to 0.01 V, demonstrating the high-quality electrochemical response provided by our critical FY19 breakthrough—the surface p^+ -doped Si wafer. These data also demonstrate that substantial current is passed prior to the crystalline Si lithiation potential (~ 115 mV), indicative of SEI growth.

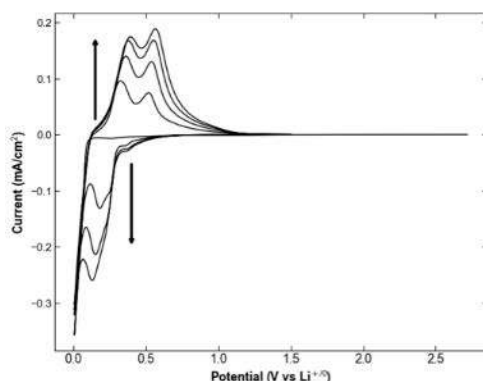


Figure II.1.B.81 Cyclic voltammograms for heavily surfaced p^+ -doped Si wafers (bulk resistivity 5–10 $\Omega \cdot \text{cm}$) in the ATR-FTIR spectroelectrochemical cell. These surface-doped wafers feature an ~ 100 nm-deep surface p^+ layer (doping density 10^{19} – 10^{20} cm^{-3}), resulting in a highly conductive working electrode (<1 $\text{m}\Omega \cdot \text{cm}$)

Our initial experiments directly targeted the SEISta FY19 Milestones by conducting potentiostatic holds at a range of potentials (open-circuit voltage, 1.0 V, 0.7 V, 0.4 V, 0.15 V, 0.1 V vs. $\text{Li}^{+/0}$) on native SiO_x -terminated p^+ -Si wafers. We found that at 0.1 V vs. Li^+/Li , lithiation of the Si wafer anode quickly eliminates its reflective nature and the ATR-FTIR signal is lost. Given that cyclic voltammograms of SiO_x -terminated Si wafers show minimal current is passed at potentials higher than 0.5 V vs. Li^+/Li (Figure II.1.B.82, left), we focused on the low potential regions of 400 and 150 mV vs. Li^+/Li for all comparative studies. Initial experiments in Q3FY19 were conducted on wafer silicon terminated with native oxide (SiO_x) by collecting in situ FTIR spectra during potentiostatic holds at early SEI growth potentials (400 and 150 mV vs. Li/Li^+), and in Q4FY19 we performed the same experiments on hydrogen-terminated silicon surfaces (SiH). Accordingly, this allowed us to discern the effects of surface termination on the near-surface electrolyte composition as a function of early-stage SEI growth.

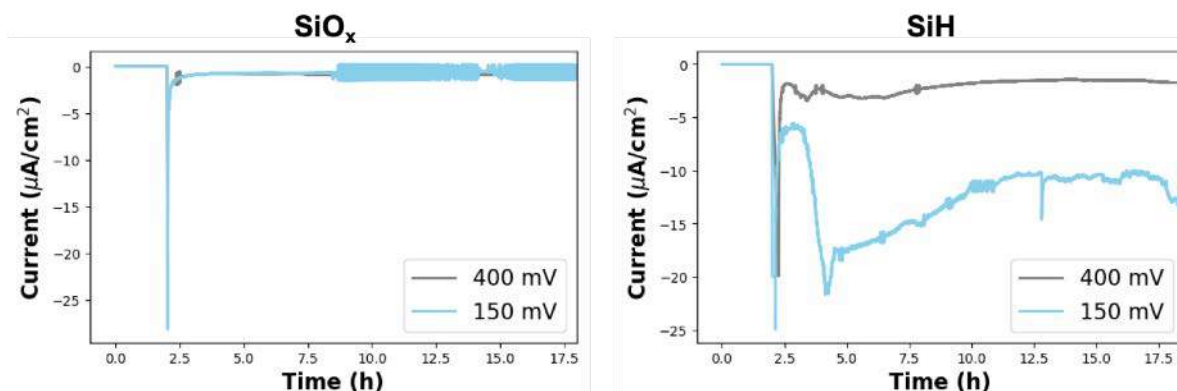


Figure II.1.B.82 Chronoamperograms of silicon wafers with native oxide (left, SiO_x) and hydrogen terminated (right, SiH) at 400 and 150 mV vs. Li/Li^+ (gray and blue, respectively). The wafers used in this experiment feature a highly p^+ -doped surface layer (doping density = 10^{19} – 10^{20} cm^{-3}) to allow for high conductivity and IR transparency. The chronoamperograms show the greater reactivity of the SiH samples compared to SiO_x .

Comparing the chronoamperograms for SiO_x - and H-terminated Si wafers shows that the SiH surface is far more reactive (shown in Figure II.1.B.82), consistent with our prior chemical reactivity studies. For the SiO_x -terminated wafers (Figure II.1.B.82, left), the current quickly decays to $-1 \mu\text{A}/\text{cm}^2$ in the first 30 min for both 400 and 150 mV vs. Li/Li^+ . In stark contrast, the SiH -terminated surfaces (Figure II.1.B.82, right) show larger currents over the entire 18 h in each experiment, signaling a much greater reactivity. The current of the SiH sample held at 400 mV vs. Li/Li^+ decays to $-2.5 \mu\text{A}/\text{cm}^2$ in the first 30 min of the potentiostatic hold, then decreased over the 18 h. At lower potentials (150 mV vs. Li/Li^+), the SiH sample exhibits a strikingly different current profile. In the first 30 min, the current density reaches $-8 \mu\text{A}/\text{cm}^2$, but instead of decaying gradually, as occurs at 400 mV, the current instead *increases* before decreasing and reaching a steady-state current of approximately $-14 \mu\text{A}/\text{cm}^2$. The results highlight the greater reactivity and slower passivation of the etched SiH surface relative to the SiO_x -terminated surface, and further confirms the major FY19 SEISa project conclusion that both SiH and SiO_x are bad actors in Si anode SEI stability.

Finally, in Q3 we determined that the in situ ATR-FTIR experiment in its present configuration is probing near-surface changes to the electrolyte, *not* the SEI itself. In Figure II.1.B.83 we show ATR-FTIR spectra of the C=O stretching region of the SiH samples corresponding to the potentiostatic holds depicted in Figure II.1.B.82. We highlight the C=O region as it contains signatures of the carbonates in the electrolyte where significant changes are observed. These data show that uncoordinated EMC is preferentially lost (as compared to coordinated EMC or uncoordinated/coordinated EC) in the near-surface electrolyte region. It is unclear whether this is due to direct decomposition of uncoordinated EMC or the result of Li^+ -coordinated EMC and subsequent equilibration (where uncoordinated EMC replaces lost Li^+ -coordinated EMC due to Le Chatlier's principle). Further, in the 150 mV vs. Li/Li^+ sample we observe an *increase* in the Li^+ -coordinated EC peak, which may be the result of a similar equilibrium process. This exciting result reveals the components of the Gen2 electrolyte that contribute to early-stage SEI growth, where it is clear that EMC is more reactive with the silicon surface and likely is a greater constituent of the early-stage SEI than EC. Future work will add additional components to this experimental configuration: (1) we will attempt to develop a similar experiment on a three-dimensional electrode composed of Si nanocrystals (NCs), thereby increasing signal to noise of the SEI relative to the background electrolyte signal; and (2) introduce additives to the electrolyte (FEC, MgTFSI, etc.) to explore how these species modify the electrolyte decomposition reactions resulting in the early-stage SEI.

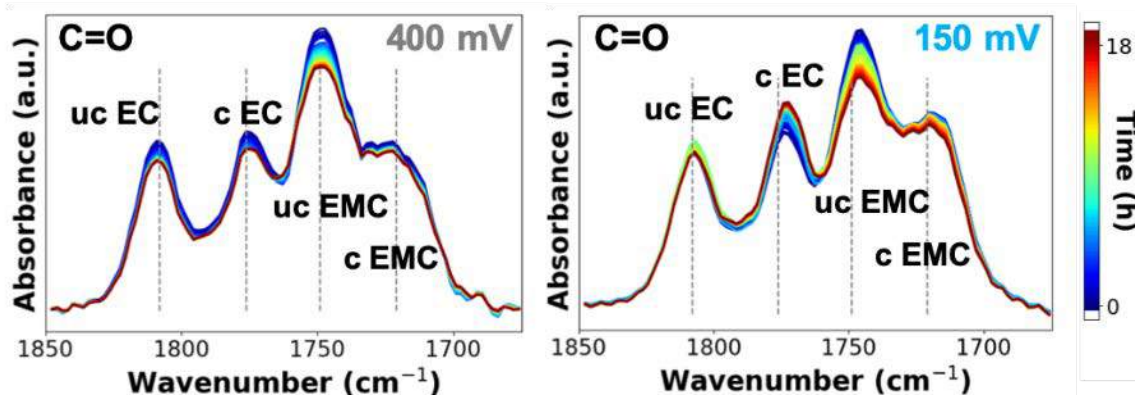


Figure II.1.B.83 Carbonyl region of FTIR spectra corresponding to the chronoamperograms shown in Figure II.1.B.82, showing loss of uncoordinated (uc) EMC relative to other electrolyte components during the 18-hour potentiostatic holds

Electrolyte Characterization via In situ Raman

Raman spectroscopy is a powerful tool for studying both electrodes and electrode-electrolyte interphase (EEI), as it provides both structural and chemical information. In addition, it is a nondestructive analysis and can characterize many types of samples including an amorphous thin film [9],[10]. In this study, we report an in situ surface-enhanced Raman spectroscopy (SERS) technique with a modified cell configuration, which enabled us to successfully monitor the reversible electrochemical behavior of the Si anode and newly formed alkyl carboxylates (R-COO^-), possibly resulting from electrolyte decomposition within the silicon-electrolyte interphase (SiEI).

Reference Spectra and Peak Assignment

To aid our analysis of the in situ Raman measurements, we first constructed a reference library of Raman spectra for components of the Gen2 electrolyte—1.2 M lithium hexafluorophosphate (LiPF_6) in ethylene carbonate (EC):ethyl methyl carbonate (EMC) (3:7 wt%),—used in this study. Detailed peak assignments for the electrolyte components and their coordination with Li^+ cations in a standard Gen2 electrolyte are presented in Table II.1.B.5.

Electrochemical Performance and Corresponding SERS Spectra

The in situ electrochemical cell (ECC-Opto-Std, EL-Cell GmbH) was assembled with a Si working electrode (amorphous Si (a-Si) thin film deposited on a Cu substrate) and a Li metal foil as counter/reference electrodes in a coin-type cell configuration. The cell was then filled with a Gen2 electrolyte. After two hours of rest (for enough wetting of Si electrodes with the electrolyte) at the open-circuit voltage (OCV), the cell was cycled galvanostatically at the current of $15 \mu\text{A}$ in the voltage range of 0.01–1.5 V (vs. Li/Li^+ , hereafter). During cycling, Raman spectra were collected at specific voltages (based on previous voltage profile studies) using a Raman microscope equipped with a 632.8-nm He-Ne laser. The results of electrochemical cycling profiles (the 1st and 2nd cycles) and corresponding Raman spectra are presented in Figure II.1.B.84 (b).

Table II.1.B.5 Raman Peak Assignments

Raman Band Center (cm ⁻¹)	Assignment	Species of Origin	Reference(s)
380		EMC	this work
401		EMC	this work
513		EMC	this work
530		EMC	this work
716	o, O-C-O	EC	[11,12]
729	o, O-C-O	EC...Li ⁺	[11,12]
741	u, P-F	PF ₆ ⁻	[11,13]
838		EMC	this work
877		EMC	this work
892	β, C-C	EC	[11,12]
904		EC...Li ⁺	[3]
932	δ, O-C-O	EMC	[5], this work
938	δ, O-C-O	EMC...Li ⁺	[5], this work
973	u, C-C	EC	[2,3]
1008		EMC	this work
1070	u, C-C	EC	[2], this work
1092		EMC	this work
1116		EMC	this work
1164		EMC	this work
1201		EMC	this work
1225	τ, CH ₂	EC	[2], this work
1275		EMC	this work
1304		EMC	this work
1455		EMC	this work
1483	δ, CH ₃	EC	[2]
1748	u, C=O	EMC	[5], this work
1771	u, C=O	EC	[2]
1795		EC...Li ⁺	this work
1802	u, C=O	EC	[2]
u = stretching; δ = bending; o = ring breathing; β = ring deformation; τ = twisting			

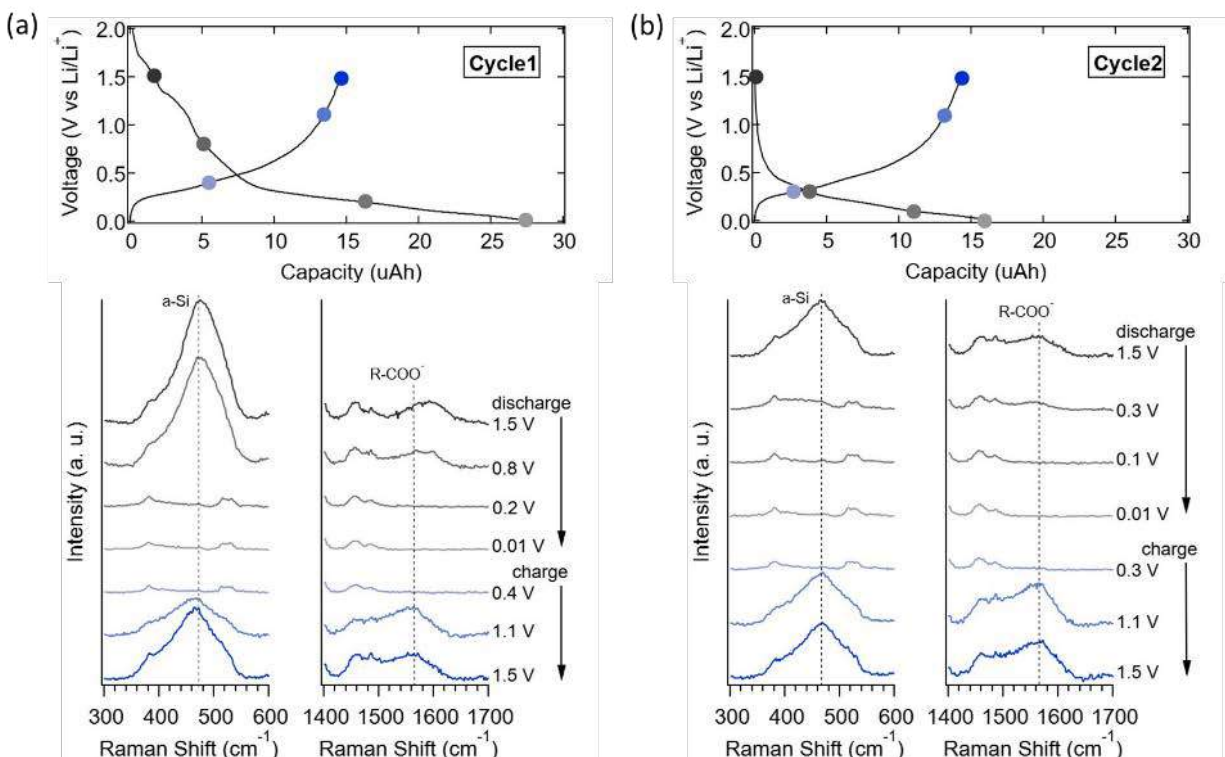


Figure II.1.B.84 Galvanostatic cycling voltage profiles and corresponding in situ Raman spectra collected at specific voltages: (a) the 1st cycle and (b) the 2nd cycle. The spectra were obtained with a 632.8-nm He-Ne laser, and all spectra were baseline corrected

The electrochemical behavior of the Si thin-film electrode agrees well with the reported literature [6], where the lithiation starts at around 0.3 V and continues until the assigned cutoff voltage (0.01 V). In addition, a significant amount of irreversible capacity loss is observed after the first delithiation, primarily due to the electrolyte reduction and subsequent SiEI formation. In the second cycle, the irreversible capacity loss is much less compared to that of the first cycle, likely due to the formation of SiEI in the first cycle, which prevents further electrolyte reduction.

In situ SERS spectra collected during the first and second cycles exhibit reversible peak intensity changes upon lithiation and delithiation. Specifically, the strong a-Si peak observed at 470 cm^{-1} prior to the lithiation disappears as the Si is lithiated (at 0.2 V) and reappears after the Si is delithiated (at 1.1 V). The same reversible behavior is observed in the second cycle. Another interesting feature is a new peak at 1,565 cm^{-1} , which evolves during the galvanostatic cycling. This 1,565 cm^{-1} peak first appears at around 0.8 V, which corresponds to the electrolyte reduction voltage [14],[15], and the peak intensity change synchronizes with that of the a-Si peak upon cycling. This peak at 1,565 cm^{-1} is assigned to the asymmetric COO^- stretching mode [9]. Additionally, according to the previous in situ FT-IR study by Shi et al., this peak is likely from lithium propionate [8]. To find additional new peaks possibly attributed to decomposed species of reduced electrolytes and/or formed SiEI components, we tried additional cycling (up to 10 cycles) and lowering the applied current ($I = 7.5 \mu\text{A}$) to increase the probability of electrolyte reduction and SiEI formation reactions. No additional new peaks, however, were observed during 10 cycles, and in situ SERS spectra with a lower current demonstrated almost the same spectral features as before. One possible explanation for limited peak detection is that it is challenging to collect Raman signal from decomposed species and/or formed SiEI components due to relatively too-strong Raman signal from both Si anode and electrolyte components. Furthermore, many of the SiEI species are soluble in the electrolyte, so they may go into solution and move away from our Raman measurement excitation volume [10],[11].

We successfully developed a novel spectroscopic technique for in situ studies of the electrode-electrolyte interphase (EEI). In situ measurements show the reversible changes in the a-Si peak intensity upon lithiation and delithiation. Moreover, alkyl carboxylate species were detected as a significant SEI component that possibly incorporated into the Si electrode surface during cycling. Our experimental setup showed a reproducible and reliable electrochemical and spectroscopic performance over multiple cycles. This method thus provides valuable information regarding the surface chemistry changes and evolution of the SEI, which can be useful for detailed understanding (and stabilization) of the SEI layer for the development of next-generation lithium-ion batteries. Finally, we emphasize that this technique is applicable to other battery systems and the EEI contained within.

In situ Evaluation of the SEI in the Presence of a Binder

Binders, particularly polyvinylidene fluoride (PVDF), are an industry standard used in composite electrodes to bind active materials and additives such as C black to the metal current collector and to promote particle-to-particle cohesion. Though the final architecture of the binder matrix is not fully understood, there are interactions between the surface of the Si and the binder. This leads to the question of how the addition of an insulating polymeric binder, added to mitigate the effect of Si expansion in composite slurries, affects the SEI formation.

We know the binder has a role in the electrochemistry regardless of the anode [16],[17]. For example, the commonly used binder PVDF doesn't work in silicon-based chemistries, but the use of polyacrylic acid (PAA) does [18],[19],[20]. PAA is composed of carboxyl groups that form a covalent bond to the hydroxyl groups present on the Si surface due to the native oxide layer [19]. Very little is known about how PAA or any other binder affects the composition and formation of the SEI. For instance, how does the insulating nature of the PAA change or alter Li conduction pathways? Or, if the Si nanoparticle is completely coated by PAA, how does the electrolyte interact with the active material? Lastly, does the SEI form on the surface of the polymer or the surface of the Si?

In addition to materials like PAA there has also been interest in electronically conductive binders in order to eliminate the need for conductive additives such as C black. One such example is Poly(2,7-9,9-dioctylfluorene-co-2,7-9,9-(di(oxy-2,5,8-trioxadecane))fluorene-co-2,7-fluorenone-co-2,5-1-methylbenzoate ester) (PEFM), which was designed to incorporate different functional groups to create an n-type conductive polymer modified to uptake electrolyte and maintain mechanical stability [21]. Similar questions exist as to how this material works and what functionality could be utilized to develop designer interfaces.

To answer these questions, we applied spin coating to prepare model electrodes with well-defined binder layers and probed their chemistry using neutron reflectometry. The absence of charge of a neutron gives rise to a deeply penetrating particle, allowing for their use as a probe to study materials in complex environments. Because of their wavelike nature they can be reflected and/or refracted off of surfaces, separating materials of different indices of refraction in a way analogous to electromagnetic radiation—that is, neutrons obey Snell's Law. This gives rise to a neutron-scattering technique sensitive to surfaces and interfaces known as neutron reflectometry (NR). Reflectometry is an elastic scattering technique, i.e., there is no energy exchange when neutrons or x-rays interact with matter. In the case of neutrons, unlike electromagnetic radiation, the indices of refraction of most materials is less than one. As a result of neutron interaction with the nucleus as opposed to the electrons, the technique is not limited by Z number. This is of particular importance in materials for energy storage due to the presence of Li and H. In addition, neutrons are sensitive to isotopes, which can be exploited to allow for contrast variation within a single experiment.

The specular reflection of neutrons off different layers of a material results in the wave vector transfer (Q) described by the following term:

$$Q = k_{f,z} - k_{i,z} = \frac{4\pi}{\lambda} \sin \vartheta$$

Equation 1. Wave vector transfer

where θ is the angle of incidence and λ the neutron wavelength. Probed length scales range from 1–500 nm with sub-nm resolution. Reflectivity (R) is a measure of the ratio of reflected neutrons to those that fall incident on the surface. Data collection results in a plot of R vs. Q . Through a fitting routine, the thickness, roughness, and/or diffuseness of the layers is determined. However, the most important parameter determined is the scattering length density (SLD), which gives information on the composition of the measured layer as defined by:

$$SLD = \beta = \frac{\rho N}{M} \sum_i b_i$$

Equation 2. Scattering length density

where ρ is the materials density, N is Avogadro's number, M is the molar mass, and b_i is the scattering length of each individual scatter within the molecular volume. Modeled data results in an SLD plot, a one-dimensional representation of the heterostructures of the system separated by the interfacial roughness between the layers. Figure II.1.B.85 shows a schematic representation of the cell and electrode configuration used for these experiments, along with an image of the cell on the beam line.

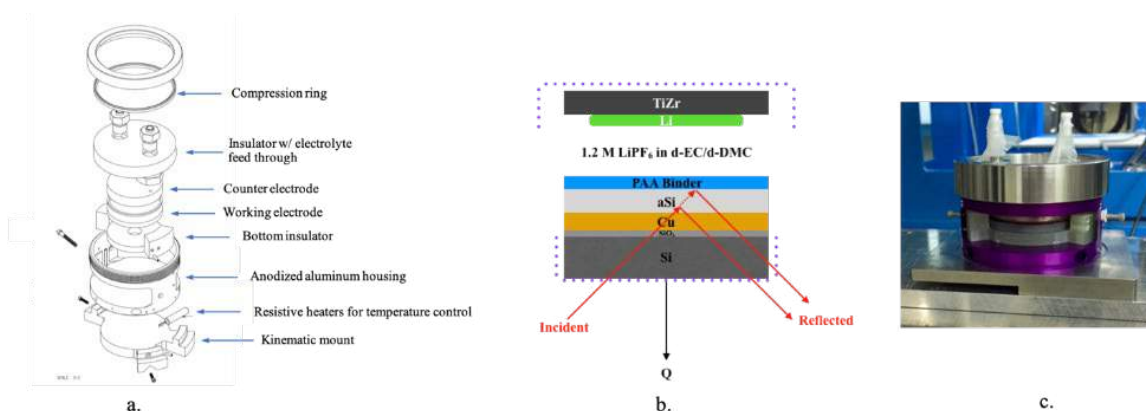


Figure II.1.B.85 Schematic (a), scattering orientation (b), and photo (c) of the in situ electrochemical cell

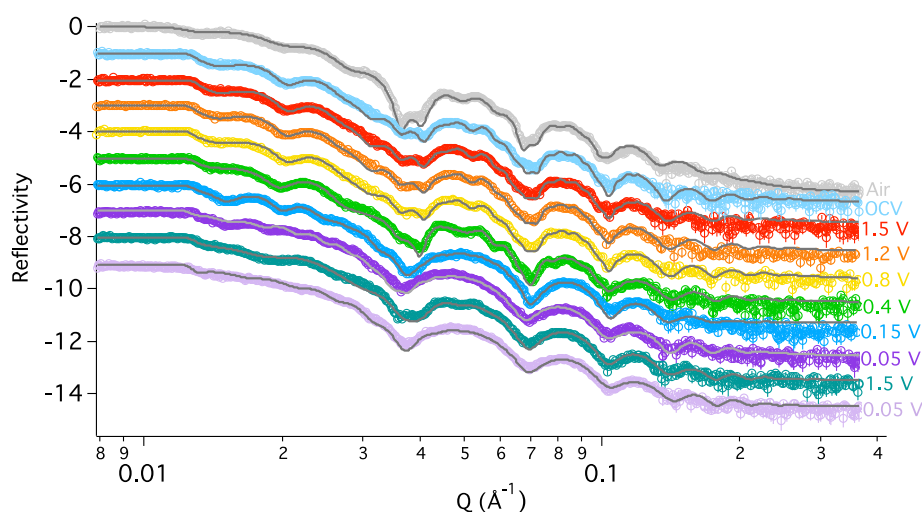
Interfacial Chemistry of PAA Binders on Amorphous Silicon

The processing conditions for the PAA layer are crucial to the cyclability of the anode. The first attempts at electrode fabrication utilized a 5 wt% solution of $M_w=450,000$ PAA, spin cast, and dried at 200°C for various amounts of time. At 200°C the PAA crosslinks and forms an anhydride [22], resulting in the PAA layer being impermeable and preventing lithiation of the a-Si (Figure II.1.B.86. ***This suggest that when casting anodes from composite slurries, the polymer binder does not fully coat Si nanoparticles' surfaces as this would prevent any cycling.*** In order to introduce the polymer to a thin-film architecture that allowed for cycling, we evaluated different processing conditions. After trying different molecular weights and drying temperatures it was determined a $M_w=1,800$ PAA dried at 140°C prevented crosslinking and enabled anode lithiation.

Figure II.1.B.86 shows the reflectivity data collected for these samples as a function of the cell potential versus $\text{Li}^{0/+}$. Figure II.1.B.87 shows the scattering length density profile measured from the fits of the reflectivity data. We constrained the parameter space for fitting the NR data by measuring the as-prepared heterostructures of the vapor-deposited layers in air. The Cu and a-Si layer thicknesses were determined to be $17.0 \text{ nm} \pm 0.01 \text{ nm}$

and $58.80 \text{ nm} \pm 0.04 \text{ nm}$, with an SLD of 6.58 ± 0.01 and 1.76 ± 0.02 , respectively (the SLD unit $\times 10^{-6} \text{ \AA}^{-2}$ will be kept off for simplicity). These values agree with uniform dense layers of Cu and H incorporating into the a-Si layer (presumably during the sputtering process). It is important to note that the SLD is a summation of each of the individual scatterers within a layer. As such, the incorporation of an element with a large scattering cross-section, such as C (6.6 fm), D (6.6 fm), P (5.13 fm), and/or F (5.7 fm) will increase the overall SLD as a result of these elements' large neutron cross-sections. Likewise, in the case of Li or H incorporation (-1.90 and -3.7 fm, respectively), a decrease in the SLD would be expected. In order to prevent water contamination, the PAA-coated sample was placed directly into the glovebox while still hot from drying. To determine the thickness and the SLD of the spin-cast PAA, witness samples were made using the same spin-coating and drying procedures directly onto the single-crystal Si substrate, which were promptly measured by NR. The PAA thickness averaged around 30 nm with an SLD of 1.8, which is slightly lower than the theoretical SLD of PAA of about 1.96, assuming a density of $1.41 \text{ g}\cdot\text{cm}^{-3}$. The SLD of the Si substrate was 2.07 and had a thin oxide layer with an SLD of 3.5, which provided contrast to the PAA layer.

Figure II.1.B.86 Neutron reflectivity curves (open circles) and fits (grey line) for PAA on a-Si thin film anode at different



states of charge (curves offset for clarity)

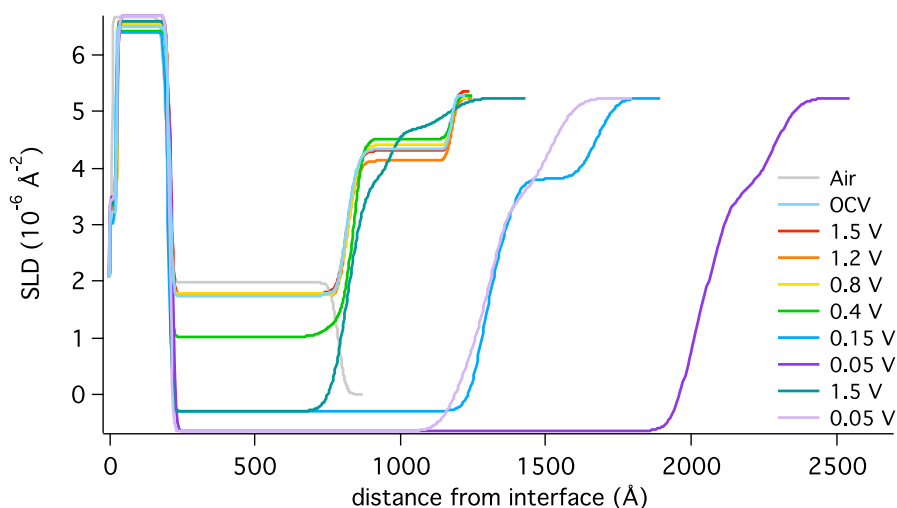


Figure II.1.B.87 The resulting SLD plots from reflectivity fitting routine representing a one-dimensional view of the film heterostructures separated by interfacial roughness

Upon cycling there are no significant changes within the system at 1.5 V, as expected. No change is evident in the PAA layer. The a-Si layer remains at $56.54 \text{ nm} \pm 0.15 \text{ nm}$ with an SLD of 1.79 ± 0.03 . At 1.2 V minimal changes were observed in the NR data, and all layers' thicknesses and SLDs remain unchanged statistically. Figure II.1.B.88 highlights the stability within the three layers, in both the SLDs and thicknesses, up to 0.8 V. Typically, at potentials more negative than 1.2 V, electrolyte reduction and SEI formation occurs [23]. This was not seen in the NR at 0.8 V; in fact, the calculated scattering profile remains unchanged.

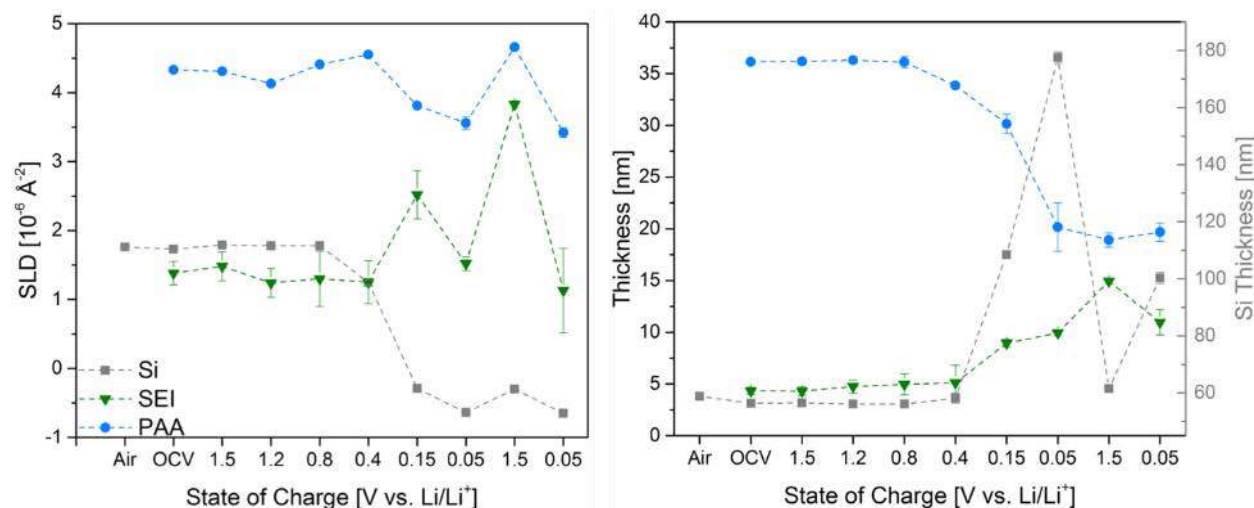


Figure II.1.B.88 A summary of the SLD (left) and thickness (right) values obtained from NR refinements

At 0.4 V the PAA layer thins down to 33.9 nm while maintaining its SLD at 4.55 ± 0.02 . There is a 2-nm increase in the a-Si layer (56 to $58.2 \text{ nm} \pm 1.8 \text{ nm}$) with a decrease in the SLD from 1.76 to 1.25 ± 0.04 (Figure II.1.B.88), indicating the beginning of lithiation of the sample, as Li is a negative scatterer. However, NR implies little lithiation from thickness changes, but electrochemically the Li to Si ratio is estimated to be $\text{Li}_{0.2}\text{Si}$. At 0.15 V the NR profile drastically changes. Here, fringes between 0.04 Å^{-1} and 0.1 Å^{-1} are smoothed (Figure II.1.B.89, dark blue), indicating changes in layer thicknesses and compositions. The a-Si layer swells to $108.4 \text{ nm} \pm 0.51 \text{ nm}$ with an SLD of -0.29 ± 0.04 , suggesting composition of $\text{Li}_{1.6}\text{Si}$ for the a-Si layer from the refined NR data. Assuming 100% Faradaic efficiency, the electrochemically derived composition is around $\text{Li}_{2.3}\text{Si}$. SEI is most likely being consumed to form the SEI layer. The oxide layer on the surface of the electrode increases in SLD from ~ 1.3 to 2.52 ± 0.35 . The increase in the SLD suggests a heavier scatter such as C, D, O, F, or P incorporating into the oxide film, as opposed to Li. *These components are all from the electrolyte, suggesting electrolyte decomposition products in the oxide layer, resulting in the formation of the SEI.* The PAA layer at the electrolyte interface continued to thin, settling at $33 \text{ nm} \pm 0.1 \text{ nm}$ from 36 nm , and decreasing in SLD from 4.3 to 3.81 ± 0.04 . Due to the polarization of the cell at 0.15 V, a significant amount of Li is being diffused into the Si and the lowering of the PAA SLD is the result of Li incorporation into the PAA layer.

Upon further lithiation the PAA layer has thinned by 10 nm at 0.05 V (30.1 nm to 20.2 nm), in addition to a change in the SLD to 3.56 ± 0.09 (from 3.8 at 0.15 V). The thinning of the PAA from the start of 0.4 to 0.05 V would suggest the PAA is dissociating into the electrolyte and is changing in composition at the beginning of lithiation ($x > 1$). This could be attributed to Li exchange within the PAAH to LiPAA . The SEI layer decreases in SLD to 1.52 ± 0.1 compared to 2.52 at 0.15 V , suggesting more Li in the film. The silicon is lithiated to $\text{Li}_{3.8}\text{Si}$, which results in a thickness of $177.54 \text{ nm} \pm 2 \text{ nm}$ and SLD of -0.64 ± 0.04 . Upon delithiation to 1.5 V , the SEI layer grows to $15 \text{ nm} \pm 0.2 \text{ nm}$ with an increase in the SLD to 3.83 ± 0.05 (from 1.52), reflecting a change in the chemistry of the layer as a result of the delithiation of the anode. The increase in the SLD and thickness would be from the incorporation of solvent molecules such as C, O, and D. The PAA

layer increases in SLD to 4.66 ± 0.03 . The Si layer thins but the SLD (-0.3) indicates the anode was not fully delithiated, and from the electrochemistry the Li:Si ratio is estimated to be $\text{Li}_{0.9}\text{Si}$. The second lithiation sees the PAA layer remain ~ 20 nm; however, the SLD returns to around 3.4 as in the first lithiation. The SEI layer shrinks to 11 nm with a decrease in the SLD to 1.13 (as opposed to 1.52 after the first lithiation). Both the SEI layer and PAA change in chemical composition and thickness based on the state of lithiation or delithiation.

The above data detail the thickness and composition of the SEI layer that forms beneath a perfect PAA binder coating. Initially, the PAA uptakes solvent within the layer, but there is no evidence of the chemical reaction between the Si and the electrolyte. This is in contrast to previous NR experiments which observed a lithium-rich layer segregating to the a-Si surface upon exposure to the electrolyte, indicating that the PAA is protecting the silicon surface at OCV [24],[25],[26],[27],[28]. Instead, under the PAA layer we observe the hydrogen-terminated oxide layer grown on the a-Si from the reaction with the atmosphere. This suggests the PAA preferentially adsorbs the solvent, excluding the salt, which will play a role in the initial SEI formation and Li transport during lithiation.

There are few changes to the thickness and composition of the interfacial layers down to 0.4 V vs. Li/Li^+ . This indicates that the PAA is effectively acting as an SEI by suppressing electrolyte decomposition while still allowing solvent to approach the silicon surface. This is in contrast to measurements collected on an amorphous silicon electrode, which revealed the formation of a 25-nm thick inorganic-like SEI layer [25],[27]. This data indicates a well-defined PAA layer prevents electrolyte decomposition above 0.4 V, which may be beneficial to other intermetallic anodes such as antimony. Below 0.4 V there are significant changes observed at the Si-PAA interface. At 0.15 V, lithium-containing species have diffused to the silicon surface where they react (beneath the PAA layer), resulting in an inorganic-like SEI layer, Li_2O and LiF , that is about 10 nm thick and the silicon electrode begins to lithiate. Simultaneously, the PAA is thinning/decomposing and uptaking lithium within the PAA layer, leading to a lithiated PAA-like composition. This inorganic SEI layer is similar to the surface measured without the PAA [25],[27]. Indeed, the composition is similar based on scattering length density (2.5 vs. 2.9), but the PAA layer is much thinner: 9 nm vs. 19 nm, respectively [25],[27]. This indicates the polymer is acting as an artificial SEI while still enabling the formation of a lithium-containing SEI [29]. These data are consistent with reports which claim that after PAA is electrochemically reduced to form LiPAA , a protective layer of binder reduction products prevents the reduction of the carbonate-based electrolyte and forms a relatively thin and more stable SEI [30]. Similar effects on graphite anodes that contain PAA have been observed, where the binder suppressed the first lithiation decomposition of the electrolyte as a result of the PAA binder coverage [31],[32]. Upon further lithiation below 0.05 V vs. Li/Li^+ , the SEI continues to change in composition as evident by the decrease in the SLD from 2.5 to 1.5. Interestingly, the thickness remains constant at 9 nm.

Interfacial Chemistry of PEFM Binders on Amorphous Silicon [28]

The a-Si anode used in the NR studies was initially measured in air to determine the as-prepared structure of the sample. The refinement of the data (Figure II.1.B.89) results in an SLD plot (Figure II.1.B.89) which represents the heterostructure of the thin-film layer versus the SLD and is separated by interfacial roughness between each layer as schematically shown on the SLD plot on the bottom of Figure II.1.B.89. From the refinement, the Si layer was determined to have a thickness of ~ 463 Å with an SLD of 2.07, which is in good agreement with the theoretical SLD of Si (2.07), indicating a uniform and dense a-Si film. There was no evidence for an oxide layer on the a-Si surface as there has sometimes been reported, or if present, was contrast matched and wasn't evident by NR [25]. The Cu film was approximately 200 Å thick with an SLD of 6.54, which is in good agreement of the theoretical value of 6.59, while the native oxide layer present on the substrate was ~ 17 Å thick. The PEFM polymer binder was spin coated to a thickness of 43.5 Å, which was ideal in order to allow lithiation and prevent creation of an insulating layer. The fit resulted in an SLD of 1.57. The SLD value of the density and areal density for the PEFM binder layer were calculated to be 0.35 g cm^{-3} and $0.15 \text{ } \mu\text{g cm}^{-2}$, respectively.

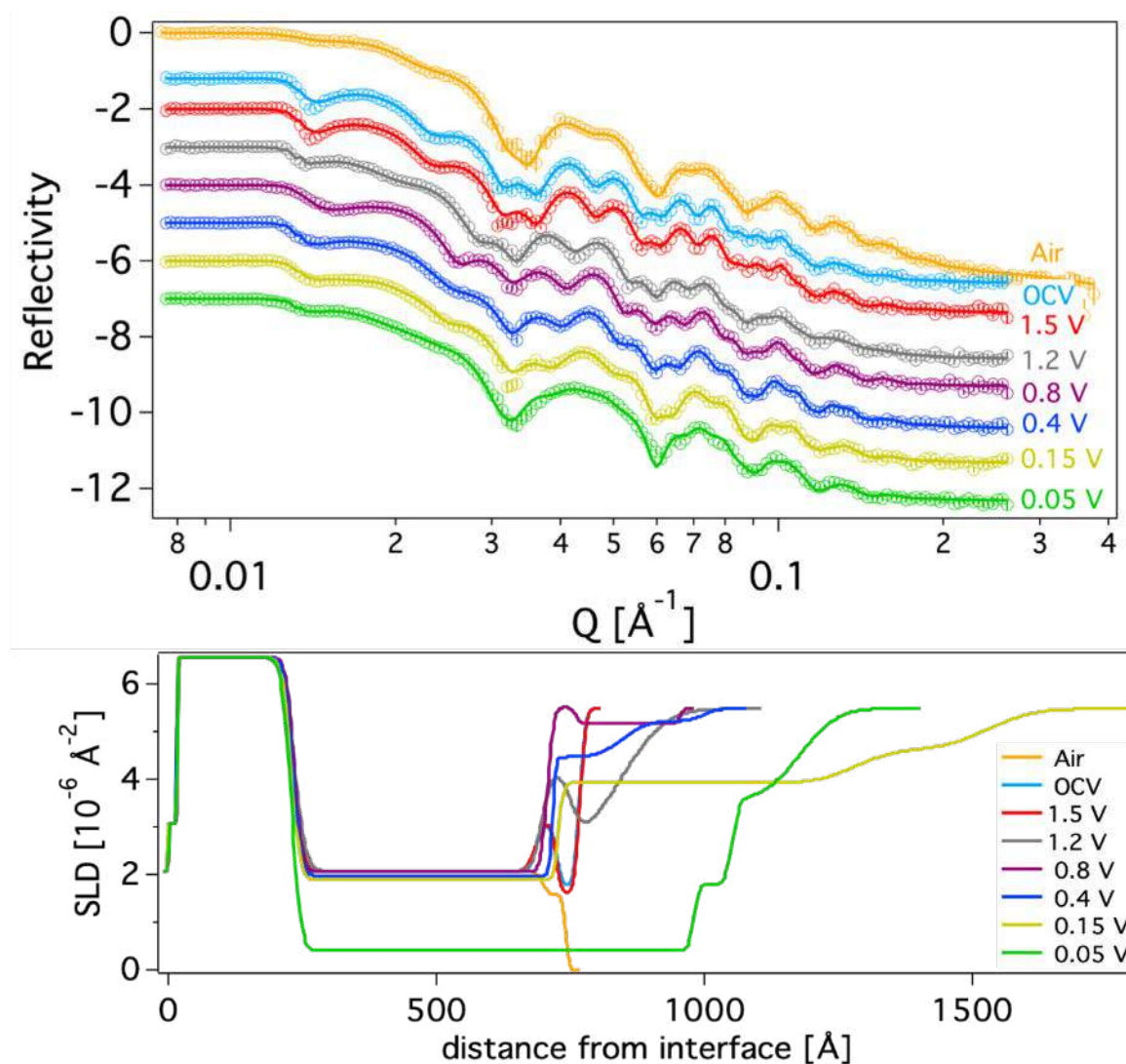


Figure II.1.B.89 Neutron reflectivity data with open holes representing collected data and the fit, shown as a solid line (top). The SLD profile from resulting fit (bottom)

After the cell was constructed and alignment complete, the electrolyte was in contact with the anode for ~30 min and the OCV equilibrated to 2.8 V (vs. Li/Li^+) before data collection. Figure II.1.B.89 shows NR data collected for the sample in the cell (top) and resulting SLD/thickness profiles (bottom). Changes in the reflectivity from air to OCV are evident, with the resulting fit indicating a decrease in the Si layer thickness (462 to 450 \AA) and the addition of a new layer on the surface of the anode. The new film is attributed to a reaction layer that forms as a result of the chemical reactivity of the active Si surface with the electrolyte, and is approximately 41 \AA thick. The SLD value was 3.01, significantly lower than the electrolyte SLD (5.46), indicating the incorporation of a component with a low coherent scattering length needed to lower the SLD. Given the elemental makeup of the electrolyte components, i.e., D, O, F, and P (6.6, 5.8, 5.1, and 5.6 fm, respectively), which have relatively high scattering lengths, the reaction layer is most likely Li rich, which has a bound coherent scattering length of -1.90 fm, coming from the LiPF_6 salt.

Refinements of the 0.8 V NR data indicate two distinct structures: the SEI layer on the surface of the anode and the PEFM on top of the SEI, depicted in Figure II.1.B.89 (purple SLD profile). The interface between the SEI and PEFM are distinct and well defined, unlike what was observed at OCV, 1.5 V, and 1.2 V, which did not show distinct interfaces between the reaction layer on the surface of the anode and the polymer layer on top

of the reaction layer. The most likely explanation is binding of Li to the PEFM, which is designed to be cathodically doped in a reducing environment where Li will attach to the F group of the polymer. In addition, at 0.8 V the reduction of the EC begins and the reaction layer becomes a true SEI layer. Interestingly, NR shows no increase in thickness for the SEI (from the previous potential), however there is a significant increase in the SLD from 4.09 at 1.2 V to 5.50, indicative of a significant change in chemistry of the SEI layer on the surface of the Si due to the reduction of the EC at this potential.

The lithiation of the a-Si layer begins at 0.4 V vs. Li/Li⁺, as indicated in the NR refinements with the increase in the Si layer from 472.4 to 484.9 Å, coupled with the lowering of the SLD to 1.97, indicating the incorporation of Li as it has a low scattering cross-section which lowers the average SLD. From previous work the extent of lithiation was estimated to be Li_{0.05}Si, a very small Li content within the Si [13]. Other Li is becoming incorporated in the SEI layer on the silicon, as a significant decrease in the SLD, from 5.5 to 4.5, was observed as well as a swelling of the layer by over 70 Å (compared to the 0.8 V thickness). There is evidence of a more intermixed layer between the polymer and SEI forming, as indicated by the SLD profile (Figure II.1.B.89) in which the distinct polymer layer seen at 0.8 V is no longer evident at 0.4 V. The SLD profile indicates a diffuse interface between the SEI and polymer layer. The large uptake of electrolyte results in a contrast match as the layers' SLDs become close to that of the electrolyte. By 0.15 V, the PEFM and SEI layers result in a gradient where the interface between the two layers is no longer distinguishable. Interestingly, the SLD of the PEFM layer has decreased from 5.21 to 4.61, similar to the SEI layer which sees the SEI settle to 3.91 (as compared to 4.46 at 0.4 V). As the potential is decreasing and more Li is moving through the system, it is most likely becoming incorporated in the PEFM as well as being consumed in the SEI, leading to the small Li:Si ratio, Li_{0.09}Si, being observed. The Si layer has only slightly changed in both thickness and SLD, further supporting small lithiation of the anode.

At 0.05 V the layer has been lithiated to Li_{0.7}Si. Due to low Li:Si ratio, the Li was most likely consumed in both the SEI and PEFM layers, which is further evidenced by a decrease in the SLD of the SEI (3.91 to 1.79) and the PEFM (4.61 to 3.55). The SEI and PEFM layers appear to swell significantly at 0.15 V; however, at 0.05 V a distinct 72.1 Å SEI layer forms on the surface of the lithiated Si with an SLD of 1.79 (Figure II.1.B.89). This would indicate a fairly Li-rich SEI due to the significant decrease in SLD from the previous two voltage states. Lithiation is also indicated by an increase in the Si layer settling to 750.8 Å and lowering of the SLD to 0.40, indicative of Li incorporation.

In summary, a distinct reaction layer forms on the surface of the a-Si anode while the PEFM stays on top of the reaction layer, and even though there is not a sharp interface between the two layers they are distinguishable up until 0.8 V (Figure II.1.B.89, bottom). The PEFM is a dynamic layer, changing in both SLD and thickness as the cell is polarized to lower potentials (vs. Li/Li⁺). A large gradient between the SEI (after 0.8 V) and the PEFM occurs at 0.4 V and 0.15 V, whereas there is no true distinction between the polymer at the electrolyte interface and the SEI on the surface of the anode. Once the cell is polarized to 50 mV, there is enough of a driving force to push the trapped Li in the binder into the anode, resulting in a reordering of the SEI and PEFM. The PEFM shrinks by ~126 Å (247 Å at 0.15 V to 121 Å at 0.05 V), forming well-defined interfaces between the SEI and binder layer (Figure II.1.B.89, bottom, green SLD plot). However, the PEFM is no longer the same chemistry as the as-prepared sample, as evidenced by changes in the SLD, most likely being a chemical makeup of decomposition products and reactants leading to an intermixed layer as summarized in Figure II.1.B.90. The PEFM binder was designed to swell in electrolyte solutions, similar to PVDF, and shown to incorporate upwards of 50 wt% of solvent within its structure [6],[14]. The PEFM layer does not inhibit the electrolyte from contacting the a-Si surface, as evidenced by the documented formation of a reaction layer, akin to a pre-SEI observed at OCV (Figure II.1.B.89), and in the 12-Å decrease in the Si layer (from in air) when in contact with the electrolyte [9],[11]. From OCV to 1.2 V there is distinct separation between the reaction layer on the surface of the Si and the PEFM on top of the reaction layer, as evidenced in the SLD plot in Figure II.1.B.89. After polarization of the cell to 0.8 V vs. Li/Li⁺, the significant change in SLD from 1.57 in air to 5.15 indicates a larger incorporation of the electrolyte into the layer.

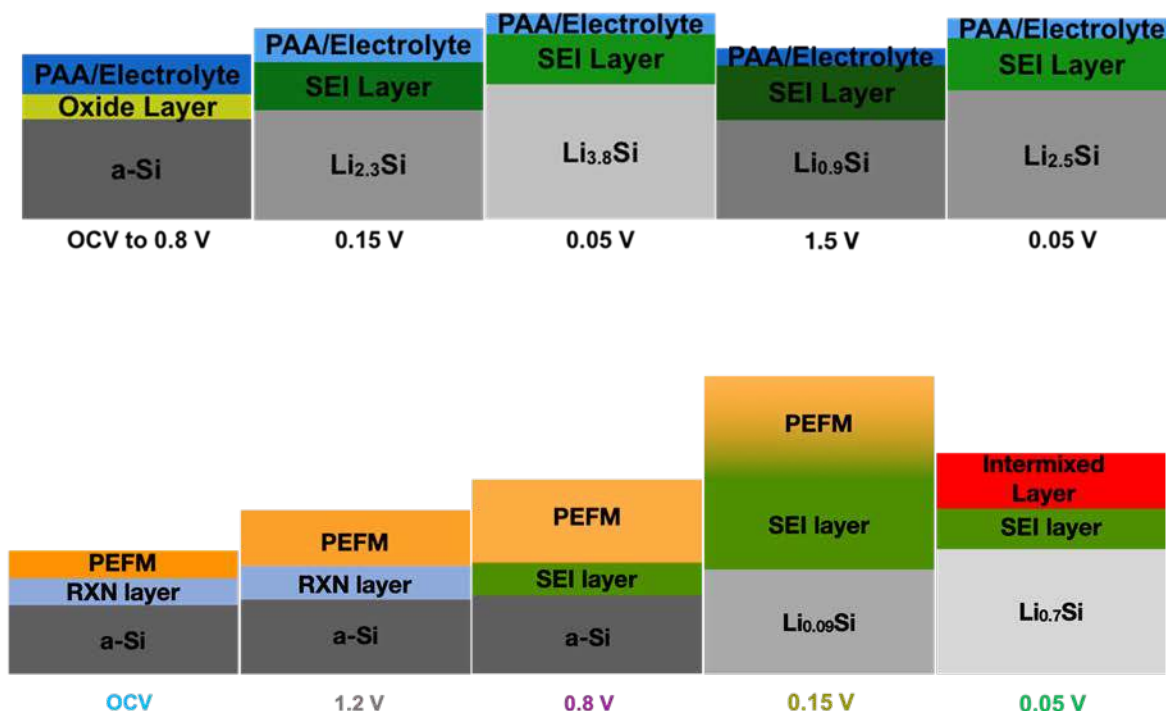
From the NR it is evident that the polymer layer is continuously changing with higher states of lithiation through interactions with the electrolyte. The large amount of electrolyte uptake within the PEFM inhibits the bulk electrolyte from contacting the Si surface. The most likely explanation for the diffuse layers, i.e., a lack of distinct interfaces and more of a gradient from the electrolyte/PEFM/SEI interfaces observed at 0.4 V and 0.15 V, is the result of electrolyte decomposition within the polymer and SEI layer altering the electrolyte composition that is interacting with the Si. The 0.05 V (vs. Li/Li⁺) SLD plot showed a distinct SEI with a low SLD (1.79) form on the surface of the Si, but is not purely LiF, which has a theoretical SLD of 2.30. This SEI layer is relatively thin at 72.1 Å. The polymer layer is most likely a composition of electrolyte decomposition products as the SLD settles to 3.55 and is no longer PEFM. The layer is 126.3 Å thick, compressing from 0.15 V (247.3 Å), which would indicate products moving out of the binder layer into the SEI or silicon.

Comparison of Binders and Binderless Electrodes [24],[25],[27],[28]

Figure II.1.B.90 graphically summarizes the structure of the SEI under the various binders, along with representative thickness and composition data measured at the same states of charge for cells with PAA and PEFM binders and cells without binders using only Gen2 electrolyte with and without FEC. Through an analysis of this data several trends can be ascertained:

1. The SEI formed on electrodes with a binder grows beneath the binder layer. Furthermore, if a binder is too “homogeneous,” then no lithium will transport through the binder coating. This is significant as it would indicate the binder needs to be heterogeneous on the silicon to enable lithiation. This points to the need to identify the “best” conditions with binder coverage to give optimal binding but still allow Li transport.
2. In all cases the SEI chemistry is dynamic. Previously we have described this effect as “breathing,” where part of the SEI is dissolved upon delithiation resulting in changes in the SEI chemistry due to loss of SEI components (e.g., LEDC). The extent of this breathing is likely correlated with capacity fade and loss of cyclability/increases in interfacial resistances. These data point to the need to design an electrolyte/SEI layer that forms insoluble species upon reduction or has strong bonding with the silicon surface to avoid dissolution.
3. The choice of solvent and binder has a dramatic influence on the SEI chemistry and composition. Figure II.1.B.90, bottom, shows representative SLD and thickness data collected for the various samples evaluated using neutron reflectivity. Several trends are observed. First, at 0.4V, after lithiation has begun, the SEI using the PAA and FEC is thin (60–99 Å), whereas samples with PEFM or no FEC have a much thicker SEI (130–250 Å). These data indicate that the choice of chemistry results in less SEI and therefore less electrolyte consumption.
4. The data collected at 0.15 V, after the start of deep lithiation, show significant changes in the thickness and composition as a function of the electrolyte/binder. Specifically, the FEC SEI is dense and has a lower SLD (2.3), indicating that it is predominantly inorganic in nature (LiF-like). The PAA has a slightly higher SLD (2.5) and thickness (89 Å) than with the FEC. Without a binder or FEC, the SEI has a higher SLD (2.9) and larger thickness (187 Å), while the PEFM has an SLD of 3.9 with a thickness of 556 Å. Following this trend, the FEC and PAA give a thinner, more inorganic SEI, while the Gen2 and PEFM lead to a thicker, more organic SEI layer. This is significant as there is more loss in structural thickness and composition for the SEI grown as a more organic composition compared to the more inorganic composition. The significance of this is that the SEI needs to be more inorganic to be stable. This points to the need to prevent the dissolution of species like LEDC.
5. There are indications that the binders are playing a role in the selective transport of electrolyte species. When compared across one another it appears that the PAA is acting to concentrate the Li ions needed to form a dense inorganic SEI, as evident by the lower SLD of the SEI layer. The PEFM appears to be acting to concentrate the solvent (as evident by its high SLD) at 0.4 V and 0.15 V. This will lead to a higher organic-content electrolyte that more readily dissolves, as evident in the loss of SEI thickness

at maximum lithiation (0.05 V). The significance of these data is that it might be wise to investigate binders that act as Li^+ transport membranes.



FEC			PAA			Si			PEFM		
Voltage	SLD	Thickness (Å)	SLD	Thickness (Å)		SLD	Thickness (Å)		SLD	Thickness (Å)	
OCV	2.6	60	4.3	80*		2.4	45		3.0	42	
1.2	2.6	58	4.1	80*		4.7	175		4.1	55	
0.4	2.6	59	4.5	99*		2.0	246		4.5	130	
0.15	2.3	68	2.5	89		2.9	187		3.9	556	
0.05			1.5	99					1.6	72	



* = Estimated based on swelling of binder in solvent

Figure II.1.B.90 Schematic of the SEI chemistry with various binders (top) and a schematic representation of the relative fraction of inorganic versus organic SEI components (bottom)

This work can be related to composite electrodes and the processing needed to make such electrodes. As is clear from this work, a fully coated Si particle behaves differently than one that has patchy coverage. If the binder fully encapsulates a Si particle and is cross-linked at high temperature from drying procedures, there will be no Li^+ transport. These data would support the need to make a heterogenous PAA/Si structure to allow some Li transport. The challenge would therefore be related to ensuring a minimally exposed silicon surface

(which would react to form larger amounts of SEI) while maintaining some pathways for electrolyte to interact with the silicon surface. It would also explain why FEC works well with PAA-based composite electrolytes, in that it is resulting in the polymeric protective layer while maintaining Li-transport pathways.

Headspace Solid-Phase Microextraction GC-MS

Gas chromatography-mass spectrometry (GC-MS) is an analytical technique widely used to study degradation mechanisms in Li-ion batteries. This technique has been used by others in the past to study electrolyte degradation and elucidate probable decomposition mechanisms [1]. Here we attempt to use GC-MS to identify SiEI components that dissolve in the electrolyte during cycling. We present three case studies: (1) silicon anode coin-cell galvanostatic cycling vs. OCV rest, (2) the effect of 50 ppm of water added to Gen2 electrolyte, and (3) Gen2 electrolyte recovered from a Si-anode lithium half-cell that was held at elevated temperature. These studies provide guidance to stabilizing the SiEI, providing mechanistic explanations of surface chemistry and various reactions/interactions within the SiEI.

It is known that lithium salts, such as lithium hexafluorophosphate (LiPF_6), are destructive to the gas chromatography column; therefore, direct liquid injection of Gen2 electrolyte samples should be avoided. We are developing methods for extracting molecular species present in the electrolyte (e.g., electrolyte solvents, degradation species, soluble SiEI components, etc.) without the uptake of the potentially hazardous LiPF_6 salt. Recently, we have employed the technique of headspace solid-phase microextraction (HS-SPME), which has already been shown to work for electrolyte analysis of aged commercial Li-ion batteries [1]. In HS-SPME, volatiles present in the headspace of a vial are diffused from the sample to the headspace, where they are adsorbed onto a polymer-coated fiber with a high affinity for the target compounds. The fiber is then transferred to the injection port of the gas chromatography column, where the volatiles are desorbed for analysis (Figure II.1.B.91). Preventing the gas chromatography column from exposure to corrosive LiPF_6 salt allows for a longer functional lifetime.

In our experiments, an 85- μm polyacrylate fiber (Supelco) was used for HS-SPME. Headspace extraction time was 10 min at room temperature. Sample analysis was performed by manual injection into an Agilent 7890B Gas Chromatograph coupled to an Agilent 5977B single quadrupole mass selective detector. We used a split ratio of 100:1 for Case Study 1, and a splitless column injection for the other two studies. Molecular species were determined by searching the mass spectra within a National Institute of Standards and Technology (NIST) database (MassHunter software).

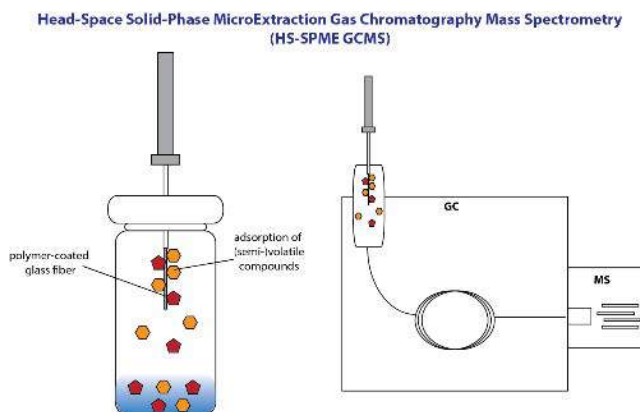


Figure II.1.B.91 Headspace Solid-Phase Microextraction Gas Chromatography Mass Spectrometry (HS-SPME GC-MS) prevents injection of LiPF_6 salt into the gas chromatographer while still providing detection of electrolyte solvents, decomposition products, and soluble SiEI components

Case Study 1: Ten Galvanostatic Cycles vs. OCV Rest. For our initial SP-ME GC-MS study, we used approximately $6.5 \times 6.5 \text{ mm}^2$ pieces of monocrystalline silicon wafer (675 μm thickness; boron-doped, 0.005 Ωcm) as the working electrodes. The counter electrodes were Li-metal foil. Celgard 2325 and Whatman GF/F

glass microfiber were used for the separators. The Gen2 electrolyte consisted of 1.2 M LiPF₆ salt dissolved in a mixture of EC:EMC (3:7 wt%), and 30 μ L was used. Half of the samples were left at OCV. After an initial 2-hr OCV rest, the others were galvanostatically cycled with an applied current of 30 μ Acm⁻² between voltage limits of 0.1 V and 1.5 V vs. Li/Li⁺ and 2-hr half-cycle time limits. After 10 cycles all cells were carefully disassembled. The separators were placed in 10-mL glass vials and then caps with polytetrafluorethylene (PTFE) septa were crimped onto the vials to seal them for subsequent HS-SPME.

Figure II.1.B.92 (b) shows the gas chromatographs of a cycled cell and one left at OCV. For comparison, we also used the same SPME method to sample the headspace above a vial containing 200 μ L of just Gen2 electrolyte. All three samples yield similar results: a large EMC signal at a retention time around 4.1 min, a large EC signal around 12.3 min, and a smaller DEC signal around 6.4 min. The presence of DEC is not surprising as it is a known byproduct of EC reduction in the presence of EMC. The inset of Figure II.1.B.92 (b) shows a zoom-in of the chromatographs between 10 and 14 min. There appear to be some small differences between samples, but the signal intensities are too low for us to confidently identify them at this time. It is likely that 10 cycles was insufficient to create enough soluble SiEI species for our detection. This led us to think about how we might increase the probability of chemical side-reactions in the cell, for example by adding a small amount of water to the Gen2.

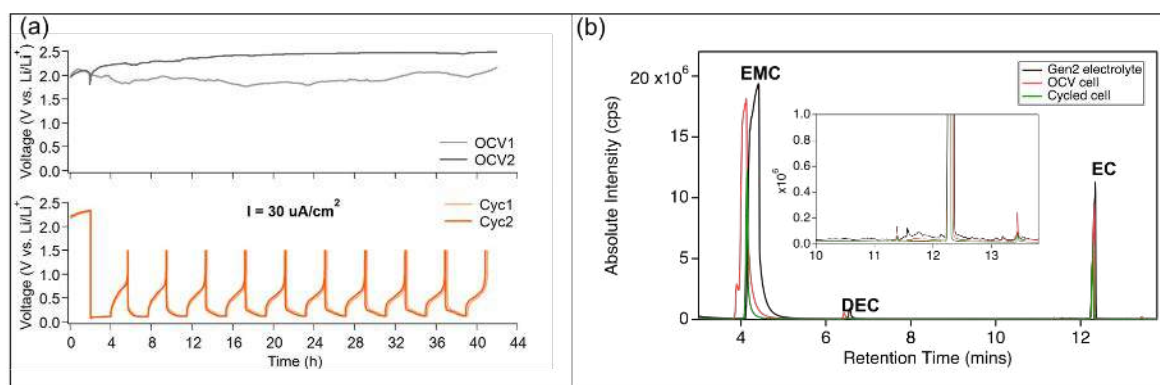


Figure II.1.B.92 (a) Electrochemical performance of coin-type cells (with Si wafer vs. Li metal): Half of the samples were rested at OCV, while the other half were galvanostatically cycled between 0.1 and 1.5 V at an applied current of 30 μ A/cm². (b) Gas chromatograms using HS-SPME to sample the headspace above the separators (red and green lines) and pristine Gen2 electrolyte for comparison (black line); inset in part (b) is a zoom-in at retention times between 10 and 14 minutes

Case Study 2: Effect of 50 ppm Water Added to Gen2 Electrolyte. To understand how the presence of water in the system affects the interfacial chemistry of the Si anodes, we evaluated the electrochemical performance of Si anodes in Gen2 (1.2 M LiPF₆ in EC/EMC (3:7, wt/wt)) with 50 ppm of water. The Si-wafer electrodes were held at 3 different voltages: 1, 0.5, and 0.2 V vs. Li/Li⁺ for 10 hours. Afterwards the cells were disassembled and the electrolyte was transferred into a 1-mL polypropylene vial with a PTFE-liner crimp cap.

Figure II.1.B.93 shows the gas chromatographs of the electrolytes recovered from the potentiostatic experiment. For the sample with 50 ppm of H₂O in Gen2 held at 1 V there is a large signal corresponding to fluorophosphates. These species are known products of the hydrolysis of PF₅. A small but interesting signal present in every sample appears at 6.53 min retention time, corresponding to ethylene decarbonate (EDC). LiEDC has been detected by others as the primary electrochemical reduction product of ethylene carbonate (EC) during battery operation. Furthermore, we observed ethyl-hexyl carbonate at 11.6 min retention time. Alkyl carbonates can be formed by radical species originating from the reduction of EC that then react with other radical fragments. Interestingly, in this case we see a greater signal intensity for 0.5-V samples, where

side reactions with the electrolyte are favored. Almost no signal is detected from the 1-V sample without water.

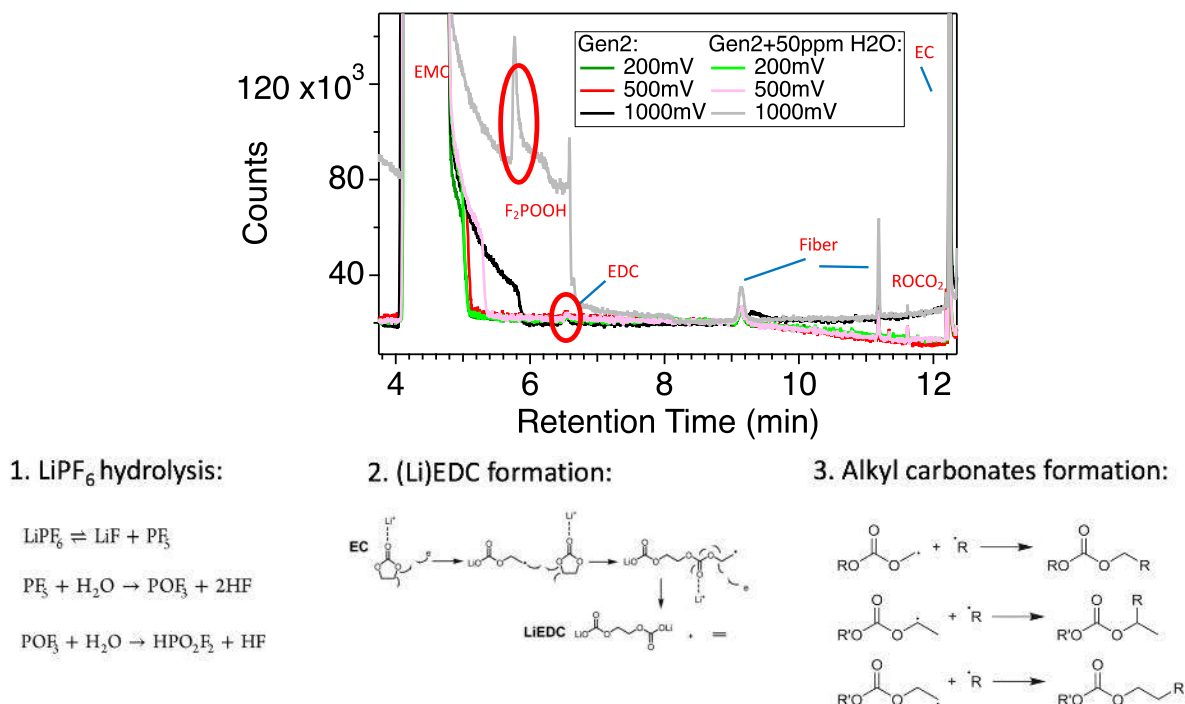


Figure II.1.B.93 (top) Comparison of GC-MS gas chromatographs of the recovered electrolyte from potentiostatic holds at 1, 0.5, and 0.2 V for 10 hrs. (bottom) Reaction mechanism for some of the soluble SiEI species detected in the GC-MS

Case Study 3: Temperature-Dependent Decomposition of Gen2. In our third study, we investigated the behavior of an a-Si anode in a lithium half-cell with Gen2 electrolyte at an elevated temperature of 60°C. The cell was held at OCV (~3.2 V vs. Li/Li⁺, at 60°C) for approximately 30–60 min. Afterwards, the cell was disassembled and the Gen2-soaked separator was sampled with HS-SPME and run through the GC-MS. Figure II.1.B.94 shows a comparison of the gas chromatographs of pristine Gen2 and the electrolyte species sampled by the HS-SPME. Gen2 electrolyte components are abundant in both cases: EMC (4.1 min) and EC (12.2 min). However, the heated electrolyte has many more peaks. Many of these peaks correspond to reactions between fluorophosphoric acid (from PF₅ hydrolysis) and silicon oxygen species, for example methanephosphonofluoridic acid. Further studies of silicon anodes in LiPF₆-based electrolytes at elevated temperatures are ongoing.

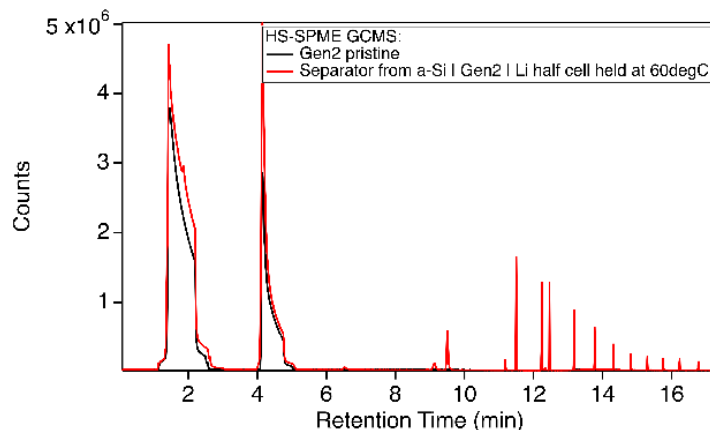


Figure II.1.B.94 Comparison of GC-MS gas chromatographs of pristine Gen2 electrolyte and the electrolyte from a half-cell containing silicon, lithium, and Gen2 held at 60 °C

In conclusion, the idea to detect soluble SiEI components with GC-MS remains promising. We show here that it is possible to analyze the volatile molecular components present in the electrolyte after battery cycling. Moving forward, we must continue to refine conditions for both the volatiles extraction (SPME time and temperature) and the GC detection (split ratio and heating). We seek to minimize the overwhelming EMC and EC solvent signals, but still detect soluble SEI species. In addition, we plan to combine our liquid analysis with gas GC-MS, as well as with analytical spectroscopy such as FTIR, to piece together a fuller picture of the SiEI formation and evolution during battery cycling. This technique will help evaluate some of the strategies emerging from other efforts in the project towards SiEI stabilization, such as silicon surface chemical modification.

Design of New Si Surfaces Based on Experimentally Validated Stable Chemical Moieties

Understanding the Role of Hydrophobic and Hydrophilic Surface Ligands on Si Nanoparticles

The SEI is important for reversible lithiation and charge storage in silicon anodes and may lead to better cycle performance. The ability of Li^+ ions to reach the Si NP surface, the electrical contact between the conductive carbon matrix and the Si surface, and the kinetics of alloying (hysteresis of alloy/dealloy) are all critical parameters which are controlled by the SEI. Therefore, it is important to systematically deconstruct the individual components of the SEI to judge their relative impact on the overall device performance. Generally, components of the SEI can be broken into two categories: inorganics (SiO_x , Li_xCO_3 , and Li_xSiO_y) and organics ($\text{C}_x\text{H}_y\text{O}_z$). In Part 1 of this report we describe our efforts to quantify the effects of inorganic layers on the Si NP surface. Here, we probe the effect of the organic surface layer hydrophobicity on the electrochemical cycling of Si NPs. To do this, we leverage our nonthermal plasma synthesis method that produces exclusively SiH_x -terminated Si NCs and covalently bind hydrophobic dodecyl ligands to the Si surface. We measure the effect of this surface functionalization against nonfunctionalized (as-prepared SiH_x -terminated NPs) in composite half-cell anode configuration.

The electrochemical cycling data for the first 16 cycles, as well as the dQdV plot for dodecyl-functionalized and unfunctionalized silicon, are shown in Figure II.1.B.95. From the cycling data for the unfunctionalized silicon (blue dots) shown in Figure II.1.B.95 (a), these anodes display typical cycling behavior observed for these SiH_x -terminated NPs: low reversible first-cycle capacity (~50% coulombic efficiency) followed by delithiation capacities around 2,000 mAh/g_{Si}. The dQdV plot for dodecyl-functionalized silicon NPs, however, displays significant differences. There is no measurable delithiation capacity at any point in the first 16 cycles. The minimal measured capacity shown in the black trace of Figure II.1.B.95 (a) is due to the conductive carbon (Timcal C65) lithiation/delithiation. We therefore can conclude that the organic component of the SEI can effectively eliminate the ability of silicon to store energy under standard cycling conditions.

Deactivation of these silicon NPs for lithiation is due to at least one of several possibilities: (1) the Si NPs are electrically insulated whereas the C65 does not form electrical contact with Si; (2) the Si NPs are ionically insulated against lithiation; (3) the composite electrode hydrophobicity inhibits GenF electrolyte from percolating through the composite network; or (4) the slurry properties of the dodecyl-functionalized Si NPs are poor and result in agglomeration and isolation of the Si. To test these hypotheses, we derived dQdV plots for the first cycles of electrochemical cycling. The SiH_x -terminated silicon, represented by the blue trace, displays the typical features for first-cycle lithiation. At ~1.2 V vs. Li/Li^+ , a sharp feature corresponding to SiH_x reduction is present which is followed closely by SEI formation (electrolyte reduction) at ~1 V. Crystalline Si lithiation is apparent by the steep feature at ~0.2 V. Upon delithiation, the Si undergoes amorphization, indicated by the two features at 0.3 V and 0.5 V. The dodecyl-functionalized Si NPs display some of the same character, but important differences exist. The feature-attributed SiH_x reduction (residual SiH_x surface species are always present after surface functionalization, as characterized by FTIR [33] and solid-state NMR spectroscopy [34]) and electrolyte reduction are both present, which indicate that the dodecyl-functionalized silicon is electrically contacted to the conductive carbon matrix, but the lithiation and delithiation features are both absent from the trace. These data indicate that the engineered hydrophobicity allows electrical contact but inhibits ionic conductivity. This important result provides critical information

about the thickness (~ 1 nm) of hydrophobic coatings that will shut down (sterically block) Li^+ ion transport to the Si surface.

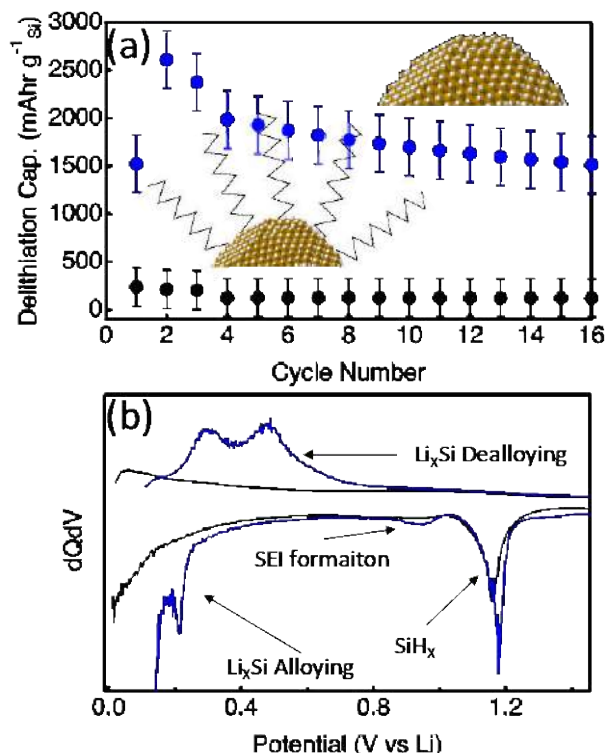


Figure II.1.B.95 (a) Cycle data for $d = 30$ nm SiH_x -terminated (black) and dodecyl-terminated (blue) in a half-cell configuration. The first three cycles are at a C-rate of C/20, and the latter 13 are C/5. The error bars represent $\pm 1 \sigma$ from the mean of three electrodes. (b) Plots the dQdV of the first cycle for the same $d = 30$ nm SiH_x -terminated (black) and dodecyl-terminated (blue) samples

We conclude that too-thick hydrophobic organic components can effectively turn off reversible lithiation of Si. From the dQdV plots, these organic moieties of the SEI affect the ionic conductivity much more than the electrical conductivity, as evidenced by the SiH_x reduction without the corresponding Li^+ alloying. These initial Q4FY19 results will be followed up with a more comprehensive investigation which probes the magnitude of the ionic insulation by varying: (1) the length of the hydrophobic chain and (2) the identity of the surface functionalization (polyethylene oxide in place of the dodecyl, etc.).

Synthesis of Functionalized Si Through Milling

It is clear that the surface functionalization of silicon will be important to forming stable electrodes as well as interface chemistry. In the above section we discussed using Plasma-enhanced chemical vapor deposition (PECVD) -grown silicon particles and reacting them in solvent to form a silicon surface. In this section we are focused on crushing boules of silicon in the presence of a sacrificial solvent. This solvent will bind to the newly exposed Si surface sites.

Figure II.1.B.96 shows representative SEM data collected for samples milled in various solvents. These materials have the same particle sizes and morphologies as the commercial silicon sources used in the Deep Dive program. More importantly, they behave fundamentally differently from the silicon materials used in the Deep Dive with respect to their surface chemistry. This is reflected in Figure II.1.B.97, which shows the zeta potential data measured for the Deep Dive silicon materials and the zeta potential for the milled silicon synthesized by the team. The Deep Dive silicon all have low zeta potential values (< 20 mV), which indicates

that they do not form stable suspensions. In contrast, the milled silicon materials in solvents have high zeta potentials (>30 mV), pointing to the ability to form stable suspensions in solution during electrode processing.

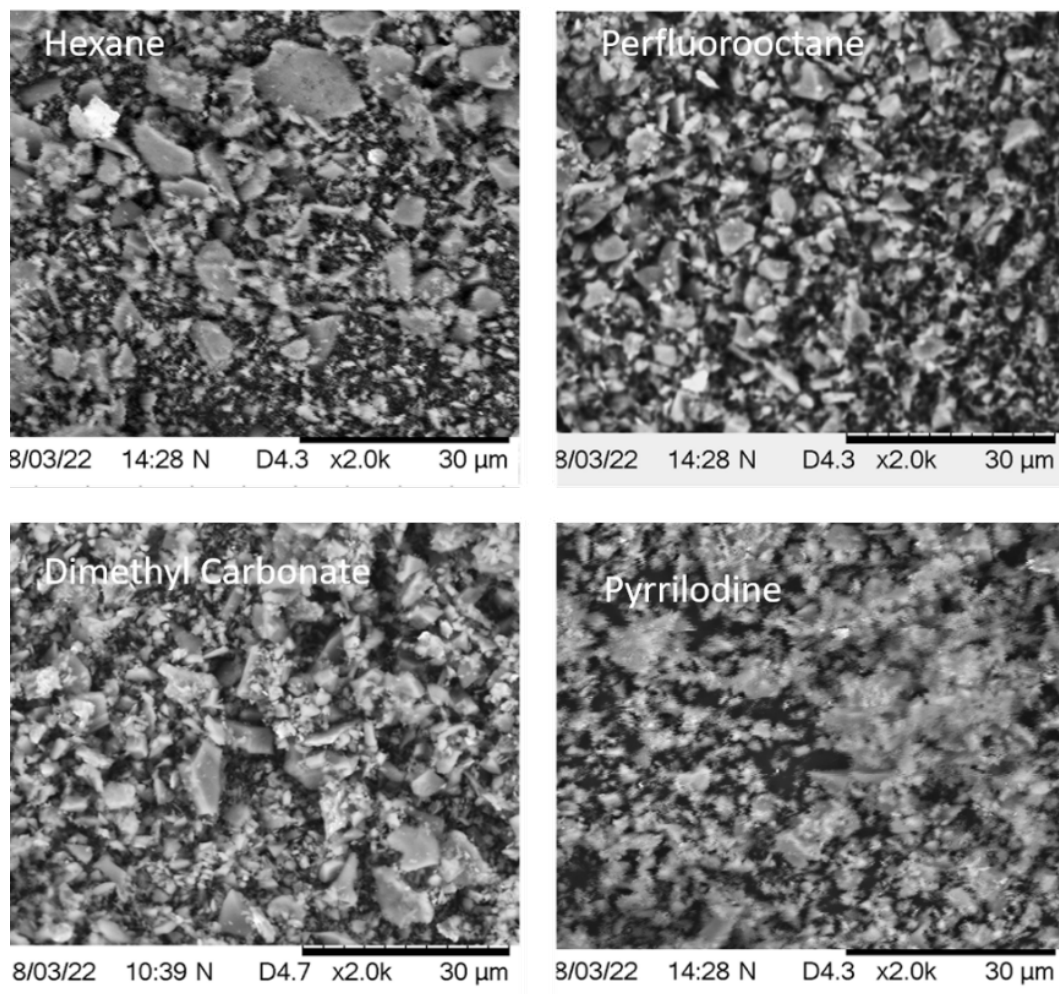


Figure II.1.B.96 SEM images of milled silicon powders

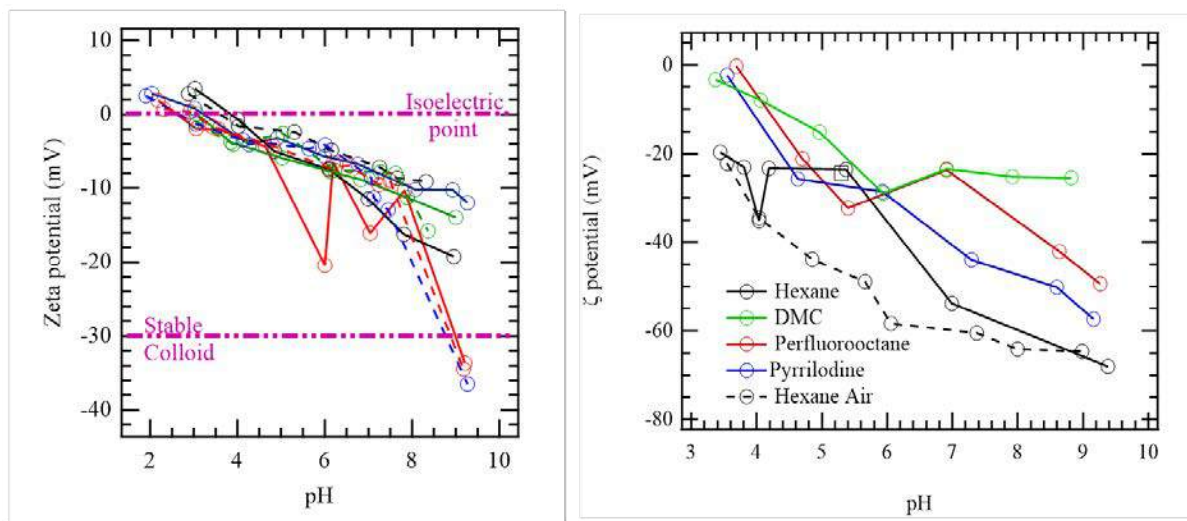


Figure II.1.B.97 Zeta potential of Deep Dive silicon (left) and milled silicon powders (right)

The resulting materials were incorporated within a cell using 80% Si, 10% carbon black (CB), and 10% binder (PAA). The cycling results are shown in Figure II.1.B.98. These data show variation in capacity retention but clearly significant changes due to changes in the surface chemistry. These changes will be explored in the future. Furthermore, the materials will be investigated using the tools and techniques discussed above.

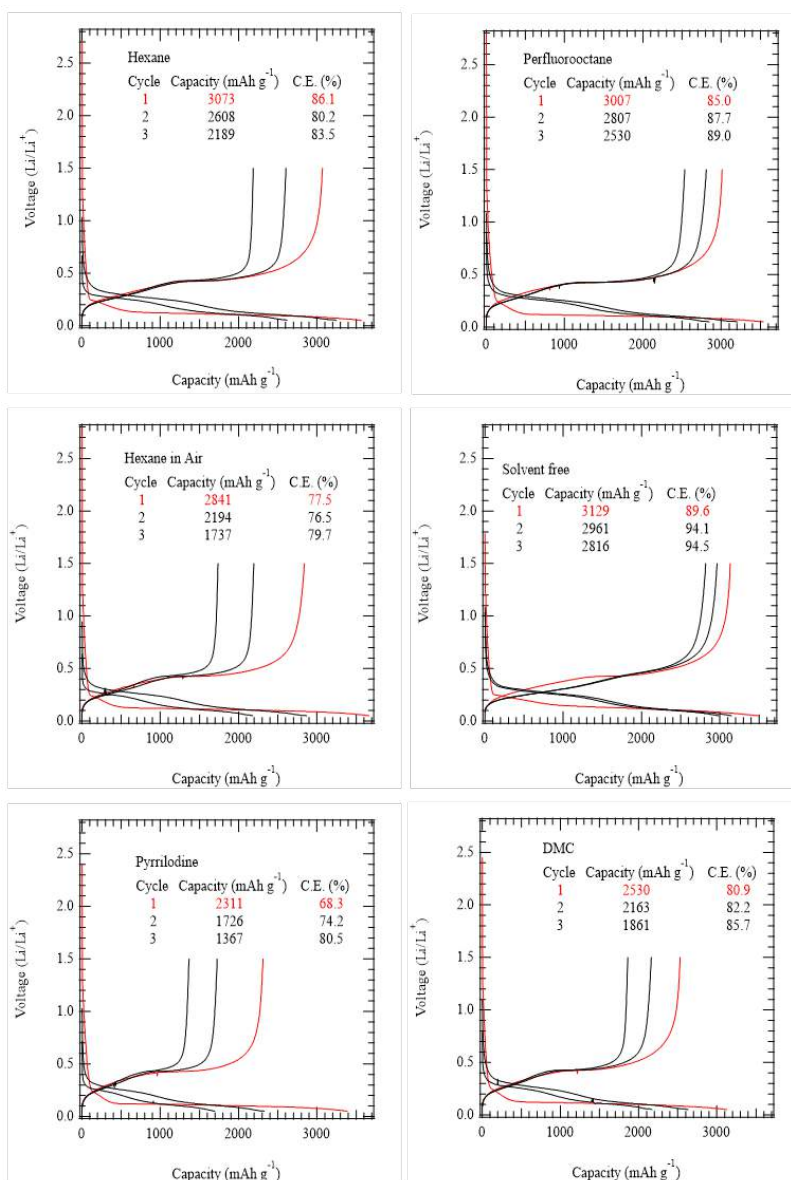


Figure II.1.B.98 Representative cycling data measured for milled silicon electrodes

Conclusions

Part 1: Studies of SiO₂ Interfaces

Our studies show that an amorphous oxide layer is preferred over a crystalline oxide in early stages of film growth; however, after ~0.3 nm, the crystalline film is thermodynamically favored. The fact that amorphous oxide films are observed in nm-thick SiO₂ suggests that the crystallization of the early-stage oxide is kinetically hindered, and the growth conditions favor the amorphous configuration. Additionally, we observe that the onset of lithiation in Si and SiO₂ films occurs at higher potentials than for bulk material.

We note that a strong dependence of lithiation on SiO₂ thickness is observed in both cycling and chronoamperometric measurements. Below 3.0-nm SiO₂, lithiation on cycling is homogeneous and occurs with high Coulombic efficiency, and holding at 0.01 V_{Li} leads to a rapid current rise that reaches steady state in under 24 h, ultimately yielding uniform lithiation. Conversely, above 3.0-nm SiO₂, initial lithiation upon both cycling and holding at 0.01 V_{Li} is very inhomogeneous, occurring at pinholes first and then spreading radially, decreasing the resistance to further lithiation as the process proceeds. This also exhibits, as exponentially in time, rising current at 0.01 V_{Li}. The thickness dependence of peak currents in CV suggests an effect of tunneling through the SiO₂ on reaction kinetics.

We note that lithiated silica tends to have lower onset potentials than unlithiated oxide, and that the onset potential scales with the degree of lithium content in the oxide film. Additionally, conductivity of the films increases with lithium content, leading to lower overpotentials for lithiation into the underlying silicon.

Localized lithiation proceeds through SiO₂ pinholes, local decrease in SiO₂, and Li spreading beneath SiO₂. Li spreads hundreds of microns or even millimeters near the Si/SiO₂ interface, whereas diffusing only a few microns in the depth of the Si wafer. This suggests very significant interfacial diffusion enhancement for Li, which could be used for battery and electrode applications.

SiO_x anodes with high oxygen content appear to form lithium silicates irreversibly during the first lithiation process. The formation of lithium silicates may suppress the electrolyte decomposition at low potential; however, it also leads to a lower first-cycle Coulombic efficiency due to its irreversibility. Raising oxygen content in the Si anode could improve its cycling performance; however, it is at the cost of lowering its reversible capacity.

The capacity fade rate of SiNP-based anodes displays a size-dependent relationship with the smallest-diameter (<10-nm) Si NPs exhibiting the best capacity retention (>99.9% CE). SiO₂ surface layers on Si NPs do not appear to affect the capacity fade rate. The capacity fade-rate trend appears to scale with the surface-area-to-volume (SA/V) ratio, indicating that both mechanical and chemical aspects may be responsible for the capacity fade. Impedance spectroscopy analysis shows significant differences in the SEI layers between Si NPs with and without surface oxidation. Despite a slower Li⁺ conduction mechanism through the SEI formed on top of SiO₂-terminated Si NPs, lithiation rates are still determined by Li⁺ diffusion in silicon, not through the SEI.

The voltage- and time-dependent formation (e.g., potentiostatic hold at specific voltage until $i \leq 5.0 \times 10^{-6}$ and/or one cycle at the voltage range of 1.5–0.01 V) and the chemical and physical nature, such as chemical composition, surface morphology, and roughness, of the Li-Mg-Si ternary phase were characterized using a variety of analytical techniques. From both spectroscopic analyses, we did not observe any specific differences between GenF and GenFM samples in terms of chemical composition; but XPS analysis revealed the possible presence of MgO (O 1s), MgF₂ (F 1s), and Mg⁰/MgF₂/MgO (Mg 2p) that may be originated from the Li-Mg-Si ternary Zintl phase. In addition, the STEM EDS atomic % maps and the corresponding sum EDS spectra are shown with Si nanoparticles being present either containing or being surrounded by a shell containing C, O, Mg, F, and P. From the Si 2p XPS spectra (in particular, from availability of Li_xSi peak), we could assume that a relatively thick and well-covered SEI layer (with possible Zintl phase) is formed in GenFM electrolyte, which may be correlated with relatively greater roughness of 200-mV, 10-mV, and 1-cycle GenFM samples from AFM analysis. To obtain a better understanding of detailed formation mechanism of the Zintl phase, we have a plan to study a Si wafer as a model electrode without additional electrode elements (e.g., conductive carbon and binder).

The novel technique VE-GITT XPS was developed and applied to study effects of lithiation on 5-nm SiO₂ / Si(001) wafer model-system anodes. Key results of these experiments include the following: As previously reported, surface silicon oxides are converted to silicate phases according to $\text{SiO}_x + y\text{Li}^+ + ye^- \rightarrow \text{Li}_y\text{SiO}_x$. Lithiation leads to a dramatic reduction of the overpotential for 5-nm SiO₂ from >0.7 V to ~0.05 V. The evolution of Li⁺ current-bias-induced BE shifts in the SiO₂ XPS peaks enable a direct correlation between lithiation overpotential and the extent of SiO₂ to Li_ySiO_x conversion. Lithium incorporation leads to a change

in near-surface doping of the Si(001) wafer from p- to n-type. Lithiation changes the magnitude of the SiO₂/Si(001) interfacial dipole by ~0.7 eV, which, in turn, shifts the valence-band offset from 5.1 eV to 5.8 eV.

Part 2: Origins of Si/Electrolyte Interface Stability

The non-passivating behavior of silicon model electrodes has been analyzed by means of electrochemical protocols specifically designed for these studies. Three model electrodes were used: amorphous Si thin films deposited on Cu, Si wafers, and Si nanoparticles. A suite of techniques were employed to determine the nature of SEI components and its physical characteristics, such as FTIR, XPS, ToF-SIMS, GITT, SSRM, and the newly developed gradient polarity solvent wash (gradient wash) technique.

Clearly, it has been shown that the non-passivating behavior of silicon thin films can be observed independently from the cracking of silicon electrodes caused by the lithiation. The main decomposition products forming the SEI have been studied, as well as the effect on the morphology and physical properties of the SEI. It appears that the composition and morphology of the SEI depends on a number of parameters such as the SOC of the electrode, the lithiation rate (scanning rate in electrochemical cycles), or the presence of contaminants (water). The latter was assessed by adding 50 ppm of water to the electrolyte. The presence of water most likely results in the hydrolysis of LiPF₆, which causes a morphologically more inhomogeneous SEI (pitted structure) and an SEI richer in fluorophosphates.

Overall, it appears that the Gen2 electrolyte is not an ideal choice for commercialization of Si-based electrodes because of its continuous decomposition upon cycling. Thus, alternative salts and solvents have been explored, and the beneficial effect of FEC and LiTFSI to improve the SEI stability is proposed in terms of mitigating the silicon corrosion. In addition, our initial studies suggest that, at prolonged galvanostatic cycling, the passivation behavior of the a-Si electrode improves by using glyme electrolyte/LiFSI salts compared to the more traditional Gen2 electrolyte.

Finally, the role of carbon coatings was analyzed. In a potential commercialization of Si-based anode materials, this aspect will also require optimization, because our studies demonstrate that drastically different Si solid-state transformation occurs during the electrochemical process due to the different types of carbon precursors and carbon coatings used on the same Si nanoparticles.

Part 3: (Re)engineering of the Si/Electrolyte Interface via Molecular Interactions

The above data demonstrate a dynamic SEI that differs depending on the electrolyte composition, surface chemistry of the electrodes, and electrolyte additives. The data show a set of complex correlations that are beginning to be unraveled using model electrodes, theory and simulation, and state-of-the-art characterization studies. The data point to the need to design new Si interfaces with electrolytes that will lead to more stable SEI layers. These are topics that are currently being pursued with new electrode chemistries that will provide avenues of research to stable Si electrodes and enable high energy-density electrodes (>350 Wh/kg).

References

Part 1: Studies of SiO₂ Interfaces

1. B. Han, C. Liao, F. Dogan, S.E. Trask, S.H. Lapidus, J.T. Vaughey, B. Key, Using Mixed Salt Electrolytes to Stabilize Silicon Anodes for Lithium-Ion Batteries via in Situ Formation of Li-M-Si Ternaries (M = Mg, Zn, Al, Ca). *ACS Appl. Mater. Interfaces* 11, 29780–29790 (2019).
2. K.N. Wood et al., *Comm.* 9, 2490 (2018).
3. A. Zur, T.C. McGill, Lattice match: An application to heteroepitaxy. *J. Appl. Phys.* 55, 378–386 (1984).
4. M. Aykol, K.A. Persson, *ACS Appl. Mater. Interfaces* 10, 3039–3045 (2018).
5. X. Chen, P.M. Vereecken. Solid and Solid-Like Composite Electrolyte for Lithium Ion Batteries: Engineering the Ion Conductivity at Interfaces. *Adv. Mater. Interfaces* 6, 1800899 (2019).

6. M. Schnabel, S. Harvey, E. Arca, G. Teeter, C. Ban, P. Stradins. Lithiation of Oxidized Silicon. Talk at the ECS conference (May 2019); Journal paper in preparation.
7. Y. Xu, C. Stetson, K. Wood, E. Sivonxay, C. Jiang, G. Teeter, S. Pylypenko, S.D. Han, K.A. Persson, A. Burrell, A. Zakutayev, Mechanical Properties and Chemical Reactivity of Li_xSiO_y Thin Films. *ACS Appl. Mater. Interfaces* 10, 38558 (2018).
8. Y. Xu, K. Wood, J. Coyle, C. Engtrakul, G. Teeter, C. Stoldt, A. Burrell, A. Zakutayev, Chemistry of Electrolyte Reduction on Lithium Silicide. *J. Phys. Chem. C* 123, 13219 (2019).
9. R. Kumar, A. Tokranov, B.W. Sheldon, X.C. Xiao, Z.Q. Huang, C.Z. Li, T. Mueller, In Situ and Operando Investigations of Failure Mechanisms of the Solid Electrolyte Interphase on Silicon Electrodes, *ACS Energy Lett.* 1, 689 (2016).
10. C.Y. Dai, C.S. Li, H.Y. Huang, Z. Wang, X.X. Zhu, X.B. Liao, X. Chen, Y. Pan, D.N. Fang, In Situ Strain Measurements and Stress Analysis of $\text{SiO}@C$ Composite Electrodes during Electrochemical Cycling by Using Digital Image Correlation, *Solid State Ionics* 331, 56 (2019).
11. R. Kumar, P. Lu, X.C. Xiao, Z.Q. Huang, B.W. Sheldon, Strain-Induced Lithium Losses in the Solid Electrolyte Interphase on Silicon Electrodes, *ACS Appl Mater Inter.* 9, 28406 (2017).
12. F. Paloukis, C. Elmasides, F. Farmakis, P. Selinis, S.G. Neophytides, N. Georgoulas, *J. Power Sources* 331, 285–292 (2016).
13. S.L. Randzio, J. Suurkuusk, A.E. Beezer (Ed.). *Biological Microcalorimetry*, Academic Press, pp. 311–341 (1980).
14. L.J. Krause, L.D. Jensen, J.R. Dahn. *J. Electrochem. Soc.* 159, A937–A943 (2012).
15. L.M. Housel et al. *ACS Appl. Mater. & Interfaces*, accepted (2019).
16. T. Gruber, D. Thomas, C. Röder, F. Mertens, J. Kortus, Raman spectroscopic studies of Li_xSi_y compounds. *Journal of Raman Spectroscopy* 44 (6), 934–938 (2013).
17. R.E. Ruther, K.A. Hays, S.J. An, J. Li, D.L. Wood, J. Nanda, Chemical Evolution in Silicon–Graphite Composite Anodes Investigated by Vibrational Spectroscopy. *ACS Applied Materials & Interfaces* 10(22), 18641–18649 (2018).

Part 2: Origins of Si/Electrolyte Interface Stability

1. E. Peled, *J. Electrochem. Soc.* 126, 2047–2051 (1979).
2. M. Winter, *Zeitschrift für Phys. Chemie.* 223, 1395–1406 (2009).
3. M.N. Obrovac, V.L. Chevrier, *Chem. Rev.* 114, 11444–11502 (2014).
4. K.N. Wood, G. Teeter. *ACS Appl. Energy Mater.* 1, 4493–4504 (2019).
5. Yoon et al., *J. Electrochem. Soc.* 164 (9), A2082 (2017).
6. Parimalan et al., *J. Phys Chem. C* 121, 22733 (2017).
7. Lu et al., *ChemElectroChem* 4, 2012–2018 (2017).
8. Phillippe et al., *Chem. Mat.* 25, 394–404 (2013).
9. Phillippe et al., *J. Am. Chem Soc.* 135, 9829–9842 (2013).
10. J.G. Lee, *J. Electrochem. Soc.* 162, A1579–A1584 (2015).
11. N. Azimi, et al, *J. Electrochem. Soc.* 162 (1), A64–A68, (2015).
12. X. Ren, et al., *Joule* 3, 1662–1676, (2019).
13. J. Miao, C.V. Thompson, *J. Electrochem. Soc.* 165, A650–A656, (2018).

14. J. Nanda, et al., *Joule* 3, 2001–2019, (2019).
15. T. Hou, et al., *Nano Energy* 64, 103881 (2019).
16. K. Xu, *Chem. Rev.* 104, 4303–4417, (2014).

Part 3: (Re)engineering of the Si/Electrolyte Interface via Molecular Interactions

1. [J. Nanda, G. Yang, T. Hou, D.N. Voylov, X. Li, R.E. Ruther, M. Naguib, K. Persson, G.M. Veith, A.P. Sokolov, Unraveling the Nanoscale Heterogeneity of Solid-Electrolyte Interphase Using Tip-Enhanced Raman Spectroscopy. *Joule* 3, 2001–2019 (2019).
2. T. Hou, G. Yang, N.N. Rajput, J. Self, S.W. Park, J. Nanda, K.A. Persson, The Influence of FEC on the Solvation Structure and Reduction Reaction of LiPF₆/EC Electrolytes and its Implication for Solid Electrolyte Interphase Formation. *Nano Energy* 64, 103881 (2019).
3. G.V. Zhuang, H. Yang, P.N. Ross, K. Xu, T.R. Jow, Lithium Methyl Carbonate as a Reaction Product of Metallic Lithium and Dimethyl Carbonate. *Electrochemical and Solid-State Letters* 9, A64–A68 (2006).
4. H. Liu, X. Wang, H. Zhou, H.D. Lim, X. Xing, Q. Yan, Y.S. Meng, P. Liu, Structure and Solution Dynamics of Lithium Methyl Carbonate as a Protective Layer For Lithium Metal. *ACS Applied Energy Materials* 1, 1864–1869 (2018).
5. G.V. Zhuang, K. Xu, H. Yang, T.R. Jow, P.N. Ross, Lithium Ethylene Dicarboxate Identified as the Primary Product of Chemical and Electrochemical Reduction of EC in 1.2 M LiPF₆/EC:EMC Electrolyte. *Journal of Physical Chemistry B* 109, 17567–17573 (2005).
6. L. Wang, A. Menakath, F. Han, Y. Wang, P.Y. Zavalij, K.J. Gaskell, O. Borodin, D. Iuga, S.P. Brown, C. Wang, K. Xu, B.W. Eichhorn, Identifying the Components of the Solid–Electrolyte Interphase in Li-Ion Batteries. *Nature Chemistry* 11, 789–796 (2019).
7. F. Shi, P.N. Ross, H. Zhao, G. Liu, G.A. Somorjai, K. Komvopoulos, A Catalytic Path for Electrolyte Reduction in Lithium-Ion Cells Revealed by In Situ Attenuated Total Reflection-Fourier Transform Infrared Spectroscopy. *J. Am. Chem. Soc.* 137, 3181–3184 (2015).
8. F. Shi, P.N. Ross, G.A. Somorjai, K. Komvopoulos, The Chemistry of Electrolyte Reduction on Silicon Electrodes Revealed by In Situ ATR-FTIR Spectroscopy. *Journal of Physical Chemistry C* 121, 14476–14483 (2017).
9. R. Baddour-Hadjean, J.P. Pereira-Ramos, Raman Microspectrometry Applied to the Study of Electrode Materials for Lithium Batteries. *Chemical Reviews* 110, 1278–1319 (2010).
10. D. Liu, Z. Shadike, R. Lin, K. Qian, H. Li, K. Li, S. Wang, Q. Yu, M. Liu, S. Ganapathy, X. Qin, Q.H. Yang, M. Wagemaker, F. Kang, X.Q. Yang, B. Li, Review of Recent Development of In Situ/Operando Characterization Techniques for Lithium Battery Research. *Adv. Mater.* 31 (2019).
11. G. Yang, I.N. Ivanov, R.E. Ruther, R.L. Sacchi, V. Subjakova, D.T. Hallinan, J. Nanda, Electrolyte Solvation Structure at Solid-Liquid Interface Probed by Nanogap Surface-Enhanced Raman Spectroscopy. *ACS Nano* 12, 10159–10170 (2018).
12. J.L. Allen, O. Borodin, D.M. Seo, W.A. Henderson, Combined Quantum Chemical/Raman Spectroscopic Analyses of Li⁺ Cation Solvation: Cyclic Carbonate Solvents-Ethylene Carbonate and Propylene Carbonate. *J. Power Sources* 267, 821–830 (2014).
13. S.D. Han, S.H. Yun, O. Borodin, D.M. Seo, R.D. Sommer, V.G. Young, W.A. Henderson, Solvate Structures and Computational/Spectroscopic Characterization of LiPF₆ Electrolytes. *J. Phys. Chem. C* 119, 8492–8500 (2015).
14. V. Etacheri, R. Marom, R. Elazari, G. Salitra, D. Aurbach, Challenges in the Development of Advanced Li-Ion Batteries: A Review. *Energy Environ. Sci.* 4, 3243–3262 (2011).

15. A. Wang, S. Kadam, H. Li, S. Shi, Y. Qi, Review on Modeling of the Anode Solid Electrolyte Interphase (SEI) for Lithium-Ion Batteries. *npj Comput. Mater* 4, 1–26 (2018).
16. C. Erk, T. Brezesinski, H. Sommer, R. Schneider, J. Janek, Toward Silicon Anodes for Next-Generation Lithium-Ion Batteries: A Comparative Performance Study of Various Polymer Binders and Silicon Nanopowders. *ACS Applied Materials & Interfaces* 5, 7299–7307 (2013).
17. S.J. Rezvani, M. Pasqualini, A. Witkowska, R. Gunnella, A. Birrozzi, M. Minicucci, H. Rajantie, M. Copley, F. Nobili, A. Di Cicco, Binder-Induced Surface Structure Evolution Effects on Li-Ion Battery Performance. *Applied Surface Science* 435, 1029–1036 (2018).
18. J. Li, R.B. Lewis, J.R. Dahn, Sodium Carboxymethyl Cellulose: A Potential Binder for Si Negative Electrodes for Li-Ion Batteries. *Electrochemical and Solid-State Letters* 10, A17–A20 (2007).
19. A. Magasinski, B. Zdyrko, I. Kovalenko, B. Hertzberg, R. Burtovyy, C.F. Huebner, T.F. Fuller, I. Luzinov, G. Yushin, Toward Efficient Binders for Li-Ion Battery Si-Based Anodes: Polyacrylic Acid. *ACS Applied Materials & Interfaces* 2, 3004–3010 (2010).
20. B.T. Young, C.C. Nguyen, A. Lobach, D.R. Heskett, J.C. Woicik, B.L. Lucht, Role of Binders in Solid-Electrolyte Interphase Formation in Lithium-Ion Batteries Studied with Hard X-Ray Photoelectron Spectroscopy. *J. Mater. Res.* 34, 97–106 (2018).
21. M. Wu, X. Xiao, N. Vukmirovic, S. Xun, P.K. Das, X. Song, P. Olalde-Velasco, D. Wang, A.Z. Weber, L.W. Wang, V.S. Battaglia, W. Yang, G. Liu, Toward an Ideal Polymer Binder Design for High-Capacity Battery Anodes. *J. Am. Chem. Soc.* 135, 12048–12056 (2013).
22. J.J. Maurer, D.J. Eustace, C.T. Ratcliffe, Thermal Characterization of Poly(Acrylic Acid). *Macromolecules* 20, 196–202 (1987).
23. K. Edström, M. Herstedt, D.P. Abraham, A New Look at the Solid-Electrolyte Interphase on Graphite Anodes in Li-Ion Batteries. *Journal of Power Sources* 153, 380–384 (2006).
24. G.M. Veith, L. Baggetto, R.L. Sacci, R.R. Unocic, W.E. Tenhaeff, J.F. Browning, Direct Measurement of the Chemical Reactivity of Silicon Electrodes with LiPF₆-Based Battery Electrolytes. *Chem. Comm.* 50, 3081–3084 (2014).
25. G.M. Veith, M. Doucet, J.K. Baldwin, R.L. Sacci, T.M. Fears, Y. Wang, J.F. Browning, Direct Determination of Solid-Electrolyte Interphase Thickness and Composition as a Function of State of Charge on a Silicon Anode. *J. Phys. Chem. C* 119, 20339–20349 (2015).
26. T.M. Fears, M. Doucet, J.F. Browning, J.K.S. Baldwin, J.G. Winiarz, H. Kaiser, H. Taub, R.L. Sacci, G.M. Veith, Evaluating the Solid-Electrolyte Interphase Formed on Silicon Electrodes: A Comparison of Ex Situ X-Ray Photoelectron Spectroscopy and In Situ Neutron Reflectometry. *Phys. Chem. Chem. Phys.* 18, 13927–13940 (2016).
27. G.M. Veith, M. Doucet, R.L. Sacci, B. Vacaliuc, J.K. Baldwin, J.F. Browning, Determination of the Solid-Electrolyte Interphase Structure Grown on a Silicon Electrode Using a Fluoroethylene Carbonate Additive. *Scientific Reports* 7, 6326 (2017).
28. K.L. Browning, J.F. Browning, M. Doucet, N.L. Yamada, G. Liu, G.M. Veith, Role of Conductive Binder to Direct Solid–Electrolyte Interphase Formation over Silicon Anodes. *Physical Chemistry Chemical Physics* 21, 17356–17365 (2019).
29. Z. Karkar, D. Guyomard, L. Roué, B. Lestriez, A Comparative Study of Polyacrylic Acid (PAA) and Carboxymethyl Cellulose (CMC) Binders for Si-Based Electrodes. *Electrochimica Acta* 258, 453–466 (2017).
30. C.C. Nguyen, T. Yoon, D.M. Seo, P. Guduru, B.L. Lucht, Systematic Investigation of Binders for Silicon Anodes: Interactions of Binder with Silicon Particles and Electrolytes and Effects of Binders

on Solid Electrolyte Interphase Formation. ACS Applied Materials & Interfaces 8, 12211–12220 (2016).

31. S. Komaba, N. Yabuuchi, T. Ozeki, K. Okushi, H. Yui, K. Konno, Y. Katayama, T. Miura, Functional Binders for Reversible Lithium Intercalation into Graphite in Propylene Carbonate and Ionic Liquid Media. Journal of Power Sources 195, 6069–6074 (2010).
32. K. Ui, D. Fujii, Y. Niwata, T. Karouji, Y. Shibata, Y. Kadoma, K. Shimada, N. Kumagai, Analysis of Solid-Electrolyte Interface Formation Reaction and Surface Deposition of Natural Graphite Negative Electrode Employing Polyacrylic Acid as a Binder. Journal of Power Sources 247, 981–990 (2014).
33. L.M. Wheeler, N.C. Anderson, P.K.B. Palomaki, J.L. Blackburn, J.C. Johnson, N.R. Neale, Silyl Radical Abstraction in the Functionalization of Plasma-Synthesized Silicon Nanocrystals. Chem. Mater. 27, 6869–6878 (2015).
34. M.P. Hanrahan, Y. Chen, R. Blome-Fernández, J.L. Stein, G.F. Pach, M.A.S. Adamson, N.R. Neale, B.M. Cossairt, J. Vela, A.J. Rossini, Probing the Surface Structure of Semiconductor Nanoparticles by DNP SENS with Dielectric Support Materials. J. Am. Chem. Soc. 141, 15532–15546 (2019).

Acknowledgements

Part 1: Studies of SiO₂ Interfaces

Contributors: Kristin Persson (LBNL), Manuel Schnabel (NREL), Chunmei Ban (NREL), Steve Harvey (NREL), Glenn Teeter (NREL), Paul Stradins (NREL), Zhifei Li (NREL), Andriy Zakutayev (NREL), Jaelyn Coyle (NREL), Kyle Fenton (SNL), Josey McBrayer (SNL), Chris Apblett (SNL), Mike Carroll (NREL), Fernando Urias (NREL), Greg Pach (NREL), Nathan Neale (NREL), Gabriel Veith (ORNL), Brenda Smith (ORNL), Rebecca McAuliffe (ORNL), Eric Allcorn (SNL), Jill Langendorf (SNL), Teal Harbour (SNL), Yeyoung Ha (NREL), Caleb Stetson (NREL), Andrew Norman (NREL), Bertrand Tremolet de Villers (NREL), Mowafak Al-Jassim (NREL), Sang-Don Han (NREL), Binghong Han (ANL), Baris Key (ANL), Jack Vaughey (ANL)

Part 2: Origins of Si/Electrolyte Interface Stability

Contributors: I. Hasa, E. Arca, S. Jurng, L. Zhang, P. Ross, G. Liu, R. Kostecki (LBNL), Y. Ha, C. Stetson, S. Harvey, G. Teeter, B. Tremolet de Villers, C.-S. Jiang, M. Al-Jassim, S.-D. Han, Y. Yin, A. Norman, M. Al-Jassim, (NREL), G. Yang, G. Veith, and J. Nanda (ORNL)

Part 3: (Re)engineering of the Si/Electrolyte Interface via Molecular Interactions

Contributors: Gabriel Veith (ORNL), Nate Neale (NREL), Jagjit Nanda (ORNL), Guang Yang (ORNL), Zhangxing Shi (ANL), Lu Zhang (ANL), Michael Carroll (NREL), Kae Fink (NREL), Yeyoung Ha (NREL), Sang-Don Han (NREL), Tingzheng Hou (UC Berkeley), Matthew Keyser (NREL), Zhifei Li (NREL), Gregory Pach (NREL), Ryan Pekarek (NREL), Kristin Persson (UC Berkeley), Shriram Santhanagopalan (NREL), Eric Sivonxay (UC Berkeley), Pauls Stradins (NREL), Bertrand J. Tremolet de Villers (NREL), Fernando Urias-Cordero (NREL), and Andriy Zakutayev (NREL), Katie Browning (ORNL), Mathieu Doucet (ORNL), James Browning (ORNL)

II.1.C Probe the Relationships between Functional Electrolytes Structure and SEI Property for Si Materials (LBNL)

Gao Liu, Principal Investigator

Lawrence Berkeley National Laboratory
1 Cyclotron Road
Berkeley, CA 94720
E-mail: gliu@lbl.gov

Brian Cunningham, DOE Technology Development Manager

U.S. Department of Energy
E-mail: Brian.Cunningham@ee.doe.gov

Start Date: October 1, 2017

End Date: September 30, 2019

Project Funding (FY19): \$400,000

DOE share: \$400,000

Non-DOE share: \$0

Project Introduction

Electrolyte decomposition products play a critical role in stabilization of the negative electrodes in lithium-ion batteries, as the negative electrode is operated outside the stability window of the electrolyte. The electrolyte decomposition products form insoluble SEI layer, which stabilizes the electrode and electrolyte interface. Silicon alloy material has large volume expansion and surface reactions with the electrolyte when it is electrochemically lithiated (charge). When delithiated (discharge), the Si alloy volume shrinks and surface area also decreases. This dynamic surface area changes during charge and discharge cause increased side reactions with the electrolyte. Moreover, some of the electrolyte decomposition products are soluble in the electrolyte rather than solid precipitates, further increasing side reactions. Surface coatings on Si materials by organic and ceramic have demonstrated improved Si surface stability towards electrolytes. Nano-sizing the Si materials can successfully prevent cracking of Si material during volume changes. The Si particles are assembled by a functional polymeric binder to improve the electrode stability in a composite electrode. Surface coating on Si, electrolyte decomposition to form SEI, or Si coating by binders during electrode processing significantly influence the performance of the Si base electrode.

Objectives

The objective of this project is to prevent the electrolyte decomposition at the electrolyte and electrode interface via electrolyte additives and materials coatings.

Approach

First, new electrolyte additive design with consideration of the SEI structures and functions on the Si materials can lead to enhanced Si performance over the traditional mixed carbonate-based electrolyte. Designing organic molecules with preferred decomposition pathways during electrochemical process can lead to controlled SEI formation on Si surface. Second, the surface coating of the Si materials and its effectiveness will be evaluated. Third, use materials design and organic synthesis to design and fabricate the interface layer, and use advanced diagnostic experiments to investigate the ion transport properties through the interface layer. This experimental investigation can lead to an in-depth understanding of the Si interface and SEI layer, and provide material solutions to reduce Si surface reactions.

Results

1. Superior carbon coating alters Si materials transformation during electrochemical process

To address the large volume change and excessive surface reaction of silicon materials during lithiation and delithiation reaction, carbon coating as an electric conductive medium and electrolyte insulating buffering layer has been widely used to encapsulate the silicon particles. Despite the reported improved capacity retention of Si-based material by carbon coating, there is relatively less investigation of the Si material

transformation with the carbon coating. Moreover, there are many different carbon precursors for performing the carbon coating, which produce carbon coatings with different chemical and morphological carbon coatings. Here, we report the drastically different Si solid state transformation during electrochemical process due to the different types of carbon precursors and carbon coatings on the same Si nanoparticles.

High temperature thermal based carbonization process is used to produce carbon coating on Si nanoparticles. Organic based precursors are used to form carbon coatings. Different precursors tend to form carbon coating with different morphologies. Two types of carbon coatings can be formed on Si, one is highly graphitized and dense coating from a polymer precursor (Si/C-P), and another is more disorder structures from sucrose precursor. The Si materials with highly graphitized and dense coating is able to deliver higher gravimetric capacity and stable cycling compared to that of the Si with disordered carbon coating. The dramatic differences come from the Si materials transformation. The Si/C-P materials maintains a two-phase reaction during delithiation in the first 30 cycles, whereas the Si/C-S forms amorphous structure after 1st cycle, and does not form clear two-phase transformation during delithiation.

Si/C electrode with compact and ordered carbon coating was prepared with polyvinylidene chloride (Si/C-P electrode), and Si/C electrode with loose and porous carbon coating was made with sucrose (Si/C-S electrode) for comparison. The cells of the Si/C electrodes were cycled at C/10 between 1.00 V and 0.01 V after a formation step at C/20 ($1C=2,000 \text{ mAh g}^{-1}$). All the reported capacities are based on the total mass of Si/C composites. Figure II.1.C.1a presents the cycling performance and Coulombic Efficiency (CE) of Si/C-P and Si/C-S. The initial Coulombic Efficiency (CE) of Si/C-P (72.7%) is much higher than that of Si/C-S (56.1%). The compact carbon structure in Si/C-P sample can protect the silicon nanoparticles from direct exposure to the electrolyte, and thus lead to improved ICE. After the formation step, the CE of Si/C-P electrode increases to above 99.0% after 10 cycles and to 99.5% after 20 cycles. On the other hand, the CE of Si/C-S electrode stays below 99.0%. Si/C-P electrode exhibits a specific charge capacity of $1219.6 \text{ mAh g}^{-1}$ with the capacity retention of 98.1% after 20 cycles at C/10, which is higher than those of Si/C-S electrode, 692.7 mAh g^{-1} and 77.0 %, respectively. At the 25th cycle, the CE of Si/C-P electrode experiences a sharp decrease, dropping from 99.8 % to 98.6 %, which is rationalized as a consequence of the fracture of the carbon coating. After the fracture of the carbon coating, the CE of the Si/C-P electrode drops to about 98%, which is very similar to that of Si/C-S electrode. During the 30-50th cycle, the Si/C-P electrode presents a gradually decreasing capacity from 1149.5 to $1078.0 \text{ mAh g}^{-1}$, and the capacity retention ratio of Si/C-P electrode during these 20 cycles is 93.8%. These results indicate that the more compact carbon coating of the Si/C-P material helps to decrease interface reaction and increase cell life. In addition, after the break-down of the carbon coating on the Si/C-P sample, the interface stability of the Si/C-P sample begins to decay.

To better understand the electrochemical behavior of the Si/C-P electrode during lithiation and de-lithiation process, the voltage profiles of Si/C-P electrode from the 2nd-50th cycles are examined in Figure II.1.C.1b. There is a major plateau at 0.43 V for the 2nd-20th de-lithiation curves, which disappears beyond the 30th cycle where the carbon coating is fractured. The disappearance of the voltage plateau at 0.43V indicates a significant bulk structure change during lithiation and de-lithiation processes due to the carbon coating fracturing. This is the first observation of the influence of compact and ordered carbon coating on bulk Si particle structure transformation during electrometrical process. Figure II.1.C.1c shows dQ/dV plots for Si/C-P electrode for 2nd-50th cycles. During the 2nd lithiation cycle, three different processes are observed. The first discharge process at $\sim 250 \text{ mV}$ is associated with the gradual lithiation of the a-Si to form $\text{Li}_{-2.0}\text{Si}$, a structure that still presents extended Si networks and large Si-Si clusters. The second process at $\sim 80 \text{ mV}$ is related to the further lithiation of $\text{Li}_{-2.0}\text{Si}$ to $\text{Li}_{-3.5}\text{Si}$. At this stage, large Si-Si clusters broke into smaller Si clusters and isolated Si anions. The third process at $\sim 35 \text{ mV}$ corresponds to the formation of the crystalline phase, c- $\text{Li}_{3.75}\text{Si}$, from a- Li_xSi . The third process is not observed beyond the 30th cycle. As for the de-lithiation process, there is a strong and sharp peak at $\sim 430 \text{ mV}$ for the 2nd-20th cycles, which is associated with the two-phase transition from c- $\text{Li}_{3.75}\text{Si}$ to Li_xSi ($x=0-2.0$). In this case, the x value is approaching 0 to reflect the dominating two-phase transition from $\text{Li}_{3.75}\text{Si}$ to almost de-lithiated amorphous Si, with minor transition from Li_xSi to a-Si phase. However, beyond the 30th cycle, where the carbon coating is fractured, two broad peaks at $\sim 280 \text{ mV}$

and ~500 mV are observed instead (no sharp peak at ~430 mV), which is indicator of solid solution reaction. This observation demonstrates that the formation of $c\text{-Li}_{3.75}\text{Si}$ is no longer the dominating process and that there is no direct transformation from $c\text{-Li}_{3.75}\text{Si}$ to amorphous Si particles. To be more specific, the two broad peaks are associated with the de-lithiation process of Li_xSi ($x=3.5\text{--}3.75$) to $\text{Li}_{-3.5}\text{Si}$ (~280 mV) and $\text{Li}_{-3.5}\text{Si}$ to $\text{Li}_{-2.0}\text{Si}$ (~500 mV). The compact and unbroken carbon coating can enhance the kinetic property of the Si alloying reaction by improving the conductivity of Si and by promoting the formation of the small Si clusters and isolated Si anions with uniformly dispersed silicon particles. And due to the enhanced alloying kinetics, the Si/C-P electrode can continuously generate $c\text{-Li}_{3.75}\text{Si}$ during lithiation process.

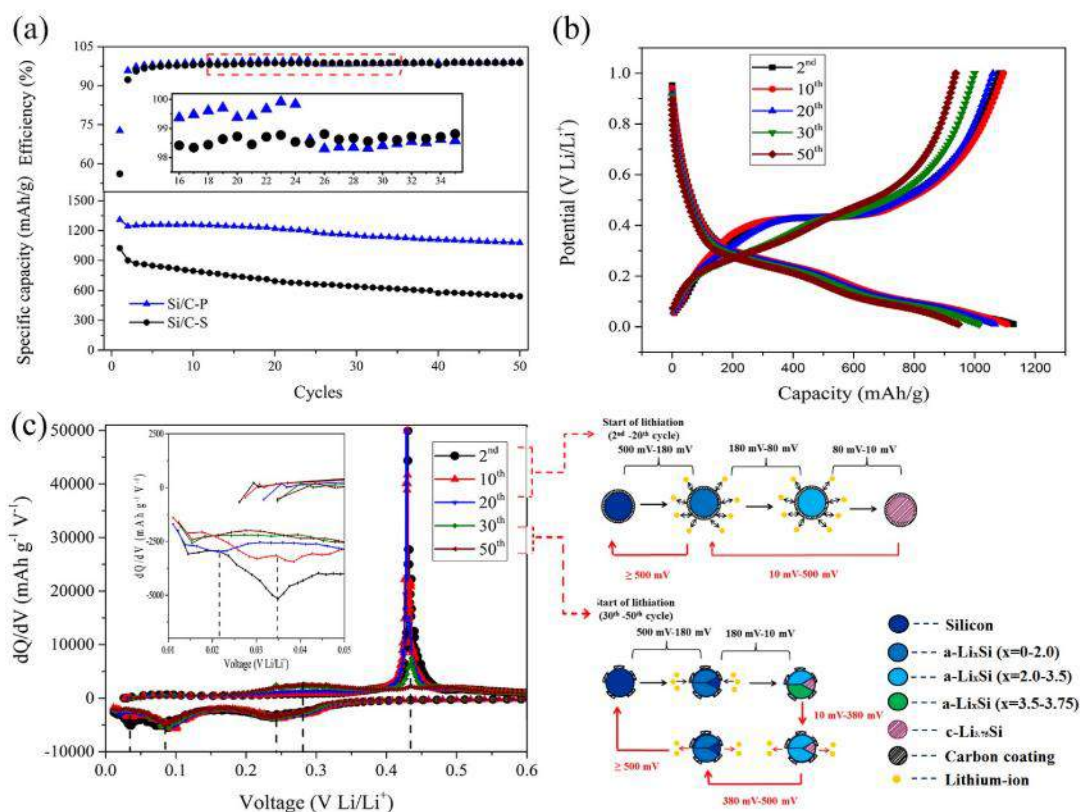


Figure II.1.C.1 (a) Cycling performances and Coulombic efficiencies of Si/C-P and Si/C-S electrodes at C/10, from 1.00V to 0.01V; (b) Galvanostatic discharge/charge profiles of Si/C-P electrode from 2nd to 50th cycles at C/10, from 1.00V to 0.01V; (c) Differential capacity vs. potential curves of Si/C-P electrode from 2nd to 50th cycles at C/10, from 1.00V to 0.01V (1C=2,000 mAh g⁻¹)

2. Electrolyte additives and detection

The solid electrolyte interphase (SEI) formed during the cycling of lithium-ion batteries by the decomposition of lithium salt and solvent molecules plays a crucial role for the device performance. However, the detailed decomposition process and distribution of products remains elusive due to the wide variety of electrochemical pathways and the lack of facile analytical methods for chemical characterization of SEIs. In this report, a gradient polarity solvent wash (gradient wash) technique involving the use of solvents with gradually increased polarities is employed to sequentially remove different SEI components from electrode surfaces and near surface. Fourier transform infrared (FTIR) spectroscopy is utilized to characterize the SEIs composition. The impacts of electrolyte additives and discharge rates over SEI formation are illustrated. This study presents a new concept of rationally controlled solvent wash technique for electrode surface analysis that can selectively remove targeted components with gradient wash of the targeted electrode (Figure II.1.C.2). The gradient wash of electrodes was performed in glass vials, where the electrodes were immersed under 5 ml solvents with gentle manual agitation. The solvents used were 0% to 100% volume ratio ethyl acetate (EA) in hexane (Hex)

solutions with 10-percent intervals (*i.e.*, 0%, 10%, 20%, 30% EA/Hex, *etc.*). After rinsing, the electrodes were immediately dried and stored under vacuum until FTIR characterization.

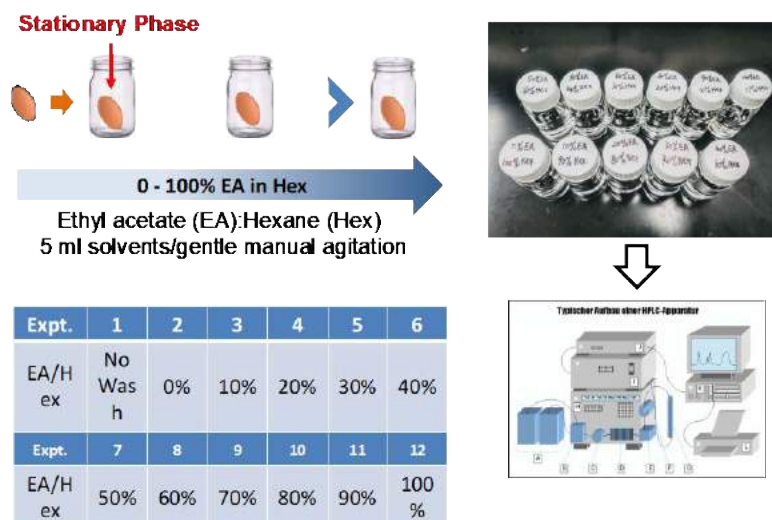


Figure II.1.C.2 Schematics of the gradient polarity solvent wash technique

We examine the SEIs and near SEIs produced with both polar methacrylate additive under different electrochemical conditions by gradient wash. Cu electrodes are electrochemically cycled with LiPF_6 ethylene carbonate/ethyl methyl carbonate (EC/EMC) electrolyte containing the additive. With a binary solvent system of a non-polar solvent and a polar solvent at various ratios, it is possible to selectively remove different SEI components. The electrode surfaces before and after each wash protocol are characterized with FTIR for identification of the decomposition products.

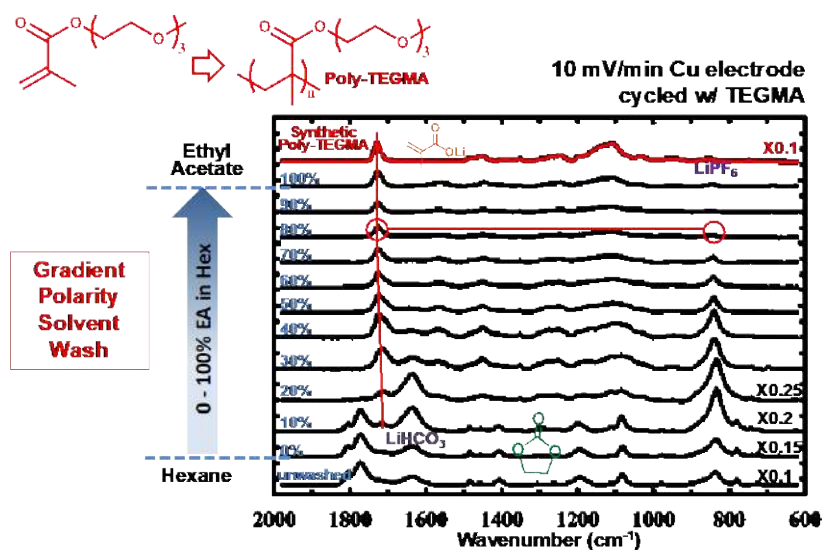


Figure II.1.C.3 Gradient polarity solvent wash was applied to a Cu electrode polarized to 10 mV Li/Li+

TEGMA additive also produced a poly-TEGMA film on the Cu electrode surface, which, due to its high polarity, did not resist adsorption of residue electrolyte (EC/EMC: LiPF_6 solvates, 1809, 1780, 1269, 1196, 1082, 833 cm^{-1}) and Li_2CO_3 (1510, 1419 cm^{-1}) as shown in Figure II.1.C.3, Spectrum I. The poly-TEGMA layer was fully exposed after gradient wash with 0-30% EA/Hex solvents. This polar polymer film also survived all remaining washing steps. Its chemical composition was confirmed with the synthetic sample. The

removal of electrolyte species with 0-30% EA/Hex solutions is consistent with the case of the base electrolyte. It is worth noting that the carbonyl peak for poly-TEGMA at 1726 cm^{-1} presented a slight red shift before removal of lithium salt species due to solvation effect.

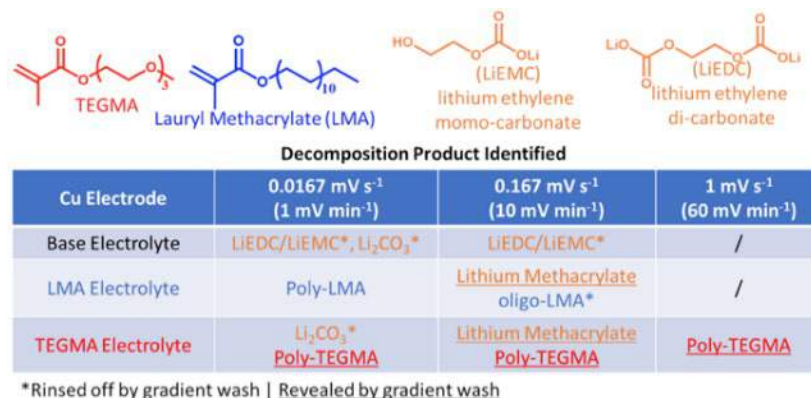


Figure II.1.C.4 Three different scanning rates of CV at 1, 10 and 60 mV min⁻¹ were applied to the Cu electrodes respectively with baseline electrolyte and two additives-based electrolytes. The Cu surface species vary due to both the additives and scan rates

The scanning rate or the potential step-down rate from 3V to 10 mV has a significant impact to the surface film (SEI) and near surface species formation (Figure II.1.C.4). At slow to medium rate of 1 to 10 mV min⁻¹, the baseline electrolyte (EC/EMC:LiPF₆) facilitates the formation of LiEDC/LiEMC salts on the Cu surface. In the two additives based electrolyte containing systems, they are predominantly additives derived polymer films on the Cu surface instead of lithium salt species. The species on the Cu surfaces can be clearly observed with gradient wash technique. However, when the voltage step rate is 60 mV min⁻¹, the Cu surface are free of deposition of decomposition products with the baseline electrolyte. A highly polar TEGMA additive tends to stick to the surface of the Cu at this fast scan rate. Therefore, the chemistry of SEI formation is dependent on the reaction rate, where lower lithiation rate favors the formation of lithium salts on the electrode surface, and faster rate promote the formation of polar organic decomposition products.

Conclusions

A compact and intact carbon matrix has been prepared by polyvinylidene chloride to encapsulate silicon nanoparticles. The Si/C-P electrode shows excellent electrochemical performance and improved CE, which reached to 99% only after 10 cycles. When the carbon matrix maintained intact, there was a two-phase reaction in Si/C-P electrode during cycling process. The Si/C-S sample prepared by sucrose presented a loose carbon structure where only one-phase reaction happened during cycling process at 0.1C. These results indicate that a compact and intact carbon matrix can improve Li⁺ migration and the integration of the electrode, which facilitates the formation of the c-Li_{3.75}Si during discharge and charge process.

Gradient polarity solvent wash of electrode surface was utilized to analyze the decomposition products of EC-based electrolyte with FTIR spectroscopy. The gradient wash technique has been proven applicable for both Cu and Si electrodes. This methodology not only can serve as an analytical tool itself, but also provides a facile surface process strategy that can fractionate SEI components. Consequently, selective removal of targeted components such as residue electrolyte molecules can be readily achieved.

Key Publications

1. Zheng, T. Y.; Zhang, T.; de la Fuente, M. S.; Liu, G., Aqueous emulsion of conductive polymer binders for Si anode materials in lithium ion batteries. *Eur. Polym. J.* 2019, 114, 265-270.
2. Zhao, H.; Wei, Y.; Wang, C.; Qiao, R. M.; Yang, W. L.; Messersmith, P. B.; Liu, G., Mussel-Inspired Conductive Polymer Binder for Si-Alloy Anode in Lithium-Ion Batteries. *Acs Applied Materials & Interfaces* 2018, 10 (6), 5440-5446.

3. Yao, K.; Ling, M.; Liu, G.; Tong, W., Chemical Reduction Synthesis and Electrochemistry of Si-Sn Nanocomposites as High-Capacity Anodes for Li-Ion Batteries. *J. Phys. Chem. Lett.* 2018, 9 (17), 5130-5134.
4. Yang, S. M.; Gu, Y. Y.; Qu, Q. T.; Zhu, G. B.; Liu, G.; Battaglia, V. S.; Zheng, H. H., Engineered Si@alginate microcapsule-graphite composite electrode for next generation high-performance lithium-ion batteries. *Electrochim. Acta* 2018, 270, 480-489.
5. Sabisch, J. E. C.; Anapolsky, A.; Liu, G.; Minor, A. M., Evaluation of using pre-lithiated graphite from recycled Li-ion batteries for new LiB anodes. *Resour. Conserv. Recycl.* **2018**, 129, 129-134.
6. Gao, X. M.; Zhu, G. B.; Qu, Q. T.; Liu, G.; Battaglia, V. S.; Zheng, H. H., Effects of Room Ionic Liquid as Solute on the Electrolyte Solution Structure and Electrochemical Performances in Ethylene Carbonate- Based Electrolyte. *J. Electrochem. Soc.* 2018, 165 (16), A3844-A3853.
7. Gao, X. M.; Ding, Y. L.; Qu, Q. T.; Liu, G.; Battaglia, V. S.; Zheng, H. H., Optimizing solid electrolyte interphase on graphite anode by adjusting the electrolyte solution structure with ionic liquid. *Electrochim. Acta* 2018, 260, 640-647.
8. Fang, S.; Li, N.; Zheng, T. Y.; Fu, Y. B.; Song, X. Y.; Zhang, T.; Li, S. P.; Wang, B.; Zhang, X. G.; Liu, G., Highly Graphitized Carbon Coating on SiO with a - Stacking Precursor Polymer for High Performance Lithium-Ion Batteries. *Polymers* 2018, 10 (6).
9. Chen, H.; Ling, M.; Hencz, L.; Ling, H. Y.; Li, G. R.; Lin, Z.; Liu, G.; Zhang, S. Q., Exploring Chemical, Mechanical, and Electrical Functionalities of Binders for Advanced Energy-Storage Devices. *Chem. Rev.* 2018, 118 (18), 8936-8982.

References

1. Li, J.-Y.; Xu, Q.; Li, G.; Yin, Y.-X.; Wan, L.-J.; Guo, Y.-G. "Research progress regarding Si-based anode materials towards practical application in high energy density Li-ion batteries." *Materials Chemistry Frontiers*, 2017, 9, 1691-1708.
2. Zuo, X.; Zhu, J.; Müller-Buschbaum, P.; Cheng, Y.-J. "Silicon based lithium-ion battery anodes: A chronicle perspective review." *Nano Energy*, 2017, 31, 113-143.
3. Ryu, J.; Chen, T.; Bok, T.; Song, G.; Ma, J.; Hwang, C.; Luo, L.; Song, H.-K.; Cho, J.; Wang, C. "Mechanical mismatch-driven rippling in carbon-coated silicon sheets for stress-resilient battery anodes." *Nature communications*, 2018, 1, 2924.
4. Higgins, T. M.; Park, S.-H.; King, P. J.; Zhang, C.; McEvoy, N.; Berner, N. C.; Daly, D.; Shmeliov, A.; Khan, U.; Duesberg, G. "A commercial conducting polymer as both binder and conductive additive for silicon nanoparticle-based lithium-ion battery negative Electrodes." *Acs Nano*, 2016, 3, 3702-3713.
5. J. R. Szczech and S. Jin, *Energy Environ. Sci.*, **4** (1), 56-72 (2011).
6. M. T. McDowell, S. W. Lee, W. D. Nix, and Y. Cui, *Adv. Mater.*, **25** (36), 4966-4985 (2013).
7. K. Xu, *Chem. Rev.*, **114** (23), 11503-11618 (2014).
8. X. Yu and A. Manthiram, *Energy Environ. Sci.*, **11** (3), 527-543 (2018).
9. K. Xu and A. von Cresce, *J. Mater. Chem.*, **21** (27), 9849-9864 (2011).
10. K. Xu, *Chem. Rev.*, **104** (10), 4303-4418 (2004).
11. L. Chen, K. Wang, X. Xie, and J. Xie, *J. Power Sources*, **174** (2), 538-543 (2007).

II.1.D Development of Si-based High-Capacity Anodes (PNNL)

Ji-Guang Zhang, Principal Investigator

Pacific Northwest National Laboratory
902 Battelle Boulevard, Mail Stop K2-44
Richland, WA 99354
E-mail: Jiguang.Zhang@pnnl.gov

Xiaolin Li, Principal Investigator

Pacific Northwest National Laboratory
902 Battelle Boulevard, Mail Stop K2-44
Richland, WA 99354
E-mail: Xiaolin.li@pnnl.gov

Brian Cunningham, DOE Technology Development Manager

U.S. Department of Energy
E-mail: Brian.Cunningham@ee.doe.gov

Start Date: October 1, 2018

End Date: September 30, 2020

Project Funding (FY19): \$500,000

DOE share: \$500,000

Non-DOE share: \$0

Project Introduction

Nano-Si, or highly porous structured Si, has been widely used to avoid pulverization of Si particles during battery cycling. However, the large surface area of nano-Si or micron-sized porous Si may also lead to a continuous reaction between lithiated Si and electrolyte. This reaction may lead to continuous growth of the SEI layer and higher cell impedance. Another possible degradation mechanism is cross talk between the Si anode and cathode. Dissolved Mn in the cathode may poison the Si anode; FEC additive, which is highly effective in forming a stable SEI layer on Si, may form a detrimental cathode-electrolyte interphase (CEI) on the cathode surface, which also increases impedance. Therefore, minimizing the surface area of Si and finding a stable electrolyte additive are critical for long-term stability of Si-based Li-ion batteries (LIBs).

Objectives

The objectives of this project are to enhance the cycle life and calendar life of Si-based LIBs by designing a stable porous Si structure. New electrolytes with more-stable salts, solvents, and additives will be developed to form a stable SEI layer on the Si anode and a stable CEI layer on the cathode to enable long-term cycling of Si-based LIBs. The degradation mechanism of Si anodes during shelf storage will be systematically investigated. New insight on these mechanisms and the new approaches developed in this work will speed up the deployment of high energy LIBs with Si-based anodes and increase market penetration of EVs and PHEVs, as required by DOE/EERE.

Approach

- Tailor carbonate-based localized high concentration electrolyte (LHCE) for Si anode.
 - LHCEs with carbonate-based solvents are investigated for improving the cycling stability of Si anodes.
- Develop nonflammable LHCE for Si anodes.
 - New LHCE design has been developed for preventing the burning hazard of electrolyte; triethyl phosphate (TEP) and bis(2,2,2-trifluoroethyl) ether (BTFE) are used as solvent and diluent, respectively.

Results

1.1 Carbonate-based localized (LHCEs) for Si anodes

Based on the effectiveness of LHCEs in stabilizing the cycle life of Si anodes found in our work last year, we have further tailored LHCE compositions for Si-based LIBs. We investigated carbonate-based LHCEs by diluting LiFSI-EC:EMC electrolyte with bis(2,2,2-trifluoroethyl) ether (BTFE). The NMC532 cathode and Si/graphite (Si/Gr) anode for the electrolyte test were obtained from ANL's CAMP facility. As shown in Table II.1.D.1, several electrolytes with different salt concentrations and molar ratios of the diluent were investigated. The electrochemical tests have shown that the carbonate-based LHCEs with BTFE can considerably improve the cycling stability and first-cycle coulombic efficiency (FCE) of full cells. As shown in Figure II.1.D.1a, electrolyte E-104 (1.8 M LiFSI in EC-EMC (3:7 by wt.)-2BTFE (molar ratio to EC/EMC) + 5 wt% FEC) enables the best overall performance of the cells considering the high specific capacity (114.8 vs. 96.3 mAh/g for the 4th cycle), improved FCE (75 vs. 60%) and good cycling stability (92.4 vs. 55% over 100 cycles) compared to the baseline electrolyte (1.2 M LiPF₆ in EC-EMC (3:7 by wt.) + 10 wt.% FEC). While other carbonate-based LHCEs with different diluents, such as TTE and TFE (Figure II.1.D.1b), were also investigated, carbonate-based LHCEs with BTFE yielded the most stable cycle life at room temperature.

Table II.1.D.1 Electrochemical Performance of NMC532 || Si/Gr (CAMP Electrodes) Full Cells in BTFE-based Electrolytes with Different Salt Concentrations

Design of experiments summary table				
	Electrolyte	FCE	Specific capacity @ 4th cycle (mAh/g)	Retention @ 100th cycle
Baseline	1.2 M LiPF ₆ in EC-EMC (3:7 by wt.) + 10 wt.% FEC	60%	96.3	55%
E-101	6 M LiFSI in EC-EMC (3:7 by wt.) + 5 wt% FEC	60%	41.8	40%
E-102	2.9 M LiFSI in EC-EMC (3:7 by wt.)-1BTFE (molar ratio to EC/EMC) + 5 wt% FEC	73%	99.1	71%
E-103	2.5 M LiFSI in EC-EMC (3:7 by wt.)-1.5BTFE (molar ratio to EC/EMC) + 5 wt% FEC	75%	117.6	67%
E-104	1.8 M LiFSI in EC-EMC (3:7 by wt.)-2BTFE (molar ratio to EC/EMC) + 5 wt% FEC	75%	114.8	95%
E-105	1.2 M LiFSI in EC-EMC (3:7 by wt.)-3BTFE (molar ratio to EC/EMC) + 5 wt% FEC	70%	82.9	71%

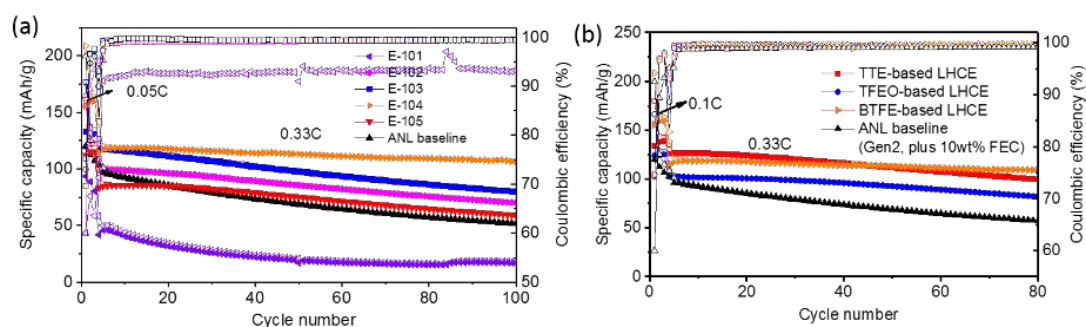


Figure II.1.D.1 (a) Cycling performance of NMC532 || Si/Gr (CAMP electrodes) in BTFE-based electrolytes with different salt concentrations; (b) cycling performance of NMC532 || Si/Gr (CAMP electrodes) in BTFE, TTE, and BTFE-based electrolytes

In the long-cycling test of the NMC532 || Si/Gr cells, superior stability was obtained in E-104 with a capacity retention of 81.8% after 200 cycles (Figure II.1.D.2a). We also investigated the high voltage stability of E-104 by testing the NMC cathode in NMC532 || Li cells with different charging cutoff voltage from 4.2 V to 4.5 V. The cells with E-104 can be charged to 4.5 V with over 25% increase in the specific capacity for 60 cycles. In contrast, a cell with baseline electrolyte cycled at a charge cutoff above 4.3 V exhibits quick capacity fading (Figure II.1.D.2b). This result implies that the LHCE electrolyte enhances the high voltage stability of NMC532 cathodes, which is highly advantageous for obtaining high energy density.

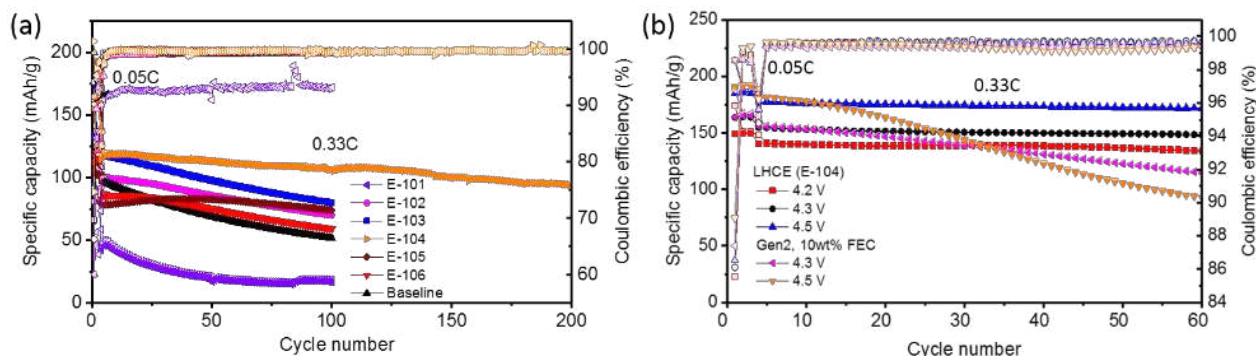


Figure II.1.D.2 (a) Cycling performance of NMC532 || Si/Gr (CAMP electrodes) in BTFE-based electrolytes with different salt concentrations at 0.05C and 0.33C; (b) high voltage stability of NMC532 || Li in E-104 and baseline electrolytes

Furthermore, as a good index for the accumulation of SEI layer during cycling, the end-of-life (EOL) swelling of electrodes was evaluated. Table II.1.D.2 shows the thickness of Si/Gr composite electrodes before testing and after the 100th cycle when fully delithiated. The average thickness of the pristine electrode was 28 μm , while the average electrode thicknesses at the 100th cycle were 52 μm in the baseline electrolyte, 42 μm in E-101, 42 μm in E-102, 40 μm in E-104, and 46 μm in E-106, respectively. These results demonstrated that E-104 can strongly suppress electrolyte decomposition and hence EOL swelling of the Si-based electrodes, which is critical to maintaining the Si electrode structure and the stability of the Si electrode and the cell during cycling. This result is in good agreement with great cycle life of NMC532 || Si/Gr cells using E-104 electrolyte.

Table II.1.D.2 Swelling of Si/Gr Anode in Different Electrolytes

	Pristine Si anode thickness (μm)	Thickness of de-lithiated Si anode (μm) at 100th cycle	Swelling at 100th cycle
Baseline	28	52	85.70%
E-101	28	42	50%
E-102	28	42	50%
E-104	28	40	42.80%
E-106	28	46	64.20%

1.2 Nonflammable LHCEs for Si anodes

To enhance the safety of high energy Li-ion batteries, we developed non-flammable triethyl phosphate (TEP)-based LHCEs tailored for Si based LIBs. Because TEP based solvent is not compatible with LiPAA binder, which is typically used in Si anode, we prepared Si-based anode using commercially available nano-

Si/graphite composite (BTR1000, BTR New Energy Materials Inc.) with polyimide (PI) binder to replace LiPAA binder. The first cycle specific reversible capacity and Coulombic efficiency of BTR1000 silicon anodes are ~1000 mAh/g and ~80%, respectively. In order to compensate the irreversible capacity loss during initial cycling, the anode was prelithiated by electrochemical cycling with Li metal as a counter electrode for 3 cycles before the full-cell assembly. The prelithiated anodes were paired with NMC333 cathodes for long term cycling.

The formulations of the electrolytes studied in this work are listed in Table II.1.D.3, along with the actual salt concentrations and the viscosities at 25°C. All of these electrolytes have similar viscosities. Both NFE-1 and NFE-2 can effectively wet the polyethylene (PE) separator, the Si/Gr anode and the NMC cathode. The measured self-extinguishing times (SETs) for these electrolytes are summarized in Table II.1.D.3. The three control electrolytes formed by adding certain amounts (2%, 5% and 10% by wt.) of FEC in the conventional 1 M LiPF₆/EC-EMC (3:7 by wt.) are still highly flammable as shown in Figure II.1.D.3a, but the two LHCE electrolytes are nonflammable due to the presence of sufficient TEP as shown in Figure II.1.D.3b.

Table II.1.D.3 Molarity, Viscosities and Self-extinguish Time (SET) of Three Baseline Electrolytes and Two Localized High Concentration Electrolytes

Samples	Electrolytes	Molarity (mol L ⁻¹)	Viscosity (cP)(25 °C)	SET (s/mL)
E-control-1	1 M LiPF ₆ in EC/EMC + 2 wt% FEC	1.0	3.02	100
E-control-2	1 M LiPF ₆ in EC/EMC + 5 wt% FEC	0.96	3.06	100
E-control-3	1 M LiPF ₆ in EC/EMC + 10 wt% FEC	0.93	3.08	100
NFE-1	1.2 M LiFSI in TEP/BTFE (1:3 by mol) (i.e., LiFSI-1.33TEP-4BTFE)	1.2	2.90	Non-flammable
NFE-2	1.2 M LiFSI in TEP/FEC/BTFE (1.2:0.13:4 by mol) (i.e., LiFSI-1.2TEP-0.13FEC-4BTFE)	1.2	2.92	Non-flammable

Commercial Si/Gr composite material with a nominal specific capacity of 1000 mAh g⁻¹ was used to investigate the long-term cycling performance of Li||Si/Gr cells in the three control electrolytes and the two LHCEs (NFE-1 and NFE-2). The areal capacity of Si/Gr electrodes was ~2.21 mAh cm⁻². The capacity of the control electrolyte with 2 wt% FEC (E-control-1) (which has the similar amount of FEC (1.2 wt%) as in NFE-2) dropped quickly only after 40 cycles (Figure II.1.D.3c). When the amount of FEC increased to 5 and 10 wt% (E-control-2 and E-control-3, respectively), the cycle life of Li||Si/Gr cells was extended to 60 cycles and 140 cycles, respectively. It is seen that the increase of FEC in the conventional electrolyte is in favor of an extension of the cycle life of Si-based anodes, which is consistent with the literature reports. The improvement, however, is only limited to a certain point. Therefore, the E-control-3 was chosen for the following comparative studies with the LHCEs. In contrast, the Si/Gr electrodes in both NFE-1 and NFE-2 LHCEs delivered a high specific capacity of 1337.8 mAh g⁻¹ with the initial Coulombic efficiency (CE) of 77.6%, and the capacity retention of the Si/Gr electrodes in NFE-1 was 66.2% after 300 cycles, while the Si/Gr electrode with FEC-containing NFE-2 LHCE showed an improved cycling stability to 73.4% capacity retention at 300th cycle and a stable CE of 99.9% (Figure II.1.D.3c).

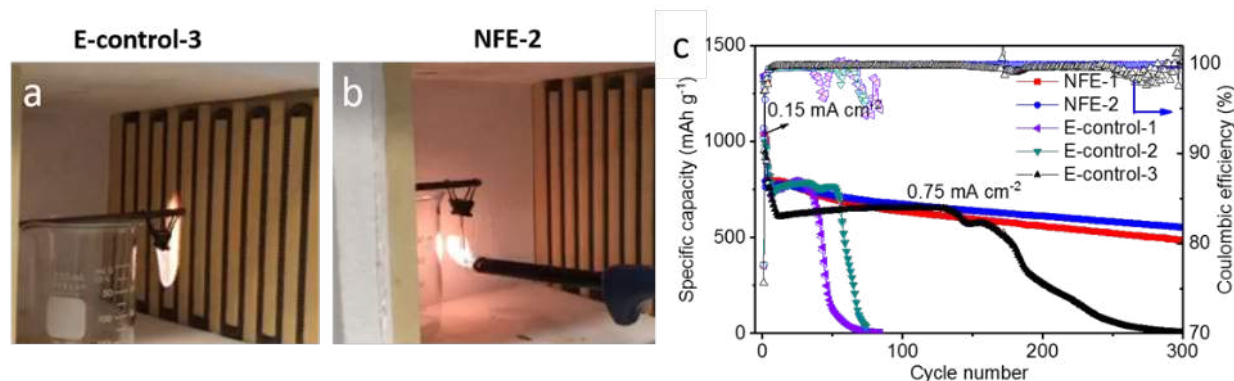


Figure II.1.D.3 Photographs of ignition tests of glass fibers saturated with E-control-3 (a) and NFE-2 LHCE. (c) Long-term cycling performance and Coulombic efficiency of Li||Si/Gr half cells in different electrolytes

Furthermore, the effects of the electrolytes on the electrode swelling at 100% state-of-charge (SOC) and end-of-life (EOL) were also evaluated and compared by using ex situ scanning electron microscopy (SEM) measurement. The average thickness of the pristine electrode was 21.4 μm , while the average electrode thickness at 1st full lithiation was 39.1 μm in E-control-3, 35.9 μm in NFE-1 and 31.2 μm in NFE-2. The electrode swelling at 100% SOC was 82.7% in electrolyte-control-3, 67.7% in NFE-1 and 45.8% in NFE-2, respectively. The average electrode thickness after 200 cycles was 44.4 μm in E-control-3, 31.2 μm in NFE-1 and 27.9 μm in NFE-2. The EOL swelling at 200th cycle is 107.5%, 45.8% and 30.4% for E-control-3, NFE-1 and NFE-2, respectively. It is demonstrated that the LHCEs can greatly suppress the full lithiation and EOL swelling of the Si-based electrodes, which is critical to the maintenance of the Si electrode structure and the stability of the Si electrode and the cell during cycling.

Considering the remarkable improvement of Li||Si/Gr cells in nonflammable LHCEs, the full cell configuration of Si/Gr with NMC333 was also investigated to further demonstrate the advantages of the nonflammable LHCEs for Si-based anodes. The NMC333 cathode had an areal capacity of 1.93 mAh cm⁻² so the ratio of the negative electrode (Si/Gr) capacity and the positive electrode (NMC333) capacity was 1.14. Given that the initial Coulombic efficiency of Si/Gr anode is only 77.6%, Si/Gr anodes were pre-cycled against Li metal in half-cells for 3 cycles to alleviate the challenges from SEI formation and then re-assembled into the Si/Gr||NMC333 full cells. Figure II.1.D.4a shows that the cells in all the three electrolytes exhibited similar reversible capacities of 150 mAh g⁻¹ (based on cathode) for the first three formation cycles at the current density of 0.15 mA cm⁻². When the current density was increased to 0.3 mA cm⁻² for charge and 0.75 mA cm⁻² for discharge in the following cycles, the cycling stability of the full cells was highly dependent on the electrolytes, showing the order from high to low of NFE-2 > NFE-1 > E-control-3. In addition, the cells with both NFE-1 and NFE-2, especially NFE-2 also displayed superior rate capability to E-control-3 (Figure II.1.D.3b). The reversible capacities of 126.5 and 112.5 mAh g⁻¹ were obtained at 5C rate with NFE-2 and NFE-1, respectively.

When carefully analyzing the long-term cycling stability of the full cells (Figure II.1.D.4a), E-control-3 led to a fast capacity decay with the capacity retention of 50.3% after 500 cycles and an obvious increase in the voltage polarization upon cycling (Figure II.1.D.4c), which can be attributed to the increase of cell resistance due to the poor interface condition between Si/Gr and electrolyte. In the case of the cells with NFE-1, the capacity retention increased to 65.7% over 500 cycles. The gradual increase of voltage polarization was also observed in the cells with NFE-1 (Figure II.1.D.4d). In contrast, the cells with NFE-2 demonstrated superior long-term cycling performance with the capacity retention of 89.8% after 600 cycles. The CE at stable cycling was close to 100% and the voltage polarization was remarkably smaller than that of E-control-3 and NFE-1 (Figure II.1.D.4e). Moreover, the full cells with NFE-2 also showed better cycling performance at the elevated temperature (Figure II.1.D.4f). The average CE of the full cells with NFE-2 at 45°C was ~99.6 and was slightly lower than that of the full cells cycled at 25°C (~100%), which is probably due to the formation of thicker films of

by-product from more decomposition of electrolyte on the electrode/electrolyte interfaces at the elevated temperature. The by-products accompanied with the formation of both thicker SEI and CEI resulted in impedance increase and capacity fading of the batteries. However, NFE-2 still allowed the capacity retention to be 90.2% over 200 cycles when the cells were tested under 45°C. In addition, the full cells with higher areal capacity of Si/Gr (3.2 mAh cm⁻²) and NMC 333 (2.8 mAh cm⁻²) were further evaluated. Following deep cycling at 0.15 mA cm⁻², the reversible areal capacity reached 3.1 mAh cm⁻². From the 4th cycle to the 100th cycle at high rates of 0.75 mA cm⁻² for charge and 0.3 mA cm⁻² for discharge, the capacity retention with NFE-2 reached up to 95.0% after 100 cycles (Figure II.1.D.4g), which indicates the successful design of electrolyte for Si-based anodes.

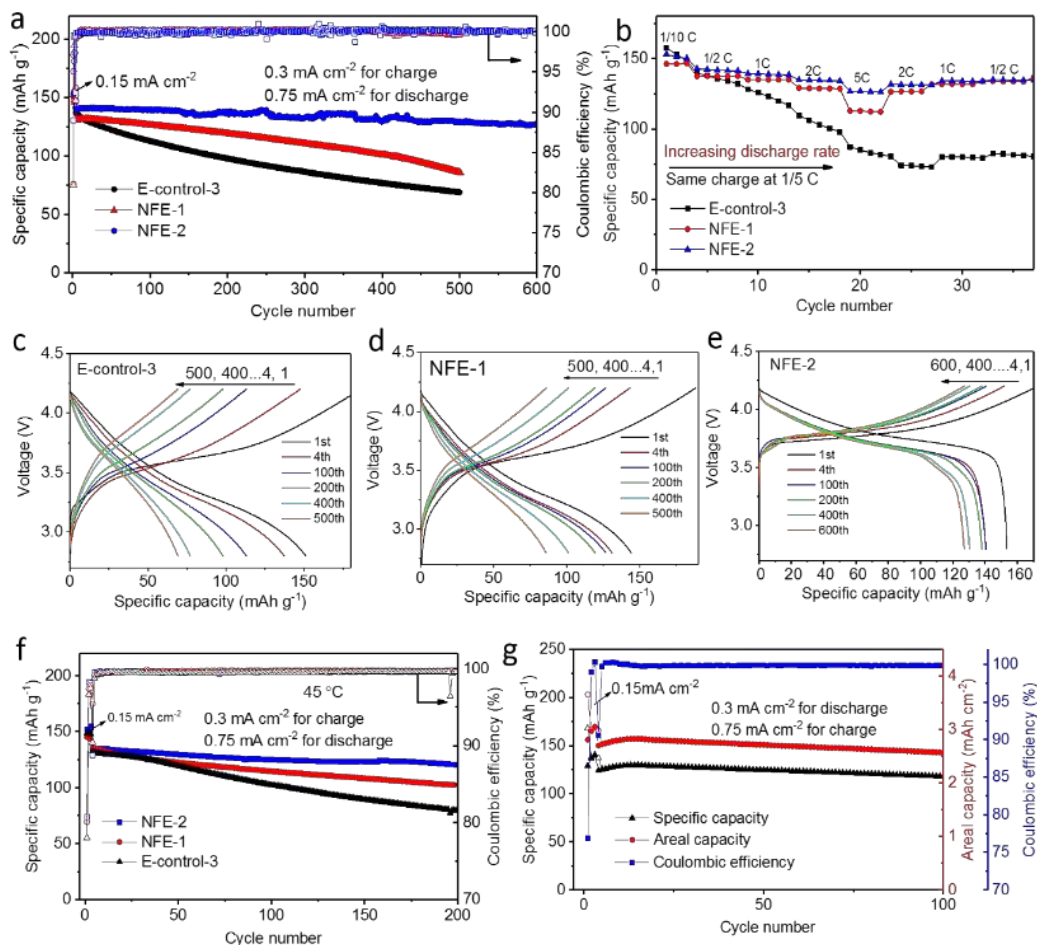


Figure II.1.D.4 Electrochemical behavior of Si/Gr || NMC333 full cells in different electrolytes. (a) Long-term cycling performance of Si/Gr || NMC333 full cells with different electrolytes at 25°C. (b) Rate capability of the Si/Gr || NMC333 cells in different electrolytes at 25°C. (c-e) Voltage profiles upon cycling in electrolyte-control-3 (c), NFE-1 (d) and NFE-2 (e). (f) Long-term cycling performance of Si/Gr || NMC333 cells cycled at 45°C in different electrolytes. (g) Cycling performance of full cell with high loading in NFE-2 at 25°C

Conclusions

LHCE electrolytes were optimized to improve cycle life of Si anodes. Different bulk solvents including carbonate, ether, and nonflammable TEP were studied. When coupled with a LiNi_{0.3}Mn_{0.3}Co_{0.3}O₂ cathode, the full cells using a nonflammable LHCE electrolyte (LiFSI-1.2TEP-0.13FEC-4BTfE) could maintain >90% capacity after 600 cycles at C/2 rate, demonstrate excellent rate capability and cycling stability at elevated temperatures and high loadings.

Key Publications/patents

1. Haiping Jia, Lianfeng Zou, Peiyuan Gao, Xia Cao, Wengao Zhao, Yang He, Mark H. Engelhard, Sarah D. Burton, Hui Wang, Xiaodi Ren, Qiuyan Li, Ran Yi, Xin Zhang, Chongmin Wang, Zhijie Xu, Xiaolin Li, Ji-Guang Zhang, Wu Xu, High-Performance Silicon Anodes Enabled By Nonflammable Localized High-Concentration Electrolytes, *Advanced Energy Materials*, 2019, 9, 1900784. DOI: 10.1002/aenm.201900784.

Acknowledgements

Key contributors include Haiping Jia, Sujong Chae, Wu Xu, Ran Yi, and Qiuyan Li.

II.1.E Pre-Lithiation of Silicon Anode for High Energy Li Ion Batteries (Stanford University)

Yi Cui, Principal Investigator

Department of Materials Science and Engineering, Stanford University
McCullough 343, 476 Lomita Mall, Stanford University
Stanford, CA 94305
E-mail: yicui@stanford.edu

Tien Duong, DOE Technology Development Manager

U.S. Department of Energy
E-mail: Tien.Duong@ee.doe.gov

Start Date: October 1, 2018

End Date: September 30, 2019

Project Funding (FY19): \$500,000

DOE share: \$500,000

Non-DOE share: \$0

Project Introduction

Rechargeable lithium-ion batteries (LIBs) are widely used for consumer electronics and exhibit great potential for electrical vehicle and grid-scale energy storage. In existing lithium-ion technology, Li is provided by Li-intercalated cathode materials. Graphite is the most commonly used anode material. Various alternative high-capacity anode materials such as silicon, with a theoretical capacity more than ten times of graphite, have been well studied and have already shown promise in potential applications. The formation of a solid electrolyte interphase (SEI) layer on the anode surfaces is a critical process that occurs prior to regular battery operations and consumes a significant amount of Li. Graphite anodes exhibit an irreversible capacity loss of 5–10% from the initial battery charging process, while for high-capacity anode materials, the first-cycle Li loss is even higher (e.g., 15–35% for Si). Low first-cycle Coulombic efficiency leads to the consumption of an excess amount of cathode material solely for the first cycle and thereby, significantly reduces the energy density. It is also challenging to effectively compensate for the Li loss through loading excessive cathode materials as a result of kinetic limitations on the cathode thickness. Accordingly, there is a strong motivation to develop high-capacity materials to prestore a large amount of Li in either cathode or anode to compensate for the initial loss. Alloy anodes with much higher capacity have been recognized as promising alternatives to graphites. Without prestored Li in anodes, the energy density is limited by the low capacity of Li metal oxide cathodes. Recently, Li metal has been revived as a high-capacity anode, but faces many challenges resulting from its high reactivity and uncontrolled dendrite growth.

Objectives

Prelithiation of high capacity electrode materials such as Si is an important means to enable those materials in high-energy batteries. This study pursues two main directions: 1) developing facile and practical methods to increase first-cycle Coulombic efficiency of lithium-ion batteries, and 2) synthesizing fully lithiated Si and other lithium compounds for pre-storing lithium.

Approach

Usually, prelithiation of cathode materials was previously achieved by treating spinel cathode materials or metal oxides with chemical reagents, like n-butyllithium, LiI, or molten Li. However, the prestored capacity is still relatively low (100–800 mAh/g). Anode materials are more attractive Li reservoirs because of the high specific capacities. In previous studies, there have been three main approaches to realize anodes with prestored Li. One approach is electrochemical prelithiation by shorting electrolyte-wetted anodes with Li foil. Another approach is to incorporate microscale stabilized lithium metal powder (SLMP; FMC Lithium Corp.) into anodes. However, synthesis of SLMP in the research laboratory is difficult. In our previous report, we showed chemically synthesized $\text{Li}_x\text{Si}/\text{Li}_2\text{O}$ core shell nanoparticles (NPs) as an effective prelithiation reagent. The NPs maintained their capacities only in the dry air but that their capacities were reduced drastically after exposure to ambient air. To further improve the environmental stability, we developed a high temperature and gas phase

surface fluorination reaction to synthesize LiF-Li_xSi NPs. The dense and crystalline LiF coating improved the stability of Li_xSi NPs in both humid air and regular slurry solvent (NMP), indicating that LiF-Li_xSi NPs were compatible with industrial electrode fabrication processes. Additionally, Li metal has been revived as a high-capacity anode, but faces many challenges resulting from its high reactivity and uncontrolled dendrite growth. Therefore, we developed an air-stable and free-standing Li_xM (M = Si, Sn, or Al) /graphene foil as an alternative to Li metal, inheriting the desirable properties of alloy anodes and pure metal anodes.

In addition, we develop a new prelithiation approach which is carried out in the electrode level and is even more facile and compitple for industry applicaiton. Moreover, the prelithiation method is heat-free and solution-free. Si electrode film was prepared by coating the slurry of Si nanoparticles, carbon black and binder mixture on copper foil through a doctor-blading method. Then Si electrode film was prelithiated by pressing a Li metal foil on top of it under a certain pressure and holding for a certain time. Then, Li_xSi electrode film can be obtained by removing the redundant Li foil through a peeling-off approach. The redundant Li foil is reusable for the next prelithiation. This electrode-level prelithiation process is also applicable to other Li alloy forming materials, such as Al, Ge and Sn.

Results

A prelithiation method achieved in the electrode level showed a specific capacity >900 mAh/g

We show that the prelithiation can be achieved in the electrode level, which is even more facile and compatible for industry application. Si electrode film was prepared by coating the slurry of Si nanoparticles, carbon black and binder mixture (the mass ratio is 8:1:1) on copper foil through a doctor-blading method. Then Si electrode film was prelithiated by pressing a Li metal foil on top of it and heating up in an argon glovebox to different temperatures (200 to 320 °C) and holding for a certain time. Then, Li_xSi electrode film can be obtained by removing the redundant Li foil through a peeling-off approach (Figure II.1.E.1). The redundant Li foil is reusable for the next prelithiation.

As shown in Table II.1.E.1, the open-circuit voltage decreases while the initial Coulombic efficiency (ICE) increases as the prelithiation temperature increases and/or the prelithiation time increases, which is due to the better prelithiaiton at a higher temperature for a longer time. Without prelithition, the ICE of the Si nanoparticle anode is less than 70%. After prelithiated under 200°C for 1h, the ICE increased to 98%. More impressively, the ICE is over 100% after being prelithiated under 320°C for only 10 min, which indicates that Si nanoparticles have been well prelithiated. It's also worth noting that the 1st cycle charge capacity of all the prelithiated Si anodes is over 2000 mAh/g. In the future, efforts will be devoted to optimizing the prelithiation temperature and duration as well as improving the air stability of the prelithiated electrode film.

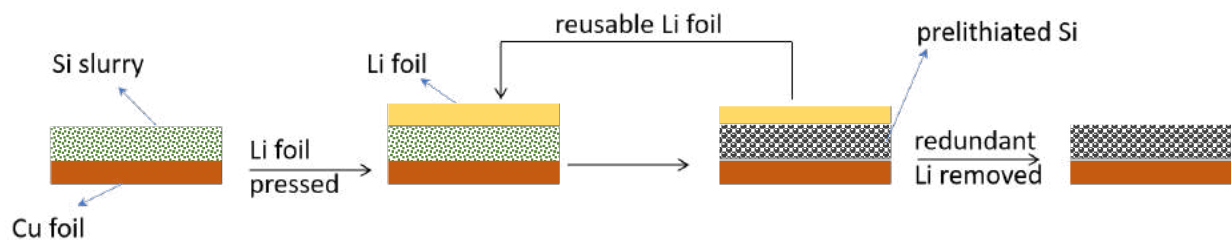


Figure II.1.E.1 Schematic illustration of the prelithiation of Si electrode film

Table II.1.E.1 Electrochemical Performance of Si Anode after being Prelithiated under Different Conditions

Prelithiation condition	Open-circuit voltage (V)	1st cycle discharge capacity /mAh g ⁻¹	1st cycle charge capacity /mAh g ⁻¹	Initial Coulombic efficiency (%)
Unprelithiated	2.05	3420	2342	68.5
200°C, 1h	0.45	2673	2165	80.9
200°C, 3h	0.30	2181	2141	98.1
200°C, 16h	0.13	2	2646	132300
260°C, 10min	0.99	4425	3372	76.2
260°C, 30min	0.44	3417	2907	85.0
260°C, 1h	0.31	644	2290	355.5
320°C, 10min	0.27	1881	2060	109.5

A heat-free and solution-free anode prelithiation method to optimize initial coulombic efficiency

We developed another prelithiation method which is heat-free and solution-free. Si electrode film was prepared by coating the slurry of Si nanoparticles, carbon black and binder mixture on copper foil through a doctor-blading method. Then Si electrode film was prelithiated by pressing a Li metal foil on top of it under a certain pressure and holding for a certain time. Then, Li_xSi electrode film can be obtained by removing the redundant Li foil through a peeling-off approach. The redundant Li foil is reusable for the next prelithiation.

As shown in Figure II.1.E.2, the initial Coulombic efficiency (ICE) increases as the pressure increases and/or the prelithiation time increases, which is due to the better Li metal-Si contact under a higher pressure and more adequate prelithiation reaction at a longer time. Without prelithiation, the ICE of the Si nanoparticle anode is around 70%. After prelithiated under 15 MPa for 5 min, the ICE increased to be over 80%. More impressively, the ICE is further increased to be over 100% after being prelithiated under 15 MPa for only 15min, which indicates that Si nanoparticles have been well prelithiated. It's also worth noting that the 1st cycle charge capacity of all the prelithiated Si anodes is over 2000 mAh/g. This prelithiation method is heat-free, solvent-free and achieved in the electrode level. In the future, efforts will be devoted to improving the air stability and electrochemical stability of the prelithiated electrode film.

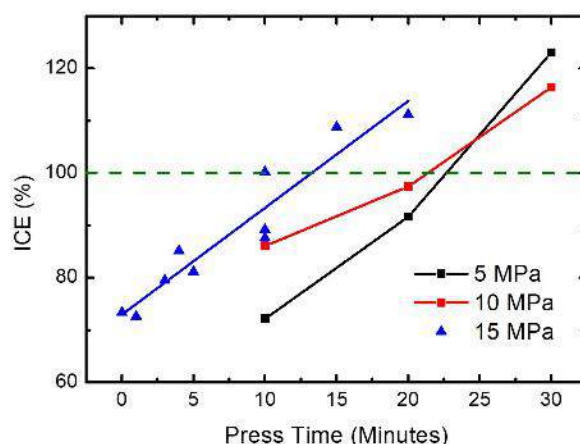


Figure II.1.E.2 The effects of pressure and pressing duration on ICE of Si anode-based half cell

Morphology and structure evolution of silicon anode after prelithiation

Si electrode film can be prelithiated through a heat-free and solution-free method, which is more facile and compatible for industry application than previously reported method. As shown in Figure II.1.E.3, before prelithiation, silicon nanoparticles are well dispersed, showing a size around 100 nm (Figure II.1.E.3a,c). After prelithiation, the size of silicon nanoparticles increased obviously, while the integrity of the structure is well maintained which is due to the initial size of silicon nanoparticle is below the critical crack size (150 nm). It's worth noting that besides Li_xSi alloy, lithium oxide and lithium metal residual can also be observed after prelithiation treatment (Figure II.1.E.3d). The upper layer with a thickness of about 1.12 μm of silicon anode are lithiated, while the below silicon nanoparticles remain unlithiated, which is due to the limited prelithiation duration and the slow diffusion speed of lithium. In the future, efforts will be devoted to improving the air stability and electrochemical stability of the prelithiated electrode film.

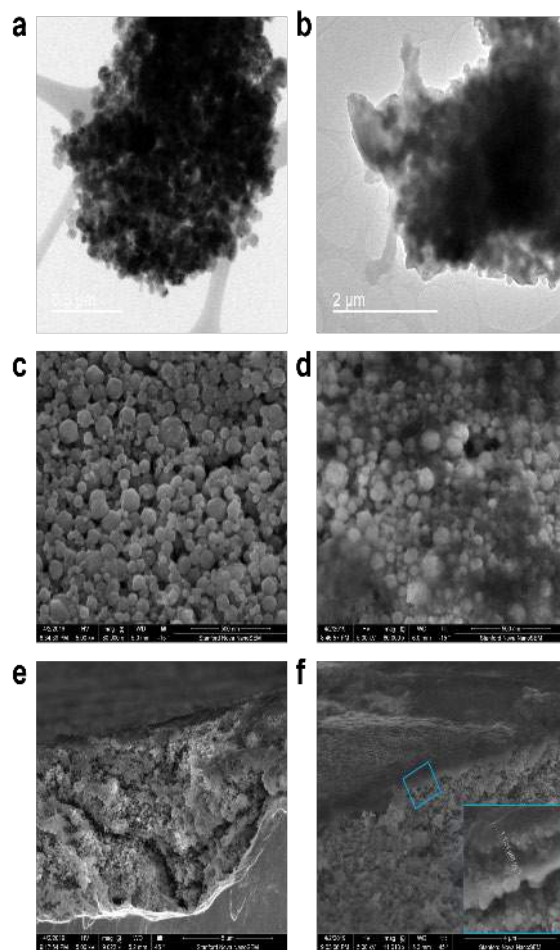


Figure II.1.E.3 Morphology evolution of Si anode before (a,c,e) and after (b,d,f) prelithiation treatment. (a,b) TEM images, (c,d) in-plane and (e,f) cross-section SEM characterization of Si anode

Prelithiated anodes show high ICE and excellent cycling stability for Li-LFP full cells

The excellent performance of prelithiated Li_xSi electrode film in half cells makes it possible to be used in full cells. We paired our prelithiated Li_xSi electrode film with a traditional LiFePO_4 cathode. Figure II.1.E.4a shows the voltage curves of the prelithiated Li_xSi - LiFePO_4 and pristine Si - LiFePO_4 full cells operated between 2.5 and 3.8 V at 1C. These two full cells show similar 1st cycle charge capacity of $\sim 2.5 \text{ mAh/cm}^2$. However, the prelithiated Li_xSi - LiFePO_4 delivers a much higher reversible discharge capacity of 2.3 mAh/cm^2 ,

corresponding to a high ICE of 91%, while the pristine Si-LiFePO₄ obtains a much lower reversible discharge capacity of 1.76 mAh/cm², corresponding to a low ICE of 70%. Figure II.1.E.4b shows the CE and capacity of the following cycles. Obviously, the prelithiated Li_xSi-LiFePO₄ achieves much higher Coulombic efficiencies than that of the pristine Si-LiFePO₄ cell for the initial several cycles, indicating a severe irreversible lithium loss of the unprelithiated Si-LiFePO₄ cell. As a result, the later-cycle capacity of the prelithiated Li_xSi-LiFePO₄ cell is much higher than that of the pristine Si-LiFePO₄ cell.

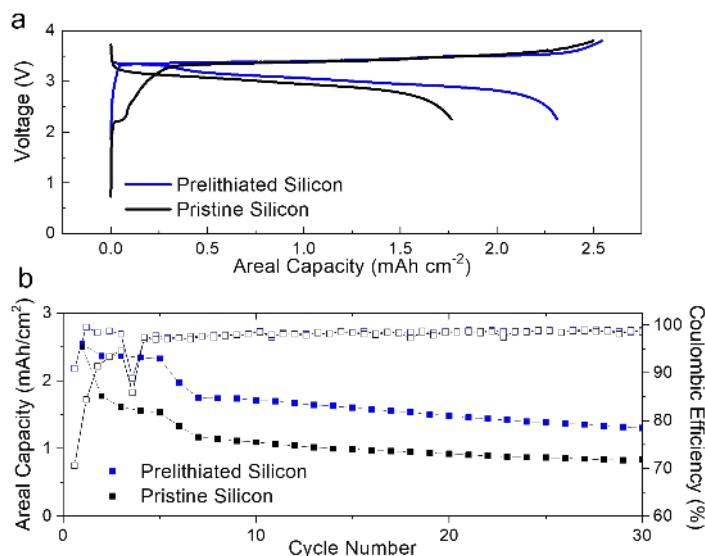


Figure II.1.E.4 (a) First cycle voltage curves and (b) cycling stability of Si-LiFePO₄ and Li_xSi-LiFePO₄ full cells operated between 2.5 and 3.8 V

Conclusions

In the past year, we have developed a new prelithiation method which can be achieved in the electrode level through a heat-free and solution-free pressing approach; it is more facile and compatible for industry application than previously reported method. The initial Coulombic efficiency of the Li_xSi-Li half cell increases as the prelithiation pressure increases and/or the prelithiation time increases, due to the better Li metal-Si contact under a higher pressure and more adequate prelithiation reaction at a longer time. In addition, we paired our prelithiated Li_xSi electrode film with a traditional LiFePO₄ cathode, the prelithiated Li_xSi-LiFePO₄ achieves much higher initial Coulombic efficiency and reversible discharge capacity than that of the pristine Si-LiFePO₄ cell. In the future, efforts will be devoted to demonstrating the Coulombic efficiency, rate capability and cycling stability of the prelithiated electrode film for Li-S full cells. In addition, this electrode-level prelithiation process will be explored and applied to other Li alloy forming materials, such as Al, Ge and Sn.

Key Publications

1. J. Zhao#, J. Sun#, A. Pei, G. Zhou, K. Yan, Y. Liu, D. Lin, and Y. Cui, "A general prelithiation approach for group IV elements and corresponding oxides", *Energy Storage Materials*, 10, 275, 2018.

II.2 Next Generation Lithium-Ion Batteries: Advanced Cathodes R&D

II.2.A Diagnostic Testing and Evaluation (ANL, ORNL, NREL)

Daniel P. Abraham, Principal Investigator

Argonne National Laboratory
9700 S Cass Avenue
Lemont, IL 46039
E-mail: abraham@anl.gov

Peter Faguy, DOE Technology Development Manager

U.S. Department of Energy
E-mail: Peter.Faguy@EE.Doe.Gov

Start Date: October 1, 2018

End Date: September 30, 2021

Project Funding (FY19): \$4,000,000

DOE share: \$4,000,000

Non-DOE share: \$0

Project Introduction

State-of-the-art Li-ion batteries (LIBs) being developed for transportation applications contain a transition metal (TM) oxide cathode and a graphite (Gr) anode; both serve as host-matrices to house Li ions during battery operation. The cathode typically contains $\text{Li}_{1+x}\text{Ni}_a\text{Co}_b\text{Al}_c\text{O}_2$ (NCA) or $\text{Li}_{1+x}\text{Ni}_a\text{Mn}_b\text{Co}_c\text{O}_2$ (NMC-abc) oxides, where $x \sim 0-0.05$ and $a+b+c = 1$. Both oxide chemistries contain Co, which is known to preserve the layered structure during Li extraction/insertion reactions. However, the possibility of a global Co shortage and soaring costs has galvanized the LIB community to seek out and explore layered oxides with lower Co contents and eventually develop Co-free cathodes, while maintaining cell performance (energy/power densities), safety and cycle/calendar life. The goal of the diagnostic testing and evaluation team is to identify constituents and mechanisms responsible for cell performance, performance degradation, and safety. Various diagnostic tools (electrochemical, physicochemical, mechanical, etc.) are used to characterize the behavior of materials (both active and inactive) contained in the electrodes and cells; this characterization may be conducted before, during, and after electrochemical cycling. Understanding the fundamental mechanisms allows the development of rational solutions to minimize performance degradation and thermal instability in the materials and electrodes, leading to safer, long-life battery cells.

Objectives

- Establish electrochemical half-cell (i.e., cells with Li-metal anodes) test protocols to characterize multiple performance aspects (capacity, rate, high voltage stability) of various cathode active materials.
- Develop in situ Mass Spectroscopy (MS) gas analysis from pouch cells using direct sampling methods and understand the impact of upper cut-off voltage (UCV) on the gas generation during aging cycles.
- Evaluate thermal stability of Ni-rich cathode materials from both chemical and structural perspectives.
- Develop Differential Scanning Calorimetry (DSC) protocols to minimize variability in the thermal stability data of various cathode active materials.
- Understand effect of cathode composition on TM dissolution and electrolyte decomposition products.
- Examine cathode-electrolyte interphase using in situ attenuated total internal reflection (ATR) Fourier transform infrared (FTIR) spectroscopy and other complimentary techniques, such as Raman and X-ray photoelectron spectroscopy (XPS).

- Obtain insights from cathode symmetric cells containing a reference electrode.
- Identify additives, which when incorporated into our baseline electrolyte (denoted as Gen2), consisting of 1.2M LiPF₆ in EC:EMC (3:7 w/w), reduces cell degradation.
- Fabricate electrodes from cathode materials and identify problems that arise during fabrication.

Approach

The objectives listed above were pursued using the following approaches:

- The half-cell protocols were designed to obtain significant information without substantial long-term cycling or fast rates, both of which can be difficult to acquire with Li-metal anodes. Two protocols were developed are referred to as the Standard Diagnostics protocol and the Rate protocol herein.
- Gas analysis was conducted on NMC-811//Gr pouch cells using a conventional GC-MS instrument. In situ gas analysis was combined with neutron diffraction to obtain information on the thermal stability of the layered oxide.
- DSC data were obtained on NMC-532 electrodes that were charged to 4.2 V after three formation cycles at a C/10 rate. The amount of electrolyte, and the ratio of electrode material to electrolyte, were varied to examine their effects on the oxide's thermal stability.
- Full-cell (Gr anode) cycling to determine TM concentrations on Gr anodes by ICP-MS and electrolyte decomposition products by HPLC. Static leaching experiments were conducted on highly-charged (4.6 V) NMC cathode materials using tetrabutyl ammonium bifluoride, (C₄H₉)₄NF·HF in EC:EMC (3:7 by wt.) solution.
- A custom cell that enabled in situ collection of ATR-FTIR spectra during electrochemical cycling was developed to observe (electro)chemical changes at the cathode-electrolyte interface.
- Reference-electrode-bearing symmetric cells, containing positive electrodes harvested from conventional oxide//Gr cells, were assembled and cycled/aged. In this configuration, potential and impedance changes of *individual oxide electrodes* can be monitored during aging, providing important information about their behavior in the absence of crosstalk.
- Electrolyte additives were synthesized in situ by simply mixing electrolyte containing LiPF₆ with additive precursors. This strategy is useful to synthesize sensitive/unstable additives and it eliminates the need for separate purification and separation processes, which can greatly reduce manufacturing costs.
- Electrodes fabricated using standard Cell Analysis, Modeling and Prototyping (CAMP) facility protocols were made available to the diagnostic team for testing and analysis.

Results

Electrochemical testing protocols in a half-cell format (Li-metal anodes)

The Standard Diagnostics protocol uses two UCVs of 4.2 and 4.5 V, as well as two potentiostatic holds, with 2.5 V used as the lower-cutoff voltage (LCV). All galvanostatic steps use a 20 mA/g current. The various steps (shown in Figure II.2.A.1) are as follows: Cycles 1-4, Low-Voltage Window (2.5- 4.2 V); Cycles 5-9, High-Voltage Window (2.5 – 4.5 V); Cycle 10: Cathode polarization and impedance are measured with current interrupts (open circuit for 15 minutes) at 25% state of charge (SOC) increments (including top of charge), on both charge and discharge steps.

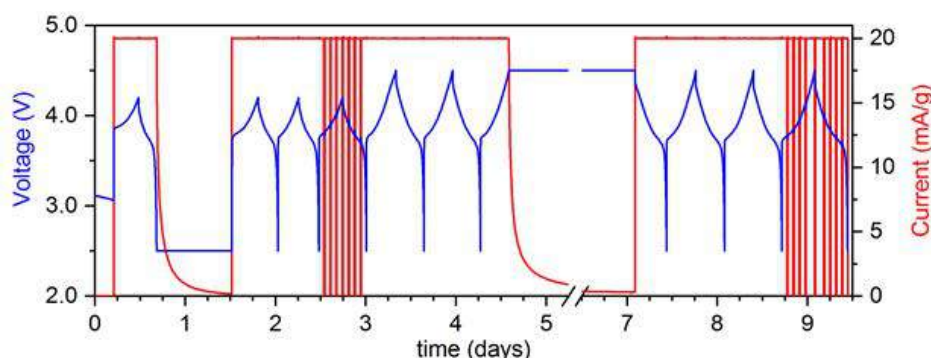


Figure II.2.A.1 Standard diagnostics protocol

Figure II.2.A.2 shows the extracted information from the first cycle of the protocol. The cycle comprises a galvanostatic charge, galvanostatic discharge, and a 20-hour potentiostatic hold at the LCV (2.5 V). With this methodology, both pre- and post-hold discharge capacities and coulombic efficiencies can be obtained. Starting with the initial (galvanostatic) charge and discharge capacities, higher Ni content is observed to be correlated to higher charge and discharge capacities. The irreversible capacity losses (ICLs, 23-30 mAh/g) and galvanostatic coulombic efficiencies (CEs, 84-87%) are approximately the same across the cathode compositions. During the low-voltage hold, ~18 mAh/g is regained by all cathodes. Adding this potentiostatic capacity to the galvanostatic discharge capacity, new CEs and ICL are obtained. The ‘true’ ICL of these compounds ranges from 5-13 mAh/g, with the CEs after the potentiostatic hold ranging from 94%-97%.

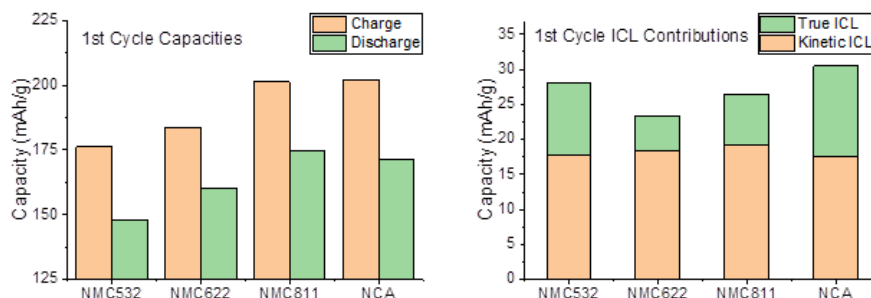


Figure II.2.A.2 (Left) Galvanostatic first-cycles capacities (without a potentiostatic hold on the discharge) and (right) sources of first-cycle capacity loss of the four cathodes examined

Figure II.2.A.3 (left) includes cycling metrics from cycles 2 and 3. Cycle 2 indicates a large ICL for all cathodes, ranging from 16-22 mAh/g. This capacity loss is on par with the kinetic losses observed on the first cycle and reveals the ‘reversibility’ of the kinetically inhibited, mostly-lithiated phase. Figure II.2.A.3 (right) shows cycling metrics from cycles 6, 7, and 9, and is an evaluation of high voltage performance and the changes that occur after exposure to a high voltage hold. The discharge capacities for cycle 6 show that roughly 40 mAh/g of capacity is gained at 4.5 V compared to 4.2 V for all NMCs (~30 mAh/g for NCA), with the discharge capacity of the NMC-532 approximately 25 mAh/g lower than NMC-811 at 4.5 V.

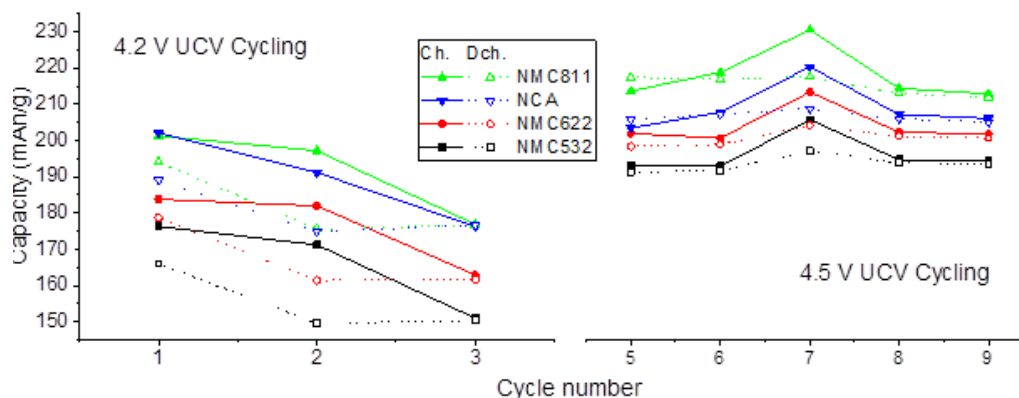


Figure II.2.A.3 “(Left) Capacity vs. cycle number for the LCV (4.2-2.5 V) cycles and (right) the UCV (4.5-2.5 V) cycles used in the standard protocol. Cycles 4 and 10 were not included. The capacity for cycle 1 includes the potentiostatic hold at the LCV of 2.5 V. Closed symbols are charge capacities and open symbols are discharge capacities

Cycle 7 metrics, shown in Figure II.2.A.4 (left), reveal that the galvanostatic portion of the charge capacity (labeled CC in the figure, left) is roughly the same as the cycle 6 charge capacity (labeled ‘Pre-hold’, in the figure, right) as expected. However, additional charge capacity is obtained during the 60-hour hold at 4.5 V (Post-hold) amounting to ~12 mAh/g for all materials. Discharge capacities for cycle 7 are greater than those for cycle 6, which reflects a greater state of charge brought about by the 60-hour hold. However, the data show that side-reaction capacity, i.e., the difference between cycle 7 Post-hold charge capacities and discharge capacities, is slightly higher for the Ni-rich NMC-811 and NCA (~12 mAh/g) than for the NMC-532 and NMC-622 (~9 mAh/g). Comparing cycle 9 discharge capacities to cycle 6 shows the effect of the high-voltage hold (Figure II.2.A.4, right). For NMC-532 and NMC-622, discharge capacities *increase* slightly by ~2 mAh/g. For the higher Ni-content cathodes, capacities *decreased* by ~5 mAh/g for the NMC-811 and 2 mAh/g for the NCA, implying that NMC-811 may be the least ‘stable’ cathode under these conditions.

Figure II.2.A.5 shows the current-interrupt polarizations of cycles 4 and 10 (before and after the high-voltage hold cycle) at 25% SOC increments. These voltages were obtained by allowing the cell to rest at open circuit for 15 minutes. For the cathodes surveyed, polarization values decreased from cycle 4 (4.2 V cycle, Pre-hold) to cycle 10 (4.5 V cycle, Post-hold), revealing that for the intermediate voltages surveyed, under the conditions here, there is no indication of significant impedance rise for any of the cathodes after the potentiostatic hold. However, the top of charge polarization is much greater than the intermediate SOC, for all cathodes, with NMC-811 showing the highest at 69 mV. This observation again suggests that the NMC-811 is the least stable composition among the cathodes tested.

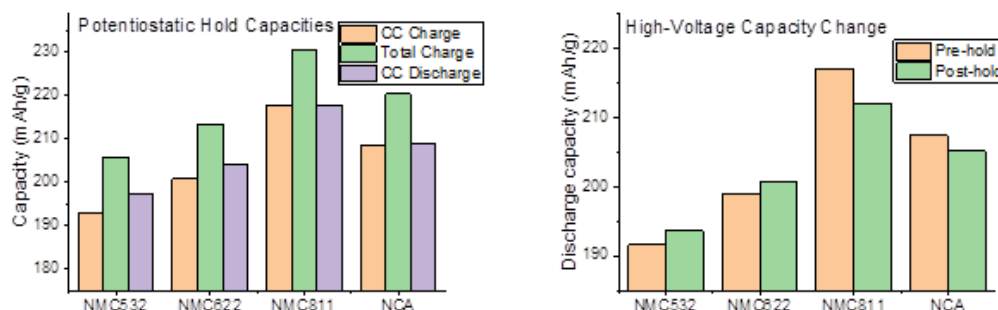


Figure II.2.A.4 (Left) Capacities during the potentiostatic-hold cycle and (right) effect of the potentiostatic hold on discharge capacities, where discharge capacities from cycles 6 and 9 are used for “Pre-hold” and “Post-hold” capacities, respectively

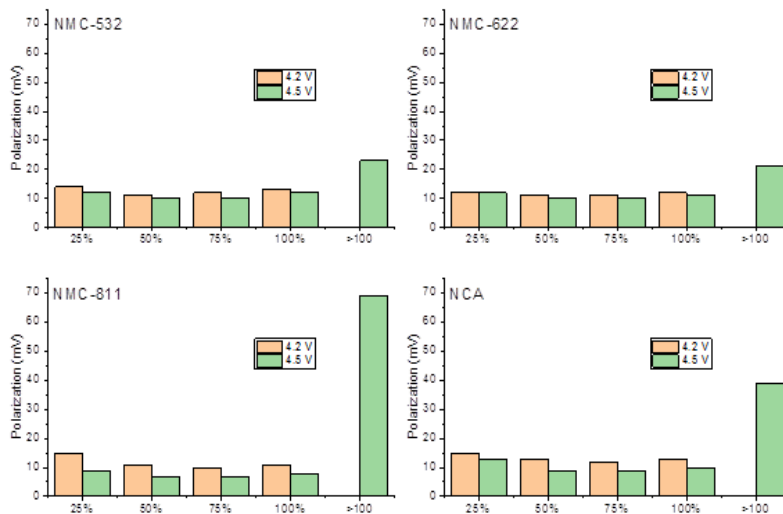


Figure II.2.A.5 Polarizations at various SOC as determined by current interrupts for cycles 4 (orange) and 10 (green).

The Rate protocol is comprised of 20 mA/g charge cycles with discharge rates of 20, 60, 100, 200, and 20 mA/g for 3 cycles each, at an UCV of 4.3 V, for a total of 15 cycles. This protocol is then repeated with an increased UCV of 4.5 V. The LCV is 2.5 V for all cycles. Figure II.2.A.6 shows the rate performance of the four cathodes surveyed. In cycles 1-15 (4.3 V UCV), the difference between the initial 20 mA/g discharge cycles and the 200 mA/g discharge cycles is about 20 mAh/g. The final 4.3 V UCV cycles at 20 mA/g are all equal or slightly greater in capacity than the initial cycles, indicating that a small 'break-in' (<5 mAh/g), or electrolyte wetting period is necessary before these systems reach peak capacity. Additionally, this highlights the stability of these cathodes at intermediate voltage, in that none of the cathodes show decreased capacity over the first half of the test at 4.3 V. Starting with cycle 16, the higher charging voltage (4.5 V) results in higher capacities, especially for the lower Ni-content cathodes. NMC-532 gains ~25 mAh/g, whereas the NCA gains only ~10 mAh/g. Furthermore, the higher-voltage cycling of the second half of the test does result in a decrease in the capacity of the higher Ni-content cathodes, where NMC-811 and NCA lose 3.1% and 2.6% of their capacity, respectively, while the NMC-532 and NMC-622 lose less than 1% capacity. A benefit of using slow (equal) rates at the beginning and end of testing at a specific UCV is the ability to evaluate damage to the cycling performance brought about by the cycling protocol. For these materials, the 4.3 V rate damage was negligible for three of the four cathodes surveyed, indicating the capacity at the end of the 4.3 V cycling protocol was similar to initial capacities. The 4.5 V rate damage (capacity change from cycle 16-18 to 28-30) is the lowest for the NMC-532, at 0.6%, increasing to 3.1% for the NMC-811.

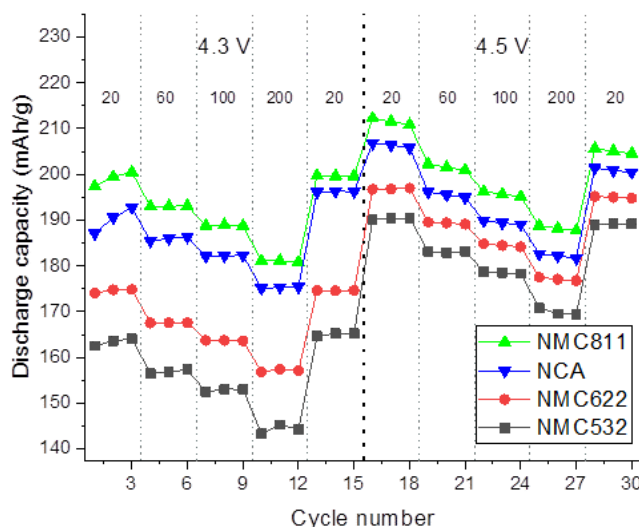


Figure II.2.A.6 Average rate performance of the four cathodes surveyed. Discharge current (mA/g) is indicated in each 3-cycle subdivision, 20 mA/g used for all charge cycles

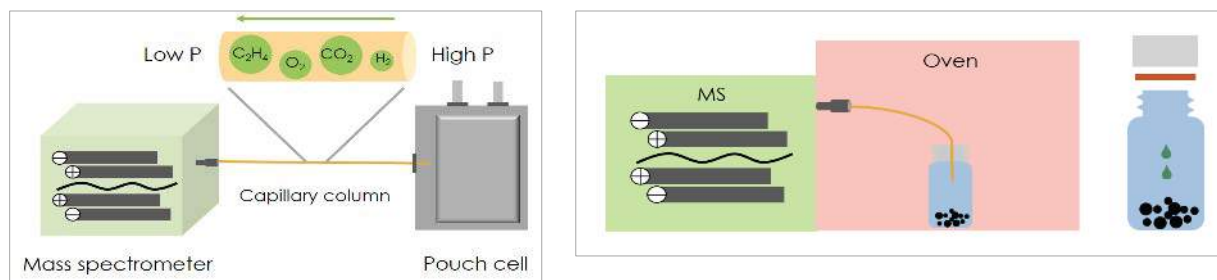


Figure II.2.A.7 Schematic of in situ MS set up for gas analysis using direct sampling method from pouch cell (left image) and for thermal stability test (right image)

Probing Cathode-Electrolyte Interface Reactions by Gas Analysis

In situ mass spectroscopy for gas analysis was conducted on NMC-811//Gr pouch cells fabricated at the U.S. DOE Battery Manufacturing Facility (BMF) at Oak Ridge National Laboratory. The set up was based on a conventional GC-MS instrument (Figure II.2.A.7-left). A glass capillary tube (Polymicro 1068150019), without any stationary phase on inner wall, was first sealed in a pouch cell and the other end of the capillary tube was connected to the MS. The optimal length of the capillary tube was determined to be 45 inches to ensure both accuracy and sensitivity. The setup developed has several advantages: (i) common pouch cells are used instead of customized electrochemical cells; (ii) practical cell configurations can be used to better assess the gas behaviors in the cells; (iii) no carrier gas is used, thus increasing the test sensitivity and preventing the electrolyte from drying out. A modified design was used to probe the gassing behavior of NMC-811 during the thermal stability test (Figure II.2.A.7-right). A sealed glass vial with a high-temperature septum was used as the container for NMC-811 electrodes.

Effect of the upper cut-off voltage (UCV): The real-time generation rate of gases along with voltage and current profiles of aging cycles, using different UCVs, is shown in Figure II.2.A.8. C_2H_4 is generated the most during the 4.2 V aging cycle, with a peak rate of around $5 \text{ nmol min}^{-1} \text{ g}^{-1}$. All other gases have a lower rate than $2 \text{ nmol min}^{-1} \text{ g}^{-1}$ in the whole process. It is hypothesized here that the hydrocarbons, including CH_4 , C_2H_4 and C_2H_6 , are from the reduction of electrolyte solvent contributing to SEI formation on the anode side. It does appear that O_2 and H_2 show a trend vs. voltage. However, the rate of these gases is far below $1 \text{ nmol min}^{-1} \text{ g}^{-1}$, making it hard to draw conclusions. H_2 is believed to be the product of residual water reduction on the anode side. For O_2 , it is well accepted that the lattice oxygen of layered TM oxides can be released during high

voltage operation. However, with an UCV of 4.2 V, it is hard to tell if the oxygen is from water oxidation on the cathode or the TM oxide crystal lattice. Significant amounts of CO and CO₂ are not observed. It is worth noting that the onset potential of all the gases are similar (around 4.2 V) and that most gases are generated during the UCV hold.

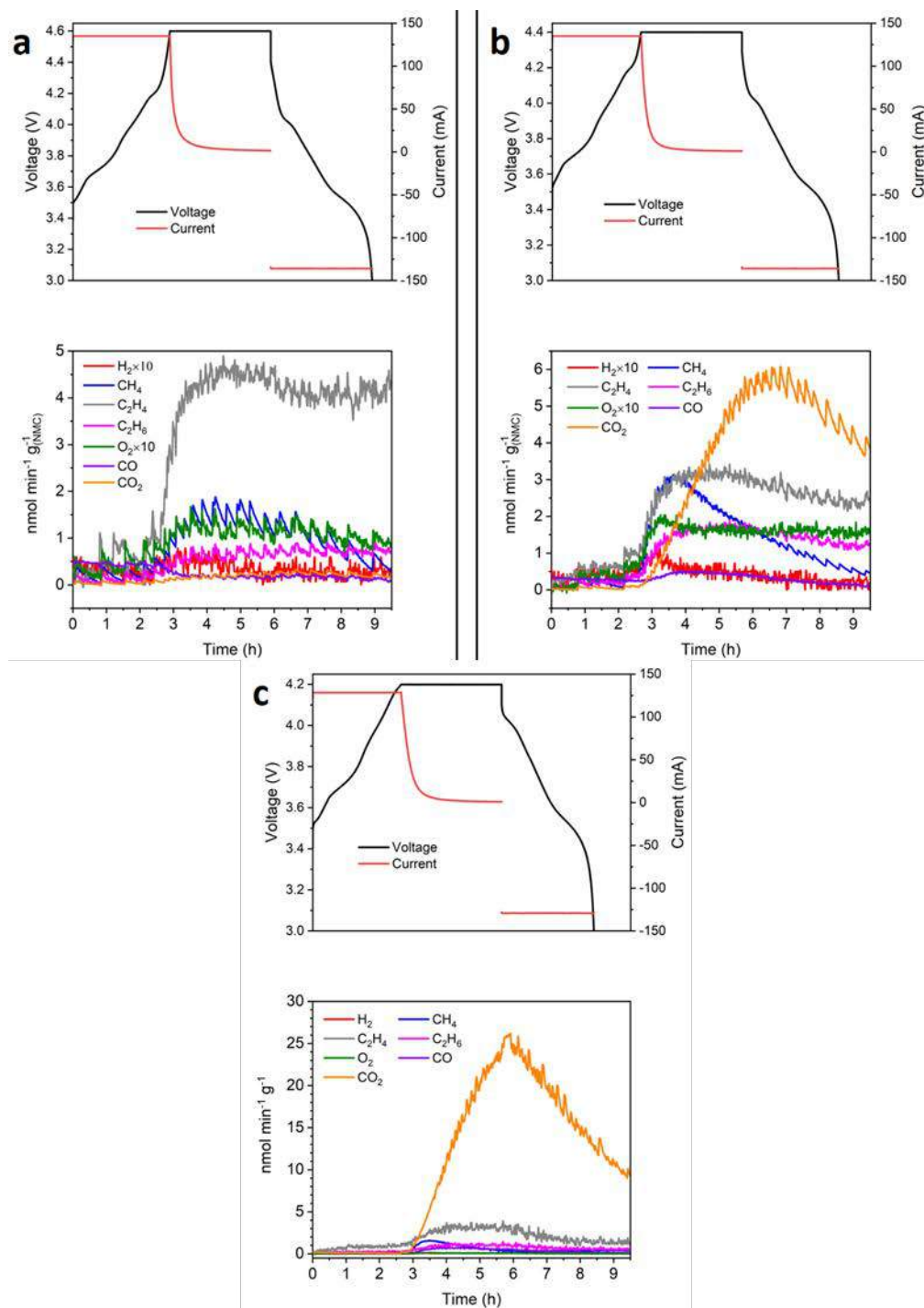


Figure II.2.A.8 Gas generation during cycling with UCVs of 4.2 V (top left panel), 4.4 V (top right panel), and 4.6 V (bottom panel)

Figure II.2.A.8b shows results with an UCV of 4.4 V; this cell has much faster capacity fade than the cell with a 4.2 V UCV, Figure II.2.A.8a. The biggest difference compared to the 4.2 V cycle is in the amount of CO_2 generated where the maximum generation rate is around $6 \text{ nmol min}^{-1} \text{ g}^{-1}$ while the rate at 4.2 V is lower than $0.5 \text{ nmol min}^{-1} \text{ g}^{-1}$. The hydrocarbon amounts are slightly lower than those in the 4.2 V cycle. A possible explanation is that the SEI layer is more complete over the 4.4 V cycle, thus making the energy barrier of electrolyte solvent decomposition higher. O_2 and H_2 have a clearer trend in terms of signal change during the 4.4 V cycle. Although the amounts of these two gases increased compared to the 4.2 V cycle, the change is incremental and does not clearly indicate if the lattice oxygen release is accelerated by the 4.4 V UCV. It can be seen that all gases again share a similar onset potential of around 4.2V, indicating that these oxidation and reduction processes are related. From these results, it is clear that CO_2 generation is very sensitive to UCV, but O_2 generation is not sensitive to the UCV above 4.2 V for this cathode and shows a different trend when compared to CO_2 .

To shed more light on the UCV effect on gassing behavior, a more extreme UCV of 4.6 V was adopted. At 4.6 V, the charge and discharge capacities are 215 mAh g^{-1} and 211 mAh g^{-1} respectively, which is 5.5% higher compared to cells with the 4.4 V UCV. All gases were generated around the onset potential of 4.2 V which is similar to the onset potential for the 4.2 V and 4.4 V cycles. CO_2 is the dominant species under this condition in this process having a peak rate of around $25 \text{ nmol min}^{-1} \text{ g}^{-1}$. Hydrocarbons including CH_4 , C_2H_4 and C_2H_6 have a very similar behavior as those for the lower UCVs. The generation rates of these hydrocarbons kept decreasing compared with previous cycles indicating the gradual completion of SEI layer formation. Interestingly, the O_2 generation level is still very low even with the high UCV of 4.6 V. More detailed studies are needed to confirm the degree of oxygen release from the TM oxide lattice.

Thermal stability study combining gas analysis and neutron diffraction: Chemical changes during thermal exposure play an important role in the long-term safety and performance of cells. Here, we combine in situ gas analysis with neutron diffraction to give a broader picture of the thermal stability of NMC-811. Four electrode samples were prepared electrochemically; $\text{Li}_{0.3}\text{Ni}_{0.8}\text{Mn}_{0.1}\text{Co}_{0.1}\text{O}_2$, $\text{Li}_{0.5}\text{Ni}_{0.8}\text{Mn}_{0.1}\text{Co}_{0.1}\text{O}_2$, $\text{Li}_{0.75}\text{Ni}_{0.8}\text{Mn}_{0.1}\text{Co}_{0.1}\text{O}_2$ and $\text{LiNi}_{0.8}\text{Mn}_{0.1}\text{Co}_{0.1}\text{O}_2$. Two sets of thermal stability test were performed; the first set was performed on the composite electrode material only while the second set was performed in the presence of GEN2 electrolyte ($1 \mu\text{l/mg}$).

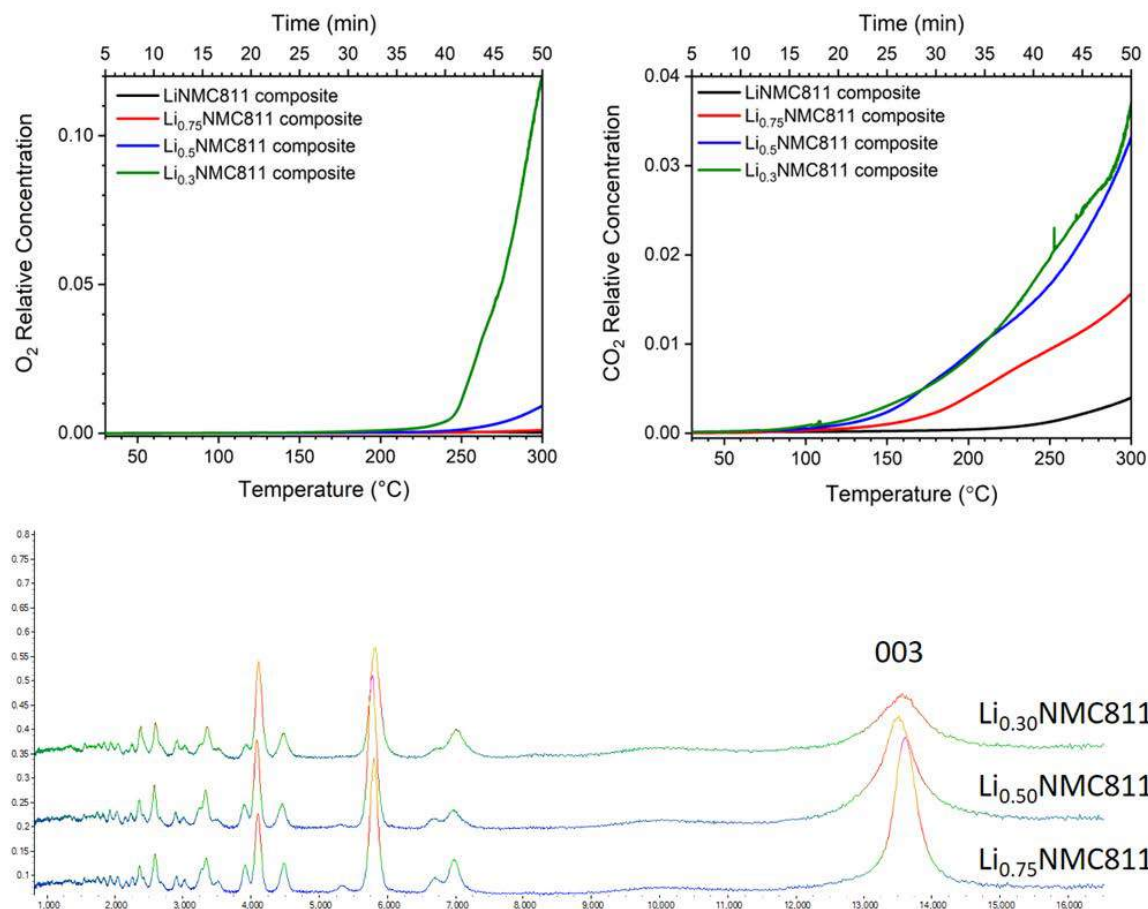


Figure II.2.A.9 O₂ (upper left) and CO₂ (upper right) generation rate during thermal stability test of composite electrode without the presence of electrolyte. Neutron diffraction of composite materials after undergoing thermal stability test (lower panel)

The gassing results are shown in Figure II.2.A.9. The level of delithiation clearly plays an important role in the thermal stability of the oxide where the *more delithiated* NMC-811 released more O₂ at an earlier onset temperature. The Li_{0.3}Ni_{0.8}Mn_{0.1}Co_{0.1}O₂ electrode released large amounts of O₂ starting around 230°C, while the Li_{0.75}Ni_{0.8}Mn_{0.1}Co_{0.1}O₂ did not release significant amounts of O₂ over the range of temperature used (300°C max). The CO₂ amounts are also shown. Without electrolyte, the generation of CO₂ is believed to be caused by the oxidation of carbonaceous materials in the electrode. The trend of CO₂ is in good agreement with the O₂ generated. Ex situ neutron diffraction was performed on the composite materials after the thermal stability test. The most notable feature from neutron diffraction pattern is broadening of the oxide's 003 peak. Greater peak broadening was observed for highly-delithiated samples indicating a higher level of cation mixing between the Li and TM elements.

The chemical interactions between the electrolyte and cathode materials was also probed (Figure II.2.A.10). In the presence of electrolyte, O₂ release was accelerated, with respect to both onset temperature and amounts for all electrodes with different delithiation levels, indicating decreased stability in the presence of electrolyte. The amount of CO₂ released is one order of magnitude higher than the amount of O₂ released and two orders of magnitude higher than the CO₂ amount released in the absence of electrolyte. These results reiterate the importance of cathode/electrolyte interactions with respect to cathode stability.

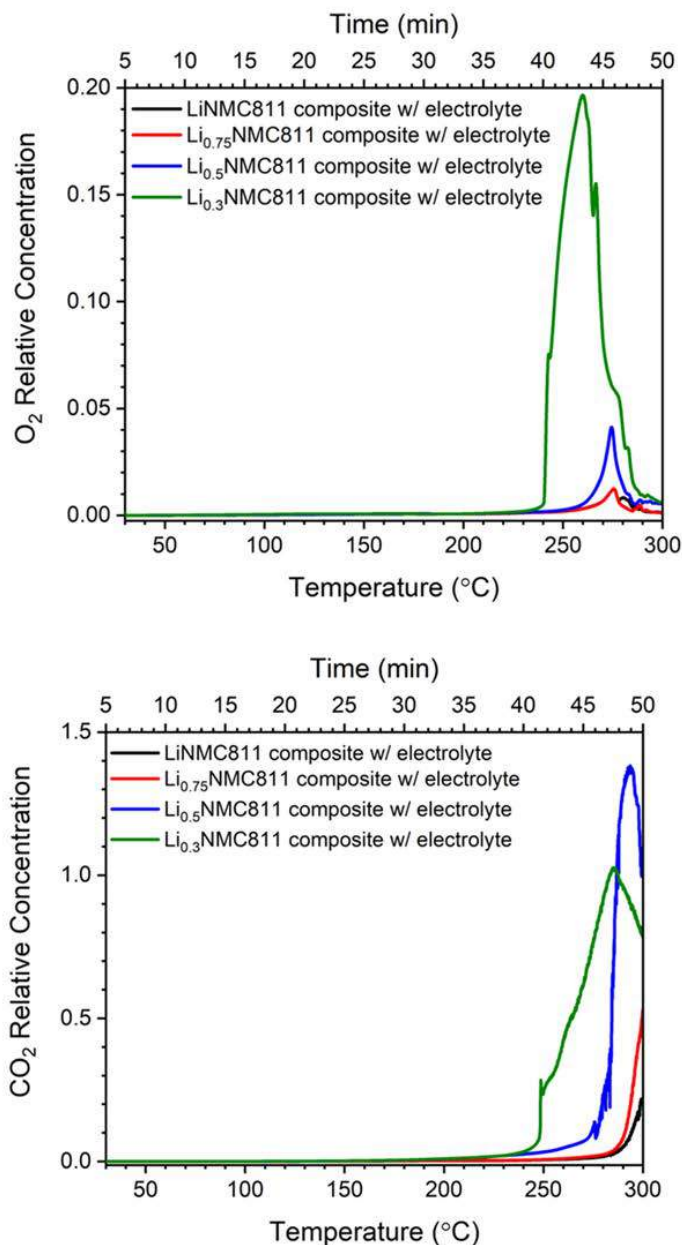


Figure II.2.A.10 O₂ and CO₂ generation rate during thermal stability test of composites with the presence of electrolyte

Developing DSC protocols

In this work, NMC-532 electrodes, made by the CAMP facility at ANL, were charged to 4.2 V after three formation cycle between 4.2 – 3.0 V, at a C/10 rate. At the end of charge a constant voltage hold was applied until the current decreased to C/20. The charged electrode was rinsed with EMC and scraped from the current collector. DSC sample capsules were loaded with various amounts of the recovered NMC-532 powders and fresh Gen2 electrolyte as listed in Table II.2.A.1. The DSC sample capsule was then sealed for measurement. The temperature was scanned from room temperature to 400 °C at a scan rate of 10 °C/min. Figure II.2.A.11 shows the heat flow results for all five samples, from top to bottom, corresponding to # 1 to #5 in the table.

Table II.2.A.1 DSC Samples with Various Amounts of Active Material and Electrolyte

Sample #	NMC-532, mg	Electrolyte, μL
1	2	2
2	1.2	1.2
3	1	1.5
4	1	2
5	0	1

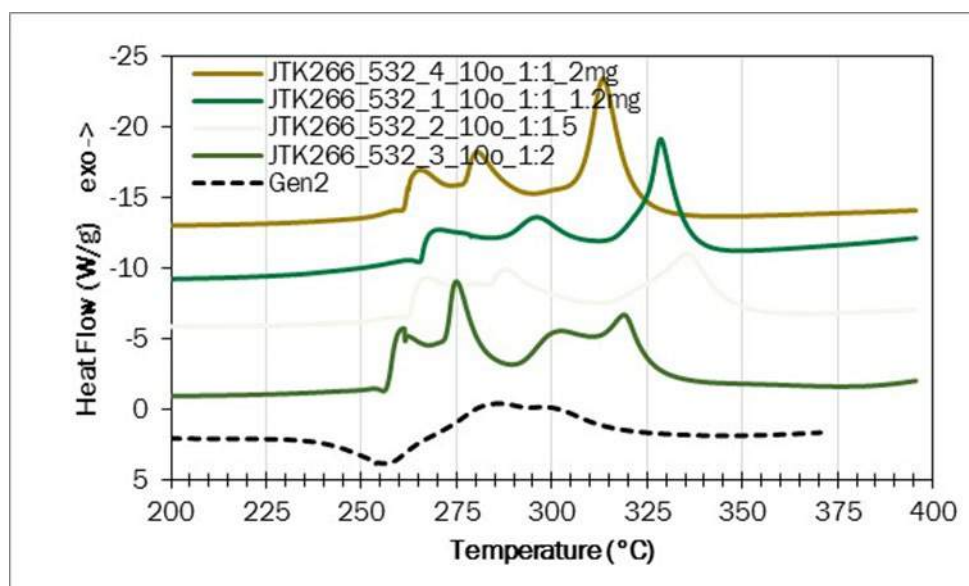


Figure II.2.A.11 DSC results of five samples with various amounts of electrode material and electrolyte

In Figure II.2.A.11, the bottom-most curve is electrolyte alone with no active material, which is used as the control. All the other curves, consisting of various amounts of active material and electrolyte, show quite similar thermal behaviors with three or four major exothermic peaks. These exothermic peaks are related phase changes and corresponding reactions between the active material and electrolyte, which reflects the intrinsic thermal properties of active materials. However, the on-set temperatures and peak temperatures change with various ratios between active material and electrolyte. The second curve from bottom has the highest electrolyte to electrode ratio, which shows the lowest on-set temperature. The on-set temperature increases with decreasing electrolyte to active material ratio. The total amount of active material also affects the on-set temperature when comparing the top two curves that have the same electrolyte to active material ratio but different amounts of total materials. The more material in the sample holder, the lower the on-set temperature. According to this study, the optimum amount of active material was determined to be 1.5– 3 mg. When desired, electrolyte is added by auto pipette with a ratio of 1 μL electrolyte per mg of laminate powder. It was found that this was a sufficient amount electrolyte to wet the powder, but not significant excess, which can affect the DSC signal. Clearly, a controlled and consistent amount electrolyte should significantly improve DSC reproducibility between groups, which will allow meaningful comparisons between cathode materials.

Electrode Cross Talk and TM Dissolution

As Ni content of the oxide-cathode increases, the concentration of $\text{Ni}(4+)$ species in the charged cathodes increases. This makes the interface between the electrolyte and the cathode even more thermodynamically unstable. A direct result of the instability may be a change in electrolyte decomposition products present in the cell, possibly making TM dissolution easier. To examine how cathode composition affects TM dissolution and electrolyte decomposition products the following two approaches were used. The first approach, referred to as

in-cell, was to cycle pouch cells containing NMC-111, NMC-532, NMC-622, and NMC-811 and subsequently determine TM concentrations deposited on the Gr by ICP-MS and to characterize the electrolyte decomposition products by high-performance liquid chromatography (HPLC). The electrolyte consisted of 1.2 M LiPF₆ in EC:EMC (3:7 by wt.; Gen2). The second approach was to use static leaching experiments on highly-charged (4.6 V) NMC cathodes using tetrabutyl ammonium bifluoride, (C₄H₉)₄NF·HF in EC:EMC (3:7 by wt.) solution. The bifluoride salt was used because it is an organic-soluble source of HF.

In-cell experiments: Three full cells containing NMC-532, NMC-622 and NMC-811 cathodes, matched with Gr anodes, were prepared in pouch cell configuration. Cells were cycled between 4.4 to 3.0 V for 100 cycles. After cycling, the cells were disassembled in an Ar-filled glove box and a portion of each anode was used for ICP-MS analysis. Aged electrolytes were carefully collected and treated for HPLC analysis.

Figure II.2.A.12a shows the quantification results of TM ions found at the anodes of cycled cells using NMC-532, NMC-622 and NMC-811 cathodes.

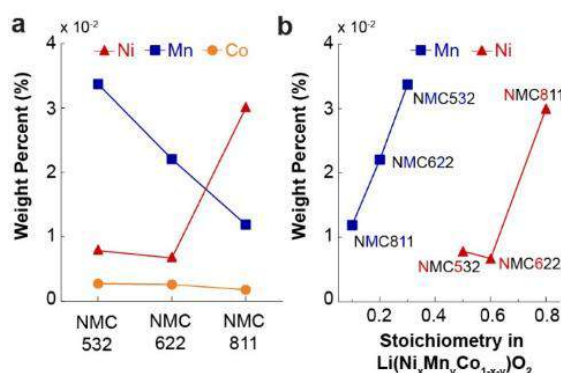


Figure II.2.A.12 ICP-MS quantification results. (a) Concentration of Mn (blue, circle), Ni (red, square) and Co (orange, diamond) from anodes cycled with various NMC cathodes. (b) Concentration of Mn and Ni from various NMC cathodes versus ideal stoichiometry in Li(Ni_xMn_yCo_{1-x-y})O₂.

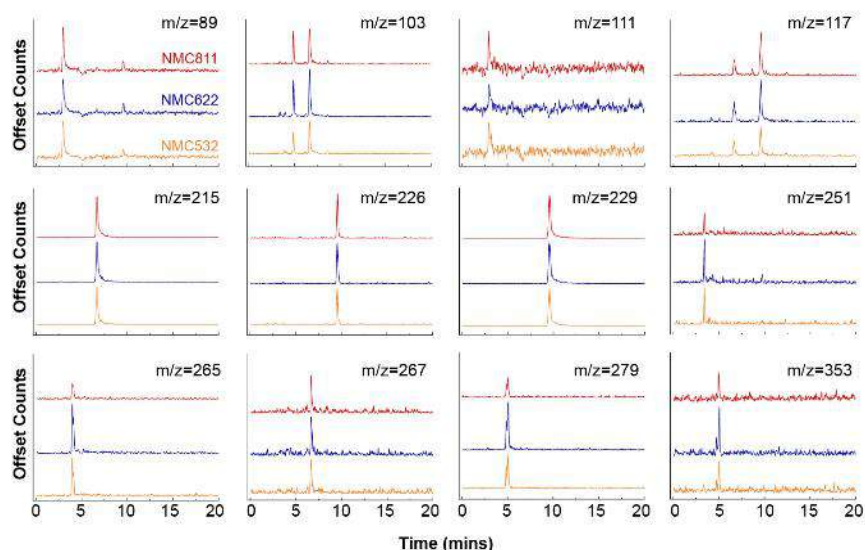


Figure II.2.A.13 SICs of m/z detected via HPLC/ESI-MS that are present in the aged Gen2 electrolyte samples from the cycled pouch cells composed of graphite anodes against NMC-532(orange), NMC-622(blue) and NMC-811(red)

It is observed that Co was detected in the lowest amounts for all 3 cells. the largest amount of Mn was observed for NMC-532 and Mn detection decreased linearly as its atomic fraction in the NMC decreased. The

relationship between Ni in solution and cathode composition was observed to be more complex. The concentration of Ni was similar for NMC-532 and NMC-622 but sharply increased with NMC-811. Figure II.2.A.12b replots the dissolution concentration of Mn and Ni versus the ideal stoichiometry of the NMC cathodes used. The quantification results revealed in this study were generally consistent with other recent reports regarding a higher Ni dissolution from Ni-rich cathodes. HPLC was utilized to investigate the aged Gen2 electrolyte extracted from the cycled pouch cells. Many peaks in the chromatogram were detected, indicating numerous decomposition species. Figure II.2.A.13 shows the single ion chromatographs (SIC) from the 12 most prominent peaks. The electrolyte from all cells had SICs that looked roughly the same. This implies that cathode composition did not alter the decomposition species detected by HPLC in the aged electrolyte and no clear relationship between migrating TM ions and electrolyte decomposition species can be discerned from the data.

Table II.2.A.2 Twelve Most Intense Ions Detected via HPLC and Corresponding Chemical Structures

m/z	M.W.	adduct	Calculated number of C	Proposed chemical structure
89	88	H+	3	Ethylene Carbonate
103	80	Na+	4.3	C ₄ H ₉ LiO
111	108	Na+	4.5	C ₅ H ₁₂ O
117	116	H+	6.0	C ₆ H ₁₂ O ₂
215	214	H+	7.7	C ₈ H ₄ F ₆
226	208	NH ₄ ⁺	10.5	C ₁₁ H ₁₂ O ₄
229	206	Na+	3.7	N/A
251	250	H+	6.2	C ₅ H ₃ F ₉ O
265	242	Na+	5.4	C ₆ H ₅ F ₇ O ₂
267	266	H+	12.8	C ₁₂ H ₂₇ O ₄ P
279	278	H+	10.2	C ₁₀ H ₁₅ F ₅ O ₃
353	330	Na+	12.5	C ₁₂ H ₂₈ O ₆ P ₂

The mass spectra corresponding to the SICs in Figure II.2.A.13 were used to determine the effective weights of the (pseudo)molecular ions and the number of carbon atoms they contained. Table II.2.A.2 lists the 12 most intense species detected in the three samples and the composition of proposed chemical structures. To identify the chemical structure and compositions of these species, it was assumed that the molecule can only be composed of C, O, F, P, and H. It was also assumed that the uncertainty in the number of carbons in the proposed molecule was ± 1 .

Static tests: The point of this work was to help understand the factors that affect TM dissolution. Figure II.2.A.14 shows the dependence of Ni, Mn, and Co in solution, with and without the bifluoride additive, for the four cathode compositions studied. It should be noted that the concentrations of these metals without the bifluoride is also shown on the plots as blue bars. These metal concentrations were, in general, too low to be seen at the micromolar scale.

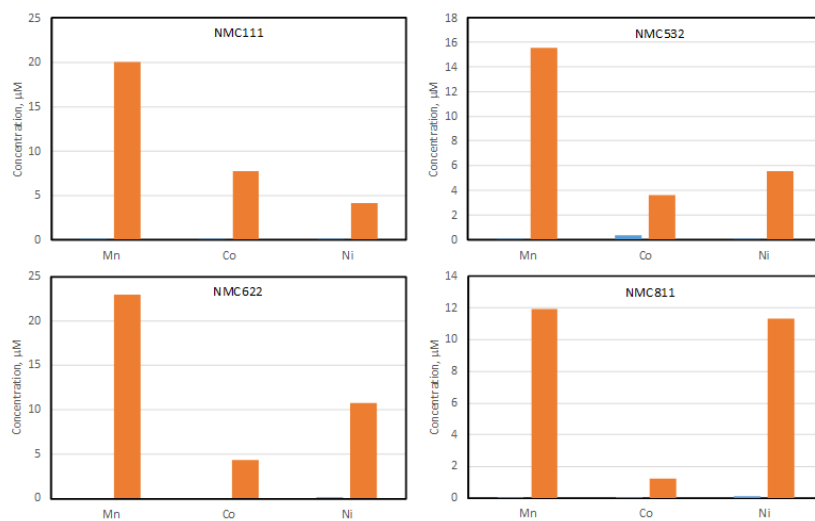


Figure II.2.A.14 Concentrations of Mn, Co and Ni in solution from the cathode materials used in this study. The concentrations of the metals without the additive are given as blue bars; and with it, as orange ones. It should be noted that, due to the large differences in the relative concentrations, the blue bar may not be visible in all plots

The relative changes, $([metal\ with\ additive] - [metal\ without\ additive]) / [metal\ without\ additive]$, was calculated from these values. The concentrations of Mn and Co in solution showed the largest change, in general, in response to the addition of the bifluoride. Relationships in the data were determined using Visual Basic for Applications in Excel®. A search algorithm was implemented to test all possible combinations of the terms shown in Eq. 1,

$$[TM] = b(X_{Mn})^{\alpha}(X_{Ni})^{\beta}(X_{Co})^{\gamma}, \quad (1)$$

where $[TM]$ is the concentration of either Ni, Mn or Co in solution; b is a constant; X_{TM} is the bulk stoichiometry of Mn, Ni, or Co; and α , β , and γ are the orders of the reaction in that component. If the component accelerated the reaction, the corresponding exponent was positive; if it inhibited the reaction, the exponent was negative. If α , β , or γ was zero, then there was no contribution from that component to the overall expression.

The actual fitting was performed using the LINEST function in Excel®. We restricted the values of α , β , and γ to be integers between -5 and 5 and $|\alpha + \beta + \gamma| \leq 5$. These restrictions arose from a consideration of the surface of the oxide, that is, how many next-nearest-neighbor atoms were TMs. Each TM center has, at most, five next-nearest-neighbor metal atoms, which limited the range of values possible for the given exponent. A fit was considered acceptable if the regression coefficient, r^2 , was greater or equal to 0.95. The results of the fitting exercise are shown in Figure II.2.A.15. It was interesting to observe that, in most cases, the relationships showed that the concentration of the TMs increased with the expression given on the x-axis of the charts. $[Mn]$ increased with $X_{Ni}X_{Co}$; $[Ni]$, with $X_{Co}(X_{Ni})^3$; and $[Co]$, with X_{Co} . However, it was found that as $(X_{Mn})^2$ increased, $[Ni]$ decreased. Taking the fitting results for Ni as an example in Figure II.2.A.15, the two expressions state that $[Ni]$ is proportional to $X_{Co}(X_{Ni})^3$ and is inversely proportional to $(X_{Mn})^2$. These expressions can be related to possible configurations of atoms on the surface of the charged cathode. If one considers the arrangements of next-nearest neighbors ($NNNs$) around a central Ni atom, a configuration with three Ni $NNNs$ and one Co NNN would be expected to accelerate the dissolution rate of Ni. On the other hand, if two of the $NNNs$ were Mn, the dissolution rate of Ni would be retarded. Similar interpretations for the fitting results for Co and Mn can be made.

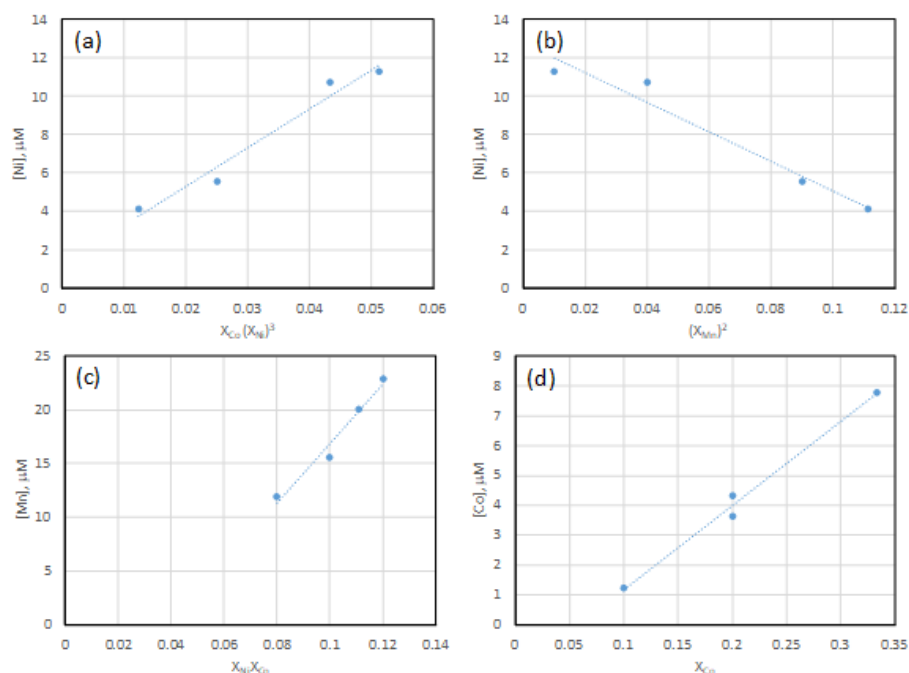


Figure II.2.A.15 Concentrations of the transition metals vs. various combinations of the ideal stoichiometries with bifluoride present. Markers represent the data, and dotted lines, the least squares fit. The regression yielded the following equations (value of r^2): (a) $[\text{Ni}] = 203.07X_{\text{Co}}(X_{\text{Ni}})^3 + 1.23$ (0.97); (b) $[\text{Ni}] = -77.04(X_{\text{Mn}})^2 + 12.76$ (0.96); (c) $[\text{Mn}] = 275.67X_{\text{Co}}(X_{\text{Ni}}) - 10.71$ (0.97); and (d) $[\text{Co}] = 28.09X_{\text{Co}} - 1.61$ (0.99)

In situ Spectroscopic Analysis of the Cathode-Electrolyte Interface

Experimental setup with an in situ ATR-FTIR cell: In order to perform ATR-FTIR measurements of the cathodes in situ while simultaneously subjecting them to galvanostatic electrochemical testing, a custom cell holder was designed (Figure II.2.A.16). The ATR-FTIR cell design concept was adapted from previous efforts by Phil Ross *et al.* to study Li-ion battery anodes.

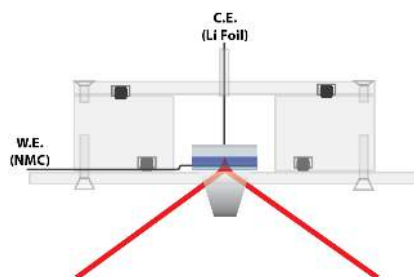


Figure II.2.A.16 In situ ATR-FTIR cell design

In the design herein, a PEEK holder and lid assembly is affixed to an ATR-FTIR prism plate, creating an air-tight seal. The porous cathode (working electrode) is placed onto the surface of the prism. Above that is approximately 40 μL of Gen2 electrolyte, a separator (Celgard 2325), a Li-metal foil (counter/reference electrode), and a stainless-steel spacer (SS316). When the lid is closed, a SS316 rod fit into the lid presses down on the “coin-type” cell to ensure good electrical contact with the counter electrode, the pressure also provides an intimate interface between the cathode surface and the ATR prism resulting in a high FTIR signal. It has been demonstrated that the cell enables reliable electrochemical testing, similar to a standard 2032 coin-type cell. The cathode sample is prepared by dipping a porous aluminum current collector into a slurry mixed

with cathode active materials, polymer binder (PVdF), conductive carbon (C45), and n-methyl pyrrolidone (NMP) as a slurry solvent. After coating both sides of the current collector, the cathode is dried in a vacuum oven at greater than 90°C for overnight and subsequently calendared between stainless steel rollers to achieve a total thickness between 50 and 100 μm . ATR-FTIR spectra were acquired with either a Thermo Nicolet 6700 or Bruker Alpha II FTIR spectrometer. Scans were collected in the range of 4000-400 cm^{-1} . Each spectrum was an average of 192 scans against a background from a blank cell that was sealed in an argon filled glove box. Spectra were baseline subtracted using either a multi-polynomial or rubber band (convex-hull) baseline fit.

In situ ATR-FTIR spectra and reference library for the electrolyte at the cathode-electrolyte interphase (CEI): During a galvanostatic cycle between 3.0-4.5 V (vs. Li/Li^+ , hereafter), the electrolyte solution structure near the cathode surface was monitored. Importantly, infrared vibrational absorptions are sensitive to a molecule's local bonding environment. This enables the distinction between electrolyte species—EMC, EC, and PF_6^- —associated with a nearby Li^+ ion or “free” species surrounded by other solvent molecules in the solution near the cathode surface. For example, a free EMC solvent molecule has an O-C-O bending mode vibrational absorption at 1266 cm^{-1} , but when solvating a Li^+ ion, the absorption shifts to 1306 cm^{-1} . Table II.2.A.3 lists the peak assignments for Gen2 molecular bond vibrational absorptions.

Table II.2.A.3 FTIR Peak Assignments for Gen2 Electrolyte

FTIR Band Center (cm^{-1})	Assignment	Species of Origin	Reference(s):
560		PF	this work
781	o, O-C-O	EC	this work
795	o, O-C-O	$\text{EC}\cdots\text{Li}^+$	this work
825	u, P-F	$\text{PF}_6^-\cdots\text{Li}^+$	[1, 2]
840	u, P-F	PF_6^-	[1, 2]
874	u, P-F	$\text{PF}_6^-\cdots\text{Li}^+$	[1, 2]
904	u, C-O	EMC	this work
940	u, C-O	$\text{EMC}\cdots\text{Li}^+$	this work
972	o	EC	[3]
1008	u, C-C-O	EMC	this work
1075	u, C-O	EC	[4]
1085	u, C-O	$\text{EC}\cdots\text{Li}^+$	[4]
1160	δ , O-C-O	EC	[4]
1200	δ , O-C-O	$\text{EC}\cdots\text{Li}^+$	[4]
1266	δ , O-C-O	EMC	[4], this work
1306	δ , O-C-O	$\text{EMC}\cdots\text{Li}^+$	[4], this work
1375	δ , CH_2	EC	[4], this work
1390	δ , CH_2	EC	[4], this work
1407	δ , CH_3	$\text{EC}\cdots\text{Li}^+$	[4], this work
1450	δ , CH_3	EMC	[4], this work
1480	δ , CH_3	$\text{EMC}\cdots\text{Li}^+$	[4], this work
1715	u, C=O	$\text{EMC}\cdots\text{Li}^+$	this work
1745	u, C=O	EMC	this work
1772	u, C=O	$\text{EC}\cdots\text{Li}^+$	[4]

FTIR Band Center (cm ⁻¹)	Assignment	Species of Origin	Reference(s):
1778	u, C=O	EC	[4]
1804	u, C=O	EC	[4]
[1] F. Shi, et al., <i>J. Am. Chem. Soc.</i> , 2015, 137, 3181-3184. [2] F. Shi, et al., <i>J. Phys. Chem. C</i> , 2017, 121, 14476-14483. [3] D.M. Seo, et al., <i>J. Phys. Chem. C</i> , 2015, 119, 14038-14046. [4] A.V. Cresce, et al., <i>Phys. Chem. Chem. Phys.</i> , 2017, 19, 574-586.			

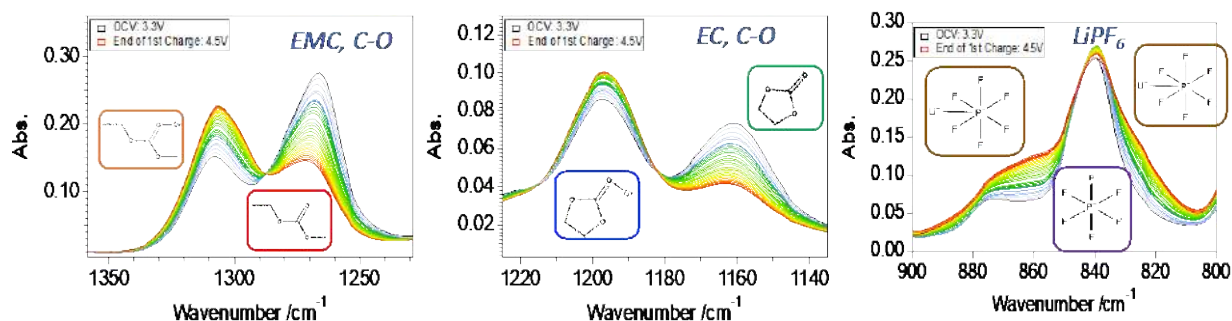


Figure II.2.A.17 ATR-FTIR spectra showing the changes in peak intensities during electrochemical delithiation of NMC-622 cathode for electrolyte components—EMC, EC, and PF₆—associated with a Li⁺ ion or “free” in the solution near the cathode surface

Figure II.2.A.17 shows in situ ATR-FTIR absorption bands for the Gen2 components during electrochemical delithiation (charging) of the NMC-622 cathode up to 4.5 V.

During charging, the local concentration of Li-ions in the solution increases, and a decrease in the free EC and free EMC solvent absorptions, and a concomitant increase in the ion-associated absorptions, are observed. For the P-F vibrational absorption of the PF₆⁻ anion, there is an increase in the contact ion pair absorptions, similar to what has been shown in other studies by varying the salt concentration in the electrolyte. A quasi-reversible behavior in solution structure is observed when the cell polarization is reversed and the battery is discharged.

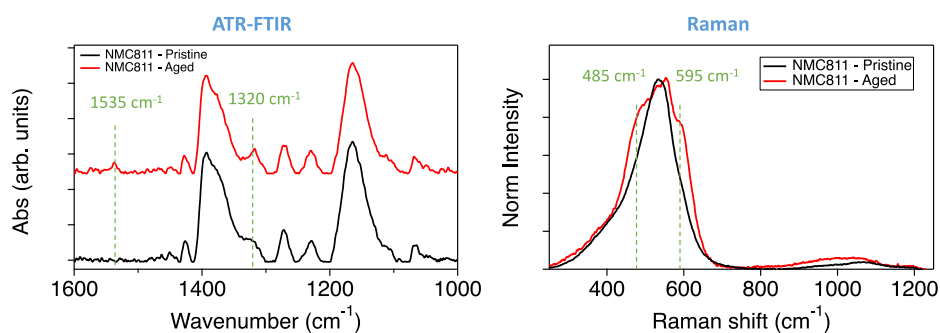


Figure II.2.A.18 ATR-FTIR and Raman spectra comparing the pristine and aged NMC-811 composite electrodes

Preliminary in situ ATR-FTIR spectra for the cathode materials: In addition to investigating the solution structure near the cathode surface, the ATR-FTIR technique is also able to probe the cathode material itself. The evanescent wave at the surface of the ATR prism extends 1-5 μm into the sample, so it should measure both the bulk and the surface of the cathode sample. To confirm this, intentionally induced surface chemical changes were introduced by oxidizing an NMC-811 composite electrode on a hot plate at 80°C with 100 % relative humidity for 395 hrs. Figure II.2.A.18 shows the ATR-FTIR (left) and Raman (right) spectra

comparing the pristine and aged sample. In the FTIR data, two new peaks are observed at 1535 cm^{-1} and 1320 cm^{-1} , corresponding to formation of carboxylate-containing surface species, which is corroborated by the emergence of shoulder bands around the main 540 cm^{-1} NMC-811 peak in the Raman scattering data.

In situ ATR-FTIR was then used to monitor the changes to an NMC-622 (as a model cathode) during a galvanostatic charge/discharge cycle (C/10 rate; $105\text{ }\mu\text{A}/\text{cm}^2$), shown in Figure II.2.A.19. The differential capacity versus voltage, dq/dV , is displayed in the inset. On the right side of the figure is the ATR-FTIR spectra taken at the specific points in the cycle: 3.35 V (open circuit voltage (OCV)), 3.8 V charging, and 3.6 V discharging. At 3.8 V during charging, in situ ATR-FTIR spectra (right, blue trace) shows a blue shift of the 583 cm^{-1} peak and increase in intensity of a peak at 595 cm^{-1} , compared to at OCV (right, black trace). This change in vibrational absorption of the TM-oxygen bonding may reflect the changes in TM-oxygen bond lengths due to oxidation. Upon discharge back to 3.6 V, the ATR-FTIR spectrum (right, gold trace) is similar to that of OCV, suggesting the bond lengths revert mostly back to their original states (NMC-622 is known to have reversible delithiation/lithiation as far as upper cutoff voltages of 4.6 V). Comparing the spectra, there is a decrease in intensity in the region of 525 cm^{-1} as the cell is cycled. This may be due to TM dissolution, such as loss of Mn from the NMC-622 during cycling.

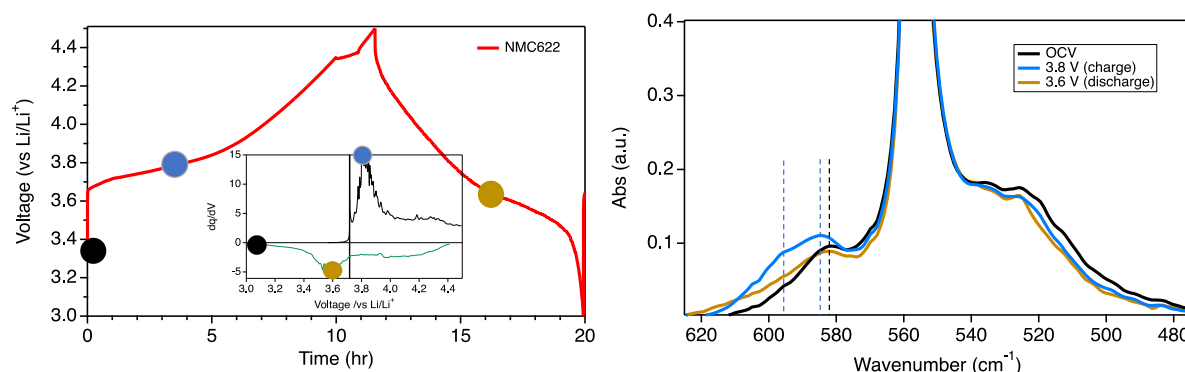


Figure II.2.A.19 (Left) C/10 galvanostatic cycle of an NMC-622 cathode (left), with dq/dV (inset). (Right) FTIR-ATR spectra

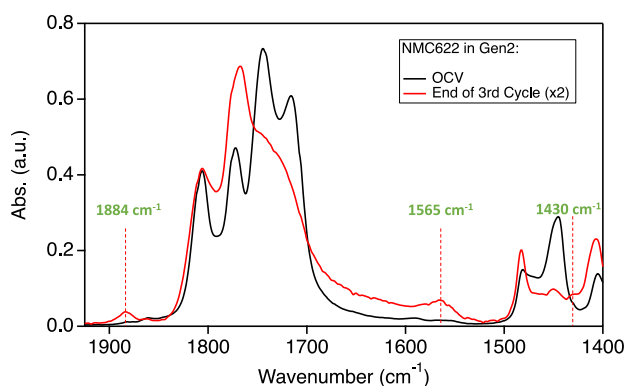


Figure II.2.A.20 ATR-FTIR spectra at OCV and after the 3rd galvanostatic charge/discharge cycles of NMC-622. After cycling, new peaks emerge that indicate formation of CEI species, containing carboxylate and carbonate functional groups

In addition to monitoring NMC-622 structural changes, formation of CEI species during cycling can also be monitored. As shown in Figure II.2.A.20, comparing the in situ ATR-FTIR spectra collected at OCV (black trace) vs. at the end of the 3rd charge/discharge cycles (red trace), a peak appears at 1565 cm^{-1} corresponding to the symmetric COO^- stretching mode of organic carboxylate species (e.g., Li propionate). The asymmetric stretch near 1430 cm^{-1} is also visible, but partly obscured by EMC solvent absorption. Another peak appears at 1884 cm^{-1} is likely due to carbonate species formed from oxidative degradation of the electrolyte solvents.

Finally, although not shown here, a broad band around 3550 cm^{-1} indicating the presence of hydroxyl species was observed.

Reference Electrodes in Symmetric Li-ion Cells with Layered Oxide Electrodes

In order to prepare the symmetric cells, NMC-532//Gr cells were cycled five times between 3.0–4.0 V at a $\sim\text{C}/20$ rate to form a stable SEI layer on the Gr electrode. The cells were then charged to 3.9 V and held at that voltage for >12 h. During this period, the oxide and Gr electrode potentials stabilized at ~ 4.0 and ~ 0.1 V vs. Li/Li^+ , respectively. The cells were then disassembled and oxide/oxide symmetric cells prepared from the harvested electrodes. Henceforth, the positive and negative electrodes in the oxide symmetric cells will be referred to as oxide(+) and oxide(-), respectively. Each symmetric cell contained a $25\text{ }\mu\text{m}$ thick Sn-coated copper wire, which was lithiated in situ to form a Li_xSn reference electrode. This probe was placed at the center of the round cell between two Celgard 2325 separators that were sandwiched between the electrodes. An auxiliary Li metal reference placed slightly to the side of the electrode sandwich was used to monitor the electrode potentials; this reference provides accurate data at open circuit or when the current flowing through the cell is small. After assembly, each symmetric cell was held at 0.0 V for a time period > 24 h to allow potential/charge equilibration between the electrodes. For the calendar (constant voltage) aging study, the oxide symmetric cell was charged to a set voltage (0.6, 0.8 or 0.95 V) at a $\sim\text{C}/20$ rate, held at this voltage for 100 h, then discharged at a $\sim\text{C}/20$ rate to 0.0 V. For the cycle aging study, the cell was cycled ten times between zero and the set voltage; the cycling rate was adjusted so that the aging period matched the aging period of the calendar-life study. These cycles were repeated multiple times to amplify the effects of aging.

Representative data from the oxide symmetric cells are shown in Figure II.2.A.21. In each cycle (Figure II.2.A.21a), the oxide(+)/oxide(-) cell is charged to 0.95 V at a $\sim\text{C}/20$ rate, held at 0.95 V for 100 h, then discharged to 0 V at a $\sim\text{C}/20$ rate. During the first cycle, as the cell voltage increases to 0.95 V, the oxide(+) potential increases to 4.678 V vs. Li/Li^+ , while the oxide(-) potential decreases to 3.728 V vs. Li/Li^+ (Figure II.2.A.21b). Interestingly, the potentials of both oxide(\pm) potentials decrease (slide) over time during the voltage hold, so that at the end of 100 h the oxide(+) and oxide(-) potentials are 4.637 and 3.687 V vs. Li/Li^+ , respectively. The electrode potentials continue to slide during the 2nd and 3rd hold cycles. Figure II.2.A.21b shows that the oxide(+) potential is 4.607 and 4.576 V before and after the 2nd 100 h hold, and 4.568 and 4.511 V before and after the 3rd 100 h hold. Hence, the oxide(+) potential is 167 mV lower (4.678 minus 4.511 V) after 300 h at 0.95 V. An identical variation is seen in the oxide(-) potential as the cell voltage is always maintained at 0.95 V. Thus, the reference electrode data indicate that the electrode cycling windows change during aging. The current flow during the 0.95 V potentiostatic hold is shown in Figure II.2.A.21c. The rapid current drop at the beginning of each hold reflects potential equilibration between the particles in the electrode. After this transition period, the current flow (necessary to maintain the cell at the hold potential) is a measure of self-discharge in the cells. For the as-prepared symmetric cells (when both electrode potentials are at ~ 4.0 V vs. Li/Li^+), the current stabilizes at values < 10 nA after ~ 5 h at 0 V. Much higher currents are observed during the 0.95 V hold (Figure II.2.A.21c). During the first 100 h hold, the current decreases to $\sim 43\text{ }\mu\text{A}$ at 25 h and then slowly increases to $\sim 84\text{ }\mu\text{A}$ at 100 h. Similar high currents ($> 40\text{ }\mu\text{A}$) are observed in the subsequent cycles (Figure II.2.A.21c).

The current flow during the potentiostatic hold is a function of the voltage (see Figure II.2.A.22). The oxide(+) and oxide(-) potentials at 0.95, 0.8 and 0.6 V cell voltages are 4.68, 4.56, 4.40 V and 3.73, 3.76, 3.8 V vs. Li/Li^+ , respectively. Note that the oxide(+) potentials are sufficiently high for electrolyte oxidation to occur, and thus a higher self-discharge (parasitic) currents are expected at higher hold voltages.

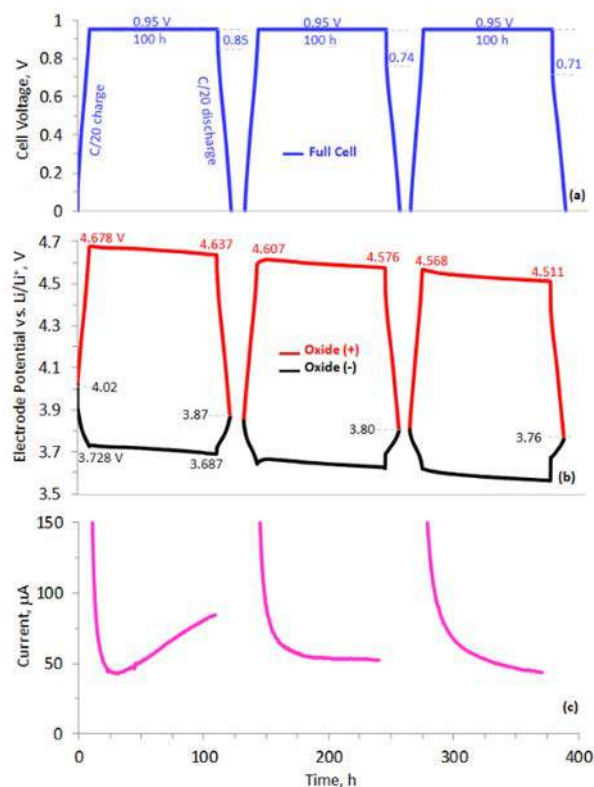


Figure II.2.A.21 Potential change during the 0.95 V potentiostatic hold in an oxide(+)/oxide(-) symmetric cell for a total of 300 h. (a) Full-cell and (b) electrode potentials. (c) Current flow through the cell during the 100 h hold cycles

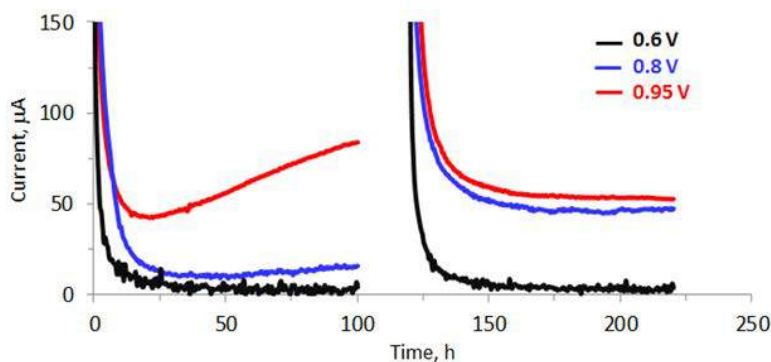


Figure II.2.A.22 Current flow through an oxide(+)/oxide(-) symmetric cell during the first (left) and second (right) 100 h potentiostatic holds at 0.6 V (black), 0.8 V (blue), and 0.95 V (red)

These expectations are met in Figure II.2.A.22. For the cell held at 0.6 V, the current stabilizes around $\sim 2 \mu\text{A}$ in ~ 20 h. In contrast, for the cell held at 0.8 V, the current decreases to $\sim 5 \mu\text{A}$ in ~ 20 h, then increases over time to $\sim 16 \mu\text{A}$ after 100 h; this behavior is similar to that seen for the 0.95 V cell. Furthermore, the currents remain relatively high for the 0.95 and 0.8 V cells, even during the 2nd 100h hold indicating the presence of parasitic reactions in the cell; these reactions are again considerably smaller for the 0.6 V hold cell.

The rapid potential decreases in the initial stages of discharge in Figure II.2.A.21a and b are indicative of increased cell impedance. This is also apparent in the Nyquist plots shown in Figure II.2.A.23. Immediately after the cell assembly (Figure II.2.A.23), all cells show similar impedance spectra with $R_{\text{tot}} \sim 17 \Omega\text{-cm}^2$. These profiles begin to diverge after cell aging. As a control, some cells were held at zero volts for an extended period, and negligible changes were observed in their EIS. Figure II.2.A.23b and c show that the impedance rise is smallest for the cell held at 0.6 V (less electrolyte oxidation) and greatest for the cell held at 0.95 V (efficient electrolyte oxidation). The increase in R_{tot} at 0.6, 0.8, and 0.95 V is 2.2, 3.2, and 4.7 times after 100 h, respectively, and 3.0, 9.3, and 19.9 times after 200 h, respectively. Note that most of the impedance rise occurs in the mid- to low-frequency arc, which suggests that the impedance rise is governed by processes occurring at the electrode-electrolyte interface.

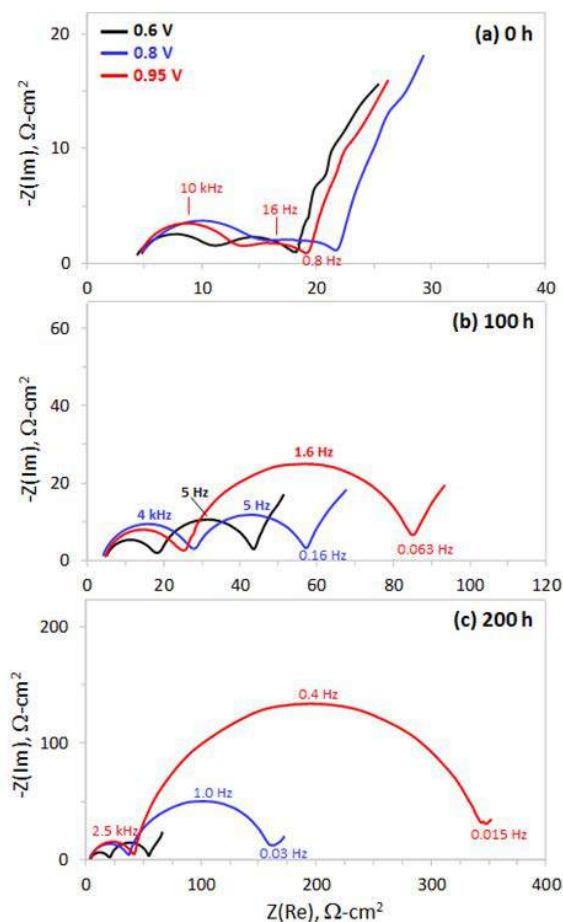


Figure II.2.A.23 Nyquist plots (100 kHz – 0.01 Hz, 30 °C, 0 V) for oxide(+)/oxide(-) symmetric cells after (a) 0 h, (b) 100 h and (c) 200 h at 0.6 V (black), 0.8V (blue) and 0.95 V (red). Mind the different scales in the three panels

Figure II.2.A.24 compares the impedance change in a cell that was *cycled* between 0-0.8 V (cycle aging) with the one that was held at 0.8 V (calendar aging). The cycling rate was chosen such that the time periods for these aging tests were the same. While the cell impedance increases on cycling, the rise during the 0-0.8 V cycles is much smaller than the rise observed during the 0.8 V hold. Furthermore, impedance changes in the two electrodes were comparable after *this* cycle ageing. These data indicate that extended electrode exposure to high potentials (conducive to electrolyte oxidation) is more deleterious than exposure to a range of potentials which occurs during the gradual cycling.

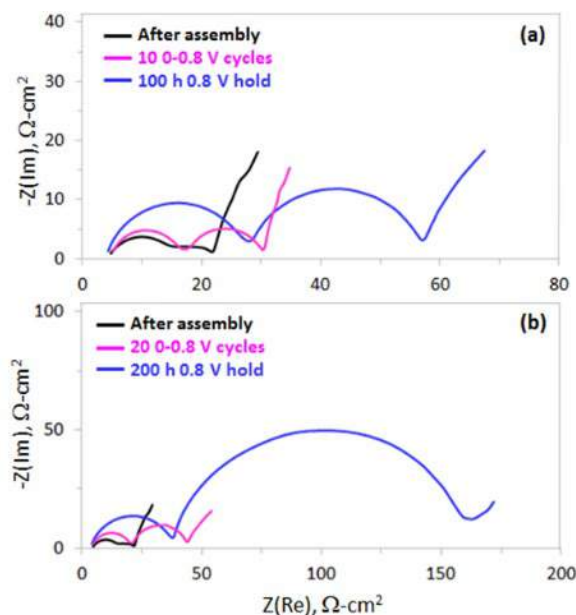


Figure II.2.A.24 Nyquist plots (100 KHz-0.01 Hz, 0 V) for oxide(+) / oxide(-) symmetric cells comparing the effect of 0-0.8 V cycling at a C/15 rate vs. 0.8 V potentiostatic hold. Panel a is for 10 cycles (100 h hold) and panel b is for 20 cycles (200 h hold)

In situ Formed Additives for High Voltage Li Ion Batteries

Previous reports demonstrated a facile in situ methodology to obtain two Li oxyfluorophosphate salts with high purity and yield for use as electrolyte additives. This methodology involved simply mixing electrolytes containing LiPF_6 with additive precursors. The resulting cyclic Li oxyfluorophosphate salts significantly enhanced the electrochemical performance of NMC-532//Gr cells, and especially reduced the impedance rise during aging. In recent work this in situ strategy has continued to extend the library of this type of additives (in situ series, abbreviated as i-series) by designing and synthesizing new additives; this set included additives with various bridging moieties as shown in Figure II.2.A.25. Second, new bifunctional additives (b-series) were introduced which could (i) scavenge residual HF and H_2O originating from electrolyte hydrolysis and (ii) stabilize the electrolyte during aging.

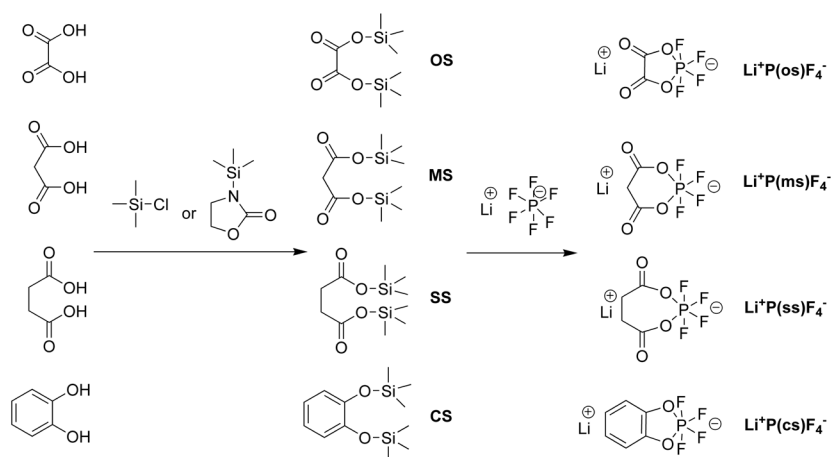


Figure II.2.A.25 In situ formed additives 2a and 2b and their precursors 1a and 1b

Synthesis of *i*-series additives: Bis(trimethylsilyl) malonate (MS) was obtained from TCI in its purest form. Bis(trimethylsilyl) oxalate (OS) and bis(trimethylsilyl) succinate (SS) were synthesized according to the literature. The 3-(trimethylsilyl)-2-oxazolidinone was used as a starting material to provide the trimethylsilyl (TMS) moiety, and the reaction was facilitated through the precipitation of 2-oxazolidinone. 1, 2-bis((trimethylsilyl)oxy)benzene (CS) was synthesized using chlorotrimethylsilane as the TMS source. NMR spectra were used to verify the formation of proposed structures and recorded on a Bruker Avance III 300 (300 MHz, ^1H ; 282.3 MHz, ^{19}F ; 121.4 MHz, ^{31}P) spectrometer. Fluorinated ethylene propylene (FEP) NMR liners (3 mm, Wilmad/VWR) were used to avoid any direct contact between the electrolytes and NMR glass tubes; the FEP tubes were carefully packed with samples and capped with the polytetrafluoroethylene (PTFE) plug and placed in a glass NMR tube (\varnothing 5 mm) containing CD_3CN for testing.

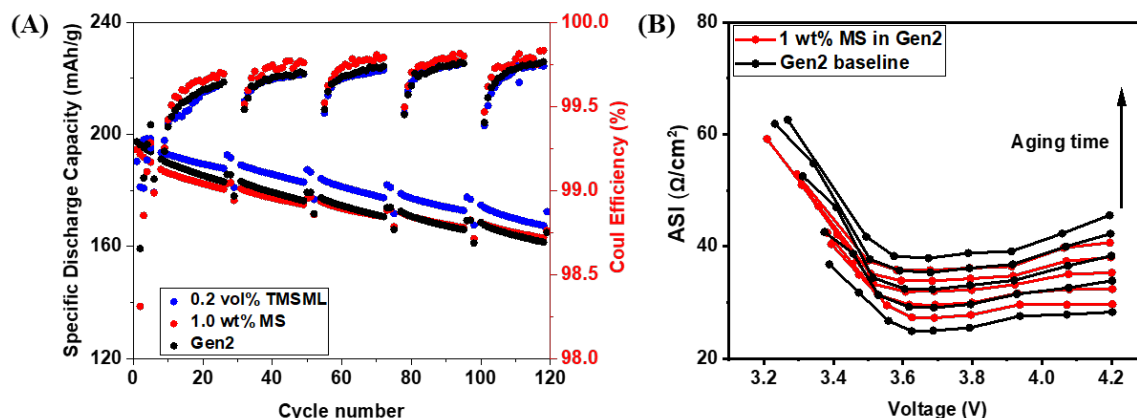


Figure II.2.A.26 (A) Specific capacity per weight of lithiated oxide of NMC-622//Gr cells containing additives and the baseline electrolyte (black line) obtained for cycling at a rate of C/3 with a 3 hour hold at the top of each charge. The discontinuities correspond to HPPC tests performed every 20th cycle. The coulombic efficiency for these cells is shown to the right; (B) Full cell area specific impedance (ASI) for the NMC-622//Gr cells with electrolyte containing 1 wt% MS and baseline Gen2 electrolyte (HPPC test). ASI of baseline Gen2 cell is shown in black while the cell containing 1 wt% MS is shown in red. The traces in the graph correspond to 7, 30, 53, 76, and 99 cycles (from bottom to the top), respectively

Bis(trimethylsilyl) succinate (SS) synthesis: *N*-Trimethylsilyl-2-oxazolidinone (40 ml, 26.7 mmol) was added to a solution of succinic acid (5.9 g, 50 mmol) in tetrachloromethane (20 ml) and the mixture was refluxed for 30 min. The mixture was cooled to 0°C , the product was filtered, and the solvent was removed in vacuum. The title compound was obtained by recrystallization of the residue from chloroform to yield a white solid (2.4 g, 73%). ^1H NMR (300M Hz, CDCl_3) δ_{H} = 2.58 (4H, s), 0.28 (18H, s).

1, 2-Bis(trimethylsilyloxy) benzene (CS) synthesis: Me_3SiCl (12.7 mL, 100 mmol) was added dropwise to a stirred solution of 1,2-catechol (4.4 g, 40 mmol) and Et_3N (16.8 mL, 120 mmol) in CH_2Cl_2 (160 mL) at 0°C , and the resulting mixture gradually warmed to 25°C over 30 min. The reaction mixture was cooled to 0°C , and saturated aqueous solution of NH_4Cl was added. This mixture was filtered through a pad of Celite[®] (eluent CH_2Cl_2) and the filtrate was washed with brine, dried, and concentrated in vacuum. The residue was triturated with Et_2O , then filtered through a pad of Celite[®] (eluent Et_2O) and concentrated in vacuum. Distillation at reduced pressure gave CS as a colorless oil (9.3 g, 78%). ^1H NMR (300M Hz, CDCl_3) δ_{H} = 0.26 (18H, s), 6.85 (4H, s). *b*-series additives, 1-(Trimethylsilyl)pyrrolidine (TMSPL) and 4-(Trimethylsilyl)morpholine (TMSML) were purchased from Sigma Aldrich and used without purification.

Cell Assembly, Testing and Results: For the *i*-series additives, 1 wt% of OS, MS, SS and CS was added to Gen2 electrolyte and the mixture was stirred at room temperature for 2-3 days. The progress of the reaction was monitored by drawing aliquots of the solution for NMR analysis. For the *b*-series additives, Gen2 electrolyte was mixed with TMSPL and TMSML before use. The test cells contained NMC-622 cathodes, Gr anodes, and Celgard 2325 separators. Galvanostatic charge/discharge cycling was carried between 3.0 and 4.4 V using a standardized protocol. The results are shown in Figure II.2.A.26. Cells with MS and TMSML have

slightly better capacity retention than that of Gen2 baseline; in addition, the MS slightly reduced impedance rise during aging.

Scavenging HF and Stabilizing Electrolytes with Bifunctional Additives: To probe whether TMSML can scavenge HF and stabilize LiPF_6 in Gen2 electrolyte, Gen2 electrolyte with intentionally added 2 vol% water with and without the additive were prepared. ^{19}F NMR spectra of these electrolytes were recorded after a pre-determined time. Representative spectra are depicted in Figure II.2.A.27b.

Gen2 electrolyte with intentionally added 2 vol% H_2O became turbid, and the glass vial was etched after 1 day, indicating the hydrolysis of LiPF_6 and generation of corrosive HF. Apparently, no such hydrolytic reaction was found in the vial of Gen2 electrolyte with 0.2 vol % TMSML (Figure II.2.A.27a), which is also confirmed by ^{19}F NMR spectra as shown in Figure II.2.A.27b. The results confirm that TMSML can effectively scavenge HF in the electrolyte, which can prevent LiPF_6 hydrolysis and stabilize the electrolyte for several weeks of storage.

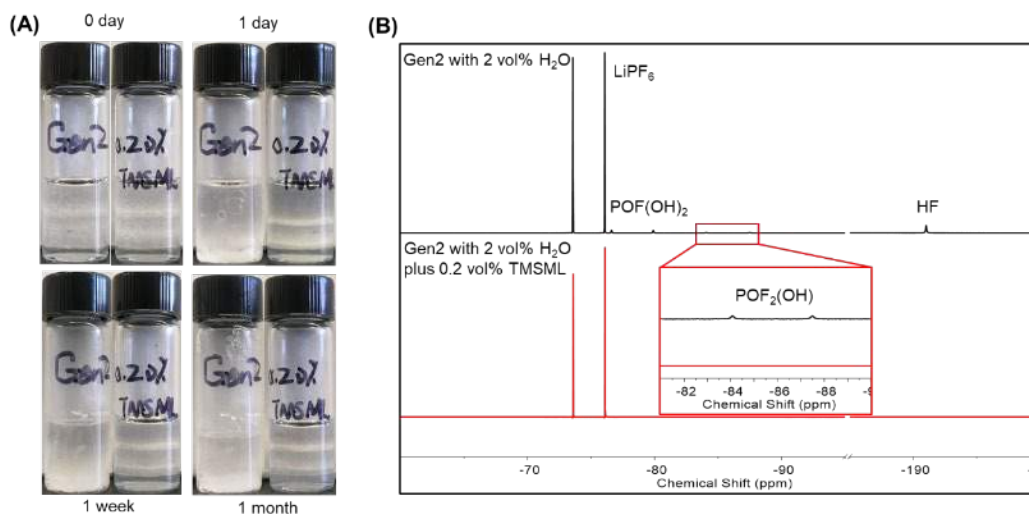


Figure II.2.A.27 (A) Pictures of the Gen2 electrolytes with intentionally added 2 vol % water without and with 0.2 vol% TMSML stored at room temperature (25 °C) original and after 1 day, 1 week and 1 month; (b) ^{19}F NMR spectra of Gen2 electrolytes with intentionally added 2 vol % water without and with 0.2 vol% TMSML stored at room temperature after 1 day

Electrode Fabrication using Cathode Powders

Two low-Co Li TM oxide powders, synthesized at Argonne, were provided to the CAMP Facility – $\text{Ni}_{0.94}\text{Co}_{0.06}$ and $\text{Ni}_{0.9}\text{Mn}_{0.05}\text{Co}_{0.05}$ (NMC-955). The pH of each powder was measured to determine if a modified slurry preparation would be necessary to minimize gelation phenomena often observed for cathodes with $\text{pH} > 12$ in the NMP/PVDF system. The measurement used 1 g of powder in 10 g of de-ionized water. The resulting pH values were 12.63 ($\text{Ni}_{0.94}\text{Co}_{0.06}$) and 12.65 ($\text{Ni}_{0.9}\text{Mn}_{0.05}\text{Co}_{0.05}$). Due to the high pH values, the CAMP Facility utilized a strategy during the slurry mixing to minimize heat. The resulting slurries had some non-ideal uniformity features due to some gelation that occurred and were apparent in the dried coating. Nevertheless, several meters of electrode were fabricated and designated for testing in both Li metal half-cells and full cells against the RNGC baseline Gr anode (A-A015). The cathode coating loadings resulted in n:p ratios of 1.08 to 1.18 (LN3174-131-6) and 1.05 to 1.18 (LN3174-132-3), based on several areal capacity factors when compared to the baseline Gr anode. These electrodes were provided to the group for characterization, performance testing, and evaluation.

Conclusions

- Two standardized electrochemical protocols using Li-metal anodes were developed for evaluation of in-house synthesized cathodes; these protocols include multiple discharge rates, three UCVs, and

potentiostatic holds in order to measure capacities, kinetics, reactivity, and stability of new materials. Cathodes from the CAMP library were evaluated with these protocols to establish benchmark performance; the expected trends, higher capacity and lower stability with higher Ni-contents, were observed.

- A novel setup to use mass spectroscopy to directly sample and analyze gases generated in Li-ion pouch cells was developed. Upper cut-off voltages of 4.2 V, 4.4 V and 4.6 V were selected to investigate the effect of voltage on the gassing behaviors of the cell. Key observations include the following: (i) CO₂ contents increase with UCV; (ii) measured O₂ levels were very low even during the 4.6 V high voltage hold; (iii) Hydrocarbons (CH₄, C₂H₄ and C₂H₆) observed are from electrolyte reduction at the anode.
- For DSC measurements, an active material amount of 1.5–3 mg is suggested. When desired, electrolyte may be added with the ratio of 1 μ L electrolyte per 1 mg of laminate powder. This volume was found to be a sufficient amount electrolyte to wet the powder, but not affect the DSC signal.
- TM dissolution and migration behavior is strongly dependent on oxide composition: higher Mn and Ni in the oxide leads to greater Mn and Ni deposition on the anode after electrochemical cycles. Co dissolution was relatively low in all tests with cathodes containing 20% or less Co. Cathode composition did not play significant role of electrolyte decomposition species detected by HPLC.
- Static leaching tests on delithiated NMC cathodes with tetrabutyl ammonium bifluoride (C₄H₉)₄NF·HF in EC:EMC (3:7 by wt.) solution suggests that surface-atom configurations of NMCs may play a role in TM dissolution.
- An in situ method for ATR-FTIR studies of cathode materials during electrochemical cycling was developed. This technique is able to probe many aspects of the cathode-electrolyte interphase including the electrolyte solution structure near the interface, structural changes in the oxide, and species that originate from cathode surface-electrolyte chemical reactions.
- For layered-oxide symmetric cells there are strong parasitic currents and a persistent slide of the electrode potential over time during calendar aging. Significant cell impedance rise, especially at higher hold voltages, is also observed. For the same test duration, magnitude of impedance rise is much larger during calendar aging than during cycle aging.
- An in situ synthesis methodology was successfully applied to extend the library of in situ formed electrolyte additives. Protective properties of the additives are related to structural features such as the rigidity of the Li oxyfluorophosphate salts. A newly developed bifunctional additive showed effectiveness in scavenging HF and stabilizing the electrolyte, resulting in an observable enhancement of cell performance.
- Electrodes with two low-Co oxide powders—Ni_{0.94}Co_{0.06} and Ni_{0.9}Mn_{0.05}Co_{0.05}, were fabricated in the CAMP Facility. Because of the high pH of the slurry, an alternative mixing strategy was used to minimize slurry gelation. The electrodes have been made available to the diagnostics team for electrochemical performance testing and detailed characterization by microscopy, spectroscopy, and diffraction.

Key Publications

1. A. Tornheim, J. Garcia, R. Sahore, I. Bloom, H. Iddir, Z. Zhang, “Decomposition of phosphorus-containing additives at a charged NMC surface through potentiostatic holds”, *J. Electrochemical Society* 166 (2019) pp. A440-A447.
2. C. Mao, R.E. Ruther, L. Geng, Z. Li, D.N. Leonard, H.M. Meyer III, R.L. Sacci, D.L. Wood III, “Evaluation of Gas Formation and Consumption Driven by Crossover Effect in High-Voltage Li-Ion Batteries with Ni-Rich NMC Cathodes”, *ACS Appl. Mater. Interfaces* (2019).

3. L. Geng, C. Mao, R.E. Ruther, D.L. Wood III, I. Belharouak, "Gas Formation and Crossover Effect in High Voltage Li-Ion Full Cells with Ni-Rich NMC Cathodes", 236th ECS Meeting, Atlanta, October 13-17, 2019.
4. K. Sahni, M. Ashuri, Q. He, R. Sahore, I.D. Bloom, Y. Liu, J.A. Kaduk, L.L. Shaw, "H₃PO₄ Treatment to Enhance the Electrochemical Properties of Li(Ni_{1/3}Mn_{1/3}Co_{1/3})O₂ and Li(Ni_{0.5}Mn_{0.3}Co_{0.2})O₂ Cathodes", *Electrochem. Acta*, 301 (2019) pp 8-22.
5. R. Sahore, F. Dogan, and I. Bloom, "Identification of Electrolyte-Soluble Organic Cross-Talk Species in a Li-Ion Battery via a Two-Compartment Cell", *Chemistry of Materials* 31 (2019) pp. 2884–2891.
6. K. Kalaga, M.T.F. Rodrigues, J. Bareño, I.A. Shkrob, D.P. Abraham, "Insights from incorporating reference electrodes in symmetric Li-ion cells with layered oxide or Gr electrodes", *Journal of Power Sources* 438 (2019) p. 227033.
7. J.R. Jokisaari, J. Guo, J. Bareno, D.P. Abraham, R.F. Klie, "Meso to Atomic Scale Microstructural Changes During Ageing of NCM Li-ion Battery Materials", *Microscopy and Microanalysis* 25 (2019) pp. 764-765.
8. K. Kalaga, M.-T. F. Rodrigues, D.P. Abraham, "In situ reference electrode: four electrode design for in-operando impedance spectroscopy", *J. Vis. Exp.* 139 (2018) e57375 (2018).
9. M.-T.F. Rodrigues, K. Kalaga, S.E. Trask, I.A. Shkrob, D.P. Abraham, "Anode-Dependent Impedance Rise in Layered-Oxide Cathodes of Li-Ion Cells", *J. Electrochem. Soc.* 165 (2018) pp. A1697-A1705.
10. J. Yang, I. A. Shkrob, Q. Liu, N. L. D. Rago, Y. Liu, K. Li, Z. Zhang, C. Liao, "Structural underpinnings of cathode protection by in situ generated Li oxyfluorophosphates. *Journal of Power Sources*, 2019, 438, 227039.
11. C. Peebles, J. Garcia, A.P. Tornheim, R. Sahore, J. Bareño, C. Liao, I. A. Shkrob, H.H. Iddir. D.P. Abraham, "Chemical Pickling of Phosphite Additives Mitigates Impedance Rise in Li Ion Batteries", *J. Phys. Chem. C* 122 (2018) pp. 122, 9811–9824.
12. I.A. Shkrob, B.H. Han, R. Sahore, A.P. Tornheim, L. Zhang, D.P. Abraham, F. Dogan, Z.C. Zhang, C. Liao, "Facile in Situ Syntheses of Cathode Protective Electrolyte Additives for High Energy Density Li-Ion Cells", *Chem. Mater.* 31 (2019) pp. 2459-2468.

Acknowledgements

Support from the U. S. Department of Energy (DOE), Vehicle Technologies Office, specifically from Peter Faguy and David Howell is gratefully acknowledged. Participation by research area: Electrochemical testing protocols in a half-cell format (Li-metal anodes) (Adam Tornheim, Daniel C. O'Hanlon, Anh Vu, Jihyeon Gim, Daniel P. Abraham, Jason R. Croy), Probing Cathode-Electrolyte Interface Reactions by Gas Analysis (Linxiao Geng, David L. Wood III, Ilias Belharouak), Developing DSC protocols (Wenquan Lu, Joel Kirner), Electrode Cross Talk and TM Dissolution (Ira Bloom, Hannah R. Morin, Donald G. Graczyk, Yifen Tsai, Susan Lopykinski, Hakim Iddir, Juan C. Garcia, Stephen Trask, LeRoy Flores, Seoung-Bum Son, Zhengcheng Zhang, Noah M. Johnson), In situ Spectroscopic Analysis of the Cathode-Electrolyte Interface (Bertrand Tremolet de Villers, Junghoon Yang, Yeyoung Ha, Sang-Don Han), Reference Electrodes in Symmetric Li-ion Cells with Layered Oxide Electrodes (Kaushik Kalaga, Marco-Tulio F. Rodrigues, Javier Bareño, Ilya A. Shkrob, Daniel P. Abraham), In situ Formed Additives for High Voltage Li Ion Batteries (Jianzhong Yang and Chen Liao), and Electrode Fabrication using Cathode Powders (Steve Trask and Andrew Jansen). Additional team members included S.J. An, Y. Cui, L. David, Z. Du, J.C. Garcia, J.A. Gilbert, D.J. Gosztola, M. He, F. D. Key, J. Li, C. Mao, V. A. Maroni, H.M. Meyer, C. Peebles, B.J. Polzin, R.E. Ruther, R. Sahore, Y. Sheng, G. Veith, M. Wood, Z. Zhang, Junghoon Yang, and Yeyoung Ha.

II.2.B Design, Synthesis, & Characterization of Low-Cobalt Cathodes (ANL, LBNL, PNNL)

Jason R. Croy, Principal Investigator

Argonne National Laboratory
9700 S Cass Avenue
Lemont, IL 46039
E-mail: croy@anl.gov

Peter Faguy, DOE Technology Development Manager

U.S. Department of Energy
E-mail: Peter.Faguy@EE.Doe.Gov

Start Date: October 1, 2018	End Date: September 30, 2021	
Project Funding (FY19): \$4,000,000	DOE share: \$4,000,000	Non-DOE share: \$0

Project Introduction

State-of-the-art Li-ion batteries (LIBs) for transportation applications contain transition metal (TM) oxide cathodes consisting of $\text{Li}_{1+x}\text{Ni}_a\text{Co}_b\text{Al}_c\text{O}_2$ (NCA) or $\text{Li}_{1+x}\text{Ni}_a\text{Mn}_b\text{Co}_c\text{O}_2$ (NMC-abc) oxides, where $x = \sim 0-0.05$ and $a+b+c = 1$. Both oxide chemistries contain Co, which has been recognized over many years of research as an important component in terms of structure, stability, and electrochemical performance. Currently, however, geopolitical concerns associated with Co mining, availability, and cost have caused the LIB community to pursue the development of low- to no-cobalt layered oxides as next-generation cathodes. The goal of this work is to show progress towards the realization of low/no-cobalt oxides having acceptable performance (energy/power densities), safety, and cycle/calendar life by way of new insights into cathode design and synthesis as they pertain to the critical roles of Co in layered oxides.

Objectives

- New insights on the critical roles of Co in layered, NMC-type oxides.
- Understanding of local ordering as a function of Co and dopant content.
- Synthesis of new, low- to no-cobalt cathodes showing promise with respect to an NMC-622 baseline.
- Synthesis and understanding of gradient cathodes with low- to no-cobalt compositions.
- Atomic-scale characterization, understanding, design, and synthesis of NiMn-based cathodes.

Approach

- Advanced characterization of low- and no-cobalt cathodes including synchrotron techniques, solid state NMR, electron microscopy, and theory/modeling.
- Large batch co-precipitation synthesis of model/new compositions for practical evaluation.
- Advanced synthesis and characterization of gradient-type cathode structures.
- Synthesis of standardized materials for distribution and study across multiple teams.

Results

Synthesis of Baseline Cathode Systems

$\text{LiNi}_{0.94}\text{Co}_{0.06}\text{O}_2$: $\text{LiNi}_{0.94}\text{Co}_{0.06}\text{O}_2$ has been demonstrated and proposed as a good candidate oxide for next-generation LIBs and is chosen in this project as a low-cobalt, Ni-rich cathode of interest¹. This composition will be studied across multiple teams in order to gain insights on such compositions with respect to synthesis, surface and thermal stability, and gassing in electrochemical cells. In addition, modifications to the system (e.g., dopants,

coatings...) will be carried out to study how they might influence the listed properties and electrochemical performance. In order to ensure quality materials in sufficient quantities, 4L continuous stirred-tank reactors (CSTR), capable of producing large batches of materials (~1kg), were set up for co-precipitation of metal hydroxide precursors. The baseline composition, $\text{Li}_{1+x}\text{Ni}_{0.94}\text{Co}_{0.06}\text{O}_2$ (hereafter noted as Ni94Co6), was first prepared as a $\text{Ni}_{0.94}\text{Co}_{0.06}(\text{OH})_2$ precursor in a batch reaction. In order to obtain the desired, secondary particle morphology, factors influencing the precursor product were carefully controlled including pH, temperature, stirring speed, feeding rate, and the molar ratio of ammonia to TM ($\text{NiSO}_4 \cdot 6\text{H}_2\text{O}$ and $\text{CoSO}_4 \cdot 7\text{H}_2\text{O}$). The as-synthesized $\text{Ni}_{0.94}\text{Co}_{0.06}(\text{OH})_2$ was dried at 60°C under Nitrogen flow and used for the preparation of the final cathode materials by mixing with $\text{LiOH} \cdot \text{H}_2\text{O}$ (1% excess). The mixture was calcined at 680°C for 12h under oxygen flow with a ramping rate of 2°C/min followed by uncontrolled cooling.

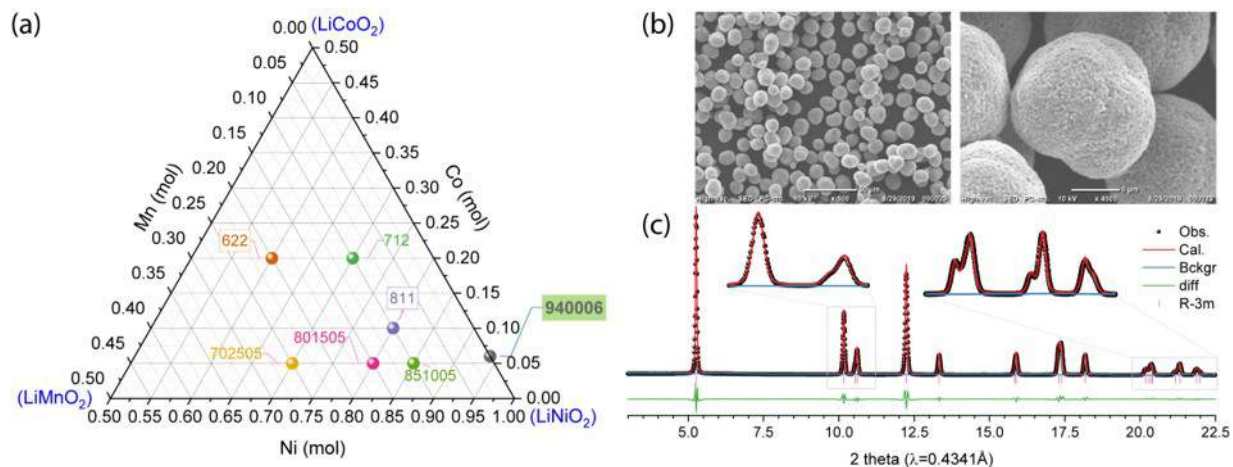


Figure II.2.B.1 (a) Ternary phase diagram of high-Nickel NMCs including the Ni₉₄Co₆ composition (gray sphere), (b) SEM-images of Ni₉₄Co₆ particles showing a narrow particle size distribution, and (c) Rietveld refinement results obtained from data taken at beamline 13-BM-C of the Advanced Photon Source (ANL)

Figure II.2.B.1(a) highlights the Ni₉₄Co₆ target composition with respect to other Ni-rich chemistries. The particle morphology of the final cathode product can be observed in the scanning electron microscopy (SEM) images of Figure II.2.B.1(b). The ~200 nm-sized primary particles are well packed forming a homogenous, spherical-shaped, secondary particle. Secondary particle size analysis was performed using dynamic light scattering to obtain D10, D50, and D90 values as summarized in Table II.2.B.1. Rietveld refinement analysis, Figure II.2.B.1(c), was conducted using synchrotron X-ray powder diffraction data collected at the Advanced Photon Source (APS) at Argonne National Laboratory and the results are reported in Table II.2.B.1. The observed pattern shows a single phase with negligible Li_2CO_3 peaks and good agreement with the calculated pattern, confirming that all peaks are well indexed to the hexagonal crystal structure with Li and TM ions (Ni and Co) located in octahedral 3a and 3b sites, respectively, with ABC (O3) stacking. The Li and TM slab distances are calculated as 2.6 Å and 2.1 Å in the layered structure with lattice parameters a (2.87 Å) and c (14.18 Å). The value of c/a above 4.9 indicates a well-defined layered structure with low cation disorder. Cation disorder between Li^+ and Ni^{2+} was calculated as 1.29 %.

Table II.2.B.1 Rietveld Refinement and Particle Size Analysis Results of $\text{LiNi}_{0.94}\text{Co}_{0.06}\text{O}_2$

Phase	$\text{LiNi}_{0.94}\text{Co}_{0.06}\text{O}_2$ ($\text{Ni}_{94}\text{Co}_6$)					
Space group	R-3m, (S.G 166)			Crystallite size, LX		132.51 nm
Lattice parameters (Å and degrees)	a: 2.87212, c: 14.18029, $\alpha=90$, $\gamma=120$			Microstrain, LY		0.1828 %
Atom	Site	Wyckoff positions			Occupancy	Uiso
Li1	3a	0	0	0	98.71	0.01266b
Ni1	3b	0	0	0.5	92.71	0.00356
Co1	3b	0	0	0.5	6	0.00356
O1	6c	0	0	0.241038	100	0.00699
Li2	3b	0	0	0.5	1.29	0.01266b
Ni2	3a	0	0	0	1.29	0.09455
	c/a	4.93723	Li-slab	2.617549Å	Transition metal-slab	2.109214Å
Reliability factors	wRp= 9.01 %, Rp= 6.99 %, aThe site occupation numbers in %, bFixed parameter as default					
Particle size analysis	Diameter, 10% (D10)	12 μm	Diameter, 50% (D50)	16 μm	Diameter, 90% (D90)	24 μm

$\text{Ni}_{94}\text{Co}_6$ cathode electrodes were prepared with an $\sim 8 \text{ mg/cm}^2$ active material loading density and Li-metal anode cells were constructed using 1.2M LiPF_6 in EC:EMC (3:7 w/w) as electrolyte. All cycles were conducted at 30°C at a $\sim \text{C}/5$ rate, results are summarized in Table II.2.B.2. To verify the impact of state of charge (SOC) on electrochemical stability, the upper cut-off voltage (UCV) on charge was controlled systematically to values of 4.2, 4.3, 4.4, and 4.45 V. Figure II.2.B.2(a) and (b) show the voltage profiles of the initial cycles with various UCVs. The specific charge capacity ranged from 235 \sim 250 mAh/g corresponding to x values of 0.85 \sim 0.91 in $\text{Li}_{1-x}\text{Ni}_{0.94}\text{Co}_{0.06}\text{O}_2$. Irrespective of the UCV, the $\text{Ni}_{94}\text{Co}_6$ material showed coulombic efficiencies of $\sim 93\text{--}95\%$ on the first cycle, implying minimal structural change and/or good kinetic properties, which might be correlated to the low cation disorder confirmed by the Rietveld refinement results.

The results above reveal the successful synthesis of the $\text{Ni}_{94}\text{Co}_6$ composition via co-precipitation. This cathode oxide has been fabricated into electrodes sheets at the Cell Analysis, Modeling, and Prototype Facility (CAMP) at ANL and electrodes and have been distributed across the project for detailed studies on the properties and performance of this cathode and its associated derivatives.

Table II.2.B.2 Summary of Electrochemical Properties of $\text{Ni}_{94}\text{Co}_6$

Upper cut-off potential (UCP)	4.2 V	4.3 V	4.4 V	4.45 v
Initial charge capacity (mAh/g)	234.7	244.01	247.93	249.91
Initial discharge capacity (mAh/g)	218.1	231.11	235.65	235.82
Initial Coulombic efficiency (%)	92.92	94.71	95.05	94.36
Capacity retention at 50 th cycle (%)	95.15	92.63	-	90.12

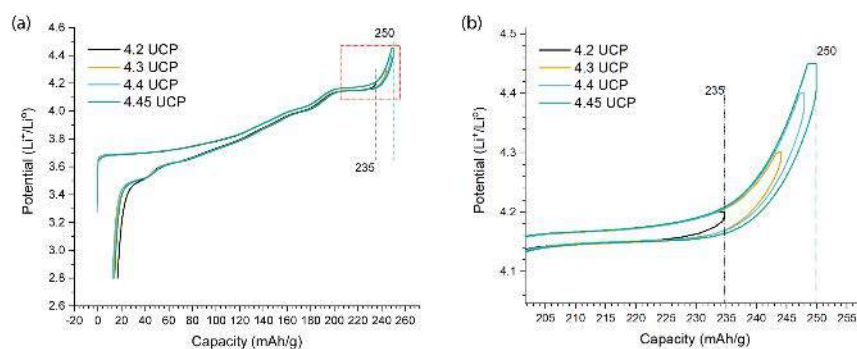


Figure II.2.B.2 (a) Initial voltage profiles and (b) magnified view of high-voltage region for the $\text{Ni}_{94}\text{Co}_6$. Cells used Li-metal anodes and were cycled at C/5 ($1\text{C}=180\text{mA/g}$) after 3 formation cycles at C/10

Concentration Gradient Materials: Using a versatile co-precipitation reactor, unique particle designs can be realized by careful control of solution feeds, pH, temperature, and so on. For example, full concentration-gradient (FCG) and CSG (core-shell concentration gradient) particles can be proposed as illustrated in Figure II.2.B.3(a) and (b). In this work, $\text{LiNi}_{0.8}\text{Mn}_{0.1}\text{Co}_{0.1}\text{O}_2$ (NMC-811) was chosen as an initial, baseline composition to help understand the properties and synthesis of gradient materials. Different metal concentration gradients, within NMC-811 hydroxides, were synthesized as illustrated in Figure II.2.B.3(c), where Norm_811 stands for the normal NMC-811 without any compositional gradient, FFCG_811 is the forward full-concentration gradient with a high-Ni core, and IFCG_811 is the inverse gradient material where a high-Ni composition is laid down near the surface. The as-synthesized precursors were mixed with lithium hydroxide monohydrate (3% excess) and calcined at 750°C for 12 hr under oxygen atmosphere with a $2^\circ\text{C}/\text{min}$ ramp. The synthesized oxides were made into laminates comprising 88 wt% active materials, 6 wt% of C-45, and 6 wt% of polyvinylidene difluoride (PVdF) binder on Al-foil current collectors. Coin-cells, using Li-metal anodes, were cycled between 4.4–2.7 V at a constant current of 100 mA/g after 3 formation cycles with a current of 20 mA/g. Figure II.2.B.3(d) shows capacity vs. cycle plots for the Norm_811, FFCG_811, and IFCG_811 cells. All variants showed good performance and similar capacity and capacity fade under these conditions using Li-metal anodes. It might be expected that performance differences between these variations will be mostly influenced by surface chemistry or particle morphology and will be amplified by full-cell (i.e., graphite anodes) and other tests. These gradient cathodes and others will be used for more detailed studies including full-cell performance, thermal stability, gassing properties, and structural characterization.

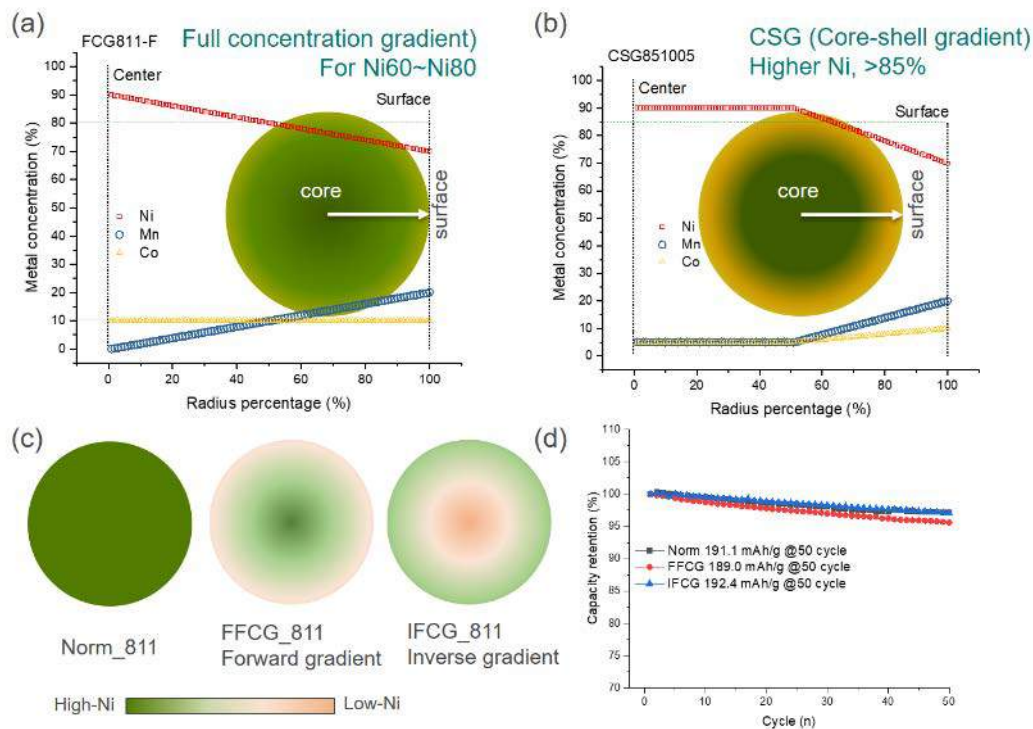


Figure II.2.B.3 (a) Illustration of concentration gradient materials using an in-house built, co-precipitation reactor for full-concentration gradient particles, (b) core-shell gradient particle, (c) a scheme of as-synthesized materials for different metal gradients with an NMC-811 composition and the corresponding capacity retention results

LiNiO₂-Based Cathodes: The most straightforward route to decreasing Co content in NMC cathodes is by increasing Ni content. Ni-rich NMCs offer both low cobalt and high energy densities and are therefore attractive options. However, many years of research and development have been spent on pure LiNiO₂ and its derivatives (e.g., >~90% Ni) and critical issues related to stability (e.g., surface/thermal) still remain. In order to gain new insights on the mechanisms and stabilization of LiNiO₂-based cathodes, a series of materials are being synthesized and distributed across the project for detailed studies. Six metal-hydroxide precursor compositions were synthesized, in various batch sizes ranging from ~300g to ~1 kg to realize final compositions of LiNiO₂, LiNi_{0.90}Co_{0.05}Mn_{0.05}O₂, LiNi_{0.90}Co_{0.10}O₂, LiNi_{0.90}Mn_{0.10}O₂ and LiNi_{0.80}Co_{0.10}Mn_{0.10}O₂ (via 1 and/or 10L Taylor Vortex Reactors (TVR)), and LiNi_{0.75}Mn_{0.25}O₂ (via a 4L CSTR), at the Materials Research and Engineering Facility (MERF) at ANL. SEM, Figure II.2.B.4, and Rietveld refinements, Table II.2.B.3, show the high quality of the obtained, final products for example compositions. Detailed studies of calcination, Li-content, washing, electrochemistry, and differential scanning calorimetry (DSC) of these Ni-rich chemistries were carried out and will be presented in future reports and publications.

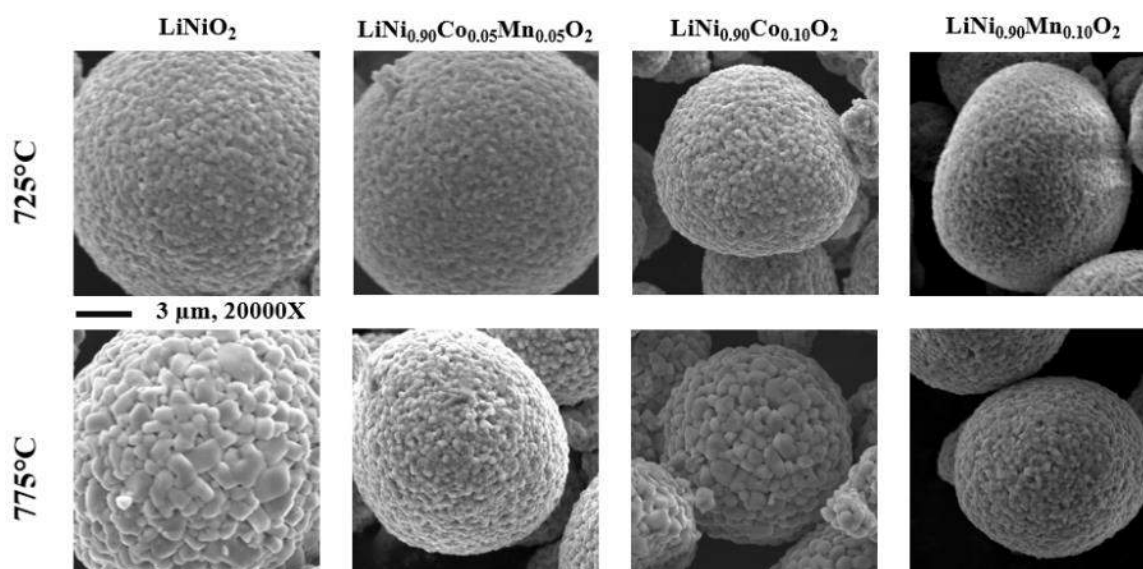


Figure II.2.B.4 SEM images of baseline, Ni-rich compositions annealed at different temperatures

Table II.2.B.3 Rietveld Refinement Analysis of Samples

Calcination Temp. (°C)	Sample	a (Å)	c (Å)	Ni/Li (%)	Crystallite size (μm)	Rw
725	LiNiO ₂	2.877	14.198	1.48	0.260	3.012
775	LiNiO ₂	2.878	14.197	2.01	0.282	3.745
725	LiNi _{0.90} Co _{0.05} Mn _{0.05} O ₂	2.872	14.194	2.03	0.142	1.688
775	LiNi _{0.90} Co _{0.05} Mn _{0.05} O ₂	2.873	14.197	1.19	0.237	2.208
725	LiNi _{0.90} Co _{0.10} O ₂	2.870	14.181	0.31	0.233	1.883
775	LiNi _{0.90} Co _{0.10} O ₂	2.870	14.178	0.23	0.266	2.241
725	LiNi _{0.90} Mn _{0.10} O ₂	2.876	14.206	6.91	0.053	2.262
775	LiNi _{0.90} Mn _{0.10} O ₂	2.877	14.217	3.71	0.145	2.185

Study of Model Cathode Materials

Surface Reconstruction of Single-Crystal NMCs: The stability of cathode particle surfaces directly exposed to the electrolyte is one of the most crucial and determining factors for cathode performance at high operating voltages. Theory has predicted a strong dependence of surface stability on chemical composition as well as surface facets of layered oxides, yet conflicting results on the correlations exist as most experimental studies focus on cycled secondary particles recovered from composite electrodes. Here, discrete platelet-shaped NMC-333 and NMC-622 crystal samples were synthesized by using a two-step process: coprecipitation of TM sulfate precursors followed by annealing of the resulting intermediates with lithium hydroxide. The as-synthesized NMC samples had an average platelet size of ~ 200 nm and a thickness of ~ 50 nm, as shown in Figure II.2.B.5(a) and (b) for NMC-333 and NMC-622, respectively. Scanning transmission electron microscopy (STEM) imaging further confirms the platelet morphology, where sharp edges of well-defined facets are clearly seen, Figure II.2.B.5(c) and (d). The single crystal nature of the samples was verified by the presence of a single orientation throughout the particles, based on a TEM/selected area electron diffraction (SAED) analysis procedure. Figure II.2.B.5(e) shows the indexed facets present on the platelet NMC crystals. The XRD patterns collected on the as-synthesized NMC-333 and NMC-622 samples, Figure II.2.B.5(f),

suggest that both samples are phase pure with the hexagonal α -NaFeO₂ structure (R-3m space group). Peak splitting in the (006)/(012) and (018)/(110) doublets were observed, confirming well-ordered, layered structures.

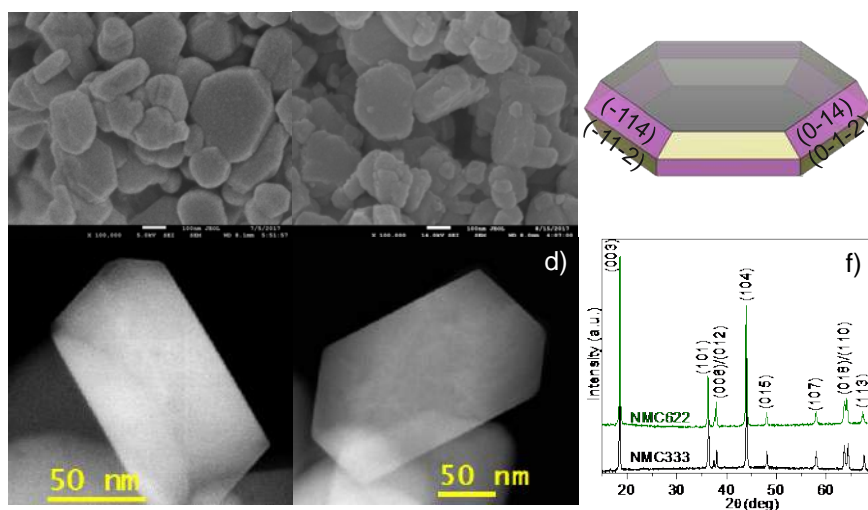


Figure II.2.B.5 (a) and (b) SEM images, (c) and (d) STEM images of pristine NMC-333 and NMC-622 crystal samples, (e) indexed facets on platelet NMC particles and (f) XRD patterns of pristine NMC-333 and NMC-622 crystal samples

The electrochemical performance of NMC-333 and NMC-622 crystal samples was evaluated by galvanostatically charging and discharging in coin cells (Li-metal anodes) at a rate of C/10, using two voltage windows of 3.0–4.3 V and 3.0–4.6 V. The evolution of the charge-discharge profiles from the 1st cycle to the 100th cycle is plotted at intervals of 10 cycles as shown in Figure II.2.B.6(a)–(d). As might be expected, capacity retention of the NMC-333 was much better than that of the NMC-622, especially when both electrodes were cycled between 3.0 and 4.3 V, where the Ni-rich 622 reaches a higher SOC. Cycling to a higher UCV of 4.6 V increases the initial discharge capacity but decreases the cycling stability of both samples, as shown in Figure II.2.B.6(e) and 2(f). This trend in capacity and stability trade-off is consistent with previous reports on NMC materials.

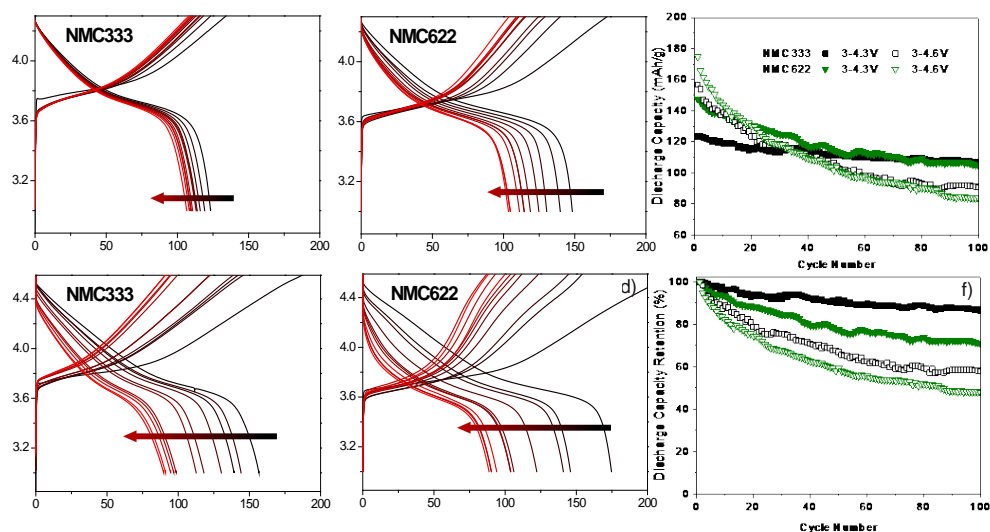


Figure II.2.B.6 First 100-cycle charge-discharge profiles of (a, c) NMC333 and (b, d) NMC622 in the voltage window of (a, b) 3–4.3 V and (c, d) 3–4.6 V. e) and f) Comparison of discharge capacity and capacity retention at a cycling rate of C/10

Layered structures with the R-3m space group were further confirmed on the pristine particles by using atomic-resolution HAADF STEM imaging. As shown in Figure II.2.B.7, the TM layers and Li layers are stacked along the c -axis. Cation disorder in the NMC-333 was negligible as bright spots were not observed in the dark Li slab regions. Thin, surface reconstruction layers (SRL) with thicknesses of ~ 1.0 nm and ~ 1.5 nm were found on the non-(001) surfaces of the pristine NMC-333 (Figure II.2.B.7(a)) and NMC-622 (Figure II.2.B.7(c)), respectively. Fast Fourier Transform (FFT) processing of the STEM images, taken in both side view [010] and top view [012] zone axes, reveals that the crystal structure of the surface layer is noticeably denser than that of the bulk, as some Li sites are occupied by the TMs to form anti-site defects, consistent with the previous reports. Depending on the surfaces examined, both ‘spinel-like’ ($Fd\bar{3}m$ space group) and ‘rock salt-type’ phases ($Fm\bar{3}m$ space group) were observed on NMC-333 and NMC-622. It should be noted that, in order to eliminate the ambiguities that can arise from the fact that materials with different structures can give similar, two-dimensional projections, it is critical to obtain three-dimensional structural information by imaging along more than one zone axis. No visible SRLs were found on the (001) planes in either sample (Figure II.2.B.7(b) and (d)), where such surfaces are terminated by Li-ion impermeable TM slabs. SRL formation on pristine NMCs also showed a composition-dependent behavior. The thickness of the SRL on NMC-333 was ~ 1 nm while it increased to ~ 1.5 nm on NMC-622.

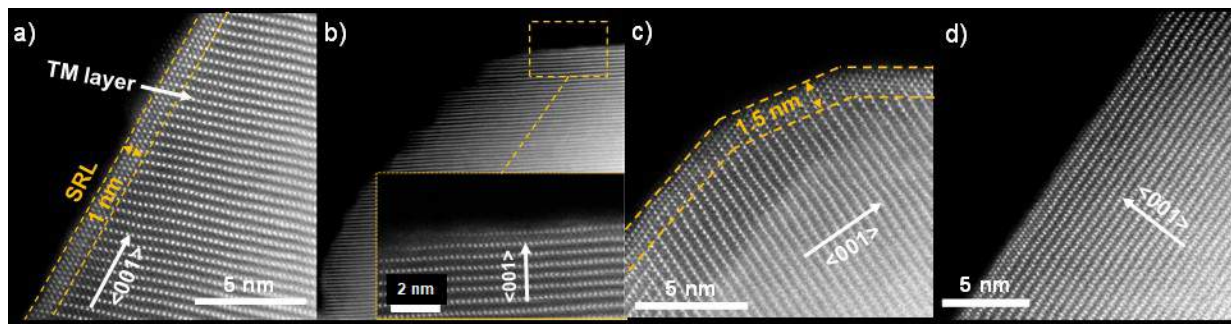


Figure II.2.B.7 HAADF STEM imaging shows facet-dependent surface reconstruction on (a, b) pristine NMC-333 and c, d) pristine NMC-622 particles. SRL was found on non-(001) surface (a, c) while no SRL was observed on (001) surfaces.

Post-modern analysis was carried out on harvested cathode particles to evaluate structural and chemical changes caused by cycling. Figure II.2.B.8 shows atomic-resolution STEM images collected on NMC-333 and NMC-622 after 100 cycles between 3.0-4.6 V. It is evident that in both samples, further SRL growth occurred during cycling, which also showed composition- and facet-dependent behavior. On the non-(001) surface, the thickness of the SRL increased from approximately 1.0 nm to 1.5 nm for NMC-333, Figure II.2.B.8(a), and 1.5 nm to 3.5 nm for NMC-622, Figure II.2.B.8(c). This corresponds to a net growth of 50% and $\sim 135\%$ after 100 cycles, nearly 3x faster in the higher-Ni content NMC-622 sample. Although no SRL was observed on the Li-impermeable (001) surfaces of pristine NMC-333 or NMC-622, cycling-induced surface transformations of (001) surfaces were observed in both materials. As shown in Figure II.2.B.8(b) and (d), thin SRLs consisting of ~ 3 atomic layers and ~ 1.5 nm were found on NMC-333 and NMC-622, respectively. Compared to the non-(001) surfaces, the growth of the SRL on the (001) surface is significantly less severe, confirming the facet-dependent nature of SRL growth due to cycling.

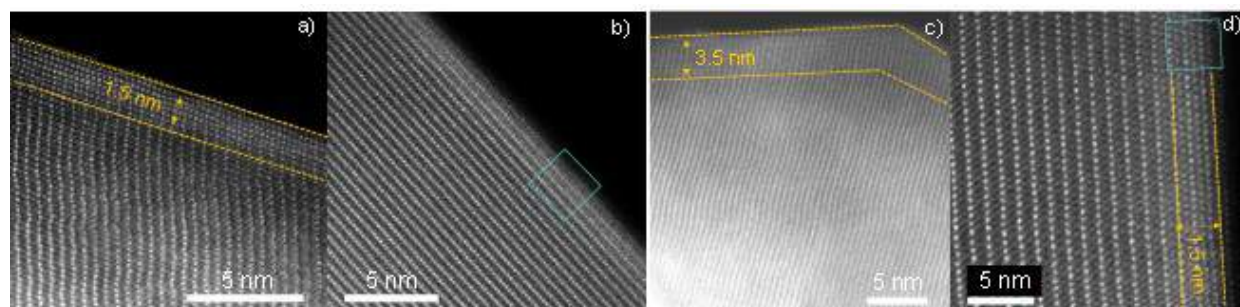


Figure II.2.B.8 Atomic-resolution HAADF STEM images of SRL formation on: non-(001) surfaces (a and c) and (001) surfaces (b and d) of cycled NMC-333 (a and b) and NMC-622 (c and d) platelet crystals

This study reveals that SRLs on pristine and cycled particles have a similar nature, both showing chemical gradients as well as composition- and surface/facet-dependent behavior. The selective surface reconstruction is likely a combined result of cation exchange (inter-plane) and cation migration (intra-plane), particularly Li/Ni exchange and Ni migration. These processes are closely related to Li loss from the lattice, which might be facilitated by high heat during synthesis, reaction with atmosphere, and/or high-voltage/SOCs and side reactions during electrochemical cycling.

The Role of Secondary Particle Structures on Surface Reconstruction: The mechanisms of nanometer thick reconstruction layers on cathode surfaces, as reported above for single crystals, and the role that these structures play in electrochemical performance, are still not fully understood. Often, electrolyte interactions are presumed to play a role, where electrochemical side reactions at electrode-electrolyte interfaces may assist in the generation of oxygen vacancies on surfaces, in turn, facilitating TM diffusion [ENREF 41](#) and disorder. In this work, a detailed study of various boundaries within secondary particles is presented. Cycling-induced surface transitions, at different crystal terminations with distinctive characteristics, representing solid-liquid, solid-gas, and solid-solid interfaces in practical cathode-electrodes have been characterized and are presented in Figure II.2.B.9. It was observed that surface transformations during cycling of a Ni-rich cathode-oxide (76% Ni, NMC76) are governed by direct contact with the liquid electrolyte. Specifically, within a secondary particle of NMC, the three-dimensional hierarchical aggregate of primary particles leads to the formation of grain boundaries of different characteristics including open grain boundaries that allow the permeation of liquid electrolyte, and closed ones that exclude liquid electrolyte penetration, Figure II.2.B.9(a)-(d). Upon battery cycling, surfaces in direct contact with the liquid electrolyte showed a SRL, Figure II.2.B.9(e)-(h); while the surfaces that did not have contact with the electrolyte showed no such reconstructions, Figure II.2.B.9(i)-(l), thereby emphasizing the vital role of solid-liquid interface reactions in controlling phase transitions.

On the other hand, oxygen vacancy formation and migration were observed to significantly affect phase transition behavior at solid-solid interfaces, where significant oxygen loss led to severe phase transitions at coherent twin boundaries and an absence of oxygen loss resulted in sluggish phase transitions at incoherent boundaries. These studies indicate that secondary particle architectures can influence phase transitions and suggest that controlling such architectures (e.g., mitigating the penetration of liquid electrolyte along grain boundaries) could be critical for enhancing cathode stability.

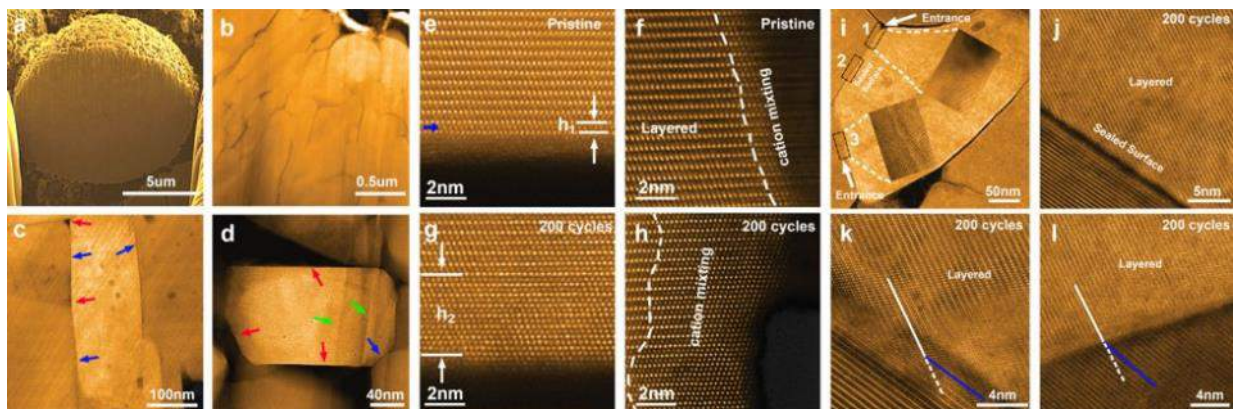


Figure II.2.B.9 Phase transitions at open surfaces, closed surfaces, and grain boundaries. (a) Cross-sectional SEM image of a secondary particle. (b) HAADF-STEM image of the NMC76, (c-d) HAADF-STEM image of the primary particles. The blue, red, and green arrows point to the inter-granular GBs, inter-granular channels, and intra-granular boundaries, respectively. (e) Surface configurations of pristine NMC76 at the basal plane. The blue arrow points to the Li layer occupied by TM ions. (f) Surface configurations of pristine NMC76 at the edge plane. (g) Surface configurations of NMC76 at the basal plane after 200 cycles. (h) Surface configurations of NMC76 at the edge plane after 200 cycles. The white dashed lines in (f) and (h) outline the boundary between the layered structure and the converted phase. h_1 represents the thickness of converted phase/cation mixed phase. (i) The construction of a typical sealed surfaces. The black rectangle, 2, outlines the sealed surface area. The black rectangles 1 and rectangle 3 indicate the entrances to the area 2. The inserts are a magnified view of the two entrances. (j) Atomic resolution imaging of the sealed surface from rectangle 2 in (i). (k-l) The configurations of incoherent boundaries after prolonged cycling. The white and blue lines indicate the (003) planes of upper and low grains

NMR studies of $\text{LiMn}_{0.5}\text{Ni}_{0.5}\text{O}_2$ -based Cathodes: Solid-state NMR is a crucial characterization technique for LIB systems as ^6Li and ^7Li magic angle spinning (MAS) NMR can directly probe Li cations and local ordering within the bulk and surfaces of NMC cathodes. This work focuses on characterization of the local structures of both surface and bulk environments of Li in order to understand local ordering, segregation, and surface lithium-bearing species in materials with different compositions prepared by different synthesis routes. Solid-state NMR is a quantitative, local structural probe and can be used to determine which species are removed on charging the battery, how the local structure changes on extended cycling, and how these changes affect electrochemical performance.

Task 1. Study of Model Systems: For FY19, solid-state NMR characterization studies have focused initially on the model, zero-cobalt system of $\text{LiNi}_{0.5}\text{Mn}_{0.5}\text{O}_2$ moving to similar compositions containing 5% Co, Al, and Mg, separately, to understand the influence of dopants on TM ordering and Li/Ni mixing. The results were compared to NMC-442 where the Ni:Mn ratio remains 1:1, but the Co content is increased in order to study its role in local ordering. The effect of cycling on the local structure for these different compositions was studied using ^6Li solid-state NMR after 120 cycles in coin-cells using Li-metal anodes.

Task 2. Study of Synthesis Conditions: In FY19, the effect of synthesis conditions on TM ordering, phase separation, Li/Ni exchange, and domain size change were also studied. Previous NMR reports and theoretical modeling studies on Li and Mn rich cathodes from this project have shown that local ordering and domain sizes are greatly affected by synthesis conditions^{2,3}. In collaboration with the cathode synthesis effort, ^6Li solid-state NMR studies were initiated on $\text{LiNi}_{0.5}\text{Mn}_{0.5}\text{O}_2$ and $\text{LiNi}_{0.41}\text{Mn}_{0.5}\text{Co}_{0.05}\text{O}_2$ compositions prepared under different calcination temperatures and cooling rates with ^6Li enriched precursors.

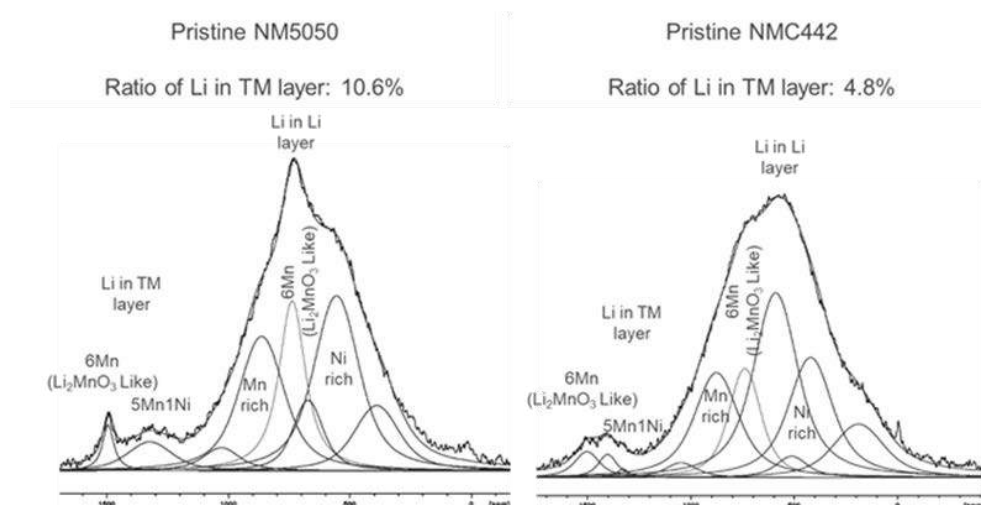


Figure II.2.B.10 ^6Li solid-state NMR analysis of pristine NiMn5050 and NMC-442 compositions

Figure II.2.B.10 shows ^6Li NMR comparisons of NiMn5050 and NMC-442 materials in the pristine state. Two groups of resonances were observed for the Li species present in the lattice; Li in Li layers around 500-800 ppm and Li in TM layers around 1300-1500 ppm. The deconvolution of the peaks observed for Li in Li layers reveals at least six different Li environments indicating different local ordering/domains and domain boundaries from Fermi-contact shifts of 1st and 2nd coordination shells for Ni, Mn, and Co rich domains. In addition, a distinct signature of Li_2MnO_3 -like domains with peaks observed at ~ 750 ppm are observed. For the octahedral Li sites in TM layers, two main resonances at ~ 1350 (Li coordinated to 5Mn) and ~ 1500 (Li coordinated to 6Mn for Li_2MnO_3 -like ordering) ppm were observed. The quantitative comparison of the data reveals that the amount of Li ions in TM layers, and the level of Li/Mn ordering (i.e., LiMn_6 , LiMn_5Ni_1 ordering), differs with the Co content of the materials.

The effect of cobalt on local ordering after cycling for NiMn5050 and NMC-442 compositions was also studied by ^6Li NMR on cycled cells (120 cycles, 3-4.7 V window, Li-metal anodes) as shown in Figure II.2.B.11. Comparing with the NMR data of the pristine samples (Figure II.2.B.10) a profound loss of order, or reordering, in the materials is observed after cycling. It is clearly seen for NiMn5050 sample that some Li ions can still be found in the 'formal' octahedral sites of the TM layers after cycling, whereas in the case of NMC-442 a total loss of Li in the TM layers is observed. Looking at the local ordering of Li in Li layers, for both samples, more Li loss is observed from Mn-rich domains.

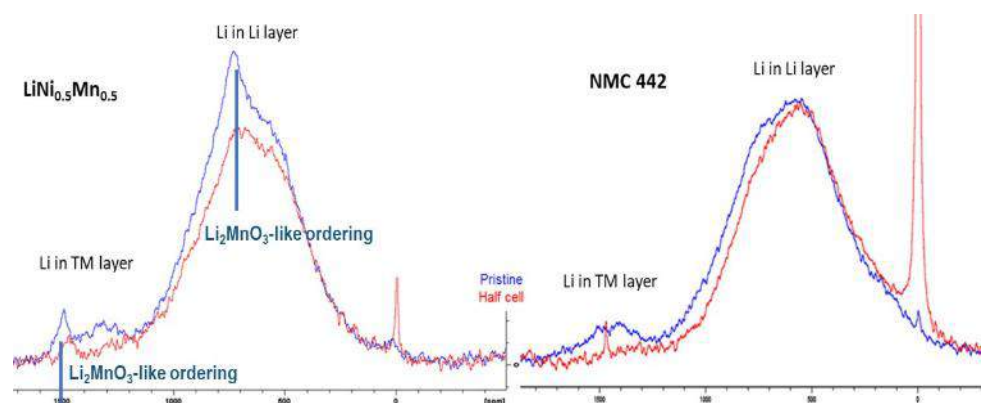


Figure II.2.B.11 Comparison of ^6Li solid-state NMR analysis of cycled and pristine NiMn5050 and NMC-442 compositions

The effect of different dopants on local ordering and Li content was further studied in NiMn5050 model systems with 5% Co, Al, and Mg as dopants, substituted for Mn. Figure II.2.B.12 shows comparisons of the pristine and cycled (120 cycles, 3-4.7 V, Li-metal anodes) materials. Although the differences look small, careful deconvolutions of each data set for pristine samples (data not shown) suggest that having Co as a dopant results in slightly lower Li content in TM layers (5%) in comparison to Al (6%) and Mg (6.5%). Similar to the previous example (NiMn5050 vs. NMC-442) the presence of Li/Mn ordering is also more pronounced for Al and Mg doped samples as opposed to Co doping. These differences can also be related to the solubility differences of Al and Mg in a Mn-rich matrix as shown by previous reports⁴. The lower solubility results in more surface species containing Al and Mg and reduces the dopant content in the bulk. This is proven by ²⁷Al NMR studies on Al-doped samples (data not shown) where both lattice and surface Al sites are seen, where surface Al may act more as a coating.

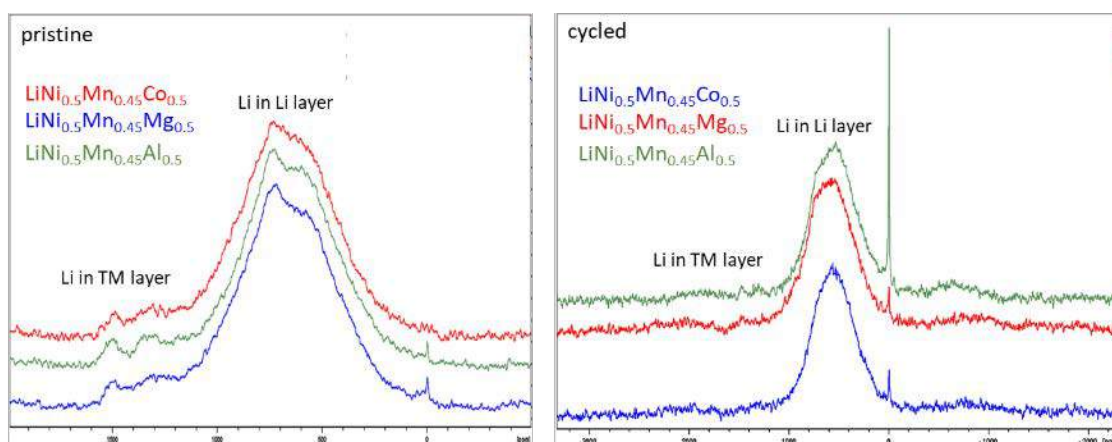


Figure II.2.B.12 Comparison of ⁶Li solid-state NMR analysis of pristine and cycled samples having different dopants

Based on theory and modeling calculations and previous studies within the project^{2,3}, synthesis conditions such as annealing temperature and cooling rate can have a significant influence on TM ordering, Li/Ni exchange, and domain sizes. In parallel with the NiMn5050 model systems studies, a new set of samples was synthesized with ⁶Li enriched precursors (to improve signal intensity for ⁶Li NMR experiments) with the conditions and compositions shown in Table II.2.B.4.

Table II.2.B.4 Model Systems Prepared with Various Synthesis Conditions for NMR Studies

Composition	Calcination temp	Ramping rate (K/min)	Cooling rate	Li blending ratio	Atmosphere
LiMn0.5Ni0.5O2	900	2	LN Quench	1.015	Air
LiMn0.5Ni0.5O2	900	2	Regular	1.015	Air
LiMn0.5Ni0.5O2	700	2	LN Quench	1.015	Air
LiMn0.5Ni0.5O2	700	2	Regular	1.015	Air
LiMn0.41Ni0.54Co0.05O2	900	2	LN Quench	1.015	Air
LiMn0.41Ni0.54Co0.05O2	900	2	Regular	1.015	Air
LiMn0.41Ni0.54Co0.05O2	700	2	LN Quench	1.015	Air
LiMn0.41Ni0.54Co0.05O2	700	2	Regular	1.015	Air

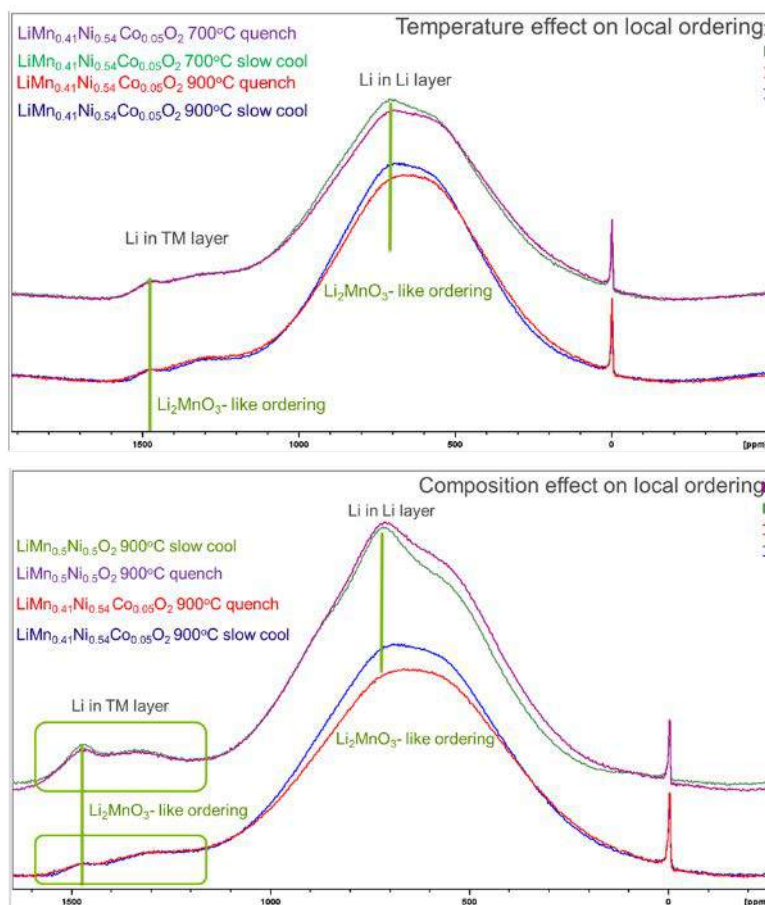


Figure II.2.B.13 Comparison of ^6Li solid-state NMR of model systems: The effect of synthesis conditions and the presence of Co on Li/Mn ordering ('clustering')

The aim of this detailed approach is to study the ordering differences (e.g., honeycomb, flower, zigzag) with different synthesis conditions. All ^6Li NMR data of the pristine samples were carefully deconvoluted and normalized to estimate the level of Li/Mn ordering (e.g., LiMn_6), Li content in TM layers, and the presence of surface impurities. The comparison of the data for all different samples are summarized in Figure II.2.B.13. Based on these results it is observed that slow cooling provides more ordering of Mn in configurations such as $\text{LiMn}_6/\text{LiMn}_5\text{Ni}_1$ (thermodynamically favored) whereas quenching results in more disorder and distribution of different local environments. The level of Li/Mn ordering is found to be dependent on annealing T with lower T resulting in more ordering. At high temperatures, and with quenching, ordering is seen to be slightly mitigated. The effect of Co is also studied as shown in Figure II.2.B.13 (bottom panel). Based on the results of individual deconvolutions and area calculations, the presence of Co in the structure results in less Li in TM layers (as shown with peak intensity differences in the green box of Figure II.2.B.13) and better mixing of TMs in the bulk which results in lower ordering of Li/Mn. As such, the presence of Co is seen to have a greater influence on Li/Mn ordering than the annealing/quenching conditions studied here.

Synthesis and Characterization of New, Low-Cobalt Cathode Compositions: Though Ni-rich cathodes currently receive considerable attention, alternatives to LiNiO_2 -based materials (e.g. > ~90% Ni) might be found in NiMn-based compositions such as $\text{LiNi}_{0.5}\text{Mn}_{0.5}\text{O}_2$. Mn is known to increase the thermal stability of layered oxides, is significantly less expensive than Co or Ni, and is one of the earth's most abundant elements. Though Mn can also introduce adverse effects, Mn-rich cathodes can achieve good performance. In this work, NiMn-based alternatives to LiNiO_2 -based compositions are explored with good success, and results describing a low-cobalt cathode within a targeted range of compositions are reported.

Previous reports have shown that Li/Ni exchange in $x\text{Li}_2\text{MnO}_3 \cdot (1-x)\text{LiMO}_2$ ($M=\text{Mn, Ni}$) compositions occurs almost exclusively within LiMO_2 -type inhomogeneities. As such, contrary to some reports, increasing x serves only to lower the overall fraction of those inhomogeneities not necessarily the Li/Ni exchange associated with them.³ The reader is referred to reference 5 for a detailed discussion of the local structures that form in the presence of excess Li in Mn-containing cathodes. In addition, it is well known that Co serves to help establish a more layered structure in NMC-type compositions that contain Mn and are rich in Ni. Furthermore, with the addition of a small amount of excess Li in the presence of Mn two things can be accomplished, 1) a few percent excess Li has been shown to improve rate capability in layered oxides, and 2) a small amount of ‘excess’ capacity might be achieved. Also, excess Li and Mn, even at very low levels, leads to a strong tendency for that Li and Mn to charge order starting at low temperatures ($\sim 400^\circ\text{C}$) during synthesis, whereas complete layering of even pure $\text{LiCo}(\text{Ni})\text{O}_2$ occurs above these temperatures. Therefore, it might be possible to better utilize small amounts of Co by ‘directing’ its effect to regions of interest (i.e., those prone to Li/Ni exchange) through the presence of a tailored amount of Li/Mn ordering. Following the above observations, it is proposed that cathodes of general composition, $x\text{Li}_2\text{MnO}_3 \cdot (1-x)\text{LiMn}_{0.5-\delta}\text{Ni}_{0.5+\delta/2}\text{Co}_{\delta/2}\text{O}_2$, with $x < \sim 0.10$, may be reasonable alternatives to LiNiO_2 -based, low-cobalt oxides. The so-called composite notation is used here to convey the concept of the different nano-scale inhomogeneities present (e.g., LiMn_6) and how each might influence cathode properties with respect to ‘excess’ Li and added Co. Herein a low-cobalt NMC (LC-NMC) composition with $x = 0.05$ and $\delta = 0.10$ is presented.

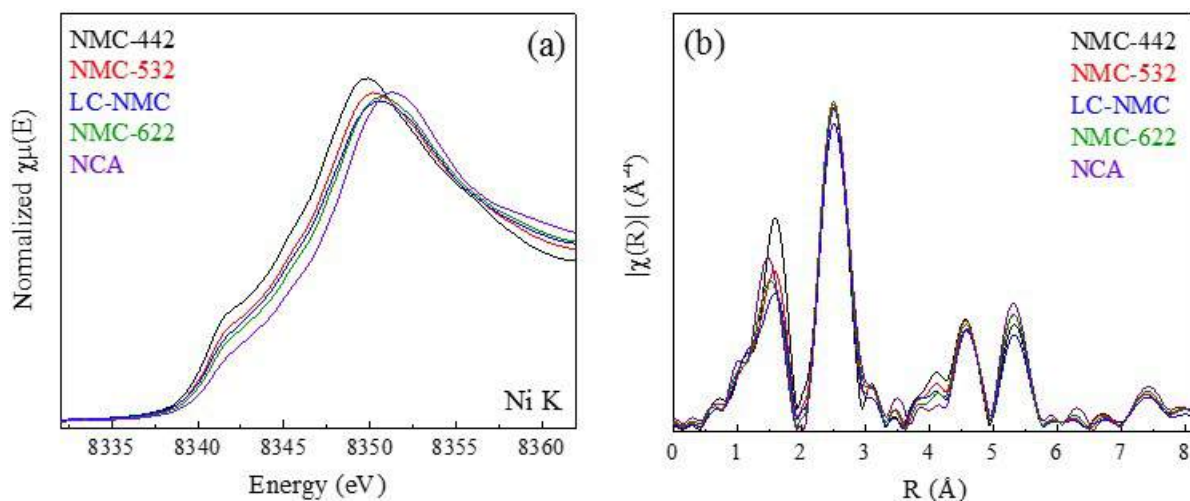


Figure II.2.B.14 (a) Ni K-edge XANES for the LC-NMC compared to data from standard NMC compositions and NCA. (b) Corresponding magnitudes of the Fourier transformed EXAFS of the samples in (a)

Figure II.2.B.14(a) shows Ni K-edge XANES data for the LC-NMC sample compared to a series of industrially prepared NMCs including NMC-442, NMC-532, NMC-622, and NCA. Here, the NMC-442 represents Ni^{2+} in a layered, R-3m oxide. The average Ni oxidation state increases with increasing Ni content from NMC-532 to NMC-622 and ending with NCA, having an average Ni oxidation state of $3+$. The Ni K-edge of the LC-NMC is situated between NMC-532 and NMC-622, giving an average oxidation of roughly $\text{Ni}^{2.5+}$. Supporting evidence for the mixed Ni oxidation state and environment can also be found in the magnitude of the Fourier-transformed EXAFS shown in Figure II.2.B.14(b). Notably, Ni^{3+} ions in these oxides reside in Jahn-Teller distorted octahedra having two distinct Ni-O bond lengths. The NMC-442, having a majority of Ni^{2+} ions with one Ni-O bond length, thus gives a large amplitude for the Ni-O bonds at $\sim 1.5 \text{\AA}$ (not corrected for photoelectron wave shift) in Figure II.2.B.14(b). For the NMC standards samples, having various proportions of $\text{Ni}^{2+/3+}$, the amplitudes are damped due to the convolution of the two different Ni-O bonds. In general, it can be seen that the LC-NMC sample herein is indicative of layered NMCs such as NMC-532 and NMC-622, but with much less Co. Mn and Co K-edges (not shown) of the LC-NMC match those of the Mn and Co K-edges from the NMC-442, 532, and 622 samples, which all closely overlap (e.g., Mn^{4+} and Co^{3+}).

Of particular significance is the amplitude of the correlations just below $\sim 4\text{\AA}$ in Figure II.2.B.14(b). The intensity here can be attributed to Ni-O-Ni bonds arising from Ni located in the lithium layers of these layered oxides and is a direct indication of Li/Ni exchange. The LC-NMC shows correlations on par with the commercial NMCs. Xiao et al.⁷ have recently quantified the Li/Ni exchange of NMC-622, 532, and 442 using neutron and magnetic measurements and found values of just $\sim 3\text{--}4\%$ for these compositions. The EXAFS data of Figure II.2.B.14 corroborates an equally well-layered structure for the LC-NMC and confirms less than 5% Li/Ni exchange. This observation is further reflected in the data of Figure II.2.B.15(a) showing the excellent rate capability of the LC-NMC. Rate data was collected between 4.45–2.5 V at 30°C with charge and discharge rates being equal, as listed in the plot (mAh g^{-1}). The LC-NMC delivers 75% of its initial capacity at a rate of 600 mA g^{-1} ($\sim 4C$, where C is defined by the actual time taken to discharge the cell at a given rate) revealing the facile diffusion of Li in structure on both charge and discharge. It has been previously established that rate performance decreases with increasing Li/metal exchange and the data of Figure II.2.B.15(a) along with the XAS data of Figure II.2.B.14 verify the well-layered nature of the LC-NMC. It should be noted here that active material loadings were kept low ($\sim 5\text{ mg cm}^{-2}$) in order to study the inherent cathode-particle properties. A Ragone plot derived from the data in Figure II.2.B.15(a) is shown in Figure II.2.B.15(b). For a rough estimate of performance, the red circle shows data of a commercial NMC-622 at the 10-hour rate (4.4V cutoff) taken from reference 7.

A systematic study on a series of oxides within the $x\text{Li}_2\text{MnO}_3 \cdot (1-x)\text{LiMn}_{0.5-\delta}\text{Ni}_{0.5+\delta/2}\text{Co}_{\delta/2}\text{O}_2$ compositional space is currently under way including dopants and surface treatments as well as scale-up and full-cell testing with graphite anodes.

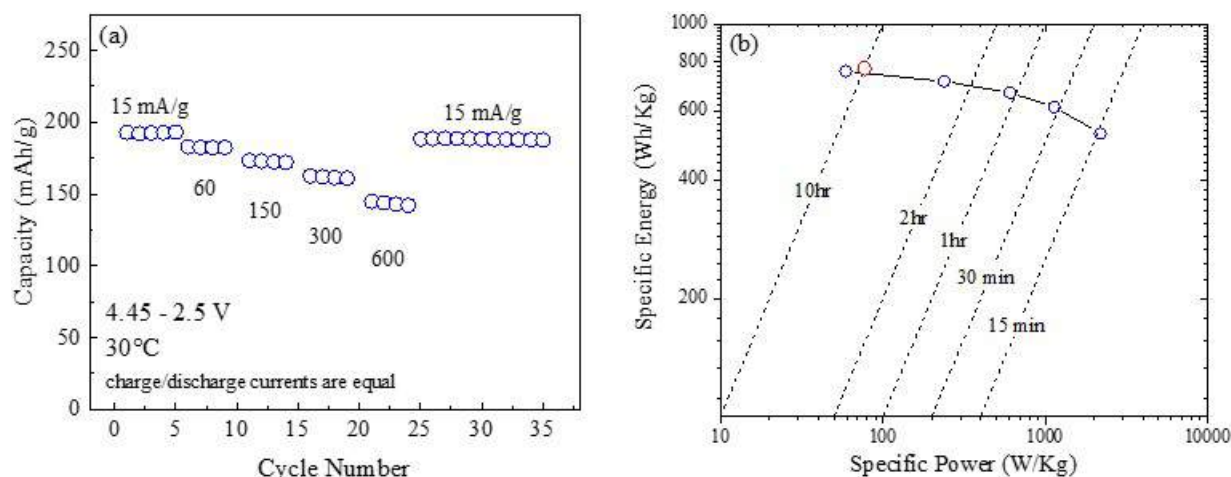


Figure II.2.B.15 (a) Rate data of the LC-NMC cathode conducted between 4.45–2.5V at 30°C . Charge and discharge currents were the same and are as listed in the plot (mA g^{-1}). (b) Ragone plot derived from the data in (a), based on active weight of the cathode only

Conclusions

- Co-precipitation reactors are being used to synthesize a series of Ni-rich cathode compositions of interest, as model and practical oxides, for distribution and study across multiple teams exploring structure, electrochemical performance/degradation, thermal properties, gassing, and surfaces.
- Tailored CSTR reactors are being used to synthesize a series of Ni-rich gradient materials having various compositions and structures.
- Well-formed, single-crystal NMCs are being studied to uncover the facet-dependent properties of cathode-oxides; namely, surface reconstruction and segregation tendencies related to synthesis, composition, and electrochemical cycling.

- Advanced microscopy/spectroscopy studies are being conducted and have revealed the critical role of secondary-particle architectures in cathode surface degradation.
- Solid-state NMR, including ^6Li NMR, is revealing new insights on the subtleties of Li and TM ordering in NMC oxides as they are influenced by dopant elements and synthesis conditions.
- Studies of the prototypical, no-cobalt, $\text{LiMn}_{0.5}\text{Ni}_{0.5}\text{O}_2$ layered oxide is leading to new insights on Li/Ni exchange and has produced a low-cobalt (5%), ‘high’ Mn (35%) composition showing preliminary performance on par with NMC-622.

Key Publications

1. J. Zhu and G. Chen, “Single-Crystal Based Studies for Correlating Properties and High-Voltage Performance of $\text{Li}[\text{Ni}_x\text{Mn}_y\text{Co}_{1-x-y}]\text{O}_2$ Cathodes”, *J. Mater. Chem. A*, 7, 2019, 54632.
2. J.R. Croy, B.R. Long, M. Balasubramanian, “A Path Towards Cobalt-Free Lithium-Ion Cathodes”, *J. Power Sources*, 440, 2019, 227113.
3. S. Sharifi-Asl, G. Chen, J. R. Croy, M. Balasubramanian, R. Shahbazian-Yassar, “Aberration-Corrected Scanning Transmission Electron Microscopy of Single Crystals and Chemically-Gradient NMC Cathodes”, *Microscopy and Microanalysis*, **24** (S1), 1536 (2018). DOI:10.1017/S1431927618008164.
4. J. Zhu and G. Chen, “Understanding Surface Reactivities on Ni-Rich Layered Oxide Cathodes”, 2018 Bay Area Battery Summit, Berkeley, CA, October 2018.

References

1. J. Li and A. Manthiram, “A Comprehensive Analysis of the Interphasial and Structural Evolution of Long-Term Cycling of Ultrahigh-Nickel Cathodes in Lithium-Ion Batteries”, *Adv. Energy Mater.* (2019) 1902731.
2. B.R. Long, J.R. Croy, F. Dogan, M.R. Suchomel, B. Key, J. Wen, D.J. Miller, M.M. Thackeray, M. Balasubramanian, *Chem. Mater.* 26 (2014) 3565.
3. J. R. Croy, K.G. Gallagher, M. Balasubramanian, B.R. Long, M.M. Thackeray, “Quantifying Hysteresis and Voltage Fade in $x\text{Li}_2\text{MnO}_3 \cdot 1-x\text{LiMn}_{0.5}\text{Ni}_{0.5}\text{O}_2$ Electrodes as a Function of Li_2MnO_3 Content” *J. Electrochem. Soc.* 161 (2014) A318.
4. F. Dogan, J.T. Vaughey, H. Iddir, and B. Key, *ACS Appl. Mater. Interfaces*, 8 (2016) 16708.
5. J.R. Croy, M. Balasubramanian, K.G. Gallagher K.G.; A.K. Burrell, “Review of the U.S. Department of Energy’s “Deep Dive” Effort to Understand Voltage Fade in Li- and Mn-Rich Cathodes”, *Acc. Chem. Res.* 48 (2015) 2813.
6. Y. Xiao, T. Liu, H. Chen, et al., “Insights into the origin of lithium/nickel ions exchange in layered $\text{Li}(\text{Ni}_x\text{Mn}_y\text{Co}_z)\text{O}_2$ cathode materials”, *Nano Energy* 49 (2019) 77.
7. S. Ahmed, S.E. Trask, D.W. Dees, P.A. Nelson, W. Lu, A. Dunlop, B.J. Polzin, A.N. Jansen, “Cost of automotive lithium-ion batteries operating at high upper cutoff voltages”, *J. Power Sources*, 403 (2018) 56.

Acknowledgements

Guoying Chen, Anh Vu, Ozge Kahvecioglu, Jihyeon Gim, Jessica Durham, Jian Zhu, Minkyung Kim, Nick Sovronec, Fulya Dogan, Binghong Han, Daniel O’Hanlon, Jack Vaughey, Shankar Aryal, Eungje Lee, Arturo Gutierrez, Mahalingam Balasubramanian, Kris Pupek, Khalil Amine, Chongmin Wang, Soroosh Sharifi-Asl, Reza Shahbazian-Yassar, Lianfeng Zou, Linze Li, Ji-Guang Zhang.

Support from the U. S. Department of Energy (DOE), Vehicle Technologies Office, specifically from Peter Faguy and David Howell is gratefully acknowledged.

II.2.C Theory and Modeling (ANL, LBNL)

Hakim Iddir, Principal Investigator

Argonne National Laboratory
9700 S Cass Avenue
Lemont, IL 46039
E-mail: Iddir@anl.gov

Peter Faguy, DOE Technology Development Manager

U.S. Department of Energy
E-mail: Peter.Faguy@EE.Doe.Gov

Start Date: October 1, 2018

End Date: September 30, 2021

Project Funding (FY19): \$4,000,000

DOE share: \$4,000,000

Non-DOE share: \$0

Project Introduction

State-of-the-art, Li-ion batteries used in electric vehicle applications rely on transition metal (TM) oxide chemistries such as $\text{LiNi}_{0.8}\text{Co}_{0.15}\text{Al}_{0.05}\text{O}_2$ (NCA) or $\text{Li}_{1+x}\text{Ni}_a\text{Mn}_b\text{Co}_c\text{O}_2$ (NMC-abc), where x is typically at, or slightly above, the stoichiometric value of $x=0$. The current generation of cathodes achieve practical oxide energy densities of about ~650 Wh/kg oxide and the intrinsically high volumetric energies for Ni-rich compositions ($a \geq 0.5$) has led to interest in developing cathodes such as NMC-811. Although progress has been steady, several major concerns exist with respect to future implementation NMC cathodes. NMC-based compositions have shown promise in meeting DOE/USABC goals for PHEV and EV applications, but only under higher voltage operation than is currently possible where definition of ‘high voltage’ is cathode-specific. Importantly, higher nickel content NMCs (e.g., NMC-811) have lower onset voltages. High-voltage oxygen instabilities are particularly critical issues for cathode surfaces and can lead to oxygen loss, facile TM dissolution, surface reconstructions, reaction with organic electrolytes, and thermal runaway. It is, therefore, widely recognized that stabilization of cathode surfaces is essential if high-voltage NMC-based cells are to be realized in application. Coupled to materials issues associated with high-energy cells is the ever-growing recognition of an unsustainable reliance on security critical materials. For NMC cathodes, the most important of these materials is cobalt. High demand, fluctuating prices, and scrutiny over the ethical and geopolitical implications related to cobalt mining has attracted interest in the possibility of competitive, cobalt-free oxides. The goal of this project is to use molecular scale modeling to gain a detailed understanding of high-energy, low Co or Co free, cathode materials with respect to design, synthesis, degradation, and stabilization.

Objectives

Atomistic simulations will be carried out using a combination of spin-polarized density functional theory (DFT) calculations, molecular dynamics (MD), simulated annealing, genetic algorithms, Kinetic Monte-Carlo and ab-initio thermodynamics approaches to determine:

- The effect of reduced Co content (<10%) on the electronic structure and bulk stability of NMC cathode materials.
- The effect of complete Co-replacement (X: X being a single or a combination of two or more TMs) and Li-content on the electronic structure, bulk stability and surface reactivity of Co-free NMX cathode materials.
- The effect of anion substitution (partial) on the electronic structure and stability of NMX materials will be investigated following the detailed approach mentioned above.

In FY29, the project focused mainly on Mn_xNi_x ($\text{LiMn}_x\text{Ni}_x\text{Co}_{1-2x}\text{O}_2$) systems, designed to understand the roles of Co in order to provide fundamental understanding on the effect of Co in high-Ni content NMCs, and provide potential substitutes for Co through the following:

- Mn_xNi_x : For these compositions, Ni should remain as Ni^{2+} only, and hence allow for separation of the effects of different Ni oxidation states from the effects of Co content.
- Electronic effects (amount of electronic charge delocalization, M -O charge density overlap, spin state).
- Minimum amount of Co to maintain the layered structure (Li-Ni exchange, Ni, Mn migration to Li layer)
- Co clustering/next neighbors, domain size/local configuration effect on layered structure stability.

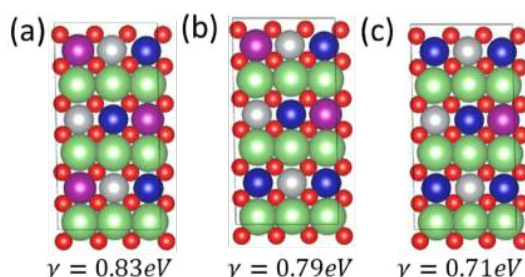


Figure II.2.C.1 Schematic representation of the slab model for NMC-111 (104) facet (top view): (a) stoichiometric amount of Co, (b) excess of one Co ion per surface, (c) excess of two Co ions per surface. Small red spheres represent oxygen, green, grey, purple and blue spheres represent Li, Ni, Mn and Co respectively

Approach

Atomistic simulations have been carried out using a combination of DFT calculations and the Nudged Elastic Band (NEB) method as implemented in the Vienna Ab Initio Simulation Package (VASP).^{1,2} The exchange-correlation potentials have been treated by the Generalized Gradient Approximation (GGA) parametrized by Perdew, Burke, and Ernzerhof (PBE).³ The interactions between valence electrons and ion cores were described by the Projected Augmented Wave (PAW) method.⁴ All the ions were allowed to relax until the total energy differences were no more than 0.003 eV. The GGA+U scheme was used to apply the onsite correlation effects among 3d electrons of the TMs, where the parameter (U-J) was set to 5.96, 5.00, and 4.84 eV for Ni, Co, and Mn, respectively.⁵ The wave functions were expanded in the plane wave basis up to a kinetic energy of 500 eV. All ions were allowed to relax until the total energy differences were no more than 0.003 eV. After geometry optimizations within the DFT+U framework, a single point calculation was used with the hybrid functional HSE06 to perform electronic relaxation.⁶ Adsorption and reaction energies (ΔE) were calculated using the following expression:

$$\Delta E = E_{\text{surf+adsorbate}} - E_{\text{surf}} - E_{\text{adsorbate}}$$

where $E_{\text{adsorbate}}$ is the energy of the isolated molecule in vacuum, E_{surf} is the energy of the bare slab, and $E_{\text{surf+adsorbate}}$ is the total energy of the molecule adsorbed on the slab. The configuration of cations in the TM layer was determined in a previous work.⁸ An index notation based on the original standard hexagonal unit cell is used. It was also assumed that the entropic and volumetric contributions were negligible. Bulk solvent effects were accounted for by using an implicit solvation model as implemented in the DFT code VASP.⁷ Previous work determined that the most reactive facet of NMC cathodes is the (012) surface.⁸ This facet was used as the prototype surface to determine cathode electrolyte interactions. To locate the atom/molecule configurations that minimize the adsorption energy on the lithiated and partially delithiated surfaces, the potential energy surface of solvent-surface interaction was explored by testing several adsorption configurations, using ab-initio Molecular Dynamics.

To provide a fundamental understanding of preferential elemental segregation, a (104) surface slab of $\text{Li}(\text{Ni}_{1-x-y}\text{Mn}_x\text{Co}_y)\text{O}_2$, with composition $x = y = 1/3$ (NMC-111) was built. The Co concentration on the surface was varied in different simulations by swapping Co atoms from the bulk to the surface, keeping the overall supercell stoichiometry constant. Figure II.2.C.1 shows a schematic of the surface layer for the symmetric slab model, which consists of 384 ions distributed in 9 layers. Each layer is stoichiometric, resulting in a non-polar surface. The octahedron formed by the metals and Li atoms with the surrounding O atoms in the central layer were kept fixed to mimic the behavior of the bulk. Figure II.2.C.1(a) represents the surface layer unit cell for the stoichiometric slab. Figure II.2.C.1(b) and Figure II.2.C.1(c) show the surface of the slab with an excess content of Co ions of one and two extra Co per surface layer (note that there are three Co atoms per surface layer for the stoichiometric NMC-111 reference supercell, respectively).

Results

Decomposition of Phosphorus-Containing Additives at a Charged NMC Surface Through Potentiostatic Holds:

DFT simulations were performed to compute the strength of the interactions between the cathode surface and additive molecules including Triethyl phosphite (TEPi), tris(trimethylsilyl) phosphite (TMSPi), and Tris(2,2,2-trifluoroethyl) phosphite (TTFP). A state of charge corresponding to 75% delithiation was used to simulate a high voltage state. To build confidence in the molecule-surface model, an initial TMSPi additive-molecule-surface configuration was calculated. This was followed by ab-initio molecular dynamic simulations at 700 K for a few ps to explore a wider set of configurations (local minima) and locate the most likely configuration with the lowest energy state. Further energy minimization was performed at the GGA+U level using the steepest descent to find the lowest energy for the additive-surface configuration. Unlike TMSPi, calculations show that TEPi readily oxidizes to TEPa. However, it is unlikely to form a passivation film on the cathode surface given the weak binding energy between TEPa and the surface. The steric effect may account for the differences between TMSPi and TEPi. For TMSPi, the scission of the TMS groups generates a smaller P-O phosphite moiety, which tends to attach to the cathode oxide surface. Another possible mechanism of TEPi decomposition is the abstraction of an oxygen atom from its alkyl group. However, the reaction energy (-0.02 eV) indicates this process is thermodynamically less favorable than the reaction with the oxide surface oxygen. Another additive considered in this study is TTFPi. H abstraction from TTFPi is not thermodynamically favorable. On the pristine NMC surface, the CF_3 groups from TTFPi do not bind to any Li, TM, or O atom. A strong interaction was observed at a higher charge state when 75% of the Li was removed from the cathode. A stable, free phosphate molecule is generated by the removal of an oxygen atom from the oxide surface, which reduces the TM ions on the oxide surface. The change in total energy is -3.1 eV, indicating a strong thermodynamic driving force for the formation of a P-O bond with covalent character. This value is very close to results of calculations on the formation of TTFPa from TTFPi in solution (-3.5 eV). Since further reaction with the surface is not expected, the phosphate form of the molecule (TTFPa) interacts weakly with the surface.

Effect of Electrolyte Composition on Rock Salt Surface Degradation in NMC Cathodes During High-Voltage Potentiostatic Holds:

DFT calculations were used to study the interaction of each electrolyte component (The TTFP additive as well as the solvent molecules EC, EMC, DFEC, and HFDEC) with the NMC (012) surface (see Figure II.2.C.2). Ab initio molecular dynamics (AIMD) were used to explore the configuration space of the molecules over the surface. Several adsorption configurations were tested in order to find atomic positions that minimized the adsorption energy on both the fully lithiated and fully delithiated top surface layers. Some of these configurations are shown in Figure II.2.C.2. The results show that the interaction of the fluorinated electrolytes is much reduced compared to interaction of non-fluorinated electrolytes (less electrolyte oxidation).

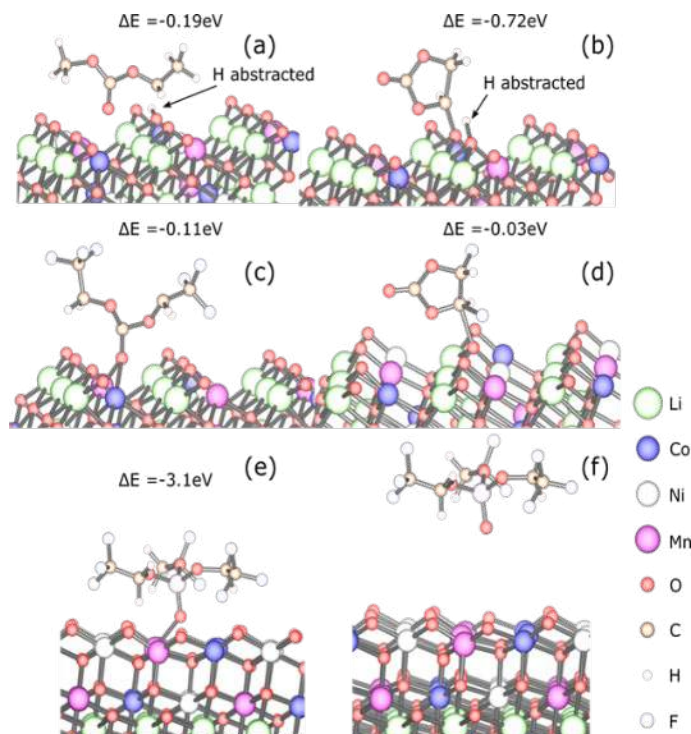


Figure II.2.C.2 Lowest energy configuration of electrolyte components at or near the (012) facet of (a-d) fully lithiated or (e-f) fully delithiated NMC-532. (a) EMC, (b) EC, (c) HFDEC, (d) DFEC, (e) TTFP on delithiated NMC, and (f) TTFPa detached from NMC surface

Revisiting the Mechanism Behind TM Dissolution from Delithiated NMC Cathodes:

The presence of water is believed to promote HF-attack and the concomitant reduction of the metal lattice. Figure II.2.C.3 shows the DFT calculated d-band projected density of states on the TMs in a fully lithiated NMC cathode. The lowest lying unoccupied states belong to the Mn ions making them more susceptible to accept extra charge in the system. This is consistent with experiments that show the presence of Mn in solution when water is added. Also, reduced Mn ions are soluble in the standard organic solvent. In a charged state, Ni ions will be reduced, promoting their subsequent dissolution as observed in the charged case. For Co, an increased amount of dissolved Co was observed in the presence of Li-acac (a salt added to the electrolyte), which can be explained by the difference in solubilities of the TM-acac complexes. DFT calculations found that the strongest complex, among all possibly formed in solution, is $\text{Co}(\text{acac})_3$ with a formation energy of -1.63 Hartrees compared with $\text{Ni}(\text{acac})_2$ -1.02 Hartrees and $\text{Mn}(\text{acac})_2$ -0.98 Hartrees. Therefore, Co tends to dissolve more despite being only 20% of the cathode material. However, the presence of TTFP also promotes a different composition in solution. As previously mentioned, TTFP oxidizes by taking an oxygen from the surface (reducing the surface), promoting further TM reduction and dissolution.

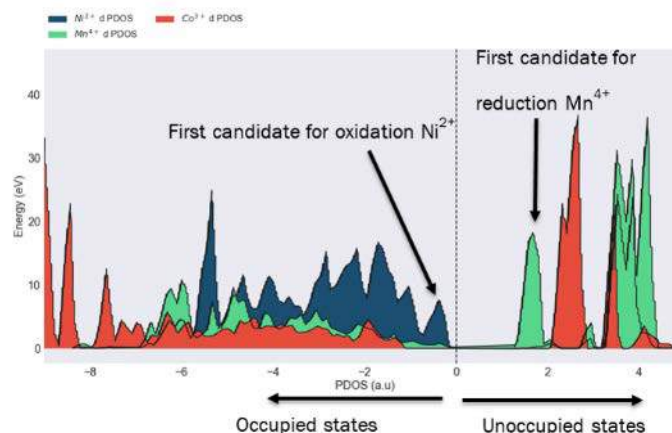


Figure II.2.C.3 Projected Density of States (PDOS) on the TMs in fully lithiated (pristine) NMC. The dashed line indicates the Fermi level

Facet-Dependent Elemental Segregation and Surface Reconstruction:

Even though TM segregation and the associated deleterious effects have been observed in many studies, a consensus on the origins and thermodynamic driving forces for such processes is still lacking. In this work, a different mechanism is proposed that involves Ni migration into the Li layer and its preference to segregate to the surface that eventually triggers spinel formation. The actual driving force for Ni enrichment near the surface is a favourable Li-Ni exchange near the surface and not Mn migration into the bulk. This mechanism is further rationalized when one considers the fact that a spinel-like phase is observed even in pristine materials. Alone, Mn segregation to the bulk would not explain the previously-observed, preferential segregation of Ni to the (012) facet and Co to the (104) facet.

Herein, facet-dependent TM segregation is proposed through a combined phase-change/segregation, stabilized by the strain on the surface reconstruction (SR). First, the stabilization effect of Co on the (104) surface is considered. Second, the formation of Li-Ni anti-site defects in different positions and configurations (see Figure II.2.C.4) are compared. Finally, the hypothesis of the strain induced stabilization of the SR is introduced.

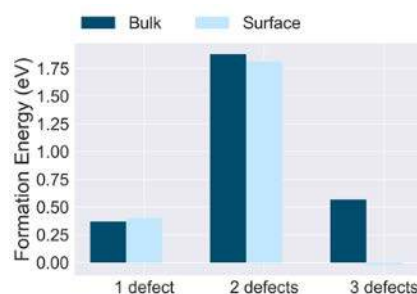


Figure II.2.C.4 Li/Ni anti-site formation energy change with number of defects. The defects are located in the same Li layer forming a row of continuous defects

The results for Co segregation to the (104) facet are shown in Figure II.2.C.1. The surface energy of (104) facet is lowered with the increase of Co surface concentration. The stabilization of the (104) surface energy is due to the increased crystal-field stabilization of Co being in intermediate spin state.

A completely different mechanism for Ni segregation is put forward, where the presence of a thermodynamic driving force for the segregation of Ni to the surface via Li-Ni exchange near the (012) surface is shown. Moreover, a stabilized pure LiNiO₂, over-lithiated thin-film, pinned to the NMC core is found when it is

allowed to relax in the perpendicular direction. This is an indication of a driving force for simultaneous Ni segregation and surface reconstruction in the (012) facet. Hence, elemental segregation and surface reconstruction-layer formation are intimately linked and are facet dependent phenomena. The global composition affects the nature and the thickness of the SR, which can impact the impedance and also necessarily the chemical stability of the cathode/electrolyte interface as well.

Effect of Co on Li-Ni Anti-Site Defect Formation in $\text{LiMn}_{0.5}\text{Ni}_{0.5}\text{O}_2$

As a cathode material, $\text{LiMn}_{0.5}\text{Ni}_{0.5}\text{O}_2$ (MN5050) exhibits rate capability issues. This is typically attributed to a high concentration of Li-Ni anti-site defects (so called Li-Ni exchange) that consequently decrease the ionic conductivity of the material. The thermodynamic equilibrium configuration of MN5050, the so-called ‘zigzag pattern’, does not exhibit Li-Ni exchange. However, a special configuration based on the hexagonal symmetry known as the ‘flower pattern’, where Li occupies the center of a hexagon surrounded by Mn in the first shell and Ni in the second shell, produces 8.3 % Li-Ni exchange, in agreement with experimental results. Based on kinetic arguments, it has been suggested that during synthesis the true thermodynamic equilibrium structure cannot be achieved. The flower pattern, being closer in structure to random configurations, is locked in during cooling, and hence does not evolve toward the low-energy zigzag pattern. To perform atomistic calculations on the effect of Co content in MN5050 compositions, a reliable starting model must be built. The thermodynamically stable model (zigzag) was used herein to conduct simulation studies of Co-containing compositions. Results show that the lowest limit in Li-Ni exchange concentration is dictated by thermodynamics and varies with the configuration.

To better design low-Co cathode materials, a better understanding of the ionic configuration and its role on Li-Ni disorder is needed. Herein, a pair of Ni-Mn ions are randomly selected and swapped. The energy is calculated using DFT and the process is repeated for hundreds of structures. The final goal is to understand TM-TM interactions. A surrogate model is fitted to predict energies for unknown structures and larger domains. Figure II.2.C.5 shows the energies for the explored configurations. The snapshots in Figure II.2.C.5 shows the arrangement of the ions in the TM layer.

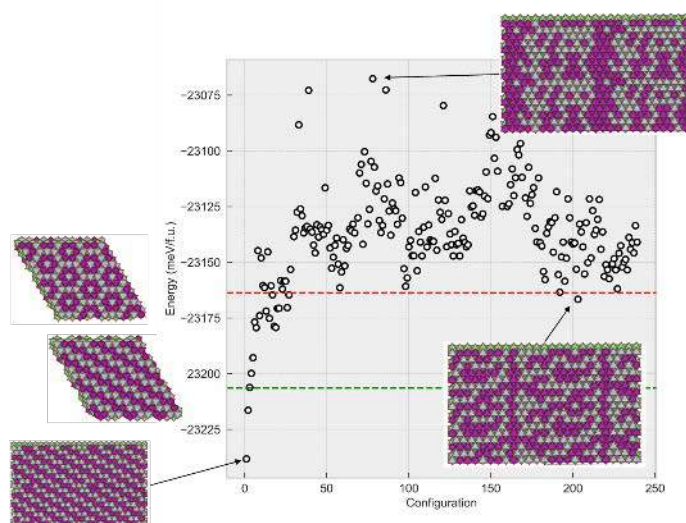


Figure II.2.C.5 Total energy of $\text{LiNi}_{0.5}\text{Ni}_{0.5}\text{O}_2$ for different ionic configurations within the transition metal layer. Grey represent Ni, purple represents Mn and green represents Li in the layer underneath the transition metal layer

Figure II.2.C.6(a) shows the configurations sorted by energies and the number of TM-TM bonds (where TM = Co, Ni, Mn). In Figure II.2.C.6(b) The total energy is plotted as a function of the number Ni-Mn bonds in the system. There is a clear correlation between the energy and the number of Ni-Mn bonds in each configuration.

The formation of clusters is not favorable and dispersion decreases the total energy. It can be noticed that there is less spread in the data when the number of Ni-Mn bonds is high, since there are less possible configurations.

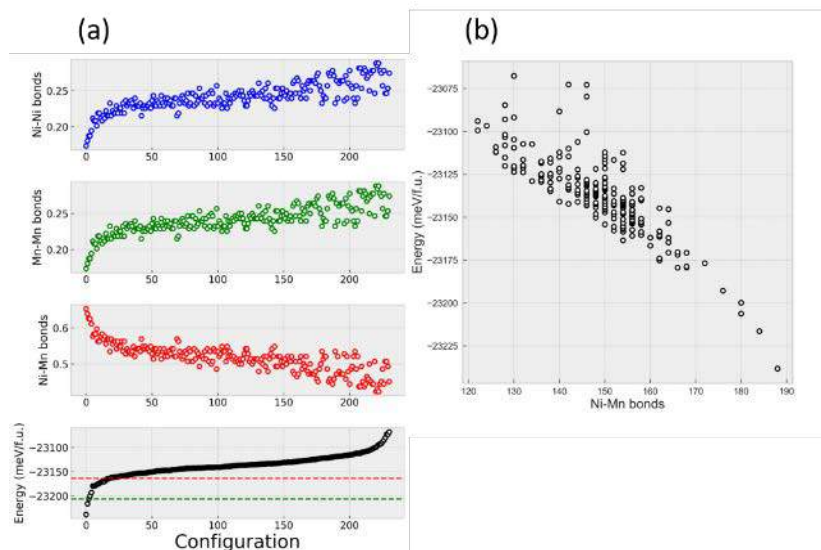


Figure II.2.C.6 Total energy of $\text{LiNi}_{0.5}\text{Ni}_{0.5}\text{O}_2$ for different ionic configurations within the transition metal layer. (a) Configurations sorted by energies and the number of TM-TM bonds (where TM = Co, Ni, Mn). (b) Total energy as a function of the number of Ni-Mn bonds in the system. Grey represents Ni, purple represents Mn and green represents Li in the layer underneath the TM layer

Figure II.2.C.7 shows the effect of Li-Ni anti-site defect concentration on the total energy of the system. The total energy decreases when one Li-Ni anti-site defect is formed in the supercell (except one configuration 33). Further increase in the defect concentration increases the total energy up to or higher than the pristine material (no Li-Ni exchange). Given the size of the supercell, 1 Li-Ni, 3 Li-Ni, and 9 Li-Ni defects represent 0.9%, 2.8% and 8.3 % concentrations, respectively. For the perfect flower and zigzag, all the tested configurations with 0.9% and 2.8% Li-Ni exchange show a decrease in the total energy where even concentrations up to ~8% would be favorable. Higher defect concentrations (>8%) can be reached at higher temperatures. After heating the system up, slow annealing should lead to 1-3 % Li-Ni exchange. The effect of Co is being investigated keeping the same Ni/Mn ratio. Preliminary results show that Co helps the dispersion of Mn and decreases the concentration of Li-Ni anti-site defects.

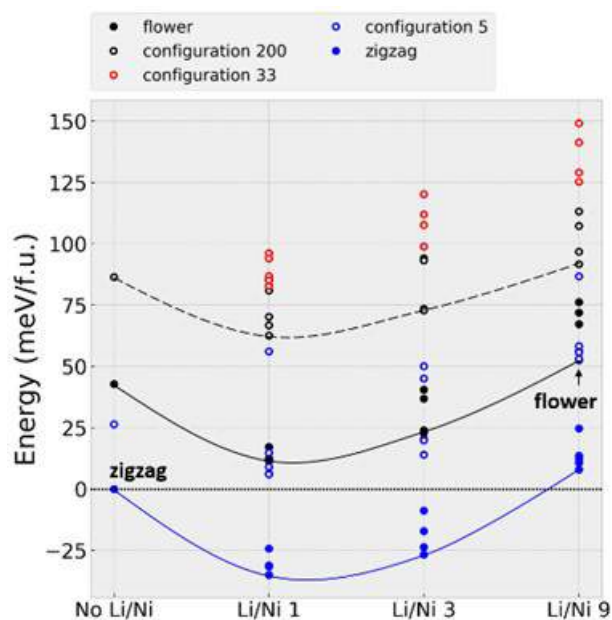


Figure II.2.C.7 Total energy change of $\text{LiNi}_{0.5}\text{Ni}_{0.5}\text{O}_2$ for five different ionic configurations within the transition metal layer, as a function of Li-Ni defect exchange concentration

Conclusions

Atomistic based modeling helped provide fundamental and mechanistic details and understanding on the interaction of additives and electrolytes with pristine and charged cathode surfaces. In the case of TMSPI, insights on the mechanism of passivation led to the design of new additives. The origin and the link between elemental surface segregation and surface reconstruction were proposed, providing new cathode design approaches that can limit surface reconstruction. Critical atomic interactions between different TMs, as well as the amount of Li-Ni exchange, is revealed via screening of a large number of configurations.

Key Publications

1. A. Tornheim, J. Garcia, R. Sahore, H. Iddir, I. Bloom, Z. Zhang. "Decomposition of phosphorus-containing additives at a charged NMC surface through potentiostatic holds." *J. Electrochem. Soc.*, 166, (2019) A440.
2. A. Tornheim, S. Sharifi-Asl, J. Garcia, J. Bareño, H. Iddir, R. Shahbazian-Yassar, Z. Zhang. "Effect of electrolyte composition on rock salt surface degradation in NMC cathodes during high-voltage potentiostatic holds." *Nano Energy*, 55 (2019) 216.
3. R. Sahore, D. O'Hanlon, A. Tornheim, C.-W. Lee, J. Garcia, H. Iddir, M. Balasubramanian. "Revisiting the mechanism behind transition-metal dissolution from delithiated $\text{LiNi}_x\text{Mn}_y\text{Co}_z\text{O}_2$ (NMC) cathodes." *J. Power Sources* (*submitted*).
4. Garcia, Juan, Adam Tornheim, Ritu Sahore, Ira Bloom, Zhengcheng Zhang and Hakim Iddir. "Decomposition of phosphorus-containing additives at a charged NMC surface: atomistic modeling insights." 2019 American Physical Society March Meeting, March 4, 2019 - March 8, 2019.
5. Garcia, Juan, Javier Bareno, Guoying Chen, Jason Croy and Hakim Iddir. "Facet dependent cation segregation in layered lithium transition-metal oxide cathode materials." 2019 American Physical Society March Meeting, March 4, 2019 - March 8, 2019.
6. Garcia, Juan, Adam Tornheim, Ritu Sahore, Ira Bloom, Zhengcheng Zhang and Hakim Iddir. "Decomposition of Phosphorus-Containing Additives at a Charged NMC Surface: Atomistic

Modeling Insights.” 2018 Materials Research Society Spring Meeting and Exhibit, April 2, 2018 - April 6, 2018.

References

1. G. Kresse and J. Furthmüller, “Efficiency of ab-initio total energy calculations for metals and semiconductors using a plane-wave basis set”, *Comp. Mater. Science*, 1996, 6, 15–50.
2. G. Kresse and J. Hafner, “Ab Initio molecular dynamics for liquid metals”, *Phys. Rev. B*, 1993, 47, 558–561.
3. J. P. Perdew, K. Burke and M. Ernzerhof, “Generalized Gradient Approximation Made Simple”, *Phys. Rev. Lett.*, 1996, 77, 3865–3868.
4. P. E. Blöchl, “Projector augmented-wave method”, *Phys. Rev. B*, 1994, 50, 17953–17979.
5. H. Iddir and R. Benedek, “First-Principles Analysis of Phase Stability in Layered–Layered Composite Cathodes for Lithium-Ion Batteries”, *Chem. Mater.*, 2014, 26, 2407–2413.
6. J. Heyd, G. E. Scuseria and M. Ernzerhof, “Hybrid functionals based on a screened Coulomb potential”, *The J. Chem. Phys.*, 2003, 118, 8207–8215.
7. K. Mathew, R. Sundararaman, K. Letchworth-Weaver, T. A. Arias and R. G. Hennig, “Implicit solvation model for density-functional study of nanocrystal surfaces and reaction pathways”, *The J. Chem. Phys.*, 2014, 140, 084106.
8. J. C. Garcia, J. Bareño, J. Yan, G. Chen, A. Hauser, J. R. Croy and H. Iddir, “Surface Structure, Morphology, and Stability of $\text{Li}(\text{Ni}_{1/3}\text{Mn}_{1/3}\text{Co}_{1/3})\text{O}_2$ Cathode Material”, *J. Phys. Chem. C*, DOI:10.1021/acs.jpcc.7b00896.

Acknowledgements

Juan Garcia, Adam Tornheim, Zhengcheng Zhang, Fulya Dogan, Jack Vaughey, Ritu Sahore, Ira Bloom, Cameron Peebles, Daniel Abraham, Guoying Chen, Jason R. Croy. Support from the U. S. Department of Energy (DOE), Vehicle Technologies Office, specifically from Peter Faguy and David Howell is gratefully acknowledged.

II.2.D Design & Synthesis of High Energy, Mn-Rich Oxides for Li-Ion Batteries (ANL)

Jason R. Croy, Principal Investigator

Argonne National Laboratory
9700 S Cass Avenue
Lemont, IL 46039
E-mail: croy@anl.gov

Peter Faguy, DOE Technology Development Manager

U.S. Department of Energy
E-mail: Peter.Faguy@EE.Doe.Gov

Start Date: October 1, 2018
Project Funding (FY19): \$900,000

End Date: September 30, 2019
DOE share: \$900,000

Non-DOE share: \$0

Introduction

This project seeks to advance the performance of Mn-rich cathode chemistries as alternatives to Ni-rich NMCs, thereby creating inexpensive, safe, energy-dense, competitive options capable of meeting DOE cost and energy targets for next-generation batteries. Manganese is one of the earth's most abundant elements, is known for its safety characteristics in Li-ion chemistries, and is ~5-30 times as inexpensive as Ni and Co, respectively, depending on current prices. Therefore, significant economic opportunities will exist, including the creation of new markets, if such chemistries can achieve performance parity with Ni-rich counterparts. In order to achieve this goal, targeted engineering of nano-scale structures within novel, Mn-rich cathodes, developed at Argonne National Laboratory, will be pursued.

Objectives

- Develop low-cost, high-energy and high-power Mn-oxide-based cathodes for lithium-ion batteries that will meet the performance, safety, and cost requirements of PHEV and EV vehicles
- Improve the design, composition, and performance of advanced electrodes with stable architectures and surfaces, facilitated by an atomic-scale understanding of electrochemical and degradation processes
- Characterization of novel, end-member compositions as tailored components of integrated electrodes structures
- Explore co-precipitation reaction variables of constant stirred-tank reactors (CSTR) in order to understand critical parameters related to the synthesis of well-controlled (morphology, size, density), Mn-rich, cathode-oxides.

Approach

1) A bottom-up approach to fabricate Mn-rich cathodes is taken whereby x , in $x\text{Li}_2\text{MnO}_3 \cdot (1-x)\text{LiNMCO}_2$ 'layered-layered' (LL) electrodes, is limited to less than ~0.25 and the composition modified by reducing the lithium content slightly to integrate spinel domains in the LL structure, thereby creating composite, 'layered-layered-spinel' (LLS) structures with Mn contents of ~50% or more. This approach represents a comprehensive strategy to address the known limitations of LL cathodes by:

- Inherently limiting the extent of Li/Mn ordering (i.e., $x < 0.25$) and, therefore, damaging effects (e.g., voltage fade) of the electrochemical activation process whereby lithium and oxygen are removed from the Li_2MnO_3 component, while still allowing for substantial capacities ($>200 \text{ mAh g}^{-1}$);
- Introducing spinel domains (especially at surfaces) to help improve rate capability and stability; and

- Introducing vacant lithium sites, by way of the spinel component, that can take up lithium on the first discharge after the activation of the Li_2MnO_3 component, thereby reducing first-cycle, irreversible capacities.
- 2) Utilize CSTR reactors to gain insights on the critical parameters influencing co-precipitation synthesis of Mn-rich cathode-oxides as practical alternatives to Ni-rich NMCs
 - 3) Utilize novel, spinel-based materials as stabilizing components of LLS electrode materials

Results

Effect of Firing Temperature on Electrochemical and Thermal Properties of LLS Oxides: Previous reports have verified the promising properties of LLS cathode electrodes where performance parity with Ni-rich NMCs such as ~NMC-532/622 was demonstrated. In an extension of that work, the critical factors related to practical synthesis of these promising Mn-rich, LLS oxides was pursued. Although co-precipitation in CSTR-type reactors is an industry standard, the control over morphology, density, and subsequent electrochemical properties of Mn-rich, LLS chemistries has not been studied. Herein, initial results are presented on the effects of annealing temperatures on electrochemical and thermal properties of a baseline, LLS cathode oxide.

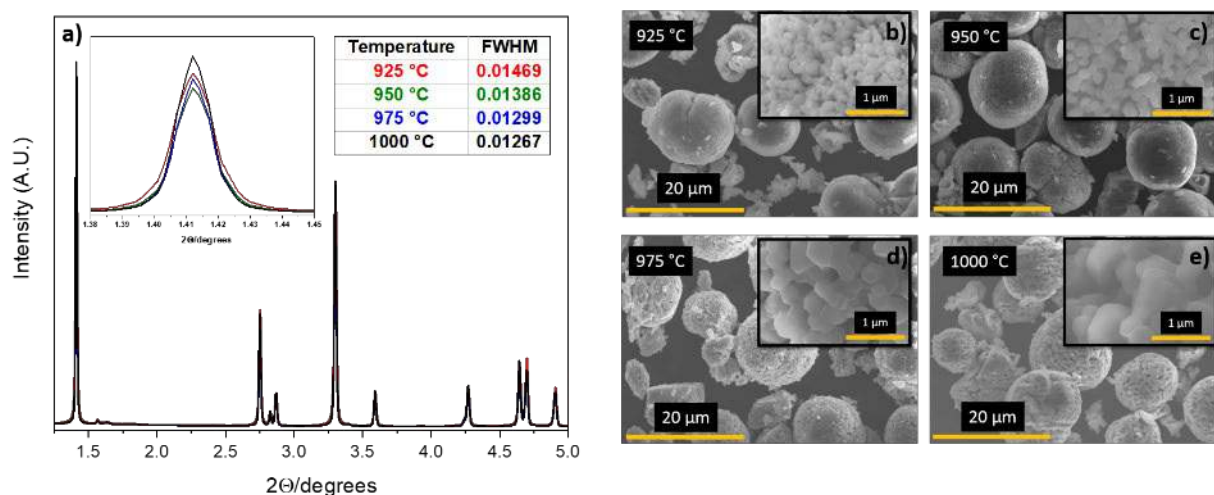


Figure II.2.D.1 (a) High resolution X-ray data on four LLS samples fired at different temperatures as noted in the figure. The inset shows a magnified view of the (003) peaks and the table shows how the full width at half maximum changes as a function of the firing temperature. SEM images showing the morphology of the primary (inset) and secondary particles of the samples fired at: (b) 925 °C (c) 950 °C (d) 975 °C and (e) 1000 °C

A baseline transition metal (TM) carbonate precursor ($\text{Mn}_{0.53}\text{Ni}_{0.28}\text{Co}_{0.19}\text{CO}_3$) was prepared using co-precipitation via a 4L CSTR. Good morphology and the targeted precursor composition were obtained. The TM carbonate was then fired with lithium carbonate at 900 °C targeting a nominal composition of $\sim \text{Li}_{1.18}\text{Mn}_{0.54}\text{Co}_{0.18}\text{Ni}_{0.28}\text{O}_x$ ($\text{Li}/\text{TM} = 1.18$), having an integrated ($\sim 6\%$) spinel component. The fired sample was then split into four batches and re-fired at different temperatures: 925 °C, 950 °C, 975 °C, and 1000 °C. ICP analysis was carried out on the four re-fired samples revealing similar composition (Li:TM ratios) for all samples: $\text{Li}_{1.18}\text{Mn}_{0.53}\text{Co}_{0.19}\text{Ni}_{0.28}\text{O}_x$ (925 °C), $\text{Li}_{1.18}\text{Mn}_{0.54}\text{Co}_{0.19}\text{Ni}_{0.27}\text{O}_x$ (950 °C), $\text{Li}_{1.17}\text{Mn}_{0.53}\text{Co}_{0.19}\text{Ni}_{0.28}\text{O}_x$ (975 °C), and $\text{Li}_{1.18}\text{Mn}_{0.53}\text{Co}_{0.19}\text{Ni}_{0.28}\text{O}_x$ (1000 °C) – referred to herein by the respective firing temperatures.

High resolution X-ray data were collected on the four samples and are shown in Figure II.2.D.1(a). All peaks could be matched to the expected R-3m and C2/m space groups. A visual inspection of the (003) peak, shown as an inset of Figure II.2.D.1(a), discloses a difference in the peak width for each of the samples. A more detailed analysis of the data using the Scherrer equation confirmed a systematic decrease in the full width at half maximum (FWHM) as the firing temperature increased. Changes to the FWHM can be caused by various

changes to the material including crystallite size, stacking fault density, stresses between grains, and others. Scanning electron microscopy (SEM) images were collected on the four samples and are shown in Figure II.2.D.1(b)-(e). As seen from the figures, the secondary particle size was not affected by the change in firing temperature. On the other hand, the primary particle size did increase as the firing temperature was increased (see insets) and is likely contributing to the differences in FWHM for the samples. The effective surface area of the samples was found to decrease as the firing temperature increased: 3.8 m²/g (925°C), 2.8 m²/g (950°C), 1.3 m²/g (975°C), and 1.0 m²/g (1000°C).

Although the chemical analysis confirmed that all samples were of similar composition, small changes in firing temperature could affect the crystallography (e.g., phase fractions or Li/Ni exchange), and in turn the electrochemistry, between the samples. Therefore, ex situ neutron powder diffraction (NPD) data were collected on the high-resolution powder diffractometer Echidna at ANSTO. Refinements were carried out and the estimates for percent C2/m phase and Li/Ni exchange with respect to firing temperature are shown in Figure II.2.D.2(a) and (b), respectively. The amount of C2/m phase nominally decreased as the firing temperature increased, though the differences were minimal and within the deviation. Similarly, the amount of Li/Ni exchange in each sample generally decreased as the firing temperature increased; nonetheless, the spread between the samples with the highest and lowest amounts of Li/Ni exchange was ~ 1%.

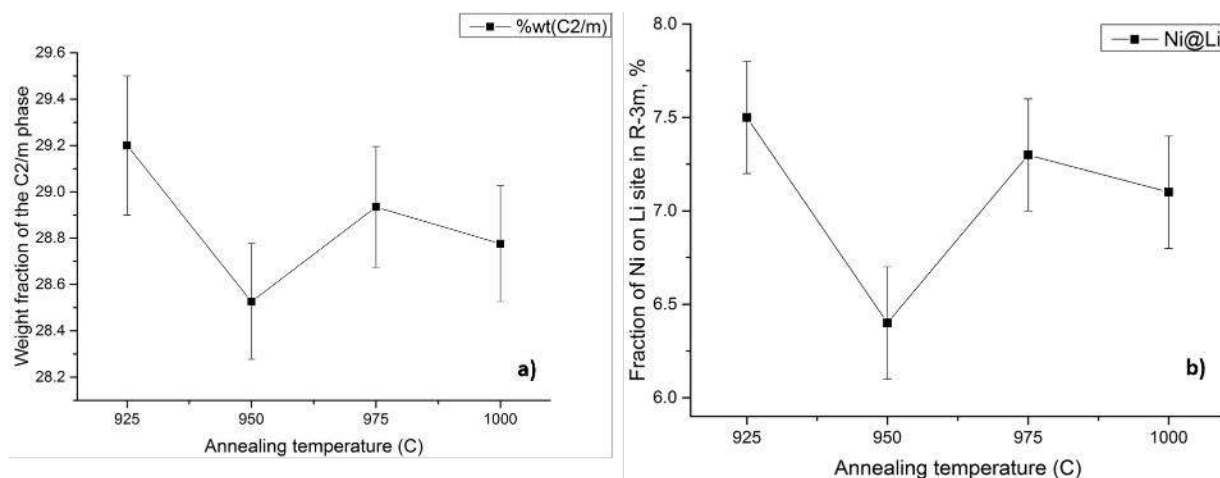


Figure II.2.D.2 Refinements neutron powder diffraction data (ANSTO) showing (a) the weight fraction of C2/m and (b) % Li/Ni exchange as a function of secondary firing temperatures

Electrochemical cycling of the samples was carried out in coin-cells using Li-metal anodes. All cells underwent an activation cycle between 4.6 – 2.5 V followed by continuous cycling between 4.5 – 2.5 V. All cycling was carried out with a current of 20 mA/g at 30°C. The capacity and coulombic efficiency for select cycles is shown in Figure II.2.D.3(a). The missing cycles in Figure II.2.D.3(a) were used to collect other information that will not be reported here. The first cycle charge capacities for the samples were very similar: 262 mAh/g (925°C), 259 mAh/g (950°C), 260 mAh/g (975°C), and 258 mAh/g (1000°C). The discharge capacities systematically decreased as the firing temperature of the cathode material increased: 230 mAh/g (925°C), 225 mAh/g (950°C), 217 mAh/g (975°C), 210 mAh/g (1000°C). As such, a decrease in first-cycle coulombic efficiency was observed as the firing temperature increased. Except for a small difference at the beginning of the first-cycle charge (Figure II.2.D.3(b)), the voltage curves for all cells overlap with each other. Similarly, the first-cycle discharge curves overlap until the voltage drops below 3.5 V, whereupon the amount of additional capacity delivered below 3.5 V increased as the firing temperature of the oxide decreased. During the subsequent cycles between 4.5 – 2.5 V, the oxides prepared with lower firing temperatures delivered higher capacities, as shown in Figure II.2.D.3(a). However, unlike the first-cycle voltage curves, there are observable differences in the 10th-cycle charging profiles of the cells, Figure II.2.D.3(c).

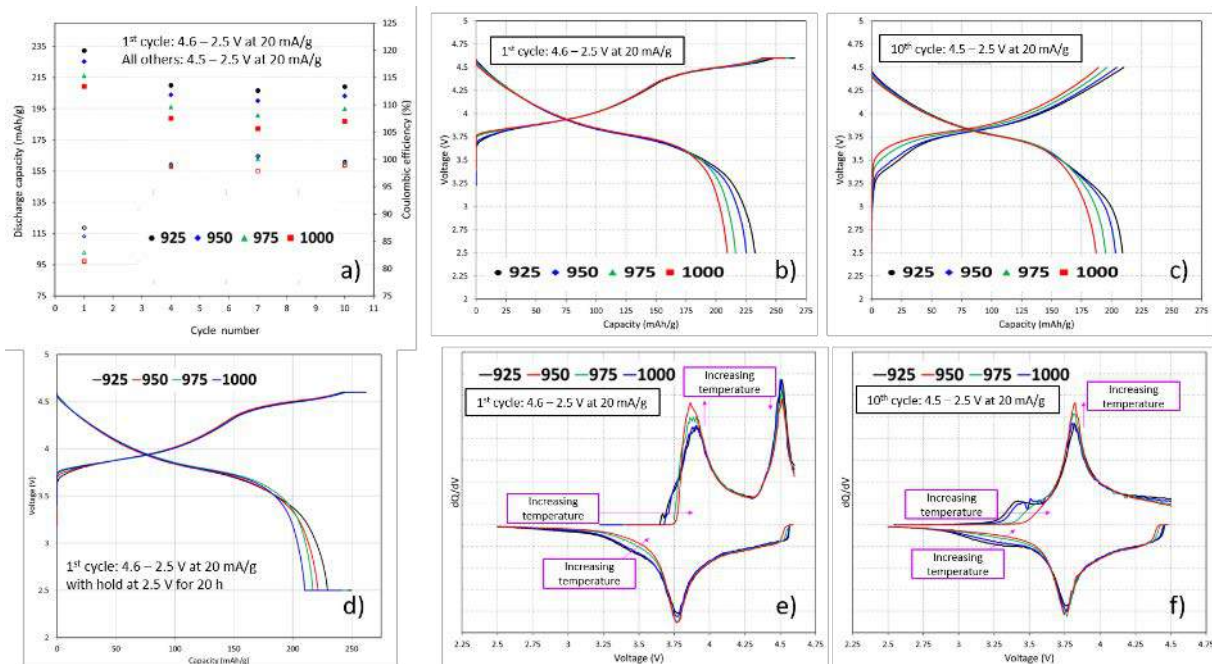


Figure II.2.D.3 Electrochemical performance of samples fired at different temperatures: 925°C, 950°C, 975°C, and 1000°C. The current for all cycles was 20 mA/g. The first cycle activation was between 4.6 – 2.5 V. All other cycles were between 4.5 – 2.5 V. (a) Capacity (filled symbols) and coulombic efficiency (open symbols) for the 1st, 4th, 7th, and 10th cycles. The charge/discharge curves for the (b) 1st cycle and (c) 10th cycle. (d) 1st cycle charge/discharge curve between 4.6 – 2.5 V at 20 mA/g with a 20 hour voltage hold at 2.5 V. dQ/dV of the (e) 1st cycle and (f) 10th cycle

The various samples were also tested under a modified first-cycle activation between 4.6 – 2.5 V, which included a 20 hour hold at 2.5 V at the end of discharge, as shown in Figure II.2.D.3(d). The amount of capacity that could be recovered due to the low voltage hold increased as the firing temperature of the sample increased: 20 mAh/g (925°C), 24 mAh/g (950°C), 29 mAh/g (975°C), 32 mAh/g (925°C). This trend is, perhaps, related to worsening kinetics with higher temperature annealing and larger primary particle sizes.

Additionally, the thermal properties of the cathode-electrodes were investigated. Each electrode sample underwent an activation cycle between 4.6 – 2.0 V followed by 3 formation cycles between 4.5 – 2.5 V, all at a C/10 rate. All cells were then taken to an equivalent state of charge ($\text{Li}_{0.3}\text{MO}_2$), disassembled in an argon-filled glove box and washed with EMC solvent to remove residual electrolyte. The electrodes were then dried and loaded into a DSC capsule with electrolyte (1.2M LiPF_6 , EC:EMC 3:7 wt.) with a ratio of 1 μL of electrolyte per 1 mg of cathode powder. The capsules were then sealed before being removed from the glove box and loaded into the DSC instrument (Perkin Elmer DSC 6000). DSC measurements were recorded between 30 – 400°C using a ramp rate of 10°C/min. Figure II.2.D.4 shows the results.

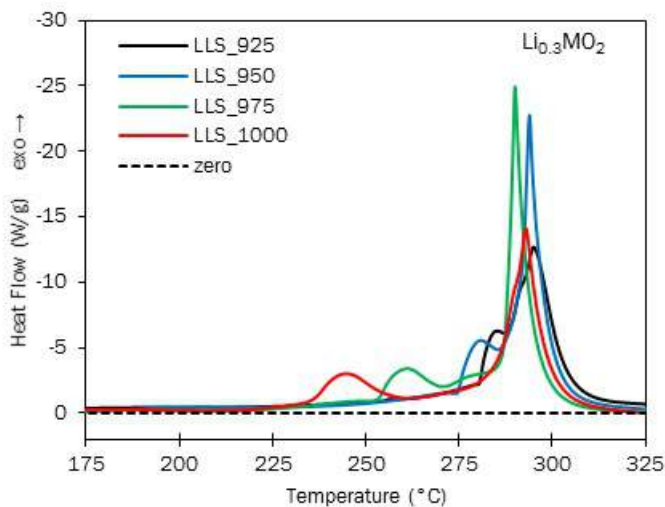


Figure II.2.D.4 Representative DSC data (baseline-subtracted, mass-normalized) from each charged cathode sample, all charged to the same calculated lithium content after formation cycles.

All samples exhibit a consistent, major exothermic peak at $\sim 295^{\circ}\text{C}$. However, each sample exhibits a ‘pre-peak’ that varies in area and onset temperature. Interestingly, samples prepared with higher annealing temperature (with larger primary particles, lower surface area) exhibit the lowest pre-peak onset temperature and the largest pre-peak areas. Samples annealed at lower temperature (smaller primary particles, higher surface area) exhibit the highest pre-peak onset temperature and lowest pre-peak areas. Studies are ongoing to better understand the thermal data and electrochemical behavior of LLS cathodes as a function of composition and synthesis.

Novel, Zero-Strain, Spinel Oxides: As shown above, and elsewhere, the incorporation of a spinel-type component in Li-/Mn-rich cathodes can have a profound effect on their electrochemical properties. Controlling the composition, properties, and integration of such components is non-trivial and systematic studies on end-member compounds have been undertaken to discover promising candidates. Previous reports have shown that the phase purity and electrochemical performance (cycle stability and rate performance) of lithiated spinel LiCoO_2 (S-LCO) can be greatly improved by partial Co substitution with cations such as Ni, Mg, Ga, and Al. Among them, Al-substituted lithiated spinel $\text{LiCo}_{1-x}\text{Al}_x\text{O}_2$ (S-LCO-Al) showed the best electrochemical performance. Herein, the structural change of S-LCO-Al is monitored by operando synchrotron XRD and surprisingly small lattice volume changes during the charge and discharge processes are confirmed. Operando synchrotron XRD data obtained during the initial charge and discharge of a Li/LT- $\text{LiCo}_{0.85}\text{Al}_{0.15}\text{O}_2$ cell are shown in Figure II.2.D.5(a). The synchrotron XRD data do not provide any significant evidence of a peak shift during the initial charge–discharge process even at a high angle, Figure II.2.D.5(b). The change to the unit cell volume is practically zero, $\Delta\text{Vol} \leq 0.02\%$, Figure II.2.D.5(c). This is quite surprising as even ‘zero-strain’ $\text{Li}_4\text{Ti}_5\text{O}_{12}$ shows small changes to the cubic unit cell parameter ($\Delta\text{Vol} \sim 0.2\%$) while the topotactic two-phase reaction process, which occurs when the $\text{Li}_4\text{Ti}_5\text{O}_{12}$ spinel structure is lithiated to form rock salt $\text{Li}_7\text{Ti}_5\text{O}_{12}$, is visible in the splitting of the XRD peaks at a high angle. Although the positions of the peaks remain unchanged in Figure II.2.D.5(a), a reversible change in the relative peak intensities is evident. For example, the intensities of the (311) and (511) peaks increased during charge while those of the (400) and (440) peaks decreased, which correlate with the movement of Li ions in the interstitial space. The corresponding Rietveld refinements of the electrode at various states of charge indicate that Li extraction occurs initially from the 16c octahedral sites of the structure and that the 8a tetrahedral sites become gradually and increasingly occupied by Li as the charge process continues, Figure II.2.D.5(d). At the end of the initial charge, at a composition close to the ideal spinel stoichiometry, $\text{Li}_{0.54}\text{Co}_{0.85}\text{Al}_{0.15}\text{O}_2$, almost all the remaining Li ions reside on the 8a tetrahedral sites of the structure.

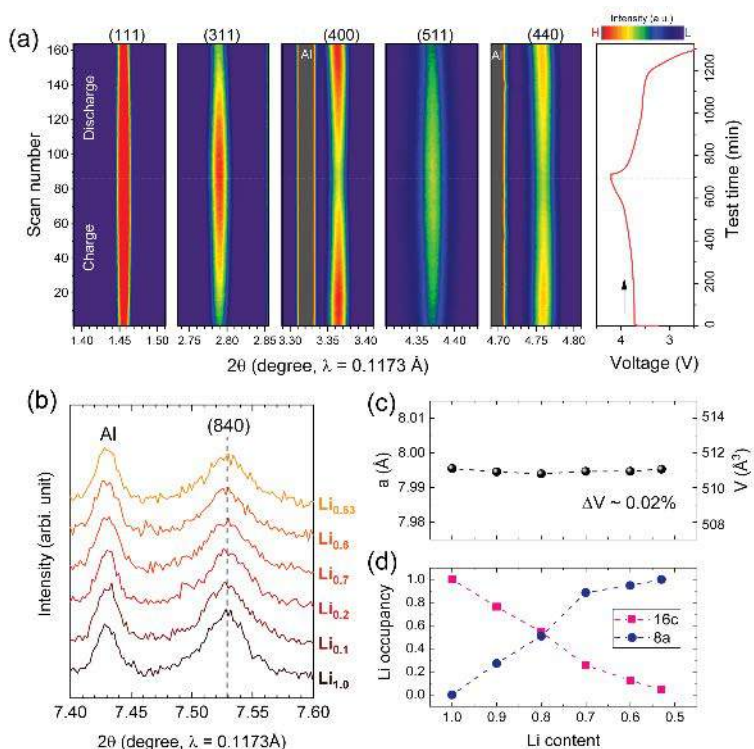


Figure II.2.D.5 Operando synchrotron XRD analysis of a Li/LT- $\text{LiCo}_{0.85}\text{Al}_{0.15}\text{O}_2$ cell cycled between 4.2 – 3.5 V vs. Li at 15 mA/g: (a) changes to strong peaks (selected regions) and corresponding initial charge/discharge profile; variation of the (b) (840) peak, (c) unit cell volumes, and (d) Li occupancies as function of Li content.

Figure II.2.D.6 and Table II.2.D.1 summarize the electrochemical properties of S-LCO-Al electrodes. The theoretical capacity of the electrode decreases with increasing Al because Al is electrochemically inactive. Interestingly, 0.5 Li could be extracted from unsubstituted S-LCO electrodes as well as S-LCO-Al that contained 10% and 20% Al. Therefore, because Al is lighter than Co, the initial charge capacity increases from 133.8 mAh/g for Al = 0 to 147.5 mAh/g for Al = 0.2, reflecting an increase in the utilization of the $\text{Co}^{3+/4+}$ redox couple from 49% to 63%. While discharge capacities of ~ 100 mAh/g were delivered by S-LCO-Al electrodes with 10–30% Al substitution, there was a significant drop in capacity and $\text{Co}^{3+/4+}$ utilization for larger Al content ($x \geq 0.4$), which is not surprising given the higher concentration of the electrochemically inactive Al ions and the formation of Al-segregated domains as revealed by magic angle spinning, nuclear magnetic resonance (MAS NMR) data (not shown here).

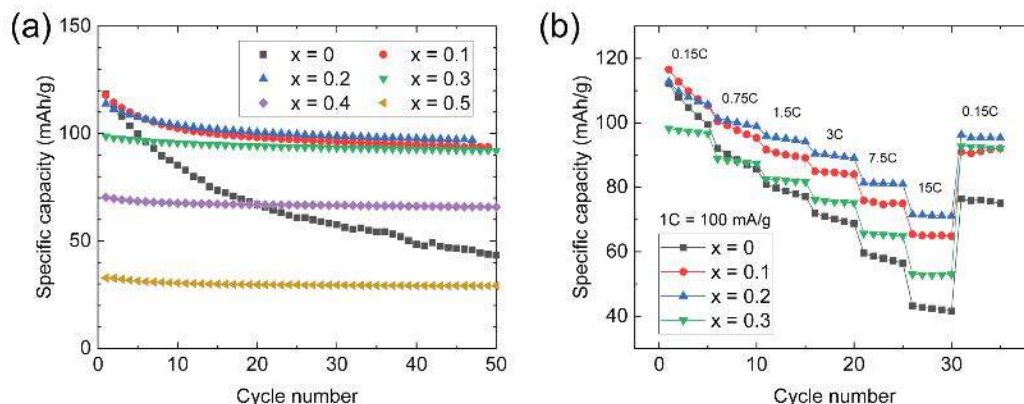


Figure II.2.D.6 (a) Capacity vs. cycle number for lithium cells with $\text{LT-LiCo}_{1-x}\text{Al}_x\text{O}_2$ electrodes ($0 \leq x \leq 0.5$), (b) rate performance data ($0 \leq x \leq 0.3$).

Table II.2.D.1 Theoretical and Experimental Properties of $\text{LT-LiCo}_{1-x}\text{Al}_x\text{O}_2$ Electrodes for $0 \leq x \leq 0.5$

Sample	Theor. cap. $\text{Co}^{3+/4+}$ redox [mAh/g]	1 st charge capacity [mAh/g]	Extracted Li [mol]	Co redox utilization [%]	1 st discharge capacity [mAh/g]	Coulombic efficiency [%]	Avg. voltage [V vs. Li]
LT-LiCoO_2	273.8	133.8	0.49	49	110.4	83	3.60
$\text{LT-LiCo}_{0.9}\text{Al}_{0.1}\text{O}_2$	254.8	141.0	0.50	55	117.9	84	3.68
$\text{LT-LiCo}_{0.8}\text{Al}_{0.2}\text{O}_2$	234.4	147.5	0.50	63	113.9	77	3.73
$\text{LT-LiCo}_{0.7}\text{Al}_{0.3}\text{O}_2$	212.5	128.8	0.42	61	98.8	77	3.76
$\text{LT-LiCo}_{0.6}\text{Al}_{0.4}\text{O}_2$	189.0	95.3	0.30	50	70.3	74	3.72
$\text{LT-LiCo}_{0.5}\text{Al}_{0.5}\text{O}_2$	163.6	66.9	0.20	41	32.8	49	3.72

It is proposed that the excellent cycling stability and rate capability of single-phase, zero-strain behavior, S-LCO-Al materials, can be attributed to an atomic arrangement in which Al cations reside predominantly on the octahedral 16d sites of the lithiated spinel (rock salt) structure with a minor fraction on the octahedral 16c sites, i.e., $[\text{Li}_{2-y}\text{Al}_y]^{16c}[\text{Co}_{2-x}\text{Al}_{x-y}\text{Li}_y]^{16d}\text{O}_4$ in which $x > y$. It is argued that any Al on the 16c sites would block the occupation of nearest-neighbor tetrahedral 8a sites by Li, thereby preventing the coordinated migration of Li from 16c sites to 8a sites and the ideal two-phase rock salt-to-spinel transition – at least during the early stages

of charge. During the latter stages of charge, when the structure becomes highly lithium-deficient, preferential occupancy of the 8a sites and localized regions of spinel within a delithiated defect rock salt matrix can be expected. It is therefore reasoned that the reversible single-phase electrochemical signature of Li/S-LCO-Al cells, particularly at the higher values of Al content, can be attributed predominantly to Li extraction from a slightly disordered lithiated-spinel (rock salt) framework structure. In the absence of Al migration from octahedral (16c) to tetrahedral (8a) sites, the formation of distinct macroscopic phase boundaries between ideal spinel and lithiated-spinel regions in $[\text{Li}_{2-y}\text{Al}_y]^{16c}[\text{Co}_{2-x}\text{Al}_{x-y}\text{Li}_y]^{16d}\text{O}_4$ electrodes can be expected to be suppressed during electrochemical cycling.

Conclusions

Lithium- and manganese-rich, layered-layered-spinel (LLS) electrodes have shown continuous improvement and can now compete with chemistries such as ~NMC-532/622. Detailed studies of practical synthesis methods, which are so far not presented in the literature, are being carried out in order to understand the critical parameters associated with the control of composition, morphology, density, thermal, and electrochemical properties of Mn-rich, LLS electrodes. Furthermore, novel, zero-strain spinel-based materials have been discovered and reported for the first time. These studies highlight the complex role of how composition and cation ordering can drastically alter the properties of lithium-metal-oxide cathodes. The results herein add to the building library of data that support a strategy of continued development of cost-effective, manganese-rich electrodes.

Key Publications

1. J. R. Croy, A. Gutierrez, M. He, B. T. Yonemoto, E. Lee, and M. M. Thackeray, "Development of Manganese-Rich Cathodes as Alternatives to Nickel-Rich NMCs," *Journal of Power Sources*, 2019, 434, 226706
2. Eungje Lee, Bob Jin Kwon, Fulya Dogan, Yang Ren, Jason R. Croy, and Michael M. Thackeray, "Lithiated Spinel $\text{LiCo}_{1-x}\text{Al}_x\text{O}_2$ as a Stable Zero-Strain Cathode," *ACS Applied Energy Materials* **2**, 6170-6175 (2019).
3. Eungje Lee, Jason R. Croy, and Michael M. Thackeray, "Exploring Cobalt-Based Lithiated Spinel Cathodes," International Battery Association Meeting, San Diego, CA, March 3-8, 2019.
4. Arturo Gutierrez, *Enabling High-Energy Lithium- and Manganese-Rich Cathodes*, AlChe Midwest Regional Conference, Chicago, IL, 18 March 2019. **Invited**
5. Arturo Gutierrez, *The Evolution of Energy Storage Demands Leading to Li-ion Use in EV Applications*, University of Illinois Chicago, Chicago, IL, 05 November 2019. **Invited**

Acknowledgements

Eungje Lee, Arturo Gutierrez, Jiajun Chen, Jinhyup Han, Joel Kirner, Yang Ren, Roy Benedek, Maxim Avdeev, Michael M. Thackeray. Support from the U. S. Department of Energy (DOE), Vehicle Technologies Office, specifically from Peter Faguy and David Howell is gratefully acknowledged.

II.2.E *In situ* Spectroscopy of Solvothermal Synthesis of Next-Generation Cathode Materials (BNL)

Feng Wang, Principal Investigator

Brookhaven National Laboratory
Sustainable Energy Technologies Department
Upton, NY 11973
E-mail: fwang@bnl.gov

Jianming Bai, Principal Investigator

Brookhaven National Laboratory
National Synchrotron Light Source II
Upton, NY 11973
E-mail: jmbai@bnl.gov

Peter Faguy, DOE Technology Development Manager

U.S. Department of Energy
E-mail: Peter.Faguy@EE.Doe.Gov

Start Date: October 1, 2018
Project Funding: \$1,500,000

End Date: September 30, 2021
DOE share: \$1,500,000

Non-DOE share: \$0

Project Introduction

Electrode performance is largely determined by the structural properties of active materials, and so can be advanced by synthesis of phase-pure materials, and control of their stoichiometry, morphology, surface/interfaces. However, synthesizing materials with desired structure and properties has proven difficult due to the complexity associated with chemical reaction and involvement of metastable intermediates. In this project, we develop *in situ* capabilities/techniques using *state-of-the-art* synchrotron facilities for real-time studies of synthesis to capture intermediates and their structural evolution, elucidating how temperature, pressure, time, and the precursors affect the kinetic reaction pathways and, consequently, the structural properties of the final products. This capability enables probing of synthesis reactions at scales varying from the bulk phases to a single particle, as well as interfaces. By coupling with electrochemical characterization of the synthesized materials, such studies elucidate how structure, composition, and synthesis affect electrochemical performance and therefore provide a basis for rational synthesis of novel cathode materials with desired structure, stoichiometry and morphology.

Objectives

The goal is to develop novel high-capacity cathodes through synthetic control of the phase, stoichiometry and morphology.

Approach

One unique approach taken in this project is to develop new battery materials through *in situ* probing and kinetic control of synthesis reaction using the world-leading facilities at Brookhaven and other national laboratories. More specifically, synchrotron x-ray, neutron-based *in situ* techniques are developed and applied to studies of synthesis reaction and kinetic pathways during preparation of high-capacity cathode materials. Insights from such studies will be used for design and synthesis of novel cathode materials with desired structure and properties.

Results

Study of the role of Co/Mn substitution in tuning cationic ordering in high-Ni cathodes In this study, a multimodal approach was employed for determination of the kinetic synthesis process, and the related cationic

ordering in preparing high-Ni $\text{LiNi}_{0.7}\text{Mn}_x\text{Co}_{0.3-x}\text{O}_2$ ($0 \leq x \leq 0.3$), via a combination of in situ synchrotron X-ray diffraction (XRD), absorption spectroscopy (XAS), neutron powder diffraction (NPD) and nuclear magnetic resonance (NMR). Quantitative analysis enables identification of the impact of Co and Mn on the kinetics and thermodynamics of cationic ordering for direct comparison to first principles calculations. Illustration of the setup and some of the main results from time-resolved XRD are presented in Figure II.2.E.1, showing the similar ordering process in the 3 different systems, $\text{LiNi}_{0.7}\text{Mn}_{0.1}\text{Co}_{0.2}\text{O}_2$ (NMC712), $\text{LiNi}_{0.7}\text{Mn}_{0.2}\text{Co}_{0.1}\text{O}_2$ (NMC721), and $\text{LiNi}_{0.7}\text{Mn}_{0.3}\text{O}_2$ (NM73), from the initial improvement to deterioration of Li/Ni ordering as they were subjected to heat treatment at 850°C . Quantitative structural analysis via Rietveld refinement was also made, with results provided in Figure II.2.E.1(E-G). At the beginning of the heating, both lattice parameters a and occupancy of Ni^{2+} at 3b sites showed an exponential decay, indicating the fast Li/Ni ordering. After holding for a certain time ($\sim 1\text{h}$ or longer), they reached minimum values and increased linearly thereafter, indicating Li/Ni disordering caused by Li/O loss. Li/Ni ordering and disordering should occur concomitantly throughout the calcination, with ordering being dominant at the beginning, and then disordering becoming dominant after long holding time (as a result of Li/O loss). As shown in Figure II.2.E.1 G or H, it took longer time for the occupancy of Ni(3b) to reach the minimum with the increase of Mn content, which indicates that Mn substitution slowed down the kinetics of Li/Ni ordering. In short, Co facilitates Li/Ni ordering; while Mn aggravates Li/Ni mixing and slows down the ordering kinetics.

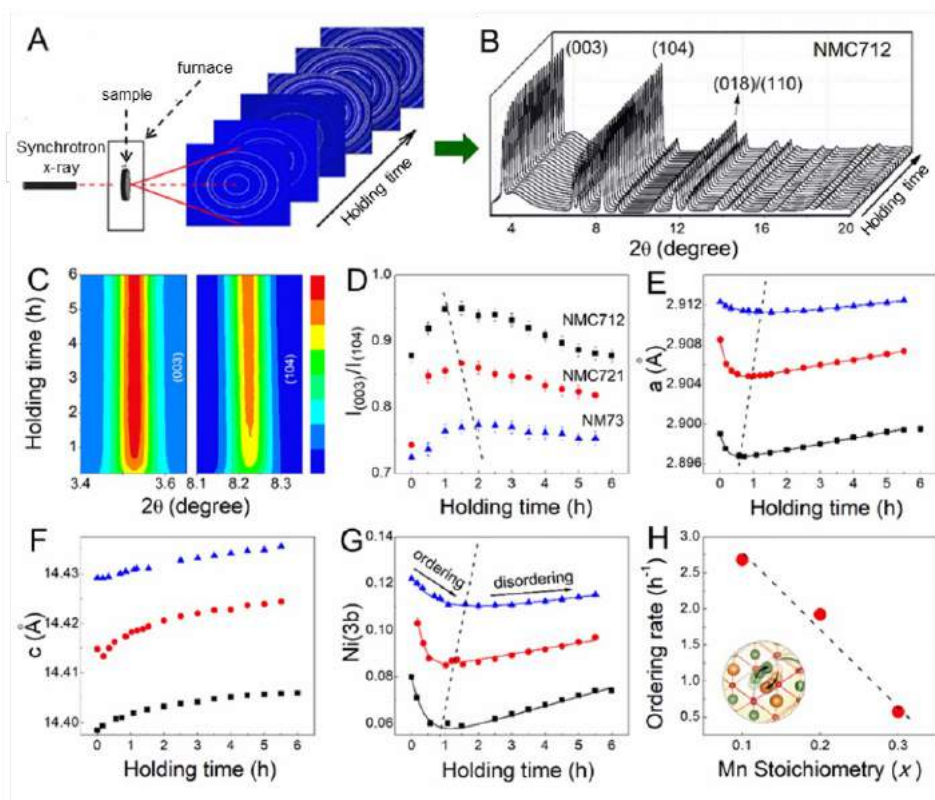


Figure II.2.E.1 In situ tracking of cationic ordering/disordering in $\text{LiNi}_{0.7}\text{Mn}_x\text{Co}_{0.3-x}\text{O}_2$ ($0 \leq x \leq 0.3$) during calcination at 850°C . (A) Schematic illustration of the experimental setup for in situ synchrotron XRD measurements. (B) Time-resolved XRD patterns recorded at 850°C during the synthesis of $\text{LiNi}_{0.7}\text{Mn}_{0.1}\text{Co}_{0.2}\text{O}_2$ (NMC712), with wavelength $\lambda = 0.2953 \text{ \AA}$. (C) Intensity maps of characteristic peaks (003), (104) in Figure 1B. (D–G) Evolution of the $I(003)/I(104)$ ratio, lattice parameter a , c , and occupancy of Ni at 3b sites, respectively, as a function of holding time for NMC712 (black square), NMC721 (red circle), and NM73 (blue triangle). The solid lines in (E, G) represent the fitting of lattice parameter a and the anti-site occupancy of Ni at 3b sites, $\text{Ni}(3b)$, as a function of time, by using an exponential-linear function $y = A\exp(-kt) + bt + y_0$; the error bars represent standard deviations derived from the Rietveld refinements. (H) Dependence of the kinetics of cationic ordering on Mn stoichiometry.

The site occupancy and local environment of lithium, transition metal elements (Ni, Mn, and Co) were further studied by combined XAS, NMR and NPD, providing direct evidence for the presence of Li both in TM (3a) and (3b) sites, and with the increase of Mn substitution, more Ni^{2+} was introduced, with most of them located in the TM(3a) sites. Co substitution led to the decrease in lattice parameters and suppression of Li/Ni mixing and further replacement of Co by Mn caused the gradual increase of both lattice parameters and Li/Ni mixing. In the whole series, NC73 shows the largest *Li-slab* distance, indicating the best ionic conductivity and rate performance among the compositions. Such composition-dependent cationic ordering was explained by *ab initio* calculations (Figure II.2.E.2), namely, the presence of Co facilitates Li/Ni ordering process by reducing the strength of magnetic frustration, strengthening intra-plane super-exchange (SE) interactions. Further substitution of Mn increases the strength of magnetic frustration and strengthens the inter-plane SE interactions, thereby aggravating Li/Ni mixing. This study demonstrated the crucial role of magnetic interactions in determining the local structural ordering of TM oxides, hence offering new insights into the synthetic design of high-Ni cathodes and, broadly, TM-based materials for various applications.

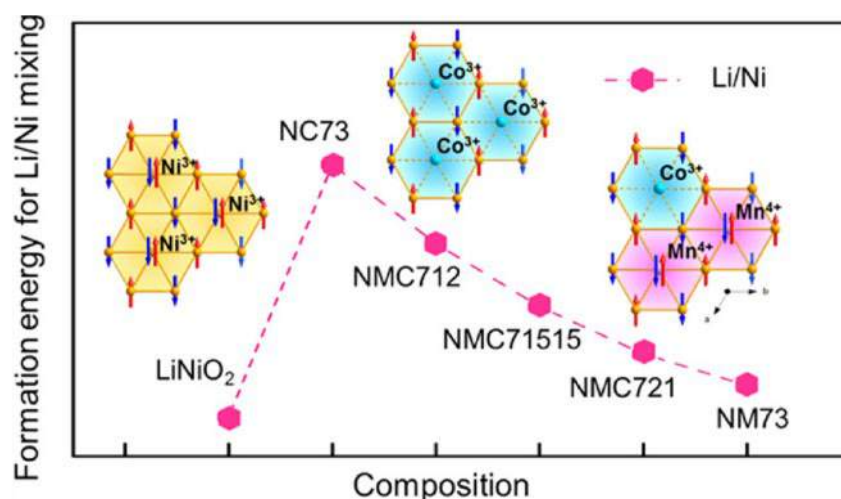


Figure II.2.E.2 Li/Ni mixing as a function of composition in the series of $\text{LiNi}_{0.7}\text{Mn}_x\text{Co}_{0.3-x}\text{O}_2$ ($0 \leq x \leq 0.3$).

Optimization of cationic ordering and surface properties during synthesis of high-Ni cathodes In this work, we have systematically explored the optimization of synthesis conditions (i.e., sintering temperature and sintering time) for $\text{LiNi}_{0.7}\text{Mn}_{0.15}\text{Co}_{0.15}\text{O}_2$ (NMC71515). Using synchrotron XRD, both structural ordering and disordering processes were quantitatively studied, revealing strong correlations between Li/Ni ordering and sintering conditions (Figure II.2.E.3). By reaching an equilibrium point where the two processes had the same reaction rate, a structure with the highest degree of structural ordering was obtained. Afterwards, the disordering reaction started to take over. Additional characterizations using thermogravimetric analysis (TGA) and X-ray photoelectron spectroscopy (XPS) further revealed an intrinsic correlation between the Li/Ni ordering and the surface reconstruction, which involves Li_2CO_3 decomposition and Li loss from the particle surface. Through tuning the sintering conditions in the range (775 ~ 850 °C), highly ordered NMC71515 cathode materials without Li-deficient phases, were synthesized. To obtain the correlation between electrochemical performance and sintering conditions, galvanostatic cycling experiments were also carried out on the NMC71515 prepared at different temperatures. Some of the main results are provided in Figure II.2.E.3 C, D, showing that high capacity (~180 mAh/g) was achieved in most of the samples at low rates (except the one synthesized at too low temperature (750 °C)). However, they showed big difference in the rate capability, which, according to the surface characterization, is attributed to the surface reconstruction. The sample synthesized at 775 °C exhibited the highest rate capability, due to the high structural ordering both in the bulk and at surface. Results from this work provides insights into synthetic design of high-Ni cathode materials.

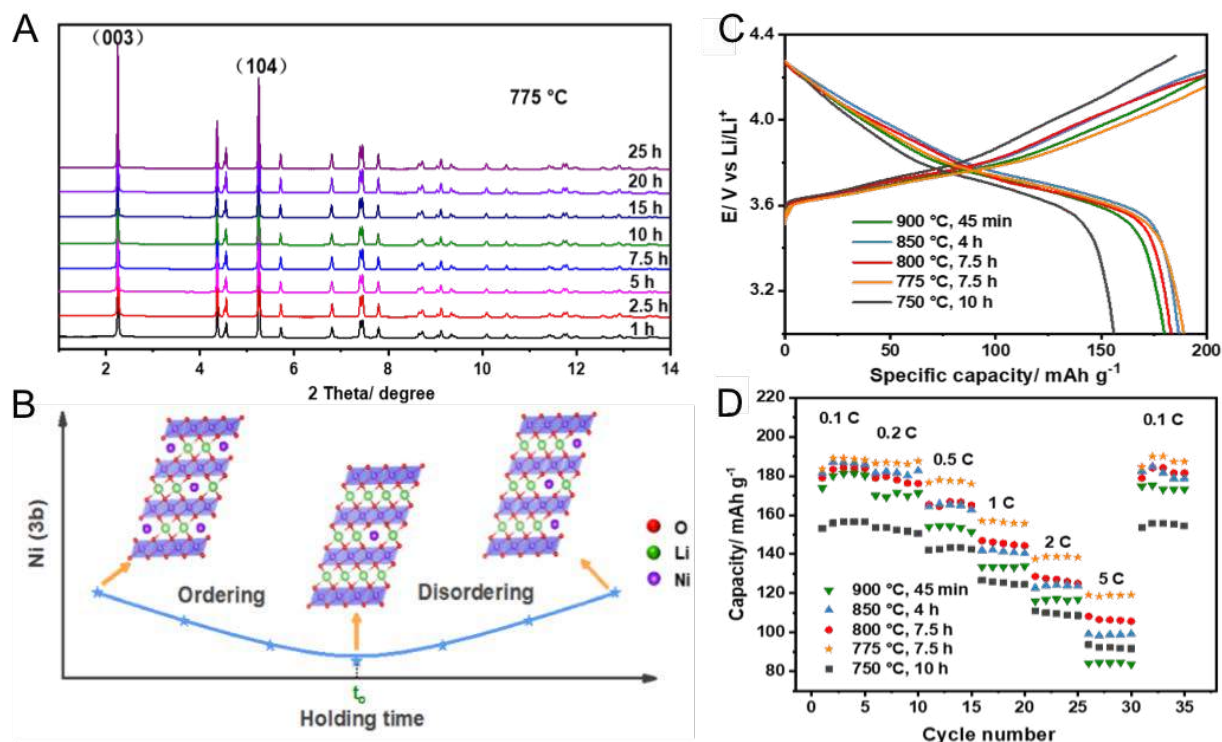


Figure II.2.E.3 Dependence of cationic ordering and electrochemical performance in NMC71515 on sintering temperature and holding time. (A) Synchrotron XRD patterns from NMC71515 sintered at 775 °C (data were also taken from samples sintered at other different temperatures and not shown here). (B) Schematic illustration of cationic ordering and disordering processes with holding time. (C, D) Galvanostatic charge/discharge profiles and rate performances of NMC 71515, respectively, sintered for optimized time at different temperatures.

Rational synthesis of surface-conditioned high-Ni cathodes Although the surface reconstruction has been identified to be a critical issue for high-Ni NMC layered oxide cathodes, it is still unclear how it occurs during synthesis as the reconstruction was observed ex situ, on the samples cooled down to room temperature. Therefore, in situ synchrotron X-ray diffraction, coupled with surface analysis, is applied to studies of the synthesis process, using NMC71515 as a representative of high-Ni layered oxides, to investigate how synthesis conditions, particularly the cooling rate, affect the structural evolution, not only in the bulk, but also at the surface. As illustrated by the scheme in Figure II.2.E.4, the insulating Li_2CO_3 and NiO-type rock salt, once formed at the surface, would cause impedance to the Li extraction/insertion. Therefore, systemic structural/electrochemical characterization was made to NMC71515 obtained through slow cooling and quenching, using multiple techniques. The whole synthesis process was tracked in situ using temperature-resolved synchrotron XRD technique, to capture all of the crystalline species, not only the main layered phases, but those formed at the surface, such as Li_2CO_3 .

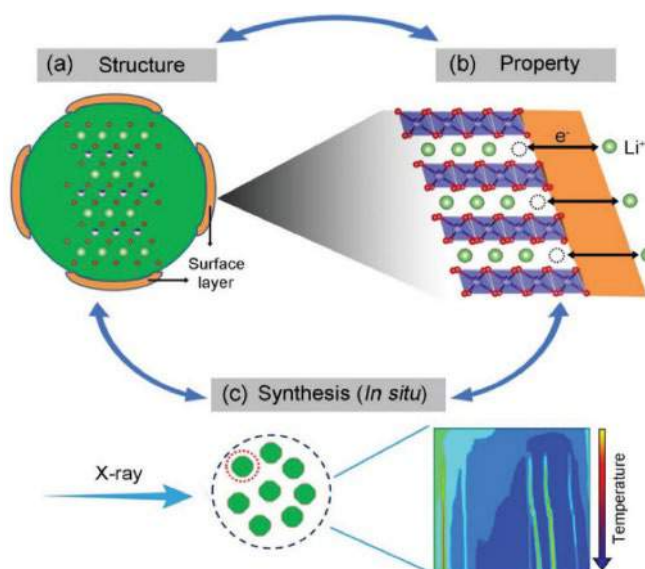


Figure II.2.E.4 Schematic illustration of the approach with a “closed” loop for rational design of synthesis in making high-Ni layered oxides, specifically, through studying the surface reconstruction and its impact to electrochemical properties, and its formation process (via in situ X-ray study). a,b) Formation of a surface layer, and the potential impact on the electrochemical performance due to impedance to the Li extraction/insertion during charging/discharging. c) In situ X-ray studies of the synthesis process using temperature-resolved synchrotron X-ray diffraction technique that has high enough detection efficiency to track the formation of Li_2CO_3 (despite its weak scattering of X-ray; inset).

Results from surface sensitive X-ray/electron microscopy/spectroscopy and electrochemical impedance spectroscopy, indicated that the sample obtained by slow cooling has better cationic ordering in the bulk, but more serious surface reconstruction compared to the sample obtained by quenching. Through quenching, NMC71515 with improved rate capability was obtained. To investigate how the cooling rate affects the kinetics of cationic ordering and surface reconstruction, comparative in situ synchrotron XRD study was performed, with the main results provided in Figure II.2.E.5.

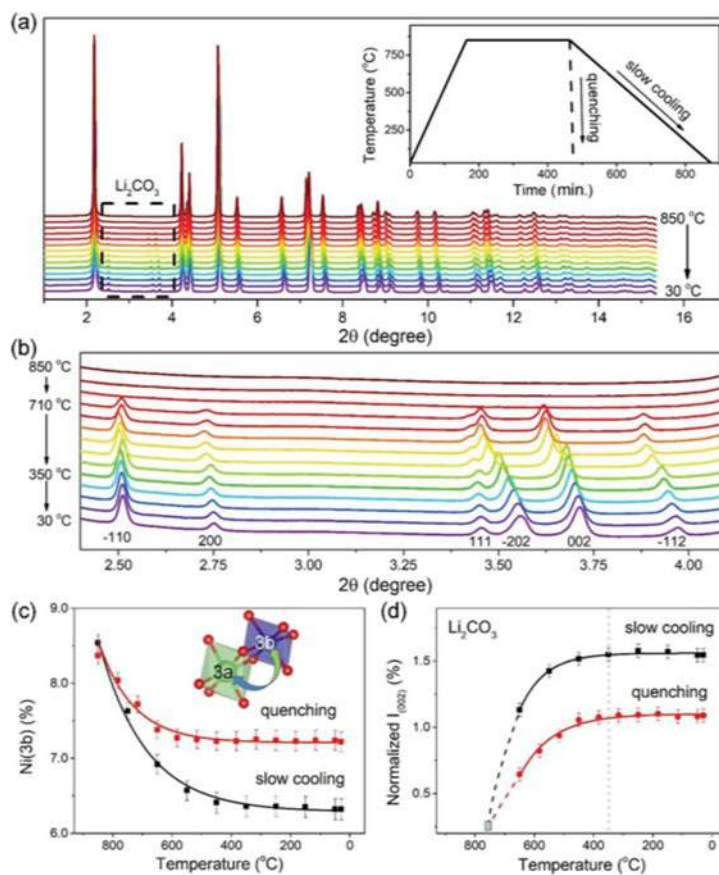


Figure II.2.E.5 In situ tracking of the structural evolution and formation of Li_2CO_3 in NMC71515 upon cooling during synthesis. a) Temperature-resolved in situ XRD patterns recorded during the slow cooling process. Inset: temperature profiles of in situ experiments during slow cooling and quenching (as labeled), using cooling rates of 2 and 200 °C min⁻¹, respectively. b) Zoom-in view of the diffraction patterns associated with Li_2CO_3 , as marked by the black dashed square in (a). c) The evolution of the percentage of Ni at 3b sites, $\text{Ni}(3b)$, as a function of temperature; Inset: schematic illustration of Li/Ni ordering process, showing inter-diffusion of Li/Ni ions between 3a sites (in the TM layers) and 3b sites (in the Li layers). d) The evolution of the integrated area of 002 peak associated with Li_2CO_3 (denoted as $I(002)$), and normalized by $I(104)$ of the layered oxides as a function of temperature. The dashed lines are extended from the fitting lines and crossed at the gray square, indicating the initial formation of Li_2CO_3 at around 750 °C. No obvious increase of the peak intensity at temperatures below 350 °C (as marked with a dotted line).

Results from this study revealed, for the 1st time, the cooling-induced surface reconstruction during synthesis of NMC71515, leading to buildup of Li_2CO_3 , formation of a Li-deficient layer and Ni reduction at the particle surface. Such surface reconstruction that occurs mainly at high temperatures (above 350 °C), is different than that during storage or electrochemical cycling. In addition, the kinetic reconstruction process is cooling rate dependent, and can be suppressed by quenching, to improve rate performance. Findings from this study, particularly the origin of surface reconstruction, and the demonstrated solutions to alleviate the issue, may inspire new strategies for design and synthesis of high-Ni layered oxide cathodes.

Conclusions

In FY19, in situ multimodal synchrotron x-ray techniques were developed and employed for studying the synthesis reaction and kinetic pathway in preparing Ni-rich NMC layered oxides. [ENREF 24](#) A combination of in situ, ex situ experimental and theoretical studies revealed the relationship between the kinetics, thermodynamics of cationic ordering and magnetic interactions (including intra-plane magnetic frustration and inter-plane super-exchange) in the $\text{LiNi}_{0.7}\text{Mn}_x\text{Co}_{0.3-x}\text{O}_2$ ($0 \leq x \leq 0.3$) system. These findings shed light on the

intrinsic roles of Mn/Co in tuning Li/Ni mixing through local magnetic interaction, and so may help to pave the way for synthetic design of high-performance layered NMC for batteries, and other TM-based materials.

In addition, investigation was made to the kinetic and thermodynamic aspects of cationic ordering during synthesis of NMC71515, showing that cationic ordering in the bulk is coupled to surface reconstruction during synthesis, which occur concomitantly and are both greatly affected by Li_2CO_3 decomposition and Li loss at the particle surface. Through tuning the sintering/cooling conditions, highly ordered NMC71515 with high capacity and excellent rate capability is synthesized. Following the efforts on in situ probing and kinetic control of cationic ordering and surface reconstruction in the bulk materials, this project will shift the focus onto synthetic control of local structural ordering and stoichiometry within individual particles, aiming at synthetic design of surface-stabilized high-Ni NMC layered oxides.

Key Publications

1. M-J. Zhang, X. Hu, M. Li, Y. Duan, L. Yang, C. Yin, M. Ge, X. Xiao, W-K. Lee, J. Y. P. Ko, K. Amine, Z. Chen, Y. Zhu, E. Dooryhee, J. Bai, F. Pan and F. Wang, “Cooling Induced Surface Reconstruction during Synthesis of High-Ni Layered Oxides” **Adv. Energy Mater.** 1901915 (2019; online: <https://doi.org/10.1002/aenm.201901915>)
2. J. Zheng, X. Yu, M.T. Nguyen, D. Lao, Y. Zhu, F. Wang, D.J. Heldebrant, Assessing the impacts of dynamic soft-templates innate to switchable ionic liquids on nanoparticulate green rust crystalline structures. **Chem. Commun.** 55, 11239 (2019).
3. J. Zheng, Y. Ye, T. Liu, Y. Xiao, C. Wang, F. Wang, and F. Pan, “Ni/Li Disordering in Layered $\text{Li}(\text{Ni}_x\text{Mn}_y\text{Co}_z)\text{O}_2$: Electrochemical Impact, Origin and Control”, **Acc. Chem. Res.** 52, 2201 (2019).
4. D. Wang, C. Xin, M-J. Zhang, J. Bai, J. Zheng, R. Kou, J.P. Ko, A. Huq, G. Zhong, C. Sun, Y. Yang, Z. Chen, Y. Xiao, K. Amine, F. Pan and F. Wang “Intrinsic Role of Cationic Substitution in Tuning Li/Ni Mixing in Ni-rich Layered Oxides” **Chem. Mater.** 31, 731 (2019).
5. Y. Duan, L. Yang, M-J. Zhang, Z. Chen, J. Bai, K. Amine, F. Pan and F. Wang, Insights into Li/Ni Ordering and Surface Reconstruction during Synthesis of Ni-rich Layered Oxides, **J. Mater. Chem. A** 7, 513 (2019).

Acknowledgements

The work was supported by the Energy Efficiency and Renewable Energy, Office of Vehicle Technologies of the U.S. Department of Energy under contract DE-SC0012704. We thank the contribution by the team members, Mingjian Zhang, J. Patrick Looney, Yandong Duan, Chong Yin, Yusuf Celebi, and by collaborators, Yu-chen Karen Chen-Wiegar, Juergen Thieme, Eric Dooryhee, Mingyuan Ge, Xianghui Xiao, Wah-Keat Lee, Lijun Wu, Yimei Zhu (Brookhaven National Laboratory), Feng Pan (Peking U.), Khalil Amine, Zonghai Chen, Yang Ren, Chengjun Sun (Argonne National Laboratory), Ashfia Huq (Oak Ridge National Laboratory), Peter Ko (Cornell High Energy Synchrotron Source).

II.2.F Lithium Batteries with Higher Capacity and Voltage (UTA)

John B. Goodenough, Principal Investigator

The University of Texas at Austin
204 E. Dean Keeton St.
Austin, TX 78712
E-mail: jgoodenough@mail.utexas.edu

Peter Faguy, DOE Technology Development Manager

U.S. Department of Energy
E-mail: Peter.Faguy@EE.Doe.Gov

Start Date: October 1, 2018

End Date: September 30, 2019

Project Funding: \$120,000

DOE share: \$0

Non-DOE share: \$0

Project Introduction

A safe alkali-metal anode that can be plated/stripped reversibly at low resistance and high rates over many thousands of charge/discharge cycles would maximize the volumetric energy density for a given cathode of a rechargeable battery for powering an all-electric road vehicle. Such a battery could also be used for stationary back-up storage of electric power from energy sources other than fossil fuels.

Objectives

The project objective is to develop an electrochemically stable alkali-metal anode that can avoid the SEI layer formation and the alkali-metal dendrites during charge/discharge. To achieve the goal, a thin and elastic solid electrolyte membrane with a Fermi energy above that of metallic lithium and an ionic conductivity $\sigma > 10^{-4} \text{ S cm}^{-1}$ will be tested in contact with alkali-metal surface. The interface between the alkali metal and the electrolyte membrane should be free from liquid electrolyte, have a low impedance for alkali-metal transport and plating, and keep a good mechanical contact during electrochemical reactions.

Approach

The project will design, make, and test cells. The approach is to introduce a solid-electrolyte interfacing the anode and a coating on the anode current collector that is wet by a lithium anode. The solid electrolyte should also be wet by the anode to create a bond that is strong enough to constrain the anode volume changes to be perpendicular to the anode/electrolyte interface.

Results

The project has been conducted in collaboration with others in my group besides those supported by the BMR project. We have reported previously only results obtained with milestones specified by this project. Here, we report results placed in the broader context of our collaboration effort.

First, we have tested a low-cost separator concept that could reduce the long-standing cost of commercial rechargeable batteries while also improving upon some of the important properties of a separator. Polymer separators have long been treated as a staple in the lithium-ion battery technology, with the majority of interest in technological advancement falling to the three main components; the cathode, the anode, and the electrolyte. However, the polymer separator is one of the major cost hurdles for large-scale productions. In order to reduce the cost of current lithium-ion battery technology, cheaper alternatives to the traditional polymer separators that still maintain the necessary properties for a separator must be explored.

We started with a survey of current literature on ceramic materials with a large electronic energy band gap large enough such that the Fermi levels of the two electrodes fall within it. This requirement coupled with a need for cheap material processing yielding a useful morphology such as uniform nanospheres left us with the obvious choice of silica, SiO_2 . Rather than sintering a pellet to attempt to serve as a separator or mixing with a

binder polymer, we developed the idea of spraying the uniform nanoparticles onto the surface of the cathode. This coating gives a much better plasticity over a sintered ceramic pellet, allowing a much more robust ceramic separator. These coated LiCoO_2 electrodes were first tested against a graphite anode with 1M LiClO_4 in EC/DMC/FEC (45:45:10) as the electrolyte for proof of concept.

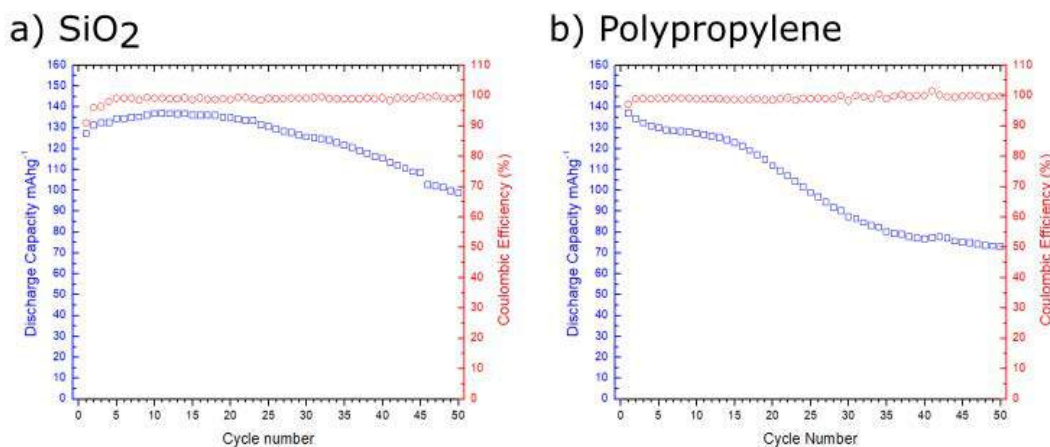


Figure II.2.F.1 Discharge capacity and coulombic efficiency of full-cells with SiO_2 electrode coating as a separator (a) and a sheet of polypropylene as a separator (b)

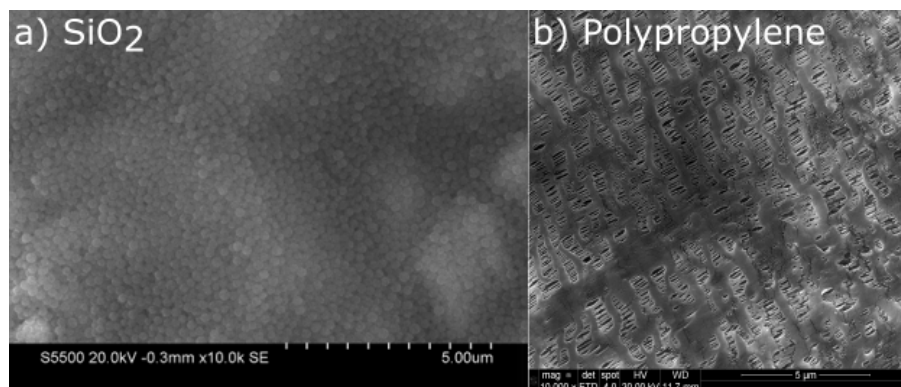


Figure II.2.F.2 SEM images of SiO_2 electrode coating and a sheet of polypropylene representative of the separator schemes used for cells in Figure II.2.F.1

Second, We have synthesized and tested a cathode material $\text{Na}_3\text{MnZr}(\text{PO}_4)_3$ with NASICON structure that could increase the energy density of current rechargeable sodium batteries while also reducing the cost through the use of earth-abundant transition-metals of manganese and zirconium. The voltage and energy density of a sodium battery is largely determined by the cathode material; the majority of research interest in sodium cathodes falls into three main categories: layered transition-metal oxides, Prussian-blue analogues, and polyanionic compounds. However, an inferior cycling stability and a low working voltage are the major issues for the current cathode candidates. In order to reduce the cost and increase the energy density of current sodium battery technology, new cathode alternatives that have a high working voltage and excellent cycling stability must be explored.

We started with a survey of current literature on the redox energies of transition metals in polyanionic compounds that deliver a charge/discharge voltage within the electrochemical stability window of traditional liquid electrolytes with organic-carbonate as the solvents. This requirement coupled with a need for low-cost material candidates having a useful and high working voltage led us to explore the redox energies of manganese in NASICON structures, $\text{Na}_3\text{MnZr}(\text{PO}_4)_3$. Rather than preparing the cathode material from a solid-

state reaction, which yields large cathode particles without a carbon coating, we developed the idea of synthesizing cathode $\text{Na}_3\text{MnZr}(\text{PO}_4)_3$ nanoparticles with an in situ generated carbon coating through a sol-gel method (Figure II.2.F.3). This method gives a much better electrical conductivity than that of micrometer-sized cathode particles prepared from solid-state reactions to give a much higher rate capability of the cathode materials. These carbon-coated $\text{Na}_3\text{MnZr}(\text{PO}_4)_3$ cathode materials were first tested against a sodium-metal anode with 1M NaClO_4 in PC/FEC (90:10) as the electrolyte for proof of concept.

Both the $\text{Mn}^{3+}/\text{Mn}^{2+}$ and $\text{Mn}^{4+}/\text{Mn}^{3+}$ redox couples are accessed in the cathode, with the average discharge voltage at 4.0 V and 3.5 V vs. Na^+/Na (Figure II.2.F.4). Half cells with a $\text{Na}_3\text{MnZr}(\text{PO}_4)_3$ cathode cycled very well at a current density of 0.5 C when compared to control cells using a standard polypropylene sheet as a separator. The experimental results coupled with theoretical calculations indicate that the excellent cycling stability exhibited by the $\text{Na}_3\text{MnZr}(\text{PO}_4)_3$ cathode is due to the structural stability of the NASICON structure and the inhibited Jahn-Teller distortion of Mn^{3+} in the intermediate phase of $\text{Na}_2\text{MnZr}(\text{PO}_4)_3$.

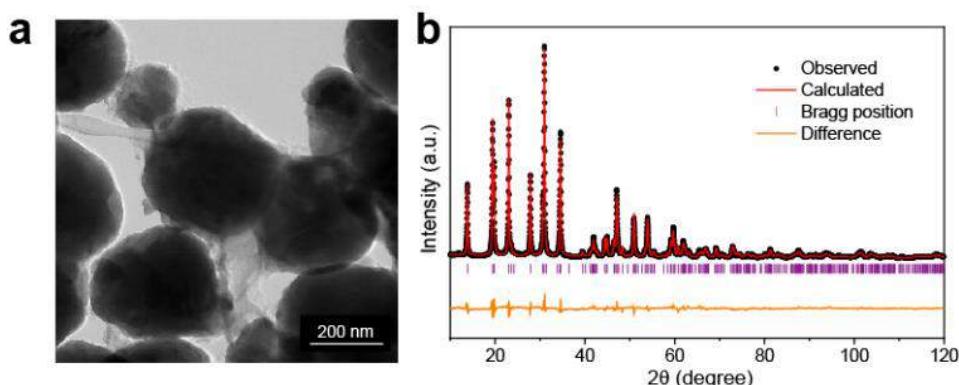


Figure II.2.F.3 (a) TEM image and (b) XRD pattern of the $\text{Na}_3\text{MnZr}(\text{PO}_4)_3$ cathode material prepared by the sol-gel method

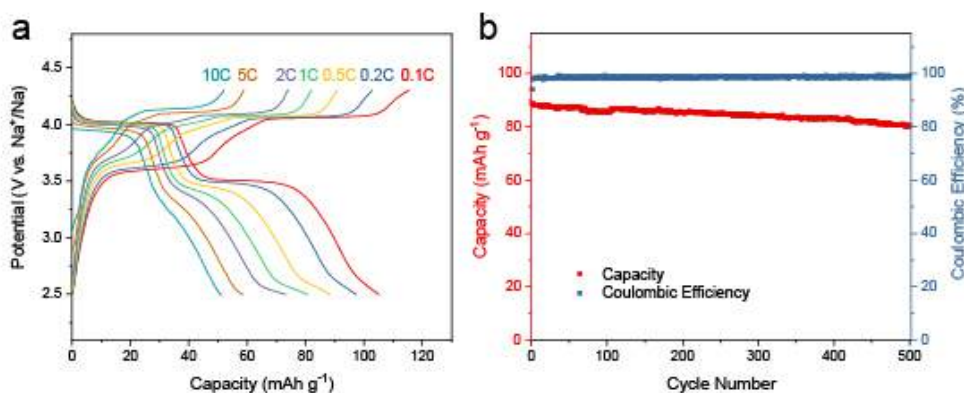


Figure II.2.F.4 (a) Charge/discharge profiles of the $\text{Na}_3\text{MnZr}(\text{PO}_4)_3$ cathode at different current densities. (b) Charge/discharge cycling performance of the $\text{Na}_3\text{MnZr}(\text{PO}_4)_3$ cathode at the rate of 0.5 C

Third, We prepared $\text{Li}_6\text{PS}_5\text{Cl}$ sulfide solid electrolyte by mechanical milling and subsequent heat-treatment; the structure and characteristic of this electrolyte were shown in Figure II.2.F.5. In Figure II.2.F.5(a), the XRD pattern of $\text{Li}_6\text{PS}_5\text{Cl}$ is the same as that of Li_7PS_6 , both of which belong to the argyrodite crystalline phase. $\text{Li}_6\text{PS}_5\text{Cl}$ is a typical representative of argyrodite. Figure II.2.F.5(b-c) were the Nyquist plots of $\text{Li}_6\text{PS}_5\text{Cl}$ electrolyte at different temperatures and the temperature dependence of the Li-ion conductivity. At ambient temperature, $\text{Li}_6\text{PS}_5\text{Cl}$ solid electrolyte exhibits an ionic conductivity of $1.29 \times 10^{-3} \text{ S cm}^{-1}$, and activation energy of 0.32 eV. We also evaluated the electrochemical stability of $\text{Li}_6\text{PS}_5\text{Cl}$ solid electrolyte with linear cyclic voltammetry of steel/SE/Li cell at a constant scan rate of 5 mV s^{-1} in the voltage window of (-0.5-5) V

(Figure II.2.F.1(d)). Except the lithium plating at -0.5 V and the lithium stripping at 0.3 V, no additional current peak is detected in the whole scanning voltage range, indicating that $\text{Li}_6\text{PS}_5\text{Cl}$ has a wide and stable electrochemical window. Figure II.2.F.5(e) was the SEM images and corresponding element mapping, the average size of $\text{Li}_6\text{PS}_5\text{Cl}$ solid electrolyte is $\sim 5\mu\text{m}$.

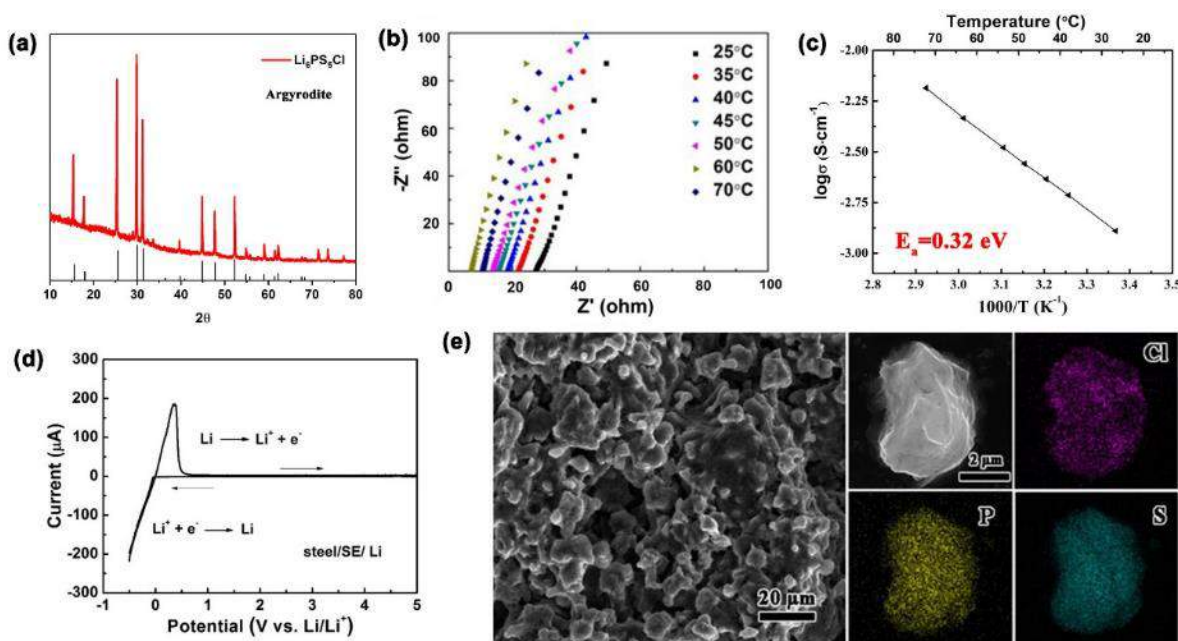


Figure II.2.F.5 The structure and characteristic of $\text{Li}_6\text{PS}_5\text{Cl}$ sulfide solid electrolyte. (a) XRD. (b) The Nyquist plots at different temperatures. (c) Temperature dependence of the ionic conductivity. (d) Cyclic voltammogram of stainless steel/SE/Li cell at a scanning rate of 0.5 mV/s between -0.5 V and 5 V. (e) SEM images and corresponding element mapping

We also evaluated the electrochemical performance of $\text{Li}_6\text{PS}_5\text{Cl}$ in an all-solid-state $\text{Li}_2\text{S}/\text{Li}_6\text{PS}_5\text{Cl}/\text{Li}$ battery (Figure II.2.F.6(a)). The capacity of this battery is 320 mAh g^{-1} at ambient temperature, and it can be increased to $\sim 600\text{ mAh g}^{-1}$ at 55°C . The optimization of the cell, especially the electrolyte/electrodes interfaces, will be studied to further improve the cycling of the cell.

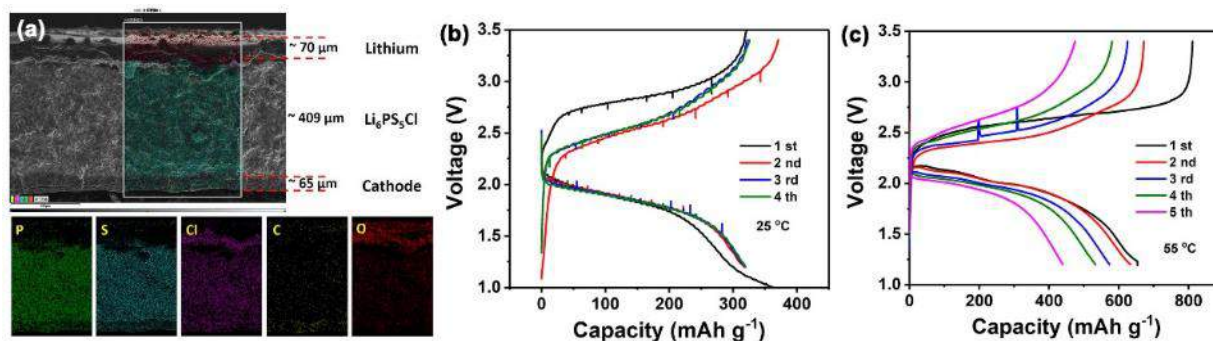


Figure II.2.F.6 (a) The structure of $\text{Li}_2\text{S}/\text{Li}_6\text{PS}_5\text{Cl}/\text{Li}$ battery. (b-c) Electrochemical performance of $\text{Li}_2\text{S}/\text{Li}_6\text{PS}_5\text{Cl}/\text{Li}$ battery at 25°C and 55°C , respectively

Lastly, prepared *P3* structure $\text{Na}_{0.6}(\text{Li}_{0.2}\text{Mn}_{0.8})\text{O}_2$ through mixing and calcining at 700°C for 24 h; the structure and characteristic of this material are shown in Figure II.2.F.7(a-b). The main peaks of the XRD pattern of nominal $\text{Na}_{0.6}(\text{Li}_{0.2}\text{Mn}_{0.8})\text{O}_2$ fit well those of a layered *P3* oxide with space group *R3m* in which the Na^+ ions occupy trigonal prismatic sites between close-packed layers of octahedral-site $(\text{Li}_2\text{Mn}_{0.8})\text{O}_{6/3}$ sharing

common edges. The *P3* and *P2* structures have, respectively, cubic and hexagonal layer stacking with Na in trigonal-prismatic sites, the *O3* structure has cubic stacking with Na in octahedral sites. Figure II.2.F.7(c-d) is the charge and discharge curves of a cell cycled between different voltages. In Figure II.2.F.7 (c), a long plateau at $V \approx 4.2$ V, which is associated with the oxidation of the O-2p band. Since the initial solid-electrolyte interphase (SEI) passivating layer of the anode contains Na^+ from the cathode, the continuing capacity fade with cycling would appear to signal an irreversible loss of alkali ions from the cathode. On cycling from 2.0 to 4.5 V at 15 mA g^{-1} , Figure II.2.F.7 (d), the total discharge capacity initially increases slightly before decreasing; but the length of the long plateau at 4.1 V on discharge decreases progressively with cycling as in Figure II.2.F.7(c).

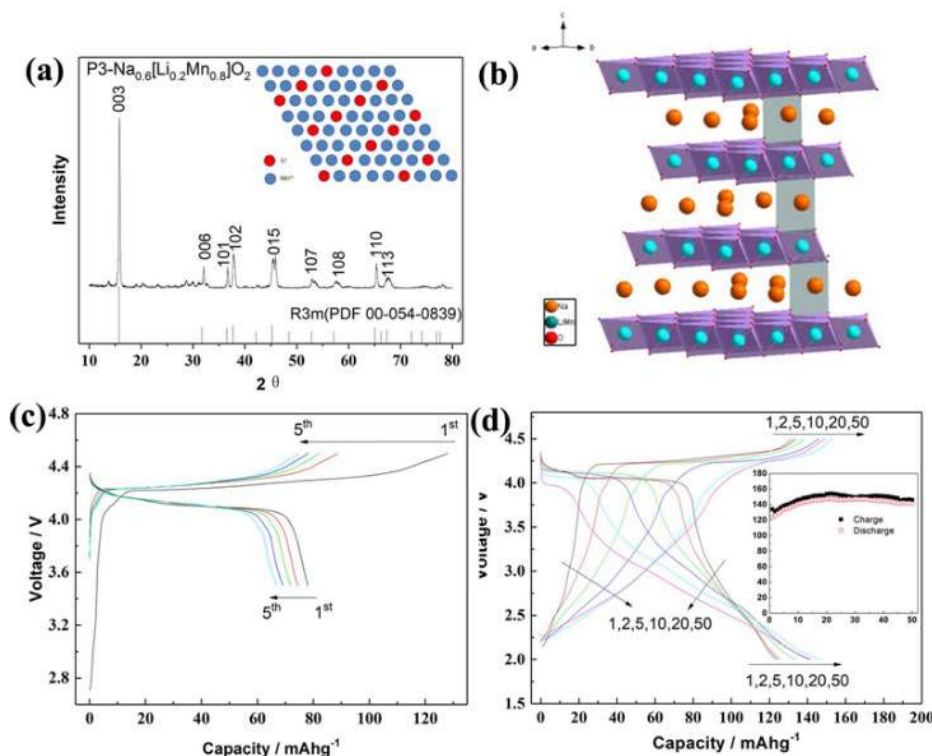


Figure II.2.F.7 Structure and electrochemical performance of $\text{Na}_{0.6}(\text{Li}_{0.2}\text{Mn}_{0.8})\text{O}_2$ (a) XRD pattern. The inset is ordered Li/Mn atoms. (b) the *P3* structure. (c) Charge and discharge profiles and cycle stability at 10 mA g^{-1} between 3.5-4.5 V. (d) Charge and discharge profiles and cycle stability at 15 mA g^{-1} between 2.0 and 4.5 V

XPS probes the electronic states at surface atoms. Figure II.2.F.8(a) shows Mn 2p XPS patterns of $\text{P3-Na}_{0.6}[\text{Li}_{0.2}\text{Mn}_{0.8}]\text{O}_2$ at five different states of the initial cycle. There is little change in the Mn XPS peaks between 3.3 and 4.5 V on charge and discharge. Figure II.2.F.8(b) compares the ex situ XRD patterns of nominal *P3*- $\text{Na}_{0.6}(\text{Li}_{0.2}\text{Mn}_{0.8})\text{O}_2$ of a dried as-prepared electrode with those taken after charge to 4 and 4.5 V, discharge to 3.9, 3.3, and 2.0 V and after 5 cycles between 3.5 and 4.5 V as well as after 50 cycles between 2.0 and 4.5 V. The *P3* structure is retained after all treatments with no evidence of the *O3* (Na in octahedral coordination) or other phases. The initial charge capacity of 128 mAh g^{-1} between 3.5 and 4.5 V corresponds to the extraction of 0.44 Na^+ per formula unit, which leaves $0.16 \text{ Na}^+/\text{f.u.}$ to stabilize the *P3* structure. It is remarkable that after 50 cycles in the voltage ranges 2.0 to 4.5 V versus Na^0 , the XRD peaks retain the as-prepared structure with no shift of the lattice parameter. The only change is the intensity of the XRD peaks of the cycled sample and a broadening of some peaks. The *P3* structure remains stable over electrochemical cycling even though oxidation on charge introduces holes primarily in the O-2p bands. This observation suggests the formation of an amorphous second phase grows with cycling.

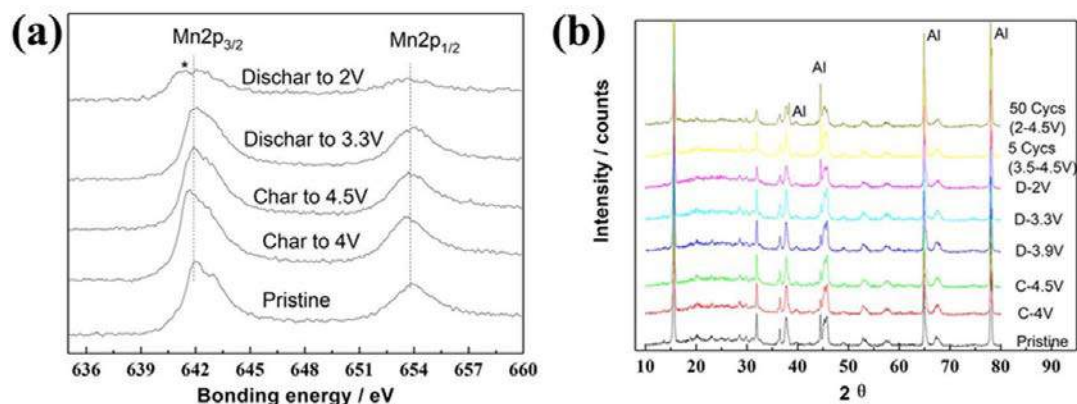


Figure II.2.F.8 (a) XPS patterns of Mn during the initial charge and discharge process. (b) Ex situ XRD patterns of P3-Na_{0.6}(Li_{0.2}Mn_{0.8})O₂ at different states

Conclusions

Investigation of a new cell concept has been performed: It consists of low-cost ceramic separator, novel NASICON-structured cathode material, solid sulfide electrolytes, and oxygen redox chemistry for reversible high-voltage Na⁺ intercalation. The SiO₂-coated separator not only can reduce the long-standing cost of commercial rechargeable batteries, but also can improve upon some of the important properties of a separator. Moreover, the new Na₃MnZr(PO₄)₃ cathode delivers a high working voltage and excellent cycling stability for sodium battery.

Key Publications

1. Gao HC, Seymour ID, Xin S, Xue LG, Henkelman G, Goodenough JB. 2018. Na₃MnZr(PO₄)₃: A High-Voltage Cathode for Sodium Batteries. *J Am Chem Soc* 140:18192-18199.
2. Gao HC, Li YT, Park K, Goodenough JB. 2016. Sodium extraction from NASICON-structured Na₃MnTi(PO₄)₃ through Mn(III)/Mn(II) and Mn(IV)/Mn(III) redox couples. *Chem Mater* 28:6553-6559.
3. Zhou WD, Xue LG, Lu XJ, Gao HC, Li YT, Xin S, Fu GT, Cui ZM, Zhu Y, Goodenough JB. 2016. Na_xMV(PO₄)₃ (M = Mn, Fe, Ni) structure and properties for sodium extraction. *Nano Lett* 16:7836-7841.
4. Gao HC, Xin S, Xue LG, Goodenough JB. 2018. Stabilizing a high-energy-density rechargeable sodium battery with a solid electrolyte. *Chem* 4:833-844.
5. Gao HC, Xue LG, Xin S, Goodenough JB. 2018. A high-energy-density potassium battery with a polymer-gel electrolyte and a polyaniline cathode. *Angew Chem Int Ed* 57:5449-5453.
6. Xue LG, Gao HC, Li YT, Goodenough JB. 2018. Cathode dependence of liquid-alloy Na-K anodes. *J Am Chem Soc* 140:3292-3298.
7. Zhou AJ, Xu ZM, Gao HC, Xue LG, Li JZ, Goodenough JB. 2019. Size-, Water-, and Defect-Regulated Potassium Manganese Hexacyanoferrate with Superior Cycling Stability and Rate Capability for Low-Cost Sodium-Ion Batteries. *Small* 15:1902420.
8. Xue LG, Zhou WD, Xin S, Gao HC, Li YT, Zhou AJ, Goodenough JB. 2018. Room-temperature liquid Na-K anode membranes. *Angew Chem Int Ed* 57:14184-14187.

II.2.G Disordered RockSalt Structured Cathode Materials: Electrochemistry and Synthesis (LBNL)

Guoying Chen, Principal Investigator

Lawrence Berkeley National Laboratory
1 Cyclotron Road
Berkeley, CA 94720
E-mail: GChen@lbl.gov

Peter Faguy, DOE Technology Development Manager

U.S. Department of Energy
E-mail: Peter.Faguy@EE.Doe.Gov

Start Date: October 1, 2018

End Date: September 30, 2021

Total Project Cost: \$1,100,000

DOE share: \$1,100,000

Non-DOE share: \$0

Project Introduction

The projected growth of Li-ion battery (LIB) production towards 1 TWh/year will require more than a million tons of Co/Ni combined, which constitutes a very sizeable fraction of the annual production of these metals. The recent development of Li-excess cation-disordered rocksalt (DRX) cathodes provides an avenue for the LIB field to develop high energy density cathodes that use more abundant and less expensive metals. DRX materials have been shown to deliver energy densities up to 1000 Wh/kg, and its cation disordered nature allows for a wide range of chemistry free of Co and/or Ni. In addition, the ability to substitute some of the oxygen by fluorine in locally Li-rich environments provides an extra handle to optimize performance through increasing metal-redox capacity in DRX. As this class of cathodes are relatively new, further materials design and development are needed in order to properly evaluate their likelihood in eventual commercialization. To do so, fundamental understanding on what controls DRX performance characteristics, particularly rate capability, cycling stability and voltage slope, is critical. This project has assembled research efforts involving modeling, synthesis, electrochemistry and characterization to tackle the challenges. The current chapter reports on the synthesis and electrochemistry components of the project.

Objectives

The goals of this project are as follows:

- Understand the factors that control DRX cycling stability, particularly to what extent cycle life is controlled by impedance growth on the surface and by bulk changes in the material
- Understand what controls the rate of DRX materials, particularly rate limitation posed by bulk transport and surface processes
- Investigate the root of voltage profile slope in DRX and develop modification strategies
- Develop Co-free high energy density DRX cathodes with improved performance.

Approach

This project focuses on three representative baseline systems and their analogues to understand the challenges and opportunities in DRX materials. The baseline systems include the following: Mn-redox based $\text{Li}_{1.2}\text{Mn}_{0.625}\text{Nb}_{0.175}\text{O}_{1.95}\text{F}_{0.05}$ (LMNOF), Ni-redox based $\text{Li}_{1.15}\text{Ni}_{0.45}\text{Ti}_{0.3}\text{Mo}_{0.1}\text{O}_{1.85}\text{F}_{0.15}$ (LNTMOF), and a high F-content $\text{Li}_2\text{Mn}_{1/2}\text{Ti}_{1/2}\text{O}_2\text{F}$ (LMTOF) that utilizes the $2e^- \text{Mn}^{2+}/\text{Mn}^{4+}$ redox couple. The following thrusts are pursued:

- Explore synthesis conditions to prepare DRX materials with optimal performance

- Establish reliable and scalable synthesis protocols
- Fabricate quality electrodes of DRX materials and establish baseline performance in pouch cells
- Develop electrochemical testing protocols and benchmark DRX performance metrics
- Develop new synthesis methods to fluorinate DRX cathodes
- Evaluate the effect of F content on electrochemical performance.

Results

1) Scalable synthesis and electrochemical performance of DRX baseline materials – Solid-state synthesis of two DRX compounds, LMNOF and LNTMOF, was optimized for 10 g scale on various synthesis parameters, including precursor mixing and high-temperature annealing. The optimized baseline samples were delivered to the various tasks in the DRX program. A good fit obtained from Rietveld refinement of LMNOF XRD pattern

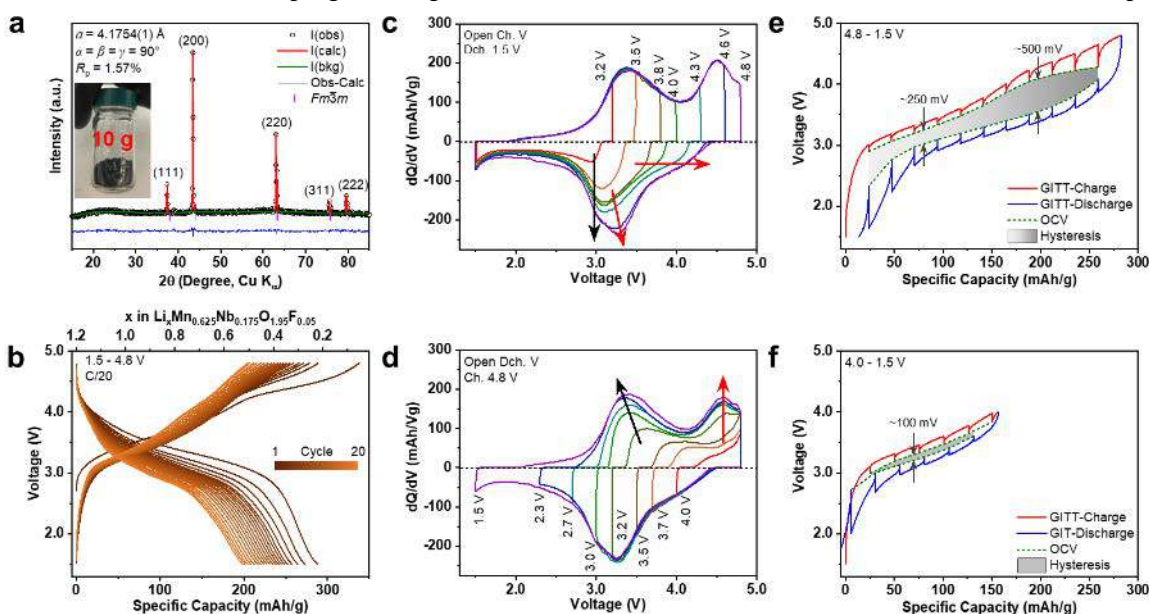


Figure II.2.G.1 Synthesis and electrochemistry of LMNOF baseline. (a) XRD pattern and Rietveld refinement of optimized cathode, (b) voltage profiles in cycle 1-20, dQ/dV curves for voltage window tests at various (c) charge and (d) discharge cutoff voltages, and GITT plots with a voltage range of (e) 4.8 – 1.5 V and (f) 4.0 – 1.5 V.

(Figure II.2.G.1a) shows pure rocksalt phase with an a lattice parameter of $4.1754(1) \text{ \AA}$. Electrochemistry of both DRX cathodes was obtained after optimization of carbon processing condition. The LMNOF baseline cathode delivered an initial discharge capacity of 288 mAh/g and a reversible capacity of 200 mAh/g after 20 cycles, corresponding to 30.6% capacity loss (Figure II.2.G.1b). To understand the redox behavior, galvanostatic cycling test was performed by progressively opening charge and discharge cutoff voltage after the full activation in the first cycle (Figure II.2.G.1c, d). Cationic Mn and anionic oxygen redox reactions have been identified from cutoff voltage tests, which involves symmetrical $\text{Mn}^{3+}/\text{Mn}^{4+}$ redox around 3.1 V and asymmetrical anionic oxygen redox that takes place at $\sim 4.5 \text{ V}$ during charge and in a voltage range from high voltage till $\sim 3.0 \text{ V}$ during discharge. Such asymmetrical anionic oxygen redox accounts for a large hysteresis in LMNOF cathode. This agrees well with galvanostatic intermittent titration technique (GITT) results (Figure II.2.G.1e, f), showing the voltage gap in the high voltage region related to anionic oxygen redox doubles that of Mn redox in the low voltage region. Meanwhile, oxygen activity in the high voltage region shows a negative impact on Mn redox, given a much smaller voltage gap for Mn redox when cycled to 4.0 V. Similar optimization strategy for solid-state synthesis and carbon processing was employed on LNTMOF cathode. Pure DRX rocksalt phase with a

lattice parameter of $4.1487(3) \text{ \AA}$ was obtained, as indicated by Rietveld refinement analysis (Figure I.1.2a). Optimal LNTMOF cathode delivered an initial discharge capacity of 276 mAh/g , with a reversible capacity of 202 mAh/g remained after 20 cycles (Figure II.2.G.2b). In contrast with LMNOF, a larger portion of discharge capacity was obtained at lower voltages, suggesting the different redox behaviors in these two DRX cathodes. Using the same testing protocols developed for LMNOF, a similar set of voltage window tests were conducted on LNTMOF cathode (Figure II.2.G.2c, d). The study showed the redox process at 2.0 V plateau during discharge is directly correlated with that in the high voltage region during charge. Additionally, a second redox process contributed to the 2.0 V discharge plateau, given the emergence of an anodic peak around 2.2 V when opening discharge cutoff voltage further below 2.5 V . Such different redox behaviors between LMNOF and LNTMOF cathodes were further revealed by GITT tests (Figure II.2.G.2e, f). In stark contrast with LMNOF, an obvious increase in voltage gap toward lower voltage region was observed, as evidenced by $\sim 300 \text{ mV}$ in the high voltage region vs. $\sim 1.1 \text{ V}$ in the low voltage region.

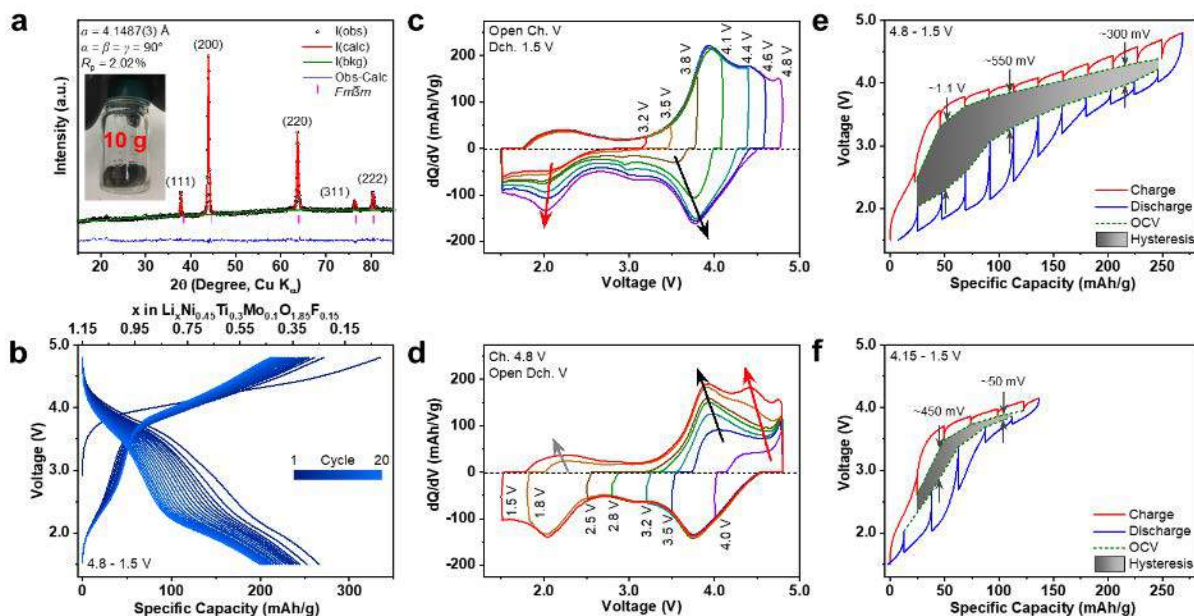


Figure II.2.G.2 Synthesis and electrochemistry of LNTMOF baseline. (a) XRD pattern and Rietveld refinement of optimized cathode, (b) voltage profiles of the baseline in cycle 1-20, dQ/dV curves for voltage window tests at various (c) charge and (d) discharge cutoff voltages, and GITT plots with a voltage range of (e) $4.8 - 1.5 \text{ V}$ and (f) $4.15 - 1.5 \text{ V}$

The high power pulse characterization (HPPC) test was performed to investigate the relationship between impedance and DOD. Figure II.2.G.2 (left) shows resistance vs. OCV plot. One can see that the resistance for the electrode during a 30 sec pulse is 5 times greater for the sample without carbon ball milling, although the resistance for both is fairly large. Closer inspection of the data is provided by examining the voltage curve during

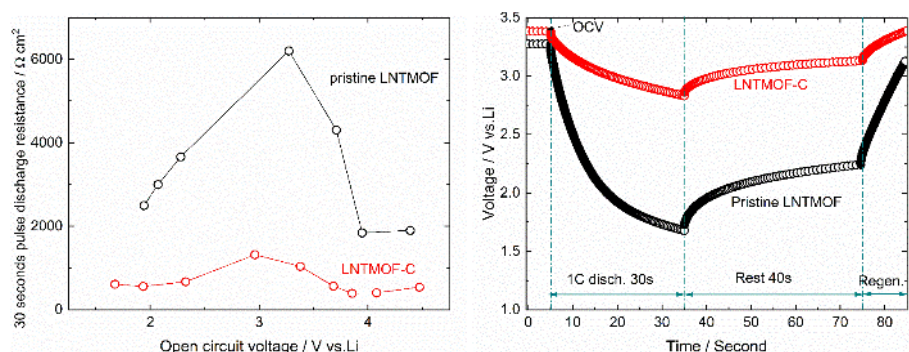


Figure II.2.G.3 Left: Cell resistance plotted against OCV for LNTMOF with and without carbon ball milling. Right: voltage profile during the 30-second pulse at an OCV close to 3.3 V.

the discharge pulse as also seen in Figure II.2.G.2 (right). The longer term diffusional resistance is poor for both but even worse for the material without ball milling with carbon. This is likely a particle size effect as ball milling significantly reduces the as-synthesized large particles and improves overall Li transport in the sample.

2) Effect of F content – In order to gather understanding on the role of F, we synthesized two sets of LMNOF baseline analogues with Nb and Ti as the redox inactive d0 metal, respectively: $\text{Li}_{1.3}\text{Nb}_{0.3}\text{Mn}_{0.4}\text{O}_2$ (L1.3M0.4NO)/ $\text{Li}_{1.3}\text{Nb}_{0.2}\text{Mn}_{0.5}\text{O}_{1.8}\text{F}_{0.2}$ (L1.3M0.5NOF) and $\text{Li}_{1.2}\text{Ti}_{0.4}\text{Mn}_{0.4}\text{O}_2$ (L1.2M0.4TO)/ $\text{Li}_{1.2}\text{Ti}_{0.2}\text{Mn}_{0.6}\text{O}_{1.8}\text{F}_{0.2}$ (L1.2M0.6TOF). In the case of the oxyfluorides, Mn content was increased to charge compensate F substitution into the O sublattice. Synthesis was carried out by using a molten-salt method where LiF was used as both precursor and self-flux. Excess LiF was removed by thoroughly washing the as-synthesized product with de-ionized water. Figure II.2.G.1 compares the structure composition as well as the particle morphology of the samples. Well-crystallized single-phase rocksalt structure was confirmed by the XRD measurements. Impurities such as LiF was not observed. SEM imaging shows single-particle morphology (Figure II.2.G.4), with a particle size of ~ 5 and $20 \mu\text{m}$ for the oxides and oxyfluorides, respectively. Further examination shows that while the oxides adopt a spherical particle shape, the oxyfluorides presents clear facets on the surface. This suggests that introducing F induces preferential growth in certain facets. All TMs, O and F were uniformly distributed at particle level, as shown in the EDX mapping results. Elemental composition was further verified by combined ICP and F-ion selective electrode measurements.

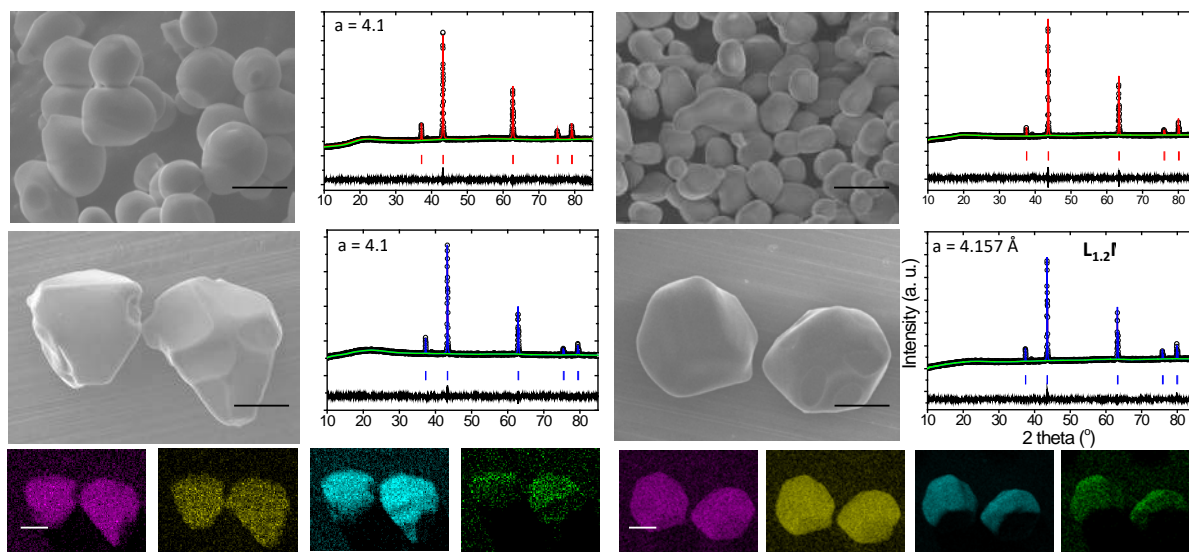


Figure II.2.G.4 SEM images and XRD patterns of a) $L_{1.3}M_{0.4}NO$, b) $L_{1.3}M_{0.5}NOF$, c) $L_{1.2}M_{0.4}TO$, and d) $L_{1.2}M_{0.6}TOF$ samples. EDX mapping results on b) and d) are shown at the bottom

The first 20-cycle voltage profiles as well as capacity and discharge voltage retention during the first 50 cycles are shown in Figure II.2.G.5. In the Nb-based samples, F substitution substantially improves the initial discharge capacity, increasing from ~ 275 mAh/g in $L_{1.3}M_{0.4}NO$ to 310 mAh/g in $L_{1.3}M_{0.5}NOF$ (Figure II.2.G.5a and Figure II.2.G.5b). Better retention in both capacity discharge voltage was achieved in the latter (Figure II.2.G.5e and Figure II.2.G.5f), leading to significantly better maintained energy density upon cycling. F improvement was also observed on the Ti-based compound (Figure II.2.G.5c and Figure II.2.G.5d), with the discharge capacity in $L_{1.2}M_{0.6}TOF$ remaining nearly constant during the first 50 cycles (Figure II.2.G.5g), and the voltage decay along with cycling reduced considerably (Figure II.2.G.5h). Compared to the Ni-based oxide and oxyfluoride, overall better electrochemical performance was achieved on the Ti-based counterparts, suggesting that redox inactive d^0 metal also plays an important role. The interplay between d^0 metal and F will be further investigated.

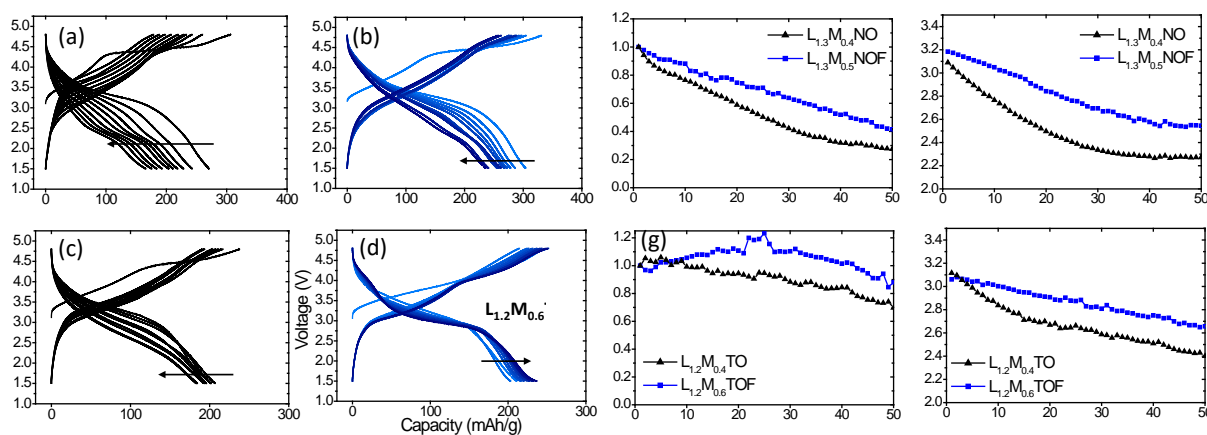


Figure II.2.G.5 a-d) First 20-cycle voltage profile of $L_{1.3}M_{0.4}NO$, $L_{1.3}M_{0.5}NOF$, $L_{1.2}M_{0.4}TO$, and $L_{1.2}M_{0.6}TOF$ half cells. e) and g) capacity retention of the half cells. f) and h) discharge voltage retention of the half cells. The current density is 10 mA/g.

Figure II.2.G.6 compares the 1st cycle dQ/dV profiles of the samples. The two-voltage region behavior is clearly reflected by the well-defined Mn³⁺/Mn⁴⁺ oxidation peak in the lower-voltage region and the O oxidation peak in the higher-voltage region. In L_{1.3}M_{0.4}NO, the O oxidation peak shows a doublet profile (Figure II.2.G.6a) where the higher-voltage peak of the doublet was previously attributed to O oxidation *via* O loss. F substitution reduces the capacity contribution from the high-voltage peak, suggesting reduced O₂ loss in L_{1.3}M_{0.5}NOF. For Ti-based oxide and oxyfluoride, the overall capacity from O oxidation was lower than that of the Nb-based samples. The incremental capacity of the higher-voltage O oxidation peak is nearly nonexistent in L_{1.2}M_{0.6}TOF (Fig. 6b).

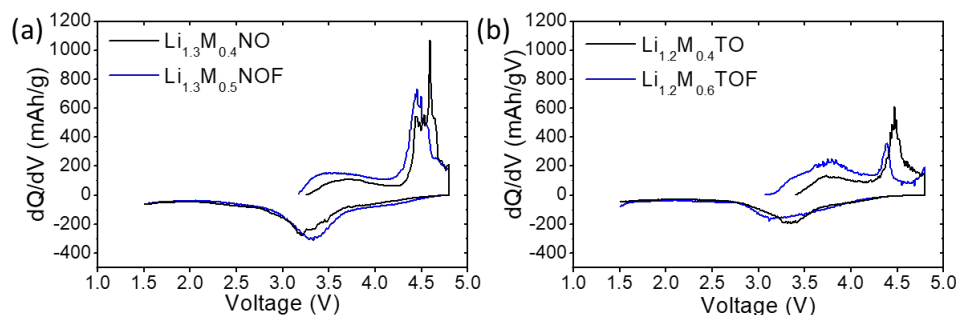


Figure II.2.G.6 First-cycle incremental capacity (dQ/dV) profiles of: a) L_{1.3}M_{0.4}NO and L_{1.3}M_{0.5}NOF half cells and b) L_{1.2}M_{0.4}TO and L_{1.2}M_{0.6}TOF half cells. The current density is 10 mA/g.

3) Novel synthesis techniques for DRX fluorination – To identify appropriate reaction conditions to incorporate F into LNTMO and optimize the cathode's fluorine content to improve its capacity retention during cycling, an in situ fluorine gas reactor was used as one strategy to incorporate fluorine in the LNTMO baseline compound. Direct fluorination reaction between a Li-rich DRX cathode LNTMO and F₂ gas using a fluidized bed reactor (Figure II.2.G.7 left) was performed. X-ray diffraction (XRD) patterns of the pristine and fluorinated powders are shown in Figure II.2.G.7 right. The mildly fluorinated samples (30min and 3hrs containing approximately 3 and 5 at% F, respectively) had a single phase rocksalt structure (space group Fm-3m) which was similar to that of the pristine material. Under more aggressive fluorination conditions (12 h corresponding to ~15 at% F content), a crystalline LiF impurity phase was formed. F content was estimated using energy dispersive X-ray spectroscopy (EDX). To better understand the F distribution and bonding environment in the cathodes, X-ray photoelectron spectroscopy (XPS) depth profiling studies were also performed (see Figure II.2.G.8). These measurements indicate that (i) direct fluorination formed a LiF-like phase near the particle surface and (ii) F content was higher near the surface compared to the bulk.

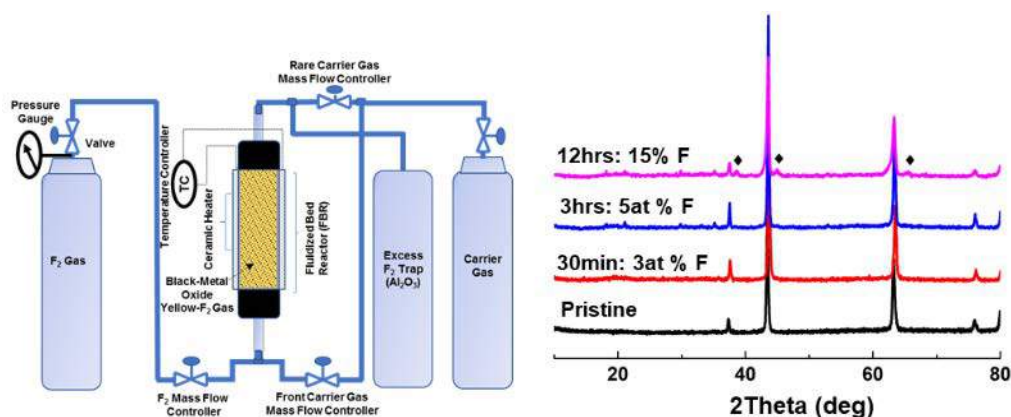


Figure II.2.G.7 Setup of the fluidized bed reactor (left) and XRD patterns of pristine LNTMO and the F- LNTMO at different conditions (right). The F content was determined by EDX analysis

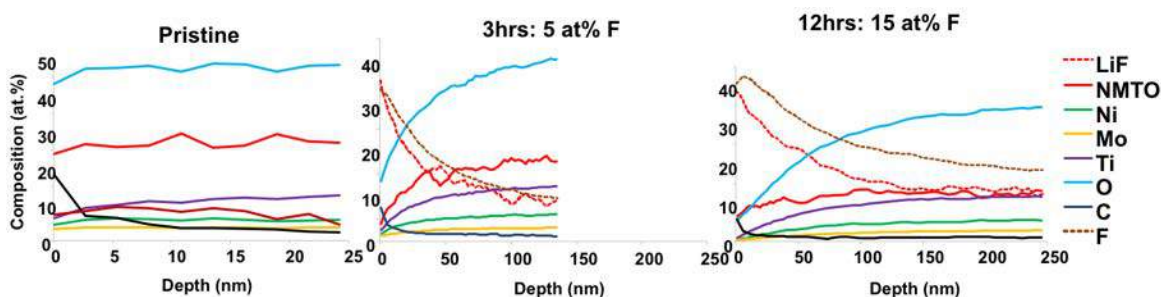


Figure II.2.G.8 Summary of XPS depth-profiling experiments for pristine and F-LNTMO

The electrochemical properties of pristine LNTMO and fluorinated LNTMO (F-LNTMO) cathodes were evaluated in half cells using a Li anode and LiPF_6 /liquid carbonate electrolyte. As shown in Figure II.2.G.9, 3 at% F substitution yielded a cathode with a reversible capacity ~ 275 mAh/g which is comparable to that of the pristine material. Under more aggressive fluorination conditions (12 h corresponding to ca. 15 at% F), the cathode exhibited a substantially lower reversible capacity (180 mAh/g), which is attributed to the LiF surface film previously discussed. Interestingly, all samples in Figure II.2.G.4 showed a single sloping voltage plateau ~ 4 V during charge and two plateaus ~ 2 and 3.5 V during discharge. The redox processes associated with each plateau are not fully understood, but these results suggest that lithiation/delithiation steps proceed through different reaction pathways. Work is in progress to determine the exact chemical state and location of F in the DRX cathode structure and its effect on the electrochemical performance.

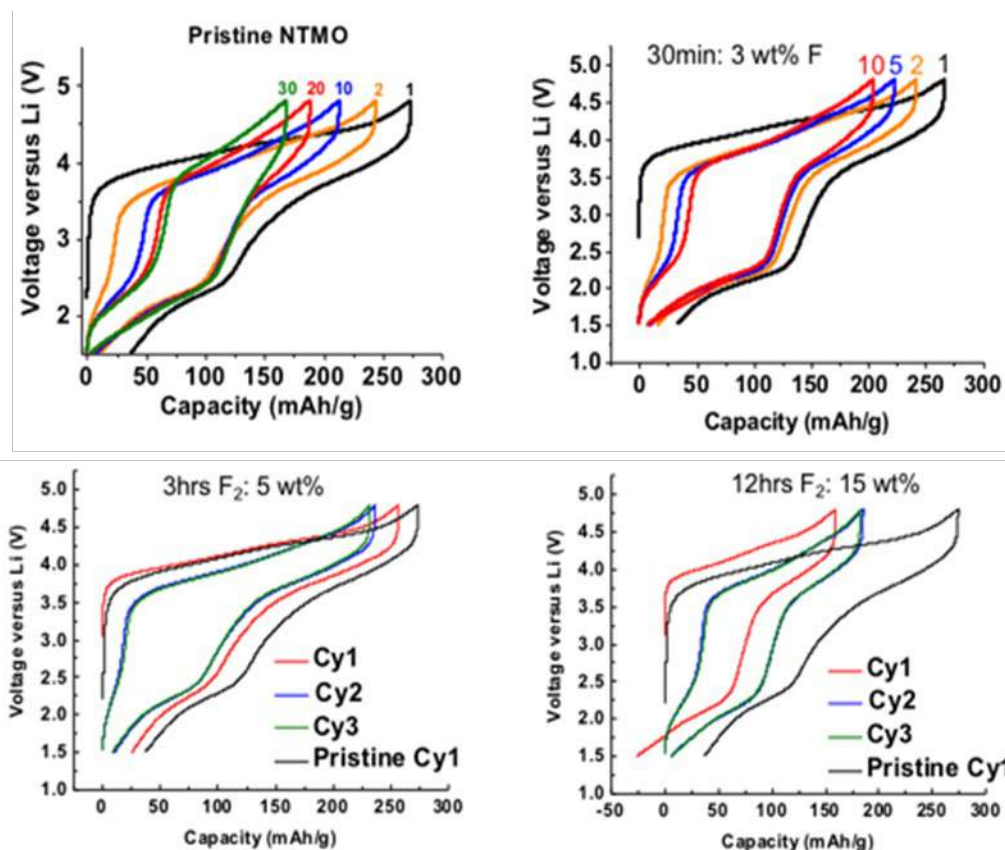


Figure II.2.G.9 Electrochemical cycling for first few cycles for pristine LNTMO and 30min, 3hrs and 12hrs F-LNTMO

Conclusions

Solid-state reaction conditions for two DRX baseline samples, LMNOF and LNTMOF, were optimized. Reliable procedures for synthesis at 10 g scale were successfully developed. Scaled-up samples were verified in quality and distributed as baseline materials for use in the various tasks within the program. DRX electrode fabrication process was investigated and electrochemical performance of the baseline samples evaluated. The effect of F substitution on electrochemical performance was evaluated through the comparison between DRX oxyfluorides and their oxide counterparts. F was found to increase capacity, reduce oxygen loss at high voltages, reduce polarization and improve the overall cycling stability. Further studies are under way to optimize the F content in DRX. A novel fluorination method using F₂ gas in a fluidized bed reactor was developed, wherein F content in the cathode can be easily varied by controlling the reaction time. This method can be applied to fluorinate a wide range of DRX compositions as they are developed.

Key Publications

1. N. Li, S. Hwang, M. Sun, Y. Fu, V. S. Battaglia, D. Su, W. Tong, Unraveling the Voltage Decay Phenomenon in Li-rich Layered Oxide Cathode of No Oxygen Activity, *Advanced Energy Materials*, accepted (2019).
2. E. C. Self, Y. Zhang, A. K. Kercher, N. D. Phillip, F. M. Delnick, J. Nanda, “Structural and Electrochemical Characterization of Thin Film Li₂MoO₃ Electrodes,” *Journal of the Electrochemical Society*, 166 (6), 2019, A1015-A1021.
3. D. Chen, J. Wu, J. K. Papp, B. D. McCloskey, W. Yang and G. Chen, “Role of Redox-Inactive Transition-Metals in the Behavior of Cation-Disordered Rocksalt Cathodes,” submitted (2019).

Acknowledgements

Vincent Battaglia, Gerbrand Ceder, Matthew Crafton, Yanbao Fu, Kenny Higa, Xiangyun Song, Yuan Yue, Wei Tong.

II.2.H Disordered RockSalt Structured Cathode Materials: Characterization and Modeling (LBNL, ORNL, PNNL, UC Santa Barbara)

Gerbrand Ceder, Principal Investigator

Lawrence Berkeley National Laboratory
1 Cyclotron Road
Berkeley, CA 94720
E-mail: gceder@berkeley.edu

Peter Faguy, DOE Technology Development Manager

U.S. Department of Energy
E-mail: Peter.Faguy@EE.Doe.Gov

Start Date: October 1, 2018
Total Project Cost: \$1,900,000

End Date: September 30, 2021
DOE share: \$1,900,000

Non-DOE share: \$0

Project Introduction

The projected growth of Li-ion battery (LIB) production towards 1 TWh/year will require more than a million tons of Co/Ni combined, which constitutes a very sizeable fraction of the annual production of these metals. The recent development of Li-excess cation-disordered rocksalt (DRX) cathodes provides an avenue for the LIB field to develop high energy density cathodes that use more abundant and less expensive metals. DRX materials have been shown to deliver energy densities up to 1000 Wh/kg, and its cation disordered nature allows for a wide range of chemistry free of Co and/or Ni. In addition, the ability to substitute some of the oxygen by fluorine in locally Li-rich environments provides an extra handle to optimize performance through increasing metal-redox capacity in DRX. As this class of cathodes are relatively new, further materials design and development are needed in order to properly evaluate their likelihood in eventual commercialization. To do so, fundamental understanding on what controls DRX performance characteristics, particularly rate capability, cycling stability and voltage slope, is critical. This project has assembled research efforts involving modeling, synthesis, electrochemistry and characterization to tackle the challenges. The current chapter reports on the modelling and characterization components of the project.

Objectives

The goals of this project are as follows:

- Understand the factors that control DRX cycling stability, particularly to what extent cycle life is controlled by impedance growth on the surface and by bulk changes in the material
- Understand what controls the rate of DRX materials, particularly rate limitation posed by bulk transport and surface processes
- Investigate the root of voltage profile slope in DRX and develop modification strategies
- Develop Co-free high energy density DRX cathodes with improved performance.

Approach

This project focuses on three representative baseline systems and their analogues to understand the challenges and opportunities in DRX materials. The baseline systems include the following: Mn-redox based $\text{Li}_{1.2}\text{Mn}_{0.625}\text{Nb}_{0.175}\text{O}_{1.95}\text{F}_{0.05}$ (LMNOF), Ni-redox based $\text{Li}_{1.15}\text{Ni}_{0.45}\text{Ti}_{0.3}\text{Mo}_{0.1}\text{O}_{1.85}\text{F}_{0.15}$ (LNTMOF), and a high F-content $\text{Li}_2\text{Mn}_{1/2}\text{Ti}_{1/2}\text{O}_2\text{F}$ (LMTOF) that utilizes the $2e^- \text{Mn}^{2+}/\text{Mn}^{4+}$ redox couple. The following thrusts are pursued:

- Use bulk, local, and surface characterization techniques to investigate structural and chemical properties

- Obtained detailed characterization on TM and O redox chemistries occurring both in the bulk and on the surface
- Use a combination of experimental and theoretical framework to understand various structural ordering features and establish how local and long-range structure affect lithium transport in DRX cathodes
- Model surface energy and particle morphology, and investigate their effect on ion transport and stability
- Understand degradation mechanisms in the bulk and at the cathode/electrolyte interface.

Results

1) Structural and chemical characterization – Due to the disordered nature, local structural probes such as solid-state NMR is an excellent characterization technique for DRX materials. Figure II.2.H.1 shows the ^7Li and ^{19}F NMR data collected on pristine LMNOF and LNTMOF samples. The ^7Li NMR data shown in Fig. 1a and 1c exhibit broad signals attributed to paramagnetic ^7Li environments in the DRX. Isotropic pj-MATPASS spectra, depicted as gray shaded regions, indicate a distribution of ^7Li chemical shifts, consistent with the large range of Li local environments in the disordered structures. In contrast, the sharp diamagnetic ^7Li signals centered at 0 ppm reveal Li-containing diamagnetic domains in the DRX or impurity phases (Li_2CO_3 , Li_2O , LiF), as exemplified by the overlaid LiF spectra (in blue). Integration of the ^7Li spectra suggests that 14% and 25% ($\pm 5\%$) of Li nuclei are in diamagnetic environments in the LMNOF and LNTMOF samples. ^{19}F NMR data collected on LMNOF are shown in Figure II.2.H.1b and exhibit broad, overlapping signals clearly distinct from the LiF signal shown in blue, indicating bulk F incorporation in the DRX structure and negligible F-containing diamagnetic impurities or domains. In the case of LNTMOF, the ^{19}F NMR data are shown in Figure II.2.H.1d. The pj-MATPASS isotropic spectrum shown as a gray shaded region reveals a broad distribution of ^{19}F chemical shifts, indicative of bulk F incorporation in the DRX. The sharp signal at -204 ppm provides evidence for LiF -like F environments, which could either arise from local diamagnetic domains due to short-range order in the DRX or from LiF impurity phases. These domains/impurities can unfortunately not be quantified from the ^{19}F NMR data, as NMR signals from F nuclei directly bonded to Ni are too broad to be observed.¹ 2D NMR technique is currently being explored to better understand short-range order in these materials. Such experiments combine ^7Li and ^{19}F chemical shift information into one correlation map and provide insight into Li-F spatial proximities, as shown in Figure II.2.H.1e for LiF . This approach remains challenging for paramagnetic DRX samples, due to very fast NMR signal decay.

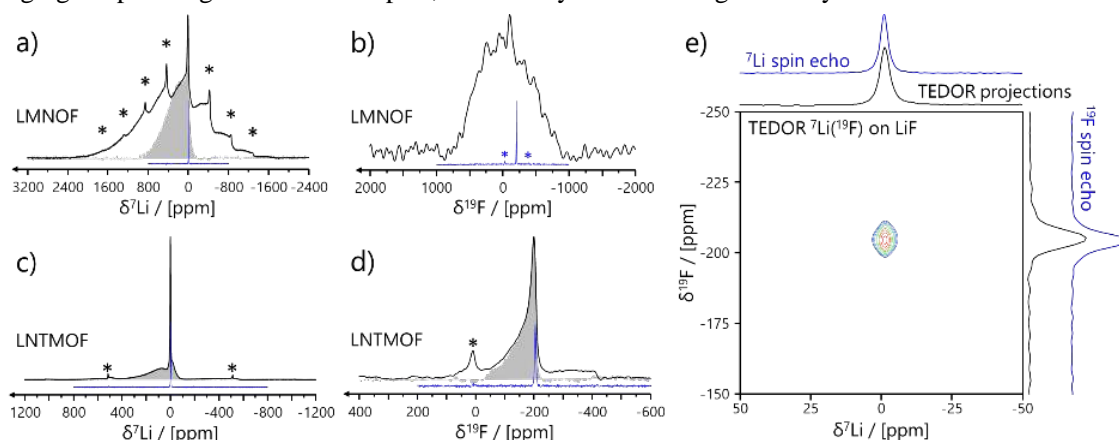


Figure II.2.H.1 ^7Li (a, c) and ^{19}F (b, d) spin echo NMR spectra of LMNOF (a, b, in black), LNTMOF (c, d, in black) and LiF (a-d, in blue) obtained at $B_0 = 7$ T and 60 kHz (a, b) or 55 kHz (c, d) magic angle spinning (MAS). Asterisks indicate spinning sidebands. Isotropic ^7Li (a, c) and ^{19}F (b) pj-MATPASS spectra collected on LMNOF (a) and LNTMOF (c, d) are represented with a gray shading. (e) $^7\text{Li}\{^{19}\text{F}\}$ 2D TEDOR spectrum of LiF obtained at $B_0 = 7$ T and 45 kHz MAS using a 45 μs recoupling time. The TEDOR projections in black are compared to LiF ^7Li and ^{19}F MAS NMR spectra in blue.

Raman spectroscopy was also used to probe local structure and chemical changes in DRX materials. Figure II.2.H.2 shows the Raman spectra of LMNOF and LNTMOF collected with a 512 nm Ar⁺ ion laser. The band at 624 cm⁻¹ can be viewed to belong to Mn-O stretching vibration of the MnO₆ group. The band is assigned to A_{1g} symmetry in the O_h⁷ spectroscopic space group. The position and half-width of the band are independent of Li concentration but sensitive to distortions in the MnO₆ octahedra. Thus, the peak shape could provide useful insights about the extent of distortion in the structure during the cycling process and also act as a rubric to measure the fluorine distribution in the powder. The intensity of the shoulder at 500 cm⁻¹ on the hand is directly correlated with ratio of Mn³⁺ and Mn⁴⁺ in the system making it an ideal candidate to study the lithiation process in the bulk or surface of the material. For LNTMOF (Figure II.2.H.2b), bands at 527 cm⁻¹ (F_{2g}) and 407 cm⁻¹ (E_g) are assigned to Ni²⁺ symmetric stretch mode. Both these bands have been shown to be sensitive to the oxidation state of Ni in the electrode and to Ni dissolution from the surface. The band observed at 816 cm⁻¹ is assigned to a doubly coordinated oxygen (Mo₂-O) stretching mode which results from cornered shared oxygen between two octahedra.

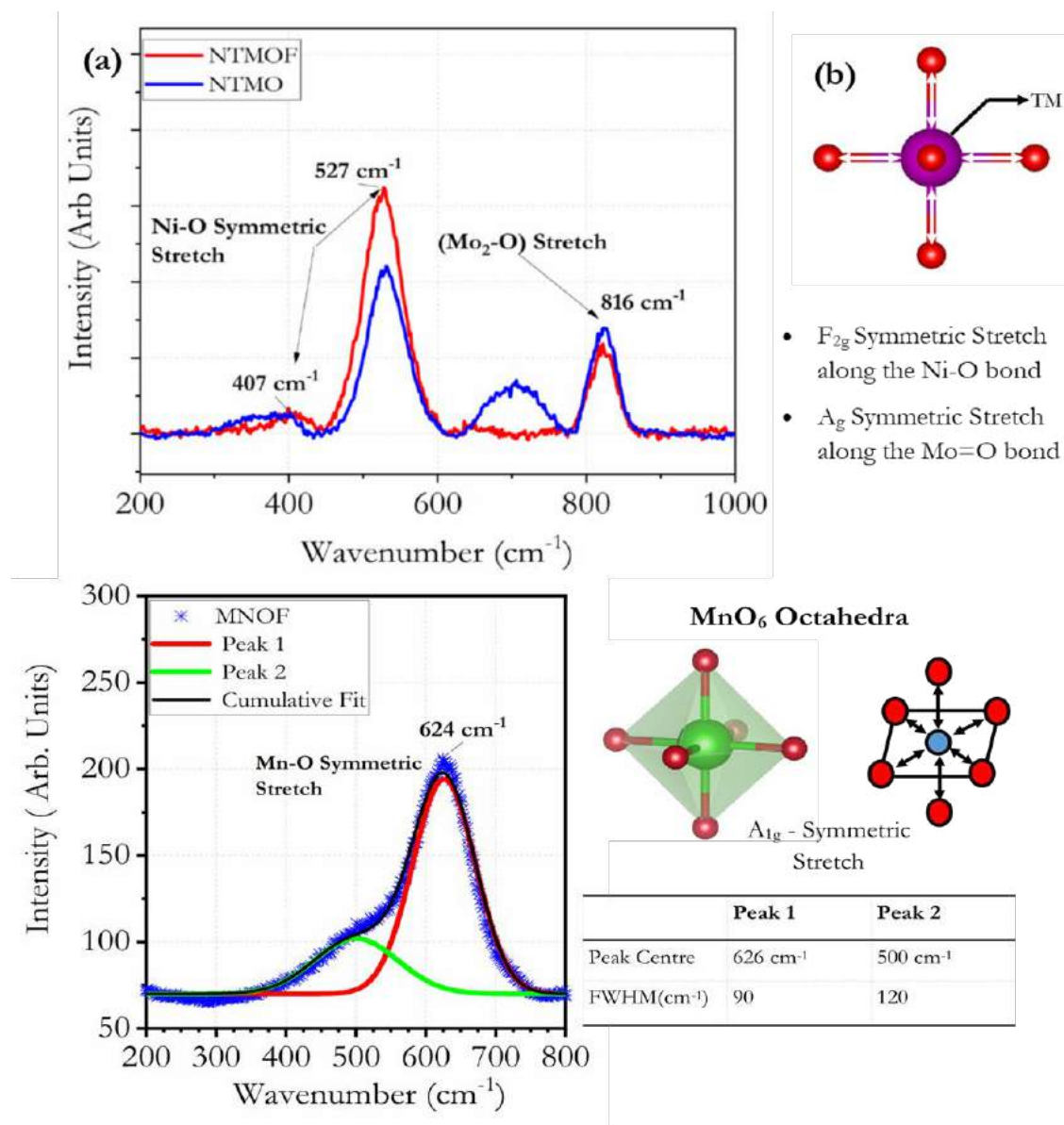


Figure II.2.H.2 Raman spectra collected on a) LMNOF and b) LNTMOF. Schematics of the Mn-O symmetric stretch are also shown

2) Redox chemistry and degradation mechanism – Understanding chemical reaction mechanisms in the bulk and on the surface is critical in addressing performance issues facing DRX materials. High-efficiency mapping of resonant inelastic X-ray scattering (mRIXS) was recently used to solve the line shape distortion issue of TM-*L* edges and to distinguish the lattice O redox states from the dominating hybridization features in O-*K* signals. In order to obtain the intrinsic oxygen redox signatures through O-*K* mRIXS, a procedure was established to avoid the X-ray radiation damage as well as the energy overlapping issue between the oxidized oxygen states and the strong hybridization features from TMs.¹ Figure II.2.H.3 shows results from representative Mn-*L* and O-*K* mRIXS studies. The experiments were performed on a series of LMNOF electrodes that were cycled to different electrochemical potentials or cycles. Oxidation states of Mn in the bulk can be quantified by fitting the signals extracted from Mn-*L* mRIXS, which is plotted in Figure II.2.H.3c (blue dashed line) during the initial charge/discharge cycle. The changes in Mn oxidation state provide direct quantification on capacity contributed by Mn redox. Signature from lattice oxidized oxygen emerges upon charging, especially at the high-voltage range, but the oxidized oxygen state clearly persists to a much lower potential during discharge.

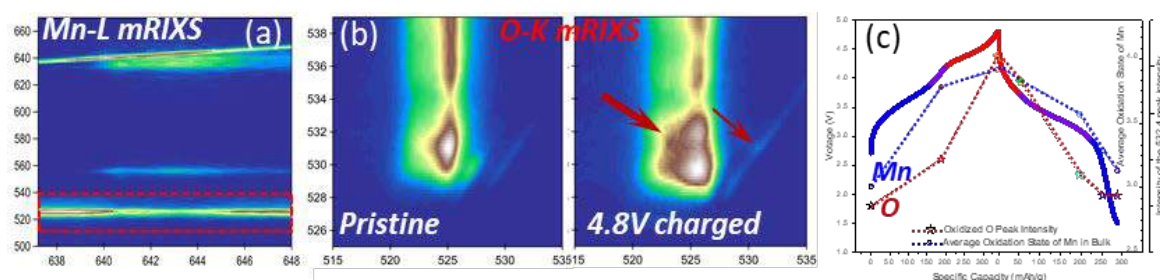


Figure II.2.H.3 mRIXS results of Mn-*L* (a) and O-*K* (b) collected on LMNOF cycled to different electrochemical potentials. The red rectangular in (a) indicates the area that non-distorted Mn-*L* spectra could be extracted for absolute quantification of the Mn redox reactions. Red arrows in (b) indicates the oxidized oxygen feature that could be quasi-quantified to reveal the reversibility and cyclability of the oxygen redox in DRX-based electrodes. The quantification results of Mn redox and the evolution of the oxidized oxygen feature are displayed in (c) in blue and red dashed lines, respectively

In general, the lattice oxygen redox probed by mRIXS displays decent reversibility, which is consistent with previous reports on this material.

The combined soft X-ray absorption spectroscopy (XAS), mRIXS and hard XAS results (not shown) also provides the information on the chemical contrast between the surface and the bulk states.

F *K*-edge XAS was used to examine the bonding environment of F and how it evolves with the cycling of cation-disordered oxyfluorides. Although F carries a nominally negative charge due to its highest electronegativity, distinctive F *K*-edge XAS spectra are produced depending on the bonding environment of F. In the simplest case, F in LiF carries a static negative charge and exists as fluoride anion. Its F *K*-edge spectrum (Figure II.2.H.4a) shows a sharp peak near 695 eV with no obvious pre-edge features. In the post-edge region, a few shallow and broad peaks can also be seen. These distinctive spectral features are the result of the highly localized charge accumulated at F centers, as illustrated in Figure II.2.H.4b. On the other hand, in oxyfluoride rocksalts such as $\text{Li}_{1.3}\text{Nb}_{0.2}\text{Mn}_{0.5}\text{O}_{1.8}\text{F}_{0.2}$ ($\text{Li}_{1.3}\text{M}_{0.5}\text{NOF}$, an analogue to LMNOF), the peak near 695 eV is much broader and no post-edge features are present (Figure II.2.H.4a). The peak broadening implies highly delocalized electron distribution, which can be understood as covalency between F and its neighbors (Figure II.2.H.4b). On the basis of this understanding, F *K*-edge XAS was performed on a series of $\text{Li}_{1.3}\text{M}_{0.5}\text{NOF}$ samples at both charged and discharged states after various cycles, and the results are shown in Figure II.2.H.4c-Figure II.2.H.4e. With the increase of cycle number, the main peak in the F *K*-edge XAS profile becomes sharper, suggesting increase of ionic character in F. Quantitative analysis was performed by using PCA, which deconvolutes the spectra into two independent components of pristine $\text{Li}_{1.3}\text{M}_{0.5}\text{NOF}$ and LiF used as the standards for covalent and ionic contributions, respectively. PCA spectral fitting are shown in Figure II.2.H.4c and Figure II.2.H.4d, and the results on ionic fraction evolution is shown in Figure II.2.H.4e. It is evident that with cycling, the ionic fraction continues to increase. After 50 cycles, ionic fraction in both

charged and discharged states is significant, at ~20% and 40%, respectively. The analysis suggests that cycling leads to changes in the chemical environment of F, which steadily evolves into more LiF-like.

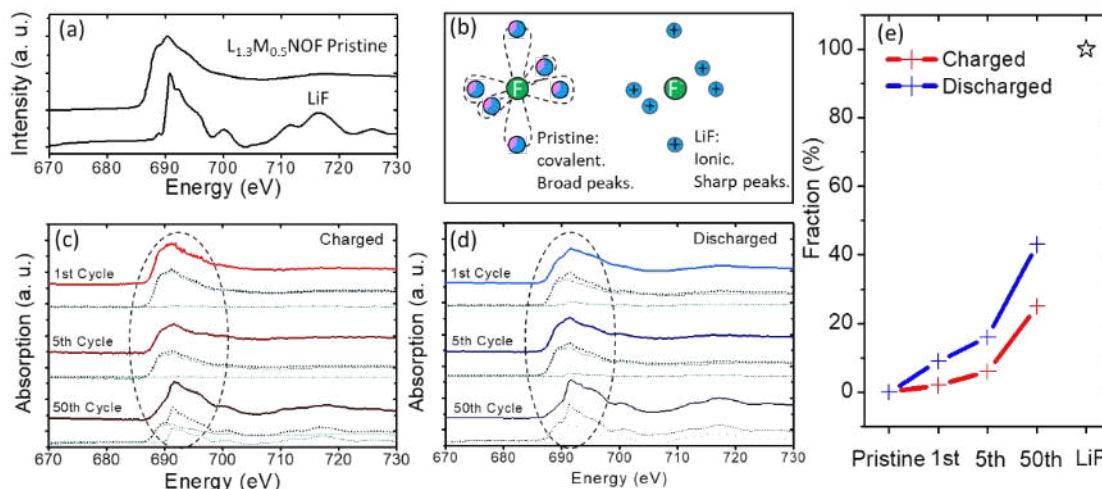


Figure II.2.H.4 a) Comparison of F K-edge XAS of pristine $L_{1.3}M_{0.5}NOF$ and LiF, b) a schematic showing covalent and ionic bonding environment of F. Comparison of F K-edge XAS of $L_{1.3}M_{0.5}NOF$ cathode after: c) charged to 4.8 V and d) discharged to 1.5 V after various cycles. All spectra were collected under TEY mode. Each spectrum was fitted via linear combination fitting of covalent and ionic components (green lines) and the fitted spectra are shown in dotted lines. e) Changes in ionic fraction as a function of cycle number

To further understand detrimental surface processes that lead to performance decay in DRX, differential electrochemical mass spectrometry (DEMS) and fluoride scavenging technique were used, which allow for the direct examination of processes such as oxygen loss, electrolyte degradation, and fluoride dissolution. By periodically sampling the gas headspace of a cell during cycling, DEMS allows the in situ observation and quantification of gas evolution from the cell. Figure II.2.H.4a shows the gas evolution from a sample DRX material observed over several electrochemical cycles. On the first cycle, a small amount of oxygen is evolved. On subsequent cycles, no oxygen is evolved. Meanwhile, CO_2 is evolved at a higher, more consistent rate throughout cycling. The first cycle displays significantly more CO_2 than subsequent ones, and CO_2 evolution occurs whenever there is a nonzero current in the cell. Monitoring the evolution of O_2 during cycling allows for the examination of irreversible oxygen loss, whereas monitoring the evolution of CO_2 provides information about electrolyte degradation. These techniques provide valuable information about the interfacial stability of DRX materials.

Fluoride-scavenging is a technique whereby an additive that reacts with fluoride is added to the cell. This technique can be used to monitor fluoride dissolution from DRX materials because the scavenger additive will not react with fluorine in the lattice of the material, but it will react with fluoride that leaches out of the material. By using a scavenger additive that produces a gas when it reacts with fluoride, fluoride-scavenging can be coupled with DEMS to measure the product of the reaction. Figure II.2.H.5b displays DEMS data for a cell containing a fluorine-scavenger. In this experiment, fluoride reacts with the scavenger to form gaseous Me_3SiF , which is then detected with DEMS. It shows a gradually decreasing background profile of Me_3SiF , accompanied by distinct peaks of Me_3SiF evolution at high voltages. The background profile may correspond to residual fluoride that remains from synthesis, which is slowly consumed. The distinct peaks at high voltages, however, represent additional fluoride dissolution from the material that occurs to a diminishing extent upon cycling. Using this measurement as a proxy for fluoride formation in the cell, fluoride dissolution from the cathode can be studied in situ.

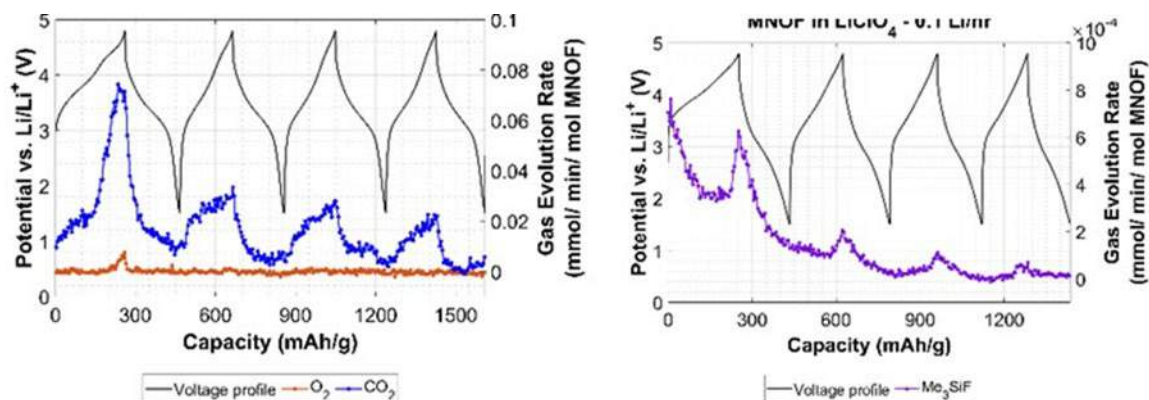


Figure II.2.H.5 a) DEMS measurements of O_2 and CO_2 evolution during cycling of LMNOF and b) fluoride-scavenging coupled with DEMS to examine fluoride dissolution from LMNOF. The cell is cycled in $LiClO_4$ instead of $LiPF_6$ to remove other sources of fluoride

Complementing the experimental studies, surface and oxygen evolution energy calculations can provide further insights on interfacial chemistry. Surface energy calculations for the [100], [110], [111] and [112] facets of Li_2MnO_2F was performed to find the Wulff shape of the particle. A unique method to achieve symmetric surfaces for this disordered material was developed for this purpose. Once the Wulff shape is determined, the oxygen evolution energy on each facet will be calculated to determine which facets and terminations are more robust to oxygen loss. Oxygen evolution energy calculations were also performed on the [100] surfaces of these materials while varying the concentration of fluorine on the surface. Oxygen retention was found to be higher on surfaces with higher concentrations of fluorine.

3) Local structural ordering and Li-transport – Recently, it was revealed that DRX systems display short-range order (SRO) but disordered over the long-range. Such cation arrangements enable Li-transport through a Li-percolating network that can be characterized by the population and spatial distribution of tetrahedral clusters composed of Li and TMs. Scanning transmission electron microscopy (STEM) and associate techniques were used to characterize the atomic structural feature in an LMNOF analogue, $Li_{1.2}Ti_{0.2}Mn_{0.6}O_{1.8}F_{0.2}$. A high-angle annular dark-field (HAADF) STEM image and the corresponding Fast Fourier transform (FFT) are shown in Figure II.2.H.6a and Figure II.2.H.6b, respectively. In the FFT, the diffracted bright spots correspond to the cubic lattice, while the diffused intensity corresponds to short-range order (SRO). By filtering the FFT using masks that only permit the diffracted spots (Figure II.2.H.6d), the atomic structures corresponding to the long-range ordered (LRO) cubic lattice are extracted by the Inverse-FFT (IFFT) image in Figure II.2.H.6c. By filtering the FFT using masks that block the diffracted spots (Figure II.2.H.6f), the ordering after the LRO is removed can be directly visualized in the IFFT image in Figure II.2.H.6e, where the green and red color correspond to lower and higher intensity, respectively. The intensity in the filtered HAADF image can be directly correlated to the cation densities within each atomic column. Since the heavy TM atoms are directly observable by HAADF imaging, the green and red color in Figure II.2.H.6h should correspond to Li-rich and TM-rich regions, respectively, as compared to the average composition. Upon examining the configurations of Li-rich and TM-rich atomic columns in Figure II.2.H.6h, it is quite surprising that a quasi-periodic pattern persisting more than several unit cells in width, typically several nanometers in dimension, such as those highlighted by the dashed rectangles, can be commonly observed. The scale of these quasi-periodic patterns is far beyond those for the commonly defined SRO, indicating a quasi-ordered state. In each of those patterns, the Li-rich channels are atomically thin and oriented along a preferred direction. At large scales, the nanosized quasi-periodic patterns jointed to result in interconnected Li-rich channels that should allow facile Li percolation along arbitrary directions. This suggests that the cation arrangements in DRX are not only short-range ordered but also quasi-ordered over long ranges. The long-range quasi-ordered states, rather than the previously regarded fully disordered structures, predominantly determine the atomic

configurations of the Li-percolation network and thus can regulate the electrochemical properties of the DRX cathodes.

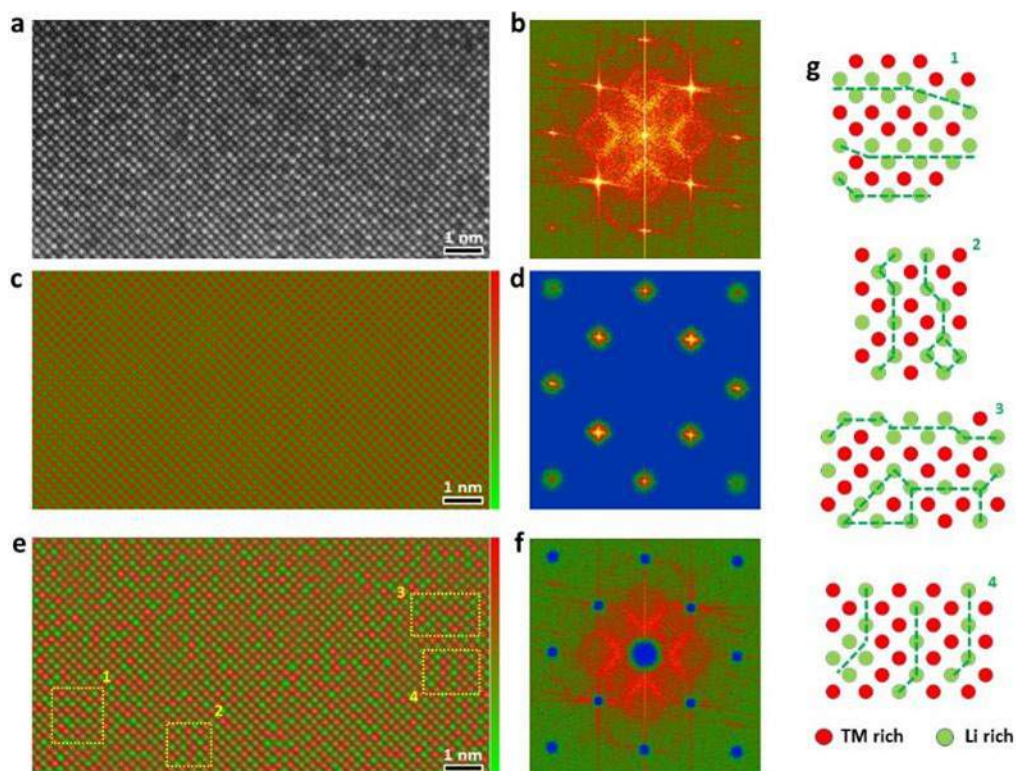


Figure II.2.H.6 Atomic structures of $\text{Li}_{1.2}\text{Ti}_{0.2}\text{Mn}_{0.6}\text{O}_{1.8}\text{FO}_{0.2}$. (a) As-captured atomic-scale HAADF STEM image and (b) corresponding Fast Fourier transform (FFT). (c) Filtered HAADF STEM image from the masked FFT pattern in (d) showing atomic structures that correspond to the long-range ordered cubic lattice. (e) Filtered HAADF STEM image from the masked FFT pattern in (f) showing the quasi-periodic pattern, as typified by the dashed line marked regions as indicated by 1-4. (g) Atomic models for 4 different nanosized regions highlighted in (e), indicating quasi-periodic patterns over long ranges

The type of SRO that appears is often determined by the different cation-cation and cation-anion interactions and is highly related to the electrochemical performance of the DRX cathodes. To better understand the complex relation between F substitution and Li percolation, Monte Carlo simulations based on an *ab initio* parameterized cluster expansion was conducted to model the cation and anion distributions in $\text{Li}_x(\text{M}, \text{M}')_{2-x}\text{O}_{2-y}\text{F}_{2y}$ systems at synthesis temperatures. Figure II.2.H.7a shows the amount of percolating Li as a function of F content in four representative DRX systems, $(\text{M}, \text{M}') = (\text{Mn}^{3+}, \text{Ti}^{4+})$, $(\text{Ni}^{2+}, \text{Ti}^{4+})$, $(\text{Ni}^{2+}, \text{Nb}^{5+})$ and $(\text{Mn}^{2+}, \text{Ti}^{4+})$, for a typical Li excess composition $x = 1.2$. For all systems, F content initially decreases the amount of percolating Li but then, around 2-8% F, increases it as more F is incorporated. Figure II.2.H.7b shows the amount of percolating Li (color scale) and the theoretical transition metal redox capacity (solid lines) as a function of both Li and F contents for the $(\text{Ni}^{2+}, \text{Ti}^{4+})$ system and serves as a design map for experimental optimization in this chemical space. This plot reveals that increasing the Li content increases the amount of percolating Li but lowers the transition metal redox capacity, which can impede long-term capacity retention. This tradeoff results in a limited region of compositional space, enclosed by the transparent oval, where DRX cathodes with a high capacity and good cyclability are likely to be synthesized. Figure II.2.H.7c shows the experimental validation of the role of F. Based on the voltage curves of samples with 0% F (LMNO), 5% F (LMNF10), and 15% F (LMNF30), the sample with 5% F exhibits the lowest capacity among the three materials, demonstrating that Li percolation can be curtailed by low F content but recovered by increased F content.

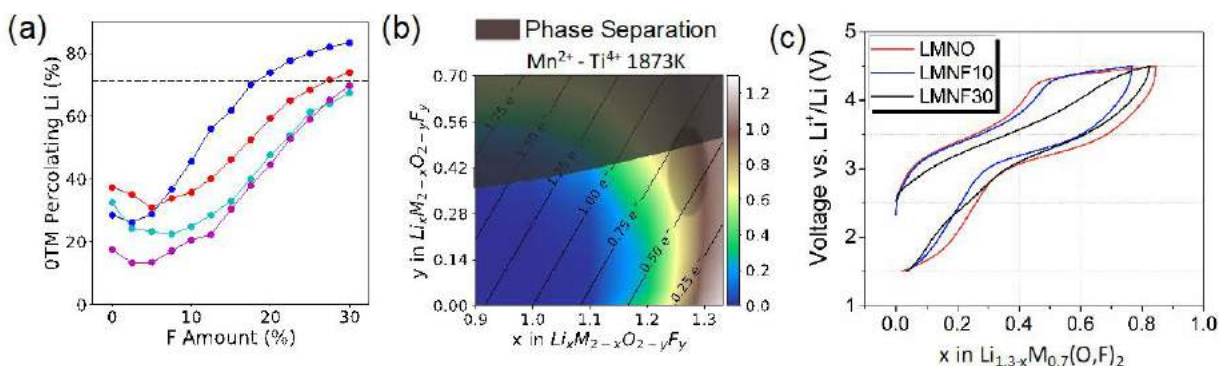


Figure II.2.H.7 (a) Evolution of the amount of percolating Li as a function of F content obtained from Monte Carlo simulations at 1873 K, a temperature representative of typical synthesis conditions for this class of materials, in four $\text{Li}_{1.2}(\text{M}, \text{M}')_{0.8}\text{O}_{2-y}\text{F}_y$ DRX systems: $(\text{M}, \text{M}') = (\text{Mn}^{3+}, \text{Ti}^{4+})$, $(\text{Ni}^{2+}, \text{Ti}^{4+})$, $(\text{Ni}^{2+}, \text{Nb}^{5+})$ and $(\text{Mn}^{2+}, \text{Ti}^{4+})$. (b) Li percolation map as a function of both Li and F contents in $\text{Li}_x(\text{Ni}^{2+}, \text{Ti}^{4+})_{2-x}\text{O}_{2-y}\text{F}_y$, obtained from Monte Carlo simulations at 1873 K. The color scale represents the amount of accessible Li through the O-TM percolation network, while solid lines indicate the theoretical $\text{Ni}^{2+}/\text{Ni}^{4+}$ redox capacity. (c) First-cycle voltage profiles of $\text{Li}_{1.3}\text{Mn}_{0.267}\text{Nb}_{0.433}\text{O}_2$ (LMNO), $\text{Li}_{1.3}\text{Mn}_{0.3}\text{Nb}_{0.4}\text{O}_{1.9}\text{F}_{0.1}$ (LMNF10), and $\text{Li}_{1.3}\text{Mn}_{0.367}\text{Nb}_{0.333}\text{O}_{1.7}\text{F}_{0.3}$ (LMNF30) within a voltage window of 1.5–4.5 V

Conclusions

DRX materials are promising Co-free cathodes with flexible cation and anion chemistry and high energy density. This project has employed a suit of bulk, local, and surface characterization techniques to gain comprehensive understanding on structural and chemical characteristics of these compounds as well as their changes associated with the battery cycling. Detailed investigation on the redox chemistry of both TM and O led to insights on materials degradation mechanisms. A combination of theory, synthesis and characterization was used to study the local and long-range structural features in F-DRX. Cation SRO is a useful handle to modify the voltage profile and Li-ion mobility, and fluorination was found to have a significant influence on both SRO and Li kinetics. For oxides with good Li kinetics, low amounts of fluorination can be detrimental and high fluorination amounts are required to improve Li percolation. In the future work, increasing fluorine and transition metal contents will be explored as strategies to reduce oxygen activities and improve cycle life. Effort to improve rate capability will focus on understanding root cause of rate limit, whether it is intrinsic to the DRX materials or related to surface densification process. SRO will be optimized through modeling and characterization, and experimental conditionals will be explored to tailor and control SRO during synthesis.

Key Publications

1. H. Ji, A. Urban, D. A. Kitchaev, D. H. Kwon, N. Artrith, C. Ophus, W. Huang, Z. Cai, T. Shi, J. C. Kim, H. Kim, G. Ceder, Hidden structural and chemical order controls lithium transport in cation-disordered oxides for rechargeable batteries, *Nat. Comm.*, 10, 592, 2019.
2. Z. Lun, B. Ouyang, Z. Cai, R. J. Clément, D. H. Kwon, J. Huang, J. K. Papp, M. Balasubramanian, Y. Tian, B. D. McCloskey, H. Ji, H. Kim, D. A. Kitchaev, G. Ceder, Design Principles for High-Capacity Mn-Based Cation-Disordered Rocksalt Cathodes, *Chem*, 6, 1, 2020.
3. B. Ouyang, N. Artrith, Z. Lun, Z. Jadidi, D. A. Kitchaev, H. Ji, A. Urban, G. Ceder, Effect of Fluorination on Lithium Transport and Short-Range Order in Disordered-Rocksalt-Type Lithium-Ion Battery Cathodes, Submitted.
4. R. J. Clément, Z. Lun, and G. Ceder, Cation-disordered Rocksalt Transition Metal Oxides and Oxyfluorides for High Energy Lithium-ion Cathodes, submitted to *Energy Environ. Sci.* (2019).
5. Zhao, E. et al. "Stabilizing the Oxygen Lattice and Reversible Oxygen Redox Chemistry through Structural Dimensionality in Lithium-Rich Cathode Oxides," *Angew Chem Int Ed Engl* **58**, 4323-4327 (2019). doi:10.1002/anie.201900444.

Acknowledgements

Guoying Chen, Juhyeon Ahn, Jordan Burns, Dongchang Chen, Guoying Chen, Raphaele Juliette Clement, Matthew Crafton, Emily Foley, Raynald Giovine, Yang Ha, Huiwen Ji, Haegyum Kim, Robert Kostecki, Linze Li, Bryan McCloskey, Jagjit Nanda, Kristin Persson, Ethan C. Self, Chongmin Wang, Wanli Yang, Yiman Zhang

II.3 Next Generation Lithium-Ion batteries: Frontier Science at Interfaces

II.3.A Molecular-level Understanding of Cathode-Electrolyte Interfaces (SLAC)

Michael F. Toney, Principal Investigator

Stanford Synchrotron Radiation Lightsource, SLAC National Accelerator Laboratory
2575 Sand Hill Road
Menlo Park, CA 94025
E-mail: mftoney@slac.stanford.edu

Peter Faguy, DOE Technology Development Manager

U.S. Department of Energy
E-mail: Peter.Faguy@ee.doe.gov

Start Date: October 1, 2018

End Date: September 30, 2021

Project Funding (FY19): \$450,000

DOE share: \$450,000

Non-DOE share: \$0

Project Introduction

Understanding the underlying chemistry and physics of the cathode-electrolyte interface (CEI) in next-generation lithium-ion batteries (NG-LIB) is crucial to overcome the present limitations and develop stabilization strategies for functional interfaces in harsh electrochemical conditions. To tackle this challenge, we will combine theoretical modeling with advanced X-ray surface scattering studies, spectroscopic and electrochemical characterization using model, thin-film, transition-metal oxide (TMO) electrodes and high purity electrolytes. The collaboration team consists of researchers from SLAC National Accelerator Laboratory, U.S. Army Research Laboratory/ARL, and Lawrence Berkeley National Laboratory/LBNL. We will combine molecular-level modeling of the interface and its evolution with advanced interface diagnostics tools using model systems. Such approach would allow sufficient in-depth modeling and characterization to develop the necessary level of understanding of the interface degradation processes and it builds on our past success in related interfacial research [1]-[8]. To achieve our goals, we have employed high-voltage TMO epitaxial thin film cathodes with controlled complexity and highly purified baseline electrolytes, and our high-precision *three-electrode* electrochemical cell. We have conducted various synchrotron x-ray studies to elucidate the surface structure of NMC thin-films and their degradation with carbonates-based electrolytes. To determine the interfacial evolution of cathode thin-films and interphase evolution pathways, we will use in situ and ex situ synchrotron x-ray measurements that characterize the structural and chemical evolution of the interface before, during and after CEI formation. These will feature simultaneous in situ surface x-ray scattering, and ex situ x-ray spectroscopies, as well as ion and electron spectroscopies. Our approach will provide fundamental knowledge about how the electrode surface and electrolyte composition dictate the reaction pathways and will help enable strategies to stabilize the interfaces.

Objectives

High-energy NG-LiB electrochemistries require the utilization of high capacity and high-voltage cathode materials (> 4.5 V vs Li/Li⁺). Their full potential has to date been hampered by the paucity of understanding the underlying chemistry and physics of the cathode interfaces. In particular, the practical implementation of NG-LiBs is to a large extent obstructed by the absence of a suitable electrolyte. While typical carbonate-based electrolytes have been reliable in current LiBs, they intrinsically and thermodynamically degrade at higher potentials. In combination with highly reactive cathode surfaces and defects, this creates an unstable cathode-electrolyte interface, which results in the evolution of CO₂, active material consumption, transition metal dissolution and increased cell impedance. This is even more problematic at elevated temperatures such as present for fast charging. While significant progress in mitigating these issues has been reported by using nitriles [9], sulfones [10],[11], ionic liquids, or fluorinated carbonates [12], stabilization of the high voltage

TMO cathode-electrolyte interface is still unresolved due to lack of mechanistic understanding of the degradation mechanism and development of the stabilization strategy. Our objective is to provide an unprecedentedly detailed picture of the underlying physics and chemistry of the cathode-electrolyte interface. This includes a detailed understanding of the molecular arrangement of electrolyte molecules and electrochemical double layer at the cathode surface and how this evolves into the CEI (e.g., the nucleation/growth mechanisms as well as CEI structure, morphology, and composition). We anticipate that our results will fill the gap in understanding of the underlying chemistry and physics of the cathode interfaces and will be disseminated *via* a number of impactful publications. This knowledge can be utilized to guide the design of optimized electrolytes and cathode surfaces, and will help to accelerate the development and deployment of NG-LIBs for electric vehicles.

Approach

Our approach is to combine molecular-scale modeling with advanced x-ray studies and precision electrochemical characterization using model thin-film electrodes and high purity electrolytes. It will start with the purification of electrolytes and the controlled growth of NMC thin-films by Pulsed laser deposition (PLD), followed by precise electrochemistry measurement in our three-electrode electrochemical cone cell, and the synchrotron-based X-ray scattering and spectroscopy studies of NMC surface. PLD-derived epitaxial thin films will be used as well-defined, high voltage cathode materials. We will utilize the high-voltage cathode material lithium nickel-manganese-cobalt-oxide (NMC, $\text{LiNi}_{0.5}\text{Mn}_{0.3}\text{Co}_{0.2}\text{O}_2$). The use of epitaxial thin films as model systems enables high resolution x-ray experiments and well-controlled electrochemical experiments that only contain contributions from the cathode of interest rather than parasitic reactions from the conductive additive or binder material. In order to reach our proposed objectives, we plan a multimodal approach, involving synchrotron-based x-ray scattering techniques (x-ray reflectivity/XRR & surface X-ray diffraction/SXRD), as well as *ex situ* x-ray spectroscopy (x-ray absorption spectroscopy/XAS) measurements at electrolyte-epitaxial thin film cathode interfaces. These are complemented by molecular dynamics (MD) simulations and density functional theory (DFT) calculations. XRR/XRD will yield information on the electron density profile, which can then be chemically interpreted in terms of the arrangement of the molecules within the electrolyte, as well as the nucleation and growth of the CEI. The *ex situ* x-ray spectroscopy will unravel complementary chemical information and composition.

Results

While traditional carbonate-based electrolytes have been widely developed, they tend to be electrochemically decomposed on cathode surface at high potentials. And the interfacial reactions between carbonate-based electrolytes and highly reactive cathode surfaces would trigger the degradation of the cathodes, leading to transition metal dissolution and the cell impedance increase. Intensive efforts have been focused on formation of stable CEI using different electrolytes, and understand the degradation mechanism of cathode surface and carbonates-based electrolytes.

To investigate the electrochemical stability of baseline carbonates (1.2 M LiPF_6 in EC : EMC), sulfones (3.25M LiFSI in sulfolane) and fluorinated carbonates (1 M LiPF_6 in FEC : EMC, and LiPF_6 in FEC : FEMC : HFE), LSV have been conducted on Pt surface using the three-electrode electrochemical cone cell (Figure II.3.A.1a). As evidenced by the significant increased current at high potentials ($>4.4\text{V}$), the carbonate-based electrolyte showed limited electrochemical stability at high potentials. However, as compared with carbonates, sulfones and fluorinated electrolytes enlarged enhanced electrochemical stability windows. This confirmed the advantage of sulfones and fluorinated electrolytes over carbonate-based electrolytes for high-voltage operation.

To understand the electrolyte degradation behaviors, DFT calculations have been conducted to probe the reaction energy of solvent and salt decomposition with half-lithiated $\text{Li}_{0.5}\text{NiO}_2$ and LiNiO_2 as model cathodes. At $\text{Li}_{0.5}\text{NiO}_2$ surface, the double H-transfer mechanism of EMC becomes the dominant mode with a reaction energy of -3.05 eV . The intermediate associated with ethylene elimination spontaneously releases H from $-\text{CH}_2$ to the surface with a reaction energy of -2.91 eV . The H-transfer from the alkyl side of FEC also have a very low energy of the intermediate state (-0.09 eV) and very favorable reaction energy of -2.90 eV relative to the chemisorbed state. The decomposition of LiPF_6 salts on LiNiO_2 surface have a reaction energy of -1.75 eV .

These theoretical modeling indicated the chemical instability of electrolytes on cathode surfaces and the influence of different electrolyte compositions - both EMC and FEC tend to decompose on the $\text{Li}_{0.5}\text{NiO}_2$, but FEC reaction is much slower (higher energy barrier).

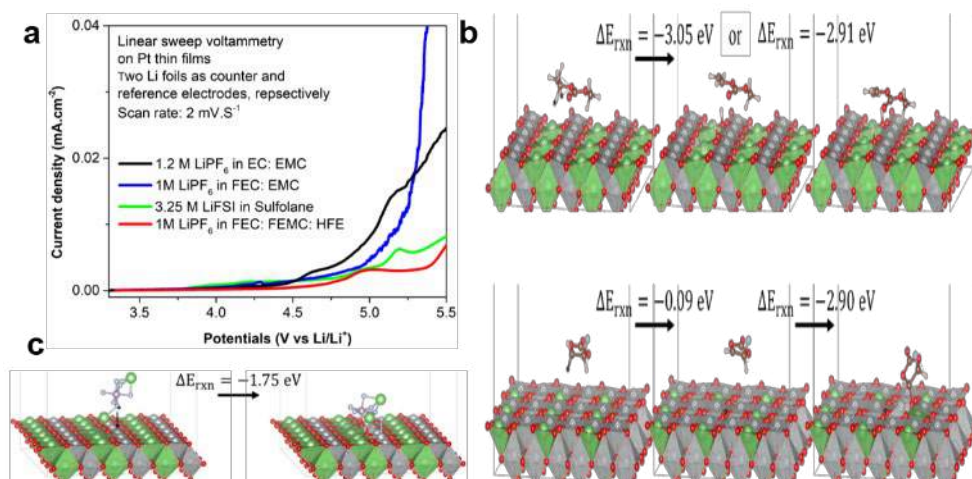


Figure II.3.A.1 The electrochemical stability window of different electrolytes and the degradation of electrolytes on cathode surface as-revealed by theoretical modeling and experiments. (a) The linear sweep voltammetry (LSV) studies of baseline carbonates (1.2 M LiPF₆ in EC/ethylene carbonate : EMC/ethyl methyl carbonate), sulfones (3.25M LiFSI in sulfolane), as well as fluorinated carbonates (1 M LiPF₆ in FEC/fluoroethylene carbonate : EMC, and LiPF₆ in FEC : FECM/methyl (2,2,2-trifluoroethyl) carbonate): HFE/2,2,2-Trifluoroethyl 1,1,2,2-tetrafluoroethyl ether); (b) The most probable decomposition reactions and the reaction energy (E_{rxn}) of EMC (top) and FEC (bottom) on $\text{Li}_{0.5}\text{NiO}_2$, respectively;. (c) The reaction energy of LiPF₆ salt decomposition on LiNiO_2 . Colors: Li (green), O (red), Ni (dark grey), F (light grey), P (light grey)

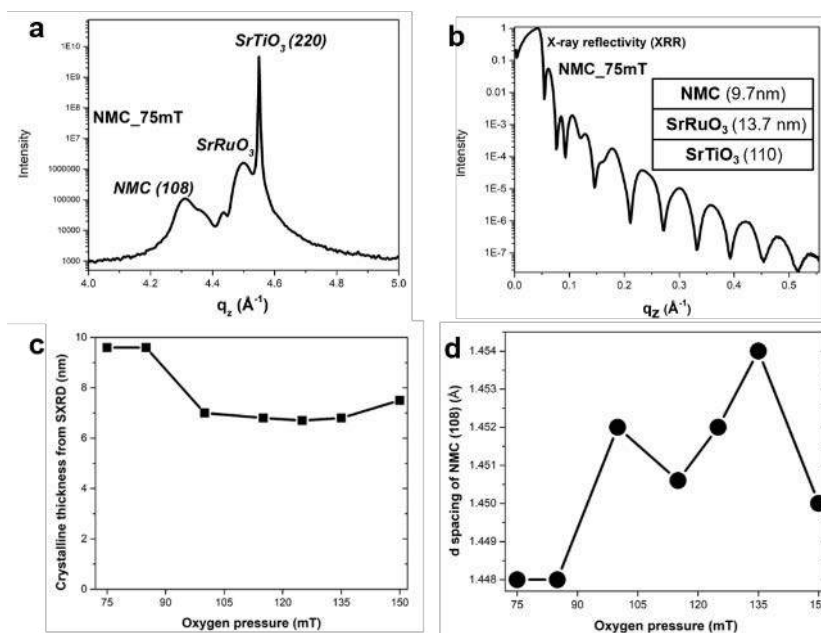


Figure II.3.A.2 Structure characterization of PLD-grown NMC thin-films with different oxygen pressure. The SXRD (a) and XRR (b) of NMC thin-films grown at an oxygen pressure of 75mT, inserted are the scheme of the structure and thickness of NMC thin-film, and SrRuO_3 buffer layers. The crystalline thickness and d spacing of (108) Bragg peak as a function of oxygen pressure conditions in PLD growth

To obtain molecular-level insights into electrolyte degradation and cathode-electrolyte interface, model cathode surfaces are needed to reduce the complexity. Therefore, we conducted PLD growth of NMC thin

films on SrTiO_3 (110) substrates with SrRuO_3 as conductive buffer layers, and explored the influence of oxygen pressure on structural parameters in thin-films. To better understand the interfacial evolution of CEI, we started with thin films of 10 nm. The crystalline structure and film thickness have been studied by the synchrotron based SXRD and XRR, respectively. The appearance of NMC (108) Bragg peak in the SXRD pattern indicated the successful growth of NMC thin-films at the oxygen pressure of 75 millitorr (mT), and the film thickness is determined by XRR, and the well-defined slope and oscillations indicated the existence of smooth interface in NMC- SrRuO_3 - SrTiO_3 (Figure II.3.A.3 a-b). The influence of oxygen pressure on the crystalline thickness and d-spacing of (108) Bragg peak is then systematically studied by SXRD and XRR (Figure II.3.A.2 c-d). It can be found that the oxygen pressure can influence the defect concentrations of as-deposited NMC thin-films during PLD growth. With the controlled growth of model thin-film cathodes, then we explored the electrochemical performances of NMC in typical carbonate-based electrolytes.

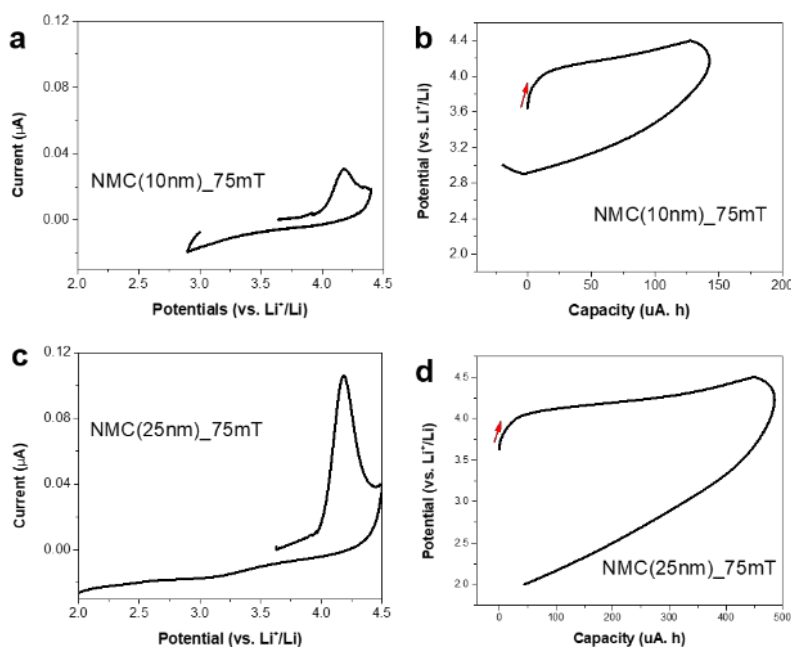


Figure II.3.A.3 The electrochemical characterization of PLD-derived NMC thin-films of different thickness. The cyclic voltammograms and potential-capacity curves of NMC thin-films grown under an oxygen pressure of 75mT in a thickness of 10 nm (a, b) and 25 nm (c, d), respectively (with a scan rate of 0.2 mV.S⁻¹ and in the electrolyte of 1M LiPF₆ in commercial EC : DMC/dimethyl carbonate)

To understand the electrochemical performance of NMC thin-films, cyclic voltammetry (CV) was conducted in our electrochemical cells. NMC in a thickness of 10 nm showed a delithiation peak centered at 4.2V, its capacity at 4.4 V reached to 13 % of its theoretical capacity. It is notable that with increased thickness to 25 nm, the capacity at 4.4 V increased to 20% of its theoretical capacity. Comparing the performances of NMC thin-films of two different thickness, we can get capacities much closer to the theoretical capacity with increased film thickness. Both films did not show obvious lithiation peaks, however, successful delithiation has been achieved in the thicker NMC films grown on Al foil (100nm) by PLD. Therefore, there is a neglected effect of film thickness on the lithiation and delithiation performances of NMC. Currently, we are working on increasing the thickness of NMC films on SrRuO_3 - SrTiO_3 and explore the neglected thickness effect on the electrochemical performance of NMC thin-films. As evidenced by many studies, NMC particles are chemical and electrochemically unstable with carbonate electrolytes, forming interfacial layers of about 10 nm upon cycling

In the ultrathin-film, the interfacial reaction between cathode surface and electrolyte has been significantly enhanced. Therefore, the degradation of NMC thin-films can happen due to the interfacial reactions between carbonate-based electrolyte and NMC.

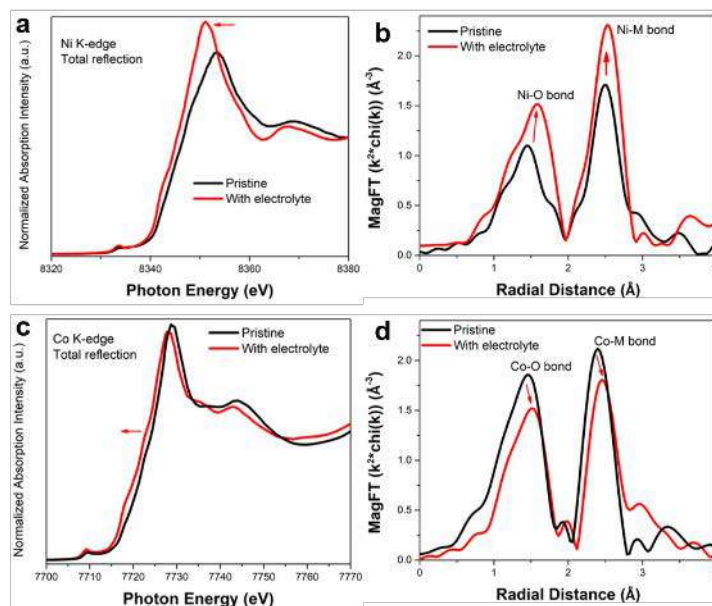


Figure II.3.A.4 The evolution of interphase from the chemical reactions between NMC and carbonate electrolytes (1M LiPF₆ in EC : DMC). The surface-sensitive total reflection X-ray absorption near edge structure (XANES) and Fourier transformed extended X-ray absorption fine structure (FT-EXAFS) of NMC thin-films with and without electrolyte at Co K-edge (a, b) and Ni K-edge (c, d), respectively

To understand the electrochemical behaviors and the transformations of NMC thin-films in carbonate-based electrolytes, we explored the chemical evolution of 10nm NMC thin-films through the total reflection X-ray absorption spectroscopy with surface and element sensitivities. As evidenced by the XANES and FT-EXAFS, both the oxidation states and coordination structures of the Co and Ni sites in the NMC thin-films have showed significant changes when they were exposed to carbonate-based electrolytes. In the XANES at Ni K-edge and Co K-edge, obvious negative shifts have been observed when NMC thin-films were soaked in 1M LiPF₆ in EC : DMC. This indicated the chemical reduction of Ni and Co sites in NMC thin-films that is induced by the carbonate-based electrolytes. Besides the chemical reduction, significant changes on the local coordination of metal-oxygen and metal-metal bonds have been also observed by FT-EXAFS for both Co and Ni sites. These results provided the evidence of the degradation of NMC thin-films with carbonate-based electrolytes. Such interfacial transformation is believed to account for the thickness effect in the electrochemical performances of NMC thin-films since the surface structure and chemistry have changed when NMC thin-films contacted with carbonate-based electrolytes. And the effects of different electrolytes and the thin-film orientation would be systematically studied and compared with the DFT calculations and MD simulations.

With a control growth of NMC thin-films of different defects concentration and thickness and better insights into the chemical degradation of NMC thin-films in carbonate-based electrolytes, we would explore the effects of advanced electrolytes on the stabilization of CEI, and the evolution of electrochemical interfaces through the ex situ and in situ SXRD/XRR and x-ray spectroscopies. And the as-formed CEI compositions will be studied by x-ray photoelectron spectroscopy/XPS and time-of-flight secondary ion mass spectrometry/TOF-SIMS. The experimental studies of cathode surfaces and CEI would be combined with theoretical modeling, therefore would provide molecular-level insights into the evolution of CEI and fundamental knowledge about how the electrode surface and electrolyte composition would dictate the reactions and will help enable strategies to stabilize the interfaces.

Conclusions

Understanding the evolution and stabilization of the high-voltage CEI is of great significance for the development of NG-LiBs. In this project, we will conduct the surface X-ray scattering and spectroscopy

studies using model epitaxial thin film cathodes in conjunction with theoretical modeling to probe key interfacial electrochemistries between thin-film cathodes and electrolytes. The electrochemical stabilities of carbonate-based baseline and advanced electrolytes have been experimentally and theoretically explored. As revealed by surface X-ray scattering, epitaxial NMC thin-films have been successfully developed by PLD growth with controlled thickness and defect concentrations. And the cathode thin-films have been subject to electrochemical cycling. We have identified the thickness effect on the electrochemical performances of NMC thin-films and the influence of the carbonate-based electrolyte on the surface transformation of NMC thin-films. We anticipate that our combined X-ray, electrochemistry, and molecular scale modeling approach will provide scalable insights into the understanding of the chemical and electrochemical stability of electrolyte at cathode surface, therefore promoting the rational design of advanced high-energy batteries.

Key Publications

1. Huang, Q.; Pollard, T. P.; Ren, X.; Kim, D.; Magasinski, A.; Borodin, O.; Yushin, G., Fading Mechanisms and Voltage Hysteresis in FeF₂-NiF₂ Solid Solution Cathodes for Lithium and Lithium-Ion Batteries. *Small* 2019, 15, 1804670-18046680;
2. J. Alvarado, M. A. Schroeder, T. P. Pollard, X. Wang, J. Z. Lee, M. Zhang, T. Wynn, M. Ding, O. Borodin, Y. S. Meng, K. Xu, Bisalt Ether Electrolytes: a Pathway Towards Lithium Metal Batteries with Ni-rich Cathodes. *Ener. Environ. Sci.* 2019, 12, 780-794;
3. O. Borodin, Challenges with Prediction of Battery Electrolyte Electrochemical Stability Window and Guiding the Electrode-Electrolyte Stabilization. *Curr. Opin. in Electrochem.* 2019, 13, 86-93.

References

1. Cao, C., H. G. Steinruck, B. Shyam, K. H. Stone, and M. F. Toney. "In Situ Study of Silicon Electrode Lithiation with X-Ray Reflectivity." *Nan. Lett.* 16, no. 12 (Dec 14 2016): 7394-401. <https://doi.org/10.1021/acs.nanolett.6b02926>.
2. Cao, C. T., H. G. Steinruck, B. Shyam, and M. F. Toney. "The Atomic Scale Electrochemical Lithiation and Delithiation Process of Silicon." *Adv. Mater. Inter.* 4, no. 22 (Nov 23 2017): 1700771. <https://doi.org/ARTN 1700771>.
3. Horowitz, Y., H. G. Steinruck, H. L. Han, C. Cao, Abate, II, Y. Tsao, M. F. Toney, and G. A. Somorjai. "Fluoroethylene Carbonate Induces Ordered Electrolyte Interface on Silicon and Sapphire Surfaces as Revealed by Sum Frequency Generation Vibrational Spectroscopy and X-Ray Reflectivity." *Nano. Lett.* 18, no. 3 (Mar 14 2018): 2105-11. <https://doi.org/10.1021/acs.nanolett.8b00298>.
4. Steinrück, Hans-Georg, Chuntian Cao, Yuchi Tsao, Christopher J. Takacs, Oleg Kononov, Jenel Vatamanu, Oleg Borodin, and Michael F. Toney. "The Nanoscale Structure of the Electrolyte-Metal Oxide Interface." *Ener. Environm. Sci.* 11, no. 3 (2018): 594-602. <https://doi.org/10.1039/c7ee02724a>.
5. Franklin, J. B., B. Zou, P. Petrov, D. W. McComb, M. P. Ryan, and M. A. McLachlan. "Optimised Pulsed Laser Deposition of ZnO Thin Films on Transparent Conducting Substrates." *J. Mater. Chem.* 21, no. 22 (2011): 8178-82. <https://doi.org/10.1039/c1jm10658a>.
6. Hartung, S., N. Bucher, J. B. Franklin, A. M. Wise, L. Y. Lim, H. Y. Chen, J. N. Weker, et al. "Mechanism of Na⁺ Insertion in Alkali Vanadates and Its Influence on Battery Performance." *Adv. Ener. Mater.* 6, no. 9 (May 11 2016): 1502336. <https://doi.org/ARTN 1502336>. [10.1002/aenm.201502336](https://doi.org/10.1002/aenm.201502336).
7. Wang, H. W., Y. Zhang, H. X. Ang, Y. Q. Zhang, H. T. Tan, Y. F. Zhang, Y. Y. Guo, et al. "A High-Energy Lithium-Ion Capacitor by Integration of a 3d Interconnected Titanium Carbide Nanoparticle Chain Anode with a Pyridine-Derived Porous Nitrogen-Doped Carbon Cathode." *Adv. Funct. Mater.* 26, no. 18 (May 10 2016): 3082-93.

8. Gauthier, M., T. J. Carney, A. Grimaud, L. Giordano, N. Pour, H. H. Chang, D. P. Fenning, et al. "Electrode-Electrolyte Interface in Li-Ion Batteries: Current Understanding and New Insights." *J Phys. Chem. Lett.* 6, no. 22 (Nov 19 2015): 4653-72. <https://doi.org/10.1021/acs.jpcllett.5b01727>.
9. Zhi, H., L. Xing, X. Zheng, K. Xu, and W. Li. "Understanding How Nitriles Stabilize Electrolyte/Electrode Interface at High Voltage." *J Phys. Chem. Lett.* 8, no. 24 (Dec 21 2017): 6048-52. <https://doi.org/10.1021/acs.jpcllett.7b02734>.
10. Alvarado, J., M. A. Schroeder, M. H. Zhang, O. Borodin, E. Gobrogge, M. Olguin, M. S. Ding, et al. "A Carbonate-Free, Sulfone-Based Electrolyte for High-Voltage Li-Ion Batteries." *Mater. Today* 21, no. 4 (May 2018): 341-53. <https://doi.org/10.1016/j.mattod.2018.02.005>.
11. Su, Chi-Cheung, Meinan He, Paul Redfern, Larry A. Curtiss, Chen Liao, Lu Zhang, Anthony K. Burrell, and Zhengcheng Zhang. "Alkyl Substitution Effect on Oxidation Stability of Sulfone-Based Electrolytes." *ChemElectroChem* 3, no. 5 (2016): 790-97. <https://doi.org/doi:10.1002/celec.201500550>.
12. Suo, L., W. Xue, M. Gobet, S. G. Greenbaum, C. Wang, Y. Chen, W. Yang, Y. Li, and J. Li. "Fluorine-Donating Electrolytes Enable Highly Reversible 5-V-Class Li Metal Batteries." *Proc. Natl. Acad. Sci. U. S. A.* 115, no. 6 (Feb 6 2018): 1156-61. <https://doi.org/10.1073/pnas.1712895115>.
13. O. Oleg, Borodin, Olguin Marco, E. Spear Carrie, W. Leiter Kenneth, and Knap Jaroslaw. "Towards High Throughput Screening of Electrochemical Stability of Battery Electrolytes." *Nanotechnology* 26, no. 35 (2015): 354003.
14. Borodin, O., and D. Bedrov. "Interfacial Structure and Dynamics of the Lithium Alkyl Dicarboxate Sei Components in Contact with the Lithium Battery Electrolyte." *J. Phys. Chem. C* 118, no. 32 (Aug 14 2014): 18362-71. <https://doi.org/10.1021/jp504598n>.
15. Borodin, Oleg, Guorong V. Zhuang, Philip N. Ross, and Kang Xu. "Molecular Dynamics Simulations and Experimental Study of Lithium Ion Transport in Dilithium Ethylene Dicarboxate." *J. Phys. Chem. C* 117, no. 15 (2013/04/18 2013): 7433-44. <https://doi.org/10.1021/jp4000494>.
16. Borodin, O., and D. Bedrov. "Interfacial Structure and Dynamics of the Lithium Alkyl Dicarboxate Sei Components in Contact with the Lithium Battery Electrolyte." *J. Phys. Chem. C* 118, no. 32 (Aug 14 2014): 18362-71. <https://doi.org/10.1021/jp504598n>.
17. Jain, A., S. P. Ong, G. Hautier, W. Chen, W. D. Richards, S. Dacek, S. Cholia, et al. "Commentary: The Materials Project: A Materials Genome Approach to Accelerating Materials Innovation." *APL Mater.* 1, no. 1 (Jul 2013): 011002. <https://doi.org/Art10.1063/1.4812323>.

II.3.B Stability of Cathode/Electrolyte Interfaces in High Voltage Li-ion Batteries (ANL)

Dusan Strmcnik, Principal Investigator

Argonne National Laboratory
9700 S Cass Avenue
Lemont, IL 60439
E-mail: strmcnik@anl.gov

Vojislav Stamenkovic, Principal Investigator

Argonne National Laboratory
9700 S Cass Avenue
Lemont, IL 60439
E-mail: vstamenkovic@anl.gov

Peter Faguy, DOE Program Manager

U.S. Department of Energy
E-mail: Peter.Faguy@EE.Doe.Gov

Start Date: October 01, 2018
Project Funding (FY19): \$500,000

End Date: September 30, 2021
DOE share: \$500,000

Non-DOE share: \$0

Project Introduction

Li-ion batteries have become very important in the last two decades and represent the power source of choice for most portable electronic devices. However, an improvement of this technology is still necessary to be durably introduced onto new markets such as electric vehicles (EVs) and hybrid electric vehicles (HEVs). One of the viable options to meet the high energy density demands of the new Li-ion technology are the high voltage Li-ion batteries, which utilize the cathode materials that can operate at voltages higher than 4.5 V vs. Li/Li⁺. A major problem with these high voltage cathode materials is the incompatibility with “conventional” Li-ion electrolytes, which commonly consist of a combination of lithium hexafluorophosphate (LiPF₆) salt with a binary solvent mixture of cyclic and linear alkyl carbonates such as ethylene carbonate (EC) and ethyl methyl carbonate (EMC). These electrolytes undergo severe degradation at high voltages which is often remedied by cathode passivation additives. Another approach, is to develop new solvents which are intrinsically stable at high voltages. Both approaches, however, demand a much better fundamental understanding of the underlying degradation mechanisms of the Li-ion cathode/electrolyte interfaces, which would be on par with understanding of aqueous electrochemical interfaces.

Objectives

The main goal of this proposal is to establish fundamental mechanistic understanding of the principles that govern the decomposition and properties of cathode/electrolyte interfaces and relate them to the performance of high voltage Li-ion cells.

In order to achieve this goal, we will divide our work into five objectives:

- Investigate the chemistries of individual electrolyte components of a Li-ion battery on a variety of materials, from well-defined metal single crystals to realistic TMO samples at high potentials, relevant for high voltage LiB. These individual components will range from different solvents, electrolyte salts to impurities that can either be present in the electrolyte from the beginning or contaminate the system during battery operation (e.g., metals from the cathode side).
- Investigate how the experimental conditions influence these individual chemistries or how they enhance or diminish individual processes in the case of overlapping chemistries.

- By utilizing both theoretical as well as experimental tools, establish thermodynamic and kinetic windows of stability of individual components. Furthermore, an attempt will be made to include mass transport effects into the understanding of the interface stability in various electrochemical environments.
- Combine the thermodynamic, kinetic and mass transport properties of a certain chemistry under specific experimental conditions to build an EEI with specific properties.
- Test the performance of the EEI in coin cells.

Approach

The number one priority of this proposal is to extend the state of the art of understanding how individual components of the cathode/electrolyte interface behave at potentials relevant for high-voltage Li-ion batteries and how these individual components interact with each other. A long-term goal, however, is to implement this knowledge into next generation high-voltage cathode materials and electrolytes. While there are many studies available in the literature exploring the electrolyte as well as cathode material decomposition, most of the attempts focused on real materials in real cells. Although such complex phenomena can be ‘tested’ in real systems, the only way to resolve, apply and connect the underlying fundamental processes with real cell performance would be possible with unique experimental-computational approach. To the best of our knowledge, a deeper fundamental understanding about the structure and properties of cathode side electrode-electrolyte-interphase at the atomic/molecular level is still lacking and would be of high importance for the development of next generation LiBs.

Our approach differs significantly from the well-established testing approach, incorporating three critical steps: (i) utilization of model well-defined systems to assess fundamental descriptors for the decomposition of the electrolyte as well as cathode components; (ii) probing more complex electrolytes and electrode materials with different morphologies; and (iii) exploring the properties of cathode materials that are currently, or are potential candidates, to be used in LIB.

Results

Deconvoluting individual degradation processes at the cathode/electrolyte interface:

Complexity of real battery electrolyte-cathode interface degradation is extremely high and involves, among others, Li^+ intercalation-deintercalation, cathode material dissolution and electrolyte decomposition. Our ability to deconvolute these processes relies on various ex situ and in situ experimental techniques suited to monitor

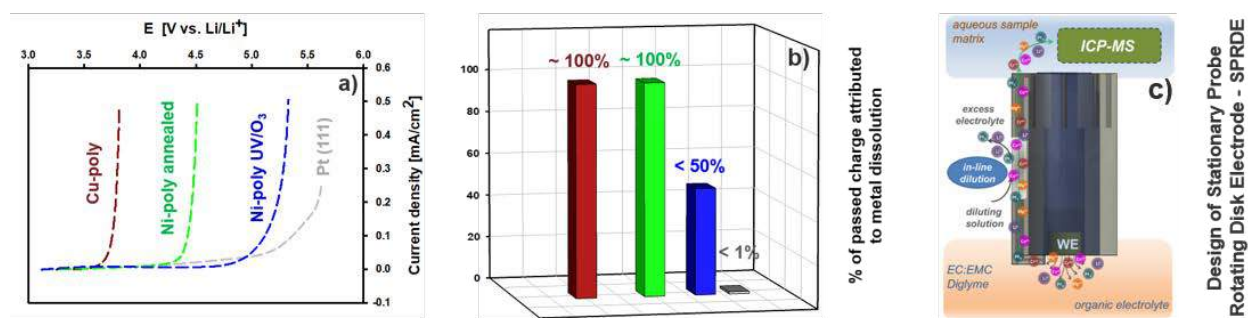


Figure II.3.B.1 a) Electrochemical response of Cu, Ni and Pt electrodes in 1 M LiPF₆ in EC/EMC 3:7w. b) % of metal dissolution in each response as measured by ICP-MS. c) Schematic of the Stationary Probe Rotating Disk Electrode (SPRDE) System Coupled to Inductively Coupled Plasma Mass Spectrometry (ICP-MS)

interface dynamics at atomic and molecular levels and, equally important, on our ability to design interfaces of lesser complexity, where these individual processes can be enhanced or isolated. In Figure II.3.B.1a, we show the electrochemical response of 4 different electrode materials in contact with 1 M LiPF₆ in EC/EMC 3:7w.

With the help of our recently developed SPRDE-ICP-MS method [11] (Figure II.3.B.1c), we are able to show, that for Cu and annealed Ni electrode, the observed current is the result of almost 100% electrode material dissolution. In the case of Pt electrode, on the other hand, the amount of dissolved electrode material is below the detection limit. Here, the observed current is exclusively tied to the electrolyte decomposition. An intermediate case is observed on ozone treated Ni, where both metal dissolution as well as electrolyte decomposition occur simultaneously. While ICP-MS can help us account for the electrons associated with electrode material dissolution, other methods are needed to account for electrons, transferred across the interface

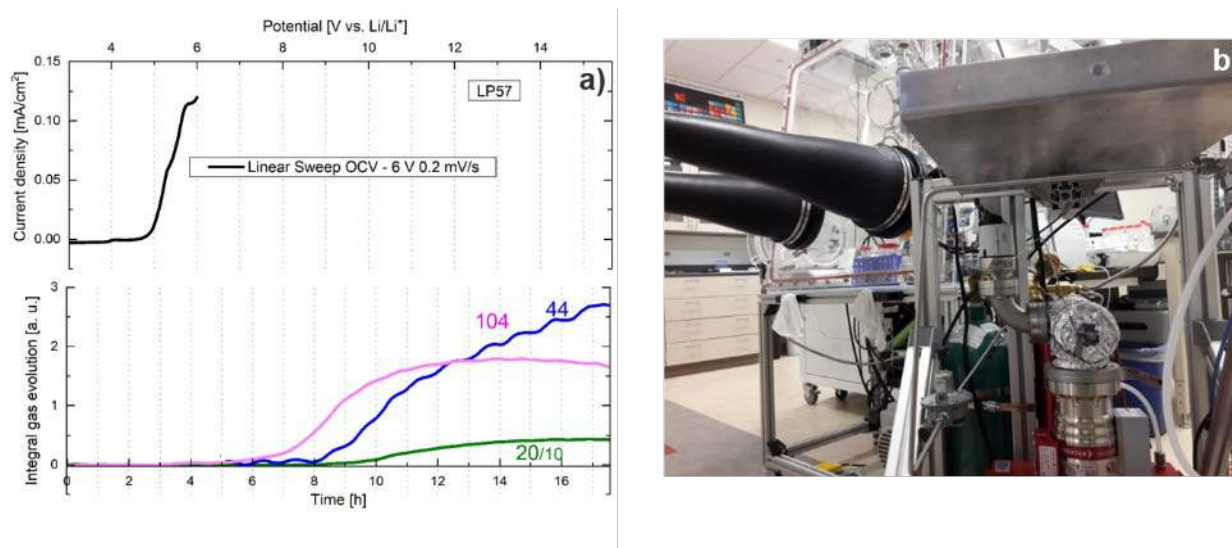


Figure II.3.B.2 Online Electrochemical Mass Spectrometry. a) Gas detection following linear potential sweep to 6 V of C-65 carbon electrode. Signals for HF, CO₂ and POF₃ are clearly visible. b) Picture of the OEMS apparatus

due to electrolyte decomposition. One of the techniques that allows us to follow gaseous products during the decomposition of the electrolyte is Online electrochemical Mass Spectrometry (OEMS) (Figure II.3.B.2), that we have recently added to our portfolio of tools. While still experiencing some technical difficulties, in preliminary results obtained for the 1 M LiPF₆ in EC/EMC 3:7w decomposition on C-65 carbon, we were able to follow the production of CO₂, HF and POF₃ (Figure II.3.B.2a). Finally, we want to be able to detect and monitor the electrolyte decomposition products, that remain in the solution. One of the simplest species, that is suggested to be produced during the solvent oxidation, is the proton [21,31]. In the following, we present a method for quantitative detection of protons in carbonate-based electrolytes.

Detection of generated protons during electrolyte decomposition:

One of the possible consequences of electron abstraction from a solvent molecule like EC is the subsequent proton generation [21,31]. The formed protons can further react with the solvent, electrolyte salt or cathode material. Our method for proton detection is based on rotating ring disk electrode RRDE electrochemical detection using Pt ring as an amperometric detector. We first validated the method using a hydrogen oxidation reaction (HOR) to produce protons on the disk, which could then be detected on the ring. Figure II.3.B.3a shows a typical electrochemical response of Pt disk electrode in Ar purged 1 M LiClO₄ in EC/EMC 3:7w electrolyte. No significant currents are detected between 2.8 and 3.5 V vs Li/Li⁺. In an H₂ purged solution, however, we observe a typical cyclic voltammogram with the anodic wave corresponding to H₂ → 2H⁺ + 2e⁻ and the cathodic wave to the 2H⁺ + 2e⁻ → H₂ reaction. The half wave potential for the HOR lies at 3.16 V, which is the RHE=0 for the given conditions. Figure II.3.B.3b summarizes the polarization curves at 4 different rotation rates between 400-1600 rpm in the H₂ purged solution and the related response on the ring. We were able to show that the collection efficiency of the ring was ~20%, which is the theoretical value for the

setup used. This means that we were able to account for all the protons created during the oxidation of hydrogen on the disk and successfully validate the method.

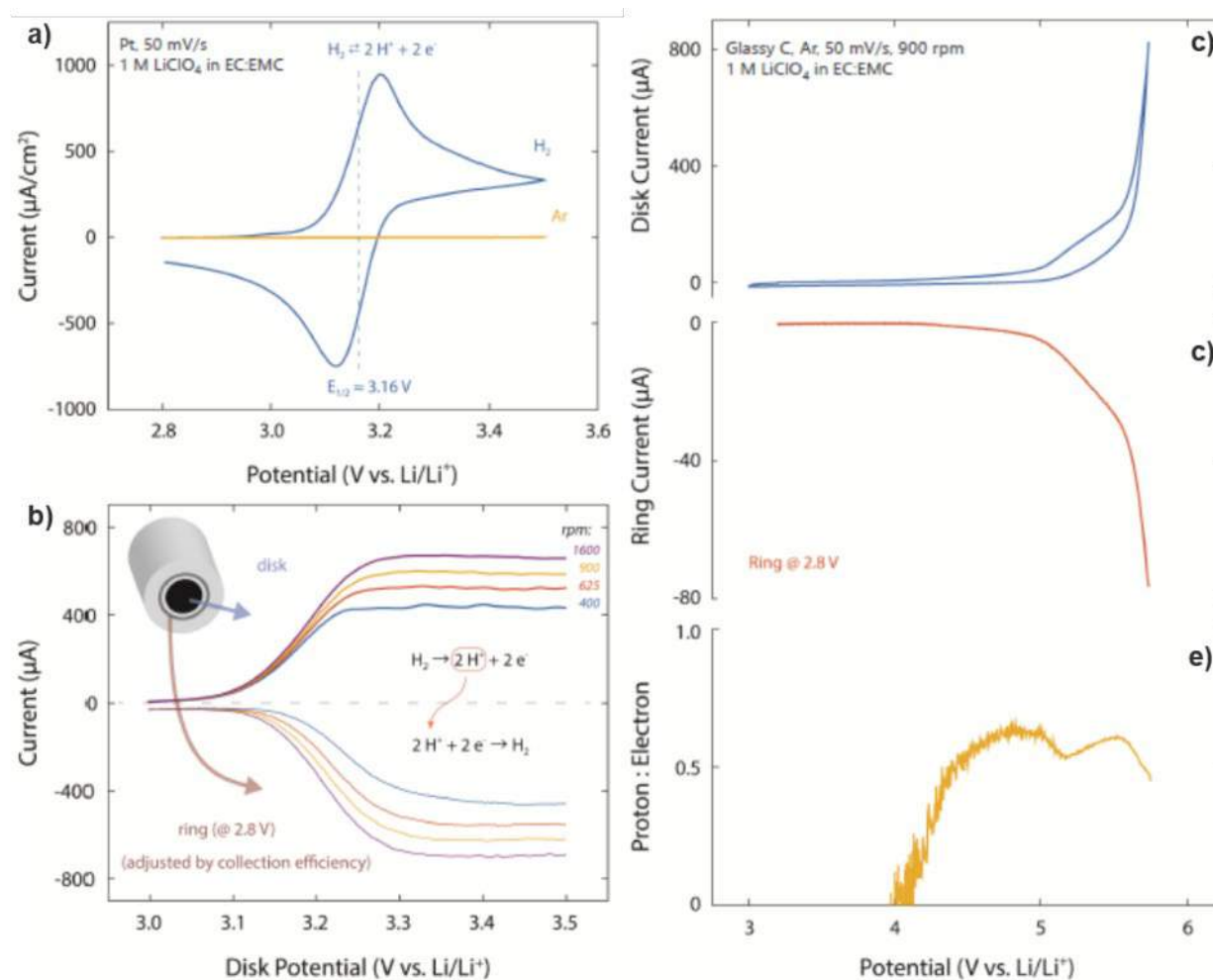


Figure II.3.B.3 Rotating ring disk proton detection method. a) Cyclic voltammogram of hydrogen oxidation/evolution reaction in a H_2 saturated electrolyte. b) Polarization curves for HOR at different rotation rates on the Pt disk and the measured responses on Pt ring. c) Electrochemical decomposition of 1 M LiClO_4 EC/EMC electrolyte on Glassy carbon electrode. d) Proton reduction current on the Pt ring. e) Proton/electron ratio obtained from disk vs. ring current, corrected for the ring collection efficiency

By changing the disk material, we are now able to track the production of protons as a result of electrolyte decomposition on any other material. In Figure II.3.B.2c, we investigate the electrochemical response on glassy carbon disk. Although an extensive electrolyte decomposition is only observed above 5 V, small currents can be measured already around 4 V. The fact that we observe matching currents on the ring as well, indicates that the process starting at $\sim 4\text{ V}$ is indeed generating protons, linked to oxidation of the solvent. Interestingly, and in contrast to the HOR measurements, the numbers of transferred electrons and measured protons do not match. Instead, in the potential range between 4.3 and 5.8 V, we can detect approximately 1 H^+ on the ring per 2 electrons transferred on the disk. This suggests that in addition to generating a proton in the oxidation process, we also consume an additional electron for a second oxidation process which at this point is still under investigation.

The influence of the electrolyte salt, solvent and electrode material on the decomposition of electrolyte:

Recent literature suggests that electrolyte oxidation processes are far more complex than previously anticipated, when most of the DFT studies focused on understanding of oxidation stability of isolated molecules and related them to the bulk electrolyte oxidation potential. However, more recent findings seem to support the idea that either solvent molecules or anions from the electrolyte can stabilize the abstraction of proton after the oxidation, i.e., first electron transfer from the solvent molecule [4]–[7]. In II.M.2.4, we demonstrate the extent of different effects on the oxidation potential in 1 M LiClO₄ in EC/EMC 3:7w and 1 M LiPF₆ in EC/EMC 3:7w. Several observations are noteworthy here: i) the potential of main oxidation process, signified by sharp exponential increase in current, depends on the nature of the solvent; ii) the substrate has a significant influence on the decomposition process, even reversing the order of solvent oxidation, as seen in the case of EC and EMC based electrolytes on Pt and graphene electrode in Figure II.3.B.4b and Figure II.3.B.4c, respectively; iii) anion seems to play an enormous role in the electrooxidation of the solvents – a 0.7 V difference is observed for LiPF₆ and LiClO₄ based electrolytes; iv) finally, smaller currents are observed at much more negative potentials than the main oxidation process – these currents are rotation dependent, suggesting a possible oxidation due to electrolyte impurities. Up to this point, we have limited ourselves mainly to observations of the effects we have to take into account when considering electrolyte decomposition. Our next step will be to collect more data with our newly acquired techniques, which is needed for understanding of each individual effect.

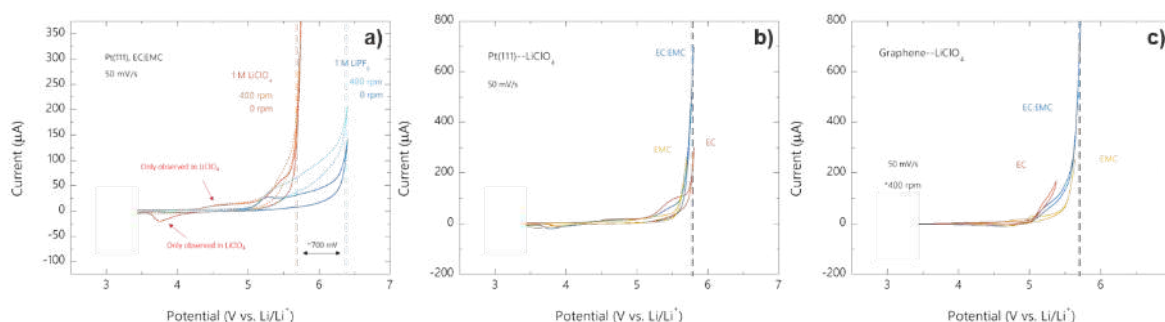


Figure II.3.B.4 Effects of anion, solvent, substrate and rotation rate on the electrolyte oxidation. a) Comparison of the electrochemical responses on Pt(111) electrode in LiClO₄ and LiPF₆ based electrolytes with and without rotation. b) Comparison of electrochemical responses in EC, EMC and EC/EMC based LiClO₄ electrolytes on Pt electrode. c) Comparison of electrochemical responses in EC, EMC and EC/EMC based LiClO₄ electrolytes on graphene electrode

Conclusions

Complexity of real battery electrolyte-cathode interface degradation is extremely high and involves, among others, Li⁺ intercalation-deintercalation, cathode material dissolution and electrolyte decomposition. Our ability to deconvolute these processes relies on various ex situ and in situ experimental techniques suited to monitor interface dynamics at atomic and molecular levels and, equally important, on our ability to design interfaces of lesser complexity, where these individual processes can be enhanced or isolated.

We have added two new techniques to our portfolio of tools that will help us resolve important questions regarding electrolyte decomposition. OEMS will help us detect gaseous products during electrolyte oxidation, while RRDE proton detection method will be able to quantitatively determine the number of protons generated per number of electrons transferred.

Finally, we were able to show that the solvent, anions, substrate and electrolyte impurities each contribute to the electrolyte decomposition. While we want to avoid quick and superficial conclusions on the underlying reasons for the role of each of these interface components in the electrochemical response, these observations set the outline of our future work.

Key Publications

1. Pietro P. Lopes, Milena Zorko, Krista L. Hawthorne, Justin G. Connell, Brian. J. Ingram, Dusan Strmcnik, Vojislav R. Stamenkovic, and Nenad M. Markovic, Real-Time Monitoring of Cation Dissolution/Deintercalation Kinetics from Transition-Metal Oxides in Organic Environments, *J. Phys. Chem. Lett.* 2018, 9, 4935–4940

References

1. Pietro P. Lopes, Milena Zorko, Krista L. Hawthorne, Justin G. Connell, Brian. J. Ingram, Dusan Strmcnik, Vojislav R. Stamenkovic, and Nenad M. Markovic, Real-Time Monitoring of Cation Dissolution/Deintercalation Kinetics from Transition-Metal Oxides in Organic Environments, *J. Phys. Chem. Lett.* 2018, 9, 4935–4940
2. Michael Metzger, Benjamin Strehle, Sophie Solchenbach, and Hubert A. Gasteiger, Origin of H₂ Evolution in LIBs: H₂O Reduction vs. Electrolyte Oxidation, *J. Electrochem. Soc.* 2016 163 A798-A809
3. Thomas M. Østergaard, Livia Giordano, Ivano E. Castelli, Filippo Maglia, Byron K. Antonopoulos, Yang Shao-Horn, and Jan Rossmeisl, Oxidation of Ethylene Carbonate on Li Metal Oxide Surfaces, *J. Phys. Chem. C* 2018, 122, 10442–10449
4. Oleg Borodin, Wishvender Behl, and T. Richard Jow, Oxidative Stability and Initial Decomposition Reactions of Carbonate, Sulfone, and Alkyl Phosphate-Based Electrolytes, *J. Phys. Chem. C* 2013, 117, 8661–8682
5. Lidan Xingab and Oleg Borodin, Oxidation induced decomposition of ethylene carbonate from DFT calculations – importance of explicitly treating surrounding solvent, *Phys. Chem. Chem. Phys.*, 2012, 14, 12838–12843
6. Oleg Borodin, Xiaoming Ren, Jenel Vatamanu, Arthur von Wald, Cresce Jaroslaw Knap, Kang Xu, Modeling Insight into Battery Electrolyte Electrochemical Stability and Interfacial Structure, *Acc. Chem. Res.* 2017, 50, 12, 2886-2894
7. Magali Gauthier, Thomas J. Carney, Alexis Grimaud, Livia Giordano, Nir Pour, Hao-Hsun Chang, David P. Fenning, Simon F. Lux, Odysseas Paschos, Christoph Bauer, Filippo Maglia, Saskia Lupart, Peter Lamp, Yang Shao-Horn, Electrode–Electrolyte Interface in Li-Ion Batteries: Current Understanding and New Insights, *J. Phys. Chem. Lett.* 2015, 6, 22, 4653-4672

II.3.C Interfacial Studies of Emerging Cathode Materials (LBNL)

Marca M. Doeff, Principal Investigator

Lawrence Berkeley National Laboratory
1 Cyclotron Road
Berkeley, CA 94720
E-mail: mmdoeff@lbl.gov

Peter Faguy, DOE Technical Development Manager

U.S. Department of Energy
E-mail: Peter.Faguy@ee.doe.gov

Start Date: October 1, 2018

End Date: September 30, 2021

Project Funding (FY19): \$300,000

DOE share: \$300,000

Non-DOE share: \$0

Project Introduction

At present, commercialized cathode materials for high-energy lithium ion batteries (LIBs) are based on transition metal oxides such as NMCs ($\text{LiNi}_x\text{Mn}_y\text{Co}_z\text{O}_2$). These are intercalation electrodes, in which transition metals such as Ni and Co undergo redox as lithium is inserted or removed from the structures. The theoretical capacities of these electrodes are about 280 mAh/g based on the transition metal redox, but, typically, only a portion of this capacity can be accessed due to practical limitations such as oxidative stability limits of the electrolytic solutions and structural stability of the electrodes. Practical capacities range from about 140-200 mAh/g depending on exact composition and usage (rates, voltage limits, etc.). Recently, the discovery that reversible or partly reversible oxygen redox processes can occur in a variety of structures has opened up a new design space for cathode materials, with the tantalizing possibility of attaining capacities well beyond the 280 mAh/g theoretical limit of traditional intercalation layered oxides. These materials include Li_2MnO_3 , [1] lithium and manganese rich NMCs (LMR-NMCs) [2] and Co-free analogs, [3] other types of lithium-rich layered oxides with structures similar to Li_2MnO_3 , [4] three-dimensional structures such as $\beta\text{-Li}_2\text{IrO}_3$, [5] and cation-disordered rock salts [6] including variants of Li_3NbO_4 [7],[8] and Li_3IrO_4 . [9] Many of these materials exhibit capacities of 300 mAh/g or more, but suffer from poor rate capability, voltage hysteresis, and fading. [10] In these cases, irreversible oxygen loss, [11] morphological [12] and structural changes [13],[14] are to blame for the performance issues. Other materials appear to cycle more stably, [5],[9] at least for a limited time, and strategies such as partial fluorine substitution for oxygen [15] appear to mitigate irreversible oxygen loss and result in improved behavior. Because oxygen loss tends to occur at particle surfaces, and is associated with the deleterious structural and morphological changes that are responsible for poor cycling and rate characteristics of some of these materials, it would be extremely useful to understand the fundamental processes occurring at the cathode/electrolyte interface and on particle surfaces better. While LMR-NMCs have been intensively characterized, [16] few studies to probe interfacial characteristics have been carried out on most of the other materials mentioned above. We now propose to study candidate materials, both those that perform well and those that perform badly, using an array of surface-sensitive, depth-profiling, and bulk techniques. These include synchrotron X-ray absorption spectroscopy (XAS), X-ray photoelectron spectroscopy (XPS), X-ray Raman (XRS) and transmission X-ray microscopy (TXM) as well as STEM/EELS (scanning transmission electron microscopy/electron energy loss spectroscopy). Materials will be investigated as a function of composition, particle size and surface area, state-of-charge, and cycling history. By the end of the project, there should be sufficient information to allow a set of recommendations to be made regarding the best way to ensure stable and robust cycling of electrodes that undergo both transition metal and oxygen redox.

Objectives

Reports of oxygen redox activity in materials with unusually high capacities are intriguing, but fairly little is known about how these materials actually work. There are a number of unanswered questions to which the work proposed here is designed to answer. First, how deep into the bulk does oxygen redox occur? Is it

primarily a surface reaction? When does oxygen release occur, as opposed to reversible redox? Does the oxygen redox or oxygen release contribute to the structural instability that is often seen, and can this be prevented by, e.g., cationic or anionic substitutions, coatings, or other strategies? How do the particle surfaces of charged or partially charged materials interact with the electrolytic solutions, and how does this contribute to capacity fading, rate limitations, and other performance issues? Once these questions are answered, strategies such as substitutions, coatings and particle morphology/size engineering can be considered to ensure robust cycling.

Approach

To answer the above questions, we will synthesize selected materials with differing particle sizes/surface areas, subject them to electrochemical charge, discharge, and cycling or chemical delithiation, and study them using an array of surface and bulk sensitive techniques including synchrotron X-ray absorption spectroscopy (XAS), X-ray photoelectron spectroscopy (XPS), transmission X-ray microscopy (TXM), X-ray Raman, and microscopy. Materials of interest include $\text{Li}_4\text{Mn}_2\text{O}_5$, [17] $\text{Li}_2\text{Ru}_x\text{M}_y\text{O}_3$ ($\text{M}=\text{Sn}, \text{Fe}, \text{Ti}$)⁴ and $\text{Li}_4\text{FeSbO}_6$. [18] Although not all of these materials are practical, the objective is to obtain information that can ultimately be used to design high capacity materials from low cost and earth-abundant elements.

Results

$\text{Li}_4\text{Mn}_2\text{O}_5$ is synthesized by mechanochemical milling of LiMnO_2 with Li_2O under argon for ten hours, followed by carbon coating to improve electronic conductivity. Figure II.3.C.1 shows the XRD pattern and a scanning electron micrograph (SEM) of the powder. The reflections can all be indexed to a rock salt structure, although peaks are very broad, consistent with nanometric particles. The material appears to be single phase, with no obvious impurities.

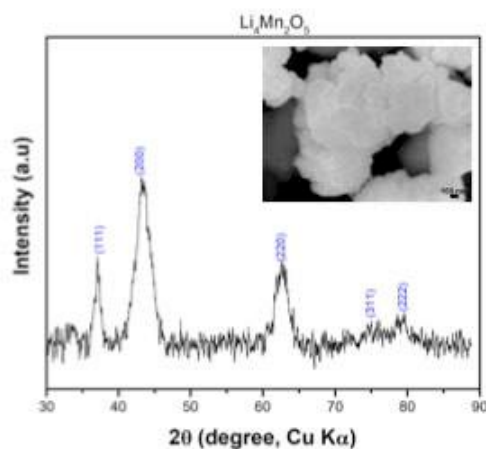


Figure II.3.C.1 XRD pattern of as-synthesized $\text{Li}_4\text{Mn}_2\text{O}_5$ with an SEM image shown in the inset

The electrochemistry is shown in Figure II.3.C.2. The initial discharge capacity, after charge to 4.8V, is nearly 350 mAh/g. The theoretical capacity based on extraction of 2 lithium ions per formula unit and oxidation of Mn^{3+} to Mn^{4+} is 246 mAh/g. The excess capacity may derive from additional extraction of lithium and partial oxidation to Mn^{5+} or oxidation of oxygen ions or some combination of these. A somewhat lower initial discharge capacity of about 310 mAh/g is attained when charge is limited to 4.4V. In either case, a rapid capacity fade, as well as voltage fading is seen to occur upon cycling. The rate of fading appears to be insensitive to the upper voltage limit, suggesting that irreversible oxidation of electrolyte (which would be less apparent upon cycling to 4.4V) is not the main cause. Limiting the lower discharge voltage cutoff to 2.0V, instead of 1.2V, yields discharge capacities of about 200–220 mAh/g, depending on what upper voltage limit is used. At present, we do not have sufficient cycling data under these conditions to assess whether this improves reversibility.

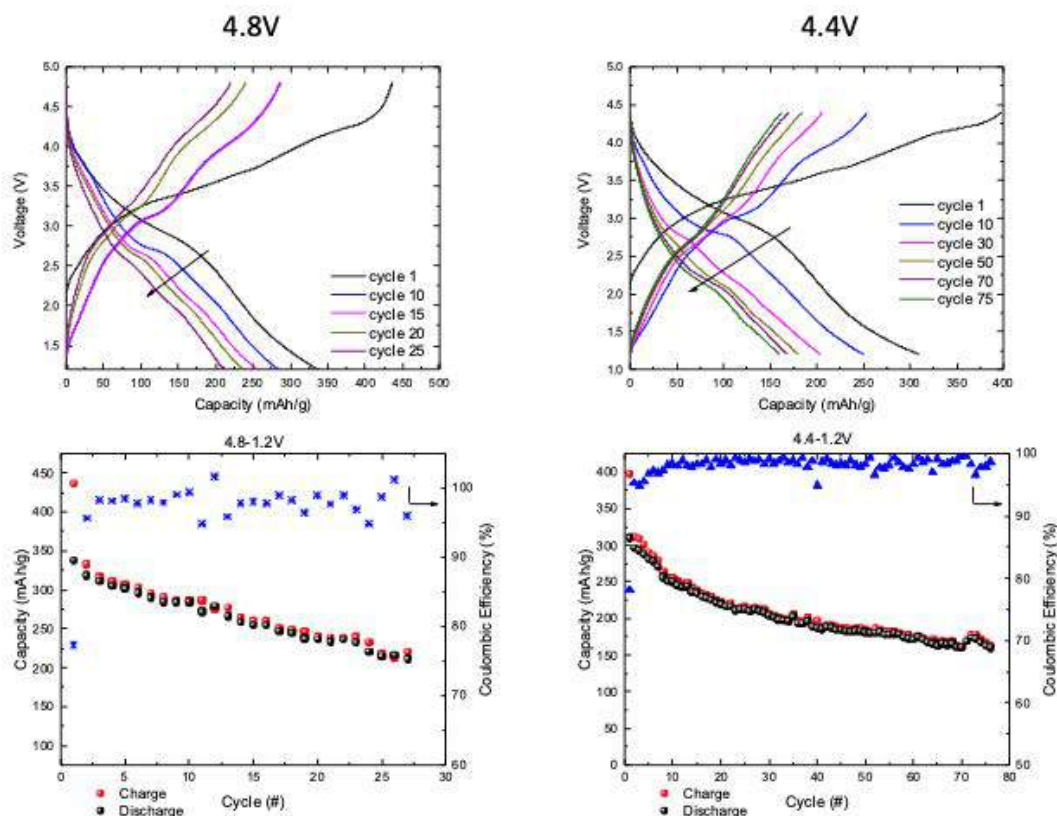


Figure II.3.C.2 Upper left: charge and discharge profiles of $\text{Li}_4\text{Mn}_2\text{O}_5$ in a lithium half cell when cycled between 4.8-1.2V and (lower left) capacity as a function of cycle number. Upper right: charge and discharge profiles of $\text{Li}_4\text{Mn}_2\text{O}_5$ in a lithium half cell when cycled between 4.4-1.2V and (lower right) capacity as a function of cycle number

X-ray Raman experiments were performed on $\text{Li}_4\text{Mn}_2\text{O}_5$ electrodes as a function of state-of-charge (first charge). This is an element-specific synchrotron technique, which probes electronic structure via non-resonant inelastic scattering of x-rays from core electrons. While it has the enhanced sensitivity of surface-sensitive soft X-ray absorption experiments, it probes into the bulk. Figure II.3.C.3 shows Mn L-edge data on electrodes charged to various potentials. Also shown is the O K-edge data. The Mn L-edge spectrum of the pristine electrode is consistent with trivalent Mn, [19] as expected. As the electrode is charged, the L_3 edge shows development of a second peak at higher energy, diagnostic of oxidation to tetravalent Mn. There is little difference in the spectra of the electrode charged to 4.4V and the one charged to 4.8V, suggesting that further oxidation of Mn does not occur between 4.4 and 4.8V, with the caveat that there is not much known about what the Mn^{5+} L-edge spectrum looks like. There are two peaks of significance in the O K-edge spectrum of the pristine electrode; one at 534 eV and another at about 532 eV. The first peak is most likely due to Li_2O (or Li_2CO_3), left over from the synthesis procedure. Because these phases are composed of light elements, they do not show up in the XRD pattern. Interestingly, this peak disappears in the charged electrodes, indicating that Li_2O dissolves or decomposes. Electrochemical decomposition of Li_2CO_3 is known to occur at high voltages and may contribute to the high first charge capacity and coulombic inefficiency. The feature near 532 eV can be attributed to oxygen bonded to manganese. As the electrode is oxidized, the intensity of this feature at first increases (up to 4.4V) and then decreases a bit upon going to 4.8V. There is a well-known correlation between the intensity of TM3d-O2p peaks and the number of oxygen hole states. As charge progresses, the number of oxygen hole states increases, but the decrease at the end of charge implies that some oxygen loss has occurred. This is, however, not proof that oxygen is being oxidized, rather it is a reflection of changes in the covalencies of the TM-O bonds in this material. To further investigate the redox behavior of $\text{Li}_4\text{Mn}_2\text{O}_5$, further experiments are planned, including X-ray Raman on discharged and cycled electrodes and soft XAS and XPS, to probe the surface behavior.

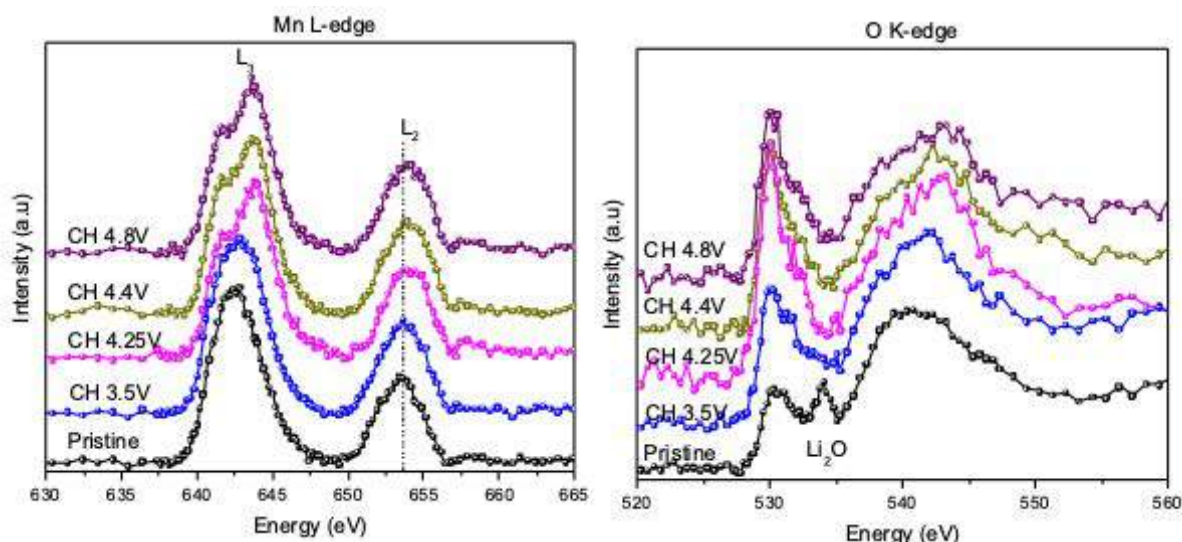


Figure II.3.C.3 Left: X-ray Raman Mn L-edge spectra on pristine and charged $\text{Li}_4\text{Mn}_2\text{O}_5$ electrodes as a function of charging potential. Right: X-ray Raman O K-edge spectra

During this fiscal year, we also initiated a study of the electrochemical behavior of $\text{Li}_2\text{Ru}_{0.75}\text{Sn}_{0.25}\text{O}_3$ and $\text{Li}_2\text{Ru}_{0.75}\text{Ti}_{0.25}\text{O}_3$. Both of these compounds were synthesized by solid-state reactions and all peaks in the XRD patterns could be indexed to the C/2m space group (Figure II.3.C.4). These are both layered materials with structures similar to that of Li_2MnO_3 , as shown in the inset in Figure II.3.C.4.

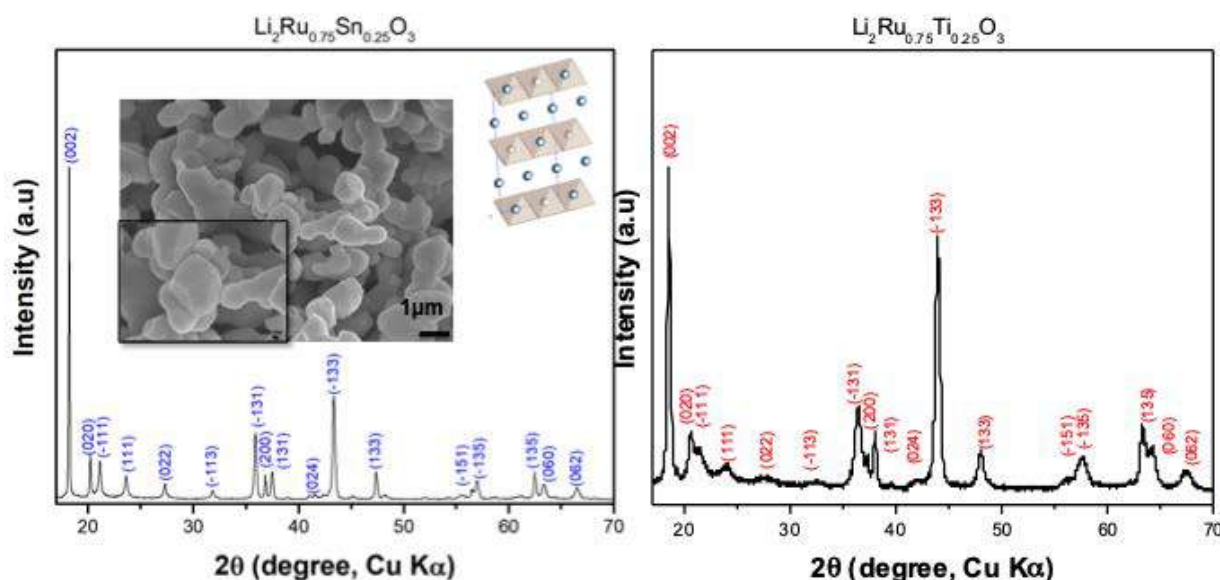


Figure II.3.C.4 Left: XRD pattern of $\text{Li}_2\text{Ru}_{0.75}\text{Sn}_{0.25}\text{O}_3$ with its structure and the particle morphology indicated in the insets. Right: XRD pattern of $\text{Li}_2\text{Ru}_{0.75}\text{Ti}_{0.25}\text{O}_3$

The electrochemistry of these two materials is shown in Figure II.3.C.5. The capacity of $\text{Li}_2\text{Ru}_{0.75}\text{Sn}_{0.25}\text{O}_3$ is about 250 mAh/g initially, when cycled between 4.6–2.0V with a capacity retention of about 65% after 100 cycles. A slightly higher capacity can be obtained initially if the charge limit is increased to 4.8V. Similar capacities are obtained for $\text{Li}_2\text{Ru}_{0.75}\text{Ti}_{0.25}\text{O}_3$ with some fading evident over initial cycles. Evident in both of these materials is the change in the voltage profile after the first cycle, possibly related to oxygen activation.

Both of these materials are good model compounds for the study of oxygen redox in emerging cathode materials.

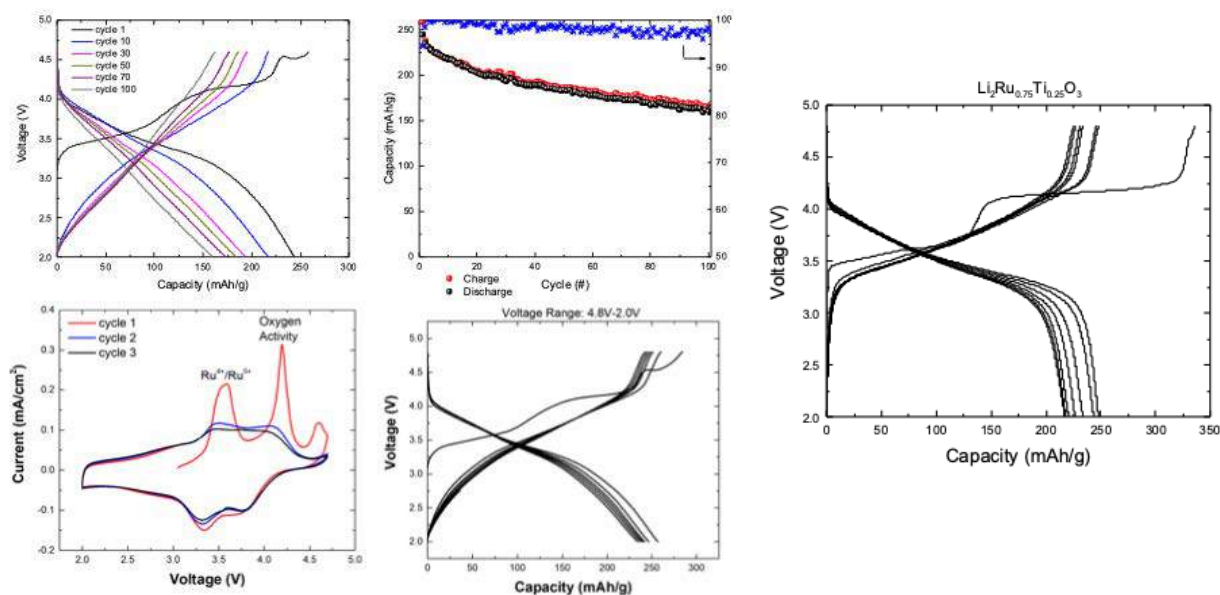


Figure II.3.C.5 Upper left: Voltage profiles of a Li/Li₂Ru_{0.75}Sn_{0.25}O₃ cell cycled between 4.6 and 2.0V. Upper middle capacity as a function of cycle number. Bottom left : cyclic voltammogram of a Li/Li₂Ru_{0.75}Sn_{0.25}O₃ cell cycled between 4.8 and 2.0V and (bottom center) voltage profiles over the same potential range. Right: Voltage profiles of a Li/Li₂Ru_{0.75}Ti_{0.25}O₃ cell between 4.8-2.0V

Conclusions

Several emerging cathode materials with very high capacities were synthesized and characterized electrochemically. Mn L-edge and O K-edge X-ray Raman experiments were carried on Li₄Mn₂O₅ electrodes as a function of state-of-charge.

Key Publications

1. Alvarado, J., Wei, C., Nordlund, D., Kroll, T., Sokaras, D., Tian, Y., Liu, Y. and Doeff, M. M., "Thermal Stress-Induced Charge and Structure Heterogeneity in Emerging Cathode Materials" *Mater. Today*, (2019) under review.

References

1. Chen, H., and Islam, M. S., "Lithium Extraction Mechanism in Li-Rich Li₂MnO₃ Involving Oxygen Hole Formation and Dimerization" *Chemistry of Materials* 28, (2016): 6656-6663.
2. Croy, J. R., Balasubramanian, M., Gallagher, K. G., and Burrell, A. K., "Review of the U.S. Department of Energy's "Deep Dive" Effort to Understand Voltage Fade in Li- and Mn-Rich Cathodes" *Acc Chem Res* 48, (2015): 2813-21.
3. Luo, K., Roberts, M. R., Guerrini, N., Tapia-Ruiz, N., Hao, R., Massel, F., Pickup, D. M., Ramos, S., Liu, Y. S., Guo, J., Chadwick, A. V., Duda, L. C., and Bruce, P. G., "Anion Redox Chemistry in the Cobalt Free 3d Transition Metal Oxide Intercalation Electrode Li[Li_{0.2}Ni_{0.2}Mn_{0.6}]O₂" *Journal of the American Chemical Society* 138, (2016): 11211-11218.
4. Sathiya, M., Rousse, G., Ramesha, K., Laisa, C. P., Vezin, H., Sougrati, M. T., Doublet, M. L., Foix, D., Gonbeau, D., Walker, W., Prakash, A. S., Ben Hassine, M., Dupont, L., and Tarascon, J. M.,

- “Reversible Anionic Redox Chemistry in High-capacity Layered-oxide Electrodes” *Nature Materials* 12 (2013): 827-835.
5. Pearce, P. E., Perez, A. J., Rousse, G., Saubanere, M., Batuk, D., Foix, D., McCalla, E., Abakumov, A. M., Van Tendeloo, G., Doublet, M. L., and Tarascon, J. M., “Evidence for Anionic Redox Activity in a Tridimensional-ordered Li-rich Positive Electrode β - Li_2IrO_3 ” *Nature Materials* 16 (2017): 580-586.
 6. Seo, D. H., Lee, J., Urban, A., Malik, R., Kang, S., and Ceder, G., “The Structural and Chemical Origin of the Oxygen Redox Activity in Layered and Cation-disordered Li-excess Cathode Materials” *Nature Chem.* 8 (2016): 692-697.
 7. Yabuuchi, N., Takeuchi, M., Nakayama, M., Shiiba, H., Ogawa, M., Nakayama, K., Ohta, T., Endo, D., Ozaki, T., Inamasu, T., Sato, K., and Komaba, S., “High-capacity Electrode Materials for Rechargeable Lithium Batteries: Li_3NbO_4 -based System with Cation-disordered Rocksalt Structure” *Proc. Natl. Acad. Sci. USA* 112, (2015): 7650-7655.
 8. Yabuuchi, N., Nakayama, M., Takeuchi, M., Komaba, S., Hashimoto, Y., Mukai, T., Shiiba, H., Sato, K., Kobayashi, Y., Nakao, A., Yonemura, M., Yamanaka, K., Mitsuhashi, K., and Ohta, T., “Origin of Stabilization and Destabilization in Solid-state Redox Reaction of Oxide Ions for Lithium-ion Batteries” *Nature Communications* 7, (2016): article no. 13814.
 9. Perez, A. J., Jacquet, Q., Batuk, D., Iadecola, A., Saubanère, M., Rousse, G., Larcher, D., Vezin, H., Doublet, M.-L., and Tarascon, J.-M., “Approaching the Limits of Cationic and Anionic Electrochemical Activity with the Li-rich Layered Rocksalt Li_3IrO_4 ” *Nature Energy* 2, (2017): 954-962.
 10. Assat, G., Delacourt, C., Corte, D. A. D., and Tarascon, J.-M., “Practical Assessment of Anionic Redox in Li-Rich Layered Oxide Cathodes: A Mixed Blessing for High Energy Li-Ion Batteries” *J. Electrochem. Soc.* 163, (2016): A2965-A2976.
 11. Xu, J., Sun, M., Qiao, R., Renfrew, S. E., Ma, L., Wu, T., Hwang, S., Nordlund, D., Su, D., Amine, K., Lu, J., McCloskey, B. D., Yang, W., and Tong, W., “Elucidating Anionic Oxygen Activity in Lithium-rich Layered Oxides” *Nature Communications* 9, (2018): article no. 947.
 12. Kan, W. H., Chen, D., Papp, J. K., Shukla, A. K., Huq, A., Brown, C. M., McCloskey, B. D., and Chen, G., “Unravelling Solid-State Redox Chemistry in $\text{Li}_{1.3}\text{Nb}_{0.3}\text{Mn}_{0.4}\text{O}_2$ Single-Crystal Cathode Material” *Chem. Mater.* 30, (2018): 1655-1666.
 13. Mikhailova, D., Karakulina, O. M., Batuk, D., Hadermann, J., Abakumov, A. M., Herklotz, M., Tsirlin, A. A., Oswald, S., Giebeler, L., Schmidt, M., Eckert, J., Knapp, M., and Ehrenberg, H., “Layered-to-Tunnel Structure Transformation and Oxygen Redox Chemistry in LiRhO_2 upon Li Extraction and Insertion” *Inorg. Chem.* 55, (2016): 7079-7089.
 14. Gent, W. E., Lim, K., Liang, Y., Li, Q., Barnes, T., Ahn, S. J., Stone, K. H., McIntire, M., Hong, J., Song, J. H., Li, Y., Mehta, A., Ermon, S., Tylliszczak, T., Kilcoyne, D., Vine, D., Park, J. H., Doo, S. K., Toney, M. F., Yang, W., Prendergast, D., and Chueh, W. C., “Coupling between Oxygen Redox and Cation Migration Explains Unusual Electrochemistry in Lithium-rich Layered Oxides” *Nature Communications* 8, (2017): article no. 2091.
 15. Lee, J., Papp, J. K., Clement, R. J., Sallis, S., Kwon, D. H., Shi, T., Yang, W., McCloskey, B. D., and Ceder, G., “Mitigating Oxygen Loss to Improve the Cycling Performance of High Capacity Cation-disordered Cathode Materials” *Nature Communications* 8, (2017): article no. 981.
 16. Wei, W., Chen, L., Pan, A., and Ivey, D. G., “Roles of Surface Structure and Chemistry on Electrochemical Processes in Lithium-rich Layered Oxide Cathodes” *Nano Energy* 30, (2016): 580-602.

17. Freire, M., Kosova, N. V., Jordy, C., Chateigner, D., Lebedev, O. I., Maignan, A., and Pralong, V. “A New Active Li-Mn-O Compound for High Energy Density Li-Ion Batteries” *Nature Mater.* 15, (2016): 173–177.
18. McCalla, E., Abakumov, A., Rousse, G., Reynaud, M., Sougrati, M. T., Budic, B., Mahmoud, A., Dominko, R., Van Tendeloo, G., Hermann, R. P. et al. “Novel Complex Stacking of Fully-Ordered Transition Metal Layers in $\text{Li}_4\text{FeSbO}_6$ Materials” *Chem. Mater.* 27, (2015):1699–1708.
19. Yang, W., Liu, X., Qiao, R. Olalde-Velasco, P., Spear, J. D., Roseguo, L., Pepper, J. X., Chuang, Y.-d., Denlinger, J. D., and Hussain, Z., “Key Electronic States in Lithium Battery Materials Probed by Soft X-ray Spectroscopy”, *J. Electron. Spectroscopy and Related Phenom.* 190, 2013): 64-74.

II.3.D Understanding and Modification of High-Energy Cathodes and Their Interfaces with Electrolytes for Next-Generation Li-Ion Batteries (PNNL)

Jie Xiao, Principal Investigator

Pacific Northwest National Laboratory
902 Battelle Boulevard
Richland, WA, 99352
E-mail: jie.xiao@pnnl.gov

Ji-Guang Zhang, Principal Investigator

Pacific Northwest National Laboratory
902 Battelle Boulevard
Richland, WA 99352
E-mail: jiguang.zhang@pnnl.gov

Peter Faguy, DOE Technology Development Manager

U.S. Department of Energy
E-mail: Peter.Faguy@ee.doe.gov

Start Date: September 1, 2018

End Date: September 30, 2019

Project Funding (FY19): \$450,000

DOE share: \$450,000

Non-DOE share: \$0

Project Introduction

As the bottleneck of the cell capacity and energy, cathode materials that have higher capacity/operating voltage and improved stability towards the electrolyte are urgently needed to enable next-generation Li-ion battery technologies for electrical vehicles (EVs).^{[1],[2],[3]} Among different cathode materials, Ni-rich NMC ($\text{LiNi}_x\text{Mn}_y\text{Co}_{1-x-y}\text{O}_2$, $x \geq 0.6$) has a specific capacity greater than 200 mAh/g, high operating voltage (ca. 3.8 V) and low cost and is therefore deemed as one of the most promising cathode candidates for high-energy Li-ion batteries. For conventional $\text{LiNi}_{1/3}\text{Mn}_{1/3}\text{Co}_{1/3}\text{O}_2$ cathode, aggregated secondary particles that consist of nano-sized primary particles are the common microstructures which have many benefits of reduced ion diffusion pathway and power capability etc. However, when Ni content is substantially increased, gas generation and moisture sensitivity become great concerns in these secondary particles which have high surface areas to accommodate side reactions with moisture and generate gas.^{[4],[5]}

Objectives

The goal of this project is to advance the fundamental understanding of the cathode/electrolyte interfaces, especially those between electrolyte and Ni-rich and low-cobalt NMC cathode (i.e., $\text{LiNi}_x\text{Mn}_y\text{Co}_{1-x-y}\text{O}_2$, $x \geq 0.6$) for next-generation Li-ion batteries. Scalable synthesis approaches will be developed to prepare single crystal Ni-rich and low-Co NMC with desired bulk and surface properties for convenient electrode preparation and cell-level integration. The dynamic interactions between cathode and electrolytes will be revisited by using micron-sized but electrochemically active single crystal as a platform to identify effective solutions to develop next-generation high-energy cathode materials.

Approach

Single crystal particles of Ni-rich cathode with increased particle size e.g., a few microns and reduced surface areas have the advantages of potentially reduced gas generation, enhanced materials stability towards moisture attack and extended cycling stability. The “cracking” issue along the phase boundaries that are usually seen in polycrystalline Ni-rich NMC particles^[1] may also be mitigated in its single crystal counterpart. The following approaches have been proposed to tackle the scientific challenges existing in Ni-rich cathodes.

- Synthesis of electrochemically active single crystal $\text{LiNi}_{0.76}\text{Mn}_{0.14}\text{Co}_{0.10}\text{O}_2$ (referred as NMC76 thereafter) with ca.200 mAh/g reversible capacity.
- Side-by-side comparison of single crystalline and polycrystalline NMC76 electrodes at relevant scales.
- Demonstration of good cycling stability from single crystal cathode in graphite/NMC full cells consisting of thick electrodes that are easily adaptable by industry.
- Probe the evolution of interface between NMC76 and electrolyte in a “living” electrochemical cell by applying in situ Atomic Force Microscope (AFM).

Results

Both polycrystalline and single crystalline NMC76 have been synthesized with similar particle sizes at ca.3 μm (Figure II.3.D.1a and Figure II.3.D.1b). While polycrystalline NMC76 is a secondary particle consisting of nano-sized prime particles (Figure II.3.D.1c), single crystal NMC76 displays quite dense structures (Figure II.3.D.1d). Cavitation and internal pores are observed along with surface films for polycrystalline NMC76 (Figure II.3.D.1e). In contrast, there is no internal grain boundaries or “cracks” seen in single crystal NMC76 and the surface of single crystal is also quite clean (Figure II.3.D.1f). Figure II.3.D.1g and 1h are the electron diffraction pattern of polycrystalline and single crystalline NMC76, respectively, both of which indicate good crystallinity of single phase of α - NaFeO_2 -type layered structure consistent with X-ray diffraction patterns (not shown here).

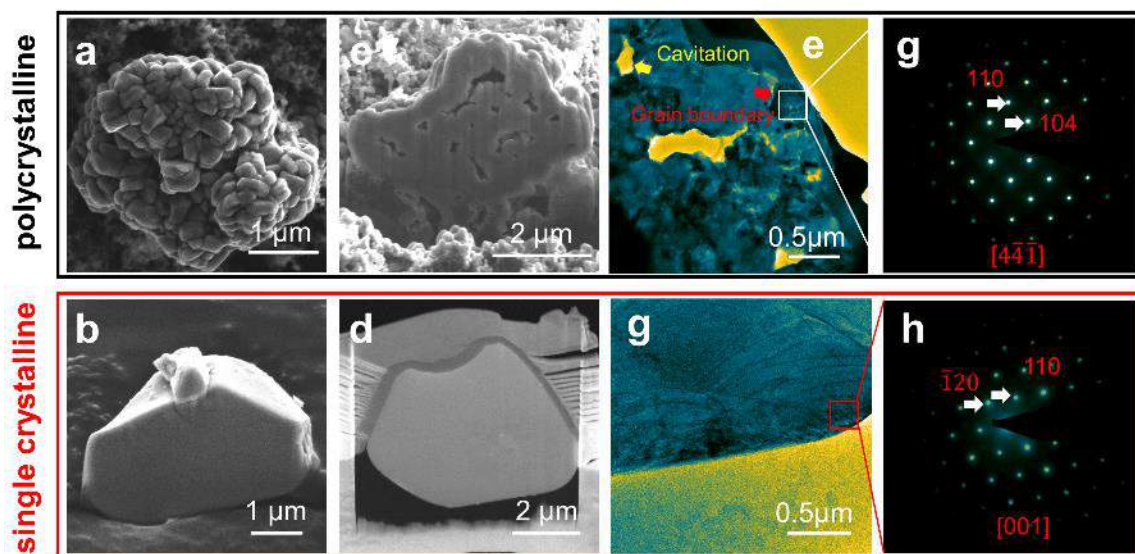


Figure II.3.D.1 Morphology and phase characterization of polycrystalline and single crystalline NMC76. (a, b) SEM images of polycrystalline and single crystalline NMC76. (c, d) Cross section images of polycrystalline and single crystalline NMC76. (e, f) STEM images of polycrystalline and single crystalline NMC76. (g, h) Selected area electron diffraction (SAED) of polycrystalline and single crystalline NMC76

NMC76 electrodes with different loadings ranging from 2 mAh/cm² to 5 mAh/cm² have been prepared to understand the relationship between particle morphologies and electrode packing density, electrode porosity and tortuosity. Figure II.3.D.2 compares the cross-sectional SEM images of electrodes with different mass loading made from polycrystalline (Figure II.3.D.2a) and single crystals (Figure II.3.D.2b). For the similar electrode thickness, more single crystals are packed into the electrode compared with polycrystalline, benefitted from increased tap density of single crystals. Without calendaring process, the porosities of polycrystalline and single crystalline electrodes are 65% and 62%, respectively. It is thereby concluded that single crystalline NMC benefits for the dense stacking of electrodes and reduction of cathode tortuosity.

Among the different mass loading of cathodes, 4 mAh/cm² areal capacity is of particular interest since it is the minimum areal capacity requirement to deliver 250 Wh/kg cell-level energy in the pouch cells based on graphite/NMC chemistry (cell design not shown here). Figure II.3.D.2c compares the electrochemical performances of 4 mAh/cm² cathodes consisting of different particle morphologies. Note that the active material content is 96% in all as-prepared electrodes convenient for future practical adoption. At such a high loading, both electrodes deliver > 200 mAh/g capacity, although there is around 19 mAh/g capacity gap between polycrystalline and single crystalline. The Coulombic efficiency of single crystal based thick cathode is 85% while the polycrystalline one is 91%, suggesting the inadequate utilization of big single crystals.

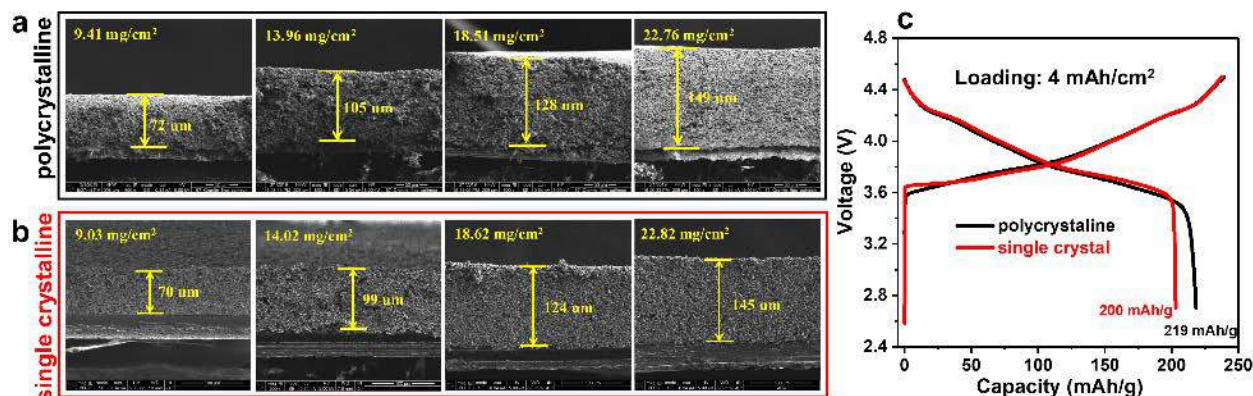


Figure II.3.D.2 (a) Cross section images of polycrystalline NMC76 cathodes with different mass loadings. (b) Cross section images of single crystalline NMC76 cathode with different mass loadings. (c) Comparison of the first charge-discharge curves for polycrystalline and single crystalline NMC76 based thick cathodes. The corresponding coulombic efficiencies of single crystalline and polycrystalline cathodes are 85% and 91%, respectively

NMC76 single crystal cathode was further tested in full cells by using graphite as the anode. Thick NMC76 cathode with 22.3 mg/cm² mass loading was prepared for coin cell testing which represents the typical necessary loading in realistic high-energy cells. N/P ratio of graphite anode and NMC76 cathode is controlled temporally at 1.4 which is still under optimization. The first cycle efficiency of the full cell is 85.6% due to the SEI formation and the slightly excessive amount of graphite in the anode. Although Li loss (low efficiency) occurs during first charge, the first discharge capacity of the single crystal NMC76 still reached ca. 200 mAh/g (Figure II.3.D.3a). Good cycling stability is also seen from graphite/NMC76 cells. After 100 cycles, the capacity retention ratio is ca. 88.3% (Figure II.3.D.3b). Note that the electrochemical performances discussed in Figure II.M.4.3 are from thick cathode (and anode) thus the results are directly transferrable to future Ni-rich cathodes in realistic batteries.

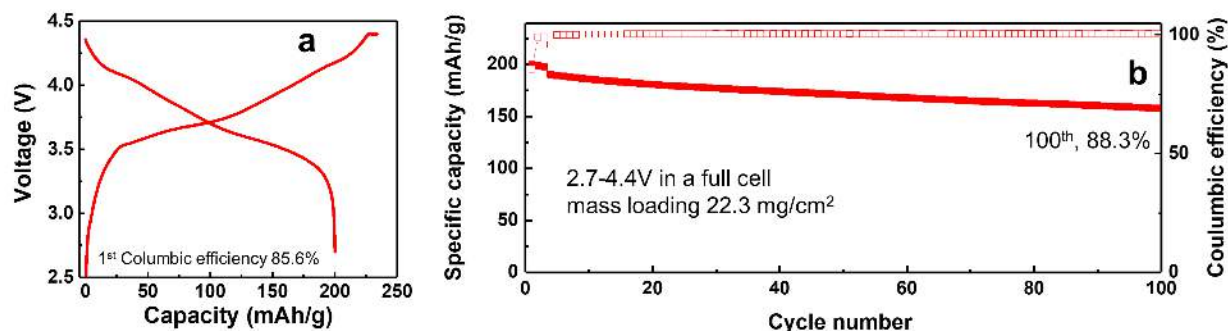


Figure II.3.D.3 (a) First charge and discharge curve of single crystal NMC76 in a graphite/NMC76 full cell between 2.7 and 4.4 V at 0.1C (1C = 200 mA/g). (b) Cycling stability of single crystal NMC76 in the graphite/NMC full cell using thick electrode. The full cell is charged at C/10 and discharged at C/3

In order to understand the interfacial reaction initiating on the surfaces of Ni-rich cathode in contacting with liquid electrolyte, in situ Atomic Force Microscope (AFM) has been applied to probe the cathode/interface evolution under the electrical field in a functioning electrochemical cell. The cyclic voltammetry curve of in situ AFM testing is shown in Figure II.3.D.4a along with the illustration of in situ AFM testing setup (inset of Figure II.3.D.4a). Figure II.3.D.4b to Figure II.3.D.4i show the corresponding AFM images of polycrystalline NMC76 at different potentials as labeled in Figure II.3.D.4a. It is noted that the some of the originally rough surfaces/planes become clean during cycling, which is presumably assigned to the decomposition of the residual carbonate salts formed during and after synthesis. Comparing Figure II.3.D.4b and 4i, regions A and B were significantly changed after the first cycle. Region A was extruded by the adjacent primary particles and region B experienced large volume expansion during the first cycle, which maybe lead to the disconnection or “cracking” between neighboring primary particles during cycling. Single crystalline NMC76 is also being investigated now by using in situ AFM technique to understand the differences of microstructural changes of two different NMC76 particles, if any.

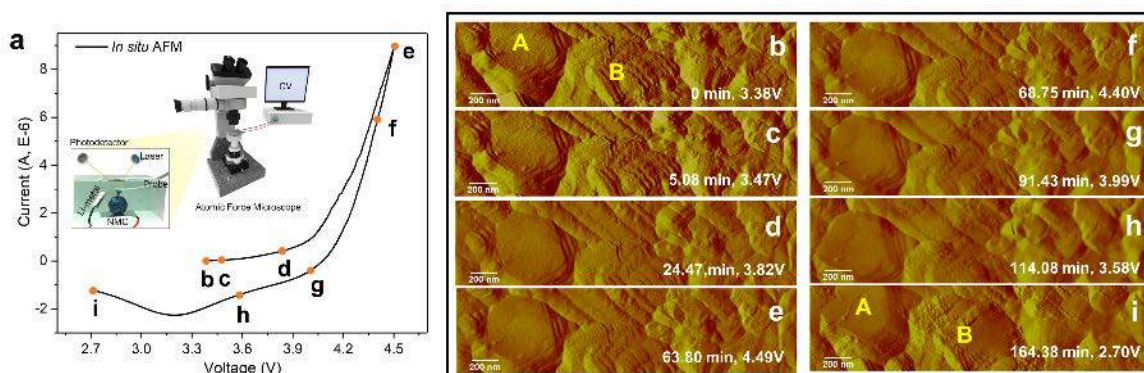


Figure II.3.D.4 (a) Cyclic voltammetry curve of polycrystalline NMC76 under in situ AFM testing, inserted figure is the demonstration of in situ AFM experimental setup. (b, c, d, e, f, g, h and i) AFM images of polycrystalline NMC76 at different potentials obtained from in situ measurements

Conclusions

Single crystalline Ni-rich cathode has been successfully synthesized and compared with its polycrystalline counterpart at relevant scales. Dense structure without cavities and surface films are observed in single crystal NMC76. Compared with polycrystalline NMC76, single crystals pack into more compact cathodes and therefore reduce the electrode porosity and tortuosity. Greater than 200 mAh/g capacity has been delivered from single crystal NMC76 with 88% capacity retention for 100 cycles in a graphite/NMC76 full cell (high mass loading). In situ AFM probing reveals that certain surfaces of polycrystalline NMC76 becomes clean after the first cycle but a significant volume expansion during discharge is also seen which may lead to the later particle segregation along phase boundaries of the secondary particles.

Key Publications

1. J. Xiao, “Ni-rich Cathode for Advanced Li-ion Batteries (invited), 236th ECS meeting, Atlanta, GA, October 15, 2019.
2. J. Hu, J. Tao, Y. Bi, Y. Xu, C. Wang, J.-G. Zhang and J. Xiao, “Understanding the Rate-limiting Step: from Thin-film to Thick Ni-Rich Cathodes”, to be submitted.
3. J. Hu, J. Tao, Y. Bi, Y. Xu, J.-G. Zhang and J. Xiao, “Probing the Cathode/Electrolyte Interface by in situ AFM”, to be submitted.
4. Y. Bi, J. Tao, J. Hu, Y. Xu, C. Wang, J.-G. Zhang and J. Xiao, “Understanding High Performance Single Crystalline Ni-rich Cathode and its Interfacial Reactions”, to be submitted.

References

1. Kim, Un-Hyuck, Hoon-Hee Ryu, Jae-Hyung Kim, Robert Mücke, Payam Kaghazchi, Chong S. Yoon, and Yang-Kook Sun. 2019. “Microstructure-Controlled Ni-Rich Cathode Material by Microscale Compositional Partition for Next-Generation Electric Vehicles.” *Advanced Energy Materials* 9 (15):1803902. doi: 10.1002/aenm.201803902.
2. Park, Kang-Joon, Hun-Gi Jung, Liang-Yin Kuo, Payam Kaghazchi, Chong S. Yoon, and Yang-Kook Sun. 2018. “Improved Cycling Stability of $\text{Li}[\text{Ni}_{0.90}\text{Co}_{0.05}\text{Mn}_{0.05}]\text{O}_2$ Through Microstructure Modification by Boron Doping for Li-Ion Batteries.” *Advanced Energy Materials* 8 (25):1801202. doi: 10.1002/aenm.201801202.
3. Deng, Tao, Xiulin Fan, Longsheng Cao, Ji Chen, Singyuk Hou, Xiao Ji, Long Chen, Shuang Li, Xiuquan Zhou, Enyuan Hu, Dong Su, Xiao-Qing Yang, and Chunsheng Wang. 2019. “Designing In situ-Formed Interphases Enables Highly Reversible Cobalt-Free LiNiO_2 Cathode for Li-ion and Li-metal Batteries.” *Joule* 3 (10):2550-2564. doi: 10.1016/j.joule.2019.08.004.
4. Weber, Rochelle, Christopher R. Fell, J. R. Dahn, and Sunny Hy. 2017. “Operando X-ray Diffraction Study of Polycrystalline and Single-Crystal $\text{Li}_x\text{Ni}_{0.5}\text{Mn}_{0.3}\text{Co}_{0.2}\text{O}_2$.” *Journal of The Electrochemical Society* 164 (13):A2992-A2999. doi: 10.1149/2.0441713jes.
5. Li, Jing, Andrew R. Cameron, Hongyang Li, Stephen Glazier, Deijun Xiong, M. Chatzidakis, Jenn Allen, G. A. Botton, and J. R. Dahn. 2017. “Comparison of Single Crystal and Polycrystalline $\text{LiNi}_{0.5}\text{Mn}_{0.3}\text{Co}_{0.2}\text{O}_2$ Positive Electrode Materials for High Voltage Li-Ion Cells.” *Journal of The Electrochemical Society* 164 (7):A1534-A1544. doi: 10.1149/2.0991707jes.

Acknowledgements

We thank the contribution from our collaborator Dr. Enyuan Hu at the Brookhaven National Laboratory on the structural analysis.

II.3.E Fluorinated Deep Eutectic Solvent (FDES)-Based Electrolytes (ANL)

Zhengcheng (John) Zhang, Principal Investigator

Argonne National Laboratory
9700 S Cass Avenue
Lemont, IL 60439
E-mail: zzhang@anl.gov

Peter Faguy, DOE Technology Development Manager

U.S. Department of Energy
E-mail: Peter.Faguy@ee.doe.gov

Start Date: October 1, 2018

End Date: September 30, 2021

Project Funding (FY19): \$350,000

DOE share: \$350,000

Non-DOE share: \$0

Project Introduction

Next-generation lithium-ion battery requires high-voltage high-energy density for long-range electric vehicle applications, therefore cathode materials with high voltage (> 4.3 V) and high capacity (>200 mAhg⁻¹) with low cost are greatly demanded. However, the performance of high-voltage high-energy cells are compromised due to the instable cathode/electrolyte interphase caused by the decomposition of electrolytes and transition metal dissolution-diffusion-deposition cycle.

Objectives

The objective of this project is to design and develop stable non-carbonate electrolyte materials that are thermodynamically stable at the cathode/electrolyte interphase, thus the new electrolyte could enable high-voltage high-energy (>4.5 V vs Li⁺/Li) cathodes such as Ni-rich, low- or Co-free cathodes, and are compatible with graphite, silicon anode and other cell components.

Approach

In the past years, the interest in deep eutectic solvents (DES) has been steadily increasing, much due to the possibilities to rationally design their special physical properties by choosing the right combination of components. In this project, we will design and develop new DES solvents based on fluorinated cations/anions to provide thermodynamic stability at cathode/electrolyte interphase at high voltages due to the incorporation of electron-withdrawing fluorine and fluorinated alkyl groups could lower the HOMO energy level, thus expand the electrochemical window up to 5.0 V vs Li⁺/Li.

Results

Physical properties and ion conformation

Deep eutectic solvents (DESs) are systems formed from a mixture of two solid organic materials that yields a free-flowing solution with a melting temperature below that of an ideal liquid mixture. As an example, 1-methyl-1-propylpiperidinium bis(fluorosulfonyl)imide (PMpipFSI) based DES solvent was prepared by one-step reaction of two solid precursors. The DES-based electrolyte was prepared with various LiFSI concentrations in an argon-filled glovebox, and their physicochemical properties (viscosity, ionic conductivity and Li⁺ transference number) are summarized in Table II.3.E.1. The viscosity and conductivity for the neat DES or special ionic liquid (IL) is 87.25 cP and 3.50×10^{-3} Scm⁻¹ respectively, which are comparable to the previous reported results. The viscosity increases, and the conductivity decreases when the LiFSI salt concentration increases from 1 M to 5 M, indicating the strong electrostatic interactions between Li⁺, PMpip⁺ cation and FSI⁻ anion. The highest viscosity and the lowest conductivity were observed for the saturated one (5 M) - i.e., 936.6 cP and 0.353×10^{-3} Scm⁻¹. As reported by other groups,^{[1],[2]} although the overall conductivity decreases, the Li⁺ transference number (t_{Li^+}) is significantly increased from 0.164 for 1 M to 0.475 for 5 M. A

high t_{Li^+} is beneficial for fast Li^+ transportation yielding high power capability of the Li-ion battery. Interestingly, when the concentration increases from 3.0 M to 4.0 M, t_{Li^+} reaches a plateau of 0.34.

Table II.3.E.1. Summary of Physical Properties, Ionic Conductivity and Li^+ Transference Number of PMpipFSI with Different LiFSI Concentrations

Denoted concentration ^a	Molarity of LiFSI (mol/L)	Molality of LiFSI (mol/kg)	Mole ratio of each ion			Viscosity (cP)	Conductivity (10^{-3} Scm^{-1})	t_{Li^+} (Li^+ trans. #)
			Li^+	PMpip ⁺	FSI^-			
-	0	0	0	0.50	0.50	87.25	3.50	-
1 M	0.93	0.76	0.10	0.40	0.50	133.5	2.24	0.164
2 M	1.7	1.5	0.16	0.34	0.50	249.0	1.25	0.185
3 M	2.4	2.3	0.21	0.29	0.50	396.0	0.819	0.340
4 M	2.9	3.0	0.25	0.25	0.50	601.3	0.555	0.344
5 M	3.4	3.8	0.28	0.22	0.50	936.6	0.353	0.475

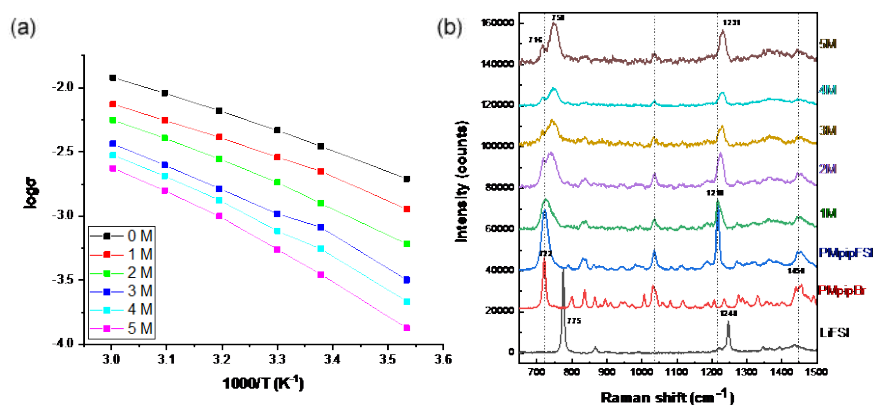


Figure II.3.E.1 (a) PMpipFSI/LiFSI electrolyte conductivity dependence on temperature measured by electrochemical impedance spectroscopy, and (b) Raman spectra (600-1500 cm^{-1}) for PMpipFSI/LiFSI electrolyte with different LiFSI salt concentrations

Figure II.3.E.1a shows the relationship of conductivity with temperature. The curvature feature of $\log(\sigma)$ vs $1000/T$ (T is temperature in Kelvin) for the high concentration electrolytes ($>3 \text{ M}$) indicates the ion transport mechanism differs from the dilute ones which follow the Arrhenius equation. This mechanism change is supported by strong interaction between Li^+ and FSI^- anion as evidenced by Raman spectra (Figure II.3.E.1b). The substantial Raman peak change occurs in the region from 650-1500 cm^{-1} , while no difference was observed in the region of 200-650 cm^{-1} and 1500-3200 cm^{-1} . The $\nu_{\text{S-N-S}}$ band in the FSI^- shows a characteristic peak at 722 cm^{-1} for the neat PMpipFSI solvent, and this peak shifts to 775 cm^{-1} for solid LiFSI salt due to the tight Li^+ and FSI^- coordination. When LiFSI was added, this peak broadens and gradually shifts to high wavenumber with increasing concentration from 1 M to 5 M. This shift reaches the maximum of 750 cm^{-1} for the 5 M electrolyte, close to the value of solid LiFSI.

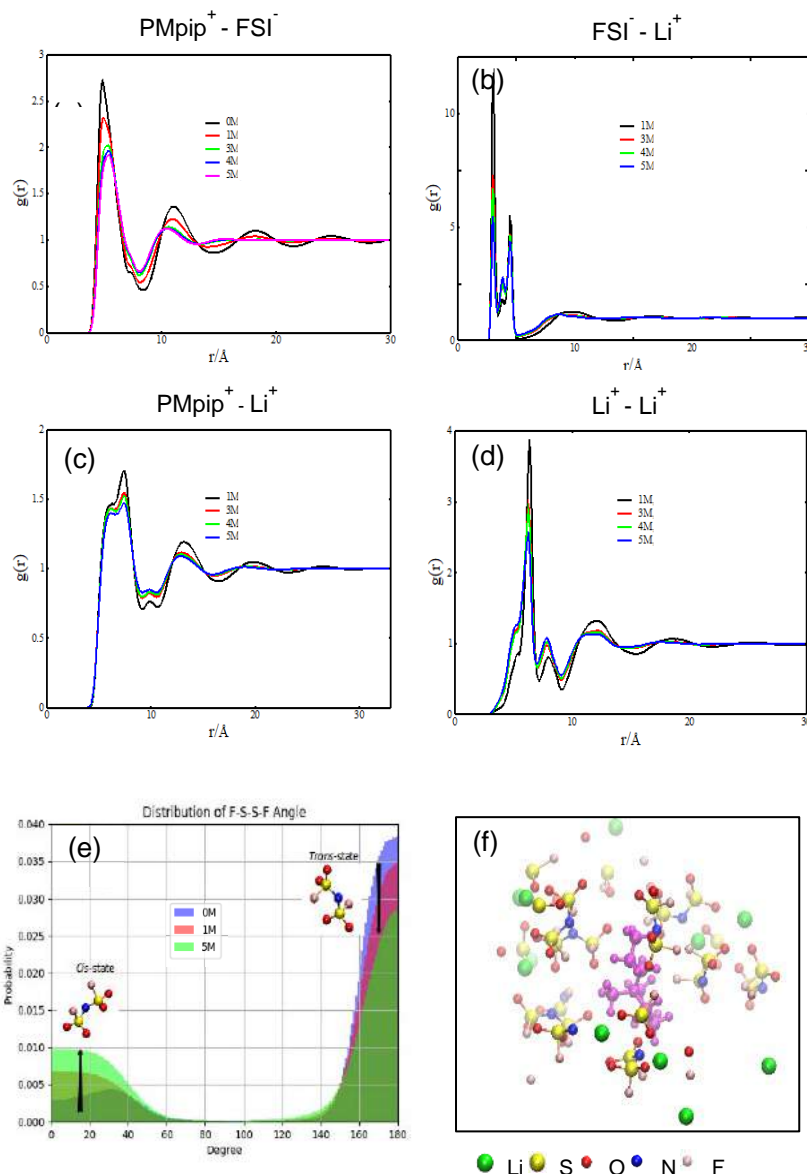


Figure II.3.E.2 (a-d) Pairwise radial distribution functions $g(r)$ computed from MD simulations. 3-4 (Strong spatial coordination between Li⁺ and FSI⁻ within 5 Å can be observed. In contrast, the coordination shells of other type ion-ion pairs extend to 10 Å and exhibit significantly weaker spatial coordination than Li⁺- FSI⁻

Figure II.3.E.2a-Figure II.3.E.2d summarizes the pairwise radial distribution functions computed from MD simulations. With the increase of Li⁺ concentration, the correlation peak of PMpip⁺-FSI⁻ pairs slowly shifts to the right, and the long-range correlation completely disappears when the LiFSI concentration reaches 3 M and higher. Meanwhile, the coordination distance between Li⁺ and PMpip⁺ exhibits corresponding slow shift while coordination shell between Li⁺ and FSI⁻ does not shift, revealing that the strong electrostatic attraction of Li⁺-FSI⁻ pairs significantly influences the binding configuration between PMpip⁺ and FSI⁻. On the contrary, the band at higher wavenumber blue shifted to 750 cm⁻¹, indicating the formation of Li⁺ and FSI⁻ ion pairs as evidenced by the significantly increased coordination number of Li⁺ around FSI⁻ (see caption of Figure II.3.E.2d). Concurrently, the $\nu_{\text{S-O}_2}$ band in Raman spectrum is also blue-shifted from 1218 cm⁻¹ to 1231 cm⁻¹ (Figure II.3.E.1b), which is in consistent with the results for $\nu_{\text{S-N-S}}$ band. In addition to the direct Raman measurement, we also observed considerable conformational transition of FSI⁻ with increasing Li⁺

concentrations by MD simulation. Figure II.3.E.2e presents the population change of *cis*- and *trans*-state of F-S-S-F “dihedral” structure in the FSI⁻ anion with increasing LiFSI concentration. Here the *cis*-state denotes a conformation where the two fluorine atoms stand on the same side of the S-S axis, while in *trans*-state the two fluorine atoms stand on the opposite side along the S-S axis. The co-existence of the two conformations is also reflected by the dual coordination peaks in the Li⁺-FSI⁻ radial distribution (Figure II.3.E.2b). However, with increasing Li⁺-FSI⁻ interactions, considerable shifting from *trans*-state (>90°) to *cis*-state (<90°) occurred. Figure II.3.E.2f illustrates a snapshot of Li⁺-FSI⁻-PMpip⁺ complexes at 5 M LiFSI concentration, centered with a PMpip⁺ cation. Tight Li⁺-FSI⁻ pairing can be clearly observed and on the other side, it can be naturally expected that the strong electrostatic repulsion between Li⁺ and PMpip⁺ expels the PMpip⁺ from FSI⁻ and screens the long-range interactions of PMpip⁺ and FSI⁻ and thus downgrades the role of PMpip⁺ in Li⁺ transport.

Oxidation stability and Al current collector passivation

However, there are two possible corrosion sources in this standard 2032-coin cell setup: Al and stainless-steel (SS). To isolate these two corrosion sources, an Al-coated 2032-coin cell setup was employed for cyclic voltammetry study. As shown in Figure II.3.E.1b, the internal side of the cathode cap (made of SS) is coated with Al and the SS spacer placed between the cathode cap and the cathode/working electrode was moved to the anode side in order to evaluate the Al corrosion/passivation behavior. Figure II.3.E.3 summarize the cyclic voltammograms of 1 M, 5 M LiFSI-PMpipFSI and Gen 2 electrolyte, respectively. For 1 M and 5 M PMpipFSI electrolytes, the Al oxidation starts at 3.2 V and 3.5 V in the first anodic scan and the corrosion current density is 50 times smaller than that obtained in the standard 2032-coin cell setup shown in Figure II.3.E.4c (Al working electrode with an adjacent SS spacer). Different from the results tested in standard 2032-coin cell setup, no corrosion reaction was observed at the 2nd and 3rd scan, indicating both 1 M and 5 M electrolyte could effectively passivate the Al and thus inhibit its corrosion. As expected, Gen 2 electrolyte showed the passivation behavior on Al as evidenced from the CV data in Figure II.3.E.3c. At this point, it is evident that both low and high concentration PMpipFSI electrolytes could effectively passivate the Al, and the large corrosion current observed in the standard 2032-coin cell setup were originated from the corrosion of SS spacer used in the cell.

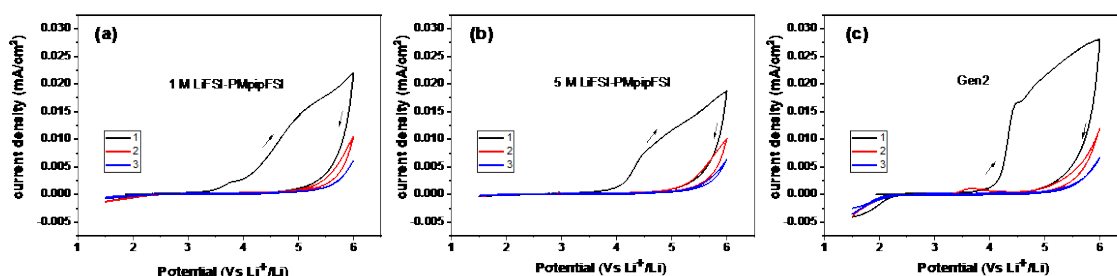


Figure II.3.E.3 Cyclic voltammograms of (a) 1 M LiFSI-PMpipFSI, (b) 5 M LiFSI-PMpipFSI and (c) Gen 2 electrolyte using Al working electrode in an Al-coated 2032-coin cell setup (Figure II.3.E.1b). (Working electrode: Al, counter and reference electrode: Li, scan rate: 10 mV/s)

Cyclic voltammetry was also performed to study the oxidation stability of ILEs. When the ILEs were anodically scanned to 6 V vs Li⁺/Li, large oxidation currents occurred with an onset voltage of 5.5 V and a corresponding reduction peak at 3 V appeared during the cathodic scan (Figure II.3.E.4a). However, when the scan window was narrowed down to 5 V, no oxidation current was observed and the corresponding reduction peak at 3 V also disappeared (Figure II.3.E.4b), indicating ILEs are thermodynamically stable up to 5 V which can support the redox of most high-voltage high-energy cathodes. Although voltage stability is a critical property for electrolyte, the capability of passivating Al current collector is equally crucial. It is widely accepted that carbonate electrolytes with amide salt such as LiTFSI and LiFSI could not passivate Al. On the

contrary, LiPF_6 salt could well passivate Al by forming insoluble AlF_3 and LiF . The passivation behavior for ILEs with amide salt is controversial. Our group recently reported a corrosion/passivation behavior of ILEs and demonstrated that the PMpipFSI with various LiFSI concentrations could sufficiently passivate Al current collector, but they all show corrosion towards stainless-steel with much suppressed corrosion for the high concentration ILEs. Therefore, to eliminate the high voltage exposure of ILE to the stainless-steel in the standard 2032-coin cells, Al-coated 2032-coin cells shown in Figure II.3.E.4c were used for all the cell testing.

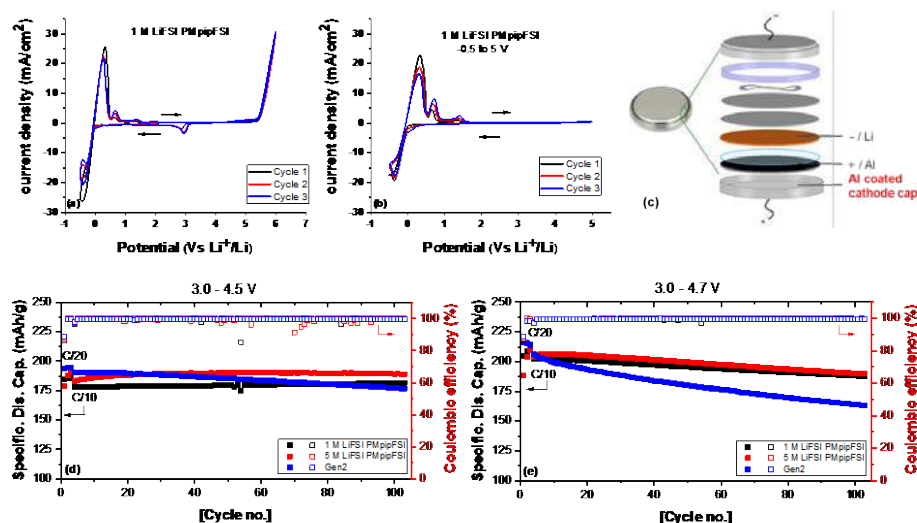


Figure II.3.E.4 (a) Cyclic voltammograms of ILEs scanned to 6.0 V vs Li^+/Li and (b) scanned to 5.0 V vs Li^+/Li using Pt as working electrode and Li as counter and reference electrode; (c) Al-coated 2032-coin cell configuration with two stainless steel spacers placed on anode side; (d) capacity retention and Coulombic efficiency of NMC532/Li cells with 1 M and 5 M ILE with a cutoff voltage 4.5 V-3.0 V, and (e) 4.7-3.0 V

NMC532 half- and full cell cycling at high voltages

Li salt concentration significantly impacts the ion conformation as revealed by Raman and MD simulation. To investigate its impact on high voltage stability, NMC532 half-cells were examined first. Figure II.3.E.4d- Figure II.3.E.4e shows the specific discharge capacity and Coulombic efficiency using 1 M and 5 M electrolyte as well as the conventional one - Gen 2 cycled between 4.5-3.0 V and 4.7-3.0 V. For 4.5 V half cells, Gen 2 electrolyte cell delivers highest initial capacity of 190.6 mAh/g, but it decays cycle by cycle with only 92% capacity retention for 100 cycles. Both PMpipFSI IL-electrolytes deliver lower initial capacity (177.9 mAh/g for 1 M and 183.1 mAh/g for 5 M), but no obvious capacity fading is observed within 100 cycles. The 5 M cell capacity slowly increased during the first 25 cycles, indicating a sluggish electrode wetting due to the increased viscosity. Surprisingly, remarkable difference in cycling performance was achieved when the cycling upper cutoff voltage was elevated to 4.7 V. The initial specific discharge capacity is comparable for all three electrolyte cells: 206.2 mAh/g for Gen 2, 202.6 mAh/g for 1 M and 203.8 mAh/g for 5 M IL-electrolyte. At this high voltage, Gen 2 shows the fastest fading rate and delivers 79% capacity retention. In contrast, both IL electrolytes outperform the Gen 2. It is worth to note that 5 M cell has a comparable or slightly better performance in terms of initial capacity and cycling stability than 1 M cell regardless of its extremely high viscosity. On the contrary, 1 M LiFSI-PMpipFSI experiences a higher overpotential than 5 M LiFSI-PMpipFSI (Figure II.3.E.2 in Supporting Information). More surprisingly, the C-rate test in NMC/Li cells showed that 5 M cell has a higher power capability than the 1 M cell regardless of the upper cutoff voltage as shown in Figure II.3.E.5a-Figure II.3.E.5b.

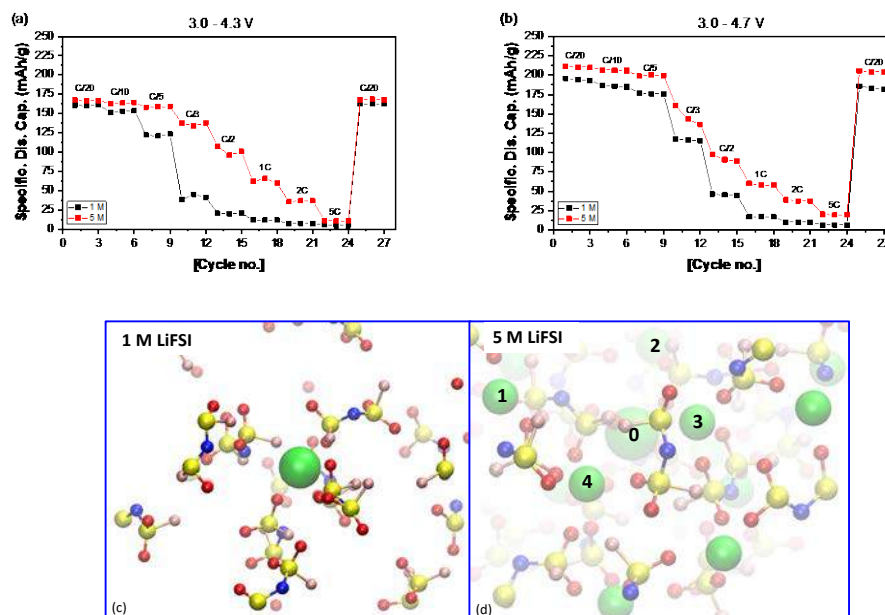


Figure II.3.E.5 C-rate capability of NMC532/Li cells with 1 M and 5 M LiFSI-PMpipFSI electrolyte cycled between (a) 4.3-3.0 V, and (b) 4.7-3.0 V; snapshots randomly selected from equilibrated MD trajectory for (c) 1 M and (d) 5 M-LiFSI concentration, respectively. (The two concentrations exhibit sharply different coordination structure, where one Li⁺ and four FSI⁻ constitute an isolated Li⁺ solvation structure at 1 M concentration while at 5 M concentration a deadlocked Li⁺-FSI⁻... Li⁺-FSI⁻... coordination network is established. For a center Li⁺ (labeled with 0), each of its four coordinated FSI⁻ also is paired with another Li⁺ (labeled by 1, 2, 3, 4))

Conclusions

In FY2019, we have demonstrated a stable electrolyte based on DES with saturated LiFSI salt. Contrary to common wisdom that ionic liquid like electrolyte are viscous and less conducting, the saturated DES electrolyte in this study exhibited a much higher Li⁺ transference number yielding high power capability of the LIB. Furthermore, after addressing the metal corrosion issue, we demonstrated its exceptional oxidation stability in 4.7 V NMC532/Li cells. Both properties are ascribed to the unique solvation structure adopted at saturated condition. Microscopic structural analysis based on MD simulations indicates the tightly coupled Li⁺-FSI⁻ pairing inhibits the motions of FSI⁻ by “doping” Li⁺ to all possible coordination sites associated with FSI⁻. Li⁺ adapts from diffusion to collective hopping transport mechanism.

Key Publications

1. Qian Liu, Trevor L. Dzwiniel, Krzysztof Z. Pupek, and Zhengcheng Zhang. Corrosion/Passivation Behavior of Concentrated Ionic Liquid Electrolytes and Its Impact on the Li-ion Battery Performance. *Journal of Electrochemical Society*, **2019**, in press.
2. Qian Liu, Wei Jiang, Maria Jose Piernas Munoz, Yuzi Liu, Zhenzhen Yang, Ira Bloom, Trevor L. Dzwiniel, Ying Li, Krzysztof Z. Pupek, and Zhengcheng Zhang. Saturated ionic liquid-based electrolytes for high-voltage NMC532/Si-graphite batteries. *Nature Materials*, **2019**, submitted.

References

1. Yoon, H.; Howlett, P. C.; Best, A. S.; Forsyth, M.; MacFarlane, D. R., Fast Charge/Discharge of Li Metal Batteries Using an Ionic Liquid Electrolyte. *J. Electrochem. Soc.* 2013, 160 (10), A1629-A1637.

2. Forsyth, M.; Girard, G. M. A.; Basile, A.; Hilder, M.; MacFarlane, D. R.; Chen, F.; Howlett, P. C., Inorganic-Organic Ionic Liquid Electrolytes Enabling High Energy-Density Metal Electrodes for Energy Storage. *Electrochim. Acta* **2016**, 220, 609-617.
3. Phillips, J. C.; Braun, R.; Wang, W.; Gumbart, J.; Tajkhorshid, E.; Villa, E.; Chipot, C.; Skeel, R. D.; Kalé, L.; Schulten, K., Scalable molecular dynamics with NAMD. *J. Comput. Chem.* **2005**, 26 (16), 1781-1802.
4. Jiang, W., Accelerating Convergence of Free Energy Computations with Hamiltonian Simulated Annealing of Solvent (HSAS). *Journal of Chemical Theory and Computation* **2019**, 15 (4), 2179-2186.

Acknowledgements

Support from Peter Faguy and David Howell at Vehicle Technologies Office (VTO), Office of Energy Efficiency and Renewable Energy, U.S. Department of Energy is gratefully acknowledged. NMC532 and Si-graphite electrodes were fabricated at Argonne's Cell Analysis, Modeling and Prototyping (CAMP) Facility, which is fully supported by VTO within the core funding of the Applied Battery Research (ABR) for Transportation Program. This research used the Leadership Computing Facility resource at Argonne, which is supported by the Office of Science, U.S. Department of Energy under Contract No. DE-AC02-06CH11357. The submitted manuscript has been created by UChicago Argonne, LLC, Operator of Argonne National Laboratory.

II.3.F Developing *In situ* Microscopies for the Model Cathode/Electrolyte Interface (NREL)

Robert Tenent, Principal Investigator

National Renewable Energy Laboratory
16253 Denver West Parkway
Golden, CO 80401
E-mail: robert.tenent@nrel.gov

Peter Faguy, DOE Technology Development Manager

U.S. Department of Energy
E-mail: Peter.Faguy@ee.doe.gov

Start Date: October 1, 2018

End Date: September 30, 2021

Project Funding (FY19): \$200,000

DOE share: \$200,000

Non-DOE share: \$0

Project Introduction

Multiple processes occurring at the cathode/electrolyte interface such as metal dissolution and oxygen evolution are known to lead to long term cell life issues for lithium ion batteries. However, many questions remain about the precise mechanisms involved in some of these processes. As an example, while manganese (Mn) dissolution is known to occur with a variety of cathode materials, there is still present debate about the oxidation state of Mn that is involved in the dissolution process.^{[1],[2]} Analysis of cells following failure as well as examination of species present in electrolyte samples from cycled cells, can tell us much about these degradation processes. However, these techniques may not capture information about chemical and/or electrochemical processes happening at or very near the cathode electrolyte interface. A need exists to develop diagnostic tools that can examine processes happening in situ immediately at the cathode/electrolyte interface.

This project is focused on using in situ probe microscopy techniques to observe and measure processes happening at the cathode/electrolyte interface. We plan to employ three forms of scanning probe microscopes including atomic force microscopy (AFM), scanning electrochemical microscopy (SECM) and a combined system that utilized both techniques. The SECM shown in Figure II.3.F.1 is a scanned probe microscope that can be used to perform electrochemical analysis of species evolving from or being consumed at an electrode surface. Analysis occurs in an active four-electrode electrochemical cell containing an electrolyte solution. The applied potential at both the substrate (model cathode material) and the sensing “tip” electrode is controlled versus the same reference and auxiliary electrode by a bi-potentiostat. The use of a small “tip” electrode (typically consisting of a < 10µm dia. metal wire) allows high speed electrochemical analytical techniques to be employed. This enables examination of species that may evolve from the cathode/electrolyte interface before they undergo subsequent reactions such as electrolyte degradation or SEI formation.

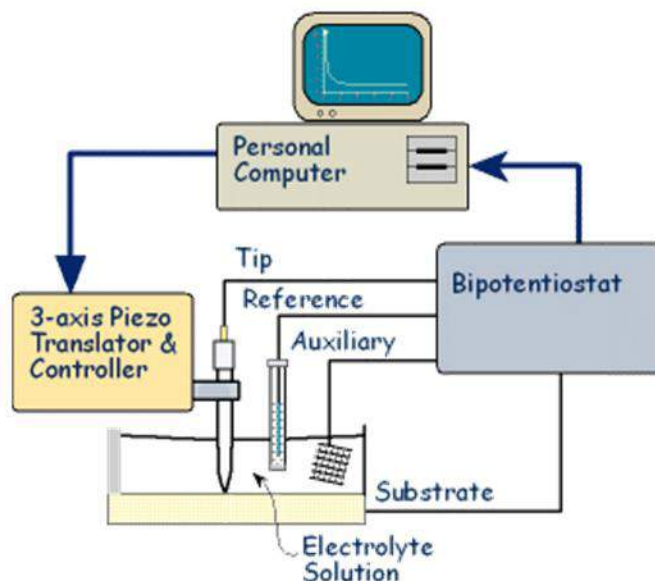


Figure II.3.F.1 Schematic representation of a scanning electrochemical microscope (SECM)

Objectives

The main objective of this work is to employ various interfacial electrochemical analytical methods to understand reaction mechanisms occurring at the cathode/electrolyte interface that influence overall battery performance. These probe microscopy-based analysis methods will be developed and demonstrated for the observation of varying degradation processes associated with the cathode/electrolyte interface. Model cathode materials including single crystal materials will be developed that can serve as baseline materials for this and other projects in the VTO portfolio.

Approach

Efforts in fiscal year 2019 have focused on the study of manganese dissolution processes from $\text{Li}_x\text{Mn}_2\text{O}_4$ (LMO) as a model system, however we seek to develop general techniques for interfacial electrochemical analysis of more complex systems including the NMC family. Particular focus will be based on developing high speed electrochemical analysis techniques that will allow us to tease out surface reaction details that may not be easily accessed with other methods. Scanning probe microscopy-based imaging techniques will also be developed that will allow spatial observation of active degradation processes. This will potentially relate cathode surface structure to observed degradation mechanisms. As a portion of this project, we will also focus on the development and demonstration of various model cathode materials that can be employed by this and other projects throughout the VTO portfolio.

As discussed earlier, initial focus has been placed on attempting to characterize byproducts of Mn dissolution from LMO. This provides us with a simplified model system that avoids further complications from additional processes occurring at the cathode/electrolyte interface for more complex systems such as the NMC family. We will demonstrate the ability to detect and measure the Mn dissolution processes in real time. Initial focus will be placed on developing methods to quantitate and differentiate various expected species including $\text{Mn}^{2+/3+}$ occurring at relevant cathode surfaces.

Model cathode systems will be developed and demonstrated using the Polymer Assisted Deposition (PAD) method. PAD provides a simple solution phase process that allows deposition of a wide variety of metal oxide materials. PAD has previously been employed to deposit various NMC formulations^[3] and can be used as a platform for providing multiple model cathode systems. Figure II.3.F.2 schematically represents the basic PAD process. PAD uses polyethyleneimine (PEI) and ethylenediaminetetraacetic acid (EDTA) to bind with soluble

metal salts (e.g., metal nitrates, chloride or acetates) to make films of various metal oxides. First-row transition metal ions such as Cu bind to PEI through coordination bonding between the lone pairs on the nitrogen atoms of PEI and cations. Other metals such as Sr bind to EDTA through covalent bonding between EDTA and metal ions, then bind to PEI through hydrogen bonding and electrostatic attraction between PEI and EDTA complex. In this process, polymers stabilize the precursor by preventing hydrolysis and condensation reactions and allowed us to obtain the viscosity required to enable a simple spin coating deposition method. These features make it feasible to grow binder-free cathode films with pure phase and low roughness over a large scale, free of cracks and imperfections. Particularly, PAD also provides a simple route to prepare epitaxial thin films by controlling the orientation of the substrate. When the deposition is applied onto a single crystal substrate, a high-quality epitaxial thin film with well-defined orientation following the substrate will be formed.

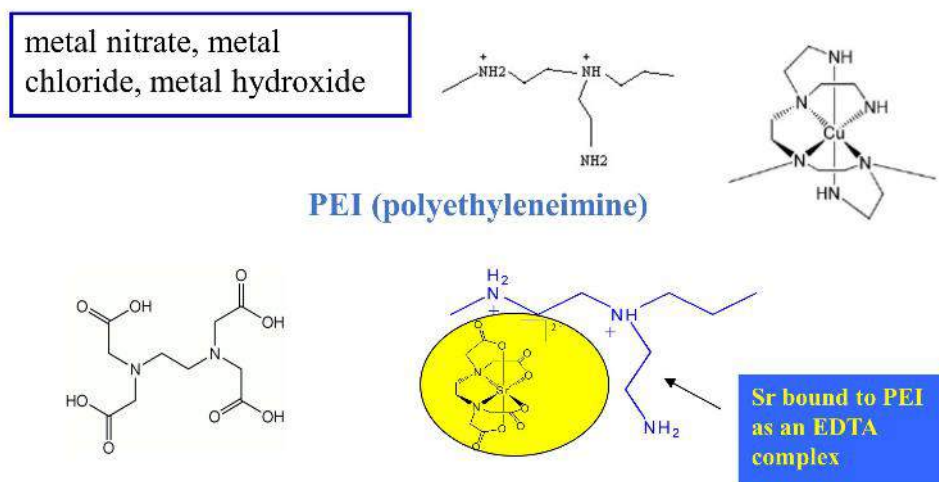


Figure II.3.F.2 Schematic Representation of the Polymer Assisted Deposition (PAD) Process

In addition to model cathode development via PAD and AFM/SECM method development, substantial work on the fundamental electrochemistry of various degradation products in relevant electrolytes will be conducted. Initially work will focus on understanding the electrochemistry of manganese in carbonate electrolytes. Variations in carbonate formulation as well as lithium salt anion will be explored to determine impact on how metal ions evolving from the cathode behave in these environments. These fundamental studies to determine relevant analytical parameters will provide the basis for later AFM/SECM studies to ensure understanding of the observed processes.

Results

Model Cathode Development and Demonstration:

LiMn₂O₄ (LMO) films on Si wafer, Stainless Steel (Pt-SS) and single-crystal SrTiO₃ (STO) were prepared via PAD. Figure II.3.F.3a presents a photograph of LMO films on Si synthesized at 600°C and the corresponding XRD and AFM data in Figure II.3.F.3b-e. In the observed XRD pattern, peaks at around 18°, 36° and 44° are attributed to the spinel LMO (111), (311) and (400) respectively, indicating the formation of LMO without impurities. AFM images confirm the films are fully and continuously covered on Si with low surface roughness (<3nm RMS).

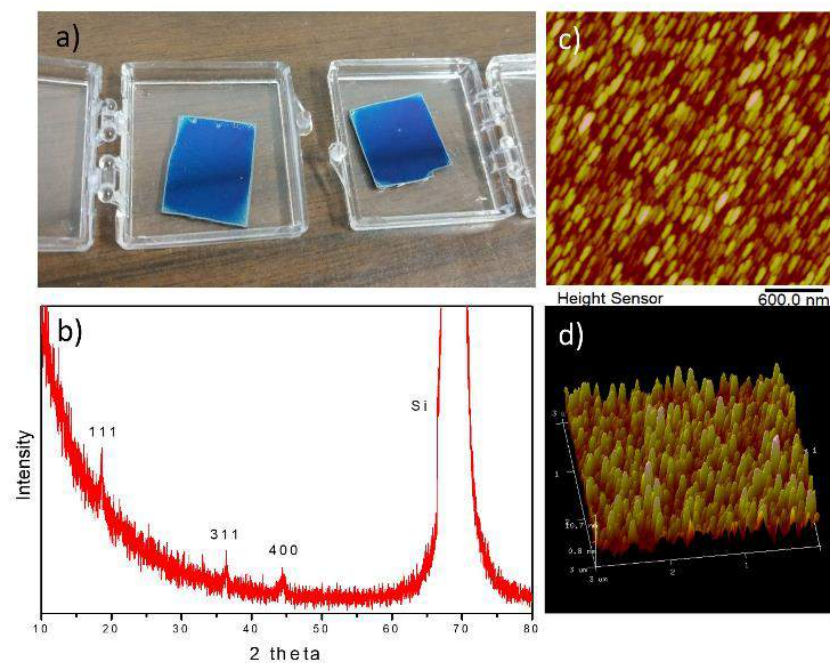


Figure II.3.F.3 (A) Photograph of PAD films coated on ~1cm² silicon samples, (B) XRD for LMO deposited on Si substrates (C) AFM of PAD LMO films on Si

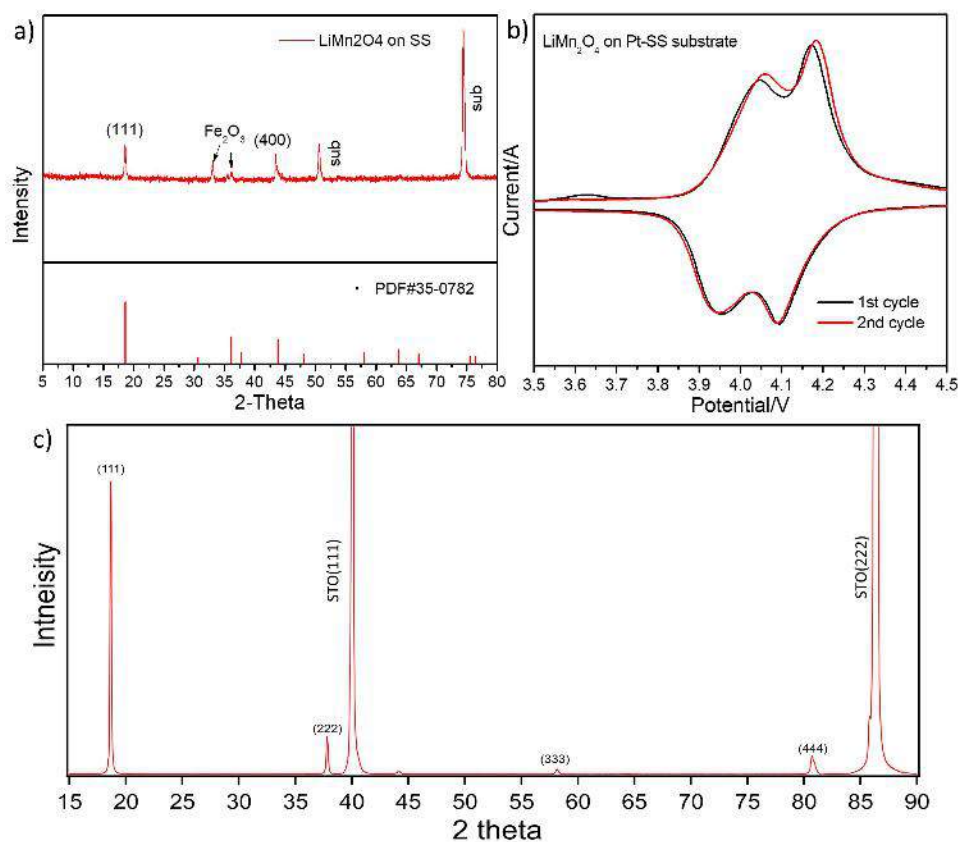


Figure II.3.F.4 (A) XRD for LMO PAD film on stainless steel (B) Cyclic Voltammetry for PAD Film on stainless steel (C) XRD of LMO(111) deposited via PAD on STO (111)

Figure II.3.F.4a demonstrates the XRD pattern of an LMO film on SS. Similar to Figure II.3.F.3a, a typical spinel LMO phase on SS is revealed. A coin cell was assembled to investigate the electrochemical property of LMO thin film by using LMO on Pt-SS as cathode electrode, Li metal as anode electrode and 1 mol L⁻¹ LiPF₆ in EC/DMC/EMC (1:1:1 in volume) as electrolyte, and its cyclic voltammetry is demonstrated in Figure II.3.F.4b. The CV was conducted from 3.5V to 4.5V at 0.1mV/s scan rate. Two pairs of peaks indicate a typical two-step reversible lithiation and delithiation process between LiMn₂O₄ and λ -MnO₂, further proving the binder-free LMO film synthesized by PAD electrode is practicable.

In order to grow single crystal LMO thin films, STO substrates were chosen based on appropriate lattice matching with LMO. Figure II.3.F.4c demonstrates the XRD of LMO on a single crystal STO <111> substrate, showing the peaks corresponding to (111), (222) (333) and (444) plane of spinel LMO phase respectively. The extinction of peaks corresponding to other orientations indicates the epitaxial nature of LMO thin film, suggesting the LMO (111) is parallel to the STO (111) surface. Single crystal LMO on STO <110> and STO <100> will be conducted.

Electrochemical Analysis:

Electrochemistry of Mn(II/III)

Based on our stated goal of detecting Mn dissolution from LMO, prior to initiating SECM work we conducted fundamental studies of the electrochemistry of manganese ions in carbonate-based electrolytes. This work forms the basis of our expected response from tip electrode measurements in planned SECM experiments. Bench level electrochemical experiments were conducted in standard three electrode cells using a 2 mm Pt disk working electrode, lithium metal reference electrode and Pt wire counter electrode. Variations in electrolyte composition have been shown to impact Mn dissolution from LMO. Specifically, the presence of HF in the electrolyte which is known to evolve from reactions of residual water with the PF₆ anion. Based on this, we examined a group of carbonate-based electrolyte formulations. We varied carbonate blends as well as the lithium salt anion to determine the impact on our observed response. Electrolyte solutions were produced using Mn(II) acetylacetonate (acac) and Mn(III) acetylacetonate (acac) to ensure the presence of Mn in the solution. Analysis of data collected from these studies clearly indicated a very diverse chemistry of the Mn ion in these electrolytes. While multiple electrolyte formulations were studied, for the sake of simplicity our discussion here will focus on our initial work with Mn acetylacetonates in 1M LiClO₄ in propylene carbonate. Later reports will include further studies of more complex electrolyte formulations.

Figure II.3.F.5 compares cyclic voltammetry results for Mn(II) (acac) and Mn(III) (acac) salts dissolved in 1M LiClO₄ in propylene carbonate. In addition to data for the Mn salts, a voltammogram for the “blank” electrolyte is shown for comparison. Data was collected at 100 mV/s scan rate. The black trace shown in Figure II.3.F.5 shows that the background electrolyte shows few appreciable faradaic processes within the examined voltage range. Upon addition of Mn(II) (acac) the CV trace (red) shows two oxidation peaks at ~ 2.8V and 3.4V with subsequent reductions at ~ 3.1V and ~ 2.2V which we attribute to Mn complexes formed with the electrolyte material. The blue trace for addition of Mn(III) (acac) shows oxidations at ~ 3.4V and ~ 3.7V and a clear reduction at ~ 3V. Interestingly, if the voltage sweep is reversed at <4.7V, another reduction peak appears at ~ 3.6V showing a quasi-reversible electron transfer couple that appears only in the presence of Mn (III). It should also be noted that both Mn acetylacetonate salt solutions show a significant increase in current above 4.8V as compared to the blank electrolyte sample. Interestingly, while all samples were prepared at a 1mM Mn salt concentration, the Mn (III) species shows significantly higher current than the Mn (II) containing sample. We are currently conducting ICP and EPR based studies of these solutions to confirm the concentration of the Mn salts as well as the oxidation state of Mn present following the procedure outlined by Aurbach¹. It is possible that the increased current could be tied to an interaction between the Mn salts and electrolyte oxidation products that may be forming at these extreme potentials. Note that the blank electrolyte trace is beginning to show current above ~ 4.2V that likely indicated initial electrolyte decomposition. It may be possible to deconvolute these effects through SECM generation/collection experiments of Mn(II/III) using Pt tip and substrate electrodes and this will be explored in future experiments. The clear finding from these

studies is that the electrochemistry of Mn salts in these electrolytes is complex and we have simplified the system to the best of our ability by using the LiClO₄:PC electrolyte blend.

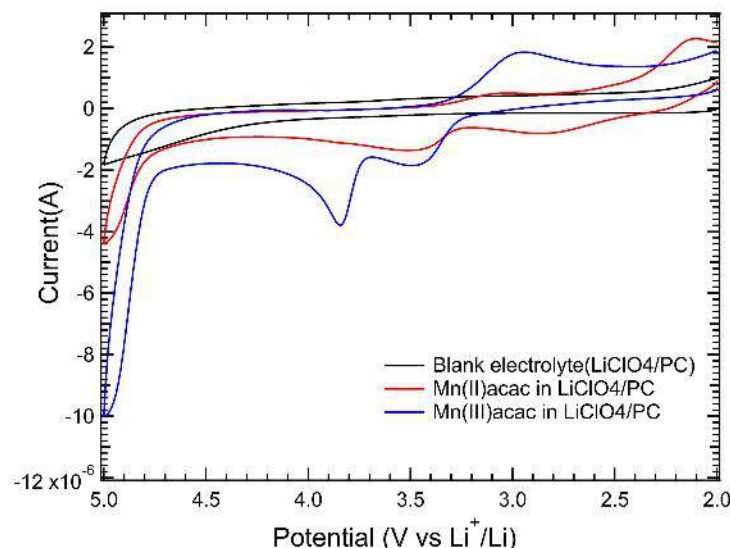


Figure II.3.F.5 Cyclic Voltammetry for a 2 mm Pt disk electrode in 1M LiClO₄:PC, with 1mM Mn(II) and Mn(III) acac

Figure II.3.F.6 shows data for our initial SECM-based experiments. These experiments were conducted by placing a 25 μm diameter Pt disk SECM tip electrode near an LMO substrate in a four electrode SECM cell. Li metal served as a reference electrode and Pt wire was used as a counter electrode. The tip electrode was positioned using the ferrocene/ferrocenium redox couple which appeared to show reversible electron transfer at the Pt tip electrode in this electrolyte solution. Tip approach curves were collected with the tip voltage set for the diffusion limited oxidation of ferrocene and the substrate electrode unbiased. This led to a “negative feedback” type response in which the tip current decreases as it approaches the substrate due to physical blocking of diffusion of the redox mediator species. The tip was allowed to approach the substrate until the tip current decreased to 75% of that measured at “infinite” distance from the LMO substrate. Based on the standard expected negative feedback approach curve, this would correlate with achieving a tip to substrate spacing of $\sim 20 \mu\text{m}$ for the 25 μm tip electrode.^[4] It should be noted that despite the lack of a deliberate voltage bias at the LMO substrate it is possible that the ferrocenium ion could be reduced and fed back to the tip to be re-oxidized. This may lead to a deviation from the model negative feedback approach curve and could make precise positioning of the tip electrode challenging in a purely SECM based experiment. Future studies with the combined AFM/SECM format will de-couple electrode positioning and electrochemical detection eliminating this challenge. However, in an attempt to repeatedly position the tip, all approach/positioning curves were collected to that 75% of the tip electrode diffusion limited current.

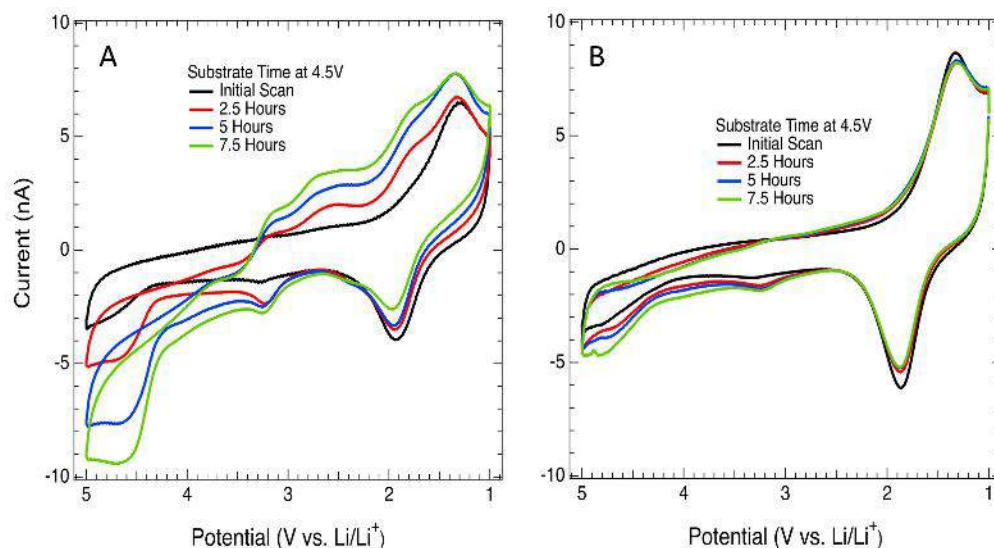


Figure II.3.F.6 SECM Tip Voltammetry collected at a 25 μm tip electrode placed near an LMO substrate. Data was collected following 30-minute intervals of holding the LMO substrate at 4.5V vs Li/Li⁺

Once the tip was positioned near the surface, the ferrocene containing electrolyte solution was removed and the cell rinsed with fresh electrolyte. Subsequent tip voltammograms were collected in order to ensure removal of any residual mediator species. Following placement of the tip near the LMO substrate and removal of the ferrocene mediator species, cyclic voltammograms were collected at the tip electrode to set a baseline background signal prior to exposing LMO to voltage bias. The LMO electrode was then held at 4.5V for 30 min intervals. Between each of these intervals the cyclic voltammetry experiment at the tip electrode was repeated in order to observe any new signals that may emerge over the earlier collected background electrolyte scans. This was repeated until the LMO substrate had been held at 4.5V for a total of 15 hours with tip voltammograms collected at each 30-minute interval. The data from this process is shown in Figure II.3.F.6A. An identical experiment was conducted using a stainless-steel substrate without LMO deposited but having gone through identical processing including a high temperature anneal. This was done in order to isolate the tip voltammetric response from the LMO as compared to any species that maybe released from the stainless-steel substrate. The oxidation and reduction peaks observed in both data sets at $\sim 1.8\text{V}$ and $\sim 1.4\text{V}$ respectively are due to a background electrolyte process that is observed with the tip far from the underlying substrate as well as in traditional “beaker” three electrode studies conducted with larger Pt electrodes. The initial trace in black shows that other than the aforementioned background process a largely featureless current-voltage response in the potential window examined prior to exposure of the LMO to high voltage holds. Subsequent tip voltammograms are shown after 2.5, 5 and 7.5 hours of holding the LMO substrate at a constant 4.5V bias. The data shown in Figure II.3.F.6A clearly shows several redox events growing into the observed tip voltammograms as a function of increased 4.5V voltage hold times for the LMO substrate. One oxidation appears to develop at $\sim 3.2\text{V}$ in the initial scan collected after 2.5 hours, but remains largely constant with increased voltage exposure. Above $\sim 4.4\text{V}$ the tip voltammograms show an increase in current that scales with increasing LMO voltage hold time. As discussed earlier, Figure II.3.F.5 appears to show increased current at voltages above $\sim 4.5\text{V}$ in the presence of either Mn (II) or Mn (III) species. This increased current also appears to be observed in Figure II.3.F.6A and is likely due to the presence of Mn in the electrolyte solution after the high voltage holds. The return voltage sweep shows multiple reduction peaks potentially indicative of electron transfer reactions to various Mn complexes formed. It should be noted that only scans which had gone above 4.4V showed these multiple peaks which may indicate that the signals obtained are from decomposition products of the species formed in the oxidation observed above 4.4V. Comparison to the data in Figure II.3.F.6B shows little change in the observed current voltage curves and none that increase with increasing time for the high voltage holds thus indicating that the observed changes observed in Figure II.3.F.6A are

likely due to the presence of the LMO substrates. Further control experiments are being conducted including ICP/EPR analysis of electrolyte solutions collected in the SECM experiments to confirm Mn dissolution as well as the likely oxidation state of Mn present in solution using the aforementioned protocol.

Conclusions

Efforts to date appear to be consistent with the detection of Mn dissolution at the Pt SECM tip electrode under our experimental conditions. Bench level electrochemical analysis as well as the SECM generation/collection experiments clearly indicate a very rich chemistry for the Mn (II/III) couple in carbonate electrolytes. Multiple control experiments have been conducted to isolate the observed signals to degradation products unique to the LMO containing cell. Additional studies are underway to verify the presence of Mn in these solutions as well as the oxidation state present. Comparison of the data presented in Figure II.3.F.5 and Figure II.3.F.6 are consistent with our conclusion of Mn detection, however questions remain about the oxidation state present. On-going studies are in process to isolate this. This information will be used to inform high resolution imaging of LMO under active bias using the AFM/SECM instrument to isolate specific surface sites that may be driving the degradation process.

Key Publications

1. Enhancing electrocatalysis of $\text{LiNi}_{0.5}\text{Co}_{0.2}\text{Mn}_{0.3}\text{O}_2$ by introducing lithium deficiency for oxygen evolution reaction - Di Huang, Jiuling Yu, Zhengcheng Zhang, Chaiwat Engtrakul, Anthony Burrell, Meng Zhou, Hongmei Luo, Robert C. Tenent; submitted to ACS Applied Materials and Interfaces.

References

1. Banerjee, A.; Shilina, Y.; Ziv, B.; Zeigelbauer, J.M.; Luski, S.; Aurbach, D.; Halalay, I.C., J. Am Chem. Soc. 2017, 139, 1738-1741.
2. Benedek, R., J. Phys. Chem. C, 2017, 121, 22049-22053.
3. Huang, D.; Shi, Y.; Tornheim, A.P.; Baren, J.; Chen, Z.; Zhang, Z.; Burrell, A.; Luo, H., Applied Materials Today 2019, 16, 342-350.
4. Bard, A.J. In Scanning Electrochemical Microscopy; Bard, A.J, Mirkin, M.V. Eds.; CRC Press: Boca Raton, FL, 2012.

Acknowledgements

The author would like to thank multiple key collaborators on this effort including Drs. Chaiwat Engtrakul, Sanjini Nanayakkara and Anthony Burrell (NREL), Professor Hongmei Luo and Mr. Di Huang (New Mexico State University).

II.3.G Advanced Lithium Ion Battery Technology – High Voltage Electrolyte (Daikin America, Inc.)

Ron Hendershot, Principal Investigator

Daikin America, Inc.
2749 Highway 20 W
Decatur, AL 35601
Email: hendershot@daikin-america.com

Joseph Sunstrom, Principal Investigator

Daikin America, Inc.
2749 Highway 20 W
Decatur, AL 35601
E-mail: sunstrom@daikin-america.com

Alec Falzone, Principal Investigator

Daikin America, Inc.
2749 Highway 20 W
Decatur, AL 35601
E-mail: afalzone@daikin-america.com

Tien Duong, DOE Technology Development Manager

U.S. Department of Energy
E-mail: Tien.Duong@ee.doe.gov

Start Date: October 1, 2018	End Date: September 30, 2021	
Project Funding (FY19): \$300,000	DOE share: \$300,000	Non-DOE share: \$0

Project Introduction

The use of electrolytes containing small fluorinated molecules to enable stable high voltage (> 4.3 V) battery operation is the focus of this project. Previously, Daikin has shown that it is possible to operate lithium ion batteries utilizing several different cathode chemistries up to 4.5 V. This is accomplished by reducing the gas generation originating from electrolyte decomposition at high voltage. The primary mechanism for this is not completely understood, but the hypothesis is that the fluorinated molecules form a film on the highly oxidizing cathode. It is known that battery cycle performance above 4.5 V drops significantly, however the source of the observed performance loss is not yet understood. The target for this project is to achieve 300 cycles above 80% capacity retention at 4.6 V. A better understanding of gas evolution, which happens above 4.3 V and the failure mode above 4.5 V, is sought in order to propose mitigation strategies which will facilitate better high voltage performance in lithium ion batteries.

The battery industry trend for cathode materials is toward reducing the overall cobalt content (i.e., higher nickel) for a variety of reasons. Some of which include: increasing cost, loss of supply, and human rights issues. The experiments proposed for this project will encompass a range of cathode materials with successfully higher nickel content. This will be performed in order to comprehend how fluorinated electrolyte interacts with various cathode surfaces. This is with the anticipation that the lithium ion battery industry will move towards nickel-rich cathodes, which can operate at higher voltage in order to achieve more energy-dense batteries.

Objectives

The three-year project can be divided into three main milestone topics, each spanning one fiscal year: 1) understanding of gassing mechanisms and kinetics, 2) examining physical and chemical aspects of film

formation, and 3) observation of chemical and structural evolution of electrode surfaces at various operating conditions. The FY2019 focus is the characterization of thickness changes in the cell (non-gassing), along with quantifying metal dissolution of the cathode as a function of various operating conditions. In addition, the absolute thickness of standard carbon films reported in FY2018 were obtained. While the qualitative understanding of gaseous components in tested cells was performed in FY2017, the capability to quantify all discovered components is established in FY2019. Quantifying these components will help develop an understanding of electrolyte decomposition at high voltage (> 4.5 V) and potentially mitigate this degradation mechanism.

Cycling cells at high voltage results in changes to the crystal structure of the $\text{LiNi}_x\text{Mn}_y\text{Co}_z\text{O}_2$ ($\text{NMC}_{xyz} = 111, 532, 622, 811$) and $\text{LiNi}_{.80}\text{Co}_{.15}\text{Al}_{.05}\text{O}_2$ (NCA) cathodes, which leads to dissolution of transition metals and irreversible capacity loss of the cell. We aim to determine which electrolyte formulation/cell chemistry limits transition metal dissolution of the cathode. Developing methods to measure cell thickness changes will aid in the understanding of relationships between cell thickness changes (non-gassing), metal dissolution, and electrochemical performance. Additional analyses of films derived from different electrolytes (i.e., hydrocarbon vs. fluoroether (HFE) vs. HFE/FEC) will correlate chemical composition at the cathode-electrolyte interface to electrolyte formulation.

Approach

The evolving composition of the electrolyte in the battery will be examined by various analytical instruments to study volatiles [gas chromatography – mass spectrometry (GC-MS)/thermal conductivity detector (TCD)], liquid [liquid chromatography MS (LC-MS)], and solid [time-of-flight secondary ion mass spectrometry (TOF-SIMS), thermogravimetric analysis MS (TGA-MS), X-ray photoelectron spectroscopy (XPS), and Auger electron spectroscopy (AES)] electrolyte decomposition products during battery operation. In the first year, the team addressed the gas composition and kinetics for both hydrocarbon and fluorocarbon as a function of several charge/discharge conditions. In the second year, the project transitioned into analysis of the solid-state electrolyte (SSE) decomposition components of its tested batteries to obtain valuable information about SEI layer formation and how it manifests change in both the anode (graphite) and cathode (LCO and NMC). The third year is focused on measuring changes in the solid state structure of the cathode following high-voltage operation along with investigating the swelling of the solid-state components (non-gassing). Quantification of any dissolved metal ions originating from the cathode (transition metals), and deposited on the anode will be obtained using inductively coupled plasma – mass spectrometry (ICP-MS). We will also study changes in the cathode structure using powder X-ray diffraction (XRD).

Results

Battery Thickness (non-gas) vs. Time/Voltage – Milestone 1

Swelling of the anode/cathode wind of 1 Ah NMC111 pouch cells was reported in previous findings (DOE EE0006437), and is a known degradation mechanism especially at high-voltage (> 4.5 V). Thickness changes as a function of time/voltage in addition to cell chemistry/electrolyte were targeted in order to understand the contributing factors to this decay pathway. It is hypothesized that this swelling is attributed to changes in the graphite anode. Initial cell thickness changes (non-gassing) were measured using Keyence GT2 series contact sensors which were secured in place using custom fabricated/machined aluminum housings. Signal from these sensors was measured through the analog output leads (Voltage/Current), and recorded using a channel on an Arbin battery tester. These contact sensors have a linear response in the 0 – 5 mm range, with a $\pm .1$ μm accuracy. Thickness standards (0 – 1 mm) were used to generate the calibration curve depicted in Figure II.3.G.1 (left). It was necessary to generate calibration curves for each sensor to account for system variability (Δ Thickness vs. Voltage). In addition, the structure of the contact sensor device setup for 200 mAh cells can also be seen in Figure II.3.G.1 (right).

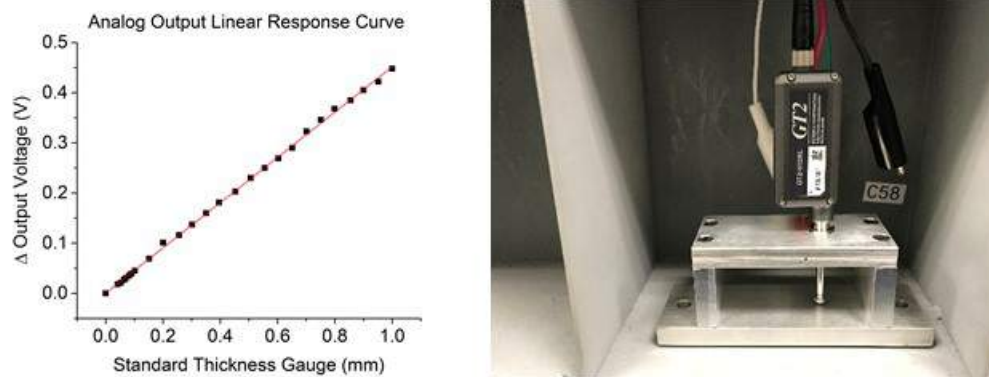


Figure II.3.G.1 Calibration curve of Keyence contact sensors in the 0 – 1 mm range (left). Custom device configuration to measure thickness changes in 200 mAh cells (right)

Initial experiments investigating NMC532 cells as a function of time/voltage/electrolyte were targeted due it being the best performing cell chemistry to date. Three electrolyte formulations were included in the first batch of cells, and cycled at 4.2, 4.5, and 4.6V. Cells contained the identical LiPF_6 concentration (1.2 M) and 1,3-propane sultone (PS) as an anti-gassing additive (1% w/w). The HFE electrolyte contains 60:20:20 (EMC:EC:HFE), HFE/FEC electrolyte contains 60:20:20, and the baseline hydrocarbon formulation is 80:20 (EMC:EC). There are minimal changes to thicknesses in NMC532 cells at 4.2V when comparing hydrocarbon to HFE electrolyte. Figure II.3.G.2 depicts the thickness changes of NMC532 cathodes as a function of electrolyte over 200 charge/discharge cycles (symmetric at 0.7C, CCCV every 10) between 3.0 and 4.6 V.

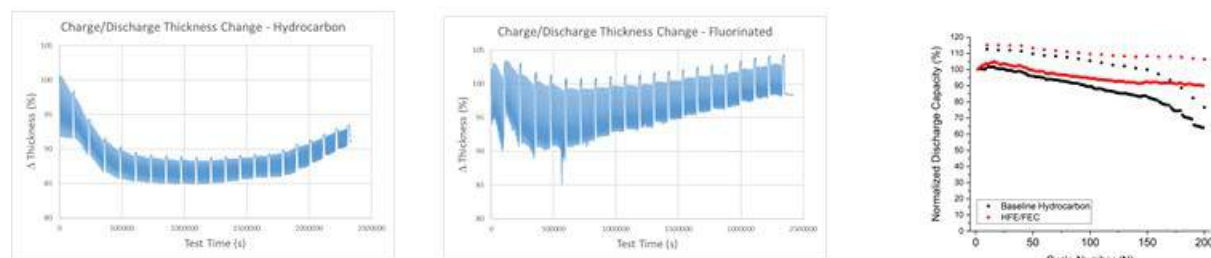


Figure II.3.G.2 Thickness changes of NMC532 cells as a function of electrolyte, with the baseline hydrocarbon (left) and HFE/FEC electrolyte (middle). Electrochemical performance of NMC532 cells normalized to 1st CC/CC cycle (right)

Upon charging, both pouch cells gain between 3-5% of overall thickness as lithium inserts into the graphite anode. As the cells lose capacity due to cathode/electrolyte degradation at high voltage, there is a measureable thickness change as a function of cycle number. There is a correlation between the accelerated thickness increase and capacity loss around cycle 150 in the NMC532 cell with the hydrocarbon electrolyte (Figure II.3.G.2, right). The chemical nature of this accelerated thickness change/capacity loss is still under investigation. One drawback to this method of measurement is that physical contact with the pouch cell causes a slight compression at the sensor/pouch interface, resulting in the negative feature in both graphs. Although small changes in thickness were observed, they do not reflect thickness measurements of the cathode/anode segments taken of the pouch cell following post-mortem analysis. To address this, cells thickness we measured using an additional method. Table II.3.G.1 depicts the thickness changes of cells using a micrometer, indicating the overall swelling of the jelly-roll is greater than the 3-5 % during a charge/discharge evident in Figure II.3.G.2 above.

Table II.3.G.1 200 mAh Cell Thickness Changes Following 200 Charge/discharge Cycles at .7C

Cell Chemistry	Upper Voltage	Electrolyte	Overall Cell Thickness Change (%)
NMC532/Graphite	4.6	Hydrocarbon (Baseline)	22.2
NMC532/Graphite	4.6	HFE	24.0
NMC532/Graphite	4.6	HFE/FEC	20.2

Swelling of the jelly roll in NMC532/graphite pouch cells following a cycle life test at high voltage was observed in all electrolytes. There was a slight difference between the three different formulations, with the HFE/FEC having the smallest change, and HFE the greatest. Cells were measured at the same SOC (100 %) for the micrometer thickness measurements. One possible explanation to this will be discussed in the next section, which explores deposited transition metals at the anode post-mortem.

Due to compression of the jelly roll at the sensor/pouch interface, an alternative method to measure cell thickness changes as a function of time/voltage has been designed. This method utilizes a fixed laser, which reflects off the surface of a fixed object at a glancing angle (29°). The position of the reflected light is tracked with time-resolved photography, calibrated to known changes in position along the z-axis. Experiments using this technique are currently ongoing and will be reported following Q2 FY2020. Figure II.3.G.3 depicts the prototype setup of the constructed apparatus along with the pixel response from the image software. This method of thickness measurement offers a $\pm 50 \mu\text{m}$ resolution, and a repeatable response.

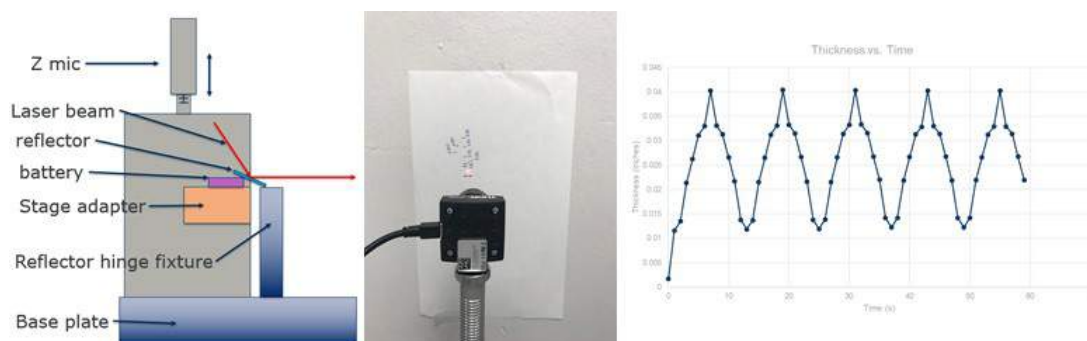


Figure II.3.G.3 Prototype setup of the non-contact thickness measurement system (left) and laser position calibration (middle). The pixels from the laser is tracker using the ImageJ software package (NIH)

Metal Dissolution vs. Time/Voltage – Milestone 2

One of the known degradation mechanisms of mixed metal oxide cathode materials is the irreversible dissolution of transition metals, especially at high voltage ($> 4.5\text{V}$). These dissolved metals migrate into solution, with some remaining dissolved in the organic electrolyte. However, the majority deposits on the anode material. Efforts in Q2FY2019 transitioned into investigating changes in this solid-state structure of materials in cells as a function of time/voltage/electrolyte. The initial approach utilizes ICP-MS to determine the concentration of dissolved metals which have deposited on the anode. Figure II.3.G.4 depicts the concentration of cobalt from tested LCO cells (4.5 and 4.6V) as a function of electrolyte composition. LCO is known to have accelerated decomposition at high voltage, with Co dissolution being a contributing factor. A baseline concentration of transition metals in the graphite anode is expected due to manufacturing processes. A dried, untested NMC532 cell was deconstructed with a portion of graphite anode digested and analyzed via

ICP-MS. Although an anode portion from other untested cell chemistries (NMC622 and LCO) were not submitted for analysis, similar concentrations of transition metals (Ni, Mn, Co) are expected.

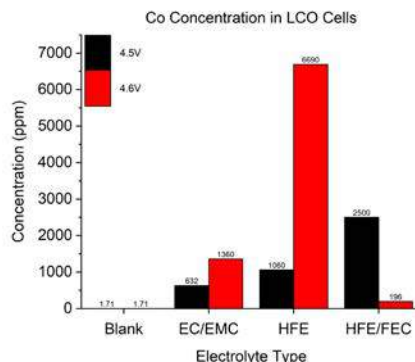


Figure II.3.G.4 Dissolved Co concentrations in tested LCO cells as a function of time (200 cycles), voltage (4.5 and 4.6V), and electrolyte (EC/EMC, HFE, HFE/FEC)

Previous electrochemical performance data demonstrated LCO's inability to be cycled at 4.5V or above. One of the proposed degradation mechanism is the dissolution of Co into the electrolyte, and ultimate deposition on the graphite anode. LCO cells exhibited significant delamination of graphite from the copper current collector at both 4.5 and 4.6V, which complicated the sample preparation prior to digestion. A significant amount (> 1000 ppm) of dissolved Co was detected in graphite anodes at high voltage. Dissolved Co was highest with just the fluorinated ether, and decreases upon the addition of FEC to the electrolyte (6690 vs. 196 ppm). This phenomenon is also seen in NMC532 and NMC622 cells as seen in Figure II.3.G.5 and Figure II.3.G.6, albeit with a smaller effect.

Figure II.3.G.5 depicts dissolved metal concentrations at the anode at both 4.2 (top row) and 4.5V (bottom row). At 4.2V, NMC532 cells have less than 100 ppm of total dissolved metals (top left), with NMC622 exhibiting a higher concentration in all electrolyte formulations (top right). Both fluorinated electrolytes contain lower amounts of all metals in both cell chemistries, demonstrating the increased stability of fluorinated electrolytes over the baseline hydrocarbon (EC/EMC) formulation. Aside from the NMC622 cell at 4.5V, cells with the HFE electrolyte contain the highest concentration of dissolved metals.

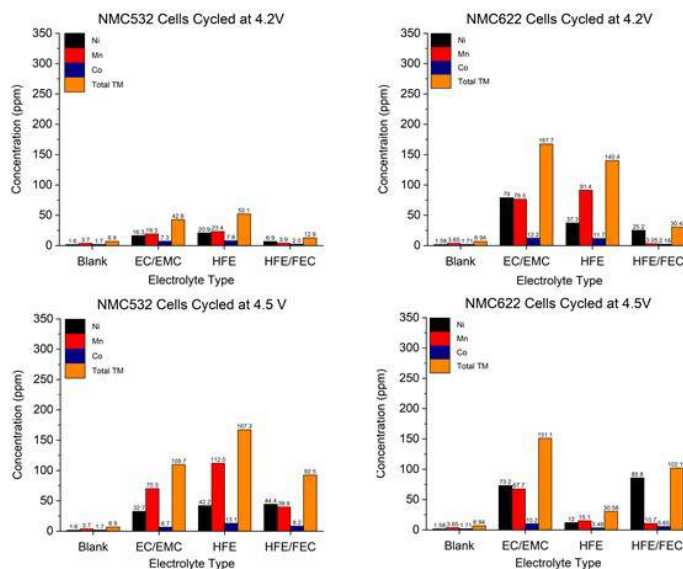


Figure II.3.G.5 Dissolved metals concentration (Ni, Mn, Co) in tested NMC532 and NMC622 cells as a function of time (200 cycles), voltage (4.2 and 4.5V), and electrolyte (EC/EMC, HFE, HFE/FEC)

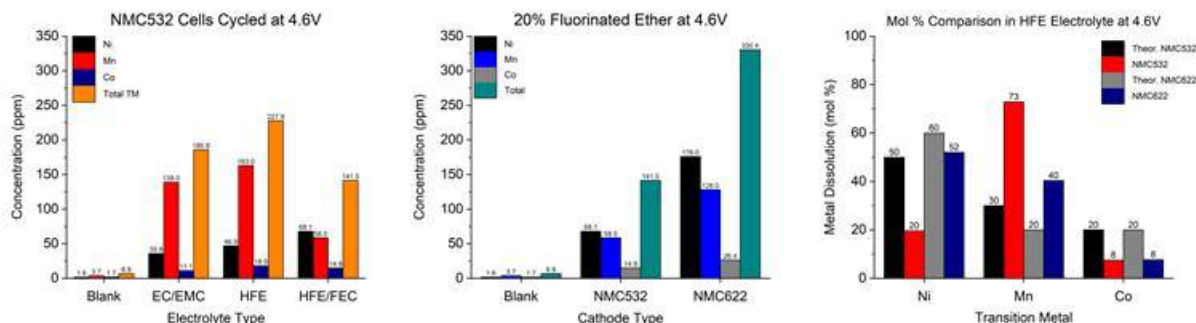


Figure II.3.G.6 Dissolved metals (Ni, Mn, Co) in tested NMC532 cells at 4.6V (left). NMC532 and NMC622 cells with the HFE electrolyte at 4.6V (middle). Stoichiometric ratios of HFE cells at 4.6V post mortem versus theoretical (right)

NMC532 cells cycled at 4.6V as a function of electrolyte are depicted in Figure II.3.G.6 (left). As seen in cells at 4.2 and 4.5V, the addition of HFE results in a more dissolved metals at the anode. However, FEC again suppresses the deposition of Ni, Mn, and Co. One explanation for this is that FEC could form coordination complexes with the corresponding metal, keeping it soluble in the liquid electrolyte. Its presence would not be detectible with ICP-MS of the graphite anode, however could be detected using HRESI-MS of the liquid.

One outstanding question we aim to answer is whether the transition metals dissolve in a stoichiometric ratio, or if there is selective dissolution of one of the components.^[1] Figure II.3.G.6 (right) depicts experimental molar ratios of dissolved metals in NMC532 (red) and NMC622 (navy) cells at 4.6V with the HFE electrolyte versus theoretical ratios (black/grey). In the NMC532 cell, the dissolution of Ni (20 %) and Co (8 %) is much lower than anticipated. Instead of being present at a 50 % mol percent as would be predicted by the stoichiometry of NMC532, Mn is present at 73 %. NMC622 exhibits similar behavior, with Ni (52 %) and Co (8 %) being present lower than stoichiometrically predicted. As seen in the NMC532 cell, Mn is also present at a higher concentration (40 %) than what would be predicted stoichiometrically.

Cathode Surface Structure vs. Time/Voltage – Milestone 3

Collaborative efforts with Dr. Julia Chan were initiated in Q4FY19 to study solid-state structural changes in high-Nickel containing cathodes as a function of electrolyte and voltage. Baseline diffraction patterns of 200 mAh cells have been established, and can be seen in Figure II.3.G.7. Based on findings from dissolved metals experiments outlined in the previous section, significant changes to the solid-state structure of the mixed metal oxide cathode would be expected. Although it is known (FY2018) that a fluorinated electrolyte forms a protective film (CEI layer) on the surface of the cathode, it remains to be seen if this protection has any effect on the solid-state structure of the material.

In addition, it has been shown that changes to structural parameters can be detected both post-mortem and in situ as a function of SOC.^{[2],[3],[4]} Our approach will investigate a variety of cathodes (NMC111, 532, 622, 811, NCA) as a function of electrolyte and SOC.

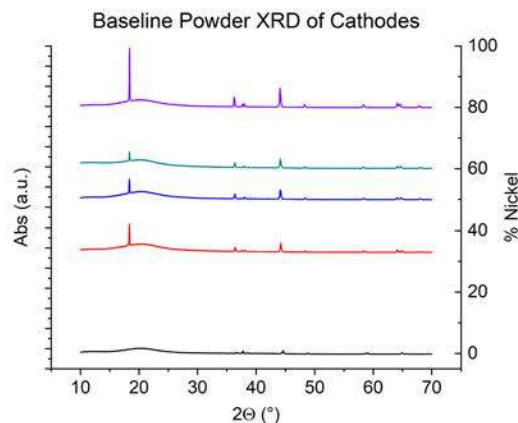


Figure II.3.G.7 Powder X-ray diffraction patterns for LCO and all NMC cathodes studied to date. LCO (**black**), NMC111 (**red**), NMC532 (**blue**), NMC622 (**teal**), and NMC811 (**violet**) are depicted

Quantitative Gas Analysis – Custom Gas Manifold

Throughout FY2017 and FY2018, the gassing kinetics of FEC was investigated as a function of voltage, electrolyte, and cell chemistry. With the addition of more FEC (10 vs. 20%), there was a larger quantity of gas produced in all chemistries. In addition, the qualitative gas composition as a function of voltage, electrolyte, and cell chemistry was reported (FY2018). Some components which were identified include: CO₂, O₂, CO, CH₄, C₂H₆, C₂H₄, H₂, CH₃F, and C₂H₅F. Commercial gas standards are commonly used to quantitate gaseous components, however standard mixtures including fluorinated components are not common. As a result, a custom gas mixing manifold was fabricated in order to create these mixtures. Figure II.3.G.8 depicts the gas mixing control plate (left) along with the individual sample cylinder design (right).



Figure II.3.G.8 Custom gas manifold control plate (left) is comprised of a series of needle and ball valves, and monitored using the digital pressure gauge ($\pm .1$ torr). A typical sample cylinder containing the desired mixture allows for the direct sampling of the gas without contaminating the bulk mixture (right)

Creating standard mixtures of components present in lithium ion batteries post-mortem will help identify a cell chemistry/electrolyte combination which minimizes this degradation mechanism. Previous reports have identified concentrations of select hydrocarbon and permanent gases in NMC-containing cells, however have not established a strong relationship between HFC's and fluorinated additives at high-voltage. [\[5\]](#)

Film Composition and Thickness – Carbon Film Standards

Building on the sputter rate standard film calibration method reported in FY2018, efforts were expanded to measure the film thickness in each standard. Knowing the exact film thicknesses of the standard films allows for a more accurate determination of the sputter rate for films on the cathode surface. Amorphous carbon was sputtered to desired thicknesses of: 50 nm, 100 nm, and 500 nm on a layer of aluminum, with a silicon wafer serving as the substrate. Samples were prepared and analyzed at Evans Analytical Group (Raleigh, NC) utilizing their FIB-SEM expertise with imaging semiconductors. Figure II.3.G.9 depicts a cross-section of each carbon film sample.

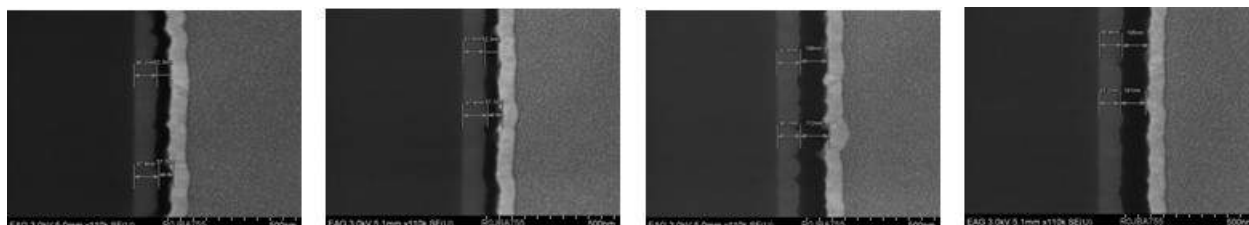


Figure II.3.G.9 Cross sections of 50 nm (far and middle-left) and 100 nm (middle and far-right) following Pt deposition and FIB milling

To analyze the samples, a layer of Pt was sputtered onto cleaved carbon film samples to aid with the FIB milling and SEM imaging. Cross-sections were then milled and mounted normal to the face of interest on a FE-SEM and imaged at various magnifications. Analysis of samples distributed throughout the wafer were performed in order to develop an understanding of the uniformity of the films. The Al thickness was determined to be 88.1 nm in the 50 nm carbon film standard, and 85.1 nm in the 100 nm analog. Carbon film thicknesses were determined to be 54.2 and 108 nm, respectively.

Conclusions

Activities in the third fiscal year transitioned away from surface chemistry analysis of the CEI layer as a function of various parameter of the cell, and into solid-state structural changes in both the cathode and anode. The project aims to determine the source swelling of the jelly roll in pouch cells, as well as suggesting ways to mitigate this degradation mechanism. Two different methods of measuring thickness changes in pouch cells were developed in FY2019, one using a physical contact sensor tracking changes in the z-direction. The other monitoring the position of reflected incident light as the pouch cell swells. Although the physical contact sensor demonstrated that cells increase in size between 3-5% as lithium inserts into the graphite, compression of the cell wind at the point of contact prohibits the measurement of bulk cell thickness changes. This limitation revealed the need for a non-contact method of thickness determination, and we look forward to analyzing the results in subsequent reports.

Dissolution of the cathode is a contributing factor to the thickness increase observed in cells post-mortem. The migration of transition metals from the solid—state structure is not a reversible process, and results in either dissolved metals remaining in the organic electrolyte or deposition at the anode. ICP-MS data from NMC532 and NMC622 cells as a function of time/voltage/electrolyte confirms the dissolution of Ni, Mn, and Co, originating from the cathode. Cycling high nickel containing chemistries at high voltage (4.5V and 4.6V) results in a larger concentration of all metals. Manganese is present at a larger concentration than what would be expected from the stoichiometry in both NMC532 (73 vs. 30 %) and NMC622 (40 vs. 20 %). We are currently awaiting results from NMC622 cells with the EC/EMC and HFE/FEC electrolyte at 4.6V, and aim to compare these with data obtained from NMC532 cells.

The migration of transition metals out of the cathode and into the organic electrolyte results in measureable changes to the solid-state structure. To investigate these changes, efforts in Q4FY2019 transition into investigating these modulations of the cathode surface structure of the mixed-metal oxide. The baseline

diffraction patterns have been established for cell chemistries studied to date, with additional experiments to be carried out post-mortem as a function of SOC and electrolyte.

The Go/No-Go milestone for FY2019 was to deliver interim cells to Idaho National Laboratory and compare the best-practice to date cells to those submitted at the beginning of the project. 14 NMC532 cells with the baseline hydrocarbon (1.2 M LiPF₆, 80% EMC, 20% EC + 1% (w/w) PS) electrolyte were submitted along with 14 of the best performing to date fluorinated electrolyte (1.2M LiPF₆, 60% EMC, 20% HFE, 15% FEC, 5% EC + 1% (w/w) PS). The testing of these cells began on 07/29/2019, and are still undergoing cycle life testing at 30°C at the time of the FY2019 Annual Report submission.

Key Publications

1. Sunstrom, J.; Falzone, A. J.; Gilmore, M.; et al. “Pushing the Energy Limits of Lithium Ion Batteries through Fluorinated Materials”, SAE Technical Paper, **2019**, 2019-01-0595
2. Falzone, A. J.; Sunstrom, J.; Meserole C.; Hendershot, R.; Grumbles, E.; Khan, F.; Flannagin, M. Daikin Advanced Lithium Ion Battery Technology – High Voltage Electrolyte, *2019 DOE-VTO AMR Meeting*, Arlington, VA, June 13, 2019

References

1. Jung, R.; Linsenmann, F.; Thomas, R.; et al. *J. Electrochem. Soc.* **2019**, *166*, A378-A389
2. Li, J.; Downie, L. E.; Ma, L.; Qiu, W.; Dahn, J. R. *J. Electrochem. Soc.* **2015**, *162*, A1401-A1408
3. Tian, C.; Nordlund, D.; Xin, H. L.; et al. *J. Electrochem. Soc.* **2018**, *165*, A696-A704
4. Bak, S.; Hu, E.; Zhou, Y.; et al. *ACS Appl. Mater. Interfaces* **2014**, *6*, 22594-22601
5. Xia, J.; Petibon, R.; Xiao, A.; Lamanna, W. M.; Dahn, J. R.; *J. Electrochem. Soc.* **2016**, *163*, A1637-A1645

Acknowledgements

We would like to thank Dr. Julia Chan (UT-Dallas) for assistance with powder XRD measurements of cathode materials.

II.4 Next Generation Lithium-Ion batteries: Low-Cobalt/No Cobalt cathodes

II.4.A Aerosol Manufacturing Technology to Produce Low-Cobalt Li-ion Battery Cathodes (Cabot)

Toivo Kodas, Principal Investigator

Cabot Corporation
157 Concord Road
Billerica, MA 01821
E-mail: Toivo.Kodas@cabotcorp.com

Peter Faguy, DOE Technology Development Manager

U.S. Department of Energy
E-mail: Peter.Faguy@ee.doe.gov

Start Date: October 1, 2018 End Date: September 30, 2019
Project Funding (FY19): \$1,397,139 DOE share: \$1,117,139 Non-DOE share: \$280,000

Project Introduction

Although considerable progress has been made with battery materials over the last 5-10 years, the cathode remains a major performance-limiting material in Li-ion battery (LIB) technology. New materials and battery chemistries will overcome some of the remaining challenges, but cathode materials must also be manufactured at a lower cost and with a smaller environmental footprint using new processes that can also enable improved control over stoichiometry, morphology and compositional homogeneity. Cabot, Argonne National Laboratory and SAFT research teams are combining their extensive expertise in particle synthesis, battery materials and cell design to develop a low-cost, flexible aerosol manufacturing technology for production of high-performance Li-ion battery cathodes. This project will develop low-Cobalt cathode materials via Reactive Spray Technology (RST) and Flame Spray Pyrolysis (FSP) to reach performance targets of < 50 mg Cobalt/Wh.

Objectives

The objective of this project is to research, develop, and demonstrate RST and FSP for production of low-Cobalt active cathode materials for use in next-generation LIBs capable of the following:

Table II.4.A.1 Project performance targets for cathode active material and cell made with this material

Beginning of Life Characteristics at 30 °C	Cell Level	Cathode Level
Useable Specific Energy @ C/3	---	≥60 Wh/kg
Calendar Life (< energy fade)	15 years	---
Cycle Life (C/3 deep discharge with <20% energy fade)	1,000	---
Cobalt Loading	<50 mg/Wh	---
Cost	≤\$100/kWh	---

Approach

To achieve the above targets, we are working towards demonstrating the production of low-Cobalt particle compositions. Cabot has shown the feasibility of $\text{LiNi}_{0.8}\text{Mn}_{0.1}\text{Co}_{0.1}\text{O}_2$ (NMC811) by RST; for this project we are extending this to even lower Co amounts. This requires us to identify approaches to solve key problems of phase stability, water sensitivity, interface degradation and others. The team is exploring particle doping, coating, morphology and size control on a robust platform that can be extended to other material

configurations. We are leveraging the flexibility of RST and FSP to produce key low-Co cathode compositions relevant for achieving scale with a further scale up pathway identified. Cabot and ANL are identifying the most suitable RST and/or FSP platform and process conditions to synthesize low-Co NCM and Li-excess disordered rocksalt (LxDRS) cathode active material compositions. The optimization of low-Co cathode electrodes is including new conductive additive formulations and development of low-Co cathode pastes containing additive formulations that ensure percolation and mechanical stability of cathode electrodes.

The team will focus on demonstrating cathode compositions with Cobalt loading $<50\text{mg/Wh}$ and $>600\text{ Wh/kg}$ specific energy at C/3. These performance goals at the cell level drive us to new compositions, lower Cobalt than NMC811, along with other materials systems comprising fluorine. Composition must be optimized for performance, cycling, stability and operation among others. Our proposed RST/FSP route will address these issues and allow doping, coating, gradients and novel particle morphologies which can solve these problems.

Results

Reactive Spray Technology (RST)

Cabot's RST is a flexible aerosol manufacturing platform capable of producing low-Cobalt cathode compositions and variety of other materials. The flexibility to achieve unique combinations of compositions and microstructures comes from the fact that the RST combines chemistries from both liquid phase and solid-state processing. The key component of RST synthesis is processing of liquid precursors at precisely controlled temperatures but with short processing times ($<50\text{ sec}$), which yields materials with preferred properties. The RST unit has been set up and commissioned in the Materials Engineering Research Facility (MERF) at ANL. During this process the cooling system, furnace (hot wall) and collection unit has been updated and optimized to process high Ni-content cathode active materials. A digital photograph of the unit is presented in Figure II.4.A.1. Cabot has demonstrated its ability to produce unique NMC materials using RST including 111, 523, 622 and 811 compositions. Characterization results indicated that particle size (related to powder tap density) and cycle life need to be improved to obtain a higher density active material and more stable Low-Co electrode. Overcoming these issues are the goals of this project.

Synthesis and Optimization of RST-made Battery Materials

A series of experiments has been performed at different RST synthesis conditions suitable for large scale manufacturing to produce NCM powders with particle size ranging from 1 to $\sim 10\text{ }\mu\text{m}$, varying degree of particle porosity and excellent compositional purity. Water-based precursors have been used to produce NCM811. Obtaining the NCM811 formulations has been achieved by simple adjustment of the stoichiometry of the precursor element salt concentrations in the solution phase. As can be seen from Figure II.4.A.2 above, morphology of the as-sprayed powder is independent of its composition. XRD spectra indicate the target crystal structure has been partially obtained after the RST step. An annealing step (under oxygen, and temperature $700\text{--}800^\circ\text{C}$) leads to the full transformation of the rock salt crystal to the layered structure. Half coin cells were made with these active materials using a standard slurry formulation and ANL GEN2 electrolyte. Two formation cycles were run at 0.1C (charge/discharge) followed by cycling at C/3 from 2.7 to 4.3 V (Figure II.4.A.2). The reversible capacity was 203 mAh/g for the samples after calcination under oxygen. After formation all cells were set to cycle at C/3, the first 20 cycles are shown in Figure II.4.A.2. Initial electrochemical testing shows very promising data. Further optimization is required to improve NCM811 cycle stability.



Figure II.4.A.1 Reactive spray technology system set up and optimized at ANL to produce cathode material

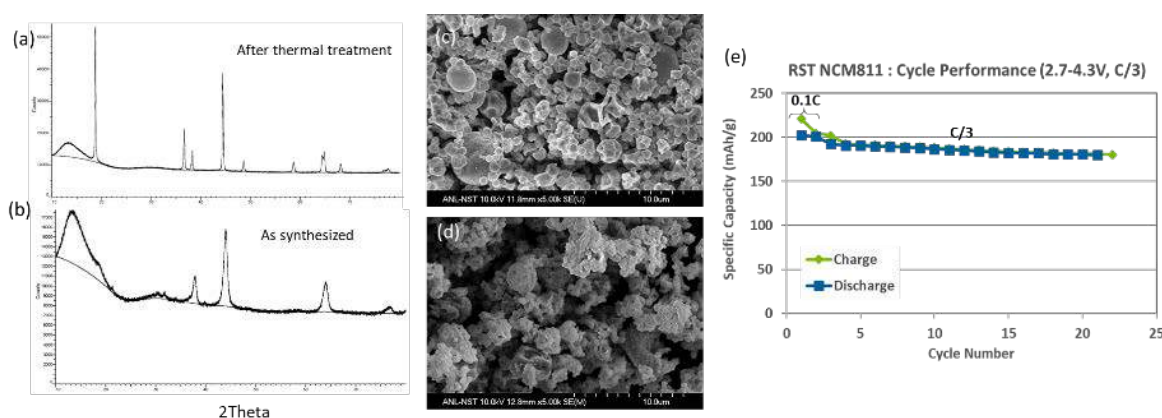


Figure II.4.A.2 (a) XRD patterns and (b) SEM pictures of the layered NCM811 by RST. (e) Formation and cycle life testing plots for NCM811 electrodes made with active material synthesized with the RST system.

Flame Spray Pyrolysis (FSP)

FSP is a subtype of aerosol synthesis techniques. Combustible solutions containing organic and/or inorganic metal salts are combusted in spray flames to yield combustion gas and solid products where the solid products are the targeted synthesized material. In FSP, precursor liquid droplets are fully combusted to atomic or molecular form after which product molecules and clusters form leading to the nucleation of individual particles. Primary particles in the size range 20-200 nm are produced in this modality. Larger size particles are achievable by primary particle coalescence and growth in post-flame in situ annealing. FSP tends to produce highly crystalline particles. The ANL FSP facility provides the ability to synthesize up to 6 unique compositions per day for coin cell level testing (10 g) as well as the ability to produce 500g per day for the amounts needed to complete project cell deliverables (>2 Ah cells).

Synthesis of High-Ni Content Cathode Active material by FSP

Initial work with FSP focused on the synthesis of small amounts of NCM cathode active materials, allowing us to understand and optimize FSP process parameters to finally produce NCM811. Over 1.5 kg of powder was synthesized, calcined, milled and classified and used to coat cathode electrodes for the fabrication of cells. The different synthesis campaigns were defined with guidance from coin cell results and analytical evaluation of the materials.

The early work at ANL was targeted to synthesize small batches of NCM 111, 622 and 811 using acetylacetonate (acac) precursors. After thermal treatment under air (NCM111) or pure oxygen (NCM622 and 811) the layered structure is formed as confirmed with XRD studies. Half coin cells were made with these

active materials using a standard slurry formulation and ANL GEN2 electrolyte. Two formation cycles were run at 0.1C (charge/discharge) followed by cycling at C/3 (2.7 to 4.3 V). Even though, the structural characteristics and electrochemical performance were within our technical targets, this precursor is expensive and will increase powder production cost. Because of that, the team explored less costly precursors as well as modified precursor conditions to synthesize cathode active material. Precursors used consisted of metal nitrates (>97% purity, Sigma-Aldrich). LiNO_3 was then added at a concentration of > 1.00 mol Li nitrate/L solution, 5-20% in excess of stoichiometry, to compensate for Li loss during synthesis and reduce $\text{Ni}^{2+}/\text{Li}^+$ mixing in the layered structure.

Half coin cells were fabricated using standard formulations described above. Structural and electrochemical analysis aided selection of the best process parameter conditions. A summary of the results is presented in Table II.4.A.2 and Figure II.4.A.3. The data obtained indicated that the nitrate precursor (water-based and low-price material) was a better option (based on powder structure, composition, electrochemical characteristics and cost) relative to the acac solutions.

Table II.4.A.2 Summary of Samples and Precursors Used to Synthesize NCM811

Sample	Precursor	1 st Disc. Cap at 0.1C (mAh/g)	C.E. (%)
FSP-04-1-S126	Acac with Li	185	84
FSP-04-3-S139	Nitrate with Li	172	85
FSP-04-3-S140	Nitrate with Li excess	186	84
FSP-04-3-S148	Acetate with acetic acid	178	86
FSP-04-3-S150	Acetate with propionic acid with Li excess	167	81
FSP-04-3-S178	Nitrate with Li excess, production run (>330g)	186	85

The process parameters used to make sample FSP-04-1-S140 (Table II.4.A.2) were selected as the best synthesis conditions and used to make larger batches (> 300g, FSP-04-3S178) followed by further physical electrochemical characterization. The ANL team used improved process parameters to make >1.5 kg of NCM811. The annealing process (batches > 100g) was also modified to consistently transform the green powder (rock-salt type) to the final layered structure. During annealing (12h at 750°C in oxygen) the particles (mainly under micron size) sinter into large secondary particles (> 100µm), that need to be reduced to be used in the production of Li-ion electrodes. To this end, the annealed product was milled and sieved (at Cabot) to reduce particle size with a D50 target not greater than 10 µm.

Like the annealing step, this process will need to be modified to accommodate ~200g of powder during milling. A planetary ball mill was employed to grind the post annealed material. Milling optimization was performed using ~20 g of powder. Parameters such as media size, ball-to-powder ratio, speed and milling time were modified to obtain a powder with particle size distribution similar commercially available NCM811 material. With minor modification these learnings will be employed to mill larger material quantities (~160g) using bigger milling jars. Sieving (classification) with different mesh sizes will be used to separate larger aggregates. During this process, we learned that the crystallite size decreases as milling energy and time increase (refer to Figure II.4.A.4).

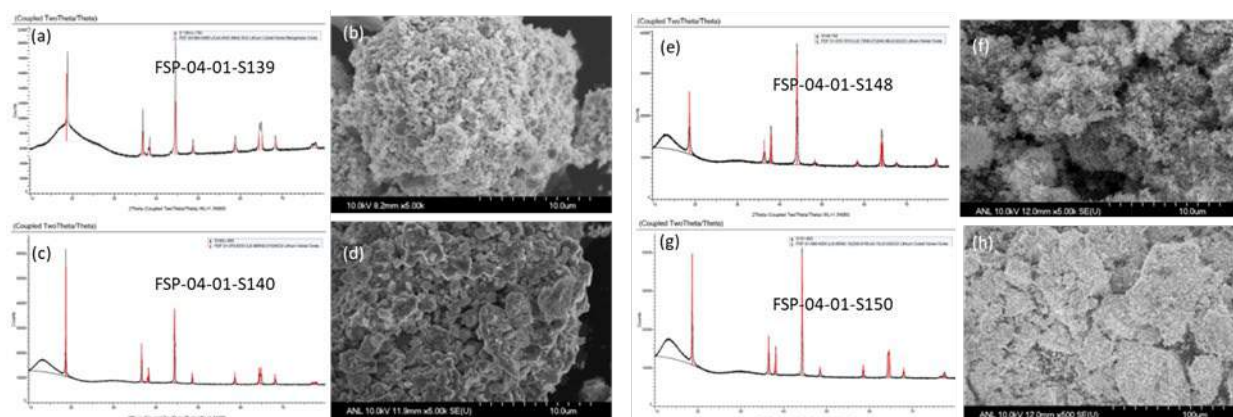


Figure II.4.A.3 NCM 811 produced by FSP with different precursor and flame conditions. XRD pattern and SEM (a) and (b) nitrate precursors, (c) and (d) nitrate precursors with excess Li, (e) and (f) nitrate precursors, acetate with acetic acid, (g) and (h) nitrate precursors, acetate with propionic acid and excess Li.

The average tap density of the latest FSP-made NCM811 powder (after milling/classification) is 2.2 g/cm^3 . The latter value meets the Go/No-Go technical target (tap density $> 2.0 \text{ g/cm}^3$). Particle size distribution was also measured: the obtained values are close to the commercial reference (NCM811): $D_{10} = 2 \mu\text{m}$, $D_{50} = 8 \mu\text{m}$ and $D_{90} = 18 \mu\text{m}$. Figure II.4.A.4 summarizes particle milling and characterization results. Additional half-cell testing was carried out after powder milling and classification, which are summarized in Figure II.4.A.5. As presented in Table II.4.A.2 the reversible discharge capacity for electrodes made from the large-scale campaign is 186 mAh/g with a first columbic efficiency of 86%. Cycling performance seems to improve with a narrow particle size distribution compared to the small scale (hand grinding). Further experiments are ongoing to understand the influence of milling conditions on electrochemical performance.

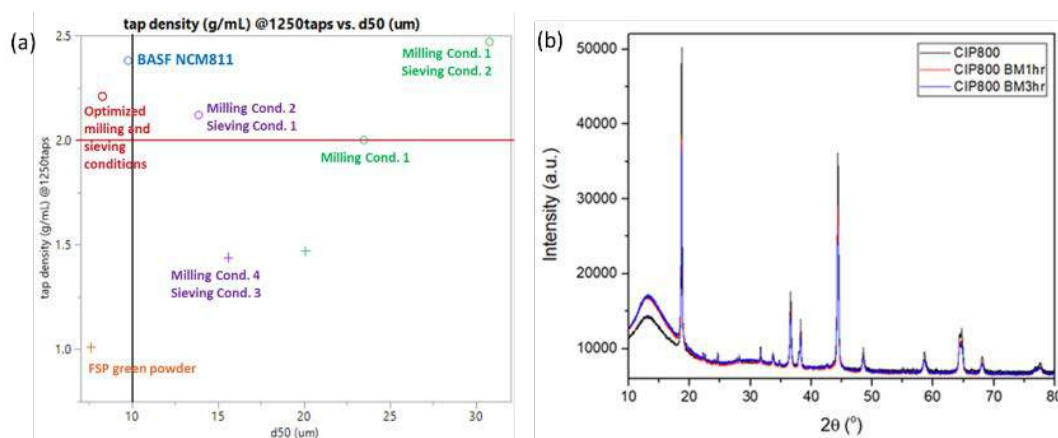


Figure II.4.A.4 (a) Different milling and sieving conditions used to post process NCM811 powder. (b) XRD pattern of NCM811 (a) as prepared, milled for (b) 1 and (c) 3 hours. Crystallite size decreases as milling energy process increases

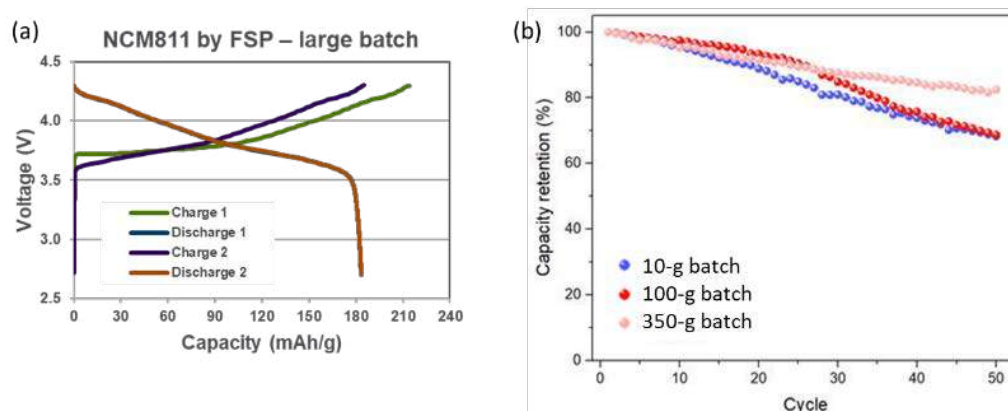


Figure II.4.A.5 Half-cell data for electrode made with NCM811 by FSP using nitrate precursors. (a) Formation data for large scale sample (>350g per batch), (b) Cycling data for sample at different scales, the larger batches were milled and classified using an improved method (better particle distribution)

Active material surface modification

In order to improve secondary particle control, processing characteristics, environmental stability and cycle stability, the team at Cabot has started exploring NCM811 surface coating. Dry coating experiments with potential for low cost were performed using different metal oxide nanoparticles (Cabot product). Small amounts (<1wt%) of nano powder were mixed with NCM811 (uncoated research grade, BASF) and then thermally treated at different conditions under air and argon. SEM micrographs were taken to observe alumina coverage over the larger NCM811 particles. The inset in Figure II.4.A.6 (a), before thermal treatment, clearly shows that the nano metal oxide is dispersed on the surface of the NCM. It is worth noting that the coverage is not conformal (as expected), which is confirmed by looking at the SEM pictures post annealing. Dark and lighter grey patches are observed (Figure II.4.A.6 (b)) over primary 811 particles and corroborate the uneven surface coating. Initial electrochemical data (Figure II.4.A.6 (c) and (d), using half coin cells) suggests that the metal oxide coating effectively improves cycle life performance. Further particle surface and electrochemical characterization are ongoing to continue with this investigation.

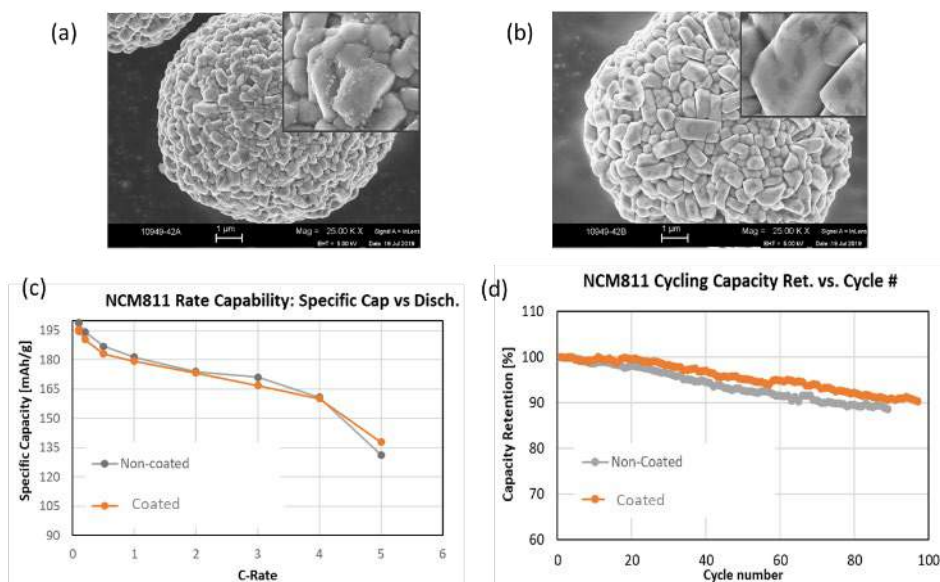


Figure II.4.A.6 Scanning electron micrographs of NCM 811 coated with 1wt% nano NCM111, (a) before and (b) after thermal treatment. Dark and light patches on particle surface may indicate uneven coating. Half coin cell for NCM811 cathodes with nano NCM111. (c) rate capability plots and (d) cycling data

Other Cell Component Selection

The SAFT team has worked to select, design and optimize anode formulation and structure, as well as selecting electrolyte and conductive additives packages. Commercially available graphite and NCM811 powder has been used to screen different electrolyte formulations. Initial screenings suggest that the LTXHP (Cabot R&D product) is a good conductive additive to be used in this high Nickel system. Twenty-one (21) 4.2 Ah pouch cells were fabricated and are under testing (to be completed early Q4). The anode composition was graphite (97wt%), CMC (1.5wt%) and SBR (1.5wt%) with a 6.28 mg/cm² mass loading. The cathode composition was: NCM (95wt%), LTXHP (3wt%) and PVDF (2wt%) with a 10 mg/cm² mass loading. Six different electrolyte compositions were used to assemble the cells. Cells were tested for: cycle life at 60°C, cycle life at 25°C and calendar life at 60°C. Experiments have been completed and cell components were selected: natural graphite, electrolyte, binder and conductive additive.

Conclusions

Our team has employed a reactive spray technology (RST) and a flame spray pyrolysis (FSP) system to demonstrate key cathode compositions and down select candidate compositions for further development in a pouch cell optimization cycle. ANL and Cabot scientists have optimized the synthesis process and postprocesses to obtain NCM811 with the right electrochemical and physical properties required to meet the EERE's Go/No-Go technical targets. ANL is working to produce enough NCM811 to produce deliverable cells. The produced powder will be used by SAFT for the fabrication of the cell deliverables. SAFT has selected other cell components to work well with NCM811. Currently, the team is working to develop appropriate surface treatments to improve high Ni-content cathode particle secondary particle control, processing characteristics, environmental stability and cycle stability. Encouraging initial data has been gathered and work will continue to validate our findings at meaningful cell formats.

Key Publications

1. "Aerosol Manufacturing Technology to Produce Low-Cobalt Li-ion Battery Cathodes", BAT411_Oljaca_2019_p, U.S. DOE Vehicle Technologies Program Annual Merit Review, AMR, 2019.

Acknowledgements

We would like to acknowledge Dr. Joseph Libera and Dr. Eungje Lee at Argonne National Laboratory, Dr. Joong Sun Park and Mrs. Carine Margez at SAFT for their valuable contribution to this project.

II.4.B Cobalt-free Cathode Materials and Their Novel Architectures (UCSD)

Ying Shirley Meng, Principal Investigator

University of California, San Diego
9500 Gilman Dr.
La Jolla, CA 92093
E-mail: shmeng@ucsd.edu

Peter Faguy, DOE Technology Development Manager

U.S. Department of Energy
E-mail: Peter.Faguy@ee.doe.gov

Start Date: October 2018	End Date: September 2021	
Project Funding (FY19): \$1,043,000	DOE share: \$834,000	Non-DOE share: \$209,000

Project Introduction

Since its discovery [1], $\text{LiNi}_{0.5}\text{Mn}_{1.5}\text{O}_4$ (LNMO) spinel-type cathode materials have long intrigued the transportation industry due to their high operating voltage (4.7 V) and capability to handle high charging rates. More recently, the strong desire to eliminate cobalt in cathode materials has sparked a renewed interest in this class of oxides. Various attempts to create LNMO/graphite batteries that exhibit high voltage, relatively high energy density, and high charging capabilities have been carried out worldwide, but they all have suffered from excessive degradation and short cycle life, especially when stored or cycled at elevated temperatures (55°C or higher) [2]. Our proposed work will solve the long-standing issues by 1) novel architecture of LNMO thick electrodes to enable 4-6 mAh/cm² loading, 2) new electrolyte formulation to suppress degradation in LNMO/Gr full cells, and 3) close collaboration among university-national lab-industry to demonstrate the feasibility of a Co free Li-ion cell with energy density exceeding 600 Wh/kg at cathode level. The main focus of this research is to solve the structural stability of LNMO and the interphase problems with electrolytes, including adopting an appropriate surface coating for the cathode; the development of a novel electrolyte (electrolyte additive, sulfone-based electrolyte); and the advancement of a new dry electrode processing method. In the past five years, our research team has made great progress on developing innovative synthesis techniques of high tap density cathode materials; conformal coating methods on powder samples; advanced characterization techniques on the atomic scale, electrode scale, and at the cell level; we have also made significant inroads on thick-electrode-architecture cell prototyping. **UT Austin** has extensive experience in the co-precipitation synthesis of LNMO cathode materials with a batch tank reactor at above the kilogram scale. **UCSD** has achieved conformal coatings on cathode particles through polymer assisted deposition. **UCSD** has also demonstrated that cryo-(S)TEM is crucial for interphase studies as it can effectively preserve CEI structure/chemistry from beam damage. **LBNL** has effective diagnostic methods for full cells at both the coin cell and pouch cell level. **Tesla, Inc.** possesses a unique dry battery electrode coating technology that offers extraordinary ionic and electronic conductivity for extremely thick electrodes. It is through these successful experiences and fundamental understanding of these high voltage cathode materials that we can successfully formulate strategies to optimize LNMO-based battery system.

Objectives

The proposed research aims to deliver a Co free Li-ion battery with energy density exceeding 600Wh/kg at the cathode active material level. More specifically, the main goal of this project is to develop a high-performance and low-cost spinel-type $\text{LiNi}_{0.5}\text{Mn}_{1.5}\text{O}_4$ electrode and novel electrolyte formulation to suppress full cell degradation at high voltage and temperature. The best combination of high voltage electrode and electrolyte will achieve higher cell energy density, better safety performance, longer battery life, and greatly reduce the overall cost of the battery. The critical success factors in achieving that goal include:

- (1) Electrolyte stability and compatibility for both the cathode and anode materials under high charge and discharge voltage;
- (2) LNMO bulk and surface stability at high working temperature 55-60°C;
- (3) High areal cathode loading with new polymer binder and a dry-processing method to ensure adequate electronic and ionic transport for fast rates.

Approach

The main focus of this research is to solve the structural stability of LNMO and the interphase problems with electrolytes, including adopting an appropriate surface coating for the cathode; the development of a novel electrolyte (electrolyte additive, sulfone-based electrolyte); and the advancement of a new dry electrode processing method. In addition, to guide our research to determine which electrolyte system is more stable and compatible for LNMO electrode materials under high voltage cycling, we will develop a series of characterization techniques such as ex situ X-ray photoelectron spectroscopy (XPS), ex situ cryogenic transmission electron microscopy (cryo-TEM), ex situ cryogenic focused ion beam microscope (cryo-FIB) and in situ time-of-flight secondary-ion mass spectrometry (TOF-SIMS).

Results

The following progress has been achieved in FY19:

LNMO cathode materials performance comparison using 3 mAh/cm² loading thick electrode

Three different samples of LNMO cathode materials were selected to conduct the comparison. LNMO electrode with loading of approximately 3 mAh/cm² was prepared by mixing LNMO with polyvinylidene fluoride (PVDF) and acetylene black (Super C65) in N-Methyl-2-Pyrrolidone (NMP) solution for 1 hour, followed by 60°C vacuum heating overnight. An additional 1 hour of vacuum heating at 120°C was adopted to remove excess NMP residue and improve adhesion. CR2032 coin cells were assembled to test performance of each LNMO sample with Li metal as the anode. Voltage range was set to be 3.5 V ~4.85 V to avoid side reactions. Cycling procedure was set to be C/10 for 2 cycles, then C/3 for the rest cycling (1C = 147 mAh/g). The first cycle charge-discharge profiles as

the basic electrochemical performance of these three materials are shown in Figure II.4.B.1, where the capacities of NEI-A, Haldor Topsoe, and LNMO-5 are 127.35, 135.72 and 133.73 mAh/g, respectively. The related energy densities of these materials are also listed in the figure. Typically, higher nickel content in the composition will lead to a longer plateau above 4.6 V both during the charge and discharge process, which will directly benefit the overall energy density in full cell level. It is obvious that LNMO-5 sample from UT Austin team delivers the highest capacity from Ni redox among these three materials. From ICP results, it can be verified that LNMO-5 has the minimum value of Mn/Ni ratio (3.060) among three samples. As for the Haldor Topsoe LNMO, the Mn/Ni ratio is 3.474, which is expected to get the largest capacity from Mn redox as well as the overall discharge capacity. Besides, due to the high discharge capacity for Haldor Topsoe and the high average voltage for LNMO-5, both of them exhibit energy density over 600 Wh/kg, which are extremely promising in the full cell level testing.

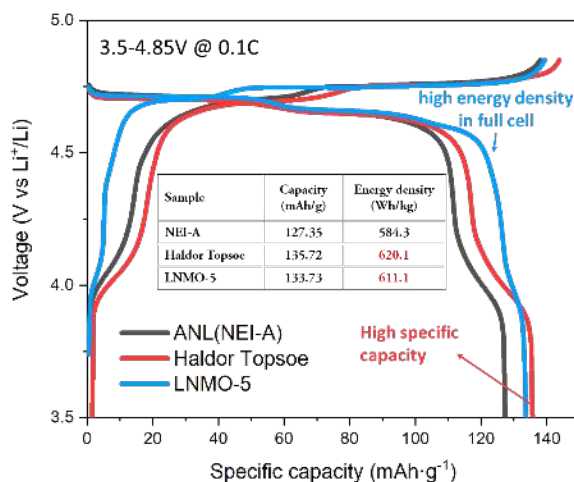


Figure II.4.B.1 Initial charge-discharge profile of different LNMO samples with 3 mAh/cm² loading thick electrode.

Novel electrolyte screening for high voltage LNMO cathode from Haldor Topsoe

ARL team has further screened novel electrolyte using LNMO from Haldor Topsoe. The following cycling study was performed in Al-clad 2032 type coin cells with a 15mm ϕ LNMO electrode and a 5/8" ϕ piece of lithium foil with a single Asahi C5 ceramic-coated PE separator and 50 μ L of electrolyte. All cell components were dried at 120°C under vacuum overnight and assembled in an Ar-glovebox. Cells were cycled according to the following protocol: 3.5-5.0 V, all charging at C/2 and discharging at 1C X 200 cycles, 4C X 50 cycles, 8C X 50 cycles, and 1C X 1000 cycles. We started screening our top-performing high voltage electrolytes with this new material at 30°C. As shown in Figure II.4.B.2, the FEC/DMC baseline initially exhibits the best performance over the first 200 cycles, but the cells are generally comparable. Interesting, both Daikin electrolytes suffer significantly during the accelerated discharge rate testing, which may be a sign of interphase impedance. After almost 500 cycles it's clear that the FEC/DMC baseline and modified formula with TMB are the top performers. The new LNMO sample can deliver a reversible capacity of 135 mAh/g at C/3, reaching the project goal of 600 Wh/kg at the cathode level.

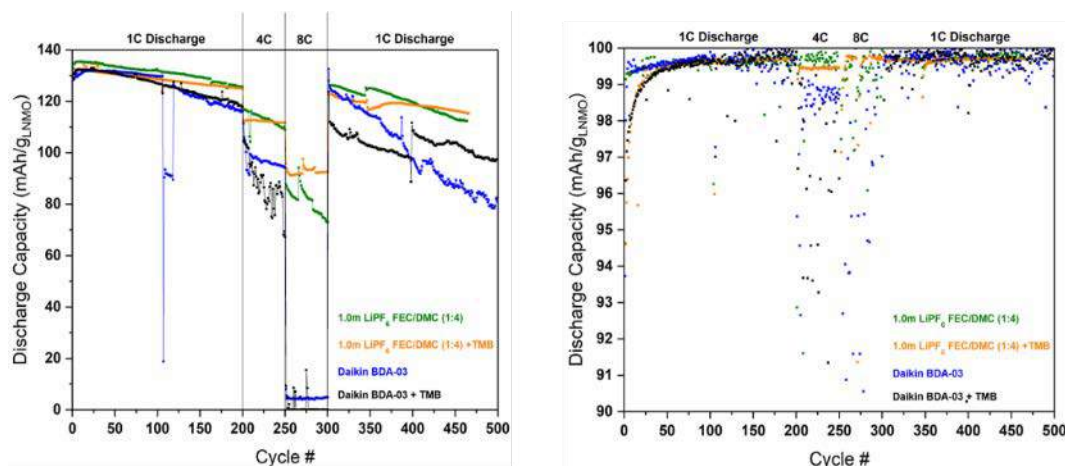


Figure II.4.B.2 Galvanostatic cycling (left) and associated Coulombic efficiencies (right) for industry-partner LNMO with different novel electrolytes in half cells

Enhancement of the electrochemical performance of LNMO cathode material

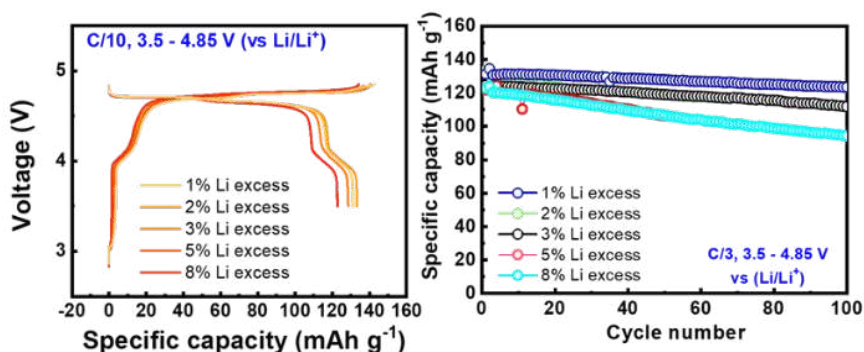


Figure II.4.B.3 Charge-discharge profiles (Left) and cycle performances at C/3 (Right) of the LNMO samples synthesized with different excess lithium in the reaction mixture

UT-Austin team continued working on the optimization of LNMO firing parameters including excess lithium amount in the reaction mixture, firing temperature, and cooling rate. As shown in Figure II.4.B.3, various excess lithium amounts (from 1 to 8 mole%) were used when firing LNMO. The cell cycling results show that the LNMO sample with 1% excess lithium delivers the best performance in both

capacity and cycling stability. As a result, 1% lithium excess will be used for future exploration and optimization. In addition, another high-performance spinel LNMO-5 has been developed. As depicted in Figure II.4.B.4, the primary particles of LNMO-5 are slightly smaller than those of LNMO-3, ranging from 400 nm to 1 μ m. Most of them show a well-shaped octahedral morphology with (111) facet exposed, which is

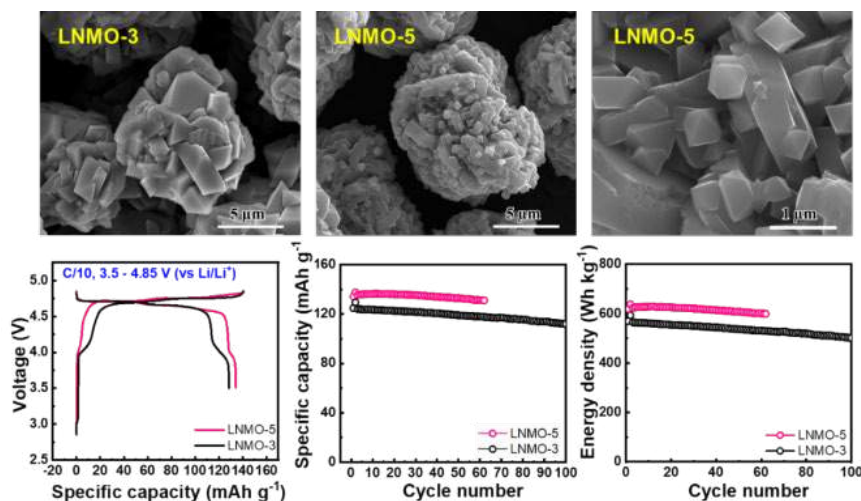


Figure II.4.B.4 SEM images of the LNMO-3 and LNMO-5 samples and the corresponding electrochemical performances in half cells.

suggested to be beneficial to electrochemical performance. Benefiting from the changes in morphology, the specific capacity of LNMO could be further increased to ~ 135 mAh/g at C/3, which corresponds to an energy density of 628 Wh/kg. Large batch of LNMO-5 sample (500 g) has been shipped to UCSD for high mass-loading electrode fabrication and full-cell evaluation.

Full cell demonstration with capacity retention >80% at C/3 rate for 300 cycles

For the LNMO spinel material, there are two primary voltage plateaus: a higher voltage process which occurs around ~4.7 V vs. Li/Li⁺ and corresponds to the Ni²⁺/Ni³⁺ and Ni³⁺/Ni⁴⁺ transitions, and a second process that occurs around 4 V which corresponds to the Mn³⁺/Mn⁴⁺ transition. The consensus in the field is that the Ni redox processes are generally very reversible, but the difference in size of the Mn³⁺/Mn⁴⁺ cations leads to Jahn-Teller distortion, straining and potentially destabilizing the lattice structure, thus leading to poor cycle life. The tradeoff to avoiding this process completely by operating within a more confined voltage window (4.4-4.9 V) is that some capacity is inaccessible. ARL team tested this behavior with the materials for this project with the areal capacity loading ~2.2 mAh/cm² and the Gen2 baseline electrolyte (1M LiPF₆ in EC/EMC 3:7 by mass). Four cells with graphite anode were cycled: two of which were operated over an expanded voltage window to gauge the cycling stability of the Mn transition and the other two of which were cycled in confined window to test the Ni redox process reversibility. The results (Figure II.4.B.5) suggest that an additional capacity of ~15-20 mAh/g LNMO is introduced by activating the Mn transition, but that it is most likely exhausted between 100 and 150 cycles, at which point the capacity retention of all four cells is very similar. More than 80% capacity retention has been achieved in the LNMO full cell within a confined voltage window after 300 cycles. Additional cycling data is needed before any conclusion regarding long term stability can be made, but at this point there does not appear to be a significant penalty. This does introduce a question regarding the merit of our capacity retention goal. The concern is whether it is better to have higher initial capacity and suffer greater capacity loss initially or if it is more appropriate to start at a lower capacity in order to generate the best stability and highest capacity retention.

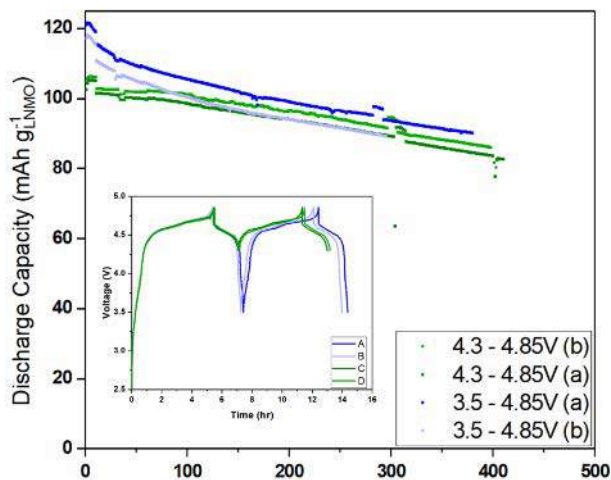


Figure II.4.B.5 Cycling results for LNMO-graphite full cells cycled within a confined (green) and expanded (blue) voltage window.

The coin-cell type full cells were also assembled at UCSD with the NEI-A LNMO as the cathode materials and the NIMTE graphite as the anode material. It is worth noting that the active material loading is around $3\text{mAh}/\text{cm}^2$ for the cathode, and the N/P ratio is well controlled between 1.05 and 1.1. The active material mass loading of the cathode is more than $20\text{mg}/\text{cm}^2$. As shown in Figure II.4.B.6, the full cell delivers 84% capacity retention after 300 cycles and 79.4% after 400 cycles. Such high retention for the cell cycling in the range from 3.3 to 4.85 V is due to the stabilized interfacial chemistry, which can be identified by the Coulombic efficiency growing to above 99.9% after 100 cycles. Additionally, the degradation of electrolytes upon high voltage regions would lead to a low Coulombic efficiency, thus setting the charging cutoff voltage to a lower value would have instantaneous effect to mitigate the unpleasant decomposition of electrolyte. So far, NEI-A LNMO with $\sim 3\text{mAh}/\text{cm}^2$ areal loading exhibits excellent capacity retention of $\sim 98.5\%$ in 50 cycles by lowering down the upper voltage cutoff from 4.85 V to 4.75 V. The extended cycles based on different cutoff voltage range will be further investigated to improve the cycling stability.

LNMO cathode characterization after long-term cycling

Figure II.4.B.7 depicts electron microscopy data from the pristine sample and cycled sample (at the discharge state after 225 cycles between 3.5 to 4.85 V). The particles show a high degree of crystallinity and well faceted surfaces. Multiple grains were selected for study and the results are consistent, therefore only representative data are shown here. Figure II.4.B.7a shows the representative HAADF-STEM

images of the pristine LNMO taken along the [110] crystallographic direction. In this

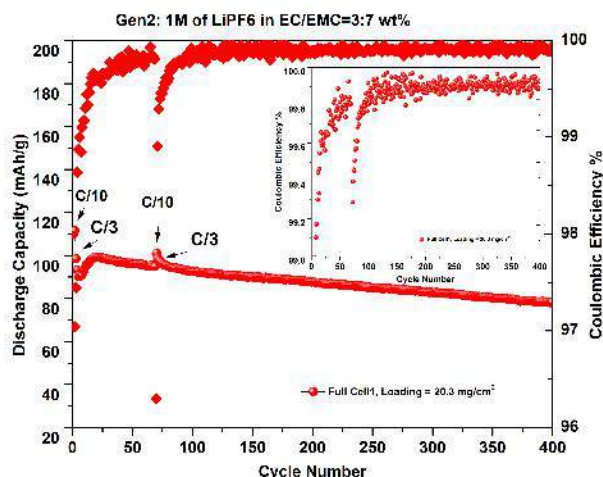


Figure II.4.B.6 Cycling results for LNMO-graphite full cells with $3\text{mAh}/\text{cm}^2$ loading and Gen2 electrolyte.

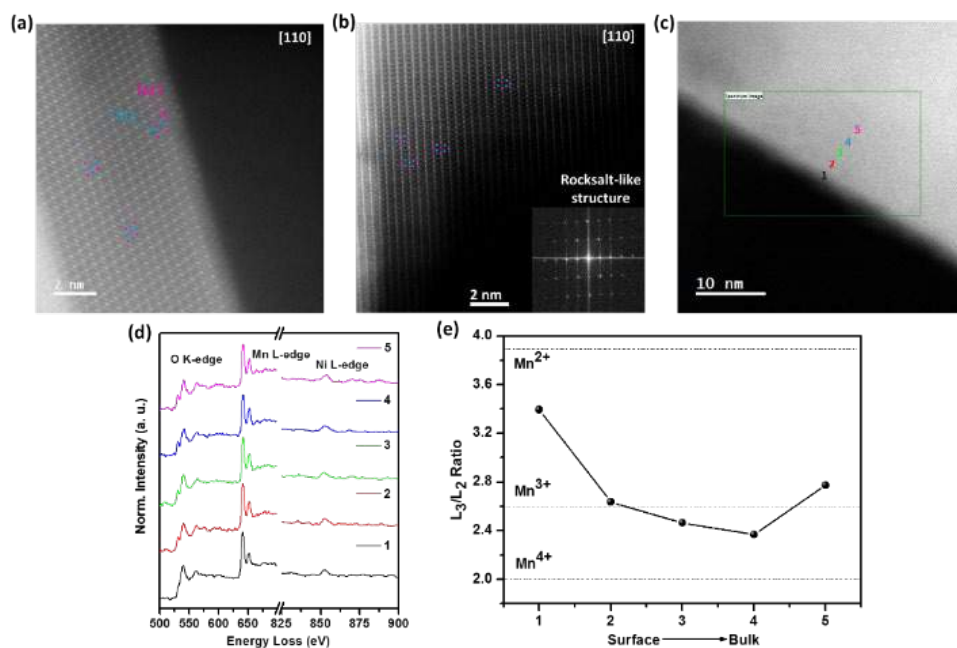


Figure II.4.B.7 STEM/HAADF images of the (a) pristine LNMO and (b) LNMO after 225 cycles in Gen2 electrolyte. (c, d) Spatially resolved EELS spectra from the surface to the bulk of the cycled LNMO in Gen2 electrolyte and (e) Mn L3/L2 ratio fit results from the EELS spectra compared to literature values for various oxidation states of Mn species.

presence of anti-site TM defects. On the other hand, the HAADF images of the cycled LNMO (Figure II.4.B.7b) shows different contrast changes from the bulk and to the surface atomic columns. Close examination of the cycled LNMO structure (Figure II.4.B.7b) indicates the presence of bright contrast in the tetrahedral Li sites and empty octahedral sites in the center of the diamond configuration. Based on the HAADF images in cycled LNMO, the TM ions migrated into two different Li atomic sites - the tetrahedral and octahedral Li sites - and resulted in rocksalt-like (MnO) structure. Spatially resolved EELS were also obtained at a step of ~2 nm from the surface to bulk and the spectra are presented in Figure II.4.B.7d. The data points are aligned with the ADF image to indicate where each spectrum was taken (Figure II.4.B.7c). There is a clear O pre-peak in the O K-edge obtained from bulk of the particle cycled in Gen2 electrolyte. This pre-peak starts to decrease when it comes to the interface region, and disappears completely in the near surface. The disappearance of the pre-peak can be ascribed to the rocksalt-like structure formation and reduction of neighboring TM which is verified by both L_3/L_2 peak intensity ratio and peak shift in the Mn L-edge. In the detailed L_3/L_2 ratio analysis shown in Figure II.5.7e, it is going to lower Mn oxidation state at point 1, while other points are going back to higher Mn oxidation state, i.e., Mn^{3+} . It is worth mentioning here that the Mn oxidation state at point 1 is close to Mn^{2+} which undergoes a dissolution, migration, and redeposition process, poisoning graphite anode side in the full cell cycling. From the STEM/EELS results, it is clear that structural degradation and composition changes occur in the sample, which impedes the Li diffusion pathway and reduces the amount of active material during cycling.

LNMO/graphite pouch cell evaluation with different novel electrolyte

LNMO/graphite full cells with three electrolytes have been tested for 300 cycles from LBNL team. The results are shown in Figure II.4.B.8. The cell with the LiDFOB additive shows the least capacity fade, after 300 cycles, its capacity retention is ~71%, but the energy efficiency is the worst of the three cells. The cell with Gen2 electrolyte shows the highest energy efficiency but the worst capacity fade and the capacity fade is generally worsening with each cycle. The cell with high voltage Daikin electrolyte shows a capacity per cycle that is leveling out and maintains a moderate energy efficiency.

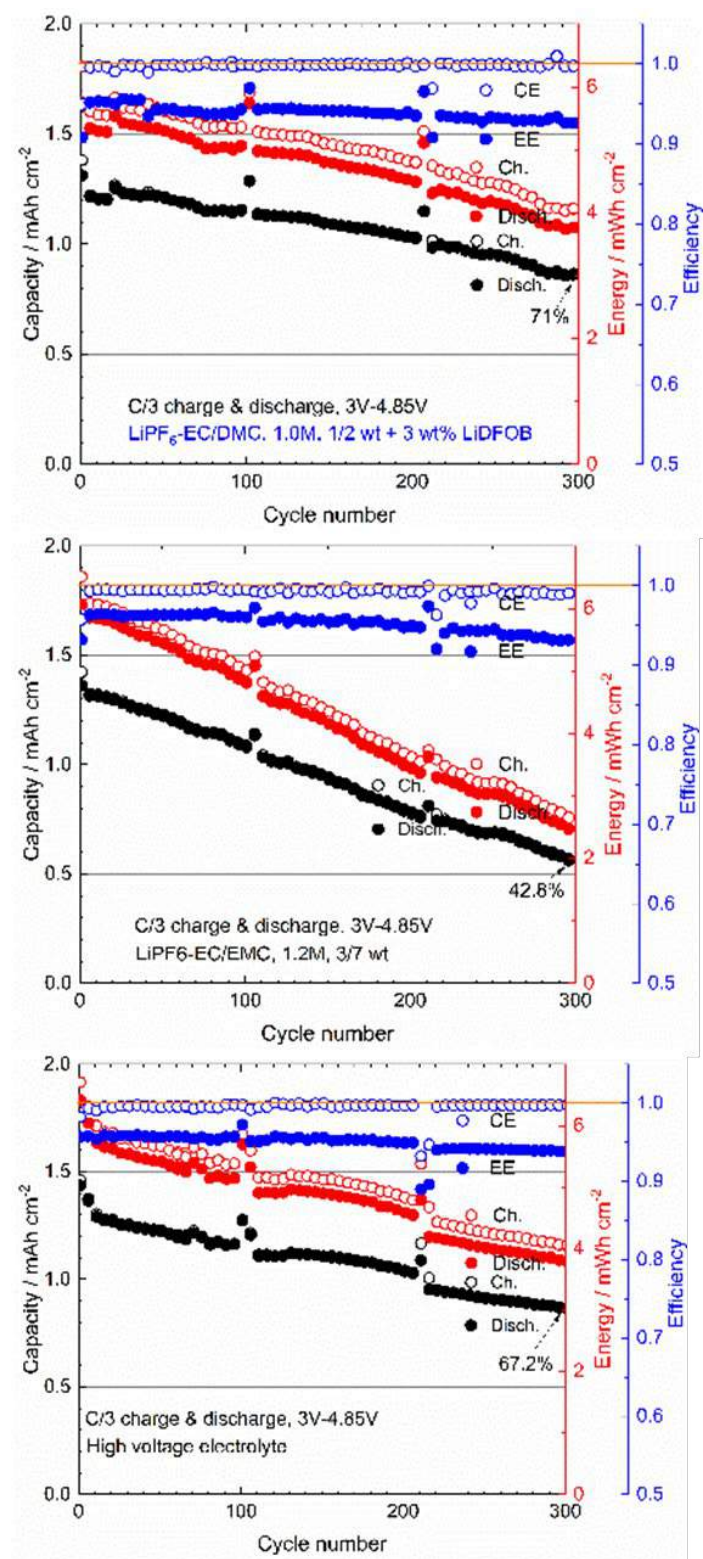


Figure II.4.B.8 Performance metrics per cycle at C/3 in terms of coulombic efficiency, energy efficiency, and energy and capacity on charge and discharge of LNM0/graphite cells with different electrolytes (electrolyte composition identified at the bottom of each figure)

Baseline performance of dry coating LNMO thick electrode with over 4 mAh/cm² loading

Tesla have successfully dry coated thick electrodes and demonstrated their initial electrochemical results using initial LNMO powders received from ANL (NEI-A). The fabricated dry electrode is about 115 microns in thickness and has a loading of approximately 30 mg/cm² (2.61 g/cc). To further enable LNMO/graphite full cell with dry coated thick LNMO electrode over 4 mAh/cm² loading, a new iteration of dry coated thick selectrode (formulation #3) was fabricated. New active material from Haldor Topsoe was used in the electrode and the ratio between active material: carbon: binder was changed from 95:2:3 to 90:6:4. The purpose of increasing carbon content in the electrode is to improve the electronic conductivity of the thick electrode. The fabricated dry electrode is about 130 microns in thickness and has an active mass loading of approximately 4 mAh/cm² as seen in Figure II.4.B.9a. EDX mapping indicates a uniform distribution of active material and carbon (Figure II.4.B.9b). CR2032 half cells of thick electrode formulation #3 against Li metal were assembled with 50 μ L Gen2 electrolyte and celgard 2325 separator. The cells were cycled between 3.5 V to 4.85 V using C/10. Representative voltage profiles in different cycles are shown in Figure II.4.B.9c, where an initial capacity about 121 mAh/g and an initial Coulombic efficiency of 78.76% is achieved. The cycling performance of thick electrode formulation #3 is shown in Figure II.4.B.9d and e. An increase of discharge capacity and energy density over first several cycles is observed in multiple cells, which indicates an activation process of the thick electrode. In the third cycle, all three cells deliver over 130 mAh/g discharge capacity (equals to 3.95 mAh/cm²) and 600 Wh/kg discharge energy density. The half cells start to decay after 4 cycles, which is largely due to the Li metal failure when cycled with thick cathode.

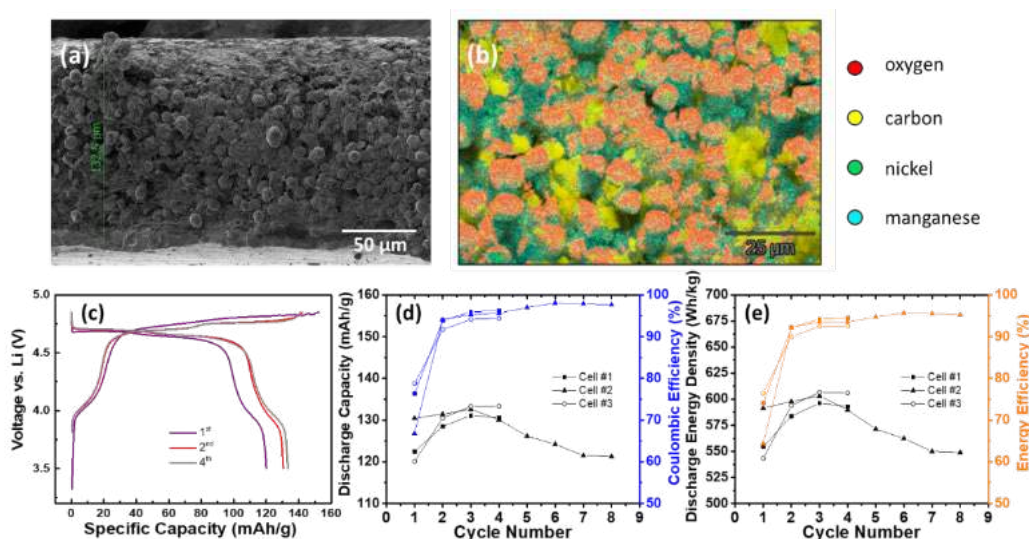


Figure II.4.B.9 (a) cross-section SEM image of dry coated LNMO thick electrode with Haldor Topsoe material. (b) EDX mapping of the cross-section of the electrode. (c) voltage profile of formulation #3 LNMO/Li half cell assembled in CR2032 with Gen2 electrolyte. (d) capacity retention and (e) energy density retention of formulation #3 LNMO/Li half cells cycled at C/10

Dry coated graphite electrode with 12.3 mg/cm^2 active loading was paired up with dry coated LNMO formulation #3 to assemble full cell. Al-clad CR2032 cases, flooded Gen2 electrolyte and glass fiber separator were used in full cell. The coin cell type full cell was cycled between 3.3 V and 4.85 V using C/10 ($1\text{C} = 147 \text{ mAh/g}$). Compared to formulation #2 (fabricated in Q3) which shows 40%-50% initial Coulombic efficiency and 40-60 mAh/g initial discharge capacity, formulation #3 exhibits great improvement. The full coin cell of formulation #3 delivers 75.7% initial Coulombic efficiency and 118 mAh/g initial discharge capacity as well as 518 Wh/kg initial energy density (Figure II.4.B.10). After 9 cycles, the full cell delivers 100 mAh/g capacity

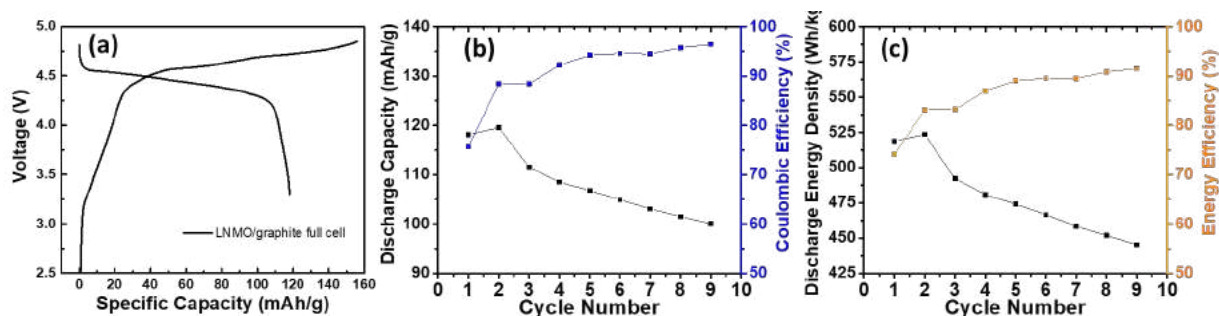


Figure II.4.B.10 (a) 1st cycle voltage profile of the LNMO/graphite full cell using formulation #3 cathode and dry coated graphite with capacity matching. Cycling performance of this full cell in terms of (b) capacity and (c) energy density are shown in the figure. The full cell was cycled between 3.3 V to 4.85 V with C/10

(85% retention) and 445 Wh/kg energy density (86% retention). To control the decay rate and increase cycling retention, further improvement in dry coated thick electrode full cell is needed. Future work will mainly focus on tuning the carbon ratio and porosity in thick electrode to ensure good electronic and ionic conductivity. Pouch cell with stable pressure control will also be introduced in testing the dry coated thick electrode.

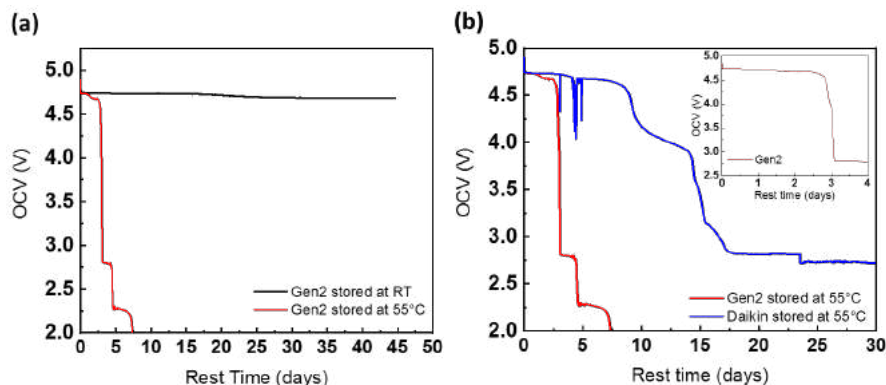


Figure II.4.B.11 (a) OCV of half cells with Gen2 stored at room temperature (black) and at 55°C (red). (b) OCV of half cells with Gen2 (red) and Daikin electrolyte (blue) as a function of the rest time. (inset) Expanded view of the OCV with Gen2 electrolyte between 0 and 4 days.

Self-discharge reaction in LNMO/Li half-cell

Self-discharge decreases the shelf life of batteries and causes them to initially have less than a full charge when actually put to use. As we have made the breakthroughs in cycling stability and thick electrode architectures, we realize that self-discharge of high voltage LNMO cathode is an important aspect that we need to look into, especially under the elevated temperature storage condition. During the testing,

the cells, which consist of LNMO cathode and Li metal anode in Gen2 or Daikin electrolyte, were fully charged at room temperature and rested at room temperature or at 55°C in a temperature-controlled chamber. Open circuit voltage (OCV) of each cell was monitored during the storage. The voltage profiles are plotted in Figure II.4.B.11 as a function of rest time. First, the OCV of the cells with Gen2 stored at room temperature and at 55°C are compared in Figure II.4.B.11a. Even after 40 days, the cell stored at room temperature still keeps high voltage ($>4.0 \text{ V}$), while the OCV of the cell stored at 55°C dropped to 2.8 V after 3 days. This implies slow self-discharging rate for the LNMO high voltage cathode at room temperature and the self-discharge reaction is accelerated at high temperature. Next, the OCV profiles with different electrolytes are

compared in Figure II.4.B.11b. This experiment was carried out under accelerated condition at high temperature to identify any difference between different electrolytes. The OCV of the cell with Gen2 electrolyte shows a similar voltage profile of a cell normally discharged with a constant current. During this experiment, the cells with an active mass loading of about 5 mg, were fully discharged after three days at 55°C. In the OCV plot in Figure II.4.B.11b, the plateaus at 4.73 V and 4.67 V correspond to the Ni reduction reaction. There is also a small plateau observed at around 4.0 V, which is related to Mn reduction from Mn^{4+} to Mn^{3+} . Even after reaching 2.8 V, which is the normal OCV after LNMO half-cell assembly, the cell keeps self-discharging. The voltage plateaus at 2.80 and 2.28 V corresponds to Mn^{3+} to Mn^{2+} reactions. The cell with Daikin electrolyte, in contrast, demonstrates a different voltage profile from that of the cell with Gen2. First, the cell with Daikin electrolyte retains high voltage (> 4.0 V) for two to three times longer than cell with Gen2 electrolyte. Second, the OCV profile shape is different than the Gen2 cell. In the cell with Daikin electrolyte, the plateau corresponding to Mn 4+/3+ redox at 4.0 V is relatively longer. In order to elucidate more details, further characterization of the LNMO structural change and the electrolyte decomposition process at each period during storage is needed.

Conclusions

Three baseline LNMO cathodes from different suppliers were systematically compared from both materials properties and electrochemical performances. The best LNMO sample can deliver a reversible capacity of 135 mAh/g at C/3, reaching the project goal of 600 Wh/kg at the cathode level. Large batch production of LNMO cathode with in-house UTX precursors has been prepared, which delivers better capacity retention compared with commercially available sample. More than 80% capacity retention has been achieved in the LNMO full cell within a confined voltage window after 300 cycles. Dry coated thick electrodes with areal loading larger than 4 mAh/cm² have been prepared and their electrochemical performance has been improved. Novel electrolytes were tested, where LiDFOB additive shows the least capacity fade in the pouch cell.

Key Publications

We have a few publications planned for 2020. None yet in 2019.

References

1. Ohzuku, T.; Takeda, S.; Iwanaga, M. Solid-State Redox Potentials for $\text{Li}[\text{Me}_{1/2}\text{Mn}_{3/2}]\text{O}_4$ (Me: 3d-Transition Metal) Having Spinel-Framework Structures: A Series of 5 Volt Materials for Advanced Lithium-Ion Batteries. *J. Power Sources* **1999**, 81-82, 90-94.
2. Lu, J.; Lee, K. S. Spinel Cathodes for Advanced Lithium Ion Batteries: A Review of Challenges and Recent Progress. *Mater. Technol.* **2016**, 31 (11), 628-641.

Acknowledgements

We thank Dr. Aaron D. Yocum (NETL manager), Dr. Ahmad Pesaran (NREL manager), and Dr. Jack Deppe (INL manager) for supporting our work. The project partners for this project included Arumugam Manthiram (The University of Texas at Austin), Hieu Duong (Tesla, Inc.), Vince Battaglia (Lawrence Berkeley National Laboratory), Kang Xu (Army Research Laboratory), and Marshall Schroeder (Army Research Laboratory).

II.4.C Novel Lithium Iron and Aluminum Nickelate (NFA) as Cobalt-Free Cathode Materials (ORNL)

Dr. Ilias Belharouak, Principal Investigator

Energy and Transportation Science Division
Oak Ridge National Laboratory
2370 Cherahala Boulevard
Knoxville, TN 37932-6479
E-mail: belharouaki@ornl.gov

Peter Faguy, DOE Technology Development Manager

U.S. Department of Energy
E-mail: Peter.Faguy@EE.Doe.Gov

Start Date: October 1, 2018	End Date: September 30, 2021	
Project Funding (FY19): \$2,100,000	DOE share: \$2,100,000	Non-DOE share: \$0

Introduction

To meet the latest DOE cost and performance targets for electric vehicles (production cost \$80/kWh), the focus of current battery research should be reoriented towards reducing the cobalt content in the cathode materials to less than 50 mg/Wh at the cell level. [1] However, achieving this target is challenging when considering that the present-day battery cathode materials such as $\text{LiNi}_x\text{Mn}_y\text{Co}_z\text{O}_2$ (NMC) or $\text{LiNi}_{0.8}\text{Co}_{0.15}\text{Al}_{0.05}\text{O}_2$ (NCA) employ considerable amounts of cobalt in their compositions. Adding to this, the price of cobalt has been in a constant state of fluctuation over the past half-decade with prices nearly tripling in the past few years. A recent report by the Cobalt Development Institute (CDI) also indicates that nearly 58% of global cobalt production is currently used in many diverse industrial and military applications (super alloys, catalysts, magnets, pigments, etc.). [2] The companies that are actively engaged in this sector can weather the cobalt price uncertainties even in the case of high shortages as it only represents a negligible part of their material costs. This scenario compounded by a supply and demand constraint would be crippling to the EV/battery manufacturing industry considering the burgeoning rate at which the EV and consumer electronics markets are expanding. While current commercial cathodes such as NCA and NMC (811) are making steady inroads into the EV market, it is worth examining the question whether cobalt is needed at all. In light of this developing scenario, the primary objective of this project is to research, develop and scale the novel lithium iron and aluminum nickelate, $\text{LiNi}_x\text{Fe}_y\text{Al}_z\text{O}_2$ (NFA: Ni, Fe, Al) class of cathodes that will free the battery manufacturing industry from cobalt while maintaining or exceeding the benefits offered by NCAs and NMCs in order to achieve the prerequisite performance targets.

Objectives

The overall goal of this work is to implement $\text{LiNi}_{0.8(0.9)}\text{Fe}_{0.2(0.1)-x}\text{Al}_x\text{O}_2$ (NFA) as novel cobalt-free cathodes in large format Li-ion cells achieving the following performance and cost targets:

1. Zero (0) cobalt loading as NFA cathodes only have nickel (80-90%), and the balance (10-20%) is a combination of iron and aluminum.
2. 650-750 Wh/kg usable specific energy at C/3 rate at the material level at the beginning of life.
3. Thousand (1000) deep charge and discharge cycles at the C/3 rate with less than 20% capacity fade in 2.3 Ah cells.
4. Less than \$100 per kWh at the cell level.

Approach

Three major approaches at the material level are being implemented in this work:

1. Optimization of the amounts of Al^{3+} which favors the stabilization of nickel in the 3+ oxidation state, which ensures the dual dimensionality and oxygen stability in the cathodes. (*good for reversibility and cycle life*)
2. Introduction of controlled amounts of Fe^{3+} (equal or less than 10%) to improve the electronic conductivity in the Ni-Al slab. (*good for power*)
3. Fine-tuning of the synthesis conditions and processes to yield highly-ordered layered NFA cathodes with higher packing densities to achieve higher energy densities without compromising cycling performance. (*good for translating the material properties and performance from bench scale to pilot scale*)

Results

The task flow of this project comprises of investigating the compositional landscape of this new NFA class of cobalt-free cathodes followed by scale-up of the best performing composition using the co-precipitation process in a Continuous Stirred Tank Reactor (CSTR). The first step involves the synthesis of the NFA class of cathodes using the Sol-Gel method to investigate the compositional landscape of these materials. Figure II.4.C.1. (A) shows the sol-gel method for synthesis of the NFA cathodes. The transition metal sources (Ni, Fe) along with

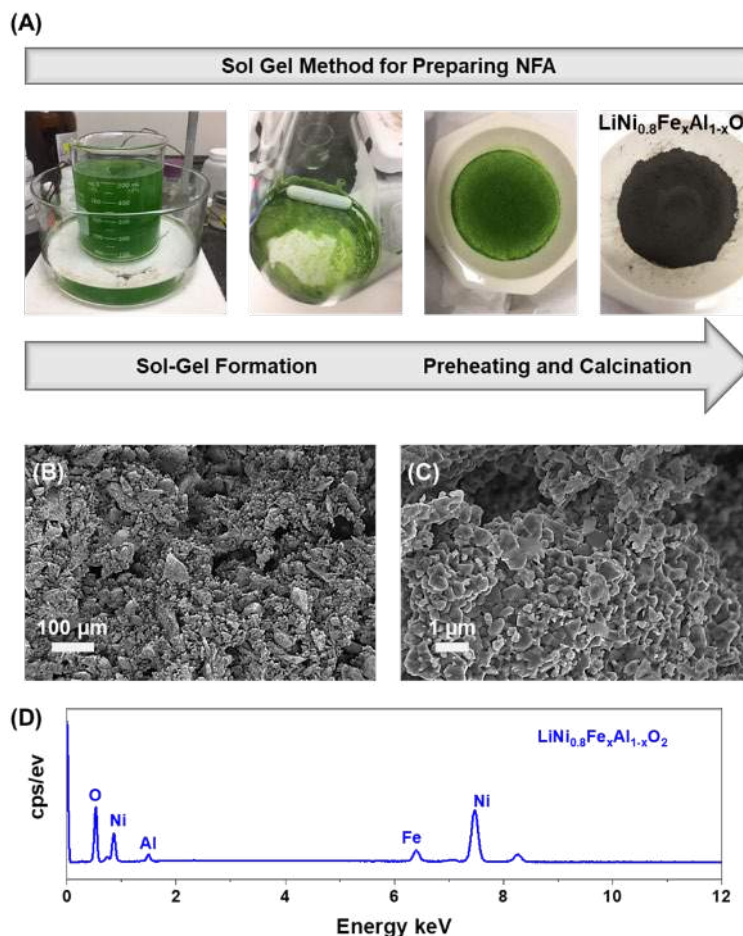


Figure II.4.C.1 (A) Sol Gel method for preparation of NFA cathode powders, (B - C) Scanning electron micrographs of the sol-gel synthesized NFA cathode powders, (D) EDS spectra of the sol-gel synthesized NFA powders

lithium and aluminum sources in appropriate molar concentrations were dissolved in DI water. Citric acid (1:1, transition metal: acid) was added to the solution mixture followed by heating at 60°C under continuous stirring to obtain a clear gel which was then evaporated to obtain the green precursor powders. The precursor powders were then subjected to heat treatment initially at 400°C to burn off organics followed by calcination in oxygen atmospheres (700 – 800°C). The calcined powders were ground using a mortar and pestle to obtain the final NFA cathode powders. By varying the amounts of iron and aluminum, three compositional variants of the NFA class (NFA - 1, NFA - F and NFA - A) were synthesized for investigation in the context of this work. Scanning electron micrographs for the synthesized powders are shown in Figure II.4.C.2. (B). The SEM micrographs show primary particles of NFA forming secondary aggregates which is a characteristic of such powders synthesized using the Sol-Gel process. [3],[4],[5] Energy Dispersive Spectroscopy (EDS) was used to analyze the elemental composition of the synthesized powders. EDS spectra shown in Figure II.4.C.3. (C) indicated the presence of constituent transition metal cations (Ni, Fe and Al) in the as synthesized powders. Though the morphological control of the powders synthesized using the sol-gel process was challenging, this process enables quick exploration of the compositional landscape of the NFA class of cathodes.

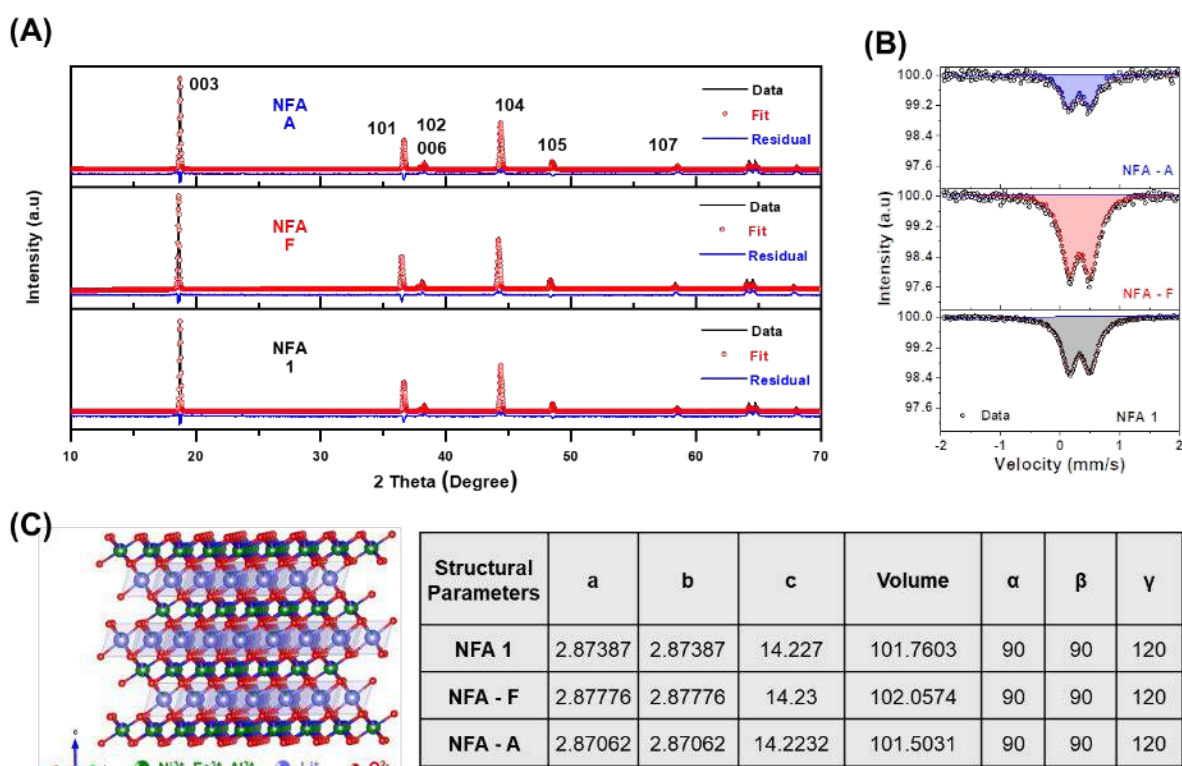


Figure II.4.C.2 Crystallographic assessment of the NFA compositional variants (A) X-Ray diffractograms, (B) Mossbauer spectra, (C) Schematic representation of the crystal structure of NFA class and with the corresponding lattice parameters

Crystallographic assessment of the three compositional variants were performed using X-Ray Diffraction technique. The X-Ray diffractograms shown in Figure II.4.C.2. (A) of the three compositional variants of the NFA class showed phase purity with well-ordered crystal structures in the R-3m space group. The observed diffraction patterns are consistent with the layered pure phase α -NaFeO₂ [6],[7]. An important parameter for nickel rich class of cathodes is the extent of cation mixing which is characterized by the presence of some Ni²⁺ ions in the Li⁺ layer owing to the similarity in their ionic radii. [8] This parameter can be assessed using the ratio between the intensities of (003) and (104) peaks observed in the diffractograms. It was observed that all the compositional variants had minimal cation mixing characterized by the high (003)/(104) ratio (>1.5 for all the variants). Further, Mossbauer spectroscopy, a technique sensitive to iron containing materials was employed to investigate the oxidation state and local environment of iron in the synthesized NFA powders.

Mossbauer spectra (Figure II.4.C.2. (B)) recorded at room temperature shows a symmetric doublet which was fitted using a single component indicating one iron site. Moreover, this also indicates that the NFA powders are paramagnetic confirming the absence of any magnetic iron impurities at room temperature. The obtained isomershifts indicate the presence of iron with +3 high spin oxidation state. Also, quadruple splitting values for the three variants indicated that the iron is present in an asymmetric environment. The absence of other peaks in the spectra indicates iron solely in +3 state without any +2 or +4 impurities [9],[10]. A schematic representation of the obtained crystal structure and the calculated lattice parameters are shown in Figure II.4.C.2. (C). Overall microstructural, spectroscopic and crystallographic assessment highlights the feasibility of synthesizing phase pure, highly ordered NFA cathode material using the sol-gel process.

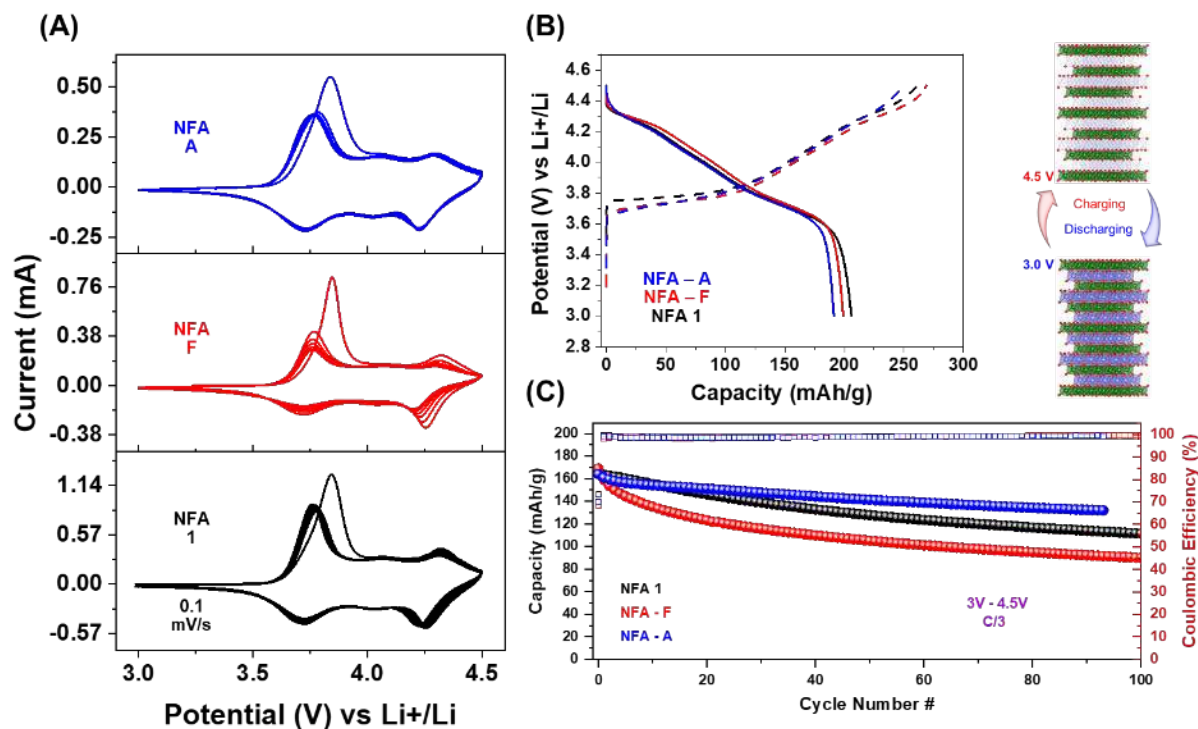


Figure II.4.C.3 Electrochemical assessment of the NFA compositional variants (A) Cyclic voltammograms, (B) Charge/Discharge curves, (C) Cycling performance

The synthesized NFA variants were assessed electrochemically by assembling 2032-coin cells with the NFA variants as the cathode (80 wt. % as synthesized powder, 10 wt. % PVDF binder and 10 wt% conductive carbon additive (Denka)), Gen-2 electrolyte and Li metal as the anode. Cyclic voltammetry (CV) tests (Figure II.4.C.3. (A)) at a scan rate of 0.1m V/s between the voltage window of 2.0 V and 4.5 V were performed. The CVs show Li-ion insertion (cathodic peaks) and extraction (anodic peaks) processes exhibited by the NFA variants with good reversibility. The voltammograms are similar to that observed for the typical cobalt containing commercial layered cathodes such as NCA and NCMs characterized by the dominant nickel redox features with distinct crystallographic transitions. It can be observed that the compositional variant NFA – F when compared to NFA - 1 and NFA – A showed faster degradation in redox peak heights suggesting degradation in performance. The variants NFA – 1 and NFA – A however, exhibited comparative stability with NFA – A exhibiting minimal degradation in performance. The charge/discharge behavior of the three NFA variants at 0.1C is shown in Figure II.4.C.3. (B) The three cobalt-free compositional variants showed similar initial capacities of around 200 mAh/g which is comparable to cobalt containing NMCs and NCA type cathode materials synthesized using similar processes. The cycling behavior of the three variants was assessed using continuous charge/discharge tests at C/3 between 3V and 4.5V as shown in Figure II.4.C.3. (C). It can be

observed that the NFA – A variant showed stable performance and capacity retention when compared to the other two NFA variants. A major cause for degradation observed could be due to the fact that these materials were cycled between 3V and a comparatively higher voltage of 4.5V. Cobalt containing cathodes such as NCAs and NCMs show capacity fading behavior at these high voltages and therefore they are operated generally between 3V and 4.3V. [11],[12] Overall, these electrochemical assessments emphasize the feasibility of the NFA class in achieving the overall project objectives.

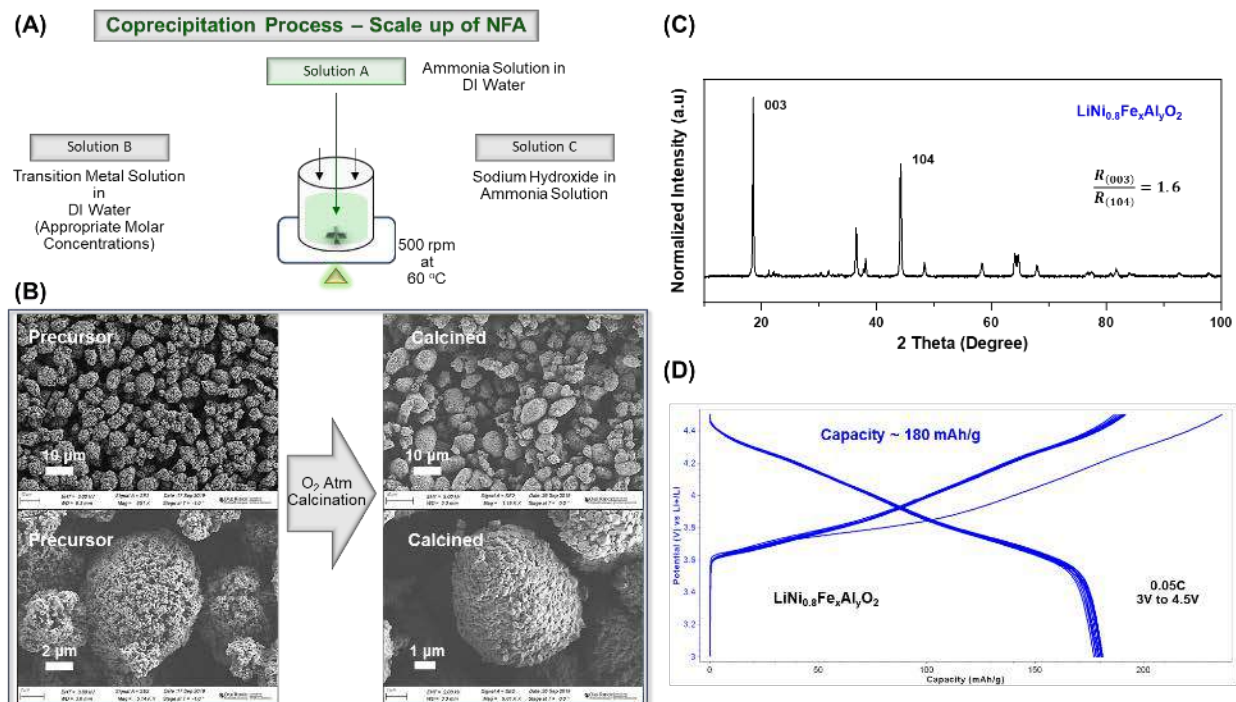


Figure II.4.C.4 (A) Schematic representation of the co-precipitation process for the scale-up of the NFA class, (B) Scanning electron micrographs of the NFA cathode powders synthesized using co-precipitation process and calcined in oxygen atmospheres, (C) X-Ray Diffractogram of the NFA powders synthesized using co-precipitation process and (D) Electrochemical assessment of the NFA powders synthesized using co-precipitation process

Table II.4.C.1 Equilibrium Reactions, Solubility Product Constant and pH of Precipitation

Equilibrium Reaction	Ksp	pH (begin to precipitate)
$\text{Ni}^{2+} + 2\text{OH}^- = \text{Ni}(\text{OH})_2$	2.00×10^{-15}	6.20
$\text{Fe}^{2+} + 2\text{OH}^- = \text{Fe}(\text{OH})_2$	1.58×10^{-15}	7.01
$\text{Fe}^{2+} + 3\text{OH}^- = \text{Fe}(\text{OH})_3$	1.31×10^{-20}	4.1
$\text{Al}^{3+} + 3\text{OH}^- = \text{Al}(\text{OH})_3$	4.57×10^{-33}	2.1

The compositional landscape of the NFA class was explored using the Sol-Gel process following which the best performing composition was scaled up using the coprecipitation process in a CSTR. A major advantage of the co-precipitation process is that large quantities of good morphologically controlled spherical NFA cathode powders can be obtained. Figure II.4.C.4. (A) shows a schematic representation of the process where the material is first synthesized in the form of a spherical precursor ($\text{Ni}_{0.8}\text{Fe}_x\text{Al}_y(\text{OH})_2$) starting from the transition metal sources in the form of sulfates, nitrates or chlorides which are pumped into the reaction vessel containing a solution of ammonia and water. The base solution containing appropriate amounts of NaOH and ammonia are added to precipitate the hydroxide precursor. PH of the process and stirring speed was maintained at a

constant value and was continuously monitored throughout the process. The NFA system has three elements which precipitate at different pH values as given by their solubility product constants (K_{sp}) in Table II.4.C.1. Due to the much smaller K_{sp} of $\text{Al}(\text{OH})_3$ compared to $\text{Ni}(\text{OH})_2$, $\text{Fe}(\text{OH})_2$ and $\text{Fe}(\text{OH})_3$, controlling the co-precipitation of Ni^{2+} , Fe^{2+} or Fe^{3+} and Al^{3+} simultaneously is challenging. To overcome this challenge, AlO_2^- was employed as the Al source, which hydrolyses into $\text{Al}(\text{OH})_3$ under appropriate pH conditions, ensuring the simultaneous co-precipitation of Ni^{2+} , Fe^{2+} and Al^{3+} . The $\text{Ni}_{0.8}\text{Fe}_x\text{Al}_y(\text{OH})_2$ precursor powder was filtered then washed with deionized water several times until the pH of the filtrate was close to 7.0. After sieving, powders with an average particle size of 10 μm were used for further analyses. The filtered powder was dried at 120°C overnight and then fired with appropriate amount of Li_2CO_3 at temperatures between 700°C and 750°C for varying periods of time in oxygen atmospheres to make $\text{LiNi}_{0.8}\text{Fe}_x\text{Al}_y\text{O}_2$. Scanning electron micrographs of the co-precipitated precursor powders and the subsequently calcined cathode material is shown in Figure II.4.C.4. (B) It can be observed that the obtained precursor powders show spherical morphology which was retained after calcination to form the final cathode material. The final material comprises of primary particles (100-400 nm) aggregated to form secondary spherical particles (5-15 μm). This co-precipitation process in a CSTR can yield cathode materials with good spherical morphology and in large quantities (~500g). X-Ray diffractogram (Figure II.4.C.4. (C)) shows the obtained NFA cathode material with minimal impurities and good ordering with lowered cation mixing. The electrochemical performance of the co-precipitated NFA was assessed using charge/discharge measurements. The obtained cathode material delivered good capacities (~180 mAh/g at 0.05C) when tested between the voltage range of 3V to 4.5V. Further morphological and electrochemical optimizations are presently underway to enable high capacities and good cycling stabilities. Overall, these approaches provide key pathways of further development and optimizations towards achieving the project objectives.

Conclusions

In summary, this work was aimed at developing a novel class of cobalt free cathode material, the NFA class of cathodes for achieving the latest battery cost and performance targets set by DOE. The cathode material was synthesized initially using sol-gel process to predominantly explore the compositional landscape of the NFA system. This latest class of cobalt free cathode material was then evaluated for compositional and phase purity, crystallographic stability and electrochemical performance. The best performing NFA cathode material was then scaled-up using the co-precipitation process in a CSTR. Microstructural characterization revealed precursors with spherical morphology which was maintained even after high temperature calcination processes. Crystallographic and Electrochemical assessments reveal comparable capacities and stabilities warranting further investigations and highlighting the potential of the NFA class of cathodes in meeting the overall project objectives. Overall, the systematic approaches described in this work provide several key directions and insights on the NFA system which shows immense promise for the development of next generation li-ion batteries.

Key Publications

1. Muralidharan, N., Essehli, R., Self, E. C., Nanda, J., & Belharouak, I. (2019, September). Investigating the
2. Origin of Cation Mixing in Nickel Rich Cathodes. In Meeting Abstracts (No. 5, pp. 289-289). The Electrochemical Society.

References

1. D. Howell, Vehicle Technologies Office Merit Review 2017: Overview of the DOE VTO Advanced Battery R&D Program, <https://www.energy.gov/eere/vehicles/downloads/vehicle-technologies-office-merit-review-2017-overview-doe-vto-advanced>
2. Sebastien Gandon, No cobalt, no Tesla?, <https://techcrunch.com/2017/01/01/no-cobalt-no-tesla/>

3. Ilango, P. Robert, T. Subburaj, K. Prasanna, Yong Nam Jo, and Chang Woo Lee. "Physical and Electrochemical Performance of $\text{LiNi}_{1/3}\text{Co}_{1/3}\text{Mn}_{1/3}\text{O}_2$ Cathodes Coated by Sb_2O_3 Using a Sol-gel Process." *Materials Chemistry and Physics* 158 (2015): 45-51.
4. Lee, Suk-Woo, Hyungsub Kim, Myeong-Seong Kim, Hee-Chang Youn, Kisuk Kang, Byung-Won Cho, Kwang Chul Roh, and Kwang-Bum Kim. "Improved electrochemical performance of $\text{LiNi}_{0.6}\text{Co}_{0.2}\text{Mn}_{0.2}\text{O}_2$ cathode material synthesized by citric acid assisted sol-gel method for lithium ion batteries." *Journal of Power Sources* 315 (2016): 261-268.
5. Xiang, Yanhong, Zhen Sun, Jian Li, Xianwen Wu, Zhixiong Liu, Lizhi Xiong, Zeqiang He, Bo Long, Chen Yang, and Zhoulan Yin. "Improved electrochemical performance of $\text{Li}_{1.2}\text{Ni}_{0.2}\text{Mn}_{0.6}\text{O}_2$ cathode material for lithium ion batteries synthesized by the polyvinyl alcohol assisted sol-gel method." *Ceramics International* 43, no. 2 (2017): 2320-2324.
6. Belharouak, I., Y-K. Sun, J. Liu, and K. Amine. " $\text{Li}(\text{Ni}_{1/3}\text{Co}_{1/3}\text{Mn}_{1/3})\text{O}_2$ as a suitable cathode for high power applications." *Journal of Power Sources* 123, no. 2 (2003): 247-252.
7. Belharouak, Ilias, Wenquan Lu, Donald Vissers, and Khalil Amine. "Safety characteristics of $\text{Li}(\text{Ni}_{0.8}\text{Co}_{0.15}\text{Al}_{0.05})\text{O}_2$ and $\text{Li}(\text{Ni}_{1/3}\text{Co}_{1/3}\text{Mn}_{1/3})\text{O}_2$." *Electrochemistry Communications* 8, no. 2 (2006): 329-335.
8. Myung, Seung-Taek, Filippo Maglia, Kang-Joon Park, Chong Seung Yoon, Peter Lamp, Sung-Jin Kim, and Yang-Kook Sun. "Nickel-rich layered cathode materials for automotive lithium-ion batteries: achievements and perspectives." *ACS Energy Letters* 2, no. 1 (2016): 196-223.
9. Delmas, C., M. Menetrier, L. Croguennec, I. Saadoune, A. Rougier, C. Poullierie, G. Prado, M. Grüne, and L. Fournes. "An overview of the $\text{Li}(\text{Ni},\text{M})\text{O}_2$ systems: syntheses, structures and properties." *Electrochimica Acta* 45, no. 1-2 (1999): 243-253.
10. Jensen, KM Ø., H. P. Gunnlaugsson, Mogens Christensen, and B. B. Iversen. "Mössbauer spectroscopy study of defects in hydrothermally synthesized LiFePO_4 cathode material." *Hyperfine Interactions* 226, no. 1-3 (2014): 73-78.
11. Liu, Hao, Mark Wolf, Khim Karki, Young-Sang Yu, Eric A. Stach, Jordi Cabana, Karena W. Chapman, and Peter J. Chupas. "Intergranular cracking as a major cause of long-term capacity fading of layered cathodes." *Nano letters* 17, no. 6 (2017): 3452-3457.
12. Ryu, Hoon-Hee, Kang-Joon Park, Chong S. Yoon, and Yang-Kook Sun. "Capacity fading of Ni-rich $\text{Li}[\text{Ni}_x\text{Co}_y\text{Mn}_{1-x-y}]\text{O}_2$ ($0.6 \leq x \leq 0.95$) cathodes for high-energy-density lithium-ion batteries: bulk or surface degradation?." *Chemistry of Materials* 30, no. 3 (2018): 1155-1163.

Acknowledgements

We would like to acknowledge Dr. Nitin Muralidharan, Dr. Rachid Essehli, Dr. Jagjit Nanda, Dr. Jue Liu, Dr. Ethan Self and Dr. Raphael Hermann for their involvement with the synthesis, characterization and useful discussions regarding this work.

II.4.D Enhancing Oxygen Stability in Low-Cobalt Layered Oxide Cathode Materials by Three-Dimensional Targeted Doping (UC Irvine)

Huolin Xin, Principal Investigator

University of California, Irvine
4129 Frederick Reines Hall
Irvine, CA 92697-4575
E-mail: huolin.xin@uci.edu

Feng Lin, Principal Investigator

Virginia Tech
Department of Chemistry
Blacksburg, VA 24061
E-mail: fenglin@vt.edu

Kristin Persson, Principal Investigator

University of California Berkeley
210 Hearst Mining Building
Berkeley, CA 94720
E-mail: kristinpersson@berkeley.edu

Wu Xu, Principal Investigator

Pacific Northwest National Laboratory
902 Battelle Boulevard
Richland, WA 99354
E-mail: wu.xu@pnl.gov

Jiang Fan, Principal Investigator

American Lithium Energy Corporation
2261 Rutherford Road
Carlsbad, CA 92008
E-mail: jfan@americanlithiumenergy.com

Peter Faguy, DOE Technology Development Manager

U.S. Department of Energy
E-mail: Peter.Faguy@ee.doe.gov

Start Date: November 1, 2018	End Date: October 31, 2021	
Project Funding (FY19): \$3,125,000	DOE share: \$2,500,000	Non-DOE share: \$625,000

Project Introduction

In this project, we propose to develop a new concept and a generic platform that can lead to the greatly enhanced stabilization of all high-energy cathode materials, and in particular high-nickel (Ni) and low-cobalt (Co) oxides. The new concept is a 3D doping technology that hierarchically combines surface and bulk doping. We will use surface doping to stabilize the surface of primary particles and also introduce dopants in the bulk to further enhance oxygen stability, conductivity, and structural stability in low-Co oxides under high voltage and deep discharging operating conditions. This new concept not only will deliver a low-cost, high-energy cathode but also will provide a generic method that can stabilize all high-energy cathodes. The proposed novel 3D doping approach is poised to resolve some longstanding challenges in fundamental doping effects on battery materials as well as to reduce Li-ion batteries' cost and improve their safety, energy density, and lifetime.

To tackle this problem, we have formed a highly complementary multi-university/national labs/industry team to enable a doping-central and systematic investigation of low-Co materials and create a knowledge base for many electrode materials to be used in advanced electric vehicles. The successful execution of the proposed project relies on five components that can be carried out by the complementary team members: (1) a theoretical investigation of surface and bulk stabilizing dopants (Persson), (2) precise synthesis of materials with targeted doping (Lin and Xin), (3) development of electrolytes for high-Ni low-Co oxides (Xu), (4) multi-scale characterization of the structures and their interfaces by scanning transmission electron microscopy (SEM) and synchrotron X-ray imaging and spectroscopy tools (Xin and Lin), and (5) pouch cell-level integration (Fan). The UCI-led project will enable a doping-central and systematic investigation of low-Co materials and create a knowledge base for many electrode materials to be used in advanced electric vehicles.

Objectives

The primary objective of this project is:

- Displace Co while maintaining high-Ni content and high energy density: Cobalt concentration < 50 mg/Wh or No-Co, Energy density > 750 Wh/kg (C/3, 2.5-4.4 V) at cathode level, Cost ≤ \$100/kWh
- Improve cycle and calendar life by retaining oxygen through a 3D doping technology: Capacity retention > 80% at 1,000 cycles, energy retention > 80% at 1,000 cycles, calendar life: 15 years
- Deliver a theoretical model: High-throughput DFT calculations that rationalize the selection of oxygen-retraining surface and bulk dopants
- Develop electrolytes with functional additives to form high-quality surface protection layers on both high-Ni/low-Co layered oxides and graphite anode to help the whole project achieve the proposed energy and capacity retention target, i.e., >80% at 1,000 cycles. The FY19 work will focus on electrolyte formulating for NMC811 baseline cathode and graphite anode.
- Offer a knowledge base by performing proactive studies of thermal stability, oxygen loss, and the degradation of the cathode/electrolyte interfaces.

Approach

- We utilize a three-dimensional (3D) doping technology that is a hierarchical combination of surface and bulk doping: (1) Surface doping stabilizes the interface between the primary particles and the electrolyte. (2) Introduction of dopants to the bulk enhances oxygen stability, conductivity and structural stability in low-Co oxides under high voltage and deep discharging operating conditions. (3) A composition controlled and thermodynamics driven synthesis will be used to accurately achieve the desired 3D doping structures.
- Use first-principle calculations to predict surface dopants for oxygen retention at surface of LiNiO₂ and rationalize the effectiveness of dopants.
- Formulate new electrolytes that stabilize the cathode/electrolyte interfaces at deep charging conditions: (1) Coin cell testing of commercial baseline materials. Perform coin cell electrochemical studies of baseline commercial NMC811 cathode and graphite (Gr) anode using the baseline electrolyte to establish coin cell-level benchmarks. (2) Coin cell testing of NMC-D. Evaluate the capacity and cycle life of the synthesized 3D doped cathode materials at the coin cell level using the baseline electrolyte. The results will be compared with the commercial NMC811 baseline. (3) Electrolyte formulating. Formulate functional localized high-concentration electrolytes (LHCEs) to improve cycle life and safety of baseline commercial NMC811 cathode and Gr anode at coin cell level, optimize electrolyte formulation for NMC-D-90532, and compare with electrolyte baseline for >200 cycles in Gr||NMC full cells at 4.4 V cutoff.
- Advanced computational and characterization techniques are developed to study: (1) dopant environment and chemistry. (2) thermal stability, oxygen loss, and the degradation of the cathode/electrolyte interfaces.

Results

1. Co-free layered oxide with 3D hierarchical Mg/Ti dual dopants

With the hierarchical distribution of Mg/Ti dual dopants in LiNiO₂, we report a Co-free layered oxide that exhibits enhanced bulk and surface stability. The soft X-ray absorption spectroscopy (XAS) revealed that the Ni oxidation state was slightly lower than Ni³⁺ (Figure II.4.D.1a). Additionally, we found that the Ti⁴⁺ dopant was fully accommodated in the layered lattice with no TiO₂ phase, as indicated by the absence of the Ti L₃-eg splitting (Figure II.4.D.1a). The presence of carbonate species was evident at the surface (Figure II.4.D.1a). Furthermore, we performed neutron diffraction (ND) and Rietveld refinement to determine that ~4% Ni occupied the Li sites (Figure II.4.D.1b). The cation-mixing was unidentifiable in the atomic-resolution annular dark-field scanning transmission electron microscopy (ADF-STEM) image of the bulk due to the small amount (Figure II.4.D.1c). Yet, a thin layer of Ni sitting at the Li sites was observed at the surface (Figure II.4.D.1d). These results suggested that the cation-mixing might prefer lodging at the surface. To further probe the Ti distribution, we performed electron energy loss spectroscopy (EELS) scanning from the particle surface to subsurface (Figure II.4.D.1e-f). The Ti⁴⁺ L-edge signal was mainly detected in the first five spectra, and the normalized Ti⁴⁺ L-edge intensity confirmed that the Ti⁴⁺ dopant was enriched at the top few nanometers of the particles (Figure II.4.D.1f-g). The energy dispersive X-ray spectroscopy (EDS) mapping results (Figure II.4.D.1h-j) revealed that Mg²⁺ was evenly distributed whereas Ti⁴⁺ was enriched at the top ~3 nm, which was consistent with the EELS mapping.

We evaluated the battery performance of the Mg/Ti-LNO cathode in half and full cells at 2.5–4.4 V vs. Li⁺/Li and 22°C. Such a high upper cutoff voltage allowed us to investigate the advantages of the dual dopants in limiting phase transformations and mitigating the cathode–electrolyte interfacial reactions under aggressive conditions. Compared with LNO, the Mg/Ti-LNO showed much smoother charge/discharge profiles (Figure II.4.D.2a, in particular within the 4.0–4.4 V and 3.7–3.5 V ranges), indicating that phase transformations and Li/vacancy ordering are suppressed. At C/10, the Mg/Ti-LNO cathode delivered a 208 mAh/g discharge capacity which was slightly lower than the baseline LNO (225 mAh/g). However, the charge/discharge profiles (Figure II.4.D.2b) of Mg/Ti-LNO after 50 cycles overlapped well with the second cycle (i.e., minimal increase of cell polarization), delivering a 95% capacity retention that was remarkably higher than the baseline LNO (73.6%, Figure II.4.D.2a). We plotted dQ/dV vs. voltage based on the charge/discharge profiles of the two cathodes (Figure II.4.D.2c). Consistent with the charge/discharge profiles, the

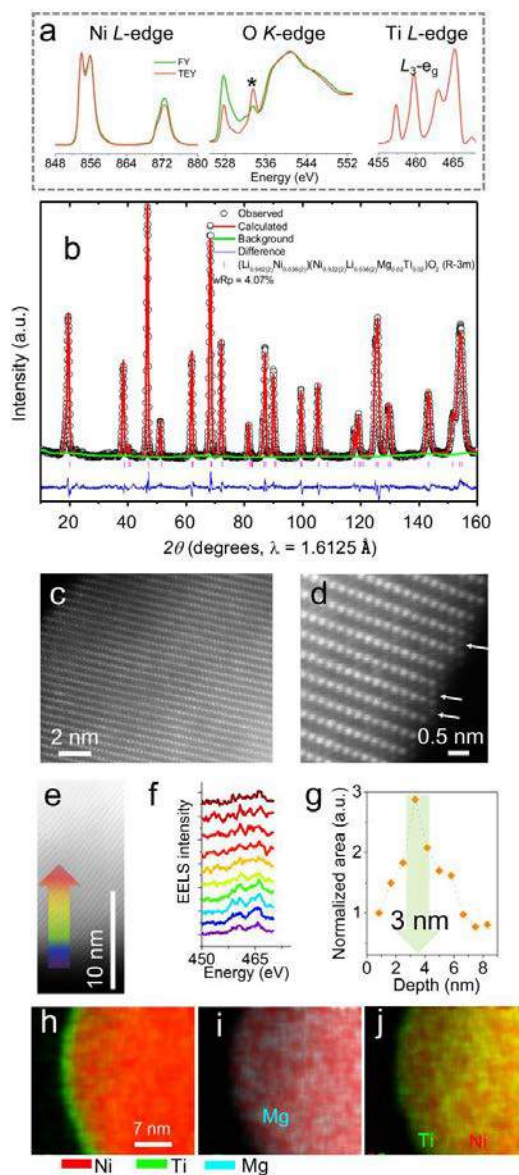


Figure II.4.D.1 Characterizations of the pristine Mg/Ti-LNO material. (a) Ni/Ti L-edge and O K-edge soft XAS spectra, the * represents carbonate species; (b) neutron diffraction and Rietveld refinement; (c-d) annular dark-field STEM images of the primary particle; (e) EELS spectra scanning pathway from the surface to subsurface with the increment of 0.8 nm for each spectrum; (f) Ti L-edge EELS spectra recorded with the scanning pathway (from the bottom purple to the top dark red spectra); (g) normalized peak area of Ti L-edge EELS as a function of the scanning depth; (h) STEM-EDS mapping of the Ni (red), and Ti (green) in the composition scale and (i-j) concentration scale on the selected particle.

Mg/Ti-LNO displayed smoother and fewer peaks than the LNO (Figure II.4.D.2c). After 50 cycles, we observed negligible changes (neither the intensity nor the peak position) in the dQ/dV vs. voltage curve of the Mg/Ti-LNO (Figure II.4.D.2c). However, the rapid fading around 3.6 V and 4.1 V was observed in the LNO, which were associated with the $H1 \rightarrow M$ and $H2 \rightarrow H3$ phase transformations, respectively. In addition, the rate capability of the Mg/Ti-LNO cathode was better than that of the LNO (the 2C capacity maintained 76% of the C/10 capacity in the Mg/Ti-LNO cathode) (Figure II.4.D.2d). At C/5, C/2 and 1C (Figure II.4.D.2e), the initial discharge capacity was 200, 180 and 175 mAh/g, respectively. The capacity retention after 150 cycles at C/5 and C/2 was 86% and 90%, respectively.

Furthermore, 85% capacity retention was achieved at 1C for 300 cycles. The material-level specific energy was ~780 Wh/kg at C/10 and C/5, and ~680 Wh/kg at C/2 and 1C (Figure II.4.D.2f), which

were higher than many reported Ni-rich NMC cathodes. The energy retention was 96%, 88%, 85%, and 77% at C/10, C/5, C/2 and 1C after their corresponding numbers of cycles shown in Figure II.4.D.2f.

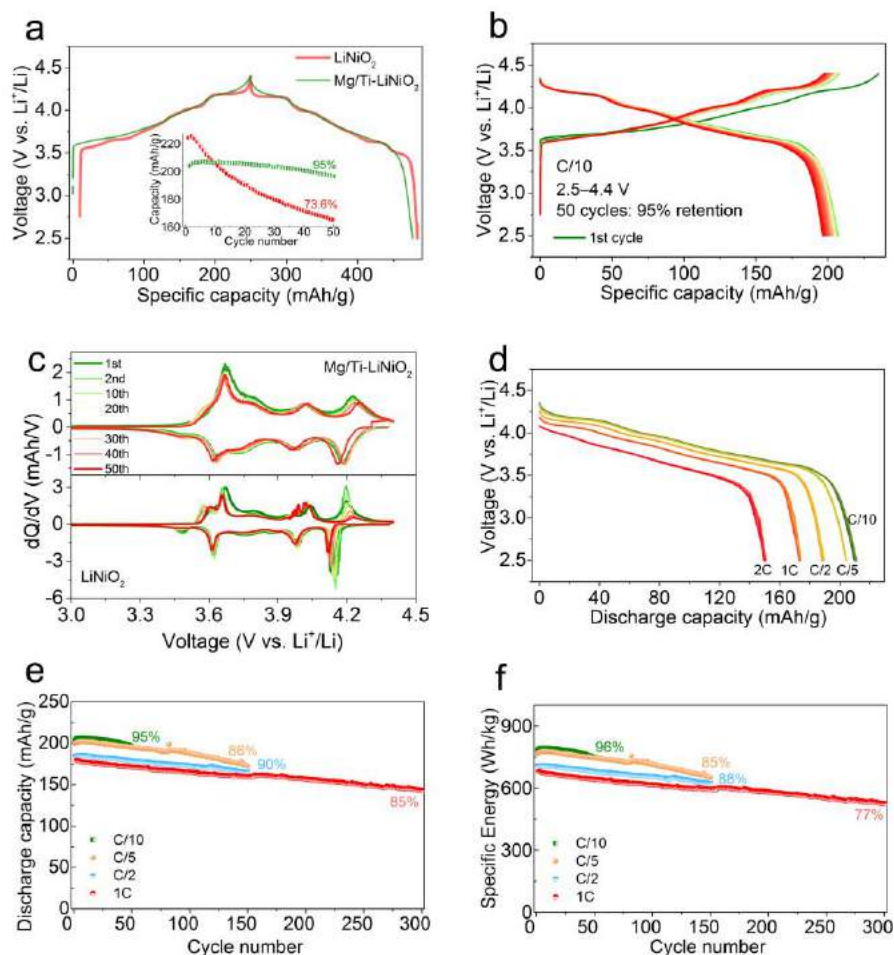


Figure II.4.D.2 Electrochemical performance of the half cells containing the Mg/Ti-LNO cathode at 22°C within 2.5–4.4 V. (a) The voltage profiles of the LNO and Mg/Ti-LNO at C/10 (20 mA/g), the insert shows the discharge capacity as a function of cycle number; (b) the voltage profiles in the first 50 cycles at C/10; (c) the dQ/dV curves of the two cathodes derived from the voltage profiles at C/10; (d) discharge voltage profiles at the symmetrical constant currents of C/10, C/5, C/2, 1C and 2C; (e) long-term cycling performance; (f) specific energy retention at different C-rates.

2. Structural characterization of the VT Gen-2 and Gen-3 material in the as-synthesized state

First, to confirm that the 3D doping profile was retained in the VT Gen 2 chemistry, we performed chemically sensitive electron tomography to map the composition of Ni, Ti and Mg in the primary particles with single nanometer resolution. The results in Figure II.4.D.3 show that there is a thin surface-dopant-rich outer layer demonstrating that the desired 3D doping structure was successfully achieved. Similarly, pristine VT Gen-3 Sb-doped LNO was also characterized. Atomic-resolution HAADF-STEM image of the pristine Sb-doped LNO (Figure II.4.D.4a) shows perfect layered structure. EDS mapping (Figure II.4.D.4b) shows that Sb was effectively doped into LNO and a thin surface-dopant-rich outer layer was also formed.

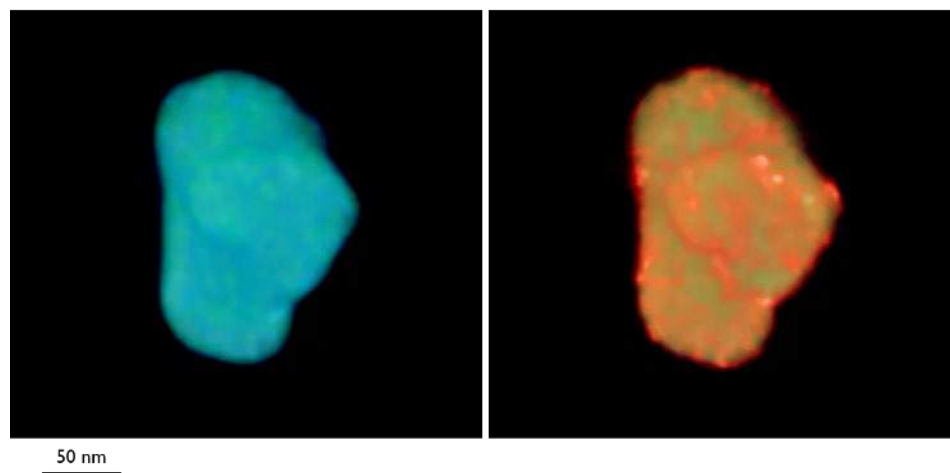


Figure II.4.D.3 STEM-EDS tomographic reconstruction of the primary cathode particles with Gen-2 chemistry. Surface dopant is shown in red, bulk dopant is shown in blue, and Ni is shown in green

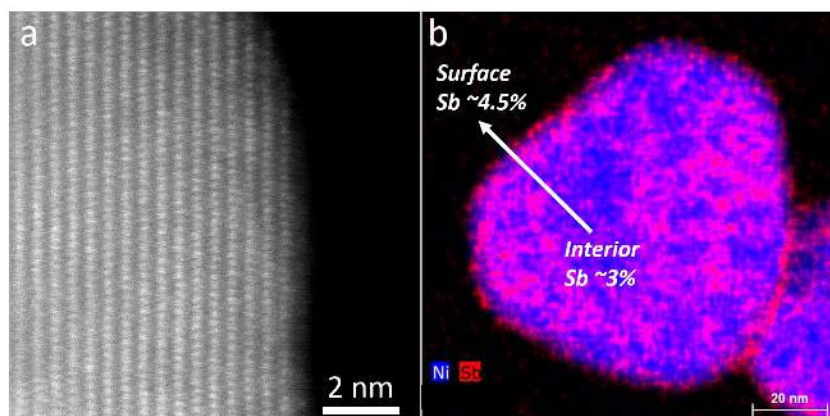


Figure II.4.D.4 (a) Atomic-resolution HAADF-STEM image of pristine VT Gen-3 Sb-doped LNO and (b) Sb distribution in VT Gen-3 Sb-doped LNO

3. *In situ* TEM investigation of degradation mechanism of LNO and TiMg-doped LNO

To understand the structural and chemomechanical degradation of high-nickel-content cathode materials, we choose the classic LNO and VT Gen2 TiMg-doped LNO as model materials and studied their degradation mechanism using in situ TEM technique. In real battery, oxygen loss occurs via interfacial reaction between delithiated lattice and electrolyte, in this study, we intentionally perform in situ heating to accelerate oxygen release and then explore the degradation dynamics and mechanism of the high nickel cathode materials. Before in situ heating, LNO and TiMg-doped LNO particles were second fully charged to 4.4 V and then loaded onto a heating chip with SiN window. Both in situ electron diffraction, atomic-resolution TEM and electron tomography were combined in our study to understand the degradation both at particle scale and atomic scale. Figure II.4.D.5a shows the atomic structure of delithiated LNO with large amount of stacking faults (O1 stackings). Upon heating at 230°C, the regions with stacking faults rapidly transform in to disordered spinel (Figure II.4.D.5b) and then rock-salt structure (Figure II.4.D.5b).

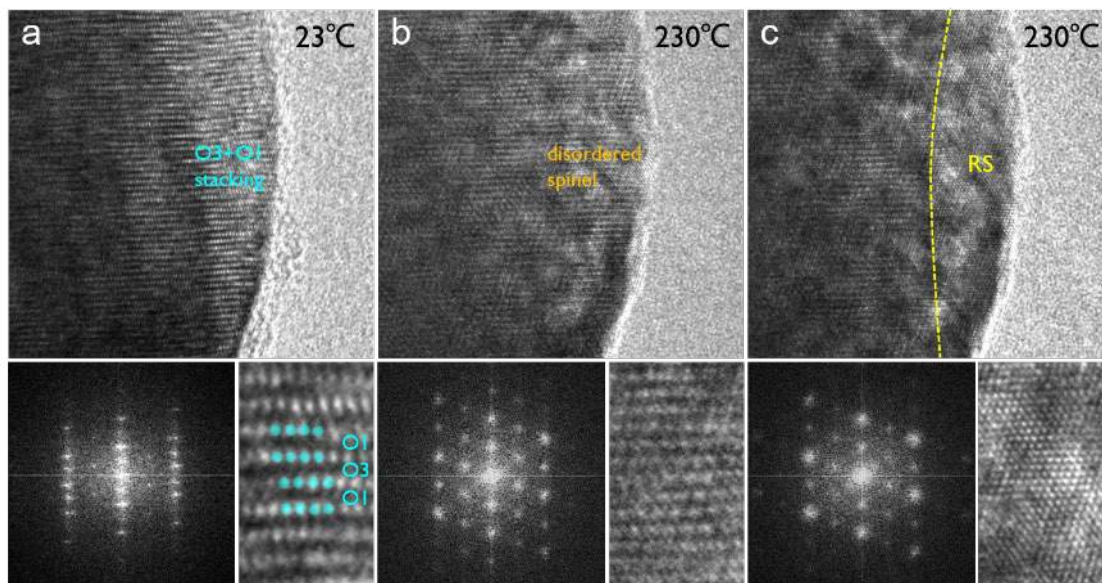


Figure II.4.D.5 In situ probing structural degradation of delithiated LNO during oxygen loss. (a) Atomic-resolution TEM image of delithiated LNO. The insets shows FFT and enlarged image showing local O1-O3-O1 stacking. (b) Layered structure to disordered spinel transformation in delithiated LNO upon heating at 230 °C. (c) Disordered spinel to rock-salt transformation with prolonged heating at 230 °C

Besides structural stability, chemomechanical stability is also important issue to address for high-nickel-content cathode materials. With continuous oxygen loss, we found that cracks will form in LNO and TiMg-doped LNO and finally lead to mechanical breakdown of the cathode materials. Using electron tomography, we deciphered the 3D configuration of these cracks and found that these cracks/pores are parallel to (003) planes of the layered structure (Figure II.4.D.6) which is closely related to oxygen loss and the structural transformation. Figure II.4.D.7a-b shows two correlated HAADF-STEM and bright-field TEM images of an delithiated TiMg-doped LNO particle. After in situ heating at 250 °C for about an hour, large amounts of pores/cracks formed in the particle. Atomic-resolution TEM image (Figure II.4.D.7c) shows alternating rock-salt and pores/ cracks formed, while the bulk regions still remain as disordered spinel. The result indicates that local aggregation of TM atoms and vacancies occurs concomitantly and finally result in simultaneous spinel to rock-salt transformation and crack nucleation.

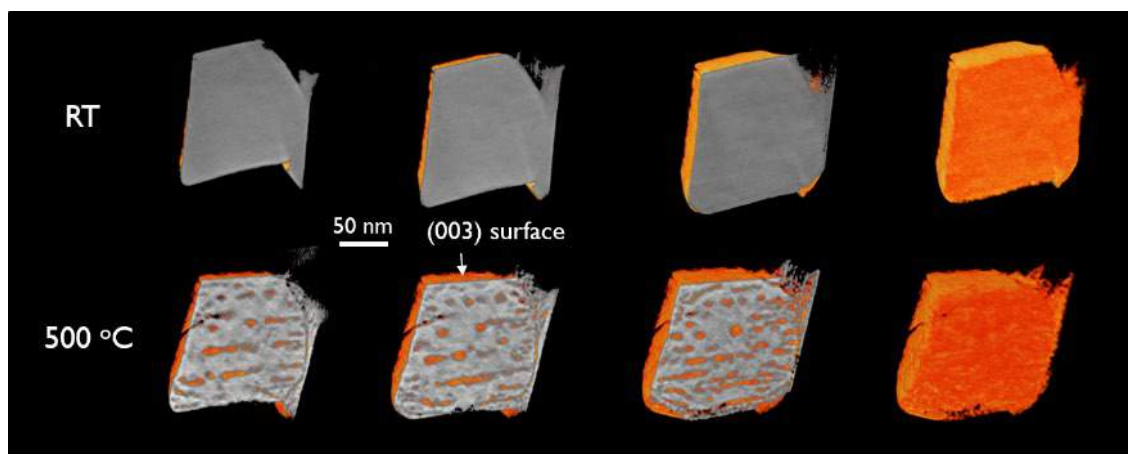


Figure II.4.D.6 (a) 3D electron tomography of a delithiated LNO particle at room temperature. (b) 3D electron tomography of the delithiated LNO with severe oxygen loss after in situ heating at 500 °C. Pores/cracks formed along (003) planes of layered structure as indicated by the arrow

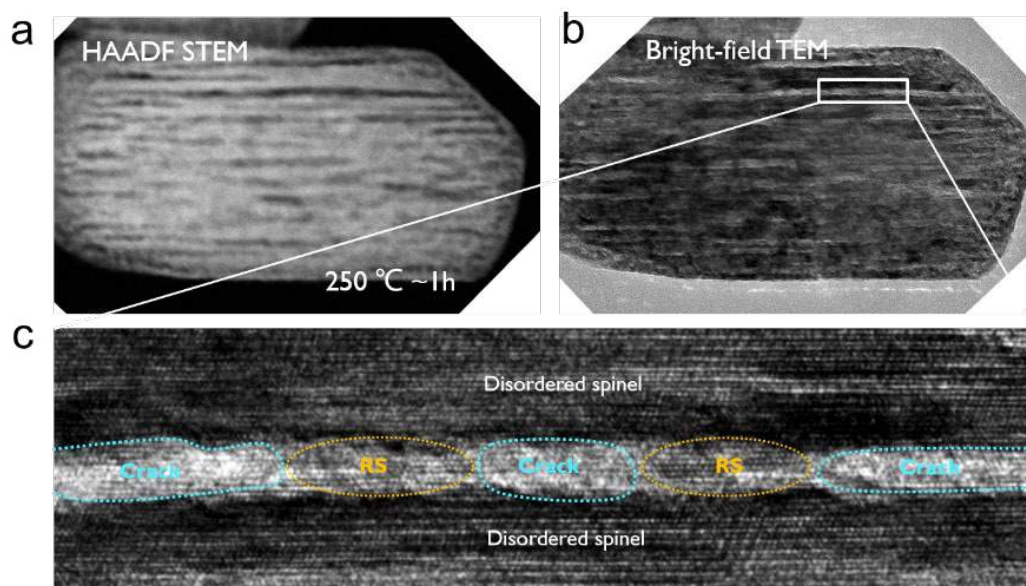


Figure II.4.D.7 (a) HAADF-STEM image and (b) Bright-field image of a delithiated TiMg-doped LNO after in situ heating at 250 for 1 h. (c) Atomic-resolution TEM image of the delithiated TiMg-doped LNO in (b)

4. Evaluation of doping elements for suppress of oxygen loss

Our initial set of doping elements consists of Al, Ti, Ta, Sb, Y, Mg and B. To evaluate each dopant's ability to suppress the surface oxygen loss, we calculated the relative oxygen release energy during delithiation of doped-LiNiO₂ with respect to the pristine phase (Figure II.4.D.8). Figure II.4.D.8b shows a surface model of doped LiNiO₂ with the (104) surface facet. We explored all the symmetrically inequivalent O sites at the surface and calculated the averaged oxygen release energy. It can be seen from Figure II.4.D.8a that the calculated oxygen release energies of Sb-, Ta-, and Ti-doped LiNiO₂ are higher than that of the pristine phase, which implies that Sb, Ta, and Ti can enhance the surface oxygen retention of LiNiO₂ and Sb is predicted to be the most promising dopant. Further insight into the nature of the dopant-oxygen bonding is provided by an electron localization function (ELF) analysis, as shown in Figure II.4.D.8c. The green regions between the Sb and O atoms correspond to shared electrons, which is a signature of covalent bonding. Therefore, a higher degree of electrons sharing between Sb and O leads to a stronger Sb-O bond and better oxygen retention.

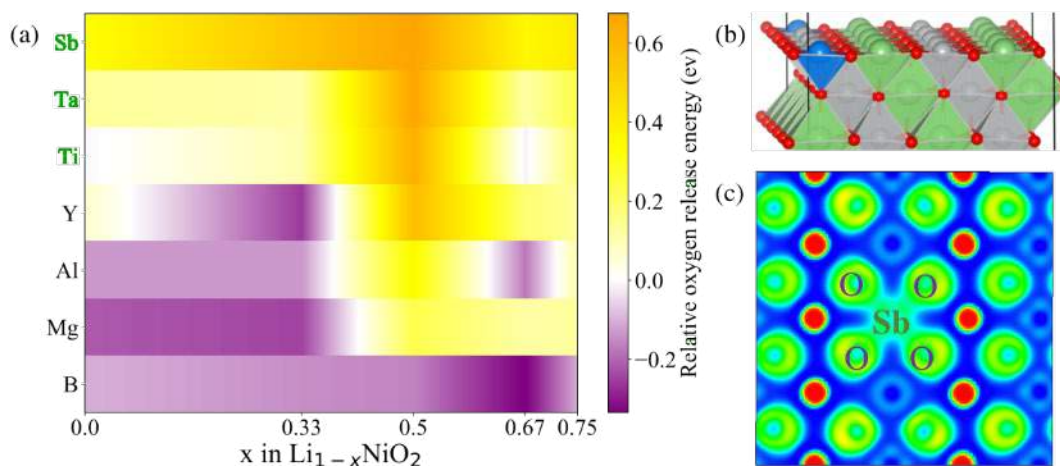


Figure II.4.D.8 (a) The relative surface oxygen release energies of doped LiNiO₂ with respect to the pristine phase. An orange color indicates an improved oxygen retention, while a purple color indicates a reduced oxygen retention as compared to the pristine phase. (b) Schematic illustration of surface doped LiNiO₂ model. Blue: dopant, green: Li, grey: Ni, red: oxygen. (c) 2D electron localization function contour plot for the surface slice of Sb-doped LiNiO₂

5. New LHCEs (AE001-AE005) development for Gr||NMC811 cells to improve cycling stability

To improve the cycle life of baseline commercial NMC811 cathode and Gr anode, five novel LHCEs (noted as AE001-AE005) and the baseline electrolyte (1 M LiPF₆/EC-EMC plus 2% VC) were evaluated in Gr||NMC811 coin cells and the electrochemical performances are shown in Figure II.4.D.9. Compared to the baseline electrolyte, all the LHCEs show similar discharge capacity at the initial cycle, but significantly improved room and high-temperatures cycling stability, charging/discharging rate capabilities up to 3C and low-temperature discharge performance. Among the LHCEs, AE003 enables the best performances: 1) the highest discharge capacity of 194.3 mAh g⁻¹ in the first formation cycle; 2) a reversible capacity of 157.9 mAh g⁻¹ with a capacity retention of 86.0% after 1,000 cycles under 25°C; 3) a reversible capacity of 183.6 mAh g⁻¹ with a capacity retention of 94.9 % after 100 cycles under 60°C; 4) good rate capabilities under fast charging or discharging up to 3C rate; and 5) high discharge capacity at -30°C with a capacity retention of 85.6 % (compared to 25°C). EIS, HRTEM and XPS characterizations of the cycled Gr and NMC811 electrodes after 100 cycles under 60°C demonstrate that the SEI on Gr anode and CEI on NMC811 cathode in LHCEs are much more homogeneous, thinner, robust and conductive, especially in AE003, enabling much better protections on both NMC811 cathode and Gr anode than E-baseline, and significantly improved battery performances even under the high cut-off voltage of 4.4 V.

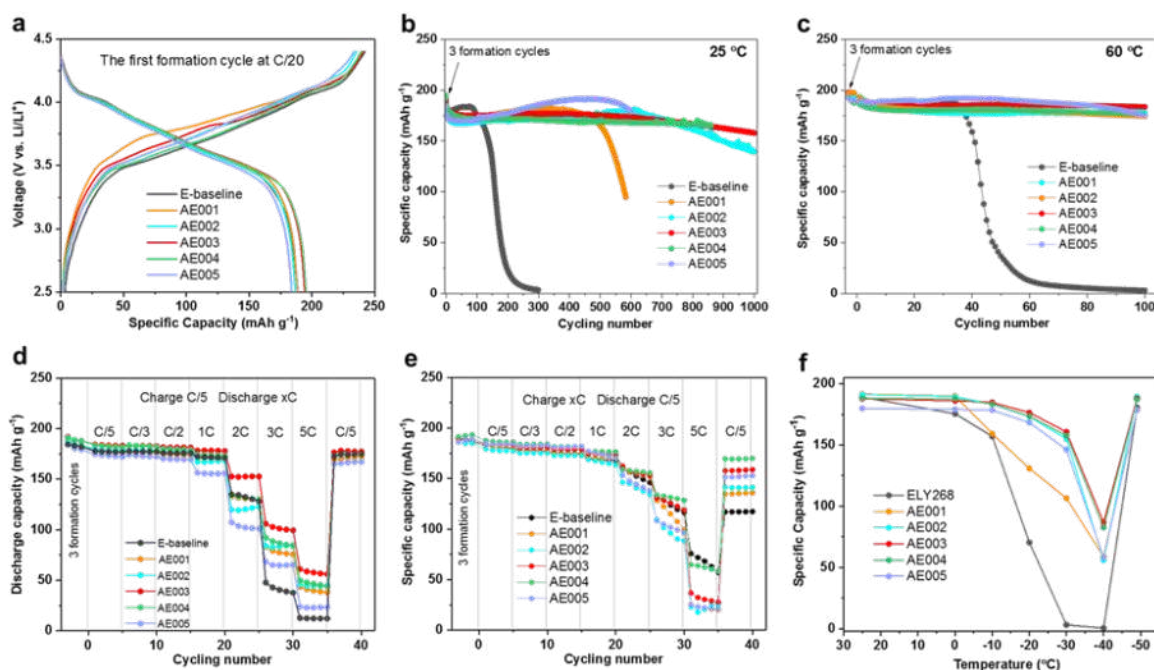


Figure II.4.D.9 Battery performances of Gr||NMC811 coin cells using different electrolytes between 2.5 and 4.4 V. (a) Voltage profiles of the first formation cycle at C/20 and 25 °C. (b-c) Long-term cycling stability at C/3 at (b) 25 °C and (c) 60 °C after three formation cycles at 25 °C. (d,e) Rate capabilities under (d) varying discharge rates (xC) with the same charge rate at C/5 and (e) varying charge rates (xC) with the same discharge rate at C/5. f, Low-temperature discharge performance at C/5 discharge rate, with all charging process at 25 °C while the discharging at 25 °C, 0 °C, -10 °C, -20 °C, -30 °C and -40 °C, and then back to 25 °C. 1C = 2.8 mAh cm⁻²

6. Nonflammable electrolytes for Li-ion batteries enabled by ultraconformal passivation interphases

To improve the safety of the baseline commercial NMC811 cathode and Gr anode at coin cell level, two nonflammable LHCEs and three control electrolytes were investigated systematically. From Figure II.4.D.10, the control electrolyte, highly flammable, gives a capacity retention of 83.0% after 300 cycles. Fast capacity decay takes place in the cell with the control + TEPA electrolyte (flame retarding), with the capacity of 97.9 mAh g^{-1} and capacity retention of 71.6% after 50 cycles. As for the electrolytes of control + TEPA + VC (flame retarding) and 1.2 M LiFSI/TEPA-BTFE, the capacities are stabilized at around 100 mAh g^{-1} that is much lower than that of the control. The best cycling performance is achieved in the cell with 1.2 M LiFSI/TEPA-EC-BTFE electrolyte, 134.8 mAh g^{-1} specific capacity retains after 300 cycles, corresponding to 85.4% capacity retention that is higher than that of the control. This is mainly attributed to the more homogenous, thin and robust SEI film formed on Gr anode in this LHCE.

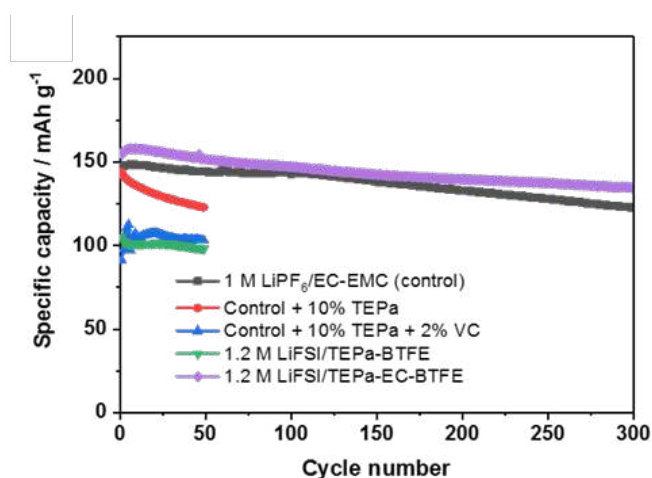


Figure II.4.D.10 Cycling performance of Gr||NMC811 coin cells with five different electrolytes. The Gr||NMC811 cells were subjected to two formation cycles at C/20 and then cycling at C/2 charge and 1C discharge in the cutoff voltage range of 2.8-4.3 V and 1C = 200 mAh g^{-1} or 1.5 mAh cm^{-2} based on the weight of the NMC811 active material.

7. Scale up of the precursors of the 3D targeted doped high-Ni low-Co NMC cathode materials (NMT)

The precursor of the VT-developed new NMT cathode material was synthesized at both small-scale size ($\sim 9 \text{ g}$) and scaled-up size ($\sim 100 \text{ g}$). Then the NMT cathode materials were prepared by calcination of the precursor material and LiOH powder. The NMT from small size precursor synthesis exhibits similar discharge capacities in both Li||NMT and Gr||NMT cells with the baseline electrolyte like the one the VT team obtained. However, the NMT from the scaled-up precursor shows lower reversible capacity than the small scale one, but both present excellent cycling stability using the newly developed AE003. When compared with the commercial NMC811, although the charge/discharge capacities of the new NMT cathode materials are lower, the cycling stability at 4.4 V and 1C rate is still very good.

8. Fabrication of Prismatic cells

Fabrication of the Project Progress Cells (PPC) were completed in this budget period. Prismatic cells with a design capacity of about 2.5 Ah minimum were fabricated in order to benchmark the performance of the baseline NMC811 material. Initial rating on the cells has been performed, and the cells are currently being cycled. Cells will be delivered for testing at the end of November. The discharge voltage profiles of the PPC at various discharge currents and at room temperature are shown in Figure II.4.D.11. The cell's first cycle discharge capacity

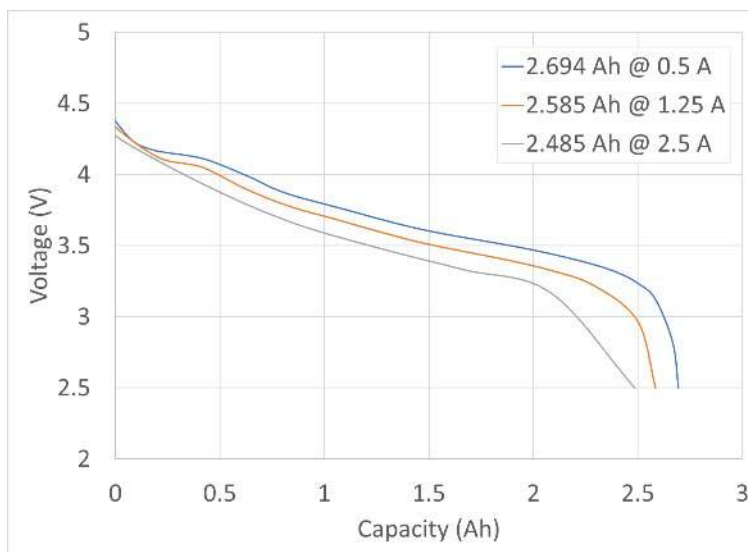


Figure II.4.D.11 Discharge voltage profiles of the Project Progress Cells (PPC) at different currents and at room temperature.

was 2.788 Ah and the first cycle discharge energy was 10.346 Wh. The positive electrode mass was 15.33 g and was 96% active, giving a cathode-level reversible specific capacity and energy of about 218.94 mAh/g, and 812.53 Wh/kg, respectively. The cell's discharge capacity at 0.5 A ($\sim C/5$) was 2.694 Ah, and the cell discharged 92.2% of its nominal ($C/5$) capacity at 2.5 A ($\sim 1C$).

The cycle life of the PPC was evaluated by charging and discharging the cell. The cell was galvanostatically charged to 4.4 V at a current of 0.833 A ($C/3$ for 2.5 Ah) and then potentiostatically charged at 4.4 V for an additional 2 hours. The cell was then galvanostatically discharged at 0.833 A ($C/3$) to 2.5 V. The charge and discharge capacities as well as the coulombic efficiency are shown in Figure II.4.D.12. In the first 10 cycles, the capacity quickly decays, losing nearly 25% of its initial capacity, before stabilizing at about 2 Ah. The degradation appears to have decelerated, and cycling is still being performed to characterize the capacity fade. Based on a linear projection of the last 20 cycles, the capacity after 100 cycles will be about 1.5 Ah, corresponding to a capacity fade of about 40% after 100 cycles.

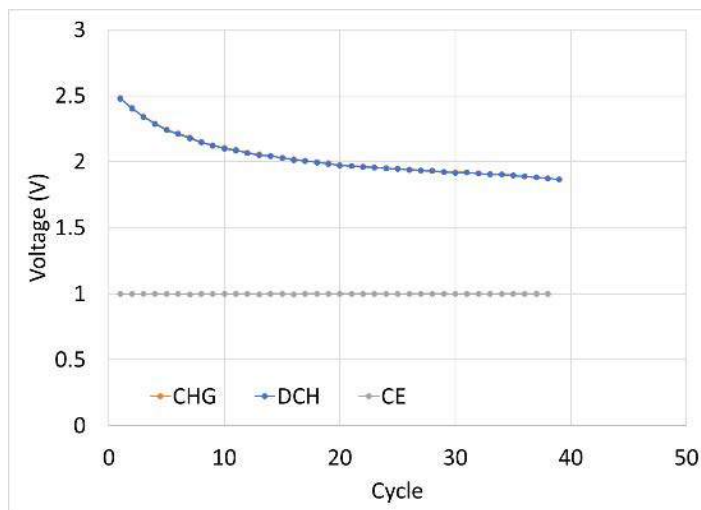


Figure II.4.D.12 Charge and discharge capacity of the Project Progress Cells (PPC) during cycling at room temperature.

Conclusions

- We expanded the conventional doping strategy and proposed the concept of manipulating the dopant distribution in battery particles to simultaneously enhance the surface and bulk stability of Co-free, LiNiO₂-based cathodes. Ti showed a gradient distribution and was enriched at the surface, whereas Mg distributes homogeneously throughout the particles. Both dopants were well accommodated in the Ni sites of the layered structure. The dual dopants in the bulk reduced the Li/vacancy ordering, smoothened voltage profiles, and suppressed irreversible phase transformations. The interfacial stability of the Mg/Ti-LNO material was improved, leading to mitigated Ni dissolution, reduced cell impedance, improved thermal stability, and better self-discharge resistance.
- Identified Sb as the most promising dopant to mitigate surface oxygen loss. In addition, Ti and Ta are also effective dopants.
- Rationalized the effectiveness of Sb, Ti and Ta based on the bond strength between the dopant and oxygen.
- New LHCEs have been developed to improve the battery performances and safety of the baseline commercial NMC811 cathode and Gr anode at coin cell level.
- The optimal LHCE, AE003, significantly enhances the Gr||NMC811 coin cells to achieve an excellent cycling stability under 4.4 V at 25°C (of 86.0% capacity retention over 1, 000 cycles) and 60°C, good rate capabilities under fast charging or discharging up to 3C rate, and high low-temperature discharge performance down to -30°C with a capacity retention of 85.6% at $C/5$ rate.
- The LHCE of 1.2 M LiFSI/TEPa-EC-BTFE is demonstrated to have not only intrinsic non-flammability, but also great battery performance, exhibiting 85.4% capacity retention after 300 cycles.

- The precursors of the 3D targeted doped NMT have been scaled up and the NMT cathode materials were also prepared. The NMT from scaled-up precursor shows slightly lower capacity than the one from the small size synthesized precursor. Need to improve the performance of the precursor scale-up.
- AE003 in Gr||NMT enables superior cycling stability (100% capacity retention after 200 cycles at 1C rate between 2.5 and 4.4 V), compared to Gr||NMT using E-baseline and the commercial Gr||NMC811 with AE003.

Key Publications

1. Mu, L.; Zhang, R.; Kan, W. H.; Zhang, Y.; Li, L.; Kuai, C.; Zydlewski, B.; Rahman, M. M.; Sun, C.; Sainio, S.; Avdeev, M.; Nordlund, D.; Xin, H.L.; Lin, F. (2019) Dopant Distribution in Co-free High Energy Layered Cathode Materials. *Chemistry of Materials*. (Accepted for publication)
2. Steiner, J.; Cheng, H.; Walsh, J.; Zhang, Y.; Zydlewski, B.; Mu, L.; Xu, Z.; Rahman, M. M.; Sun, H.; Michel, F.; Sun, C.; Nordlund, D.; Luo, W.; Zheng, J.; Xin, H.; Lin, F. (2019) Targeted Surface Doping with Reversible Local Environment Improves Oxygen Stability at the Electrochemical Interfaces of Nickel-Rich Cathode Materials. *ACS Applied Materials & Interfaces*. 11, 41, 37885-37891
3. Berkeley Electrochemistry Seminar Series, Berkeley, California (Oct 7, 2019): “Investigate Li Intercalation Stability of Ni-Rich Cathodes from First-Principles”; J. Cheng
4. Xia Cao, Yaobin Xu, Linchao Zhang, Mark H Engelhard, Lirong Zhong, Xiaodi Ren, Haiping Jia, Bin Liu, Chaojiang Niu, Bethany E Matthews, Haiping Wu, Bruce W Arey, Chongmin Wang, Ji-Guang Zhang*, and Wu Xu*, Nonflammable Electrolytes for Lithium Ion Batteries Enabled by Ultraconformal Passivation Interphases, *ACS Energy Letters*, 2019, **4**, 2529-2534. DOI:10.1021/acsenenergylett.9b01926.

Acknowledgements

This material is based upon work supported by the U.S. Department of Energy’s Office of Energy Efficiency and Renewable Energy (EERE) under the Award Number: DE-EE0008444.

II.4.E High-Nickel Cathode Materials for High-Energy, Long-Life, Low-Cost Lithium-Ion Batteries (UTA)

Arumugam Manthiram, Principal Investigator

University of Texas at Austin
Texas Materials Institute, University of Texas at Austin
Austin, TX 78712
E-mail: manth@austin.utexas.edu

Shriram Santhanagopalan, Principal Investigator

National Renewable Energy Laboratory
Golden, CO 80401
E-mail: shriram.santhanagopalan@nrel.gov

Peter Faguy, DOE Technology Development Manager

U.S. Department of Energy
E-mail: Peter.Faguy@EE.Doe.Gov

Start Date: October 1, 2018	End Date: March 31, 2022	
Project Funding (FY19): \$3,000,000	DOE share: \$2,400,00	Non-DOE share: \$600,000

Project Introduction

By virtue of high energy content, lithium-ion batteries occupy a privileged position in the energy storage landscape, from portable electronics to electric vehicles (EV). In spite of this success, energy and cost requirements of lithium-ion batteries are extremely stringent, especially for transportation applications. To this end, there is a need to further enhance the energy content of state-of-the-art nickel-based layered oxides ($\text{Li}[\text{Ni}_a\text{Co}_b\text{Mn}_c]\text{O}_2$ with $a + b + c = 1$, denoted as NCM-*abc* and $\text{Li}[\text{Ni}_{1-x-y}\text{Co}_x\text{Al}_y]\text{O}_2$, denoted as NCA) deployed in passenger electric vehicles, which will be the cathode material of choice for passenger electric vehicles at least through the next decade. In addition, the substantial dependence on cobalt in these cathodes (*e.g.*, 12 wt.% Co in NCM-622), a scarce and costly metal primarily mined from Central Africa with geopolitical concerns, must be lowered for sustained mass market penetration of electric vehicles. If nothing changes in the current cathode formulations, demand for Co could outstrip supply by 2030 with surging global EV production, setting the stage for far higher prices. Though Co-free commercial cathodes exist, *i.e.*, lithium iron phosphate (LiFePO_4) and lithium manganese oxide (LiMn_2O_4), they offer much lower energy contents and cannot meet the requirements of next-generation automotive batteries for passenger electric vehicles.

This project aims to address these challenges and develop low-cobalt and cobalt-free, high-nickel $\text{LiNi}_{1-x}\text{M}_x\text{O}_2$ ($\text{M} = \text{Mn, Al, Mg, Zr, Ta, etc.}$ and $x \leq 0.15$) layered oxides as cathode materials for lithium-based automotive batteries. Through compositional tuning, high energy, high power, long lifetime over a wide temperature range, as well as excellent safety under abuse can be prioritized for varying market needs. In addition, these efforts will reduce or even eliminate the dependence on cobalt of commercial layered oxide cathodes, thus leading to more secure supply chains, lower cost, and less adverse impacts on the environment. The cathode materials developed in this project will contribute to future designs of low-cobalt or cobalt-free, high-energy rechargeable lithium-based batteries, including both lithium-ion and lithium-metal chemistries.

Objectives

The objective of this project is to produce Li-ion cells capable of the following performance (see Table II.4.E.1):

Table II.4.E.1 Performance Targets

Beginning of Life Characteristics at 30 °C	Cell Level	Cathode Level
Useable Specific Energy @ C/3		≥ 600 Wh/kg
Calendar Life (<. energy fade)	15 Years	
Cycle Life (C/3 deep discharge with < 20% energy fade)	1,000	
Cobalt Loading		≤ 50mg/Whr
Cost	≤ \$100/kWh	

Approach

Low-cobalt and cobalt-free high-nickel $\text{LiNi}_{1-x}\text{M}_x\text{O}_2$ ($\text{M} = \text{Mn, Al, Mg, Zr, Ta, etc.}$ and $x \leq 0.15$) layered oxides are assessed as cathodes for lithium-ion batteries. A model cathode $\text{LiNi}_{0.94}\text{Co}_{0.06}\text{O}_2$ is first investigated with atomic layer deposition (ALD) coatings and compatible ethylene carbonate (EC)-free electrolyte systems (*e.g.*, replaced with 3 % vinylene carbonate (VC)). Subsequently, low-cobalt, high-nickel $\text{LiNi}_{1-x-y}\text{Co}_y\text{M}_x\text{O}_2$ ($y < 0.06$ and $x \leq 0.15$) compositions are surveyed. The total content of Mn and other dopants (*e.g.*, Al, Mg, Zr, Ta, *etc.*) can reach up to 15 % through either hydroxide co-precipitation or lithiation annealing to maintain good thermal and cycling stability while achieving the 600 Wh kg^{-1} energy goal. Based on the results, an optimal cathode material is selected to produce twenty-one 2 Ah pouch cells for Go/No-Go decisions and to deliver to DOE for independent evaluation/validation. Detailed experimental approaches are below:

1. Dopant Survey: A survey of different dopants and electrode formulations of $\text{LiNi}_{0.94}\text{Co}_{0.06}\text{O}_2$
2. Conducting Salt Survey: A survey of various conducting salts for EC-free electrolyte systems, with a selection of top systems for scale-up and further component optimization
3. ALD Coating Survey: ALD coatings on top-performing $\text{LiNi}_{0.94}\text{Co}_{0.06}\text{O}_2$ formulations with baseline and EC-free electrolyte systems
4. Cell Results (Go/ No Go). ≥ 2 Ah pouch cells, capable of 600 W h kg^{-1} (cathode level) and ≥ 80 % energy retention after 1,000 cycles with cobalt content below 50 mg Co/Wh

Results

A series of metal ions, including nickel, cobalt, manganese, aluminum, and magnesium, have been co-precipitated together at UT Austin, and the obtained hydroxide precursors show consistent particle morphology and size distribution (Figure II.4.E.1). We used a similar co-precipitation routine for all the compositions for a consistent comparison of electrochemical performance. The samples were then dried overnight, and TGA was applied to determine the proper lithium vs. metal ratios for these various compositions. After a careful calcination optimization (data not shown here), we assembled pouch cells and Figure II.4.E.2 shows pouch-cell cycling performance for three compositions (NCA-900505, NMA-900505, and NCMAM-9004040101). The NCMAM-9004040101 pouch cells have already been cycled for > 700 times and seen a 10.8% fade in specific energy. Assuming the energy fade remains linear as cycling proceeds, these cells will reach 80% of their original specific energy after ~ 1390 charge-discharge cycles. For the NCA-900505 and NMA-900505 pouch cells, cycling performance is somewhat worse, estimated to be ~ 610 and 710 cycles, respectively.

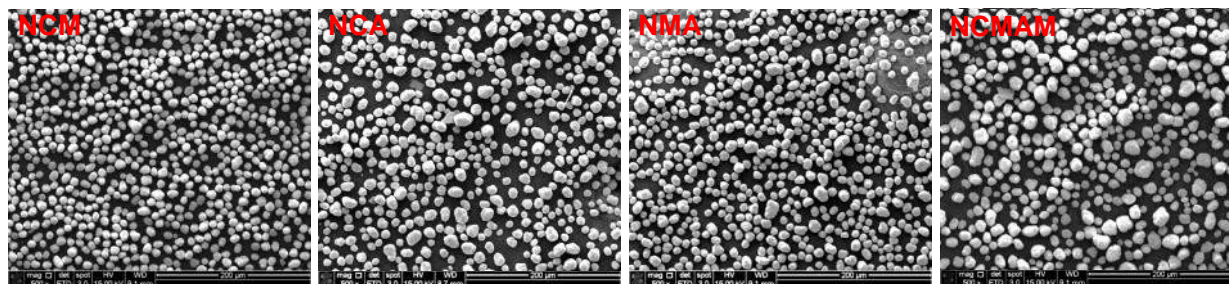


Figure II.4.E.1 SEM images of various low-cobalt or cobalt-free, high-nickel compositions prepared through metal hydroxide co-precipitation, *i.e.*, NCM-900505 ($\text{LiNi}_{0.9}\text{Co}_{0.05}\text{Mn}_{0.05}\text{O}_2$), NCA-900505 ($\text{LiNi}_{0.9}\text{Co}_{0.05}\text{Al}_{0.05}\text{O}_2$), NMA-900505 ($\text{LiNi}_{0.9}\text{Mn}_{0.05}\text{Al}_{0.05}\text{O}_2$), and NCMAM-9004040101 ($\text{LiNi}_{0.9}\text{Co}_{0.04}\text{Mn}_{0.04}\text{Al}_{0.01}\text{Mg}_{0.01}\text{O}_2$)

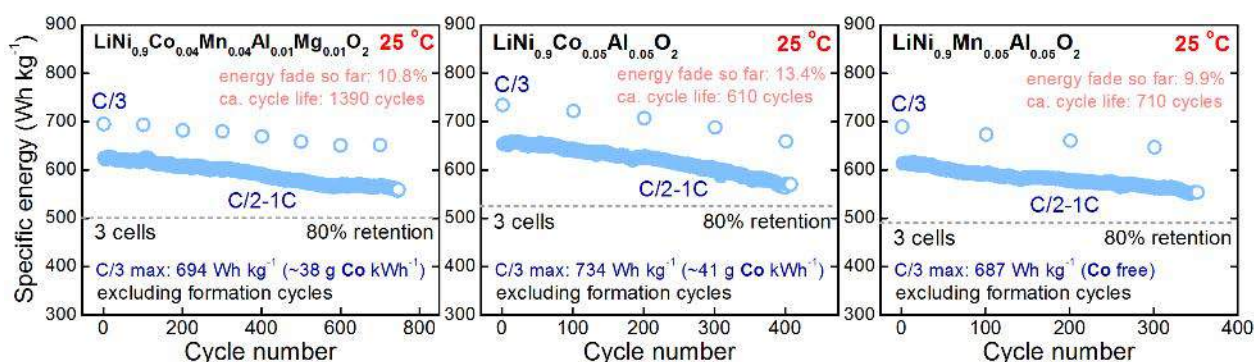


Figure II.4.E.2 Pouch cell cycling performances of NCMAM-9004040101, NCA-900505, and NMA-900505 (voltage window 2.5 – 4.2 V; active material loading: 2.0 mAh cm⁻²; single stack)

Based on the pouch cell performance in Figure II.4.E.2, we have synthesized a low-cobalt cathode with the composition $\text{LiNi}_{0.85}\text{Co}_{0.05}\text{Mn}_{0.075}\text{Al}_{0.02}\text{Mg}_{0.005}\text{O}_2$ (Ni-85) through hydroxide co-precipitation and calcination (~1.8 kg). As shown in Figure II.4.E.3, the cathode consists of spherical particles of substantially uniform size distribution (~11 μm). With a laboratory-scale tube furnace, we can only calcine ~200 g of Ni-85 per batch. Several iterations of calcination were, therefore, used to collect ~1.8 kg. UT Austin has carefully evaluated the properties of $\text{LiNi}_{0.85}\text{Co}_{0.05}\text{Mn}_{0.075}\text{Al}_{0.02}\text{Mg}_{0.005}\text{O}_2$ of each calcination batch. Figure II.4.E.4 (left) shows their coin cell performance from Batches 3 – 9. Pouch cells with representative batches (4 & 5) were also assembled, and preliminary cycling results are shown in Figure II.4.E.4 (right). Through this process, we made sure to only send samples with good and consistent electrochemical performance to Tesla, Inc. for making thirty 2 Ah pouch cells.

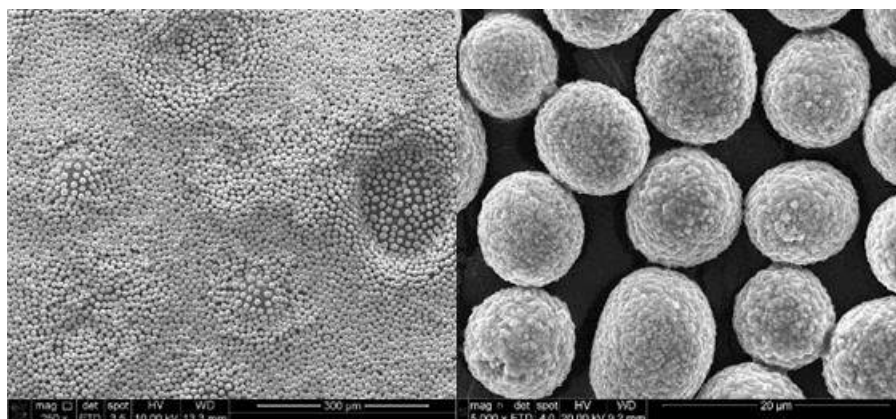


Figure II.4.E.3 SEM images of $\text{LiNi}_{0.85}\text{Co}_{0.05}\text{Mn}_{0.075}\text{Al}_{0.02}\text{Mg}_{0.005}\text{O}_2$ prepared through metal co-precipitation, which has been delivered to Tesla, Inc. for making thirty 2 Ah pouch cells for performance evaluation by DOE

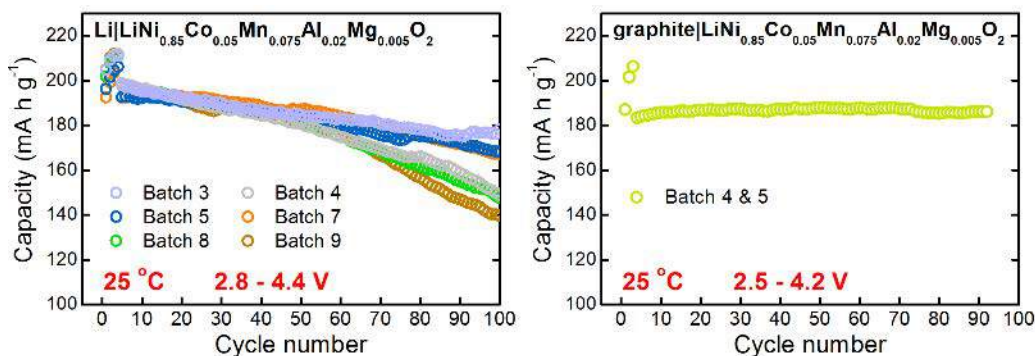


Figure II.4.E.4 Coin cell performances of LiNi_{0.85}Co_{0.05}Mn_{0.075}Al_{0.02}Mg_{0.005}O₂ (Ni-85): (left) coin-cell performance evaluation of samples from varying 200 g batches; (right) pouch-cell performance evaluation of samples from batches 4 & 5

We have also explored doping of metal cations in low-cobalt, high-nickel layered oxides through calcination. This enables us to choose more diverse dopants, since it is generally challenging for metal cations to be uniformly co-precipitated along with nickel without seriously disrupting particle size and morphology. Dopants investigated in Year 1 include Ta⁵⁺, Zr⁴⁺, and Sn⁴⁺ on a baseline material, lithium nickel oxide (LiNiO₂). The top-performing preliminary results from doping of Ta⁵⁺ are depicted in Figure II.4.E.5. Ta⁵⁺ was doped at 0.5, 1.0, and 2.0 at.%, forming LiNi_{0.995}Ta_{0.005}O₂, LiNi_{0.99}Ta_{0.01}O₂, and LiNi_{0.98}Ta_{0.02}O₂. The precursors were calcined at different temperatures and tested in half cells to find the optimal calcination temperatures. Then, pouch full cells were fabricated from the optimized calcination temperatures.

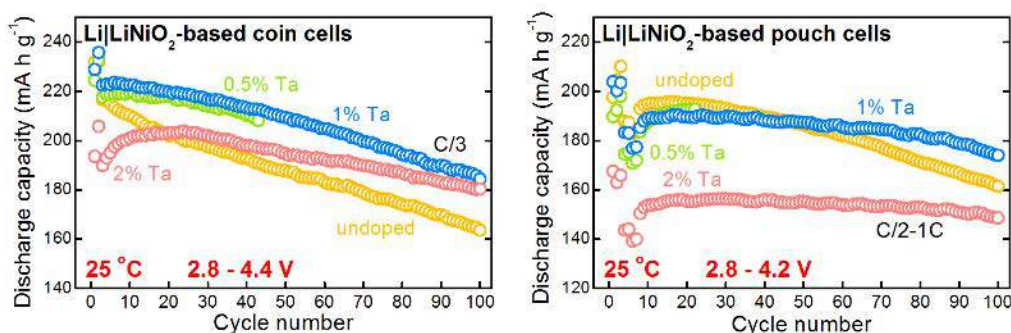


Figure II.4.E.5 Preliminary cycling performances of Ta⁵⁺-doped LiNiO₂ in both coin and pouch cells

In Year 1, we have explored a variety of EC-free nonaqueous electrolytes adopting various lithium conducting salts for low-cobalt high-nickel, layered oxide cathode materials for enhanced lifetime performance. In our previous research published in *Advanced Energy Materials* (2019, 9, 1901152), we explored two electrolyte systems with LiPF₆ and lithium bis(fluorosulfonyl)imide (LiFSI) as the Li conducting salts and ethyl methyl carbonate (EMC) as the solvent. Vinylene carbonate (VC) was employed in the EC-free electrolytes as SEI-forming additive. Assembled graphite|LiNi_{0.94}Co_{0.06}O₂ pouch full cells in EC-free electrolytes showed high initial discharge capacities of ~ 220 mA h g⁻¹ and enhanced cyclability over long-term cycling. Based on these results, we have now further explored the use of lithium difluoro(oxalato)borate (LiDFOB) as an electrolyte additive instead of VC. In the LiFSI/EMC-based solution with VC, a necessary amount of LiPF₆ (0.5 M) is needed for corrosion inhibition of the Al cathode current collector during battery cycling. LiDFOB is known to effectively passivate the Al current collector even in trace amounts. Here, we designed a series of electrolyte compositions using LiFSI as the conducting salt and EMC as the solvent, containing different amounts of LiDFOB from 1 to 10% by weight (Figure II.4.E.6). A control electrolyte with pure LiDFOB as the conducting salt was also tested. It appears that 3 wt.% LiDFOB in the LiFSI/EMC solution is sufficient to passivate fully the Al cathode current collector during full-cell operation, as evidenced by stable cycling performance over 300 cycles.

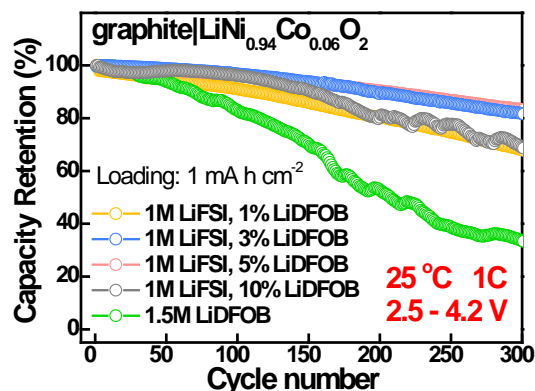


Figure II.4.E.6 Cyclability of graphite|LiNi_{0.94}Co_{0.06}O₂ pouch cells in LiFSI/EMC-based electrolyte with lithium difluoro(oxalato)borate (LiDFOB) as the SEI-forming additive

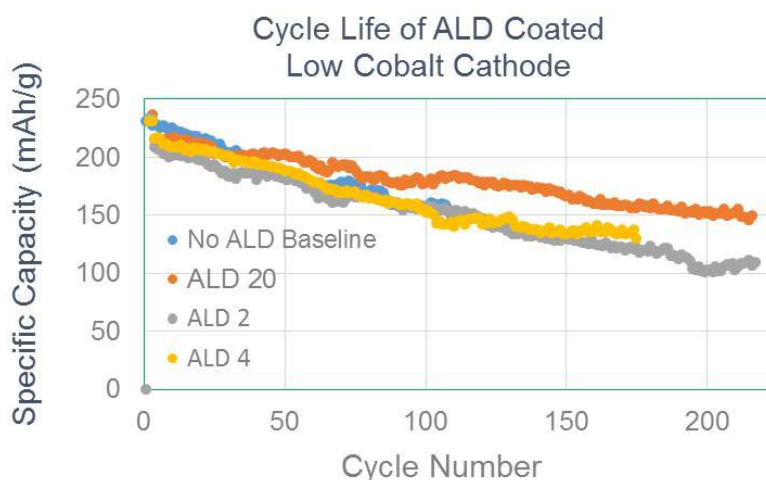


Figure II.4.E.7 Cycling performances in coin cells of LiNi_{0.94}Co_{0.06}O₂ treated with various ALD coating cycles

For the proposed ALD coating study, UT Austin supplied NREL with ~ 500 g of a baseline low-cobalt, high-nickel cathode material, LiNi_{0.94}Co_{0.06}O₂ (NC-9406). ALD coatings were performed in a BENEQ fluidized bed ALD chamber attached to a glovebox. NC-9406 was coated with trimethylaluminium (TMA) as a precursor and with 2, 4 and 20 ALD layers at 200 °C. The coated cathode powders were then mixed into a standard electrode slurry and made into half coin cells, results below (Figure II.4.E.7). 20 iterations of the coating process correspond to an approximately 2 nm thick ALD coating of Al₂O₃. The specific discharge capacity retained after 200 cycles increased by nearly 25% with 20 layers of ALD while 2 and 4 layers of ALD coating showed no statistically significant improvement over the baseline.

In the third and fourth quarters, NREL performed process development of roll-to-roll coating NC-9406 material onto an 8-inch-wide Al foil. The total solid content in the slurry was varied between 30 and 40% across these different runs. The different conditions chosen reflect tradeoffs between conductivity of the dry slurry (based on the carbon to cathode active material ratio) and the viscosity of the slurry (PVdF to

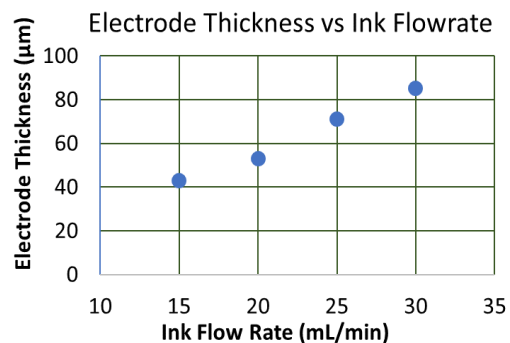


Figure II.4.E.8 Electrode thickness as a function of Ink flow rate. Web rate was held at 0.7 m/min.

NMP ratio). Ink recipes were stirred with various methods to avoid congealing of the ink and bubble formation during roll-to-roll coating. The congealing of the cathode slurry was traced to the excess lithium content in the respective batch of materials. Coating thickness was also characterized as a function of ink flow rate (Figure II.4.E.8) and had a relatively uniform thickness across the width of the web ($\pm 3 \mu\text{m}$ before calendaring). The web rate was held fixed at 0.7 m/min. The thickness of the electrode coating shows a linear increase with the flow rate of the ink, for this range. Final electrode coatings showed few defects (Figure II.4.E.9). Thickness uniformity across the web was $\pm 5 \mu\text{m}$. Cell level performance will be reported in subsequent reports.



Figure II.4.E.9 Roll of NC-9604 on an 8-inch-wide Al foil. 10 x 10 cm wide defect free electrodes were punched out of the roll

Conclusions

In Year 1, UT Austin has explored various low-cobalt or cobalt-free, high-nickel compositions prepared through co-precipitation of metal hydroxides. Based on these results, we have synthesized a low-cobalt, high-nickel layered oxide cathode material through upscaling of lithiation calcination, which has been delivered to Tesla, Inc. for making twenty one 2 Ah pouch cells. Fifteen of these pouch cells will be delivered to DOE for performance evaluation. In addition, UT Austin has explored the electrochemical performance of a model cathode ($\text{LiNi}_{0.94}\text{Co}_{0.06}\text{O}_2$, NC-9406) in ethylene carbonate (EC)-free nonaqueous electrolytes adopting various lithium conducting salts. With NC-9406 supplied by UT Austin, NREL has investigated the effect of ALD coating on the electrochemical performance, including impedance and cycling stability. In addition, NREL has established roll-to-roll coating of NC-9406 for fabricating large-format pouch cells. These results laid solid foundation for our continuing efforts in the development of low-cobalt or cobalt-free, high-nickel layered oxide cathodes for automotive batteries throughout this project.

Key Publications

Reports:

1. DOE EE8445 Quarterly Report-01-19 (January 30, 2019)
2. DOE EE8445 Quarterly Report-04-19 (April 16, 2019)
3. DOE EE8445 Quarterly Report-07-19 (July 23, 2019)
4. DOE EE8445 Quarterly Report-10-19 (October 28, 2019).

Publications:

1. W. Li, E. M. Erickson, and A. Manthiram, "High-nickel Layered Oxide Cathodes for Lithium-based Automotive Batteries," *Nature Energy* (accepted).

Presentations:

1. A. Manthiram, “Advanced Materials for Next-generation Batteries,” 2019 *Nankai-Cambridge International Symposium on Advanced Materials*, Nankai University, Tianjin, China, May 19 – 21, 2019 (invited).
2. A. Manthiram, “High-nickel Layered Oxide Cathodes for Lithium-ion Batteries,” 22nd *International Conference on Solid State Ionics (SSI-22)*, PyeonChang, South Korea, June 16 – 21, 2019 (invited keynote talk).
3. A. Manthiram, “High-nickel, Low-cobalt Cathodes for Lithium-ion Batteries,” 19th *Advanced Automotive Battery Conference*, San Diego, CA, June 24 – 27, 2019 (invited)
4. A. Manthiram, “High-nickel Layered Oxide Cathodes for Lithium-ion Batteries,” *Tesla*, Menlo Park, CA, July 25, 2019 (invited).
5. A. Manthiram, “Low-cobalt Cathodes for Lithium-ion Batteries,” *Fall 2019 American Chemical Society Meeting*, San Diego, CA, August 25 – 29, 2019 (invited).
6. A. Manthiram, “High-Nickel Layered Oxide Cathodes for Lithium-ion Batteries: Complexities and Prospects,” 2019 *Lithium Battery Discussion Meeting*, Arcachon, France, September 15 – 20, 2019 (invited plenary talk).

II.4.F Cobalt-Free Cathodes for Next Generation Li-Ion Batteries (Nexceris)

Neil Kidner, Principal Investigator

Nexceris LLC
404 Enterprise Drive
Lewis Center, OH 43035
E-mail: n.kidner@nexceris.com

Peter Faguy, DOE Technology Development Manager

U.S. Department of Energy
E-mail: Peter.Faguy@ee.doe.gov

Start Date: October 1, 2018
Project Funding: \$3,083,213

End Date: December 31, 2019
DOE share: \$2,466,547

Non-DOE share: \$616,666

Project Introduction

As the largest distributed source of CO₂ emissions, the transportation sector is currently experiencing a rapid transition to electric mobility and the adoption of electric (EV) vehicles, with 100-million EVs targeted by 2020. The increased demand for EVs will drive demand for battery materials. Current state-of-the-art lithium-ion batteries (LiBs) are based on cobalt-containing cathode chemistries. Speculation over a future global shortage of cobalt has led to a rapid increase in cobalt prices and renewed interest in increasing battery performance with reduced or cobalt-free cathode formulations. This provides an opportunity to reestablish U.S. dominance in batteries and prevent us from going from one dependency on oil to another in cobalt.

One of the most attractive approaches to improve battery energy density is to increase the battery voltage. There is, therefore, a need for next-generation, high-potential and high-capacity cathode materials. The spinel formulation LiNi_{0.5}Mn_{1.5}O₄ (LNMO) is a very promising candidate based on its high specific energy (650 Wh/kg-cathode level) and cobalt-free formulation. Unfortunately, the adoption of this material has been limited by its poor cycle life, caused by oxidative decomposition of the electrolyte and a series of parasitic reactions occurring at the electrode-electrolyte interface, which prevents its commercial adoption.

Objectives

The project goal is to develop a next-generation LiB based on a cathode material that can meet the following specifications: Useable specific energy (cathode level) of at least 600 Wh/kg @ C/3

- 15 years of calendar life
- 1000 cycles (C/3 deep-discharge rate) with less than 20 percent energy fade
- Compatibility with cell cost of less than \$100/kWh

LNMO is an attractive candidate cathode material, which already satisfies two of the specifications. The goal of this project is to develop and validate a stabilized Ti-substituted lithium manganese nickel-oxide, LiNi_{0.5}Mn_{1.2}TiO_{0.3}O₄ (LNMTO) with improved cycle and calendar life. The cell chemistry, including electrode and electrolyte formulations, will be optimized for stable performance under aggressive high-voltage operating conditions. Technical feasibility will be demonstrated through the fabrication and testing of 2 Ah-cells. In 2019 the project focus is on establishing a performance baseline for the LNMTO cathode derived from solid-state processing that will serve as a starting point for the LNMTO core/shell work. To support this development a parallel co-precipitation synthesis approach will be developed to manufacture LNMO and LNMTO spinel powders. The manufacturing approaches chosen will be readily scalable and demonstrate a roadmap to high volume production and achieving the target cell cost of < \$100 /kWh.

Approach

The proposed project approach is shown schematically in Figure II.4.F.1. The cycle and calendar life of high-voltage will be improved by developing a novel core-shell microstructure that enables the formation of a solid-electrolyte interface that effectively passivates the cathode surface. The microstructural enhancements of the cathode material focus on preferentially enriching the surface with titanium. In parallel, new, optimized electrode binder and electrolyte chemistries will be incorporated to address degradation mechanisms associated with high-voltage systems.

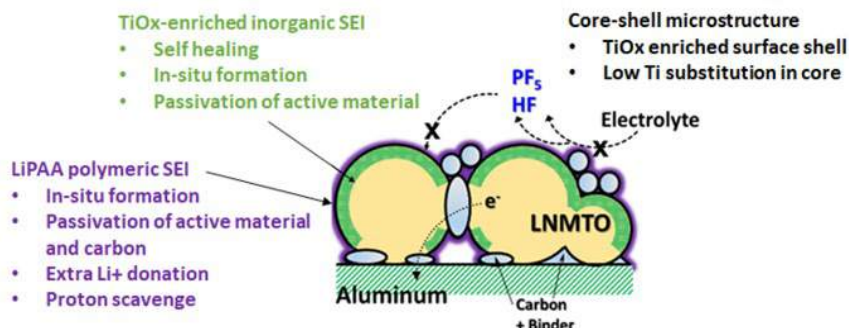


Figure II.4.F.1 Schematic of the technical approach for creating high-performance LNMTMO Li-ion cathodes

Commercially-practiced solid-state and chemical co-precipitation methods will be used to scale-up production of the LNMTMO powder and demonstrate its performance in large-format 2-Ahr cells. In parallel, microstructural enhancement of the LNMTMO powder will be completed to create novel core-shell structures where Ti is preferentially located at the surface to provide additional passivation and minimize capacity loss from Ti substitution in the bulk.

Finally, to address additional degradation mechanisms associated with the operation of carbon conducting powders at high-voltages, advanced cell chemistries, including binder and electrolyte additives will be developed and optimized for the LNMTMO cathode material.

Results

Nexceris has successfully identified and scale-up a solid-state process for manufacturing high-voltage cathode spinels, including LNMTMO and LNMO. The primary unit operations and key process variables that have been optimized are shown in Figure II.4.F.2. Solid-state process development has focused on achieving a homogeneous cathode powder with minimal impurity phases through the identification of an appropriate mixing and calcination and particle size reduction strategies

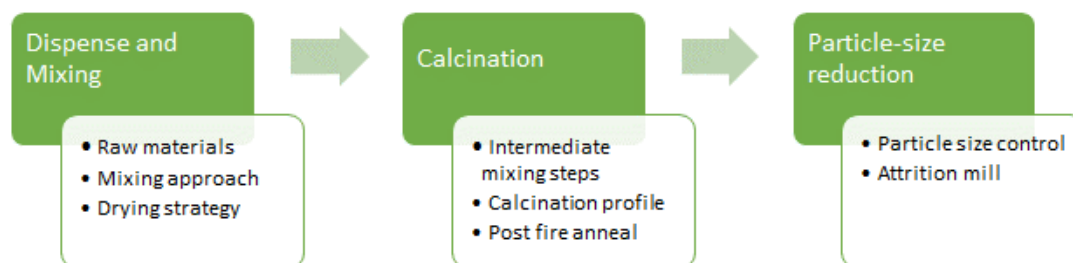


Figure II.4.F.2 Key unit operations and process variables for the solid-state synthesis of high voltage spinel cathode powders

XRD Rietveld analysis was used to quantify the homogeneity of the LNMTMO (and LNMO) powders. Table II.4.F.1 shows a steady improvement in LNMTMO homogeneity achieved during solid-state synthesis process development. The reduction in the second spinel and rock-salt impurity phases indicate the successful implementation of process modifications to achieve a more uniform composition.

Table II.4.F.1 Rietveld Analysis of LNMTO Cathode Powders

	April	Early May	Late May	June
Main Spinel (wt. %)	87.5.0	87.0	90.0	94.2
2 nd spinel (wt. %)	9.9	9.7	6.6	4.6
Rock salt Impurity (wt. %)	2.6	3.2	3.4	1.2

The baseline solid-state LNMTO process is a cost-effective process that uses commercially-practiced processes and is readily scalable to larger batch sizes. To support the manufacture of the Project Progress Cells (PPCs) the process has been successfully scaled to kilogram scale batch sizes. Figure II.4.F.3 shows half-cell charge/discharge curves and discharge capacity versus cycle number for half-cells made with LNMTO cathode powder manufactured from different batch sizes from 20 g to 2 kg.

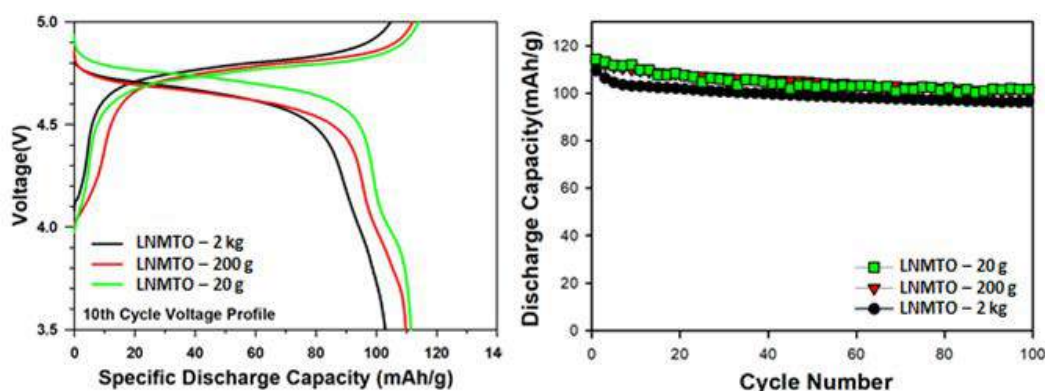


Figure II.4.F.3 Charge/Discharge-voltage profiles and cycle performance for coin-type half-cells at 25°C made with LNMTO cathodes from different production size batches, 20 g, 200 g, and 2 kg. Electrolyte 1 M LiPF₆ in 1:1 wt. EC/EMC (no additive). Cycling conditions: Cycle 1: C/10 then C/5 (Ch) and C/2 (dis)

In addition to the baseline solid-state process, Nexceris has developed a modified two-step solid-state process that further improves LNMTO powder homogeneity and as shown in Figure II.4.F.4 results in enhanced initial discharge capacity. Unfortunately, the modified solid-state approach was difficult to scale and the performance improvement was unable to be replicated with larger batch sizes.

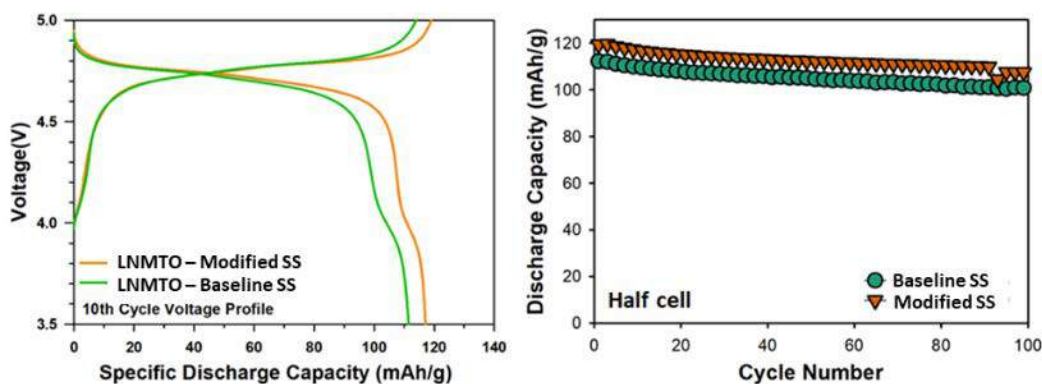


Figure II.4.F.4 Charge/Discharge-voltage profiles and cycle performance for coin-type half-cells at 25°C with LNMTO cathodes made with baseline and modified solid-state processes. Electrolyte 1 M LiPF₆ in 1:1 wt. EC/EMC (no additive). Cycling conditions: Cycle 1: C/10 then C/5 (Ch) and C/2 (dis)

In parallel to scaling the solid-state process, an alternative co-precipitation approach has been developed. Leveraging existing co-precipitation techniques from the literature [1],[2],[3],[4],[5], LNMO powders have been successfully synthesized. In addition, a novel co-precipitation approach has been developed to synthesize LNMTO powder. Figure II.4.F.5 compares the charge/discharge and cycling behavior of LNMO and LNMTO powders made from solid-state and co-precipitation routes. The co-precipitation process produces a compositionally more uniform powder which results in improved performance.

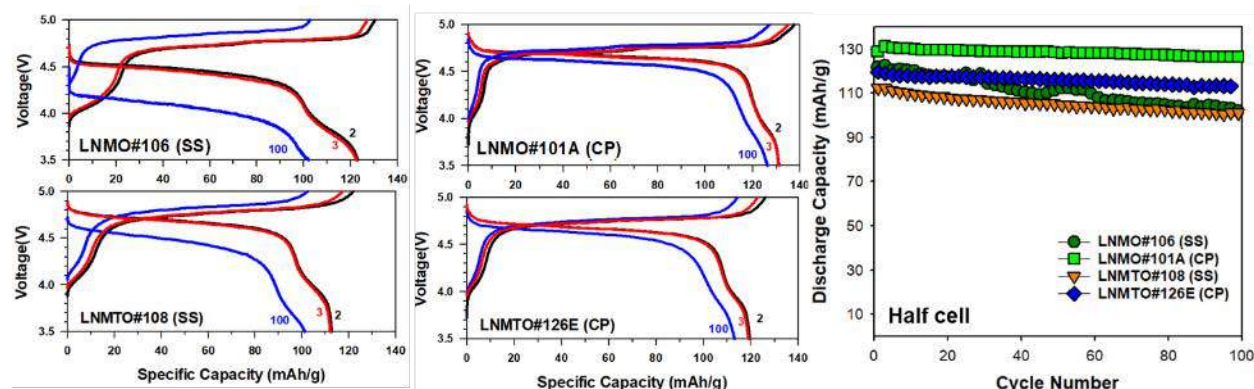


Figure II.4.F.5 Charge/Discharge-voltage profiles and cycle performance coin-type half-cells made with LNMO and LNMTO cathodes synthesized using solid-state (SS) and co-precipitation (CP) processes. Electrolyte 1 M LiPF₆ in 1:1 wt. EC/EMC (no additive). Cycling conditions: Cycle 1: C/10 then C/5 (Ch) and C/2 (dis)

Nexceris has begun some preliminary core/shell work. Initial results are extremely encouraging and indicate the potential to build on the Year 1 baseline with significant performance improvements. Figure II.4.F.6 shows the improvement in half-cell, and full-cell performance (discharge capacity and cycling) for an initial core-shell LNMTO cathode compared to baseline solid-state LNMTO cathode. The result indicates that a core-shell microstructure can achieve both a higher initial discharge capacity than LNMTO (by maintaining an LNMO based core) while preserving the improved cycle life through the formation of a protective Ti enriched surface.

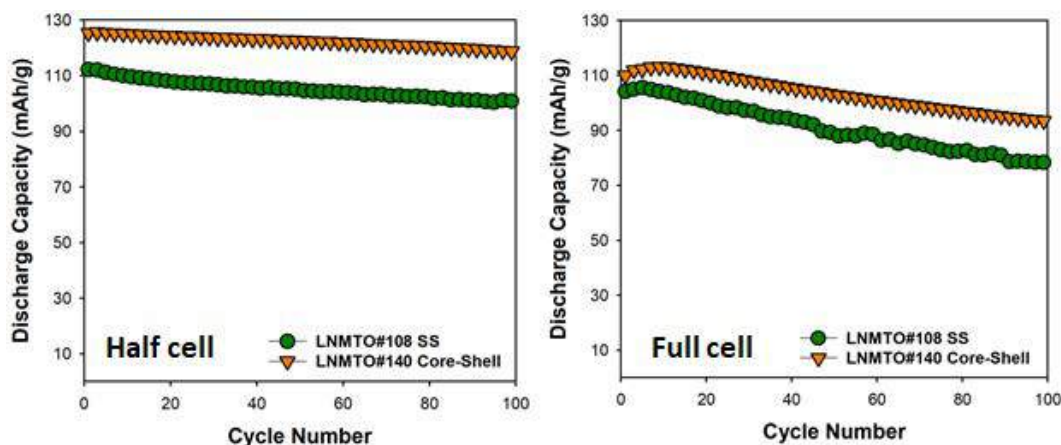


Figure II.4.F.6 Comparison of the cycle performance of half-cell and full-cells made with baseline solid-state (SS) LNMTO cathode and preliminary core/shell LNMTO cathode. Anode: Li (half) and graphite (full) Electrolyte 1 M LiPF₆ in 1:1 wt. EC/EMC (no additive). Cycling conditions: Cycle 1: C/10 then C/5 (Ch) and C/2 (dis)

Optimization of the solid-state and co-precipitation synthesis approaches was based on efficient screening through XRD analysis and half and full-cell coin-cell testing. To mitigate the risk and understand the issues with scaling to the larger-format 2-Ah PPCs, promising candidate cathodes and cell chemistries were transitioned single-layer pouch cell (SLPC) testing. SLPC testing allowed the project team to more effectively assess the effect of changes to cell chemistry (electrode and electrolyte formulation). Figure II.4.F.7 shows a

comparison of the cycling behavior of multiple coin-type full-cell and SLPC using the same baseline solid-state LNMTO cathode powder with LiPAA binder and baseline electrolyte (1M LiPF₆ in 1:1 wt. EC:EMC) with no additives. Although there is some cell-to-cell variation the coin full-cell and SLPC behavior is in general agreement.

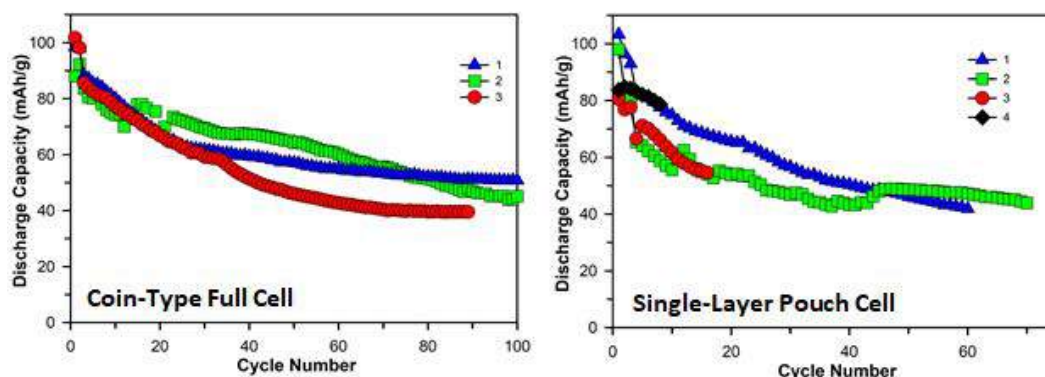


Figure II.4.F.7 Cycle performance of coin-type full-cells and single-layer pouch cells at 25°C made with the baseline LNMTO cathode with LiPAA binder, Electrolyte 1 M LiPF₆ in 1:1 wt. EC/EMC (no additive) and graphite anode. Cycling conditions Cycle 1: C/20, Cycle 2/3: C/10 rate, then coin-cell: C/5 (Ch) and C/2 (dis), and pouch cell: C/3 (Ch) and C/3 (dis)

Once a robust SLPC fabrication process was developed it was used to investigate different cell chemistries and identify electrolyte binder and electrolyte formulations that would help stabilize the high-voltage cell. Figure II.4.F.8 shows the performance of SLPCs made with a range of different electrolyte additives. Several promising additives, including LiBOB and LiDFOB have been identified and optimization of the additive concentration for larger format cells is in progress.

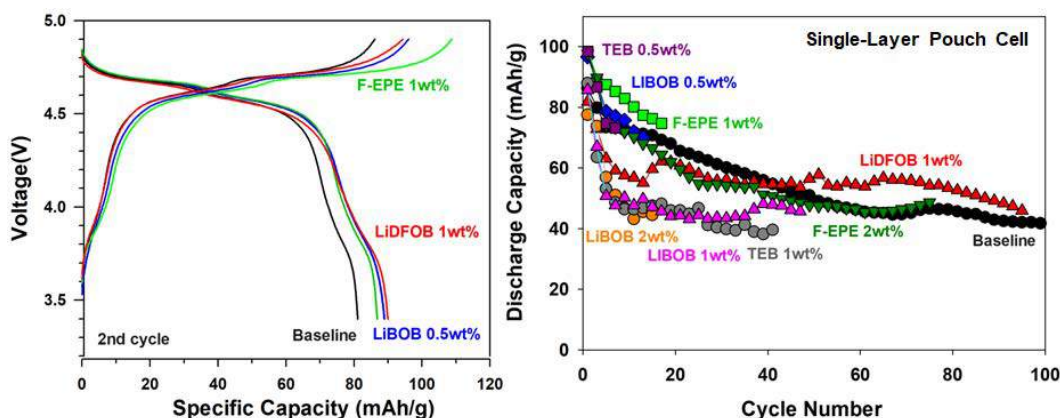


Figure II.4.F.8 Charge/Discharge-voltage profiles and cycle performance of SLPC with baseline LNMTO cathode with LiPAA binder, Electrolyte 1 M LiPF₆ in 1:1 wt. EC/EMC (with additive) and graphite anode. Cycling conditions Cycle 1: C/20, Cycle 2/3: C/10 rate, then coin-cell: C/5 (Ch) and C/2 (dis), and pouch cell: C/3 (Ch) and C/3 (dis)

Conclusions

Nexceris has successfully developed a scalable solid-state process for manufacturing LNMTO cathode powder and validated its performance through coin-type half-cell and full-cell testing, and single-layer pouch cells. To stabilize this high-voltage cathode material alternative electrode binder and electrolyte additive formulations have been evaluated. 2 Ah cells will be manufactured using a down-selected LNMTO cathode material and cell chemistry and tested to establish a performance baseline. In parallel an alternative co-precipitation synthesis approach has been developed that achieves high powder homogeneity and cell performance.

References

1. L. Quispe et al., “Synthesis of Spinel $\text{LiNi}_{0.5}\text{Mn}_{1.5}\text{O}_4$ by a Wet Chemical Method and Characterization for Lithium-Ion Secondary Batteries,” *Journal of the Ceramic Society of Japan*, vol. 123, no. 1, pp. 38-42, 2015.
2. H. Lin et al., “Crystallographic facet- and size-controllable synthesis of spinel $\text{LiNi}_{0.5}\text{Mn}_{1.5}\text{O}_4$ with excellent cyclic stability as cathode of high voltage lithium-ion battery,” *Journal of Materials Chemistry A*, vol. 2, pp. 11987-11995, 2014.
3. C. Wattanawikkam, W. Pecharapa and K. Ishihara, “X-ray absorption spectroscopy analysis and magnetic properties of M-doped TiO_2 nanoparticles (M= Co, Mn, Ni, and Zn) prepared by co-precipitation method,” *Ceramics International*, vol. 43, pp. S397-S402, 2017.
4. J. S. Jang, W. Li, S. Oh and J. Lee, “Fabrication of CdS/TiO_2 nano-bulk composite photocatalysts for hydrogen production from aqueous H_2S solution under visible light,” *Chemical Physics Letters*, vol. 425, pp. 278-282, 2006.
5. D. Dambournet, I. Belharouak and L. Amine, “Tailored Preparation Methods of TiO_2 Anatase, Rutile, Brookite: Mechanism of Formation and Electrochemical Properties,” *Chemistry of Materials*, vol. 22, pp. 1173-1179, 2010.

Acknowledgements

Nexceris would like to acknowledge the support of their project partners, Dr. Jung-Hyun Kim at The Ohio State University, and Navitas Systems. Dr. Kim’s team has provided excellent technical guidance and support for cell chemistry development and cell testing. Navitas Systems has provided feedback on the large-format cell manufacturing and is working to fabricate and test the 2 Ah cells.

Nexceris would also like to thank the project’s NETL manager, Adrienne Riggi for her project support and management, and Dr. Jack Deppe and Dr. Ahmad Pesaran for their technical guidance.

II.4.G High-Performance Low-Cobalt Cathode Materials for Li-ion Batteries (PSU)

Donghai Wang, Principal Investigator

Professor of Mechanical Engineering
The Pennsylvania State University
University Park, PA 16802
E-mail: dwang@psu.edu

Chao-Yang Wang, Principal Investigator

Professor of Mechanical Engineering
The Pennsylvania State University
University Park, PA 16802
E-mail: cxw31@psu.edu

Nanda Jagjit, Principal Investigator

Chemical Sciences Division
Oak Ridge National Laboratory
Oak Ridge, TN 37831
E-mail: nandaj@ornl.gov

Chongmin Wang, Principal Investigator

Environmental Molecular Sciences Laboratory
Pacific Northwest National Laboratory
Richland, WA 99352
E-mail: chongmin.wang@pnnl.gov

Peter Faguy, DOE Technology Development Manager

U.S. Department of Energy
E-mail: Peter.Faguy@ee.doe.gov

Start Date: October 1, 2018

End Date: December 31, 2021

Project Funding (FY19): \$850,434

DOE share: \$680,347

Non-DOE share: \$170,087

Project Introduction

The layer-structured $\text{Li}[\text{Ni}_x\text{Co}_y\text{Mn}_{1-x-y}]\text{O}_2$ (NCM) cathode materials have been the best choice for increasing the driving distance per charge of electric vehicles.[1],[2],[3] The high Ni layered oxide represents successfully commercialized NCM cathodes (such as NCM622[4] and NCA[5]) in lithium-ion batteries (LIBs) for EV applications due to their high energy density and acceptable cycling stability. The price of cobalt, a key element within LIBs for stability, has nearly tripled over the past few years due to increased demand from the cell phone industry, current materials shortage, increased adoption of electrical vehicle, and speculation for a future global shortage,[6],[7],[8] as mentioned in the DOE Funding Opportunity Announcement. To meet the requirement and sustainability of the next-generation long-range and low cost EVs, developing cathode materials with very low Co content to achieve higher energy density and lower cost is both essential and urgent.

Objectives

The overarching objective of this proposed work is to develop stabilized NCM cathode materials with low Co content (namely $\text{LiNi}_x\text{Co}_y\text{Mn}_{1-x-y}\text{O}_2$, $y \leq 0.04$) so as to meet DOE's goal of reducing Co loading to below 50 mg Wh^{-1} , while maintaining energy density greater than 600 Wh kg^{-1} based on cathode material. The obtained NCM cathode paired with graphite anode shall deliver batteries with a high initial specific energy density of over 240 Wh kg^{-1} and low capacity fading rate of less than 20% in 1000 cycles under C/3 discharge rate.

Approach

To accomplish this goal, a multidisciplinary team with several co-investigators has been formed from three organizations: The Pennsylvania State University (PSU), Oak Ridge National Laboratory (ORNL), and Pacific Northwest National Laboratory (PNNL). The PI and co-investigators are Dr. Donghai Wang (PI) from PSU with expertise on synthesis of nanostructured materials and manipulation of interfacial properties of electrochemically active materials, Dr. Jagjit Nanda with substantial knowledge of and expertise in state-of-the-art cathodes from ORNL, Dr. Chao-Yang Wang with significant experience in advanced cell design and fabrication and cell diagnostics from PSU, and Dr. Chongmin Wang with world-wide known expertise of advance atomic scale characterization of electrode materials from PNNL. Furthermore, this project will leverage off and synergistically work with the current DOE-funded programs on battery materials at PSU and ORNL, and electrode materials characterization at PNNL.

Results

We have achieved the following progress:

High-nickel $\text{LiNi}_{0.83}\text{Co}_{0.11}\text{Mn}_{0.06}\text{O}_2$ and low-cobalt $\text{LiNi}_{0.92}\text{Co}_{0.055}\text{Mn}_{0.025}\text{O}_2$ (NCM92) materials

We mainly focused on synthesis and surface protection techniques of NCM cathode material $\text{LiNi}_{0.83}\text{Co}_{0.11}\text{Mn}_{0.06}\text{O}_2$. In this way, we will not only be able to study the coating material and coating process based on NCM811 particle, but also to integrate surface coating process into the synthesizing process of NCM cathode material. By mixing NCM precursor (Ni : Co : Mn = 0.83 : 0.11 : 0.06) and $\text{LiOH} \cdot \text{H}_2\text{O}$ in a mortar and afterwards a two-step heat treatment at various high temperatures, a series of $\text{LiNi}_{0.83}\text{Co}_{0.11}\text{Mn}_{0.06}\text{O}_2$ cathode materials were successfully synthesized. The effect of heat treatment process at different temperature was investigated. X-ray diffraction patterns (Figure II.4.G.1) and scanning electron microscopy (SEM) images (Figure II.4.G.2) verified the successful synthesis of desired materials. All materials exhibits a well-formed layered structure according to XRD patterns, and the sample calcined at 750°C shows the largest ratio of $I_{(003)}/I_{(104)}$, which is the (003) peak intensity over that of (104) peak. The larger $I_{(003)}/I_{(104)}$ is, the better layered structure the sample shows, which is good for the specific capacity and cyclability of the cathode material. The $I_{(003)}/I_{(104)}$ values of all the as-synthesized materials are listed in Table II.4.G.1.

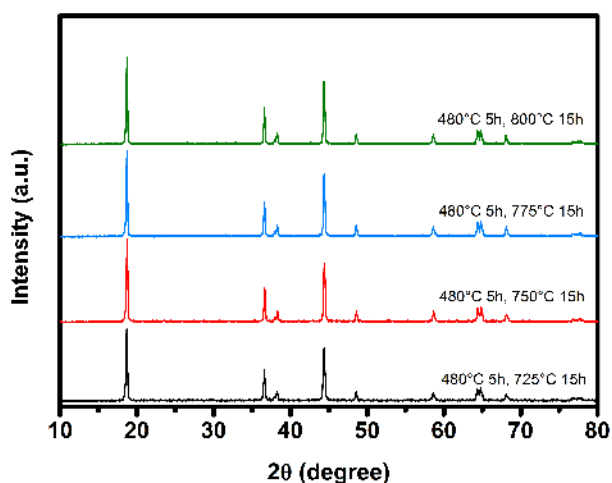


Figure II.4.G.1 XRD patterns of $\text{LiNi}_{0.83}\text{Co}_{0.11}\text{Mn}_{0.06}\text{O}_2$ materials calcined at 480°C first, and then at various high temperatures from 725°C to 800°C

Besides morphology and structural analysis, the electrochemical test have also been carried out. The detailed optimization results in terms of cycling performance are shown below in Figure II.4.G.3a. Here we employed conventional carbonate electrolyte LP57 (1 M LiPF₆ in EC:EMC = 3:7, BASF) and lithium metal for half-cell testing between 2.7 to 4.3 V. According to the data, the material synthesized at 750°C delivers the best electrochemical performance with the initial discharge capacity of 193 mAh g⁻¹ and the capacity retention of 91% after 100 cycles. In addition, we have also demonstrated LiNi_{0.83}Co_{0.11}Mn_{0.06}O₂ cathode materials coated with different amount of LFP. 5%, 10% and 15% wt LFP were mixed with LiNi_{0.83}Co_{0.11}Mn_{0.06}O₂ by ball-milling (150 rpm, 2 h), respectively. Among all materials, the one with 10% LFP coating shows the best electrochemical performance with the initial discharge capacity of 192 mAh g⁻¹ and the capacity retention of 95% after 100 cycles, as exhibited in Figure II.4.G.3b.

Table II.4.G.1 $I_{(003)}/I_{(104)}$ Values of the LiNi_{0.83}Co_{0.11}Mn_{0.06}O₂ Materials Synthesized at Various Temperatures

Synthesis temperature (°C)	725	750	775	800
$I_{(003)}/I_{(104)}$ value	1.35	1.42	1.35	1.34

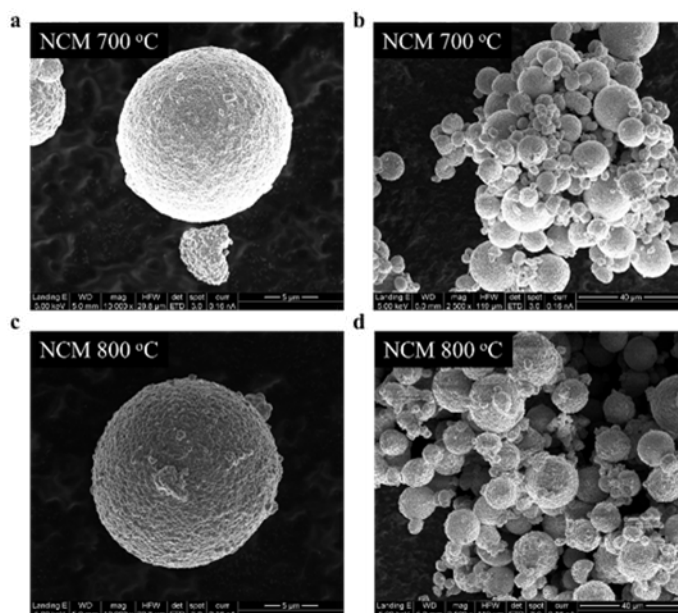


Figure II.4.G.2 SEM images of as-synthesized LiNi_{0.83}Co_{0.11}Mn_{0.06}O₂ material at 700 °C (a and b) and 800 °C (c and d)

We also continue to cycle the 2.5 Ah pouch cells consisted of NCM811 cathode coated with 10 wt% LFP and graphite anode, with the cathode loading of 17.5 mg/cm² and the negative/positive ratio of 1.1. These cells are cycled at 40°C as well as room temperature, as shown in Figure II.4.G.4. The cycling conditions are: 1C constant current and then constant voltage (CCCV) to 4.2V till C/5, and aged cells are characterized at room temperature condition every 200 cycles, i.e., C/3 CCCV to 4.2V till C/20. It can be seen that LFP coated NCM811 is very stable at room temperature, with the capacity retention at C/3 of 80.1% after 3800 cycles. The cell achieves 4941 cycles at 72.4% capacity retention while still showing signs of a healthy cell capable of cycling stably (no perceptible gassing or lithium plating). Even at 40°C, the cell can cycle nearly 2,000 at 20% capacity loss of C/3. This LFP coated NCM material was further characterized to investigate its morphology and functioning mechanism. According to HAADF-STEM image and EDX elemental maps shown in Figure II.4.G.5, LiFePO₄ mainly distributed at the surface of NCM particle, and no evidence was found to show the infusion of LiFePO₄ along the grain boundary.

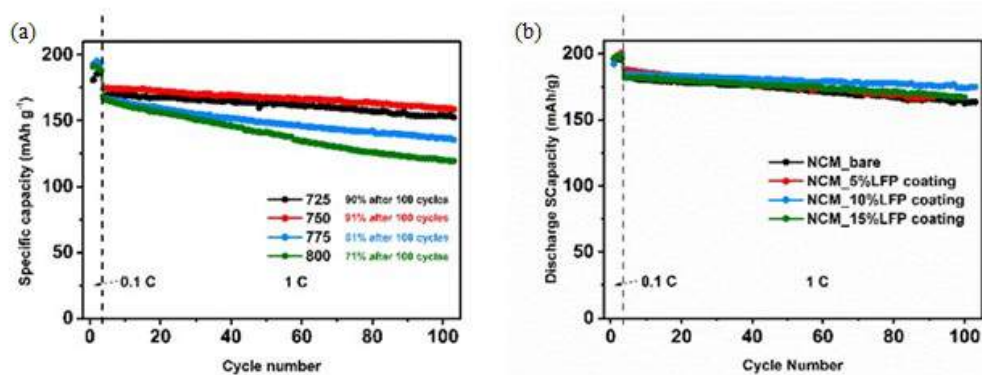


Figure II.4.G.3 a) Capacity retention of $\text{LiNi}_{0.83}\text{Co}_{0.11}\text{Mn}_{0.06}\text{O}_2$ synthesized at various temperatures. b) Capacity retention of LFP-coated $\text{LiNi}_{0.83}\text{Co}_{0.11}\text{Mn}_{0.06}\text{O}_2$ with different LFP amount

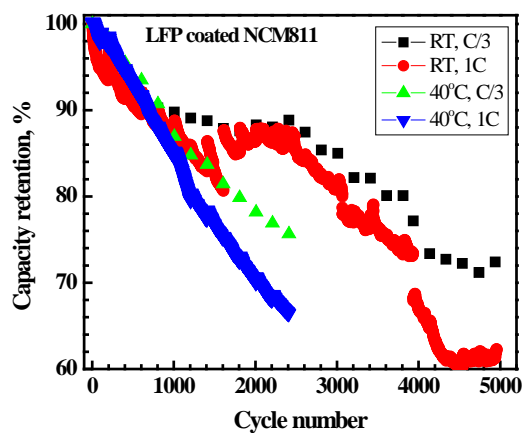


Figure II.4.G.4 Capacity retention of the LFP-coated NCM/Graphite full-cells during 1 C cycling at room temperature and 40°C

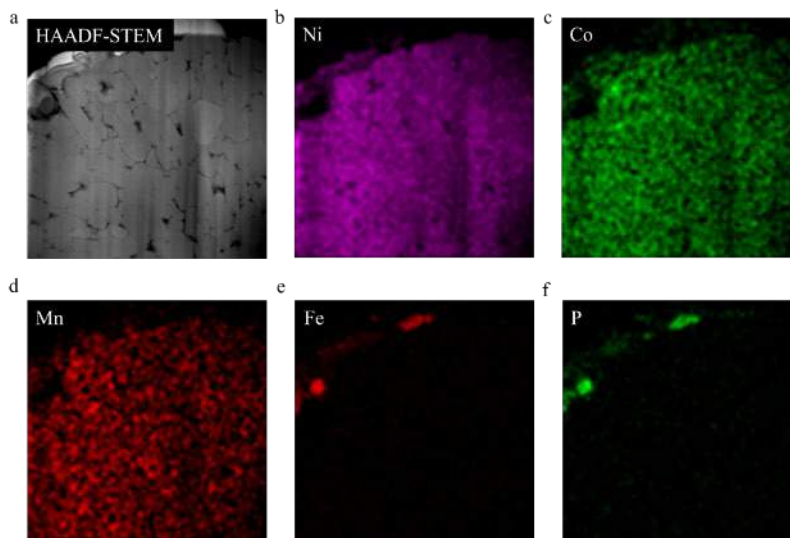


Figure II.4.G.5 (a) HAADF-STEM image of LFP-NCM and (b-f) corresponding EDX elemental maps

Additionally, in this quarter we fabricated 20 pouch cells to be delivered to Idaho National Laboratory, as shown in Figure II.4.G.6. The capacity was measured, as shown in Table II.4.G.2. The cell capacity is uniform and in the range of 2.460-2.478 Ah. C-rate performance was measured as shown in Figure II.4.G.7. The C-rate performance of two different cells are almost the same, which can deliver 87% of cell capacity at 3C discharge rate and at room temperature.

Table II.4.G.2 C/3 Capacity of the Cells Measured at Room Temperature

Cell number	Capacity (Ah)	Cell number	Capacity (Ah)
1	2.466	11	2.464
2	2.468	12	2.468
3	2.464	13	2.469
4	2.473	14	2.464
5	2.460	15	2.475
6	2.463	16	2.462
7	2.465	17	2.468
8	2.466	18	2.467
9	2.469	19	2.463
10	2.478	20	2.472



Figure II.4.G.6 Image of twenty cells to be delivered to Idaho National Laboratory

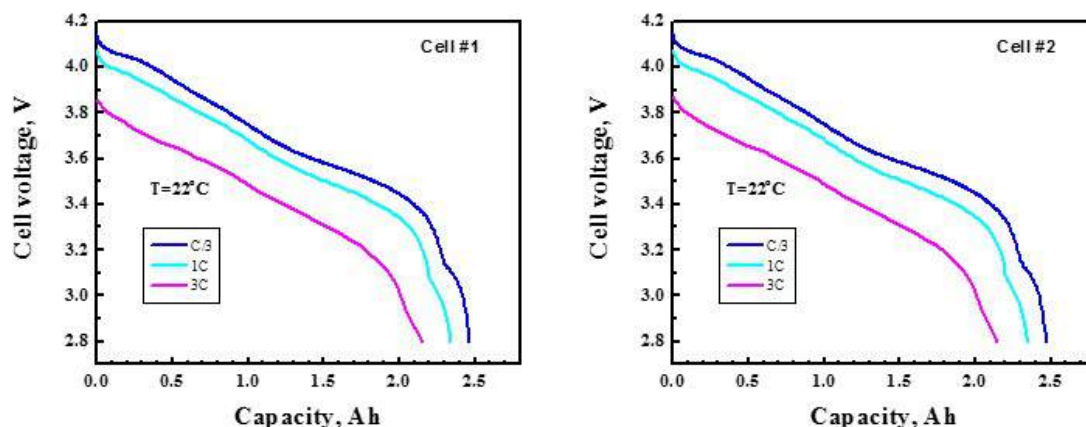
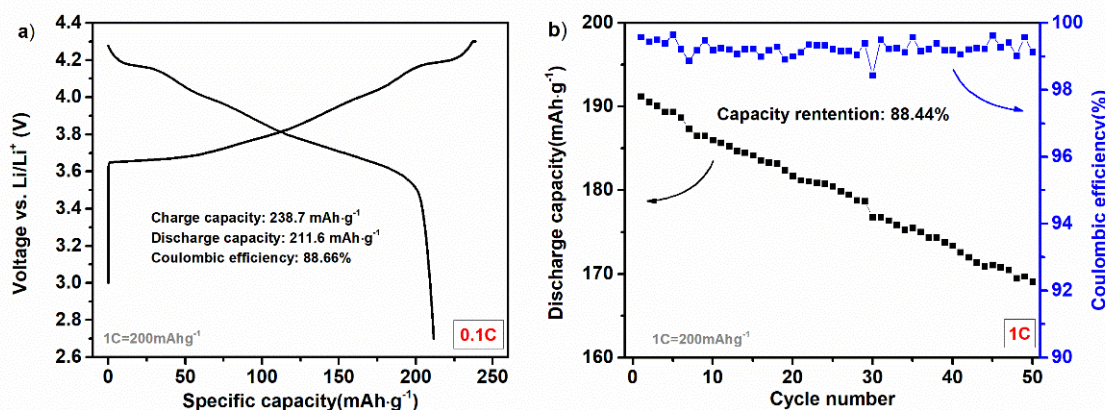


Figure II.4.G.7 C-rate performance of Cells #1 and #2

As for low-cobalt $\text{LiNi}_{0.92}\text{Co}_{0.055}\text{Mn}_{0.025}\text{O}_2$ (NCM92) materials, the material has been successfully synthesized at 715°C . The electrochemical properties of the material are also being tested (Figure II.4.G.8). The initial discharge capacity is 211 mAh g^{-1} , and the initial coulombic efficiency is 88.6%. The cell also shows a good cycling performance, and the capacity retention is 88% over 50 cycles after the activation process.

Figure II.4.G.8 a) Charge/discharge curves b) capacity retention and coulombic efficiency of the low-cobalt material $\text{LiNi}_{0.92}\text{Co}_{0.055}\text{Mn}_{0.025}\text{O}_2$ synthesized at 715°C

Cobalt-free Mo doped $\text{LiNi}_{1/2}\text{Mn}_{1/2}\text{O}_2$ (LNMO) cathode materials

We have worked on synthesis and electrochemical optimization of Mo doped $\text{LiNi}_{1/2}\text{Mn}_{1/2}\text{O}_2$ (LNMO) compositions. LNMO compositions traditionally have poor capacity retention due to cation mixing between Ni^{2+} and Li^+ layers. It was hypothesized that presence of small fraction of Mo^{6+} (between 0.5 – 2 wt %) would reduce the cation mixing and provide stable capacity retention. Further, Mo^{6+} being a d^0 cation could provide higher oxidation stability under lithiation enabling higher voltage and capacity.

$\text{LiNi}_{0.5-x/2}\text{Mn}_{0.5-x/2}\text{Mo}_x\text{O}_2$ (where $x = 0, 0.01, 0.03, 0.05$) were prepared as follow: stoichiometry amount of $\text{Li}(\text{OCOCH}_3)_2 \cdot 2\text{H}_2\text{O}$, $\text{Ni}(\text{OCOCH}_3)_2 \cdot 4\text{H}_2\text{O}$, $\text{Mn}(\text{OCOCH}_3)_2 \cdot 4\text{H}_2\text{O}$, $(\text{NH}_4)_6\text{Mo}_7\text{O}_{24}$ and citric acid were dissolved in deionized water. The solution was heated to 60°C while stirring until the water is evaporated and produce dry gel. The dry gel was grounded before first phase heating at 400°C for 4 hr ($5^\circ\text{C}/\text{min}$ ramp

rate) under the air atmosphere followed by the second phase heating at 850°C for 15 hr in air (5°C/min ramp rate).

Figure II.4.G.9 shows the XRD pattern of LNMO and different contents of Mo-doped LNMO. It can be observed that there is no difference between LNMO and 1% Mo doped LNMO. With increase in molybdenum (Mo-3% and Mo-5%), there is a formation of secondary phase such as Li_2MoO_4 and superposition of Li-Mo-O and Mn_3O_4 . All the material shows a broad peak at about 2θ range of 20° - 24° which corresponds to Li_2MnO_3 structure having a space group $C2/m$. With increase in Mo, we can observe that there is a peak at 30° correspond to the superposition of Li-Mo-O and Mn_3O_4 compound, where Mo is in +6 valence states which suggest that excess Mo combine with excess Li and O atom to form compound on the surface. For LNMO and 1% Mo doped-LNMO XRD pattern, it can be seen that there is no clear separation of (108)/(110) and (006)/(102) doublet reflection compared to higher molybdenum content LNMO. The 3 and 5 wt% Mo doped samples showed some impurities.

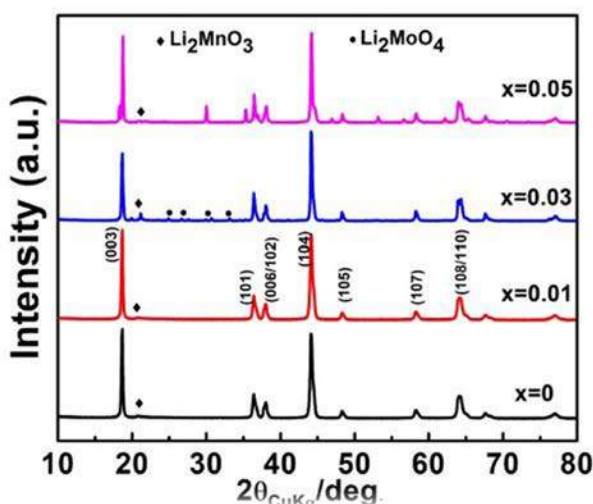


Figure II.4.G.9 XRD patterns of various Mo content in $\text{LiNi}_{0.5-x/2}\text{Mn}_{0.5-x/2}\text{Mo}_x\text{O}_2$ (where $x = 0, 0.01, 0.03, 0.05$)

Figure II.4.G.10 shows the 1st, 2nd, 3rd, 10th, 20th, 50th and 100th cycle for undoped and 1 wt% doped LNMO in the voltage range of 2.0-4.5V at 20mA/g. LNMO shows the first discharge capacity of $\sim 155 \text{ mAh g}^{-1}$ which decreases to $\sim 123 \text{ mAh g}^{-1}$ after 10 cycles with the capacity loss of $\sim 21\%$, whereas Mo-doped electrode shows $\sim 179 \text{ mAh g}^{-1}$ and decreases to $\sim 164 \text{ mAh g}^{-1}$ (10th cycle) with the capacity loss of only $\sim 8.3\%$. Further, the Irreversible Capacity Loss (ICL) for LNMO and Mo-doped LNMO shows $\sim 11.93\%$ and $\sim 8.97\%$ respectively for the first cycle. Mo doped demonstrate less ICL values due to less electrode and electrolyte side reaction caused by the presence of Mo^{6+} - modified electrode interface.

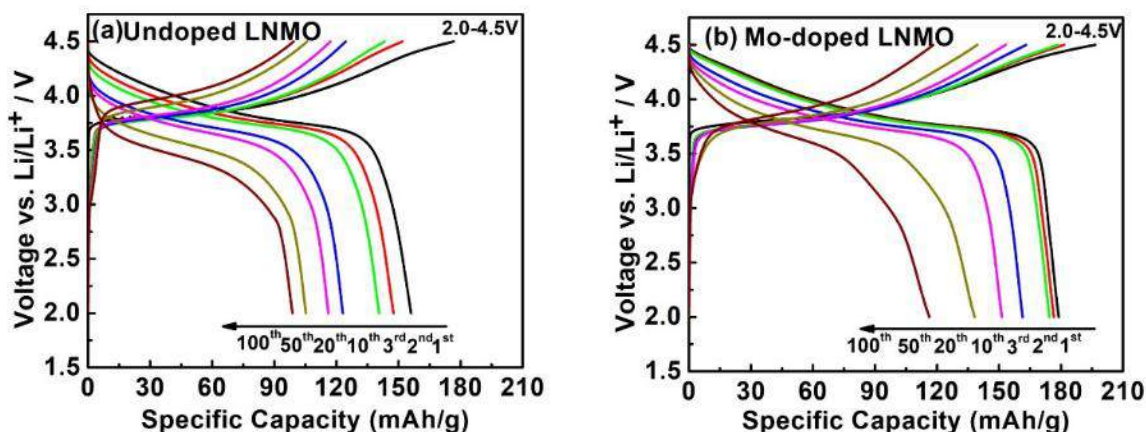


Figure II.4.G.10 Charge and discharge curves at different cycles in the voltage range between 2.0-4.5 V at current density of 20mA/g for (a) Undoped LNMO and (b) Mo-doped LNMO

To further reveal the functionality of Mo doping in enhancing stability of $\text{LiNi}_{0.5}\text{Mn}_{0.5}\text{O}_2$, microscopy and spectroscopy characterization techniques were used to gain more insights. Transmission electron microscopy (TEM), STEM images and corresponding EDS maps were collected as shown in Figure II.4.G.11. EDS elemental mapping reveals that Mo at the level of 1 at% is uniformly distributed in the lattice of $\text{LiNi}_{0.5}\text{Mn}_{0.5}\text{O}_2$. In addition, further analysis through HAADF-STEM imaging (Figure II.4.G.12d-g) reveals that Mo doping will lead to mitigation of transition metal migration to Li layer. In addition, EELS analysis shown in Figure II.4.G.12h-j shows that Mo doping leads to decreased valence of Mn, while decreased valence of Ni. Moreover, HAADF-STEM image of the material before and after cycling (Figure II.4.G.13) demonstrates that Mo doping could prevent the layered to the rock salt structure transition upon the cycling of the $\text{LiNi}_{0.5}\text{Mn}_{0.5}\text{O}_2$ cathode.

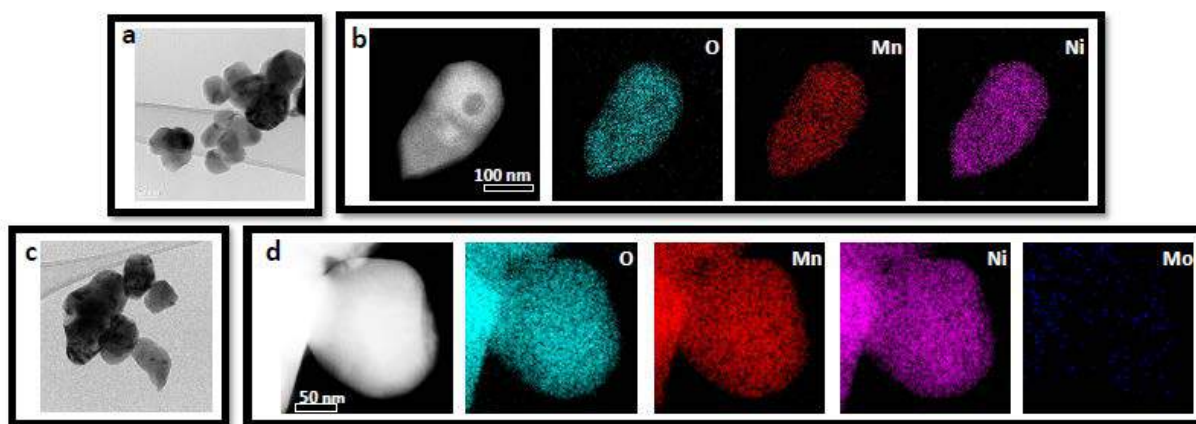


Figure II.4.G.11 TEM images, STEM images and corresponding EDS maps of (a, b) $\text{LiNi}_{0.5}\text{Mn}_{0.5}\text{O}_2$ and (c, d) $\text{LiNi}_{0.4995}\text{Mn}_{0.4995}\text{O}_2$

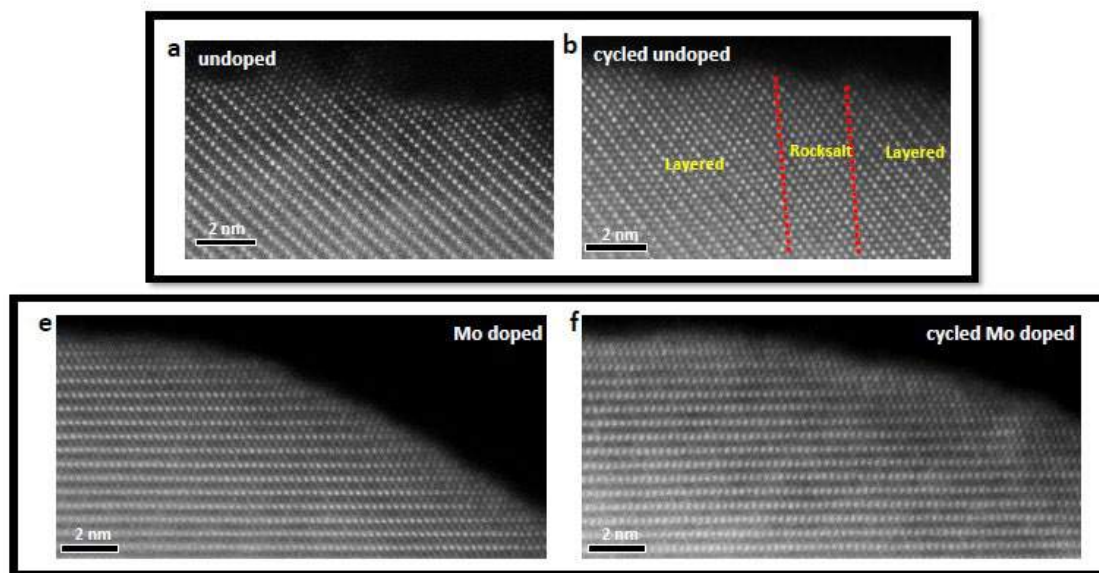


Figure II.4.G.12 HAADF-STEM and EELS analysis of Mo doped and undoped $\text{LiNi}_{0.5}\text{Mn}_{0.5}\text{O}_2$.

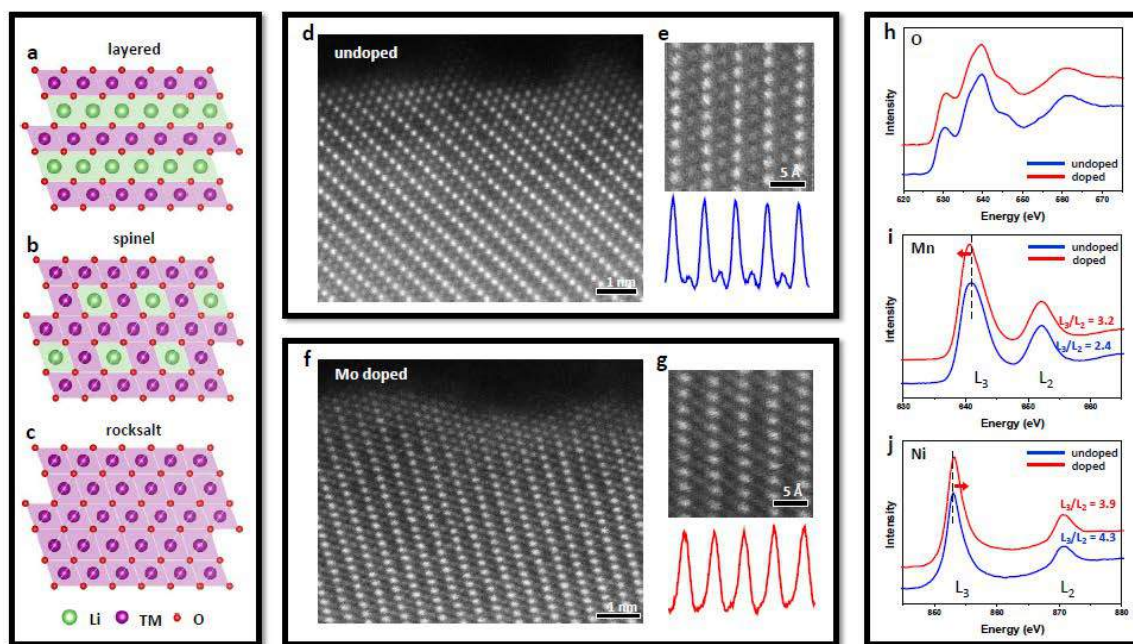


Figure II.4.G.13 STEM-HAADF images of $\text{LiNi}_{0.5}\text{Mn}_{0.5}\text{O}_2$ (a) before and (b) after cycling. STEM-HAADF images of Mo-doped $\text{LiNi}_{0.5}\text{Mn}_{0.5}\text{O}_2$ (e) before and (f) after cycling

As mentioned above, 1 at% Mo substitution in LNMO increased the reversible capacity from 150 to 180 mAh/g, but higher dopant levels yielded poor cycling performance due to formation of impurity phases (e.g., Li_2MoO_4). Therefore, new synthesis methods are developed to incorporate early transition metal dopants (e.g., Mo) into $\text{LiNi}_{1/2}\text{Mn}_{1/2}\text{O}_2$ (LNMO) cathodes.

$\text{LiNi}_{0.5-x/2}\text{Mn}_{0.5-x/2}\text{Mo}_x\text{O}_2$ cathodes ($x = 0, 0.005$, and 0.0075) were prepared using a sol-gel reaction route. All materials were phase-pure with the desired layered structure (R-3m symmetry) as determined by X-ray

diffraction (results not shown). The cathodes' electrochemical properties were evaluated in half cells containing a Li metal anode and liquid carbonate electrolyte (1.2 M LiPF₆ in EC/EMC, 3/7 by weight). Figure II.4.G.14 shows the cathodes' cycling performance collected at 20 mA/g between 2.0 – 4.5 V vs. Li/Li⁺. Compared to undoped LNMO, 0.5 – 0.75 at% Mo substitution did not significantly impact the initial reversible capacity (~150 mAh/g) but dramatically improved the cycling stability (e.g., 85 vs. 66% capacity retention after 65 cycles for 0.5 at% Mo and undoped LNMO, respectively). The Mo doped cathodes also exhibited excellent rate capabilities. As shown in Figure II.4.G.15, when cycled at 100 mA/g, the sample with 0.5 at% Mo showed a reversible capacity of 105 mAh/g compared to only 90 mAh/g for undoped LNMO.

Based on the 1 at% Mo material, the functioning mechanism of Mo doping is further uncovered. A key question for the Co-free cathode is the surface structure and cation mixing in the bulk lattice. One way to mitigate the cation mixing is to use lattice doping. However, it is far from clear as how a dopant can effectively mitigate the cation mixing. To answer these questions herein, the effects of Mo dopant (~1 at%) on the structural stability of LiNi_{0.5}Mn_{0.5}O₂ is explored using a combination of atomic-resolution scanning transmission electron microscopy (STEM) imaging and first principle density functional theory (DFT) calculations. The structures of the undoped and Mo-doped cathode particles, before and after cycling, are directly compared to reveal the doping effects at the atomic scale. The observed enhancement of structural stability induced by Mo doping can be directly correlated to the improved capacity and cycling performance measured in the doped cathodes.

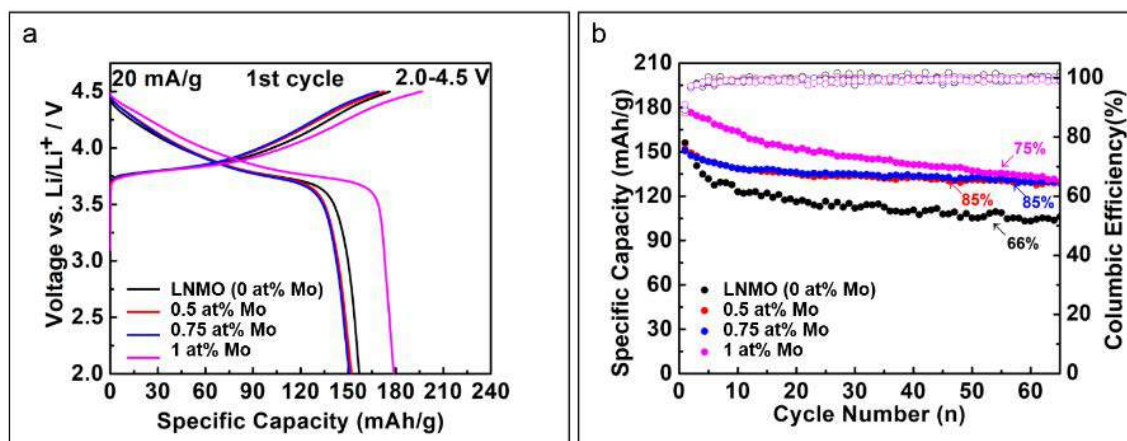


Figure II.4.G.14 Electrochemical performance of LNMO with 0 – 1 at% Mo substitution showing: (a) Galvanostatic charge/discharge curves collected during the first cycle and (b) capacity stability over 65 cycles. Cells were cycled between 2.0 – 4.5 V vs. Li/Li⁺ at a specific current of 20 mA/g

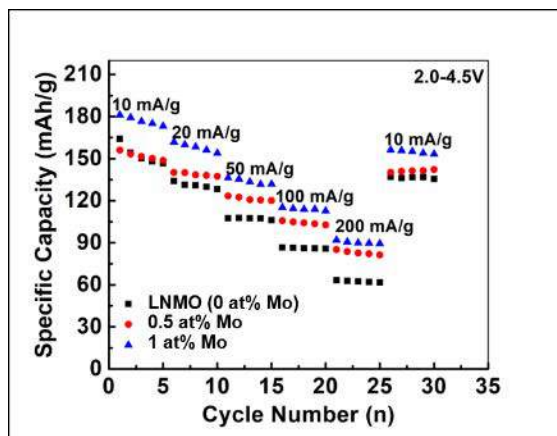


Figure II.4.G.15 Rate capabilities of LNMO with 0 – 1 at% Mo substitution when cycled between 2.0 – 4.5 V vs. Li/Li⁺ at specific currents of 10 – 200 mA/g

High-angle annular dark-field (HAADF) STEM images of representative nanoscale regions near the surfaces of the undoped and Mo-doped LNMO particles prior to cycling are shown in Figure II.4.G.16a and d, respectively. Corresponding magnified regions aligned with STEM-image intensity profiles for both materials are shown in Figure II.4.G.16b and e. The layered structure consisting of alternating Li layers and TM layers is evident in both undoped and Mo-doped LNMO. A major difference of these two structures, however, is the enhanced image contrast at the atomic columns in the Li layers in the undoped LNMO (Figure II.4.G.16b) as compared to the Mo-doped LNMO (Figure II.4.G.16e). In a HAADF STEM image, since the image contrast is proportional to the atomic number Z as $\sim Z^{1.7}$, only the heavy atoms (*i.e.*, Ni, Mn, and Mo) are directly observable while the light atoms (*i.e.*, Li and O) are invisible. Therefore, the contrast at the Li layers should be attributed to the migration of heavy atoms into these layers. In fact, Mn and Ni exist as tetravalent Mn^{4+} and bivalent Ni^{2+} cations in LNMO. Since the Ni^{2+} cations have an ionic radius similar to that of Li^+ (0.69 and 0.76 Å, respectively), the Ni^{2+} cations in the transition metal layers can easily replace their positions with the Li^+ cations in the Li layers, resulting in cation mixing. Such cation mixing impedes the Li^+ ion diffusion in the Li layers and thus reduces the reversible capacity and is detrimental to high-rate performances of the cathodes. Our observations here clearly show that the degree of cation mixing is reduced in the Mo-doped LNMO.

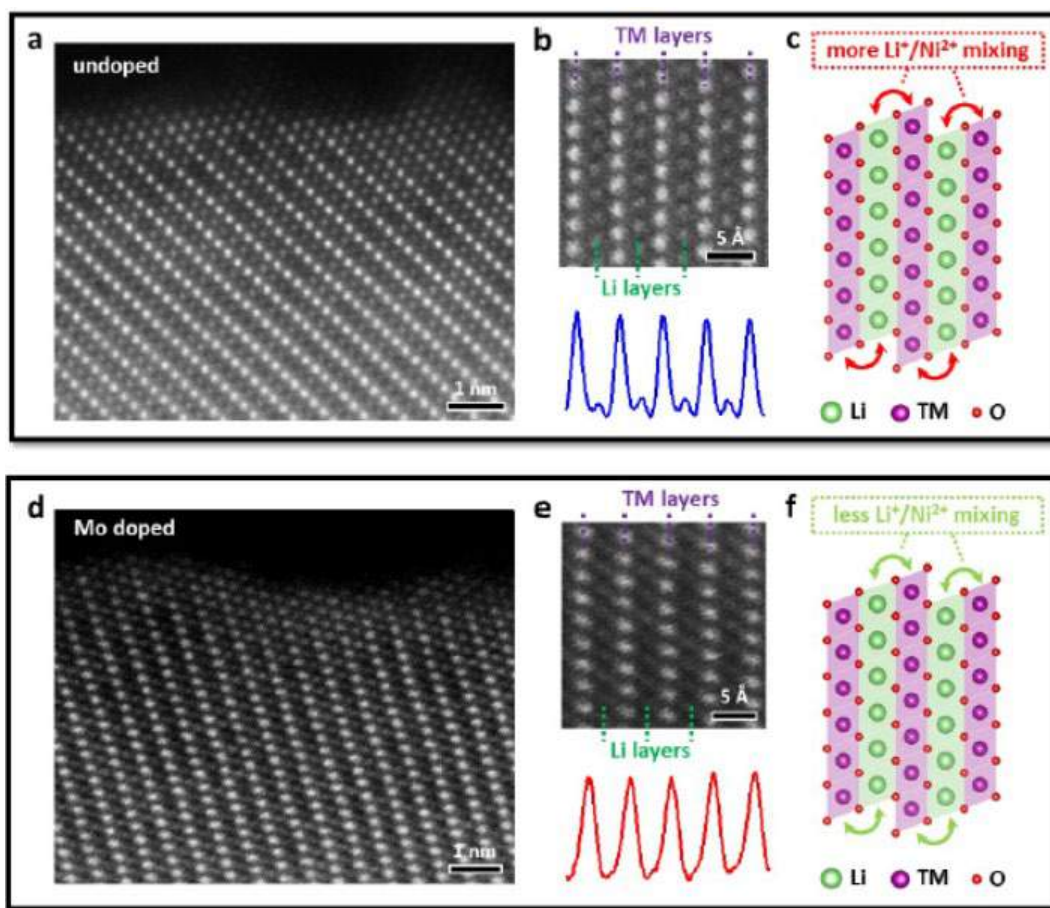


Figure II.4.G.16 Atomic structures of pristine undoped and Mo-doped LNMO. (a) HAADF STEM image of a near-surface region in undoped LNMO. (b) Magnified HAADF STEM image of undoped LNMO aligned with STEM-image intensity profiles. (c) Corresponding atomic model the layered LNMO structure marked with strong cation mixing. (d) HAADF STEM image of a near-surface region in Mo-doped LNMO. (e) Magnified HAADF STEM image of Mo-doped LNMO aligned with STEM-image intensity profiles. (f) Corresponding atomic model the layered LNMO structure marked with weak cation mixing

Atomic-resolution STEM image of doped and undoped LNMO particles after 100 cycles has been carried out. We found that Mo doping significantly reduces the degree of $\text{Li}^+/\text{Ni}^{2+}$ cation mixing which increases the cathode's reversible capacity and improves its structural stability during cycling. We also show that layered-to-rocksalt phase transitions can initiate at intragranular spinel-like grain boundaries inside the particle bulk, which challenges the current understanding that such phase transitions are initiated at the particle surface. (Figure II.4.G.17c) Since similar grain boundaries likely exist in many layered oxides, this mechanism may be applicable to a wide range of cathodes materials.

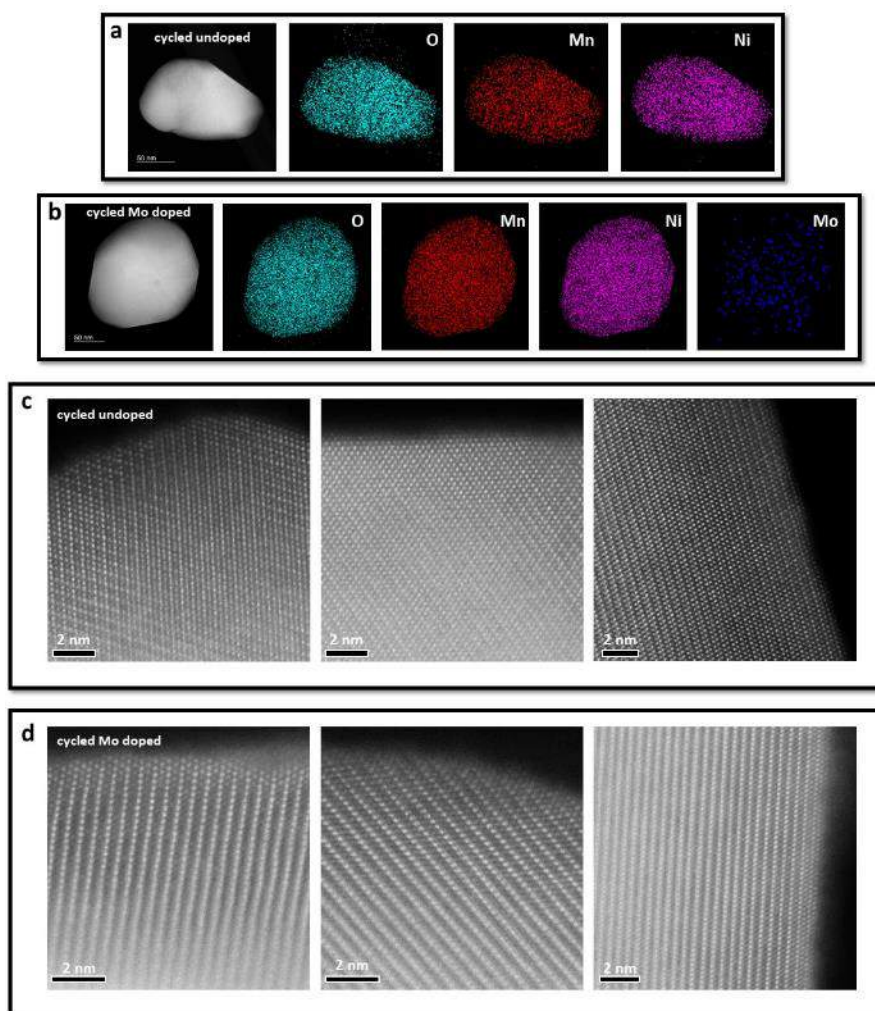


Figure II.4.G.17 Morphology, composition, and atomic structures of cycled undoped and Mo-doped LNMO particles. (a) STEM image and corresponding EDS elemental maps of an undoped LNMO particle after 100 cycles. (b) STEM image and corresponding EDS elemental maps of a Mo-doped LNMO particle after 100 cycles. (c) Atomic-resolution STEM image of local regions in 3 different undoped LNMO particles after 100 cycles, in which strong cation mixing and phase transitions (layered-to-spinel-like or layered-to-rocksalt) are observed. (d) Atomic-resolution STEM image of local regions in 3 different Mo-doped LNMO particles after 100 cycles. The layered structures were well-preserved without any significant cation mixing or phase transitions

Conclusions

In conclusion, high-nickel $\text{LiNi}_{0.83}\text{Co}_{0.11}\text{Mn}_{0.06}\text{O}_2$ and low-cobalt $\text{LiNi}_{0.92}\text{Co}_{0.055}\text{Mn}_{0.025}\text{O}_2$ (NCM92) materials have been successfully synthesized with good layered structure. $\text{LiNi}_{0.83}\text{Co}_{0.11}\text{Mn}_{0.06}\text{O}_2$ synthesized at 750°C exhibits the best electrochemical performance, with the initial discharge capacity of 193 mAh g^{-1} and the capacity retention of 91% after 100 cycles. After LiFePO_4 coating, the electrochemical performance is further

improved. The material with 10% LFP coating shows the initial discharge capacity of 192 mAh g⁻¹ and the capacity retention of 95% after 100 cycles. For low-cobalt NCM92 materials, the material synthesized at 715°C can deliver an initial discharge capacity of 211 mAh g⁻¹, and the capacity retention is 88% over 50 cycles. In addition, 10 wt% LFP coated NCM811 were used for cell assembly with graphite, which shows a capacity retention at C/3 of 80.1% after 3800 cycles, and 72.4% after 4941 cycles. This result have already fulfilled the objective.

We have also systematically studied the stability of Co-free cathode with a composition of LiNi_{0.5}Mn_{0.5}O₂ (LNMO), which is not stable upon cycling. We found that even 1at% Mo doping can enhance the cycling stability. We revealed that the Mo dopant is uniformly distributed in the lattice, which can mitigate the cation interlayer mixing. We further revealed that upon cycling, the Mo dopant can prevent the Ni-Li layers intermixing, therefore enhancing the lattice stability for better cycling stability. Our findings shed light on key structure/performance correlations in Co-free layered oxide cathodes and provide atomic-scale mechanisms which explain the improved electrochemical properties and enhanced structural stability caused by cation doping.

Key Publications

1. Linze Li, Jianguo Yu, Devendrasinh Darbar, Ethan C. Self, Donghai Wang, Jagjit Nanda, Indranil Bhattacharya and Chongmin Wang, “Atomic-Scale Mechanisms of Enhanced Electrochemical Properties of Mo-Doped Co- Free Layered Oxide Cathodes for Lithium-Ion Batteries”, *ACS Energy Lett.* 2019, 4, 2540–2546.

References

1. S.-T. Myung, F. Maglia, K.-J. Park, C. S. Yoon, P. Lamp, S.-J. Kim, Y.-K. Sun, *Nickel-Rich Layered Cathode Materials for Automotive Lithium-Ion Batteries: Achievements and Perspectives*, *ACS Energy Letters* **2017**, 2, 196.
2. A. Konarov, S.-T. Myung, Y.-K. Sun, *Cathode Materials for Future Electric Vehicles and Energy Storage Systems*, *ACS Energy Letters* **2017**, 2, 703.
3. F. Schipper, E. M. Erickson, C. Erk, J.-Y. Shin, F. F. Chesneau, D. Aurbach, *Review—Recent Advances and Remaining Challenges for Lithium Ion Battery Cathodes: I. Nickel-Rich, LiNixCoyMnzO2*, *Journal of The Electrochemical Society* **2017**, 164, A6220.
4. D. Ren, Y. Shen, Y. Yang, L. Shen, B. D. A. Levin, Y. Yu, D. A. Muller, H. D. Abruña, *Systematic Optimization of Battery Materials: Key Parameter Optimization for the Scalable Synthesis of Uniform, High-Energy, and High Stability LiNi0.6Mn0.2Co0.2O2 Cathode Material for Lithium-Ion Batteries*, *ACS Applied Materials & Interfaces* **2017**, 9, 35811.
5. M. Guilmard, C. Poullierie, L. Croguennec, C. Delmas, *Structural and electrochemical properties of LiNi0.70Co0.15Al0.15O2*, *Solid State Ionics* **2003**, 160, 39.
6. W. Bernhart, in *Lithium-Ion Batteries*, (Ed: G. Pistoia), Elsevier, Amsterdam **2014**, 553.
7. D. Larcher, J. M. Tarascon, *Towards greener and more sustainable batteries for electrical energy storage*, *Nature Chemistry* **2014**, 7, 19.
8. C. Vaalma, D. Buchholz, M. Weil, S. Passerini, *A cost and resource analysis of sodium-ion batteries*, *Nature Reviews Materials* **2018**, 3, 18013.

Acknowledgements

The work was supported by the Department of Energy, Office of Energy Efficiency and Renewable Energy (EERE), Vehicle Technology Office, under Award Number DE- EE0008447. We appreciated the support from Colleen Butcher at National Energy Technology Laboratory.

II.5 Next Generation Lithium-Ion Batteries: Diagnostics

II.5.A Interfacial Processes (LBNL)

Robert Kostecki

Lawrence Berkeley National Laboratory
1 Cyclotron Road
Berkeley, CA 94720
E-mail: r_kostecki@lbl.gov

Tien Duong, DOE Technology Development Manager

U.S. Department of Energy
E-mail: Tien.Duong@ee.doe.gov

Start Date: October 1, 2015

End Date: September 30, 2019

Project Funding (FY19): \$440,000

DOE share: \$440,000

Non-DOE share: \$0

Project Introduction

Li-based batteries are inherently complex and dynamic systems. Although often viewed as simple devices, their successful operation relies heavily on a series of complex mechanisms, involving thermodynamic instability in many parts of the charge/discharge cycle and the formation of metastable phases. This paradigm of Li-battery system operation usually drives the battery toward irreversible physical and chemical conditions that lead to battery degradation and failure.

The requirements for long-term stability of Li batteries are extremely stringent and necessitate control of the chemistry at a wide variety of temporal and structural length scales. Progress towards identifying the most efficient mechanisms for electrical energy storage and the ideal material depends on a fundamental understanding of how battery materials function and what structural/electronic properties limit their performance. This in turn necessitates the development and use of new characterization tools to monitor these processes.

The design of the next generation of Li batteries requires a fundamental understanding of the physical and chemical processes that govern these complex systems. Although some significant advances have been made to prepare and utilize new materials efforts towards the understanding of their operation mechanisms and degradation modes have been insufficient and/or unsuccessful.

Instability and/or high resistance at the interface of battery electrodes limit electrochemical performance of high-energy density batteries. A better understanding of the underlying principles that govern these phenomena is inextricably linked with successful implementation of high energy density materials in Li-based cells for PHEVs and EVs. Pristine and cycled composite and thin film model electrodes are investigated using a variety of state-of-the-art techniques to identify, characterize and monitor changes in materials structure and composition that take place during battery operation and/or storage. This project constitutes an integral part of the concerted effort within the BMR Program and it supports development of new electrode materials for high-energy Li-metal based rechargeable cells.

Objectives

This collaborative project involves the development and application of advanced experimental methodologies to study and understand the mechanism of operation and degradation of high capacity materials for rechargeable cells for PHEV and EV applications. The main objective of this task is to develop and apply in situ and ex situ far- and near-field optical multifunctional probes and synchrotron-based advanced x-ray techniques to obtain detailed insight into the electrode and electrolyte active material structure and the physio-chemical phenomena at electrode/electrolyte interfaces at a spatial resolution that corresponds to the size of basic chemical or structural building blocks. Through an integrated synthesis, characterization, and

electrochemistry effort, we aim to develop an understanding of which structural and chemical features of the electrode and electrolyte materials control these performance characteristics so that rational decisions can be made as to their further development into commercially viable cathode materials. The primary goal of these studies are:

- (i) Understand the factors that control charge/discharge rate, cyclability, and degradation processes
- (ii) Design and apply new diagnostic techniques and experimental methodologies that are capable to unveil the structure and reactivity at hidden or buried interfaces and interphases that determine material, composite electrode and full cell electrochemical performance and failure modes, and
- (iii) Propose effective remedies to address inadequate Li-metal based battery calendar/cycle lifetimes for PHV and EV applications.

Approach

- Develop, apply and couple advanced characterization techniques, such as optical (Raman, ATR-FTIR) and scanning probe spectroscopy and microscopy (near-field IR) with standard electrochemical methods to determine function, operation and degradation of materials, electrodes and battery cells.
- Design and manufacture model thin-film and composite LLZO and LPS solid-state electrolytes by pulsed laser deposition (PLD) as model systems for fundamental electrochemical studies of Li-metal battery systems. Construct ultra-smooth, defined model electrodes and solid electrolytes by pulsed laser deposition (PLD) to permit the use of novel investigative techniques during operation.
 - Characterize the bulk and surface structure of Li anode, NMC cathode electrodes and solid-state electrolytes and its relation to electrochemical and interfacial properties.
 - Characterize the chemistry of solid-state electrolyte/Li and electrolyte/cathode interfaces with ex situ near field IR, XAS and XPS.
 - Design and develop new XAS/XPS experimental setup to characterize in situ solid/solid (e.g., NMC/SSE Li/SSE) interfaces.
- Work closely with other investigators in the ABMR Program to support development of new electrode materials for high-energy Li-metal based rechargeable cells.

Results

We carried out diagnostic studies of chemical and electrochemical reactions at electrode/electrolyte interfaces in all-solid-state-battery systems. Model cells were assembled with NCM cathodes, lithium thiophosphate (LPS-Li₃PS₄) solid-state electrolyte and graphite anode. The cathode was assembled by pressing ion-conductive LPS solid-state electrolyte with NMC powder and slight amount of conductive carbon additive, whereas the anode was manufactured by mixing and pressing LPS and graphite powder. NCM cathodes with different nickel contents i.e., NCM333, NCM523 and NCM811 and LiNbO₃-coated NCM811 were built, tested and characterized with x-ray absorption spectroscopy (XAS) in the Advanced Light Source user facility in LBNL. The all-solid-state spectro-electrochemical cell was cycled between 2.5-4 V at 0.1 C. The cell assembly and electrochemical measurements were carried out under Ar atmosphere to avoid any possible interference of side reactions with oxygen or moisture.

Sulfur K-edge and phosphorous K-edge XAS spectra of the pristine and cycled NMC electrode were recorded ex situ (Figure II.5.A.1). The S K-edge XAS spectrum of pristine LPS electrolyte shows the absorption peak at 2470.2 eV, which corresponds to the occupied S 1s orbital. The chemical shift of the S K-edge is sensitive to changes in the ground state charge density around sulfur atom. It can be used to obtain information about the chemical bonding environment and related changes upon chemical reaction(s) between LPS and NCM.

X-ray absorption spectra of NMC/LPS composites recorded after 1 day storage in Ar glove box (Figure II.5.A.1a) show that the S K-edge shifts to higher energies with increasing nickel content in NCM. This effect is due to a decreasing shielding and lower negative net charge and electron density of the sulfur atom e.g., PS_4^{3-} (ortho-thiophosphate) may be transformed to other thiophosphates, such as $\text{P}_2\text{S}_7^{4-}$ (pyro-thiodiphosphate), $\text{P}_2\text{S}_6^{4-}$ (hypo-thiophosphate) and $\text{P}_2\text{S}_6^{2-}$ (meta-thiophosphate). In ortho-thiophosphates, a negative net charge of three electrons is distributed equally over the four sulfur atoms. While for pyro-thiophosphates only two electrons over three sulfur atoms are distributed, one P–S–P bridge exists, which can affect photoelectron transition from occupied S 1s orbitals to unoccupied S 3p s* antibonding orbitals. However, the fact that no shift can be observed for the NCM811 coated with LiNbO_3 demonstrates that interfacial side reactions can be effectively inhibited.

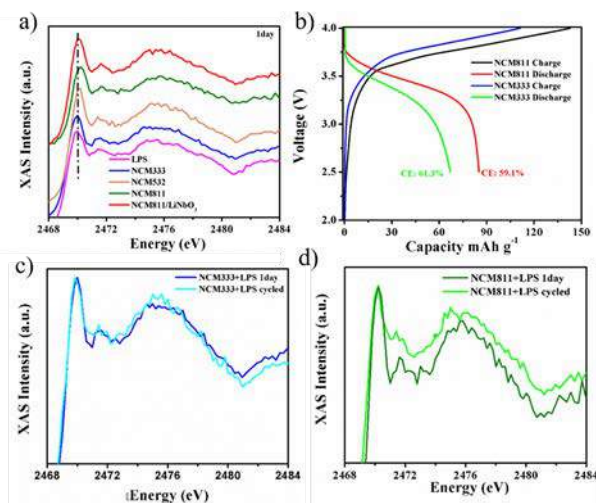


Figure II.5.A.1 (a) S K-edge XANES spectra of LPS mixed with NCM333, 523, 811 and 811 coated with LiNbO_3 , (b) 1st cycle charge and discharge profile of NCM333 and NCM811 cathode. S K-edge XANES spectra of cycled solid state batteries which assembled with (c) LPS-NCM333 and (d) LPS-NCM811

The first charge discharge cycle of NMC333 and NMC811-based cells show rather low active material utilization ca. 46% and poor coulombic efficiency ca. 60 %, which may results from the inadequate electronic connectivity in the electrode composite and/or active material/electrolyte due to side reactions (Figure II.5.A.1b). However, the corresponding XAS spectra after 1 cycle (Figure II.5.A.1c ad Figure II.5.A.1d) look nearly identical to the pristine electrodes i.e., no clear evidence of additional LPS decomposition reactions was observed as compared to the pristine electrode after 1 day of storage.

The high solubility of intermediate products in Li/S batteries i.e., lithium polysulfide and the resultant shuttle effect lead to a rapid capacity fading along with a low coulombic efficiency. We studied the effect of a co-block polymer binder to mitigate some of these issues. The PEO unit in the co-block polymer can strongly bond with the lithium polysulfide and suppress the active materials dissolution, whereas the insoluble PS polymer chain can maintain the mechanical strength of the binder in the DOL/DME electrolyte.

In situ UV–vis spectroscopy of 0.02 g PVdF and co-block polymer in 5 mL 0.5 mmol/L polysulfide in 1,3-dioxolane (DOL)/1,2-di-methoxyethane (DME) solution (1:1 v/v) over 24 h is shown in Figure II.5.A.2. In the presence of co-block polymer binder the polysulfide absorption bands at 287, 316 and 430 nm continuously decrease during the test. These results indicate that the ethylene oxide group in PEO can bind polysulfide and remove them from the solution.

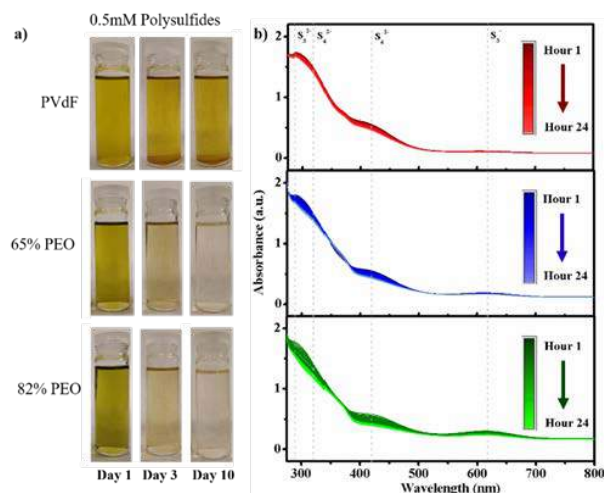


Figure II.5.A.2 Optical images (a) and UV-vis absorbance spectra (b) of and PVdF co-block polymer (65% PEO, 82% PEO) binder in 0.05 mmol/L polysulfide solution in DOL/DME

The galvanostatic cycling of Li/S coin cells show (Figure II.5.A.3a) that co-block polymer-based (65% PEO, 82% PEO) cathodes exhibit higher cell capacity and coulombic efficiency than PVdF-based cathodes. The Li⁺-conductive PEO enhances sulfur utilization and better capacity retention during the electrochemical charge-discharge process. The *in operando* S K-edge XAS spectra (Figure II.5.A.3 c-e) show peaks at 2472.2 and 2480.0 eV, which are attributed to polysulfides and sulfonyl groups in LiTFSI, respectively. The increase of the polysulfide peak intensity is suppressed in the presence of the co-block polymer binder. This observation suggests the 65% PEO co-block polymer binder inhibits dissolution of polysulfides into the electrolyte during electrochemical charge-discharge process.

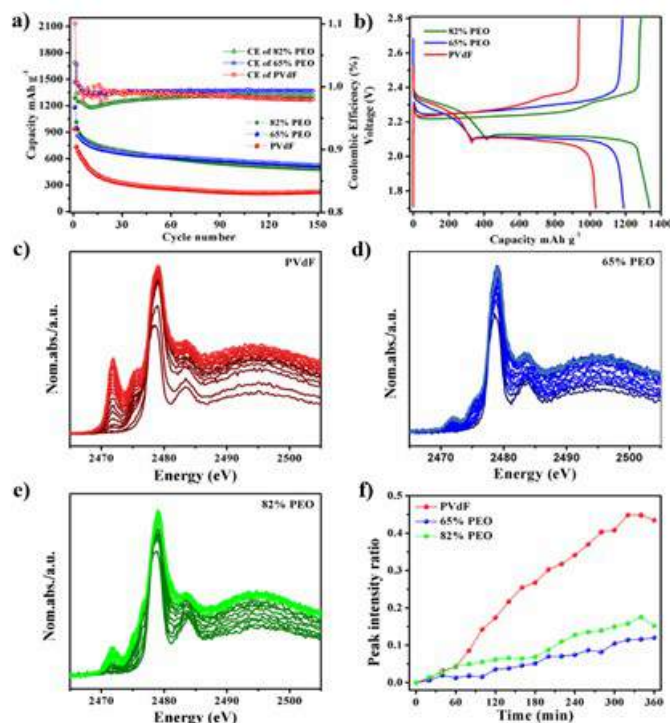


Figure II.5.A.3 Discharge capacity and coulombic efficiency at 0.2 C (a), and discharge/charge voltage profiles at 0.05 C of sulfur composite cathodes with PVdF and co-block polymer binder. In operando sulfur K-edge XAS spectrum of PVdF (c) and co-block polymer-based (d,e) composite cathodes after 1st discharge. 2472 eV polysulfides peak normalized intensity (f)

Fluorescent species are formed during cycling of lithium batteries as a result of electrolyte decomposition due to the instability of the non-aqueous electrolytes and side reactions that occur at the electrode surface. The increase in the background fluorescence due to the presence of these components makes it harder to analyse data due to the spectroscopic overlap of Raman scattering and fluorescence. We pioneered the use of Kerr gated Raman spectroscopy for the isolation of the scattering effect from the fluorescence enabling the collection of the Raman spectra of LiPF_6 salt and LiPF_6 -based organic carbonate electrolyte, without the interference of the fluorescence component.

Kerr gate Raman is also an effective technique to suppress the fluorescence background in Raman experiments [1],[2],[3],[4], thereby providing extra sensitivity via use of lower wavelength laser excitation in order to allow detection of surface layers and solid electrolyte interphase compounds on battery electrodes. Kerr gate Raman is based on the different time-dependence of fluorescence and Raman scattering signals upon short-pulse optical excitation. While fluorescence has a finite lifetime in the order of hundreds of picoseconds (ps) to nanoseconds (ns), Raman scattering is instantaneous and follows in time the initiating laser pulse within picoseconds (ps) or femtoseconds (fs). Such distinct time-domains for these two processes opens up a technical opportunity for separating them, provided an ultra-fast gating mechanism of the optical signal is coupled with the excitation pulse.

We have demonstrated with proof-of-concept experiments that the background fluorescence emission in the scattering spectrum of LiPF_6 as salt and in the conventional battery electrolyte with EC/DMC solvents can be minimised or completely suppressed by Kerr gated Raman (Figure II.5.A.4). Fluorescent species are formed during cycling of lithium ion batteries as a result of electrolyte decomposition due to the instability of the non-aqueous electrolytes and side reactions that occur at the electrode surface. The increase in the background fluorescence due to the presence of these components makes it harder to analyse data due to the spectroscopic overlap of Raman scattering and fluorescence. It has been demonstrated that Kerr gate Raman is an effective technique for the isolation of the scattering effect from the fluorescence enabling the investigation of the decomposition of battery electrolyte components and potentially identifying the source of the fluorescent background from trace organics left over from the recrystallization of LiPF_6 . In the spectra collected for water contaminated LiPF_6 salt, not only was it possible to detect peaks within the region for those associated with PF_6^- , but also to POF_3 , a well-known degradation compound resulting for hydrolysis of LiPF_6 . Crucially this result highlights how Kerr gated Raman can be used to evaluate degradation reaction pathways as well as providing a method of quality control in detecting the surface speciation on LiPF_6 salt samples before electrolyte preparation.

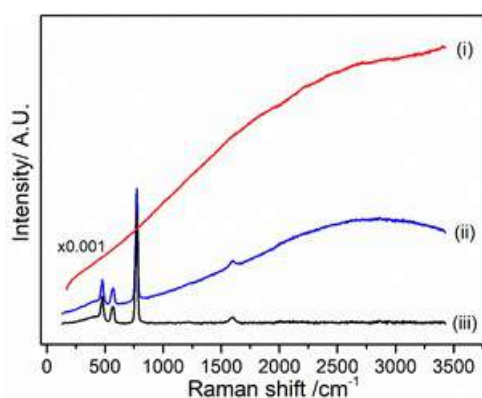


Figure II.5.A.4 Raman spectrum of pristine LiPF_6 salt collected with a 400 nm laser wavelength in (i) CW, (ii) Kerr gated mode, (iii) baseline correction of Kerr gated spectrum. The intensity of the (i) CW spectrum has been scaled by $\times 0.001$ in order to observe all three spectra on the same axis

Kerr gated measurements of 1M LiPF_6 in EC/DMC electrolyte showed bands associated with each of the components when aged in air and a broad band at 3500 cm^{-1} and a change in the relative intensity ratio of the bands related to $\text{C}=\text{O}$ were observed due to the coordination of the water molecules after addition of water.

The present study highlights Kerr gated Raman as a powerful technique that can be applied in the investigation of electrode/electrolyte interfaces and the speciation of the solid electrolyte interphase of battery systems in ex situ or operando studies, even in the presence of fluorescent species formed during cycling due to the suppression of the background emission

Conclusions

1. Ethylene oxide-polystyrene co-block polymer binders can prevent dissolution of Li-polysulfides in the electrolyte and help improve long-term electrochemical performance of Li-S batteries.
 - 65% ethylene oxide unit co-block polymer binder inhibits Li-polysulfides dissolution and maintain mechanical integrity of the sulfur cathode during cycling.
 - High content of ethylene oxide (82%) in the co-block polymer lead to dissolution of the binder and Li-polysulfides into electrolyte and its accumulation on the surface of Li-anode.
2. Carried out proof-of-concept Kerr gated Raman experiments to investigate electrolyte degradation processes Li and Li-ion batteries.
 - The present study shows for the first time that Kerr gate Raman can be applied ex situ or in situ in the investigation of electrode/electrolyte interfaces of battery systems even in the presence of fluorescent species formed during cycling.

Key Publications

1. Laura Cabo-Fernandez, Alex Neale, Filipe Braga, Igor Sazanovich, Robert Kostecki, Laurence Hardwick, “Kerr gated Raman spectroscopy of a LiPF₆-based organic carbonate electrolyte for Li-ion batteries”, Physical Chemistry Chemical Physics, DOI: [10.1039/C9CP02430A](https://doi.org/10.1039/C9CP02430A)
2. Ulrike Boesenberg, Dimosthenis Sokaras, Dennis Nordlund, Tsu-Chien Weng, Evgeny Gorelov, Thomas J. Richardson, Robert Kostecki, Jordi Cabana “Electronic structure changes upon lithium intercalation into graphite – Insights from ex situ and operando x-ray Raman spectroscopy”, Carbon, 143, 371-377 (2019). <https://doi.org/10.1016/j.carbon.2018.11.031>
3. Atetegeb Meazah Haregewoin, Lydia Terborg, Liang Zhangb, Sunhyung Jurng, Brett L. Lucht, Jinghua Guo, Philip N. Ross, Robert Kostecki, “The electrochemical behavior of poly 1-pyrenemethyl methacrylate binder and its effect on the interfacial chemistry of a silicon electrode”, Journal of Power Sources 376 (2018) 152–160, <https://doi.org/10.1016/j.jpowsour.2017.11.060>
4. Ivana Hasa, Atetegeb Haregewoin, Hans Bechtel, Jinghua Guo, Philip N. Ross, Liang Zhang, Robert Kostecki, “On the Origins of Interfacial Instability of Intermetallic Anodes”, International Coalition for Energy Storage and Innovation and Pacific Power Source Symposium Joint Meeting, January 9, 2019, Waikaloa Village, HI, USA
5. Ivana Hasa, Atetegeb Meazah Haregewoin, Lydia Terborg, Liang Zhang, Sunhyung Jurng, Brett L. Lucht, Jinghua Guo, Philip N. Ross, Robert Kostecki, “On the Origins of Interfacial Instability of Intermetallic Li-ion Anodes”, E-MRS 2018 Fall Meeting, Warsaw, Poland, September 17-20, 2018, (invited talk).
6. Atetegeb Meazah Haregewoin, Lydia Terborg, Liang Zhang, Sunhyung Jurng*, Brett L. Lucht*, Jinghua Guo, Philip N. Ross, Robert Kostecki, “The Electrochemical Behavior of Binders and their Effect on the Interfacial Chemistry of a Silicon Electrode”, 69th Annual ISE Meeting, Bologna, Italy, September 2-7.
7. R. Kostecki, I. Hasa, A. Haregewoin, L. Zhang, P. Ross, “ Surface reactivity of Li-ion intermetallic electrodes in organic carbonate electrolyte.”, 256th ACS National Meeting, Boston, MA, August 19-23, 2018 (invited talk)

8. Robert Kostecki, ““Understanding Charge and Mass Transport across Interfaces and Interphases in Rechargeable Batteries”, 2nd International conference on Electrochemical Energy Science and Technology 2018 (EEST2018), Niagara Falls, Canada, August 13-17, 2018 (kenote lecture)
9. Robert Kostecki, “Studies of interfacial instability of intermetallic anodes”, Telluride Workshop on “Interfacial Chemistry and Charge Transfer for Energy Storage and Conversion, July 23-27, 2018, Telluride, CO (invited talk)

References

1. A. Guéguen, D. Streich, M. He, M. Mendez, F. F. Chesneau, P. Novák and E. J. Berg, Decomposition of LiPF₆ in High Energy Lithium-Ion Batteries Studied with Online Electrochemical Mass Spectrometry, *J. Electrochem. Soc.*, 2016, **163**, A1095–A1100.
2. P. Matousek, M. Towrie and A. W. Parker, Fluorescence background suppression in Raman spectroscopy using combined Kerr gated and shifted excitation Raman difference techniques, *J. Raman Spectrosc.*, 2002, **33**, 238–242.
3. P. Matousek, M. Towrie, C. Ma, W. M. Kwok, D. Phillips, W. T. Toner and A. W. Parker, Fluorescence suppression in resonance Raman spectroscopy using a high- performance picosecond Kerr gate, *J. Raman Spectrosc.*, 2001, **32**, 983–988.
4. P. Matousek, M. Towrie and A. W. Parker, Efficient Rejection of Fluorescence from Raman Spectra Using Picosecond Kerr Gating, *Appl. Spectr.*, 1999, **53**, 1485–1489.

Acknowledgements

This work has been performed in close collaboration with V. Battaglia (ABMR program leads), ABMR Cathode and Anode Task Groups (ANL, LBNL, SUNY, UP, HQ, NREL, UU), R-C. Lee, J. Franklin, G. Chen, M. Doeff, K. Persson, V. Zorba, W. Yang, C. Ban, N. Balsara, B. McCloskey, Advanced Light Source (H. Bechtel, E. Rotenberg, E. Crumlin), University College London (P. Shearing, J. Franklin), University of Liverpool (UK) (L. Hardwick), Central Laser Facility, Research Complex at Harwell (UK), University of California, Berkeley, and Umicore, Farasis Energy, Inc.

II.5.B Advanced in situ Diagnostic Techniques for Battery Materials (BNL)

Xiao-Qing Yang, Principal Investigator

Chemistry division, Brookhaven National Laboratory
Bldg. 555
Upton, NY 11973
E-mail: xyang@bnl.gov

Seongmin Bak, Principal Investigator

Chemistry division, Brookhaven National Laboratory
Bldg. 555
Upton, NY 11973
E-mail: smbak@bnl.gov

Tien Duong, DOE Technology Development Manager

U.S. Department of Energy
E-mail: Tien.Duong@ee.doe.gov

Start Date: October 1, 2018

End Date: September 30, 2019

Project Funding (FY19): \$500,000

DOE share: \$500,000

Non-DOE share: \$0

Project Introduction

This project will be focused on the development of advanced diagnostic characterization techniques for the following issues: obtaining in-depth fundamental understanding of the mechanisms governing the relationship between the structure and the performance of battery materials; providing guidance and approaches to improve the properties of battery materials. The unique approach of this project is the development and application of combined synchrotron based in situ X-ray techniques such as x-ray diffraction (XRD), pair distribution function (PDF), hard and soft x-ray absorption (XAS and SXAS), together with other imaging and spectroscopic tools such as transmission electron microscopy (TEM), scanning transmission electron microscopy (STEM), mass spectroscopy (MS), X-Ray fluorescence microscopy (XRF) and transmission x-ray microscopy (TXM), as well as neutron-based techniques, such as neutron diffraction and neutron PDF (NPDF). For advanced Li-ion battery technologies, the revolutionary approaches using new generation of materials for cathode, anode, electrolyte, and separator are in the horizon. The new generation of cathode materials such as high voltage spinels ($\text{LiMn}_{2-x}\text{Ni}_x\text{O}_4$), Li-rich high energy density $\text{Li}_{1+x}(\text{NiMnCo})\text{O}_2$ (NMC) composite materials, high Ni content NMC cathode materials, and high energy density S-based cathode materials, together with high energy density lithium metal anode materials will significantly increase the energy density of the beyond lithium-ion battery systems. However, many technical barriers must be overcome before the large-scale commercialization of these new materials can be realized. This project will use the time-resolved x-ray diffraction TR-XRD and absorption (TR-XAS) developed at BNL to study the kinetic properties of these materials with structural sensitivity (TR-XRD) and elemental selectivity (TR-XAS). This project will develop and apply the HRTEM, TXM and PDF techniques, as well as neutron diffraction and neutron PDF to study the mechanisms of capacity and performance fading of cathode and anode materials. Another important issue is the thermal stability of new cathode materials which is closely related to the safety of the batteries. This problem will be studied using the combined TR-XRD, TR-XAS with mass spectroscopy (MS). This project also proposes to develop a novel in situ and ex situ X-ray fluorescence (XRF) microscopy combined with X-ray absorption spectroscopy (XAS) technique, which will enable us to track the morphology and chemical state changes of the electrode materials during cycling. In summary, this project supports the goals of VTO, the Battery and Electric Drive Technologies, and BMR program of by developing new diagnostic technologies and applying them to the beyond lithium-ion battery systems and by providing guidance for new material development.

Objectives

The primary objective of this project is to develop new advanced in situ material characterization techniques and to apply these techniques to support the development of new cathode and anode materials with high energy and power density, low cost, good abuse tolerance, and long calendar and cycle life for the next generation of lithium-ion batteries (LIBs) to power plug-in hybrid electric vehicles (PHEV). The diagnostic studies will be focused on issues relating to capacity retention, thermal stability; cycle life and rate capability of advanced Li-ion batteries.

Approach

- Using nano-probe beamline at NSLSII to study the elemental distribution of new solid electrolyte materials for Li-ion and Na-ion batteries
- Using the pair distribution function (PDF) to study the high energy density LiCoO_2 with high charging voltage limit. Using both x-ray (x-PDF) and neutron (n-PDF) probes to study the mechanism of anionic redox reaction (ARR) in cathode materials for Li-ion batteries and explore the potential of using this material for high energy density cells.
- Using transmission x-ray microscopy (TXM) to do multi-dimensional morphological/chemical imaging of cathode materials
- Using a combination of time resolved X-ray diffraction (TR-XRD) and mass spectroscopy (MS), together with in situ soft and hard X-ray absorption (XAS) during heating to study the thermal stability of the electrode materials
- Using in situ XRD and XAS, to study the new concentration gradient cathode materials to improve the cycle life of Li-ion batteries
- Design and carry out three-dimensional (3D) STEM tomography experiments to study high energy density $\text{Li}_{1.2}\text{Ni}_{0.15}\text{Co}_{0.1}\text{Mn}_{0.55}\text{O}_2$ cathode materials at pristine state and after multiple cycling.

Results

In FY2019, BNL has been focused on the ex situ soft x-ray absorption (sXAS) studies at oxygen and sulfur K-edge of novel organic disulfide cathode material for Li-S batteries at different charged and discharged states. At BNL, we have design and synthesized novel organodisulfide electrode material 2,3,4,6,8,9,10,12- Octathia biscyclopenta [b,c]-5,11-antraquinone-1,7-dithione (TPQD) for LIBs. As shown in Figure II.5.B.1, TPQD structure dithiolane group coordinated to a molecular benzoquinone skeleton through 1,4-dithiane, here four-electron redox of disulfides and two-electron redox of 1-4-benzoquinone (BQ) are expected with a theoretical capacity of 324 mAh g^{-1} . Our electrochemical results indicated that the TPQD electrode exhibits a high initial capacity of 251.7 mAh g^{-1} , which is corresponding to the 4.7 electron redox per formula unit. Thanks to the fast kinetics of BQ and π -conjugation structure, TPQD also delivers good high rate capability (150 mAh g^{-1} at 5C) with stable cyclic performance. O K-edge XANES spectra were measured and shown in Figure II.5.B.2 to confirm the electrochemical mechanism of BQ in TPQD electrode. For the as-prepared TPQD, a sharp peak at 531 eV is observed, which is corresponding to the $\text{O}1s-\pi^*$ ($\text{C}=\text{O}$) excitation that originates from the quinone. It can be clearly observed for the spectra at the 1st and 2nd discharge state that the peaks located at 531 eV markedly disappeared, meanwhile two new peaks appeared at around 534 and 539 eV, attributing to the $\text{O}1s-\sigma^*$ ($\text{O}-\text{C}=\text{C}$) and $\text{O}1s-\sigma^*$ ($\text{O}-\text{Li}$) excitation, respectively. That means a successful transformation from $\text{C}=\text{O}$ to $\text{C}=\text{C}-\text{O}-\text{Li}$ during the lithiation process. When the electrodes are recharged back 3V, the characteristic peaks at 534 and 539 eV are obviously weakened and a strong peak at 531 eV appeared again, indicating the reformation of $\text{C}=\text{O}$ bonding.

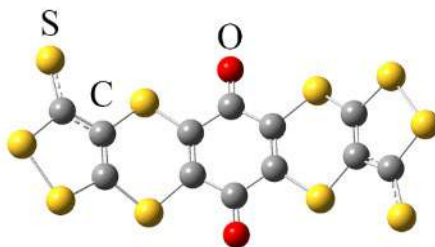


Figure II.5.B.1 Optimized structure and bond length of TPQD obtained by DFT calculation (grey denotes to the carbon, yellow for sulfur and red for oxygen)

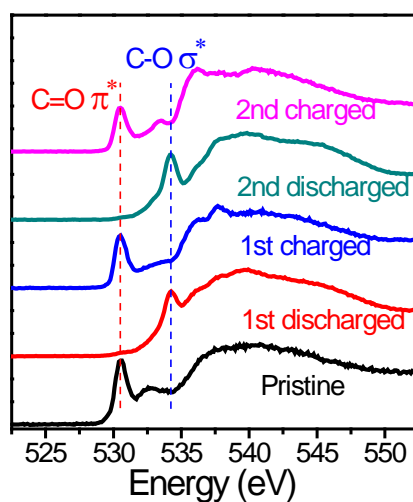


Figure II.5.B.2 O K-edge XANES spectra of TPQD electrodes at the different states of charge

To study the redox behavior of the disulfide bond ($-S-S-$) in the dithiolane, S K-edge XAS spectra of TPQD electrodes were collected at pristine, after the first discharge, and after first charge states, as shown in Figure II.5.B.3 b. For all three spectra, there are three main peaks located at 2469.5 eV, 2472.0 eV, and 2473.6 eV, which are assigned to the transition from S 1s to $S=C \pi^*$ (marked as 3), $S-S \sigma^*$ (marked as 4), and $S-C \sigma^*$ (marked as 5) states, respectively. No changes of peak 3 before and after discharge and charge were observed, indicating $S=C$ groups in the TPQD are not involved in the charge storage process at all. By comparing the spectra of the discharged samples with that of the pristine one, two significant changes can be found: (1) the intensity of peaks 4 and 5 decreased; (2) a new broad peak appeared at 2479.8 eV. A slight decrease in the intensity of peaks 4 and 5 is related to the breakage of disulfide bonds (i.e., $-C-S-S-C$) and its lithiation (i.e., formation of $-C-S-Li$). The newly formed feature at 2479.8 eV can be assigned to the transition from S 1s to the $S-O \sigma^*$ in SO_3^{2-} or $COSO_2^-$, which are possibly formed by a side reaction between the $-C-S-C$ bond and DOL.

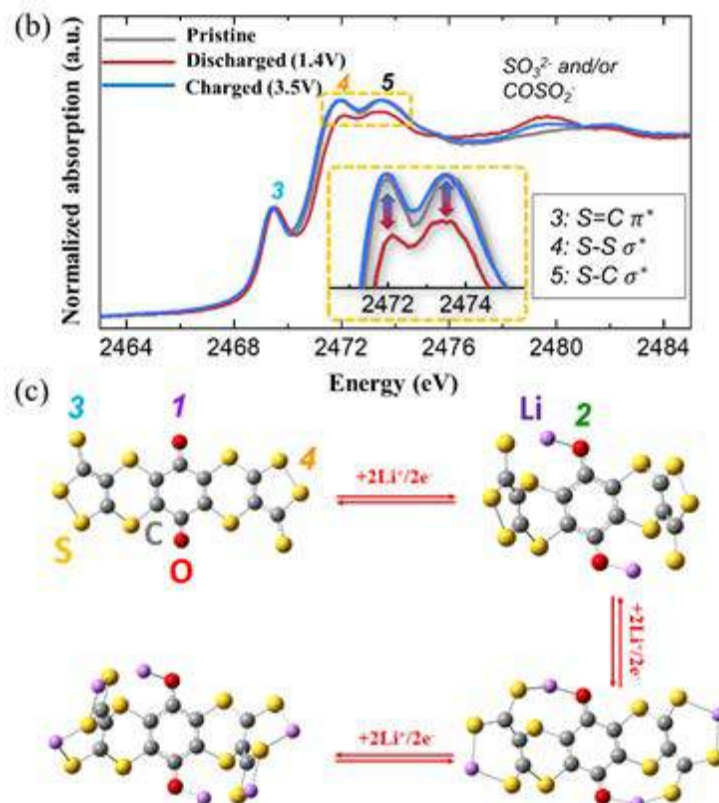


Figure II.5.B.3 (b) S-K edge XAS spectra of TPQD electrodes at different state of charge. (c) The structural evolution of TPQD electrodes during the lithiation process

In FY2019, BNL also carried out the ex situ X-ray microprobe. X-ray fluorescence microscopy (XRF) and sulfur K-edge X-ray absorption spectroscopy (XAS) studies of high energy density Li-S pouch cells. Chemical information of the sulfur species regarding the composition and distribution were studied using XRF. Figure II.5.B.4 depicts XRF and XAS spectra results from R1-R3 regions (Figure II.5.B.4 a) of the cycled sulfur cathode. Figure II.5.B.4b shows XRF image collected at R1 (7×7 mm) below an energy of 2469 eV, which only detects sulfur species with relatively low absorption energies. Apparently, this area is covered mainly by the low-valence sulfur species (in yellow color), with randomly distributed uncovered spots (in blue color). Further XAS analysis reveals that the low-valence sulfur species (from yellow area) are composed of Li polysulfides and Li sulfides; while the high valent species (from blue spots) are mainly sulfone and sulfate (Figure II.5.B.4 d). When the X-ray beam energy is increased to 2480 eV, more sulfur species with a wider valence range from S²⁻ to S⁴⁺ can be detected. In contrast to XRF at 2469 eV, more uniform mapping was observed at 2480 eV (Figure II.5.B.4 c). It means that the whole R1 area is evenly covered by sulfur species with a wider valence range. The comparison of Figure II.5.B.4 b and Figure II.5.B.4 c presents variation of the sulfur species in both oxidation states and distribution in the local R1 area, which suggests random distributed reaction areas in the region. Similar results i.e., randomly distributed reaction areas were observed in the R3 region (Figure II.5.B.4 h, Figure II.5.B.4 i and Figure II.5.B.4 j). However, more significant differences were found in the center region of the electrode (R2). Compared to R1 and R3, R2 experiences much more serious inhomogeneous reactions as proved by the uneven XRF mapping at both 2469 and 2480 eV (Figure II.5.B.4 e and Figure II.5.B.4 f). In addition, high contents of sulfone from TFSI, and S⁶⁺ from SO₄²⁻ were detected by XAS (Figure II.5.B.4 g), which are either from the residual of LiTFSI salt, or oxidation of the sulfur species by LiNO₃. This may be caused by earlier solvent depletion in R2 compared to R1 and R3 regions, which exacerbate polarization and thus decrease the reaction extent locally.

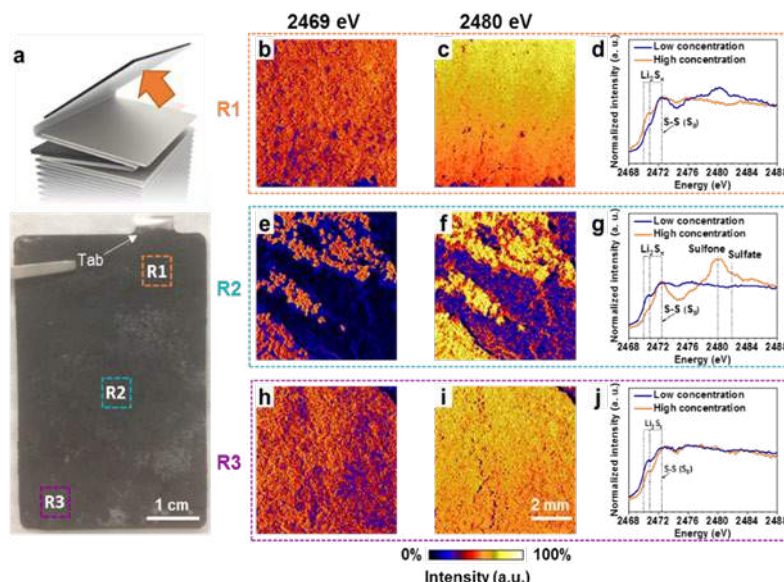


Figure II.5.B.4 Digital photograph for sulfur cathode obtained from the cycled pouch cell (schematic illustration) with indicating boxes for three selected spots of interest; outer region nearby electrode-tab (R1), central region (R2) and outer corner region (R3). Corresponding mappings of XRF at two different energy levels (2469 and 2480 eV) to investigate the status and distribution of sulfur species at the regions of R1 (b and c), R2 (e and f), and R3 (h and i). XAS spectra (d, g, and j) within an energy scanning range of 2468–2488 eV at two strong contrasted areas in XRF image respectively

Figure II.5.B.5 depicts XRF and XAS spectra results from R1-R3 regions (Figure II.5.B.5) of the cycled lithium metal anode. Figure II.5.B.5 shows XRF image collected at R1 (7×7 mm) below an energy of 2469 eV, which only detects sulfur species with relatively low absorption energies. Apparently, this area is covered mainly by the low-valence sulfur species (in yellow color), with randomly distributed uncovered spots (in blue color). Further XAS analysis reveals that the low-valence sulfur species (from yellow area) are composed of Li polysulfides and Li sulfides; while the high valent species (from blue spots) are mainly sulfone and sulfate. When the X-ray beam energy is increased to 2480 eV, more sulfur species with a wider valence range from S^{2-} to S^{4+} can be detected. In contrast to XRF at 2469 eV, more uniform mapping was observed at 2480 eV. It means that the whole R1 area is evenly covered by sulfur species with a wider valence range. Sulfur, polysulfide, Li_2S , SO_3^{2-} , $COSO_2^-$, SO_4^{2-} could be observed from Li metal anode side. This indicates the shuttling effect of lithium polysulfide as well as SEI formation with sulfur contained electrolyte. (also, heterogeneity of SOC). Similar as for cathode results reported in our Q3 report, the middle part of Li metal anode side also shows more heterogeneous distribution of sulfur species. Region 3 where the region most far from the tab shows much uniform chemical distribution.

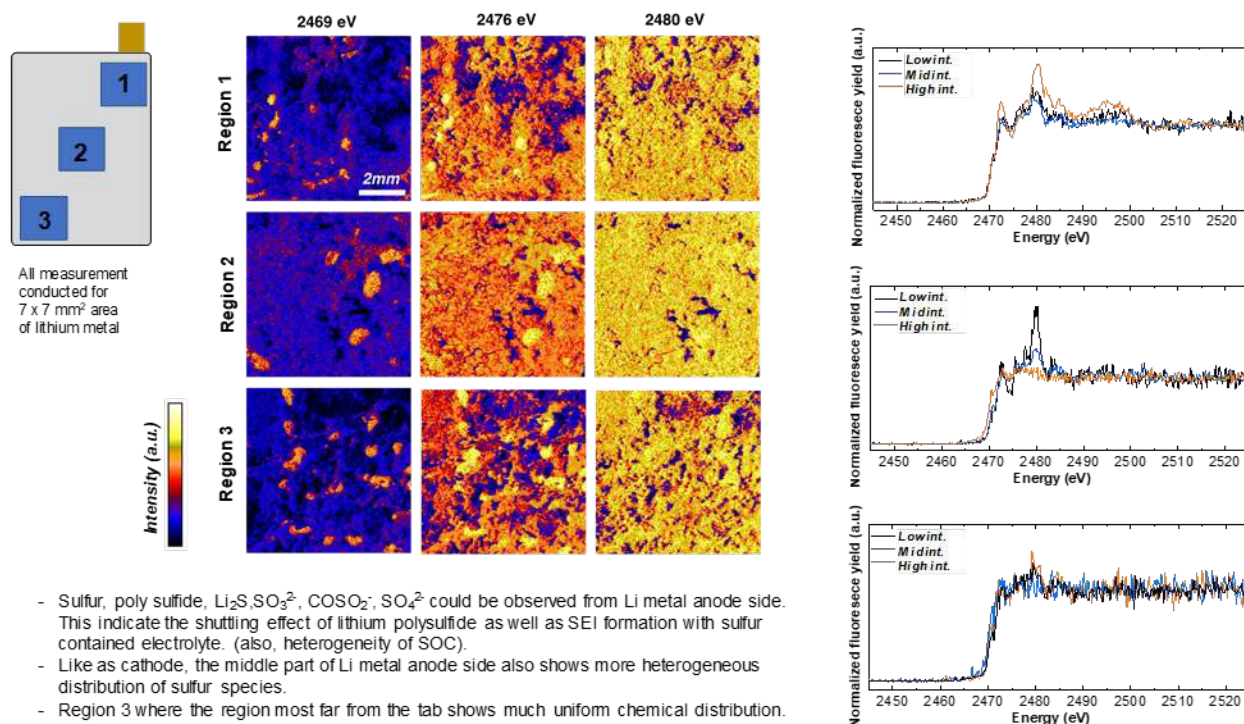


Figure II.5.B.5 Spatially-resolved XAS and XRF imaging for cycled Li metal anode (inner side)

Conclusions

This project, Advanced in situ Diagnostic Techniques for Battery Materials (BNL), has been successfully completed in FY2019. All milestones have been completed. The publication records are very good. Extensive collaboration with other national labs, U.S. universities and international research institutions were established.

Key Publications

Publications

1. Fei Wang, Enyuan Hu, Wei Sun, Tao Gao, Xiao Ji, Xiulin Fan, Fudong Han, Xiao-Qing Yang*, Kang Xu* and Chunsheng Wang*, "A rechargeable aqueous Zn^{2+} -battery with high power density and a long cycle-life", *Energy Environ. Sci.*, 2018, DOI: 10.1039/C8EE01883A, Publication date: October 3rd, 2018
2. Sol Yun, Seong-Min Bak, Sanghyeon Kim, Jeong Seok Yeon, Min Gyu Kim, Xiao-Qing Yang, Paul V. Braun*, Ho Seok Park*, "Rational Design of Hierarchically Open-Porous Spherical Hybrid Architectures for Lithium-Ion Batteries", *Adv. Energy Mater.*, DOI: 10.1002/aenm.201802816, Publication Date: December 20, 2018
3. Yejing Li, Xuefeng Wang, Yurui Gao, Qinghua Zhang, Guoqiang Tan, Qingyu Kong, Seongmin Bak, Gang Lu, Xiao-Qing Yang, Lin Gu, Jun Lu, Khalil Amine, Zhaoxiang Wang*, and Liquan Chen, "Native Vacancy Enhanced Oxygen Redox Reversibility and Structural Robustness", *Adv. Energy Mater.*, DOI: 10.1002/aenm.201803087, Publication Date: December 05, 2018
4. Yuwei Mao, Xuelong Wang, Sihao Xia, Kai Zhang, Chenxi Wei, Seongmin Bak, Zulipiya Shadike, Xuejun Liu, Yang Yang, Rong Xu, Piero Pianetta, Stefano Ermon, Eli Stavitski, Kejie Zhao, Zhengrui Xu, Feng Lin, Xiao-Qing Yang, Enyuan Hu and Yijin Liu, "High-Voltage Charging-Induced Strain, Heterogeneity, and Micro-Cracks in Secondary Particles of a Nickel-Rich Layered Cathode Material", *Adv. Funct. Mater.*, DOI: 10.1002/adfm.201900247, Publication Date: March 07, 2019

5. Zulipiya Shadike, Hung-Sui Lee, Chuanjin Tian, Ke Sun, Liang Song, Enyuan Hu, Iradwikanari Waluyo, Adrian Hunt, Sanjit Ghose, Yongfeng Hu, Jigang Zhou, Jian Wang, Paul Northrup, Seong-Min Bak, and Xiao-Qing Yang, "Synthesis and Characterization of a Molecularly Designed High-Performance Organodisulfide as Cathode Material for Lithium Batteries", *Adv. Energy Mater.*, DOI: 10.1002/aenm.201900705, Publication Date: April 10, 2019.
6. Ruoqian Lin, Enyuan Hu, Mingjie Liu, Yi Wang, Hao Cheng, Jinpeng Wu, Jin-Cheng Zheng, Qin Wu, Seongmin Bak, Xiao Tong, Rui Zhang, Wanli Yang, Kristin A. Persson, Xiqian Yu, Xiao-Qing Yang and Huolin L. Xin, "Anomalous metal segregation in lithium-rich material provides design rules for stable cathode in lithium-ion battery", *Nature Communications*, DOI: 10.1038/s41467-019-09248-0, Publication Date: April 09, 2019.
7. Dongqing Liu, Qipeng Yu, Shuai Liu, Kun Qian, Shuwei Wang, Wei Sun, Xiao-Qing Yang, Feiyu Kang, and Baohua Li*, "Evolution of Solid Electrolyte Interface on TiO₂ Electrodes in an Aqueous Li-Ion Battery Studied Using Scanning Electrochemical Microscopy", *J. Phys. Chem. C* 2019, 123, 20, 12797-12806, DOI: <https://doi.org/10.1021/acs.jpcc.9b01412>, Publication Date: May 1, 2019.
8. Qi-Qi Qiu, Zulipiya Shadike, Qin-Chao Wang, Xin-Yang Yue, Xun-Lu Li, Shan-Shan Yuan, Fang Fang, Xiao-Jing Wu, Adrian Hunt, Iradwikanari Waluyo, Seong-Min Bak*, Xiao-Qing Yang*, and Yong-Ning Zhou*, "Improving the Electrochemical Performance and Structural Stability of the LiNi_{0.8}Co_{0.15}Al_{0.05}O₂ Cathode Material at High-Voltage Charging through Ti Substitution", *ACS Appl. Mater. Interfaces*, 2019, 11, 26, 23213-23221, DOI: 10.1021/acsami.9b05100, Publication Date: June 11, 2019.
9. Shaofeng Li, Sang-Jun Lee, Xuelong Wang, Wanli Yang, Hai Huang, Daniel S. Swetz, William B. Doriese, Galen C. O'Neil, Joel N. Ullom, Charles J. Titus, Kent D. Irwin, Han-Koo Lee, Dennis Nordlund, Piero Pianetta, Chang Yu, Jieshan Qiu, Xiqian Yu, Xiao-Qing Yang, Enyuan Hu*, Jun-Sik Lee*, and Yijin Liu*, "Surface-to-Bulk Redox Coupling through Thermally Driven Li Redistribution in Li- and Mn-Rich Layered Cathode Materials", *J. Am. Chem. Soc.*, DOI: 10.1021/jacs.9b05349, Publication Date (Web): July 9th, 2019.
10. Shuai Liu, Zepeng Liu, Xi Shen, Xuelong Wang, Sheng-Chieh Liao, Richeng Yu, Zhaoxiang Wang*, Zhiwei Hu, Chien-Te Chen, Xiqian Yu, Xiaoqing Yang, Liquan Chen, "Li-Ti Cation Mixing Enhanced Structural and Performance Stability of Li-Rich Layered Oxide", *Adv. Energy Mater.*, DOI: 10.1002/aenm.201901530, Publication Date (web): July 15, 2019.
11. Ming-Hui Cao, Zulipiya Shadike, Seong-Min Bak, Tian Wang, Enyuan Hu, Steven Ehrlich, Yong-Ning Zhou*, Xiao-Qing Yang*, Zheng-Wen Fu*, "Sodium storage property and mechanism of NaCr_{1/4}Fe_{1/4}Ni_{1/4}Ti_{1/4}O₂ cathode at various cut-off voltages", *Energy Storage Materials*, DOI: 10.1016/j.ensm.2019.07.022, publication date (Web): July 22, 2019.
12. Enyue Zhao, Minghao Zhang, Xuelong Wang, Enyuan Hu, Jue Liu*, Xiqian Yu*, Marco Olguin, Thomas A Wynn, Ying Shirley Meng*, Katharine Page, Fangwei Wang, Hong Li, Xiao-Qing Yang, Xuejie Huang, Liquan Chen, "Local structure adaptability through multi cations for oxygen redox accommodation in Li-Rich layered oxides", *Energy Storage Materials*, DOI: 10.1016/j.ensm.2019.07.032, publication date (Web): July 25, 2019.
13. Tao Deng, Xiulin Fan*, Longsheng Cao, Ji Chen, Singyuk Hou, Xiao Ji, Long Chen, Shuang Li, Xiuquan Zhou, Enyuan Hu, Dong Su, Xiao-Qing Yang, Chunsheng Wang*, "Designing In situ-Formed Interphases Enables Highly Reversible Cobalt-Free LiNiO₂ Cathode for Li-ion and Li-metal Batteries", *Joule*, DOI: 10.1016/j.joule.2019.08.004, Publication Date (web): September 4, 2019.

Presentations

1. Zulipiya Shadike, Ruoqian Lin, Enyuan Hu, Seong-Min Bak, Xiao-Qing Yang*, Hung-Sui Lee, Xiqian Yu, Yong Chu, and Yijin Liu, "Using Synchrotron X-ray and Neutron Based Scattering as well

as TXM and TEM Imaging Techniques to Study the New Cathode Materials for Batteries and Studies on Li Metal Anode Protections”, presented at Materials Science and Engineering Colloquium, at Department of Applied Physics & Applied Mathematics, Columbia University, New York, USA, November 16, 2018. **Invited**

2. Ruoqian Lin, Zulipiya Shadike, Seong-Min Bak, Enyuan Hu, Huolin Xin, Xiaojing Huang, YoungHo Shin, Hung-Sui Lee, Yong S. Chu, and Yijin Liu, and Xiao-Qing Yang*, “Using multi-modal and multi-scale TEM and TXM imaging techniques to study the structural stability of high Ni-content cathode materials”, presented at 2018 MRS Fall Meeting, Boston, USA, November 29, 2018. **Invited.**
3. Enyuan Hu, Yijin Liu, Huolin Xin, and Xiao-Qing Yang. “Identification and Visualization of Chemical Outliers through Scientific Data Mining in Nanoscale Spectro-microscopic Study of NMC Electrode”, 2019 TMS Annual Meeting & Exhibition, San Antonio, TX, USA, March 10-15, 2019. **Invited.**
4. Ruoqian Lin, Zulipiya Shadike, Seong-Min Bak, Enyuan Hu, Huolin Xin, Xiaojing Huang, YoungHo Shin, Hung-Sui Lee, Yong S. Chu, Yijin Liu, and Xiao-Qing Yang*, “Understanding capacity fade in high-nickel content cathode materials for lithium batteries:”, presented at U.S.-China Clean Energy Research Center for Clean Vehicles (CERC-CVC), Xining, China, June 23, 2019. **Invited.**

II.5.C Advanced Microscopy and Spectroscopy for Probing and Optimizing Electrode-Electrolyte Interphases in High Energy Lithium Batteries (UCSD)

Ying Shirley Meng, Principal Investigator

University of California, San Diego
9500 Gilman Drive
La Jolla, CA 92093
E-mail: shmeng@ucsd.edu

Tien Duong, DOE Technology Development Manager

U.S. Department of Energy
E-mail: Tien.Duong@ee.doe.gov

Start Date: October 1, 2018

End Date: January 31, 2020

Project Funding (FY19): \$364,000

DOE share: \$327,600

Non-DOE share: \$36,400

Project Introduction

The earliest developed LiCoO₂ layered oxide cathode material sparked the development of other layered cathode materials, dominating the positive electrode materials for lithium ion batteries. Within the practical operating conditions of today, the current generation layered oxide materials do not meet the future energy storage demands of 350 Wh kg⁻¹ at cell level. Li-rich layered oxide (LRLO) materials have the potential to meet the high energy demands. Unlike the classical layered oxides, LRLO materials exhibit capacities that go beyond conventional topotactic mechanistic theoretical values [1]. Despite its high capacities, this material has several challenges (voltage fading, structural instability, sluggish kinetics, cathode electrolyte

interphase instability, etc.) that must be overcome in order to reach commercialization. In the past five years, our research group has made great progress on developing advanced characterization techniques coupled with atomic scale modeling to properly characterize the dynamic phenomena that govern the performance limitations of LRLO materials. Furthermore, our efforts have guided the material synthesis and surface modification to improve capacity retention. By carefully controlling the oxygen activities through the creation of uniform oxygen vacancies, we were able to avoid structural decomposition in LRLO. Our materials deliver a discharge capacity as high as 306 mAh g⁻¹ with an initial coulombic efficiency of 90.6% [2]. Furthermore, they do not exhibit obvious capacity decay with a reversible capacity over 300 mAh g⁻¹ after 100 cycles at 0.1 C-rate. Our approach demonstrates the critical needs for advanced diagnosis and characterization. It is through the in-depth understanding of these high voltage cathode materials at atomistic and molecular level and their dynamic changes during the operation of batteries; we can successfully formulate strategies to further optimize this class of cathode materials, especially for the voltage instabilities. The diagnostic tools developed here can also be leveraged to study anode materials such as Li metal anode. The challenge of probing Li metal is the low dose tolerance (high beam sensitivity) of Li metal. We will have to apply cryogenic method (low-temperature) and low-dose electron microscopy and specialized camera to enable the characterization of the lithium metal.

Objectives

The proposed research aims to develop advanced microscopy and spectroscopy tools to probe, understand, and optimize the anion activities that govern the performance limitations such as capacity and voltage stabilities in high energy Li-excess transition metal (Ni, Co, Mn, etc.) oxides cathode materials. Our approach uniquely combines atomic resolution scanning transmission electron microscopy (STEM), electron energy loss spectroscopy (EELS), operando Bragg Coherent Diffraction Imaging (BCDI), and first principles computation to probe anion redox and oxygen evolutions in Li-excess NMC materials. Furthermore, we will track the lithium and oxygen dynamics under electrochemical testing via operando neutron diffraction which will enhance the understanding of the overall structural changes due to anion activities. Ultimately, this will hone in

on the synthesis efforts to produce the modified materials with the optimum bulk compositions and surface characteristics at large scale for consistently good performance. The above-mentioned characterization tools will be extended to diagnose various anode types, such as Li metal anode.

Approach

This unique approach combines STEM/EELS, operando BCDI, and *Ab initio* computation as diagnostic tools for probing anion redox and oxygen evolutions in Li-excess NMC materials. This allows for pinning down the atomistic/molecular mechanism of anion oxidation and determining the speciation compositions and surface characteristics for enabling high rate and long life in the proposed materials. Neutron enables the characterization of bulk material properties to enhance and further optimize high energy electrode materials. This work funds collaborations on EELS (Miaofang Chi, Oakridge National Laboratory); neutron diffraction (Ke An, ORNL); soft XAS (Marca Doeff, Lawrence Berkeley National Laboratory). It supports collaborative work with Zhaoping Liu and Yonggao Xia at Ningbo Institute of Materials Technology and Engineering China. It also supports collaboration with Battery500 consortium.

Results

The following progress has been achieved in FY19:

Benchmark modified LRLO cathodes performance

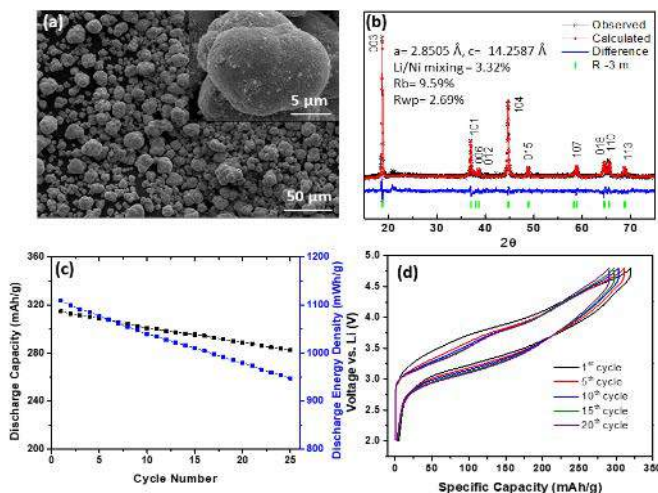


Figure II.5.C.1 (a). SEM images taken at different magnifications. (b). Rietveld refinement of the XRD pattern of LR-NCM. (c). The discharge capacity and energy density of the modified LR-NCM. (d). Voltage profiles of the modified LR-NCM at different cycle numbers.

a discharge capacity of 314 mAh/g and an energy density of 1109 mWh/g at the 1st cycle. The improved electrochemical performance is ascribed to the efficient utilization of oxygen activity through the creation of surface oxygen vacancies in the modified LR-NCM. After 25 cycles, the modified LR-NCM remains a specific capacity of 283 mAh/g (90.1% of the initial cycle) and an energy density of 940 mWh/g (84.7% of the initial cycle). The hysteresis between Li insertion and removal in the modified LR-NCM is shown in Figure II.5.C.1d. An increase of the hysteresis over cycling can be observed. Overall, the GSIR modified LR-NCM has been chosen as the benchmark cathode for its high specific capacity and coulombic efficiency. Further improvement is needed to evade the decrease in energy density and the increase of hysteresis over cycling. Novel electrolyte will be introduced to create a more stable cathode electrolyte interface (CEI) in the system. One strategy is to add electrolyte additives such as LiBOB and LiDFOB. Another strategy will be using carbonate-free, sulfone-based electrolyte with high Li salt concentration, which could support system's fast ion

A gas-solid interface reaction (GSIR) was introduced to achieve delicate control of oxygen activity in LRLO.

Li[Li_{0.144}Ni_{0.136}Co_{0.136}Mn_{0.544}]O₂ (denoted as LR-NCM) was synthesized through co-precipitation method (Figure II.5.C.1a). Carbon dioxide gas was used to create uniform oxygen vacancies on LR-NCM particles' surface without affecting structural integrity. Figure II.5.C.1b shows the Rietveld refined XRD pattern of LR-NCM after GSIR, in which all the peaks can be well indexed to R-3m space group. Li/Ni mixing of the sample is 3.32%. Element ratio of the modified LR-NCM was confirmed as Li:Ni:Co:Mn=1.155:0.128:0.141:0.535 by ICP-OES. The discharge capacity and energy density over cycling of the modified LR-NCM are shown in Figure II.5.C.1c. All the cells were charge/discharge at C/20 (1C=250mAh/g) for two cycles as an activation process before the cycling at C/10 rate. After activation, it delivers

exchange over large voltage window. Both strategies are expected to improve the cycling performance in LR-NCM through the modification of CEI.

Electrolyte additive LiBOB for the cycling performance improvement of LRLO cathodes

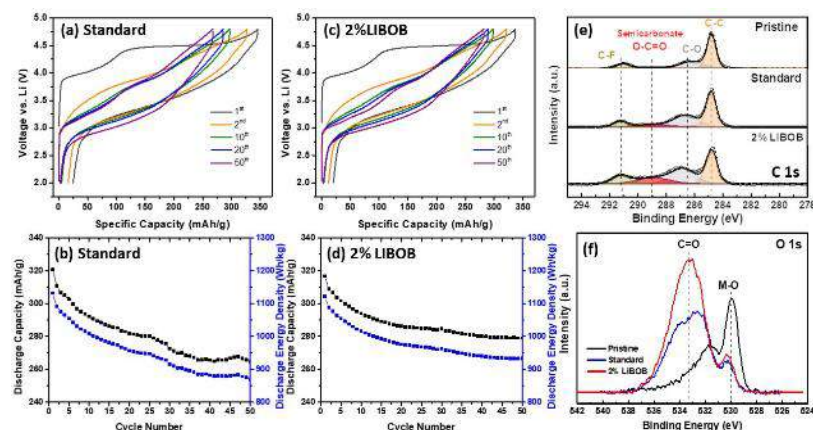


Figure II.5.C.2 (a). Voltage profiles and (b). cycling performance of the LR-NCM cycled in standard electrolyte. (c). Voltage profiles and (d). cycling performance of the LR-NCM cycled in 2% LiBOB electrolyte. (e). XPS C 1s and (f). XPS O 1s comparison of pristine LR-NCM electrode and LR-NCM cycled in different electrolyte after 50 cycles.

cells were charge/discharged at C/20 (1C=250 mAh/g) for two cycles and C/10 for the rest of the cycles. For the first cycle, LR-NCM delivers a discharge capacity of 321 mAh/g and an energy density of 1133 Wh/kg in Standard electrolyte. The LR-NCM cycled in 2% LiBOB exhibits slightly lower capacity of 317 mAh/g and energy density of 1123 Wh/kg. After 50 cycles in the Standard electrolyte, LR-NCM remains a specific capacity of 264 mAh/g (82.2% retention) and an energy density of 870 mWh/g. In comparison, the LR-NCM cycled in 2% LiBOB exhibits much better cycling stability with capacity of 279 mAh/g (88.0% retention) and energy density of 933 Wh/kg after 50 cycles. XPS was conducted to the pristine LR-NCM electrode and LR-NCM after 50 cycles in different electrolyte. Figure II.5.C.2e shows the XPS C 1s spectra where 4 different carbon types are detected, including C-C peak at 284.8 eV, C-O peak at 286.5 eV, O-C=O peak at 289.1 eV, and C-F (from PVDF) at 291.1 eV. A noticeable feature for the cathode cycled in 2% LiBOB is the appearance of the 289.1 eV peak. This can be attributed to the semi-carbonate species produced by the LiBOB decomposition. A more intense peak corresponding to C=O at around 533.2 eV in O 1s spectra is thus observed for LR-NCM cycled in 2% LiBOB, indicating the formation of a stable CEI layer [3]. Future work will focus on investigating other novel electrolyte systems for LR-NCM and further characterizations of the CEI layer through STEM-EELS.

GSIR modified $\text{Li}[\text{Li}_{0.144}\text{Ni}_{0.136}\text{Co}_{0.136}\text{Mn}_{0.544}]\text{O}_2$ was chosen as our benchmark cathode material for its high specific capacity and coulombic efficiency. To further optimize this material, a novel electrolyte with LiBOB additive (lithium bis(oxalato) borate) is introduced to the system. The baseline electrolyte used in this study is 1M LiPF_6 in EC: DMC=3:7 by volume (denoted as Standard); the novel electrolyte is 0.98M LiPF_6 +0.02M LiBOB in EC: DMC=3:7 by volume (denoted as 2% LiBOB). The voltage profiles and cycling performances of LR-NCM with different electrolyte are shown in Figure II.5.C.2a-d. All the

Cryo-EM and XPS comparison of cycled LRLO in different electrolyte

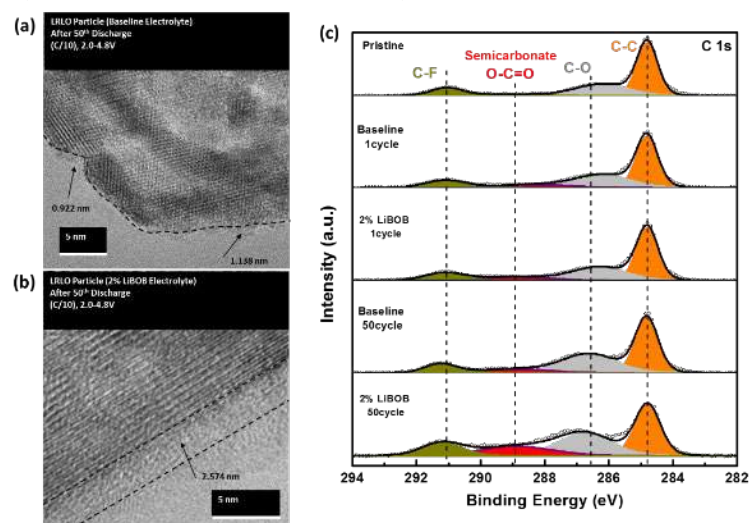


Figure II.5.C.3 Cryo-TEM images of the (a). cycled LR-NCM in the Baseline electrolyte and (b). in 2% LiBOB electrolyte. (c). XPS spectra of the pristine and cycled LR-NCM.

LR-NCM cycled in 2% LiBOB exhibits better cycling stability compared with that of LR-NCM cycled in the Baseline electrolyte. To explain the performance improvement, the CEI structure and chemistry were characterized with cryo-TEM and XPS. Note that TEM under cryo temperature is necessary to preserve CEI structure/chemistry and avoid electron beam damage. After the 50th discharge, the CEI structure in the Baseline electrolyte, shown in Figure II.5.C.3a, exhibits significant variations in thickness and uniformity, with open sections of minimal coverage allowing direct exposure of the electrolyte to the cathode particle surface. Conversely, the CEI generated on the LR-NCM particle after 50 cycles with the 2% LiBOB appears much more uniform in thickness and conformal in surface coverage

(Figure II.5.C.3b). XPS was then conducted to the pristine LR-NCM electrode and LR-NCM after different cycles in different electrolyte. Figure II.5.C.3c shows the XPS C1s spectra where 4 different carbon types are detected. A noticeable feature for the cathode cycled in 2% LiBOB is attributed to the semicarbonate species produced by the LiBOB decomposition, indicating the formation of a stable CEI layer. This is in approximate agreement regarding thickness with another CEI study [3], albeit for a different cathode material and lower voltage cutoff. Due to this stable CEI layer, the cycling performance of LR-NCM is largely improved with the LiBOB additive.

STEM and EELS comparison of cycled LRLO in different electrolyte

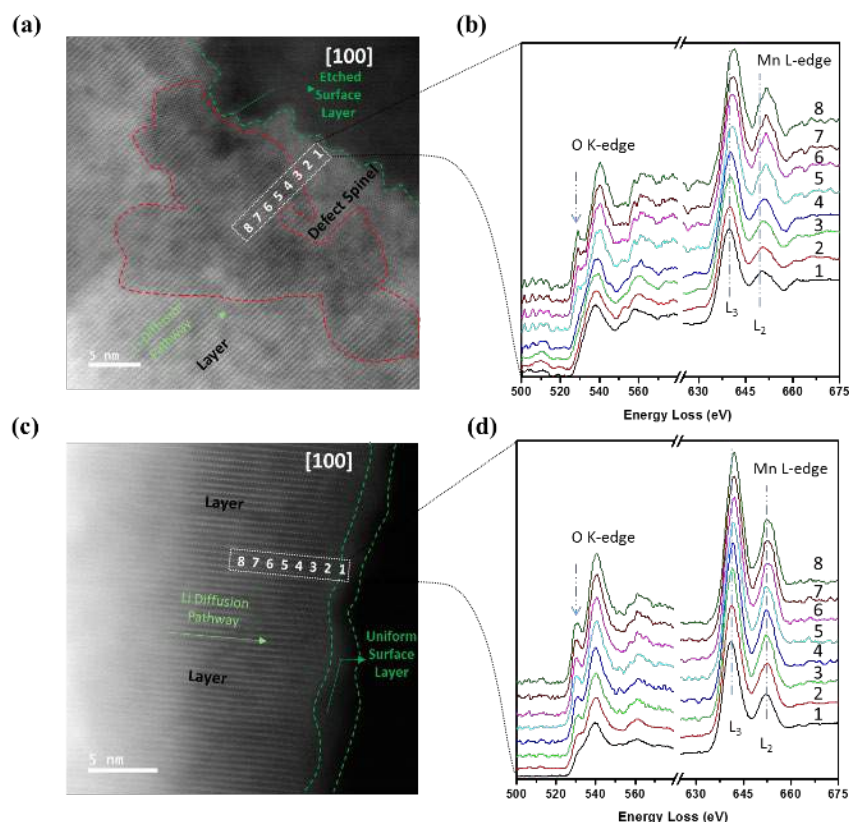


Figure II.5.C.4 STEM/HAADF images of the (a). cycled LR-NCM in the Baseline electrolyte and (b). cycled LR-NCM in 2% LiBOB electrolyte. Spatially resolved EELS spectra from the surface to the bulk of the (c). cycled LR-NCM in the Baseline electrolyte and (d). cycled LR-NCM in 2% LiBOB electrolyte.

STEM/HAADF images were collected for the samples cycled 50 times in different electrolyte to explain the performance improvement at atomic scale. For the sample cycled in the Baseline electrolyte (Figure II.5.C.4a), we clearly observed bulk structural degradation which is featured by the nucleation of nanovoids in the bulk lattice, as representatively revealed by the red dashed circle. TM ions were found in the Li layer in the subsurface regions, forming a defect spinel structure that is different from the layered structure in bulk. In addition, an etched surface was observed, which can be attributed to the defective CEI layer formed during cycling in the Baseline electrolyte. In sharp contrast, the cycled sample obtained from 2% LiBOB electrolyte shows uniform contrast across the entire grain (Figure II.5.C.4c), which corresponds to a well-defined layered structure after 50 cycles.

The formation of a more uniform CEI layer well prevents the structural transformation and degradation from particle surface to bulk. Spatially resolved EELS were also obtained at a step of ~ 0.8 nm from the surface to bulk and the spectra are presented in Figure II.5.C.4b and d. The data points are aligned with the HAADF image to indicate where each spectrum was taken. There is a clear O pre-peak in the O K-edge obtained from bulk of the particle cycled in the baseline electrolyte. This pre-peak starts to decrease when it comes to the interface region of the spinel-like phase, and disappears completely in the near surface. The disappearance of the pre-peak can be ascribed to the oxygen vacancy formation and reduction of neighboring TM which is verified by both L_3/L_2 peak intensity ratio and peak shift in the Mn L-edge. The same spectra evolution was only found in a thin surface region (less than 2 nm) for the cycled sample in LiBOB electrolyte. From the STEM/EELS results, it is clear that structural degradation and composition changes occur in the sample where the CEI is not well formed, which impedes the Li diffusion pathway and reduces the amount of active material during cycling. As a result, electrolyte additive LiBOB shows an improvement in both the rate performance and cycling stability of LR-NCM.

Comparison of cycled LRLO and classical layered oxides under heat treatment

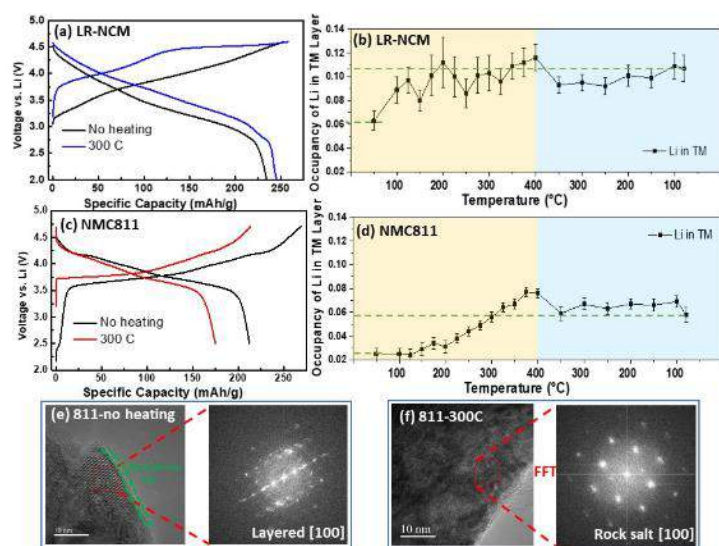


Figure II.5.C.5 Electrochemical performance of the (a). initially cycled LR-NCM and (c). initially cycled NMC811 with or without heat treatment. The changes in the occupancy of Li in TM layer during heat treatment in the (b). initially cycled LR-NCM and (d). initially cycled NMC811 obtained from operando neutron diffraction. HRTEM images and corresponding FFT pattern of the (e). 10-cycled NMC811 and (f). 10-cycled NMC811 after annealing at 300°C for 1 hour.

In FY18, we explored the voltage and structural recovery of LRLO under heat treatment, which provides an insight in optimizing the performance of LR-NCM. After annealing under 300°C for 1 hour, the cycled LR-NCM exhibits the characteristic “oxygen plateau” around 4.5 V (Figure II.5.C.5a). To further study the recovery behavior in LRLO, a classical layered oxide material $\text{LiNi}_{0.8}\text{Mn}_{0.1}\text{Co}_{0.1}\text{O}_2$ (denoted as NMC811) is introduced for comparison. NMC811 samples after first cycle was also annealed under 300°C for 1 hour. It is clearly shown in Figure II.5.C.5c that the cycled NMC811 sample after heat treatment has a lower capacity and larger polarization. In operando neutron diffraction reveals that heat treatment assists Li migration into the transition metal (TM) layer for both the cycled LR-NCM and NMC811 (Figure II.5.C.5b and d). The increase of Li occupancy in TM layer for cycled LR-NCM recovers the ordered structure and the local Li-excess environment. While, the increase of Li in

TM layer for cycled NMC811 results in the structure disordering. Figure II.5.C.5e and f compare the single particle structure difference of the cycled NMC811 before and after heat treatment. Layered phase of NMC811 is well maintained after cycling but transformed to rock salt structure after heat treatment. This comparison once more manifests that voltage and structure recovery is a unique feature for anionic redox related cathode materials.

Characterization of SEI on electrochemically deposited lithium metal with new electrolyte systems

As the Coulombic efficiency of Li metal varies greatly with electrolyte properties and current density, we compared two representative electrolytes, a high-concentration electrolyte (HCE; 4 M lithium bis(fluoro sulfonyl)imide (LiFSI) and 2 M lithium bis(trifluoromethane sulfonyl)imide (LiTFSI) in 1,2-dimethoxyethane (DME)) and a commercial carbonate electrolyte (CCE; 1 M LiPF_6 in ethylene carbonate/ethyl methyl carbonate (EC/EMC)), at three stripping rates (0.5 mA cm^{-2} , 2.5 mA cm^{-2} and 5.0 mA cm^{-2} ; all plating at 0.5 mA cm^{-2} for 2 hours). To elucidate the formation mechanism of inactive Li, we use cryo-TEM to explore the nanostructure of the inactive Li in HCE and CCE after stripping at 0.5 mA cm^{-2} . Sheet-like inactive Li appears in the HCE sample (Figure II.5.C.6a), whereas inactive Li in the CCE retains a whisker-like morphology (Figure II.5.C.6e). Based on the (110) lattice plane distance of body-centered cubic Li, the region that contains crystalline metallic Li^0 is highlighted in green in the high-resolution TEM (HRTEM) images for both electrolytes (Figure II.5.C.6b and f). Compared with the inactive Li obtained from CCE, a much smaller area of metallic Li^0 component is observed in HCE. This indicates that most of the deposited metallic Li^0 in HCE has been successfully stripped, corresponding to the high Coulombic efficiency. Whisker-like unreacted metallic Li^0 up to about 80 nm in length remains in the CCE sample and is well isolated by the surrounding SEI. The SEI components were determined by matching the lattice spacing in HRTEM images with their fast Fourier transform (FFT) patterns (Figure II.5.C.6c and g). Consistent with the XPS results (Figure II.5.C.6d and h), Li_2CO_3 and Li_2O constitute the majority of the SEI, which also contains LiF as well as other amorphous organic species for both electrolytes. Further examining the SEI components in HCE and CCE by

XPS, we found that stripping rates have negligible impact on the relative contributions from SEI components. The cryo-TEM analysis and XPS results indicate that the contribution from the SEI Li^+ to the global content of inactive Li is not as large as commonly believed from previous studies.

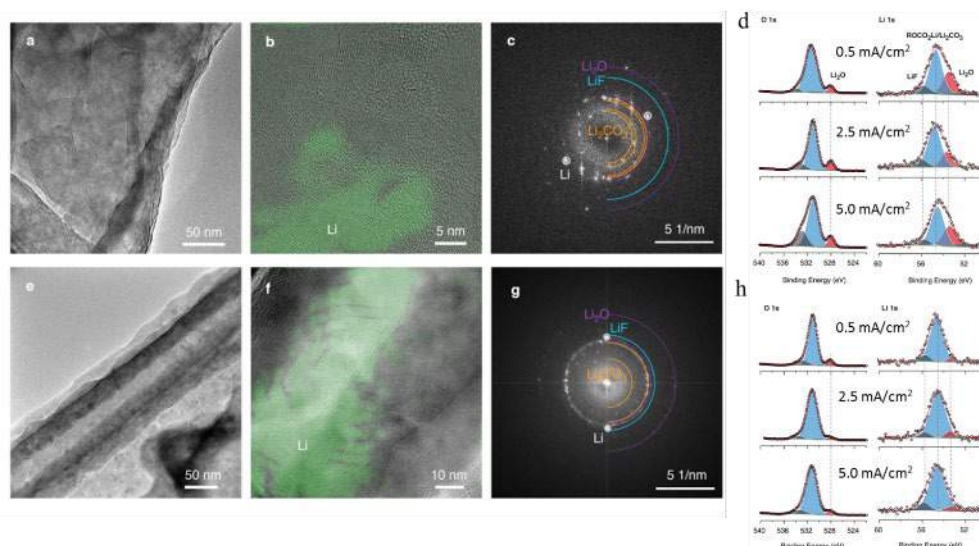


Figure II.5.C.6 (a-c), results for HCE. (e-g), results for CCE. (a, e), Inactive Li morphology at low magnifications for both electrolytes. (b, f), HRTEM shows that a different amount of metallic LiO is wrapped by SEI in the two types of electrolyte. (c, g), FFT patterns of corresponding HRTEM indicate the SEI component, which contains crystalline Li_2CO_3 , Li_2O , and LiF . (d, h), XPS analysis of inactive Li SEI components formed in HCE (d) and CCE (h) for various stripping rates

Conclusions

A novel electrolyte with LiBOB additive is introduced to further improve the electrochemical performance of modified LRLO. Through rigorous characterization methods, stable CEI layer is confirmed on the cycled sample with the novel electrolyte, which prevents the active material corrosion as well as surface structure transformation. The thermal effect comparison between cycled LRLO and classical layered oxides manifests that voltage and structure recovery is a unique feature for anionic redox cathode materials. The cryo-EM results on EDLi indicate that the contribution from the SEI Li^+ to the global content of inactive Li metal is not as large as commonly believed from previous studies. We conclude that cryogenic imaging methodology is effective for probing and optimizing electrode-electrolyte interphases in high energy lithium batteries.

Key Publications

1. C. Fang, X. Wang, and Y. S. Meng, "Key Issues Hindering a Practical Lithium-Metal Anode", *Trends in Chemistry*, 2019, 1, 152.
2. M. Zhang, M. Olguin, Y. S. Meng, et al., "Advanced Characterization Tools for Probing Anionic Redox in Layered Cathode Materials" IBA Meeting, 2019, San Diego, U.S., Poster Presentation.
3. E. Zhao, M. Zhang, Y. S. Meng, et al., "Local Structure Adaptability through Multi Cations for Oxygen Redox Accommodation in Li-Rich Layered Oxides", *Energy Storage Materials*, 2019, in print.
4. Y. S. Meng and M. Zhang, "Oxygen Redox Activities in Li-Rich Layered Oxides: Pushing the Limit of Intercalation" American Chemical Society Meeting, 2019, San Diego, U.S., Invited talk.
5. B. Qiu, M. Zhang, Y.S. Meng, et al., "Structural Metastability and Reversibility in Anionic Redox-based Cathode for Next Generation High Energy Rechargeable Battery", *Cell Reports Physical Science*, 2019.

6. M. Zhang and Y. S. Meng, “Toward the Stable and Reversible Lattice Oxygen Redox in Li-Rich Layered Oxides” Electrochemical Society Meeting, 2019, Atlanta, U.S., Postdoctoral Associate Research Award talk.

References

1. B. Qiu, M. Zhang, Y. Xia, Z. Liu, Y. S. Meng, *Chemistry of Materials* 29 (2017): 908-915.
2. B. Qiu, M. Zhang, L. Wu, J. Wang, Y. Xia, D. Qian, H.D. Liu, S. Hy, Y. Chen, K. An, Y. Zhu, Z. Liu, Y. S. Meng, *Nature Communications* 7 (2016): 12108.
3. S. Ha, J. Han, Y. Song, M. Chun, S. Han, W. Shin, N. Choi, *Electrochimica Acta* 104 (2013): 170-177.

Acknowledgements

We thank Dr. Aaron D. Yocum (NETL manager) for supporting our work.

II.5.D Microscopy Investigation on the Fading Mechanism of Electrode Materials (PNNL)

Chongmin Wang, Principal Investigator

Pacific Northwest National Laboratory
902 Battelle Boulevard, Mail Stop K8-93
Richland, WA 99352
E-mail: Chongmin.wang@pnnl.gov

Tien Q. Duong, DOE Technology Development Manager

U.S. Department of Energy
E-mail: Tien.Duong@ee.doe.gov

Start Date: October 1, 2015

End Date: September 30, 2019

Total Project Cost: \$1,300,000

DOE share: \$1,300,000

Non-DOE share: \$0

Project Introduction

Rechargeable batteries are indispensable component of our daily life, ranging from portable electronics, tools to electrification of cars. One of the most important goals for these applications of rechargeable batteries is to further improve their capacity, cycle life, safe operation, make them environmental-friendly and more affordable. During the operation of a rechargeable battery, structural and chemical evolution of cathode, anode, electrolyte and the corresponding interfaces formed among them are critical factors that control the performance of the batteries. An in depth understanding of these structural and chemical evolution and their correlation with battery performance will be the key for designing electrode materials with better properties. This project will focus on establishing the structure and property relationship in rechargeable batteries using advanced in situ and ex situ microscopy and spectroscopy tools. This study will provide feed-back to the battery materials development group for designing of better materials with better properties. The project includes two tasks: Task 1 will focus on high capacity anode and interfaces and Task 2 will focus on Ni-rich Cathode and interfaces.

Objectives

The objective of this work will be using a combination of ex situ, in situ and operando and cryo high-resolution transmission electron microscopy (TEM) and spectroscopy to probe the fading mechanism of both Li and Si as high capacity anode and Ni-rich NMC as high capacity cathode. For high capacity anode, the research task will focus on revealing how Li and Si interact with liquid electrolyte to critically affect their fading process. For the Ni-rich NMC cathode, the research task will focus on delineating the structural and chemical evolution of the Ni-rich NMC as their dependence on the operating voltage, charge rate and chemistry of electrolyte. To complement the high resolution TEM study, in situ liquid cell SIMS and XPS will also be used to gain structural and chemical evolution of cathode and anode and correlate the structural and chemical evolution with battery performance. The diagnosis work will be in close combination with calculation and atomic level modeling.

Approach

In the proposed research, aberration-corrected STEM-HAADF and cryo-TEM imaging combined with EELS/EDX chemical analysis will be used to probe the microstructural and chemical evolution of the Ni-rich NMC layered cathode before and after cycling. EELS/EDX mapping, time-of-flight secondary ion mass spectrometry (TOF-SIMS), nano-SIMS, and XPS will be used to explore the elemental distribution and the thickness of SEI layer formed on the surface of the cathode material. Direct correlation of the structural and chemical information with battery properties will provide insight on the capacity degradation mechanism of the layered materials with different compositions and performance improvement mechanism with lattice doping/surface modification/electrolyte additives. These characterization results will be used to guide the materials optimization process and establish a solid knowledge base on the correlation between materials selections and structure evolution in the Ni-rich NMC layered cathode materials.

Results

(1) Correlation of oxygen loss, anionic redox, vacancy injection and lattice stability of Li rich cathode

Oxygen loss is a well perceived degradation mechanism for layer structured cathode, contributing to the capacity loss and structural instability of the lattice. However, it is far from clear as how the oxygen loss happens. Here, we reveal the oxygen loss process of lithium rich transition metal oxide (LTMO) layer cathode, giving direct information on the evolution of cathode lattice during battery cycling at a high charging cutoff voltage as the anionic redox process is triggered.

We used focused ion beam (FIB) lift-out techniques to prepare cross sectional transmission electron microscopy (TEM) specimens to capture the surfaces and interiors of LTMO cathode particles as battery cycling proceeded. The STEM-HAADF images in Figure II.5.D.1 show that nano-void formation and lattice transformation start from the particle surface and gradually propagate towards the center as the battery is cycled. Computational simulations show that triggering anionic redox processes lead to lowering of both the formation energy of oxygen vacancy and the diffusion barrier of oxidized oxide ions, therefore facilitating inward migration of oxygen vacancies. Our work highlights that although oxygen anions offer the opportunity to access extra capacity during high-voltage cycling in LTMO cathodes, they also trigger a degradation mechanism that is believed to play a significant role during prolonged battery cycling.

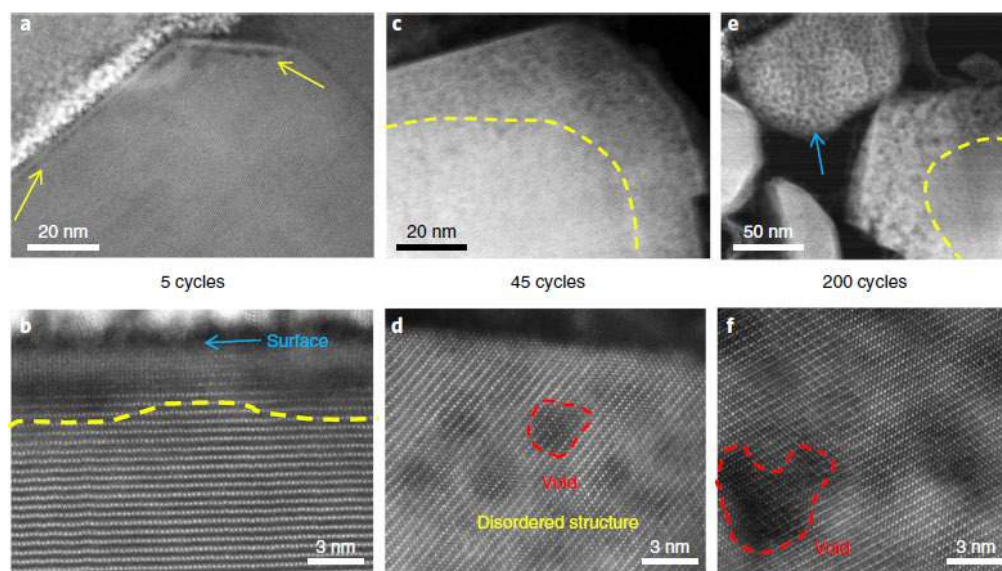


Figure II.5.D.1 Spatial and temporal evolution of structural degradation from the surface into the bulk STEM-HAADF images of the $\text{Li}_{1.2}\text{Mn}_{0.6}\text{Ni}_{0.2}\text{O}_2$ cathode show the gradual propagation of the nanovoid-populated zone from the particle surface towards the interior of the particle with increasing cycles of the battery. a,b, After five cycles, formation of the nanovoid-populated region at the particle surface region is indicated by the yellow arrows in a, where the nanovoid shows as a dark contrast. c,d, After 45 cycles, the nanovoid-populated zone thickens. The red dashed line in d indicates a nanovoid. e,f, After 200 cycles, further thickening of the nanovoid-populated zone occurs. Note that the small particle as indicated by the blue arrow in e has been fully populated by nanovoids. The dashed yellow lines in b, c and e mark the boundary between the nanovoid-populated zone near the surface and the region free of nanovoids within the bulk lattice

We prepared a needle-shaped TEM specimen of a $\text{Li}_{1.2}\text{Mn}_{0.6}\text{Ni}_{0.2}\text{O}_2$ electrode that had been cycled 300 times at a high charging cutoff voltage of 4.8 V. By collecting a tilting series of STEM-HAADF images ranging from -76° to $+78^\circ$, we built a 3D tomography of this grain. Fragmentation analysis of the tomography data allowed direct visualization of the spatial distribution of the nano-voids. We estimated the nano-void volume ratio to be 24% for this needle, indicating substantial mass loss and lattice reconstruction during cycling.

Our cross-sectional STEM observations and 3D tomography reconstructions offer a unique opportunity for understanding bulk lattice degradation of LTMO cathodes. This bulk degradation involves nano-void

formation and lattice structure transformation, which are consequences of electrochemically driven oxygen vacancy formation at particle surfaces and subsequent injection into the bulk lattice and a condensation process, which is sharply contrasted with the case of a thermally driven process. Although an anionic redox reaction coupled with a cationic redox reaction has been demonstrated to be a new route for developing a high-capacity cathode, excitation of anionic redox-induced lattice instability as revealed in this work indicates the conflicting roles of oxygen redox activity during high voltage cycling. The progressive surface-to-bulk degradation indicates that the suppression of oxygen vacancy generation at the particle surface is the key factor for curtailing subsequent injection of vacancies.

(2) Functioning mechanism of Al in NCA on enhanced cycling stability

Doping of trace amount of Al in lithium nickel cobalt oxide (NCA) has been noticed to dramatically enhance the cycling stability. However, the functioning mechanism of Al dopant remains unclear. Using atomic level imaging, spectroscopic analysis and DFT simulation, we reveal that the Al dopant in NCA is partially dissolved in the bulk lattice and partially exist as Al_2O_3 particles that epitaxially dressed on the cathode particle surface. The Al_2O_3 particles play a role similar to those of surface coating at the site they reside. The Al substitution lowers transition metal (TM) redox energy level and consequently promotes the formation of a stable cathode electrolyte interphase (CEI) layer, which prevents the dissolution of TM from cathode, and therefore eliminates the otherwise deposition of TM on anode through cross talking upon battery cycling.

In specific, we use two Ni rich cathodes, one with the formula of $\text{LiNi}_{0.94}\text{Co}_{0.06}\text{O}_2$ (NC) and the other with 2 at% addition of Al in the NC materials ($\text{LiNi}_{0.92}\text{Co}_{0.06}\text{Al}_{0.02}\text{O}_2$, termed as NCA), to elucidate the origin of Al for enhanced cycling stability of NCA. We reveal that the Al dopant enhanced cycling stability from two aspects: improve the electrode structural stability and modify the cathode electronic property and thus reactivity. Our STEM observations coupled with EDS mapping reveal that part of Al segregated on the cathode surface, which leads to the formation of Al_2O_3 islands with a size of a few nanometers. The atomistic simulations reveal that the Al dopant facilitates the formation of phosphate containing cathode electrolyte interface (CEI) layers in the Ni-rich cathode, resulting from the dopant induced down shift of Fermi level. The CEI layers coupled with the scattered Al_2O_3 nano-islands work in synergy and enhance the battery performance.

Through systematic comparison study of NC and NCA, we reveal that the dramatically improved cycling stability of NCA, as contrasted with that of NC, is originated from Al dopant governed enhancement of cathode-electrolyte interface stability, due to the modification of both crystallographically structural stability and electronical energy of cathode. Compared to the NC, the NCA group demonstrates a significantly improved interface behavior associated with several concurrent events: a much reduced TM metal dissolution and re-precipitation; a significantly thinner surface re-construction layers; a less severe secondary particle pulverization upon the prolonged cycling; and a much reduced SEI thickness in the graphite anode, illustrating the vital roles of the Al doping in mitigating the detrimental reactions occurring at the cathode electrolyte interface. Two consequences originated from Al doping contribute to the improvement of interfacial reactivity: the development of epitaxial Al_2O_3 nano-islands arising from the Al segregation, and the formation of CEI layers upon cycling. The results extend the understanding of dopant effects from bulk to solid liquid interface, and may be applicable in more general cathode systems.

(3) Cryo-TEM to reveal the role of VC on enhanced cycling stability of lithium ion battery

Batteries using lithium (Li) metal as anode are considered promising energy storage systems because of their high specific energy densities. The crucial bottlenecks for Li-metal anode are Li dendrites growth and side reactions with electrolyte inducing low Coulombic efficiency (CE) and short cycle life. Vinylene carbonate (VC), as an effective electrolyte additive in Li-ion batteries, has been noticed to significantly enhance the CE, while the origin of such an additive remains unclear.

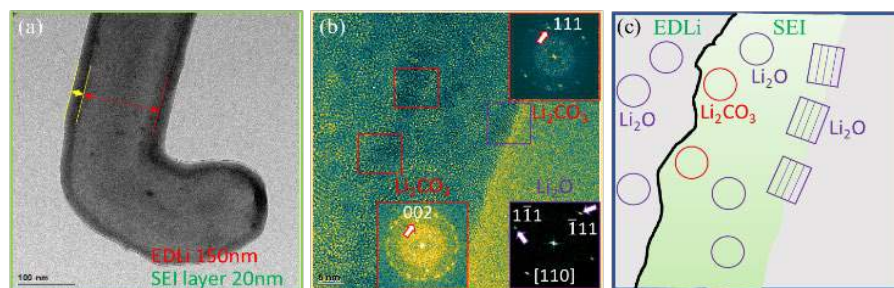


Figure II.5.D.2 Atomic-resolution TEM of electrochemically deposited Li metal (EDLi) and SEI interface. (a) Bright-field TEM image of the EDLi at a low magnification. (b) Atomic-resolution image of the EDLi and SEI interface. (c) Schematic of the observed SEI formed on EDLi

Here we use cryo-TEM imaging combining with EDS elemental and EELS electronic structure analyses to reveal the role of VC additive. We discovered that the electrochemically deposited Li metal (EDLi) in VC-containing electrolyte is slightly oxidized with the SEI being a nanoscale-mosaic like structure comprised of organic species, Li_2O and Li_2CO_3 ; while the EDLi formed in VC-free electrolyte is featured by a combination of fully oxidized Li with Li_2O SEI layer and pure Li metal with multilayer nano-structured SEI. These results highlight the possible tuning of crucial structural and chemical features of EDLi and SEI through additives and consequently direct correlation with electrochemical performance, providing valuable guidelines to rational selection, design and synthesis of additives for new battery chemistries.

In order to understand the contribution of VC additive to the electrochemical performance of Li metal anode, the electrolytes of 1.2 M LiPF_6 in ethylene carbonate (EC)-ethyl methyl carbonate (EMC) (3:7 by wt.) with and without 5 wt.% VC were used to electrochemically deposit Li metal. The baseline electrolyte (without VC) exhibits a Li CE of only 63.0%, mainly due to the excessive side reactions between the porously deposited Li metal and the electrolyte components. Adding 5 wt.% VC into the baseline electrolyte could significantly improve the Li CE to 94.3%.

We preserve and image beam sensitive Li growth and SEI with atomic resolution, revealing detailed nanostructures and their changes in different electrolyte environments by using cryo-TEM, EDS and EELS. The electrolyte of $\text{LiPF}_6/\text{EC-EMC}$ without VC additive gives very low Li CE but high interfacial ionic conductivity, while the addition of 5 wt.% VC additive in the electrolyte could dramatically improve the CE of Li metal electrode but increase the interfacial impedance as well. From the microcosmic point of view, we reveal that the EDLi formed in VC-containing electrolyte has slightly oxidized Li metal, while some of the EDLi formed in VC-free electrolyte is pure Li_2O , which is the main reason for low Li CE (Figure II.5.D.2). In addition, the SEI structures formed in VC-free and VC-containing electrolytes are also different. The SEI formed in VC-containing electrolyte is a mosaic like structure, which is the main reason that the impedance is high in VC-containing electrolyte. On the contrary, the SEI formed in VC-free electrolyte is similar to multilayer structure containing LiF. The results establish the correlation between the electrochemical performance (CE and interfacial impedance) and the structure of deposited Li and SEI layer formed in VC-free and VC-containing electrolytes, which will help designing new electrolytes and additives for the emerging battery chemistries that operate at even more extreme conditions.

Conclusions

Using the state-of-the-art electron microscopy, we have revealed some key new insights that correlate with battery performance. We found that, during operation of a rechargeable battery, oxygen vacancies produced at the surfaces of lithium-rich layered cathode particles migrate towards the inside lattice. This process is associated with a high cutoff voltage at which an anionic redox process is activated. First-principle calculations reveal that triggering of this redox process leads to a sharp decrease of both the formation energy of oxygen vacancies and the migration barrier of oxidized oxide ions, therefore enabling the migration of oxygen vacancies into the bulk lattice of the cathode. This work unveils a coupled redox dynamic that needs to be

taken into account when designing high-capacity layered cathode materials for high-voltage lithium-ion batteries. We revealed aluminum dopants in lithium nickel cobalt aluminum oxide are partially dissolved in the bulk lattice with a tendency of enrichment near the primary particle surface and partially exist as aluminum oxide nano-islands that are epitaxially dressed on the primary particle surface. The aluminum concentrated surface lowers transition metal redox energy level and consequently promotes the formation of a stable cathode-electrolyte interphase. This work demonstrates a general principle as how the trace dopants modify the solid-liquid interfacial reactions for enhanced performance. We discovered that the electrochemically deposited Li metal (EDLi) in VC-containing electrolyte is slightly oxidized with the SEI being a nanoscale-mosaic like structure comprised of organic species, Li_2O and Li_2CO_3 ; while the EDLi formed in VC-free electrolyte is featured by a combination of fully oxidized Li with Li_2O SEI layer and pure Li metal with multilayer nano-structured SEI. These results highlight the possible tuning of crucial structural and chemical features of EDLi and SEI through additives and consequently direct correlation with electrochemical performance, providing valuable guidelines to rational selection, design and synthesis of additives for new battery chemistries.

Key Publications

1. Lianfeng Zou, Jianyu Li, Zhenyu Liu, Guofeng Wang, Arumugam Manthiram & Chongmin Wang, "Lattice doping regulated interfacial reactions in cathode for enhanced cycling stability", **Nature Communications**, **10:3447 (2019)**.
2. Pengfei Yan, Jianming Zheng, Zhen-Kun Tang, Arun Devaraj, Guoying Chen, Khalil Amine, Ji-Guang Zhang, Li-Min Liu and Chongmin Wang, "Injection of oxygen vacancies in the bulk lattice of layered cathodes", **Nature Nanotechnology**, **14, 602-608 (2019)**.
3. Xia Cao, Yaobin Xu, Linchao Zhang, Mark H. Engelhard, Lirong Zhong, Xiaodi Ren, Haiping Jia, Bin Liu, Chaojiang Niu, Bethany E. Matthews, Haiping Wu, Bruce W. Arey, Chongmin Wang, Ji-Guang Zhang, and Wu Xu, "Nonflammable Electrolytes for Lithium Ion Batteries Enabled by Ultraconformal Passivation Interphases", **ACS Energy Lett.** **4, 2529-2534 (2019)**.
4. Runwei Mo, Fan Li, Xinyi Tan, Pengcheng Xu, Ran Tao, Gurong Shen, Xing Lu, Fang Liu, Li Shen, Bin Xu, Qiangfeng Xiao, Xiang Wang, Chongmin Wang, Jinlai Li, Ge Wang and Yunfeng Lu, "High-quality mesoporous graphene particles as high-energy and fast-charging anodes for lithium-ion batteries", **Nature Communications**, **10:1474 (2019)**.
5. Jaegeon Ryu, Ji Hui Seo, Gyujin Song, Keunsu Choi, Dongki Hong, Chongmin Wang, Hosik Lee, Jun Hee Lee and Soojin Park, "Infinitesimal sulfur fusion yields quasi-metallic bulk silicon for stable and fast energy storage", **Nature Communications**, **10:2351(2019)**.
6. Gyujin Song, Jun Young Cheong, Chanhon Kim, Langli Luo, Chihyun Hwang, Sungho Choi, Jaegeon Ryu, Sungho Kim, Woo-Jin Song, Hyun-Kon Song, Chongmin Wang, Il-Doo Kim and Soojin Park, "Atomic-scale combination of germanium-zinc nanofibers for structural and electrochemical Evolution", **Nature Communications**, **10:2364(2019)**.
7. Chaojiang Niu, Huilin Pan, Wu Xu, Jie Xiao, Ji-Guang Zhang, Langli Luo, Chongmin Wang, Donghai Mei, Jiashen Meng, Xuanpeng Wang, Ziang Liu, Liqiang Mai and Jun Liu, "Self-smoothing anode for achieving high-energy lithium metal batteries under realistic conditions", **Nature Nanotechnology**, **14, 594-601(2019)**.
8. Lianfeng Zou, Zhenyu Liu, Wengao Zhao, Haiping Jia, Jianming Zheng, Yong Yang, Guofeng Wang, Ji-Guang Zhang and Chongmin Wang, "Solid-Liquid Interfacial Reaction Triggered Propagation of Phase Transition from Surface into Bulk Lattice of Ni-Rich Layered Cathode", **Chem. Mater.** **30, 7016-7026 (2018)**.

II.5.E *In Operando* Thermal Diagnostics of Electrochemical Cells (LBNL)

Ravi Prasher, Principal Investigator

Lawrence Berkeley National Laboratory
1 Cyclotron Road
Berkeley, CA 94720
E-mail: RSPrasher@lbl.gov

Tien Duong, DOE Technology Development Manager

U.S. Department of Energy
E-mail: Tien.Duong@ee.doe.gov

Start Date: October 1, 2018

End Date: September 30, 2021

Project Funding (FY19): \$300,000

DOE share: \$300,000

Non-DOE share: \$0

Project Introduction

Effective heat dissipation in batteries is important for many reasons, such as performance, reliability, and safety (Wang et al. 2016; Bandhauer, Garimella, and Fuller 2011; Palacin and de Guibert 2016; Keyser et al. 2017; Liu, Zhu, and Cui 2019). Currently, the thermal management of battery cells is provided at the system level by either forced air or liquid cooling. This engineering solution has many shortcomings, such as a reduction in the energy density at the system level and complex system designs to allow for fluid flow. In spite of such high importance, so far no thermal transport measurements or diagnostics have been performed inside electrochemical batteries under operating conditions. An understanding of thermal transport through various interfaces within the electrochemical cell is of particular importance as interfacial thermal transport typically plays the dominant role (up to 90% of the overall thermal resistance according to our preliminary measurements) in determining the internal temperature rise and temperature gradients within various devices. Currently, no thermal model exists that can predict the spatially resolved internal temperature rise within an operating battery, accurate to the true heterogeneous multilayered internal structure of the battery.

Objectives

We will measure the dominant thermal resistances within the multilayered stack comprising the full battery cell. These measurements will be performed *operando* on a fully assembled and functioning battery. This will identify the layer(s) and layer interface(s) that dominate the total thermal resistance to heat flow within an operating battery, even if they are buried deep within the bulk of the battery cell, and quantify their contributions. From these measurements we will build a spatially resolved theoretical thermal model of the internal heat transfer within a battery. This model can then be used to accurately predict the internal temperature rise and temperature profile of a battery under various operating conditions, such as fast charging. This model can also be used to guide the thermal optimization of battery design and battery control software to improve performance, reliability, and safety. Such a model does not currently exist.

Approach

The thermal measurements will be achieved using a customized derivative of the 3-omega technique (Cahill 1990; Dames and Chen 2005). This technique uses microfabricated sensors placed on the outer surfaces of the electrochemical cell stack (see Figure II.5.E.1) to launch thermal waves at multiple frequencies into the battery and interrogate the thermal transport properties at various depths within the bulk of the cell. Our technique simultaneously measures thermal transport properties as a function of depth into the cell as well as temperature. Because the measurement is performed in the frequency domain and not the time domain, it is very robust against ambient noise. Our design enables *operando* measurement during battery operation because our sensors and measurements are immune to both electrical interference from the battery and thermal interference from any heat generated by the battery's own operation.

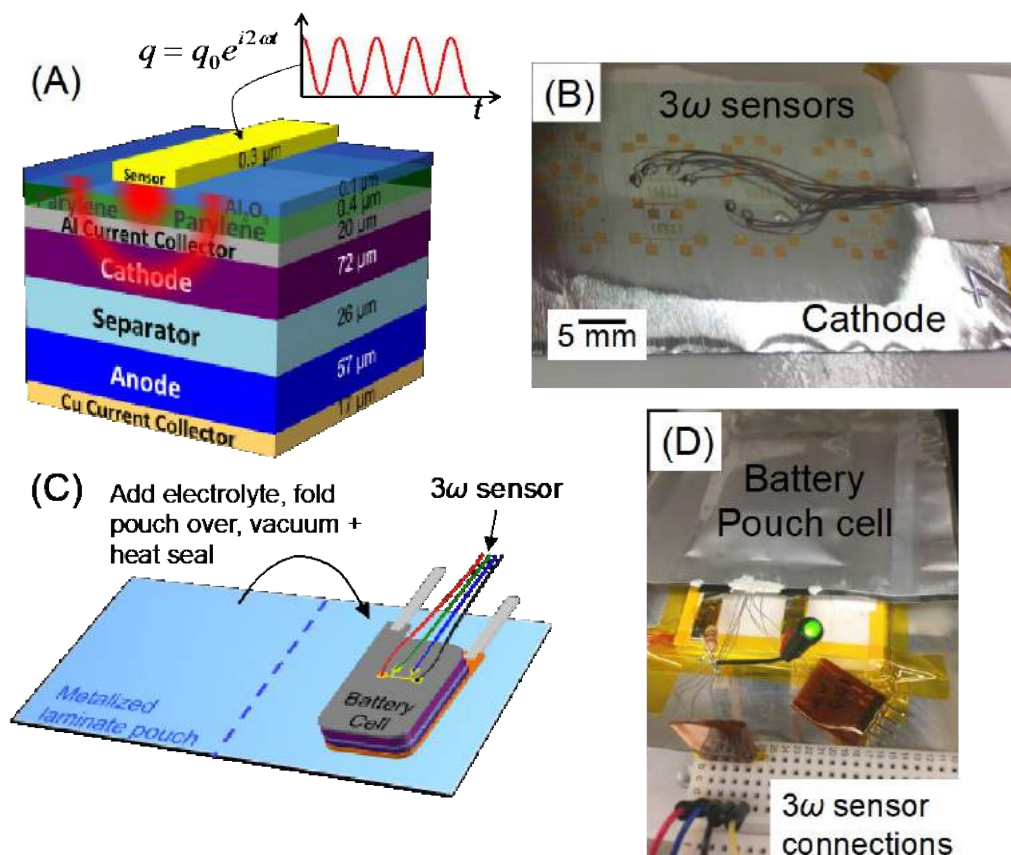


Figure II.5.E.1 Design of 3-omega thermal sensors and how they are incorporated into an electrochemical battery pouch cell for *in-operando* measurements. (A) Sensor and sample design and operation. (B) Sensors fabricated on a cathode. (C) Sensors embedded within pouch cell; assembled in a glove box. (D) *Operando* measurement of a battery while it powers an LED (for illustrative purposes only; actual data collected using battery cyclers, not LED)

We are working with the Battaglia group at LBNL in order to make lithium-ion electrochemical pouch cells inside of which we embed our sensors, and to perform electrical measurements on the batteries in addition to our thermal measurements. Because our sensors probe the interior of the battery from the surface of the multilayer stack, the sensors are non-invasive and do not disturb the local environment of the electrochemical multilayer stack. Sending in thermal waves at many different frequencies allows us to separate out the thermal transport properties at different locations throughout the depth profile of the cell.

Prior to performing any measurements, we fully simulate each experiment and numerically optimize the thermal design of the housing of our battery samples so as to maximize sensitivity to the properties of interest and minimize sensitivity to the outside environment and noise. All sensors are designed and fabricated in-house.

Results

We have successfully performed *operando* measurements of the spatially resolved internal thermal resistance of cycling pouch cells, analyzed the data using in-house measured model input parameters, and created a physics model to explain the high thermal contact resistances observed. The summary of the project's results is given in Figure II.5.E.2.

We found that the dominant thermal resistance in the battery is the thermal contact resistance (TCR) between the separator and the electrodes ($TCR_{s-e} = TCR_{separator-anode} + TCR_{separator-cathode}$). It was not possible to fit the data using a model that attributed the thermal resistance anywhere else in the battery. As the battery ages and undergoes formation cycling, these interfaces account for the majority of the total thermal resistance in the battery. Therefore, mitigating thermal problems within the battery will necessitate improving the thermal transport across this interface.

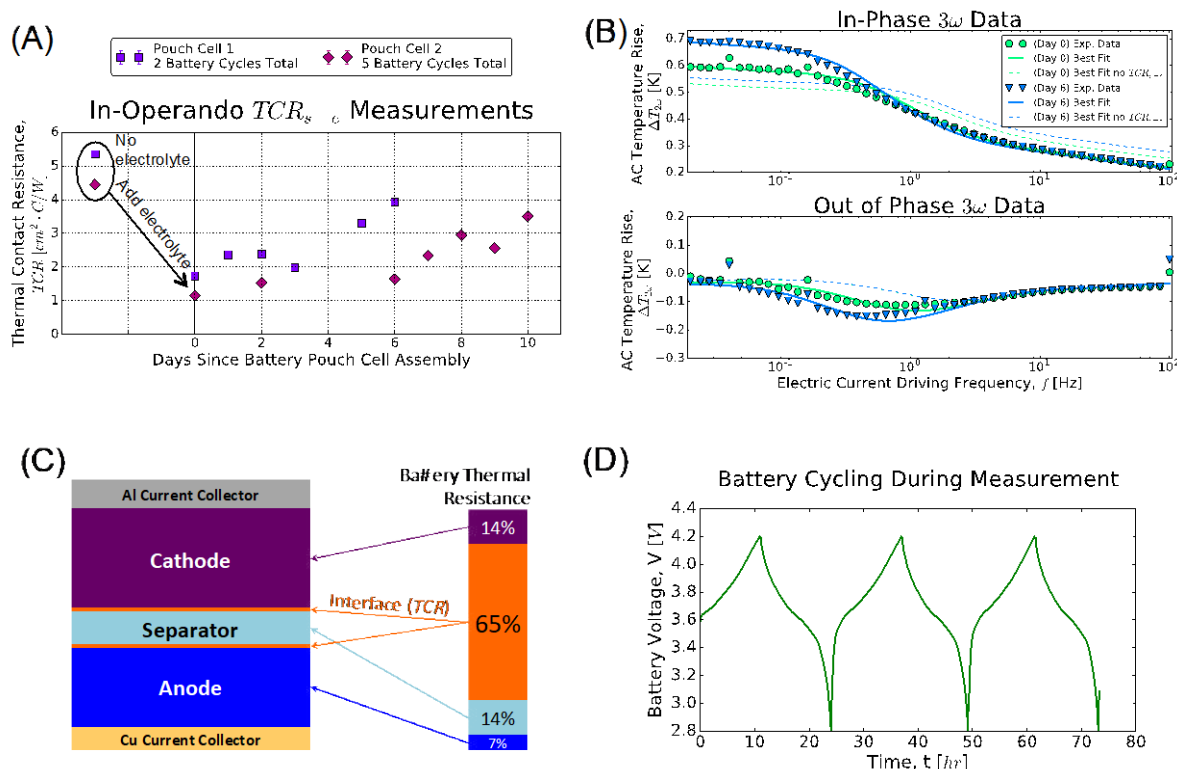


Figure II.5.E.2 Results of *operando* measurements. (A) Thermal contact resistance (TCR) between separator and electrodes as a function of pouch age during formation cycling. (B) Representative raw 3-Omega data for pouch cell 1 before and after 2 formation cycles, showing it is not possible to fit data without including a TCR. (C) Breakdown of relative contribution of each battery layer to total thermal resistance. (D) Representative voltage traces of battery cycling during 3-omega measurement.

We developed a physics model to explain why the TCR_{s-e} is so high. At the interface between the electrode and the separator, heat travels in parallel through the solid-solid contacts of the electrode particles and also through the liquid electrolyte. The heat transfer through the particles is constricted through small contact points between the particles and the separator, even after accounting for deformation of the separator and the particles. Our model suggests heat transfer across the interface could likely be improved by reducing the particle sizes or by improving the thermal conductivity of the electrolyte.

Conclusions

Our measurements reveal for the first time that the thermal resistance of an operating lithium-ion battery gets worse with cycling and is dominated by the thermal contact resistances between the separator and electrodes. We note that while we measured the thermal properties of a single battery “unit cell,” this electrode-separator sandwich is repeated dozens of times within the full stack of commercial battery geometries. The TCR_{s-e} is therefore also repeated dozens of times volumetrically throughout the full cross section of a battery where its deleterious effect on the internal heat transfer is magnified proportionately. Our analysis shows that most of the

heat flows through the liquid electrolyte at the separator-electrode interface, which means mitigation strategies proposed in the literature such as increasing the carbon loading to increase the thermal conductivity of electrodes (Keyser et al. 2017) will have minimal impact. A better strategy will be geometry modification such as decreasing the size of the active particles or increasing the thickness of the electrodes to reduce the TCR_{s-e} or its relative impact, respectively.

Key Publications

1. This work has been presented in part at the 2019 International Technical Conference and Exhibition on Packaging and Integration of Electronic and Photonic Microsystems (InterPACK).

References

1. Bandhauer, Todd M., Srinivas Garimella, and Thomas F. Fuller. 2011. "A Critical Review of Thermal Issues in Lithium-Ion Batteries." *Journal of The Electrochemical Society* 158 (3): R1. <https://doi.org/10.1149/1.3515880>.
2. Cahill, David G. 1990. "Thermal Conductivity Measurement from 30 to 750 K: The 3ω Method." *Review of Scientific Instruments* 61 (2): 802–8. <http://scitation.aip.org/content/aip/journal/rsi/61/2/10.1063/1.1141498>.
3. Dames, Chris, and Gang Chen. 2005. " 1ω , 2ω , and 3ω Methods for Measurements of Thermal Properties." *Review of Scientific Instruments* 76 (12): 124902. <https://doi.org/10.1063/1.2130718>.
4. Keyser, Matthew, Ahmad Pesaran, Qibo Li, Shriram Santhanagopalan, Kandler Smith, Eric Wood, Shabbir Ahmed, et al. 2017. "Enabling Fast Charging – Battery Thermal Considerations." *Journal of Power Sources* 367: 228–36. <https://doi.org/10.1016/j.jpowsour.2017.07.009>.
5. Liu, Yayuan, Yangying Zhu, and Yi Cui. 2019. "Challenges and Opportunities towards Fast-Charging Battery Materials." *Nature Energy*. <https://doi.org/10.1038/s41560-019-0405-3>.
6. Palacin, M. R., and A. de Guibert. 2016. "Why Do Batteries Fail?" *Science* 351 (6273): 1253292–1253292. <https://doi.org/10.1126/science.1253292>.
7. Wang, Chao Yang, Guangsheng Zhang, Shanhai Ge, Terrence Xu, Yan Ji, Xiao Guang Yang, and Yongjun Leng. 2016. "Lithium-Ion Battery Structure That Self-Heats at Low Temperatures." *Nature* 529 (7587): 515–18. <https://doi.org/10.1038/nature16502>.

Acknowledgements

We thank Dr. Sean Lubner, Dr. Suman Kaur, Dr. Yanbau Fu, and Dr. Vince Battaglia for their help in carrying out the research in this project.

II.5.F Solid Electrolyte Interphases on Lithium Metal for Rechargeable Batteries (General Motors)

Xingcheng Xiao, Principal Investigator

General Motors Research and Development Center
30470 Harley Earl Boulevard
Warren, MI 48092-2031
E-mail: xingcheng.xiao@gm.com

Tien Duong, DOE Technology Development Manager

U.S. Department of Energy
E-mail: Tien.Duong@ee.doe.gov

Start Date: October 1, 2016	End Date: September 30, 2019	
Project Funding (FY19): \$580,174	DOE share: \$464,139	Non-DOE share: \$116,035

Project Introduction

Lithium (Li) metal-based batteries, including Li-air, Li sulfur batteries, and solid-state batteries, are among the most promising candidates of high energy density batteries, due to their ultrahigh capacity (3860 mAh g^{-1}), lowest reduction potential ($\sim 3.04 \text{ V}$ vs. S.H.E), and low density (0.534 g cm^{-3}). However, Li typically goes through large volume expansion and contraction during stripping/plating processes, leading to coupled mechanical/chemical degradation at multiple length scales, including the formation of mossy structures and dendrite growth. The mossy structure leads to low cycle efficiency due to the continuous decomposition of electrolyte. Dendrite formation leads to current shortage and sometime catastrophic failure. Both failures are initiated from the damage of the solid electrolyte interphase (SEI).

The fundamental understanding of the coupled mechanical/chemical degradation of the SEI layer during lithium cycling will enable the project to identify the desirable mechanical properties on SEI/lithium as a system and the specific transport properties that enable the homogenous lithium stripping/plating while avoiding the mossy structure. Furthermore, it will allow the project to develop a highly impactful strategy to protect lithium metal and achieve dendrite free high cycle efficiency, which can dramatically increase the energy density of lithium batteries for EV applications.

Objectives

The project objective is to develop a comprehensive set of in situ diagnostic techniques combined with atomic/continuum modeling schemes to investigate and understand the coupled mechanical/chemical degradation of the SEI layer/lithium system during lithium cycling. The goal of this understanding is to develop a new coating design strategy to achieve high cycle efficiency/dendrite free and extend the cycle life of high-energy-density batteries with lithium as the anode for EV application.

Approach

Different in situ techniques, including AFM, nano-indentor, dilatometer, and stress-sensor, will be developed to investigate the mechanical compatibility between SEI and soft lithium and the relationship between surface morphology and current density distribution that results in an inhomogeneous lithium plating/stripping process. Multiple strategies will be developed to tailor the mechanical and transport properties of SEI and to properly engineer the protective coating/lithium interface.

Results

During the past year, we have further investigated the coupled mechanical/electrochemical behaviors of SEI/Li during stripping/plating processes, including the impact of artificial SEI on the stress evolution of Li during plating and stripping process, and the impact of applied pressure on Li morphologies. Combining with

multiscale modeling, we further optimized the coating design strategy and developed a series of polymer-based surface coating to protect Li metal electrodes to achieve high cycle efficiency/dendrite free electrode.

Impact of Artificial Passivating Layer on Stress Evolution in Lithium Metal Electrodes

Our previous study on bare lithium metal electrode strongly supports the idea that the stress response is largely dominated by the surface Li/SEI composite layer rather than the underlying plated Lithium. Putting an artificial SEI will allow us to decouple the stress response between the SEI and lithium metal further, allowing us to analyze the nature of superior cycling performance provided from artificial SEI with mechanistical insight. In these studies, the soft (PEO) artificial SEI was applied directly onto the current collector via spin-coating a PEO-based solution, and the hard (LiF) artificial SEI was deposited onto the current collector via sputtering.

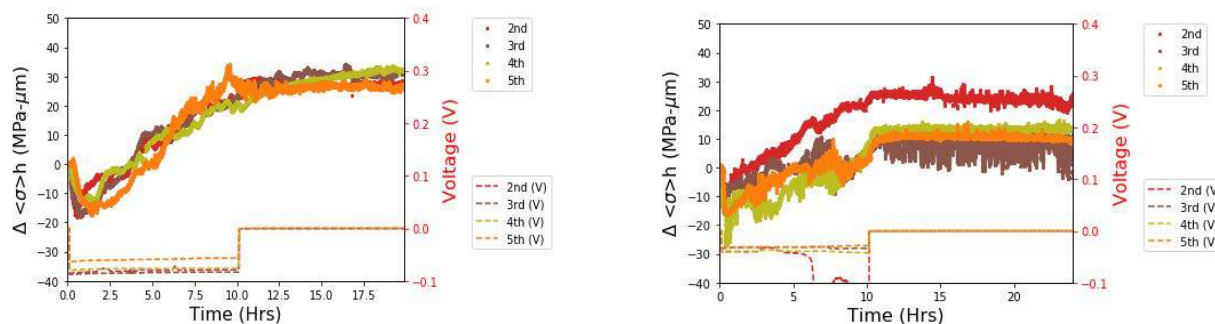


Figure II.5.F.1 Change in stress-thickness vs. time for respective cycles from the MOSS studies. Left plot is the response with soft (PEO) artificial layer. Right plot is the response with stiff (LiF) artificial layer.

As seen in Figure II.5.F.1, the initial transient compressive stress we previously observed in samples without protection does not appear from 2nd ~ 5th cycle. The initial transient stress from bare Au sample was a dominant stress trend, which was attributed to the surface phenomena associated with SEI formation reaction. With PEO or LiF protection, however, this initial transient stress is relatively small, and a steady-state, linear growth stress behavior is instead seen throughout the entire plating sequence. Figure II.5.F.1 further shows that with an artificial SEI protection, the dominant compressive stress that arises from reaction between Lithium and the liquid electrolyte can be suppressed, and the stress response becomes more “growth-stress dominant” from the plated lithium metal instead. The stress evolution from MOSS measurements indicate that both soft and hard (PEO and LiF) artificial SEI layers suppress the compressive initial transient stress and the relaxation behavior associated with surface layer formation. The results indicate that these artificial layers act as a barrier from further SEI decomposition reaction. Using both in situ stress measurements with a complimentary data set of improved performance, a chemo-mechanical solution will be developed to enhance the performance of lithium metal anodes.

Established a strategy to quantify the interfacial strength between artificial SEI and Li metal.

We used PAA as the artificial SEI and calculated the work of separation/delamination of the Li/polymer interface, $W_{sep}(\text{polymer})$ based on DFT calculations of simpler Li/oligomers interfaces. As shown in Figure II.5.F.2, for each PAA oligomer (tetramer, hexamer, and nanomer), five fully relaxed adsorption configurations were studied. It was found that the major chemical bonds formed at the Li/PAA-oligomers interface include: a) the O atoms in the PAA bond with multiple surface Li atoms; b) deprotonation reactions lead to enhanced Li-O ionic bonding and H incorporation into the Li substrate. For interface delamination, three possible delamination routes were considered for each interface (a) breaking all Li-O bonds, (b) breaking all Li-Li bonds (Li decohesion), and (c) breaking all Li-O bonds and Li-Li bonds, as shown in Figure II.5.F.1a-c. The DFT calculated $W_{sep}(\text{Oligomer})$ (Figure II.5.F.2d) reveals that the likely route when PAA is delaminated tends to involve breaking partial Li-O bonds and partial Li-Li bonds, especially the surface Li atoms that are ionized and those are bonded with two O atoms in the PAA oligomers tend to delaminate along with the PAA

oligomer. Since it is impossible to sample all the configurations at an Li/PAA polymer interface, we first calculated the average adhesion energy contribution from each bonded O at the interface, $\langle E_{BO} \rangle$, by fitting the lowest $W_{sep}(\text{Oligomer})$ as a linear function of the number of O bonded with Li, N_{BO} . As shown in Figure II.5.F.1d, $\langle E_{BO} \rangle$ is ~ 1.40 eV/per bonded O. Then, the $W_{sep}(\text{Oligomer})$ is estimated based on $\langle E_{BO} \rangle \times A_{BO}(\text{Polymer})$, where A_{BO} is the areal density of O that is bonding with Li surface. Based on the density of PAA polymer (1.41 g/mL), the oxygen number density is $0.024 \text{ O}/\text{\AA}^3$. Assuming in an interface thickness region that is similar to Li-O bond length, the areal density of O is $0.057 \text{ O}/\text{\AA}^2$. Based on our DFT relaxed oligomers/Li interface structures, $\sim 76\% \pm 13\%$ O atoms in this region form Li-O interfacial bond. Therefore, A_{BO} is estimated to be $0.043 \text{ O}/\text{\AA}^2$, leading to a $W_{sep}(\text{Oligomer})$ of 0.97 J/m^2 .

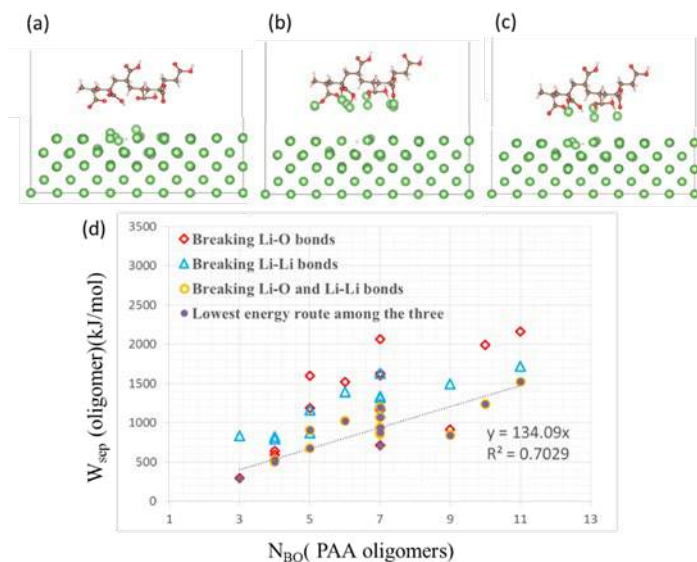


Figure II.5.F.2 Delamination of PAA oligomers by (a) breaking all Li-O bonds, (b) breaking all Li-Li bonds, and (c) breaking mixed Li-O and Li-Li bonds. (d) The work of separation in terms of energy,

Investigated influence of externally applied pressure on the microstructure of electroplated mossy Li

The experiment was using Li|Li symmetric cells in a Swagelok configuration. Under a low pressure of 0.05 MPa, many Li chunks remain on the stripping side after 8 cycles (Figure II.5.F.3), while no residual Li chunks were found on the stripping side of the cells under higher pressures, e.g., 0.11 and 0.17 MPa. The average thickness of the mossy Li layer decreases with increasing pressure. The mossy Li layer of the cell under a pressure of 0.05 MPa has an average thickness of $79.6 \mu\text{m}$, which is about 1.6 times larger than that of the cell under a pressure of 0.17 MPa. Mossy Li with a smaller thickness has a more compact microstructure and better electronic connections among dendrites, highlighting the effects of external pressure on the cycling stability of Li metal electrodes.

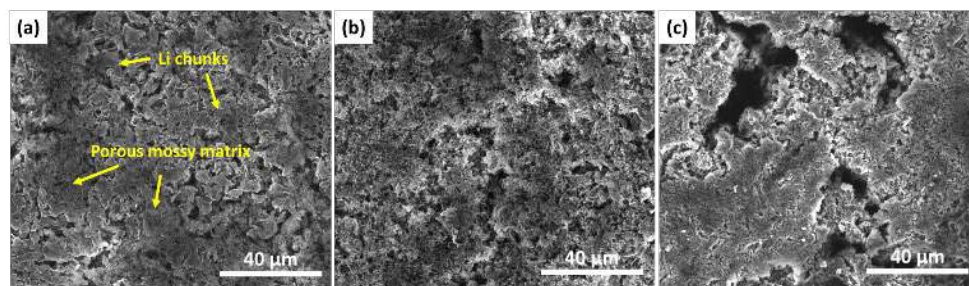


Figure II.5.F.3 The microstructure of mossy Li on the stripping side under different pressures: (a) 0.05 MPa, (b) 0.11 MPa, and (c) 0.17 MPa. The current density is 1 mA/cm^2 and the areal capacity of plating and stripping is 4 mAh/cm^2

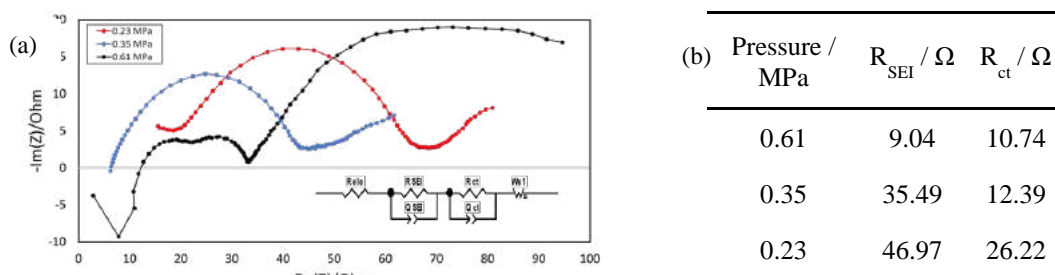


Figure II.5.F.4 (a) EIS curves for the three pressures of 0.23, 0.35, and 0.61 MPa. (b) EIS results

To further study the effects of pressure, higher pressures of 0.23, 0.35, and 0.61 MPa were investigated. The largest overpotential was observed for the cell under 0.61 MPa. Electrochemical impedance spectroscopy (EIS) measurements reveal the resistance of the SEI layer, R_{SEI} , and the charge transfer resistance, R_{ct} , both decrease with applied pressure. As the pressure increases, a larger portion of long, thin, and wispy mossy lithium was replaced by thick, compact lithium. High aspect ratio and wispy mossy lithium can be seen in all three samples. The 0.23 MPa sample has a higher percentage of the high aspect ratio mossy lithium while the 0.61 MPa sample displayed a higher percentage of thick, compact lithium than the other two pressures. The presence of the different mossy lithium morphologies found on each sample could be caused by a variation of stress locally. One possible reason could be the irregular and rough surface of the separator which will be investigated in the future. This study along with previous reports provides valuable insight into the influence of pressure on the performance of lithium metal electrodes.

Investigated effects of current density on the structure and mechanical properties of mossy Li

The experiments were conducted using scanning electron microscopy (SEM) and an environmental nanoindentation system equipped with a flat punch indenter. The size of Li chunks/dendrites decreases from 12.7 to 6.3 μm as the current density increases from 1 to 10 mA/cm^2 in the DOL-DME electrolyte, as shown in Figure II.5.F.5. The porosity of mossy Li increases with current density. For example, the porosity of mossy Li electroplated at 1.0 and 10 mA/cm^2 is 22.4% and 41.5%, respectively.

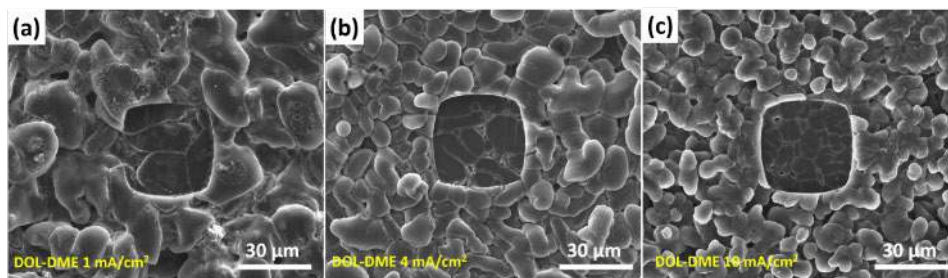


Figure II.5.F.5 The microstructure of mossy Li electroplated at different current densities in the DOL-DME electrolyte

Both dendrite size and porosity can influence the creep behavior of mossy Li. As evaluated by flat punch indentation in an argon-filled glovebox, the steady-state impression velocity (v_{cind}) of mossy Li increases with decreasing current density. In addition, v_{cind} of mossy Li is much smaller than that of bulk Li under the same punching stress due to different dominant creep mechanisms. The creep of bulk Li is dominated by the dislocation climb mechanism at room temperature, while diffusion-mediated mechanisms may dominate the creep behavior of mossy Li because (1) dislocation starvation or dislocation multiplication-induced entanglements is more likely to occur in the micro-sized Li dendrites, (2) v_{cind} of the mossy Li electroplated at 4 mA/cm^2 in the EC-DEC electrolyte is almost the same as that induced by bulk diffusion and surface diffusion of Li. Since the size effect is more pronounced for small Li dendrites, v_{cind} decreases with decreasing dendrite size, i.e., increasing current density.

Established a new coating strategy to protect lithium metal electrode.

For a high efficiency protecting and practical operation, the chemical used for surface treatment should react with lithium surface fast and in high yield. Chlorosilane is a good candidate at this point. It has been demonstrated that treating the lithium metal electrode with chlorotrimethylsilane (TMCS) to form an alkyl siloxane is a simple and effective method to avoid the side reactions between lithium and electrolyte, however, this protecting film cannot survive in high current density cycling, which makes it less practicable to use. The densely packing of small alkyl siloxane molecules resulted from the reaction of TMCS and lithium surface (LiOH , Li_2O) enables the effective isolation of lithium and electrolyte, but the alkyl siloxanes have a low Young's modulus and individually packed in the film, therefore the film is easy to break under high current density cycling. Considering these facts, we used chloro(dimethyl)-phenylsilane (PhDMCS) to treat lithium surface, in which one methyl group of TMCS was replaced with one phenyl ring. The reaction product of aryl siloxanes had much higher Young's modulus due to the rigid phenyl ring structures. The simulation results showed the adjacent phenyl rings of siloxane molecules organized in an edge-to-face structure, indicating a strong electrostatic attraction due to π - π interaction (Figure II.5.F.6). The double reinforcement of the aryl siloxane film due to high rigidity of phenyl ring structures and the π - π interaction of adjacent phenyl rings, dramatically increased the battery cycling life even under high current density and areal capacity cycling (Figure II.5.F.7).

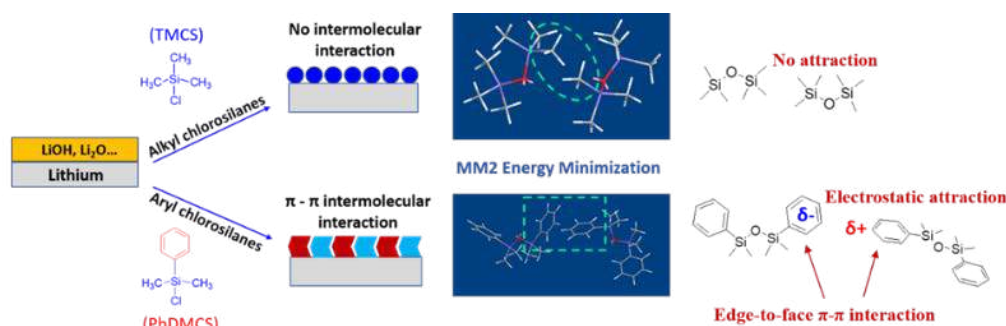


Figure II.5.F.6 The reaction mechanism of lithium surface treatment with chlorosilanes and simulation results of intermolecular interaction in resulted siloxane coating film on lithium surface

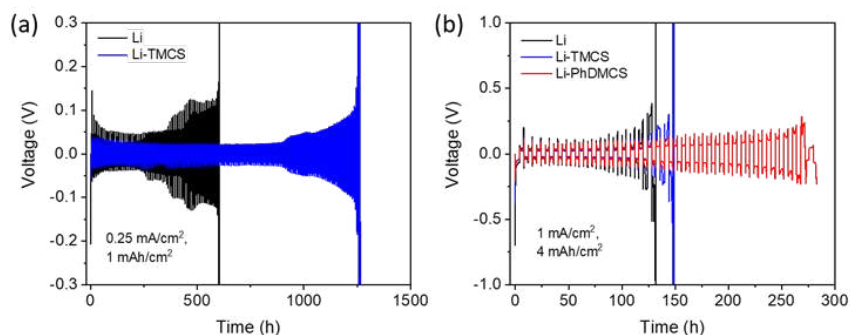


Figure II.5.F.7 Galvanostatic cycling voltage profiles for symmetric cells using coated (TMCS or PhDMCS modified) or uncoated lithium electrodes under (a) low (0.25 mA/cm^2 , 1 mAh/cm^2) and (2) high (1 mA/cm^2 , 4 mAh/cm^2) current density and areal capacity

The success of this surface coating with aryl siloxanes provided us an ideal system to figure out the mechanism of SEI protecting by comparing the in situ characterization results of coated and uncoated lithium metal electrodes, and thus to develop and optimize the in situ diagnostic techniques. The preliminary results by in situ impedance measurement indicated the PhDMCS-coated lithium electrode had much smaller impedance increase during storage and cycling comparing with uncoated lithium due to surface stabilization (Figure II.5.F.8a & Figure II.5.F.8b). The in situ height changes of lithium electrode by dilatometer showed the uncoated lithium electrode had much fast height increase comparing the PhDMCS-coated one under high current density cycling, indicated more dead lithium and SEI residues generated on uncoated lithium surface (Figure II.5.F.8c & Figure II.5.F.8d). Further in situ characterization, such as SEM, nanoindentation, MOSS stress evolution is in progress, which combined with simulation results, will help us to understand the relationship of SEI components and their impact to battery performance, inversely develop the best in situ diagnostics techniques for lithium metal rechargeable batteries.

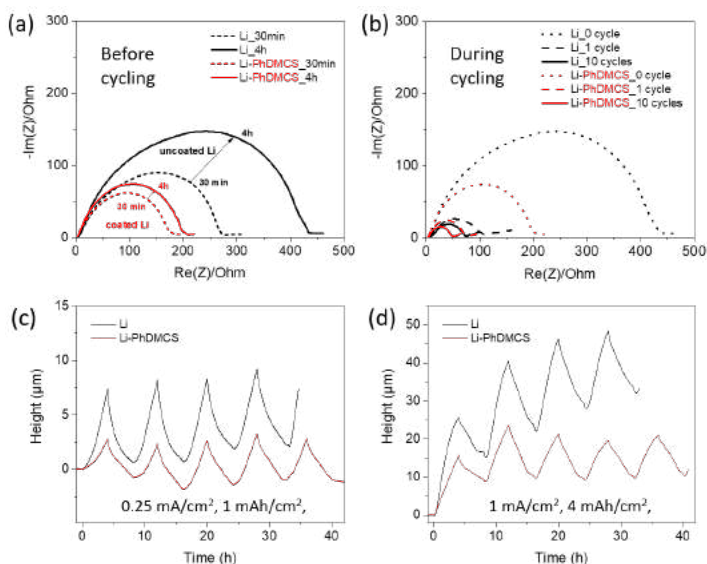


Figure II.5.F.8 in situ characterization of symmetric cells using PhDMCS treated or untreated lithium electrodes. (a) and (b): Impedance before and during cell cycling. (c) and (d): Height change by dilatometer.

Conclusions

- The artificial SEI layer plays a critical role for the stress evolution. Typical, softer layer would suppress the initial transient stress because the soft matrix buffers the stress from additional SEI formation.
- The external pressure can impact the formation of Li mossy structure: higher external pressure typically leads to a thinner layer of mossy Li with more compact microstructure and better electronic connections among dendrites, which potentially extends cycle life.
- The atomic-scale modeling shows the interfacial mechanical strength is highly dependent of the chemical bonds formed between coating and Li metal. Li-O bonds would provide much higher work of separation than Li-F bonds (1.1 vs. 0.23 J/m^2).
- We demonstrated a strategy to use the aryl siloxane film as an artificial SEI layer to protect lithium electrode by treating the lithium with phenyl substituted chlorosilanes. We have shown that high modulus of phenyl ring structures and the extra reinforcement by the π - π interaction of siloxane molecules through edge-to-surface organization of neighboring phenyl rings can enhance the stability of the SEI layer on lithium.

Key Publications

Peer viewed Journals

1. W. Zhang, T. H. Cai, and B. W. Sheldon, The Impact of Initial SEI Formation Conditions on Strain-Induced Capacity Losses in Silicon Electrodes, *Adv. Energy Mater.* 2018, 1803066

2. Dong, X., Lin, Y.X.*, Li, P., Ma, Y., Huang, J., Guo, Z., Bin, D., Wang, Z., Wang, Y.G., Qi, Y., Xia, Y.Y., High Energy Rechargeable Metallic Lithium Battery At -70°C Enabled by A Co-Solvent Electrolyte, *Angew. Chem. Int. Ed.* (2019), <https://doi.org/10.1002/ange.201900266>
3. K. Guo, W. Zhang, B.W. Sheldon, H. Gao, Concentration dependent properties lead to plastic ratcheting in thin island electrodes on substrate under cyclic charging and discharging, *Acta Materialia*, vol. 164, (2019): 261-271
4. Y. Liu, K. Guo, C. Wang, H. Gao, Wrinkling and ratcheting of a thin film on cyclically deforming plastic substrate: Mechanical instability of the solid-electrolyte interphase in Li-ion batteries, *J. Mech. Phys. Solids*, 123 (2019): 103-118.
5. Y. Wang, D. Dang, D. Li, J. Hu, Y.T. Cheng. Influence of polymeric binders on mechanical properties and microstructure evolution of silicon composite electrodes during electrochemical cycling. *J. Power Sources* 425 (2019): 170-178.
6. Y. Wang, D. Dang, M. Wang, X. Xiao, and Y. Cheng, Mechanical behavior of electroplated mossy lithium at room temperature studied by flat punch indentation, *Appl. Phys. Lett.* 115, 043903 (2019); <https://doi.org/10.1063/1.5111150>
7. J. Cho, X. Xiao, K. Guo, Y. Liu, H. Gao, B.W. Sheldon, Stress evolution in lithium metal electrodes, *Energy Storage Materials* (2019) DOI: 10.1016/j.ensm.2019.08.008
8. J. Xu, H. Tian, J. Qi, Y. Qi, and X. Xiao, Mechanical and Electronic Stabilization of Solid Electrolyte Interphase with Sulfite Additive for Li Metal Batteries, *J. Electrochem. Soc.*, 166 A3201-A3206 (2019)
9. B. Li, J. Xu, X. Xiao, A Reinforced Composite Film on Lithium Metal Electrodes through Aryl Chlorosilane Treatment, *Langmuir*, 2019, (accepted)

Patents

1. B. Li, X. Xiao, In situ Polymerization to Protect Lithium Metal Electrodes, P048616, 2019
2. X. Xiao, Methods for manufacturing electrode including fluoropolymer based solid electrolyte interface layers, P049559-US-NP, 2019
3. X. Xiao, Electrode including fluoropolymer based solid electrolyte interface layers and batteries and vehicles utilizing the same. P049933-US-NP

Acknowledgements

The PI would like to acknowledge co-PIs: Prof. Brian W. Sheldon, Prof. Huajian Gao at Brown University, Prof. Yue Qi at Michigan State University, Prof. Yang-Tse Cheng at University of Kentucky, Dr. Qinglin Zhang at General Motors R&D Center, graduate students and postdocs: Dr. Binsong Li, Kai Guo, Yuxiao Lin, Yikai Wang, Andrew Meyer, and Dingyin Dan.

The team would like to also acknowledge the support from Program Managers Tien Duong at DoE, Patricia Smith at NAVSEA-Carderock, and Aaron Yocum at NETL.

II.5.G High-Conductivity, Low-Temperature Polymer Electrolytes for Lithium-Ion Batteries (LBNL)

Bryan D. McCloskey, Principal Investigator

Lawrence Berkeley National Laboratory and University of California, Berkeley
201-D Gilman Hall
Berkeley, CA 94720
E-mail: bmcclusk@berkeley.edu

Tien Duong, DOE Technology Development Manager

U.S. Department of Energy
E-mail: Tien.Duong@ee.doe.gov

Start Date: October 1, 2015	End Date: September 30, 2019	
Project Funding (FY19): \$250,000	DOE share: \$250,000	Non-DOE share: \$0

Project Introduction

As initially described by Doyle, Fuller, and Newman, the development of high Li^+ transference number (t_{Li}) electrolytes, those in which the ionic current is carried either predominantly or entirely by Li^+ (instead of a combination of Li^+ and its necessary counteranion), could dramatically enhance cell-level energy densities by reducing transport limitations within porous electrodes. Traditional binary salt electrolytes, i.e., those in which a Li salt is dissolved into a liquid electrolyte, typically have reasonable low temperature ion conductivity and anode impedance, but suffer from ionic concentration polarization due to movement of the electrochemically inactive anion. Therefore, the ionic concentration within the porous battery cathode, where Li ions are consumed, continuously decreases until it reaches zero at some shallow depth within the electrode, thereby limiting the ultimate electrode thickness. High t_{Li} electrolytes could significantly reduce, or perhaps eliminate, concentration polarization at high discharge rates, enabling thicker electrodes to be used, which would increase the ratio of electrochemically active battery components to passive cell components (such as the electrolytes), thereby increasing the energy density of the cell, particularly at high current rates desirable for electric vehicles. The challenge with high t_{Li} polymer electrolytes is their low ionic conductivity at operational temperatures of interest to car manufacturers. The overall objective of our proposed research is to design an ionomer-based electrolyte with desirable ion transport and interfacial impedance characteristics sufficient for a practical Li-ion battery for mobile applications. If successful, the materials developed in this project would reduce Li-ion battery volume and improve battery safety, thereby ushering mass-market penetration of electric vehicles.

Objectives

Design of electrolytes with enhanced transport properties compared to conventional liquid organic electrolytes is key to improving the rate at which a Li-ion battery can be discharged or charged. Ideally, electrolytes would allow high mobility for lithium ions and disallow mobility of inactive ions (for example, the counteranion of the Li^+). However, current liquid electrolyte compositions usually provide higher mobility for the counteranion than Li^+ , which results in high concentration polarization that disallows fast charging, particularly in batteries that employ thick porous electrodes, as is necessary for EVs to provide high energy densities. The project objective is to develop a high Li^+ transference number (t_{Li} , the fraction of ionic current carried by Li^+ in an electrolyte of uniform composition) polymer-based electrolyte that, when used in a Li-ion battery, can support current rate capabilities sufficient for EV propulsion at room temperature.

Approach

Lowering the operating temperature of polymer electrolytes has been cited as an important challenge to their viability as Li-ion battery electrolytes. The project will address this challenge by using Li^+ neutralized anionically charged polymers as salts in conventional liquid solvents. Using these so-called polyelectrolyte

solutions, initial results indicate that the project can access t_{Li} values typical of single-ion conducting polymer electrolytes ($t_{\text{Li}} > 0.9$) and conductivity values (> 1 mS/cm at room temperature) that approach those of traditional battery electrolytes. We have designed polyelectrolyte solutions in which highly charged polymers based on two chemistries, sulfonated polysulfones and polystyrene with appended imides, have been engineered to fully dissolve in Li-ion battery-relevant liquid carbonate solvents. During FY19, we have focused on characterizing and optimizing the Li^+ transport in these systems by developing electrochemical methods to accurately measure the full set of transport coefficients under Newman's concentrated solution theory. We have explored additive engineering to improve ion dissociation, and have demonstrated that an optimized polyelectrolyte solution can be used in a Li-ion battery electrolyte.

Results

Our work in FY19 primarily focused on investigations of fundamental polyelectrolyte solution properties to inform the design of high transference number solutions in a battery-relevant ethylene carbonate/dimethyl carbonate (EC/DMC) blend solvent, as opposed to dimethylsulfoxide (DMSO) as has been used previously.

The vast majority of polyelectrolyte solution literature has investigated the properties of water-based solutions, with very few studies focused on non-aqueous transport properties. No study has reported behavior of any charged polymer dissolved in EC/DMC. In general, polyelectrolyte theory would suggest that the dielectric constant of the solvent is the most important factor determining solution behavior, and thus we would expect EC/DMC to behave similarly to the DMSO solutions that we have previously studied given their similar dielectric properties. As DMSO co-intercalates with lithium into graphite electrodes, ideally EC/DMC would be used as solvent. To investigate the transport properties of an EC/DMC solution (as shown in Figure II.5.G.1), we utilize a sulfonated polysulfone/poly(ethylene glycol) copolymer (PSf-co-PEO), whose composition is shown in Figure II.5.G.2. We investigated the transport properties of this polymer as a function of polymer concentration, solvent type (EC/DMC vs DMSO), and as a function of added lithium bis(trifluoromethylsulfonyl)imide salt (Figure II.5.G.1). The conductivity of these solutions is plotted here for DMSO and EC/DMC. We found that the conductivity of all solutions increases with added small molecule salt ("LiTFSI Added" on the x-axis), but we see significant differences between EC/DMC and DMSO. The polymer solution without added salt has much lower conductivity in EC/DMC than in DMSO. Further, while the polymer/salt solutions in DMSO have higher conductivity than pure LiTFSI (the "0M Polymer" line), in EC/DMC the conductivity of the polymer-containing solutions is actually lower than with just LiTFSI. Through direct observation of the ^7Li NMR peak width, and computational calculations performed in collaboration with Kristin Persson's group, we found that the reason for this difference is poor dissociation of the sulfonate/lithium ion pair on the polymer backbone. This study indicates the need for strategies to improve salt dissociation in carbonate-based polyelectrolyte solutions, either through new polymer chemistries or additive engineering.

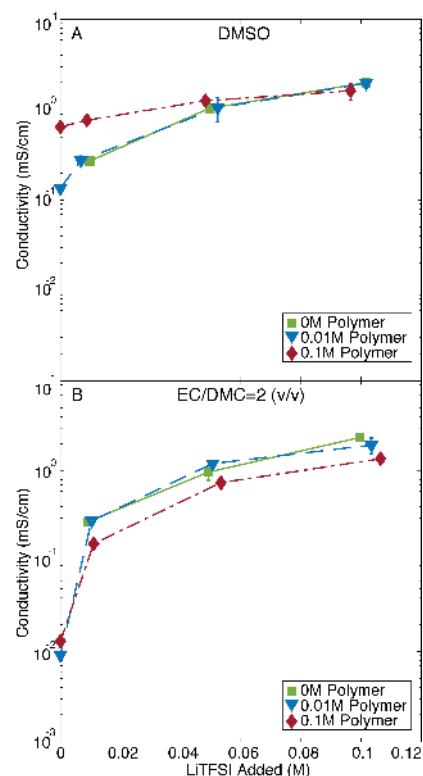


Figure II.5.G.1. Conductivity of Li^+ -neutralized sulfonated PSf-co-PEO polymer solutions with added LiTFSI salt. Polymer concentration is reported as sulfonate concentration.

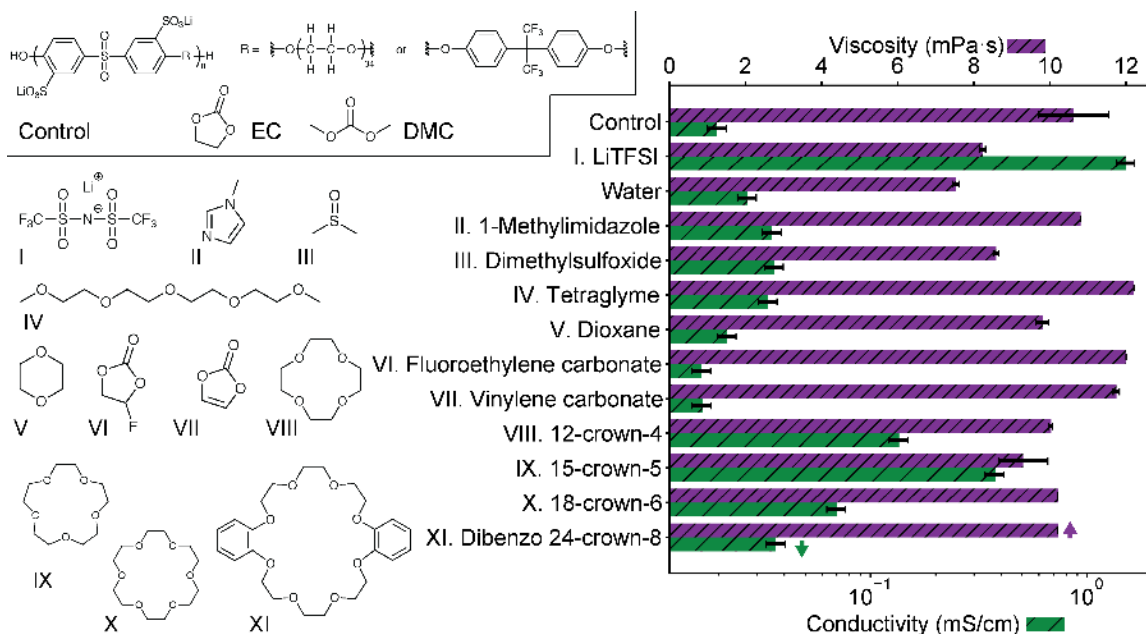


Figure II.5.G.2. Conductivity and viscosity of a range of potential additives to improve conductivity of the control 0.1 M polymer in 2:1 (vol.) EC:DMC. Each additive is introduced at 0.1 M to match the lithium content of the solution. The structure of the polymer, EC, and DMC in the control solution are also included.

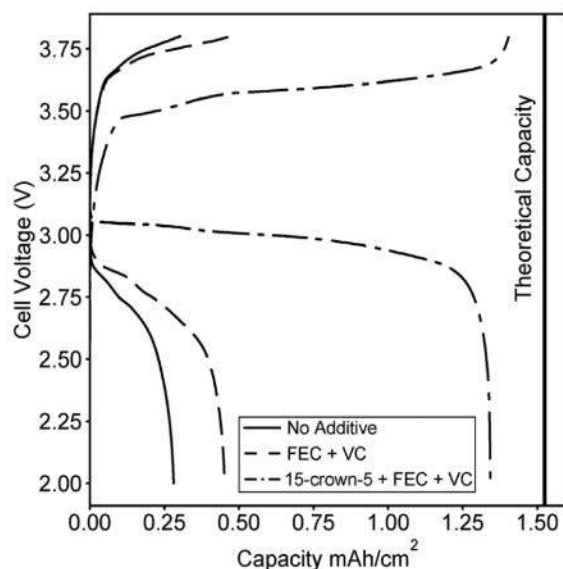


Figure II.5.G.3. Second charge and discharge curves at C/20 for batteries fabricated with the 0.1 M polymer in 2:1 (vol.) EC:DMC solution containing no additives (control), containing stabilizing additives FEC and VC, and containing 15-crown-5 and the stabilizing additives. The calculated theoretical maximum capacity of the cell is also shown.

comprised of a porous 1.52 mAh/cm² lithium iron phosphate cathode and a 2.64 mAh/cm² graphite anode, both purchased from MTI).

When using the sulfonated polymer shown in Figure II.5.G.2, we found that the polymer was fully soluble in a 2:1 (vol.) ethylene carbonate:dimethyl carbonate (EC:DMC) solution, but that the sulfonate-Li⁺ ion pair remained strongly associated in solution, resulting in very poor solution conductivity (~0.02 mS/cm, Figure II.5.G.2 control). We therefore pursued additive engineering in an attempt to attain higher conductivity in carbonate-based polyelectrolyte solutions to make them useful in batteries.

We screened a range of potential additives to improve dissociation, and hence conductivity, of a Li⁺-neutralized, sulfonated polymer studied in our group (shown in the upper left hand corner of Figure II.5.G.2), finding that 15-crown-5 ether is able to increase polyelectrolyte conductivity by over an order of magnitude (see Figure II.5.G.2, which presents conductivity and viscosity of polyelectrolyte solutions prepared from the polymer shown in EC:DMC with various additives). We demonstrated that this is due to increased dissociation of lithium through pulsed field gradient nuclear magnetic resonance measurements. We further showed that the optimized 15-crown-5 ether-containing solution enables operation of a battery composed of commercial electrodes (see Figure II.5.G.3, where the cell is

This study is the first report of a polyelectrolyte solution functioning as the electrolyte in a lithium-ion battery. There is a wide array of charged polymers that have never been tested as a polyelectrolyte solution within a lithium ion battery, and we will continue to seek optimized versions of these materials as battery electrolytes. This study provided clear proof of concept for the idea of polyelectrolyte solutions as battery electrolytes.

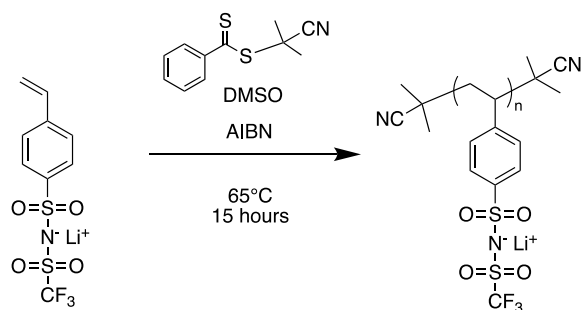


Figure II.5.G.4. RAFT polymerization synthesis scheme for triflimide-based styrene polymer (PS-LiTFSI)

We also focused on the synthesis and initial characterization of a polymer with an appended anion that more readily dissociates, namely, the triflimide-based styrene polymer (PS-LiTFSI). These polymers were produced via a straightforward one-step synthesis using reversible addition-fragmentation polymerization (RAFT, Figure II.5.G.4). Characterization of the raw polymers via gel-permeation chromatography and NMR showed the successful synthesis of a polymer with a targeted molecular weight of 13,700 and polydispersity of 1.28 based on polystyrene standards. No side reactions were observed and expected lithium content was confirmed via ^7Li NMR spectroscopy.

Polyelectrolyte solutions were produced, with both TFSI-based polymers showing good solubility up to at least 3 M in a 2:1 ethylene carbonate/dimethyl carbonate mixture. Conductivity and viscosity measurements were performed on these solutions, showing both promising conductivity, over 1 mS/cm, and low viscosity (see Figure II.5.G.5). Initial Pulsed-Field Gradient NMR (PFG-NMR) diffusion measurements on the PS-LiTFSI in carbonate polyelectrolyte solution show significantly higher diffusion coefficients for lithium species than for the polymer backbone with values on the order of $2 \times 10^{-6} \text{ cm}^2/\text{s}$ and $5 \times 10^{-7} \text{ cm}^2/\text{s}$, respectively.

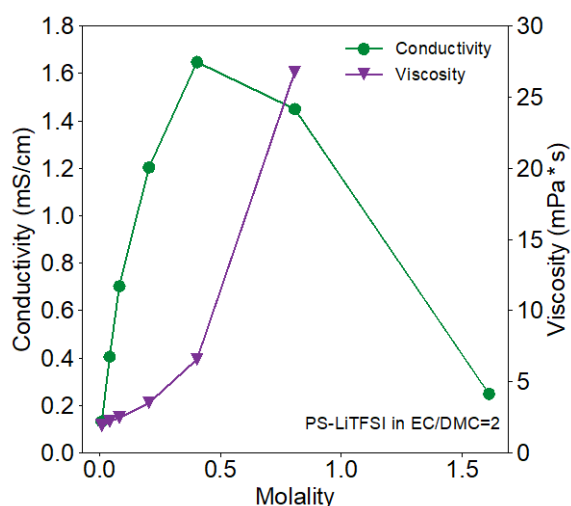


Figure II.5.G.5. Conductivity (mS/cm) & viscosity (mPa s) as a function of concentration for PS-LiTFSI in carbonate solutions.

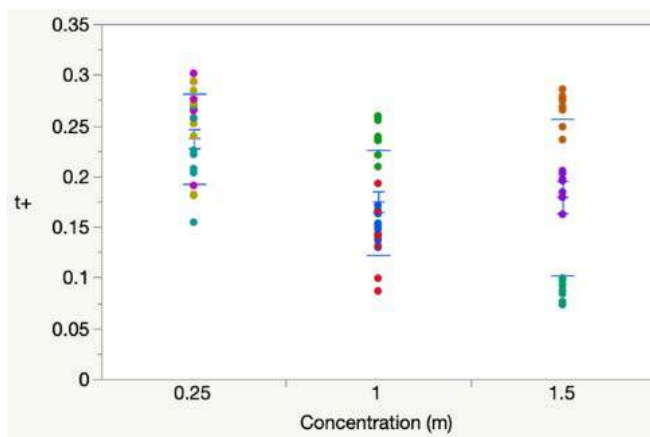


Figure II.5.G.6. Ideal transference number versus Li concentration (molal) for LiTFSI in EC:EMC (3:7). Each color represents a separate cell, with each cell polarized subsequently to ± 5 , ± 10 , ± 15 , & ± 20 mV.

Furthermore, we reported on lithium stability issues that hindered ideal transference number measurements of liquid electrolytes via the Bruce-Vincent method. By using electrolyte-lean systems of lithium bis(trifluoromethyl sulfonamide) (LiTFSI) in ethylene carbonate: ethyl methyl carbonate (EC:EMC, 3:7 w/w), we were able to attain more stable current responses to applied polarization (Figure II.5.G.6). All cells were first conditioned for 6 cycles at $20 \mu\text{A}/\text{cm}^2$ after which we observed a stable current-voltage response. Bruce-Vincent measurements were then performed on these cells with the interfacial resistance monitored throughout the measurement via impedance spectroscopy. The interfacial resistance appeared stable throughout all

measurements. A variability analysis was run using concentrations ranging from 0.25–1.5 molal LITFSI in EC:EMC system with polarization potentials from 5mV – 20 mV. We found no clear dependence of the obtained ideal transference number on the applied potential, however moderate cell-to-cell variability is still noted (see Figure II.5.G.5), although values reported are reasonable compared to similar values in the literature. We found that the current or length of the preconditioning cycle had little effect on the cell-to-cell repeatability.

Conclusions

In summary, we continue to develop liquid carbonate based polyelectrolyte solutions as potential high transference number electrolytes for Li-ion batteries. Enabling a high transference number electrolyte, one in which the lithium is more mobile than the anion, could enable fast charging and higher energy density batteries by a reducing deleterious concentration gradients. Prior to this year, the only report of a polyelectrolyte in battery-relevant carbonate solvents demonstrated very poor conductivity due to poor dissociation of the appended sulfonate anion from lithium ions. We therefore screened a range of potential additives to improve conductivity, finding that crown ethers were able to increase conductivity by over an order of magnitude, and further showed that the optimized solution enables operation of a battery composed of commercial electrodes. Additionally, we have explored the use of an appended ion chemistry that dissociates readily in carbonate solvents without the inclusion of additives. We continue to be interested in understanding the influence of solution and polymer composition on Li⁺ transport, and therefore are also developing electrochemical methods to fully characterize transport properties using Newman's concentrated solution theory.

Key Publications

1. McCloskey, B. D.; Xu, K. "Current trends in electrolytes." *Editorial comment for special issue, ECS Interface* (2019) 28(2), 47.
2. Diederichsen, K. M.; McCloskey, B. D. "Additive engineering to enable nonaqueous polyelectrolyte solutions for lithium ion batteries." *Molecular Systems Design and Engineering*, accepted (online).
3. Fong, K. D.; Self, J.; Diederichsen, K. D.; Wood, B. M.; McCloskey, B. D.; Persson, K. A. "Ion transport and the true transference number in nonaqueous polyelectrolyte solutions for lithium-ion batteries." *ACS Central Science* (2019) 5(7), 1250-1260.
4. Diederichsen, K. M.; Fong, K.; Persson, K. A.; McCloskey, B. D. "Investigation of solvent type and salt addition in high transference number nonaqueous polyelectrolyte solutions for lithium-ion batteries." *Macromolecules* (2018) 51(21), 8761-8771.

Acknowledgements

B.D.M. gratefully acknowledges his colleagues- Kyle Diederichsen, Kara Fong, Helen Bergstrom, and Rickey Terrell- who performed this work, as well as the fruitful computational collaboration with Prof. Kristin Persson.

II.5.H Development of High Energy Battery System with 300Wh/kg (ANL)

Khalil Amine, Principal Investigator

Organization: Argonne National Laboratory

Address: 9700 S Cass Avenue

Lemont, IL 60439

E-mail: amine@anl.gov

David Howell, DOE Program Manager

U.S. Department of Energy

E-mail: David.Howell@ee.doe.gov

Start Date: September 30, 2018

End Date: September 30, 2019

Project Cost (FY19): \$1,730,000

DOE share: \$700,000

Non-DOE share: \$1,030,000

Project Introduction

Transformational changes in battery technologies are critically needed to enable the effective use of renewable energy sources, such as solar and wind, and to allow for the expansion of the electrification of vehicles. For these applications, batteries must store more energy per unit volume and weight, and they must be capable of undergoing many thousands of charge-discharge cycles. Therefore, developing high-performance batteries is critical to meet these requirements, which certainly relies on material breakthroughs. In the meantime, to enhance the performance and lifetime of batteries (specifically lithium-ion batteries), it is very critical to understand, for example, the formation of the solid-electrolyte interphase (SEI) layer, and the degradation mechanisms in battery electrodes, oftentimes, at the nanometer scale. Under this circumstance, various state-of-the-art in-situ and operando characterization tools are very critical to understanding battery behavior and could help address all the major issues of lithium batteries and beyond. The collaborative work with our colleagues from china will consist of the following:

- Development of advanced in situ characterization tools to understand failure mechanism in different battery systems with focus on high voltage high energy cathode (230mAh/g)
- Characterization of Silicon-Based Anode Materials and their Solid-Electrolyte Interphase (SEI)
- Characterization of Lithium Sulfur Batteries
- Investigation of the safety of batteries at the component and pack level
- Characterization and development of new catalysts to improve the efficiency of Li-O₂ batteries and/or Zinc ion Battery.

Objectives

This project will conduct research on rechargeable Li-ion battery and beyond lithium ion to help develop the next generation of advanced batteries that can help expedite electrification of vehicles and enable smart grids. The main objective is to understand and develop advanced battery chemistries based on lithium ion and beyond lithium ion that meet 300Wh/kg energy density.

Approach

Tasks 1 Development of advanced in situ characterization tool to understand failure mechanism in different battery systems with focus on high voltage high-energy cathode (230mAh/g).

For most of battery systems, there is a significant reactivity both at the bulk and the interface of electrodes that are not well understood and are the major cause of both poor cycle life, poor safety and poor efficiency. One task of this project is going to focus on developing advanced in-situ techniques at ANL, BNL and PNNL in

collaboration with our Chinese partners at Tsinghua University, Xiamen University, Peking University and BIT by making use of the advanced user facilities at the above organizations. The techniques developed includes synchrotron based in situ X-ray techniques (x-ray diffraction, hard and soft x-ray absorption) with other imaging and spectroscopic tools such as high resolution transmission electron microscopy (HRTEM), Scanning transmission electron microscopy (STEM), mass spectroscopy (MS), X-Ray fluorescence microscopy (XRF) and transmission x-ray microscopy (TXM). We use the time-resolved x-ray diffraction TR-XRD and absorption (TR-XAS) developed at ANL and BNL to study the kinetic properties of electrode materials with structural sensitivity (TR-XRD) and elemental selectivity (TR-XAS). In-situ XANES is used to monitor oxidation state of active metal ions in cathode. This technique can be used to understand failure mechanism of high voltage, and high energy cathode which will help us develop high capacity high voltage and stable cathode. Another important issue is the thermal stability of new cathode materials which is closely related to the safety of the batteries. This problem is studied using the combined TR-XRD, TR-XAS with mass spectroscopy (MS). This project also proposes to develop a novel in situ X-ray fluorescence (XRF) microscopy combined with X-ray absorption spectroscopy (XAS) technique, which will enable us to track the morphology and chemical state changes of the electrodes and the SEI layer formation and decomposition during cycling.

Task 2 Characterization of Silicon-Based Anode Materials and their Solid-Electrolyte Interphase (SEI)

This work is to investigate Si-based material as the anode including development of in-depth understanding of the SEI protective layer that can be formed on these materials and characterization of the lithium alloying properties of the bulk that will influence the formation of the SEI layers. Finding electrolyte additives that can provide a good protective SEI for silicon-based anodes, as well as operate at higher voltages, would provide for stable cycling performance needed for high energy and high power lithium ion batteries for PHEV and EV applications. The team combine characterization of silicon anode material, electrolytes and electrolyte additives to meet the desired criteria for high energy density Li ion batteries. For the characterization of SEI properties and formation mechanisms on the Si anode materials, we have access to and expertise in the following techniques: SEM, TEM, AFM and STEM. Scanning electron microscopy (SEM), transmission electron microscopy (TEM), and scanning tunneling electron microscopy (STEM) are available through the electron microscopy center (EMC) and CNM. Atomic force microscopy (AFM) with electrochemical capability is available in our group. AFM study inside of a dry box is possible. The AFM can be used to study the formation of SEI layer, its thickness, morphology, and mechanical strength, etc.

XPS and SIMS Analysis X-ray photoelectron spectroscopy (XPS) is an ideal tool for surface characterization. Survey scans and high-resolution scans of the Si 2p, C 1s, O 1s, F 1s, Li 1s, and P 2p energy spectra are very informative for the identification of the compounds present on the surface, especially the solid electrolyte interface (SEI). Secondary ion mass spectrometry (SIMS) is a technique to analyze the composition of solid surfaces and thin films by sputtering the surface of the specimen with a focused primary ion beam and collecting and analyzing ejected secondary ions. These secondary ions are measured with a mass spectrometer to determine the elemental, isotopic, or molecular composition of the surface and films. SIMS is the most sensitive surface and thin film analysis technique, being able to detect elements present in the parts per billion range.

XANES X-ray absorption at near edge spectroscopy (XANES) of Si K-edge on a series of discharge and charge Si-based samples can be carried out at Canadian Light Source (CLS). Our preliminary results using the XANES technique showed that the Si-containing species are involved in the SEI formation over Si anode, but it seems that the Si-containing SEI is dependent of the discharge and charge process, i.e. the potential applied.

Results

1. Simultaneously Dual Modification of Ni-rich Layered Oxide Cathode for High-energy Lithium-ion Batteries

Layer-structured Ni-rich materials have been considered as promising cathode candidate for the next-generation lithium ion batteries (LIBs) owing to their high energy density compared with LiFePO_4 and LiCoO_2 . However, these materials are still facing significant challenges for commercialization in large scale.

One of the major problems is known as interfacial instability, which means that upon cycling, the electrode/electrolyte interface of Ni-rich materials suffers from severe side reaction at a highly delithiated state. In addition, bulk structural degradation is another vital factor that deteriorates the electrode capacity. To overcome these problems, we need to simultaneously dual modification on surface and bulk of Ni-rich cathode.

In collaboration with our Chinese partners at Xiamen University, the Argonne team together with BNL rationally designed and synthesized Ti-doped, and $\text{La}_4\text{NiLiO}_8$ -coated $\text{LiNi}_{0.8}\text{Co}_{0.1}\text{Mn}_{0.1}\text{O}_2$ cathode materials, via a simple and convenient dual-modification strategy of synchronous synthesis and in-situ modification. Based on the theoretical calculation of the migration energy difference between La and Ti from the surface to the inside of NCM, it is reasonable that compared to the La atoms, Ti atoms are more likely doped into the bulk NCM (). Thus, the Ti-doped and LaMO-coated $\text{LiNi}_{0.8}\text{Co}_{0.1}\text{Mn}_{0.1}\text{O}_2$ could be synchronously synthesized in-situ under the same temperature. In addition, this route avoids the detrimental exposure of NCM powders to air and water during the modification process. More importantly, the attained dual-modified architecture inherits the advantages of both $\text{La}_4\text{NiLiO}_8$ coating and Ti doping. The $\text{La}_4\text{NiLiO}_8$ coating functions as a protector and can effectively prevent the electrolyte attack, leading to a significant improvement of the NCM surficial stability and conductivity. The Ti^{4+} (0.74 Å) ions, which pose similar ion radius with Ni^{2+} (0.69 Å), serve as pillars and electrons accumulators that reduce the degree of cation mixing and detrimental H2-3 phase transition during cycling, and further suppress the formation of intergranular cracks. These results contribute to the significant enhancement in electrochemical performance in term of improved rate performance, capacity retention and largely suppressed voltage fading, even under exertive conditions such as at elevated temperature (60°C) and under extended cut-off voltage (4.5 V).

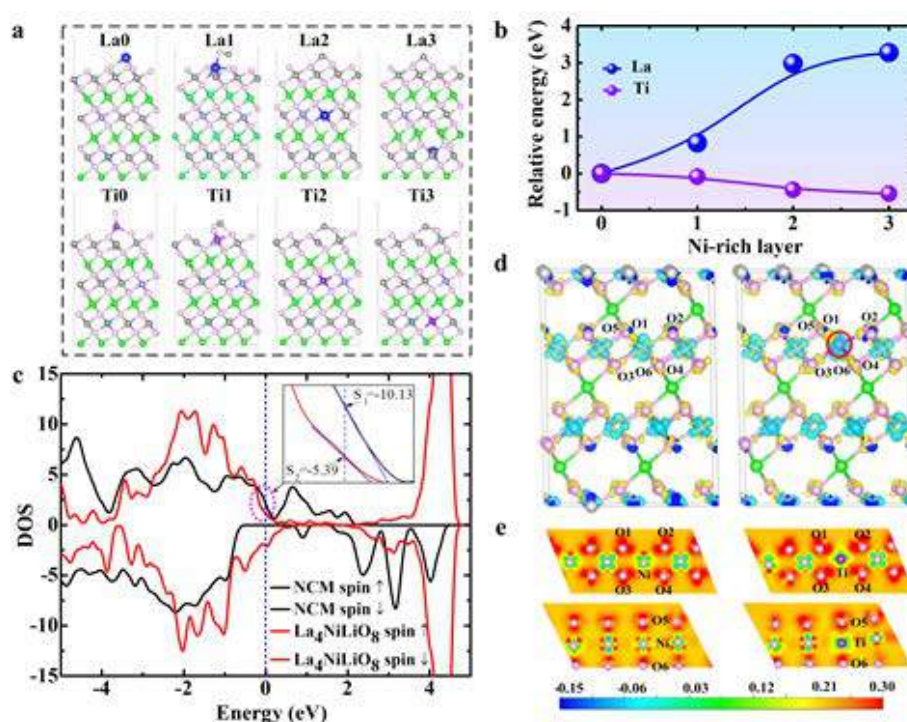


Figure II.5.H.1 Theoretical design of the roadmap for an advanced Ti & LaMO dual modification

The cyclability of the synthesized dual modified composite also outperforms many Ni-rich materials. By in-house designed full-field transmission X-ray microscopy (TXM) and nano-XANES, ex-nuclear magnetic resonance (NMR), ex-X-ray diffraction (XRD) and transmission electron microscopy (TEM), we elucidated the capacity degradation mechanism of NCM and revealed that the inhomogeneity of Ni^{3+} distribution within a particle and among particles for the NCM after cycling. (Figure II.5.H.2) Our finding in this work demonstrated

that the dual-modification strategy is quite effective in suppressing bulk mechanical degradation and inconsistent evolution of surficial structural degradation.

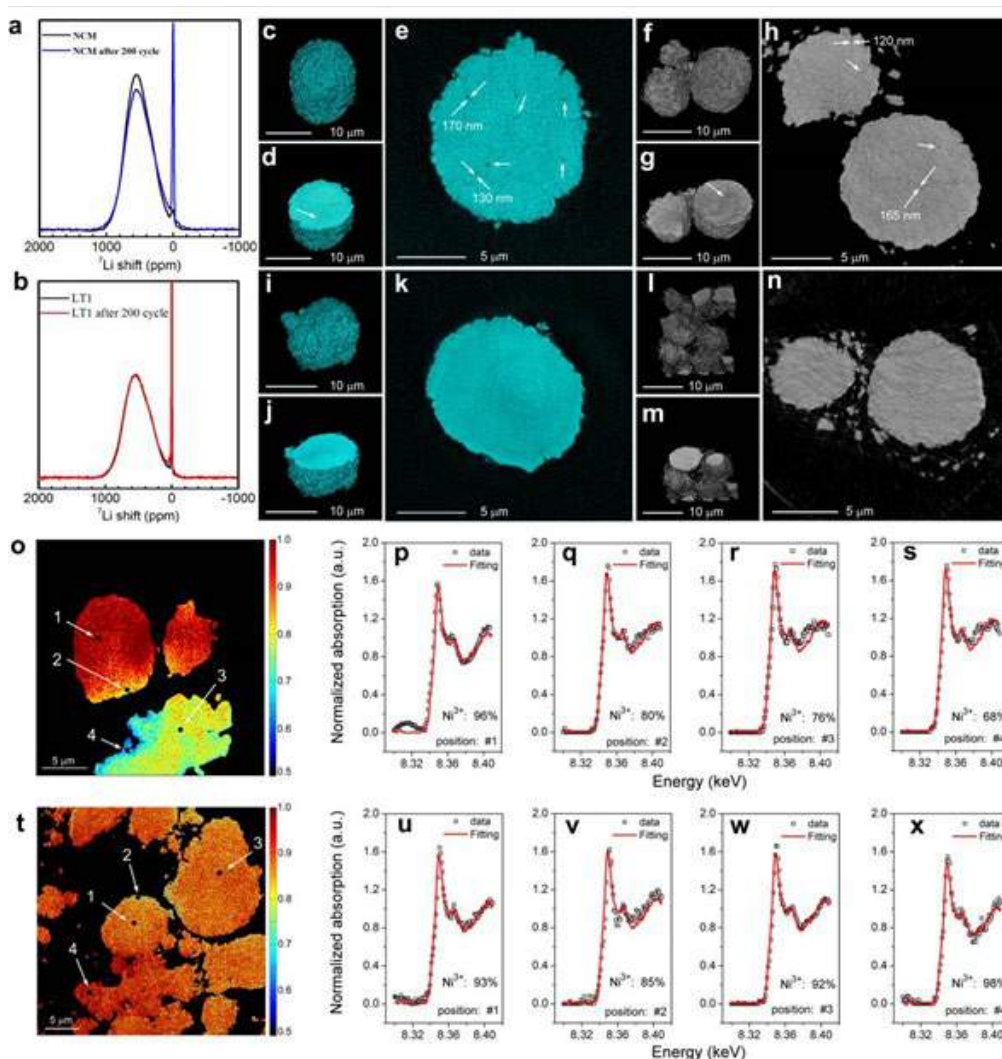


Figure II.5.H.2 ^7Li MAS NMR spectra obtained before cycling and after cycling of NCM and NCM with modification. Morphology characterization of NCM and NCM with modification using TXM

This work has been published in *Advanced Functional Materials*, 29, 1808825, (2019)

1. Building ultraconformal protective layers on both secondary and primary particles of layered lithium transition metal oxide cathodes

In collaboration with The Hong Kong Polytechnic University and Tsinghua University, we demonstrate the ultraconformal poly(3,4-ethylenedioxythiophene) skin facilitates the transport of lithium ions and electrons, significantly suppresses the undesired layered to spinel/rock-salt phase transformation and the associated oxygen loss, mitigates intergranular and intragranular mechanical cracking, and effectively stabilizes the cathode–electrolyte interface. This approach remarkably enhances the capacity and thermal stability under high-voltage operation. Building a protective skin at both secondary and primary particle levels of layered oxides offers a promising design strategy for Ni-rich cathodes towards high-energy, long-life and safe lithium-ion batteries.

At first, by using an oxidative chemical vapour deposition (oCVD) technique, an ultraconformal, highly electronically conductive and ionically permeable poly(3,4-ethylenedioxythiophene) (PEDOT) skin was successfully built on both secondary and primary particles of layered oxide cathode materials. To confirm the capability of oCVD in building PEDOT skin at both primary and secondary particle levels, characterizations using Fourier-transform infrared spectroscopy, Raman spectroscopy and X-ray photoelectron spectroscopy, and transmission electron microscopy (TEM) with scanning transmission electron microscopy-high-angle annular dark-field imaging (STEM-HAADF) and Energy-dispersive X-ray spectrometry (EDS) element mapping were carried out. The thickness increased from 7 to 14, 20 and 28 nm with 20, 40, 60 and 80 min of oCVD, respectively.

The in situ high-energy X-ray diffraction (HEXRD) during charge/discharge shown that the protective skin facilitated the a highly reversible phase transformation during delithiation–lithiation process. In contrast, for the bare cathode, many peaks have deviated from their original 2 θ positions after the first cycle. The PEDOT skin coating can also suppress the undesired layered to spinel/rock-salt structural evolution during high-voltage charge. The capacity retention rate at C/10 over 50 cycles can be improved to 76.7, 85.2, 96.6 and 95.8% from 67.6% (for bare NCM) with 20, 40, 60 and 80 min of oCVD, respectively. The cycle stability of the layered Ni-rich LiNi_{0.85}Mn_{0.05}Co_{0.10}O₂ cathode and Li-rich Li_{1.2}Mn_{0.54}Ni_{0.13}Co_{0.13}O₂ cathode can also be significantly improved by building an ultraconformal PEDOT skin, demonstrating the broad application of this approach in the development of better materials towards high-energy and long-life rechargeable batteries. For the cathode safety, the delithiated 60-PEDOT@NCM111 cathode, the major exothermic peak related to the phase transformation was not observed, indicating that the artificial PEDOT skin can effectively suppress the undesired layered to spinel phase transition under a thermal driving force.

Our result demonstrated a strategy to significantly improve the electrochemical and thermal stability of layered oxide cathode materials by building an ultraconformal conductive polymer skin at both secondary and primary particle levels. This surface engineering approach demonstrates significant breakthroughs over the previously reported oxide and solid electrolyte coatings in terms of stabilizing the crystal/interfacial structure over long-term cycling and high-temperature heating.

These significant findings are summarized in a paper that was recently published by *Nature Energy*.

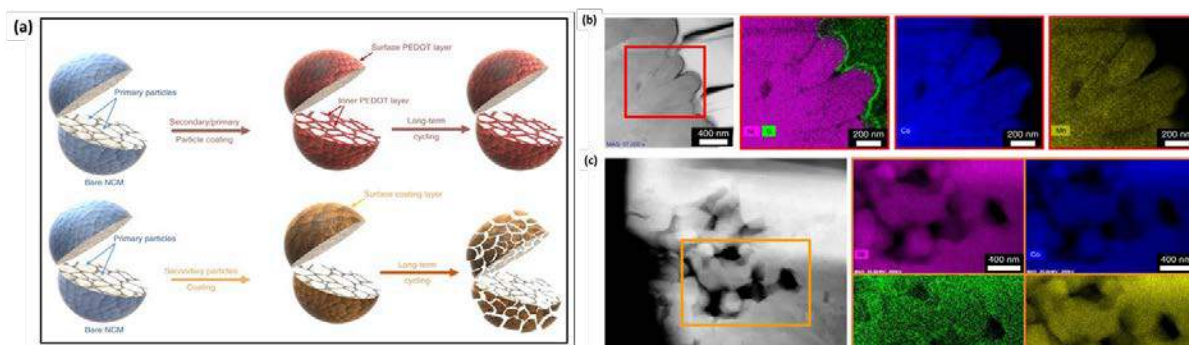


Figure II.5.H.3 The ultrafine coating on both primary and secondary particle surface for the cathode

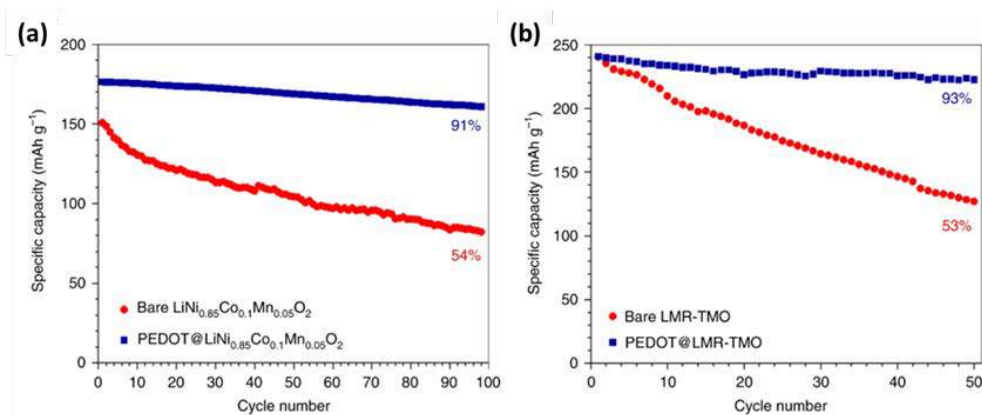


Figure II.5.H.4 The effects of PEDOT coating on electrochemical performance

2. *Correlation between Mn Manganese Dissolution and Dynamic Phase Stability in Spinel-based Lithium-Ion Battery*

Performance improvement of cathode materials represent one of the most critical technological challenges for lithium ion batteries (LIBs), as existing cathode materials exhibit underachieved cycling stability and severe capacity loss. Historically long accepted to be the singular root cause of capacity fade, transition metal dissolution and its subsequent anode deposition have been reported to interfere with Li intercalation and destroy the anode solid electrolyte interface. However, the effect of TM dissolution on the cathode electrochemical performance has been seldom investigated in previous studies. The TM loss from the cathode could very likely lead to some irreversible structural transformation, which potentially produces resultant effects on cathode structural stability. These are significant factors in cathode cycling performance improvement, but currently still not completely understood.

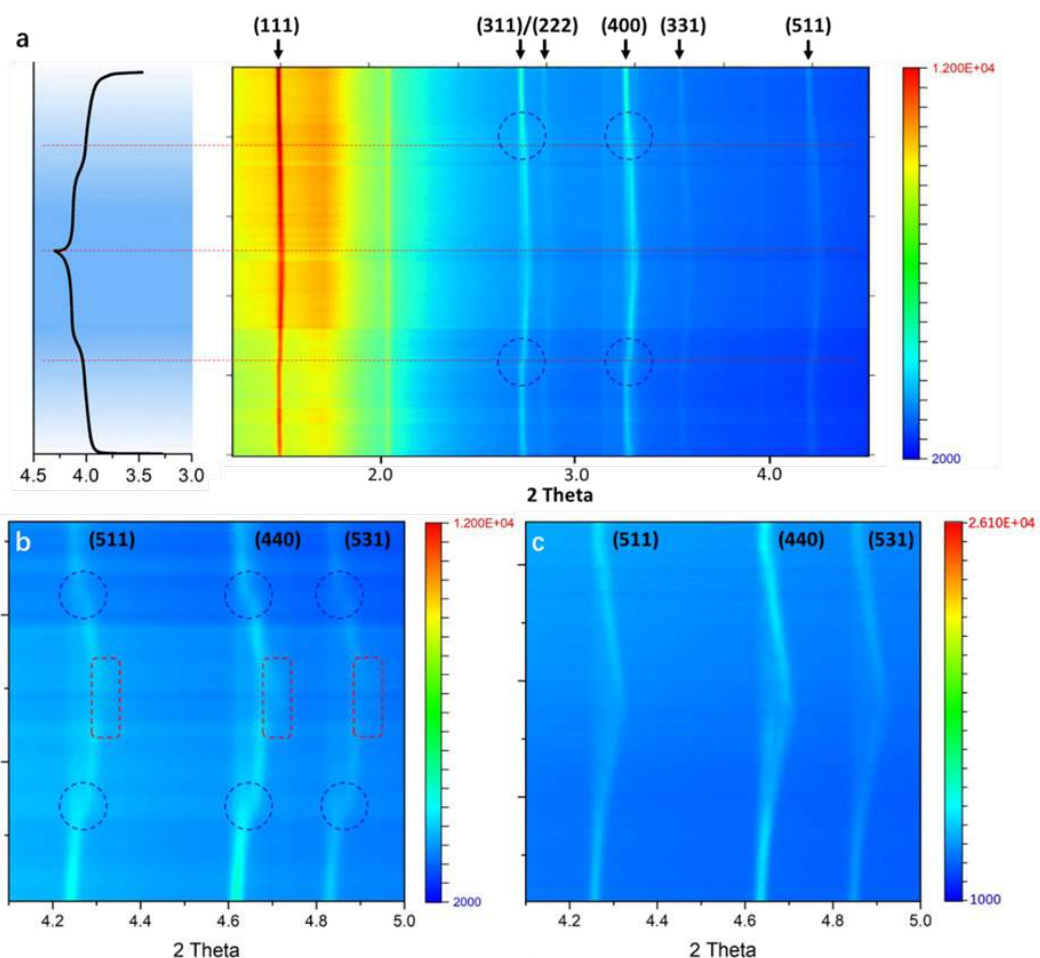


Figure II.5.H.5 In situ synchrotron HE-XRD characterization on the structural evolution of LMO and LR-LMO during the first charge/discharge

In collaboration with Peking University, we employed spinel LiMn_2O_4 as a model system with control experiments to explicitly demonstrate what cathode structural evolutions are involved in charge/discharge process, as well as how structural evolutions interact with Mn dissolution. Through the combination of in-situ/ex-situ high energy X-ray diffraction (XRD) and scanning transmission electron microscopy (STEM), it is evident that LiMn_2O_4 suffers from severe irreversible phase evolutions, which surprisingly produces a soluble Mn_3O_4 phase driven by Mn(III) disproportionation at charging, an over-lithiated $\text{Li}_2\text{Mn}_2\text{O}_4$ at high discharge potential (3.4V), and particle cracks with cycling. These side reactions are the predominated reasons for the fast Mn dissolution of LMO. Meanwhile, the cooperation between fast Mn dissolution and the Jahn-Teller distortion, continuously triggers the generation of over-lithiated $\text{Li}_2\text{Mn}_2\text{O}_4$ on the surface, in turn facilitating the irreversible phase transformation and particle cracks. These unprecedented findings unambiguously enable us to draw a much deeper understanding for the mechanism of spinel LiMn_2O_4 capacity fade: continuous irreversible phase transition and Mn dissolution form a vicious cycle that constantly consumes the capacity of LMO. Consequently, we were able to utilize state-of-the-art techniques to reproduce the atomic structural advantages of Li-rich LiMn_2O_4 with Li/Mn disordering and surface reconstruction, effectively mitigating the irreversible phase transition, and thus suppressing Mn dissolution and particle cracks as well. These new insights provide essential understandings for cathode capacity decay and can serve as design principles for future discovery of improved structurally stable cathode materials for LIBs.

These unprecedented discoveries are summarized in a paper that was recently published by *Nature Communications*.

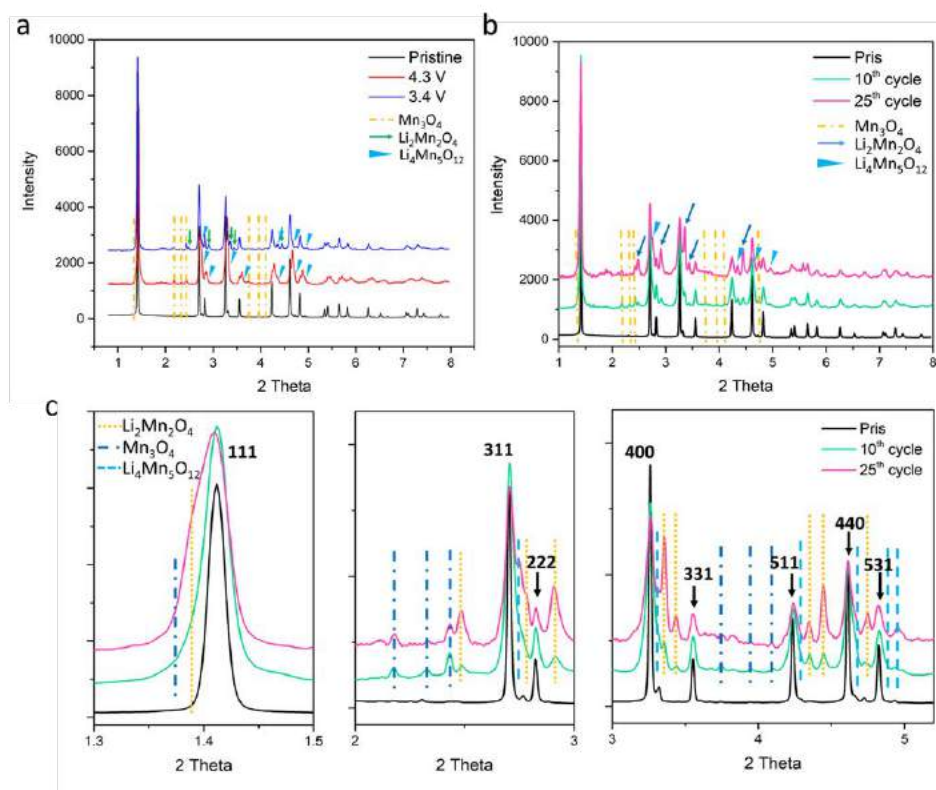


Figure II.5.H.6 Qualitative structural analysis of LMO with different potentials and cycles

Conclusions

1. Through probing from surface to bulk, from individual to the whole ensembles of particles, we show that the average valence states of each type of transition metal cations are continuously reduced, which is attributed to the oxygen release from LMR. Such reductions activate the new lower voltage $\text{Mn}^{3+}/\text{Mn}^{4+}$ and $\text{Co}^{2+}/\text{Co}^{3+}$ redox couples in addition to the original ones like $\text{Ni}^{2+}/\text{Ni}^{3+}$, $\text{Ni}^{3+}/\text{Ni}^{4+}$, and O^{2-}/O^- , directly leading to the voltage fade. We also show that the oxygen release causes microstructural defects such as the formation of large pores within particles which also contributes to the voltage fading.
2. We developed a concerted approach to quantitatively monitor the interphasial components as they deposit on electrode surface at various potentials steps.
3. We demonstrated that the chemical crosstalk is the hidden reason of the battery TR. To design a safe high-energy-density automotive battery, the released oxygen from the cathode is the most critical factor to consider. If the cathode is vulnerable to high temperature, an advanced separator cannot guarantee the safety (or a battery with solid-state electrolyte). The rational design of the reliable high energy density battery needs careful verification at both the material level and automotive cell level.

Key Publications

1. Huiping Yang, Hong-Hui Wu, Mingyuan Ge, Lingjun Li, Yifei Yuan, Qi Yao, Jie Chen, Lingfeng Xia, Jiangming Zheng, Zhaoyong Chen, Junfei Duan, Kim Kisslinger, Xiao Cheng Zeng, Wah-Keat Lee, Qiaobao Zhang, Jun Lu, "Evolution of redox couples in Li- and Mn-rich cathode materials and

- mitigation of voltage fade by reducing oxygen release”, *Advanced Functional Materials*, 29, 1808825, 2019
2. Xu, G. L.; Liu, Q.; Lau, K.; Liu, Y.; Liu, X.; Gao, H.; Zhou, X.; Zhuang, M.; Ren, Y.; Li, J.; Shao, M.; Ouyang, M.; Pan, F.; Chen, Z.; Amine, K.; Chen, G., Building ultraconformal protective layers on both secondary and primary particles of layered lithium transition metal oxide cathodes. *Nature Energy*, 4, 484-494, 2019
 3. Tongchao Liu, Alvin Dai, Jun Lu, Yifei Yuan, Yinguo Xiao, Lei Yu, Matthew Li, Jihyeon Gim, Lu Ma, Jiajie Liu, Chun Zhan, Luxi Li, Jiabin Zheng, Yang Ren, Tianpin Wu, Reza Shahbazian-Yassar, Jianguo Wen, Feng Pan, Khalil Amine, “Correlation between Manganese Dissolution and Dynamic Phase Stability in Spinel-based Lithium-Ion Battery”, *Nature Communications*, 10(1), 1-11, 2019
 4. Zhang, M.J., Hu, X., Li, M., Duan, Y., Yang, L., Yin, C., Ge, M., Xiao, X., Lee, W.K., Ko, J.Y.P. and Amine, K., 2019. Cooling Induced Surface Reconstruction during Synthesis of High-Ni Layered Oxides. *Advanced Energy Materials*, 9(43), 1901915, 2019
 5. Duan, Y., Yang, L., Zhang, M.J., Chen, Z., Bai, J., Amine, K., Pan, F. and Wang, F., 2019. Insights into Li/Ni ordering and surface reconstruction during synthesis of Ni-rich layered oxides. *Journal of Materials Chemistry A*, 7(2), 513-519, 2019
 6. Li, Y., Wang, X., Gao, Y., Zhang, Q., Tan, G., Kong, Q., Bak, S., Lu, G., Yang, X.Q., Gu, L. and Lu, J., 2019. Native vacancy enhanced oxygen redox reversibility and structural robustness. *Advanced Energy Materials*, 9(4), 1803087, 2019
 7. Xiong, B.Q., Zhou, X., Xu, G.L., Liu, Y., Zhu, L., Hu, Y., Shen, S.Y., Hong, Y.H., Wan, S.C., Liu, X.C. and Liu, X., 2019. Boosting Superior Lithium Storage Performance of Alloy-Based Anode Materials via Ultraconformal Sb Coating-Derived Favorable Solid-Electrolyte Interphase. *Advanced Energy Materials*, 1903186, 2019
 8. Zheng, S., Hong, C., Guan, X., Xiang, Y., Liu, X., Xu, G.L., Liu, R., Zhong, G., Zheng, F., Li, Y. and Zhang, X., 2019. Correlation between long range and local structural changes in Ni-rich layered materials during charge and discharge process. *Journal of Power Sources*, 412, 336-343, 2019.
 9. Jiang, Z.L., Xu, G.L., Yu, Z., Zhou, T.H., Shi, W.K., Luo, C.S., Zhou, H.J., Chen, L.B., Sheng, W.J., Zhou, M. and Cheng, L., 2019. High rate and long cycle life in Li-O₂ batteries with highly efficient catalytic cathode configured with Co₃O₄ nanoflower. *Nano Energy*, 64, 103896, 2019
 10. Dai, Alvin, Qidong Li, Tongchao Liu, Khalil Amine, and Jun Lu. “Fundamental Understanding of Water-Induced Mechanisms in Li–O₂ Batteries: Recent Developments and Perspectives.” *Advanced Materials*, 31, 1805602, 2019
 11. Danni Lei, Yan-Bing He, Huijuan Huang, Yifei Yuan, Guiming Zhong, Qiang Zhao, Xiaoge Hao, Danfeng Zhang, Chen Lai, Siwei Zhang, Jiabin Ma, Yinping Wei, Qipeng Yu, Wei Lv, Yan Yu, Baohua Li, Quan-Hong Yang, Yong Yang, Jun Lu, Feiyu Kang Cross-linked beta alumina nanowires with compact gel polymer electrolyte coating for ultra-stable sodium metal battery. *Nature Communications*, 10(1), 1. 2019.
 12. Li, Q.; Liu, Z.; Zheng, F.; Liu, R.; Lee, J.; Xu, G. L.; Zhong, G.; Hou, X.; Fu, R.; Chen, Z., Identifying the Structural Evolution of the Sodium Ion Battery Na₂FePO₄F Cathode. *Angew. Chem. Int. Ed.*, 57, 11918-11923, 2018.
 13. Cao, Y., Li, M., Lu, J., Liu, J. and Amine, K., 2019. Bridging the academic and industrial metrics for next-generation practical batteries. *Nature Nanotechnology*, 14, 200–207, 2019
 14. Chuan Wu, Sichen Gu, Qinghua Zhang, Ying Bai, Matthew Li, Yifei Yuan, Huali Wang, Xinyu Liu, Yanxia Yuan, Na Zhu, Feng Wu, Hong Li, Lin Gu, Jun Lu, “Electrochemically activated spinel manganese oxide for rechargeable aqueous aluminum battery”, *Nature Communications*, 10: 73, 2019

II.5.I Correlative Microscopy Characterization of Oxide Electrodes (SLAC National Accelerator Laboratory)

William C. Chueh, Principal Investigator

SLAC National Accelerator Laboratory
2575 Sand Hill Road
Menlo Park, CA 94025
E-mail: wchueh@stanford.edu

Tien Duong, DOE Technology Development Manager

U.S. Department of Energy
E-mail: Tien.Duong@ee.doe.gov

Start Date: January 1, 2016

End Date: September 30, 2019

Project Funding (FY19): \$450,000

DOE share: \$450,000

Non-DOE share: \$0

Project Introduction

A new cross-technique characterization platform will be developed to track lithiation dynamics at the single-particle level in Lithium- Manganese-rich Nickel Cobalt Oxide (LMR-NMC). Fundamental insights from this new diagnostic capability are expected to increase the power density and cycle life of oxide electrodes by improving electrode utilization, reducing electrochemical hotspots, decreasing capacity and voltage fade, and enhancing safety, which all improve the viability of lithium-ion batteries for vehicle transportation. By understanding lithiation at the single-particle level, this project's success will contribute to improving on-vehicle battery management, such as charging/discharging protocol, state-of-charge and state-of-health monitoring.

Due to the cost of Co, substituting Ni, Mn, Al, Mg, or Cr in the layered oxide cathode LiCoO₂ has become the focus of much research. LMR-NMC is of significant interest for use in electric vehicle applications due to its balance of cost and performance, with demonstrated specific capacities of 230- 280 mAh g⁻¹. Recharging time, power density, voltage/capacity fade, and thermal stability are important performance matrices for these battery chemistries to gain widespread use in vehicle transportation. Rational engineering of electrode chemistry and microstructure is expected to greatly increase these aspects of battery performance. However, due to the wide range of length scales involved – spanning nanometers to millimeters – a comprehensive understanding of kinetics and degradation in battery electrodes is lacking, especially at the single-primary-particle level. Part of the challenge lies in the characterization of lithiation dynamics across a wide range of length scales of realistic batteries during cycling.

This project is carried out in collaboration with scientists at Advanced Light Source and the Molecular Foundry, users facilities at Lawrence Berkeley National Laboratory.

Objectives

This study aims to develop and utilize a correlative microscopy platform to investigate the lithiation dynamics of LMR-NMC, with the specific goal of understanding factors that determine the rate capability and degradation mechanisms at the single primary particle length scale. By developing a nanoscale and single-particle understanding of lithiation, the project addresses specific engineering problems including electrochemical hotspot, electrode utilization, safety, and capacity/voltage fade. Chemistry-sensitive soft transmission X-ray microscopy, operating in standard and in ptychography mode, will be carried out on cycling electrodes in a liquid electrolyte using a microfluidic cell. A platform to transfer the identical electrode to the transmission electron microscope and Raman microscope will be developed to integrate the X- ray, electron and optical characterization with the goal of achieving a comprehensive understanding of the lithiation dynamics at the single-particle level. Ex-situ spectro- ptychography on electrodes cycled at low (-20 °C) and

high (+80 °C) temperatures will be conducted to understand the temperature dependence of lithiation dynamics, hotspots, and degradation in single particles.

Approach

Chemistry-sensitive soft transmission X-ray microscopy, operating in standard and in ptychography mode, will be carried out on cycling electrodes in a liquid electrolyte using a microfluidic cell while the electrode is cycled between the charged and the discharged state. The expected spatial resolution is 5 nm (ptychography mode) and 50 nm (standard mode). To attain even higher spatial resolution, a platform to transfer the same electrode to the transmission electron microscope will be developed. Finally, Raman microscopy, which is sensitive to the vibrational nature of chemical bonds, will also be used to characterize the same electrode. With the seamless integration the X-ray, electron and optical characterization, the goal is to achieve a complete understanding of the lithiation dynamics at the single-particle length scale.

Results

Anion Redox

We continued the investigation of model anion redox compound $\text{Li}_{2-x}\text{Ir}_{1-x}\text{Sn}_x\text{O}_3$ from FY18. Understanding why Sn substitution gives rise to these phenomena is central to uncovering the origin of the coupling between anion redox and metal migration/vacancy formation. Since the defect concentration is more reliably quantified in LISO25 ($x = 0.25$), we focus our DFT analysis on this composition. First, we examined the evolution of the computed DOS in the control case of ordered, $\text{M}_{\text{Li}}/\text{V}_{\text{M}}$ -free LISO25 as a function of Li stoichiometry. We observe that no unhybridized O $2p$ states are depopulated in the fully delithiated O1 structures – only hybridized Ir–O states are accessed, giving Ir a formal oxidation state of at least 6+, which is inconsistent with our XAS results. Thus, simple delithiation and the O3-O1 stacking change does not explain the high voltage redox process in LISO. Importantly, our DFT calculations suggest that O redox cannot occur in LISO25 or LISO50 after delithiating 1.5 Li per formula unit if $\text{M}_{\text{Li}}/\text{V}_{\text{M}}$ defects are not allowed to form.

Next, we introduce the experimentally-observed $\text{Sn}_{\text{Li}}/\text{V}_{\text{M}}$ defects and examine their effect on the electronic structure and charge distribution of LISO. Out-of-plane Sn migration into a Li layer site creates a cation vacancy, V_{M} , and neighboring single-coordinate (dangling) oxygen atoms. Note that we use the term “single-coordinate” to refer to the number of covalent bonding partners – i.e. counting Ir or Sn, but not Li. We find this stabilizes the delithiated structure significantly by 1.34–1.36 eV, whereas the formation of $\text{Ir}_{\text{Li}}/\text{V}_{\text{M}}$ defect pairs are predicted to have a much smaller driving force of 0.02 eV.

We attribute the $\text{Sn}_{\text{Li}}/\text{V}_{\text{M}}$ stabilization to the response of the resulting M–O dangling bonds, which undergo one of two major transformations. As shown in Figure 1, when $\text{M} = \text{Ir}$, these bonds contract substantially, changing from ~ 1.94 Å to ~ 1.77 Å. Figure 1b shows that the bond contraction accompanies a splitting of the previously unhybridized O $2p$ states (shaded, top panel), with some states moving above the Fermi level and becoming oxidized (shaded, bottom panel) – i.e. oxygen redox. The shifted states, approximately 1.5 eV higher in energy, rehybridize with the Ir $5d$ states. These observations suggest the formation of short Ir–O π bonds (equivalently, terminal oxo ligands) through donation of oxygen lone pair electrons, approaching Ir=O double bonds (Figure 1b).

When $\text{M} = \text{Sn}$, on the other hand, the single-coordinate oxygens are predicted to instead pair up to form short (~ 1.44 Å) O–O dimers that straddle the V_{M} (Figure II.5.I.1c). Again, this transformation results in a shift of the previously buried NB O $2p$ states from below to above the Fermi level along with donation of electron density from O to a neighboring Ir. We stress that these localized dimers are distinct from the long (~ 2.5 Å) dimers previously proposed for this material in that they are well within the range of typical bond lengths for O_2^{n-} species and, crucially, do not form in the absence of cation migration.

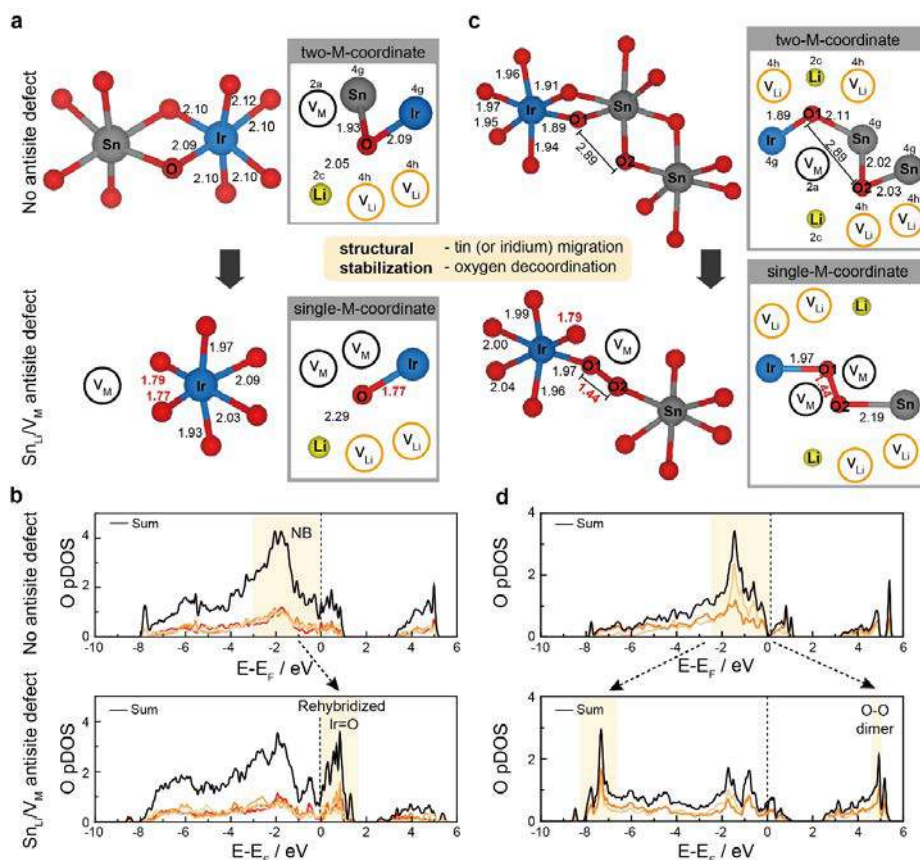


Figure II.5.I.1 Computational predictions of M-O decooordination and Ir=O/O-O mediated anion redox. (a) Local coordination environments predicted by DFT in a $\text{Li}_{0.5}\text{Ir}_{0.75}\text{Sn}_{0.25}\text{O}_3$ structure showing the consequence of SnLi/VM defect formation when the vacancy neighbors only Ir: contraction of the Ir-O bonds (left) and the resulting changes in local oxygen environment (right). Note that the presence of Li neighboring O negligibly affects the O 2p states due to minimal hybridization between Li and O. (b) Projected DOS of the individual oxygen atoms involved in the Ir-O bond contraction before (top) and after (bottom) forming the SnLi/VM defect, demonstrating the shift of the O 2p states above the Fermi level, indicating oxygen redox. (c) Local coordination environments when the migrating Sn initially neighbors another Sn, resulting in the formation of a 1.44 Å O-O dimer. (d) Projected DOS of the individual oxygen atoms involved in the O-O bond formation before (top) and after (bottom) forming the SnLi/VM defect and O-O dimer, also showing a shift of the O 2p states above the Fermi level

LMR-NMC Degradation

We report on characterization of LMR-NMC as a function of cycle number using scanning transmission X-ray microscopy. In order to preserve the microstructure of the cathodes, we employed ultramicrotomy to cross-section secondary particles. Subsequently, Ni L-edge X-ray absorption spectroscopy was carried out to assess the local state-of-charge. Because LMR-NMC undergoes anion redox, O K-edge spectroscopy was used additionally to assess the anion redox extent. Because high state-of-charge cathodes are sensitive to air, samples were transferred with minimal exposure to air.

Figure II.5.I.2 shows that the relative Ni oxidation state varies quite substantially throughout the electrode in the charged state (4.6V) after 125 cycles. As clearly shown, the entire electrode microstructure is preserved, from primary particles, to secondary particles to the porous electrode. The spectroscopic signature of oxidized oxygen in the O K edge remains strong even after 125 cycle. We note that there is a clear dependence on primary particle thickness (which is estimated by the extent of absorption at each pixel), with the thinner particles oxidizing much less. The heterogenous state-of-charge also exists within secondary agglomerates, in addition to primary particles. Because a constant voltage hold was performed, we do not believe this state-of-

charge distribution is due to slow kinetics. Instead, it may be attributed to presence of point defects of secondary phases near the surface.

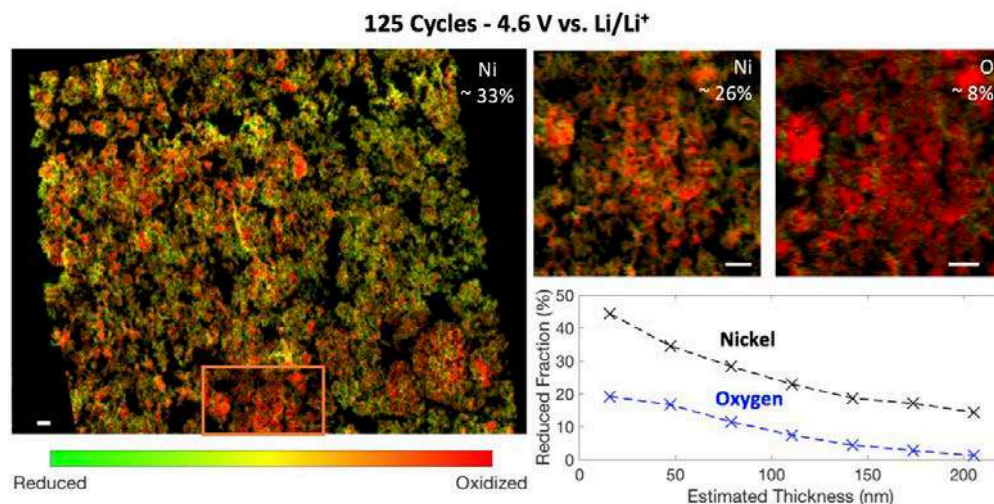


Figure II.5.I.2 Spatial distribution of the Ni and O oxidation state in the charged state after 125 cycles determined through STXM. The far left shows the distribution over an “electrode scale” ($\sim 30 \times 30 \mu\text{m}$) determined with only three energies, while the zoomed in images show the distribution within the boxed region determined by fitting of spectra containing > 40 energies. The reduced fraction as a function of thickness is taken using the zoomed in images, although there is no qualitative difference when using the “electrode scale” Ni map instead. The scale bar in each image is 1 micron

NMC Intercalation Dynamics

We characterized NMC111 cathode platelet particles synthesized via molten salt route. Such a microstructure is ideal for studying Li transport during charging and discharging because transport occurs along the in-plane direction during microscopy measurements. Similarly, this geometry allows phase boundary movement along the fast transport axis of layered oxides to be directly visualized. Open-circuit voltage is essentially the same as those synthesized from standard routes. We note that these particles exhibit modest rate capability (approximately ten times worse than those from coprecipitation synthesis), likely due to the low edge and basal facets in the platelet geometry.

As proof-of-concept, we performed high-resolution scanning transmission X-ray microscopy measurements on these particles at various states-of-charge (Figure 1). Ni oxidation state was used to infer the state-of-charge. We have shown that Ni is an effective indicator of SOC because it is the main redox partner in NMC111. Imaging was carried out in standard transmission mode as well as in ptychography mode (scanning coherent diffractive imaging). As can be seen, high spatial resolution in ptychography mode was achieved. Two types of experiments were carried out. First, ex-situ imaging whereby particles were cycled to a predefined SOC, stopped, battery cell disassembled, and electrodes rapidly dried. This procedure is carried out in around one minute, and prevents the re-distribution of Li between particles, though it does not preclude Li rearrangement within a given particle. Second, operando imaging was carried out, whereby the particles were cycled electrochemically while imaged. In both experiments, beam-induced damage (in terms of redox state change) was negligible.

Conclusions

We have successfully developed a suite of in-situ and post mortem diagnostic tools for investigating cycling and degradation of anion-redox cathodes such as LMR-NMC as well as conventional NMC. We discovered the structure-redox link in Li-rich oxides that gives rise to the high capacity as well as the voltage fade. We also developed a platelet morphology for cathodes suitable for studying intercalation in-situ.

Key Publications

1. J. Hong, W. E. Gent, P. Xiao, K. Lim, D.-H. Seo, J. Wu, P. M. Csernica, C. J. Takacs, D. Nordlund, C.-J. Sun, K. H. Stone, W. Yang, D. Prendergast, G. Ceder, M. F. Toney, W. C. Chueh. Metal-Oxygen Decoordination Stabilizes Anion Redox in Li-rich Oxides. *Nature Mater.* **18**, 256-265 (2019).
2. K. Dai, J. Wu, Z. Zhuo, Q. Li, S. Sallis, J. Mao, G. Ai, C. Sun, Z. Li, W.E. Gent, W.C. Chueh, Y. Chuang, R. Zeng, Z. Shen, F. Pan, S. Yan, L.F.J. Piper, Z. Hussain, G. Liu, and W. Yang. High Reversibility of Lattice Oxygen Redox Quantified by Direct Bulk Probes of Both Anionic and Cationic Redox Reactions. *Joule* **3**, 518-541 (2019).
3. J. Wu, Q. Li, S. Sallis, Z. Zhuo, W. E. Gent, W. C. Chueh, S. Yan, Y.-D. Chuang, W. Yang. Fingerprint Oxygen Redox Reactions in Batteries through High-Efficiency Mapping of Resonant Inelastic X-ray Scattering. *Condens. Matter.* **4**, 5 (2019).

Key Publications

This project was led by a SLAC team consisting of Yi Cui, William C. Chueh, and Michael F. Toney.

II.6 Next Generation Lithium-Ion batteries: Modeling Advanced Electrode Materials

II.6.A Electrode Materials Design and Failure Prediction (ANL)

Venkat Srinivasan, Principal Investigator

Argonne National Laboratory
9700 S Cass Avenue
Lemont, IL 60439
E-mail: vsrinivasan@anl.gov

Tien Q. Duong, DOE Technology Development Manager

U.S. Department of Energy
E-mail: Tien.Duong@ee.doe.gov

Start Date: October 1, 2018	End Date: September 30, 2019	
Project Funding (FY19): \$1,460,000	DOE share: \$1,460,000	Non-DOE share: \$0

Project Introduction

Solid-state electrolytes (SSEs) for lithium ion batteries (LIBs) are being actively investigated because it has the potential to enable lithium (Li) metal anodes and substantially enhance the energy density of existing LIBs. Adoption of SSEs can also increase the safety of the existing Li-ion cells, because it can completely replace the flammable liquid electrolytes. However, realistic implementation of SSEs face interfacial issues at both the positive and negative electrode sides. Formation of Li dendrites during the charging process prevents the usage of these SSEs with Li metal anodes under low temperature ($< 30^{\circ}\text{C}$) and high current density conditions. Experimentalists have observed Li dendrites within the grain-boundary (GB) region. Several experimental observations and theoretical calculations have reported the GB conductivity to be smaller than that observed in grain-interior (GI). This points to the fact that there should be current focusing in GI, and not in the GB domain. In the present project, from the reaction kinetics perspective, a theoretical understanding has been developed that explains the formation and propagation of Li dendrites within the GB region in spite of smaller conductivity within GB. In the present project Li dendrite growth within LLZO SSEs has been investigated. The cathode/SSE interface also experiences the following issues that can decrease the cyclable capacity and increase the cell resistance: a) Inter-diffusion of transition-metal cations from the cathode particles to the SSE, and b) Delamination between the cathode and SSE during repeated charge–discharge process. The issues associated with interfacial delamination have been addressed in the present project. The reason behind this detachment phenomenon between cathode and solid electrolyte, and how this impacts the interfacial charge transfer resistance is of great importance to the scientific community. Here, the delamination between LLZO electrolyte and NMC 111 cathode particles has been investigated.

Objectives

The main objective of this project is development of computational models for understanding the various degradation mechanisms for next-generation Li-ion batteries. This year's goal is to use the continuum-based mathematical model to (1) investigate interfacial stability between electrodes and ceramic-based SSEs, and (2) experimentally measure and understand the impedance observed at the cathode/SSE interface. Ceramic-based SSEs are expected to enable high energy density and liquid-free, safe, next-generation Li-ion batteries. Li-metal anodes should be incorporated due to their substantially larger specific capacity, as compared to present day graphite-based anodes. During deposition, lithium dendrite growth through the SSEs and subsequent short circuit has been a major issue, limiting the successful implementation of SSEs. Similarly, on the cathode side, diffusion of TMs into the SSEs and delamination between cathode and SSE lead to increased interfacial resistance. The developed computational model will be used to investigate the impact of microstructural (grain size), physical (mechanical stiffness), and transport (conductivity) properties of the SSE on the overall

interfacial degradation observed at both the cathode and anode sides. Due to the SOC-dependent electrochemical and mechanical properties of the cathode, an attempt will be made to experimentally measure the SOC dependent impedance at the cathode/SSE interface. The main focus of this project will be to elucidate the interfacial issues, observed at both anode and cathode sides, and devise strategies to enable the successful implementation of SSE in next-generation Li-ion batteries.

Approach

To address the problems mentioned earlier, a computational methodology have been developed, based on a combination of finite element method, lattice spring method and finite volume method, that can capture the evolution of potential field and mechanical stress within the SSEs, and predict the potential pathway for crack and dendrite propagation. The same methodology can be used to predict the extent of delamination that occurs at the cathode/SSE interface. Butler-Volmer based reaction current have been assumed at the electrode/electrolyte interface for both cathode and anode. The impact of mechanical stress induced electrochemical potential on the reaction kinetics has also been taken into account.

Results

Investigate the impact of grain-interior(GI)/grain-boundary(GB) microstructure on the overall dendrite growth observed at SSE/lithium interface:

Even though the mechanical stiffness of the ceramic based electrolytes are very high, lithium dendrite growth through SSEs has been one of the major bottlenecks preventing their widespread implementation in next generation LIBs. Inhomogeneous GI/GB microstructure, variation in conductivity through the two different phases, difference in their elastic stiffness, all of these factors contribute to the overall non-uniform current distribution observed at the Li/SSE interface. Majority of the experimental studies and DFT based lower length scale calculations indicate that the conductivity of lithium through the GB region is smaller in magnitude than the GI. However, several experimental observations reported enhanced lithium deposition at the GB regions. In the present research, using the concept of mechanical stress induced change in electrochemical potential, we provide an explanation why current focusing at the GB is possible in spite of slower ionic transport. Following the pioneering work conducted by Monroe and Newman (JES 2004, A880), we derived a modified version of the Butler-Volmer equation that takes into account the stress induced change in electrochemical potential, and is also applicable to ceramic based single ion conducting SSEs. Magnitude of mechanical stress has been estimated assuming deposition of a monolayer of lithium at the Li/SSE interface. Since, newly deposited lithium metal pushes the existing metal electrode and the SSE in opposite directions, compressive stress evolves in both of them. The modified Butler-Volmer equation indicates that higher compressive stress prevents lithium deposition. Since the elastic modulus of the GB region is a few orders of magnitude smaller than the elastic modulus of GI, lower compressive stress develops there. This result in enhanced lithium deposition at the GBs. Smaller magnitude of GB conductivity tends to minimize the current focusing, but the net current density at GB still remains higher than the GI. Figure II.6.A.1(a) and Figure II.6.A.1(b) demonstrates two different GI/GB microstructures that have been used to analyze the effect of grain size on the current focusing. Figure II.6.A.1(c) clearly depicts that smaller sized grains, with multiple GBs, leads to uniform distribution of currents and reduced focusing at GBs.

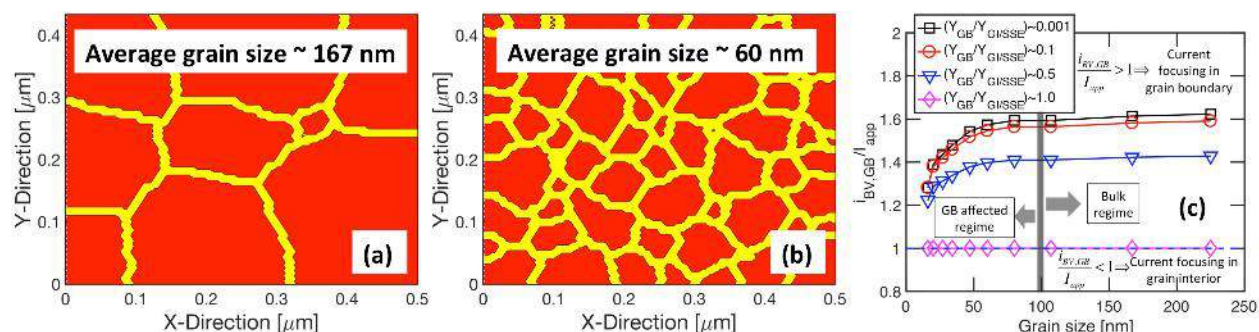


Figure II.6.A.1 (a) GI/GB microstructure with average grain size 167 nm. (b) GI/GB microstructure with average grain size 60 nm. (c) Current focusing observed at the GB region plotted with respect to grain size. Decrease in grain size helps to distribute the current and reduce the current focusing observed at the GB regions

Figure II.6.A.2 clearly demonstrates that enhanced lithium deposition at the GB region has the potential to initiate crack fronts, which can propagate through the brittle ceramic SSE and eventually short the cell. Explanation of enhanced lithium deposition and crack initiation at GB region satisfies the milestone for the first quarter.

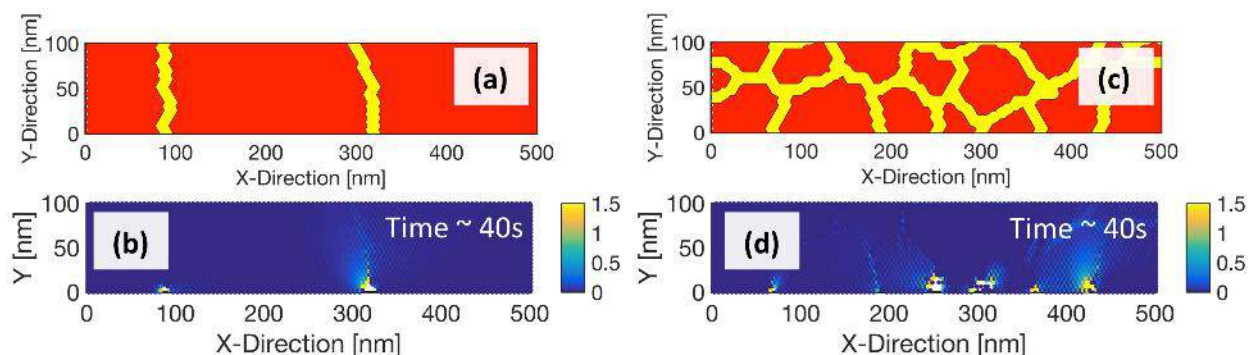


Figure II.6.A.2 (a) GI/GB microstructure with larger grains (LG). (b) Strain energy (SE) and cracking at GB for LG. (c) GI/GB microstructure with small grains (SG). (d) SE and cracks at GB for SG

Analyze the effect of delamination at the cathode/solid-state-electrolyte interface as a mode of degradation:

In order to improve the energy density and safety of next generation lithium ion batteries, it is necessary to use lithium metal anodes and solid state electrolytes (SSEs). However, to build a successful electrochemical cell, good cathode materials must also be incorporated as the positive electrode of the battery. Conventional cathode materials, for example, LCO, NMC, etc., store lithium atoms through intercalation mechanism. During the charge process, lithium ions go out of these cathode particles, which result in their shrinkage. Similarly, during discharge, lithiation of these cathode materials result in their expansion. Usually, during the synthesis process, lithium ion cells are fabricated in a discharged state, which means that the cathodes are assembled in a lithiated condition. During the formation cycles, the cells are charged for the first time, which leads to the delithiation of the cathode particles. The initial delithiation gives rise to tensile stresses at the cathode/SSE interface, which may lead to interfacial delamination based on the amount of volume contraction of cathode, compliance of the SSE, and binding energy between the cathode and the SSE. Also, oxide based SSEs (such as, LLZO) demonstrates grain interior (GI) and grain boundary (GB) microstructure. Since, the GBs demonstrate lower mechanical stiffness than the GIs, stresses of different magnitude evolve at the GI and GB regions. The reaction current at the cathode/SSE interface is given by the Butler-Volmer equation (i_{BV}), which takes into account the mechanical stress induced changes in the electrochemical potential ($\Delta\mu_e$). The overpotential is defined as, $\eta_s = \phi_s - \phi_e + (\Delta\mu_e - F)$, and the Butler-Volmer equation is written as, $i_{BV} = i_0 \exp(\Delta\mu_e - /2RT) [\exp(F\eta_s/2RT) - \exp(-F\eta_s/2RT)]$. Here, i_0 is the exchange current density, which

depends on the concentration of lithium at the cathode/SSE interface and also the activation energy barrier for lithium transportation between cathode and SSE. In the present analysis, a constant magnitude of i_0 has been assumed. Figure II.6.A.3 shows the LLZO/NMC interface modeled in the present study and current focusing at the grain boundaries during both charge and discharge processes.

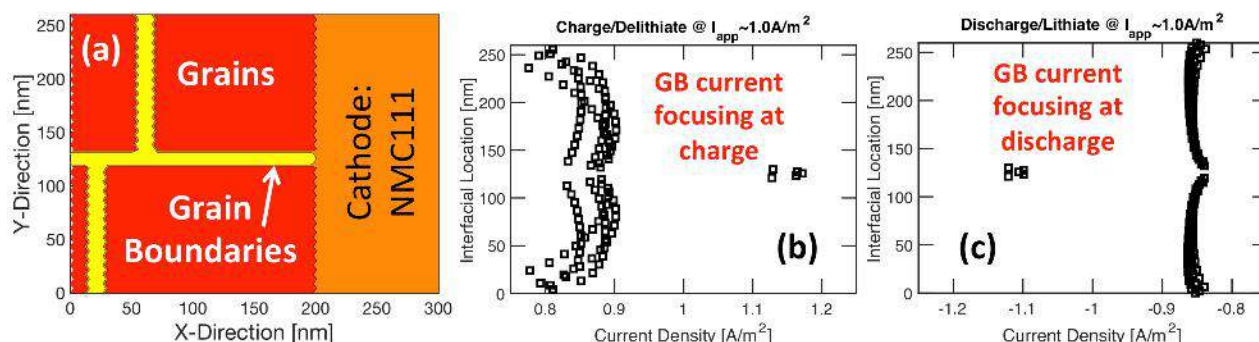


Figure II.6.A.3 (a) Computational domain of the cathode/SSE interface with presence of grain boundaries (GB). (b) Distribution of current density at the interface during the charge process (magnitude of current is positive, because anodic current is active). (c) Distribution of current density at the interface during the discharge process (magnitude of current is negative, because cathodic current is active)

Schematic representation of a NMC/SSE interface is demonstrated in Figure II.6.A.4(a), which clearly shows that delamination may occur at the time of delithiation due to the shrinkage of cathode. Such detachment may lead to decrease in electrochemically active surface area, and increase in cell resistance. The charge-discharge curves obtained at 10 A/m^2 , shown in Figure II.6.A.4(b), demonstrates the fade in first discharge capacity due to delamination during the first charge step. Successfully capturing the degradation at cathode/SSE interface, and predicting its impact on cell performance, completes the milestone for the second quarter.

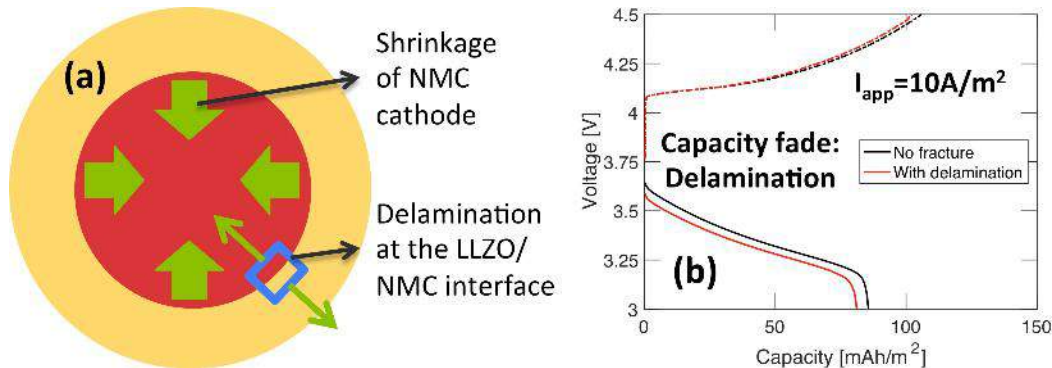


Figure II.6.A.4 (a) Schematic diagram of the cathode/SSE interface where delamination can occur during the first charge or delithiation process. (b) Charge and discharge curves obtained during the first delithiation and lithiation of the cathode particles. Delamination during the charge process manifests as a capacity fade during discharge

Investigate the impact of grain size of the electrolyte on the mechanical degradation occurring at the cathode/SSE interface:

In the last quarter, we demonstrated that the lithium insertion/extraction induced swelling and contraction of the NMC based cathode material can lead to delamination at the cathode/solid-electrolyte interface. This loss of interfacial contact can eventually lead to a decrease in the total amount of electrochemically active surface area, effectively reducing the discharge capacity of the solid-electrolyte cells. Impact of solid-electrolyte microstructure on the interfacial delamination induced capacity fade has been investigated in the present quarter. Different LLZO microstructures have been generated with various grain sizes. Figure II.6.A.5(a) and Figure II.6.A.5(b) shows two such LLZO/NMC interfaces, where the average LLZO grain size has been assumed to be around 150nm and 75nm, respectively. By conducting charge-discharge cycle on top of these

LLZO/NMC microstructures, interfacial delamination induced capacity fade has been estimated. From Figure II.6.A.5(c), it is evident that the magnitudes of capacity fade decreases with smaller grain sizes. This can be attributed to the fact that within LLZO microstructures with smaller grains, there exist multiple grain boundary domains. The grain-boundaries demonstrate smaller elastic modulus, and higher deformability, as compared to the grain-interiors. With larger number of mechanically soft grain-boundary domains, the ceramic electrolyte is able to better accommodate the volume changes experienced by the cathode materials. Hence, within LLZO microstructures with small grains, smaller magnitude of strain energy evolves at the interface, which leads to less interfacial delamination, and subsequently lesser capacity fade.

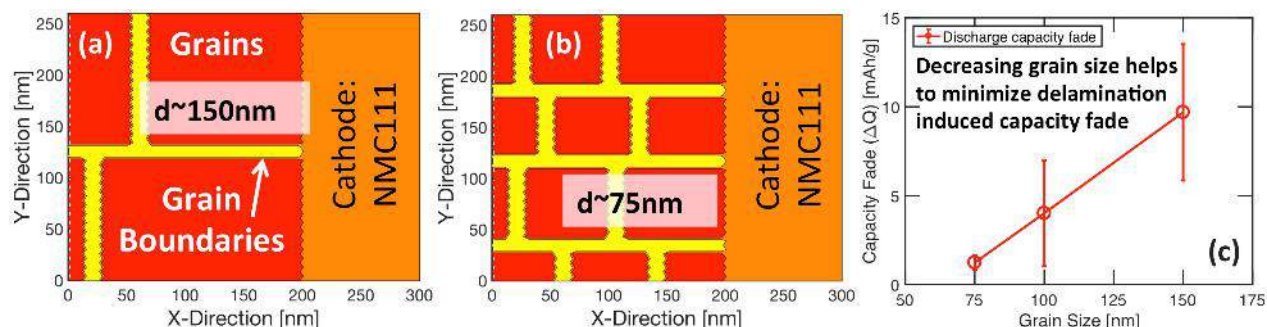


Figure II.6.A.5 (a) Computational domain with large grain size of approximate diameter around 150nm. (b) Computational domain with smaller grain sizes of diameter approximately 75nm. In both (a) and (b), the orange portion indicates cathode (NMC 111), the red domain denotes grain interior, and the yellow region stands for the grain-boundary. (c) Capacity fade due to interfacial delamination as observed in different LLZO microstructures with various grain sizes. Decreasing the grain size helps to minimize capacity fade

As a continuation of the earlier efforts, we also investigated the impact of long term cycling on the interfacial delamination induced capacity fade. All the LLZO/cathode microstructures, with different electrolyte grain sizes, have been subjected to ten CCCV-charge and CC-discharge cycles. The applied current density for the CC process is 1A/m^2 , whereas the cutoff voltage during charging has been assumed to be 4.4V. The CV process has been stopped as soon as the current becomes less than 10% of the initial applied current density. The performance curves for the first, third and the ninth cycle has been demonstrated in Figure II.6.A.6(a). Whereas, the overall capacity fade is shown in Figure II.6.A.6(b). The LLZO microstructures with smaller grains experience capacity fade at a slower rate. Analysis of interfacial delamination induced capacity fade with different LLZO grain sizes concludes the milestone for the third quarter.

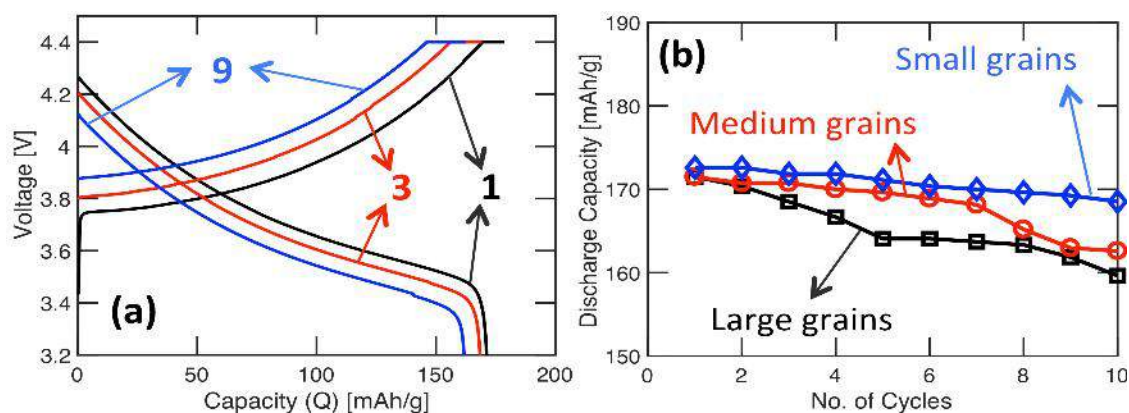


Figure II.6.A.6 (a) The voltage vs. capacity performance curves as observed during the first, third and ninth CC-CV charge and CC discharge cycle as observed in the LLZO microstructures with large grain sizes. (b) Interfacial delamination induced capacity fade observed in three different LLZO microstructures with large, medium and small grain sizes. The rate of capacity fade is much less in the smaller grain, due to the limited mechanical degradation observed there

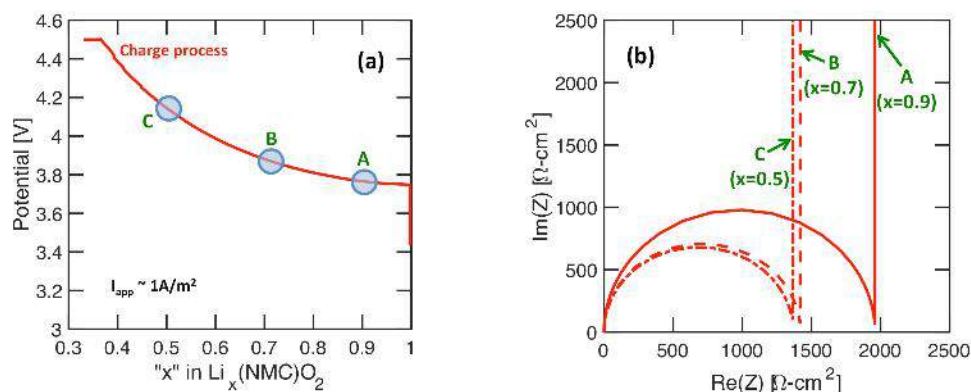


Figure II.6.A.7 (a) Demonstration of change in potential with stoichiometry of Li in NMC cathodes during the charge process. Impedance analysis has been conducted at three different SOC values. (b) The impedance curves at three different points denoted by A, B and C

Estimate SOC-dependent impedance at cathode/SSE interface. If not possible, proceed with impedance measured at fixed SOC:

The earlier mesoscale computational model used a planar NMC cathode, and a LLZO electrolyte with different grain sizes. Volume change during the lithiation and delithiation of NMC cathodes lead to delamination at the cathode electrolyte interface, which can effectively increase the charge transfer resistance. In the present analysis, once the cathode delaminates from the electrolyte, it is assumed to be an irreversible process. In the impedance model, the ionic and electronic conductivity of LLZO electrolyte and NMC cathode are assumed to be infinitely large, which makes their contribution to the overall impedance curve negligible. The semicircle from charge transfer resistance, and the low frequency tail due to diffusion within the cathode has been modeled here. Figure II.6.A.1(a) demonstrates a potential vs. SOC curve as obtained during charge. Impedance plots have been generated at three different SOC values of 0.9, 0.7 and 0.5, which are also denoted as A, B and C, respectively. The corresponding impedance diagrams are shown in Figure II.6.A.1(b), where it is evident that the diffusion process within the cathode is extremely fast, and does not contribute to the overall impedance at all. This fast diffusion of Li atoms is attributed to the extremely small length of the cathode domain, only 100 nm. However, the charge transfer resistance decreases with increasing SOC. This is due to the dependence of exchange current density on the concentration of Li at the cathode surface. The charge transfer resistance is also inverse to the exchange current density. Impact of delamination on the charge transfer resistance did not become obvious even at 50% SOC.

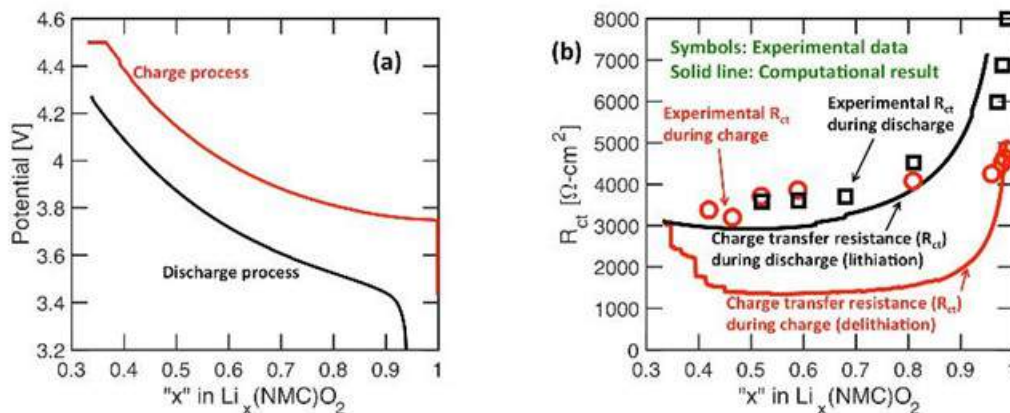


Figure II.6.A.8 (a) Potential vs. Li stoichiometry curves as obtained during the charge and discharge processes. (b) Variation in charge transfer resistance with Li stoichiometry during charge (red) and discharge (black) process. The experimental results are denoted by symbols

Voltage profile during the charge (red) and discharge (black) process, with respect to SOC, have been demonstrated in Figure II.6.A.8(a). The corresponding charge transfer resistance (R_{ct}) has been plotted in Figure II.6.A.8(b). The red solid line denotes R_{ct} during charge process, which initially decreases, and later increases because of interfacial delamination. The increase in R_{ct} due to delamination becomes obvious only at SOC values lower than 0.5. The black line indicates R_{ct} during discharge process, which changes mostly due to the variation in Li concentration at the cathode surface. These theoretical predictions correlate qualitatively with experimental observations shown in Figure II.6.A.8(b) by the red and black symbols. Estimation of SOC dependent impedance curve successfully completes the milestone for the fourth quarter. Since the charge transfer resistance changes substantially with SOC, SOC dependent impedance must be used in the future.

Conclusions

In the present research, issues at the electrode/SSE interface have been investigated using a continuum based mesoscale model. The major conclusions are summarized below:

1. Mechanical stress induced electrochemical potential at the Li-metal/SSE interface leads to difference in reaction kinetics at the GI and GB regions, which leads to enhanced Li deposition at GB. These deposits at the GB can also cause fracture within the SSE through which Li dendrites can grow and eventually short the cell.
2. During the charge process Li ions move out of the NMC cathode particles. This causes the cathodes to shrink, which effectively leads to formation of tensile stress at the cathode/SSE interface, which causes interfacial fracture. This delamination phenomenon effectively decreases the electrochemically active surface area, and the charge transfer resistance increases. Also, the magnitude of charge transfer resistance depends on the SOC of the operating cell, and SOC dependent impedance must be taken into account for successful estimation of performance in cathode/SSE cells.

Using LLZO electrolytes with very small grain size, or amorphous solid electrolytes, can minimize current focusing at the Li metal anode. Small grains contain multiple GBs, which distribute the current focusing uniformly throughout the metal anode. Adoption of similar small-grained SSEs can help to minimize the interfacial delamination observed at the cathode/SSE interface. Since, GBs have lower elastic modulus than the bulk electrolyte, they act as sites of strain energy release, and helps to decrease the extent of detachment. Usage of zero strain cathodes can also help to prevent interfacial delamination at cathode/SSE interface.

Key Publications

Publications

1. P. Barai, K. Higa, A. T. Ngo, L. A. Curtiss, and V. Srinivasan. Mechanical Stress Induced Current Focusing and Fracture in Grain Boundaries. *Journal of the Electrochemical Society* (2019) **166** A1752 – A1762.

Presentations

1. P. Barai, and V. Srinivasan. Impact of Solid-Electrolyte-Interphase (SEI) Stiffness on Lithium Dendrite Growth. Presented at ECS spring Meeting 2019, Dallas, TX.

II.6.B Design and Synthesis of Advanced High-Energy Cathode Materials (LBNL)

Guoying Chen, Principal Investigator

Lawrence Berkeley National Laboratory
1 Cyclotron Road
Berkeley, CA 94720
E-mail: GChen@lbl.gov

Tien Duong, DOE Technology Development Manager

U.S. Department of Energy
E-mail: Tien.Duong@ee.doe.gov

Start Date: October 1, 2016
Total Project Cost: \$500,000

End Date: September 30, 2019
DOE share: \$500,000

Non-DOE share: \$0

Project Introduction

To meet DOE targets for Li-ion batteries intended for vehicular applications, electrode materials with higher energy density and higher stability are needed. Critical performance issues associated with electrode structural and morphological instabilities, side reactions with the electrolyte, and transport limitations are sensitive to material's properties such as chemical compositions, crystal structures, surface facets, and particle sizes. Advances in materials development, therefore, require a better understanding of the relationships between properties and functions, yet this has been difficult to achieve on conventional aggregated secondary particles. This project addresses the challenges in a systematic way, by synthesizing single-crystal version of the commercially promising yet complex electrode materials, obtaining new insights into the materials utilizing state-of-the-art analytical techniques that are mostly inapplicable or ineffective on conventional secondary particles, and subsequently establishing the relationships between structure and function. The goal is to use these findings to rationally design and synthesize advanced electrode materials with improved performance.

Objectives

This project will use a rational, non-empirical approach to design and synthesize next-generation high-energy, high-voltage cathode materials. Combining a suite of advanced diagnostic techniques with model cathode materials and model electrode/electrolyte interfaces, the project will perform systematic studies to achieve the following goals: 1) obtain new insights into solid-state chemistry, particularly cationic and/or anionic redox activities during charge and discharge of lithium transition-metal oxides, 2) gain fundamental understanding on cathode/electrolyte interfacial chemistry and charge transfer process as well as the impact of operating voltage window, 3) reveal performance- and stability-limiting properties and processes in high-energy, high-voltage cathodes, and 4) develop strategies to mitigate the structural and interfacial instabilities.

Approach

Prepare single crystals of Li-rich transition-metal oxides with well-defined physical attributes. Perform advanced diagnostic and mechanistic studies at both bulk and single-crystal levels. Global properties and performance of the samples will be established from the bulk analyses, while the single-crystal based studies will utilize time- and spatial-resolved analytical techniques to probe material's redox transformation and failure mechanisms.

Results

Owing to the capacity boost from oxygen redox activities, Li-rich cation-disordered rocksalts (LRCDS) represent a new class of promising high-energy Li-ion battery cathode materials. Redox-inactive transition-metal (TM) cations, typically d^0 TM (i.e., fully oxidized refractory metal), are essential in the formation of rocksalt phases, however, their role in electrochemical performance and cathode stability is largely unknown. Here three Mn-based LRCDS, $\text{Li}_{1.3}\text{Nb}_{0.3}\text{Mn}_{0.4}\text{O}_2$ (LNMO), $\text{Li}_{1.25}\text{Nb}_{0.15}\text{Ti}_{0.2}\text{Mn}_{0.4}\text{O}_2$ (LNTMO) and $\text{Li}_{1.2}\text{Ti}_{0.4}\text{Mn}_{0.4}\text{O}_2$ (LTMO), were prepared and

systematically investigated for the effect of d^0 TM on their redox behavior. The content of redox-active Mn was fixed at 0.4 to ensure that d^0 TM is the only cation variable. All samples consisted of well-formed large primary particles with an average particles size of approximately 5 μm . Rietveld refinement of the X-ray diffraction (XRD) patterns collected on the oxides show well-crystallized rocksalt structure in the absence of impurities. Figure II.6.B.1 shows the electrochemical evaluation of the synthesized rocksalts. Cyclic voltammetry (CV) measurements were used to analyze the redox behavior and monitor the changes in redox couples with cycling. As shown in Figure II.6.B.1a-c, the overall features of the CV profiles are essentially the same. In the first cycle, the first anodic peak corresponds to the oxidation of Mn^{3+} to Mn^{4+} while the second strong anodic peak arises from O oxidation. With extensive cycling, the peak corresponding to Mn oxidation gradually shifted to higher voltage while the intensity of the peak corresponding to O oxidation gradually diminished. During the cathodic process, the primary reduction process (including both TM and O) occurred at 3.2 V in the first cycle. The current of this reduction peak gradually decreased while an additional lower-voltage peak gradually increased with cycling. This leads to an increase in the voltage gap between the cathodic and anodic peaks and reduced total redox current densities. With different d^0 TM, these changes in the CV profile occur at a different rate, with the slowest rate observed on LTMO. The voltage profiles measured within 50 cycles are shown in Figure II.6.B.1d-f while the 1st cycle incremental capacity (dQ/dV) profiles are shown in Figure II.6.B.1g-i. On the dQ/dV profile, the two-voltage region behavior is clearly reflected by the well-defined Mn^{3+} - Mn^{4+} oxidation peak in the lower-voltage region and the O oxidation peak in the higher-voltage region. The most significant differences among the rocksalts lie in the O oxidation peak. The observation implies that Nb facilitates the involvement of O oxidation more effectively than Ti, leading to a higher 1st cycle discharge capacity of ~ 280 mAh/g (equivalent of 0.94 Li^+ reintercalation) in LNMO. The discharge capacity of LTMO is significantly lower, at ~ 200 mAh/g (equivalent of 0.61 Li^+ reintercalation). For LNTMO, about 0.90 Li^+ reinserted during 1st discharge (~ 280 mAh/g), which is only slightly lower than that of LNMO. It is clear that the d^0 TM plays a significant role in regulating the redox chemistry of the Mn-based rocksalt cathodes. The effect of d^0 TM, however, appears to be nonlinear and certain synergy exists. A clear understanding on the role of d^0 TM, therefore, is critical in order to properly design the oxide cathodes to achieve balanced capacity and capacity retention.

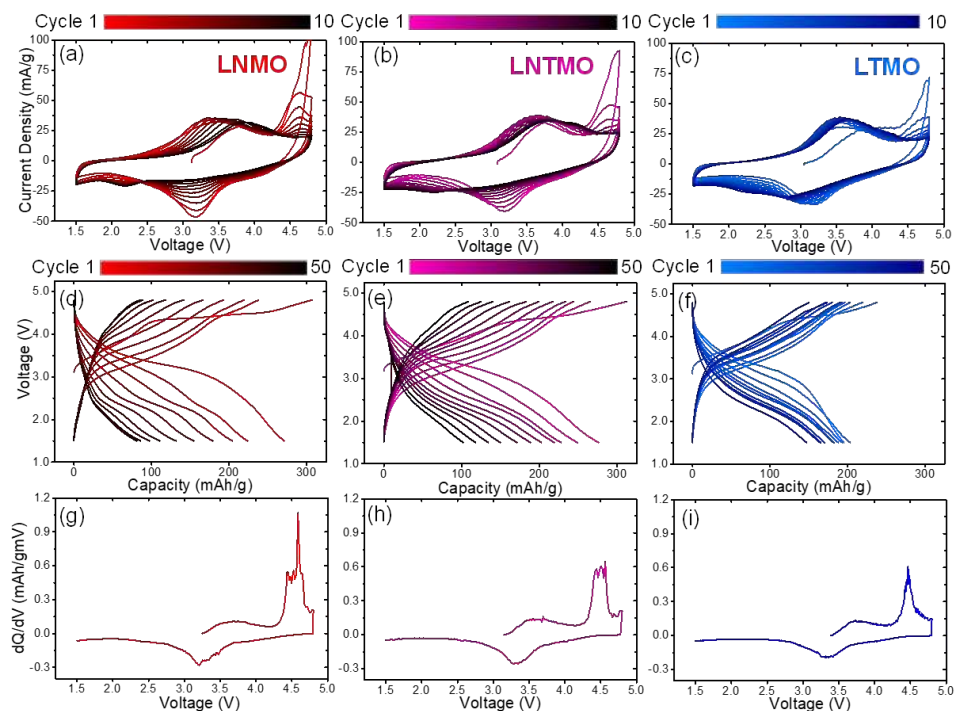


Figure II.6.B.1 a-c) Cyclic voltammograms of LNMO, LNTMO and LTMO half cells in the first 10 cycles. The scan rate is 5 mV/min. d-f) Voltage profiles of LNMO, LNTMO and LTMO half cells in the first 50 cycles. Data plotted in every 5 cycles. g-i) First-cycle incremental capacity (dQ/dV) profiles of the half cells. Half-cell cycling current density is 10 mA/g

Two separate analytical techniques were used to investigate the effect of d^0 TM on oxygen redox activities in our model samples: differential electrochemical mass spectroscopy (DEMS) was used to probe irreversible oxygen loss through evaluating gas release during charge and discharge, while reversible oxygen redox was probed by O K -edge mapping of resonant inelastic X-ray scattering (mRIXS) measurements. Figure II.6.B.2 compares the DEMS measurement results from LNMO and LTMO half cells. To better correlate the charge storage and gas evolution, the release rates of O_2 and CO_2 as a function of voltage are plotted together with differential capacity profiles (dQ/dV). The cumulative amount of O_2 generation is also shown. For both DEMS cells, after the broad Mn oxidation peak, O oxidation occurred around 4.2 V which produced a much stronger peak in the dQ/dV profiles. Ti-based rocksalt delivered considerably lower O oxidation capacity than that of the Nb-based cathode, at approximately 50%. For both rocksalts, within the Mn oxidation region (i.e., prior to 4.2 V), no obvious O_2 generation was observed. After 4.2 V, O_2 release totaling 7.5 mmol/mol was observed on LNMO (Figure II.6.B.2a), while the O_2 release from LTMO remained much lower at 0.42 mmol/mol (approximately 6% of that in LNMO, Figure II.6.B.2b). This corresponds to an irreversible capacity contribution (from O_2 evolution) of approximately 8.9 mAh/g and 0.55 mAh/g for LNMO and LTMO, respectively. A gap between the maximum O_2 release and the center of the O oxidation peak on the dQ/dV profile was observed in both oxide cathodes, suggesting a “delay effect”. This is because most O^{n-} ($0 < n < 2$) anions are generated around the peak voltage while maximum O_2 release occurs at the highest O^{n-} concentration in the lattice, which is after the peak voltage. We further compared the amount of O_2 release when the same amount of Li^+ was extracted from the oxide cathodes, which was achieved by charging the LNMO DEMS cell to 4.5 V while charging the LTMO DEMS cell to 4.8 V. Under these conditions, the cumulative O_2 release for LNMO is 0.73 mmol/mol, nearly twice of the cumulative O_2 amount for LTMO even at 4.8 V. Such comparison confirms that Ti has a stabilizing effect on O redox by preventing irreversible loss through O_2 gas formation.

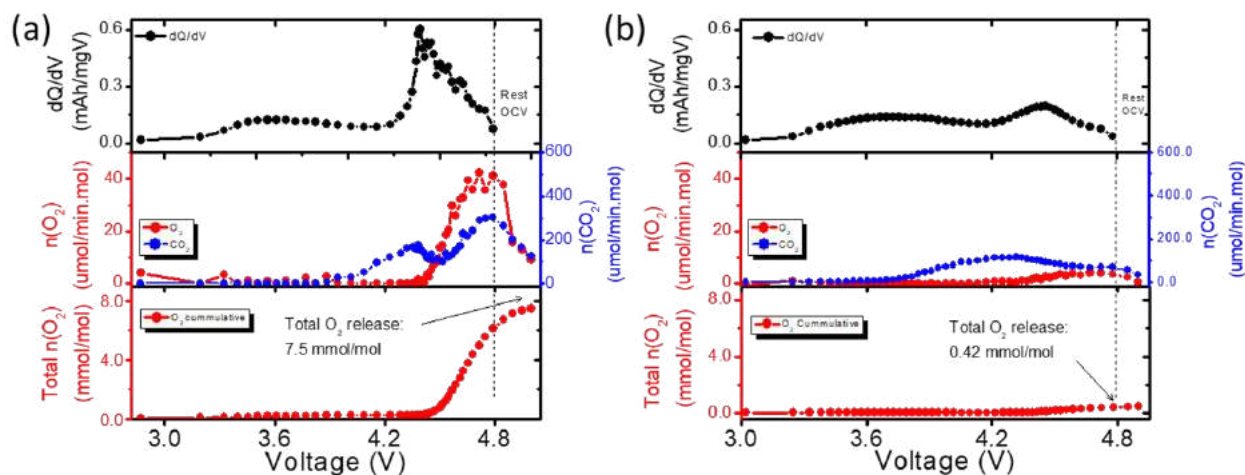


Figure II.6.B.2 Comparison of operando DEMS measurements on a) LNMO and b) LTMO half-cells. The dQ/dV profiles (top panel) during the 1st charge are added to correlate with the gas analysis. Middle panels show gas evolution as a function of cell voltage while bottom panels show the cumulative O_2 evolved during the 1st charge. The charge rate is 25 mA/g

With the ability to detect oxidized oxygen at a specific emission energy that is different from where the TM-O hybridization signals dominate, O- K mRIXS has been recognized as the most direct and reliable spectroscopic tool to fingerprint O redox reaction in oxide electrodes. Specifically, oxidized oxygen in the lattice was found to typically display fingerprint features around 523.7 eV and 531 eV in emission and excitation energies in mRIXS, respectively. Unlike the conventional O- K XAS, such features from the oxidized oxygen are easily distinguished from the stronger and broader TM-O hybridization signals around 525 eV emission energy. Here, O- K mRIXS collected on LNMO and LTMO at the pristine state (P) as well as after various cycling, including 1st charged and discharged (1Ch and 1D), 5Ch and 5D, 50Ch and 50D are shown in Figure II.6.B.3. A strong and broad horizontal feature around 524-526 eV emission energy (vertical axis) is observed in all samples. As stated before, this broad feature originates from the TM-O hybridization and is of TM character, corresponding to the so-called

“pre-edge” feature in the O-K XAS profile. After the 1st charge, the characteristic spectroscopic signature of oxidized oxygen with the emission energy of ~523-524 eV clearly emerges on both LNMO and LTMO, as indicated by the black-colored ovals in Figure II.6.B.3. Upon the 1st discharge, such feature disappears, suggesting that lattice oxygen redox reaction takes place in both cathode materials. The process with this feature emerging in the charged state and disappearing in the discharged state continued in the following cycles, however, the extent of the reversibility varied. In LNMO, a significant intensity reduction was seen only after 5 cycles, as shown in the 5th charged sample in Figure II.6.B.3a. This suggests large decay in the lattice oxygen redox process. In contrast, the peak feature is largely maintained in the charged LTMO electrode even after 50 cycles (Figure II.6.B.3b).

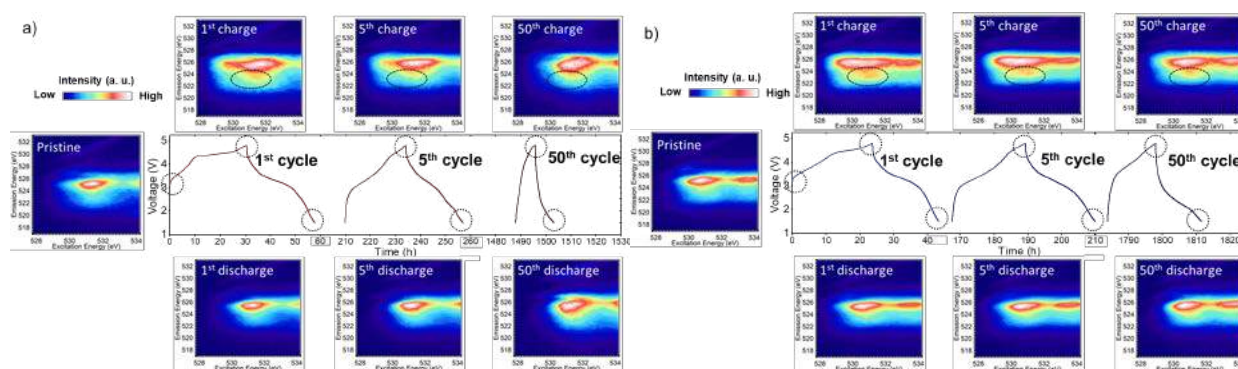


Figure II.6.B.3 O K-edge mRIXS maps collected at pristine (P), charged (Ch) and discharged (D) states after various cycles: a) LNMO and b) LTMO. The voltage profiles of the selected cycles are also shown

Further comparison in oxygen redox stability is achieved by comparing the RIXS cuts around the characteristic excitation energy of 531 eV. Fig. 4a illustrates the RIXS cut emission spectral profile with an excitation energy of 531 eV extracted from the mRIXS map plotted with the same color scale. The spectral component with the highest intensity corresponds to the TM-O hybridization while the “shoulder” component corresponds to the oxidized oxygen feature. Figure II.6.B.4b and Figure II.6.B.4c display the RIXS cuts with an excitation energy of 531 eV for LNMO and LTMO electrodes at pristine and various charged/discharged states, respectively. All RIXS spectra were normalized based on the maximum intensity around 525 eV. The shaded area between the charged and discharged states in the emission energy range of 521 to 525 eV represents the intensity contrast of the O^{n-} ($n < 2$) feature. In comparison with LNMO in Figure II.6.B.4b, the relatively stable oxygen redox activity in LTMO is evident in Figure II.6.B.4c. The retention of such an intensity contrast between charged and discharged electrodes for both LNMO and LTMO is further summarized in Figure II.6.B.4d. In the 1st

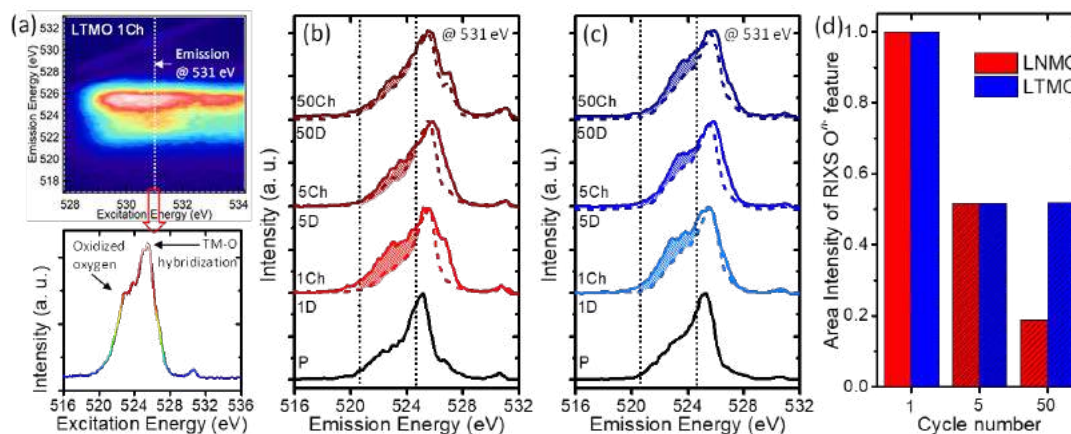


Figure II.6.B.4 a) mRIXS map and the corresponding RIXS cut emission spectrum collected at the excitation energy of 531 eV, b) and c) RIXS cut spectra of LNMO and LTMO collected at the pristine state and after various cycles, and d) changes in area intensity of RIXS O^{n-} feature as a function of cycle number

cycle, considerable shaded intensity contrast presents in both LNMO and LTMO. From the 1st to 5th cycle, the intensity contrast decays at a similar level of approximately 49%. We note that the observed stronger shoulder intensity in Figure II.6.B.4c was in fact due to the extension of the broad Ti-O hybridization signals (also at 531 eV excitation energy). By directly comparing the intensity contrast between the charged and discharged electrodes, this effect was effectively eliminated. After the 50th cycle, LTMO shows a much better retention in the O²⁻ feature at charged state, with the shaded intensity remained at ~ 52% of the value in the 1st cycle. On the other hand, RIXS cut spectra differences between charged and discharged states of LNMO is minor after 50 cycles. The shaded intensity is only about 18 % of the initial intensity, 3x less than that in LTMO. Such distinct contrast between LTMO and LNMO confirms that oxygen redox is more reversible in LTMO than that in LNMO, and Ti is a better d^0 TM in terms of improving O²⁻ cyclability during cell operation.

In order to probe the effects of d^0 TM on chemical stability, systematic studies using X-ray absorption spectroscopy were conducted. Soft X-ray absorption spectroscopy with the total electron yield (TEY) detection mode allows surface sensitive analysis, probing approximately top 5 nm of the particles, as illustrated in Fig. 5a. Complementing the surface analysis, Mn K-edge X-ray near-edge absorption spectroscopy (XANES) was also performed to evaluate the bulk chemical properties, as shown in the schematic in Figure II.6.B.5b. Figure II.6.B.5c-f summarizes the effect of cycling on the changes in Mn oxidation state. Surface Mn valence state in the samples was calculated *via* systematic linear combination analysis while bulk Mn valence state was obtained by interpolating the XANES edge energies of the samples in the calibration curve established from the oxide standards. Overall, surface Mn is more reduced than the bulk, both at the charged and discharged states. At the charged state (Figure II.6.B.5c and Figure II.6.B.5d), bulk Mn in LNTMO and LTMO remained nearly constant at 4+ while a reduction in LNMO was observed in the first 5 cycles. After the 50th cycle, bulk Mn was reduced to an average of 3.1+ in LNMO and 3.5+ in LTMO, while the surface Mn fell below 3+. Particularly, surface Mn valence state approached 2+ in LNMO. At the discharged state (Figure II.6.B.5e and Figure II.6.B.5f), bulk Mn valence state decreased from 3+ in the pristine to 2.7+ in LTMO and 2.5+ in LNMO during the first 50 cycles. On the surface, Mn valence of all rocksalts was close to 2+. Compared to LNMO, Mn reduction was significantly less in both Ti based oxides. Furthermore, structural evaluation by synchrotron X-ray diffraction (XRD) showed that compared to the pristine samples, all cycled cathodes showed significant peak shift toward lower angles as well as peak broadening and splitting, suggesting lattice expansion and the existence of multiple rocksalt phases. While the extent of lattice expansion in LNTMO and LNMO are comparable, this was much reduced in LTMO. These results suggest that redox-inactive d^0 TM is not only capable of tuning the reversibility of O redox, it also impacts the chemical and structural stabilities of redox-active TM (namely Mn) during electrochemical cycling.

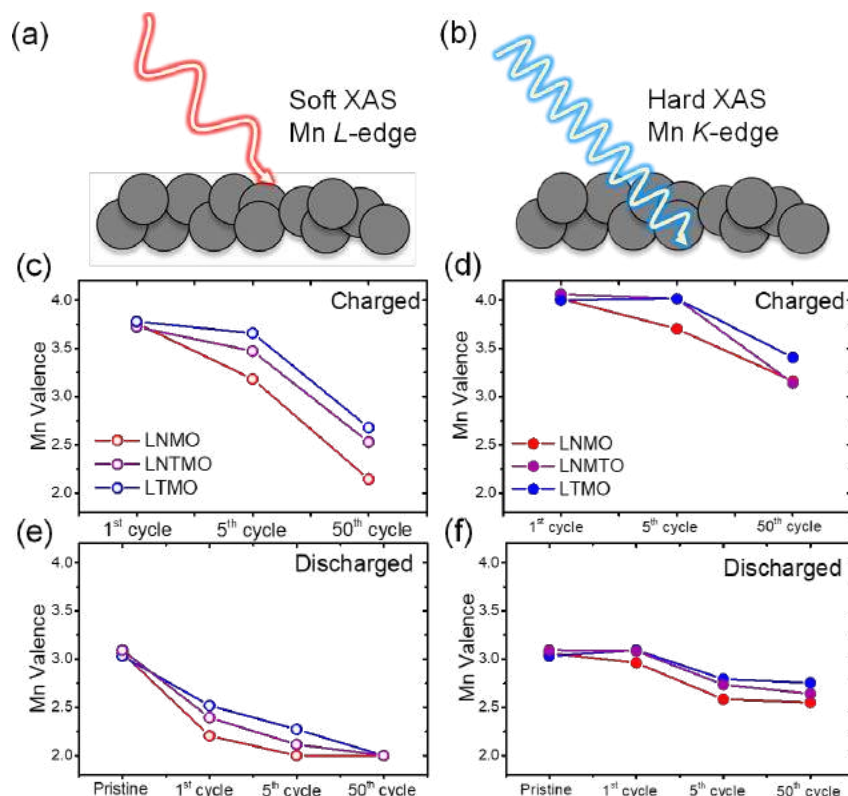


Figure II.6.B.5 a, b) Schematics showing the probing depth of hard XAS (for Mn K-edge XANES) and soft XAS (for Mn L-edge), c, e) average Mn oxidation states derived from K-edge XANES edge energy of spectra collected on charged and discharged electrodes after various cycles, respectively, d, f) average Mn oxidation states derived from PCA analysis of Mn L-edge sXAS spectra collected on charged and discharged electrodes after various cycles, respectively

The effect of d^0 TM on the performance and stability of rocksalt cathodes is summarized in the schematic shown in Figure II.6.B.6. As Li cations are removed from the lattice during charging, Mn and O oxidation occur consecutively to compensate the total charge at different voltages. Capacity contribution from $\text{Mn}^{3+}/\text{Mn}^{4+}$ redox was determined by the Mn content, approximately 120-130 mAh/g in LNMO, LNTMO and LTMO with a Mn content of 0.4. The difference lies in the initial capacity contribution from O redox, which were ~ 150 and 70 mAh/g for LNMO and LTMO, respectively. Although d^0 TM cation is not redox active, it does have a significant impact on the extent of oxygen oxidation initially. More importantly, d^0 TM is capable of regulating the stability of the oxidized oxygen, by adjusting the ratio of irreversible loss *via* O_2 gas release and reversible redox participation of the oxidized O^{n-} in the lattice. As shown in Figure II.6.B.6, the ability of Ti in stabilizing the oxidized oxygen leads to less surface densification and reduced cathode degradation, accompanied by much improved chemical and structural stabilities as well as enhanced cycling stability in LTMO. Modifying the cationic sublattice via properly adjusting the redox-inactive d^0 TM, therefore, presents an important route in materials design to achieve balanced capacity and stability of LRCDS.

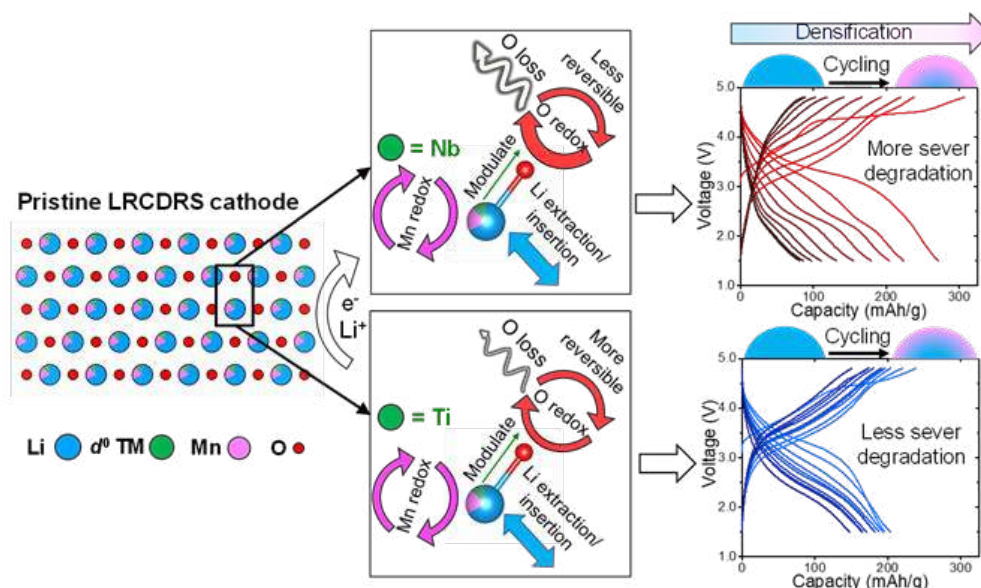


Figure II.6.B.6 Schematics showing the effect of d^0 TM on O redox behavior and subsequent degradation of the Mn redox-active cation-disordered rocksalt cathodes

Conclusions

The role of redox-inactive d^0 TM in the redox chemistry and performance degradation of Mn-based LRCDRS was systematically investigated. Although d^0 TM is not electrochemically active, it serves as a modulator for oxygen redox. Nb was found to promote oxygen oxidation while Ti intrinsically stabilize the oxidized oxygen, leading to much less oxygen release and more reversible O redox for charge storage. As a result, considerable differences were observed on chemical and structural stabilities as well as cycling stability of the LRCDRS cathodes. Our study suggests that by properly designing redox-inactive TMs, a balanced capacity and stability may be achieved in LRCDRS cathodes, opening new possibilities in utilizing O redox for charge storage in practical LIB cells. This may also have an implication in other classic and novel electroactive functional materials where the role of redox-inactive component and its interaction with redox-active component should be closely examined.

Key Publications

1. W. H. Kan, C. Wei, D. Chen, T. Bo, B.-T. Wang, Y. Zhang, Y. Tian, J.-S. Lee, Y. Liu and G. Chen, "Evolution of Local Structural Ordering and Chemical Distribution upon Delithiation of Rock-Salt Structured $\text{Li}_{1.3}\text{Ta}_{0.3}\text{Mn}_{0.4}\text{O}_2$ Cathode," *Advanced Functional Materials*, 1808294 (2019). DOI: 10.1002/adfm.201808294.
2. D. Chen, W. H. Kan and G. Chen, "Understanding Performance Degradation in Cation-Disordered Rock-Salt Oxide Cathodes," *Advanced Energy Materials* 1901255 (2019). DOI: 10.1002/aenm.201901255.
3. D. Chen, W. H. Kan and G. Chen, "In-depth Analysis of Performance Degradation Mechanism in Cation-Disordered Rocksalt Cathodes" *Materials Views China* 40063 (2019). DOI: materialsviewschina.com/2019/09/40063.
4. P. Yan, M. Su, J. Zheng, N. Song, A. Devaraj, B. Liu, Y. Wang, G. Chen, X. Li, Z. Xu, K. Amine, J.-G. Zhang, and C.-M. Wang, "Anionic Redox Enhanced Vacancy Injection and Condensation in Bulk Lattice of Layered Cathodes," *Nature Nanotechnology* **14**, 602 (2019). DOI: 10.1038/s41565-019-0428-8.
5. G. Chen, "Li-Rich Rock-Salt Oxides as High-Energy LIB Cathodes," IBA 2019, La Jolla, CA, March 2019.

6. D. Chen and G. Chen, “Unraveling the Origin of Performance Degradation in High-Capacity Cation-Disordered Oxide Cathodes,” 235th ECS Meeting, Dallas, TX, May 2019.
7. G. Chen, “Model System Diagnostics for High-Energy Cathode Development,” 2019 Vehicle Technologies Office Annual Merit Review Meeting, Arlington, VA, June 2019.
8. G. Chen, “Development of Li-Rich Cation-Disordered Rocksals as High-Energy Cathodes,” ACS Fall 2019 National Meeting & Expo, San Diego, CA, August 2019 (invited).
9. D. Chen and G. Chen, “Understanding Performance Degradation in Cation Disordered Rock-Salt Cathodes *via* Synchrotron X-ray characterizations,” 2019 SSRL/LCLS Users' Meeting, Menlo Park, CA, September 2019.

II.6.C Design of High-Energy, High-Voltage Lithium Batteries through First-Principles Modeling (LBNL)

Kristin A. Persson, Principal Investigator

Lawrence Berkeley National Laboratory
1 Cyclotron Road
Berkeley, CA 94720
E-mail: kapersson@lbl.gov

Tien Duong, DOE Technology Development Manager

U.S. Department of Energy
E-mail: Tien.Duong@ee.doe.gov

Start Date: October 1, 2018

End Date: September 30, 2019

Project Funding (FY19): \$350,000

DOE share: \$350,000

Non-DOE share: \$0

Project Introduction

This project supports VTO programmatic goals by modeling next-generation, high energy cathode materials and enabling stable cathode operation at high voltages through functional coatings and rational design of electrolytes. To enhance the performance of future as well as current Li-ion systems, improvements on both the cathode and the electrolyte side are needed. We aim to improve understanding of the atomistic mechanisms underlying the performance of the respective materials, with the goal to suggest improvement strategies, such as optimal coating and electrolyte formulations. During the past year, we focused on an amorphous coating design to improve cathode oxygen retention while promoting Li⁺ diffusivity. Amorphous coating layers tend to be conformal, with reduced grain boundaries, or other defective regions that exist in polycrystalline coating layers. Hence, amorphous coatings are likely to reduce the kinetics of metal and/or oxygen ion transport. We have studied the ionic transport through various amorphous coating formulations using large-scale *ab initio* molecular dynamics (AIMD) and density functional theory (DFT) simulations. This allowed us to understand the coordination environments that promote or de-promote Li⁺ and oxygen mobility, respectively.

Furthermore, fundamental studies of electrolyte conductivity and transport mechanisms, as a function of solvent and salt concentrations, and components have been conducted. The largely unexplored superconcentrated regime of carbonate electrolytes provides new opportunities for improving Li-ion cell electrolytes. However, the transport and solvation mechanisms in such electrolytes are unknown: insight into them may allow improving transport and bulk conductivity properties.

Objectives

- Understanding of the factors that govern charge transport in non-aqueous superconcentrated liquid electrolytes
- Critical surface coating design and optimization strategies that will improve cycling of Li-ion battery cathodes by reducing cathode degradation from oxygen loss.

Approach

- Perform first-principles calculations to model the solid-state electrode material thermodynamics and kinetics.
- Model liquid electrolytes through coupled classical MD and first-principles methods to accurately capture solvation structure as well as reactivity of liquid system.
- Examine different transport models to study the electron and ion mobility through the amorphous coating layer.

- Analyze the Li and O trajectories and investigate the coordination environments that cause the ion diffusion bottlenecks.

Results

Experimentally, conformal ultrathin coatings consisting of Al_2O_3 and ZnO are realized by atomic layer deposition (ALD), where the defect chemistry and impurity content can lead to off-stoichiometry, trapped charges and some electronic leakage. Therefore, the exact composition and electronic state of the material may not be known and requires us to broadly consider three possible scenarios for Li diffusion in conformal coatings (see Figure II.6.C.1): (1) **the electron conducting model**, where Li^+ diffuses accompanied by an electron through the coating. In this scenario, Al^{3+} or Zn^{2+} is reduced during the Li^+ diffusion; (2) **the electrolyte model**, where the electronically insulating coating acts as an electrolyte where Li^+ moves with a ‘solvation shell’ of compensating negative charge. In this case, the coating cations (Al, Zn) are not reduced during the Li diffusion; (3) **the space charge model**, where Li^+ tunnels through the electronically insulating coating and a space charge builds up at the surface.

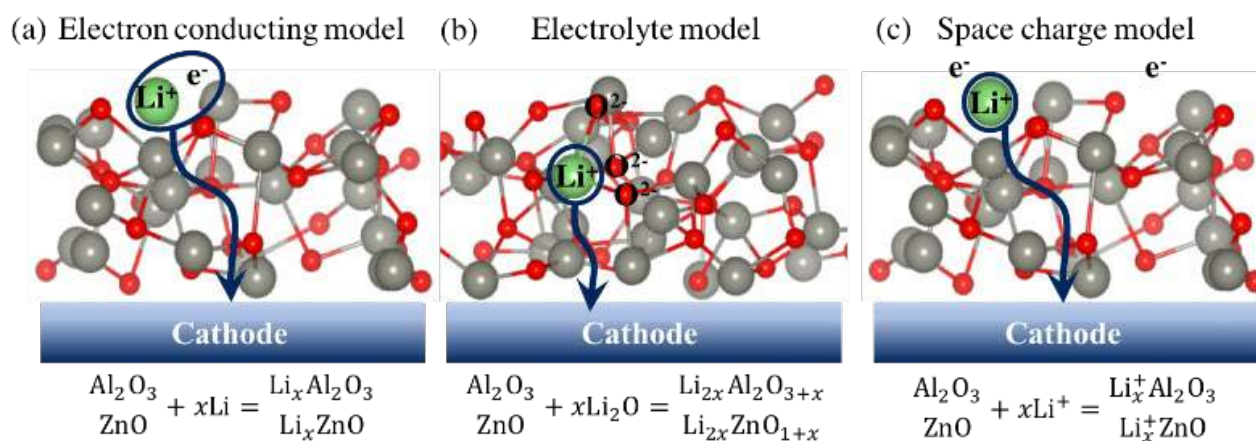


Figure II.6.C.1 Schematic illustrations of different Li transport models in amorphous coating.

The space charge model was ruled out as the build-up overpotential exceeds the dielectric breakdown strength of both Al_2O_3 as well as ZnO , for all relevant coating thicknesses.^[5] Therefore, we focused on the first two Li diffusion scenarios, which can be seen in Figure II.6.C.1a, b. To simulate an electron conducting model, we inserted extra Li^0 into amorphous Al_2O_3 and ZnO to generate $\text{Li}_x\text{Al}_2\text{O}_3$ and Li_xZnO , respectively. To simulate the electrolyte model, we inserted Li_2O as representing a solvated Li^+ cation into amorphous Al_2O_3 and ZnO to generate $\text{Li}_{2x}\text{Al}_2\text{O}_{3+x}$ and $\text{Li}_{2x}\text{ZnO}_{1+x}$, respectively. In the electrolyte model, there are two transport mechanisms for Li^+ diffusion, similar to the diffusion of Li^+ in a liquid electrolyte: (1) vehicular transport, where Li^+ diffuses with its coordination shell as a lithium complex; (2) structural transport, where the Li^+ diffuses by exchanging O^{2-} anions in its coordination shell. These two diffusion mechanisms can also be applied to O^{2-} diffusion, where the O^{2-} is accompanied by Al^{3+} or Zn^{2+} as the coordinating species.

The amorphous structure is generated by implementing a “liquid-quench” process, in which heating, equilibration, and quenching are done through series of AIMD simulations. To generate a liquid phase of the amorphous structure, the structure is heated at a temperature that is higher than the material’s melting point. A sequence of AIMD simulations in the *NVT* ensemble are employed to equilibrate the amorphous structure until both energy and pressure are converged. The equilibrium structure is then quenched to 0K to obtain the optimized atomic positions in the amorphous structure. To investigate Li^+ and O^{2-} diffusion at different temperatures, the amorphous structure is heated to several specific temperatures and its equilibrium structures are obtained by repeating the AIMD equilibration routine described above. Then, the trajectories of amorphous structure under different temperatures are collected for diffusion analysis. The self-diffusion coefficients D of Li and O in amorphous structure at $T = 300\text{K}$ are calculated from the Einstein relation $D = \langle r^2 \rangle / 6t$, where

$\langle r^2 \rangle$ is the mean square displacement. We determine $\langle r^2 \rangle$ values of Li^+ and O^{2-} ions from the collected trajectories and calculate D at each T . Finally, the D value at $T = 300\text{K}$ is extrapolated from the values at higher T using Arrhenius plot. The procedure described above is broadly applicable to evaluate Li^+ and O^{2-} diffusion in various amorphous materials.

Figure II.6.C.2a shows the trajectory of one Li^+ ion in $\text{Li}_{0.3}\text{Al}_2\text{O}_{3.15}$ (electrolyte model) for 40 ps at 2000K from the *ab initio* molecular dynamics (AIMD) simulations. We implemented a density-based spatial clustering (DBSCAN) to differentiate the vibrational and translational motions for Li trajectories, which are represented by the yellow and green dots in Figure II.6.C.2a, respectively. For each time step, we also analyzed the number of nearest neighbors for the Li^+ during the vibrational and translational motions to elucidate the promoting/limiting factors for diffusion. Figure II.6.C.2b shows that the number of nearest O neighbors during translation is smaller than that during vibration, which implies that the oxygen content of the coating is one of the limiting factors for Li^+ diffusion.

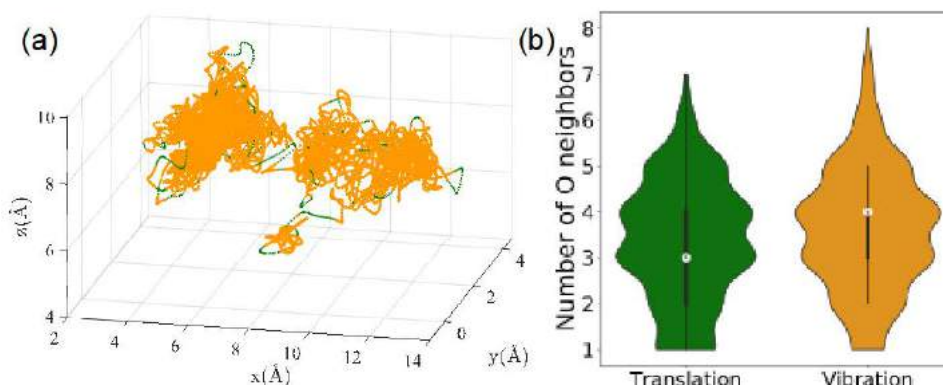


Figure II.6.C.2 (a) Trajectory of one Li^+ atom in $\text{Li}_{0.3}\text{Al}_2\text{O}_{3.15}$ (electrolyte model) for 40 ps at 2000K. Yellow and green dots represent vibrational and translational motions, respectively. (b) Number of O^{2-} neighbors during Li translational and vibrational motions. The white dots represent the median values.

An additional goal of the current BMR project is the study of the specific modes of transport in superconcentrated electrolytes via validated classical molecular dynamics simulations, for which time scales are commensurate with relevant diffusional modes. The specific systems are LiPF_6 and LiBF_4 in PC. In the superconcentrated regime (3 M), there is an absence of solvent exfoliation otherwise present at lower concentrations [2] as well as a reported ability for fast charging and higher anodic stability [4]. However, concurrently, there is a significant decrease in the bulk conductivity. A bottom-up, molecular-level rational design of superconcentrated requires an atomistic understanding of the solvation structure and charge transport in said systems. Therefore, a validated methodology for molecular dynamics simulation in the superconcentrated regime is desirable.

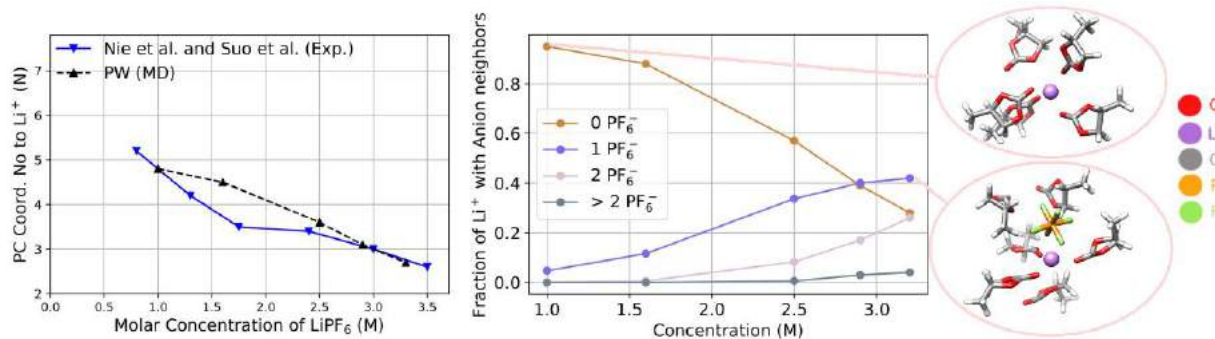


Figure II.6.C.3 Coordination number of Li^+ with PC computed in the present work and compared to experimental values (left) and fraction of Li^+ with $n \text{PF}_6^-$ anions (middle). Representative solvation structures are shown on the right

Assessment of electrolyte molecular-level structure was done via comparison to experiment of molecular dynamics simulation-obtained coordination number of Li^+ to the PC solvent, shown in Figure II.6.C.3 (left). There is good agreement to experimental values from Nie et al. [2], indicating a proper representation of concentration-dependent solvation structures in the molecular dynamics simulations. The number of neighboring counter anions to the Li^+ is shown in Figure II.6.C.3 (center) as a function of LiPF_6 concentration. The solvation environment of the Li^+ is significantly altered in the superconcentrated regime, where a much larger fraction of Li^+ cations are surrounded by anions in their primary solvation shell, consistent with the reported decrease in coordination number. However, even in the superconcentrated regime, there is still a non-negligible fraction of Li^+ with no anions in their primary solvation shell. Representative solvation structures are illustrated in Figure II.6.C.3 (right).

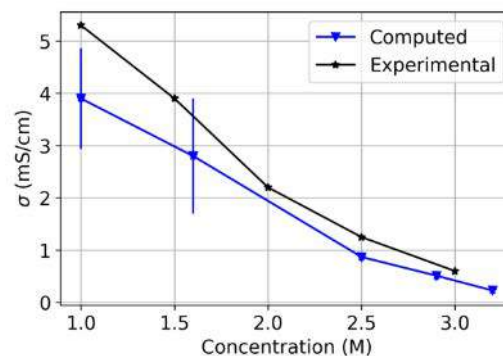


Figure II.6.C.4 Bulk electrolyte conductivity of LiPF_6 electrolyte as a function of salt concentration. Experimental data taken from Takeuchi et al. [3]

The molecular dynamics simulations ability to model transport of electrolyte species was validated by comparison of computed bulk conductivity σ to experimental σ , shown in Figure II.6.C.4. There is good agreement between computed values and experiment, indicating that the herein employed methods are satisfactory for modeling such systems, thus providing a framework for further work in the molecular-level understanding and design of superconcentrated electrolytes.

The diffusion of Li^+ in superconcentrated LiBF_4 /propylene carbonate electrolyte has been speculated as differing from LiPF_6 in propylene carbonate due to specific ion-hopping processes [1]. Figure II.6.C.5 shows the diffusion constants for the ionic species, computed herein as a function of concentration from 1 M to 3 M. The employed methodology can allow both qualitative and quantitative agreement with experiment for LiBF_4 in propylene carbonate, which will allow further analysis and elucidation of the specific modes of transport and conductivity.

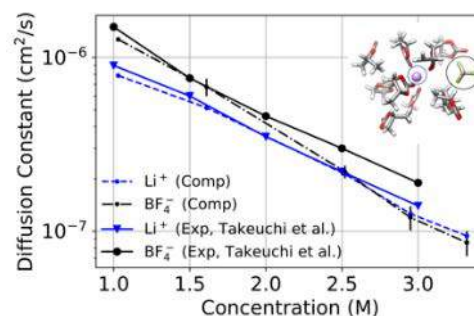


Figure II.6.C.5 Diffusion constants of Li^+ and BF_4^- in propylene carbonate as a function of concentration

Conclusions

In summary, we have elucidated the Li^+ solvation structure change (more anion rich) for LiPF_6 in propylene carbonate as the electrolyte enters the superconcentrated regime. Moreover, we have benchmarked the calculation of transport properties of superconcentrated LiPF_6 and LiBF_4 in propylene carbonate, allowing us to move towards characterizing the diffusional modes. In addition, we have studied the ion transports in amorphous Al_2O_3 and ZnO . The amorphous structure is generated by implementing a “liquid-quench” process, which is realized by a series of AIMD simulations. Ion trajectory analysis shows that the bottleneck for Li diffusion is the number of nearest O neighbors. The Li ion is trapped at its equilibrium vibration site by the neighboring O ions, and its translation to another vibration site is initiated by the Li-O bond breaking/making process.

Key Publications

1. “Investigate Li Intercalation Stability of Ni-Rich Cathodes from First-Principles”; Berkeley Electrochemistry Seminar Series, Berkeley, California (Oct 7, 2019): J. Cheng.

2. “Transport in Superconcentrated LiPF₆ and LiBF₄/Propylene Carbonate Electrolytes”, Julian Self, Kara D. Fong, Kristin A. Persson, ACS Energy Letters, 2019. 10.1021/acsenenergylett.9b02118

References

1. Hwang, Sunwook, Dong-Hui Kim, Jeong Hee Shin, Jae Eun Jang, Kyoung Ho Ahn, Chulhaeng Lee, and Hochun Lee. 2018. “Ionic Conduction and Solution Structure in LiPF₆ and LiBF₄ Propylene Carbonate Electrolytes.” *The Journal of Physical Chemistry C* 122 (34): 19438–46.
<https://doi.org/10.1021/acs.jpcc.8b06035>.
2. Nie, Mengyun, Daniel P. Abraham, Daniel M. Seo, Yanjing Chen, Arijit Bose, and Brett L. Lucht. 2013. “Role of Solution Structure in Solid Electrolyte Interphase Formation on Graphite with LiPF₆ in Propylene Carbonate.” *The Journal of Physical Chemistry C* 117 (48): 25381–89.
<https://doi.org/10.1021/jp409765w>.
3. Takeuchi, Munetaka, Yasuo Kameda, Yasuhiro Umebayashi, Sari Ogawa, Takaaki Sonoda, Shin-ichi Ishiguro, Miho Fujita, and Mitsuru Sano. 2009. “Ion–Ion Interactions of LiPF₆ and LiBF₄ in Propylene Carbonate Solutions.” *Journal of Molecular Liquids* 148 (2–3): 99–108.
<https://doi.org/10.1016/j.molliq.2009.07.003>.
4. Yamada, Yuki, and Atsuo Yamada. 2015. “Review—Superconcentrated Electrolytes for Lithium Batteries.” *Journal of The Electrochemical Society* 162 (14): A2406–A2423.
5. Xu, Shenzhen, Ryan M. Jacobs, Ha M. Nguyen, Shiqiang Hao, Mahesh Mahanthappa, Chris Wolverton, and Dane Morgan. 2015. “Lithium Transport through Lithium-Ion Battery Cathode Coatings.” *Journal of Materials Chemistry A* 3, no. 33: 17248–72.

Acknowledgements

This work was intellectually led by the Battery Materials Research (BMR) program under the Assistant Secretary for Energy Efficiency and Renewable Energy, Office of Vehicle Technologies of the U.S. Department of Energy, Contract DE-AC02-05CH11231. This research used resources of the National Energy Research Scientific Computing Center, a DOE Office of Science User Facility supported by the Office of Science of the U.S. Department of Energy under Contract No. DE-AC02-05CH11231. This research also used the Lawrence Livermore computational cluster resource provided by the IT Division at the Lawrence Berkeley National Laboratory (Supported by the Director, Office of Science, Office of Basic Energy Sciences, of the U.S. Department of Energy under Contract No. DE-AC02-05CH11231)

II.6.D First Principles Investigation of Existing and Novel Electrode Materials (LBNL)

Gerbrand Ceder, Principal Investigator

Lawrence Berkeley National Laboratory
1 Cyclotron Road, MS: 33-146
Berkeley, CA 94720
E-mail: gceder@berkeley.edu

Tien Duong, DOE Technology Development Manager

U.S. Department of Energy
E-mail: Tien.Duong@ee.doe.gov

Start Date: October 1, 2018
Project Funding (FY19): \$400,000

End Date: September 30, 2019
DOE share: \$400,000

Non-DOE share: \$0

Project Introduction

An all-solid-state battery is one of the most promising directions for next-generation energy storage, because of its expected safety and potentially high energy density. However, there are important scientific and engineering obstacles to be addressed for realizing a commercial all-solid-state battery. In particular, the development of a solid-state electrolyte with 1) high ionic conductivity, 2) phase stability for facile synthesis, and 3) good chemical/electrochemical stability against Li metal anode as well as cathode material is essential [1],[2],[3]. Sulfide electrolytes are intensively studied owing to their high ionic conductivity [4],[5],[6] and good contact with electrode materials due to their mechanical softness [7],[8]. However, no solid-state electrolyte satisfying all the required conditions has been developed [9],[10],[11].

In this part of the BMR program, crystalline and amorphous Li-P-S materials and coating materials are studied to better understand the relation between structure and transport properties. The temperature-dependent Li-P-S phase diagram is constructed using density functional theory (DFT) to predict the synthesizability of known and unknown crystalline phases. Amorphous Li-P-S phases are modelled with melt-and-quench structures which are in good agreement with experimentally determined structure functions for the amorphous state. In addition, coating materials which can improve the chemical/electrochemical stability against Li metal anode and cathode materials are explored using high-throughput DFT calculations.

Objectives

The project objective is to determine the design principles needed to create SSEs with high Li-ion conductivity while also achieving stability against common Li-ion cathodes and Li-metal anodes.

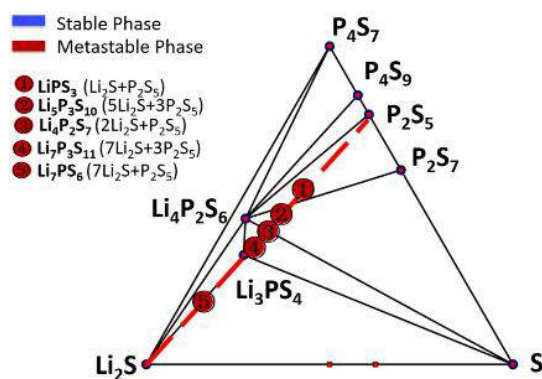
Approach

First principles methods are used to screen suitable solid electrolyte with high electrochemical stability and high ionic conductivity. Ionic conductivity and amorphous structures are studied with ab initio molecular dynamics (AIMD). Thermodynamic interface stability is assessed from ab initio computed grand potential phase diagrams in which the lithium voltage can be controlled. Kinetic limits for solid electrolyte decomposition are assessed by topotactic lithium insertion and removal from the solid electrolyte.

Results

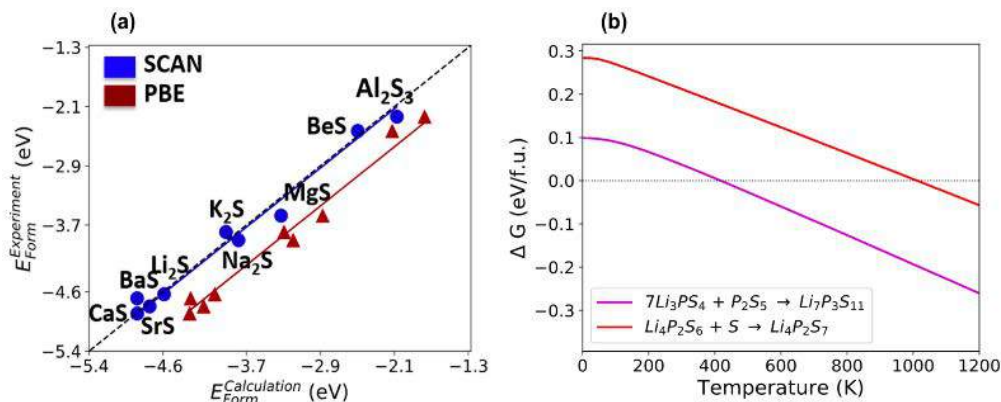
Modeling of the temperature-dependent Li-P-S phase diagram for solid state electrolytes

The SCAN meta-GGA exchange correlation functional [12],[13] is used to construct the ground state phase diagram within the $\text{Li}_2\text{S-P}_4\text{S}_7\text{-S}$ compositional space, which is shown in Figure II.6.D.1.

Figure II.6.D.1 Calculated Li_2S - P_4S_7 - S phase diagram using SCAN functional

According to the phase diagram, $\text{Li}_4\text{P}_2\text{S}_6$ and Li_3PS_4 are the only two stable phases at 0K, while the remaining five metastable phases are marked by red points. We found that to achieve accurate phase stability predictions in this chemical space with disperse anions, such as Sulfur, it is important to use novel DFT functionals such as SCAN. The formation energy data in Figure II.6.D.2a shows that the SCAN functional performs superior in several aspects to the classic PBE-GGA: The binary sulfide formation energy calculated by PBE has a systematic error of -0.54 eV as compared to experiment. Since SCAN captures the bonding strength of S with non-transition metal atoms much better than PBE, SCAN gives a systematic error of only -0.03 eV. In addition, Figure II.6.D.2a shows that there is no need for any sulfide correction when using the phase diagram or energetic data calculated from SCAN, which has been a problem for previous functionals such as PBE.

The SCAN functional also performs better in ranking the Li-P-S polymorphs. For example, PBE predicts the ground state of Li_3PS_4 to have $\text{P}\bar{4}3\text{m}$ symmetry. However, this is inconsistent with the synthesis reports in the literature, since the real ground state of Li_3PS_4 is the γ phase with $\text{Pmn}2_1$ space group. This deviation of PBE prediction from experimental results may arise from the fact that the PBE functional always over-stabilizes surfaces [14]. The SCAN functional also properly captures finite temperature variations in phase stability. Even though $\text{Li}_7\text{P}_3\text{S}_{11}$ and $\text{Li}_4\text{P}_2\text{S}_7$ are both metastable phases as shown in the 0K phase diagram, they become thermodynamically stable above 420K and 1010K as a result of vibrational entropy effects (Figure II.6.D.2b). These calculation results are consistent with experimental synthesis reports [15]. This data gives us confidence to use SCAN for the study of conductivity in amorphous phases.

Figure II.6.D.2 (a) Comparison of binary sulfide formation energy calculated from PBE and SCAN with experimental measurement. (b) ΔG vs. T for $\text{Li}_7\text{P}_3\text{S}_{11}$ & $\text{Li}_4\text{P}_2\text{S}_7$

Modelling the structure of amorphous Li_3PS_4

Lithium thiophosphate (LPS) glasses and glass-ceramics, $x\text{Li}_2\text{S} \cdot (1-x)\text{P}_2\text{S}_5$ ($x = 0.7-0.8$), have a high ionic conductivity (0.2–3.0 mS/cm) [15],[16] and are easy to process. Amorphous models for the composition $0.75\text{Li}_2\text{S} \cdot 0.25\text{P}_2\text{S}_5$ –corresponding to the ortho-thiophosphate stoichiometry Li_3PS_4 – have been generated via AIMD [17] by applying different melt-and-quench and simulated annealing protocols to a unit cell with 128 atoms. All computed structures display PS_4 tetrahedra, both isolated and connected through S bridges (P_2S_7) or P-P bonds (P_2S_6), as well as “atypical” structural motives such as sulfur chains and tri-coordinated phosphorus. In Figure II.6.D.3a the pair distribution functions (PDFs) for the computational amorphous LPS model is compared with experimental X-Ray scattering data (see Figure II.6.D.3a), showing good agreement.

The peak superposition in the measured total PDF does not allow unambiguous confirmation of “anomalous” structural motives we observe in the simulation. To answer this question, and thus uniquely characterize the amorphous LPS structure, it is necessary to resort to the additional support of spectroscopic data, e.g., Raman spectra. Because groups of atoms have a specific vibrational fingerprint, Raman spectra can identify such groups in the amorphous structure. We have calculated the Raman spectra of some crystalline reference structures as shown in the Figure II.6.D.3b. These enabled us to identify and factorize vibrational contributions from atomic groups involving P and S atoms that are specific to the different crystalline frameworks, namely $[\text{PS}_4]^{3-}$ for Li_3PS_4 , $[\text{P}_2\text{S}_7]^{4-}$ for $\text{Li}_7\text{P}_3\text{S}_{11}$ and $[\text{P}_2\text{S}_6]^{4-}$ for $\text{Li}_4\text{P}_2\text{S}_6$.

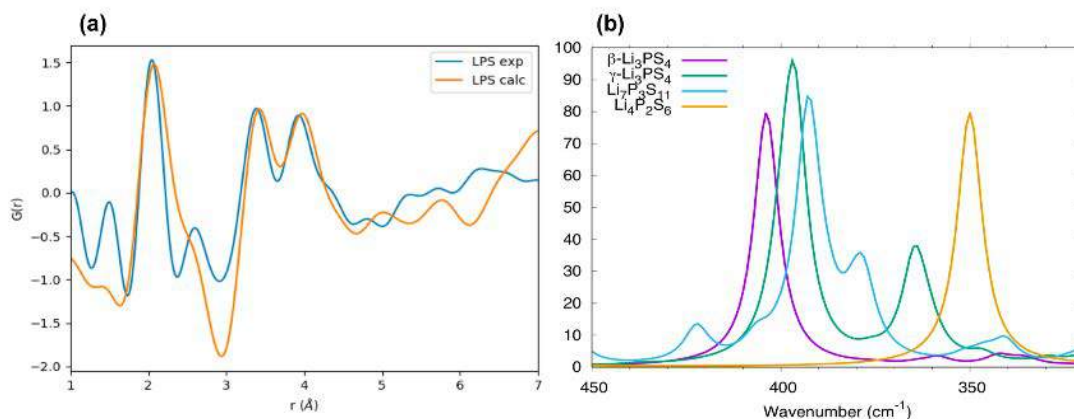


Figure II.6.D.3 (a) Comparison between calculated and experimental PDFs for amorphous LPS. (b) Raman spectra calculated for different LPS crystalline phases

Exploring coating materials for stabilizing interface between the Li-P-S electrolyte and NCM cathode

At the LPS/cathode interface LPS can decompose due to the high voltage which extracts lithium from the conductor, or by chemical reaction with the oxide cathodes. One way to mitigate these issues is the use of a cathode coating which act as a buffer layer between the cathode and LPS. An ideal cathode coating should have an oxidation stability limit above 4 V and a reduction limit below 2.7 V to overlap with the stability window of LPS, and low chemical reactivity with both the cathode and LPS. Figure II.6.D.4a shows the computed electrochemical stability of stable Li-containing materials categorized by their anion chemistries. It can be observed that fluorides have the highest oxidation limits, followed by chlorides, polyanionic oxides, and non-polyanionic oxides. Compounds in the “Others” category (e.g., bromides, nitrides and phosphides) generally have the lowest oxidation limits, below 2.5 V. The green box in Figure II.6.D.4a represents the stability window of interest, which contains 302 compounds, most of which are halides, polyanionic oxides, and non-polyanionic oxides.

The calculated chemical reactivity of these candidate coatings with LPS and a typical oxide cathode $\text{LiNi}_x\text{Co}_y\text{Mn}_{1-x-y}\text{O}_2$ (NCM) is plotted in Figure II.6.D.4b. We found that although the non-polyanionic oxides have a low reactivity (defined by $|\Delta E_{\text{rxt}}|$) below 50 meV/atom with oxide cathodes, they often have high reactivity above 100 meV/atom with the LPS electrolyte. In contrast, in the green box in Figure II.6.D.4b

defined by reactivity below 100 meV/atom with both NCM and LPS, the 184 compounds mostly consist of halides and polyanionic oxides. Due to the ease of synthesis and application of oxides, we consider polyanionic oxides to be the most promising cathode coating materials that can effectively protect LPS from high-voltage oxide cathodes.

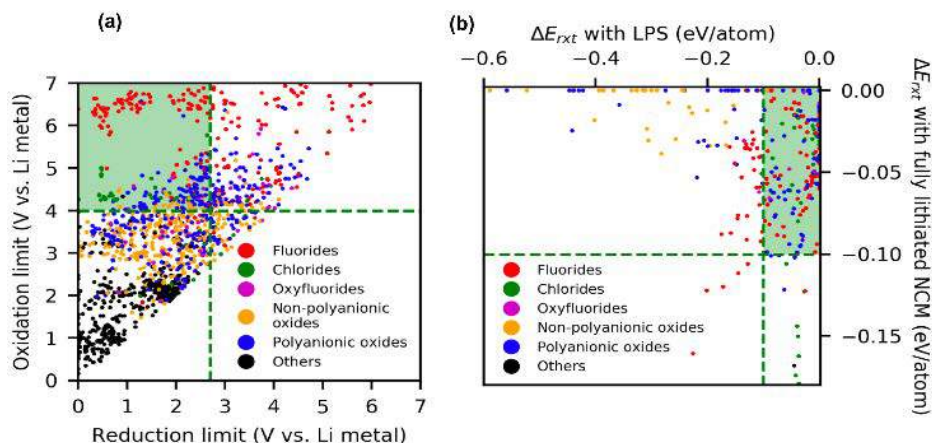


Figure II.6.D.4 (a) Electrochemical stability windows of 1,600 phase-stable materials categorized by anion chemistry. (b) Chemical reaction energy ΔE_{rxt} with LPS and fully lithiated NCM for the 302 screened materials enclosed in the green box in (a) [18].

Elucidating the role of local structure on the ionic conductivity in amorphous Li-P-S system

The amorphous Li-P-S phase generally shows higher intrinsic ionic conductivity than the corresponding crystalline phase with the same composition [10]. Recent experimental work shows that amorphous Li-P-S consists of anion blocks such as PS_4^{3-} , $\text{P}_2\text{S}_6^{4-}$ and $\text{P}_2\text{S}_7^{4-}$ [15]. To verify the exact role of each anion building block, amorphous structures consisting of different types of building blocks have been prepared by a high temperature anneal and quench Molecular Dynamics (MD) technique. In order to separate the effect of the Li ion concentration from that of the structure, the atomic composition of the structures is fixed to $\text{Li}:\text{P}:\text{S} = 3:1:4$. The density is kept constant at 2 g cm^{-3} for all samples. The reference structure, which only contains PS_4^{3-} anions, is generated by annealing the $\beta\text{-Li}_3\text{PS}_4$ phase at 1000K. This leads to amorphization without breaking of P-S bonds during the annealing timescale (10 ps). The structures with $\text{P}_2\text{S}_6^{4-}$ and $\text{P}_2\text{S}_7^{4-}$ building blocks are created through a stoichiometric substitution from the reference structure 1) $2x \cdot \text{PS}_4^{3-} \rightarrow x \cdot \text{P}_2\text{S}_7^{4-} + x \cdot \text{S}_2^{2-}$ and 2) $2y \cdot \text{PS}_4^{3-} \rightarrow y \cdot \text{P}_2\text{S}_6^{4-} + y \cdot \text{S}_2^{2-}$. Figure II.6.D.5 shows the structures of the reference, $x=1$, $x=2$ and $y=1$ substitution. Diffusion constants of Li ions are obtained from AIMD simulations (>250 ps) on these materials.

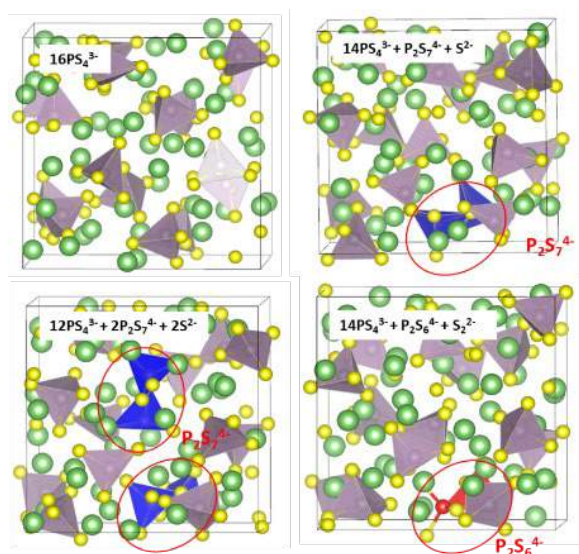


Figure II.6.D.5 Computational structures of the amorphous Li-P-S systems including different types of anion building blocks at same composition. Green, purple and yellow balls denote Li, P and S ion, respectively

As shown in Figure II.6.D.6, the activation barriers of diffusion are determined to be 485, 347, 282 and 289 meV for the reference, $x=1$, $x=2$, and $y=1$ substitution respectively. These results clearly indicate that modification of PS_4^{3-} into $\text{P}_2\text{S}_6^{4-}$ or $\text{P}_2\text{S}_7^{4-}$ reduces the activation barrier for Li diffusion. The difference between the top right and bottom left plot also indicate that an increasing concentration of substitution ($x=1$ to $x=2$) further reduces the activation barrier. Therefore, the structure and composition of the anion building blocks affect the diffusion of Li ions in LPS in a substantial way, even though there is no long-range order in the structures and no chemical composition change.

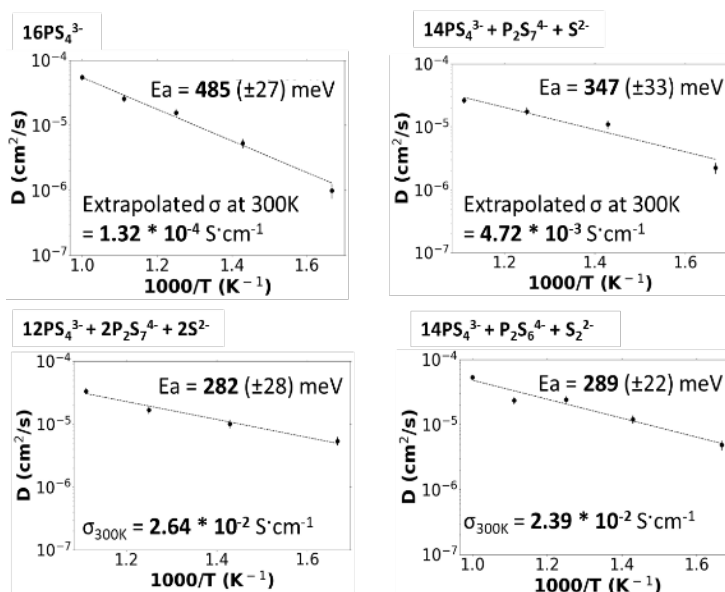


Figure II.6.D.6 Arrhenius plots of AIMD simulation on the Li-P-S systems with different concentrations of anion building blocks, PS_4^{3-} , $\text{P}_2\text{S}_6^{4-}$ and $\text{P}_2\text{S}_7^{4-}$

Conclusions

Using first principles calculations, we calculated the ground states in the Li-P-S phase diagram, and successfully predict the experimental synthesis temperature of known materials such as $\text{Li}_4\text{P}_2\text{S}_7$ and LiPS_3 . In addition, the unknown phase, $\text{Li}_4\text{P}_2\text{S}_7$, is predicted to be stable above 1000K.

With high-throughput DFT calculation, we found 302 candidate coating materials with electrochemical stability between 2.7 V and 4 V. Further filtering on chemical stability against amorphous LPS and NCM led to 184 materials with reaction energy lower than 100 meV against both the electrolyte and cathode materials. These candidate coating materials mostly consist of halides and polyanionic oxides, and are predicted to outperform existing coating materials.

To analyze amorphous Li-P-S an atomistic model of Li:P:S=3:1:4 composition was constructed using a computational melt-and-quench process. The model contains polyanions such as $[\text{PS}_4]^{3-}$, $[\text{P}_2\text{S}_7]^{4-}$ and $[\text{P}_2\text{S}_6]^{4-}$, successfully reproducing the structural feature observed in the experiments. Generated PDF also matches well with the experimental X-Ray scattering data. Based on this result, the effect of polyanions on the ionic conductivity was examined by constructing hypothetical amorphous Li-P-S structures with different local environment, revealing that modification of $[\text{PS}_4]^{3-}$ into $[\text{P}_2\text{S}_6]^{4-}$ or $[\text{P}_2\text{S}_7]^{4-}$ reduces the activation barrier up to 200 meV.

Key Publications

1. Ji, H., Kitchaev, D. A., Lun, Z., Kim, H., Foley, E., Kwon, D. H., ... & Clément, R. J. (2019). Computational Investigation and Experimental Realization of Disordered High-Capacity Li-Ion Cathodes Based on Ni Redox. *Chemistry of Materials*, 31(7), 2431-2442.
2. Ji, H., Urban, A., Kitchaev, D. A., Kwon, D. H., Artrith, N., Ophus, C., ... & Kim, H. (2019). Hidden structural and chemical order controls lithium transport in cation-disordered oxides for rechargeable batteries. *Nature communications*, 10(1), 592.
3. Lun, Z., Ouyang, B., Cai, Z., Clément, R. J., Kwon, D. H., Huang, J., ... & Ji, H. (2019). Design Principles for High-Capacity Mn-Based Cation-Disordered Rocksalt Cathodes. *Chem*.
4. Hong, J., Gent, W. E., Xiao, P., Lim, K., Seo, D. H., Wu, J., ... & Stone, K. H. (2019). Metal–oxygen decoordination stabilizes anion redox in Li-rich oxides. *Nature materials*, 18(3), 256.
5. Yihan Xiao, et al. “Understanding interface stability in solid-state batteries”. *Nature Reviews Materials*, in press (2019).

References

1. Wang, Y., Richards, W. D., Ong, S. P., Miara, L. J., Kim, J. C., Mo, Y., & Ceder, G. (2015). Design principles for solid-state lithium superionic conductors. *Nature materials*, 14(10), 1026.
2. Richards, W. D., Miara, L. J., Wang, Y., Kim, J. C., & Ceder, G. (2015). Interface stability in solid-state batteries. *Chemistry of Materials*, 28(1), 266-273.
3. Zhu, Y., He, X., & Mo, Y. (2016). First principles study on electrochemical and chemical stability of solid electrolyte–electrode interfaces in all-solid-state Li-ion batteries. *Journal of Materials Chemistry A*, 4(9), 3253-3266.
4. Chen, S., Xie, D., Liu, G., Mwizerwa, J. P., Zhang, Q., Zhao, Y., ... & Yao, X. (2018). Sulfide solid electrolytes for all-solid-state lithium batteries: structure, conductivity, stability and application. *Energy Storage Materials*, 14, 58-74.
5. Seino, Y., Ota, T., Takada, K., Hayashi, A., & Tatsumisago, M. (2014). A sulphide lithium super ion conductor is superior to liquid ion conductors for use in rechargeable batteries. *Energy & Environmental Science*, 7(2), 627-631.

6. Kamaya, N., Homma, K., Yamakawa, Y., Hirayama, M., Kanno, R., Yonemura, M., ... & Mitsui, A. (2011). A lithium superionic conductor. *Nature materials*, 10(9), 682.
7. Deng, Z., Wang, Z., Chu, I. H., Luo, J., & Ong, S. P. (2016). Elastic properties of alkali superionic conductor electrolytes from first principles calculations. *Journal of The Electrochemical Society*, 163(2), A67-A74.
8. Sakuda, A., Hayashi, A., & Tatsumisago, M. (2013). Sulfide solid electrolyte with favorable mechanical property for all-solid-state lithium battery. *Scientific reports*, 3, 2261.
9. Hayashi, A., Hama, S., Morimoto, H., Tatsumisago, M., & Minami, T. (2001). Preparation of Li₂S–P₂S₅ amorphous solid electrolytes by mechanical milling. *Journal of the American Ceramic Society*, 84(2), 477-79.
10. Zheng, F., Kotobuki, M., Song, S., Lai, M. O., & Lu, L. (2018). Review on solid electrolytes for all-solid-state lithium-ion batteries. *Journal of Power Sources*, 389, 198-213.
11. Tian, F., Radin, M. D., & Siegel, D. J. (2014). Enhanced charge transport in amorphous Li₂O₂. *Chemistry of Materials*, 26(9), 2952-2959.
12. Sun, J., Ruzsinszky, A., & Perdew, J. P. (2015). Strongly constrained and appropriately normed semilocal density functional. *Physical review letters*, 115(3), 036402.
13. Kitchaev, D. A., Peng, H., Liu, Y., Sun, J., Perdew, J. P., & Ceder, G. (2016). Energetics of MnO₂ polymorphs in density functional theory. *Physical Review B*, 93(4), 045132.
14. Patra, A., Bates, J. E., Sun, J., & Perdew, J. P. (2017). Properties of real metallic surfaces: Effects of density functional semilocality and van der Waals nonlocality. *Proceedings of the National Academy of Sciences*, 114(44), E9188-E9196.
15. Dietrich, C., Weber, D. A., Sedlmaier, S. J., Indris, S., Culver, S. P., Walter, D., ... & Zeier, W. G. (2017). Lithium ion conductivity in Li₂S–P₂S₅ glasses—building units and local structure evolution during the crystallization of superionic conductors Li₃PS₄, Li₇P₃S₁₁ and Li₄P₂S₇. *Journal of Materials Chemistry A*, 5(34), 18111-18119.
16. Mizuno, F., Hayashi, A., Tadanaga, K., & Tatsumisago, M. (2006). High lithium ion conducting glass-ceramics in the system Li₂S–P₂S₅. *Solid State Ionics*, 177(26-32), 2721-2725.
17. Perdew, J. P., Burke, K., & Ernzerhof, M. (1996). Generalized gradient approximation made simple. *Physical review letters*, 77(18), 3865.
18. Xiao, Y., Miara, L. J., Wang, Y., & Ceder, G. (2019). Computational Screening of Cathode Coatings for Solid-State Batteries. *Joule*, 3(5), 1252-1275.

II.6.E Addressing Heterogeneity in Electrode Fabrication Processes (Brigham Young University)

Dean Wheeler, Principal Investigator

Brigham Young University
Department of Chemical Engineering
330 Engineering Building
Provo, UT 84602
E-mail: dean_wheeler@byu.edu

Brian Mazzeo, Principal Investigator

Brigham Young University
Department of Electrical and Computer Engineering
450 Engineering Building
Provo, UT 84602
E-mail: bmazzeo@byu.edu

Tien Duong, DOE Technology Development Manager

U.S. Department of Energy
E-mail: Tien.Duong@ee.doe.gov

Start Date: October 1, 2016

End Date: September 30, 2019

Project Funding (FY19): \$350,000

DOE share: \$350,000

Non-DOE share: \$0

Project Introduction

A lack of fundamental understanding about the relationships between fabrication parameters, microstructure, and performance prevents appropriate feedback and hurts the development of next-generation battery materials and process improvement in battery manufacturing. For instance, one problem with large-format batteries is ensuring uniformity in the manufacturing process, so that all components perform equally well and no component contributes unduly to performance limitations and failure. This improvement in manufacturing will not be possible without additional information on the nature of heterogeneities and how they relate to electrode fabrication steps. Even more beneficial is if the information is made available in a timely manner through the use of convenient and reliable experimental and modeling tools.

Objectives

The goal of this work is to better understand connections between fabrication conditions and undesired heterogeneity of thin-film electrodes by means of new non-destructive inspection techniques and computer models. This work resulted in new diagnostic and modeling tools for rapidly and conveniently interrogating how well homogeneity has been maintained in electrodes during fabrication and in subsequent cycling. Real-time measurement of heterogeneity will enable manufacturer quality control improvements. The measurement and modeling tools will further enable researchers to compare different electrodes, improve formulations and processes, and anticipate cell performance of new designs.

Approach

Two non-destructive inspection techniques were developed and improved which will characterize electrochemical and mechanical uniformity of the electrodes. The first tool is a flexible contact probe on a polymer substrate for rapidly measuring local electrical conductivity across electrodes of any geometry. The second tool is a new acoustic probe that measures local elasticity and density of the composite film. These two prototyping efforts are tied together by a particle-based microstructure model that allows prediction and correlation of electrode conductive and mechanical properties with fabrication conditions. Each of these tools involved one or more quarterly milestones. In addition to model and tool development, the tools were used to

examine electrodes sourced from other researchers, including from industry, in order to assess the effects of mixing and composition changes, and the effects of cycling.

Results

This final year of the project focused on continuing innovations to allow localized measurements of electrode properties to enable quantification of heterogeneity. For instance, localized ionic conductivity measurements were made for the first time. An improved drying model was developed and likewise used to describe heterogeneity.

The following established FY 19 Milestones were completed:

1. Quantify microstructure heterogeneity effects on overall cell performance.
2. Create localized ionic electrode conductivity maps.
3. Create design package for commercialization of the conductivity probe including controls and hardware.
4. Investigate the physics of the drying process with the smoothed particle hydrodynamics drying model.

Milestone 1. Quantify microstructure heterogeneity effects on overall cell performance.

This project has established by multiple means that there are heterogeneities on mm and larger length scales present even in commercial-grade Li-ion electrodes. However, it had not previously been quantified how such heterogeneities would affect cell performance. For instance, it is possible that such heterogeneities average out and thus do not need to be of concern. On the other hand, these variations could adversely affect battery performance and lifetime as a result of non-uniform current, temperature, state of charge (SOC), and aging. Thus an activity this year was to establish this connection through developing a preliminary full-cell heterogeneity model.

The model was based on a series of Newman-type models operating in parallel. Newman-type models are well-used in the battery community due to their physical realism and fidelity to experimental charge and discharge behavior. However, traditional Newman-type models are based on using homogenized or averaged properties such as ionic and electronic conductivity. This means that they ignore heterogeneity and cannot predict such effects. While other 3D electrode models have been created to remedy this problem, they in turn require extensive experimental microstructures as input and also require a great deal of computational effort to produce single charge or discharge curves.

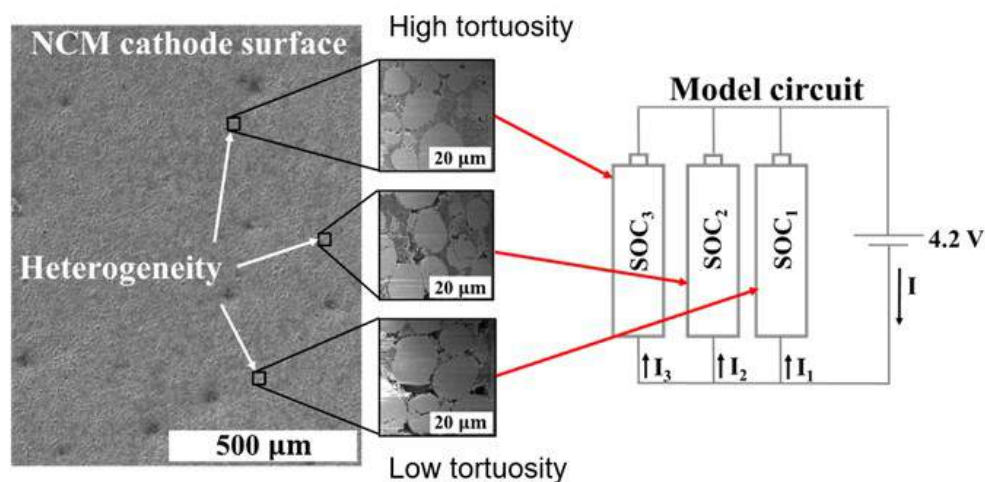


Figure II.6.E.1 A Newman-type model was adapted to rapidly predict the effects of heterogeneity by placing dissimilar regions in parallel. The model is able to show why lithium plating occurs preferentially in some regions.

The proposed model married the computational efficiency of the Newman-type models with the possibility of heterogeneous description of electrode behavior. This is illustrated in Figure II.6.E.1. In essence, multiple Newman-type models are run in parallel, each describing a different representative region of the electrode and providing voltage and current feedback to each other by means of the current collector. Because each submodel represents a different region of the electrode film, it can have its own transport properties and possibly material loading, i.e., properties that vary from one location to another in a realistic heterogeneous electrode. Both positive and negative electrodes were combined in the model to generate full-cell behavior. The model was used to assess the effects of fast-charge regimes on causing localized degradation in the electrodes.

Variations in the positive and negative electrodes were examined according to whether the different resistances were aligned or misaligned. The results for different charge and discharge rates show that higher rates increase non-uniformities of dependent properties such as temperature, current density, positive and negative electrode states of charge, and charge and discharge capacities, especially in the case of charging. As an illustration, Figure II.6.E.2 shows curves of state of charge (SOC), temperature, and other properties for the three regions running in parallel during a 5C charge. Sensitivity analysis for this case shows that structural heterogeneity affects the charge capacity to the greatest extent and temperature to the least extent.

Moreover, the results suggest that degradation takes place faster and to higher degree during charging due to more non-uniformity compared to the results from comparable discharging case. In addition, for the discharging cases, the results show that the misaligned active material loading case has more negative effects on the cell performance and lifetime. In this case, the results suggest that high degradation takes place during discharge in the negative electrode.

In conclusion, adequate homogeneity is needed in electrodes to enable fast charging capability with a good cycle life. Additional work is needed to experimentally confirm these model results.

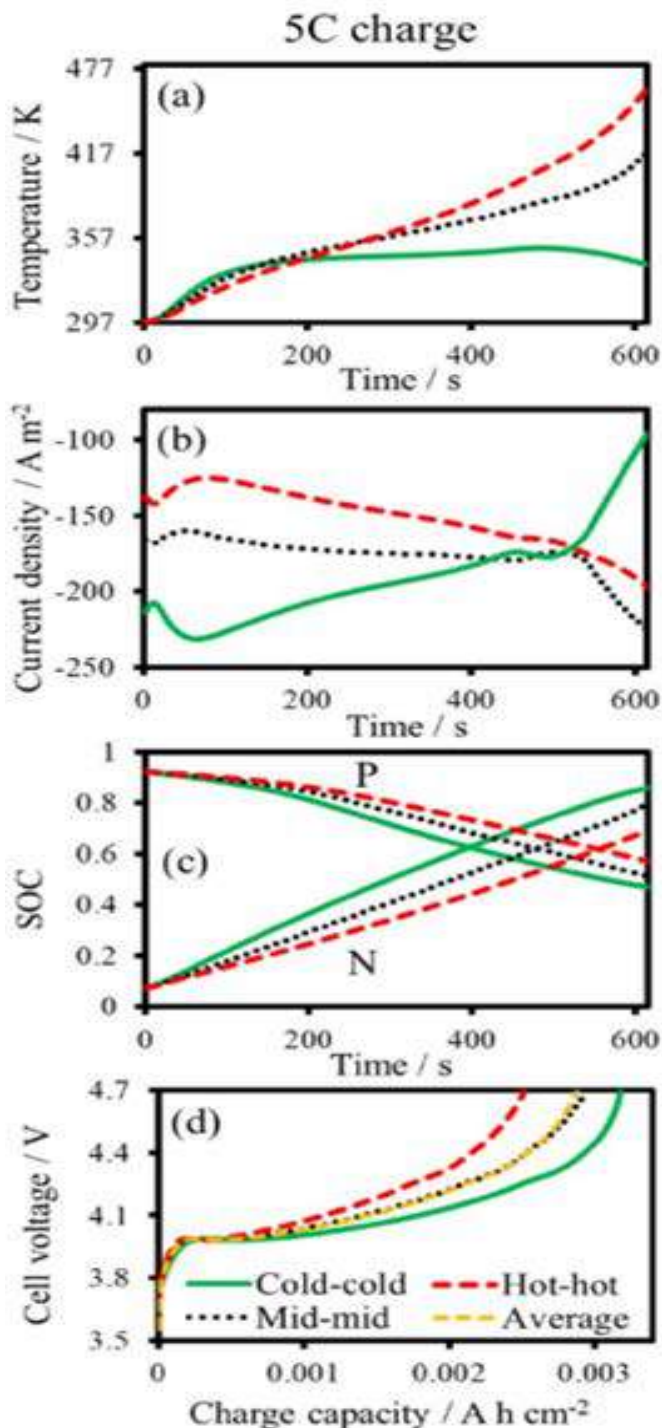


Figure II.6.E.2 Temperature, current, and positive and negative electrodes states of charge (SOCs) distributions, along with charge curves for the charging aligned resistances case (hot-hot, middle-middle, and cold-cold)

Milestone 2. Create localized ionic electrode conductivity maps.

In addition to electronic conductivity measurements, and perhaps of more concern to manufacturers, the ionic conductivity of battery electrode is crucial for performance of cells. However, estimating the ionic conductivity of electrode films is often performed over large areas on the order of square centimeters. Past work at BYU has demonstrated the use of probes fabricated for electronic conductivity to perform ionic conductivity measurements. The major obstacle with the use of these probes was that the deposited films often were not sufficiently robust for repeated use. Therefore, a renewed effort and redesign was needed in order to generate reliable localized ionic conductivity maps of electrode films.

Figure II.6.E.3. shows the concept of the new conductivity probe as well as the realized probe attached to a computer-controlled stage. At each location on the surface of the battery electrode sample, an electrochemical impedance spectroscopy (EIS) experiment is conducted in combination with a non-lithium-containing electrolyte. A detailed impedance model in cylindrical coordinates is needed to interpret the experiments and generated effective ionic conductivities. This too was completed during FY 19.

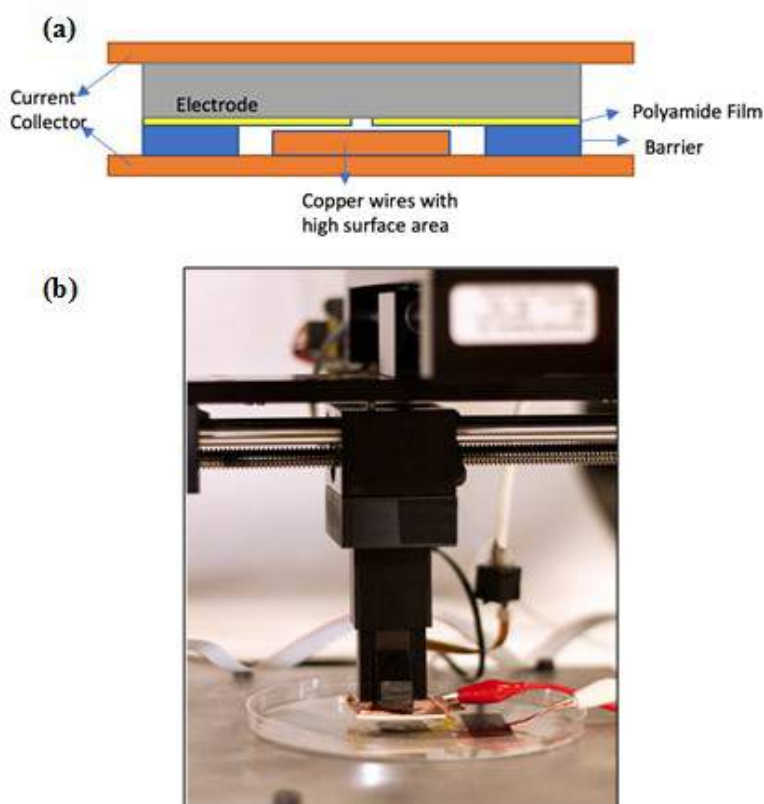


Figure II.6.E.3 (a) Conceptual geometry (not to scale) of revised local conductivity probe and (b) XYZ stage for automated measurement of local conductivity

Figure II.6.E.4 illustrates an early result from the newly constructed probe. A 4 x 4 grid of points with 6 mm offsets was used to sample a commercial LCO electrode. Subsequent work has shown similar results for other electrodes, including NMC cathodes. The results suggest that the relative amount of variation in ionic conductivity and diffusivity is significant, though typically less than for electronic conductivity. The newly created tool is suitable for ongoing laboratory use. Anticipated analysis in subsequent EERE-funded work will include sampling on graphite anodes to understand limitations of fast charging.

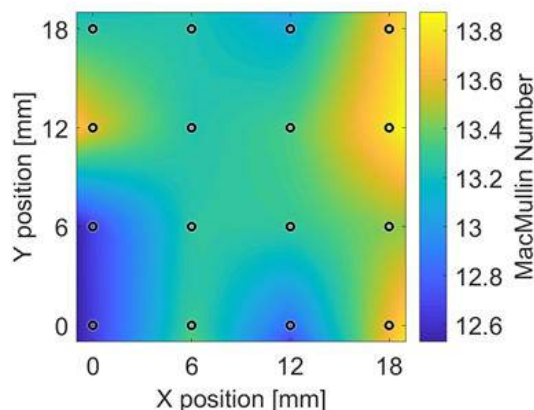


Figure II.6.E.4 An example localized conductivity measurement with ionic conductivity given in terms of dimensionless MacMullin Number, for a commercial LCO electrode

Milestone 3. Create design package for commercialization of the conductivity probe including controls and hardware.

The electronic conductivity probe developed under prior EERE funding and improved under the present EERE project has proven to be a unique tool for analyzing electrodes during manufacture. It has also been used to determine changes in conductivity and contact resistance after formation and cycling (after harvesting of electrodes from cells). The team at BYU has received electrodes for analysis from many organizations including universities, national laboratories, and companies. In order to increase throughput and accessibility to this tool, a portion of the budget for FY 19 was devoted to funding a student team to improve the design of the electronic conductivity probe. This was done under the auspices of the BYU Engineering Capstone Program. The team designed and built a self-contained testing unit (see Figure II.6.E.5), with a combination of off-the-shelf and customized parts, and associated operating software. Additionally, probes and software (not the complete system) were sold to Missouri S&T and UC Irvine this year. Discussions with multiple companies are ongoing to further commercialize the conductivity probe.

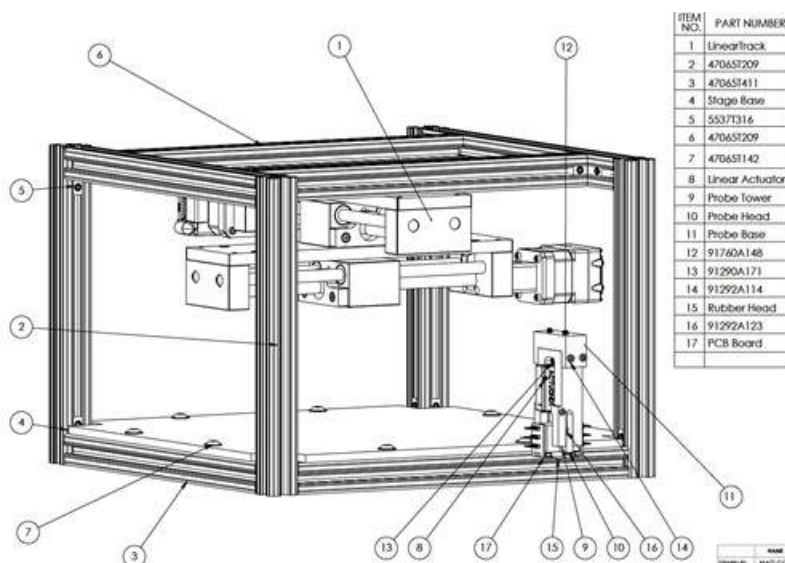


Figure II.6.E.5 Schematic of XYZ stage and head unit for local electronic conductivity probe. This unit was adapted for use in measuring ionic conductivity as well, as shown in the adjacent figure (b).

Milestone 4. Investigate the physics of the drying process with the smoothed particle hydrodynamics drying model.

One of the major activities of this project was to build a physically accurate particle simulation model. The model needed to be able to handle liquid-solid and liquid-gas interfaces to enable simulations of the slurry coating and drying processes. This involved making significant changes to a prior particle-based model. Specifically, the researchers at BYU began using a technique known as smooth particle hydrodynamics (SPH). SPH has previously been used to imitate fluid motion, but there has not been significant effort to use the method to simulate slurry behavior and soft-solid behavior (porous electrodes, though composed of hard active

materials, have overall mechanical properties similar to polymers and other soft solids). Therefore, adaptation of the SPH model required additional work under this project.

Figure II.6.E.6 illustrates results from the new SPH model during drying and calendaring steps. The model can imitate gradients in composition that have been experimentally observed in our laboratory by means of SEM/EDS on cross sections of dried electrodes. The model is also able to show how heterogeneities in the microstructure develop from small differences in the starting configuration, illustrating how heterogeneities can develop not only from poor quality control, but also as a result of structural instabilities inherent to the drying process. Finally, experimental measurements of mechanical properties of the slurries and dried electrodes were made to assist in validating the model and understanding the relevant physics.

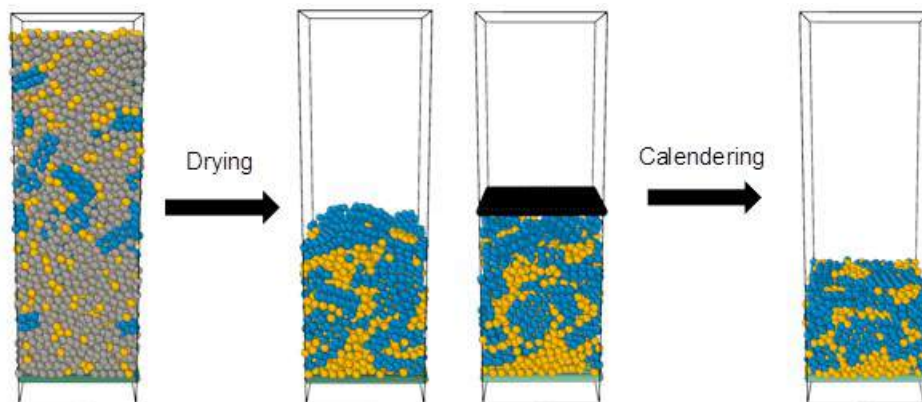


Figure II.6.E.6 Snapshots of beginning and ending particle configurations for drying and calendaring SPH simulations. The colored spheres indicate active material (blue), carbon/binder (yellow), and solvent (gray)

Conclusions

This last year of a multiyear project has demonstrated a complete set of tools for analyzing the transport performance of composite electrodes on the length scales 100 μm and larger. The tools include both computer models and localized conductivity probes. It is anticipated that these tools will enable continuing improvement in our understanding of heterogeneity and potential remedies. Interest in these tools by other researchers including by commercial battery producers has demonstrated the potential value of this unique understanding.

Key Publications

The following publications were made during FY 19 under EERE support. Several additional manuscripts based on this year's work are in preparation.

1. J. Yao, J. Cassler, D.R. Wheeler, and B.A. Mazzeo, "Characterization of mechanical properties of thin-film Li-ion battery electrodes from laser excitation and measurements of zero group velocity resonances," *J. Applied Phys.* 126, (2019), 085112.
2. J.E. Vogel, M.M. Forouzan, E.E. Hardy, S.T. Crawford, D.R. Wheeler, and B.A. Mazzeo, "Electrode microstructure controls localized electronic impedance in Li-ion batteries," *Electrochimica Acta* 297, (2019), 820-825.

The following presentations at scientific conferences were based partially on this funding.

1. F. Pouraghajan, F. Sun, B.A. Mazzeo, and D.R. Wheeler, "The interplay of electrode heterogeneity, SEI growth, and Li plating in Li-ion batteries," 236th Meeting of the Electrochemical Society, Atlanta, GA (2019).
2. E.E. Hunter, J.E. Vogel, D.R. Wheeler, and B.A. Mazzeo, "The impact of calendaring on the electronic conductivity heterogeneity of lithium-ion electrode films," 236th Meeting of the Electrochemical Society, Atlanta, GA (2019).

3. K. Nielsen, B. Liu, B.A. Mazzeo, and D.R. Wheeler, "Heterogeneity of ionic conductivity in lithium-ion battery electrodes," 236th Meeting of the Electrochemical Society, Atlanta, GA (2019).
4. B. Liu, K. Nielsen, B.A. Mazzeo, and D.R. Wheeler, "Instrument for measuring local ionic conductivity of porous electrodes," 236th Meeting of the Electrochemical Society, Atlanta, GA (2019).
5. A.I. Thompson, F. Pouraghajan, B.A. Mazzeo, and D.R. Wheeler, "The effects of cycling on ionic and electronic conductivities of 18650 Li-ion cells," 236th Meeting of the Electrochemical Society, Atlanta, GA (2019).
6. J.G. Sederholm, J.E. Vogel, B.A. Mazzeo, and D.R. Wheeler, "Factors affecting contact resistance between electrode and current collector," 236th Meeting of the Electrochemical Society, Atlanta, GA (2019).
7. N. Clemens, D.R. Wheeler, and B.A. Mazzeo, "Alignment of conductive additive in Li-ion battery electrodes through use of electric fields," 236th Meeting of the Electrochemical Society, Atlanta, GA (2019).
8. M. Nikpour, N. Barrett, C.A. Harrison, D.R. Wheeler, and B.A. Mazzeo, "Microscale simulations of drying and calendaring processes to manufacture porous electrodes," 236th Meeting of the Electrochemical Society, Atlanta, GA (2019).

Acknowledgements

Partners in this effort included Ram Subbaraman (Bosch), Daniel Abraham (ANL), Andrew Colclasure (NREL), Kandler Smith (NREL), Bryant Polzin (ANL), Chisu Kim (Hydro-Québec), and Henning Dreger (TU Braunschweig). Other commercial parties provided materials, discussions, or both, but do not wish to be publicly identified at this time.

II.6.F Large scale *ab initio* molecular dynamics simulation of liquid and solid electrolytes (LBNL)

Lin-Wang Wang, Principle Investigator

Lawrence Berkeley National Laboratory
One cyclotron road, MS-66
Berkeley, CA 94760
E-mail: lwwang@lbl.gov

Tien Duong, DOE Technology Development Manager

U.S. Department of Energy
E-mail: Tien.Duong@ee.doe.gov

Start Date: October 1, 2018

End Date: September 30, 2019

Total Project Cost: \$225,000

DOE share: \$225,000

Non-DOE share: \$0

Project Introduction

One major obstacle for lithium sulfur battery is the dissolution of the lithium polysulfide in the electrolytes. The goal of this project is to use large scale *ab initio* calculation and molecular dynamics simulations to study the discharge mechanism in Li sulfur battery, especially for polysulfide interaction with liquid electrolyte solvent molecules, and cathode materials, as well as Li diffusion mechanism in superionic crystal solid electrolytes. We like to search for cathode materials and designs to prevent the dissolution based on thermodynamic principles. The long term goal is to use such theoretical understanding to provide guidance to develop better electrolyte and cathode systems to overcome the bottlenecks which currently prevent the commercialization of the Li/S battery.

Objectives

The long term goal of this project is to understand the atomistic mechanism and process of Li/S battery through theoretical simulations. We like to use such understanding to design new Li/S cathode materials, as well as new electrolytes. Another goal is to test the theoretical limit of different approaches of the Li/S cathodes designs, compare the pros and cons of different designs. For example, there are different strategies to design Li/S battery cathodes: physical confinement and encaging of S; thermal dynamical attachment of Li polysulfide to some substrates; polymer binder attachment of LiS; 2D material attachment of LiS; and amorphous LiS solids. They can face different challenges: the limited theoretical capacity; the electric conductivity; the Li diffusion in the material; the thermodynamic stability. In order to compare the pros and cons of different designs, we have studied different systems. The purpose is to provide a theoretical guidance to the experiments in this field. A related topic is to study both solid and liquid electrolytes, which are critical to the work of Li/S battery. This might include the Li diffusion in a narrow porous environment intruded with liquid electrolyte; liquid Li electrolyte not dissolving Li polysulfide.

Approach

In many designs of Li/S cathode materials, the system is often disordered and amorphous. This poses great challenges for *ab initio* simulations of such systems. We have both used conventional *ab initio* methods, as well as developing new methods to study such systems. Most of our calculations are based on density functional theory (DFT). One approach is to use genetic algorithm to search for the minimum energy structure. This is important for Li-S battery since the cathode material and the binding morphology is usually not in simple crystal structure, instead it is more likely to be a cluster or amorphous. Another issue is the dealing of the solvent effects for liquid electrolyte. We have used both the implicit solvent model, as well as explicit electrolyte molecules simulations. For the solvent model, a continue medium representing the dielectric response of the electrolyte is used. The parameters of this solvent model are fitted to reproduce the experimental voltages at the different stages of dissolved Li polysulfide Li_2S_n . This can thus provide the

reliable thermodynamic energy of the Li_2S_n in the electrolyte, as well as the Li/S clusters attached to some substrates. However, such implicit model will not be able to describe the Li^+ ion diffusion in the electrolyte, especially in some confined environment. In order to do that, we have used explicit solvent molecules in a molecular dynamics (MD) simulation. Such MD can be carried out under DFT, but can also be done using classical force field for large systems. The challenge for classical force field MD is the lack of reliable force field. In that regards, we are testing the development of machine learning force field (ML-FF) based on ab initio DFT calculation data. That is one of the future research topic in this project. Besides Li^+ ion diffusion in liquid electrolyte, Li diffusion in solid electrolyte, or potential cathode material is another major topic. For Li diffusion in solid electrolyte we are using the nudged elastic band (NEB) method to calculate the barrier height. However, the NEB is only applicable for systems with well defined structures and local minima (e.g., in crystal structures), it cannot be applied to complicated amorphous systems as in some of the lithium sulfur cathode materials we are studying. There are two approaches to overcome this difficult. One is to do a direct DFT MD at elevated temperatures, then do an extrapolation to yield the room temperature Li diffusion result. This can often be done for solid electrolyte. However, for some LiS cathodes, e.g., the amorphous like cathode, raising the temperature can melt the material, hence causing a phase change. As a result, the diffusion property in a high temperature phase (e.g., liquid) cannot be extrapolated to predict the diffusion in the lower temperature solid phase. For such cases, we have tested new approaches. One is to apply a force on one lithium atom, forcing it to move along one direction. Some local heating is provided to the pulled upon Li atom, so it can thermodynamically explore the local environment, meanwhile not to melt the system. The resulting potential landscape is analyzed to get the information for the barrier height. We find this is a useful approach to study the Li diffusion in an amorphous environment, which is often the case for realistic Li/S cathode materials.

Results

In the past year, we have carried out theoretical studies in three areas: (1) Solid electrolyte Li diffusion model; (2) Li^+ diffusion in the liquid electrolyte near the surface; (3) LiS amorphous 3D cathode design; (4) Sulfur vulcanization in polymer as a sulphur Cathode.

(1) **Solid electrolyte Li diffusion:** we have studied the cooperative Li transport in Thio-LISICON [1]. It is found that the coordinated transport of two Li atom moving together has a lower barrier than the movement of each Li atom by itself. One of the reason is that, the energy of one Li atom can be transferred to the second Li atom when the first Li is going downhill in energy while the second Li is doing uphill in energy. As a result, the total energy balance out, resulting in smaller potential barrier. Such complex movement of the Li atom in solid electrolyte has modified our understanding of the microscopic movement in the solid electrolyte system.

In order to search possible solid electrolytes in the vast crystal database, we have developed an algorithm which can identify the Li diffusion pathway in a crystal [2]. Traditionally, the diffusion pathway can be theoretically investigated ab initio either through transition barrier calculations using NEB method, or through direct ab initio MD. However, such simulations are rather expensive, thus cannot be used for high throughput screening. To overcome this, we have developed a fast empirical method, which can be used to quickly reveal the Li transition pathway. This method is based on the bond valence (BV) method. In the BV method, the energy of Li at a given spatial location is estimated by the charge neutrality principle. More specifically, the charge transfer between an anion and the Li is assumed to exponentially depend on their distance with coefficients depending on the electron negativities and the radius of the anion. The total charge transfer from the Li to neighboring anions should sum up to 1. However, this method ignores the long range

Coulomb interactions, as well as the repulsion between Li and other nearby positive cations in the system. That can lead to erroneous path. We have thus added the Ewald energy on top of the BV model. This Ewald energy takes into account the Coulomb interactions, and the cation-Li repulsion. Proper mixing of the BV term and the Ewald energy term is used to take into account both effects. We have used the resulting formula to evaluate the Li transition paths in dozens of known crystal. We found that this BV-Ewald method provide qualitatively similar path compared with ab initio results, but with computations thousands of times faster. Figure II.6.F.1 shows the comparison between the BV-Ewald revealed Li pathway and the ab initio calculated Li transition pathways. Using this BV-Ewald method, we have investigated 34 known solid state electrolytes. Although they are known as solid state Li electrolyte, not all of their paths are known. Using BV-Ewald method, we have identify some of them as 3D electrolyte (with all three directions connected with Li channels), while some others are 2D and 1D electrolytes (with only 2D or 1D channels).

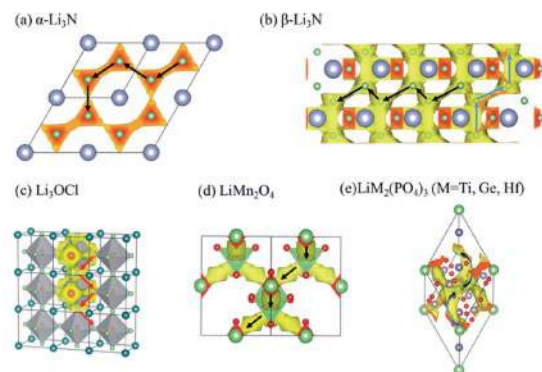


Figure II.6.F.1 The Li diffusion pathways for different solid electrolytes (the yellow isosurfaces), compared with the ab initio calculated transition pathways (the arrows)

(2) Li⁺ diffusion in the liquid electrolyte near the surface. In many of the actual Li/S battery design, porous carbon are used as conductive substrate to bind with S particle and to confine Li polysulfide to some extent. The liquid electrolyte is intruding inside such porous carbon to deliver the Li⁺ ion. If the porous size become very small in nanometer scale, one fundamental issue is: how fast the Li⁺ ion can diffuse inside such system. We have studied related problems for Li⁺ diffusion close to a surface. Using ab initio molecular dynamics, we have simulated Li⁺ diffusion in liquid electrolyte, especially when the Li⁺ ion is close to LiF surface. The electrolyte is consisted with DMC and EC molecule, the salt is Li⁺PF₆⁻, and the simulation is carried out in 600K, up to 60ps. In this simulation, (Figure II.6.F.2(a), (b)) Li⁺ and PF₆⁻ are always close to each other, as shown in the Li-F correlation function in Figure II.6.F.2(d). The diffusion between these two species are correlated. We have investigated the local structure of Li-O and Li-F. The related correlation functions are shown in Figure II.6.F.2(c).

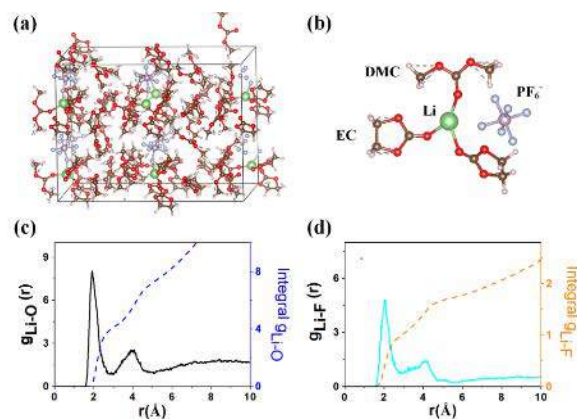


Figure II.6.F.2 (a) Side view of schematic representation of liquid electrolytes. (b) One representative local structures of the coordination environments around a Li-ion. (c) Li-O and (d) Li-F pair correlation functions (solid lines) and their integrals (dash lines) for LE from NVT AIMD simulation at 600 K

The electrolyte system is then placed on top of a LiF slab, with LiF(100) surface (Figure II.6.F.3). If the Li^+ is close to the surface, it tends to bind to surface F. The Li^+ diffusion mobility depends sensitively on the distance between Li^+ and LiF surface. If the Li-LiF distance is short, the diffusion constant is significantly reduced. It gradually increases to bulk value with the Li-LiF distance approach to 20 Å. This has implication for the Li^+ diffusion in the liquid electrolyte in a confined space. We plan to investigate more of such behavior, include more systematic study of Li diffusion in a confine cavity or porous structure.

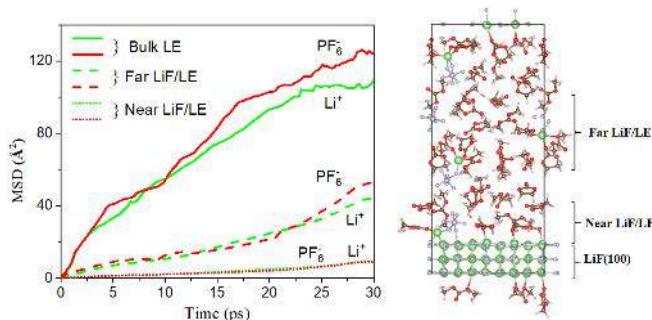


Figure II.6.F.3 mean square displacement (MSD) plots of Li-ion and PF_6 -ion taken from 30 ps NVT at 600 K simulations in bulk LE and LiF/LE interface.

(3) **3D Li/S electrode design:** although the theoretical Li-S battery gravitational capacity is high, it is based on the final product of solid Li_2S . If there are heavy substrate (e.g., used to anchoring LiS cluster), the gravitational capacity will be significantly reduced. Besides, the volumetric capacity is also a major challenge if 2D materials, or polymer binders are used to anchoring the LiS cluster. To overcome these difficulty, one approach is to design 3D LiS bulk material. Due to the lack of appropriate crystal structure, we have tested the use of 3D amorphous structure. In order to have electric conductivity, and to have strong binding to prevent the electrolyte dissolution, we have mixed Li_xS_y amorphous with microporous coordination polymers (2D hexaaminobenzene based coordinated polymer, 2D-HAB-CP). We have constructed a Li_xS_y /2D-HAB-CP alternating stacking structure as shown in Figure II.6.F.5. One major issue for such a structure is the Li diffusion in such a system. Only like the intercalation system where a clear Li diffusion path can be defined, here the Li_xS_y layer is amorphous, the diffusion of Li requires the breaking and forming of Li-S bonds and S-S bonds. It is thus not clear whether the Li can diffuse at all in such a system. Using our atom-pulling algorithm, we have calculated the typical diffusion barrier heights. The resulting distribution of the barrier height (due to the amorphous feature of the system) at different lithiation levels are shown in Figure II.6.F.4(a). We see the majority of the barriers are in the order of 0.5 eV. Our estimated diffusion constants at different lithiation levels as functions of temperature are shown in Figure II.6.F.4(b). We see that, as the lithiation increase from Li_5S_8 to Li_{15}S_8 , the diffusion constant of Li decreases. However, at low level of lithiation, the mobility is

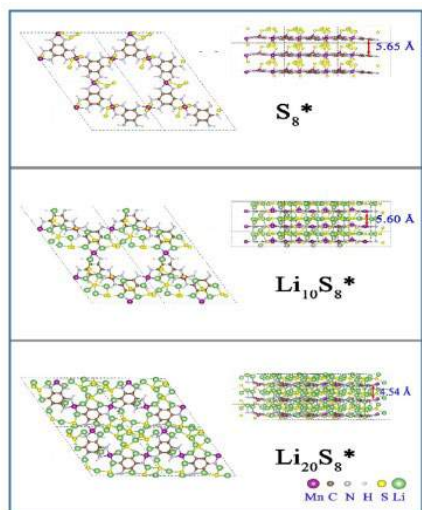


Figure II.6.F.4 the stacking structure of Li_xS_y /2D-HAB-CP at different level of lithiations.

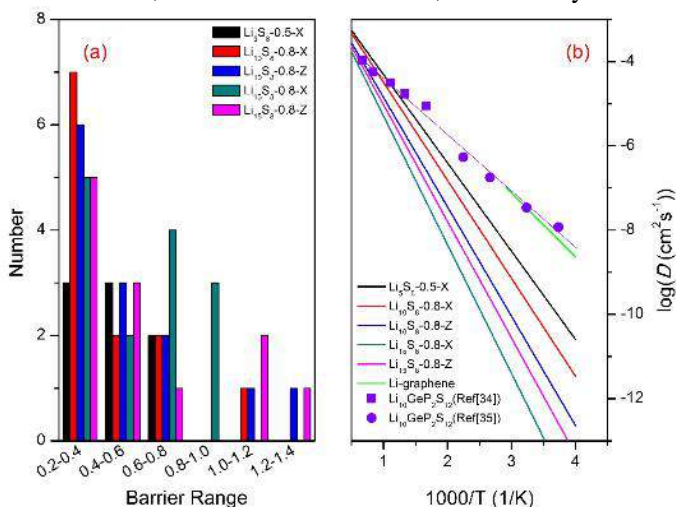


Figure II.6.F.5 Li-migration barriers distribution (a) and diffusion coefficients as a function of temperature (b) of Mn-HAB- Li_5S_8 , Mn-HAB- Li_{10}S_8 , and Mn-HAB- Li_{15}S_8 , in the X and Z-directions. The diffusion coefficients curves of Li on graphene and $\text{Li}_{10}\text{GeP}_2\text{S}_{12}$ are also presented as a reference.

relatively large at room temperature (10^{-8} cm²/s). The reduced Li diffusion at high lithiation is due to steric hindrance effect where it is difficult for Li to form new bonds. This point out the future direction to design such 3D bulk Li/S cathode: a more porous and less dense structure.

(4) **Sulfur vulcanization in polymer as a sulphur cathode:** Sulfur vulcanization is well-known process which converts natural rubber or related polymers into materials of a variety of hardness, elasticity, and mechanical durability by heating them with sulfur. One possibility is to take the advantage of this process, using the sulfur in such materials for Li-S battery application. Polymers with properly designed structure and specific properties can be used to hold the sulfur chains for applications in Li-S batteries. For this purpose, we have tried to theoretically design proper polymers for easy vulcanization with maximum amount of sulfur to gain better energy capacity. Since polymer based Li-S cathode materials often suffer from low capacity, one question is: what is the maximum amount of S and Li-S one can use in a conjugated polymer system. The increase of sulfur amount in such a system can be achieved by adjusting the functional groups in the polymer. In the Figure II.6.F.6, we try to find out different factors that favor the vulcanization. We have compared the vulcanization energy of 5-Decene in two methods (cycloaddition and crosslinking) with different S chains. By calculating the vulcanization energies, we find that crosslinking is thermodynamically favorable for vulcanization and the length of S chains is 6. Meanwhile, the edge C=C is better than middle position C=C bonds in terms of attaching the S chains.

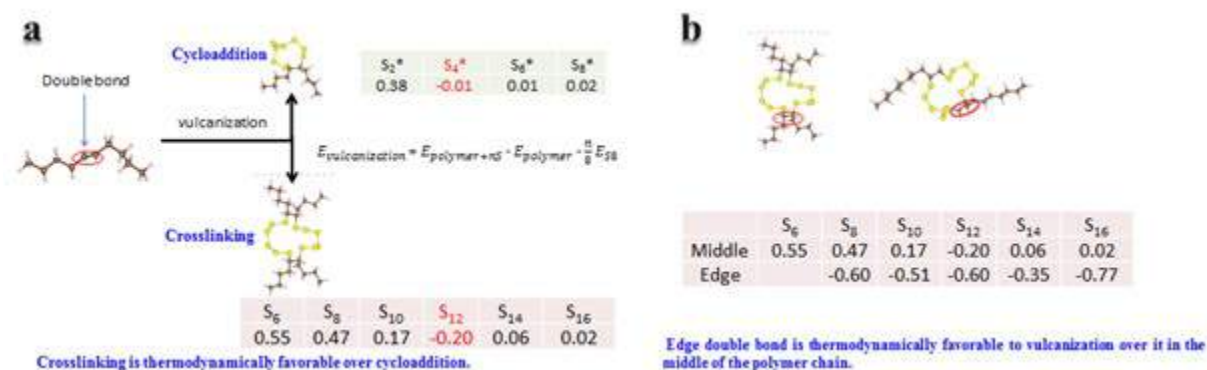


Figure II.6.F.6 (a) vulcanization of 5-Decene in two methods (cycloaddition and crosslinking); (b) two different positions of C=C in Decene are considered as vulcanization sites. The numbers in the table are the vulcanization energies in eV for different S chains and different binding configurations

Figure II.6.F.7 plots the lithiation process of S vulcanized 5-Decene. During the lithiation process, the Li atoms break long S chains into isolated S mixing with Li atoms. Meanwhile the structures of 5-Decene is well-preserved. The formation energy is linearly proportional to the number of Li added into the complex with a slope of -1.45, indicating a stable energy provided with a voltage of 1.45 V during the discharge process. The voltage is lower than the theoretical voltage of pure lithium polysulfide (2.1~2.4 V). The gravimetric capacity is 530.35 Wh/Kg.

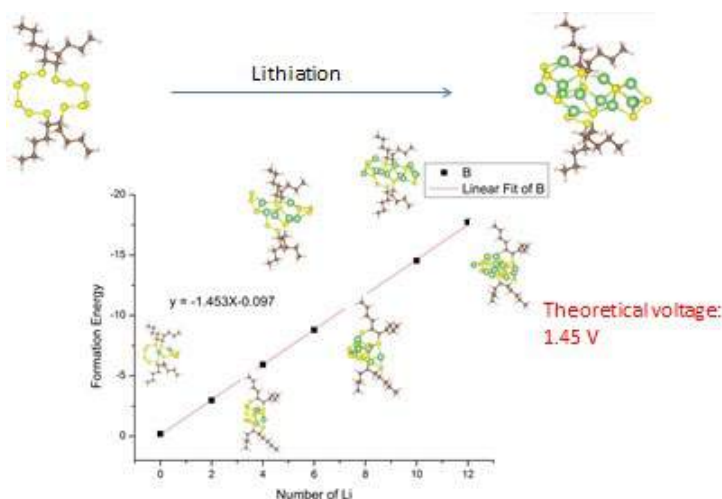


Figure II.6.F.7 the lithiation process of S vulcanized 5-Decene

In the future, we plan to investigate other structures, especially to increase the voltage, perhaps through the use of bigger sulfur clusters. We also need to study bigger systems to investigate the structure of the overall polymer system, especially to understand whether the polyphenylene will still be electrically conductive in such an environment. To understand that, electronic structures and hopping conductivities of the polymer backbone systems will be calculated.

Conclusions

In conclusion, we have studied different systems, both electrolytes and Li-S cathode materials. For the solid electrolyte, we have investigated the coordinated diffusion pattern of two Li atoms. We have developed a model to quickly scan the crystal data base for the Li diffusion path in each crystal structure. For the liquid electrolyte, we have used ab initio molecular dynamics to calculate the Li^+ diffusion, especially we observed significant diffusion constant when the Li^+ is close to the surface of LiF crystal. For the Li-S cathode material, we have designed an amorphous $\text{Li}_x\text{S}_y/2\text{D-HAB-CP}$ stacking material. The goal is to investigate such 3D cathode material for increased volumetric capacity. We have developed a special computational method to study the Li diffusion in such a system. We found that, when the amount of lithiation is small, the Li diffusion in such amorphous 3D system is reasonable. But when the system is fully lithiated, the mobility becomes small. We have also studied the vulcanization of polymer as potential Li-S cathode material. Different binding configurations are studied using S chains. We found that the cross link of the S chain has a strongly ability to bind with Li ions. The theoretical voltage of such a cross linked polymer is 1.35 V. We plan to investigate bigger systems, with aggregated polymers for the maximum possible vulcanization and Li binding capacity.

Key Publications

1. B. Zhang, L. Yang, L.W. Wang, F. Pan, "Cooperative transport enabling fast Li-ion diffusion in Thio-LISICON $\text{Li}_{10}\text{SiP}_2\text{S}_{12}$ solid electrolyte", *Nano Energy* 62, 844 (2019).
2. D. Chen, J. Jie, M. Weng, S. Li, D. Chen, F. Pan, L.W. Wang, "High throughput identification of Li ion diffusion pathways in typical solid state electrolytes and electrode materials by BV-Ewald method", *J. Mat. Chem. A*, 7, 1300 (2019).
3. G. Gao, F. Pan, L.W. Wang, "Theoretical investigation of 2D hexaaminobenzene coordination polymers as Li-S battery", *Adv. Energy Mat.* 8, 1801823 (2018)
4. S. Banerjee, X. Zhang, L.W. Wang, "Motif based design of a mixed oxygen-sulfur framework towards improved stability and record high Li-ion conductivity", *Chemistry of Materials*, 2019, DOI/10.1021/acs.chemmater.9b01639.

II.6.G Dendrite Growth Morphology Modeling in Liquid and Solid Electrolytes (MSU)

Yue Qi, Principal Investigator

Michigan State University
3509 Engineering Building
East Lansing, MI 48824
E-mail: yueqi@egr.msu.edu

Tien Duong, DOE Technology Development Manager

U.S. Department of Energy
E-mail: Tien.Duong@ee.doe.gov

Start Date: January 1, 2017
Project Funding: \$1,135,125

End Date: December 31, 2019
DOE share: \$999,843

Non-DOE share: \$135,282

Project Introduction

In this project, we will first develop a phase-field model to incorporate the electrochemical driving forces predicted from first principles simulations in liquid electrolytes and then incorporate mechanical driving forces to simulate dendrite growth in solid electrolytes with resolved microstructures. The μm -thick solid electrolytes will allow easier, direct comparison of modeling and experimental results, thus facilitating the validation of the electrochemical-mechanically driven Li-dendrite growth model. Last but not least, the computational model for solid electrolytes can also be applied to study and design nm-thin artificial SEI on Li metal surface. Therefore, this atomically-informed phase-field model will allow us to design the desired properties of artificial SEI coating to suppress dendrite growth in liquid-electrolyte and the microstructure of a solid-electrolyte to be dendrite-resistant during cycling. This model will enable the design of durable and safe Li-anodes for Li-S, Li-air, all-solid Li-ion batteries, as well as high energy density Li-ion batteries, lead to batteries that meet DOE's target for the high energy batteries cell density ($>350 \text{ Wh/kg}$) for EV applications and cost below \$100/kWh.

Objectives

The ultimate goal of this project is to develop a validated model to predict Li dendrite morphology evolution in both liquid and solid electrolytes during electrodeposition and stripping, in order to accelerate the adoption of Li metal electrodes in current and emerging battery technologies. To achieve this goal, the project has four objects:

- 1) formulate a general framework that captures the electrochemical-mechanical driving forces for Li morphology evolution;
- 2) consider the role of the nm-thin SEI in liquid-electrolytes as well as the microstructures of mm-thick solid-electrolytes for Li morphology evolution;
- 3) connect micron-scale phase-field models and atomic-scale DFT-based simulations via parameter- and relationship-passing in order to predict Li dendrite nucleation and growth kinetics and morphology; and
- 4) validate the key input parameters and main conclusions of the multi-scale model as new capabilities being developed step-by-step.

Approach

This project will develop a multi-scale model that connects micron-scale phase-field models and atomic-scale DFT-based simulations via parameter- and relationship-passing in order to predict Li-metal dendrite morphology evolution, in both liquid and solid electrolytes. The key innovation of this project is to capture the

electrochemical-mechanical driving forces and incorporate the roles of nm-thin solid electrolyte interphase (SEI) in liquid electrolytes as well as of the microstructures of μm -thick solid electrolytes for all-solid-state batteries. Our strategy to study Li dendrite morphology in both liquid and solid electrolytes allows us to share many similar governing equations and common mechanisms, to gradually increase the complexity of the model, and to validate the model step-by-step for its crucial input parameters and main conclusions through tailored experiments.

Results

Li dendrite growth in solid electrolytes of all-solid batteries

In order to reveal the origin of Li dendrite growth inside solid electrolytes (SE), we have developed a multi-scale Li-dendrite growth model in solid electrolytes with microstructure and internal extended defects. First, Density Functional Theory (DFT) calculations were used to evaluate the effect of surface electronic properties. Four promising SEs, cubic- $\text{Li}_7\text{La}_3\text{Zr}_2\text{O}_{12}$ (c-LLZO), $\beta\text{-Li}_3\text{PS}_4$, $\text{Li}_{1.17}\text{Al}_{0.17}\text{Ti}_{1.83}(\text{PO}_4)_3$ (LATP), and $\text{Li}_2\text{PO}_2\text{N}$ were compared. The total and local density of states (TDOS and LDOS) and the distribution of excess electrons on the surfaces were investigated and showed a large variation in different SE materials. To demonstrate the electronic impacts on the Li dendrite morphological evolution, we further developed a general phase field model of Li plating in a polycrystalline SE environment incorporating the Butler-Volmer kinetics, solid mechanics, and explicit lithium nucleation process. The DFT calculated concentration of excess electrons on one of the surfaces served as an input to the phase field simulations. Since the electronic structures of GB of LLZO are still beyond normal DFT calculations, in the phase field model, the GBs adopt the electronic properties of the surfaces at the moment. The influence of the grain size of the polycrystalline SE and the excess electron density in the internal surfaces on the lithium dendrite penetration depth will be discussed. The model captured several observed lithium dendrite growth trends in all-solid-state batteries, i.e., Li dendrite intergranular growth, the isolated Li-metal formation within pores and grain boundaries, and a sudden increase of Li-dendrite penetration depth.

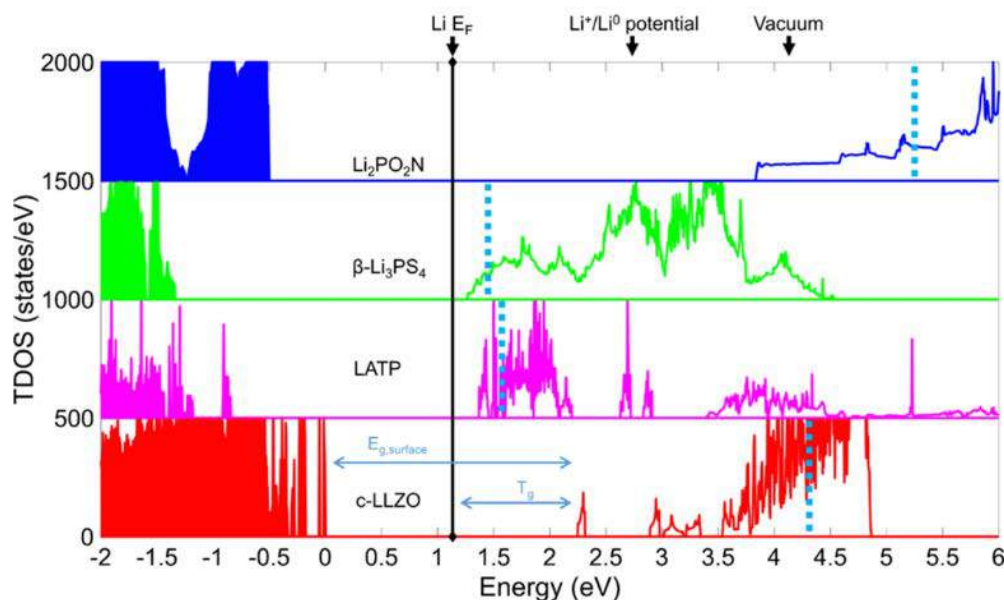


Figure II.6.G.1 The calculated total density of states (TDOS) for the four SE surface structures aligned with the vacuum level. The position of CBM of the corresponding bulk structure is labeled as the cyan dot lines. The position of the vacuum level, and the Fermi level of Li metal ($\text{Li } E_F$), and the potential corresponding to the Li^+/Li^0 deposition are labeled. $E_{g,\text{surface}}$ stands for the surface bandgap, and T_g is the energy difference from Li-metal in vacuum to the CBM of the SE.

Figure II.6.G.1 shows the aligned TDOS for the four SE materials. The $\text{Li}_2\text{PO}_2\text{N}$ surface still has a large bandgap of around 4.35 eV, while c-LLZO surface shows a considerable drop in bandgap from 4.30 eV of bulk to 2.20 eV of the surface due to the existence of surface states. On the other hand, there is no apparent change of bandgap on the $\beta\text{-Li}_3\text{PS}_4$ and LATP surfaces, and both have a small decrease of around 0.2 eV in bandgap from bulk to surface structure. As the intrinsic carrier (electrons/holes) concentration and electronic conductivity increase with decreased surface bandgap, the TDOS results suggest that the surfaces of c-LLZO, LATP, and $\text{Li}_2\text{PO}_2\text{N}$ are more conductive than their bulk structure that is electronically insulating, but $\text{Li}_2\text{PO}_2\text{N}$ surface could still be insulating due to its large bandgap. The reduced surface band gap can also push the conduction bands below the Li plating potential, so electrons can transfer from Li-metal to the solid electrolyte. Therefore, both the bulk and surface CBM are below the Li-plating voltage for $\beta\text{-Li}_3\text{PS}_4$ and LATP, allowing electron transfer. Although the CBM for bulk c-LLZO is above the Li^+/Li^0 potential, the surface state is not. Therefore, the surface state in c-LLZO is critical for the electron transfer from Li to LLZO.

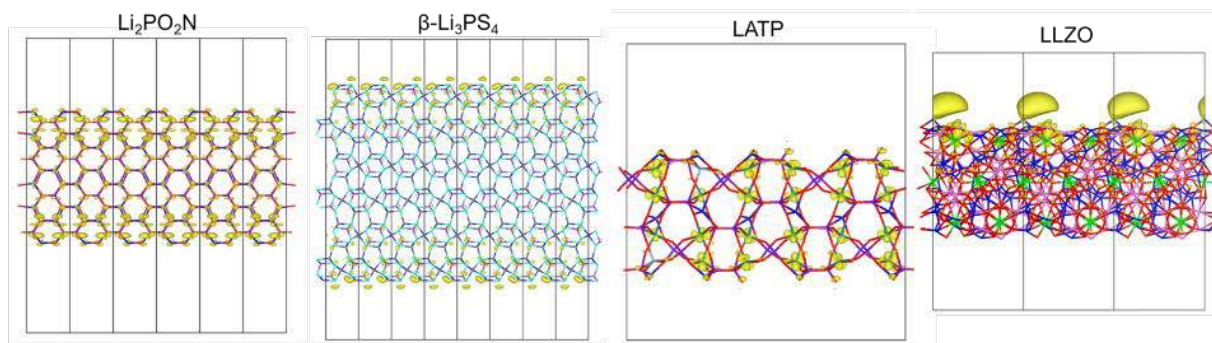


Figure II.6.G.2 The distribution of additional electrons (yellow region), which is calculated from the difference in charge density before and after inserting additional electrons.

Figure II.6.G.2 mimics the situation of excess electrons arriving on the surfaces by calculating the charge density difference before and after inserting the electrons at a density of $0.0046/\text{\AA}^2$ for all the solid electrolyte slab models. The distribution of the excess electrons was plotted as the yellow region at the selected isosurface that ensures the plotted charge density is the same across different materials. It can be seen that the additional electrons are localized mostly on the c-LLZO surface. However, for $\text{Li}_2\text{PO}_2\text{N}$, $\beta\text{-Li}_3\text{PS}_4$, and LATP, those excess electrons seem to stay mainly underneath the surface. This is consistent with experimental observations that the Li dendrites in c-LLZO and $\beta\text{-Li}_3\text{PS}_4$ seem to grow in the pores and crack surfaces and grain boundaries. This analysis of the excess electron distribution could be used to evaluate how likely the additional electrons localize on the surface, which would make reducing Li-ions to Li-metal possible. Based on this result, it is suggested that the c-LLZO surface would be more likely to have Li-ions reduced on the surface than the other three solid electrolytes because the additional electrons are localized on the c-LLZO surface.

The Li electrodeposition processes in SEs of grain sizes ranging from 75 to $500\mu\text{m}$ were simulated in identical $500\mu\text{m} \times 500\mu\text{m}$ 2D half-cells with a constant electric overpotential of -0.1V. To directly demonstrate the influence of excess surface electrons on electrodeposition, we compared two idealized scenarios of surface electronic states: “real” LLZO polycrystalline SEs referring to the extended internal defects with excess surface electron concentration ($c_e = 0.337\text{ mol/L}$) and “ideal” LLZO SEs referring to the extended internal defects with no surface electrons, while both have identical structures. In both cases, the Li dendrite growth is driven electrochemically by the applied overpotential. The location of dendrite penetration is governed by SE local mechanical strength, which is weaker at GBs and extended defects. The spatial and temporal evolution of the multiphase morphology, Li ion concentration, and electric potential during electrodeposition were tracked over the simulation time of 800 s. Based on the phase morphology, the far most position of Li-metal phase toward the Li-anode surface is defined as the Li-dendrite penetration depth.

The final morphologies of 800s electrodeposition (Figure II.6.G.3) show a larger amount of metallic Li and deeper dendrite penetration depth in real LLZO than the ideal LLZO for all SE grain sizes. This difference is due to the additional electrochemical driving force from excess surface electrons in real LLZO. The contrast between the real and ideal cases becomes more prominent when isolated nucleation of metallic Li took place in the real SEs with the grain sizes of 75 μm and 150 μm . This is because the additional electrodeposition sites provided by the isolated nucleation inside SE significantly increase the intergranular dendrite penetration depth and growth rate. A clear comparison is quantitatively demonstrated by the dynamic evolution curves of the total amount of Li (corresponding to capacity loss) and the dendrite penetration depth in SEs, where the two abrupt rising steps in the penetration depth and the sudden deviations in the Li dendrite amount increasing rates highlighted by red arrows, indicate the initiation of isolated nucleation (Figure II.6.G.3 k1). Without the trapped electrons at the GBs, the Li growth is continuous. With the electrons on GB, the dendrite growth can be discontinuous. We also observed an increasing trend in the total amount of metallic Li in SE and potentially a higher probability of isolated nucleation. This is because the SE of finer grain size or lower mass density contains higher volumetric percentages of internal extended defect surface, e.g., from pores, cracks and grain boundaries. Therefore, they create more space and driving force for intergranular growth and more sites for isolated nucleation, leading to the observed trends. The model captured several major reported trends of lithium dendrite growth in all-solid-state batteries, i.e. Li dendrite intergranular growth, the isolated Li-metal formation within pores and grain boundaries, and the sudden increase of Li-dendrite penetration depth. These simulated electrodeposition behaviors can further lead to the observation of the abrupt rise in charging current (under constant voltage condition) and effective electronic conductivity of SEs, and will eventually cause accelerated capacity loss during cycling and a higher risk of short-circuiting. [1],[2]

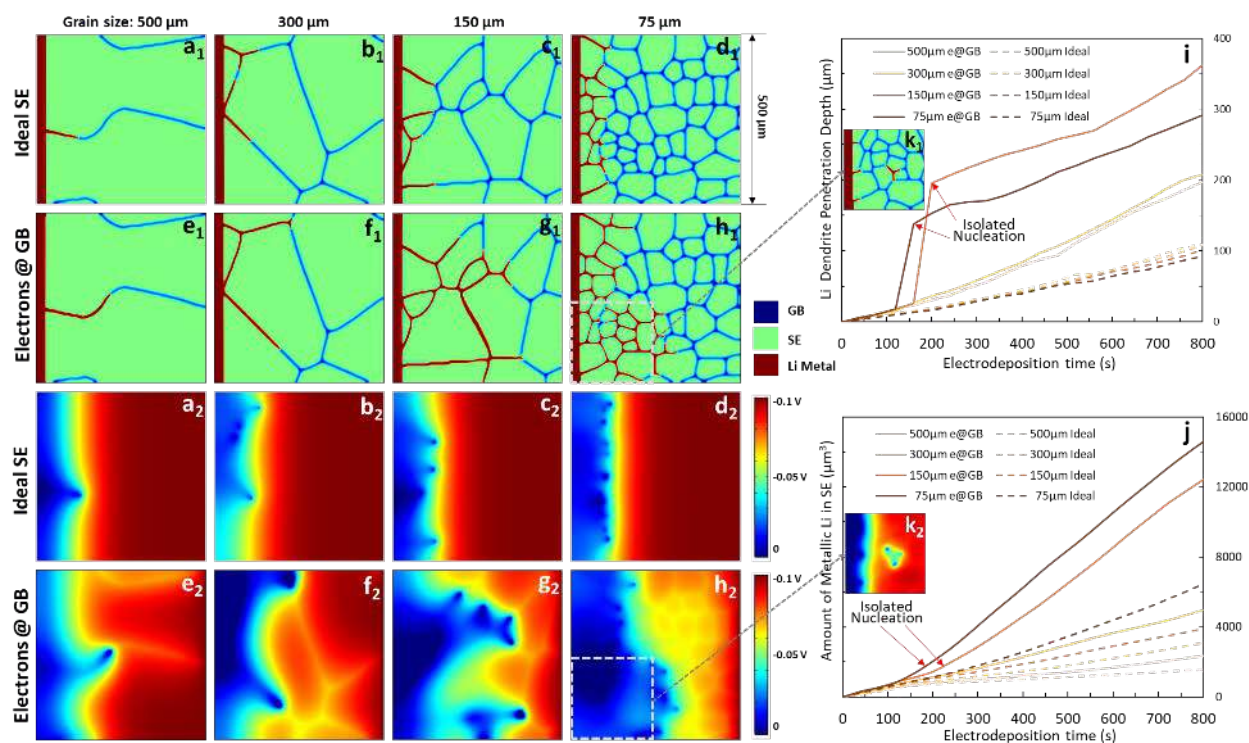


Figure II.6.G.3 Phase-field simulation results on the impacts of surface trapped electrons and grain size on the morphologies and electric potential distributions after 800s Li electrodeposition. A comparison of the final phase morphologies in (a1-d1) the ideal SEs with excess electron-free surfaces and (e1-h1) the real SEs with the calculated surface electron concentrations from DFT, in a series of grain sizes. And a comparison of their corresponding final electric overpotential distributions for the SEs in (a1-h1). The dynamic evolution of (i) the Li dendrite penetration depths and (j) the total amount of metallic Li in SEs of different grain sizes. The initiation of isolated dendrite nucleation is demonstrated by (k1) the phase morphology and (k2) the corresponding electric potential distribution in the SE of the 75 μm grain size at 200s.

Finally, we compared the basic materials properties of these SE materials (Table II.6.G.1), including the shear modulus, the reduction voltage, the bulk bandgap, the surface bandgap, energy gap to Li-metal, and the location of the excess electrons, in order to identify the key material properties that impact Li dendrite growth inside of the solid electrolytes. Using the surface electronic property as the criteria, the ranked Li dendrite growth resistance in these SE materials is: $\text{Li}_2\text{PO}_2\text{N} > \beta\text{-Li}_3\text{PS}_4 \approx \text{LATP} > \text{LLZO}$, consistent with a broad range of experimental observations, including the measured electron conductivity and the Li dendrite growth rate. Thus, these DFT-computable properties can be used to screen solid electrolyte materials with high Li dendrite resistance via high throughput calculations.

Table II.6.G.1 Comparison of the Intrinsic Material Properties of Different Solid Electrolytes

	Shear Modulus (GPa)	Fracture Energy (J/m ²)	Reduction Potential vs. Li (V)	GGA-PBE			HSE			Location of excess electrons
				E _{g,bulk} (eV)	E _{g,surface} (eV)	T _g (eV)	E _{g,bulk} (eV)	E _{g,surface} (eV)	T _g (eV)	
Li₂PO₂N	30	0.92	0.87	5.98	4.35	2.69	6.92	5.61	2.88	Bulk - O
β-Li₃PS₄	6	0.38	1.71	2.82	2.67	0.13	3.49	3.38	0.25	Bulk - S,P
LATP	56	0.88	2.16	2.42	2.24	0.47	3.31	3.05	0.07	Bulk - Ti
c-LLZO	59	1.72	0.05	4.30	2.20	1.11	5.46	2.19	1.23	Surface - La

The Li dendrite growth in liquid electrolytes of all-solid batteries

To further figure out the impact of SEI on Li dendrite evolution, an isotope exchange experiment was designed. The process is to first deposit a $\sim 5\mu\text{m}$ ^7Li layer in an ether electrolyte (4 M $^7\text{LiFSI}$ DME) then deposit another $\sim 5\mu\text{m}$ ^6Li layer in carbonate electrolyte (1 M $^6\text{LiPF}_6$ EC/DEC) under a range of current densities from 0.2 to 3 mA cm⁻². TOF-SIMS depth profile was used to analyze the SEI composition in the top ~ 100 nm. The TOF-SIMS data shows the organic components are generally located near the surface of SEI as indicated by organic species HCOO⁻ and C₂H₂O⁺. The inorganic species, S and P, are from the two independent Li salts, $^7\text{LiFSI}$ and $^6\text{LiPF}_6$, respectively. Thus, S indicates the pre-formed SEI on the first ^7Li layer and P indicates the SEI formed during the second ^6Li layer deposition. For all the samples, S and P have close intensities. Therefore, we conclude that the 2nd Li deposition mainly occurs underneath the pre-formed SEI layer, as predicted in our charge transfer model.^[3] While the 2nd Li layer morphology and Coulombic efficiency changed monotonically with the current density (higher current density led to rougher morphology and lower Coulombic efficiency), the $^6\text{Li}/^7\text{Li}$ ratio in the top ~ 100 nm did not change monotonically with the current density. The $^6\text{Li}/^7\text{Li}$ ratio ratios were very close to each other for current densities 1, 2, 3 mA cm⁻² and became the highest at the current density of 0.5 mA cm⁻². It was speculated that the SEI formation rate and the current rate jointly determined the composition of the newly deposited SEI-covered Li metal. The top SEI layer had mixed compositions from the pre-formed SEI (^7Li) and the newly formed SEI (^6Li). This indicates that electrolyte decomposition reactions continue to occur inside, instead of on top, of the pre-formed SEI layer, requiring detailed modeling of the inhomogeneity in SEI.

The modeling of the impact of SEI on Li dendrite growth in liquid electrolyte turned its focus on the inhomogeneity at GBs or heterogeneous interfaces in the SEI, particular for the initial stage of dendrite nucleation at Li metal anode. It has been shown in our model that the space charge layer is formed at heterogeneous interfaces in SEI, the actual length scale of space charge distribution can be strongly associated with the grain size and defect density in the SEI or artificial coating layer. The impact of space charge length scale on Li electrodeposition morphologies was investigated via the implicit SEI phase-field model. Based on the phase-field simulation results, conclusions can be drawn that (1) Li dendrite growth during plating can be suppressed by decreased space charge length scale at anode surface, and that (2) when the space charge length

scale is reduced to around the same order of anode surface protuberance size (initial roughness), smooth electrodeposition morphology can be achieved. One key inhomogeneity in the SEI is the grain boundaries (GB). A systematic study of the electronic properties of GBs has been conducted via density functional theory (DFT) calculations. It was found that all the investigated GBs reduced the bandgaps and the tilt GBs reduced the bandgaps to a larger extent than the twist GBs. Aligning the band structure with the Li-metal suggested that all the conduction bands of these GBs were still above the Li-metal reduction potential, thus would not be occupied. However, electron tunneling is more likely to occur through the GBs with reduced tunneling barriers.

Conclusions

We developed a multiscale modeling integration DFT calculation and phase field simulation to investigate the Li dendrite formation and growth inside solid electrolytes with microstructures and internal defects. Through DFT calculations, we discovered that the bandgap of surfaces (pores and cracks) is lower than that in bulk in solid electrolytes. The reduced bandgap pushed unoccupied state below the Li-plating potential and facilitate electron transfer from Li-metal to the surface state. Especially, in c-LLZO, the surface atoms can trap excess electrons. Also, we incorporated the new electron trapping mechanism in the phase-field model by introducing surface electron density and dendrite nucleation process, and revealed that the electrons trapped on the internal defect surfaces accelerate the Li dendrite growth and allow isolated Li nucleation to occur, leading to non-uniform dendrite growth. It also suggested that the solid electrolytes with finer grain size or higher volumetric percentage of internal defect surface have a higher probability of isolated Li nucleation. This causes an abrupt increase in dendrite penetration growth depth and growth rate. The DFT-predicted resistance of solid electrolytes to Li dendrite growth inside was ranked as: $\text{Li}_2\text{PO}_2\text{N} > \beta\text{-Li}_3\text{PS}_4 \approx \text{LATP} > \text{LLZO}$. The results are consistent with the experimental results in the literature. With this model, we can further determine the critical material properties that impact Li dendrite growth inside of the solid electrolytes, which are the internal defect surfaces (pores, grain boundaries, and junction) and their electronic conducting properties. Furthermore, via these DFT-computable electronic properties of surfaces, high throughput calculations are desirable to provide the design direction for Li dendrite resistant solid electrolyte materials. The model was extended to investigate the role of SEI in Li dendrite growth in a liquid electrolyte, while the focus of the current model emphasizes the inhomogeneities in the SEI layer.

Key Publications

1. G. Li, Z. Liu, Q. Huang, Y. Gao, M. Regula, D. Wang, L-Q. Chen, D. Wang, "Stable metal anodes enabled by electrokinetic effects in high-zeta-potential porous structures", *Nature Energy*, 3 1076 (2018).
2. Y.S. Li and Y. Qi, "Energy Landscape of the Charge Transfer Reaction at the Complex Li/SEI/Electrolyte Interface." *Energy Environ. Sci.* 12, 1286-1295 (2019)
3. H-K. Tian, Z. Liu, Y. Ji, L-Q. Chen, Y. Qi, "Interfacial Electronic Properties Dictate Li Dendrite Growth in Solid Electrolytes", *Chem. Mater.* 31, 7351-7259 (2019).
4. J. Xu, H-K. Tian, J. Qi, Q. Zhang, Y. Qi, and X.X. Xiao. "Mechanical and Electronic Stabilization of Solid Electrolyte Interphase with Sulfite Additive for Lithium Metal Batteries", *J. of Electrochem. Soc.* 166 (14), A3201-A3206 (2019)
5. G. Li, Z. Liu, D. Wang, X. He, S. Liu, Y. Gao, A. AlZahrani, S. H. Kim, L-Q. Chen, D. Wang, "Electrokinetic Phenomena Enhanced Lithium-Ion Transport in Leaky Film for Stable Lithium Metal Anodes", *Adv. Energy. Mater.* 9(2), 1900704 (2019).
6. B. Xu, Z. Liu, J. Li, X. Huang, B. Qie, T. Gong, L. Tan, X. Yang, D. Paley, X. Liao, Q. Cheng, H. Zhai, X. Chen, L-Q. Chen, C-W. Nan, Y-H. Lin, Y. Yang, "Engineering Interfacial Adhesion for High-performance Lithium Metal Anode", *Nano Energy* (2019), <https://doi.org/10.1016/j.nanoen.2019.104242>.

7. J. Wan, J. Xie, X. Kong, Z. Liu, K. Liu, F. Shi, A. Pei, W. Chen, J. Chen, H. Chen, X. Zhang, L. Zong, J. Wang, L-Q. Chen, J. Qin, Y. Cui, “Ultrathin, flexible, solid polymer composite electrolyte enabled with aligned nanoporous host for lithium batteries”, *Nature Nanotechnol.* 14, 705–711(2019).

References

1. Han, F., *et al.*, *Nat Energy* 4, 187–196 (2019)
2. Song, Y., *et al.*, *Adv. Energy Mater.* 9, 1900671 (2019)
3. Li, Y.S. and Qi, Y., *Energy Environ. Sci.* 12, 1286 (2019)

Acknowledgments

The Co-PIs for the project include Prof. Long-Qing Chen (Penn State University), Dr. Xingcheng Xiao and Dr. Qinglin Zhang (General Motors).

II.7 Beyond lithium-Ion R&D: Metallic Lithium

II.7.A Mechanical Properties at the Protected Lithium Interface (ORNL)

Nancy Dudney, Principal Investigator

Oak Ridge National Laboratory
PO Box 2008, MS6124
Oak Ridge, TN 37831
E-mail: dudneynj@ornl.gov

Erik Herbert, Principal Investigator

Michigan Technological University
604 M&M Building, 1400 Townsend Dr.
Houghton, MI 49931
E-mail: eherbert@mtu.edu

Jeff Sakamoto, Principal Investigator

University of Michigan
2350 Hayward Avenue
Ann Arbor, MI 48109
E-mail: jeffsaka@umich.edu

Tien Duong, DOE Technology Development Manager

U.S. Department of Energy
E-mail: Tien.Duong@ee.doe.gov

Start Date: January 1, 2015

End Date: March 30, 2019

Project Funding (FY19): \$500,000

DOE share: \$500,000

Non-DOE share: \$0

Project Introduction

A stable lithium anode is critical to achieve high energy density with excellent safety, lifetime and cycling efficiency. Instability and/or high resistance at the interface of lithium metal with various solid electrolytes limit the use of the metallic anode for batteries with high energy density batteries, such as Li-air and Li-S, as well as for solid-state batteries with solid composite cathodes. The critical impact of this endeavor is a much deeper analysis of the degradation for both the lithium metal and the solid electrolyte, so that materials can be chosen and engineered to fulfill the target level of performance for EV batteries, namely 1000 cycles and 15 year lifetime, with adequate pulse and charge power.

While other programs look at changes in the lithium morphology and the electrochemical performance with soft or liquid electrolytes, this project focuses on the mechano-electrochemical properties of the lithium metal at the interface with inorganic ceramic or glass solid electrolytes. Interestingly, the evolution of the lithium interface with cycling appears to differ for glass and ceramic electrolytes, but separating the nature of the solid electrolyte from the many other factors related to the rates and cycled capacity is complex. Degradation processes under investigation includes the formation of metallic Li filaments or dendrites that may cause catastrophic short circuits to form across solid electrolytes. Also, Li-solid electrolyte interfaces may fail due to physical separation of Li from the solid electrolyte. There are different mechanisms proposed for these failure processes. The mechanical properties of the lithium metal, the solid electrolyte, and the interface will influence the contact area and adhesion, the formation and growth of cracks and dendrites, and changes in the microstructure and defects. Indeed, the structure and mechanical properties of the Li / solid electrolyte interface may evolve in complex ways depending on details of the battery cycling and age. Detailed and quantitative study of the mechanical properties for both the Li metal and solid electrolytes is essential for

efforts to model the properties and potential degradation of the Li metal in a solid state battery. The properties need to be evaluated at different and relevant length scale, time (current) scale, and temperatures.

Objectives

The practical objective for this project is to understand the evolution of the lithium metal upon cycling in contact with a model inorganic solid electrolyte under various intrinsic and extrinsic conditions to develop informative and predictive stability maps. Of importance is to clarify conditions that risk catastrophic failure. Different constructions for the stability maps are explored which illustrate the predominate mass transport process and defect structure evolution in the lithium metal. Simple maps address the current density, areal capacity, and layer thickness. Maps extending to many other cell designs, interfacial factors and duty cycle parameters are envisioned for future works. A key activity is to develop experimental tools with which to probe the lithium morphology in real time. Our work interprets experimental results with models of the kinetic processes.

Key materials properties and mechanical insights needed to construct stability maps are determined. In particular, micrometer-scale properties of the electrolytes and lithium metal are needed. Mechanical, transport, and even thermodynamic properties depend on microstructure and defect properties that may differ with size and crystal orientation at the interface. This project expands our understanding of the Li metal-solid electrolyte interface through state-of-the-art nanoindentation studies and precision bulk mechanical tests. Experimental tools are refined to probe the structure, mechanical properties, and interfaces relevant to thin solid electrolyte membranes and ultra-thin lithium films required to achieve high energy density. Methods include mechanical and imaging observations *during* mass transport and relaxation. As lithium has a low melting temperature, annealing of the defects and grain structure in the lithium is continuously underway. Our objective is to provide the critical information that will enable transformative insights into the complex coupling between the microstructure, lattice and interface defects and the mechanical behavior of Li metal anodes when subjected to relevant battery operating conditions (e.g., cycling rate, pressure, temperature, DOD, etc.).

Approach

We are testing the mechanical properties of the solid electrolyte (SE) and the lithium independently, as well as for the interfaces of lithium against solid electrolyte. The cycling of the lithium across the interface is conducted via symmetric Li cells or full cells with an intercalation cathode. The sample configurations are dictated by the processing of the solid electrolytes which include a glassy lithium phosphorus oxynitride (Lipon) electrolyte, prepared by sputter deposition of a thin film, and a ceramic lithium lanthanum zirconium oxide (LLZO) electrolyte, prepared by hot-pressing a green pellet or cast sheet. The lithium metal is applied to the cleaned solid electrolyte surfaces by either vacuum vapor deposition (at ORNL) or by melt processing (at UM) using protocols developed to ensure that the interface is as clean and smooth as possible. In all cases the samples were well protected from air and humidity during tests.

Various impedance and imaging methods are used to characterize the evolution in the Li-solid electrolyte interface structure as the lithium is plated and stripped. These are standard tests to determine the average properties and features of the buried Li-SE interface. The incorporation of mechanical tests set our program apart. On the macro-scale approach, most tests are conducted with an Instron housed within a glovebox. The impedance or DC current tests are recorded under load and Instron test provide average measures of the interface and bulk measures of the lithium. Incorporation of a reference electrode provides for separation of the electrical properties from plating and stripping. For micron-scale information, nanoindentation is conducted with the tool + microscope in a dedicated, temperature stable glovebox. Large arrays of indents are recorded rapidly and automatically, as statistical analysis is required. The micron-scale is most relevant to consideration of the inhomogeneity and flaws at the buried Li interface. Illustrations of cracks, dendrites hot spots and pores are all presumed to initiate with local accumulation of stress and defects.

Results

1. *Li-LLZO interface studies by macro-scale Instron and electrochemical tests.*

Several different studies were conducted to evaluate critical conduction leading to Li dendrite formation or alternatively to loss of contact at the Li-LLZO interface upon Li stripping.

Li plating. To understand the relation between the critical current density and electrochemical potential leading to formation of metallic Li filaments, three-electrode cells were assembled and tested to evaluate the Li-LLZO interface at and below 0 V vs Li/Li⁺. This study controlled the potential and measured the current. At low under potentials, stable cycling was observed in which the Li-LLZO interface exhibited Ohmic behavior, confirmed by EIS measurement. However, at greater under potentials, deviation from Ohmic behavior was observed. We hypothesize that there is a critical voltage above which electronic conduction occurs within the solid electrolyte leading to internal lithium metal precipitation. The mechanism could be governed by quantum mechanics. This work can help understand the conditions under which Li metal penetrates ceramic electrolyte and enable solutions to stabilize metal anodes. Additionally, band structure and density of state (DOS) first-principle calculations were performed to validate the experimental results. The manuscript discussing the results is under preparation.

Several interface studies considered the formation of interface defects such as pores or initiation of Li dendrites by comparing the diffusion rate of lattice defects through the Li metal with the current density across the interface imposed by electrochemical cycling. In the first study, consideration of the self-diffusivity in the Li metal indicates that current densities up to 1 mA/cm² could be accommodated at room temperature without defect accumulation leading to hot spots that may initiate dendrites. This increases by 7-fold at 100°C which agrees with the observed dependence of the critical current density associated with short circuit failures as a function of cycling temperature.[\[1\]](#)

In further imaging studies, we take advantage of abnormal grain growth to view large single crystals and bicrystals harvested from LLZO hot pressed pellets. These were used for Li isotope studies tracer diffusion studies to examine the Li transport within the crystal and along the grain boundaries by neutron imaging. The data set is undergoing further statistical analysis to compare the different pathways for Li (ions and atoms) in LLZO grain boundaries and grains.

Li stripping. In a follow up study, the correlation between stack pressure and stripping current density has been established for Li contacts on LLZO pellets.[\[2\]](#) The plating and stripping contacts were separated with the addition of a reference electrode plated on the side of the LLZO pellet. An example of the results is shown in Figure II.7.A.1 comparing the strain rate from stack pressure with that required of the applied current. When the stack pressure is too low for the applied current, impedance spectroscopy indicates that voids are forming at the interface. This is the basis for generating a stability map describing the different defects generated in the Li as function of discharge current and stack pressure. Together, these results demonstrate how self-diffusion and mechanical deformation of the Li anode on a macroscopic scale are correlated to the failure of these systems. However, to design Li metal batteries that can operate in realistic environments, the mechanics of the Li metal at the length scales of these intrinsic defects (cracks, pores, grain boundaries) needs to be well understood.

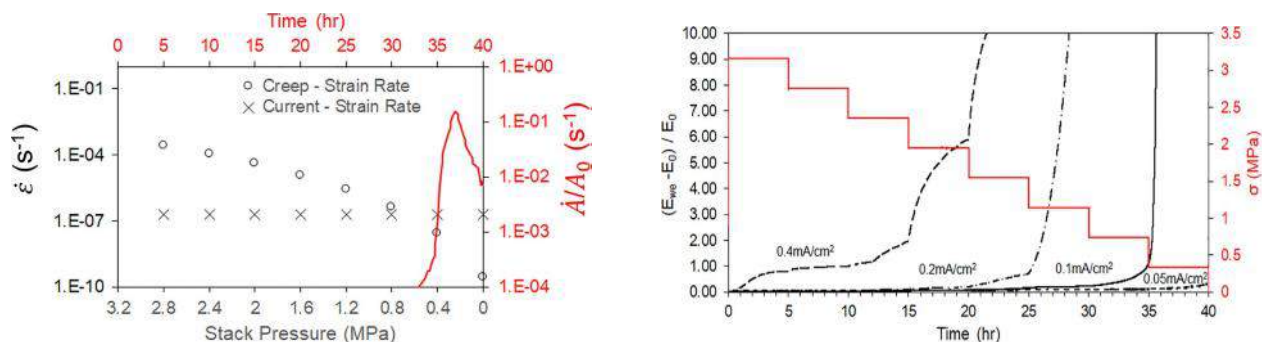


Figure II.7.A.1 Discharge of the Li-solid electrolyte interface is sensitive to pressure. Comparison (left) of the pressure-induced creep-strain rate and the current-induced strain rate for stripping Li at 0.1 mA/cm². The point where the current-induced strain rate becomes dominant is when unstable void growth occurs at the Li interface, reducing the contact area, A. Stepwise reduction in stack pressure (right) while stripping Li at different currents identifies the maximum discharge rate that can be accessed for a stack pressure.

2. Nano-indentation results of lithium and glassy Lipon interface.

In earlier work [3],[4],[5], extensive experiments using dynamic nanoindentation have found surprising mechanical behavior for thin Li films. As found for a variety of metals examined at small length scales such as nanofibers and pillars, ‘smaller is stronger,’ as small volumes of material may be defect-free compared to larger bulk samples. From our results of nanoindentation at the free surface of lithium films, we reported that Li can support pressures ranging from 80-350 times the yield strength of bulk polycrystalline lithium. Similar results have been reported for micro-pillars of Li metal.[6] This year a detailed analysis and model based on these experiments was constructed. A stability map, described here, illustrates the stress generated at the interface as a function of the current density and local inhomogeneity of Li plating.

Representative load-displacement curves from the nanoindentation experiments are shown in Figure II.7.A.2a. As the applied load monotonically increases, the mean pressure the surface can support (hardness) is quite high, as only diffusion processes can relieve the stress. The sudden punch-in (abrupt transition) depends on the strain rate and varies from indent to indent. This is attributed to the probability of finding a preexisting dislocation multiplication source within the stressed volume that can relieve the pressure by initiating plastic flow via a dislocation avalanche. The hardness is lower after this transition. While holding at the maximum load, the indenter continues to creep well into the lithium. Extensive statistical analysis, including a 3-term Weibull model, leads us to hypothesize that at these ‘small’ length scales, the lithium flow (stress relief) depends directly on the competition between diffusional creep and dislocation multiplication/nucleation. The volume of the stressed material determines both the diffusion length and the probability of finding a dislocation source that has sufficient room to physically operate.

An analytical model, recently published,[7] describes the two-dimensional state of stress at the lithium/SE interface as a function of current density. Figure II.7.A.2 illustrates the undulating surface proposed in the model leading to the deformation mechanism map, shown in Figure II.7.A.2c. Similar results are obtained if the interface is physically flat but is impacted by the same variation in the local current density. To illustrate the utility of the map, the dashed vertical line identifies the critical interface defect dimensions and volume most likely to promote the development of a mode I tensile stress in the solid electrolyte that is capable of initiating fracture and catastrophic failure. Left of the line, the defect volume is small enough to alleviate the pressure by diffusional flow (shorter diffusion length). To the right, the stress relief mechanism changes to dislocation mediated flow because the defect volume is sufficiently large to find and activate a dislocation multiplication source.

The SE failure of course depends on the nature of the solid electrolyte. New results characterize the creep behavior of the glassy Lipon electrolytes. In contrast, ceramic electrolyte including the garnet LLZO are brittle with no measurable tendency for plastic deformation. These are additional considerations that will be incorporated into future analyses.

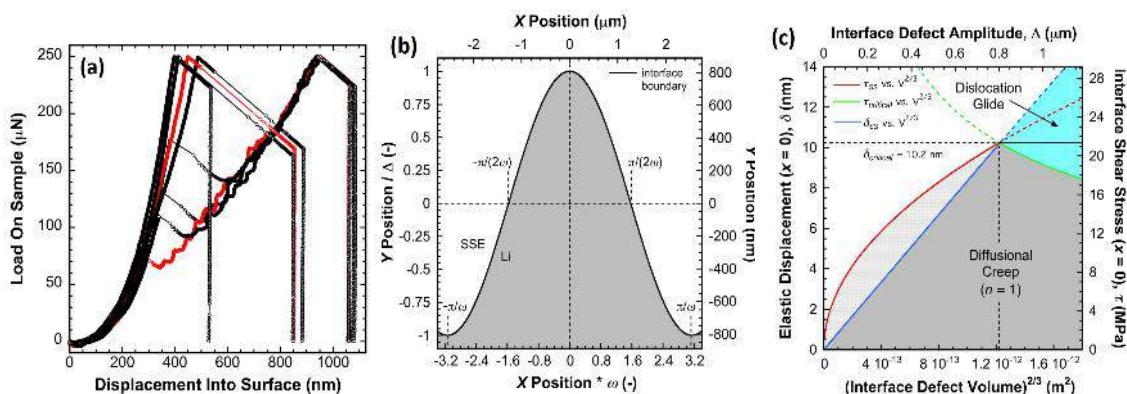


Figure II.7.A.2 Typical load displacement curves (a) show the punch-in displacement that occurs at a range of displacement. An undulation in the surface (b) is proposed to model an interface defect and the corresponding state of stress as a function of the electrochemical cycling conditions. The model yields the deformation mechanism map for Li (c). Here the average current density at the interface and the Young's modulus of Li are taken to be 1 mA/cm² and 9 GPa, respectively.

Conclusions

The investigations presented in this work address the formation of defects at the Li-solid electrolyte interface under different current densities, temperature, critical dimensions and stack pressures. Our work includes macro- and micron-scale experiments and models, yielding two different views of how lithium metal responds to stress, whether generated internally by lithium plating or externally by a stack pressure. Future analyses should include the solid electrolyte properties, which vary from strong, brittle ceramics to glasses that can respond by creep.

This work provides some of the key pieces needed to construct a grand map of the intrinsic and extrinsic deformation and fracture processes active under conditions for cycling of a battery with a lithium anode. The basic mechanisms by which lithium and the solid electrolyte can accommodate the stresses from battery cycling, via lattice and grain boundary diffusion, elastic or plastic relaxation processes, is being elucidated at the relevant dimension and time (current) scales. There is still much to learn to fully understand the behavior as Li is plated and stripped, particularly at high rates, and to predict evolution of the buried interface for extended and variable cycling conditions.

Key Publications

1. Michael J. Wang, Rishav Choudhury, Jeff Sakamoto, "Characterizing the Li-Solid-Electrolyte Interface Dynamics as a Function of Stack Pressure and Current Density," *Joule* 3 (2019) 2165-2178.
2. Jeff Sakamoto, "Solid-State Batteries - More pressure needed," *Nature Energy -News and Views*, 4 (2019) 8270828.
3. M. Wang and J. Sakamoto, "Temperature Dependent Flux Balance of the Li / Li₇La₃Zr₂O₁₂ Interface," *Journal Electrochemica Acta* 296 (2019) 842-7.
4. E.G. Herbert, N.J. Dudney, M. Rochow, V. Thole, S.A. Hackney, "On the mechanisms of stress relaxation and intensification at the lithium/solid-state electrolyte interface". *J. Mater. Res.*, 34, (2019)3593-3616.

References

1. M. Wang and J. Sakamoto, “Temperature Dependent Flux Balance of the Li / $\text{Li}_7\text{La}_3\text{Zr}_2\text{O}_{12}$ Interface,” *Journal Electrochemica Acta* 296 (2019) 842-7.
2. Michael J. Wang, Rishav Choudhury, Jeff Sakamoto, “Characterizing the Li-Solid-Electrolyte Interface Dynamics as a Function of Stack Pressure and Current Density,” *Joule* 3 (2019) 2165-2178.
3. E.G. Herbert, S.A. Hackney, N.J. Dudney, P.S. Phani, “Nanoindentation of high purity vapor deposited lithium films: The elastic modulus,” *J. Mater. Res.*, 33, 1335-1346 (2018).
4. E.G. Herbert, S.A. Hackney, N.J. Dudney, V. Thole, P.S. Phani, “Nanoindentation of high purity vapor deposited lithium films: A mechanistic rationalization of diffusion-mediated flow.” *J. Mater. Res.*, 33, 1347-1360 (2018).
5. E.G. Herbert, S.A. Hackney, N.J. Dudney, V. Thole, P.S. Phani, “Nanoindentation of high purity vapor deposited lithium films: A mechanistic rationalization of the transition from diffusion to dislocation-mediated flow.” *J. Mater. Res.*, 33, 1361-1368 (2018).
6. C. Xu, Z. Ahmad, A. Aryanfar, V. Viswanathan, J.R. Greer, “Enhanced strength and temperature dependence of mechanical properties of Li at small scales and its implications for Li metal anodes,” *PNAS*, 114 (2017) 57-61.
7. E.G. Herbert, N.J. Dudney, M. Rochow, V. Thole, S.A. Hackney, “On the mechanisms of stress relaxation and intensification at the lithium/solid-state electrolyte interface.” *J. Mater. Res.*, 34, (2019) 3593.

Acknowledgements

Prof. Steve Hackney (Michigan Technological University) played a key role in interpreting and developing models of the indentation studies for the lithium metal.

II.7.B Composite Electrolytes to Stabilize Metallic Lithium Anodes (ORNL)

Nancy Dudney, Principal Investigator

Oak Ridge National Laboratory
PO Box 2008, MS6124
Oak Ridge, TN 37831
E-mail: dudneynj@ornl.gov

XI (Chelsea) Chen, Principal Investigator

Oak Ridge National Laboratory
PO Box 2008, MS6124
Oak Ridge, TN 37831
E-mail: chenx@ornl.gov

Tien Duong, DOE Technology Development Manager

U.S. Department of Energy
E-mail: Tien.Duong@ee.doe.gov

Start Date: October 1, 2018

End Date: September 30, 2019

Project Funding (FY19): \$400,000

DOE share: \$400,000

Non-DOE share: \$0

Project Introduction

A stable lithium anode is critical to achieve high energy density batteries with excellent safety, lifetime and cycling efficiency. This study will identify the key design strategies that should be used to prepare composite electrolytes to meet the challenging combination of mechanical and chemical and manufacturing requirements to protect and stabilize the lithium metal anode for advanced batteries. The composites are composed of two solid electrolytes, a ceramic component for high ionic conductivity and high elastic modulus plus a small volume fraction of a polymer electrolyte to provide processability of a very thin, light weight and flexible electrolyte membrane.

In previous years we limited the choice of electrolyte materials to those that were well characterized and readily available. This allowed us to focus on how to process and characterize the thin dense composite membrane, and more importantly, this strategy allowed us to determine what factors determine the control the ionic conductivity across the polymer-ceramic interface. This interface is critical for good performance of simple composite structures. The design rules and approaches from earlier studies are now being applied to composites using alternative and novel electrolyte materials which will improve the composite solid electrolyte performance. While the interfaces between the polymer and ceramic electrolytes is still a key challenge, attention is also directed towards stability of the lithium and cathode electrode interfaces. Success in this program will enable these specific DOE technical targets: 500-700Wh/kg, 3000-5000 deep discharge cycles, robust operation.

Objectives

The overall objective of this program is to prepare composites of polymer and ceramic electrolyte materials as thin membranes which have the unique combination of electrochemical and mechanical properties required to stabilize the metallic lithium anode while providing for good power performance and long cycle life. If successful, this composite electrolyte will help eliminate failure mechanisms including the formation of lithium dendrites, delamination of the lithium or cathode electrodes, and the gradual consumption of lithium due to side reactions or physical isolation.

In a solid-state Li metal battery built on a composite solid electrolyte, a number of interfaces need to be optimized to maximize performance. The interfaces include exterior interfaces (cathode/electrolyte and Li/electrolyte) and interior interfaces (polymer/ceramic and ceramic particle/ceramic particle). We aim to

develop a fundamental understanding of ion transport across these interfaces and search for practical solutions to optimize them.

For the interior interfaces, we want to characterize and compare the ion transport between a variety of polymers with different ion transport mechanism and several model ceramics. This will allow design of new polymer systems capable of forming synergistic interfaces with the ceramic. At the same time, we aim to develop practical approaches to decrease the ceramic particle/particle contact resistance. While developing the composite electrolytes, we aim at using ready-to-scale-up processing techniques and making them into commercially relevant form factors (thin and large area).

At the cell level, we seek to understand how the chemical and mechanical properties of the electrolyte affects cell performance, failure mechanism and formation of Li filaments. We also seek solutions to reduce the interfacial resistance between the electrode and the electrolyte and undesired side reactions.

Approach

Our earlier approach was to spray coat a slurry containing the ceramic powder along with a Li salt and dissolved polyethylene oxide (PEO). This was subsequently dried and pressed to densify the film into a homogeneous membrane with high ceramic loading of discrete particles with polymer filling the interstices. Composites were also formed by hot-pressing the dry mixtures of the ceramic, Li salt and PEO as this provided a more rapid sample fabrication to shape. For either processing route, only when the PEO was plasticized with a small organic molecule was the ceramic-polymer interface sufficiently conductive for the composite to achieve our goal for an acceptable Li ion conductivity. The interface properties were carefully confirmed by using ideal laminated structures of the same materials used in the composites. Clearly other materials and methods were needed to further improve the composite electrolyte.

Alternatives for both the ceramic and the polymer phase are being explored with goals to: improve the percolated connectivity of ceramic, improve the Li ion conduction across polymer-ceramic interface, and enhance the Li ion transference number conductivity in polymer. Various polymer materials were synthesized and tested, including cross-linked and gelled polymer electrolytes and single ion conducting polymers with anions bound to the polymer structure. Impedance spectroscopy together with a host of other characterizations methods are used to determine the ion associations and polymer dynamics as they affect the Li⁺ conductivity in both the neat polymer phase and in the ceramic composites. For ceramic phase, the processing methods and performance of thin sintered membranes is explored, initially with glass-ceramic LATP-based powders from Ohara Corporation, LICGCTM, then with alternatives including the garnet LLZO. The sintering process is intended to ensure a fully 3D connected pathway of the ceramic phase across and along the membrane. The porosity in the ceramic membrane will then be filled with the polymer electrolyte. If Li⁺ ion transport between the ceramic and polymer was facile, this would improve the overall homogeneity of Li ion current across the separator membrane. X-ray tomography and electron microscopy are used to determine the microstructure, and various dynamic and stress-strain tests to determine mechanical properties.

While the scientific goals are focused on addressing the composite electrolyte and interfaces, fabricating and cycling electrochemical cells is an important way to characterize the stability with Li and mechanical integrity of the electrolyte. We are seeking to identify practical processing routes to fabricate full batteries using the composite electrolytes with a composite cathode and thin lithium metal anode. The addition of a very thin single ion conducting layer, such for Lipon, may play important role to eliminate the salt concentration polarization and provide a smooth interface for the lithium anode. These studies increase the complexity of the program, but are practical approaches to improve performance and advance our appreciation for challenges to come with implementation of the solid electrolyte and Li anode technology

Results

Results are summarized for four topics: 1. development of a three-dimensional interconnected polymer/ceramic composite as a thin film solid electrolyte. 2. Gel composite electrolytes with improved Li⁺

transference number and cycling performance. 3. Composite electrolytes with single-ion-conducting polymer matrix. 4. Cycle tests of full and symmetric cells with metallic lithium anode.

1. A three-dimensional interconnected polymer/ceramic composite as a thin film solid electrolyte.

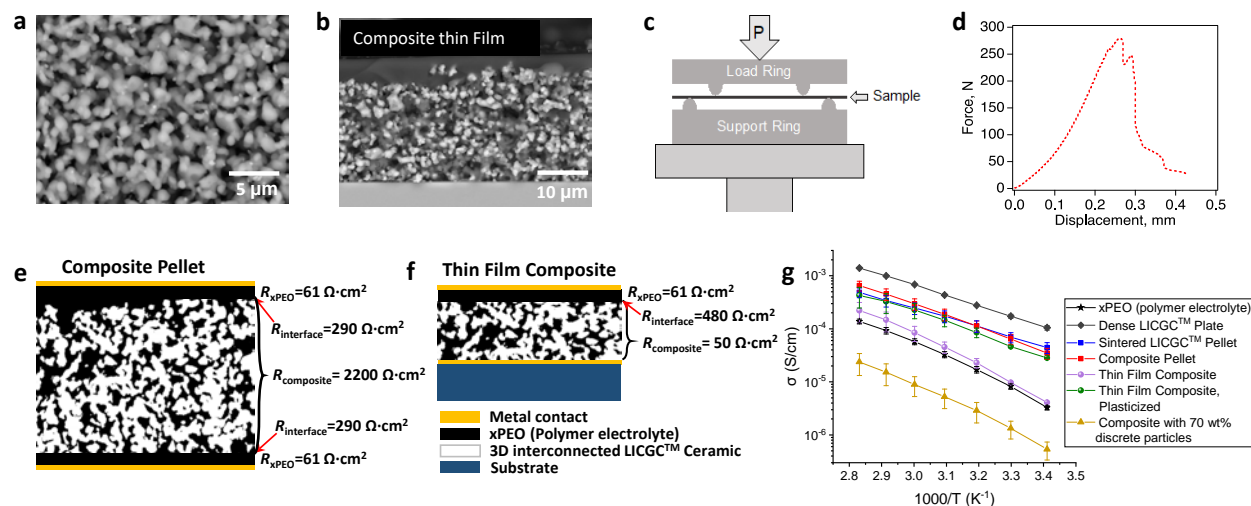


Figure II.7.B.1 **a**, In-plane scanning electron microscopy (SEM) image of sintered LICGC™ thin film. **b**, cross-section view of the LICGC™/xPEO composite thin film. **c and d**, equibiaxial flexural strength measurement of the composite electrolyte. **e and f**, schematics of the composite pellet (e) and thin film (f), showing that the effects of surface xPEO layer and interfacial resistance. Schematics are not drawn to scale. **g**, the ionic conductivity of composite pellet and thin film as a function of inverse temperature, compared to neat polymer, pristine ceramic, and a composite without the interconnected ceramic structure.

Our past work indicated when making a composite electrolyte with discrete ceramic particles, even with a loading that is above the ceramic percolation threshold, ion transport through the ceramic fillers is not efficient due to the large interparticle contact resistance and insufficient particle-particle contact area. Therefore, the traditional method mixing discrete ceramic particles into a polymer matrix fails to take advantage of the high ionic conductivity of the ceramic.

This year we developed an approach to fabricate a solid composite electrolyte film that is thin, ionically conductive, and mechanically robust with good potential for manufacturability. First LICGC™ ceramic thin film with thickness of ~25 μm is formed by aqueous spray coating, a scalable process. The film is partially sintered to form a three-dimensionally interconnected structure with a dense backbone (Figure II.7.B.1a). It is then backfilled with a cross-linkable poly(ethylene oxide)-based polymer electrolyte, referred to as xPEO (Figure II.7.B.1b). The flexural strength of the composite was measured by equibiaxial deformation in a ring-on-ring setup (Figure II.7.B.1c). The load-displacement curve is shown in Figure II.7.B.1d. The resulting equibiaxial strength was calculated to be 19.5 MPa. The composite electrolyte with the 3D ceramic network exhibited significantly increased mechanical strength compared to neat xPEO and the polymer phase decreased the brittleness of the composite.

We performed thorough analysis of the ionic conductivity of the composite electrolyte with a three-dimensional interconnected ceramic network. An area specific resistance of $50 \Omega \cdot \text{cm}^2$ was achieved for the thin film composite layer. This was determined by comparing the impedance spectra of 1 mm thick composite pellet with the spray-coated 25 μm thin film. A surface polymer-rich overlayer (Figure II.7.B.1e and f) increased the total resistance of each sample by about 300-500 $\Omega \cdot \text{cm}^2$. This interfacial resistance can be minimized by finding a way to remove the excess xPEO layer or by the addition of TEGDME plasticizer. The plasticized composite thin film had an exceptionally high ceramic loading of ~77 wt.% and gives an ionic conductivity of 3.5×10^{-5} S/cm at 20°C, an order of magnitude larger than the neat polymer electrolyte and about two orders of magnitude larger than randomly dispersed ceramic particles in polymer with a similar loading (Figure II.7.B.1g).

2. Gel composite electrolytes with improved Li^+ transference number and cycling performance.

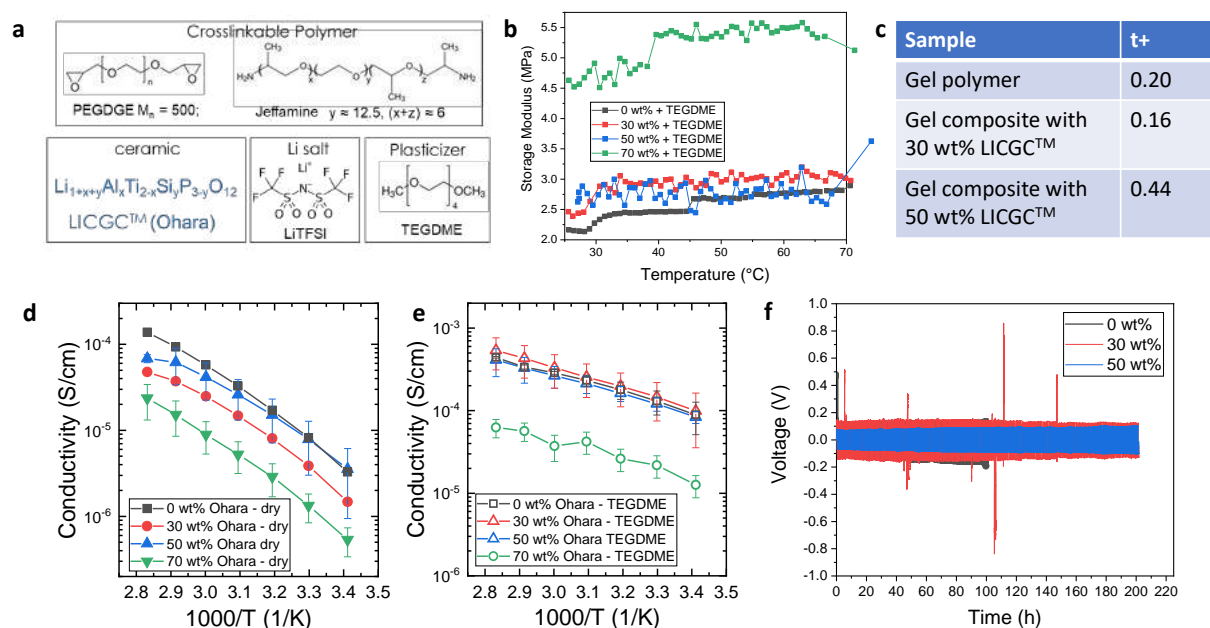


Figure II.7.B.2 **a**, composition of the gel composite electrolyte. **b**, storage moduli of gel composite electrolytes as a function of temperature, measured by dynamic mechanical analysis. **c**, Li^+ transference number of the gel composite electrolytes. **d** and **e**, ionic conductivity in the dry (**d**) and plasticized states (**e**). **f**, Li symmetrical cell cycling at room temperature.

So far we have been limiting the use of plasticizer to a small amount. Given the positive effects of the plasticizers in increasing the ionic conductivity of the polymers as well as decreasing the interfacial resistance between the polymer and the ceramic electrolyte, this year, we expanded the polymer/plasticizer design and developed a hybrid electrolyte that is heavily doped with plasticizers. A one pot synthesis containing oligomers, lithium salt and ceramic powder was performed (Figure II.7.B.2a). The resulting membrane was a very homogenous and mechanically flexible membrane. We characterized the conductivity, mechanical modulus, transference number and lithium symmetrical cell performance of gel composite electrolytes (GCE) with 3 ceramic loadings, 30 wt.%, 50 wt.% and 70 wt.% (GCE-30, GCE-50 and GCE-70) (Figure II.7.B.2) Before infusing the plasticizer TEGDME, both dry polymer and composite electrolytes showed low room-temperature ionic conductivity ($< 10^{-5}$ S/cm). The conductivity of plasticized GCE-30 and GCE-50 was the same as the gel polymer electrolyte (GPE) without any ceramic. GCE-70 showed 1 order of magnitude lower ionic conductivity. The storage modulus of GCE-30 and GCE-50 was merely slightly higher than GPE. The lithium symmetrical cell of GCE-50 showed the best performance, featuring smaller overvoltage and higher rate capability (rate data not shown). We attribute this to an increased Li^+ transference number with the presence of LICGC™ ceramic.

3. Composite electrolytes with single-ion-conducting polymer matrix.

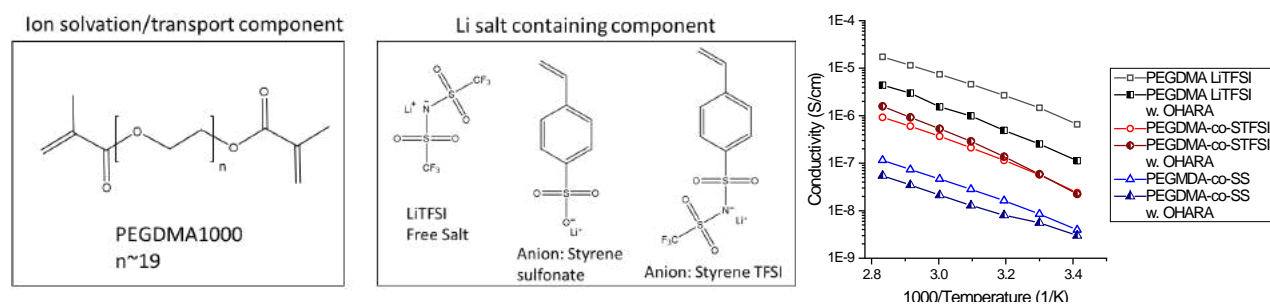


Figure II.7.B.3 Composites consisting of LICGTM ceramic and 3 different polymers: PEGDMA crosslinked with LiTFSI free salt, with covalently bound styrene sulfonate anion and with covalently bound styrene TFSI anion. Right, ionic conductivity of the polymers and their respective composite with 50 wt% Ohara ceramic.

We expanded our polymer portfolio and examined three polymers (collaboration with Prof. Jennifer Schaefer). The ion solvation/transporting component of these polymers is polyethylene glycol dimethacrylate (PEGDMA). The methacrylate group can be covalently connected to an anion-containing component. We compared three different types of anions: TFSI free anion, covalently bound styrene sulfonate anion (SS⁻) and covalently bound styrene TFSI anion (STFSI⁻) (Figure II.7.B.3). The ionic conductivity of the dry polymers and their composites with 50 wt.% Ohara ceramic is shown in Figure II.7.B.3, right. An order of magnitude decrease in the conductivity was observed in the composite containing free LiTFSI salt compared to the neat polymer – this is consistent with our past results on dry composites. Interestingly, we observed an increase in the conductivity of the composite containing Ohara ceramic and PEGDMA-co-LiSTFSI polymer compared to the neat polymer.

4. Cycle tests of full and symmetric cells with metallic lithium anode

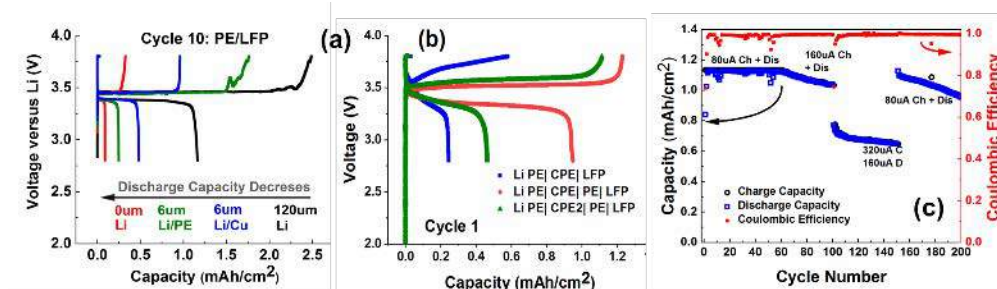


Figure II.7.B.4 Cycling of Li/LiFePO₄ solid state cells with dry composite and polymer electrolytes. **a**, cells at cycle 10 with different thicknesses of excess Li, 0–120 μm; **b**, reduced polarization when thin PEO+salt fills interface between the cathode and electrolyte composites; **c**, one of the longest cycling cells with Lipon at the cathode interface.

A variety of cells were fabricated to evaluate: the enhanced cycle life attributed to excess Li capacity, the effect of a single ion conductor coating on the cathode, and thin polymer layers to provide full contact between composites. Examples of results are illustrated in Figure II.7.B.4. The composite electrolytes are limited to those with dispersed ceramic particles at high ceramic loading. The polymer electrolytes are well dried and free of plasticizers. Compared to earlier work, we have eliminated one variable by using optimized LiFePO₄ dry composite cathodes prepared industrially with areal capacity of 1.1 mAh/cm². One recurring complication is that for many cells there are a limited number of cycles with charge capacities greater than the theoretical areal capacity. This is believed to be attributable to soft dendrite shorts, perhaps aggravated by misalignment of the anode and cathode; this is under investigation. The best cycling and rate performances to date are for cells that have a thin 300nm Lipon layer added to the cathode interface.

Conclusions

- In order to take advantage of the high ionic conductivity of the ceramic particles, one approach is to try to decrease the interfacial resistance between the polymer and the ceramic. An alternative approach is to create a three-dimensional interconnected ceramic network as the base to form composite electrolytes. The main ion transport pathway in this type of composite is through the ceramic network. Owing to the interconnected structure of the ceramic, the composite electrolyte exhibits much improved mechanical strength.
- With discrete ceramic particles dispersed in a polymer matrix, their effect on the mechanical modulus below the percolation threshold is limited. On the other hand, in heavily plasticized gel composite electrolytes, they can help significantly increasing the Li^+ transference number. They also help improve the flexibility and handleability of the otherwise soft and brittle membranes.
- The interfacial transport is much improved between LICGCTM and single-ion conducting crosslinked polymer matrix (PEGDMA-co-STFSI), compared to crosslinked polymer with free Li salt. However, due to the intrinsically low conductivity of single-ion-conducting polymer, composite with such polymers cannot be used at room temperature. Going forward we want to explore the tradeoff between ionic conductivity and transference number of the hybrid electrolytes.
- When fabricating and evaluating full batteries with composite electrolytes, we find that: a thin polymer layer reduces the impedance between the composite cathode and composite electrolyte, limiting the amount of Li metal at the anode helps to quickly reveal degradation, and cells with thin Lipon barrier at the cathode-electrolyte interface provide some of the best cycling to date.

Key Publications

Publications

1. X. C. Chen*, X. Liu, A. S. Pandian, K. Liu, F. M. Delnick, N. J. Dudney*, *Determining and Minimizing Resistance for Ion Transport at the Polymer/Ceramic Electrolyte Interface*, ACS Energy Letters, **2019**, 4, pp 1080–1085.
2. Max Palmer, Sergiy Kalnaus, Marm Dixit, Andrew Westover, Kelsey Hatzell, Nancy Dudney, X. Chelsea Chen, *A Three-Dimensional Interconnected Polymer/Ceramic Composite as a Thin Film Solid Electrolyte*, submitted.

Patents

1. U.S. provisional application no. 62/912,667, Oct. 9, 2019. Thin Solid Composite Electrolyte with Zero Interparticle Resistance. S. Kalnaus, X. S. Chen, M. J. Palmer, A. S. Westover, N. J. Dudney

Acknowledgements

These researchers provided important insight and assistance with the program: Laura Merrill, student of Prof. Jennifer Schaefer, Notre Dame; Kelsey Hatzell, student of Prof. Marm Dixit, Vanderbilt University; and Drs. Sergiy Kalnaus and Andrew Westover, staff members at Oak Ridge National Laboratory.

II.7.C Lithium Dendrite Prevention for Lithium Batteries (PNNL)

Wu Xu, Principal Investigator

Pacific Northwest National Laboratory
902 Battelle Boulevard
Richland, WA 99354
E-mail: wu.xu@pnnl.gov

Ji-Guang Zhang, Principal Investigator

Pacific Northwest National Laboratory
902 Battelle Boulevard
Richland, WA 99354
E-mail: jiguang.zhang@pnnl.gov

Tien Duong, DOE Technology Development Manager

U.S. Department of Energy
E-mail: Tien.Duong@ee.doe.gov

Start Date: October 1, 2018

End Date: September 30, 2020

Project Funding (FY19): \$400,000

DOE share (FY19): \$400,000

Non-DOE share: \$0

Project Introduction

Lithium (Li) metal batteries (LMBs) have been regarded as the ‘holy grail’ for the next generation high-energy-density rechargeable batteries due to the use of Li metal anode (LMA) with low redox potential (-3.040 V vs. standard hydrogen electrode), high theoretical specific capacity (3860 mAh g^{-1}), and low density (0.534 g cm^{-3}). However, the applications of LMBs have been hindered by two main problems. One is the growth of Li dendrites during repeated charge/discharge processes, which can penetrate the separator and cause safety hazards. Another is the low Coulombic efficiency (CE) of Li plating/stripping because Li metal is thermodynamically unstable in organic electrolytes, causing the depletion of electrolyte and the consumption of LMA, thus shortening the cycle life of the batteries using LMA. In our previous work, the effects of Li salt mixtures, solvents, additives, and surface coating on polymer separators have been systematically studied. Those previous works mainly focus on liquid electrolytes. In FY19, our researches have been extended to polymer electrolytes, including the effects of such polymer electrolytes on oxidation stability, ionic conductivity, Li CE, Li anode morphology, battery performance and compatibility with $\text{LiNi}_x\text{Mn}_y\text{Co}_z\text{O}_2$ (NMC) cathodes. Furthermore, the ex situ protective coating for LMAs has also been studied. The findings will guide the development of polymer electrolytes and protection of LMAs to achieve higher Li CE and suppress Li dendrites.

Objectives

1. Stabilize Li anode in rechargeable LMBs for long cycle life.
2. Investigate effects of various organic solvents and polymers on ionic conductivity, Li CE, Li deposition morphology, and battery performances in terms of cycling stability and rate capability at both room temperature and elevated temperatures.
3. Develop protective layers to enhance the stability of LMAs with electrolytes.

Approach

The following approaches have been used to reach the objectives outlined above. First, three types of superconcentrated electrolytes (SCEs) based on organic carbonate, ether and phosphate solvents were investigated to get a suitable electrolyte with high ionic conductivity, high electrochemical stability, high Li CE and dendrite-suppressed morphology. Second, a new type of polymer electrolyte with high oxidative

stability was developed through polymer-in-”quasi-ionic liquid” strategy. The compatibility of such electrolytes with high-Ni NMC cathode was investigated. Third, a uniform Ag-embedded interlayer was pre-formed to protect Li metal. Various characterization technologies, including high-resolution scanning electron microscopy (SEM), transmission electron microscopy (TEM) and X-ray photoelectron spectroscopy (XPS) were used to analyze the morphology and composition of the interfacial films on Li-metal surfaces.

Results

1. Superconcentrated electrolytes (SCEs)

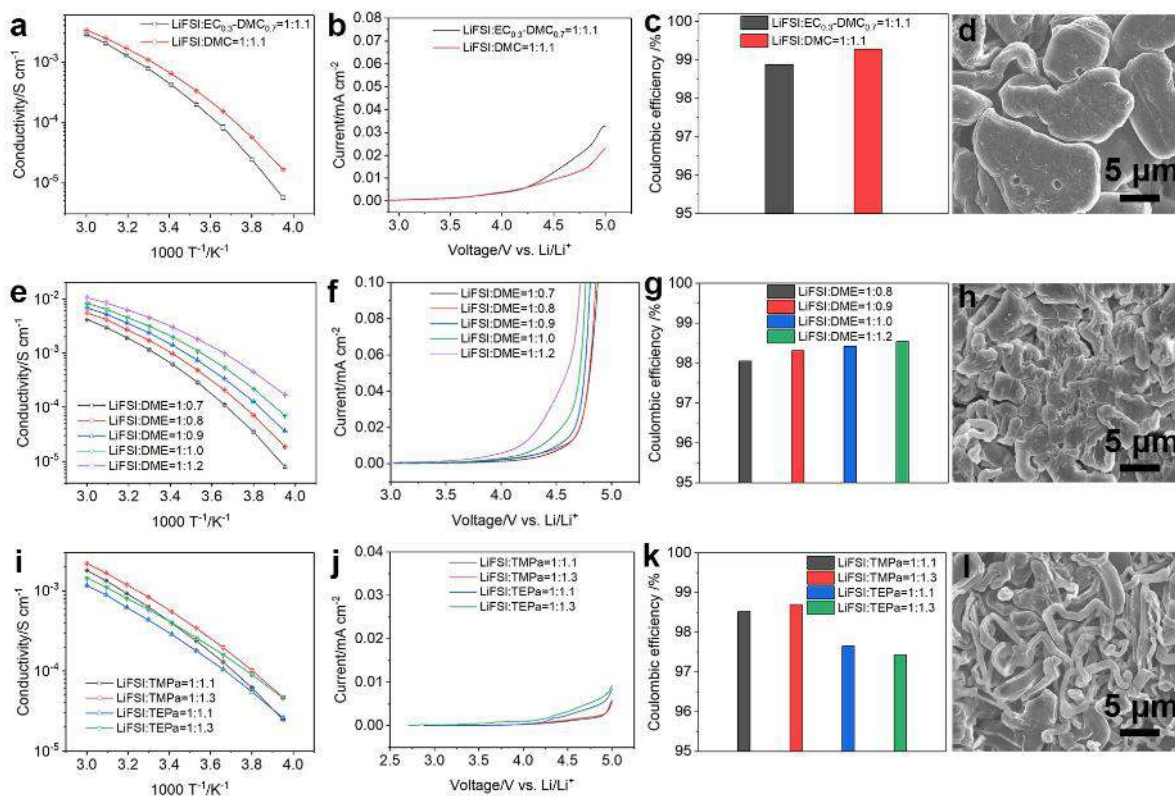


Figure II.7.C.1 Temperature dependence of ionic conductivity of (a) carbonate SCEs, (e) ether SCEs, (i) alkylphosphate SCEs. Electrochemical stability of (b) carbonate SCEs, (f) ether SCEs, (j) alkylphosphate SCEs in Li|Li|Pt cells at a scan rate of 0.5 mV s⁻¹ and room temperature. CE of Li|Cu cells at 0.5 mA cm⁻² with (c) carbonate SCEs, (g) ether SCEs, (k) alkylphosphate SCEs. SEM images of deposited Li particles at 0.1 mA cm⁻² with capacity of 1.5 mAh cm⁻² with (d) LiFSI-1.1DMC, (h) LiFSI-1.2DME, (l) LiFSI-1.3TMPa

SCEs are beneficial to the stable cycling of LMAs. The conductivity, electrochemical stability, Li CE and deposited Li morphology of three types of SCEs were investigated. LiFSI-1.1DMC has slightly higher conductivity of 1.1 mS cm⁻¹ at 30°C, electrochemical oxidation voltage of 4.6 V vs. Li/Li⁺ and average Li CE (99.3%) than LiFSI-1.1(EC0.3-DMC0.7) that has a conductivity of 0.8 mS cm⁻¹ at 30°C, oxidation voltage of 4.4 V and Li CE of 98.8%. Large nodule-like and compact Li particles can be obtained for LiFSI-1.1DMC (Figure II.7.C.1a-d). For the SCEs of LiFSI-nDME at different molar ratios, the increase of solvent content increases the conductivity (from 1.2 to 4.5 mS cm⁻¹ at 30°C for 1:0.7 to 1:1.2) and Li CE (from 98.0% for 1:0.8 to 98.5% for 1:1.2), but decreases the oxidation voltage from 4.6 V for 1:0.7 to 4.2 V for 1:1.2. Li particles deposited in all SCEs with DME are very compact (Figure II.7.C.1e-h). For the alkylphosphates-based SCEs, LiFSI-1.1TMPa and LiFSI-1.3TMPa have slightly higher conductivities than TEPA ones, 0.6 and 0.8 mS cm⁻¹ at 30°C vs 0.4 and 0.6 mS cm⁻¹, respectively. Both TMPa-based SCEs exhibit 5.0 V stability while the TEPA-based SCEs are stable only up to 4.7 V, but their stabilities are still much higher than those of the carbonate-based HCEs and DME-based SCEs. Highest CE (98.7%) is obtained in LiFSI-1.3TMPa. Fibrous

and nodule-like Li particles can be observed and the deposited Li film is looser than those formed in carbonate and ether SCEs (Figure II.7.C.1i-l).

2. Polymer-in-“quasi-ionic liquid” electrolytes (PQILEs)

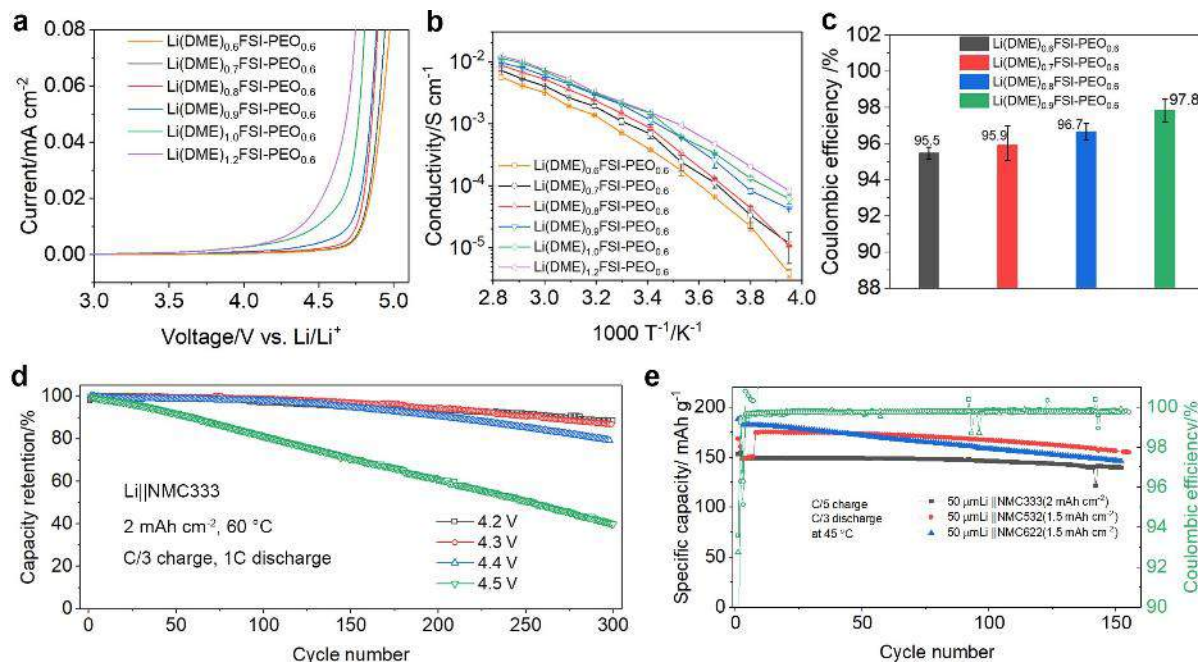


Figure II.7.C.2 (a) Linear sweep voltammetry curves of PQILEs of $\text{Li}(\text{DME})_x\text{FSI-PEO}_{0.6}$ on Pt electrode in a three-electrode cell with a scan rate of 0.5 mV s⁻¹. (b) Temperature dependence of ionic conductivity of $\text{Li}(\text{DME})_x\text{FSI-PEO}_{0.6}$. (c) Average Li CE values of $\text{Li}(\text{DME})_x\text{FSI-PEO}_{0.6}$ at 60 °C with Celgard 3501. (d) Cycling performance of Li||NMC cells using $\text{Li}(\text{DME})_{0.7}\text{FSI-PEO}_{0.6}$ under different charge cut-off voltages. (e) Cycling performance of Li||NMC cells with different cathode materials and the optimal PQILE cycled in the voltage range of 3.0-4.3 V

In LiFSI-*n*DME (where *n* ranges from 0.7 to 1.2), ligand molecules are strongly coordinated with the cations. It's a type of “quasi-ionic liquids” (QILs). The polymer-in-“quasi-ionic liquid” electrolytes (PQILEs) can further increase the oxidation stability of the PEO-based electrolytes and retain their high conductivity as well. With the decrease of the molar ratio (*x*) of the DME solvent in PQILEs of $\text{Li}(\text{DME})_x\text{FSI-PEO}_{0.6}$, the anodic stability limit shifts to a more positive potential (where the initial oxidation voltage is defined as the voltage value when the current density reaches 5 μA cm⁻²). The irreversible oxidative current for $\text{Li}(\text{DME})_{1.2}\text{FSI-PEO}_{0.6}$ starts to flow at around 4.2 V vs. Li/Li⁺, while the oxidation voltage of $\text{Li}(\text{DME})_{0.7}\text{FSI-PEO}_{0.6}$ is increased to above 4.5 V (Figure II.7.C.2 (a)). Raman spectra show that no free DME and EO exist in $\text{Li}(\text{DME})_{0.7}\text{FSI-PEO}_{0.6}$. The DME and EO oxygen both donate their lone electron pairs to the Li⁺ cation, which has improved the oxidation stability of the gel polymer electrolyte. As the molar ratio of DME (*x*) increases, the ionic conductivity increases, and they all show a conductivity higher than 1 mS cm⁻¹ at 30 °C. The $\text{Li}(\text{DME})_{0.7}\text{FSI-PEO}_{0.6}$ shows a conductivity of 1.1 mS cm⁻¹ at 30 °C (Figure II.7.C.2 (b)). The Li CEs of $\text{Li}(\text{DME})_x\text{FSI-PEO}_{0.6}$ with Celgard 3501 are 95.5%, 95.9%, 96.6% and 97.8% for $x = 0.6, 0.7, 0.8$ and 0.9 respectively. Li metal cells with a NMC333 cathode were cycled with different cut-off voltages. A capacity retention of 88.4% after 300 cycles is achieved with a charge cutoff voltage of 4.2 V at C/3 charge rate and 1C discharge rate (where 1C = 2 mA cm⁻²). With a charge cutoff voltage of 4.3 V, the cell shows a capacity retention of 86.7% after 300 cycles. Even when the cell is charged to 4.4 V, it still retains 79.2% of the initial capacity after 300 cycles. When the cell charge voltage is further increased to 4.5 V, a continuous capacity fading is observed and the capacity decreases to ~40% in 300 cycles, indicating the decomposition of the electrolyte (Figure II.7.C.2 (d)). The cycling stabilities of Li||NMC batteries using the optimal PQILE $\text{Li}(\text{DME})_{0.7}\text{FSI-PEO}_{0.6}$ with thin LMA and three different cathode materials were investigated. Under C/5

charge and C/3 discharge in the voltage range of 3.0 ~ 4.3 V, the Li||NMC cells with 50 μm Li after 150 cycles show the capacity retention of 93.5% for NMC333, 88.6% for NMC532 and 80.2% for NMC622, indicating the decreased cycling stability of the NMC cathode material with the increase of the Ni content (Figure II.7.C.2 (e)).

3. Reasons behind high voltage stability of PQILEs

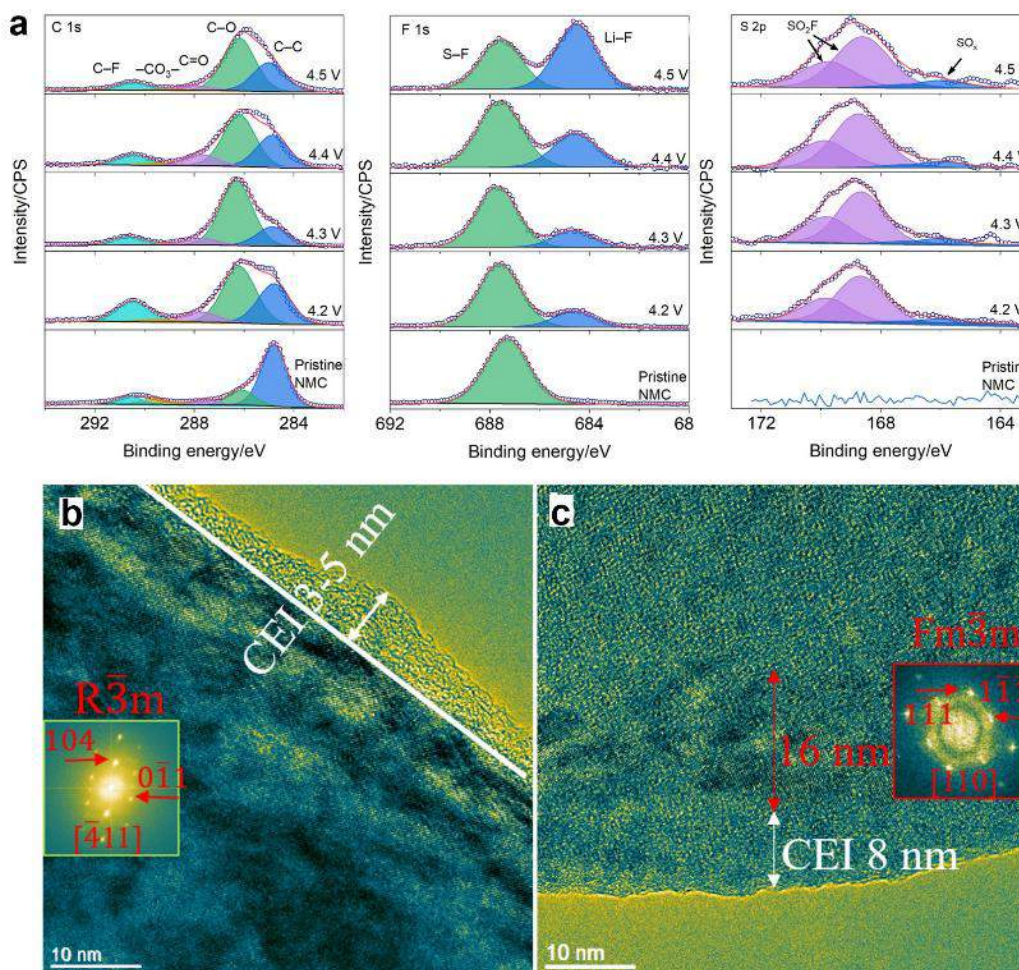


Figure II.7.C.3 (a) XPS profiles of the pristine NMC333 cathode and NMC333 cathodes after 300 cycles with different charge cut-off voltages of 4.2, 4.3, 4.4 and 4.5 V. TEM images of NMC cathodes after 300 cycles at 60 °C with the charge cutoff voltage of (b) 4.4 V and (c) 4.5 V. Insets are the fast Fourier transform (FFT) patterns of selected regions

For the high voltage stability of PQILEs, the cycled Li anodes and NMC333 cathodes were fully analyzed. The main difference is that the contents of LiF and oxidized sulfur species in the cathode electrolyte interphase (CEI) layers increase largely when the charge cutoff voltage is increase from 4.4 V to 4.5 V. For example, when the charge cutoff voltage increases from 4.2 V to 4.3 V, 4.4 V and 4.5 V, the LiF content in CEI increases from 20.4% to 21.8%, 33.8% and 56.8%, respectively; while the oxidized sulfur species change from 9.4% to 10.3%, 10%, and 13.1%, respectively (Figure II.7.C.3 (a)). Such changes suggest that when the charge cutoff voltage reaches 4.5 V, more PEO, DME and FSI⁻ are decomposed, leading to more oligomers, LiF and oxidized sulfur species on NMC surface, which cause the faster capacity decay. The charge cutoff voltage of 4.4 V does not cause serious decomposition of the PQILE so the CEI is still stable enough to maintain good cycling stability. More understanding of the reasons for the high voltage stability of the PQILE can be obtained from the TEM images of the cycled NMC. The NMC cathode charged to 4.4 V still remains the R3m structure

(Figure II.7.C.3 (b)). By contrast, the NMC cathode charged to 4.5 V has a thick layer of the rock-salt phase under the CEI layer, which is different from the R3m structure of the bulk NMC (Figure II.7.C.3 (c)).

4. Ag-embedded interlayer for Li metal protection

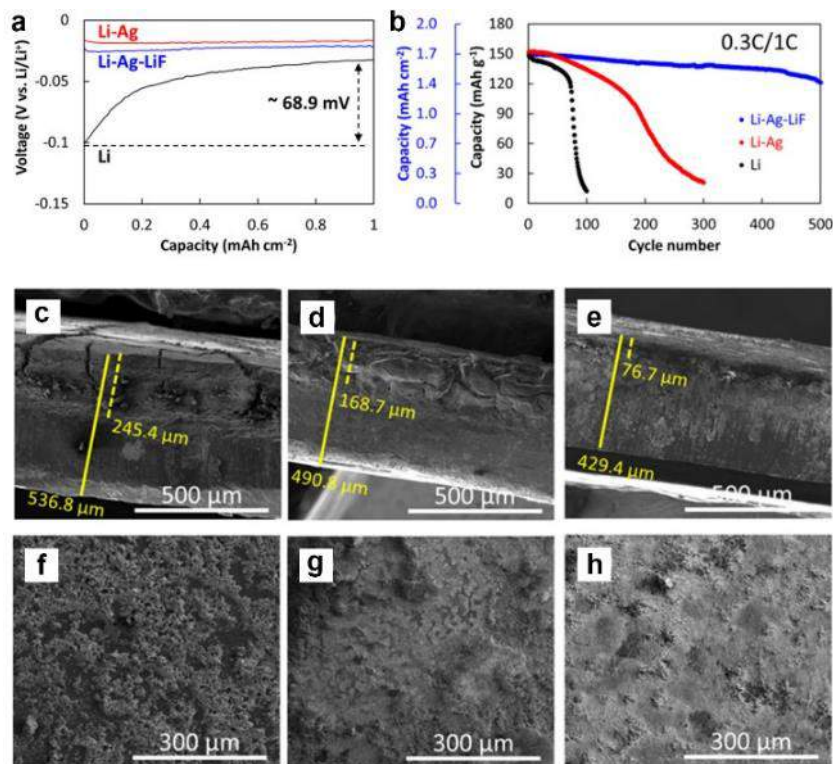


Figure II.7.C.4 (a) Nucleation overpotentials of Li plating on Li, Li-Ag, and Li-Ag-LiF surfaces in a carbonate electrolyte of 1 M LiPF_6 in EC-DMC (1:2 by vol.) (b) Cycling performance of Li||NMC333 full cells. SEM images of the cycled (c, f) Li, (d, g) Li-Ag/Li, and (e, h) Li-Ag-LiF/Li anodes disassembled from the Li||NMC333 full cells after 100 cycles at 1C/1C rates

The Li metal was treated with a silver-ion (Ag^+) precursor solution consisting of AgTFSI in DME and FEC mixture. Due to the strong oxidant nature of Ag^+ ions, abundant Ag nanoparticles could be formed on the Li surface. Density functional theory (DFT) calculations show that the binding energies of Li atom adsorption on different facets of an Ag surface are generally higher than those on a Li surface. Thus, Ag particles could act as nucleation sites for Li deposition with reduced overpotential, which would lead to high exchange current density and very uniform Li plating/stripping morphology. Meanwhile, the Li^+ ions released during Ag^+ reduction could efficiently react with F^- ions cleaved from FEC to form a cross-linked LiF-rich interphase, leading to a LiF-rich solid electrolyte interphase (SEI) layer during initial cycling that would efficiently protect the LMA for long-term cycling. The Li anodes decorated with Li-Ag-LiF clusters (denoted as Li-Ag-LiF/Li here) can be plated/stripped with low-overpotential (Figure II.7.C.4 (a)), high CE and long cycling stability. The Li||NMC333 cells with the Ag-LiF decorated Li anode retained >80% capacity over 500 cycles (Figure II.7.C.4 (b)), with a very smooth surface and a thin passivation layer ($\sim 76.7 \mu\text{m}$). From the disassembled anodes, a very thick, porous layer of $\sim 245.4 \mu\text{m}$ is observed on the cycled untreated Li anode, which is $\sim 45.7\%$ of the total thickness ($\sim 536.8 \mu\text{m}$, Figure II.7.C.4 (c)). The cycled Li-Ag/Li anode shows a thinner passivation layer ($\sim 168.7 \mu\text{m}$) (Figure II.7.C.4 (d)). In contrast, a very smooth surface is obtained for the Li-Ag-LiF/Li with a thin passivation layer ($\sim 76.7 \mu\text{m}$, Figure II.7.C.4 (e)). Massive dendrites are generated on the bare Li surface (Figure II.7.C.4 (f)), consistent with the thick porous layer observed in cross-section. In contrast, uniform granular morphologies are observed on both Li-Ag/Li (Figure II.7.C.4 (g)) and Li-Ag-LiF/Li (Figure II.7.C.4 (h)) anodes due to the presence of Ag nanoparticles as nucleation sites.

Conclusions

1. Among the three SCEs, both LiFSI-1.1DMC and LiFSI-nDME have conductivity larger than 1 mS cm^{-1} , oxidation stability over 4.5 V, CE higher than 98% and compact Li particles.
2. The optimal PQILE, $\text{Li}(\text{DME})_{0.7}\text{FSI-PEO}_{0.6}$, can greatly improve the oxidation stability of PEO due to the donation of lone electron pairs of the ether oxygen atoms (from PEO and DME) to the Li^+ cation. A moderate conductivity of 1.1 mS cm^{-1} at 30°C can be obtained in the PQILE because of the ion transport in the QIL $\text{Li}(\text{DME})_{0.7}\text{FSI}$. LMBs with NMC333 cathode and the optimized PQILE have a capacity retention of 79.2% after 300 cycles when the cells are charged to 4.4 V. The PQILE is also compatible with NMC532 and NMC622. However, when cells are charged to 4.5 V, there are some local crystal structure changes in NMC and more serious electrolyte decomposition, resulting in unstable CEI and SEI, which are the reasons behind fast decay of the LMBs at high voltage (4.5 V).
3. A uniform Ag nanoparticle-decorated LMA for high-performance LMBs was demonstrated. This effective treatment can lead to well controlled nucleation and formation of a stable SEI. Ag nanoparticles embedded in the surface of LMA induced uniform Li plating/stripping morphologies with reduced overpotential. More importantly, cross-linked LiF-rich interphase formed during Ag^+ reduction enables a highly stable SEI layer. Based on the Ag-LiF decorated anodes, LMBs with NMC333 cathode ($\sim 1.8 \text{ mAh cm}^{-2}$) can retain >80% capacity over 500 cycles.

Key Publications and Presentations

1. H. Wu, Y. Xu, X. Ren, B. Liu, M. H. Engelhard, M. S. Ding, P. Z. El-Khoury, L. Zhang, Q. Li, K. Xu, C. Wang, J.-G. Zhang*, W. Xu*, “Polymer-in-”Quasi-Ionic Liquid” Electrolytes for High-Voltage Lithium Metal Batteries”, *Adv. Energy Mater.*, 2019, **9**, 1902108. (DOI:10.1002/aenm.201902108)
2. Z. Peng, J. Song, L. Huai, H. Jia, B. Xiao, L. Zou, G. Zhu, A. Martinez, S. Roy, V. Murugesan, H. Lee, X. Ren, Q. Li, B. Liu, X. Li, D. Wang*, W. Xu*, J.-G. Zhang*, “Enhanced Stability of Li Metal Anodes by Synergetic Control of Nucleation and the Solid Electrolyte Interphase”, *Adv. Energy Mater.*, 2019, **9**, 1901764. (DOI:10.1002/aenm.201901764)
3. W. Xu, J.-G. Zhang, “Lithium dendrite prevention for lithium batteries”, Oral presentation at *BMR Electrolyte Discussion*, Berkeley, CA, October 11, 2018.
4. W. Xu, “Advancing Lithium Metal Batteries”, Featured presentation at *2019 International Battery Seminar & Exhibit*, Fort Lauderdale, Florida, March 26-27, 2019.
5. X. Li, J. Tao, D. Hu, M.H. Engelhard, W. Zhao, J. Zhang, and W. Xu, “Effects of Separators on Lithium Metal Batteries”, at *International Battery Association 2019*, La Jolla, California, March 03-08, 2019.
6. H. Wu, Y. Xu, X. Ren, B. Liu, M. Engelhard, M. Ding, P. El-Khoury, L. Zhang, Q. Li, K. Xu, C. Wang, J.-G. Zhang, and W. Xu, “Polymer-in-”quasi ionic liquid” electrolytes for high-voltage lithium metal batteries”, *235th ECS Meeting*, Dallas, Texas, May 26-30, 2019.
7. W. Xu and J.-G. Zhang, “Lithium dendrite prevention for lithium batteries”, *2019 DOE VTO Annual Merit Review Meeting*, Arlington, Virginia, June 10-13, 2019.
8. H. Wu, Y. Xu, X. Ren, B. Liu, M. Engelhard, M. S. Ding, P. Z. El-Khoury, L. Zhang, Q. Li, C. Wang, K. Xu, C. Wang, J.-G. Zhang, and W. Xu, “High-voltage lithium-metal batteries enabled by PEO-based gel electrolytes”, *Beyond Lithium Ion XII*, Golden, Colorado, June 25-27, 2019.

Acknowledgements

Key contributors Drs. Haiping Wu and Zhe Peng are greatly appreciated.

II.7.D Understanding and Strategies for Controlled Interfacial Phenomena in Li-Ion Batteries and Beyond (TAMU, Purdue)

Perla B. Balbuena, Principal Investigator

Texas A&M University
3122 TAMU
College Station, TX 77843
E-mail: balbuena@tamu.edu

Jorge Seminario, Principal Investigator

Texas A&M University
3122 TAMU
College Station, TX 77843
E-mail: seminario@tamu.edu

Partha Mukherjee, Principal Investigator

Purdue University
585 Purdue Mall
West Lafayette, IN 47907-2088
E-mail: pmukherjee@purdue.edu

Tien Duong, DOE Technology Development Manager

U.S. Department of Energy
E-mail: Tien.Duong@ee.doe.gov

Start Date: October 1, 2016
Project Funding: \$1,333,335

End Date: September 30, 2019
DOE share: \$1,200,000

Non-DOE share: \$133,335

Project Introduction

This project focuses on elucidating the roles of the electrolyte and electrode on the formation and evolution of the SEI layer and cell electrochemical performance on silicon and on Li metal anodes. For Si nano/microstructures we evaluate lithiation, volume changes, reactivity, and chemo-mechanical transformations as functions of nanoparticle size, shape, presence of coatings, electrolyte composition, electron leakage to the electrolyte, and cycling. For Li metal anodes we provide a detailed analysis of the electrode and electrolyte effects on reactivity and as a function of microstructural evolution and underlying stochasticity as dendrites nucleate and grow. We thoroughly investigate and test how the chemistry of the various components of the electrolyte and the electrode architecture may affect the electrochemical reactions as well as cell degradation. The analysis of Si electrodes was reported in the previous year. This report focuses on Li metal anodes issues characterization and analysis.

Objectives

The knowledge gained by developing fundamental understanding of the issues associated with metal electrodeposition and stripping are aimed to elaborate strategies for solving practical issues associated with SEI instability, electrode expansion, and dendrite formation. These strategies emerge from electrolyte formulation and electrode morphology design.

Approach

A comprehensive multiscale modeling approach including first-principles ab initio static and dynamics, classical molecular dynamics, and coarse-grained mesoscopic models is used to characterize the roles of the electrolyte chemical, structural, and dynamical properties and of the electrode micro- and nanostructure on the formation and evolution of the SEI layer and associated electrochemical performance on silicon and on Li

metal anodes. For Si nano/microstructures we evaluate lithiation, volume changes, reactivity, and chemo-mechanical transformations as functions of nanoparticle size, shape, presence of coatings, electrolyte composition, electron leakage to the electrolyte, and cycling. For Li metal anodes we focus on a detailed analysis of the electrolyte effects on reactivity leading to solid electrolyte interphase formation, and as a function of electrode microstructural evolution and underlying stochasticity as dendrites are formed.

Results

Mechanisms of Li cation deposition on a Cu(001) surface

A practical limit for the solvent concentration around each Li^+ ion-containing salt molecule was found to be given by the cation-oxygen polyhedral structure. Cation reduction at the Cu(001) surface is an insufficient condition for Li growth, given the endothermic nature of such deposition reaction (Figure II.7.D.1a). The deposition process is a two-step mechanism. The 1st step is driven by kinetics, and the 2nd involves the dissociation of the cation-containing salt. In the presence of an external electric field, surface polarization orbitals increase the cation-metal coulombic interaction (Figure II.7.D.1b, c), leading to an overall exothermic deposition process (Figure II.7.D.1d). However, reductive stability of the cation is not completely achieved, due to the noble character of the Cu(001) surface.

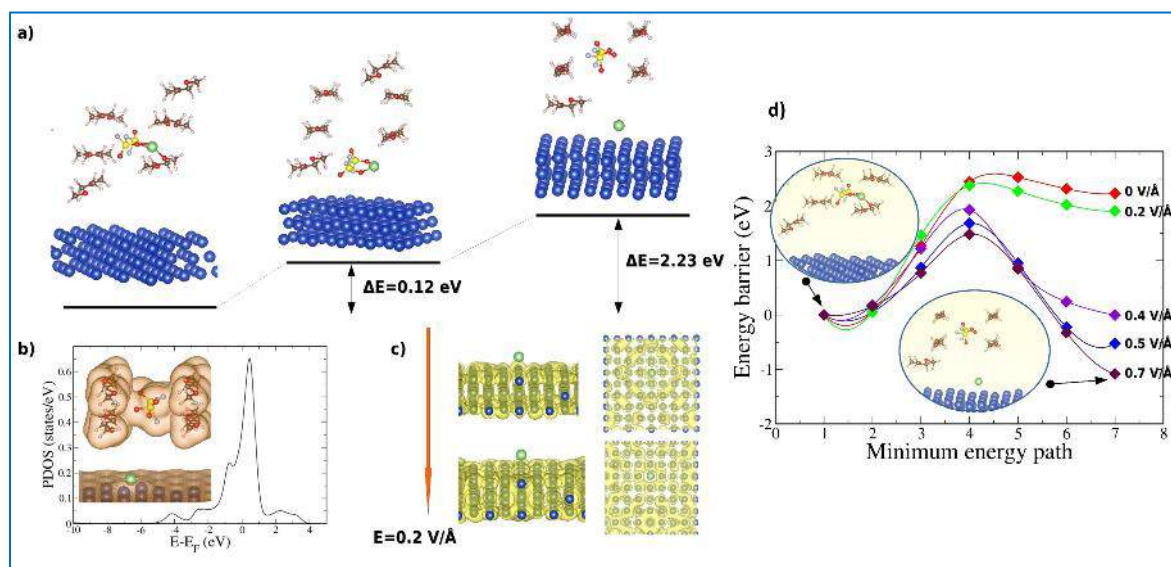


Figure II.7.D.1 (a) Energy profile of Li deposition on Cu(001) from DME-solvated LiFSI in absence of an external field. ΔE values are energies relative to the initial configuration shown at the left. (b) Projected density of states (DOS) of the partially reduced Li 1s orbital, after adsorption on Cu(001). The Li 1s orbital is usually located in the unoccupied region, right of the Fermi level. At the surface, the Li 1s peak shifts toward the Fermi level, indicating partial reduction. The inset shows the charge density distribution. (c) Polarization orbitals (yellow) created on the Li/Cu(001) system by an external electric field of 0.2 V/\AA . (d) Electric field dependence of the kinetic energy profile of Li deposition on Cu(001). Substrate and molecules are placed between two electrodes (not shown), within the Effective Screening Medium framework. Adapted from J. Mater. Chem. A, 7, 8527-8539, (2019)

AIMD simulations showed that the formation of an intermediate DME– Li^+ composite is the key to Li deposition, and the use of low solvent densities (high salt concentration or localized high concentration) becomes crucial to allow the growth of uniform Li layers. Simulations set as an electrochemical cell revealed that externally applied bias largely determines cation deposition mechanisms. Considering different salt/solvent combinations and two sets of potential regimes indicated that solvent structures with symmetric charge density, such as DOL, exert less influence on cation deposition, whereas salts with a large electric dipole moment, such as LiNO_3 , quickly prompt the formation of salt–solvent intermediate composites. For a low potential regime, low solvent (high salt) concentrations also result in fast salt adsorption with no solvent interaction. Such adsorbed structures always entail the formation of a surface–oxygen bond, as well as

different Li^+ -O polyhedra, depending on the salt/solvent pair. High potentials always result in accelerated deposition reactions, leading to adsorption of salt-solvent composites, even with DOL as solvent. Thus, moderate voltage windows and rapid deposition times (controlling the driving force given by electrolyte concentration and/or current rate) are suggested as the optimal choice for cation deposition and uniform growth of metal anode layers, in order to achieve stable electrode-electrolyte interfaces. Details are in *J. Mater. Chem. A*, 7, 8527-8539, (2019).

Charge environment surrounding fluorinated compounds

Fluorinated compounds are sought as important battery material components. Moreover, they are supposed to be part of the best solid electrolyte interphases (natural or artificial). Understanding their physical-chemical properties is crucial. Evaluation of molecular electrostatic potentials (MEPs) helps elucidating bulk or interfacial molecular behavior. We introduced a new visualization technique for the σ -hole region of molecules containing covalently bonded atoms of groups IV–VII. It consists in isolating a single potential surface surrounding the molecule and comparing its shape and coverage to other surfaces generated on a logarithmic scale from ~ 3 mV to 3 V. This allows a complementary inspection of the electrostatic behavior of the molecule with isodensity MEP maps displaying potential as a colored spectrum along the desired surface. For molecules with multiple potential regions existing at the same isopotential value like in the case of PF_6 , a typical counter-ion in present Li-ion batteries, a clear separation appears, and it displays behavior effectively. Compounds with F substituents that do not conform with the original σ -hole progression of the halobenzene series (fluorobenzene, neutral PF_5 and PF_6 , and the PF_6 anion), have a σ -hole appearing over generally smaller ranges. However, the range sizes are enough to determine the structure of interesting materials with nonbonded interactions affecting drift currents of Li-ions during battery charge and discharge. Details are in *J. Mol. Model.* 25, (2019).

Modeling plating and stripping

A Kinetic Monte Carlo (KMC) model was developed to investigate the competition between reaction and diffusion of Li ions during plating and stripping. The model showed the effect of the rates of the various events on the development of nucleation morphologies (Figure II.7.D.2). A non-dendritic interface morphology results under reaction and ionic transport controlled scenarios. Otherwise, mossy, dendritic, whisker or needle-like structures may grow with the main characteristic being the propensity for undesirable vertical growth. During discharging, a pitted interface may be formed along with bulk dissolution. Surface diffusion is a key determinant controlling the extent of dead Li formation, including a higher probability of the same when the effect of surface diffusion is comparable to that of ionic diffusion in the electrolyte and interface reaction. Details are in *J. Mater. Chem. A*, 7 (9), 4668-4688 (2019).

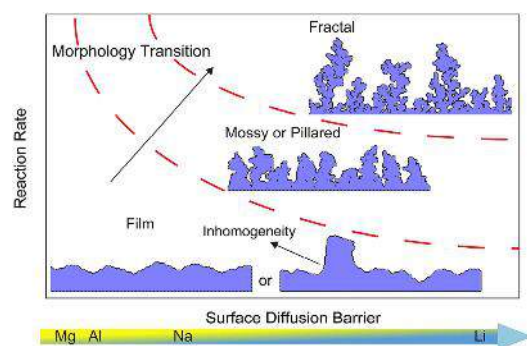


Figure II.7.D.2 Effects of reaction rate and surface diffusion barrier on the development of metal nucleation morphology as calculated from KMC simulations. From *Energy Storage Materials*, 20, 1 (2019)

A similar KMC model employed to emulate the cationic shield effect, when other cations (such as Cs^+) are added to the solution to moderate the Li electrodeposition mode, revealed that the use of additive cations forms an electrostatic shield at the dendrite tip, hindering dendrite growth. KMC results demonstrate that dendrite suppression depends on the concentration of additive cations, as well as the competition between the reaction

kinetics and transport of additive cations. Furthermore, the electrostatic shield helps regulate dendrite growth in the transport-limited regime, leading to relatively uniform dendrite height over the electrode width compared to that without additive cations. Additional details are *J. Mater. Chem. A*, 7, 18442-18450, (2019), and *Energy Storage Materials*, 20, 1 (2019).

Role of native SEI layer on reactivity of Li metal surfaces

A combined experimental and theoretical-computational study was carried out to determine the effect of native SEI layers (LiOH , Li_2O , Li_2CO_3) on the reactivity of Li metal surfaces. The composition and thickness of the simulated layers were determined by a controlled soft-landing experiment that allows depositing specific anions on the electrode surface and characterizing their decomposition via XPS experiments performed by our collaborators at PNNL. Our AIMD simulations clearly showed the differences in reactivity imposed by the presence of specific SEI layers covering Li metal. These differences arise because of the chemical and structural differences of the layers. For example, Li_2O is a crystalline ordered material that in thicknesses of $\sim 1\text{nm}$ is able to store and transfer charge to the TFSI anion without major structural changes. In contrast, both LiOH and Li_2CO_3 are molecular crystals with dipoles that reorient responding to the effect of the field imposed by the Li metal substrate (Figure II.7.D.3).

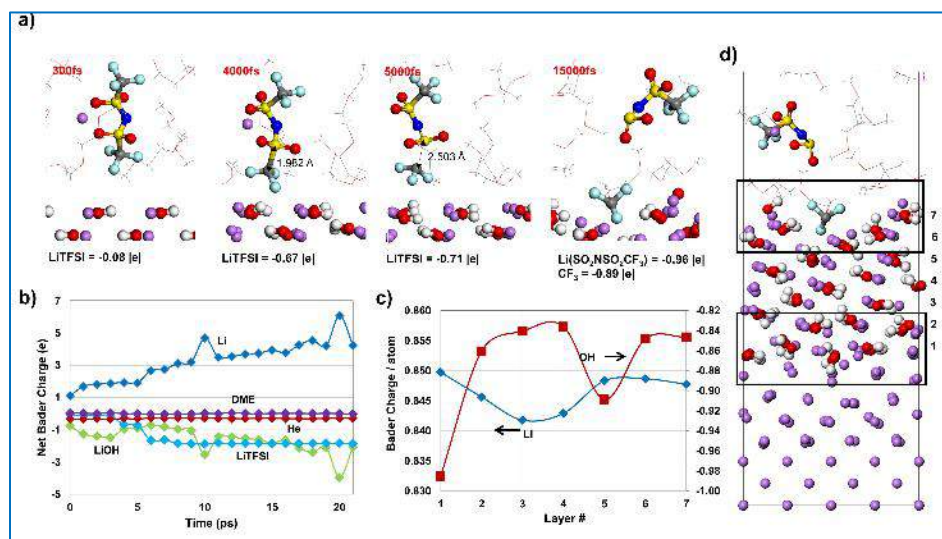


Figure II.7.D.3 LiTFSI decomposition on LiOH/Li. (a) Snapshots illustrating decomposition dynamics. (b) Net Bader charges of system components for DME and 1 M LiTFSI with Li/LiOH. (c) Bader charges of elements in Li and OH layer by layer, numbered as in (d). (d) Snapshot of the system at the end of dynamics. Color code: Li: purple; O: red; S: yellow; N: blue; F: light blue; C: gray

These structural changes also affect the electron transfer through the films. The Li_2O layer is more receptive for electronic charge transfer from the Li metal. Despite the high electronic charge transfer, the structural rearrangement within the Li_2O layer is minimal. The LiOH system behaves as the least-receptive passivation layer for electron transfer from the Li metal but displays large internal structural rearrangements (Figure II.7.D.3). In addition, the transferred electron from the Li metal appears mostly delocalized in the immediate OH layer at the metal interface, leading to a more positively charged top-surface layer of LiOH . The lack of electronic charge stored on the surface of LiOH is evident from the relatively slow decomposition of the LiTFSI molecule through a $2e^-$ reduction process. The stability of the LiTFSI molecule relies on its structural orientation with respect to the LiOH layer, indicating the dampened electron transfer process. The Li_2CO_3 layer shows the exchange of electronic charge leading to an oscillatory electronic density inside the layer in conjunction with the parent Li metal slab. This unique and fast (ps) electron exchange behavior is accompanied by significant structural rearrangements. The Li_2CO_3 layer also mediates faster kinetics in the LiTFSI molecule decomposition reactions compared with the decomposition reactions compared with the LiOH and Li_2O layers. For example, the LiF phase formation through a three-step reaction pathway is only observed in the presence

of the Li_2CO_3 surface layer within the time scale of our AIMD simulations. Additional details are in *ACS Appl. Mater. Interfaces*, 11, 31467-31476, (2019).

Reactivity and mechanical effects in solid electrolyte/Li metal interfaces

$\text{Li}_9\text{N}_2\text{Cl}_3$ is a solid electrolyte material of the family of choro-nitrides. AIMD study of an electrochemical interface between this material and a Li-metal surface was performed to analyze interfacial electrochemical instability. An external applied electric field emulates the interface under charging conditions (Figure II.7.D.4).

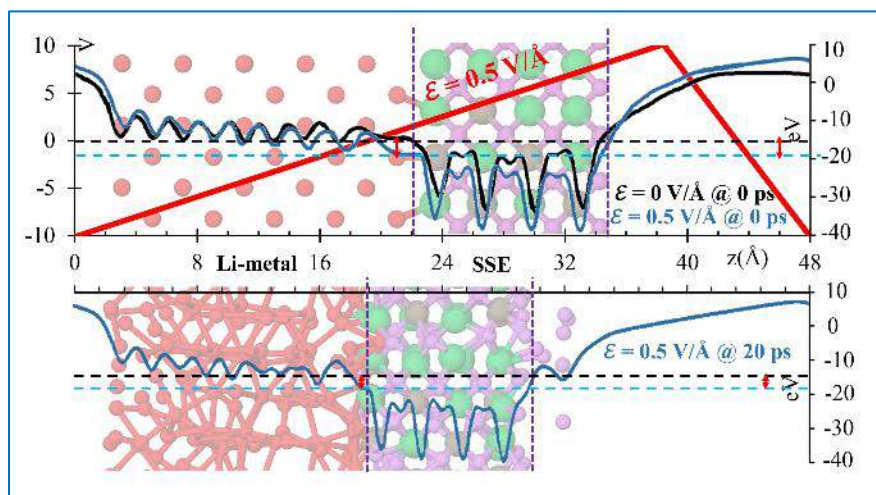


Figure II.7.D.4 Simulation cell contains Li metal surface (red atoms) interfacing with a solid-state electrolyte $\text{Li}_9\text{N}_2\text{Cl}_3$ (Li: purple, N: brown, Cl: green). (a) Input potential (red line) and potential energy profile with (black line) and without (yellow line) the application of an external electric field at 0 ps. (b) Potential energy profile (black line) at 20 ps under an external electric field along the z-axis pointing to the right. The asymptotic slope of the input potential along the slab tends to the external field of 0.5 V/Å

At open circuit, electrochemical stability existed at both sides of the interface, in good agreement with reported experiments. However, a structural re-accommodation takes place at both sides of the interface. Some oxidation of the surface Li-atoms takes place when Cl and N anions capture Li from the metal to complete octahedral structures. Charge and electron density analyses explain the difference between Cl and N behavior. At the interface with the $\text{Li}_9\text{N}_2\text{Cl}_3$ (002) facet, a larger negative charge on low-coordinated N atoms retains more Li atoms than the Cl atoms do. At charging conditions applying an external electric field (0.5 V/Å), no major changes are observed in atomic diffusion or structural changes at the interphase; except for changes of the Li-metal crystal structure. Due to migration of Li from the metal anode to the electrolyte, vacancies are created on the anode, causing a structural re-arrangement at the anode surface. In comparison with our previous studies on solid-state sulfide based electrolytes, this electrolyte is much more stable. Interesting insights were found about mechanisms of Li migration under the electric field via cooperative effect of the almost-immobile anions. Additional details are given in *J. Electrochem. Soc.* 166, A2048-A2057, (2019).

In solid electrolytes, mechanical stability is crucial. Reaction-driven interfacial growth causes significant strain in layered architectures accompanied by mass transfer and moving boundaries. An analytical model of the stress generated in a multilayer film incorporating the elastic-plastic strain of the growth layer, suggested its strong dependence on the mechanical properties and thickness. This analytical formalism was applied to a layered all-solid-state lithium battery architecture. The following conclusions were obtained: (1) In the early stage of Li plating, the Li metal electrode undergoes elastic deformation. To avoid the failure of materials, the positive electrode film requires high stiffness and the external elastic constraints on the multilayer film should be small to release the volumetric changes of electrode materials. (2) Stress can be significantly reduced by using porous hosts for Li electrodeposition due to relatively low Li molar volume. Porous hosts could also increase the active sites and thus avoid Li dendrite growth at high current density. (3) Li dendrite penetration through the solid electrolyte separator can be alleviated by increasing the fracture toughness of solid

electrolytes, reducing the surface flaw size, and applying internal battery pressure. Details of this analysis are in *Phys. Rev. Appl.*, 11 (3), 034038 (2019).

Cathode stability

Metal-oxide cathodes suffer from structural/thermal instability that lead to the release of their lattice O under non-equilibrium conditions and safety concerns in Li-ion and Li-metal batteries. Our combined experimental and theoretical study showed that an atomically thin layer of reduced graphene oxide (rGO) can suppress oxygen release from Li_xCoO_2 (LCO) particles and improve their structural stability. Experiments suggested that O release is hindered at high cutoff voltage cycling when the cathode is coated with rGO, and reduction of Co species from the graphene-coated samples is delayed when compared with bare cathodes. DFT and AIMD simulations showed that the rGO layers could suppress O_2 formation more effectively due to the strong C-O cathode bond formation at the interface of rGO/LCO where low coordination oxygen atoms exist. Experiments were performed by collaborators at the University of Illinois at Chicago. Additional details are given in *Adv. Funct. Mater.*, 1901110, (2019).

Conclusions

New first-principles atomistic-level methodologies demonstrated the effect of electric fields on cation electrodeposition in the presence of liquid or solid electrolytes. The applied field affects the thermodynamics and kinetics of Li electrodeposition, but the mechanisms for electrodeposition are less dependent on the actual value of the field. For liquid electrolytes, the nature and concentration of both salt and solvent determine the details of the desolvation and deposition events. In solid electrolytes, the effect depends on the “softness” and electrochemical stability of the electrolyte. For relatively stable solid electrolytes, the only noticeable effect is a faster kinetics. Simulations also allowed the identification of ionic transport mechanisms in solid electrolytes under applied fields. Further Li nucleation events take place in longer time and length scales. Coarse-grained methods revealed the Li nucleation morphology evolution as a function of surface diffusion, ionic diffusion, and interfacial reactions. Differences in Li metal reactivity due to native SEI layers were examined with an integrated experimental/computational study. Charge storage and release by the different layers was found to be highly dependent on their structural and polarizability characteristics. Mitigation strategies based on an atomically thin reduced graphene oxide coating layer were tested regarding O_2 release from oxide cathodes during battery operation. The protective effect of the graphene oxide layer on partially delithiated cathodes is due to the bonding of the under-coordinated lattice O to C atoms of the coating, which limits O_2 evolution.

Key Publications

1. Galvez-Aranda, D. E.; Varma, A.; Hankins, K.; Seminario, J. M.; Mukherjee, P. P.; Balbuena, P. B., “Chemical and Mechanical Degradation and Mitigation Strategies for Si Anodes”, *J. Power Sources*, 419, 208-218, (2019).
2. D. Tewari, P. P. Mukherjee, “Mechanistic Understanding of Electrochemical Plating and Stripping of Metal Electrodes”, *J. Mater. Chem. A*, 7 (9), 4668-4688 (2019).
3. F. Hao, W. Wang, and P.P. Mukherjee, “Electrochemical-Reaction-Driven Interfacial Stress in a Solid-Solid Layered Architecture,” *Phys. Rev. Appl.*, 11 (3), 034038 (2019).
4. R. C. Longo, L. E. Camacho-Forero, and P. B. Balbuena, “Charge-Mediated Cation Deposition on Metallic Surfaces,” *J. Mater. Chem. A*, 7, 8527-8539, (2019).
5. Sharifi-Asl, F. A. Soto, Y. Yuan, T. Foroozan, P. Abbasi, R. Deivanayagam, R. Rojaee, B. Song, A. Salehi-khojin, K. Amine, J. Lu, P. B. Balbuena, R. Shahbazian-Yassar, “Anti-Oxygen Leaking LiCoO_2 ,” *Adv. Funct. Mater.*, 1901110, (2019).
6. R. J. Alaminosky and J. M. Seminario, “Sigma-Holes from Iso Molecular Electrostatic Potential Surfaces,” *J. Mol. Model.* 25, (2019).
7. D. E. Galvez-Aranda and J. M. Seminario, “Ab Initio Study of the Interface of the Solid-State Electrolyte $\text{Li}_9\text{N}_2\text{Cl}_3$ with a Li-Metal Electrode,” *J. Electrochem. Soc.* 166, A2048-A2057, (2019).

8. Hao, A. Verma, and P. P. Mukherjee. "Electrodeposition stability of metal electrodes." *Energy Storage Materials*, 20, 1 (2019).
9. E. P. Kamphaus, S. Angarita-Gomez; X. Qin; M. Shao; M. Engelhard; K. Mueller; V. Murugesan,; P. B. Balbuena, "Role of inorganic surface layer on solid electrolyte interphase evolution at Li-metal anodes," *ACS Appl. Mater. Interfaces*, 11, 31467-31476, (2019).
10. F. Hao, A. Verma, and P. P. Mukherjee, "Cationic Shield Mediated Electrodeposition Stability in Metal Electrodes," *J. Mater. Chem. A*, 7, 18442-18450, (2019).

II.7.E Engineering Approaches to Dendrite Free Lithium Anodes (University of Pittsburgh)

Dr. Prashant N. Kumta, Principal Investigator

University of Pittsburgh
815C Benedum Hall, 3700 O'Hara Street
Pittsburgh, PA 15261
E-mail: pkumta@pitt.edu

Dr. Moni Kanchan Datta, Principal Investigator

University of Pittsburgh
815C Benedum Hall, 3700 O'Hara Street
Pittsburgh, PA 15261
E-mail: mkd16@pitt.edu

Dr. Oleg I. Vellkokhatnyi, Principal Investigator

University of Pittsburgh
815C Benedum Hall, 3700 O'Hara Street
Pittsburgh, PA 15261
E-mail: olv3@pitt.edu

Tien Duong, DOE Technology Development Manager

U.S. Department of Energy
E-mail: Tien.Duong@ee.doe.gov

Start Date: October 1, 2016	End Date: September 30, 2019	
Project Funding (FY19): \$539,268	DOE share: \$431,160	Non-DOE share: \$108,108

Project Introduction

Lithium (Li) cycling under normal conditions in a lithium metal battery (LMB) witnesses a non-planar Li/electrolyte interface (cellular/dendritic microstructure) primarily responsible for controlling the performance, safety and reliability of LMBs. Dendrite formation in electrochemical systems occurs due to inhomogeneous current densities coupled with local diffusion gradients, surface roughness, and kinetic roughening of the surface of the anode systems. However, as complex and ubiquitous as it seems, the phenomenon of Li dendrite nucleation and growth are not very well-understood. It is reported that a planar front is stable only if the current density is sufficiently small, and/or the transference number as well as/or chemical diffusivity of Li ion in the electrolyte is sufficiently large. Since the surface microstructures form a major link connecting the performance and electrodeposition/plating conditions, it is important to develop scientific understandings of how the Li metal plating conditions, as well as the electrolyte and the current collector properties influence the resulting microstructures of the plated Li metal. This is important in order to predict, modify, and control the microstructure of the deposited Li metal by meticulously designing the appropriate battery components as well as the Li metal electrodeposition/plating conditions. Adding to the complexity and increasing the enigmatic nature is the formation of the solid-electrolyte interphase (SEI). Control and elimination of Li metal dendrite formation is a veritable challenge and, if overcome, would render the universal adoption of lithium metal batteries (LMB) for stationary and transportation electric vehicle (EV) applications. The current project is thus a scientific study of novel approaches undertaken and implemented to address the highly complex but ubiquitous problem of dendrite formation in LMBs, combined with electrolyte decomposition, and associated cell-failure. Development of dendrite free high-performance Li anodes will enable the use of Li-free cathodes (e.g., Li-S, Li-air) opening up a myriad possibilities pushing the envelope in terms of achieving the desired cathode capacity and battery energy density with cost $\leq \$75$ (kWh)⁻¹.

Objectives

This project will yield lithium metal anodes with specific capacity ≥ 2000 mAh/g (≥ 4 mAh/cm²), cycling stability of ~ 1000 cycles, coulombic efficiency loss $\leq 0.01\%$, coulombic efficiency: $\geq 99.99\%$ combined with superior rate capability. The goal is to systematically characterize the different approaches for generation of dendrite-free Li-metal anodes while also providing an understanding of the scientific underpinnings, as well as evaluating the microstructure and electrochemical performance of the dendrite free Li metal anodes. The morphological stability/instability criterion analysis will be developed based on the concept of “*the constitutional under-potential plating*” (CUP) and perturbation analysis occurring at the Li-metal/electrolyte interface to understand the driving force as well as resistance to perturbation for the formation of the nonplanar interface microstructure. Finally, the effects of battery cycling parameters such as current density and potential gradient on the morphology and size of Li microstructures (e.g., dendrite tip radius, dendrite arm spacing) will be developed which will predict, modify, and control the microstructure of the deposited Li metal by designing appropriate battery component systems and electrodeposition conditions. Generation of high performance dendrite free Li metal anodes will successfully demonstrate generation of novel sulfur cathodes affording the fabrication of Li-S batteries meeting the targeted gravimetric energy densities ≥ 350 Wh/kg and ≥ 750 Wh/l with a cost target \$125/kWh and cycle life of at least 1000 cycles for meeting the next generation EV everywhere blueprint.

Approach

This is a multi-year project comprised of three major phases to be successfully completed in three years.

- Phase – 1 (Year 1): Synthesis, characterization and scale up of suitable porous metal foams (PMFs) for use as current collectors for lithium anodes and Li-ion conductor (LIC) materials to prepare multilayer porous foams (MPFs).
- Phase – 2 (Year 2): Development of Li-rich structurally isomorphous alloy (SIA) anodes and Generation of composite multilayer anodes (CMAs).
- Phase-3 (Year 3): Advanced high energy density, high rate, and extremely cyclable cell development.

The project will involve collaboration with Dr. Moni Kanchan Datta (UPitt) and Dr. Oleg I. Velikokhatnyi (UPitt) as Co-PIs. In addition, collaborations will be undertaken and continued with Dr. D. Krishnan Achary (UPitt) for solid-state nuclear magnetic resonance (MAS-NMR) characterization.

Results

A systematic theoretical and experimental study was performed to understand the formation of non-planar interface microstructure to determine the condition needed for eliminating dendrite formation during Li metal plating [1]. It is predicted that if the equilibrium potential gradient (mG_c) at the electrode/electrolyte interface arising due to concentration gradient at the interface (G_c) is higher than the true potential gradient (G_L) at the electrolyte ($mG_c > G_L$) (Figure II.7.E.1a), the electrolyte in front of the interface will be in an underpotential state leading to a nonplanar interface.

The developed perturbation theory as well as the dendrite kinetic theory including interfacial/adhesion energy and Gibbs Thomson parameter (GTP) serve to lower the perturbation parameter in addition to the driving force for perturbation ($mG_c - G_L$) successfully predicting the effect of concentration gradient and interfacial energy on the formation of planar/non-planar interface structure (PCT/US2018/041210) [2]. Accordingly, identification of a suitable current collector exhibiting desired adhesion energy/capillarity as well as high wettability with Li metal is thus expected to increase the energy required to perturb the interface with high curvature, and consequently, improve the cycle life of LMBs.

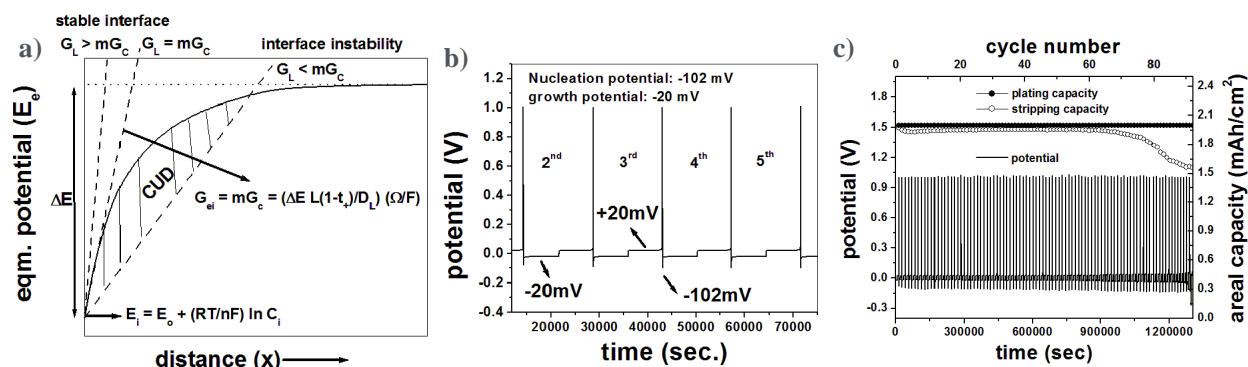


Figure II.7.E.1 (a) Equilibrium plating potential of Li arising due to compositional variation at the Li-metal/electrolyte interface illustrating the condition for dendrite formation. (b) Variation of Li metal plating and stripping potential for 5th-10th cycles of positive interfacial energy current collector. The plot shows large nucleation underpotential (-100 mV) with growth potential of -21 mV cycled at a current density of 1 mA cm^{-2} with plating areal capacity 2 mAh cm^{-2} (c) Plating and stripping potential variation with time for 92 cycles, and areal capacity 2 mAh/cm^2 with cycle number for positive interfacial energy current collector showing poor cycle life after 60 cycles

It must be mentioned here that identification of suitable current collector exhibiting excellent wettability ($\theta < 30^\circ$, θ is wetting angle) with Li metal also improves the nucleation kinetics by minimizing the nucleation barrier and improving the nucleation rate to yield conditions for homogeneous deposition of Li metal across the current collector [1],[2]. Metal alloys exhibiting low interfacial energy or adhesion energy with Li metal are expected to form dendritic structures and correspondingly, delaminate from the current collector resulting in poor cycle life.

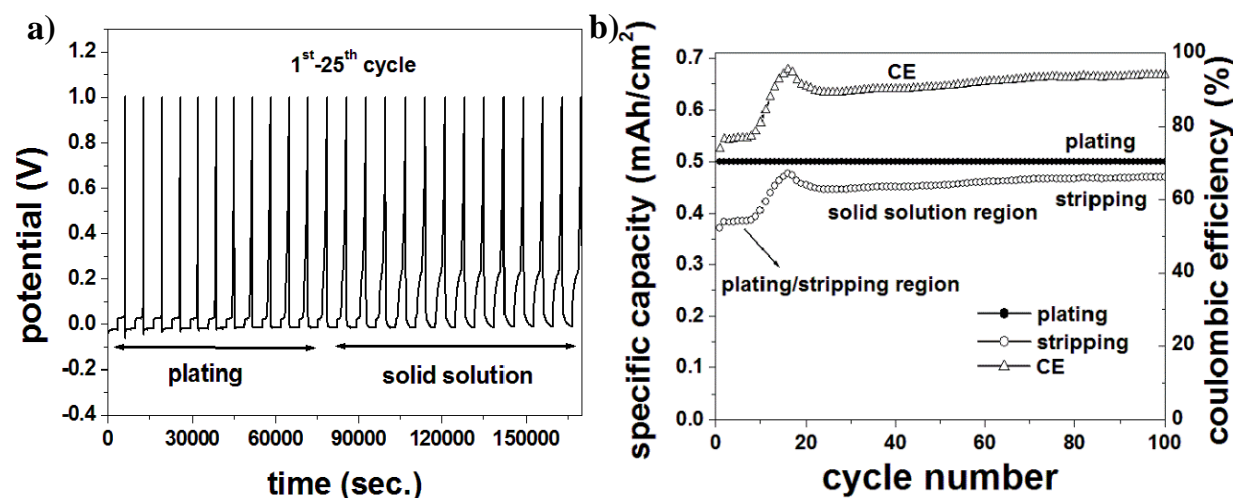


Figure II.7.E.2 (a) Variation of Li metal plating and stripping potential for 25th cycles of SIA cycled at a current density of 1 mA cm^{-2} with plating areal capacity 0.5 mAh cm^{-2} (b) Variation areal capacity with cycle number of SIA showing excellent cycle life, however, low CE for first 10th cycles due to low Li ion diffusivity

One of the alloys developed by the PIs exhibiting low interfacial energy ($+90 \text{ kJ mol}^{-1}$) cycled at a plating current density of 1 mA cm^{-2} with a charge density 2 mAh cm^{-2} shows a high nucleation underpotential (-100 mV) (Figure II.7.E.1b). The system also shows poor cycle life/coulombic efficiency after 60 cycles due to the formation of dendritic structure and subsequently causing delamination of the Li metal from the current collector (Figure II.7.E.1c). Therefore, suitable alloy design of current collector exhibiting non-reactivity to Li metal along with high interfacial energy and excellent lattice registry as well as good wetting with Li metal is highly desirable. Several promising structurally isomorphous alloys (SIAs), multicomponent alloys (MCA) and interface engineered Cu current collectors (IES) have been developed keeping in mind the above aspects conducive for effective Li metal plating/stripping for achieving the desired microstructural control. To

determine the Li growth front morphology after significant crystal growth ($\sim 10\text{-}20\mu\text{m}$ thickness) of the nucleated Li, and study the long term cycling performance of Li metal at a charge density of $1\text{mAh}/\text{cm}^2$ - $4\text{mAh}/\text{cm}^2$, the Li metal plating/stripping was carried out at a current density of $0.5\text{mA}/\text{cm}^2$ - $1\text{mA}/\text{cm}^2$ for 1h-4h up to 100-300 cycles tested in $1.8\text{M LiTFSI}+0.2\text{M LiNO}_3$ in DOL:DME electrolyte.

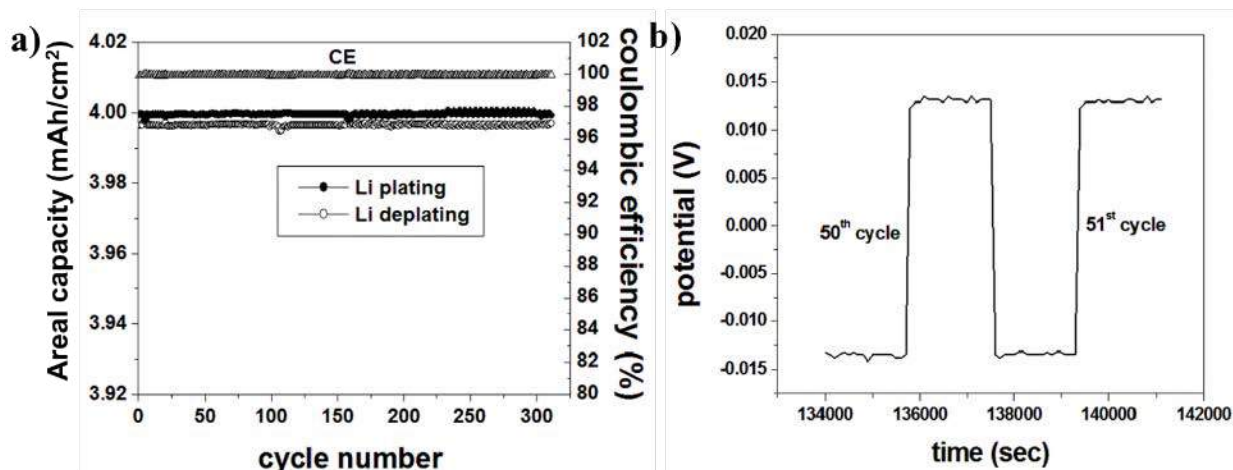


Figure II.7.E.3 (a) Variation areal capacity with cycle number of MCA showing excellent cycle life with CE $\sim 99.9\%$ cycled at $1\text{mA}/\text{cm}^2$. (b) Variation of Li metal plating and stripping potential for 50 $^{\text{th}}$ cycles of MCA showing zero nucleation underpotential and 15mV growth potential

The developed SIAs/MCAs/IESs with excellent Li metal lattice registry and large GTP in particular, serve as next generation current collectors displaying excellent cyclability obviating cellular or dendritic structure formation promoting long cycle life (Figure II.7.E.2, Figure II.7.E.3 and Figure II.7.E.4). SIA alloys show low CE ($\sim 80\%$) for first few cycles (Figure II.7.E.2) due to low diffusivity of Li and SEI formation of highly reactive SIAs with the electrolyte. Therefore, a systematic theoretical study based on DFT calculation is needed to identify suitable alloying elements to improve the Li ion diffusivity in SIA alloys. On the other hand, the developed MCA alloys show excellent cyclability upto 300 cycles with zero nucleation underpotential cycled at a current density of $1\text{mA}/\text{cm}^2$ yielding an areal capacity $\sim 4\text{mAh}/\text{cm}^2$ (Figure II.7.E.3).

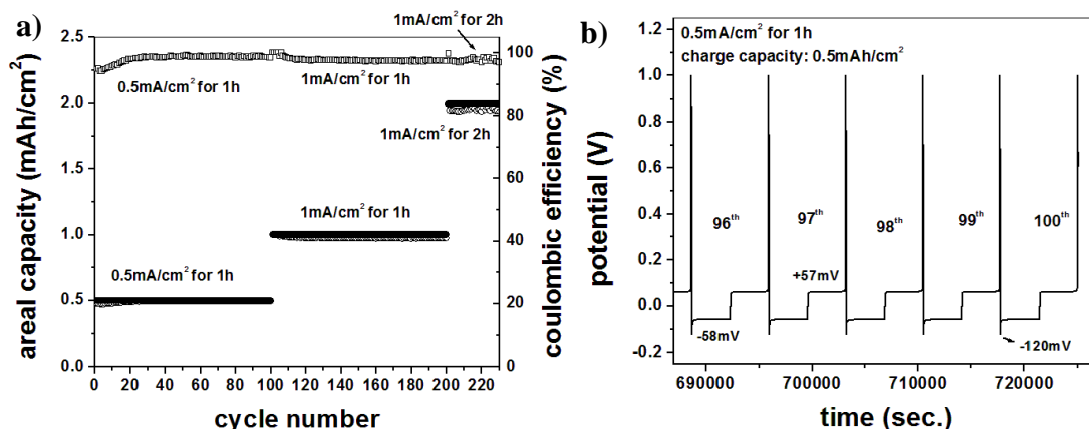


Figure II.7.E.4 (a) Variation areal capacity with cycle number of IES showing excellent cycle life with CE $\sim 99.4\%$. (b) Variation of Li metal plating and stripping potential for 96 $^{\text{th}}$ -100 $^{\text{th}}$ cycles showing 58mV growth potential

The plating/stripping behavior of Li metal using the novel “zero nucleation underpotential” MCAs (Figure II.7.E.3) also shows a coulombic efficiency $\sim 100\%$. The SEM micrograph of the Li metal growth front obtained after 100 cycles for MCA, shown in Figure II.7.E.5, indicates the evolution of a planar morphology with no presence of dendritic structures. Similarly, IES on Cu current collector shows excellent cyclability

(Figure II.7.E.4). The variation of areal capacity with cycling (Figure II.7.E.4) up to 220 cycles of studied IES coated Cu foil tested at a different current density shows excellent cyclability with CE >99.5% after 10th cycle whereas traditional Cu current collector exhibits poor cyclability after few cycles. Figure II.7.E.4 also shows absence of intermetallics formation during Li metal plating suggesting the Li ion non-reactivity of IES to form intermetallics or solid solution. Further, the growth potential of Li metal (Figure II.7.E.5b), cycled at a current density of 0.5mAh/cm² for 1h, show no significant growth potential change (~58 mV) with time or cycling, suggesting minimal potential hysteresis of IES coated Cu foil. The above results clearly suggest that the novel materials developed exhibiting high Li ion absorption (i.e., minimizing the driving force of perturbation) and high Gibbs Thomson parameter current collector are a promising way to improve the Li metal battery performance without formation of dendrites.

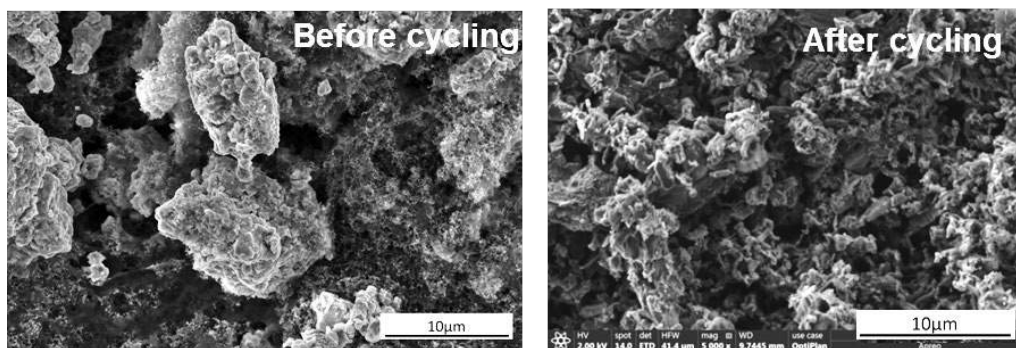


Figure II.7.E.5 SEM micrograph of Li metal growth front obtained after 100 cycles.

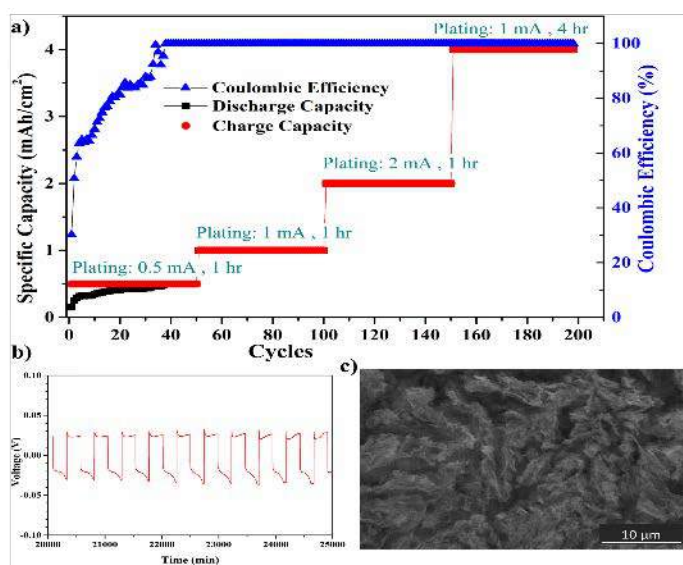


Figure II.7.E.6 a) Electrochemical cycling, b) Voltage profile after 40 cycles, c) SEM after 200 cycles showing absence of dendrites, scale bar 10 microns

In addition, different effective nucleating agents (ENA) are alloyed with effective host alloy (EHA) to form effective nucleating host alloys (ENHA) transforming the Li plating field towards uniform homogenous nucleation and growth regime. High energy mechanical milling (HEMM) was used to synthesize these new materials and the evolution of the phases was accordingly studied using X-ray diffraction. Subsequently, ENHA was studied for Li plating/stripping in a CR2025 coin cell using Li as counter/reference electrode and 1M LiPF₆ in EC:DEC:FEC as the electrolyte at different areal current/charge densities as shown in Figure II.7.E.6 (a). ENHA exhibits improvements in the electrochemical processes of reversible Li plating/stripping yielding a high coulombic efficiency of ~99.6% at the end of 200 cycles (Figure II.7.E.6a). The

plating/stripping potential decreases ~20-40 mV as the electrode stabilizes after 40 cycles (Figure II.7.E.6b). Post cycled SEM images of the electrode (Figure II.7.E.6c) indicates absence of dendrites due to the efficient nucleation and uniform growth of Li during the plating and stripping processes of ENHA alloy.

Carbon Based Nanostructures for stable lithium metal plating:

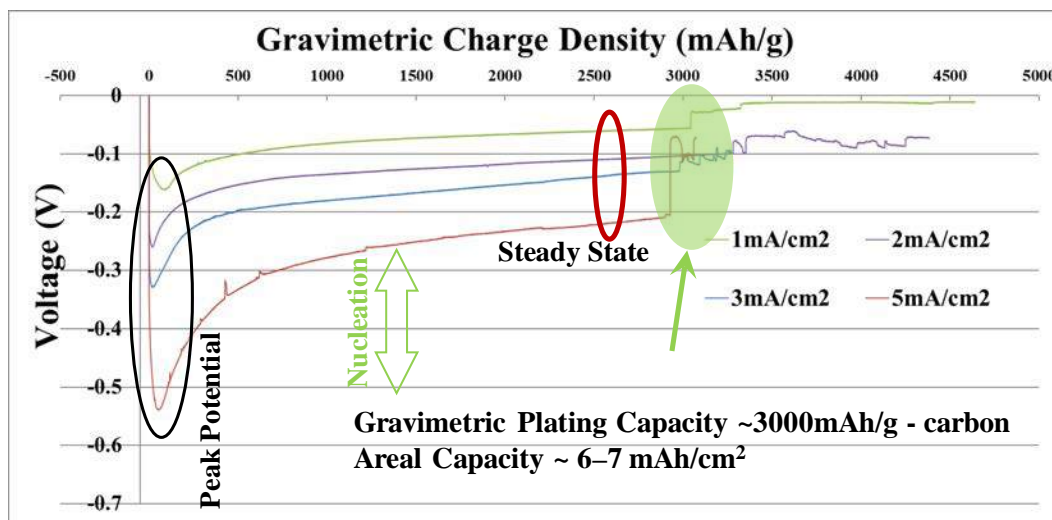


Figure II.7.E.7 Nucleation and growth behavior of carbon nano -architectures at different current rates.

The major fundamental issues associated with Li plating is the high over potential of plating (both nucleation and growth) followed by inefficient electron transfer due to formation and growth of electronically non conducting SEI layer. Hence, a novel nanostructured carbon-based electrode was designed and fabricated to control the electron transfer phenomenon in the substrate and Li^+ transfer from the solvent to the growing lithium site. The surface of these nanostructured electrode provides uniform deposition sites resulting in homogenous growth resulting in coalescence of growth sites and reduces the electron transfer resistance within the electrode from the surface of the Li growth site.

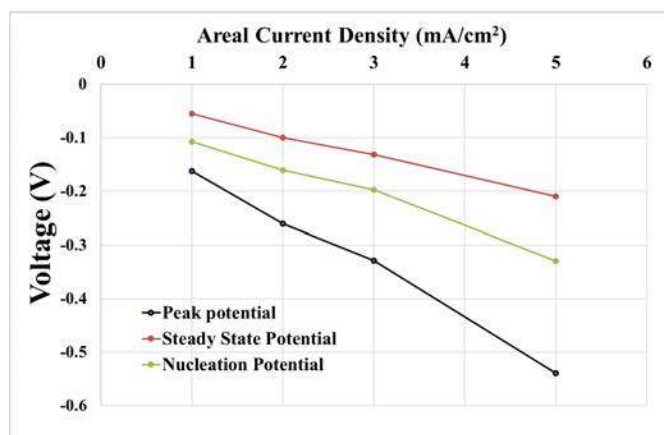


Figure II.7.E.8 Variation of potentials of Li plating on carbon nanoarchitectures at different current densities

Lithium intercalation and deintercalation reaction with these carbon-based electrodes accordingly show a capacity contribution of ~100-150mAh/g and ~40-50mAh/g at low (25mA/g) and high (4A/g) current rates, respectively, with a capacity loss of ~250-300mAh/g during the initial cycles. Subsequently, Sand's time experiment for single plating experiment was carried out in a two-electrode pressure less system to study the stability of Li plating (Figure II.7.E.7). The electrodes show a stable plating capacity of ~3000mAh/g with an

areal capacity of $\sim 6\text{--}7\text{mAh/cm}^2$ before approaching the undesired mossy / fractal Li plating for an active material loading of $\sim 2\text{--}3\text{mg/cm}^2$. The steady state growth region shows minimal fluctuations (data point recorded @ 0.5mV voltage fluctuation) indicating uniform growth front. Even at high current density of 5mA/cm^2 the system shows a low nucleation overpotential $\sim 0.33\text{V}$ (Figure II.7.E.8). This carbon - based nano architecture also shows a columbic efficiency of $\sim 95\text{--}97\%$ during initial cycles followed by $\sim 99.71\text{--}99.87\%$ for over 200 cycles for a plating charge of 4mAh/cm^2 and current densities of 1mA/cm^2 and 4mA/cm^2 (Figure II.7.E.9).

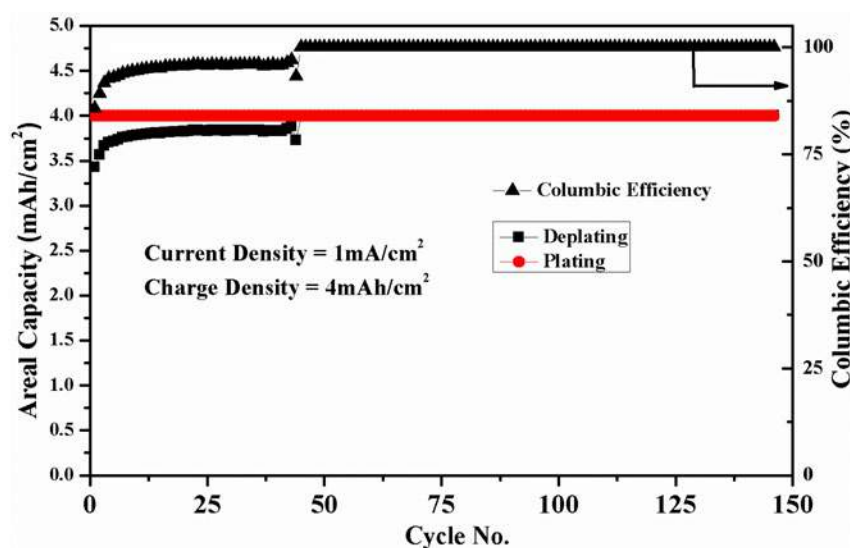


Figure II.7.E.9 Columbic Efficiency of Li plating and deplating @ 1mA/cm^2 , 4mAh/cm^2 in Li/Li+ cell

Hence, a study of this transition region has been conducted to see the voltage profile in this region for short circuiting phenomenon. A study of the voltage profile for this cell (Figure II.7.E.10) between the 40th – 50th cycles (between 350h – 400h) indicates a distinct region with the system transitioning from nucleation and growth to plating regime without nucleation. Following this, the plating phenomenon uses pre-existing nucleation sites without creating new plating regions.

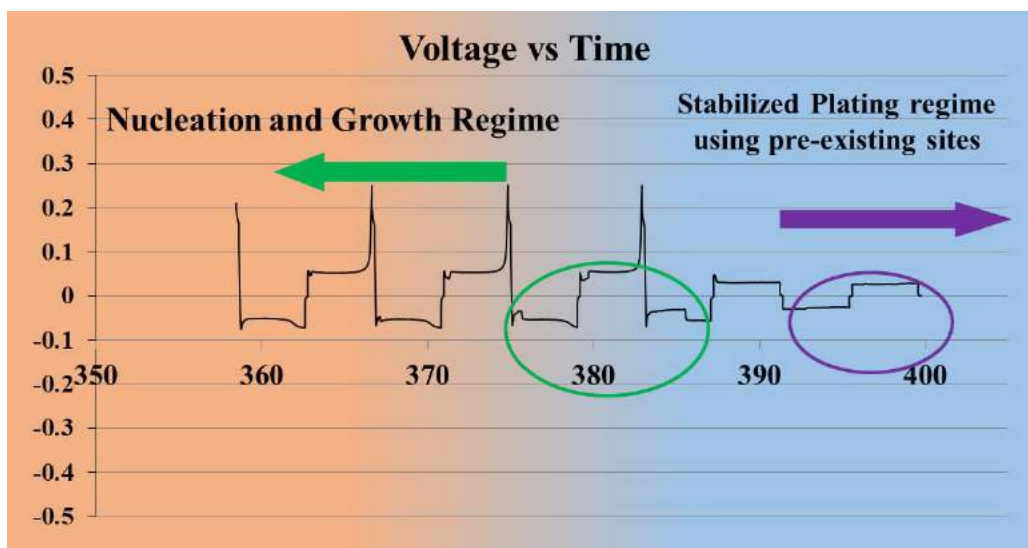


Figure II.7.E.10 Voltage vs. time (hours) profile of carbon-based electrodes at the transition region in traditional coin cell testing

Additionally, in normal coin cell testing (the Li foil area is smaller than the working copper electrode area), the Li plating hence, spreads with each cycle due to resistance to plating created by the formation of the SEI layer. Hence, the system shows false results of stable Li plating for 30–80 cycles depending on the current/charge density. A new insulated coin cell design was introduced confining the Li plating on the copper working electrode and correspondingly, recording the actual performance of the electrodes by insulating the stainless steel in the coin cell from the electrolyte contact while preserving its electrical continuity with the copper working electrode (Figure II.7.E.11). The CE of the Cu foil decreases to ~75 – 80% within the first 5 cycles in the insulated coin cell compared to traditional testing where the Cu foil shows stable plating for 50 cycles. This testing method provides rapid experimental technique to study the actual performance of the materials for Li plating accelerating the study, reducing the characterization time along with providing a scientifically accurate testing method in coin cells.

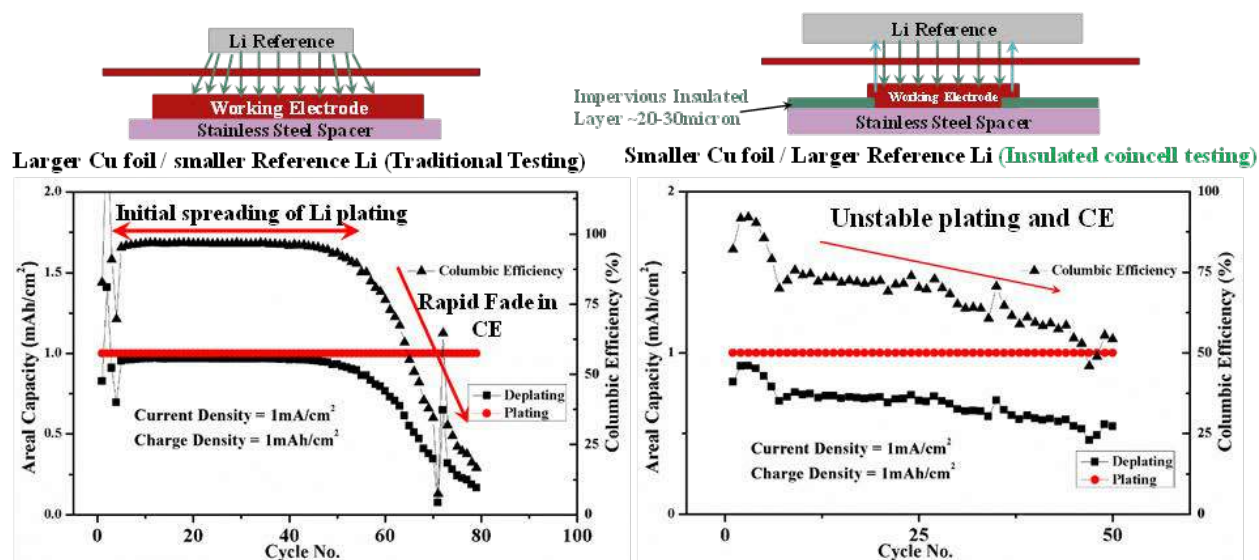


Figure II.7.E.11 Schematic of the traditional and insulated coin cell testing along with the recorded performance for copper foils

Hence, carbon-based architectures in traditional coin cell testing show an initial low CE of plating (~95-97%) due to spreading of the Li plating marked by distinct nucleation and growth regimes during each cycle after which the spread of Li plating saturates. Subsequently, the system shows a CE of ~99.71-99.87% representing the actual performance of the carbon nano architectures. Carbon nano – architected electrodes thus, tested in an insulated coin cell (Figure II.7.E.12) show a high CE of >99.85% in the first 10 cycles of Li plating and deplating @4mA/cm², 4mAh/cm² and a high CE of >99.9% for over 500 cycles upon long term cycling. CE fluctuations observed in the initial 10 cycles is due to activation of new regions in the nanostructures.

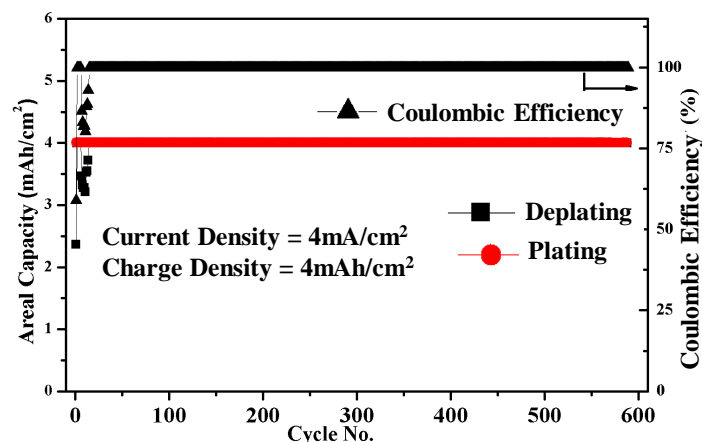


Figure II.7.E.12 Coulombic Efficiency of Li plating and de-plating @4mA/cm², 4mAh/cm² in Li/Li+ cell (Insulated coin cell).

Conclusions

A rigorous theoretical study based on mass transfer and charge transfer of Li ions under the combined influence of potential gradient (G_L), named as migrational Li ion flux, and concentration gradient (G_c), named as diffusional flux, has been conducted. It is predicted that if the equilibrium potential gradient generated at the electrode/electrolyte interface ($G_L = mG_c$) arising due to concentration gradient at the interface is higher than the true potential gradient in the electrolyte ($mG_c > G_L$), the electrolyte in front of the interface will be in an underpotential region and as a result, a non-planar interface will be formed. In addition to the driving force to perturbation ($mG_c - G_L$) parameter, the developed perturbation theory as well as dendrite kinetic theory successfully predicts the effect of interfacial energy (γ) or Gibbs Thomson parameter (Γ) as resistance to the perturbation parameter on the formation of planar interface structure. The detailed theoretical analysis herein brings to the forefront the intricate connections between the concentration and the potential gradients with the current density such that one can predict, modify, and control the microstructure of the electrochemically deposited Li metal by designing appropriate current collector, electrolyte and cycling conditions to prevent the deleterious influence of formation of dendrites thus enabling an anode-free LMB system. Identification of suitable current collectors, exhibiting desired interfacial energy/capillarity with Li metal (high Gibbs Thomson parameter (Γ)) are in line with the theoretical analyses, and as a result, offer a novel approach to dendrite-free anode less LMB system with improved cycle life. The current project was successful in developing several systems (SIA, MCA, IES, ENHA) exhibiting zero nucleation underpotential and no intermetallic formation with the Li metal. The developed alloys clearly suggest that novel materials exhibiting high Li ion absorption (i.e., minimizing the driving force of perturbation) and high Gibbs Thomson parameter current collector are a promising way to improve the Li metal battery performance without formation of dendrites over long cycles (~300 cycles).

Additionally, novel nanostructured carbon electrode structures were developed along with an accurate framework for the electrochemical characterization of the Li plating and deplating processes. These carbon-based nanostructures showed a high coulombic efficiency of ~99.71-99.87% for over 600 cycles when tested in insulated coin cell at current densities of ~1 – 6 mA/cm² and areal charge densities of 4 – 6 mAh/cm².

Key Publications

1. Moni K. Datta, Bharat Gattu, Ramalinga Kuruba, Pavithra Shanthi, and Prashant N. Kumta, "Constitutional Under-potential Plating (CUP) – New Insights for Predicting the Morphological Stability of Deposited Lithium Anodes in Lithium Metal Batteries", J. Power Sources (2019) under review.
2. P. N. Kumta, "Engineering approaches to dendrite free Li-metal anodes", Presentation given to GGB Bearings, September 9, 2019

3. Piyathip Thanapisitikul, Bharat Gattu, Moni Kanchan Datta, Bandi Ramalinga and Prashant N. Kumta, Hybrid Ceramic Solid State Electrolyte for High Performance Solid State Batteries, Presentation, 236th ECS meeting, Atlanta, GA, Oct 2019.

References

1. Moni K. Datta, Bharat Gattu, Ramalinga Kuruba, Pavithra Shanthi, and Prashant N. Kumta, “Constitutional Under-potential Plating (CUP) – New Insights for Predicting the Morphological Stability of Deposited Lithium Anodes in Lithium Metal Batteries”, J. Power Sources (2019) under review.
2. Jampani, P.H., Shanthi, P. M., Gattu, B., Datta, M K, Velikokhatnyi, O.I., Kumta, P.N., “High capacity, air-stable, Structurally Isomorphous lithium Alloy (SIA), Multilayer Porous Foams (MPFs) and Composite Multilayer Anodes (CMAs) for dendrite-free lithium metal anodes for Li-ion batteries”, U.S. Provisional Patent Appln. No. 62/529,588 (2017).

Acknowledgements

Research fully supported by the U.S. Department of Energy OVT-DE-EE0006825. Partial support from the Edward R. Weidlein Chair Professorship Funds, Nanomaterials for Energy Conversion and Storage Technology (NECST) Laboratories, and the Center for Complex Engineered Multifunctional Materials (CCEMM) from the University of Pittsburgh is also acknowledged for assistance and help with procuring the electrochemical equipment and facilities used in this research work.

II.7.F Electrochemically Responsive Self-Formed Li-ion Conductors for High Performance Li Metal Anodes (Penn State University)

Donghai Wang, Principal Investigator

The Pennsylvania State University
134 Energy and the Environment Laboratory Building
University Park, PA 16802
E-mail: dwang@psu.edu

Tien Duong, DOE Technology Development Manager

U.S. Department of Energy
E-mail: Tien.Duong@ee.doe.gov

Start Date: October 1, 2016	End Date: September 30, 2019	
Project Funding (FY19): \$1,266,050	DOE share: \$1,139,317	Non-DOE share: \$126,733

Project Introduction

The project will develop and optimize organo- Li_xS_y , organo- $\text{Li}_x\text{P}_y\text{S}_z$, and organo- $\text{Li}_x\text{S}_y/\text{organo-Li}_x\text{P}_y\text{S}_z$ composite materials as protective layers for Li metal anodes in Li-S batteries. The core focus will be on synthesis methods and precursors for new organic/inorganic hybrid Li-ion conductors, protective layer composition, and protective layer fabrication methods. This will be accompanied by property measurement and characterization (conductivity, mechanical properties, etc.) for the protective layer on Li metal, as well as detailed diagnostics and cell testing. At the conclusion of the project, twelve ~300 mAh pouch cells will be delivered which use the optimal protection layer.

Objectives

The objective of this project is to develop and deliver an electrochemically responsive self-formed hybrid Li-ion conductor as a protective layer for Li metal anodes, enabling Li metal anodes to cycle with a high efficiency of ~99.7% at high electrode capacity ($>6 \text{ mAh/cm}^2$) and high current density ($>2 \text{ mA/cm}^2$) for over 500 cycles. The project will also demonstrate prototype ~300 mAh Li-S battery cells with energy densities of ~200 Wh/kg and ~80% capacity retention for ~300 cycles at ~80% depth of discharge (DOD) using Li metal anodes with this protective layer.

Approach

The novel multiphase organo- Li_xS_y or organo- $\text{Li}_x\text{P}_y\text{S}_z$ hybrid ion conductors with tunable multi-functional organic components and controlled Li_xS_y and $\text{Li}_x\text{P}_y\text{S}_z$ inorganic components will be designed and prepared, and thus enable safe use of lithium metal with high CE. In the third year, the team will develop the organo- $\text{Li}_x\text{S}_y/\text{organo-Li}_x\text{P}_y\text{S}_z$ composite lithium protection layers with tuned functionality: (1) finding appropriate composition, (2) developing appropriate synthesis and fabrication methods, and (3) optimizing organo- $\text{Li}_x\text{S}_y/\text{organo-Li}_x\text{P}_y\text{S}_z$ components in a protection layer to further improve CE and Li-S battery performance.

Results

We develop a three-dimensional cross-linked polyethylenimine lithium-ion-affinity sponge (3D PPS) as the Li metal anode host and use electrokinetic phenomena to mitigate the issues of Li metal anode. We show that electrokinetic surface conduction and electroosmosis within the high-zeta-potential sponge (Figure II.7.F.1a) change concentration and current density profiles, enabling dendritic-free plating/stripping of lithium with high Coulombic efficiency (CE) at high deposition capacities and current densities, even at low temperatures. The use of lithium-hosting sponge leads to a significantly improved cycling stability of lithium-metal batteries with a limited amount of lithium (e.g., N/P ratio = 0.6) at commercial-level areal capacity.

3D PPS was prepared directly on Cu foil by an ice-templating method through crosslinking of branched polyethylenimine (PEI) by 1, 4-butanediol diglycidyl ether (BGE) (Figure II.7.F.1c). Scanning electron microscopy (SEM) investigation of the 3D PPS host on Cu foil (3D PPS@Cu) along top and cross-section views (Figure II.7.F.1d and e, respectively) reveals sponge-like porous structure containing irregularly shaped pores. The pores in 3D PPS have a high interconnectivity. The 3D PPS has a pore volume of $\sim 5.5 \text{ cm}^3 \text{ g}^{-1}$ and a porosity of 87%, and therefore can accommodate deposited Li as high as 74.6 wt% within the sponge host. 3D PPS has a lot of polar groups (amine and ether) which have strong affinity with Li ions and self-concentrate Li ions (self-concentrating feature). The Li-ion-affinity groups direct the formation of EDL in 3D PPS with a high zeta potential of approximately +42 mV in the electrolyte (1.0 M lithium

bis(trifluoromethanesulfonyl)imide (LiTFSI) in 1, 3-dioxolane (DOL) and 1, 2-dimethoxyethane (DME) with a volume ratio of 1:1). The existence of EDL promotes electrokinetic phenomena, such as electrokinetic surface conduction and electroosmosis (electrokinetic pumping feature), within the sponge under an electric field. the Li-ion electrokinetic self-concentrating and pumping features of the 3D PPS can synergistically overcome diffusion limited current (Figure II.7.F.2a), reduce the concentration polarization (Figure II.7.F.2b-h), and therefore regulate the Li-ion concentration difference in deionization area to enable a uniform Li-ion distribution (Figure II.7.F.2f).

Benefiting from the Li-ion electrokinetic self-concentrating and pumping effects of 3D PPS, dendrite-free Li plating/stripping on 3D PPS@Cu at both high deposition capacity and high current density is achieved in a variety of electrolytes. Compared with bare Cu electrode typical of mossy dendritic structure of Li (Figure II.7.F.3a-b), 3D PPS@Cu exhibits a uniform, compact and dendrite-free Li conformally deposited within 3D PPS at various deposition capacities and current densities in ether-based electrolyte (2 mA h cm^{-2} and 2 mA cm^{-2} in Figure II.7.F.3c-f; 2 mA h cm^{-2} and 4 mA cm^{-2} in Figure II.7.F.4a-d; 4 mA h cm^{-2} and 4 mA cm^{-2} in Figure II.7.F.4e-h; 4 mA h cm^{-2} and 6 mA cm^{-2} in Figure II.7.F.4i-l). Remarkably, at extremely high deposition capacities and current densities (6 mA h cm^{-2} and 6 mA cm^{-2} in Figure II.7.F.3i-l; 4 mA h cm^{-2} and 12 mA cm^{-2} in Figure II.7.F.5a-d; 4 mA h cm^{-2} and 20 mA cm^{-2} in Figure II.7.F.5e-h), the deposited Li still shows a uniform, compact morphology and a conformal structure within 3D PPS. Strikingly, even at low temperatures, uniform and dendrite-free Li deposition is still observed within 3D PPS at a high current density of 20 mA cm^{-2} and a deposition capacity of 4 mA h cm^{-2} (0°C and -10°C as shown in Figure II.7.F.6 and Figure II.7.F.7, respectively).

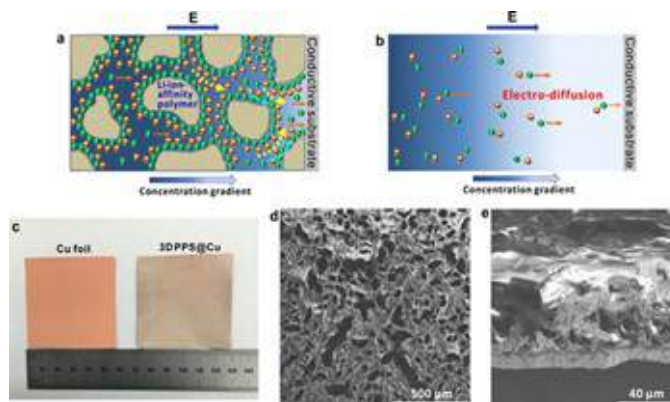


Figure II.7.F.1 (a) Electrokinetic phenomena (e.g. electrokinetic surface conduction and electroosmosis) in 3D PPS under electric field. (b) Electro-diffusion of Li ions in traditional cells under electric field. (c) Photograph of bare Cu foil and 3D PPS@Cu. (d) SEM morphology of 3D PPS@Cu (top view). (e) SEM morphology of 3D PPS@Cu (cross-section view).

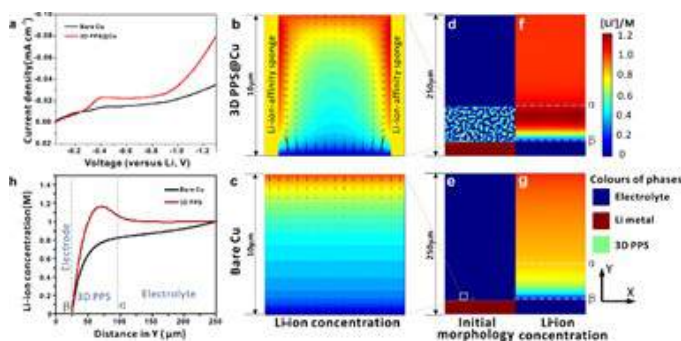


Figure II.7.F.2 The Li-ion electrokinetic self-concentrating and pumping features of the 3D PPS. (a) Linear sweep voltammograms of 3D PPS@Cu and bare Cu electrode, (b,c) Equilibrium Li-ion concentration profiles with constant-reaction-current electrode surfaces at the enlarged $10 \times 10 \mu\text{m}^2$ sponge-pore scale for (b) 3D PPS@Cu and (c) bare Cu electrode. (d,e) Initial phase morphologies of $250 \times 250 \mu\text{m}^2$ (d) 3D PPS@Cu and (e) bare Cu half-cell systems. (f,g) Equilibrium Li-ion concentration profiles with constant-reaction-current electrode surfaces at the $250 \times 250 \mu\text{m}^2$ scale for (f) 3D PPS@Cu and (g) bare Cu electrode. (h), 1D cross-sectional equilibrium Li-ion concentration profiles along Y direction in 3D PPS@Cu and bare Cu electrode.

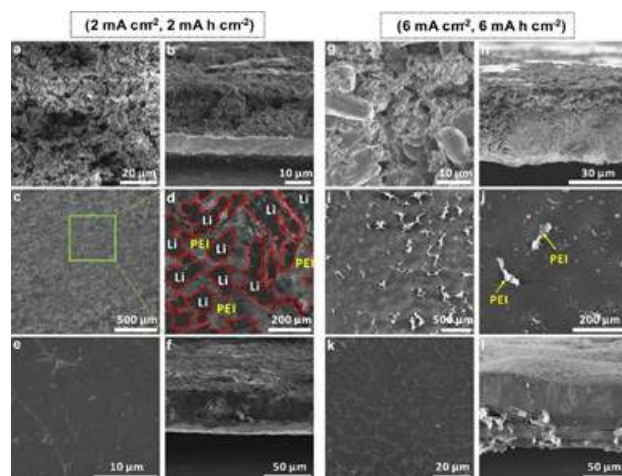


Figure II.7.F.3 The morphology of Li metal deposited on the different electrodes. SEM images of Li metal deposited on the bare Cu electrode (a-b) and 3D PPS@Cu (c-f) at a deposition capacity of 2 mA h cm^{-2} and current density of 2 mA cm^{-2} . SEM images of Li metal deposited on the bare Cu electrode (g-h) and 3D PPS@Cu (i-l) at a deposition capacity of 6 mA h cm^{-2} and current density of 6 mA cm^{-2} . The electrolyte used here is 1.0 M LiTFSI in DOL and DME ($V/V = 1$) with 1 wt\% LiNO_3 .

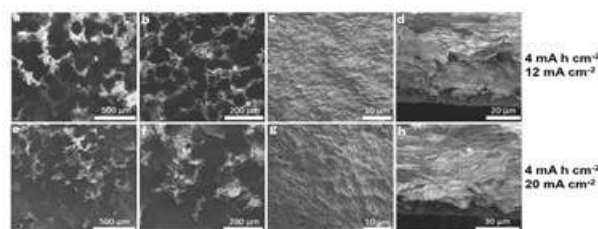


Figure II.7.F.5 The morphology of Li metal deposited on the 3D PPS@Cu at extremely high current densities and a deposition capacity of 4 mA h cm^{-2} . (a-d) At a current density of 12 mA cm^{-2} . (e-h) At a current density of 20 mA cm^{-2} . The electrolyte used here is $1.0 \text{ M LiTFSI/DOL+DME+1 wt\% LiNO}_3$.

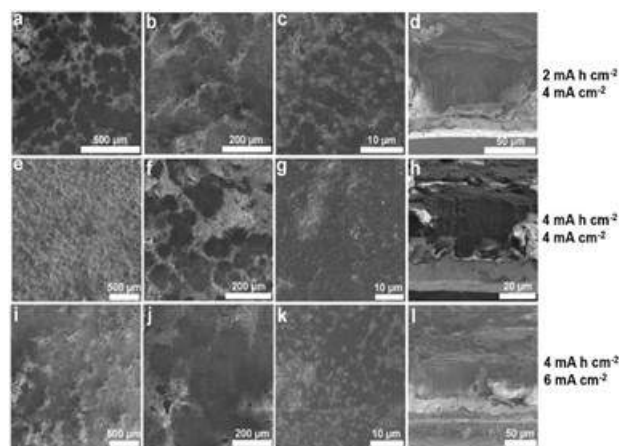


Figure II.7.F.4 The morphology of Li metal deposited on the 3D PPS@Cu at different deposition capacities and current densities. $\text{LiTFSI/DOL+DME+1 wt\% LiNO}_3$.

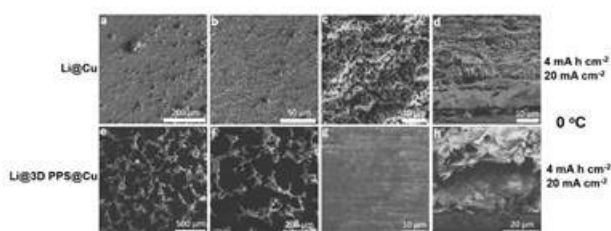


Figure II.7.F.6 The morphology of Li metal deposited on the bare Cu electrode and 3D PPS@Cu at -10°C with a high current density of 20 mA cm^{-2} and a deposition capacity of 4 mA h cm^{-2} .

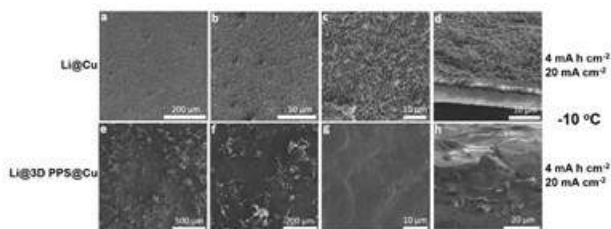


Figure II.7.F.7 The morphology of Li metal deposited on the bare Cu electrode and 3D PPS@Cu at -10°C with a high current density of 20 mA cm^{-2} and a deposition capacity of 4 mA h cm^{-2} .

The uniform and dendrite-free of Li within 3D PPS@Cu leads to significantly improved CE and cycling stability of Li plating/stripping. When measured at a deposition capacity of 2 mA h cm^{-2} and a current density of 2 mA cm^{-2} , the cells with 3D PPS@Cu electrodes exhibit a long cycle life over 800 cycles with an average CE as high as 99.1% (Figure II.7.F.8a). When elevating the deposition capacity to 4 mA h cm^{-2} and the current density to 4 mA cm^{-2} , a high average CE of 99% over 450 cycles is achieved (Figure II.7.F.8b). More notably, under extremely high deposition capacity and current density (6 mA h cm^{-2} and 6 mA cm^{-2}), the 3D PPS@Cu electrodes show a peerless Li plating/stripping performance undemonstrated to date with an average CE of 98.9% for more than 300 cycles (Figure II.7.F.8c).

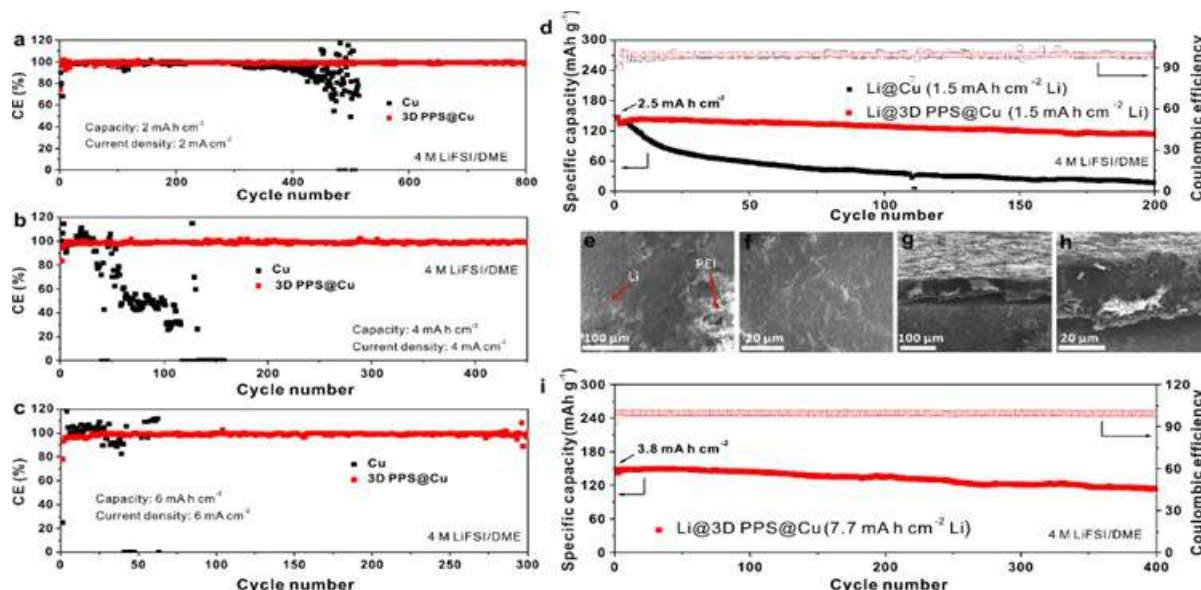


Figure II.7.F.8 (a), CE of Li deposition on 3D PPS@Cu and bare Cu electrode at a current density of 2 mA cm⁻² and a deposition capacity of 2 mA h cm⁻². (b), CE of Li deposition on 3D PPS@Cu and bare Cu electrode at a current density of 4 mA cm⁻² and a deposition capacity of 4 mA h cm⁻². (c), CE of Li deposition on 3D PPS@Cu and bare Cu electrode at a current density of 6 mA cm⁻² and a deposition capacity of 6 mA h cm⁻². (d), Cycling performance of full cells (N/P ratio: 0.6) using 1.5 mA h cm⁻² Li on 3D PPS@Cu and bare Cu electrode as anodes, respectively. (e-h), SEM images of Li@3D PPS@Cu in full cell after 50 cycles. (i), Cycling performance of full cells (N/P ratio: 2) using 7.7 mA h cm⁻² Li on 3D PPS@Cu as anodes and high-areal-capacity LiFePO₄ as cathodes (3.8 mA h cm⁻²)

The high CE of Li plating/stripping within 3D PPS@Cu allow us to fabricate 3D PPS@Cu with limited amount of Li (designated as Li@3D PPS@Cu) as anode, potentially achieving a high-energy-density Li metal battery with excellent cycling life. We demonstrated this advantage in full cells assembled using Li@3D PPS@Cu anodes and LiFePO₄ cathodes. At a low N/P ratio of 0.6 (areal Li amount ratio of negative to positive electrodes, termed N/P ratio), the full cell exhibits an initial capacity of 146.7 mA h g⁻¹ (areal capacity of 2.5 mA h cm⁻²) and maintains a stable cycling performance over 200 cycles with an average CE of ~99.7% (Figure II.7.F.8d). We attributed the excellent cycling performance of full cells to stable Li@3D PPS@Cu anodes confirmed by their dendrite-free morphology after 50 cycles, as shown in SEM images (Figure II.7.F.8e-h). When the high-areal-capacity LiFePO₄ cathodes (3.8 mA h cm⁻²) were used. The full cells deliver an initial capacity of 149 mA h g⁻¹ and show excellent cyclability of 400 cycles with average CE of ~99.78% at a N/P ratio of 2 (Figure II.7.F.8i), confirming excellent cycling stability of Li@3D PPS@Cu anodes in a practical cycling condition.

We also synthesized a multifunctional sulfur-containing polymer (MSCP) containing P_xS_y components (polymer-P_xS_y) through the reaction of sulfur anion (S_n⁻) containing trifunctional crosslinker lithium polysulfidophosphate with a chlorine-rich polymer. During Li plating/stripping, the polymers react with Li metal and in situ release Li sulfides and Li_xP_yS_z at the interface of polymer and Li metal to form organo-Li_xS_y/organo-Li_xP_yS_z composite protection layer. Figure II.7.F.9a shows the image of a just mixed solution of chlorine-rich polymer and sulfur anion (S_n⁻) containing

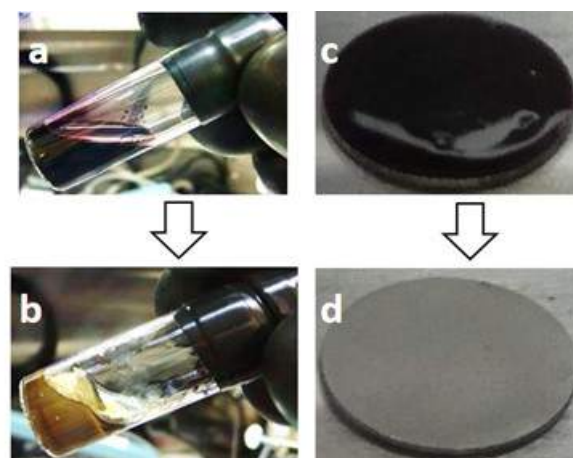


Figure II.7.F.9 Optical images of (a) just mixed solution of starting materials, (b) after 10 h. Optical images of (c) just mixed solution of starting materials on SS foil and (d) after drying overnight under vacuum.

trifunctional crosslinker lithium polysulfidophosphate in a molar ratio of 1.1/1 between Cl-C bond on chlorine-rich polymer and S_n^- , which appeared as a dark red solution. After standing at room temperature for 10 h, the color of system turned into pale yellow and gel-like solid formed (Figure II.7.F.9b), indicated the happening of crosslinking reaction between these two starting materials. For the fabrication of composite film, 50 μ L mixed solution of chlorine-rich polymer and sulfur anion (S_n^-) containing trifunctional crosslinker lithium polysulfidophosphate was dropped onto a stainless steel (SS) and dried under vacuum overnight. After drying, it can be seen that the coated dark red solution (Figure II.7.F.9c) changed into a solid and uniform off-white film (Figure II.7.F.9d).

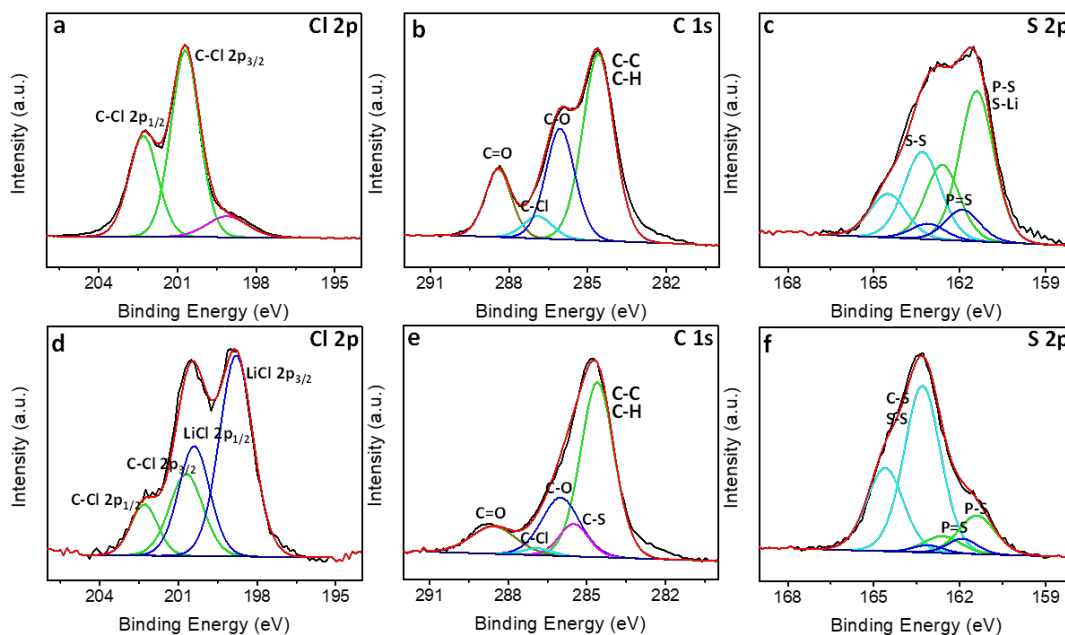


Figure II.7.F.10 High-resolution XPS spectra of Cl 2p, C 1s and S 2p for (a and b) pure chlorine-rich polymer, (c) S_n^- -containing trifunctional crosslinker lithium polysulfidophosphate and (d-f) polymer- P_xS_y film

X-ray photoelectron spectroscopy (XPS) was performed to further demonstrate the successful crosslinking reaction between the starting materials and the results are shown in Figure II.7.F.10. From the Cl 2p spectra of chlorine-rich polymer and polymer- P_xS_y (Figure II.7.F.10a and d), we can see clearly that peaks correspond C-Cl bond decreased and new peaks corresponding to LiCl formed, which is a reaction product between the starting materials. Accordingly, from the C 1s spectra of chlorine-rich polymer and polymer- P_xS_y (Figure II.7.F.10b and e), we can see that peak corresponds to C-Cl bond of chlorine-rich polymer decreased after reacting with S_n^- -containing trifunctional crosslinker lithium polysulfidophosphate and new peak corresponds to C-S bond formed for the polymer- P_xS_y . Moreover, from the comparison of S 2p spectra of S_n^- -containing trifunctional crosslinker lithium polysulfidophosphate and polymer- P_xS_y (Figure II.7.F.10c and f), we can see that peak at 161.4 corresponds to P-S and S-Li bonds in S_n^- -containing trifunctional crosslinker lithium polysulfidophosphate decreased significantly, while peak at 163.3 corresponds to S-S and C-S bonds increased apparently. The obvious changes of C 1s, Cl 2p and S 2p spectra between precursors and the as-prepared polymer- P_xS_y film strongly demonstrate the successful reaction between the starting materials. The crosslinking structure of polymer- P_xS_y would ensure its good mechanical strength and integrity so that to provide effective protection for the in situ formed robust SEI layer.

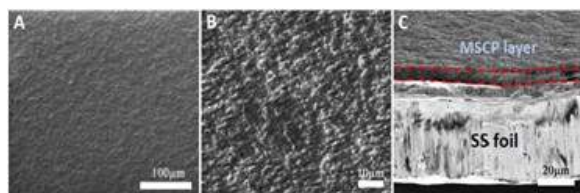


Figure II.7.F.11 (a,b) Top-view and (c) side-view SEM images of the as-prepared MSCP film on SS foil

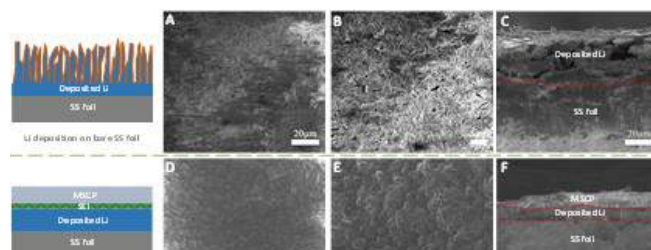


Figure II.7.F.12 (a,b) Top-view and (c) side-view SEM images of deposited Li on bare SS foil after 10 cycles. (d,e) Top-view and (f) side-view SEM images of deposited Li on MSCP protected SS foil after 10 cycles. The cells were cycled at 2 mA cm^{-2} and 2 mAh cm^{-2}

The morphology of MSCP was investigated by using SEM. As shown in Figure II.7.F.11, the optimized MSCP film appears to have a uniform coating layer on the substrate with a thickness of around $6.0 \mu\text{m}$. The morphology of deposited Li with an MSCP protection film was investigated. As shown in Figure II.7.F.12, for Li deposition on the MSCP film protected SS foil, the MSCP layer on the top surface keeps intact and uniform after cycling (Figure II.7.F.12d, e). Also, a sandwich cross-section structure can be observed that consists of a top layer of the MSCP film, a middle layer of the deposited dense Li, and a bottom layer of the SS foil (Figure II.7.F.12f). The results demonstrate that the MSCP protective layer can provide effective protection for Li metal anode and enable a dendrite-free Li plating/stripping after long-term cycling.

Chemical components of the SEI layer (MSCP-SEI) using MSCP protection film has been investigated by the XPS characterization. As shown in Figure II.7.F.13 and Figure II.7.F.14, the chemical components of MSCP-SEI and control SEI layers are analyzed through the deconvoluted S 2p, P 2p, Cl 2p, Li 1s, C 1s, F 1s, and N 1s XPS spectra. In MSCP-SEI, peaks at 160.5 and 161.3 eV in S 2p spectra (Figure II.7.F.13a) can be ascribed to the inorganic sulfide components Li_2S , Li_2S_2 , and Li_3PS_x . The existence of Li_3PS_x components can be confirmed from the P 2p spectra (Figure II.7.F.13b). The peak at 163.3 eV in S 2p spectra corresponding to S–S and C–S bonds can be ascribed to the inorganic polysulfides (Li_2S_n , $n \geq 3$) and the polymertethered organo(poly)sulfide. The existence of polymer-tethered organo-(poly)sulfide can also be verified from the C–S bond in C 1s spectra (Figure II.7.F.14a). In addition, inorganic salts such as LiCl , LiF , and Li_xNO_y can be observed from Cl 2p (Figure II.7.F.13c), F 1s (Figure II.7.F.14b), and N 1s (Figure II.7.F.14c) spectra, respectively. The existence of multiple Li salts and Li sulfides can be also confirmed from the Li 1s spectra (Figure II.7.F.13d). The MSCP-SEI shows a higher content of C (36.82%), S (10.16%), P (3.48%), and Cl (1.19%), but a lower content of O (28.24%), Li (16.52%), N (1.51%), and F (2.08%), compared with that of control SEI (C 11.63%, S 3.16%, P 0%, Cl 0%, O 42.14%, Li 35.44%, N 11.63%, and F 5.83%) (Figure II.7.F.3i). The higher content of C in MSCP-SEI implies polymer dominant SEI rather than inorganic-dominant SEI, which is attributed to a significant participation of MSCP into the SEI formation. The contribution of MSCP to MSCP-SEI also manifests at a higher content of sulfur species in MSCP-SEI due to chemical/electrochemical decomposition of the sulfur species from MSCP at the interfaces. The higher content of P species in MSCP-SEI particularly indicates the presence of Li_3PS_x

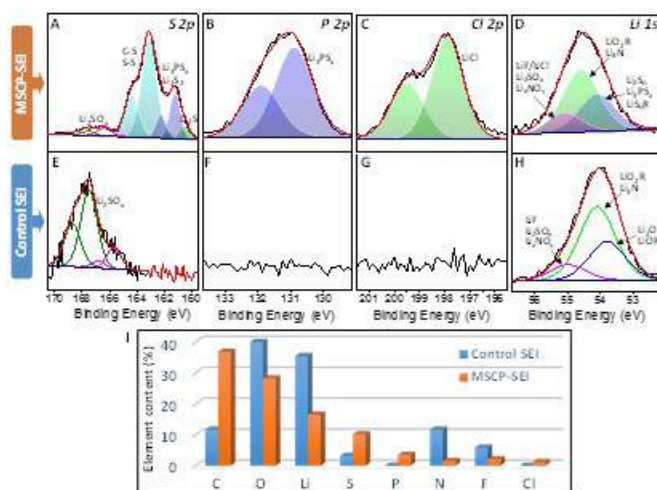


Figure II.7.F.13 S 2p, P 2p, Cl 2p, and Li 1s XPS spectra of (a)–(d) MSCP-SEI and (e)–(h) control SEI. (i) Elemental composition comparison of control SEI and MSCP-SEI calculated on the basis of the XPS spectra

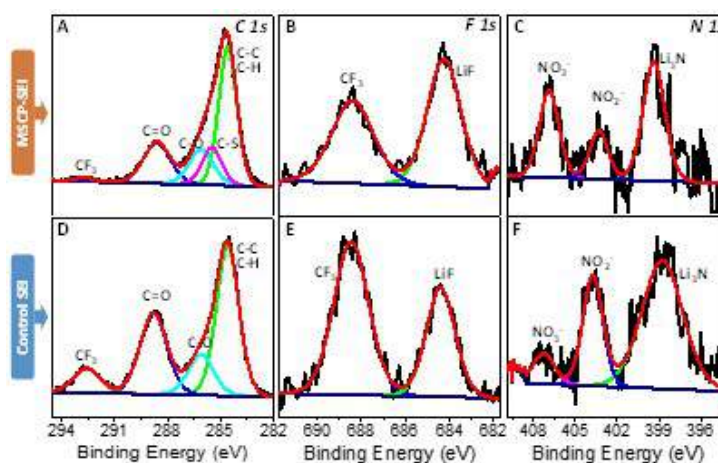


Figure II.7.F.14 C 1s, F 1s, and N 1s XPS spectra of (a-c) MSCP-SEI and (d-f) control SEI.

species in the SEI. On the other side, the lower c content of N and F in MSCP-SEI indicates an alleviated decomposition of LiTFSI and LiNO_3 salts by using MSCP, as LiTFSI is the only source of F and both LiTFSI and LiNO_3 are the only source of N in the electrolyte. Furthermore, the lower content of Li and O in MSCP-SEI indicates a reduced consumption of the Li salt as well as electrolyte by using MSCP.

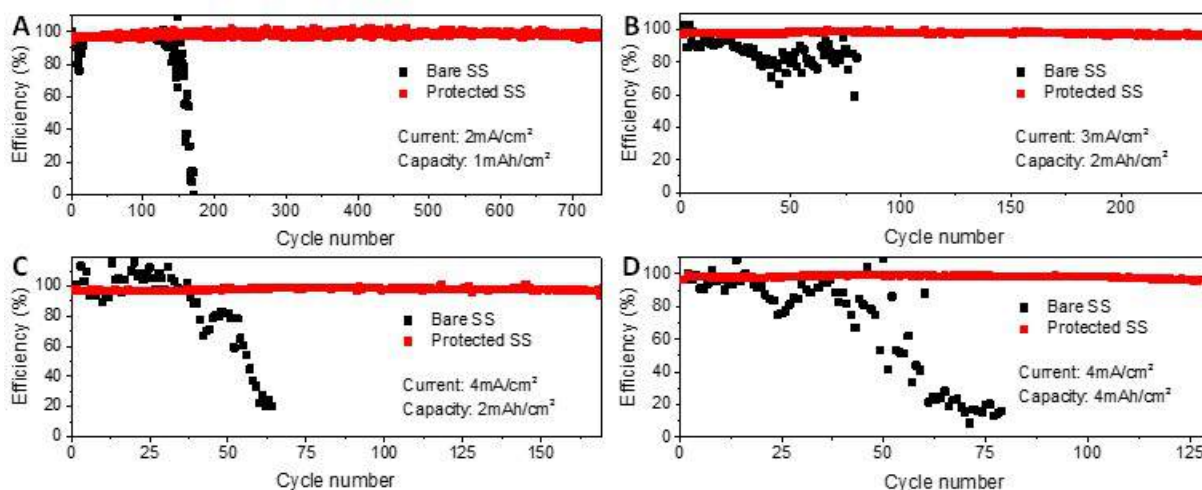


Figure II.7.F.15 CEs of cells using bare (black) and MSCP protected (red) SS foil versus cycle number at (a) 1 mA cm^{-2} and 1 mAh cm^{-2} , (b) 2 mA cm^{-2} and 2 mAh cm^{-2} , (c) 2 mA cm^{-2} and 3 mAh cm^{-2} , and (d) 2 mA cm^{-2} and 4 mAh cm^{-2}

We evaluate the electrochemical cycling performance of Li deposition using the MSCP protection layer to illustrate its advantages. As shown in Figure II.7.F.15, compared with the fast drop of CEs using bare SS foil, cells using MSCP protected SS foil can maintain high CEs for a prolonged cycle life. Specifically, an average CE of 98.7% for over 950 cycles at 1 mA cm^{-2} and 1 mAh cm^{-2} (Figure II.7.F.15a) and an average CE of 98.5% for over 460 cycles at 2 mA cm^{-2} and 2 mAh cm^{-2} (Figure II.7.F.15b) can be achieved for cells using the MSCP protected SS foil. Even at higher capacities of 3 and 4 mAh cm^{-2} , very stable cycling can also be achieved (Figure II.7.F.15c,d), respectively. Figure II.7.F.16a shows voltage profiles as a function of time of two Li||Li symmetric cells using bare or MSCP protected Li metal foils. The cell using MSCP protected Li metal foils shows lower voltage overpotential ($<120 \text{ mV}$) and stable cycling for more than 800 h without an obvious voltage fluctuation compared with control cells. Finally, the MSCP protection for Li metal anode was further evaluated in full cells using LFP ($\sim 2.4 \text{ mAh/cm}^2$) cathode and the MSCP protected Li metal anode. As shown in Figure II.7.F.16b, the cell with MSCP protected Li metal anode shows significantly increased cycling performance with a capacity retention of $\sim 89.4\%$ even after 500 cycles and an improved average CE of $\sim 99.9\%$. Furthermore, we found that an anode-free cell using MSCP protected SS foil as anode and LFP as cathode shows remarkably improved cycling stability than that in a bare SS foil anode-free cell (Figure II.7.F.16c).

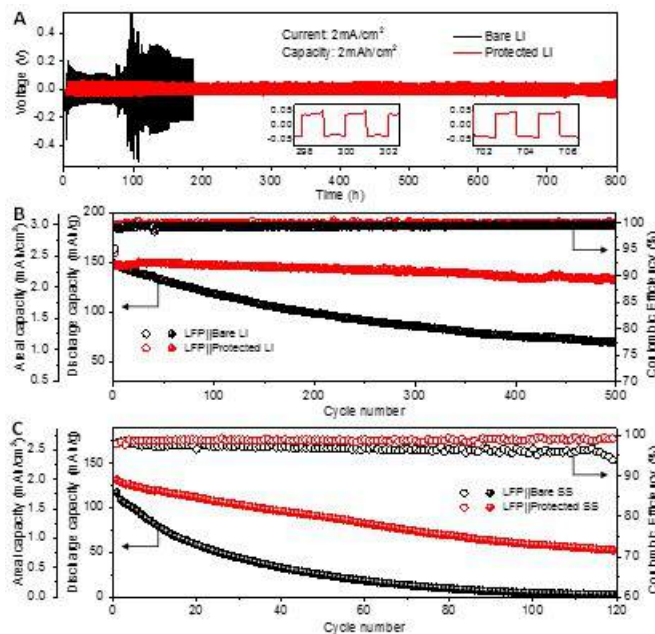


Figure II.7.F.16 (a) Cycling performance of symmetric cells using bare (black) or MSCP protected (red) Li metal foils cycled at 2 mA cm^{-2} and 2 mAh cm^{-2} . (b) Cycling performance of Li||LFP full cells using bare (black) and MSCP protected (red) Li metal as anode at 0.5 C ($1 \text{ C} = 170 \text{ mAh/g}$). (c) Cycling performance of anode-free SS||LFP cells using bare SS foil (black) and MSCP protected (red) SS foil as anode at 0.5 C

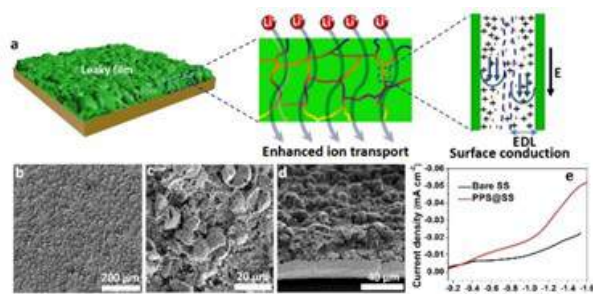


Figure II.7.F.17 (a) Electrokinetic phenomena (i.e. electrokinetic surface conduction) enhance Li-ion transport in the leaky film under applied electric field in the electrolyte. (b-d) SEM morphology of the PPS leaky film. e) The linear sweep voltammeteries of PPS@stainless steel (PPS@SS) and bare SS electrodes

We also develop a high-zeta-potential porous film containing nano/submicron-sized pores, called a leaky film, to promote electrokinetic phenomena for enhancement of the Li-ion transport (Figure II.7.F.17a) and enable uniform deposition of Li metal anodes. The leaky film was composed of crosslinked polyethylenimine (PEI)-based polyurea (PEIPU), poly(ethylene oxide) (PEO), and SiO₂ nanoparticles (PEIPU-PEO-SiO₂, designated as PPS). PPS leaky films on Cu or Li substrates (designated as PPS@Cu or PPS@Li, respectively) were prepared by successive coating of PEI-SiO₂-PEO colloidal solution and hexamethylene diisocyanate (HDI) solution onto the substrate, followed by in situ crosslinking between PEI and HDI. Scanning electron microscopy (SEM) images (Figure II.7.F.17b-d) display a rough surface morphology of the polymer composite film on the Cu foil containing submicron-sized pores, which endow the film with “leaky” property, the measured leaky rate is $\approx 2.82 \text{ mL cm}^{-3} \text{ s}$. Due to the unique chemical structure and Li-ion affinity, the PPS leaky film can not only self-concentrate the Li ion, but also induce the electrokinetic phenomena to enhance the Li-ion transport, which can be directly demonstrated by linear sweep voltammetry (LSV). As shown in Figure II.7.F.17e, the higher current density of PPS leaky film electrode at voltages of $-0.4 - 1.1 \text{ V}$ is attributed to the improved local Li-ion concentration in the leaky film, owing to its Li-ion affinity to adsorb Li ion. The Li-ion affinity also drives the formation of EDL on the leaky film surfaces, evidenced by the measured zeta potential of $+36 \text{ mV}$ in the electrolyte (1.0 M lithium hexafluorophosphate (LiPF₆) in ethylene carbonate (EC) and diethyl carbonate (DEC) (V/V = 1)). The existence of EDL induces electrokinetic surface conduction within the leaky film under an electric field. The electrokinetic surface conduction can enhance the Li-ion transport to

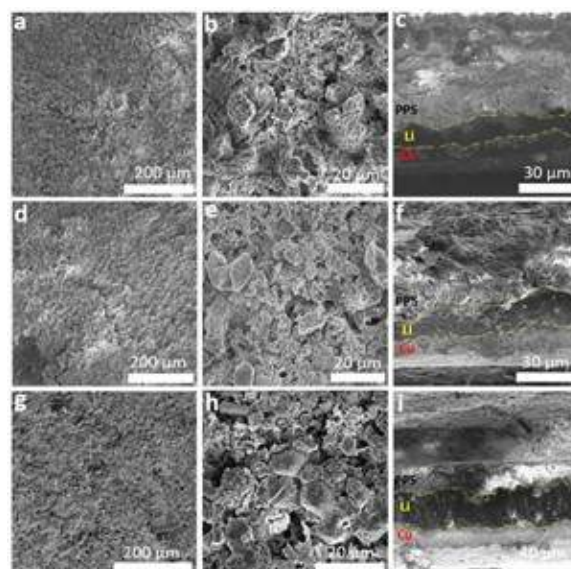


Figure II.7.F.18 The morphologies of Li metal deposited on the PPS@Cu at (a-c) a deposition capacity of 2 mAh cm^{-2} and a current density of 1 mA cm^{-2} , (d-f) a deposition capacity of 4 mAh cm^{-2} and a current density of 2 mA cm^{-2} , (g-i) a deposition capacity of 6 mAh cm^{-2} and a current density of 2 mA cm^{-2}

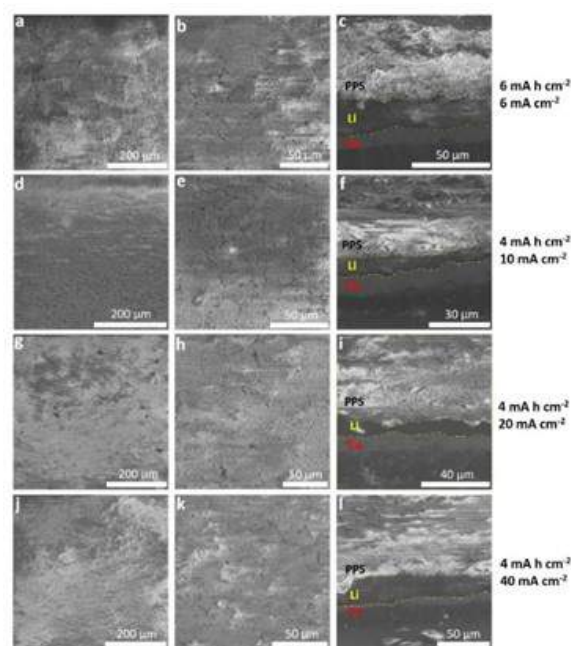


Figure II.7.F.19 The morphology of Li metal deposited on the PPS@Cu at different deposition capacities and current densities. (a-c) 6 mAh cm^{-2} and 6 mA cm^{-2} . (d-f) 4 mAh cm^{-2} and 10 mA cm^{-2} . (g-i) 4 mAh cm^{-2} and 20 mA cm^{-2} . (j-l) 4 mAh cm^{-2} and 40 mA cm^{-2}

overcome the diffusion-limited current under strong Li ion depletion conditions, which is manifested by the dramatic increase of current density of PPS leaky film electrode above -1.1 V in LSV.

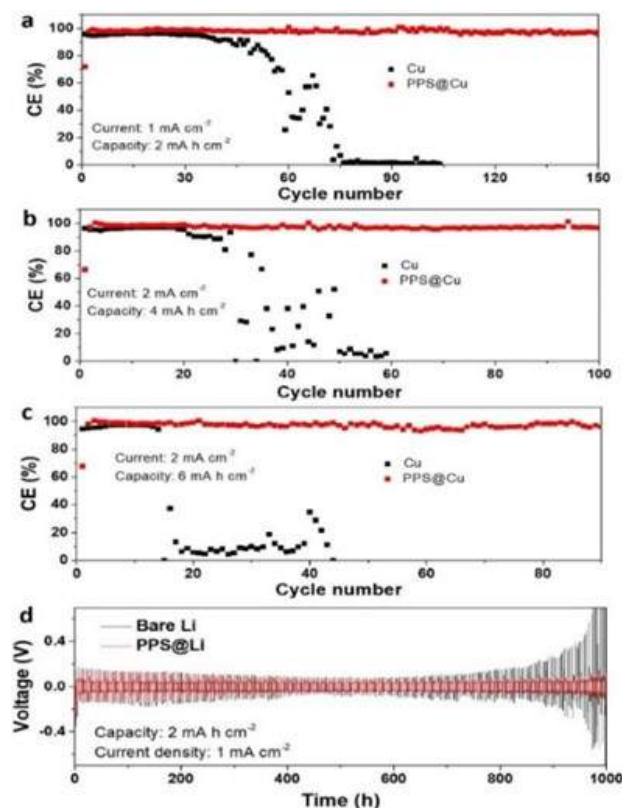


Figure II.7.F.20 Electrochemical performance of PPS@Cu and bare Cu foil electrodes. CE of Li plating/stripping on PPS@Cu and bare Cu foil at a current density of 1 mA cm^{-2} and a deposition capacity of 2 mA h cm^{-2} (a), at a current density of 2 mA cm^{-2} and a deposition capacity of 4 mA h cm^{-2} (b), and at a current density of 2 mA cm^{-2} and a deposition capacity of 6 mA h cm^{-2} (c). (d) Cycling stability of symmetric cells using PPS leaky film protected Li metal as electrodes

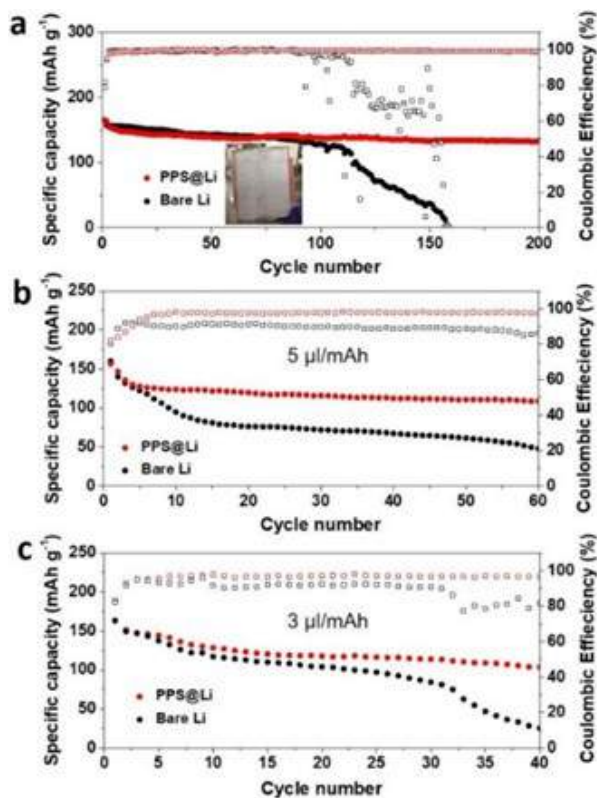


Figure II.7.F.21 Cycling performance of full cells using PPS leaky film protected Li metal as anodes and NCM-811 as cathodes. (a) Flooded electrolyte. (b) Lean electrolyte of $5 \mu\text{l/mAh}$. (c) Lean electrolyte of $3 \mu\text{l/mAh}$. The photo image of Li foil protected by PPS leaky film ($20 \text{ cm} \times 15 \text{ cm}$) is shown as an inset in (a), the thickness of Li foil is $120 \mu\text{m}$. The areal capacity of NCM-811 cathode is around 4.2 mA h cm^{-2}

The Li-ion transport enhancement PPS leaky film can effectively suppress the growth of dendritic Li at high deposition capacities and high current densities in a carbonate-based electrolyte. As shown in SEM images, the deposited Li demonstrates a uniform, compact and dendrite-free morphology without penetrating the PPS layer under various deposition capacities and current densities (2 mAh cm^{-2} , 1 mA cm^{-2} in Figure II.7.F.18a-c; 4 mAh cm^{-2} , 2 mA cm^{-2} in Figure II.7.F.18d-f; 6 mAh cm^{-2} , 2 mA cm^{-2} in Figure II.7.F.18g-i; 6 mAh cm^{-2} , 6 mA cm^{-2} in Figure II.7.F.19a-c). Notably, even at high rates of 2.5 C (4 mAh cm^{-2} , 10 mA cm^{-2} in Figure II.7.F.19d-f), 5 C (4 mAh cm^{-2} , 20 mA cm^{-2} in Figure II.7.F.19g-i) and 10 C (4 mAh cm^{-2} , 40 mA cm^{-2} in Figure II.7.F.19j-l), the uniform and compact Li layer can still be achieved under the PPS leaky film. The uniform and dendrite-free deposition of Li enabled by PPS leaky film leads to an improvement of the Li plating/ stripping CE. At a deposition capacity of 2 mAh cm^{-2} and a current density of 1 mA cm^{-2} , the cells containing PPS leaky film deliver an enhanced average CE of 97.8% over 150 cycles (Figure II.7.F.20a). When the deposition capacities increased to 4 mAh cm^{-2} (Figure II.7.F.20b) and 6 mAh cm^{-2} (Figure II.7.F.20c) at a current density of 2 mA cm^{-2} , the cells containing PPS leaky film still maintained high average CEs of 97% over 100 cycles and 96.9% over 90 cycles, respectively. In contrast, the bare Cu electrodes show

very poor CE and cycling stability. Figure II.7.F.20d shows the cycling stability of symmetric Li metal cells at a current density of 1 mA cm^{-2} and a deposition capacity of 2 mAh cm^{-2} . Compared with the bare Li metal anodes exhibiting a gradual increase in hysteresis over cycles by almost 250% after 800 h, Li metal anodes with PPS leaky film show good cycling stability with a low overpotential at $\approx 40 \text{ mV}$ for over 1000 h.

The stable Li metal anodes enabled by the PPS leaky film ensure their high performance in Li metal batteries. Full cells were assembled using thin PPS@Li foil ($\approx 120 \text{ }\mu\text{m}$) as anodes and high-areal-capacity NCM-811 ($\approx 4.2 \text{ mAh cm}^{-2}$) (PPS@ Li|NCM-811) as cathodes. When flooded electrolyte was used (Figure II.7.F.21a), the cells with PPS@Li delivered a high initial discharge capacity of 165.4 mAh g^{-1} , and still maintained the capacity of 132.8 mAh g^{-1} after 200 cycles (80.3% capacity retention) with an average CE of 99.4%, while the control cells show a fast capacity decay after 100 cycles. Under lean electrolyte conditions, it is expected that the cells exhibit worse cycling performance than that of cells with flooded electrolyte, as the reduced electrolyte greatly decreases the cycling life. We found that the cells with PPS@Li anodes still exhibit improved cycling stability, capacity retention and CE compared with control cells under the lean electrolyte condition, as shown in Figure II.7.F.21b ($5 \text{ }\mu\text{L mAh}^{-1}$) and Figure II.7.F.21c ($3 \text{ }\mu\text{L mAh}^{-1}$).

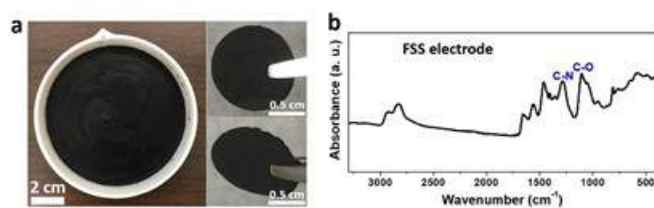


Figure II.7.F.22 (a) The photos of prepared FSS electrodes. (b) FT-IR spectra of FSS electrode

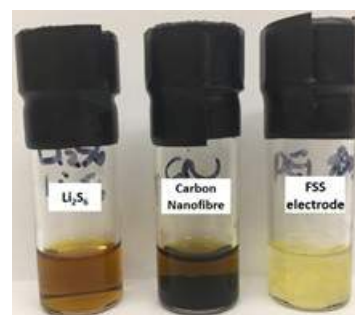


Figure II.7.F.23 Li_2S_6 adsorption of FSS electrodes

For sulfur cathodes, we develop a functional porous sponge sulfur (FSS) electrode to eliminate the self-discharge and enable a high performance of Li-S battery. The FSS electrode is fabricated by an ice-templating method through cross-linking reaction between Li-ion-affinity polymers. Figure II.7.F.22a shows the pictures of as-prepared FSS electrodes, which can be peeled off and cut into different sizes. The FSS electrodes contains a lot of functional groups (C-N, C-O), evidenced by FT-IR spectra (Figure II.7.F.22b). These functional groups have strong Li-ion affinity and endow the electrodes with strong Li polysulfides (LiPS) chemisorption. Figure II.7.F.23 shows the ability of FSS electrodes to adsorb the LiPS.

The strong LiPS chemisorption and the unique structure can enable the FSS electrode with excellent performance. As shown in Figure II.7.F.24a, at an E/S ratio of $10 \text{ }\mu\text{L mg}^{-1}$, the FSS electrodes with various S mass loading of 6.0, 8.78 and 10 mg cm^{-2} deliver high initial capacities of 1180.2, 1149.9 and $1132.9 \text{ mA h g}^{-1}$, respectively, indicating high S utilization even under high S mass loading, and maintain stable cycling over 200 cycles with good capacity retention. At the conditions of high S mass loading (11 mg cm^{-2}) and low E/S ratio ($\leq 5 \text{ }\mu\text{L mg}^{-1}$) (Figure II.7.F.24b), the FSS electrode delivers an initial discharge capacity of $973.8 \text{ mA h g}^{-1}$, corresponding to a high areal capacity of $10.63 \text{ mA h cm}^{-2}$ and an energy density of $\sim 250 \text{ W h kg}^{-1}$ (considering the total mass of the cathode, anode and electrolyte). At a much lower E/S ratio of $3 \text{ }\mu\text{L mg}^{-1}$ (Figure II.7.F.24c), the FSS electrode still exhibits an initial discharge capacity of $973.8 \text{ mA h g}^{-1}$ (areal capacity: $10.45 \text{ mA h cm}^{-2}$), corresponding to a much higher energy density of 308 W h kg^{-1} , and maintains a stable cycling over 100 cycles.

We further use organosulfide as the additive in the electrolyte to push the energy density to a much higher level. As shown in Figure II.7.F.25a, at an E/S ratio of $5 \text{ }\mu\text{L mg}^{-1}$, the FSS electrode with a S mass loading of $\sim 11.7 \text{ mg cm}^{-2}$ exhibits a high energy density of 412 Wh kg^{-1} and good cycling stability for 100 cycles. When

the E/S ratio is further reduced to $3.5 \mu\text{l mg}^{-1}$ (Figure II.7.F.25b), the FSS electrode shows an initial energy density of 432 Wh kg^{-1} , the highest energy density can reach 460 Wh kg^{-1} .

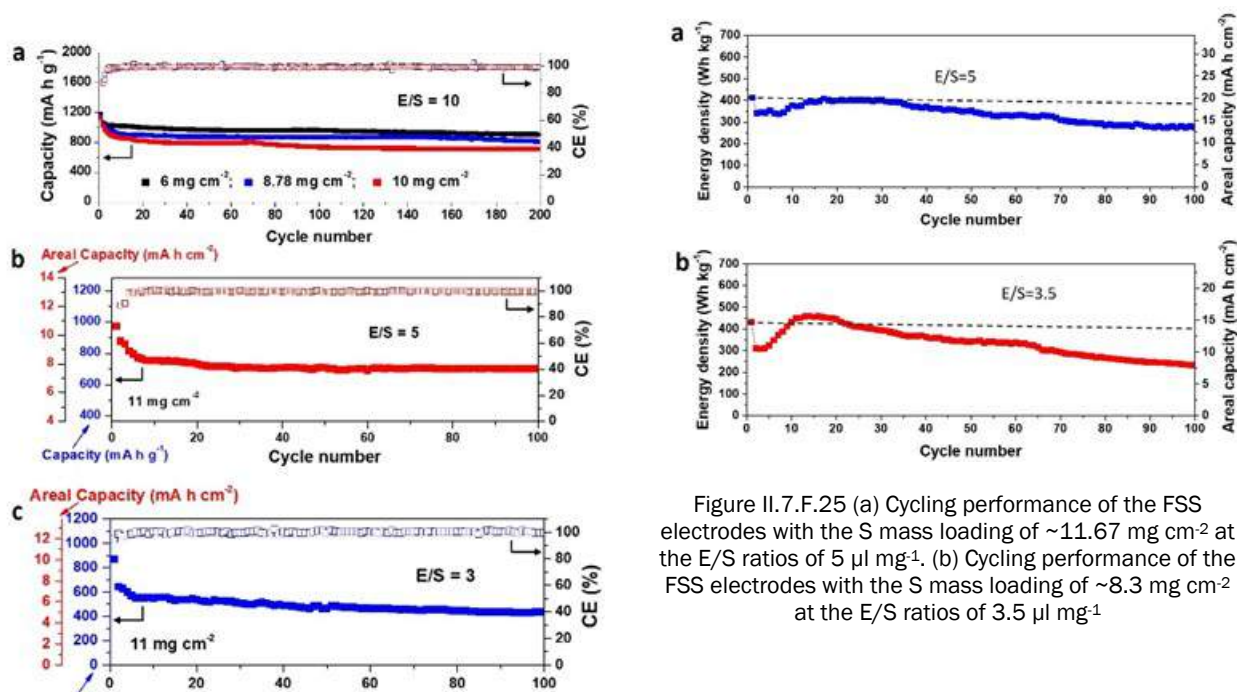


Figure II.7.F.25 (a) Cycling performance of the FSS electrodes with the S mass loading of $\sim 11.67 \text{ mg cm}^{-2}$ at the E/S ratios of $5 \mu\text{l mg}^{-1}$. (b) Cycling performance of the FSS electrodes with the S mass loading of $\sim 8.3 \text{ mg cm}^{-2}$ at the E/S ratios of $3.5 \mu\text{l mg}^{-1}$

Figure II.7.F.24 (a) The cycling performance of the FSS electrode with various S mass loading of 6, 8.78 and 10 mg cm^{-2} at an E/S ratio of $10 \mu\text{l mg}^{-1}$. The cycling performance of the FSS electrodes with the S mass loading of 11 mg cm^{-2} at the E/S ratios of $5 \mu\text{l mg}^{-1}$ (b) and $3 \mu\text{l mg}^{-1}$ (c). The electrolyte used here is 1 M LiTFSI/DOL+DME+4 wt% LiNO₃

Conclusions

We successfully developed a 3D Li-ion affinity porous sponge and Li-ion affinity leaky film to promote electrokinetic effects to enable stable metal battery anodes. The strong Li-ion affinity and electrokinetic effects significantly improve the Li-ion transport and fundamentally change the Li-ion transport behavior, which in turn leads to a uniform deposition of Li metal anodes, even at harsh conditions (e.g., high deposition capacity, high deposition current density, high rate, low temperature). We also successfully developed a multifunctional sulfur-containing polymer, during Li plating/stripping, the polymers react with Li metal and in situ release Li sulfides and Li_xPyS_z at the interface of polymer and Li metal to form organo-Li_xS_y/organo-Li_xPyS_z composite protection layer. Using this protection layer, Li anodes were effectively protected without any dendritic and mossy lithium, high Coulombic efficiency (CE) of lithium plating/stripping was achieved. For sulfur cathodes, we develop a functional porous sponge sulfur (FSS) electrode to eliminate the self-discharge and enable a high performance of Li-S battery.

Key Publications

- Li, G. X., Liu, Z., Huang, Q. Q., Gao, Y., Regula, M., Wang, D. W., Chen, L. Q., Wang, D. H., Stable metal battery anodes enabled by polyethylenimine sponge hosts by way of electrokinetic effects, *Nat. Energy*, 2018, 3, 1076-1083.
- Zhao, Y. M., Li, G. X., Gao, Y., Wang, D. W., Huang, Q. Q., Wang, D. H., Stable Li Metal Anode by a Hybrid Lithium Polysulfidophosphate/Polymer Cross-Linking Film, *ACS Energy Letters*, 2019, 4, 1271-1278.

3. Li, G. X., Liu, Z., Wang, D. W., He, X., Liu, S., Gao, Y., AlZahrani, A., Kim, S. H., Chen, L. Q., Wang, D. H., Electrokinetic Phenomena Enhanced Lithium-Ion Transport in Leaky Film for Stable Lithium Metal Anodes, *Advanced Energy Materials*, 2019, 9, 1900704.

Acknowledgements

The work was supported by the Department of Energy, Office of Energy Efficiency and Renewable Energy (EERE), Vehicle Technology Office, under Award Number DE-EE0007795. We appreciated the support from Colleen Butcher at National Energy Technology Laboratory.

II.7.G Integrated Multiscale Modeling for Design of Robust 3D Solid-State Lithium Batteries (LLNL)

Brandon C. Wood, Principal Investigator

Lawrence Livermore National Laboratory
7000 East Avenue
Livermore, CA 94550
E-mail: wood37@llnl.gov

Tien Q. Duong, DOE Technology Development Manager

U.S. Department of Energy
E-mail: Tien.Duong@ee.doe.gov

Start Date: November 1, 2018

End Date: October 30, 2021

Project Funding (FY19): \$357,000

DOE share: \$357,000

Non-DOE share: \$0

Project Introduction

Architected 3D solid-state batteries have a number of intrinsic performance and safety advantages over conventionally processed 2D batteries based on liquid organic or polymer electrolytes (Arthur et al. 2011). First and foremost, functionality and architecture of component materials in principle can be tuned for optimal energy and power density. In addition, the use of solid-state electrolytes offers increased safety and potential compatibility with higher-voltage and higher-energy-density electrode materials, which can further enhance capacity. Nevertheless, proper design of 3D solid-state batteries remains a formidable challenge. Solid-state batteries tend to suffer from high interfacial resistance arising from poor physical contacts (McOwen Dennis et al. 2018), as well as the formation of intermediate phases at the often-unstable interface between the cathode and electrolyte. They also suffer from non-uniform mechanical responses that can promote stress cracking in response to lithium uptake during cycling. For 3D architectures, these issues can become even more problematic, since the complex morphologies tend to introduce additional non-uniformities in electric fields and current densities (Hart et al. 2003, Long et al. 2004) at the numerous component interfaces. The use of 3D printing and other additive manufacturing methods offer the promise of directed engineering of architectures to improve structural and chemical integrity, but such approaches also introduce other difficulties, including microstructures that are notoriously difficult to control and vary widely according to the specific processing condition.

To realize the ultimate goal of designing and printing optimized 3D solid-state batteries, it is critical to understand the interfacial losses and instabilities that impede performance and promote failure at multiple scales. Validated modeling and simulation have a unique role to play in pursuit of this aim, since they can directly probe structure-property relations and provide guidance for optimizing function of component materials. In general, existing modeling strategies tend to suffer from one of two shortcomings. Some fail to address the multi-physics nature of the various processes active in 3D batteries, which range from electrical to chemical to mechanical responses that are often coupled. Others fail to address the multiscale nature of the battery materials and their integration, ignoring the fact that atomistic, microstructural, and cell-level processes must be considered to understand how processing and architecture affect performance. This project leverages advanced computational models to address these shortcomings and investigate diffusion kinetics limitations in ceramic 3D solid-state battery materials. This can be viewed as a first step towards enabling future optimization of 3D battery designs.

Objectives

This project aims to develop a multiscale, multi-physics modeling framework for probing the effects of materials microstructure and device architecture on ion transport within 3D ceramic solid-state battery materials, with the goal of enhancing performance and reliability. We have three primary objectives: (1) integrate multi-physics and multiscale model components; (2) understand interface- and microstructure-derived limitations on ion transport; and (3) derive key structure-performance relations for enabling future optimization.

Approach

Our approach integrates simulations at three scales to predict ion transport limitations within the ceramic solid-state electrolyte $\text{Li}_7\text{La}_3\text{Zr}_2\text{O}_{12}$ (LLZO), as well as across the interface between LLZO and LiCoO_2 cathodes. A particular focus is on understanding the effects of microstructures and architectures resulting from processing of 3D solid-state batteries, as well as their mechanical and chemical evolution at different stages of cycling. First-principles and classical molecular dynamics simulations are used to compute fundamental Li-ion diffusion within bulk solid electrolyte and cathode materials, along/across grain boundaries of the electrolyte, and along/across electrolyte/cathode interfaces. Next, phase-field simulations are used to generate digital representation of realistic microstructures of the materials, which are combined with the atomistic simulation results to parameterize mesoscale effective property calculations and to establish microstructure-property relationships for ion transport. Finally, these relationships inform a cell-level macroscopic electro-chemo-mechanical modeling framework, which can be used to optimize the performance of ceramic 3D solid-state Li batteries based on LLZO solid electrolytes.

Results

Atomistic simulations of stress-, composition-, and structure-dependent Li diffusion. The dominance of interfaces in 3D all-solid-state batteries requires incorporation of interfacial effects into our description of ion transport at the atomistic scale. Using atomistic simulations, we are pursuing three specific factors that can be modified by the presence of interfaces and may be relevant for ion transport: interfacial mechanical stresses, compositional variations, and structural disordering.

First, we employed atomistic simulations to establish baseline elastic and mass transport properties of LiCoO_2 electrodes and LLZO solid electrolytes, as well as their interdependence of stress and diffusion. Elastic constants for cubic LLZO, Li metal, and hexagonal LiCoO_2 were first calculated using density functional theory, with results summarized in Table II.7.G.1. The activation energy for Li-ion hopping in LiCoO_2 as a function of strain was then calculated using density functional theory, combined with the nudged elastic band (NEB) method. It has been proposed that Li-ion can diffuse in LiCoO_2 through either single vacancy or di-vacancy mechanism; accordingly, we evaluated strain-dependent activation energies for Li-ion hopping in LiCoO_2 based on these two mechanisms. As shown in Table II.7.G.2, applying compressive strain along the *c*-axis will substantially increase the activation energy for Li diffusion, indicating that diffusion kinetics are highly dependent on the stress state and the orientation of the cathode-electrolyte interface.

Table II.7.G.1 Calculated elastic constants for Li metal, cubic LLZO and hexagonal LiCoO_2

Material	Bulk modulus (GPa)	C_{11} (GPa)	C_{12} (GPa)	C_{44} (GPa)
Li metal (bcc)	13.7	14.2	13.5	11.5
LLZO (sc)	110	180	75	73

Material	Bulk modulus (GPa)	C_{11} (GPa)	C_{12} (GPa)	C_{13} (GPa)	C_{33} (GPa)	C_{44} (GPa)
LiCoO_2 (hex)	154	380	119	110	279	125

Table II.7.G.2: Calculated strain-dependent activation energy of Li-hopping in LiCoO_2

Mechanisms	Uniaxial strain, a	Uniaxial strain, b	Uniaxial strain, c
Single vacancy	25 meV/%	17 meV/%	64 meV/%
Di-vacancy	9.4 meV/%	9.4 meV/%	53 meV/%

Second, we began exploring Li-ion diffusion in LLZO as a function of Li composition, which can vary near interfaces in real 3D solid-state battery configurations. Diffusion barriers were initially evaluated by the nudged elastic band (NEB) method at zero temperature based on three different diffusion mechanisms: single-

ion hopping, dimer, and trimer concerted motion. Table II.7.G.3 shows that the activation energy of Li-ion diffusion in LLZO highly depends on local Li concentration near the diffusion pathways. Because all of these mechanisms can contribute to Li-ion diffusion simultaneously, these results established the necessity of a fully dynamical approach that can evaluate the effects of composition on the overall Li-ion mobility. To this end, in collaboration with Prof. Adelstein at San Francisco State University, we used classical molecular dynamics to examine composition-dependent Li-ion diffusivity in LLZO, finding that the lowest activation energy for Li-ion diffusion, ~ 0.22 eV, is for composition $\text{Li}_{6.5}\text{La}_3\text{Zr}_2\text{O}_{12}$. Further simulations exploring the composition dependence of ion diffusion are underway.

Third, we initiated simulations to explore the effects of structural disorder at interfaces and grain boundaries on ion diffusion. Working with our collaborators, we used molecular dynamics simulations to derive ionic diffusivities of atomically disordered LLZO models as proxies for generic high-angle grain boundaries of LLZO. Preliminary values were used to parameterize our mesoscale model to compute the effective Li diffusivity of polycrystalline LLZO.

Table II.7.G.3: Effects of vacancy on the activation energy of Li-ion diffusion in cubic LLZO

Compositions	Single-ion	Dimer	Trimer
Full Li+ occupation	0.15 eV	0.10-0.15 eV	0.16 eV
Single-vacancy near diffusion pathway	0.34 eV	0.38-0.54 eV	0.31-0.49 eV

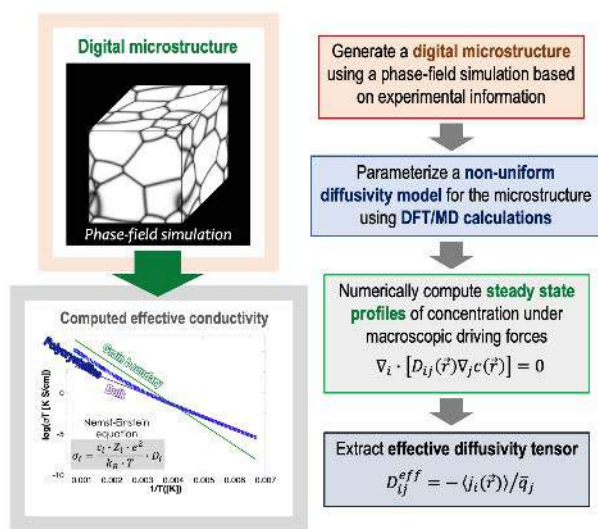


Figure II.7.G.2. Workflow for computing the effective ionic diffusivity/conductivity of reconstructed digital representation of a solid electrolyte microstructure

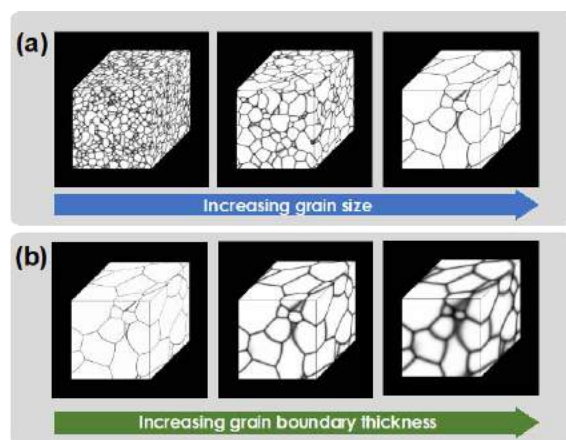


Figure II.7.G.1. Examples of generated digital microstructures of polycrystalline LLZO with (a) different grain sizes; and (b) different grain boundary thicknesses

Mesoscale modeling of Li transport through complex microstructures.

This year's mesoscale modeling efforts focused on three subtasks: 1) establishment of a mesoscale modeling framework for predicting effective ion transport as a function a microstructure; 2) parameterization of the framework for polycrystalline LLZO; and 3) investigation of the impacts of specific microstructural features on ion transport. As illustrated in Figure II.7.G.2, we established a workflow for efficiently computing the effective ionic diffusivity/conductivity of a realistic solid electrolyte microstructure. We first generated 3D digital microstructures of polycrystalline LLZO using phase-field simulations. Figure II.7.G.1 shows examples of generated microstructures with different grain sizes and grain boundary thicknesses. These simulated complex microstructures were then used as inputs to compute the effective ion diffusion calculations. Corresponding position-dependent Li diffusivity models for the microstructures were parameterized by bulk

and grain boundary diffusivities derived from our team's classical molecular dynamics simulations. Based on these inputs, we have begun performing computations of effective Li ionic conductivities of a series of systematically generated microstructures as a function of temperature.

In Figure II.7.G.3(a), we show one example of how microstructure is predicted to affect ionic conductivity. Using preliminary values from our atomistic simulations, the computed effective conductivity of polycrystalline LLZO is predicted to undergo a transition from bulk-dominant to the grain boundary-dominant behaviors. To characterize this transition for the given microstructure, we define the “*kink temperature* (T_{kink})” where this transition occurs, which is a function of temperature, grain size, and grain boundary thickness, among other factors (see inset, Figure II.7.G.3(a)). Figure II.7.G.3 (a) and (b) show the characterized kink temperatures as functions of grain size and grain boundary thickness, respectively. The extracted kink temperatures exhibit nonlinear and nontrivial behaviors with varying grain size and grain boundary thickness, with implications for performance. In addition, we note that the kink temperature is highly sensitive to those two microstructural features, indicating the possible tunability of Li conductivity characteristics/behaviors by controlling LLZO microstructures. In future quarters, parameters will be refined and validated by partnering with microstructural and impedance data from our experimental collaborators to connect processing routes to performance.

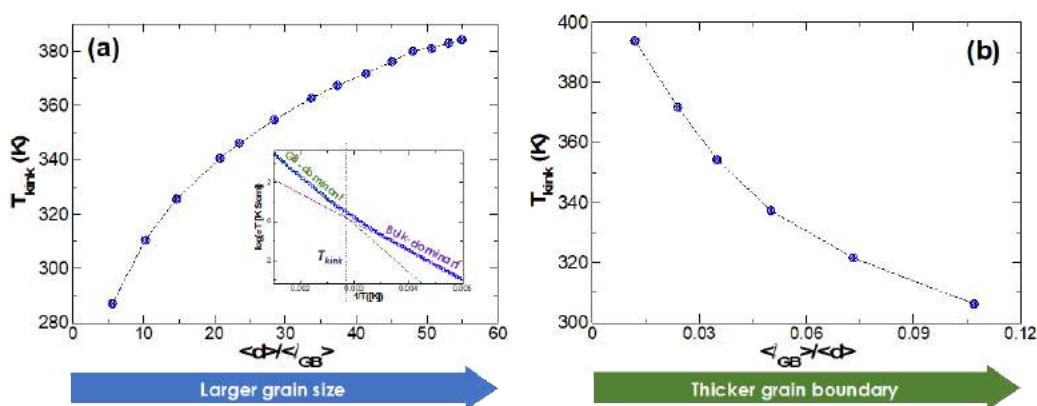


Figure II.7.G.3. Characterized kink temperatures of computed temperature-dependent ionic conductivities of polycrystals with (a) increasing grain size; and (b) increasing grain boundary thickness

Conclusions

This quarter's activities laid the foundation for a new capability to simulate the effects of microstructure on ionic conductivity in LLZO solid electrolytes. This is critical for understanding interface-dominated 3D batteries, for which processing conditions and architectures may alter microstructure, and by extension interfacial impedance. Our atomistic simulations showed how diffusion properties in LLZO and LiCoO_2 depend on strain, compositional variation, and structural disordering induced by these interfaces. In addition, our mesoscale simulation framework was constructed and successfully tested on polycrystalline LLZO. Early results show that microstructure may have a significant effect on ionic conductivity. In outlying quarters, we will work to fully integrate the interdependencies from our atomistic simulation results into the model and to use our framework to understand and predict electrochemical impedance spectroscopy performed by our partners.

Key Publications

1. L. Wan, "Atomistic modeling of interfaces in solid-state batteries," KIST-LLNL Workshop, Livermore, CA (September 2019).
2. T.W. Heo, "Mesoscale approach for modeling solid-state electrodes and electrolytes," KIST-LLNL Workshop, Livermore, CA (September 2019).

3. A. Jana, “Electrochemomechanics of lithium dendrite growth,” KIST-LLNL Workshop, Livermore, CA (September 2019).
4. B.C. Wood, “Integrated Multiscale Modeling for Design of Robust 3D Solid-State Lithium Batteries,” VTO Annual Merit Review (June 2019).

References

1. Arthur, T. S., D. J. Bates, N. Cirigliano, D. C. Johnson, P. Malati, J. M. Mosby, E. Perre, M. T. Rawls, A. L. Prieto, and B. Dunn. 2011. “Three-dimensional electrodes and battery architectures.” *Mrs Bulletin* 36 (7):523-531. doi: 10.1557/mrs.2011.156.
2. Hart, R. W., H. S. White, B. Dunn, and D. R. Rolison. 2003. “3-D microbatteries.” *Electrochemistry Communications* 5 (2):120-123. doi: 10.1016/s1388-2481(02)00556-8.
3. Long, J. W., B. Dunn, D. R. Rolison, and H. S. White. 2004. “Three-dimensional battery architectures.” *Chemical Reviews* 104 (10):4463-4492. doi: 10.1021/cr020740l.
4. McOwen Dennis, W., Shaomao Xu, Yunhui Gong, Yang Wen, L. Godbey Griffin, E. Gritton Jack, R. Hamann Tanner, Jiaqi Dai, T. Hitz Gregory, Liangbing Hu, and D. Wachsman Eric. 2018. “3D-Printing Electrolytes for Solid-State Batteries.” *Advanced Materials* 30 (18):1707132. doi: 10.1002/adma.201707132.

Acknowledgements

This work was performed under the auspices of the U.S. Department of Energy by Lawrence Livermore National Laboratory under contract DE-AC52-07NA27344.

Collaborations. The LLNL computational modeling team includes Tae Wook Heo, Liwen Wan, and Aniruddha Jana. The project also collaborates with Dr. Adelstein from San Francisco State University (atomistic diffusion modeling) and Dr. Ye from LLNL (3D printing of solid-state battery materials). We are also partnered with Dr. Ellen Ivers-Tiffée from KIT (impedance spectroscopy of solid-state electrolytes), Dr. Peter Zapol from Argonne (modeling of solute segregation in LLZO), and Prof. Dina Fattakhova-Rohlfing from FZJ (controlled synthesis of LLZO with varying densities and microstructures) as part of the U.S.-Germany partnership on solid-state battery research.

Impact: Completion of this project will lead to understanding of interfacial losses and instabilities that impede performance and promote failure of solid-state batteries. The multiscale and multi-physics modeling framework developed in this work will address shortcomings of existing modeling strategies that either lack coupling of the multi-physics nature of various processes active in 3D batteries or fail to incorporate processes at different length scales to understand function. Ultimately, the tools and understanding generated by this project can be utilized to realize optimization of interface-dominated 3D batteries.

Out-Year Goals. Future activities will focus on refining our atomistic interface models for improved fidelity of ion transport simulations through crystalline and amorphous LLZO and across heterogeneous interfaces between the solid electrolyte and the cathode. We will also work with our collaboration partners to reconstruct microstructures of 3D printed materials and apply them to determine effective stresses and ion transport through the polycrystalline materials.

II.7.H 3D Printing of All-Solid-State Lithium Batteries (LLNL)

Jianchao Ye, Principal Investigator

Lawrence Livermore National Laboratory
7000 East Avenue
Livermore, CA 94550
E-mail: ye3@llnl.gov

Tien Duong, DOE Technology Development Manager

U.S. Department of Energy
E-mail: Tien.Duong@ee.doe.gov

Start Date: November 20, 2018

End Date: November 19, 2021

Project Funding: \$1,125,000

DOE share: \$1,125,000

Non-DOE share: \$0

Project Introduction

Traditional batteries are composed of two-dimensional films that are stacked and/or rolled. Thin film batteries display high power density while their thick film counterparts show good energy density, but it has proven difficult to concurrently achieve both within these planar form factors. In addition, conventional Li-ion batteries based on liquid organic electrolytes or gel polymer electrolytes have raised severe safety concerns due to the intrinsic flammable properties of the organic electrolytes. They are also not ideal for the use of high energy density metallic lithium (Li) anodes due to Li dendrite growth, or sulfur cathodes due to shuttling effects that result in fast capacity fade. There is an urgent need to develop safe, high-performance solid-state batteries (SSBs) with advanced electrolyte and separator technologies. Although in recent years a series of superionic conductors have been developed for electrolytes and separators [1],[2],[3], their performance does not satisfy demanding criteria due to large impedance from poor solid electrolyte-electrode contact and questionable electrochemical and mechanical stability. Unlike the well-established roll-to-roll fabrication of conventional Li-ion batteries, the processing of SSBs is unique due to the brittleness of solid state electrolytes (SSEs). The commercially available or lab-developed SSE discs are usually very thick (hundreds of micrometers to millimeters) to overcome their brittle nature, which unfortunately increases the cell impedance and accounts for the majority of the overall cell weight and volume, leading to dramatically decreased power and energy densities. [4]

In this project, we will investigate 3D printing techniques to overcome safety, fabrication, mechanical, and electrochemical issues in SSBs. 3D printing builds complex structures in a layer-by-layer fashion, which allows rapid production of hierarchical architectures, gradient and multi-material structures, and multi-component assemblies. 3D printing is an emerging area that could fundamentally transform energy storage devices. For example, 3D printing can produce batteries with arbitrary form factors to fit a product's specific volume requirements and can create interwoven electrode arrangements over a wide range of length scales to improve transport and increase power density for a given energy density. For SSBs, 3D printing may dramatically reduce the separator thickness from ~1 mm (by hydraulic pressing) to tens of micrometers or less. In addition, the interfacial contact area between the electrolyte and the electrode may be increased via 3D interdigitated designs. Hence, we expect a significant reduction of the overall cell impedance and enhancement of both energy and power densities of SSBs by harnessing an array of 3D printing technologies being developed at Lawrence Livermore National Laboratory (LLNL).

The major R&D challenge in 3D printing of batteries is to develop a fabrication scheme that exhibits good printability, processability, and compatibility while achieving the ideal 3D layouts and feature resolution necessary to improve properties and performance. Batteries are complex systems that typically involve assembly of multiple components—for example, active materials (anode and cathode), electrolyte, separator, electrically conductive additives, binders, current collectors, and packaging. To be economically viable, the assembled system must meet many stringent requirements, such as high weight percentage of active materials,

high ionic and electronic conductivities, and good mechanical and thermal properties. To print a battery, the feedstocks (e.g., inks, resins, powders, suspensions, etc.) must also meet certain process requirements, such as exhibiting proper flow characteristics (or rheology), being stable and predictable, or perhaps even being photocurable for some specific 3D printing approaches. In addition, the multi-material nature of batteries is a nontrivial problem for 3D printing, and aspects such as varied particle morphologies and surface chemistry place increased importance on properly tuning the feedstock properties. For the case of SSBs, the solid state electrolyte (SSE) is included in three battery components, the anode, cathode, and separator, which increases the difficulty in the feedstock development as multiple interactions between different solid components (e.g., solid electrolyte, conductive filler, and active materials) need to be considered. In the case of extrusion-based 3D printing processes, such as Direct Ink Writing (DIW) and Fused Deposition Modeling (FDM), particle aggregation or agglomeration in the ink can limit the minimum feature size that can be achieved due to jamming and nozzle clogging, which hinders the enhancement of power characteristics in 3D batteries. To realize the full potential of 3D printing, feedstocks for each component must be created that are suitable for the particular printing approach, multi-material printing methods must be developed, and material compatibility during post-processing steps must be addressed. With respect to the latter, sintering is a typical post-processing method used to improve the ionic conductivity of SSE separators. Yet, co-sintering with active materials could facilitate undesired reactions that may increase the interfacial impedance. [5],[6] Furthermore, stresses that develop during post-processing due to dimensional changes and volume reductions could lead to cracking and fracturing. We aim to solve these materials, manufacturing, and processing challenges to create 3D multi-material batteries and will first focus on the printing of SSEs. In addition, we will strive to develop materials and 3D printing approaches for SSBs that eliminate the need for sintering steps.

Objectives

- Objective 1: Tuning microstructures of 3D printed SSE separators
- Objective 2: Process compatibility with cathode printing
- Objective 3: 3D printing of sinter-free SSE separators.

Approach

The project will focus on 3D printing the solid-state electrolyte to tackle materials, manufacturing and processing challenges. In the first year, we will develop feedstock materials based upon state-of-the-art Li-ion conductors for SSBs. Next, we will explore a range of LLNL 3D printing methods to determine feedstock compatibility, complexity of 3D structure, and minimal feature size. We will focus on DIW, but other AM techniques will also be explored throughout the three-year timeline as long as budget allows. We will consider the scalability of these approaches and strive to develop high throughput methods that could be economically viable. In addition, material and processing compatibilities will be considered throughout the project. For example, we will verify the compatibility of our printed SSEs with typical SSB cathode materials during post-processing, specifically during sintering. Recognizing that sintering could be a limiting factor, both from a technological but also from a business standpoint, we will develop sintering-free feedstocks and 3D printing techniques to eliminate the possible compatibility issues during post-processing.

Results

Powder feedstock development

The particle size, morphology, and composition of solid-state electrolyte powders are critical for both ink printing and post-sintering. We evaluated two commercial Ta doped LLZO (LLZTO) powders and chose one with ~ 5 μm particle size as the starting material for further modifications. The raw powders cannot be printed due to large agglomerates and require high packing density and a high sintering temperature ($\geq 1100^\circ\text{C}$) for densification. We reduced the particle size by high energy ball milling. It was found that the milling environment is important to break down the particles. As shown in Figure II.7.H.1, dramatic particle size reduction is observed only for solvents that can mix well with LLZTO and have low viscosity—the alcohol-based solvents and aprotic solvents with proper surfactants. Although ethanol and IPA can effectively mill

down the particle size, both XRD and ICP-OES (Figure II.7.H.2 (a)) suggest H^+/Li^+ exchange occurs during high energy ball milling and results in Li loss. As a result, a secondary phase (e.g., $La_2Zr_2O_7$) is formed after sintering of ethanol milled powder (Figure II.7.H.2 (b)), and the pellet sintered at 1100°C is still highly porous (Figure II.7.H.2 (d)). Instead, acetonitrile/Triton X-100 ball milled (MT-milled) powders show no XRD peak shift and much less Li loss. The corresponding sintered pellets are pure cubic phase and show a high degree of densification.

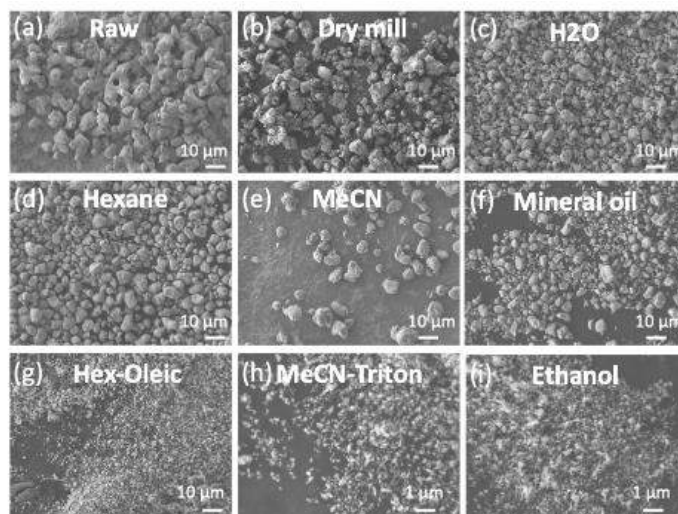


Figure II.7.H.1 Morphology of LLZTO powders under various high-energy ball milling conditions. (a) Raw powders purchased from MTI Corporation. (b) Dry milled powders. (c-i) powders milled in medium including (c) H_2O , (d) hexane, (e) acetonitrile, (f) mineral oil, (g) hexane with oleic acid, (h) acetonitrile with Triton X-100, (i) ethanol. Milling beads are 0.1-0.2 mm YSZ, time is 60 min

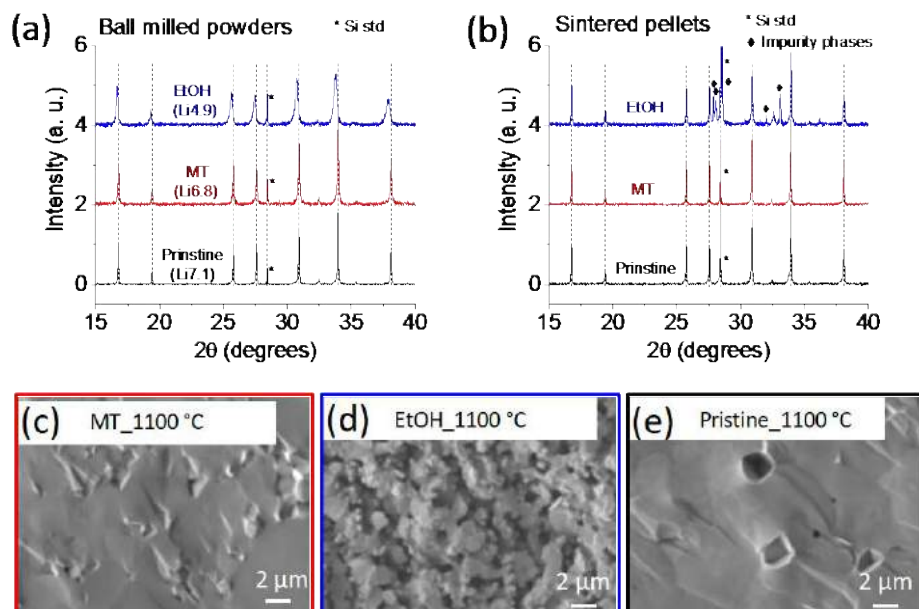


Figure II.7.H.2 (a) XRD of powders before ball milling (black), and after ball milling in acetonitrile/Triton X-100 (red) and ethanol (blue). x values in (Li_x) represent Li contents in $Li_xLa_3Zr_{1.4}Ta_{0.6}O_7$ measured from ICP-OES. (b) XRD of corresponding 1100°C sintered pellets. (c-e) SEM images of corresponding 1100°C sintered pellets

Furthermore, the sintering temperature was lowered by 150°C with no Li loss by using high energy ball milled powders with reduced particle size, as shown in Figure II.7.H.3 (a-i). These MT-milled powders can be

sintered at temperatures as low as 950°C and produce relative densities of 96%-98% when sintered in the temperature range 950°C to 1100°C. Different microstructures were obtained using different starting particle sizes and sintering temperatures. The ionic conductivity (Figure II.7.H.3 (j)) of the sintered pellets made of MT-milled powders with density > 95% is comparable to that of well-sintered raw powder pellets, reaching $\sim 8 \times 10^{-4}$ S/cm at 30°C.

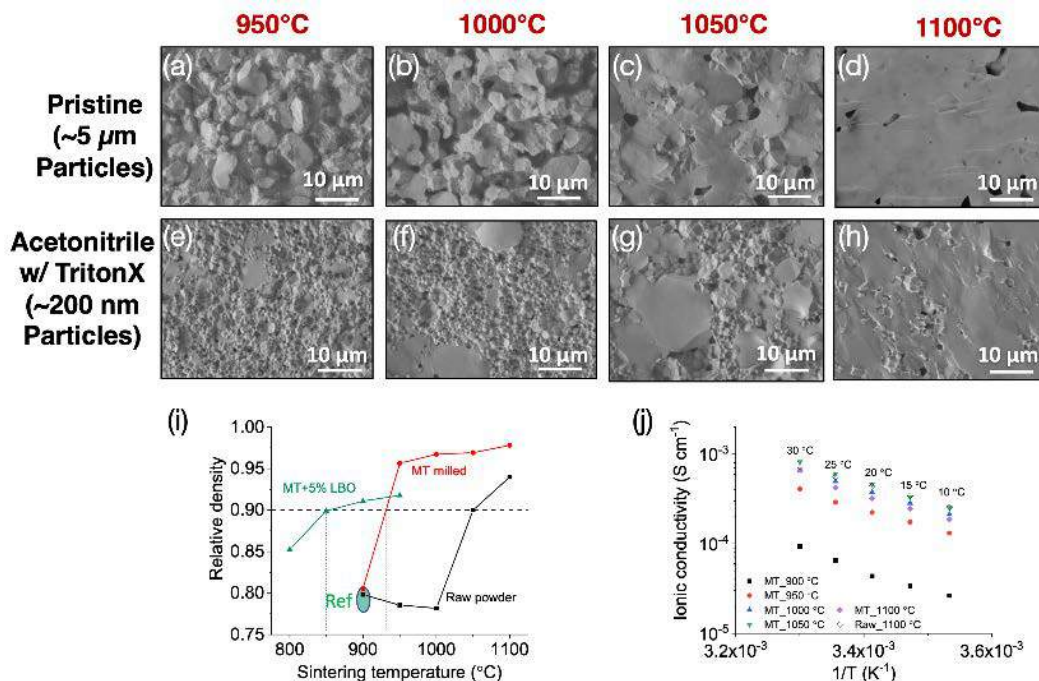


Figure II.7.H.3 (a-d) and (e-h) are SEM images of pristine and MT-milled LLZTO powder pellets sintered at 950°C, 1000°C, 1050°C, and 1100°C, respectively. (i) Relative density of LLZTO pellets (black: raw powder; Red: MT-milled powder; Green: ball milled LLZTO with 5 wt% Li₃BO₃ powder) sintered at different temperatures. The green circle is the density of sintered LLZO with Li₃BO₃ additive reported in the literature. [7]

Ink recipe development and 3D printing

Based on the MT-milled powders, various ink recipes were developed for 3D printing. Table II.7.H.1 lists several ink recipes developed thus far under this project. They are divided into three categories: solvent-based, solvent/binder-based, and resin-based inks. Pure solvent (i.e., NMP)-based inks can be densified after sintering. However, extra care is needed to avoid drying-induced cracking. The addition of polymer binders removes cracks. The poly(ethylene glycol) diacrylate (PEGDA) recipe enables flexible mechanical properties in the green film and UV/thermal curing for fast shape forming. It can be printed using two printing techniques: direct ink writing (DIW) and paste projection microstereolithography (paste PuSL). Therefore, a significant amount of effort was put into this versatile recipe.

Table II.7.H.1 Development of Ink Recipes for 3D Printing

Types of Inks	Compositions	Notes
Solvent-based	NMP/LLZTO	High solid content. Slippery ink. Easy cracking after drying. Can be densified.
	Ethylene glycol/LLZTO	<60 wt% solid content. Viscous but homogeneous ink. Easy cracking after drying. No success yet in densification.
Solvent-based with binders	Cyclohexanone/cellulose /LLZTO	Slippery ink. No success yet in 3D printing.
	Ethylene glycol/cellulose /LLZTO	Uniform ink; slow drying. No success yet in densification.
	Acetonitrile/PEO/LLZTO	DIW printable. Fast drying.
	NMP/Acetonitrile/PEGDA/LLZTO	DIW printable. Can be densified.
Resin-based	PEGDA/LLZTO	UV/thermal curable; DIW printable. Can be densified.

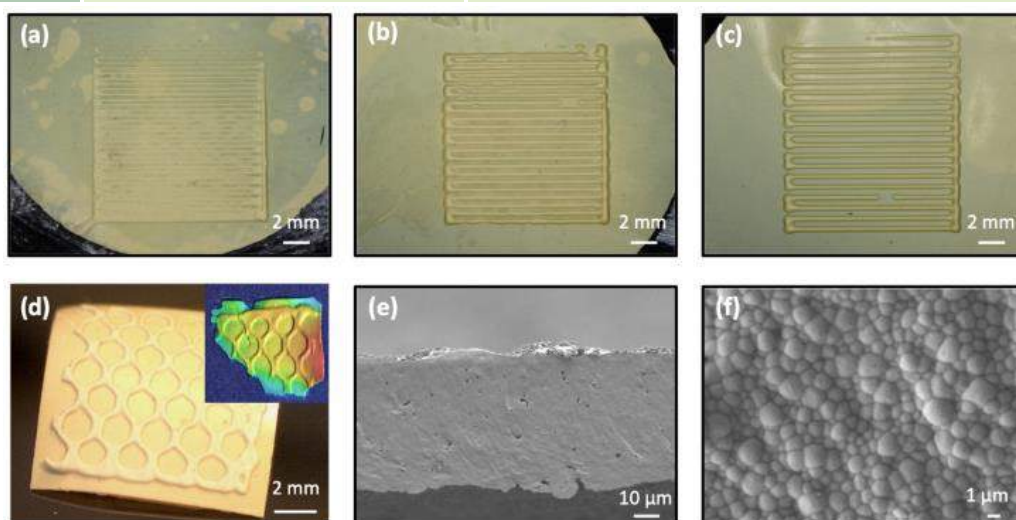


Figure II.7.H.4 PEGDA recipe: 3D printing and post sintering. PEGDA/LLZTO ink was first printed as a thin film using the paste PuSL system, and then zig-zag structures with varying spacings (a-c) were printed on top using DIW. (d) A honeycomb structure on a film substrate. Inset is an 3D optical image of a piece after 1100 °C sintering. (e) Cross-section SEM image of the printed film after sintering, showing high densification with thickness of ~ 50 μm. (f) Surface

To produce thin and uniform SSE separator films with high efficiency, PuSL is much faster than DIW. PEGDA/LLZTO inks with solid contents from 50 wt% to 85 wt% were developed and printed using a house-made Paste PuSL system. The PEGDA is crosslinked by shining a UV light for 7-30 seconds. For thin film fabrication, an area UV projection is utilized. Selective polymerization can also be developed by using computer-designed light patterns and optimizing initiator/absorbent/inhibitor content, which will be explored in our next plan. For now, we employed DIW to write simple structures on top of PuSL printed films (Figure II.7.H.3 (a-d)) to determine proper sintering conditions for densification.

Post sintering for densification

The initial solid content of the PEGDA/LLZTO ink used for printing and sintering (shown in Figure II.7.H.4) is 60 wt%. Even with such low LLZTO content, the use of ~ 200-nm MT-milled nanopowders allows the film to be densified at proper sintering conditions (Figure II.7.H.4 (e-f)) without commonly-used pre-pressing techniques to improve initial packing density. Conversely, films made from raw powder (~ 5 μm particle size) using either the PEGDA/LLZTO or NMP/LLZTO recipe cannot be densified well after sintering even with 83 wt% solid content, as shown in Figure II.7.H.3a. By replacing the raw powder with MT-milled powder, an NMP/LLZTO film with 73 wt% solid content can be densified in a tube furnace at 1100°C for 6 hours (Figure II.7.H.5 (b)).

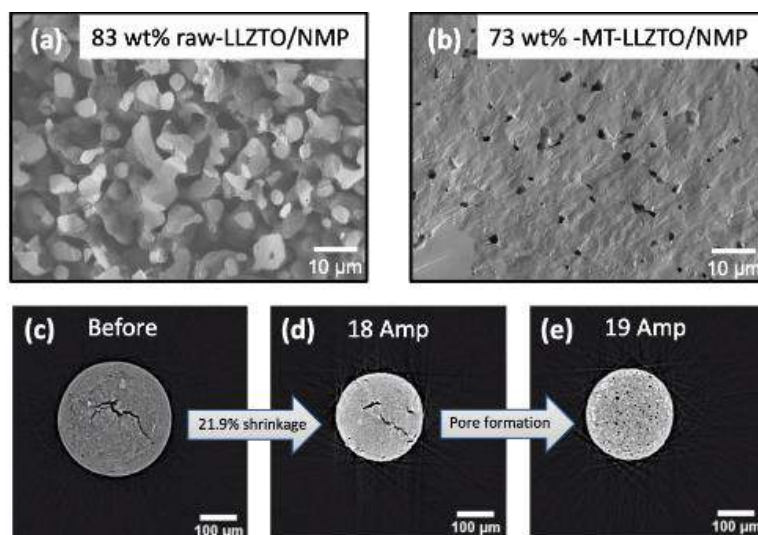


Figure II.7.H.5 Sintering of DIW-extruded LLZTO filaments. (a) 1100 °C furnace-sintered filament from raw powder LLZTO/NMP (83 wt%) ink. (b) 1100 °C furnace-sintered filament from ball milled LLZTO/NMP (73 wt%) ink. (c-e) In situ tomography results from halogen lamp sintering of ball milled LLZTO filament. Sintering temperature is proportional to the applied current of the lamp heating source

In situ synchrotron radiography/tomography was conducted to reveal sintering kinetics. A DIW-extruded filament was used for these experiments, and a halogen lamp provided the heating source. As shown in Figure II.7.H.5 (c-e), the diameter of the filament shrinks 21.9% within one minute of infrared light irradiation. Further increasing the temperature leads to the evolution of pores, which indicates decomposition and needs further investigation.

Although the densification of printed parts has been demonstrated, there are still problems to be solved after sintering, such as cracking and warpage (especially for thin films), that hinder the measurement of ionic conductivity and the integration with other battery components. These issues are currently being tackled through various stress/strain management methods. The sintering temperature is also higher for printed films than hydraulic pressed pellets due to the lower initial packing density. Recently, we introduced Li_3BO_3 as a sintering agent and found that the densification was accelerated dramatically, with 90% relative density obtained at 850°C, as shown in Figure II.7.H.3 (i), well above literature reported density values. [7]

Conclusions

LLZTO powders with reduced particle size (~200 nm) were successfully prepared using optimized high-energy ball milling conditions. The use of milled powders improves printing quality and accelerates densification during furnace sintering. Over 97% relative density and $8 \times 10^{-4} \text{ S/cm}$ ionic conductivity has been achieved. Simple geometries such as thin films (< 100 μm) and films with architected interfaces have been printed using Paste PuSL and DIW techniques. Printed samples with relatively low solid content can still be densified at certain sintering conditions, and the densification can be accelerated by adding Li_3BO_3 as a sintering agent.

References

1. N. Kamaya, K. Homma, Y. Yamakawa, M. Hirayama, R. Kanno, M. Yonemura, T. Kamiyama, Y. Kato, S. Hama, K. Kawamoto, A. Mitsui, A lithium superionic conductor, *Nat. Mater.* 10(9) (2011) 682-686.
2. W.S. Tang, A. Unemoto, W. Zhou, V. Stavila, M. Matsuo, H. Wu, S. Orimo, T.J. Udovic, Unparalleled lithium and sodium superionic conduction in solid electrolytes with large monovalent cage-like anions, *Energy Environ. Sci.* 8(12) (2015) 3637-3645.
3. Y. Wang, W.D. Richards, S.P. Ong, L.J. Miara, J.C. Kim, Y.F. Mo, G. Ceder, Design principles for solid-state lithium superionic conductors, *Nat. Mater.* 14(10) (2015) 1026-1032.
4. Y. Kato, S. Hori, T. Saito, K. Suzuki, M. Hirayama, A. Mitsui, M. Yonemura, H. Iba, R. Kanno, High-power all-solid-state batteries using sulfide superionic conductors, *Nat. Energy* 1 (2016) 1-7.
5. Y. Ren, T. Liu, Y. Shen, Y. Lin, C.-W. Nan, Chemical compatibility between garnet-like solid state electrolyte $\text{Li}_{6.75}\text{La}_3\text{Zr}_{1.75}\text{Ta}_{0.25}\text{O}_{12}$ and major commercial lithium battery cathode materials, *J. Materiomics* 2(3) (2016) 256-264.
6. L. Miara, A. Windmüller, C.-L. Tsai, W.D. Richards, Q. Ma, S. Uhlenbruck, O. Guillon, G. Ceder, About the compatibility between high voltage spinel cathode materials and solid oxide electrolytes as a function of temperature, *ACS Appl. Mater. Interfaces* 8(40) (2016) 26842-26850.
7. R.A. Jonson, P.J. McGinn, Tape casting and sintering of $\text{Li}_7\text{La}_3\text{Zr}_{1.75}\text{Nb}_{0.25}\text{Al}_{10}\text{O}_{12}$ with Li_3BO_3 additions, *Solid State Ionics* 323 (2018) 49-55.

Acknowledgements

We would like to acknowledge our team members including Xiaosi Gao, Marissa Wood, Siwei Liang, Jean-Baptiste Forien, Cheng Zhu, Jose Ali Espitia, and Leonardus Bimo Bayu Aji for their great contributions to the project. We also express our thanks to our Deputy Division Leader Tony Van Buuren, the point of contact for energy storage materials, and E-program manager Dan Flowers. This work was performed under the auspices of the U.S. Department of Energy by Lawrence Livermore National Laboratory under Contract DE-AC52-07NA27344.

II.7.I Advanced Polymer Materials for Batteries (Stanford University)

Zhenan Bao, Principal Investigator

Stanford University
443 Via Ortega, Shriram Center
Stanford, CA 94305
E-mail: zbao@stanford.edu

Yi Cui, Principal Investigator

Stanford University
476 Lomita Mall, McCullough Building
Stanford, CA 94305
E-mail: yicui@stanford.edu

Tien Duong, DOE Technology Development Manager

U.S. Department of Energy
E-mail: Tien.Duong@ee.doe.gov

Start Date: October 1, 2018
Project Funding (FY18): \$450,000

End Date: September 30, 2019
DOE share: \$450,000

Non-DOE share: \$0

Project Introduction

Li easily reacts with electrolyte components to form a natural SEI, which is full of defects and ‘hot spots’ with higher current density. This leads to faster Li deposition and formation of dendrites. Additionally, large volume change of Li metal anodes during stripping/plating will expose fresh Li surface to electrolyte. The irreversible and uncontrollable parasitic reactions between Li metal and electrolyte components aggravate Li consumption, further forming dead Li, lowering the CE, and devastating the cycle life of Li metal anodes. [1],[2],[3] These problems are major obstacles against their practical application. With the implementation of a polymer-based protective layer which functions as an artificial SEI with desired properties, we were able to enhance the performance of Li metal electrodes.

Objectives

This project will develop new polymer materials for batteries. The team will develop polymer coatings with specific mechanical properties that can accommodate the volume expansion and contraction of the Li-metal anode associated with deposition and stripping (charging and discharging).

Approach

The project uses soft polymer coatings with dynamic crosslinking to give the resulting polymers liquid-like rheological properties and stretchable and self-healing properties. In previous work, the project has shown that such coatings resulted in uniform deposition/stripping of lithium metal and improved cycling stability of Li-metal electrodes. To understand the design rules for effective polymer coatings, we chose a few representative polymers to systematically understand structure property relationships. Here, we investigate the correction between surface energy of the polymer and exchange current for lithium deposition.

Results

The development of lithium metal batteries is currently hindered by the high reactivity of lithium metal with the electrolyte. In addition, inhomogeneous deposition of lithium leads to high surface area dendritic growth that further exacerbates reaction with the electrolyte. Designing the electrode-electrolyte interface and controlling the lithium deposition morphology is therefore of great importance. Currently, we have focused on the design of polymer coatings that function to limit the electrolyte (polar solvent and salt) accessibility to the electrode surface, thereby limiting undesired reactions. First, we use a model liquid system to allow us to understand the effect of Li ion solvation on Li deposition. We design a nonpolar:polar electrolyte mixture

where nonpolar alkanes can limit the accessibility of the polar solvent to the electrode surface. We show that hexane and cyclohexane addition to ether solvents (1,3-dioxolane and 1,2-dimethoxyethane) reduce the Li ion solvation, halves the nucleation and growth overpotentials for lithium deposition, increases the cell coulombic efficiency, improves the lithium deposition morphology, increases the electrolyte oxidative stability ($> 0.2\text{V}$), and doubles the cycle life – even when compared to a widely used fluorinated ether. Then we used this knowledge to apply to polymer coating design.

1. Liquid model system

Rationale for molecule selection and study

Lithium metal is stable in the presence of linear alkane media such as mineral oil. Mineral oil is highly viscous; hence we focused on shorter chain alkanes such as *n*-hexane with a similar chemical structure to mineral oil, but with low molecular weight and viscosity. Because hexane is nonpolar (and cannot solvate ions), we need a polar solvent that is miscible with hexane, but can also dissolve lithium salts. 1,3-dioxolane (DOL) and 1,2-dimethoxyethane (DME) were chosen for this work because they have been heavily explored for lithium metal deposition and stripping, and have been shown to yield higher coulombic efficiencies than carbonate-based solvents used in Li-ion batteries. Fluorinated solvent additive – TTE – was chosen to serve as the comparison to the hexane system because TTE has been heavily explored for lithium metal use. Unlike hexane, TTE is expected to react with lithium metal, and should give insight into reactive vs nonreactive additives and their effect on lithium deposition and stripping. The molecular structures of these compounds are shown in Figure II.7.I.1a.

Influence on electrochemistry

The influence of the electrolyte mixtures on lithium deposition and stripping was studied. Figure II.7.I.1b shows that the nucleation overpotential required to deposit lithium is lowest for the DOL:hexane mixture and highest for the TTE mixture. Furthermore, the time (or capacity) required for the nucleation event is lowest for the DOL:hexane mixture and highest for the DOL:TTE mixture. More importantly, the growth overpotential for continued lithium deposition and stripping is lowest in the hexane mixture and is a function of hexane content (Figure II.7.I.1c). As the cosolvent amount is increased with hexane addition, the nucleation overpotential is decreased compared to DOL and DOL:TTE mixture.

To better understand the effect of the nonpolar alkanes on the electrochemistry, we fabricated Li/Cu cells and studied the initial lithium deposits using scanning electron microscopy (SEM). Figure II.7.I.2a shows that when 0.1 M DOL is used as the electrolyte, clear dendrites are formed. These dendrites span the entire electrode. However, when a 0.1 M DOL:hexane electrolyte is used (Figure II.7.I.2a), the density of dendrites present on the electrode surface is much lower. The lack of dominant dendrite formation may help explain the longer cycling lifetime observed in Figure II.7.I.1b-c. Our original hypothesis for exploring these nonreactive nonpolar solvents is that they can limit the accessibility of the polar solvent to the electrode surface; hence prolonging cycle life through a mechanism different from reactive additives that instead passivate the surface. However, this hypothesis – termed the surface coverage effect – does not help explain the decrease in nucleation and growth overpotentials.

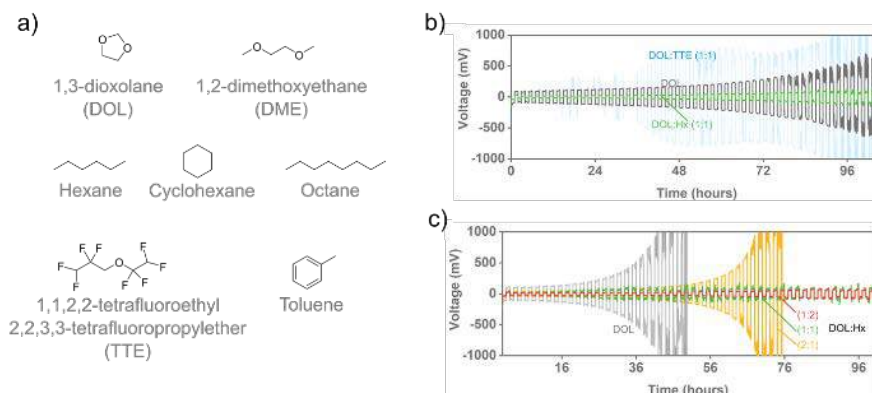


Figure II.7.I.1 (a) Chemical structures of the liquid compounds studied in this work. (b) Lithium/Lithium cycling at 0.5 mA/cm² to 0.5 mAh/cm² as a function of electrolyte content. (c) Li/Li cycling at 1 mA/cm² to 1 mAh/cm² as a function of hexane content in the electrolyte. The ratios (e.g., 1:1) represent volume ratios. Salt concentration: 0.1 M LiTFSI

Solvation effect

To better explain the decrease in nucleation and growth overpotentials, we probe the lithium-ion solvation environment in the different electrolyte mixtures. ¹H, ⁷Li, and ¹⁹F nuclear magnetic resonance (NMR) spectroscopy were used to study the solvation changes. Figure II.7.I.2b shows the ⁷Li NMR spectra of a 0.1 M LiTFSI in DOL solution as the hexane volume content is increased. Despite maintaining the same salt concentration, the lithium peak shifts significantly downfield as a function of hexane content. Downfield shift (shift to higher frequencies) is observed due to deshielding of the electron cloud surrounding the nuclei of interest – a decrease in the electron cloud that opposes the externally applied magnetic field. Therefore, there is less ion pairing and a decrease in Lewis basicity around the lithium ion. In contrast, TTE binds to the Li⁺ within the Li⁺–DOL solvation shell and hence increases the electron density around the lithium ion, leading to an upfield shift in the ⁷Li NMR spectrum.

The solvation free energy of a lithium-ion solvated by different electrolyte mixtures was computed using classical molecular dynamics. Upon hexane and cyclohexane addition to DOL, the magnitude of the lithium solvation free energy continually decreases. For TTE, the magnitude of the solvation free energy increases with higher TTE concentration. These MD simulations corroborate the NMR results in that they show looser Li⁺ coordination and solvation with hexane or cyclohexane addition, and stronger Li⁺ solvation with TTE addition. The ionic solvation behavior strongly correlates with the electrochemistry.

Knowledge obtained from this work about the utility of limiting polar electrolyte accessibility to the lithium metal electrode can yield new design approaches regarding polymer selection for lithium metal coatings. The polymer should be designed to frustrate lithium ion solvation within the electrolyte (reduce solvation free energy) and be chemically stable against contact with lithium metal.

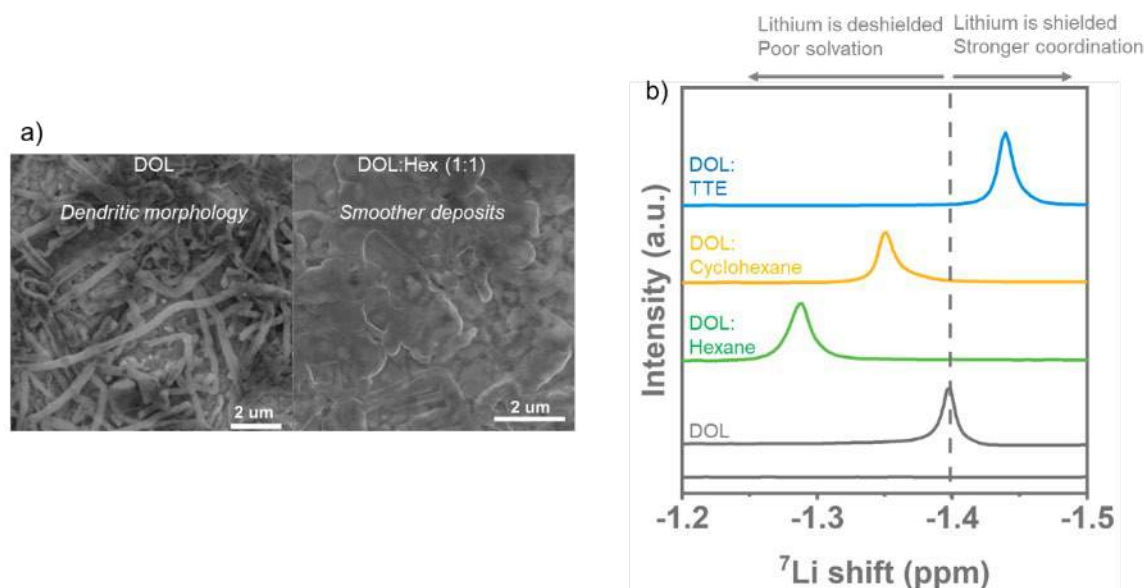


Figure II.7.I.2 (a) SEM image of the lithium deposition morphology at a current rate of 1 mA/cm² to 0.1 mAh/cm² as a function of electrolyte content. (b) ^7Li NMR chemical shifts of 0.1 M LiTFSI in the respective electrolytes. The dashed line in (b) demarcates the ^7Li chemical shift of LiTFSI in DOL, and the 'deshielding' and 'shielding' is made with respect to the peak

2. Self-healable polymeric architectures

We hypothesize that stimuli-responsive polymeric architectures can be effective in preventing morphological instabilities during electrodeposition compared to covalently bonded rigid polymers and crosslinked elastomers, when used as artificial interfaces between the electrode and electrolyte. The fundamental working mechanism of the dynamic polymeric coatings can arise from the spontaneous structural response of the polymer in response to the roughening electrode during electrodeposition. As the polymer coating is free to flow, if there is a 'hotspot' (uneven deposit) on the surface of the lithium metal, the dynamic polymer coating can rearrange and cover these regions resulting in increased overpotential. Thus, successively Li⁺ ions deposit on the flatter regions resulting in uniformity of deposition. Furthermore, the tortuous pathway in the polymeric interface can enable uniform distribution of lithium ions during charging process, thus leading to uniform deposition.

In this work, we synthesize a series of different supramolecular polymers will be designed comprising of various content of non-covalent interactions and polymer entanglements using polymerization of PDMS with urea linkages. Figure II.7.I.3a shows the chemical structure of the self-healing polymer (SHP) comprising of a PDMS soft block where n (number of siloxane monomers) was changed from 10 to 350, while the urea linkages were formed using isophrone diisocyanate units. The variation in the ratios between urea units and PDMS blocks are useful in understanding the effect of elasticity and the self-healing property. We characterized the molecular properties of the SHP using Infrared Spectroscopy as shown in Figure II.7.I.3b. It is observed that the shift in the wavenumber in the $-\text{NH}$ and $-\text{C}=\text{O}$ bond stretching (representing the strength of H-bonding) is nearly identical for all the three co-polymers. However, the abundance of the H-bonding units are significantly different in the three samples.

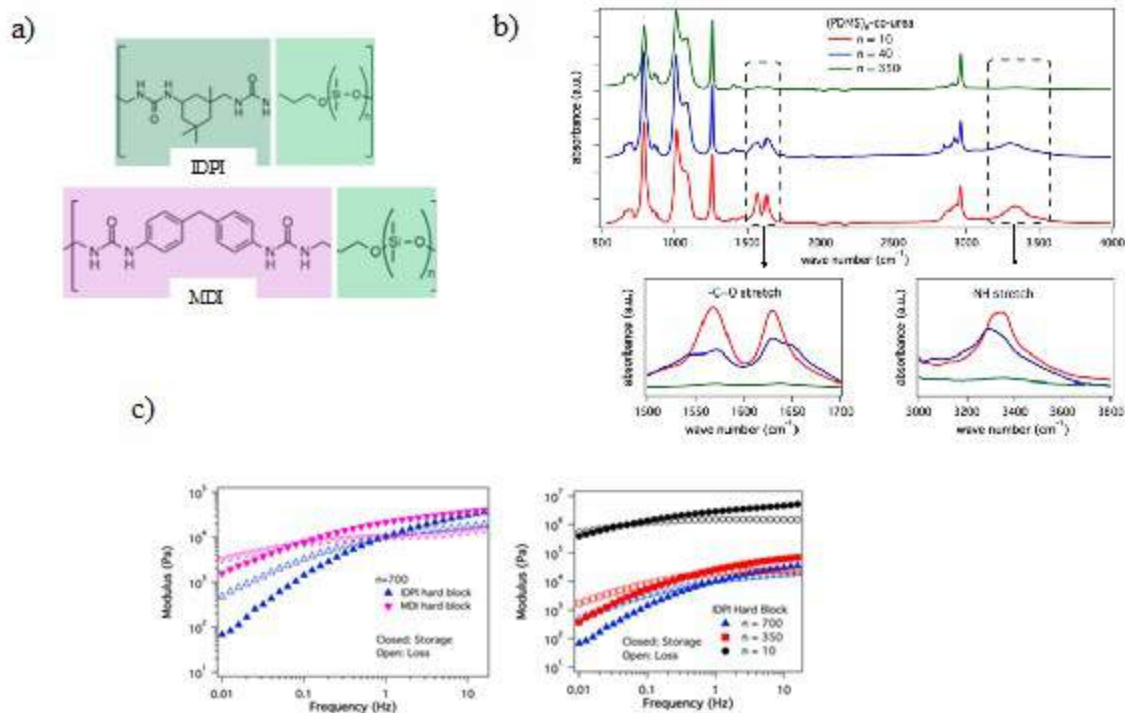


Figure II.7.I.3 **a**, Chemical structure of PDMS Self-Healing Polymer (SHP). **b**, FTIR Spectra of the PDMS-IDPI with varying size of PDMS soft block in the co-polymer. **c**, Oscillatory shear measurements at strain 1% for the different PDMS based self-healing polymers

We performed the frequency dependent oscillatory shear measurements to analyze the mechanical and molecular properties of the supramolecular polymers. Specifically, we utilized a strain of 1% and temperature 25°C. The high frequency regime corresponds to the elastic behavior of the material, while the low frequency corresponds to the viscous effects. It can be seen that changing the hard unit from IDPI to MDI increases the cross-over frequency storage and loss modulus, reflecting a higher relaxation time (Figure II.7.I.3c). Also, variation of the number of monomers in the soft unit (PDMS from 10 to 700), leads to decrease in the elastic modulus of the polymer by about three orders of magnitude. Thus, the range of the polymers show wide differences in the molecular properties, reflective in the macroscopic relaxation behavior as well as the modulus.

We analyzed the electrochemical characteristics of the PDMS self-healing polymer using coulombic efficiency measurements in a Li||PDMS-IDPI SHP@Cu cells. Specifically, the current density used in this experiment was 0.5mA/cm² and the capacity being 1mAh/cm², while the electrolyte utilized was 1M LiPF₆ in EC/DMC along with 10%FEC additives. Figure II.7.I.4a shows the comparison of the lithium plating efficiency for the different PDMS-SHP coatings with varying size of PDMS blocks. It is observed that the coulombic efficiency values for all the coatings were nearly identical at values between 90-95%. However, there appears to be a trend in the relative lifetimes of the cells. It is seen that the PDMS-IDPI SHP with the shortest PDMS co-block (n=10) outperforms the other coatings. This indicates that a higher degree of dynamic bonding is essential for the stabilization of electrodeposition. Furthermore, we compared the performance of the Li||Cu cells with that of control electrolyte in Figure II.7.I.4b, where it is clear that while the control cell fails within 100 cycles, the PDMS-SHP coating enables stable cycling for over 150 cycles.

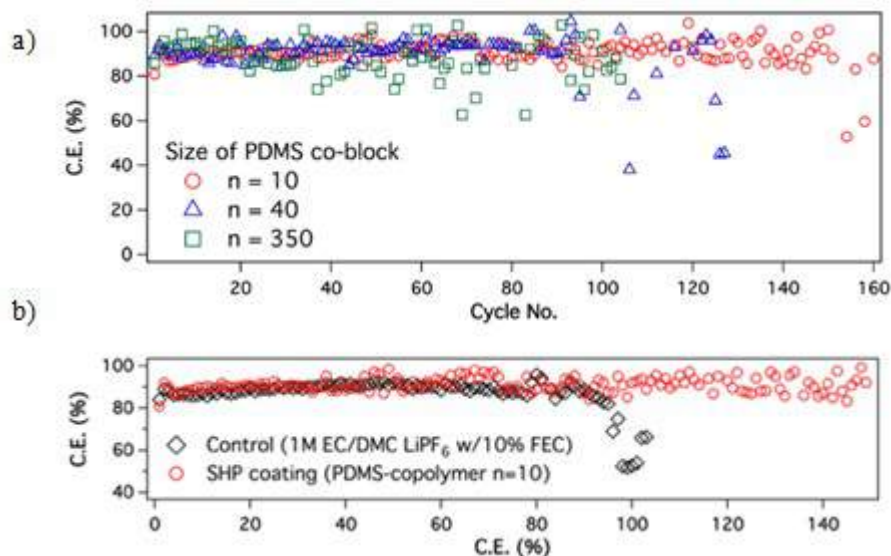


Figure II.7.I.4 **a**, Chemical structure of PDMS-IDPI Self-Healing Polymer. **b**, FTIR Spectra of the PDMS SHP with varying size of PDMS soft block in the co-polymer

We further analyzed the coulombic efficiencies in a Li||PDMS-SHP@Cu cells. In this measurement, a fixed amount of lithium was deposited onto the copper electrode, followed by repeated stripping and plating for shorter timeframes. Thereafter, the amount of lithium remaining from the copper electrode was quantified for obtaining the coulombic efficiency of electrodeposition. The electrolyte utilized in this experiment was 1M DOL/DME LiTFSI with 1% LiNO₃. Figure II.7.I.5a shows the typical voltage profile in the measurement. While Figure II.7.I.5b compared the coulombic efficiency of the different PDMS-SHP coatings with varying size of PDMS blocks and different molecular weights. It is observed that the coulombic efficiency values for all the coatings were nearly identical at values between 90-95%, except for the stiffest polymer ($n=10$). However, there appears to be a trend in the relative lifetimes of the cells. It is seen that the PDMS-SHP with the higher flowability outperforms the polymers with higher stiffness. Furthermore, the higher H-bonding units have higher CE as seen from the differences between the MDI vs. IDPI hard block based PDMS SHP. Thus our results indicate that a higher degree of electrodeposition stabilization is achievable by incorporating polymer coating with high flowability and abundance of strong dynamic bonding units.

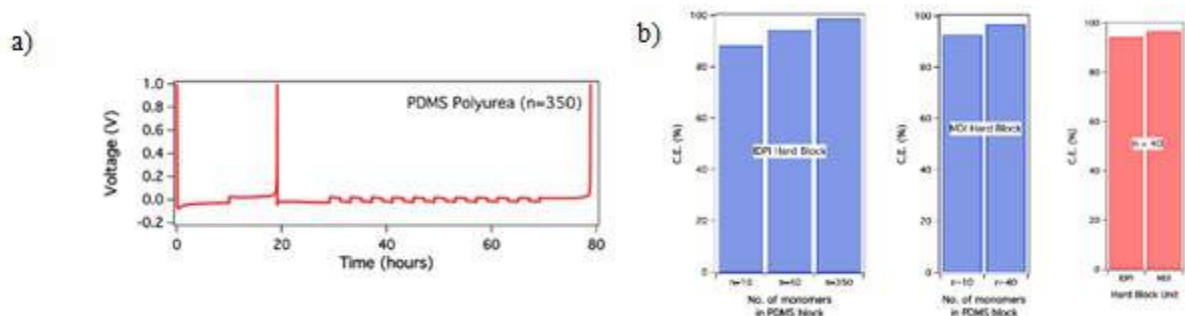


Figure II.7.I.5 **a**, Typical voltage profile of Li||PDMS-SHP@Cu cells. **b**, Coulombic efficiency comparisons of the PDMS SHP with varying size of PDMS soft block as well as H-bonding strengths in the co-polymer

Figure II.7.I.6b compares the coulombic efficiency of the polymer coatings with varying H-bonding strength. It is observed that the coulombic efficiency of the lithium deposition is higher for the polymer coated copper compared to the bare. It is important to note here that previous reports on polymer coatings have been shown to be effective in only ether-based electrolytes and not in carbonate-based systems which are more desirable for high voltage batteries. Thus, improved C.E. with the current polymer coating is interesting and

encouraging. The figure also shows the values for all the coatings show a trend that at lower levels of MDI content in the polymer coating show higher coulombic efficiency than the ones with higher MDI content. Also, it is apparent that the coulombic efficiency is higher for the polymers below the gel-point in comparison to stiffer polymers. Our results clearly demonstrate that improved dynamicity in the polymers enable stable deposition, which is a deviation from the long-standing concept in solid electrolytes which states that high modulus is important to prevent dendrites.

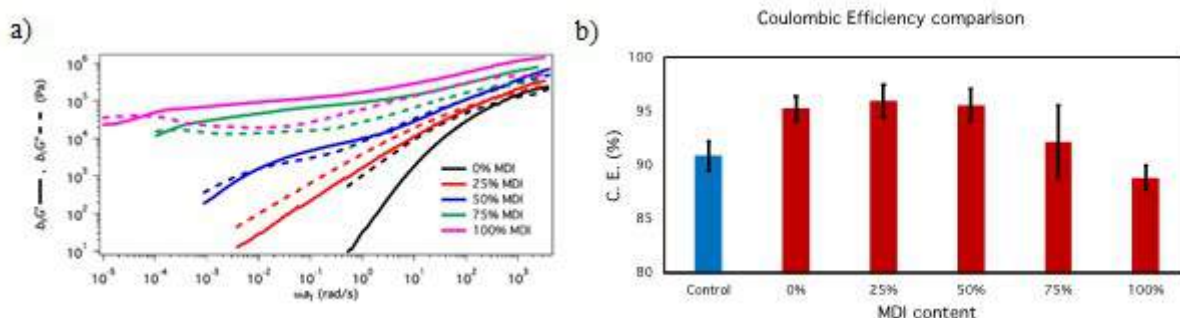


Figure II.7.1.6 **a**, Oscillatory shear measurements at strain 1% for the different self-healing polymers. **b**, Coulombic efficiency comparisons of the polymer SHP with varying H-bonding strengths in the co-polymer

Conclusions

Rational design of the electrode-electrolyte interphase is essential to stabilize electrodeposition of metallic lithium. Thus, it is important to design an artificial interfacial layer that can accommodate the stress generation due to the volume changes during battery operation and at the same time maintain ionic continuity. Using model liquid electrolyte additives, we learned that the utility of limiting polar electrolyte accessibility to the lithium metal electrode can yield new design approaches regarding polymer selection for lithium metal coatings. The polymer should be designed to frustrate lithium ion solvation within the electrolyte (reduce solvation free energy) and be chemically stable against contact with lithium metal. This knowledge led to the choice of a non-polar PDMS polymer backbone with dynamic H-bonding of different strengths and concentration. Such polymer systems allow access of a variety of mechanical properties. We found more stable cycling could be obtained with a higher degree of dynamic bonding. The coulombic efficiency was higher for the polymers below the gel-point in comparison to stiffer polymers. Our results clearly demonstrate that improved dynamicity in the polymers enable stable deposition, which is a deviation from the long-standing concept in solid electrolytes which states that high modulus is important to prevent dendrites. The insights provided here should serve as a starting point for further systematic investigation into soft organic coatings that can potentially help to enable the uniform and reversible deposition of lithium metal at high rates and over long times.

Key Publications

1. Yuchi Tsao, Minah Lee, Elizabeth C. Miller, Guoping Gao, Jihye Park, Shucheng Chen, Toru Katsumata, Helen Tran, Lin-Wang Wang, Michael F. Toney, Yi Cui, Zhenan Bao, Designing a quinone-based redox mediator to facilitate Li₂S oxidation in Li-S batteries, *Joule*, 3, 872-884, 2019.
2. Chibueze V. Amanchukwu, Xian Kong, Jian Qin, Yi Cui, and Zhenan Bao. Nonpolar alkanes modify lithium-ion solvation for improved lithium deposition and stripping. *Advanced Energy Materials*. 2019. <https://doi.org/10.1002/aenm.201902116>
3. Zhiao Yu, David Mackanic, ..., Yi Cui, and Zhenan Bao. A dynamic, electrolyte-blocking, and single-ion-conductive network for stable lithium-metal anodes. *Joule*. 2019. <https://doi.org/10.1016/j.joule.2019.07.025>

References

1. Xu, W. et al. Lithium metal anodes for rechargeable batteries. *Energy Environ. Sci.* 7, 513–537 (2014).
2. Lin, D., Liu, Y. & Cui, Y. Reviving the lithium metal anode for high-energy batteries. *Nat. Nanotechnol.* 12, 194–206 (2017).
3. Xu, K. Electrolytes and Interphases in Li-Ion Batteries and Beyond. *Chem. Rev.* 114, 11503–11618 (2014).

II.8 Beyond Lithium-Ion R&D: Solid-State Batteries

II.8.A Solid-State Inorganic Nanofiber Network-Polymer Composite Electrolytes for Lithium Batteries (WVU)

Nianqiang Wu, Principal Investigator

West Virginia University
P.O. Box 6106
Morgantown, WV 26506
E-mail: nick.wu@mail.wvu.edu

Tien Duong, DOE Technology Development Manager

U.S. Department of Energy
E-mail: Tien.Duong@ee.doe.gov

Start Date: October 1, 2016
Project Funding: \$1,400,193

End Date: September 30, 2019
DOE share: \$1,244,012

Non-DOE share: \$156,181

Project Introduction

Safety is of concern regarding the currently commercial lithium batteries due to the use of highly volatile and flammable organic solvent-based electrolytes. Use of solid-state electrolytes is an alternative solution to the safety issue; and it improves the chemical and thermal stability of lithium batteries due to their good mechanical strength and potentially good electrochemical stability. [1],[2]

Objectives

The project objective is to develop the solid-state electrolytes based on the highly-conductive inorganic nanofibrous network in the polymer matrix for lithium-ion batteries.

Approach

Integration of the highly Li⁺-conductive inorganic nanofiber network into the polymer matrix not only provides the continuous Li⁺ transport channels, but also inhibits crystallization from the amorphous state of polymer electrolyte. The inorganic nanofibers are fabricated with an electrospinning technique. The ionic conductivity of inorganic nanofibers is improved by chemical substitution or doping. Highly ionic-conductive polymers are developed by cross-linking and/or creation of a block-copolymer structure. The composition and microstructure of the composite electrolyte are designed to suppress the lithium dendrite formation.

Results

Flexible electrolyte-cathode bilayer framework with stabilized interface for room-temperature all-solid-state lithium-sulfur batteries

In a bilayer framework, a three-dimensional (3D) carbon nanofiber/sulfur (CNF/S) cathode was integrated with Li_{0.33}La_{0.557}TiO₃ (LLTO) nanofiber-polyethylene oxide (PEO) solid composite electrolyte, which served as both the cathode and the electrolyte for room-temperature all-solid-state Li-S batteries. The LLTO/PEO composite electrolyte exhibited the decomposition potential of around 4.5 V vs. Li|Li⁺ and the ionic conductivity of 2.3×10^{-4} S cm⁻¹ at room temperature with 13 wt% LLTO nanofibers.

The all-solid-state lithium-sulfur batteries based on the bilayer framework were tested at room temperature without addition of any liquid electrolyte. The full-cell exhibited stable cycling performance with Coulombic efficiency over 99% after 50 cycles. The battery was able to charge/discharge at higher current density up to 0.2C at room temperature with reversible capacities of 384,358 and 262 mAhg⁻¹ at current density of 0.05C, 0.1C and 0.2C, respectively, as shown in Figure II.8.A.1).

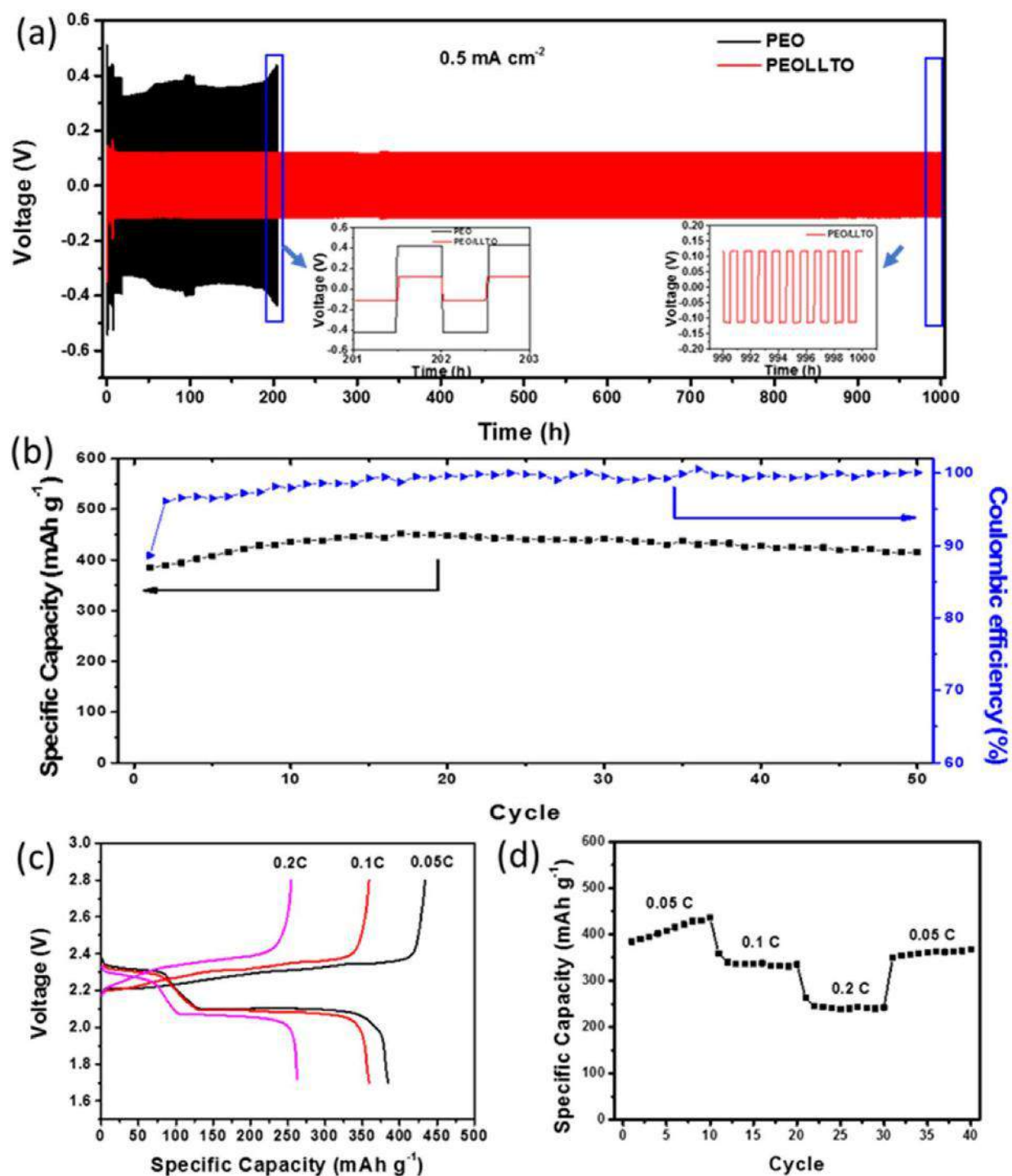


Figure II.8.A.1 (a) Voltage profiles of Li plating/stripping cycling with a current density of 0.5 mA cm^{-2} at room temperature (inserted: voltage profiles of PEO and PEO/LLTO tested at 201–203 cycles - left; voltage profile of PEO/LLTO at 990–1000 cycles - right). (b) Cycling performance of full-cell battery tested at 0.05 C (0.084 mA cm^{-2}) with a sulfur loading of 1.27 mg cm^{-2} . (c) Charge/discharge curves and (d) rate capability of the full cell tested at 0.05 C (0.084 mA cm^{-2}), 0.1 C (0.168 mA cm^{-2}) and 0.2 C (0.335 mA cm^{-2})

Garnet-rich Composite Solid Electrolytes for Dendrite-free, High-rate, Solid-state Lithium-metal Batteries

A new type of composite solid electrolytes composed of silane-modified $\text{Li}_{6.28}\text{La}_3\text{Al}_{0.24}\text{Zr}_2\text{O}_{12}$ (s@LLAZO) nanofibers and poly(ethylene glycol) diacrylate (PEGDA) were developed. The ionic conductivity of the composite electrolyte reached $4.9 \times 10^{-4} \text{ S cm}^{-1}$ with 60 wt.% of s@LLAZO nanofiber content. The oxidized decomposition onset started at 5.3 V for s@LLAZO-60PEGDA composite electrolyte.

Such a composite electrolyte was used to assemble the all-solid-state batteries with pure Li metal as anode and LiFePO_4 as cathode, which demonstrated the discharge capacities of 147 and 78 mAh g^{-1} at a rate of 0.5C and 5C, respectively, and excellent cycling stability at 0.5C with extraordinarily high rate capability up to 10C at ambient temperature. In short, the novel design of composite electrolyte with s@LLAZO nanofibers has opened an alternative avenue for development of all-solid-state Li ion batteries.

Chemical Interaction and Enhanced Interfacial Ion Transport in Ceramic Nanofiber-Polymer Composite Electrolyte for All-Solid-State Lithium Metal Battery

A solid-state ceramic/polymer composite electrolyte was developed based on 3D electrospun aluminum-doped LLTO nanofiber network embedded in the polyvinylidene fluoride-hexafluoropropylene (PVDF-HFP) matrix. In addition, lithium phosphate has been coated on the LLTO nanofiber surface before the nanofibers were embedded into the polymer matrix. The flexible LLTO/ Li_3PO_4 /polymer composite electrolyte exhibited ionic conductivity of $5.1 \times 10^{-4} \text{ S/cm}$ at room temperature and an electrochemical stability window of 5.0 V vs. $\text{Li}|\text{Li}^+$. Strong chemical interaction occurred between the nanofibers and the polymer matrix. Solid-state nuclear magnetic resonance (NMR) spectra revealed that lithium ions transport via three pathways: (i) intra-polymer transport, (ii) intra-nanofiber transport, and (iii) interfacial polymer/nanofiber transport.

The $\text{LiFePO}_4|\text{PVDF-HFP}/\text{LLTO}/\text{Li}_3\text{PO}_4|\text{Li}$ cell delivered the specific discharge capacity of 130.7 mA h g^{-1} at a current rate of 0.5C and retained 87.8% (114.7 mA h g^{-1}) of the initial capacity after 160 cycles. The Coulombic efficiency remained over 99.4% after 160 cycles. The discharging capacity was measured to be 158, 147, 133, 98, and 76 mAh g^{-1} at rate of 0.1C, 0.2C, 0.5C, 1C and 2C, respectively. When the current rate was switched back to 0.1 C, the cell exhibited a reversible capacity of 149 mA h g^{-1} .

Plastic crystal-added solid polymer- Garnet composite electrolytes

A plastic crystal-added solid polymer electrolyte was developed based on poly(ethylene glycol) methacrylate and pentaerythritol tetraacrylate (PETA) cross-linked polymer with addition of puccinonitrile (SN) plasticizer. This polymer electrolyte showed ionic conductivity of $8.3 \times 10^{-4} \text{ S cm}^{-1}$ at room temperature, and an electrochemical stability window of 4.7 V vs. $\text{Li}|\text{Li}^+$. After addition of 20 wt.% LLAZO nanofibers, the composite electrolyte demonstrated ionic conductivity of $8.5 \times 10^{-4} \text{ S cm}^{-1}$ at room temperature, and an electrochemical stability window of 5.0 V vs. $\text{Li}|\text{Li}^+$.

Conclusions

1. A composite bilayer framework was fabricated, in which the LLTO ceramic nanofiber/PEO composite electrolyte was coupled to a 3D flexible carbon nanofiber/sulfur (CNF/S) cathode. The full cell battery with the bilayer framework demonstrated very good electrochemical performance at room temperature with the Coulombic efficiency of over 99%.
2. A new type of composite solid electrolyte composed of silane-modified $\text{Li}_{6.28}\text{La}_3\text{Al}_{0.24}\text{Zr}_2\text{O}_{12}$ (s@LLAZO) nanofibers and PEGDA were developed. The ionic conductivity reached $4.9 \times 10^{-4} \text{ S cm}^{-1}$ with 60 wt.% of s@LLAZO nanofiber content. The oxidized decomposition onset potential started at 5.3 V for the s@LLAZO-60PEGDA composite electrolyte. The all-solid-state battery with such a composite electrolyte demonstrated stable cycling performance for 200 cycles and excellent rate capability (up to 10C) at room temperature due to the improved utilization of fast Li^+ conductor (LLAZO) in the composite structure.
3. The LLTO nanofibers were doped with aluminum and then coated with lithium phosphate to help form a continuous lithium-ion-conducting network, improving the lithium ion mobility at the LLTO nanofiber. The ionic conductivity of the PVDF-HFP/LLTO/ Li_3PO_4 reached $5.1 \times 10^{-4} \text{ S/cm}$. The full-cell battery with

this electrolyte and the lithium metal anode exhibited good cycling performance and rate capability. This work showed that interfacial synergy between the ceramic nanofibers and the polymer played an important role in the electrochemical performance of the composite electrolyte.

Key Publications

1. Zhu, Pei, Chaoyi Yan, Mahmut Dirican, Jiadeng Zhu, Jun Zang, R. Kalai Selvan, Ching-Chang Chung et al. “ $\text{Li}_{0.33}\text{La}_{0.557}\text{TiO}_3$ ceramic nanofiber-enhanced polyethylene oxide-based composite polymer electrolytes for all-solid-state lithium batteries.” *Journal of Materials Chemistry A* 6, no. 10 (2018): 4279-4285.
2. Zhu, Pei, Chaoyi Yan, Jiadeng Zhu, Jun Zang, Ya Li, Hao Jia, Xia Dong et al. “Flexible electrolyte-cathode bilayer framework with stabilized interface for room-temperature all-solid-state lithium-sulfur batteries.” *Energy Storage Materials* 17 (2019): 220-225.
3. Yan, Chaoyi, Pei Zhu, Hao Jia, Jiadeng Zhu, R. Kalai Selvan, Ya Li, Xia Dong et al. “High-Performance 3-D Fiber Network Composite Electrolyte Enabled with Li-Ion Conducting Nanofibers and Amorphous PEO-Based Cross-Linked Polymer for Ambient All-Solid-State Lithium-Metal Batteries.” *Advanced Fiber Materials* 1, no. 1 (2019): 46-60.
4. Yan, Chaoyi, Zhu, Pei, Jia, Hao, Du, Zhuang, Zhu, Jiadeng, Dong, Xia, Wu, Nianqiang, Dirican, Mahmut, Zhang, Xiangwu. “Garnet-rich Composite Solid Electrolytes for Dendrite-free, High-rate, Solid-state Lithium-metal Batteries”, submitted.
5. Yang, Hui, Bright, Joeseeph, Chen, Banghao, Zheng, Peng, Gao, Xuefei, Liu, Botong, Kasani, Sujan, Zhang, Xiangwu, Wu, Nianqiang, “Chemical Interaction and Enhanced Interfacial Ion Transport in Ceramic Nanofiber-Polymer Composite Electrolyte for All-Solid-State Lithium Metal Battery”, submitted.

References

1. Yang, Chunpeng, Kun Fu, Ying Zhang, Emily Hitz, and Liangbing Hu. “Protected Lithium-Metal Anodes in Batteries: From Liquid to Solid.” *Advanced Materials* 29, no. 36 (2017): 1701169.
2. Sun, Chunwen, Jin Liu, Yudong Gong, David P. Wilkinson, and Jiujuun Zhang. “Recent advances in all-solid-state rechargeable lithium batteries.” *Nano Energy* 33 (2017): 363-386.

II.8.B Improving the Stability of Lithium-Metal Anodes and Inorganic-Organic Solid Electrolytes (LBNL)

Dr. Nitash P. Balsara, Principal Investigator

Department of Materials Sciences
Lawrence Berkeley National Laboratory
University of California, Berkeley
Berkeley, CA 94720
E-mail: nbalsara@berkeley.edu

Tien Duong, DOE Technology Development Manager

U.S. Department of Energy
E-mail: Tien.Duong@ee.doe.gov

Start Date: October 1, 2018

End Date: September 30, 2019

Project Funding (FY19): \$400,000

DOE share: \$400,000

Non-DOE share: \$0

Project Introduction

Polymer electrolytes offer increased stability in lithium batteries in comparison to more widely used liquid electrolytes. Nanostructured electrolytes containing both soft, ion-conducting domains and rigid non-conducting domains offer the opportunity to tune both mechanical and electrical properties separately. Such electrolytes are conveniently made by block copolymer self-assembly. Most of the block copolymer electrolytes studied thus far comprise organic polymer chains for both the conducting and rigid domains. We aim to synthesize new electrolytes that simultaneously display low resistance to ion transport and have greater stability against lithium in comparison to organic diblock copolymers. The project objective is to establish a new hybrid electrolyte that will be stable against cells with a Li-metal anode.

Objectives

The project will synthesize a new hybrid electrolyte that is designed to be stable against lithium metal. The material is a block copolymer, wherein, acryloisobutyl polyhedral oligomeric silsesquioxane (POSS) is covalently bonded to PEO chain, which is a conventional polymer electrolyte. Electrochemical characterization of this polymer will include measurement of three transport properties including ionic conductivity, salt diffusion coefficient, and the cation transference number. Knowledge of all three parameters as a function of salt concentration is required to fully characterize the electrolyte. In addition, a key indicator of electrolyte performance is the limiting current of the electrolyte, *i.e.*, the maximum current that can be safely passed through the electrolyte before failure. We measure the limiting current through chronopotentiometry experiments. The stability against lithium metal will be evaluated by impedance spectroscopy to quantify the interfacial resistance and cyclic voltammetry (CV). We also investigate the possibility the lithium physically dissolves (*i.e.*, non-electrochemically) from the electrode into the PEO phase. Finally, X-ray tomography experiments will be used to visualize the electrolyte and probe failure mechanisms in cycling experiments (using a lithium-polymer-lithium cell configuration) to prove the effectiveness of the electrolyte.

Approach

First, the team synthesized hybrid diblock copolymers by incorporating monomers that contain an inorganic component. Then, electrolytes are prepared by mixing the diblock copolymers with salt. Electrochemical and mechanical characterization of these materials are performed before carrying out cycling X-ray tomography experiments. The combination of these approaches enables rational design of materials that exhibit improved stability against lithium metal and high performance.

Results

Determine limiting current in solid electrolytes

The limiting current of a hybrid triblock copolymer electrolyte, POSS-PEO-POSS (structure show in Figure II.8.B.1) was measured. A 5-35-5 [kg/mol] membrane was fabricated with salt concentration $[Li]/[EO] = 0.04$. A routine to test the limiting current of POSS-PEO-POSS was performed and shown in Figure II.8.B.1. The measurement was performed by sandwiching a 30-micron thick solid organic-inorganic polymer electrolyte between Li electrodes. The Li-polymer-Li cells were then polarized to electrodeposit Li from one electrode to the other. The current density was increased systematically until the potential diverged, or the cell short-circuited. The results in Fig 1 show that the POSS-PEO-POSS hybrid triblock electrolyte demonstrated a limiting current above 3.0 mA cm^{-2} . Further experiments on this cell showed an exceptionally high limiting current between 4.5 and 6.0 mA cm^{-2} for a membrane of $30 \mu\text{m}$ thickness. For the first time, we were able to experimentally achieve the estimated limiting current of 4.5 mA cm^{-2} based on Monroe and Newman's equation (Eq. 1) without an immediate short-circuit.[1]

$$i_L = \frac{2c_B D F}{L(1-t_{Li})} \quad (\text{Eq. 1})$$

In all previous experiments on all-organic block copolymer electrolytes, the practical limiting current was reached well before the estimated limiting current based on Eq. 1 was reached. We also note that the estimate of limiting current is not based on complete characterization of solid polymer electrolytes using the Newman approach. The limiting current is implicated as a normalization factor in Barai et al.'s model of the propagation of lithium protrusions through solid polymer electrolytes.[2],[3] Thus, it is of relevance to study the effect of current density on the nucleation and growth of lithium protrusions. Due to limitations in triblock polymer material, the systematic study of current density effects was conducted with PS-PEO (115-172), which has been shown to have indistinguishable cycle life compared to equivalent cells fabricated with POSS-PEO-POSS (5-35-5).

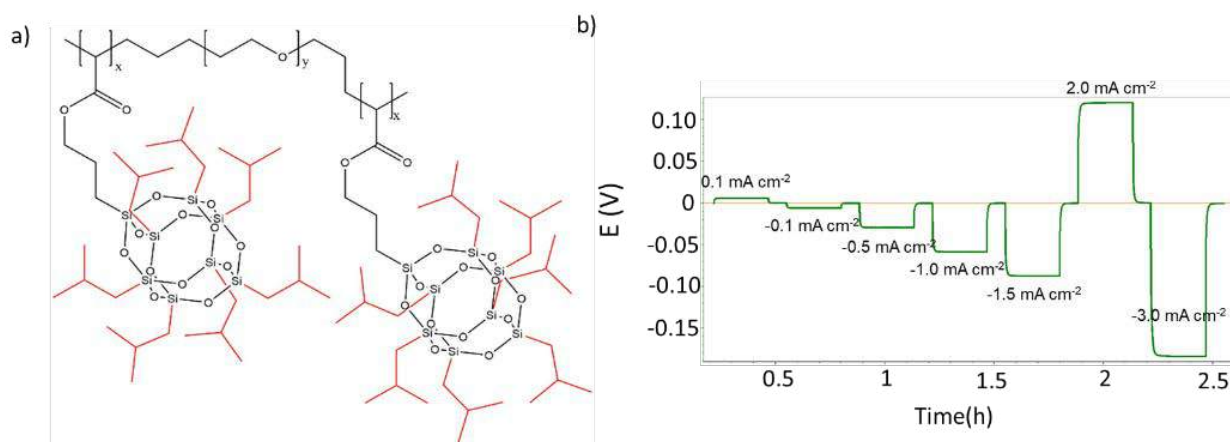


Figure II.8.B.1 (a) POSS-PEO-POSS (5-35-5) chemical structure (b) Example of a routine used to test the limiting current of POSS-PEO-POSS (5-35-5)

- (1) Monroe, C.; Newman, J. J. *Electrochem. Soc.* **2003**, 150 (10), A1377–A1384.
- (2) Barai, P.; Higa, K.; Srinivasan, V. *J. Electrochem. Soc.* **2017**, 164 (2), 180–189.
- (3) Barai, P.; Higa, K.; Srinivasan, V. *Phys. Chem. Chem. Phys.* **2017**, 19, 20493–20505.

Interfacial resistance in lithium-solid electrolyte-lithium cells: The nature of the lithium/electrolyte interface in hybrid block copolymer electrolytes was probed using impedance spectroscopy. Lithium symmetric cells were fabricated using a triblock POSS-PEO-POSS (5k-35k-5k) electrolyte with $r = \frac{[Li]}{[EO]} = 0.04$. Cells were conditioned using a current density of 0.02 mA cm^{-2} for 10 cycles, with each cycle consisting of 4 hours of

charge, 45 minutes of rest, 4 hours of discharge, and 45 minutes of rest. Figure II.8.B.2 shows that the effective resistance of the electrolyte during conditioning cycles was stable for 10 cycles. Figure II.8.B.3 is a Nyquist plot showing bulk and interfacial resistance components before and after the 10 conditioning cycles shown in Figure II.8.B.1. The bulk resistance is unchanged, and the interfacial resistance increases by approximately 10% and stabilizes.

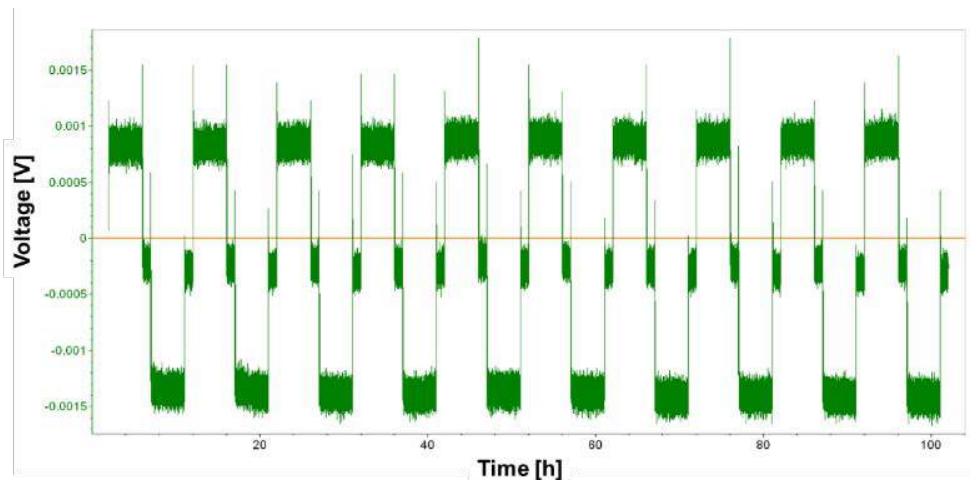


Figure II.8.B.2 Voltage as a function of time during preconditioning cycles for a lithium symmetric cell and a POSS-PEO-POSS/LiTFSI $r = 0.04$ electrolyte. This cell was cycled at a current density of 0.02 mA cm^{-2} without significant increase in resistance over 10 cycles

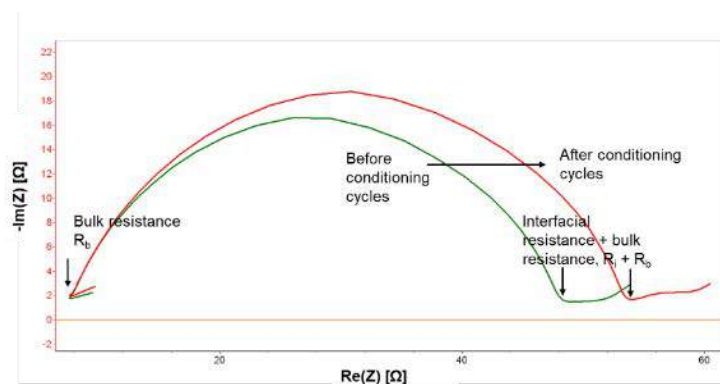


Figure II.8.B.3 Nyquist plot of a lithium symmetric cell before and after the conditioning cycles shown in Fig. 1. Bulk resistance was unchanged and interfacial resistance increased by approximately 10%. Frequencies sampled were 1 Hz to 1 MHz with 30 mV perturbations

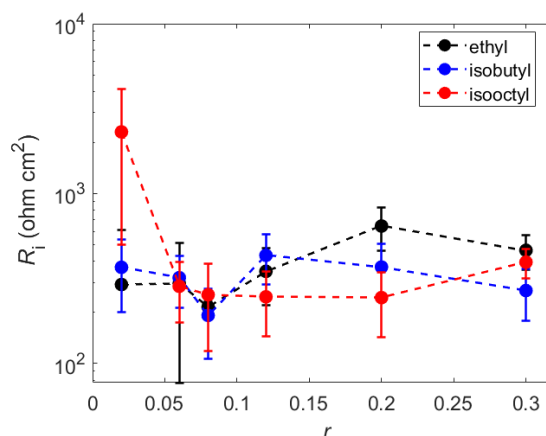


Figure II.8.B.4 Interfacial resistance of PEO-POSS 5k-1k with ethyl, isobutyl, and isooctyl end groups as a function of salt concentration

The lithium/electrolyte interface was also probed in PEO-POSS electrolytes with approximate molecular weight (5k-1k) while changing end groups (-ethyl, -isobutyl, -isooctyl) on the POSS component to see if the end groups on the POSS component have significant interactions with lithium at the electrode/electrolyte interface. Interfacial resistance was measured with impedance spectroscopy as a function of salt concentration. The results are demonstrated in Figure II.8.B.4. It appears that the interfacial resistance is not a strong function of POSS end group or salt concentration.

Physical dissolution of lithium metal in PEO

As the conducting phase of PEO-POSS and POSS-PEO-POSS electrolytes is PEO, a study was completed to better understand the nature of the electrode-electrolyte interface with homopolymer PEO. A remarkable property of the interface between PEO-based electrolytes (both homopolymers and block copolymers) and lithium metal is the observation that good mechanical and electrical contact are maintained even when tens of micrometers of lithium are displaced during cycling. This is especially surprising in block copolymers with high elastic moduli which contradicts that adhesion strength declines with increasing modulus [1]. The underpinnings of this observation may be explained by a surprising result: lithium metal is sparingly soluble in PEO. While the solubility of alkali metals in polar solvents is well known [2], a solution of a metal and a polymer has not been previously reported.

To demonstrate this, we annealed PEO samples with various molecular weights at 130°C against lithium metal and performed ⁷Li NMR on the PEO after removing the excess lithium foil. A reference solution of bis(trifluoromethylsulfonyl)amine lithium salt (LiTFSI) in tetraglyme was used to quantify the dissolved lithium concentration in molality, m . The results are shown in Figure II.8.B.5. In Figure II.8.B.5a-c, we show the ⁷Li NMR spectra for the dissolved lithium/PEO sample in a coaxial configuration with the reference solution in the outer compartment. The sharp peak at roughly -0.2 ppm is due to the LiTFSI in tetraglyme (this peak is not present in samples without the reference). By fitting the data (red lines), we obtain the integrated intensity of the two peaks and calculate the molar concentration of lithium in the PEO sample. We plot m as a function of PEO molecular weight in Figure II.8.B.5d.

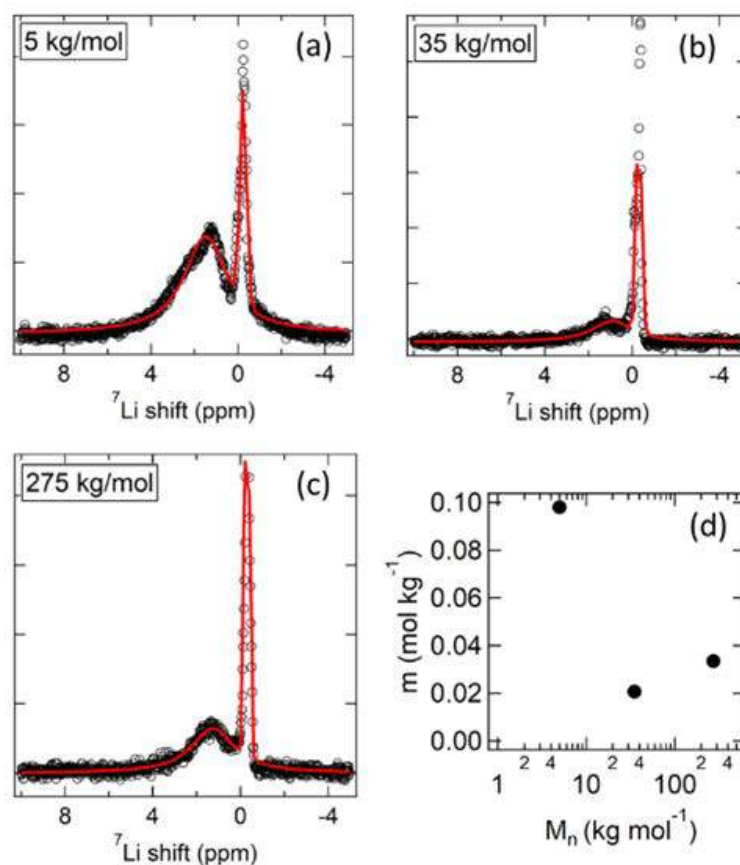


Figure II.8.B.5 ^7Li NMR spectra (open circles) of (a) 5 kg mol $^{-1}$ (b) 35 kg mol $^{-1}$ and (c) 275 kg mol $^{-1}$ PEO annealed against lithium metal for 12 days at 130°C in a coaxial NMR tube with a reference solution in the outer compartment. Red lines are fits to the experimental data. (d) Lithium molality as a function of PEO molecular weight

The dissolved lithium species also affects the conductivity of the PEO. We assembled lithium/PEO/lithium cells and measured the conductivity over time while annealing the cell at 120°C and compared the result to cells with stainless steel electrodes. The PEO initially contained no lithium salts. The results are shown in Figure II.8.B.6. There is a sharp increase in the conductivity of the cells with lithium electrodes, which we attribute to the dissolved lithium species. The result suggests that the lithium species exists in solution as a lithium cation and solvated electron. This conclusion is consistent with reports of lithium solubility in liquid ammonia³ and other alkali metals in ether solvents [4],[5]

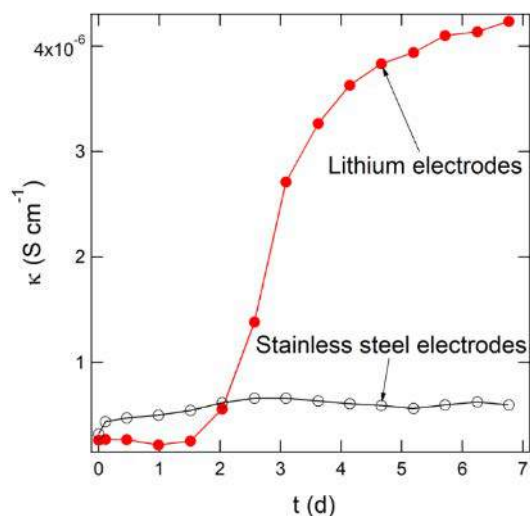


Figure II.8.B.6 Conductivity of 35 kg mol⁻¹ PEO, containing no lithium salts, annealed at 120 °C in a lithium symmetric cell (closed symbols) and a stainless-steel symmetric cell (open symbols) as a function of time

We have also seen evidence of lithium dissolution in PEO-containing block copolymers. The observation of lithium dissolution in PEO provides new insight to the lithium/electrolyte interface. When a solid is immersed in a solvent in which it is soluble, the interface is not well defined. Because the kinetics of dissolution are slow and/or the solubility is low (resulting in the low concentrations reported in Figure II.8.B.4d), we still observe a well-defined interface macroscopically. While, at first glance, the solubility of lithium metal in PEO may seem problematic, it may be the underlying phenomenon that allows dendrite-preventing block copolymers with high moduli to be implemented in lithium metal battery applications.

1. Stone, G. M.; Mullin, S. A.; Teran, A. A.; Hallinan, D. T.; Minor, A. M.; Hexemer, A.; Balsara, N. P. *J. Electrochem. Soc.* **2012**, 159 (3), A222–A227.
2. Dye, J. L. *Philos. Trans. R. Soc., A* **2015**, 373 (2037), 20140174.
3. Seely, C. *Chem. News* **1871**, 23 (594), 169–170.
4. Cafasso, F.; Sundheim, B. R. *J. Chem. Phys.* **1959**, 31 (3), 809–813.

Study the effect of lithium metal purity and failure mechanisms:

Impurities in the lithium metal electrode material were imaged using X-ray tomography at beamline 8.3.2 at the Advanced Light Source, as shown in Figure II.8.B.7.

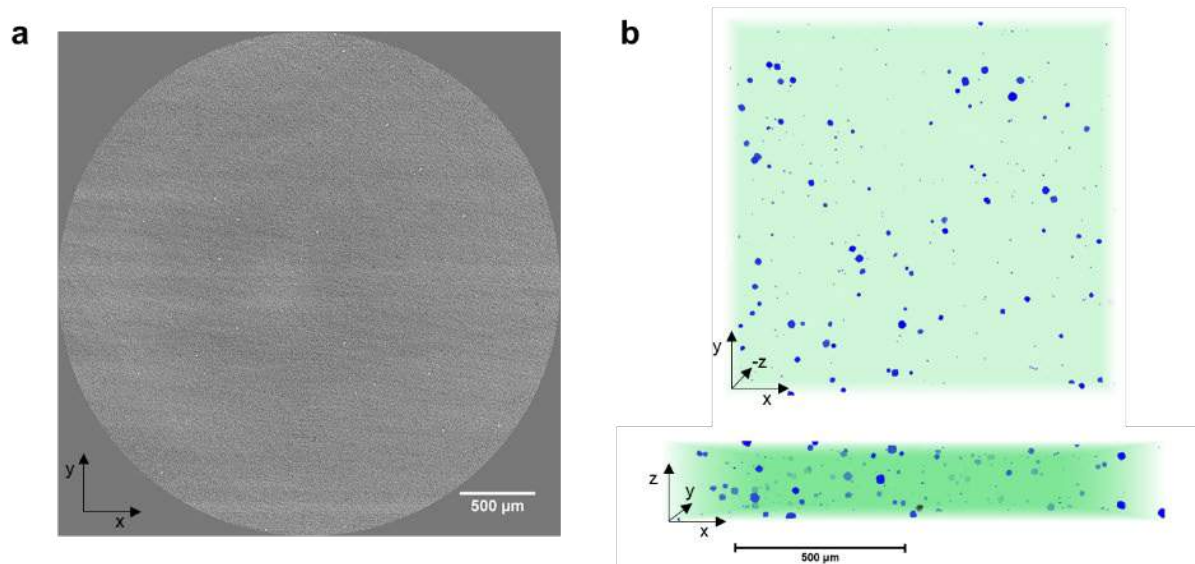


Figure II.8.B.7 (a) Impurities are present in lithium as-received. Cross-sectional slice through cell with additional cross section of pure lithium showing impurity particles. (b) Volume reconstruction of volume of lithium as-received with highlighted impurity particles and a volume density

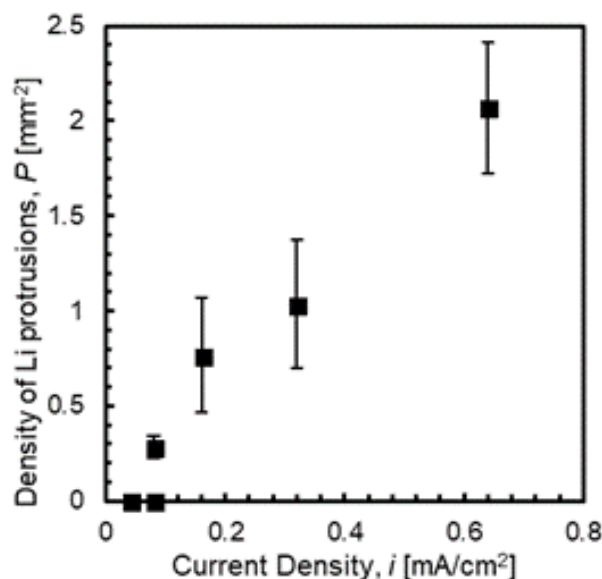


Figure II.8.B.8 Correlation between current density and defect density in failed cells. The areal density of protruding defects, P , increases with current density

Last year, we found that the density of lithium protrusions increased with current density in an analogous block copolymer electrolyte, shown in Figure II.8.B.8.

We also found that protruding structures were nucleated in the POSS-PEO-POSS (5-35-5) triblock in the vicinity of these impurity particles, shown in Figure II.8.B.9. As a result, we hypothesized a treatment for lithium symmetric cells containing a block copolymer electrolyte to move impurity cells away from the electrode-electrolyte interface. This may be accomplished by plating planar lithium at a low current density to use the electrolyte to “filter” out impurity particles (impurity particles do not go through the electrolyte). A schematic is shown in Figure II.8.B.10a. The goal of this treatment is to reduce nucleation of lithium protrusions by reducing the concentration of impurity particles at the electrode-electrolyte interface. A plot of

current, voltage, and time during a treatment step is shown in Figure II.8.B.10b. Figure II.8.B.10c shows a cross-section by X-ray tomography of a cell before this treatment. Figure II.8.B.10d and Figure II.8.B.10e show the results of the treatment: most impurity particles are successfully removed from the interface, although some remain adhered.

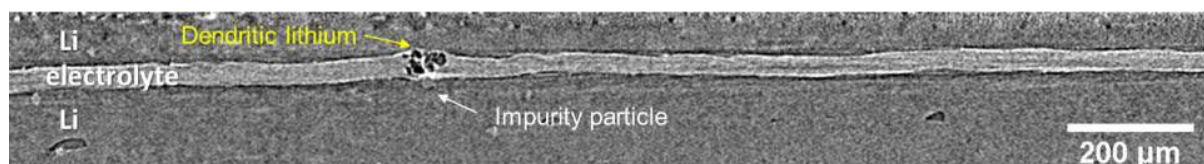


Figure II.8.B.9 Slice through a reconstructed volume imaged using X-ray tomography. This Li/POSS-PEO-POSS/Li cell was cycled at 0.175 mA cm^{-2} and failed after 17 cycles

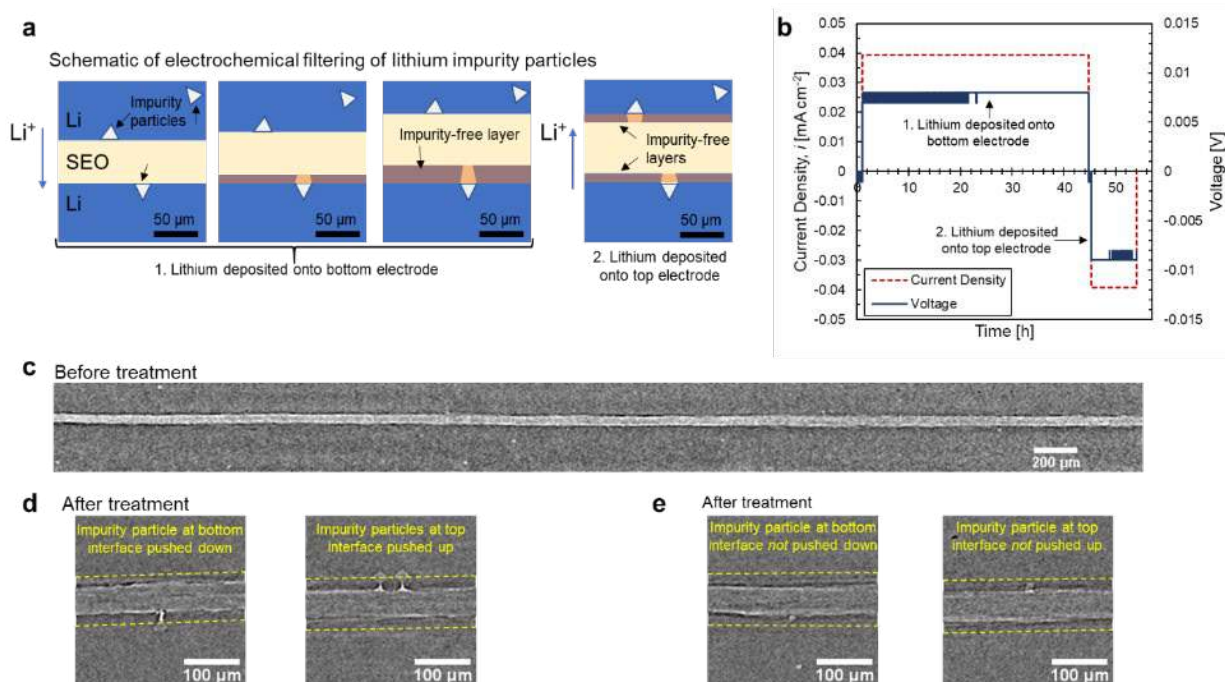


Figure II.8.B.10 Strategy of the electrochemical filtering treatment to push impurity particles away from the interface. (a) Schematic of the electrochemical filtering treatment. After symmetric cell fabrication, some impurity particles, shown as white triangles, lie at the electrode-electrolyte interface. Step 1: with a sufficiently low current density, new planar lithium, highlighted in orange, can be deposited onto the bottom electrode to create a layer free of impurity particles. Step 2: by reversing the direction of current, planar lithium may be plated on to the upper electrode, such that the both electrodes now have a layer of impurity-free lithium at the electrode-electrolyte interface. (b) Current density and voltage of one electrochemical treatment over time. Lithium was charged at 0.04 mA cm^{-2} for 43.75 h (8.5 μm of Li calculated) and discharged at the same current density for 8.75 h (1.7 μm of Li calculated). (c) Slice through a reconstructed volume of a symmetric cell as-fabricated after 14 conditioning cycles. No inhomogeneities were observed at the interfaces. (d) Slices through a reconstructed volume of the symmetric cell in Fig. 2c after an electrochemical filtering treatment. Yellow dashed lines indicate the calculated height of lithium after the treatment. This cell charged a calculated 38 μm of lithium, and discharged a calculated 19 μm of lithium. Impurity particles are visibly pushed away from the electrode-electrolyte interface. (e) Slices through a reconstructed volume of the symmetric cell in Fig. 2d after an electrochemical filtering treatment. Yellow dashed lines indicate the calculated height of lithium after the treatment. Some impurity particles still remain adhered to the polymer electrolyte after the treatment

The cells were then cycled at a constant current density in order to determine the effects of treatment on lifetime. The treated cells passed an average of 52-390% more charge before failure compared to control cells. Further work is underway to determine the nature of this improvement.

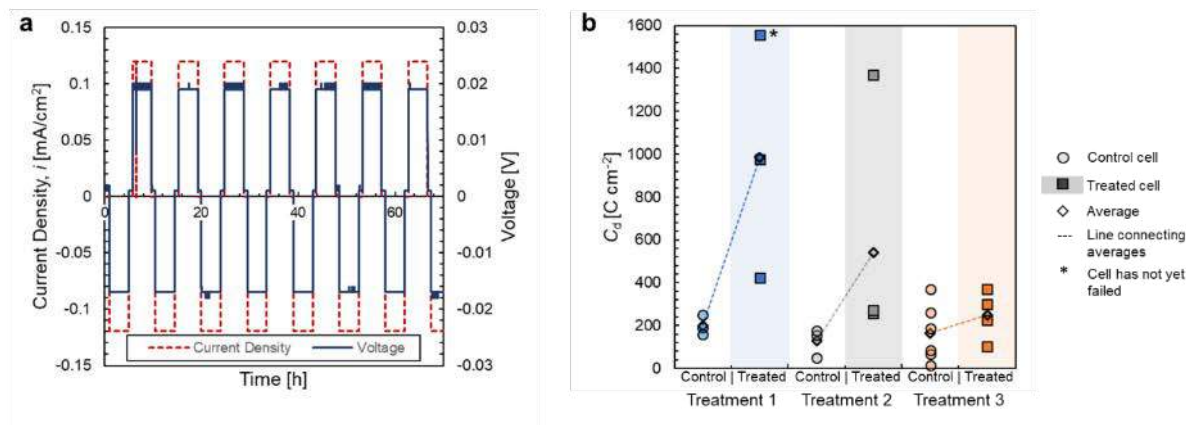


Figure II.8.B.11 Galvanostatic cell cycling example and results. (a) Current density and voltage of the first cycles at 0.12 mA cm⁻² for one cell. During each cycle, current was applied for 4 h at -0.12 mA cm⁻² (2.3 μ m of Li calculated), no current was applied for 45 minutes, current was applied for 4 h at 0.12 mA cm⁻², and no current was applied for 45 minutes. (b) Charge passed before failure, C_d , plot for each group's control and treated cells. Details of the electrochemical filtering treatment are found in Figure II.8.B.4. The transparent circles indicate control cells, while the filled-in squares indicate treated cells. Hollow diamonds indicate the average of cells in the column. Dashed lines connect the averages of control and treated cells in each group. The asterisk indicates a cell which has not yet failed. Treatment 1 cells were cycled at 0.12 mA cm⁻², while Treatment 2 and 3 cells were cycled at 0.175 mA cm⁻²

Determine parametric range over which stable lithium electrodeposition is obtained

It is important to determine the conditions under which stable lithium electrodeposition can be obtained for multiple applications. Stable electrodeposition can also be described as reversible deposition: that is, deposition in which stripping occurs uniformly from a planar lithium surface and plating results planar lithium. This plated lithium should not be mossy or include lithium protrusions or other features. Perfectly stable deposition during cycling should lead to infinite cycle life. Stable electrodeposition was observed in an all-organic poly(ethylene oxide)-based rigid block copolymer electrolyte at a low current density: 0.04 mA cm⁻² (Figure II.8.B.12). Although this current density is too low to be used in practical applications, one might imagine we could leverage stable deposition at low current density to pre-treat lithium cells to extend cycle life at high current density.

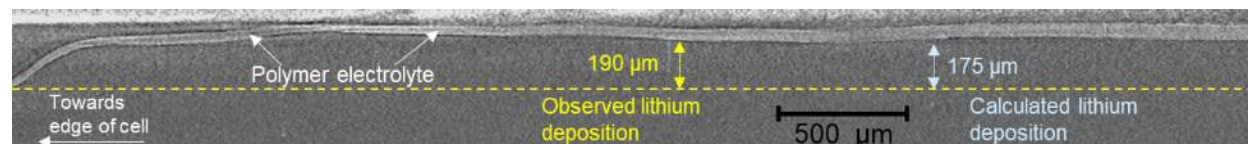


Figure II.8.B.12 Representative cross section of cell polarized at $i = 0.04$ mA cm⁻² for $t = 900$ h acquired using X-ray tomography. Lithium was deposited downward through the polymer electrolyte, which appears as a light band extending across the cell near the top of the cross-section. No lithium protrusions were observed. This cell did not short circuit. The yellow arrow shows the thickness of the electrochemically deposited lithium, 190 μ m, at a representative location based on the analysis of the tomograms, using the electrolyte's original position at the edge of the cell as a reference point. The light blue arrow shows for comparison the estimated thickness of electrochemically deposited lithium, 175 μ m, based on the current passed through the cell

Further, we have measured higher limiting currents in hybrid-inorganic-organic block copolymer electrolytes than all-organic block copolymer electrolytes (Figure II.8.B.13).

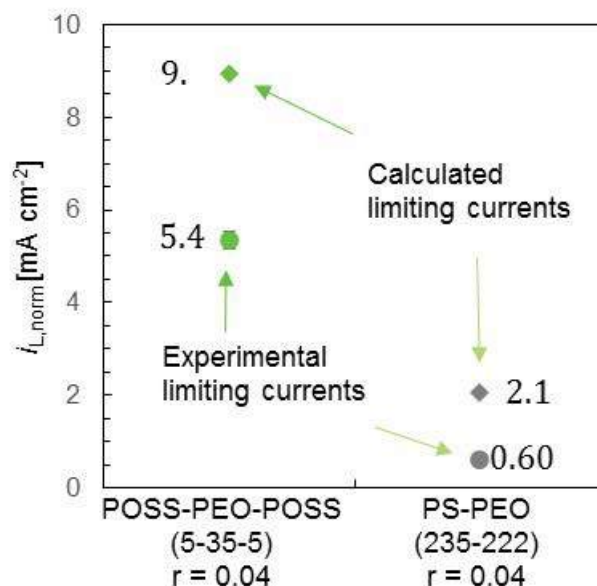


Figure II.8.B.13 Comparison of the calculated and experimental limiting currents of a POSS-PEO-POSS hybrid inorganic-organic block copolymer electrolyte and a PS-PEO all-organic block copolymer electrolyte. In each case, the calculated limiting current is higher than the experimental limiting current due to considerations for transport in the concentrated solution regime. The limiting current of the POSS-PEO-POSS electrolyte is both higher and proportionally closer to its calculated limiting current than the PS-PEO

Stable electrodeposition has been linked to the current density through the electrolyte normalized by the limiting current density of the electrolyte. Thus, we may achieve stable electrodeposition at higher current density in hybrid inorganic-organic electrolytes: if the limiting current ratio is proportional to the ratio of critical current densities at which stable electrodeposition is achieved, we may expect to see a 9-fold improvement in the critical current density.

Conclusions

In the present research, the stability of hybrid organic-inorganic copolymer electrolyte against lithium metal has been investigated. The major conclusions are summarized below:

1. The hybrid triblock electrolyte demonstrated an exceptionally high limiting current between 4.5 and 6.0 mA cm⁻² for a membrane of 30 μ m thickness. For the first time, we were able to experimentally achieve the estimated limiting current of 4.5 mA cm⁻² based on Monroe and Newman's model.
2. Investigations of a PEO homopolymer and lithium metal interface reveal that lithium metal is sparingly soluble in PEO.
3. In order to improve lithium/electrolyte interface, a simple procedure to plate planar lithium at a low current density is performed to use the electrolyte to "filter" out impurity particles. Using this treatment, most impurity particles are successfully removed from the interface.
4. Stable electrodeposition has been linked to the current density through the electrolyte normalized by the limiting current density of the electrolyte. Thus, we may achieve stable electrodeposition at higher current density in hybrid inorganic-organic electrolytes:

Key Publications

1. M.D. Galluzzo, D.M. Halat, W.S. Loo, S.A. Mullin, J.A. Reimer, N.P. Balsara. "Dissolution of Lithium Metal in Poly(ethylene oxide)" *ACS Energy Lett.*, 2019, 4, pp 903–907.
2. Gribble, D. A., Frenck, L., Shah, D. B., Maslyn, J. A., Loo, W. S., Mongcopa, K. I. S., Pesko, D. M., Balsara, N. P. "Comparing Experimental Measurements of Limiting Current in Polymer Electrolytes

with Theoretical Predications”. *Journal of the Electrochemical Society*, 2019, 166 (14), pp A3228-A3234.

3. Maslyn, J.A., Frenck, L., Loo, W. S., Parkinson, D. Y., Balsara, N. P. “Extended Cycling through Rigid Block Copolymer Electrolytes Enabled by Reducing Impurities in Lithium Metal Electrodes.” *ACS Appl. Energy Mater.* 2019, Published Nov. 7, 2019. DOI: 10.1021/acsaem.9b01685.

Presentations

1. American Physical Society (APS) March Meeting, Boston, Massachusetts (March 4-8, 2019): “Dissolution of Lithium Metal in Poly(ethylene oxide)” ; M. D. Galluzzo, N. P. Balsara.
2. American Physical Society (APS) March Meeting, Boston, Massachusetts (March 4-8, 2019): “The effect of chemical structure on the morphology, ion transport, and modulus of hybrid inorganic-organic diblock copolymer electrolytes” ; K. Gao, N. P. Balsara.
3. American Physical Society (APS) March Meeting Boston, MA: Sethi, G., Villaluenga, I., & Balsara, N. (2019). “Phase Behavior of Hybrid Inorganic-Organic Diblock Copolymer Electrolytes.”
4. Berkeley Electrochemistry Seminar Series, Berkeley, California (May 20, 2019). “Dissolution of Lithium Metal in Poly(ethylene oxide)” ; M. Galluzzo.
5. Berkeley Electrochemistry Seminar Series, Berkeley, California (June 24, 2019). “Factors Influencing Lithium Protrusion Nucleation and Cycle Life in Solid Polymer Electrolytes for Battery Applications” ; J. Maslyn.
6. American Chemical Society (ACS) Fall 2019 National Meeting & Exposition, San Diego, CA: Chakraborty, S., Sethi, G., Villaluenga, I., & Balsara, N. (2019). “Self-Assembly Behavior of Organic-Inorganic Hybrid Triblock Copolymer Solid Electrolyte.

II.8.C U.S.-German Cooperation on Energy Storage: Lithium-Solid-Electrolyte Interfaces (ORNL)

Nancy Dudney, Principal Investigator

Chemical Sciences Division, Oak Ridge National Laboratory
1 Bethel Valley Road
Oak Ridge, TN 37830
E-mail: dudneyj@ornl.gov

Andrew S. Westover, Principal Investigator

Chemical Sciences Division, Oak Ridge National Laboratory
1 Bethel Valley Road
Oak Ridge, TN 37830
E-mail: westoveras@ornl.gov

Tien Duong, DOE Technology Development Manager

U.S. Department of Energy
E-mail: Tien.Duong@ee.doe.gov

Start Date: June 1, 2019

End Date: September 30, 2023

Project Funding (FY19): \$200,000

DOE share: \$200,000

Non-DOE share: \$0

Project Introduction

Key requirements for next generation batteries include the combination of higher energy density, longer life, reliable safety, lower cost and sustainable production. Solid state batteries can meet these goals if the materials are used efficiently, if they provide stable operation and if manufacturing can be streamlined. There are significant challenges, but success will help electrify transportation and other industries. In this program we address the significant challenges presented to stabilize the Li metal anode contacting the battery's solid electrolyte. Li metal offers a high energy density if, and only if, there is little excess Li added to the battery beyond that required by the full energy of the cathode. Li is also highly reactive, and few solid electrolytes are either thermodynamically or kinetically stable in contact with the metal. Further, flaws at the interface likely present sites for initiation of Li incursion, crack formation or rupture of the electrolyte particularly at high current densities. All of these challenges are related to the interface for which we know relatively little. Success of Li metal batteries depends on advancing our understanding of this buried Li to solid electrolyte interface and how it changes upon driving large amounts of Li across the interface and back at high current densities. Because of this challenge, a program of cooperative research with German laboratories has been developed. Here fundamental understanding will be accelerated by bringing together a vast array of characterization tools and experts in the field to study a few, promising and well-established model materials that can be shared across the team. Through our collective efforts and results, new insights will emerge that will guide further advances in solid state lithium metal batteries.

Only researchers at ORNL are funded by this AOP program, but collaborators funded individually include researcher from 5 U.S. National Laboratories and 6 U.S. universities, with a similar number of sister organizations in Germany. The team will share common materials and protocols for making the Li - solid electrolyte interface. Samples will be tailored for specific characterization approaches. Results will be aggregated, analyzed and used to develop predictive theoretical models. This will inform and educate other scientists and technologists about the opportunities and challenges for practical development and use of solid-state batteries for vehicles and other applications of interest to the U.S. DOE and energy sector.

Objectives

1. Identify the quality and homogeneity for different sources of Lithium metal.

When reducing the amount of excess lithium, it is likely that the purity and quality of the Li will become critical. There is little known about the effects of impurities, although antidotal observations raise concern for Na and other contaminants and formation of impurity aggregates. The expected outcome is an informative evaluation of the purity and uniformity of the thin lithium foils or coatings, both bulk and at buried and exposed interfaces, as obtained from different fabrication routes, research laboratories and commercial sources.

2. Develop tools to probe the structure and composition of the buried interface

This characterization is important to evaluate the quality of the interface. Most work is limited to ionic transport studies, such as impedance spectroscopy, vacuum characterizations of very thin Li on the solid electrolyte surface, and post-cycling cross sections by microscopy. New methods are needed to reveal reactions and variations in the microstructures at the buried interface. Protection, even from vacuum exposure, is important to accurately probe the interface, particularly if variations from the bulk are subtle. The expected outcome for this objective is a suite of characterization methods designed to elucidate the performance of Li metal protected by a solid electrolyte.

3. Compare the interfaces formed with different Li sources with the model solid state electrolytes

As will be readily shown in task 2, the quality of the Li can vary greatly from Li source to Li source. In particular Li that is directly evaporated onto an electrolyte will have a clean buried interface. If Li is applied in any other way, there will be a thin (or not so thin) layer on the surface of the Li which will affect the interface formation. The goal of this objective is to understand the differences such surfaces layers have on the final battery performance. The expected outcome will be key insights into the requirements for lithium purity and processing for stable interface formation.

4. Determine the evolution of the Li-solid electrolyte interface with cycling.

During cycling the Li is repeatedly removed and then re-plated. This will have a dramatic effect on the morphology of the Li anode. As this Li anode continues to evolve, defects including grain boundaries will be in a constant state of flux. Understanding how the Li changes, its effect on filament formation and its relation to ultimate battery failure is important. The expected outcome of this objective is a deeper understanding of the mechanisms affecting the evolution of the interface properties under different application.

Approach

For the first year, objectives 1 and 2 will be addressed. With good understanding of the protocols and materials to be examined, experiments addressing objectives 3 and 4 will examine how the interface fabrication and cycling influence the interface structure and transport properties.

1. Identify the purity and homogeneity for different sources of Lithium metal.

The team at ORNL has long experience with preparing very thin films of Li metal by vacuum deposition, preferably directly onto the solid electrolyte surface to ensure highest purity. Several other partners also prepare Li films in-house. Commercially, Li is supplied as thin self-supporting foils or as Li coated onto a metal foil current collector. Characterization of the lithium is not routine. Results will be compared using different characterization tools available at ORNL to understand differences in phase purity, composition, density, texture and microstructure, of the pristine material (bulk and surface). Characterizations will include microscopy (x-ray tomography, diffraction, low voltage TEM/SEM); spectroscopy (XPS, EDX, ICP, FTIR, Raman) and physical properties (nanoindentation, gas pycnometry). Samples will be exchanged with partner institutions for complementary characterizations. Processing may be adjusted to probe the sensitivity of the solid electrolyte interface to various properties (density, purity, microstructure) of the lithium.

2. Develop tools to probe the structure and composition of the buried interface

Several different tools at ORNL will be pioneered to assess the information that can be provided about the interface. Initially, work will use thin film Li and electrolytes available at ORNL, comparing glassy, ceramic and polymer electrolytes. As the shared-model materials identified for the collaboration, specifically LLZO ceramics and Rotaxanes, become available, these will take priority over ORNL materials. Through our initial experiments, we can provide sample fabrication protocols to prepare the model electrolytes and lithium anodes suitable for characterization at ORNL. The tools we are eager to investigate at ORNL include: (1.) precision electroanalytic measure of the maximum Li consumption. (2.) Dynamic impedance spectroscopy to capture the reversible and non-reversible interface changes upon formation and initial cycles of the Li. (3.) Time of flight secondary ion mass spectrometry to determine the gradients of the interface reaction. (4.) Neutron reflectometry to similarly characterize any interface reaction. (5.) Local adhesion of the lithium to the solid electrolyte by nanoindentation with a flat probe.

3. Compare the interfaces formed with different Li sources.

Using the most revealing tools adopted in task 2, we next examine the interfaces with Li introduced in different ways. We anticipate that the contact area, adhesion, purity and uniformity will be sensitive to whether the Li is vapor deposited, electrodeposited, or laminated onto the solid electrolyte surface. The interface will also depend on the surface preparation of the solid electrolyte including cleaning, polishing, or perhaps activation. We anticipate using the model electrolytes supplied by collaborating partners. Further, as research progresses, processing of the lithium may be adjusted to probe the sensitivity of the solid electrolyte interface to various properties (density, purity, microstructure) of the lithium, through for example, intentional addition of a suspect impurity.

4. Determine the evolution of the Li-solid electrolyte interface with cycling.

During cycling both the Li and solid electrolyte are likely to change. This will depend on the temperature, current density, and other details of the duty cycle and interface fabrication. Electroanalytic, dynamic impedance and neutron reflectometry will be used to follow changes during cycling. To list of characterization methods above, nanoindentation with a Berkovich tip will also be used to follow the evolution and anneal of defects in the thin film lithium anode, as lithium is plated and stripped. This follows earlier work in collaboration with Erik Herbert (Michigan Technological University) where unique time and length scale creep mechanisms were examined for Li metal films. Plans for examining the buried interface during the active cycling will be coordinated with other researchers in the program. Additionally, advanced tools will be used to examine the interface and materials for changes comparing the initial state with the plating and stripping.

Results

For this new project, initial work has commenced on Objective 1: “Identify the quality and variation for different sources of Lithium metal” and Objective 2: “Develop tools to probe the structure and composition of the buried interface”. For Objective 1, Li samples have been prepared for X-ray tomography studies in collaboration with the Nitash Balsara group (also a key participant in the larger German-U.S. program). For Objective 2 we have nearly completed a key study to develop a tool for determining the stability of Li metal with solid state electrolytes. To understand interface stability, we are adapting a coulombic efficiency technique where the stability of Li at the electrolyte interface is then determined by measuring the Coulombic efficiency of repeated plating and stripping of the lithium onto a metal current collector. [\[1\]](#) For a solid-state electrolyte, this technique has been used by the group of Jurgen Janek (also a participant in the German-U.S. collaboration) for LLZO based solid state electrolytes but it has not been fully developed. [\[2\]](#)

In our case, we started by depositing a thin Ni current collector on a smooth sapphire wafer. This was followed by a Lipon thin film and a Li electrode. Based on our system there was a brief air exposure between each deposition resulting in a thin Ni-O layer between the Ni and the Lipon. To test the interfacial stability Li was plated on the Ni current collector and then stripped from the current collector. With this technique we can precisely determine how much Li was lost on the first cycle. Although there are other possibilities, it is presumed that a majority of the Li metal that is lost reacts to form an interfacial layer between Lipon and Li

metal. By assuming full thermodynamic decomposition of the Lipon according to the equation $8 \text{Li} + \text{Li}_3\text{PO}_{3.4}\text{N}_{0.4} \rightarrow \text{Li}_3\text{P} + 3.4 \text{Li}_2\text{O} + 0.4 \text{Li}_3\text{N}$, we can estimate the thickness of the interfacial layer that is formed.

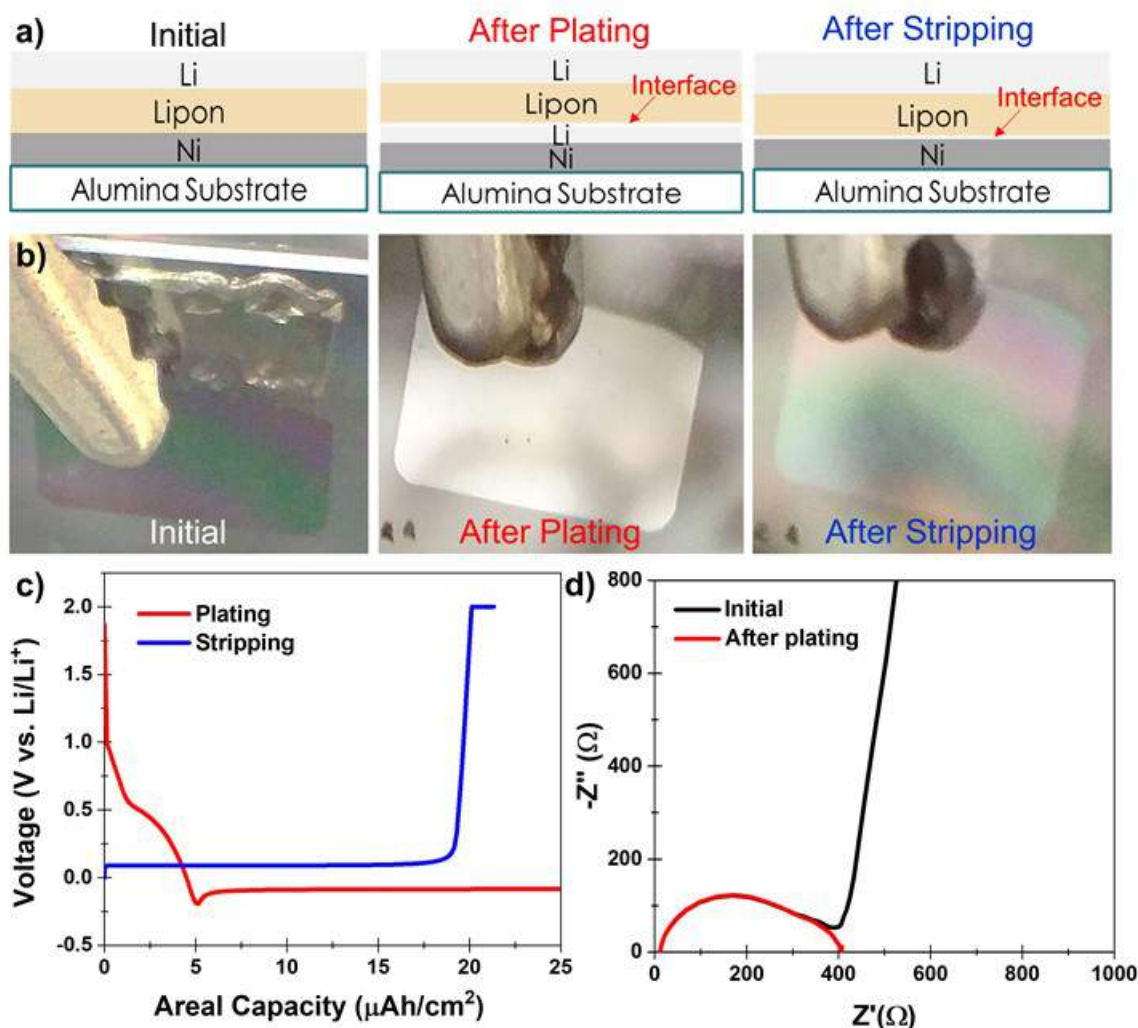


Figure II.8.C.1 (a) Schematic of the experimental design in the initial state, after plating Li on the Ni current collector and after interface formation and stripping of the Li. (b) Photographs of one cell taken through the Sapphire wafer in the initial state, after the first plating, and after the first stripping cycle. (c) Plating and stripping curves for a representative cell. (d) Nyquist plots for electrochemical impedance spectroscopy (EIS) of the cell in (c) in its initial state and after plating Li metal

Figure II.8.C.1 gives a basic illustration of the technique and results for a representative sample. Figure II.8.C.1a is a schematic of the cells used to perform the technique. In Figure II.8.C.1b there are three photographs of a representative cell taken through the sapphire wafer. We can see the Li cathode with the optical interference from the Ni and Lipon thin films. After plating we can see the Li metal has formed a complete conformal layer with a mirrorlike finish implying there is little to no roughness in the film. After we subsequently strip the Li we can see that virtually all of the Li is removed and we have returned to what optically looks like the initial state. Although it is difficult to conclusively determine if all of the Li has been stripped, we can confirm that we plated enough Li to conformally plate the Li metal and thus our area normalization is accurate. In Figure II.8.C.1c we can see both the plating and stripping curve for the film. We can see that the initial OCV is at about ~2V vs. Li/Li⁺ which is due to the potential difference between the Ni-O surface layer and the Li metal. Upon applying a current Li first intercalates into the Ni-O surface layer accounting for ~4.4 μAh/cm² from ~2V to ~0V vs. Li/Li⁺ out of a total of 25 μAh/cm². In turn Li was then

stripped. Assuming the end of Li stripping occurs at $\sim 0.2\text{V}$ vs. Li/Li^+ . We are able to strip $\sim 19.5\text{ }\mu\text{Ah/cm}^2$. Considering the Li lost to the Ni-O layer this leaves a capacity of $\sim 1.1\text{ }\mu\text{Ah/cm}^2$ lost during this first cycle. Assuming all this lost Li went into an interfacial layer, the interface would have consumed $\sim 5.3\text{ nm}$ of Li and 2.5 nm of Lipon to form an interfacial layer that is approximately $\sim 4.9\text{ nm}$ thick. Although the results differ slightly with different test setups, substrates and conditions, virtually all the measurements predict a Li loss of $\sim 5\text{ nm}$ or less. We are still working out some of the small experimental details to determine the best substrate and to eliminate as many sources of error as possible, including the presence of the Ni-O layer and to provide a statistical analysis. With an interfacial layer that is $\sim 4.9\text{ nm}$ or less, Lipon is one of the most stable electrolytes for Li metal batteries. This is confirmed with electrochemical impedance spectroscopy (EIS) presented in Figure II.8.C.1d. In the initial state we see the bulk semicircle corresponding to the Lipon ionic resistance, second small semicircle that may correspond to the initial Lipon-Li interface and a capacitance due to the Ni-NiO-Lipon interface. After deposition we see that the capacitance disappears, but there is no change in the two semicircles. This suggests that the interface formed has a very low resistance. This does not change after many consecutive charge/discharge measurements. For comparison a recent paper by Shirley Meng's group tested a wide range of liquid electrolytes. The very best of these electrolytes had a 1st cycle Coulombic efficiency of 97.1% of 1 mAh/cm^2 charge. This results in a 1st cycle capacity loss of $29\text{ }\mu\text{Ah/cm}^2$. Assuming that the oxide capacity was similar to our Ni foil at $\sim 5\text{ }\mu\text{Ah/cm}^2$, they lost at least 116 nm of Li.

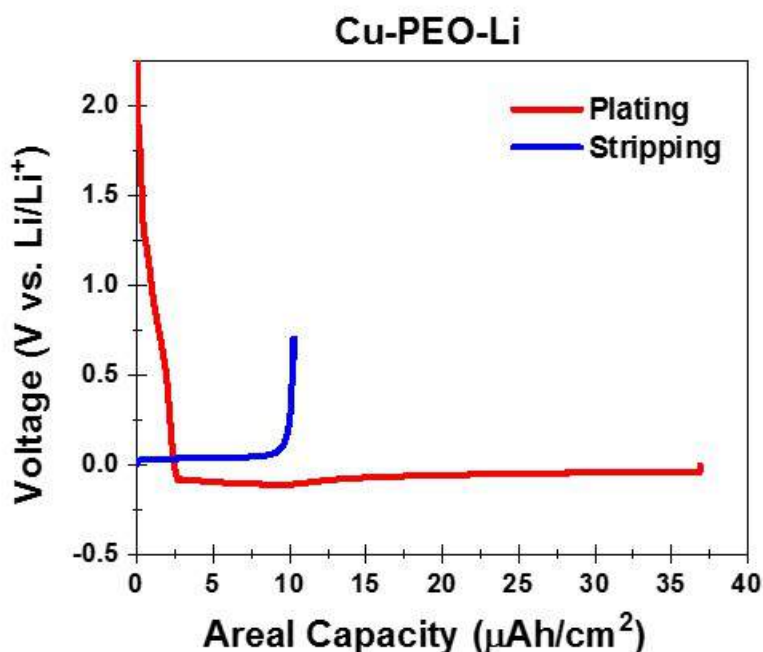


Figure II.8.C.2 Plating and stripping profile of a Cu foil/PEO-LiTFSI/Li metal cell

We anticipate that this will be a robust method to test the stability of virtually any solid-state electrolyte with Li metal. Once all the key experimental procedures are determined with the Li-Lipon system, we plan to adapt this technique to study the key model electrolytes chosen for the joint U.S.-German collaboration. We have performed preliminary tests for the PEO-LiTFSI electrolyte. These results are presented in Figure II.8.C.2. We again see the initial Li intercalation into the Cu-O with a capacity of $\sim 2.45\text{ }\mu\text{Ah/cm}^2$, we then subsequently plated $\sim 34.5\text{ }\mu\text{Ah/cm}^2$ of Li. When we tried to strip the Li from this cell, we were only able to recover $10.3\text{ }\mu\text{Ah/cm}^2$. This corresponds to a Li loss of $\sim 117\text{ nm}$. This is comparable with the very best liquid electrolyte tested by the Meng group. [\[2\]](#)

Conclusions

In summary, we have developed a simple method for testing the stability of solid-state electrolytes with Li metal. The technique relies on a simple plating and stripping of Li onto a metal current collector. By counting the number of electrons lost on the first and subsequent cycles we can determine how stable the electrolyte is with Li metal. For Lipon we demonstrated that the interface formed with Li metal is less than 5nm thick. For the polymer electrolyte PEO-LiTFSI the electrolyte layer is much thicker and corresponds to a Li loss of ~117 nm which is comparable to the very best of the liquid electrolytes.

Going forward we will continue to develop techniques to understand the purity of Li metal and the stability of solid-state electrolytes with Li metal. Ongoing work includes X-ray tomography of evaporated Li metal, TOF-SIMS analysis, and continued plating and stripping stability studies. In the next year we will continue to develop these techniques and begin applying them to the model systems that will be studied by all of the program participants.

References

1. Fang, C.; Li, J.; Zhang, M.; Zhang, Y.; Yang, F.; Lee, J. Z.; Lee, M.-H.; Alvarado, J.; Schroeder, M. A.; Yang, Y., Quantifying inactive lithium in lithium metal batteries. *Nature* 2019, 572 (7770), 511-515.
2. Krauskopf, T.; Dippel, R.; Hartmann, H.; Pepler, K.; Mogwitz, B.; Richter, F. H.; Zeier, W. G.; Janek, J., Lithium-Metal Growth Kinetics on LLZO Garnet-Type Solid Electrolytes. *Joule* 2019, 3 (8), 2030-2049.

Acknowledgements

Xi Chelsea Chena and Laura Merrill assisted with making and testing PEO-LiTFSI cells.

II.8.D Lithium Thiophosphate-Based Solid Electrolytes and Cathodes for All-Solid-State Batteries (ORNL)

Jagjit Nanda, Principal Investigator

Oak Ridge National Laboratory
1 Bethel Valley Road
Oak Ridge, TN, 37831
E-mail: nandaj@ornl.gov

Tien Duong, DOE Technology Development Manager

U.S. Department of Energy
E-mail: Tien.Duong@ee.doe.gov

Start Date: October 1, 2018

End Date: September 30, 2019

Project Funding (FY19): \$400,000

DOE share: \$400,000

Non-DOE share: \$0

Project Introduction

Advances in solid electrolytes (SEs) with superionic conductivity and stable electrode/electrolyte interfaces are key enablers for all solid-state batteries (SSBs) to meet the energy density and cost targets for next generation batteries for electric vehicles. This project utilizes various electrochemical and structural characterization methods to address key technical barriers associated with lithium thiophosphate-based SEs. Compared to their oxide counterparts, thiophosphate SEs offer several key advantages, including: (i) exceptionally high Li^+ conductivities up to 10^{-2} S/cm (comparable to nonaqueous liquid electrolytes), (ii) availability of low temperature and inexpensive synthesis routes to produce glass, glass-ceramic, and crystalline structures, and (iii) soft mechanical properties which facilitates material processing. Among their drawbacks, these materials have narrow electrochemical stability windows and hence limited stability against lithium metal anodes and high voltage cathodes. They also suffer from poor chemical stability and are highly sensitive to moisture. This project aims to enable SSB research targeted toward VTO's BATT 500 goal of 500 Wh/kg (cell level) for 1,000 cycles.

Objectives

- I. Undertake synthesis and structural characterization of lithium thiophosphate and related superionic conductors.
- II. Produce thiophosphate SEs with Li^+ conductivities in the range of 1×10^{-3} – 1×10^{-4} S/cm at room temperature by optimizing the synthesis method, dopant concentration, and surface properties.
- III. Evaluate SE passivation at cathode interfaces by combining electrochemical characterization with vibrational spectroscopy.
- IV. Develop interfacial coatings and new cathode chemistries to obtain an area specific resistance (ASR) $< 10 \text{ ohm cm}^2$.

Approach

Studies in FY2019 focused on the synthesis and characterization of lithium thiophosphate-based SEs and cathodes. These materials were prepared using solution-based processing routes previously developed at ORNL[1], and their structure was evaluated using X-ray diffraction (XRD) and vibrational spectroscopy. Electrochemical measurements were performed on pelletized solid electrolytes (approximately 13 mm diameter, 1 mm thickness) using either blocking (carbon-coated Al) or non-blocking (Li metal) electrodes sandwiched between stainless steel current collectors (see Figure II.8.D.1a). The lithium storage properties of several thiophosphate cathode candidates were screened using chemical titrations with a lithium biphenyl

anion radical ($\text{Li}^+\beta^\bullet$) solution. Appropriate precautions were taken to avoid exposing the materials to ambient conditions during synthesis and characterization.

Results

$\beta\text{-Li}_3\text{PS}_4$: A Model Lithium Thiophosphate Solid Electrolyte

Li_3PS_4 was synthesized by mixing Li_2S and P_2S_5 in tetrahydrofuran (THF) followed by drying under vacuum at 25–140°C overnight. As shown in Figure II.8.D.1a, the material dried at room temperature contained co-crystallized THF (denoted as $\text{Li}_3\text{PS}_4 \cdot 3\text{THF}$), and crystalline $\beta\text{-Li}_3\text{PS}_4$ was obtained after drying at 140°C. The Raman spectrum of $\beta\text{-Li}_3\text{PS}_4$ contained a sharp band at 426 cm^{-1} which is attributed to the symmetric P-S stretch of the isolated PS_4^{3-} tetrahedra (see Figure II.8.D.1b and Figure II.8.D.1c).^[2] No impurities, residual precursors, or coordinated THF were detected in the powder heated at 140°C.

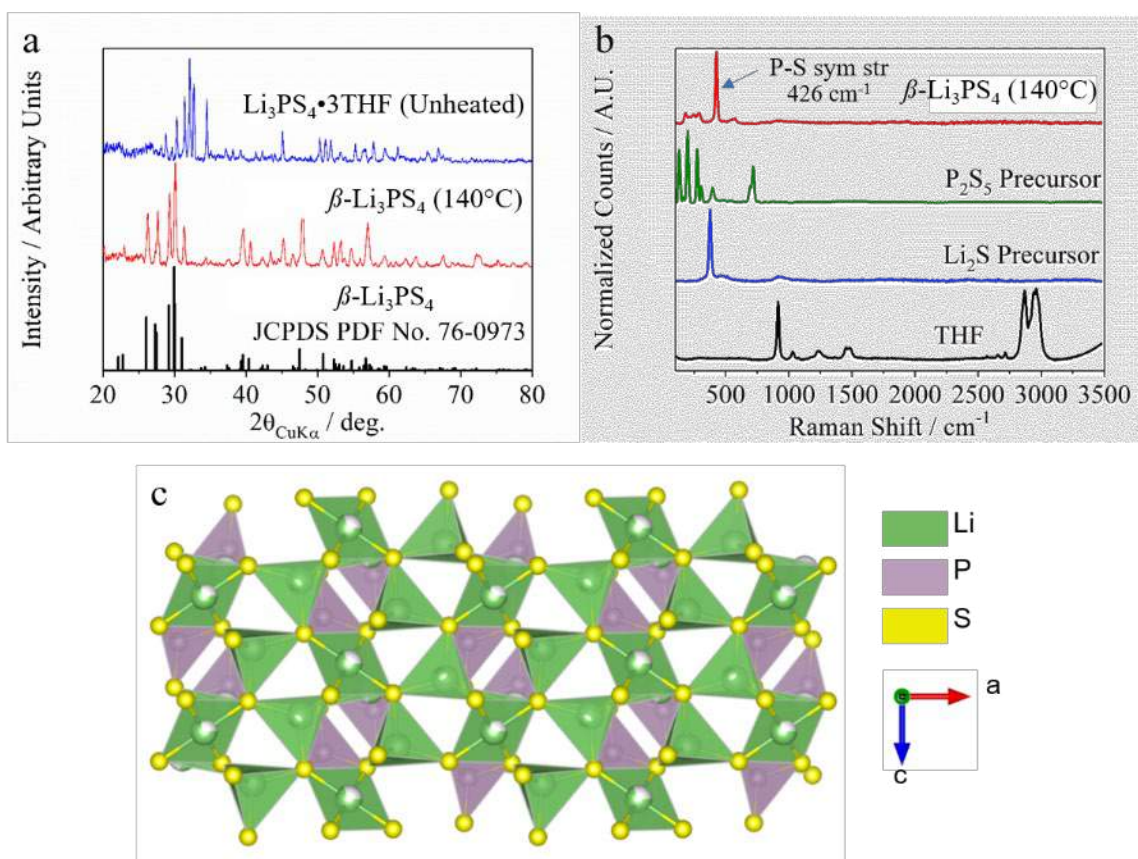


Figure II.8.D.1 Structural characterization of $\beta\text{-Li}_3\text{PS}_4$ prepared through a solution-based route showing (a) X-ray diffraction (XRD) patterns and (b) Raman spectra of the precursors and annealed powders. (c) Crystallographic structure of $\beta\text{-Li}_3\text{PS}_4$. In (b), the broad background at $2\theta < 30^\circ$ are due to the Kapton film which was used to prevent air exposure during the XRD measurements

To evaluate the electrochemical properties of $\beta\text{-Li}_3\text{PS}_4$, SE pellets (ca. 13 mm diameter, 1 mm thickness) were pressed at 560 MPa at room temperature. The resulting pellets had a density of 1.65 g/cm^3 which is 12% lower than the theoretical density of $\beta\text{-Li}_3\text{PS}_4$ (1.87 g/cm^3), indicating the materials likely contained voids and/or lower density amorphous phase(s). The Li^+ conductivity of $\beta\text{-Li}_3\text{PS}_4$ was measured via AC impedance spectroscopy using the cell design illustrated in Figure II.8.D.2a. Corresponding Nyquist plots (see Figure II.8.D.2b) exhibited vertical capacitive tails (skew angle $< 5^\circ$) at low frequencies due to charge accumulation near the SE/electrode interfaces. The synthesized $\beta\text{-Li}_3\text{PS}_4$ displayed a high Li^+ conductivity of $1.5 \times 10^{-4} \text{ S}/\text{cm}$ at room temperature and activation energy of 0.34 eV which is consistent with previous reports.^{[1],[2],[3]} Notably, cells containing either blocking or nonblocking electrodes (i.e., carbon-coated

aluminum and lithium metal, respectively) yielded identical Li^+ conductivities (within measurement error) which indicates the resistance of any passive film at the $\text{Li}_3\text{PS}_4/\text{Li}$ interface was negligible compared to the resistance of the $\beta\text{-Li}_3\text{PS}_4$ pellet.

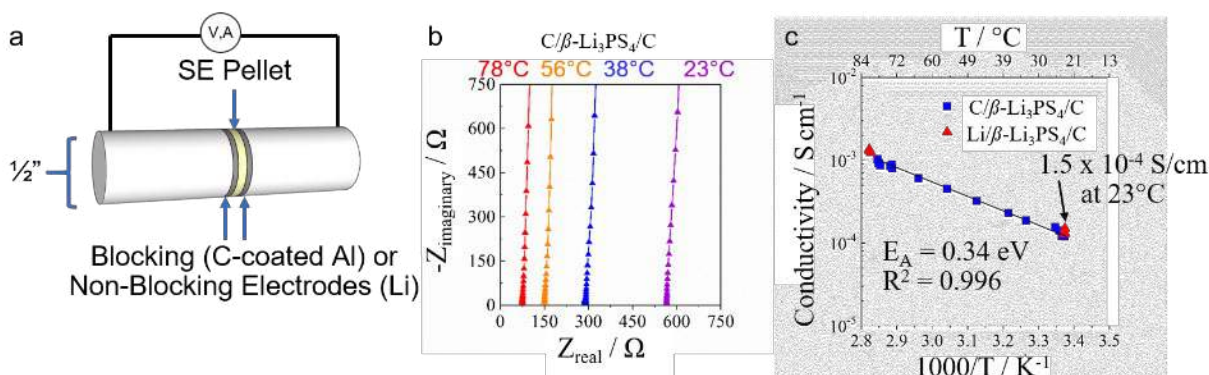


Figure II.8.D.2 Ionic conductivity measurements of $\beta\text{-Li}_3\text{PS}_4$ solid electrolyte pellets. (a) Conductivity cell configuration, (b) representative Nyquist plots of a $\text{C}/\beta\text{-Li}_3\text{PS}_4/\text{C}$ cell at 23–78 °C, and (c) Arrhenius plots showing ionic conductivity as a function of temperature for $\text{C}/\beta\text{-Li}_3\text{PS}_4/\text{C}$ and $\text{Li}/\beta\text{-Li}_3\text{PS}_4/\text{C}$ cells

In addition to their Li^+ conductivity, the electrochemical stability window of SEs can also be determined using AC impedance spectroscopy. To illustrate this approach, the impedance of a $\text{Li}/\beta\text{-Li}_3\text{PS}_4/\text{C}$ cell (open-circuit potential = 2.215 V) was measured as a function of the C cathode potential (see Figure II.8.D.3). As expected, the high frequency intercept associated with ionic resistance of the $\beta\text{-Li}_3\text{PS}_4$ pellet was unchanged throughout these measurements. As the cell was polarized from 2.2 – 2.6 V vs. Li/Li^+ , the total capacitance gradually increased from ~ 0.5 to $1.0 \mu\text{F}/\text{cm}^2$, presumably due to higher charge carrier concentrations near the electrode/electrolyte interfaces. At potentials > 2.6 V vs. Li/Li^+ , the capacitance sharply decreased to $0.6 \mu\text{F}/\text{cm}^2$ which is attributed to formation of a passive film consisting of Li_3PS_4 oxidation products on the cathode surface.^[4] The resistance of this film was apparently much less than that of the Li_3PS_4 pellet since the high frequency resistance did not increase under these oxidizing conditions. Overall, these results illustrate that Li_3PS_4 is thermodynamically unstable at the operating potential of common Li-ion battery cathodes (> 3 V vs. Li/Li^+), and thus formation of kinetically stabilized passive films at SE/cathode interfaces is critical for sulfide-based SSBs. Studies in FY2020 will evaluate the composition and structure of passive films formed between thiophosphate SEs and various cathodes (e.g., LiFePO_4 and LiMO_2 , $\text{M} = \text{Ni}$, Mn , and/or Co).

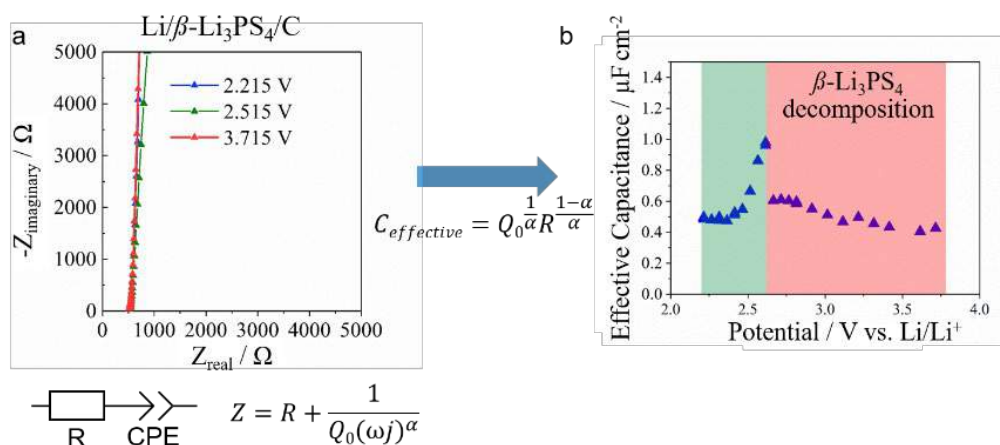


Figure II.8.D.3 AC impedance measurements on a $\text{Li}/\beta\text{-Li}_3\text{PS}_4/\text{C}$ cell used to determine the oxidative stability limit of the $\beta\text{-Li}_3\text{PS}_4$ solid electrolyte. (a) Nyquist plots collected by polarizing the C electrode between 2.2 – 3.7 V vs. Li/Li^+ and (b) effective total cell capacitance as a function of cathode potential. The sharp decrease in capacitance at potentials > 2.6 V vs. Li/Li^+ is attributed to formation of a passive film at the C electrode

Amorphous Li_3PS_4 /Poly(ethylene oxide) (PEO) Solid Electrolytes

A major bottleneck for $\beta\text{-Li}_3\text{PS}_4$ SEs is the lack of scalable processing methods to produce SE thin films which should be ca. 10-25 μm for practical SSBs. Furthermore, the nano-/polycrystalline structure of $\beta\text{-Li}_3\text{PS}_4$ films/pellets may cause nonuniform current densities across the SE/Li interface and exacerbate Li dendrite propagation during battery operation. To address these issues, we developed a new class of composite SEs consisting of amorphous Li_3PS_4 dispersed in poly(ethylene oxide) (denoted as a- Li_3PS_4 +PEO). These materials were synthesized by mixing Li_2S , P_2S_5 , and PEO (600 kDa, 0.2 – 56 wt% in the composite) in acetonitrile followed by annealing at 25 – 250°C. As shown in Figure II.8.D.4a and Figure II.8.D.4b, the composites were largely amorphous and did not contain either crystalline $\beta\text{-Li}_3\text{PS}_4$ or crystalline PEO phases. We attribute this result to strong coordination between the PEO and $\text{Li}_2\text{S}/\text{P}_2\text{S}_5$ precursors which inhibited crystallization of $\beta\text{-Li}_3\text{PS}_4$ at elevated temperatures. Residual Li_2S was detected in composites with 0.2 – 5 wt% PEO, indicating these samples contained Li deficient thiophosphate phase(s) [e.g., $\text{Li}_{3-x}(\text{PS}_4)_{1-x}$].

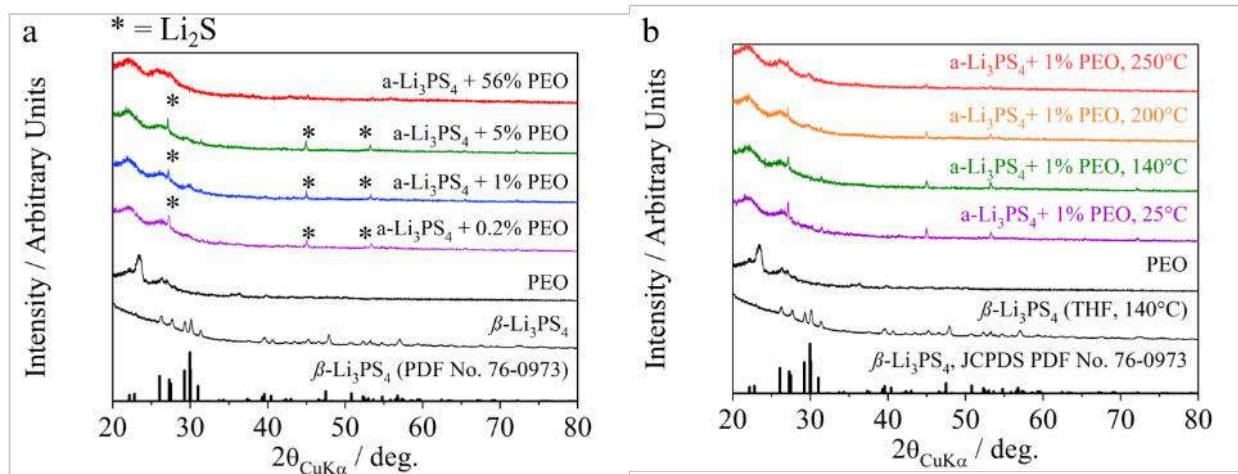


Figure II.8.D.4 Structural characterization of a- Li_3PS_4 + PEO composite solid electrolytes. (a) XRD patterns of composites containing 0.2 – 56 wt% PEO. (b) XRD patterns of a- Li_3PS_4 + 1 wt% PEO after heating for 12 h at 25 – 250°C. The broad background at $2\theta < 30^\circ$ are due to the Kapton film which was used to prevent air exposure during the XRD measurements

Raman spectra of amorphous composites containing 1 wt% PEO heated at 25 – 250°C for 12 h are given in Figure II.8.D.5. Unlike $\beta\text{-Li}_3\text{PS}_4$ which showed a single band at 426 cm^{-1} , the a- Li_3PS_4 +1% PEO composites exhibited multiple convoluted bands at 394, 407, and 428 cm^{-1} which indicates a distribution of P-S bonding environments (e.g., PS_4^{3-} , $\text{P}_2\text{S}_6^{4-}$ and $\text{P}_2\text{S}_7^{4-}$ polyanions).^[5] Moreover, the relative intensity of these bands changed depending on the heat treatment. Interestingly, C-H stretches associated with coordinated acetonitrile were clearly present in the sample dried at 25°C (see Figure II.8.D.5b), but these bands were not observed in the materials heated at 140 – 250°C due to their strong fluorescence background. After heating at 250°C, the composite showed a weak band at 1,440 cm^{-1} which is attributed to thermal decomposition product(s). These results demonstrate that the structure of the a- Li_3PS_4 /PEO composites is very sensitive to the drying/annealing conditions. Neutron scattering experiments to be performed in FY2020 are expected to provide more insight on the materials' local structure.

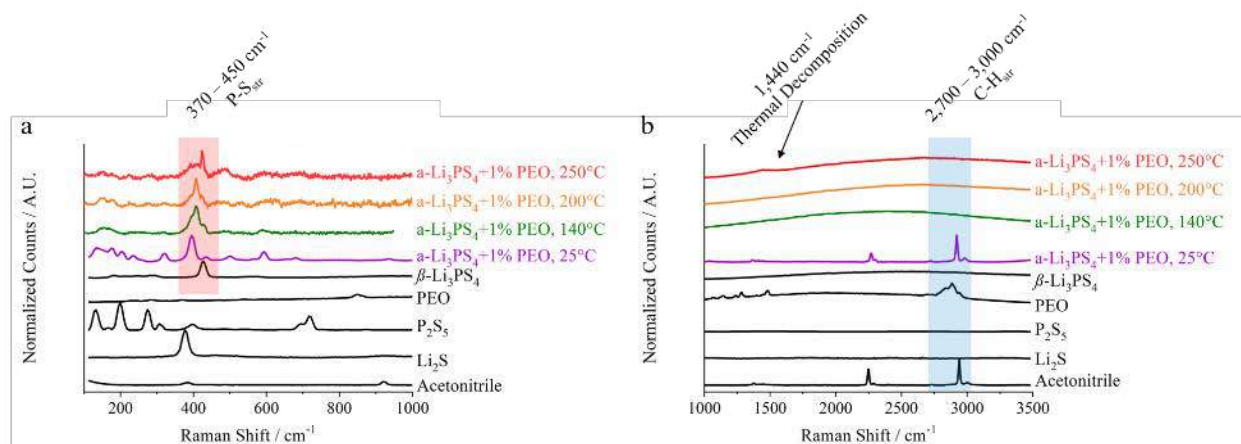


Figure II.8.D.5 Raman spectra of a-Li₃PS₄ + 1 wt% PEO after heating for 12 h at 25 – 250 °C showing (a) 100–1,000 cm⁻¹ and (b) 1,000 – 3,500 cm⁻¹ regions

Figure II.8.D.6 summarizes the Li⁺ conductivity measured for a-Li₃PS₄+PEO composites containing 1 – 56 wt% PEO. Samples with high PEO content (25 – 56 wt%) exhibited very low conductivities (< 1 × 10⁻⁹ S/cm at room temperature) due to the insulating nature of PEO. At lower PEO concentrations (1 – 5 wt%), the composite's conductivity was moderate (~2 × 10⁻⁶ S/cm at room temperature). Interestingly, incorporating a lithium salt (lithium trifluoromethanesulfonate, LiTFS) into the sample with 5 wt% PEO increased the room temperature conductivity nearly 1 order of magnitude. Although their Li⁺ conductivities were lower than that of β-Li₃PS₄, the composite a-Li₃PS₄+PEO SEs may offer advantages in terms of processability (e.g., to produce thin, flexible SE films) and Li dendrite suppression (e.g., by preventing preferential Li conduction along specific crystallographic facets). Symmetric Li/SE/Li and Li/SE/cathode cells will be tested in FY2020 to explore these potential advantages.

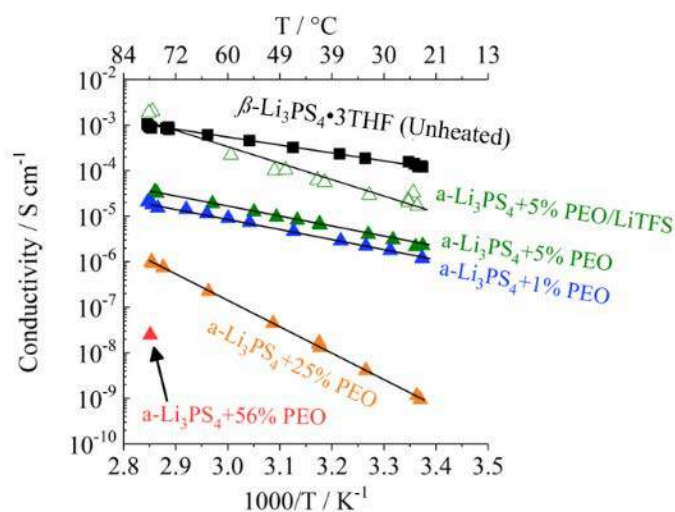
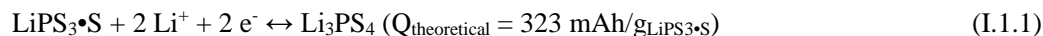


Figure II.8.D.6 Li⁺ conductivity for several a-Li₃PS₄ + PEO composite solid electrolytes. The sample denoted a-Li₃PS₄ + 5% PEO/LiTFS contained PEO/lithium trifluoromethanesulfonate (LiTFS) in a 12/1 molar ratio, and the total PEO+LiTFS content was 5 wt%. Li⁺ conductivity of crystalline β-Li₃PS₄ is shown for comparison

Catenated Sulfur Cathodes

In addition to our work on superionic SEs, we also developed a synthesis route to produce new lithium thiophosphate compounds which are promising candidates for high capacity/high energy density cathodes. Figure II.8.D.7a shows a Li-P-S ternary phase diagram which highlights several compounds of interest. The

present work investigated catenation of 1 S onto LiPS_3 to produce $\text{LiPS}_3\cdot\text{S}$. Unlike sulfur cathodes which often exhibit poor reversibility (e.g., due to formation of an insulating Li_2S phase), $\text{LiPS}_3\cdot\text{S}$ is expected to form the superionic conductor Li_3PS_4 during discharge (see Equation I.1.1 and the green line in Figure II.8.D.6a). This favorable charge/discharge mechanism is anticipated to produce a cathode with good rate capabilities and cyclability.



The LiPS_3 moiety was first synthesized using a solution-based method in which Li_2S and P_2S_5 were mixed in either tetrahydrofuran (THF) or acetonitrile (AN) followed by thermal annealing at 140 – 270°C. As shown by the X-ray diffraction (XRD) patterns in Figure II.8.D.7b, either crystalline or amorphous LiPS_3 were produced depending on the synthesis conditions. Sulfur catenation was then performed by reacting the LiPS_3 with elemental S in THF followed by thermal annealing. Interestingly, the catenated $\text{LiPS}_3\cdot\text{S}$ compounds were completely amorphous regardless of whether a crystalline or amorphous LiPS_3 precursor was utilized. The catenated compounds remained amorphous after heating to 260°C and thermally decomposed at 320°C. Vibrational spectroscopic studies are underway to resolve the local bonding and structure of these amorphous materials.

The lithium storage properties of several LiPS_3 and $\text{LiPS}_3\cdot\text{S}$ compounds were screened using chemically mediated reactions. In this setup, the cathode powders were chemically reduced using a titrant solution containing lithium biphenyl anion radical ($\text{Li}^+\text{B}^{\cdot-}$) dissolved in diglyme. As titrant was added dropwise to the cathode powders, the solution changed from dark blue (indicating the presence of $\text{Li}^+\text{B}^{\cdot-}$) to translucent yellow (indicating the absence of $\text{Li}^+\text{B}^{\cdot-}$). The total titrated capacities for LiPS_3 and $\text{LiPS}_3\cdot\text{S}$ are listed in Table II.8.D.1. While the amorphous LiPS_3 had a relatively low lithium capacity (206 mAh/g), the crystalline LiPS_3 exhibited an 8-fold higher capacity (1,683 mAh/g) which indicates this material was fully reduced to form Li_2S + Li_3P (see Equation I.1.2). The discrepancy between the measured and theoretical capacities is within the measurement error. Overall, these results illustrate that the cathode's structure has a dramatic impact on its electrochemical properties.

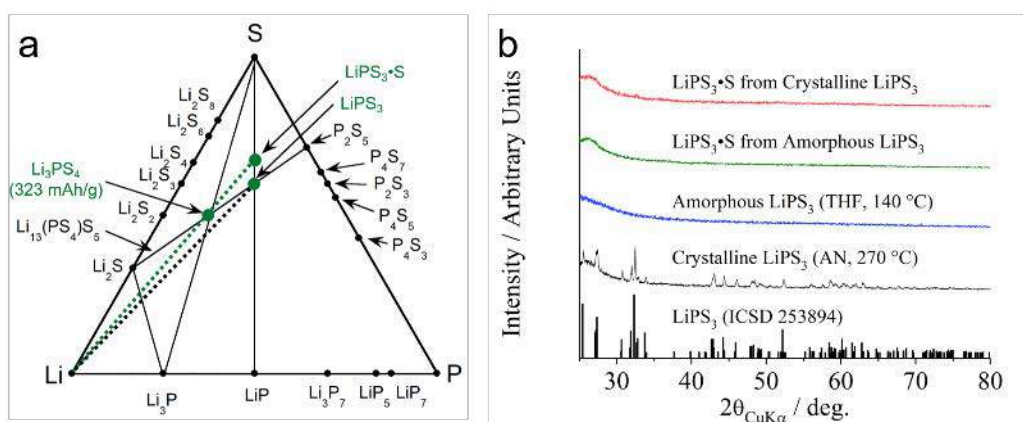
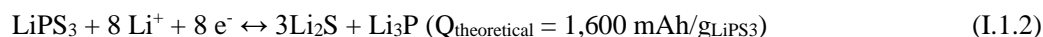


Figure II.8.D.7 (a) Li-P-S ternary phase diagram. Due to limited available thermodynamic quantities (e.g., free energies of formation), not all tie lines are known for this system. (b) X-ray diffraction (XRD) patterns of LiPS_3 and catenated $\text{LiPS}_3\cdot\text{S}$ cathode powders. The sloping profiles at $2\theta < 30^\circ$ are due to the Kapton film which was used to prevent air exposure during the XRD measurements

Compared to LiPS_3 , the catenated cathodes exhibited modest capacities ranging from 340 – 400 mAh/g which indicates these materials were not fully reduced to form Li_2S + Li_3P . The measured capacities are reasonably close to that expected for $\text{LiPS}_3\cdot\text{S}$ reduction to Li_3PS_4 (323 mAh/g, see Equation 1), although more work is

needed to determine the reduction mechanism. Future work will investigate the electrochemical properties of these materials in SSBs containing a Li metal anode and thiophosphate-based solid electrolyte.

Table II.8.D.1 Chemically Titrated Capacities of LiPS₃ and LiPS₃•S cathode powders

Cathode	Chemically Titrated Lithium Capacity (mAh/g)
LiPS ₃ (amorphous)	206
LiPS ₃ (crystalline)	1,680
LiPS ₃ •S (from amorphous LiPS ₃)	401
LiPS ₃ •S (from crystalline LiPS ₃)	339

Titration were performed by reducing the active material powder using a lithium biphenyl anion radical species (Li⁺β[•]) dissolved in diglyme. The electrochemical potential of the titrant solution was approximately 0.2 V vs. Li/Li⁺.

Conclusions

A model lithium thiophosphate solid electrolyte (β-Li₃PS₄) was synthesized using a solution-based route. The material exhibited a high Li⁺ conductivity (e.g., 1.5 × 10⁻⁴ S/cm at room temperature) using either blocking or non-blocking electrodes which indicates the resistance of the passive film at the Li anode was negligible compared to that of the SE pellet. Additional AC impedance measurements demonstrated that β-Li₃PS₄ is oxidatively unstable at potentials > 2.6 V vs. Li/Li⁺. The composition and structure of passive films which form at various β-Li₃PS₄/cathode interfaces will be evaluated in FY2020.

In addition to our studies on crystalline β-Li₃PS₄, a new class of composite Li₃PS₄/poly(ethylene oxide) SEs which are completely amorphous and exhibit Li⁺ ionic conductivities up to 1 × 10⁻⁶ S/cm at room temperature were also developed. The presence of the PEO component facilitates the material's processability and suppresses crystallization of the β-Li₃PS₄ phase, thus enabling fabrication of amorphous SEs with a wide range of compositions. The performance of SSBs containing β-Li₃PS₄ vs. α-Li₃PS₄/PEO SEs will be compared in FY2020.

A synthesis method to catenate sulfur onto LiPS₃ was explored to fabricate high energy density cathodes with the formula LiPS₃•S. The resulting compounds were amorphous, and chemical titrations showed that the cathodes' lithium capacity was closely linked to their structure. As such, future work in FY2020 will utilize a suite of characterization methods [e.g., vibrational spectroscopy, neutron scattering, and nuclear magnetic resonance (NMR)] to better understand how the materials' local structure impacts their electrochemical properties.

Key Publications

1. F. M. Delnick, E. C. Self, and J. Nanda, High Capacity Catenated Polysulfidophosphate Cathodes for Lithium Batteries, ORNL Invention Disclosure 81913074, **2019**.

References

1. Liu, Z.; Fu, W.; Payzant, E. A.; Yu, X.; Wu, Z.; Dudney, N. J.; Kiggans, J.; Hong, K.; Rondinone, A. J.; Liang, C., Anomalous high ionic conductivity of nanoporous beta-Li₃PS₄. J. Am. Chem. Soc. 2013, 135 (3), 975-8.
2. Lin, Z.; Liu, Z.; Fu, W.; Dudney, N. J.; Liang, C., Lithium polysulfidophosphates: a family of lithium-conducting sulfur-rich compounds for lithium-sulfur batteries. Angew Chem Int Ed Engl 2013, 52 (29), 7460-3.

3. Hood, Z. D.; Wang, H.; Pandian, A. S.; Peng, R.; Gilroy, K. D.; Chi, M.; Liang, C.; Xia, Y., Fabrication of Sub-Micrometer-Thick Solid Electrolyte Membranes of β -Li₃PS₄ via Tiled Assembly of Nanoscale, Plate-Like Building Blocks. *Adv. Energy Mater.* 2018, 8 (21), 1800014.
4. Richards, W. D.; Miara, L. J.; Wang, Y.; Kim, J. C.; Ceder, G., Interface Stability in Solid-State Batteries. *Chem. Mater.* 2015, 28 (1), 266-273.
5. Dietrich, C.; Weber, D. A.; Sedlmaier, S. J.; Indris, S.; Culver, S. P.; Walter, D.; Janek, J.; Zeier, W. G., Lithium ion conductivity in Li₂S–P₂S₅ glasses – building units and local structure evolution during the crystallization of superionic conductors Li₃PS₄, Li₇P₃S₁₁ and Li₄P₂S₇. *J. Mater. Chem. A* 2017, 5 (34), 18111-18119.

Acknowledgements

Frank M. Delnick is project Co-PI, and team members include Ethan C. Self, Guang Yang, and Teerth Brahmabhatt. This research is sponsored by the United States Department of Energy through the Office of Energy Efficiency and Renewable Energy (EERE) and Vehicle Technologies Office (VTO, Program Manager: Tien Duong).

II.8.E Advancing Solid-State Interfaces in Lithium-Ion Batteries (ANL)

Nenad M. Markovic, Principal Investigator

Argonne National Laboratory
9700 South Cass Avenue
Lemont, IL 60521
E-mail: nmmarkovic@anl.gov

Larry A. Curtiss, Principal Investigator

Argonne National Laboratory
9700 South Cass Avenue
Lemont, IL 60521
E-mail: curtiss@anl.gov

Tien Duong, DOE Technology Development Manager

U.S. Department of Energy
E-mail: Tien.Duong@ee.doe.gov

Start Date: October 1, 2016
Project Funding: \$1,200,000

End Date: September 30, 2019
DOE share: \$1,200,000

Non-DOE share: \$0

Project Introduction

The proposed work will develop and exploit a variety of ex situ and in situ experimental optical and surface sensitive techniques and electrochemical methods to explore and explain bulk and interfacial properties of the selected materials. The results will serve to unravel many puzzling bulk and interfacial properties of $S_{\text{Li}}\text{-}S_{\text{EL}}\text{-}S_{\text{C}}$ systems, including various types of ceramic and glass materials. As one example, cubic garnet $\text{Li}_7\text{La}_3\text{Zr}_2\text{O}_{12}$ (LLZO) stabilized with Al, Nb or Ta dopants is a particularly promising solid electrolyte for all-solid-state lithium metal batteries. Another material, $\text{Li}_{0.33}\text{La}_{0.55}\text{TiO}_3$ (LLTO) is a solid electrolyte with a pseudoperovskite structure with ordered La rich (Li poor) and La poor (Li rich) planes that make it suitable for studying orientation dependence of interface properties.

Objectives

The project objectives are multifaceted, including development of a new mechanically and chemically stable and Li-ion conductive ($\geq 2 \times 10^{-4}$ S/cm at 298 K) solid electrolyte for a solid-state battery encompassing a Li-metal anode, Li-oxide-based cathode, and nonflammable crystalline and amorphous solid electrolytes that can operate at cathode potentials > 5 V (denoted as a $S^{\text{Li}}\text{-}S^{\text{EL}}\text{-}S^{\text{C}}$ system). This year, our objectives are (1) to use surface and bulk sensitive techniques, spectroscopic methods and computational tools to (a) understand the impact of different dopants in LLZO (Nb vs. Ta vs. Al) on reactivity and (b) determine the impact of solid electrolyte crystallinity (single crystal vs. polycrystalline vs. amorphous) on electrolyte reactivity, and (2) distinguish chemical vs. electrochemical reactivity at the interface and bulk of model solid-state electrochemical systems with Li metal anodes by electrochemical testing and characterization. The out-year goals are to use and develop the physical and chemical synthesis methods for design of solid-solid interfaces with unique chemical/mechanical/conductivity properties.

Approach

The project proposes to develop and use interdisciplinary, atomic-/molecular-level insight obtained from integrating both experimental- and computational-based methodologies to define the landscape of parameters that control interfacial properties for a new generation of the Li-ion solid-solid battery systems. The strategy will involve transferring knowledge gained from well-characterized thin-film materials to real-world materials. This strategy forms a closed loop wherein the knowledge gained from model systems is used to design more

complex, real-world materials, and vice versa. The work will focus on utilizing existing in-house synthesis and characterization methods to enable rapid transition from fundamental science to realistic cells.

Results

LLZO-Li Bulk Stability

We have previously shown that the intrinsic reactivity of interface between lithium metal and cubic $\text{Li}_7\text{La}_3\text{Zr}_2\text{O}_{12}$ (LLZO) stabilized with Al, Nb or Ta dopants is dopant dependent. We have determined that some degree of Zr reduction takes place for all three dopants, as well as that significant reduction of Nb takes place for Nb-doped LLZO. To determine whether the redox reaction is surface-limited, we have used XPS and synchrotron x-ray techniques to determine valence changes in the bulk of the doped LLZO after its reaction with Li metal. LLZO samples reacted with lithium were polished to remove surface layers and XPS measurements of re-polished samples were performed revealing significant reduction of Nb species in the bulk of Nb doped LLZO (Figure II.8.E.1a). This suggests that Li inserts into the Nb-doped LLZO bulk as a result of the reaction with Li metal, transforming LLZO from a solid electrolyte into a cathode material. In contrast to the Nb species, there is only Zr^{4+} observed in the Zr 3d core level spectrum of Al, Nb or Ta doped re-polished samples (Figure II.8.E.1b), indicating that the reduction of Zr observed at the surface does not proceed further into the bulk. Due to relatively low Al dopant concentration and overlap of its XPS spectrum with stronger Cu 3s peak from Cu impurities in the Li target, it was not possible to analyze the Al valence state in Al doped LLZO with XPS. Therefore, soft X-ray absorption measurements in total fluorescence yield mode characterization were used to scan Al K edge to track valence change of Al. XAS spectra taken before and after reaction with lithium metal (Figure II.8.E.1c) showed no significant differences. This result suggests that unlike Nb, the Al species are stable at least in the bulk ($\sim 50\text{nm}$ from surface) of LLZO, which indicates that the reaction of Li with Al-doped LLZO is surface-limited.

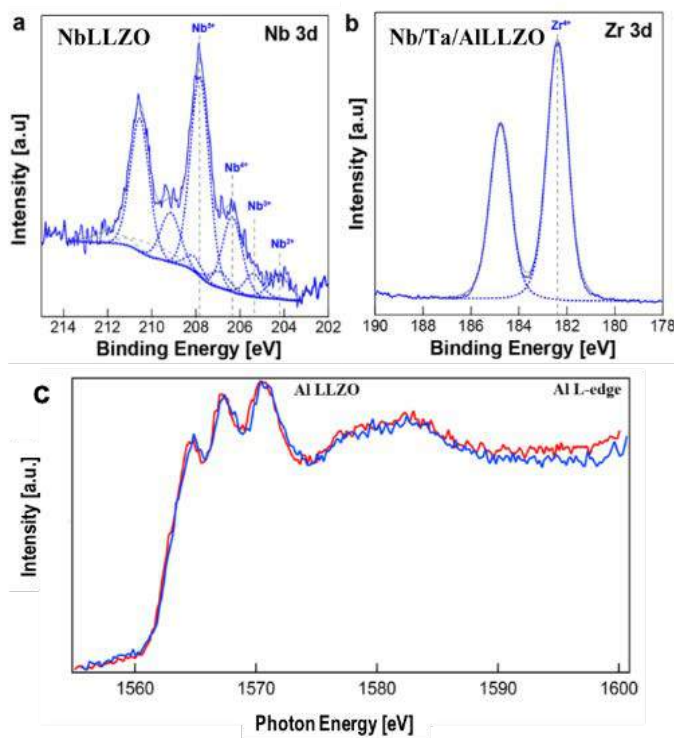


Figure II.8.E.1 Bulk Stability of doped-LLZO in Contact with Metallic Li: (a) Nb 3d and (b) Zr 3d core level XPS spectra and (c) Al L-edge XAS spectra reveals (a) the reduction of Nb, (b) no reactivity of Zr for all doped LLZO, and (c) no reactivity of Al

Li-LLZO Symmetric Cell Cycling

We carried out electrochemical testing of Li/LLZO interfaces with different dopants in order to compare interfacial and bulk changes during electrochemical cycling with the chemical reactivity observed from UHV Li deposition studies. Electrochemical cycling was done in the symmetric (Li-S_{EL}-Li) coin cell configuration. Thicker lithium films were vacuum-deposited on both sides of UHV-annealed LLZO pellets using our Li-LLZO interface preparation procedure, and a clean Li foil was placed on the freshly deposited Li films. Symmetric cells were then assembled inside the glove box and tested at room temperature without any stack pressure applied. Galvanostatic cycling of Li/doped LLZO/Li at 8 $\mu\text{A cm}^{-2}$ and 2 mA cm^{-2} exhibit Ohmic behavior for both Al- and Ta- doped samples (based on the charge transfer resistance, ≈ 50 and $\approx 25 \Omega \text{ cm}^2$, respectively). This indicates that Al and Ta doped-LLZO are stable against Li during high current density cycling. Nb-doped LLZO (initial charge transfer resistance $\approx 400 \Omega \text{ cm}^2$) displayed higher polarization and significantly longer cycle times needed to reach quasi-steady-state conditions, consistent with the chemical reactivity with Li observed previously. Al-doped LLZO cells were even further cycled at current densities as high as 4 mA cm^{-2} without failure for >300 cycles with 0.5 μm Li plated/stripped per cycle (Figure II.8.E.2 a), which is the highest current density for a planar LLZO membrane reported to date. Similar to cycling at 2 mA cm^{-2} , initially present 10mV overpotentials (Figure II.8.E.2 b) gradually decrease to a stable and flat voltage profile for the remainder of the cycling (Figure II.8.E.2 c). Our results show that introducing a thin film of vacuum-deposited Li metal improves electrochemistry at the Li/LLZO interface, yielding a low charge transfer resistance and enabling higher critical current densities during cycling than have been demonstrated thus far. After cycling with high current density (>2 mA cm^{-2}), symmetric cells were opened inside a glove box for characterization. LLZO was separated from Li foil and then polished to remove ~ 300 microns of material from the surface and access the bulk. La, Zr and dopant core level XPS spectra were collected to see if the high current density cycling causes chemical changes inside the solid electrolyte. There is no obvious reduction of Zr or La for all three doped LLZO samples. Nb-doped LLZO showed discoloration and XPS revealed significant reduction of Nb. However, the reduction of Nb in the bulk is not necessarily the result of high current cycling, as the same reduction and discoloration happened for Nb-doped LLZO in contact with Li foil over 3 days as well. Overall, XPS characterization showed Al- and Ta-doped LLZO are chemically stable to cycling at high current densities when the Li-LLZO interface is generated using Li thin films. LLZO pellets extracted from coin cells after extended cycling at high current density exhibit no discoloration related to dendrite formation, consistent with the ohmic response during cycling and with our previous observations of self-limiting surface reactions and stable interfacial behaviour of Al- and Ta-doped LLZO.

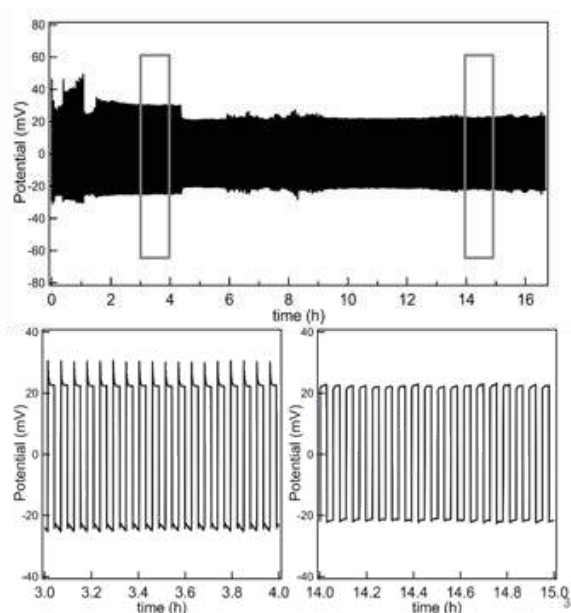


Figure II.8.E.2 Galvanostatic cycling of Al-doped LLZO: a) Symmetric Li/Al-LLZO /Li coin cell cycled with the current density of 4 mA cm⁻² b) Charge and discharge voltage profiles after 3h of cycling c) Charge and discharge voltage profiles after 14h of cycling

Effect of LLTO(hkl) Orientation

Li_{0.33}La_{0.55}TiO₃ (LLTO) is a solid electrolyte that crystallizes in a pseudo-perovskite structure with ordered La rich (Li poor) and La poor (Li-rich) planes normal to the c-axis in a tetragonal structure. Previous characterization (Annual Report 2018) showed after depositing ~20 nm of Li on epitaxial LLTO(hkl) thin films, LLTO(100) exhibits ~33% Ti reduction in the bulk, whereas LLTO(001) films only exhibit ~13 % Ti reduction. The differences in the extent of bulk Ti reduction are likely due to the ordering of La-rich and Li-rich planes either parallel or normal to the substrate c axis, the former provides a faster Li diffusion path into LLTO along the (100) direction. To confirm this, XRD scans were performed along film's surface normal and in-plane directions, and show that that the layer ordering was preserved in epitaxial LLTO thin films after reaction with Li. XRD L-scan along the out-of-plane direction showed that the majority of LLTO (001) films have the c-axis out of plane (c-domain), resulting in stronger half-order peak intensity associated with the ordering. In contrast, (100)-oriented films have much weaker half-order peaks in XRD L-scan, suggesting a minority c-domain component in (100) film. Similarly, for the XRD H-scan along the in-plane direction, the (100) films exhibit a stronger half-order peak signal than (001) films, suggesting that (100) films have a larger in-plane c-axis component than (001) films. In conclusion, XRD scans indicate that, as proposed above, it is easier for Li to diffuse into (100) oriented film, with ordered Li-rich planes along the surface normal. However, (001) films also have a minority in-plane c-axis component, allowing some amount of Li diffusion into the structure and explaining the small amount of bulk reduction observed in these films.

Effect of LLTO Crystallinity

Although LLTO exhibits orientation-dependent differences in bulk reactivity after short-term exposure to deposited Li thin films as shown above, long-term reaction (~3 days) with excess Li eventually results in identical bulk reduction behavior regardless of orientation (Figure II.8.E.3 a). XAS spectra collected for four different orientations of LLTO(hkl) films reveal a similar amount of Ti reduction ($\text{Ti}^{3+}/\text{Ti}^{4+}$) and lattice expansion for all four orientations, indicating that the orientation-dependent differences observed above are kinetic, rather than thermodynamic in origin. This stands in contrast to *amorphous* LLTO thin films, which surprisingly exhibit no evidence of surface reactivity after deposition of thin Li films (XPS, Figure II.8.E.3 b). Even more surprisingly, no reactivity is observed in the bulk (XAS, Figure II.8.E.3 c) even after 3 days of contact with excess Li. As the same LLTO PLD target was used to deposit amorphous and LLTO(hkl) films, we expect no significant differences in stoichiometry resulting in the observed differences in reactivity. As amorphous LLTO has previously been reported to have similar ionic conductivity to its crystalline counterpart ($\sim 10^{-5}$ S/cm), this suggests that amorphous materials may represent a promising path forward towards realizing conductive solid electrolytes with reduced interfacial reactivity.

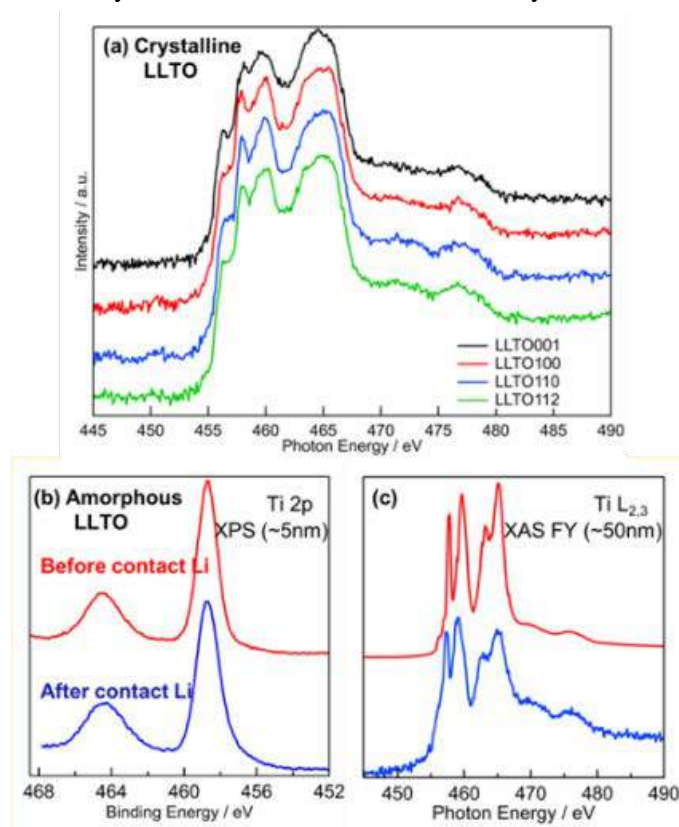


Figure II.8.E.3 Effect of LLTO Crystallinity on Reactivity with Metallic Li (a) XPS and (b) XAS spectra of amorphous LLTO film after contacting with Li metal. (c) XAS of crystalline LLTO films after reaction with Li

Li-LLTO *Ab Initio* Molecular Dynamics (AIMD)

Our calculations for $\text{Li}/\text{La}_{0.55}\text{Li}_{0.33}\text{TiO}_3$ interfaces performed using different terminations for three different interfaces $\text{Li}/(001)$ LLTO, $\text{Li}/(100)$ LLTO and $\text{Li}/\text{amorphous LLTO}$. The (001) and (100) orientations are distinguished by preferential layering of Li and La in LLTO parallel and perpendicular to the surface, respectively. Amorphous structure was prepared by equilibrating molten LLTO for 10 ps, then quenching it to melting temperature for 20 ps and quenching it further to 300K for 20 ps, all using NPT ensemble, and equilibrating for 10 ps using NVT ensemble. Atomic density distribution for all species with distance from the interface remained relatively unchanged during the simulations. For the $\text{Li}/(100)$ LLTO interface considerable Li exchange between the metallic Li and Li in LLTO was observed (Figure II.8.E.4) with Li ions hopping

across the interface and along Li-rich planes of LLTO. For the Li/(001) LLTO interface, there was no Li exchange between Li metal and LLTO at the simulation timescale. For the Li/amorphous LLTO interface, Li motion was localized within LLTO, despite higher volume per formula unit compared to the ordered LLTO. Our experimental results indicated that the crystalline LLTO orientation with La layers parallel to the interface with Li metal shows much less reactivity than the interface with La layers oriented normal to the interface. The AIMD simulations provide support for these observations by evidence of considerably faster Li ion diffusion along the Li-rich layers parallel to La layers in crystalline LLTO. The AIMD results on amorphous LLTO indicate no redistribution of atomic species or Li exchange in LLTO.

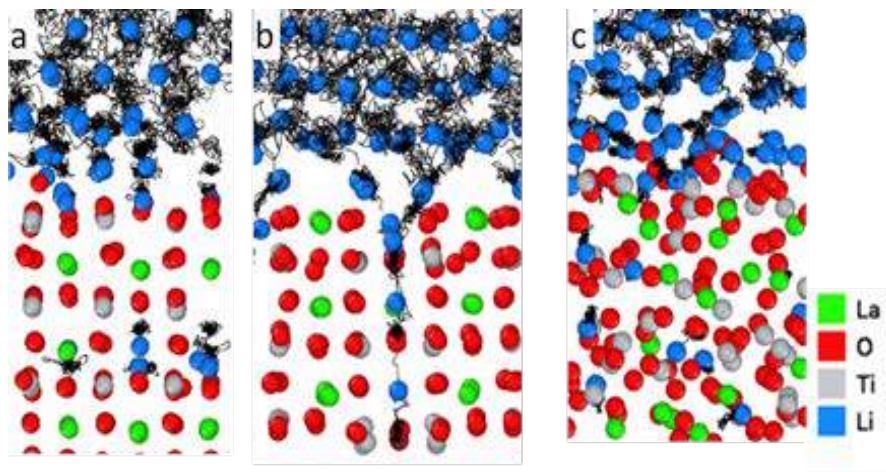


Figure II.8.E.4 Li-LLTO Ab Initio Molecular Dynamics: AIMD trajectories for (a) Li/LLTO (001) interface; (b) Li/LLTO (100) interface and (c) Li/amorphous LLTO interface. Initial atomic positions are shown with balls, and Li ion trajectories are shown with black lines

Conclusions

We continued our work on intrinsic stability of LLZO with different dopants in contact with metallic lithium and demonstrated that some degree of Zr reduction takes place for all three dopant types as well as significant reduction of Nb for Nb-doped LLZO. To determine whether the redox reaction is surface-limited, valence changes in the bulk were characterized and our results suggest that unlike Nb, the Al species are at least stable in the bulk (~50nm from surface) of LLZO and indicating that the reaction is surface-limited. Time-dependent chemical reactivity was investigated on the basis of charge transfer resistance obtained by electrochemical impedance spectroscopy. We examined cycling performance of the symmetric cells made of Al and Ta doped LLZO that were created via an interface design strategy, which leverages the combination of vacuum annealing of LLZO and vacuum deposition of Li metal to realize significant improvements in electrochemical performance. We are proposing that maximizing interface contact area with lithium metal will lead to a more homogeneous flux of lithium and the prevention of nucleation hot spots. LLZO pellets extracted from coin cells after extended cycling at high current density exhibit no discoloration related to dendrite formation, consistent with our previous observations of self-limiting surface reactions and stable interfacial behaviour of Al- and Ta-doped LLZO. Furthermore, X-ray absorption spectroscopy measurements give no indication of reduction in the bulk of the LLZO material, further confirming the stability of these materials to extended cycling at high current densities.

Continuing with our work on LLTO thin films, we have confirmed with XRD observed orientation-dependent differences in surface reactivity after short-term exposure to thin Li films. We demonstrated that long-term reaction (~3 days) with excess Li eventually results in identical bulk reduction behavior for crystalline LLTO regardless of orientation. XAS spectra collected for four different orientations of LLTO (hkl) films reveal a similar amount of Ti reduction ($\text{Ti}^{3+}/\text{Ti}^{4+}$) and lattice expansion in the bulk for all four orientations. This indicates that the orientation-dependent differences observed above are kinetic, rather than thermodynamic in

origin. This stands in contrast to amorphous LLTO thin films, which surprisingly exhibit no evidence of surface or bulk reactivity after deposition of Li thin films. The AIMD simulations indicate faster Li ion diffusion from interface of LLTO (100) surface with Li metal into the bulk crystalline LLTO along the Li-rich atomic planes compared to LLTO (001) surface with Li-rich planes normal to the interface. The Ab Initio Molecular Dynamics (AIMD) results on amorphous LLTO indicate no redistribution of atomic species or Li exchange between Li metal and LLTO demonstrating that Li motion was localized within LLTO, despite higher volume per formula unit compared to the ordered LLTO. Overall, AIMD simulations suggest that the observed reactivity of LLTO films towards Li metal correlates with feasibility of Li ion exchange in LLTO.

Key Publications

Patent:

1. Interface Design For High Current Density Cycling Of Solid State Battery Yisi Zhu, Sanja Tepavcevic, Justin Connell, Peter Zapol and Nenad Markovic, ANL Case #IN-19-084

Publications:

1. **Dopant-Dependent Stability of Garnet Solid Electrolyte Interfaces with Lithium Metal** Zhu, Y., Connell, J. G., Tepavcevic, S., Zapol, P., Garcia-Mendez, R., Taylor, N. J., Sakamoto, J., Ingram, B. J., Curtiss, L. A., Freeland, J. W., Fong, D. D., Markovic, N. M., *Adv. Energy Mater.* **2019**, 9, 1803440.
2. **Interface Design for High Current Density Cycling of Solid State Battery** S. Tepavcevic, Y. Zhu, J. G. Connell, P. Zapol, J. W. Freeland, D. D. Fong, J. Sakamoto, L. Curtiss, V. R. Stamenkovic and N. M. Markovic, in preparation (2019)
3. **Comparison of Chemical Reactivity of Amorphous LLTO to Epitaxial Films of Different Orientation towards Metallic Li Anode** Y. Zhu, S. Tepavcevic, P. Zapol, J. G. Connell, J. W. Freeland, D. D. Fong, L. A. Curtiss, and N. M. Markovic, in preparation (2019).

Acknowledgements

Zhu, Y., Connell, J. G., Tepavcevic, S., Zapol, P. are acknowledged for their contributions in carrying out work described in this report. Garcia-Mendez, R., Taylor, N. J., Sakamoto, J., Ingram, B. J., Freeland, J. W., Fong, D. D are acknowledged for their collaboration in this project.

II.8.F Self-Forming Thin Interphases and Electrodes Enabling 3-D Structures High Energy Density Batteries (Rutgers, The State University of New Jersey)

Glenn G. Amatucci, Principal Investigator

Rutgers, The State University of New Jersey
671 U.S. Highway 1
North Brunswick, NJ 08902
E-mail: gamatucc@soe.rutgers.edu

Tien Duong, DOE Technology Development Manager

U.S. Department of Energy
E-mail: Tien.Duong@ee.doe.gov

Start Date: October 1, 2016	End Date: September 30, 2019	
Project Funding (FY19): \$399,903	DOE share: \$334,334	Non-DOE share: \$65,569

Project Introduction

This project remains extremely relevant with the potential to bring a step change in energy density, cost, safety and high voltage scalability of battery technology compared to the current state of the art secondary battery technologies. The technology is based on an in situ formed solid-electrolyte battery leading to high energy metal fluoride vs. lithium metal chemistry in a planar battery electrode format and provides the following advantages: 1) enabling the use of lithium metal electrodes via solid-state electrolytes, 2) eliminating Li metal in fabrication and handling of cells, 3) providing the highest practical energy density electrochemical system, and 4) enabling a unique pathway to high voltage systems.

Objectives

The objective of this research was to establish a pathway to scalable fabrication of electrolytically formed high energy density fluoride-lithium batteries. Within the confines of the 2019 objectives addressed by this report our focus was to identify and address transport limitations which are unique to this novel system and lay the ground work for a viable and cost effective technology development.

Approach

The in situ self-formed battery enables the formation and implementation of high energy density Li/metal fluorides by simple polarization of a LiF-based bi-ion conducting glass between a positive and a negative reactive current collector. These solid state in situ batteries are fabricated with a maskless scalable patterning technique. The rationale is that such maskless scalable patterning technique offers a pathway to high throughput, low material loss and fabrication of complex architectures. The resulting solid state in situ cells have shown transport barriers in positive electrode that need to be addressed in order to optimize utilization and discharge rate and achieve our objectives.

Good electron and ion transport properties are critical throughout all levels of the solid-state electrochemical cells to achieve high performance and durability. It is especially true for self-formed batteries which rely on the interactions between the conducting glass electrolyte and the metal reactive current collectors to form the metal fluoride positive electrode and the lithium metal negative electrode separated by the electrolyte. Indeed, the quality of this initial formation will affect the performance of the cell upon subsequent cycling. As such, ionic and electronic transport and diffusion limitations, as described in Figure II.8.F.1, constitute major challenges that have been addressed systematically both in the single and 12 V cell configurations. Indeed, the ion transport limitations occurred due to the poor diffusion of the F^- ions in order to replace ions utilized at the electrode-electrolyte interface during the formation reaction between the conducting glass electrolyte and the reactive current collectors. This created barriers at the interface prohibiting further electrolyte reactions and capacity loss. In the case of electron transport, the outer shell of the current collectors formed the active

electrodes while the core remained the current collectors for the cell. As a result, the electron progression through the newly formed positive electrode active material from the current collectors will be more difficult due to the lower electronic conductivity of metal fluorides.

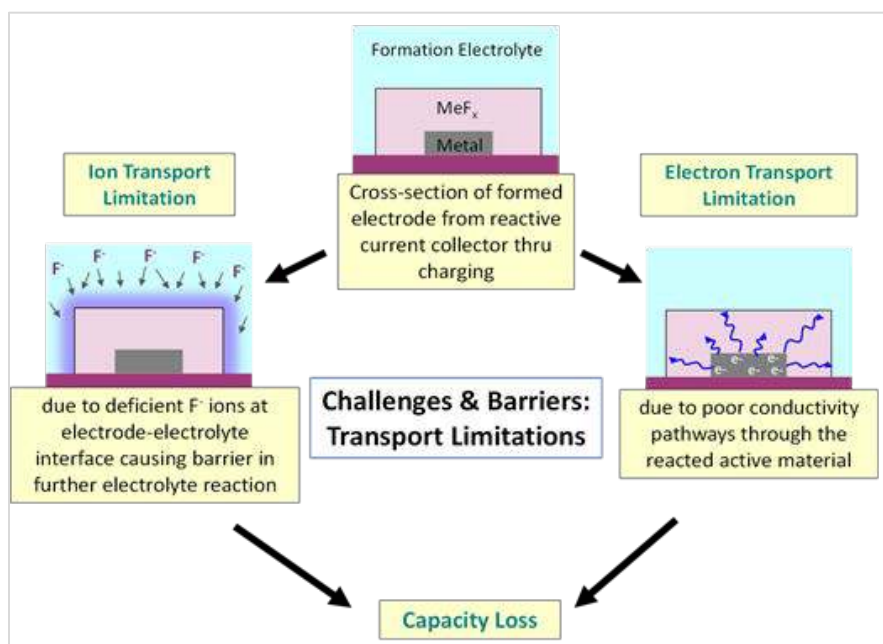


Figure II.8.F.1 Illustration of transport challenges, both ionic and electronic identified and addressed in this work

Figure II.8.F.2 illustrates the rationale for our research and development plan to address the ion and electron transport challenges and improve the self-formed battery system electrochemical performance. Electrodes of modified aspect ratio (Figure II.8.F.2B) provide electrodes of lower electrode width and height to increase the surface area in order to reduce diffusion distances and thereby improve transport compared to the standard design shown in Figure II.8.F.2A. In addition, excess electrolyte (Figure II.8.F.2C) to provide excess F^- and Li^+ ions for interactions with the reactive current collectors was used to ensure the formation reaction is not fluorine limited. Finally, cells comprised electrodes with modified aspect ratios, excess spacing and also shorter electrode spacing (Figure II.8.F.2D) to improve the diffusion within the electrolyte. All approaches are discussed herein.

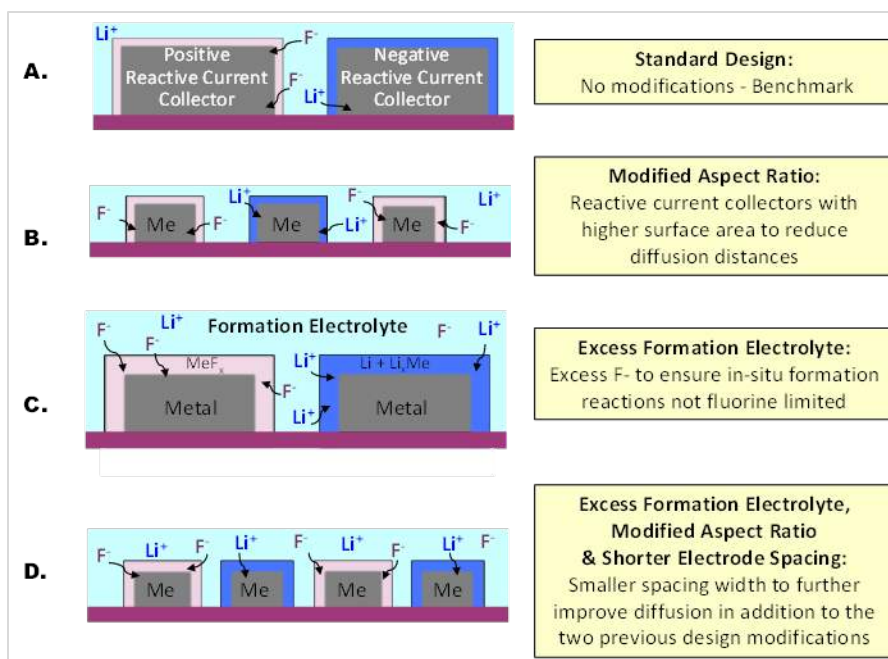


Figure II.8.F.2 Illustration of the transport challenges, both ionic and electronic identified and addressed in this work

Results

12 V Planar Cell Transport Improvements: Stepped cycling protocols to alleviate stress

Formation cycles with lower charge capacity cutoffs of 13% and 26% based on the theoretical capacity were utilized for the first and second cycles to limit or avoid mechanical stresses developed during phase transformations. Subsequent cycles were charged to a capacity cutoff of 52%, which was used as the targeted depth of reaction for all previous studies. These studies also utilized a modified electrode aspect ratio configuration (described in Figure II.8.F.2B). This cycling protocol is believed to produce progressive formation of the electrochemical cell which likely alleviates stresses induced by phase transformation. As such, the cycling stability of the 12 V planar cell increased from 1-2 cycles to > 8 cycles as shown in Figure II.8.F.3.

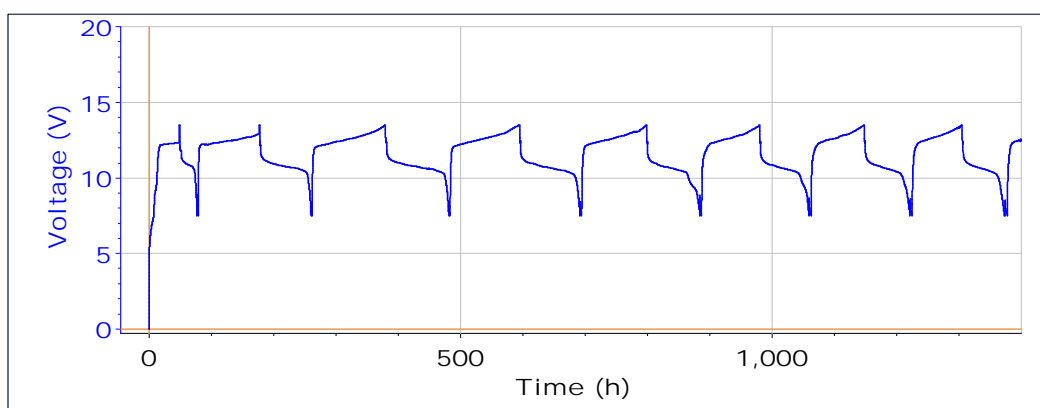


Figure II.8.F.3 Voltage profile of a 12 V cell architecture with a modified electrode aspect ratio. The cell cycled between 7.5 V and 13.5 V following a charge protocol with incremental capacity cutoffs of 13%, 26%, and 52% of the theoretical capacity in the first 3 cycles and maintaining its maximum cutoff after the 3rd cycle

12 V Planar Cell Transport Improvements: Electrolyte additives

Electronic conductive additives were incorporated to the conducting glass electrolyte in order to further improve conductivity and promote more interactions between the electrolyte and reactive current collectors. Such electrolyte additives were evaluated in 12 V planar cells with electrodes of modified aspect ratio design (Figure II.8.F.2B) using the stepped cycling protocol. The electrolyte additives revealed performance advancements by 30% in capacity and 10% in utilization as shown in Figure II.8.F.4.

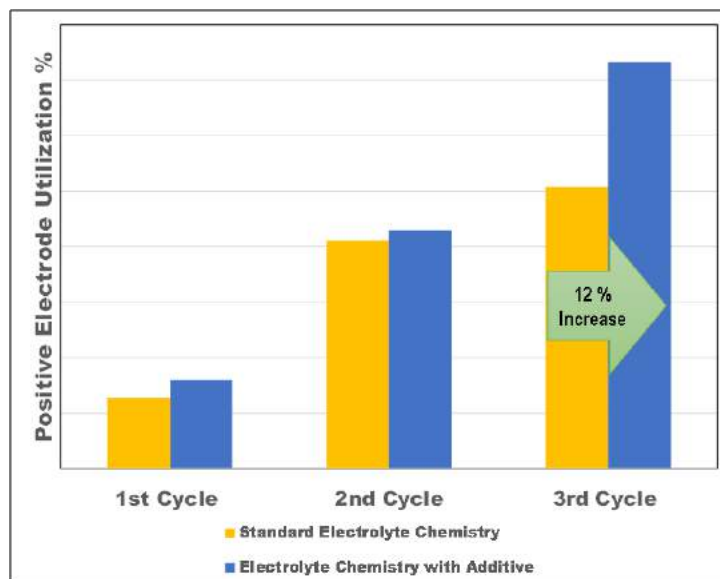


Figure II.8.F.4 Impact of electrolyte additive on the utilization of the positive electrode for 12 V self-formed cells cycled between 7.5 and 13.5 V. The cells were charged at constant voltage with incremental capacity cutoffs of 13%, 26%, and 52% of the theoretical capacity in the first 3 cycles showing that when the capacity limitation is lifted, the solid state electrolyte additive improves the performance appreciatively

12 V Planar Cell Transport Improvements: Cell design modifications to the electrode and spacing widths

Two pathways were undertaken to shorten the diffusion length to improve transport properties and increase electrochemical performance of 12 V planar cells. Electrode width was further reduced to promote accessibility of active material within the positive electrode as described in Figure II.8.F.2B. However, electrochemical properties were either equal or less favorable than those based on standard electrode widths. Such results implied the thinner electrode mechanical integrity may be approaching its limit with the current fabrication process. In the second approach, spacing between the electrodes was reduced to decrease diffusion length of reactive electrolyte as described in Figure II.8.F.2D. These adjustments did not improve performance most likely due to engineering challenges regarding morphology of the electrode structure in conjunction with the complexity of the 12 V planar design. However, research from a previous project revealed close to 100% positive utilization with 70% less spacing between the electrodes. As such, we focused on cell designs based on further lowering electrode spacing.

Optimized cell orientation and cell design for the 12 V planar and single cell configurations

As mentioned above, the cell structure and design dimensions were reassessed to utilize simple and shorter pathways to increase the formation electrolyte's ion diffusion and transport. For the 12 V planar cell configuration, we studied the effects of increasing the electrolyte reserve capacity with reduced electrode spacing and modified aspect ratio (Figure II.8.F.2D). Electrode spacing was reduced from 90 microns in our standard design to 60 microns in our advanced design. Additionally, a modified aspect ratio 4 times smaller than the standard was applied to increase accessible positive reactive electrode material. Figure II.8.F.5 compares the positive electrode utilization and the electrode pairs' energy densities of the advanced 12 V cell design in comparison with earlier designs. The thicker electrolyte and shorter electrode spacing had a positive outcome resulting in the best performance achieved with the 12 V planar cell configuration at 44% positive

electrode utilization and 1059 Wh/L for the energy density based on the electrode pair. Driving the electrode spacing to even smaller dimensions may further improve the cell performance but that is beyond the capabilities of our fabrication equipment.

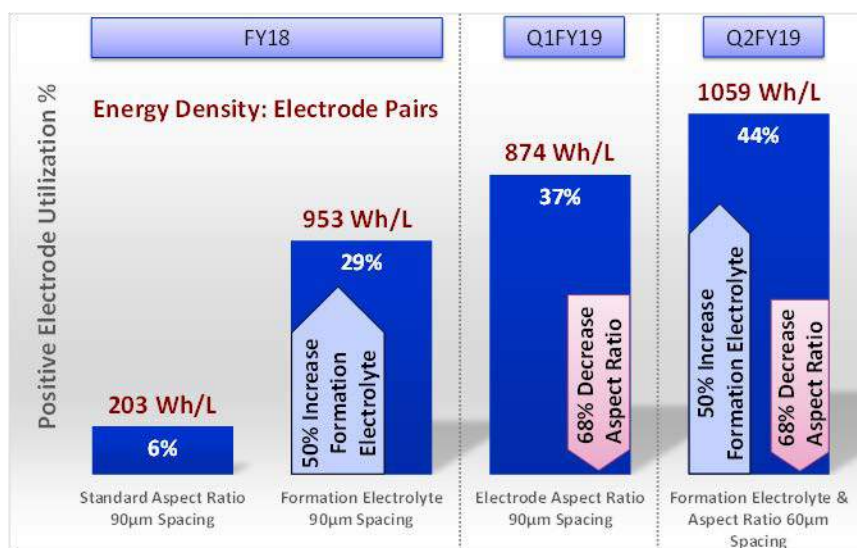


Figure II.8.F.5 Comparison of the positive electrode utilization and electrode pairs' energy density for the 12 V cell configuration with variations on the cell design. The variations that were tested include electrode aspect ratio, electrolyte thickness, and electrode spacing

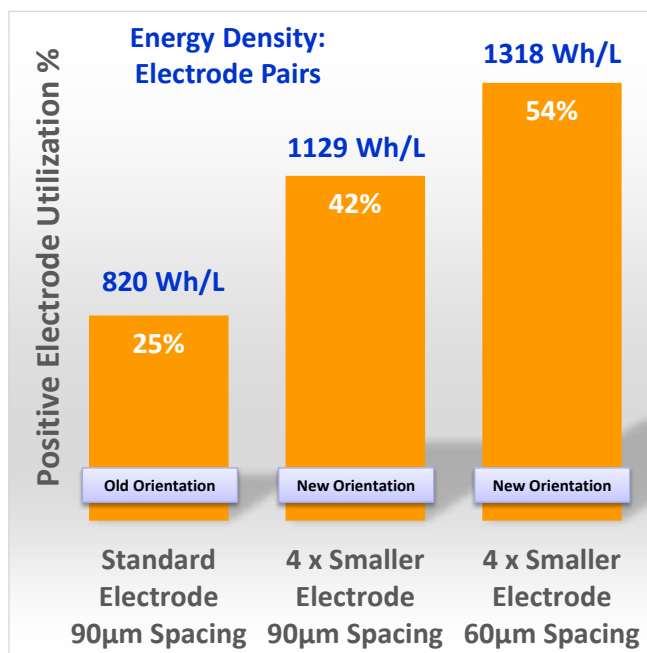


Figure II.8.F.6 Comparison of the positive electrode utilization and electrode pairs' energy densities for the single cell configuration with variations in cell design. Variations include orientation, electrode aspect ratio and electrode spacing

To better understand the effects of cell design on performance, we returned to our single cell configuration for the remainder of our effort to eliminate cell complexity associated with the 12 V design as a factor on cycling performance. In the single cell configuration, the orientation of the cell architecture was reengineered to match similar design features of the 12 V planar cell. The electrode spacing and electrode aspect ratio were also

decreased similarly to the 12 V planar cell. Figure II.8.F.6 compares results of such evaluation. In comparison to the original design, the smaller aspect ratio, 60 micron electrode spacing and new orientation design yielded some of our single best results with 54% positive electrode utilization and 1318 Wh/L energy density based on electrode pairs. These results provided an improvement of approximately 116 % in utilization and about 60 % in energy density from our standard original design. This cell design optimization demonstrated that the aspect ratio and/or the cell orientation have the largest effect on the cell performance. Shorter electrode spacing is also a critical design parameter to achieve good cell performance. Further reduction of electrode spacing may promote additional advances in cell performance, however these are beyond our current fabrication equipment capabilities.

Single cell configuration transport improvements: Localized lithium enrichment to improve formation efficiency

The optimized cell design for the single cell configuration was combined with varying quantities of localized Li^+ ion enrichment, non-inclusive of the F^- ions typically found in the formation electrolyte. This enrichment process is believed to provide the necessary access to Li^+ ions without the complexity of other interactions from the formation electrolyte. Three Li-contents have been evaluated: a standard Li^+ enrichment composition, and 1.8x and 3.3x the standard Li^+ enrichment amount. Results using single cell configurations cycled from 1.5 to 3.5 V are shown in Figure II.8.F.7. The standard Li^+ ion dopant had an advantageous outcome for the first cycle, reaching the highest achieved positive electrode utilization for the single cell design at 89%. In contrast, further enrichment at 1.8x and 3.3x the standard composition had detrimental impact on the positive electrode utilization and performance. Physical review of each cell revealed that adding excessive Li^+ ion enrichment structurally compromised the mechanical integrity of the cell by loss of adhesion. As such, the impact of increased lithium salt concentration may be masked by a mechanical component of failure.

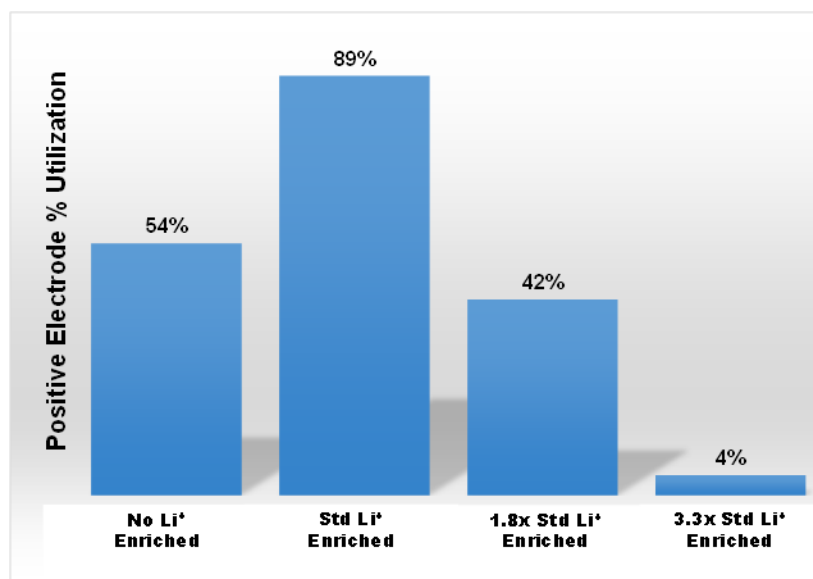


Figure II.8.F.7 Positive electrode utilization (%) for single cell configurations with different lithium ion dopant quantities, in the first cycle. The cells were cycled between 1.5 V and 3.5 V

Single cell configuration transport improvements: Nanolayered multicomponent electrode compositions with optimized cell design

To improve the accessibility of the active material and address both the Li^+ and F^- ion limitation, the optimized cell design with the nanolayered electrode composition was compared with the standard as seen in Figure II.8.F.8. The positive electrode utilization was increased to 82% from 54%. In addition, irreversible losses were improved achieving second cycle positive electrode utilization of 69%. It was concluded that the nanolayered multicomponent electrode structurally provided more pathways for access to F^- ions and maintained conductivity pathways but were deficient in Li^+ ions as the Li^+ to F^- ratio was kept at a constant.

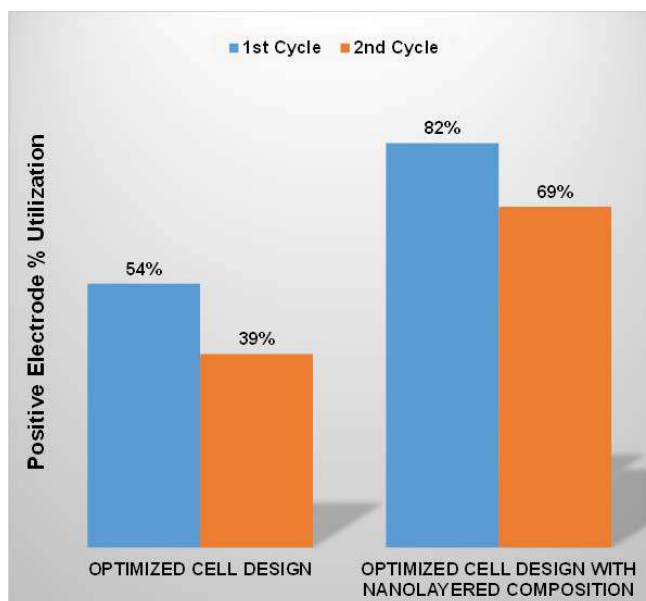


Figure II.8.F.8 Positive electrode utilization (%) of optimized single cell designs, without and with nanolayered multicomponent electrodes in the first two cycles. Cells were cycled between 1.5 V and 3.5 V

Single cell configuration transport improvements: Hybrid electrolytes to promote ion transport capabilities

The hybrid electrolyte comprised of our standard solid state electrolyte and a controlled amount of ionic liquid applied to the surface prior to cell formation. Four different hybrid electrolyte compositions were evaluated with the optimized cell orientation and modified aspect ratio for the single cell configuration. Figure II.8.F.9 compares the positive electrode utilization results obtained with the hybrid electrolytes versus the standard solid electrolyte cell composition for the 90 micron electrode spacing. The interactions of hybrid electrolytes A and B had neutral effects without prominent change in electrode utilization in comparison to the standard solid electrolyte. Hybrid electrolyte chemistries C and D both provided significant gains in the positive electrode utilization increasing to 68% and 85% respectively. It was concluded that these chemistry compositions provided the best interactions to promote F^- and Li^+ ion mobility leading to higher active material conversion and reaction.

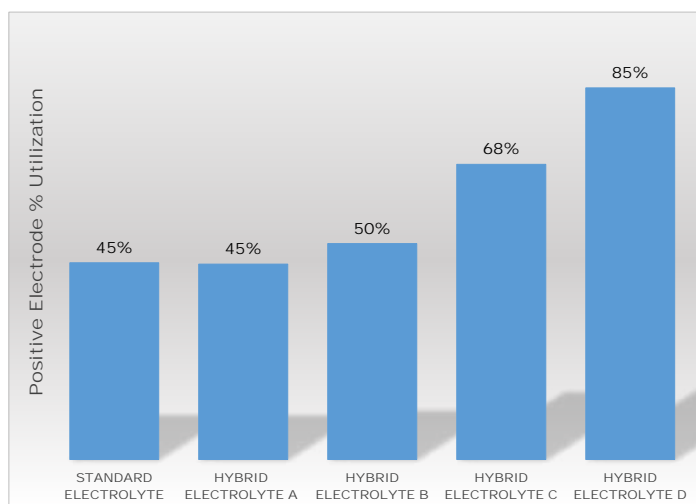


Figure II.8.F.9 Positive electrode utilization (%) for the first cycle of single cell configurations with 90 micron spacing and different hybrid electrolyte compositions. The cells were cycled between 1.5 V and 3.5 V

Single cell configuration transport improvements: Controlled cycling charge depth

In a final attempt to analyze the cycling stability of the cell configurations with combined transport improvement methods, cells were cycled with three different charge capacity cutoffs. The cell configuration combined the standard lithium enrichment and optimized cell design with the multicomponent nanolayered electrode structure. All cells were cycled from 1.5 to 3.5 V. Three cycling protocols were investigated: 1) 75% charge capacity cutoff based on the theoretical capacity, for all cycles, 2) 75% cutoff for the first cycle only, 25% charge cutoff for all subsequent cycles, and 3) 25% charge capacity cutoff, for all cycles. Figure II.8.F.10 depicts the efficiency of the first four cycles for each protocol. The best results occurred when the cells were charged up to 75% upfront followed by shallower cycling. This may be due to the higher charge capacity allowing deeper access to active material for formation of the electrode, but then confining cycling to this material at the lower capacities. Cycling with a charge capacity cutoff at 75% theoretical for all cycles induces deteriorating cycling ability due to decreasing transport and diffusion properties limiting accessible active material. Cycling with a capacity cutoff at 25% theoretical for all cycles had mediocre efficiencies because not enough active material was accessed initially to maintain prolonged cycling.

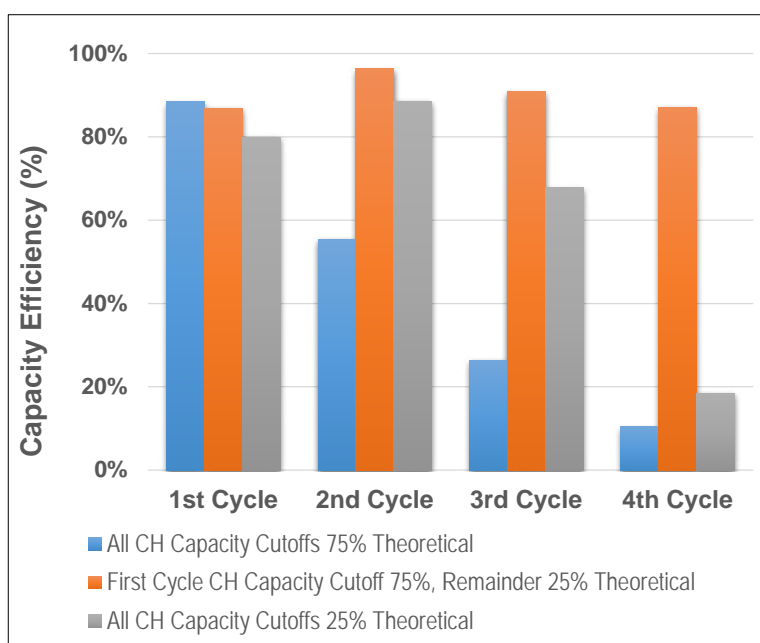


Figure II.8.F.10 Cycling efficiency (%) comparison for the first four cycles of single cell configurations with lithium enrichment, nanolayered electrode composition, and the optimized cell design. The charge capacity cutoffs were varied. The cells were cycled between 1.5 V and 3.5 V

In summary, it would be worthwhile to use the higher capacity cutoff simply as a formation step and combine the cell configuration with smaller electrode spacings but those investigations are beyond our current capabilities.

Conclusions

Several avenues have been investigated to promote advancements in cell performance for our unique high energy density self-forming battery system. The biggest challenges of this project were overcoming the transport and diffusion barriers that presently suppress solid state batteries from surpassing currently used technology. The 12 V planar configuration achieved 44% positive electrode utilization and 1049 Wh/L energy density based on electrode pairs by increasing the electrolyte thickness and developing an optimized cell design with better accessible active material. Further investigations with the single cell configuration allowed us to establish positive electrode utilizations in the range of 82-89% and 1318 Wh/L for the pairs. The highest achieved utilization resulted from lithium enrichment with the optimized cell design. Controlling the depth of

charge after initial formation was identified as beneficial for prolonged discharge capacity efficiency. Ultimately, the development of this self-forming battery system holds great potential but requires improved equipment capable of reaching finer degrees of resolution and precision to properly push the limits of this technology, both in energy density and cycle life.

II.8.G U.S.-German Co-operation: Lillint (ANL)

Chi Cheung Su, Principal Investigator

Argonne National Laboratory
9700 S Cass Avenue
Lemont, IL 60439
Email: csu@anl.gov

Khalil Amine, Principal Investigator

Argonne National Laboratory
9700 S Cass Avenue
Lemont, IL 60439
Email: kamine@anl.gov

Tien Duong, DOE Technology Development Manager

U.S. Department of Energy
E-mail: Tien.Duong@ee.doe.gov

Start Date: July 1, 2019

Project Funding (FY19): \$370,000

End Date: September 30, 2019

DOE share: \$370,000

Non-DOE share: \$0

Project Introduction

Owing to the exceptionally low electrochemical potential and extremely high specific capacity of lithium metal anode, lithium metal batteries (LMBs) have received tremendous attention recently. [1],[2],[3] However, the successful commercial application of LMBs is still impeded by severe safety problems originated from the instability of the interface between lithium metal and electrolyte. [4],[5] As a result, it is crucial to develop a reliable electrolyte system in order to realize the operation of LMBs. Since solvent solvation heavily influences the electrochemistry of an electrolyte system, it is essential to understand the lithium solvating ability of each individual solvent in designing useful functional electrolyte system. [6],[7] The change in the solvation state of electrolyte solvents can not only alter the redox potential of the electrolyte system, but also reshape the electrode-electrolyte interfacial reaction pathway, leading to the formation of very different solid-electrolyte interfaces (SEI). [8],[9]

In this project, we are going to perform in-depth solvation study about the electrolyte systems used by LMBs. Vibrational spectroscopy such as FTIR and Raman will be coupled with novel internally referenced diffusion-ordered spectroscopy (IR-DOSY) NMR technique to reveal the details of the solvation status of individual component in an electrolyte system. The correlation of SEI chemistry and the electrolyte chemistry will be investigated and unveiled. Furthermore, study will be carried out to understand the relationship between the SEI chemistry and the lithium plating morphology.

Objectives

To understand the role of lithium metal-liquid electrolyte interface from the electrolyte chemistry perspective, we propose the following aspects:

1. Reveal the connection between the solvation status of organic solvents/additives/salts and the SEI chemistry on lithium metal anode.
2. Understand the mechanism of the SEI layer growth and reformation tracing back to the subtle molecular structure of organic electrolyte components.
3. Correlate the SEI chemistry and the growth morphology of Li deposits.

4. Carry out theoretical quantum chemistry simulation to reveal the different decomposition pathways in various solvation statuses of the electrolyte solvents.

This project is focused on establishing a fundamental understanding of the mechanism behind the stabilization of lithium metal anode by liquid electrolytes, which can surely enable the rational design of reliable electrolyte system.

Approach

Our approach to meet the objectives is to use our newly developed internally referenced diffusion-ordered spectroscopy (DOSY) technique to characterize the detailed solvation status of individual components in various electrolytes. A combination of experimental techniques such as vibrational spectroscopy (Raman & FTIR) and surface-sensitive spectroscopy (XPS & TEM), as well as advanced computational techniques such as density functional theory calculation and molecular dynamics simulation that are available to the U.S.-German team members, will be deployed to decode the correlation between the solvation state of electrolyte components and the SEI chemistry.

Conventional electrolyte (1.2M LiPF₆ in EC/EMC) with vinylene carbonate (VC) additive was selected as our baseline electrolyte due to its high popularity in lithium-ion batteries. The addition of VC significantly improves the stability of the lithium metal-liquid electrolyte interface. The evolution of SEI will be monitored by various spectroscopic techniques such as in situ SEM and EIS, while the chemical composition of SEI will be analyzed by FTIR, NMR, EDX and XPS. The solvation status of individual component in the electrolyte will be revealed by novel internally referenced DOSY NMR technique. Extensive research on the connection between the solvation statuses of electrolyte components and the chemical composition of SEI on lithium metal will be carried out.

Collaborators include Jeff Lopez (MIT), Yang Shao-Horn (MIT), Perla Balbuena (TAMU), Simon Wiemers-Meyer (MEET) and Stefano Passerini (KIT) and Rachid Amine (ANL).

Results

Preparation of review articles contributed by U.S.-German team members

Two review papers focusing on 1. The composition of SEI on lithium metal anode and its function & 2. The morphology of lithium metal anode upon cycling, will be written by our U.S.-German team members.

Solvation study of additives vinylene carbonate (VC) and vinyl ethylene carbonate (VEC) by IR-DOSY

The values of relative solvating power (χ) of VC and VEC were determined by internally referenced diffusion-ordered spectroscopy and diffusion coefficient-coordination ratio (D- α) analysis. [9] Relative solvating power (χ) is defined as the ratio between the coordination percentage of a test solvent (α) and the coordination percentage of a reference solvent (α_0). Electrolyte solvent with large value of relative solvating power has a higher tendency to coordinate with lithium cation.

Due to the distinctive separation of proton resonance peaks, IR-DOSY offers an effective way to determine the solvation state of electrolyte solvents. [10] Toluene was added as an internal reference into the VC:EMC 1:1 and LiPF₆:VC:EMC 1:4:4 (molar ratio) solution because of its non-coordinating nature. [10] As depicted in Figure II.8.G.1a, VC and EMC diffuses at a very similar rate before the addition of LiPF₆ salt. However, the diffusion coefficient of EMC decreases significantly after the addition of LiPF₆ and is smaller than that of VC, as illustrated in Figure II.8.G.1b, implying that EMC has a higher affinity toward lithium cations than VC. Table II.8.G.1 summarizes the coordination ratio (α) of EMC and VC in the LiPF₆:VC:EMC 1:4:4 solution and the ratio of diffusion coefficients of toluene, VC and EMC before and after the addition of LiPF₆. The relative solvating power of VC is calculated to be 0.49, which is similar to the χ value of FEC (0.63). The low lithium solvating ability of VC is originated from the conjugation of C=C bond to the carbonate group within the cyclic ring. Such conjugation lowers the electron density of the lone pair on the oxygen atom of the carbonyl group, resulting in the decrease of the solvating ability of VC. On the contrary, the relative solvating power of

VEC (1.28), a cyclic carbonate with vinyl side chain attached, is significantly higher than that of EMC. Figure II.8.G.1c and Figure II.8.G.1d displays respectively the ^1H DOSY-NMR spectra of VEC:EMC 1:1 and LiPF_6 :VEC:EMC 1:4:4 solution. The ratio of diffusion coefficients of VEC before and after the addition of LiPF_6 is larger than the ratio of EMC as depicted in Table II.8.G.2, suggesting that higher percentage of VEC was solvating the lithium cations. Since the $\text{C}=\text{C}$ bond of VEC is not conjugated to the carbonate group, it has little effect on the electron density of the lone pair on the oxygen atom of the carbonyl group. Thus, the relative solvating power of VEC is similar to that of EC.

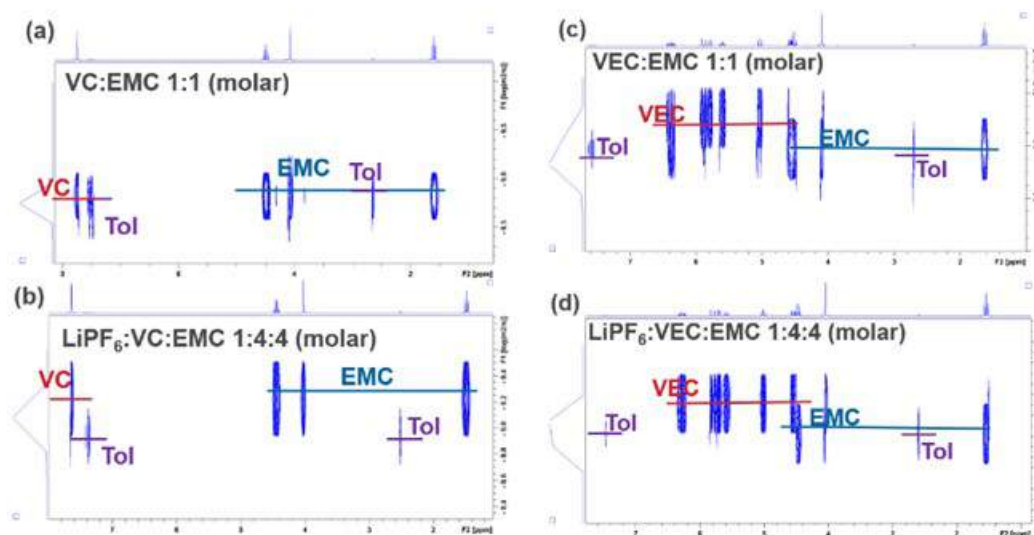


Figure II.8.G.1 ^1H DOSY-NMR spectra of (a) 1:1 VC:EMC, (b) 1:4:4 LiPF_6 :VC:EMC, (c) 1:1 VEC:EMC and (d) 1:4:4 LiPF_6 :VEC:EMC with toluene added as an internal reference

Table II.8.G.1 Coordination Ratio α and the Ratio of Diffusion Coefficients of Toluene, VC and EMC Before and After the Addition of LiPF_6

Compound	Coordination ratio α	$D_{\text{unsalted}}/D_{\text{salted}}$
Toluene	N/A	2.48
EMC	0.55	3.65
VC	0.27	2.95

Table II.8.G.2 Coordination Ratio α and the Ratio of Diffusion Coefficients of Toluene, VEC and EMC Before and After the Addition of LiPF_6

Compound	Coordination ratio α	$D_{\text{unsalted}}/D_{\text{salted}}$
Toluene	N/A	2.78
EMC	0.40	3.77
VEC	0.51	3.99

Li/Li symmetric cell of VC and VEC as electrolyte additives

The Li/Li symmetric cell was used to evaluate the plating/stripping stability of the Li metal anode when 2 weight percentage of VC or VEC was added to conventional Gen2 electrolyte (1.2M LiPF_6 in EC/EMC 3/7 weight ratio) as the electrolyte additive. A current density of 2 mA cm^{-2} was used to cycle the cell. As

illustrated in Figure II.8.G.2, the cell cycled in the Gen2 electrolyte with 2% VC additive shows a random voltage fluctuation and high voltage polarization, indicating the growth of the lithium dendrite. In the meantime, the cell cycled in the Gen2 electrolyte with 2% VEC additive displays good cycling stability, suggesting reversible plating-stripping of Li^+ on the lithium metal electrode. Compared to VC in Gen2 electrolyte, a significantly higher amount of VEC is coordinated with the lithium cations in the VEC in Gen2 electrolyte due to its high relative solvating power. Since lithium-coordinated solvent molecule is preferentially reduced on the lithium metal anode, less VC was reduced on the lithium metal anode compared to VEC, when VC or VEC was added to Gen2 electrolyte with the same weight %. Therefore, the VEC in Gen2 electrolyte demonstrated enhanced cycling stability in the Li/Li symmetric cell test.

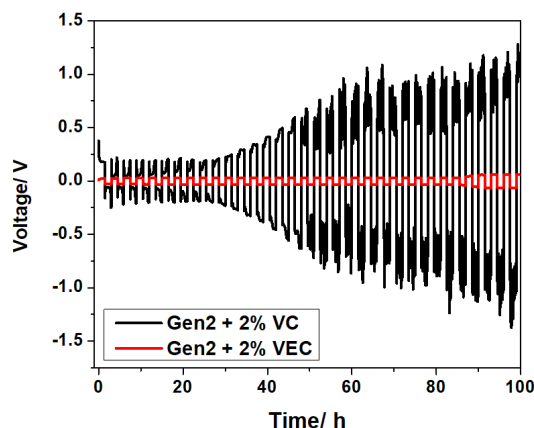


Figure II.8.G.2 Voltage profiles for Li/Li symmetric cells cycled at 2 mA cm^{-2} with Gen2 with 2% VC and Gen2 with 2% VEC electrolytes

Conclusions

The novel IR-DOSY technique was demonstrated to be highly effective in determining the solvation status of individual electrolyte components. Despite the structural similarity between VC and VEC, there is a distinctive difference in lithium solvating ability between the two compounds. The relative solvating power of VC is 0.49, which is significantly lower than that of VEC (1.28). The conjugation of the C=C double bond with the carbonate group in VC largely reduces electron density of the electron lone pairs on the oxygen atom of the carbonyl group, leading to a remarkable decrease of lithium solvating ability of VC. As a result, when VC is used as an electrolyte additive, the amount of coordinated VC in Gen2 electrolyte is relatively small compared to that of VEC. Since lithium-coordinated solvent molecule is preferentially reduced on the lithium metal anode, less VC was reduced on the lithium metal anode compared to VEC, when VC or VEC was added to Gen2 electrolyte with the same weight %. These results clearly demonstrate the importance of the solvation status of electrolyte components during the formation of SEI layer and how the solvation state of electrolyte solvent alters the SEI composition.

Future research will be focusing on the establishment of the connection between the solvation state of electrolyte components and the SEI chemistry on the lithium metal. Meanwhile, we are going to collaborate with other U.S.-German team members in using advanced computational techniques to provide information about a series of solvents able to easily form high quality SEI on lithium metal and the reaction pathway of the SEI formation.

References

1. Xu, W.; Wang, J.; Ding, F.; Chen, X.; Nasybulin, E.; Zhang, Y.; Zhang, J.-G., Lithium Metal Anodes for Rechargeable Batteries. *Energy Environ. Sci.* **2014**, 7 (2), 513–537.

2. Li, X.; Zheng, J.; Engelhard, M. H.; Mei, D.; Li, Q.; Jiao, S.; Liu, N.; Zhao, W.; Zhang, J. G.; Xu, W., Effects of Imide-Orthoborate Dual-Salt Mixtures in Organic Carbonate Electrolytes on the Stability of Lithium Metal Batteries. *ACS Applied Materials & Interfaces* **2018**, *10* (3), 2469–2479.
3. Chen, S.; Zheng, J.; Mei, D.; Han, K. S.; Engelhard, M. H.; Zhao, W.; Xu, W.; Liu, J.; Zhang, J. G., High-Voltage Lithium-Metal Batteries Enabled by Localized High-Concentration Electrolytes. *Advanced Materials* **2018**, *30* (21), e1706102.
4. Zheng, J.; Yan, P.; Mei, D.; Engelhard, M. H.; Cartmell, S. S.; Polzin, B. J.; Wang, C.; Zhang, J.-G.; Xu, W. Highly Stable Operation of Lithium Metal Batteries Enabled by the Formation of a Transient High-Concentration Electrolyte Layer. *Advan. Ener. Mater.* **2016**, *6* (8), 1502151.
5. Qian, J.; Xu, W.; Bhattacharya, P.; Engelhard, M.; Henderson, W. A.; Zhang, Y.; Zhang, J.-G. Dendrite-Free Li Deposition Using Trace-Amounts of Water as an Electrolyte Additive. *Nano Energy* **2015**, *15*, 135–144.
6. Xing, L.; Zheng, X.; Schroeder, M.; Alvarado, J.; von Wald Cresce, A.; Xu, K.; Li, Q.; Li, W., Deciphering the Ethylene Carbonate-Propylene Carbonate Mystery in Li-Ion Batteries. *Accounts of Chemical Research* **2018**, *51* (2), 282–289.
7. Chapman, N.; Borodin, O.; Yoon, T.; Nguyen, C. C.; Lucht, B. L. Spectroscopic and Density Functional Theory Characterization of Common Lithium Salt Solvates in Carbonate Electrolytes for Lithium Batteries. *J. Phys. Chem. C* **2017**, *121* (4), 2135–2148.
8. Su, C.-C.; He, M.; Amine, R.; Chen, Z.; Sahore, R.; Dietz Rago, N.; Amine, K., Cyclic carbonate for highly stable cycling of high voltage lithium metal batteries. *Energy Storage Materials*. **2019**, *17*, 284-292.
9. Su, C.-C.; He, M.; Amine, R.; Rojas, T.; Cheng, L.; Ngo, A. T.; Amine, K., Solvating power series of electrolyte solvents for lithium batteries. *Energy & Environmental Science* **2019**, *12* (4), 1249-1254.
10. Su, C. C.; He, M.; Amine, R.; Chen, Z.; Amine, K., Internally Referenced DOSY-NMR: A Novel Analytical Method in Revealing the Solution Structure of Lithium-Ion Battery Electrolytes. *J. Phys. Chem. Letters* **2018**, *9* (13), 3714–3719.

Acknowledgements

The following individuals' contribution to this project is gratefully acknowledged: Rachid Amine (ANL), Jiayan Shi (ANL), Jeff Lopez (MIT), and Simon Wiemers-Meyer (MEET).

II.8.H U.S.-German Co-operation: CatSE (ANL)

Larry Curtiss, Principal Investigator

Argonne National Laboratory
9700 S Cass Avenue
Argonne, IL 60516
Email: curtiss@anl.gov

Tien Duong, DOE Technology Development Manager

U.S. Department of Energy
E-mail: Tien.Duong@ee.doe.gov

Start Date: August 1, 2019
Project Funding: \$600,000

End Date: September 30, 2021
DOE share: \$600,000

Non-DOE share: \$0

Project Introduction

Solid-state batteries (SSBs) are regarded as promising candidates to increase safety, cycle life, energy and power density compared with conventional liquid electrolyte based Li ion batteries. However, achieving these targets still poses significant challenges especially at the interfaces of electrodes and electrolyte. While in the beginning the low Li-ion conductivities of the solid electrolytes were considered as a bottleneck for the development of SSBs, the continuous material optimization lead to competitive solid electrolyte materials that can nowadays compete with their liquid analogs. Solid-state oxide electrolytes offer high chemical stabilities with wide electrochemical potential windows enabling use of high voltage cathode materials and lithium metal anodes, which may drastically increase the energy density of the SSBs.

Therefore, assuring a stable interface between the solid electrolyte and active electrode material with good ionic transport is considered as one of the major remaining challenges in the realization of practical SSBs. Synthesis and processing of SSB materials at high temperatures, up to 1000°C, results in possible ion diffusion at the interface and the formation of possible interphases that could raise interfacial resistance.

For example, previous combined experimental and DFT studies [2] revealed that a combination of LLZO and with high voltage spinel cathode materials ($\text{Li}_2\text{NiMn}_3\text{O}_8$, $\text{Li}_2\text{FeMn}_3\text{O}_8$, LiCoMnO_4) will react and form interphases at temperatures below 600°C. Similarly, LiCoO_2 (LCO) cathode material [4],[5] was reported to react with LLZO above 700°C in air resulting in new phases such as La_2CoO_4 and/or LaCoO_3 . The formation of interphases at the interfaces between LLZO and cathode materials could lead to large increases in the charge-transfer resistance across the interface and reduce the overall cell performance. By investigating properties of cathode- solid state electrolyte interfaces using computational methods in close connection with experimental studies, this U.S.-German project aims to mitigate the effects of chemical reactivity at the interface on stability of the interface and conductivity across the interface.

Objectives

The main goal of this joint U.S.-German project is to understand the fundamental properties of the interface between a solid ceramic ionic conductor (exemplified by a LLZO) and a solid cathode in order to enable the development of ceramic lithium cell with minimized total resistance, high total capacity and high power performance. LMNO cathodes will be used, which are isostructural to the LLZO electrolyte. In addition LCO will serve as reference for the class of the layered oxide materials. The project aims at investigating the fundamental properties of “ideal” LLZO/cathode interfaces to understand how the compositional, structural, and potential gradients at and across the interface impact its stability and charge transfer/transport mechanisms. The specific questions we are going to address in this joint U.S.-German project is how does the solid-solid interface evolve during charge/discharge cycling, how does it impact the cycling stability and how can electro-chemo-mechanical changes be accommodated to achieve the stable cycling performance. This will be

addressed both experimentally and theoretically. This project is focused on developing a fundamental understanding of these contributions to enable rational design of stable solid/solid interfaces with minimized impedance. Investigation of solid-solid interfaces is complicated by the multiple types of interfaces (both surface and buried, such as grain boundaries and heterojunctions), materials (crystalline and amorphous inorganic solids as well as polymers), phenomena (chemical, electrochemical and mechanical) as well as time and length scales of the processes involved.

Approach

Computational modeling combined with experimental studies are an important avenue for investigating interfacial phenomena and resulting performance limitations in SSBs. In this U.S.-German project we will use computational approaches for modeling SSBs that complement characterization studies in the U.S.-German collaboration. In the field of atomistic modeling, density functional theory (DFT) calculations, molecular dynamics and kinetic Monte Carlo calculations will be applied to predict thermodynamic stability of doped LLZO materials and investigate interfacial transport properties for comparison with experiment. For example, previous computational studies have addressed Li transport in LLZO grain boundaries, site preference and defect energies for possible dopants in bulk LLZO, and thermodynamic stability of cathode/electrolyte interfaces. [\[1\]](#), [\[2\]](#), [\[3\]](#) Effects of interfacial orientations, inhomogeneous dopant concentrations, and protective layers on transport across interfaces and material stability are still investigated in combination with experimental studies.

Results

This U.S.-German Co-op is a new project, which was just initiated. A U.S.-German workshop was held in July 2019 to plan specific systems for investigations. As a model cathode material, LMNO was chosen due to its structural similarity to the substrate material LLZO. In addition, LCO will serve as a reference cathode system for the class of the layered oxides, in order to be consistent with other thrusts in the U.S.-German collaboration, which have their focus on layered cathode materials with different fractions of transition metal cations (Co, Mn and Ni). The layered reference provides important insight into the structural compatibility of isostructural and non-isostructural combinations. The collaboration will include studies of solid state electrolytes with layered cathode materials with different fractions of transition metal cations (Co, Mn and Ni).

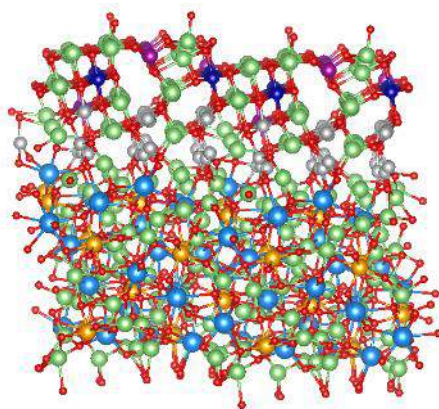


Figure II.8.H.1 Structure of LLZO (001) and NMC (10 –14) interface that is calculated using density functional theory.

The project is using a combination of complementary experimental, analytical and computational techniques available to the U.S.-German team members who have unique and complementary experimental and theoretical expertise. As part of the project we will use computational studies of interfaces using density functional theory, and ab initio and classical molecular dynamics to investigate chemical reactivity and charge transfer at interfaces, including grain boundaries, to determine their charge transport properties and stability. Understanding the chemical environment at the interface will be aided by direct spectroscopic simulations,

which will be compared with experimental measurements to refine the model. The chemical and atomic structural environment of the interface will be evaluated from first principles calculations and compared with analogous experiments. Interfacial energies will be estimated, along with diffusion barriers for Li^+ ions across these interfaces. These data will be used to parameterize larger-scale transport models. The interface models will be also used to compute the expected degree of chemo-mechanical strain as a function of Li content in the cathode materials. Other electrolyte/electrode interfaces will be studied using these computational approaches to collaborate with experimental studies as needed. Initial modeling of LLZO electrolyte at the density functional theory level and build model interfaces with model cathode materials. An example of one such interface between NMC and LLZO that will be used in investigate the effect of dopants such as Al is shown in Figure II.8.H.1.

Conclusions

This U.S. German Co-op project was initiated at the end of FY19. We have initiated collaborations with our partners.

References

1. Yu, S. et al., Chem. Mater. (2017), 29, 9639-9647
2. Miara, L. et al., ACS Applied Materials & Interfaces (2016), 8, (40), 26842-26850.
3. Zhu, Y. et al, J. Mater. Chem. A (2016) 4, 3253-3266
4. Kim, K. H. et al., Journal of Power Sources (2011), 196, 764-767.
5. Uhlenbruck, S. et al., Journal of Electroceramics (2017) 38, 197-206.

II.8.1 Dual Function Solid State Battery with Self-forming Self-healing Electrolyte and Separator (Stony Brook University)

Distinguished Professor Esther Takeuchi, Principal Investigator

Stony Brook University
1000 Innovation Road
Stony Brook, NY 11794-6044
E-mail : esther.takeuchi@stonybrook.edu

Kenneth J. Takeuchi, Principal Investigator

Stony Brook University
1000 Innovation Road
Stony Brook, NY 11794-6044
E-mail: kenneth.takeuchi.1@stonybrook.edu

Amy C. Marschilok, Principal Investigator

Stony Brook University
1000 Innovation Road
Stony Brook, NY 11794-6044
E-mail: amy.marschilok@stonybrook.edu

Tien Duong, DOE Technology Development Manager

U.S. Department of Energy
E-mail : Tien.Duong@ee.doe.gov

Start Date: October 1, 2016
Project Funding: \$1,200,000

End Date: September 1, 2019
DOE share: \$1,065,975

Non-DOE share: \$134,025

Project Introduction

The goal of this project is to demonstrate a solid-state rechargeable battery based on a lithium metal anode and iodine cathode with a self-forming, self-healing electrolyte and separator. The presence or formation of dendrites or pin holes can result in compromised cell performance or even failure for solid state cells which would be avoided by the proposed new technology. The theoretical energy density of the Li/I₂ couple is 560 W·h/kg, which provides the opportunity to meet or exceed the DOE target of 250 W·h/kg at the battery level.

Objectives

The project objective is to demonstrate a solid-state rechargeable battery based on a Li-metal anode and iodine cathode with a self-forming, self-healing electrolyte and separator with high gravimetric and volumetric energy density.

Approach

The proposed concept is a dual function rechargeable solid-state battery utilizing LiI as the electrolyte, with lithium metal as the anode and iodine as the cathode with a self-forming, self-healing separator/electrolyte. The battery will be assembled in the discharged state where the anode and cathode will be created during the first formation (charge) step. Initially, with the formation of the battery, lithium ion (Li⁺) will form a Li-metal layer at the anode, with generation of iodine at the cathode. LiI will remain and serve as both the separator and electrolyte.

This is a multiyear program where the effort is divided into three major tasks.

- Year 1 involves electrolyte preparation and characterization including preparation of SSEs and conductivity measurements.

- Year 2 will focus on cell construction and testing including both in situ and ex situ analysis.
- Year 3 will focus on cell characterization. Under the program, cycle life, efficiency, energy density, and the functional capacity of cells will be determined.

Table II.8.I.1 Quarterly Milestones and Verification for FY19.

	Q1	Q2	Q3	Q4
Milestone	Determine functional capacity and energy density of construction A cells	Determine functional capacity and energy density of construction B cells	Destructive analysis of construction A cells	In situ analysis of select A/B cells
Verification	Galvanostatic charge-discharge cycling	Galvanostatic charge-discharge cycling	Cross-sectioning, SEM/TEM	EDXRD Analysis

Results

In the last year, two different cell designs (A and B) were both tested with four different interface varieties (I – IV). Interface modification led to marked decreases in resistance and an accompanying decrease in the overpotential during the first charge step wherein the anode and cathode (iodine) form in situ. After the initial charge step, the cells maintained the lowered resistance throughout cycling. This was further examined through impedance measurements before and after cycling under increasing environmental temperatures from room temperature to 50 C. At 50 C, Cell design B, interface III shows the largest decrease in impedance overall both after charge and discharge. Extended cycling at room temperature determined an increase in the Coulombic efficiency (CE) of all cell types during the first 3 cycles through interface modification. Cell design B, interface I (with lithium) had the overall highest CE between 90 – 100%. Destructive analysis of the cells and examination with X-ray diffraction identified an $\text{I}_2\text{-LiI(HPN)}_2$ complex at the cathode interface in the charged state, confirming the presence of charge separation.

In addition to the two previous cell designs, a new electrolyte process was implemented to further reduce charge transfer resistance. The initial impedance of Process III was reduced to $1/8^{\text{th}}$ the impedance of our previous electrolyte method (Process I) and after the initial charging step, this was further reduced by 1.5 orders of magnitude. Furthermore, changing the processing of the electrolyte led to an increase in lithiation potential, allowing the cell to deliver a significant increase in discharge capacity and energy.

Finally, all cell designs and electrolyte processes were capable of self-healing shorts created during the charging process, improving the overall safety of the cells and lengthening their lifetime.

Determination of functional capacity and energy density of construction A cells

Functional capacity was initially determined in construction A cells. The cell design A included the composite LiI solid electrolyte with $\text{LiI(3-hydroxypropionitrile)}_2$ (LiI(HPN)_2) additive. Cell design A was constructed with four interface variations: A-Interface I, II, III, IV (AI-I to -IV). Variation of the interface was studied to evaluate its effects on Coulombic efficiency during charge-discharge cycling.

Before charging, Electrochemical Impedance Spectroscopy (EIS) was obtained. AI-I had an impedance value that was $> 2X$ that of AI-II ($1.8 \text{ v. } 0.85 \text{ M}\Omega\text{cm}^{-1}$) (Figure II.8.I.1A). Initially the cells were activated by a charge step, by charging at constant current ($10 \mu\text{A}/\text{cm}^2$) to 5% state of charge. Upon charging, (arrow, Figure II.8.I.1B), there is a notable difference ($\sim 0.7\text{V}$) in overpotential observed between the two cell constructions, however, as charge continues the potentials of the two cells become more similar.

Additionally, new interfaces (AI-III and AI-IV) were evaluated. Pre- and post- charge impedance was obtained, (Figure II.8.I.3A, post-charging denoted by arrow) where a substantial decrease after charge was noted. Cells were tested by stepwise charging, where they were charged at $5 \mu\text{A}/\text{cm}^2$, $10 \mu\text{A}/\text{cm}^2$, $20 \mu\text{A}/\text{cm}^2$ to 5% theoretical capacity then discharged for a total of five charge-discharge cycles (Figure II.8.I.3C). The

resistance (in $k\Omega$) was shown as a function of charge or discharge with respect to the cycle number (Figure II.8.I.3B), where the resistance was determined by the intersection of the semi-circle on a point on the x-axis in the low frequency region of a Nyquist plot.

While there was an increase in the impedance after discharge, the values remained far lower than the initial impedance of the as prepared cells. The Coulombic efficiency for each cycle was determined and some differences were observed between cell constructs, however cell construction A cells demonstrated Coulombic efficiencies of $\leq 30\%$ (Figure II.8.I.3D). The energy density of the solid state was determined based on utilization of the LiI active material in the cell. With full utilization of the LiI in the current electrolyte/cell chemical composition, the energy density is 450 Wh/kg.

Determination of functional capacity and energy density of construction B cells

Cell design B was constructed with four interface variations with the same composite LiI solid electrolyte with LiI(HPN)₂ additive: B-Interface I-IV. Variation of the interface was studied to evaluate its effects on Coulombic efficiency during charge-discharge cycling. Longer term cycling was conducted where different cell design B constructs (B I- IV) were compared with cell design A I. The Coulombic efficiency of the cells over 60 cycles is reported in Figure II.8.I.23. Interestingly, three of the B type cell designs (I, II, and III) show a significant increase in efficiency over the first 10 cycles. This is similar to the behavior observed in cell design A I. Notably, cell design B I shows Coulombic efficiencies of between 90 and 100% throughout the testing regime. With full utilization of the LiI of the current electrolyte/cell chemical composition, the energy density is ~450 Wh/kg. Cell design B, constructs I, III, IV, were subsequently cycled at elevated temperatures and compared with cell design A I. The Coulombic efficiency of the cells over 10-12 cycles at higher and lower depths of charge (DoD) is shown in Figure II.8.I.4A-B. At higher DoD, the cell

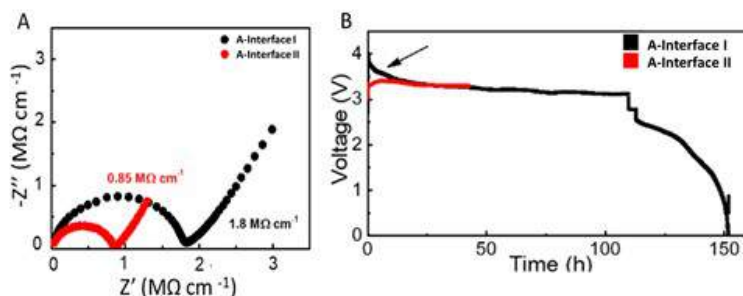


Figure II.8.I.1 Cell Design A: (A) pre-charge AC Impedance, (B) Comparison of first cycle charge curve.

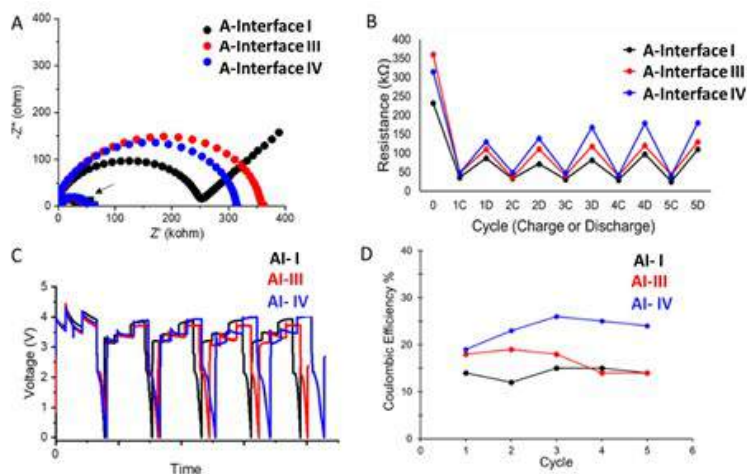


Figure II.8.I.3 Cell Design A: (A) EIS (B) Resistance v. cycle, (C) Cycling, (D) Coulombic efficiency v. cycle number.

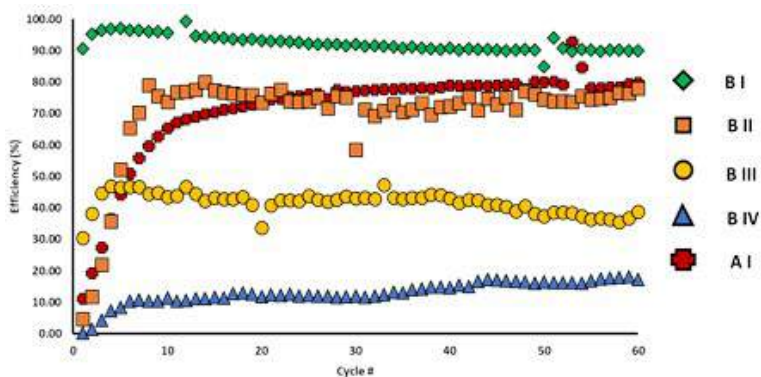


Figure II.8.I.2 Coulombic efficiency under extended cycling in cell constructions B I-B IV with comparison to A I.

types that contain a lithium interface, i.e., B I and A I, continue to exhibit a significant increase in efficiency over the first 10 cycles. At lower DoD cycling, the sequential improvement is smaller before stabilizing at values similar to that observed during longer term cycling. In contrast, cell types without an additional lithium interface, (B III and B IV), show minimal change at lower and higher DoD, before stabilizing at values similar to that observed during longer term cycling.

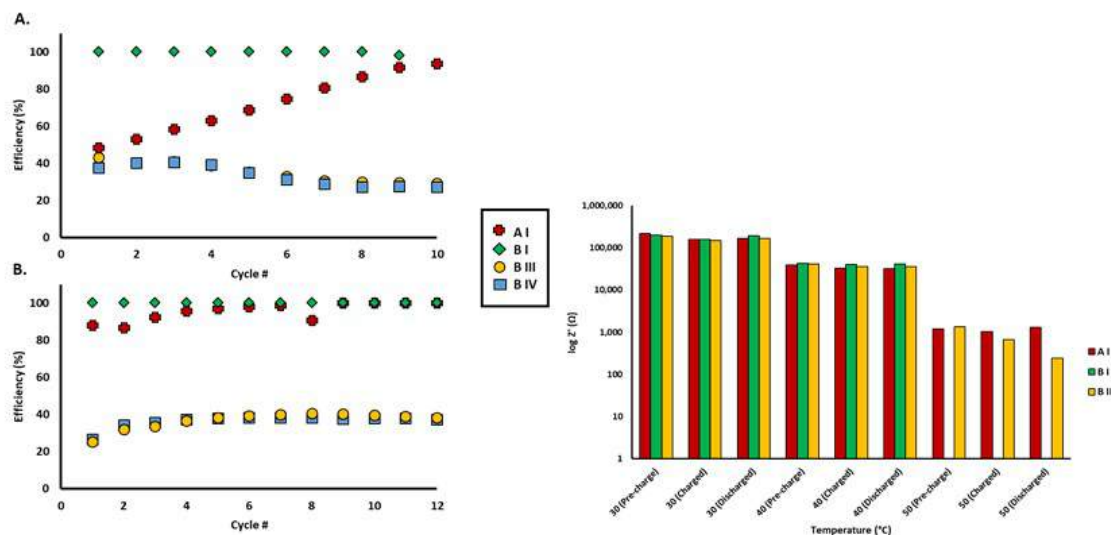


Figure II.8.I.4 Coulombic efficiency in cell constructions B I, B III, B IV and A I at (A) higher and (B) lower DoD at 40 °C and Impedance measurements at elevated temperature prior to charging, charged, and fully discharged for cell designs B I, B III, and A I.

Destructive Analysis of Cells

Solid state cells in cell configuration A were charged to ~ 50% of theoretical capacity. The cells were then disassembled and examined using x-ray diffraction. The diffraction pattern of the composite electrolyte prior to cell assembly is shown in Figure II.8.I.5A indicating the presence of LiI, LiI·H₂O, and LiI(3-hydroxypropionitrile)₂. After charge, as shown in Figure II.8.I.5B, the same three components can be identified along with the presence of I₂·LiI(3-hydroxypropionitrile)₂ affirming the generation of iodine at the cathode interface of the solid electrolyte after charge. SEM/EDS was also conducted to show morphology of cycled cells, Figure II.8.I.6.

In situ analysis of LiI Cells

Energy dispersive X-ray diffraction (EDXRD) utilizes white beam radiation combined with a 'wiggler' insertion device to produce high energy radiation capable of penetrating the stainless-steel casing of a conventional coin cell, enabling in situ and operando data collection. Coin cells, were incrementally moved through the beam on a

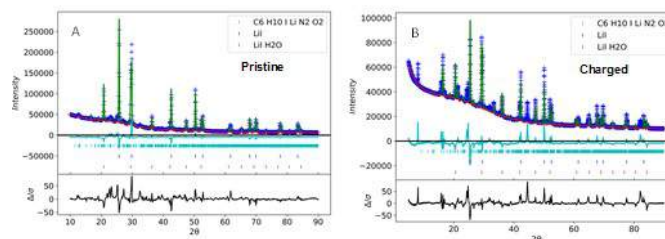


Figure II.8.I.5 X-ray diffraction of composite solid electrolyte A) Prior to cell assembly, B) Removed from cell after charge

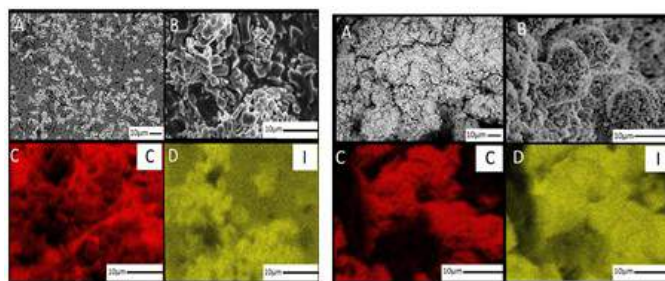


Figure II.8.I.6 SEM/EDS analysis of cells post charge, L) Cathode side, R) Anode side

motorized stage, providing spatial resolution. (Figure II.8.I.7). A vertical resolution of 20 μm was utilized, in combination with location sampling to study the differences in ion diffusion between the edge and the center of an electrode.

Impact of the New Electrolyte Process on Cell Impedance

A new electrolyte process for cell construction A is under exploration. Variations in processing progress from the least processed (Process I), to the most processed (Process III). All types were compared to a Control (no additional processing). The hypothesis was that the modified process would impact the cell resistance, and thus the cells were tested with electrochemical impedance spectroscopy (EIS), which revealed that further processing of the electrolyte indeed induced a decrease in the impedance of the pristine cells (Figure II.8.I.8A). Little difference was seen between Process I and II, but Process III is 1 order of magnitude lower in impedance than the Control cell. Notably, Process II has approximately $1/8^{\text{th}}$ the impedance of our previous electrolyte method. Upon charging to as little as 0.5% of their theoretical capacity, all cells show a significant decrease in impedance consistent with the formation of a more conductive Li^0 metal layer at the negative electrode interface (Figure II.8.I.8B). Process III again has the lowest impedance of all the cells, and 1.5 orders of magnitude less than Process I. This further exemplifies that our new electrolyte processing method significantly lowers the resistance of the cell in both the pristine and charged states. Additionally, as the level of processing is increased, the lithiation potential increases as well, allowing the cell to deliver a significant increase in discharge capacity and total energy (Figure II.8.I.8C). The processing decreased the particle size, thereby decreasing diffusion path length per particle improving ionic diffusion.

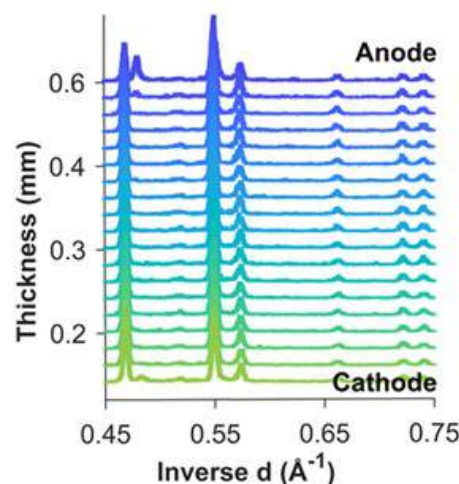


Figure II.8.I.7 EDXRD stack plot for uncharged LiI solid electrolyte with LiI(HPN)₂ additive

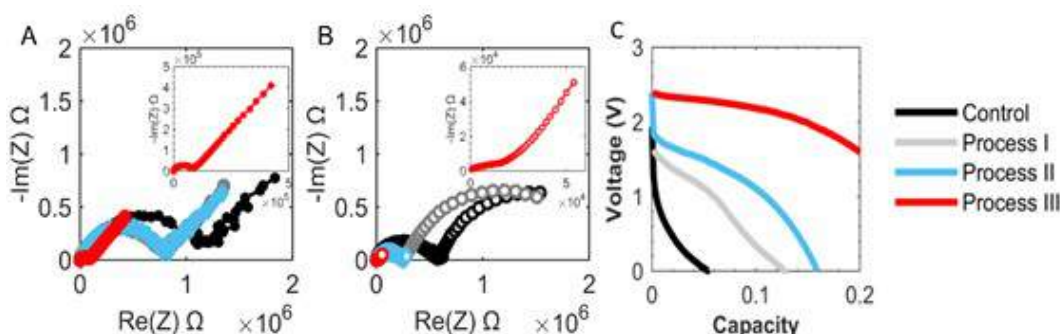


Figure II.8.I.8 EIS of Control, Process I, II, III A) Before charge, B) After charge to 0.5%, and C) Discharge profile

Demonstration of Self-Healing

The hypothesis put forward as part of the initial concept for the project was that the cell chemistry would be self-healing. If a lithium dendrite formed during charge of the cell and reached the iodine cathode, the reaction of the lithium dendrite with the iodine would consume the tip of the dendrite to form lithium iodide, more of the solid electrolyte. The formation of the solid electrolyte would allow the cell to recover and continue to function. Exploration of this concept was conducted as shown in Figure II.8.I.9 where a cell was cycled under a sufficiently high current density to induce the growth of dendrites and internal shorts, Figure II.8.I.9A. The same cell is shown in Figure II.8.I.9B cycled under a reduced current density after the initial test. The cell demonstrates no evidence of internal shorts and continues to function effectively.

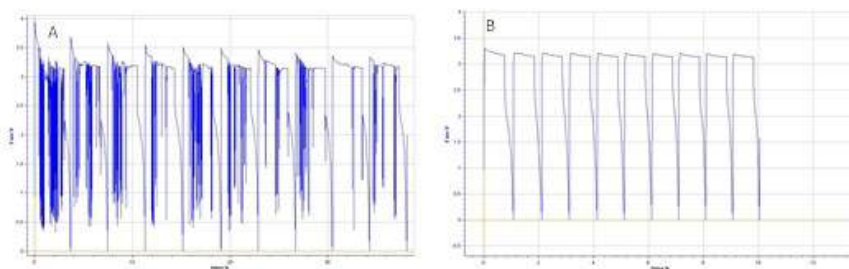


Figure II.8.I.9 Demonstration of self-healing A) Under high current density, B) Same cell cycled under lower current density

Conclusions

- Cell construction A noted the importance of the interface by observations in overpotential and ACI
- Cell construction B tested modified interfaces and observed notable increases in efficiency
- Electrode material processing method improved subsequent discharge capacity
- Self-healing was demonstrated by continued cycling after normally catastrophic shorting events.

Key Publications

1. Abraham, M. R. Dunkin, J. Huang, B. Zhang, K. J. Takeuchi, E. S. Takeuchi, A. C. Marschilok, "Interface effects on self-forming rechargeable Li/I₂ based solid state batteries", MRS Communications, **9**, 657-662 (2019).
2. C. A. Stackhouse, A. Abraham, K. J. Takeuchi, Esther S. Takeuchi, A. C. Marschilok, "Progress and Outlook on Few Component Composite Solid State Electrolytes," MRS Advances, 1-6, (2019). Advance online publication. DOI: 10.1557/adv.2019.264

Presentations

1. Spring, 2019 American Chemical Society, *invited*. "High-energy density solid-state rechargeable battery based on Li/I₂", "DIVISION: Division of Energy and Fuels, SESSION: Innovative Chemistry & Materials for Electrochemical Energy Storage, Orlando, FL.
2. Presentation: A. Abraham, J. Huang, P. F. Smith, A. Marschilok, K. Takeuchi, E. Takeuchi "Demonstration of a self-forming solid-state rechargeable Li/I₂ battery", MRS Fall 2018, Boston, MA.
3. Esther S. Takeuchi, Kenneth J. Takeuchi, Amy C. Marschilok, Alyson Abraham, Chavis Stackhouse, Andrea M. Bruck, Mikaela R. Dunkin, Jianping Huang, Paul F. Smith, "Dual Function Solid State Battery with Self-Forming, Self-Healing Electrolyte and Separator", 2019 DOE Vehicle Technologies Office Annual Merit Review (AMR), June 10-13, 2019, Arlington, VA 22202.
4. Chavis A. Stackhouse, Alyson Abraham, Mikaela Dunkin, Jianping Huang, Bingjie Zhang, Amy C. Marschilok, Esther S. Takeuchi, Kenneth J. Takeuchi, "Lithium Iodide Based Batteries: Complex Interfacial Chemistry and Progress In Self-Healing", Summer, 2019 National Institutionalized Research and Career Development Award Meeting. POSTER SESSION: Chemistry and Biochemistry, Ann Arbor, MI. *Award received*

II.9 Beyond Lithium-Ion R&D: Lithium Sulfur Batteries

II.9.A Novel Chemistry: Lithium-Selenium and Selenium-Sulfur Couple (ANL)

Khalil Amine, Principal Investigator

Argonne National Laboratory
9700 South Cass Avenue
Lemont, IL 60439-4837
E-mail: amine@anl.gov

Tien Duong, DOE Technology Development Manager

U.S. Department of Energy
E-mail: Tien.Duong@ee.doe.gov

Start Date: October 1, 2017

End Date: September 30, 2019

Project Funding (FY19): \$500,000

DOE share: \$500,000

Non-DOE share: \$0

Project Introduction

Lithium/sulfur (Li/S) batteries have attracted extensive attention for energy storage applications due to the high theoretical energy density (2600 Wh kg^{-1}) and earth abundance of sulfur.^[1] Recently, selenium and selenium-sulfur systems have also received considerable attention as cathode materials for rechargeable batteries because of the high electronic conductivity (20 orders of magnitude higher than sulfur) and high volumetric capacity (3254 mAh cm^{-3}) of selenium.^[2] Selenium-sulfur mixtures are miscible in a wide concentration range, and many Se-S composites can be prepared, including Se_5S , Se_5S_2 , Se_5S_4 , SeS , Se_3S_5 , SeS_2 , SeS_7 , and even materials with a small amount of Se such as SeS_{20} .^[2] These Se-S composites offer higher theoretical specific capacities than Se alone and improved conductivity compared to pure S. However, similar to Li/S batteries, two major obstacles resulting from lithium polysulfides/polyselenides shuttle and lithium dendrite formation remain huge challenges for long-life Li/Se-S batteries.^[3] The former is due to the dissolution and migration of polysulfides/polyselenides intermediates in the conventional ether-based electrolytes, which could induce severe parasitic reactions with Li metal and hence formation of porous or mossy Li metal. The latter is originated from the parasitic reactions of lithium metal with the electrolytes, leading to the formation of fragile solid electrolyte interphase (SEI) on Li metal, further uncontrolled lithium dendrite growth and eventually dead lithium. These parasitic reactions are the direct cause for the rapid capacity fade and poor coulombic efficiency of Li/S and Li/Se-S batteries.

Via advanced diagnostic tools including synchrotron X-ray probes and computational modeling, the team led by Dr. Khalil Amine at Argonne National Laboratory (ANL) is focusing on the development of rational cathode structure designs and exploration of novel electrolytes to effectively eliminate these parasitic reactions and suppress simultaneously the shuttle effect and lithium dendrite formation during long-term cycling.

Objectives

The objective of this project is to develop novel Li/Se-S batteries with high energy density (500 Wh kg^{-1}) and long life (>500 cycles) along with low cost and high safety.

Approach

To prevent the dissolution of polysulfides and increase the active material utilization, S or Li_2S is generally impregnated in a conducting carbon matrix. However, this approach makes it difficult to increase the loading density of practical electrodes. It is proposed here to solve the above barriers by the following approaches: (1) partial replacement of S with Se, (2) confinement of the SeS_x in a porous conductive matrix with high pore volume, and (3) exploration of advanced electrolytes that can suppress shuttle effect and lithium dendrite growth.

Results

Identifying correlation between parasitic reactions and solvation-ion-exchange in Li/S and Li/Se-S batteries

The conventional electrolytes for Li/S and Li/Se-S batteries are 1 M Lithium LiTFSI in a mixture of low-donor-number solvents such as 1,3-dioxolane (DOL) and 1,2-dimethoxyethane (DME). However, they have high polysulfides/polyselenides solubility and cannot sustain a stable lithium plating/stripping during prolonged cycling, leading to continuous occurrence of parasitic reactions during charge/discharge and hence shorten cycle life.^[4] It is reported that the interaction between free solvents, polysulfides/polyselenides and lithium metal play a critical role on the parasitic reactions. However, a fact that has been ignored for a long time is the solvating power difference among different cations/anions (e.g., Li^+ , TFSI^- and S_x^{2-}), which could initiate a solvation-ion-exchange (SIE) process and lead to the regeneration of free solvents. Through experimental and computational study, we have identified a unprecedented correlation between parasitic reactions and SIE process in Li/S and Li/Se-S batteries. We have reported a new class of concentrated siloxane based electrolytes to effectively eliminate the SIE process and achieve zero parasitic reactions in Li/S and Li/Se-S batteries.

Computational and experimental understanding of solvation-ion-exchange chemistries in cathode chemistry

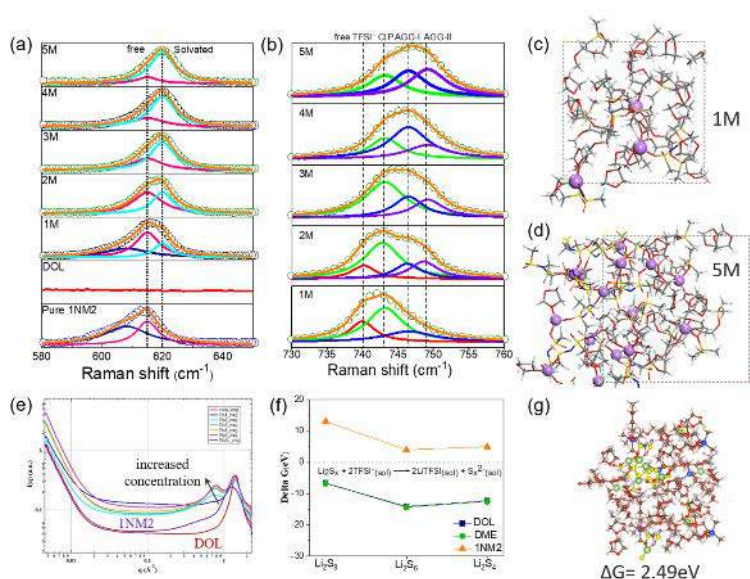


Figure II.9.A.1 Raman spectra of siloxane, DOL and siloxane-based electrolytes with increased concentration in the Raman shift range of (a) 580-650 cm^{-1} and (b) 730-760 cm^{-1} . Typical snapshot of the optimized structures of (c) 1M and (d) 5M siloxane-based electrolytes using ab initio molecular dynamics (AIMD) simulation. (e) Small angle X-ray scattering (SAXS) result of siloxane-based electrolytes with increased concentration. (f) calculated solvation-ion-exchange energy in different solvents. (g) Snapshot of simulated structure of Li_2S_6 in 5M siloxane-based electrolyte determined by AIMD simulation

Figure II.9.A.1a and Figure II.9.A.1b shows the Raman spectra of siloxane based electrolytes with increased concentration. The Raman band between 580 and 650 cm^{-1} is ascribed to the Si-O-C stretching in the siloxane solvent, while the Raman band between 730 and 760 cm^{-1} is due to the coupled CF_3 bending and S-N stretching in TFSI $^-$. As shown, with an increased LiTFSI concentration, the free siloxane and TFSI $^-$ diminished to form CIPs and AGGs with strong coulombic interactions with multiple Li^+ cations. We further applied AIMD simulation to have an atomic-scale understanding of the solvation structure around the Li^+ and TFSI $^-$. Figure II.9.A.1c and Figure II.9.A.1d shows the snapshot from the AIMD trajectories for 1M and 5M siloxane based electrolytes. The result showed that with increased concentration, the ratio of coordinated O atoms has been increased by 2-fold. Moreover, the Li coordination number is decreased from 4.0 to 3.6 simultaneously.

The results indicated that there are no free solvents that can interact with selenium-sulfur. The SAXS result of siloxane-based electrolytes in Figure II.9.A.1e showed a continuous intensity increase in the q range from 0.3 to 1 \AA^{-1} , confirming the formation of aggregate when increasing the concentration. We further calculated the SIE energies in different solvents and found that the SIE process could occur in the DOL and DME solvents ($\Delta G < 0$), but be prohibited in the siloxane solvents ($\Delta G > 0$). This result was further confirmed by the AIMD simulation on the interaction of Li_2S_6 with 5M siloxane-based electrolytes, which showed no chemical bond breaking of Li_2S_6 with a ΔG of 2.49 eV (the reaction is unfavorable).

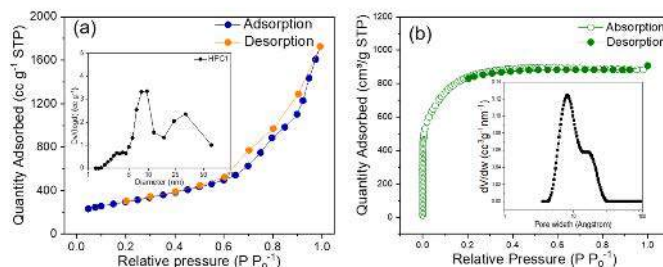


Figure II.9.A.2 BET measurement results of two highly porous carbon (HPC) hosts in this study: (a) HPC1 and (b) HPC2

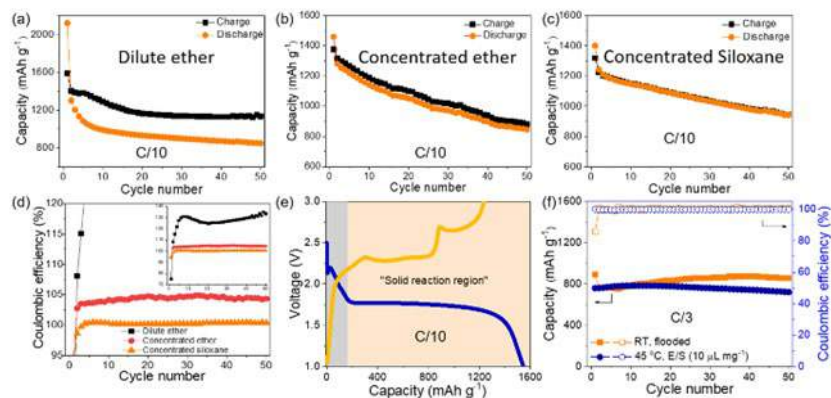


Figure II.9.A.3 Cycle performance of S-HPC1 (70 wt.% S) composite in (a) dilute ether, (b) concentrated ether and (c) concentrated siloxane electrolytes. (d) Coulombic efficiency comparison in different electrolytes. (e) Charge/discharge profiles and (f) cycling performance of S-HPC2 (70 wt.% S) composite in concentrated ether electrolytes

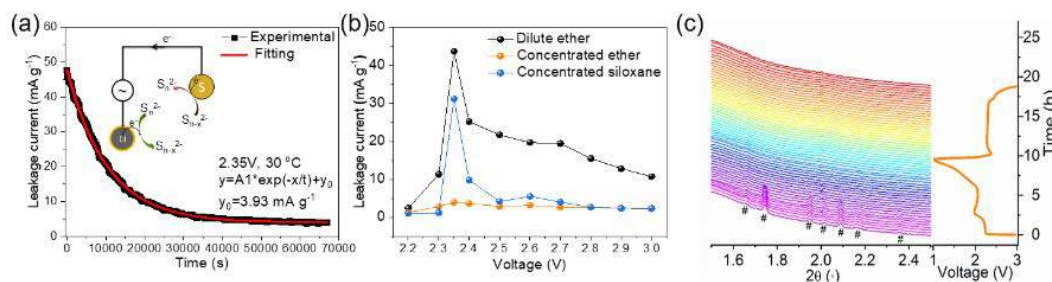


Figure II.9.A.4 (a) Representative current relaxation curve collected to extract the static leakage current. (b) Leakage current measurement of S-HPC1 composite in different electrolytes. (c) in situ HEXRD characterization on S-HPC1 composite in concentrated ether electrolytes

In order to evaluate the effect of solvation-ion-exchange on the electrochemical performance of Li/S and Li/Se-S batteries, we have prepared three different electrolytes including dilute ether (DE), concentrated ether (CE) and concentrated siloxane (CS) electrolytes. To exclude the effect of cathode confinement, we have

chosen a porous carbon (HPC1) with relatively larger pore size of 33 nm (Figure II.9.A.2a), and synthesized a S/HPC1 composite with 70 wt.% S loading. The electrochemical test results (Figure II.9.A.3a-Figure II.9.A.3c) showed that despite low cathode confinement, the S-HPC1 composite not only demonstrated better cycle stability, but also demonstrated much lower parasitic reactions (no gap between charge and discharge capacities) in the CS electrolytes. This can be confirmed from the coulombic efficiency comparison in Figure II.9.A.3d, which showed that the CS electrolytes demonstrated almost 100% coulombic efficiency, outperforming CE (~105%) and DE (>120%). It is also noted that although most of the ether solvents were solvated by Li^+ and TFSI $^-$ in the concentrated ether electrolytes, it still exhibited parasitic reactions, which is because of the higher solvating power of S_x^{2-} towards ether solvents than Li^+ and TFSI $^-$, hence triggering the SIE process. The effect of cathode confinement was further investigated by using a microporous carbon (HPC2, Figure II.9.A.2b), which could alter the sulfur transformation pathway from the typical solid-liquid-solid to quasi solid-solid process (Figure II.9.A.3e), and hence directly bypass the formation of polysulfides/polyselenides in the CS electrolytes. The S-HPC2 (70 wt.%S) composite could also demonstrate stable cycle performance with high coulombic efficiency of nearly 100% in the CS electrolytes under flooded and low E/S ratio condition.

We have further used a home-built high precision leak current measurement system to compare the parasitic reactions of S-HPC2 composite in different electrolytes. The measured static current is proportional to the rate of parasitic reactions and can be correlated with the capacity fading of Li-S and Li/Se-S batteries. Figure II.9.A.3a shows a typical current relaxation curve collected; an exponential decay function was used to extract the static current (y_0). Figure II.9.A.3b compares the measured static current of in different electrolytes. As shown, the leakage current in the CS electrolyte is much lower than that in the DE and CE electrolytes. This indicates that the parasitic reactions have been significantly suppressed in the CS electrolytes. In situ HEXRD characterization on the S-HPC1 cathode in the CS electrolytes showed that the crystalline sulfur was directly converted into amorphous Li_2S , which is different from the results in the ether based electrolytes,^[5] indicating much less formation of polysulfides.

Understanding solvation-ion-exchange chemistries on Li metal plating/stripping behavior

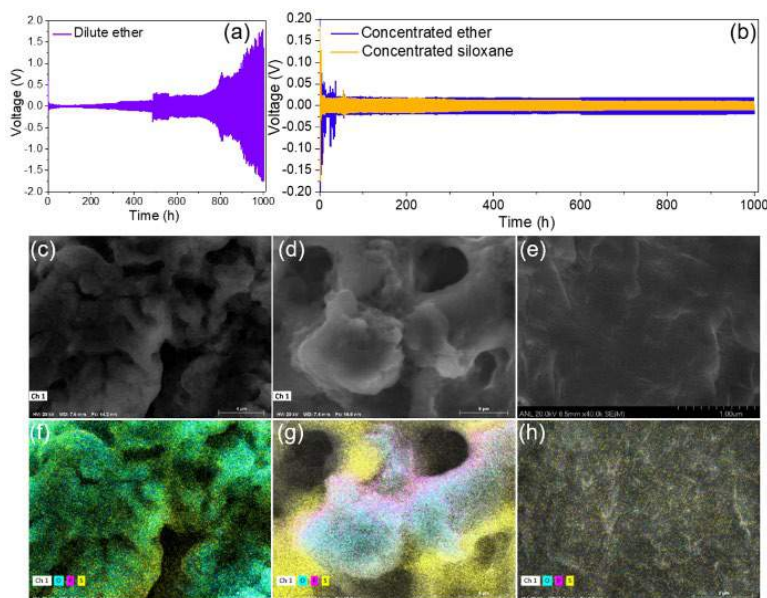


Figure II.9.A.5 Li metal plating/stripping in Li/Li symmetric cells in (a) dilute ether and (b) concentrated electrolytes at 1.25 mA cm^{-2} with an areal capacity of 1.25 mAh cm^{-2} . SEM image of Li metal and corresponding EDX mapping in different electrolytes: (c, f) dilute ether, (d, g) concentrated ether and (e, h) concentrated siloxane electrolytes

The effect of different electrolytes on the Li plating/stripping process was also investigated. Figure II.9.A.5a-5b compares the voltage profiles of Li/Li symmetric cells in different electrolytes. As shown, it presented dramatically increased voltage polarization after 400 h in the DE electrolytes, which is due to the severe reactions between Li metal and free ether solvents or migrated polysulfides. On the contrary, it could present stable Li plating/stripping in both concentrated electrolytes within 1000 h due to significantly decreased free solvents. Noted that CS presented a lower voltage polarization than CE. However, due to the SIE process in the CE electrolytes, the reformed polysulfides would react with Li metal, and hence alter the Li deposition process. As shown in Figure II.9.A.5c-Figure II.9.A.5h, after 20 cycles of charge/discharge in DE and CE electrolytes, the surface of cycled Li metal become very rough and porous, corresponding to severe Li corrosion. The corresponding EDX mapping on Li metal confirmed the domination of sulfur species on Li metal. In contrast, the surface of cycled Li metal remained relatively flat, and very few F, O and S species from SEI layer can be detected, indicating very few parasitic reactions of Li metal with either polysulfides or electrolytes.

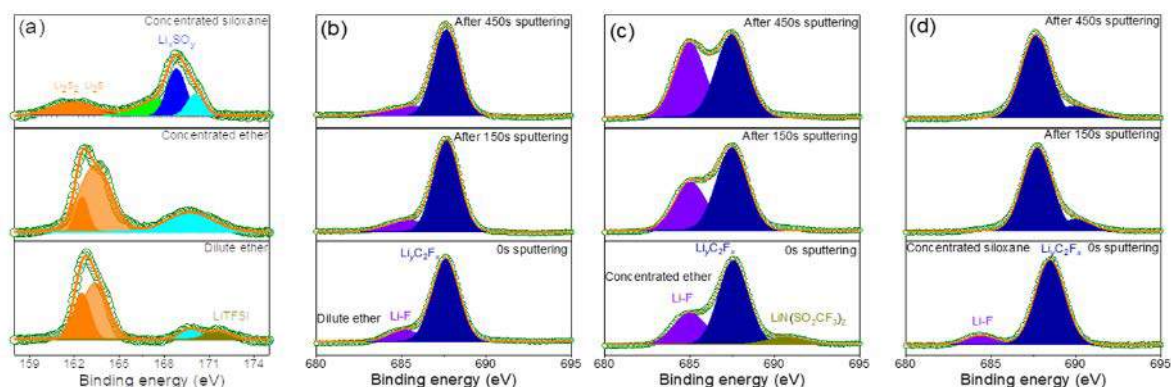


Figure II.9.A.6 (a) S 2p spectra of Li metal in the Li/S-HPC1 cells after 20 cycles in different electrolytes at C/10. F 1s spectra of Li metal in Li/S-HPC1 cells after 20 cycles in different electrolytes: (b) dilute ether; (c) concentrated ether and (d) concentrated siloxane

It has been found that the formation mechanism and the nature of the SEI layers derived from concentrated electrolytes could be fundamentally different from that formed in the dilute electrolytes. To elucidate the distinct SEI layer as a function of depth in different electrolytes, we have conducted XPS characterization using Ar sputtering at various times. Figure II.9.A.6a shows the S 2p spectra of cycled Li metal in different electrolytes. As shown, in the ether based electrolytes (both DE and CE), we can observe a severe accumulation of $\text{Li}_2\text{S}/\text{Li}_2\text{S}_2$ on the surface of Li metal, while the amount of $\text{Li}_2\text{S}/\text{Li}_2\text{S}_2$ is significantly suppressed in the CS electrolytes. This is a clear indicator for the formation of polysulfides during cycling in the DE and CE electrolytes. Furthermore, the depth profiles analysis in Figure II.9.A.6b-Figure II.9.A.6d showed that the SEI layer in the DE and CE electrolytes are much thicker than that in the CS electrolyte. Even after 450 s sputtering, LiF, a common SEI component derived from the decomposition of LiTFSI, still existed in the SEI layer of cycled Li metal in the DE and CE electrolytes. Correspondingly, the SEI after cycling in the CS electrolyte is much denser but thinner, while the SEI layers in the DE and CE electrolytes are much thicker and porous. This could be attributed to the suppressed reactivity of Li metal in the CS electrolytes by regulating solvation-ion-exchange process.

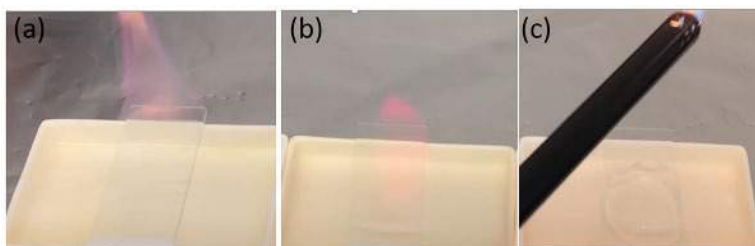
Highly non-flammable concentrated siloxane based electrolytes for high safety

Figure II.9.A.7 Flammability test: (a) dilute ether; (b) concentrated ether and (c) concentrated siloxane

The ether solvents such as DOL and DME are highly volatile and have very low flash point ($< 2^{\circ}\text{C}$). As a result, they can trigger severe safety risks for batteries especially when operating at elevated temperatures. We have hence compared the flammability of three electrolytes by ignition test. As shown in Figure II.9.A.7, the DE electrolytes got fire after 1 ignition, CE electrolytes got fire after 2 ignition, while CS electrolytes did not get fire even after 10 ignition. This is because of the high flash point of siloxane solvents ($> 100^{\circ}\text{C}$). As a result, a better safety could be expected from the CS electrolytes.

Conclusions

In summary, we have reported a new class of concentrated siloxane based electrolytes for Li/S and Li/Se-S batteries, which demonstrated significant advantages over the conventional ether based electrolytes (both dilute and concentrated). It was found that the siloxane electrolytes can effectively eliminate the solvation-ion-exchange process and can thereby simultaneously revoke the dissolution of polysulfides/polyselenides and lithium dendrite growth. Therefore, we can enable zero parasitic reactions in Li/S and Li/Se-S batteries, corresponding to almost 100% coulombic efficiency, even for non-encapsulated cathodes. In addition, due to their high flash point, the concentrated siloxane electrolytes are highly non-flammable. The insights in this study may provide a new solution for stable and safe lithium metal batteries with high efficiency.

Key Publications

Publications/Patents

1. Xu, G. L. et al., *Adv. Energy Mater.* 2019, 9, 1802235.
2. Zhuang, M. H. et al., *Nano Energy*, 2019, 58, 660-668.
3. Xu, G. L. and Amine, K. Novel Chemistry for automotive application: Lithium-selenium and selenium-sulfur couple. Abstract of papers of the American Chemical Society, 2019, 257.
4. Xu, G. L. et al., Zero parasitic reactions in lithium-sulfur batteries by regulating cations/anions solvation chemistries, under submission.
5. Xu, G.L.; Chen, Z.; Liu, J; Amine, K., Poly (alkylene oxide) siloxane-based electrolytes for rechargeable batteries, U.S. Patent Application no. US20190044181A1.
6. Xu, G. L.; Amine, K., NON FLAMMABLE ELECTROLYTES, U.S. Patent Application 16/660.968.

Invited Talks

1. Khalil Amine, Jun Lu, Gui-Liang Xu, Zonghai Chen, Larry Curtiss. Advanced Energy Storage Systems for Enabling Electrification of Vehicles “Lithium Ion & Beyond”. 236th ECS meeting, October 13-17, 2019, Atlanta, USA (Battery Division Research Award).
2. Gui-Liang Xu, Zonghai Chen and Khalil Amine. Novel Chemistry for Automotive Application: Lithium-Selenium and Selenium-Sulfur Couple. Spring 2019 ACS National Meeting. Mar 31st–Apr 4th, Orlando, FL, USA.

References

1. Seh, Z. W., Y. M. Sun, Q. F. Zhang, and Y. Cui. “Designing High-Energy Lithium-Sulfur Batteries.” *Chemical Society Reviews* 45, no. 20 (2016): 5605-34. DOI:10.1039/c5cs00410a
2. Abouimrane, A., D. Dambournet, K. W. Chapman, P. J. Chupas, W. Weng, and K. Amine. “A New Class of Lithium and Sodium Rechargeable Batteries Based on Selenium and Selenium-Sulfur as a Positive Electrode.” *Journal of the American Chemical Society* 134, no. 10: 4505-08. DOI: 10.1021/ja211766q.
3. Cui, Yanjie, Ali Abouimrane, Jun Lu, Trudy Bolin, Yang Ren, Wei Weng, Chengjun Sun, et al. “(De)Lithiation Mechanism of Li/SeS_x (X = 0-7) Batteries Determined by in Situ Synchrotron X-Ray Diffraction and X-Ray Absorption Spectroscopy.” *Journal of the American Chemical Society* 135, no. 21: 8047-56. DOI: 10.1021/ja402597g.
4. Qian, Jiangfeng, Wesley A. Henderson, Wu Xu, Priyanka Bhattacharya, Mark Engelhard, Oleg Borodin, and Ji-Guang Zhang. “High Rate and Stable Cycling of Lithium Metal Anode.” *Nature Communications* 6, no. 1: 6362. DOI:10.1038/ncomms7362.
5. Conder, Joanna, Renaud Bouchet, Sigita Trabesinger, Cyril Marino, Lorenz Gubler, and Claire Villevieille. “Direct Observation of Lithium Polysulfides in Lithium-Sulfur Batteries Using Operando X-Ray diffraction.” *Nature Energy* 2, no. 6 (2017). DOI: 10.1038/nenergy.2017.69.

Acknowledgements

Support from Tien Duong of the U.S. DOE’s Office of Vehicle Technologies Program is gratefully acknowledged. I would like to thank Dr. Guiliang Xu at ANL for the major contribution to this project. The collaborations included those with Dr. Yang Ren and Dr. Chengjun Sun at APS of ANL (in Synchrotron X-ray characterization) and with Dr. Larry Curtiss and Dr. Anh Tuan Ngo at MSD of ANL (in Computational modeling).

II.9.B Development of High Energy Lithium-Sulfur Batteries (PNNL)

Dongping Lu, Principal Investigator

Pacific Northwest National Laboratory
902 Battelle Boulevard
Richland, WA 99354
E-mail: dongping.lu@pnnl.gov

Jun Liu, Co-Principal Investigator

Pacific Northwest National Laboratory
902 Battelle Boulevard
Richland, WA 99354
E-mail: jun.liu@pnnl.gov

Tien Duong, DOE Technology Development Manager

U.S. Department of Energy
E-mail: Tien.Duong@ee.doe.gov

Start Date: October 1, 2015

End Date: September 30, 2020

Project Funding (FY19): \$400,000

DOE share (FY19): \$400,000

Non-DOE share: \$0

Project Introduction

Lithium-sulfur (Li-S) battery has a high theoretical energy ($\sim 2300 \text{ Wh kg}^{-1}$) while an extremely low cost, making it one of the most promising battery technologies to meet the DOE target of $< \$80/\text{kWh}$ for vehicle electrification. High energy Li-S batteries ($> 350 \text{ Wh/kg}$) have been demonstrated experimentally; however, the cycle life of these batteries is still very limited. In order to reach a cell energy greater than 350 Wh/kg for a cell with a capacity of $< 3\text{Ah}$, the cathode loading and E/S (electrolyte/sulfur) ratio of Li-S batteries should be $> 6 \text{ mg S/cm}^2$ and $< 3 \text{ }\mu\text{L/mg}$, respectively. Unfortunately, under those conditions, both the sulfur utilization rate and cell life are very limited. It was verified in our previous reports that electrode passivation from irreversibly deposited $\text{Li}_2\text{S}/\text{Li}_2\text{S}_2$ and surface blocking effects from polymer binders contribute significantly to the cell polarization increase and capacity decay. These detrimental effects are further escalated when only a lean amount of electrolyte is used. The lack of Li-ion conduction induced by the lean electrolyte, as well as its continuous consumption, is believed to be the intrinsic reason for the shortened cycle life of the cells. Therefore, one of the key challenges to enable a long-cycle-life, high energy Li-S battery is how to construct and maintain stable Li-ion conductive networks without depending solely on consumable liquid electrolyte for Li^+ transport. To minimize the dependence of Li^+ ion transport solely on liquid electrolyte, a second phase of solid Li^+ conductors was proposed to be introduced into the electrode architectures, forming the solid/liquid electrolyte hybrid Li^+ conductive networks (Figure II.9.B.1). To realize such a design, several scientific challenges need to be addressed simultaneously: 1) Highly conductive solid Li^+ conductors to enhance fast sulfur and sulfides conversion reactions, 2) low electrode porosity design to reduce liquid electrolyte amount and suppress free polysulfide redistribution, 3) feasible electrode processing method to realize preparation of high-mass-loading sulfur electrode with uniformly distributed solid Li^+ conductors, and 4) liquid electrolytes compatible with both the Li^+ conductor and the sulfur to minimize the interfacial contact resistance of the cathode.

In FY19, our main efforts focus is to design and prove the concept of a liquid-solid hybrid sulfur cathode by 1) the development of highly conductive and air stable solid Li^+ conductors and 2) a solvent-free electrode preparation method that enables the incorporation of the Li^+ conductors in high-loading sulfur electrodes. The research will also incorporate our previously developed electrode materials (U.S. Patent No. 9577250) and

electrode additives (U.S. Pat. App. No. 15/334240) to achieve high-loading electrodes with optimized microstructures.

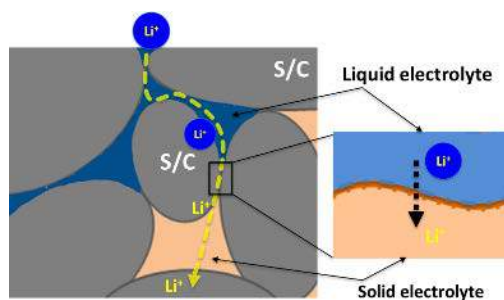


Figure II.9.B.1 Schematic of the hybrid electrode design, in which solid electrolyte and liquid electrolyte are filled in the big voids and small pores of electrode, respectively, to enable the robust Li-ion conduction networks in sulfur cathode.

Objectives

- Develop solid Li^+ conductors that possess high Li^+ conductivity, acceptable air stability, and acceptable interfacial compatibility with sulfur to construct solid Li^+ conduction networks for the hybrid electrode design.
- Develop a solvent-free electrode preparation method to realize the fabrication of solid Li^+ conductors contained sulfur cathode with a very lean binder content.

Approach

1. Develop halogen substituted sulfide based solid-state Li^+ conductors with a room temperature ionic conductivity of >1 mS/cm.
2. Study the halogen substitution effects on the electrochemical window, air sensitivity, and interfacial properties of the Li^+ conductors.
3. Develop a solvent-free processing method for the preparation of Li^+ conductors contained sulfur cathode (>4 mg S/cm²) with a very lean amount of binder (<5 wt.%).
4. Evaluate compatibility of liquid electrolytes towards the Li^+ conductors and identify key criteria for liquid electrolyte selection.

Results

1. Development of superionic low-temperature phase sulfide based Li^+ conductors ($\text{Li}_7\text{P}_2\text{S}_8\text{Br}_{0.5}\text{I}_{0.5}$) (LT-LPSBI) with room temperature conductivity >1 mS/cm.

Under the practical conditions of a high-loading cathode and a lean amount of electrolyte, the cycle life of a Li-S battery is very limited. The excessive electrolyte consumption during deep Li metal stripping/plating causes early electrolyte insufficiency. This leads to both capacity decay and a shortened cell cycle life. To minimize the dependence of Li^+ transport on liquid electrolyte, a second phase of solid Li^+ conductors was needed to be introduced into the electrode architectures, forming the solid/liquid electrolyte hybrid Li^+ conductive networks. To realize such a design, it is key to develop solid state Li^+ conductors that possess high Li^+ conductivity. For this task, we identified and synthesized a new low-temperature phase of $\text{Li}_7\text{P}_2\text{S}_8\text{Br}_{0.5}\text{I}_{0.5}$ (LT-LPSBI) solid electrolyte. The precursor mixtures were completely reduced to the amorphous state after mechanically ball-milling as shown in Figure II.9.B.2a. Upon heating, the amorphous product underwent two exothermic events according to the DTA analysis, with onsets at around 180°C and 230°C, respectively. The two events correspond to the crystallization of the metastable LT-LPSBI phase and the crystallization of high temperature phase LPSBI (HT-LPSBI). In order to minimize the conversion to HT-LPSBI, LT-LPSBI was obtained by annealing at 160°C for 60h. Three major broad diffraction peaks were observed at 20.0°, 23.6° and 29.3°, which are ascribed to the diffraction of the LT-LPSBI phase (Figure II.9.B.2a) with nanocrystals or

amorphous phase as proved by the scanning transmission electron microscopy (STEM) and selected area electron diffraction (SAED) characterization (Figure II.9.B.2c-Figure II.9.B.2e). The ionic conductivities of the glass, LT-LPSBI and HT-LPSBI were characterized by impedance spectroscopy. A typical impedance plot consisted of a straight line that intercepts with the real axis at a high frequency, representing the electrode response. The ionic conductivity of LT-LPSBI was measured at 4.7 mS/cm at room temperature (r.t.) (Figure II.9.B.2b), which is comparable to LGPS-type materials or crystalline $\text{Li}_7\text{P}_3\text{S}_{11}$ in a cold pressed state. In comparison, the r.t. conductivities of the glass phase and HT-LPSBI were 0.8 mS/cm and 0.05 mS/cm, respectively. The activation energy E_a of the three phases was calculated based on the Arrhenius equation, $\sigma = \sigma_0/T \exp(-E_a/kT)$, and the E_a of the three phases follows the inverse trend of the ionic conductivities: 0.31 eV, 0.26 eV and 0.20 eV for HT, glass and LT, respectively.

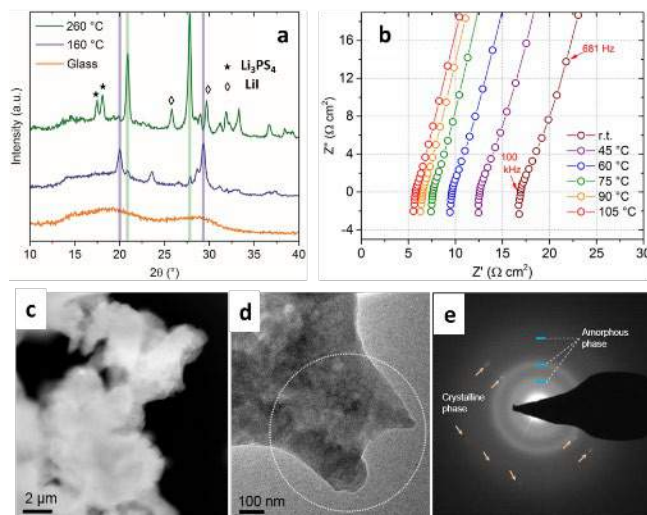


Figure II.9.B.2 (a) XRD patterns of the glass phase (bottom), LT-LPSBI (middle) and HT-LPSBI (top). (b) Nyquist plot of an In-SE-In (SE = LT-LPSBI) cell tested at various temperatures. (c) STEM of LT-LPSBI powder. (d) Low magnification TEM image of the primary particle edge. (e) Electron diffraction of the circled region in panel d

2. Exceptional air stability and interfacial properties of $\text{Li}_7\text{P}_2\text{S}_8\text{Br}_{0.5}\text{I}_{0.5}$ (LT-LPSBI)

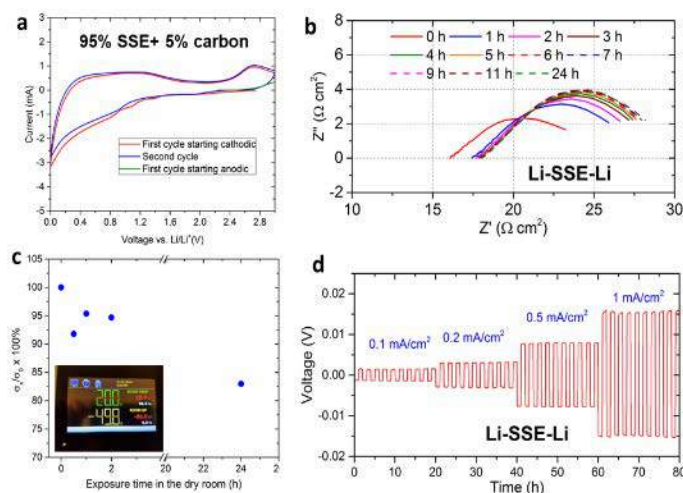


Figure II.9.B.3 (a) Cyclic voltammogram for a C-SSE/SSE/Li cell at a scan rate of 5 mV/s (SSE=LT-LPSBI). (b) Nyquist plots of a Li/SSE/Li cell at room temperature as a function of time (voltage modulation was 5 mV). (c) The effect of exposure to dry room atmosphere on the ionic conductivity of LT-LPSBI. σ_{Li} is the ionic conductivity at x h. (d) Li/SSE/Li cell cycling at different areal current densities with 1h duration for each step

To verify the availability of the prepared solid Li^+ conductors for the hybrid sulfur cathode design, key material properties such as electrochemical window, air stability, and interfacial stability with the Li anode were studied systematically. The electrochemical window of LT-LPSBI was characterized by cyclic voltammetry (CV) (Figure II.9.B.3a). Rather than adopting the conventional configuration of M/SE/Li (M standards for an electrochemically inert planar metal electrode such as Pt), conductive carbon (5 wt.%) was mixed with SE for the working electrode to mimic the real scenario in an electrode. Scanning towards the negative direction (0 V vs. Li), the onset of substantial increase in cathodic current was around 1.4 V. On the reverse scan, two broad peaks spanning from 0.2 V to 1.7 V and a relatively narrow peak at 2.7 V were observed. All peaks corresponded to the oxidation of the reduction products during the forward scan, since the scan starting towards the positive direction showed no anodic current at 2.7 V. These results indicate 1.4–2.7 V is a reasonably stable electrochemical window for LT-LPSBI, which falls within the operational window of the Li-S battery. The interfacial transport behavior of LT-LPSBI with Li anode was evaluated using potentiostatic EIS in two-electrode Li/SE/Li cells by monitoring the impedance change over time (Figure II.9.B.3b). The left intercept of the impedance and the span increased with time, with change being greatest between 0 h and 1 h. The change slowed down with time and the impedance eventually became relatively stable after a few hours. The dependence of the impedance on time is typical of the growth of SEI layers that are kinetically stable, which can be attributed to the lack of metal or semiconductor elements in the LT-LPSBI. The moisture stability of the LT-LPSBI was tested in the dry room atmosphere and the conductivity decreased by only 5% within 2 h and by 15% in 24 h (Figure II.9.B.3c). Therefore, the LT-LPSBI can be handled in the dry room for a reasonable amount of time without substantial degradation. Li/SSE/Li symmetric cells were subject to DC polarization to evaluate the Li cycling stability (Figure II.9.B.3d). The critical current density can reach as high as 1 mA/cm^2 . At 0.5 mA/cm^2 , the polarization stayed relatively constant during the cycling; the areal interfacial resistance at 0.5 mA/cm^2 was measured $5 \Omega \cdot \text{cm}^2$, which is among the smallest SSE/Li interfacial resistances observed for all of the reported solid electrolytes. The Li/SSE/Li cell can be cycled for 800 hours at 0.5 mA/cm^2 .

3. Solvent-free processing for the fabrication of the Li-ion conductor contained sulfur electrode ($S > 4 \text{ mg/cm}^2$, $S \text{ content} > 75 \text{ wt\%}$, and electrode density $> 1 \text{ g/cm}^3$)

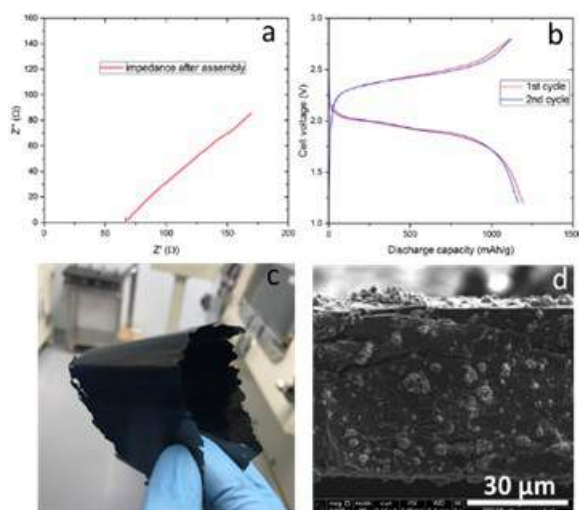


Figure II.9.B.4 (a) Nyquist plot of a S-SE/SE/Li cell at room temperature for the frequency range of 100 kHz to 0.01 Hz (voltage modulation was 5 mV, SE=LT-LPSBI). (b) First two cycle charge/discharge curves of the S/SE/Li cell. (c) Photo image of the high-loading and free-standing sulfur cathode. (d) Cross-section SEM of the S electrode ($S \text{ } 4.4 \text{ mg/cm}^2$)

In order to build the solid/liquid hybrid Li^+ conduction networks for a high energy sulfur cathode, a new solvent-free processing method was developed. To facilitate sulfur conversion reactions, an optimal contact among the triple phases of active sulfur, carbon additive, and the Li^+ conductor is required. The availability of LT-LPSBI for the building of an efficient Li^+ ion conduction network in high-loading sulfur cathodes was

verified in an all-solid-state Li-S cell. It was found that the types of sulfur host materials and carbon conductors, as well as the material mixing procedures all play critical roles in the improvement of the sulfur utilization rate while maximizing the sulfur content in the whole electrode. Figure II.9.B.4a shows a typical Nyquist plot of the solid Li-S cell at optimized conditions. The low overall cell resistance indicates optimal triple-phase contact inside the electrode with the carefully selected materials and optimized composition. With a sulfur content of 44 wt% and a mass loading of 3.8 mg/cm^2 , the solid Li-S cell delivers a reversible capacity $>1200 \text{ mAh/g}$ at 0.1 mA/cm^2 at room temperature, demonstrating the effectiveness of the LPSBI in building effective Li^+ conduction frameworks. The fully overlapped charge/discharge curves (Figure II.9.B.4b) indicate a robust electrode structure and stable S/C/SSE interfaces. Of note, the content of LT-LPSBI in the solid cell is still high (40 wt.%), which is expected to be reduced to a reasonably low level through the proposed hybrid electrode design. A significant challenge of using the sulfide-based Li^+ ion conductors is the complicated electrode preparation procedure due to their moisture sensitivity. In particular, it is very difficult to prepare thin and flexible electrodes due to the very limited binders and solvents that are compatible with sulfide-based electrolytes. The solvent-free approach was developed for the sulfur cathode preparation after successfully addressing the binder compatibility and distribution problems. With only 1~5 wt.% binder, free standing and flexible sulfur electrodes can be prepared with controllable sulfur mass loadings. Figure II.9.B.4c shows a photo image of such a flexible sulfur cathode, which has a sulfur loading $> 4.4 \text{ mg/cm}^2$ and a measured electrode density of $\sim 2 \text{ g/cm}^3$. The cross section SEM image (Figure II.9.B.4d) reveals a dense electrode architecture with uniformly distributed LT-LPSBI particles, which is critical for sulfur reactions through a solid-solid pathway.

4. Compatible liquid electrolytes with the solid Li-ion conductor and Li metal anode

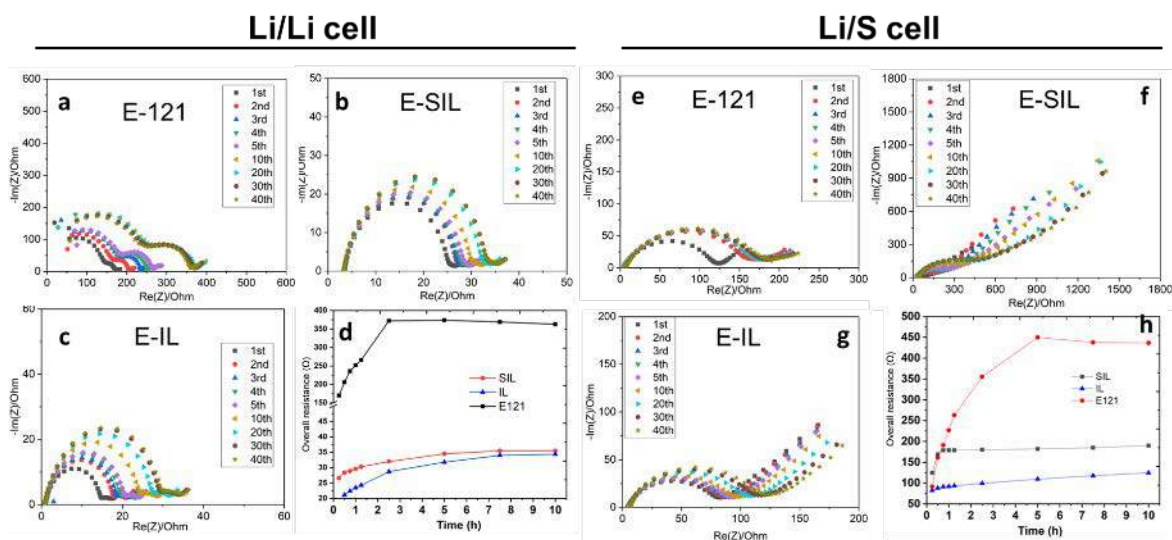


Figure II.9.B.5 Interfacial stability of liquid electrolytes with Li anode and SSE contained sulfur cathode. Nyquist plots of Li/Li symmetric cells with (a) 1M LiTFSI/DOL/DME+0.3M LiNO_3 (E-121), (b) solvated ionic liquid electrolyte (E-SIL), (c) room temperature ionic liquid electrolyte (E-IL), and (d) corresponding overall resistance evolution with a test duration of 10 hours. Nyquist plots of Li-S cells with (a) E-121, (b) E-SIL, (c) E-IL, and (d) corresponding overall resistance evolution with a test duration of 10 hours

One key step to the realization of the hybrid Li-S battery design is to identify appropriate liquid electrolytes (LE) that are stable towards both the Li anode and the SSE. Upon contact with certain liquid electrolytes/additives, a Li anode can be eventually stabilized by forming an effective solid electrolyte interface (SEI). However, it is challenging to maintain the stability of a sulfide-based SSE in the presence of liquid electrolytes. This is due to the highly reactive nature of the sulfide-based SSE towards the conventional polar organic solvents. Selection of compatible liquid electrolytes can be rationalized by tuning the solvent

solubility to sulfide and nucleophilic reactivity with the SSE. Three different categories of liquid electrolytes (conventional liquid electrolyte (E-121), solvated ionic-liquid like electrolyte (E-SIL), and room temperature ionic liquid electrolyte (E-IL)) were prepared. To study the compatibility of $\text{Li}_7\text{P}_2\text{S}_8\text{Br}_{0.5}\text{I}_{0.5}$ with LE in a practical electrode scenario, high-loading sulfur cathodes ($\text{S} > 6 \text{ mg/cm}^2$) with a S/C: SSE: binder ratio of 84:15:1 were prepared using the solvent-free processing method and used as model electrodes. The electrolyte amount was controlled at $\text{E/S}=2 \text{ mL/g}$ for each Li-S cell. The stability of the liquid electrolytes with the Li anode was studied first. Figure II.9.B.5a-c compare the EIS evolution of the Li anode in contact with different electrolytes during the 10 hours' rest (acquired 40 EIS spectra with a 15-min interval). The results obtained with the same cell configuration indicate that IL and SIL are prone to forming a lower resistance interface on the Li anode compared to the E-121. This corroborates excellent stability of the IL based electrolytes towards Li metal and suggests that less free-solvent would be desirable for the electrolyte design in pursuit of a low resistance and stable Li anode interface. However, the SSE containing S electrodes exhibit different responses when exposed to those electrolytes. The cell using the conventional E-121 electrolyte quickly reaches a stable interface within one hour (Figure II.9.B.5e); while the cell with the E-SIL needs > 5 hours to establish a stable interface with a very high resistance (Figure II.9.B.5f). Those observations can be explained by both the permeability and the reactivity of the LE. During the EIS measurement period, the LE was involved in the simultaneous processes of cathode infiltration and side reactions with SSE and Li anode. The former process improves electrode wetting, thus lowering cell impedance, while the side reactions contribute to the increased overall cell resistance. For E-121, its viscosity is much lower than the other two, so it requires a shorter time to complete the electrolyte infiltration process in the low-porosity sulfur electrode and establish stable interfaces on both electrodes through passivation reactions. In the case of the SIL electrolyte with high viscosity, the electrolyte infiltration process and the associated side reactions are both slowed down. It was noticed that the residual free solvent in the SIL is very reactive with SSE, generating high interfacial resistance and even blocking the electrode after 5 hours. The IL shows well balanced permeability and interfacial stability with both the Li anode (Blue in Figure II.9.B.5d) and the SSE (Blue in Figure II.9.B.5h). These findings will be used as a principle for further optimization of the electrolyte for the hybrid Li-S demonstration.

Conclusions

- 1) A low temperature phase sulfide-based Li-ion conductor $\text{Li}_7\text{P}_2\text{S}_8\text{Br}_{0.5}\text{I}_{0.5}$ (LT- LT-LPSBI) was prepared by mechanochemical approach; high ionic conductivity of 4.7 mS/cm was demonstrated at room temperature.
- 2) Exceptionally stable and low-resistance interface of $5 \Omega \text{ cm}^2$ was realized towards the Li anode; long term cycling of Li/ LT-LT-LPSBI /Li cell was achieved for $>800 \text{ h}$ at a current density of 0.5 mA/cm^2 .
- 3) A solvent-free processing method was developed and applied for the preparation of sulfide solid-electrolyte containing sulfur cathodes with $<5 \text{ wt\%}$ of binder; sulfur utilization rate of $>1300 \text{ mAh/g}$ was realized in high S loading electrodes.
- 4) Selection of compatible liquid electrolytes with a sulfide solid electrolyte can be rationalized by tuning the solvent solubility to sulfide, component nucleophilic reactivity with the SSE, and electrolyte wettability/ viscosity; ionic liquid and solvated ionic-liquid like electrolytes are more suitable liquid electrolytes for the hybrid Li-S cell design.

Key Publications

1. Wang Y, Lu D, Xiao J, He Y, Harvey GJ, Wang C, et al. Superionic Conduction and Interfacial Properties of the Low Temperature Phase $\text{Li}_7\text{P}_2\text{S}_8\text{Br}_{0.5}\text{I}_{0.5}$. *Energy Storage Materials*, 2019, 19, 80-87.
2. Lu D, Xiao J, Shi L, Baranovskiy A, Zhang J and Liu J, Development of high energy Lithium-sulfur Batteries: from Materials to Pouch cell, 2019 International Coalition for Energy Storage and Innovation (ICESI) and Pacific Power Source Symposium (ICESI-PPSS 2019), January 2019, Waikoloa Village, HI

3. 3. Shi L, Lu D, Niu C, Xiao J, and Liu J, Extending the Cycle Life of Li-S Cells at Practical Conditions, Battery500 Review Meeting, April 17-18, 2019, Seattle, WA
4. 4. Lu D and Liu J, Development of High Energy Lithium-sulfur Batteries, DOE 2019 Annual Merit Review (AMR), June 10-13, 2019, Arlington, Virginia
5. 5. Shi L, Lu D, Niu C, Ren X, Xiao J, and Liu J, Understanding of Failure Mechanism of High Energy Lithium-Sulfur Pouch Cells, 235th ECS meeting, May 26-30, Dallas, TX
6. 6. Lu D, Wang Y, Yu Z, Zhang J, Xiao J, and Liu J, Highly Conductive Sulfide Based Solid Electrolyte for Lithium-sulfur Batteries, Advanced Lithium Batteries for Automobile Applications (ABAA 12), Oct. 6-9, Ulm, Germany.
7. 7. Xiao J, Lu D, and Liu J, Understanding Lithium Sulfur Batteries at Different Scales, 236th ECS meeting, Oct. 13-17, Atlanta, GA.

II.9.C Nanostructured Design of Sulfur Cathodes for High Energy Lithium-Sulfur Batteries (Stanford University)

Yi Cui, Principal Investigator

Stanford University

Department of Materials Science and Engineering, Stanford University

Stanford, CA 94305

E-mail: yicui@stanford.edu

Tien Duong, DOE Technology Development Manager

U.S. department of Energy

E-mail: Tien.Duong@ee.doe.gov

Start Date: October 1, 2018

End Date: September 30, 2019

Project Funding (FY19): \$500,000

DOE share: \$500,000

Non-DOE share: \$0

Project Introduction

Lithium-sulfur batteries can bring about significant improvements to the current state-of-the-art battery technologies due to its high specific energy density and cost saving. However, probing sulfur electrochemistry has multiple challenges that include: a) sulfur and its reduced species are extremely sensitive to vacuum, electron beam irradiation and X-ray irradiation, which limits the diagnostic tools one can use; b) sulfur has a large family of intermediate species connected by interwoven reaction pathways, which could be easily disturbed by added indicators or labels; c) the materials easily change upon removing from native electrolyte, hence often requiring *in operando* study. We therefore build in situ characterization platform to monitor nucleation/dissolution of sulfur, and provide avenues to the development of advanced Li-S batteries. We demonstrate an electrochemical approach to generate and observe super-cooled sulfur. Our methodology combines darkfield microscopy, a transparent electrochemical cell, and a fast camera to visualize the process at single microdroplet with millisecond time resolution. This new platform may open up new opportunities for studying super-cooled liquids as the droplets approach either homogeneous nucleation to the crystalline state or enter into the glass transition. Relevant to understanding lithium-sulfur battery chemistry, liquid sulfur is observed, for the first time, to form in the electrochemical cell and elucidates a long-debated reaction pathway for sulfur redox reaction in this environment.

Objectives

The charge capacity limitations of conventional transition metal oxide cathodes are overcome by designing optimized nano-architected sulfur cathodes. This study aims to enable sulfur cathodes with high capacity and long cycle life by developing sulfur cathodes from the perspective of nanostructured materials design, which will be used to combine with lithium metal anodes to generate high-energy lithium-sulfur batteries. A non-invasive imaging method was developed with sub-micron, sub-second resolution for Li-S battery in label-free, native organic liquid electrolyte. Substrate-dependent electrochemical formation of super-cooled liquid sulfur and crystals, as well as rapid solidification of a super-cooled sulfur droplet was demonstrated. Direct evidence about a long-debated reaction pathway of surface mechanism vs. solution mechanism for sulfur and the current collector effect on sulfur evolution was provided. The sulfur growth behaviors on different current collectors were investigated and the results with their electrochemical performance were correlated. Direct real-time observation of sulfur species evolution at the microscale and investigation of their reaction kinetics are under developing.

Approach

The approaches refer to three main parts: (I) advanced nanostructured sulfur cathodes design and synthesis, including (1) engineer empty space into sulfur cathode to solve the problem of electrode volume expansion; (2) develop novel sulfur nanostructures with multi-functional coatings for the confinement of sulfur/lithium polysulfides to address the issues of active materials loss and low conductivity; (3) develop/discover optimal nanostructured materials that can capture the polysulfide dissolved in the electrolyte; (4) develop space efficiently packed nanostructured sulfur cathode to increase the volumetric energy density and rate capability; (5) identify the interaction mechanism between sulfur species and different types of oxides/sulfides, and find the optimal material to improve the capacity and cycling of sulfur cathode. (II) Structure and property characterization, including (1) ex situ scanning electron microscopy; (2) XPS analysis; (3) in operando X-ray diffraction and optical microscopy. (III) Electrochemical testing including (1) coin cells and pouch cells; (2) A set of electrochemical techniques.

Results

We combine dark-field light microscopy (DFLM) and a planar electrochemical cell fabricated on a glass slide to visualize sulfur electrochemistry *in operando*, and a metal grid electrode (1 μm in line width, 50 nm in height) was deposited on a glass substrate via e-beam lithography for galvanostatic charging/discharging at room temperature (Figure II.9.C.1a-d). During electrochemical cycling, liquid-like sulfur microspheres form on Ni grids towards the end of charging (formation starts at ~ 2.8 V), and reversibly reduce into soluble polysulfide upon discharging (Figure II.9.C.1e-i). Well-separated nickel grids allow sulfur microspheres to be individually resolved and monitored. The microspheres are spherical, semi-transparent to light, and form over the entire surface of nickel grid electrode. As they grew larger and approached each other, neighboring droplets occasionally merged into larger droplets that relaxed rapidly to a spherical shape to minimize surface energy (Figure II.9.C.1j-k). To confirm the chemical composition of microdroplets, micro Raman spectroscopy was performed on the same sealed electrochemical cell. The Raman spectrometer had sufficient spatial resolution to collect spectra on individual sulfur microdroplets (Figure II.9.C.1l). The spectra of the droplets match that of solid sulfur powders but not polysulfides, indicating the liquid droplets are chemically cyclo-sulfur (S_8). Eutectic alloys of sulfur with other elements can significantly alter the freezing temperature, but the Raman spectra rule out this possibility. On the other hand, it is well known that small amounts of impurities serve as heterogeneous nucleation sites that limit the degree of supercooling. Sulfur in its molten state is also known to form polymeric chains, but earlier Raman spectroscopy investigations of the polymerization of S_8 monomers into higher order S_n polymers concluded that polymerization occurs at temperatures greater than 140°C .

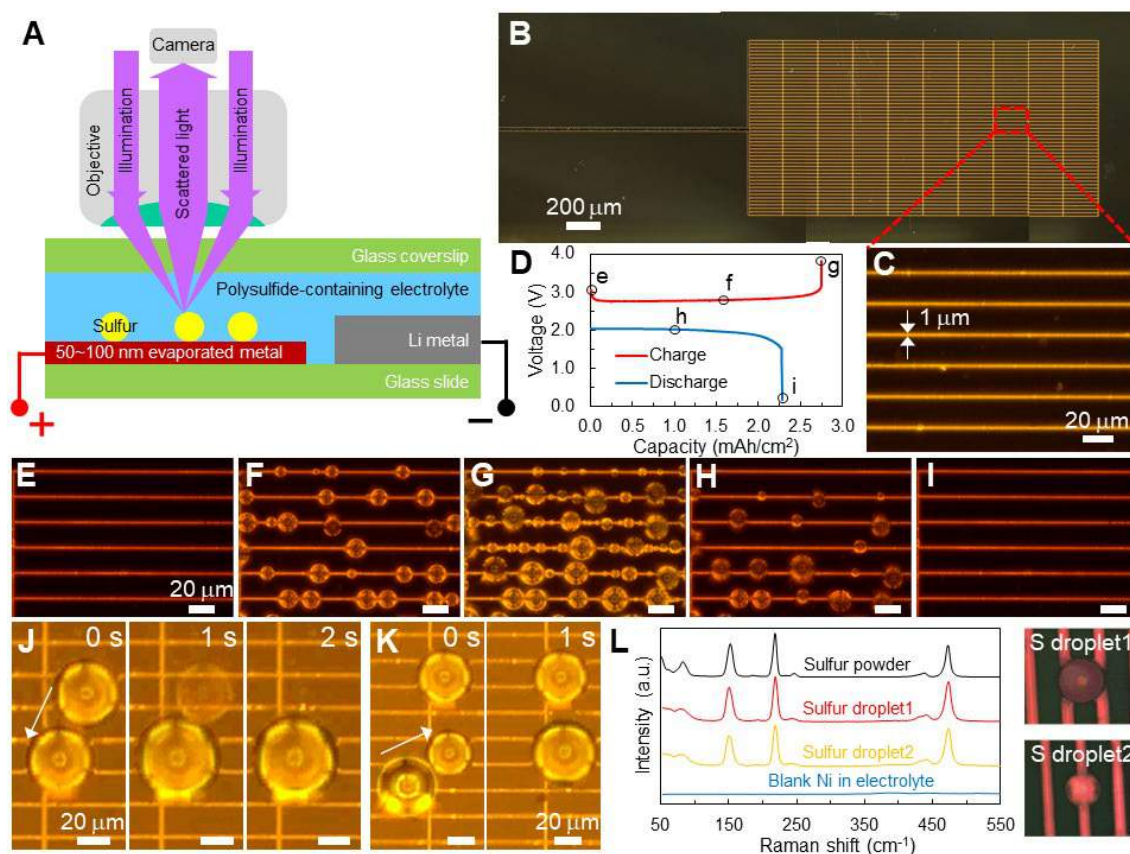


Figure II.9.C.1 (a) Schematic of the electrochemical cell design that allows in-operando dark field light microscopy (DFLM) observation. (b and c) DFLM images of the metal grid (50 nm thick, 1 μm wide) fabricated on glass slide as a substrate for the electrochemical cell. (d) Voltage profile of the cell. Time-lapse DFLM images (e-i) showing the formation and dissolution of super-cooled sulfur droplets. (j, k) Two sets of time-lapse images showing rapid merging of neighboring droplets and relaxation to spherical shape within one second, indicating the liquid nature of sulfur. (l) In situ Raman spectra of super-cooled sulfur droplets. Corresponding bright field light microscopy images captured by the Raman microscope are shown on the right. The spectra match that of solid S_8 powder, and the signals are not from electrolyte or substrate

In addition to nickel, these super-cooled liquid sulfur microdroplets electrochemically form on various other metal-containing substrates, including palladium, platinum, indium tin oxide (ITO), and cobalt sulfide (CoS_2) (Figure II.9.C.2a). In contrast, carbon substrate (polished glassy carbon) leads to the formation of irregular crystalline solid sulfur particles that do not undergo significant changes when contacting with each other (Figure II.9.C.2b). Therefore, the electrochemical formation of super-cooled sulfur is both generic and substrate-dependent. It should be noted that the super-cooling reported here is unlikely to stem from a size effect. Liquid-like behaviors have been shown to accompany extremely small (< 10 nm) particles, but the droplets reported here are micron-scale, whose melting point is close to bulk according to Gibbs-Thomson equation.

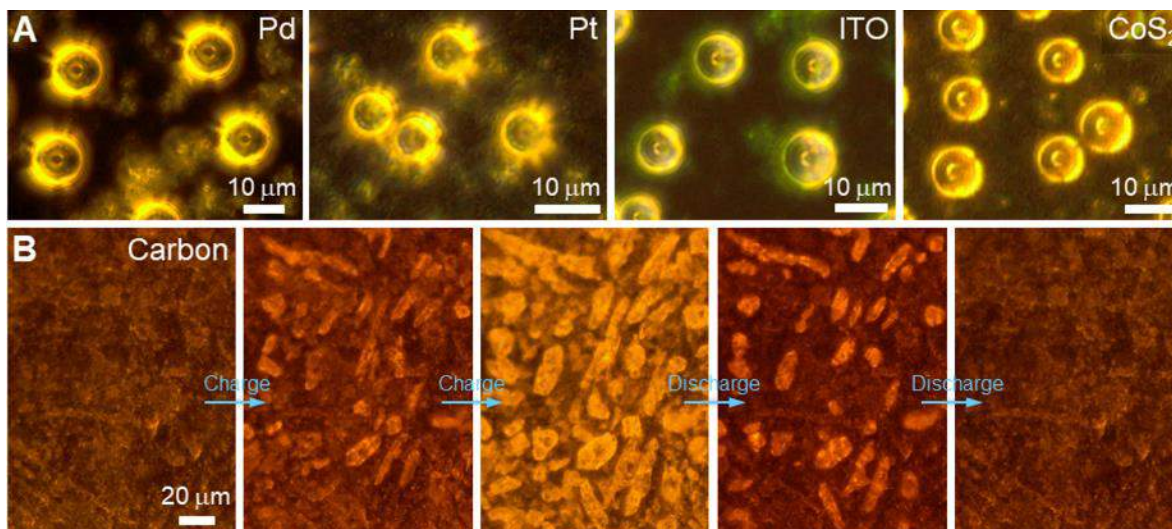


Figure II.9.C.2 (a) *In-operando* DFLM images of sulfur droplets electrochemically formed on Pd, Pt, indium tin oxide (ITO) and cobalt sulfide (CoS₂) substrates. (b) Time-lapse *in-operando* DFLM images of crystalline sulfur formation and dissolution on glassy carbon substrate

Super-cooled liquids usually solidify quickly after the onset of nucleation. The electrochemically generated super-cooled sulfur droplets do not solidify by themselves over an observation window of 1 hour. We induced nucleation at the microscale, to verify their meta-stability. We spread exfoliated graphite nano-platelets on Ni metal grids Figure II.9.C.3a and b) to electrochemically generate both sulfur droplets and crystals in one cell (Figure II.9.C.3c) and recorded events when a sulfur crystal grown from graphite touches a sulfur droplet grown on Ni. As shown in the time-lapse images in Figure II.9.C.3d-h, the sulfur microdroplets turned from transparent to frosted within one second upon the touch of a growing sulfur microcrystal, indicating the solidification of sulfur droplet. The rapid solidification preserved the spherical shape of the sulfur droplet (Figure II.9.C.3g). Upon further growth (Figure II.9.C.3h), the surface of the sulfur particle becomes rougher, indicating its solid and polycrystalline nature. A chain of such solidification events was also observed, confirming the meta-stability of electrochemically generated super-cooled sulfur droplets. Note that trace amounts of guest species may dope inside the liquid sulfur droplets and could originate from catalytic reactions of sulfur at metal-containing surfaces. However, the melting temperature of these solidified electrochemically generated sulfur microdroplets is similar to that of pure S₈ powders, indicating the purity of these super-cooled droplets is high.

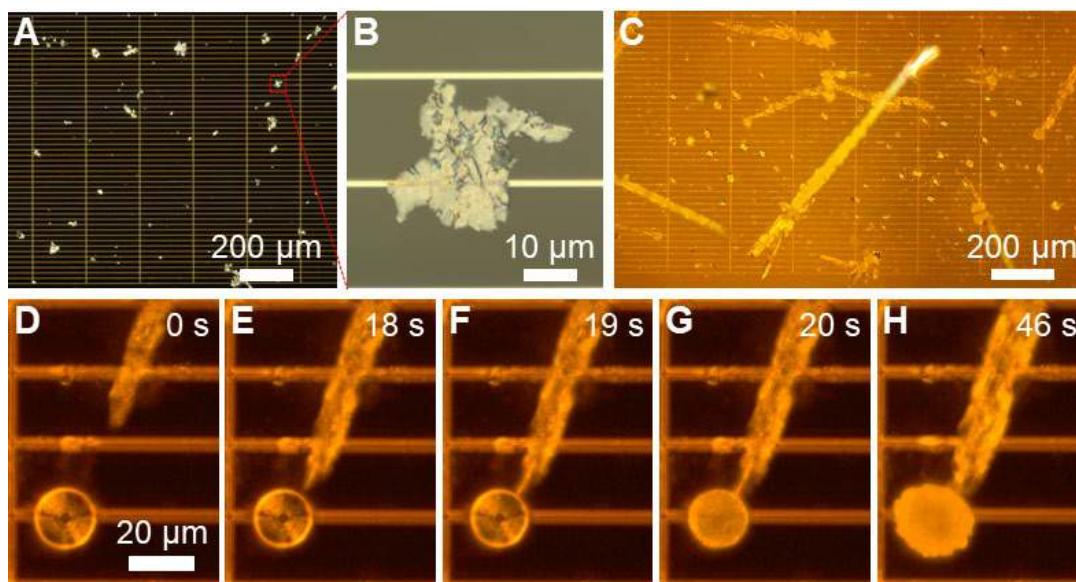


Figure II.9.C.3 (a) DFLM image of exfoliated graphite nano-platelets dispersed on Ni metal grid for growing solid and liquid sulfur in the same cell. (b) High-magnification bright field light microscopy image of a single nano-platelet sitting on Ni grid, as shown in the red box in (a). (c) *In-operando* DFLM image of the cell after charging, showing co-existing needle-shaped sulfur microcrystals and metastable sulfur droplets. (d-h) Time-lapse DFLM images showing the approaching of a needle-shaped sulfur microcrystal towards a sulfur microdroplet and its rapid solidification upon touching

While most sulfur microdroplets form on the conductive Ni line (Figure II.9.C.4a), we observed a few instances when they form on the insulating glass next to the Ni line (Figure II.9.C.4b). This suggests that sulfur could electrochemically form via a solution mechanism, in addition to the traditionally hypothesized surface mechanism. As shown in Figure II.9.C.4c, in surface mechanism, polysulfide anion transfers electrons to electrode and deposit locally, whereas in solution mechanism, electron transfer first generates soluble intermediate species which diffuse off the conducting substrate before depositing. We hypothesize the diffusive intermediate specie to be S_8 molecule, because it is slightly soluble in the DOL/DME electrolyte. The surface mechanism will have the issue of electrode surface being fully covered by the insulating charge/discharge product (sulfur/ Li_2S) and limit the areal capacity. The solution mechanism, however, allows the product to form off the electrode surface, therefore maintains the accessibility of electrode surface to electrolyte and enables high areal capacity and rate capability. The solution mechanism also applies to the reverse process of solid sulfur dissolution upon discharging. Large sulfur crystals dissolved isotropically, regardless of the accessibility of electron. And after they broke into segments, the electrically disconnected sulfur still reacted. This finding contradicts the common belief in Li-S battery that for insulating sulfur to be electrochemically active, it needs to have small size and be electrically connected to current collector.

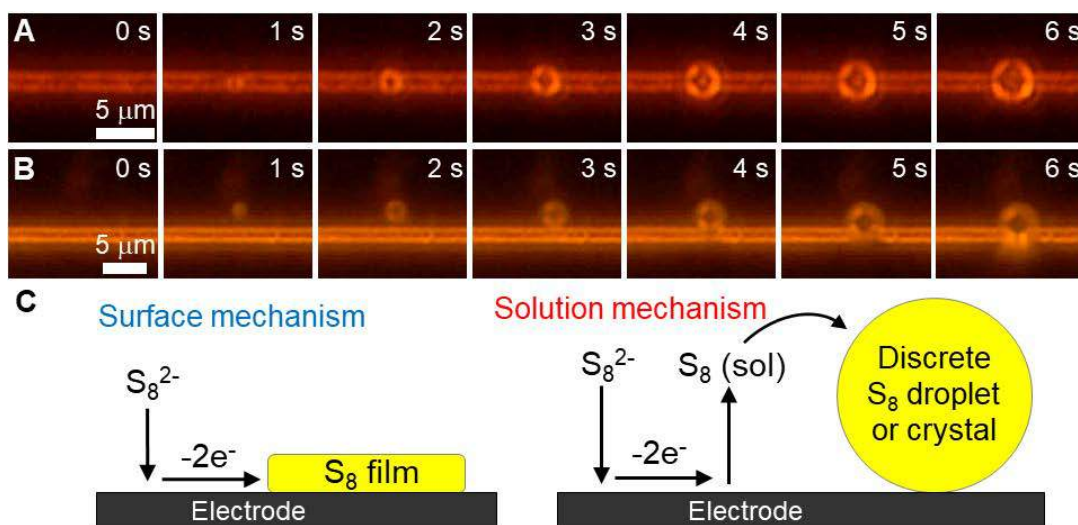


Figure II.9.C.4 (a and b) Time-lapse light microscopy images of the initial formation of sulfur droplets, one on the Ni grid (a) and another off the Ni grid on glass (b). (c) Two general mechanisms for the nucleation and growth of sulfur on electrodes. The solution mechanism is consistent with the results in both (a) and (b)

To evaluate the effect of current collector material on electrochemical performance, Ni-coated (~50 nm) aluminum (Al) foil was fabricated through e-beam evaporation (denoted as Ni), commercial carbon-coated Al (denoted as C) and Al foils were used as current collectors for Li-S batteries. Coin cells were assembled with lithium polysulfide catholyte using Li metal as the anode and different planar current collectors at the cathode. The cycling performance of Li-S batteries based on Ni, C, and Al electrodes are shown in Figure II.9.C.5a. A capacity of 0.98 mAh cm^{-2} was delivered for the Ni electrode at a current density of 0.05 mA cm^{-2} , which retained 95% of its capacity (0.93 mAh cm^{-2}) after 50 cycles (Figure II.9.C.5b), demonstrating good cycling stability. However, the capacity decayed quickly from 1.12 to 0.16 mAh cm^{-2} for the C electrode with a capacity retention of only 14% when tested at the same conditions. This capacity decay is mainly ascribed to the weak binding between carbon and lithium polysulfides causing the dissolution of polysulfides. Meanwhile, almost no redox reactions occurred on the Al surface which showed a capacity close to zero after three cycles, indicating the non-active surface of Al foil. When the current density was increased 5 times to 0.25 mA cm^{-2} , the battery with a Ni electrode still delivered a capacity of 0.77 mAh cm^{-2} , 69% of the capacity obtained at 0.05 mA cm^{-2} (Figure II.9.C.5c), indicating a fast charge/discharge capability, while C and Al electrodes could not work at this current density. Electrochemical impedance spectroscopy (EIS) was performed to further understand the charge transfer and resistance of these electrodes. Figure II.9.C.1d and inset show the Nyquist plots of the cells with Ni, C, and Al electrodes at open circuit before cycling. The depressed semicircle represents the charge transfer resistance (R_{ct}) on the electrode surface. It can be clearly seen that the R_{ct} of the Ni electrode is much lower than that of the C and Al electrodes (Figure II.9.C.5d). The smaller resistance indicates that the Ni layer exhibits faster charge transfer compared to that of the other electrodes, which will be further confirmed by theoretical calculations of the lithium ion charge transfer kinetics in later discussion.

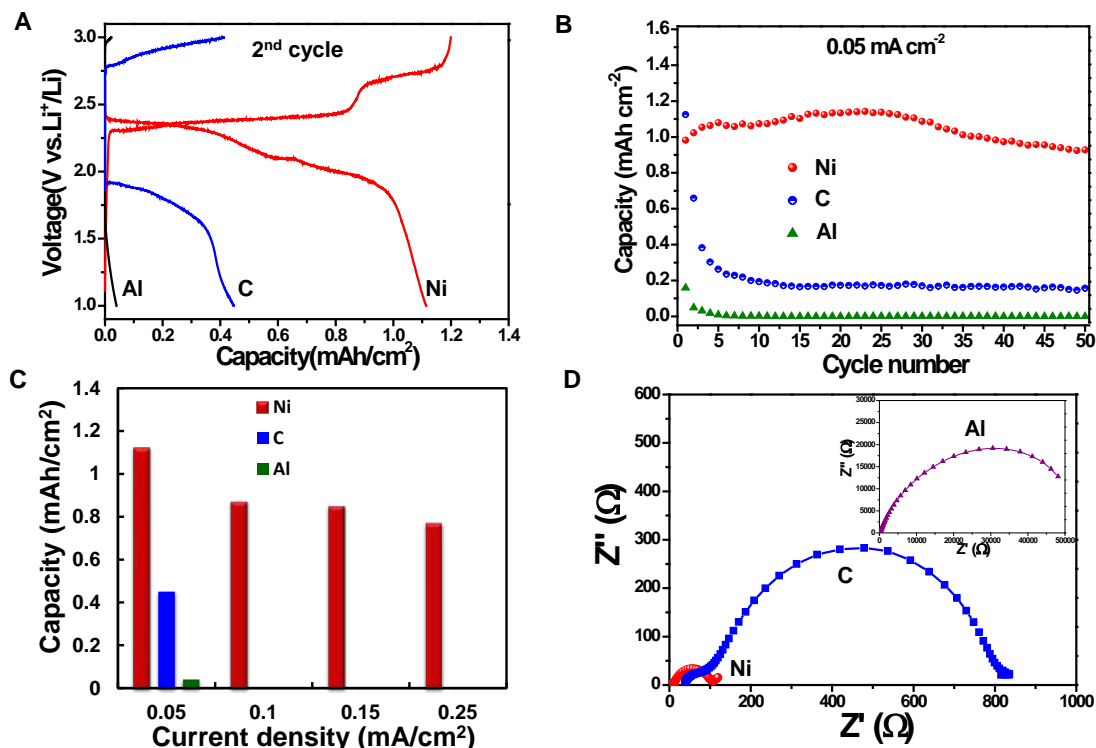


Figure II.9.C.5 (a) Charge/discharge voltage profiles of the Ni, C, and Al electrodes at a current density of 0.05 mA cm^{-2} . (b) Cycling stability of the Ni, C, and Al electrodes at a current density of 0.05 mA cm^{-2} for 50 cycles. (c) Comparison of the rate capacity of the Ni, C, and Al electrodes. (d) Nyquist plots of the Ni and C electrodes at open circuit before cycling at room temperature. Inset is the Nyquist plot of the Al electrode at open circuit before cycling at room temperature

To further understand the significantly different battery performance of these electrodes, in situ optical observation and ex situ experimental characterizations are combined to reveal the underlying mechanism. As sulfur species are sensitive to the atmosphere (*e.g.*, water and oxygen), electron beam, and X-ray irradiation, in situ optical microscopy is a mild and effective methodology to monitor the morphology evolution of sulfur species on different current collectors. As demonstrated in Figure II.9.C.6, distinct sulfur growth behaviors were observed on Ni, C, and Al electrodes. As seen from Figure II.9.C.6a-c, there was no sulfur growth or Li_2S deposition on the surface of Al over the entire range of applied voltage (from 1.0 to 3.0 V), suggesting the inertness of Al surface for sulfur redox. In contrast, many sulfur crystals (highlighted by the red circle) emerged and grew on the surface of the C electrode during charging (Figure II.9.C.6e). The subsequent discharge process was also monitored and a large number of flocculent, blurry particles precipitated out during the process (Figure II.9.C.6f). Most strikingly, spherical liquid sulfur droplets gradually nucleated and grew on the Ni substrate during charging, and all of the sulfur droplets dissolved and finally disappeared from the Ni surface during the discharging process (Figure II.9.C.6g-i). No clear features of Li_2S were visible after discharge, suggesting that the size of the Li_2S is possibly below the resolution limit of the optical microscope. Therefore, scanning electron microscopy (SEM) was employed to investigate the morphology change for the sulfur species on different substrates.

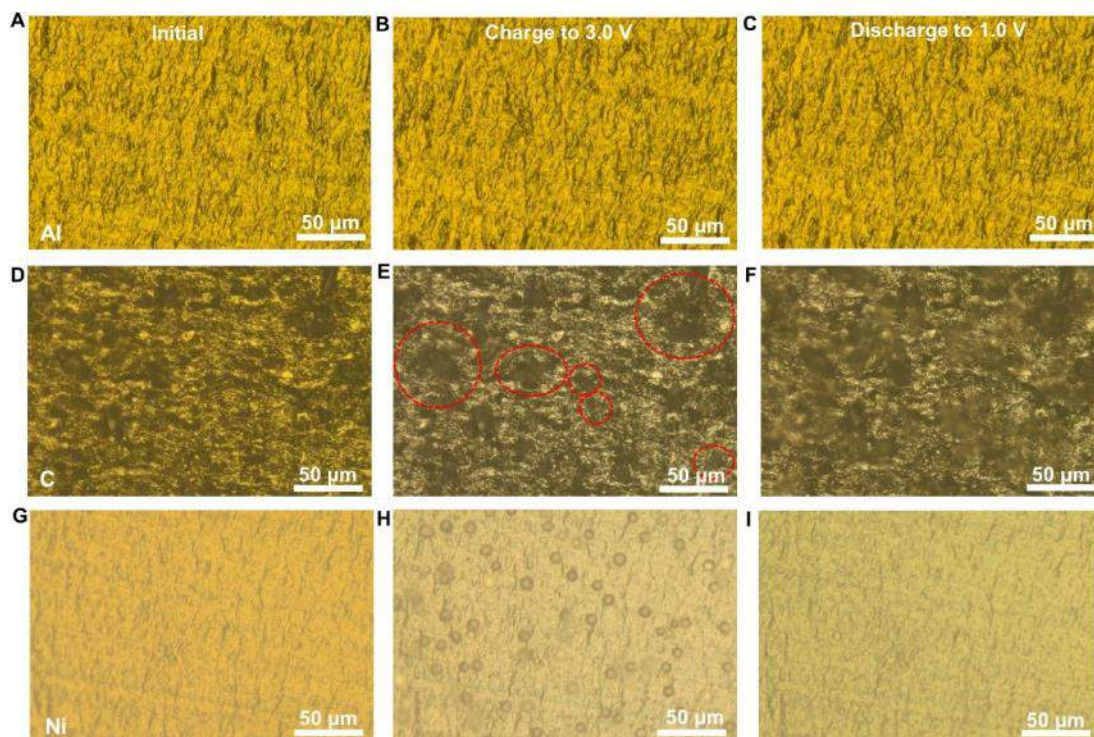


Figure II.9.C.6 Optical images of the Al electrode in lithium polysulfide electrolyte (a) at initial state, (b) after charging to 3.0 V, and (c) after discharging to 1.0 V. Optical images of the C electrode in lithium polysulfide electrolyte (d) at initial state, (e) after charging to 3.0 V, and (f) after discharging to 1.0 V. Optical images of the Ni electrode in lithium polysulfide electrolyte (g) at initial state, (h) after charging to 3.0 V, and (i) after discharging to 1.0 V

The cells based on the Ni, C, and Al electrodes were disassembled in the glovebox at the charged state (3.0 V) or the discharged state (1.0 V), washed using dioxolane, and examined by SEM. The morphologies of the sulfur species are displayed in Figure II.9.C.7. The Al surface is relatively inert with an ultra-low capacity, and with only a thin layer of sulfur/Li₂S coating the surface during charging and discharging (Figure II.9.C.7a and d). This is confirmed by the energy dispersive X-ray spectrometry (EDS) elemental analysis which shows a very weak sulfur signal coexisting with peaks from aluminum and oxygen. In contrast, large amounts of flower-shaped Li₂S particles composed of small sheets with sizes of about 2~3 μm were observed under SEM that randomly deposited on the surface of the C electrode during discharging (Figure II.9.C.7b). After charging to 3.0 V, in addition to the sulfur crystals produced by oxidation of Li₂S, some of the insoluble, flower-like Li₂S deposits remained on the carbon surface (inset of Figure II.9.C.7e). These insoluble Li₂S causes capacity decay due to irreversible sulfur conversion reactions, which is consistent with the cycling results. More interestingly, high density of vertically grown Li₂S nanosheets were observed for the Ni electrode during the discharging process (Figure II.9.C.7c), and the SEM image (Figure II.9.C.7f) combined with EDS spectrum indicate the complete conversion from Li₂S nanosheets to sulfur on the Ni surface after charging to 3.0 V. This reversible deposition/dissolution of the sulfur species on the Ni surface is critical to maintain efficient charge transfer kinetics and achieve a long term cycling stability for Li-S batteries.

In order to obtain a more detailed understanding of the Li₂S oxidation process, X-ray photoelectron spectroscopy (XPS) was used to analyze the products on Ni and C substrates at the charged states. In the high-resolution Li 1s spectrum, it is worth noting that no obvious features can be observed in the lithium signal from the Ni sample, indicative of the absence/little of lithium polysulfide intermediates or Li₂S after the charging process (Figure II.9.C.7g). However, the distinct lithium signal at around 55.3 eV can be clearly seen from the C sample (Figure II.9.C.7g), implying the existence of lithium sulfides that match well with the SEM results (Figure II.9.C.7e). As for the S 2p spectrum of the charged C electrode shown in Figure II.9.C.7h, other than

the peaks which correspond to elemental S (162.7 and 163.9 eV), the appearance of S^{2-} peaks (160.6 and 161.8 eV) in the XPS spectra, corresponding to Li_2S , indicates the existence of remaining Li_2S covering the surface of the carbon current collector. As for the Ni current collector, all the peaks can be ascribed to S^0 , confirming the complete conversion of polysulfides to sulfur (Figure II.9.C.7h). Therefore, the Ni layer speeds up not only the electron transfer but also the redox reaction of the polysulfide conversion on the electrode surface, which is expected to promote the reversibility of sulfur chemistry and enable high power capability for Li-S batteries.

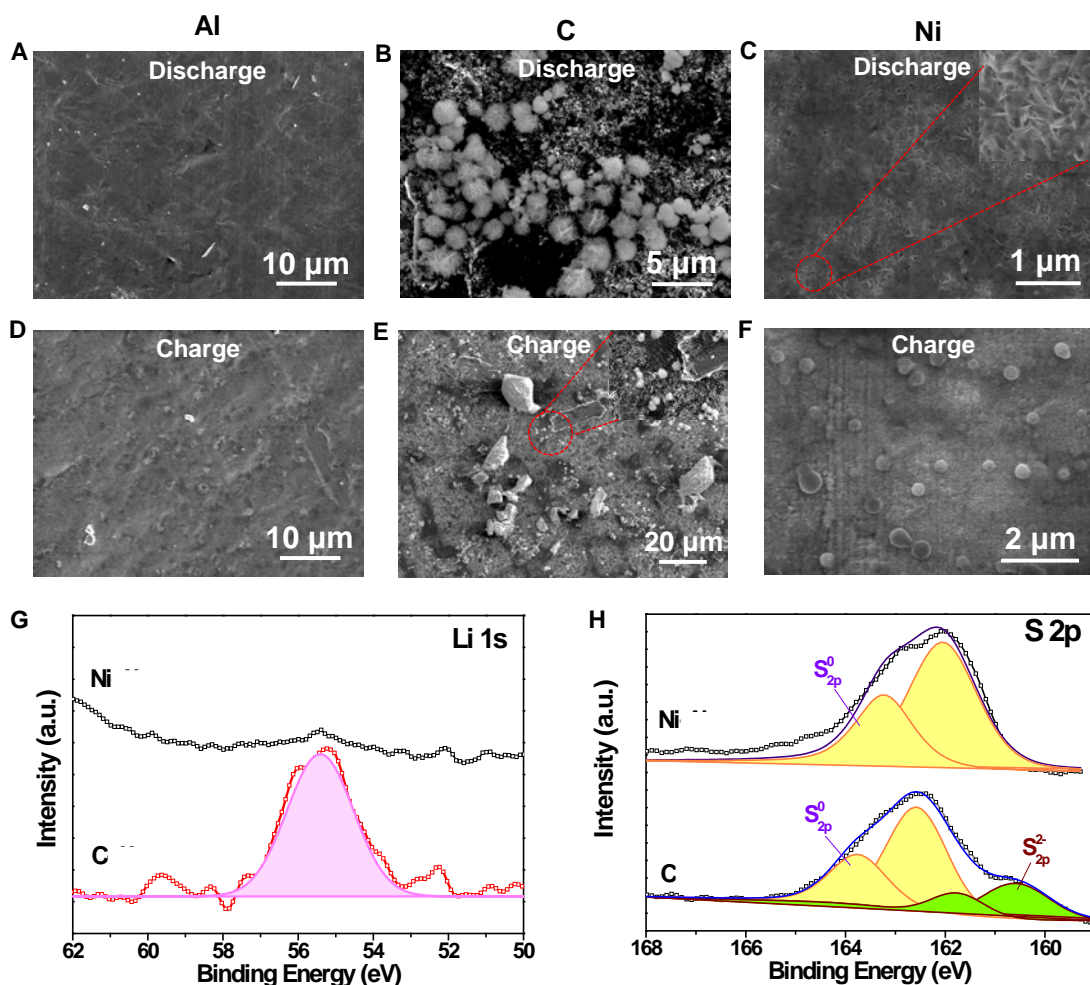


Figure II.9.C.7 SEM images of the discharging products formed on the (a) Al, (b) C, and (c) Ni substrates. Inset in (c) is the magnified area indicated by the red circle. SEM images of the charging products formed on the (d) Al, (e) C, and (f) Ni substrates. Inset in (e) is the magnified area indicated by the red circle. (g) Li 1s XPS spectra of the Ni and C substrates. (h) S 2p XPS spectra of the Ni and C substrates

Based on the above discussion, Figure II.9.C.8a-c present schematics of the sulfur species evolution on Ni, C, and Al substrates during the charging and discharging processes. During the charging process, some sulfur droplets start to nucleate on the surface of the Ni electrode. These liquid droplets are generated at small sizes, then grow up and merge together into larger sizes after touching each other. The liquid sulfur droplets leave plenty of unoccupied current collector surface as electrochemically active sites for polysulfide conversion, which enables the high area capacity on the Ni surface. Upon discharging, the liquid sulfur droplets reversibly reduce into soluble polysulfides and finally form sheet-like Li_2S depositing on the Ni surface (Figure II.9.C.8a). In contrast, on the C substrate, the accumulation of insulating Li_2S and disconnected sulfur crystals during repeated cycling will block charge transport across the electrode/electrolyte interface and cause active material loss, resulting in poor reaction kinetics and fast capacity decay (Figure II.9.C.8b). For Al substrates,

there is generally a thin and dense oxidation layer (Al_2O_3) on the surface, which weakens the adsorption of sulfur species on the interface, rendering the surface inert to sulfur conversion. Therefore, the thin layer of insulating sulfur/ Li_2S on the inactive interface passivates the electrode, terminating further accumulation of sulfur species and leading to the negligible capacity in charging/discharging processes (Figure II.9.C.8c).

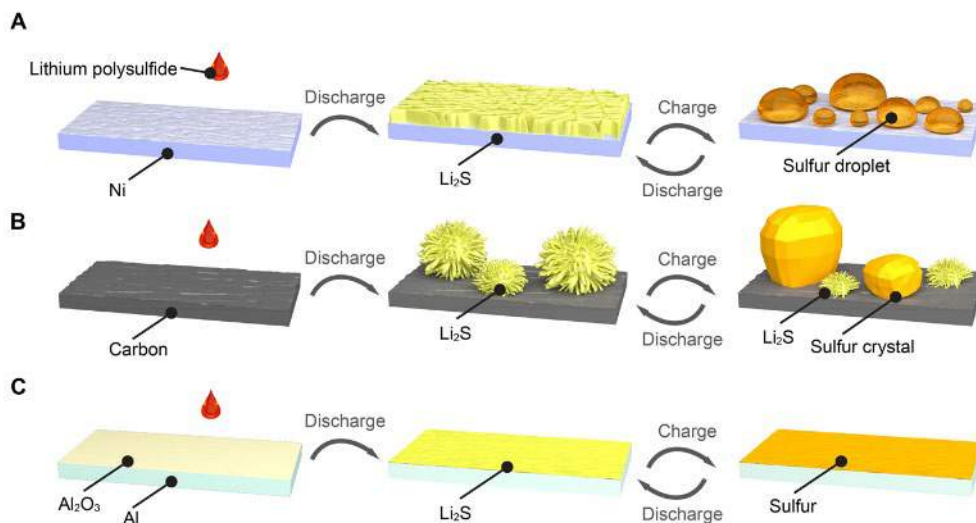


Figure II.9.C.8 Schematic illustration of the sulfur species evolution on (a) Ni, (b) C, and (c) Al substrates during charging and discharging processes

Conclusions

In all, in the past one year, we have made great progress in understanding the mechanism of Li-S batteries. In situ characterization platform to monitor nucleation/dissolution of sulfur/ Li_2S_n was built, which is a non-invasive imaging method with sub-micron, sub-second resolution for Li-S battery in label-free, native organic liquid electrolyte. Super-cooled liquid sulfur microdroplets were directly generated from polysulfide electrochemical oxidation on various metal-containing electrodes. The Sulfur droplets remain liquid at 155°C below sulfur's melting point ($T_m = 115^\circ\text{C}$), with fractional super-cooling change, $(T_m - T_{sc})/T_m$, larger than 0.40. *In operando* light microscopy captured the rapid merging and shape relaxation of sulfur droplets, indicating their liquid nature. Micropatterned electrode and electrochemical current allow precise control of the location and size of super-cooled microdroplets, respectively. Using this new platform, we initiated and observed the rapid solidification of super-cooled sulfur microdroplets upon crystalline sulfur touching, which confirms super-cooled sulfur's meta-stability at room temperature. In addition, the formation of liquid sulfur in electrochemical cell enriches lithium-sulfur-electrolyte phase diagram and potentially may create new opportunities for high-energy Li-S batteries. We also visualize the distinct sulfur growth behaviors on Al, carbon-coated Al (C), and Ni-coated Al (Ni) current collectors: no sulfur grows on the surface of Al, while solid sulfur crystals emerge on the carbon surface and supercooled liquid sulfur droplets appear on the Ni substrate during charging at room temperature. Through in situ optical microscopy, ex situ experimental characterization, as well as theoretical calculations, we demonstrate (1) liquid sulfur generated on Ni provides higher reversible capacity, faster kinetics and better cycling life compared to solid sulfur and (2) Ni facilitates the phase transition (e.g., Li_2S decomposition).

Key Publications

1. Nian Liu, Guangmin Zhou, Ankun Yang, Xiaoyun Yu, Feifei Shi, Jie Sun, Jinsong Zhang, Bofei Liu, Chun-Lan Wu, Xinyong Tao, Yongming Sun, Yi Cui*, Steven Chu*, Direct electrochemical generation of supercooled sulfur microdroplets well below their melting temperature, *PNAS*, 2019, 116, 765.

II.9.D Mechanistic Investigation for the Rechargeable Li-Sulfur Batteries (University of Wisconsin)

Deyang Qu, Principal Investigator

University of Wisconsin Milwaukee
3200 N Cramer Street
Milwaukee, WI 53211
E-mail: qud@uwm.edu

Xiao-Qing Yang, Principal Investigator

Chemistry Department
Bldg. 555, Brookhaven National Laboratory
Upton, NY 11973
E-mail: xyang@bnl.gov

Tien Duong, DOE Technology Development Manager

U.S. Department of Energy
E-mail: Tien.Duong@ee.doe.gov

Start Date: September 1, 2018

End Date: August 30, 2019

Total Project Cost: \$300,000

DOE share: \$300,000

Non-DOE share: \$0

Project Introduction

Rechargeable lithium sulfur (Li-S) batteries are considered potential candidates to replace cutting edge Li-ion batteries in EV due to their high theoretical energy density ($1672\text{mAh}\cdot\text{g}^{-1}$), safety, and low cost. However, the capacity loss for a rechargeable Li-S battery remains a major obstacle. The equilibrium reactions between dissolved polysulfides and elemental sulfur (polysulfide shuttle), are the major reason for the continuous decay of the capacity during cycling and high self-discharge during storage. This is especially true for the Li-S batteries with elemental sulfur as the redox materials and lithium salts in organic solvents as the liquid electrolytes.

In the past few years, we successfully developed a method to qualitatively and quantitatively determine all the dissolved polysulfides during the charge and discharge of a Li-S cell for the first time. The mechanisms for the sulfur redox reaction were revealed and the processes were better understood. Also, an in situ electrochemical-microscopic technique for the in situ investigation of the Li anode during cycling was established, so the interaction between dissolved polysulfide ions and Li-anode were investigated real time. Taking the advantages of the advancements of in situ diagnostic technologies, the effectiveness of many potential inhibitors was investigated, the stability of cell components in polysulfide electrolyte was also studied.

With these better understandings of the mechanisms for Li-S chemistry, in 2018 we firstly, further investigated the sulfur redox reaction in various electrolytes with the focus on the inhibition for the “shuttle effect” (one of the major conclusions during the past work was that sacrificial additives like LiNO_3 which can slow down the “shuttle effect” initially cannot solve the problem since they eventually are consumed). Secondly, synthesized and tested many composite sulfur compounds e.g., polymer sulfide compounds to replace the elemental sulfur as cathode active material. Thirdly, tailored the physical properties of the sulfur (sulfide) composites, developed and improved electrode making processes to increase the aerial capacity and aerial rate capability of the cathode. Finally, explored various alternative anode materials to replace metallic Li in order to eliminate the chemical reactions between the anode and dissolved polysulfides in the electrolyte.

We will continue to engage in the fundamental in situ electrochemical investigations of the sulfur redox mechanisms so better approaches can be found to mitigate the problem of the “shuttle effect” e.g., proper

electrolyte composition and additives. We will also engage in the creative engineering design of electrode manufacturing processes to suit the new composite cathode materials. Potentially, Li-S batteries could enable competitive market entry of electric vehicles by reducing the cost and extending the driving distance per charge.

Objectives

The primary objectives are:

- To continue conducting focused fundamental research on the mechanism of “shuttle effect” inhibition for rechargeable Li-S batteries;
- To continue developing the electrode and electrolyte systems which can mitigate the “shuttle effect” so the low self-discharge and long cycle life can be achieved.
- To synthesize sulfur composite materials. In this objective, special attentions will be focus on polymer sulfur composite materials.
- To develop creative electrode making processes to improve processability and aerial capacity, e.g., polymeric sulfur composite may not be suitable for the traditional slurry casting process.

The ultimate goal for the project is to develop a practical rechargeable Li-S battery to meet the challenges of powering the next generation of electric vehicles beyond Li-ion technologies.

Approach

1. In situ High Performance Liquid Chromatography (HPLC)/Mass Spectroscopy (MS)-Electrochemical method. The overall electrochemical and chemical reactions of dissolved polysulfides can be monitored in real time.
2. Ex situ X-ray diffraction (XRD) and X-ray photoelectron spectroscopy (XPS) to investigate the surface of the sulfur cathode and Li anode to elucidate the surface changes during the Li-S battery operation.
3. In situ 3D microscope and electrochemical measurement in a specially designed cell to detect dendrite growth during cell operation.
4. Synthesis of polymer sulfur composite materials to limit the dissolved polysulfide ion migration.
5. Dry method to make high aerial capacity electrodes.
6. Extended collaboration with other U.S. and international academic institutions and U.S. industrial partners.

Results

Figure II.9.D.1 shows our thinking of how to mitigate the “shuttle-effect” of the dissolved polysulfide ions. The main purposes are firstly to localize the dissolved polysulfide ions in the cathode matrix, and secondly to prevent the chemical reactions between the anode and dissolved polysulfide ions. We are exploring a way to bond the polysulfide species on the backbone materials, and new anode materials.

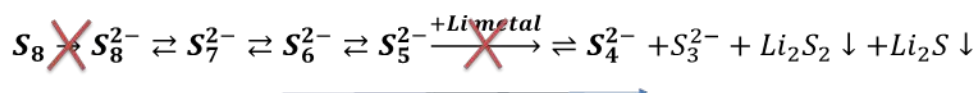


Figure II.9.D.1 Prevent dissolution of the polysulfide ions and their reaction with the anode

1, Synthesis and test of polymeric sulfur compound as cathode materials with high rate and good cycle performance.

In order to better localize the polysulfide in the cathode matrix and prevent them from diffusing into the bulk electrolyte and making contact with the Li anode, we tried to bond the polysulfide species onto the backbone materials, either modified carbon or polymers through chemical bonds. Based on findings from the literature research, polymer sulfur materials were synthesized and tested as Li-S cathode. An example of a typical synthesis mechanism of a sulfur-polymer is shown in Figure II.9.D.2, and selective unsaturated cross-linkers for sulfur containing polymers in Figure II.9.D.3. In order to make sure the entrapment of all polysulfides in the cathode matrix, the binding energy between polysulfides and backbone (polymer) of the matrix must be stronger than the solvation energy of polysulfide and Li ion with solvent. Cross linking is an effective way for the restriction of polysulfides within the electrode matrix, since the mobility of polysulfides can be limited by chemical bonding or relatively strong Van de Waals forces. However, there remains some engineering challenges, especially in material processing. The copolymer compounds are elastic in nature and therefore have a low packing density. Many of those compounds are also difficult to dissolve in solvent, so the traditional slurry casting technique widely used in Li-ion electrode manufacturing may not be adequate for making sulfur copolymer electrodes. Table II.9.D.1 and Figure II.9.D.4 show the performance of the ten copolymer cathodes synthesized in 2019, made with improved processes. Improvement can be demonstrated.

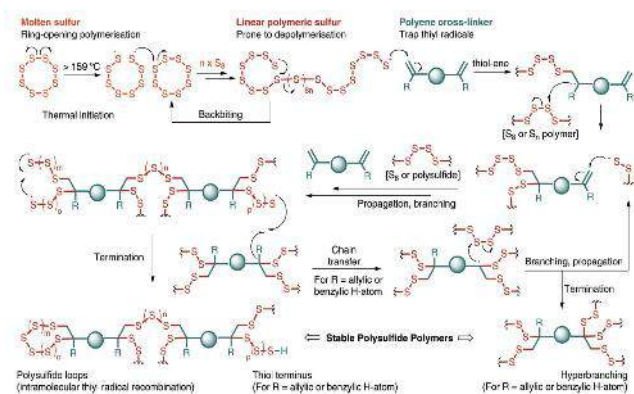


Figure II.9.D.2 Example of synthesis route of a sulfur co-polymer compound. Chalker et al, Green Chem. 2017,19,2748

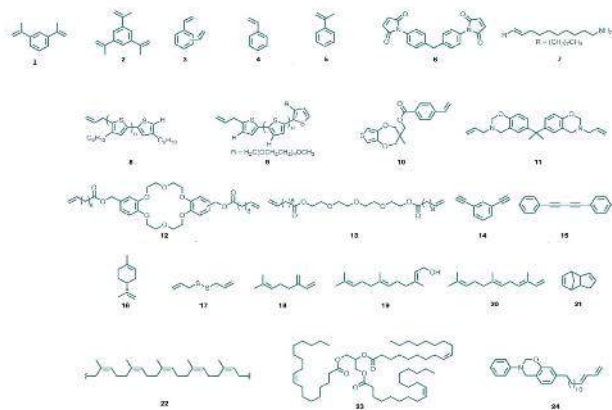


Figure II.9.D.3 The selection of possible cross-linking groups for the co-polymers

Table II.9.D.1 Test results of ten synthesized co-polymer electrodes in 2018, but with improved electrode processes.

	1 st Discharge Capacity (mAh/g)	100 th Discharge Capacity (mAh/g)	200 th Discharge Capacity (mAh/g)
1	632.9	467.8	340.7
2	671.2	359.3	371.8
3	783.2	374.8	n/a
4	252.3	242.3	201.1
5	1091.8	580.7	n/a
6	210.9	68.5	56.7
7	696.6	323.4	2744.8
8	749.9	319.0	178.7
9	227.3	190.3	133.4
10	743.5	374.9	290.2
S8	1365.0	300.9	207.5

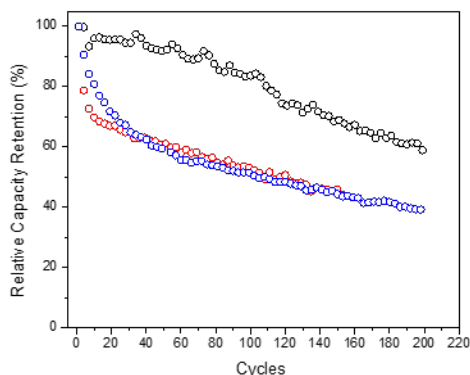


Figure II.9.D.4 Comparison of relative capacity retention of three selected copolymer cathodes

We continued the chemical synthesis of different new sulfur containing copolymer materials. For example, the procedures for the synthesis of the conductive crosslinked Polysulfur-random-PPV copolymer cathode material was further refined. The synthesis route and mechanism to copolymerize sulfur with p-Phenylene vinylene derivative is shown in Figure II.9.D.5. The sulfur content can be adjusted during the synthesis according to the conditions. The physical properties of the resulting material vary with the percentage of sulfur in the copolymer. Although the cycle life was significantly improved, the volumetric density is still lower than traditional sulfur/carbon cathode due to the intrinsic elastic nature of the polymer, and the copolymer did not dissolve well in organic solvents to form a slurry. New electrode fabrication methods are under development to replace the slurry coating method.

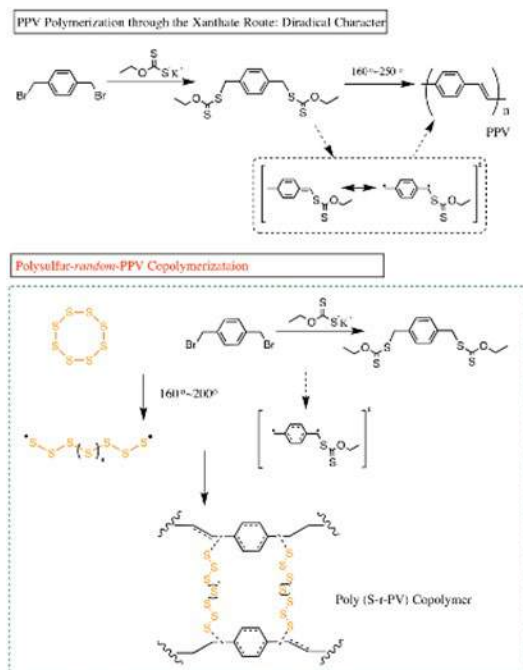


Figure II.9.D.5 Copolymerize sulfur with p-Phenylene vinylene to form crosslinked sulfur-rich S/Xant- copolymer

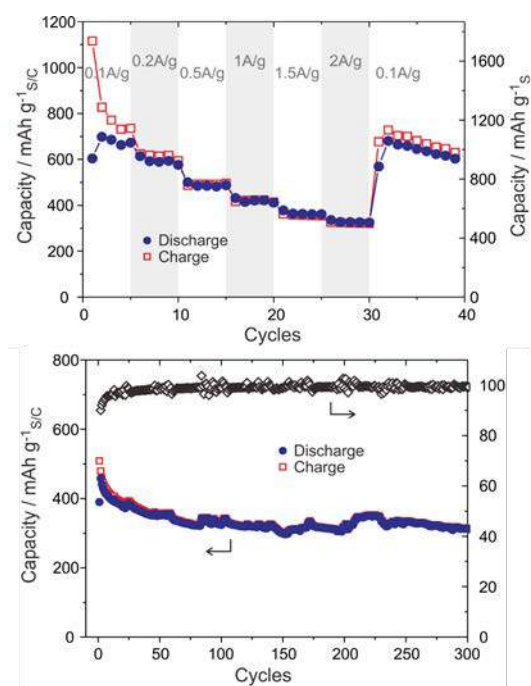


Figure II.9.D.6 Rate performance of a coin cell made of fully prelithiated Phosphorus anode and 75% Sulfur/carbon cathode (up); the cyclability of the cell (low). copolymer

2, Development of Li containing anode which does not react with the dissolved polysulfide ions - prelithiated P/C anode and sulfur Batteries.

In order to mitigate the chemical reactions between the Li anode and the polysulfide ions, alternative Li containing anode materials are also under investigation. A prelithiated P/C electrode was obtained by immersing the pristine P/C electrode into 1 M Li-Bp/THF. Apart from compensating for the initial capacity loss due to the consumption of active Li ions during the formation of the SEI layer, the anode prelithiation also enabled the P/C electrode to pair with the Li-free sulfur cathode due to the fact that reversible Li can also be pre-loaded into P/C matrix. Due to the less negative potential of a prelithiated P/C electrode against Li, when a fully-prelithiated P/C electrode is used to replace the Li metal anode, the “shuttle” effect may be limited due to less reactive anode with dissolved polysulfides. Figure II.9.D.6 shows the performance of a coin cell made with a fully prelithiated phosphorus anode paired with a sulfur-carbon cathode (75% sulfur). The resulting P/S coin cell exhibited a good rate capability and cycling stability even with a more limited lithium source than that in a metallic Li anode. At 1 A/g discharge rate, it delivered an initial capacity of 460 mAh g⁻¹, based on sulfur and carbon weight (S/C). The P/S cell retained a reversible capacity of 312 mAh g⁻¹(S/C) after 300 cycles, with a capacity decrease of 0.10% per cycle and an average coulombic efficiency over 99%. It demonstrated discharge capacities of 686, 589, 485, 421, 363, and 327 mAh g⁻¹(S/C) at 0.1, 0.2, 0.5, 1, 1.5, and 2 A g⁻¹, respectively. When the current density was back to 0.1 A g⁻¹, it delivered a reversible capacity of 681 mAh g⁻¹(S/C). The new configured S/P cell can provide a theoretical maximum energy density of 967 Wh kg⁻¹ based on the theoretical capacity of sulfur, fully prelithated phosphorous and slightly lower discharge voltage of the cell. An energy density of 358 Wh kg⁻¹ has been realized based on the total weight of cathode and anode at the discharge capacity at 0.1 A g⁻¹. In Figure II.9.D.7, the concept for a full cell made with a fully-prelithiated P/C anode and a S/C cathode is schematically illustrated. Good rate and cycling performance of a prelithiated P/C electrode is also demonstrated in the Figure II.9.D.7. In a full S/P cell, a good rate capability and cycling stability are shown in the figure despite a limited Li source. At 1 A/g, it delivered an initial capacity of 460 mAh g⁻¹_{S/C} and retained a reversible capacity of 312 mAh g⁻¹_{S/C} after 300 cycles, with a capacity decrease of 0.10% per cycle and an average CE over 99%. The S/P cell exhibited a similar voltage profile as a S/Li cell except at different voltages, displaying two discharge plateaus at 1.4 V and 1.1 V. Despite the output voltage being a little low, the newly configured S/P cell could provide a theoretical maximum energy density of 967 Wh kg⁻¹. An energy density of 358 Wh kg⁻¹ has been realized in a not-optimized coin cell, based on the total mass of active materials (P/C and S/C). In addition, both S and P are cheap and environmentally abundant.

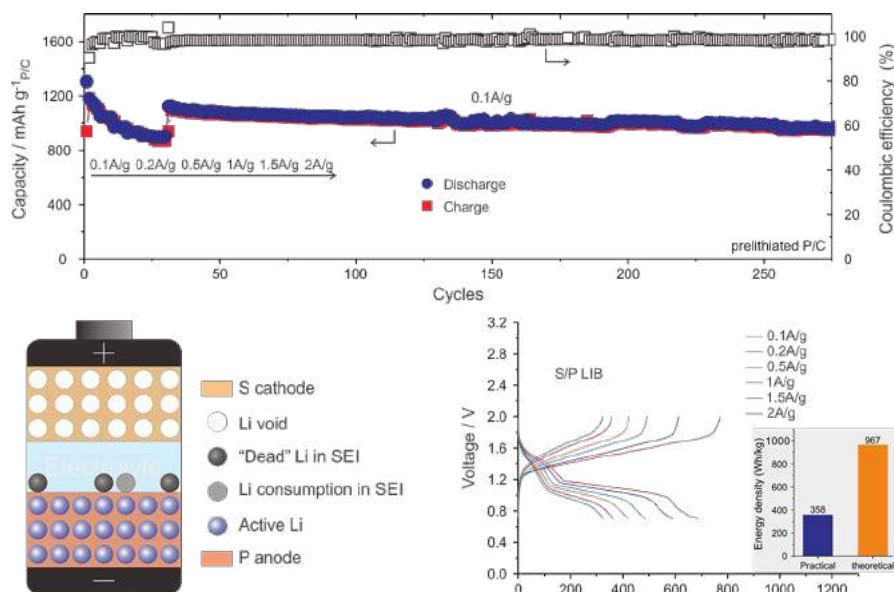


Figure II.9.D.7 Schematic illustration of the S/P batteries (low/left); rate and cycling performance of a fully prelithiated P/C anode prepared through patented chemical methods (up); typical voltage profiles at different current densities (d). Insert is the theoretical and practical energy densities of the S/P LIB (low/right)

3, Evaluation and testing electrolyte additives in Li/S cells

Seven small organic sulfides were investigated: CH₃SCH₃, C₂H₅SC₂H₅, C₃H₇SC₃H₇ (mono-sulfide); CH₃SSCH₃, C₂H₅SSC₂H₅, C₃H₇SSC₃H₇ (di-sulfide) and CH₃SSSCH₃ (tri-sulfide). Two types of sulfur cathodes were tested: a typical elemental sulfur cathode (prepared by infusing elemental sulfur S₈ into carbon matrix at 170°C) was tested as a control; a polymeric sulfur cathode (prepared by polymerizing sulfur and monomer organic substrate under heated condition) was also tested. Figure II.9.D.8A and B show the cycling results for the control and the polymeric sulfur cathodes, respectively. Evidentially, small organic sulfides, including dimethyl sulfide (DMS), diethyl sulfide (DES), dipropyl sulfide (DPS), dimethyl disulfide (DMDS), diethyl disulfide (DEDS), dipropyl disulfide (DPDS), and dimethyl trisulfide (DTS) were shown to *have little influence on the cycle-performance of Li-S (S₈) and Li-PS(polymeric sulfur) batteries*. The results are shown in Figure II.9.D.8.

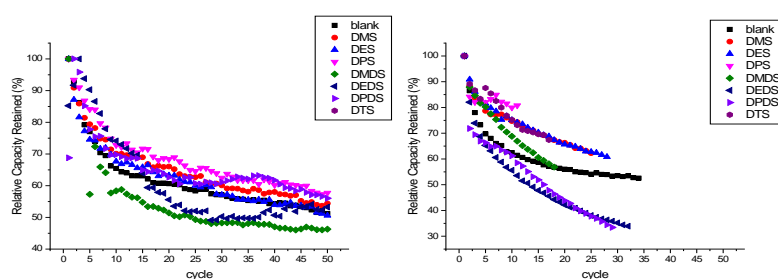


Figure II.9.D.8 (A) The sulfur cathode is a polymeric sulfur (co-polymerization with monomer) electrode, the averaged capacity is 0.805 mAh discharge/charge; (B) The sulfur cathode is an elemental sulfur electrode, the averaged capacity is 2.075 mAh discharge/charge at 50uA between 1.8 to 2.8V

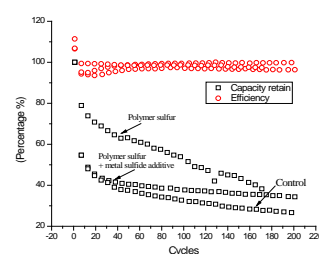


Figure II.9.D.9 Cycle life of sulfur and polymer sulfur cathodes with metal sulfide additives

Due to the specific interactions between some transition metals such as Hg, Ag, and Cu with elemental sulfur and polysulfides, it's conceivable that sulfides or polysulfides of those metal elements, as a cathode additive, could either effect the redox mechanism of sulfur, or localize the polysulfide intermediates within the cathode

matrix. Either way, the polysulfide “shuttle effect” could be alleviated. As shown in Figure II.9.D.9, the Hg/Sulfur mixture as an additive has observable influence on the cycling performance of Li-S batteries. For the polymeric sulfur cathode without an additive, the capacity kept decreasing throughout the whole duration of cycling, even though the initial capacity retention was better. The capacity decay of a polymeric sulfur cathode with an additive was mainly observed at beginning. After the 50th cycle, however, the capacity remained relatively steady. The mechanisms of such improvements are still under investigation.

Conclusions

1. Various sulfur containing co-polymers were synthesized and tested. The hypothesis that the strong chemical bonding in the co-polymers can limit the dissolution of polysulfide ions in the electrolyte. Thus, reducing the “shuttle-effect”.
2. Alternative Li-containing anode materials can significantly reduce the chemical interaction between the anode and dissolved polysulfide ions, which also can reduce the “shuttle-effect”.
3. Additives to the electrolyte are not conclusive.
4. It has been proven that the in situ HPLC-MS electrochemical essays developed to quantitatively and qualitatively determine the polysulfide ions are very useful for Li-S investigation.

Key Publications

Gongwei Wang, Feifei Li, Dan Liu, Dong Zheng, Caleb J Abegglen, Yang Luo, Xiao-Qing Yang, Tianyao Ding, Deyang Qu “High performance lithium-ion and lithium–sulfur batteries using prelithiated phosphorus/carbon composite anode” *Energy Storage Materials* <https://doi.org/10.1016/j.ensm.2019.08.025>.

II.9.E Electrochemically Stable High Energy Density Lithium Sulfur Batteries (University of Pittsburgh)

Dr. Prashant N. Kumta, Principal Investigator

University of Pittsburgh
815C Benedum Hall, 3700 O'Hara Street
Pittsburgh, PA 15261
E-mail: pkumta@pitt.edu

Dr. Moni K. Datta, Principal Investigator

University of Pittsburgh
815C Benedum Hall, 3700 O'Hara Street
Pittsburgh, PA 15261
E-mail: mkd16@pitt.edu

Dr. Oleg I. Velikokhatnyi, Principal Investigator

University of Pittsburgh
815C Benedum Hall, 3700 O'Hara Street
Pittsburgh, PA 15261
E-mail: olv3@pitt.edu

Tien Duong, DOE Technology Development Manager

U.S. Department of Energy
E-mail: Tien.Duong@ee.doe.gov

Start Date: October 1, 2018	End Date: September 30, 2019	
Project Funding (FY19): \$439,129	DOE share: \$395,197	Non-DOE share: \$43,932

Project Introduction

Lithium–sulfur battery (LSB) technology is widely investigated as an attractive alternative to currently used Li-ion battery (LIB) chemistries for the EV/PEV industry due to the superior theoretical capacity (1674 mAh/g) and specific energy density (2600 Wh/kg) of elemental sulfur. Moreover, the natural abundance of sulfur in the earth's crust makes it a more economical and highly attractive proposition compared to currently existing intercalation-based LIB cathode materials systems. However, the dissolution of sulfur via formation of soluble polysulfides (PSs) (i.e., poor capacity retention) and the inferior electronic conductivity of S (barrier to complete active materials utilization) are one of the primary limitations of LSBs along with the concomitant development of the Li metal anode which together continue to hinder the much-awaited commercialization of the system. Current generation sulfur cathodes show low reversible specific storage capacity, very poor charging rates and low loading densities. There is hence, a vital need for conducting research to overcome the major issues impeding the development of high energy density LSB technology to enable next generation systems meeting the Battery 500 objectives.

Objectives

This project is a scientific study to obviate the primary problems of (a) low overall electrode capacity (mAh/g-active material) occurring due to low electronic conductivity of sulfur (b) poor cycling stability owing to polysulfide (PS) dissolution (c) voltage drop due to PS transport across and the deposition at the lithium anode (d) poor coulombic efficiency (CE). The target of the Battery500 seedling projects is in-line with the overall objectives of the program with the target being to deliver either lithium metal/sulfur cells or lithium/NMC cells exhibiting in excess of 500 Wh/kg energy density and stable cycling over 1000 cycles shown in Table II.9.E.1 below. The proposed innovative and engineered strategies involving polysulfide confinement, sulfur electrocatalyst (SEC), directly derived sulfur assembled (DDSA) electrodes of electronically conducting

nanostructured doped sulfur yielding high sulfur loadings $> 10 \text{ mg/cm}^2$ will yield sulfur cathodes displaying specific capacity $\geq 1200 \text{ mAh/g}$ (electrode-level capacity), at $\geq 2.2 \text{ V}$ generating $\sim 600 \text{ Wh/kg}$ energy density systems higher than the target objectives. Full cells meeting the required deliverables will be made and performance tested in pouch cells. Successful completion of the proposed program will yield: (a) Targeted lithium-sulfur battery (LSB) specific energy ($\geq 500 \text{ Wh/kg}$) and energy density ($\geq 750 \text{ Wh/l}$), (b) Compact light-weight LSB, (c) Economical and scalable precursors; (d) Excellent life-cycle (~ 1000 cycle), calendar life (~ 15 years) and fast recharge-ability. Finally, full cells with optimized sulfur cathodes and dendrite free lithium metal anodes (LMA) will be generated with the following performance metrics: Specific energy $> 500 \text{ Wh/kg}$, cyclability (> 1000 cycles), loss per cycle $< 0.01\%$, Coulombic Efficiency (CE): $> 90\%$ capable of meeting MIL-STD-810G and IEC62133 industry safety standards.

Table II.9.E.1 Battery Specifications for the Battery 500 Program

Energy Storage Performance Requirements		Battery500
Characteristics	Unit	
Specific Energy	Wh/kg	> 500
Energy Density	Wh/l	> 750
Electrode Sulfur Loading	Mg/cm^2	> 10
Specific Capacity	mAh/g	≥ 1200
Voltage	V	≥ 2.2
Calendar Life	Year	~ 15
Cycle Life	Cycles	> 1000
Loss Per Cycle	%	< 0.01
Coulombic Efficiency	%	$> 90\%$

Approach

(i) Generation of novel high sulfur loading directly doped sulfur architecture (DDSA) binder free cathodes and unique polysulfide trapping agent (PTA) configurations (S1), (ii) Generation of novel inorganic framework materials (IFM) enabling high sulfur loading and polysulfide (PS) confinement (S2), (iii) Development of organic Complex Framework Materials (CFMs) serving as improved sulfur hosts using wet-chemical methods (S3), (iv) Generation of high Li-ion conducting (LIC) and PS dissolution resistant coatings on sulfur nanoparticles. (v) Identification of functional catalysts (FCs) for rapid conversion of PS to Li_2S and Li_2S to Li and S.

To achieve the Batt 500 goals for the selected systems, studies in Phase 2 will involve three main thrust areas:

Thrust 1: Improvement of selected materials performance and scale up

The proposed technology involves improving the selected materials performance to be executed in the following fashion: S1: (a) Extended cycle life (~ 1000 cycles) testing using Batt 500 protocol; (b) if the capacity fade is $\geq 30\%$, S1 will be coated with conjugated lithium polymer (CLiP), sulfur containing polymer (SCP) and LIC coatings, (c) Increase S loading in S1 by optimizing the process and LIC coating parameters for direct testing to achieve the targeted cycle life (~ 1000 cycles) and areal capacity $\geq 6 \text{ mAh/cm}^2$; (d) fabricate large area electrode ($\sim 20 \text{ cm}^2$) for pouch cell testing. For S2 and S3: (a) Similar to S1, S2 and S3 materials will be coated with CLiP-SCP-LIC to achieve the targeted cycle life; (b) incorporation of functional catalysts (FCs) identified in Phase 1 to promote rapid PS to Li_2S conversion kinetics and improve cycle life; and (c) Synthesis

of highly porous, economic, and electronically conductive FC based IFM and new CFMs infiltrated by S (CFM-S) to yield the targeted capacity ($\geq 1000 \text{ mAh/g}$) and cycle life (~ 1000 cycle).

Thrust 2: Electrode Fabrication of targeted areal capacity (6 mAh/cm^2)

Fabrication, characterization and optimization of high S loading electrodes of S2 and S3 will achieve the targeted areal capacity ($\geq 6 \text{ mAh/cm}^2$) and cycle life (~ 1000 cycles) with fade in capacity of $\sim 0.01\%$ loss per cycle. Computational modeling of the electrode will be conducted using Finite Elements methodology to identify electrode geometrical parameters. Morphological engineering of S2 and S3 electrodes exploiting 3D printing and electrospinning will be performed to achieve low charge transfer resistance, and high Li ion conductive multi-layer 3D architectures electrodes leading to high rate-capacity cells.

Thrust 3: Pouch cell fabrication and testing technology

The optimized large area electrodes ($\sim 20 \text{ cm}^2$) exhibiting targeted areal capacity and cycle life will be used in the assembling of pouch cell with CPE systems as separators developed in Phase 1 and in-house synthesized Li metal alloy anodes ($\sim 100 \mu\text{m}$).

Results

The current project involved identification and synthesis of functional catalysts (FCs) for rapid conversion of polysulfides (PS) to lithium disulfide as well as optimization of the high loading directly doped sulfur architecture (DDSA) electrodes.

To accelerate the polysulfide (PS) conversion forward to Li_2S and backward to form pure Li and S, functional catalyst materials were identified to facilitate both, the forward and backward reactions (**Reactions 1 and 2**) (**Equation 1**) and correspondingly, significantly decrease or even completely eliminate the PS dissolution. Several compounds as potential functional catalysts (FCs) have been chosen for the present study.

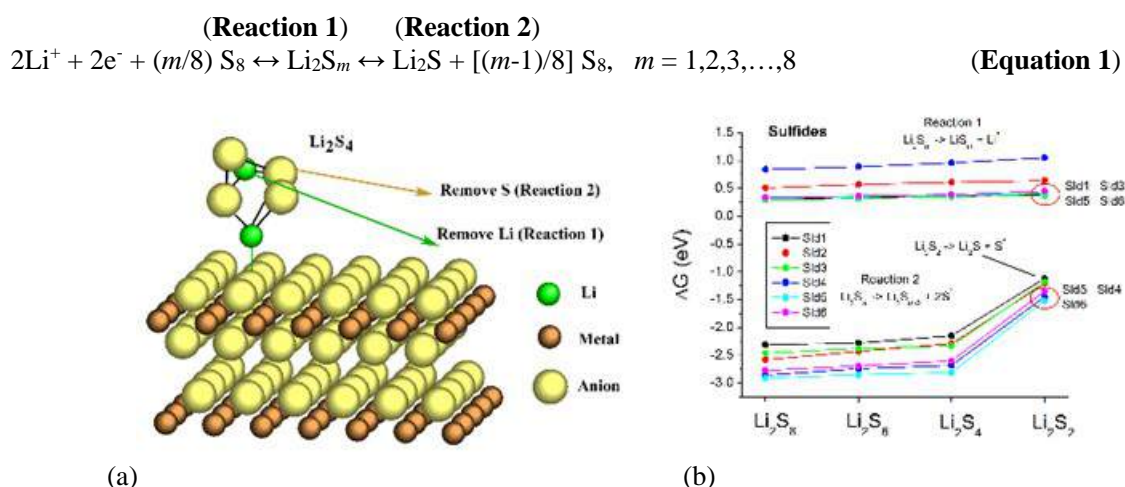


Figure II.9.E.1 Schematic representation of the FC surface with attached polysulfide molecule (removal of Li or S atom represents reaction 1 or 2, respectively) and free energies of reaction 1 and 2 for different FCs and polysulfides

A schematic representation of the FC surface with the attached polysulfide molecule is shown in Figure II.9.E.1a. The decomposition energy ΔG of the various PSs is different for the different FCs (see Figure II.9.E.1b). The best catalysts for **Reaction 1** are Sld1, Sld3, Sld5, and Sld6, while for **Reaction 2** are Sld4, Sld5, and Sld6. Thus, for both reactions, Sld5 and Sld6 are the best. The FCs identified in this work will be evaluated experimentally and reported subsequently.

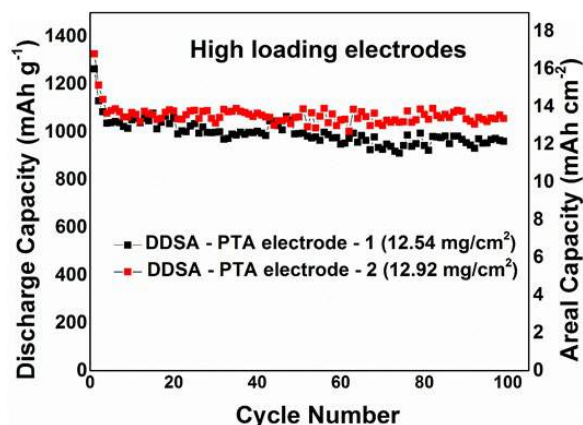


Figure II.9.E.2 Electrochemical cycling of PTA-DDSA electrode using the Batt 500 lean electrolyte protocol

The research work also involved electrochemical testing of PTA coated DDSA electrodes using the Batt 500 protocol (lean electrolyte-3 μ l/mg S). Both forms of the DDSA electrodes, PTA-DDSA-1 and PTA-DDSA-2 electrodes show an initial capacity of 1263 mAh/g and 1326 mAh/g respectively, when cycled at C/20 rate. Upon prolonged cycling, both PTA-DDSA-1 and PTA-DDSA-2 show a capacity of 1023 mAh/g and 986 mAh/g respectively after 100 cycles at C/5 rate.

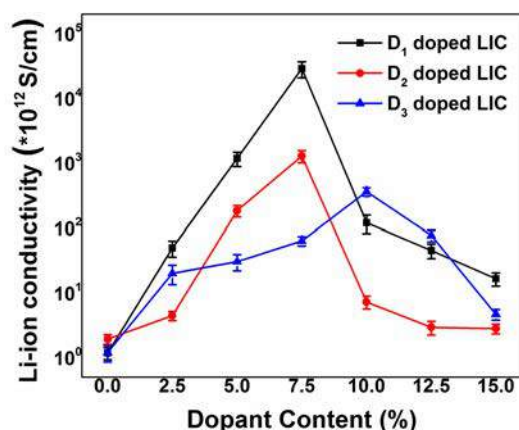


Figure II.9.E.3 Li ion conductivity of the doped LICs predicted by theoretical analysis using DFT

Research conducted during FY2019 period of the current project involved electrochemical performance study of the doped lithium ion conductors (LICs) identified in Phase 1 (Figure II.9.E.3) and explore their polysulfide shielding properties. The doped and undoped LICs coated thick nano sulfur pelletized electrodes (~ 7.5 mg-S/cm²) were tested in a Li-S battery and the changes in the charge transfer resistance (R_{ct}) before cycling at open circuit potential was analyzed by electrochemical impedance spectroscopy (EIS) (Figure II.9.E.4a). EIS test shows a steady R_{ct} decrease for the LIC coated electrodes with dopant additions due to higher lithium ion conductivity of the doped LICs contrasted with undoped LIC predicted by the DFT calculations. Doped and undoped LIC coated S electrodes were then cycled at a charge and discharge rate of 0.2C for 100 cycles to assess the influence of the dopants on the cycle life. Cycling results (Figure II.9.E.4b) show improved cycling stability for the doped LIC coated electrodes compared to undoped LIC coated electrodes. D₁ doped LIC in fact, yielded a capacity of 553 mAh/g while undoped LIC displays only 247 mAh/g after 100 cycles. These initial results reveal the ability of the doped LICs to improve the sulfur cathodes cycling stability by decreasing the interface impedance and also anchoring the polysulfides from entering the electrolyte.

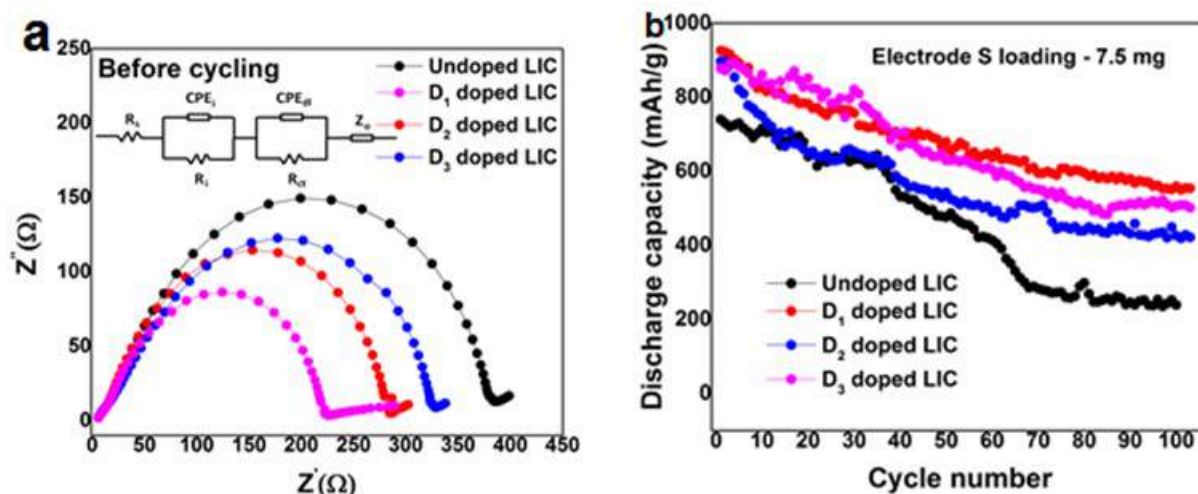


Figure II.9.E.4 a) EIS analysis of the Li-S batteries fabricated using the doped LIC coated sulfur electrodes as cathodes; Figure b) Cycle life performance of the doped and undoped LIC coated sulfur cathodes cycled at a rate of 0.2C

Subsequently, sulfur infiltrated sulfur-copper-bipyridine derived complex framework material (S-Cu-bpy-CFM) developed in Phase 1 (Figure II.9.E.5) were evaluated for their performance as cathodes. Correspondingly, the doped and undoped LICs coated on S-Cu-bpy-CFM pellet electrodes (~ 3.8 mg-S/cm²) were tested in coin cells with Li metal in lean (~ 3 ul/mg) electrolyte conditions.

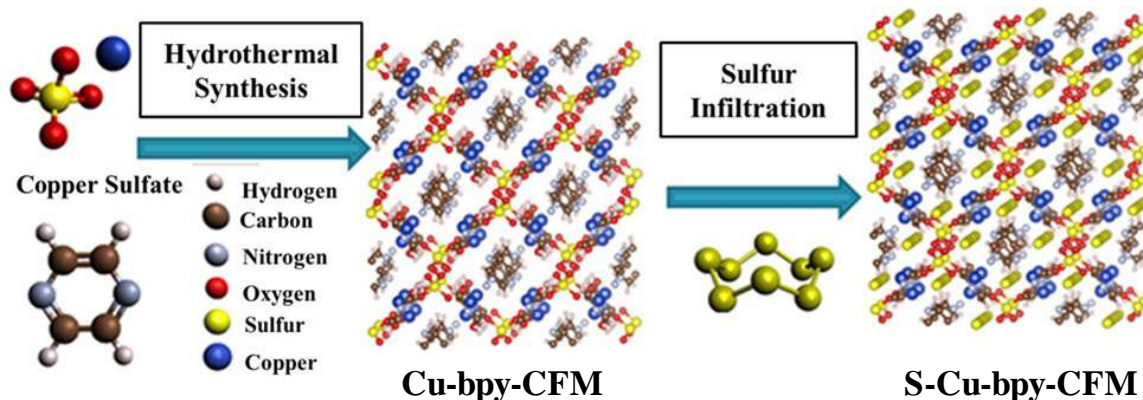


Figure II.9.E.5 Synthesis of Cu-bpy-CFM and sulfur infiltrated S-Cu-bpy-CFM electrodes (EnergyTechnol.2019, 1900141, <https://doi.org/10.1002/ente.201900141>)

Effect of doping on cycling stability of the S-Cu-bpy-CFM cathodes cycled at 100 mA/g current (Figure II.9.E.6a) and rate capability (Figure II.9.E.6b) were evaluated by comparing the cycling of doped and undoped LIC coated S-Cu-bpy-CFM cathodes. Undoped LIC coated S-Cu-bpy-CFM cathodes display an initial capacity of 873 mAh/g and a stable capacity of 583 mAh/g after 100 cycles. The doped LIC coated S-Cu-bpy-CFM cathodes on the other hand, showed much better cycling and rate capability due to higher Li-ion conductivity of the doped LICs. Electrodes with D₁ doped LIC show an initial capacity of 871 mAh/g stabilizing to 702 mAh/g after 100 cycles. These results support the theory that doped LICs enhance the cycling stability and rate capability of S-Cu-bpy-CFM cathodes by improving the sulfur utilization and anchoring polysulfides from

entering the electrolyte. Results of ongoing work on different porous, cost effective functional catalysts based inorganic framework materials and carbon based CFM will be described in the subsequent reports to follow.

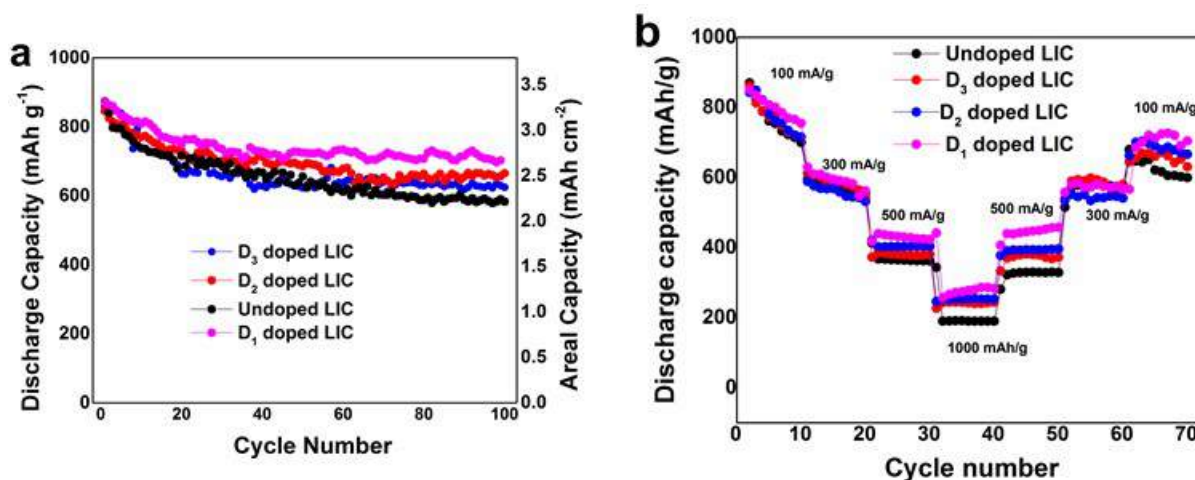


Figure II.9.E.6 (a): Cycling performance of doped and undoped LIC coated S-Cu-bpy-CFM cathodes cycled at a rate of 100 mA/g. Figure II.9.E.2(b): Rate capability performance of the doped and undoped LIC coated S-Cu-bpy-CFM cathodes

Continued research in FY 2019 involved development of electronic conductor (EC) and lithium ion conductor (LIC) coated complex framework materials (CFMs), the results of which are described herein. As a continuation of the work on novel doped lithium ion conductors (LICs) in Phase 1, work conducted in FY 2019 involved chemically coating these lithium ion conducting LICs and ECs onto porous CFMs to improve their electronic conductivity ($\sim 10^{-3}$ S/cm) along with room-temperature lithium ion conductivity ($\sim 10^{-4}$ S/cm). High sulfur loading (~ 4.5 - 7 mg/cm²) cathodes with ~ 64 wt% sulfur content were prepared from sulfur infiltrated EC-CFM and LIC-CFM. These cathodes were cycled against lithium metal using 1.8M LiTFSI and 0.2M LiNO₃ solution under lean electrolyte conditions ($\sim 4 \mu$ l/mgS). The EC-CFM-S cathodes exhibited a stable specific capacity of 678 mAh/g and areal capacity of 3.8 mAh/cm² after 70 cycles when cycled at C/10 rate (Figure II.9.E.7a&b). The LIC-CFM-S cathodes on the other hand, exhibited a stable specific capacity of 662 mAh/g and areal capacity of 4.04 mAh/cm² after 70 cycles when cycled at C/10 rate. These results are in alignment with the Battery500 requirements for Phase II and current research efforts are focused on further improving this initial promising performance.

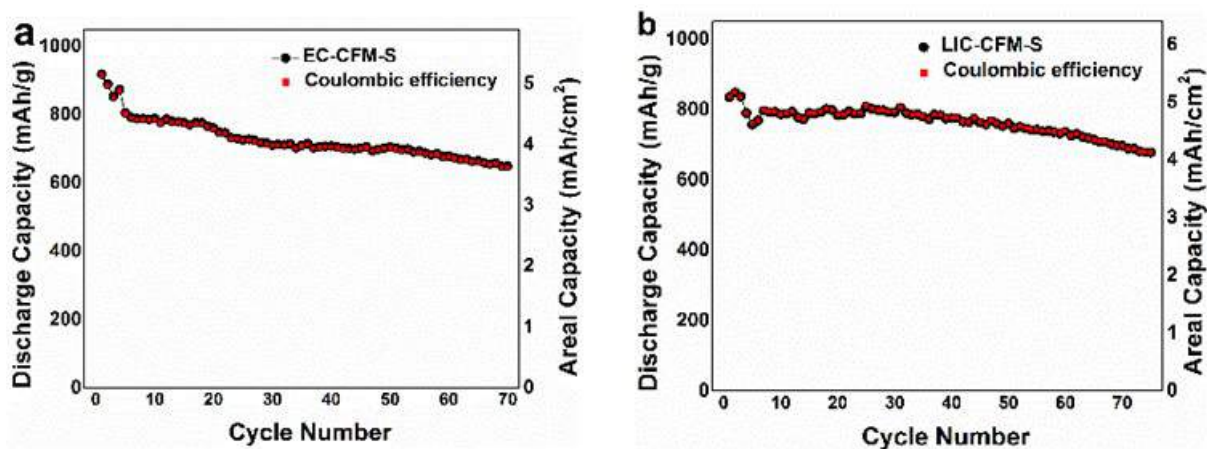


Figure II.9.E.7 a: Cycling performance of EC-CFM-S and 7b: Cycling performance of LIC-CFM-S

During the last phase of FY 2019, the project also involved conducting DFT based study to identify prospective functional catalysts (FCs) for rapid conversion of polysulfides to Li_2S and to $\text{Li}+\text{S}$. As a continuation of the study initiated in the previous phases of FY 2019, another type of prospective functional catalysts have been explored using this approach. At present, the computation has been performed for both reactions (1) and (2) at six different metal oxide surfaces. The decomposition energies ΔG of the various polysulfides are different for the different oxides as shown on Figure II.9.E.8. For both reactions oxides 1, 3, and 6 are the best. Theoretical consideration of various other inorganic systems as potential functional materials will be conducted in the near future followed by the experimental validation of the theoretical findings. Results of these findings will be reported in subsequent reports.

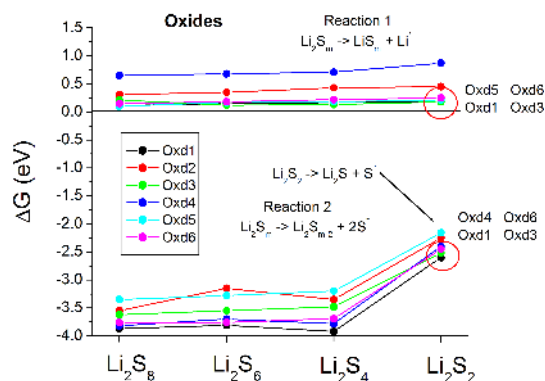


Figure II.9.E.8 Free energies of reaction 1 and 2 for different metal oxides as functional catalytic materials and polysulfides

Conclusions

The aim of Phase-2 in 2019 was to improve the cycling characteristics and reduce the polysulfide dissolution in Li-S batteries by using solid state lithium ion conductors (LICs) using DFT calculations. Undoped LIC coated S-Cu-bpy-CFM cathodes display an initial capacity of 873 mAh/g and a stable capacity of 583 mAh/g after 100 cycles. The doped LIC coated S-Cu-bpy-CFM cathodes on the other hand, showed much better cycling and rate capability due to higher Li-ion conductivity of doped LICs. Electrodes with D₁ doped LIC show an initial capacity of 871 mAh/g stabilizing to 702 mAh/g after 100 cycles. In addition, work was directed at developing sulfur architectures by infiltrating sulfur into chemically coupled conducting complex framework materials (CFMs). By implementing such a unique approach various complex framework materials system (EC-CFM-S and LIC-CFM-S) were derived and evaluated as cathodes in lithium sulfur batteries. The EC-CFM-S showed a stable discharge capacity of 678 mAh/g after 70 cycles at C/10 rate, LIC-CFM-S exhibited a high discharge capacity of 662 mAh/g after 70 cycles at C/10 rate.

Key Publications

1. Jampani, P.H.; Gattu, B.; Shanthi, P.M.; Damle, S.S.; Basson, Z.; Bandi, R.; Datta, M.K.; Park, S.K.; Kumta, P.N. Flexible sulfur wires (Flex-SWs) – A Versatile platform for lithium-sulfur batteries, *Electrochimica Acta* Vol. 212, pp. 286 - 293 (2016)
2. Shanthi, P.M.; Jampani, P.H.; Gattu, B.; Sweeney, M.; Datta, M.K.; Kumta, P.N. Nanoporous Non-Carbonized Metal Organic Frameworks (MOFs): Understanding the Origin of Irreversible Capacity loss in Non-Carbonized Carbonate – based Metal Organic Framework (MOF) Sulfur hosts for Lithium – Sulfur battery, *Electrochimica Acta*, Vol, 229, pp 208–218 (2017)
3. Shanthi, P.M., Jampani, P.H., Gattu, B., Albuquerque T., Datta, M.K., Kumta, P.N., “Novel electrospun PVdF – HFP Composite Polymer Electrolytes (CPEs) with enhanced Ionic Conductivities for Lithium – Sulfur batteries”, *ACS Applied Energy Materials*, 2018, 1 (2), 483–494. 1.

4. Pavithra M Shanthi, Oleg Velikokhatnyi, Prashanth J Hanumantha, Bharat Gattu, Moni K Datta, Prashant N Kumta, "Density functional theory and experimental strategies for improving the lithium-ion conductivity of doped Li_4SiO_4 " – under review.
5. Pavithra M Shanthi, Prashanth J Hanumantha, Kuruba Ramalinga, Bharat Gattu, Moni K Datta, Prashant N. Kumta, "Sulfonic Acid – based Metal Organic Frameworks (MOFs) – New Polysulfide Immobilizing Systems for Lithium – Sulfur battery", J. Electrochem. Society, 2019
6. Pavithra M Shanthi, Prashanth J Hanumantha, Kuruba Ramalinga, Bharat Gattu, Moni K Datta, Prashant N Kumta, "Spectroscopic investigations of Cu-bpy and Cu-pyz Metal Organic Framework (MOF) systems for Lithium – Sulfur battery" – Energy Technology, 2019.
7. Jampani, P.H.; Gattu, B.; Shanthi, P.M.; Kumta, P.N. Novel electro-spun sulfur wires for fabricating mattes of lithium-sulfur batteries, International Patent Number: WO 2016/145429 A1, U.S. Provisional Patent, Application Number: PCT/US2016/022283 (Filing date: 03/14/2016)
8. Shanthi, P. M, Jampani, P.H., Gattu, B.; Datta, M K, Velikokhatnyi, O. I., Kumta, P.N., "Electrospinning of PVdF-HFP: Novel Composite Polymer Electrolytes (CPEs) with enhanced ionic conductivities for Lithium-Sulfur batteries." U.S. Provisional Appln. Serial No. 62/529,638 (2017).
9. Jampani, P.H., Shanthi, P. M., Gattu, B., Datta, M K, Velikokhatnyi, O.I., Kumta, P.N., "High capacity, air-stable, Structurally Isomorphous lithium Alloy (SIA), Multilayer Porous Foams (MPFs) and Composite Multilayer Anodes (CMAs) for dendrite-free lithium metal anodes for Li-ion batteries", U.S. Provisional Patent Appln. No. 62/529,588 (2017).

Acknowledgements

Colleen Butcher (U.S. Department of Energy/NETL) served as the program manager for this project. Research fully supported by the U.S. Department of Energy OVT-DE-EE0006825. Partial support from the Edward R. Weidlein Chair Professorship Funds, Nanomaterials for Energy Conversion and Storage Technology (NECST) Laboratories, and the Center for Complex Engineered Multifunctional Materials (CCEMM) from the University of Pittsburgh is also acknowledged for assistance and help with procuring the electrochemical equipment and facilities used in this research work.

II.9.F New electrolyte binder for Lithium sulfur battery (LBNL)

Gao Liu, Principal Investigator

Lawrence Berkeley National Laboratory
1 Cyclotron Road
Berkeley, CA 94720
E-mail: gliu@lbl.gov

Tien Q. Duong, DOE Technology Development Manager

U.S. Department of Energy
E-mail: Tien.Duong@EE.DOE.GOV

Start Date: October 1, 2018

End Date: September 30, 2019

Project Funding (FY19): \$400,000

DOE share: \$400,000

Non-DOE share: \$0

Project Introduction

A strong demand for low-cost and high-energy-density rechargeable batteries has spurred lithium-sulfur (Li-S) rechargeable battery research. First, sulfur is an abundant and low-cost material. Second, the Gibbs energy of the lithium (Li) and sulfur reaction is approximately 2,600 Wh/kg, assuming the complete reaction of Li with sulfur to form Li_2S , more than five times the theoretical energy of transition metal oxide cathode materials and graphite coupling. With these advantages, Li-S batteries could be both high energy density and low cost, satisfying demand in energy storage for transportation application. The major obstacle is the loss of sulfur cathode material as a result of polysulfide dissolution into common electrolytes, which causes a shuttle effect and significant capacity fade. The polysulfide shuttle effect leads to poor sulfur utilization and fast-capacity fade, which have hindered widespread use of rechargeable Li-S batteries. This work is focused on developing polymer composite to confine and capture of the polysulfide to enable stable Li-S rechargeable batteries.

Objectives

This project aims to identify and develop new electrode composition and functional adhesive binders for Li-S battery. The properties of the ideal sulfur electrode would have high electronic conductivity, have good ion conductivity, be stable towards polysulfide, and promote the polysulfide affiliation with the electrode substrate to prevent polysulfide dissolution.

Approach

The chemical confinement both at material and electrode level alleviates the diffusion of polysulfides and the shuttle effect. Covalently bond sulfur polymer composite is developed to immobilize sulfur species. A polyisoprene-sulfur (PIPS) copolymer and nano-sulfur composite materials are synthesized through inverse vulcanization of PIP polymer with sulfur micron size particles for high areal capacity lithium sulfur batteries. The composite forms polycrystalline structure and sulfur nanodomain in the copolymer matrix. PIP polymer is also used as binders for the electrode to further capture the dissolved polysulfides. This approach enables scalable materials production and high sulfur utilization in the cell level.

Results

We demonstrate a copolymer based on grafted sulfur on polyisoprene (PIP) as the electroactive materials to realize high areal capacity sulfur electrodes in Li-S batteries, and the same PIP polymers is used as electrode binders to further capture the dissolved polysulfide and provide additional stability. A toluene solution-based copolymerization is chosen to avoid evolution of gaseous byproducts (e.g., H_2S and other volatile sulfur rich molecules). Meanwhile, vulcanization catalysts, i.e., tetramethylthiuram disulfide and zinc oxide, were added to promote the polysulfide addition to the polymer to form the sulfur and PIP copolymer (vulcanization) without overheating the reaction. To optimize vulcanization conditions, the effects of temperature, amount of catalyst, reaction time and feed ratios of sulfur and PIP were all explored. The copolymerization enables high

sulfur content polyisoprene-sulfur (PIPS) copolymer and confined nano-sulfur phases (90 wt% sulfur) as shown in Figure II.9.F.1. The confinement mechanism of dissolved polysulfides is also illustrated in Figure II.9.F.1. After copolymerization, the C-S bonds can trap the long chain Li_2S_n to avoid further shuttle effect, which is also beneficial to overcome the volume expansion.

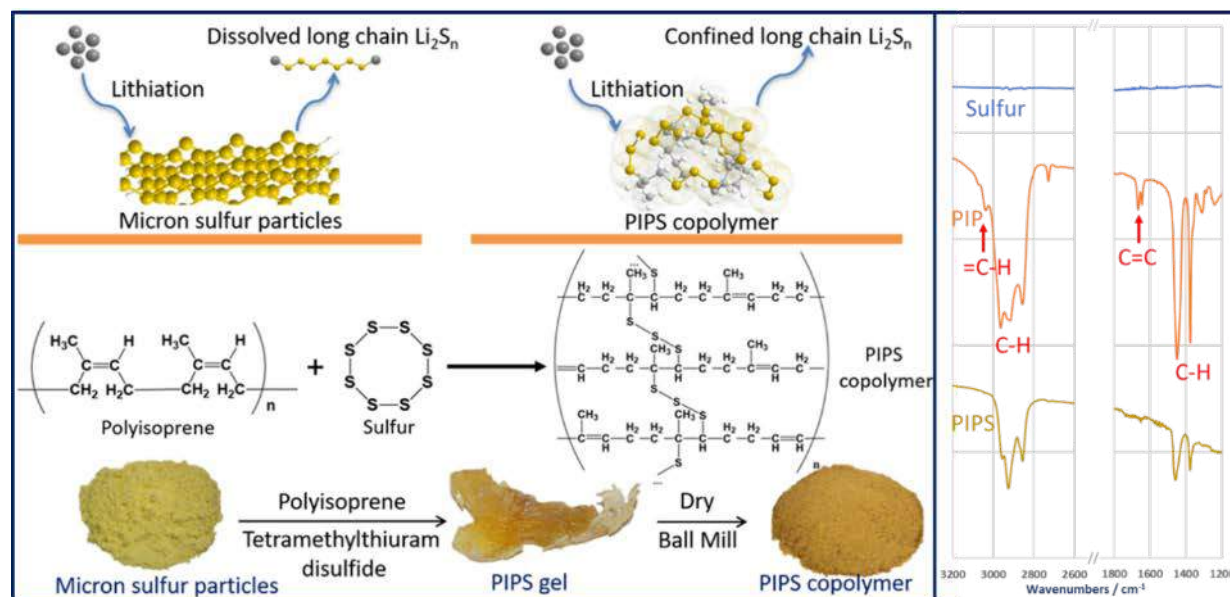


Figure II.9.F.1 Left section. Long chain polysulfides confinement mechanism is illustrated at the upper part: the C-S bonds generated after vulcanization provide a reservoir for long chain polysulfides so that the polysulfides would not directly diffuse into electrolyte. The chemical transformation and material processing for PIPS preparation are shown at the lower part: polysulfides are immobilized in the polymer network. Right section. FT-IR spectra of starting materials sulfur (blue) and PIP (orange), and product PIPS (yellow).

The synthesized PIPS was examined with FT-IR. As shown in Figure II.9.F.1 (right section), the FT-IR spectrum of the starting material PIP shows a peak at 3036 cm^{-1} , indicating presence of =C-H bonds; correspondingly, the peaks at 1665 and 1643 cm^{-1} are observed for the C=C bonds. Disappearance of these peaks from the IR spectrum of PIPS demonstrates successful transformation from PIP to PIPS. The PIPS spectrum still presents very similar alkane C-H peaks as those of PIP, excluding the possibility of material decomposition.

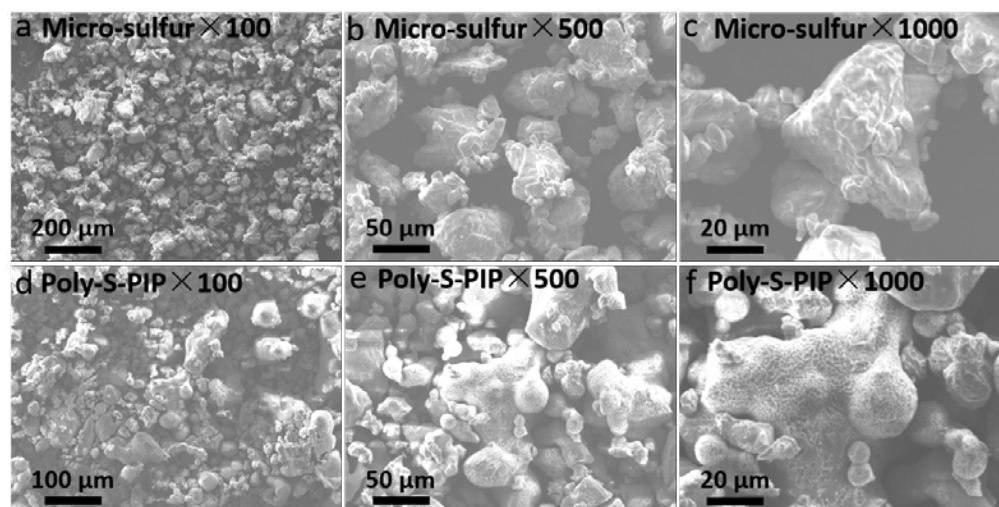


Figure II.9.F.2 SEM images of (a, b, c) commercially available micron sulfur and (d, e, f) vulcanized PIPS and sulfur nanocomposite materials particles. The particle sizes of the samples vary from several microns to tens of microns. The PIPS and sulfur nanocomposite materials particles show evident network structure on the surface.

To evaluate the properties of PIPS and sulfur nanocomposite materials, high-resolution transmission electron microscopy (HRTEM) images are collected as shown in Figure II.9.F.2. Here, a typical polycrystalline structure, Debye rings in Figure II.9.F.2b and Figure II.9.F.2e, is presented through inverse fast Fourier transform (FFT). The Debye rings originated from Figure II.9.F.2a and d clearly demonstrated the success of copolymerization and the incorporation of nano domain sulfur in connection with the sulfur crosslinkers. The homogeneous distribution at nano-scale is verified by the randomly distributed polycrystalline without preferred orientation. At the micro-scale, the morphology is recorded through scanning electron microscopy (SEM) as shown in Figure II.9.F.3. The size of sulfur particles used for our controlled cells range from several microns to tens of microns. The dried PIPS copolymer material after ball mill is around the same particle size distribution as the sulfur precursors in Figure II.9.F.3a-c. The electrochemical stability of PIP was tested using cyclic voltammetry (CV), as shown in Figure II.9.F.1, which demonstrates that the PIS is inactive between 1.7 and 2.8 V. The binder coats the surface of the sulfur composite and may impede the lithium ion diffusion. Hence, the wettability of the binder is also evaluated as demonstrated in Figure II.9.F.2. The total electrolyte uptake is about 22% of the final swelling weight. This number is similar to the traditional polyvinylidene fluoride binder. Afterwards, thermalgravimetric analysis (TGA) ramping to 600 °C in nitrogen at the rate of 5°C/min is conducted as shown in Figure II.9.F.2. The TGA profiles of PIPS and sulfur nanocomposite materials reveal that 30 wt% residues remain at 600°C, which implies better thermal stability. The better thermal stability of the copolymer is a necessary condition for battery operation.

High areal capacity is critical when considering practical application. A high sulfur loading is necessary for reaching a high areal capacity. The sulfur loading ($7.0 \text{ mg}_{\text{sulfur}}/\text{cm}^2$) in this study is approximately 5-10 times higher than in most other nanostructured carbon-sulfur electrodes published recently ($0.7\text{-}1.5 \text{ mg}_{\text{sulfur}}/\text{cm}^2$). The battery performance is studied in two-electrode coin cells with lithium metal as the counter electrode. Figure II.9.F.3a and b portray the galvanostatic cycling performance, in terms of gravimetric and areal capacity, as a function of sulfur loading. The areal delithiation capacity of PIPS and sulfur nanocomposite materials based electrode remains above $6.5 \text{ mAh}/\text{cm}^2$ for ca. 30 cycles. The reason for the limited cycles is due to the dendrite growth in the lithium metal side. In addition to the high areal capacity, the initial lithiation specific capacity reaches $1262 \text{ mAh}/\text{g}$, and is stabilized at $850 \text{ mAh}/\text{g}$ on cycling at such a high loading. It is worth to note that a polysulfide reactive binder also plays an important role to stabilized the thick sulfur electrodes during the cell operation. Polyisoprene can also directly react with the dissolved polysulfides to form a grafted polysulfide chain on the PIP polymers to further retain and confine polysulfide as shown in Figure II.9.F.2a. When the polyisoprene binder is replaced by PVDF, the capacity retention decreases even for PIPS and sulfur

nanocomposite materials based electrodes. The Coulombic efficiency for all PIP based electrodes is above 95%. However, the PVDF binder and elemental sulfur control electrode has much lower CE. The low CE of the controlled cells is due to the large amount of dissolution of reduced polysulfide species, which oxidized during the following delithiation process. The higher CE of PIPS based electrode proves the effective control of polysulfide diffusion of PIPS and sulfur nanocomposite materials based electrode.⁴⁴ Panels d, e, f show typical lithiation/delithiation profiles of the elemental sulfur and PIPS and sulfur nanocomposite materials based electrodes. The lithiation profile show two plateaus at around 2.3 and 2.1 V versus Li/Li⁺. The plateau at ca. 2.3 V is corresponded to the reduction of sulfur to higher-order lithium polysulfides. The plateau at ca. 2.1 V is corresponded to the transformation of higher order lithium polysulfides to low-order lithium polysulfides.

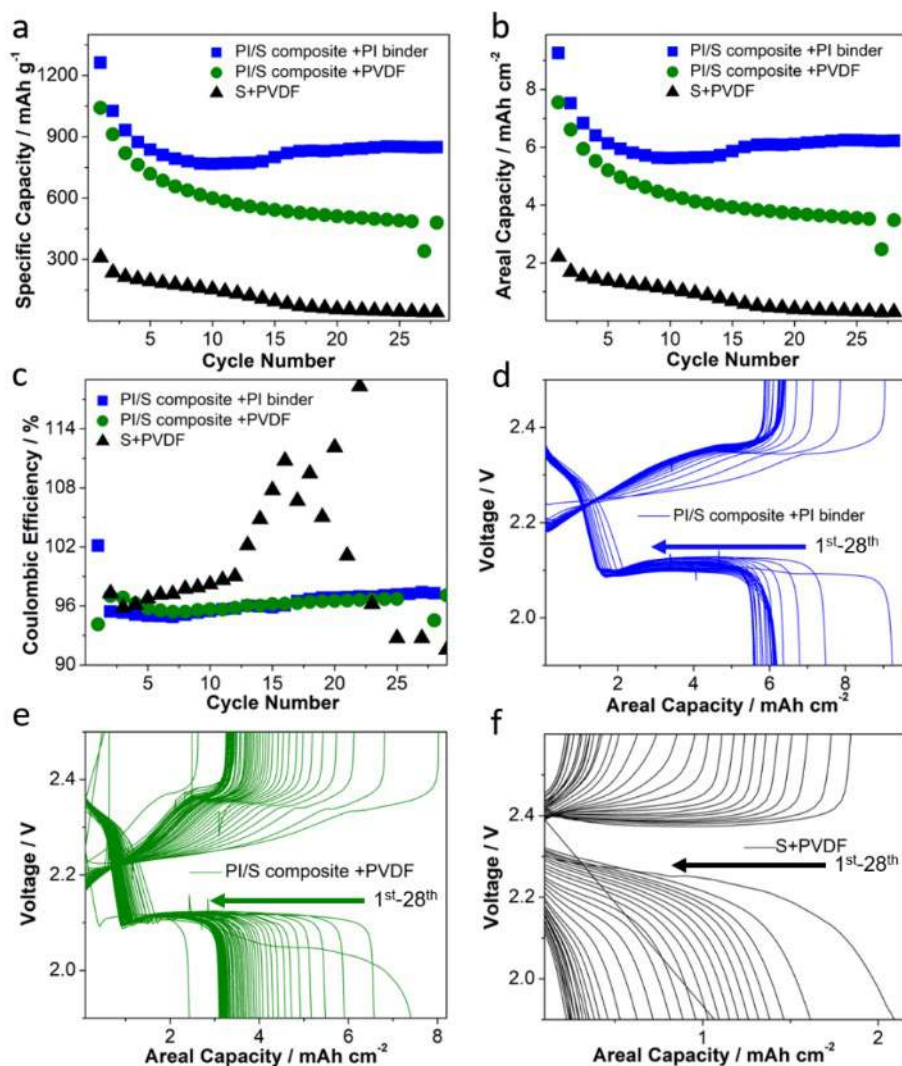


Figure II.9.F.3 Electrochemical characterization of PIPS and sulfur nanocomposite materials based sulfur electrode and comparison to micron sulfur based electrode. The composition of cathode is PIPS and sulfur nanocomposite materials: C45:Graphene:binder=6:2:1:1 (weight ratio). The sulfur content in PIPS and sulfur nanocomposite materials is 90 wt%. a, b, c, Cycling stability comparison of PIPS and sulfur nanocomposite materials based sulfur electrode versus micron sulfur based electrode at around 0.47 mA/cm² at 30 °C. d, e, f galvanostatic lithiation and delithiation.

Conclusions

In summary, the electrochemical lithiation process of vulcanized polyisoprenes that contain covalently immobilized sulfur chains were examined, and a significant performance enhancement was observed by comparing the results to those of the isolated elemental sulfur particles. The lithiation/delithiation shuttle factor is proved to be low enough even at a very small lithiation/delithiation current. The vulcanized strategy presents a promising areal capacity of 6.5 mAh/cm² during cycling. We also expect that further optimization of the copolymers structure can lead to better performance of the polymer based sulfur electrode system.

Key Publications

1. ChangAn Yang, QiaoKun Du, Zeheng Li, Min Ling, Xiangyun Song, Vincent Battaglia, Xiaobo Chen, Gao Liu In situ covalent bonding of polysulfides with electrode binders in operando for lithium-sulfur batteries, *Journal of Power Sources* 402 (2018) 1–6
2. Zeheng Li, Chen Fang, Chao Qian, Shudong Zhou, Xiangyun Song, Min Ling, Chengdu Liang, and Gao Liu Polyisoprene Captured Sulfur Nanocomposite Materials for High- Areal-Capacity Lithium Sulfur Battery *ACS Appl. Polym. Mater.* (2019) 1, 1965–1970
3. Chen Fang, Guangzhao Zhang, Jonathan Lau, and Gao Liu Recent advances in polysulfide mediation of lithium-sulfur batteries via facile cathode and electrolyte modification *APL Mater.* (2019) 7, 080902

References

1. Bresser, D.; Passerini, S.; Scrosati, B., Recent progress and remaining challenges in sulfur-based lithium secondary batteries - a review. *Chem. Commun.* **2013**, 49, 10545-10562.
2. Manthiram, A.; Fu, Y. Z.; Chung, S. H.; Zu, C. X.; Su, Y. S., Rechargeable Lithium-Sulfur Batteries. *Chem. Rev.* **2014**, 114, 11751-11787.
3. Lin, C. N.; Chen, W. C.; Song, Y. F.; Wang, C. C.; Tsai, L. D.; Wu, N. L., Understanding dynamics of polysulfide dissolution and re-deposition in working lithium-sulfur battery by in-operando transmission X-ray microscopy. *J. Power Sources* **2014**, 263, 98-103.
4. Mikhaylik, Y. V.; Akridge, J. R., Polysulfide shuttle study in the Li/S battery system. *J. Electrochem. Soc.* **2004**, 151, A1969-A1976.
5. Ai, G.; Dai, Y.; Ye, Y.; Mao, W.; Wang, Z.; Zhao, H.; Chen, Y.; Zhu, J.; Fu, Y.; Battaglia, V.; Guo, J.; Srinivasan, V.; Liu, G., Investigation of surface effects through the application of the functional binders in lithium sulfur batteries. *Nano Energy* **2015**, 16, 28-37.
6. Chen, W.; Lei, T. Y.; Lv, W. Q.; Hu, Y.; Yan, Y. C.; Jiao, Y.; He, W. D.; Li, Z. H.; Yan, C. L.; Xiong, J., Atomic Interlamellar Ion Path in High Sulfur Content Lithium-Montmorillonite Host Enables High-Rate and Stable Lithium-Sulfur Battery. *Adv. Mater.* **2018**, 30, 1804084.
7. Yao, N. P.; Heredy, L. A.; Saunders, R. C., Secondary Lithium-Sulfur Battery. *J. Electrochem. Soc.* **1970**, 117, C247-&.
8. Heredy, L. A.; Parkins, W. E., Lithium-Sulfur Battery Plant for Power Peaking. *Ieee T. Power. Ap. Syst.* **1972**, Pa91, 1731-&.
9. Lei, T. Y.; Chen, W.; Lv, W. Q.; Huang, J. W.; Zhu, J.; Chu, J. W.; Yan, C. Y.; Wu, C. Y.; Yan, Y. C.; He, W. D.; Xiong, J.; Li, Y. R.; Yan, C. L.; Goodenough, J. B.; Duan, X. F., Inhibiting Polysulfide Shuttling with a Graphene Composite Separator for Highly Robust Lithium-Sulfur Batteries. *Joule* **2018**, 2, 2091-2104.
10. Chen, W.; Lei, T. Y.; Wu, C. Y.; Deng, M.; Gong, C. H.; Hu, K.; Ma, Y. C.; Dai, L. P.; Lv, W. Q.; He, W. D.; Liu, X. J.; Xiong, J.; Yan, C. L., Designing Safe Electrolyte Systems for a High-Stability Lithium-Sulfur Battery. *Adv. Energy Mater.* **2018**, 8, 1702348.

II.9.G Multifunctional, Self-Healing Polyelectrolyte Gels for Sulfur Cathodes in Li-S Batteries (University of Washington)

Alex K-Y. Jen, Principal Investigator

University of Washington
Seattle, WA 98195
Email: ajen@u.washington.edu

Jihui Yang, Principal Investigator

University of Washington
Roberts Hall 315, Box 352120
Seattle, WA 98195
Email: jihuiy@u.washington.edu

Tien Duong, DOE Technology Development Manager

U.S. Department of Energy
E-mail: Tien.Duong@ee.doe.gov

Start Date: January 1, 2017
Project Funding: \$1,388,888

End Date: December 31, 2019
DOE share: \$1,250,000

Non-DOE share: \$138,888

Project Introduction

The current electric vehicle (EV) battery market is dominated by lithium-ion batteries (LIBs). However, conventional LIBs based on lithium metal oxide cathodes and graphite anode have begun to reach their performance limits after progressive materials and device optimization over the past two decades. In order to meet EV Everywhere goals of 75% cost reduction and 50% weight reduction in electric vehicle batteries by 2022, radically new strategies must be employed.

One tantalizing solution is to look beyond traditional lithium-ion intercalation chemistry towards “beyond-lithium” systems such as the lithium-sulfur (Li-S) battery. A sulfur cathode has a theoretical gravimetric specific capacity of 1673 mAh/g at ~2V vs Li/Li⁺, rendering a theoretical energy density improvement of 500% as compared to the lithium metal oxide cathodes found in LIBs. This increase can be matched on the anode side by using lithium metal, which has an intrinsic theoretical gravimetric specific capacity of 3860 mAh/g—an order of magnitude higher than graphite. Additionally, sulfur is cheap and earth-abundant, making this redox couple highly attractive for EV battery use.

However, a commercially-viable Li-S battery has remained elusive due to technical challenges. Many of them stem from the formation of polysulfides (Li₂S_x, 3 ≤ x ≤ 8) which are highly soluble in organic electrolytes, leading to self-discharge, passivation of the lithium anode, low coulombic efficiency due to the escape of polysulfides into the electrolyte, and voltage hysteresis from differences in forward and backward reaction mechanism. In addition, both the starting material (sulfur) and end products (Li₂S, Li₂S₂) are highly insulating, necessitating the use of a large amount of conductive carbon in the electrode. Furthermore, because the overall reaction is accompanied by a large volume change, this composite matrix is prone to cracking, resulting battery failure. Finally, on the anode side, lithium metal tends to form dendrites upon repeated stripping and plating, which puncture the cell separator and cause internal shorting.

Researchers have addressed these issues, to a certain degree of success, using a variety of strategies, introducing ionic liquid electrolytes, solid electrolyte interphase (SEI)-improving additives, mesoporous carbon hosts, advanced binders, and many others. Still, despite these myriad strategies, a safe Li-S battery with long cycle life based on scalable fabrication techniques remains elusive, as no single strategy or even combination of several has proven to be totally effective at both stopping efficiency/capacity loss due to dissolution of polysulfides and preventing dendrite growth.

Objectives

The project objective is to develop self-healing and polysulfide-trapping polyelectrolyte gels containing room-temperature ionic liquid (RTIL) for the Li-S battery system. The Li-S battery will be capable of achieving gravimetric and volumetric energy densities of ≥ 800 Wh/kg and ≥ 1000 Wh/L, respectively.

The project will achieve the following performance targets (all cycles at C/10 rate unless otherwise specified):

- A cathode gravimetric specific capacity of ≥ 675 mAh/g after 10 charge/discharge cycles between 2.8 and 1.7 V vs Li/Li⁺
- An average coulombic efficiency $\geq 99\%$ for the 10th cycle through the 100th
- $\geq 90\%$ capacity retention after 100 cycles as compared to the capacity of the 10th cycle.
- $\geq 30\%$ capacity retention when cycled at a C/2 rate, as compared to the capacity at C/10
- Ability to operate at temperatures between -20°C and 50°C.

Approach

We have developed Li-S coin cells that utilize self-healing, interpenetrated ionomer gel electrolytes in both the cathode and separator. The team has synthesized necessary starting materials and fabrication procedures of components of these gels while testing their relevant electrochemical and mechanical properties. All components are combined into interpenetrating structures, which are being tested both alone and in cell configurations. Device performance data have been collected and used to further optimize designs of both materials and cells, to optimize Li-S battery design capable of doubling the energy density of traditional LIBs. In this program, the team has focused on (1) design and synthesis of a variety of precursors for gel electrolytes, (2) fabrication and testing of both reference materials and novel materials made from these precursors, and (3) iterative validation and improvement of our design principles through both materials and device testing.

During Budget Period 1 (quarters 1-6), we have synthesized a variety of starting materials for gel electrolytes and self-healing polymers, fabricated them into films both individually and together, and then tested their electrochemical/mechanical properties relevant to use in a Li-S battery. Additionally, we have synthesized a variety of sulfur/carbon (S/C) composites, utilizing mesoporous carbons with varying properties and various functionalities placed onto their surfaces.

Organic synthesis includes naphthalene diimide (NDI) and pyrene (Py) containing materials, as well as monomers for the polyelectrolyte phase. Materials have been synthesized using established synthetic routes and characterized by nuclear magnetic resonance (NMR), gel permeation chromatography, and/or solution-phase cyclic voltammetry (CV). Synthesis of S/C composites was achieved by mixing of sulfur and carbon at above the melting point of sulfur, and characterized by Brunauer–Emmett–Teller (BET) surface area and pore size analysis to confirm successful integration of sulfur into the pore structure. Surface functionality has been studied by thermal gravimetric analysis (TGA) and x-ray photoelectron spectroscopy (XPS).

Fabrication and testing of ionomer gels with varying ratios of ionic liquid (IL) and molecular starting materials have been performed. Basic electrochemical and mechanical properties of each gel composition have been tested and used to determine structure-property relationships, then gel compositions with favorable properties underwent more detailed testing on long-term interfacial stability with Li foil, Li dendrite suppression, and polysulfide diffusion. Conductivity and thermal properties have been assessed by A/C impedance, TGA, and differential scanning calorimetry. Tensile stress tests were carried out to determine mechanical properties. Li/gel/Li symmetric cells have been constructed and analyzed for development of interfacial resistance and dendrite suppression using cyclic stripping/plating method. Polysulfide trapping ability were quantified by measuring UV-vis absorption spectra from a fixed-concentration solution.

Fabrication and testing of self-healing films, made from various structures and ratios of NDI and Py containing moieties, were performed. Mechanical and self-healing properties have been tested, as well as ionic conductivity. Static and dynamic mechanical testing have been carried out to determine tensile modulus, toughness modulus, and storage and loss modulus. Self-healing properties were measured by slicing films in two, contacting the pieces, and annealing at fixed temperature, followed by repeating tensile stress tests. This was followed by fabrication and testing of gel electrolytes containing both physically-crosslinked (self-healing) and chemically-crosslinked (ionomer) materials. All of the tests detailed above were performed in order to determine how the performance of individual components of the gel translates into an interpenetrated structure containing all components.

Parallel to materials development efforts, we undertook fabrication and testing of small-capacity coin cells utilizing a variety of cell design concepts, including organic electrolytes, IL electrolytes, non-self-healing polyelectrolyte gels, and interpenetrating gels in order to benchmark performance and demonstrate interpenetrating materials system capable of significantly improved performance. Cells were cycled for short periods (≤ 100 cycles) at rates ranging from C/100 or C/50 to C/2. A/C impedance spectra have been collected at various points in order to observe the evolution of internal impedances during cell cycling. Voltages traces during charge and discharge were observed and correlated to internal processes such as polysulfide speciation and buildup of insulating $\text{Li}_2\text{S}/\text{Li}_2\text{S}_2$ deposits. The origins of undesirable cell performance were investigated using a combination of experimental techniques, including targeted cycling, CV measurements, A/C impedance measurements, scanning electron microscopy, and x-ray diffraction (XRD).

During Budget Period 2 (quarters 7-12), we have continued synthesis of molecular components of gels and S/C composites from raw starting materials. Synthesis have been performed according to literature, as well as any modifications in order to produce materials more efficiently. We have continued testing of gel electrolytes containing both physically-crosslinked and chemically-crosslinked ionomer materials, as well as development of self-healing polymer films based on physical-crosslinking. Basic electrochemical and mechanical (including self-healing) behavior have been characterized, and gel compositions with favorable properties underwent more detailed testing on long-term interfacial stability with Li foil, Li dendrite suppression, and polysulfide diffusion. Systematic structural and compositional adjustments have been made to the gel electrolyte formulation based on cell performance details.

We have fabricated coin cells with sulfur-based cathodes and lithium metal anodes which utilize electrolyte materials in the cell structure and studied their performance as a function of material design. Initially, low-mass-loading demonstration cells was constructed, followed by practical-loading cells. This task culminated directly in the production of deliverable 10 mAh Li-S cells for DOE testing. All of the experiments previously mentioned for cell testing have been performed as cell design is optimized. We have utilized instrumentation at the Washington Clean Energy Testbeds on the University of Washington campus, the University of Washington Molecular Analysis Facility, and NMR/microscopy instrumentation available at the Environmental Molecular Sciences Laboratory at the Pacific Northwest National Laboratory.

Results

Multifunctional Ionomer Gel Polyelectrolytes / Gel Cathodes

Previously, we have described the integration of our solvate ionogel (SIG) materials into both the cathode and separator of Li-S batteries. This resulted in quasi-solid-state cells which showed excellent specific capacity and retention upon cycling at 23°C, but with a significant overpotential, and voltage features that are a typical of cells with organic electrolytes. In the first quarter of this year, we have developed improved formulations and fabrication procedures for our gel cathodes and composite separators, and also performed extensive testing on these materials—both in and outside of full-cell configurations—to gain insight into the origins of full-cell cycling behavior.

Figure II.9.G.1a shows the capacity of Li-S concept cells ($\sim 1\text{mg}_{\text{sulfur}}/\text{cm}^2$) over 100 cycles at 30°C. At C/10 rate. We found that quasi-solid-state cells containing SIG showing better capacities than the control material

system (PVdF binder + organic liquid electrolyte (DOL/DME) in Celgard 2500), but by a slight amount (~ 100 mAh/g), and exhibit long-term capacity fading at a similar rate. By contrast, cells of typical construction with Li(G4)TFSI solvate ionic liquid (SIL) electrolyte showed poorer initial capacity, but with reduced fading. Examining voltage profiles (3rd cycle) for these cells at varying rate revealed major differences between cell types (Figure II.9.G.1b-c). We found that the discharge overpotentials of SIG/SIL cells are almost uniformly larger than the control electrolyte, especially during the low-voltage region that accounts for most of the cell capacity. The transition from higher to lower voltage also occurs more gradually for these cells, although the voltage minimum at this transition point, characteristic of a polysulfide-induced “dip” in liquid electrolyte conductivity, is absent for the SIG cells. Similarly, overpotential for SIG/SIL cells during recharge is generally larger, and more sloped for SIG cells. Also notable is the maximum in voltage observed upon initiation of recharge, well-known to be associated with activation of solid Li_2S deposits. This “bump” is significant for the SIL case, but far less prominent in the SIG case and entirely absent from the control.

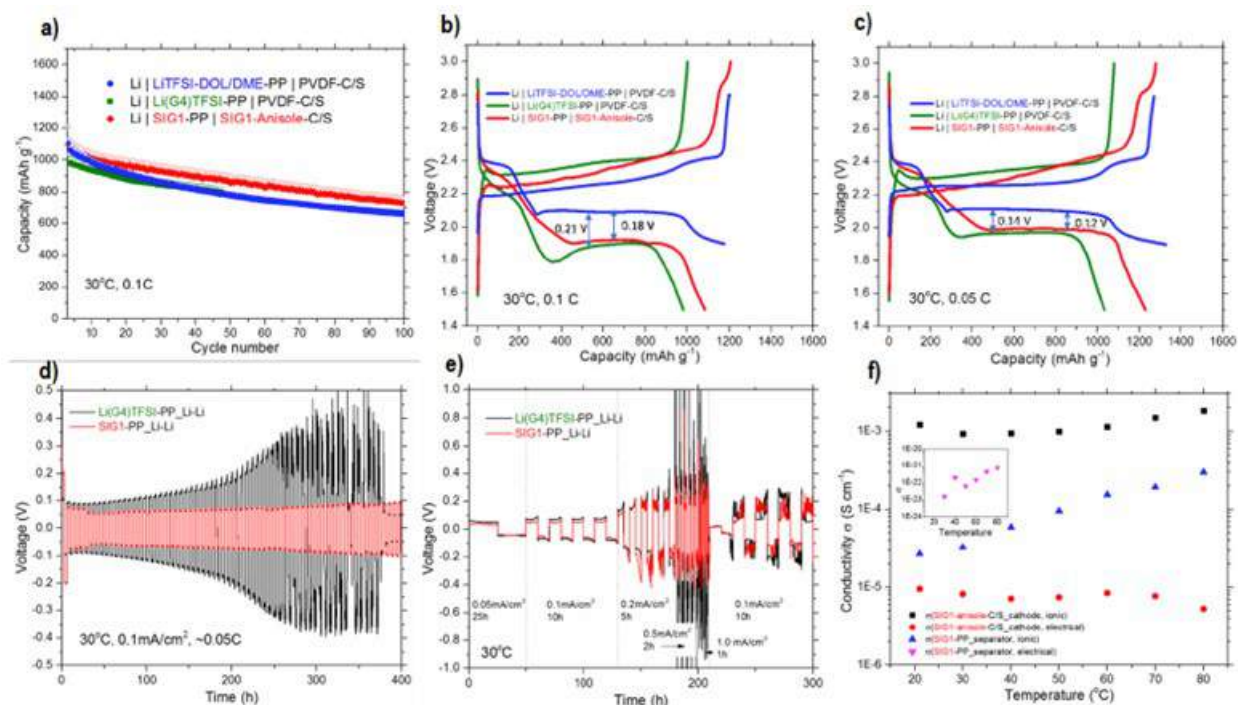


Figure II.9.G.1 a) Specific capacity (mAh/G_{sulfur}) for Li-S cells of indicated cell structure [anode | electrolyte-separator | binder/gel-cathode] during Galvanostatic cycling at 0.1C (calculated based on 1672 mAh/G_{sulfur} theoretical capacity). b) 3rd cycle voltage profiles for indicated cells at 0.1C. c) 3rd cycle voltage profiles for indicated cells at 0.05C. d) Cycling of symmetric cells [electrolyte-separator-electrodes] at ± 0.1 mA/cm² using a 6h cycle period. e) Cycling of symmetric cells [electrolyte-separator-electrodes] with varying current density and cycle period. f) Ionic/electrical conductivity vs temperature for gel cathodes and gel separators, extracted from frequency-dependent impedance between stainless steel blocking electrodes

In order to gain further insight, we have fabricated Li|Li symmetric cells containing either SIG composite separators or Celgard 2500 wetted with a similar total volume of SIL. Cyclic stripping/plating at 30°C and 0.1 mA/cm² (Figure II.9.G.1d), roughly equivalent to the current density of the above cells at 0.05C, reveals uniformly lower and more-stable overpotential for the SIG separators (~ 50 mV vs. ~ 100 mV). This trend roughly holds at larger current densities (Figure 1e), although the potentials become erratic at 0.2 mA/cm² or higher, indicating unstable behavior that will eventually lead to dendrite-related short-circuiting.

These differences at the anode/seperator may explain the increased overpotential of full-cells with SIL electrolyte as compared to SIG, they cannot explain the differences of both compared to the control, even assuming the anode/seperator resistance of the control cell is negligible. While many of these differences may

instead relate to altered conversion chemistries in the cathode, a significant portion of the overpotential in the SIG cells may be due to poor electrical conductivity in the cathode as well. Impedance analysis of a typical gel cathode sample between blocking electrodes revealed a very poor through-film electrical conductivity of $<10^{-5}$ S/cm (Figure 1f), corresponding to ~ 125 mV cell polarization at C/10 rate.

Previously, we have noticed unique changes to the discharge voltage traces in QSS cells (less-distinct and lengthened upper plateau, downward shift of the lower plateau), and ruled out the influence of anode or separator processes as being the primary source of these changes, leaving the cathode as the most likely source. However, it was still unclear whether the behavior we observed was due to overpotentials in the cathode—whether ohmic and/or state-of-charge-dependent—or a reflection of changes to the chemical pathways for sulfur conversion *i.e.*, thermodynamic changes brought on by the SIG electrolyte.

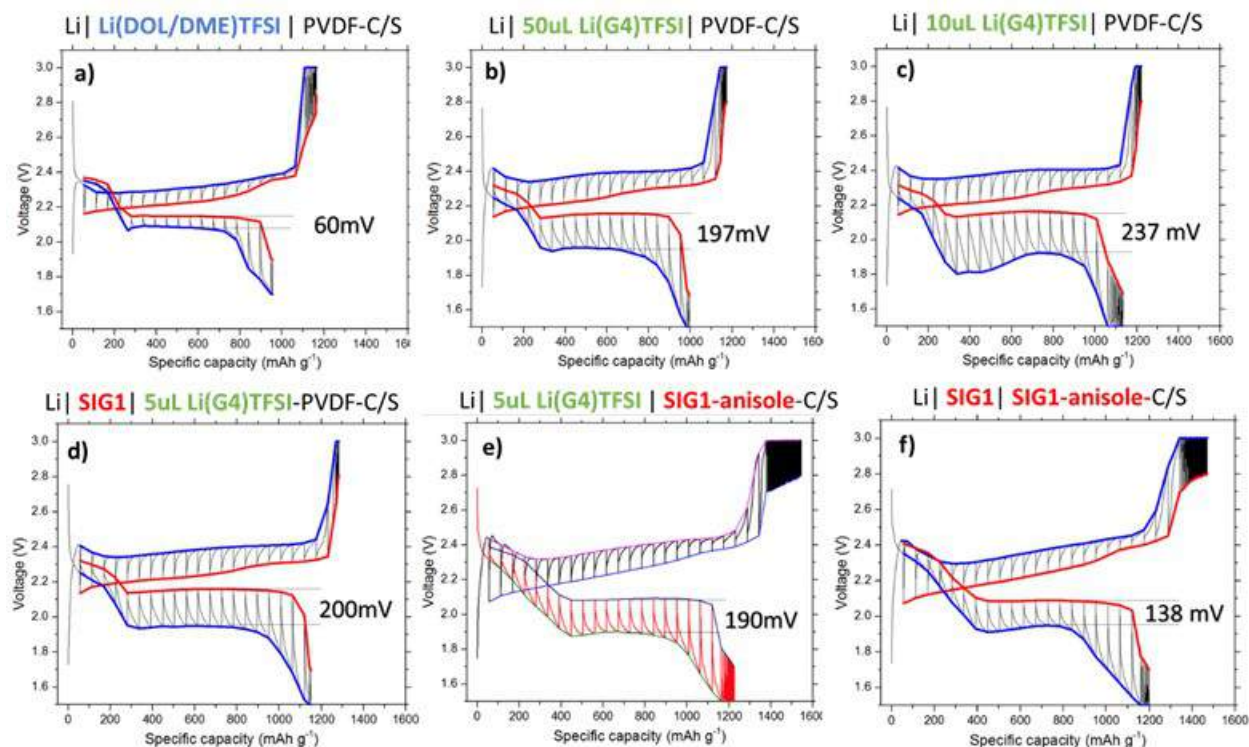


Figure II.9.G.2 GITT results for six different Li-S coin cell designs, with the cell structure indicated as Li | (electrolyte) | (cathode). All data was collected at 30 °C and C/10 rate (assuming 1672 mAh/g_s), with GITT being performed on the 3rd cycle. All cathodes have ~ 1 mg_s/cm² areal loading. The blue and red curves connect the current-applied voltages and open-circuit voltages, respectively, measured directly before current interruption and after a 1hr rest, respectively. Their difference represents the cell overpotential at that point of charge/discharge. The point of minimum overpotential during the lower discharge plateau of each cell is labeled on the corresponding graphs

In order to clarify the influence of these disparate factors on QSS cell behavior, we have performed Galvanostatic Intermittent Titration Technique (GITT) measurements on Li-S cells of varying design (Figure II.9.G.2a-f). This experiment allowed us to calculate the overpotential for each cell as a function of state-of-charge, and thus determine the open-circuit or “true” thermodynamic shape of the charge/discharge curves in each case. Since open circuit voltage depends solely on the chemical potentials of reactive species within the cell, this provides insight into the chemistry of our SIG cathodes, and also suggests areas of improvement within the design. For the sake of a clear comparison, we have marked the point of least overpotential during the lower discharge plateau of each cell. First, we may compare these discharge overpotentials amongst cell designs. Unsurprisingly, the control cell with organic electrolyte (Figure II.9.G.2a) requires the least overpotential, and the cell with a traditional cathode (S/C/PVDF) and limited volume of SIL (Figure II.9.G.2c) requires the most overpotential. This is due to significantly-increased charge transfer resistance at both the

anode and cathode for the latter case and highlights the limitations of “dropping in” a new electrolyte without considering its effects on the entire battery system. Adding a large excess of SIL electrolyte (Figure II.9.G.2b) alleviates this effect slightly, most likely due to improved wetting of the cathode and total capacity of the electrolyte to dissolve lithium polysulfides. On the other hand, replacing half of the volume of SIL with a SIG composite separator (Figure II.9.G.2d) gives a similar result without requiring an increase in total electrolyte volume. This is almost certainly related to decreased anode overpotential, as we have previously observed for SIG composite separators.

Cells containing SIG-based cathodes, on the other hand, outperform all cell designs based on S/C/PVDF cathodes and SIL electrolyte, with the lowest overpotential observed for the QSS cell (Figure II.9.G.2f). We can partially attribute this to the improved wetting of the cathode achieved by our fabrication technique, as well as the influence of polysulfide-solvating diluent anisole. Overall, this result indicates that the internal resistance of our QSS design can only partially explain its altered discharge characteristics. By process of elimination, this implies that some fundamental change to the chemical pathway of discharge has also occurred in SIG-based cathodes. Comparing open circuit voltage traces (red curves in Figure II.9.G.2) further implicates this hypothesis. We note that merely switching from an organic electrolyte to SIL electrolyte in the cathode has very little effect on the open circuit behavior, mostly manifesting as a slight decrease in the upper plateau voltage and less-sharp transition to the lower plateau. The differences in current-applied voltage between these cells can therefore mostly be attributed to overpotential. On the other hand, the open-circuit behavior of cells with SIG-based cathodes closely resembles their current-applied behavior, starting with a broad, extended, downward-sloping region that begins at a *higher* voltage than the upper plateau of traditional designs but ends at a *lower* voltage. This is followed by a lower plateau that is downward shifted by ~50mV from the other cells.

While we cannot yet identify the exact changes in cathode chemistry that cause these features, it seems safe to say that our SIG-based electrolyte has a dramatic effect on the sulfur conversion chemistry. These results also suggest that the increased overpotential associated with ionic liquid electrolytes in Li-S cells can be successfully mitigated to acceptable levels. We have accomplished this in our design through use of a solvating diluent (anisole), a cathode fabrication process which circumvents electrolyte wetting problems, and a gel composite separator that successfully restricts polysulfide migration without incurring large overpotentials or significant extra weight/volume. We have successfully fabricated test coin cells with higher cathode loadings (≥ 4 mgS/cm²) based on these strategies and adjusted our design accordingly in order to retain favorable cycling characteristics whilst minimizing overpotential.

We have tested the robustness of our QSS design towards self-discharge, which Li-S batteries are particularly susceptible to. A reference cell, fabricated using PVDF binder in the cathode and liquid organic electrolyte (1M LiTFSI in DOL:DME 1:1 v/v + 1wt% LiNO₃), was also tested for comparison. After two “formation cycles” at C/20, cells were cycled at C/10 until the 7th discharge, at which point 300 mAh/gS capacity was discharged, followed by a 100h rest. Discharge was then resumed, and cycling continued as normal. Figure 3a depicts the results: the cell with organic electrolyte (“OE”) lost 185 mAh/gS (18.3%) to self-discharge relative to the previous cycle, while the QSS cell lost only 108 mAh/gS (8.9%). Interestingly, the OE cell recovered 63 mAh/gS in the following cycle, bringing the total two-cycle loss to 12.1%, while the QSS cell lost an additional 44 mAh/gS for a similar total of 12.5%. However, the OE charge/discharge capacities rapidly diverged after this point, strongly suggesting an accelerated redox shuttle effect. The QSS cell did not exhibit this behavior, instead cycling its remaining capacity stably with a coulombic efficiency of ~98%. This result is especially encouraging given the lack of anode-passivating additives in the QSS system. Hence, while we have observed that both designs are similarly susceptible to irreversible capacity loss during self-discharge, we have found that the QSS system is more resistant to continued degradation caused by the redistribution of sulfur species during prolonged rest.

Examining the voltage profiles of each cell before, during, and after the self-discharge test (Figure 3b and 3c) provides some insight into the cause of capacity loss. First, we find that the general shape and voltage of each

discharge/charge region remains mostly unaffected following self-discharge; however, in each case, the irreversible capacity loss is mostly localized to the lower plateau, corresponding to the conversion of soluble polysulfides into insoluble Li_2S_2 and Li_2S . Prior literature suggests that the lower plateau capacity is often limited by the passivation of conducting surfaces with these insoluble products, rather than the total availability of reducible sulfur. Our previous GITT results also support this interpretation. In light of this, the capacity which is irreversibly lost by both cells following self-discharge may be related to the disproportionation of soluble polysulfides during the rest period, resulting in the production of insoluble sulfides and accelerated passivation of cathode surfaces. Further study is needed to confirm this mechanism and investigate its prevention.

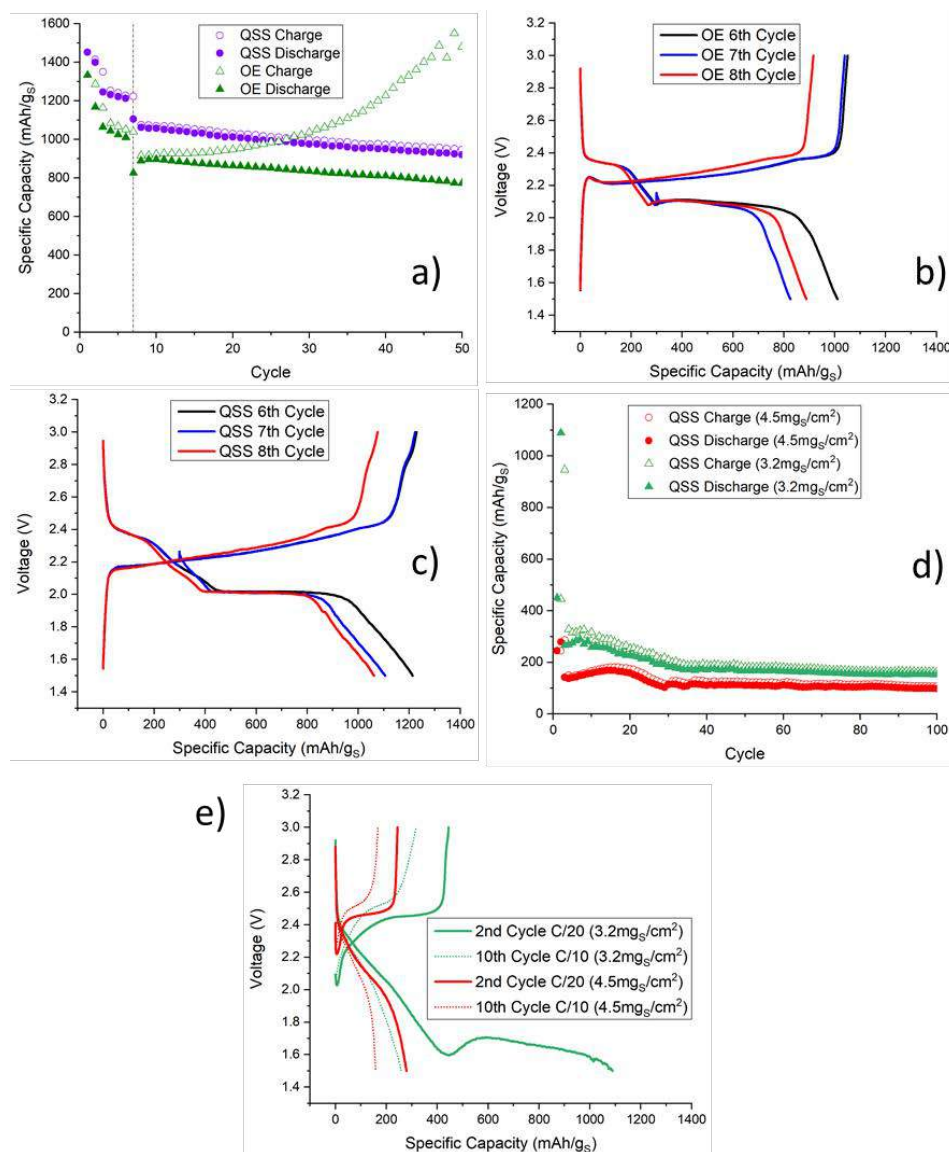


Figure II.9.G.3 a) Cycling performance of QSS and OE cells, with a 100h rest during 7th cycle discharge. Some irreversible capacity loss is observed for both designs, but the OE cell exhibits accelerated redox shuttling after the self-discharge test, while the QSS cell continues to cycle stably; b) OE voltage profiles for the 6th, 7th, and 8th cycles; c) QSS voltage profiles for the 6th, 7th, and 8th cycles; d) Cycling performance of two representative high-loading QSS cells. Available capacity is quite low at C/10 due to large internal resistance in the thick cathodes; e) 2nd and 10th voltage profiles for the representative high-loading cells. Increasing resistance during discharge prevents the cells from accessing their lower plateau capacity, especially at C/10

We also focused significant effort this year on fabricating and testing QSS cells with higher cathode areal loadings, with the goal of attaining reasonable performance at 4-5 mg_s/cm². Since our gel cathodes are blade coated from a precursor-containing slurry, we were able to achieve increased loading simply by casting films at increased height. However, the downside of this “cure in place” method is that high loading cathodes were exceptionally thick—over 0.5mm in some cases. Predictably, this produced significant internal resistance in the final QSS cells. As shown in Figure II.9.G.3d, the capacity available during the initial two cycles at C/20 was commonly much larger than that available at C/10, which was generally 100-200 mAh/g_s in all cases. Examining the voltage profiles in Figure II.9.G.3e reveals that the cause of this low capacity is an inability to reach the lower plateau prior to the safety cutoff of 1.5V, due to rapidly growing internal resistance during the initial stages of discharge. We have also tested a number of improved gel cathode formulations with the goal of minimizing required thickness for high loading and reducing the cathode charge transfer overpotential.

Higher-loading cathodes (>3mg_s/cm²) were fabricated by increasing the coating thickness; however, these cathodes performed poorly due to their extreme thickness (approaching 1mm). In order to reduce the thickness of such cathodes without compromising their sulfur content, we have revised our SIG sulfur/carbon (S/C) slurry composition (see Table II.9.G.1 below) to increase the overall solids content prior to curing-in-place. To compensate for this, we also increased the amount of diluent solvent anisole relative to Li(G4)TFSI solvate ionic liquid in order to reduce viscosity of slurry and promote improvement in mixing. Much of the diluent was evaporated during the casting process and therefore acts merely as a processing solvent. The remaining anisole was meant to promote faster ion transport in the final cathode as a solvent diluent in the SIG electrolyte.

Table II.9.G.1 Breakdown of SIG/S/C slurry (and subsequent cathode) composition by weight. The demonstration cell formula was used for QSS cells with ~1 mg_s/cm² cathode loading, while the updated formula is intended for high-loading (4-5 mg_s/cm²) cells.

SIG/S/C Slurry Composition (1g basis)		
	Demonstration Cell Formula	Updated High-Loading Formula
Solid Components	0.1g	0.2g
S ₈	117.5mg	133mg
MJ430	117.5mg	57mg
MWCNT	65mg	70mg
Liquid Components	0.9g	0.8g
PEGDMA (750Da)	153.4mg	143.9mg
Radical Initiator	3.1mg	2.9mg
Li(G4)TFSI	650.9mg	458.8mg
Anisole	92.6mg	195.5mg
(Addt'l Anisole, evap.)	9.3mg	219.6mg

This updated slurry composition did indeed produce cathodes with 4-5mg_s/cm² loading at only ~400-500μm thickness. However, we found that casted cathode films from the composition were not mechanically robust and did not survive the die-cutting process without significant crumbling and/or delamination from the carbon-coated aluminum substrate. This is almost certainly due to the reduced amount of PEDGMA crosslinker relative to solids content. We have adjusted the ratio of liquid components in our slurry to produce a robust cathode with high loading and reduced thickness, as well as attempting to introduce our self-healing polymers into the slurry for additional robustness and electrochemical performance enhancement.

Self-Healing Polymer Binders for S/C Composite Cathodes

Following our previous characterization of the PENDI-350/triPy (PP) self-healing polymer system, including its tunable mechanical/self-healing behavior and useful Li^+ conductivity, we have continued our efforts to characterize the effects of this material in a Li-S battery system. As reported earlier, performance improvements are expected from the two primary functions of the polymer system: the polysulfide-trapping effect of naphthalene diimide (NDI) moieties, and self-healing of mechanical damages of materials during cycling. The PP polymer when used as a binder for S/C composite cathode has shown to increase the capacity retention significantly from 43.5% to 74.2% after 100 cycles at C/20. The capacity retention reached close to 100% after 100 cycles at 1C, which demonstrated the polysulfide trapping property of the PP polymer.

We have performed CV and UV-Vis studies of dibutyl-NDI (dbNDI) and Li_2S_8 as model compounds to understand the details of polysulfide-trapping mechanism. By simply mixing dbNDI with Li_2S_8 in DOL/DME, the color changed immediately from yellow of Li_2S_8 to black of mixture of polysulfide with various compositions (Figure II.9.G.4a). The color change suggests strong interaction/reaction between dbNDI and Li_2S_8 . UV-vis studies were conducted of solutions with various ratio between dbNDI and Li_2S_8 . As shown in Figure II.9.G.4b, dbNDI (red line) shows characteristic peak of neutral state at 379 nm. After adding Li_2S_8 with molar ratio of 1:1, the peak of the neutral dbNDI (379 nm) decreases slightly and a peak at 483 nm increases, which corresponds to the existence of dbNDI mono-anion. When the ratio of Li_2S_8 :dbNDI increase to 2:1, more of the neutral dbNDI is reduced into dbNDI mono-anion. Meanwhile, the peak of dbNDI $^{2-}$ di-anion appears at 407 nm which increase rapidly with increasing Li_2S_8 . In short, the NDI moiety enhance the capacity retention in two different ways: first, it can be reversibly reduced into NDI $^{2-}$ di-anions which can trap polysulfides via strong ion-dipole interaction (Figure II.9.G.4d); second, it can also function as a redox-mediator (Figure II.9.G.4e), which promotes the charge transfer and finally increases the utilization of sulfur during discharge process. Further characterization of this effect is ongoing in Li-S cell with practical loading sulfur cathode.

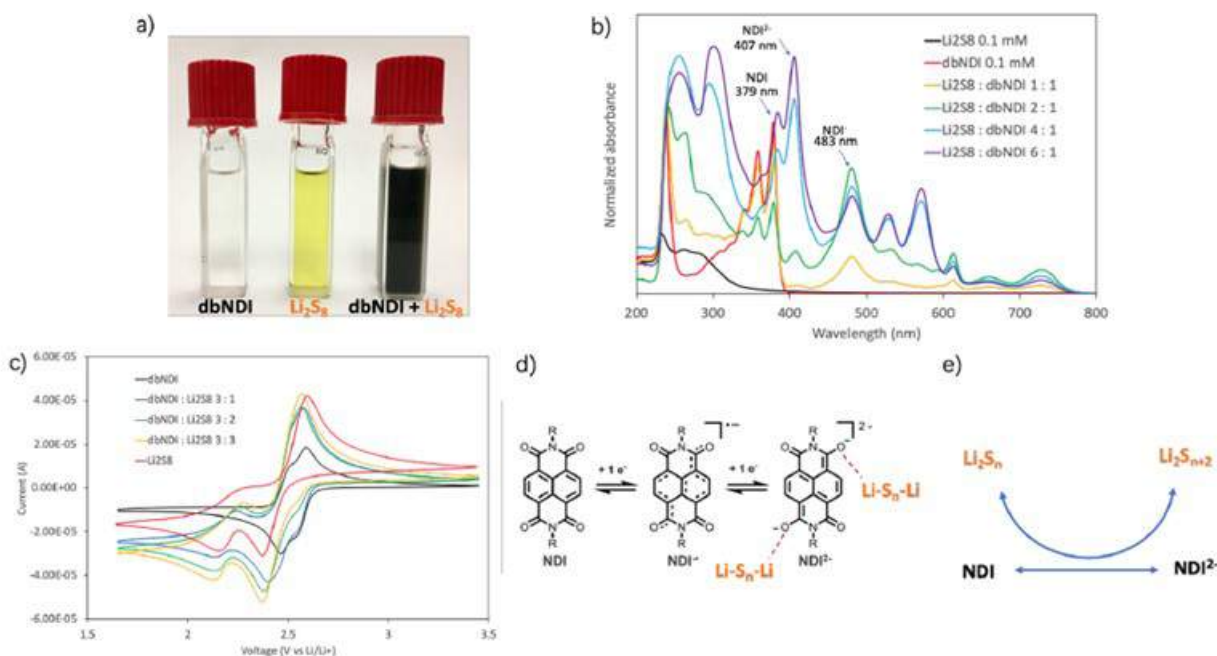


Figure II.9.G.4 a) Visual test of the reaction/interaction between Li_2S_8 (1 mM) in DOL/DME (1:1, v:v) with 1 M LiTFSI. b) UV-vis spectra of solutions with various ratio between dbNDI and Li_2S_8 in DOL/DME (1:1, v:v) with 1 M LiTFSI. The concentration of dbNDI was kept constant as 0.1 mM in the mixture. c) CV spectra of dbNDI (10 mM) and Li_2S_8 in DOL/DME (1:1, v:v) with 1 M LiTFSI (scan rate = 10 mV/s). d) Two-step reductions of NDI moiety and illustration of ion-dipole interaction between NDI moiety and polysulfides. e) Schematic illustration of redox-mediator effect of NDI moiety

With the significant improvement of capacity retention at low S loading (around 1 mg/cm^2), we have refocused our efforts on fabricating cathode with higher S loading ($> 4 \text{ mg/cm}^2$). We have fabricated high loading S cathode via systematic design of the S cathode components, including current collector, ratio design between PENDI-350 and tri-Py, choose of carbon conductive additive, and even the loading amount of S/C composite. Carbon coated Al foil was used as current collector which improves the adhesion between current collector with S cathode. Multi-wall carbon nanotubes were used as conductive additive to replace black carbon. The 1D structure of carbon nanotube known to assist forming interpenetrating conductive 3D network, which improves not only mechanical integration but also electrical conductivity of S cathode. The S ratio of S/C composite was improved to 70%. Based on the new composition, we have fabricated cathodes with PP and PVDF as binder (shown in Figure II.9.G.5a). After 40 cycles, the discharge capacity of cathode with PP binder retains as high as 1070 mAh/g (capacity retention of 92%). On the contrary, the capacity retention of cathode with PVDF binder after 40 cycles is about 76% (909 mAh/g). Meanwhile, we have noticed the decrease of coulombic efficiency, especially for cathode based on PVDF. We attributed this to the side reactions on the anode.

Besides, we have carefully optimized the ratio between PENDI-350 and tri-Py to achieve high loading S cathode with mechanical integration. As mentioned, a more robust binder system is needed to mitigate the increasing mechanical stress for S cathode with higher loading. As shown in Figure II.9.G.5b, the S cathode with PENDI-350:tri-Py ratio of 3:1 is prone to cracking as the S loading amount increases to around 4 mg/cm^2 . After increasing the amount of tri-Py by changing the ratio to 1:1, a continuous S cathode was achieved even with S loading amount greater than 4.2 mg/cm^2 . The cycling performances of cathode with PP binder (PENDI-350 : tri-Py = 1:1) with varying S loading is shown in Figure II.9.G.5c. The initial capacity of cathode with loading of 4.2 mg/cm^2 is around 800 mAh/g and remains almost constant within first several cycles. This implies the successful operation of S cathode with high S loading and good capacity retention. However, a sudden drop of capacity happens following the decrease of coulombic efficiency. The side reaction on the anode is a possible failure mechanism of S cathode with high S loading. We are investigating the detailed mechanisms and developing methods to protect the anode further.

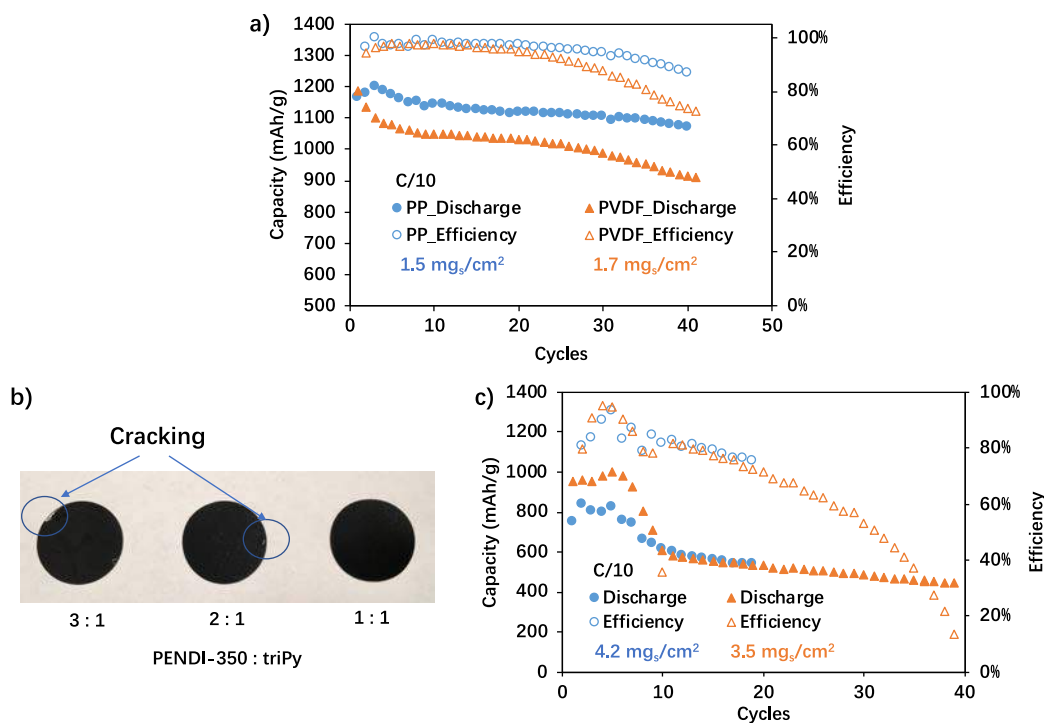


Figure II.9.G.5 a) Cycling performances of S cathodes with PP and PVDF as binder, respectively; b) S cathodes fabricated using PP as binder with different ratio between PENDI-350 and tri-Py; c) Cycling performances of S cathodes with PP (PENDI-350: tri-Py = 1 : 1) as binder with different loading amount of S

As described above, although the cathode exhibited high and stable cycling capacity around 810 mAh/g in the first several cycles, sudden drop happened in the following cycles. Therefore, we have focused our research on understanding the failure mechanism of cathode, including studies of lower coulombic efficiency and cathode cracking in this system. Coulombic efficiency is related to the dissolution of lithium polysulfides and therefore capacity retention. In our design, PENDI-350 is used to trap the polysulfides.

First, pure PENDI-350 was used as binder to compare with reference binder PVDF. As shown in Figure II.9.G.6a, cathode with PENDI-350 as binder shows better capacity retention and much higher coulombic efficiency than case of PVDF. Specifically, the trends of capacity change are different. The dramatic capacity decrease in the first several cycles of cathode with PVDF as binder implies the quick dissolution of the polysulfides into the electrolyte. Then the shuttle effect becomes more significant, leading to constant decay of capacity and lowering of the coulombic efficiency. On the contrary, cathode with PENDI-350 as binder has stable capacity around 1000 mAh/g in the first three cycles, which implies the significant trapping of the polysulfides. The coulombic efficiency stays constant around 98% even after around 60 cycles. The capacity stays almost constant after 30th cycles. Therefore, we think these two cathodes have different capacity failure mechanism: cathode with PVDF as binder loses capacity due to the dissolution of the polysulfides; although cathode with PENDI-350 as binder traps polysulfides efficiently, cathode cracking can lead to the loss of sulfur by isolation. To prove this, SEM images of these cathodes were taken after cycling 20 cycles. As shown in Figure II.9.G.6b, cathode with PVDF as binder showed continuous surface without significant cracking. However, there is cracking with width of 15 micron in the surface of cathode when PENDI-350 was used as binder, due to its higher rigidity most likely. Besides, the morphologies of the two film are quite different: in the case of cathode using PENDI-350 binder, the surface is smoother. This suggests better compatibility of PENDI-350 binder with carbon/sulfur composite possibly resulting a layer of PENDI-350 film formation on the surface of cathode during the cycling process.

Second, due to the different failure mechanism, it is possible that the mechanical integration of electrode materials can be improved by adding PVDF into PENDI-350. As shown in Figure II.9.G.6c, after adding PVDF (with weight ratio between PVDF and PENDI-350 as 1:3), the capacity retains around 962 mAh/g after 40 cycles with sulfur loading of 2.5 mg/cm². However, the coulombic efficiency is worse than pure PENDI-350. We think that although PVDF helps improve the mechanical integration, it may also interfere the interactions between PENDI-350 and PENDI-350 or between PENDI-350 and sulfur/carbon composite. The SEM image of cathode with PENDI-350/PVDF as binder after 20 cycles is shown in Figure II.9.G.6c. It is found that the surface of cathode is less smooth than the cathode with pure PENDI-350 as binder. This suggests that less polymer film is formed on the surface of cathode, which means part of PENDI-350 may dissolved into the electrolyte. The lack of PENDI-350 may leads to the dissolution of the polysulfides and low coulombic efficiency. Therefore, we can simply increase the thickness of sulfur cathode to alleviate the dissolution problem of PENDI-350. As shown in Figure II.9.G.6d, the cathode with sulfur loading of 3.7 mg/cm² and PENDI-350/PVDF as binder was fabricated. It shows stable capacity around 800 mAh/g after 32 cycles. And the coulombic efficiency was higher than 98%, which may due to the trapping effect of PENDI-350 and the physical blocking of thick cathode. Therefore, by improving the mechanical property and alleviating the dissolution of PENDI-350, high loading sulfur cathode with high capacity retention and coulombic efficiency has been achieved. Although the capacity is stable, it needs to be improved further. More systematic investigation of the failure mechanism of PP binder is ongoing.

Although we have fabricated the cathode with S loading of 3.70 mgS/cm² by using PENDI-350/PVDF as a composite binder, the coulombic efficiency and discharge capacity of the composite decrease quickly after around 30 cycles. We thought that PVDF may interfere with the interactions between PENDI-350 chains or between PENDI-350 and S/C composite. On the other hand, although we have demonstrated the effect of PENDI-350 on lithium polysulfides trapping, and possible redox reaction between NDI units and the polysulfides, we thought a more detailed investigation of the reaction pathways of LiPS in the presence of such binder is necessary. Here, we have focused our efforts on stabilizing capacity retention of the cathode, understanding and modulating interactions between the polysulfides and NDI units of the binder to improve the performance further.

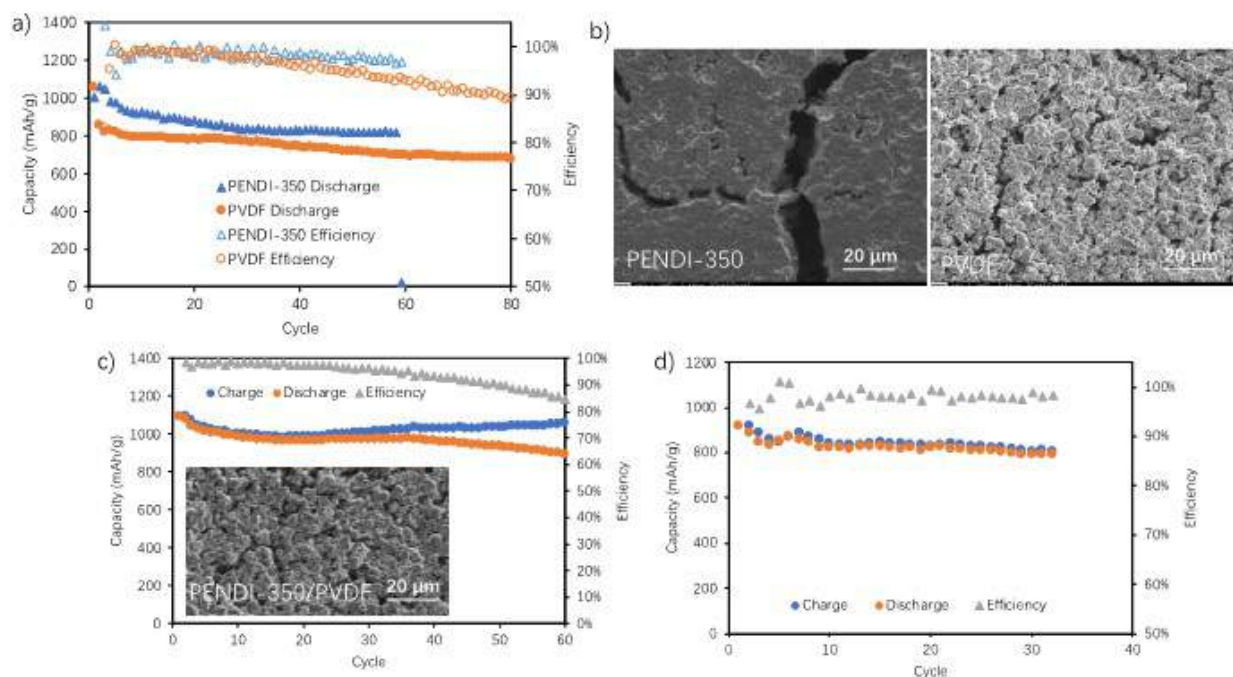


Figure II.9.G.6 a) Cycling performances of S cathodes with PENDI-350 (2.0 mgS/cm²) and PVDF (3.1 mgS/cm²) as binder, respectively; b) SEM images of cathodes with PENDI-350 and PVDF as binder after 20 cycles; c) Cycling performance of sulfur cathode with PENDI-350/PVDF as binder and the SEM image of the cathode after 20 cycles; d) Cycling performance of sulfur cathode with PENDI-350/PVDF

First, we have replaced PVDF with PEO to form a polymer blends of PENDI-350 and PEO as a binder for S/C cathode. As shown in Figure II.9.G.7a, we have fabricated test cells with S/C cathode using PENDI-350/PEO (weight ratio = 3:1) as binder with loading of 3.71 mgS/cm². It shows that the cell capacity remains at 718 mAh/g after 100 cycles at 1C. The capacity retention is as high as 91% (based on the 6th cycle with capacity of 789 mAh/g). We attribute this improved capacity retention to the flexibility of long-chain PEO (Mw = 1000 K) as well as its good compatibility with PENDI-350 resulting well dispersed polymer blends. To improve the mechanical properties further, we have added tri-Pyrene cross-linker that can form reversibly crosslinked network structures with PENDI-350 *via* quadrupolar aromatic pi-pi stacking between NDI and Pyrene units. In the PENDI-350/triPy/PEO (PPP binder) the flexible PEO chains could entangle to form inter-penetrating network structures. As shown in Figure II.9.G.7b, test cells with S/C cathode with a PPP (PENDI-350:triPy:PEO = 3 : 2 : 1 by weight) binder was fabricated with S loading of 2.91 mgS/cm². The capacity remains around 918 mAh/g after 30 cycles with relative capacity retention of 97% (based on 6th cycle with capacity of 954 mAh/g). We have also fabricated Li-S cells with the S/C cathode with relatively high loading of 5.04 mgS/cm² without cracking (Figure II.9.G.7c).

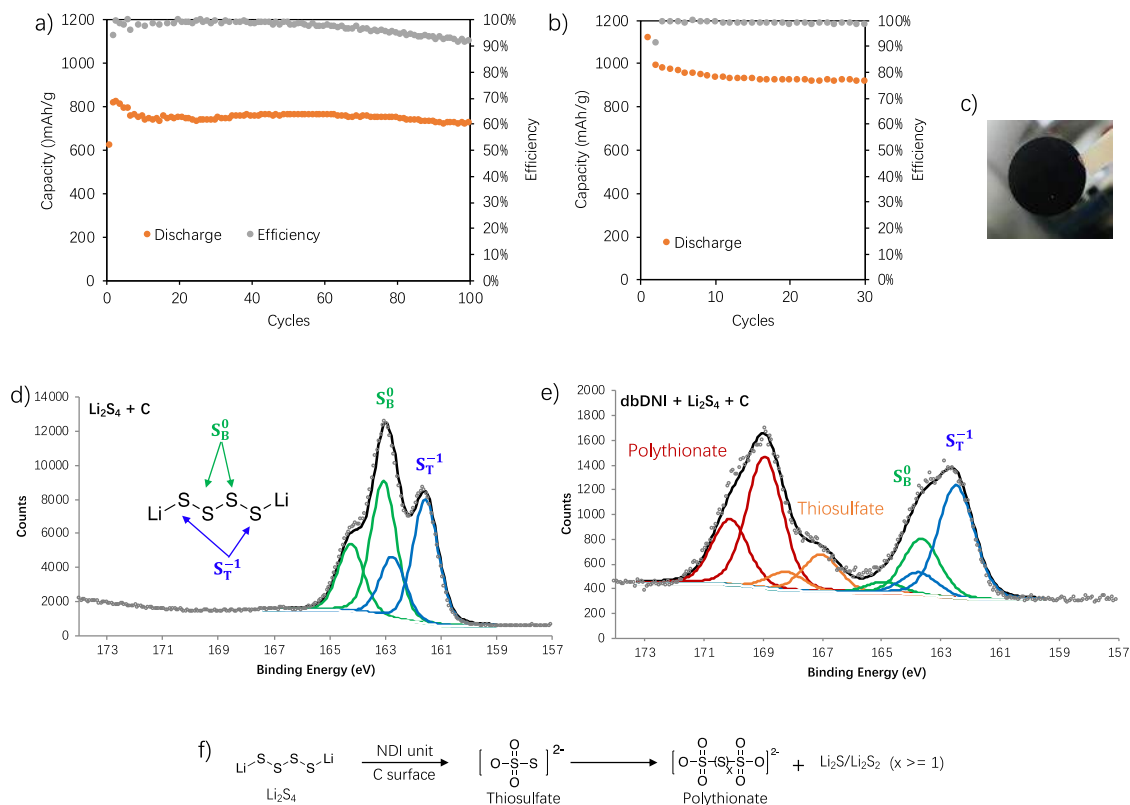


Figure II.9.G.7 Cycling performances of cells with S cathodes with a) PENDING-350/PEO as binder (3.71 mgS/cm²) and b) PENDING-350/triPy/PEO (PPP) as binder (2.91 mgS/cm²). All cells were cycled with C rate of C/10 in the first 5 cycles and then 1C in the remaining cycles; c) Image of S cathode using PPP as binder (5.04 mgS/cm²); XPS spectrum of d) Li₂S₄ reacted with mesoporous carbon and e) Li₂S₄ and dbNDI mixture reacted with mesoporous carbon; f) Possible reaction route of lithium polysulfides in the presence of NDI

Meanwhile, we have performed series of XPS studies to understand the interaction mechanism between the polysulfides and NDI units. Li₂S₄ was employed as a representative long-chain LiPS, which was synthesized by stoichiometric mixing of S₈ and Li₂S₂ in DME. Didutyl-NDI (dbNDI) was used as a NDI model compound to react with Li₂S₄ before XPS test. Mesoporous carbon surface was functionalized with thiophenols using diazonium chemistry to enhance interactions with S species, and the mesoporous carbon was added into Li₂S₄ solution to mimic the cell operation condition. As shown in Figure II.9.G.7d, the XPS spectrum of Li₂S₄ interacted with the carbon shows two S2p_{3/2} contributions at 161.6 and 130.0 eV with relative peak ratio of around 1:1, referred to as terminal (S_T⁻¹) and bridging (S_B⁰) sulfur atoms. A typical XPS spectrum of Li₂S₄ from the test suggests that the existence of mesoporous carbon doesn't change the state of Li₂S₄. However, after adding dbNDI, as shown in Figure II.9.G.7e, XPS spectra show two more sulfur species. The new S2p_{3/2} peaks at 166.9 eV and 168.8 eV are in accord with the binding energy of thiosulfate and polythionate complex. As proposed in Figure II.9.G.7f, Li₂S₄ can be oxidized into polythionates and short chain polysulfides in the presence of NDI units in the binder. The additional electrochemical contribution of NDI can help to explain the exceptional performance enhancement of sulfur cathodes made of NDI containing PPP binder.

Conclusions

Multifunctional Ionomer Gel Polyelectrolytes / Gel Cathodes

- We have developed fabrication procedures for all-solid-state Li-S cells containing solvate ionogel in both the cathode and separator and demonstrated the potential of this system to produce good capacity retention and coulombic efficiency during galvanostatic cycling.

- Cyclic stripping/plating measurements revealed uniformly lower and persistent overpotential for the SIG separators. The differences at the anode/separator may explain the increased overpotential of full-cells with SIL electrolyte as compared to SIG.
- The increased overpotential associated with ionic liquid electrolytes in Li-S cells can be successfully mitigated to acceptable levels by using a diluent solvent (anisole), a cathode fabrication process which circumvents electrolyte wetting problems, and a gel composite separator that successfully restricts polysulfide migration without incurring large overpotentials or significant extra weight/volume.
- Unique changes to the discharge voltage traces in QSS cells (less-distinct and lengthened upper plateau, downward shift of the lower plateau) has studied in detail using GITT measurements on Li-S cells of varying design. Results indicated that the internal resistance of our QSS design can only partially explain its altered discharge characteristics, and some fundamental change to the chemical pathway of discharge has also occurred in SIG-based cathodes.
- Robustness of our QSS design towards self-discharge has been tested and found that the system is more resistant to continued degradation caused by the redistribution of sulfur species during prolonged rest.
- We have also focused significant effort on fabricating and testing QSS cells with higher cathode areal loadings, with the goal of attaining reasonable performance at 4-5 mgS/cm². A series of improved gel cathode formulations were tested with the goal of minimizing required thickness for high loading, and reducing the cathode charge transfer overpotential, as well as attempting to introduce our self-healing polymers into the slurry for additional robustness and electrochemical performance enhancement. This optimized slurry composition did indeed produce cathodes with 4-5mgS/cm² loading at only ~400-500μm thickness.

Self-Healing Polymer Binders for S/C Composite Cathodes

- Following our previous characterization of the PENDI-350/triPy (PP) self-healing polymer system, including its tunable mechanical/self-healing behavior and useful Li⁺ conductivity, we have continued our efforts to characterize the effects of this material in a Li-S battery system.
- The PP polymer when used as a binder for S/C composite cathode has shown to increase the capacity retention significantly from 43.5% to 74.2% after 100 cycles at C/20. The capacity retention reached close to 100% after 100 cycles at 1C, which demonstrated the polysulfide trapping property of the PP polymer.
- We have performed CV and UV-Vis studies dibutyl-NDI (dbNDI) and Li₂S₈ as model compounds to understand the details of polysulfide-trapping mechanism. The NDI moiety in the PP polymer enhance the capacity retention in two different ways: first, it can be reversibly reduced into NDI²⁻ di-anions which can trap polysulfides via strong ion-dipole interaction; second, it can also function as a redox-mediator, which promotes the charge transfer and finally increases the utilization of sulfur during discharge process.
- We have fabricated high loading S cathode via systematic design of the S cathode components, including current collector, ratio design between PENDI-350 and tri-Py, choice of carbon conductive additive, and the loading amount of S/C composite. Carbon coated Al foil was used as current collector which improves the adhesion between current collector with S cathode. Multi-wall carbon nanotubes were used as conductive additive to replace black carbon. The S ratio of S/C composite was improved to 70%. Based on the new composition, we have fabricated cathodes with PP and PVDF as binder. After 40 cycles, the discharge capacity of cathode with PP binder retains as high as 1070 mAh/g (capacity retention of 92%).

- Robust binder system is needed to mitigate the increasing mechanical stress for S cathode with higher loading. The S cathode with PENDI-350:tri-Py ratio of 3:1 is prone to cracking as the S loading amount increases to around 4 mg/cm². After increasing the amount of tri-Py by changing the ratio to 1:1, a continuous S cathode was achieved even with S loading amount greater than 4.2 mg/cm².
- In our binder, PENDI-350 is used to trap the polysulfides. Cathode with PENDI-350 as binder has stable capacity around 1000 mAh/g in the first three cycles, which implies the significant trapping of the polysulfides. The coulombic efficiency stays constant around 98% even after around 60 cycles. The capacity stays almost constant after 30th cycles. SEM studies suggest improved compatibility of PENDI-350 binder with carbon/sulfur during the cycling process. Although cathode with PENDI-350 as binder traps polysulfides efficiently, cathode cracking can lead to the loss of sulfur by isolation.
- The dramatic capacity decrease in the first several cycles of cathode with PVDF as binder implies the quick dissolution of the polysulfides into the electrolyte. However, cathode with PVDF as binder showed continuous surface without significant cracking. Due to the different failure mechanism, it is possible that the mechanical integration of electrode materials can be improved by adding PVDF into PENDI-350.
- We have fabricated test cells with S/C cathode using PENDI-350/PEO (weight ratio = 3:1) as binder with loading of 3.71 mgS/cm². The capacity retention was as high as 91% (based on the 6th cycle with capacity of 789 mAh/g). We attribute this improved capacity retention to the flexibility of long-chain PEO (Mw = 1000 K) as well as its good compatibility with PENDI-350 resulting well dispersed polymer blends. To improve the mechanical properties further, we have added tri-Pyrene cross-linker that can form reversibly crosslinked network structures with PENDI-350 *via* quadrupolar aromatic pi-pi stacking between NDI and Pyrene units.
- In the PENDI-350/triPy/PEO (PPP binder) the flexible PEO chains could entangle to form inter-penetrating network structures. Test cells with S/C cathode with a PPP (PENDI-350:triPy:PEO = 3 : 2 : 1 by weight) binder was fabricated with S loading of 2.91 mgS/cm². The capacity remains around 918 mAh/g after 30 cycles with relative capacity retention of 97% (based on 6th cycle with capacity of 954 mAh/g). We have also fabricated Li-S cells with the S/C cathode with relatively high loading of 5.04 mgS/cm² without cracking.

Key Publications

1. Hubble D., Qin J., Lin F., Murphy I. A., Jang S.-H., Yang J., Jen A. K.-Y., "Designing Lithium Solvate Ionogels with Very High Conductivity and Lithium Transference Number." *J. Mater. Chem. A*, **2018**, 6, 24100–24106. DOI: 10.1039/C8TA08808J.
2. Qin J., Lin F., Hubble D., Wang Y., Li Y., Murphy I. A., Jang S.-H., Yang J., Jen A. K.-Y., "Tuning Self-healing Properties of Stiff, Ion-conductive Polymers." *J. Mater. Chem. A*, **2019**, 7, 6773–6783. DOI: 10.1039/C8TA11353J.
3. Li Y.,* Murphy I. A.,* Chen Y., Lin F., Wang X., Wang S., Hubble D., Jang S.-H., Mueller K. T., Wang C., Jen A. K.-Y., Yang J., "A Multi-functional Interface Derived from Thiol-modified Mesoporous Carbon in Lithium-sulfur Batteries" *J. Mater. Chem. A*, **2019**, 7, 13372-13381. DOI: 10.1039/C9TA02743B.
4. Lin, F. Design and Synthesis of Organic Functional Materials for Energy Conversion and Storage Applications (Ph.D. Thesis). University of Washington, Seattle, WA, September **2019**.
5. Hubble, D. From Solvate to Cell: A Molecular Engineering Approach to the Li-S Battery (Ph.D. Thesis). University of Washington, Seattle, WA, November **2019**.

Acknowledgements

Project team includes a senior research scientist Dr. Sei-Hum Jang, Ph.D. candidate students Dion Hubble, Jiaxu Qin, Ian Murphy, and Francis (Ray) Lin from the Jen group, as well as Dr. Shanyu Wang and Yun (April) Li from the Yang group. Special thanks to *PNNL personals.* Dion Hubble acknowledges government support under and awarded by the Department of Defense, Air Force Office of Scientific Research, National Defense Science and Engineering Graduate (NDSEG) Fellowship, 32 CFR 168a.

II.10 Beyond Li-ion R&D: Lithium-Air Batteries

II.10.A Rechargeable Lithium-Air Batteries (PNNL)

Ji-Guang Zhang, Principal Investigator

Pacific Northwest National Laboratory
902 Battelle Boulevard
Richland, WA 99354
E-mail: jiguang.zhang@pnnl.gov

Wu Xu, Principal Investigator

Pacific Northwest National Laboratory
902 Battelle Boulevard
Richland, WA 99354
E-mail: wu.xu@pnnl.gov

Tien Duong, DOE Technology Development Manager

Vehicle Technologies Office
U.S. Department of Energy
E-mail: Tien.Duong@ee.doe.gov

Start Date: October 1, 2015

End Date: September 30, 2020

Project Funding (FY19): \$200,000

DOE share: \$200,000

Non-DOE share: \$0

Project Introduction

It is well known that the state-of-the-art (SOA) lithium (Li)-ion batteries are a mature technology and may reach their practical limit on specific energy ($\sim 300\text{--}350\text{ Wh kg}^{-1}$) soon. Therefore, a worldwide effort has been made to explore new battery chemistries that may far exceed the specific energies of Li-ion batteries. Among the alternative energy storage systems, Li-air batteries have caught worldwide research interest since the first report of a nonaqueous Li-air battery in 1996 due to their extremely high theoretical specific energy density ($\sim 5,200\text{ Wh kg}^{-1}$ when the weights of Li and O_2 are included). However, before the commercialization of Li-air batteries, considerable challenges need to be overcome. These challenges include electrolyte instability, high overpotential, and severe corrosion of Li anodes. These problems cause poor round-trip efficiency and short cycle life in SOA Li-air batteries. To enable ultrahigh-energy-density Li-air batteries suitable for electric vehicle applications, it is critical to develop electrolytes that are more stable against reactive oxygen species and Li metal anodes, design alternative catalysts and carbon-based or carbon-free air electrodes, stabilize Li metal anodes, and seek new insights into the mechanisms of oxygen reduction/evolution reactions (ORR/OER).

Objectives

The objective of this project is to develop rechargeable Li-oxygen (Li-O_2) batteries with long-term cycling stability through in-depth research on more stable electrolytes and highly efficient catalysts for air electrodes, protection of Li metal anodes, and deeper insight into the ORR/OER mechanisms behind the electrochemical performance of Li-O_2 cells. In FY19, we focused on Li anode stabilization and building stable Li-O_2 batteries using protected Li anodes and optimized air electrodes to improve cycling stability of Li-O_2 batteries.

Approach

Stability of Li metal anodes when exposed to an oxygen-saturated, nonaqueous electrolyte is critical for the cycle life of Li-O_2 batteries. Highly elastic and stable protective composite layers, cross-linked gel-polymer electrolytes, and 3D host structures were applied for stabilization of Li anode under oxygen atmosphere in Li-O_2 batteries. A stable solid electrolyte interphase (SEI) layer was formed in situ using selected electrolytes and treatment protocols before Li-O_2 cell operation. In addition, in situ electrochemical pretreatment was

conducted to redistribute ruthenium oxide (RuO_2) catalyst on air electrodes and optimize the catalytic effects. The electrochemical performance of Li- O_2 batteries using the protected Li metal anodes and the optimized carbon/catalyst composite air electrodes based on carbon nanotubes (CNTs) and transition metal oxides such as RuO_2 were evaluated.

Results

Significant progress has been made in protection of electrodes (both carbon-based air electrode and Li anode) and optimization of efficient catalysts in Li- O_2 batteries in FY19. The details are described below.

1. Cross-linked gel-polymer electrolytes with high concentration electrolytes to protect Li metal anodes in Li- O_2 batteries

Cross-linked gel-polymer electrolytes composed of lithium trifluoromethanesulfonate (LiTf), tetraethylene glycol dimethyl ether (TEGDME), and polyethylene oxide (PEO) were designed for protection of Li metal anodes in Li- O_2 batteries. Li- O_2 cells composed of Li metal anodes and CNT air cathodes with three liquid electrolytes, 1 M LiTf-TEGDME electrolyte with 5% PEO (PEO with diluted electrolyte), 3 M LiTf-TEGDME electrolyte with 5% PEO (PEO with highly concentrated electrolyte (HCE)), and 3 M LiTf-TEGDME electrolyte (HCE with no PEO) were fabricated (Figure II.10.A.1a). They were cycled at 25°C at a current density of 0.1 mA cm^{-2} under a capacity control protocol of 1,000 mAh g^{-1} (Figure II.10.A.1b). The

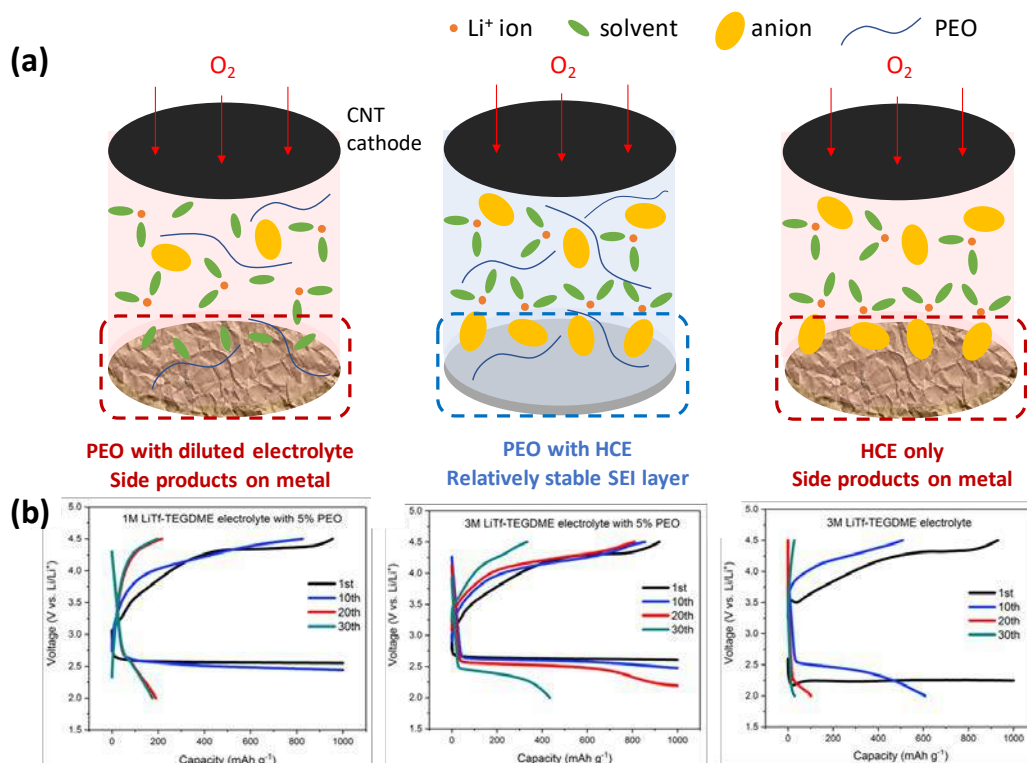


Figure II.10.A.1 (a) Schematic images of Li- O_2 cells composed of Li metal anodes and CNT air cathodes with different electrolytes: PEO with 1 M LiTf-TEGDME (left), PEO with 3 M LiTf-TEGDME (center), and 3 M LiTf-TEGDME (right). (b) Cycling stability performance of the above Li- O_2 cells at 25°C at a current density of 0.1 mA cm^{-2} under a capacity protocol of 1,000 mAh g^{-1}

Li- O_2 cells with Li anodes protected by PEO with diluted electrolyte exhibited limited cycle life, as shown on the left in Figure II.10.A.1b. In contrast, the cycle life of the Li- O_2 cells increased when the salt concentration in the liquid electrolyte for the cross-linked PEO electrolyte was increased to 3 M (Figure II.10.A.1b, center). However, Li- O_2 cells with 3 M LiTf-TEGDME electrolyte but without PEO exhibit the worst cycling stability (Figure II.10.A.1b, right) compared to Li- O_2 cells with the two other polymer-based electrolytes. This indicates

that addition of 5 wt.% PEO polymer in the electrolytes can increase the cycle life of Li-O₂ cells. After 30 cycles, the morphological changes of cycled Li metal anodes with different electrolytes were investigated. Some black side-reaction products were found on Li metal surfaces cycled in PEO with diluted electrolyte. Much less corrosion product was found on Li metal anodes recovered from Li-O₂ cells cycled in PEO with concentrated electrolyte (3 M LiTf-TEGDME). However, without PEO in the electrolyte, a much thicker corrosion layer was observed on cycled Li metal anodes recovered from Li-O₂ cells cycled in HCE with 3 M LiTf-TEGDME. These results indicate that a small amount of PEO can form a stable SEI layer on Li metal anodes and effectively suppress the corrosion of Li metal anodes in an oxygen-rich environment, thus greatly enhancing the cycling stability of Li-O₂ cells. It is worth noting that there is no efficient catalyst was used to decorate CNT-based air cathodes in the cells.

2. Highly elastic polymer-based protective layer to stabilize Li metal anodes in Li-O₂ batteries

An elastic polymer-based protective layer composed of polydimethylsiloxane (PDMS), lithium bis(fluorosulfonyl)imide (LiFSI), and DME was developed. Usually, many small grooves were observed on the as-received commercial Li foil surface, which are generated during manufacturing of Li foil. When free-standing membranes are used to cover the surface of Li metal anodes, many voids between the Li foil (with grooves) and the protective membrane will naturally occur, as shown in Figure II.10.A.2a. This gap will increase the interfacial resistance of the Li metal anodes (Figure II.10.A.2a, top). To avoid this problem, a composite solution of the polymer, Li salt, and solvent were directly coated on the Li surface, then thermally solidified to enable good contact between Li and the cross-linked polymer layer (CPL) and to decrease the interfacial resistance on Li metal (Figure II.10.A.2a, bottom). After casting, this uniform and highly elastic CPL coated on the Li anode functions as a reliable protection for the whole Li metal surface during Li-metal battery cycling. This novel CPL was effective against highly reactive Li metal after one week, even at elevated temperature (60°C). The ionic conductivity of this CPL is $1.1 \times 10^{-4} \text{ S cm}^{-1}$ at 25°C. In addition, cyclic stability tests of Li||Li symmetric cells with or without the CPL on Li metal containing 1 M LiFSI-DME electrolyte were conducted at a current density of 0.2 mA cm^{-2} at 25°C (Figure II.10.A.2b). The Li||Li symmetric cell (using PP separator) without CPL protection exhibits significant plating/stripping polarity increase during cycling due to the continuous side reaction between Li metal and the liquid electrolyte. In contrast, stable cycling beyond 550 h with very low hysteresis has been obtained in the Li||Li cells with CPL protection on the Li surface. These

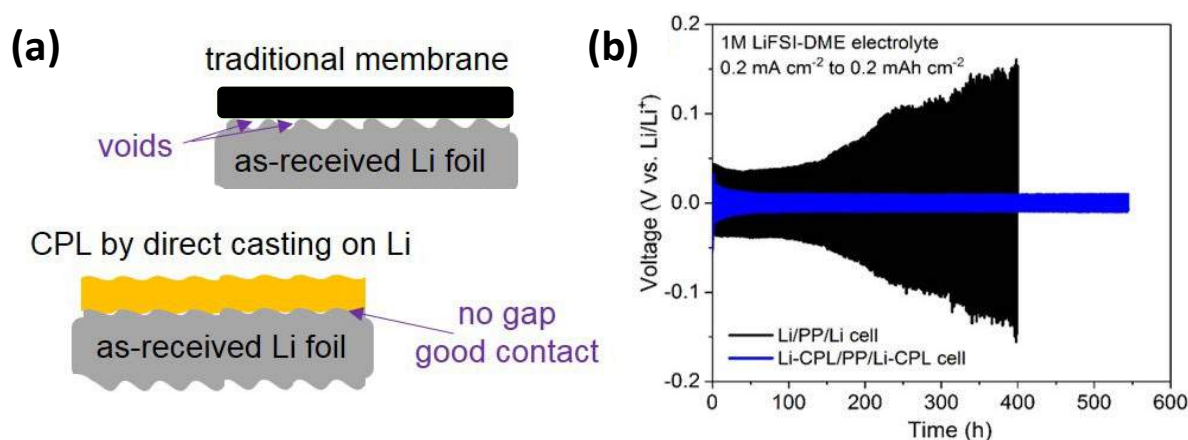


Figure II.10.A.2 (a) Schematic of traditional artificial membrane on as-received Li foil surface and current CPL applied by direct casting on Li foil. (b) Cyclic stability tests based on Li||Li cells with or without CPL on Li metal containing 1 M LiFSI-DME electrolyte at 25°C. Current density: 0.2 mA cm^{-2}

results clearly demonstrate that the CPL developed in this work can effectively extend the cycle life of Li metal anode. However, further tests of these CPL-protected Li anodes did not indicate significant improvement in the performance of the Li-O₂ cells using the same electrolyte of LiFSI in DME because LiFSI is unstable against reduced oxygen species. Therefore, further optimization of electrolytes is necessary.

3. Development of inorganic/polymeric composite as protective layer with 3D carbon host structure to stabilize anode in Li-O₂ batteries

To more evenly distribute Li⁺ ion flux on Li anode and stabilize the Li surface, the host structure and protective layer for Li metal anodes in Li-O₂ batteries were investigated (Figure II.10.A.3a). Porous carbon paper was used as a conductive 3D matrix; it was treated with ammonium hydroxide solution for 24 h to functionalize its surface for facile Li metal soaking. After the carbon fabric was functionalized, it was transferred into an argon (Ar)-filled glovebox and soaked in molten Li metal at 300°C for 30 min. After Li infiltration, excess Li was removed from the surface, and the Li/C composite was cooled to ambient temperature. A Nafion-Al₂O₃ composite layer (NCL) was prepared and coated on the Li/C composite as a stable protective composite layer to protect the Li/C composite anode in oxygen-rich environments. Nafion was selected because it can form a stable polymer against reactive oxygen. To understand the effect of host structure and protection layer for anodes in Li-O₂ batteries, Li-O₂ cells composed of Li metal foil, Li/C composite anode, or NCL-protected Li/C composite anode were cycled at 25°C at a current density of 0.1 mA cm⁻² under a capacity protocol of 1,000 mAh g⁻¹. RuO₂-CNT air electrodes and 1 M LiTf-TEGDME electrolyte were used for all the cells to minimize variables. More stable cycle performance of Li-O₂ cells can be obtained with NCL-protected 3D Li/C composite anodes (Figure II.10.A.3b, right) compared to those of Li-O₂ cells using bare Li metal foil (Figure II.10.A.3b, left) and Li/C composite anodes without protection (Figure II.10.A.3b, center).

However, the cycle life of Li-O₂ cells was limited to about 40 cycles although the protected Li/C composite was used as a host for Li anodes. To reveal the failure mechanism in these Li-O₂ batteries, the morphological change of protected Li/C composite anodes after 40 cycles was investigated; The amount of Li in the Li/C composite under the protective layer was significantly reduced after cycling. This means that some Li was irreversibly lost due to the side reaction on the cathode side and cannot return to the anode side during cycling.

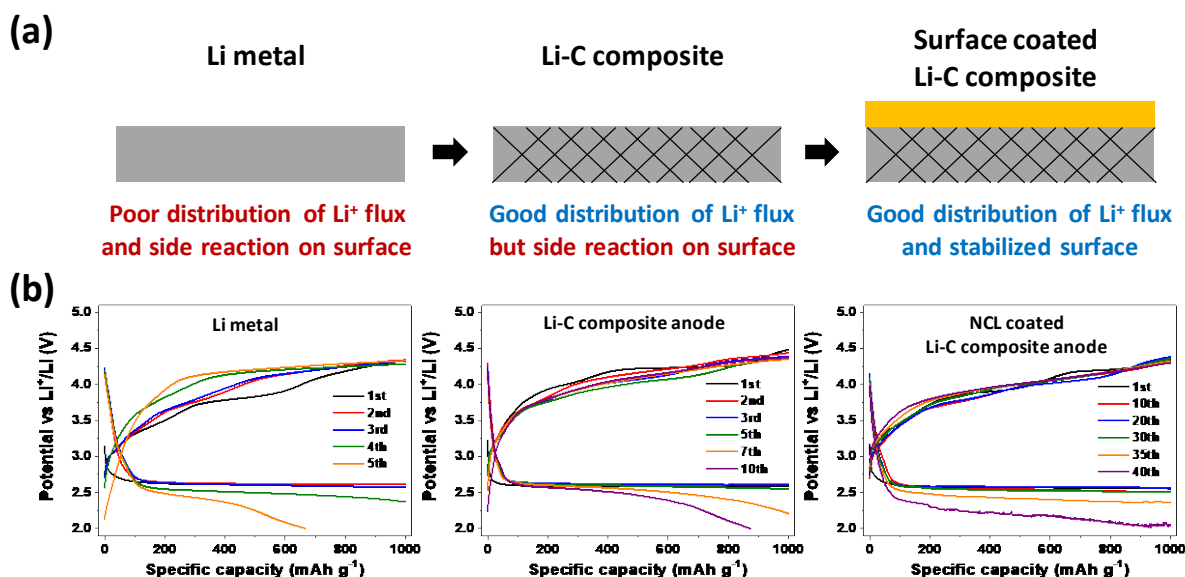


Figure II.10.A.3 (a) Schematic images of different anodes and improvement by 3D carbon host for Li/C composite anodes and protective layer (NCL) coating for surface stabilization. (b) Cyclic stability tests based on Li-O₂ cells composed of RuO₂-CNTs air cathodes and 1 M LiTf-TEGDME electrolyte at 25 °C at a current density of 0.1 mA cm⁻² under a capacity protocol of 1,000 mAh g⁻¹ with Li metal anode (left), Li/C composite anode (center), and NCL-protected Li/C composite anode (right)

In other words, it is confirmed that reversibility of Li anodes depends not only on the anode/electrolyte reaction, but also on the cathode/electrolyte/O₂ reaction. In addition, an in situ formed, stable SEI layer between the protective layer and the Li metal surface was required for higher stability of Li/C composite anodes. Therefore, to improve the stability of Li anodes in Li-O₂ batteries, optimization of the full cell

structure, including improvement of cathode reversibility and formation of stable SEI layer (formed either in situ or ex situ), on Li anode surface are required.

4. Li-O₂ batteries using protected Li-C composite anode and optimal RuO₂/CNT air electrodes

In our previous work, we developed a low cost, one-step electrochemical pre-charging strategy to simultaneously generate protective thin films on both the CNT air electrode and Li metal anode in Ar atmosphere. In this work, we combined the pretreatment strategy developed previously with a protective coating developed recently to further improve the stability of Li-O₂ batteries. The Li-O₂ cells using RuO₂/CNT air electrodes and NCL-protected Li/C composite anodes were pretreated electrochemically by discharging and recharging the cells under Ar atmosphere (D 0.8 V-C 4.3 V). After the pretreatment, large particles of RuO₂ (see Figure II.10.A.4a) had redistributed and formed ultrafine RuO₂ catalyst (see Figure II.10.A.4b) which can largely improve the catalytic efficiency and lead to reduced overvoltage, as was shown in subsequent evaluation in oxygen environment. In addition, as we described in our previous work, this in situ electrochemical pretreatment can also stabilize the surface of Li/C anodes under the NCL-protected layer.

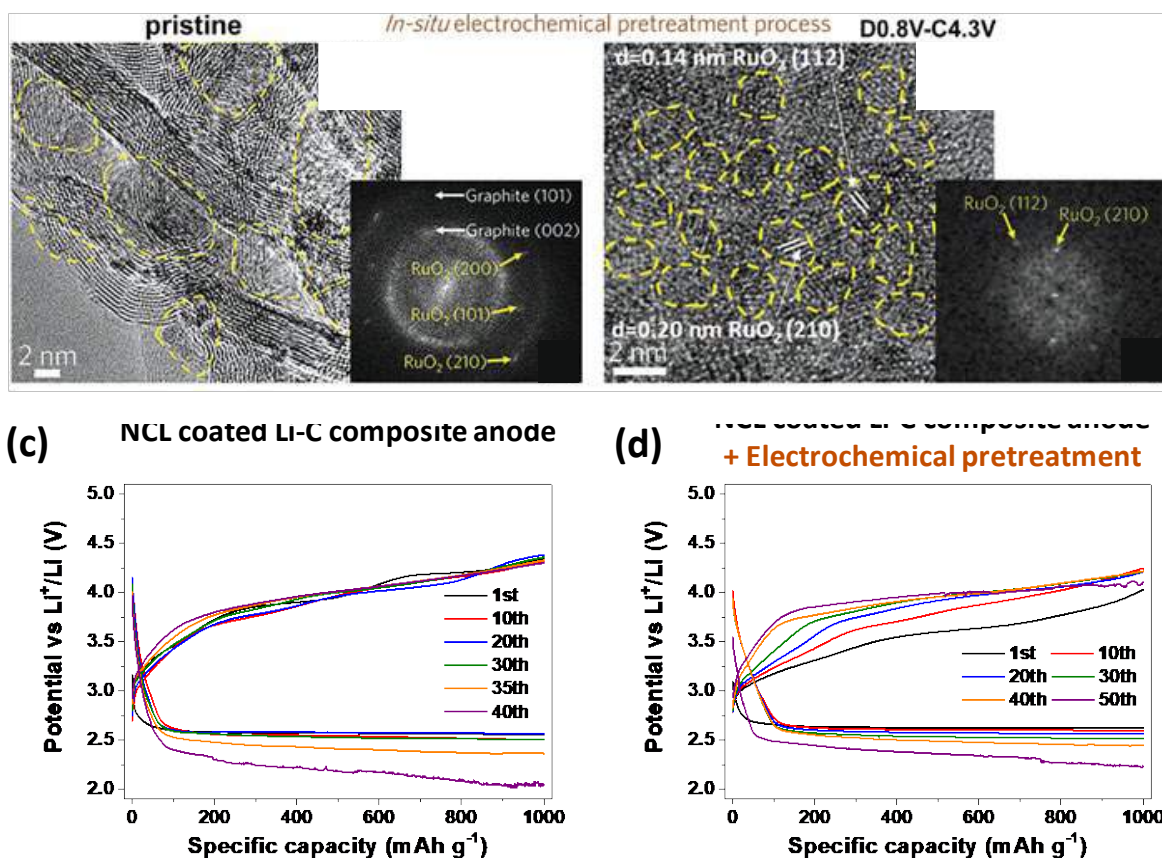


Figure II.10.A.4 (a, b) TEM image and corresponding FFT pattern of (a) pristine RuO₂/CNT electrode and (b) pretreated electrode. (c, d) Cyclic stability tests of Li-O₂ cells composed of RuO₂/CNTs air cathodes, 1 M LiTf-TEGDME electrolyte, and protected Li/C composite anode at 25 °C at a current density of 0.1 mA cm⁻² under a capacity limited protocol of 1,000 mAh g⁻¹ (c) without or (d) with electrochemical pretreatment

Using this optimized RuO₂/CNT air electrode and NCL-protected Li/C composite anode with in situ formed SEI and cathode electrolyte interphase layers, cycling performance of Li-O₂ cells was evaluated and compared with the cell without pretreatment at 0.1 mA cm⁻² under a capacity-limited protocol of 1000 mAh g⁻¹ based on the total mass of RuO₂ and CNTs (Figure II.10.A.4c and d). The voltage profiles of the Li-O₂ cells clearly demonstrate that the pretreatment enhanced the catalytic effect of RuO₂ on the air electrode, which induced lower charge potential. In addition, more stable cycling performance of Li-O₂ cells can be obtained with

pretreatment via improved stability of the Li/C anode with a stable SEI layer. To further improve the performance of Li-O₂ cells, electrolytes with more stable organic solvents against highly reactive reduced oxygen species will be developed.

Conclusions

- Cross-linked gel-polymer electrolytes composed of HCE (3 M LiTf-TEGDME) with a small amount of PEO (5%) were designed to protect Li metal anodes and effectively suppress their corrosion in an oxygen-rich environment, which enhances the cycling stability of Li-O₂ cells.
- Direct coatings of Li metal anodes by polymeric protective layers using PDMS or Nafion were successfully developed to prevent voids between the Li metal and protective layers. These protective layers improved the stability of Li metal anodes during electrochemical tests.
- A protected Li/C composite anode was prepared by Li infiltration into a surface-functionalized 3D carbon host and covered with a stable Nafion-Al₂O₃ composite layer (NCL). With the protection layer and the 3D Li/C structure, the cycle life of Li-O₂ cells was more than quadrupled (from 6~10 cycles to >40 cycles).
- Cycling performance of Li-O₂ cells with optimized RuO₂/CNT air electrodes and protected Li anodes protected by in situ electrochemical pretreatment was successfully evaluated. The combination of the optimized, efficient air electrode and the protected Li/C composite anode have further enhanced the cycling stability of Li-O₂ batteries.
- Although stable artificial protective layers or in situ formed SEI layers are formed on Li anodes in Li-O₂ batteries, stable solvent and electrolyte are still urgently needed for long term cycling stability of Li-O₂ cells.

Key Publications and Patent Application

1. B. Liu, W. Xu, L. Luo, J. Zheng, X. Ren, H. Wang, M. H. Engelhard, C. Wang, and J.-G. Zhang, "Highly Stable Oxygen Electrodes Enabled by Catalyst Redistribution through an In Situ Electrochemical Method," *Advanced Energy Materials* **2019**, 9, 1803598. DOI: 10.1002/aenm.201803598.

Acknowledgements

Key contributors include Drs. Won-Jin Kwak and Bin Liu are greatly appreciated.

II.10.B Li-Air Batteries (ANL)

Khalil Amine, Principal Investigator

Argonne National Laboratory
9700 S Cass Avenue
Argonne, IL 60516
Email: amine@anl.gov

Larry Curtiss, Principal Investigator

Argonne National Laboratory
9700 S Cass Avenue
Argonne, IL 60516
Email: curtiss@anl.gov

Jun Lu, Principal Investigator

Argonne National Laboratory
9700 S Cass Avenue
Argonne, IL 60516
Email: junlu@anl.gov

Tien Duong, DOE Technology Development Manager

U.S. Department of Energy
E-mail: Tien.Duong@ee.doe.gov

Start Date: October 1, 2017

End Date: September 30, 2019

Project Funding (FY19): \$500,000

DOE share: \$ 500,000

Non-DOE share: \$0

Project Introduction

Lithium-oxygen batteries are of much interest because they offer, in principle, ten times the energy density of conventional lithium-ion systems. The inherent energy potential of lithium metal approaches that of gasoline, but there are challenges that remain to be able to unlock this potential. While today's lithium-ion batteries may provide acceptable power for hybrid electric vehicles and all-electric vehicles, they do not as yet provide sufficient energy for driving distances desired by consumers. A breakthrough in Li-oxygen battery technology would significantly increase the possibility of extending the electric range of these vehicles with the added advantages of reducing battery cost and weight. [1]

The successful implementation of non-aqueous Li-air cells has been hampered because of severe materials problems that have limited electrochemical performance. These include (1) the non-aqueous electrolytes can be unstable under both the charge and discharge conditions, thereby seriously limiting cycle life; (2) during discharge, the solid and insoluble Li_2O_2 and/or other lithium oxide products are deposited on the surface or within the pores of the carbon cathode, thereby passivating the surface as well as clogging the pores and restricting oxygen flow; (3) degradation of the lithium anode due to oxygen crossover destroys the integrity and functioning of the cell; and (4) commonly used transition metal cathode catalysts, do not access the full capacity of the oxygen electrode or enable sufficiently high rates.

The team led by Dr. Khalil Amine, Dr. Larry Curtiss, and Dr. Jun Lu at Argonne National Laboratory is working on problems that limit the electrochemical performance of the Li-oxygen battery, including the stability of the organic electrolytes, development of new cathode catalysts, and the stability of the lithium anode under oxygen-crossover conditions. This effort will lead to the development of a reversible lithium oxygen battery that provides much higher energy density than state-of-the-art lithium ion batteries for electric vehicles.

Objectives

The objective is to develop new cathode architectures for lithium air batteries to lower the charge overpotential, improve the cell efficiency, and increase cycle life. Commonly used carbons and cathode catalysts do not access the full capacity of the oxygen electrode and can cause significant charge overpotentials, which lowers efficiency and limits cycle life. Therefore, there is a need for improved catalysts and how they can control the discharge product morphology, which affects the overpotentials. New more stable electrolytes are also needed to prevent gradual electrolyte decomposition that occurs in the presence of the reduced oxygen species. Another goal is to develop methods to protect the lithium anode from corrosion such as for example by the oxygen crossover effect, which can reduce the cycle life. This project will develop new cathode materials and electrolytes for Li-air batteries for long cycle life, high capacity, and high efficiency.

Approach

This project addresses the challenges of Li-O₂ batteries through experimental and theoretical investigation of (a) the discharge formation mechanism, (b) investigation of the morphology and composition of the discharge product, and (c) investigation of electrolyte decomposition mechanisms. This understanding is being used to (1) develop new cathode materials to promote formation of discharge morphologies such as those involving superoxides with better conductivity to decrease charge overpotentials, (2) cathode materials that do not degrade with cycling and (c) methods to protect the lithium anode. The experimental work to create advanced electrolytes, carbons, catalysts, cathodes, and anodes is guided by theory and modeling. The experimental results are thoroughly analyzed with very sophisticated analytical techniques such as in situ XRD and Raman. These characterization results are used to fine-tune the computational studies. Fundamental understanding of the underlying principles will be provided to greatly facilitate the next steps in the development cycle.

Collaborators include Professor Kah Chun Lau (University of California-Norridge), Professor Yiying Wu (Ohio State University), Dr. Dengyun Zhai (China). We utilize several facilities at Argonne National Laboratory including the Advanced Photon Source, the Center for Nanoscale Materials, and the Argonne Leadership Computing Facility.

Results

New Catalyst Development

Catalysts play a very important role in the oxygen evolution reaction (OER) of lithium peroxide in Li-O₂ batteries and the right catalyst can reduce the overpotential during charge and increase efficiency. So far, attractive OER performances are mostly reported for catalysts using expensive noble metals such as Ir, Ru, Pt, and Pd, which could limit the large scale applications of Li-O₂ batteries. Hence, it is desirable to explore low-cost and effective alternative catalysts for the OER. We have investigated two types of new catalysts this year: a low cost Co based catalyst and a thin film Pd catalyst; these are described below.

Transition metal-based catalysts such as Co₃O₄, NiO, Co(OH)₂, and Ni(OH)₂ have attracted much attention because of their low cost and earth abundance. However, most of the synthesis methods not only involve multiple processes, but also have problems with the aggregation or contamination of catalysts. We designed a simple approach to prepare ultrafine cobalt and nickel nanoparticles dispersed in a porous LiOH structure (denoted as Co₂Ni@LiOH) by an in situ lithiation strategy. We lithiated cobalt–nickel layered double hydroxide (Co–Ni LDH) nanoplates by a discharge process under argon in a Swagelok cell, which leads to the formation of cobalt and nickel metal nanoparticles in a LiOH composite (Co₂Ni@LiOH). Then, the Co₂Ni@LiOH composite-based electrode was directly employed as the cathode in a Li-O₂ cell after filling the glass chamber with pure oxygen. The metal particles have ultrafine size (~2 nm) and the composite has a uniform 3D porous structure with enhanced surface area and good electrical conductivity.

As the oxygen cathode for the Li–O₂ cell, the Co₂Ni@LiOH exhibits a discharge voltage of 2.7 V and a very low charge potential of 3.4 V at a current density of 50 $\mu\text{A cm}^{-2}$, which results in a much higher roundtrip efficiency of $\sim 79\%$ compared with that of pristine Co–Ni LDH ($\sim 59\%$). This high roundtrip efficiency is comparable to that of the well-known noble metals. The Co₂Ni@LiOH-based Li–O₂ cell is stable and can last 40 cycles with a 3.6 V charge potential at the current density of 50 $\mu\text{A cm}^{-2}$. We investigated the discharge and charge products in the Li–O₂ cell from different cycles at a current density of 50 $\mu\text{A cm}^{-2}$.

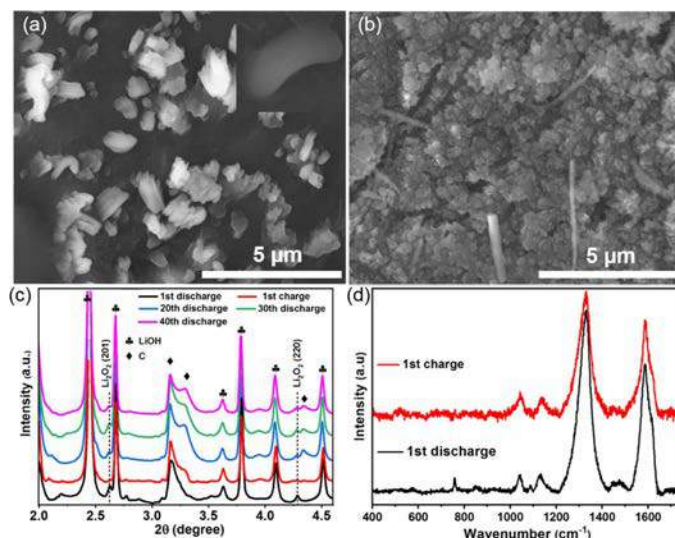


Figure II.10.B.1 SEM of (a) 1st discharge and (b) charge products in Li–O₂ batteries with the Co₂Ni@LiOH cathode. (c) XRD of the 1st, 20th, 30th, and 40th discharge and the 1st charge products, (d) Raman spectrum of the 1st discharge and charge products in Li–O₂ battery (Amine et al, ACS Applied Materials & Interfaces, 11, 811–818 (2019))

After the 1st discharge, the SEM image (Figure II.10.B.1a) shows that the Co₂Ni@LiOH electrode is covered by toroidal structures, which is the common morphology for Li₂O₂. After charging the cell, all the toroidal structures disappeared and the interconnected structure is exposed, which is Co₂Ni@LiOH (Figure II.10.B.1b). The XRD and Raman spectra for various cycles are shown in Figure II.10.B.1c and Figure II.10.B.1d. The well-aligned network facilitates the oxygen diffusion and the electrolyte penetration into the electrode. The enhanced electrical conductivity network improves the charge transport kinetics and more active sites are exposed, which facilitate the adsorption and dissociation of oxygen during the oxygen reduction reaction and the oxygen evolution reaction. This new catalyst design is important for the development of effective non-noble metal catalysts for Li–O₂ batteries.

The second catalyst we investigated was based on a wet impregnation chemistry method to form a very thin layer of palladium nanoparticles on the surface of carbon, which largely suppresses the electrolyte side reactions through a selective coating on the carbon defect sites. Simultaneously, the Pd films serve as an electrocatalyst enabling the decomposition of lithium peroxide at a very low overpotential. This rational design of the cathode catalyst is found to improve overall cell efficiency and extends the cycle life of the lithium-oxygen battery. The as-prepared Pd-coated carbon sample was tested in a Li–O₂ cell together with the pristine carbon as the control. The charge potential of pristine carbon cathode (4.2 V) was found to be substantially higher than that of the Pd/carbon sample (3.2 V), indicating that the coated Pd film served as a good OER catalyst to facilitate the decomposition of the Li₂O₂. After only 15 cycles, the cell fails with the charge voltage exceeding the 5.0 V cut off. The increase of the overpotential is likely due to the accumulation of the products from the side-reactions occurring on the carbon defect sites. In contrast, the Pd/carbon cathode has a low first cycle charge potential of 3.2 V with good cyclability. The cell fails at about 50 cycle. In the case of the Pd/carbon cathode, the discharge product is confirmed to be largely Li₂O₂ according to scanning electron microscope, Raman spectroscopy and high-energy X-ray diffraction results.

This work demonstrated that the defect sites on conductive carbon supports can be leveraged as deposition sites for Pd films, serving the dual purpose of mitigating carbon degradation while reducing the OER overpotential to ~ 0.2 V. Compared with pristine carbon electrodes, the Pd deposited carbon exhibited less side reactions, lowered overpotentials and ultimately higher cycle stability. This work provides a new method for achieving high-performance Li-O₂ batteries and will be used with new electrolytes for longer cycle life in these batteries.

Control of Discharge Product Morphologies

The underlying reason for the evolution of Li₂O₂ morphology are not well understood in Li-O₂ batteries and is important for their development. In particular, the effect, if any, of the surface structure of the oxygen cathode on the morphology of the grown Li₂O₂ is still not clear, nor is the effect of Li₂O₂ formation on the mass and charge transport in the O₂ cathode. In order to clarify this, we have carried out a systematic experimental and theoretical modeling study on the evolution of Li₂O₂ morphology at different stages of the discharge-charge cycle in a Li-O₂ cell.

To suitably monitor the evolution of Li₂O₂, i.e., the discharge product morphology during discharge, we fabricated Li-O₂ cells to minimize variations in the cell construction since variations in the cathode weight, temperature, moisture, and electrolyte wetting can lead to significant changes in the cell performance. TEGDME with 1M LiCF₃SO₃ was selected as the electrolyte since it has been demonstrated to be relatively stable towards the discharge product Li₂O₂, during the discharge reaction. The cells were discharged to different specific capacities with a constant current density, and subsequently subjected to scanning electron microscopy observation, impedance measurements, and XRD investigation. SEM images of the discharged cathodes after the 1st, 2nd, and 10th discharge cycles indicate that the discharge products on the carbon cathode are toroid particles and it seems that the particle size and quantity increase with the cycle number. We also carried out DFT calculations of the evolution of Li₂O₂ clusters and O₂ mobility.

From this study it was clear that the morphology and particle size of the discharge product changes significantly as a function of the depth of the discharge as well as the cycle number. The impedance spectroscopy showed a gradual increase in the resistance with an increase in the depth of discharge, which might be an indication of the build-up of an insulation layer of Li₂O₂. This phenomenon was confirmed by fitting of the impedance, which showed a lower O₂ diffusion, possibly due to the clogging caused by the insulating layer of Li₂O₂. The limitation in the mobility of O₂ was confirmed by ab initio molecular dynamics calculations. Furthermore, a sustainable mass transport of the diffusive active species (e.g., O₂ and Li⁺) and evolution of the underlying interfaces are critical to dictate desirable oxygen reduction (discharge) and evolution (charge) reactions in the porous carbon electrode of a Li-O₂ cell.

Electronic conductivity in Li-O₂ discharge products

The electronic conductivity of discharge products in Li-O₂ batteries and effect on charge potentials is not well understood and is important for making advances in this type of battery. In order to clarify this, we have carried out a careful experimental study of effect of composition on electronic conductivity using cathode materials that can control composition. Theoretical calculations have demonstrated increased electronic conductivity of LiO₂ compared to Li₂O₂, but there has been no experimental evidence reported for this. Electrochemical impedance spectroscopy (EIS) can be used to quantify the increase in charge transfer resistance of the ORR reactions in Li-O₂ batteries due to discharge product passivation of the cathode. In this work the first experimental evidence indicating that LiO₂ has increased electronic conductivity compared with Li₂O₂ has been found. Galvanostatic discharge and charge experiments coupled with three electrode impedance measurements were used to investigate the charge transfer impedance for LiO₂ discharge product compared to that of Li₂O₂, which is insulating in the bulk form. Iridium-rGO (Ir-rGO) was used as a cathode material, which we have previously shown gives LiO₂ as the discharge product. [2]

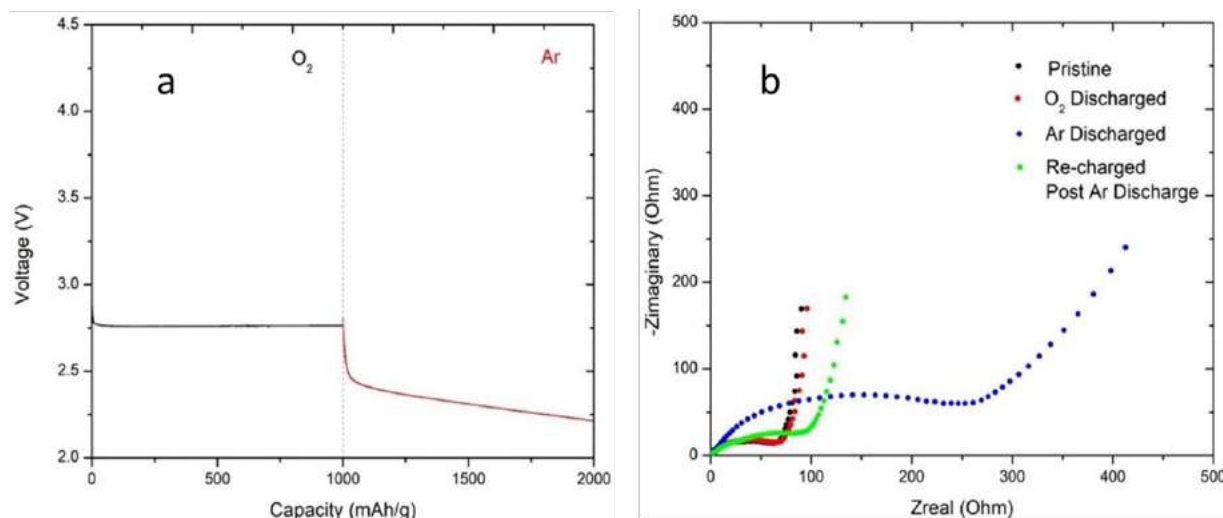


Figure II.10.B.2 (a) Discharge profile of Ir-rGO under O₂ followed by discharge profile under Ar flow (b) PEIS measurements performed on pristine cathode, after O₂ discharge, after Ar discharge and after re-charge of the discharged cathode

In the experiment shown in Figure II.10.B.2 the discharge was carried out first in O₂ ($\text{O}_2 + \text{Li}^+ + \text{e}^- \rightarrow \text{LiO}_2$) to form LiO₂ and then in Ar ($\text{LiO}_2 + \text{Li}^+ + \text{e}^- \rightarrow \text{Li}_2\text{O}_2$) to form Li₂O₂. The observed cathode potential during the O₂ discharge was constant at approximately 2.75 V vs Li/Li⁺ with a discharge capacity of 1000 mAh/g. Upon discharge in Ar, the voltage readily dropped to 2.2 V vs Li/Li⁺ with a discharge capacity of 1000 mAh/g. The discharge capacity above 2.0 V vs Li/Li⁺ of the same cathode in Ar, without a prior discharge in O₂ is <100 mAh/g. This indicates that the capacity obtained during the Ar discharge in Figure II.10.B.2a is derived from the reduction of the LiO₂ discharge species formed during the prior O₂ discharge. Raman and titration analysis were performed and indicated that LiO₂ was formed during discharge with O₂ and that it was converted to Li₂O₂ by the discharge in Ar.

Nyquist plots show that the impedance spectra of the cathode after the O₂ discharge is similar to the pristine cathode as shown in Figure II.10.B.2b. The impedance of the cathode after discharge in Ar is larger than the impedance measured after the initial O₂ discharge. The impedance of the cathode measured after re-charge is reduced in comparison to the impedance of the discharged cathode. These impedance results demonstrate that the impedance increase in Figure II.10.B.2b is a result of the change from LiO₂ to Li₂O₂. Investigation of other Li-O₂ cells without Ir, where Li₂O₂ is formed as the discharge product, have confirmed this increase in impedance. The key conclusion of this work from the EIS studies is the increased electronic conductivity of LiO₂, which can lead to reduced charge over-potentials in batteries forming this discharge product found in previous studies.

Conclusions

Two new catalysts have been investigated. We designed a simple approach to prepare ultrafine cobalt and nickel nanoparticles dispersed in a porous LiOH structure (denoted as Co₂Ni@LiOH) by an in situ lithiation strategy. The well-aligned network facilitates the oxygen diffusion and the electrolyte penetration into the electrode. The enhanced electrical conductivity network improves the charge transport kinetics and more active sites are exposed. This new catalyst design is important for the development of effective non-noble metal catalysts for Li-O₂ batteries. The work on the second catalyst demonstrated that the defect sites on conductive carbon supports can be leveraged as deposition sites for Pd films, serving the dual purpose of mitigating carbon degradation while reducing the OER overpotential to ~0.2 V. Compared with pristine carbon electrodes, the Pd deposited carbon exhibited less side reactions, lowered overpotentials and ultimately higher cycle stability. We have also carried out studies that have revealed new insights into how the Li₂O₂ morphology evolves and the nature of the electronic conductivity of different lithium oxides. The key

conclusion of the latter work is the increased electronic conductivity of LiO_2 , which can lead to reduced charge over-potentials in batteries forming this discharge product.

Key Publications

1. “In situ Formed Ir_3Li Nanoparticles as Active Cathode Material in Li-Oxygen Batteries,” Avik Halder, Anh T. Ngo, Xiangyi Luo, Hsien-Hau Wang, J. G. Wen, Pedram Abbasi, Mohammad
2. Asadi, Chengji Zhang, Dean Miller, Dongzhou Zhang, Jun Lu, Paul C. Redfern, Kah Chun Lau,
3. Rachid Amine, Rajeev S. Assary, Yun Jung Lee, Amin Salehi-Khojin, Stefan Vajda, Khalil Amine,
4. Larry A. Curtiss, *J. Phys. Chem. A* (2019) <https://doi.org/10.1021/acs.jpca.9b06875>
5. “Lithiation induced non-noble metal nanoparticle for Li- O_2 batteries,” Yuanyuan Guo, Zhengfei Dai, Jun Lu, Xiaoqiao Zeng, Yifei Yuan, Xuanxuan Bi, Lu Ma, Tianpin Wu, Qingyu Yan, Khalil Amine, *ACS Applied Materials & Interfaces*, 11, 811–818 (2019).
6. Deactivation of redox mediators in lithium-oxygen batteries by singlet oxygen, W. J. Kwak, H. Kim, Y. K. Petit, C. Leypold, T. T. Nguyen, N. Mahne, P. Redfern, L. A. Curtiss, H. G. Jung, S. M. Borisov, S. A. Freunberger, Y.-K. Sun, *Nature Communications*, **10**, 1380 (2019). DOI: 10.1038/s41467-019-09399-0
7. Fundamental Understanding of Water-Induced Mechanisms in Li- O_2 Batteries: Recent Developments and Perspectives, A Dai, Q Li, T Liu, K Amine, J Lu, *Advanced Materials*, 1805602 (2018).
8. Study of the Li-Oxygen Battery Discharging and Charging Process using In situ TEM, K He, Y Yuan, X Bi, T Foroozan, J Lu, R Shahbazian-Yassar, *Microscopy and Microanalysis* 24 (S1), 328-329 (2018)

References

1. “Aprotic and aqueous Li- O_2 batteries,” J. Lu, L. Li, J. B. Park, Y. K. Sun, F. Wu, K. Amine, *Chem Rev* 2014, **114**, 5611.
2. “A lithium-oxygen battery based on lithium superoxide,” J. Lu, Y. J. Lee, X. Luo, K. C. Lau, M. Asadi, H.-H. Wang, S. Brombosz, J. G. Wen, D. Zhai, Z. Chen, D. J. Miller, Y. S. Jeong, J.-B. Park, Z. Z. Fang, B. Kumar, A. Salehi-Khojin, Y.-K. Sun, L. A. Curtiss, K. Amine, *Nature* 2016, **529**, 377.

II.10.C Lithium Oxygen Battery Design and Predictions (ANL)

Larry Curtiss, Principal Investigator

Argonne National Laboratory
9700 S Cass Avenue
Argonne, IL 60516
Email: curtiss@anl.gov

Amin Salehi, Principal Investigator

University of Illinois at Chicago
Department of Mechanical and Industrial Engineering
842 West Taylor Street
Chicago, IL 60607
Email: salehikh@uic.edu

Ahn Ngo, Principal Investigator

Argonne National Laboratory
9700 S Cass Avenue
Argonne, IL 60516
Email: ango@anl.gov

Tien Duong, DOE Technology Development Manager

U.S. Department of Energy
E-mail: Tien.Duong@ee.doe.gov

Start Date: October 1, 2019
Project Funding: \$1,500,000

End Date: September 30, 2021
DOE share: \$1,500,000

Non-DOE share: \$0

Project Introduction

Lithium(Li)-oxygen batteries are considered as a potential alternative to Li-ion batteries for transportation applications due to their high theoretical specific energy. The high energy density of Li-O₂ batteries is made possible because of the formation of the Li₂O₂ product, which can store significantly higher amounts of energy compared to other energy storage systems because of the Li-O bonds. However, the challenge is that the decomposition of Li₂O₂ during the charge process requires charge transfer, which is difficult because of the large band gap of solid Li₂O₂ likely covering catalytic sites. This leads to a sluggish charge process requiring higher potentials for Li₂O₂ decomposition, which in turn reduces the energy efficiency of the battery and puts the electrolyte at risk of degradation. Additionally, the charge potential can depend on the morphology and size of Li₂O₂ product. The major issues with the existing Li-O₂ systems include degradation of the anode electrode, reactions with air components, clogging of the cathode, and electrolyte instability.

Objectives

The objective of this work is to develop new materials for Li-O₂ batteries that give longer cycle life and improved efficiencies in an air environment. New electrolytes blends and additives are being investigated that can reduce clogging and at the same time can promote the cathode functionality needed to reduce charge overpotentials. The cathode materials are based on the 2-dimensional transition metal dichalcogenides (TMDCs) that we have found to be among the best oxygen reduction and evolution catalysts. The objective is to design and predict new electrolytes that work with these catalysts to give longer cycle life, high charge rates, good efficiencies, and high capacities needed to make scale up possible for these types of batteries.

Approach

The experimental strategy is to use cathode materials based on 2-dimensional transition metal dichalcogenides (TMDCs) that we have found to be among the best oxygen reduction and evolution catalysts.¹ These cathode materials will be combined with new electrolyte blends and additives that can work in synergy to reduce charge potentials and increase the stability of the Li-air system. Density functional theory and ab initio molecular dynamics simulations are used to gain insight at the electronic structure level of theory of the electrolyte structure and function both in the bulk and at interfaces with the cathode, anode, and discharge product. Classical molecular dynamics are used to obtain understanding at longer length and time scales of processes occurring in the electrolyte and growth mechanisms of discharge products. Computations play a key role in the design and predictions of new electrolytes as well as characterization for understanding. We will also utilize a high throughput screening strategy based on experiment and theory to develop a large database of properties and outcomes of electrolyte combinations that can be analyzed using machine learning to predict electrolytes and additives that will have the best performance.

Results

New Electrolyte Blends

Recently, we demonstrated a Li-O₂ battery comprised of a lithium carbonate-based protected anode, a molybdenum disulfide (MoS₂) cathode, and dimethyl sulfoxide(75%)/ionic liquid(25%) electrolyte that all work together to give a cycle long life and that can run in an air-like atmosphere for the first time², although it required a high charge potential (~4 V). As first step in improving the efficiency of this battery, i.e., lowering the charge potential we have investigated modifying the electrolyte of the Li-O₂ cell based on the molybdenum disulfide cathode. As an initial experiment we used pure O₂ with no other air components for this systematic study on reducing the charge potential by changes in the electrolyte. In this work we explored adding

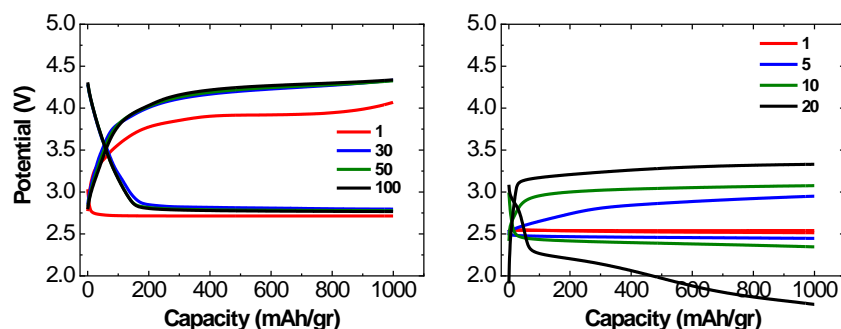


Figure II.10.C.1 Voltage profiles for Li-O₂ battery with LiNO₃ salt (left), and LiI redox mediator (right)

separately two salts to the electrolyte blend including lithium nitrate and lithium iodide. These two salts were chosen as they have been found to be beneficial in some Li-O₂ systems. Lithium nitrate has been found to provide lithium anode protection in Li-S systems and lithium iodine has been found to act as a redox mediator in some Li-O₂ systems. Each of these was used in combination with a LiTFSI salt. The voltage profiles for both additives are shown in Figure II.10.C.1. The results for lithium nitrate indicate that it provides for long cycle life as it ran for 100 cycles and is probably due to the formation of a protective coating on the anode. The results for lithium iodine indicate that it gives a low charge potential, but poor cycle life.

We then investigated a Li-O₂ cell configuration based on the molybdenum disulfide cathode with 25% ionic liquid in an electrolyte blend with 75% tetraglyme (TEGDME) containing both LiNO₃ and LiI salts at the same time. This cell was able to achieve a low charge potential (~3.4 V) and a long cycle life (100 cycles). A unique aspect of this electrolyte is the large concentrations of both LiNO₃ and LiI used in it. These large concentrations along with the use of both salts at the same time seems to be an effective way to both reduce the charge potential and increase cycle life at the same time, which is not possible when used separately. The voltage profile is shown in Figure II.10.C.2. In addition, various techniques have been used to characterize the

discharge product including Raman spectra, XPS, and high resolution TEM (HRTEM). All techniques show the presence of Li_2O_2 as the discharge product. The Raman spectra is shown in Figure II.10.C.2. The Li anode has been found to an amorphous coating from HRTEM studies that results from the LiNO_3 and protects the anode from degradation.

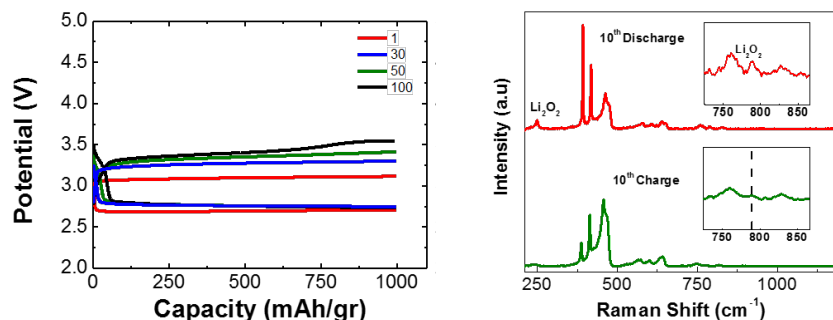


Figure II.10.C.2 (left) Voltage profiles for Li-O₂ battery with 1M LiNO₃ and 1M LiI in 75% TEGDME/ 25% IL; (right) Raman spectra showing the presence of Li₂O₂ in the discharge product

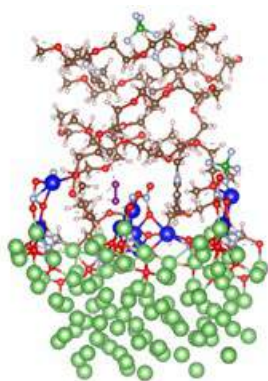


Figure II.10.C.3 AIMD simulation of eight LiNO₃ molecules added to electrolyte showing them forming a layer on the lithium anode

We carried out computations to help investigate the role of these specific salts in the Li-O₂ cell. This has included ab initio molecular dynamics (AIMD) simulations of the interface between the electrolyte and a lithium metal surface when lithium nitrate is added. Figure II.10.C.3 shows the result when eight lithium nitrate molecules are added to the electrolyte near the Li surface. The lithium nitrate molecules react strongly with the lithium surface to form a layer on the lithium surface. We also added an oxygen molecule to the system and it was found that the lithium nitrate layer prevented the reaction of O₂ with the lithium surface, which occurs if it is free to interact with the surface. This strong reaction with the lithium surface of the lithium nitrate is consistent with the experimental results showing that lithium nitrate gives long cycle life. We also carried out DFT computational simulations to investigate the role of the LiI as a redox mediator in the Li-O₂ cell. This included simulations of LiI₃, the oxidized product of LiI at the interface between the electrolyte and a Li₂O₂ interface. It is found that the LiI₃ becomes three LiI moieties at the interface and helps to decompose the Li₂O₂ with a low barrier to decomposition. The reaction pathways for this decomposition are being explored.

While the LiNO₃/LiI system showed improved performance for cycle life and efficiency, it is not capable of operating in an air environment and its cycle life is limited to about 100 cycles. We found that replacement of the two salts by InI₃ greatly improved the performance of the Li-O₂ cell. An optimal electrolyte include InI₃ as a salt enabled us to operate the battery in a dry air environment with a capacity of 1Ah/g at high rate of 1A/g up to 475 cycles. It had a polarization gap of less than ~0.7 for more than 200 cycles. The average discharge and charge potentials for 200 cycles are 2.75 V and 3.5 V, respectively. Also, the capacity loss of the battery is less than 10% after more than 200 cycles. Different characterization techniques have been used to show the discharge product and all of them verify the presence of Li₂O₂ including Raman spectra, XRD, XPS, and high resolution TEM (HRTEM). Figure II.10.C.2 shows the Raman and XRD characterizations on the cathode side. Also, XPS characterization shows the formation of Li-In alloy on the anode surface, which apparently provides excellent lithium anode protection.

Systematic study of redox mediators

Redox mediators are additives that can homogeneously dissolve in the electrolyte solutions to assist oxidation of discharge products (Li₂O₂), i.e., by having oxidation potentials less than 3.5 V. There have been numerous investigations of existing RMs. However, none of these have systematically investigated the

performance of a large number of redox mediators within one specific Li-O₂ battery system. We have studied twenty four redox mediators in terms of their chemical characteristics such as redox potential with DMSO and TEGDME electrolytes. We also collected data on the separation of cathodic and anodic peaks and intensities of the peaks, which correlates with reversibility and electron transfer rates. Results for redox potentials collected from electrochemical cyclic voltammetry (CV) experiments for DMSO electrolyte for 18 of the RMs are shown in Figure II.10.C.4.

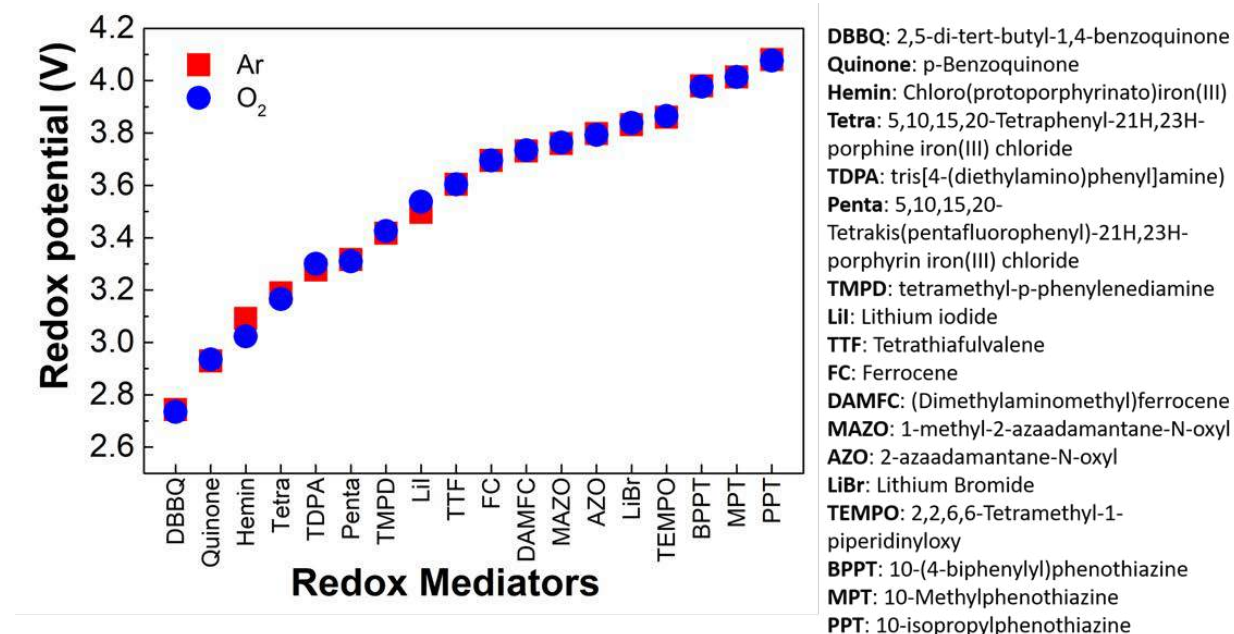


Figure II.10.C.4 Redox potentials (vs Li⁺/Li) of redox mediators measured from CV experiments in DMSO

Nine of the best RMs were selected based on an integrated comparison of different results from the CV studies. Galvanostatic cycling tests on these nine RMs (FC, LiI, TMPD, DAMFC, LiBr, Quinone, TTF, TDPA, DBBQ) were performed in Li-O₂ batteries in Swagelok cells. The results for all nine show that halides such as LiI and LiBr exhibit much better performance compared with the organic based on the charge potentials. The organic ones and transition metal complexes tend to have increasing charge potentials with number of cycles such as shown in Figure II.10.C.4 for TDPA and FC. This may be due to the reaction with singlet O₂, which may be present charge. However, the presence of the discharge plateau (reduction of I₃⁻ to I⁻) at higher concentrations of LiI and LiBr (not shown here) restrict their state of charge when compared to other RMs. For solving the issue, we reported from the second quarter by using LiNO₃ as an additive to bypass the non-functional fraction of capacities. Selected organic RM such as TTF and TDPA reveal more effective results than halides for suppressing charge over-potentials, yet their instabilities is a major challenge especially in the presence of singlet oxygen that may be formed during discharge.

We have also carried out density functional calculations on the RMs considered in the experimental studies. This has included calculation of the redox potentials, which were in agreement with the experimental measurements. In addition, for the organic RMs having oxidation potentials less than 3.5 V we used these as base molecules for adding functional groups to expand the set of possible RMs. Some of these have oxidation potentials less than 3.5 V and may be effective as redox mediators.

Li-CO₂ Battery

Lithium-CO₂ batteries are attractive energy storage systems for fulfilling the demand of future large-scale applications such as electric vehicles due to their high specific energy density compared to lithium-ion

batteries. However, a major challenge with Li-CO₂ batteries is attaining reversible formation and decomposition of the Li₂CO₃ and other carbon discharge products, along with a lack of fundamental mechanistic understanding of the associated charge and discharge reactions. We have developed a fully reversible Li-CO₂ battery having overall carbon neutrality using molybdenum disulfide nanoflakes as a cathode catalyst combined with an ionic liquid and dimethyl sulfoxide hybrid electrolyte. This combination of materials produces a multicomponent composite (Li₂CO₃/C) product rather than formation of separated carbon and Li₂CO₃ nanoparticles. The battery shows a superior long cycle life of 500 cycles for a fixed 500 mAh/g capacity per cycle. The long cycle life demonstrates for the first time that covalent C-O bond making and breaking chemical transformations can be used in energy storage systems, in addition to the widely studied alkali metal (Li, Na, K) – oxygen ionic-bond making and breaking transformations. Density functional calculations were used to deduce a mechanism for the reversible discharge/charge processes and explain how the carbon interface with Li₂CO₃ provides the electronic conduction needed for the oxidation of Li₂CO₃, as well as the carbon to generate the CO₂ on charge. The achievement of a reversible, long cycle life Li-CO₂ battery opens the way for use of CO₂ in advanced energy storage systems.

Conclusions

In summary we have explore various combinations of salts to improve the overall performance of Li-O₂ batteries using 2-dimensional MoS₂ nanoflakes as catalysts. We explored adding separately two salts to the electrolyte blend including lithium nitrate and lithium iodide. Each of these was used in combination with a LiTFSI salt. The results for lithium nitrate indicate that it provides for long cycle life as it ran for 100 cycles and is probably due to the formation of a protective coating on the anode. The results for lithium iodine indicate that it gives a low charge potential, but poor cycle life. However, by using both the lithium iodide and lithium nitrate salts at the same time we were able to achieve a low charge potential and a relatively long cycle life. A unique aspect of this electrolyte is the large concentrations of both LiNO₃ and LiI used in it. The use of both salts at the same time seems to be an effective way to both reduce the charge potential and increase cycle life at the same time, which is not possible when used separately. An alternative approach was also found to be effective for obtaining good performance as well as being able to operate in a dry air environment. We found that replacement of the two salts by InI₃ enabled us to operate the battery in a dry air environment at high rate of 1A/g up to 475 cycles with a small polarization gap.

In other work we have systematically investigated the performance of a large number of redox mediators within one specific Li-O₂ battery system. We have studied twenty four redox mediators in terms of their chemical characteristics such as redox potential with DMSO and TEGDME electrolytes that will help enable studies of redox mediators. Finally, we have developed a fully reversible Li-CO₂ battery having overall carbon neutrality using molybdenum disulfide nanoflakes as a cathode catalyst combined with an ionic liquid and dimethyl sulfoxide hybrid electrolyte. This combination of materials produces a multicomponent composite (Li₂CO₃/C) product rather than formation of separated carbon and Li₂CO₃ nanoparticles. The long cycle life demonstrates for the first time that covalent C-O bond making and breaking chemical transformations can be used in energy storage systems.

Key Publications

1. “A Long-Cycle-Life Lithium-CO₂ Battery with Carbon Neutrality”, A. Ahmadiparidari, R.E. Warburton, L. Majidi, M. Asadi, A. Chamaani, J.R. Jokisaari, S. Rastegar, Z. Hemmat, B. Sayahpour, R.S. Assary, B. Narayanan, P. Abbasi, P.C. Redfern, A. Ngo, M. Voros, J. Greeley, R. Klie, L.A. Curtiss, A. Salehi-Khojin, *Adv Mater*, 1902518 (2019). DOI: 10.1002/adma.201902518
2. “Lowering Charge Potentials Without Capacity Loss in High Rate Lithium-Oxygen Batteries,” Alireza Ahmadiparidari, Shadi Fuladi, Leily Majidi, Samuel Plunkett, Paul C Redfern, Jianguo Wen, Tao Li, Anh Tuan Ngo, Fatemeh Khalili-Araghi, Larry Curtiss, Amin Salehi-Khojin, submitted.

References

1. New Class of Electrocatalysts Based on 2D Transition Metal Dichalcogenides in Ionic Liquid, L. Majidi, P. Yasaei, R. E. Warburton, S. Fuladi, J. Cavin, X. Hu, Z. Hemmat, S. B. Cho, P. Abbasi, M.

- Vörös, L. Cheng, B. Sayahpour, I. L. Bolotin, P. Zapol, J. Greeley, R. F. Klie, R. Mishra, F. Khalili-Araghi, L. A. Curtiss, A. Salehi-Khojin, *Adv Mater*, **31**, 1804453 (2019).
2. Lithium-Oxygen Batteries with Long Cycle Life in a Realistic Air Atmosphere, M. Asadi, B. Sayahpour, P. Abbasi, A. T. Ngo, K. Karis, J. R. Jokisaari, C. Liu, B. Narayanan, M. Gerard1, P. Yasaei, X. Hu, A. Mukherjee, K. C. Lau, R. S. Assary, F. Khalili-Araghi, R. F. Klie, L. A. Curtiss, Amin Salehi-Khojin, *Nature*, **555**, 502–506

II.11 Beyond Lithium-Ion R&D: Sodium-Ion Batteries

II.11.A Exploratory Studies of Novel Sodium-Ion Battery Systems (BNL)

Xiao-Qing Yang, Principal Investigator

Brookhaven National Laboratory
Chemistry Division, Bldg. 555
Upton, NY 11973
E-mail: xyang@bnl.gov

Enyuan Hu, Principal Investigator

Brookhaven National Laboratory
Chemistry Division, Bldg. 555
Upton, NY 11973
E-mail: enhu@bnl.gov

Tien Duong, DOE Technology Development Manager

U.S. Department of Energy
E-mail: Tien.Duong@ee.doe.gov

Start Date: October 1, 2018
Project Funding (FY19): \$400,000

End Date: September 30, 2019
DOE share: \$400,000

Non-DOE share: \$0

Project Introduction

The next generation of rechargeable battery systems with higher energy and power density, lower cost, better safety characteristics, and longer calendar and cycle life need to be developed to meet the challenges to power electrified vehicles in the future. Na-ion battery systems have attracted more and more attention due to the more abundant and less expensive nature of Na resources. However, building a sodium battery requires redesigning battery technology to accommodate the chemical reactivity and larger size of sodium cations. Since Na-ion battery research is an emerging technology, new materials to enable Na electrochemistry and the discovery of new redox couples and the related diagnostic studies of these new materials and redox couples are quite important. This project will use the synchrotron based in situ x-ray diagnostic tools developed at BNL to evaluate the new materials and redox couples, to explore in-depth fundamental understanding of the reaction mechanisms aiming to improve the performance of these materials and provide guidance for new material developments. This project will also focus on developing advanced diagnostic characterization techniques for these studies. The synchrotron based in situ x-ray techniques (x-ray diffraction, or XRD, x-ray pair distribution function, or xPDF, and x-ray absorption spectroscopy, or XAS) will be combined with other ex situ tools such as transmission electron microscopy (TEM), scanning transmission electron microscopy (STEM), mass spectroscopy (MS), transmission x-ray microscopy (TXM), as well as neutron diffraction (ND) and neutron PDF (nPDF). In FY2019, this BNL team has performed several successful experimental studies at various beamlines of National Synchrotron Light Source II (NSLSII) such as hard x-ray nanoprobe (HXN), x-ray Powder diffraction (XPD), and inner-shell spectroscopy (ISS) beamlines. By collaborating with Dr. Huolin Xin, this team also has carried out studies using the 3d TEM tomography and STEM-EELS on the new cathode materials for Na-ion batteries. The BNL team has been closely working with top scientists on new material synthesis at ANL, LBNL, SLAC, and PNNL, with U.S. industrial collaborators, and international collaborators in Japan and South Korea.

Objectives

The primary objective of this proposed project is to develop new advanced in situ material characterization techniques and apply these techniques to explore the potentials, challenges, and feasibility of new rechargeable battery systems beyond the lithium-ion batteries, namely the sodium-ion battery systems for electrified

vehicles, such as plug-in hybrid electric vehicles (PHEV) and battery electric vehicles (BEV). In order to meet the challenges of powering PHEVs and BEVs, new rechargeable battery systems with high energy and power density, low cost, good abuse tolerance, and long calendar and cycle life need to be developed. This project will use the synchrotron based in situ x-ray diagnostic tools, combined with TEM, STEM, and TXM imaging techniques developed at BNL to evaluate the new materials and redox couples to obtain fundamental understanding of the reaction mechanisms of these material aiming to the improvement and to provide guidance for new material and new technology development regarding Na-ion battery systems.

Approach

This project will use the synchrotron based in situ x-ray diagnostic tools developed at BNL to evaluate the new materials and redox couples to enable a fundamental understanding of the mechanisms governing the performance of these materials and provide guidance for new material and new technology development regarding Na-ion battery systems. These techniques include:

- Using nano-probe beamline at NSLS II to study the elemental distribution of new solid electrolyte materials for Na-ion batteries
- Using transmission x-ray microscopy (TXM) to do multi-dimensional mapping of cathode materials of Na-ion batteries
- Using a combination of time resolved X-ray diffraction (TR-XRD) and mass spectroscopy (MS), together with in situ soft and hard X-ray absorption spectroscopy (XAS) during heating to study the thermal stability of the cathode materials for Na-ion batteries
- Design and carry out three-dimensional (3d) STEM tomography experiments to study new cathode materials for Na-ion batteries at pristine state and after multiple cycling.

Results

In FY2019, BNL has been focused on the in situ XRD studies on the structural evolution of $\text{Na}_{0.7}[\text{Cu}_{0.15}\text{Fe}_{0.3}\text{Mn}_{0.55}]\text{O}_2$, and $\text{Na}_{0.7}[\text{Cu}_{0.2}\text{Fe}_{0.2}\text{Mn}_{0.6}]\text{O}_2$ materials. The in situ XRD results for $\text{Na}_{0.7}[\text{Cu}_{0.15}\text{Fe}_{0.3}\text{Mn}_{0.55}]\text{O}_2$ during the first cycle are shown in Figure II.11.A.1a. The (002) peak located at 15.8° continuously shifts to lower 2θ angle, suggesting a solid-solution reaction. Along with the deintercalation of Na^+ ion, the c lattice parameter increases significantly, which is caused by the increased Coulombic repulsion between two adjacent O layers. However, when the in situ cell is further charged to 4.2 V, the (002) peak shifts back to higher 2θ angles quickly, indicating new phase formation during the high voltage charge process. In contrast, the in situ XRD results for $\text{Na}_{0.7}[\text{Cu}_{0.2}\text{Fe}_{0.2}\text{Mn}_{0.6}]\text{O}_2$ shown in Figure II.11.A.1c have different structural evolution than $\text{Na}_{0.7}[\text{Cu}_{0.15}\text{Fe}_{0.3}\text{Mn}_{0.55}]\text{O}_2$, no new diffraction peaks beyond P2 structure were observed during sodium deintercalation and intercalation at high charging cut-off voltage, but only gradual shift of peak position. This suggests a solid-solution reaction mechanism during the full charge/discharge process in the voltage range of 2.5V and 4.2V, which is consistent with CV results and electrochemical charge/discharge curves.

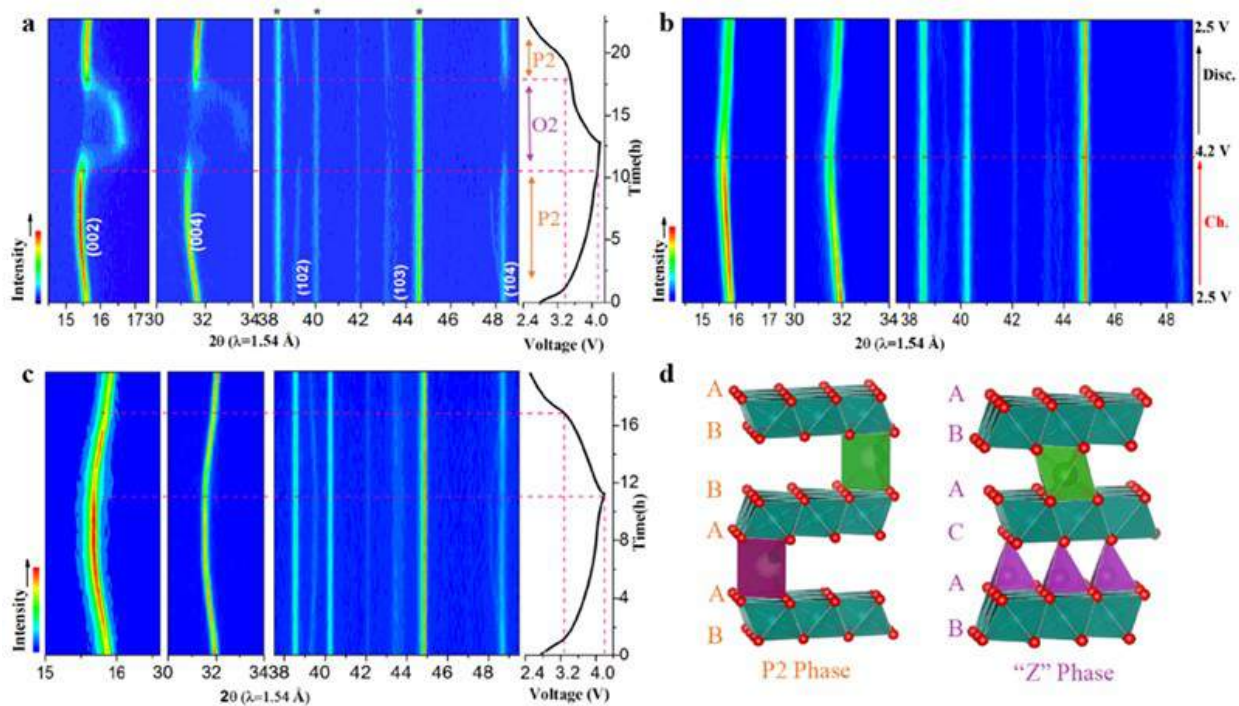


Figure II.11.A.1 Structure evolution during Na extraction and insertion. In situ XRD patterns of $\text{Na}_{0.7}[\text{Cu}_{0.15}\text{Fe}_{0.3}\text{Mn}_{0.55}]\text{O}_2$ electrode collected during **a)** the first and **b)** the fifth charge/discharge process. **c)** In situ XRD patterns of $\text{Na}_{0.7}[\text{Cu}_{0.2}\text{Fe}_{0.2}\text{Mn}_{0.6}]\text{O}_2$ electrode collected during the first charge/discharge. All cycled between 2.5 and 4.2 V under a current rate of C/15

In FY2019, BNL also carried out the Synchrotron based XAS studies and XAS analysis of $\text{Na}_{0.7}[\text{Cu}_{0.15}\text{Fe}_{0.3}\text{Mn}_{0.55}]\text{O}_2$ and $\text{Na}_{0.7}[\text{Cu}_{0.2}\text{Fe}_{0.2}\text{Mn}_{0.6}]\text{O}_2$ electrodes at different state-of-charge (SOC) at Fe K-edge, Cu K-edge and Mn K-edge. The XAS results for $\text{Na}_{0.7}[\text{Cu}_{0.15}\text{Fe}_{0.3}\text{Mn}_{0.55}]\text{O}_2$ at the first and the 11th cycles are shown in Figure II.11.A.2. To have a deep insight into the voltage fade, the K-edge XAS tests of electrodes cycled after 10 cycles were also performed and results are shown in Figure II.11.A.2a. No obvious difference is found around the absorption edge. However, the pre-edge intensity of both 11th charged and 11th discharged is higher than that of the first cycle. It can be concluded that more Fe ions transport to the interlayer after the 11th charge and more Fe ions remained at the interlayer tetrahedral sites after the 11th discharge. The gradual accumulation of Fe in interlayer leads to relative larger polarization, but such accumulation tends to stabilize within subsequent cycles and the voltage fading phenomenon will weaken correspondingly. However, the pre-edge peak of the 1st charged or the 11th charged $\text{Na}_{0.7}[\text{Cu}_{0.2}\text{Fe}_{0.2}\text{Mn}_{0.6}]\text{O}_2$ electrode at Fe-edge shows almost no changes compared with the pristine one (Figure II.11.A.2d). It means that very few of Fe ion in the charged $\text{Na}_{0.7}[\text{Cu}_{0.2}\text{Fe}_{0.2}\text{Mn}_{0.6}]\text{O}_2$ electrode migrate from the TM layer to the interlayer tetrahedral site, thus the structure maintained P2 stacking mode all around the circulations. The XANES spectra at Cu K-edge of $\text{Na}_{0.7}[\text{Cu}_{0.15}\text{Fe}_{0.30}\text{Mn}_{0.55}]\text{O}_2$ and $\text{Na}_{0.7}[\text{Cu}_{0.20}\text{Fe}_{0.20}\text{Mn}_{0.60}]\text{O}_2$ electrodes were also measured during the first cycle and are displayed in Figure II.11.A.2b and Figure II.11.A.1e, respectively. Both absorption edges of these two electrodes show negligible shift below 4.0 V and an apparent shift between 4.0-4.2 V, indicating the oxidation of Cu^{2+} proceeds above 4.0 V. Moreover, the weak single pre-edge peak of Cu K-edge doesn't change obviously, which indicates that the octahedral coordination of Cu is maintained very well even charged to a high voltage. Figure II.11.A.2c, 1f display the normalized XANES spectra in $\text{Na}_{0.7}[\text{Cu}_{0.15}\text{Fe}_{0.30}\text{Mn}_{0.55}]\text{O}_2$ and $\text{Na}_{0.7}[\text{Cu}_{0.20}\text{Fe}_{0.20}\text{Mn}_{0.60}]\text{O}_2$ electrodes at different SOC during the 1st and 11th cycles respectively.

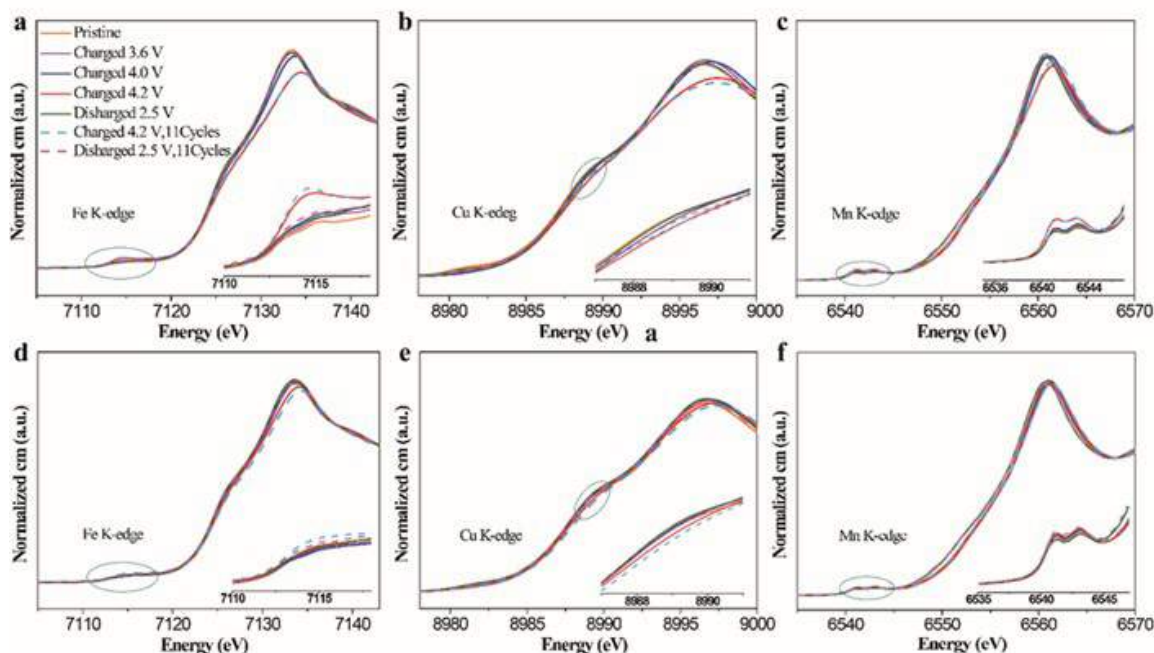


Figure II.11.A.2 XAS analysis of a-c) $\text{Na}_{0.7}[\text{Cu}_{0.15}\text{Fe}_{0.3}\text{Mn}_{0.55}]\text{O}_2$ and d-f) $\text{Na}_{0.7}[\text{Cu}_{0.2}\text{Fe}_{0.2}\text{Mn}_{0.6}]\text{O}_2$ electrodes at different SOC during the 1st and 11th cycle: XANES spectra at a), d) Fe K-edge, b), e) Cu K-edge and c), f) Mn K-edge

In FY2019, BNL carried out the synchrotron based soft XAS studies and XAS analysis of $\text{Na}_{0.7}[\text{Cu}_{0.15}\text{Fe}_{0.3}\text{Mn}_{0.55}]\text{O}_2$ and $\text{Na}_{0.7}[\text{Cu}_{0.2}\text{Fe}_{0.2}\text{Mn}_{0.6}]\text{O}_2$ electrodes at different SOC. In order to gain more fundamental insights into the correlation between different TM elements and oxygen participation in electrochemical reactions. Soft XAS was performed on the TM L-edge as well as O K-edge of both $\text{Na}_{0.7}[\text{Cu}_{0.15}\text{Fe}_{0.3}\text{Mn}_{0.55}]\text{O}_2$ (Figure II.11.A.3 a–c) and $\text{Na}_{0.7}[\text{Cu}_{0.2}\text{Fe}_{0.2}\text{Mn}_{0.6}]\text{O}_2$ (Figure II.11.A.3 d–f) electrodes. Detailed results on Cu L-edge, Fe L-edge and O K-edge spectra of the two electrodes at different states of charge in both the 1st and 15th cycle are shown in Figure II.11.A.3 a–f. To highlight the spectral differences in battery cycling, only the L3 edge, which evolves due to $2p_{3/2}$ – $3d$ state transition of TM L-edge XAS, is shown. As for Cu L-edge and Fe L-edge XAS, the most evident change is the rise and decay of a metal to ligand charge transfer (MLCT) feature, as shown in the shaded area. Such a MLCT feature has been verified in previous reports in TM oxide systems and is supported by theoretical simulations. It should be noted that the increase in Cu content in the lattice will enhance the MLCT effect between Cu and O, but relatively mitigate such an effect between Fe and O. Therefore, Cu–O becomes the redox center to compensate for charge neutrality upon deep desodiation at high charging voltage. O K-edge XAS further supports the perturbation on the TM–O hybridization feature upon Na removal with excess Cu doping. The surface-sensitive total electron yield (TEY) results, as shown by dotted lines, are in contrast to the bulk-sensitive total fluorescence yield (TFY) results, implying particular surface layer-formation upon battery cycling. In the case of $\text{Na}_{0.7}[\text{Cu}_{0.2}\text{Fe}_{0.2}\text{Mn}_{0.6}]\text{O}_2$, where drastic voltage decay occurs, it was found that the 15th charged cathode at 4.3 V basically reproduced the 1st charge 3.9 V state, which is consistent with the dynamic origin of the voltage decay phenomenon. Based on sXAS characterization, it can be concluded that superior battery performance in $\text{Na}_{0.7}[\text{Cu}_{0.2}\text{Fe}_{0.2}\text{Mn}_{0.6}]\text{O}_2$ can be interpreted from interactive correlation among inherent Fe, substituting TM elements and ligand oxygen.

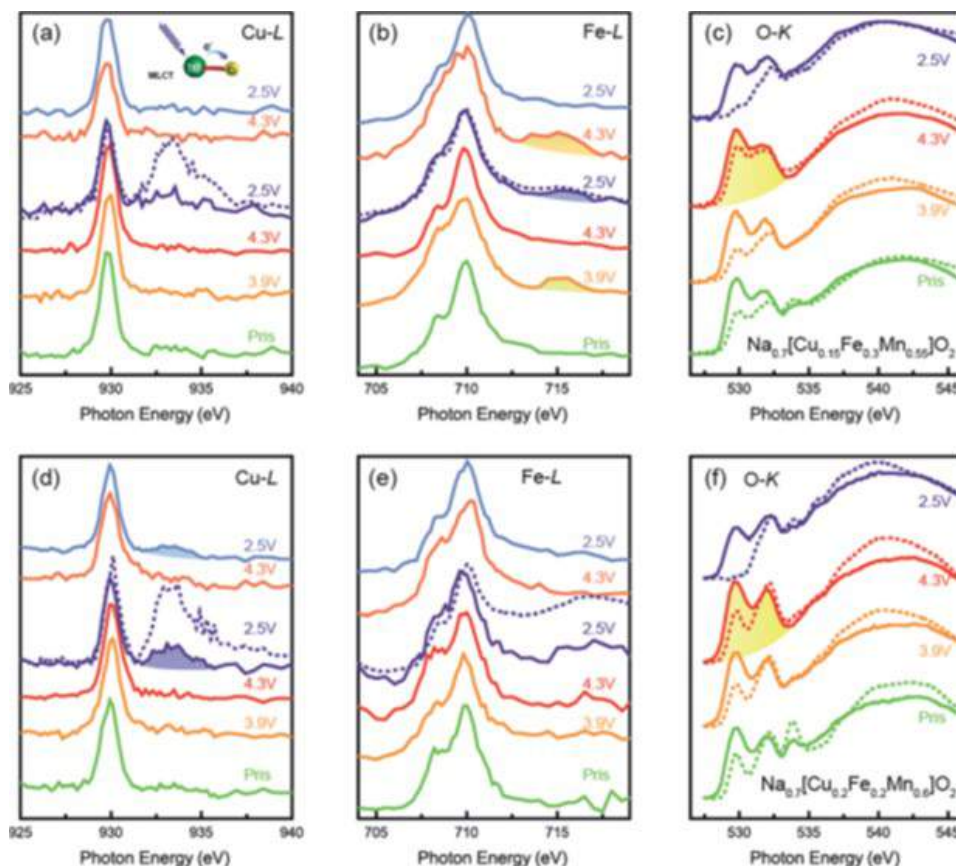


Figure II.11.A.3 xAS of $\text{Na}_{0.7}[\text{Cu}_{0.15}\text{Fe}_{0.30}\text{Mn}_{0.55}]\text{O}_2$ (a–c) and $\text{Na}_{0.7}[\text{Cu}_{0.20}\text{Fe}_{0.20}\text{Mn}_{0.60}]\text{O}_2$ (d–f) samples. The Cu L-edge, (a and d), Fe L-edge (b and e), and O K-edge (c and f) xAS data for the $\text{Na}_{0.7}[\text{Cu}_x\text{Fe}_y\text{Mn}_{1-x-y}]\text{O}_2$ cathode were collected at different cycle states, including pristine, charge 3.9 V, charge 4.3 V, and discharge 2.5 V during the first cycle and charge 4.3 V and discharge 2.5 V during the 15th cycle. The spectra in solid lines were collected in TFY mode, while those in dotted lines demonstrate xAS collected in TEY mode. Schematic of metal to ligand charge transfer (MLCT) is shown in the inset of (a). The spectral evolution is highlighted with shaded areas

In FY2019, BNL also carried out the synchrotron based XRD studies of a new P2-type $\text{Na}_{0.72}[\text{Li}_{0.24}\text{Mn}_{0.76}]\text{O}_2$ cathode material for Na-ion batteries (NIB), which exhibits exceptionally high initial charge capacity of about 210 mAh/g (0.72 Na) based on a pure anionic redox reaction (ARR). Surprisingly, global P2 structure can be maintained with minimal volume change (1.35%) upon complete removal of Na^+ ions. This is due to the reduced Coulombic repulsion associated with ARR and consequent suppression of the phase transition as observed in other P2 materials. We revealed for the first time that ARR has the functionality of stabilizing the structure, in addition to its role in increasing its already known capacity. This would pave the way for the further improvement of high-energy-density NIBs. To investigate the structural evolution of $\text{Na}_{0.72}[\text{Li}_{0.24}\text{Mn}_{0.76}]\text{O}_2$ upon Na^+ deintercalation and intercalation, we performed in situ XRD measurements, the results of which are displayed in Figure II.11.A.4. It could be observed that on initial Na deintercalation process, the (002) peak first shifts to a lower angle and then slightly shifts to a higher angle, while (100), (102), and (104) peaks continuously shift to higher angles. No notable sign of the formation of O2 or OP4 phase (or Z phase), as reported in $\text{Na}_{0.67}[\text{Ni}_{0.33}\text{Mn}_{0.67}]\text{O}_2$ or $\text{Na}_x[\text{Fe}_{0.5}\text{Mn}_{0.5}]\text{O}_2$ can be observed. The phase evolution proceeds in a reverse manner in general over the discharge process, and no new peak can be observed. This result is also confirmed by the ex situ XRD analysis.

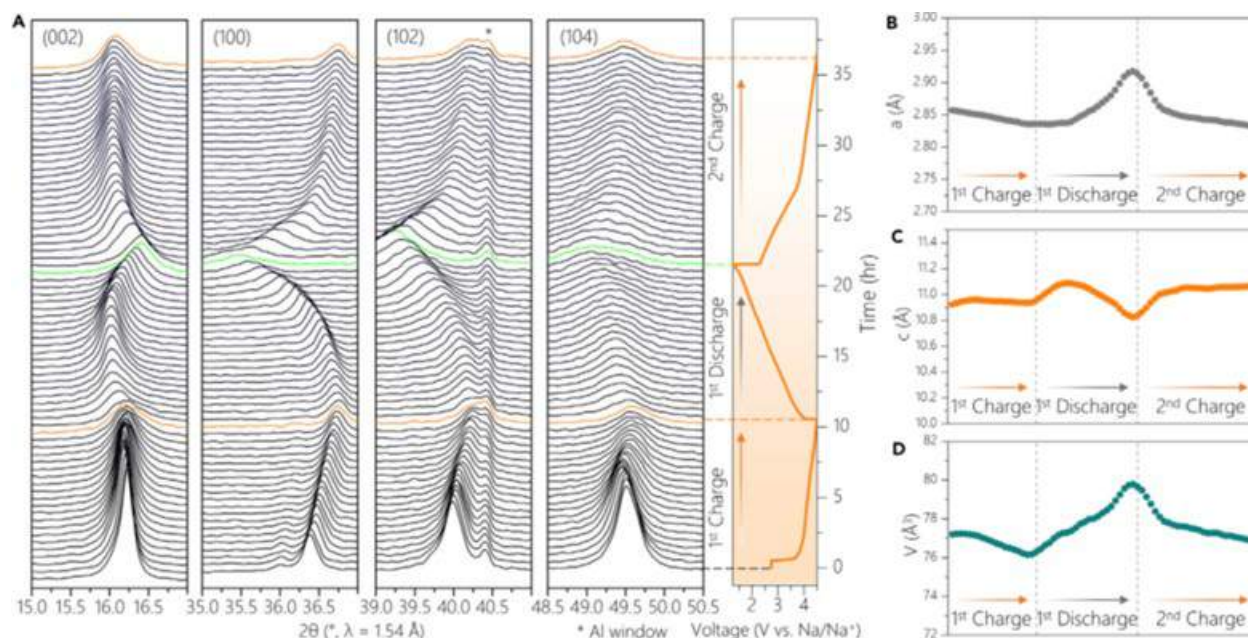


Figure II.11.A.4 Crystal Structural Evolution of Na_{0.72}[Li_{0.24}Mn_{0.76}]O₂ Electrodes. (A) In situ XRD patterns collected during the first charge/discharge and the second charge of the Na_{0.72}[Li_{0.24}Mn_{0.76}]O₂. (B–D) Evolution of the lattice parameters during the charge/discharge process: a axis (B); c axis (C); and unit cell volume (D)

Conclusions

This project, “Exploratory Studies of Novel Sodium-Ion Battery Systems (BNL)”, has been successfully completed in FY2019. All milestones have been completed. The publication records are very good. Extensive collaboration with other national Labs, U.S. universities and international research institutions were established.

Key Publications

Publications

1. Bohang Song, Enyuan Hu, Jue Liu*, Yiman Zhang, Xiao-Qing Yang, Jagjit Nanda, Ashfia Huq* and Katharine Page*, “A novel P3-type Na_{2/3}Mg_{1/3}Mn_{2/3}O₂ as high capacity sodium-ion cathode using reversible oxygen redox”, *J. Mater. Chem. A*, DOI: 10.1039/C8TA09422E, Publication date: December 10th, 2018
2. Qin-Chao Wang, Jing-Ke Meng, Xin-Yang Yue, Qi-Qi Qiu, Yun Song, Xiao-Jing Wu, Zheng-Wen Fu, Yong-Yao Xia, Zulipiya Shadike, Jinpeng Wu, Xiao-Qing Yang, and Yong-Ning Zhou*, “Tuning P2-Structured Cathode Material by Na-Site Mg Substitution for Na-Ion Batteries”, *Journal of American Chemical Society (JACS)*, DOI: 10.1021/jacs.8b08638, Publication Date (Web): December 18, 2018
3. Xiaohui Rong, Enyuan Hu, Yaxiang Lu, Fanqi Meng, Chenglong Zhao, Xuelong Wang, Qinghua Zhang et al. “Anionic Redox Reaction-Induced High-Capacity and Low-Strain Cathode with Suppressed Phase Transition.” *Joule* 2019, 3, 503. Publication Date: February 20, 2019. DOI: 10.1016/j.joule.2018.10.022.
4. Yejing Li, Xuefeng Wang, Yurui Gao, Qinghua Zhang, Guoqiang Tan, Qingyu Kong, Seongmin Bak, Gang Lu, Xiao-Qing Yang, Lin Gu, Jun Lu, Khalil Amine, Zhaoxiang Wang, Liquan Chen. “Native Vacancy Enhanced Oxygen Redox Reversibility and Structural Robustness.” *Adv. Energy Mater.* 2019, 9, 1803087. Publication Date: January 24, 2019. DOI: 10.1002/aenm.201803087.

5. Bohang Song, Mingxue Tang, Enyuan Hu, Olaf J. Borkiewicz, Kamila M. Wiaderek, Yiman Zhang, Nathan D. Phillip, Xiaoming Liu, Zulipiya Shadike, Cheng Li, Likai Song, Yan-Yan Hu, Miaofang Chi, Gabriel M. Veith, Xiao-Qing Yang, Jue Liu*, Jagjit Nanda*, Katharine Page*, Ashfia Huq*, “Understanding the Low-Voltage Hysteresis of Anionic Redox in $\text{Na}_2\text{Mn}_3\text{O}_7$ ”, *Chem. Mater.* 201931103756-3765, DOI: 10.1021/acs.chemmater.9b00772, Publication Date: May 1, 2019
6. Ming-Hui Cao, Zulipiya Shadike, Seong-Min Bak, Tian Wang, Enyuan Hu, Steven Ehrlich, Yong-Ning Zhou*, Xiao-Qing Yang*, Zheng-Wen Fu*, “Sodium storage property and mechanism of $\text{NaCr}_{1/4}\text{Fe}_{1/4}\text{Ni}_{1/4}\text{Ti}_{1/4}\text{O}_2$ cathode at various cut-off voltages”, *Energy Storage Materials*, DOI: 10.1016/j.ensm.2019.07.022, publication date (Web): July 22, 2019.

Presentations

1. Enyuan Hu, Ruoqian Lin, Xiqian Yu, Zulipiya Shadike, Seongmin Bak, Hung Sui Lee, Yijin Liu, Katherine Page, Jue Liu, Huolin Xin, Xuelong Wang, Xiao-Qing Yang*, “Using Synchrotron X-ray and Neutron Based Scattering combined with TEM and TXM imaging Techniques to Study the New Cathode Materials for Batteries”, presented at Hong Kong Symposium of Batteries, at The Hong Kong Polytechnic University, Hong Kong, December 17, 2018. **Invited**

II.11.B Development of Advanced High-energy and Long-life Sodium-ion Battery (ANL)

Khalil Amine, Principal Investigator

Argonne National Laboratory
9700 South Cass Avenue
Lemont, IL 60439
E-mail: amine@anl.gov

Christopher Johnson, Principal Investigator

Argonne National Laboratory
9700 South Cass Avenue
Lemont, IL 60439
E-mail: cjohnson@anl.gov

Tien Duong, DOE Technology Development Manager

U.S. Department of Energy
E-mail: Tien.Duong@ee.doe.gov

Start Date: January 1, 2019

End Date: December 31, 2024

Project Funding (FY19): \$680,000

DOE share: \$680,000

Non-DOE share: \$0

Project Introduction

Considering the natural abundance and low cost of sodium resources, sodium-ion batteries (SIBs) have received much attention for large-scale electrochemical energy storage. [1] However, the larger ionic radius of Na^+ (1.02 Å) than Li^+ (0.67 Å) brings more challenges on the development of good Na-host materials with optimal electrochemical properties. On one hand, despite most SIBs cathode materials are either imitating or duplicating from lithium analogues, there are significant differences in the intercalation chemistries between sodiation and lithiation. The layered oxides cathodes deliver very high energy density, but undergo more complex phase transition during charge/discharge, resulting in severe capacity fade during prolonged cycling. [2] On the other hand, the absence of suitable anode materials has obstructed progress in the development of SIBs. Two of the most promising anode materials, graphite and silicon have limited sodium storage capability. Hard carbon can demonstrate reversible sodiation/de-sodiation, but the capacity is lower than 300 mAh g⁻¹, significantly limited the energy density of SIBs. [3],[4] Alloying anode materials such as phosphorus can deliver high capacity, but suffer from huge volume changes and severe parasitic reactions with the electrolytes, resulting in rapid capacity degradation during long-term cycling. [5]

Via advanced diagnostic tools including synchrotron X-ray probes and computational modeling, the team led by Dr. Khalil Amine and Dr. Christopher Johnson at Argonne National Laboratory (ANL) is focusing on the development of rational cathode materials, anode materials and electrolytes to develop long life and high energy SIBs with low cost and high safety.

Objectives

The project objective is to develop high-energy SIBs with long life, low cost and high safety. The energy density target is 200 Wh kg⁻¹ and/or 500 Wh L⁻¹, wherein the anode and cathode capacity targets are 600 mAhg⁻¹ and 200 mAhg⁻¹, respectively.

Approach

In a team approach, the Na-ion battery group will create a versatile Na-ion battery chemistry with beneficial advantages such as low cost, safety, recycling, and sustainability of materials used. The team will work in a synergistic way so that the final design is the culmination of advances in phosphorus carbon composites mated with optimized lead or other highly dense metalloids, such as tin and/or antimony and derivatives thereof, for the recyclable anode. Synthesis and optimization of such blended composite anodes will be conducted in

parallel to diagnostic characterization of structures, phase formation, and cycling stability. Cathode work will begin at the end of the first year and will involve (1) gradient cathodes consisting of Fe-Mn compositions, and (2) intergrowths of layer stacking sequenced oxides. If resources allow, the team also will attempt to stabilize cathode surfaces using ALD methods, particularly for the benefit of staving off dissolution of manganese and iron/electrolyte reactivity.

Results

The first year of this project is focusing on the development of high performance anode materials. We have reported two class of novel anode materials for sodium-ion batteries with stable cycle life.

High capacity phosphorus-based anode materials for SIBs

Phosphorus based anode materials, are considered as the most appealing candidate because of their attractive theoretical capacities of up to 2596 mAh g^{-1} . However, stable host materials are usually required to overcome the large volume changes induced during repeated charge/discharge to achieve long-term cycle stability. At Argonne, we have developed an advanced strategy by ball-milling to mitigate the interfacial and mechanical issue for phosphorus anode material. We have synthesized a nanostructured black phosphorus (BP)/Ketjenblack-multiwalled carbon nanotubes composite (referred to as BPC). The BPC composite was prepared by high-energy ball milling of black phosphorous (70 wt.%), ketjenblack, and multiwalled carbon nanotubes. The BP, Ketjenblack (EC-600JD) and MWCNTs used in this work are all commercially available. The phosphorus nanoparticles interact with the highly conductive ketjenblack, forming secondary micro-sized particles. The high surface area of Ketjenblack ($1400 \text{ m}^2 \text{ g}^{-1}$) could enable a uniform distribution of BP in the BPC composite, while the high conductivity of Ketjenblack and MWCNTs yields a dual conductive network that facilitates electron transport within the BPC composite.

The XRD in Figure II.11.B.1a show that after ball milling, the strong diffraction peaks of bulk BP became broad, indicating the formation of nanocrystalline BP. Similar result was seen in the Raman test (Figure II.11.B.1b). The microstructures of the BP and BPC composite were characterized by electron microscopy (Figure II.11.B.1c-Figure II.11.B.1f). The particle size of bulk BP is about hundreds of micrometer (Figure II.11.B.1c). After high energy ball milling, these large BP particles cannot be observed. They are homogeneously assembled with Ketjenblack and MWCNTs and form a unique nanostructure. Secondary particles with a particle size of about hundreds of nm to $1 \mu\text{m}$ can be observed (Figure II.11.B.1d). The high-magnification TEM image of the BPC composite in Figure II.11.B.1e clearly shows that BP nanoparticles with crystal lattices (marked by dashed circles) uniformly distributed in the amorphous carbon matrix, confirming the nanocrystalline property of BP in the BPC composite. The interval between lattices was measured to be 0.334 nm from the high resolution TEM image (Figure II.11.B.1f), coinciding with the d-spacing for the (021) plane of black phosphorus (PDF no. 76-1962).

The electrochemical performance of the BPC composite anode was evaluated by assembling them into coin cells with sodium as reference and counter electrode. The optimal electrolyte was 1 M NaPF_6 in propylene carbonate (PC) with 2 vol.% fluorinated ethylene carbonate (FEC), in which FEC has been widely used as additives to protect the electrolyte decomposition. The initial charge/discharge profile of the BPC anode is shown in Figure II.11.B.2a. The initial discharge capacity was measured to be $2206.7 \text{ mAh g}^{-1}$, corresponding to 85% phosphorus utilization compared to the theoretical capacity of phosphorus. The first reversible capacity was $2011.1 \text{ mAh g}^{-1}$, corresponding to an initial coulombic efficiency as high as 91.1%. Such a high coulombic efficiency is very important when coupling an anode with a cathode material in a full cell system. And the average working voltage of the BPC anode is around 0.5 V vs. Na/Na^+ , which is good for the consideration of both energy density and reactivity towards electrolytes. Figure II.11.B.2b illustrates cyclic voltammetry of the BPC anode. A weak and broad peak occurs at around 1.0 V in the first cathodic scan, and is attributed to the reduction of electrolytes to form the SEI layer. In the subsequent scans, a new peak centered at around 0.95 V appeared, which should be attributed to the initial sodiation of BP. When the potential was further scanned from 0.8 to 0.01 V , a major cathodic peak appeared at about 0.45 V , which corresponds to

sodium ion insertion and formation of Na_xP ($1 < x \leq 3$). The curves overlapped after the 2nd cycle, indicating excellent cycle stability.

As shown in Figure II.11.B.2c, the BPC anode maintained very stable capacities of around 2000 mAh g⁻¹ within 50 cycles at 0.416 A g⁻¹. At a much higher charge/discharge current density of 1.3 A g⁻¹, the BPC anode illustrates excellent cycle stability, which could deliver a very high reversible capacity of about 1700 mAh g⁻¹ after 100 cycles (Figure II.11.B.2d). The effect of Na salts on the cycle performance of BPC anode has been also examined. As shown in Figure II.11.B.2e, the BPC anode demonstrates higher reversible capacity and better cycle stability in the NaPF₆-based electrolytes than NaClO₄-based electrolytes. This is probably due to the higher ionic conductivity and better stability of NaPF₆. Due to the high cost of black phosphorus, we also examined the electrochemical performance of red phosphorus-carbon (RPC) composite using similar synthetic process. Figure II.11.B.2f showed that the RPC anode exhibits lower initial coulombic efficiency (87.8%), lower reversible capacities, and higher capacity fading rate in 50 cycles, which may be due to its lower electronic conductivity than BPC. However, it should be noted that the sodium storage performance of RPC anode is still comparable to most of P/C composites, convincing the advantages of Ketjenblack-MWCNTs network used in this work. Also, the results indicate that a blend of black and red phosphorus could achieve both high capacity and lower the cost simultaneously.

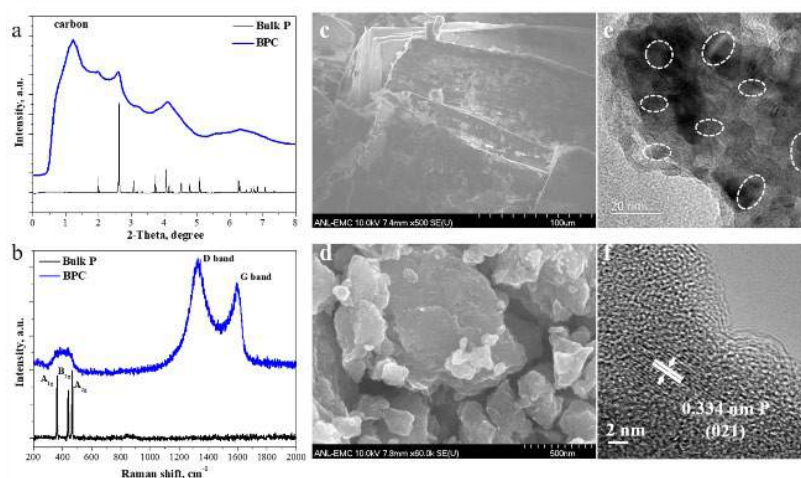


Figure II.11.B.1 (a) X-ray Diffraction and (b) Raman spectra of Black Phosphorus-Carbon Composite. SEM images of (c) Bulk phosphorus and (d) black phosphorus-carbon composite, (e) High magnification and (f) high resolution TEM images of BPC composite

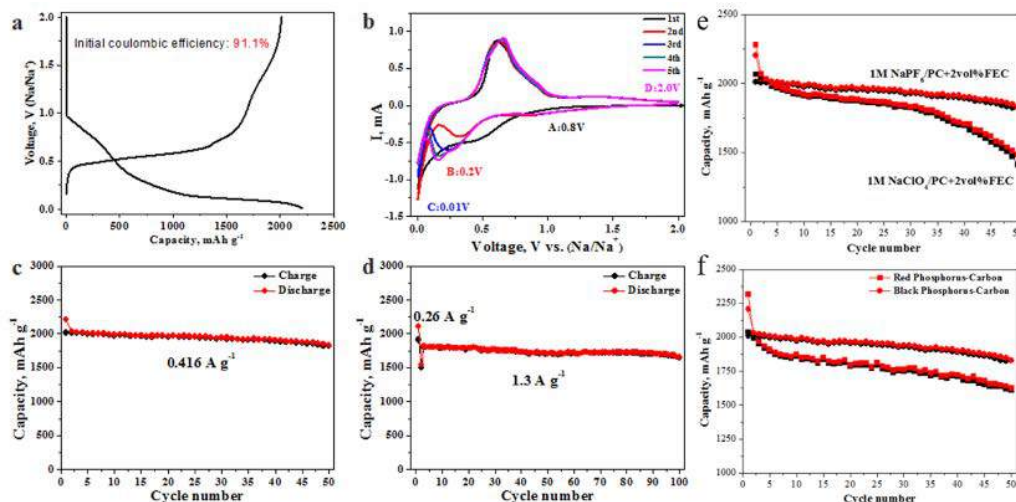


Figure II.11.B.2 (a) Initial voltage profile of black phosphorus-carbon composite at 0.416 A g^{-1} ; (b) Cyclic voltammogram of black phosphorus-carbon composite at 0.1 mV s^{-1} ; Cycle performance of black phosphorus-carbon composite anode at (c) 0.416 A g^{-1} and (d) 1.3 A g^{-1} . The specific capacities were calculated based on the mass of BP. (e) The effect of Na salts on the cycle performance of BPC anode using different electrolytes at 0.416 A g^{-1} . (f) Comparison for the cycle performance of red phosphorus-carbon and black phosphorus-carbon composite at 0.416 A g^{-1} .

Lead (Pb), Pb-oxides/C composite anode with high volumetric energy density

Process optimization of Pb-PbO-C composite anodes

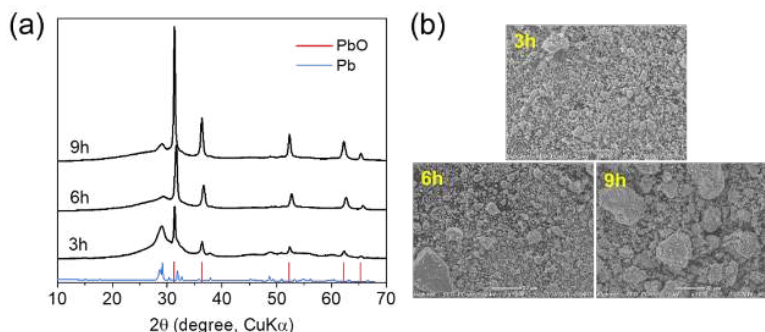


Figure II.11.B.3 (a) XRD patterns and (b) SEM images of the Pb-PbO-C composite samples prepared by SPEX mill with various milling times

The synthesis and process optimization of Pb-containing anodes for SIBs has been conducted through varying the following parameters: (1) starting lead oxide (PbO and Pb_2O_3) materials, (2) lead oxide/carbon ratio, (3) milling time, (4) electrode binder (PVDF), and (5) the electrolyte and additives. This optimization is designed to maximize the stability and promote higher capacity of Pb-based SIB anodes.

The relative fractional amounts of Pb and PbO phases and the particle morphologies in the final products are affected by the starting type of lead oxides, lead oxide/carbon ratio, and milling time. Figure II.11.B.3 shows the effect of milling time as an example. As the milling time increases, the fractional amounts of metallic Pb increases (Figure II.11.B.3a). Longer milling also resulted in kneading of soft Pb metal powders together to form a larger aggregate (SEM; Figure II.11.B.3b). The right choice of binder appears to be critical for stable cycling of the conversion-alloying electrodes like Pb oxides. An improved cycle stability is observed when the PVDF content is increased. A PAA-based binder, while useful for Si-alloying anodes in Li-ion batteries, in the presence of the Pb-Pb oxide anodes caused slurry gelling. The addition of FEC improved electrochemical performance (specific capacity and cycle stability) in the sodium cells.

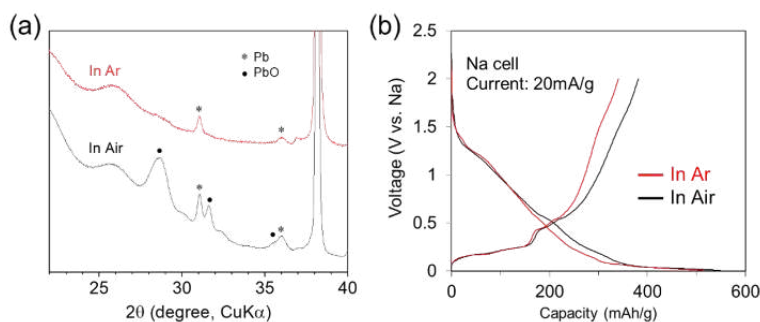
Air stability

Figure II.11.B.4 (a) XRD and (b) initial voltage profiles of the Pb-O-C electrodes prepared in air and in Ar-filled glove box

As-synthesized Pb-PbO-C composite powder, which was freshly coming out of the milling jar, contains high

Pb/PbO ratio. However, the sample is gradually oxidized when stored in air. We suspect that the fresh metallic Pb nanoparticles have highly active surfaces that easily oxidize in contact with oxygen in air. The high Pb/PbO ratio could be maintained by fabricating the electrode laminates inside of Ar-filled glove box as depicted in the stable XRD shown in Figure II.11.B.4a.

Figure II.11.B.4b shows the initial voltage profiles of the electrodes prepared in air and in a glove box. It is clear that the electrode preparation atmosphere (i.e., difference in the Pb/PbO ratio) has only a marginal effect on the electrochemical performance. Slightly increased capacity for the air prepared electrode corresponds to the higher theoretical capacity of PbO and the conversion of PbO to Li_2O plus Pb during the cycling.

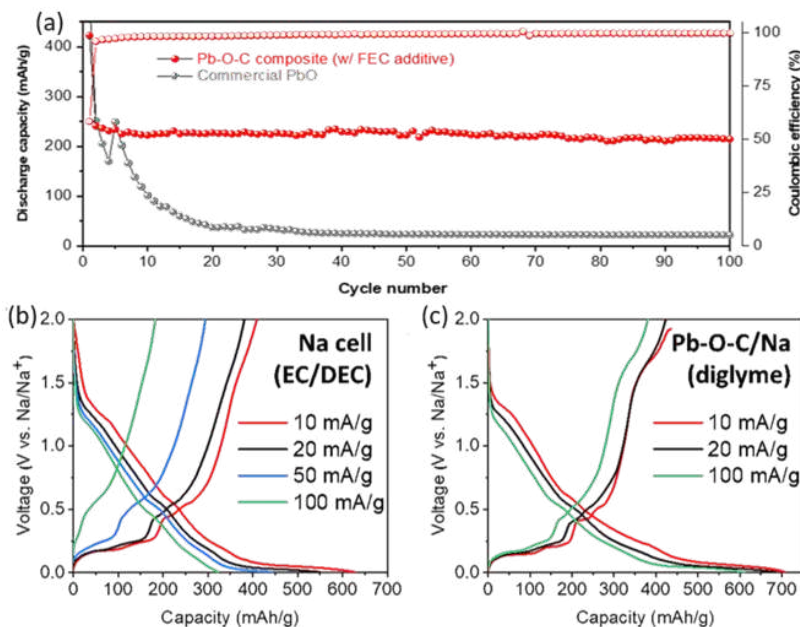
Sodium insertion/extraction kinetics

Figure II.11.B.5 (a) Cycle performance of optimized Pb-PbO-O anode in sodium half cells. Carbonate electrolytes are used and 100 mA g⁻¹ current density was applied. Initial voltage profiles of the Pb-PbO-C nanocomposite anode cycled in different electrolytes: (a) 1M NaPF₆ in EC/DEC, and (b) 1M NaTFSI in TEGDME

Figure II.11.B.5a compares the optimized coin cell performances of Pb-PbO-C in lithium and sodium cells. Conventional electrolytes (NaPF₆ dissolved in carbonate solvent) were used and a moderate current density (100 mA g⁻¹) was applied for the comparison. As shown, the optimal Pb-PbO-C electrode can deliver a stable capacity of 200 mAh g⁻¹ within 100 cycles, demonstrating much better performance than commercial PbO powder. Because of the high mass per volume density of the Pb-Pb oxide/C composite, the volumetric capacity equates to about 1600 mAh cc⁻¹.

The coin cell tests conducted at varying current density revealed that the lower specific capacity for the sodium cell shown in Figure II.11.B.5a is due to the inability to sodiate all the way down to Na₁₅Pb₄ at a low voltage of 0.1 V (vs. Na) from Na₉Pb₄. The high cell impedance seen at high current density of 100 mA g⁻¹ is the reason for the lower capacity. Figure II.11.B.5b shows that at low current densities, the sodium cell has higher cell impedance and slower sodium cycling makes the 0.1 V plateau accessible and increases the specific capacity significantly. In Figure II.11.B.5c, the sodium coin cell prepared with an ether-based electrolyte (1M NaTFSI dissolved in TEGDME) has much better cell impedance behavior and thus the high discharge capacity is obtained even at 100 mA g⁻¹ current density. Ether-based electrolyte is reported to have better cathodic stability and form thinner SEI layer on the anodes.

Conclusions

In summary, we have demonstrated two class of alloying type anode materials by scalable high-energy ball milling process. Both high specific capacity, high volumetric capacity and stable cycle life has been demonstrated by significantly suppressed volume changes. The phosphorus based anode we developed has an ultra-high initial coulombic efficiency of > 90%, high reversible capacity of ~ 2000 mAh g⁻¹ and excellent cycle stability. The Pb based anode could deliver high volumetric capacity of 1600 mAh cc⁻¹ and good cycle stability. However, in order to further extend the cycle life, a robust SEI is necessary to effectively suppress the parasitic reactions with the electrolyte solvents.

Key Publications

Publications

1. Biwei Xiao, Kuan Wang, Gui-Liang Xu, Junhua Song, Zonghai Chen, Khalil Amine, David Reed, Manling Sui, Vincent Sprenkle, Yang Ren, Pengfei Yan and Xiaolin Li, *Advanced Materials*, 2019, 31, 1805889.
2. Dan Sun, Dan Huang, Haiyan Wang, Gui-Liang Xu, Xiaoyi Zhang, Rui Zhang, Yougen Tang, Deia Abd El-Hady, Wael Alshitari, Abdullah Saad AL-Bogami, Khalil Amine, and Minhua Shao, *Nano Energy*, 2019, 61, 361-369.
3. Minghao Zhuang, Gui-Liang Xu, Li-Yong Gan, Yubing Dou, Cheng-Jun Sun, Xuewu Qu, Yingying Xie, Zhenjing Liu, Yuting Cai, Yao Ding, Irfan Haider Abidi, Abhishek Tyagi, Khalil Amine and Zhengtang Luo, *Nano Energy*, 2019, 58, 660-668.

Patents and Patent applications

1. Gui-Liang Xu, Zonghai Chen, Khalil Amine, High performance layered cathode materials for high voltage sodium-ion batteries, US10325730B2.
2. Gui-Liang Xu, Zonghai Chen and Khalil Amine, Phosphorus-carbon composites as battery anode materials, U.S. Patent App. 15/006, 456, pending.

Talks

1. "Challenges and strategies to advance sodium-ion battery towards higher energy density", Gui-Liang Xu and Khalil Amine, 2019 ICNaB, Naperville, IL, USA, Nov 4-7, 2019

2. “Where are Sodium-ion Batteries Headed? An Analysis of their Future”, Christopher Johnson, 2019 Fall American Chemical Society Meeting, San Diego, CA, USA, August 25-29, 2019.
3. “An Evaluation of Electrochemical Properties for a Series of Sodium-Ion Battery Anodes“, Christopher Johnson, 236th The Electrochemical Society Meeting, Atlanta, GA, Oct. 12-17, 2019
4. “Pb-Based Nanocomposite Anodes for Li- and Na-Ion Batteries”, Jinhyup Han, Jehee Park, Youngsik Kim, Shabbir Ahmed, Eungje Lee, Christopher Johnson, 236th The Electrochemical Society Meeting, Atlanta, GA, Oct. 12-17, 2019

References

1. Yabuuchi, Naoaki, Kei Kubota, Mouad Dahbi, and Shinichi Komaba. 2014. “Research Development on Sodium-Ion Batteries.” *Chemical Reviews* 114 (23):11636-11682. doi: 10.1021/cr500192f.
2. Han, Man Huon, Elena Gonzalo, Gurpreet Singh, and Teofilo Rojo. 2015. “A comprehensive review of sodium layered oxides: powerful cathodes for Na-ion batteries.” *Energy & Environmental Science* 8 (1):81-102. doi: 10.1039/c4ee03192j.
3. Wen, Y., K. He, Y. J. Zhu, F. D. Han, Y. H. Xu, I. Matsuda, Y. Ishii, J. Cumings, and C. S. Wang. 2014. “Expanded graphite as superior anode for sodium-ion batteries.” *Nature Communications* 5. doi: Artn 403310.1038/Ncomms5033
4. Huang, Shaozhuan, Lixiang Liu, Yun Zheng, Ye Wang, Dezhi Kong, Yingmeng Zhang, Yumeng Shi, Lin Zhang, Oliver. G. Schmidt, and Hui Ying Yang. 2018. “Efficient Sodium Storage in Rolled-Up Amorphous Si Nanomembranes.” *Adv. Mater.* 30 (20):1706637. doi: 10.1002/adma.201706637.
5. Kang, Hongyan, Yongchang Liu, Kangzhe Cao, Yan Zhao, Lifang Jiao, Yijing Wang, and Huatang Yuan. 2015. “Update on anode materials for Na-ion batteries.” *Journal of Materials Chemistry A* 3 (35):17899-17913. doi: 10.1039/c5ta03181h.

Acknowledgements

Support from Tien Duong of the U.S. DOE’s Office of Vehicle Technologies is gratefully acknowledged. Dr. Guiliang Xu and Dr. Eungje Lee at ANL were major contributors to this project.

II.11.C High Capacity, Low Voltage Titanate Anodes for Sodium Ion Batteries (LBNL)

Marca Doeff, Principal Investigator

Lawrence Berkeley National Laboratory
1 Cyclotron Road
Berkeley CA 94720
E-mail: mmdoeff@lbl.gov

Tien Duong, DOE Technology Development Manager

U.S. Department of Energy
E-mail: Tien.Duong@ee.doe.gov

Start Date: January 1, 2019

End Date: September 30, 2021

Project Funding (FY19): \$300,000

DOE share: \$300,000

Non-DOE share: \$0

Project Introduction

Cost and supply security issues with lithium [1] are compelling reasons to develop sodium-ion batteries as potential alternatives to the better-known lithium-ion analogs. Identification of a suitable anode material for sodium ion cells remains the critical challenge to further progress, as graphite (the anode material used in lithium ion batteries) does not intercalate sodium to an appreciable extent. Recently, several sodium titanates [2],[3],[4] have been found to undergo reversible sodium intercalation processes at potentials much lower than 1V vs. Na^+/Na , making them attractive candidates for use as anodes in sodium ion systems. These materials have stepped layered structures but show very different electrochemical behaviors depending on composition and step size. Work on this project is directed towards understanding these differences through an array of synthetic, electrochemical, and structural characterization techniques, and overcoming practical impediments to their use, such as the high first cycle coulombic inefficiencies that are currently observed. The ultimate goal of the project is to produce a 200-250 mAh/g anode that cycles reversibly. Such a material would be an enabling technology for a practical high-energy sodium ion battery.

Objectives

The planned work is conceived to overcome the main obstacle to the practical realization of sodium-ion batteries; the lack of a suitable anode material. Experiments are designed to improve the practical reversible capacities and overcome the high first cycle coulombic inefficiencies of promising low voltage sodium titanates, as well as to assess the stabilities of the sodiated (partially and fully discharged) products of the electrochemical reactions. Some effort is devoted to consideration of electrolytes and understanding of the electrolyte/anode interface, which must go hand-in-hand with anode development. The ultimate goal is to produce a high capacity (200-250 mAh/g), stable and reversible low voltage anode material suitable for use in a sodium-ion battery configuration.

Approach

Candidate stepped layered titanates will be synthesized by appropriate routes (hydrothermal, solid state routes, etc.). Materials will then be characterized electrochemically and physically. Structure-function relationships will be built to correlate the effect of changing structure (for example, step size) on electrochemical properties. Synchrotron methods such as soft and hard X-ray absorption spectroscopy and XPS are used to probe electronic structures and particle surfaces of pristine and cycled materials.

Results

The structures of three classes of titanate materials of interest to this project are shown in Figure II.11.C.1. They all exhibit stepped layered structures. $\text{Na}_2\text{Ti}_3\text{O}_7$, shown on the left, has a step size of 3 and was recently shown to insert sodium ions at 0.3V vs. Na^+/Na , exhibiting a flat voltage profile indicative of a two-phase reaction. The middle structure, with a step size of 6, is known as “sodium nonatitanate” or NNT and has the

composition $\text{NaTi}_3\text{O}_6(\text{OH}) \cdot 2\text{H}_2\text{O}$ in the as-made state. Both water and sodium ions are present in the interlayer spacings, but the material can be dehydrated at elevated temperatures and does not take up water again after drying. It exhibits a somewhat sloping voltage profile with an average potential of about 0.3V vs. Na^+/Na . Lepidocrocite-structured titanate is shown on the right. This class of material exhibits corrugated structures (step size 1) and in the as-made state has compositions of $\text{A}_x\text{Ti}_{2-y}\text{M}_y\text{O}_4$; A = K, Rb, or Cs, and M represents a vacancy or a wide variety of substituents including Li, Mn, Mg, Zn, Cu, and Co. Titanium in these structures is always tetravalent, and the stacking of the corrugated layers varies depending on what occupies the interlayer spacings. These materials also exhibit sloping voltage profiles at low potentials in sodium half-cells, with the capacity a function of composition.

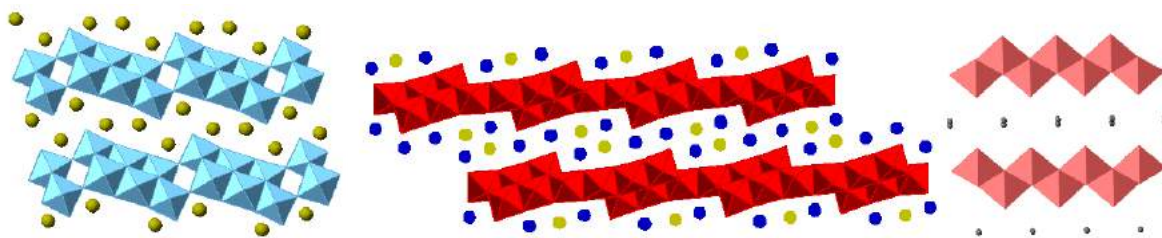


Figure II.11.C.1 Structures of $\text{Na}_2\text{Ti}_3\text{O}_7$ (left), $\text{NaTi}_3\text{O}_6(\text{OH}) \cdot 2\text{H}_2\text{O}$ or NNT (middle) and lepidocrocite -type titanate $\text{A}_x\text{Ti}_{2-y}\text{M}_y\text{O}_4$ (right)

Of these three types of structures, NNT and lepidocrocite-type titanates appear to have better reversibility in sodium cells than $\text{Na}_2\text{Ti}_3\text{O}_7$, which may be a function of their sloping voltage profiles (there is some evidence that the end-member $\text{Na}_4\text{Ti}_3\text{O}_7$ produced upon reduction of $\text{Na}_2\text{Ti}_3\text{O}_7$ is not stable with respect to spontaneous loss of sodium and oxidation. Because the reaction is two-phase throughout nearly the whole discharge, it is impossible to avoid making this material). Our work this year focused primarily on NNT, as it can be prepared hydrothermally and does not require ion-exchange, in contrast to many of the lepidocrocite-type titanates.

Our initial results on NNT, reported in reference [3] showed a sloping and rather featureless voltage profile when this material was discharged in either sodium or lithium cells, with no obvious differences in potentials. This raised the question of what the redox mechanism actually is; whether it is intercalation and charge transfer or some sort of pseudo-capacitive mechanism. Changes in the X-ray diffraction (XRD) patterns of pristine and discharged electrodes indicated that sodium intercalation does occur in this structure. [5] Further evidence for charge transfer is shown in Figure II.11.C.2, along with the first and second discharge profile in a sodium cell (taken from reference [3]). A carbon-free electrode is white in color, consistent with the existence of Ti in the tetravalent state. When the electrode was discharged, it turned dark blue, diagnostic of some reduction to trivalent titanate. More quantitative evidence is provided in the hard X-ray absorption spectra (XAS) of pristine and discharged electrodes, where shifts in the absorption peaks are consistent with charge transfer and reduction to Ti^{3+} . Similar shifts consistent with titanium reduction are seen in the soft XAS spectra (not shown). While some pseudo-capacitance may contribute to the capacity of these electrodes, this evidence, along with the XRD patterns indicate that the main redox mechanism is reductive intercalation of sodium electrodes.

The initial results published on this system, while encouraging, showed that there were some kinetic limitations, resulting in lower-than-expected capacities for the NNT electrodes in sodium cells. Improvements were also needed in cycle life. By changing the conditions of the hydrothermal reaction used to make NNT, two different morphologies were produced. Spherical clusters were produced at 200°C after 20 hours, and very long nanowires after 96 hours. Better results were observed with the clusters than the nanowires, although kinetic limitations were observed for both. The discharge characteristics were further improved when the binder was changed to CMC from PVDF and nanowires were carbon-coated (Figure II.11.C.3). C-coated dehydrated nanowire NNT electrodes with CMC binders could be discharged nearly 200 mAh/g and showed significant improvement in cycle life.

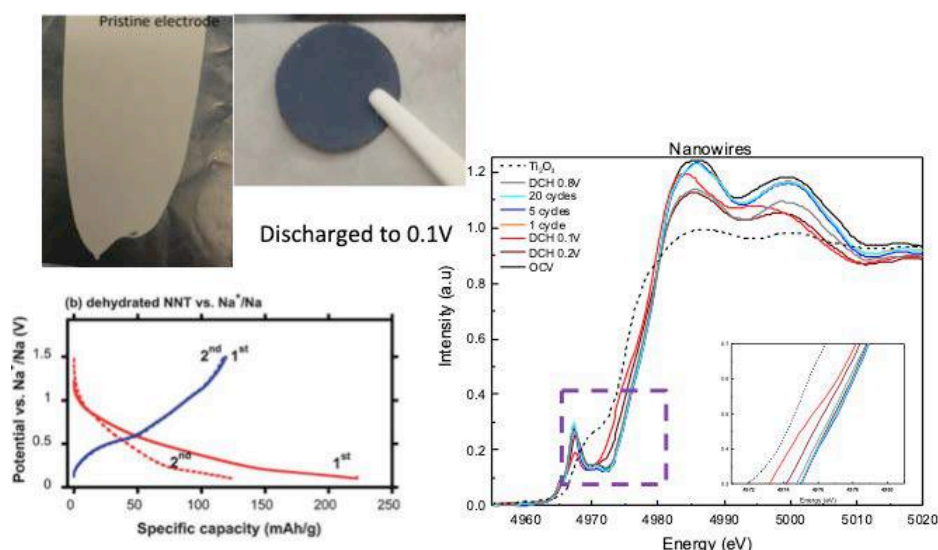


Figure II.11.C.2 Top left: images of a pristine carbon-free electrode containing NNT, and a carbon-free electrode discharged to 0.1V. The color change is a qualitative indicator of reduction to trivalent titanium. The first and second discharge profiles of a Na/NNT cell is shown at bottom left (taken from reference [3]) showing the sloping voltage profile. Ti K-edge hard XAS spectra of pristine, cycled, and discharged NNT electrodes are shown on the right. These results are also consistent with $\text{Ti}^{3+}/\text{Ti}^{4+}$ redox.

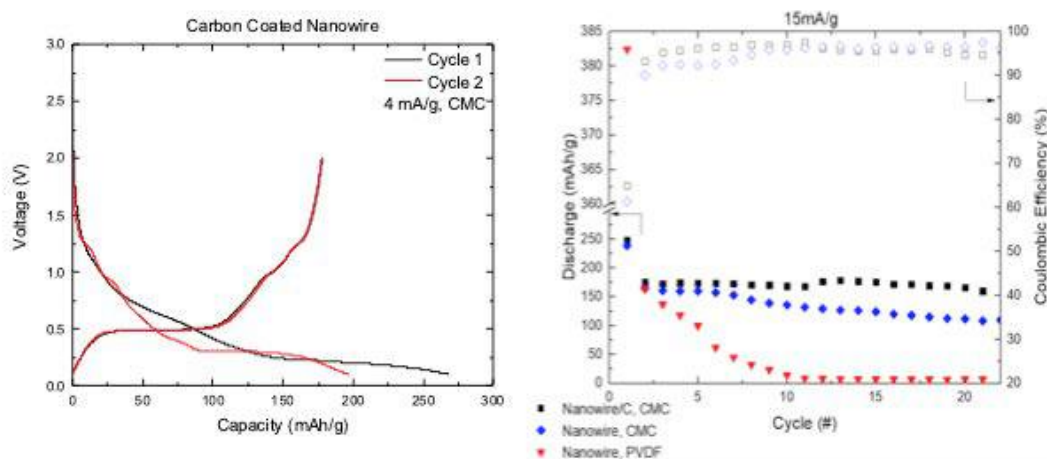


Figure II.11.C.3 First and second cycles of a carbon coated nanowire NNT electrode made with CMC binder (left) discharged in a sodium half cell at low rates. Cycling behavior of nanowire electrodes with PVdF binder (red), CMC binder (blue) and carbon coated with CMC binder (black) in sodium half cells at moderate rates

Interestingly, several new features are observed in the discharge profiles of these improved electrodes in sodium half-cells compared to the earlier results. Small plateaus are observed at about 1.25V and 0.95V and there appears to be more capacity below about 0.4V than seen previously. An electron diffraction pattern obtained on NNT dehydrated at 600°C (Figure II.11.C.4) resembles that of $\text{Na}_2\text{Ti}_6\text{O}_{13}$, a tunnel compound with very different discharge characteristics. [6] While the reversibility of $\text{Na}_2\text{Ti}_6\text{O}_{13}$ is excellent, the capacity is only about 60 mAh/g at an average potential of about 0.9V vs. Na^+/Na , close to where one of the small plateaus appears in the profile of Na/NNT cells. Furthermore, the XRD pattern of heated NNT still resembles that of the parent compound, although with smaller interlayer spacings consistent with the removal of water.

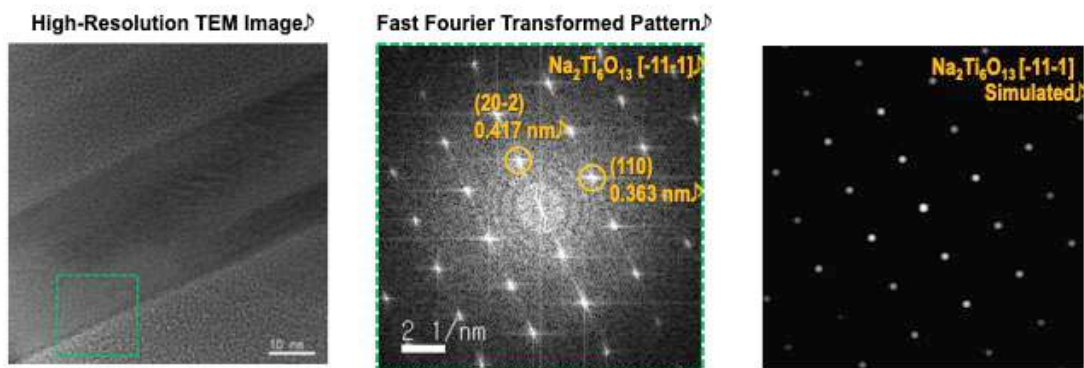


Figure II.11.C.4 High-resolution TEM image of NNT dehydrated at 600°C (left), its electron diffraction pattern (middle) and a simulated pattern for $\text{Na}_2\text{Ti}_6\text{O}_{13}$ (right)

To study this further, NNT samples were dried at several different temperatures and the discharge characteristics studied in sodium half-cells (Figure II.11.C.5).

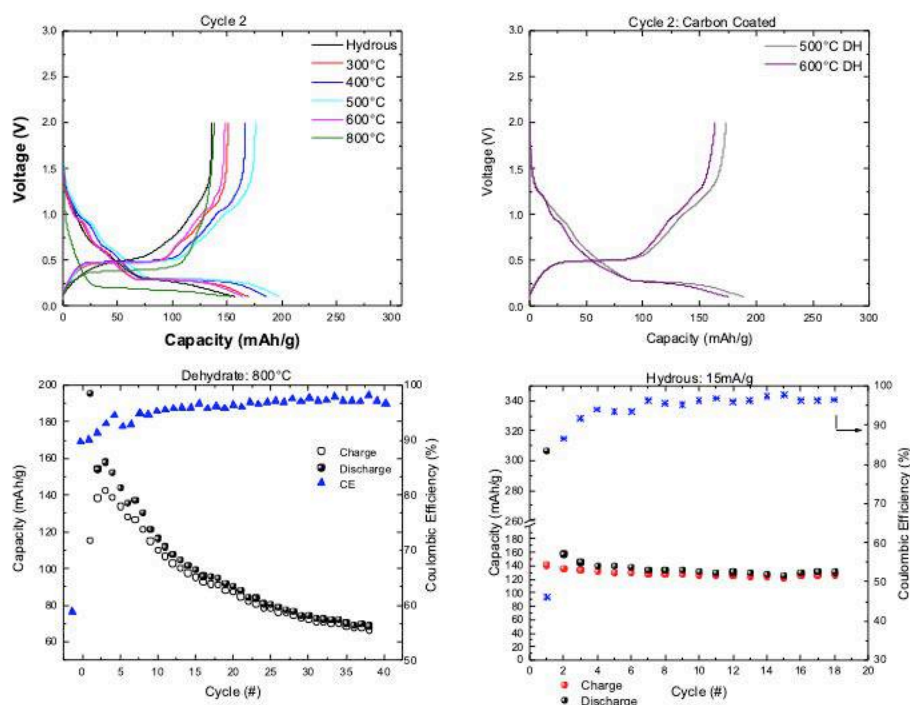


Figure II.11.C.5 Second cycle discharge profiles of NNT heated to different temperatures (upper left) in sodium half cells. Comparison of second cycle discharge profiles of NNT heated to 500°C and 600°C (upper right). Cycling data for NNT heated to 800°C (lower left) and that of the hydrous (unheated) sample, lower right

All of the samples except for NNT heated to 800°C show similar second cycle discharge profiles such as small plateaus in the sloping sections as well as significant capacity below about 0.4V. NNT heated to 800°C decomposes to form $\text{Na}_2\text{Ti}_6\text{O}_{13}$ and $\text{Na}_2\text{Ti}_3\text{O}_7$, and the voltage profile shows characteristics of both phases, with some capacity at higher voltages and a flat section near 0.3V typical of $\text{Na}_2\text{Ti}_3\text{O}_7$. This phase mixture cycles poorly (Figure II.11.C.5, lower left), dominated by the behavior of $\text{Na}_2\text{Ti}_3\text{O}_7$, which exhibits poor reversibility. The highest capacity is observed for NNT heated to 500°C, which is somewhat greater than that

of the 600°C sample at moderate discharge rates (Figure II.11.C.5, upper right) and close to 200 mAh/g, the targeted capacity. Somewhat surprisingly, the as-made (hydrous) NNT shows excellent capacity retention upon cycling, although the capacity is somewhat lower than that seen for the heated samples. This shows the importance of proper electrode engineering (CMC binder instead of PVDF, and carbon coating) for good performance for this particular material, as hydrous NNT electrodes with PVDF binder show poor cycling behavior. [3]

The electrochemical and XRD results indicate that NNT heated to 600°C has not fully converted to $\text{Na}_2\text{Ti}_6\text{O}_{13}$ although the electron diffraction pattern seems to suggest this. However, NNT in the as-made state is somewhat disordered, exhibiting not only stacking faults but edge dislocations that give it some tunnel-like characteristics. [7] Upon heating to 600°C, water is removed and “pinch points” form where the steps of two adjacent layers nearly join, [3] even more reminiscent of tunnel structures, although the corrugated layers are largely retained. At higher temperatures, conversion to tunnel-structured $\text{Na}_2\text{Ti}_6\text{O}_{13}$ and $\text{Na}_2\text{Ti}_3\text{O}_7$ is completed. We speculate that NNT heated to 600°C resembles an intergrowth between something that looks like $\text{Na}_2\text{Ti}_6\text{O}_{13}$ and the original layered structure. The fortuitous effect is a combination of excellent reversibility attributable to the tunnel structure but with higher capacity attributable to the layered portion. We will be carrying out more characterization experiments and preparing a paper on this system soon.

Some portion of the work this year was also devoted to a lepidocrocite-structured titanate, $\text{Na}_{0.7}\text{Ti}_{1.825}\square_{0.175}\text{O}_4$ (where \square indicates vacancies) prepared by ion-exchange from the Cs-containing analog. This electrode exhibits the sloping voltage profile typical of lepidocrocite titanates, [4] and shows excellent cycling behavior and rate capability (Figure II.11.C.6). The initial capacity (second discharge) of 175 mAh/g falls slightly short of our goals, but it should be possible to synthesize a material with fewer vacancies and more titanium, which would give a higher capacity.

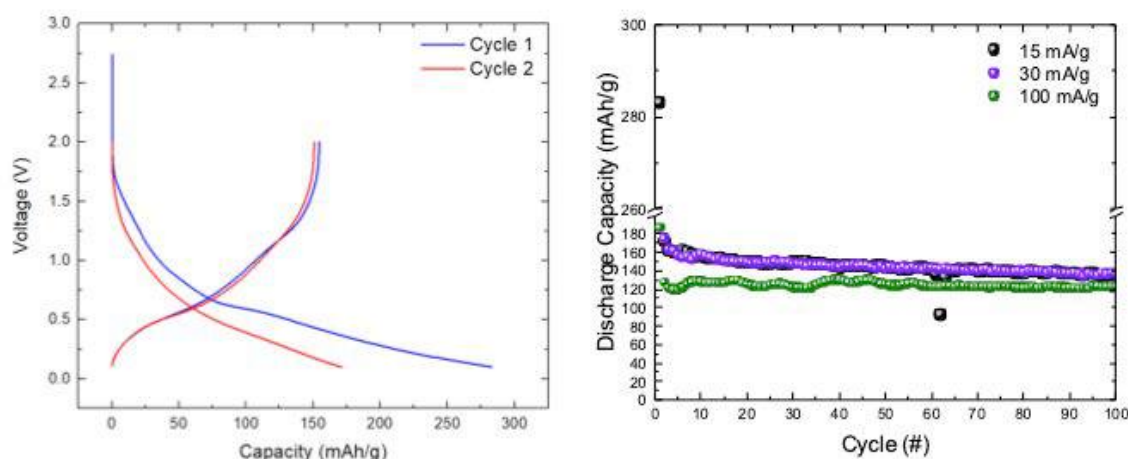


Figure II.11.C.6 First and second cycle discharge profiles of $\text{Na}_{0.7}\text{Ti}_{1.825}\square_{0.175}\text{O}_4$ in sodium half cells (left). Cycling data at different rates on right

Conclusions

Electrodes based on NNT deliver capacities close to 200 mAh/g and cycle reversibly when 1) the synthesis and heat treatment is optimized, and 2) when effective electrode engineering (binder and carbon coating) is used. This can be attributed to its structural characteristics. These share some features of robust tunnel compounds like $\text{Na}_2\text{Ti}_6\text{O}_{13}$, which cycles extremely well, but has limited capacity. The material, however, mostly retains a corrugated layered structure, imparting higher capacities than obtained with tunnel compounds. This combination of features results in much better cycling than is found with $\text{Na}_2\text{Ti}_3\text{O}_7$, a related structure with a step size of 3 rather than the 6 found in NNT. Observed color changes upon reduction and Ti K-edge X-ray

absorption spectroscopy on pristine, discharged, and cycled electrodes confirm that Ti redox occurs. Another system with excellent cycling characteristics are the lepidocrocite titanates, which are corrugated layered structures with a step size of 1 (zigzag structure). One of these systems, $\text{Na}_{0.7}\text{Ti}_{1.825}\square_{0.175}\text{O}_4$, was studied this year, and can deliver about 175 mAh/g reversibly at moderate rates. Higher capacities may be achievable by increasing the amount of Ti and decreasing the number of vacancies in this structure. An advantage of NNT over the lepidocrocite structures is that the former does not need to be ion-exchanged. Work in the upcoming year will continue on these two promising systems, with some attention paid to reducing the first cycle coulombic inefficiency, which probably arises from SEI formation and irreversible reactions with added carbon in the electrodes.

Key Publications

1. Alvarado J. and Doeff M., "Understanding the Properties that Affect the Reversibility of Sodium Titanate Anodes" (invited talk given by Judith Alvarado) 236th meeting of the Electrochemical Society, Atlanta GA, Oct. 13-17th, 2019.

References

1. Vaalma, C., Buchholz, D., Weil, M., and Passerini, "A Cost and Resource Analysis of Sodium-Ion Batteries" *S., Nature Rev. Mater.* 3, (2018): article number 18013.
2. Senguttuvan, P., Rousse, G., Seznec, V., Tarascon, J.-M., and Palacin, "Na₂Ti₃O₇; The Lowest Voltage Every Reported Oxide Insertion Electrode for Sodium Ion Batteries" *M. R Chem. Mater.*, 23, (2011): 4109-4111.
3. Shirpour, M., Cabana, J., and Doeff M., "New Materials based on a Layered Sodium Titanate for Dual Electrochemical Na and Li Intercalation Systems" *Energy & Environ. Sci.*, 6, (2013): 2538- 2547.
4. Shirpour, Mona, Cabana, Jordi, and Doeff, Marca "Lepidocrocite-type Layered Titanate Structures: New Lithium and Sodium Ion Intercalation Anode Materials", *Chem. Mater.* 26, (2014): 2502-2512.
5. Seshadri, Dhruv, Shirpour, Mona, and Doeff, Marca "Electrochemical Properties of Electrodes Derived from NaTi₃O₆OH•2H₂O in Sodium and Lithium Cells", *J. Electrochem. Soc.* 162, (2015): A52-A59.
6. Rudola, A., Kuppan, S., Devaraj, S., Gong, H. and Balaya, P. "Na₂Ti₆O₁₃; a Potential Anode for Grid-Storage Sodium-Ion Batteries" *Chem. Commun.* 49, (2013): 7451-7453.
7. Andrusenko, I., Mugnaioli, E., Gorelik, T. E., Koll, D., Panthofer, M., Tremel, E., and Kolb, U. "Structure Analysis of Titanate Nanorods by Automated Electron Diffraction Tomography" *Acta Crystal. B* 67, (2011): 218-225.

II.11.D Electrolytes and Interfaces for Stable High-Energy Sodium-ion Batteries (PNNL)

Ji-Guang Zhang, Principal Investigator

Pacific Northwest National Laboratory
902 Battelle Boulevard
Richland, WA 99354
E-mail: jiguang.zhang@pnnl.gov

Tien Duong, DOE Technology Development Manager

U.S. Department of Energy
E-mail: Tien.Duong@ee.doe.gov

Start Date: October 1, 2018

End Date: September 30, 2021

Project Funding (FY18): \$400,000

DOE share (FY18): \$400,000 Non-DOE share: \$0

Project Introduction

The sodium (Na)-ion battery (NIB) is regarded as one of the most promising alternative power sources for lithium-ion batteries due to the natural abundance of sodium in the earth's crust and similarities between the electrochemical properties of Na^+ and Li^+ ions. However, practical performance of NIBs largely depends on the properties of electrode materials and electrolytes. In recent years, a series of potential electrode materials (both anode and cathode) have been developed with good capacity and electrochemical windows, but the electrochemistry of NIBs, especially the stability of electrode-electrolyte interfaces in these batteries, is still not fundamentally understood. One of the essential challenges for NIBs is to understand the electrode/electrolyte interphases formed on the electrode materials and design a functional, stable interface for long-term cycling of NIBs. The Na^+ -ion diffusion kinetics in electrode materials also need to be improved for enhanced coulombic efficiency (CE) and power rate of NIBs. In this regard, design of advanced electrolytes is critical to enable the formation of an effective solid electrolyte interphase (SEI) and cathode electrolyte interphase (CEI), especially during the initial cycles of NIBs. A stable SEI/CEI layer will determine the long-term cycling stability and the rate capability of the NIBs. In FY19, our work focused on systematic study of different electrolytes (including salts, solvent, and additives) and their effects on the electrochemical performance of electrode materials in an effort to stabilize the electrode-electrolyte interface with fast ion transport and high CE. The results obtained in this work will guide electrolyte optimization and stabilize both anode and cathode, and thereby enable high energy and stable cycling of NIBs.

Objectives

- Investigate various sodium salts, solvents, and additives for their effects on ionic conductivity, solvation structure, Na CE, and stability against hard carbon (HC) anodes and high voltage cathodes to enable long-term cycling stability of NIBs.
- Obtain a fundamental understanding of the electrolyte/electrode interface and correlate electrochemical performance of NIBs with the interface properties to guide electrolyte development.

Approach

The following approaches have been used to reach the objectives outlined above. First investigated were the effects of solvent composition (mixtures of linear and cyclic carbonate) and sodium salts (NaPF_6 , NaTFSI , NaFSI , NaOTf) on the capacity and CE of electrode materials for Na batteries (including Na metal anode, hard-carbon anode, and layered transition metal oxide cathode). Second, the electrolyte components and salt concentration were optimized to improve the electrochemical stability of the electrolytes. In parallel, new, functional, nonflammable, phosphate-based electrolytes were developed to maximize the electrode capacity utilization and cycling performance. Finally, various characterization methods, including in situ and ex situ spectroscopy methods will be used to identify the origin of the SEI at the dynamic interface, providing

guidance for the electrolyte and interface design and enabling high achievable capacity and long life of Na-ion batteries.

Results

1. Effects of carbonate solvent composition and sodium salts on hard-carbon performance

Nonaqueous electrolytes comprising organic solvent and sodium salt are critical for enhancing the interfacial stability during battery cycling. Electrolytes are known to react with anode/cathode surfaces to form SEI or CEI, which are the key factor for NIBs. For carbonate-based electrolytes, ionic conductivity of the electrolytes exhibits the following sequence: EC+DMC (1:1 by mass) > PC+DMC (1:1 by mass) > EC+PC (1:1 by mass) > PC > DMC. This is independent of the electrolyte salt used. The salt effect was further studied in the optimal cosolvent of EC+DMC (1:1 by mass). The electrolytes with different salts exhibit the following sequence in ionic conductivity: NaFSI ~ NaPF₆ > NaTFSI > NaOTf. Raman spectroscopy and ¹³C NMR were used to investigate the solvation of sodium ions in different carbonate-based electrolytes. Raman spectra of EC-DMC-based electrolytes show a peak shift and appearance of new vibration bands at high frequency due to coordination between Na⁺ and carbonyl oxygen nuclei (Figure II.11.D.1a). The distinct band and peak shifting of EC is more obvious than those of DMC, indicating stronger cation-solvent interaction between EC and Na ("EC-Na⁺"). In addition, the chemical shift of EC-based electrolytes is greater than that of DMC. All these results indicate that the chemical coordination ability of solvents exhibits the following order: PC ~ EC > DMC (Figure II.11.D.1b).

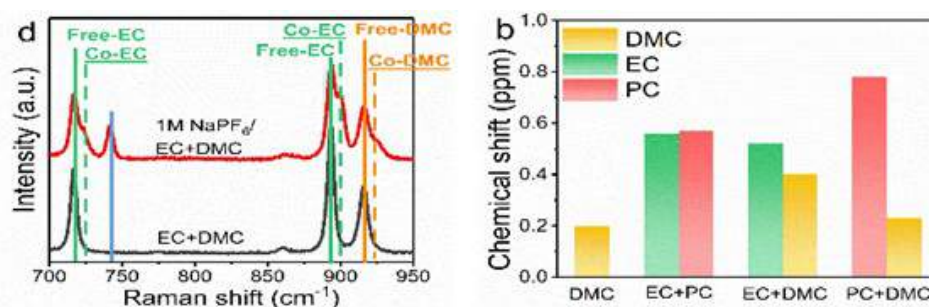


Figure II.11.D.1 (a) Raman spectra of EC-DMC mixed solvent and 1 M NaPF₆/EC-DMC electrolyte. (b) ¹³C Chemical shift deduced from ¹³C NMR spectra of different carbonates based electrolyte

Na||HC cells were used for initial evaluation of electrolytes (Figure II.11.D.2). The solvent has significant effect on capacity and rate performance of HC anodes. EC in cosolvent is critical for formation of a stable SEI on the HC anode, which leads to higher CE and fast ion transport. The electrolyte of 1 M NaPF₆/EC+DMC (1:1 by mass) exhibited the best overall performance, with the highest reversible capacity of 313 mAh g⁻¹ in the first cycle at 0.1C, the highest initial-cycle coulombic efficiency of 85.2%, and the best rate performance of 243 mAh g⁻¹ at 1C (Figure II.11.D.2a, Figure II.11.D.2b). In situ three-electrode EIS measurement was done to study the stability of cathode/electrolyte and anode/electrolyte interfaces separately. EIS results in the first cycle indicate that the HC has the smallest electrochemical impedance in EC+DMC mixture (1:1 by mass) among different electrolytes with 1 M NaPF₆ (Figure II.11.D.2c). The rate performance of HC follows a sequence of NaPF₆ > NaOTf > NaFSI > NaTFSI (all at 1 M) in electrolytes with the same solvent of EC+DMC (1:1 by mass), as shown in Figure II.11.D.2d.

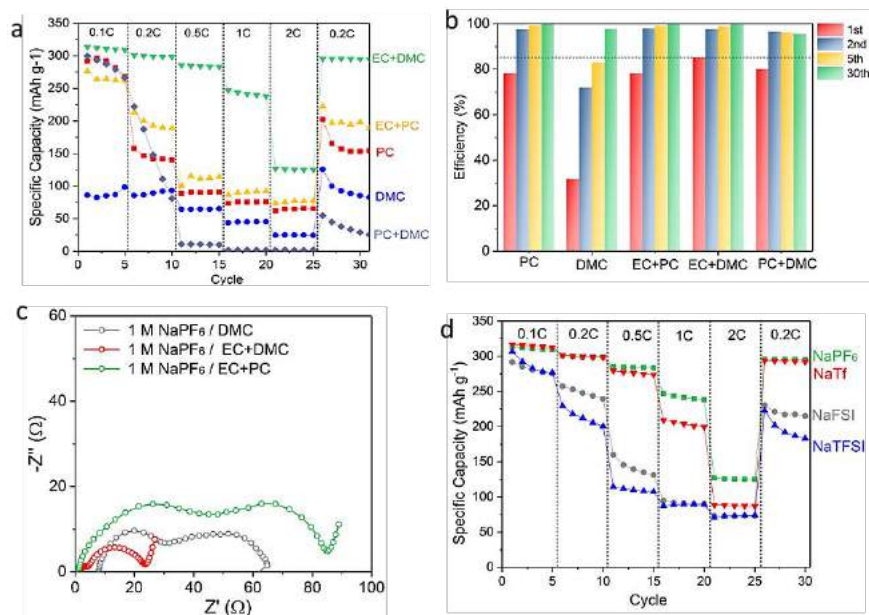


Figure II.11.D.2 (a) Rate performance and (b) Coulombic efficiency of Na || HC cells (HC electrode: HC:PVDF:CB = 90:5:5; mass loading: 2–3 mg. cm⁻²) in 1 M NaPF₆ electrolyte with different solvents (c) Three-electrode EIS measurement for HC electrodes in different electrolytes. (d) Rate performance of HC in electrolytes with different salts (1 M) in EC+DMC mixture (1:1 by mass)

2. Optimized long-term cycling of hard-carbon anode

To investigate the effect of binder on the performance of HC anodes, two different binders (PVDF dissolved NMP and alginate acid dissolved in water) were used in the anode casting process. The coated electrodes were cycled at 0.2 C in the optimal electrolyte of 1 M NaPF₆/EC+DMC (1:1 by mass) (Figure II.11.D.3a) identified in our work discussed above. After 250 cycles, the HC anode coated with PVDF binder exhibited a reversible capacity of 218.0 mAh g⁻¹. In contrast, the anode with alginate acid aqueous binder demonstrated a much higher capacity of 261.2 mAh g⁻¹, with a CE of 87.7% for the first cycle and >99.9% for long-term cycling. The charge–discharge profiles of the HC anode with alginate acid aqueous binder at different cycle numbers further revealed stable cycling performance, as shown in Figure II.11.D.3b.

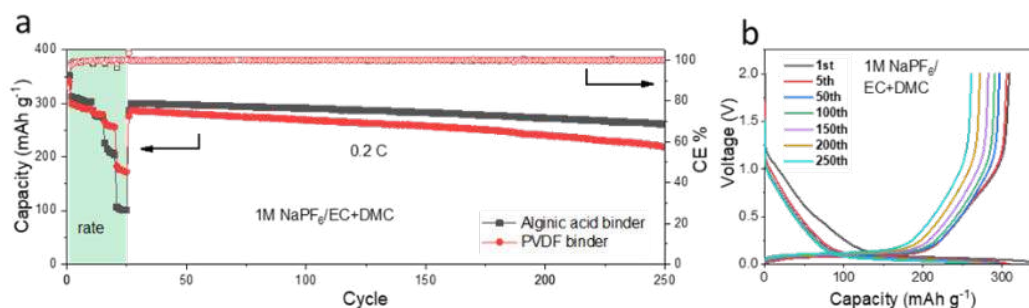


Figure II.11.D.3 (a) Cycling stability of Na || HC cells (HC electrode, HC:binder:CB = 90:5:5; mass loading: 2–3 mg. cm⁻²) in 1 M NaPF₆/EC+DMC electrolyte. (b) Charge profile of Na || HC cells (HC coated with alginate acid binder)

3. Functional nonflammable phosphate-based electrolytes

Phosphate solvents with distinctive properties like high oxidation window, high thermal stability and nonflammability are very promising for electrolyte application because of their safety. Functional phosphate-based electrolytes using triethyl phosphate (TEP) or trimethyl phosphate (TMP) with different solvent: salt (NaFSI) molar ratios (8:1, 4:1, 2:1, 1.8:1) were prepared. A highly concentrated electrolyte (HCE) of

TEP:NaFSI (2:1) exhibited slightly higher ionic conductivity ($\sim 4 \text{ mS cm}^{-1}$ at 25°C) than that of TMP:NaFSI (2:1). The TTE diluent in TEP:NaFSI (2:1) does not have significant effect on the ionic conductivity of the electrolyte, while the BTFE diluent leads to $\sim 30\%$ increase in the ionic conductivity of the electrolytes (Figure II.11.D.4a, Figure II.11.D.4b, Figure II.11.D.4c).

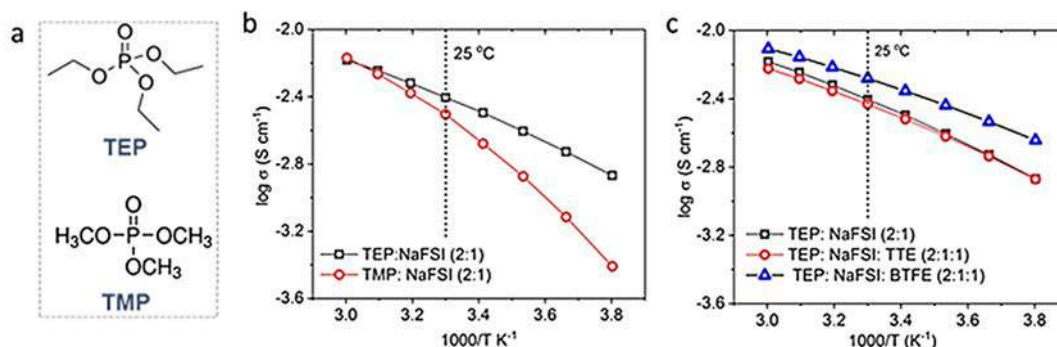


Figure II.11.D.4 (a) Molecular structure of TEP and TMP (b) Ionic conductivity of TEP:NaFSI and TMP:NaFSI (2:1) at different temperatures (c) The effect of BTFE or TTE diluent on the conductivity of TEP-based electrolyte

^{13}C NMR and Raman spectroscopy were used to investigate the solvation phenomena of sodium ions in phosphate-based electrolyte (Figure II.11.D.5). As the salt concentration increased, the ^{13}C NMR peak position shifted to higher frequency, indicating an increase of coordination number between Na^+ ions and TEP. In addition, the TEP peak at 737 cm^{-1} in Raman spectra shows a blue shift corresponding to the stronger interaction between Na^+ and TEP when NaFSI salt concentration in the electrolyte increases. The reduction in free TEP solvent in HC electrolyte inhibits further decomposition of TEP. In locally highly concentrated electrolytes (LHCEs), diluent bis(2,2,2-trifluoroethyl) ether (BTFE) or 1,1,2,2-tetrafluoroethyl-2,2,3,3-tetrafluoropropyl ether (TTE) does not induce any significant modification on the solvation structure. Indeed, there is no clear changes can be identified in ^{13}C NMR spectra (peak at 64.6 ppm) or Raman spectra after different amount of diluent (BTFE or TTE) were added to the electrolytes.

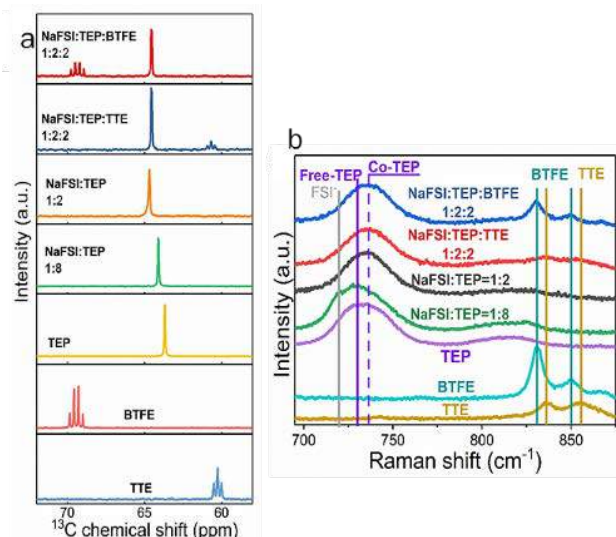


Figure II.11.D.5 (a) ^{13}C NMR spectra (b) Raman spectra of TEP-based electrolyte and with TTE or BTFE diluent

Nonflammable phosphate-based LHCEs exhibited not only a lower overall salt molarity, lower viscosity, and greater safety, but they could also preserve the Na^+ -coordinated TEP solvation structure. In charge-discharge tests, Na||HC cells with LHCE electrolytes demonstrated a capacity of 270 mAh g^{-1} and CE of 80.4% at 0.1 C

rate. After the initial cycle, the CE quickly rose to 99.9%. The cycling performance was quite stable for almost 100 cycles without any observable capacity fade, as shown in Figure II.11.D.6.

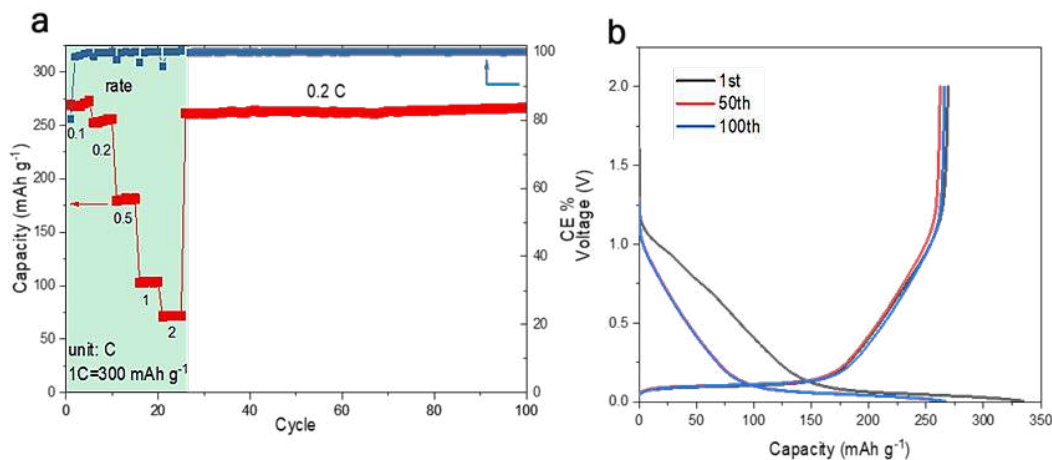


Figure II.11.D.6 (a) Cycling performance at different discharge rates and (b) Charge-discharge profiles of Na||HC in phosphate-based LHCE (NaFSI:TEP:TTE= 1:2:2). The HC electrode consists of HC:PVDF:CB = 90:5:5; mass loading: 2–3 mg. cm⁻²

Conclusions

1. In carbonate-based electrolyte, solvent (species and ratio) and sodium salt have significant effects on the CE of Na cycling and the stability of the electrolytes against electrode materials. EC is a critical component of the electrolytes for forming stable SEIs on both HC anodes and Na metal.
2. The HC anode showed excellent cycling stability in the optimized carbonate electrolyte 1 M NaPF₆/EC-DMC (1:1 by mass). Using this electrolyte, an HC anode with alginate binder demonstrated a high CE and high capacity during long-term cycling (261.2 mAh g⁻¹ and 99.9 % CE after 250 cycles).
3. Nonflammable phosphate-based HCE and LHCE were developed for NIB electrolyte. LHCE with BTFE or TTE diluent is highly compatible with HC anodes and outperforms HCE electrolytes.

Key Publications, Presentations and Patent

1. J.-G. Zhang, H. Pan, P. M. Le, T. D. Vo, Y. Jin, N. Sabi. "Electrolytes and Interfaces for Stable High-Energy Na-Ion Batteries", *DOE Na-ion Workshop*, Richland, WA, August 27, 2019.
2. Jin Y., H. Pan, P. Le, T.D. Vo, and J.-G. Zhang. "Non-flammable Localized High Concentration Electrolytes for Stable High Voltage and High Loading Sodium Batteries." *International Conference on Sodium Batteries (ICNaB-2019)*, Naperville, IL, November 5–7, 2019.

Acknowledgements

Key contributors include Dr. Huilin Pan, Dr. Yan Jin, Dr. Phung Le, Thanh Vo, and Noha Sabi.

II.12 Beyond Lithium-Ion R&D: Battery500

II.12.A Battery500 Innovation Center (PNNL, SLAC)

Jun Liu, Principal Investigator

Pacific Northwest National Laboratory
902 Battelle Boulevard
Richland, WA 99354
E-mail: jun.liu@pnnl.gov

Yi Cui, Principal Investigator

Stanford University/SLAC
450 Serra Mall
Stanford, CA 94305
E-mail: yicui@stanford.edu

Tien Duong, DOE Technology Development Manager

U.S. Department of Energy
E-mail: Tien.Duong@ee.doe.gov

Start Date: October 1, 2018	End Date: September 30, 2019	
Project Funding (FY19): \$8,000,000	DOE share: \$8,000,000	Non-DOE share: \$0

Project Introduction

Lithium (Li)-ion batteries play a critical role in modern day technologies, but their specific energy (Wh/kg) and energy density (Wh/L) are approaching the maximum practically achievable values based on existing technology with the conventional cathode and anode materials. The large scale deployment of electric vehicles and ever-increasing demand of modern technologies require further increase in cell energy and cost reduction. Rechargeable Li-metal batteries are regarded as “Holy Grail” of high-energy-density systems because Li metal has an ultrahigh theoretical specific capacity (3860 mAh/g), an extremely low redox potential (-3.040 V vs. standard hydrogen electrode), and a very low gravimetric density (0.534 g/cm³). However, the practical application of Li metal anode (LMA) still faces several big challenges, including safety concerns due to Li dendrite growth, limited cycle life because of low Li Coulombic efficiency (CE), and infinite volume change during Li stripping and redeposition if a two-dimensional (2D) flat Li foil is used. In addition, developing the next generation rechargeable Li metal batteries with a specific energy higher than 300 Wh/kg, up to 500 Wh/kg, is still a significant challenge. Many groups are focusing on the fundamental breakthroughs in electrode materials and control the unnecessary side reactions in such new battery concepts. Solid-state Li batteries using solid electrolytes have recently received wide attention due to the inherent high safety and decent energy. There have been intense efforts to improve the bulk conductivity, interfacial charge transport and stability for the manufacturing of the solid-state cells. A very desirable strategy is to take advantage of the electrode materials that are commercially or nearly commercially available and introduce the least perturbation to the cell configuration and manufacturing process of the current technologies. Based on these considerations, two battery chemistries, high nickel content lithium nickel-manganese-cobalt oxide (high-Ni LiNi_xMn_yCo_zO₂ (NMC), Ni>60%), coupled with LMA, and Li-sulfur (S) chemistry, with the potential to achieve a specific energy higher than 500 Wh kg⁻¹ are selected for this Battery500 innovation center project.

Objectives

The Battery500 Consortium aims to develop commercially viable Li battery technologies with a cell level specific energy of 500 Wh/kg through innovative electrode and cell designs that enable the extraction of the maximum capacity from advanced electrode materials. In addition, the project aims to be able to achieve 1000 cycles for the developed technologies.

Approach

The Battery500 Consortium will utilize first class expertise and capabilities in battery research in the United States and develop an integrated and multidisciplinary approach to accelerate the development and deployment of advanced electrode materials in commercially viable high energy batteries. The LMA combined with compatible electrolyte systems and two types of cathodes—one high-Ni NMC and another S—will be studied and developed to reach high specific energy. The project focus is to design novel electrode and cell architectures to meet the 500 Wh/kg goal. The Consortium will work closely with R&D companies, battery/materials manufacturers and end-users/OEMs to ensure that the developed technologies are aligned with industry needs and can be transferred to production. The out-year goals for FY2019 include: (1) Synthesize high-nickel layered oxide cathodes (Ni content > 90%) with a capacity of > 210 mAh/g and test such materials using Battery500 protocols; (2) Implement Li protection approaches to demonstrate 20% cycle life improvement; (3) Fabricate and test a pouch cell capable of 350 Wh/kg and 250 cycles; and (4) Fabricate and test a pouch cell capable of 400 Wh/kg and 30 cycles. All of these goals have been successfully achieved in FY2019.

Results

Keystone project 1: Materials and interfaces

Li Metal Anode and High Ni Content Cathode

In FY 2019, the consortium focused on developing further understanding of the SEI layer to inform further conception of advanced electrolyte systems, electrode design, and interfacial engineering and to support efforts on improving current pouch cell performance to reach the project goal of 500 Wh/kg specific energy.

Characterization of SEI formation at different potentials: The consortium recognizes the critical dependence of battery performance on the nanostructure and electrochemical properties of the SEI. However, knowledge of how the SEI nanostructure forms and its impact on ionic transport is limited due to difficulties in direct probing. Using cryogenic-electron microscopy (cryo-EM) and electrochemical impedance spectroscopy (EIS), we tracked the voltage-dependent, stepwise evolution of the SEI formed on CuO nanowires in carbonate electrolytes. We find that the SEI in 1 M LiPF₆/EC-DEC electrolyte forms as a 3 nm thick amorphous layer at 1.0 V vs. Li/Li⁺ and grows in thickness with decreasing anode potential, to a thickness of 8 nm upon reaching 0.0 V vs Li/Li⁺ (Figure II.12.A.1, a-c). With the addition of 10% fluoroethylene carbonate (FEC) to the electrolyte, the SEI thickness evolves similarly (Figure II.12.A.1, d-f). However, the nanostructure of the layer changes in the presence of the FEC additive; with 10% FEC, an inverted multilayer structure forms, whereas with no additives, a mosaic-type structure is formed instead (Figure II.12.A.1c,f). By correlating the observed nanostructures with refined EIS measurements, we find that the mosaic nanostructure causes continuous increase in impedance during growth (Figure II.12.A.1g), while the inverted layered nanostructure formed with FEC improves SEI conductivity and maintains its interfacial impedance (Figure II.12.A.1h).

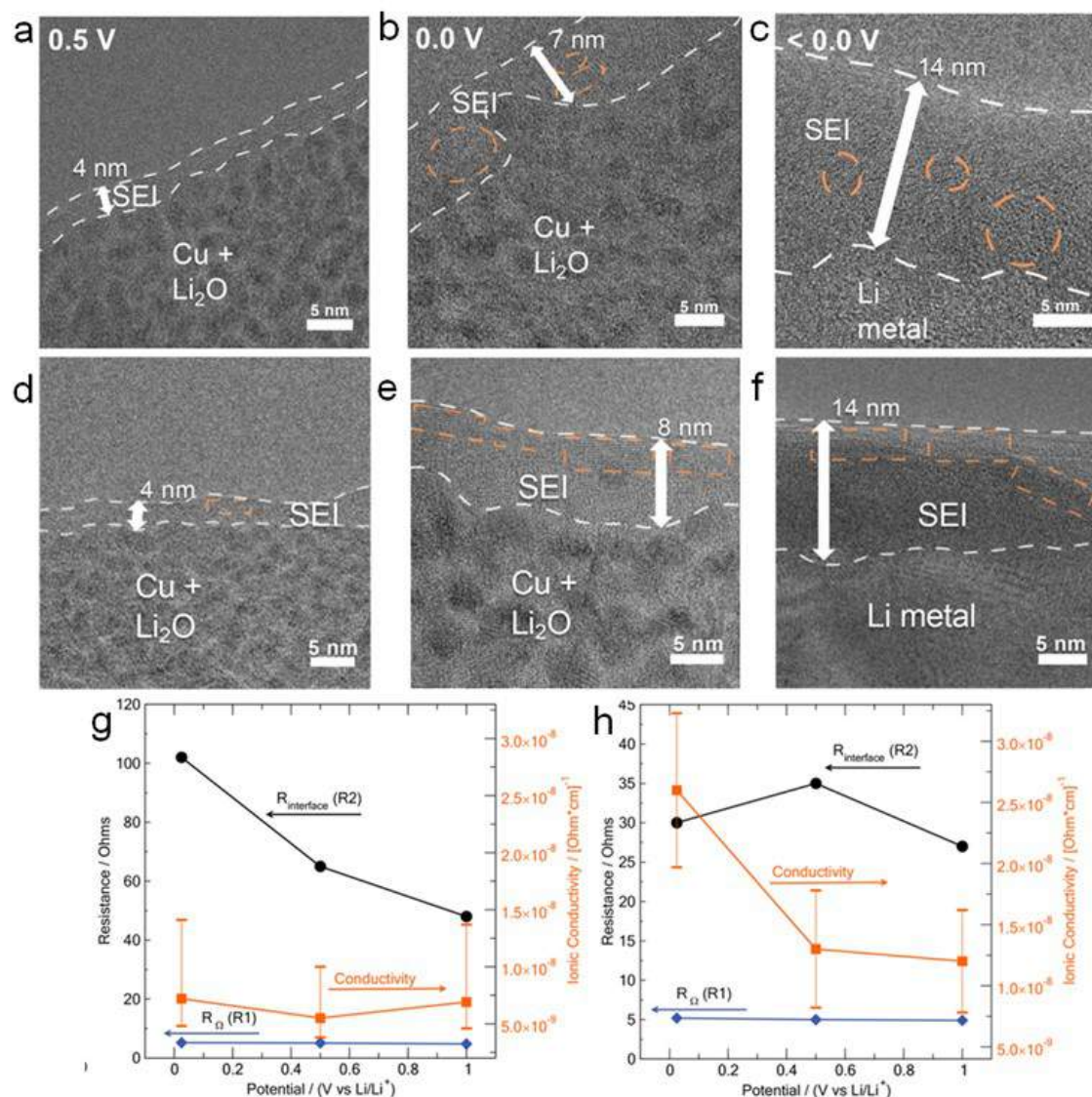


Figure II.12.A.1 (a-c) Cryo-EM images of SEI formed in 1M LiPF₆ in EC/DEC without FEC on CuO nanowires at electrode potentials of (a) 0.5 V, (b) 0.0 V, and (c) below 0.0 V vs. Li/Li⁺. (d-f) Cryo-EM images of SEI formed in 1M LiPF₆ in EC/DEC with 10% FEC on CuO nanowires at electrode potentials of (a) 0.5 V, (b) 0.0 V, and (c) below 0.0 V vs. Li/Li⁺. (g,h) Series resistance (R1), SEI ionic conductivity, and interfacial resistances (R2) extracted from EIS measurements for SEI formed in electrolyte (g) without and (h) with 10% FEC additive. Na_{0.7}[Cu_{0.2}Fe_{0.2}Mn_{0.6}]O₂ electrode collected during the first charge/discharge. All cycled between 2.5 and 4.2 V under a current rate of C/15

Keystone 1 project also has investigated an LMA on which dendrite-free Li can be plated/stripped rapidly at a relatively low impedance from either a liquid or a solid electrolyte. The design of electrochemical cell used in Operando XRD approaches and simulation approaches have been further improved. The origin of the 1st cycle capacity loss of high-Ni NMC and approaches to mitigate it are also proposed. An LMA on which dendrite-free Li can be plated/stripped rapidly at a relatively low impedance from either a liquid or a solid electrolyte has been demonstrated in coin cells by Goodenough's group at University of Texas at Austin (UTA). The anode is fabricated in a glove box by incorporating graphite fluoride (GF) in molten Li at 250°C. The Li bonds strongly with the GF to form a LiF layer, and the hydrophobic GF-LiF SEI protects the Li metal from reaction with moist air. Such formed GF-LiF-Li composite then can be removed from the glove box and assembled in a cell in ambient air. The GF-LiF composite is stable on contact with an organic liquid-carbonate electrolyte

and bonds with metallic-Li to form a dendrite-free GF-LiF-Li composite anode. The GF-LiF-Li composite anode can reduce fabrication costs, enable a fast charge, increase cycle life, and increase the energy density in safe rechargeable Li-metal batteries. The results of this study is shown in Figure II.12.A.2.

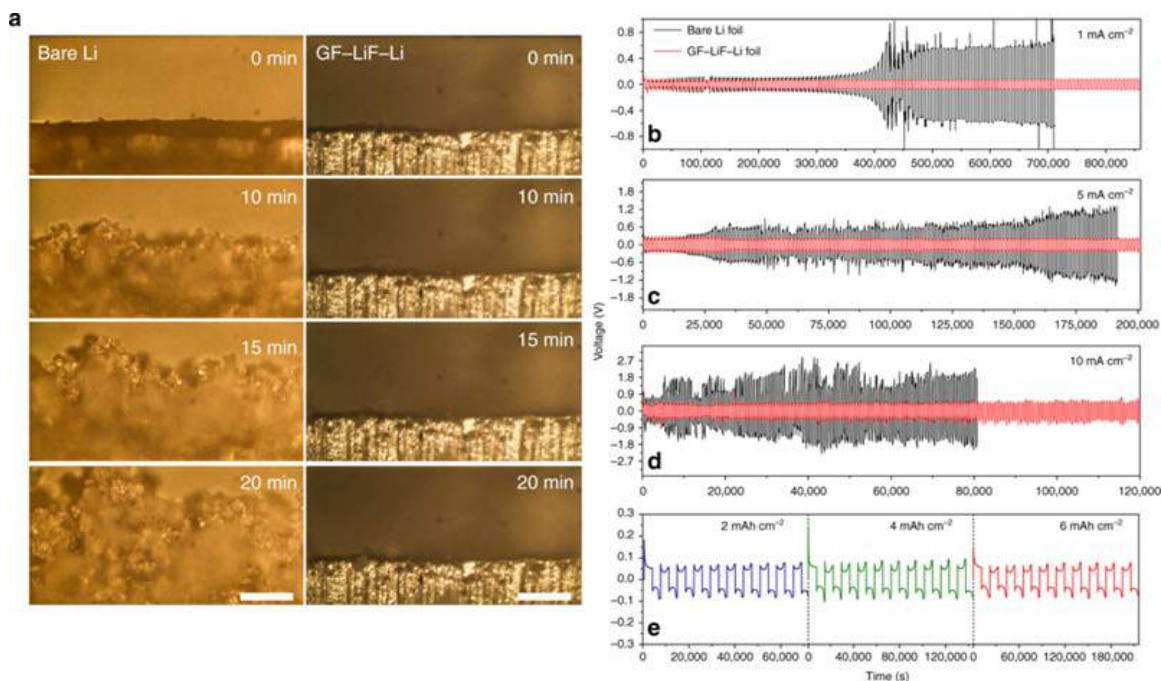


Figure II.12.A.2 In situ optical microscopy used to visualize the electrodeposition of Li and long-term cycling on symmetric cells. (a) The optical images of the bare Li (left column) and GF-LiF-Li (right column) interfaced with electrolyte after 0, 10, 15, and 20 minute Li plating at a current rate of 3 mA cm⁻². The scale bars are 200 μm. (b) to (d) Cycling curves in symmetric cells for bare Li foil (black) and GF-LiF-Li (red) at various current densities: (b) 1 mA cm⁻², (c) 5 mA cm⁻², and (d) 10 mA cm⁻². The specific capacity of the cell is 1 mAh cm⁻². (e) Cycling performance of symmetric GF-LiF-Li cells cycled at 2 mA cm⁻² rates for 2, 4, and 6 mAh cm⁻² capacity cells

To understand and quantify sources causing reduced CE during cycling, in operando XRD studies were carried out and the design of electrochemical cell used was modified by Toney's group (SLAC) to provide better control over electrochemical surface area. The sources identified include 'dead' Li, reduction of the electrolyte to form the SEI, and corrosion of the Li metal. A pouch cell holder with well-controlled pressure applied to the cell was designed to be compatible for X-ray measurements. Therefore, the methodology of X-ray measurements of Li metal can be extended to a realistic cell. The initial results in this controlled pressure cell indicate that the compression has a large influence on over potential and some of the 'dead' Li can be re-activated. The baseline 1 M LiPF₆ in EC/DMC electrolyte (LP30) with controlled amounts of HF additive is being studied in Li||Cu cells as a model system to investigate the mechanistic link between electrolyte composition, solid electrolyte interphase (SEI) properties, and Li metal morphology. Results have determined that there is an optimum concentration range (~100 ppm) of HF additive which induces columnar growth, while lower and higher concentrations yielding less ordered morphologies. Initial AFM studies have shown the promise of this technique in producing valuable operando data even for very low capacity cell to visualize the link between the initial SEI formation on Cu and initial Li metal nucleation. The voltage profiles of a Li||Cu symmetric cell has been simulated by Subramanian's group (UW) and compared with experimental data obtained by operando XRD as shown in Figure II.12.A.3a. The variation of overpotentials as a function of time is shown in Figure II.12.A.3b. The fitted polynomials predict a sharp drop in overpotential at the Cu electrode, in addition to a smaller increase at the Li electrode. The anodic signature is likely due to the transition between 'fast' and 'slow' pathways. At the Li electrode, this may be the exhaustion of electrochemically deposited Li and their associated faster kinetics, and gradual transition to stripping from the bulk. The sharp drop at the Cu electrode is more pronounced than at the Li electrode, suggesting a transition in Li deposition from growing of

the existing deposits to the formation of new nuclei, possibly due to passivation by SEI formation. This likely explains the sudden drop followed by a gradual rise in overpotential. The trends in electrode polarization track the variations in fitted exchange current density. The increase in polarization of both electrodes is due to the reduction in effective exchange current densities, establishing the consistency of the model.

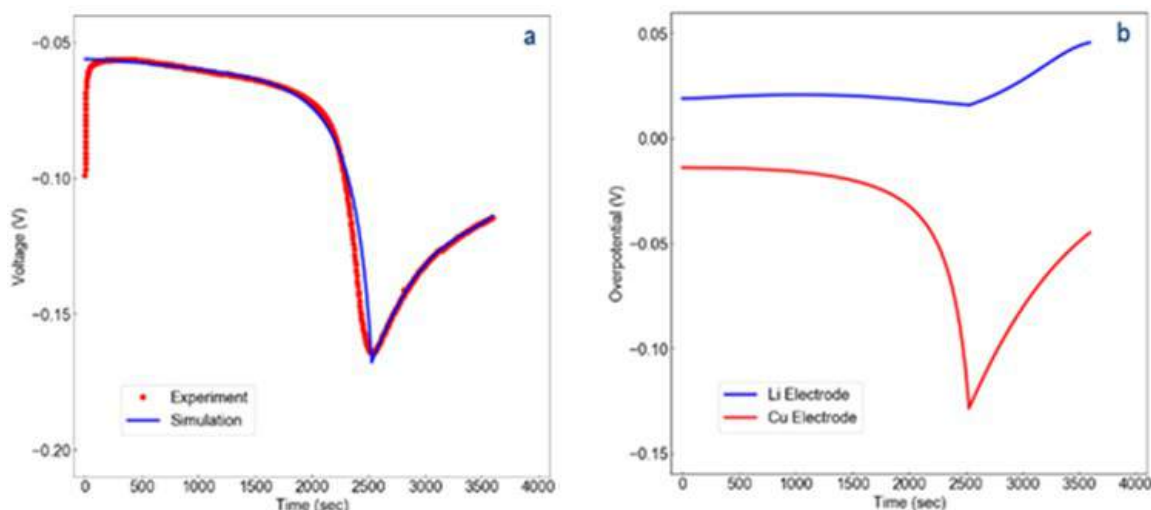


Figure II.12.A.3 (a) Comparison between model prediction and experimental voltage response for lithium symmetric cells. (b) Simulated electrode overpotentials as a function of time

The origin of the 1st cycle capacity loss of high-Ni NMC has been investigated by Whittingham's group (Binghamton). It was found that the slow in-diffusion of Li ions was the main contributor to the 1st cycle capacity loss for NMC811. As shown in Figure II.12.A.4a-b, increasing the temperature to 45°C significantly decreased this loss. This is indicative of a diffusion-limited reaction. This study also indicated that there are additional side-reactions for the highest charging voltaged cells, such as increased cycling hysteresis and discharge capacity loss. Elemental substitution in lattice and surface coatings might be mitigations to be used. In addition, it was also found that calendaring decreases the 1st cycle loss and conductive carbon types and amount used have no impact (electrode conductivity is not an issue). In addition, cathode active material loading also has no impact. In a separate effort, the effect of separator coating on the performance of Li||NMC811 cells was investigated by Yang's group (UW). As shown in Figure II.12.A.4c, excellent cycling stability of cells using $\text{Li}_{1.3}\text{Al}_{0.3}\text{Ti}_{1.7}(\text{PO}_4)_3$ (LATP)-coated PP separator has been demonstrated in a pouch cell prepared at PNNL. The cell using the LATP-coated PP separator has a reversible capacity of $\sim 200 \text{ mAh g}^{-1}$ and a CE of 99.5% at 0.33 C rate cycling, higher than those of the cells using the bare PP separator ($\sim 195 \text{ mAh g}^{-1}$ and 98.5%).

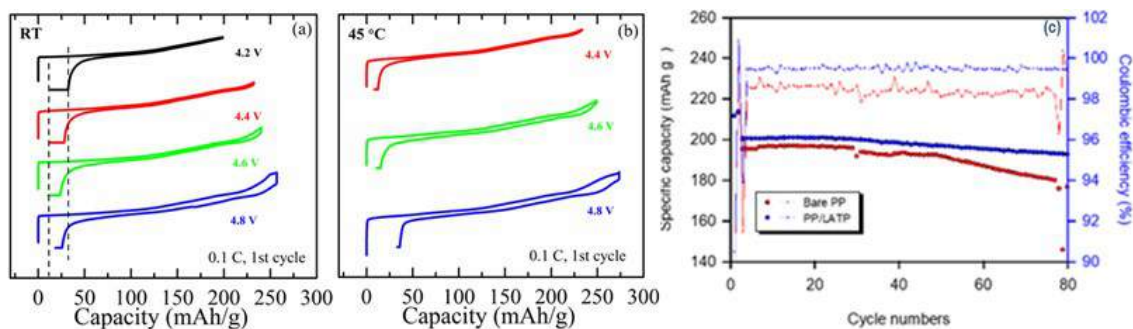


Figure II.12.A.4 Compare of 1st cycle of ECOPRO NMC811 vs. Li with cycled with different upper limit voltages (2.8 ~ 4.4, 4.6 and 4.8 V) at (a) room temperature (RT) and (b) 45 °C. (c) Cycling performance of the Li || NMC811 pouch cells using bare PP and LATP-coated PP separators

Most of the research performed to-date used commercial sources of 622 and 811 NMC. A goal of the Battery500 effort was to shift to an in-house source of material so that any coatings or lattice substitutions are known (vendors do not normally disclose this information). Figure II.12.A.5 shows that large batches, 220 g, of NMC811 can now be made that show the same behavior as small batches.

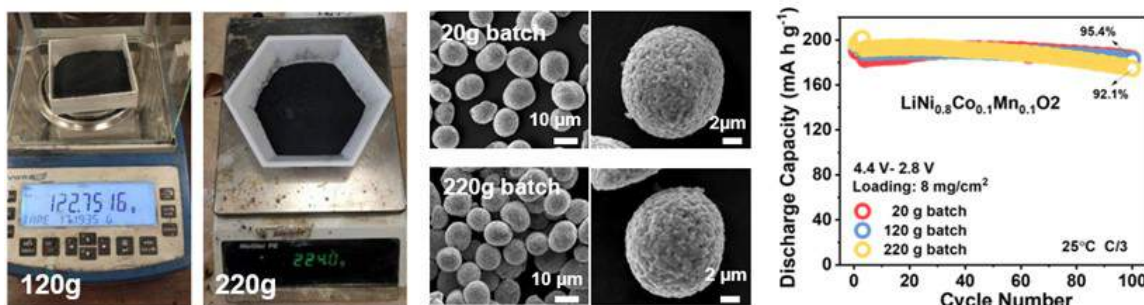


Figure II.12.A.5 Large scale synthesis of NMC811, showing (left) the material formed; (center) the uniformity of the “meatballs” formed, top is 20 g batch and bottom is 220 g batch; and (right) the consistency of discharge capacity and capacity retention between the different size batches

The use of thick electrodes demands that the team builds the capabilities to study their behavior. Many of these capabilities are now in place, and are described in Figure II.12.A.6.

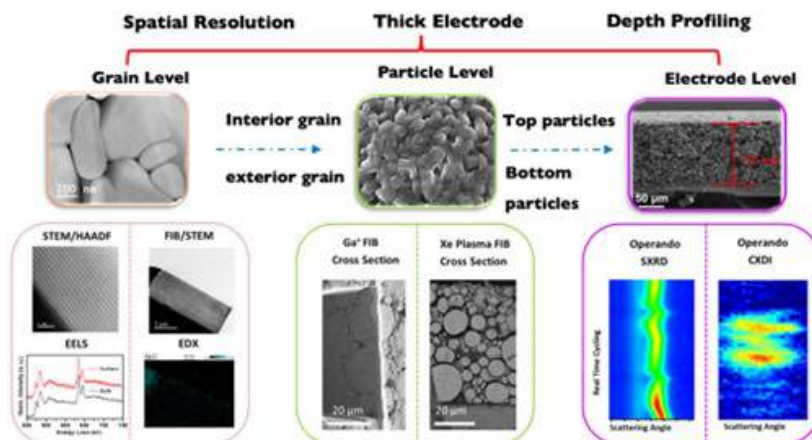


Figure II.12.A.6 Schematic of the tools Battery500 are employing to study thick electrodes

An anomalously large d-spacing peak at 7 Å is observed for NMC622 cathode material at highly charged state (> 4.5 V) (see Figure II.12.A.7a). This unique feature has never been reported before. Neutron pair distribution function (nPDF) analysis combined with Reverse Monte Carlo simulation reveal that significant structural heterogeneity is induced by deep charging (see Figure II.12.A.7b-c). This in turn leads to structural modulation in the transition metal layer, meaning that transition metal cations deviate from the ideal crystallographic 3b site (0, 0, 0.5) and the extent of deviation varies periodically. Such structural modulation is directly observed in high-resolution TEM study (Figure II.12.A.7d). It shows that such modulation gives rise to a large spacing at around 7 Å. Such structural feature is unique to the Ni-rich layered materials and only appears at highly charged state. This study provides structural insight into the potential problems of high-voltage charging, which is beneficial for higher energy-density cathode materials.

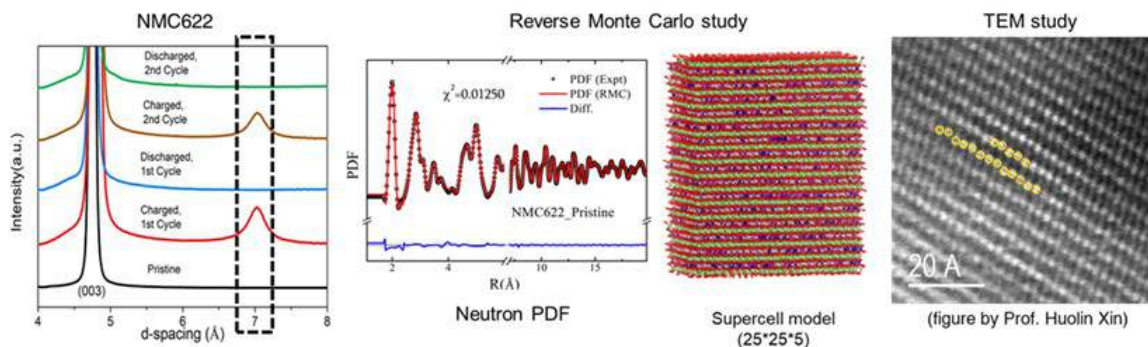


Figure II.12.A.7 Abnormal d-spacing observed in NMC622 cathode material at highly charged state (> 4.5 V). (a) Large d-spacing peak at 7 Å. (b) Neutron pair distribution function (nPDF) analysis with (c) supercell model. (d) TEM observation of the abnormal structure formed at highly charged state

New electrolytes

Keystone 1 developed ether-based liquid electrolytes for the Li||NMC811 cells that are enabling to attain long life and high energy density, determined the impact of coatings on the NMC811 electrode and developed the capability to make large batches of NMC811 in-house. An ether-based localized high concentration electrolyte (LHCE) has been developed that can greatly enhance the stability of a Ni-rich NMC811 cathode under 4.4 V and 4.5 V with an effective protection interphase enriched in LiF. Four electrolytes were investigated: conventional electrolyte 1 M LiPF₆ in EC-EMC (3:7 by wt.) with 2 wt.% of VC; dilute electrolyte (LiFSI-9DME); high concentration electrolyte (HCE, LiFSI-1.2DME), and LHCE (LiFSI-1.2DME-3TTE). Li||NMC811 cells with a medium high cathode areal loading of 1.5 mAh cm⁻², a thick Li anode and an excess electrolyte were first assembled and cycled under high voltages. Figure II.12.A.8a shows, for the Li||NMC811 cells charged to 4.4 V, the superior behavior of the LHCE over the conventional electrolyte. The synergistic effect between the LiFSI salt and the DME solvent plays an important role in stabilizing the highly reactive NMC811 cathode. The LHCE also shows the highest Coulombic efficiency. Even at a cutoff voltage of 4.5 V, the LHCE was superior, holding over 82% of the initial capacity after 250 cycles. XPS data further indicate that more stable SEI layer and CEI layer are formed on the LMA and NMC811 cathode in LHCE. The superior stability of Li anode and NMC811 cathode in this electrolyte enables dramatically improved cycling performances of Li||NMC811 batteries under highly challenging conditions, 1.1 times excess Li anode and an extremely limited electrolyte amount.

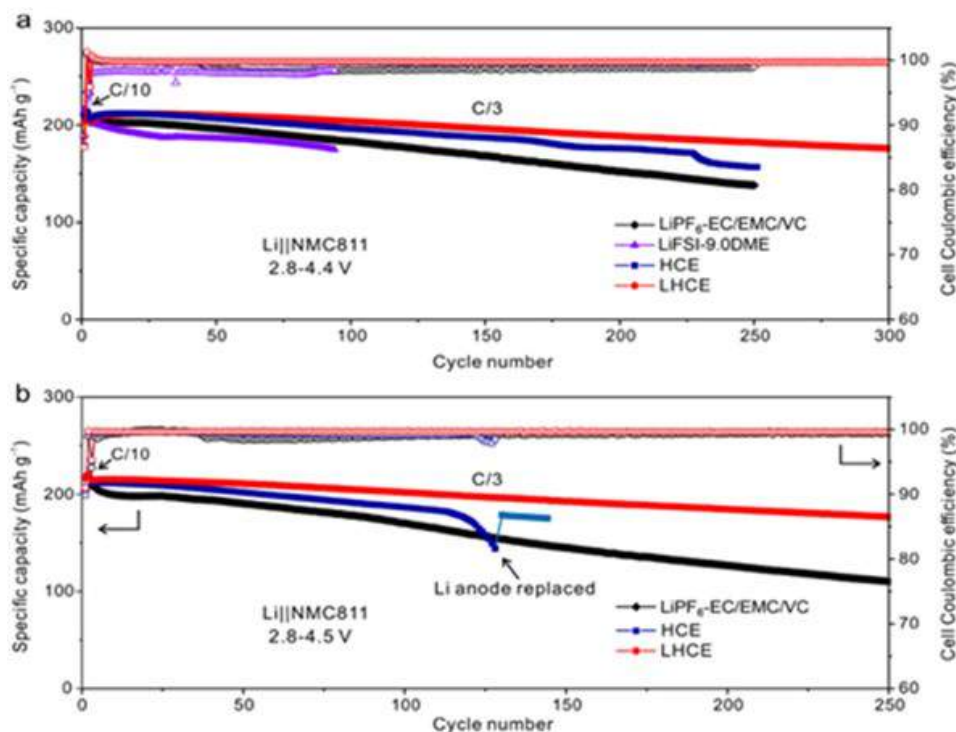


Figure II.12.A.8 Cycling performances of Li||NMC811 batteries in different electrolytes (conventional electrolyte (1 M LiPF₆ in EC-EMC (3:7 by wt.) with 2 wt.% of VC); dilute electrolyte (LiFSI-9DME); HCE (LiFSI-1.2DME), and LHCE (LiFSI-1.2DME-3TTE) under the charge cutoff voltage of 4.4 V (a) and 4.5 V (b), respectively. The electrolyte amount in each coin cell is 75 μ l

Another LHCE based on a class of fluorinated solvents, hydrofluoroorthoformate has also been developed, which leads to a CE of Li cycling up to 99.5%. One example of hydrofluoroorthoformate-based LHCEs is 1 M LiFSI in DME-TFEO (1:9 by wt. and 1.2:3 by mol., named as 1 M LiFSI/DME-TFEO). TFEO diluent has a much higher boiling point (145°C) than that of BTFE (63°C) diluent used in previous work and largely improves the stability of the electrolyte. The SEI formed during cycling in this electrolyte exhibits a monolithic feature by Cryo-TEM images (see Figure II.12.A.9a-1d), which is in sharp contrast to the widely-reported mosaic- or multilayer-type SEIs that are not homogeneous and could lead to uneven Li stripping/plating and fast Li and electrolyte depletion over cycling. The highly homogeneous SEI, not only prevents dendritic Li formation, but also minimizes Li loss and volumetric expansion. Furthermore, this electrolyte strongly suppresses the phase transformation of the NMC811 from layered structure to rock salt and stabilizes the structure. Tests of high-voltage Li||NMC811 cells show long-term cycling stability and high rate capability, as well as reduced safety concerns. The dashed lines in Figure II.12.A.9c shows a consistent SEI thickness of \sim 10 nm on the Li surface. Interestingly, the dominant components of this SEI layer are amorphous inorganic compounds. This SEI is proved to be not only uniform in horizontal coverage, but also in depth through the SEI from the surface to the bottom (close to Li metal). This electrolyte leads to a CE of up to 99.5% as measured in Li||Cu cells. This is one of the best values reported for Li metal anodes. It can also form a stable cathode electrolyte interface (CEI) layer at high voltage cathodes. Figure II.12.A.9e shows the Li||NMC811 cell using this electrolyte exhibits a capacity retention of 80% after 300 cycles and a high CE of 99.7% over cycling.

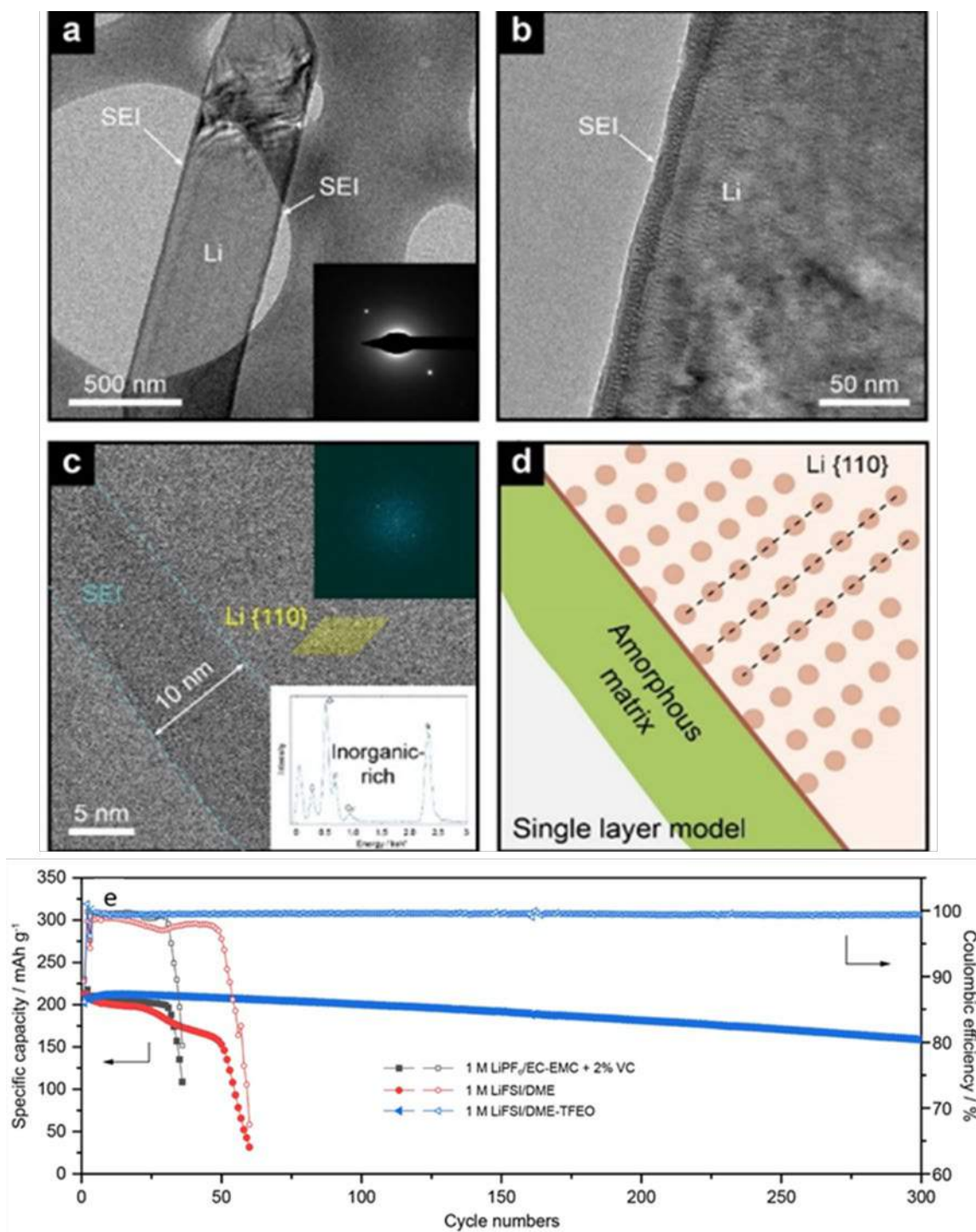


Figure II.12.A.9 SEI on Li metal anode. (a)–(c) Cryo-EM images of Li deposited on a TEM grid at different scales. Insert in (a) shows corresponding selected area electron diffraction (SAED) pattern. Insert in (c) shows corresponding reduced fast Fourier transform (FFT) (up) and the energy-dispersive X-ray spectroscopy (EDS) spectra (bottom) of the SEI layer, where the yellow lines show the lattice space of the crystalline Li. (d) Schematic of the observed single-layer SEI structure on deposited Li in the 1 M LiFSI/DME-TFEO electrolyte. (e) Li||NMC811 cell cycling performances of the investigated electrolytes, where the lines with full and hollow circles represent specific capacity and CE of the cells, respectively

As noted in previously quarterlies, high-Ni NMC is very reactive with both the environment and the electrolytes, and also has a large capacity loss, 10-15%, on the first cycle. In order to remediate this, a range of coatings and surface substitution studies were performed. As shown schematically to the right, these can be just a coating or a coating with penetration into the surface layers. Niobium and boron based coatings were studied. The results of cell performances are shown in Figure II.12.A.10. The use of a niobium oxide coating/substitution reduced the 1st cycle loss, whilst at the 1% level slightly increasing the capacity of the cell. The capacity retention and rate capability were also improved. The use of a boron coated NMC811, using LiDFOB (Li difluoro oxalato borate), resulted in higher rate capability and capacity retention. A boron based coating was also found to protect an ultra-high Ni NMC, $\text{LiNi}_{0.94}\text{Co}_{0.06}\text{O}_2$, against environmental degradation. Figure II.12.A.10 compares the superior rate capability of the boron coated NMC versus the uncoated NMC after storage. The capacity is also improved.

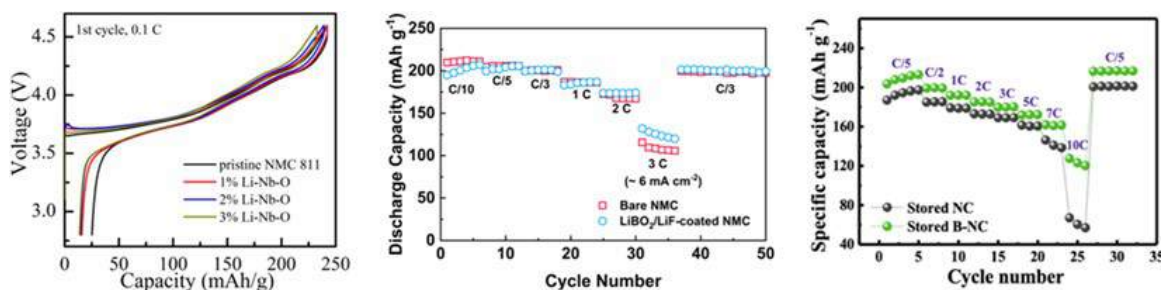


Figure II.12.A.10 (Left) 1st cycle behavior of NMC811 in voltage range 2.8-4.6 V; (middle) rate capability of NMC811 with a LiBO₂/LiF coating in voltage range 2.8-4.6 V, and (right) rate capability of LiNi_{0.94}Co_{0.06}O₂ after storage in voltage range 2.8-4.4 V

Li-S batteries

Redox mediator for Li₂S activation in Li-S cells: The initial oxidation of Li₂S in cathodes of Li-S batteries is characterized by an undesirable high overpotential barrier during charging. By engineering the functional groups and structure of small molecule quinones, we designed a redox mediator molecule to improve the efficiency and fast initial activation of Li₂S microparticles. By tailoring the quinone derivative properties, such as oxidation potential, solubility, and electrochemical stability, initial charging of Li₂S electrodes occurs below 2.5 V at a 0.5C rate with a subsequent discharge capacity as high as 1300 mAh/g (Figure II.12.A.11). Furthermore, we find that deposition of dead, disconnected Li₂S is effectively prevented with the addition of

the redox mediator, avoiding the primary cause of increasing polarization and decreasing reversible capacity of Li-S batteries upon cycling.

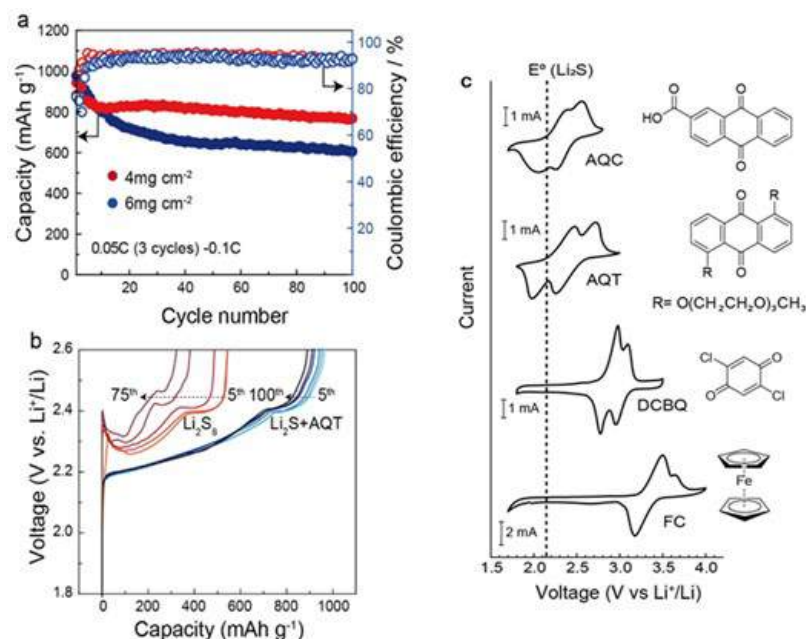


Figure II.12.A.11 a) Cycle performance of Li₂S electrodes with high sulfur mass loading. (b) Voltage profiles of Li₂S charging with and without quinone redox mediator. (c) Comparison of redox potentials of different redox mediator candidates

Keystone project 2: Electrode architectures

Architecture design of thick cathodes

The goal of the Keystone 2 is to design, model, fabricate and characterize the effects of electrode architecture on electrode and cell performance in support of reaching the project of 500 Wh/kg cell specific energy.

Included in this Keystone are architecture design of thick cathodes (UCSD), Li metal electrode architectures (PNNL and Stanford), inorganic (UT-Austin) and polymer (Stanford) electrolytes, and electrode performance modeling (UW).

Groups of Meng and Liu at UCSD carefully examined the electrochemical performances of thick electrodes, which are necessary to achieve a cell level energy density of 400 Wh/kg, by studying the influence of active mass loading and porosity for both NMC622 and NMC811 as shown in Figure II.12.A.12. To further improve the rate performance of the NMC811 cathode, the Liu's Group recently performed chemical modification of the carbon additive. While the improvement under C/3 rate is minor vs the baseline, at a C/2 rate, the benefit becomes more pronounced.

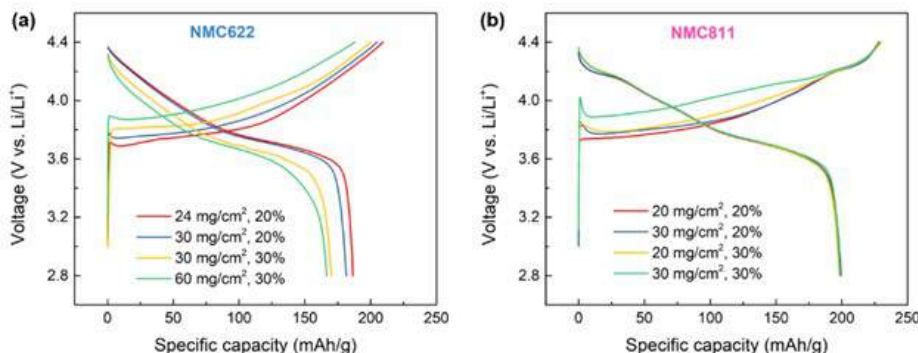


Figure II.12.A.12 First cycle voltage profiles of (a) NMC622 and (b) NMC811 thick electrodes with various active mass loading and porosity, at C/10, 2.8 – 4.4 V. Electrodes are provided by Maxwell Technologies

In order to statistically study the thick electrode evolution during cycling and its influence on electrochemical performance, Xe Plasma FIB (PFIB) was applied to NMC811 thick electrode for large volume serial section tomography. Emerging Xe+ PFIB-SEM technology led by Thermo Fisher Scientific offers materials removal rates at least 60 times greater than conventional Ga+ FIB which has limited imaging volumes. As shown in Figure II.12.A.13a, the pristine NMC811 thick electrode with 30 mg/cm² loading and 20% porosity was PFIB cut at voltage of 30 kV and current density of 60 nA. The cutting width was 130 microns with rocking mill at +/-3 degree. Slices were cut every 25 nm and imaging was recorded every 4th slice, so the slice thickness in the image stack is 100 nm. Secondary particles cracking is observed even from the pristine state (see Figure II.12.A.13b). Segmentation of some phases is straightforward due to the difference in brightness ranges, other phases appear in identical intensities in the PFIB-SEM images are differentiated based on their relative location. As shown in Figure II.12.A.13c, the PFIB-SEM images are segmented into four separate phases: vacuum, bulks of particles, cracks, and additives. By volume fraction, these four phases occupy 10.64%, 60.32%, 5.35%, and 23.69% of the total reconstructed volume, respectively. In addition, EDX mapping of the NMC811 thick electrode on one serial section shows uniform distribution of active materials, PVDF binder, and conductive carbon (Figure II.12.A.13 d). This method of large volume tomography based on PFIB-SEM enables the monitoring of crack formation before and after cycling, which is being investigated.

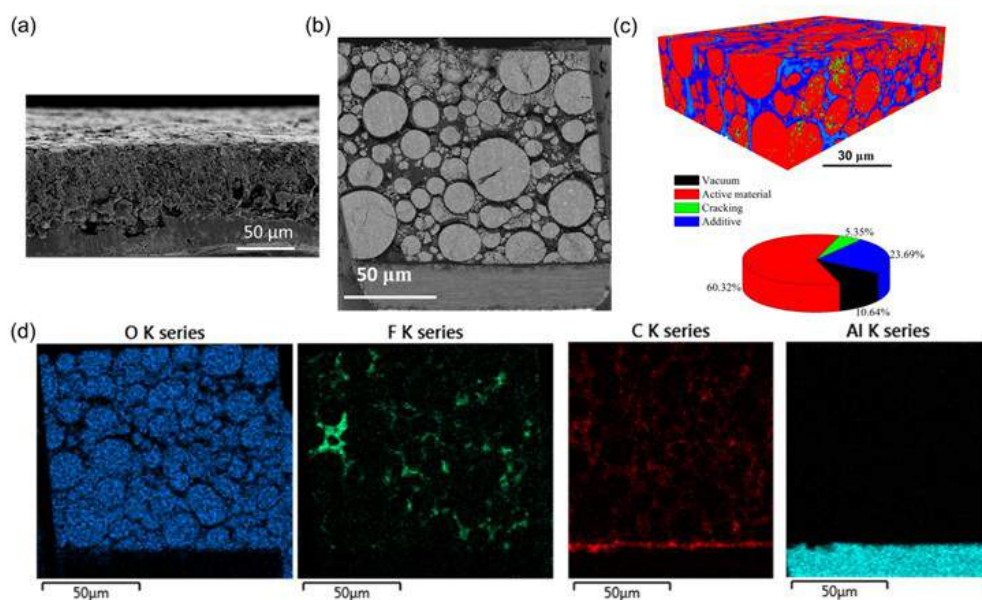


Figure II.12.A.13 (a) SEM cross-section image of pristine NMC811 thick electrode, (b) PFIB large volume serial section of the thick electrode, (c) 3D reconstructed volume and phase segmentation calculated using the PFIB-SEM data, and (d) EDX mapping of NMC811 thick electrode on one serial section obtained from PFIB

Lithium metal electrode architecture

Work at Stanford on the Li electrode architecture is the use of pyrolyzed eggplant (EP) to serve as a Li metal host to take advantage of its aligned channels. Further, the host is coated with LiF (EP-LiF) to improve the interfacial stability in an ether electrolyte. Figure II.12.A.14 illustrates the fabrication process of EP-LiF. A fresh EP was first frozen and dried to get rid of all the water in the structure without shrinkage. Then the dry EP was cut into thin pieces and punched into round shape. Then the freeze-dried EP was carbonized under 1000°C and Ar atmosphere for 4 h to form carbonized EP. The channel-like structure could be maintained after carbonization. This structure is also schematically illustrated in Figure II.12.A.14. Energy-dispersive X-ray spectroscopy (EDS) and X-ray photoelectron spectroscopy (XPS) results confirm that the carbonized EP is composed essentially of carbon framework.

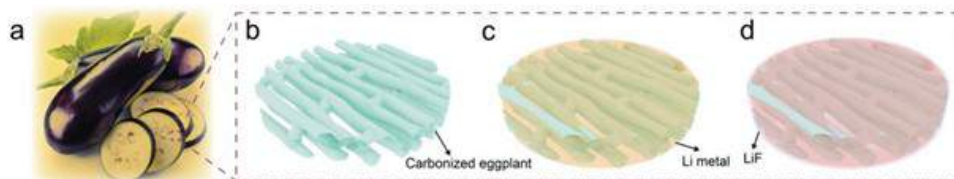


Figure II.12.A.14 (a) Photo of an eggplant and its cross-section morphology. (b) Schematic illustration for a carbonized EP with interconnected channel-like structure. (c) Carbonized EP after Li metal melt infusion. (d) Carbonized EP-Li metal composite anode further coated with a layer of LiF thin film NMC811 thick electrode on one serial section obtained from PFIB

Li metal morphology after cycling in a symmetric cell setup was observed under SEM. Figure II.12.A.15a shows the top view image of an EP-LiF electrode after one symmetric cell cycle with current density of 1 mA cm⁻² and areal capacity of 1 mAh cm⁻², while Figure II.12.A.15 c shows that of a Li foil. Dendritic growth could be clearly observed for bare Li foil. Li metal filaments with diameter from 200 nm to 2 μm tangled together, increasing Li metal exposure area to the electrolyte and aggravating Li metal capacity decay. On the contrary, EP-LiF was able to achieve a rather homogeneous Li metal deposition morphology. The grain boundary on the EP-LiF anode surface confirmed that the observed Li metal was indeed freshly plated with high homogeneity instead of the initial infused Li metal. Li metal plating morphology after longer cycling was also characterized. Figure II.12.A.15 b shows the top view image of an EP-LiF anode after 10 symmetric cell cycles under 1 mA cm⁻² and 1 mAh cm⁻² areal capacity while Figure II.12.A.15 d shows that of a Li foil. Li metal dendrites on bare Li foil became thinner. This is because the continuous cycling created much dead Li and also SEI shells from previous cycling. The thinner Li metal dendrites not only exacerbated fresh Li metal consumption, but also would increase the possibility of short circuit and severe battery thermal runaway. As for EP-LiF, although the surface was roughened slightly, the plated Li metal still maintained an intact piece without much increased surface area. After 100 cycles under 1 mA cm⁻² and 1 mAh cm⁻², EP-LiF was still able to maintain a rather uniform morphology.

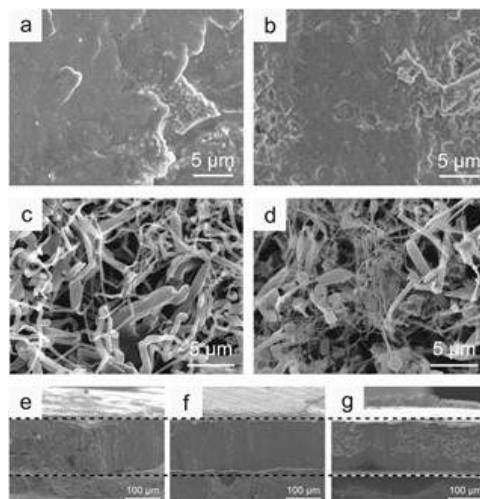


Figure II.12.A.15 Top view SEM image of EP-LiF anode after (a) 1 cycle and (b) 10 cycles under 1 mA cm^{-2} and 1 mAh cm^{-2} in a symmetric cell. Top view SEM image of Li foil anode after (c) 1 cycle and (d) 10 cycles under 1 mA cm^{-2} and 1 mAh cm^{-2} in a symmetric cell. Cross section of (e) a pristine EP-LiF electrode, (f) an EP-LiF electrode after stripping $\approx 10 \text{ mAh cm}^{-2}$ of capacity and (g) an EP-LiF electrode after stripping $\approx 10 \text{ mAh cm}^{-2}$ of capacity and plate it back anode further coated with a layer of LiF thin film NMC811 thick electrode on one serial section obtained from PFIB

Work at the Meng Group at UCSD has focused on the development of a methodology to quantify how much of the Li is lost to reactions with electrolyte to form the solid electrolyte interface and how much is lost as metallic Li to electrical isolation. The method is based on analyzing hydrogen gas production after reacting the electrode with water; only isolated Li metal will produce hydrogen. The method is applied to correlate the origin of inactive Li with the CE in Li||Cu cells. Two representative electrolytes, the high-concentration electrolyte (HCE, $4.6 \text{ m LiFSI} + 2.3 \text{ m LiTFSI}$ in DME) and commercial carbonate electrolyte (CCE, 1 M LiPF_6 in EC/EMC), were compared at three stripping rates (0.5 , 2.5 and 5.0 mA cm^{-2} , all plating was done at 0.5 mA cm^{-2} for 1 mAh cm^{-2}). Figure II.12.A.16 a and b show their average CE and representative voltage profiles during the first cycle. The small error bars indicate good consistency among the cells. As expected, the HCE exhibits higher CE than the CCE. The total amount of inactive Li is equal to the capacity loss between the plating and stripping processes, displaying a linear relationship with CE in Figure II.12.A.16d. The content of the metallic Li^0 was directly measured by the hydrogen evolution method. As summarized in Figure II.12.A.16c, in the HCE, the capacity loss from inactive metallic Li^0 is about 60% at different stripping rates. This is consistent with the similar CE at various stripping rates. Whereas in the CCE, it contributes over 90%, especially at high stripping rate. Surprisingly, the amount of unreacted metallic Li^0 exhibits a linear relationship with loss of CE, as shown in Figure II.12.A.16e, which is almost independent from the testing conditions. This implies that the CE loss is governed by the formation of inactive metallic Li^0 . Thus, the SEI Li^+ amount (Figure II.12.A.16f) deducted from above remains low and relatively constant under various stripping rates. Based on these analyses, we identify the unreacted metallic Li^0 , rather than the (electro)chemically formed Li^+ in SEI, as the dominating cause for the inactive Li and capacity loss in LMBs, clearing the long-term misconception in the field that the low CE is caused by the continuous repairing of SEI fracture which consumes both electrolyte and active Li.

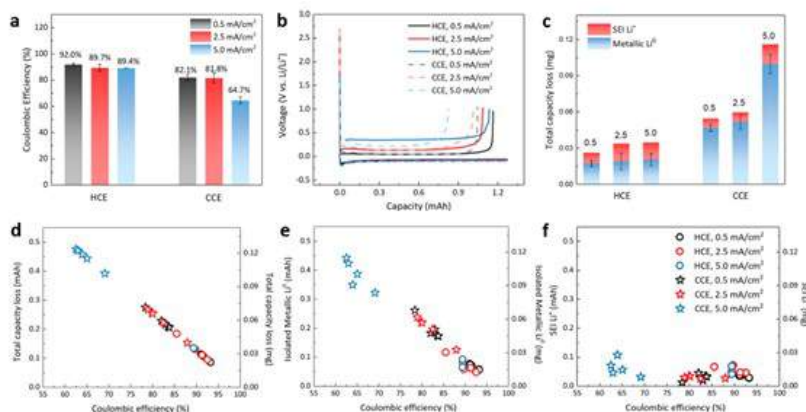


Figure II.12.A.16 Quantitative differentiation of inactive Li by the hydrogen evolution method. (a) Average CE of Li||Cu cells under different testing conditions. (b) Representative voltage profiles of Li||Cu cells under different testing conditions in the first cycle. (c) Summarized quantitative contribution of capacity loss from the SEI Li⁺ and metallic Li⁰. (d) Total capacity loss as a function of CE. (e) Inactive metallic Li amount measured by the TGC method as a function of CE. (f) Calculated SEI Li⁺ amount as a function of CE

The analysis results obtained at UCSD thus argue for approaches to effectively connect Li metal in order to prevent the formation of isolated metallic Li. In this regard, PNNL developed a mesoporous carbon framework that is highly lithiophilic which encourages the filling of the mesopores with Li metal thus promoting self-wetting and self-smoothing. As a result, a Li metal battery with a NMC811 cathode showed excellent cycle life even in lean electrolyte and low N/P ratio conditions (Figure II.12.A.17).

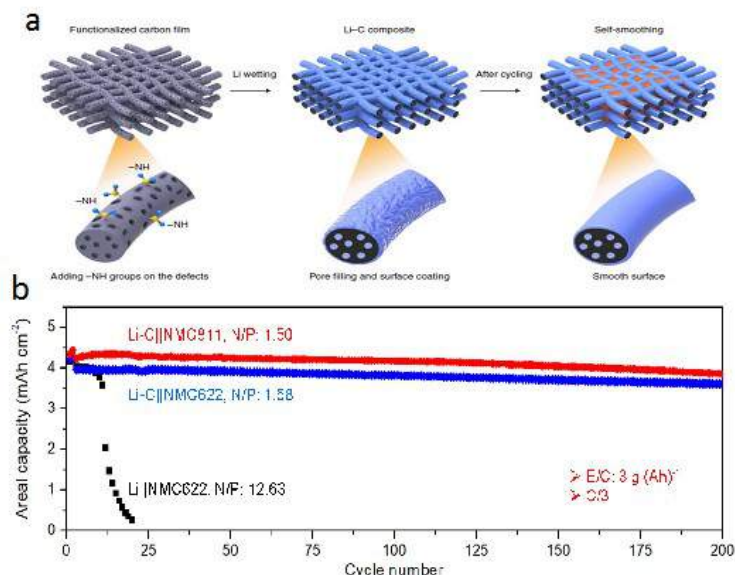


Figure II.12.A.17 (a) Schematic of the structure of a 3D mesoporous carbon host that encourages Li wetting and pore filling. (b) Capacity retention of Li||NMC cells with cycling. NMC622 is LiNi_{0.6}Co_{0.2}Mn_{0.2}O₂, NMC811 is LiNi_{0.8}Co_{0.1}Mn_{0.1}O₂, E/C is electrolyte/capacity ratio

In a collaboration between Stanford and PNNL, another 3D host employed a silicon pillared graphene oxide, or SirGO. Silicon makes the host more lithiophilic and prevents the collapse of the GO structure upon Li metal stripping. This design is proven to be effective in ensuring Li metal incorporation into the host rather than on the outer surface. Upon removal of Li, the thickness of the electrode is maintained, demonstrating the effectiveness of design Figure II.12.A.18).

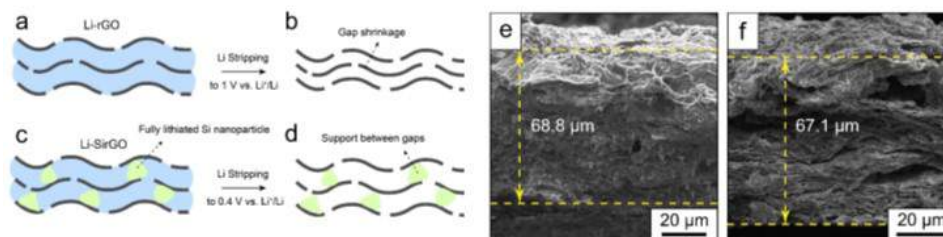


Figure II.12.A.18 A schematic comparison of the structure of Li-rGO (reduced graphene oxide) and Li-SirGO where the presence of silicon between the GO layers helps to maintain the gaps (a-d); SEM images of electrode cross-section demonstrating that the Li-SirGO structure maintains its overall thickness after removal of 1 mAh/cm² of lithium

Meng's group at UCSD utilized Cryo-EM techniques to study different Li morphologies under different conditions and their correlations to Li anode failure. Cryogenic focused ion beam-scanning electron microscopy (Cryo-FIB-SEM) was used to explore the microstructures of inactive Li. High concentration ether-based electrolyte (HCE) and commercial carbonate electrolyte (CCE) samples under different stripping rates were chosen for the morphological study. They found that as the stripping rate increases, the morphology of inactive Li in HCE evolves from uniform sheets to local clusters (Figure II.12.A.19a-c) with a thickness increased from 500 nm to 2 μm Figure II.12.A.19d-f). For the CCE, the deposited whisker-like Li becomes thinner after stripping (Figure II.12.A.19g-i), and turns thicker in cross-section along with the increased stripping rates (Figure II.12.A.19j-l), corresponding to the increased loss of CE at high rates. It is worth noting that these residues exhibit poor connection to the current collector, indicating the loss of electronic conductive pathways.

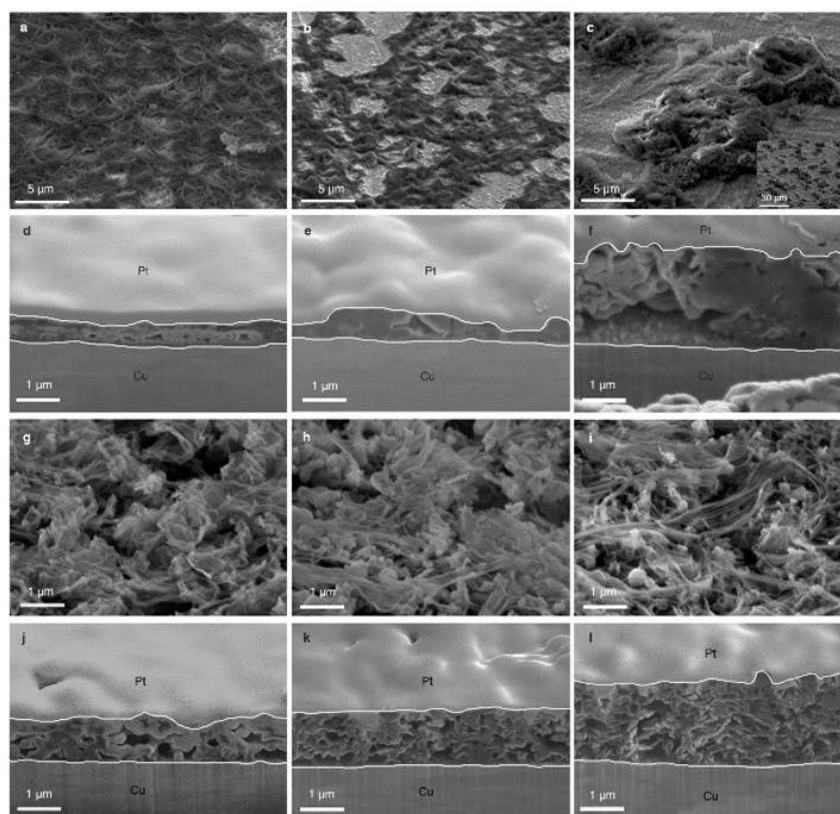


Figure II.12.A.19 Microstructures of inactive Li generated in HCE (a-f) and CCE (g-l) imaged by Cryo-FIB-SEM. (a-c) and (g-i) are top view of the inactive Li at 52° tilted stage. (d-f) and (j-l) are cross-sections obtained by cryo-FIB. Each column represents a stripping rate. (a, d, g and j) are at 0.5 mA cm⁻². (b, e, h and k) are at 2.5 mA cm⁻². (c, f, i and l) are at 5.0 mA cm⁻²

They further used Cryo-TEM to investigate the nanostructure of the inactive Li in HCE and CCE after stripping at 0.5 mA cm^{-2} . Sheet-like inactive Li appears in the HCE sample (Figure II.12.A.20a), while inactive Li in the CCE remains a whisker-like morphology (Figure II.12.A.20e). Based on the (110) lattice plane distance of bcc Li, the region that contains crystalline metallic Li^0 is highlighted in green in the high-resolution TEM (HRTEM) images for both electrolytes (Figure II.12.A.20b, f). Compared with the inactive Li obtained from CCE, a much smaller area of metallic Li^0 component is observed in HCE. This indicates that most deposited metallic Li^0 in HCE has been successfully stripped, corresponding to the high CE. Whisker-like unreacted metallic Li^0 as large as $\sim 80 \text{ nm}$ in length remains in the CCE sample and is well isolated by the surrounding SEI. The SEI components were determined by matching the lattice spacing in HRTEM images with their FFT patterns (Figure II.12.A.20c, g). Li_2CO_3 and Li_2O constitute the major part of SEI, which also contains LiF as well as other amorphous organic species for both electrolytes. The above observations from Cryo-TEM are summarized in the schematic plot (Figure II.12.A.20d, h), which reveal the form of inactive Li with two different morphologies at nanoscale.

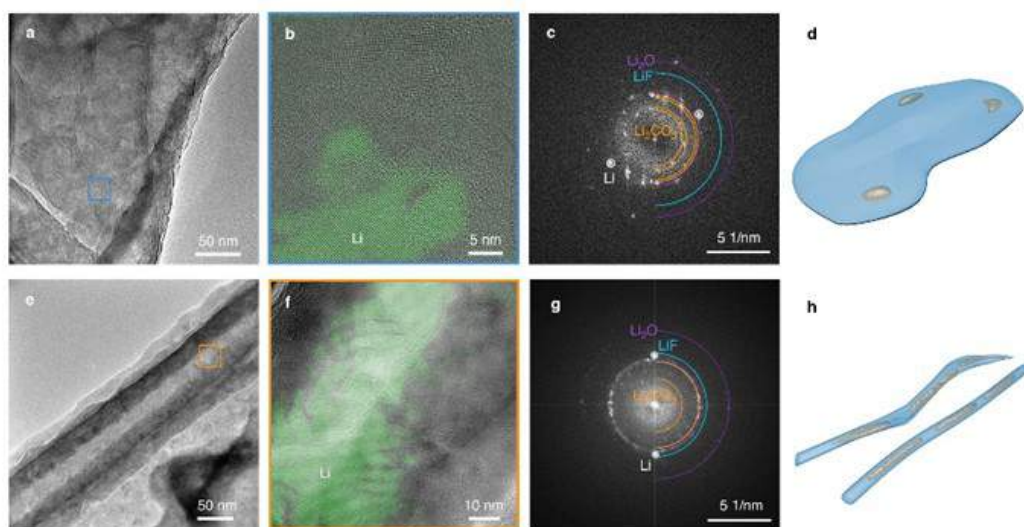


Figure II.12.A.20 Nanostructures of inactive Li generated in HCE (a-d) and CCE (e-h) by Cryo-TEM. a, e, inactive Li morphology at low magnifications for both electrolytes. b, f, HRTEM shows a different amount of metallic Li^0 is wrapped by SEI in the two types of electrolytes. The highlighted metallic Li^0 region in green is identified through FFT-mask filtering-inverse FFT-image overlay process. c, g, FFT patterns of corresponding HRTEM indicate the SEI component which contains crystalline Li_2CO_3 , Li_2O , and LiF . d, h, Schematic of inactive Li nanostructure in both electrolytes. Small area of metallic Li^0 is embedded in a sheet-like SEI layer for HCE, while a large bulk of metallic Li^0 is isolated in whisker-like SEI layer in CCE

A new artificial SEI layer based on a polymeric network with both self-healability and high Li^+ single-ion conductivity has been developed in Bao's group at Stanford (Figure II.12.A.21). An ideal artificial SEI must have several key properties. First, flowability and self-healability are desirable so that the SEI can adapt to huge volume changes during Li stripping/deposition and prevent dead Li from detaching. Second, high Li^+ single-ion conductivity in the artificial SEI is beneficial to reduce 'hot spots', increase critical Li deposit size, and stabilize the Li metal anode. Last but not the least, the SEI needs to be both chemically and electrochemically inert in presence of liquid electrolyte (insoluble and unreactive) as well as Li metal to minimize deleterious side reactions. To date, several attempts have been made to design artificial SEIs with some of the desirable properties such as viscoelasticity, self-healability, or high ion conductivity. However, few are able to combine all of these properties. Additionally, the majority of the reported Li-metal artificial SEIs are only compatible with ether-based electrolytes, making them impractical when paired with high-voltage, high-energy-density Ni-rich NMC cathodes that are used in today's commercial Li-ion batteries. In this newly developed polymeric network, tetrahedral $\text{Al}(\text{OR})_4^-$ anions are introduced as a novel dynamic motif with freely transporting Li^+ counter ions that are directly introduced during the reaction. With this self-healable single-ion-conductive network (Figure II.12.A.21a, SSN) as the Li-metal artificial SEI, over 400 stable

plating/stripping cycles have been obtained in Li||Cu cells using a commercial carbonate-based electrolyte. More importantly, >85% capacity retention for over 160 cycles in a Li||NMC full battery was achieved. To our knowledge, this is the first time that self-healability and single-ion conductivity are incorporated into one chemical structure to create an effective artificial SEI for Li metal batteries.

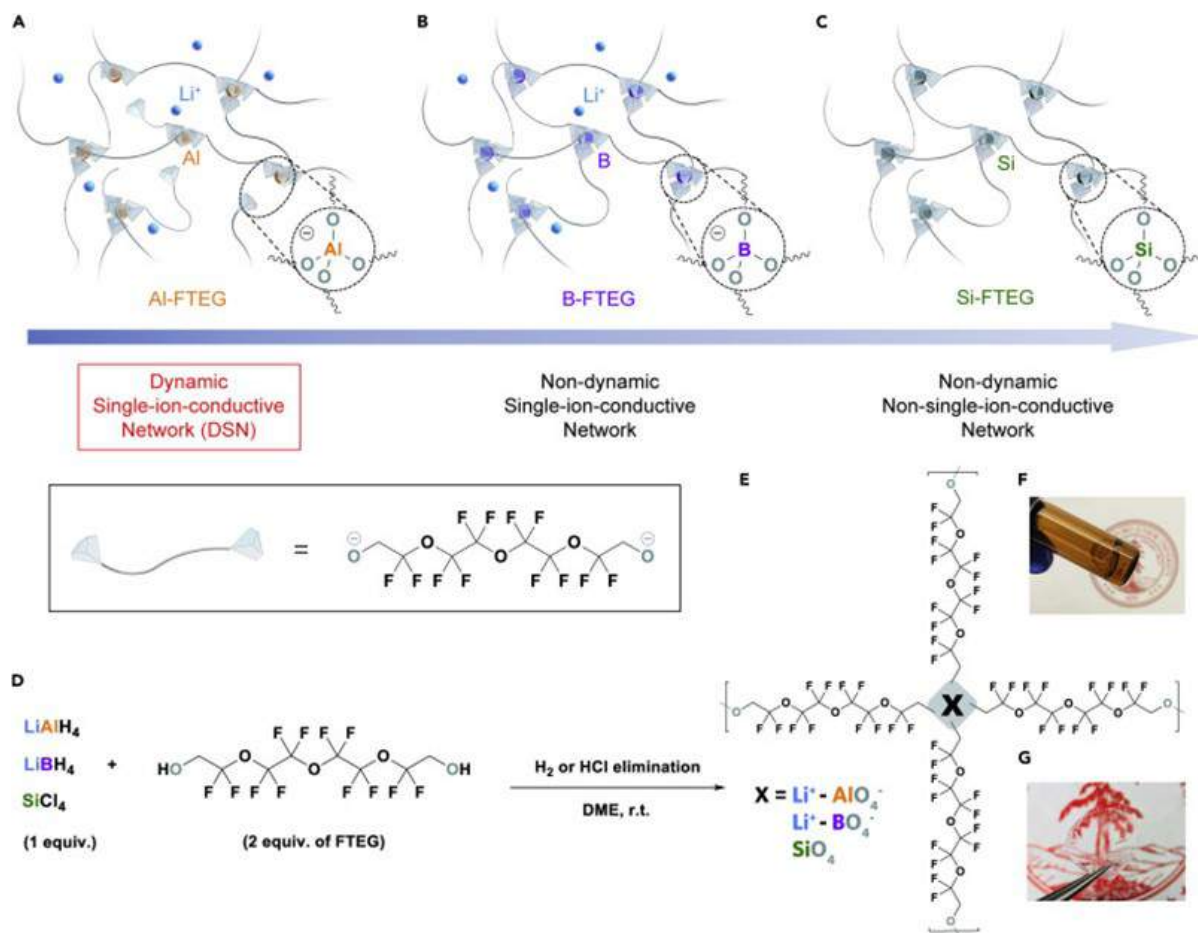


Figure II.12.A.21 Molecular design and chemical structures of SSN and derivatives. (a-c) Conceptual sketch of SSN (a), B-SSN (b), and Si-SSN (c). Blue spheres: Li⁺; orange spheres: Al; purple spheres: B; olive spheres: Si; tetrahedra: anion centers; grey chains: soft ligands. (d) The reaction to synthesize SSN. (e) Detailed chemical structure of SSN. (f, g) Photos of an as-synthesized viscous SSN/DME solution (f) and a free-standing SSN film (g)

Keystone project 3: Cell fabrication, testing and diagnosis

In FY2019 Keystone project 3 worked to refine understanding on safety for Li metal cells including both Li handling and evaluation of testing protocols. Other areas of advancement were on diagnostics and characterization of performance fade for Li metal systems including characterization of cells undergoing both calendar and cycle life evaluation.

Characterization of cells and electrodes is necessary to understand the reasons for performance fade and highlight key challenges in achieving high cycle life. A key outcome when performing post-testing evaluation of a cell which started testing in FY17, which had a specific energy of 310 Wh/kg and completed 200 cycles was that low levels of state-of-charge variation in the NMC622 cathode were observed (Figure II.12.A.22). Despite less than 3% variation in distribution across the electrode as determined using ex situ XRD lateral mapping analysis, specific areas on the electrode were not fully lithiated during discharge of the cell near the end of life. Based on the electrochemical cycling data and other post-test analysis, this variation is likely due to distinct and evolving heterogeneity in the cell during cycling which results in poor transport and hence low

capacity (0.15 Ah at C/3) at moderate rates, but which enables relatively high retention at low rates (1.0 Ah at C/20) at the end of cycling (Figure II.12.A.22A).

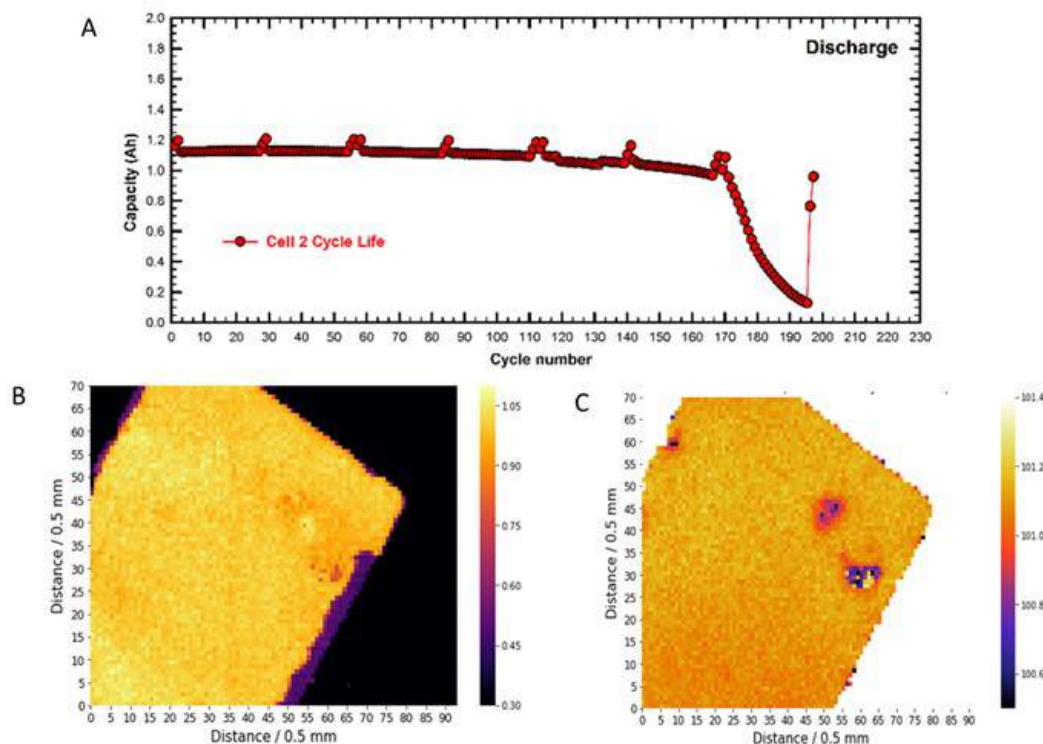


Figure II.12.A.22 A) Cycling data for a Li/NMC622 cell developed in FY17. The cell achieved 200 cycles. B) Variation in NMC loading content from ex-situ XRD analysis following the completion of testing C) SOC in the NMC cathode from ex-situ XRD analysis

Evaluation continued for cells developed to meet the FY2019 milestone which have a specific energy of 400 Wh/kg continue to cycle and have over 30 cycles with greater than 85% capacity retention (<15% fade). Calendar life evaluation of Li||NMC cells has shown that over the course of more than a year that less than 7% fade is observed. The FY2019 milestones for Keystone 3 are related to refining the understanding on safety and disseminating best practices to the Battery500 consortium. Along those lines a compilation of practices and concerns was presented to the Battery500 team and a draft report was prepared. Both focused on understanding safety thresholds and means to minimize risk to research personnel spanning from the receipt of Li to post-test activities. It included safety both with respect to use of Li and to testing of larger 1 Ah+ cells. One key consideration which was highlighted was understanding the state of the Li metal after disassembly as the potential for shorting the cell (even if in an Ar-filled glovebox) is enhanced due to loose Li as shown in Figure II.12.A.23. As seen in the post-test image key areas where Li is disconnected from the Cu current collector provide opportunity to short the cell and hence added caution is needed during characterization to minimize the risk to researchers.

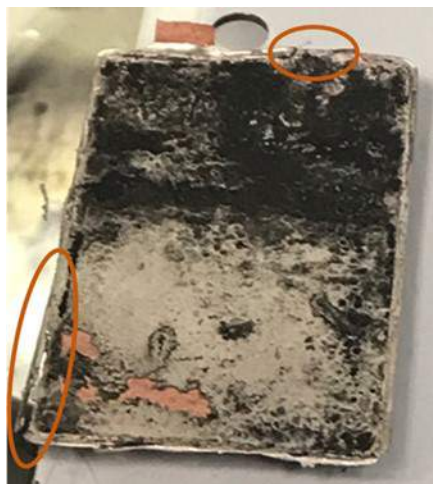


Figure II.12.A.23 Post-test Li metal electrode at the completion of 200+ cycles. Circles indicate areas of disconnected Li after cycling

Through collaborations between Xiao's group (PNNL) and Yang's group (BNL), polysulfide redistribution during the pouch cell cycling was visually studied and it was discovered that even on the same cathode layer the electrochemical reaction is highly inhomogeneous. The work highlighted that not only were various polysulfide species generated, the relative concentration of these polysulfide species was different across the surface of the positive electrode (Figure II.12.A.24). It seems that the center of S cathode inherits the original microstructures more than the marginal parts, suggesting the reaction is not complete in the center. This spatial variation in reaction front is likely related to the wetting of the thick sulfur cathodes used in this cell to achieve high specific energy. Achieving uniform wetting is a key challenge which will need to be addressed at the pouch cell level for future work. To more uniformly enhancing electrode wetting, future work will reduce the sulfur loading and cell parasitic weight simultaneously so the cell-level energy will not be sacrificed. Further improvement of sulfur utilization will benefit the balance between high-energy and extended cycling of Li-S batteries.

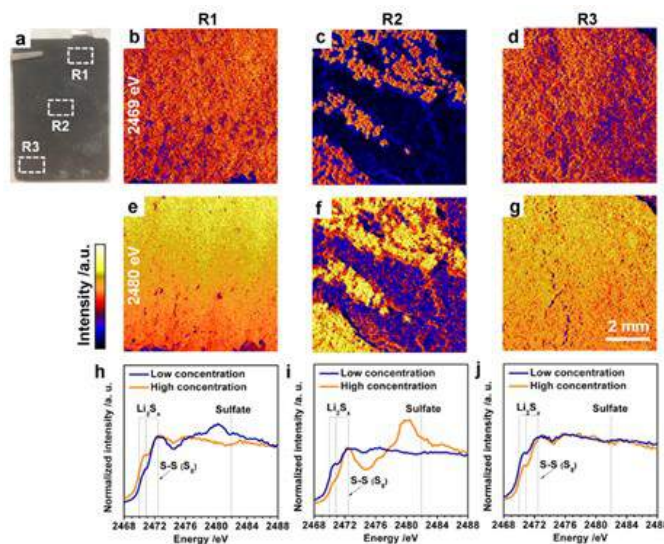


Figure II.12.A.24 Uneven reaction was identified by XRF (b ~ g) and XAS spectra (h ~ i) at different locations of sulfur cathodes harvested from the cycled Li-S pouch cell. (a) Photo image of the cycled cathode with labeled locations for XRF and XAS analysis: R1(b, e, and h), R2 (c, f, and i) and R3 (d, g, and j). b, c, and d are XRF collected at 2469 eV. e, f and g are XRF collected at 2480 eV. h, i, and j are XAS collected in the b, c, and d, respectively within a energy range of 2468-2488 eV. Yellow and blue lines in the XAS spectra were collected at the yellow and blue dots of corresponding XRF image at 2469 eV

The other research focus area was on the role of pressuring during cycling for Li||NMC811 cells. It was found that in a quasi-fixed gap setting that the pressure during cycling changed significantly across each cycle and that the cycle life for cells was significantly increased as elevated pressure was applied to the exterior of the cell. When comparing the difference between 1 psi of external pressure and 21 psi of external pressure it was found that the cycle life increased by slightly more than 3-fold. In addition to increasing the cycle life of the cells the application of higher pressure resulted in a more linear increase and decrease in pressure and in less cycle-to-cycle variation in pressure as shown in Figure II.12.A.25. The uniformity in pressure and the linearity of the increase is likely due to greater utilization of Li metal deposited during charging of the cell. Activities are currently underway to understand evolution over longer cycling and to further increase the external pressure to understand limitations on increasing cycle life.

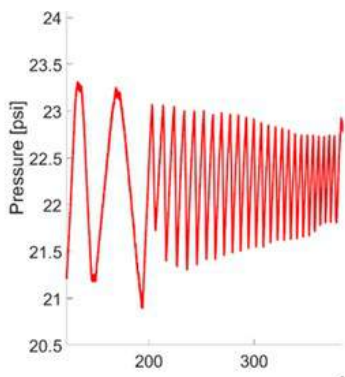


Figure II.12.A.25 Pressure evolution over the first 28 cycles for a cell with 21 psi of external pressure applied. Similar, but more pronounced variation was observed at lower pressures which also exhibited decreased cycle life

Understanding cycle life and ways to life extension is a key concern for enabling high-energy, rechargeable Li metal batteries and it was what Keystone project 3 has been focused on for the 3rd quarter of FY2019. Using different sets and designs for Li||NMC cells the Battery500 team has been focusing on ways to extend cycle life using multiple routes and cell characterization approaches. The current result of these activities has been the development of a 2.5 Ah cell with 350 Wh/kg capable of 250 cycles with less than 20% fade (Figure II.12.A.26). The Keystone project 3 team is currently in the process of validating this performance and in developing an early understanding of the state of calendar life for this round of cells. Initial work on previous designs has shown over one year of calendar life with low capacity fade. As part of the validation activities and prior assessment of calendar and cycle life key differences in performance are being evaluated.

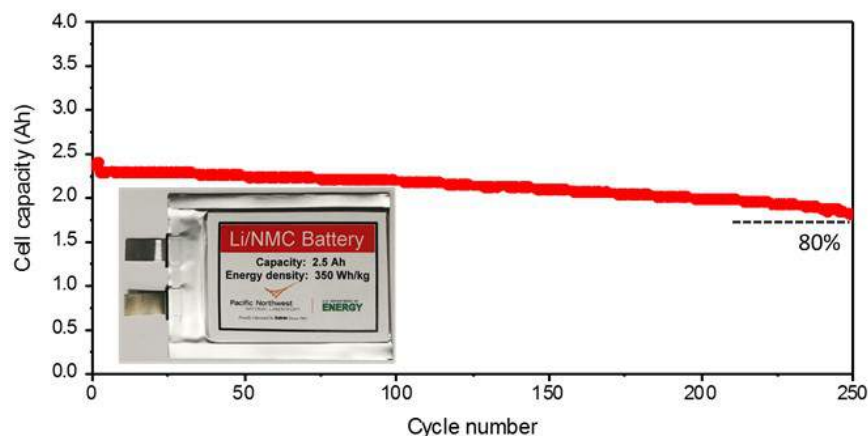


Figure II.12.A.26 Cycle life data for a 2.5 Ah Li||NMC cell. Cycling was at a C/10 charge and a C/3 discharge

One area that has helped facilitate the long cycle life in full pouch cells has been a refined understanding of pressure and pressure conditions for fixturing cells. A key finding from earlier in FY19 which was applied to the 2.5 Ah pouch cell was the uniform use of pressure and tracking pressure evolution as cycling advanced. In response to the realization that as activities related to cell design and use conditions has evolved, the team has developed additional standard testing protocols including single layer pouch cell procedures. The combination of coin cell and single layer pouch cell procedures provide a joint means to better understand both materials processes as well as means to more directly understand charging and mechanical differences in cell design. The standard procedures for single layer pouch cells include prescribed cathode loading, electrolyte volume similar to the standard coin cell procedures. The single layer pouch procedures also include means for fixturing cells and additional safety related information. As shown in Figure II.12.A.27 the team is now starting to more discretely evaluate pressure uniformity as a function of the materials being used in the cell and how the associated design impacts electrochemical performance. On the left side differential capacity for cells at three different pressures shows a distinct shift in response and utilization as cycling progresses. On the right computational assessment of the impact of surface roughness on local current density is shown. For the assessment, characterization of the electrode surface roughness was used to import into the model. As shown in Figure II.12.A.27 increasing the roughness of the electrode leads to current density variation which subsequently increases the localized pressure distribution in the cell during cycling.

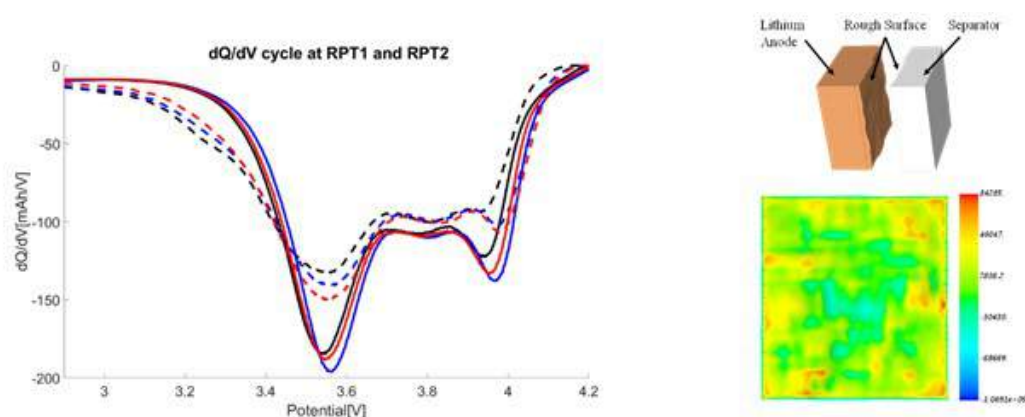


Figure II.12.A.27 Left) Differential capacity analysis on the impact of three different pressure regimes for cycling of a single layer Li||NMC pouch cell. Right) Model framework and predicted, local current density for real electrode during early cycling

Keystone 3 efforts have been focusing on increasing stability of NMC811 to stabilize NMC811 at high voltages but extend cycle life. Recent work at U. Washington showed that with proper coating such as LiF/LiBO₂-coated NMC811 cathode, higher stability can be obtained at 4.6 V cutoff to retain similar capacity as the pristine cathode (Figure II.12.A.28). The better stability of the coated NMC811 cathode also demonstrated in the differential scanning calorimetry (DSC) experiment with smaller heat release and higher onset temperature than the pristine cathode. The conductivity measurements on the cathode materials indicated that the coating reduced the conduction on the NMC811 surface to minimize electrolyte decomposition. The coating does not increase the polarization of the cell, thus a high specific energy could be achieved with longer cycle life.

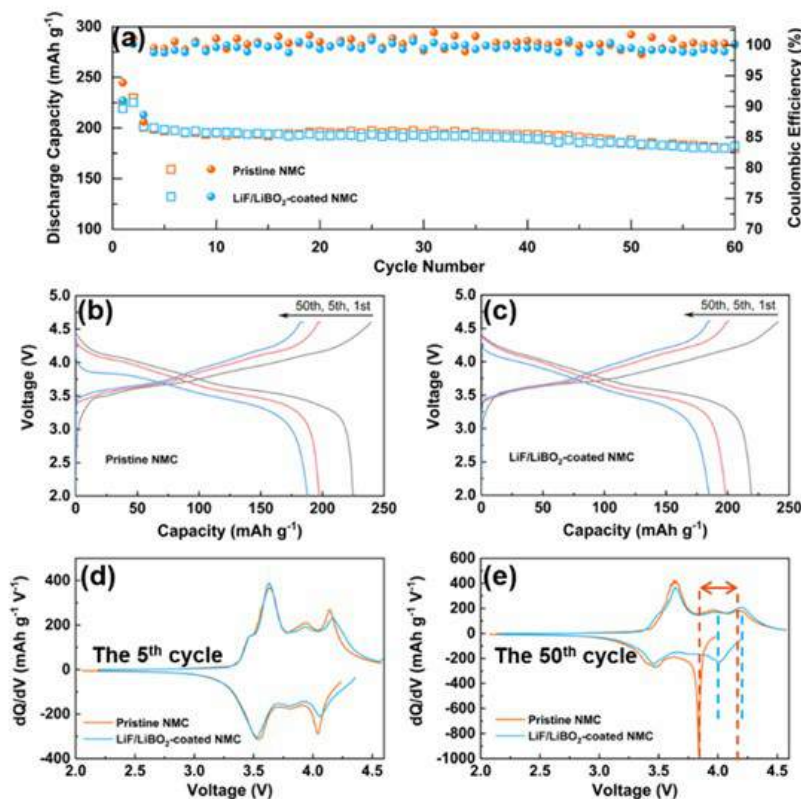


Figure II.12.A.28 (a) Cycling performance of the pristine and LiF/LiBO₂-coated NMC811 cathodes. Selected charge–discharge curves of (b) the pristine and (c) LiF/LiBO₂-coated NMC811 cathodes. The dQ/dV plot of the pristine and LiF/LiBO₂-coated NMC811 thick electrodes at the (d) 5th and (e) 50th cycles. The tests were conducted using the Battery500 testing protocol at 20 °C within the voltage range of 2.8–4.4 V at C/3. There was a 4-h rest between charge and discharge regimes during cycle aging. The formation was performed at C/10 for two cycles with 1-h rest between charging and discharging

Deeper understanding of the capacity fade and its attributes on cell failure was also progressed well. A novel electrochemical analytical diagnosis (eCAD) technique was developed at INL to dissect capacity fade attributes into a number of identifiable failure modes (e.g., loss of active materials (LAM), artifact by IR-drop, and under-utilization of the active materials in NMC622 (UAM)), and their effect and impact on cell capacity (e.g., $Q_{F_{LAM}}$, $Q_{F_{IR}}$ and $Q_{F_{UAM}}$) can now be monitored and quantified by eCAD and using NMC622 cathode as an internal reference. Currently, this eCAD approach has been validated with a build of 14 coin cells using Li | standard electrolyte | NMC622 configuration. Figure II.12.A.29 shows the contributions of the capacity fade attributes to the loss of active materials ($Q_{F_{LAM}}$), IR-drop ($Q_{F_{IR}}$), and under-utilization of the active materials in NMC622 ($Q_{F_{UAM}}$) in the charge retention of an early failed cell during C/3 cycle aging at 25 °C. The eCAD technical also allowed us to estimate the amount of loss of Li inventory ($Q_{F_{LLI}}$), as shown in Figure II.12.A.29a. The revelation of the significant impact of LLI on charge retention, the inability of measuring $Q_{F_{LLI}}$ directly by testing, and the ability to estimate such factor in quantitative details are a critical breakthrough in diagnosis. Figure II.12.A.29b exhibits the SEM micrographs of the Li metal electrode morphology obtained from the aged cells at the end of the test. The significant amount of dead Li on the failed cell indicates the eCAD analysis indeed revealed the correspondence of the impact from dead Li on LLI. Protect Li from loss in cycle aging is key to long cycle life. The application of eCAD to other cell configurations and associated stress factors (e.g., pressure on the pouch cells) is under way and will be reported in subsequent reports.

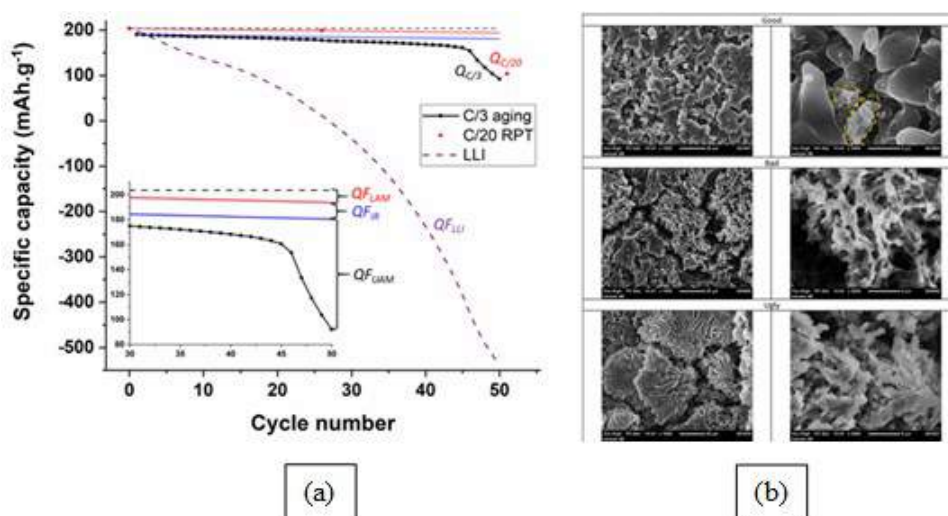


Figure II.12.A.29 The electrochemical analytical diagnosis (eCAD) technique revealed (a) the attributes to the capacity fade of an early failed Li | standard electrolyte | NMC622 coin cell and the significant impact from the loss of Li inventory. (b) The SEM micrographs showed the impact of the dead Li on the Li inventory that failed the cell

Conclusions

This project has been successfully completed in FY2019. All milestones have been completed. The publication records are very good: 2 patent applications were filed by the Battery500 team member institutions. 55 peer reviewed papers were published and more than 111 invited presentations were delivered in FY2019. Extensive collaboration within the consortium and with seedling teams, as well as other national Labs and U.S. universities has been well established and very fruitful.

Key Publications

Patents and patent applications:

1. S. Wang, H. Pan, J. Xiao, J. Liu, and J. Yang, "Battery Separator with Lithium Ion Conductor Coating", International Patent Application No. PCT/US2019/037988, June 19, 2019. (filed by University of Washington)
2. Jie Xiao, Chaojiang Niu, Dianying Liu and Jun Liu, "Cell Design and Fabrication of Li Metal Pouch Cells with cell-level energy of 300 Wh/kg or higher", Patent application filed by PNNL in August 2019. PNNL IPID: 31510-E.

Publications

1. Xiaoyun Yu, Guangmin Zhou, Yi Cui, "Mitigation of shuttle effect in Li-S battery using a self-assembled ultrathin molybdenum disulfide interlayer", *ACS applied materials & interfaces*, DOI: 10.1021/acsami.8b19354, Publication Date (Web): December 27, 2018.
2. W. Huang, D. T. Boyle, Y. Li, Y. Li, A. Pei, H. Chen, and Y. Cui, "Nanostructural and Electrochemical Evolution of the Solid-Electrolyte Interphase on CuO Nanowires Revealed by Cryogenic-Electron Microscopy and Impedance Spectroscopy" *ACS Nano*, vol. 13, no. 28, pp. 737-744, Publication Date (Web): December 27, 2018.
3. Y. Li, Y. Li, and Y. Cui, "Catalyst: How Cryo-EM Shapes the Development of Next-Generation Batteries" *Chem*, vol. 4, no. 10, pp. 2250-2252, Publication Date (Web): October 11, 2018.
4. Liang Yin, Gerard Mattei, Zhuo Li, Jianming Zheng, Wengao Zhao, Fredrick Omenya, Chengcheng Fang, Wangda Li, Jianyu Li, Qiang Xie, Ji-Guang Zhang, M. Whittingham, Y. Shirley Meng, Arumugam Manthiram, and Peter G. Khalifah, "Extending the limits of powder diffraction analysis:

- diffraction parameter space, occupancy defects, and atomic form factors”, *Rev. Sci. Instru.*, 2018 Sep;89(9):093002, DOI: 10.1063/1.5044555
5. Sol Yun, Seong-Min Bak, Sanghyeon Kim, Jeong Seok Yeon, Min Gyu Kim, Xiao-Qing Yang, Paul V. Braun*, Ho Seok Park*, “Rational Design of Hierarchically Open-Porous Spherical Hybrid Architectures for Lithium-Ion Batteries”, *Adv. Energy Mater.*, DOI: 10.1002/aenm.201802816, Publication Date: December 20, 2018
 6. Yejing Li, Xuefeng Wang, Yurui Gao, Qinghua Zhang, Guoqiang Tan, Qingyu Kong, Seongmin Bak, Gang Lu, Xiao-Qing Yang, Lin Gu, Jun Lu, Khalil Amine, Zhaoxiang Wang*, and Liquan Chen, “Native Vacancy Enhanced Oxygen Redox Reversibility and Structural Robustness”, *Adv. Energy Mater.*, DOI: 10.1002/aenm.201803087, Publication Date: December 05, 2018
 7. J. Li, W. Li, Y. You, and A. Manthiram, “Extending the Service Life of High-Ni Layered Oxides by Tuning the Electrode-Electrolyte Interphase” *Advanced Energy Materials*, vol. 8, no. 29, pp. 1801957, Publication Date (Web): October 15, 2018.
 8. H. Xu, Y. Li, A. Zhou, N. Wu, S. Xin, Z. Li, and J. B. Goodenough, “Li₃N-Modified Garnet Electrolyte for All-Solid-State Lithium Metal Batteries Operated at 40°C” *Nano letters*, vol 18, no. 11, pp. 7414–7418, Publication Date (Web): October 23, 2018.
 9. H. Lee, H.-S. Lim, X. Ren, L. Yu, M.H. Engelhard, K. S. Han, J. Lee, H.-T. Kim, J. Xiao, J. Liu, W. Xu*, J. Zhang*. “Detrimental Effects of Chemical Crossover from the Lithium Anode to Cathode in Rechargeable Lithium Metal Batteries.” *ACS Energy Letters*, 2018, 3(12), 2921-2930. DOI:10.1021/acseenergylett.8b01819. Publication Date (Web): November 9, 2018
 10. H. Lee, S. Chen, X. Ren, A. Martinez, V. Shutthanandan, V. Murugesan, K.S. Han, Q. Li, J. Liu, W. Xu*, J. Zhang*. “Electrode Edge Effects and the Failure Mechanism of Lithium-Metal Batteries.” *ChemSusChem*, 2018, 11(21), 3821-3828. DOI: 10.1002/cssc.201801445 Publication Date: October 11, 2018.
 11. Shrikant C. Nagpure, Tanvir R. Tanim, Eric J. Dufek, Vilayanur V. Viswanathan, Alasdair J. Crawford, Sean M. Wood, Jie Xiao, Charles C. Dickerson, and Boryann Liaw “Impacts of lean electrolyte on cycle life for rechargeable Li metal batteries” *Journal of Power Sources* 407, (2018): 53-62 Publication Date (Web) October. 23, 2018.
 12. J. Liu*, Z. Bao, Y. Cui, E. J. Dufek, J. B. Goodenough, P. Khalifah, Q. Li, B. Y. Liaw, P. Liu, A. Manthiram, Y. S. Meng, V. R. Subramanian, M. F. Toney, V. V. Viswanathan, M. S. Whittingham, J. Xiao, W. Xu, J. Yang, X.-Q. Yang, and J.-G. Zhang, “Pathways for practical high-energy long cycling lithium metal batteries”, *Nature Energy*, 2019, 4(3), 180-186, Publication date (web): February 25, 2019.
 13. F. Xin, H. Zhou, Q. Yin, Y. Shi, F. Omenya, G. Zhou, and M. S. Whittingham*, “Nanocrystal Conversion-Assisted Design of Sn–Fe Alloy with a Core–Shell Structure as High-Performance Anodes for Lithium-Ion Batteries”, *ACS Omega*, 2018, 4, 4888-4895. Publication date (web): March 5, 2019.
 14. Q. Xie, W. Li, and A. Manthiram, “A Mg-doped High-nickel Layered Oxide Cathode Enabling Safer, High-energy-density Li-ion Batteries,” *Chem. Mater.*, 2019, 31(3), 938-946, Publication Date (Web): January 22, 2019.
 15. W. Li, H. Y. Asl, Q. Xie, Q., and A. Manthiram, “Collapse of LiNi_{1-x-y}CoxMnyO₂ Lattice at Deep Charge Irrespective of Nickel Content in Lithium-Ion Batteries,” *J. Am. Chem. Soc.*, 2019, 141(13), 5097-5101, Publication Date (Web): March 19, 2019.
 16. N. Dawson-Elli, S. Kolluri, K. Mitra and V. R. Subramanian, “On the Creation of a Chess-AI-Inspired Problem-Specific Optimizer for the Pseudo Two-Dimensional Battery Model Using Neural Networks”, *J. Electrochem. Soc.*, 2019, 166(6), A886-A896, Publication Date (web): March 15, 2019.

17. J. Alvarado[†], M. A. Schroeder[†], T. P. Pollard[†], X. Wang, J. Z. Lee, M. Zhang, T. Wynn, M. Ding, O. Borodin*, Y. S. Meng* and K. Xu*, “Bisalts Ether Electrolyte: A Pathway Towards Lithium Metal with Nickel-Rich Cathodes”, *Energy Environ. Sci.*, 2019, **12**(2), 780-794, publication date (web): January 25, 2019
18. H. Wang, D. Lin, J. Xie, Y. Liu, H. Chen, Y. Li, J. Xu, G. Zhou, Z. Zhang, A. Pei, Y. Zhu, K. Liu, K. Wang, and Y. Cui*, “An Interconnected Channel-Like Framework as Host for Lithium Metal Composite Anodes”, *Adv. Energy Mater.*, 2019, DOI: 10.1002/aenm.201802720, Publication Date (Web): January 2, 2019.
19. N. Liu, G. Zhou, A. Yang, X. Yu, F. Shi, J. Sun, J. Zhang, B. Liu, C.-L. Wu, X. Tao, Y. Sun, Y. Cui*, and S. Chu, “Direct electrochemical generation of supercooled sulfur microdroplets well below their melting temperature”, *Proc. Natl. Acad. Sci.*, 2019, 116(3), 765-770, Publication Date (Web): January 15, 2019.
20. D. Lin, Y. Liu, Y. Li, Y. Li, A. Pei, J. Xie, W. Huang, and Y. Cui*, “Fast galvanic lithium corrosion involving a Kirkendall-type mechanism” *Nature Chemistry*, 2019, **3**, 382-389, Publication Date (Web): January 21, 2019.
21. Y. Tsao, M. Lee, E. C. Miller, G. Gao, J. Park, S. Chen, T. Katsumata, H. Tran, L.-W. Wang, M. F. Toney, Y. Cui*, and Z. Bao*, “Designing a Quinone-Based Redox Mediator to Facilitate Li₂S Oxidation in Li-S Batteries”, *Joule*, 2019, **3**, 872-884, Publication Date (Web): January 22, 2019.
22. H. Wang, Y. Li, Y. Li, Y. Liu, D. Lin, C. Zhu, G. Chen, A. Yang, K. Yan, H. Chen, Y. Zhu, J. Li, J. Xie, J. Xu, Z. Zhang, R. Vila, A. Pei, K. Wang, and Y. Cui*, “Wrinkled Graphene Cages as Hosts for High-Capacity Li Metal Anodes Shown by Cryogenic Electron Microscopy”, *Nano Lett.*, 2019, **19**(2), 1326-1335, Publication Date (Web): January 24, 2019.
23. Z. Liang, K. Yan, G. Zhou, A. Pei, J. Zhao, Y. Sun, J. Xie, Y. Li, F. Shi, Y. Liu, D. Lin, K. Liu, H. Wang, H. Wang, Y. Lu, and Y. Cui*, “Composite lithium electrode with mesoscale skeleton via simple mechanical deformation”, *Sci. Adv.*, 2019, **5**, eaau5655, Publication Date (Web): March 15, 2019.
24. Y. Mao, X. Wang, S. Xia, K. Zhang, C. Wei, S. Bak, Z. Shadike, X. Liu, Y. Yang, R. Xu, P. Pianetta, S. Ermon, E. Stavitski, K. Zhao, Z. Xu, F. Lin, X.-Q. Yang*, E. Hu and Y. Liu, “High-Voltage Charging-Induced Strain, Heterogeneity, and Micro-Cracks in Secondary Particles of a Nickel-Rich Layered Cathode Material”, *Adv. Funct. Mater.*, 2019, DOI: 10.1002/adfm.201900247, Publication Date: March 07, 2019
25. Y. Cao, M. Li, J. Lu, J. Liu, and K. Amine, “Bridging the Academic and Industrial Metrics for Next-Generation Practical Batteries”, *Nature Nanotech.*, 2019, **14**(3), 200-207. Publication Date: February 18, 2019.
26. C. Niu, H. Pan, W. Xu, J. Xiao, J.-G. Zhang, L. Luo, C. Wang, D. Mei, J. Meng, X. Wang, Z. Liu, L. Mai, J. Liu*, “Self-smoothing Anode for Achieving High-Energy Lithium Metal Batteries under Realistic Conditions,” *Nature Nanotech.*, 2019, DOI:10.1038/s41565-019-0427-9. March 13, 2019.
27. X. Ren, L. Zou, S. Jiao, D. Mei, M. Engelhard, Q. Li, H. Lee, C. Niu, B. Adams, C. Wang, J. Liu, J. Zhang*, and W. Xu*, “High-Concentration Ether Electrolytes for Stable High-Voltage Lithium Metal Batteries.” *ACS Energy Lett.*, 2019, **4**(4), 896–902. Publication Date (Web): March 20, 2019.
28. S. Chen, C. Niu, H. Lee, Q. Li, L. Yu, W. Xu, J.-G. Zhang, E. J. Dufek, M. S. Whittingham, S. Meng, J. Xiao*, J. Liu*, “Critical Parameters for Evaluating Coin Cells and Pouch Cells of Rechargeable Li-Metal Batteries”, *Joule*, 2019, **3**(4), 1094-1105. Publication Date (Web): February 28, 2019
29. A. W. Abboud, E. J. Dufek, and B. Liaw, “Implications of Local Current Density Variations on Lithium Plating Affected by Cathode Particle Size”, *J. Electrochem. Soc.*, 2019, **166**(4), A667-A669 53-62 Publication Date (Web) March 2, 2019.

30. Z. Shadike, H.-S. Lee, C. Tian, K. Sun, L. Song, E. Hu, I. Waluyo, A. Hunt, S. Ghose, Y. Hu, J. Zhou, J. Wang, P. Northrup, S.-M. Bak, and X.-Q. Yang, “Synthesis and Characterization of a Molecularly Designed High-Performance Organodisulfide as Cathode Material for Lithium Batteries”, *Adv. Energy Mater.*, DOI: 10.1002/aenm.201900705, Publication Date (Web): April 10, 2019.
31. R. Lin, E. Hu, M. Liu, Y. Wang, H. Cheng, J. Wu, J.-C. Zheng, Q. Wu, S. Bak, X. Tong, R. Zhang, W. Yang, K. A. Persson, X. Yu, X.-Q. Yang and H. L. Xin, “Anomalous metal segregation in lithium-rich material provides design rules for stable cathode in lithium-ion battery”, *Nature Commun.*, 2019, 10, 1650. DOI: 10.1038/s41467-019-09248-0, Publication Date: April 09, 2019.
32. D. Liu, Q. Yu, S. Liu, K. Qian, S. Wang, W. Sun, X.-Q. Yang, F. Kang, and B. Li*, “Evolution of Solid Electrolyte Interface on TiO₂ Electrodes in an Aqueous Li-Ion Battery Studied Using Scanning Electrochemical Microscopy”, *J. Phys. Chem. C*, 2019, 123 (20), 12797-12806, DOI: <https://doi.org/10.1021/acs.jpcc.9b01412>, Publication Date: May 1, 2019.
33. Q.-Q. Qiu, Z. Shadike, Q.-C. Wang, X.-Y. Yue, X.-L. Li, S.-S. Yuan, F. Fang, X.-J. Wu, A. Hunt, I. Waluyo, S.-M. Bak*, X.-Q. Yang*, and Y.-N. Zhou*, “Improving the Electrochemical Performance and Structural Stability of the LiNi_{0.8}Co_{0.15}Al_{0.05}O₂ Cathode Material at High-Voltage Charging through Ti Substitution”, *ACS Appl. Mater. Interfaces*, 2019, 11 (26), 23213-23221, DOI: 10.1021/acsami.9b05100, Publication Date: June 11, 2019.
34. H. Chen, A. Pei, D. Lin, J. Xie, A. Yang, J. Xu, K. Lin, J. Wang, H. Wang, F. Shi, D. Boyle, and Y. Cui. “Uniform High Ionic Conducting Lithium Sulfide Protection Layer for Stable Lithium Metal Anode”, *Adv. Energy Mater.* 2019, 9 (22), 1900858. Publication Date (Web): April 30, 2019.
35. W. Li, A. Dolocan, J. Li, Q. Xie, and A. Manthiram, “Ethylene Carbonate-free Electrolytes for High-nickel Layered Oxide Cathodes in Lithium-ion Batteries”, *Adv. Energy Mater.*, 2019, 1901152, Publication date (Web): June 25, 2019.
36. R. Bewley, E. J. Dufek, S. E. Egan, D. J. Jamison, C. Ashton, C. H. Ho, M. C. Evans and T. L. Bennett, “Safety Aspects of Energy Storage Testing”, *J. Electrochem. Soc.*, 2019, 166 (8), E263-265. Publication Date: May 21, 2019
37. C. Fang, X. Wang and Y. S. Meng*, “Key Issues Hindering a Practical Lithium-Metal Battery”, *Trends in Chem.*, 2019, 1, 152-158. Publication Date: May 2019.
38. H. Zhou‡, H. Liu‡, Y. Li, X. Yue, X. Wang, M. Gonzalez, Y. S. Meng, and P. Liu*, “In situ formed polymer gel electrolytes for lithium batteries with inherent thermal shutdown safety features”, *J. Mater. Chem. A*, 2019,b7, 16984-16991, Publication Date: June 25, 2019
39. N. Dawson-Elli, S. Kolluri, K. Mitra and V. R. Subramanian, “On the Creation of a Chess-AI-Inspired Problem-Specific Optimizer for the Pseudo Two-Dimensional Battery Model Using Neural Networks”. *J. Electrochem. Soc.*, 2019, 166 (6), A886-A896. Publication Date: March 15, 2019
40. X. Ren, L. Zou, X. Cao, M. H. Engelhard, W. Liu, S. D. Burton, H. Lee, C. Niu, B. E. Matthews, Z. Zhu, C. Wang, B. W. Arey, J. Xiao, J. Liu, J.-G. Zhang,* W. Xu,* “Enabling High-Voltage Lithium-Metal Batteries under Practical Conditions”, *Joule*, 2019, 3, 1662-1676. DOI:10.1016/j.joule.2019.05.006. Publication date (Web): June 5, 2019.
41. C. Niu, H. Lee, S. Chen, Q. Li, J. Du, W. Xu, J.-G. Zhang, M. S. Whittingham, J. Xiao*, J. Liu*, “High-energy lithium metal pouch cells with limited anode swelling and long stable cycles”, *Nature Energy*, 2019, 4, 551-559. DOI:10.1038/s41560-019-0390-6. Publication date (Web): May 13, 2019.
42. Hui Zhou, Fengxia Xin, Ben Pei, and M. Stanley Whittingham*, “What Limits the Capacity of Layered Oxide Cathodes in Lithium Batteries?”, *ACS Energy Letters*, 2019, 4, 1902-1906. DOI: 10.1021/acsenerylett.9b01236. July 18, 2019

43. Fengxia Xin, Hui Zhou, Xiaobo Chen, Mateusz Zuba, Natasha Chernova, Guangwen Zhou, and M. Stanley Whittingham*, “Li–Nb–O Coating/Substitution Enhances the Electrochemical Performance of the LiNi_{0.8}Mn_{0.1}Co_{0.1}O₂ (NMC 811) Cathode”, *ACS Applied Materials & Interfaces*, 2019, **11**, 34889-34894. DOI: 10.1021/acsami.9b09696. August 30, 2019
44. Fredrick Omenya, Nikolas Zagarella, Jatinkumar Rana, Hanlei Zhang, Carrie Siu, Hui Zhou, Bohua Wen, Natasha Chernova, Louis F. J. Piper, Guangwen Zhou, and M. Stanley Whittingham*, “Intrinsic Challenges to the Electrochemical Reversibility of the High Energy Density Copper (II) Fluoride Cathode Material”, *ACS Applied Energy Materials*, 2019, **2**, 5243-5253, DOI: 10.1021/acsaeem.9b00938. June 14, 2019
45. ZhiaoYu, David G. Mackanic, Wesley Michaels, Minah Lee. Allen Pei. Dawei Feng, Qihong Zhang, Yuchi Tsao, Chibueze V. Amanchukwu, Xuzhou Yan, Hansen Wang, Shucheng Chen, Kai Liu, Jiheong Kang, Jian Qin, Yi Cui*, Zhenan Bao*, “A dynamic, electrolyte-blocking, and single-ion-conductive network for stable lithium-metal anodes”, *Joule*, 2019. DOI: [10.1016/j.joule.2019.07.025](https://doi.org/10.1016/j.joule.2019.07.025). Publication Date (Web): August 26 2019.
46. Jiewen Xiao, Guangmin Zhou, Hetian Chen, Xiang Feng, Dominik Legut, Yanchen Fan, Tianshuai Wang, Yi Cui, and Qianfan Zhang, “Elaboration of Aggregated Polysulfide Phases: From Molecules to Large Clusters and Solid Phases”, *Nano letters*, 2019, **19**, 7487-7493. Publication Date (Web): September 11, 2019.
47. Chibueze V. Amanchukwu, Xian Kong, Jian Qin, Yi Cui*, Zhenan Bao*, “Nonpolar Alkanes Modify Lithium-Ion Solvation for Improved Lithium Deposition and Stripping”, *Advanced Energy Materials*, 2019, 1902116. Publication date: September 23, 2019
48. Xia Cao, Xiaodi Ren, Lianfeng Zou, Mark H. Engelhard, William Huang, Hansen Wang, Bethany E. Matthews, Hongkyung Lee, Chaojiang Niu, Bruce W. Arey, Yi Cui, Chongmin Wang, Jie Xiao, Jun Liu, Wu Xu*, and Ji-Guang Zhang*, “Monolithic solid–electrolyte interphases formed in fluorinated orthoformate-based electrolytes minimize Li depletion and pulverization”, *Nature Energy*, 2019, **4**, 796–805. Publication Date (Web): September 13, 2019
49. Ji-Guang Zhang, “Anode-less”, *Nature Energy*, 2019, **4** (8), 637-638.
50. Shaofeng Li, Sang-Jun Lee, Xuelong Wang, Wanli Yang, Hai Huang, Daniel S. Swetz, William B. Doriese, Galen C. O’Neil, Joel N. Ullom, Charles J. Titus, Kent D. Irwin, Han-Koo Lee, Dennis Nordlund, Piero Pianetta, Chang Yu, Jieshan Qiu, Xiqian Yu, Xiao-Qing Yang, Enyuan Hu*, Jun-Sik Lee*, and Yijin Liu*, “Surface-to-Bulk Redox Coupling through Thermally Driven Li Redistribution in Li- and Mn-Rich Layered Cathode Materials”, *Journal of the American Chemical Society*, 2019, **141**, 12079-12086. DOI: 10.1021/jacs.9b05349, Publication Date (Web): July 9, 2019.
51. Shuai Liu, Zepeng Liu, Xi Shen, Xuelong Wang, Sheng-Chieh Liao, Richeng Yu, Zhaoxiang Wang*, Zhiwei Hu, Chien-Te Chen, Xiqian Yu, Xiaoqing Yang, Liquan Chen, “Li-Ti Cation Mixing Enhanced Structural and Performance Stability of Li-Rich Layered Oxide”, *Advanced Energy Materials*, 2019, **9**, 1901530. DOI: 10.1002/aenm.201901530, Publication Date (web): July 15, 2019.
52. Enyue Zhao, Minghao Zhang, Xuelong Wang, Enyuan Hu, Jue Liu*, Xiqian Yu*, Marco Olguin, Thomas A Wynn, Ying Shirley Meng*, Katharine Page, Fangwei Wang, Hong Li, Xiao-Qing Yang, Xuejie Huang, Liquan Chen, “Local structure adaptability through multi cations for oxygen redox accommodation in Li-Rich layered oxides”, *Energy Storage Materials*, 2019, DOI: 10.1016/j.ensm.2019.07.032, publication date (Web): July 25, 2019.
53. Tao Deng, Xiulin Fan*, Longsheng Cao, Ji Chen, Singyuk Hou, Xiao Ji, Long Chen, Shuang Li, Xiuquan Zhou, Enyuan Hu, Dong Su, Xiao-Qing Yang, Chunsheng Wang*, “Designing In situ-Formed Interphases Enables Highly Reversible Cobalt-Free LiNiO₂ Cathode for Li-ion and Li-metal Batteries”, *Joule*, 2019, DOI: 10.1016/j.joule.2019.08.004, Publication Date (web): September 4, 2019.

54. Chengcheng Fang, Jinxing Li, Minghao Zhang, Yihui Zhang, Fan Yang, Jungwoo Z. Lee, Min-Han Lee, Judith Alvarado, Marshall A. Schroeder, Yangyuchen Yang, Bingyu Lu, Nicholas Williams, Miguel Ceja, Li Yang, Mei Cai, Jing Gu, Kang Xu, Xuefeng Wang and Ying Shirley Meng*, “Quantifying Inactive Lithium in Lithium Metal Batteries”, *Nature*, 2019, **572**, 511-515. DOI: 10.1038/s41586-019-1481-z, Publication Date (web): August 21, 2019.
55. Yangyuchen Yang, Daniel M. Davies, Yijie Yin, Oleg Borodin, Jungwoo Lee, Chengcheng Fang, Marco Olguin, Yihui Zhang, Ekaterina S. Sablina, Xuefeng Wang, Cyrus S. Rustomji* and Ying Shirley Meng*, “High Efficiency Lithium Metal Anode Enabled by Liquefied Gas Electrolyte”, *Joule*, 2019, **3**, 1986-2000. DOI: 10.1016/j.joule.2019.06.008, Publication Date (web): July 1, 2019.

Invited Presentations

1. Jun Liu, “Materials Science Challenges for High Energy Li Cells,” 2018 MRS Fall Meeting, Nov 25-30, 2018.
2. Jun Liu, “Electrolyte Chemistry for Li and Zn Batteries,” 2018 MRS Fall Meeting, Nov 25-30, 2018.
3. X. Cao, S. Chen, X. Ren, J. Zheng, L. Yu, W. Xu, and J. Zhang. “Stabilization of Metal Anodes by Localized High Concentration Electrolytes.” Presented by Jason Zhang at 2018 MRS Fall Meeting, Boston, Massachusetts, 11/27/2018.
4. J. Xiao and J. Liu, The 6th International Renewable and Sustainable Energy Conference, “Fundamental Challenges of Rechargeable Lithium Metal Batteries”, Rabat, Morocco, December 2018. (**keynote speaker**)
5. J. Xiao and J. Liu, The 11th International Conference on Advanced Lithium Battery for Automobile Applications, “Challenges and Opportunities of Employing Li Metal Anode for the Next-Generation Battery Technologies”, Huzhou, China, October 2018.
6. Zulipiya Shadike, Ruoqian Lin, Enyuan Hu, Seong-Min Bak, Xiao-Qing Yang*, Hung-Sui Lee, Xiqian Yu, Yong Chu, and Yijin Liu, “Using Synchrotron X-ray and Neutron Based Scattering as well as TXM and TEM Imaging Techniques to Study the New Cathode Materials for Batteries and Studies on Li Metal Anode Protections”, presented at Materials Science and Engineering Colloquium, at Department of Applied Physics & Applied Mathematics, Columbia University, New York, USA, November 16, 2018.
7. Ruoqian Lin, Zulipiya Shadike, Seong-Min Bak, Enyuan Hu, Huolin Xin, Xiaojing Huang, YoungHo Shin, Hung-Sui Lee, Yong S. Chu, and Yijin Liu, and Xiao-Qing Yang*, “Using multi-modal and multi-scale TEM and TXM imaging techniques to study the structural stability of high Ni-content cathode materials”, presented at 2018 MRS Fall Meeting, Boston, USA, November 29, 2018.
8. Enyuan Hu, Ruoqian Lin, Xiqian Yu, Zulipiya Shadike, Seongmin Bak, Hung Sui Lee, Yijin Liu, Katherine Page, Jue Liu, Huolin Xin, Xuelong Wang, Xiao-Qing Yang*, “Using Synchrotron X-ray and Neutron Based Scattering combined with TEM and TXM imaging Techniques to Study the New Cathode Materials for Batteries”, presented at Hong Kong Symposium of Batteries, at The Hong Kong Polytechnic University, Hong Kong, December 17, 2018.
9. M. Stanley Whittingham, “Can Multi-Electron Intercalation Batteries replace today’s Li-Ion Batteries? (The Ultimate Limits of Intercalation, as exemplified by NMC and 2e Cathodes)”, 11th AABA Conference, Huzhou, China, October 14th, 2018.
10. M. Stanley Whittingham, “Approaching 50 Years of Li -Ion Batteries (From Solid State Ionics to Domination of Portable Storage)”, Energy Storage Review, Nanjing, China, October 16th, 2018.
11. M. Stanley Whittingham, “Solid State Ionics – The Key to the Discovery and Domination of Lithium Batteries”, Director’s Lecture, PNNL, Richland WA. October 30th, 2018.

12. M. Stanley Whittingham, "What are the Materials Limitations to Advancing Li-Batteries to the Next Level", Harvard University, Cambridge MA, Nov. 14th, 2018.
13. M. Stanley Whittingham, "Materials for High Energy Li and Li-Ion Batteries", MRS Meeting, Boston, Nov. 26th, 2018.
14. M. Stanley Whittingham, MRS David Turnbull Award Lecture: "Solid State Ionics – The Key to the Discovery and Domination of Lithium Batteries for Portable Energy Storage Leading to a Multi-Billion Dollar Industry", MRS Meeting, Boston, Nov. 27th, 2018.
15. Y. Shirley Meng "1D, 2D and 3D Defect Dynamics in Li Intercalation Compounds", 2018 MRS Fall Meeting&Exhibit, November 29, 2018 in Boston, Massachusetts USA.
16. B. Liaw, Departmental Seminar, Materials Science and Engineering, University of Washington, Seattle, WA, November 19, 2018."Future Mobility – How Battery Changes Electrification".
17. B. Liaw, 9th Annual Battery Safety Conference, Arlington, VA, October 30-31, 2018."Cross-Platform Analysis to Improve Cell Design for Safety". Featured presentation.
18. B. Liaw, Departmental Seminar, Electrical Engineering, San Diego State University, San Diego, CA, October 19, 2018, "A Broad Perspective on Future Mobility – How Battery Changes Electrification".
19. Y. Cui, "Nanomaterials Design for Energy Storage and Catalysis" Northwestern University, Materials Science Seminar, October 2, 2018. **I**
20. Y. Cui, "Nanomaterials Design for Energy and Environment", The 19th Annual Vanderbilt Nanoscience and Nanotechnology Forum, Vanderbilt University, October 3, 2018. **Keynote Talk.**
21. Y. Cui, "Nanomaterials Design for Energy and Environment" The 6th Nano Israel conference, Jerusalem, Israel, October 10–11, 2018. **Plenary Talk**
22. Y. Cui, "Fibers Across Multiple Length Scale from Energy, Environment to Electronics"2018 Fall Fiber Society Conference at University of California, Davis, October 29-31, 2018. **Plenary Talk**
23. Y. Cui, "How Far Can Batteries Go" Global Energy Forum, Stanford University, November 1-2, 2018.
24. Y. Cui, "Batteries Now and Future". The Stanford Chinese Faculty & Family Club (SCFFC), Quarterly Speaker Series, Nov. 4, 2018.
25. Y. Cui, "Pathways of Batteries Towards Sustainable Electric Transportation and Stationary Storage", Stanford University, Department of Energy Resources Engineering Seminar, November 5, 2018.
26. Y. Cui, "Materials Technology Innovation and Commercialization" 2018. International Symposium on Functional Materials for Energy Storage and Conversion – Carbon Energy, Wenzhou, China, November 12-13, 2018. **Plenary Talk**
27. Y. Cui, "Nanotechnology for Energy and Environment", University of Chinese Academy of Sciences seminar, Beijing, China, November 14, 2018.
28. Y. Cui, "Hollow Materials Design for Energy", Xiangshan Meeting on Hollow Materials, Beijing, China, November 15-16, 2018. **Keynote talk.**
29. Y. Cui, "Nanoscale Design for Lithium-Sulfur Batteries", Materials Research Society Fall Meeting, Symposium ET09, Boston, November 25-30, 2018.
30. Y. Cui, "Nanoscale Composite Polymer Electrolyte Batteries", Materials Research Society Fall Meeting, Symposium ET01, Boston, November 25-30, 2018.

31. Y. Cui, “Nanomaterials and Interfacial Design for Energy Storage”, The 4th International Symposium on Energy Chemistry & Materials (ISECM 2018), Xiamen University, December 10-13, 2018.
Plenary Talk
32. W. C. Chueh, “Understanding the Many Length Scales of Ion Insertion Solids”, Materials Research Society Meeting, Boston, USA, November 28, 2018.
33. M. F. Toney, “X-rays Show How Sustainable Energy Materials Function”, Sandia National Laboratories Colloquium, December 17th, 2018.
34. M. S. Whittingham, “Can Multi-Electron Intercalation Systems Supplant NMC Cathodes?”, ICESI-PPSS Meeting, Kona, HA, January 9th, 2019.
35. M. S. Whittingham, “What are the Materials Limitations to Advancing Li-Batteries to the Next Level?”, ECS San Francisco Section, Oakland, CA, January 23rd, 2019.
36. M. S. Whittingham, “Materials for High Energy Density Li and Li-Ion Batteries” IBA Meeting, La Jolla, CA, March 8th, 2019.
37. M. S. Whittingham, “Pros and Cons of High Ni NMCAs vs 2 Li Systems”, 14th China-U.S. EV and Battery Technology Exchange, Shaoxing, China, March 30th, 2019.
38. A. Manthiram, “Near-term and Long-term Perspectives of Battery Technologies,” Battery India – 2019, Goa, India, January 5 – 7, 2019. **Plenary Talk**
39. A. Manthiram, “Battery Technologies: Near-term and Long-term Perspectives,” 12th International Symposium on Advances in Electrochemical Science and Technology (iSAEST-12), Chennai, India, January 8 – 10, 2019. **Plenary Talk**
40. A. Manthiram, “A Perspective on Electrical Energy Storage,” SRM University, Chennai, India, January 9, 2019.
41. A. Manthiram, “A Perspective on Next-generation Battery Chemistries,” Seoul National University, Seoul, South Korea, January 28, 2019. **Distinguished Lecture**
42. A. Manthiram, “A Deep-dive on High-nickel Lithium-ion Batteries and Lithium-sulfur Batteries,” Seoul National University, Seoul, South Korea, January 29, 2019. **Distinguished Lecture**
43. A. Manthiram, “A Path Forward to Low-cobalt or Cobalt-free Cathodes for Lithium-ion Batteries,” International Battery Association Meeting, San Diego, CA, March 3 – 8, 2019. **Keynote Talk**
44. A. Manthiram, “Battery Technologies for Grid Storage and E-Mobility,” India Smart Grid Forum, New Delhi, India, March 12 – 15, 2019. **Plenary Talk**
45. J. Xiao and J. Liu. “Lithium Sulfur Batteries: From Fundamental Understanding to Pouch Cell Integration”, International Battery Association (IBA) Meeting, March 2019, San Diego, CA.
46. J. Xiao and J. Liu. DOE/Office of Electricity Workshop on “Non-Aqueous Redox Flow Cells”, “Standardizations of rechargeable lithium metal battery research”, Santa Fe, NM, 2019.
47. J. Xiao and J. Liu. “Battery500 Consortium: Fundamental Research to Enable Next-generation Battery Technologies”, Detroit Section of The Electrochemical Society (ECS), Detroit, MI, 2019.
48. J. Xiao and J. Liu. “Challenges and Opportunities of Lithium Metal Anode”, Seminar at General Motor Global R&D Center, Warren, 2019.
49. W. Xu. “Advancing Lithium Metal Batteries.” Presented at 2019 International Battery Seminar & Exhibit, Fort Lauderdale, Florida. 03/26/2019. **Featured presentation.**

50. W. Xu, X. Ren, S. Jiao, and J.-G. Zhang. "Ether-Based Electrolytes for High-Voltage Lithium Metal Batteries." Presented by W. Xu at 2019 International Coalition for Energy Storage and Innovation and Pacific Power Source Symposium Joint Meeting, Big Island, Hawaii. 01/09/2019.
51. G. Pawar, X. Wang, E. Dufek, S. Meng and B. Liaw, "Lithium Plating: Understanding of a Very Complicated Phenomena". International Battery Association 2019, La Jolla, CA, March 3-8, 2019.
52. B. Liaw, "Can Failure Mode and Effect Analysis Redefine Battery Safety?", Invited presentation to GM at General Motor Warren Technology Center, March 26, 2019.
53. E. Dufek, "Cell Variability: Implications for high power and energy cell design", Pacific Power Sources Symposium, Waikoloa, Hawaii, Jan. 9, 2019.
54. Y. Cui, "Exploring New Chemistries for Stationary Storage: H₂ Gas Batteries and Molten Lithium Metal Batteries" International Coalition for Energy Storage and Innovation and Pacific Power Source Symposium Joint Meeting, Big Island of Hawaii, at the Hilton Waikoloa Village, January 5-10, 2019, **keynote**.
55. Y. Cui, "Nanomaterials Design for Energy, Environment and Textile" Wilson College of Textiles, North Carolina State University, Feb. 2, 2019.
56. Y. Cui, "Nanomaterials and Interface Design for Electrochemical Energy Technology" Gordon Research Conference on Nanomaterials for Applications in Energy Technology, Ventura Beach Marriott Ventura, California, Feb 24 - Mar 1, 2019, **keynote**.
57. Y. Cui, "Designing Lithium Metal Anodes: Host Materials and Solid Electrolyte Interphase" International Battery Association 2019 Meeting, La Jolla, San Diego, California, Mar 3 to 8, 2019, **keynote**.
58. Y. Cui, "Materials and Interface Design for Electrochemical Energy Storage" California Institute of Technology, Inorganic-Electrochemistry Seminar Series, Mar 11, 2019.
59. Y. Cui, "Nanomaterials Design for Energy and Textile" Cornell Energy Systems Institute: Distinguished Lecturer, Cornell University, Mar 14, 2019.
60. Y. Cui, "Emerging Materials Selection and Design for Batteries with High Energy Density, Ultralong Cycle Life and Excellent Safety", International Battery Seminar, Fort Lauderdale, March 25-28, 2019.
61. Y. Cui, "Lithium Metal anode host and interface material design" The 14th U.S.-China Electrical Vehicle and Battery Technology Conference, Shaoxing, China, Mar 29-31, 2019.
62. J.-G. Zhang, "Stabilization of Metal Anodes by Localized High Concentration Electrolytes," 2019 International Coalition for Energy Storage and Innovation (ICESI) and Pacific Power Source Symposium (ICESI-PPSS 2019) joint meeting, Waikoloa, Hawaii, January 5-10, 2019.
63. Y. Shirley Meng, "Advanced Diagnosis and Characterization for Next Generation Energy Storage Materials" Materials Science and Engineering Department Seminar, University of California Irvine, May 24th, 2019.
64. Ping Liu, "Chemistry and architectures for energy storage", University of California, Santa Cruz, Department of Chemistry, April 1st, 2019.
65. Ping Liu, "Long life and safe lithium batteries", Advanced Automotive Battery Conference, San Diego, June 24th, 2019.
66. Wu Xu, Xiaodi Ren, Shuhong Jiao, and Ji.Guang Zhang. "Stable High-Voltage Lithium Metal Batteries Enabled by Ether-Based Electrolytes". Presented by W. Xu at 2019 MRS Spring Meeting, Phoenix, Arizona. 04/26/2019.

67. Wu Xu, Xiaodi Ren, Shuhong Jiao, and Ji-Guang Zhang. “Enabling Ether-Based Electrolytes for High Voltage Lithium Metal Batteries”. Presented by W. Xu at 257th ACS National Meeting, Orlando, Florida. 04/02/2019.
68. Ji-Guang Zhang, Xia Cao, Xiaodi Ren, and Wu Xu, “The Fundamental Mechanism behind the Stability of Li Metal Anodes in Non-aqueous Electrolytes”, presented by J.-G. Zhang at the 235th ECS meeting in Dallas, TX, May 26-31, 2019.
69. Ji-Guang Zhang, “Non-Flammable Electrolytes for Lithium Metal Batteries,” presented at Beyond Li-ion Symposium XII, Golden, CO, June 25-27, 2019.
70. Enyuan Hu, Yijin Liu, Huolin Xin, and Xiao-Qing Yang. “Identification and Visualization of Chemical Outliers through Scientific Data Mining in Nanoscale Spectro-microscopic Study of NMC Electrode”, 2019 TMS Annual Meeting & Exhibition, San Antonio, TX, USA, March 10-15, 2019.
71. Ruoqian Lin, Zulipiya Shadike, Seong-Min Bak, Enyuan Hu, Huolin Xin, Xiaojing Huang, YoungHo Shin, Hung-Sui Lee, Yong S. Chu, Yijin Liu, and Xiao-Qing Yang*, “Understanding capacity fade in high-nickel content cathode materials for lithium batteries:”, presented at U.S.-China Clean Energy Research Center for Clean Vehicles (CERC-CVC), Xining, China, June 23, 2019.
72. M. S. Whittingham, “What are the Materials Limitations to Advancing Lithium Batteries to the Next Level?”, CESI, Chemical Engineering, Cornell U., April 10th 2019.
73. M. S. Whittingham, ““What are the Chemistry and Materials Limitations to Advancing Lithium Batteries to the Next Level?”, Syracuse, April 16th 2019. Prins Memorial Lecture.
74. M. S. Whittingham, “Key Parameters for Solid Electrolytes – Learnings from Beta-Alumina and Future Opportunities”, MRS Meeting, Phoenix, April 2019.
75. M. S. Whittingham, “How Far Can We Push the Limits of Intercalation Batteries?”, CCMR, Cornell U., May 22nd, 2019.
76. Jie Xiao and Jun Liu, 2019 Spring Biannual Meeting Electric Flight Batteries, “Battery500 Consortium: Revisiting and Addressing the Fundamental Challenges of Rechargeable Li Metal Batteries”, University of Maryland, College Park, June 14th, 2019.
77. Jie Xiao and Jun Liu, 235th ECS Spring Meeting, “Battery500 Consortium: Addressing the Fundamental Challenges to Enable High-Energy Rechargeable Li Metal Batteries”, Dallas, TX, May 27th, 2019.
78. Yi Cui, “Nanomaterials Design for Energy and Environment”, Nanotechnology Seminar organized by Graduates in Nanotechnology, Georgia Institute of Technology, April 8, 2019.
79. Yi Cui, “Thermal Materials and Science in Textile and Batteries” Materials Research Society Spring Meeting, Symposium QN05, Phoenix, Arizona, Apr 22-26, 2019.
80. Yi Cui, “Lithium Metal Anode: Host Materials Design and Solid Electrolyte Interphase” 4th Lithium Battery International Summit (LBIS), Shenzhen, China May 6-9, 2019.
81. Yi Cui, “Nanomaterials Design for Energy, Environment and Textile” Donghua University Seminar, May 8, 2019.
82. Yi Cui, “Nanomaterials and Interface Design for Energy Storage” Seoul National University, Department of Materials Science and Engineering Seminar, May 9, 2019.
83. Yi Cui, “Reinventing Batteries: What’s Possible?” Miller Institute Symposium 2019, Marconi Conference Center, Jun 7-9, 2019.
84. Yi Cui, “Nanomaterials Design for Energy and Environment” The 6th Nano Today Conference, June 16-20, 2019, Lisbon, Portugal, **Plenary**.

85. Yi Cui, “Nanomaterials Design for Energy Storage” Dan Maydan Prize in Nanoscience, Jun 18, 2019, The Hebrew University of Jerusalem, **Award Talk**.
86. Jun Liu, “Next generation High Energy Batteries”, presented at the World New Energy Vehicles Congress, Hainan, China, June 30, 2019.
87. Jun Liu, “Addressing Li Problems in High Energy Batteries”, presented at the Advanced Automobile Battery Conference (AABC), San Diego, USA, June 23, 2019.
88. Jun Liu, “Next Generation High Energy Batteries for Electrification”, presented at the Euro Mediterranean Conference on Materials and Renewables, Marrakesh, Morocco, June 14, 2019.
89. A. Manthiram, “Next-generation Battery Technologies,” *Huazhong Agricultural University*, Wuhan, China, May 6, 2019.
90. A. Manthiram, “A Perspective on Electrical Energy Storage,” *Zhengzhou University*, Zhengzhou, China, May 7, 2019.
91. A. Manthiram, “Advanced Materials for Next-generation Batteries,” 2019 *Nankai-Cambridge International Symposium on Advanced Materials*, Nankai University, Tianjin, China, May 19 – 21, 2019.
92. A. Manthiram, “High-nickel Layered Oxide Cathodes for Lithium-ion Batteries,” 22nd *International Conference on Solid State Ionics (SSI-22)*, PyeonChang, South Korea, June 16 – 21, 2019, **Keynote Talk**.
93. A. Manthiram, “High-nickel, Low-cobalt Cathodes for Lithium-ion Batteries,” 19th *Advanced Automotive Battery Conference*, San Diego, CA, June 24 – 27, 2019.
94. Boryann Liaw, “Battery technology and safety.” 2019 CIE/USA-DFW and AAEOY International Technology & Leadership Conference (ITLC), Dallas, TX, August 17, 2019.
95. M. Stanley Whittingham, “What are the Materials Limitations to Advancing Lithium Batteries to the Next Level?”, U. Colorado, Mechanical Eng., Boulder, CO, September 16th 2019.
96. M. Stanley Whittingham, “Past, Present and Future of High Energy Batteries”, BatteryNext, Boulder, CO, September 17th, 2019.
97. M. Stanley Whittingham, “What are the Materials Limitations to Advancing Lithium Batteries to the Next Level?”, Virginia Tech., Chemistry, Blacksburg, VA, September 20th 2019.
98. Yi Cui, “Nanomaterials Design and Interphases for Batteries” The 5th International Conference on Energy Conversion and Storage, Beijing, China, Aug 15-16, 2019. **Keynote**.
99. Yi Cui, “Nanomaterials Design for Energy and Environment” International Forum on Advanced Materials 2019 (IFAM2019), Wuhan, China, Sep 24-26, 2019. **Plenary**.
100. Yi Cui, “Fiber and Textile Materials for Energy, Environment and Electronics”, 15th Asian Textile Conference (ATC-15), Hangzhou, China, Sep 27-29, 2019. **Plenary**.
101. Yi Cui, “Materials and Interface Design for Batteries” ACS Forum “Nanomaterials for Energy and Life Sciences”, Yonsei University, Sep. 30-Oct. 1, 2019.
102. Arumugam Manthiram, “High-nickel Layered Oxide Cathodes for Lithium-ion Batteries,” Tesla, Menlo Park, CA, July 25, 2019,
103. Arumugam Manthiram, “High-energy-density Cathodes for Lithium-based Batteries,” Institute of Chemistry, Chinese Academy of Sciences, Beijing, China, August 14.

104. Arumugam Manthiram, “High-Nickel Layered Oxide Cathodes for Lithium-ion Batteries: Complexities and Prospects,” 2019 Lithium Battery Discussion Meeting, Arcachon, France, September 15 – 20, 2019, **Plenary Talk**.
105. Ji-Guang Zhang, “Localized High-Concentration Electrolytes for Li Metal Batteries”, 2019 International Conference on Electrochemical Energy, Sydney, Australia, Aug. 4-8, 2019.
106. Ji-Guang Zhang, “A Monolithic SEI Layer Prevents Li Depletion and Pulverization”, ACS 2019 Fall meeting in San Diego, CA on Aug. 26, 2019.
107. Jun Liu, “Understanding Rechargeable Lithium Sulfur Pouch Cells”, International Conference on Lithium-Sulfur Batteries, Beijing, August 12-15, 2019.
108. Peter Khalifah, “Clockwork inside cathodes – unparalleled insights into defects and inhomogeneities”, presented at Stevens Institute of Technology, September 2019.
109. Peter Khalifah, “New innovations for operando diffraction studies of battery electrodes with spatial and temporal resolution”, presented at American Chemical Society ENFL conference, August 2019.
110. Peter Khalifah, “Thermodynamic relationships between composition and defect concentration in NMC cathodes resolved using novel high-precision powder diffraction methods”, presented at American Chemical Society ENFL conference, August 2019.
111. Y. Shirley Meng, “Advanced Diagnosis and Characterization for Next Generation Energy Storage Materials” BASF Seminar, Shanghai, July 5th, 2019.

II.12.B Battery 500 Seedling: Composite Cathode Architecture for Solid-State Batteries (LBNL)

Marca M. Doeff, Principal Investigator

Lawrence Berkeley National Laboratory
1 Cyclotron Road
Berkeley, CA 94720
E-mail: mmdoeff@lbl.gov

Guoying Chen, Principal Investigator

Lawrence Berkeley National Laboratory
1 Cyclotron Road
Berkeley, CA 94720
E-mail: gchen@lbl.gov

Stephen Sofie, Principal Investigator

Department of Mechanical and Industrial Engineering
Montana State University
Bozeman, MT 59717
E-mail: ssofie@montana.edu

Tobias Glossmann, Principal Investigator

Mercedes-Benz Research and Development, North America
12120 Telegraph Road
Redford, MI 48239
E-mail: tobias.glossmann@daimler.com

Tien Duong, DOE Technology Development Manager

U.S. Department of Energy
E-mail: Tien.Duong@ee.doe.gov

Start Date: April 1, 2019

End Date: March 31, 2021

Project Funding (FY19): \$167,902

DOE share: \$150,972

Non-DOE share: \$16,930

Project Introduction

Currently, all solid-state batteries (ASSBs) with lithium metal anodes are fabricated in thin film formats, with cathode areal capacities much lower than the several mAh/cm² used in LIBs. [1] The vacuum technologies used to produce these devices are costly and the thin film configurations result in practical energy densities much lower than DOE targets or theoretical values. To overcome these deficiencies, it is necessary to find ways to fabricate thicker cathodes using scalable and lower cost technologies. Successful design of thick cathodes for all solid-state batteries that scale performance without transport losses would represent a breakthrough enabling adoption of this technology for traction applications.

In lithium-ion batteries (LIBs), the devices of choice for electric vehicles, cathodes are typically 20-100 μm thick, with thicker electrodes the most desirable option for high-energy cell designs. To overcome ionic and electronic conductivity limitations of active materials, electrodes are typically made in composite form and contain carbon and binder, which helps to ameliorate volume changes associated with charge and discharge processes. Approximately 25 vol% electrolytic solution is added to the porous composite electrode to impart sufficient ionic conductivity for successful operation in LIBs. For all solid-state batteries, the electrolyte must be introduced during the electrode fabrication process rather than added to a porous structure afterwards. For this work, we are proposing thick composite electrodes consisting of Ni-rich lithium nickel manganese cobalt

oxide (NMC) active material, the solid electrolyte material LLZO (Al-substituted $\text{Li}_7\text{La}_3\text{Zr}_2\text{O}_{12}$), and an electronically conductive polymer such as polyaniline, which would double as a binder able to accommodate volume changes. Carbon may also be added, if needed. For this project, we first fabricate a porous scaffold of LLZO by freeze-casting [2] and then infiltrate the pores with the other components needed to make composite electrodes. Freeze casting allows unparalleled control of porosity by changing processing variables such as slurry loading, solvent, and temperature. [3] Freeze tapecasting (FTC), a variant of this process, allows thin components (hundreds of microns thick or less) to be fabricated in a continuous fashion.

The technical barriers addressed by this work include the following: 1) inadequate energy density due to thickness limitation of the cathode electrode, 2) slow charging rate due to poor ionic and electronic conduction in solid state batteries, and 3) high cost of cell manufacturing. We address these barriers by 1) improving ion transport kinetics with a scaffolding porous structure of solid electrolyte and improving electronic conduction with conductive polymer, 2) enabling thick electrodes and reducing cost by using a novel, easy to scale up freeze casting technique, and 3) improving gravimetric and volumetric energy density by reducing inactive components, specifically reducing current collector contribution and using conductive polymer for both electronic conduction and binder.

Objectives

The aim of this project is to design and make composite cathode architectures combining a solid-state ion conductor, a conductive polymer additive, and a high energy density cathode material such as Ni-rich NMC. Using novel freeze tape-casting and sintering methods that are large-area scalable, potentially very low-cost and environmentally sustainable, we fabricate composite cathodes with thickness, areal loading, mechanical properties, electronic and ionic conductivities comparable to the traditional electrodes used in lithium-ion batteries with a liquid electrolyte. Success in this project will enable safe, all solid-state lithium batteries with specific energies approaching 500 Wh/kg.

Approach

We utilize novel freeze casting and freeze tape-casting techniques to produce porous scaffolds of LLZO (variants of $\text{Li}_7\text{La}_3\text{Zr}_2\text{O}_{12}$). The unidirectional pores of the scaffolds are then infiltrated with Ni-rich NMC powders and a conducting polymer such as polyaniline (or PVdF and carbon) to form thick ($\sim 100\ \mu\text{m}$) composite cathodes, which ultimately can be used in all solid-state configurations. Bilayer structures are also fabricated by combining the porous structure with a dense layer of electrolyte, [4] with lithium foil added to complete the solid-state cell. (Current collectors can be added by sputtering thin layers of metal on the composite electrodes). Another configuration of interest is that of a trilayer, in which the dense layer is sandwiched between two porous layers, one of which contains cathode material and the other an anode material such as $\text{Li}_4\text{Ti}_5\text{O}_{12}$ or lithium metal, to form the device. Some effort is also devoted to fabrication of NMC scaffolds and infiltration of LLZO into these structures, essentially the reverse of the procedure discussed above.

Results

Phase 1 of this project (Aug. 2017-March 2019) was devoted to demonstrating the principle of using infiltrated freeze cast LLZO scaffold electrodes in a hybrid cell [5] (i.e., one containing liquid electrolyte) and developing appropriate FTC processing parameters for LLZO. [6] The latter proved to be challenging due to the reactivity of LLZO with water, used in the slurry formulation. By adjusting the slurry loading and formulation, it was possible to produce scaffolds with porosities of about 70% after sintering, close to the targeted goal. While LLZO is protonated by water and forms lithium carbonate, heating easily reverses the reaction. During Phase 2, we devoted some effort to tape casting thin dense layers of LLZO and characterizing their electrochemical properties in symmetrical cells with lithium electrodes. The tapes are very sensitive to sintering conditions, with microstructure and the degree of lithium loss a function of both the tape thickness and temperature/time. By adding an excess of a lithium source such as lithium carbonate during sintering, phase-pure layers approximately 95% dense and 25-44 μm thick with the requisite cubic LLZO polymorph could be produced reliably in all layers. Interface-engineered symmetrical cells were produced by sputtering gold onto the LLZO

tapes, which promotes adhesion of the lithium foils (Figure II.12.B.1). The symmetrical cells showed very low interfacial impedance and could sustain a critical current density of about $100 \mu\text{A}/\text{cm}^2$.

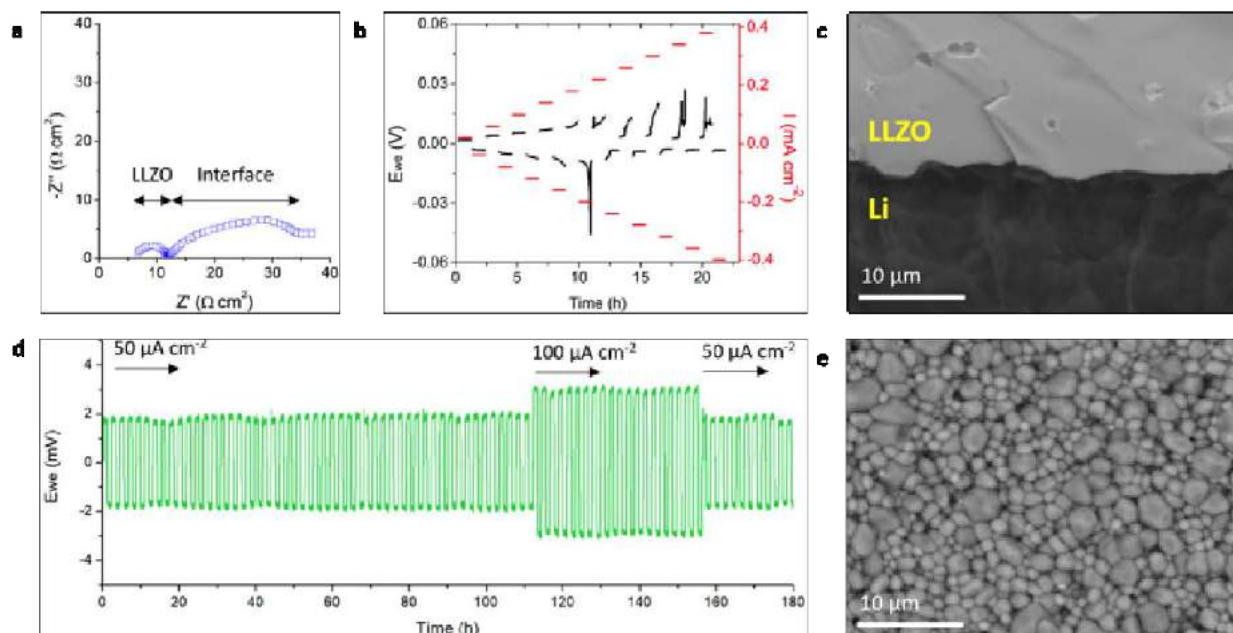


Figure II.12.B.1 (a) Nyquist plot of Au interface engineered Li/LLZO/Li cell. (b) DC cycling of Au interface engineered Li/LLZO/Li cell with a step current of $20 \mu\text{A cm}^{-2}$ starting from $20 \mu\text{A cm}^{-2}$. (c) SEM fracture surface image showing superior interfacial bonding of Li and LLZO. (d) DC cycling of Au interface engineered Li/LLZO/Li cell at selected current densities. (e) SEM surface image of typical sintered LLZO thin films

Work was also directed towards fabrication of porous/dense bilayers and porous/dense/porous trilayers. Images of these structures are shown in Figure II.12.B.2. For these, FTC and tape cast green tapes were stacked together and sintered. Thinner dense layers (down to $14 \mu\text{m}$ thick) could be used than for the free-standing films because the porous layers act as mechanical supports for the otherwise fragile thin dense films. FTC green tapes made with 10 vol% LLZO were used, resulting in 70% porosity after sintering. Trilayers are particularly advantageous here because the symmetry allows for uniform shrinkage during densification. Also shown in Figure II.12.B.2 is an optical image of a typical trilayer and a 3D reconstruction of a micro-computed tomography (CT) scan. A video of the trilayer (not shown) indicates that the pores are unidirectional and are not closed. Fracture surface images show what might appear to be pore blockages but are due to LLZO rods extending from one wall to another. The top surface image in Figure II.12.B.2g shows clearly that the pores are not blocked. This is important because blocked pores can interfere with effective infiltration of electrode components. Another advantage to the trilayer structure has been demonstrated recently in symmetrical cells where lithium was infiltrated into both of the porous layers with a random pore structure on each side. [7] A much higher critical current density (up to $10 \text{ mA}/\text{cm}^2$) can be achieved with this design compared to devices with planar interfaces because of the large contact area between the electrolyte and the lithium metal.

Solid-state cells using a porous/dense layer bilayer framework were constructed. A slurry containing NMC-622, carbon black and PVdF binder was infiltrated into the porous layer, followed by solvent removal (Figure II.12.B.3). Fracture surface micrographs show that the slurry penetrated into the porous LLZO layer. A conductive solid was then melt-infiltrated into the structure. Upon cooling, the conductive solid, which is waxy and soft forms a conductive bridge between the NMC-622 and the LLZO framework, and helps to maintain contact among the components as the cell is cycled.

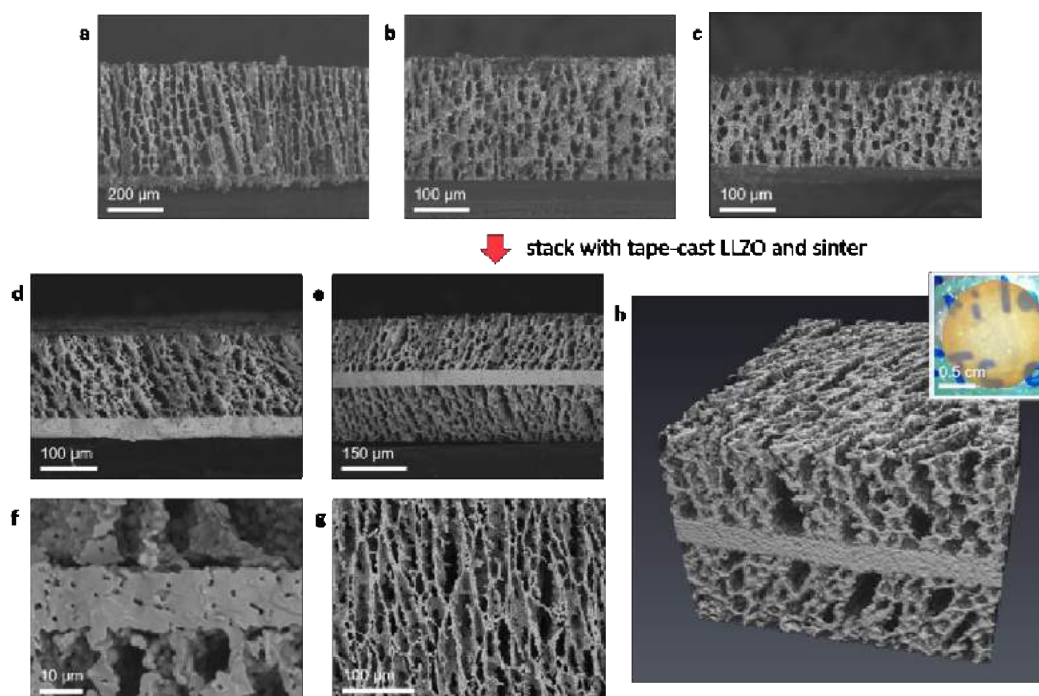


Figure II.12.B.2 Fracture surface SEM micrographs of green tapes freeze tape cast from slurries containing (a) 7.5 vol.% LLZO / 400 μm , (b) 10 vol.% LLZO / 220 μm , and (c) 10 vol.% LLZO / 150 μm . Fracture surface micrographs of (d) sintered porous/dense (140/36 μm) bilayer, (e) porous/dense/porous (130/37/130 μm) trilayer, and (f) porous/dense/porous trilayer with a 14 μm dense layer. (g) Surface SEM micrograph of the porous layer. (h) 3D reconstruction of micro-CT scan of the trilayer. Subvolume size is 400 (width) \times 280 (height) \times 530 (depth) μm^3 . Inset shows an optical image of a typical trilayer

All solid-state batteries with lithium foil electrodes showed total room temperature impedances of $\sim 350 \Omega\text{-cm}^2$, (Figure II.12.B.3d), the lowest ever reported for liquid-free solid-state batteries using LLZO as the electrolyte. As shown in Figure II.12.B.1, the impedances of the dense LLZO layer and Li/LLZO interface are very low, so that the main contributor is the composite cathode, which is about 120-130 μm thick. The solid-state cells were cycled between 2.5-4.4V at 0.1C (1C=175 mAh/g) rate and showed discharge capacities of 125-135 mAh/g. In order to ensure infiltration, it was necessary to grind the NMC-622, which has a somewhat deleterious effect on performance. [8] The results here are comparable to what is obtained in cells with liquid electrolytes containing milled NMC-622.

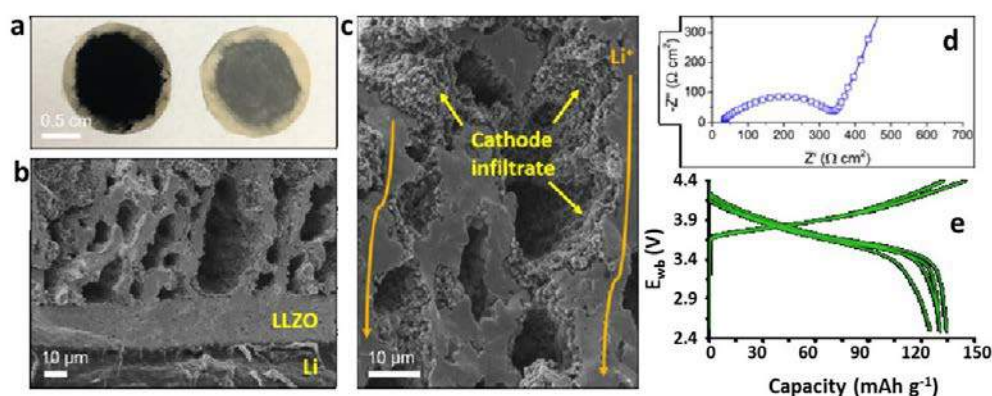


Figure II.12.B.3 (a) Optical image of cathode infiltrated LLZO bilayer. Cathode infiltrated porous layer surface (left) and dense layer surface (right) are shown. (b) SEM fracture surface image of cathode infiltrated bilayer (c) Same cell at higher magnification showing cathode infiltrate. (d) Nyquist plot of the constructed all solid state battery. (e) Initial charge/discharge profiles of the ASSB at room temperature

Reference [9] contains a comprehensive list of attempts to cycle batteries with LLZO electrolytes. Many of these cells contain some liquid electrolyte, were cycled at elevated temperatures, or were fabricated using form factors that are not relevant for vehicular applications (e.g., ultra-thin vacuum-deposited electrodes). Based on this survey, we can confidently claim that this is the first report of successful room temperature cycling of a bulk type all solid-state battery using a LLZO separator and composite electrode in a practical form factor.

While this can be considered a breakthrough in the technology, more work needs to be done. At present, only limited cycling can be obtained for reasons that are not clear. The infiltration process and/or pore sizes in the scaffold need to be optimized so that grinding can be avoided, to achieve better performance. Alternatively, NMC-622 with smaller particle sizes should be used (i.e., micro-sized single crystal NMC, which currently has limited availability commercially) or solution precursors can be infiltrated into the structures with controlled heating to allow the NMC phases to form. Our calculations indicate that the thicker the electrodes ($>200\text{ }\mu\text{m}$) and the higher the LLZO porosities, the better the practical energy densities, but it is unknown whether these configurations can be discharged at reasonable rates. The promise of high energy density also requires that only a small excess of lithium be used; it remains to be seen whether cells with this small excess can be cycled repeatedly without failure. Our work in upcoming months will be directed towards addressing these issues, as well as exploring alternative methods mentioned in the objectives and approach sections.

Conclusions

We have demonstrated a proof-of-principle all solid-state battery, which can be discharged at room temperature, *without the addition of any liquids*. The success of the all solid-state battery constructed here can be ascribed to several factors, including the use of a thin, dense LLZO separator layer, seamless Li/LLZO contact, a low tortuosity pore structure, and intimate NMC-622/LLZO contact via the use of a secondary soft solid conductor. A significant advantage to the last point is that it obviates the need for co-sintering to ensure good contact among the components. Co-sintering introduces difficulties associated with reactions between components at high temperatures. Additionally, the concept of combining a rigid scaffold with a soft, yet solid, conductor is quite general, and can be expanded to other types of solid electrolytes, including those that conduct, e.g., sodium.

Key Publications

1. Shen, H. Yi, E., Amores, M., Cheng, L., Tamura, N., Parkinson, D., Chen, G., Chen, K. and Doeff, M. M. "Oriented Porous LLZO 3D Structures Obtained by Freeze Casting for Battery Applications" *J. Mater. Chem. A*, (2019): DOI: 10.1039/C9TA06520B.
2. Shen, H., Yi, E., Cheng, L., Amores, M., Chen, G., Sofie, S. and Doeff, M. "Solid State Electrolyte Considerations for Electric Vehicle Batteries", *Sust. Energy & Fuels* 3, (2019): DOI: 10.1039/c9se00119k.

References

1. Bates, J.B., Dudney, N. J., Neudecker, B., Ueda, A. and Evans, C.D. "Thin-film Lithium and Lithium-ion Batteries" *Solid State Ionics* 135, (2000): 33-45.
2. DeVille, S. "Freeze-Casting of Porous Ceramics: A Review of Current Achievements and Issues" *Adv. Eng. Mater.* 10, (2008): 155-169.
3. Driscoll, D., Weisenstein, A. J., and Sofie, S. W., "Electrical and flexural anisotropy in freeze tape cast stainless steel porous substrates" *Mater. Lett.*, 65 (2011): 3433-3435.
4. Yi, E., Wang, W., Kieffer, J., and Laine R. M., "Flame made nanoparticles permit processing of dense, flexible, Li⁺ conducting ceramic electrolyte thin films of cubic-Li₇La₃Zr₂O₁₂ (c-LLZO)," *J. Mater. Chem. A*, (2016): DOI: 10.1039/c6ta04492a.
5. Shen, H. Yi, E., Amores, M., Cheng, L., Tamura, N., Parkinson, D., Chen, G., Chen, K. and Doeff, M. M. "Oriented Porous LLZO 3D Structures Obtained by Freeze Casting for Battery Applications" *J. Mater. Chem. A*, (2019): DOI: 10.1039/C9TA06520B.

6. Shen, H., Yi, E., Heywood, S., Parkinson, D., Chen, G., Tamura, N., Sofie, S., Chen, K., and Doeff, M. M. “Scalable Freeze Tape Casting Fabrication and Pore Structure Analysis of 3D LLZO Solid-State Electrolytes”, *ACS Appl. Mater. & Interfaces*, (2019) under review.
7. Hitz, G. T., McOwen, D. W., Zhang, L., Ma, Z., Fu, Z., Wen, Y., Gong, Y., Dai, J., Hamann, T. R., Hu, L., and Wachsman, E.D., “High-Rate Lithium Cycling in a Scalable Trilayer Li-Garnet-Electrolyte Architecture” *Mater. Today* 22, (2019): 50–57.
8. Pan, T., Alvarado, J., Zhu, J., Yue, Y., Xin, H. L., Nordlund, D., Lin, F., and Doeff, M. M. “Structural Degradation of Layered Cathode Materials in Lithium-Ion Batteries Induced by Ball Milling” *J. Electrochem. Soc.* 166, (2019): A1964–A1971.
9. Samson, A. J., Hofstetter, K., and Thangadurai, V. “A Bird’s-Eye View of Li-Stuffed Garnet-Type $\text{Li}_7\text{La}_3\text{Zr}_2\text{O}_{12}$ Ceramic Electrolytes for Advanced All-Solid-State Li Batteries” *Energy Environ. Sci.* (2019): DOI: 10.1039/c9ee01548e.

II.12.C Battery500 Seedling Projects

Tien Duong, DOE Technology Development Manager

U.S. Department of Energy

E-mail: Tien.Duong@ee.doe.gov

Start Date: October 1, 2017
Project Funding: \$8,000,000

End Date: September 30, 2020
DOE share: \$8,000,000

Non-DOE share: \$0

Introduction/Objectives

Proof-of-concept or seedling projects were awarded to support the Battery500 Program. The projects are high-risk, high-payoff efforts that if successful will provide an infusion of novel technology into the Consortium's effort. The objective of the Battery500 Consortium is to research, develop, and demonstrate lithium battery technologies capable of achieving a cell specific energy of ≥ 500 Wh/kg and 1,000 cycles. The two electrochemistries being developed are lithium metal/sulfur and lithium metal/high nickel lithium nickel manganese cobalt (NMC) cells, using solid or concentrated liquid electrolytes. Promising phase I awardees are competitively down-selected at the end of 18 months for a second phase of research.

Approach

The goal of the Battery500 seedlings is to jump-start emerging technologies that could lead to a cell delivering an energy density of 500 Wh/kg over 1,000 cycles.

In 2016 fifteen Phase I seedling projects were awarded to complement the Battery500 Program. The projects were considered high-risk, high-payoff efforts that if successful would provide an infusion of novel technology into the Consortium's effort.

In FY2019, ten of those projects were allowed to move forward. They included:

Design, Processing, and Integration of Pouch-Format Cell for High-Energy Lithium-Sulfur Batteries (Mei Cai, General Motors)

This work aims to develop the design and processing method for Li-S batteries to achieve high energy density and long cycle life. The sulfur cathode will be optimized to achieve the desired loading and porosity. Novel electrode fabrication processes will be developed to provide continuous cathode production. The electrolyte formulation will be modified and tuned to further improve the electrochemical performance of the optimized cathode and stability toward lithium anode. With the development of each major component, integration and full cell design will proceed through the combined efforts of the pilot cell validation and the algorithm modeling tool that was developed inside GM. The pouch-format cell will be fabricated accordingly. The final deliverable in this phase will be a moderate-sized pouch-format cell (for example, ≥ 2 Ah) with a high energy density of ≥ 500 Wh/kg and a long cycling life of ≥ 1000 cycles.

Electrochemically Stable High Energy Density Lithium-Sulfur Batteries (Prashant N. Kumta, University of Pittsburgh)

This project is a fundamental and applied scientific study to obviate the primary problems plaguing Li-S batteries (LSBs) namely, (a) low overall electrode capacity (mAh/g-active material) occurring due to low electronic conductivity of sulfur (b) poor cycling stability owing to polysulfide (PS) dissolution in the electrolyte (c) voltage drop due to PS transport across and accompanying deposition at the lithium anode (d) poor coulombic efficiency (CE). Successful completion of the proposed program will yield: (a) Targeted lithium-sulfur battery (LSB) specific energy (≥ 500 Wh/kg) and energy density (≥ 750 Wh/l), (b) Compact light-weight LSB, (c) Economical and scalable precursors affording ease of manufacturability; (d) Excellent life-cycle (~ 1000 cycle), calendar life (~ 15 years) and fast ability to recharge. The project involves development of innovative and engineered approaches to achieve the targeted objectives. These include the following: (a) Generation of novel high-sulfur loading directly deposited sulfur architecture (DDSA) systems offering binder

free cathodes juxtaposed with unique polysulfide trapping agent (PTA) configurations, (b) Generation of novel inorganic framework materials (IFM) and heterostructured electron and Li-ion conducting composite architectures enabling high sulfur loadings and polysulfide (PS) binding as well as confinement within the electrode, (c) Development of novel organic functionalities based Complex Framework Materials (CFMs) serving as improved sulfur hosts using economic and scalable solution-chemistry methods, (d) Generation of high Li-ion conducting (LIC) and PS dissolution resistant coatings on sulfur nanoparticles, and finally, (e) Identification of novel oxide and non-oxide functional catalysts (FCs) for promoting rapid conversion kinetics of PS to Li_2S and Li_2S to Li and S utilizing chemical interactions of polysulfides with transition metal (TM) oxides as well as non-oxides to trap and bind of the electrochemically active sulfur within the porous carbon structures. In all of the above approaches, the goal is to increase sulfur utilization yielding high areal capacity in excess of 4mAh/cm^2 while translating the design into scalable electrode fabrication for pouch cells with high sulfur loadings to deliver high overall electrode capacity. Another approach to reduce polysulfide dissolution is electrolyte modification utilizing novel composite polymer electrolyte (PE) replacements.

Highly Loaded Sulfur Cathode, Coated Separator, and Gel Electrolyte for High-Rate Lithium-Sulfur Batteries (Yong L. Joo and Jin Suntivichi, Cornell University; Trung Nguyen, EIC Labs)

The project objective is to research, develop, and demonstrate a 1-Ah Li-S battery prototype capable of achieving an energy density of $\geq 500\text{ Wh/Kg}$ while achieving a cycle life of ≥ 300 cycles at the 0.5 C discharge rate. The key features of the project's approach are the development of layered cathode with high sulfur loading and of a polymer/ceramic separator coated with graphene for Li-S battery systems. The Li-S batteries that incorporate such cathode materials and the high-rate, thermally stable separator with graphene will stop/minimize the "shuttle effect" and have the potential to achieve the theoretical specific energy and energy density of the Li-S battery. Gel electrolyte based on ceramic crosslinker will be incorporated in the high-rate polymer/ceramic separator to enhance safety without compromising rate capability. Rigorous abuse tests of Li-S batteries will provide insight into the safety of Li-S batteries.

Controlled Interfacial Phenomena for Extended Battery Life (Perla Balbuena and Jorge Seminario, Texas A&M University)

This project aims to use highly accurate computational modeling to guide optimal material screening for a Li/S battery. The effort seeks to reduce time and cost associated with trial and error experimentation. The effort seeks to use integrated computations and experiments to gain understanding and characterization of interfacial phenomena. First-principles simulations and *in situ* experimentation and analysis constitute the basis of this project. The innovation aspects are: (a) detailed DFT and *ab initio* molecular dynamics (AIMD) analysis and characterization at the interfaces coupled with well-designed XPS, X-ray absorption spectroscopy (XAS), NMR, and electrochemical tests of half cells and complete cells; and (b) use of classical molecular dynamics (CMD) simulations that extend the length and time scales of the interfacial models integrated with the microscopic chemical information regarding reactivity and composition of interphases obtained from DFT, AIMD, XPS, NMR, and chemical imaging techniques and that will allow characterization of slower kinetics phenomena not usually properly addressed.

3D Printed, Low Tortuosity Garnet Framework for Beyond 500 Wh/kg Batteries (Eric Wachsman and Liangbing Hu, University of Maryland)

This project aims to fabricate controlled 3D porous solid-state electrolyte (SSE) structures that are ordered and act as electrode supports, facilitating fast ion transport within the electrodes. This will enable higher battery C-rates and thicker electrodes for higher loading. The 3D structures can also increase the mechanical strength of the solid-state battery (SSB). In parallel, 3D solid-state ionic and electronic transport models will be developed to determine achievable C-rates as a function of structure. With this information, high-performance Li-S and Li-NMC batteries will be fabricated using the 3D SSE structures. LLZ (lithium lanthanum zirconate) garnet inks will be developed to 3D print solid electrolyte high-porosity, low-tortuosity patterns, including lines, grids, and columns. Using 3D printing enables rapid comparison of different electrolyte structure types as well as variations in structure characteristics (such as column height and width). These structures will be used in porous-dense-porous trilayer structures and assembled into batteries for testing. At the same time, 3D solid-

state ionic and electronic transport models will be developed to understand how the 3D structure affects the ionic and electronic transport rates and how to increase electrode loading while maintaining high C-rates. The models will be validated by experiment, and used to optimize the 3D electrolyte structure.

Composite Cathode Architectures Made by Freeze-Casting for All-Solid-State Lithium Batteries (Marca Doeff and Guoying Chen, Lawrence Berkeley National Laboratory; Stephen Sofie, Montana State University; Tobias Glossmann, Mercedes Benz R&D North America, Inc.)

This project will develop composite cathode architectures combining a solid-state ion conductor, a conductive polymer additive, and a high-energy-density cathode material such as Ni-rich NMC. Using novel freeze tape-casting and sintering methods that are large-area scalable, potentially very low-cost, and environmentally sustainable, the team will fabricate composite cathodes with thickness, areal loading, mechanical properties, and electronic and ionic conductivities comparable to the traditional electrodes used in Li-ion batteries with a liquid electrolyte. The project will utilize novel freeze-casting and freeze tape-casting techniques to produce porous scaffolds of LLZO (variants of $\text{Li}_7\text{La}_3\text{Zr}_2\text{O}_{12}$). The unidirectional pores of the scaffolds will be infiltrated with Ni-rich NMC powders and a conducting polymer such as polyaniline, or polyvinylidene difluoride (PVDF) and carbon, to form thick (20-100 μm) composite cathodes that can be used in all solid-state configurations.

High-Energy Solid-State Lithium Batteries with Organic Cathode Materials (Yan Yao, University of Houston)

The project objective is to research, develop, and demonstrate a multi-electron organic insertion material (OIM) for solid-state lithium batteries capable of achieving an energy density $\geq 500 \text{ Wh/Kg}$ while achieving a ≥ 500 cycle life. The team plans to use high-energy OIMs to systematically address the general property-mismatch dilemma faced by organic cathode materials, thereby ensuring that the high specific energy demonstrated from the active material level is maintained at the cell level. The project will be divided into two parts: first, the team will explore strategies to achieve a favorable microstructure of the OIM-electrolyte composites; second, OIMs with higher specific energy than that achieved in Phase 1 will be developed. The team expects more advanced OIMs, along with optimized microstructure, to achieve Battery500 targets.

Solvent-Free and Non-Sintered 500 Wh/kg All Solid-State Battery (Michael Wixom, Navitas; Chunsheng Wang, University of Maryland; David Wood, Oak Ridge National Laboratory)

The project aims to develop a solid-state battery (SSB) through a highly conductive stable solid-state electrolyte (SSE), a composite high energy cathode, a surface protected lithium anode, and a roll-to-roll film fabrication process. The goal is scalable production of large format all SSB ($\geq 2 \text{ Ah}$) able to deliver 500 Wh/kg and achieve life of 1000 charge/discharge cycles. This effort will address both material limitations and process challenges facing large-format SSB production. At present, sulfide SSEs have two major limitations to be solved before being adopted for large-scale battery production: (1) low (electro)chemical stability against air and common cathode materials, and (2) lack of scalable fabrication processes. This project will address the first by modifying the sulfide structure to improve its stability and will address the second challenge by adopting and scaling a Dry Process Electrode Fabrication technology developed successfully at Navitas.

Multifunctional Lithium-Ion Conducting Interfacial Materials for Lithium-Metal Batteries (Donghai Wang, Pennsylvania State University)

The project objective is to research, develop, and demonstrate multifunctional LIC interfacial materials as a protective layer for Li-metal anodes in Li-ion batteries, enabling Li-metal anodes to cycle with a high efficiency of $\sim 99.5\%$ at high electrode capacity ($> 6 \text{ mAh/cm}^2$) and high current density ($> 2 \text{ mA/cm}^2$) for over 500 cycles. The project will demonstrate Li-metal battery cells with an energy density of $\geq 500 \text{ Wh/kg}$ and $\geq 80\%$ capacity retention over 500 cycles using Li-metal anodes with this protective layer. The overall approach will focus on development and optimization of synthesis methods and precursors for multifunctional LIC interfacial materials, protective layer composition, and protective layer fabrication methods. This will be accompanied by property measurement and characterization (conductivity, mechanical properties, etc.) for the protective layer on lithium metal, along with cell testing.

Advanced Electrolyte Supporting 500 Wh/kg Lithium-Carbon/NMC Batteries (Chunsheng Wang, University of Maryland)

The objective of this project is to research, develop, and demonstrate a unique Li-C/NMC battery system supported by novel all-fluorinated and ionic liquid electrolytes as well as a micro-sized Li/C composite anode capable of achieving an energy density ≥ 500 Wh/Kg while achieving a 1,000-cycle life. The goal is to provide the critical information that will enable transformative insights into the complex coupling between the microstructure, host, and composition of the SEI layer, cycling CE, and cycling stability of Li-metal anodes. Meanwhile, the electrolytes should also be able to support the high-voltage NMC cathode materials. By tuning the salts, solvents, and concentrations in electrolytes, the team maximizes the cycling CE and cycling stability of lithium anodes. Meanwhile, they also enhance oxidation stability of the electrolytes on the NMC and LNO cathodes. Understanding of the degradation processes of lithium anode and high-voltage cathode will guide design of next-generation electrolytes. The element (such as cobalt and fluorine) doping will be used to enhance the electrochemical stability of Co-free LNO.

Results

Design, Processing, and Integration of Pouch-Format Cell for High-Energy Lithium-Sulfur Batteries (Mei Cai, General Motors)

The cathode loading, sulfur content, and cathode porosity were systematically studied to determine their impact on capacity. An optimized cathode composition (80 wt% sulfur content, 5-6 mg/cm² loading, 60% porosity) was identified that yielded a capacity of 800 mAh/g. Efforts also focused on the development of polysulfide trapping medium to improve the capacity retention and cyclability.

A new “electrostatic coating” method that can effectively coat a uniform thin layer (<50 μm) of nano TiO₂ (~20 nm) onto separator was developed. TiO₂ nano-particles contain surface O-2 defect sites which carry positive charge. When the TiO₂ coated separator is used in Li-S batteries, the long chain polysulfide species with negative charge can be electrostatically adsorbed onto TiO₂. Preliminary results indicate that the new TiO₂ coated separators can be a promising approach to improving the cycle life of Li-S cells. To improve the practical energy density of Li-S pouch cells, a further increase in the areal sulfur loading in the sulfur cathode (e.g. > 6 mg/cm²) may be necessary. However, cracking of electrode coating is typically observed in high mass loading electrodes > 6 mg/cm². Therefore, a new double-layers slurry coating method was developed to further increase the cathode coating thickness.

Electrochemically Stable High Energy Density Lithium-Sulfur Batteries (Prashant N. Kumta, University of Pittsburgh)

The following achievements were made: 1. PTA coated DDSA electrodes tested using Battery500 protocol (lean electrolyte 3 $\mu\text{l}/\text{mg}$ S) show an initial capacity of ~1326 mAh/g at C/20 and ~1023 mAh/g capacity after 100 cycles at C/5. 2. Electrochemical study of aliovalent substituted lithium ion conductors (LICs) as PTAs identified using Density Functional Theory (DFT). Testing of thick nano sulfur pellets (~7.5 mg-S/cm²) indicated improved stability of substituted LICs over pure LIC. Thus, LICs coated sulfur infiltrated sulfur-copper-bipyridine derived CFM, (S-Cu-bpy-CFM) pellet electrodes (~3.8 mg-S/cm²) tested in coin cells with Li metal in lean (~3 ml/mg) electrolyte conditions cycled at 100 mA/g display an initial capacity of ~873 mAh/g and a stable capacity of ~583 mAh/g after 100 cycles. Substituted LIC coatings show an initial capacity of ~871 mAh/g stabilizing to ~702 mAh/g after 100 cycles. 3. Explore electronic conductor (EC, electronic conductivity ~10⁻³ S/cm) and LIC (Li-ion conductivity ~10⁻⁴ S/cm) coated CFMs for confining sulfur and as effective PTAs. High sulfur loading (~4.5-7 mg/cm²) EC-CFM-S cathodes with ~64wt% sulfur content cycled against lithium under lean electrolyte conditions (~4 $\mu\text{l}/\text{mg}$ S) exhibited stable specific capacity of ~678 mAh/g and areal capacity of ~3.8 mAh/cm² after 70 cycles when cycled at C/10. The LIC-CFM-S cathodes exhibited a stable specific capacity of ~662 mAh/g and areal capacity of ~4.04 mAh/cm² under identical conditions in line with Battery500 requirements. 4. Finally, DFT study identified functional catalysts (FCs) promoting rapid conversion of PS to Li₂S and Li+S, and correspondingly eliminate PS dissolution. Experimental synthesis and testing of FCs validating theory are underway.

Highly Loaded Sulfur Cathode, Coated Separator, and Gel Electrolyte for High-Rate Lithium-Sulfur Batteries (Yong L. Joo and Jin Suntivichi, Cornell University; Trung Nguyen, EIC Labs)

Two failure mechanisms of the sulfur/carbon cathode (surface passivation and diffusion limit) have been analyzed via a newly developed model with a cascade of polysulfide reactions, mass transport, nucleation, and adsorption, and are verified in various sulfur/carbon cathodes to optimize the morphology/structure of the highly loaded sulfur cathode. Hybrid separators obtained by gas-assisted electrospinning of polymer/ceramic blends significantly enhances the rate capability, exhibiting the capacity of 800 mAh/g at 2C charge/discharge rate. Recent work on gel electrolyte demonstrated that gel network created by the ceramic cross-linker can effectively trap soluble polysulfides, leading to a better capacity retention than liquid electrolyte.

Controlled Interfacial Phenomena for Extended Battery Life (Perla Balbuena and Jorge Seminario, Texas A&M University)

Investigations focused on characterizing the structure and reactivity of current best localized high-concentration electrolytes (formulations provided by our PNNL colleagues) for Li-metal batteries, and the composition and structure of their SEI. In addition the roles of the electrolyte solvation properties (from dilute solutions, to highly concentrated, to localized high concentrated via addition of a diluent), and correlating these properties to their electronic structure and redox behavior for both anode and cathode reactions were elucidated. The findings from these efforts were used for developing of a new screening methodology where we aim to characterize the optimal formulations for both Li metal anode and high voltage metal oxide cathode. Optimized formulations are currently being tested following the newly developed methodology (best cases will be tested at PNNL). Interfaces between sulfide solid electrolytes and C/S cathodes have been exhaustively investigated to determine possible benefits and/or challenges of the sulfide electrolyte. An advanced yet simple method was developed and implemented to characterize Li dendrite growth with simultaneous electrolyte reduction. The simple method is able to predict Li growing morphologies from first principles. We expect the method to be very helpful for designing appropriate anode substrate morphologies.

3D Printed, Low Tortuosity Garnet Framework for Beyond 500 Wh/kg Batteries (Eric Wachsman and Liangbing Hu, University of Maryland)

LLZ inks were formulated and multiple line, grid, and column 3D printed structures fabricated using these inks on top of bilayer (dense-separator/random-porous-support) garnet structures. Li metal fills the random-porous side of the bilayer structure and sulfur and NMC have been infiltrated into the 3D printed structures. With initial un-optimized ~70 μm high NMC-cathode grid structures a cell energy density of 120 Wh/kg was achieved. Models for energy density and power capability have also been developed and demonstrate increasing C-rate capability and energy density with decreasing diameter and increasing height, respectively. By continued improvement of the printing processes the height of the 3D printed multilayer grids structures and column heights have since been increased. To date maximum column heights of ≥ 200 μm have been achieved with ~60 μm diameter columns and filled with NMC achieving ≥ 200 μm high NMC/garnet solid-state cathode structures that are now ready for cell cycling and comparison with model performance predictions.

Composite Cathode Architectures Made by Freeze-Casting for All-Solid-State Lithium Batteries (Marco Doeff and Guoying Chen, Lawrence Berkeley National Laboratory; Stephen Sofie, Montana State University; Tobias Glossmann, Mercedes Benz R&D North America, Inc.)

Porous scaffolds of LLZO with porosities in excess of 70% have been successfully fabricated using freeze tape casting, and pore size analysis carried out. The best results were obtained using slurries containing 7.5 vol. % LLZO; higher loadings either resulted in some bridging or did not produce the desired porous structures. Pores were acicular, had effective diameters about 30 μm across, and tortuosity close to 1. Composites consisting of LLZO scaffolds and PEO-LiTFSI showed higher room temperature conductivities than either the polymer electrolytes alone or mixtures of polymer electrolyte with LLZO powder, showing the beneficial effects of a low tortuosity porous scaffold on ionic conductivity. Cells consisting of porous LLZO scaffolds infiltrated with NMC-622, carbon, PVdF binder and a secondary soft solid ionic electrolyte as cathodes, thin (~

14 μm thick) dense LLZO separators, and lithium foil anodes could be charged and discharged at C/10 rate at room temperature. This is the first example of successful operation of a completely liquid-free solid-state battery with a realistic form factor based on LLZO. Two papers describing these results have just been accepted for publication, one in ACS Applied Materials & Interfaces, and another in ACS Applied Energy Materials.

High-Energy Solid-State Lithium Batteries with Organic Cathode Materials (Yan Yao, University of Houston)

Direct mixing of OIM and solid electrolyte particles has afforded solid-state composite cathodes with a specific capacity of 407 mAh/g when the active material ratio is 20 wt%. This performance is not sustained at higher active material ratios, such as 40 wt%. Preliminary studies indicated that such performance drop originated from the formation of unfavorable microstructures of the composite electrode, which has decreased ionic conduction within the cathode. Therefore methods to improve the microstructures were explored. One of the most effective ways that identified so far is wet-mixing where the solid electrolyte is mixed with OIM as a solution instead of solid particles. Together with particle size control of OIM particles, the active material ratio was increased from 20 to 40 wt% without compromising the specific capacity. The origin of the improvement has been investigated with imaging techniques at different length scale. Scanning electron microscopy (SEM) observation of the morphology of OIM-solid electrolyte composite powders revealed that the dry-mixed powders show large agglomerates and apparent phase segregation, while the wet-mixed powders show much finer particles and a more uniform feature distribution. 3-Dimensional profiling of Li^+ in dry- and wet-mixed electrodes with secondary ion mass spectrometry with time-of-flight mass analysis (TOF-SIMS) shows large aggregates of the solid electrolyte in the former while more uniform solid electrolyte distribution in the latter. SEM observation of the cross-section of the electrodes revealed a continuous solid-electrolyte network in the wet-mixed electrode while a discontinuous one for the dry-mixed one.

Solvent-Free and Non-Sintered 500 Wh/kg All Solid-State Battery (Michael Wixom, Navitas; Chunsheng Wang, University of Maryland; David Wood, Oak Ridge National Laboratory)

The synthesis of Li_3PS_4 (LPS) solid state electrolytes (SSE) by introducing co-dopant of CaO and P_2O_5 in the mechanical milling procedure was optimized. The obtained LPS electrolyte exhibited a much higher stability (up to 4 hours) in a dry room and an ionic conductivity of $0.5 \times 10^{-3} \text{ S cm}^{-1}$ at 25 $^\circ\text{C}$ and $1 \times 10^{-3} \text{ S cm}^{-1}$ at 50 $^\circ\text{C}$. This enables a large-scale film fabrication process in a dry-room and a reasonably high charge and discharge rate of solid-state batteries. Other on-going optimization efforts, such as using non-oxide dopants and post annealing, further improved the ionic conductivity. Surfaced-coated LCO/LPS/Li solid-state batteries in Swagelok cell format showed good reversible specific capacity of $>120 \text{ mAh/g}$ and cycle life of 250 at 0.025C rate and about 100 cycles at 0.1C rate and room temperature. A flexible, solid-state electrolyte and cathode-composite film was successfully prepared in large area through a Navitas-developed dry-electrode process, but the ionic conductivity needs to be further improved for a practical solid-state pouch cell. Efforts are underway to use special additives and novel processing technology to reduce the content of the polymer binder in the cathode and electrolyte film to improve ionic conductivity without debasing mechanical strength. Previous results has shown that the surface protection on Li metal could stabilize the Li/SSE interphase. A new solid-state cell containing the recently optimized LPS solid-state electrolyte, cathode composite film and a surface-protected Li anode is being assembled for an improved cell performance.

Multifunctional Lithium-Ion Conducting Interfacial Materials for Lithium-Metal Batteries (Donghai Wang, Pennsylvania State University)

Stable operation of rechargeable lithium (Li)-based batteries is highly dependent on the solid-electrolyte interphase (SEI) on Li metal anode. New SEI techniques, other than using electrolyte additives, were developed. Based on our previous efforts of using reactive polymeric composites for Li metal protection, the practical application of a polymer composite on Li anode was explored. A scalable process of coating a polymer film by in situ crosslinking onto large pieces of Li metal foil (4 cm by 5 cm in size) was successfully developed. The coating thickness is as thin as $\sim 3 \mu\text{m}$. Full cells were assembled using the protected Li foil ($\sim 50 \mu\text{m}$) as anodes and LCO ($\sim 2 \text{ mAh cm}^{-2}$) as cathodes. The cells demonstrated excellent capacity retention

after 200 cycles (82.6%) using a conventional electrolyte, while the control cells show a fast capacity decay after only 40 cycles. An SEI technique, utilizing a self-assembled monolayer of electrochemically active molecules to regulate the nanostructure and composition of SEI and deposition morphology of Li metal anodes was also developed. A multilayer SEI containing a LiF-rich inner phase and amorphous outer layer was shown to effectively seal the Li surface in contrast to the conventional impassive SEI at low temperatures. Consequently, galvanic Li corrosion and self-discharge were suppressed; stable Li deposition was realized from -60° to 45°C ; and a Li|LiCoO₂ cell with a capacity of 2.0 mAh cm^{-2} displayed a 200-cycle life at -15°C with a recharge time of 45 minutes.

Advanced Electrolyte Supporting 500 Wh/kg Lithium-Carbon/NMC Batteries (Chunsheng Wang, University of Maryland)

To improve the substrate Li affinity, Bi and graphite were mixed and coated on Cu for Li deposition. Initial investigations evaluated the Li stripping/plating behavior and Li deposition morphologies on the designed substrate in Li||Bi-Gr cells. Electrochemically, three-step reaction during Li plating/stripping process were observed: Bi alloying/dealloying, graphite Li intercalation/deintercalation and plating/stripping. A short plateau at approximately 0.7 V was attributed to BiLi alloying while a sloping range from 0.2 to 0 V was associated with Li intercalation of graphite. A dominant long plateau around 0 V was attributed to Li depositing/dissolution. It is worth noting that Bi-Gr substrate showed no spike at initial lithiation. The charge/discharge curves overlap well, indicating 1) Bi-Gr substrate is stable and 2) there is not much overpotential increase over the 200 testing cycles. More importantly, the cycling efficiency reaches 99.83+% at 0.5 mA cm^{-2} and 1.0 mAh cm^{-2} . This result is as good as those reported for Bi@Graphite, but with much easier substrate fabrication process. The electrochemical performance of NMC 622||Li cells was evaluated in the ionic liquid electrolyte at 0.5 mA cm^{-2} using 1.5 mAh cm^{-2} with cut-off potential at 4.3 V vs. Li. The capacity retention was determined to be ~ 90% after 80 cycles. The capacity loss in the half cell was due to irreversible structural change of the active materials as reported in literatures. A Li-free NMC 622 || Cu cell was also demonstrated with over 80% capacity retention after 150 cycles, demonstrating exceptional high Coulombic efficiency. In future studies, additives and coating method will be tested to further enhance the Li performance in the electrolyte. The SEI and electrolyte properties that enables stable Li anode will be studied.

Acknowledgements

The goal of the Battery500 seedlings is to jump-start emerging technologies that could lead to a cell delivering an energy density of 500 Wh/kg over 1,000 cycles. Patricia H. Smith, Ph.D., from the NAVSEA-Carderock, Non-Metallic Materials Research & Engineering Branch, 617 served as the Project Coordinator in the preparation of this section of the report.

(This page intentionally left blank)

